META'17 Incheon - Korea

The 8th International Conference on Metamaterials, Photonic Crystals and Plasmonics

Proceedings

ISSN 2429-1390

metaconferences.org


인천광역시
Incheon Metropolitan City
MPK
GeePS
nCOMS
Photonics
Applied Physics A
LINBOU
WILEY
CASE
원천관광공사
WITec
HIGUARD
Live Cell Instrument
BRUKER
scinco
Edmund
Park
NANO
convergence
L2K

META'17 Incheon - Korea

The 8th International Conference on Metamaterials, Photonic Crystals and Plasmonics

Please share your comments, photos & videos !

www.facebook.com/metaconference

@metaconference

Edited by

Said Zouhdi | Paris-Sud University, France
Junsuk Rho | POSTECH, Korea
Hakjoo Lee | CAMM, Korea

CONTENTS

META'17 ORGANIZATION

Said Zouhdi, General Chair
Paris–Sud University, France

Junsuk Rho, General Co-Chair
POSTECH, Korea

Hakjoo Lee, General Co-Chair
CAMM, Korea

INTERNATIONAL ADVISORY COMMITTEE

Harry Atwater, USA
Federico Capasso, USA
Andre de Lustrac, France
Nader Engheta, USA
Teruya Ishihara, Japan
Tatsuo Itoh, USA
Yuri Kivshar, Australia
Graeme W. Milton, USA
Raj Mittra, USA
Manuel Nieto-Vesperinas, Spain
Susumu Noda, Japan
Masaya Notomi, Japan
Yahya Rahmat-Samii, USA
Vladimir Shalaev, USA
Ari Sihvola, Finland
David R. Smith, USA
J(Yiannis) Vardaxoglou, UK
Martin Wegener, Germany
Xiang Zhang, USA
Nikolay Zheludev, UK

TECHNICAL PROGRAM COMMITTEE

Pierre-Michel Adam, France
Ishwar Aggarwal, USA
Javier Aizpurua, Spain
Xavier Begaud, France
Svetlana V. Boriskina, USA
Alberto Bramati, France
Kurt Busch, Germany
Bernard Casse, USA
Che Ting Chan, Hong Kong
Debashis Chanda, USA
Pai-Yen Chen, USA
Johan Christensen, Spain
Naresh Das, USA
Alfredo De Rossi, France
Mohamed Farhat, Qatar
Monika Fleischer, Germany
Michael A. Fiddy, USA
Monika Fleischer, Germany
Wolfgang Fritzsche, Germany
Francisco Garcia-Vidal, Spain
Alexander Govorov, USA
Ortwin Hess, United Kingdom
Joachim Krenn, Austria
Laura M. Lechuga, Spain
Howard (Ho Wai) Lee, USA
Jensen Li, Hong Kong
Jichun Li, USA
Haitao Liu, China
Anatole Lupu, France
Bumki Min, Korea
Fernando Moreno, Spain
Teri Odom, USA
Namkyoo Park, Korea
Dorota Pawlak, Poland
Min Qiu, China
Kazuaki Sakoda, Japan
Luca Sapienza, UK
Mohamed Swillam, Egypt
Takuo Tanaka, Japan
Giorgos P. Tsironis, Greece
Augustine Urbas, USA
Hong Wei, China
Joel K. W. Yang, Singapore
Anatoly V Zayats, UK
Lei Zhou, China

SPECIAL SYMPOSIA ORGANIZERS

Alexander Govorov
USA

Xing Yi Ling
Singapore

Jerome Plain
France

Konstantin Vytovtov
Russia

SPECIAL SESSIONS ORGANIZERS

Fahhad H. Alharbi, Qatar
Christos Argyropoulos, USA
Henri Benisty, France
Palash Bharadwaj, USA
Shah Nawaz Burokur, France
Alessandro Casaburi, UK
Lucia Caspani, UK
Debashis Chanda, USA
Kuo-Ping Chen, Taiwan
Pai-Yen Chen, USA
Zhi Ning Chen, Singapore
Qiang Cheng, China
Tae In Choi, Korea
Wonshik Choi, Korea
Aurelien Cuche, France
Artur Davoyan, USA
Andre de Lustrac, France
Qingguo Du, China
Kofi Edee, France
Mohamed Farhat, Qatar
Laure Huitema, France
Kin Hung Fung, Hong Kong
Hayk Harutyunyan, USA
Chen-Bin Huang, Taiwan
Jer-Shing Huang, Taiwan
Teruya Ishihara, Japan
Themos Kallos, Canada
Eugene Kamenetskii, Israel
Mercedeh Khajavikhan, USA
Pilhan Kim, Korea
Yoon Young Kim, Korea
Panagiotis Kosmas, UK
Yun Lai, China
Howard Lee , USA
Qiang Li, China
Yue Li, China
Ji-Seok Lim, Korea
Ko-Wei Lin, Taiwan
Haitao Liu, China
Hui Liu, China
Wei Liu, Singapore
Yu Luo, Singapore
Anatole Lupu, France
Guancong Ma, Hong Kong
Ren-Min Ma, China
Marco Miniaci, France
Andrey Miroshnichenko, Australia
Rhiannon Mitchell-Thomas, UK
Khaled Mnaymneh, Canada
Jong G. Ok, Korea
Namkyoo Park, Korea
Dorota Pawlak, Poland
Virginie Ponsinet, France
Ilya Razdolski, Germany
Fangfang Ren, China
Almas Sadreev, Russia
Kazuaki Sakoda, Japan
Neha Sardana, India
Sebastian Schulz, Canada
David Schmool, France
Alexey Slobozhanyuk, Australia
Vasily Temnov, France
Andrea Toma, Italy
Din Ping Tsai, Taiwan
Vincent Paillard, France
Remo Proietti Zaccaria, Italy
Guido Valerio, France
Jian Wang, China
Hong Wei, China
Qi Ye Wen, China
William Whelan-Curtin, UK
Steve Hang Wong, Hong Kong
Jeong Weon Wu, Korea
Jianjia Yi, China
Hao Yu, Singapore
Kuang Zhang, China
Jie Zhu, China
Xuefeng Zhu, China

PLENARY SPEAKERS

Federico Capasso

Harvard University, USA

Metaoptics in the visible

Federico Capasso is the Robert Wallace Professor of Applied Physics at Harvard University, which he joined in 2003 after 27 years at Bell Labs where he was Member of Technical Staff, Department Head and Vice President for Physical Research. He is visiting professor at NTU with both the School of Physical and Mathematical Sciences and Electrical and Electronic Engineering. His research has focused on nanoscale science and technology encompassing a broad range of topics. He pioneered band-structure engineering of semiconductor nanostructures and devices, invented and first demonstrated the quantum cascade laser and investigated QED forces including the first measurement of a repulsive Casimir force. His most recent contributions are new plasmonic devices and flat optics based on metasurfaces. He is a member of the National Academy of Sciences, the National Academy of Engineering, the American Academy of Arts and Sciences. His awards include the King Faisal Prize, the IEEE Edison Medal, the SPIE Gold Medal, the American Physical Society Arthur Schawlow Prize in Laser Science, the Jan Czochralski Award for lifetime achievements in Materials Science, the IEEE Sarnoff Award in Electronics, the Materials Research Society Medal, the Wetherill Medal of the Franklin Institute, the Rank Prize in Optoelectronics, the Optical Society Wood Prize, the Berthold Leibinger Future Prize, the Julius Springer Prize in Applied Physics, the European Physical Society Quantum Electronics Prize.

Dirk Englund

MIT, USA

Towards Scalable Semiconductor Quantum Networks

Dirk Englund received his BS in Physics from Caltech in 2002. Following a Fulbright year at TU Eindhoven, he earned an MS in electrical engineering and a PhD in Applied Physics in 2008, both from Stanford University. He was a postdoctoral fellow at Harvard University until 2010, when he started his group as Assistant Professor of Electrical Engineering and of Applied Physics at Columbia University. In 2013, he joined the faculty of MIT's Department of Electrical Engineering and Computer Science. Dirk's research focuses on quantum technologies based on semiconductor and optical systems. Recent recognitions include the 2011 Presidential Early Career Award for Scientists and Engineers, the 2011 Sloan Research Fellowship in Physics, the 2012 DARPA Young Faculty Award, the 2012 IBM Faculty Award, an 2016 R&D100 Award, the OSA's 2017 Adolph Lomb Medal , and the 2017 ACS Photonics Young Investigator Award.

Ortwin Hess

Imperial College London, UK

Active Quantum Nanoplasmonics : From Single Molecule Strong Coupling to Stopped-Light QED and Lasing

Ortwin Hess currently holds the Leverhulme Chair in Metamaterials in the Blackett Laboratory (Department of Physics) at Imperial College London. He obtained the PhD degree from the Technical University of Berlin (Germany) in 1993 and the Habilitation at the University of Stuttgart in 1997. From 2003 to 2010 he was professor at the University of Surrey (Guildford, UK) and visiting professor at Stanford University (1997/98) and at the Ludwig-Maximilians University of Munich (1999/2000). Ortwin's research interests bridge theoretical condensed matter physics with photonics and are focused on light-matter interaction in nano-photonics, metamaterials and spatio-temporal nano-laser dynamics. He discovered the 'trapped-rainbow' principle, had the idea of stopped-light lasing and made defining contributions to the fields of spatio-temporal dynamics of semiconductor lasers, ultraslow light in metamaterials, complex quantum dot photonics and photonic crystals and strong coupling in nanoplasmonics. Ortwin pioneered active nanoplasmonics and optical metamaterials with quantum gain for which he is awarded the 2016 Royal Society Rumford Medal.

Satoshi Kawata

Osaka University, Japan

Tip-enhanced Raman scattering microscopy : plasmonic molecular imaging beyond the limits

Satoshi Kawata has been a Professor (currently Distinguished Professor) of Applied Physics and Frontier Biosciences at Osaka University since 1993, and also a Chief Scientist in RIKEN from 2002 to 2012. He has served as the President of Japan Society of Applied Physics, the President for Spectroscopical Society of Japan, Editor of Optics Communications, and a Director of Board of OSA. Professor Kawata is one of pioneers in near field optics (the inventor of aperture-less near-field scanning optical microscope and tip-enhanced Raman microscopy), two-photon engineering (the inventor of 3D fabrication with two-photon polymerization, isomerization, photo-refraction, and reduction). He has published a number of papers and books on three-dimensional and nano-resolution microscopy, vibrational spectroscopy, bio-imaging, signal recovery and photon pressure on nano-structures. The "8-micron bull" fabricated with his invented two-photon polymerization has been awarded in Guinness World Record Book 2004 Edition. He is a Fellow of OSA, SPIE, IOP, and JSAP.

Yong-Hee Lee

Korea Advanced Institute of Science and Technology (KAIST), Korea

Squeezing of Photonic Energy into A Point-like Space

Yong-Hee Lee received his master degree in Applied Physics and Ph.D degree in Optical Sciences at Korea Advanced Institute of Science and Technology (KAIST) and at the University of Arizona, respectively. During his stay at AT&T Bell Laboratories, he pioneered and demonstrated the first proton-implanted VCSELs in 1990 and holds the original patent on this industrial VCSEL. In 1991 he joined the Department of Physics of KAIST where he continued his research on VCSELs and started new research on photonic crystal nano-lasers. His laboratory demonstrated various forms of photonic crystal laser including the first electrically-driven photonic crystal laser. His recent interest lies in on the physics of light-matter interaction at the nano-scale and the ultimate light source for photonic integrated circuits and quantum information science. From 2003 to 2004 he was an IEEE LEOS Distinguish Lecturer. Prof. Lee served as an Associate Editor of Optics Express. He is a Fellow of IEEE and the Optical Society of America. Domestically he received numerous awards including the National Academy of Science Award, Korea Scientist Award and the most recent Korea Best Scientist and Engineer Award. In 2014 He received the Humboldt Research Award and the IEEE Photonics Society Engineering Achievement Award. He co-authored more than 180 international journal papers and patents related to nanophotonics. He advised and produced over 40 PhD's in physics during his stay at KAIST.

Franco Nori

RIKEN, Japan & University of Michigan, USA

Parity-Time-Symmetric Optics, extraordinary momentum and spin in evanescent waves, and the quantum spin Hall effect of light

Franco Nori is a RIKEN Chief Scientist, as well as Group Director of the "Quantum Condensed Matter Research Group" at CEMS (Center for Emergent Matter Science). Also, he is a Team Leader of the Interdisciplinary Theoretical Science Program at RIKEN (the Japanese National Laboratory). Also, since 1990 he has been a faculty member of the Physics Department at the University of Michigan, Ann Arbor, USA. Prior to this, he did postdoctoral research work at the Institute for Theoretical Physics, at the University of California, Santa Barbara. He received a PhD in Physics from the University of Illinois. He has co-authored over 80 papers in Physical Review Letters as well as over 30 in Science and Nature journals, and has been cited over 29K times, with an h-index of 84. He is an Elected Fellow of the American Physics Society (APS), Institute of Physics (IoP), Optical Society of America (OSA), and the American Association for the Advancement of Science (AAAS). He received the 2014 Prize for Research in Physics, from the Matsuo Foundation, Japan ; and the 2013 Prize for Science, by the Minister of Education, Culture, Sports, Science and Technology, Japan. Also, an "Excellence in Research Award" and an "Excellence in Education Award" from the University of Michigan.

Eli Yablonovitch

UC Berkeley, USA

Optical Antennas ; Spontaneous Emission Faster Than Stimulated Emission

Eli Yablonovitch introduced the idea that strained semiconductor lasers could have superior performance due to reduced valence band (hole) effective mass. With almost every human interaction with the internet, optical telecommunication occurs by strained semiconductor lasers. He is regarded as a Father of the Photonic BandGap concept, and he coined the term "Photonic Crystal". The geometrical structure of the first experimentally realized Photonic bandgap, is sometimes called "Yablonovite".

Prof. Yablonovitch is elected as a Member of the National Academy of Engineering, the National Academy of Sciences, the American Academy of Arts & Sciences, and is a Foreign Member of the Royal Society of London. He has been awarded the Buckley Prize of the American Physical Society, the Isaac Newton Medal of the UK Institute of Physics, the Rank Prize (UK), the Harvey Prize (Israel), the IEEE Photonics Award, the IET Mountbatten Medal (UK), the Julius Springer Prize (Germany), the R.W. Wood Prize, the W. Streifer Scientific Achievement Award, and the Adolf Lomb Medal. He also has an honorary Ph.D. from the Royal Institute of Technology, Stockholm, & the Hong Kong Univ. of Science & Technology, and is honorary Professor at Nanjing University.

Eli Yablonovitch is the Director of the NSF Center for Energy Efficient Electronics Science (E3S), a multi-University Center headquartered at Berkeley. He received his Ph.D. degree in Applied Physics from Harvard University in 1972. He worked for two years at Bell Telephone Laboratories, and then became a professor of Applied Physics at Harvard. In 1979 he joined Exxon to do research on photovoltaic solar energy. Then in 1984, he joined Bell Communications Research, where he was a Distinguished Member of Staff, and also Director of Solid-State Physics Research. In 1992 he joined the University of California, Los Angeles, where he was the Northrop-Grumman Chair Professor of Electrical Engineering. Then in 2007 he became Professor of Electrical Engineering and Computer Sciences at UC Berkeley, where he holds the James & Katherine Lau Chair in Engineering.

Xiang Zhang

UC Berkeley, USA

Parity-time Symmetry Breaking Lasing and Anti-Lasing

Xiang Zhang is the Ernest Kuh Chaired Professor at the University of California, Berkeley and Director of Materials Science Division at Lawrence Berkeley National Laboratory (LBNL). He is also the Director of the NSF Nano-scale Science and Engineering Center (SINAM). He is an elected member of the US National Academy of Engineering (NAE), Academia Sinica and foreign member of Chinese Academy of Sciences. His research in optical metamaterials was selected by Times Magazine as "Top 10 Scientific Discoveries in 2008". Xiang Zhang was a recipient of many awards including the NSF CAREER Award, Fred Kavli Distinguished Lecturehip, Fitzroy Medal, Charles R. Richards Memorial Award, the Max Born Award, the Julius Springer Prize for Applied Physics. He received his BS/MS in physics in Nanjing University, China, and Ph.D from UC Berkeley in 1996 and was on faculty at Pennsylvania State University and UCLA prior returning Berkeley faculty in 2004.

Nikolay Zheludev

University of Southampton, UK & NTU, Singapore

Metamaterials, anapoles and flying donuts

Nikolay Zheludev's research interest are in nanophotonics and metamaterials. He is the Director of the Centre for Photonic metamaterials and Deputy Director of the Optoelectronics Research Centre in Southampton University, UK. He is also co-Director of The Photonics Institute and directs the Centre for Disruptive Photonic Technologies at Nanyang Technological University. His personal awards include the Thomas Young medal (IOP) for "global leadership and pioneering, seminal work in optical metamaterials and nanophotonics", the Leverhulme Trust Senior Research Fellowship ; Senior Research Professorship of the EPSRC ; The Royal Society Wolfson Research Merit Award & Fellowship. He is a Fellow of the European Physical Society (EPS), the Optical Society (OSA) and the Institute of Physics (London). He is Editor-in-Chief of the Journal of Optics (IOP) and an Advisory Board Member for Nanophotonics, ACS Photonics and Nature Publishing Group Scientific Reports. In 2007 created European Physical Society international meeting at the crossroads of nanophotonics and metamaterials, NANOMETA. He was among a small group of research community leaders who provided initial impetus to the International Year of Light, declared by United Nations for 2015.

KEYNOTE SPEAKERS

Harry Atwater
CALTECH, USA

Dynamic Wavefront Control and Imaging with Active Nanophotonic Structures

Che Ting Chan
HKUST, Hong Kong

Pseudo-spins and their consequences in classical waves

Andrei Faraon
California Institute of Technology, USA

Flat and conformal optics with dielectric metasurfaces

Michael Farle
University of Duisburg-Essen, Germany & Immanuel Kant Baltic Federal University, Russia

Functionalized Hybrid Nanomagnets : New Materials for Innovations in Energy Storage and Medical Theranostics

Peer Fischer
Max Planck Institute, Germany

Chiral plasmonic nanostructures

Jean-Jacques Greffet
Institut d'Optique Graduate School, France

Quantum plasmonics

Yurii Gun'ko
Trinity College Dublin, Ireland

Chiral nanomaterials and their applications

Teruya Ishihara
Tohoku University, Japan

Second order optical nonlinearity in metamaterial

Chennupati Jagadish

The Australian National University, Australia

Semiconductor Nanowires and Metastructures for Optoelectronic Device Applications

Yoon Young Kim

Seoul National University, Korea

Extreme elastic anisotropy – realization by metamaterials

Byoungho Lee

Seoul National University, Korea

Metasurfaces for in-plane plasmonic arbitrary pattern generation

Stefan Maier

Imperial College London, UK

Hybrid nanostructures for sub-wavelength imaging, nonlinear optics, and chemistry

Namkyoo Park

Seoul National University, Korea

Acoustic omni meta-atom for decoupled access to all octants of a wave parameter space.

Markus Raschke

University of Colorado Boulder, USA

Seeing with the nano-eye : accessing structure, coupling, and dynamics in matter on its natural length and times scales

Mu Wang

Nanjing University, China

Making Structured Metal Transparent for Ultra-Broadband Electromagnetic and Acoustic Waves

META'17 VENUE

META'17 will be held at the **Songdo Convensia**, 123 Central-ro, Yeonsu-gu, 21998, **Incheon**, Korea.
Tel. : +82-32-210-1037
Fax : +82-32-210-1005
Website : www.songdoconvensia.com

GETTING TO VENUE

Address

Songdo Convensia, 123 Central-ro, Yeonsu-gu, 21998, **Incheon**, Korea.
Tel. : +82-32-210-1037
Fax : +82-32-210-1005
Website : www.songdoconvensia.com

Seoul (Downtown) -> Songdo Convensia

- By Subway

Subway Station	Information
University of Incheon (Incheon Line)	Take Seoul subway line number 1 and get off at Bupyeong Station Transfer Bupyeong Station to Incheon subway and get off at University of Incheon Station Take a walk around 10-15minutes to Songdo ConvensiA (next to Sheraton Hotel)
Dongmak Station (Incheon Line)	Take Seoul subway line number 1 and get off at Bupyeong Station Transfer Bupyeong Station to Incheon subway and get off Dongmak Station Through exit 3, take bus 8, 6, 780 to Songdo ConvensiA Bus Stop

- By Taxi

Fee	Taxi Fare ranges from 60,000 – 90,000 KRW ※ Receipt can be collected from driver if needed
Hours	Available 24hours
About	Ask Taxi Driver for 'Songdo ConvensiA' (at Songdo of Incheon City nearby Sheraton Hotel)

Incheon International Airport (ICN) -> Songdo Convensia

1) By KAL-limousine (~40 min, 7,000 KRW)

- Board the limousine bus (6707B) at the platform 4A

- Get off at **Sheraton Grand Incheon Hotel** (last stop)

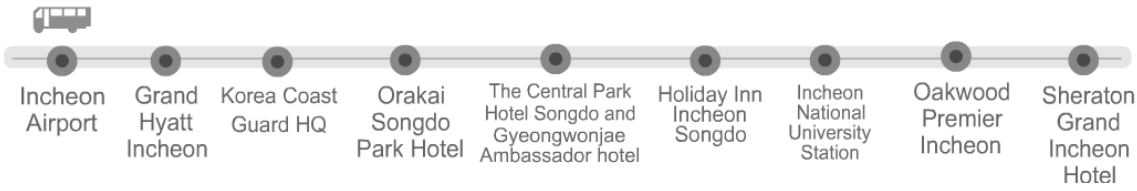

Time schedule

Departure Point Incheon Airport (Bus Stop #4A) Arrival Point Sheraton Grand Incheon Hotel

Please be advised that actual times may vary depending on traffic conditions.

Travel Time : 30min

Departure time					
05:53	06:21	06:58	07:33	08:13	08:58
09:38	10:23	11:13	12:03	12:53	13:43
14:33	15:23	16:14	17:03	17:43	18:22
19:03	19:53	20:42	21:30	22:11	

- For more information, please visit, https://www.kallimousine.com/eng/guide01_en.html or http://www.airport.kr/pa/en/a/3/1/1/index.jsp#none

2) By Bus (~1 hour, ~3,000 KRW)

- Board a bus line 303 at the platform 13A

- Get off at **Songdo The Sharp First World (East gate)** station (~40 mins)
- Walk 450m (~7 mins on foot)
- 

Time schedule

To Incheon	first	05:00	To CAT	first	05:40
	last	21:30		last	23:00
Interval	15min.		Transit time	210분(MI)	
Type	Local City		Fare	KRW 2,800	

GUIDELINES FOR PRESENTERS

ORAL PRESENTATIONS

Each session room is equipped with a stationary computer connected to a LCD projector. Presenters must load their presentation files in advance onto the session computer. Technician personnel will be available to assist you.

Scheduled time slots for oral presentations are 15 mn for regular, 20 mn for invited presentations, 30 mn for keynote talks and 35 mn for plenary talks, including questions and discussions. Presenters are required to report to their session room and to their session Chair at least 15 minutes prior to the start of their session.

The session chair must be present in the session room at least 15 minutes before the start of the session and must strictly observe the starting time and time limit of each paper.

POSTER PRESENTATIONS

Presenters are requested to stand by their posters during their session. One poster board, A0 size (118.9 x 84.1 cm), in portrait orientation, will be available for each poster (there are no specific templates for posters). Pins or thumbtacks are provided to mount your posters on the board. All presenters are required to mount their papers 30mn before the session and remove them at the end of their sessions. Posters must prepared using the standard META poster template (available on the conference website).

PRE-CONFERENCE TUTORIALS

Frontier's Lectures on Metamaterials and Plasmonics

July 24 (Mon.), Seoul National University
Room 118, Building 301, Dept. of ECE

Lecturer	Session	Title
	08:50-09:00	**Opening**
Thomas Zentgraf	09:00-10:00	**Nonlinear Metasurfaces**
Jensen Li	10:00-11:00	**Spin-enabled optics with metamaterials and metasurfaces**
Yongmin Liu	11:00-12:00	**Reconfigurable Plasmonics and Metamaterials**
	12:00-13:30	**Lunch**
Mu Wang	13:30-13:55	**Meet Editors – Physical Review Letters**
Zachary Lapin	13:55-14:20	**Meet Editors – Nature Communications**
Ling Lu	14:20-15:20	**Topological Photonic Crystals**
	15:20-15:30	**Coffee Break**
Andrey Miroshnichenko	15:30-16:30	**Multipole decomposition and nonradiating sources in nanophotonics/metamaterials**
Renmin Ma	16:30-17:30	**Plasmonic nanolasers: fundamental, application and challenges**
Cristian Ciracì	17:30-18:30	**The optics of film-coupled nanoparticles: a bridge to the quantum realm**

Tutorial is free of charge, but registration is required. Please follow the link below to register:
https://docs.google.com/forms/d/1w4N8SrZSUlfRWgeuqDhmHoIDmMCgp9L7xEoPc5kowBI/edit

Chairs:

Namkyoo Park
Seoul National University

Hakjoo Lee
CAMM

Junsuk Rho
POSTECH

Session will be held in **Multimedia Room 118 of Building 301**
Lunch will be served at the faculty **cafeteria, first floor of Building 301**

Access to Meta Pre-conference
- Rm. 118, Building 301, Seoul National University

● From '*Incheon*' or '*Gimpo*' International Airport

- **By public transportation** [~2 hours: KRW ~10,200 (Incheon),~1.5 hour: KRW ~5,200 (Gimpo)]
o Board the limousine bus line number **6003** (The bus stop is **6A,12B in Incheon and 6 in Gimpo**).
o Get off at the front gate of Seoul National University.
o Board a bus line **5511 or 5513, or take a taxi.**
o Get off at either bus stop number 9 or 10 which are in front of buildings 301 and 302 (**last stop**).
- By taxi [~1 hour, KRW ~49,000 (Incheon), ~1 hour, KRW ~19,600 (Gimpo)]

● From Seoul Station

- **By public transportation** [~1 hour, KRW ~1300]
o Take the subway (**line No. 4**) **from Seoul station to Sadang station.**
o Transfer the subway line from No. 4 to No. 2.
o Take the subway (**line No. 2**) **from Sadang to Nakseongdae station.**
o Get out of **Exit 4**, turn left around the GS gas station, and board a bus line **02**.
o Get off in front of buildings 301 and 302 (**last stop**).
- By taxi [~45 minutes, KRW ~13,500]

● From Songdo Convensia, Incheon

- **By public transportation** [~1 hour, KRW ~2,000]
o Take the subway (**line Incheon No. 1**) **from Incheon Nat'l Univ station to Bupyeong station.**
o Transfer the subway line from 'Incheon No. 1' to 'No. 1' (not Incheon No. 1!).
o Take the subway (**line No. 1**) **from Bupyeong to Sindorim station.**
o Transfer the subway line from 'No. 1' to 'No. 2'.
o Take the subway (**line No. 2**) **from Sindorim to Nakseongdae station.**
o Get out of **Exit 4**, turn left around the GS gas station, and board a bus line **2**.
o Get off in front of buildings 301 and 302 (**last stop**).
- By taxi [~45 minutes, KRW ~32,500]

Campus Map of Seoul National University

Accommodation

No.	Name	Distance	Rates	
1	**Hoam Faculty House**	4km (Bus #02, to the last stop: 15 minutes)	Standard Double (KRW 104,500) Standard Twin (KRW 104,500) Deluxe Double (KRW 148,500) Deluxe Twin (KRW 148,500)	http://www.hoam.ac.kr/
2	**Novotel Ambassador Seoul Doksan**	10km (~1 hour)	Superior Double (KRW 125,000) Superior Twin (KRW 125,000)	https://www.ambatel.com/main.amb?null
3	**Shilla Stay Guro**	10km (~1 hour)	Standard Double (KRW 126,000) Standard Twin (KRW 126,000) Deluxe Double (KRW 137,000)	http://www.shillastay.com/guro/index.do
4	**Sheraton Seoul Palace Gangnam Hotel**	14km (~1 hour)	Deluxe Double (KRW 147,250) Deluxe Twin (KRW 147,250)	http://www.sheratonseoulpalace.com/overview
5	**Mercure Ambassador Gangnam**	13.5km (~1 hour)	Standard Double (KRW 132,300) Standard Twin (KRW 132,300) Superior Double (KRW 146,300)	https://mercure.ambatel.com/gangnam/meeting/hallInfo.amb?brand_code=M0456&gnbCode=040000&lnbCode=040200&menu_se=M1244

*Hotel information is just for your reference. You have your own responsibility to reserve your accommodation.

Nonlinear Metasurfaces

Thomas Zentgraf
Department of Physics
Ultrafast Nanophotonics
Paderborn University, Germany
Email: thomas.zentgraf@uni-paderborn.de

For efficient nonlinear processes the engineering of the nonlinear optical properties of media becomes important. In particular, the phase relation between the fundamental and the nonlinear waves plays here an important role. The most well-known technique for spatially engineering nonlinear properties is the quasi-phase matching scheme for second-order processes like second harmonic generation (SHG). The quasi-phase matching leads to efficient frequency conversion compared to a homogeneous nonlinear medium by providing the extra momentum to compensate the phase mismatch between the fundamental and harmonic waves. The so-called 'poling' is the most widely employed technique for achieving quasi-phase matching. By periodically reversing the crystalline orientation of ferroelectric materials, the sign of the $\chi^{(2)}$ nonlinear susceptibility can be spatially modulated along the propagation direction. However, such a poling only leads to a binary state for the nonlinear material polarization, which is equivalent to a discrete phase change of π of the nonlinear polarization.

Here I will discuss a novel nonlinear metamaterial with homogeneous linear optical properties but continuously controllable phase of the local effective nonlinear polarizability. For the demonstration we use plasmonic metasurfaces with various designs for the meta-atom geometry together with circular polarized light states. The controllable nonlinearity phase results from the phase accumulation due to the polarization change along the polarization path on the Poincare Sphere (the so-called Pancharatnam-Berry phase) and depends therefore only on the spatial geometry of the metasurface. By using a fixed orientation of the meta-atom the nonlinear phase can be spatially arbitrarily tailored over the entire range from 0 to 2π. In contrast to the quasi-phase matching scheme the continuous phase engineering of the effective nonlinear polarizability enables complete control of the propagation of harmonic generation signals, and therefore, it seamlessly combines the generation and manipulation of the harmonic waves for highly compact nonlinear nanophotonic devices. We will demonstrate the concept of phase engineering for the manipulation of the SHG and THG from metasurfaces and the restriction on the symmetry properties of the geometry.

Furthermore, I will discuss a nonlinear Berry phase in the time domain which arises from the rotational Doppler shift that can be observed on spinning metasurfaces. The rotational Doppler shift in nonlinear optics was predicted nearly 50 years ago and recently demonstrated at nonlinear crystals. The Doppler frequency shift was determined for the SHG of a circularly polarized beam passing through a spinning nonlinear optical BBO crystal with three-fold rotational symmetry. In our experiments we found that the SHG signal with a circular polarization opposite to that of the fundamental beam experiences a Doppler shift of three times the rotation frequency of the optical crystal. This finding is of fundamental significance in nonlinear optics and also for tailored nonlinearities, as it provides a further degree of freedom with the design of nonlinear materials, in particular for moving media. We will briefly discuss how this rotational Doppler Effect can be also utilized for spinning metasurfaces in the nonlinear regime.

Biography: Professor Thomas Zentgraf received his bachelor's degree of Engineering from University of Applied Sciences Jena, Germany, in 2001 and a master's degree of Physics of the Technical University Clausthal, Germany, in 2002. After that, he joined the University of Stuttgart, Germany, where he under the supervision of Professor Harald Giessen received his PhD in the 2006. Prof Zentgraf was honored with a Feodor-Lynen-Fellowship by the Alexander von Humboldt Foundation in 2007 and joined as a research fellow the group of Professor Xiang Zhang at the Mechanical Engineering Department at University of California at Berkeley, USA. In 2011 he returned to Germany and became full professor for Applied Physics at the Department of Physics, University of Paderborn, where he is head of the Ultrafast Nanophotonics Group. His research interests focus on using ultrafast spectroscopy to study linear and nonlinear effects in plasmonic and dielectric metamaterials and plasmonic-hybrid materials.

Spin-enabled optics with metamaterials and metasurfaces

Jensen Li
School of Physics and Astronomy
University of Birmingham, United Kingdom
Email: j.li@bham.ac.uk

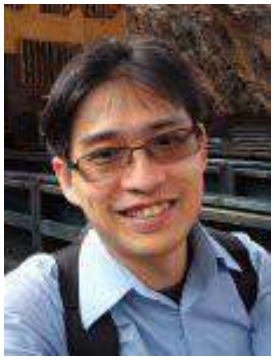

Light, similar to other vector waves such as elastic waves, has a spin-degree of freedom in its propagation. The interaction between spin and motion provides an interesting way to manipulate the orbital motion of light, in addition to the driving force from a refractive index gradient in conventional optics. In this tutorial, I will give an introduction of geometric phase and the associated optical-spin Hall effect in a systematic approach and will show its applications and new opportunities in metamaterials and metasurfaces. For example, the optical spin-Hall effect can be utilized to control dynamically the generation of surface plasmon on a plasmonic metasurface by putting a tailor-made array of anisotropic metamaterial atoms on a surface. When these anisotropic metamaterial atoms are assembled into a three dimensional material, I will also show how these can be used to generate a pseudo-magnetic field or gauge field for photon, which can guide light into cyclotron motion, as if it is a real magnetic field acting on electron motion. These discussions provide a feasible route to spin-enabled optics.

Biography: Dr. Jensen Li received his BEng degree with first class honours in electrical and electronic engineering from the University of Hong Kong in 1998 and his MPhil, PhD degree in physics from the Hong Kong University of Science and Technology in 2000 and 2004. In this period of time, he worked on the zero-th order photonic band gap and the theoretical proposal of acoustic negative index metamaterials.

From 2005 to 2007, Jensen worked in Imperial College London, with support from a Croucher Foundation postdoctoral fellowship, where he developed a theoretical scheme of carpet cloaking.

From 2007 to 2009, he was a postdoctoral researcher at the University of California at Berkeley, participated in the realization of carpet cloaking at infrared frequencies. He also started to work on acoustic metamaterials with super-resolution there.

From 2009 to 2013, he was an assistant professor at the City University of Hong Kong. He continued his research in metamaterials and also worked on alternative schemes in achieving acoustic negative indices without local resonance from theory to realization.In 2013, he joined University of Birmingham as a senior lecturer.

Reconfigurable Plasmonics and Metamaterials

Yongmin Liu
Assistant Professor
Department of Mechanical and Industrial Engineering
Department of Electrical and Computer Engineering
Northeastern University, Boston, USA
Email: y.liu@neu.edu
Group Website: http://www.northeastern.edu/liulab

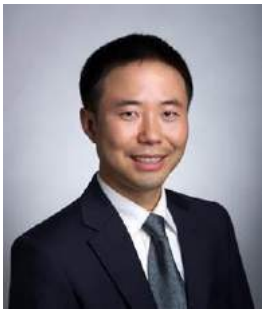

Plasmonics has become a very important branch in nano optics. It allows us to concentrate, guide, and manipulate light at the deep subwavelength scale, promising enhanced light-matter interaction, next-generation optical circuits, sub-diffraction-limited imaging, and ultrasensitive biomedical detection [1-3]. Furthermore, the assembly of judiciously designed metallic structures can be used to construct metamaterials and metasurfaces with exotic properties and functionalities, including anomalous refraction/reflection, strong chirality and invisibility cloak [4,5]. There is a pressing need of tunability and reconfigurability for plasmonics and metamaterials, in order to perform distinctive functionalities and miniaturize the device footprint. In this talk, I will present our recent work in reconfigurable plasmonics and metamateirals. First, I will discuss the first demonstration of reconfigurable plasmonic lenses operating in microfluidic environment, which can dynamically diverge, collimate and focus surface plasmons [6]. Second, I will present a novel graphene metasurface to fully control the phase and amplitude of infrared light with very high efficiency. It manifests broad applications in beam steering, biochemical sensing and adaptive optics in the crucial infrared wavelength range [7]. Finally, I will discuss origami-based, dual-band chiral metasurfaces at microwave frequencies. The flexibility in folding the metasurface provides another degree of freedom for geometry control in the third dimension, which induces strong chirality from the initial, 2D achiral structure [8]. These results open up a new avenue towards lightweight reconfigurable metadevices.

References: [1] S. A. Maier, "Plasmonics: fundamentals and applications", Springer Science+ Business Media (2007); [2] T. Zentgraf et al., "Plasmonic Luneburg and Eaton lenses", **Nature Nanotechnology** 6, 151 (2011); [3] Y. M. Liu, et al., "Compact magnetic antennas for directional excitation of surface plasmons", **Nano Letters** 12, 4853 (2012); [4] Y. M. Liu and X. Zhang, "Metamaterials: a new frontier of science and technology", **Chemical Society Reviews** 40, 2494 (2011); [5] K. Yao and Y. M. Liu, "Plasmonic metamaterials", **Nanotechnology Review** 3, 177 (2014); [6] C. L. Zhao et al., "A reconfigurable plasmofluidic lens", **Nature Communications** 4:2350 (2013); [7] Z. B. Li et al., "Graphene plasmonic metasurfaces to steer infrared light", **Scientific Reports** 5, 12423 (2015); [8] Z. Wang et al., manuscript in preparation.

Biography: Dr. Yongmin Liu obtained his Ph.D. from the University of California, Berkeley in 2009. He joined the faculty of Northeastern University at Boston in fall 2012 with a joint appointment in the Department of Mechanical & Industrial Engineering and the Department of Electrical & Computer Engineering. Dr. Liu's research interests include nano optics, nanoscale materials and engineering, plasmonics, metamaterials, biophotonics, and nano optomechanics. He has authored and co-authored over 50 journal papers, including *Science*, *Nature*, *Nature Nanotechnology*, *Nature Communications*, *Physical Review Letters* and *Nano Letters*. Dr. Liu received Office of Naval Research Young Investigator Award (2016), 3M Non-Tenured Faculty Award (2016), Air Force Summer Faculty Fellowship (2015), and Chinese Government Award for Outstanding Students Abroad (2009). Currently he serves as an editorial board member for *Scientific Reports*, *EPJ Applied Metamaterials* and *Nano Convergence*.

Topological Photonic Crystals

Ling Lu
Institute of Physics, Chinese Academy of Sciences, Beijing, China

Due to the recent discovery of topological insulators, it has been recognized that topology is indispensable in distinguishing phases of matter. Similarly, new optical material systems are being discovered with non-trivial topologies of their global wave-functions in the momentum space, whose interfaces support novel states of light with ideal transport properties such as the robustness to large disorder or fabrication imperfections.

In this talk, I will show experimental realizations and theoretical predictions of 2D and 3D photonic crystals with topologically protected edge and surface states. Specifically, I will discuss single and multimode one-way waveguides, the observation of Weyl points, a single Dirac cone surface state immune to random disorder and topological one-way fibers. This research can be extended to phonons, plasmons and other bosons. These new degrees of freedom in bosonic band topologies promise wide exciting opportunities in both fundamental physics and technological outcomes.

Biography: Ling Lu is a professor in the Institute of Physics of Chinese Academy of Sciences in Beijing China. He obtained his bachelor in Physics in 2003 from Fudan University in Shanghai, China. He got his Ph.D. in Electrical Engineering in 2010 at University of Southern California in Los Angeles. His thesis work, advised by Prof. John O'Brien, was on photonic crystal nanocavity lasers. He was a postdoc and later a research scientist in the Physics Department of Massachusetts Institute of Technology, where he worked with Prof. Marin Soljačić and John Joannopoulos and collaborated with Prof. Liang Fu. His current research focuses on topological photonics.

Multipole decomposition and nonradiating sources in nanophotonics and metamaterials

Andrey Miroshnichenko
Associate Professor
Nonlinear Physics Centre
Research School of Physics and Engineering
Australian National University
Acton, ACT, 2601, Australia

Email: andrey.miroshnichenko@anu.edu.au
Website: andreysquare.com

Multipole decomposition is indispensable tool in analyzing the optical response of nanoscale structures consisting of finite size elements. In general, there are two complementary approaches based on Cartesian (current) multipoles and Spherical (scattered field) multipoles. For subewavelength elements they produce similar description. But for larger elements certain deviations might occur. In this tutorial, I will provide the basic description of both methods and specify kind of complementary information they provide. I will also introduce the concept of nonradiation sources, provide specific examples of so-called *anapole* modes and demonstrate the importance of toroidal dipole moments.

References:

1. Kaelberer, M. et al., *Science* **330**, 1510, (2010).
2. Chen, J. et al., *Nature Photonics* **5**, 531 (2011).
3. Grahn, P. et al., *New J. Phys.* **14** 093033 (2012).
4. Miroshnichenko, A. E. et al., *Nature Comm.* **6**, 8069 (2015).

Biography: A/Prof. Andrey Miroshnichenko obtained his PhD in 2003 from the Max-Planck Institute for Physics of Complex Systems in Dresden, Germany. In 2004 he moved to Australia to join the Nonlinear Physics Centre at ANU. During this time A/Prof. Miroshnichenko made fundamentally important contributions to the field of photonic crystals and bringing the concept of the Fano resonances to photonics. In 2007 A/Prof. Miroshnichenko was awarded by APD Fellowship from the Australian Research Council. It allowed him to initiate the research on a new class of tunable photonic structures infiltrated with liquid crystals. Later, in 2011 he was awarded by Future Fellowship from the Australian Research Council. During this period, he pioneered the research of high-index dielectric nanoparticles in the visible range, including one of the first demonstrations of the optically induced magnetic response in silicon nanoparticles. The current topics of his research are nonlinear nanophotonics, topologiccal photonics, and resonant interaction of light with nanoclusters, including optical nanoantennas and metamaterials.

Plasmonic nanolasers: fundamental, application and challenges

Renmin Ma
School of Physics
State Key Lab for Mesoscopic Physics
Collaborative innovation center of quantum matters
Peking University, China
Email: renminma@pku.edu.cn

Plasmonic nanolasers are a new class of quantum amplifiers that deliver coherent surface plasmons well below the diffraction barrier which brings fundamentally new capabilities to biochemical sensing, super-resolution imaging and on-chip optical communication. In this talk, I will review fundamental, application and challenges of this emergent device.

Biography: Ren-Min Ma is an assistant professor in the School of Physics, Peking University. He received his PhD from Peking University. His dissertation was focused on semiconductor physics and devices in low dimensional structures and received the National Top 100 Ph.D. dissertations of China Award. He was a postdoc researcher at UC Berkeley during 2009-2014. He developed the first room temperature semiconductor plasmon laser, directionally emitted waveguide embedded plasmon laser and applied plasmon lasers to sensing field. His current research interests include nanophotonics and nanomaterials.

The optics of film-coupled nanoparticles: a bridge to the quantum realm

Cristian Ciracì
Center for Biomolecular Nanotechnologies, Istituto Italiano di Tecnologia,
Via Barsanti 14, 73010 Arnesano, Italy
Email: cristian.ciraci@iit.it

Metals support surface plasmons at optical wavelengths and have the ability to localize light to sub-wavelength regions. The film-coupled nanoparticle system—in which plasmonic nanoparticles are separated nanometer distances from a metal film by an insulating spacer—has unique properties that make it useful for a variety of processes depending on the nanoparticle shape. Nanospheres that are coupled to a film, for example, have been predicted to produce enormous field enhancements—as much as thousands of times that of the incident radiation—in the separating region between nanoparticle and film. For the narrowest (<1 nm) gaps, light can be so tightly confined that the nonlocality associated with the dielectric response of the metal and quantum effects can have a strong impact on the scattering properties of the system, placing strict bounds on the ultimate field enhancement.

Another interesting system is that of nanocubes or planar structures, which support transmission line-like modes between the two planar metal contact regions. Collective scattering of film-coupled nanocubes can strongly modify reflectance properties of the underlying surfaces, creating a nearly ideal absorber at desired wavelengths. The controlled reflectance of the surface might provide a means for enhancing nonlinearity, for example by allowing potentially all of a fundamental beam to be converted into higher harmonics. Moreover, we numerically find a sub-nm gap regime in which nonlocal effects can dramatically enhance the nonlinear optical response of the metal by several order of magnitude.

All mentioned structures can be easily and cheaply fabricated using colloidal nanoparticles, surface chemistries, or atomic layer deposition lithography, allowing for near angstrom-scale control over the spacer thickness and large-area uniformity. At the same time, a reliable way to theoretically describe and numerically model optical properties of plasmonic nanostructures with different length scales requires methods beyond classical electromagnetism. In this tutorial I will present an implementation of the hydrodynamic model that takes into account the nonlocal behavior of the electron response by including the electron pressure and it is generalized so that it can describe electron spill-out and tunneling effects, including nonlocal broadening near metal surfaces.

Biography: Cristian Ciracì obtained his BSc in Computer Science Engineering in February 2005 and his MSc in Science for Engineering in July 2007 at Sapienza, University of Rome (Italy). He received his Ph.D. in Condensed Matter Physics from University of Montpellier, France, with honor degree in September 2010. In November 2010 he joined the Center for Integrated Metamaterials and Plasmonics at **Duke University (U.S.)** as a Postdoc. In March 2014 he joined the Center for Biomolecular Nanotechnologies at the **Istituto Italiano di Tecnologia (IIT)**, Italy, where he currently holds a position as Researcher. His main research activities concern numerical modeling and investigation of electromagnetic propagation in complex media, with particular emphasis on nonlinear optical phenomena. During the years of his research activity he has co-authored several publications on top-tier scientific journals and has been invited to several international conferences. In 2012 his work was featured on the **cover of Science Magazine**.

TABLE OF CONTENTS

Plenary Presentation

Keynote Presentation

Hybrid Optically Active Nanomaterials

Recent Advances in Complex Materials and Nanophotonics

Toroidal Electrodynamics and Toroidal Metamaterials

Nano-Plasmonics for Sensing

Functional Materials and Devices for Acoustic and Elastic Waves

Nanophotonics on Silicon Platform

Metasurfaces and 2D Metamaterials in microwave region

Singularity Points in Acoustic Metamaterials: Physics and Applications

Photonic topological insulators: fundamental physics â€

Transformation Optics concept and applications

Advanced passive and active metasurfaces

A bottom-up approach towards metamaterials and plasmonics

Active, Nonlinear, Quantum, and Reconfigurable Plasmonics and Metamaterials

New concepts for energy harvesting and photon management

Hybrid Plasmonics with Quantum Confined Materials and Devices

Fano resonances in optics and microwaves: Physics and application

Parity-Time and related symmetries in Photonics, Plasmonics, Acoustics

Plasmonic Nanocircuits: Fundamentals and Devices

Classical and Quantum Applications using Fast and Slow Light Photonics

Towards integrated quantum photonics: materials, designs, technologiesâ€¦

META-magnetism and interdisciplinary applications

Nanophotonics and plasmonics for information applications

Metamaterial Structures for Healthcare Applications

Near, Mid and Far Infrared Photonics

Periodic Systems with Glide Symmetry

Advances in Nanolasers

Photo/Thermal Conversions and Their Applications

THz metamaterial and metasurface

Acousto-elastic metamaterials and phononic crystals

Metamaterials in Communication Systems

Plasmonic Sensor for Biomedical Device

Alternative plasmonic materials

Coupling of magnetic and electric dipoles to magneto-electric resonancesâ€¢

Novel photonic and plasmonic structures: theory and applications

Recent Progress in Novel Functionalities of Plasmonic and Metamaterial Structures

Advanced numerical and theoretical tools as applied to modern nano photonics â€

Optically-assisted mechanical systems for advanced photonicsâ€

Wideband metamaterials for antennas and related applications

Structural Color for Displays and Imaging

Military Applications of Metamaterials

Innovative Metamaterials

Applications of nanophotonics and metamaterials in bio-imaging

Plasmonics and nanophotonics

Metamaterials and negative index materials

Photonic crystals

Laser and cavities

Acoustic metamaterials

Materials for photonics (Graphene, MoS2, WS2, etc)

Photonics based on 2D materials

Chiral and bianisotropic materials

Plasmonics-based devices

Metamaterial-based devices

Metasurfaces and flat optics

Optical antennas

Plasmon-enhanced photovoltaics, photocatalysis, and solar fuels

Topological photonics

Quantum photonics

Parity time symmetry

Nanobiophotonics

Near-field optics and nano-optics

Super-resolution imaging

Transformational electromagnetics, cloaking

FSS, HIS and Extraordinary transmission

Modeling, Computational Techniques and Verification of Theory

Emerging applications: Quantum photonic devices, Biophotonics, Plasmonics for health, â€¦

Nanofabrication Technology, Lithography and etching techniques, Growth and deposition, Self-organized

Plenary Presentation

Metamaterials, anapoles and flying donuts

N. I. Zheludev
Optoelectronics Research Centre, University of Southampton &
The Photonics Institute, Nanyang Technological University, Singapore
niz@orc.soton.ac.uk

Abstract-Electromagnetic toroidal multipoles can be represented as currents flowing on the surfaces of tori were recently experimentally observed in metamaterials and nanoparticles. They provide physically significant contributions to the basic characteristics of matter including absorption, dispersion, and chirality. They give rise to dynamic anapoles, illusive non-radiating charge-current configurations recently detected in matter. Toroidal excitations also exist in free space as spatially and temporally localized electromagnetic pulses propagating at the speed of light and interacting with matter in a way different from conventional electromagnetic transvers pulses. We discuss these recent findings and the role of localized and propagating electromagnetic toroidal excitations in light-matter interactions, spectroscopy and telecommunications.

REFERENCES

1. N. Papasimakis, V. Fedotov, V. Savinov, T. A. Raybould, and N. I. Zheludev. **Electromagnetic toroidal excitations in matter and free space**. Nature Mater. 15, 263 (2016)
2. T. A. Raybould, V. A. Fedotov, N. Papasimakis, I. J. Youngs, and N. I. Zheludev. **Focused electromagnetic doughnut pulses and their interaction with interfaces and nanostructures.** Opt. Express 24(4), 3150 (2016)
3. M. Gupta, V. Savinov, N. Xu, L. Cong, G. Dayal, S. Wang, W. Zhang, N. I. Zheludev, and R. Singh**. Sharp toroidal resonances in planar terahertz metasurfaces.** Adv. Mater. 28, 8206 (2016)
4. D. W. Watson, S. D. Jenkins, J. Ruostekoski, V. A. Fedotov, and N. I. Zheludev. **Toroidal dipole excitations in metamolecules formed by interacting plasmonic nanorods**. *Phys. Rev. B* **93**, 125420 (2016)
5. T. A. Raybould, V. A. Fedotov, N. Papasimakis, I. Kuprov, I. J. Youngs, W. T. Chen, D. P. Tsai, and N. I. Zheludev. **Toroidal circular dichroism.** Phys. Rev. B 94(3), 035119 (2016)
6. V. Savinov, V. A. Fedotov, and N. I. Zheludev. **Toroidal dipolar excitation and macroscopic electromagnetic properties of metamaterials**. Phys. Rev. B 89, 205112 (2014)
7. P. C. Wu, W.-L. Hsu, W. T. Chen, Y.-W. Huang, C. Y. Liao, A. Q. Liu, N. I. Zheludev, G. Sun and D. P. Tsai. **Plasmon coupling in vertical split-ring resonator metamolecules**. *Scientific Reports* **5**, 9726 (2015)
8. A. A. Basharin, M. Kafesaki, E. N. Economou, C. M. Soukoulis, V. A. Fedotov, V. Savinov, N. I. Zheludev. **Dielectric metamaterials with toroidal dipolar response.** *Phys. Rev. X* **5**, 011036 (2015)
9. V. Savinov, V. A. Fedotov, and N. I. Zheludev. **Toroidal dipolar excitation and macroscopic electromagnetic properties of metamaterials.** *Phys. Rev. B* **89**, 205112 (2014)
10. V. A. Fedotov, A. V. Rogacheva, V. Savinov, D. P. Tsai, N. I. Zheludev. **Resonant transparency and non-trivial non-radiating excitations in toroidal metamaterials.** *Scientific Reports* **3**, 2967 (2013)
11. Y. W. Huang, W. T. Chen, P. C. Wu, V. A. Fedotov, N. I. Zheludev and D. P. Tsai. **Toroidal lasing spaser.**

Sci. Rep. **2**, 1237 (2013)

12. Y. W. Huang, W. T. Chen, P. C. Wu, Y. Z. Ho, D. P. Tsai, V. Fedotov, V. Savinov, N. I. Zheludev and Y. F. Chau. **Plasmonic toroidal resonance at optical frequencies.** *SPIE Newsroom* (2012)
13. Y. W. Huang, W. T. Chen, P. C. Wu, V. Fedotov, V. Savinov, Y. Z. Ho, Y.F. Chau, N. I. Zheludev, and D. P. Tsai. **Design of plasmonic toroidal metamaterials at optical frequencies** *Opt. Express* **20**(2), 1760 (2012)
14. T. Kaelberer, V. A. Fedotov, N. Papasimakis, D. P. Tsai, and N. I. Zheludev. **Toroidal dipolar response in a metamaterial.** *Science* **330**, 1510 (2010)
15. N. Papasimakis, V. A. Fedotov, K. Marinov, and N. I. Zheludev. **Gyrotropy of a metamolecule: wire on a torus.** *Phys. Rev. Lett.* **103**, 093901 (2009)
16. K. Marinov, A. D. Boardman, V. A. Fedotov, and N. Zheludev. **Toroidal metamaterial** *New J. Phys.* **9**, 324 (2007)
17. A. D. Boardman, K. Marinov, N. Zheludev, and V. A. Fedotov. **Dispersion properties of nonradiating configurations: finite-difference time-domain modeling.** *Phys. Rev. E* **72**(3), 036603 (2005)

Squeezing of Photonic Energy into A Point-like Space

Y. H. Lee[1,*] **and M. K. Kim**[2]

[1]Department of Physics, KAIST, Daejon, Korea

[2]KU-KIST Graduate School of Converging Science and Technology, Korea University, Seoul, Korea

[*]corresponding author: yhlee@kaist.ac.kr

Abstract – A three-dimensionally tapered metallic nano-gap resonator with modal volume of ~1.0×10^{-7} λ^3 is to be discussed. From a 5-nm-air-gap gold resonator, strong second harmonic signals are generated at a point-like space where electromagnetic energy is highly concentrated. The nonlinear signal is found to be stronger than that from a 100-nm-gap counterpart by a factor of >27,000. Rich nonlinear characteristics observed from quantum dots and nm-scale proteins trapped in the nano-gap will also be discussed.

Metaoptics in the Visible

Federico Capasso

John A. Paulson School of Engineering and Applied Sciences, Harvard University, USA

capasso@seas.harvard.edu

Abstract- Metasurfaces based on sub-wavelength patterning have major potential for arbitrary control of the wavefront of light by achieving local control of the phase, amplitude and polarization and allowing greater functionality and more compact devices. We have introduced a new CMOS compatible technology based on atomic layer deposition of TiO_2 which has enabled high performance metalenses, achromatic lenses, immersion objectives, axicons, vortex plates, holograms and ultracompact spectrometers for a wide range of applications.

Parity-Time-Symmetric Optics, extraordinary momentum and spin in evanescent waves, and the quantum spin Hall effect of light.

Franco Nori [1,2]
[1] *RIKEN, Saitama, Japan.* [2] *University of Michigan, Ann Arbor, USA*

(1) Optical systems combining balanced loss and gain provide a unique platform to implement classical analogues of quantum systems described by non-Hermitian parity–time (PT)-symmetric Hamiltonians. Such systems can be used to create synthetic materials with properties that cannot be attained in materials having only loss or only gain. We report PT-symmetry breaking in coupled optical resonators. We observed non-reciprocity in the PT-symmetry-breaking phase due to strong field localization, which significantly enhances nonlinearity. In the linear regime, light transmission is reciprocal regardless of whether the symmetry is broken or unbroken. We show that in one direction there is a complete absence of resonance peaks whereas in the other direction the transmission is resonantly enhanced, which is associated with the use of resonant structures. Our results could lead to a new generation of synthetic optical systems enabling on-chip manipulation and control of light propagation.

Related references:

B. Peng, et al., *Parity-time-symmetric whispering-gallery microcavities,* Nature Physics **10**, 394-398 (2014). [PDF][Link][arXiv]. Supplemental: [PDF][Link]; "News & Views": [PDF][Link]

B. Peng, et al., *Loss-induced suppression and revival of lasing,* Science **346**, 328-332 (2014). [PDF][Link][arXiv]

B. Peng, Ş.K. Özdemir, W. Chen, F. Nori, L. Yang, *What is and what is not electromagnetically induced transparency in whispering-gallery microcavities*, Nature Communications **5**, 5082 (2014). [PDF][Link][arXiv]

H. Jing, Ş.K. Özdemir, X.Y. Lu, J. Zhang, L. Yang, F. Nori, *PT-Symmetric Phonon Laser*, Phys. Rev. Lett. **113**, 053604 (2014). [PDF][Link][arXiv]

F. Monifi, J. Zhang, Ş.K. Özdemir, B. Peng, Y.X. Liu, F. Bo, F. Nori, L. Yang, *Optomechanically induced stochastic resonance and chaos transfer between optical fields,* Nature Photonics, 10, 399–405 (2016). [PDF][Link]. Also its cover story. Featured in a News and Views.

(2) Maxwell's equations, formulated 150 years ago, ultimately describe properties of light, from classical electromagnetism to quantum and relativistic aspects. The latter ones result in remarkable geometric and topological phenomena related to the spin-1 massless nature of photons. By analyzing fundamental spin properties of Maxwell waves, we show that free-space light exhibits an intrinsic quantum spin Hall effect—surface modes with strong spin-momentum locking. These modes are evanescent waves that form, for example, surface plasmon-polaritons at vacuum-metal interfaces. Our findings illuminate the unusual transverse spin in evanescent waves and explain recent experiments that have demonstrated the transverse spin-direction locking in the excitation of surface optical modes. This deepens our understanding of Maxwell's theory, reveals analogies with topological insulators for electrons, and offers applications for robust spin-directional optical interfaces.

Main reference:

K.Y. Bliokh, D. Smirnova, F. Nori, *Quantum spin Hall effect of light*, Science 348, 1448-1451 (2015). [PDF] [Link] [arXiv]. Highlighted in a Perspectives [Science 348, 1432 (2015)].

Some related work by our group can be found in the following references:

K.Y. Bliokh, F. Nori, *Transverse spin of a surface polariton*, Phys. Rev. A **85**, 061801 (2012). [PDF][Link][arXiv]

K.Y. Bliokh, A.Y. Bekshaev, F. Nori, *Dual electromagnetism: helicity, spin, momentum, and angular momentum*, New J. Phys. **15**, 033026 (2013). [PDF][Link][arXiv] ISI Highly cited paper 2013-2014.

K.Y. Bliokh, J. Dressel, F. Nori, *Conservation of the spin and orbital angular momenta in electromagnetism*, New J. Phys. **16**, 093037 (2014). [PDF][Link][arXiv]

K. Y. Bliokh, Y. S. Kivshar, F. Nori, *Magnetoelectric Effects in Local Light-Matter Interactions*, Phys. Rev. Lett. **113**, 033601 (2014). [PDF][Link][arXiv]

K. Y. Bliokh, A. Y. Bekshaev, F. Nori, *Extraordinary momentum and spin in evanescent waves*, Nature Communications **5**, 3300 (2014). [PDF][Link][arXiv] ISI Highly cited paper.

A.Y. Bekshaev, K.Y. Bliokh, F. Nori, *Transverse spin and momentum in two-wave interference*, Phys. Rev. X **5**, 011039 (2015). [PDF][Link][arXiv]

J. Dressel, K.Y. Bliokh, F. Nori, *Space-time algebra as a powerful tool for electromagnetism*, Physics Reports 589, 1–71 (2015).

K.Y. Bliokh and F. Nori, *Transverse and longitudinal angular momenta of light*, Physics Reports, Volume 592, 26 (August 2015), Pages 1–38 (2015). A 38-pages review, including some of our results. URL: [PDF][Link][arXiv]

K.Y. Bliokh, F.J. Rodriguez-Fortuno, F. Nori, A.V. Zayats, *Spin-orbit interactions of light*. Nature Photonics 9, p. 796–808 (2016). 13-pages review, including some of our results. [PDF][Link][arXiv]

M. Antognozzi, et al., *Direct measurements of the extraordinary optical momentum and transverse spin-dependent force using a nano-cantilever,* Nature Physics, 3732 (2016). [PDF][Link][arXiv]

Z.P. Liu, et al., *Metrology with PT-Symmetric Cavities: Enhanced Sensitivity near the PT-Phase Transition,* Phys. Rev. Lett. **117**, 110802 (2016). [PDF][Link][arXiv]

D. Leykam, K.Y. Bliokh, C. Huang, Y.D. Chong, F. Nori, *Edge Modes, Degeneracies, and Topological Numbers in Non-Hermitian Systems,* Phys. Rev. Lett. **118**, 040401 (2017). [PDF][Link][arXiv][Supplementary information]

Tip-enhanced Raman scattering microscopy: plasmonic molecular imaging beyond the limits

Satoshi Kawata
Osaka University, Japan
Kawata@ap.eng.osaka-u.ac.jp

Abstract
Tip-enhanced Raman scattering (TERS) microscopy as a version of near-field scanning optical microscopy has been widely used for analyzing molecular distribution of nanomaterials and biomaterials In this presentation, mechanisms of super-resolution and field enhancement of TERS microscopy will be discussed and recent progress of TERS microscopy beyond the limits, such as nanometer resolution, 3D imaging, and deep UV imaging, will be shown.

Raman microscopy has been a convenient tool for analyzing and imaging various materials as it provides richer information than other imaging techniques based on topographic information. However, Raman scattering is a weak phenomenon and the spatial resolution in any optical microscopy is usually restricted by the diffraction limit of the probing light. Both these problems can be overcome by use of surface plasmons, which confines optical field in the near field of probe tip [1], resulting in local enhancement of light [2] as well as super spatial resolution [3]. The spatial resolution in imaging is limited around 10 nm due to the necessity of a reasonable diameter of metallic tip to excite collective electron oscillation and due to the contribution of imaginary part of dielectric constant of probe metal in visible range [4]. The factor of enhancement is also limited due to the necessary of covering the spectrally broad band for the excitation and Raman scattering shift of sample [5]. The effective spectral range is also limited to near UV to near infrared for silver and gold. In this presentation, I will show our research progress in TERS microscopy beyond the limitations. The spatial resolution has been drastically improved by applying pressure on to the sample with a tip to introduce the localized structural deformation in sample [6]. The broadband enhancement by cascading the probe antennae [7], the deep UV resonant Raman TERS [8] without photo-degradation wit use of lanthanide ions [0], and 3D Raman imaging with a gold nano-particle inside a living cell [10] will be discussed.

REFERENCES

[1] S. Kawata, ed. "Near Fiel Optics and Surface Plasmon Polaritons," Springer, 2001
[2] S. Kawata, Y. Inouye, P. Verma, ***Nature Photon.. 3***, 388 (2009).
[3] S. Kawata, et. al. ***Chem. Rev., 117***, in press, (2017).
[4] S. Kawata, ***Jpn. J. Appl. Phys. 53***, 010001 (2013).
[5] A. Taguchi, S. Kawata, P. Verma, ***Nano Scale. 7***, 17424 (2015).
[6] T. Yano et al., ***Nature Photonics***, ***3***, 473 (2009).
[7] S. Kawata, A. Ono, P. Verma, ***Nature Photon.***, ***3***, 473, 2009.
[8] A. Taguchi, et. al., ***J. Raman Spectrosc. 40,*** 1324, 2009.
[9] Y. Kumamoto, et. al., ***Biomed Opt. Express. 7***,158 (2015).
[10] J. Ando, et. al, ***Nano Lett. 11***, 5344 (2011).

Active Quantum Nanoplasmonics:
From Single Molecule Strong Coupling to Stopped-Light Lasing

O. Hess
The Blackett Laboratory, Imperial College London, Prince Consort Road, London, SW7 2AZ, UK
o.hess@imperial.ac.uk

Abstract- Nanoplasmonic cavities create a unique environment for controlled spatio-temporal dynamics of light strongly coupled with single quantum emitters (molecules, quantum dots) providing a basis for strong coupling at room temperature, strong coupling quantum spectroscopy and paving the way for few- or single-molecule lasing.

Nanoplasmonic (meta-)materials and nanophotonics have the unique ability to confine light in extremely sub-wavelength volumes and thereby strongly enhance the effective strength of electromagnetic fields. Fundamentally, such high-field enhancement can alter the local density of states experienced by a photoactive molecule to unprecedented degrees and control its exchange of energy with light. For a sufficiently strong field enhancement, one enters the strong-coupling regime, where the energy exchange between the excited states of molecules/materials and plasmons is faster than the de-coherence processes of the system. As a result, the excitonic state of the molecule becomes entangled with the photonic mode, forming hybrid excitonic-photonic states. These hybrid-states are part light, part matter and allow for characteristic Rabi oscillations of atomic excitations to be observed. Until recently, the conditions for achieving strong-coupling were most commonly met at low temperatures, where de-coherence processes are suppressed. As a major step forward, we have recently demonstrated room-temperature strong coupling of single molecules in a plasmonic nano-cavity [1] which was achieved using a host-guest chemistry technique, controlling matter at the molecular level. Concurrently, linking nano-spectroscopy of quantum dots with strong coupling allows to lithographically realise a strong-coupling set-up that couples dark plasmonic modes and quantum dots [2]. Remarkably, through strong coupling we obtain spectroscopic access to otherwise veiled states (such as the charged trion state) enabled through a strong-coupling induced speed up of the radiative dynamics of the quantum dot states [2]. Considering the key importance of strong coupling in quantum optics our findings pave the road for a wide range of ultrafast quantum optics experiments and quantum technologies at ambient conditions. Moreover, the pronounced position-dependent spectral changes may lead to new types of quantum sensors and near-field quantum imaging modalities.

References

[1] R. Chikkaraddy, B. de Nijs, F. Benz, S. J. Barrow, O. A. Sherman, E. Rosta, A. Demetriadou, P. Fox, O. Hess and J. J. Baumberg, Nature **535**, 127 (2016).
[2] H. Gross, J. M. Hamm, T. Tuffarelli, O. Hess and B. Hecht, under review, (2017).

Parity-time Symmetry Breaking Lasing and Anti-Lasing

Xiang Zhang
UC Berkeley, USA

Abstract: Optical loss is usually undesirable. Recently, judiciously designed balanced gain and loss structures, so called parity-time (PT) symmetric synthetic materials, are explored due to their extraordinary properties. In this talk I will discuss the notion of PT symmetry in optical systems. Especially I will discuss how to achieve nano-scale spectrometer by designing an anti-Hermitian light matter interactions. This will be also useful for spectrum splitting in solar applications. Finally, I will discuss a single mode lasing scheme using PT symmetric periodically modulation in a micro ring lasers, and lasing and anti-lasing in a single cavity.

Optical Antennas;
Spontaneous Emission Faster Than Stimulated Emission.

Eli Yablonovitch
University of California, Berkeley

Abstract-Antennas emerged at the dawn of radio for concentrating electromagnetic energy into a volume much smaller than the wavelength cubed, allowing for nonlinear radio detection. Such coherent detection is essential for radio receivers, and has been used since the time of Hertz. Conversely, an antenna can efficiently extract radiation from a sub-wavelength source, such as a small cellphone.

Over 100 years after the radio antenna, we finally have tiny "optical antennas" which can extract radiation from molecules and quantum dots. With optical antennas, spontaneous light emission can become faster than stimulated emission. Antenna physics has been poorly covered in education. It does not require plasmonics; nor the Purcell effect.

Towards Scalable Semiconductor Quantum Networks

Dirk Englund
Department of Electrical Engineering and Computer Science, MIT, USA
*corresponding author: englund@mit.edu

Abstract-The Internet is among the most significant inventions of the 20th Century. We are now poised for the development of a quantum internet to exchange quantum information and distribute entanglement among quantum memories (and ultimately quantum computers) that could be great distances apart. This kind of quantum internet would have a range of applications that aren't possible in a classical world, including long-distance unconditionally-secure communication, certain types of precision sensing and navigation, and distributed quantum computing. But we still need to develop or perfect many types of components and protocols to build such a quantum internet. This talk will consider some of these components, focusing on photonic integrated circuits, diamond spin-based quantum memories, and prototype networks. Specifically, the first part of this talk will review our recent progress in adapting one of the leading PIC architectures—silicon photonics—for different types of quantum secure communications protocols. The second part of the talk will consider how photonic integrated circuits technology may extend the reach of quantum communications through all-optical and memory-based quantum repeaters, as well as extensions to modular quantum computers.

Keynote Presentation

Metasurfaces for in-plane plasmonic arbitrary pattern generation

Byoungho Lee
School of Electrical and Computer Engineering, Seoul National University, Seoul 08826, Korea
*byoungho@snu.ac.kr

Abstract- Plasmonic metasurfaces with distributed nanoslits are demonstrated to generate in-plane plasmonic arbitrary patterns based on holographic approach. Utilizing extremely anisotropic scatterings of surface plasmon polaritons (SPPs) at nanoslits, holographic reconstructon and modulation of plasmonic wavefront are achieved by designing spatial distributions and rotations of nanoslits. Polarization-dependent modulations of in-plane SPP wavefront are thoroughly studied for focusing, switching, and multiplexing in-plane plasmonic waves. Moreover, manipulation of complex plasmonic field in terms of phase and amplitude is proposed for complete control of arbitrary holographic SPP patterns.

Plamonics and metasurface are the major research topics which have led the boom of nanophotonics recently. Plasmonics have emerged as a powerful route to subwavelength optical technologies by using surface plasmon polaritons (SPPs) which are surface bound electromagnetic waves propagating along a metal-dielectric interface. Meanwhile, metasurfaces, which are planar metamaterials, have been extensively studied to manipulate properties of light abruptly in anomalous manner. Particularly, as an ultra-thin flat optical component for coherent light manipulation, metasurface has been attracting much interest as a promising candidate to replace conventional bulky optic components. Moreover, metasurfaces have been found to enable coherent control of plasmonic waves as well as light waves propagating in the free space.

In this presentation, metasurfaces for arbitrary plasmonic wavefront generation and polarization dependent modulations will be presented. Firstly, physical mechanisms of nanoslits as anisotropic SPP scatterers will be explained. Then, design methods to assign phase profiles on nanoslit distributions are presented in case of various polarization states [1]. Plasmonic waves are focused, switched, multiplexed, and steered depending on polarization state modulations [1-3]. Lastly, arbitrary complex plasmonic field generation with manipulation of both phase and amplitude is introduced with an example of plasmonic Airy beam generation [4].

Acknowledgments National Research Foundation (NRF) of Korea (21A20131612805)

REFERENCES

1. S.-Y. Lee *et al*., “Plasmonic meta-slit: shaping and controlling near-field focus,” *Optica*, Vol. 2, No. 1, pp. 6-13, 2015.
2. S.-Y. Lee *et al*., “Polarization-multiplexed plasmonic phase generation with distributed nanoslits,” *Opt. Express*, Vol. 23, No. 12, pp. 15598-15607, 2015.
3. G.-Y. Lee *et al*., "Near-field focus steering along arbitrary trajectory via multi-lined distributed nanoslits," *Sci. Rep.*, Vol. 6, No. 33317, 2016.
4. E.-Y. Song *et al*., "A double-lined metasurface for plasmonic complex-field generation," *Laser Photon. Rev.*, Vol. 10, No. 2, pp. 299-308, 2016.

Hybrid nanostructures for sub-wavelength imaging, nonlinear optics, and chemistry

S. A. Maier[1]

[1] Imperial College London, London SW7 2AZ, UK

Abstract **– We demonstrate how controlled emission of hot electrons in plasmonic nanoantennas leads to highly localized nanochemistry. This scheme is utilized for the assembly of hybrid metallic nanoantennas consisting both of top-down fabricated elements, and nanosized colloids. The second part of the talk will show new results for dielectric and hybrid metallic/dielectric antennas, based on Si, Ge and GaP, for highly enhanced harmonic generation and surface-enhanced sensing.**

Plasmonic nanoantennas with nanoscale gaps act as efficient transducers of electromagnetic energy from the far to the near field at optical frequencies, creating hot spots of field energy utilized extensively in surface-enhanced spectroscopy and sensing. Using a super-resolution localization scheme, we demonstrate direct imaging of these electromagnetic hot spots via single-molecule emission events, paying careful attention to coupling between molecular emission and antenna modes, in order to determine the true position of the single emitters [1]. We then introduce the notion of "reactivity hot spots" — nanosized regions in plasmonic antennas where hot electrons generated via plasmon decay are emitted. We demonstrate that control over this emission process can lead to highly localized surface chemistry [2], allowing the positioning of colloidal nanospheres around bow tie antennas with high accuracy (Figure 1). A combination of experimental imaging of these reactivity hot spots and ab initio theory will be used to elucidate this process.

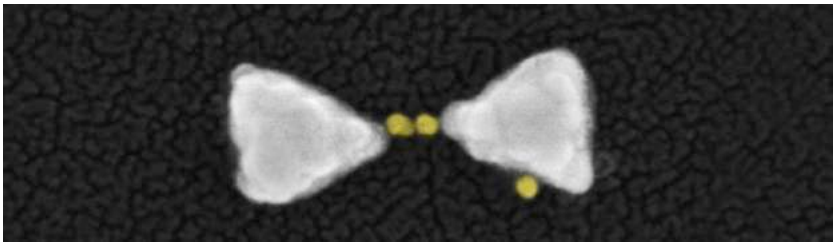

Fig. 1. Gold nanospheres arranged in the gap of a silver bow tie antenna via localized hot electron emission [2]. SEM image false-coloured to distinguish between the two materials. The diameter of the gold spheres is 15 nm.

In the second part of the talk, we will present new results on dielectric and hybrid dielectric/metallic nanoantennas, focusing on highly enhanced harmonic generation and surface-enhanced spectroscopy under low-loss conditions. As an example, GaP nanopillars allow to utilize the advantages of dielectric antennas in terms of low loss and high field confinement throughout the visible regime [3]. We will further show new, unpublished results on hybrid Si/plasmonic antennas, as highly efficient nanoscale sources of third harmonic radiation.

REFERENCES

[1] Mack et al., "Decoupling absorption and emission processes in super-resolution localization of emitters in a plasmonic hot spot", Nature Communications 8, 14513 (2017)

[2] Cortés et al., "Plasmonic hot electron driven site-specific surface chemistry with nanoscale special resolution", Nature Communications (accepted 2017)

[3] Cambiasso et al, "Bridging the gap between dielectric nanophotonics and the visible regime with effectively lossless GaP antennas", Nano Letters (accepted 2017)

Acoustic omni meta-atom for decoupled access to all octants of a wave parameter space

Sukmo Koo, Choonlae Cho, Jun-ho Jeong, and Namkyoo Park*
Photonic Systems Laboratory, Department of ECE, Seoul National University, Seoul 08826, Korea
*corresponding author: nkpark@snu.ac.kr

Abstract-Although the decoupling of fundamental wave parameters has been envisaged as an ideal platform towards the top–down and deterministic reconfiguration of the meta-atom (Pendry, Science 312, 2006), its feasibility has remained as a plausible idea. In this talk we present our recent proposal for a new design strategy for the meta-atom (Koo et. al., Nat. comm. 13012, 2016). Focusing on an acoustic platform, the criteria for the decoupling of wave parameters are derived, and an omni meta-atom that achieves independent, broad-range access to all octants of the wave parameter space (ρ, B^{-1}, Ξ) is demonstrated. With the precision access for target parameters, we also demonstrate new meta-devices, including bianisotropic meta-surfaces for independent beam shaping of transmission / reflection-waves.

Extreme elastic anisotropy – realization by metamaterials

Yoon Young Kim

Seoul National University
School of Mechanical and Aerospace Engineering
E-mail address: yykim@snu.ac.kr, Tel:02-880-7154

While extreme effective material properties, such as negative or very large density and stiffness, have been explored significantly, studies on the realization of extreme anisotropy has not received much attention. Particularly for elastic media that are characterized by 4^{th}-order tensor field, a wide spectrum of material anisotropy can be envisioned. As illustrative cases of extreme anisotropy, one can make shear modulus equal to or even larger than longitudinal modulus for which unique wave phenomena known as conical refraction or polarization anomaly can take place. Natural materials alone may not achieve the desired anisotropy but specially designed elastic metamaterials made of either single or multiple phases can. In this talk, we discuss a recent progress made towards the design of extreme anisotropic elastic metamaterials. Also, their potential applications will be discussed.

Second order optical nonlinearity in metamaterials

Teruya Ishihara
Department of Physics, Graduate School of Science,
Tohoku University, Sendai, Japan
*corresponding author: t-ishihara@m.tohoku.ac.jp

Abstract-By designing sub-wavelength structure, it is possible to endow a new response that is not obtained in nature. In this paper, various second order optical nonlinearities including second harmonic generation, optical rectification and electro-optic effects are discussed in the same platform for metamaterials.

Even in centrosymmetric materials, second-order optical nonlinearity exists at the surface where permittivity environment changes abruptly. In the oblique incident configuration, surface polarization is excited which generates second harmonic generation (SHG) and photo-rectification. For normal incidence it does not give SHG unless the surface has a structure which breaks the symmetry in the plane. The structure can be endowed by artificially carving the surface by using e-beam lithography for example. This structure can be considered as a new type of metamaterial where second order optical nonlinearity is designed. Earlier we have shown that by breaking the symmetry, it is possible to observe SHG in semiconductor embedded structure [1] and photorectification in metal-based metamaterials [2,3]. Recently sub-wavelength shape dependent SHG was investigated and analyzed in terms of effective susceptibility concept [4-7]. By appropriately design the subwavelength structure, it may be possible to produce extremely nonlinear metamaterial beyond the empirical Miller's rule [8], which sets the ceiling limit for nonlinear response.

In this paper, we will discuss examples of the second order optical nonlinearities in the same platform for artificially designed metamaterial films.

Acknowldgements
This work is based on stimulating discussions with my collaborators, K. Koshino, X. Luo, S.G. Tikhodeev, N.A. Gippius, N. Nishimura, M. Onoda, M. Iwanaga, S. Ohno, M. Matsubara, M. Lein, M. Nakagawa and my previous students, H. Nakajima, T. Hatano, H. Kurosawa, M. Saikawa, Y. Hachiya and present students, M. Akbari, K. Iwata and Y.B. Habibullah.

REFERENCES

[1] T. Ishihara, K. Koshino, and H. Nakashima, "Second Harmonic Generation due to Quadrupole Interaction in a Photonic Crystal Interaction: Angle Dependence and the Symmetry of the Unit Cell," Phys. Rev. Lett. Vol. 91, 2003, 203901:1-4.
[2] T. Hatano, B. Nishikawa, M. Iwanaga and T. Ishihara, "Optical rectification effect in 1D metallic photonic crystal slabs with asymmetric unit cell, " OPTICS EXPRESS 16 , 8236-8241 (2008).
[3] H. Kurosawa, T. Ishihara, N. Ikeda, D. Tsuya, M. Ochiai and Y. Sugimoto , "Optical rectification effect due to surface plasmon polaritons at normal incidence in a nondiffraction regime," OPTICS LETTERS 37, 2793-2795 (2012).

[4] S. Roke, M. Bonn and A.B. Petukhov, “Nonlinear optical scattering: The concept of effective susceptibility,” Phys. Rev. B Vol.70, 2004, 1150106:1-10.
[5] K. O’Brien, H. Suchowski, J. Rho, A. Salandrino, B. Kante, X. Yin, and X. Zhang, “Predicting nonlinear properties of metamaterials from the linear response,” Nature Materials Vol.14, 2014, 379-383.
[6] J. Butet and O.J.F. Martin, “Evaluation of the nonlinear response of plasmonic metasurfaces: Miller’s rule, nonlinear effective susceptibility method, and full-wave computation,” Journal of the Optical Society of America B, 33 (2016) A8-15.
[7] M. Saikawa, Y. Hachiya, K. Iwata, M. Matsubara, and T. Ishihara, “Second Harmonic Generation from sub-wavelength Triangular Hole Array in Au Thin Film, ” Session 2A21, META2017.
[8] R.C. Miller, “Optical second harmonic generation in piezoelectric crystals,” Appl. Phys. Lett. 5, 17-19 (1964).

Electronically Tunable Materials and Metasurfaces: Exploring Quantum Materials and Device Designs for Dynamic Wavefront Control

Harry A. Atwater

Thomas J. Watson Laboratory of Applied Physics and Kavli Nanoscience Institute
California Institute of Technology, Pasadena, California 91125, USA
E-mail address: haa@caltech.edu

Abstract- Tuning the complex dielectric function of low-dimensional materials and metasurfaces enables scientific exploration of quantum materials such graphene, phosphorene and topological insulators and, as well plasmonic and nanophotonic device applications for dynamic wavefront control including electronic phase and amplitude modulators for the near infrared (conducting oxides) and mid infrared (graphene). We discuss light-matter interactions in emerging quantum materials and report dynamically tunable metasurfaces in the near-infrared and mid-infrared with $>\pi$ phase modulation and 'perfect' absorption approaching 100%.

We have explored the photonic properties of thin electrostatically gated phosphorene and $(Bi_{1-x}Sb_x)_2Te_3$ topological insulators using mid-infrared spectroscopy measurements. We combine these optical experiments with transport measurements and ARPES to identify the observed spectral modulation as a combination of gate-variable Pauli-blocking of bulk interband optical transitions at higher energies and modulation of intraband transitions associated with both topological surface stated (TSS) and the bulk free carrier density.

In the domain of device applications, we experimentally demonstrate a gate-tunable metasurface that enables dynamic electrical control of the phase and amplitude of plane wave reflection. Tunability arises from field-effect modulation of the complex refractive index of conducting oxide layers incorporated into metasurface antenna elements which are configured in a reflectarray geometry. We measure a phase shift of $>\pi$ and ~ 30% change in the reflectance by applying 2.5 V gate bias. Additionally, we demonstrate modulation at frequencies exceeding 10 MHz, and electrical switching of +/-1 order diffracted beams, a basic requirement for electrically tunable beam-steering phased array metasurfaces.

We further demonstrate electronically tunable mid-infrared transmission that utilizes resonant absorption in graphene plasmonic ribbons to modulate the extraordinary optical transmission effect in subwavelength metallic slit arrays. Resonant absorption in plasmonic modes of nanoscale monolayer graphene ribbons situated inside subwavelength metallic slits can efficiently block the coupling channel for extraordinary optical transmission, leading to a strong suppression of transmission. Full wave simulations predict a transmission modulation of 95.7% via this mechanism. Measurements reveal a transmission modulation of 96%, yielding an experimental realization of 'perfect' absorption in monolayer graphene.

Quantum Plasmonics

B. Vest[1], M.-C. Dheur[1], E. Devaux[2], A. Baron[3], E. Rousseau[4], J.-P. Hugonin[1], G. Messin[1], F. Marquier[1] and J.J. Greffet

[1]Laboratoire Charles Fabry, Institut d'Optique, CNRS, Université Paris-Saclay, 91127 Palaiseau cedex, France.

[2]Institut de Science et d'Ingénierie Supramoléculaire, CNRS, Université de Strasbourg, 67000 Strasbourg,France.

[3]Centre de Recherche Paul Pascal, CNRS, 33600 Pessac, France.

[4]Laboratoire Charles Coulomb, UMR CNRS-UM 5221, Université de Montpellier, 34095 Montpellier, France.
[*]corresponding author: jean-jacques.greffet@institutoptique.fr

Abstract-In this talk, we report experiments aiming at exploring the physics of surface plasmons in the single plasmon regime. In other words, we revisit quantum optics using surface plasmons: tests of the wave-particle duality of surface plasmons, observation of entanglement between a photon and a plasmon and two photon interference on a lossy beam splitter. In the latter case, we observe both a correlation dip and a correlation peak at the outputs of a beamsplitter.

Chiral plasmonic nanostructures

P. Fischer[1,2,*]

[1]Max Planck Institute for Intelligent Systems, Heisenbergstr. 3, Stuttgart, Germany

[2]Institute for Physical Chemistry, University of Stuttgart, Pfaffenwaldring 55, Stuttgart, Germany

[*]fischer@is.mpg.de

Abstract-How can one see gold nanoparticles in strongly absorbing blood? I will describe that this is possible with plasmonic nanohelices. Moreover, I will show that record local plasmon resonance (LSPR) sensitivities can be achieved when plasmonics and chirality are combined. We use a general fabrication scheme to rapidly grow chiral nanostructures from plasmonic and magnetic materials, in a way that lets us tailor their dielectric function. We thereby realize metafluids whose optical properties can be tuned and dynamically switched.

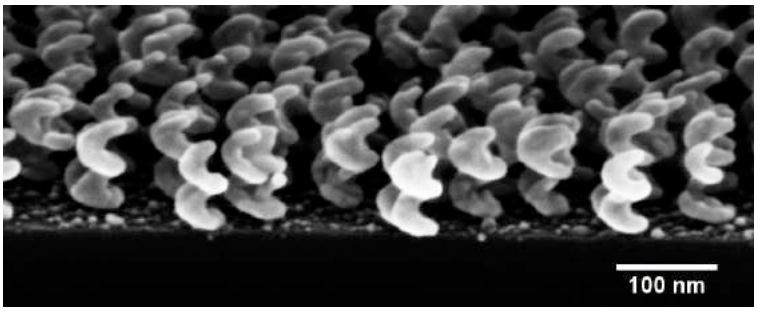

Fig. 1. Surface with chiral nanostructures (adapted from [1])

References

1. Mark, A.M.; Gibbs, J.G.; Lee, T.-C.; Fischer, P. *Nature Mat.* **2013**, 12, 802.

2. Jeong, H.-H.; Mark, A.M.; Alarcón-Correa, M.; Kim, I.; Oswald, P.; Lee, T.-C.; Fischer, P. *Nature Comm.* **2016**, 7, 11331.

3. Jeong, H.-H.; Mark, A.M.; Lee, T.-C., Alarcón-Correa, M.; Eslami, S.; Gibbs, J.G.; Fischer, P. *Nano Lett.* **2016**, 16, 4887.

Ultrafast nanoscopy: imaging structure, function, and dynamics of matter on its natural length and times scales

Markus B. Raschke

Department of Physics, Department of Chemistry, and JILA, University of Colorado, Boulder, USA
*Email address: markus.raschke@colorado.edu

Abstract: I will present the advances in multimodal linear, nonlinear, and spatio-temporal nano-imaging for the study of fundamental optical and plasmonic phenomena, coupled single molecule or quantum dynamics, with unprecedented nanometer spatial and femtosecond resolution, sensitivity and precision [1-6]. To gain the desired *simultaneous nanometer spatial resolution with spectroscopic specificity and femtosecond temporal resolution* we combine plasmonic and optical antenna concepts with ultrafast and shaped laser pulses to precisely control optical excitation on femtosecond time and nanometer length scales from the visible to THz spectral range. In the implementation with scattering scanning near-field microscopy (*s*-SNOM) or other tip-enhanced microscopy modalities with nonlinear, ultrafast, and IR and Raman vibrational spectroscopies, the resulting enhanced and qualitatively new forms of light-matter interaction enable deep-subwavelength spatially resolved imaging of heterogeneities and nano-confinement as they define the properties of most functional materials. I will present several new concepts extending tip-enhanced spectroscopy into the nonlinear and ultrafast regime for nano-scale imaging and spectroscopy of surface molecules and nano-solids. Examples include the adiabatic nano-focusing for nm-resolved imaging of the few-fs plasmon coherence [1] (Fig. 1), ultrafast and nonlinear probing of structure and dynamics in quantum materials [2-4], vibrational nano-imaging of molecular structure, coupling, and dynamics down to the single molecule level [5,6] (Fig. 2), and the transition from classical to quantum plasmonic emitter coupling and femtosecond control for electron wavepackets for ultrafast electron imaging and STM.

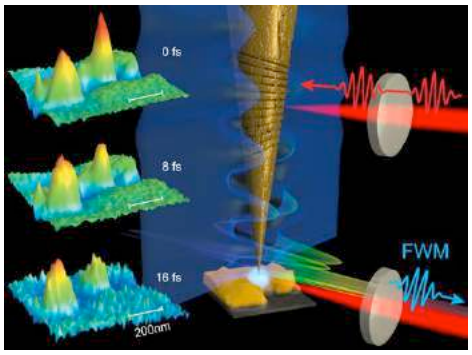

Fig. 1. Nonlinear four-wave mixing nano-focused imaging of coherent plasmon dynamics with few femtosecond and nanometer resolution [1]

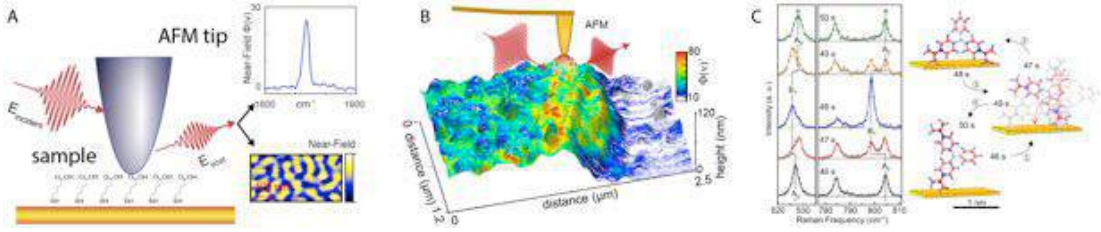

Fig. 2. Tip-enhanced/tip-scattering vibrational Raman and IR nano-spectroscopy and -imaging probing structure, order, and dynamics in self-assembled monolayer (A), molecular electronic materials (B), and intra- and intermolecular vibrational redistribution in single molecule spectral diffusion (C).

References:

[1] V. Kravtsov, R. Ulbricht, R., J. M. Atkin, , and M. B. Raschke, M. B. Plasmonic nanofocused four-wave mixing for femtosecond near-field imaging. *Nature Nanotechnol.* **11**, 459-464 (2016).

[2] B. T. O'Callahan, J. M. Atkin, A. C. Jones, J. H. Park, D. Cobden, and M. B. Raschke. Inhomogeneity in the ultrafast insulator-to-metal transition dynamics of VO_2. *Nature Commun.* **6**, 6849 (2015).

[3] S. Berweger, C. C. Neacsu, A. Mao, H. Zhou, S. S. Wong, M. B. Raschke. Optical nanocrystallography with tip-enhanced phonon Raman spectroscopy", *Nature Nanotechnol.* **4**, 496 (2009).

[4] J. M. Atkin, S. Berweger, A. C. Jones, and M. B. Raschke. Nano-optical imaging and spectroscopy of order, phases, and domains in complex solids. *Advances in Physics* **61**, 745 (2012).

[5] E. A. Muller, B. Pollard, H. A. Bechtel, P. van Blerkom, M. B. Raschke. Infrared vibrational nano- crystallography and – imaging. *Science Advances* **2** (2016) e160106.

[6] B. Pollard, E. A. Muller, K. Hinrichs, M. B. Raschke, Vibrational nano-spectroscopic imaging correlating structure with intermolecular coupling and dynamics. *Nature Commun*. **5** (2014) 3587.

Pseudo-spins and their consequences in classical waves

C.T. Chan[1*]
[1]Hong Kong University of Science and Technology, Hong Kong, China
[2]Author Affiliation, Country
[*]corresponding author: phchan@ust.hk

Abstract- Classical wave systems such as photonic crystals and metamaterials can exhibit pseudospin physics. The pseudospin in such systems gives rise to unique transport properties such as super-Klein tunneling. In addition, the conventional Anderson localization picture needs to be revised for waves propagating in 1D disordered systems carrying pseudospins. The localization length in such systems reaches a minimum value at a critical random strength and any additional disorder beyond this critical strength only makes the waves less localized.

Many of the novel properties of graphene can be described by a "massless Dirac equation" with a pseudospin of ½. The term "pseudospin" here refers to the two degrees of freedom given by the two atomic sites in a unit cell of graphene's honeycomb lattice, not to the intrinsic spin of electron,.

The natural question to ask is then whether we can construct systems with a higher pseudospin. Previous work in ultracold atom systems suggested that this is possible in some artificial lattices, and such systems can support striking transport properties. However, ultracold atom systems usually demand extremely low temperature and hence technically difficult to realize in experiments. We find that certain classical wave systems with special dispersions near the zone center correspond to a pseudospin-1 system, which offers the opportunity to study the pseudospin physics in classical wave systems with experimentally realizable materials and in room temperature. Here, the pseudospin of 1 does not refer to the intrinsic spin of photons, but the three degrees of freedom of the spatial wavefunction of photon near the Dirac-like point of the photonic crystal. Interesting properties of such photonic pseudospin-1 system includes "super Klein tunneling" and "super-collimation". While both "Klein tunneling" and "collimation" are known effects for graphene (and pseudospin of ½ in general), these effects become more robust and pronounced when the pseudospin becomes 1.

In addition, the conventional Anderson localization picture needs to be revised for waves propagating in 1D disordered systems carrying pseudospins. In conventional disordered system, localization length decreases with disorder. The localization length in psuedospin systems reaches a minimum value at a critical random strength and any additional disorder beyond this critical strength only makes the waves less localized. More importantly, for pseudospin-1 systems, there exists a sharp transition at the critical random strength which separates the localization behavior into two distinct regimes with different localization characteristics. These novel phenomena have never been seen before in ordinary disordered systems. The localization characteristics are also depends strongly on the details of the disorder potential, which is again not seen in ordinary materials.

We will also compare the localization characteristics of systems carrying pseudospins 1and pseudospins of ½.

Making Structured Metal Transparent for Ultra-Broadband Electromagnetic and Acoustic Waves

Mu Wang
National Laboratory of Solid State Microstructures and Department of Physics,
Nanjing University, Nanjing 210093, China
*Email: muwang@nju.edu.cn

Abstract- In this talk, I will present our recent studies on making structured metals transparency for ultrabroadband electromagnetic waves and acoustic waves via surface excitations. First, I will show the effect that periodic, quasiperiodic, and disordered metallic gratings can become transparent and completely antireflective for extremely broadband electromagnetic waves at oblique incidence. Further, we develop an approach to design oblique metal gratings that are transparent for broadband electromagnetic waves (including optical waves and terahertz ones) with normal incidence. Thirdly, we demonstrate that the principles of broadband transparency for structured metals can be extended from one-dimensional metallic gratings to two-dimensional scenario. Finally we point out that similar phenomena can be observed in sonic artificially metallic structures, demonstrating transparency for broadband acoustic waves. With this series of studies we try to provide guidelines to develop novel broadband metamaterials, which are promising for applications of transparent conducting panels, antireflective conducting solar cells, broadband acoustic imaging and sensing, etc.

REFERENCES

1. Ren X. P., *et al*, "Non-periodic metallic gratings transparent for broadband terahertz waves", *Phys. Rev. B* 91, 045111, 2015

2. Qi D. X., et al., "Broadband enhanced transmission of acoustic waves through serrated metal gratings", *Appl. Phys. Lett*. 106, 011906, 2015

3. Fan R. H., et al. "Making structured metals transparent for ultrabroadband electromagnetic waves and acoustic waves", *Annals of Physics*, 358, p5-19, 2015

4. Fan R. H., et al., "Oblique metal gratings transparent for broadband terahertz waves", *Appl. Phys. Lett*. 102, 171904, 2013

5. Fan R. H., et al., "Broadband antireflection and light-trapping enhancement of plasmonic solar cells", *Phys. Rev. B* 87, 195444, 2013

6. Qi D.-X., et al., "Multiple-band transmission of acoustic wave through metallic gratings", *Appl. Phys. Lett*. 101, 061912, 2012

7. Huang X.-R., R.-W. Peng, and R.-H. Fan, "Making metals transparent for white light by spoof surface plasmons", *Phys. Rev. Lett*. 105, 243901, 2010.

8. Fan R. H., et. al., "Transparent metals for ultrabroadband electromagnetic waves", *Adv. Mater.*, 24, 1980, 2012

Hybrid Optically Active Nanomaterials

Penetration Effect in Uniaxial Anisotropic Metamaterials

K. Vytovtov[1*] and S. Zouhdi[2]
[1]Department of Information Technology, Astrakhan State Technical University, Russia
[2]Polytech Paris-Sud, Paris-Sud University, France
[*]corresponding author: vytovtov_konstan@mail.ru

Abstract - We consider a plane harmonic wave propagating parallel to an interface between a standard isotropic medium and an anisotropic metamaterial. It is proved analytically that part of the wave power propagates into the anisotropic metamaterial. Reflection and transmission coefficients are obtained.

An interesting behavior of a plane wave propagating parallel to an interface between isotropic and anisotropic media has been considered in [1]. It has been shown analytically that a bulk wave is excited within the anisotropic medium at grazing incidence. This phenomenon has been defined as the "penetration effect". The hypothesis about reflected wave propagation perpendicularly to an interface was also presented in [2] but this problem has not been studied in detail.

Here we study a semi-infinite uniaxial anisotropic metamaterial described by the permittivity dyadic

$$\overleftrightarrow{\varepsilon} = \begin{vmatrix} \varepsilon_{11} & 0 & 0 \\ 0 & \varepsilon_{11} & 0 \\ 0 & 0 & \varepsilon_{33} \end{vmatrix} \qquad (1)$$

and a scalar permeability μ. Here ε_{11}, ε_{33}, μ have negative values. It is assumed that the anisotropy axis is in the plance of incidence. It is also assumed that a plane harmonic wave propagates parallel to the interface between a standard isotropic medium, free space, and the anisotropic metamaterial. The geometry of the problem is shown in Fig.1.

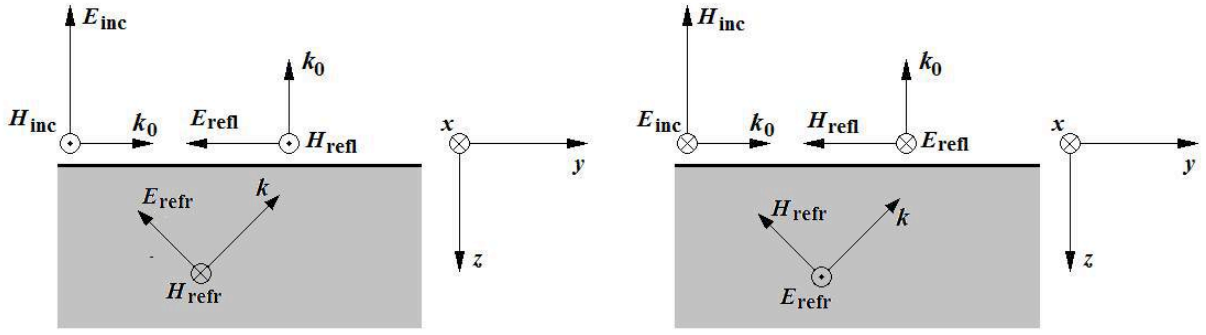

a) b)

Fig.1. Geometry of the problem: a) for TE-wave, b) for TM-wave

After algebraic transformation we obtain the permittivity dyadic (1) in the *xyz*-system

$$\overleftrightarrow{\varepsilon} = \begin{vmatrix} \varepsilon_{xx} & 0 & 0 \\ 0 & \varepsilon_{yy} & \varepsilon_{yz} \\ 0 & \varepsilon_{zy} & \varepsilon_{zz} \end{vmatrix} \quad (2)$$

which can be considered as a two-dimensional metamaterial. In the general case of a lossy medium, the elements of (2) are complex.

We show that the plane wave propagating parallel to the interface can excite a bulk wave propagating under an arbitrary angle within the anisotropic metamaterial. We found that the normal components of the wave vector and the Poyting vector are non-zero.

To describe the reflected wave behavior one should take into account the fact that the tangential components of the wavenumbers of incident, reflected, and refracted waves must be equal to each other and also equal to wavenumber in the isotropic medium. The reflected wave can propagate along the interface or perpendicular to it. Moreover the magnetic filed of the refracted wave has a tangential component for an ordinary wave and electric field has a tangential component for an extraordinary wave. Therefore these components must be also present in the reflected wave since they were not present in the incident wave.

Based on these considerations, we assume that a reflected linearly polarized wave should propagate perpendicular to the interface between the isotropic and the anisotropic medium. The reflection and transmission coefficients are obtained for this case.

For an ordinary wave the reflection coefficient is equal to zero (R=0) and the transmission coefficient is equal to one (T=0). Thus the reflected wave is absent for this type of waves. The surface current at the interface is also nil.

For an extraordinary wave the reflection and transmission coefficients are:

$$R = \frac{\omega\left(\varepsilon_{yy}\varepsilon_{zz} - \varepsilon_{yz}\varepsilon_{zy}\right)}{\omega\left(\varepsilon_{yy}\varepsilon_{zz} - \varepsilon_{yz}\varepsilon_{zy}\right) - k_z\varepsilon_{zz} - k_y\varepsilon_{yz}} \qquad T = \frac{k_z\varepsilon_{zz} + k_y\varepsilon_{yz}}{\omega\left(\varepsilon_{yy}\varepsilon_{zz} - \varepsilon_{yz}\varepsilon_{zy}\right) - k_z\varepsilon_{zz} - k_y\varepsilon_{yz}}$$

More interestingly, in this case the reflection and transmission coefficients do not depend on the frequency if there is no frequency dispersion in the material parameters. Additionally a surface polarization change occures at the interface. These changes are a result of molecular polarization caused by the electromagnetic field.

REFERENCES

1. Vytovtov K., Mospan L. Penetration effect in gyrotropic slab: theory and applications, *Journal of Optical Society of America*. V. 29, N 6, 2012, pp. 877-882, 2012.
2. Vytovtov K., S. Zouhdi *S.* Exotic reflection of plane waves by anisotropic structures, *Metamaterials'2012: The 6th International Congress on Advanced Electromagnetic Materials in Microwaves and Optics*, St. Petersburg, Russia, 2012, pp.432-434.

Bimetallic Nanocatalysts with Integrated Functions of Plasmonics and Catalysis toward Energy Conversion

C.-H. Kuo[1*], Y.-C. Chuang[2*], B. T. Sneed[3] and D. A. Cullen[4]

[1] Institute of Chemistry, Academia Sinica, Taipei 11529, Taiwan

[2] National Synchrotron Radiation Research Center, Hsinchu 30076, Taiwan

[3]Center for Nanophase Materials Sciences and [4]Materials Science and Technology Division, Oak Ridge National Laboratory, Oak Ridge, Tennessee 37831-6496, United States

[*]corresponding author: chunhong@gate.sinica.edu.tw

Abstract Wearing Pt on Cu nanocubes to form the bimetallic nanocatalysts is demonstrated. By heterogeneous coating of Pt, the ultimate rhombic dodecahedral core-frame nanostructures were obtained. Turning the amount of Pt atoms, the frames evolved at the 100 corners to form the vertex-stretching ones. The corresponding nanoframes could be obtained after removing the Cu cores. The nanoframes showed superior performances in the ORR and the photoreduction of 4-nitrophenol , rendering them the cost-efficient alternatives for noble metal catalysts.

The noble metal Pt was successfully coated on the surfaces of the Cu nanocubes by virtue of efficient thermal reduction. The reduced Pt atoms deposited on the Cu surfaces to form Cu-CuPt core-frame nanocrystals The CuPt alloy frames were generated due to co-reduction of Pt(II) and residual Cu(I) ions in the supernatant of Cu nanocube solution and the diffusion of Cu atoms at the core-shell interfaces. The alloying induced the {100} face evolution on the Cu nanocubes and resulted in the rhombic dodecahedral (RD) shape to minimize the crystal energy. Raising the added amount of Pt precursor, the vertices at the {100} corners of the RD core-frame nanocrystals grew out as stretching tips in that sufficient reduced Pt atoms kept growing into the vertices. After removing the Cu cores from the core-frame nanocrystals, the CuPt alloy nanoframes in regular and vertex-stretching (V-S) RD shape were obtained and verified in the Pt/Cu ratios of 26/74 for the regular RD NFs, and 41/59 for the V-S ones (Figure 1).

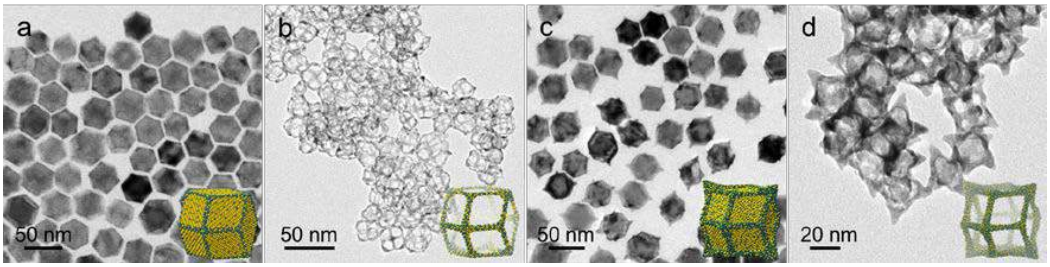

Figure 1. (a) Regular core-frame nanocrystals, (b) regular nanoframes, (c) vertex-stretching core-frame nanocrystals, and (d) vertex-stretching nanoframes in rhombic dodecahedral shapes.

More importantly, abundant surface defects such as terraces and adatoms on both the NFs render them highly active catalysts. In ORR, the V-S NFs showed very superior ECSA activity, 1.3 and 3 times high than those of the regular NFs and the commercial Pt/C. However, it decayed after ADT for 1,200 cycles due to the

surface reconstruction on the defected stretching tips. The Pt mass activity of V-S NFs presented a lower value than that of the regular NFs which indicated the higher content of Pt in the V-S structures. In reduction reactions of 4-nitrophenol, both NFs displayed excellent activities than that of the commercial Pt NPs in dark. Furthermore, their activities were improved at least 1.3 times high under irradiation of visible light, attributed to the effect of SPR enhancement contributed by the nanophase Cu crystal domains in the Cu-rich skeletons.

Acknowledgements We are grateful for the technical support from NanoCore, the Core Facilities for Nanoscience and Nanotechnology at Academia Sinica in Taiwan. A portion of the electron microscopy was performed as part of a user project through Oak Ridge National Laboratory's Center for Nanophase Materials Sciences, which is a U.S. Department of Energy (DOE) Office of Science User Facility and using instrumentation provided by the U.S. DOE Office of Nuclear Energy, Fuel Cycle R&D Program, and the Nuclear Science User Facilities. We specially thank Ms. Mei-Ying Chung, the technician in the Institute of Chemistry at Academia Sinica in Taiwan, for carrying out SEM analyses and measurements of ICP-OES. This work is financially supported by the Ministry of Science and Technology, Taiwan (MOST 104-2113-M-001-007-MY2), and Academia Sinica, Taiwan (Program of Nanotechnology No. 2393).

REFERENCES

1. Huang, X. Q.; Li, Y. J.; Chen, Y.; Zhou, H. L.; Duan, X. F.; Huang, Y., "Plasmonic and Catalytic AuPd Nanowheels for the Efficient Conversion of Light into Chemical Energy," *Angew. Chem. Int. Ed.*, Vol. 52, No.23, 6063-6067, 2013.
2. Hsu, S. C.; Chuang, Y. C.; Sneed, B. T.; Cullen, D. A.; Chiu, T. W.; Kuo, C. H., "Turning the Halide Switch in the Synthesis of Au-Pd Alloy and Core-Shell Nanoicosahedra with Terraced Shells: Performance in Electrochemical and Plasmon-Enhanced Catalysis," *Nano Lett.*, Vol.16, No.9, 5514-5520, 2016.
3. Yu, X. F.; Wang, D. S.; Peng, Q.; Li, Y. D., "High performance electrocatalyst: Pt-Cu hollow nanocrystals," *Chem. Commun.*, Vol. 47, No.28, 8094-8096, 2011.

Electronic structure and optical gain of $InAs_{1-x}Bi_x/InP$ pyramidal quantum dots

Zhi-gang Song[1,2], Sumanta Bose[1] , Weijun-Fan[1,*], Xiaohong Tang[1], and Shushen Li[2]

[1] School of Electrical and Electronic Engineering,

Nanyang Technological University, Singapore 639798, Singapore

[2] SKLSM, Institute of Semiconductors, Chinese Academy of Sciences, P.O. Box 912, Beijing 100083, China

* ewjfan@ntu.edu.sg

Here, we'll show our simulation results on the electronic structure and optical gain of the $InAs_{1-x}Bi_x/InP$ pyramidal quantum dots (QDs). We have taken the valence band anticrossing (VBAC) model into our calculation following our previous work of $GaN_xBi_yAs_{1-x-y}/GaAs$ QDs[1]. The Hamiltonian of the QD is given by

$$H = \begin{pmatrix} H_{8\times8} & H_{8\times6} \\ H_{6\times8} & H_{6\times6} \end{pmatrix} \qquad (1)$$

Where $H_{8\times8}$ is the Kane Hamiltonian, $H_{6\times6}$ is the Bi-state related Hamiltonian and the $H_{8\times6}$ is the interaction between host material and Bi-states. The optical gain is obtained by

$$G(E) = \frac{\pi e^2 \mathrm{h}}{m_0^2 \varepsilon_0 n_r c E} \sum_{n_c, n_v} \frac{1}{V} \left| M^{cv} \right|^2 \left(f_c + f_v - 1 \right) B_{cv}(E - E_{cv}) \qquad (2)$$

All details of the theoretical model can be found in our previous paper [1]. The parameters in model are taken from Refs [2],[3].

FIG.1 shows the variation of conduction band (CB), valence band (VB) and band gap energy with the concentration of Bi and the height of QD. It is clearly shows that the band gap can be tuned less than 400 meV which means that the wavelength of photon will exceed 3μm when the concentration of Bi is more than 7% for the QD with height of 20 in unit of lattice constant. The VB increases obviously when more Bi atoms are incorporated due to the VBAC effect. The CB decreases slowly as compared with VB, resulting from the combination of strain effect and virtual crystal effect. Although the compressive strain effect introduced by Bi drives the CB to go up, the virtual crystal effect drives the CB to go down more quickly. Quantum size effect can be seen as the band gap decreases with the increasing the height of the QDs.

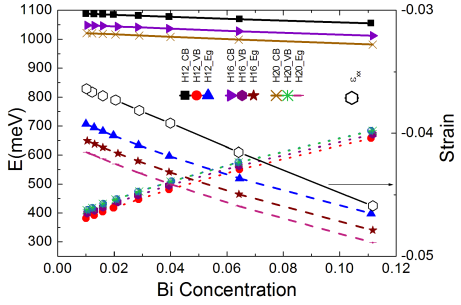

FIG.1. The variety of CB, VB and Eg with the Bi concentration and the height of QD.

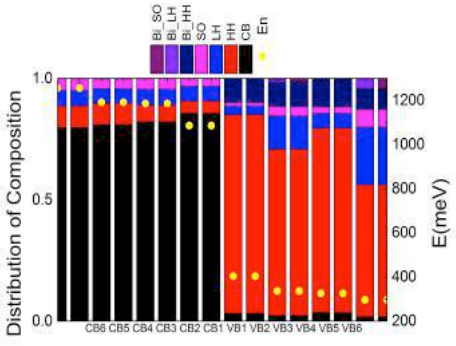

FIG.2. Distribution of compositions for the first six CBs, VBs of H12 QD with Bi of 1.6%.

FIG.2 shows the composition of the first six CBs and VBs. The majority of VB states are the HH states and some Bi_HH states also are mixed.

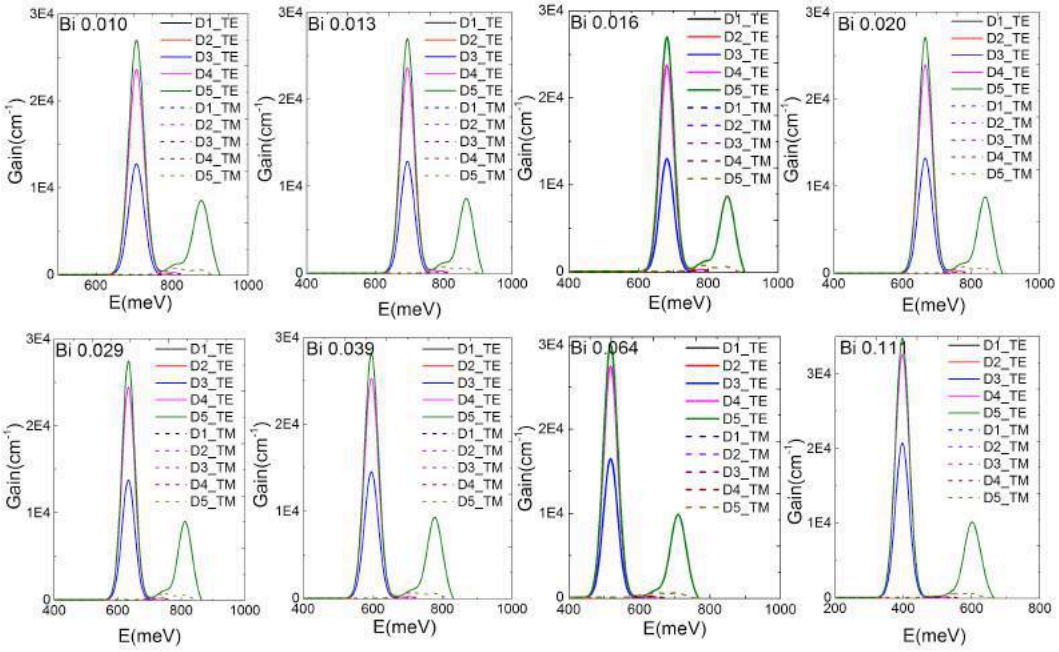

FIG.3. The optical gain of the H12 QDs for different carrier densities and different Bi composition. Here the D2_TE means that the carrier concentration is 2 X10^{18}cm^{-3} for TE mode.

FIG.3 shows the optical gain of the QD for TE and TM modes with different carrier densities in the unit of $10^{18}\mathrm{cm}^{-3}$ and different Bi concentration. The location of the primary peak is red-shift as the concentration of Bi increases. The photon wavelength will exceed 2μm when the concentration of Bi is larger than 3% for the H12 QD. For the sufficiently high carrier density, we obtain a secondary peak in addition to the primary peak.

In summary, the Bi indeed decreases the band gap of the $InAs_{1-x}Bi_x$/InP pyramidal QDs and thus may achieve the 2 and 3μm laser emission. This is important for 2 and 3μm laser devices. The wavelength can be tuned by controlling the concentration of Bi.

W.J. Fan would like to thank the funding support from Singapore MOE AcRF Tier 1 RG182/14, and RG176/16.

Reference:

[1] Zhi-gang Song, Sumanta Bose, Wei-Jun Fan and Shu-Shen Li, J.Appl.Phys. **119**, 143103(2016).
[2] I. Vurgaftman, J. R. Meyer and L. R. Ram-Mohan, J. Appl. Phys. **89**, 5815 (2001).
[3] D.P.Samajdar and S.Dhar, The Scientific World Journal, **2014**, 704830 (2014).

Emergent Nanophotonic Technologies For Chemical Applications

Affar S. Karimullah, , Calum Jack, Ryan Tullius, Vincent M. Rotello[A], Graeme Cooke, Nikolaj Gadegaard[B], Laurence D. Barron, Malcolm Kadodwala,*.

School of Chemistry, Joseph Black Building, University of Glasgow, Glasgow, G12 8QQ, UK.

[B]School of Engineering, Rankine Building, University of Glasgow, Glasgow, G12 8QQ, UK.

[A]Department of Chemistry, 710 Nt. Pleasant Street, University of Massachusetts Amherst, MA 01003, USA.

.

Chirality, the property of an object to lack mirror symmetry and thus be able to exist in two non-superimposable mirror image forms, is a ubiquitous property in nature. Indeed, the building blocks of life, amino acids and sugars are chiral, and this sense of handedness propagates in to the complex structures of life. In this talk I will discuss how near fields with chiral asymmetries, generated by light scattering from chiral nanostructures, can uniquely characterise higher order biological structure which is invisible to conventional spectroscopy. I will demonstrate how the interaction of chiral nanostructures and biomaterials can be understood using concepts from physical chemistry and atomic and molecular physics; orbital hybridisation and quantum interference phenomenon such as electromagnetic induced transparency (EIT).

Nanoplasmonics for ultra-high resolution colours prints and DNA-programmable nanoplasmonics

Xiao Ming Goh[1*], Lin Xi[2], Gomathy Sandhya Subramanian[1], Ng Jia Hong Ray[3], Joel K. W. Yang[1, 3], and Shawn J. Tan[1]

[1]Institute of Materials Research and Engineering, A*STAR

[2]Molecular Engineering Lab, A*STAR

[3]Singapore University of Technology and Design

[*]corresponding author: gohxm@imre.a-star.edu.sg

Abstract- Metal nanostructures can be designed to exhibit specific plasmonic resonances in their optical reflectance spectra through the control of nanostructure material and geometry. This unique spectral control and tunability is attractive for ultra-high resolution colour printing, or for producing security elements for anti-counterfeiting. Their enhanced sensitivity can be combined with the programmability of DNA to develop active plasmonic systems. Here, economical ways of making high resolution colour prints and integrating lithographically-defined nanostructures on solid substrates with DNA will be discussed.

Plasmonic nanostructures can support highly efficient, resonances within gaps or cavities [1-3]. The strong dependence of this phenomenon on geometry and local environment has been exploited for nanoscale manipulation of electromagnetic fields, allowing for extreme local field confinement and enhancement. By lithographically defining nanostructures, one can tune their characteristic resonances to produce wide colour tunability in the visible spectrum. Previously, we demonstrated an approach to ultra-high resolution colour printing in arrays of dielectric pillars capped with a thin layer of metal [4-6]. Multiple layers of optical information can also be encoded within the same area by employing different shapes and/or orientations of nanostructures illuminated by orthogonally polarised light to elicit Surface-Plasmon-induced changes in the colour spectra [6]. This unique spectral control and tunability is particularly attractive for applications such as ultra-high resolution colour printing or for producing unique security elements in anti-counterfeiting technologies.

The enhanced sensitivity afforded by plasmonic nanostructures can further be combined with the programmability of DNA to develop new-generation DNA-based active plasmonic systems. Practical means for active control of these nanoplasmonic systems will open up vast possibilities for downstream applications, such as plasmonic-electronics and solid-state chemical and biological sensing, but has remained elusive. While DNA has previously been shown to enable control over plasmonic resonances in nanoparticle-based systems, the lack of means for precise spatial positioning of these nanoparticles presents challenges for systems integration and readout. The use of programmable DNA to actively control the nanogap between nanoparticles and lithographically defined nanostructures is a strategy that can potentially provide a sensitive plasmonic platform for biomolecule detection as well as a means of dynamically controlling plasmonic colours. Here, I will discuss results including economical ways of making high resolution colour prints, plasmonic pixels that can encode dual images, and combining lithographically-defined nanostructures on solid substrates with DNA programmability towards DNA-nanoplasmonic hybrid systems.

Acknowledgements: The authors would like to acknowledge the funding support from the Joint Council Office (JCO), Agency for Science, Technology and Research (A*STAR).

REFERENCES

[1] D. P. Fromm, A. Sundaramurthy, P. J. Schuck, G. Kino, and W. E. Moerner, "Gap-Dependent Optical Coupling of Single 'Bowtie' Nanoantennas Resonant in the Visible," *Nano Lett*., vol. 4, no. 5, pp. 957–961, May 2004.
[2] P. Mühlschlegel, H.-J. Eisler, O. J. F. Martin, B. Hecht, and D. W. Pohl, "Resonant optical antennas.," *Science*, vol. 308, no. 5728, pp. 1607–9, Jun. 2005.
[3] H. Fischer and O. J. F. Martin, "Engineering the optical response of plasmonic nanoantennas," *Opt*. *Express*, vol. 16, no. 12, p. 9144, Jun. 2008.
[4] K. Kumar, H. Duan, R. S. Hegde, S. C. W. Koh, J. N. Wei, and J. K. W. Yang, "Printing colour at the optical diffraction limit," *Nat*. *Nanotechnol*., vol. 7, no. 9, pp. 557–561, 2012.
[5] Shawn J. Tan, et. al., Plasmonic Color Palettes for Photorealistic Printing with Aluminum Nanostructures, *Nano Letters*, Vol. 14, no. 7, pp. 4023-4029, 2014.
[6] Xiao Ming Goh, et. al., Three-dimensional plasmonic stereoscopic prints in full colour, Vol. 5, 5361, *Nature Communications*, 2014.

Novel Magnetoplasmonic Nanoparticle and its Assembled Structures; Synthesis, Colorometry, and Multi-photon Imaging

Jaebeom Lee*, Van Tan Tran, Junyoung Kwon

Department of Cogno-Mechatronics Engineering, Pusan National University, Busan, 609-735, Republic of Korea

*Corresponding author: E-mail: jaebeom@pusan.ac.kr

Abstract

Controlling and understanding the assembly of colloidal nanoparticles remain a challenging issue for optimizing magnetic-plasmonic devices for various applications including sensors, displays, bio-imaging and therapy. A magnetic field is successfully utilized to induce the fabrication of multidimensional structures composed of magnetite coated silver core/shell ($Ag@Fe_3O_4$) particles, which exhibit intriguing optical properties. Also we report a proof-of-concept experimental results using biocompatible FeSe QDs and femtosecond infrared laser, leading to remarkable excitation-dependent photoluminescence in two-photon luminescence (2PL). An effective and highly controlled dip-coating technique for fabrication of one-dimensional (1D) structure of magnetoplasmonic particles on large-area surface is proposed by combining electrostatic and magnetic dipole interactions. This technique is demonstrated to be a very powerful approach to modulate optical properties of magnetoplasmonic particles. Moreover, a magnetic-field assisted coating technique for fabrication of two-dimensional (2D) amorphous photonic crystal (APC) film of the magnetoplasmonic particles on a filter membrane is proposed. The magnetoplasmonic 2D APC exhibits strong dual reflected colors caused by structural scattering and plasmon resonance scattering.

Plasmonic Liquid Marbles for In-situ Monitoring of Picoliter-scale Reactions

Xing Yi Ling

Division of Chemistry and Biological Chemistry, School of Physical and Mathematical Sciences, Nanyang Technological University, 21 Nanyang Link, Singapore 637371.

*corresponding author: xyling@ntu.edu.sg

Abstract- Current microscale tracking of chemical kinetics is limited to destructive ex-situ methods, which are also unable to provide real-time reaction monitoring at a molecular level. In this talk, I will discuss our group's development using highly flexible plasmonic liquid marbles as pico-liter analytical sensors. By using the ultrasensitive surface-enhanced Raman scattering (SERS) capability imparted by the plasmonic shell of the Ag nanoparticles of the liquid marbles, the liquid marbles are capable of quantitative examination of multiple analyte(s), even at trace level. Simultaneous two-phase analyte detection at the interfacial of aqueous and organic solvents can also be achieved using our marble. Recently, we extend the usage of our flexible liquid marbles as picoreactor, which is also capable of providing in-situ identification of reaction dynamics in their native reaction environment and at molecular level. One unique property of the liquid marbles is that they can be submerged at liquid–liquid interface. We exploit the interfacial property to monitor the interfacial reaction of dimethyl yellow (p-dimethylaminoazobenzene (DY)) across aqueous and organic phases. Using this soft plasmonic platform, we have successfully resolved the presence of two isomeric products with very similar physical properties, which would otherwise be indiscernible by other analytical methods. Ultimately, our ability to precisely decipher molecular-level reaction dynamics sketches new horizons to develop more efficient processes in synthetic chemistry and nanotechnology.

Ultrafast optical responses of photoexcited electrons and excitons in hybrid nanomaterials

G. P. Wiederrecht[1]
[1]Center for Nanoscale Materials, Argonne National Laboratory, Argonne, IL 60439, USA
[*]corresponding author: wiederrecht@anl.gov

Abstract- The ultrafast optical responses of two types of hybrid nanomaterials are described. The first is the ultrafast hot electron response of plasmonic gap mode metamaterial nanostructures, in which two plasmonic nanostructures are separated by a thin layer of semiconducting or insulating material, with impact on understanding and using energetic electrons. The second describes ultrafast exciton generation and migration in porphyrin-based self-assembled biomimetic nanomaterials, with ramifications for optical light harvesting in self-healing structures.

In this talk I will describe the ultrafast optical responses of two types of hybrid nanomaterials. For the first topic, optically excited plasmonic nanostructures can produce energetic, hot electrons before thermalization that are of great interest for driving new photophysical or photochemical processes. However, new approaches are needed to generate hot electrons with higher efficiency and to easily detect them optically. It is also important to understand their decay processes in order to better harness extremely energetic hot electrons for applications before losing energy to thermalization. I describe our advances in this area using gap-mode plasmonic metamaterials that incorporate atomic layer deposition of semiconductor or insulating materials to precisely control the gap distance in the hybrid structures.[1] The gap modes create unusually high electromagnetic fields that are efficient at creating energetic electrons. New approaches to spectroscopically recognize the presence of hot electrons as well as to model the kinetics of hot electron decay are described.

Second, I describe the study of porphyrin-based biomimetic hybrid nanostructures that self assemble into structures capable of supporting exciton migration and excitonic light harvesting behavior. The ultrafast transient optical absorption and emission responses are monitored in order to characterize exciton migration. The importance of the environmental structural response in realizing efficient and long-range exciton transport is described. Sensitization of the porphyrin-based system with excitonic nanostructures to utilize a broader portion of the solar spectrum is also found to significantly enhance the yield of mobile excitons. The ability of these structures to operate as light harvesters with self-healing properties is evaluated.

Acknowledgements - The use of the Center for Nanoscale Materials, an Office of Science user facility, was supported by the U.S. Department of Energy, Office of Science, Office of Basic Energy Sciences, under Contract No DE-AC02-06CH11357.

REFERENCES

1. Harutyunyan, H., Martinson, A. B. F., Rosenmann, D., Khorashad, L. K., Besteiro, L. V., Govorov, A. O., Wiederrecht, G. P., "Anomalous ultrafast dynamics of hot plasmonic electrons in nanostructures with hot spots," *Nat. Nanotech.* Vol. 10, 770-775, 2015.

Plasmonic Titanium Nitride for Solar Energy Conversion

A. Naldoni[1,2*], **U. Guler**[1], **H. Reddy**[1], **A. O. Govorov**[3], **A. Kildishev**[1], **A. Boltasseva**[1], **V. M. Shalaev**[1]
[1]School of Electrical & Computer Engineering and Birck Nanotechnology Center, Purdue University, West Lafayette, IN-47907, USA
[2]CNR - Istituto di Scienze e Tecnologie Molecolari, Via Golgi 19, 20133 Milan, Italy
[3]Department of Physics and Astronomy, Ohio University, Athens, Ohio, 45701, USA
[*]corresponding author: analdoni@purdue.edu

Abstract-Refractory titanium nitride (TiN) is an emerging alternative plasmonic material with resonances in the visible and near-infrared. Its exceptional stability in corrosive chemical environment and its durability at high temperature enable the use of TiN for a wide range of solar energy conversion applications. We will present our recent results on the use of plasmonic TiN for photocatalysis, solar/thermophotovoltaics, and our progress on the large-scale fabrication of refractory plasmonic nanostructures.

The use of plasmonic nanostructures in solar energy conversion has recently attracted great attention.[1,2] Recent demonstrations have been mainly limited to nanostructures made of gold and silver. While they show excellent optical properties for plasmonic applications, major issues are related to their high cost, poor chemical (Ag) and thermal stability (Au, Ag). Aluminum is an alternative plasmonic material that provides high optical performance at low cost [3] Nevertheless, its low melting point (around 300-400°C for nanostructures) and its poor chemical stability under alkaline conditions preclude Al from operating under either thermal or chemical harsh conditions.

On the contrary, transition metal nitrides such as titanium nitride (TiN) and zirconium nitride (ZrN) exhibit optical properties similar to Au and can be utilized as plasmonic materials in the visible and near-infrared regions. [4] Combining refractory material properties with plasmonic properties, transition metal nitrides offer a unique solution to material-related problems in applications where high temperature durability and/or chemical stability are needed. We will present the use of colloidal plasmonic nanoparticles of TiN in solar water splitting, lithographically-patterned TiN metamaterials for solar/thermophotovoltaics (STPV), and a newly-developed approach for the large-area fabrication of plasmonic TiN nanostructures.

In particular, we will present our recent results on superior photocurrent generation for solar water splitting by using TiN nanoparticles (NPs) on TiO_2 nanowires (NWs) as compared to using gold (Figure 1a). Through a combined experimental and theoretical approach, we will show that the superior performance of TiN is due to the broadband hot electron generation and improved electrical junction at the metal-semiconductor interface.[5] The design and implementation of refractory TiN metamaterials for STPV applications will be also discussed. This technology requires extremely high temperatures and suffers from material thermal stability. Refractory TiN metamaterials can be a solution to this limitation. Recent results on TiN nanostructures for broadband absorption and selective emission for STPV will be discussed.[6] The schematic of our design and a comparison on the thermal stability of TiN over Au are shown in Figure 1b. Finally, our recent results on large-scale fabrication of refractory plasmonic nanostructures will be discussed.[7] Figure 1c shows the morphology plasmonic resonances of tilted TiN NWs obtained by using a TiO_2 NWs array precursor deposited through

glancing angle deposition. We will also show that plasmonic TiN can be obtained after nitridation of TiO_2 nanoparticles, lithographically-patterned TiO_2 and more complex TiO_2 nanostructures highlighting the potential of this approach, not only for solar energy applications, but also for lasing and flat nanophotonics.

Our results show that plasmonic TiN enable enhanced performance for solar energy conversion holding promise for its implementation in stable and cost-effective devices.

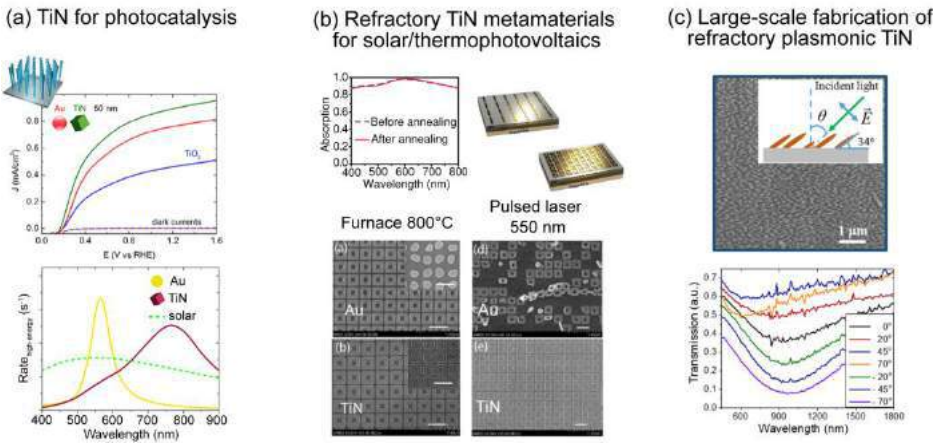

Figures 1: (a) Increased plasmon-enhanced water splitting in TiN/TiO_2 over Au/TiO_2 (upper plot) due to a broadband hot electron generation of plasmonic TiN nanoparticles (NPs) (lower plot).(25) (c) A plasmonic TiN metamaterial for solar/thermophotovoltaics. TiN survives at both high temperatures and more intense light illumination than Au. (c) Large-scale fabrication of novel plasmonic TiN nanostructures from TiO_2 nitridation.

REFERENCES

1. Brongersma, M. L., N. J. Halas and P. Nordlander, "Plasmon-induced hot carrier science and technology," *Nat*. *Nanotech*., 10, 25–34, 2015.
2. Atwater H. A. and A. Polman, "Plasmonics for improved photovoltaic devices," *Nat*. *Mater*., 9, 205–213, 2010.
3. Knight, M. W., N. S. King, L. Liu, H. O. Everitt, P. Nordlander and N. J. Halas, "Aluminum for plasmonics," *ACS Nano*, 8, 834–840, 2014.
4. Guler, U., A. Boltasseva and V. M. Shalaev, "Refractory plasmonics," *Science*, 344, 263–264, 2014.
5. Naldoni, A., U. Guler, Z. Wang, M. Marelli, F. Malara, X. Meng, L. V. Besteiro, A. O. Govorov, A. V Kildishev, A. Boltasseva and V. M Shalaev, "Broadband hot electron collection for solar water splitting with plasmonic titanium nitride," *Adv*. *Opt*. *Mater*., accepted, 2017.
6. Li, W., U. Guler, N. Kinsey, G. V. Naik, A. Boltasseva, J. Guan, V. M. Shalaev and A. V. Kildishev, "Refractory plasmonics with titanium nitride: broadband metamaterial absorber," *Adv*. *Mater*., 26, 7959–7965, 2014.
7. Guler, U., D. Zemlyanov, J. Kim, Z. Wang, R. Chandrasekar, X. Meng, E. Stach, A. V. Kildishev, A. Boltasseva and V. M. Shalaev, "Plasmonic titanium nitride nanostructures via nitridation of nanopatterned titanium dioxide," *Adv*. *Opt*., DOI: 10.1002/adom.201600717, 2017.

Fluorescence enhancement with metal, dielectric and metal-dielectric hybrid platforms

P. Bai[*1], S. Sun[1,2], L. Wu[1], and C. E. Png[1]

[1]Electronics and Photonics Department, Institute of High Performance Computing, Agency for Science, Technology and Research, 1Fusionopolis Way, Singapore 138632

[2]Microsystem & Terahertz Research Center, China Academy of Engineering Physics, No.596, Yinhe Road, Shuangliu, Chengdu, China 610200

[*]corresponding author: baiping@ihpc.a-star.edu.sg

Abstract- Metallic nanoparticles, dielectric nanoparticles and metal-dielectric hybrid dimers have been investigated for fluorescence enhancement. Results show that the metallic nanoparticles have better fluorescence enhancement in high-index media (e.g. water), whereas the dielectric nanoparticles have higher fluorescence enhancement in low-index media (e.g. air). The hybrid dimers show 40% higher electric field enhancement comparing with dielectric dimers and 30% lower loss comparing with metallic dimers, yielding a fluorescence enhancement 30% higher than that of the pure dielectric dimers.

Fluorescence is a wide spread optical technique for the detection of molecular analytes in chemistry, biology and medicine[1]. The optical signal from a single fluorophore is generally weak, limiting the sensitivity. Metallic nanoparticles have been proved to be a versatile platform in fluorescence enhancement due to surface plasmon resonance. Up to date, over three-order fluorescence enhancement by the metallic nanoparticles has been achieved. However, the metallic nanoparticles suffer from parasitic losses, decreasing the quantum yields and resulting in the quenching of the fluorophores when they close to the metal surface. As an alternative, high permittivity dielectric nanoparticles are recently proposed to enhance the fluorescence. They can also generate the field enhancement near the nanoparticles although the physical mechanism is different. The lossless nature of dielectric material does not compromise the fluorescence quantum yield. The question is which are better, metallic or deictic nanoparticles? A dimer nanoantenna has demonstrated unprecedented capabilities to confine light into deep-subwavelength regime[2], which is promising for a variety of emerging applications. To simultaneously satisfy the growing demand in both high electric field enhancement and low loss features, a natural way is to construct a metal-dielectric hybrid dimer that automatically integrates the advantages of both platforms.

We will first present a comprehensive evaluation on the capabilities and applicability of the mettalic and dielectric nanoparticles in the fluorescence enhancement, including the different physical mechanisms of the fluorescence enhancement by the two material platforms, the investigation of the nanoparticle enhancement for different fluorophores in both air and water media, and a fair comparison between the respective optimized situations where the resonance wavelengths of both dielectric and plasmonic nanoparticles are shifted to the same. The results show that the metallic nanoparticles have better fluorescence enhancement in the higher index medium (e.g. water), whereas the dielectric nanoparticles have higher fluorescence enhancement in the lower

index medium (e.g. air)[3].

Then we integrate the metallic and dielectric nanoparticles to enhance the fluorescence with hybrid dimers. When the hybrid dimer under plane wave excitation, we discovered that the coupling between metal plasmonic mode and dielectric electric-dipole-mode creates a hybridized mode due to the direct electric-electric dipole-dipole interaction between the nanoparticles. Between the plasmonic mode and dielectric magnetic-dipole-mode, there is no direct but indirect coupling, which happens between the primary resonances excited by the incident light and the secondary resonances induced by the primary resonances. When the hybrid dimer is radiated by a quantum emitter, we found that the electric/magnetic dipole selectively excites the electric/magnetic (magnetic/electric) resonances of the dimer when the emitter orients parallel (perpendicular) to the dimer axis.

By placing fluorescence dyes to the low loss dielectric side of the hybrid dimer, 40% higher electric field enhancement comparing the dielectric dimer and 30% lower loss comparing with the metallic dimer can be simultaneously achieved, yielding a fluorescence enhancement 30% higher than that of the pure dielectric dimer. On top of that, the hybrid dimer directs 20% more radiation towards the dielectric side due to its unique asymmetrical structure (e.g. permittivity and size contrast between the constituent nanoparticles), thereby significantly enhancing the antenna directivity.

Our studies show that both metal and dielectric have their own advantages, and the hybrid dimer possesses the potential to be an optical antenna simultaneously achieving high field enhancement, low loss and good directivity features. The fundamental coupling mechanism between metallic and dielectric nanoparticles can also be extended to other structures, paving the way in the design of complex hybrid systems.

Acknowledgements, This work was supported by Agency for Science and Technology Research (A*STAR) Singapore with Pharos project: Dielectric Nanoantennas, Grant no.: 152-73-00025; and Quantum Technologies for Engineering (QTE) Program (Project 5: Frequency Conversion of Single Photons for Quantum Networking), Grant no.: A1685b0005.

REFERENCES

1. Gauglitz, G. Point-of-Care Platforms. Annu. Rev. Anal. Chem., Vol. 7, 297-315, 2014.
2. Aćimović, S. S., Kreuzer, M. P., González, M. U., Quidant, R., Plasmon Near-Field Coupling in Metal Dimers as a Step toward Single-Molecule Sensing. ACS Nano. Vol. 3, 1231-1237, 2009
3. Sun, S., Wu, L., Bai P. and Png C. E., Fluorescence enhancement in visible light: dielectric or noble metal? Physical Chemistry Chemical Physics, Vol.18, 19324-19335, 2016.

Blinking surface-enhanced Raman scattering and fluorescence from polyamino acid or dye molecules on the same silver nanoaggregate

Y. Kitahama
[1]Department of Chemistry, Kwansei Gakuin University, Japan
[*]corresponding author: kitahama@kwansei.ac.jp

Abstract Blinking of surface-enhanced Raman scattering (SERS) and surface-enhanced fluorescence (SEF) from the same silver nanoaggregate with poly-L-lysine or thiacarbocyanine were simultaneously observed at different wavelengths. Intensities of the SERS were plotted against those of the SEF at the same times. The SERS of poly-L-lysine was emitted while no SEF of silver atomic cluster on the silver surface was observed. This result suggests single molecule detection. We compared the blinking statistics of poly-L-lysine to that of the dye molecules.

SERS and SEF can be applied a sensitive measurement enough to detect a single molecule adsorbed on a noble metal, because enhanced electromagnetic (EM) field is induced at a junction of the metal nanoaggregate by excitation light via localized surface plasmon resonance (LSPR). At single molecule level, blinking is observed. It has disturbed an application of SERS and SEF in terms of a reproducibility of the spectra and a tracking of the emitter. It is thought that the blinking is induced by the molecule goes in and out of the enhanced EM field. However, there is a possibility that the reason of the blinking is fluctuation of the EM field.

We observed blinking SERS and SEF from silver nanoaggregate with poly-L-lysine or thiacarbocyanine. The silver nanoaggregate were dispersed on glass slide by spin coating and then were excited by using a diode-pumped solid-state laser beam (λ = 532 nm). The signal were collected with an objective lens of an inverted microscope and was split into a short and long wavelength area through W-VIEW Gemini (Hamamatsu) in which a dichroic mirror and band-pass filters were inserted. Then, the video was taken by an inverted microscope coupled with a cooled digital CCD camera (ORCA-AG, Hamamatsu).

For poly-L-lysine, intensities of the signal in the short wavelength area were plotted against those in the long wavelength area at the same times as shown in Fig. 1. They express “L”-shaped distribution; namely, the SERS was emitted while no SEF was observed. In the spectrum of poly-L-lysine, the SERS peaks are attributed to poly-L-lysine, while the broad band in the long wavelength area is assigned to fluorescence due to emissive silver atomic cluster, which formed by photo reduction of silver oxide on the nanoaggregate [1]. Thus, when poly-L-lysine goes into the junction of the nanoaggregate, the silver atomic cluster cannot enter the EM field. It is noted that the result suggests single molecular detection.

Also for thiacarbocyanine, the intensities of the signal in the short wavelength area were plotted against those in the long wavelength area at the same times. They express “/”-shaped distribution. Thus, the SERS was emitted while the SEF was observed, because the SERS and SEF in the spectrum originate from the same dye molecule. In the case of the dye molecules formed J-aggregate, the variances of the plotted intensities of SERS against those of SEF are different from those for the dye formed H-aggregate. The result may be due to different adsorption between the dye molecules formed J- and H-aggregate [2], because the intensities of SERS and SEF are influenced by distance from the metal surface; the latter is quenched by an energy transfer to the surface.

In a similar way of the previous our studies [3], statistics of the blinking SERS and SEF were analyzed by a truncated power law. The probability distributions for duration of the bright and dark event against the duration $P_{on/off}(t)$ are fitted by

$$P_{on}(t) = At^{\alpha_{on}} \quad (1)$$

and

$$P_{off}(t) = Bt^{\alpha_{off}} \exp(-t/\tau), \quad (2)$$

where $\alpha_{on/off}$ is the power law exponent for bright/dark events, respectively, and τ is the truncation time. These parameters for the blinking SERS were plotted against those for the blinking SEF from the same nanoaggregates. For the dye formed J-aggregate, the power law exponents, which are influenced by a random walk model of the molecule on the metal surface, for the SERS were derived to be more various values than those for the SEF. On the other hand, the opposite trend was shown for the dye formed H-aggregate. The truncation times for the SERS of poly-L-lysine are longer than those for the SEF, while those for the SERS of thiacarbocyanine molecules are shorter than those for the SEF. In the present case, the truncation time is affected not by a speed of the molecule, but by an energy barrier from the dark state to the bright state of SERS and SEF, which are different in the enhancement process.

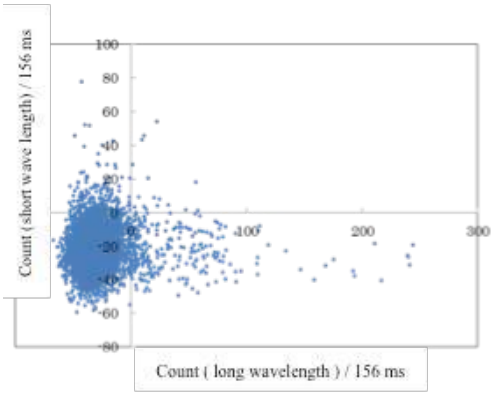

Fig. 1 Signal intensities observed simultaneously in the short and long wavelength area from the same blinking spot.

Acknowledgements This work was supported by KAKENHI (No. 16K05671) from the Ministry of Education, Culture, Sports, Science, and Technology of Japan. The author thanks Y. Nishiyama and Prof. Y. Ozaki for their cooperation.

REFERENCES

1. Kitahama, Y., T. Nagahiro, Y. Tanaka, T. Itoh and Y. Ozaki, *J. Raman Spectrosc.*, DOI: 10.1002/jrs.5079.
2. Kitahama, Y., A. Ogawa, Y. Tanaka, S. Obeidat, T. Itoh, M. Ishikawa and Y. Ozaki, *Chem. Phys. Lett.,* **493**, 309–313 (2010).
3. Kitahama, Y., In "*Frontiers of Plasmon Enhanced Spectroscopy Volume 1 (ACS Symposium series Vol. 1245)*" ACS publication, Washington DC, Chap. 4, (2016).

Generalized Theory of Foerster-Type Nonradiative Energy Transfer in Nanostructures with Mixed Dimensionality: Confinement Dimension vs Stacking Dimension

Pedro Ludwig Hernandez Martinez[1,2*], **Alexander O. Govorov** [3], **and Hilmi Volkan Demir** [1,2*]

[1]LUMINOUS! Centre of Excellence for Semiconductor Lighting and Display, School of Electrical and Electronics Engineering,
Physics and Applied Physics Division, School of Physical and Mathematical Sciences,
Nanyang Technological University, Singapore 639798, Singapore

[2]Department of Physics, Department of Electrical and Electronics Engineering,
UNAM - National Nanotechnology Research Center and Institute of Materials Science and Nanotechnology, Bilkent University, Ankara 06800, Turkey

[3] Department of Physics and Astronomy, Ohio University, Athens, OH, 45701, USA

[*]corresponding authors: pedro@ntu.edu.sg, HVDEMIR@ntu.edu.sg

Abstract-We report a generalized theory for the Foerster-type nonradiative energy transfer (NRET), which includes the derivation of the effective dielectric function due to the donor in different confinement geometries and the derivation of transfer rates distance dependencies due to the acceptor in different confinement geometries, including mixed dimensionality in arrays. These accounts for the transfer rates in all possible combinations of different confinement geometries and assembly architectures. Thus, we obtain a unified picture of NRET in assembled nanostructures arrays.

To obtain the confinement effects of the dielectric function on the Förster-type nonradiative energy transfer (NRET), the effective dielectric function, in the long distance approximation, for the spherical geometry (Nanoparticle (NP) case), cylindrical geometry (Nanowire (NW) case) and planar geometry (Quantum well (QW) case) were obtained (Table 1) by calculating the electric potential for these geometries.

α-direction	NP	NW	QW
X	$\varepsilon_{eff_D} = \frac{\varepsilon_{NP_D} + 2\varepsilon_0}{3}$	$\varepsilon_{eff_D} = \frac{\varepsilon_{NW} + \varepsilon_0}{2}$	$\varepsilon_{eff} = \varepsilon_0$
Y	$\varepsilon_{eff_D} = \frac{\varepsilon_{NP_D} + 2\varepsilon_0}{3}$	$\varepsilon_{eff} = \varepsilon_0$	$\varepsilon_{eff} = \varepsilon_0$
Z	$\varepsilon_{eff_D} = \frac{\varepsilon_{NP_D} + 2\varepsilon_0}{3}$	$\varepsilon_{eff_D} = \frac{\varepsilon_{NW} + \varepsilon_0}{2}$	$\varepsilon_{eff} = \varepsilon_0$

Table 1. Effective Dielectric Function Summary: Effective dielectric constant expressions for the cases of NP, NW and QW in the long distance approximation.

The NRET rate was calculating using equation (1)

$$\gamma_{trans} = \frac{2}{\mathrm{h}} \mathrm{Im}\left[\int dV \left(\frac{\varepsilon_A(\omega)}{4\pi} \right) \mathbf{E}_{in}(\mathbf{r}) \cdot \mathbf{E}_{in}^{*}(\mathbf{r}) \right] \tag{1}$$

where the integration is taken over the acceptor volume, $\varepsilon_A(\omega)$ is the dielectric function of the acceptor, and $\mathbf{E}_{in}(\mathbf{r})$ includes the effective electric field created by an exciton at the donor side. The average NRET rate (at room temperature) is calculated as

$$\gamma_{trans} = \frac{\gamma_{x,trans} + \gamma_{y,trans} + \gamma_{z,trans}}{3} \tag{2}$$

where $\gamma_{\alpha,trans}$ is the transfer rate for the α-exciton $(\alpha = x, y, z)$. We found that the energy transfer rate is

$$\gamma_{trans} \propto \frac{1}{d^n} \tag{3}$$

where *n = 6, 5, 4* and *3* for 3D confinement (QD case), 2D confinement (NW case), 1D confinement (QW case) and 0D confinement (bulk case), respectively.

In conclusion, we present a complete picture and unified understanding of the nonradiative energy transfer for nanostructures of mixed dimensionality and in assembled nanostructures arrays. We obtain the analytical expressions for the energy transfer rate in the long distance approximation. Our findings show that the acceptor quantum confinement dimension sets the generic NRET distance dependence and the donor geometry dimension modifies the effective dielectric function. This generic distance dependence can be remodified by arraying (stacking) the nanostructures. Therefore, the functional distance dependency of the NRET rate is determined by the quantum confinement as well as array stacking dimensionality of the acceptor. The NRET results obtained in this work can be used to design and optimize new solid-state devices for high efficiency light generation and harvesting. The formalism developed here is convenient to estimate the NRET rates in experimental studies involving assembled nanostructure arrays.

REFERENCES

1. Hernández-Martínez, P. L., Govorov, A. O., and Demir, H. V., "Generalized Theory of Förster-type Nonradiative Energy Transfer in Nanostructures with Mixed Dimensionality", *J. Phys. Chem. C*, Vol 117, No 19, 10203−10212, 2013.
2. Hernández-Martínez, P. L., Govorov, A. O., and Demir, H. V., "Förster-type Nonradiative Energy Transfer for Assemblies of Arrayed Nanostructures: Confinement Dimension vs. Stacking Dimension", *J. Phys. Chem. C*, Vol. 118, No. 9, 4951–4958, 2014.

Observation of Isotopic Effect on Hydrogen Evolution Process using *In-situ* Electrochemical Surface Enhanced Raman Scattering.

Hiro Minamimoto*, and Kei Murakoshi
Department of Chemistry, Faculty of Science, Hokkaido University, North 10 West 8, Kita-ku, Sapporo, Hokkaido 060-0810, Japan
*corresponding author: minamimoto@sci.hokudai.ac.jp

Abstract- *In-situ* electrochemical surface enhanced Raman scattering measurements were performed for the investigation of the isotopic effect for the hydrogen evolution reactions. Using various mixed ratio of H_2O and D_2O, curious behavior for the heavy water was observed depending on the electrode potential. Through the analysis of the obtained SERS spectra, it was revealed that the highly ordered structures of water molecules formed at the surface of the electrode during hydrogen evolution process.

The strong optical field is generated by the excitation of the localized surface plasmon resonance (LSPR) under the light illumination onto plasmon active nano-metal structures.[1] It is well known that the generated strong optical field leads several interesting phenomena such as chemical reactions or surface-enhanced Raman Scattering (SERS). SERS is a very useful tool for observing a small number of molecules in the progress of the electrochemical reactions with ultra-high sensitivity.[2] Up to date, several groups have been focusing on the water molecule behavior during electrochemical hydrogen evolution reactions using electrochemical SERS measurements. In their great efforts, it was found that SERS intensity depends on the metal species, electrode potentials, and the supporting electrolyte species.[3] Although various studies have been reported, there is a still room for discussion, such as scattering enhancement mechanism.

Hydrogen evolution reactions (HER) is the one of the well examined electrochemical reactions. Especially for the case of the HER in the mixed solution of H_2O and D_2O, the ratio for the generated H_2 and D_2 depends on the over potential, the mixed ratio, or solution temperature. Although, various examinations have been carried out, at the present stage, the specific factor for the control of the isotopic effect for HER is still unclear. In this study, we have investigated the isotopic effect for HER process via *in-situ* electrochemical SERS measurements. Through the use of various mixed ratios and electrode potential, several new and curious phenomena were observed.

The silver and gold wire electrode were used for SERS measurements. Before SERS measurements, two oxidation reduction cycle (ORC) procedures were performed in order to obtain the atomically roughened surface. Electrochemical SERS measurements were conducted with the electrochemical three electrode cell as shown in Fig. 1. The electrolyte solution was 0.1 M Na_2SO_4 aq. which was halide free solutions. All electrochemical Raman spectra from the surface of roughened metal electrodes

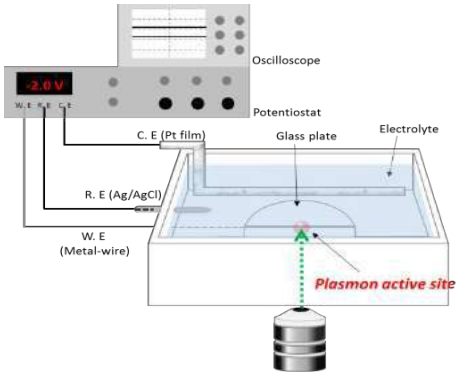

Fig.1 Schematic illustration for *in-situ* electrochemical SERS measurement system.

were obtained by the inverse Raman microscope. The excitation wavelength for acquiring spectra were 514 (2.41 eV) and 785 (1.58 eV) nm.

SERS spectra obtained from the mixed solutions of H_2O and D_2O on Ag electrode surface were shown in Fig. 2. The excitation wavelength was 514 nm. The broad bands at around 500 and 3400 (2400) cm^{-1} are assigned to the libration and OH (OD) stretching mode (σ(OH)). The representative Raman band for SERS of water is the sharp band at 1600 (1400) cm^{-1} corresponding to the OH (OD) bending mode (δ(OH)) which appears in only HER over potential region. It should be mentioned that the scattering intensities for water/ deuterium band becomes relatively weak with the case for Au electrode or λ_{ex} = 785 nm. Apparently, the scattering intensity becomes stronger as the negative potential polarization. This behavior can be explained by the charge transfer effect to induce effective resonance of the scattering. Generally, the scattering intensity of each Raman band reflects the composition of the bulk solutions. However, in the present case, the scattering intensity for σ(OH) ignores the mixed ratio of the bulk solution. From this result, it can be said that the composition of the bulk solution drastically changed at the localized position during the process for HER. In addition to this result, we have observed the various highly ordered structures of deuterium oxide during the HER process. Through the all attempts, we have confirmed that the very unique behavior of the deuterium oxide at the strong optical field during HER process. The present results would be the key for understanding the principle of the isotopic effect on HER.

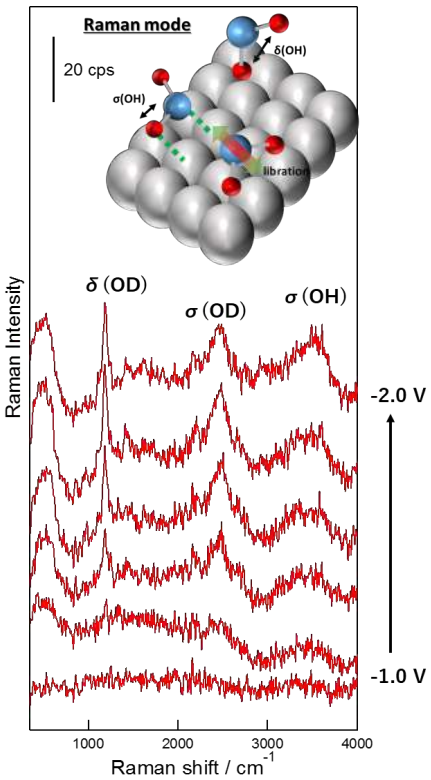

Fig. 2 *In-situ* electrochemical SERS spectra obtained from mixed solution. The ratio of H_2O and D_2O was 1 to 10. The electrode potential was scanned from −1.0 to −2.0 V vs. Ag/AgCl from bottom to top. The electrode and excitation wavelength were Ag and λ_{ex} = 514 nm, respectively.

REFERENCES

1. Minamimoto, H., Toda, T., Futashima, R., Li, X., Suzuki, K., Yasuda, S., Muraskoshi, K., Visualization of Active sites for plasmon-Induced Electron Transfer Reactions Using Photoelectrochemical Polymerization of Pyrrole, *J. Phys. Chem. C*, 120(29)**,** 16051, 2016.,
2. Yonezawa, Y., Minamimoto, H., Nagasawa, F., Takase, M., Yasuda, S., Murakoshi, K., Observation of Molecule Catalysis for the Hydrogen Evolution Reaction using In-Situ Electrochemical Surface-Enhanced Raman Scattering, *J. Electroanal. Chem.*, in revision.
3. Chen, Y. X., Tian, Q. Z., “Dependence of surface enhanced Raman scattering of water on the hydrogen evolution reaction” *Chem. Phys. Lett*, 281, 379–383, 1997.

Exciton-plasmon coupling of single quantum dots and a metal nanowire

Hong Wei*
Institute of Physics, Chinese Academy of Sciences, Beijing 100190, China
*corresponding author: weihong@iphy.ac.cn

Abstract-We studied the coupling of single quantum dots and a metal nanowire. By exciting a single quantum dot, single surface plasmons are generated in the nanowire with the quantum efficiency dependent on the distance between the quantum dot and the nanowire. The single quantum dots can also be excited by the propagating surface plasmons in the nanowire. We demonstrate the selective excitation of two quantum dots within diffraction-limited area by modulating the electric field using the interference of surface plasmons.

Benefiting from the subwavelength confinement feature of surface plasmons (SPs), plasmonic waveguides can perform the function of optical fibers at the deep subwavelength scale and construct plasmonic devices for nanophotonic circuitry. Metal nanowires (NWs) can support multiple SP modes, which are the physical origins of various phenomena for the propagating SPs in the NWs. The electric field confinement and propagation of the SPs also make metal NWs attractive for investigating light–matter interactions in NW-emitter coupled systems. The coupling of single quantum emitters and a metal NW generates single SPs propagating in the NW, opening the prospects of using quantum optical techniques to control single SPs and designing novel quantum plasmonic devices.

We studied the exciton-plasmon interaction in the coupled system of single quantum dots (QDs) and a silver nanowire [1, 2]. The decay rates of all the exciton recombination channels were experimentally obtained. Thus we obtained the quantum efficiency of single QD exciting single SP. By using Al_2O_3 film of different thickness to control the QD-NW separation, we revealed the distance dependence of the exciton decay rates and the SP quantum yield. We also show that the intensity and lifetime of the QD emission can be modified by creating a nanogap between the silver NW and a silver nanoparticle with the QD located in the nanogap. Moreover, the QD on the NW can be excited by the propagating SPs, enabling a remote excitation technique. By using the interference of SPs to modulate the electric field on the NW, we demonstrate the selective excitation of two QDs within diffraction-limited area.

Acknowledgements This work was supported by the Ministry of Science and Technology of China (Grant No. 2015CB932400), the National Natural Science Foundation of China (Grant Nos. 11422436 and 11374012), and the New Star of Science and Technology Program of Beijing Municipal Science and Technology Commission (Grant No. xx2015B078).

REFERENCES

1. Li, Q., Wei, H., and Xu, H. X., "Resolving single plasmons generated by multiquantum-emitters on a silver nanowire", *Nano Lett.*, 14, 3358-3363, 2014.

2. Li, Q., Wei, H., and Xu, H. X., “Quantum yield of single surface plasmons generated by a quantum dot coupled with a silver nanowire”, *Nano Lett.*, 15, 8181−8187, 2015.

Tailoring light-matter interaction in integrated silicon-organic hybrid devices for high-efficiency THz emission

K. M. Schulz[1*], J. Hoffman[1], A. Rusche[1], Jingdong Luo[2], A. Petrov[1,3] and M. Eich[2,4]

[1]Institute of Optical and Electronic Materials, Hamburg University of Technology, Hamburg, D-21073, Germany

[2]Department of Material Science and Engineering, University of Washington, Seattle, Washington 98195-2120, USA

[3]ITMO University, 49 Kronverkskii Ave., 197101, St. Petersburg, Russia

[4]Institute of Materials Research, Helmholtz-Zentrum Geesthacht, Geesthacht, D-21502, Germany

[*]corresponding author: marvin.schulz@tuhh.de

Abstract- Silicon waveguides functionalized with non-linear organic cladding material are a versatile integrated platform to provide long-range interaction of high-intensity confined light with non-linear material. Here, we show that such waveguides can be utilized for high efficiency, integrated and compact THz sources based on non-linear frequency mixing. Light-matter interaction in these systems is modelled and optimized by analytical and numerical means.

THz science is a rapidly growing filed with applications in information and communications technology, biology and medical sciences, non-destructive evaluation and quality control, security, environmental monitoring and more [1,2]. Despite the recent progress in the field, it still remains challenge to produce continuous wave THz radiation with integrated, compact, room-temperature stable and tunable devices [3].

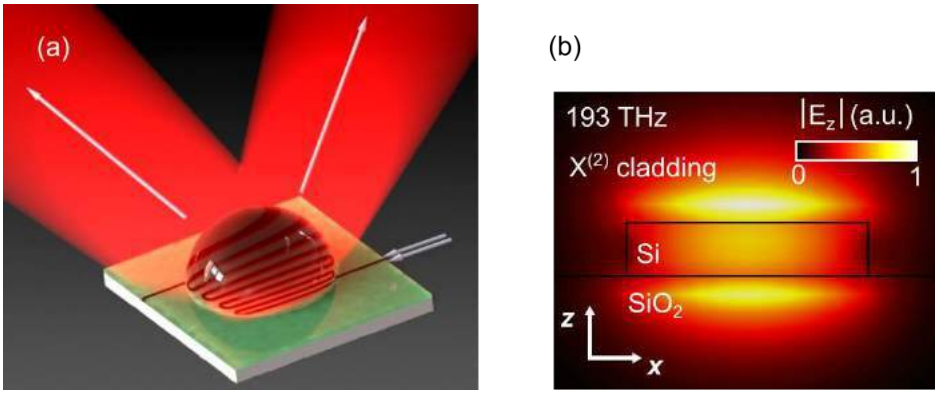

Figure 1. (a) folded silicon waveguide covered with non-linear material (green) and a half-spherical high-index THz lens. Two inclined THz beams are emitted from the device. (b) Mode profile of an optical TM-mode at NIR Frequency in a silicon waveguide covered with organic non-linear cladding material. A large percentage of the optical field intensity is confined in the non-linear material leading to strong light-matter interaction.

Here, we present concept for high- efficiency integrated THz sources. The concept is based on non-linear frequency mixing of two near infrared (NIR) modes guided in the same silicon waveguide that is cladded with non-linear organic polymers. Such materials can be well combined the with silicon photonic platform [4]. In the non-linear cladding material, evanescent fields of the two (NIR) modes mix and produce the difference frequency which can be tuned to any deliberate frequency in the THz range.

A high-index half-spherical THz lens is for phase matching in a Cherenkov scheme (cf. Fig. 1 (a)). Compact devices can be obtained by folding waveguides into a meander line structure. Due to the large refractive index contrast, silicon waveguides strongly confine light with low optical loss which can be exploited to realize a long interaction length of high-intensity light with the non-linear cladding material (cf. Fig. 1 (b)).

The non-linear conversion efficiency, besides phase matching considerations and the intensity of the input light, is governed by the optical environment of the polarization sources at THz frequencies - an effect that is often referred to as Purcell effect. Employing numerical [5] and analytical tools we show that the emitted THz power can be increased as a result of the Purcell effect by appropriately choosing the refractive index of the coupling material and the dispersion of the optical waveguides. We find that a THz output power in the order of 1μW (CW) can be obtained as a consequence of the long interaction length provided by the low-loss silicon waveguide and the engineered Purcell effect in the system.

Acknowledgements: We gratefully acknowledge support from CST, Darmstadt, Germany with their MICROWAVE STUDIO software.

REFERENCES

1. Nagatsuma, T., G. Ducournau and C. C. Renaud, “Advances in terahertz communications accelerated by photonics,” *Nat. Photon.*, Vol. 10, 371–379, 2016.
2. Tonouchi, M. “Cutting-edge terahertz technology,” *Nat. Photon.*,, Vol. 1, 97 - 105, 2007.
3. Lewis, R. A., “A review of terahertz sources,” *J. Phys. D: Appl. Phys.*, Vol. 47, 374001 (11pp), 2014.
4. Schulz K. M., S. Prorok, D. Jalas, S. R. Marder, J. Luo, A. K.-Y. Jen, R. Zierold, K. Nielsch and M. Eich “Mechanism that governs the electro-optic response of second-order nonlinear polymers on silicon substrates,” *Opt. Mater. Express*, Vol. 5, 1653-1660, 2015.
5. Schulz, K. M., H. Vu, S. Schwaiger, A. Rottler, T. Korn, D. Sonnenberg, T. Kipp and S. Mendach, “Controlling the Spontaneous Emission Rate of Quantum Wells in Rolled-Up Hyperbolic Metamaterials,” *PRL*, Vol. 117 , 085503, 2016.

Improving the photocatalytic water reducing activity of $LaTi_2O_7$ by tuning the crystal facets and composing with plasmonic Au

Junying Zhang
Department of Phyiscs, Beihang University, Beijing 100191, China
e-mail:zjy@buaa.edu.cn

The photocatalytic activity of $La_2Ti_2O_7$ (LTO) is limited by the large band gap and poor electron mobility. These problems can be conquered by hybridization with materials with visible-near infrared (vis-NIR) light absorption and high charge carrier transport. Firstly, we synthesized a 2D composite with g-C_3N_4 nanosheets and nitrogen doped LTO nanosheets (NLTO). The composite exhibited high photocatalytic activities for H_2 production under UV and visible light irradiation [1]. Secondly, Au/LTO was composited with black phosphorus (BP). The broad absorption of BP and plasmonic Au contribute to the enhanced photocatalytic H_2 production in the visible and NIR light regions [2].

LTO nanosteps (NSP) with successive surface heterojunctions were synthesized, which have high photocatalytic hydrogen generation performance. The LTO NSP uniformly packed with MoS_2 shell exhibited further improved activity and good stability. Moreover, UV to NIR light induced photocatalytic water reduction was achieved by introducing plasmonic Au nanorods to LTO NSP.

References

[1] Xiaoyan Cai, Junying Zhang, Mamoru Fujitsuka, Tetsuro Majima, Appl. Catal. B: Environ. 202 (2017)191–198

[2] Mingshan Zhu, Xiaoyan Cai, Mamoru Fujitsuka, Junying Zhang, Tetsuro Majima, Angew. Chem. 129 (2017) 2096 –2100

Macroscale ultrasharp nanocone metamaterials – optical properties and applications

M. Cordova-Castro[1], W. P. Wardley[1], M. E. Nasir[1], G. A. Wurtz[2], A. Krasavin[1], A. V. Zayats[1] and W. Dickson[1*]

[1]King's College London, United Kingdom

[2]Unviersity of North Florida, USA

[*]corresponding author: wayne.dickson@kcl.ac.uk

Abstract-Self-assembled hyperbolic metamaterials comprised of gold nanorod arrays deposited via anodic aluminium oxide templates have received significant attention due to the broad tunability of the optical properties due to the template geometry and the scalable fabrication approach. In this work we describe a method to create ultrasharp nanocone arrays using the broad beam argon ion milling of gold nanorod metamaterials. Such materials support localized plasmonic resonances characterized by strong electromagnetic field enhancement at the cone apex.

Plasmonic metamaterials fabricated using bottom-up approaches are inherently scalable and inexpensive. Template based fabrication benefits from low size dispersity and the ability to finely tune the dimensions of the porous structure over a wide range (inter-rod separation 55–100 nm, diameter>9 nm and thickness from 20–500 nm).[1] This flexibility enables the production of large area arrays of metallic nanorods with user specified dimensions providing designer optical properties.[1] The spectral position of the dipolar plasmonic resonances in such arrays depend both on the geometry of the individual nanorods but also on their separation; the electromagnetic coupling between adjacent rods modifies the field intensity distribution which reaches a maximum between the rods.[2] Due to their high refractive index sensitivity these materials have been used as optical sensors for biological molecules[3], ultrasound[4] and hydrogen[5] and the ability to engineer all-optical control of their optical properties makes these suitable candidates for ultrafast active devices.[2]

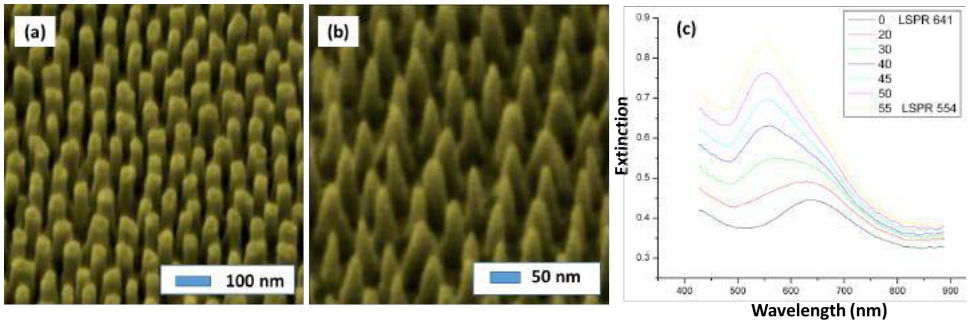

Figure 1: SEM images of (a) Nanorods having a diameter of 45 nm and separation of 90 nm after the removal of the alumina matrix and (b) Nanocone metamaterial formed from (a) after oblique incidence argon ion milling. (c) Extinction spectra of the nanocone metamaterial acquired with TM polarized light at various angles of incidence (legend).

In this paper we present a new type of optical metamaterial based on large area arrays of ultrasharp

nanocones. Notwithstanding the scalable fabrication process, such nanostructuring provides an extra degree of freedom to tailor the optical properties of the arrays, which support localized plasmonic resonances that can be tuned in wavelength, by varying the nanocone geometry, and that exhibit high electromagnetic field enhancement at the cone apex. Here we will describe the fabrication process and optical properties of these materials, highlighting the spectral tunability of the resonances and the achievable field enhancement. Prospects for the use of these novel metamaterials in nonlinear and reactive devices will be elaborated.

Acknowledgements, A. Zayats and W. Dickson would like to note that this work was partly funded by the EPSRC EP/M013812/1.

REFERENCES

1. Nasir, M.; Peruch, S.; Vasilantonakis, N.; Wardley, W.; Dickson, W.; Wurtz, G.; Zayats, A., Tuning the effective plasma frequency of nanorod metamaterials from visible to telecom wavelengths. *Appl. Phys. Lett.* **2015,** *107* (12), 121110.

2. G. A. Wurtz; R. Pollard; W. Hendren; G. Wiederrecht; D. Gosztola; V. A. Podolskiy; Zayats, A. V., Designed ultrafast optical nonlinearity in a plasmonic nanorod metamaterial enhanced by nonlocality. *Nat Nanotechnol* **2011,** *6*, 107.

3. Kabashin, A. V.; Evans, P.; Pastkovsky, S.; Hendren, W.; Wurtz, G.; Atkinson, R.; Pollard, R.; Podolskiy, V.; Zayats, A., Plasmonic nanorod metamaterials for biosensing. *Nat Mater* **2009,** *8*, 867-871.

4. Yakovlev, V. V.; Dickson, W.; Murphy, A.; McPhillips, J.; Pollard, R. J.; Podolskiy, V. A.; Zayats, A. V., Ultrasensitive Non‐Resonant Detection of Ultrasound with Plasmonic Metamaterials. *Adv. Mater.* **2013,** *25* (16), 2351-2356.

5. Nasir, M. E.; Dickson, W.; Wurtz, G. A.; Wardley, W. P.; Zayats, A. V., Hydrogen Detected by the Naked Eye: Optical Hydrogen Gas Sensors Based on Core/Shell Plasmonic Nanorod Metamaterials. *Adv. Mater.* **2014**.

Enhancement of the Activity of Plasmonic Photocatalysts

J. Zhang[1], J. P. Claverie[1*], X. Yu and L. Razzari[2]
[1]Université de Sherbrooke, Canada
[2]Institut National de la Recherche Scientifique, Énergie, Matériaux et Télecom, Canada
[*]corresponding author: jerome.claverie@usherbrooke.ca

Abstract-Plasmonic photocatalysts are widely popular as they permit an efficient utilization of the solar spectrum in photocatalysis. However, they usually require a noble metal component, which precludes a large scale deployment of such devices. We present here two strategies to increase their activity, and thus to reduce the amount of noble metal.

Semiconducting metal oxides, such as TiO_2, form an important class of photocatalsyts, as they are widely available at low cost, they are quite stable, but they are usually only active in the ultraviolet (UV) and lower wavelength part of the solar spectrum. Plasmonic photocatalysts constituted of metal nanoparticles exhibiting surface plasmon resonance (SPR) and a semiconducting metal oxide have been extensively investigated, because they can extend the activity of the photocatalyst to higher wavelength illumination. However, from an economic point of view, the large-scale use of such photocatalysts will be curtailed by the prohibitive cost and availability of noble metals. We propose here two strategies to reduce the amount of such metals.

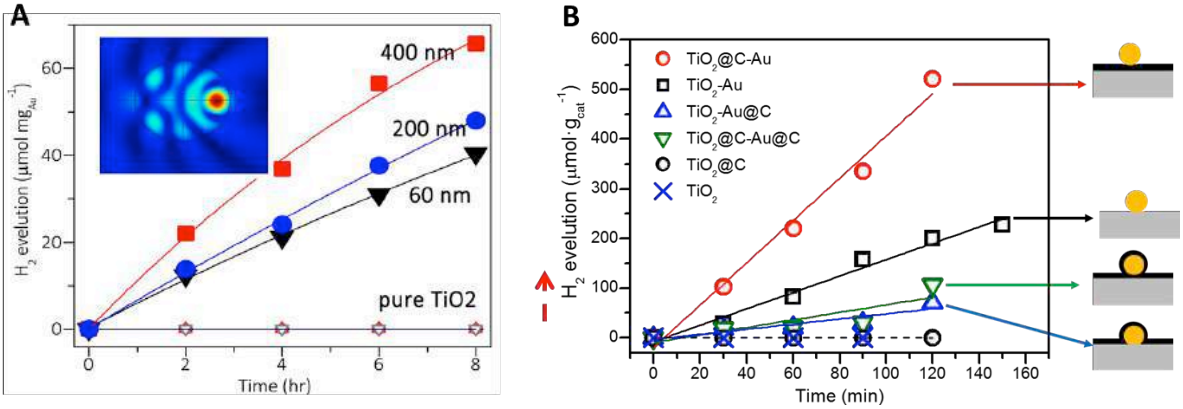

Figure 1. A. Hydrogen evolution from a TiO_2 sphere of increasing diameter (60, 200 and 400 nm) decorated with one Au nanoparticle (d = 60 nm).[1] The inset shows the WGM induced EM field (mode 4) within a 400 nm TiO_2 sphere. B. Hydrogen evolution from a plasmonic Au-TiO_2 photocatalyst decorated with carbon, for various arrangements of C, Au and TiO_2.[2] All experiments are performed with the same amount of Au, TiO_2 and C, under the same conditions.

In the first one, we demonstrate that the activity of the photocatalyst can be tuned by exploiting whispering gallery mode (WGM) resonances expressed within the semiconductor (Fig. 1a). Using the right size and architecture combination for TiO_2 and Au nanoparticles, the activity of the photocatalyst can be enhanced by a factor of fourty. The role of these WGM resonances is to enhance the absorption and interfacial field of the plasmonic Au NPs in Au−TiO_2 hybrids. Thus, by exploiting the combination of WGM resonances and SPR, one

can easily construct photocatalysts that are active in a broad spectral range, for example, from 400 up to 800 nm and further.

In the second one, we demonstrate that carbon can play a synergestic role in the development of the photocatalytic activity of an Au-TiO_2 composite plasmonic photocatalyst (Fig. 1b). We prepared three TiO_2-C-Au structures with different Au and C arrangements, but keeping the same amount of each component. Remarkably, the activity of the photocatalyst is not only highly dependent of on the architecture of the catalyst, but also on the type of reaction investigated. Photocatalytic degradation of dyes, PEC and IPCE measurements all point toward the fact that a sandwich structure, whereby Au is sandwiched between graphene leaflets at the surface of TiO_2, gives the highest activity. However, for hydrogen production, the TiO_2@C-Au catalyst exhibits an activity which is five times greater than TiO_2@C, indicating a synergistic action of plasmonic Au NPs and graphene. Thus, although the presence of carbon can result in a significant increase of the activity of the catalyst, this increase can only be achieved if the spatial arrangement of the Au and C on TiO_2 is finely controlled.

REFERENCES

1. Zhang, J., Jin, X., Morales-Guzman, P. I., Yu, X., Liu, H., Zhang, H., Razzari, L. and J. P. Claverie, "Engineering the Absorption and Field Enhancement Properties of Au–TiO_2 Nanohybrids via Whispering Gallery Mode Resonances for Photocatalytic Water Splitting," *ACS Nano*, Vol 10, No. 4, 4496–4503, 2016.
2. Zhang, J., Vasei, M. Sang, Y., Liu, H., Claverie, J. P. "TiO_2@Carbon Photocatalysts: The Effect of Carbon Thickness on Catalysis," *ACS Appl. Mater. Interfaces*, Vol 8, No. 3, 1903–1912, 2016.

Ultrahigh Enhancement of Electromagnetic Fields by Exciting Localized Surface Plasmon with Propagating Surface Plasmon

Shuzhou Li[1*]
[1]School of Materials Science and Engineering, Nanyang Technological University, Singapore
[*]corresponding author: li@ntu.edu.sg

Abstract-We demonstrated that the localized surface plasmon resonances of a gold sphere can be excited by the extended surface plasmon of a silver thin film. The finite-difference time domain simulations have shown that the electromagnetic field enhancement in this configuration can be up to three orders higher than direct plane wave excitation. This huge enhancement has also been observed in surface-enhanced fluorescence and surface-enhanced Raman spectroscopy. These results show high potential for enhanced spectroscopic sensing and other optoelectronic application.

Excitation of localized surface plasmons (LSPs) of metal nanoparticles (NPs) residing on a flat metal film has attracted great attentions recently due to the enhanced electromagnetic (EM) fields found to be higher than the case of NPs on a dielectric substrate. In the present work, it is shown that even much higher enhancement of EM fields is obtained by exciting the LSPs through extended surface plasmons (ESPs) generated at the metallic film surface using the Kretschmann-Raether configuration. We show that the largest EM field enhancement and the highest surface-enhanced fluorescence intensity are obtained when the incidence angle is the ESP resonance angle of the underlying metal film. The finite-difference time-domain simulations indicate that excitation of LSPs using ESPs can generate 1-3 orders higher EM field intensity than direct excitation of the LSPs using incidence from free space. The ultrahigh enhancement is attributed to the strong confinement of the ESP waves in the vertical direction. With this unique configuration, we also found that an array of particles shows a critical importance of the inter-particle gap on the enhancement factor, which was confirmed experimentally using surface-enhanced Raman scattering (SERS). A monomolecular layer of 4-Aminothiophenol sandwiched in between the silver film and the gold nanoparticles showed SERS enhancement factor of the order of 10^{10} per molecule in the hotspots. It is demonstrated that the ultra-high SERS enhancement does occur only when the ESP is coupled to the LSP at an optimized inter-particle gap. Further, highly sensitive detection of glycerol in ethanol is demonstrated using the optimum structure with detection limit of the order of 10^{-12} to the weight percentage of ethanol, which is equivalent to a few molecules detection. This ultrahigh enhancement is useful in realizing various highly sensitive biosensors when strong enhancement is required as well as in highly efficient optoelectronic and energy devices.

Acknowledgements, This research is conducted by NTU-HUJ-BGU Nanomaterials for Energy and Water Management Programme under the Campus for Research Excellence and Technological Enterprise (CREATE), that is supported by National Research Foundation, Prime Minister's Office, Singapore. This research is also supported by Academic Research Fund Tier 1 (RG107/15).

REFERENCES

1. Li, A., S. Isaacs, I. Abdulhalim, and S. Li, “Ultrahigh Enhancement of Electromagnetic Fields by Exciting Localized with Extended Surface Plasmons,” *J. Phys. Chem. C*, *119*, 19382, 2015
2. Srivastava S. K., A. Li, S. Li, and I. Abdulhalim, Optimal Interparticle Gap for Ultrahigh Field Enhancement by LSP Excitation via ESPs and Confirmation Using SERS, *J. Phys. Chem. C*, *120*, 28735, 2016.
3. Li, A., S. K. Srivastava, I. Abdulhalim, and S. Li, “Engineering the Hot Spots in Squared Arrays of Gold Nanoparticles on a Sliver Film,” *Nanoscale*, *8*, 15658, 2016

Time-dynamical model for the lasing of homogeneous and core-shell plasmonic nanoparticles coupled to an active medium

A. Cathey[1], A. Veltri[1*], A. Chipouline[2] and A. Aradian[3*]

[1]Colegio de Ciencias y Ingeniera, Universidad San Fransisco de Quito, Quito, Ecuador

[2]Institute for Microwave Engineering and Photonics, Technische Universität Darmstad, Darmstad, Germany

[3]Centre de Recherche Paul Pascal, CNRS & Univ. Bordeaux, Pessac, France

[*]corresponding author: aradian@crpp-bordeaux.cnrs.fr

Abstract-We propose a full time-dynamical and space-dependent theoretical description of the optical response of plasmonic nanoparticles coupled to gain (active medium) in two geometries homogeneous spheres immersed in a gain medium, and gain core-metal shell nanoparticles. We are able to calculate the lasing threshold and the initial stages of the lasing instability, and for the latter geometry, we solve the long-term dynamics which we show to be only dipolar, calculating the emission width of the nanolaser as well as exploring other relevant features of the system.

We here explore the features of nanolasers using, for the first time, a time-dependent model, which integrates a quantum formalism to describe the gain and a classical treatment for the metal. Our model also fully takes into account the influence of the system geometry (shape of the plasmonic resonator).

We start with studying the case of a homogeneous, metallic, spherical nanoparticle immersed in an active medium (gain) using a fully multipolar approach [1,2]. We calculate the lasing threshold value for all multipoles of tthe spaser, as well as the onset of the lasing instability, in the linear dipolar regime, with and without external field forcing. We also calculate the behaviour of the system *below* the lasing threshold, with the external field, demonstrating the existence of an amplification regime where the nanoparticle's plasmon is strongly enhanced but stable: this corresponds to partial loss compensation. Figure 1 shows the initial temporal evolution of the dipolar moment of the nanoparticle, in a stable case (below the threshold), displaying plasmon amplification, and in the unstable case, above threshold. Finally, for later, non-linear stages of the dynamics and the approach to the steady-state of the spaser; in particular, it is shown that, for the considered geometry, the spasing is necessarily multi-modal, i.e., multipolar modes are always activated, irrespective of how small the nanoparticle is with respect to the wavelength [2].

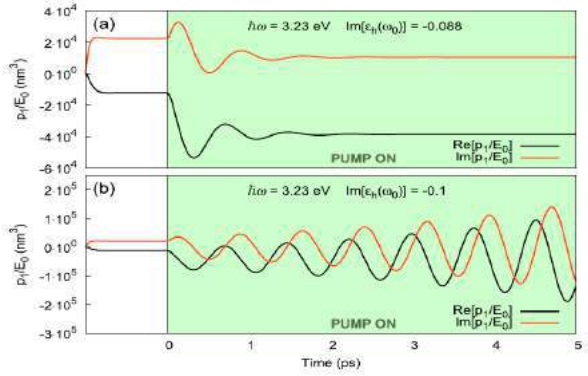

Figure 1. (a) Amplification regime below threshold: the dipole moment converges to a stable state with values which are greater in absolute value than those observed when the pump is off ($t < 0$). **(b)** Unstable lasing state, obtained above threshold.

We then move on [3] to a geometry closer to actual experiments and practical applications: a nanoparticle containing an active core and a plasmonic shell. It can be demonstrated that, in this case, the emission is mono-modal with only the dipolar mode activated. We then study the lasing threshold as well as the rise of the instability when gain values exceed it. For later times, however, significant differences appear with respect to the previous case, the most prominent one being that higher-order modes are never activated. We then solve the full time dynamics and look for non-linear, long-term states which are dominated by the interplay the nanolaser emission and the depletion of the population inversion in the active medium, which will then limit the growth of the laser. This leads in most cases to stationary states, which are reached via damped oscillations on the emission. We sometimes also observe, in restricted areas of the parameter space, richer features like bistability, where the system hesitates between a linear attractor state and a non-linear attractor. Figures 2 shows the normalized intensity value of the field calculated near the particle surface as the gain level is varied in the system.

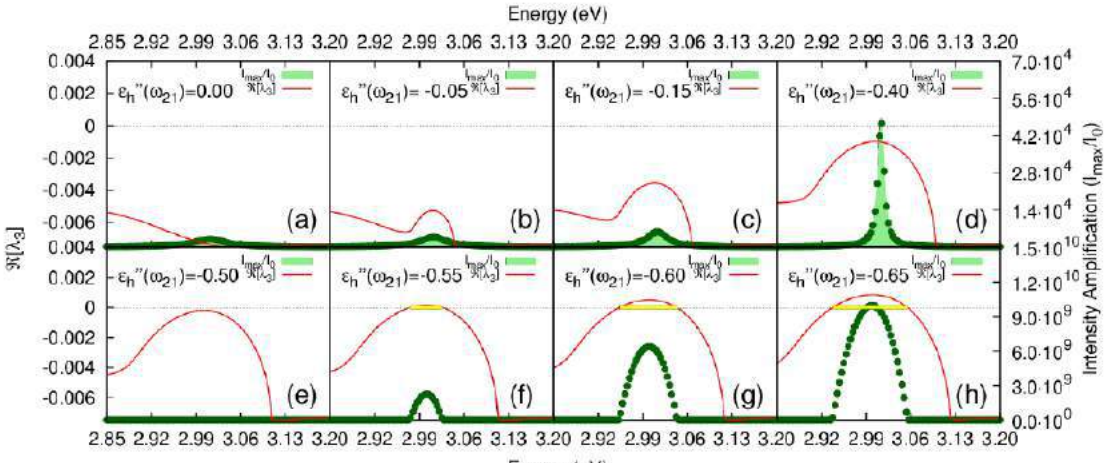

Figure 2. (a) Green points: intensity near the particule surface for increasing gain values in the particle's core from (a) to (h). From (a) to (d) the response is linear with partial loss compensation, while on (e) the lasing threshold is attained. From (f) to (g), one can observe the nonlinear emission state, and calculate the spectral width.

Acknowledgements. This work was supported by the LabEx AMADEus (ANR-10-LABX-42) in the framework of IdEx Bordeaux (ANR-10-IDEX-03-02), France.

REFERENCES

1. Veltri, A. and A. Aradian, "Optical response of a metallic nanoparticle immersed in a medium with optical gain," *Phys. Rev. B*, Vol. 85, 115429, 2012
2. Veltri, A., A. Chipouline and A. Aradian, "Multipolar, time-dynamical model for the loss compensation and lasing of a spherical plasmonic nanoparticle spaser immersed in an active gain medium," *Sci. Rep.*, Vol. 6, 33018 (2016).
3. Cathey, A., A Veltri and A. Aradian "Theoretical properties of the lasing of core-shells," *in preparation*.

Compact plasmonic resonance shift sensors

A. Horrer[1], J. Haas[1], P. S. Blach[1], V. Henken-Mellies[1], S. El-Asfar[1], V. Wedler[1], S. Rau[2], K. Krieg[2], K. Freudenberger[2], L. Leidner[2], G. Gauglitz[2], D. P. Kern[1], and M. Fleischer[1*]

[1]Institute for Applied Physics and Center LISA[+], Eberhard Karls University Tuebingen, Germany

[2]Institute of Physical and Theoretical Chemistry, Eberhard Karls University Tuebingen, Germany

[*]corresponding author: monika.fleischer@uni-tuebingen.de

Abstract- Different fabrication approaches for nanostructured localized surface plasmon resonance (LSPR) sensors will be presented and their sensitivities evaluated. A miniaturized setup based on gradient index lenses will be shown.

Plasmonic nanostructures can be used as sensors for the local index of refraction. Under illumination, localized surface plasmon resonances (LSPRs) occur depending on the permittivity of the surroundings. The sensing concept relies on the high sensitivity of the LSPR wavelength to changes of the refractive index in their immediate vicinity. Such optical resonance-shift sensing can offer a marker-free alternative to e.g. fluorescence based detection [1]. Shifts in the intensity maximum of the LSPR spectrum can be evaluated to determine the refractive index of a bulk liquid of known composition, as e.g. demonstrated in Figure 1. While the method as such is unspecific, it can be made selective by functionalizing the nanostructure surface. In this case, the local refractive index can e.g. be changed by receptor-antibody-binding processes.

In this presentation the nanofabrication and plasmonic modes of arrays of nanodiscs, nanorods and vertical dimers will be discussed [2]. The nanostructures are implemented in microfluidic channels within fluidic PDMS cells. Examples for resonance-shift sensing based on changes of the refractive index of the bulk liquid will be shown. The biosensing capability is demonstrated by functionalizing the nanostructure surface and observing resonance-shifts due to the specific binding of testosterone antibody from solution. The overall setup is miniaturized by preparing nanostructures directly on the planar surfaces of gradient index lenses, which are then integrated within the fluidic cells as the optical detection element.

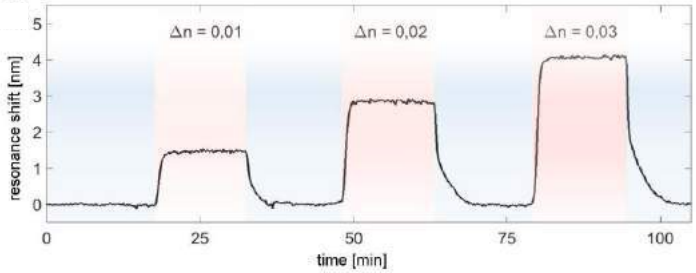

Figure 1: Measured resonance shifts for alternating water and water/glycerol mixtures.

Acknowledgements

This work was performed in the context of the COST Action MP1302 Nanospectroscopy. Financial support by Baden-Württemberg Foundation in the research program Optical Technologies and by Deutscher Akademischer Austauschdienst (DAAD) within the scope of the program PROCOPE is gratefully acknowledged.

REFERENCES

1. Di Fabrizio, E., S. Schlücker, J. Wenger, R. Regmi, H. Rigneault, G. Calafiore, M. West, S. Cabrini, M. Fleischer, N. van Hulst, M.F. Garcia-Parajo, A. Pucci, D. Cojoc, C.A.E. Hauser and M. Ni, "Roadmap on biosensing and photonics with advanced nano-optical methods", *J. Opt.* Vol. 18, 063003, 2016.
2. Horrer, A., K. Krieg, K. Freudenberger, S. Rau, L. Leidner, G. Gauglitz, D. P. Kern and M. Fleischer, "Plasmonic vertical dimer arrays as elements for biosensing", *Anal. Bioanal. Chem.,* Vol. 407, No. 27, 8225-8231, 2015.

Chiral nanomaterials and their applications

Yurii K. Gun'ko,[1,2*] Finn Purcell-Milton,[1] Olan Cleary,[1] Alex Loudon,[1] Vera Kuznetsova,[1] Maria V. Mukhina,[2] Ivan V. Korsakov,[2] Vladimir G. Maslov,[2] Anvar Baimuratov,[2] Ivan Ruhlenko,[2] Alexander Baranov,[2] and Anatoly Fedorov [2]

[1] School of Chemistry and CRANN, Trinity College Dublin, Dublin 2, Ireland.
[2] Saint Petersburg ITMO University, 197101 Saint Petersburg, Russia.
[*]corresponding author: igounko@tcd.ie

Abstract: The main goal of our work is to develop new types of inorganic nanoparticulate materials possessing optical activity and chirality, study their properties, investigate their nature and explore their applications. We have developed new chiral nanomaterials including chiral II-VI semiconducting nanoparticles (quantum dots) and chiral nanoparticles of technologically important metal oxides. We have also demonstrated potential applications of chiral quantum dots for chiral recognition and luminescent chemo- and bio- sensing.

Symmetry and chirality are properties commonly found throughout the natural world. Chirality is one of the most important factors in molecular recognition, with chiral compounds having a major role in chemistry, biology and medicine. Chirality has also been envisaged to play an important role in nanotechnology. Over the last years the area of chiral nanoparticles has received a great deal of attention due to the range of potential applications offered by these materials [1-5].

The main aim of our work is to develop new types of technologically important inorganic nanoparticulate materials possessing optical activity and chirality, study their properties, investigate their nature and explore their applications (Figure 1).

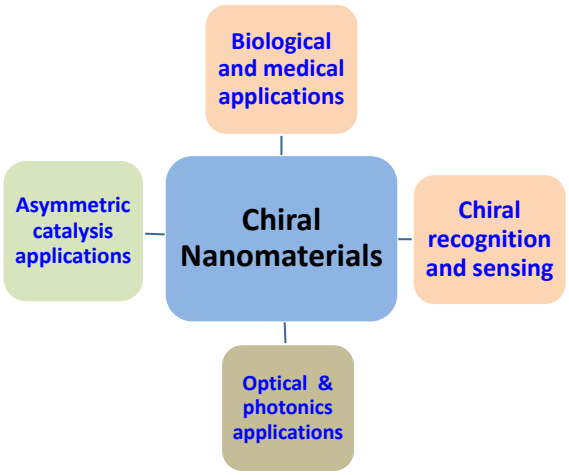

Figure 1. Potential applications of chiral nanomaterials.

We have developed new chiral nanomaterials including chiral II-VI semiconducting nanoparticles (quantum dots) and chiral nanoparticles of technologically important metal oxides. In addition we started to explore the properties of novel anisotropic chiral nanomaterials. The new nanomaterials have shown a very interesting optical activity and unusual chiral morphologies which were confirmed by various instrumental techniques. We have found that in some nanocrystals (e.g. CdSe/ZnS QDs and quantum rods) the chirality and corresponding optical activity are intrinsic features that can occur even without the presence of chiral ligands. The intrinsic chirality of the CdSe based nanocrystals is caused by the presence of intrinsically occurring chiral defects such as dislocations or point defects in these nanostructures. The use of chiral ligands enabled us to separate these nanostructures into different phases and enhance their chiroptical activity. We have also demonstrated potential applications of chiral quantum dots for chiral recognition and luminescent chemo- and bio- sensing. We have also found that live cells demonstrate an enantioselective uptake of chiral quantum nanostructures. It is expected that chiral nanomaterials will find applications in sensing, nanomedicine, asymmetric synthesis, catalysis and other areas.

Acknowledgements

The authors gratefully acknowledge financial support from the Science Foundation of Ireland (Grant SFI 12/IA/1300) and the Ministry of Education and Science of the Russian Federation (Grant No. 14.B25.31.0002).

REFERENCES

1. Govorov, A. O. , Gun'ko, Y. K., Slocik, J. M., Gerard, V. A., Fan Z. Y. and Naik R. R., "Chiral Nanoparticle Assemblies: Circular Dichroism, Plasmonic Interactions, and Exciton Effects", *J. Mater. Chem*., Vol. 21, 16806-16818, 2011.
2. Ben-Moshe, A., Maoz, B. M. , Govorov A. O. and Markovich G., "Chirality and chiroptical effects in inorganic nanocrystal systems with plasmon and exciton resonances", *Chem.Soc. Rev*., Vol. 42, 7028-7041, 2013.
3. Milton, F. P., Govan, J., Mukhina, M. V. and Gun'ko, Y. K., "The chiral nano-world: chiroptically active quantum nanostructures", *Nanoscale Horizons*, Vol. 1, 14-26, 2016.
4. Mukhina, M. V., Maslov, V. G., Baranov, A. V., Fedorov, A. V., Orlova, A. O., Purcell-Milton, F.; Govan, J., Gun'ko, Y. K., "Intrinsic Chirality of CdSe/ZnS Quantum Dots and Quantum Rods", *Nano Letters*, Vol.15, 2844–2851, 2015.
5. Moloney, M. P., Govan, J., Loudon, A., Mukhina, M. and Gun'ko, Y. K., "Preparation of chiral quantum dots", *Nature Protocols*, Vol. 10, 558-573, 2015.
6. J. Govan and Y. K. Gun'ko, "Recent progress in chiral inorganic nanostructures", *RSC Nanoscience & Nanotechnology ser*., *Nanoscience*, Vol. 3, 1–30, 2016.
7. Baimuratov, A. S.; Rukhlenko, I. D.; Gun'ko, Y. K.; Baranov, A. V.; Fedorov, A. V., "Dislocation-Induced Chirality of Semiconductor Nanocrystals", *Nano Letters,* Vol. 15, 1710-1715, 2015.

Magnetic and Electric Resonances in Core/Shell Nanostructures

J. Parker[1,2], N. F. Scherer[2*], and S. K. Gray[3*]

[1]The James Franck Institute and Department of Physics, The University of Chicago, Chicago, IL 60637, USA
[2]The James Franck Institute and Department of Chemistry, The University of Chicago, Chicago, IL 60637, USA
[3]Center for Nanoscale Materials, Argonne National Laboratory, Argonne, IL 60439, USA
[*]corresponding authors: nfscherer@uchicago.edu and gray@anl.gov

Abstract- The optical responses of core/shell nanostructures composed of silica cores and numerous small silver nanoparticles composing an outer shell are studied with a finite-difference time-domain (FDTD) approach. Light scattering cross sections are decomposed via a multipolar analysis in order to reveal their magnetic and electric multipolar character. The analysis is presented for core-shell structures illuminated by a variety of scalar and vector incident light beams, showing how various modes can be selectively excited.

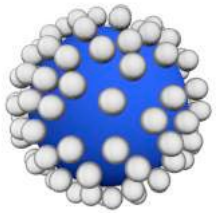

Figure 1. A core-shell nanostructure. In this work we typically study silica cores with diameters of 330 nm surrounded by up to 160 silver nanoparticles with diameters of 40 nm.

Creating negative-index metamaterials requires both negative permittivity and permeability at the excitation frequencies of interest and this is tantamount to creating strong electric and magnetic resonances. Core-satellite structuresare known to exhibit magnetic modes at optical frequencies and their characterization is relevant for the development of metamaterials and metafluids[1].

We study the optical responses of silica-silver nanoparticle core/shell nanostructures (**Figure 1**) using the FDTD method. We introduce a method of multipolar analysis for FDTD simulations and apply it to better understand the interaction of both linearly polarized or scalar and vector beams with silica-silver core-satellite structures at a new level of detail[2]. The method can be used to identify the multipolar nature of scattering peaks and provide angular scattering intensity for better comparison to experimental results. The types of vector beams considered have radial, azimuthal or shear polarization.

Azimuthally polarized light is shown to selectivity excite the magnetic modes of the core-satellite nanostructures, in addition to enhancing their scattering intensity and spatially rotating the mode. Similarly, radially polarized light selectively excites and enhances the electric modes and shear polarized light selectively excites and enhances quadrupolar and higher order modes. We also find that linearly and azimuthally polarized light excite magnetic dipolar and magnetic quadrupolar modes that can spatially interfere with each other, which can be an important consideration for experimentally-observed angular scattering. In addition, nanoparticle placement and arrangement is shown to be an important aspect of scattering by these systems.

ACKNOWLEDGEMENT

The authors would like to acknowledge support from the Vannevar Bush Faculty Fellowship program sponsored by the Basic Research Office of the Assistant Secretary of Defense for Research and Engineering and funded by the Office of Naval Research through grant N00014- 16-1-2502. This work was performed, in part, at the Center for Nanoscale Materials, a U.S. Department of Energy Office of Science User Facility under Contract No. DE-AC02-06CH11357.

The submitted manuscript has been created by UChicago Argonne, LLC, Operator of Argonne National Laboratory ("Argonne"). Argonne, a U.S. Department of Energy Office of Science laboratory, is operated under Contract No. DE-AC02-06CH11357. The U.S. Government retains for itself, and others acting on its behalf, a paid-up nonexclusive, irrevocable worldwide license in said article to reproduce, prepare derivative works, distribute copies to the public, and perform publicly and display publicly, by or on behalf of the Government.

REFERENCES

1. Sheikholeslami, S. N., Alaeian, H., Koh, A. L. and Dionne, J. A., *Nano Letters*, Vol. 13, 4137-4141, 2013.
2. Parker J., Gray, S. K. and Scherer, N. F., in preparation, 2017.

Plasmonic nanostructures in thin film generated by laser induced self-organization processes

N. Destouches[1*], Z. Liu[1], J. Siegel[2], M. Vangheluwe[1], S. Bakhti[3], D. Slaughter[3], A. Belkacem[3]

[1]Univ Lyon, UJM-Saint-Etienne, CNRS, Laboratoire Hubert Curien UMR 5515, F-42023, Saint-Etienne, France

[2] Laser Processing Group, Instituto de Optica, Serrano 121, 28006 Madrid, Spain

[3] Chemical Sciences Division, Lawrence Berkeley National Laboratory, Berkeley, California 94720, USA

*nathalie.destouches@univ-st-etienne.fr

Abstract- Controlling plasmonic systems with nanometre resolution over large non-planar areas with high flexibility and speed is of strategic importance for spreading their use in various industrial fields. Using light to trigger self-organization processes controlled by non-linear feedback mechanisms is a unique strategy to meet this challenge. Here, we open a new route for the ultrafast laser-induced self-organization of metallic nanostructures in 3D, we characterize the self-organization processes through time-resolved polarization imaging and we demonstrate that this laser marking technique offers a powerful tool for the engineering of plasmonic colors.

Different strategies have recently been developed to create plasmonic colors based on the control of localized surface plasmon resonances, such as gap plasmons and hybridized disk–hole plasmons.[1] Most of them have been implemented by electron beam lithography, a powerful tool to produce well-controlled nanostructures but still prohibitive in terms of time and cost for many applications. Other techniques such as nanoimprint or self-assembly are more appropriate for producing large-scale nanostructured materials, but they lack versatility. In contrast, laser techniques offer the advantage of controlling plasmonic systems over large non-planar areas with high-speed and flexible processes. We especially demonstrated that cw laser light could trigger self-organization processes of metallic nanoparticles in thin films resulting in plasmonic nanopatterns exhibiting singular dichroic colors.[2]

In this presentation we demonstrate the high efficiency of ultrashort laser pulses to produce a full range of plasmonic colors while controlling thermal effects. The laser color marking technique is based on triggering self-organization processes of metallic nanoparticles in a protective thin inorganic film. Beyond the generation of planar nanostructures, we show that 3D self-organization can be activated and controlled in nanocomposite films by ultrashort laser irradiation, resulting in plasmonic nanostructured films with highly regular periodic lattices located at different depths. Such a 3D self-organization is shown to originate from the simultaneous excitation of independent optical modes at different depths in the film and to be activated by the plasmon-induced charge separation and thermally-induced NP growth mechanisms. We implement time-resolved polarization imaging to characterize the different self-organization processes that appear to occur at different time scales at different depths depending on local phase changes or diffusion limited growth processes.

REFERENCES

1. Kristensen, A., Yang, J.K., Bozhevolnyi, S.I., Link, S., Nordlander, P., Halas, N.J. and Mortensen, N.A. Plasmonic colour generation. *Nat. Rev. Mater.* **2**, 16088 (2016).

2. Destouches, N., Crespo-Monteiro, N., Vitrant, G., Lefkir, Y., Reynaud, S., Epicier, T., Liu, Y., Vocanson, F. and Pigeon, F., 2014. Self-organized growth of metallic nanoparticles in a thin film under homogeneous and continuous-wave light excitation. *J. Mater. Chem. C* **2**, 6256-6263 (2014).

Optical chirality generation and amplification in achiral plasmonic nanostructures assembled with chiral biomolecules

Dangyuan Lei[1,2]

[1]Department of Applied Physics, The Hong Kong Polytechnic University, Hong Kong, China
[2]Shenzhen Research Institute, The Hong Kong Polytechnic University, Shenzhen, China
E-mail: dylei@polyu.edu.hk

Abstract – I will discuss our recent study on the generation and amplification of optical chirality in achiral metal nanostructures assembled with chiral biomolecules. I will show how an individual plasmonic nanostructure interacts with chiral biomolecules, which enables switching and amplifying the molecular optical activity and probing the conformational evolution of the chemisorbed molecules. I will also show how a cluster of plasmonic nanostructures can be assembled with chiral molecules to produce plasmon-induced circular dichroism response in both UV and visible-NIR regions.

Main text – Recent studies demonstrate that conjugation of noble metal nanoparticles (NPs) with chiral molecules can switch the molecular optical activity, which is usually located in the UV region, to the visible wavelength region. The new circular dichroism (CD) response appears at the localized surface plasmon resonance (LSPR) band of the metal NPs and thus is termed plasmon-induced CD [1]. This phenomenon is of particular importance for determining and manipulating the optical chirality and activity in the visible and near infrared (NIR) regions and has numerous applications in the fields of biochemical sensing, enantioselective catalysis, biomedicine chirality separation, and chiroptical nanodevices. In this talk, I will show how an individual plasmonic nanostructure interacts with chiral biomolecules, which enables switching and amplifying the molecular optical activity and, more importantly, probing the conformational evolution and structural rearrangement of the chemisorbed molecules on the nanostructure surface, thus constituting a promising stereo-chemically attuned nano-sensor. I will also show how a cluster of achiral plasmonic nanostructures can be assembled with chiral molecules to produce plasmon-induced CD response in both UV and visible-NIR regions. The induced CD resonance position can be adjusted from ~340 nm to above 900 nm through altering the aspect ratio and/or the assembling pattern of the hybrid nanostructures. Detailed theoretical calculations elucidate the electromagnetic interaction mechanisms responsible for the observed CD in both cases.

References

1. W. Zhang, A. O. Govorov, G. W. Bryant, Physical Review Letter 97, 146804 (2006).

2. Z. Y. Bao *et al*., Angewandte Chemie International Edition 129, 1303-1308 (2017).

Circularly Polarized Luminescence from Chiral Lanthanide Phosphate Nanocrystals

U. Hananel, A. Ben Moshe, and G. Markovich*
[1]School of Chemistry, Tel Aviv University, Tel Aviv 6997801, Israel
*corresponding author: gilmar@post. Tau.ac.il

Abstract- We prepared colloidal chiral lanthanide phosphate nanocrystals using chiral molecular templates and studied their chirality through circularly polarized luminescence at the lanthanide emission lines. Some of these emission lines exhibited very large degree of circular polarization, up to ~50%. High enantiomeric purity of the nanocrystals was obtained using tartaric acid molecular templates.

Following our recent work on enantioselective synthesis of α-HgS,[1] and Te, Se nanocrystals,[2] using thiolated chiral ligands (cysteine, penicillamine, glutathione), we have moved to a very different system of inorganic nanocrystals of chiral space group: lanthanide phosphate hydrates (Rhabdophanes, $LnPO_4 \cdot H_20$). We synthesized Eu^{3+} doped $TbPO_4 \cdot H_2O$ nanocrystals, which correspond to a chiral space group ($P3_121$), in the presence of chiral ligands. We have measured circularly polarized luminescence (CPL) at the lanthanide emission lines (see Figure 1). On using pure L- or D-tartaric acid ligands we observed substantial CPL values for these nanocrystals, of up to 20-50% for certain emission lines. Surprisingly, on preparing the nanocrystals with L- and D-tartaric acid mixtures at different enantiomeric excess values, we observed almost complete enantioselectivity in the product nanocrystals already at ~20-30% enantiomeric excess of the tartaric acid. The sensitivity of the resulting nanocrystal handedness to the enantiomeric excess of the tartaric acid depended on the synthesis temperature and pH.

The successful control of nanocrystal handedness by the tartaric acid molecules probably indicates collective effects involving a large number of ligand molecules at the nucleation stage or at the handedness determining stage in the growth of these nanocrystals.

This is an interesting model system for studying the formation and handedness control of chiral crystals. The CPL is a very useful tool for studying the formation of such chiral crystals and following their evolution kinetics.

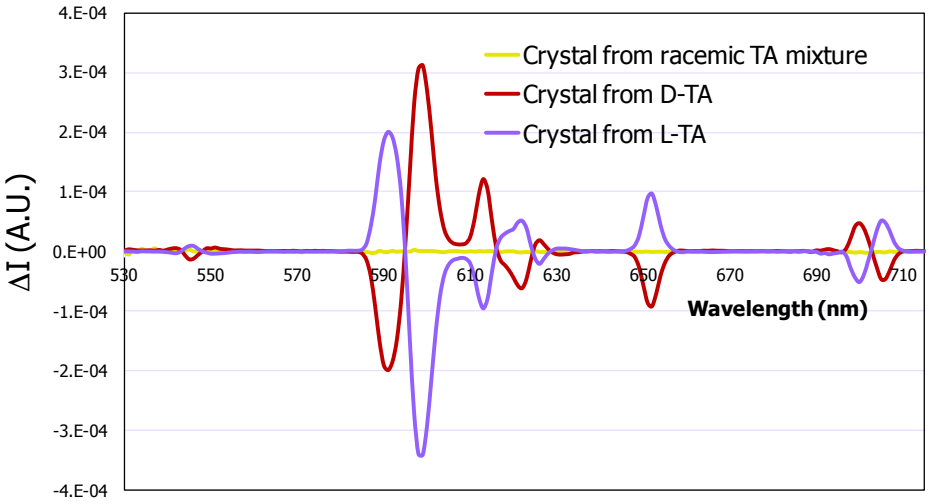

Figure 1. CPL spectra of the Eu^{3+} doped $TbPO_4 \cdot H_2O$ nanocrystals prepared with pure L- and D-tartaric acid (L-TA and D-TA) and with a racemic mixture of the two.

Acknowledgements: This research was supported by The Israel Science Foundation grant no. 507/14.

REFERENCES

1. Ben-Moshe, A., Govorov, A. O. and Markovich, G. "Enantioselective Synthesis of Intrinsically Chiral Mercury Sulfide Nanocrystals", *Angew. Chem. Int. Ed.* Vol. 52, 1275-1279, 2012.
2. Ben-Moshe, A., Grayer Wolf, S., Bar Sadan, M., Houben, L., Fan, Z. Govorov, A. O. and Markovich, G. "Enantioselective control of lattice and shape chirality in inorganic nanostructures using chiral biomolecules", *Nature Comm.* Vol. 5, 4302, 2014.

Local electromagnetic flip-flop in plasmonic infrared trimer nanoantenna

Yinping Zhang[1], Guillaume Demersy[2], Davy Gérard[1], Stephanie L. Dodson[3], Qihua Xiong[3], Jérôme Plain[1], Nicolas Bonod[2] and Renaud Bachelot[1]*

[1] ICD/LNIO CNRS UMR 6281, Université de Technologie de Troyes, France
[2] Institut Fresnel, CNRS France
[3]Nanyang Technological University, Singapore
*Corresponding author: renaud.bachelot@utt.fr

Abstract- we investigated light spatial localization in an infrared nanoantenna consisting of a gold trimer. The study is based on two-photon molecular motion in azobenzene-containing photopolymers. It is shown that different electromagnetic hot spots can be tuned and controlled, on demand, with an external plane wave. 4-digit plasmonic combination was also discussed.

Metallic Nanostructures (MN) offer the possibility of strong spatial confinement, down to the nanometer scale. In this context, easy remote control of electromagnetic hot spot constitutes an important challenge. In particular, rational control of MN geometry and incident beam shaping (including phase and angle of incidence) can produce a large variety of near-field distribution that can be exploited in the future, e.g. for photonic computing.

Recently, It was theoretically demonstrated that that symmetric and antisymetric modes can be excited, on demand by a propagating plane wave in a linear trimer of identical gold nanoparticles[1]. In this paper, we experimentally demonstrate this effect on plasmonic infrared trimer nanoantenna. Two novelties are emphasized. First, we report direct near-field observation of mode balancing and localization of hot spots in trimer plasmonic nanoantenna. Second, we have used for the first time two-photon absorption in azobenzene moieties for plasmonic nano-imaging of infrared nanoantenna, opening the route to near-field investigation of coupled systems based on molecular probing. The studied nanostructure is shown in Fig. 1(a).

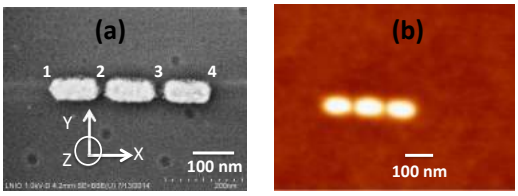

Figure 1. Studied gold nanotrimer

To investigate the optical near-field, we used a specific approach that has been developed over the past decade[2].

Azobenzene molecules that are covalently attached to a polymeric backbone are used as optically driven molecular nanomotors. After exposure to the light, an atomic force microscope (AFM) is used to measure the resulting topography that is related to the near-field intensity pattern to be characterized. Fig. 1(b) shows the plasmonic structure after photopolymer deposition, before any exposure. Figure 2 shows examples of AFM images taken after exposure (at λ=900 nm) with different incident angles and polarizations. Topographical depletions correspond to electromagnetic hot spots that triggered molecular migration. The results were analyzed and compared with electrodynamics calculation allowing us to discuss field spatial localization.

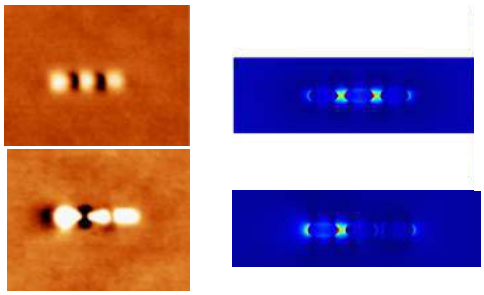

Figure 2. Examples of hot spot localization. Left: AFM images taken after exposure (λ=900 nm). Right: corresponding calculated field maps.

Interestingly, by considering hot spots at both cavities and trimer extremities (named 1, 2, 3, 4 in Fig. 1(a)), we demonstrated the partial activation of a four-digit plasmonic code (cf. example in Fig. 3)
This study opens the avenue to near-field plasmonic circuits and information that are controlled by simple far-field optical commands.

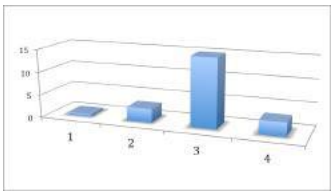

Figure 3. Example of 4-digit plasmonic configuration. 1, 2, 3, 4 stand for the locations pointed out in Fig. 1(a). The heights correspond to depletions in nm observed at each location.

Acknowledgements

This work was supported by the ANR through the HAPPLE project

REFERENCES

1. A. Devilez, B. Stout, and N. Bonot "Mode Balancing far-field control of light localization in nanoantenna," *Phys. Rev. B*, Vol. 81, 215128, 2010.
2. J. Plain, G. P. Wiederrecht, S. K. Gray, P. Royer and R. Bachelot, "Multiscale Optical Imaging of Complex Fields Based on the Use of Azobenzene Nanomotors," *J. Phys. Chem. Lett.*, Vol. 4, 2124–2132, 2013.

III-V Semiconductor Nanowires for Optoelectronics Applications

Chennupati Jagadish
Electronic Materials Engineering
Research School of Physics and Engineering
The Australian National University, Canberra, ACT0200, Australia
Email: c.jagadish@ieee.org

Semiconductors have played an important role in the development of information and communications technology, solar cells, solid state lighting. Nanowires are considered as building blocks for the next generation electronics and optoelectronics. In this talk, I will introduce the importance of nanowires and their potential applications and discuss about how these nanowires can be synthesized and how the shape, size and composition of the nanowires influence their structural, electronic and optical properties. I will present results on axial and radial heterostructures and how one can engineer the optical properties to obtain high performance optoelectronic devices. I will discuss the role of surface non-radiation recombination and how the quantum efficiency of these nanowires will be discussed. I will also present the crystal phase control of nanowires and implications for polarization properties of these nanowires.

Plasmonic cavities and how one can enhance the quantum efficiency of nanowires using plasmonic cavities will be discussed.

I will present results on room temperature operation of GaAs/AlGaAs nanowire multi quantum well lasers and also wurtzite InP nanowire lasers.

I will also present results on GaAs/AlGaAs and InP nanowire THz detectors. These detectors have shown excellent signal to noise ratio similar to bulk ZnTe detectors despite sub-wavelength dimensions. Bandwidth of these detectors will be discussed.

Nanowire solar cells have drawn considerable attention in recent times and I will present results on nanowire solar cells and identify the challenges in improving the efficiency of the solar cells.

I will discuss how Nanowires can be used to engineer neural networks towards creating brain on a chip.

Future prospects of the semiconductor nanowires will be discussed.

Metal nanostructures characterization by digital holography: applications to thermoplasmonics and electrochemistry

A. Lalisse[1,3], V. Brasiliense[1,2], M.C. Nguyen[1,2], P. Berto[1], R. Kuszelewicz[1], F. Kanoufi[2], J. Plain[3], G.Tessier[1]

[1] Neurophotonics Laboratory, CNRS-UMR 8250, Université Paris Descartes, 45 rue des Saints-Pères, 75006, Paris, France

[2] ITODYS, CNRS-UMR 7086, Université Paris Diderot, 15 rue J. A. de Baif, 75013 Paris, France

[3] ICD/LNIO, UMR 6281, CNRS, Technological University of Troyes, 10004 Troyes, France

[*]corresponding author: gilles.tessier@parisdescartes.fr

Abstract- Heterodyne digital holography is a powerful tool to study optically scattering objects. It allows the reconstruction of 3D images, and the superlocalization of individual objects with 3x3x10 nm^3 precision. Associated to heterodyning, it can also measure modulated phenomena like the scattering efficiency changes thermally induced by the modulated excitation of plasmonic nanoantennas. We will illustrate the possibilities of this technique to study electrochemical processes in single metallic nanoparticles, and to obtain quantitative thermal mapping in thermoplasmonics.

Heterodyne digital holography is an interferometric technique which gives access to both the amplitude and phase of the optical field, allowing the reconstruction of 3D images. We have recently shown that the concept of superlocalization, initially proposed to pinpoint the position of fluorescent molecules, can be applied to the coherent field scattered by metallic nanoobjects: using holography, individual nanoparticles separated by more than the width of the microscope point spread function can be localized in 3D with an accuracy of 3x3x10 nm^3 over relatively large volumes. Real-time holograms are reconstructed in order to superlocalize and track several individual NPs, which finds interesting application in electrochemical nanoimpacts monitoring.

This emerging field of research is based on the time-resolved detection of stochastic collisions of individual NanoParticles, (NPs) on micro-electrodes or in nano-confined electrochemical cells [1] to measure electron transfer processes associated to single NP impacts. We will illustrate the possibilities of this coupled system in several chemical systems, where 3D particle tracking can provide a NP size estimate during the Brownian approach of the particle (through its mean square displacement). During chemical reactions on the metal interface, we will show that holography and spectroscopy, associated to an optical model of the scattering, give access to relevant information on the size, position, and chemical composition of the NPs [2].

Associated to heterodyning, digital holography also allows the study of rapidly modulated phenomena. This includes the modulated optical excitation of nanofabricated plasmonic nanoantennas, which induces a localized heating in lossy metals, and a refractive index change. The optical and thermal properties of these objects strongly depend on the morphology of the nanostructure and its dielectric environment. Both can be efficiently monitored by digital holography, which provides the 3D optical scattering pattern of the structures and gives access to quantitative thermal imaging. We will illustrate the possibilities of the method on various nanofabricated systems, with the aim of modelling, characterizing and optimizing the thermal properties of metallic nanostructures.

REFERENCES

1. Zhou, Y.; Reels, N.; Compton, R.C. *Angew. Chem. Int. Ed.* **2011**, *50*, 4219-4221; 2) Xiao, X.; Bard, A. J. *J. Am. Chem. Soc.* **2007**, 129, 9610-9612; 3) Kang, M.; Perry, D.; Kim Y.; Colburn A.W.; Lazenby, R. A.; Unwin P.R. *J. Am. Chem. Soc.*, **2015**, *137*, 10902–10905
2. Batchelor-McAuley, C.; Martinez-Marrades, A.; Tschulik, K.; Patel, A.N.; Combellas, C.; Kanoufi, F.; Tessier, G.; Compton, R.G. *Chem. Phys. Lett.* **2014**, *597*, 20–25. 2) Patel, A.N.; Martinez-Marrades, A.; Brasiliense, V. ; Koshelev, D. ; Besbes, M. ; Kuswelewicz, R. ; Combellas, C. ; Tessier, G.; Kanoufi, F. *Nano Lett.*, **2015**, *15*, 6454–6463.

Hybrid plasmonic-dielectric metamaterials for enhanced nonlinear response

Hayk Harutyunyan[1,*]
[1]Department of Physics, Emory University, Atlanta 30322 GA, USA
[*]corresponding author: hayk.harutyunyan@emory.edu

Abstract- Since its discovery in the 1960s, nonlinear optics has revolutionized optical technologies and laser industry. Development of efficient nanoscale nonlinear sources will pave the way for new applications in photonic circuitry, quantum optics and biosensing. However, nonlinear signal generation at dimensions smaller than the wavelength of light brings new challenges. These include the reduced light-matter interaction volume, the overlap of the fundamental and the nonlinear modes at the nanoscale and the outcoupling of the nonlinear signal to the far-field. Here, we develop hybrid plasmonic – dielectric metamaterials that overcome these limitations and demonstrate ~10^{-4} nonlinear signal conversion efficiency at visible frequencies.

In the first part of my talk I will introduce new type of 3-dimensional, non-planar plasmonic metasurface and demonstrate 3 orders of magnitude enhancement of second harmonic generation (SHG) compared to doubly-resonant plasmonic nanowire gratings. The metasurface consists of an array nanowires with characteristic plasmonic and photonic (diffraction grating) resonances. The geometry of the metamaterial design minimizes the destructive interference of nonlinear emission into the far-field, provides independently tunable resonances both for fundamental and harmonic frequencies, a good mutual overlap of the modes and a strong interaction with the nonlinear material [1,2]. In the second part of my talk I will describe our recent efforts to combine localized plasmon modes with propagating photonic waveguide modes. The hybridized mode that is formed as a result of such coupling can exhibit the desirable feature of plasmonic modes such as high Purcell factors and large field enhancement but with reduced losses.

Our findings can enable the development of efficient nanoscale single photon sources, integrated frequency converters and other nonlinear devices.

REFERENCES

1. J. Butet, P.F. Brevet, and O. J. F. Martin. “Optical second harmonic generation in plasmonic nanostructures: From fundamental principles to advanced applications”. *ACS Nano*, 9, 10545-10562, **2015**.
2. K. O'Brien, H. Suchowski, J. Rho, A. Salandrino, B. Kante, X. Yin, and X. Zhang. Predicting nonlinear properties of metamaterials from the linear response. *Nature Mat.,* 14, 379, **2015**.
3. H. Harutyunyan, G. Volpe, R. Quidant, and L. Novotny. Enhancing the nonlinear optical response using multifrequency gold-nanowire antennas. *Phys. Rev. Lett.,* 108, 217403, **2012**.

Active control of strong plasmon–exciton coupling in two-dimensional atomic semiconducting crystals

Jinxiu Wen[1,3], **Hao Wang**[1,3], **Huanjun Chen**[1,2*]

[1]State Key Laboratory of Optoelectronic Materials and Technologies, Guangdong Province Key Laboratory of Display Material and Technology, Sun Yat-sen University, Guangzhou 510275, China.

[2]School of Electronics and Information Technology, Sun Yat-sen University, Guangzhou 510006, China.

[3]School of Physics, Sun Yat-sen University, Guangzhou 510275, China.

[*]corresponding author: chenhj8@mail.sysu.edu

Abstract-We report on the strong plasmon–exciton coupling in monolayer WS_2 coupled to individual plasmonic gold nanorods. Due to the high oscillator strength and larger binding energy of the 2D exciton of WS_2, we have obtained large Rabi splitting energy of 91 meV ~ 133 meV at ambient condition which was associated with only 5 ~ 18 excitons. In addition, the strong coupling can be dynamically tuned either by electrostatic gating or temperature scanning.

Strong light–matter coupling of quantum emitters with optical cavities have attracted much interest for its importance in the fundamental cavity quantum-electrodynamics research and great potentials in quantum information applications. In the strong coupling regime, the rate of energy exchange between the exciton transition and photon is faster than both of their dissipation rates, which results in the formation of hybrid light-matter states manifested by a Rabi splitting energy. Metallic plasmonic nanocavities have been shown as an excellent platform to realize the strong coupling at room temperature with dye molecules or quantum dots due to their ability to confine light at the deep subwavelength.[1,2] On the other hand, two-dimensional semiconducting transition-metal dichalcogenides (TMDs) have recently emerged as promising candidates for facilitating the light–matter interaction due to the high oscillator strength and large banding energy of their tightly bound 2D excitons. Although several studies have reported the strong coupling in TMD monolayers integrated with optical microcavities as well as plasmonic nanostructures, they all involved plenty of excitons due to the large size of the optical cavities.[3,4] Furthermore, active control on the strong coupling by taking advantage of the exceptional excitonic properties of the TMDs has yet to be demonstrated. Here, we investigate all-solid-state, room-temperature strong coupling with active control in heterostructure composed of monolayer WS_2 and an individual plasmonic gold nanorod.

Figure 1a schematically shows the gold nanorod–WS_2 monolayer heterostructure studied in our work. The single-crystalline monolayer WS_2 flake was grown by chemical vapor deposition (CVD) method with the thickness of ~ 1 nm and exhibited an exciton emission centering at 1.95 eV with a narrow linewidth (γ_{ex}) of 57 meV (Figure 1b). The gold nanorods were synthesized with different aspect ratios to enable the spectral overlap with the exciton transition, and Figure 1c shows the scattering spectrum of a typical gold nanorod with aspect ratio of 2.2, which exhibits a longitudinal plasmon resonance with the plasmon resonance energy of 1.97 eV with and linewidth (γ_{pl}) of 149 meV (Figure 1c). A well-defined mode splitting can be observed in the scattering spectrum from the gold nanorod coupled to the WS_2 monolayer with the formation of the high- and low-energy hybrid states (Figure 1d), which indicates the coherent plasmon–exciton coupling. Furthermore, we have

observed the anti-crossing behavior on the scattering energy diagram of the heterostructures by measuring the spectra of various gold nanorods with different detunings between plasmon frequencies and exciton transition. The Rabi splitting energy, $\hbar\Omega$ is ~ 106 meV, which fulfills the criterion where the strong coupling can occur ($\hbar\Omega > (\gamma_{pl} + \gamma_{ex})/2$). Due to small mode volume of gold nanorod and 2D structure of the monolayer WS_2, the plasmonic field is strongly confined and enhanced at the WS_2 surface, with the strongest enhancements locating near the two apexes of the nanorod (Figure 1e), which is occupied by few excitons since the WS_2 exciton extends several unit cells (Figure 1f). The Rabi splitting energies can be tuned from ~ 133 meV to ~ 91 meV by precisely reducing the nanorod volume while fixing the plasmon resonance frequency at the exciton energy, which only involve 18 to 5 excitons. Most importantly, the WS_2 excitons are sensitive to external stimulus, which enables the active control on the strong coupling via electrostatic gating as well as temperature scanning.

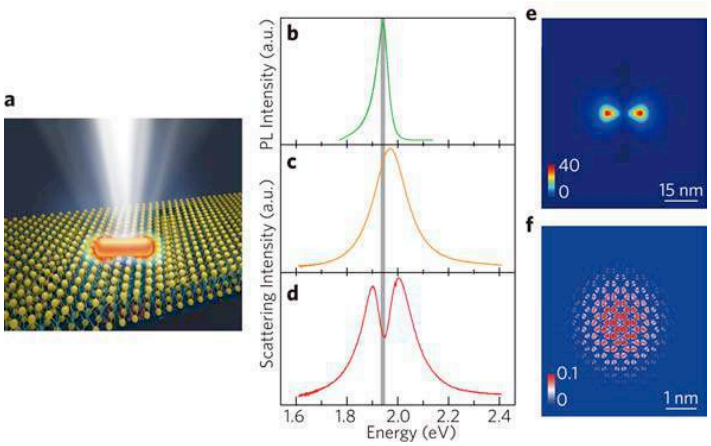

Figure 1. a) Schematic showing the heterostructure composed of an individual gold nanorod coupled to the WS_2. **b)** Photoluminescence spectrum of the monolayer WS_2. Scattering spectra of **c)** individual gold nanorod, and **d)** nanorod coupled to the WS_2. **e)** Near-field enhancement contour of an individual gold nanorod placed onto the WS_2 monolayer. The electric field contour is drawn on the WS_2 plane underneath the gold nanorod. **f)** Modulus-square of the real-space wavefunction of the WS_2 exciton.

In summary, we have demonstrated all-solid-state, room-temperature, and active controllable strong coupling in monolayer WS_2 coupled to a single plasmonic gold nanorod. This strong coupling system hold a great promise for future on-demand quantum optics devices.

REFERENCES

1. Lastname, F. M., *Book Title*, Wiley-Interscience, New York, 1986. 1. Santhosh, K., Bitton, O., Chuntonov, L. and Haran, G., "Vacuum Rabi splitting in a plasmonic cavity at the single quantum emitter limit," *Nat. Commun.*, Vol. 7, 11823, 2016.
2. Chikkaraddy, R., de Nijs, B., Benz, F., Barrow, S. J., Scherman, O. A., Rosta, E.; Demetriadou, A., Fox, P., Hess, O. and Baumberg, J. J., "Single-molecule strong coupling at room temperature in plasmonic nanocavities," *Nature*, Vol. 535, No. 7610, 127-30, 2016.
3. Wang, S., Li, S., Chervy, T., Shalabney, A., Azzini, S., Orgiu, E., Hutchison, J. A., Genet, C., Samori, P. and Ebbesen, T. W., "Coherent coupling of WS_2 monolayers with metallic photonic nanostructures at room temperature," *Nano Lett.*, Vol. 16, No. 7, 2016.
4. Lundt, N., Klembt, S., Cherotchenko, E., Betzold, S., Iff, O., Nalitov, A. V., Klaas, M., Dietrich, C. P., Kavokin, A. V., Hofling, S. and Schneider, C., "Room-temperature Tamm-plasmon exciton-polaritons with a WSe_2 monolayer," *Nat. Commun.*, Vol. 7, 13328, 2016.

Constructing Plasmonic Soft Interfaces at the Microliter-scale for Multiplex Sensing and In-situ Reaction Monitoring

Hiang Kwee LEE,[1,2] Yih Hong LEE,[1] Xuemei HAN,[1] In Yee PHANG,[2] Xing Yi LING[1*]

[1]Division of Chemistry and Biological Chemistry, School of Physical and Mathematical Sciences, Nanyang Technological University, Singapore 637371 (Singapore)

[2]Institute of Materials Research and Engineering, Agency for Science, Technology and Research (A*STAR), 2 Fusionopolis Way, Innovis, No. 08-03, Singapore 138634

[*]corresponding author: xyling@ntu.edu.sg

Abstract- Liquid marbles have been studied extensively as isolated microreactors, as micropumps, and in sensing. However, current liquid-marble-based sensor and reactor are limited to qualitative colorimetry-based detection and ex-situ characterizations, respectively. Herein we fabricate plasmonic liquid marble[1] (PLM) as a substrate-less surface-enhanced Raman spectroscopy (SERS) platform for multiplex and ultrasensitive molecular detections simultaneously across two separate phases, with detection limits as low as 0.3 fmol. PLM also serves as a multi-functional reactor for in-situ and non-invasive reaction monitoring.

Acknowledgements X.Y.L. thanks the financial support from National Research Foundation, Singapore (NRF-NRFF2012-04) and Nanyang Technological University's start-up grant. H.K.L. appreciates the A*STAR Graduate Scholarship support from A*STAR, Singapore.

REFERENCES

1. Lee, H. K., Lee, Y. H., Phang, I. Y., Wei, J., Miao, Y., Liu, T. and Ling, X. Y. Plasmonic liquid marble: A miniature substrate-less SERS platform for quantitative and multiplex ultratrace molecular detection, Angew. Chem. Int. Ed., 53(20), 5054-5058, 2014.
2. Han, X., Lee, H.K., Lee, Y.H., Hao, W., Liu, Y., Phang, I.Y., Li, S., Ling, X.Y. Identifying enclosed chemical reaction and dynamics at the molecular level using shell-isolated miniaturized plasmonic liquid marble, J. Phys. Chem. Lett., 2016, 7, 1501

Selective Trapping and Fixation of DNAs Using Plasmonic Optical Tweezers

!

Yasuyuki Tsuboi

[1]Graduate School of Science, Osaka City University, Japan

*e-mail address: twoboys@sci.osaka-cu.ac.jp

!

1. Introduction

Optical manipulation of small biomolecules is an important issue in bioscience. Plasmon-based optical tweezers (POT) has attracted significant interests as a novel efficient trapping method, since it enhances a radiation force and enables us to trap smaller biomolecules. Recently, we have demonstrated POT of DNA. A micro-ring of optically trapped DNAs was formed on a plasmonic substrate upon resonant light irradiation. Also, we found that the micro-ring was permanently fixed on the substrate [1, 2]. Presumably, the micro-ring formation originates from four physical phenomena:

① Radiation force (trapping DNAs as an attractive force)
② Thermophoresis (carrying DNAs from hotter to colder regions)
③ Thermal convection (supplying DNAs from outside of plasmon excitation area to inside)
④ Coulomb's force (fixing DNAs onto a plasmonic substrate)

Since radiation force and thermophoresis strongly depend on the size of DNAs, DNAs with different base pairs (bp) should be optically separated and then fixed as micro-rings with different diameters on a plasmonic substrate. In the present study, we discuss a mechanism of the micro-ring formation and propose a new separation technique of DNAs with different number of bp (plasmonic chromatography, Fig. 1).

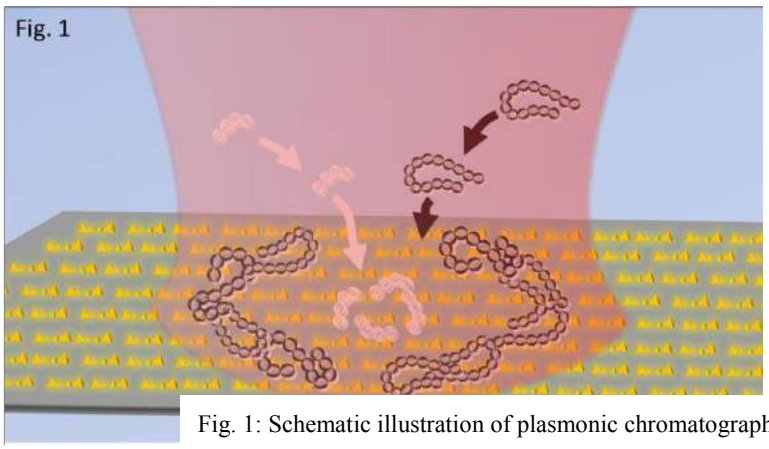

Fig. 1: Schematic illustration of plasmonic chromatography for DNAs. DNAs with different number of base pairs trap at desired positions, leading to multiple-rings formation.

2. Experiments

For a plasmonic substrate, we fabricated gold nanopyramidal dimer arrays on a glass substrate. The plasmonic substrate has a broad absorption band around 800 nm that is ascribed to a gap-mode plasmonic resonance. As trapping targets, λ-DNA (48 kbp) was labelled with YOYO-1 (λ_{em} = 509 nm) and T4-DNA (166 kbp) was labelled with DAPI (λ_{em} = 461 nm), respectively. These DNAs were mixed in an aqueous buffer solution. We used a cw near-infrared (NIR) laser (λ = 808 nm) for LSP excitation and a cw near-ultraviolet and visible lasers (λ = 375, 473 nm) for fluorescence excitation. Trapping behavior was followed using a fluorescence microscope.

3. Results & discussion

The plasmon excitation resulted in formation of two micro-rings (inner and outer rings) on a plasmonic substrate as shown in Fig. 2(a). These rings were permanently fixed on the substrate. Fluorescence spectra of the inner ring were safely assigned to YOYO-1, indicating that the inner ring consisted of λ–DNA (Fig. 2(b)). On the other hand, fluorescence spectra of the outer ring were surely assigned to DAPI, showing that the outer ring consisted of T4-DNA (Fig. 2(c)).

The position of micro-ring formation depends on the intensity of thermophoresis (repulsive force) and radiation force (attractive force). Thermophoresis repelling from the focal spot exerted DNAs, while radiation force exerted DNAs for trapping. Thermophoresis exerted DNA significantly increase with increasing the number of base pairs. As a result, DNAs with different number of base pairs formed the double micro-rings.

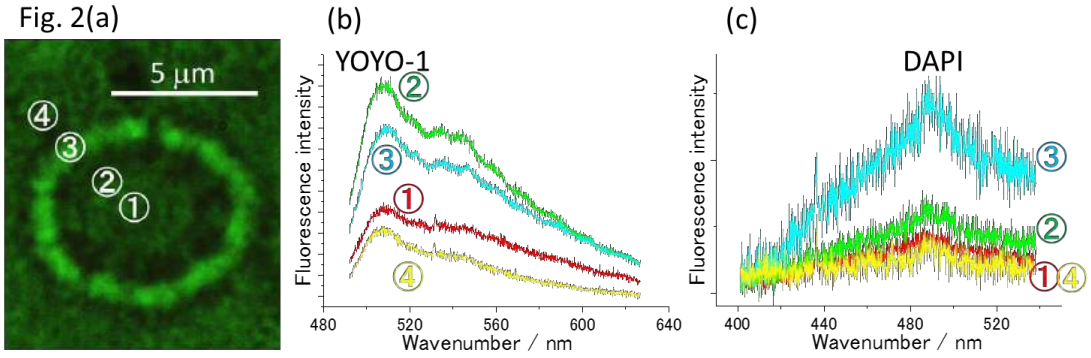

Fig. 2: (a) Optical micrographs of two micro-rings (②: inner ring, ③: outer ring) fixed on a plasmonic substrate by near-infrared laser irradiation. (b), (c) Fluorescence spectra at each positions of a plasmonic substrate. (b): YOYO-1 in λ-DNA (c): DAPI in T4-DNA

4. Conclusion

We successfully separated and fixed DNAs with different number of base pairs on a plasmonic substrate using plasmonic optical tweezers.

References

1. Shoji, T., J. Saito, N. Kitamura, F. Nagasawa, K. Murakoshi and Y. Tsuboi, "Journal of the American Chemical Society," *J. Am. Chem. Soc.*, Vol. 135, No. 17, 6643-6648, 2013.
2. Shoji, T. and Y. Tsuboi, "The Journal of Physical Chemistry Letters," *J. Phys. Chem. Lett.* Vol.5, 2957-2967, 2014.

Organizing Shape-Controlled Plasmonic Nanoparticles into Large-Area 2-Dimensional and 3-Dimensional Metacrystals

Yih Hong Lee,[1] Hiang Kwee Lee,[1,2] Yijie Yang,[1] Ruibin Jiang,[3] Jianfang Wang,[3] Xing Yi Ling[1*]

[1] Division of Chemistry and Biological Chemistry, School of Physical and Mathematical Sciences, Nanyang Technological University, Singapore 637371.

[2] Institute of Materials Research and Engineering, A*STAR (Agency for Science, Technology and Research) 2 Fusionopolis Way, Innovis, Singapore 138634.

[3] Department of Physics, The Chinese University of Hong Kong, Shatin, Hong Kong SAR, China.

[*]corresponding author: xyling@ntu.edu.sg

Abstract. One of the grand challenges in nanotechnology is controlling the organization of nanoparticles into scalable superlattices with tunable crystal structures. Here, we present a bottom-up approach to direct the self-assembly of shape-controlled plasmonic nanoparticles into multiple large-area 2-dimensional (2D) and 3-dimensional (3D) metacrystals. Using Ag octahedra and nanocubes, we demonstrate the ability to assemble each particle morphology into 3 distinct 2D metacrystals with areas larger than 50 cm^2. We further show the importance of crystal design in surface-enhanced Raman scattering.

Shape-controlled nanoparticles can be assembled into structurally diverse superlattices. However, it remains challenging to control the organization of one nanoparticle morphology into multiple superlattices over large areas. In this presentation, we demonstrate the concept of 'one nanoparticle, multiple plasmonic metacrystals' using Ag octahedra and nanocubes. We tailor the nanoscale surface chemistry of the Ag octahedra [1] and nanocubes [2] using a family of thiol-terminated molecules, enabling us to control their surface wettability. Subsequent assembly of these nanoparticles at the oil/water interface gives rise to multiple plasmonic metacrystals (Figure 1). Increasing the surface hydrophobicity of the nanoparticle surfaces leads to increasingly open metacrystals with packing densities as low as 33 %. At this packing density, the nanoparticles are standing on their vertices in their respective plasmonic metacrystals. Notably, we can achieve large areas of these plasmonic metacrystals despite their structural instability.

Our ability to achieve such large-area plasmonic metacrystals also enable a structure-to-function characterization for these metacrystals. We find that the lowest packing density metacrystals generates the highest surface-enhanced Raman scattering (SERS) enhancement factors for both the metacrystals of nanocubes and octahedra. Numerical simulations indicate that this strong enhancement arises from the large-area field delocalization within the metacrystals (Figure 1). Our findings here indicate the importance of crystal design in creating efficient SERS substrates. Furthermore, our findings imply that packing the highest number of nanoparticles within a given area will not always generate the strongest SERS enhancement. With these findings in mind, we proceed to build 3D plasmonic metacrystals possessing dual structures within a single supercrystal and demonstrate its superiority over a uniform supercrystal in SERS.

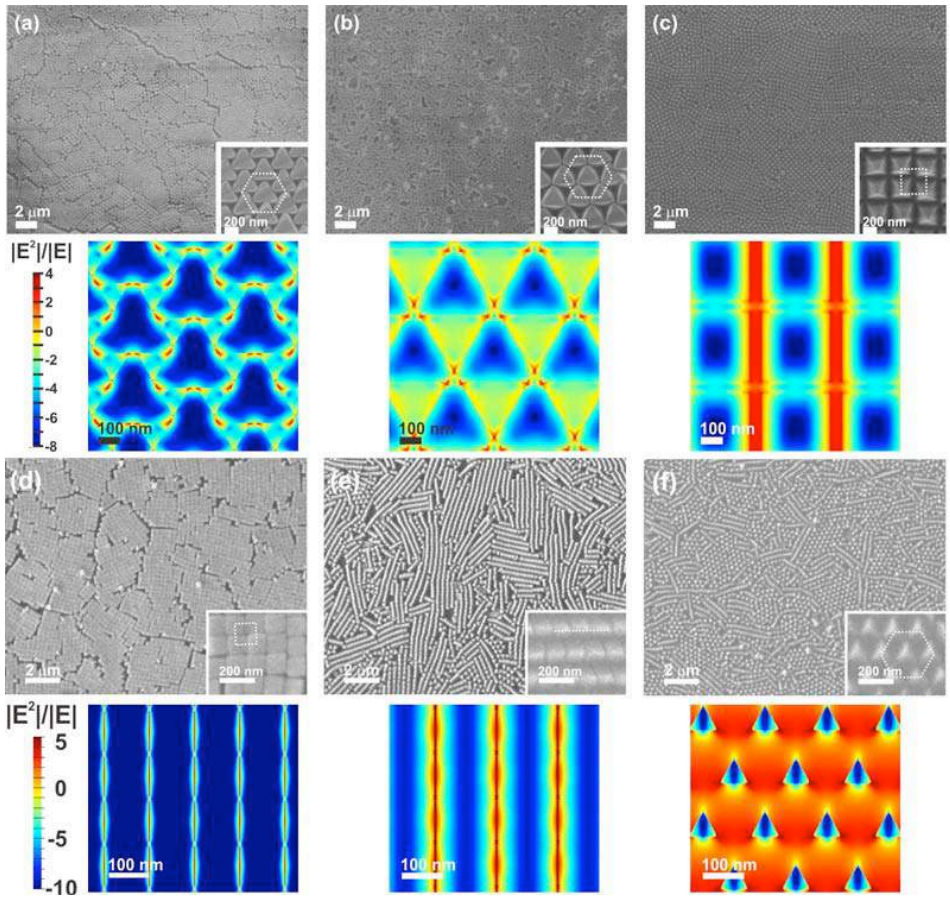

Figure 1. One nanoparticle morphology, multiple plasmonic metacrystals. Ag octahedra assemble into (a) hexagonal close-packed, (b) open hexagonal, and (c) square metacrystals, together with their corresponding local electromagnetic field enhancements at 532 nm. Ag nanocubes assemble into (d) square planar, (b) wire-like, and (f) hexagonal metacrystals, together with their corresponding local electromagnetic field enhancements at 532 nm. In (c) and (f), nanoparticles are standing on their tips within the metacrystals.

Acknowledgements. X.Y.L. and Y.H.L. thank the support from National Research Foundation, Singapore (NRFNRFF2012-04), Nanyang Technological University's start-up grant (M4080758). H.K.L. acknowledges A*STAR Graduate Scholarship support from A*STAR, Singapore. J.W. thanks the financial support from Hong Kong RGC CRF (CUHK1/CRF/12G).

REFERENCES

1. Lee, Y. H.; Shi, W. X.; Lee, H. K.; Jiang, R.; Phang, I. Y.; Cui, Y.; Isa, L.; Yang, Y.; Wang, J. F.; Li, S.; Ling, X. Y. Nanoscale Surface Chemistry Directs the Tunable Assembly of Silver Octahedra into Three 2D Plasmonic Superlattices. *Nat. Commun.* 6, 6990, 2015.
2. Yang, Y.; Lee, Y. H.; Phang, I. Y.; Jiang, R. B.; Sim, Y. F. H.; Wang, J. F.; Ling, X. Y. A Chemical Approach to Break the Planar Configuration of Ag Nanocubes into Tunable Two-dimensional Metasurfaces. *Nano Lett.* 16, 3872-3878, 2016.

Nitrogen fixation using plasmonic photoanode composed of n-semiconductor and metal nanostructures

T. Oshikiri[1*]
[1]Research Institute for Electronic Science, Hokkaido University, Japan
[*]corresponding author: oshikiri@es.hokudai.ac.jp

Abstract-Ammonia has received considerable attention as a potential energy carrier and as a fuel in addition to its use as a fertilizer because it is a non-carbon-based chemical that is easily condensed into a liquid. In this study, we introduce the nitrogen fixation to obtain ammonia using plasmonic photoanode composed of n-semiconductor and gold nanostructures. The plasmonic photoanode can synthesize ammonia from nitrogen, water, and visible light.

Plasmon-induced charge transfer has been studied as one mechanism for plasmonic energy conversion. When plasmonic metallic nanostructures make intimate contact with n-type semiconducting materials, the localized surface resonance(LSPR)-excited intraband and interband transitions of electrons can be directly injected from the plasmonic metallic nanoparticles (NPs) into the conduction band of the semiconductor, via overcoming the Schottky barrier between the metallic NP and semiconductor. One of the attractive features of this approach is the circumvention of the semiconductor bandgap-limited absorption energy band edge by harvesting the energy of photoelectrons ejected from plasmonic metallic NPs. This discovery has led to the widespread development of photocurrent generation[1-3] and photoelectrochemical water splitting systems[4,5] using visible light energy.

Ammonia has received considerable attention as a potential energy carrier and as a fuel in addition to its use as a fertilizer because it is a non-carbon-based chemical that is easily condensed into a liquid. Previously, we achieved plasmon-induced ammonia synthesis via photoelectrochemical reduction of nitrogen using a strontium titanate photoelectrode loaded with gold nanoparticles (Au-NPs) and co-catalyst via plasmon-induced charge separation.[6,7] However, the electric properties and the reaction mechanism are still unclear because the previous study only analyzed the chemical products. Furthermore, the reaction efficiency was still poor because of the limitation of ion and electron transport path. In this study, we report on a quantitative evaluation of ammonia photoelectrochemical synthesis on a two-electrodes system with the Au-NPs loaded strontium titanate as a plasmon photoanode and a zirconium as a cathode.

The photoelectrochemical nitrogen reduction device using Au-NPs/niobium-doped strontium titanate (Nb-$SrTiO_3$) plasmon photoanode was fabricated as follows. Au-NPs were fabricated on a 0.05wt% Nb-$SrTiO_3$ single crystalline substrate (110) using a sputtering and annealing method. The nitrogen reduction device comprised reaction cells with two reaction chambers separated by ion exchange membrane. The Au-NPs/Nb-$SrTiO_3$ photoanode was installed in the one chamber, and a zirconium coil as a co-catalytic cathode was put in another chamber. The both chambers were filled with an H_2SO_4 aqueous solution without a sacrificial donor. The Au-NPs/Nb-$SrTiO_3$ photoanode was irradiated by a xenon lamp using the visible light, and the cathodic chamber was bubbled with nitrogen gas during the reaction. The photoelectric properties and chemical products of the reaction were monitored simultaneously.

As the results, we have successfully evaluated ammonia photoelectrochemical synthesis quantitatively, such as bias effect, stoichiometry, and intermediate. Also, a novel reaction mechanism of plasmon-induced ammonia

synthesis is proposed.

Acknowledgements Financial supports from KAKENHI Grant Nos. 23225006, 15K17438, 25107501, the Nanotechnology Platform (Hokkaido University), and the Dynamic Alliance for Open Innovation Bridging Human, Environment and Materials (Five-Star Alliance) of MEXT are highly acknowledged.

REFERENCES

1. Nishijima, Y., K. Ueno, Y. Yokota, Y., K. Murakoshi, H. Misawa, "Plasmon-assisted photocurrent generation from visible to near-infrared wavelength using a Au-nanorods/TiO_2 electrode," *J. Phys. Chem. Lett.* Vol. 1, No.13, 2031–2036, 2010.
2. Shi, X., K. Ueno, T. Oshikiri and H. Misawa, "Improvement of plasmon-enhanced photocurrent generation by interference of TiO_2 thin film," *J. Phys. Chem. C* Vol. 117, No. 6, 24733–24739, 2013.
3. Nakamura, K., T. Oshikiri, K. Ueno, Y. Wang, Y. Kamata, Y. Kotake and H. Misawa, "Properties of Plasmon-Induced Photoelectric Conversion on a TiO_2/NiO p-n Junction with Au Nanoparticles", *J. Phys. Chem. Lett.* Vol. 7, No. 6, 1004–1009, 2016.
4. Zhong, Y., K. Ueno, Y. Mori, X. Shi, T. Oshikiri and H. Misawa, "Plasmon-assisted water splitting using two sides of the same $SrTiO_3$ single-crystal substrate: Conversion of visible light to chemical energy," *Angew. Chem. Int. Ed.* Vo. 53, No. 39,10350–10354, 2014.
5. Takakura, R., T. Oshikiri, K. Ueno, X. Shi, T. Kondo, H. Masuda and H. Misawa, "Water splitting using a three-dimensional plasmonic photoanode with titanium dioxide nano-tunnels" *Green Chem.*, published on the web, DOI: 10.1039/c6gc03217f.
6. Oshikiri, T., K. Ueno and H. Misawa, "Plasmon-induced ammonia synthesis through nitrogen photofixation with visible light irradiation," *Angew. Chem. Int. Ed.* Vol. 53, No. 37, 9802–9805, 2014
7. Oshikiri, T., K. Ueno and H. Misawa, "Selective Dinitrogen Conversion to Ammonia Using Water and Visible Light through Plasmon-induced Charge Separation," *Angew. Chem. Int. Ed.* Vol. 55, No. 12, 3942–3946, 2016.

Surface-enhanced Raman spectroscopy of single-molecules at nanometer and at angstrom-scale

Hyun-Hang Shin, Gyujin Yeon, and Zee Hwan Kim*

Department of Chemistry, Seoul National University

*corresponding author: zhkim@snu.ac.kr

Abstract : A common wisdom of surface-enhanced Raman scattering (SERS) is that the optical property is *completely* determined by the overall geometry of nanostructures (sizes, shapes, and gap-distances) and dielectric constants, despite the fact that real metallic surfaces have atomic surface defect structures and diffuse electron densities extending beyond metallic boundaries. This classical picture of plasmonics leads to the belief that plasmonic length-scale (size of localized field distribution) cannot usually go below ~10 nm. I will demonstrate the use of single-molecule SERS to follow individual chemical reaction events[1], and also spectroscopic evidences that the plasmonic hotspots can be as small as 1 angstrom. I will further discuss its implication in molecular spectroscopy, photochemistry, and nano-scale imaging.

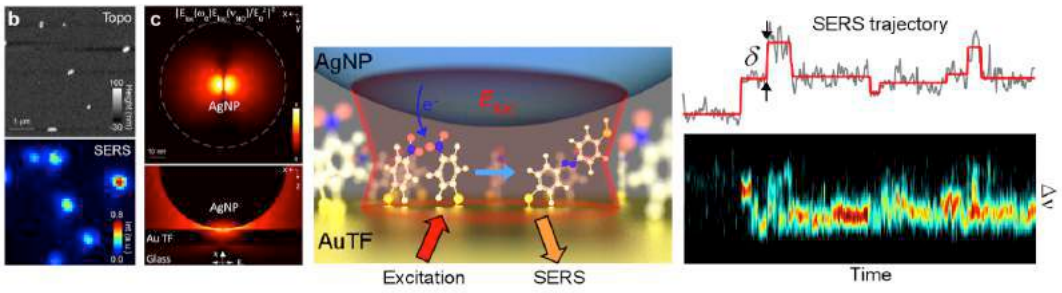

Figure1: Surface-enhanced Raman scattering of individual molecules driven by a plasmonic gap of nanoparticle and a thin film.

REFERENCES

1. Choi, H-. K, Park, W-. H., Park, C-. G., Shin, H-. H., Lee, K. S., and Z. H. Kim, "Metal-Catalyzed Chemical Reaction of Single Molecules Directly Probed by Vibrational Spectroscopy", J. Am. Chem. Soc. Vol. 138, No. 13, 4673-4684, 2016.

Composite honeycomb films based on carboxylated nitrocellulose and silver nanoparticles

Viktoryia. I. Kulikouskaya[1], Vladimir E. Agabekov[1], Nikolai S. Kazak[2*], Serge E. Kozik [2], Vladimir N.Belyi[2*]

[1]Institute of Chemistry of New Materials of National Academy of Sciences of Belarus, Minsk, Belarus
[2]Institute of Physics of National Academy of Sciences of Belarus, Minsk, Belarus
*corresponding author, E-mail: lod@dragon.bas-net.by

Abstract

Composite materials with ordered honeycomb-patterned morphology containing Ag^0 nanoparticles on the surface of carboxylated nitrocellulose matrix were fabricated by a simple solvent-evaporation method at the air/water interface. By annealing initial honeycomb composite structures, thin ordered films of silver nanoparticles were formed. The simulation of optical properties of the obtained structures was carried out and compared to measured spectra.

1. Introduction

Microstructured honeycomb polymer films are of great interest for such fields as microelectronics, biotechnology, and optics, in development of new catalytic systems, sensor devices, and membranes for various functional purposes [1–3]. Honeycomb-structured films with uniform cell size, based on macromolecular compounds, can be prepared by such methods as lithography and microcontact printing [4]. They are based on transfer of a definite pattern from one support to another using a phototemplate or a master [4]. The main advantage of this approach is good reproducibility of the results. However, the process is time-consuming, requires sophisticated expensive equipment and a template, and in the case of lithography is also power-consuming, which restricts its application. It is more promising to prepare honeycomb-structured films by self-assembly of water microdroplets under the action of humid air on a liquid polymer film formed on the water surface [1–3].

Nanoheterogeneous composite materials with metal nanoparticles entrapped in the dielectric polymer matrix deserve attention in electronics and photonics due to their unusual photo- and electric properties caused by the mutual influence of the matrix and nanoparticles. The methods for forming metal coatings on polymeric materials are quite varied: thermal vacuum [5], electrolytic [6], and chemical deposition of metals [7]. One of the promising methods is the chemical metallization, which allows to obtain a uniformly thick coating on the surface of products of not only planar, but of complex form, as well as to apply a metal by selective surface activation.

2. Fabrication procedure

Honeycomb-patterned polymer films were prepared by water-assisted method [8] from carboxylated nitrocellulose (CNC). On the first stage, CNC solution (2 wt.%) in binary solvent (*i* amylacetate:*n*-buthanol at a volume ratio 3:1) was cast on a surface of cooled water (1-3°C), spread and formed thin polymer film on the water surface. On the second stage, formed liquid polymer film was blown by humid air (relative humidity was 75 %). Water microspheres are formed by the condensation of water microdroplets from humid air at the air:polymer solution interface. The honeycomb-like porous structure of polymer appears after complete evaporation of organic solvent. Such hexagonal packing results from the tending of the system to free surface energy minimization.

Deposition of silver nanoparticles on the surface of honeycomb films was carried by electroless plating. Polymer film was immersed into silver nitrate solution (10 mg/ml, 5 min) followed by the reduction of the adsorbed Ag^+ by sodium tetraborate (0.5 mg/ml, 5 min):

$Ag^+ + BH_4^- \rightarrow Ag^0 + BH_3$.

Morphology of formed films was studied by atomic force microscopy (AFM) using scanning probe microscope (Multimode III, VEECO Metrology Group, USA) in tapping mode. Scanning conditions: TappingMode Etched Silicon Probes with stiffness in the 20-80 N/m, a resonance frequency of 330 kHz and tip radius of 8 nm. Scanning electron photomicrographs of the samples was obtained on microscope S4800 (Hitachi, Japan), equipped with a module for X-ray fluorescence analysis (XRF, Avalon-8000, Japan).

3. Structural characterization

Realization of honeycomb structure is a result of self-organizing process during condensation of water microdroplets on the evaporative cooling surface of the polymer solution. Because of the larger density of water than a polymer solution, microdroplets are dipped into a

liquid polymer film and kept in it by surface tension forces. The water microspheres pack in hexagonal array on the surface of polymer solution in self-organization process induced by thermocapillary convection in the evaporating polymer solution. Figure 1 shows an AFM image of the obtained honeycomb film having open spaced hexagonal structure. The structure consists of circular pores of nominal pore diameter about 0.8 μm, separated by a distance about 0.5 μm (Fig. 1).

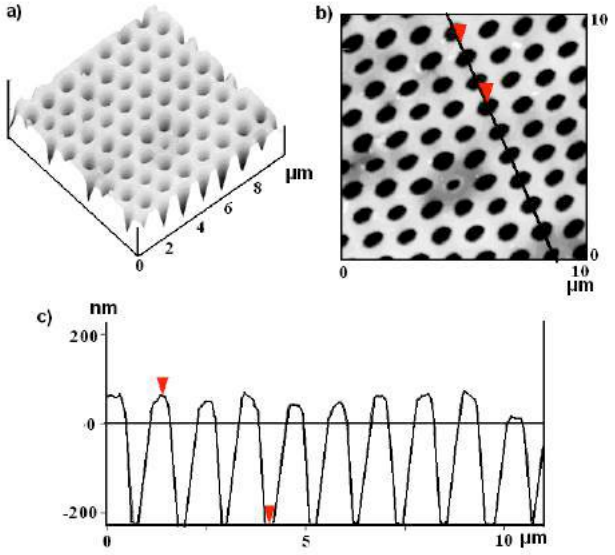

Figure 1: 3D (a) and two-dimensional (b) AFM images of an ordered honeycomb film along with a section profile of surface (c).

The surface of formed ordered honeycomb film was modified with silver nanoparticles by chemical reduction of Ag^+, adsorbed on the polymer matrix (Fig. 2). It was determined that a key factor which affects the selectivity of the Ag^0 deposition on the surface of honeycomb film is the duration of its treatment with $AgNO_3$ solution. Thus, the optimal conditions of modification of ordered honeycomb films by silver nanoparticles are the treatment the initial polymer films with silver nitrate solution for 5 minutes with subsequent treatment with reducer (sodium tetraborate) for 5 min. Such composite films represent the honeycomb polymer matrix the surface of which is covered with a uniform layer of silver nanoparticles.

According to atomic force microscopy (AFM) data the obtained composite samples represent polymer film coated with silver nanoparticles having the pore size of 700-800 nm, the depth of the cells of 650-700 nm and the distance between them 450-490 nm (Fig 2a). Silver nanoparticles with a diameter of ~ 20 nm are also visualized on the surface of the polymer honeycomb films on scanning electron micrographs of the modified samples (Fig. 2b).The presence of silver nanoparticles is also confirmed by X-ray fluorescence analysis. As compared with the XRF spectrum of the initial polymer honeycomb film, in the spectrum of modified sample appears characteristic lines of silver (Fig. 3).

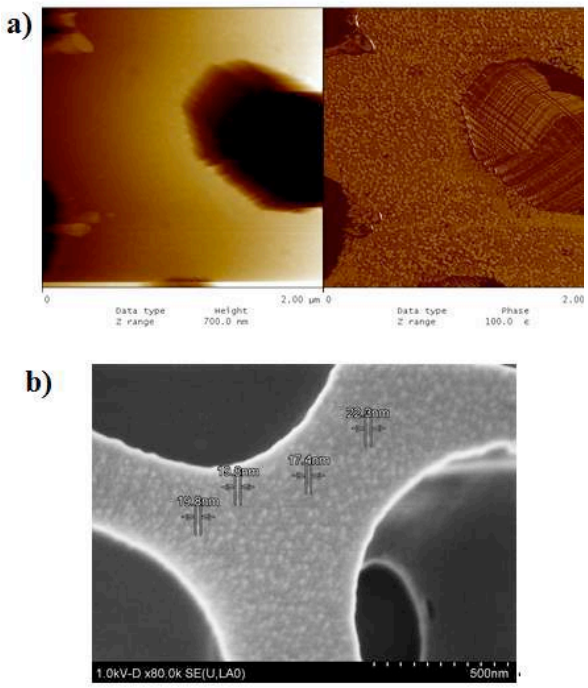

Figure 2: AFM (a) and SEM images of composite honeycomb CNC film with Ag nanoparticles

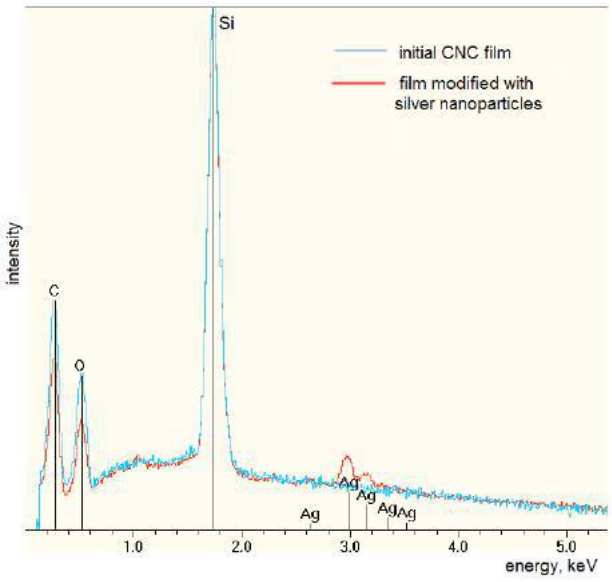

Figure 3: XRF spectra of initial and modified by silver nanoparticles honeycomb CNC films

Thermal decomposition of the polymer matrix results in forming of single-layer film of silver nanoparticles. Thus, after the annealing of honeycomb CNC film modified with

Ag nanoparticles at 200 ºC for 1 hour a layer of silver (thickness is about 15 nm) we produced a nanoparticle distribution that had periodic pattern replicating the projection of initial ordered structure of polymer film on a substrate (Fig. 4).

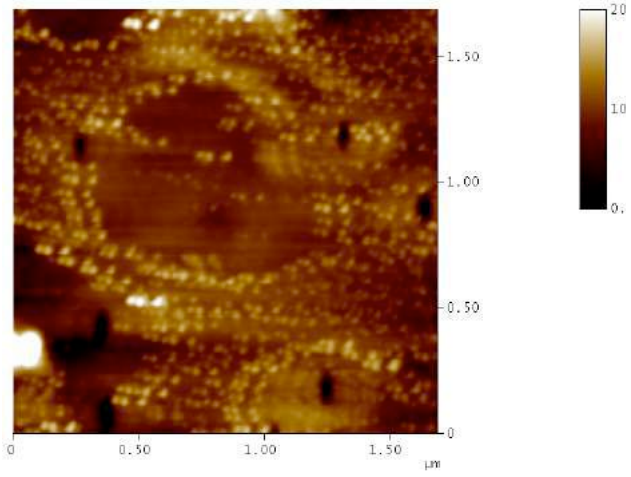

Figure 4: AFM-image of CNC film modified with Ag nanoparticles after annealing at 200 ºC for 1 hour

4. Simulation

Simulation of optical characteristics of the structure was made using FS in CST with periodical boundary conditions. The configuration of an elementary cell with a periodic structure is shown in Fig. 5.

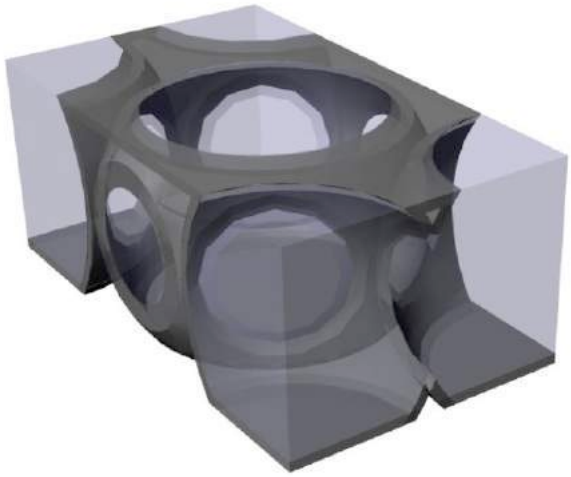

Figure 5: 3D model of polymer carcass coated with silver for simulation of optical properties

The structure is a polymer carcass with spherical crossing pores inside. The carcass is coated with the silver layer with the thickness of 20 nm. The model design describes the structure presented in Fig. 2.

In reflection and absorption spectra (Fig. 6) small region of total absorption within the wavelength of 500-550 nm is presented. For wavelengths smaller than 500 nm resonance peaks are observed, which are conditioned by the ideal periodicity of the simulated structure, and will not be observed in experimentally obtained samples having random deviations in pore gratings.

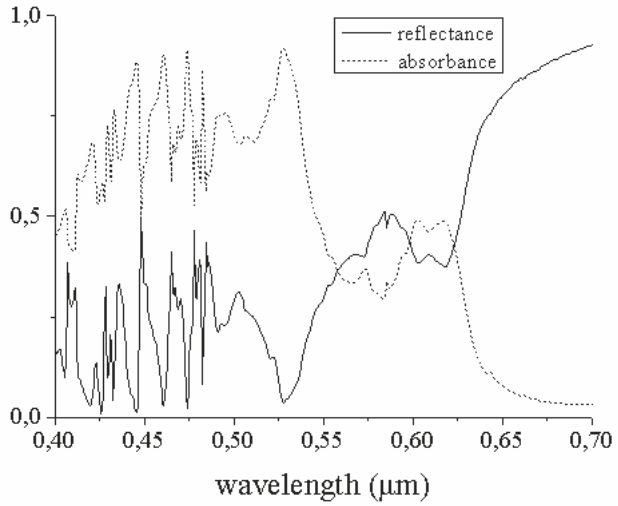

Figure 6: Reflectance and transmittance spectra for the structure shown in Fig. 5

After annealing the particles settle the substrate and form a pattern, which repeats the configuration of pores. The design of an elementary cell, which shows the structure after annealing, is given in Fig. 7.

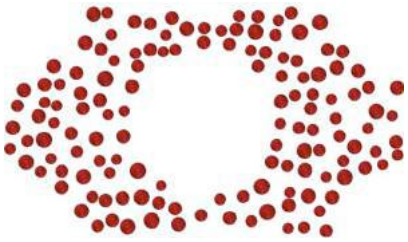

Figure 7: Model of unit cell for simulation optical properties of annealed structures

The diameter of silver particles varied within the region of 40-60 nm. Reflection and transmissions spectra of the structure on the basis of silver nanoparticles were calculated (Fig.7). Using these spectra the efficient refraction coefficient was calculated (Fig.8.).

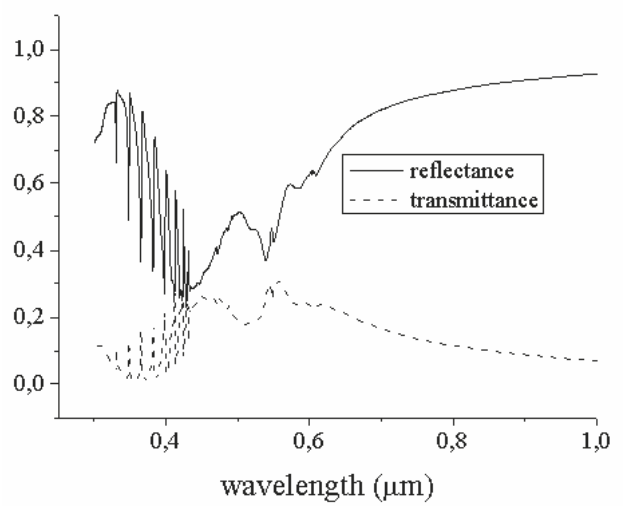

Figure 8: Simulated reflectance and transmittance spectra for the structure shown in Fig.7

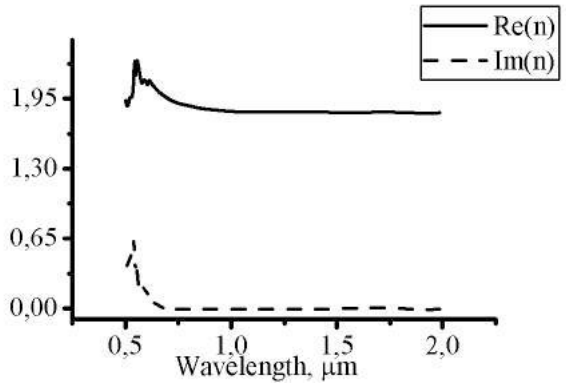

Figure 9: Simulated effective refractive index of the structure after annealing.

In plots (Fig. 8, 9) the structure on the basis of a monolayer of nanoparticles does not possess the expressed resonance peculiarities. In the plot in Fig. 9 it is seen that in infra-red region the structure behaves as a dielectric with efficient refraction index of about 1.8. To increase extremum of the refraction index within the region of 0.5-0.55 μm it is necessary to enhance the concentration of silver in the structure.

5. Conclusions

Using the solvent-evaporation method composite materials with ordered honeycomb films based on carboxylated nitrocellulose and silver nanoparticles were fabricated. For simulation of optical properties of the obtained structure 3D model of polymer carcass with silver was used.
Simulated reflectance and transmittance spectra for the model structure were compared with the measured spectra.

Acknowledgements

This work was partially supported by The King Abdulaziz City for Science and Technology (KACST) of The Kingdom of Saudi Arabia (grant N 814-33).

References

[1] J.F. Kadla, F.H. Asfour, B. Bar-Nir, Micropatterned thin film honeycomb materials from regiospecifically modified cellulose, *Biomacromolecules* 6: 161–165, 2007

[2] Ch. Yu, J. Zhai, X. Gao, M. Wan, L. Jiang, T. Li, Z. Li Water-Assisted Fabrication of Polyaniline Honeycomb Structure Film, *J. Phys. Chem. B*. 108: 4586–4589, 2004.

[3] W. Kasai, T. Kondo, Fabrication of honeycomb-patterned cellulose films, *Macromol. Biosci*. 4:17–21, 2004.

[4] H.-G. Braun, E. Meyer, Microprinting – a new approach to study competitive structure formation on surfaces, *Macromol. Rapid Commun*. 20:325–327, 1999.

[5] M.M. Gol'dberg, A.V. Koryukin, E.K. Kondrashov, *Pokrytiya dlya polimernykh materialov* (Coverings for the Polymer Materials), Khimiya, Moscow. 1980.

[6] H. Yabu, Yu. Hirai, M. Shimomura, Electroless Plating of Honeycomb and Pincushion Polymer Films Prepared by Self-Organization, *Langmuir* 22: 9760–9764, 2006.

[7] A.D. Pomogailo, A.S. Rozenberg, N.E. Uflyand, *Nanochastitsy metallov v polimerakh* (Metal Nanoparticles in Plymers), Khimiya, Moscow, 2000.

[8] V.I. Shadrina, I.A. Bashmakov, E.A. Gracheva, V.E. Agabekov, F.N. Kaputskii, Influence of the conditions of formation of nitrocellulose honeycomb-structure films on their morphology, *Russian Journal of Applied Chemistry* 83: 1318–1324, 2010.

Recent Advances in Complex Materials and Nanophotonics

A controlled-NOT gate based on THz metamaterials

F.-F. Ren*, W.-Z. Xu, and J.-D. Ye

School of Electronic Science and Engineering, Nanjing University, Nanjing 210093, China
*corresponding author: ffren@nju.edu.cn

Abstract- We demonstrate a double-layer bi-anisotropic metamaterial showing strong asymmetric polarization rotation, which can realize a controlled-NOT gate logical transformation between two orthogonal linear polarizations around 0.53 THz. Such a 3D chiral metamaterial opens up new opportunities for the construction of high efficiency optical logic processors towards ultrafast data transmission and information processing.

Logical operation based on polarization encoding of light is important for future data transmission and information processing [1]. However, in the terahertz (THz) region, chiral materials with large optical activity are not available in nature, and achieving effective manipulation of polarization states remains challenging [2]. In this work, we propose and demonstrate a 3D asymmetric THz polarizer composed of a double-layer metamaterials by the combination of a planar spiral structure and a cut-wire structure, separated by a highly stable and low-loss polyimide dielectric layer. The excellent transformation properties between polarizations transmitted through this structure demonstrate a superior CNOT gate functionality [3], which offers a new approach for future all-optical ultrafast computing technology.

Theoretical design and device fabrication. The transmission properties of coherent light through the proposed asymmetric metapolarizer can be studied in terms of a complex Jones matrix [4]. To realize asymmetric polarization rotation and its application as a polarization-encoded CNOT logic gate, a possible way is to have $|T_{yx}| > |T_{xy}|$ when $|T_{yy}| \approx |T_{xx}|$. Based on simulations with the commercial software CST MICROWAVE STUDIO, the designed parameters can be chosen and optimized. The fabrication procedure is performed on on 500 μm-thick quartz substrate with standard photolithography and lift-off technique. which is quite simple and importantly compatible with processing techniques used in traditional semiconductor industries.

Asymmetric transmission measurement. The transmission coefficient measurements were conducted with Advantest TAS7500SP THz TDS system utilizing two femtosecond lasers. The transmitted THz signal was collected by a photoconductive antenna-based THz detector, in which the pulse component was synchronized with another femtosecond laser pulse. When THz radiation propagates along the +z direction, the simulated cross-polarization transmission coefficient |Txy| in the spectral range from 0.4 to 0.7 THz is compressed below 0.22 and reaches its minimum value of 0.06 at 0.53 THz. At the same time, the cross-polarization transmission coefficient |Tyx| yields a transmission peak at the frequency of 0.53 THz with maximum value of 0.62, indicating effectively asymmetric transmission of linearly polarized waves.

Properties of the CNOT gate. On the basis of the characteristics of transmission spectra, the potential application of the metamaterials as a basic optical CNOT gate can be explored. For each of the four possible

logical basis input states |C>|T>=|CT>=|00>, |01>, |10>, and |11>, the output states would be |00>, |01>, |11>, and|10> correspondingly, which indicates that the behaviors of our scheme satisfies the criteria for two-qubit optical logic gate and works as a CNOT gate very well.

Acknowledgements. The authors would like to thank the funding support from the Natural Science Foundation of Jiangsu Province, China (No. BK20161401).

REFERENCES

1. Caulfield H. J. and Dolev S., Why future supercomputing requires optics. *Nature Photonics*, Vol. 4, 261-263, 2010.
2. Tonouchi M., Cutting-edge terahertz technology. *Nature Photonics*, Vol. 1, 97-105, 2007.
3. O'Brien J. L., Pryde G. J., White A. G., Ralph T. C., and Branning D., Demonstration of an all-optical quantum controlled-NOT gate. *Nature*, Vol. 426, 264-267, 2003.
4. Menzel C., Rockstuhl C., and Lederer F., Advanced Jones calculus for the classification of periodic metamaterials. *Phys. Rev. A*, Vol. 82, 053811, 2010.

Dimer and trimer nanoantennas from a transformation optics perspective

V. Pacheco-Peña[1], A.I. Fernández-Domínguez[2], M. Beruete[1,3], Y. Luo[4], and M. Navarro-Cía[5*]

[1]Antennas Group-TERALAB, Universidad Pública de Navarra, Spain

[2]Departamento de Física Teórica de la Materia Condensada and Condensed Matter Physics Centre (IFIMAC), Universidad Autónoma de Madrid, Spain

[3]Institute of Smart Cities, Universidad Pública de Navarra, Spain

[4]School of Electrical & Electronic Engineering, Nanyang Technological University, Singapore

[5]School of Physics and Astronomy, University of Birmingham, United Kingdom

[*]corresponding author: m.navarro-cia@bham.ac.uk

Abstract-Understanding and controlling the light-matter interaction is of fundamental importance for science and technology. Scenarios involving nanoemitters and nanoantennas are nowadays routinely measured in the lab. However, interpretation of the observations is not always straightforward. We will show here how conformal transformation can be used to provide an analytical description of the commonly used bowtie nanoantenna and its trimer counterpart.

Most recent effort in nanophotonics and nanoplasmonics has been directed toward fabrication advancements. Very complex structures have been realized experimentally and their properties are routinely measured [1]. In combination with simulations the community has gained significant insight on the physics at the nanoscale [2],[3]. However, further insight could be gained if analytical descriptions of practical scenarios are laid down. In addition, an analytical frame would speed up the design procedure.

Transformation optics attracted the attention of the research community when it was used as a design tool for invisibility cloaking [4]. More recently, this technique has shown great promise to understand plasmonic nanoantennas [5], bridging the void of analytical tools at the nanoscale. Motivated by this, we looked at conformal transformation to provide an analytical description of two-dimensional bowtie nanoantennas [6]. Here, we extend this work on bowtie nanoantennas and investigate the underlying physics in trimers. We restrict ourselves to two-dimensional nanoantennas operating in quasi-statics to keep the analytical character of the results.

The bowtie nanoantenna and its trimer counterpart are complex geometries to handle analytically. However, by applying the conformal transformation $z = \ln(z')$, where z and z' are the spatial coordinates in the transformed and original frame respectively, the nanoantennas are mapped into an infinite array of metal slabs. If the nanoantennas are excited by a single nanoemitter modelled as a line dipole, such line dipole is transformed into an array of line dipoles; for the bowtie, the unit cell with periodicity 2π in the transformed space will be comprised of two metal slabs, whereas for the trimer, it will include three metal slabs. By virtue of the conformal transformation and the quasi-static treatment, the power dissipated in the original and transformed frames are identical. The latter can be computed by simply evaluating the electric field at the dipole position:

$$P_{nr} = P_{abs}^{(x',y')} = P_{abs}^{(x,y)} = -\frac{1}{2}\omega \mathrm{Im}\{p_x E_{1x} + p_y E_{1y}\} \quad (1)$$

where P_{nr} is the nonradiative power emission by the dipole, ω is the angular frequency, p_x and p_y are the components of the emitter dipole moment along x and y directions, and E_{1x} and E_{1y} are the components of the electric field along x and y in the region of the z plane where the line dipole is located.

Figure 1 shows the nonradiative Purcell enhancement (P_{nr} normalized to the 2D dipole radiation $P_0 = 1/16\omega^3\mu_0|p|^2$; μ_0 is the free-space permeability and $|p|$ the magnitude of the dipole moment) for an aluminum bowtie and its trimer counterpart as a function of the nanoemitter orientation. The extra arm of the trimer yields a significant increase of the nonradiative Purcell enhancement and makes the nanoantenna more robust to the dipole orientation [7].

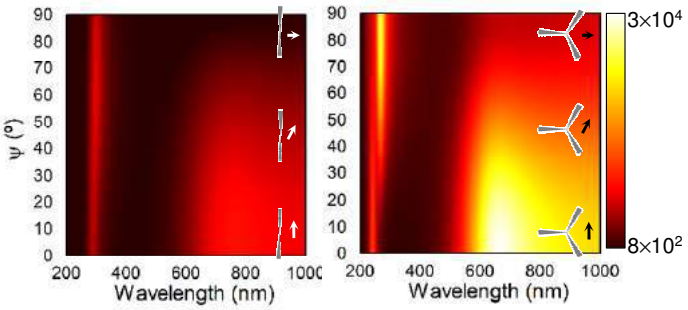

Figure1. Nonradiative Purcell enhancement spectra for an 8nm-arm aluminum dimer (left) and trimer (right) under different emitter orientation excitation.

Acknowledgements, work supported by the Spanish Government [TEC2014-51902-C2-2-R]; V.P.-P. was sponsored by the Spanish MECD [FPU AP-2012-3796]; A.I.F.-D. by EU 7th Framework Programme [FP7-PEOPLE-2013-CIG-63099] and the Spanish MINECO [FIS2015-64951-R]; M.B. by the Spanish Government [RYC-2011-08221]; Y.L. by the Singapore Ministry of Education [MOE2015-T2-1-145], NRF-CRP grant [NRF2015NRF-CRP002-008] and NTU-A*STAR Silicon Technologies Centre of Excellence [11235150003]; M.N.-C. by University of Birmingham [Birmingham Fellowship].

REFERENCES

1. Novotny, L. and B. Hecht, *Principles of Nano-Optics*, Cambrdige University Press, UK, 2012.
2. Aouani, H., M. Rahmani, M. Navarro-Cía and S. A. Maier, "Third-Harmonic-Upconversion Enhancement from a Single Semiconductor Nanoparticle Coupled to a Plasmonic Antenna," *Nature Nanotech.*, Vol. 9, No. 4, 290-294, 2014.
3. Chikkaraddy, R., *et al.*, "Single-molecule strong coupling at room temperature in plasmonic nanocavities," *Nature*, Vol. 535, No. 7610, 127-130, 2016.
4. Schurig, D., J.J. Mock, B. J. Justice, S.A. Cummer, J.B. Pendry, A.F. Starr and D.R. Smith, Metamaterial electromagnetic cloak at microwave frequencies, *Science*, Vol. 314, No. 5801, 977-980, 2006.
5. Pendry, J.B., A.I. Fernández-Domínguez, Y. Luo and R. Zhao, "Capturing Photons with Transformation Optics," *Nat. Physics*, Vol. 9, No. 8, 518-522, 2013.
6. Pacheco-Peña, V., M. Beruete, A.I. Fernández-Domínguez, Y. Luo and M. Navarro-Cía, "Description of bow-tie nanoantennas excited by localized emitters using conformal transformation," *ACS Photon.*, Vol. 3, No. 7, 1223-1232, 2016.
7. Pacheco-Peña, V., A.I. Fernández-Domínguez, Y. Luo, M. Beruete and M. Navarro-Cía, "Aluminum Nanotripods for Light-Matter Coupling Robust to Nanoemitter Orientation," *submitted.*

Non-reciprocal optical effects in nanostructured materials.

T. Verbiest*, T. Swusten, and W. Brullot
University of Leuven, Chemistry department, Belgium
*corresponding author: Thierry.verbiest@fys.kuleuven.be

Abstract-We will discuss nonreciprocal optical effects that we have observed in (chiral) nanostructured materials composed of Au, Ag and Fe_3O_4 nanoparticles.

Hybrid nanomaterials that combine different functionalities are currently of great interest. We recently developed a self-assembly method to prepare multi-layered nanostructures composed of Ag, Au and Fe_3O_4 nanoparticles that are linked together by organic molecules. Such structures combine plasmonic and (superpara)magnetic properties and they can show unusual optical properties that cannot be observed in classical materials (1).

We are particularly interested in nonreciprocal optical effects such as Faraday rotation. In this case an external magnetic field is used to induce optical rotation. The effect is non-reciprocal since the optical rotation adds up when the light travels back and forth through the sample. Faraday rotation is heavily used in optical isolators. We will show that our hybrid materials exhibit extremely strong Faraday rotation due to the presence of the superparamagnetic iron oxide and strong plasmonic enhancement due to gold and silver. Possible applications are extremely small optical isolators or magnetic field sensors.

Faraday rotation is not the only nonreciprocal optical effect that can be observed. Another one is asymmetric light transmission i.e., the dependence of optical transmittance on the direction of light propagation in the material. The effect is induced by the presence of strong quadrupolar interactions in these plasmonic materials and no magnetic field is required. We observed asymmetric transmission effects as large as 10%. The effect can be used in optical isolators or photonic circuits.

When the hybrid structures are impregnated with chiral molecules, additional nonreciprocal optical effects can be observed: in addition to natural optical rotation (which is reciprocal) we also observed a nonreciprocal optical rotation component that is of the same order of magnitude as the natural optical rotation. Like for asymmetric transmission, the origin of the nonreciprocal natural optical rotation is the existence of strong quadrupolar interactions in the material.

REFERENCES

1. Brullot, W., Swusten, T., Verbiest, T. (2015). Broadband Nonreciprocal Quadrupolarization-Induced Asymmetric Transmission (Q-AT) in Plasmonic Nanoparticle Aggregates. *Advanced Materials* **27**, art.nr. adma.201405409
2. Brullot, W; Strobbe, R; Bynens, M; Bloemen, M; Demeyer, PJ; Vanderlinden, W; De Feyter, S; Valev, VK; Verbiest, T (2014). Layer synthesis and tunable optical properties of hybrid magnetic-plasmonic nanocomposites using short bifunctional molecular linkers, *Materials Letters,* **118**, 99-102

Exploiting complex media with random nanoparticles with the principle of inverse scattering

Y. K. Park[1*]
[1]Department of Physics, KAIST, Daejeon, Republic of Korea
[*]corresponding author: yk.park@kaist.ac.kr

Abstract- We will present the applications of inverse scattering principles with digital holography. Scattering of light in complex media or biological samples can be reversed and controlled by actively controlling the wavefront of incident beams. Utilizing multiple light scattering on purpose, we demonstrate 3-D holographic microscopy, the sub-wavelength focusing and imaging, the reference-free optical phase conjugation, the reference-free holographic camera, and ultra-high definition dynamic 3D holographic display

In this talk, we will present the applications of inverse scattering principles with digital holography. First, I will present the recently developed 3-D holotomography setup using a dynamic mirror device, which is an optical analogous to X-ray computed tomography. In particular, I will discuss the visualization of 3D refractive index distributions of biological cells and tissues measured with the 3-D holotomography using the transfer function method. For a weakly scattering sample, such as biological cells and tissues, a three-dimensional refractive index tomogram of the sample can be reconstructed with the inverse scattering principle from multiple measurements of two-dimensional holograms. The outcome demonstrates outstanding visualization of 3D refractive index maps of live. In addition, we also discuss the applications of inverse scattering principle for highy scattering layers. With wavefront shaping techniques using digital holography, we demonstrate ultra-high-definition dynamic holographic display exploiting large space-bandwidth in volume speckle. Exploiting light scattering in diffusers, we also demonstrate the holographic image sensor which does not require for the use of a reference beam.

REFERENCES

1. Lee, K. et al. “Time-multiplexed structured illumination using a DMD for optical diffraction tomography,” arXiv preprint:1612.00044, 2016.
2. Lee, K. and Park, YK, “Exploiting the speckle-correlation scattering matrix for a compact reference-free holographic image sensor,” *Nat. Comm.*, Vol.7, 13359, 2016.
3. Yu, H. et al., “Ultrahigh-definition dynamic 3D holographic display by active control of volume speckle fields,” *Nat. Photon*, in press.
4. Park, J. et al., “Scattering optical elements: stand-alone optical elements exploiting multiple light scattering,” *ACS NANO,* Vol. 10(7), 6871–6876, 2016.
5. Lee K. et al., “One-wave optical phase conjugation mirror by actively coupling arbitrary light fields into a single-mode reflector,” *Phys. Rev. Lett.,* Vol. 15(15), 153902, 2015.

Three-dimensional Plasmonic Metadevices

J.-W. Chen[1], H.-H. Hsiao[1], Y. H. Chen[1], H. J. Wu[2], C. H. Chu[2], M.-K. Chen[1], W.-Y. Tsai[1], T. L. Chung[1] and D. P. Tsai[1,2*]

[1]Department of Physics, National Taiwan University, Taipei 10617, Taiwan

[2]Research Center for Applied Sciences, Academia Sinica, Taipei 11529, Taiwan

[*]corresponding author: dptsai@sinica.edu.tw

Abstract- The resonant properties arose from the electric and magnetic interactions between the vertical split-ring resonators (VSRRs) and light are theoretically and experimentally studied. Particularly, the magnetic resonance plays a key role in plasmon coupling in VSRRs. We perform several VSRR-based metadevices for practical applications in optical communication frequency such as Fano-resonance, highly sensitive nanoplasmonic sensor, isotropic absorber *etc*.

Split-ring resonator (SRR), a kind of building block for metamaterial unit cell, has attracted wide attentions due to both the electric and magnetic dipolar responses can be excited under proper conditions. Here, different from prior works, fundamental resonant properties and potential applications in novel three dimensional vertical split-ring resonators (VSRRs) are theoretically and experimentally studied. Beside a single VSRR [1], tuning the structural configuration of VSRR unit cells is able to generate various coupling phenomena in VSRRs, such as plasmon hybridization and Fano resonance [2, 3]. Subsequently, the VSRR-based refractive index sensor will be demonstrated. Due to the unique structural configuration, the enhanced plasmon fields localized in VSRR gaps can be lifted away from the dielectric substrate, allowing for the increase of sensing volume and enhancing the sensitivity [4]. We further perform a VSRR based metasurface for light manipulation at optical communication frequency, in which the 2π phase modulation is from the changing of prong length along z-direction [5]. Finally, isotropic VSRRs are introduced by optimizing the structural arrangement within a unit cell for realizing isotropic VSRR-based perfect absorbers [6, 7].

REFERENCES

1. Chen, W. T. et. al., "Optical magnetic response in three-dimensional metamaterial of upright plasmonic meta-molecules," *Opt. Express* 19, 12837-12842 (2011).
2. Wu, P. C. et. al., "Magnetic plasmon induced transparency in three-dimensional metamolecules," *Nanophotonics* 1, 131-138 (2012).
3. Wu, P. C. et. al., "Plasmon coupling in vertical split-ring resonator metamolecules," *Sci. Rep.* 5, 9726 (2015).
4. Wu, P. C. et. al., "Vertical split-ring resonator based nanoplasmonic sensor," *Appl. Phys. Lett.* 105, 033105 (2014).
5. Hsu, W.-L. et. al., "Vertical split-ring resonator based anomalous beam steering with high extinction ratio," *Sci. Rep.* 5, 11226 (2015).
6. Chen, C.-C. et. al., "Uniaxial-isotropic metamaterials by three-dimensional split-ring resonators," *Adv. Opt. Mater.* 3, 44-48 (2015).
7. Wu, P. C. et. al., "Isotropic absorption and sensor of vertical split-ring resonato," *Adv. Opt. Mater.* DOI: 10.1002/adom.201600581 (2016).

Translation Matrix for Anisotropic Metamaterials

K. Vytovtov[1*], S. Zouhdi[2] E. Barabanova[1]
[1]Department of Information Technology, Astrakhan State Technical University, Russia
[2]Polytech Paris-Sud, Paris-Sud University, France
[*]corresponding author: vytovtov_konstan@mail.ru

Abstract-Stratified anisotropic metamaterials with *N* cells within a period were *N* is an arbitrary number are studied in this paper. Bandgap structure of such materials is under our consideration. The accurate analytical method of investigating is obtained for the first time. The new sign-functions are introduced. It is found that change of the arrangement of cells doesn't affect bandgap structure of metamaterials. It also is shown that boundaries between passband and stopband are resonance characteristics of plane parallel resonator filled by stratified metamaterial. Moreover change of a layer arrangement doesn't affect the resonance characteristic of a device. Analogous properties are observed in Bragg filters and periodic waveguide structures.

Periodic anisotropic metamaterial are very important to produce various microwave, optical devices, and nanostructures [1,2] therefore investigation of these is relevant now.

To study various anisotropic periodic structures the translation matrix method is most widely used. However the matrix has been obtained and analyzed in detail for double-layered period as rule. The translation matrix for a *N*-layered isotropic structure has been presented in [3] and for a longitudinal magnetized ferrite it has been given in [4]. Bianisotropic stratified media have been described by using such a matrix in [5].The translation matrix for a stratified anisotropic metamaterial structure has been offered in [6]. However in that work the matrix has been written for a single layer. Moreover the authors have considered uniaxial anisotropy only. But metamaterials obviously are bi-axial anisotropic. It is very important advantage that the method presented here is accurate analytical and the translation matrix is obtained in elementary functions.

In this paper we study wave behavior within stratified anisotropic metamaterial. Each sell of a structure is described by the dyadics

$$\bar{\bar{\varepsilon}} = \begin{vmatrix} \varepsilon_{xx} & \varepsilon_{xy} & 0 \\ -\varepsilon_{yx} & \varepsilon_{xx} & 0 \\ 0 & 0 & \varepsilon_{zz} \end{vmatrix} \quad \bar{\bar{\mu}} = \begin{vmatrix} \mu_{xx} & \mu_{xy} & 0 \\ -\mu_{yx} & \mu_{xx} & 0 \\ 0 & 0 & \mu_{zz} \end{vmatrix} \tag{1}$$

with negative components ε_{xx}, μ_{xx}, ε_{zz} and μ_{zz}. In general case the dyadic components can be complex values. Note that here we take into account the effective parameters of a medium only.

In our work the translation matrix in the accurate analytical form is presented for the first time. The offered method can be used for various metamaterial structures as the translation matrix of a single sell is the same for them. The translation matrix is written here as the sum of the 2^N matrix group. Each group contains the 2^{N-1} matrix. Therefore we can say about 2^{2N-1} independent waves within a structure that is devided in 2^N group. On other words we can say about a *q*-th independent wave of a *p*-th group. Let us call these waves as equivalent waves. The contribution of each wave is presented by the coefficient that we call as the contribution rate. Here we also use two sign-functions

$$f_{q,j} = \text{sign}\left\{\sin\frac{\pi}{2^{N+1-j}}(2q-1)\right\} \quad (2)$$

$$F_{p,j} = \frac{1}{2}\left(1 + (-1)^{k_j+1} \times \text{sign}\left\{\sin\frac{\pi}{2^{N+1-j}}(2q-1)\right\}\right) \quad (3)$$

The function (2) has been described in [3] in detail by us. The function (3) has been introduced in [5], but it will be described here for the first time. The equivalent waves are the result of interaction of sell eigenwaves as the electromagnetic thicknesses of these are the algebraic sum of the thicknesses of the eigenwaves. Herein two eigenwaves of a same sell don't interact with each other. The function (3) establishes the arrangement of eigenwave interaction. Within each group, the wave electromagnetic thickness and the contribution ratios are different. These values are depended on a sign, which is taken for the sell electromagnetic thickness. It is obtained that within each group the signs vary in binary law. These changes take into account by the sign function (2).

Here it is found that change of sell arrangement does not affect bandgap structure if a period length is invariable. The analytical proof of this phenomenon for an isotropic medium has been presented in [6]. Now we also have obtained the accurate analytical foundation of this property for an anisotropic metamaterial.

The property described for an infinite anisotropic metamaterials can find the practical applications. Indeed Bragg filter based on an anisotropic metamaterial is a periodic structure and wave behavior in such a structure can be described by the differential equations. Therefore bandgap structure can be found from analysis of eigennumbers of the translation matrix. It is important that geometry of a studied filter can be more complicate than it has been studied early. Here a period is N-layered. Analogously a waveguide with variable section and a waveguide filled by periodic anisotropic metamaterial are described by constitutive relations (1) can be described by the obtained translation matrix.

It is found that the boundaries between passband and stopband are the resonance characteristics of a plane parallel resonator filled by inhomogeneous anisotropic metamaterial. Accurate mathematical proof of this property will be given here.

REFERENCES

1. Veselago V. G., "Electrodynamics of substances with simultaneously negative values of sigma and mu," *Soviet Phys*. *Uspekhi-ussr* **10**, 509–514 (1968).
2. Pendry J. B., Schurig D., and. Smith D. R, "Controlling electromagnetic fields," *Science* 312, 1780–1782 (2006).
3. Vytovtov K.A. Analytical Investigation of Statified Isotropic Media, *Journal of Optical Society of America A* **22** (4), 689-696 (2005).
4. Terent'ev Yu., Vytovtov K. 'Investigation of Behaviour of Waves Within Periodically Magnetized Ferrite', *International conference on antenna*. *Theory and techniques*. Kyiv, Ukraine, 1997, pp.279-281
5. Vytovtov K. A., 'The Analytical Method of Investigation of Periodic Layered Media With Uniaxial Bianisotropy' *Journal of Communications Technology and Electronics*, 46 (2), pp.159–166 (2001)
6. Hao J. and Zhou L. Electromagnetic wave scatterings by anisotropic metamaterials: Generalized 4x4 transfer-matrix method Phys. Rev B 77, 094201, 2008

High-throughput nanoscale optical positioning of single quantum dots for high-performance single-photon generation

Jin Liu[1,2], Yu-ming He[3], Luca Sapienza[4], Kumarasiri Konthasinghe[5], Sebastian Maier[3], Monika Emmerling[3], Stefan Gerhardt[3], José Vinícius De Miranda Cardoso[1], Jin Dong Song[6], Antonio Badolato[7], Christian Schneider[3], Sven Höfling[3], Marcelo Davanço[1], and Kartik Srinivasan[1]

[1]*Center for Nanoscale Science and Technology, National Institute of Standards and Technology, Gaithersburg, MD, USA 20899*
[2]*Maryland Nanocenter, University of Maryland, College Park, MD, USA 20742*
[3]*Technische Physik and Wilhelm Conrad Röntgen Research Center for Complex Material Systems, Physikalisches Institut, Universität Würzburg, Am Hubland, D-97074 Würzburg, Germany*
[4]*Department of Physics and Astronomy, University of Southampton, Southampton SO17 1BJ, UK*
[5]*Department of Physics, University of South Florida, Tampa, Florida 33620, USA*
[6]*Center for Opto-Electronic Convergence Systems, Korea Institute of Science and Technology, Seoul 136-791, South Korea*
[7]*Department of Physics and Astronomy, University of Rochester, Rochester, NY 14627, USA*
liujin23@mail.sysu.edu.cn

Abstract: We present a wide-field, high-throughput optical technique for locating solid-state quanutm emitters with <10 nm accuracy, and apply it in the creation of micropillar sources with near-optimal single-photon emission.

Solid-state quantum emitters, especially epitaxial quantum dots (QDs) with large optical oscillator strength, are a promising candidate for future on-chip quantum devices. However, the deterministic creation and eventual scalability of single QD devices greatly suffers from the random nature of the QD positions produced in their self-assembled growth. To address this, a variety of approaches for locating such QDs prior to device fabrication have been reported, and mostly rely on scanning techniques (such as confocal microscopy [1] or cathodoluminescence [2]), resulting in relatively low throughput and long acquisition time. Among different positioning methods, photoluminescence imaging is particularly appealing as it can combine high accuracy, short integration time, and wide-field capability in a simple setup [3, 4]. Here, we present a new high-performance system for nanoscale location of QDs based on photoluminescence imaging. This system exhibits improved positioning uncertainty and shorter acquisition time (3× lower and 100× shorter, respectively) than the first generation setup reported in Ref. [4]. We demonstrate its use in the creation of state-of-the-art single-photon sources, based on micropillar cavities, that emit bright, pure, and Purcell-enhanced indistinguishable photons [5, 6].

In our approach, schematically depicted in Fig. 1(a), a 630 nm LED is used to excite all of the QDs within the system's field of view (typically $\approx$ 60 μm × 60 μm), while a long wavelength LED simultaneously illuminates the sample. Emitted light from the QDs and reflected light off the sample are directed through one or more filters to reject light from the short wavelength LED before going into a sensitive electron-multiplied charge-coupled device (EMCCD) camera, or are coupled into a single mode fiber and sent to a grating spectrometer for spectral analysis. Placing the objective in close proximity to the sample allows for the use of a high NA (0.9), which both increases the solid angle over which emitted photons are collected, and also increases the LED intensity at the sample, ensuring that

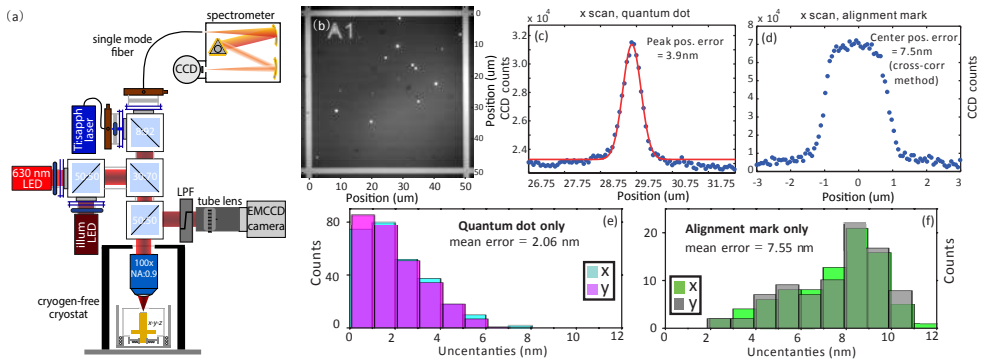

Fig. 1. (a) Schematic of the photoluminescence imaging system. The sample is on a x-y-z positioning stack within a 4 K closed-cycle cryostat. Hanging above the sample, within the cryostat, is a 100× magnification, 0.9 NA microscope objective. Two different color LEDs are combined on a 50:50 beamsplitter and sent into the objective to excite the quantum dots (QDs) and illuminate the sample, respectively. (b) Typical image of the QD photoluminescence and alignment marks taken by the setup. (c)-(d) One-dimensional line cut (along the x-axis) of the (c) QD emission and (d) light reflected off an alignment mark. (e),(f) Histograms of the uncertainties in the QD and alignment mark locations across multiple samples.

saturation of all QDs within the field of view can be achieved. Furthermore, the absence of optical windows between the objective and the sample leads to higher quality imaging. One example of an optical image used for positioning is shown in Fig. 1(b), where the image is taken within 1s and without EM gain. Figures 1(c)-(d) show horizontal line cuts through the QD and alignment mark from the image. Through maximum likelihood estimation and a cross-correlation method, uncertainties of 3.9 nm and 7.5 nm in the center positions of the QD and alignment mark have been obtained, respectively. We also show the statistics of our positioning technique in Fig 1(e),(f), where the mean uncertainties for QD and alignment mark are 2.06 nm and 7.55 nm respectively.

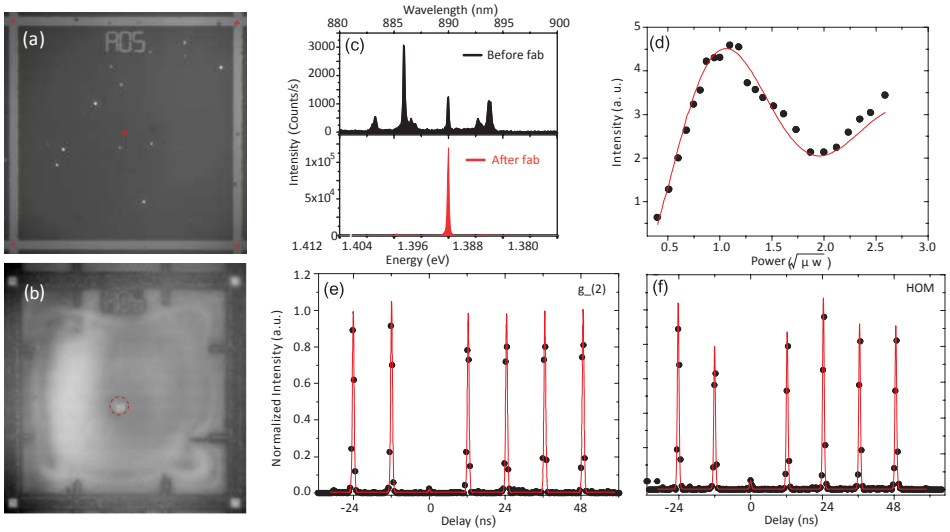

Fig. 2. (a) Photoluminescence image for quantum dot (QD) position extraction. The four alignment mark centers and center of the field are denoted by the red crosses and star, respectively. (b) Photoluminescence image of a micropillar highlighted by the red circle with a single QD in the center. (c) Spectra of the selected QD before (above) and after (below) fabrication of the micropillar. (d) Measured count rate on the spectrometer versus the pulse area of the resonant driving laser field. (d) 2^{nd} order autocorrelation histogram for pulsed resonant excitation with a π-pulse. (e) Histogram of HOM interference with the 12.2 delay time. Photons with parallel polarization are prepared here.

We apply our approach to the creation of micropillar cavities that contain a single QD in their centers, for use in triggered single-photon generation. Figure 2(a)-(b) shows the optical images of our device before and after the micro-pillar etching process. Before fabrication, individual QDs can be clearly identified while only the selected QD is located in the center of the pillar after the dry etching process (this QD was chosen based on its spectral location corresponding to the expected resonance location of the micropillar cavity). A direct comparison of micro-photonluminescence spectra of the positioned dot before and after fabrication suggests that the targeted exciton emission is greatly enhanced by the micropillar cavity structure, as shown in Fig 2(c). Lifetime measurements (not shown) further support this point, with a radiative lifetime of $\approx$ 100 ps corresponding to a Purcell factor of $\approx$ 7.8. Resonantly exciting the QD with a picosecond pulse, we observe characteristic Rabi-oscillation behavior as a function of the square root of the pump power, which is the key signature for the pulsed coherent driving of the two level system, shown in Fig. 2(d). Figures 2(e)-(f) present the second-order correlation and Hong-Ou-Mandel (HOM) interference measurements of the emitted single-photon pulses from the fully population-inverted QD excited by π-pulses at a repetition rate of 83 MHz. $g^{(2)}(0) = 0.015 \pm 0.009$, indistinguishability of (98.5 ± 3.2) %, and an extraction efficiency of (49 ± 4) % within the same device confirms an accurate placement of the QD in the center of the micropillar.

[1] A. Dousse, at al., Phys. Rev. Lett. **101**, 267404 (2008).
[2] M. Gschrey, at al., Nat. Comm. **101**, **6**, 7662 (2015).
[3] T. Kojima, K. Kojima, T. Asano, and S. Noda, Appl. Phys. Lett. **102**, 011110 (2013).
[4] L. Sapienza, M. Davanco, A. Badolato, and K. Srinivasan, Nat. Comm. **6**, 7833 (2015).
[5] X. Ding, et al., hys. Rev. Lett. **116**, 020401 (2016).
[6] N. Somaschi, at al., Nat. Photon. **10**, 340-345 (2016).

Enhancement and Inhibition of Spontaneous Photon Emission by dielectric photonic nanoantennas

Mathieu Mivelle,[1,2*] Dorian Bouchet,[1] Julien Proust,[3] Bruno Gallas,[4] Igor Ozerov,[5] Maria F. Garcia-Parajo,[2,6] Yannick De Wilde,[1] Nicolas Bonod,[3] Valentina Krachmalnicoff[1] and Sébastien Bidault[1]

[1]ESPCI Paris, PSL Research University, CNRS, Institut Langevin, 1 rue Jussieu, F-75005, Paris, France

[2]ICFO-Institut de Ciencies Fotoniques, The Barcelona Institute of Science and Technology, 08860 Castelldefels (Barcelona), Spain

[3]Aix-Marseille Université, CNRS, Centrale Marseille, Institut Fresnel, UMR 7249, 13013 Marseille, France

[4]Sorbonne Universités, UPMC Univ Paris 06, CNRS UMR 7588, Institut des Nanosciences de Paris, 75005 Paris, France

[5]Aix-Marseille Université, CNRS, CINAM, UMR 7325, 13288 Marseille, France

[6]ICREA-Institució Catalana de Recerca i Estudis Avançats, 08010 Barcelona, Spain

* mathieu.mivelle@insp.upmc.fr

Abstract- In this report, we provide the first experimental demonstration that silicon-based nanoantennas can either enhance or inhibit spontaneous emission from fluorescent molecules at the nanoscale. Using scanning probe microscopy, we analyse quantitatively the near-field interaction between a fluorescent nanosphere and silicon nanodisks in three dimensions.

Mie resonators, or high-index dielectric nanoparticles, have recently been proposed as new building blocks to produce metamaterials[1], metasurfaces[2] or optical antennas[3]. However, all prior studies have focused on the passive resonant scattering properties of dielectric particles without demonstrating their influence on active materials, a property that is crucial for nanoscale photon management. In this report, we provide the first experimental demonstration that silicon-based nanoantennas can either enhance or inhibit spontaneous emission from fluorescent molecules at the nanoscale (**Figure 1**).

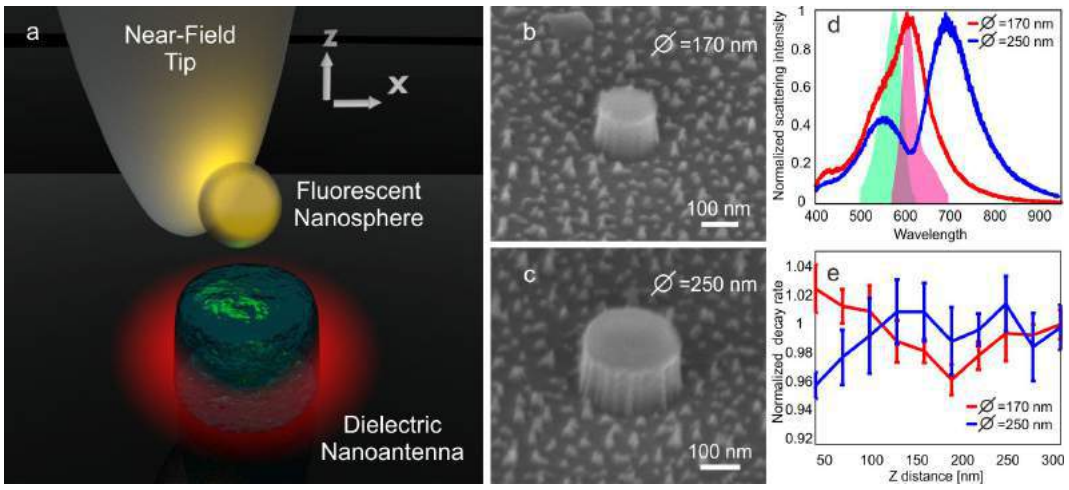

Figure 1: (a) Principal of the experiment: a fluorescent nanosphere is attached at the end of a near-field tip and placed in close proximity to a dielectric photonic antenna. (b, c) Two dimensions of dielectric antennas are considered to be either on resonance or out of resonance at the emission wavelength of the fluorescent nanosphere (d). (e) Enhancement or inhibition of the fluorescent nanosphere spontaneous emission in the vicinity of the dielectric nanoantennas.

Using scanning probe microscopy, we analyse quantitatively the near-field interaction between a fluorescent nanosphere and silicon nanodisks in three dimensions and at the nanoscale. Furthermore,

in this study we highlight the ability of dielectric nanoantennas to increase the far-field collection of spontaneously emitted photons, in excellent agreement with numerical simulations. These results are an essential contribution to the new field of Mie resonators, at the crossroads of plasmonics and dielectric microcavities, as they demonstrate the ability of high-index dielectric nanostructures to manipulate solid-state emitters at the nanoscale and at room temperature.

REFERENCES

1. Moitra, P., Yang, Y., Anderson, Z., Kravchenko, I. I., Briggs, D. P. and Valentine, J. “Realization of an all-dielectric zero-index optical metamaterial”, *Nat. Photon.* **7**, 791, 2013.
2. Spinelli, P., Verschuuren, M. A. and Polman, A. “Broadband omnidirectional antireflection coating based on subwavelength surface Mie resonators” *Nat. Commun.* **3**, 692, 2012.
[3] Fu, Y. H., Kuznetsov, A. I., Miroshnichenko, A. A., Feng Yu, Y. and Luk’yanchuk, B.“Directional visible light scattering by silicon nanoparticles” *Nat. Commun.* **4**, 1527 (2013).

Optimized nanostructures via direct laser writing: physical and chemical approaches

E. H. Waller[1], **J. Hering**[1], **and G. von Freymann**[1,2]

[1] Physics Department and Research Center OPTIMAS, University of Kaiserslautern, 67663 Kaiserslautern, Germany

[2] Fraunhofer Institute for Industrial Mathematics (ITWM), 67663 Kaiserslautern, Germany

ewaller@rhrk.uni-k.de

Abstract— We present recent advances in direct laser writing (DLW) of 3D nanostructures. These require on the one hand sophisticated control of all optical parameters in a DLW system, especially the excitation mode, on the other hand detailed knowledge of the photosensitive material and the structure formation process within this material. Here, we introduce our recent efforts on both: the optics side, including automated aberration correction and stimulated-emission-depletion DLW; the material side, encompassing proximity effect characterization and direct additive metal printing.

Direct laser writing (DLW) [1] – already one of the most versatile technologies for fabrication of 3D nano- and microstructures – has enabled a variety of structures encompassing a large range of applications, including but not restricted to metamaterials, photonic crystals and micro-optics [2]. It is based on tightly focussing a laser beam into a photo sensitive material where via two photon absorption a material change takes place and a structure forms. Despite already being widely applied, there is a demand of yet higher resolution, finer feature details, greater design fidelity, more robustness and specific material properties of these structures. Therefore, ongoing effort is put into improving the DLW system, especially the optical modes [3] (physical approach), and into understanding all processes that lead to structure formation [4] as well as into the development of new photo sensitive materials - the chemical approach.

Here, we present selected routes followed in our group that encompass both, the physical as well as the chemical approach.

On the physical side we introduce a spatial-light modulator (SLM) into the DLW setup. The phase shaping capabilities of the SLM allow sophisticated control of the focal mode. We present automated aberration correction which is applicable in high numerical aperture DLW systems. The iterative correction routine takes the intensity measured in the focal volume as feedback and pre-compensates all major aberrations present in the system using the SLM. We show that the aberration corrected excitation mode allows for substantially increased resolution of grating structures compared to the uncorrected mode.

The SLM not only enables aberration correction of the excitation mode but may be used in stimulated-emission-depletion (STED) inspired lithography. There, a second STED laser mode is overlayed with the excitation mode [5]. The STED mode locally depletes the excited photo initiator and thus locally prevents structure formation. By specifically shaping these modes into, e.g., so-called doughnut or bottle beam modes, finer feature details and higher resolution may be obtained. Here, we show that both, shaping the depleting modes as well as aberration correction of these modes, is possible using the SLM, and that both is necessary to obtain the desired resolution increase in the final structure.

On the chemical side we make use of SLM generated multi foci [6] to take a closer look at the proximity effect. We show that feature sizes and resolution is not only determined by the excitation mode. Rather, the proximity effect plays an important role and contributes to feature sizes in a distinct diffusive spatial and temporal manner [4].

Finally, we present our recent efforts in DLW of metal structures. Hereby, photo sensitive metal salt solutions are developed that undergo a photo induced reduction to neutral metal which then locally agglomerates to form a metal structure [7]. A number of effects, such as charge of metal particles, thermal heating of and scattering by the evolving structure, need to be precisely controlled or avoided.

In conclusion, SLM-based DLW enables accurate control and automated improvement of excitation and depletion modes leading to higher resolution and finer feature details of nanostructures. Furthermore, it allows for determination of spatio-temporal characteristics of the proximity effect which follows a diffusive characteristic in various photo resists. In addition, DLW systems may be used for additive manufacturing of metal structures. There, the reaction leading to the metal structure needs to be photo-initiated and thermal heating needs to be controlled.

ACKNOWLEDGMENT

The authors thank the Nano Structuring Center (NSC) for access to their clean room and scanning electron microscope. We acknowledge support by the Deutsche Forschungsgemeinschaft (DFG) in the framework of SFB 926.

REFERENCES

1. Maruo, S., Nakamura, O. and S. Kawata "Three-dimensional microfabrication with two-photon-absorbed photopolymerization," *Opt. Lett.*, Vol. 22, No. 2, 132–134, 1997.
2. Hohmann, J. K., Renner, M., Waller, E. H. and G. von Freymann "Three-Dimensional μ-Printing: An Enabling Technology," *Adv. Opt. Mater.*, Vol. 3, No. 11, 1488–1507, 2015.
3. Hering, J., Waller, E. H., and G. von Freymann, "Automated aberration correction of arbitrary laser modes in high numerical aperture systems," *Opt. Expr.*, Vol. 24, No. 25, 28500–28508, 2016.
4. Waller, E. H. and G. von Freymann, "Spatio-Temporal Proximity Characteristics in 3D μ-Printing via Multi-Photon Absorption," *Polymers*, Vol. 8, No. 8, 297–310, 2016.
5. Fischer, J., von Freymann, G., and M. Wegener "The Materials Challenge in Diffraction-Unlimited Direct-Laser-Writing Optical Lithography," *Adv. Mater.*, Vol. 22, No. 32, 3578–3582, 2010.
6. Waller, E. H. and G. von Freymann, "Multi foci with diffraction limited resolution," *Opt. Expr.*, Vol. 21, No. 18, 21708–21713, 2013.
7. Tanaka, T., Ishikawa, A., and S. Kawata, "Two-photon-induced reduction of metal ions for fabricating three-dimensional electrically conductive metallic microstructure," *Appl. Phys. Lett.*, Vol. 88, 081107, 2006.

Emission properties of second-harmonic generation in AlGaAs optical nanoantennas

L. Ghirardini,[1] L. Carletti,[2] V. Gili,[3] G. Pellegrini,[1] L. Duò, [1] M. Finazzi,[1] D. Rocco,[2] A. Locatelli,[2] C. De Angelis,[2] I. Favero,[3] M. Ravaro,[3] G. Leo,[3] A. Lemaître,[4] and M. Celebrano[1,*]

[1] *Department of Physics, Politecnico di Milano, Piazza Leonardo Da Vinci 32, 20133 Milano, Italy*
[2] *Department of Information Engineering, University of Brescia, Via Branze 38, 25123 Brescia, Italy*
[3] *Matériaux et Phénomènes Quantiques, Université Paris Diderot - Sorbonne Paris Cité, 10 rue A. Domon et L. Duquet, 75013 Paris, France*
[4] *Centre de Nanosciences et de Nanotechnologies, CNRS-UMR9001, Route de Nozay, 91460 Marcoussis, France*
**Corresponding author: michele.celebrano@polimi.it*

Abstract - We demonstrate extremely efficient second harmonic generation (SHG) from monolithic aluminum gallium arsenide (AlGaAs) nanoantennas suspended on a transparent aluminum oxide substrate. When exciting with a pump laser centered at 1554 nm, we obtained SHG with a conversion efficiency of about 10^{-5} for a 1.6 GW/cm^2 pump intensity.

Metal-less nanophotonics has recently raised an increasing interest because the optical response of high-permittivity dielectric nanoparticles exhibits negligible dissipative losses and strong magnetic multipole resonances [1–3] in the visible and near-IR. Here we propose all-dielectric $Al_{0.18}Ga_{0.82}As$-on-AlOx nanodisks, on which we measure second harmonic generation (SHG) with conversion efficiency up to 10^{-5} for a 1.6 GW/cm^2 pump in the optical telecom wavelength range [4].

Our samples were fabricated from a [100] GaAs wafer, with a 400nm layer of $Al_{0.18}Ga_{0.82}As$ on top of an aluminum-rich substrate (see Fig. 1a). The result is an array of nanopillars on an aluminum-oxide (AlOx) substrate. The linear and nonlinear optical response of such nanoantennas are modeled by using frequency-domain finite element simulations in COMSOL [5]. We numerically predict a SH conversion efficiency higher than 10^{-5} for a pump wavelength between 1500 nm and 1700 nm. To experimentally investigate the nonlinear properties of the fabricated nanopillars, we excited them with an ultrafast Erbium-doped fiber laser centered at 1554 nm (150 fs pulses, 80 MHz repetition rate).

The SHG signal was collected from an array of nanocylinders with radius varying from 175 to 225 nm, using single-photon avalanche photodiodes. The dependence of the detected SHG on the radius of the nanocylinders is in excellent agreement with the numerical simulations (see Fig. 1b). The polarization of the emitted SHG, reported in Fig. 1c as a function of the nanodisks radius, is also in very good agreement with the numerical simulations (see Fig. 1d), demonstrating the strong dependence of the SHG polarization from the nanocavity modes involved for specific nanostructures dimensions [6-7].

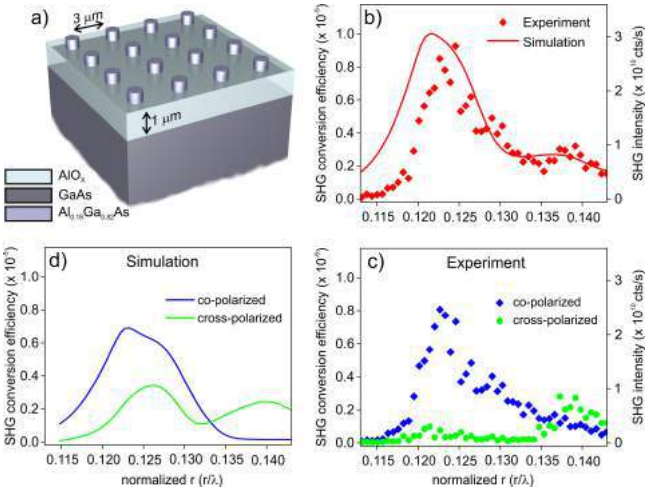

Figure 1. a) Scheme of the fabricated sample of AlGaAs nanodisks on top of a transparent (AlOx) layer. b) SHG conversion efficiency (left) and overall SHG intensity emitted by the nanodisks as a function of the normalized radius (r/λ). Polarized experimental (c) and simulated (d) SHG conversion

Our results allow gaining further insight in the mechanisms underlying the polarized nonlinear emission in these systems, showing the potential of AlGaAs-on-insulator all-dielectric platforms in the nonlinear manipulation of light properties at the nanoscale.

Acknowledgments, the authors warmly thank Prof. P. Biagioni, Prof. D. Neshev and Prof. A. Zayats for fruitful discussions and acknowledge the experimental support from Prof. C. Ricolleau and Dr. G. Wang.

This work was carried out in the framework of the Erasmus Mundus NANOPHI (2013 5659/002-001) project and of the NanoSpectroscopy COST Action (MP1302). The authors would also like to acknowledge financial support from CARIPLO Foundation SHAPES project (2013-0736) and "Double Culture" PhD Program of Sorbonne Paris Cité (V. F. Gili).

REFERENCES

[1] A. I. Kuznetsov, A. E. Miroshnichenko, Y. H. Fu, J. Zhang, and B. Lukyanchuk, "Magnetic light," *Sci. Rep*. **2**, 1–6 (2012).

[2] A. B. Evlyukhin, S. M. Novikov, U. Zywietz, R. L. Eriksen, C. Reinhardt, S. I. Bozhevolnyi, and B. N. Chichkov, "Demonstration of magnetic dipole resonances of dielectric nanospheres in the visible region," *Nano Lett.* **12**, 3749–3755 (2012).

[3] S. Person, M. Jain, Z. Lapin, J. J. Sáenz, G. Wicks, and L. Novotny, "Demonstration of zero optical backscattering from single nanoparticles," *Nano Lett.* **13**, 1806–1809 (2013).

[4] V. F. Gili, L. Carletti, A. Locatelli, D. Rocco, M. Finazzi, L. Ghirardini, I. Favero, C. Gomez, A. Lemaître, M. Celebrano, C. De Angelis, and G. Leo, "Monolithic AlGaAs second-harmonic nanoantennas," *Opt. Expr.* **24**, 15965-15971 (2016).

[5] L. Carletti, A. Locatelli, O. Stepanenko, G. Leo, and C. De Angelis, "Enhanced second-harmonic generation from magnetic resonance in AlGaAs nanoantennas," *Opt. Expr.* **23**, 26544–26550 (2015).

[6] L. Ghirardini, L. Carletti, V. Gili, G. Pellegrini, L. Duò, M. Finazzi, D. Rocco, A. Locatelli, C. De Angelis, I. Favero, M. Ravaro, G. Leo, A. Lemaître, and M. Celebrano, *Opt. Lett.* **42**, 559-562 (2017).

[7] L. Carletti, D. Rocco, A. Locatelli, C. De Angelis, V. F. Gili, M. Ravaro, I. Favero, G. Leo, M. Finazzi, L. Ghirardini, M. Celebrano, G. Marino, A. V. Zayats, "Controlling second-harmonic generation at the nanoscale with monolithic AlGaAs-on-AlOx antennas", *Nanotechnology* **28**, 114005 (2017).

Quantum dots interfaced with alkali atoms: filtering, delaying and quantum interfering single photons

H. Vural[1], S. L. Portalupi[1], M. Müller[1], J. Weber[1], J. Maisch[1], S. Kern[1], M. Widmann[2], R. Löw[3], J. Wrachtrup[2], M. Jetter[1], I. Gerhardt[2] and P. Michler[1]

[1]Institut für Halbleiteroptik und Funktionelle Grenzflächen, Center for Integrated Quantum Science and Technology (IQ^{ST}) and SCoPE, University of Stuttgart, Allmandring 3, 70569 Stuttgart, Germany

[2]3. Institute of Physics, University of Stuttgart, IQ^{ST} and SCoPE, Pfaffenwaldring 57, 70569 Stuttgart, Germany

[3]5. Institute of Physics, University of Stuttgart, IQ^{ST} and SCoPE, Pfaffenwaldring 57, 70569 Stuttgart, Germany

Abstract: We present recent results in the field of hybrid quantum systems. Single photons generated by the resonant pumping of a semiconductor quantum dot are interfaced with alkali atoms in order to realize an efficient variable delay up to a record value of 28 ns. After delaying, two successive single photons are used to perform quantum interference measurements: when only one photon is delayed the indistinguishability is fully conserved while when both are delayed the two-photon interference visibility further increases.

Hybrid quantum systems are attracting increasing attention thanks to their capability of merging the strengths of different complementary fields. In the present case, semiconductor quantum dots (QDs) are interfaced with alkali atoms. QDs are well known to be bright sources of on-demand single and indistinguishable photons. A crucial limitation is set by the relatively short coherence time that can be overcome by using alkali atoms, which display a very long coherence time and can take advantage from the properties of QD-based non-classical light sources [1].

In this direction, we have recently proven an efficient QD-to-atom interface, by filtering two consecutive single photons generated by a resonantly excited QD using of a Cs-based Faraday anomalous dispersion optical filter (FADOF) [2]. The intrinsic tunability of the Mollow triplet allowed tuning the two sidebands in resonance with the Cs-D_1 transition: a simultaneous filtering of both spectral features with more than 10% transmission was achieved, while suppressing all other components below the noise level.

The present study [3] represents a step further in the hybrid QD-atom interface, where the Cs vapor is used as variable optical delay. A tunable, resonantly excited QD is used as source of on-demand single photons, in resonance with the Cs-D_1 transition. We will report on the effect of vapor temperature on the achievable delay for single photons with many different linewidth. A record delay of 28 ns was observed for almost 100% of the transmitted photons (Fig.1 a). The ideal single-photon nature of the emitted photons was proven by autocorrelation measurements ($g^{(2)}(0) \approx 0$) after the interaction of the photons with the atomic vapor.

Photon indistinguishability is another fundamental property for quantum information purposes. In the present study we performed Hong-Ou-Mandel measurements under several different conditions (Fig. 1 b), using the alkali vapor as variable delay line. When both successively emitted photons are delayed, an increase of the photon indistinguishability is observed: we attribute this finding to a photon wavepacket "filtering" effect. It is worth noting that when only one photon is delayed ($\Delta t \approx 3$ ns) the HOM visibility is fully maintained. These findings prove that photons coherence properties are preserved after interacting with the atomic vapor, opening the way to the implementation of vapor-based quantum memories for single and indistinguishable QD photons.

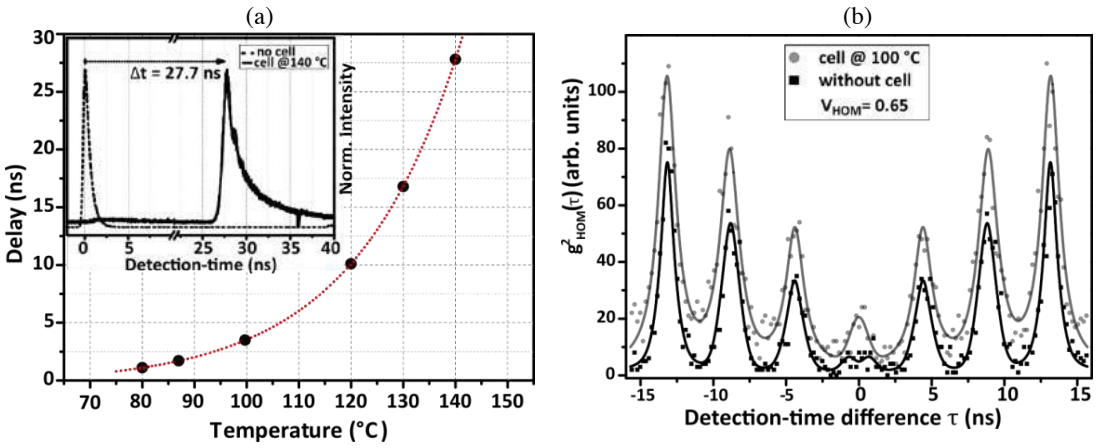

Fig.1 (a) Photon delay as a function of vapour temperature: in the inset the record delay with respect to non-delayed photons is also shown. **(b)** HOM visibility. The black curve shows the reference HOM visibility. Delaying one photon with the vapour and making it interfering with a non-delayed photon results in the HOM in grey. Both visibilities are around 0.65.

References

[1] N. Akopian, L. Wang, A. Rastelli, O. G. Schmidt, and V. Zwiller, "Hybrid semiconductor-atomic interface: slowing down single photons from a quantum dot", Nat. Photon. **5**, 230-233 (2011).

[2] S.L. Portalupi, M. Widmann, C. Nawrath, M. Jetter, P. Michler, J. Wrachtrup, and I. Gerhardt, "Simultaneous Faraday filtering of the Mollow triplet sidebands with the Cs-D1 clock transition-Supplementary", Nat. Commun. **7**, 13632 (2016).

[3] H. Vural, S. L. Portalupi, M. Müller, J. Weber, J. Maisch, S. Kern, M. Widmann, R. Löw, J. Wrachtrup, M. Jetter, I. Gerhardt, and P. Michler, in preparation (2017).

Optoelectronic metasurfaces

Jeremy N. Munday[1,2*]

[1] Department of Electrical and Computer Engineering, University of Maryland, College Park, MD, 20742, USA

[2] Institute for Research in Electronics and Applied Physics, University of Maryland, College Park, MD, 20742, USA

[*]corresponding author: jnmunday@umd.edu

Abstract- Metasurfaces consist of flat, ultrathin optical components that can have a functionality resembling that of optical structures that are over an order of magnitude larger in size. These layers enable a significant change in the amplitude and/or phase of the electromagnetic wave within a deeply subwavelength thickness. Separately, photodetectors and other optoelectronic devices are used to detect photons through creation of charge carriers in a semiconductor. In this talk, I combine these concepts and discuss the use of lossy, ultrathin film metasurfaces for the generation of hot carriers, and their subsequent collection, enabling compact polarization and wavelength selective optoelectronic components.

Perhaps the simplest form of a metasurface is an ultrathin, lossy film, which can enable a nontrivial phase change upon reflection that differs significantly from zero or pi. With proper design, these structures can enable nearly complete absorption in an ultrathin film. In cases where the absorption leads to excited free charge carriers, so-called hot carriers, optoelectronic devices can be designed to take advantage of these carriers. When a photon is absorbed within the metallic structure, its energy is transferred to an electron, which is promoted to a higher state within the conduction band (a similar phenomenon can occur for holes depending upon the incident photon energy and the density of states of the material [1]). These excited carriers can typically travel for a few tens of nanometers before collisions cause thermallization. Some fraction of carriers will be able to make it to an interface and, for a metal-semiconductor interface, be injected into the semiconductor, causing current. We have found similar results for thin metal-insulator-TCO (transparent conducting oxide) structures [2-4].

In this talk, I will discuss our recent work on the theory, fabrication, and testing of optoelectronic devices based on metasurfaces. By tailoring the absorption properties of these ultrathin films, both broadband and wavelength selective IR detectors can be fabricated on a Si-based platform. I will also present results of various imaging detectors based on these concepts.

Acknowledgements: this work is funded by an ONR YIP Award N00014-16-1-2540 and an NSF CAREER Award #1554503.

REFERENCES

1. Tao Gong and Jeremy N. Munday, "Materials for hot carrier plasmonics [Invited]," *Opt. Mat. Express.*, **5**, 2501-2512, 2015.
2. Tao Gong and Jeremy N. Munday, "Angle-Independent Hot Carrier Generation and Collection Using Transparent Conducting Oxides," *Nano Lett.*, **15**, 147–152, 2015.
3. Tao Gong and Jeremy N. Munday, "Aluminum-based hot carrier plasmonics," *Appl. Phys. Lett.* **110**, 021117 2017.
4. Tao Gong, Lisa Krayer, and Jeremy N Munday, "Design concepts for hot carrier-based detectors and energy converters in the near ultraviolet and infrared," Journal of Photonics for Energy 6, 042510-042510, 2016.

Active plasmon injection assisted negative index flat lens for noise free for sub-diffraction limited imaging.

A. Ghoshroy[1], **W. Adams**[1], **X. Zhang**[1], **and D. Ö. Güney**[1*]

[1]Department of Electrical and Computer Engineering, Michigan Technological University, 1400 Townsend Dr. Houghton MI 49931 − 1295, USA
*email: dguney@mtu.edu

Abstract— We illustrate an active loss compensation scheme for a non-ideal negative index flat lens (NIFL), based on the recently developed plasmon injection or PI scheme. The scheme is applied to an image spectra where, noise similar to real imaging systems, is artificially added. An external auxiliary source is used to amplify high spatial frequency features of the object. The compensation scheme improves SNR and has the potential to be extended to higher spatial frequencies.

Theoretically, a slab of negative (refractive) index material (NIM) can be used to amplify and focus evanescent fields which contain information about the sub-wavelength features of an object [1]. This presents an unprecedented opportunity to overcome Rayleigh's diffraction limit and achieve super-resolution imaging. However, since NIMs are artificially realized with metamaterials which are inherently lossy, compensation of these losses becomes a critical limitation especially under the deep sub-wavelength regime where the Fourier components of the image spectra are suppressed under the noise. A recently developed compensation scheme dubbed plasmon injection [2], was conceptualized with surface plasmon driven NIM [3] and provides loss compensation without using a gain medium or non-linear effects. This scheme was then applied passively as a post-processing technique to reconstruct an object with sub-wavelength features [4]. However, passive compensation (PC) is inherently prone to noise amplification under the deep sub-wavelength regime.

Here, we demonstrate that an external auxiliary source can be used to overcome noise amplification and recover high spatial frequency features of the object, which are buried under the noise. We call this "active" compensation (AC) to distinguish it from passive as in [4]. We define the NIFL imaging system by it's relative permittivity and permeability, $\epsilon_r = \epsilon^{'} + i\epsilon^{''}$ and $\mu_r = \mu^{'} + i\mu^{''}$, with $\epsilon^{'} = -1$ and $\mu^{'} = -1$ and $\epsilon^{''} = -0.1$ and $\mu^{''} = -0.1$. We construct an auxiliary source whose Fourier spectra is

$$A(k_y) = 1 + P_o \cdot exp\bigg[- \frac{(\frac{k_y}{k_o} - k_c)^2}{2\sigma^2} \bigg]. \tag{1}$$

The spatial distribution of the auxiliary is $A(y) = \mathcal{F}^{-1}\{A(k_y)\}$, where $\mathcal{F}$ is the Fourier transform operator, is convolved with the object $O(y)$. The new object, denoted by $O^{'}(y)$, is called the total object and is

$$O^{'}(y) = \int_{-\infty}^{\infty} O(y) \cdot A(y - \alpha) d\alpha. \tag{2}$$

The corresponding image spectra is then determined with the finite element software package COMSOL Multiphysics. Noise is added to the spatial frequency distribution of the image. The noise process is a circular Gaussian random variable at each spatial frequency component. The noisy Fourier spectra obtained from the image plane is

$$I_N^{'}(k_y) = T_P(k_y) \cdot O(k_y) + T_P(k_y) O(k_y) \cdot P_o \cdot exp\bigg[- \frac{(\frac{k_y}{k_o} - k_c)^2}{2\sigma^2} \bigg] + N(k_y) \tag{3}$$

where $N(k_y)$ is the noise. The second term of Eq. 3 represents an amplification effect provided by the auxiliary source. This can be used to recover the spatial frequency components of the image spectra that are buried under the noise by simply controlling the characteristics of the auxiliary, such as its central frequency k_c, the amplification strength P_0 or its full width at half maximum σ.

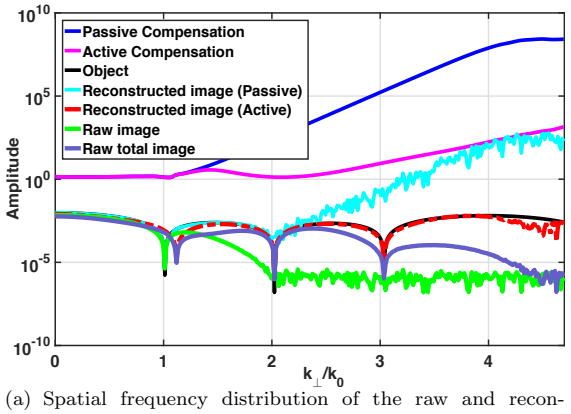

(a) Spatial frequency distribution of the raw and reconstructed images.

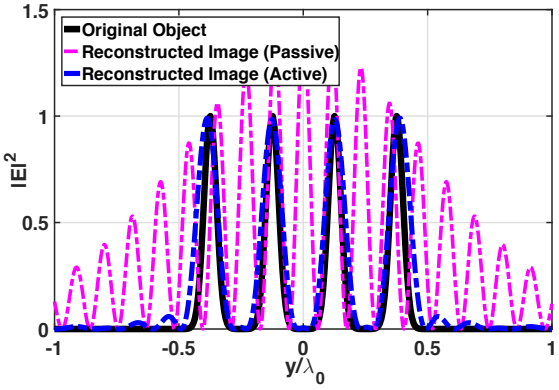

(b) Electric field intensity distribution.

Figure 1: (a) Passive $[T_P]^{-1}$ and active compensation $[T_A]^{-1}$ schemes. PC results in noise amplification in the reconstructed spectra unlike AC. The reconstructed images are obtained by multiplying the raw images with the corresponding compensation filter. (b) AC allows image reconstruction in the deep sub-wavelength regime unlike PC. Note that the passive compensated image has been scaled down by 10^7.

The image spectra given by Eq. 3 is then compensated by the inverse of the active transfer function denoted by $T_A(k_y)$

$$T_A(k_y) = T_P(k_y) + T_P(k_y) \cdot P_o \cdot exp\Big[- \frac{(\frac{k_y}{k_o} - k_c)^2}{2\sigma^2} \Big] \tag{4}$$

to reconstruct the object. The inverse of $T_A(k_y)$ is the active compensation shown in 1(a). $T_P(k_y)$ is the passive compensation in the absence of an auxiliary or when $P_0 = 0$. The resulting compensated Fourier spectra and spatial intensity distribution are shown respectively in figure 1(a) and (b), which shows how AC can reconstruct deep sub-wavelength features while PC fails. Figure 1(a) also shows how AC reveals a spatial frequency feature at $\frac{k_y}{k_o} = 3$ from the noise floor which goes undetected under PC. Moreover, AC significantly reduces noise amplification when compared with its passive counterpart thereby improving the signal to noise ratio of the imaging system.

The AC scheme makes the NIFL imaging system more versatile and opens up new avenues of high resolution imaging in the deep sub-wavelength regime where noise affects the image spectra. We have also identified some potential methods to implement convolution in the spatial domain, metasurfaces being the primary candidate. A more detailed analysis on how to design such a metasurface which can be used to convolve the object with the pump will be the focus of our future research endeavors.

ACKNOWLEDGMENT

This work was supported by Office of Naval Research(award N00014-15-1-2684).

REFERENCES

1. Pendry, J. B. (2000). “Negative Refraction Makes a Perfect Lens.” Physical Review Letters 85(18): 3966-3969.
2. Sadatgol, Mehdi and Özdemir, K. and Yang, Lan and Güney, Durdu Ö. (2015). “Plasmon injection to compensate and control losses in negative index metamaterials”. Physical review letters, 115(3), 035502.
3. Aslam, Muhammad I. and Güney, Durdu Ö. (2011). “Surface plasmon driven scalable low-loss negative-index metamaterial in the visible spectrum.” Physical Review B 84(19): 195465.
4. Adams, Wyatt and Sadatgol,Mehdi and Zhang,Xu and Güney, Durdu Ö. (2016). “Bringing the perfect lens into focus by near-perfect compensation of losses without gain media.” New Journal of Physics, 18(12), 125004.

Chirality of topological gap solitons in bosonic dimer chains

D. D. Solnyshkov[1*], O. Bleu[1], B. Teklu[1], and G. Malpuech[1]
[1]Institut Pascal, University Clermont Auvergne, Clermont-Ferrand, France
[*]corresponding author: dmitry.solnyshkov@univ-bpclermont.fr

Abstract-We study gap solitons which appear in the topological gap of 1D bosonic dimer chains within the mean-field approximation. We find that such solitons have a non-trivial texture of the sublattice pseudospin. We reveal their chiral nature by demonstrating the anisotropy of their behavior in presence of a localized energy potential.

A 1-dimensional (1D) periodic lattice with 2 different tunneling coefficients leading to the "dimerization" of the lattice is one of the simplest configurations exhibiting topological properties [1]. The dispersion of such system shows a splitting of a single *s*-type band into two bands, corresponding to the bonding and anti-bonding states of the individual dimers. These subbands are characterized by a topological invariant (the Zak phase [2]). The topology of the gap between them is determined by the Zak phase of the band below. Combining the topology of the lattice with the topology of the excitations of a quantum fluid, such as a Bose-Einstein condensate, is a particularly interesting problem of modern physics.

The properties of nonlinear solutions existing in the internal gap of the *s*-band of the 1D dimer chain can be expected to be strongly affected by its topology. The Su-Schrieffer-Heeger (SSH) soliton is perhaps one of the most famous examples of topologically nontrivial solutions [3] for a dimer chain. However, it involves dynamical dimerization, that is, modification of the properties of the lattice itself (displacement of the lattice sites or modification of tunneling coefficients): this soliton is a domain wall between two distinct lattices, each with its own dimerization order. Such dimerization domains can be observed not only in electronic systems (polymers, as in the original SSH work), but also in artificially created in photonic chains [4]. Recently, chiral solitons of the SSH type were observed in double chains [5].

But there also exist solitonic non-linear solutions, called gap solitons, that do not require the modification of the lattice and do not close the gap, contrary to the chiral edge states and the SSH soliton. Many of them have been studied in dimerized and zigzag lattices in acoustics [6], Bose condensates [7], and photonic systems [8,9], with a particularly interesting recent experimental observation [10]. However, the crucial role played by the anisotropy of the Bloch part of the soliton wavefunction with respect to the two different atoms forming the lattice (and defining the sublattice pseudospin) has remained unnoticed.

In this work [11], we demonstrate that a gap soliton in a single dimer chain can exhibit chirality. We study a gap soliton in the topological gap of a dimer chain, first using the tight-binding variational approach, and then by direct solution of the Gross-Pitaevskii equation with a periodic potential. This solution is strongly different from the chiral SSH soliton [5], because it does not involve the modification of the lattice itself. It is also different from the dark-bright solitons [12], because it does not involve neither the polarization degree of freedom, nor an extended condensate. The topological gap soliton (TGS) is a typical localized solution, appearing from the states at the boundary of a topological gap. We demonstrate that such solitons exhibit a nontrivial pattern of sublattice pseudospin due to pseudospin-anisotropic interactions. We determine their sublattice-polarization degree and demonstrate the chiral nature of these solitons via their asymmetric behavior with respect to a localized defect

(see Figure 1), which gives a striking contrast with the isotropic behavior of non-topological gap solitons (GS). These results are confirmed by direct calculations. A closer look at recent experimental data in a photonic dimer chain [10] confirms our predictions for the chiral nature of the TGS. Our results are valid for any photonic system, such as coupled waveguides [4, 10], and also for atomic condensates out of thermal equilibrium.

We acknowledge the support of the project "Quantum Fluids of Light" (ANR-16-CE30-0021).

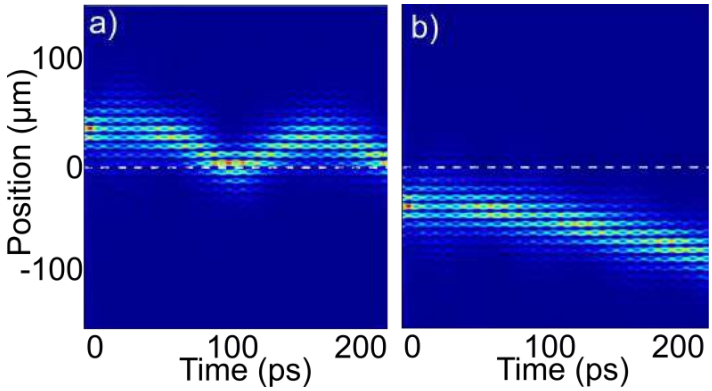

Figure 1. Chiral TGS trajectories plotted as the particle density as a function of position and time, depending on the initial position: a) oscillations b) free acceleration.

REFERENCES

1. Asboth, J. K., L. Oroszlany and A. Palyi, *A Short Course on Topological Insulators* (Springer International Publishing, 2016).
2. Zak, J., "Berry's phase for energy bands in solids", *Phys. Rev. Lett.*, Vol. 62, 2747, 1989.
3. Su, W. P., J. R. Schrieffer and A. J. Heeger, "Soliton excitations in polyacetylene", *Phys. Rev. B*, Vol. 22, 2099, 1980.
4. Blanco-Redondo, A. et al, "Topological Optical Waveguiding in Silicon and the Transition between Topological and Trivial Defect States", *Phys. Rev. Lett.*, Vol. 116, 163901, 2016.
5. Cheon, S. et al, "Chiral solitons in a coupled double Peierls chain", *Science*, Vol. 350, 182, 2015.
6. Kivshar, Y. S., N. Flytzanis, "Gap solitons in diatomic lattices", *Phys. Rev. A*, Vol. 46, 7972, 1992.
7. Haddad, L. H., C. M. Weaver and L. D. Carr, "The nonlinear Dirac equation in Bose–Einstein condensates", *New Journal of Physics*, Vol. 17, 063033, 2015.
8. Efremidis, N. K., D. N. Christodoulides, "Discrete solitons in nonlinear zigzag optical waveguide arrays with tailored diffraction properties", *Phys. Rev. E*, Vol. 65, 056607, 2002.
9. Vincencio, R. A., M. Johansson, "Discrete gap solitons in waveguide arrays with alternating spacings", *Phys. Rev. A*, Vol. 79, 065801, 2009.
10. Kanshu, A. et al, "Observation of discrete gap solitons in one-dimensional waveguide arrays with alternating spacings and saturable defocusing nonlinearity", *Optics Letters*, Vol. 37, 1253, 2012.
11. Solnyshkov, D. D., O. Bleu, B. Teklu and G. Malpuech, "Chirality of Topological Gap Solitons in Bosonic Dimer Chains", *Phys. Rev. Lett.*, Vol. 118, 023901, 2016.
12. Solnyshkov, D. D., A. V. Nalitov and G. Malpuech, "Kibble-Zurek Mechanism in Topologically Nontrivial Zigzag Chains of Polariton Micropillars", *Phys. Rev. Lett.*, Vol. 116, 046402, 2016.

Surface plasmon polariton mediated light-matter interactions in monolayer molybdenum diselenide-nanoantenna hybrid structures

Geeta Sharma[1], Astha Singh[1] and Parinda Vasa[1,*]

[1]Department of Physics, Indian Institute of Technology Bombay, Mumbai 400 076, India

[*]corresponding author: parinda@iitb.ac.in

Abstract*:* We report a simple approach to growing large area monolayer molybdenum diselenide films on different substrates using chemical vapor deposition technique. We have investigated surface plasmon mediated light-matter interactions in monolayer molybdenum diselenide-gold nanoantenna hybrid nanostructures. Our results show significant changes in the lattice constant, bandgap energy, photoluminescence lifetime and Raman lines as a direct manifestation of the Purcell effect in MoS_2-nanoantenna hybrid structures. Preliminary studies also offer indications of strong coupling in optimized sample configurations.

Layered materials show remarkable properties when thinned down to monolayer limit because of their two dimensional nature and strong electron confinement [1]. Two-dimensional (2D) monolayers of transition metal dichalcogenides, such as molybdenum diselenide (MoS_2) are currently being paid increasing attention, due to their promising future in next generation electronics and photonics. Particularly, atomically thin MoS_2 films have drawn significant interest due to the remarkable transition from an indirect bandgap to direct bandgap semiconducting material [2,3]. In conventional approaches, MoS_2 layers are synthesized by various techniques such as micromechanical exfoliation assisted by scotch tape, intercalation assisted exfoliation, solution exfoliation, physical vapor deposition, hydrothermal synthesis, sulfurization of molybdenum trioxides, etc. However, the size of MoS_2 monolayers obtained using most of these methods is limited to only a few tens of micrometers, which is not suitable for large-scale integrated device applications. Recently, chemical vapor

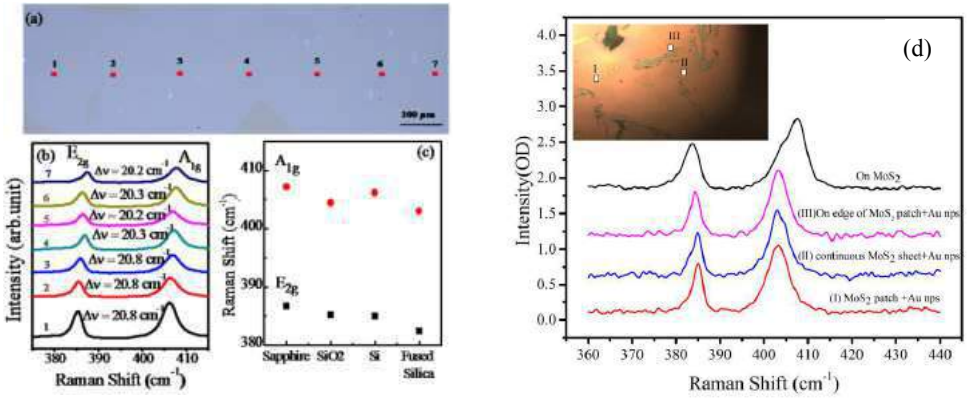

Figure: 1 (a) A large area monolayer MoS_2 film grown using chemical vapor deposition. (b,c) Characterization of the film using Raman spectroscopy, and (d) changes in Raman spectrum of a MoS_2 monolayer due to surface plasmon polariton mediated light-matter interactions.

deposition route has been extensively explored to achieve scalable synthesis of high quality MoS_2 monolayers for the development of practical devices. We have developed a simple chemical vapor deposition approach to growing large area monolayer MoS_2 films on different substrates [Fig. 1(a-c)] by sulfurization of MoO_3 in ambient pressure. Our technique involves relatively lower temperature synthesis [4], and does not require any kind of seeding or elaborate treatment of the substrate surface.

The focus of this work is to investigate nanoscale surface plasmon mediated light matter interactions in MoS_2 monolayer-gold antenna hybrid nanostructures. Elliptical and rod-shaped gold nanoparticles supporting localized surface plasmon (LSP) resonances act as efficient nano-antenna. Due to the strong plasmonic field localization offered by these nanoparticles, we have observed significant changes in the lattice constant, bandgap, photoluminescence lifetime and position as well as the width of Raman lines [Fig. 1(d)]. Our observations are a direct manifestation of the Purcell effect in these MoS_2-nanoantenna hybrid structures [5]. The changes in the bandgap energy, and thus the absorption spectra are also supported by the bandstructure calculations, which take into account the lattice distortions caused by the plasmonic fields. Preliminary studies offer indications of strong coupling in optimized sample configurations [6,7].

REFERENCES

1. K. F. Lee, C. Hone, J. Shan, T. F. Heinz, *Phys. Rev. Lett.* **105** 136805 (2010).
2. Q. H. Wang, K. Kalantar-Zadeh, A. Kis, J. N. Coleman, M. S. Strano, *Nat. Nanotechnol*. **7** 699 (2012).
3. B. Radisavljevic, M. B. Whitwick, A. Kis, *ACS Nano.* ***5*** 9934 (2011).
4. P. K. Mohapatra, S. Deb, B. P. Singh, P. Vasa, and S. Dhar, *App. Phys. Lett.* **108** 042101 (2016).
5. W. Wang, P. Vasa, R. Pomraenke, R. Vogelgesang, A. De Sio, E. Sommer, M. Maiuri, C. Manzoni, G. Cerullo, and C. Lienau, *ACS Nano* **8**, 1056 (2014).
6. P. Vasa, R. Pomraenke, S. Schwieger, Y. I. Mazur, V. Kunets, P. Srinivasan, E. Johnson, J. E. Kihm, D. S. Kim, E. Runge, G. Salamo, and C. Lienau, *Phys. Rev. Lett.* **101**, 116801 (2008).
7. P. Vasa, W. Wang, R. Pomraenke, M. Lammers, M. Maiuri, C. Manzoni, G. Cerullo, and C. Lienau, *Nature Photon.* **7**, 128 (2013).

Dispersion of the Nonlinear Susceptibility in Single Gold Nanoantennas.

V. Knittel[1], M. P. Fischer[1], A. Leitenstorfer[1], and D. Brida[1,*]
Department of Physics and Center for Applied Photonics, University of Konstanz, 78457 Konstanz, Germany
[*]corresponding author: daniele.brida@uni-konstanz.de

Abstract- We compare the third harmonic generation and incoherent photoluminescence contributions to the nonlinear optical response obtained in individual gold nanoantennas upon illumination with near-IR femtosecond pulses. With this procedure we could extract the dispersion of the nonlinear susceptibility.

Nanoantennas are excellent tools for accessing the nonlinear response of metals owing to the strong enhancement of light-matter interaction occurring in the near-field. For example, excitation of gold nanostructures with intense radiation triggers both coherent and incoherent phenomena such as third-harmonic generation (THG) [1] and multi-photon photoluminescence (MPPL), respectively [2,3]. In this work, we study the interplay between these frequency conversion mechanisms in order to unveil the effective $\chi^{(3)}$ nonlinear response of metals.

In our experiment, we exploit tuneable near-infrared pulses from a femtosecond Er:fiber laser system to excite individual gold nanorods. The resonant antennas are fabricated via electron beam lithography with subsequent evaporation of gold and lift-off. The inset in Fig. 1 (a) shows a typical rod structure resonant at 2000 nm. This simple geometry is chosen since its influence on the spectral shape of the MPPL is well understood [3]. The resulting nonlinear emission of the nanorods under illumination is spectrally resolved, as depicted in Fig. 1 (a), showing the prominent THG peak residing on a broad MPPL output.

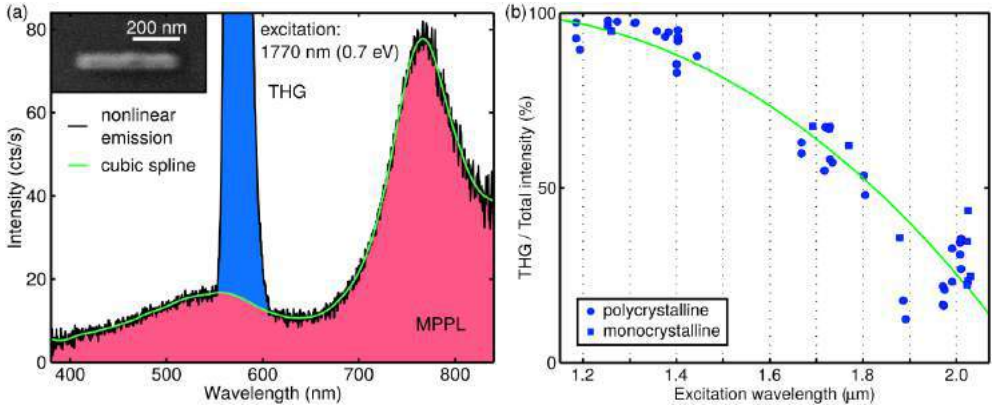

Fig. 1 (a) Typical nonlinear emission spectrum of single polycrystalline nanoantenna (black). The green line separates the coherent THG peak (blue) from the incoherent MPPL contribution (red), so that they can be integrated individually. A SEM micrograph of the corresponding nanoantenna is shown in the inset. (b) Ratio of the integrated THG output vs. the total nonlinear emission. Each data point represents the result from a single individual antenna. The green line serves as a guide to the eye.

The assessment of the nonlinear response of metallic nanostructures is complicated by the simultaneous occurrence of THG and MPPL combined to a field enhancement that cannot be determined with sufficient precision. We circumvent this problem by comparing the yield of the two nonlinear processes in individual gold nanoantennas illuminated by resonant optical pulses. This approach allows us to directly evaluate the susceptibility of gold since the field enhancement is identical for the two processes that are measured experimentally on the very same emitter. Figure 1(b) shows the ratio between the THG and the total nonlinear emission for a large set of antennas, all excited resonantly with pulses of the same temporal duration and peak intensity. This parameter is investigated as a function of the driving wavelength. The experimental results show an overwhelming contribution of the THG to the nonlinearity for short wavelength excitation.

In summary, we have investigated the nonlinear emission of single gold nanorods. By comparing the yield coherent and incoherent processes occurring on the same specimen, we overcome the dependence on the field enhancement. With this procedure we could obtain a fundamental insight in the origin of the nonlinear response by observing a strong dispersion of $\chi^{(3)}$ in THG that becomes more favourable when the fundamental excitation approaches a three photon resonance for the direct excitation of electrons from the d-band to the Fermi level.

REFERENCES

1. Hanke, T., J. Cesar, V. Knittel, A. Trügler, U. Hohenester, A. Leitenstorfer, and R. Bratschitsch, "Tailoring Spatiotemporal Light Confinement in Single Plasmonic Nanostructures," Nano Letters 12, 992 (2012).
2. Biagioni, P., M. Celebrano, M. Savoini, G. Grancini, D. Brida, S. Mátéfi-Tempfli, M. Mátéfi-Tempfli, L. Duò, B. Hecht, G. Cerullo, and M. Finazzi, "Dependence of the two-photon photoluminescence yield of gold nanostructures on the laser pulse duration," Phys. Rev. B 80, 045411 (2009).
3. Knittel, V., M. P. Fischer, T. de Roo, S. Mecking, A. Leitenstorfer, and D. Brida, "Nonlinear Photoluminescence Spectrum of Single Gold Nanostructures." ACS Nano 9, 894 (2015).
4. Knittel, V., M. P. Fischer, M. Vennekel, A. Leitenstorfer, and D. Brida, "Dispersion of nonlinear susceptibility in gold nanoantennas," submitted.

Reversible Switching of Highly Confined Phonon-Polaritons with an Ultrathin Phase-change Material

Peining Li[1], Xiaosheng Yang[1], Tobias W. W. Maß[1], Julian Hanss[1], Martin Lewin[1], Ann-Katrin U. Michel[1], Matthias Wuttig[1] and [*]Thomas Taubner[1]

[1]Institute of Physics (IA), RWTH Aachen University, 52056 Aachen, Germany

[*]corresponding author: taubner@physik.rwth-aachen.de

Abstract- We use phase-change materials (PCMs) as a switchable dielectric environment for infrared antennas and surface polaritons. Specifically, we combine an ultrathin film of PCMs with a substrate hosting surface phonon polaritons and realize the all-optical, non-volatile, and reversible switching of resonators for these ultra-confined polaritons.

The strong confinement and enhancement of light when coupled to surface waves or nanoparticles is key for various applications in nanophotonics such as sensing, imaging or other devices that enable the manipulation of light fields. In the mid-infrared spectral range, metallic nanoantennas and materials supporting surface phonon polaritons (SPhPs) can be used as building blocks of such devices. In both cases, the optical functionality is usually only obtained at a fixed wavelength, determined by the geometric design and the material properties.

In the first part of this talk, I will present our latest results on active mid-infrared plasmonics, i.e. the tuning of nanoantennas resonances via variation of the refractive index *n* of an embedding medium based on phase-change materials (PCMs) [1,2]. PCMs offer a huge contrast in the refractive index *n* due to a phase transition from amorphous to crystalline state, which can be thermally, optically or electrically triggered. I will show thermal and optical large-area switching of IR antenna resonances as well as individually addressable switching of single structures. Application potential for switchable chirality [3] and switchable detectors [4] will also be presented.

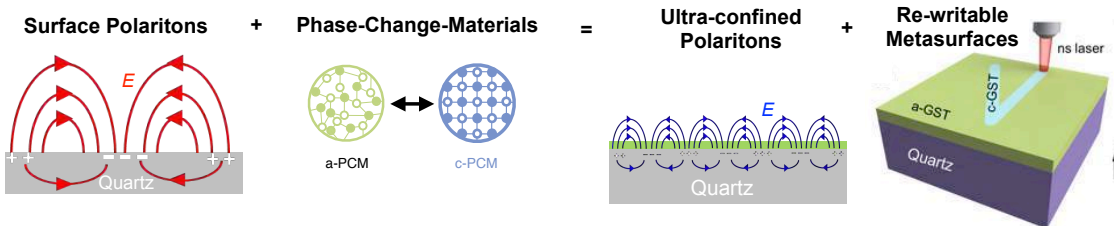

Figure 1: Sketch of our concept of combining Surface Phonon Polaritons (SPhPs) with a thin, switchable layer of Phase-Change-Materials (PCM) for achieving ultra-confined Polaritons and re-writeable metasurfaces.

In the second part, I will introduce Phonon-Polariton-based IR antennas made from polar dielectrics which

exhibit lower losses and larger Q-values compared to metallic nanoantennas. Specifically, we employ a PCM as a switchable dielectric environment for loading the SPhPs [5]. This allows us to realize all-optical, non-volatile, and reversible switching of the SPhPs by controlling the structural phase of the PCM. We experimentally demonstrate that single nanosecond (ns) laser pulses can locally switch an ultra-thin PCM (down to 7 nm, < $\lambda/1200$) for exciting ultra-confined SPhPs (polariton wavevector $k_p > 70k_0$, $k_0 = 2\pi/\lambda$) in quartz. This offers a new, elegant way to prepare all-dielectric, optically rewritable SPhP resonators without the need of complex fabrication methods.

Our approach of combining PCMs and SPhPs (Fig. 1) opens up new possibilities for non-volatile, rewritable and active nanophotonics, in particular for re-configurable, digital and memory metamaterials, flat optics and metasurfaces.

REFERENCES

1. Michel, A.-K. U. , D. N. Chigrin, T. W. W. Maß, K. Schönauer, M. Salinga, M. Wuttig, T. Taubner. „Using Low-Loss Phase-Change Materials for Mid-Infrared Antenna Resonance Tuning," *Nano Lett.,* Vol. 13, 3470-3475, 2013.
2. Michel, A.-K. U., P. Zalden, D. N. Chigrin, M. Wuttig, A. M. Lindenberg, T. Taubner, „Reversible Optical Switching of Infrared Antenna Resonances with Ultrathin Phase-Change Layers Using Femtosecond Laser Pulses,"*ACS Phot.*, Vol. 1, 833-839, 2014.
3. Yin, X. , M. Schäferling, A.-K. U. Michel, A. Tittl, M. Wuttig, T. Taubner, H. Giessen, „Active Chiral Plasmonics," *Nano Lett,.* Vol. 15, 4255-4260, 2015.
4. Tittl, A., A.-K. U. Michel, M. Schäferling, X. Yin, B. Gholipour, L. Cui, M. Wuttig, T. Taubner, F. Neubrech, H. Giessen, „A Switchable Mid-Infrared Plasmonic Perfect Absorber with Multispectral Thermal Imaging Capability." *Adv. Mat.* Vol. 27, 4597-4603, 2015.
5. Li, P., X. Yang, T. W. W. Maß, J. Hanss, M. Lewin, A.-K. U. Michel, M. Wuttig, T. Taubner, „Reversible Optical Switching of Highly Confined Phonon–Polaritons with an Ultrathin Phase-Change Material." *Nat. Mat.,* Vol. 15, 870-875, 2016.

Observation of a chiral mode at the exceptional point of a polariton laser

T. Gao,[1] G. Li,[2] E. Estrecho,[1] L. Pfeiffer,[3] K. West,[3] M. Steger,[4]
D. Snoke,[4] A. Kavokin,[2] A. G. Truscott,[1] and E. A. Ostrovskaya[1]

[1]*Research School of Physics and Engineering, The Australian National University, Canberra ACT 2601, Australia*
[2]*School of Physics and Astronomy, University of Southampton, Southampton SO17 1BJ, United Kingdom*
[3]*Department of Electrical Engineering, Princeton University, Princeton, New Jersey 08544, USA*
[4]*Department of Physics, University of Pittsburgh,*
3941 O'Hara Street, Pittsburgh, Pennsylvania 15218, USA

(Dated: February 24, 2017)

Bose-Einstein condensates show many remarkable properties, like superfluidity and excitation of quantized vortices [1]. Exciton polaritons in a semiconductor microcavity provide the opportunities to study Bose-Einstein condensation at a relatively high temperature with direct spectroscopic imaging and optical controllability. Exciton polariton is a hybrid light-matter quasiparticle, therefore the effects of the particle-particle interaction can be explored through its exciton component, while the photon component results in a relatively high decay rates and the need for a continuous pump to maintain the population. Due to the spatial and temporal coherence of the condensed exciton polaritons, their radiative decay results in a coherent photoluminescence of the microcavity, thus forming a polariton laser [2]. The driven-dissipative nature of exciton polaritons offers a platform for investigation of non-Hermitian properties [3] of Bose-Einstein condensate, which can be utilized to study both the fundamental properties of an open non-equilibrium quantum system and future novel optoelectronic or photonic micro-devices.

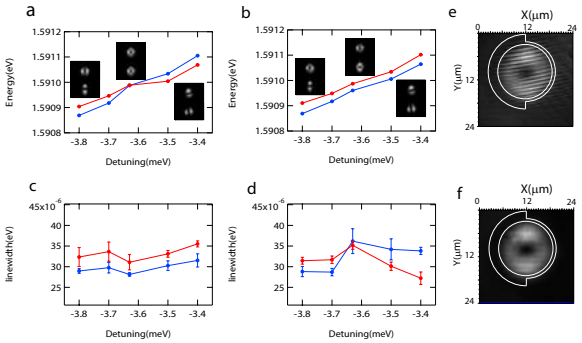

FIG. 1: Experimentally observed crossing-anticrossing transition of the real (a,b) (energy) and imaginary (c,d)(linewidths) parts of the eigenenergies with changing width of the optically-induced potential (white line), schematically shown in (e,f). A vortex mode forms in the vicinity of the exceptional point, as confirmed by the image of spatial polariton density distribution (e) and interference (f) with the reference beam.

In this work, we show the existence of a chiral mode in the form of a single charge vortex in an optically engineered ring resonator. The resonator is formed by a spatially shaped optical pump beam which induces a non-Hermitian trapping potential for exciton-polaritons. The two half rings have different widths, shown schematically in Fig.1(e,f), which affects the overlap of exciton-polariton condensate with the gain region. By adjusting the width of the half-ring and the detuning between the microcavity photon and exciton resonance, we observe the transition from crossing to anticrossing of complex eigen-energies, which signals the existence of an exceptional point. Furthermore, we confirm the formation of a chiral mode - a charge one vortex - at the exceptional point, in analogy with microwave [4] and optical [5] resonators. The fine manipulation of the relative phase between the two dipole modes (see Fig.1(a,b)) offers a new opportunity to control the vorticity and realize the mode switch in a macroscopic quantum system. Our method can be extended to generate high-order orbital angular momentum states through coalescence of multiple non-Hermitian degeneracies, which can find application in optical switching and information processing.

[1] K. G. Lagoudakis *et al.,* Nature Physics **4**, 706 (2008)
[2] A. Imamoglu *et al.,* Physical Review A **53**, 4250 (1996)
[3] T. Gao *et al.,* Nature **526**, 554 (2015)
[4] C. Dembowski *et al.,* Physical Review Letters **90**, 034101 (2003)
[5] P.Miao *et al.,* Science **353**, 464 (2016)

Near-field imaging of chiral optical fields on plasmonic materials

H. Okamoto[1,2*], **S. Hashiyada**[1,2], **T. Narushima**[1,2], **and Y. Nishiyama**[1,3]
[1]Institute for Molecular Science, Japan
[2]The Graduate University for Advanced Studies (Sokendai), Japan
[3]Present address: Institute of Science and Engineering, Kanazawa University, Japan
[*]corresponding author: aho@ims.ac.jp

Abstract To investigate internal structures of chiral optical responses in nanomaterials, we developed near-field optical activity imaging systems, and observed near-field CD images of two-dimensional gold nanostructures. Local CD signals with amplitudes as large as 100 times the macroscopic CD signals of the same samples were obtained, even for achiral structures. Furthermore, local linearly polarized near-field excitation of highly symmetric circular disks (that give no local CD signals) yielded circularly polarized scattering fields.

Chirality is a broad concept that characterizes structures of systems in almost all hierarchy of materials in natural sciences. Chirality also plays a key role in nanomaterials science. It is of fundamental importance to investigate internal structures of chiral optical responses in nanomaterials, to design functionality of chiral features of the materials. We developed near-field optical activity (typically circular dichroism, CD) imaging systems, and observed near-field CD images of two-dimensional gold nanostructures fabricated with electron beam lithography technique. We found local CD signals with amplitudes as large as 100 times the macroscopic CD signals of the same samples, for two-dimensional chiral gold nanostructures.[1] Even highly symmetric achiral structures (as typified by rectangular nanostructures) gave locally very strong CD signals,[2,3] as shown in Figure 1. In this case, average of the signal over the nanostructure yielded roughly null CD intensity.

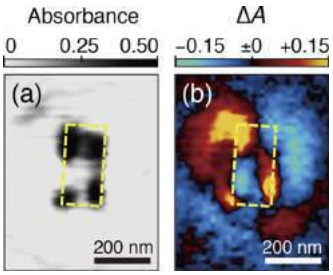

Figure 1. Near-field optical images (at 633 nm) of a gold rectangle.[2] (a) Transmission image. (b) CD image.

While even achiral nanostructures showed local CD activities, circularly symmetric two-dimensional nanostructures, such as circular disks, never give CD at any local positions. However, when the circular disk is illuminated with linearly polarized light, the circular symmetry is broken, and it potentially yields locally chiral optical fields. We extended the near-field CD microscope and conducted measurements of local optical activity for gold nanodisks. It has been found that the disk scattered circularly polarized optical fields when it was illuminated locally with linearly polarized excitation light, and that the ellipticity and the polarization azimuth angle of the scattered field depended on the incident polarization angle and relative position on the disk. The results obtained here may provide basic principle to get highly chiral optical fields, which may give us a chance to pioneer analytical applications of chiral optical fields.

Acknowledgements. This work was supported by Grants-in-Aid for Scientific Research (KAKENHI)

(Grant Nos JP15K13683, JP15H02161, and JP16H06505) and by Core-to-Core Program (A. Advanced Research Networks) from JSPS, and by the Photon Frontier Network Program of MEXT.

REFERENCES

1. Narushima, T. and Okamoto, H. “Strong Nanoscale Optical Activity Localized in Two-Dimensional Chiral Metal Nanostructures,” *J. Phys. Chem. C*, Vol. 117, 23964–23969, 2013.
2. Hashiyada, S., Narushima, T. and Okamoto, H., “Local Optical Activity in Achiral Two-Dimensional Gold Nanostructures,” *J. Phys. Chem. C*, Vol. 118, 22229–22233, 2014.
3. Nishiyama, Y. and Okamoto, H., “Near-Field Nonlinear CD Imaging of Single Gold Nanostructures,” *J. Phys. Chem. C*, Vol. 120, 28157–28162, 2016.

Analysis of of gravity-like interactions induced by fluctuating random fields

Jorge Luis-Hita[3], Manuel I. Marqués[1,2,*] , Víctor José López Pastor[1] ,Nuno de Sousa[5], Luis S. Froufe-Pérez[4], Frank Scheffold[4] and Juan José Sáenz[5]

[1].Departamento de Física de Materiales, UAM. Madrid, Spain
[2] IFIMAC & Instituto Nicolás Cabrera, UAM, Madrid, Spain
[3] Departamento de Física de la Materia Condensada, UAM, Madrid, Spain
[4] Department of Physics, University of Fribourg, Fribourg, Switzerland
[5]Donostia International Physics Center (DIPC), San Sebastian, Spain

[*]corresponding author: manuel.marques@uam.es

Abstract- The gravitational-like interactions induced by radiation are analyzed analytically a numerically for the particular case of two electric dipoles illuminated with a fluctuating random field

The idea of gravity like interactions induced by radiation dates back to works by Spitzer in 1941 [1]. More recently, the analyses of the interaction between two dipolar particles in isotropic random electromagnetic fields have shown how regions with gravitational like potentials may show up at short distances [2,4]. The interaction between two particles illuminated by artificially generated random fields has been very recently found experimentally [4] and theoretical and numerical analyses have shown that the diffusion properties of a dipole may be tuned also by using random light illumination [5,6].

In this work, we extend the analysis of gravitational-like interactions to more complicated systems [7] and we analyze the dynamics of dipoles explicitly illuminated with a group of fluctuating plane waves with wave vectors, polarizations and phases randomly distributed. Molecular dynamics simulations are implemented, in order to look for the existence of Kepler orbits in such a system.

REFERENCES

1. Spitzer Jr, L. The dynamics of the interstellar medium. ii. radiation pressure. Astrophys. J. 94, 232 (1941).

2. Thirunamachandran, T. Intermolecular interactions in the presence of an intense radiation field. Mol. Phys. 40, 393 (1980).

3. Sukhov, S., Douglass, K. M. & Dogariu, A. Dipole-dipole interaction in random electromagnetic fields. Opt. Lett. 38, 2385 (2013).

4 Bruggër G., Froufe-Pérez L.S., Scheffold F., Sáenz J.J, Controlling dispersion forces between small particles with artificially created random light fields. Nature Comm. 6:7460 (2015).

5 Marqués M.I. Dynamics of a small particle in a fluctuating random light field. Opt. Lett. 41, 796 (2016).

6 Marqués M.I. Crossover from superdiffusive to diffusive dynamics in fluctuating light fields. Phys. Rev. A 93, 063815 (2016).

7 Luis-Hita J. et al., to be published.

Coherent absorption of light by graphene and other plasmonic structures.

A. Tredicucci[1,2,3 *]

[1]Dipartimento di Fisica "E. Fermi," Università di Pisa, Largo Pontecorvo 3, 56127 Pisa, Italy

[2]Fondazione Bruno Kessler (FBK), Via Sommarive 18, 38123 Povo, Trento, Italy

[3]NEST, Istituto Nanoscienze-CNR and Scuola Normale Superiore, Piazza S. Silvestro 12, 56127 Pisa, Italy

[*]corresponding author: alessandro.tredicucci@unipi.it

Abstract - Coherent perfect absorption (CPA) and coherent perfect transparency (CPT) is discussed in 2D structures for instance based on graphene or intersubband transitions of a semiconductor heterostructure. In particular, asymmetric devices are analyzed, either relying on plasmonic resonances, properly engineered in a metal-dielectric metamaterial, or, more simply, constituted by an optically conductive surface on top of a substrate.

The light absorption properties of a system are typically considered an intrinsic material feature, mostly determined by its dielectric constant, thickness, etc. It has recently been shown, however, that full interferometric control of absorption can instead be accomplished by varying the relative phase of two coherent optical fields. Depending on the phase relation, the system can become totally opaque (coherent perfect absorption – CPA) or tuned to complete transparency (coherent perfect transparency – CPT).

These phenomena are now starting to be widely investigated at a fundamental level (CPA is actually considered the time-reversed process of lasing) and in view of innovative applications in plasmonics, or even in diagnostics and imaging techniques where the high selectivity provided by the interferometric absorption control could prove highly beneficial. Here I will discuss CPA and CPT in devices relying on polaritonic resonances, properly engineered in a metal metamaterial on top of a quantum well semiconductor heterostructure. Using diffraction gratings on Gallium Arsenide suspended membranes, "two-beam absorbance" measurements in a counter-propagating Mach Zehnder geometry reveal the absorption phase modulation. Furthermore, we report on experiments of coherent absorption on turbostratic multilayer graphene grown on silicon carbide substrate. From the analysis of the experimental data, the graphene conductance G can be deduced independently of the substrate and, thus, the number of layers N_G can be directly quantified.

For a proper interpretation of the experimental results, a general theory of CPA in linear two-port systems is constructed, without any symmetry requirements except for reciprocity; it demonstrates that optical absorption describes an ellipse as function of the difference between the intensities of the incident beams. The model is interpreted in the polariton case within a standard coupled-mode theory, and allows casting the graphene results in the more general landscape of optically conductive surfaces.

REFERENCES

1. Baldacci, L., Zanotto, S., Biasiol, G., Sorba, L., and Tredicucci, A., "Interferometric control of absorption in thin plasmonic metamaterials: general two port theory and broadband operation," *Opt. Express*, Vol. 23, No. 17, 9202–9210, 2014.

2. Zanotto, S., Mezzapesa, F. P., Bianco, F., Biasiol, G., Baldacci, L., Vitiello, M. S., Sorba, L., Colombelli, R., and Tredicucci, A., "Perfect energy-feeding into strongly coupled systems and interferometric control of polariton absorption," *Nature Phys.*, Vol. 10, No. 11, 830–834, 2014.
3. Zanotto, S., Bianco, F., Miseikis, V., Convertino, D., Coletti, C., and Tredicucci, A., "Coherent absorption of light by graphene and other optically conducting surfaces in realistic on-substrate configurations," *APL Photonics*, Vol. 2, No. 1, 016101, 2017.

Rhodium Nanocubes as building blocks for UV-plasmonics

Y. Gutiérrez[1], **D. Ortiz**[1], **J. M. Saiz**[1], **F. González**[1], **H. O. Everitt**[2,3] **and F. Moreno**[1]

[1] Group of Optics, Department of Applied Physics, University of Cantabria, Avda. Los Castros s/n. 39509 - Santander (Spain)

[2] Deparment of Physics, Duke University, Durham, North Carolina 27708, United States

[3] U.S. Army Aviation and Missile RD& E Center, Redstone Arsenal, Alabama 35898, United States

gvelay@unican.es

Abstract— Extending nanoplasmonics to the UV-range has awaken a great interest due to the current and potential applications in biological sensing, photocatalysis or spectroscopy. Very recently, rhodium (Rh) has been proposed as a promising candidate for this purpose. Its low tendency to oxidize overcomes the main problem with metals such as aluminum or magnesium. In addition, it presents outstanding catalytic properties. As the synthesis of rhodium nanocubes has been recently reported and because of its UV-plasmonic performance interest, in this research we present an analysis of the plasmonic behaviour of Rh nanocubes aggregates.

Plasmonics in the UV range results of interest in fields such as biological sensing, photocatalysis or spectroscopy [1, 2, 3]. Sanz et al. [4] studied several metals in order to find those whose properties made them more promising for UV-plasmonics. Two of the most compelling metals for this purpose are aluminum (Al) [5] and magnesium (Mg) [6]. However, nanoparticles (NPs) made of these two metals suffer from the formation of a native oxide layer whose thicknes strongly depends on the ambient conditions. Rhodium (Rh) has been proposed as an alternative due to competitive plasmonic performance and its promising properties [7]. On the one hand, it is a non-oxidizing catalytic metal. On the other hand, it is possible through chemical means to synthesize NPs with sharp edges like cubes [8] and tripod stars[9, 7], with sizes down to 10 nm.

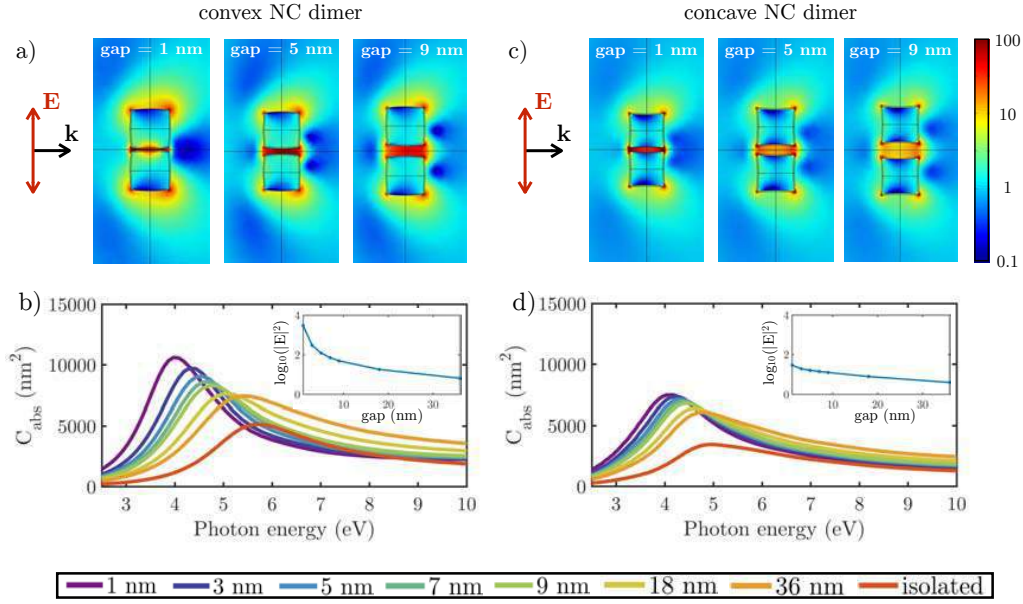

Figure 1: (a,c) Logarithmic scale $|E|^2$ images at the resonant energy and (b,d) spectral absorption cross-section C_{abs} for convex (left) and concave (right) NC dimers of several gaps, varying from 1 to 36 nm, illuminated under normal incidence with P polarization. The inset in (b,d) indicates the electric field intensity ($|E|^2$) at the center of the gap as a function of the inter-particle distance.

In this work we report a detailed numerical analysis of Rh nanocubes (NCs), paying special attention to the coupling and cooperative effects that appear when aggregates of NCs are considered. We will analyze the effect of different deviations from the perfect shape that can be seen in TEM images of synthesized Rh NCs, i.e. rounded edges and/or either concavity or convexity of their faces [8]. The hot spots created in the region between two interacting NCs (dimer) are of particular interest in SERS-like applications [10]. In this investigation we will study the dependence of UV plasmon resonances and hot spots of Rh NCs dimers on their geometry, shape, and also on electromagnetic parameters of the incident radiation like angle of incidence (AOI) and polarization when they are on substrates.

ACKNOWLEDGMENT

This research has been supported by MICINN (Spanish Ministry of Science and Innovation, project FIS2013-45854-P). Research was sponsored by the Army Research Laboratory and was accomplished under Cooperative Agreement Number W911NF-17-2-0023. Y. G. wants to thank the University of Cantabria for her FPU grant.

REFERENCES

1. Jeffrey N Anker, W Paige Hall, Olga Lyandres, Nilam C Shah, Jing Zhao, and Richard P Van Duyne. Biosensing with plasmonic nanosensors. *Nature materials*, 7(6):442–453, 2008.
2. Kadir Aslan, Joseph R. Lakowicz, and Chris D. Geddes. Plasmon light scattering in biology and medicine: new sensing approaches, visions and perspectives. *Current Opinion in Chemical Biology*, 9(5):538–544, oct 2005.
3. Chao Zhang, Hangqi Zhao, Linan Zhou, Andrea E. Schlather, Liangliang Dong, Michael J. McClain, Dayne F. Swearer, Peter Nordlander, and Naomi J. Halas. AlPd Nanodisk Heterodimers as AntennaReactor Photocatalysts. *Nano Letters*, 16(10):6677–6682, oct 2016.
4. J. M. Sanz, D. Ortiz, R. Alcaraz de la Osa, J. M. Saiz, F. González, a. S. Brown, M. Losurdo, H. O. Everitt, and F. Moreno. UV Plasmonic Behavior of Various Metal Nanoparticles in the Near- and Far-Field Regimes: Geometry and Substrate Effects. *The Journal of Physical Chemistry C*, 117(38):19606–19615, sep 2013.
5. Mark W. Knight, Nicholas S. King, Lifei Liu, Henry O. Everitt, Peter Nordlander, and Naomi J. Halas. Aluminum for plasmonics. *ACS Nano*, 8(1):834–840, 2014.
6. Florian Sterl, Nikolai Strohfeldt, Ramon Walter, Ronald Griessen, Andreas Tittl, and Harald Giessen. Magnesium as Novel Material for Active Plasmonics in the Visible Wavelength Range. *Nano Letters*, 15(12):7949–7955, dec 2015.
7. Anne M Watson, Xiao Zhang, Rodrigo Alcaraz de la Osa, Juan Marcos Sanz, Francisco González, Fernando Moreno, Gleb Finkelstein, Jie Liu, and Henry O Everitt. Rhodium nanoparticles for ultraviolet plasmonics. *Nano letters*, 15(2):1095–100, feb 2015.
8. Xiao Zhang, Pan Li, Ángela Barreda, Yael Gutiérrez, Francisco González, Fernando Moreno, Henry O. Everitt, and Jie Liu. Size-tunable rhodium nanostructures for wavelength-tunable ultraviolet plasmonics. *Nanoscale Horiz.*, 1(1):75–80, 2016.
9. R. Alcaraz de la Osa, J. M. Sanz, a. I. Barreda, J. M. Saiz, F. González, H. O. Everitt, and F. Moreno. Rhodium Tripod Stars for UV Plasmonics. *The Journal of Physical Chemistry C*, 119(22):150519105943006, jun 2015.
10. Bhavya Sharma, Renee R. Frontiera, Anne-Isabelle Henry, Emilie Ringe, and Richard P. Van Duyne. SERS: Materials, applications, and the future. *Materials Today*, 15(1-2):16–25, 2012.

Integrated III-V Photonic Crystal – Si waveguide platform with tailored Optomechanical coupling

Victor TSVIRKUN[1], Alessandro SURRENTE[1], Fabrice RAINERI[1,2], Grégoire BEAUDOIN[1], Isabelle ROBERT-PHILIP[1], Rémy BRAIVE[1,2*]

[1] Centre de Nanosciences et de Nanotechnologies, CNRS, Univ. Paris-Sud, Université Paris-Saclay, C2N Marcoussis, 91460 Marcoussis, France

[2] Université Paris Diderot, Sorbonne Paris Cité, 75207 Paris Cedex 13, France

[*]corresponding author: remy.braive@c2n.upsaclay.fr

Abstract- The optomechanical response of a heterogeneously integrated two-dimensional photonic crystal defect cavities on top of silicon-on-insulator waveguides is investigated and evidences an optomechanical coupling involving both dispersive and dissipative mechanisms. By controlling the optical coupling between the constituting elements, we were able to vary and understand the relative strength of these couplings. This scalable platform allows for unprecedented control on the optomechanical coupling mechanisms, with a potential benefit in cooling experiments, and for optomechanical circuits for optomechanically-driven signal-processing applications.

Optomechanical systems, in which the vibrations of a mechanical resonator are coupled to an electromagnetic radiation, have permitted the investigation of a wealth of novel physical effects. Typically for the most of these systems, optomechanical coupling originates from a dispersive dependence of the nanocavity resonance frequency on its geometry, which is modulated by mechanical motion. Dissipative optomechanical coupling consists in the modulation of the lifetime of the cavity photons through the motion of a mechanical oscillator. Very recently, it has been demonstrated that this effect is observed in a wide variety of devices [1-2]. Dissipative couplings may significantly enhance the detection sensitivity in optomechanically-based sensing schemes [3] and open new possibilities in optomechanical control with systems featuring both types of coupling mechanisms [4], where a tailored coupling strength is highly desired.

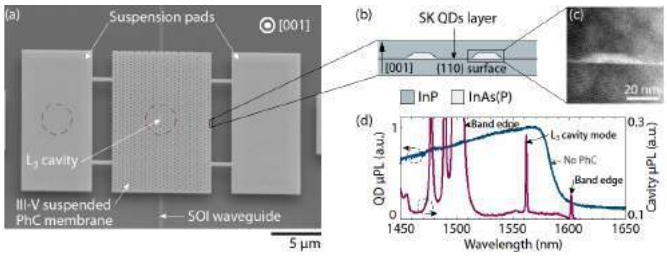

Figure 1. (a) S.E.M. picture of the photonic crystal membrane with an L3 cavity in the center above a Silicon waveguide. Inside the membrane, InAs(P) Stranski-Krastanov Quantum Dots (SK-QD) have been incorporated (b) in the InP membrane. A T.E.M. image is shown in (c). The emission spectrum of these QD is represented in blue (Fig. 1d) and the spectrum of the L3 cavity is in purple.

To fully exploit these phenomena in realistic devices or circuits, the integration of optomechanical resonators on a standard semiconductor platform is required. Here, we propose a novel approach to heterogeneously integrate arrays of two-dimensional photonic crystal defect cavities on top of silicon-on-insulator waveguides (Fig 1a). Added to that, quantum dots (QD) are incorporated in the middle of the III-V photonic crystal membrane with an emission spectrum around 1.55 μm (Fig 1b-d).

We are able to extract the dissipative and dispersive contributions of the optomechanical coupling of these devices. Tailoring of different contributions was demonstrated using external mean or integrated controls on the geometry of the optical access channel to the nanocavity

REFERENCES

1. M.Li et al, "Reactive Cavity Optical Force on Microdisk-Coupled Nanomechanical Beam Waveguides", *Physical Review Letters*, 103, 223901 (2009)
2. M. Wu et al, "Dissipative and Dispersive Optomechanics in a Nanocavity Torque Sensor", *Physical Review X*, vol. 4, pp. 021052, 2014
3. S. Forster et al, "Cavity Optomechanical magnetometer", *Physical Review Letter*, 108 120801 (2012)
4. T. Weiss et al, "Quantum limits of laser cooling in dispersively and dissipatively coupled optomechanical systems", *Physical Review A*, 88, 023850 (2013)
5. V. Tsvirkun et al, "Integrated III-V Photonic Crystal – Si waveguide platform with tailored optomechanical coupling", *Scientific Report*, 5, 16526 (2015)
6. V. Tsvirkun et al, "External control of dissipative coupling in heterogeneously integrated photonic crystal – SOI waveguide optomechanical system", *Photonics*, 3, 52 (2016)

Broadband polarization-independent antireflection coatings for solar cells from Mie resonators in silicon metasurfaces

Xiaoou Mao[1,2*], Michael Cada[1] and Eftymios Kallos[2]
[1]Dalhousie University, Canada
[2]Metamaterial Technologies Inc., Canada
[*]corresponding author: xz513853@dal.ca

Abstract- Mie-type leaky mode resonances supported by Semiconductor nanowires (NWs) can produce an antireflective response for certain polarization and wavelengths of light. This paper presents the design and simulations of 3D silicon nano pillars as Mie resonators canceling reflection from a silicon substrate, which offers a broadband (400-600nm) near unity transmission and an average reflectivity in the visible range (400-800nm) as low as 2.2% under unpolarized illumination. The results are of interest to the solar cell community.

I. INTRODUCTION

Reflection is an essential factor limiting solar cell efficiencies. It is especially important for materials with high refractive index like silicon, which is broadly used as an absorption material in solar cells. The subwavelength scale of a metamaterial unit cell makes them a great candidate as a functional light management component for ultra-thin solar cells. Metamaterials are normally constructed from resonant metallic nanostructures and many efforts have been made in design metallic metasurfaces for light management purposes, which suffer from intrinsic loss of metal in the operating wavelength of solar cells. In recent years, researchers have proved semiconductor and dielectric nanostructures can also realize similar optical functionalities based on optical resonances [1], which naturally avoid the loss from metallic materials.

This paper presents the design and simulation of 3D silicon nano pillars as Mie resonators canceling reflection from silicon substrate, which offers a broadband (400-600nm) near unity transmission and an average reflectivity in the visible range (400-800nm) as low as 2.2% under unpolarized illumination.

II. DESIGN AND SIMULATION

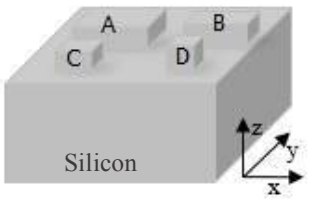

Figure 1 Unit cell of designed structure. The four pillars with different size atop the silicon substrate are marked as ABCD.

Semiconductor nanowires (NWs), especially silicon NWs, support Mie-type leaky mode resonances and have been explored and demonstrated in recent years [2,3]. These resonances can produce an antireflective response for certain polarization and wavelengths of light, depending on their size and geometrical shape. Based on the same physical mechanism, a metasurface constructed by four 3D nanopillars with different widths on top of a semi-infinite silicon substrate has been simulated and optimized to act as a broadband antireflection layer for unpolarized light, such as sunlight.

Fig. 1 shows the unit cell of the investigated structure with four differently-sized parallelepiped pillars marked as A, B, C, D. The optimized thickness of the pillars is identical and fixed at 77nm.

To better understand how the pillar size affects the reflection from the structure, a simulation was first conducted using a structure with same sized nanopillars (see inset of Fig. 2(a)). Fig. 2(a) shows the simulated reflection spectra for pillar sizes of either 52 nm or 80 nm with normal incidence of unpolarized light, and unit cell periodicity is 217 nm. Reflection of bared silicon is shown as reference. Different reflection minima can be observed for two different pillar sizes. The smaller pillar gives resonance and reflection minima at shorter wavelength and vice versa. The larger pillar size tends to affect the reflection more in the wavelength range(400-900nm) we are investigating.

Fig. 2(b) presents the reflection spectra for the nanostructure shown in Fig. 1 with different distribution of sizes (see inset and legend of Fig. 2(b)). The unit cell periodicity is 217 nm. We observe a broadband (400-600 nm) of near-zero reflectivity from the simulated reflection spectra for several different carefully designed size distribution of the silicon nanopillars. In addition, a tradeoff of reflection at shorter and longer wavelength range can be seen in Fig. 2(b) by only adjusting one of the pillar's size.

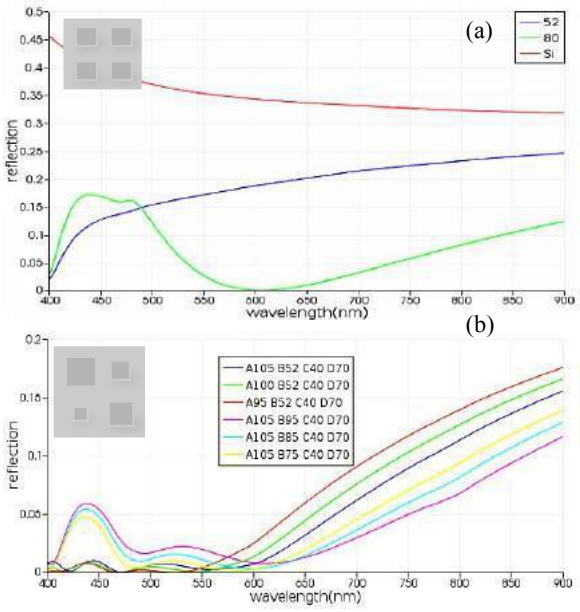

Figure 2. (a) Simulated reflection from the structure shown in the inset for two different pillar sizes 52nm(blue) and 80nm(green). Reflection of bared silicon is shown as reference(red). The unit cell periodicity is 217 nm. (b) Reflection spectra of structure in Fig.1 with four pillars with different width. Designed pillar sizes are shown in the legend with corresponded location ABCD as shown in Fig.1. The unit cell periodicity is 217nm. Insets are the view of the structure

III. CONCLUSIONS

In conclusion, we showed simulations of a broadband polarization-independent antireflection coating by carefully designed silicon nanopillars on silicon substrate (Fig. 1). The goal is to reduce the reflection of light for solar cells. The average reflection in the visible range (400-800nm) of the proposed silicon-patterned metasurfaces could reach as low as 2.2%. At the same time, from 400nm to 600nm, which is in the peak solar energy wavelength range, a near unity transmission is observed.

Acknowledgements, the author acknowledge support from CREATE ASPIRE, Mitacs Accelerate and Metamaterial Technologies Inc.

IV. REFERENCES

1. Brongersma, M. L., Cui, Y. & Fan, S., "Light management for photovoltaics using high-index nanostructures," *Nat. Mater*, Vol. 13, 452–460, 2014.
2. Cao, L. et al. "Engineering light absorption in semiconductor nanowire devices," *Nat. Mater*, Vol. 8, 643–647, 2009.

3. Spinelli, P., Verschuuren, M. a & Polman, a., “Broadband omnidirectional antireflection coating based on subwavelength surface Mie resonators,” *Nat. Commun,* 3, 692, 2012.

Hybrid Chiral Plasmonic Structures for Sensing

A. Karimullah,[1] M. Kadodwala[1]

[1]School of Chemistry, Joseph Black Building, University of Glasgow, G12 8QQ, Glasgow, UK

[*]corresponding author: Affar.Karimullah@glasgow.ac.uk

Abstract- Our work on sensing with chiral plasmonic systems has led us to develop new hybrid structures that display unique optical properties such as large optical rotation and plasmonic induced transparency. The optical properties are dependent on the strong coupling between individual components of the structures and are used to develop new sensing paradigms for biomolecular structure and surface orientation not perceivable by classical spectroscopic techniques. Here in we will describe the unique high-throughput fabrication method of these structures, their optical properties and their applications to chiral plasmonic sensing.

Chiral Plasmonic sensing utilizes superchiral near fields generated by chiral nanostructures to sense asymmetry in material.[1] Such materials are predominantly biomolecules such as proteins that have an inherent chiral structure due to the amino acid building blocks. However the chirality is further propagated in the higher order structure of the protein which are important in biochemical, pharmaceutical and medical research. In order to detect these changes, we require new forms of more sensitive plasmonic systems that are able to detect the increasingly complicated properties of biomolecules. We have developed new forms of plasmonic systems utilizing an inverse and solid structure of various patterns thus forming a hybrid structure. These effectively disposable plasmonic systems show enhanced optical properties and strong coupling effects between individual elements.[2] Tullius et al [1] have demonstrated the ability of such hybrid plasmonic systems to detect higher order structure of proteins and detect changes in the structure due to binding interactions. In this work we will describe properties of such hybrid structures and demonstrate that ability to sense biomolecular structure arises from the strong coupling effects present within the nanostructures.

Acknowledgements: We would like to acknowledge financial support from the Engineering and Physical Sciences Research Council (EPSRC EP/K034936/1), National Science Foundation (NSF grant CHE-1307021), JSPS Core to Core, and the Leverhulme Trust.

REFERENCES

1. R. Tullius, A. S. Karimullah, M. Rodier, B. Fitzpatrick, N. Gadegaard, L. D. Barron, V. M. Rotello, G. Cooke, A. Lapthorn, and M. Kadodwala, ""Superchiral" Spectroscopy: Detection of Protein Higher Order Hierarchical Structure with Chiral Plasmonic Nanostructures", *Journal of the Americal Chemical Society*. Vol. 137, 8380-8383, 2015.
2. A. S. Karimullah, C. Jack, R. Tullius, V. M. Rotello, G. Cooke, N. Gadegaard, L. D. Barron, and M. Kadodwala, "Disposable Plasmonics: Plastic Templated Plasmonic Metamaterials with Tunable Chirality", *Advanced Materials*, Vol. 27, 5610-5616, 2015.

Refractory Plasmonic Core-shell Nanostructures

Mugahid Ali[1]and Fumin Huang[2]
[1]EPSRC CDT, Photonic Integration and Advanced Data Storage, Queen's University Belfast & University of Glasgow, UK.
[2]Centre for Nanostructured Media, School of Mathematics and Physics, Queen's University Belfast, UK.
Corresponding authors: mali05@qu.ac.uk, f.huang@qub.ac.uk

Abstract- We present experimental and numerical investigation of core-shell plasmonic nanostructures composed of noble metals and refractory oxides. A variety of nanostructures of different geometries, including nanospheres, nanospheroids, and nanodisks, and a range of oxides, such as SiO_2, Al_2O_3, ZrO_2 and TiO_2, were investigated, which exhibit tunable optical properties across broad ranges of wavelengths and significantly enhanced chemical and thermal stability. The results provide important insight for developing effective optical nanodevices for applications in high-temperature environment.

Refractory plasmonic devices are highly in demand in applications in high-temperature environment, such as in data storage, solar thermophotovoltaics and nanoscale heat transfer systems [1]. Alternative plasmonic materials, such as refractory nitrides TiN and ZrN, are being under focused research due to their excellent thermal properties and competent optical properties comparable to that of gold. However, these materials have larger absorption cross-sections than those of noble metals. This generates much stronger self-heating effect which is undesirable in many applications where high degrees of thermal, optical, and morphological stabilities are crucial.

Here, we present the results of systematic investigations on core-shell nanostructures of various geometries composed of noble metals and a range of refractory oxides such as SiO_2, Al_2O_3, ZrO_2 and TiO_2. We compared the optical and thermal properties for spherical, spheroidal and disk-shape core-shell nanostructures where noble metals being either the core or the shell. All the nanostructures exhibit localized surface plasmon resonances (LSPR) that are tunable across a broad range of wavelengths by varying the geometry and materials of either the cores or shells. The results of a spherical Au nanoparticle coated with various thickness refractory oxides are shown in Fig.1(a), which demonstrate how the optical properties can be readily tuned with various coating materials and thicknesses. On the other hand, the refractory oxides coating can provide enhanced thermal stability due to their high melting points and low thermal expansion coefficients which help shielding the noble metal in the core. A thick coating layer of refractory oxides is found to increase the electric field intensity enhancement on the surface of metal core significantly (Fig.1b, c). This could cause stronger self-heating effect which is undesirable in some applications, for instance, in the heat assisted magnetic recording (HAMR) antennas. However, it can be very useful in other applications requiring high field enhancements such as in surface enhanced Raman scattering (SERS). We found that using oxides as cores and noble metals as shells can significantly reduce the optical absorption and mitigate the self-heating effect, which in addition is strongly

related to the size and the aspect ratio of the core-shell structure, thus opening multiple pathways for engineering the structures to minimize or optimize the heat generation for various applications.

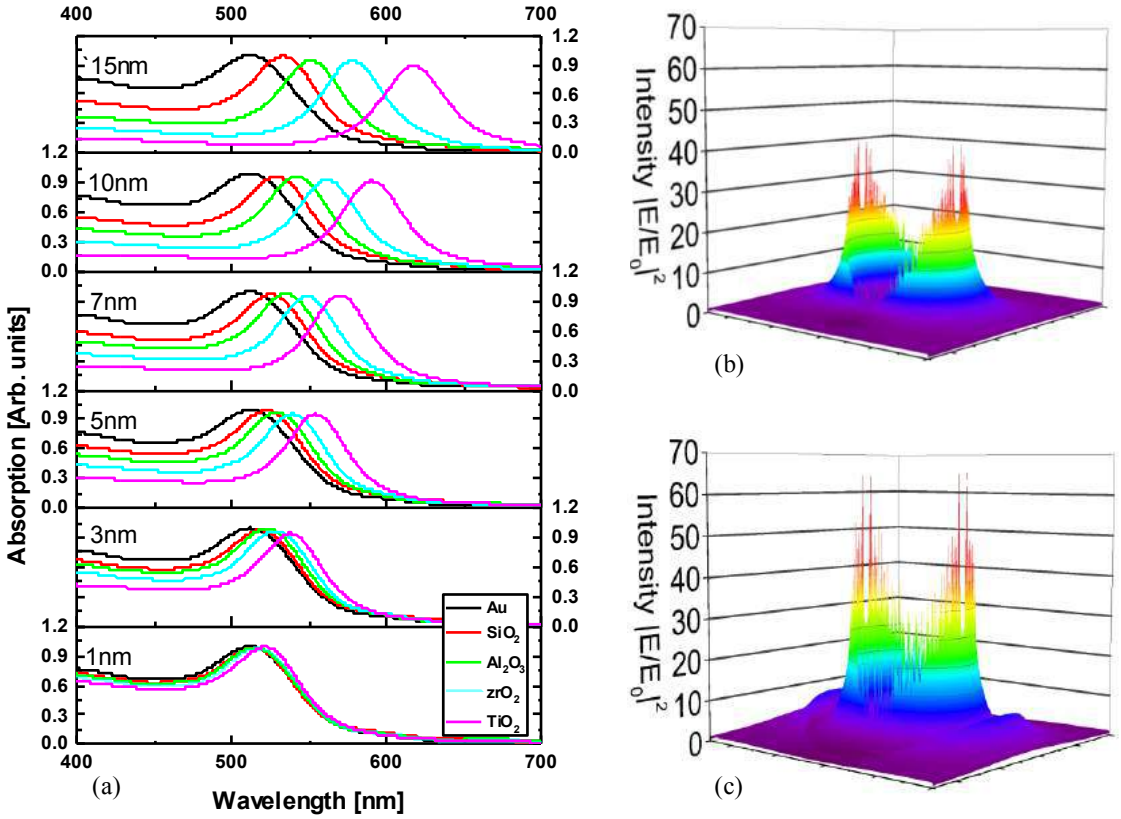

Figure 1 (a) Calculated plasmonic absorption spectra of a variety of core-shell structures (the black curves are for a bare Au sphere of 40 nm in diameter; coloured curves are for Au nanoparticles coated with various oxides), indicating the strong dependency of plasmonic resonance on the thickness and materials of shells. (b) and (c) are simulated field enhancements of (b) a bare spherical Au nanoparticle of 40 nm and (c) coated with 15 nm SiO_2 layer, respectively.

We also experimentally investigated the optical properties and thermal stability of the core-shell nanostructures, which were strongly impacted by the materials and structures. The results will provide important insight for developing effective optical nanodevices for applications in high-temperature environments.

Acknowledgements

This work was supported by EPSRC (UK) Centres for Doctor Training (CDT) grant EP/L015323/1.

REFERENCES

1. Guler, U., A. Boltasseva and V. M. Shalaev, "Refractory plasmonics", *Science* 344, 263, 2014.

Long-tailed superthermal light in coupled photonic crystal nanolasers

M. Marconi[1], J. Javaloyes[2*], P. Hamel[1], F. Raineri[1,3], J. A. Levenson[1] and A. M. Yacomotti[1]

[1] Centre de Nanosciences et de Nanotechnologies, CNRS, Univ. Paris-Sud, Univ. Paris Saclay, C2N-Orsay, 91405 Orsay Cedex France.

[2] Departament de Fisica, Universitat de les Illes Baleares, c/Valldemossa km 7.5, 07122 Mallorca, Spain

[3] Université Paris-Diderot, 75205 Paris Cedex13, France.

[*]corresponding author: mathias.marconi@u-psud.fr

Abstract- We generate long-tailed superthermal light on the non-lasing mode of a nanophotonic ensemble formed by two coupled nanolasers. An original and simple experimental technique is implemented in order to access the full probability distribution of output pulse energies. We interpret our results on the basis of a mean field theory and find, through an analogy with out-of-equilibrium thermodynamics, a new route for the generation of superthermal light statistics as a rapid cooling, quenching, of mode fluctuations.

In modern semiconductor optical cavities, non-trivial photon statistics may result from complex light-matter interaction at the nanoscale. As an example, superthermal fluctuations ($g^{(2)}(\tau = 0) > 2$) have been observed in single mode micropillar cavities as a result of superradiant quantum dot emission [1], as well as polarization mode switching in two-orthogonal polarization devices [2]. In the latter, mode competition has been identified as the main ingredient leading to non-gaussian (bimodal) probability distributions and hence superthermal light.

Evanescently coupled micro/nano lasers gather particular interest in the context of multimode nonlinear active cavity arrays. The possibility to engineer the coupling strength –both intercavity and intermode- has made possible the observation of nonlinear bifurcations such as spontaneous symmetry breaking between cavities [3] or asymmetric scattering from the blue (symmetric (S), in-phase) mode to the red (anti-symmetric (AS), out-of-phase) mode [4]. The following question arises: to what extent non-equilibrium dynamics and mode interaction in coupled nanolasers enables controlling the full photon statistics, i.e. beyond low order moments ? In this work we investigate a route for the generation of superthermal light with heavy-tailed distributions on the non-lasing mode of our coupled nanolasers systems.

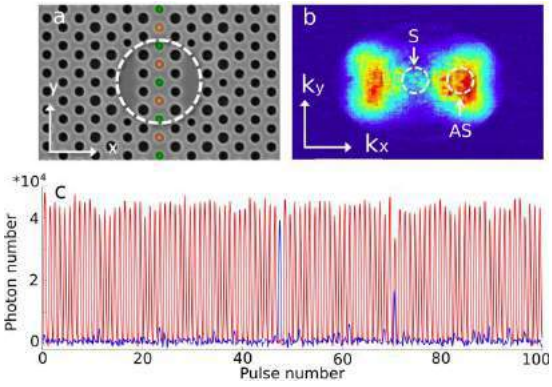

Figure 1: a) Coupled PhC nanolasers with barrier engineering (colored holes). Dashed circle: pump spot. b) Fourier plane. c) Sequence of output pulses on AS (red) and S (blue) modes.

Our experiment consists in two evanescently coupled photonic crystal (PhC) nanolasers etched in a semiconductor (InP) semiconductor free-standing membrane containing InGaAs/InGaAsP quantum wells (Fig 1a).

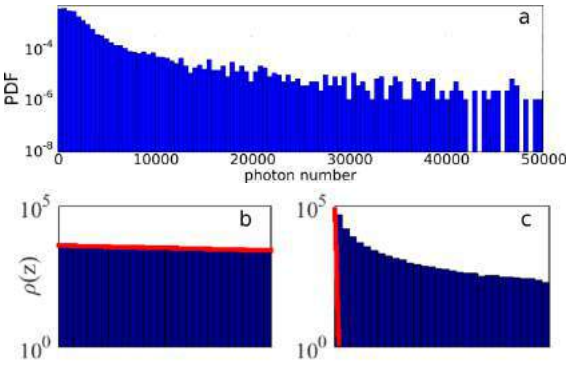

Figure 2: a) Histogram obtained from the n-time series on mode S of Fig. 2. b,c) Numerical density of photons on mode B before (b) and at the pulse maximum intensity (c). Red line: Fokker-Planck equation equilibrium distribution.

The sample is optically pumped with a pulsed laser (λ = 800 nm, 100 kHz repetition rate, 100 ps duration) leading each time to the optical emission of a single fluctuation. The AS mode, having lower optical losses, is lasing at threshold. The emission is collected with a N.A. = 0.95 microscope objective and its back focal plane is imaged through a lens to obtain the far-field pattern. In order to detect the light output, from each mode we use two single mode fibers as pinholes to simultaneously select a small region around k = 0 (mode S) and shifted along the x direction for the AS mode (Fig. 1b). Signals are sent to two Avalanche Photodiodes that deliver photocurrents proportional to the pulse energy. Typical n-time series contain 10^4 pulses. Fig. 1c shows a segment of two simultaneous n-time series showing both the AS and the S mode signals for $P = 6*P_{th}$. These n-time series allow us to obtain photon number PDFs. While the AS mode shows poissonian fluctuations, the S mode develops superthermal ($g^{(2)}(0) = 3.5$) fluctuation. This value obtained from the n-time series is confirmed by a Hanbury Brown and Twiss measurement. More importantly the superthermal statistics is associated to a heavy-tailed distribution as apparent in Fig. 2a.

We provide a complete theoretical interpretation for the appearance of the heavy tail in the photon number distributions from an analogy with out-of-equilibrium rapid cooling (quenching). In this framework each output pulse is a different stochastic realization. which can is eventually formalized by solving the associated Fokker-Planck equation [5]. We show that passing through the lasing threshold corresponds to an abrupt decrease of the contribution of spontaneous emission –that plays the role of an effective temperature- during which the statistics of the trajectories in phase space are dominated by nonlinear transport. Tuning the duration of this out-of-equilibrium quenching phase allows to obtain long-tailed distributions (Fig 2b,c).

Besides a surprising analogy with our experiment, we show that this out-of-equilibrium transformation, in which nonlinear transport dominates over diffusion fully explains the occurrence of heavy-tailed superthermal distributions on the non-lasing mode of our coupled nanolasers. We then open the road to an intuitive way to generate photon extra-bunching and, more generally, to mold the statistics of emitted photons in a nanolaser device.

REFERENCES

1. Janhke F. et al., “Giant photon bunching superradiant pulse emission and excitation trapping in quantum- dot nanolasers”, *Nat. Comm.*, Vol. 7, 11540, 2016.
2. Leymann H. A. M et al., “Intensity fluctuations in bimodal micropillar lasers enhanced by quantum-dot gain competition”, *PRA*, Vol.87, 053819, 1986.
3. Hamel P. et al., “Spontaneous mirror-symmetry breaking in coupled photonic crystal nanoalsers”, *Nat. Phot.*, Vol. 9, 311-315, 2015.
4. Marconi M., “Asymmetric mode scattering in strongly coupled photonic crystal nanolasers”, *Opt. Lett.*, Vol. 41, 5628-5631, 2016.
5. Arecchi T. et al., “Properties of laser radiation during a transient buildup”, *PRA*, Vol. 3, 1108-1124, 2008.

Extreme nonlinear optics from graphene plasmons

J. D. Cox[1]* and F. J. García de Abajo[1,2]

[1]ICFO-Institut de Ciencies Fotoniques, The Barcelona Institute of Science and Technology, Castelldefels, 08860 Barcelona, Spain

[2]ICREA-Institució Catalana de Recerca i Estudis Avançats, Passeig Lluís Companys 23, 08010 Barcelona, Spain

*corresponding author: joel.cox@icfo.eu

Abstract-The large incident electric field intensities required to achieve extreme nonlinear optical phenomena can be realized through plasmonic near-field enhancement in doped graphene nanostructures. Here we show that the combination of strong local fields and a pronounced intrinsic nonlinearity can result in efficient broadband high-harmonic generation and a dramatic modulation in the optical absorption associated with plasmon resonances in graphene, paving the way for compact ultraviolet and ultrafast light sources and all-optical switching in nanophotonic devices.

The remarkably high intrinsic optical nonlinearity of graphene can be pushed even further when the frequency of impinging light matches that of its long-lived and electrically-tunable plasmon resonances [1,2]. Through their enhanced absorption cross-sections, plasmons in doped graphene provide the means to concentrate electromagnetic energy on extreme subwavelength scales, thereby generating enormous local electric fields. Here we explore extreme nonlinear optical phenomena that are enabled by plasmonic enhancement in graphene. In particular, we investigate (1) high-harmonic generation (HHG) and (2) transient absorption arising from the elevated electronic temperature in the carbon layer upon ultrafast optical pumping. Our studies of these plasmon-assisted nonlinear effects are based on rigorous time-domain simulations, wherein graphene nanoribbons and nanoislands are described atomistically, adopting a tight-binding description of their electronic states combined with the random-phase approximation [3].

HHG usually necessitates cumbersome laser amplification schemes to reach the enormous incident electric field intensities it requires. In the case of doped, nanostructured graphene, our results indicate that high harmonics can be emitted with unprecedentedly large intensity by tuning the incident light to localized plasmon resonances of ribbons and finite islands, which in turn can be modulated via electrical gating. In contrast to HHG in atomic systems, we observe no cutoff in harmonic order, while a comparison of graphene plasmon-assisted HHG to recent measurements in solid-state systems suggests that the HHG yields from bulk semiconductors can be produced by graphene plasmons using 3-4 orders of magnitude lower pulse fluence [4]. Our findings support the strong potential of nanostructured graphene as a robust, electrically-tunable platform for HHG.

In contrast to the instantaneous nonlinear response that is commonly explored in the graphene optics community, where input and output fields maintain relative coherences, a delayed nonlinearity also takes place as a consequence of the strong dependence of the graphene response on the temperature of its conduction electrons [1,5]. We demonstrate that strong transient modulation of the optical absorption associated with plasmonic excitations in graphene nanostructures can occur when electrons are optically pumped to an elevated temperature. We systematically investigate the effect of the transient chemical

potential and electron temperature on the absorption of (1) cw illumination, (2) individual ultrafast pulses, and in (3) pump-probe schemes, where a pump pulse is used to modulate the absorption of a delayed probe pulse. Our results indicate that plasmons in doped graphene nanostructures hold great promise for all-optical switching applications in nonlinear nanophotonic devices.

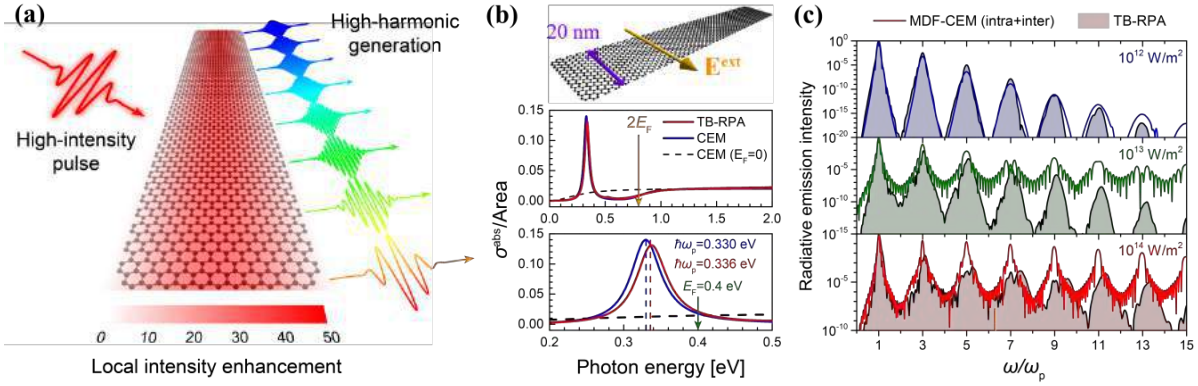

Figure 1. High-harmonic generation (HHG) assisted by graphene plasmons. (a) Schematic illustration of a doped graphene nanoribbon illuminated by an intense optical pulse that is resonant with the ribbon transverse dipole plasmon. The latter produces strong in-plane electric field intensity enhancement (see color scale) that boosts the generation of high-harmonics. (b) Absorption cross-section of a 20-nm wide armchair edge-terminated graphene nanoribbon doped to a Fermi energy E_F=0.4 eV, as predicted by atomistic tight-binding/random phase approximation (TB-RPA, red curves) and classical electrodynamic (CEM, local-RPA conductivity at 300 K, blue curves) simulations for transverse light polarization (see upper graphic). The prominent resonance feature corresponds to the transverse dipolar plasmon within the $2E_F$ optical gap. The dashed curve shows the classical simulation for the undoped ribbon. (c) Spectral decomposition of the light emission energy under illumination by a normally-incident pulse (100 fs FWHM duration, centered at the frequency ω_p of the ribbon plasmon), as calculated in the time-domain for three different pulse peak intensities (see legend) within the atomistic (TB-RPA, filled curves, $\hbar\omega_p$=0.336 eV) and massless Dirac fermion/classical electromagnetic (MDF-CEM, unfilled curves, $\hbar\omega_p$=0.330 eV) descriptions. Each curve is normalized to its own maximum value around the fundamental frequency.

REFERENCES

1. Hendry, E. et al., "Coherent nonlinear optical response of graphene," *Phys. Rev. Lett.*, Vol. 105, No. 9, 097401, 2010.
2. García de Abajo, F. J., "Graphene plasmonics: Challenges and opportunities," *ACS Photon.*, Vol. 1, No. 3, 135– 152, 2014.
3. Cox, J. D. and García de Abajo, F. J., "Electrically tunable nonlinear plasmonics in graphene nanoislands," *Nat. Commun.*, Vol. 5, 5725, 2014.
4. Cox, J. D., Marini, A. and García de Abajo, F. J., "Plasmon-assisted high-harmonic generation in graphene," *Nat. Commun.*, Vol. 8, 14380, 2017.
5. Jadidi, M. M. et al., "Nonlinear terahertz absorption of graphene plasmons," *Nano Lett.* Vol. 16, No. 4, 2734-2738, 2016.

Optical antennas – mode distributions and directionality

N. Verellen[1*], J. Li[1,2], A. Frolov[3], D. Vercruysse[1,2], D. Denkova[4], Maxim Shcherbakov[3], H. Paddubrouskaya[2], A. Fedyanin[3], V. V. Moshchalkov[2], and P. Van Dorpe[1,2]

[1]imec, Kapeldreef 75, Leuven, Belgium

[2]KU Leuven, Dept. of physics and astronomy, Leuven, Belgium

[3]Faculty of Physics, Lomonosov Moscow State University, Moscow 119991, Russia

[3]ARC Centre of Excellence for Nanoscale BioPhotonics (CNBP), Macquarie University, Sydney NSW, Australia

[*]corresponding author: niels.verellen@imec.be

Abstract- In recent years, nanotechnology and nanoscience have been expanding their toolbox dramatically. Metallic nanoantennas – also known as plasmonic resonators – can be considered as one of these novel tools providing an effective route to couple photons in and out of nanoscale volumes. Emerging as a promising alternative are all-dielectric resonant nanoantennas which demonstrate similar light concentration and manipulation capabilities yet benefiting from negligible Ohmic losses. The higher the level of control over the way an optical antenna interacts with light, the more effective this tool becomes and the further its applications will reach. Essential to this end is a detailed knowledge of such an antenna's supported modes and scattering characteristics. Especially in nanophotonics applications where every photon counts, one immediately benefits from directed photon routing for efficient photon collection.

We present a study of the modal field distribution in both plasmonic (i.e metallic) and all-dielectric rod-shaped nanoantennas. Using experimental near-field mapping in combination with finite-difference-time domain simulations, standing-wave TE and TM modes are revealed in these antennas operating at visible and near-infrared frequencies. [1-3]

Symmetry-breaking of these resonators allows the coupling of dipolar resonance modes with higher order (odd or even parity) modes. Interestingly, this effect gives rise to far field radiation patterns that can strongly deviate from the omni-directional dipole radiation. Reducing the rod-shaped antenna's symmetry into a V-shape allows the standing-wave modes observed in the near-field to generate highly directional radiation patterns. Additionally, the dielectric antenna even allows bi-directional color routing. We reveal the basic mechanisms behind this phenomena for both plasmonic [5-6] and dielectric V-antennas. [7]

The obtained insight in how directional emission and scattering are generated and how different modes come together to form far-field properties of a nanoantenna is indispensable to create new nanoscale optical devices for, e.g., sub-wavelength color routing, self-referenced directional sensing, metamaterials and flat optics.

Acknowledgements, the authors acknowledge the Methusalem funding by the Flemish Government and the F.W.O. (Flanders) for financial support.

REFERENCES

1. Denkova, D. et al., "Mapping Magnetic Near-Field Distributions of Plasmonic Nanoantennas", *ACS Nano* 7, 3168, 2013

2. Denkova, D. et al., “Lateral Magnetic Near-Field Imaging of Plasmonic Nanoantennas With Increasing Complexity”, *Small* 10(10), 1959–1966, 2014
3. Frolov, A. et al., “Near-field mapping of optical Fabry-Perot resonances in dielectric antennas
4. ”, *in preparation*, 2017
5. Vercruysse, D. et al. “Unidirectional Side Scattering of Light by a Single-Element Nanoantenna” *Nano Lett. 13* (8), 3843–3849, 2013
6. Vercruysse, D. et al. “Directional Fluorescence Emission by Individual V-Antennas Explained by Mode Expansion”, *ACS Nano 8*(8), 8232–8241, 2014
7. Li J. et al. “All-Dielectric Antenna Wavelength Router with Bidirectional Scattering of Visible Light” *Nano Letters*, *16* (7), pp 4396–4403, 2016

Optimizing the Growth of Strontium Molybdate Thin Films for Plasmonic and Nanophotonic Applications

Matthew P. Wells[1], Bin Zou[1], Brock Doiron[2], Andrei P. Mihai[1], Neil McN. Alford[1], Stefan A. Maier[2], & Peter K. Petrov[1*]

[1]Imperial College London, Department of Materials, Prince Consort Road, London SW7 2BP, UK

[2]Imperial College London, Department of Physics, Prince Consort Road, London SW7 2BP, UK

[*]corresponding author: p.petrov@imperial.ac.uk

Abstract- Strontium molybdate thin films have been studied by means of ellipsometry, XRD, and DC resistivity measurements in order to evaluate their potential use in the advancing field of plasmonics and nanophotonics. $SrMoO_3$ (SMO) thin films were grown by pulsed laser deposition on three types of substrate: $LaAlO_3$, MgO, and $SrTiO_3$. It is shown that $SrMoO_3$ exhibits tunable plasmonic behaviour at wavelengths above 600 nm with losses comparable to those of gold.

Plasmonic phenomena are expected to have a significant impact in applications such as nanoscale imaging, biological sensing, energy harvesting, and communication systems in the coming years. Traditionally, the research into plasmonics has been focused on the noble metals Au and Ag as a result of their high carrier concentrations in the near infrared[1]. However both materials are subject to excessive losses at optical frequencies[2], are incompatible with silicon-based electronics[1], and are unsuitable for high temperature applications[3], hence there arises a need for research into alternative plasmonic materials.

$SrMoO_3$ (SMO) is a compound with a perovskite-type crystal structure which has been shown previously to exhibit both metallic and Pauli paramagnetic properties. Furthermore, the bulk material shows temperature stability up to approximately 1000 K while thin films of SMO have been studied with a view to electrode applications as a result of their low room temperature resistivity. With a cubic lattice constant of 3.975 Å SMO is theoretically well-suited to growth on substrates such as $SrTiO_3$ (STO), MgO and $LaAlO_3$ (LAO), though its potential for plasmonic and nanophotonics applications has never previously been reported.

With such electronic properties in mind this article considers the potential for plasmonic and nanophotonics applications of $SrMoO_3$. We consider the optical, structural, and electrical properties of SMO thin films grown on substrates of STO, LAO and MgO with film thicknesses ranging from 50 - 200 nm. Having studied the effects of changes to the substrate temperature, laser energy, film thickness and deposition rate we observe that the ENZ crossover can be lowered to 600 nm, though this is should not be considered a lower limit. In particular, the optical properties of samples are shown to have strong dependency on the residual strain in the samples, controlled by both film thickness and deposition rate (Fig. 1). It was found that a higher ENZ frequency could be achieved by reducing the residual strain e.g. depositing thicker films at a lower deposition rate. In addition, it is noted that, as the ENZ frequency is increased, the optical losses present in SMO decrease (Fig. 2) and so compare favourably to those of gold and TiN.

Thus, SMO is a promising alternative material for plasmonics and nanophotonics applications operating in the visible to near infrared spectral regions.

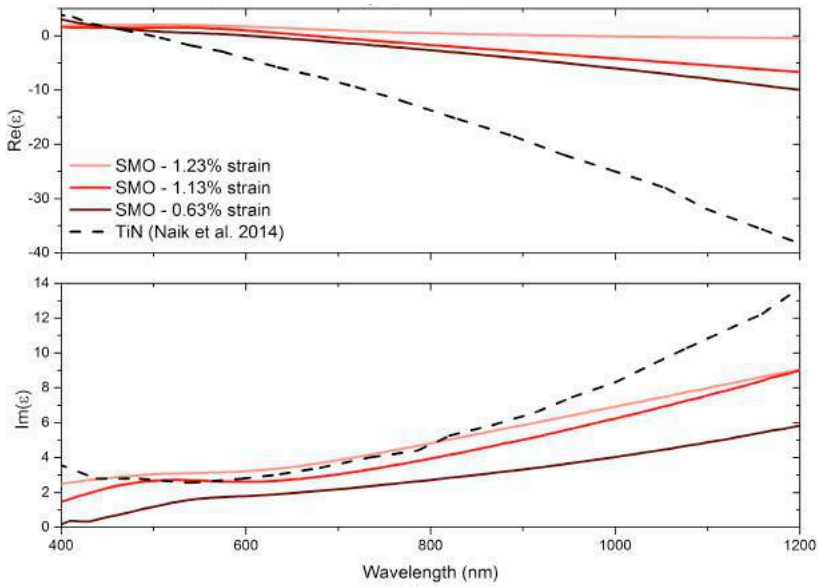

Figure 1. Dependence of $SrMoO_3$ optical properties on residual strain.

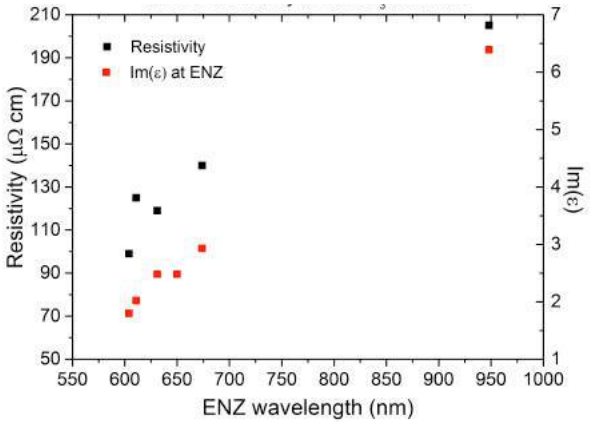

Figure 2. Relationship between ENZ frequency, optical losses and DC resistivity in Dependence of $SrMoO_3$ thin films.

Acknowledgements, This work was partly supported by Engineering and Physical Sciences Research Council (EPSRC), UK.

REFERENCES

1. Boltasseva, A. "Empowering plasmonics and metamaterials technology with new material platforms". *MRS Bull.* **39,** 461–468 (2014).
2. Johnson, P. B. & Christy, R. W. "Optical constants of the noble metals" *Phys. Rev. B* **6,** 4370–4379 (1972).
3. Braic, L. *et al.* "Optimizing strontium ruthenate thin films for near-infrared plasmonic applications" *Sci. Rep.* **5,** 9118 (2015).

Hot Carrier Extraction with Plasmonic Broadband Absorbers

Charlene Ng,*,†,‡ Jasper J. Cadusch,□ Svetlana Dligatch,§ Ann Roberts,□

Timothy J. Davis,□ Paul Mulvaney,□and Daniel E. Gomez*,†,‡,•

†Manufacturing, CSIRO, Private Bag 33, Clayton, Victoria 3168, Australia

‡Australian National Fabrication Facility, Melbourne Centre for Nanofabrication, Clayton Victoria 3168, Australia

□School of Physics and □Bio21 Institute & School of Chemistry, The University of Melbourne, Parkville, Victoria 3010, Australia §Manufacturing, CSIRO, PO Box 218, Lindfield New South Wales 2070, Australia

•RMIT University, Melbourne, Victoria 3000, Australia.

E-mail address: Daniel.Gomez@rmit.edu.au

Abstract- Hot charge carrier extraction from metallic nanostructures is a very promising approach for applications in photocatalysis, photovoltaics, and photo-detection. Here we demonstrate that a monolayer of Au nanoparticles can be assembled on a multi-stack layered configuration to achieve broadband, near-unity light absorption. We show that this enhanced light absorption leads to a 40-fold increase in the photon-to-electron conversion efficiency in photo-electrochemical cells. The measured data is interpreted with a model that enables us to establish that efficient hot carrier extraction is limited to spectral regions where (i) the photons have energies higher than the Schottky barrier at the gold-semiconductor junction and (ii) the absorption of light is localized on the metal nanoparticles.

It is expected that the rate of plasmonic hot charge carrier relaxation can be substantially increased under conditions where the metal nanostructures absorb nearly all incident photons across a broad spectral bandwidth [1,2]. Figure 1A shows the metal−semiconductor−nanoparticle structures, which consist of an optically thick metal film (200 nm) and a single layer of Au nanoparticles, separated by a thin 50 nm TiO_2 layer. These samples were made by means of sequential physical vapour deposition of materials.

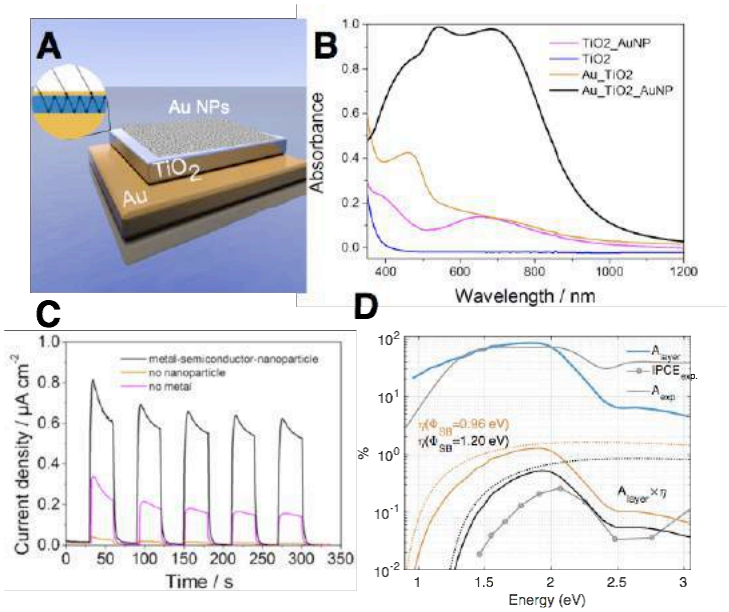

Figure 1: Plasmonic Perfect Absorber. A Diagram and SEM of the multi-stack structure. B Absorption spectra. C Photo-current vs time for different stacks. D Comparison of the measured IPCE (dots) to the derived model (black lines).

Figure 1B shows that for the multilayer stack (black line), the absorbance (measured *via* specular and diffuse transmission and reflectance) approaches 100% for some wavelengths and has a wide bandwidth. Figure 1C shows that the increased absorbance leads to increase photocurrent in photoelectrochemical cells made with these samples as photo-anodes. The efficiency (IPCE) also increases some 40x (when compared to non super-absorbing samples) and the IPCE spectrum can be well described by a model that we have developed [1].

Acknowledgements, This work was performed in part at the Melbourne Centre for Nanofabrication (MCN) in the Victorian Node of the Australian National Fabrication Facility (ANFF). C.N. was supported by an OCE Fellowship from CSIRO. D.E.G. acknowledges the ARC for support through a Future Fellowship (FT140100514). D.E.G. and T.J.D. acknowledge the ANFF for the MCN Technology Fellowships.

REFERENCES

1. C. Ng, J. Cadusch, S. Dligatch, A. Roberts, T. J. Davis, P. Mulvaney, and D. E. Gomez *ACS Nano* **10**, 4704 2016
2. C. Ng, L. W. Yap, A. Roberts, A. R. W. Cheng, and D. E. Gomez *Adv. Funct. Mater* 10.1002/adfm.201604080, 2016

Volume plasmon polariton modes in semiconductor hyperbolic metamaterials

D. Wei[1], C. Harris[2], and S. Law[1*]
[1]University of Delaware, USA
[2]Lincoln University, USA
[*]corresponding author: slaw@udel.edu

Abstract- This paper describes the first observation of volume plasmon polariton (VPP) modes in semiconductor hyperbolic metamaterials (HMMs). The metamaterials are grown using molecular beam epitaxy, after which gold gratings are fabricated on top. These gratings allow light to couple to the high-wavevector VPP modes in the HMM. Experimental data is compared to simulations, and a good agreement is found; the experimental VPP dispersion curve matches predictions. Potential applications of VPPs include subdiffraction focusing and waveguiding.

Hyperbolic metamaterials (HMMs) can be created using a superlattice of alternating subwavelength metal and dielectric layers. We have previously demonstrated HMMs grown with molecular beam epitaxy (MBE) using heavily doped InAs as the metallic component and undoped InAs as the dielectric component [1]. HMMs have a variety of unique properties, including the ability to support high-wavevector modes, sometimes called volume plasmon polaritons (VPPs). VPPs arise from the coupling of surface plasmon polaritons at every metal/dielectric interface. As more interfaces are added, more VPP modes are available. The high-wavevector of the VPP modes means that they can be harnessed for a variety of applications, including subdiffraction focusing and waveguiding. In this paper, we present data showing the successful excitation of VPP modes in semiconductor HMMs.

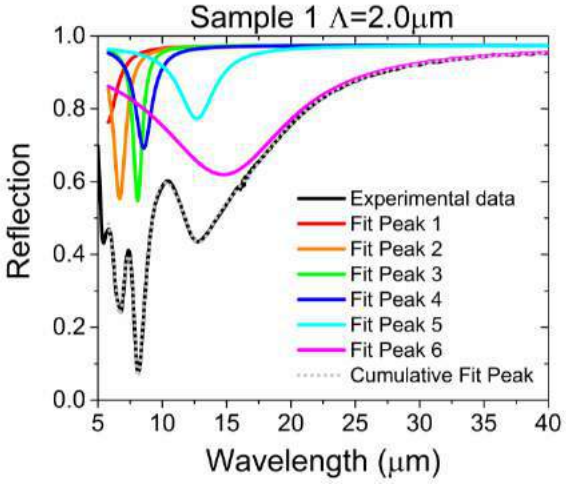

Figure 1. TM-polarized reflection as a function of wavelength for Sample 1 with grating period Λ=2.0μm. Black is experimental data, which is fit from the plasma wavelength (5.8μm) to 40μm using six Lorentzians (colored curves). The cumulative fit is shown as a gray dotted line.

HMMs were grown using MBE and standard photolithography and liftoff techniques used to fabricate gold gratings on Samples 1 and 3, as discussed previously in [1]. These samples had HMM onset wavelengths of 5.8μm and 9.5μm, respectively. The grating periods varied from Λ=1.8–4.6μm and the fill factor was held constant at 0.5. The gratings are necessary in order to match the wavevector of the incident light to the large wavevector of the VPP modes. A variety of gratings were fabricated to trace the dispersion of the VPPs. The samples were then placed in a Fourier transform infrared spectrometer and polarized reflection data was taken at a 10˚ incident angle. The data exhibited a variety of absorption features, an example of which is shown in Fig. 1. The data was then fitted using multiple Lorentzians to extract the positions of the resonances. COMSOL, a finite element modeling program, was used to simulate the optical properties of the samples, taking into account the precise shape of the band structure in the superlattice. In Fig. 2, the simulated TM reflectivity is shown in grayscale, while the extracted positions of the resonances are shown as colored dots. Different colors and shapes indicate different grating periods. Some resonances exhibit a constant wavelength, regardless of grating period; these are structural Fabry-Perot type resonances. However, for both samples, high-wavevector VPP modes can be observed. Sample 1 shows three distinct modes, while Sample 3 shows two. The resonant wavelength of these modes is strongly dependent on the wavevector in the material, as expected for VPP modes.

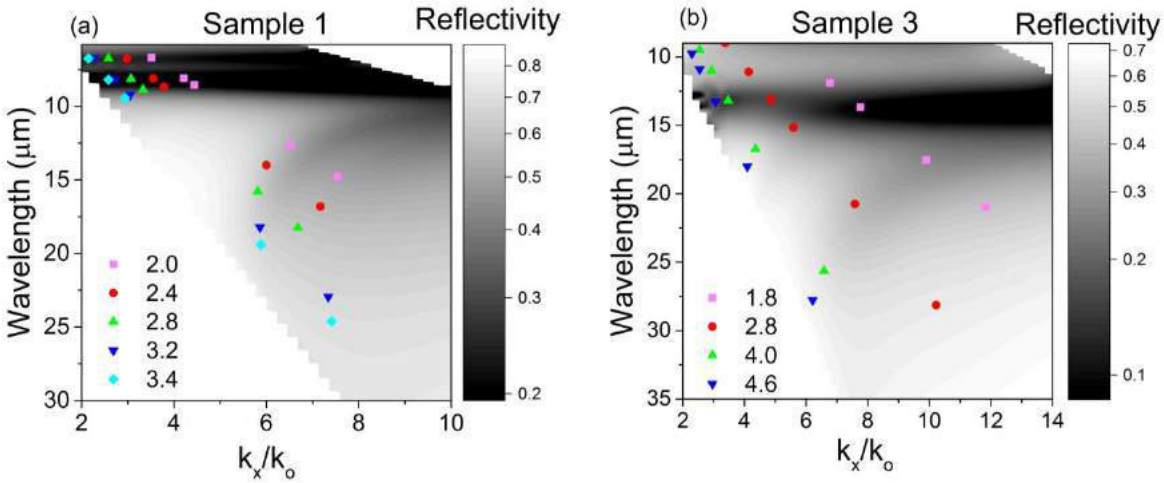

Figure 2. Simulation (grayscale) of reflection as a function of wavelength and wavevector in the HMM normalized to air for Sample 1 (a) and Sample 3 (b). Colored points indicate experimental position of VPP resonances for gratings with periods as indicated in the legend.

To our knowledge, this is the first successful excitation of VPP modes in a semiconductor HMM, and the first such experiment to be performed using a grating coupler. Now that the dispersion of these modes is understood, they can be leveraged for applications in infrared waveguiding, focusing, and imaging.

D. W. and S. L. acknowledge funding from the National Science Foundation, Division of Materials Research, under Award No. 1606673.

REFERENCES

[1] Wei, D., C. Harris, C. C. Bomberger, J. Zhang, J. Zide, and S. Law, “Single-material semiconductor hyperbolic metamaterials,” *Opt. Express*, Vol. 24, No. 8, 8735–8745, 2016.

Four-wave mixing of dispersive and solitary waves in polariton waveguiding systems.

A. Yulin [1*]

[1]ITMO University, 197101, Kronverksky pr. 49, St. Petersburg, Russian Federation

[*]corresponding author: alex.v.yulin@gmail.com

Abstract-Different regimes of resonant scattering of quasi-linear excitations on solitary waves in polariton systems are considered. One and two dimensional waveguides are studied by numerical simulations. It is shown that the efficient new frequencies generation can take place in these systems at low intensities of the pump. The resonance condition for the scattering is derived and compared against the results of the numerical modeling. The recoil of the scattering on dynamics of the solitary waves is also addressed.

Recently it was shown that solitary optical waves can form in exciton-polarton systems in weak coupling regime [1]. The advantage of these systems is that strong nonlinear effects can be observed at very low intensity of the pump. Apart from pure fundamental interest the systems under consideration can also find practical application for example for new frequency generation.

In this work we theoretically study the interactions between strong and weak waves in polariton systems described by the coupled equations for the optical E and exciton φ fields. In the dimensionless variables they have the form

$$\partial_t E - \partial_t E + \gamma_1 E + \sigma\varphi = f(x,t), \quad (1)$$

$$\partial_t \varphi + \gamma_2 \varphi + \alpha i|\varphi|^2\varphi + \sigma E = 0, \quad (2)$$

where γ_1 and γ_2 account for the losses in the photon and the exciton subsystems, σ is the coupling strength, α is the nonlinearity coefficient and $f(x,t)$ is the complex amplitude of the exciting optical field.

Choosing the appropriate shape and the intensity of the spatially localized driving force $f(x,t)$ it is possible to excite propagating solitary waves very much similar to the nonlinear pulses studied in [1]. In experiments the shape of the driving force is controlled by the shape of the optical pump and by the structure of the coupler. To study the interaction between the solitary and the dispersive wave we need the second low intensity component of the pump having a different frequency. The mixing between the solitary waves and the quasi-linear excitations results in the generation of new frequencies.

We would like to notice that the second source can be either resonant or non-resonant. In the latter case the excitation efficiency is very low and practically no propagating waves are excited. However the induces non-resonant field can interact with the solitary wave and this mixing couple a wave with detuned frequency into the wavegude. This process is illustrated in Fig. 1 showing the interaction of such a kind. In panel (a) the temporal evolution of the field is shown. The narrow intense line is the solitary wave which at $t \approx 200$ hits the area excited by the non-resonant part of the pump. At this moment generation of the propagating scattered wave starts. Panel (b) shows this process in spectral representation. The patterns corresponding to the soliton, to the non-resonant excitations and to the scattered wave are clearly visible. It is seen that the frequency and the wavenumber of the scattered wave are connected by the dispersion relation for the linear waves. We would like

to remark here that as it is seen in panel (a) of Fig.1 the trajectory of the solitary wave is changed because of the interaction with the non-resonant field. This means that the weak excitations can be used to control the parameters of the solitons in polariton systems.

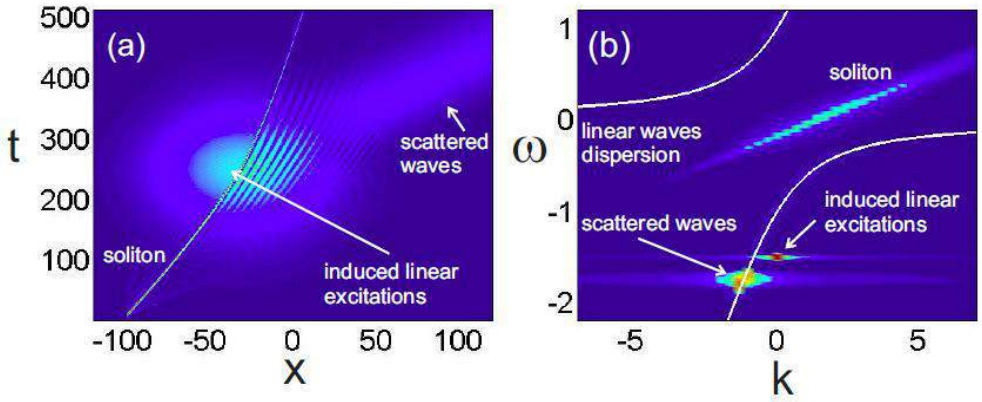

Figure 1. Panel (a) shows temporal evolution of the photon field in the system excited by a weak non-resonant pump and by a strong resonant pump leading to the formation of a solitary wave. The non-resonant pump is delayed by $t \approx 130$. The spectral representation of the field is shown in panel (b).

In one-dimensional case it is difficult to provide efficient scattering of the propagating dispersive waves on the solitons because either the scattering or the scattered wave experiences high losses. However in two-dimensional case this kind of scattering can be obtained.

Acknowledgements. This work was financially supported by the Government of the Russian Federation (Grant 074-U01) through ITMO Early Career Fellowship scheme.

REFERENCES

1. P.M. Walker, L. Tinkler, D.V. Skryabin, A. Yulin, B. Royall, I. Farrer, D.A. Ritchie, M.S. Skolnick and D.N. Krizhanovskii, "Ultra-low-power hybrid light–matter solitons", *Nature Comm*., 6, Article number: 317, 2015

Chemical modification of plasmonic nanostructures for biosensing.

S. Mackowski[1,2], **J. Niedziolka-Jonsson**[2,3*]

[1]Institute of Physics, Faculty of Physics, Astronomy and Informatics, Nicolaus Copernicus University, Grudziadzka 5, 87-100 Torun, Poland

[2]Baltic Institute of Technology Baltech, Al. Zwyciestwa 96/98, Gdynia, Poland

[3]Institute of Physical Chemistry, Polish Academy of Sciences, Kasprzaka 44/52, 01-224 Warsaw, Poland

[*]corresponding author: jniedziolka@ichf.edu.pl

Abstract-The key point in constructing biosensors based on metallic nanostructures concerns proper modification of their surfaces with defined (bio)receptors. This important tasks involves not only reproducible synthesis of homogenous nanostructures, but also establishing reliable methods for functionalization of the nanostructures that would enable efficient exploitation of plasmonic interactions in such a hybrid system. In the presentation we describe several architectures where successful control of biosensor activity of metallic nanostructures has been demonstrated.

In this work we present several ways of modification of metallic nanostructures for applying them as optical biosensors. One example concerns immobilization of an antibody for the bacteriophage T7 on gold nanospheres. The nanospheres were chosen to have the localised surface plasmon resonance in the visible range, i.e. at 520 nm, while the T7 bacteriophage was used as a model system of mammalian viruses belonging to the family of adenoviruses. In the presence of the target virus, which forms an immunocomplex with the antibody, the nanospheres tend to agglomerate. The resulting shift of the plasmon absorption band can be easily be detected by eye as the sample suspension changes its colour. The efficiency of this effect scales with the virus concentrations. An alternative approach employs a biopolymer with selected functional groups instead of antibodies as the biorecognition element. These relatively simple modifications of the metal nanoparticle surfaces resulted in fast and sensitive immunotests with detection limits in the range of pM [1] or fM [2]. We also showed that properly modified metal particles can have reasonable selectivity against non-specific viruses, in this case the M13 bacteriophage.

Metallic nanowires, due to their ability to efficiently transport excitations, are also very suitable nanostructures to construct biosensors. Moreover, diameters of such nanowires, which are in the range of 100 nm, are small enough to exhibit plasmonic effects in the visible spectral range, while their lengths exceeding tens of micrometers make them visible with a standard optical microscope. We intend to discuss selected properties of silver nanowires synthesized using a wet-chemistry approach [3]. The surface of the nanowires is amenable to a large array of surface functionalisation techniques, for example using thiol reactions. In the experiment focused on attaching photosynthetic pigment-protein complexes to the nanowires we demonstrate strong enhancement of fluorescence of these complexes due to plasmonic interactions by combining advanced fluorescence microscopy techniques. This is the first observation of metal-enhanced fluorescence in such a bioconjugated hybrid nanostructure.

Acknowledgements, The research was partially financed by the National Science Centre Poland within OPUS grant no 2016/21/B/ST3/02276 and the project 2/DOT/2016 funded by the City of Gdynia, Poland.

REFERENCES

1. Lesniewski, A.; Łos, M., Jonsson-Niedziolka, M., Krajewska, A., Szot, K., Los, J. and Niedziolka-Jonsson, J., "Antibody modified gold nanoparticles for fast and selective, colorimetric T7 bacteriophage detection", *Bioconjugate Chem.*, Vol. 25, 644-648, 2014.
2. Kannan, P., Los, M., Los, J. and Niedziółka-Jönsson, J.," T7 bacteriophage induced change of gold nanoparticle morphology; Biopolymer capped gold nanoparticles as a versatile probe for sensitive plasmonic biosensor", *Analyst*, Vol. 139, No. 14, 3563 – 3571, 2014.
3. M. Olejnik, B. Krajnik, D. Kowalska, M. Twardowska, N. Czechowski, E. Hofmann, S. Mackowski, *Applied Physics Letters* **102**, 083703 (2013).

Lasing in dark and bright modes of a finite-sized plasmonic lattice

T. K. Hakala, H. T. Rekola, A. I. Väkeväinen*, J.-P. Martikainen, M. Nečada, A. J. Moilanen, and P. Törmä

COMP Centre of Excellence, Department of Applied Physics, Aalto University School of Science, FI-00076 Aalto, Finland

*corresponding author: aaro.vakevainen@aalto.fi

In the presentation, I will show our results on lasing in plasmonic nanoparticle arrays at visible wavelengths [1]. The most startling result is that the lasing action occurs simultaneously in two modes at different energies, namely the bright and dark modes of the plasmonic lattice. We have found an intriguing out-coupling mechanism through which the dark mode can radiate to the far field. The out-coupling mechanism is based on the finite size of the array and is explained with gradual built-up of dipole moments in nanoparticles towards the array edges.

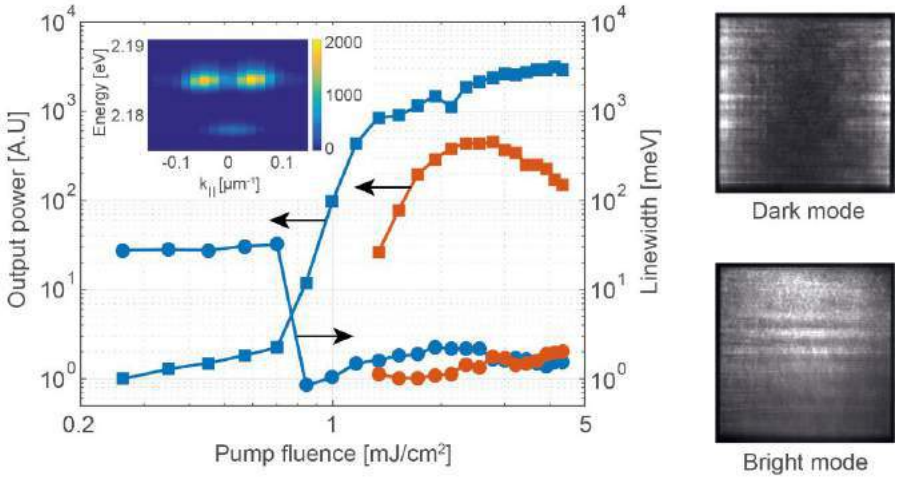

Figure 1. Left: Measured output power and linewidth of the dark mode (blue) and the bright mode (red) as a function of pump fluence. Inset: the momentum-energy distribution of the emission above threshold. Here, k_{II} refers to the in-plane momentum along one of the principal directions of the square lattice. Right: Real space distribution of the laser emission of the dark and bright mode, respectively.

We use an organic dye, Rhodamine 6G, as the gain material. The arrays consist of cylindrical silver nanoparticles with a diameter of 60 nm and a height of 30 nm, arranged in a square lattice. The periodicity is varied between 370 – 390 nm and the samples exhibit lasing in the wavelength range of 560 – 595 nm. We achieve a remarkably narrow linewidths of < 0.2 nm, beam divergence of 0.3° and a spatial coherence across the whole 100 x 100 μm^2 sized array. The results demonstrate a novel access to the dark mode and pave the way for studies of strong light-matter interaction and condensation phenomena in plasmonic lattices. In the presentation, I will also discuss recent advances related to this work.

[1] T. K. Hakala et al., *Nature Communications* **8**, 13687 (2017), doi:10.1038/ncomms13687.

Dyakonov plasmons in mid-IR

A. A. Bogdanov[1,3], **O. Takayama**[2], **E. Shkondin**[2], **M. E. Aryaee Panah**[2], **K. Golenitskii**[3], **P. Dmitriev**[1], **T. Repan**[2], **R. Malureanu**[2], **P. Belov**[1], **F. Jensen**[2], **A. V. Lavrinenko**[1,2]

[1] ITMO University, Russia
[2] Technical University of Denmark, Denmark
[3] Ioffe Institute, Russia
a.bogdanov@metalab.ifmo.ru

Abstract— In this work, we theoretically analyze Dyaknov surface plasmons (DPs) and bulk plasmon waves in CMOS compatible hyperbolic metamaterial slab. The slab consists of alternate layers of Si and aluminium-doped ZnO (AZO). We have shown that the dispersion and directivity of the analyzed waves can be efficiently tailored in the mid-IR by change of geometrical parameters of the structure and doping level of AZO layers.

Research on surface waves has intensified in the last decade due to their unique properties of surface sensitivity and field localization, which lead to improved nanophotonic devices for sensing, light-trapping, and imaging based on near-field techniques. Conventional Dyakonov surface waves supported by the interface between anisotropic and isotropic dielectrics could propagate in a very narrow range of directions because of weak optical anisotropy of natural materials [1, 2]. Using of artificial media it is possible to achieve strong anisotropy and, therefore, substantially increase the range of allowed propagation directions for Dyakonov waves [3]. In the extreme anisotropic cases, when the hyperbolic regime manifests [4], the Dyaknov surface waves transform into Dyakonov plasmons [5, 6, 7, 8]. Here, theoretically analyzed the spectrum of CMOS compatible photonic structure exhibiting properties of hyperbolic media in the mid-IR and supporting Dyaknov plasmons (DPs).

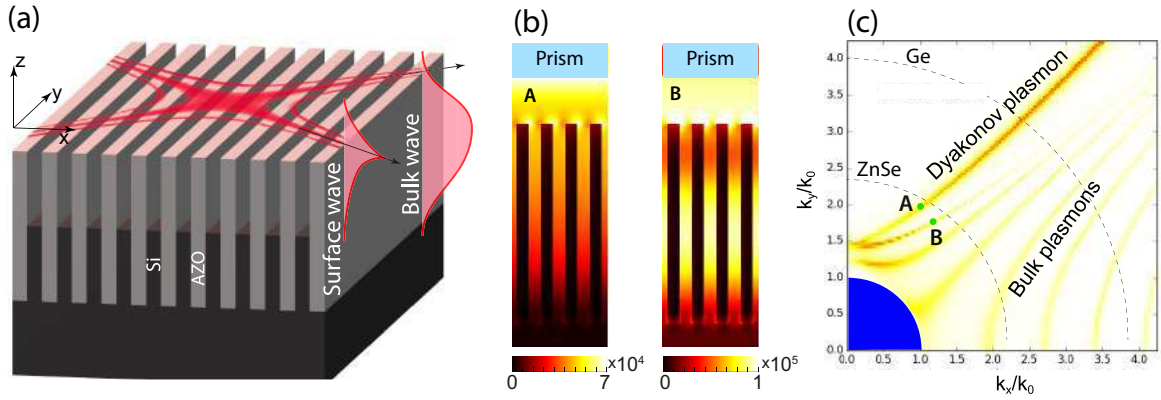

Figure 1: (a) Sketch of Si/AZO trench structure. (b) Electric field distribution ($|\mathbf{E}|$) for Dyaknov surface plasmon and fundamental bulk plasmon modes. (c) Simulation of the equal-frequency contours for Dyakonov and bulk plasmons at wavelength 3 μm.

The structure shown in Fig. 1(a) represents a high-aspect ratio (1:20) aluminium-doped ZnO (AZO) trenches partially filled by silicon. The thicknesses of AZO and silicon layers are the same and equal to 200 nm, the thickness of the slab is 4 μm.

The equal-frequency contours were found numerically by simulations of the reflectance spectra in the Otto geometry with high-index ZnSe prism. The reflectance map [Fig. 1(c)] plotted in the Fourier plane shows presence of several waveguide modes with hyperbolic dispersion. The analysis of the field profiles [see Fig. 1(b)] makes clear that these are surface (Dyakonov plasmons) and bulk plasmon modes. Dispersion and directivity of the Dyakonov plasmons and bulk plasmon modes can be effectively tailored by change of doping level of AZO, thickness of the layers and Si amount in the trenches.

In conclusion, we have proposed the CMOS compatible photonics structure supporting Dyakonov and bulk plasmon modes. Flexibility of the optical properties of the analyzed structures makes them very prospective for a plethora applications in photonics and biosensing. The obtained results provide useful guidelines for practical implementations of structures supporting Dyaknov plasmons in the mid-IR.

ACKNOWLEDGMENT

This work is supported by the Russian Science Foundation (Grant No. 15-12-20028).

REFERENCES

1. Dyakonov, M. I., "New type of electromagnetic wave propagating at an interface," *JETP*, Vol. 67, No. 4, 714–716, 1988.
2. Takayama, O., Crasovan, L., Artigas, D. and Torner, L., "Observation of Dyakonov Surface Waves," *Phys. Rev. Lett.*, Vol. 102, No. 4, 43903, 2009.
3. Miret, J. J., Zapata-Rodríguez, C. J., Jakšić, Z., Vuković, S. and Belić, M. R., "Substantial enlargement of angular existence range for Dyakonov-like surface waves at semi-infinite metal-dielectric superlattice," *J. Nanophotonics*, Vol. 6, No. 1, 63525, 2012.
4. Poddubny, A., Iorsh, I. V., Belov, P. and Kivshar, Yu. "Hyperbolic metamaterials," *Nat. Photonics*, Vol. 7, No. 12, 948957, 2013.
5. Jacob, Z. and Narimanov, E. E., "Optical hyperspace for plasmons: Dyakonov states in metamaterials," *Appl. Phys. Lett.*, Vol. 93, No. 22, 221109, 2008.
6. Vuković, S. M., Miret, J. J., Zapata-Rodríguez, C. J. and Jakšić, Z., "Oblique surface waves at an interface between a metaldielectric superlattice and an isotropic dielectric," *Phys. Scr.*, Vol. T149, 14041, 2012.
7. Zapata-Rodríguez, C. J., Miret, J. J., Vuković, S., and Belić, M. R., "Engineered surface waves in hyperbolic metamaterials," *Opt. Express*, Vol. 21, No. 16, 19113, 2013.
8. Takayama, O., Artigas, D. and Torner, L., "Practical dyakonons," *Opt. Lett.*, Vol. 37, No. 20, 4311, 2012.

Measuring Topological Orders and Band Inversion in a Photonic Peierls Chain with Non-Hermitian Parity-Time Symmetry.

Jun Jiang[1], **Weiwei Zhu**[1], **Hong Chen**[1], **and Jie Ren**[1,2*]
[1] School of Physics Science and Engineering, Tongji University, 200092 Shanghai, P. R. China
[2] Center for Phononics and Thermal Energy Science, The Institute for Advanced Study, Tongji
[*]corresponding author: xonics@tongji.edu.cn

Abstract--We demonstrate that the photonic Peierls chain, in which couplings alternate between electric and magnetic, has different topological phases with different boundaries. Furthermore, we measure the density of states, the symmetry type of the band-edge states and the topological winding number with the aid of experimentally measured dispersion and mode characteristics. These results are powerful evidences to demonstrate the topological phases trivial or not. This is the first time to measure the winding number since the proposal of topological metamaterials.

One-dimensional finite models with topological band structures represent a simple and versatile platform to demonstrate novel topological concepts. Here we present a periodic photonic system made of split ring resonator elements to study topological phenomena. The photonic Peierls chain, in which couplings alternate between electric and magnetic, has different topological phases with different boundaries. Furthermore, we measure the density of states, the symmetry type of the band-edge states and the topological winding number with the aid of experimentally measured dispersion and mode characteristics. These results, in turn, are powerful evidences to demonstrate the topological phases of states trivial or not. It is worth mentioning that, this is the first time to measure the winding number since the proposal of topological metamaterials.

Figures: .

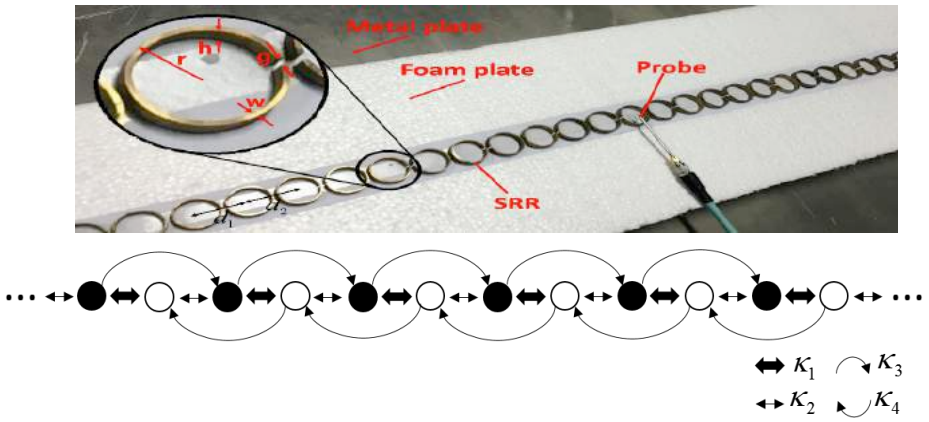

Fig. 1 The schematic illustration of the photonic Peierls chain. In this photonic Peierls chain, the couplings between the split ring resonators alternate between electric and magnetic (negative and positive). The appearance of the non-mutual next-nearest coupling causes the non-Hermitian nature with Parity-Time symmetry.

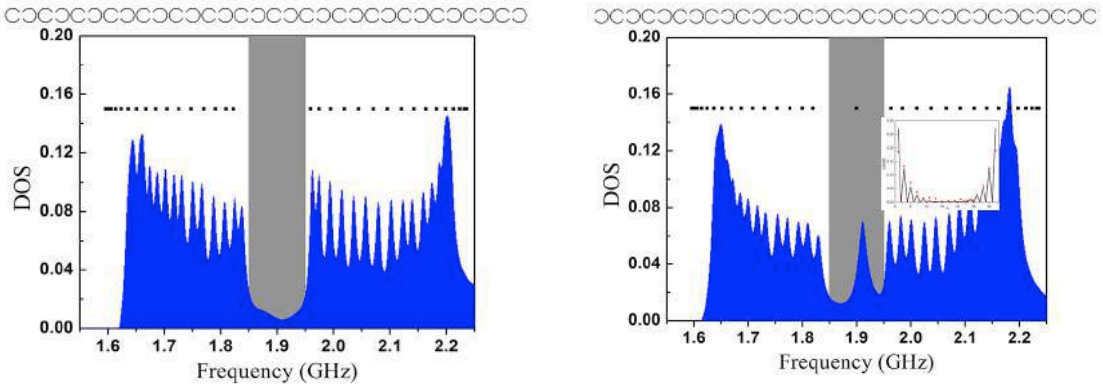

Fig. 2: The experimentally measured densities of states for different split ring reasonators with different boundaries, so as with different topologies. The topological non-trivial phase shows clearly a "zero-energy" state within the gap that corresponds to the topolgoical edge state.

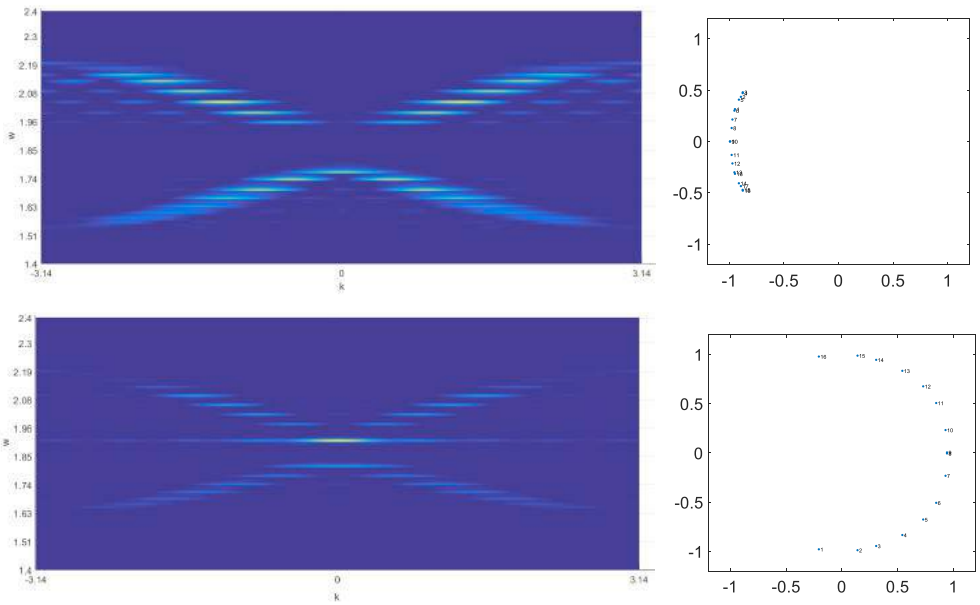

Fig. 3: The experimentally measured band dispersion and winding number for the photonic Peierls chains with two different boundaries. The lower two sub-figurs show clearly the "zero-energy" mode and the nonzero (unit 1) winding number for the topological non-trivial phase.

Acknowledgements: This work is supported by the National Basic Research Program of China (No. 2011CB922001), the NSFC (No. 11474220 and No. 11234010), the National Youth 1000 Talents Program in China, and the startup Grant (205020516074) at Tongji University.

REFERENCES

1. J. Jiang, W. Zhu, H. Chen, and J. Ren. "Measuring Topological Orders and Band Inversion in a Photonic Peierls Chain with Non-Hermitian Parity-Time Symmetry" *submitting*.

Fiber-chip surface grating couplers engineered by nanophotonic sub-wavelength grating metamaterials

Daniel Benedikovic[1,*], Carlos Alonso-Ramos[1], Pavel Cheben[2], Jens H. Schmid[2], Shurui Wang[2], Dan-Xia Xu[2], Boris Lamontagne[2], Jean Lapointe[2], Siegfried Janz[2], Robert Halir[3], Alejandro Ortega-Moñux[3], Juan-Gonzalo Wangüemert-Pérez[3], Inigo Molina-Fernández[3], Jean-Marc Fédéli[4], Milan Dado[5], Laurent Vivien[1]

[1]Centre de Nanosciences et de Nanotechnologies, CNRS, Univ. Paris-Sud, Université Paris-Saclay, C2N – Orsay, 91405 Orsay cedex, France

[2]National Research Council Canada, Information and Communication Technologies, Canada

[3]Dpto. de Ingeniería Comunicaciones, ETSI Telecomunicación, Universidad de Málaga, Spain

[4]CEA-LETI, Minatec, CEA-Grenoble, France

[5]University of Žilina, Department of Telecommunications and Multimedia, Slovakia

[*]daniel.benedikovic@u-psud.fr

Abstract-We present our recent advances in the development of high-efficiency fiber-chip surface grating couplers engineered by sub-wavelength grating nano-structuration. The intriguing technological concept of sub-wavelength grating refractive index engineering affords an additional design freedom in the development of high-quality optical coupling interfaces for sub-micrometric silicon-on-insulator technology. We present an overview of various demonstrations of high-efficiency surface grating couplers, particularly develop for applications in silicon photonics across the near-infrared wavelengths.

We have demonstrated by both designs and experiments a set of different fiber-chip surface grating couplers engineered by sub-wavelength grating metamaterials, requiring only a one step of lithography patterning and reactive ion etching, while providing the state-of-the-art fiber-chip coupling performance [1-7]. In particular, we have reported on apodized single-etch grating couplers with optimized thin film interference pattern. Those grating couplers are implemented in a conventional 220-nm-thick silicon photonics platform, with a coupling efficiency of up to -2.2 dB and -2.5 dB for wavelengths near 1.55 and 1.3 μm, respectively [3-5]. In addition, a sub-decibel fiber-chip coupling efficiency of -0.70 dB has been experimentally realized by utilizing the CMOS-compatible manufacturing via backside metallization [5].

We have also developed a flexible grating coupler concept with an ultra-high intrinsic directionality. The grating couplers can be fabricated by using only two, deep and shallow, etching levels, typically used in silicon photonic foundries [6, 7]. This coupling structure obviates the need of using typically complex fabrication processes such as high-index overlays, customized etch depths, and bottom mirrors. In particular, we have shown that the blazing effect can directly be implemented in any conventionally used silicon-on-insulator substrates, with a negligible dependence on the thickness of the BOX layer. We reported an experimental coupling efficiency of -1.3 dB near 1.55 μm in a standard 220-nm-thick silicon platform [7].

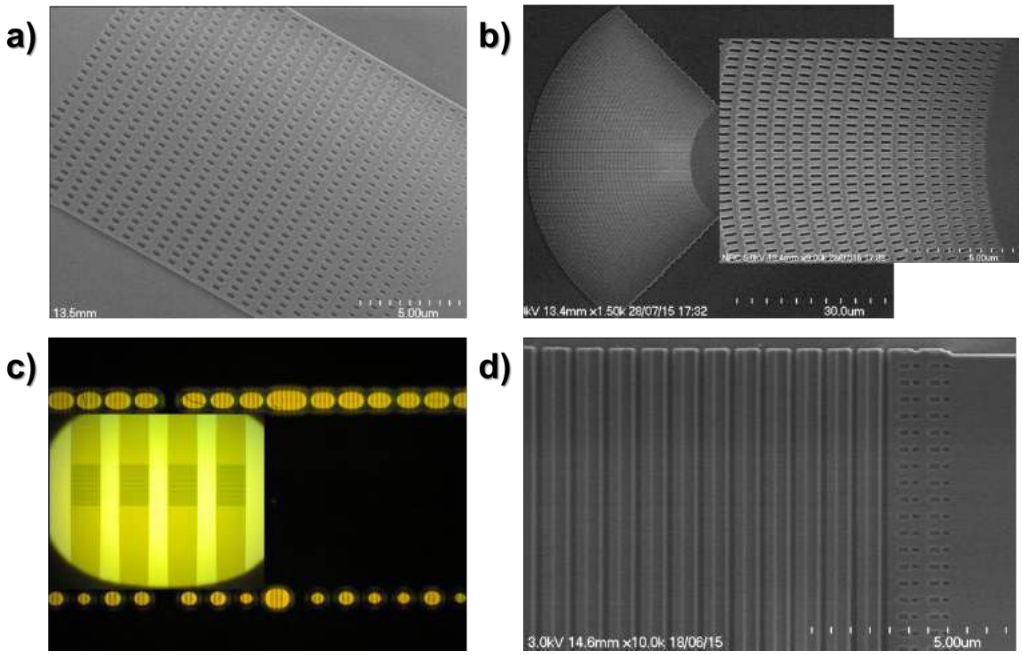

Figure: Single-etch step apodized surface grating couplers in (a) linearly-tapered and (b) curved layout configurations, and subwavelength grating nanostructure inside the trenches. (c) Optical micrograph image of the surface grating couplers layout with metal reflector underneath. (d) Dual-etch surface grating coupler with interleaved deep and shallow etched trenches and subwavelength grating index-matching region.

REFERENCES

1. Halir, et al., "Waveguide sub-wavelength structures: a review of principles and applications," *Laser Photon Rev*, Vol. 9, No. 1, 25–49, 2015.
2. Halir, et al., "Continuously apodized fiber-to-chip surface grating coupler with refractive index engineered subwavelength structure," *Opt. Letters*, Vol. 35, No. 19, 3243–3245, 2010.
3. Benedikovic, D., et al., "High-efficiency single etch step apodized surface grating coupler using subwavelength structure," *Laser Photon Rev*, Vol. 8, No. 6, 93–97, 2014.
4. Benedikovic, D., et al., "Single-etch subwavelength engineered fiber-chip grating couplers for 1.3 μm datacom wavelength band," *Opt. Express*, Vol. 24, No. 12, 12893-12904, 2016.
5. Benedikovic, D., et al., "Subwavelength index engineered surface grating coupler with sub-decibel efficiency for 220-nm silicon-on-insulator waveguides," *Opt. Express*, Vol. 23, No. 17, 22628–22635, 2015.
6. Alonso-Ramos, C., et al., "Fiber-chip grating coupler based on interleaved trenches with directionality exceeding 95%," *Opt. Letters*, Vol. 39, No. 19, 5351–5354, 2014.
7. Benedikovic, D., et al., "High-directionality fiber-chip grating coupler with interleaved trenches and subwavelength index-matching structure," *Opt. Letters*, Vol. 40, No. 18, 4190–4193, 2015.

Electromechanically Tunable Metal-Air-Metal Nanocavity

J. Takahara[1,2*]
[1]Photonics Advanced Research Center, Osaka University, Japan
[2] Graduate School of Engineering, Osaka University, Japan
[*]corresponding author: takahara@ap.eng.osaka-u.ac.jp

Abstract- We demonstrate an electromechanically tunable metal-air-metal structure based on a gold nanowire suspended on a gold substrate in visible range. By applying voltage to the nanowire, the suspended nanowire can be pull down by the electrostatic force, resulting in scattering spectral change due to Fabry-Perot resonance of a plasmonic nanocavity. Such nanocavity provides a promising route for achieving dynamical control of the interaction between surface plasmon and inserted objects such as fluorescent molecules or quantum dots in the gap.

Metal-Insulator-Metal (MIM) structure is a fundamental structure for plasmonics. In recent years, MIM structures have been applied to an efficient light absorber as a component for plasmonic metasurfaces. In such applications, a finite-length MIM structure, i.e. an MIM resonator plays a crucial role to control the efficient interaction between surface plasmon to light. Recently, electromechanically reconfigurable plasmonic metamaterials have been proposed for achieving tunable plasmonic characteristics [1]. More recently, we have reported static gap plasmon resonance in various gap sizes of a plasmonic nanowire (NW) suspended on a metal substrate [2]. Such structure, so called Metal-Air-Metal (MAM) structure, has a great potential for the dynamic control of gap plasmon resonance. Achieving electrical tuning of plasmon resonances in visible range remains a challenge, in contrast to the great success of tunable plasmonic nanostructures in the other spectral regimes.

In this paper, we demonstrate electromechanically tunable MAM structure in visible range, which is capable of dynamically tuning the resonant properties of the nanocavity [3]. In addition, we report our recent results about the modulation of light emission from colloidal quantum dots placed inside the MAM resonator.

Figure 1 shows a SEM image of a 500-nm-wide and 150-nm-thick gold NW suspended over Al_2O_3 coated (20 nm thick) Au film (80 nm thick) with a suspended length of 13.4 μm and an initial air gap of ~250 nm [3]. The suspended NW was fabricated using a probe-based pick-and-place method capable of arranging NWs on a substrate.

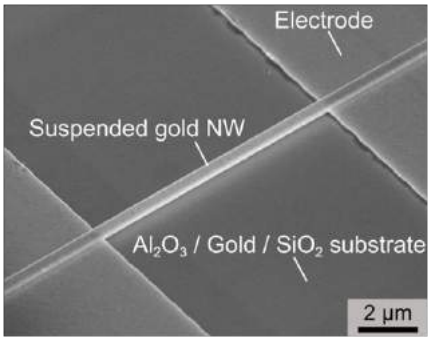

Fig. 1 SEM image of the suspended gold NW. The scale bar is 2μm.

We measured dark field image of the NW under applying voltage to the NW and performed spectroscopy. We observed the scattering color of the NW was changed with decreasing of the gap distance between the NW and the substrate from 250nm (initial) to 100nm. Hence, the gap distance can be tuned by applying voltage, resulting in controlling Fabry-Perot resonance of MAM nanocavity.

In conventional MIM nanocavity, the spacing insulating layer prevents access to the enhanced filed spot in the gap, making them limit to use in static applications. Such dynamic MAM nanocavity provides a promising route for achieving dynamical control of the interaction between surface plasmon and inserted objects such as

fluorescent molecules or quantum dots in the gap. We have placed colloidal quantum dots (CQDs) inside the MAM resonator and observed the light emission from CQDs. We report our recent results about the modulation of light emission.

REFERENCES

1. N.I. Zheludev and E. Plum, "Reconfigurable nanomechanical photonic metamaterials," *Nat. Nanotech.* Vol. 11, 16 (2016).
2. M. Miyata, A. Holsteen, Y. Nagasaki, M.L. Brongersma and J. Takahara, "Gap Plasmon Resonance in a Suspended Plasmonic Nanowire Coupled to a Metallic Substrate," *Nano Lett.*, Vol. 15, 5609 (2015).
3. M. Miyata, A. Kaijima, Y. Nagasaki and J. Takahara. "Electromagnetically Tunable Plasmonic Nanowires Operating in Visible Wavelength," *ACS Photonics*, Vol. 3, No. 12, 2268 (2016).

Au/Ni hybrid nanostructures: tuning the plasmon resonance under control.

Silvère Schuermans[1], **Thomas Maurer**[1], **Alexander Govorov**[2] **and Jérôme Plain**[1*]

[1]LNIO/ICD, University of technology of Troyes and CNRS, France

[2] Ohio University , Department of Physics and Astronomy, Clippinger Research Labs , Athens OH 45701

[*]corresponding author: jerome.plain@utt.fr

Abstract- We report on the fabrication of plasmonic hybrid Ni-Au nanoantennas. The optical properties of such nanostructure depend on the applied magnetic field and/or the temperature. Thus, we tune under control the plasmon resonance using external stimuli.

Over the past two decades, metallic nanoparticles have attracted increasing interest because of their varied and complex optical properties. These properties are mainly governed by the collective oscillations of conduction electrons called "plasmons". In particular, the excitation of the latter by optical fields leads to a local exaltation of the electromagnetic field on the surface of the nanoparticle. This very intense nanosource makes it possible to envisage nanometric optical concepts by controlling, manipulating and amplifying light at this scale. In recent years, a new challenge is the control and manipulation of optical properties using an external stimulus [1].

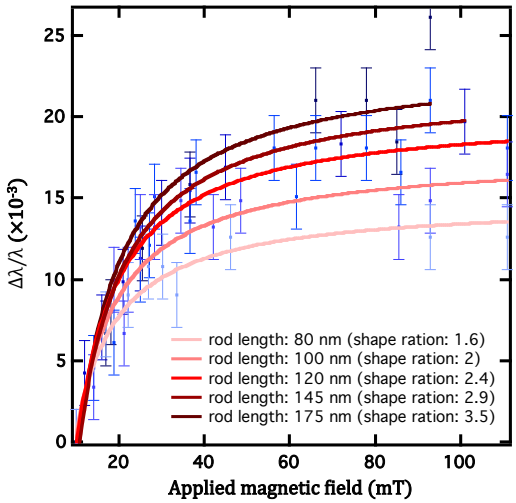

In this context, we developed Ni-Au plasmonic nanoantennas which exhibit an optical response that can be modulated either by the application of an external magnetic field or by a change in temperature. Thus, we are able to control the plasmon resonance of such individual nanoobjects over several tens of nanometers as shown in figure 1.

Figure 1. Relative shift of the plasmon resonance as a function of the applied magnetic field.

Acknowledgements, The authors thank the Nanomat platform, the LABEX ACTION and the NATO project.

REFERENCES

1. Berthelot J. et al. "Tuning of an Optical Dimer Nanoantenna by Electrically Controlling Its Load Impedance », *Nanoletters*, Vol. 9, No 11, 3914–3921, 2009.

Advantages of MDM plasmonics waveguide for Kerr nonlinearities

Stefano Palomba[1], Guangyuan (Clark) Li[1,2], and C. Martijn de Sterke[1,2]

1. Institute of Photonics and Optical Science (IPOS), School of Physics, Univ. of Sydney, NSW 2006, Australia.

2. Centre for Ultrahigh bandwidth Devices for Optical Systems (CUDOS), Univ. of Sydney, NSW 2006, Australia

stefano.palomba@sydney.edu.au

Abstract: Photonics structures are currently the leading platform for on-chip nonlinear optical application. However, limitations in compactness, interfacing with electronics and broadband operations have open the path to complementing and competing platforms such as the base based on plasmonic structures. These are promising for nonlinear optics because they strongly confine light at the nanoscale, enhancing in this way the light-matter interactions. Although Ohmic losses are an impediment to the full success of plasmonic-base structures, we showed here how plasmonic structures perform better than any other platform by harnessing efficiently the material nonlinearities manly thanks to a slow-light effect, exhibiting a different behavior than the one in dielectrics.

The Kerr effect leads, amongst other things, to a variation Δn of the refractive index with light intensity I. In turn, this leads to an intensity-dependent nonlinear phase shift $\Delta\phi_{NL}$. The key challenge that needs to be overcome in nonlinear optics is that these effects are weak and so it is crucial to use materials with the strongest possible nonlinearity and geometries which maximize these effects in small volumes, compatible with modern chip-based devices. For many years, metal-based (i.e., plasmonic) devices have promised to meet this challenge[1-3], but though the metal can compress the light very strongly, leading to huge intensities, they are also lossy, quickly dissipating these high intensities upon propagation.

Here we report which characteristics make plasmonic metal-dielectric-metal (MDM) structures the most promising nanoscale platform for nonlinear optical signal generation. After reviewing our previous work where we introduced a simple figure of merit, $F = \gamma P_{th} L_{ATT}$,[4] where $L_{ATT} = 1/\alpha$ with α the absorption coefficient, we then show that for MDM structures $F \propto 1/n^{\beta}$ with $1 \leq \beta \leq 3$, where β depends on the detailed properties of the device and n is the refractive index of the nonlinear medium. It is thus very advantageous to use nonlinear materials with low refractive index in this geometry.

We then introduce the concept of nonlinear effectiveness EFF_{NL}, in order to quantify the ability of a waveguide mode to make use of the material nonlinearity, i.e., to convert a material's nonlinear index change into a nonlinear phase shift. The EFFNL is defined as $EFF_{NL} = \Delta\varphi_{NL,mode} \Big/ \Delta\varphi_{NL,pw} = f_l \cdot S \cdot \rho_{NL}$, where the numerator and the denominator represent respectively the nonlinear phase shifts for the mode and for a plane wave in bulk, and therefore for a plane wave in bulk material, $EFF_{NL} = 1$. The nonlinear effectiveness is also proportional to a factor f_l, which represents the loss of the waveguide structure; $f_l = 1$ for a lossless mode and $f_l \equiv 2/(3\ln(3))$ for a lossy mode. The second factor S represent the slow-light effect, and the third, ρ_{NL}, is the field overlap with the nonlinear medium, which quantifies the fraction of energy in the mode that contributes to the nonlinear effects and the degree to which it does so ($0 \leq \rho_{NL} \leq 1$). Figure 1a shows the EFF_{NL} comparison between the best plasmonic structure for nonlinear optics, the MDM, and the one for all-dielectric waveguide, the Si-slot waveguide. Here the nonlinear effectiveness is plotted versus the thickness of the central layer for the MDM structure (dark blue) and an all-dielectric silicon slot waveguide (pink), Si-slot waveguide.

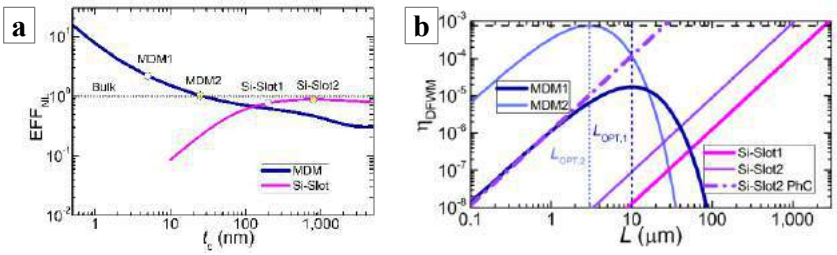

Figure 1. (a) Nonlinear effectiveness versus t_c for MDM structures (dark blue), the MDH structures (red) and an all-dielectric silicon slot waveguide (pink). (b) Four-wave mixing efficiency versus propagation length for five devices.

The nonlinear effectiveness of the MDM structure is superior to that of the Si-slot waveguide as $t_c \rightarrow 0$. This is because the field remains confined in this limit while the presence of slow-light effects contributes to the efficient use of the nonlinear refractive index change. In contrast, Si-slot waveguides exhibit modest slow light effects and cannot confine the light when the low-index layer becomes too thin.

In Figure 2b we compare the nonlinear performance for five structures, showing η_{max} versus propagation length. We consider two MDM structures with t_c=25 nm (dark blue) and t_c=5 nm (light blue); two silicon slot waveguides, with t_c=800 nm (purple) and t_c=200 nm (pink), and a silicon slot waveguide with a slow-down factor of S=6 (dashed), which mimics typical photonic crystal waveguides. The silicon slot waveguides consist of a nonlinear central layer with thickness t_c, surrounded by two 100 nm thick silicon layers (n=3.47), surrounded by air. Each of these is driven at the maximum power level of the thin MDM structure. Note that the thin MDM structure reaches $\eta_{max} \approx 10^{-3}$ after only 2.5 μm of propagation length, while all other devices require at least an order of magnitude more propagation lengths to reach the same efficiency.

Furthermore, we show that the slow-light effect mechanism is substantially different between an MDM and an all-dielectric waveguide such as a photonic crystal structure. The slow-light effect in MDMs arise because the energy in the metal propagates backwards due to its negative permittivity. This mechanism differs from that for slow-light effects in photonic crystals which rely on a narrow band structural resonance. Since the metal and dielectric permittivity have opposite signs over a large wavelength range, the slow-light effects and thus the MDM's nonlinear effectiveness are intrinsically broadband.

We have investigated the merits of plasmonic structures for degenerate four-wave mixing. We find that the MDM structure has the highest performance thanks to a combination of strong field confinement and slow light effects, but is limited by the damage threshold of the nonlinear material. Such structures beat all-dielectric structures if the required efficiency is low. The performance scales linearly with the damage threshold, and can thus be improved by using better nonlinear materials.

References

1. Kauranen, M.; Zayats, A. V. *Nature Photonics* 2012, 6, (11), 737-748.Palomba, S.; Danckwerts, M.; Novotny, L. *Journal of Optics A: Pure and Applied Optics* 2009, 11, (11), 114030.
2. Palomba, S.; Harutyunyan, H.; Renger, J.; R.Quidant; Hulst, N. F. v.; Novotny, *L. Philosophical Transactions of the Royal Society A* 2010, 369, 3497.
3. Li, G.; de Sterke, C. M.; Palomba, *S. Laser & Photonics Reviews* 2016, 10, (4), 639-646.

Material-induced chiroptical response of a single mirror-symmetric nanostructure

P. Woźniak[1,2], S. Nechayev[1,2], S. Sorayya[1,2], U. Mick[1,2], I. De Leon[3,4], R. W. Boyd[3,5,6], G. Leuchs[1,2,3], and P. Banzer[1,2,3]

[1]Max Planck Institute for the Science of Light, Germany
[2]Institute of Optics, Information and Photonics, Department of Physics, Friedrich-Alexander-University Erlangen-Nuremberg, Germany
[3]Max Planck University of Ottawa Centre for Extreme and Quantum Photonics, Canada
[4] School of Engineering and Sciences, Tecnológico de Monterrey, Mexico
[5] Department of Physics, University of Ottawa, Canada
[6] Institute of Optics, University of Rochester, USA
pawel.wozniak@mpl.mpg.de

Abstract— Chirality, an exciting property of objects lacking in mirror symmetry, provides the ability to sense the handedness of light's polarization. Instead of following the conventional apporach based on purely geometrical aspects, we now introduce a novel and versatile concept realized by a heteromaterial composition of nanostructures. Here, we report on our experimental and numerical observation of optical activity of geometrically symmetric nanoassemblies enabled by heteromaterial selection.

According to the definition introduced by Lord Kelvin [1], chirality refers to a lack of mirror symmetry of a *geometrical figure, or group of points*. Such objects can be found in nature and, when inetracting with light, are capable of distinguishing between right- and left-handed circular polarization [2]. Recently, optical activity of a variety of different artificial chiral 3D and planar nanostructures has been reported [3, 4]. However, so far a chiral optical behavior has been induced by a non-mirror-symmetric geometry of the studied structures.
Here, we present a novel concept of chiral optical response induced by heteromaterial composition of a single nanoassembly. To this end, we investigate a geometrically mirror-symmetric particle-arrangement, composed of equally sized and shaped achiral building-blocks [5] (see also Fig. 1a). In such assemblies, the choice of different materials and a proper arrangement break the symmetry of the system and enable its optical activity. The chiral behavior originates from the interaction of the multipolar responses of the individual constituents. Depending on the input polairzation state (right- or left-handed circularly polarized light) and, therefore, the phase between the linear polarization components of the illumination, indiviudal particles interact differently with their respective neighbor in the assembly due to the heteromaterial composition. The mutual interference of the multipolar modes will, therefore, result in different interaction schemes and, eventually, in a chiral response.

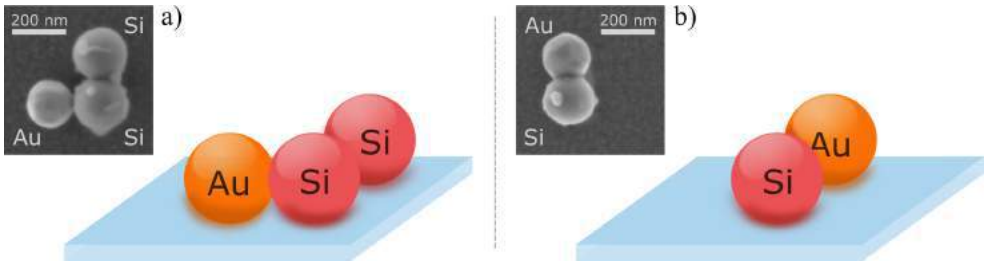

Figure 1: Sketches and SEM images of optically chiral three- (a) and two-particle (b) assemblies built from gold and silicon nanospheres.

For a proof-of-principle experimental demonstration, we recently measured the optical activity of a geometrically symmetric trimer [5] (see Fig. 1a). The trimer was assembled from gold and

silicon nanospheres on a glass substrate, utilizing a pick-and-place technique developed in-house [6]. For normal incidence, circular dichroism, i.e., the differential absorption of right- and left-handed circularly polarized light is observed. The experimental results are in excellent agreement with the numerically calculated optical response of the nanotrimer.

The heteromaterial-driven chiroptical effects can be further tailored by involving particles made of many different materials, changing the number of particles or changing their arrangement. We envision that heteromaterial selection will allow for the development of many different geometries of nanostructures exhibitng a chiral optical response. Even simpler geometries than the one described above may feature optical activity. Indeed, our recent studies confirm that optical activity can be induced also in a heterogeneous two-particle-assembly (Fig. 1b). Details will be discussed in the presentation.

In summary, we propose and investigate experimentally and numerically a new concept of chiral optical activity of a single nanostructure. In contrast to the studies reported so far, the chiral behavior originates from heterogeneous material selection of the individual constituents of the geometrically symmetric nanoassembly. Our concept of the heteromaterial-driven chiroptical response provides a new degree of freedom for precisely designing the chiral properties of individual structures at the nanoscale.

ACKNOWLEDGMENT

P.B. acknowledges financial support provided by the Alexander von Humboldt Foundation and the Canada Excellence Research Chair (CERC) in Quantum Nonlinear Optics. U.M. acknowledges financial support by the DFG via the Research Training Group GRK1896.

REFERENCES

1. Lord Kelvin, *Lectures on Molecular Dynamics and the Wave Theory of Light*, University Press Warehouse, London, 1904.
2. Gratzer, W. B. and D. A. Cowburn "Optical activity of biopolymers," *Nature*, Vol. 222, 426–431, 1969.
3. Schäferling, M., D. Dregely, M. Dregely and H. Giessen "Tailoring enhanced optical chirality: design principles for chiral plasmonic nanostructures," *Phys. Rev. X*, Vol. 2, 031010, 2012.
4. Valev, V. K., J. J. Baumberg, C. Sibilia and T. Verbiest "Chirality and chiroptical effects in plasmonic nanostructures: fundamentals, recent progress, and outlook," *Adv. Mater.*, Vol. 25, No. 18, 2517–2534, 2013.
5. Banzer, P., P. Woźniak, U. Mick, I. De Leon and R. W. Boyd "Chiral optical response of planar and symmetric nanotrimers enabled by heteromaterial selection," *Nat. Commun.*, Vol. 7, 13117, 2016.
6. Mick, U., P. Banzer, S. Christiansen and G. Leuchs "AFM-based pick-and-place handling of individual nanoparticles inside an SEM for the fabrication of plasmonic nano-patterns," in *CLEO: 2014*, San Jose, USA, June 2014, 171-176.

Experimental demonstration of a negative Kerr nonlinearity of graphene through chirped-pulse-pumped self-phase modulation

D. Castelló-Lurbe[1], J. Van Erps[1], J. L. Cheng[1,2], I. Pasternak[3], A. Krajewska[3], T. Ciuk[3], W. Strupinski[3], H. Thienpont[1], and N. Vermeulen[1]

[1]Brussels Photonics Team, Department of Applied Physics and Photonics, Vrije Universiteit Brussel, Pleinlaan 2, 1050 Brussel, Belgium

[2]Department of Physics, University of Toronto, 60 St. George Street, Toronto, Ontario M5S 1A7, Canada

[3]Institute of Electronic Materials Technology, Wolczynska 133, 01-919 Warsaw, Poland

dcastell@b-phot.org

Abstract— A negative Kerr nonlinearity of quasiundoped graphene at telecom wavelengths is demonstrated experimentally based on our novel chirped-pulse-pumped self-phase modulation approach. Since a positive Kerr nonlinear index had been assumed for graphene so far, our result will modify considerably strategies for exploiting waveguide nonlinearity enhancement induced by graphene layer deposition.

Graphene became a topic of intense research since its isolation [1] due to the panoply of applications relying on the unusual band structure of this 2D honey comb lattice of carbon atoms [2]. Particularly, graphene is a promising material for nonlinear optical applications due to the extremely large magnitude of its Kerr nonlinear index, n_2 (five orders of magnitude larger than n_2 of silicon, which is one of the largest available in integrated photonics), as was demonstrated earlier using four-wave mixing (FWM) experiments [3]. Although the sign of n_2 does not affect the (optimum) conversion efficiency of FWM, a positive n_2 had been tacitly assumed for graphene [4].

In this work, we carry out self-phase modulation (SPM) experiments where graphene-covered silicon-on-insulator (SOI) waveguides are pumped with positively and negatively chirped pulses in order to determine both magnitude and sign of the waveguide nonlinear coefficient, γ_K. Moreover, n_2 of graphene can be extracted since the nonlinear coefficient of bare SOI waveguides is also measured. A new analytical model that accounts for SPM and linear losses but also the interplay between SPM and the input chirp is used to fit the experimental spectral broadening induced by SPM and as such extract γ_K. Based on this analysis, we conclude that quasiundoped graphene possesses a negative n_2 at $1.55\,\mu$m, while its magnitude is in accordance with previous reports [3].

Our chirped-pulse-pumped SPM method relies on the following equation that governs the evolution of the root-mean-square (RMS) spectral width, μ_2, of the pulse along the waveguide (in the $z-$direction):

$$\frac{\mu_2(z)}{\mu_2(0)} = 1 + \frac{2\gamma_K P_0 \Delta z_{\text{eff}} C_0 \sigma_{31} + (\gamma_K P_0 \Delta z_{\text{eff}})^2 \sigma_{41}}{1 + 4\,C_0^2 \sigma_{21}}, \tag{1}$$

where P_0 refers to the input pulse peak power, Δz_{eff} is the effective length, C_0 accounts for the input pulse chirp and σ-coefficients are positive-valued dimensionless shape-factors [5]. This equation shows how the spectrum can broaden or get narrower depending on the sign of $\gamma_K C_0$ in the low-power regime, namely, when the term that depends linearly on P_0 becomes important compared to the term that depends quadratically on P_0. This model allows determining γ_K, including its sign, by means of measurements of μ_2 for different $z-$lengths, provided C_0 is known.

The most important features of the graphene-covered SOI waveguides and the laser sources employed in our experiments are described in Fig. 1. Further information about the laser sources, graphene deposition and patterning to vary the length of the graphene sections can be found in [5] and references therein. The relative spectral broadening is measured for six SOI waveguides covered by a graphene section with a length varying from 0 (*i.e.*, no graphene coverage) to $250\,\mu$m. When Source (1) is used [see Fig. 1(b)], 1.2 ps, 1.8 W pulses at $1.55\,\mu$m with $C_0 = 0.8$ are injected into the on-chip waveguides. In this case, the laser source provides directly positively chirped pulses. In contrast, to provide negatively chirped pulses at the waveguide input, the (slightly positively chirped) pulses emitted by an optical parametric oscillator (OPO) are sent through a negative-dispersion fiber with properly chosen length. As a result, 3 ps, 1.7 W pulses with $C_0 = -0.25$ excite the waveguides when Source (2) is considered.

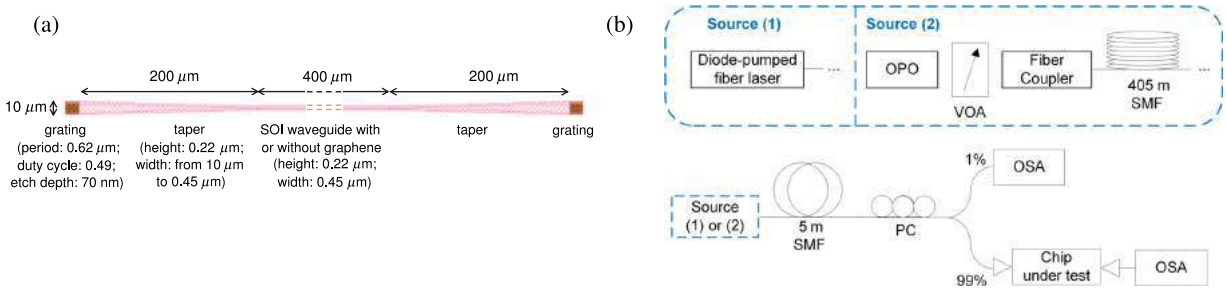

Figure 1: (a) Outline of the waveguides used in our experiments. (b) Experimental setup for the SPM measurements. The acronyms refer to variable optical attenuator (VOA), single-mode fiber (SMF), polarization controller (PC), and optical spectrum analyzer (OSA). Note that the input and output spectra are measured simultaneously using two OSAs.

Our experimental results are shown in Fig. 2. The experimental broadening factors for both positive and negative input-chirp cases can be fitted on the basis of Eq. (1) with γ_K as only fitting parameter. This fit provides $\gamma_K = -1.4\,\mathrm{W}^{-1}\,\mathrm{mm}^{-1}$ in the graphene-covered sections, which yields $n_2 = -10^{-13}\,\mathrm{m}^2\,\mathrm{W}^{-1}$ for graphene. In Fig. 2, the red lines are the theoretical curves for the case where the graphene-covered sections would have the same (positive) nonlinearity as that of bare SOI waveguides. The poor correspondence between these hypothetical curves and the experimental data showcases the strong impact of graphene on γ_K. Although the magnitude of the n_2 that we find agrees with previous works [3], this previously unreported negative n_2 of graphene changes drastically present approaches that pursue larger γ_K through graphene layer deposition.

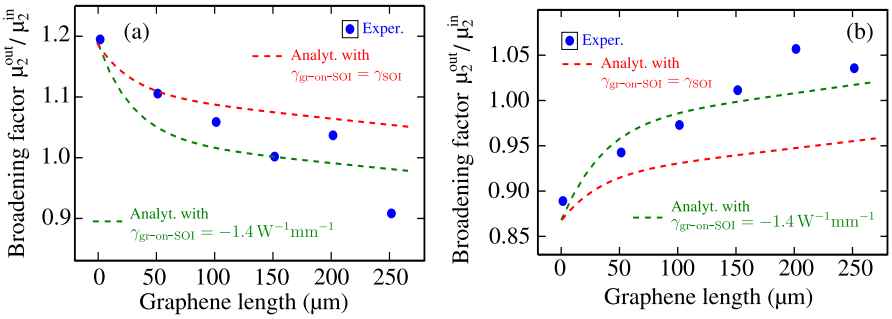

Figure 2: (a) Experimental measurement of γ_K for a positively chirped input pulse. (b) Experimental measurement of γ_K for a negatively chirped input pulse.

ACKNOWLEDGMENT

This work is supported by the ERC-FP7/2007-2013 Grant No. 336940, the EU-FET GRAPHENICS Project No. 618086, the Hercules-stichting Grant No. UABR/007/09, the FWO Project No. G.A002.13N, the EU-FP7 Graphene Flagship 604391, VUB-OZR, BELSPO-IAP, and Methusalem.

REFERENCES

1. Novoselov, K. S., A. K. Geim, *et al.* "Electric field effect in atomically thin carbon films," *Science*, Vol. 306, 666–669, 2004.
2. Bonaccorso, F., Z. Sun, *et al.* "Graphene photonics and optoelectronics," *Nature Photon.*, Vol. 4, 611–622, 2010.
3. Hendry E., P. J. Hale, *et al.* "Coherent nonlinear optical response of graphene," *Phys. Rev. Lett.*, Vol. 105, 097401, 2010.
4. Ji, M., H. Cai, *et al.* "Enhanced parametric frequency conversion in a compact silicon-graphene microring resonator," *Opt. Express*, Vol. 23, No. 14, 18679–18685, 2015.
5. Vermeulen, N., D. Castelló-Lurbe, *et al.* "Negative Kerr nonlinearity of graphene as seen via chirped-pulse-pumped self-phase modulation," *Phys. Rev. Applied* , Vol. 6, 044006, 2016.

Light on Wheels –
Transverse Angular Momentum as a Tool for Nanophotonics.

P. Banzer
Max Planck Institute for the Science of Light, Erlangen, Germany
Institute of Optics, Information and Photonics, Department of Physics, Friedrich-Alexander-University Erlangen-Nuremberg, Erlangen, Germany
*corresponding author: peter.banzer@mpl.mpg.de

Abstract-We discuss the concept of *photonic wheels*, i.e., light carrying an angular momentum (density) perpendicular to the propagation direction, as a versatile and very flexible tool for nanophotonics. We review recent studies involving transverse angular momenta.

Evanescent fields, waveguide modes, propagating surface plasmons and focused light beams share an intriguing feature. As a direct consequence of the spatial confinement they are resulting from, components of the field oscillating along the propagation direction are formed, which are usually dephased by $\pm\pi/2$ with respect to their transverse counterparts [1]. Hence, the electric or magnetic field (or both) are elliptically polarized with the polarization ellipse coinciding with a plane of propagation. Richards and Wolf first recognized this subtle detail for tightly focused light beams [2] and Huard and Vigoureux for evanescent waves [3]. In the notation of the angular momenta of light, such confined fields therefore exhibit components of the spin, which are orthogonal to the propagation direction [1] in contrast to the conventional case of circularly polarized light. This research area of transverse angular momenta was initiated in 2009 [4] and, since then, received considerable attention (see for instance [1] for a review). In some cases, the angular momentum (spin) density or the net angular momentum might be even purely transverse [4-7].

The most flexible scheme for which this phenomenon of transverse angular momentum in general and transversely spinning fields in particular can be observed and even, more importantly, also spatially tailored is the framework of nonparaxial propagation in free-space. By properly choosing the input beams to be tightly focused, tailored landscapes of locally varying transverse and longitudinal angular momenta can be created at the nanoscale [1,5-7,12]. The resulting field distributions can be used, e.g., to selectively excite individual nanoparticles or other nanoscopic systems and to control their emission. In this context it was shown that an electric field spinning around an axis parallel to a nearby interface results in highly directional emission across a dielectric interface or directional coupling to plasmons [1,6-11], with the emission direction depending on the spinning sense. The latter one can be controlled easily by placing the nanoparticle in the focal field of a tightly focused light beam where the local spin (density) depends on the relative particle position [6,7].

This effect of transverse angular momentum components in focused light beams in combination with the aforementioned directional emission of a spinning dipole across an interface paves the way for a wide range of different applications and effects [1,5-11], some of which will be discussed in this presentation.

REFERENCES

1. A. Aiello, P. Banzer, M. Neugebauer, G. Leuchs, ”From transverse angular momentum to photonic wheels,” Nat. Photon. 9, 789-795 (2015).
2. B. Richards & E. Wolf, “Electromagnetic diffraction in optical systems. II. Structure of the image field in an aplanatic system,” Proc. R. Soc. Lond. A 253, 358–379 (1959).
3. S. Huard & J. M. Vigoureux, “Mise en evidence de la polarisation d'une onde de surface par absorption atomique,” Opt. Commun. 25, 5–8 (1978).
4. A. Aiello, N. Lindlein, C. Marquardt, G. Leuchs, “Transverse angular momentum and geometric spin Hall effect of light,” Phys. Rev. Lett. 103, 100401 (2009).
5. P. Banzer, M. Neugebauer, A. Aiello, C. Marquardt, N. Lindlein, T. Bauer, G. Leuchs, “The photonic wheel - demonstration of a state of light with purely transverse angular momentum,” J. Eur. Opt. Soc, Rapid Publ. 8, 13032 (2013).
6. M. Neugebauer, T. Bauer, P. Banzer, G. Leuchs, “Polarization Tailored Light Driven Directional Optical Nanobeacon,” Nano Lett. 14, 2546 (2014).
7. M. Neugebauer, T. Bauer, A. Aiello, P. Banzer, “Measuring the Transverse Spin Density of Light,” Phys. Rev. Lett. 114, 063901 (2015).
8. J. P. B. Mueller & F. Capasso, “Asymmetric surface plasmon polariton emission by a dipole emitter near a metal surface,” Phys. Rev. B 88, 121410 (2013).
9. F. J. Rodríguez-Fortuño, G. Marino, P. Ginzburg, D. O’Connor, A. Martínez, G. A. Wurtz, A. V. Zayats, “Near-Field Interference for the Unidirectional Excitation of Electromagnetic Guided Modes,” Science 340, 328 (2013).
10. C. Junge, D. O’Shea, J. Volz, A. Rauschenbeutel, “Strong Coupling between Single Atoms and Nontransversal Photons,” Phys. Rev. Lett. 110, 213604 (2013).
11. H. Pichler, T. Ramos, A. J. Daley, P. Zoller, “Quantum optics of chiral spin networks,” Phys. Rev. A 91, 042116 (2015).
12. A. Aiello & P. Banzer, ”The ubiquitous photonic wheel,” J. Opt. 18, 085605 (2016).

Photo-thermal control of gold nanoparticle loaded microgels

D. N. Chigrin[1, 2*]

[1]DWI - Leibniz Institute for Interactive Materials, Aachen, Germany

[2]Institute of Physics (IA), RWTH Aachen University, Aachen, Germany

[*]corresponding author: chigrin@dwi.rwth-aachen.de

Microgels are cross-linked polymeric chains with dimensions ranging from several hundreds of nano- to a few tens of micro-meters. Microgels are highly sensitive to the environmental changes. Their shape and volume can experience a dramatic change in response to external stimuli such as temperature, pressure and ionic strength. This ability has attracted a lot of attention due to potential applications as micro-sensors, micro-actuators, micro-valves and drug delivery devices. In particular, temperature-responsive microgels can exhibit extremely large deformation in response to a variation of temperature of the environment. Combining photo-thermal materials (plasmonic nano-particles) with microgels opens a unique opportunity to design micro-dynamical systems, which can be controlled all-optically. In this presentation, we discuss our recent advances in the development of physical models capable to describe optically controlled, gold nanoparticle loaded microgel systems. Appropriate consideration involves self-consistent coupling of diffusion, elasticity, heat transfer and electrodynamic models. Using simple examples, we discuss how shape and volume of microgels can be controlled using light.

Plasmonic Enhancement of Light-matter Interaction in Planar Materials

Hossein Taghinejad, Syed Hamed Shams Mousavi, Tianren Fan, Mohammad Taghinejad, Ali A. Eftekhar, and Ali Adibi

School of Electrical and Computer Engineering

Georgia Institute of Technology

Two-dimensional metal dichalcogenides (2D TMDCs) have been of great interest lately due to their unique potentials for forming new optoelectronic devices. This talk is focused on the integration of 2D TMDC nanostructures with plasmonic nanostructures to considerably enhance their optical properties for enabling new devices for light emission and detection. It is shown that by using a carefully engineered plasmonic nanocavity, orders of magnitude improvement in light-matter interaction in these hybrid materials can be achieved. Supported by theoretical calculations, this technique will be experimentally presented for a variety of hybrid nanostructures, and its prospects for forming practical nanophotonic devices will be discussed.

Nonlinear plasmonics at anisotropic metal-dielectric interfaces.

I. Razdolski[1], **A. L. Chekhov**[2], **and T. V. Murzina**[2]

[1]Fritz Haber Institute of Max Planck Society, 14195 Berlin, Germany
[2]Department of Physics, Moscow State University, 119991 Moscow, Russia
razdolski@fhi-berlin.mpg.de

Abstract— We show sensitivity of second harmonic generation to the surface plasmon propagation direction at anisotropic Au/dielectric interfaces. The symmetry of the iron garnet enables interplay between even and odd components of the nonlinear susceptibility leading to a 95% asymmetry of the second harmonic output. Illustrating this interplay with a simple two-component model, we discuss its applicability to nonlinear magneto-plasmonics and nanophononics.

Featuring strong electromagnetic field localization, surface plasmon-polariton (SPP) excitations are key building blocks of modern nanophotonics. Recently, nonlinear plasmonics [1] benefited from numerous observations of SPP-enhanced second harmonic generation (SHG). Often isotropic interfaces between air and polycrystalline noble metal films are considered, where the optical properties are independent of the SPP propagation direction. Prominent SHG sensitivity to the symmetry breaking suggests its applicability for probing excitations at anisotropic interfaces where new intriguing phenomena can be expected. SHG non-reciprocity with respect to the SPP propagation also holds promise for nonlinear magneto-plasmonics [2].

In this work, we probe SPP-assisted SHG from an anisotropic interface in Bi,Tm-doped iron garnet/Au hybrid plasmonic crystals. We observe strong variations of the SHG response when the SPPs are propagating in the opposite directions, in a striking contrast to the negligible variations of the linear transmittivity. In the vicinity of the SPP resonance at the anisotropic Au/garnet interface, the modulation of the SHG intensity reaches 95%. We consider a two-source model where SHG is generated at the Au/air and Au/garnet interfaces [3]. When the SPP is excited, the relative SHG efficiency at the two interfaces changes, and the interference results in a complex shape of the SHG response. The results of the SHG phase measurements allowed us to consider SPP-induced resonant enhancement of the fundamental field as $E_\perp = E_\perp^{NR} + E_\perp^{R}$. The crystalline anisotropy of the garnet film enables both even and odd $\chi^{(2)}$ components with respect to the angle of incidence θ. Within this approach, the outgoing SHG field takes the following form:

$$P_\parallel^{2\omega}(\theta) = \chi^{(2)}_{1,\perp\parallel\parallel} E^2_{1,\parallel} \sin(\pm\theta) + \chi^{(2)}_{2,\parallel\perp\perp} (E^{\mathrm{NR}}_{2,\perp} + E^{\mathrm{R}}_{2,\perp})^2 \cos\theta, \quad (1)$$

where the lower indices 1,2 stand for the Au/air and Au/garnet interfaces, respectively.

This interference of the SHG contributions with different parity with respect to θ holds high potential for rapidly growing fields of nonlinear magneto-plasmonics and nanophononics. Firstly, interface anisotropy can be utilized to enhance variations of the SPP-driven SHG output upon the magnetization reversal in garnet. Furthermore, anisotropic interfaces constitute a popular playground in nanophononics where surface phonon-polaritons (SPhPs) in polar dielectrics are excited instead of SPPs in metals. In particular, interplay of anisotropy-driven phonon modes with SPhPs was shown to strongly enhance the SHG output in the mid-infrared [4].

REFERENCES

1. Kauranen, M. and Zayats., A. V. "Nonlinear plasmonics," *Nature Photon.*, Vol. 6, No. 1, 737–748, 2012.
2. Razdolski, I., Makarov, D., Schmidt, O. G., Kirilyuk, A., Rasing, Th. and Temnov, V. V., "Nonlinear Surface Magnetoplasmonics in Kretschmann Multilayers," *ACS Photon.*, Vol. 3, No. 2, 179–183, 2016.
3. Chekhov, A. L., Razdolski, I., Kirilyuk, A., Rasing, Th., Stognij, A. I. and Murzina, T. V., "Surface plasmon-driven second-harmonic generation asymmetry in anisotropic plasmonic crystals," *Phys. Rev. B*, Vol. 93, No. 16, 161405(R), 2016.
4. Razdolski, I., Chen, Y., Giles, A. J., Gewinner, S., Schllkopf, W., Hong, M., Wolf, M., Giannini, V., Caldwell, J. D., Maier, S. A. and Paarmann, A., "Resonant Enhancement of Second-Harmonic Generation in the Mid-Infrared Using Localized Surface Phonon Polaritons in Subdiffractional Nanostructures," *Nano Lett.*, Vol. 16, No. 11, 6954–6959, 2016.

Enhancement of Electrocataytic Activity of Octahedoral Au-Core/Pt-Shell Nanoparticles by Visible Light Irradiation

T. Kameyama, K. Sato, and T. Torimoto
Graduate School of Engineering, Nagoya University, Japan
kameyama@apchem.nagoya-u.ac.jp

Abstract Octahedral Au-core/Pt-shell (Au@Pt) nanoparticles were successfully prepared via a galvanic replacement of Cu monolayer underpotentially deposited on Au core with a Pt monolayer. The visible-light irradiation to Au@Pt nanoparticles-immobilized electrodes enlarged a cathodic current of oxygen reduction reaction (ORR), suggesting that the electrocatalytic activity of Pt shell layer was enhanced by the photoexcitation of localized surface plasmon resonance peak of octahedral Au-core particles.

Noble metal nanoparticles (NPs), exhibiting localized surface plasmon resonance (LSPR) in visible-light region, have attracted much attention because their optical properties can be tuned by precise control of their shape and size.[1,2] Recently, the enhancement of catalytic properties by the plasmonic properties of metal NPs has been intensively investigated, because hot carriers could be created in plasmonic metal NPs by the photoexitation of LSPR.[3] In this study, we try to improve the catalytic activity of Pt with LSPR of octahedral Au NPs. An electrochemical technique is used for preparing Pt shell layer on octahedral Au NPs, resulting in the formation of Au@Pt core-shell NPs. The photoexcitation of LSPR peaks of octahedral Au core in Au@Pt NPs can modify the catalytic activity of Pt shell layer for oxygen reduction reaction (ORR) as a model reaction.

Octahedral Au NPs were prepared by reduction of $HAuCl_4$ in diethylene glycol containing poly(diallyldimethylammonium chloride) at 230 °C for 1 h. The underpotential deposition (UPD) of Cu monolayer onto octahedral Au NPs immobilized on an HOPG electrode was carried out with constant potential application at 0.26 V vs. RHE in an aqueous solution containing 1.0 mmol dm^{-3} $CuSO_4$ and 0.1 mol dm^{-3} H_2SO_4. Thus-obtained Cu-deposited Au NPs on HOPG substrate immersed in aqueous solution containing 0.5 mmol dm^{-3} K_2PtCl_4 for 10 min to replace Cu monolayer by Pt, resulting in the core-shell structure of octahedral Au@Pt NPs.

The Pt shell deposition on Au surface increased the average edge length of octahedral NPs from 65 nm to 66.5 nm without significant change in shape as observed in the SEM image of Fig. 1a and b. To elucidate the surface Pt coverage on the particles, we obtained the electrochemical active surface area (ECSA) of octahedral Au@Pt NPs by measuring cyclic voltammograms. The deposition of Pt layer on Au NPs

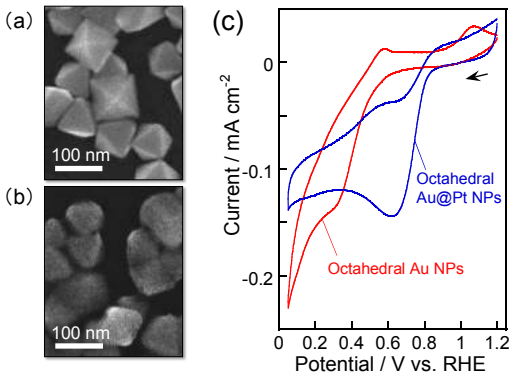

Figure 1. SEM images of octahedral (a) Au NPs and (b) Au@Pt NPs. (c) Cyclic voltammograms of octahedral Au and Au@Pt NPs in O_2 saturated 0.1 mol dm^{-3} $HClO_4$ aqueous solution.

decreased the peak current assignable to the reduction of Au oxide layer (ca. 1.15 V vs. RHE). In contrast, the peaks originating from the reduction of Pt oxide layer and the H_2 desorption on Pt surface were newly observed for Au@Pt NPs at 0.65 and 0.05V vs. RHE, respectively. These results indicated the surface of octahedral Au NPs was partially coated by the Pt shell layer. The Pt surface coverage was determined to be 85 % on octahedral Au@Pt NPs from ECSA.

Figure 1c shows the cyclic voltammograms of the octahedral Au and Au@Pt NPs for ORR in a dark condition. The cathodic current for ORR on octahedral Au@Pt NPs was observed at more negative potential than ca. 0.85 V vs. RHE, the onset potential of which was more positive than that of bare octahedral Au NPs, indicating that the electrocatalytic activity for ORR was much larger on the surface of Pt shell layer than on the bare Au surface. Furthermore the visible-light irradiation to octahedral Au@Pt NPs twice enlarged the cathodic current density of ORR at 0.7 V vs. RHE from -0.12 to -0.21 mA cm^{-2}. These results suggested that the LSPR excitation of the Au core in Au@Pt NPs greatly modified the electrocatalytic activity of the Pt shell layer for ORR.

REFERENCES

1. Sun, Y. G., and Xia, Y. N. “Shape-controlled synthesis of gold and silver nanoparticles”, *Science*, Vol. 298, 2176-2179, 2002.
2. Sawai, Y., Takimoto, B., Nabika, H., Ajito, K. and Murakoshi, K. “Observation of a small number of molecules at a metal nanogap arrayed on a solid surface using surface-enhanced Raman scattering”, *J. Am. Chem. Soc.*, Vol. 129, No. 6, 1658-1662, 2007.
3. Wnag, Q., Zheng, W., Chen, H., Zhang, B., Su, D., and Cui, Z., “Plasmonic-induced inhibition and enhancement of the electrocatalytic activity of Pd-Au hetero-nanoraspberries for ethanol oxidation” *J. Power Sou.*, Vol. 316, 29-36, 2016.

Vis and NIR nanoplasmonic active and passive materials by eutectic solidification and NanoParticle Direct Doping

D. A. Pawlak[1,2], R. Nowaczynski[1,2], M. Kurowska[1], A. Antolik[1], P. Paszke[1,2], M. Gajc[1], K. Sadecka[1], P. Osewski[1], B. Surma[1]

[1]Institute of Electronic Materials Technology, Warsaw, Poland

[2]Centre of New Technologies, University of Warsaw, Warsaw, Poland

[*]corresponding author: Dorota.Pawlak@itme.edu.pl

Abstract- We report on developments in fabricating nanoplasmonic volumetric isotropic and anisotropic materials with plasmonic resonances at visible and infrared wavelength ranges. We push the melt-based crystal growth techniques for developing novel methods as the NanoParticle Direct Doping method enabling doping dielectric matrices simultaneously with plasmonic nanoparticles and quantum dots or rare earth ions. We also push the methods utilizing the self-organization mechanism as in directional solidification of eutectic composites.

Two types of materials will be discussed: (i) based on directional solidification of eutectic composites [1, 2], and (ii) directional solidification of dielectrics directly doped with functional nanoparticles of various sizes, shapes and chemical composition (metallic-plasmonic, quantum dots) as well as various additional elements as rare earths, obtained by the NanoParticles Direct Doping, NPDD [3, 4].

It has been shown previously that with self-organization mechanism during the eutectic crystallization various shapes pertinent to metamaterials can be obtained as the 'split-ring resonator' geometry [1], rodlike [5] or lamellar structures which can be used as hyperbolic metamaterials [6], or for subwavelength transmission of electromagnetic waves [7, 8]. It has been also shown that porous three-dimensional structures can be obtained [9] as well as curved multilayer structure obtained by rotation during the eutectic growth - resembling necessary structure for metamaterial hyperlens [10]. Recently we demonstrated eutectic-based tunable nanoplasmonic materials for the first time in visible [11, 12, 13], and we have demonstrated a composite with plasmonic resonances at infrared wavelengths [to be published].

Acknowledgements, The authors thank the National Science Centre of Poland HARMONIA Project (2013/10/M/ST5/00650) and MAESTRO Project (2011/02/A/ST5/00471), and Air Force Office for Scientific Research of US NOE Project (14RT0477) for support of this work.

REFERENCES

1. D. A. Pawlak, S. Turczynski, M. Gajc, K. Kolodziejak, R. Diduszko, K. Rozniatowski, J. Smalc, I. Vendik, "How far are we from making metamaterials by self-organization? The microstructure of highly anisotropic particles with an SRR-like geometry," *Adv. Funct. Mat.*, Vol. 20, pp. 1116-1124, 2010.
2. A. M. Urbas, et al. "Roadmap on optical metamaterials," *J. Opt.* pp. 1-69, 2016.
3. M. Gajc, B. H. Surma, A. Klos, K. Sadecka, K. Orlinski, A. E. Nikolaenko, K. Zdunek, "Nanoparticle Direct Doping: novel method for manufacturing three-dimensional bulk plasmonic nanocomposites," *Adv. Funct.*

Mat. Vol. 23, 3443–3451, 2013.

4. https://www.facebook.com/fmlaboratory/videos/608375495898423/ - demonstration of the plasmonic resonance in materials obtained by NanoParticle Direct Doping method.
5. D. A. Pawlak, K. Kolodziejak, S. Turczynski, J. Kisielewski, K. Rożniatowski, R. Diduszko, M. Kaczkan, M. Malinowski," Self-organized, rod-like, micron-scale microstructure of Tb3Sc2Al3O12-TbScO3:Pr eutectic," *Chem. Mat.* Vol. 18, pp. 2450-2457, 2006.
6. A. Reyes-Coronado, M. F. Acosta, R. I. Merino, V. M. Orera, G. Kenanakis, N. Katsarakis, M. Kafesaki, Ch. Mavidis, J. Garcia de Abajo, E. N. Economou, C. M. Soukoulis, "Self-organization approach for THz polaritonic metamaterials," *Optics Express*, Vol. 20, pp. 14663-14682, 2012.
7. V. Myroshnychenko, A. Stefanski, A. Manjavacas, M. Kafesaki, R. I. Merino, V. M. Orera, D. A. Pawlak, F. J. Garcia de Abajo, "Interacting plasmon and phonon polaritons in aligned nano- and microwires", *Opt. Express* Vol. 20, pp.10879-10887, 2012.
8. M. F. Acosta, S. G. Rodrigo, L. Martín-Moreno, C. Pecharromán, R. I. Merino, "Micropillar Templates for Dielectric Filled Metal Arrays and Flexible Metamaterials," *Adv. Opt. Mat.* Vol. 5, pp. 1600670, 2017.
9. J. Kim, L. K. Aagesen, J. H. Choi, J. Choi, H. S. Kim, J. Liu, Ch-R. Cho, J. G. Kang, A. Ramazani, K. Thornton, P. V. Braun, "Template-directed directionally solidified three-dimensionally mesostructured AgCl-KCl eutectic photonic crystals," Adv. Mat. Vol. 27, pp. 4551-4559, 2015.
10. S. Akamatsu, S. Bottin-Rousseau, M. Serefoglu, G. Faivre, "Lamellar eutectic growth with anisotropic interphase boundaries: Experimental study using the rotating directional solidification method," *Acta Materialia* Vol. 60, pp. 3206–3214, 2012.
11. K. Sadecka, M. Gajc, K. Orlinski, H. B. Surma, I. Jozwik-Biala, A. Klos, K. Sobczak, P. Dluzewski, J. Toudert, D. A. Pawlak, "When eutectics meet plasmonics: Nanoplasmonic volumetric, self-organized silver-based eutectic," *Adv. Opt. Mat.* Vol. 3, pp. 381–389, 2015.
12. K. Sadecka, J. Toudert, H. B. Surma, D. A. Pawlak, "Temperature and atmosphere tunability of the nanoplasmonic resonance of a volumetric eutectic-based Bi2O3-Ag metamaterial," *Opt. Express* Vol. 23, pp. 19098-19111, 2015.
13. R. Deska, K. Sadecka, J. Olesiak-Bańska, K. Matczyszyn, D. A. Pawlak, M. Samoć, "Nonlinear plasmonics in eutectic composites: second harmonic generation and two-photon luminescence in a volumetric eutectic-based Bi2O3-Ag metamaterial," *Appl. Phys. Lett.* Vol. 110, pp. 031102-031105, 2017.

The Talbot Effect in a Metamaterial

H. Nikkhah*, T. J. Hall
University of Ottawa, Canada
*hnikk057@uottawa.ca

Abstract- The effect of anisotropy and spatial dispersion of a metamaterial on the Talbot effect may be engineered in principle. This has profound implications for applications of the Talbot Effect such as the design of multimode interference coupler (MMI). The presentation reports findings on the design of a metamaterial, and its approximation by a Kronig-Penney material that is designed to suppress the modal phase error, which limits the scaling of MMI port dimension.

The (fractional) Talbot effect describes the longitudinally spatially periodic (multiple) self-imaging of transversely spatially periodic in free-space. The theory of the Talbot effect assumes Fresnel diffraction, equivalently of a spectrum of plane wave modes concentrated on-axis, and the phase relation between the self-images predicted evinces an intimate relationship with number theory [1]. The free-space Talbot effect may be mapped to a description of the self-imaging properties of a planar multimode waveguide. The theory of the waveguide Talbot effect follows that of the free-space Talbot effect once account is taken of the (near) zero of the field introduced by the waveguide sidewalls. This somewhat complicates the phase relations. The free-space Talbot effect extends naturally to a homogenous medium and, consequently, to metamaterials.

There have been significant improvements in MMI design to improve performance (uniformity, efficiency, bandwidth) and to reduce the size of its foot-print. However, the performance of MMI on a high index contrast platform decreases significantly as the number of ports is increased. The modal phase error scales with the number of ports. This can be ameliorated by the use of a low index contrast platform [2] but this expedient conflicts with the requirement for high quality fractional self-imaging that the modal expansion is close to a Fourier series. It is modal phase errors caused by the failure of the paraxial approximation that impair performance, whether introduced by coupling of the access-waveguides or by failure of the paraxial approximation in a multimode section.

Additional degrees of freedom are needed to tune the individual phases of the intermediate modes, which might be introduced by appropriate patterning of the geometrical or optical properties of the multimode section. The perturbation of the lateral refractive index profile in the multimode section to reduce the modal phase errors has been considered theoretically [3]. Shallow etching of the multimode region can also reduce the effective index contrast [4], but these solutions have the demerit of requiring a multiple etch steps in the fabrication process. MMIs formed using a subwavelength grating waveguides (SWG) structure offer a solution requiring only a single etch step. In this way, the lateral refractive index contrast may be reduced by using SWG in the lateral cladding regions of the multimode section while the high index contrast on the access waveguides remains to be able to place them closely to reduce the size of MMIs when the number of ports increases [5]. Moreover, the modal birefringence of the waveguide can be controlled by depositing low and high index layers with the subwavelength pitch on the top of the waveguide [6]. MMIs that make use of the anisotropy of SWG structure to achieve ultra-compact footprints have been reported recently [7] and an MMI with ultra-broad bandwidth of 450 nm and phase deviation below 3 degrees has been achieved [8] by engineering the dispersion

properties of the multimode region using SWG to mitigate the wavelength dependence of the Talbot distance.

Homogenised bulk SWG behave as strongly anisotropic materials with a c-axis normal to the layers of a 1D multi-layer (Kronig-Penney) or for a 2D photonic crystal in 3D along the axis of uniformity. A Kronig-Penney structure is uniaxial as is a 2D square or hexagonal lattice of circular cylindrical holes in 3D. Anisotropy can help reduce the Talbot length but temporal and spatial dispersion is necessary to control the modal phase error and the wavelength dependence of the Talbot length. Anisotropy and, even more so, spatial dispersion complicate the theoretical description of waveguide structures. The metamaterial can result in a Talbot length substantially independent of vacuum wavelength – thereby permitting broadband operation [7]. In principle, the paraxial approximation may be made exact in the metaxial regime and therefore modal phase error eliminated – thereby permitting the scaling of MMI port dimensions.

The presentation reports findings on the design of a metamaterial, and its approximation by a Kronig-Penney material that is designed to suppress the modal phase error, which limits the scaling of MMI port dimension. The findings may enable the realisation of photonic integrated circuits components of unprecedented performance. For example, a compact broadband MMI with large port counts would constitute a breakthrough in integrated passive coupler / splitter components enabling, for example, single component discrete space passive DFT functions and large cross-overs with accurate port phase relations.

REFERENCES

1. Auslander, L., and R. Tolimieri. "Is computing with the finite Fourier transform pure or applied mathematics?." *Bulletin of the American Mathematical Society 1*, no. 6 (1979): 847-897.
2. Huang, J. Z., R. Scarmozzino, and R. M. Osgood. "A new design approach to large input/output number multimode interference couplers and its application to low-crosstalk WDM routers." *IEEE Photonics Technology Letters 10*, no. 9 (1998): 1292-1294.
3. Molina-Fernández, Inigo, Alejandro Ortega-Moñux, and Juan Gonzalo Wangüemert-Pérez. "Improving multimode interference couplers performance through index profile engineering." J*ournal of Lightwave Technology 27*, no. 10 (2009): 1307-1314.
4. Halir, Robert, Günther Roelkens, A. Ortega-Moñux, and J. G. Wangüemert-Pérez. "High-performance 90 hybrid based on a silicon-on-insulator multimode interference coupler." *Optics letters 36*, no. 2 (2011): 178-180.
5. Ortega-Monux, A., L. Zavargo-Peche, A. Maese-Novo, I. Molina-Fernández, R. Halir, J. G. Wanguemert-Perez, P. Cheben, and J. H. Schmid. "High-performance multimode interference coupler in silicon waveguides with subwavelength structures." *IEEE Photonics Technology Letters 23*, no. 19 (2011): 1406-1408.
6. Pérez-Galacho, D., R. Halir, A. Ortega-Moñux, C. Alonso-Ramos, R. Zhang, P. Runge, K. Janiak, H-G. Bach, A. G. Steffan, and Í. Molina-Fernández. "Integrated polarization beam splitter with relaxed fabrication tolerances." *Optics express 21*, no. 12 (2013): 14146-14151.
7. Halir, Robert, Pavel Cheben, Jose Manuel Luque-González, Jose Darío Sarmiento-Merenguel, Jens Schmid, Gonzalo Wangüemert-Pérez, Dan-Xia Xu, Shurui Wang, Alejandro Ortega-Moñux, and Íñigo Molina-Fernández. "Ultra broadband waveveguide coupler using an anisotropic sub-wavelength metamaterial." *arXiv preprint arXiv*:1606.03750 (2016).
8. Maese-Novo, A., R. Halir, S. Romero-García, D. Pérez-Galacho, L. Zavargo-Peche, A. Ortega-Moñux, I. Molina-Fernández, J. G. Wangüemert-Pérez, and P. Cheben. "Wavelength independent multimode interference coupler." *Optics express 21*, no. 6 (2013): 7033-7040.

Investigation of Locally Resonant Nanophononic Metamaterials with Ultralow Thermal Conductivity

B. Li[1], K. T. Tan[1*], and J. Christensen[2]

[1]Department of Mechanical Engineering, The University of Akron, Akron, OH 44325-3903, USA

[2]Instituto Gregorio Millan Barbany, Universidad Carlos III de Madrid, ES-28916 Legans (Madrid), Spain

[*]corresponding author: ktan@uakron.edu

Abstract-We present theoretical and numerical investigations on the locally resonant nanophononic metamaterials with ultralow thermal conductivity. The anomalous dynamics and thermal transport properties induced by various hybridizations between the local resonances of the branched nanopillars and the bulk modes of the host nanowires are verified by finite element analysis. A cantilever-in-mass model is proposed to theoretically analyze and control the resonance hybridization band. Particularly we report on near-zero thermal coefficients at local resonances with flat dispersion curves.

Analogous to locally resonant acoustic/elastic metamaterials, an emerging concept of nanophononic metamaterials (NPM) has been proposed recently for thermoelectric energy conversion [1]. Based on the local resonances of the nanopillars built on the surface of a host membrane, NPM can reduce the thermal conductivity without causing undesirable obstruction to the electron transport and thermoelectric conversion efficiency. Various numerical investigations on NPM have been conducted by using lattice dynamics (LD) calculations and molecular dynamics (MD) simulations [2, 3]. Little work has been reported about the analytical model of this emerging nanostructure. In this work, to theoretically investigate the dynamics and thermal transport properties of a side branched NPM (see Figure 1(a)), we propose a cantilever-in-mass model to describe the one-side branched nanowire. As shown in Figure 1(b), the host nanowire can be represented by an outer mass of m_1, and the side branched nanopillar can be enacted by a mass-less cantilever beam with an effective length of L_{eff} and an inner mass of m_2. This cantilever-in-mass model can be further transformed into a classical spring mass-in-mass model [4]. On basis of Euler–Bernoulli beam theory, we can calculate the equivalent spring stiffness of the nanopillar as $k = 3EI_z / L_{eff}^3$, where I_z is the moment of inertia about the bending z-axis or y-axis. Using the spring mass-in-mass model, we obtain the effective mass of the one-side branched nanowire as

$$m_{eff1} = m_1 + \frac{\omega_2^2 m_2}{\omega_2^2 - \omega^2} \tag{1}$$

where ω_2 is the locally resonant frequency of the internal resonator and can be written as

$$\omega_2 = \sqrt{\frac{Ea^2}{4L_{eff}^3 \rho L_h}} \tag{2}$$

The phonon dispersion relation of a one-side branched nanowire is illustrated in Figure 1(c). The mode

shapes at three representative frequencies (I, II and III) around different flat bands are visualized. It is observed that within the flat bands, the branched nanopillars exhibit distinct resonant profiles whereas the host wire does not confine any vibrations. Strong resonance coupling and hybridization between host structure and nanopillars induce the flat bands, which further result in a distinct reduction in group velocity. Using the Equations (1) and (2), we can theoretically analyze and control the first resonance hybridization bands. By modifying the resonator size, the thermal conductivity of the NPM can be further theoretically manipulated and tailored, which could be potentially significant in thermoelectric conversion.

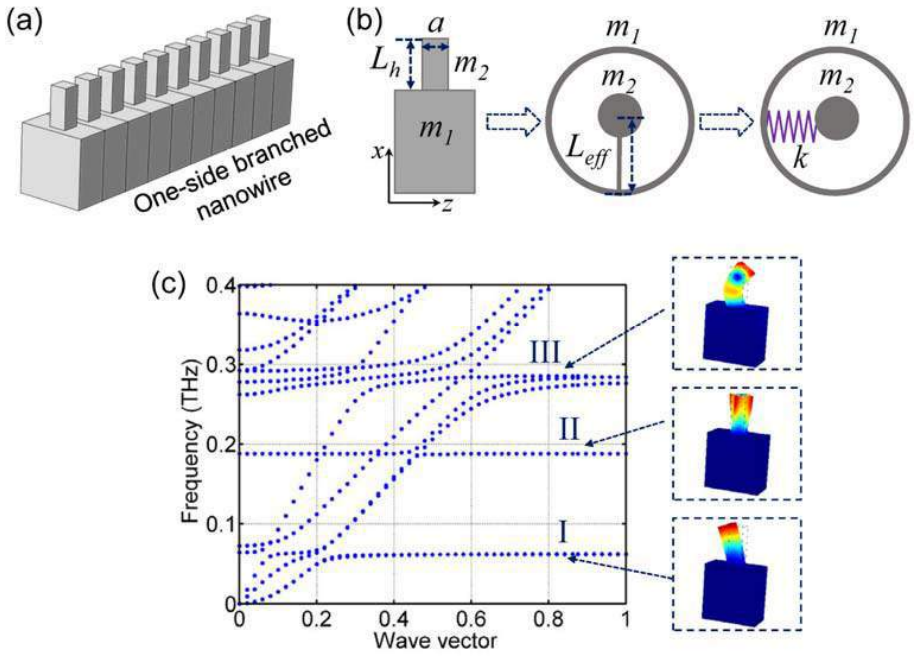

Figure 1. (a) Schematic diagram, (b) equivalent cantilever-in-mass model and (c) phonon dispersion relation for a one-side branched nanowire.

Acknowledgements

K.T. Tan acknowledges the Faculty Start-Up Grant support from The University of Akron. J. C. gratefully acknowledges financial support from the MINECO through a Ramón y Cajal grant (RYC-2015-17156).

REFERENCES

1. Davis, B. L. and M. I. Hussein, "Nanophononic metamaterial: thermal conductivity reduction by local resonance," *Phys Rev Lett*, Vol. 112, No. 5, 055505, 2014.
2. Xiong, S., K. Sääskilahti, Y. A. Kosevich, et al., "Blocking phonon transport by structural resonances in alloy-based nanophononic metamaterials leads to ultralow thermal conductivity," *Phys Rev Lett*, Vol. 117, No. 2, 025503, 2016.
3. Honarvar, H. and M. I. Hussein, "Spectral energy analysis of locally resonant nanophononic metamaterials by molecular simulations," *Phys Rev B*, Vol. 93, No. 8, 081412, 2016.
4. Qureshi, A., B. Li and K.T. Tan, "Numerical investigation of band gaps in 3D printed cantilever-in-mass metamaterials," *Sci Rep*, Vol. 6, 28314, 2016.

Ultrafast imaging of acoustic wave propagation in microsphere-based metamaterial structures

P. H. Otsuka[1], S. Mezil[1], V. Gusev[2], O. Matsuda[1], M. Tomoda[1], T. Gan[3], N. Boechler[4], A. A. Maznev[3], N. Fang[3], and O. B. Wright[1*]

[1]Division of Applied Physics, Faculty of Engineering, Hokkaido University, Sapporo 060-8628, Japan

[2]Laboratoire d'Acoustique de l'Université du Maine, UMR CNRS 6613, 72085 Le Mans Cedex 9, France

[3]Department of Mechanical Engineering, Massachusetts Institute of Technology, Cambridge, Massachusetts 02139, USA

[4]Department of Mechanical Engineering, University of Washington, Seattle, Washington 98195, USA

[*]corresponding author: olly@eng.hokudai.ac.jp

Abstract-We perform spatiotemporal imaging of acoustic waves in a metamaterial based on silica microspheres arranged in different patterns on a glass substrate, including waveguides. An ultrafast optical pump-probe system is used to obtain time-resolved two-dimensional images of both surface and bulk acoustic wave interactions with the microspheres. We also identify the metamaterial frequency band-gap regions through a detailed examination of the experimentally and theoretically obtained acoustic dispersion relations.

Materials consisting of two-dimensional arrays of particles demonstrate interesting effects on macro- and micro-scales [1,2]. Such materials exhibit a number of vibrational resonances corresponding to different types of particle motion and their mutual interactions. In particular, metamaterial structures consisting of microspheres on a glass substrate have lately been investigated by examining their interaction with propagating surface acoustic waves (SAWs), allowing the elucidation of the nature of the particle contacts and the demonstration of metamaterial band gaps corresponding to different resonances [2–4].

Arranging acoustic metamaterials in different patterns to form structures such as waveguides and cavities, in a similar way to analogous phononic-crystal and photonic-crystal structures, allows the construction of devices to control acoustic wave propagation. Such structures are ideally suited to spatiotemporal imaging studies. However, such real-time imaging has not been performed in acoustic metamaterials. In the case of particle arrays, the interaction of the particles with surface and bulk modes is expected to exhibit metamaterial band gaps.

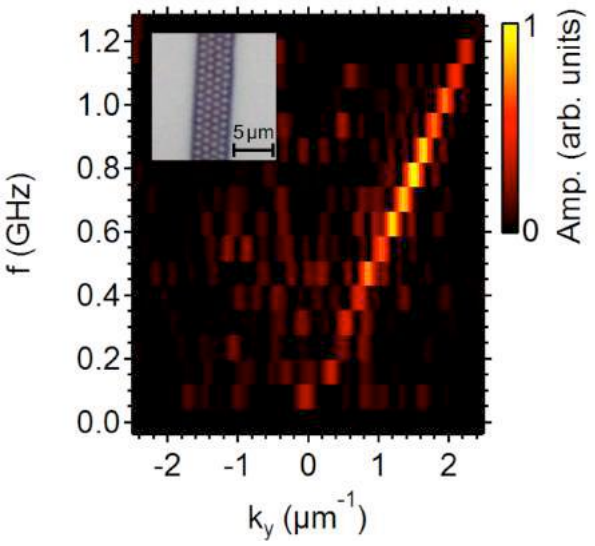

Fig. 1 Dispersion relation (frequency f vs wave number k_y along the propagation direction) of SAW propagation in a metamaterial arranged in the form of a linear waveguide. Inset: optical micrograph of a section of the sample.

However, gaps formed by bulk modes have not been experimentally studied in detail.

Here we experimentally investigate the interaction of propagating acoustic waves in a float-glass substrate with a surface structure consisting of a monolayer of 1.08 μm diameter silica spheres, demonstrating interactions with both SAWs and surface-skimming longitudinal bulk waves (SSLWs). These are excited and detected using an optical pump-probe set-up with a Ti:sapphire femtosecond laser operating at 75.6 MHz [5]. The glass substrate is coated with a 0.1 μm aluminum film for coupling with the laser pulses. The probe pulses, of wavelength 830 nm and duration ~200 fs, detect the out-of-plane surface particle velocity of the propagating waves. The beams are focused to spots of about 1 μm in diameter, and images are generated over areas up to ~200×200 μm^2, allowing animations of the surface motion to be obtained at acoustic frequencies up to ~1 GHz. Time-resolved images show acoustic waves—in particular SAWs and SSLWs—propagating along the sample surface.

Fourier analysis allows the propagation to be visualized at different frequencies, and allows the acoustic dispersion relation to be determined. In this connection, **k**-space images of the wave propagation on homogeneous samples show the presence of two acoustic modes, representing the SAWs and the faster SSLWs. Figure 1 shows the dispersion relation of SAW propagation for an arrangement of particles in the shape of a linear waveguide, in which case only the SAW mode appears. The inset of the figure shows an optical micrograph of the metamaterial waveguide sample, which consists of a column about 4 μm wide of closely packed microspheres. There is a pronounced dip in amplitude around ~300 MHz, corresponding to a wavelength of ~12 μm—considerably larger than the particle diameter—as expected for metamaterial-related resonances for this type of structure. This dip corresponds to the metamaterial band gap, a region in which the wave vector is a complex quantity.

The dispersion relation of a uniform array of microspheres is investigated by means of an analytical theory based on the interaction of the acoustic waves in the substrate with the particle vibrational resonances. We find good agreement with this theory and the experimentally determined dispersion relation of such a uniform array.

This work demonstrates the application of ultrafast laser imaging to microscale metamaterials. Future perspectives include the investigation of anisotropic effects in ordered structures and crystalline substrates, as well as the investigation of wave propagation in more complex 2D heterogeneous structures.

REFERENCES

1. Liu, Z., Zhang, X., Mao, Y., Zhu, Y.Y., Yang, Z., Chan, C.T. and Sheng, P., "Locally Resonant Sonic Materials", *Science*, Vol. 289, No. 5485, 1734–1736, 2000.
2. Boechler, N., Eliason, J.K., Kumar, A., Maznev, A.A., Nelson, K.A. and Fang, N., "Interaction of a Contact Resonance of Microspheres with Surface Acoustic Waves", *Phys. Rev. Lett.*, Vol. 111, No. 3, 036103, 2013.
3. Wallen, S. P., Maznev, A. A., and Boechler, N., "Dynamics of a monolayer of microspheres on an elastic substrate", *Phys. Rev. B*, Vol. 92, 174303, 2015.
4. Hiraiwa, M., Abi Ghanem, M., Wallen, S. P., Khanolkar, A., Maznev, A. A., Boechler, N., 2016. "Complex Contact-Based Dynamics of Microsphere Monolayers Revealed by Resonant Attenuation of Surface Acoustic Waves", *Phys. Rev. Lett.*, Vol. 116, 198001, 2016
5. Matsuda, O., Kaneko, S., Wright, O. B. and Tomoda, M., "Time-resolved gigahertz acoustic wave imaging at arbitrary frequencies", *IEEE. Trans. Ultrason. Ferroelec. Freq. Contr.*, Vol. 62, No. 3, 584–595, 2015.

Magneto-plasmonic nanostructures with broken symmetry for effective magneto-optical response

A. N. Kalish[1*] **and V. I. Belotelov**[1]
[1]Russian Quantum Center, Russia
[2]Lomonosov Moscow State University, Faculty of Physics, Russia
[*]corresponding author: kalish@physics.msu.ru

Abstract-The work is devoted to the development of the novel design of magnetoplasmonic nanostructures for improvement of magneto-optical properties. Namely, we propose (1) magneto-plasmonic crystals with broken symmetry for obtaining the Kerr effects at normal incidence, and (2) magneto-plasmonic quasicrystals with the broadband magneto-optical response.

Resent research has demonstrated the enhancement of magneto-optical effects in structured media. In particular, the attention has been paid to plasmonic crystals which are periodic structures supporting surface plasmon polaritons. It was demonstrated that the transverse Kerr effect and the Faraday effect are resonantly enhanced in magnetoplasmonic crystals, and also novel promising effects arise, namely the longitudinal intensity effect. As a rule, these effects are of resonant nature, due to their relation to the excitation of eigenmodes, which leads to narrow spectral range of magneto-optical response.

A specific kind of nanostructures that attracts attention is plasmonic quasicrystals [1], that demonstrate broadband optical response and, moreover, it is polarization-independent for 2D structures. We investigate magneto-optical effects in plasmonic quasicrystals formed by a uniform magnetic dielectric and a quasiperiodic 1D or 2D metallic lattice. Theoretical approach is developed and experimental results are presented. The experiments were performed with two types of structures: (i) the 1D quasi-periodic grating specially designed for obtaining plasmonic resonances at certain range of frequencies, and (ii) the 2D structure with 10-fold rotational symmetry. The Faraday effect as well as the transverse Kerr effect demonstrate broadband enhancement. We also find the conditions for the enhancement of the longitudinal magneto-photonic intensity effect.

Due to symmetry reasons linear effects associated with in-plane magnetization (such as the transverse Kerr effect) are prohibited at normal incidence. However, for practical reasons it would be useful to observe the transverse Kerr effect at normal incidence. For that reason, the spatial symmetry of the structure should be broken. To achieve that we investigate a plasmonic crystal formed by a uniform magnetic dielectric and a non-symmetrical metallic lattice. The obtained results for the transverse Kerr effect measurements at normal incidence are consistent with the theoretical considerations.

Acknowledgements: The work is supported by the Russian Foundation for Basic Research (project 16-52-45061) and the Russian Presidential Grant MK-2047.2017.2.

REFERENCES

1. Kasture S., A. P. Ravishankar, V. J. Yallapragada, R. Patil, N. V. Valappil, G. Mulay, and V.G. Achanta, "Plasmonic quasicrystals with broadband transmission enhancement," *Sci. Rep.* Vol. 4, 5257(1–6), 2014.

Parallelization of single nanoparticle biosensors

Wolfgang Fritzsche*, David Zopf, Jacqueline Jatschka, Sophie Thamm, André Dathe, Andrea Csáki, Matthias Thiele, Gabriele Schmidl, Li Guangrui and Ondrej Stranik

Department of Nanobiophotonics, Leibniz Institute of Photonic Technology (IPHT) Jena, Germany

*corresponding author: wolfgang.fritzsche@ipht-jena.de

There is steady increasing demand for a reliable and sensitive detection of a broad range of biomolecules. Among various different approaches for detection, our group is interested in the use of localized surface plasmon resonances (LSPR) as a transducing principle for the biomolecular binding. The LSPR occurs in metallic nanostructures, where the spectral position and shape of the resonance can be engineered by the shape of the structure. We have used several approaches with a different degree of complexity for the customized formation of the nanostructures such as microfluidic synthesis of anisotropic particles [1,2], double concentric structures by colloidal lithography [3], pyramidal structures by template stripping and colloidal lithography [4] or by thermal annealing of thin continuous metal layers [5]. The reliable readout of the spectral position of the LSPR with very low noise is one of the key challenges in the biosensing process. The relatively simple detection can be realized on nanoparticles ensembles, but the step to the spectroscopy of a single particle is challenging [6]. Often only single or a small number of nanostructures can be measured at once and therefore a parallelization of these measurements is very time consuming. In our approach we have established hyper-spectral imaging combined with microscopy imaging system, which allows to record spectral properties of many particles simultaneously [7]. We were able to map spatial variation of the protein adsorption and to demonstrate the limitation of the ensemble LSPR measurement caused by the shape variation of the metallic nanostructures.

REFERENCES

1. Thiele M, Soh J Z E, Knauer A, Malsch D, Stranik O, Müller R, Csáki A, Henkel T, Köhler J M and Fritzsche W 2016 Gold nanocubes – Direct comparison of synthesis approaches reveals the need for a microfluidic synthesis setup for a high reproducibility *Chemical Engineering Journal* 288 432–40
2. Combination of microfluidic high-throughput production and parameter screening for efficient shaping of gold nanocubes using Dean-flow mixing *Lab on a Chip* 2017 Advance Article DOI: 10.1039/C7LC00109F
3. Li G, Zopf D, Schmidl G, Fritzsche W and Stranik O 2016 Concentric dot-ring metal nanostructures prepared by colloidal lithography *Applied Physics Letters* 109 163101
4. Schmidl G, Dellith J, Dellith A, Teller N, Zopf D, Li G, Dathe A, Mayer G, Hübner U, Zeisberger M, Stranik O and Fritzsche W 2015 Silicon template preparation for the fabrication of thin patterned gold films via template stripping *Journal of Micromechanics and Microengineering* 25 125005
5. Schmidl G, Dellith J, Schneidewind H, Zopf D, Stranik O, Gawlik A, Anders S, Tympel V, Katzer C, Schmidl F and Fritzsche W 2015 Formation and characterization of silver nanoparticles embedded in optical transparent materials for plasmonic sensor surfaces *Materials Science and Engineering*: B 193 207–216
6. Jatschka J, Dathe A, Csáki A, Fritzsche W and Stranik O 2016 Propagating and localized surface plasmon resonance sensing — A critical comparison based on measurements and theory *Sens Bio-Sens Res* 7 62–70
7. Zopf D, Jatschka J, Dathe A, Jahr N, Fritzsche W and Stranik O 2016 Hyperspectral imaging of plasmon resonances in metallic nanoparticles *Biosensors and Bioelectronics* 81 287–93

Collective nano-optomechanics

E. Gil-Santos[1], W. Hease[1], A. Lemaître[2], M. Labousse[1], C. Ciuti[1], G. Leo[1] and I. Favero[1]

[1]*Matériaux et Phénomènes Quantiques, Université Paris Diderot - CNRS, 10 rue Alice Domon et Léonie Duquet, 75013 Paris, France*

[2] *Centre de Nanosciences et Nanotechnologies, CNRS, Université Paris Saclay, Route de Nozay, Marcoussis, France*

[*]ivan.favero@univ-paris-diderot.fr

Abstract- We introduce a new technique to resonantly post-tune ensembles of nanophotonic resonators with light. The method is scalable, highly precise, and compliant with on-chip structures. Building on the method, we develop medium-scale nano-optomechanical architectures where first collective phenomena do emerge. We report as first example the light-mediated frequency locking of multiple nanomechanical oscillators.

The interaction between light and mechanical motion, at the core of optomechanics, is boosted in lightweight nano-optomechanical resonators. After landmark experiments realized on single resonators, the investigation of collective phenomena now requires controlling vast ensembles of coupled resonators, with the coupling mediated by light or vibrations. This evolution towards collective nano-optomechanics bears potential for a variety of sensing applications of course, but for quantum or topological photonics as well. It is however impeded by the residual disorder imposed by nanofabrication techniques, which naturally detunes high-Q resonators and precludes resonant interactions between them.

Here we present a new technique to tune ensembles of nanophotonic/mechanical resonators. Light resonantly injected into the optical mode of a first resonator immersed in a fluid (gas or liquid) triggers an etching process, leading to a fine-tuning of the resonator's dimensions. The evolution of dimensions is monitored continuously by tracking the resonator's optical resonance with a laser. This tuning process, dubbed resonant photo-electrochemical etching, is naturally scalable to multiple resonators and allows us to tune small ensembles (2 to 5 resonators). We demonstrate the versatility of the process and discuss its implementations in various contexts.

Second, we present a first application of this tuning technique, by exploring the resonant optical interaction of multiple nano-optomechanical systems. We observe a first form of collective behavior involving several distant resonators, where a unidirectional flow of light frequency-locks a chain of nano-optomechanical oscillators.

REFERENCES

1. Gil-Santos, E., et al. "Scalable high-precision tuning of photonic resonators by resonant cavity-enhanced photoelectrochemical etching," *Nature Communications* 8, 14267 (2017).
2. Gil-Santos, E., et al. "Light-mediated cascaded locking of multiple nano-optomechanical oscillators," *Phys Rev Lett* 118, 063605 (2017).

CONNECTION BETWEEN NEGATIVE INDUCED ABSORPTION AND NEGATIVE INDEX OF REFRACTION FOR IRON DOPED POTASH-ALUMINA-BORATE GLASSES SUBJECTED TO THERMAL-RADIATION TREATMENT

A.N. Salakhitdinov[1], E.M. Ibragimova[2], M.K. Salakhitdinova[3]

[1-] Tashkent University of Information Technologies, Samarkand branch, Uzbekistan;
[2-] Institute of Nuclear Physics Academy of Science Republic of Uzbekistan;
[3]-Samarkand State University, Uzbekistan;
E-mail: smaysara@gmail.com

Abstract. This work experimentally revealed, that ^{60}Co-gamma-irradiation of potash-alumina-borate glasses doped with 2 mass.% of iron oxide to the dose of 1.7 MR in the temperature range of 150-300 ^{o}C induced differential optical density changes within $-5.7 \le \Delta D_{\lambda} \le -3$ in the wave length range of 300÷350 nm, which is characteristic for meta-material. Calculations have shown that variation of optical refraction index within $-0.66 \le \partial n / n_0 \le 0.1$ due to microstructure transformation causes changes in the differential absorption coefficient of the glass $-7.86 < \Delta\alpha_{\sim} < 0.11$.

Introduction. Besides synthesis of metamaterials [1], alternative possible way is the dynamic nonlinear effect – self-organization of multielement disordered matrix under simultaneous influence of heating and ionizing irradiation radiative effects.

Levy P.W. [2] showed that it is possible to present the radiation induced absorption formed by superposition of several individual absorption bands, in the form of Gaussian for each color center α (E) in the glasses as coefficient of absorption of photons with energy E:

$$\alpha(E)=\alpha_m \exp[- (4\ln 2/\Delta E_{1/2})(E - E_0)^2], \qquad (1)$$

where α_m – absorption coefficient at the maximum of Gaussian curve; $\Delta E_{1/2}$ – width on half-height maximum. Dexter D.L. [3] studied absorption of light by atoms in ionic crystals and improved Smakula's formula for the concentration of color centers, but this one can be use for oxide glasses

$$N_i \cdot f = 0.87 \cdot 10^{17} \cdot [n/(n^2+2)^2] \cdot \Delta E_{1/2} \cdot \alpha_m, \quad \alpha_m = (2{,}303/d) \cdot D \qquad (2)$$

where f–oscillator force, n- optical refraction index, D-optical density, d–sample thickness in cm.

The purpose of this work is to study "meta" – like optical properties related with structural transformations at thermal radiation treatment of multi-component oxide glasses.

Theoretical background. Earlier we showed that for borosilicate glasses [4] proceeding from doses dependences of optical density (D) it is possible to estimate the number of color centers N_i

Considering dispersive curves and their relation through (1) and (2): $\alpha_m=\alpha_m$ (E), n = n(E), for changes of α_m and n we can write

$$[d\alpha_m(E)/dn(E)] = [d\alpha_m(E)/dE] / [dn(E)/dE]. \qquad (3)$$

Let's assume that $$n(E)=n_0 + \delta n_E = n_0(1+(\delta n_E/n_0)), \qquad (4)$$

where n_0 - constant index of refraction, $\delta n_E/n_0$– the relative index of refraction taking into account dispersion. Replacing, for simplicity $\alpha_m(E) = \alpha_\sim$; $n_E = n_\sim$ and considering (2) and (3) for derivative $[d\alpha_\sim / dn_\sim]$ we find:

$$\left[d\alpha_\sim / dn_\sim\right] = C \cdot \left[N / \Delta E_{1/2}\right] \cdot \left\{(d / dn_\sim)\left[\left(n_0^2 + 2\right)/\left(n_0 + n_\sim\right)\right) + \left((2n_0 + n_\sim)/(n_0 + n_\sim)\right)\right\} \quad (5)$$

For simplicity we will designate $\left(n_\sim / n_0\right) = n_\sim^{'}$ and finally obtain

$$\left[d\alpha_\sim / dn_\sim^{'}\right] = \Delta\alpha_\sim = \left[2/\left(1 + n_\sim^{'}\right)\right] - \left[\left(1 + \left(2/n_0^2\right)\right)/\left(1 + n_\sim^{'}\right)^2\right] - \left[\left(2n_\sim^{'}\right)/\left(n_0\left(1 + n_\sim^{'}\right)^2\right)\right] \quad (6)$$

For meta-material [5] it is possible to accept limits of change $-0{,}66 \leq \partial n / n_0 \leq 0{,}1$ and calculate according to (6) $-7.86 < \Delta\alpha_\sim < 0.11$. Thus, due to the thermal-radiation effect, the negative value of absorption coefficient caused by results in a negative value of optical refraction index of the oxide glass. It means physically self-transparency under certain experiment conditions.

Objects of research and experimental results. We studied experimentally KAB-50 glass matrix with the composition ($50B_2O_3 25Al_2O_3 25K_2O$) mol. % doped with 2 mass.% Fe_2O_3. The samples were irradiated in ^{60}Co gamma-source at the dose rate of 236 R/s to the dose of 1.7 MR in the temperature range of 150-300 ^oC. Figure 1 shows the differential absorption spectra of the glass samples irradiated at various temperatures. The particular feature occurs in the wavelength range of 300÷350 nm, where the differential optical density becomes negative and changes in the range of $-5.7 \leq \Delta D_\lambda \leq -3$. In other words the glass sample after the treatment and additional irradiation becomes the similar of metamaterial, the same time the thermo-radiative processes can be considered as a non-linear self-transparency of glasses.

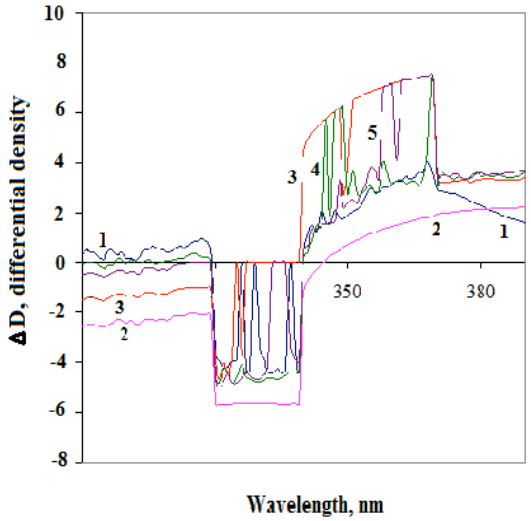

Fig. 1. Differential absorption spectra of the iron doped glasses ^{60}Co γ-irradiated at: 1-150 ^0C; 2 –200 ^0C; 3 - 250 ^0C; 4 - 300 ^0C

Acknowledgements This research is supported by the national grant A-4-9 by Ministry of High Education Republics of Uzbekistan.

References

1. Smith D.R., Padilla W.J., Veir D.C., Nemat-Nasser S.C., Schultz S. Phys.Rev.Lett. 2000, vol.84, iss.18, pp.4181-4187.
2. Levi P.W. J.Amer.Ceram. Soc.1960, 45, № 8, pp.389-395.
3. 3 D.L. Dexter. Phys. Rev. 1956, vol.101, iss.1, pp.48-55
4. Salakhitdinov A.N., Salakhitdinova M.K.,Yusupov A.A. Uzbek Journal of Physics, 2014, vol.16, iss.2, pp.144-148.
5. Panchenko V.A., Gizatillin M.G. Nanoantennas. Publisher “Radiotechnics”, Moscow, 2010, 87 p.

Self-assembled optical metamaterials.

X. Wang[1], S. Gomez-Graña[2], M. Treguer-Delapierre[2], A. Baron[1], A. Aradian[1], P. Richetti[1*], P. Barois[1*], and V. Ponsinet[2]

[1]University of Bordeaux, CNRS, CRPP, UPR 8641, 115 avenue Schweitzer, 33600 Pessac, France

[2]University of Bordeaux, CNRS, ICMCB, UPR 9048, 87 avenue Schweitzer, 33600 Pessac, France

[*]corresponding author: ponsinet@crpp-bordeaux.cnrs.fr

Abstract- Self-assembled metamaterials constitute a promising platform towards bulk optical materials with unusual effective properties. Reporting on several experimental systems, we show that they can reach unprecedented values of bulkiness and homogeneity figures of merit. This is achieved by assembling plasmonic nanoparticles into dense 3D structures, in which the localized surface plasmon resonances of the particles provide specific optical responses. We produce self-assembled hyperbolic metamaterials and self-assembled bulk nanocomposites presenting optical magnetism at visible wavelengths.

Among the exciting emerging functional nanomaterials, metamaterials are artificial composites presenting unusual properties of light propagation thanks to a specific structure at a length scale smaller than wavelength. The search for meta-properties in the visible domain has been mostly focused on nanostructured plasmonic systems. This has led to the search for new and versatile fabrication methodologies, among which nanochemistry and self-assembly have become promising routes. Two experimental systems will be discussed here, using self-assembly of metallic nanoparticles into dense organized structures, in which tailored localized surface plasmon resonances (LSPR) of the nanoparticles provide large amplitude and specific properties of the optical responses.

We produce anisotropic nanocomposites by the assembly of gold nanoparticles templated with spontaneously ordered matrices of diblock copolymers. In particular, we study periodic lamellar stacks of alternating layers of pure polymer (dielectric) and layers of composite of polymer loaded with a high density of gold nanoparticles (see Figure 1). The spectral variation of their anisotropic effective dielectric permittivity is determined by variable-angle spectroscopic ellipsometry using appropriate effective medium models.

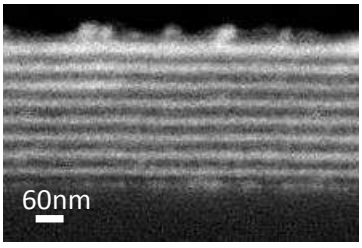

Figure 1. Side view (SEM) of a lamellar metal-dielectric

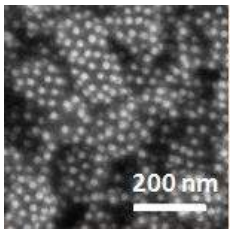

Figure 2. Top view (SEM) of assembled plasmonic raspberries

For large gold loading, the lamellar stack presents a frequency domain, in which the ordinary and extraordinary components of the dielectric function are of opposite signs. This peculiar property, called "hyperbolic", allows for the propagation of large magnitude wavevectors, carrying details finer than half the wavelength, otherwise corresponding to evanescent non-propagative waves in a usual dielectric. We therefore demonstrate for the first time the possibility of using a self-assembly methodology for the fabrication of bulk hyperbolic metamaterial[1].

We obtain plasmonic nanoclusters made of metallic satellites surrounding a dielectric core (so-called "plasmonic raspberries") by colloidal engineering. We measure both the electric dipolar and the magnetic dipolar scattering cross-section of these plasmonic raspberries vs. wavelength with a polarization resolved spectroscopic light scattering experiment. The raspberry-like nanoclusters are subsequently assembled to form a bulk metamaterial (see Figure 2), with an effective permeability parameter probed by spectroscopic ellipsometry at variable incidence, found to take values between 0.8 and 1.4, over the visible light wavelength range[2]. We thus created the first nanostructured metamaterial exhibiting a strong isotropic artificial optical magnetism in visible light.

We will discuss these results and how they can open new routes for metamaterial fabrication.

Acknowledgements. This work is supported by the LabEx AMADEus (ANR-10-LABX-42) in the framework of IdEx Bordeaux (ANR-10-IDEX-03-02), France.

REFERENCES

1. Wang, X., K. Ehrhardt, C. Tallet, M. Warenghem, A. Baron, A. Aradian, M. Kildemo, and V. Ponsinet, "Hyperbolic-by-design self-assembled metamaterial based on block copolymers lamellar phases," *J. Opt. & Laser Techn*., Vol. 88, 85-95, 2017.
2. Gomez-Graña, S., A. Le Beulze, M. Treguer-Delapierre, S. Mornet, E. Duguet, E. Grana, E. Cloutet, G. Hadziioannou, J. Leng, J.-B. Salmon, V. G. Kravets, A. N. Grigorenko, N. A. Peyyety, V. Ponsinet, P. Richetti, A. Baron, D. Torrent, and P. Barois, "Hierarchical self-assembly of a bulk metamaterial enables isotropic magnetic permeability at optical frequencies," *Materials Horizons*, Vol. 3, 596-601, 2016.

Photonic Band Gaps in Amorphous Gyroid Structures

M. Florescu
Advanced Technology Institute and Department of Physics,
University of Surrey, Guildford, GU2 7XH, United Kingdom

Abstract-We introduce a new class of photonic band gap materials based on amorphous gyroid networks. The amorphous gyroid networks are created using the concept of local-self uniformity that controls spatial correlations of on a wide range of length scales.

The fundamental correlations between the geometrical/topological characteristics of photonic materials and the advanced optical functionalities they provide is a fundamental problem in the field of structured photonic materials. To this end we introduce a new metric, local self-uniformity (LSU) [1] as a measure of the structural order of photonic network architectures of predefined valency.

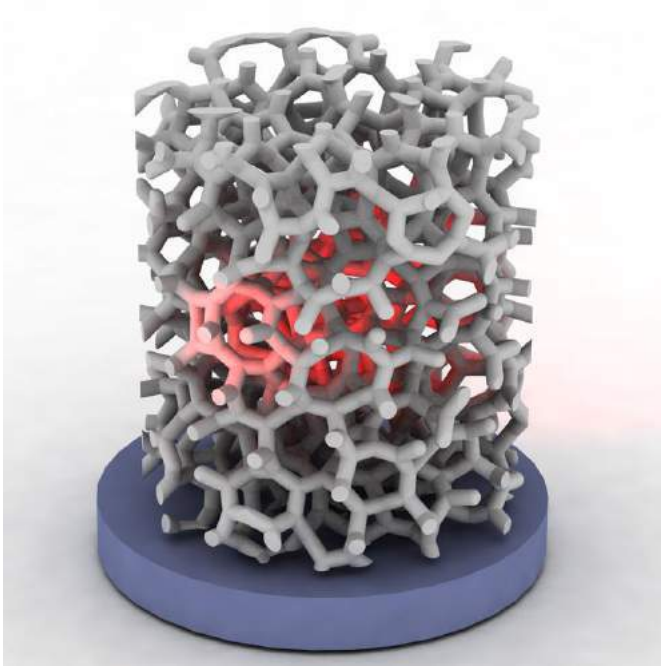

Figure 1: Schematic design of an amorphous gyroid photonic network.

The LSU metric can quantify the correlation between uniformity of the local environments and the overall photonic band gap properties and provides a new paradigm in the design of aperiodic media. LSU can be employed to uniquely classify photonic networks with a precisely defined upper limit reached for the only known strongly isotropic structures, the trivalent (SRS-gyroid) and tetravalent (diamond) networks. The lower reaches of the scale describe an interesting minimal local self-uniformity, or maximal self-dissimilarity. The LSU concept enables us to explore photonic band gap formation in a completely new architecture, the

amorphous gyroid network and to show that very distinct photonic architectures presenting large photonic band gaps, be they periodic or aperiodic, all are characterized by high values levels of local self-uniformity. The LSU metric renders the exact nature of their underlying seed patterns, whether crystalline, quasicrystalline, or hyperuniform, irrelevant.

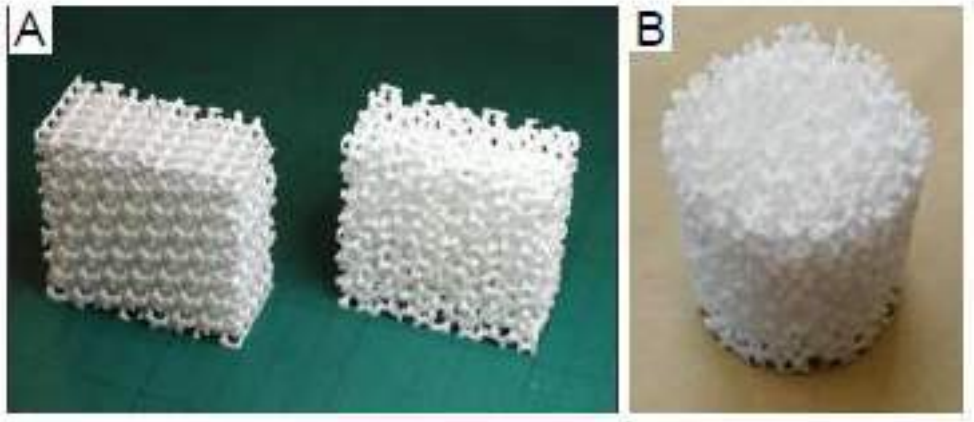

Figure 2 Alumina 3D-printed networks. The single network gyroid and amorphous gyroid blocks (A). Completed cylinder (B) assembled from the two semi-cylindrical pieces.

The new amorphous gyroid network is of significant interest for photonic applications. Amorphous gyroid is a three-dimensional continuous random network (CRN) characterized by 3-fold connected vertices and short range structural correlations whose strength decays with distance. By analogy with the well-known glassy disordered honeycomb and amorphous diamond networks, the network structure about a given vertex in amorphous gyroid should be a low symmetry realization of its structure in crystalline single network gyroid. We can expect that an amorphous gyroid structure possessing these properties should, like other glassy networks, exhibit substantial local self-uniformity. The realization and study of amorphous gyroid thus presents an opportunity to investigate the possible connection between local self-uniformity and the formation of sizeable photonic band gaps (PBGs) in high refractive index disordered structures.

The physical concept behind amorphous gyroid networks, local self-uniformity directly links a network's physical structure to its optical properties. It describes a fundamental mechanism of photonic band gap formation. Local self-uniformity, however, has significant relevance beyond this. It illuminates a subtlety in structural coloring architectures that has so far escaped detection. Further, an appreciation of a material's local electromagnetic resonances, and the control that local self-uniformity allows over the way they couple, represents a new paradigm in complex optical material design.

Acknowledgements This work was partially supported by the University of Surrey's FRSF and IAA awards to MF, the EPSRC (United Kingdom) DTG Grant No. EP/J500562/1, EPSRC (United Kingdom) Strategic Equipment Grant No. EP/L02263X/1 (EP/M008576/1) and EPSRC (United Kingdom) Grant EP/M027791/1.

REFERENCES

1. S. Sellers, W. Man, S. and M. Florescu, "Local self-uniformity in photonic networks", " Nature Communications, 8, 14439 (2017).

Nanostructured Si photonics for applications in the near- and mid-infrared

Invited Presentation

C. Alonso-Ramos[1,*], D. Pérez-Galacho[1], D. Oser[1], X. Le Roux[1], D. Benedikovic[1], F. Mazeas[2], W. Zhang[1], S. Serna[1], V. Vakarin[1], E. Durán-Valdeiglesias[1], L. Labonte[2], S. Tanzilli[2], P. Cheben[3], E. Cassan[1], D. Marris-Morini[1], L. Vivien[1]

[1] Centre de Nanosciences et de Nanotechnologies, CNRS, Université Paris-Sud, Université Paris-Saclay, C2N – Orsay, 91405 Orsay cedex, France.

[2] Université Côte d'Azur, CNRS, Institut de Physique de Nice, Parc Valrose, 06108 Nice Cedex 2, France

[3] National Research Council, Ottawa, K1A 0R6, Canada.

[*]corresponding author: carlos.ramos@u-psud.fr

Abstract- We report our advances in the development of subwavelength engineered structures for on-chip photonics circuits, including Si membrane waveguides for sensing applications in the near- and mid-infrared, and high pump-rejection filters for quantum photonics.

The large transparency window of silicon (1.1 - 8 μm wavelength range) makes it a promising material for the implementation of a wide range of applications, including datacom, sensing, nonlinear and quantum optics. Patterning silicon with features smaller than half of the wavelength (well within the capabilities of standard silicon fabrication processes) has proven to be a powerful tool to tailor material properties, allowing the realization of Si devices with unprecedented performances [1].

Here, we exploit the new degrees of freedom leveraged by subwavelength engineering to implement two types of high-performance Si filters for nonlinear optics, quantum and sensing applications in the near- and mid-infrared. First, we will present subwavelength engineered Bragg filters based on a novel differential corrugation width configuration allowing narrow-band rejection with a single etch step and relaxed fabrication constraints [2]. These filters feature a rejection bandwidth of 1.1 nm and an extinction ratio exceeding 40 dB. Then, we will show an integrated Bragg grating waveguide filter for single-mode operation in near- and mid-IR. A 500-nm-thick and 1100-nm-wide silicon waveguide allows single-mode propagation in the mid-IR, while a specific waveguide corrugation is used to radiate out the higher order modes in the near-IR. This results in an effectively single-mode operation in near-IR. Building upon this concept, we demonstrated efficient waveguide Bragg grating filters for several applications. Our achievements pave the way towards the development of new types of on-chip functionalities in silicon based on the principle of subwavelength waveguide engineering.

REFERENCES

1. R. Halir, P. Bock, P. Cheben, A. Ortega-Moñux, C. Alonso-Ramos, J. H. Schmid, J. Lapointe, D.-X. Xu, J. G. Wangüemert-Pérez, I. Molina-Fernández, S. Janz, "Waveguide sub-wavelength structures: principles and applications," *Laser & Photon. Rev.* 9(1), L25 (2014).

2. D. Pérez-Galacho, C. Alonso-Ramos, F. Mazeas, X. Le Roux, D. Oser, W. Zhang, L. Labonté, S. Tanzilli, E. Cassan, D. Marriz-Morini, L. Vivien, “Optical pump-rejection filter based on silicon sub-wavelength engineered photonic structures,” *Opt*. *Lett*. 42(8), 1468 (2017).

Deterministic Quantum Dot Microlenses: Building Blocks for Photonic Quantum Networks

A. Thoma[1], P. Schnauber[1], S. Fischbach[1], A. Kaganskiy[1], R. Schmidt[1], S. Burger[2], F. Schmidt[2], A. Carmele[3], A. Knorr[3], A. Strittmatter[1], T. Heindel[1], S. Rodt[1], and S. Reitzenstein[1*]

[1]Institut für Festkörperphysik, Technische Universität Berlin, Berlin, Germany

[2]Zuse-Institut Berlin (ZIB), Berlin, Germany

[3]Institut für Theoretische Physik, Technische Universität Berlin, Berlin, Germany

[*]corresponding author: stephan.reitzenstein@physik.tu-berlin.de.

Abstract We report on deterministic quantum light sources for applications in quantum communication systems. The sources are based on single quantum dot - microlenses fabricated by by in-situ electron-beam lithography. These quantum devices show close to ideal single photon purity with $g^{(2)}(0)<0.01$, high photon indistinguishability with V>90%, and high potential for quantum repeater networks based on entanglement distribution. Moreover, quantum dot – microlenses can be used for efficient twin-photon emission and allow for the development of stand-alone fiber-coupled single-photon sources.

The realization of building blocks for quantum networks has become one of the driving forces for the development of advanced nanophotonic device concepts and nanofabrication technologies. Within this field, significant progress has been achieved regarding for instance the fabrication of efficient quantum dot (QD) based single-photon sources. This work has almost elusively been performed on self-assembled QDs, which is explained by their superb optical and quantum optical properties. However, due to the self-assembled growth, both the position and the emission energy of individual QDs are controlled, which leads to a very low yield of usable optical devices when standard nano-processing schemes are used. This issue strongly limits the applicability upscaling of single QD based photon sources in practical systems such as multi-partite quantum networks.

In this contribution we will present a nanotechnology platform for the deterministic fabrication of high quality quantum light sources based on self-assembled QDs. Our technique is based on in-situ electron-beam lithography which allows us to integrate pre-selected quantum dots into photonic devices with nm-accuracy and flexible device design [1, 2]. In this way we realize deterministic QD microlenses (see Fig. on the right) which can act as non-classical light sources with superb optical and quantum-optical properties in terms of the photon extraction efficiency, the single photon purity and the degree of photon indistinguishability [3]. I will also discuss effects limiting the photon indistinguishability and show how they can be explored by delay-time and temperature dependent Hong-Ou-Mandel experiments [4]. The talk will conclude with recent work

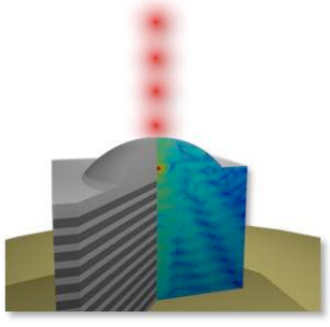

Fig. 1: Schematic view of a single-QD microlens.

and an outlook towards entanglement swapping using QD based quantum light sources [5], twin-photon emission [6] and direct fiber coupling of a QD-microlens the realize a stand-alone and user-friendly single photon source [7].

REFERENCES

1. Gschrey, M. et al., "In situ electron-beam lithography of deterministic single-quantum-dot mesa-structures using low-temperature cathodoluminescence spectroscopy," Appl. Phys. Lett. 102, 251113, 2013
2. Gschrey, M. et al., "Resolution and alignment accuracy of low-temperature in situ electron beam lithography for nanophotonic device fabrication," J. Vac. Sci. Technol. B 33, 021603, 2015
3. Gschrey, M. et al., „Highly indistinguishable photons from deterministic quantum-dot microlenses utilizing three-dimensional in situ electron-beam lithography," Nat. Comms. 6, 7662, 2015
4. Thoma, A. et al., "Exploring Dephasing of a Solid-State Quantum Emitter via Time- and Temperature-Dependent Hong-Ou-Mandel Experiments," Phys. Rev. Lett., 116, 033601, 2016
5. Thoma, A. et al., "Two-photon interference from remote deterministic quantum dot microlenses,"Appl. Phys. Lett. 110, 011104, 2017
6. Heindel, T. et al., "A bright triggered twin-photon source in the solid state, ", Nat. Commun, in press, arXiv:1608.02768
7. Schlehahn, A. et al., „A stand-alone fiber-coupled single-photon source ," arXiv:1703.10536

Engineering stimulated light-sound scattering in silicon

Peter T. Rakich[1]
[1]Yale University, Department of Applied Physics, New Haven CT, USA
[*]corresponding author: peter.rakich@yale.edu

Abstract- Brillouin nonlinearities permit stimulated light-sound scattering through optomechanical three-wave interactions. In conventional silicon waveguides, material response and poor acoustic confinement effectively stifle Brillouin nonlinearities. However, new optomechanical waveguides—that control both light and sound—have recently transformed Brillouin interactions into the strongest and most tailorable nonlinearities in silicon. In this paper, we use theory and experiment to demonstrate a variety of stimulated light-scattering processes. We also harness these interactions to realize light-amplification, signal filtering, and laser technologies.

Optical confinement and wave-guidance within optical fibers has allowed us to harness and enhance silica's intrinsic Kerr, Raman, and Brillouin nonlinearities. As a result, the silica fiber-optic is perhaps one of the most versatile nonlinear devices in existence [1]. These same principles have been applied in silicon photonics to yield a new class of highly nonlinear devices on a chip. For example, tight modal confinement has been used to radically enhance intrinsic Kerr and Raman nonlinearities in nanoscale silicon waveguides[2], [3].

Counterintuitively, Brillouin nonlinearities—which far surpass both Kerr and Raman nonlinearities in optical fibers—are exceedingly weak within these highly nonlinear silicon waveguides[4]. Within conventional silicon waveguides, material response and poor acoustic confinement effectively stifle Brillouin nonlinearities [4]. However, new optomechanical waveguides—that control both light and sound—have recently transformed Brillouin interactions into the strongest and most tailorable nonlinearities in silicon [5]–[8].

In this paper, we demonstrate a range of highly engineerable new stimulated Brillouin interactions in silicon waveguides by controlling both light and sound within a growing ecosystem of Brillouin-active optomechanical waveguides. In particular, we describe the recent realization of high performance Brillouin amplifiers in silicon [8] using forward intra-modal Brillouin interactions. We show how the unusual properties of forward-Brillouin interactions can be used to create microwave-photonic filtering technologies that have no analogue in all-optical signal processing [9], [10].

Building on these concepts, we introduce a new type of multi-mode optomechanical waveguide that creates phonon-mediated coupling between optical modes with distinct spatial profiles[11]. This process, termed stimulated inter-modal scattering, produces unusual new nonlinear dynamics[12], [13]. From a technology perspective, this process is intriguing because the incident and scattered fields propagate in distinct spatial modes, permitting unique forms of mode-multiplexing and dynamical mode conversion [11]. We show that this interaction opens the door to a range of Brillouin processes that enable everything from slow-light, to Brillouin-induced transparency, to new laser technologies in silicon.

REFERENCES

[1] G. Agrawal, *Nonlinear Fiber Optics*. Academic Press, 2012.
[2] H. Rong, A. Liu, R. Nicolaescu, M. Paniccia, O. Cohen, and D. Hak, "Raman gain and nonlinear optical

absorption measurements in a low-loss silicon waveguide," *Applied Physics Letters*, vol. 85, no. 12, pp. 2196–2198, Sep. 2004.

[3] M. A. Foster, A. C. Turner, J. E. Sharping, B. S. Schmidt, M. Lipson, and A. L. Gaeta, "Broad-band optical parametric gain on a silicon photonic chip," *Nature*, vol. 441, no. 7096, pp. 960–963, Jun. 2006.

[4] P. T. Rakich, C. Reinke, R. Camacho, P. Davids, and Z. Wang, "Giant Enhancement of Stimulated Brillouin Scattering in the Subwavelength Limit," *Phys. Rev. X*, vol. 2, no. 1, p. 011008, Jan. 2012.

[5] H. Shin *et al.*, "Tailorable stimulated Brillouin scattering in nanoscale silicon waveguides," *Nat Commun*, vol. 4, p. 1944, Jun. 2013.

[6] R. Van Laer, B. Kuyken, D. Van Thourhout, and R. Baets, "Interaction between light and highly confined hypersound in a silicon photonic nanowire," *Nat Photon*, vol. 9, no. 3, pp. 199–203, Mar. 2015.

[7] R. V. Laer, A. Bazin, B. Kuyken, R. Baets, and D. V. Thourhout, "Net on-chip Brillouin gain based on suspended silicon nanowires," *New J. Phys.*, vol. 17, no. 11, p. 115005, 2015.

[8] E. A. Kittlaus, H. Shin, and P. T. Rakich, "Large Brillouin amplification in silicon," *Nat Photon*, vol. advance online publication, Jun. 2016.

[9] H. Shin, J. A. Cox, R. Jarecki, A. Starbuck, Z. Wang, and P. T. Rakich, "Control of coherent information via on-chip photonic–phononic emitter–receivers," *Nat Commun*, vol. 6, p. 6427, Mar. 2015.

[10] A. Casas-Bedoya, B. Morrison, M. Pagani, D. Marpaung, and B. J. Eggleton, "Tunable narrowband microwave photonic filter created by stimulated Brillouin scattering from a silicon nanowire," *Opt. Lett., OL*, vol. 40, no. 17, pp. 4154–4157, Sep. 2015.

[11] E. A. Kittlaus, N. T. Otterstrom, and P. T. Rakich, "On-chip Inter-modal Brillouin Scattering," *arXiv:1611.03556 [physics]*, Nov. 2016.

[12] M. S. Kang, A. Brenn, and P. St.J. Russell, "All-Optical Control of Gigahertz Acoustic Resonances by Forward Stimulated Interpolarization Scattering in a Photonic Crystal Fiber," *Phys. Rev. Lett.*, vol. 105, no. 15, p. 153901, Oct. 2010.

[13] M. S. Kang, A. Butsch, and P. S. J. Russell, "Reconfigurable light-driven opto-acoustic isolators in photonic crystal fibre," *Nature Photonics*, vol. 5, no. 9, pp. 549–553, Aug. 2011.

Time-variant metasurfaces as a frequency converting platform

Bumki Min

[1]Department of Mechanical Engineering, Korea Advanced Institute of Science and Technology (KAIST), Republic of Korea

[*]corresponding author: bmin@kaist.ac.kr

Abstract- Rapidly time-varying metasurfaces are proposed as a frequency converting platform. The proposed metasurface is designed for sudden merging of two distinct resonances into a single resonance upon ultrafast optical excitation. From this dispersion-engineered temporal boundary onward, the merged resonance frequency component can be radiated.

A few years before the experimental demonstration of coherent nonlinear optical effect, Morgenthaler contemplated an alternate route towards the conversion of light frequency via velocity modulation of the wave, i.e. temporal variations of permittivity and/or permeability of the media [1]. Afterwards, continual theoretical efforts have been made to understand this linear frequency conversion. Experimental verifications followed then in the field of plasma physics; notable examples were the observation of frequency shift in rapidly growing plasma from laser ionization of gases and semiconductors. However, it was not until a group of researchers proposed chip-scale dynamic photonic structures, such as photonic crystals [2-5], micro-ring resonators [6], and waveguides [7] for the observation of wavelength conversion that the phenomena became the subject of engineering.

Active resonant metamaterials, in which the resonating meta-atoms are hybridized with electrically or optically reconfigurable natural materials, can be thought of as an optimal platform that can be spatiotemporally rearranged. Here, we propose rapidly time-varying metasurfaces as a frequency converting platform and demonstrate their efficacy experimentally at terahertz frequencies. Since our proposed conversion scheme does not rely on a nonlinearity of comprising materials, the conversion efficiency is invariant with respect to the intensity of an input wave. Therefore, this method would be beneficial especially for the frequency conversion of waves with weak intensities. Furthermore, the frequency of a converted wave and its efficiency is tailorable to a large degree as the conversion process does not require energy conservation between participating waves.

REFERENCES

1. Morgenthaler, F. R. “Velocity modulation of electromagnetic waves,” *IRE Trans. Microwave Theory Tech.* Vol. 6, 167-171, 1958.
2. Yacomitti, A. M. et al. “Nonadiabatic dynamics of the electromagnetic field and charge carriers in high-Q photonic crystal resonators,” *Phys. Rev. Lett.* Vol. 96, 093901, 2006.
3. Notomi, M. and Mitsugi, S. “Wavelength conversion via dynamic refractive index tuning of a cavity,” *Phys. Rev. A.* Vol.73, 05180, 2006.
4. Tanabe, T., Notomi, M., Taniyama, H., and Kuramochi, E. “Dynamic release of trapped light from an ultrahigh-Q nanocavity via adiabatic frequency tuning,” *Phys. Rev. Lett.* Vol. 102, 043907, 2009.
5. Kampfrath, T. et al. “Ultrafast adiabatic manipulation of slow light in a photonic crystal,” *Phys. Rev. A.* Vol. 81, 043837, 2010.

6. Preble, S. F., Xu, Q. and Lipson, M. “Changing the colour of light in a silicon resonator,” *Nat. Photon.* Vol. 1, 293-296, 2007.
7. Fan, L. et al. “Integrated optomechanical single-photon frequency shifte,” *Nat. Photon.* Vol. 10, 766-770, 2016.

Quantum Optics with Nanowires

V. Zwiller[‡§], A. Elshaari[‡], K. Jöns[‡], M. Versteegh[‡], L. Yang[‡], A. Fognini[§], I. Esmaeil Zadeh[§], L. Schweickert[‡], J. Zichi[‡], K. Zeuner[‡], T. Lettner[‡]

[‡]*Quantum Nano Photonics, Applied Physics Department, KTH, Stockholm, Sweden*
[§]Kavli Insitute of Nanoscience, TU Delft, The Netherlands

Nanowires offer new opportunities for nanoscale quantum optics; the quantum dot geometry in semiconducting nanowires as well as the material composition and environment can be engineered with unprecedented freedom to improve the light extraction efficiency.

Quantum dots in nanowires are shown to be efficient single photon sources, in addition because of the very small fine structure splitting, we demonstrate the generation of entangled pairs of photons from a nanowire.

Another type of nanowire under study in our group is superconducting nanowires for single photon detection, reaching efficiencies, time resolution and dark counts beyond currently available detectors. We will discuss our first attempts at combining semiconducting nanowire based single photon emitters and superconducting nanowire single photon detectors on a chip to realize integrated quantum circuits.

Tuning directional scattering through external magnetic fields in magneto-optical disordered media

Tiago J. Arruda[1], Felipe A. Pinheiro[2], and Alexandre S. Martinez[3,4]

[1]São Carlos Institute of Physics (IFSC), University of São Paulo (USP), São Paulo, Brazil,
[2]Institute of Physics, Federal University of Rio de Janeiro (UFRJ), Rio de Janeiro, Brazil,
[3]Ribeirão Preto Faculty of Philosophy, Sciences and Languages (FFCLRP), USP, São Paulo, Brazil,
[4]National Institute of Science and Technology in Complex Systems, Rio de Janeiro, Brazil.
*corresponding author, E-mail: tiagojarruda@gmail.com

Abstract

We analytically study light scattering of normally irradiated magneto-optical coated cylinders [1]. We show that the application of an external magnetic field along the cylinder axis, consisting of silica core and InSb shell, induces a drastic decrease in absorption and negative values of scattering anisotropy. This preferential backscattering response results in an anomalous regime of multiple light scattering from a collection of magneto-optical microcylinders, in which the scattering mean free path is larger than the transport mean free path.

1. Introduction

Preferential backscattering, which hardly occurs in natural media, is characterized by negative values of the asymmetry parameter, the average of the cosine of the scattering angle, $\langle \cos\theta \rangle$ [2]. Negative $\langle \cos\theta \rangle$ has been reported in ferromagnetic particles [3] and lossless dielectric nanospheres made of moderate permittivity materials, such as silicon or germanium nanospheres in the infrared region [4]. In these cases, negative asymmetry parameters have been show to lead to an unusual regime in multiple light scattering, in which the scattering mean free path is larger than the transport mean free path [4]. This peculiar transport regime has also been demonstrated for multiple scattering systems with correlated disorder under certain conditions [5].

Here, we propose an alternative, versatile strategy to achieve not only preferential backscattering (negative $\langle \cos\theta \rangle$) but also to control the scattering direction with an external parameter [6], which can be either an applied magnetic field or the temperature [1, 7]. We consider an infinitely long core-shell magneto-optical cylinder, normally irradiated by p waves, i.e., the magnetic field is parallel to the cylinder axis. The cylinder is embedded in vacuum (ε_0, μ_0) and consists of a dielectric core made of silica (SiO_2) ($\varepsilon_1 = 2.25\varepsilon_0$ and $\mu_1 = \mu_0$ in the far-infrared) of radius a coated with a cylindrical shell of indium antimonide (InSb) of radius b, which is a magneto-optical material strongly dependent of the external magnetic field and the temperature [9]. The complete analytical and numerical study of this system can be found in Ref. [1].

2. Results and discussion

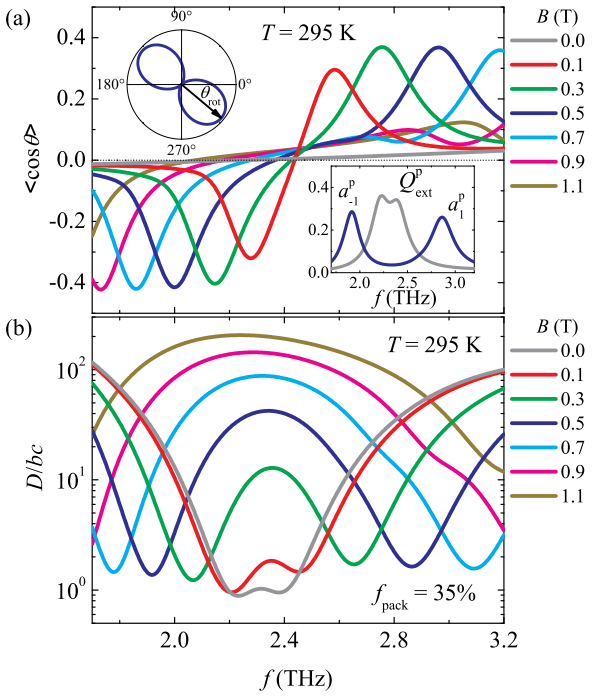

Figure 1: Light scattering by a SiO_2 microcylinder ($\varepsilon_1 = 2.25\varepsilon_0$) coated with InSb shell. The system is normally irradiated by p waves and is subjected to an external magnetic field $\mathbf{B} = B\hat{\mathbf{z}}$. (a) $\langle \cos\theta \rangle$ as a function of the frequency f, for various magnetic field amplitudes B, with the scatterer radius being $b = 2.5$ μm ($kb \ll 1$), and aspect ratio $S = a/b = 0.35$ at room temperature ($T = 295$ K). The insets show the extinction efficiency Q_{ext} for $B = 0.0$ T ($a_1^{\text{p}} = a_{-1}^{\text{p}}$) and $B = 0.5$ T ($a_1^{\text{p}} \neq a_{-1}^{\text{p}}$) and the corresponding scattering pattern for $B = 0.5$ T and $f = 2.0$ THz, where $a_{\pm 1}^{\text{p}}$ is the Lorenz-Mie coefficient for p waves. (b) The diffusion coefficient D for a collection of parallel and identical magneto-optical cylinders with packing fraction $f_{\text{pack}} = 35\%$, where c is the speed of light.

Figure 1(a) shows that the application of an external magnetic field $\mathbf{B}$ strongly affects the scattering directionality [8]. Indeed, the presence of $\mathbf{B}$ breaks the scattering isotropy of dipolar scattering, in contrast to what occurs for non-Faraday-active materials in the Rayleigh regime ($kb \ll 1$). For magneto-optical materials the Lorenz-Mie coefficient are not degenerate ($a_1^{\rm p} \neq a_{-1}^{\rm p}$) for $B \neq 0$, leading to a strongly asymmetric, magnetic field-dependent scattering pattern, as it can be seen in Fig. 1(a). In Fig. 1(b), we investigate the impact of tunable scattering anisotropy in light transport in planes composed of identical, infinitely-long magneto-optical core-shell cylinders. The parameters are the same as the Fig. 1(a): $b = 2.5$ μm, $S = a/b = 0.35$, and $T = 295$ K. Figure 1(b) reveals that the application of an external magnetic field up to $B \approx 1.0$ T leads to an increase in the diffusion coefficient $\mathcal{D}$.

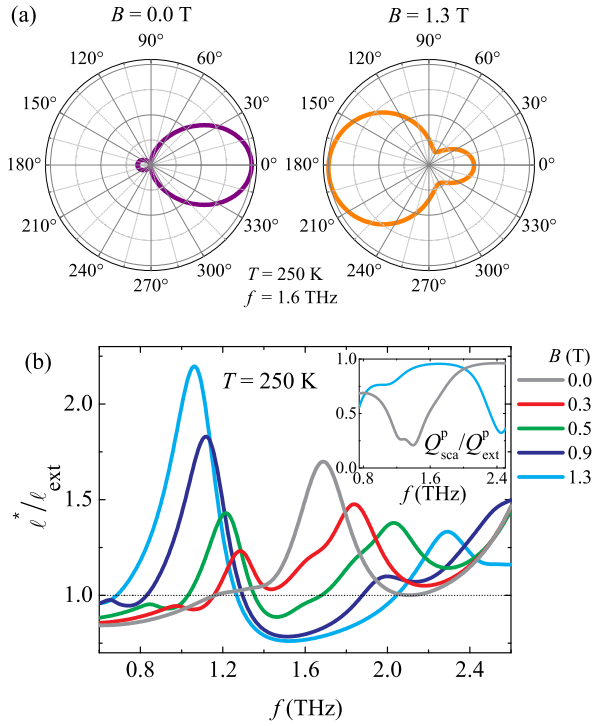

Figure 2: Light scattering by (SiO_2) core-shell (InSb) cylinders with outer radius $b = 25$ μm and aspect ratio $S = a/b = 0.5$. (a) Normalized differential scattering efficiency $\partial Q(\phi)/\partial\phi$ for a fixed frequency $f = 1.6$ THz ($kb \approx 0.84$) at temperature $T = 250$ K, for $B = 0.0$ T and $B = 1.3$ T. (b) The ratio between the transport mean free path and the extinction mean free path for a collection of cylinders.

Figures 2(a) and 2(b) demonstrate that it is possible to achieve directional scattering, which can be tuned by applying an external magnetic field, beyond the Rayleigh limit. The interference between electric and magnetic dipole contributions leads to a minimum in the internal energy around $f \approx 1.6$ THz as $\mathbf{B}$ increases. As it can be seen from Fig. 2(b), this interference induces a band (1.3 THz to 2.0 THz) of anomalous scattering in which $\ell^\star < \ell_{\rm ext}$. Moreover, for $B = 1.3$ T, $\ell^\star \approx \ell_{\rm sca}/(1 - \langle\cos\theta\rangle)$ since absorption becomes very small in this frequency range, as it can be verified in the inset of Fig. 2(b). This implies that there exists a transport regime in which $\ell^\star < \ell_{\rm sca}$, with $\ell^\star \approx 0.8\ell_{\rm sca}$.

It is worth mentioning that the application of the external magnetic field can suppress absorption in this frequency range, resulting in $Q_{\rm sca}/Q_{\rm ext} \approx 1$, as it can be seen in the inset of Fig. 2(b). In addition, for a fixed frequency and material parameters, Fig. 2(a) shows we can effectively tune the directional scattering pattern by applying $\mathbf{B}$. More details of this study can be found in Ref. [1].

3. Conclusion

Using the Lorenz-Mie theory, we have investigated the electromagnetic scattering by magneto-optical core-shell microcylinders. We have shown that the application of an external magnetic field induces a drastic decrease in electromagnetic absorption in a frequency window in the THz, where absorption is maximal in the absence of the magnetic field. We have demonstrated not only that the scattering anisotropy can be externally tuned by applying a magnetic field, but also that it can reach negative values in the THz even in the dipolar regime. This leads to an anomalous regime of multiple light scattering in a collection of magneto-optical core-shell cylinders, in which the scattering mean free path is larger than the transport mean free path in specific ranges in the THz. In our approach, we have demonstrated an unprecedented degree of external control of multiple light scattering, which can be tuned by either applying an external magnetic field or varying the temperature.

Acknowledgement

The authors acknowledge the Brazilian agencies for financial support. T.J.A holds grants from FAPESP (2015/21194-3) and CAPES/PNPD (1564300). A.S.M holds grants from CNPq (307948/2014-5). F.A.P holds grants from CNPq (303286/2013-0) and CAPES (BEX 1497/14-6). F.A.P thanks The Royal Society (Newton Advanced Fellowship NA150208) for financial support.

References

[1] T.J. Arruda, A.S. Martinez, F.A. Pinheiro, Electromagnetic energy and negative asymmetry parameters in coated magneto-optical cylinders: Applications to tunable light transport in disordered systems, *Phys. Rev. A* 94: 033825, 2016.

[2] C.F. Bohren, D.R. Huffman, *Absorption and Scattering of Light by Small Particles*, Wiley, New York, 1983.

[3] F.A. Pinheiro, A.S. Martinez, L.C. Sampaio, New effects in light scattering in disordered media and coherent backscattering cone: system of magnetic particles, *Phys. Rev. Lett.* 84: 1435, 2000.

[4] R. Gomez-Medina, L.S. Froufe-Perez, M. Yepez, F. Scheffold, M. Nieto-Vesperinas, J.J. Saenz, Negative scattering asymmetry parameter for dipolar particles: Unusual reduction of the transport mean free path and radiation pressure, *Phys. Rev. A* 85: 035802, 2012.

[5] G.M. Conley, M. Burresi, F. Pratesi, K. Vynck, D.S. Wiersma, Light transport and localization in two-dimensional correlated disorder, *Phys. Rev. Lett.* 112: 143901, 2014.

[6] A.S. Martinez, R. Maynard, Faraday effect and multiple scattering of light, *Phys. Rev. B* 50: 3714, 1994.

[7] W.J.M. Kort-Kamp, F.S.S. Rosa, F.A. Pinheiro, C. Farina, Molding the flow of light with a magnetic field: plasmonic cloaking and directional scattering, *J. Opt. Soc. Am. A* 31: 1969, 2014.

[8] W.J.M. Kort-Kamp, F.S.S. Rosa, F.A. Pinheiro, C. Farina, Tuning plasmonic cloaks with an external magnetic field, *Phys. Rev. Lett.* 111: 215504, 2013.

[9] S.C. Howells, L.A. Schlie, Transient terahertz reflection spectroscopy of undoped InSb from 0.1 to 1.1 THz, *Appl. Phys. Lett.* 69: 550, 1996.

Bound states in the continuum with high orbital angular momentum in dielectric rod with periodically modulated permittivity.

E. N. Bulgakov and A. F. Sadreev
Kirensky Institute of Physics, 660036 Krasnoyarsk, Russia

Abstract— We consider bound states in the radiation continuum (BSC) in single dielectric rod with with periodically modulated permittivity. Because of rotational and translational symmetries the BSCs are classified by orbital angular momentum m, Bloch wave vector β directed along the rod and the polarization. The BSCs with high orbital angular momentum $m \neq 0$ and mixed polarizations constitutes the most interesting class of the BSCs because of high localization of EM fields near surface of the rod.

Recently confined electromagnetic modes above the light line were shown to exist in various periodical arrays of long dielectric cylindrical rods, photonic crystal slabs and two-dimensional periodical structures on the surface of material (see reviews [1, 2]). Among these different systems the one-dimensional array of spheres possesses by rotational symmetry that gives rise to the bound states in the continuum (BSCs) with orbital angular momentum [3] as shown in Fig. 1 (a). That reflects in unique properties of the scattering of plane waves by the array for the frequency nearby the BSC frequency [2, 3]. However fabrication of infinite array or at least more than hundred identical spheres [3] and arranged into a periodical array is a challenge because of technological fluctuations of shape of the spheres. Here we consider the single dielectric rod with with periodically stepwise modulated permittivity along the rod's axis z as shown in Fig. 1 (b). We consider that the permittivity takes two values $\epsilon > 1$ and $\epsilon_0 = 1$. Then the rod is equivalent to the one-dimensional array of dielectric discs with the permittivity ϵ. This system preserves the main feature of the array of dielectric spheres which is rotational and translational symmetry, however the single rod with modulated permittivity is much easier to fabricate. Each dielectric disk has two geometrical parameters, the radius R and thickness d that essentially expands the domain of existence of the BSCs for substantially lower permittivity compared to the case of dielectric spheres.

Figure 1: Infinite periodic arrays of (a) dielectric spheres and (b) discs.

In what follows we refer all length quantities in terms of the period h of the array. Because of rotational symmetry the total system splits onto the independent sectors classified by integer $m = 0, \pm 1, \pm 2, \ldots$, orbital angular momentum (OAM) which defines the BSCs which are degenerate relative to the sign of m. All components of the σ-th BSC can be expressed through auxiliary function

$$\left[\frac{\partial^2}{\partial r^2} + \frac{1}{r}\frac{\partial}{\partial r} - \frac{m^2}{r^2} + \frac{\partial^2}{\partial z^2} + U_\sigma(z)\right]\psi_\sigma(z, r) = 0, \tag{1}$$

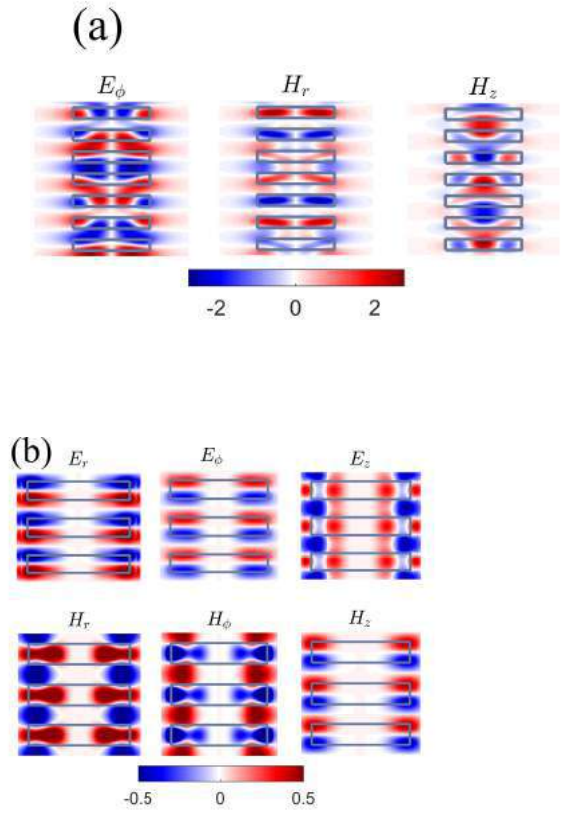

Figure 2: Patterns of the Bloch TE BSC with $m = 0, \beta = 1.08676$ at $R = 1$ and frequency $k_{0c} = 3.88423$ (a) and the BSC with high OAM $m = 5, \beta = 0$ at tuned radius of rod $R = 1.875$ and frequency $k_{0c} = 5.143873$ (b). Other parameters: $\epsilon_2 = 3, \epsilon_2 = 1, d = 0.5$.

where $\sigma = TE, TM$, $m = 0, 1, 2, \ldots$ is the orbital angular momentum and

$$U_{TE}(z) = \epsilon(z)k_0^2,$$
$$U_{TM}(z) = \epsilon(z)k_0^2 - \frac{3}{4}\left(\frac{\epsilon'(z)}{\epsilon(z)}\right)^2 + \frac{1}{2}\frac{\epsilon''(z)}{\epsilon(z)}.$$

That consideration for $m = 0$ and $\sigma = TM$ is completely equivalent to that performed by Li and Engheta in a plasmonic nanowire with periodic permittivity variation [4].

ACKNOWLEDGMENT

This work was supported by Russian Science Foundation through Grant 14-12-00266.

REFERENCES

1. Chia Wei Hsu, Bo Zhen, Stone A.D., Joannopoulos J.D. and Soljačić M., "Bound states in the continuum", *Nature Rev. Mat.*, Vol. 1, 16048, 2016.
2. Bulgakov, E.N., Sadreev, A.F., and Maksimov, D.N., "Light Trapping above the Light Cone in One-Dimensional Arrays of Dielectric Spheres", *Appl. Science*, Vol. 7, 147–172, 2017.
3. Bulgakov, E.N. and Sadreev, A.F., "Trapping of light with angular orbital momentum above the light cone in a periodic array of dielectric spheres", *Adv. EM*, Vol. 6, 1–10, 2017.
4. Li J. and Engheta N., " Subwavelength plasmonic cavity resonator on a nanowire with periodic permittivity variation", Phys. Rev. B, Vol. 74, 115125, 2006.

Toroidal Electrodynamics and Toroidal Metamaterials

Engineering anapole mode for the generation of toroidal dipole moment

H.-H. Hsiao[1], J.-W. Chen[1], Y. H. Chen[1], H. J. Wu[2], C. H. Chu[2], M.-K. Chen[1], W.-Y. Tsai[1], T. L. Chung[1] and D. P. Tsai[1,2*]

[1]Department of Physics, National Taiwan University, Taipei 10617, Taiwan

[2]Research Center for Applied Sciences, Academia Sinica, Taipei 11529, Taiwan

[*]corresponding author: dptsai@sinica.edu.tw

Abstract- A novel three-dimensional plasmonic metamaterial which is able to generate a transverse toroidal dipole moment under normal illumination is presented in the optical region. In addition to the toroidal dipolar response, a non-radiating anapole mode resulting from the destructive interference between toroidal and electric dipoles is also observed. Different from the previous works, it is a specifically designed and fabricated plasmonic metamaterials for the generation of both transverse toroidal dipole moments and associated anapole mode, and readily available for feasible applications.

Natural toroidal molecules, such as biomolecules and proteins, possess toroidal dipole moments that are hard to be detected [1], which leads to extensive studies of artificial toroidal materials. Recently, toroidal metamaterials [2] have been widely investigated to enhance toroidal dipole moments while the other multipoles are eliminated due to the spacial symmetry. However, most of generated toroidal dipole moments are either aligned vertically to the substrate surface or embedded in a dielectric, which is a critical constraint for further applications of toroidal metamaterials.

In this talk, we will show several cases on the plasmonic toroidal excitation by engineering the near-field coupling between metamaterials. The gain-assistant toroidal resonance is subsequently studied for realizing toroidal lasing spaser. In addition, a novel design for a toroidal metamaterial with multi-layered structures is also studied. Because the induced toroidal dipole moment is oscillating at the interface between metallic structure and free space, this design overcomes the challenge in detecting the scattering of the induced toroidal dipole and provides a possibility of coupling with other dipolar moments. Besides, the non-radiating anapole mode [3, 4] results from the destructive interference between toroidal and electric dipoles are realized through such proposed toroidal metamaterials. To our best knowledge, this is the first proof-of-concept demonstration of anapole mode though coupled plasmonic metamaterials which offers a promising way for the investigation of optical properties with complicated electromagnetic fields.

REFERENCES

1. Kovall, R. and Matthews, B. W., "Toroidal structure of λ-exonuclease," *Science* 277, 1824-1827 (1997).
2. Kaelberer, T. et. al., "Toroidal dipolar response in a metamaterial," *Science* 330, 1510-1512 (2010).
3. Miroshnichenko, A. E. et. al., "Nonradiating anapole modes in dielectric nanoparticles," *Nat. Commun.* 6, 8069 (2015).
4. Kuznetsov, A. et. al., "Optically resonant dielectri nanostructures," *Science.* 354, 2472 (2016).

On an exact multipole expansion and the implications for dynamic toroidal multipoles.

I. Fernandez-Corbaton[1], R. Alaee[2], and C. Rockstuhl[1,3*]

[1]Institute of Nanotechnology, Karlsruhe Institute of Technology, 76021 Karlsruhe, Germany

[2]Max Planck Institute for the Science of Light, Erlangen 91058, Germany

[3]Institute of Theoretical Solid State Physics, Karlsruhe Institute of Technology, 76131 Karlsruhe, Germany

[*]corresponding author: carsten.rockstuhl@kit.edu

Abstract-To perform a multipole expansion of a charge-current distribution is a key procedure when doing research on light-matter-interaction. Usually, expressions valid only for small particles are considered. Here, we derive exact expressions for electric and magnetic multipole moments, which are valid irrespective of the particle size. We show that the usually called toroidal multipole moments emerge in higher order terms of a Taylor expansion of these exact expressions. The physical implications of this Taylor expansion are discussed.

Quantifying the optical properties of artificial meta-atoms in terms of multipole moments is a key quantity to understand their optical action and to consider them in a broad range of applications in the slip-stream of nanoplasmonics, optical antennas, and metamaterials. The multipole moments, in general, represent elementary excitations into which the response of the meta-atom upon stimulus by an external illumination can be expanded. Usually, two approaches are used for this purpose. In a first one, the scattered field is taken and projected onto the vector spherical harmonics, being eigenmodes to the wave equation in spherical coordinates. Alternatively, the currents (either conductive or displacement current) induced in the meta-atom can be expanded in an orthonormal base. Since the radiated fields are completely determined by the current sources, the expansion of the currents must contain all the information that can be obtained by the expansion of the fields. However, this is usually obscured by an additional small argument approximation, valid only for scatterers having a size much smaller than the wavelength that is done to simplify the expressions for multipole moments on the base of the current distributions. The emerging approximate expression, e.g. for the electric dipole moment, read as

$$p_\alpha \approx -\frac{1}{i\omega}\left\{\int d^3\mathbf{r} J_\alpha^\omega + \frac{k^2}{10}\int d^3\mathbf{r}\left[(\mathbf{r}\cdot\mathbf{J}_\omega)\, r_\alpha - 2r^2 J_\alpha^\omega\right]\right\} \qquad (1)$$

where we have included the two lowest order terms of the Taylor expansion. Here, α is any of the three coordinates x, y, and z and the current distribution for a time-harmonic excitation is given in real space. This small argument approximation, however, ceases to be applicable for most meta-atoms of interest [1,2,3]. The second order term in the Taylor expansion of the exact electric dipole moment is often called the toroidal dipole moment. We shall emphasize that the expression is only approximate and an infinite number of terms in the Taylor expansion exists that have to be considered to restore the exact electric dipole moment.

However, the separation and the individual consideration of these terms in this Taylor expansion have some implications. Based on the pioneering work of Devaney and Wolf [4], it can be shown that the current distribution as a whole does not contribute to the radiated field. Instead, only an infinitely thin shell of the

current distribution if transformed into momentum space, for which $|\mathbf{p}|=\omega/c$ holds, contributes. ω is here the considered frequency and c being the speed of light [2]. The truncation of the Taylor series in Eq. 1 in real space causes out-of-shell components of the current distribution in momentum space to contribute to the approximate multipole moment. These approximate multipole moments are hence unsuitable for a quantitative analysis, as current contributions are considered for their evaluation that do not radiate and that do not interact with radiation. The contribution of these out-of-shell components is suppressed if the infinite number of terms in the Taylor expansion is added up. Therefore, all terms have always been taken into account to obtain physically meaningful results.

However, this Taylor expansion does not need to be considered. Instead, exact expressions for the multipole moments can be used that do not rely on the small argument approximation. We emphasize that exact expressions are readily found in literature [Eq. (7.20) in 5 or Eq. (9.165) without the magnetization current therein in 6]. Our contribution was to bring them in a form where they resemble their approximate counterparts of Eq. 1 [1,3]. This makes the approximations done in Eq. 1 much more evident.

In our contribution, we outline the derivation of these new expressions for the multipole moments on the base of the current distributions from first principles. Our expressions are exact and simple, i.e. comparable in complexity to those approximate expressions valid only for small objects and identical to those multipole moments extracted from the scattered field. For the electric dipole moment they read, e.g., as

$$p_\alpha = -\frac{1}{i\omega}\left\{\int d^3\mathbf{r} J_\alpha^\omega j_0(kr) + \frac{k^2}{2}\int d^3\mathbf{r}\left[3(\mathbf{r}\cdot\mathbf{J}_\omega) r_\alpha - r^2 J_\alpha^\omega\right]\frac{j_2(kr)}{(kr)^2}\right\} \qquad (2)$$

More general expressions will be presented at the conference, even though most important will be expressions for the dipolar and quadrupolar contributions. We show how these new expressions provide more accurate predictions to analyze meta-atoms. This has implications, and we will discuss this, on the ability to predict effective properties of metamaterials, to study the optical force acting on meta-atoms, and to study the response from meta-surfaces. Our results can be applied in the many areas where the multipole moments of current sources are used.

REFERENCES

1. Fernandez-Corbaton I., S. Nanz, R. Alaee, and C. Rockstuhl, *Opt. Express*, Vol. 23, No. 26, 33044-33064, 2015.
2. Fernandez-Corbaton I., S. Nanz, and C. Rockstuhl, *arXiv preprint*, arXiv:1507.00755 (2016).
3. Alaee R., C. Rockstuhl, and I Fernandez-Corbaton, *arXiv preprint*, arXiv:1701.00755 (2017).
4. Devaney A. and E. Wolf. Phys. Rev. D, Vol. 8, No. 4, 1044-1047 (1973).
5. J. D. Walecka, *Theoretical Nuclear and Subnuclear Physics* (World Scientific, 2004).
6. J. D. Jackson, *Classical Electrodynamics* (Wiley, 1998).

Progress in anapole metamaterials

Alexey A. Basharin[1,2]

1 National University of Science and Technology (MISiS), The Laboratory of Superconducting metamaterials, 119049 Moscow, Russia

2 National University of Science and Technology (MISiS), Department of Theoretical Physics and Quantum Technologies, 119049 Moscow, Russia

*corresponding author: Alexey.basharin@gmail.com

Abstract-Dynamic anapole is separated type of excitation. One of the most promising cases of anapole excitation has been observed in metamaterials and nanophotonics, which we discuss in this work. We show the peculiar properties of planar metamaterials, like extremely high Q-factor and strong electric and magnetic field localization, tunable toroidal metamaterials. Moreover, we discuss anapole excitation in dielectric metamaterials. Especially we discuss the role of losses in toroidal and anapole metamaterials: radiating and non-radiating nature and show that the playing between them can be crucial for effects of high Q-factor applications. We demonstrate our experimental and theoretical results in microwave, THz and optics.

Optical force on toroidal nanostructures: source representation versus field representation

Xu-Lin Zhang[1], **C. T. Chan**[1*]

[1] Department of Physics and Institute for Advanced Study, The Hong Kong University of Science and Technology, Clear Water Bay, Hong Kong, China

[*]corresponding author: phchan@ust.hk

Abstract- In the electrodynamic multipole expansion, all the charge and current distributions can be expanded into a complete set of contributions from electric, magnetic, as well as toroidal multipoles. However, the radiated far field from all these three types of source can be completely described in terms of electric and magnetic multipoles only, excluding the toroidal ones. We employ optical forces to address this confusion by studying the force acting on toroidal nanostructures in both source representation and field representation.

The notion of toroidal moments has always been confusing or even controversial in electromagnetics. The standard treatment of electromagnetics requires only two families of moments, namely electric and magnetic moments, to describe radiation fields for the reason that two sets of functions are complete because the fields are divergenceless in the source free homogeneous region. However, some authors showed that in addition to electric and magnetic moments, there is a third set of toroidal moments [1,2]. This issue was usually brushed aside as most electromagnetic structures do not have observable toroidal moments and so the argument of their existence is just "academic". However, due to recent advances in material fabrication, the toroidal metamaterials were theoretically predicted [1] and experimentally demonstrated at microwave frequencies [2], followed by various studies on their intriguing properties [3,4].

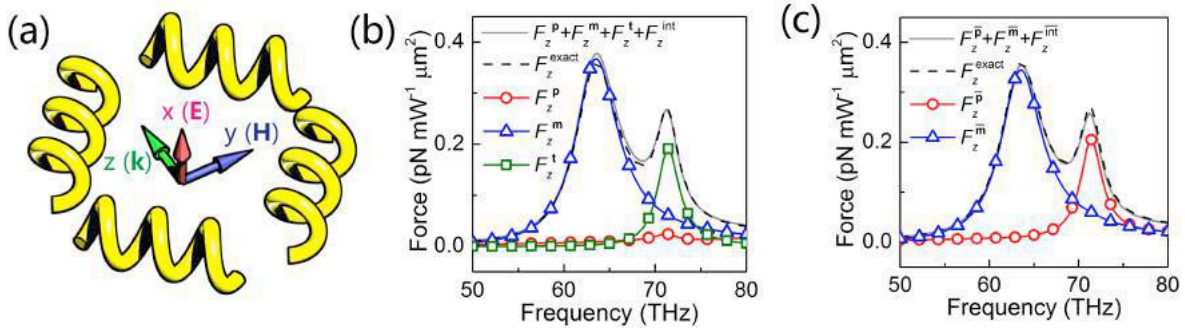

Figure 1 (a) Schematic diagram of the designed nanostructure that supports a toroidal dipole resonance. (b)-(c) Calculated optical forces acting on the toroidal nanostructure based on the source representation (b) and field representation (c).

Our main purpose in this work is to use optical force as a means to clarify whether toroidal moment is an indispensable or useful concept. Optical force is an excellent platform for such a consideration because mechanical effect is the most intuitively obvious consequence of abstract notions such as toroidal moments. We

found that there are two possible ways to understand the optical force. If we envision the optical force as a consequence of the incident wave interacting with the induced currents in a complex resonant structure, then the notion of toroidal moment is useful and indispensable. However, if we interpret the optical force as a momentum transfer between light and matter and we compute the momentum transfer by considering the scattered field in the far zone, then the toroidal moment does not appear in the description (see Figure 1). Both descriptions are correct and they complement each other, depending on whether we focus our attention on the near field or the far field. We also show that optical force enables the observation of the toroidal response of a nanostructure even when its effect on scattering power is overwhelmed by the conventional multipoles.

Acknowledgements: This work is supported by the Hong Kong Research Grants Council through grant AoE/P-02/12.

REFERENCES

1. Marinov, K., A. D. Boardman, V. A. Fedotov, and N. Zheludev, "Toroidal metamaterial," *New Journal of Physics*, Vol. 9, 324, 2007.
2. Kaelberer, T., V. A. Fedotov, N. Papasimakis, D. P. Tsai, and N. I. Zheludev, "Toroidal dipolar response in a metamaterial," *Science*, Vol. 330, 1510–1512, 2010.
3. Huang, Y., W. T. Chen, P. C. Wu, V. Fedotov, V. Savinov, Y. Z. Ho, Y. Chau, N. I. Zheludev, and D. P. Tsai, "Design of plasmonic toroidal metamaterials at optical frequencies," *Optics Express*, Vol. 20, No. 2, 1760-1768, 2012.
4. Basharin, A. A., M. Kafesaki, E. N. Economou, C. M. Soukoulis, V. A. Fedotov, V. Savinov, and N. I. Zheludev, "Design of plasmonic toroidal metamaterials at optical frequencies," *Physical Review X*, Vol. 5, 011036, 2015.

Toroidal cavity resonance in metal-dielectric-metal nanoantenna

Jun-Jun Xiao
College of Electronic and Information Engineering, Shenzhen Graduate School, Harbin Institute of Technology, Shenzhen 518055, China
E-mail: eiexiao@hit.edu.cn

Abstract- We show that in judiciously designed metal-dielectric-metal (MDM) nanoantenna, the toroidal dipole resonance may arise and dominate. Furthermore, toroidal-like cavity resonances can be excited and controlled. More interestingly, it is possible to tune the coupling interactions between such cavity modes and the antenna mode, yielding significant scattering enhancement and suppression of the MDM nanoantenna. The results are interpreted as Fano-like and/or electromagnetically-induced transparency like phenomena by a coupled oscillator model.

Dielectric nanoantennas: exploiting anapole modes and low-loss behavior for near-field localization of near-infrared and visible radiation

S. A. Maier[1]

[1] Imperial College London, London SW7 2AZ, UK

Abstract **– We discuss avenues for near-field focusing of electromagnetic radiation in the visible and near-infrared regime of the electromagnetic spectrum. A special focus will lie on the exploitation of anapole modes — coherent superpositions of electric and toroidal dipolar modes — in order to efficiently localize electric field energy in dielectric nanostructures. Materials systems to be presented include Ge, GaP, and hybrid dielectric/metallic nanoantennas.**

Dielectric nanostructures can localize electromagnetic radiation via the excitation of low-order Mie electric and magnetic modes. While not breaking the limit of diffraction, and providing a lower local field enhancement than their plasmonic counterparts, such structures show the advantage of low absorption losses due to the absence of free electron scattering. The first part of the talk will focus on the exploitation of anapole modes in order to efficiently maximize electric field enhancement in thin Ge nanodisks [1, 2], for applications in higher-harmonic generation. The nature of both first and higher-order anapole modes will be discussed, and the mode profile directly imaged using third-harmonic generation.

The second part of the talk will focus on GaP nanostructures, which due to the large bandgap show negligible absorption loss in the visible part of the spectrum [3]. Finally, hybrid dielecric/metallic nanoantennas allow the hybridization of anapole modes with plasmonic modes [4], boosting the local electric field enhancement.

REFERENCES

[1] Grinblat, G., Nielsen, M.P., Oulton, R.F., & Maier, S.A., Enhanced third harmonic generation in single Germanium nanodisks excited at the anapole mode, Nano Letters 16, 4635 (2016) doi:10.1021/acs.nanolett.6b01958

[2] Grinblat, G., Li, Y., Nielsen, M.P., Oulton, R.F., & Maier, S.A., Efficient third harmonic generation and nonlinear subwavelength imaging at a higher-order anapole mode in a single Germanium nanodisk, ACS Nano 11, 953 (2017)

[3] Cambiasso, J., Grinblat, G., Li, Y., Rakovich, A., Cortés, E., & Maier, S.A., Bridging the gap between dielectric nanophotonics and the visible regime with effectively lossless GaP antennas, Nano Letters 17, 1219 (2017)

[4] Shibamuna, T., Grinblat, G., P., Albella, P, & Maier, S.A., Efficient third harmonic generation from metal-dielectric hybrid nanoantennas, Nano Letters (2017)

On-chip Ultrafast Sources Based on Near-field Anapole Lasers

Juan Sebastian Totero Gongora[1], Andrey E. Miroshnichenko[2], Yuri S. Kivshar[2] and Andrea Fratalocchi[1]

[1]PRIMALIGHT, King Abdullah University of Science and Technology (KAUST), Thuwal 23955-6900, Saudi Arabia

[2]Nonlinear Physics Centre, Research School of Physics and Engineering, Australian National University, Canberra, ACT 2601, Australia

andrea.fratalocchi@kaust.edu.sa

Abstract— We discuss an all-dielectric integrated source of ultrafast optical pulses by finely tuning the mutual interaction and synchronization of near-field nanolasers emitting at the anapole frequency.

The generation of ultra-short pulses is standardly achieved by the mutual synchronization among a large number of cavity modes of the system, which, in most cases, is achieved by introducing external active components, such as Q-switching, saturable absorbers or optical modulators. Such components, due to their the required optical setups are complex and expensive and, more importantly, they are difficult to integrate at the nanoscale. As a result, the development of on-chip ultrafast pulsed nanolasers is still a challenging task [1].

In order to address these difficulties, we propose an integrated source based on the spontaneous synchronization of several near-field nanolasers emitting at the anapole frequency [2]. Anapoles, which have been experimentally demonstrated in silicon nanoparticles [3], are characterized by a radiation pattern which is entirely confined to the near-field, and they play a key role in the generation of scattering suppression states in dielectric nanostructures [4]. Due to their near-field emission, an ensemble of anapole-based nanolasers can be employed to investigate and engineer spontaneous synchronization phenomena in a silicon-compatible framework, as their mutual non-linear interaction is strictly confined to the near-field and can be precisely controlled within standard nanofabrication tolerances.

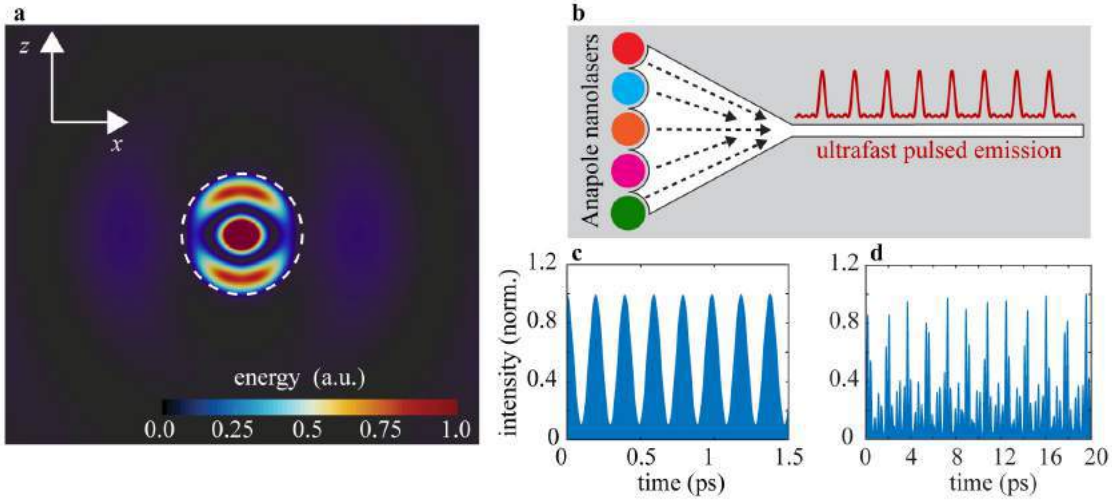

Figure 1: **Generation of ultrafast pulses from a chain of anapole-based nanolasers. (a)** Near-field emission from a three-dimensional anapole nanolaser. **(b)** Schematic representation of our ultrafast generation device, composed of an ensemble of nanolasers (green) and a Si waveguide (gray). **(c,d)** Steady-state emission from the system. The properties of the pulsed emission ranges from optical pulses of $\approx 100fs$ (b) to more complex configurations with *ps* optical pulses.

Results

We investigated the emission properties of an ensemble of anapole-based nanolasers with our Finite-Differences in Time-Domain simulator NANOCPP [5, 6, 7]. By solving a fully-dispersive set of Maxwell-Bloch equations with no approximations, we considered three-dimensional integrated nanolasers based on III-V semiconductors [8, 9]. In the Maxwell-Bloch model, the amplifying material is expressed in terms of a set of complex-valued density matrix equations. By optimizing the geometrical parameters of the system, we induced the formation of an anapole state in correspondence of the emission frequency of the amplifying semiconductor, obtaining a nonlinear emission composed of purely evanescent waves (Fig. 1-a). By combining different anapole nanolasers, the system behaves as an integrated ultrafast pulse generation device (Fig. 1-b), in which the collective emission of the interacting sources is convoyed into silicon waveguide. Due to the spontaneous synchronization of the anapole emitters, the system achieves a stable mode-locked state characterized by optical pulses of less than 100fs (Fig. 1-c). Interestingly, the pulse duration and the repetition rate of the emission can be finely tuned by acting on the spatial distribution of the anapole emitters, as shown in Fig. 1-d where we optimized the system to achieve *ps* optical pulses.

REFERENCES

1. B. Mayer, L. Janker, B. Loitsch, J. Treu, T. Kostenbader, S. Lichtmannecker, T. Reichert, S. Morkötter, M. Kaniber, G. Abstreiter, C. Gies, G. Koblmüller, and J. J. Finley. Monolithically Integrated High-β Nanowire Lasers on Silicon. *Nano Letters*, 16(1):152–156, January 2016.
2. Juan S. Totero Gongora, Andrey E. Miroshnichenko, Yuri S. Kivshar and A. Fratalocchi Anapole nanolasers for mode-locking and ultrafast pulse generation. *Nature Communications*, to appear, 2017.
3. Andrey E. Miroshnichenko, Andrey B. Evlyukhin, Ye Feng Yu, Reuben M. Bakker, Arkadi Chipouline, Arseniy I. Kuznetsov, Boris Lukyanchuk, Boris N. Chichkov, and Yuri S. Kivshar. Nonradiating anapole modes in dielectric nanoparticles. *Nature Communications*, 6:8069, August 2015.
4. Wei Liu, Jianfa Zhang, Bing Lei, Haojun Hu, and Andrey E. Miroshnichenko. Invisible nanowires with interfering electric and toroidal dipoles. *Optics Letters*, 40(10):2293, May 2015.
5. C. Liu, R. E. C. van der Wel, N. Rotenberg, L. Kuipers, T. F. Krauss, A. Di Falco, and A. Fratalocchi. Triggering extreme events at the nanoscale in photonic seas. *Nature Physics*, 11(4):358–363, April 2015.
6. Juan S. Totero Gongora, Andrey E. Miroshnichenko, Yuri S. Kivshar, and Andrea Fratalocchi. Energy equipartition and unidirectional emission in a spaser nanolaser. *Laser & Photonics Reviews*, 10(3):432–440, May 2016.
7. Henning Galinski, Gael Favraud, Hao Dong, Juan S. Totero Gongora, Favaro Gregory, Max Döbeli, Ralph Spolenak, Andrea Fratalocchi, and Federico Capasso. Scalable, ultra-resistant structural colors based on network metamaterials. *Light Science and Applications*, 6:e16233, 2017.
8. Juan S. Totero Gongora and Andrea Fratalocchi. Ab-initio techniques for light matter interaction at the nanoscale. In *Computational Chemistry Methodology in Structural Biology and Material Sciences*. Apple Academic Press, Oakville, 2016.
9. A. Fratalocchi, C. Conti, and G. Ruocco. Three-dimensional ab initio investigation of light-matter interaction in mie lasers. *Physical Review A*, 78(1), 2008.

Steering light by tailored excitation of nano-antennas and applications to nano-metrology

Zheng Xi and H.P. Urbach*
Optics Research Group, Department of Imaging Physics, Faculty of Applied Sciences
Delft University of Technology, Delft, The Netherlands
*corresponding author: h.p.urbach@tudelft.nl

Abstract- Far field methods based on the interaction of spatial mode of light with ultra-compact resonant optical antenna are proposed to measure deep subwavelength displacement. The realm of combining optical antenna theory with spatial modes will open intriguing applications in nano-metrology and provide new insights into fundamental far field subwavelength detection technique.

The field of nano optics involves the study of light and matter interactions at nano-scale. One of the key elements is nano-antenna: nano-scaled particle that interacts resonantly with free space light[1,2]. Using the so-called antenna effect, free space light can be focused down to extremely small point, and then reemitted in a highly directional way through the interference of different antenna modes. The reshaping of the light field by nano-antennas has propelled many intriguing applications ranging from holography to imaging devices.

Attractive ideas have been developed to use different spatial modes of light for the excitation of different antenna modes[3-8]. For example, it has been shown cylindrical vector beams such as radially polarized beam and azimuthally polarized beam can excite the electric and magnetic resonances of the nano-antenna respectively[5]. However, the true power of this selective excitation lies in designing the excitation field on purpose for better antenna directivity. This would require optimization of the excitation field in terms of polarization, amplitude and phase.

If the nano-antenna is placed in a strongly inhomogeneous field, its far-field scattering directivity can be largely changed depending on its relative position[6-9]. If the incoming field contains rapidly changing features, the displacement sensitivity of the nano-antenna within the field can be extremely large. In this talk, we will talk about our recent works on this subject. In particular, we will show that extremely high far-field scattering sensitivity for a displacement much smaller than the wavelength can be achieved using the optimized illumination and nano-antenna structures. This method could bring about important understandings of super-resolution technique involving spatial modes of light as well as interesting applications in optical subwavelength metrology.

REFERENCES

1. Bharadwaj, P., B. Deutsch, and L. Novotny, Optical antennas. Advances in Optics and Photonics, 2009. 1(3): p. 438-483.
2. Novotny, L. and N. Van Hulst, Antennas for light. Nature photonics, 2011. 5(2): p. 83-90.
3. Bauer, T., et al., Nanointerferometric amplitude and phase reconstruction of tightly focused vector beams. Nat Photon, 2014. 8(1): p. 23-27.
4. Lin, J., et al., Polarization-Controlled Tunable Directional Coupling of Surface Plasmon Polaritons.

Science, 2013. 340(6130): p. 331-334.
5. Xi, Z., et al. "Broadband active tuning of unidirectional scattering from nanoantenna using combined radially and azimuthally polarized beams." Optics Letters 2016 41(1): 33-36.
6. Neugebauer, M., et al., Polarization Tailored Light Driven Directional Optical Nanobeacon. Nano Letters, 2014. 14(5): p. 2546-2551.
7. Neugebauer, M., et al. "Polarization-controlled directional scattering for nanoscopic position sensing." Nat. Comm. 2016 7: 11286.
8. Xi, Z., et al. Accurate Feeding of Nanoantenna by Singular Optics for Nanoscale Translational and Rotational Displacement Sensing Phys. Rev. Lett. 2016, 117, 113903
9. Xi. Z. and Urbach.H.P. Magnetic dipole scattering from metallic nanowire for ultrasensitive deflection sensing. Phys. Rev. Lett. Accepted

Nano-Plasmonics for Sensing

Tunable plasmonic sensing through enhanced Raman spectroscopy

Bikas Ranjan[1,2], **Akihiro Kuno**[1], **Takayuki Umakoshi**[1], **and Prabhat Verma**[1*]
[1]Department of Applied Physics, Osaka University, Osaka, Japan
[2]RIKEN, Wako, Saitama, Japan
[*]corresponding author: verma@ap.eng.osaka-u.ac.jp

Abstract-Plasmonic enhancement is the key phenomenon for sensing a molecule or a sample that has weak scattering, through enhanced Raman spectroscopies, such as SERS or TERS. In such techniques, there can be two different resonances, one associated with the oscillations of the localized surface plasmons and the other associated with the Raman scattering. If the two resonances are tuned to the same wavelength, the resultant enhancement can be huge and hence makes a better sensing device. We will discuss how tuning the plasmon resonance to the resonance in Raman allows one to achieve better sensing at nanoscale.

Both surface-enhanced Raman spectroscopy (SERS) and tip-enhanced Raman spectroscopy (TERS) have been utilized as plasmonic techniques for sensing and detecting tiny amount of specific molecules, as well as for spectroscopy and imaging at the nanoscale. The most important phenomenon in such measurements is the enhancement of Raman signal, which makes it possible to detect or study a sample that is extremely small in size or weak in scattering. A large amount of research in both SERS and TERS has therefore been dedicated to improve the enhancement factor. Since the localized surface plasmon polariton resonance (LSPR) depends on the size and shape of the metallic nanoparticles, as well as on the kind of the metal, it is very crucial to properly design the surface roughness for SERS substrate or the metallic nanoparticle at the apex of the tip in TERS. Further, if the LSPR is tuned to match the resonance in Raman scattering of the given sample, then one would expect even better enhancement as both resonance effect would work together. Once one decides the sample to be measured to detected, the incident wavelength for resonant Raman scattering from that sample is known. Now, one can design the plasmonic nanostructure in such a way that the LSPR of that plasmonic nanoparticle matches with the wavelength of resonant Raman scattering. In this way, when the decided wavelength is used as the incident light, both LSPR and resonant Raman scattering are simultaneously invoked.

In order to demonstrate this phenomenon, we designed a plasmonic nano-tip for TERS measurement, where a small triangular silver nanoparticle was attached to the tip apex. By changing the size of this silver nano-triangle, we confirmed through both simulation and experimental results that one can easily tune the LSPR within the entire visible spectrum. We demonstrated that for different size of the nano-triangle, the enhancement in Raman scattering can be obtained for different incident wavelengths, confirming the tenability in LSPR for better enhancement. We further demonstrated the selective detection of the presence of pesticide molecules on a food item, such as on an orange, by tuning the LSPR to the resonant wavelength of Raman scattering. For this, we design gold and silver nanorods and control their lengths to tune the LSPR at a desired wavelength that matches with the resonant Raman scattering from the pesticide. We showed that we were able to detect very tiny amount of pesticides, which was not detectable by conventional techniques.

Ag/SiN_x sub-10 nm gap for ultra-sensitive SERS detection

R. H. Pan[1], Y. J. Wang[1], S. Li[2], Y. W. Su[2], Z. Liu[1], Y. Yang[1], J. J. Li[1*], and C. Z. Gu[1,3*]

[1] Beijing National Laboratory for Condensed Matter Physics, Institute of Physics, Chinese Academy of Sciences, Beijing 100190, China

[2] State Key Laboratory of Nonlinear Mechanics, Institute of Mechanics, Chinese Academy of Sciences, Beijing 100190, China

[3] Collaborative Innovation Center of Quantum Matter, Beijing 100871, China

[*]corresponding author: jjli@iphy.ac.cn and czgu@iphy.ac.cn

Abstract-SiN_x sub-10nm nanogap is fabricated by stress induced cracking of SiN_x nanobridge. The width of the gap is determined by the shape of nanobridge and Ag coating thickness. FDTD simulation shows that there is a "bulk effect" of the suspending nanogap, making the nanogap to be better than traditional metal gap in light confinement. Take rhodamine 6G as a probe, this structure performs very good in SERS even at an ultra-low concentration of 10^{-16} M.

Nanogap has been widely used in surface-enhanced Raman scatting (SERS) or surface enhanced infrared absorption (SEIRA), for its ability to confine light in a point or line-shape space[1-3], especially for the application of SERS. However, it is still a challenge to achieve large-area sub-10 nm nanogaps based on the existing techniques. Although a series of methods such as "break junctions" have been reported[4], problems still exists. For SERS devices applied in industry or medicine, the sub-10 nm nanogaps should be large-scale and stable. Stress induced film breaking is a promising technique to meet these requirement, however the existing technique can only be applied for brittle material[5], which restricting its application in metal structures for SERS application.

In this paper, stress induced SiN_x cracking method is introduced to achieve nanogaps with large-area, good repeatability and controllability. The bow-tie-shape is first fabricated by electron beam lithography (EBL) and reaction ion etching (RIE) on SiN_x film. TMAH is used to etch the substrate for suspending nanobridge, and in this process the stress concentrated on narrowest part of the nanobridge can release and result in SiN_x crack. By altering the shape of SiN_x nanobridge (Figure 1), the width of nanogap changes correspondingly. The gap width increases with the increasing of the bridge length and decreasing of the bridge width. In order to apply it on localized enhancement of electromagnetic, metallic nanogap is prepared by Ag deposition. Finite-different time-domain (FDTD) simulation shows that the suspending Ag/SiN_x nanogap provides strong electrical field than suspending Ag gap (Figure 2). R6G with an ultra-low concentration (10^{-16} M) can be detected.

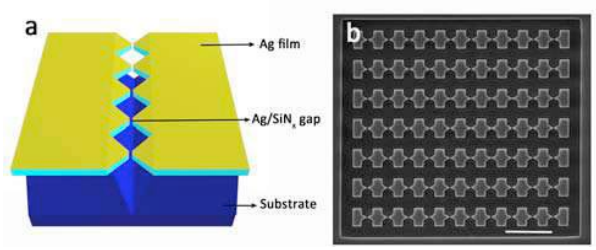

Figure 1 Schematic of Ag/SiN$_x$ nanogaps and SEM image of large-area samples.

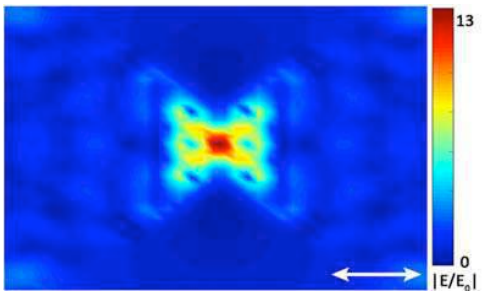

Figure 2 Field distribution of Ag/SiN$_x$ 8 nm-gap.

Acknowledgements: This work was supported by the National Natural Science Foundation of China (Grants Nos 91323304, 11174362, 61390503, 11574369, 11434017 and 11504414) and the Knowledge Innovation Project of CAS (Grant No. KJCX2-EW-W02).

REFERENCES

1. Brown, L. V. et al. “Fan-shaped gold nanoantennas above reflective substrates for surface-enhanced infrared absorption (SEIRA),” Nano Lett., Vol.15, 1272-1280, 2015.
2. Leem, J., Wang, M. C., Kang, P. & Nam, S. “Mechanically Self-Assembled, Three-Dimensional Graphene-Gold Hybrid Nanostructures for Advanced Nanoplasmonic Sensors,” Nano Lett., Vol.15, 7684-7690, 2015.
3. Zhu, C. et al. “A Hierarchically Ordered Array of Silver-Nanorod Bundles for Surface-Enhanced Raman Scattering Detection of Phenolic Pollutants,” Adv. Mater., Vol.28, 4871-4876, 2016.
4. Perrin, M. L. et al. “Large negative differential conductance in single-molecule break junctions, ” Nature nanotechnology, Vol.9, 830-834, 2014.
5. Dubois, V., Niklaus, F. & Stemme, G. “Crack‐Defined Electronic Nanogaps, ” Adv. Mater., Vol.28, 2178-2182, 2016.

Virus detection with silver nanowires

J. Grzelak[1*], A. Lesniewski[2], E. Rozniecka[2], L. Richter[2], M. Los[3], A. Voss[1], M. Jonsson-Niedziolka[2], K. Kwasniecka[3], S. Mackowski[1,4], J. Niedziolka-Jonsson[2,4]

[1]Institute of Physics, Faculty of Physics, Astronomy and Informatics, Nicolaus Copernicus University, ul. Grudziadzka 5/7, 87-100 Torun, Poland
[2]Institute of Physical Chemistry Polish Academy of Sciences, ul. Kasprzaka 44/52, 01-224 Warszawa, Poland
[3]Department of Molecular Biology, University of Gdansk, ul. Wita Stwosza 59, 80-308 Gdansk, Poland
[4]Baltic Institute of Technology Baltech, Al. Zwyciestwa 96/98, Gdynia, Poland
[*]corresponding author: justynag@fizyka.umk.pl

Abstract Fluorescence microscopy provides simple recipe to specific virus detection. Functionalized silver nanowires (AgNWs) with antibodies specific for T7 bacteriophage can be well seen in an optical microscope. By correlating fluorescence images of marked viruses with optical image of the silver nanowires we can efficient and easy define the presence of specific virus in a sample. The fluorescence will be concentrated around the viruses if the virus binds to the antibody-modified nanowires. Otherwise it will be distributed over the sample.

Sensitive detection of viruses and other relevant species has been considered recently as one of the most interesting and attractive research fields, both from fundamental and applied perspectives. The driving force behind these efforts is a need to prevent incubation and spreading of diseases among humans, animals, and plants. Binding of specific antibodies to targeted antigens is perhaps the most popular of all biosensor designs [1]. Among the numerous methods of detecting viruses are optical immunosensors based on surface plasmon resonance phenomenon, fluorescence detection or the application of optical fibers.

Since viruses labeled with fluorescent dyes are rather very small objects (20-300 nm) they cannot be directly observed using an optical microscope, however we can apply other nanostructures as “fishing rods” to detect them. While silver nanostructures have already been used to detect viruses [2], our idea was to apply silver nanowires as a geometric platform to hitch on antibodies and detect viruses by combining fluorescence and optical microscopy.

In our research we used two different bacteriophages: T7-SYBRGreen-intercalated and T4-SYTO62-intercalated. First bacteriophages are specific and the second are not-specific with respect to the antibody.

In the case with unmodified AgNWs there is no clear position correlation between the nanowires and the fluorescence spots (even for overnight incubation). Thus no specific interaction between viruses and nanowires took place. In ocntrast, for specifically functionalized AgNWs, where antibodies were attached that can bind T7-SYBRGreen intercalate bacteriophages, we observe clear correlation between these two images, as shown in Fig. 1. This effect is the most apparent after overnight incubation. We conclude that fluorescence microscopy imaginig indicates conjugtion of the antibodies attached to silver nanowires via specific attachment with T7-SYBRGreen intercalate bacteriophages. In many instances attachment of single wiruses can be demonstrated.

We belive that such an architecutre based on silver nanowires can be used for effective virus detection.

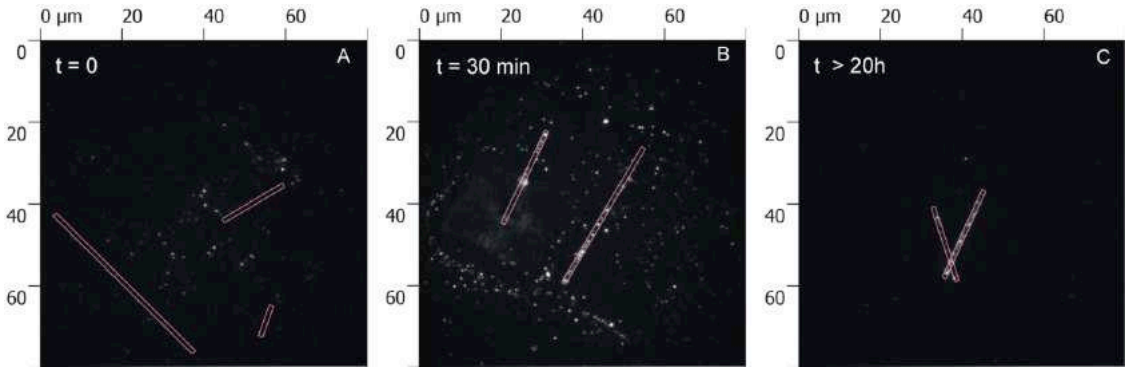

Fig. 1 Fluorescence intensity maps obtained using wide-field microscopy for T7-SYBRGreen intercalate bacteriophages mixed with AgNWs modified with anti-T7-tag antibodies after t = 0 (A), t = 30 min (B), t > 20 h (C). For excitation we used wavelength of 485 nm.

Acknowledgements

This work was supported by the Foundation for Polish Science for financial support through the FOCUS Programme no F3/2010/P/2013. The research was partially financed by the National Science Centre Poland within OPUS grant no 2016/21/B/ST3/02276 and the project 2/DOT/2016 funded by the City of Gdynia, Poland

REFERENCES

1. Lee, J-H., Kim, B-C., Oh, B-K., Choi, J-W. "Highly sensitive localized surface plasmon resonance immunosensor for label-free detection of HIV-1," *Nanomedicine: NBM* 9, 1018–1026, 2013.
2. Shanmukh, S., Jones, L., Driskell, J., Zhao, Y., Dluhy, R., Tripp, R.A. "Rapid and sensitive detection of respiratory virus molecular signatures using a silver nanorod array SERS substrate," *Nano Letters* 6, 2630-2636, 2006

Hybrid photonic-plasmonic crystal nanocavities sensors

Y. C. Ku[1], Z. T. Huang[1], P. J. Cheng[2], C. K. Chiang[3], J. C. Hsu[4*], and T. R. Lin[1,3*]

[1]Department of Mechanical and Mechatronic Engineering, National Taiwan Ocean University, Taiwan

[2]Research Center for Applied Sciences, Academia Sinica, Taiwan

[3]Institute of Optoelectronic Sciences, National Taiwan Ocean University, Taiwan

[4]Department of Mechanical Engineering, National Yunlin University of Science and Technology, Taiwan

[*]corresponding author: hsujc@yuntech.edu.tw; trlin@ntou.edu.tw

Abstract-We propose and investigate a hybrid photonic-plasmonic crystal nanocavity consisting of a silicon grating nanowire. The resonant defect mode exhibits a high quality factor of 567 and an ultrasmall mode volume of 1.9×10^{-3} $(\lambda/n)^3$. The cavity mode also reaches a sensitivity of 443 nm/*RIU* and a FWHM of 3.4 nm aiming at applications such as biosensing.

Plasmonic nanocavities that integrate surface plasmon polariton (SPP) with optical cavities usually significantly lower the effective mode volume (V_m) [1]. With the advantage of SPPs, various plasmonic cavities, especially utilizing the gap mode of SPP, have been proposed recently [2-4]. However, the quality factor of this type of cavities is compromised by parasitic loss of metal substrate..In this work, we propose and study a hybrid photonic-plasmonic nanocavity containing a silicon nanowire (*NW*) photonic crystal (*PhC*) near a metal substrate using finite-element method (*FEM*). With the periodic dielectric lattice atop the metal layer, hybrid plasmonic crystals are formed to support a complete two-dimensional band-gap [5] for the hybrid plasmonic gap structure. A defect is then introduced into the *PhC NW* to build up a nanocavity.

The proposed hybrid plasmonic nanocavity is illustrated in Fig. 1 (a). The structure consists of a patterned silicon *NW* and a silicon dioxide gap layer on silver substrate. The Si *NW*-SiO2-silver film structure supports hybrid plasmonic gap modes. These modes are coupled to the dielectric *NW PhC* Bloch modes to form a hybrid plasmonic crystal. The hybrid plasmonic structure as high-low-index dielectrics on a metal substrate brings about even small footprint inside the low-index region. Several dimensions of the proposed structure such as the *NW* etch depth *d*, the gap layer thickness *h*, and lattice constant Λ are varied to achieve the optimal design of high *Q*-factor and low mode volume. In addition, to achieve high-reflection Bragg diffraction, we look for the high refractive index contrast along the *NW*s.

In order to lower the mirror losses, different number of periods of each side by the cavity is varied to resolve the corresponding reflectivity by using three-dimensional (*3D*) *FEM* and orthogonality theorem [3]. The result shows that the reflectivity is proportional to the number of periods and gradually convergent. We obtain sufficiently small mirror loss when the cavity is accompanied with a pair of gratings of 8 periods. We then look into the field profiles of the high-*Q* resonant mode at λ = 1550 nm. As shown in Fig. 1 (b), the side view (*y*-*z* plane) of the field profiles of the cavity eigenmode reveals strong localization below the *NW*, whereas the top-view (*x*-*z* plane) shows that the field quickly decays inside the mirror region. Only one resonant mode with even symmetry along the z-axis is supported in this cavity. In addition, we solved for the quality factor *Q* of the nanocavity. In *3D FEM* calculations, we excited the nanocavity with a *y*-polarized plane wave. The spatial

integration of the squared magnitude of the electric field inside the gap region at various wavelengths was then recorded in the Fig. 1 (c). Next, resolving the field distributions of the resonance modes enables us to evaluate the mode volume V_m. A high sensitivity is essentially required for the better performance of an index sensor. We immerse the proposed nanocavities into water (n_c) or other aqueous solutions to examine the sensitivity S, as shown in Fig. 1 (d).

We proposed a hybrid photonic-plasmonic crystal nanocavity containing a silicon grating nanowire near a metal substrate with a gain gap between. We analyzed the modal characteristics of the hybrid plasmonic waveguide modes using finite-element method. We also numerically solved the band structure of the hybrid crystal modes. As a single defect is introduced to the photonic crystal, a resonant defect mode forms and exhibits strong confinement inside the gap region. For such cavities with a short defect length, a high quality factor near 567 and ultrasmall modal volume lower than 1.9×10^{-3} $(\lambda/n)^3$ are achievable. The results demonstrate that the defect mode can reach a sensitivity of 443 nm/*RIU* at the wavelength around 1550 nm aiming at biosensing applications.

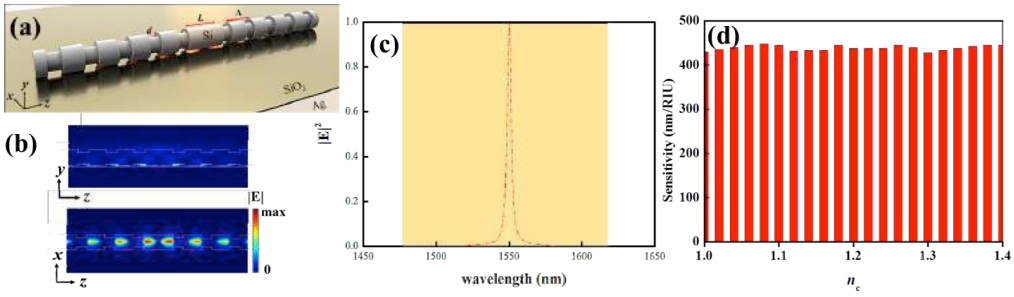

Figure 1 (a) The proposed photonic-plasmonic crystal nanocavity. (b) Side views of the defect resonant mode profiles by 3D FEM (c) The resonance line shape corresponds to a FWHM of 2.7 nm and the Q factor is 566.5. (d) The sensitivity S as function of the refractive indexes of the surrounding environments.

Acknowledgements, this work was sponsored by National Taiwan Ocean University, Research Center for Applied Sciences, Academia Sinica, Taiwan, National Yunlin University of Science and Technology, and Ministry of Science and Technology (MOST), Taiwan under Grant number MOST 105-2221-E-019-049-MY3.

REFERENCES

1. Chou, Y. H. *et al.*, "Ultrastrong mode confinement in ZnO surface plasmon nanolasers," *ACS Nano*, Vol. 9, No. 4, 3978–3983, 2015.
2. Jiang, H. A. *et al.*, "High-Q/V_{eff} gap-mode plasmonic FP nanocavity," *Opt. Express*, Vol. 21, 4752–4757, 2013.
3. Cheng, P. J. *et al.*, "Plasmonic gap-mode nanocavities with metallic mirrors in high-index cladding," *Opt. Express*, Vol. 21, 13479–13491, 2013.
4. Oulton, R. F. *et al.*, "Plasmon lasers at deep subwavelength scale," *Nature*, Vol. 461, 629–632, 2009.
5. Yang, X. *et al.*, "Hybrid photonic-plasmonic crystal nanocavities," *ACS Nano*, Vol. 5, 2831–2838, 2011.

Nanoantennas for Enhanced THz Radiation – Matter Interaction

L. Razzari[1,*]

[1] INRS-EMT, 1650, Boul. Lionel-Boulet, Varennes, Quebec, J3X 1S2, Canada

[*]razzari@emt.inrs.ca

Abstract- We present our recent investigations regarding the interaction of localized terahertz (THz) radiation with nanomaterials. Details about the design of resonant metallic nanostructures for THz field confinement will be given, together with some examples of applications.

During the last few years, we have explored the use of metallic nanoantennas for applications in THz science and technology. We have shown that these devices can confine THz radiation well beyond the diffraction limit and are characterized by a large electric field enhancement close to their extremities [1,2]. We have also demonstrated that such properties can be further optimized (reaching enhancement values > 1,000) exploiting the end-to-end coupling of THz nanoantennas through nanogaps (down to 20 nm in width). The effective absorption of an object scales with the local electric field squared, and it can thus be increased by several orders of magnitude within antenna nanocavities. This can be used to enhance the interaction of THz radiation with nanomaterials and molecules. In particular, we have recently studied the coupling between the phonon resonance of semiconducting nanocrystals and the plasmon resonance of nanoantenna arrays. When the two resonances are matched, the combined system shows a clear destructive-interference feature in THz extinction measurements. We have first employed this effect to perform enhanced THz spectroscopy of a single layer of cadmium selenide quantum dots [3]. Intensified THz radiation - matter interactions within nanoscale volumes are also found to lead to other interesting phenomena that will be discussed on site.

Acknowledgements L.R. is grateful for financial support from the Natural Sciences and Engineering Research Council (NSERC) of Canada and PRIMA Quebec.

REFERENCES

1. L. Razzari et al., "Extremely large extinction efficiency and field enhancement in terahertz resonant dipole nanoantennas," *Opt. Express* Vol. 19, 26088, 2011.
2. L. Razzari et al., "Terahertz Dipole Nanoantenna Arrays: Resonance Characteristics," *Plasmonics* Vol. 8, 133, 2013.
3. A. Toma et al., "Squeezing Terahertz Light into Nanovolumes: Nanoantenna Enhanced Terahertz Spectroscopy (NETS) of Semiconductor Quantum Dots," *Nano Lett.* Vol. 15, 386, 2015.

Laser nano-engineered functional surfaces for high-performance organic optoelectronic devices

Hong-Bo Sun[1*], Xu-Lin Zhang[1], Jing Feng[1]

[1] State Key Laboratory on Integrated Optoelectronics, College of Electronic Science and Engineering, Jilin University, 2699 Qianjin Street, Changchun 130012, China

[*]corresponding author: hbsun@jlu.edu.cn

Abstract- We report high-performance organic optoelectronic devices including organic light-emitting devices (OLEDs) and organic solar cells (OSCs) employed with laser nano-engineered functional surfaces. The proposed laser induced functional surfaces can help manipulate light-structure interactions in these devices. As a result, the electroluminescence efficiency of OELDs and photon-to-electron conversion efficiency of OSCs are considerably improved.

Organic optoelectronic devices such as organic light-emitting devices (OLEDs) and organic solar cells (OSCs) have been attracting various attentions owing to their merits of lightweight, low cost, stretchable, and ultraportable. The electroluminescence efficiency of OLEDs and photon-to-electron conversion efficiency of OSCs are key factors for their commercial applications. Manipulating the surface profiles using laser micro-nano fabrication techniques is an effective way to improve their performance. Here we report some of our recent works related to this topic.

Stretchable OLEDs are becoming more and more important in the fields of wearable displays and health-monitoring technology. We report a laser-programmable buckling process to introduce micrometer gratings into OLEDs [1]. We realized a highly stretchable OLED with mechanical robustness and unprecedented efficiency. The strained device luminous efficiency, 70 cd A^{-1} under 70% strain, is the largest to date, which may pave the way for commercial applications of stretchable OLEDs. The loss of surface plasmon-polaritons (SPPs) in OLEDs employed with metallic electrodes always sets obstacles for high efficiency of the devices. To deal with this issue, we patterned the electrodes using a laser assisted soft nano-imprinting lithography. SPPs could then be extracted successfully and the device efficiency is considerably increased [2].

Broadband absorption enhancement is an effective way to improve the performance of OSCs. We introduced two-dimensional nanostructured electrodes into OSCs to excite SPPs supported in the cathode/organic interface. We performed numerical simulations and experiments and found that light absorption in the active layer can be enhanced in broadband due to the effect of SPP-induced field enhancement [3].

To conclude, we have proposed various laser induced micronanostructured surfaces in OLEDs and OSCs, which may pave the way for the commercial applications of high performance organic optoelectronic devices.

REFERENCES

1. Yin, D., J. Feng, R. Ma, Y. F. Liu, Y. L. Zhang, X. L. Zhang, Y. G. Bi, Q. D. Chen, and H. B. Sun, "Efficient and mechanically robust stretchable organic light-emitting devices by a laser-programmable buckling process," *Nature Communications*, Vol. 7, 11573, 2016.

2. Liu, Y. F., M. H. An, X. L. Zhang, Y. G. Bi, D. Yin, Y. F. Zhang, J. Feng, and H. B. Sun, "Enhanced efficiency of organic light-emitting devices with corrugated nanostructures based on soft nano-imprinting lithography," *Applied Physics Letters*, Vol. 109, 193301, 2016.
3. Bi, Y. G., J. Feng, Y. Chen, Y. S. Liu, X. L. Zhang, Y. F. Li, M. Xu, Y. F. Liu, X. C. Han, and H. B. Sun, "Dual-periodic-corrugation-induced broadband light absorption enhancement in organic solar cells," *Organic Electronics*, Vol. 27, 167-172, 2015.

Nanoscale optical force spectroscopy in the vicinity of plasmonic and dielectric nanostructures

Taka-aki Yano[1,2*], **and Masahiko Hara**[1,2]
[1] Tokyo Institute of Technology, Yokohama, Japan
[2] RIKEN, Saitama, Japan
[*]yano@echem.titech.ac.jp

Abstract- We performed atomic force microscope (AFM)-based optical force spectroscopy to quantitatively characterize optical forces generated in the vicinity of plasmonic and dielectric nanostructures. The optical forces were either attractive or repulsive, which was controlled by size- and shape-dependent unique optical resonances of the nanostructures.

Plasmonically-induced optical forces in the vicinity of metallic nanostructures have received considerable attention because of their applications in local positioning and manipulation of nano-objects. There have been a variety of works on nano-optical forces controlled by various geometric configurations of metallic nanostructures [1].

Here in this work, we proposed the use of AFM-based near-field optical techniques [2] with high force detection sensitivity in order to quantitatively and qualitatively characterize optical forces generated in the proximity of various metallic nanostructures. In particular, the optical forces exerted between two metallic nanostructures were experimentally characterized, and were found to be either attractive or repulsive depending on the separation distance, incident angle, incident polarization and excitation wavelength. Furthermore, we also applied the plasmonically-induced optical forces for controlling biomolecular recognition reaction (ligand-receptor binding).

In addition to plasmonic materials, dielectric materials with high indices of refraction and low energy losses have recently been recently regarded as promising resonant scatterers to generate strong optical forces [3]. Among the high index materials, silicon (Si) nanoparticles with diameters of 100–200 nm have gained much attention owing to their multiple electromagnetic resonances in the visible region [4, 5]. We performed nanoscale optical force spectroscopy of a silicon nanodimer, and found that multiple excitation of electric- and magnetic-dipoles in the Si nanostructures played a crucial role in achieving the reversed optical binding force of the Si nanodimer.

REFERENCES

1. M. L. Juan, M. Righini, and R. Quidant, Nat. Photonics 5, 349 (2011).
2. T. Yano et al., Appl. Spectroscop. 70, 1239 (2016).
3. T. Yano et al., Optics Express 25, 431 (2017).
4. Y. Tsuchimoto, T. Yano et al., Optics Express 24, 14451 (2016).
5. Y. Tsuchimoto, T. Yano et al., Small, 11, 4844–4849 (2015).

Harnessing interband and intraband nonlinearities in transparent conducting oxides via two-colour excitation

M. Clerici[1], **N. Kinsey**[2,3], **C. DeVault**[4], **J. Kim**[2], **E. Carnemolla**[5], **L. Caspani**[5,6], **A. Shaltout**[2], **D. Faccio**[5],**V. Shalaev**[2], **A. Boltasseva**[2], **and M. Ferrera**[5]

[1]School of Engineering, University of Glasgow, Glasgow, G12 8LT, UK
[2]School of Electrical and Computer Engineering and Birck Nanotechnology Center, Purdue University, West Lafayette, IN, 47907, USA
[3]Dep. of Electrical and Computer Engineering, Virginia Commonwealth University, Richmond, Virginia 23220, USA
[4]Dept. of Physics and Astronomy and Birck Nanotechnology Center, Purdue University, West Lafayette, IN, 47907, USA
[5]Institute of Photonics and Quantum Sciences, Heriot-Watt University, SUPA, Edinburgh, EH14 4AS, UK
[6]Institute of Photonics, Department of Physics, University of Strathclyde, Glasgow G1 1RD, UK

Abstract— We investigated the effect of combined interband and intraband nonlinearities in aluminium zinc oxide thin films. We show that suitably timed two-colour pulsed excitations increase the material modulation bandwidth at near-infrared wavelengths and unlock novel functionalities including ultrafast modulation of the transmitted and reflected radiation frequency.

1. INTRODUCTION

Transparent conductive oxides (TCOs) are wide-bandgap semiconductors supporting large doping values ($\simeq 10^{21}$ cm^{-3}) and low effective electron mass, thus presenting a metallic response in the near-infrared (NIR) spectral region and high optical transmission in the visible part of the spectrum. This class of materials recently acquired a relevant role for nano-photonics for the large extent their optical properties can be controlled during the fabrication process and dynamically, via optical or electrical excitations [1, 2, 3]. Transparent conductive oxides also feature an epsilon-near-zero (ENZ) condition in the near-infrared spectral region, in the technologically relevant telecommunication band. At the ENZ wavelength, the effect of optical nonlinearities is enhanced [4, 5, 6], enabling ultrafast photonics applications such as all-optical switching [7]. Aluminium zinc oxide (AZO) is a TCO with reduced optical losses and low fabrication costs compared to other TCOs, showing strong, sub-picosecond interband nonlinear effects at the ENZ wavelength when excited by an above-bandgap optical pulse (UV, 325 nm) [7]. Even faster nonlinear effects have been observed when AZO is driven by longer wavelength pulses, as a consequence of the interband carrier dynamics [6]. Here, we show that the optical properties of AZO at the ENZ wavelength can be tailored in unique ways by a properly shaped two-colour optical excitation.

2. RESULTS

We experimentally investigated the change in the transmission and reflection at $\simeq 1300$ nm (ENZ wavelength) of a 900 μm thick AZO film when simultaneously excited by above ($\lambda = 262$ nm) and below ($\lambda = 787$ nm) bandgap ultrashort pulses ($\simeq 100$ fs), with a controllable relative delay. The time-resolved reflection and transmission measurements reported in Fig. 1 show that the two nonlinearities can be combined to increase or cancel the film nonlinear response. We also observed that the two-colour excitation enables to increase the modulation bandwidth above the limits of a single-pulse excitation. Further, we experimentally investigated the effect of such an ultrafast modulation on the transmitted and reflected pulse at the ENZ wavelength, reporting tunable wavelength shifts.

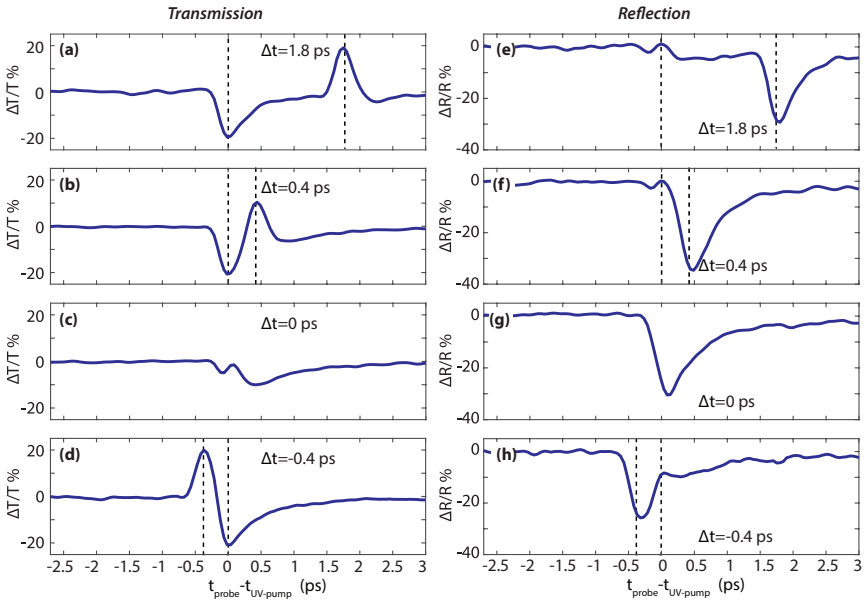

Figure 1: Relative changes in the transient transmission (a)-(d) and reflection (e)-(h) of an optical pulse at $\lambda = 1300$ nm from a 900 μm thick AZO film as a function of the delay between the UV pump and the 1300 nm probe pulse ($t_{probe} - t_{UV\text{-}pump}$). Different panels show the measured quantities for various relative delays Δt between the UV and the NIR pump pulses.

In conclusion, we shall report our measurements performed on AZO films and other commercial TCOs, and discuss the novel opportunities provided by the combination of intraband and interband nonlinearities, such as optical three-state logic and ultra-fast routing of the transmitted near-infrared radiation.

ACKNOWLEDGMENT

This work was supported by the NSF MRSEC Grant DMR-1120923, AFOSR Grant FA9550-14-1-0138DEF, and AFOSR Grant FA9550-14-1-0389. D.F. acknowledges funding from the European Research Council under the European Union's Seventh Framework Programme (FP/2007-2013)/ERC GA 306559 and EPSRC (UK, grant EP/M009122/1). M.C. acknowledges support from EPSRC (EP/P009697/1 and EP/P51133X/1). L.C. acknowledges the support from the People Programme (Marie Curie Actions) of the European Union's FP7 Programme, REA GA 627478.

REFERENCES

1. M. A. Noginov, Lei Gu, J. Livenere, G. Zhu, A. K. Pradhan, R. Mundle, M. Bahoura, Yu A. Barnakov, and V. A. Podolskiy. *Applied Physics Letters*, **99,** 021101 (2011).
2. G. V. Naik, J. Liu, A. V. Kildishev, V. M. Shalaev, and A. Boltasseva. *Proceedings of the National Academy of Sciences*, **109,** 8834 (2012).
3. J. Kim, G. V. Naik, A. V. Gavrilenko, K. Dondapati, V. I. Gavrilenko, S. M. Prokes, O. J. Glembocki, V. M. Shalaev, and A. Boltasseva. *Physical Review X*, **3,** 041037 (2013).
4. A. Capretti, Y. Wang, N. Engheta, and L. Dal Negro. *Optics Letters*, **40,** 1500 (2015).
5. M. Z. Alam, I. De Leon, and R. W. Boyd. *Science*, **352,** 795 (2016).
6. L. Caspani, R. P M Kaipurath, M. Clerici, M. Ferrera, T. Roger, J. Kim, N. Kinsey, M. Pietrzyk, A. Di Falco, V. M. Shalaev, A. Boltasseva, and D. Faccio. *Physical Review Letters*, **116,** 233901 (2016).
7. N. Kinsey, C. DeVault, J. Kim, M. Ferrera, V. M. Shalaev, and A. Boltasseva. *Optica*, **2,** 616 (2015).

Campanile Near-Field Probes Fabricated by Nanoimprint Lithography.

Alexander Koshelev[1], Giuseppe Calafiore[1], Thomas P. Darlington[2], Nicholas J. Borys[2], Alexander Weber-Bargioni[2], P. James Schuck[2], Keiko Munechika[1], Stefano Cabrini[2*]

[1] aBeam Technologies, Hayward, CA, USA

[2] The Molecular Foundry, Lawrence Berkeley National Laboratory, Berkeley, CA 94720, USA

[*]corresponding author: scabrini@lbl.gov

Abstract-Optical transformer is a plasmonic antennas that can focus the light in few nanometers space efficiently and broadband. By means of Nano Imprinting Lithography, it has been fabricated on top of an optical fiber in a configuration called "Campanile Tip". It is an efficient probe tip for Scanning Near Field Optical Microscopy and Spectroscopy. We will show the fabrication process, the optical characterization and the performances as high resolution SNOM tip.

One of the major challenges to the widespread adoption of plasmonic and nano-optical devices in real-life applications is the difficulty to mass-fabricate nano-optical antennas in parallel and reproducible fashion, and the capability to precisely place nanoantennas into devices with nanometer-scale precision [1]. In this talk, we present a solution to this challenge using the state-of-the-art ultraviolet nanoimprint lithography (UV-NIL) to fabricate functional optical transformers [2,3] (figure 1) onto the core of an optical fiber[4,5] in a single step, mimicking the 'campanile' near-field probes. Imprinted probes were fabricated using a custom-built imprinter tool with co-axial alignment capability with sub < 100 nm position accuracy, followed by a metallization step (figure 2) [6,7]. Scanning electron micrographs confirm high imprint fidelity and precision with a thin residual layer to facilitate efficient optical coupling between the fiber and the imprinted optical transformer. This novel nano-fabrication approach promises a low-cost, high-throughput, and reproducible manufacturing of advanced nano-optical devices. We demonstrate the capability to imprint 3D structures with sub-70 nm scale features and sub-100 nm positioning precision, creating functional 'campanile' near-field probes. The functionality of the imprinted probes was validated by performing hyperspectral nano-PL mapping of a dispersed film of 40 nm polystyrene fluorescent beads. Both the topography scans and the PL maps exhibited features consistent with the behavior of traditional FIB-fabricated optical transformer probes. Results show that imprinted campanile probes enable sub-diffraction-limit imaging with a resolution of ~ 80 nm, determined by the gap size at the tip apex. The fabrication process presented here can be scaled and parallelized for higher throughput and offers a promising route for mass production of nano-optical devices.

Acknowledgements This work is supported by the U.S. Department of Energy, Office of Science, Basic Energy Sciences, under Award Number DE-C0013109. Work at the Molecular Foundry was supported by the Office of Science, Office of Basic Energy Sciences, of the U.S. Department of Energy under contract no. DE-AC02- 05CH11231.

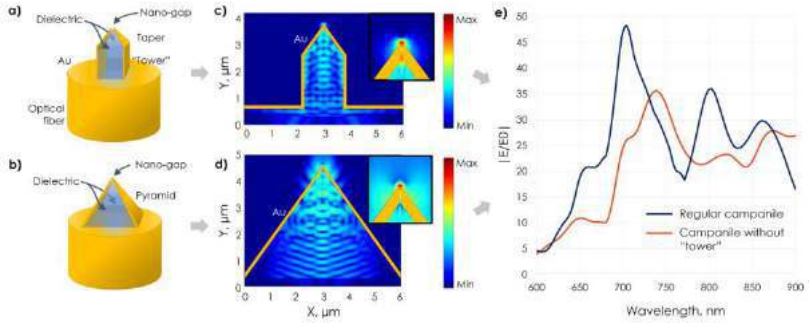

Figure 1 Campanile probe geometry and simulations. Geometries of the regular (a) and "tower-less" campanile probe. FDTD simulations of the electric field amplitude inside the campanile for a regular (c) and "tower-less" (d) campanile. Comparison of field enhancements as a function of wavelength for both configurations (e).

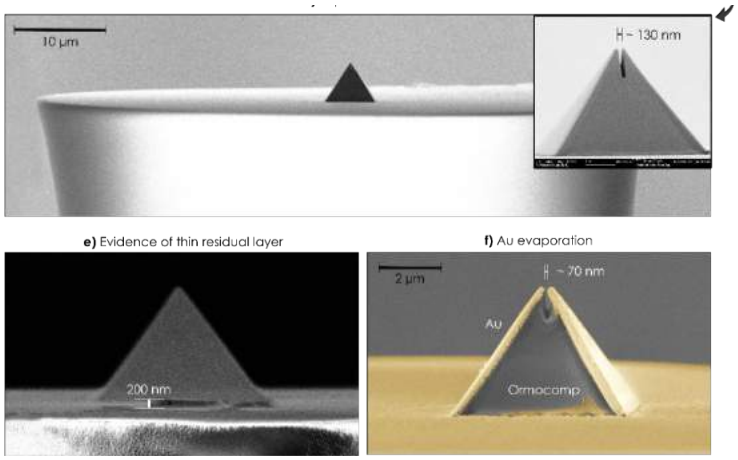

Figure 2 Tilted-view SEM of the pyramid imprinted on an optical fiber. The inset shows a close-up of the campanile that has a gap of about 130 nm in width at the apex. e. shows a residual layer of about 200 nm. f. False-color SEM image of the completed campanile probe after side-evaporation of Au with a final gap of about 70 nm.

REFERENCES

1 Schuller, J. A. *et al*. Plasmonics for extreme light concentration and manipulation. *Nature Materials* **9**, 193-204, doi:10.1038/nmat2630 (2010).

2 Stockman, M. I. Nanofocusing of Optical Energy in Tapered Plasmonic Waveguides. *Physical Review Letters* **93**, 137404 (2004).

3 Choo, H. *et al*. Nanofocusing in a metal-insulator-metal gap plasmon waveguide with a three-dimensional linear taper. *Nat Photon* **6**, 838-844, doi:10.1038/nphoton.2012.277 (2012).

4 Polyakov, A. *et al*. Coupling model for an extended-range plasmonic optical transformer scanning probe. *Light Sci Appl* **3**, e195, doi:10.1038/lsa.2014.76 (2014).

5 Bao, W. *et al*. Visualizing nanoscale excitonic relaxation properties of disordered edges and grain boundaries in monolayer molybdenum disulfide. *Nature Communications* **6**, (2015).

6 Calafiore, G. *et al*. Nanoimprint of a 3D structure on an optical fiber for light wavefront manipulation. *Nanotechnology* **27**, 375301 (2016).

7 Koshelev, A. *et al*. High refractive index Fresnel lens on a fiber fabricated by nanoimprint lithography for immersion applications. *Opt. Lett.* **41**, 3423-3426, (2016).

Dynamic color displays based on catalytic metasurfaces

Xiaoyang Duan[1,2], Simon Kamin[1], Marcus Matuschek[1], Frank Neubrech[2], and Na Liu[1,2]

[1]Max Planck Institute for Intelligent Systems, Heisenbergstrasse 3, 70569 Stuttgart, Germany
[2]Kirchhoff Institute for Physics, University of Heidelberg, Im Neuenheimer Feld 227, 69120 Heidelberg, Germany

[*]corresponding author: laura.liu@is.mpg.de

Abstract-Plasmonic color generation based on metallic metasurfaces provides resolutions far beyond the diffraction limit of light enabling new possibilities for printing color images or high-density optical data storage. However, the realization of dynamic plasmonic displays remains a challenging task. In the present paper, we utilize catalytic magnesium nanostructures, which change their optical properties during exposure to hydrogen, to demonstrate dynamic color generation. The technique could pave the way for animating high resolution images and could provide new routes for encrypting information or detecting counterfeits.

Plasmonic color printing based on tailored metallic metasurfaces provides resolutions several times higher than conventional printing techniques.[1] Due to its unprecedented subwavelength resolution, applications such as high-density optical data storage, stereoscopic imaging, or anticounterfeiting features are within reach. However, the realization of dynamic plasmonic color generation for displays with advanced functionalities still remains a challenging task.

In the present paper, we demonstrate two approaches of dynamic plasmonic displays exploiting catalytic magnesium nanostructures arranged in engineered metasurfaces.[2] First, brilliant colors are generated by tailoring the particles' sizes as well as their interparticle distances.[3] Secondly, dynamic displays based on cavity modes in a nanostructured dielectric layer, which is coated with magnesium, are demonstrated. In both approaches, a controlled hydrogenation and dehydrogenation of the magnesium trigger a metal to dielectric phase transition resulting in a dramatic change of their optical properties.

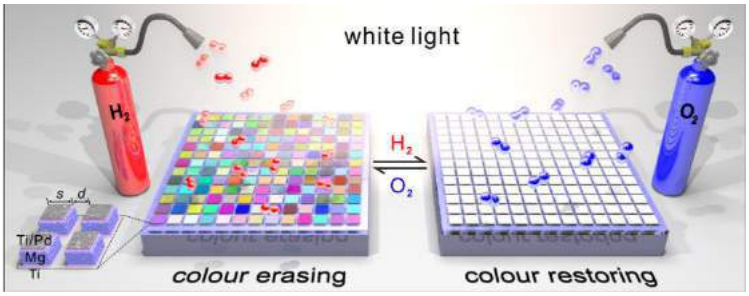

Figures 1 Schematic of the plasmonic metasurface composed of hydrogen-responsive magnesium metasurfaces interacting with incident unpolarized white light. Hydrogen loading is achieved by exposing the display to H_2 whereas dehydrogenation is achieved by oxygen exposure.

The technique could pave the way for animating ultra-high-resolution images as we demonstrated by reversibly erasing and restoring plasmonic color paintings. Furthermore, through a smart design of the nanostructures, information can be encoded on selected pixels enabling secure encryption.

Acknowledgements: The projects were supported by the Sofja Kovalevskaja grant from the Alexander von Humboldt-Foundation, the Marie Curie CIG grant, and the European Research Council (ERC Dynamic Nano) grant.

REFERENCES

1. Kumar, K. *et al*. "Printing colour at the optical diffraction limit." *Nature Nanotechnol*. **7,** 557–561 (2012).
2. Duan, X. *et al*. "Hydrogen-regulated chiral nanoplasmonics." *Nano Lett*. **16,** 1462–1466 (2016).
3. Duan, X *et al*. "Dynamic plasmonic colour display." *Nature Commun*. **8,** 14606 (2017).

Functional Materials and Devices for Acoustic and Elastic Waves

Parity Time Synthetic Phononic Media.

J. Christensen
[1]Universidad Carlos III de Madrid, Spain
corresponding author: johan.christensen@uc3m.es

Abstract- Classical systems containing cleverly devised combinations of loss and gain elements constitute extremely rich building units that can mimic non-Hermitian properties, which conventionally are attainable in quantum mechanics only. Parity-time (PT) symmetric media, also referred to as synthetic media, have been devised in many optical systems with the ground breaking potential to create nonreciprocal structures and one-way cloaks of invisibility. Here we demonstrate a feasible approach for the case of elasticity where the most important ingredients within synthetic materials, loss and gain, are achieved through electrically biased piezoelectric semiconductors [1]. We study first how wave attenuation and amplification can be tuned, and when combined, can give rise to a mechanical PT synthetic media with unidirectional suppressed reflectance, a feature directly applicable to evading sonar detection [2].

REFERENCES

1. J. Christensen, M. Willatzen, V. R. Velasco, and M.-H. Lu, Phys. Rev. Lett. 116, 207601 (2016)
2. S. A. Cummer, J. Christensen, and A. Alu, Nature Reviews Materials 1, Article number: 16001 (2016)

Beating Diffraction Limit using a three-dimensional metamaterial absorber

Guancong Ma[1,2 *], Xiying Fan[2], Fuyin Ma[2], Ping Sheng[1,2], Mathias Fink[1,3]

1 Institute for Advanced Study, Hong Kong University of Science and Technology, Clear Water Bay, Kowloon, Hong Kong, China

2 Department of Physics, Hong Kong University of Science and Technology, Clear Water Bay, Kowloon, Hong Kong, China

3 Institut Langevin, ESPCI Paris Tech, CNRS UMR 7587, PSL Research University, 1 rue Jussieu, Paris 75005, France

*corresponding author: phmgc@ust.hk

Abstract- Focal spot of a wave is bounded by diffraction limit, which has a dimension of half of the wavelength. This limit arises through the destructive interference between converging and diverging waves, which eliminate the singularity at the center of the focal spot, and gives rise to its sinc-function shape. We design a three-dimensional sub-wavelength absorber using acoustic metamaterial, and show with a time-reversal focusing experiments that by reducing the diverging waves, the focal spot is smaller than the diffraction limit.

We form a focal spot by converging, from the far-field regime, a spherical wavefront $P_{in} = \exp(-ikr - i\omega t)/r$ to a point defined as $r = 0$. Here, $k = 2\pi/\lambda$ is the incoming wave vector. However, after reaching the point $r = 0$, the wave does not disappear, instead it diverges, forming another spherical wavefront $P_{out} = \exp(ikr - i\omega t)/r$. Note that a singularity can be found in the spatial distribution of both the incoming and outgoing wavefronts *alone* at $r = 0$, at which point the wave's amplitude diverges. However, this singularity does not usually exist. This is because the total wave field in the medium given by the superposition of the two wavefronts

$$P = P_{in} - P_{out} = \left(\frac{e^{-ikr}}{r} - \frac{e^{ikr}}{r}\right)e^{-i\omega t} = \frac{2i\sin(kr)}{r}e^{-i\omega t}$$

It follows that the destructive interference between the incoming and outgoing waves eliminates the singularity at $r = 0$. The resultant total wave field takes a finite value at the origin, and the major peak of the focal spot has a FWHM of $\sim\lambda/2$. This interference process is also responsible for the formation of side lobes.

The above analysis suggests that one may restore the singularity by simply modifying the ratio of P_{in} and P_{out}. In the extreme case that $P_{out} = 0$, i. e., the wave converges to $r = 0$ but without subsequently diverging, interference no longer occurs, therefore side lobes of the

focal spot vanishes, and the singularity at $r = 0$ shall be restored.

We construct a subwavelength acoustic metamaterials that is highly absorbing for a spherical wavefront. By using this metamaterial absorber, we are able to significantly reduce the outgoing waves of thereby successfully observe that a wave can be focused to dimension smaller than the diffraction limit. Experimental evidence also show signs of singularity at the center position.

Optimal Sound-Absorbing Structures*

Ping Sheng
Department of Physics, HKUST, Clear Water Bay, Kowloon, Hong Kong, China
and
Institute for Advanced Study, HKUST, Clear Water Bay, Kowloon, Hong Kong, China
sheng@ust.hk

Causal nature of the acoustic response dictates an inequality that relates the absorption spectrum of the sample to its thickness. We use the causal constraint to delineate what is ultimately possible for sound absorbing structures, and denote those which can attain near-equality for the causal constraint to be "optimal." By using acoustic metamaterial as backing to conventional porous absorbers, a design strategy is presented for realizing structures with target-set absorption spectra and a sample thickness close to the minimum value as dictated by causality. By using this approach, we have realized a 10.86 cm-thick structure that exhibits broadband, near-perfect flat absorption spectrum starting at around 400 Hz, while the minimum sample thickness as calculated from the causal constraint is 10.36 cm. To illustrate the versatility of the approach, two additional optimal structures with different target absorption spectra are presented. This "absorption by design" strategy would enable the tailoring of customized solutions to difficult room acoustic and noise remediation problems.

*Work done in collaboration with Min Yang, Shuyu Chen, and Caixing Fu.

Topological creation of acoustic pseudospin multipoles in a flow-free symmetry-broken metamaterial lattice

Zhiwang Zhang[1], **Qi Wei**[1], **Ying Cheng**[1,2,*], **Ting Zhang**[1], **Dajian Wu**[3] and **Xiaojun Liu**[1,2,†]
[1]Key Laboratory of Modern Acoustics, Department of Physics and Collaborative Innovation Center of Advanced Microstructures, Nanjing University, Nanjing 210093, China
[2]State Key Laboratory of Acoustics, Chinese Academy of Science, Beijing 100190, China
[3]School of Physics and Technology, Nanjing Normal University, Nanjing 210046, China
Email: [*] chengying@nju.edu.cn; [†]liuxiaojun@nju.edu.cn

Abstract-Due to the spinless nature of sound, the "spin-like" degree of freedom crucial to topological states in acoustic systems is commonly realized with circulating background flow or pre-set coupled resonator ring waveguides, which drastically increases the engineering complexity. Here we realize the acoustic pseudospin multipolar states in a simple flow-free symmetry-broken metamaterial lattice. Topologically protected edge states and reconfigurable topological one-way transmission for sound are further demonstrated.

The application of topology, the mathematics of conserved properties under continuous deformation, is creating a range of new opportunities in acoustic systems. This field was inspired by the discovery of topological insulator which shew insulating behavior in the bulk and transmission states without dissipation in the interface. Because of the spinless nature of sound, the "spin-like" degree of freedom crucial to topological states in acoustic systems is commonly realized with circulating background flow[1,2] or pre-set coupled resonator ring waveguides[3], which drastically increases the engineering complexity.

In this paper, we demonstrate the "spin-like" degree of freedom crucial to topological states in a simple flow-free metamaterial lattice, without using any complicated material or structure. Starting with the honeycomb acoustic metamaterial lattice, we make the primitive cell rotated and enlarged to obtain a metamolecule, which constructs double Dirac cone at the center of the 1st Brillouin zone. We make sound circulating in the lattice and the direction of sound propagation within each hexagonal cluster (i.e., clockwise or anticlockwise) plays the role of pseudospin (i.e., pseudospin-down or pseudospin-up). Tuning the strength of intermolecular coupling by simply contracting/expanding the metamolecule can induce band inversion effect between pseudospin dipole and quadrupole, which leads to a topological phase transition (shown in Fig. 1).

As a result of the spin-orbital coupling, these artificial pseudospin multipoles can support topologically protected one-way transmission, in which the route of sound propagation can be reconfigured to whatever you want. The two pseudospin states will not affect each other at the same frequency and between different frequencies. What is worth noting is that the pseudospin modes will not change after encountering the local defects. These results open new avenues for the novel acoustic topological insulators with versatile applications, such as acoustic modulators, transducers and isolators.

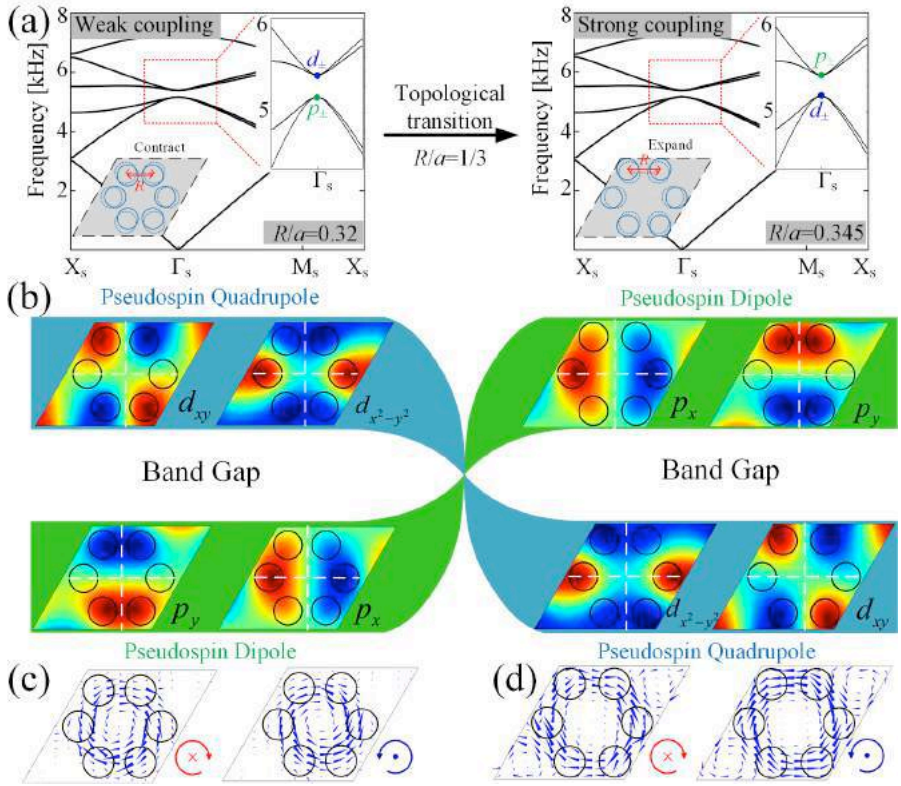

FIG. 1. (a) Topological transition as the coupling strength is tuned from weak (*Left*: R/a=0.320) to strong (*Right*: R/a=0.345). Critical coupling appears at R/a=1/3 with double Dirac cone. (b) Topological modes inversion underlying the transition. Sound intensity I associated with pseudospin-down and pseudospin-up modes below the band gap in the (c) trivial regime (R/a=0.320) and (d) nontrivial regime (R/a=0.345). The rainbow colour represents the amplitude of acoustic pressure, and the arrows show the direction and amplitude of the intensity.

This work was supported by the National Basic Research Program of China (2012CB921504), NSFC (11674172, 11574148, 11474162 and 11274171), SRFDP (20130091130004), and Jiangsu Provincial NSF (BK20160018 and BK20150562).

REFERENCES

1. Khanikaev, A.B., Fleury, R., Mousavi, S.H. & Alu, A. Topologically robust sound propagation in an angular-momentum-biased graphene-like resonator lattice. *Nat. Commun.* **6**, 8260 (2015).
2. Yang, Z. et al. Topological acoustics. *Phys. Rev. Lett.* **114**, 114301 (2015).
3. He, C. et al. Topological phononic states of underwater sound based on coupled ring resonators. *Appl. Phys. Lett.* **108**, 031904 (2016).

Anisotropic metasolids for elastic wave control

Yong Cheng, Jiahui Huang, Hongkuan Zhang and Xiaoming Zhou*
Key Laboratory of Dynamics and Control of Flight Vehicle, Ministry of Education and
School of Aerospace Engineering, Beijing Institute of Technology, Beijing 100081, China
*corresponding author: zhxming@bit.edu.cn

Abstract-We have proposed a structured metasolid, which can be homogenized into an elastic continuum with both stiffness and inertial anisotropy. Effective medium parameters have been retrieved from band structure results and have shown the orthotropic properties in elasticity and inertial mass. This anisotropic metasolid fulfills the requirement of transformation elastic mediums under some special coordinate transformations in which the Navier elastodynamic equation retains its original form. We study some elastic wave controlling examples based on the proposed metasolids.

Transformation method has now been recognized as a powerful tool for generating parameter inhomogenity in order to manipulate wave propagation in ways as one will. The concept is initiated in electromagnetics realm [1,2], and later extended rapidly to acoustics[3] and elastic waves[4]. In elasticity, Navier elastodynamic equation doesn't retain its original form under a general coordinate transformation; however elastic wave controlling based on special form-invariant transformation is still significant, which requires both elastic and inertial anisotropy in solids. The practical design of this solid can be made possible based on the metamaterial concept.

Based on the recent advances of elastic metamaterial design [5-8], we have proposed a preliminary version of the anisotropic metasolid. The element consists in a periodic hexagonal frame structure, inside which the resonator-like inclusions are inserted. Anisotropic stiffness is realized by the non-regular hexagon geometry of the frame structure. Anisotropic inertial mass is achieved due to the different resonant frequencies in two perpendicular principle directions. Band structures of the periodic lattice have been calculated, which have shown the purely longitudinal and transverse branches of our interest at a finite frequency range. Utilizing the modal fields of band structure results, we have defined average stress and strain fields for the cell structure, and retrieved all orthotropic effective parameters according to macroscopic elasticity and inertial motion equations. Effective medium analysis has been fully conducted, from which the influence of microstructure geometry to the overall anisotropy is well identified.

As an example of elastic wave controlling, we have considered a wave beam shifting medium, obtained by using the linear transformation. The parameters of this transformation device are anisotropic in both stiffness and mass, thereby can be readily realized by the proposed metasolids. The cell structures of the beam shifting metasolids have been designed with their anisotropic parameters strictly satisfying the transformation results. Full-wave simulations have been conducted to verify the beam shifting performance of the designed device.

As a conclusion, this work has proposed the microstructure model of metasolids with both elastic and inertial anisotropy. The beam shifting effect achieved by the proposed metasolids is exampled. The study is expected to find potential applications in seismic wave protection.

Acknowledgements This work was supported by the National Natural Science Foundation of China (Grant Nos. 11622215, 11572039, and 11521062), and 111 project (B16003).

REFERENCES

1. Greenleaf, A., Kurylev, Y., Lassas, M. and Uhlmann, G., "Full-Wave invisibility of active devices at all frequencies," *Commun. Math. Phys.*, Vol. 275, 749-789, 2007.
2. Pendry, J.B., Schurig, D., Smith, D.R., "Controlling electromagnetic fields," *Science*, Vol. 312, 1780-1782, 2006.
3. Norris, A.N., "Acoustic cloaking theory," *Proc. R. Soc. London Ser. A*, Vol. 464, 2411-2434, 2008.
4. Milton, G.W., Briane, M., Willis, J.R., "On cloaking for elasticity and physical equations with a transformation invariant form," *New J. Phys.*, Vol. 8, 248-248, 2006.
5. Milton, G.W., Willis, J.R., "On modifications of Newton's second law and linear continuum elastodynamics," *Proc. R. Soc. London Ser. A*, Vol. 463, 855-880, 2007.
6. Lai, Y., Wu, Y., Sheng, P., Zhang, Z.Q., "Hybrid elastic solids," *Nature Mater.*, Vol. 10, 620-624, 2011.
7. Zhu, R., Liu, X.N., Huang, G.L., Huang, H.H., Sun, C.T., "Microstructural design and experimental validation of elastic metamaterial plates with anisotropic mass density," *Phys. Rev. B*, Vol. 86, 144307, 2012.
8. Ma, G., Fu, C., Wang, G., del Hougne, P., Christensen, J., Lai, Y., Sheng, P., "Polarization bandgaps and fluid-like elasticity in fully solid elastic metamaterials," *Nature Communications*, Vol. 7, 13536, 2016.

Topological transport of sound vortices

Shubo Wang[1] **and C. T. Chan**[1*]
[1]Department of Physics and Institute for Advanced Study,
The Hong Kong University of Science and Technology, Hong Kong, China
[*]corresponding author: phchan@ust.hk

Abstract- We theoretically and experimentally demonstrated the geometric phase effect for sound using a helical waveguide. We show that the geometric phase can be used to control the flow of sound vortices inside an interferometer structure, resulting in geometric-phase-based sound vortex filter.

When a physical system undergoes a cyclic evolution, a non-integrable phase can arise in addition to the normal dynamical phase. This phase, depending only on the geometry of the path traversed in the parameter space and hence named geometric phase (also called Berry phase), has profound impact in both quantum-mechanical and classical physics, resulting in exotic phenomena such as Aharonov–Bohm effect [1] and light spin-Hall effect [2-3]. It has been experimentally observed for light travelling with a helical trajectory [4]. We show that it is possible for sound to manifest a similar effect, which may seem rather counter-intuitive as sound is a scalar wave without transverse polarization.

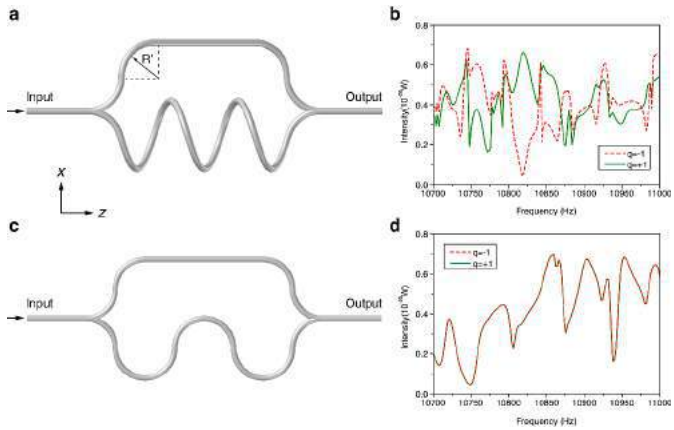

Figure 1. Designed interferometers with [(a)] and without [(c)] geometric phase. (b) and (d) show the transmissions of q = ±1 sound vortices for the configurations in (a) and (c), respectively.

Consider sound propagating inside a waveguide with hard boundary. For high-order waveguide modes such as dipole, the corresponding pressure field has a non-uniform phase on the transverse plane and hence plays a similar role as the transverse polarization field of light. The linear combination of two orthogonal dipole components is essentially a sound vortex carrying topological charge q = ±1. When the waveguide is slowly bended into a helical shape, the dynamics of the sound vortices inside are governed by an equation that is formally identical to the one describing the spin evolution under a slowly varying magnetic field [5]. The helical shape of the waveguide induces a Berry curvature (effective gauge field) that corresponds to an effective

magnetic monopole located at the origin of the momentum space, which leads to a geometry phase with a sign dependence on the topological charge of the sound vortex. So opposite sound vortices have different transmissions when they propagate through an interferometer (Fig.1a,b). However, if the waveguide has in-plane bending feature, the geometry phase vanishes and one get equal transmission for opposite vortices (Fig.1c,d).

The study here demonstrates that scalar waves such as sound also have interesting topological features that can be used for designing structures to modulate wave transport.

Acknowledgements This work was supported by Hong Kong RGC (AOE/P-02/12). We thank Prof. Z. Q. Zhang for valuable comments and suggestions.

REFERENCES

1. Aharonov Y. and D. Bohm, "Significance of Electromagnetic Potentials in the Quantum Theory," *Phys. Rev. Lett*., Vol. 115, 485, 1959.
2. Onoda M., S. Murakami and N. Nagaosa, "Hall effect of light," *Phys. Rev. Lett*. Vol. 93, 083901, 2004.
3. Hosten O. and P. Kwiat, "Observation of the spin Hall effect of light via weak measurements," *Science* Vol. 319, 787-790, 2008.
4. Tomita A. and R. Y. Chiao, "Observation of Berry topological phase by use of an optical fiber," *Phys. Rev. Lett*., Vol. 57, 937-940, 1986.
5. Wang S., G. Ma and C. T. Chan, "Geometric phase mediated topological transport of sound vortices", arXiv:1608.03976, 2016.

A metamaterial approach to the cochlear wave

M. Rupin[1], G. Lerosey[1], J. de Rosny[1], and F. Lemoult[1*]
[1]Institut Langevin, CNRS UMR 7587, ESPCI Paris, PSL Research University, 1 rue Jussieu, 75005 Paris, France
[*]corresponding author: fabrice.lemoult@espci.fr

Abstract- We show that the physics of the inner ear, responsible for the mammalian's audition, can be modelled by a one-dimensional active metamaterial. More precisely, quarter wavelength resonators, with a gradient in their resonance frequency, side coupled to a main waveguide, give rise to the travelling wave typical of the dead cochlea. By introducing a feedback loop in each resonator, we then reproduce all of the salient non-linear properties of the living cochlea.

The human ear is a fascinating sensor, capable of detecting sounds over three decades of frequency and twelve orders of magnitudes. The ability of the cochlea to enhance low-amplitude sounds is referred to as the cochlear amplification effect [1,2]. This effect is attributed to the hair cells of the organ of Corti which lies on the basilar membrane that are believed to work as subwavelength non-linear resonator operating at the particular regime of the so-called Hopf bifurcation. In this work, we propose to implement this model experimentally to study an artificial cochlea based on an active metamaterial [3], and we show that it reproduces all of the salient characteristics of the mammalian's living cochlea [4].

To mimic the frequency-dependent cochlear response, we take our inspiration from the so-called rainbow trapping effect, initially proposed in optics and more recently in acoustics [5]. The basis of our method lies in the realization of a gradient of the propagation properties, resulting in the spatial encoding of the frequency information through the slow light/sound effect. This is achieved in an elegant way using so-called locally resonant metamaterials: these propagating media are composed of an assembly of subwavelength resonators, each of which causes interferences near its respective resonance frequency [6]. Due to these local resonators, wave propagation through the metamaterial is macroscopically observed to be strongly dispersive. Then, using a different resonance frequency at every resonator location, one can obtain the desired gradient for the effective propagating wave. Experimentally, this strategy is simply implemented by side coupling quarter wavelength resonators made of rigid-walled pipes to a single mode airborne acoustic waveguide and we phenomenologically well-reproduce the tonotopic mapping of the dead cochlea (Figure 1).

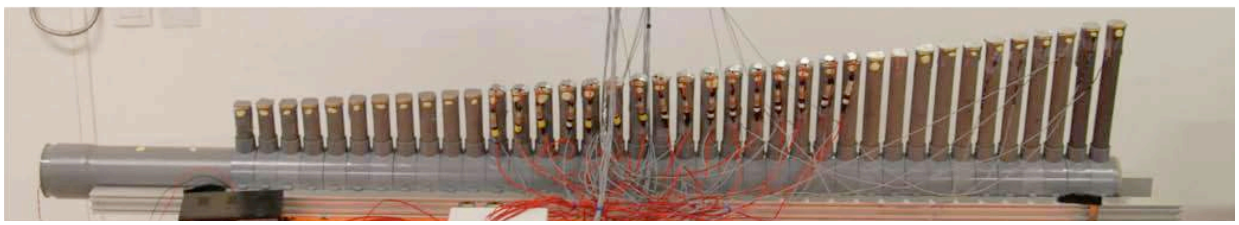

Figure 1: Photograph of the experimental gradient-index metamaterial for airborne sounds, made from 38 quarter-wavelength acoustic resonators of different heights.

Then, following a proposed biophysical model [2] which has yet to be universally accepted, we mimic a living cochlea using an active acoustic metamaterial. Each subwavelength resonator constituting the previous metamaterial is turned to an active one by adding a feedback loop with a speaker emitting sound linked to the field measured inside the resonator with a microphone. By choosing the parameters of the loop we build resonators that operate near a Hopf-bifurcation as the biophysical model of the cochlea requires. The dynamical response of the medium now becomes non-linear as it is the case for the response of the living basilar membrane. Among all of the non-linear effects that have been reported, we focus here on the cochlear amplification. By measuring the dynamical response for different amplitudes of excitation we can extract the sensitivity curve of Figure 2 which is very similar to the characteristic response of living cochleae.

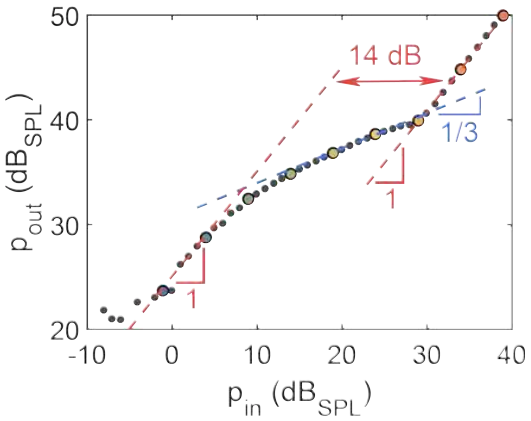

Figure 2: Non-linear dynamic of the evolution of the acoustic pressure in one resonator as a function of the excitation amplitude. This curve is analogous to experimental measurements realized on living cochleae

To conclude, we would like to emphasize that very few ingredients are necessary to reproduce the active cochlear wave. First, an adequately dissipative gradient-index locally resonant metamaterial well mimics the passive travelling wave. The active processes, as a price to pay for hyper-sensitivity to low-amplitude sounds, are created simply by replacing the resonant unit cells of the metamaterial by active resonators. As a result, the response of the medium becomes dependent on the excitation amplitude, and we have clearly reproduced the active amplification of low level sounds that characterizes the mammalian hearing abilities.

REFERENCES

1. Reichenbach, T. and A. J. Hudspeth, "The physics of hearing: fluid mechanics and the active process of the inner ear," *Rep. Prog. Phys*, Vol. 77, 76601, 2014.
2. Duke, T. and F. Jülicher, "Active traveling wave in the cochlea," *Phys. Rev. Lett.*, Vol. 90, 158101, 2003.
3. Cummer, S. A., Christensen, J. C. and A. Alu, "Controlling sound with acoustic metamaterials," *Nat. Rev. Mater.*, Vol. 1, 16001, 2016.
4. Rupin, M., Lerosey, G., de Rosny, J. and F. Lemoult, "Mimicking the cochlea with an active acoustic metamaterial," submitted to *Nat. Mat.*, 2017.
5. J. Zhu et al., "Acoustic rainbow trapping," *Sci. Rep.*, Vol. 3, 1–6, 2013.
6. Lemoult, F., Kaina, N., Fink, M. and G. Lerosey, "Wave propagation control at the deep subwavelength scale in metamaterials," *Nat. Phys.*, vol. 9, 55–60, 2013.

Negative refraction experiments in acoustic metafluids

T. Brunet[1*], A. Kovalenko[2], B. Tallon[1], O. Mondain-Monval[2] and O. Poncelet[1]
[1]Université de Bordeaux – CNRS – Bordeaux INP, I2M, Talence, France
[2]Université de Bordeaux – CNRS, CRPP, Pessac, France
[*] thomas.brunet@u-bordeaux.fr

Abstract- Negative refraction is observed at ultrasonic frequencies in underwater acoustic experiments. The phenomenon is evidenced through the deflection of an ultrasonic beam emerging from a prism-shaped negative-index metafluid composed of soft porous micro-beads randomly dispersed in a water-based gel matrix. These experiments are compared with theoretical predictions based on multiple scattering theory models revealing a good agreement for various volume-fractions of particles.

In most (negative) refraction experiments, the conventional way consists in measuring the scattering angle of the transmitted beam through a *prism* fabricated with the (negative index) material. By using this configuration, the first experiments were conducted at microwave frequencies in 2D resonant structures in 2001 [1]. Then, many other experiments were reported in optics [2] until the fabrication of 3D optical metamaterials in 2008 [3]. In the same year, negative refraction was also observed using a prism-shaped phononic crystal in acoustics [4]. Since then, negative refraction has been reported in various (non resonant) periodic systems [5] but no experiment has been conducted in random acoustic metamaterials up to now.

In this talk, we report negative refraction experiments performed at ultrasonic frequencies by using a soft 3D acoustic metafluid with a negative acoustic index [6]. This metafluid, composed of soft porous micro-beads randomly dispersed in an aqueous matrix, was confined in a prism-shape box deposited on the surface of an ultrasonic transducer. Then, the scattering angle of the transmitted ultrasound beam emerging from the prism was measured at different frequencies, evidencing negative refraction around 160 kHz as shown in the figure.

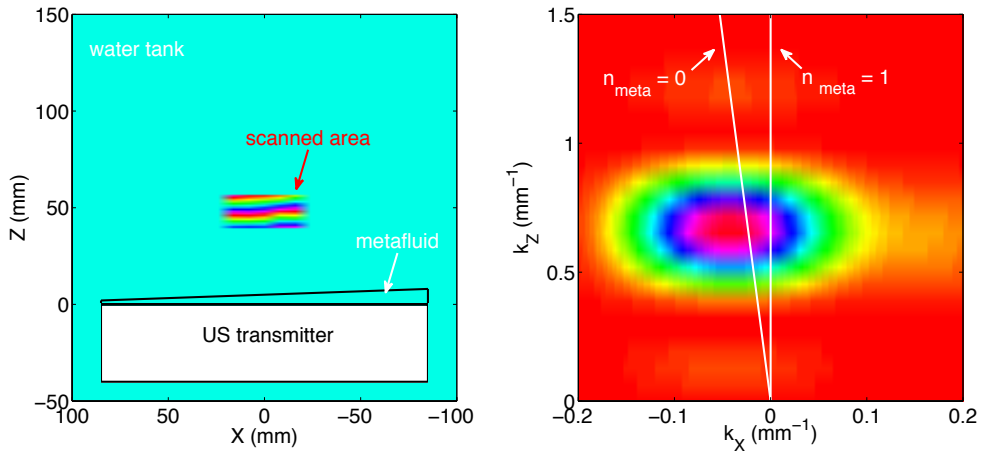

Figures: (left) spatial acoustic-field mapping at 160 kHz, (right) corresponding spatial-frequency content

(obtained by a 2D Fast Fourier Transform).

Acknowledgements: This work was funded and performed within the framework of the Labex AMADEUS ANR-10-LABEX-0042-AMADEUS with the help of the French state Initiative d'Excellence IdEx ANR-10-IDEX-003-02.

REFERENCES

1. Shelby, R. A. *et al.*, "Experimental verification of a negative index of refraction," *Science*, Vol. 292, No. 5514, 77–79, 2001.
2. Shalaev, V. M. "Optical negative-index metamaterials," *Nat. Photon.*, Vol. 1, No. 1, 41-48, 2007.
3. Valentine, J. *et al.*, "Three-dimensional optical metamaterial with a negative refractive index," *Nature*, Vol. 455, No. 7211, 376–379, 2008.
4. Sukhovich, A. *et al.*, "Negative refraction and focusing of ultrasound in two-dimensional phononic crystals," *Phys. Rev. B*, Vol. 77, No. 1, 014301, 2008.
5. Page, J. H., "Focusing of ultrasonic waves by negative refraction in phononic crystals," *AIP Adv.*, Vol. 6, No. 12, 121606, 2016.
6. Brunet, T. *et al.*, "Soft 3D acoustic metamaterial with negative index," *Nat. Mater.*, Vol. 14, No. 4, 384-388, 2015.

Topological sound in active liquid metamaterials

Liquids composed of self-propelled particles have been experimentally realized using molecular, colloidal, or macroscopic constituents. These active liquids can flow spontaneously even in the absence of an external drive. Unlike spontaneous active flow, the propagation of density waves in confined active liquids is not well explored. Here, we exploit a mapping between density waves on top of a chiral flow and electrons in a synthetic gauge field to lay out design principles for artificial structures termed topological active metamaterials. We design metamaterials that break time-reversal symmetry using lattices composed of annular channels filled with a spontaneously flowing active liquid. Such active metamaterials support topologically protected sound modes that propagate unidirectionally, without backscattering, along either sample edges or domain walls and despite overdamped particle dynamics. Our work illustrates how parity-symmetry breaking in metamaterial structure combined with microscopic irreversibility of active matter leads to novel functionalities that cannot be achieved using only passive materials.

Non-reciprocal acoustic systems: from sound isolation to topological propagation

R. Fleury
Laboratory of Wave Engineering, EPFL, Station 11, 1015 Lausanne, Switzerland
*corresponding author: romain.fleury@epfl.ch

Abstract-We discuss the possibility to largely break Rayleigh reciprocity in compact, linear acoustic systems with broken time-reversal symmetry. These subwavelength systems can be used as building blocks to construct non-reciprocal metamaterials. Interestingly, the obtained metamaterials support one-way edge modes that are topologically protected against defects and disorder, highlighting a fruitful design strategy, from engineering non-reciprocal acoustic metamolecules to building acoustic Chern topological insulators.

Non-reciprocal acoustic systems that let sound flow in one direction but block it in another may be of fundamental interest in many application fields, from underwater communication to imaging systems. However, largely violating reciprocity is not an easy task in a compact acoustic system as it requires either strong non-linear effects or a breaking of time-reversal symmetry or time invariance[1].

We discuss two different solutions to achieve large acoustic non-reciprocity in a linear subwavelength device by coupling a weak external time-odd bias to an acoustic resonance. The first system consists of a ring acoustic resonator filled with air and coupled to three output waveguides, in which we impart a slow rotating air motion (Fig. 1a). We demonstrate experimentally 30 dB of acoustic isolation for airborne audible sound in a subwavelength device[2]. The second system consists of a resonant acoustic trimer, which undergoes a weak rotating temporal modulation of the acoustic index, at a frequency much slower than the acoustic frequency (Fig. 1b). This device allows for more than 40 dB, with 0.3 dB insertion loss in a system whose total size does not exceed a sixth of a wavelength[3].

Finally, we investigate the intriguing properties of non-reciprocal metamaterials built from a periodic arrangement of these non-reciprocal metamolecules. We obtain a metamaterial that behaves as the acoustic equivalent of Chern topological insulators, in which a nontrivial topology is initiated by a breaking of time-reversal symmetry[4]. These artificial materials are characterized by the fact that they do not support acoustic propagation in their bulk, but possess one-way topological edge modes (Fig. 1c). Like their electronic counterpart, since local perturbation to the edge cannot affect the topology of the bulk, these states are topologically protected against a large class of defects and even disorder. We also discuss an acoustic equivalent of Floquet topological insulators, built from a hexagonal lattice of time-modulated, non-reciprocal trimers (Fig. 1d). This last design presents interesting robustness to site-to-site disorder in the modulation phase[5].

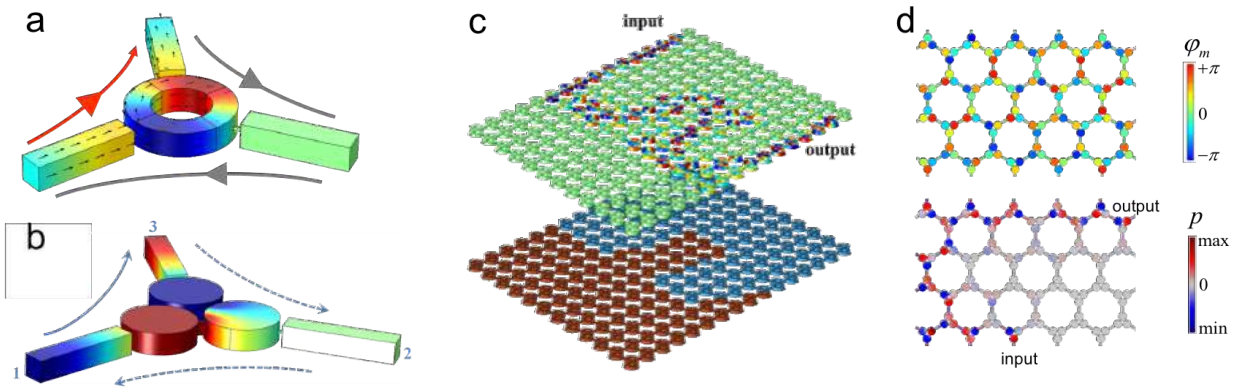

Figure 1: a) An acoustic circulator built from a resonant ring in which we rotate the air in the clockwise direction strongly breaks Rayleigh reciprocity. b) An ultrasonic circulator achieves the same functionality without resorting to motion, but using a rotating temporal modulation. c) An array of non-reciprocal elements like the ones in a) makes an acoustic Chern insulator, obtaining one-way robust reconfigurable acoustic waveguides. d) An array of non-reciprocal metamolecules like the one in b) makes the acoustic equivalent of a Floquet topological insulator, and supports some level of disorder in the modulation phase (top) and non-reciprocal Floquet edge mode propagation.

Conclusions- Compact, non-reciprocal acoustic systems can therefore be used to build non-reciprocal metamaterials that possess non-trivial topological properties, in particular one-way edge modes with topological robustness. Compared to their constituting metamolecules, such topological materials may offer significant advantages in their bandwidth of operation, robustness, and reconfigurability. Our study provides the opportunity to increase our ability to control sound propagation with broadband, backscattering-immune, reconfigurable acoustic waveguides that are immune to defects and disorder.

REFERENCES

1. Fleury, R., D. Sounas, M. Haberman, and A. Alù, "Nonreciprocal Acoustics," *Acoustics Today*, Vol. 11, 14–21, 2015.
2. Fleury, R., D. Sounas, C. Sieck, M. Haberman, and A. Alù, "Sound isolation and giant linear nonreciprocity in a compact acoustic circulator," *Science*, Vol. 343 (6170), 516-519, 2014.
3. Fleury, R., D. Sounas, and A. Alù, "Subwavelength ultrasonic circulator based on spatiotemporal modulation," *Phys. Rev. B*, Vol. 91, No. 17, 174306, 2015.
4. Khanikaev, A., R. Fleury, S. Hossein Mousavi and A. Alù, "Topologically robust sound propagation in an angular-momentum-biased graphene-like resonator lattice," *Nat. Commun.*, Vol. 6, 8260, 2015.
5. Fleury, R., A. Khanikaev and A. Alù, "Floquet topological insulators for sound," *Nat. Commun.*, Vol. 7, 11744, 2016.

Tailoring locally resonant metamaterials: from local modifications to metamaterial crystals

Nadège Kaina[1], Fabrice Lemoult[1], Simon Yves[1], Romain Fleury[1,2], Thomas Berthelot[3], Mathias Fink[1] and Geoffroy Lerosey[1]

[1]Institut Langevin, ESPCI Paris & CNRS, Paris, France
[2] Laboratory of Wave Engineering, EPFL, Station 11, route cantonale, 1015 Lausanne, Switzerland
[3] CEA Saclay, IRAMIS, NIMBE, LICSEN, UMR 3685, F-91191, Gif sur Yvette, France
[*]corresponding author: geoffroy.lerosey@espci.fr

Abstract- Starting from the very simple example of a soda can metamaterial (an acoustic medium made of Helmholtz resonators), we explain the propagation of waves in locally resonant media without involving homogenized parameters. This allows us to highlight the importance of multiple scattering even at this deep subwavelength scale. This, in turns, permits to envisage exotic phenomena such as subwavelength control of waves, slow waves, negative refraction with a single negative medium or topological metamaterial crystals.

In this talk, we will show how going beyond the paradigm usually introduced in the context of locally resonant metamaterials, namely to consider them as homogeneous materials presenting effective properties, permits to enrich the physics associated with them in a drastic way. We will first show, using a microscopic approach based on the transfer matrix, that the properties of many metamaterials made out of resonant unit cells are strictly governed by interferences, propagation effects and multiple scattering.

Then we will demonstrate how this observation allows one to tailor locally this kind of composite media at the scale of the unit cell, hence going much further than in the homogenization approximation. We will show how this allows to design various components such as cavities, waveguides, filters, that present deep subwavelength dimensions, much smaller than that of their phononic crystal counterparts. We will also demonstrate the possibility to slow down waves drastically using this kind of components, while keeping reasonable bandwidths, hence achieving delay bandwidth products 10 times higher than the state of the art in photonics or phononics.

Concentrating now on structural modifications, we will explain how a single negative metamaterial can turn double negative simply thanks to multiple scattering, provided that it is judiciously structured, hence introducing the concept of metamaterial crystals. We will show that this approach is very rich and can be used to demonstrate various analogs of solid state crystals in acoustics, such as an acoustic equivalent of graphene, or acoustic metamaterials that present topological properties at the deep subwavelength scale. We will finally show that these ideas can be straightforwardly transposed to the electromagnetic domain.

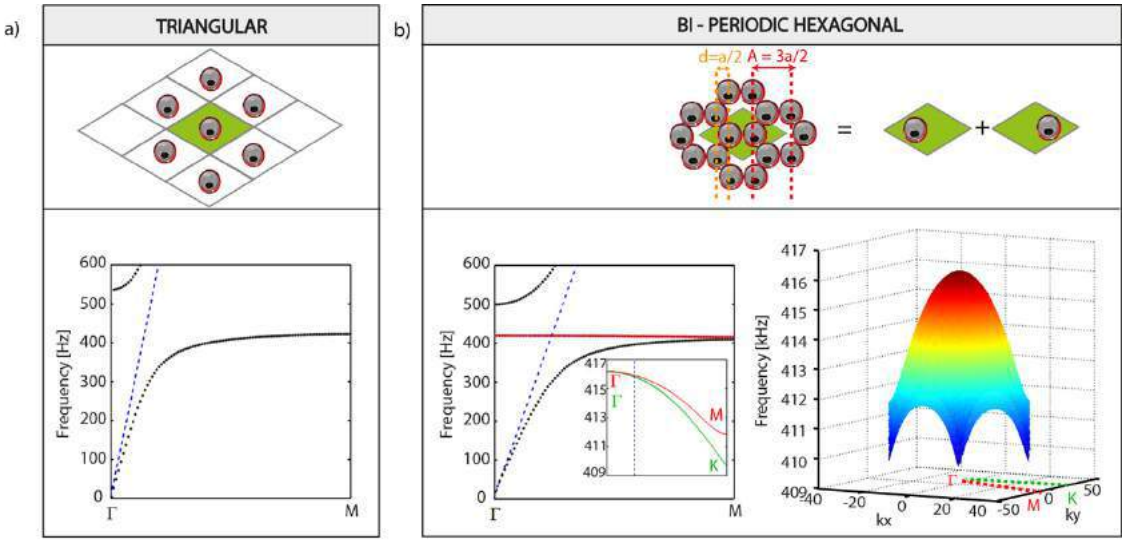

Fig. 1. A triangular Helmholtz resonator based single negative metamaterial can be turned double negative, acquiring its negative index from its symmetry broken structure.

Acknowledgements. The research leading to these results has received funding from the People Program (Marie Curie Actions) of the European Union's Seventh Framework Program (FP7/2007-2013) under REA grant agreement n. PCOFUND-GA-2013-609102, through the PRESTIGE program coordinated by Campus France. This work is also supported by LABEX WIFI (Laboratory of Excellence within the French Program "Investments for the Future") under references ANR-10-LABX-24 and ANR-10-IDEX-0001-02 PSL* and by French National Research Agency under reference ANR-13-JS09-0001-01. S.Y. acknowledges funding from French Direction Générale de l'Armement.

REFERENCES

1. Lemoult, F., Kaina, N., Fink, M. & Lerosey, G. Wave propagation control at the deep subwavelength scale in metamaterials. *Nat. Phys.* **9**, 55–60 (2013).
2. Kaina, N., Lemoult, F., Fink, M. & Lerosey, G. Ultra small mode volume defect cavities in spatially ordered and disordered metamaterials. *Appl. Phys. Lett.* **102**, 144104 (2013).
3. Kaina, N., Lemoult, F., Fink, M. & Lerosey, G. Negative refractive index and acoustic superlens from multiple scattering in single negative metamaterials. *Nature* **525**, 77–81 (2015).
4. Lemoult, F., Kaina, N., Fink, M. & Lerosey, G. Soda Cans Metamaterial: A Subwavelength-Scaled Phononic Crystal. *Crystals* **6**, 82 (2016).
5. Yves, S., Fleury, R., Berthelot, N., Fink, M., Lemoult, F. & Lerosey, G. Crystalline metamaterials for topological properties at subwavelength scales. Under review, *Nature Communications* (2017).
6. Yves, S., Fleury, R., Fink, M., Lemoult, F. & Lerosey, G. Topological acoustic polaritons: robust sound manipulation at the subwavelength scale. Under review, *New Journal of Physics* (2017).
7. Yves, S., Fink, M., Lemoult, F. & Lerosey, G. An acoustic metamaterial crystal with graphene-like dispersion. Submitted to *Phys. Rev. Lett.* (2017).

An acoustic metamaterial crystal with a graphene-like dispersion

S. Yves[1], F. Lemoult[1], M. Fink[1], and G. Lerosey[1*]
[1]Institut Langevin, CNRS UMR 7587, ESPCI Paris, PSL Research University, 1 rue Jussieu, 75005 Paris, France
[*]corresponding author: simon.yves@espci.fr

Abstract-Graphene, a honeycomb lattice of carbon atoms ruled by tight-binding interaction, exhibits extraordinary electronic properties, due to the presence of Dirac cones within its band structure. Here we explain how we induced tight-binding coupling within a locally resonant metamaterial made of mere soda cans (Helmholtz resonators) and how it allows to obtain an acoustic analog of graphene. These numerical and experimental results demonstrate the potential of crystalline metamaterials as a tabletop platform for the study of solid state physics.

In this talk, we will show how going beyond the usual description of locally resonant metamaterials in terms of effective parameters allows to construct a classical acoustic analog of graphene[1]. First we show that a triangular lattice of empty cans creates a hybridization bandgap. Within this bandgap, we then place resonant defects simply made by increasing the resonance frequency of resonators, which is easily done filling cans with water[2]. Because of the absence of propagating waves thanks to the bandgap created by the initial triangular lattice, these defects are solely linked by nearest neighbors interactions, that is tight-binding coupling[2,3]. Therefore, we design a honeycomb lattice of resonant defects around the previous triangular lattice in order to emulate the physics of graphene in such a crystalline metamaterial.

After presenting the concept behind this work, we show the experimental setup we used and the results we obtained. We compare the field maps we measure and the corresponding analytically calculated ones for a tight-binding model of graphene. This demonstrate a very good matching between both: monitoring the structure and the composition of a metamaterial[4] is indeed a powerful strategy to create an acoustic analogue of graphene.

Then, we show that the properties of the bandgap within the metamaterial permits to change easily the strength of the coupling between the defects. We present several experimental band structures and their numerical counterparts realized for different volume of water within the defect cans. Hence, this simple change allows to study a transition between a tight-binding and a polaritonic coupling within the lattice of defects. We finally show that these ideas can be straightforwardly transposed to the electromagnetic domain.

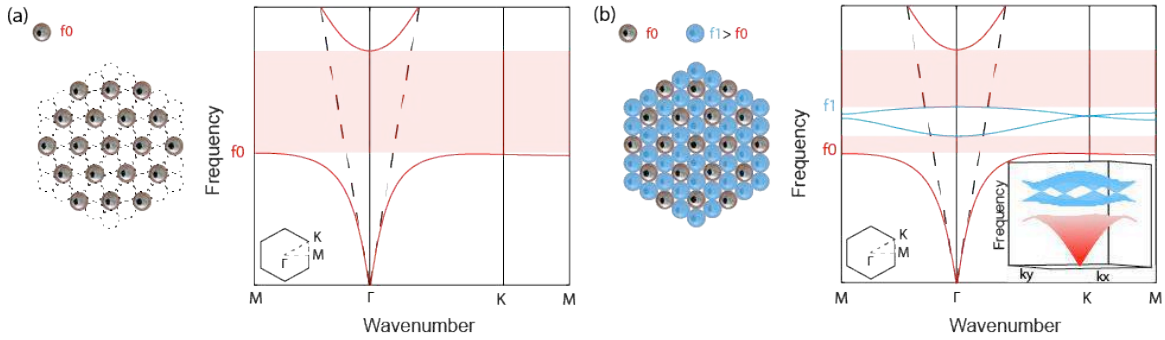

Fig. 1. A triangular lattice of empty soda cans creates a hybridization bandgap (a). This allows to induce tight-binding coupling within the honeycomb lattice of filled cans and to mimic the band structure of electronic graphene (b).

Acknowledgements. This work is supported by LABEX WIFI (Laboratory of Excellence within the French Program "Investments for the Future") under references ANR-10-LABX-24 and ANR-10-IDEX-0001-02 PSL* and by French National Research Agency under reference ANR-13-JS09-0001-01. S.Y. acknowledges funding from French Direction Générale de l'Armement.

REFERENCES

1. Yves, S., F. Lemoult, M. Fink and G. Lerosey, "An acoustic metamaterial crystal with graphene-like dispersion", Submitted to *Phys. Rev. Lett.* (2017).
2. Lemoult F., N. Kaina, M. Fink and G. Lerosey. "Wave propagation control at the deep subwavelength scale in metamaterials", *Nat. Phys.* **9**, 55–60 (2013).
3. Lemoult, F., N. Kaina, M. Fink and G. Lerosey, "Soda Cans Metamaterial: A Subwavelength-Scaled Phononic Crystal", *Crystals* **6**, 82 (2016).
4. Kaina, N., F. Lemoult, M. Fink and G. Lerosey, "Negative refractive index and acoustic superlens from multiple scattering in single negative metamaterials", *Nature* **525**, 77–81 (2015).

Tailoring the microstructure of bubble metamaterials for super absorption or negative refraction of water-borne acoustic waves.

John H. Page[1*], Reine-Marie Guillermic[1], Maxime Lanoy[1], Anatoliy Strybulevych[1], Eric J.S. Lee[1], Fabrice Lemoult[2], Geoffroy Lerosey[2], Valentin Leroy[3], and Arnaud Tourin[2]

[1]Department of Physics and Astronomy, University of Manitoba, Winnipeg, Manitoba, Canada

[2]Institut Langevin, ESPCI Paris Tech, PSL Research University, CNRS (UMR 7587), Paris, France

[3]Laboratoire MSC, Université Paris-Diderot, CNRS (UMR 7057), Paris, France

[*]corresponding author: john.page@umanitoba.ca

Abstract-Two- and three-dimensional bubble metamaterials can be tuned to enable a variety of interesting functionalities for acoustic waves by exploiting the low-frequency Minnaert resonance of the bubbles. Here we show how a broadband coherent perfect absorber for ultrasonic waves can be created from a bubble metalayer, and how doubly negative behaviour can be realized in three-dimensional bubble metamaterials.

Bubbles in a yield-stress fluid or soft solid are excellent candidates for creating acoustic metamaterials, as they exhibit a strong low-frequency monopolar resonance, which can lead to interesting effective acoustic properties at wavelengths that can be hundreds of times larger than the radius of the bubbles. Since bubbles are strongly coupled to water-borne acoustic waves, bubble metamaterials are especially well suited for applications in underwater acoustics, where, for example, ultrathin metalayers consisting of a single layer of bubbles entrapped in a soft elastic solid have been shown to act as very effective reflectors or absorbers of ultrasound [1,2]. In this presentation, we show how a bubble metalayer can be optimized to create a coherent perfect absorber for acoustic waves, and then consider how three-dimensional structures assembled from spatially correlated bubble pairs can be designed to exhibit a transparency window with a negative index of refraction.

Since the concept of a coherent perfect absorber, or "anti-laser", was first proposed in optics [3], there has been growing interest in developing coherent perfect absorbers for acoustic waves [4,5]. Such a device can be implemented by coherently illuminating a metamaterial or metalayer using two oppositely propagating incident beams. For water-borne acoustic waves, a metalayer consisting of a single layer of bubbles has several advantages for realizing an acoustic coherent perfect absorber experimentally. An important first step is to develop a soft matrix, into which the bubbles can be embedded, that is impedance-matched to the water surrounding the metalayer, so that water-matrix reflections can be eliminated; this has been achieved by mixing sub-micron TiO_2 particles into PDMS so that the longitudinal velocity and density of the cured mixture leads to the same acoustic impedance as water. It is also crucial to optimize the structure of the bubble layer so that the magnitude of the amplitude reflection and transmission coefficients (r and t) of the layer are equal to 0.5 (they are intrinsically of opposite sign), a process that was guided by the predictions of a simple analytic model whose accuracy has been tested previously [1,2]. For the optimized structure, the critical coupling condition is satisfied so that the bubble layer's radiative and dissipative damping are equal, implying a unique relation between the bubble radius a and separation d, which is given by $a^3/d^2 = 4\eta/\pi Z$, where η is the viscosity of the matrix. When two counter-propagating coherent beams of equal amplitude and phase are incident on a

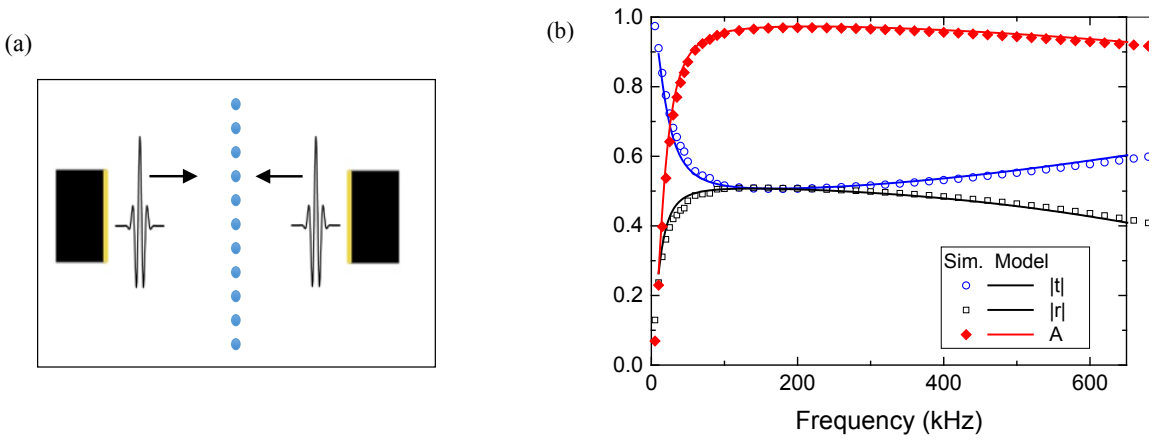

Fig.1: **(a)** Experimental setup for turning an optimized bubble metalayer (blue circles) into an acoustic coherent perfect absorber. Two ultrasonic transducers (gold and black rectangles, on the left and right) emit coherent counter-propagating pulses that arrive from opposite directions with the same incident phase at the metalayer.
(b) Predictions from finite element simulations and the analytic model for an example of a metalayer with a square array of bubbles with a = 50 μm, d = 240 μm, and η = 5.1 Pa s. Here $|r|$ and $|t|$ are the magnitudes of the amplitude transmission and reflection coefficients, and A is the absorption. For these parameters, broadband absorption is predicted to be greater than 97% for 150 kHz < f < 300 kHz, and greater than > 95% for 90 kHz < f < 510 kHz.

well-optimized metalayer, virtually all of the incident radiation is absorbed, as illustrated for one choice of model parameters in Fig. 1. This example compares the model predictions with finite element simulations, and shows that broadband near-perfect absorption can be achieved.

For three-dimensional structures with pair-wise correlated bubbles ("bi-bubbles"), strikingly different behaviour can be observed when the bubble pairs are arranged in either random or periodic arrays. Then, overlap between monopolar and dipolar resonances can lead to a frequency band with a negative refractive index, demonstrating how deeply-subwavelength spatial patterning of inclusions in metamaterials can play a crucial role in determining material properties and functionality [6]. Predictions for both types of structure will be presented and the influence of dissipation on doubly negative behaviour discussed.

REFERENCES

1. Leroy, V., A. Strybulevych, M. G. Scanlon, and J. H. Page, "Transmission of ultrasound through a single layer of bubbles", *Eur. Phys. J. E,* Vol. 29, 123-130, 2009.
2. Leroy, V., A. Strybulevych, M. Lanoy, F. Lemoult, A. Tourin, and J. H. Page, "Super-Absorption of Acoustic Waves with Bubble Meta-Screens", *Phys. Rev. B*, Vol. 91, 020301(R), 2015.
3. Chong, Y. D., L. Ge, H. Cao and A. D. Stone, "Coherent Perfect Absorbers: Time-Reversed Lasers", *Phys. Rev. Lett.*, Vol. 105, 053901, 2010.
4. Song, J. Z., P. Bei, Z. H. Hang and Y. Lai, "Acoustic coherent perfect absorbers", *New J. Phys*., Vol. 16, 033026, 2014.
5. Wei, P., C. Cröenne, S.T. Chu and J. Li, "Symmetrical and anti-symmetrical coherent perfect absorption for acoustic waves", *Appl. Phys. Lett*. Vol. 104, 121902, 2014.
6. Kaina, N., F. Lemoult, M. Fink and G. Lerosey, "Negative refractive index and acoustic superlens from multiple scattering in single negative metamaterials," *Nature*, Vol. 525, pp. 77-81, 2015.

A route to acoustic Landau levels

Zhaoju Yang[1] and Baile Zhang[1,2*]

[1]*Division of Physics and Applied Physics, School of Physical and Mathematical Sciences, Nanyang Technological University, Singapore 637371, Singapore.*

[2]*Centre for Disruptive Photonic Technologies, Nanyang Technological University, Singapore 637371, Singapore.*

**To whom correspondence should be addressed:*

E-mail: blzhang@ntu.edu.sg

Abstract

The emerging field of topological acoustics that explores novel gauge-field-related phenomena for sound has drawn attention in recent years. However, previous approaches constructing synthetic gauge field for sound predominantly relied on a periodic system, being unable to form a uniform effective magnetic field, thus lacking access to some typical magnetic-induced quantum phenomena such as Landau energy quantization. Here we introduce strain engineering, previously developed in graphene electronics and later transferred to photonics, into an aperiodic two-dimensional acoustic structure in order to form a uniform effective magnetic field for air-borne acoustic wave propagation. Landau levels in the energy spectrum can be formed near the Dirac cone region. We also propose an experimentally feasible scheme to verify the existence of acoustic Landau levels with acoustic measurement.

Air-borne sound waves have no intrinsic spins and do not respond to magnetic field. Recently several approaches of synthetic gauge field construct magnetic-like effects (such as quantum Hall effect) for sound, which have enabled the emergence of a new field of topological acoustics [1-5]. However, previous approaches constructing synthetic gauge field for sound predominantly relied on a periodic system, being unable to form a uniform effective magnetic field, thus lacking access to some typical magnetic-induced quantum phenomena such as Landau quantization [6].

Here we introduce strain engineering into a two-dimensional acoustic structure in order to effectively form a uniform magnetic field for air-borne acoustic wave propagation, and consequently, acoustic Landau levels. Typical acoustic Landau levels (labelled with numbers of 0, ±1, ±2) are shown in panel (a) of the following figure. Panels (b-e), which show the change of acoustic pressure with increase of frequency, demonstrate the process of localization (b) – spreading (c) – localization (d) – spreading (e), as a clear evidence of acoustic 0^{th}-order and $\pm1^{st}$-order Landau levels and the significant band gaps between them. As a new freedom of constructing synthetic gauge field for sound, our study has offered a path to previously inaccessible magnetic-like effects in traditional periodic acoustic structures.

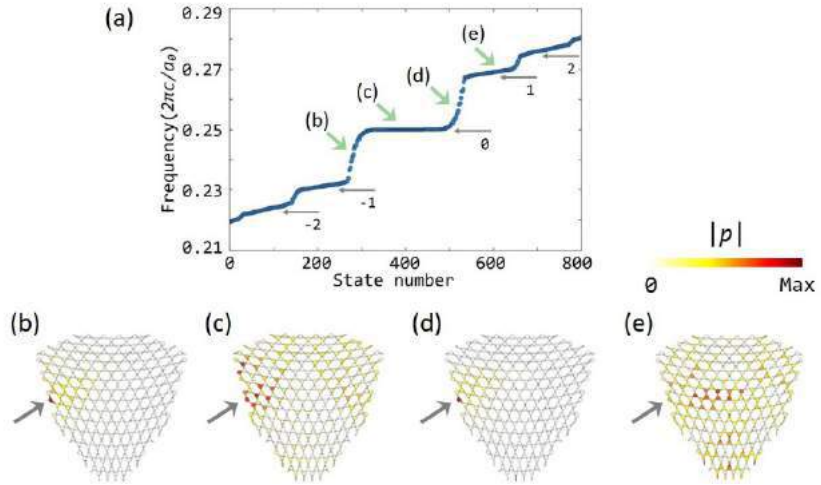

Figure 1. Landau levels in acoustic structures.

Acknowledgements

This work was sponsored by Nanyang Technological University under NAP Start-Up Grants, and Singapore Ministry of Education under Grant No. MOE2015-T2-1-070 and Grant No. MOE2011-T3-1-005.

Reference

1. E. Prodan, and C. Prodan, "Topological phonon modes and their role in dynamic instability of microtubules," Physical review letters **103**, 248101 (2009).
2. A. B. Khanikaev, R. Fleury, S. H. Mousavi, and A. Alù, "Topologically robust sound propagation in an angular-momentum-biased graphene-like resonator lattice," Nature communications **6**, 8260 (2015).
3. M. Xiao, W.-J. Chen, W.-Y. He, and C. T. Chan, "Synthetic gauge flux and Weyl points in acoustic systems," Nature Physics **11**, 920-924 (2015).
4. N. Xu, H. Cheng, S. Xiao-Chen, L. Xiao-ping, L. Ming-Hui, F. Liang, and C. Yan-Feng, "Topologically protected one-way edge mode in networks of acoustic resonators with circulating air flow," New Journal of Physics **17**, 053016 (2015).
5. Z. Yang, F. Gao, X. Shi, X. Lin, Z. Gao, Y. Chong, and B. Zhang, "Topological Acoustics," Physical review letters **114**, 114301 (2015).
6. K. von Klitzing, "The quantized Hall effect," Reviews of Modern Physics **58**, 519-531 (1986).

Observation of topological interface state of elastic wave in a silica 1D phononic crystal

***Ingi Kim[1], Satoshi Iwamoto[1,2], and Yasuhiko Arakawa[1,2]**
[1]Institute of Industrial Science, University of Tokyo, Japan
[2]Institute for Nano Quantum Information Electronics, University of Tokyo, Japan
*corresponding author: kim-ingi@iis.u-tokyo.ac.jp

Abstract-We demonstrate a topological interface state of elastic wave in solid-structured 1D phononic crystals (PnCs). Two PnCs with different structural parameters can possess a common phononic bandgap with different topological nature. At the interface between the two PnCs, a topologically confined state of elastic wave in the bandgap appears. We observe the topologically confined mode with a quality factor of ~5,650 in the transmission experiment, while no interface state exists at the interface between PnCs with the same topological characteristic.

There is currently a great interest in the study of topological properties in metamaterials that draw inspiration from quantum spin Hall and quantum Hall effects in solid state physics. Recently, some pioneering demonstrations of topological edge states in acoustic systems have been reported [1,2]. On the other hand, controlling elastic waves in solids using topological properties will pave the way to practical high-speed phononic applications. Although some theoretical studies aiming the control of elastic waves in solids have been reported [3,4], there is a lack of experimental study demonstrating such topological edge states even in one-dimensional periodic systems. Here we report the experimental realization of topological interface state in solid-structured quasi 1D PnC.

In this study, we use quasi 1D PnCs [5] made of fused silica. As shown in Fig. 1(a), each unit cell with period $D = 16$ mm along with x-direction has two wider blocks sandwiching an inner block. We designed topologically distinct PnCs, U1 ($W_{in}/D = 0.3, d_{in}/D$ =0.59) and U2 ($W_{in}/D = 0.501, d_{in}/D$ =0.72), by tuning the structural parameters of unit cells. In a 1D periodic system, the topological invariant of Bloch bands, so called Zak phase, characterizes the property of bulk band. The phononic band diagrams shown in Fig. 1(b) and (c) indicate that two

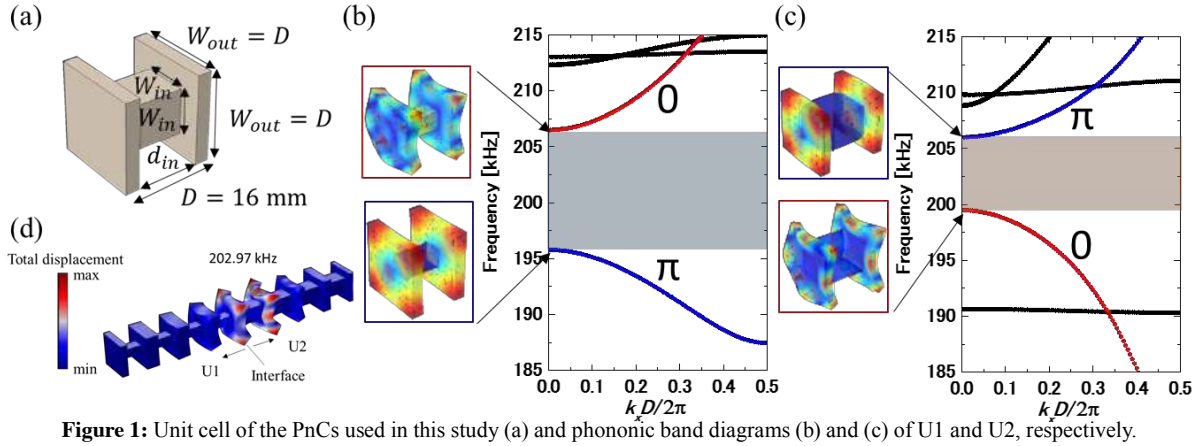

Figure 1: Unit cell of the PnCs used in this study (a) and phononic band diagrams (b) and (c) of U1 and U2, respectively. Mode shapes at the center of the Brillouin zone are shown in the insets, which exhibit the inversion of the two related bands. (d) Displacement distribution of the topological interface mode at the interface between U1 and U2.

PnCs, U1 and U2, have a topologically distinct bandgap. The characters of the bands at the upper and lower bandgap edges are inverted as shown in the insets and the Zak phase of the bands changes, resulting in a change in the topological properties of the bandgap. Therefore, at the interface of these two PnCs, a topologically protected mode is predicted to exist inside the overlapped bandgap from bulk-edge correspondence principle. Figure 1 (d) shows the displacement distribution of the topological interface mode at the interface of U1 and U2 where the each PnC has the number of period N=4. The interface mode is well confined at the interface and works as a cavity of elastic wave.

The pictures on the left of Fig. 2 (a) and (b) show the samples having a non-trivial junction of two topologically distinct PnCs (U1+U2) and a trivial junction composed of two PnCs with same topological characteristic of the bandgap (U1+U1′), respectively. Both samples were made of fused silica by ultrasonic machining process. U1′ has a slightly thicker inner block than that of U1 but a topologically identical bandgap with U1, which expects that no topological interface state exists. We measured transmission spectrum of elastic waves through the samples by a network analyzer. In the measured transmission spectrum for U1+U2 (Fig. 2 (a)), a peak indicating the topologically confined state is clearly observed in the bandgap. The topological interface state is observed at 202.38 kHz with mechanical quality factor of ~5,650. In contrast, no such peak was measured for U1+U1′ (see Fig. 2 (b)) since they have the topologically identical bandgap. The measured spectra for both samples show good agreement with numerical simulations also shown in the same figures.

In conclusion, we experimentally demonstrate a topological interface state of elastic wave in a solid-structured 1D system. Higher operating frequency above MHz can be achieved by scaling down the size of structures. Our result is an important step for the advanced control of elastic wave in solid structures by their topological characters.

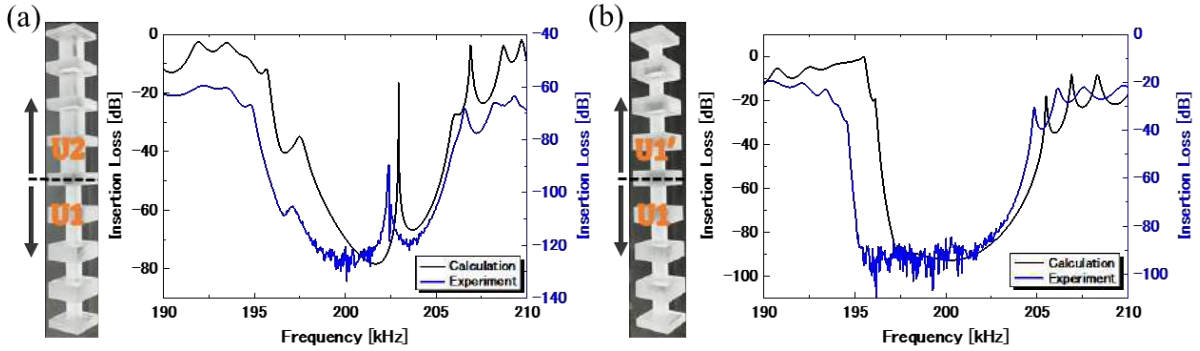

Figure 2: Measured (blue) and calculated (black) transmission spectra in the case of (a) non-trivial and (b) trivial topological PnC junctions consisting of two different 1D PnCs. respectively. Each picture on the left shows the sample used in the measurement.

Acknowledgements This work was partially supported by MEXT KAKENHI Grant Number JP26630147, JP15H05700, and by the Ono Acoustics Research Fund.

REFERENCES

1. Xiao, M., Ma, G., Yang, Z., Sheng, P., Zhang, Z.Q. and Chan, C.T., "Geometric phase and band inversion in periodic acoustic systems," *Nat. Phys.*, Vol. 11, 240-244, 2015.
2. He, C., Ni, X., Ge, H., Sun, X.-C., Chen, Y.-B., Lu, M.-H., Liu, X.-P., and Chen, Y.-F. "Acoustic topological insulator and robust one-way sound transport," *Nat. Phys.*, Vol. 12, 1124-1129, 2016.
3. Mousavi, S.H., Khanikaev, A.B. and Wang, Z. "Topologically protected elastic waves in phononic metamaterials," *Nat. Commun.*, Vol. 6, 8682, 2015.
4. Pal, R.K. and Ruzzene, M. "Edge waves in plates with resonators: an elastic analogue of the quantum valley Hall effect," *New J. Phys.*, Vol. 19, 025001, 2017.
5. Kim, I., Iwamoto, S. and Arakawa, Y., "Design of quasi-one-dimensional phononic crystal cavity for efficient photoelastic modulation," *Jpn. J. Appl. Phys.*, Vol. 55, 08RD02, 2016.

Production and control of acoustic orbital angular momentum (OAM) by metamaterials

Jianchun Cheng, Bin Liang, Xue Jiang

Collaborative Innovation Center of Advanced Microstructures and Key Laboratory of Modern Acoustics, MOE, Institute of Acoustics, Department of Physics, Nanjing University, Nanjing 210093, P. R. China

Likun Zhang

National Center for Physical Acoustics and Department of Physics and Astronomy, University of Mississippi, University, Mississippi 38677, USA

Chengwei Qiu

Department of Electrical and Computer Engineering, National University of Singapore

In this talk, I will introduce some of our latest works on production and manipulation of acoustic OAM with the aid of metamaterials. We have designed and fabricated an acoustic vortex emitter with multi-arm coiling slits that utilize diffraction effect to generate vortex beam, with broadband functionality and stable topological charge. Based on this, we further propose a new mechanism for producing acoustic OAM by converting acoustic resonances to OAM. As an implementation, we have designed and fabricated a thin planar device with high efficiency to verify our scheme. In comparison with existing ways for OAM production by phased spiral sources that need sophisticated electronic control and by physically spiral sources that need screw profiles and may also have a bulky size, our acoustic resonance-based OAM production bears the advantages of high efficiency, planar profile, compact size, no spiral structure and can be freely tuned to produce different orders of OAM. I will also briefly discuss the potential of acoustic OAM devices to revolutionize various applications such as in medical ultrasound or acoustic communication.

Ultra-thin Acoustic Metasurface-Based Schroeder Diffuser

Yifan Zhu[1], Xudong Fan[1], Bin Liang[1], Jianchun Cheng[1], and Yun Jing[2]

[1]Key Laboratory of Modern Acoustics, MOE, Institute of Acoustics, Department of Physics, Collaborative Innovation Center of Advanced Microstructures, Nanjing University, Nanjing 210093, P. R. China

[2]Department of Mechanical and Aerospace Engineering, North Carolina State University, Raleigh, North Carolina 27695, USA

Abstract - "Schroeder diffuser" is a classical design, proposed over 40 years ago, for artificially creating optimal and predictable sound diffuse reflection. It has been widely adopted in architectural acoustics and it has also shown substantial potential in noise control, ultrasound imaging, microparticle manipulation, among others. The conventional Schroeder diffuser, however, has a considerable thickness on the order of one wavelength, severely impeding its applications for low frequency sound. In this paper, a new class of ultra-thin and planar Schroeder diffusers are proposed based on the concept of acoustic metasurface. Both numerical and experimental results demonstrate satisfactory sound diffuse reflection produced from the metasurface-based Schroeder diffuser despite it being one order of magnitude thinner than the conventional one. The proposed design not only offer promising building blocks with great potential to profoundly impact architectural acoustics and related fields, but also constitutes a major step towards real-world applications of acoustic metasurfaces.

Topological subspace induced bound states in continuum

Yi-Xin Xiao[1], **Guancong Ma**[1], **Zhao-Qing Zhang**[1], **C. T. Chan**[1]
[1]Department of Physics and Institute for Advanced Study, The Hong Kong University of Science and Technology, Hong Kong, China
[*]corresponding author: phchan@ust.hk

Abstract-We propose a new kind of bound states in continuum[1-3] (BIC) in a class of systems constructed by coupling multiple identical one-dimensional (1D) chains each with inversion symmetry. The BIC existence is enabled by a specific separation of the Hilbert space into topological and non-topological subspaces. Bulk-boundary correspondence in the topological subspace guarantees the existence of a localized interface state which can lie in the continuum of extended states in the non-topological subspace, forming a BIC. Such topological BIC is observed experimentally in a coupled-acoustic-resonators system.

We couple two identical Su-Schrieffer-Heeger (SSH) chains in a way so that the chains outnumbers the coupling channels between them. With only one coupling channel, two bands remain topological characterized by quantized Berry phase, despite the overall inversion symmetry is broken by the introduction of coupler chain. A bound state occurs at the interface between two topologically different phases due to bulk-boundary correspondence. By choosing appropriate system parameters, we can make the topological interface state to overlap with the continuous spectrum of the extended states in the non-topological subspace. In this way, a BIC is formed. We emphasize this is a new scheme which relies on bulk-boundary correspondence to construct a BIC. We experimentally demonstrated our proposal in a system consisting of coupled acoustic resonators. The dipole modes of acoustic resonators are used to represent the orbitals.

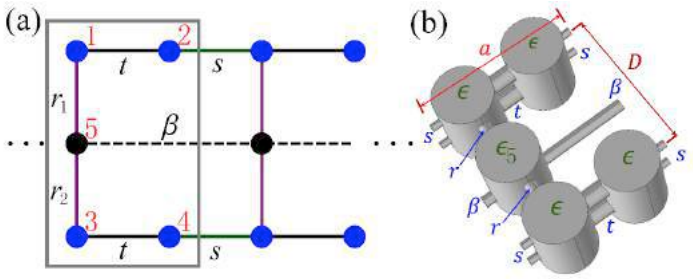

Fig. 1 (a) Two identical SSH chains coupled by a coupler "atom" per unit cell. The hopping parameters and indices of the "atom" orbitals are labeled. The on-site energies are $\varepsilon_1 = \varepsilon_2 = \varepsilon_3 = \varepsilon_4 = 0$ and ε_5. (b) A unit cell consisting of coupled acoustic cavities.

REFERENCES

1. Plotnik, Y. et al. Experimental Observation of Optical Bound States in the Continuum. Phys. Rev. Lett. 107, 183901 (2011).
2. Hsu, C. W. et al. Observation of trapped light within the radiation continuum. Nature 499, 188–191 (2013).
3. Hsu, C. W., Zhen, B., Stone, A. D., Joannopoulos, J. D. & Soljačić, M. "Bound states in the continuum". Nature Reviews Materials 1, 16048 (2016).

Analytic Materials

G. W. Milton[1],

[1]Department of Mathematics, The University of Utah, Salt Lake City, Utah, U.S.A.
milton@math.utah.edu

Abstract— This talk presents new classes of inhomogeneous media for which one can easily get exact solutions for the fields. They are called analytic materials, as the moduli involve analytic functions. The partial differential equations solved by the fields are reduced to a set of ordinary differential equations. We present explicit examples of analytic materials for elastodynamics and for electromagnetism. This greatly expands the array of examples of exactly solvable materials that one can obtain using other techniques, such as the transformation optics technique introduced by Dolin in 1961.

The theory of inhomogeneous analytic materials is developed. These are materials where the coefficients entering the equations involve analytic functions. Three types of analytic materials are identified. The first two types involve an integer p. If p takes its maximum value then we have a complete analytic material. Otherwise it is incomplete analytic material of rank p. For two-dimensional materials further progress can be made in the identification of analytic materials by using the well-known fact that a 90 degrees rotation applied to a divergence free field in a simply connected domain yields a curl-free field, and this can then be expressed as the gradient of a potential. Other exact results for the fields in inhomogeneous media are reviewed.

ACKNOWLEDGMENT

The author thanks the National Science Foundation for support through grant DMS-1211359.

REFERENCES

1. Milton, G. W., "Analytic Materials," *Proc. Roy. Soc. A*, published online DOI: 10.1098/rspa.2016.0613, 2016.

Underwater acoustic cloak with pentamode material

Y. Chen, M.Y. Zheng, X.N. Liu, G.K. Hu
School of Aerospace Engineering, Beijing Institute of Technology, Beijing 100081, China
*corresponding author: hugeng@bit.edu.cn

Abstract-A cylindrical underwater acoustic cloak is designed from pentamode material that mimics meta-fluid with anisotropic modulus. The machined cloak is tested in a designed 2D waveguide through transient cylinder wave experiments. Experiment results verify excellent cloaking performance over a broadband frequency range 9-15 kHz, and therefore confirm superior wave manipulating capability of pentamode metamaterial particularly for underwater acoustics.

Inertial acoustic cloak requires anisotropic density to deflect wave trajectory to achieve invisibility, however conventional metamaterial technique, such as perforated plate or alternating fluid layer, cannot offer sufficient anisotropy in dense fluid like water and also suffers from the infinite mass catastrophe[1]. To circumvent these difficulties, an alternative approach using pentamode material is adopted[1, 2] in this research to design cloak for underwater acoustics. Pentamode material, specially designed microstructure solid, can mimic anisotropic modulus meta-fluid, and has much stronger anisotropy than available in density through any conventional metamaterial technique. Numerical investigations[3] have shown its broadband performance for acoustic manipulation, while experiment has never been reported. Here, we experimentally demonstrate superior wave steering ability of pentamode material by designing a broadband underwater acoustic cloak[4].

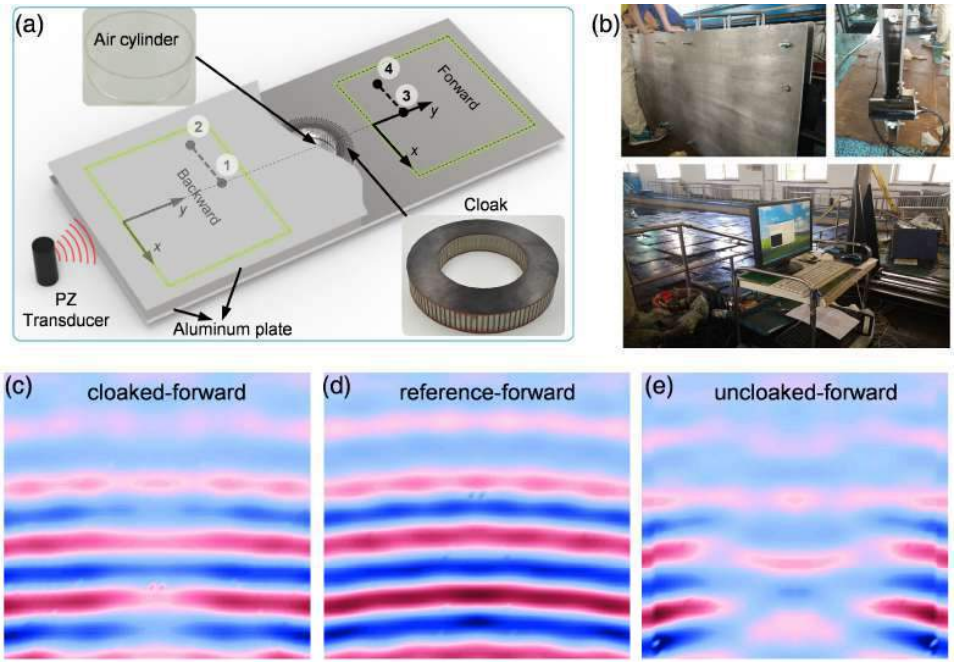

Figure 1. (a) Experiment setup demonstration; (b) Experiment test platform; (c) (d) (e) Snapshot of measured acoustic pressure field in forward region for cloaked, reference and uncloaked cases, respectively.

A new geometry is first proposed as pentamode unit cell with larger effective parameters space. A cylindrical cloak, aim at underwater acoustic wave, is designed from proposed unit cell using transformation approach as well as optimization algorithm. Geometry of pentamode cell in the cloak has been calibrated to acquire effective material parameter required by transformation approach. The cloak is finally machined from an aluminum block using advanced electric discharging machining technology with high accuracy.

Due to small size of the fabricated cloak in height direction, a 2D underwater waveguide is also proposed to test the cloak. Transient cylindrical wave emitted from a piezoelectric transducer is used to verify broadband performance of fabricated cloak. Scanned acoustic pressure field indicates obvious difference between uncloak and cloaked air scatter in both forward and backward regions. Strong scattering effect, due to severe impedance mismatch between air and background water, has been substantially eliminated when the scatter is covered with cloak, and the rectified pressure field approaches that of reference case with empty waveguide. Target Strength Reduction (TSR) has been calculated from measured signal at specific backward location, and also shows excellent cloaking performance of designed cloak over remarkable frequency range, with an averaged reduction 6.3dB in TSR over 9-15 kHz.

The experiment proves expected excellent and broadband wave steering capability of pentamode material with cloak application for the first time. It should be noted, although measurements here only indicate excellent performance of designed cloak over the given range owing to transducer frequency limitation, the designed cloak can in principle work from zero frequency, since only quasi-static material properties are employed, in contrast to inertial cloaks based on local resonance mechanism. Solid and broadband advantages together with achievable strong anisotropy make pentamode material a perfect candidate for controlling acoustic wave propagation, and may bring forth new applications, such as wave bender, metasurface, particular for underwater acoustics.

REFERENCES

1. A. N. Norris. “Acoustic cloaking theory,” *P. Roy. Soc. A-Math. Phy.*, Vol. 464, No. 2097, 2411-2434, 2008.
2. G. W. Milton, A. V. Cherkaev. “Which elasticity tensors are realizable?,” *J. Eng. Mater-T. Asme*, Vol. 117, No. 483, 1995.
3. Y. Chen, X. Liu, G. Hu. “Latticed pentamode acoustic cloak,” *Sci. Rep.*, Vol. 5, 15745, 2015.
4. Y. Chen, M. Zheng, Y. Bi, Z. Sun, X. Liu, P. Xiang, J. Yang, G. Hu. “Broadband solid cloak for underwater acoustics,” *arXiv:1611.00506*, 2016.

Experiments on asymmetric acoustic transmission devices.

T. Devaux[1,2], A. Cebrecos[2], O. Richoux[2], V. Pagneux[2], and V. Tournat[2]

[1]Division of Applied Physics, Faculty of Engineering, Hokkaido University, Sapporo 060-8628, Japan
[2]LAUM, UMR CNRS 6613, Université du Maine, Le Mans 72000, France
thibaut.devaux@eng.hokudai.ac.jp

Abstract— Building architectures able to demonstrate asymmetric transmission became a real challenge in the last decades. Here, we propose two devices with capabilities of breaking acoustic reciprocity. The first device uses nonlinear conversion in granular matter meanwhile the second allows to avoid frequency conversion during the propagation process. Helping by the experimental results, the advantages and drawbacks of each architecture are compared. The possibility to break the reciprocity introduces new capabilities for information processing and for improving acoustic imaging.

For breaking the reciprocity of a wave system, i.e. allowing the transmission through the device in one direction of propagation but not in the other [1, 2], the most common solution consists to use frequency conversion process combined with a frequency filtering process [3]. An other common solution consists to introduce a energy bias like gravity or circulating air flow [4]. The main drawback of these existent solutions is their narrow frequency band working regime where these asymmetric proprieties are obtained. Moreover, using conversion process or external energy supply is not promising for long term and energy efficiency applications in information processing. Here, we report on the design and experiments on two different architectures of asymmetric acoustic devices with and without frequency conversion process to going beyond the previous limits.

The first architecture is based on the nonlinear self-demodulation process in a one-dimensional structure made of a nonlinear granular medium and a phononic multilayer solid as shown on Fig. 1.

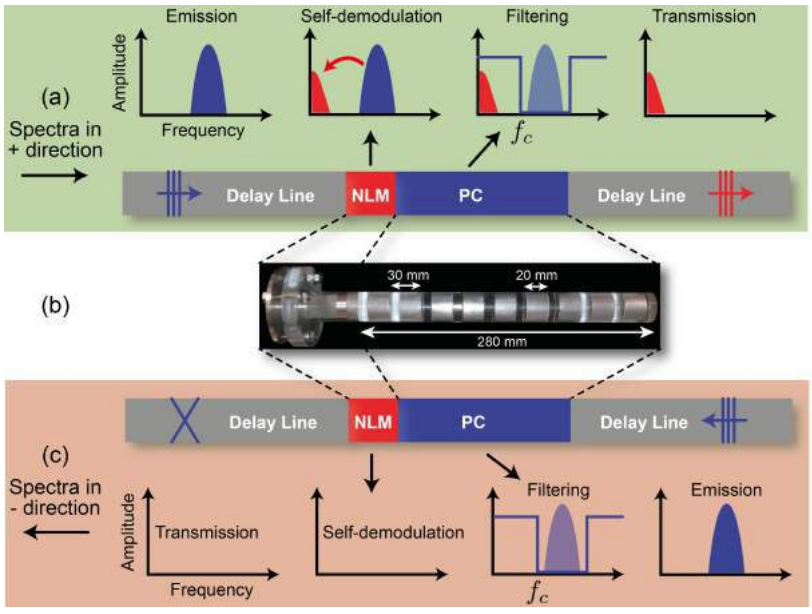

Figure 1: **(a)** Schematics of the proposed acoustic rectifier in "+" direction. **(b)** Picture of the experimental system. **(c)** Schematics in "-" direction.

Implementing upstream and downstream ultrasonic delay lines, we characterized first the two parts of this rectifier. The conversion part is assumed by 3D unconsolidated granular medium which consists of a layer with a thickness of 3.0 cm of steel powder (Fe3Cr1Mo0.5Mn0.2V) with

an average grain diameter of $d = 300$ μm. Alternating nine layers of Lucite with ten layers of aluminum, we built the phononic crystal (i.e. the selection part) where thicknesses are $d_p = 10$ mm and $d_a = 20$ mm, respectively, along with diameters of 30 mm. After characterized the two parts of this rectifier, we analyze the broadband character of this asymmetric effect, which could allow for information processing in the future. With the help of the delaylines, we also measure quantitatively the incident, reflected and transmitted wave packets, and demonstrate a ratio larger than 10^6 in transmitted acoustic wave energies for the two opposite directions of operation. The drawbacks of this device are a modification of the transmitted signal spectrum and a weak transmitted amplitude compared to the incident one.

In the second part of the presentation, we present a solution to avoid the frequency conversion process involved in the most part of asymmetric device as the first proposed using the granular matter. Interestingly, this architecture mimics the intrinsic behavior of the most known asymmetric device: the electrical diode. After detailing all processes and mechanisms involved in this asymmetric device, we demonstrate experimentally a very high efficiency with an energy transmission ratio of ! 10^6 between the two direction of propagation, as well as tunability and broadband characteristics. The most interesting aspect is that the transmitted signal does not show signs of distortion without external energy supply. Moreover, the transmitted amplitude in the allowed propagation direction is close to 1. Due to simple design and the mechanisms involved, the proposed device is also able to become a key element to realize an acoustical switch.

In conclusion, we propose two new architectures for asymmetric propagation of acoustic waves to overcome the limits of the recent proposed architectures. Combining a granular layer with a phononic crystal, we demonstrate with the first architecture, the possibility to rectifying the energy for the wide band signal with a high contrast ratio σ ! 10^6. Secondly, we propose an another architecture to avoid the conversion process trough the propagation without energy supply. The second device is able to transmit almost all the energy in the allowed propagation direction without distortion effect. These experimental results on two proposed devices for asymmetric transmission extend the previously demonstrated effects (transmission ratio, frequency bandwidth, transmitted amplitude). The designs and tests of these architectures contribute to the field of acoustic diodes, which could open avenues for novel acoustic devices aiming at controlling waves.

REFERENCES

1. D. Jalas et al., "What is - and what is not - an optical isolator". *Nat. Phot.* **7**, 579, 2013.
2. A. A. Maznev, A. G. Every, and O. B. Wright, "Reciprocity in reflection and transmission: what is a phonon diode?", *Wave Motion* **50**, 776 (2013).
3. B. Liang, B. Guo, J. Tu, D. Zhang, and J. C. Cheng, "An acoustic rectifier.", *Nat. Mater.* **9**, 989, 2010.
4. R. Fleury, D.L. Sounas, C.F. Sieck, M.R. Haberman, and A. Al, "Sound isolation and giant linear nonreciprocity in a compact acoustic circulator". *Science* **343**, 516, 2014.

Novel Topological Concepts for Reliable Mechanical Wave-guiding

Marc Serra-Garcia[1], Roman Süsstrunk[1], Osama R. Bilal[1,2], and Sebastian D. Huber[1]

[1] Institute for Theoretical Physics, ETH Zurich, 8093 Zurich, Switzerland
[2] Division of Engineering and Applied Sciences, California Institute of Technology, Pasadena, CA 91125, USA
sebastian.huber@phys.ethz.ch

Abstract – **Guiding mechanical energy in a reliable way between two points in space is an important ingredient for many technological applications such as energy harvesting or in mechanical computing. In particular, wave guides that are free from backscattering and can hence be bent without any losses would be a most welcome addition to the metamaterials toolbox. Here, we present a new design principle for wave-guides with exactly these properties. Owing to the intricate structure of the Bloch-wave structure of the bulk mechanical vibrations, surface modes with highly specialized properties are arising. We discuss a general formalism for the theoretical description of such "topological surface modes" and provide experimental implementations of two corner stones for topological wave guiding [1]. First, we introduce a mechanical analog of the quantum spin Hall effect, where a two-dimensional material nucleates one-dimensional surface states that can transport energy in a unidirectional fashion [2]. Second, we provide the first experimental observation of a quadruple (or higher order) topological insulator, where a n–dimensional systems stabilizes stable (n-2)–dimensional corner modes. This corner modes pave the way to concrete materials where stable one–dimensional waveguides are built in a three–dimensional sample.**

REFERENCES

[1] R. Süsstrunk and S.D. Huber, Proc. Natl. Acad. Sci. USA, 113, E4767, 2016
[2] R. Süsstrunk and S.D. Huber, Science, 349, 47, 2015.
[3] M. Serra-Garcia, R. Süsstrunk, O.R. Bilal, and S.D. Huber in preparation, 2017.

Nanophotonics on Silicon Platform

Purcell effect in low-dimensional photonic structures

M. F. Limonov[1,2], A. B. Pevtsov[1], S. F. Mingaleev[3], Y. S. Kivshar[2,4], and M. V. Rybin[1,2]

[1]Ioffe Institute, St. Petersburg 194021, Russia
[2]ITMO University, St.Petersburg 197101, Russia
[3]VPI Development Center, Belarus Hi-Tech Park, Minsk 220037, Belarus
[4]Nonlinear Physics Center, Research School of Physics and Engineering, Australian National University, Canberra ACT 2601, Australia
m.rybin@mail.ioffe.ru

Abstract— We analyze the Purcell effect in a waveguide with a side-coupled microcavity and demonstrate that it can be considered as an interference phenomenon. Also we describe a growth of photoluminescence intensity at the low-frequency edge of the band-gap in a photonic crystal composed of alternating amorphous hydrogenated silicon with carbon and silica layers and attribute this with the Purcell effect. We suggest that Green's function calculated by the transfer-matrix method allows describing the Purcell effects in low-dimensional photonic structures.

In many applications of photonics the light is radiated from an energy source that can be either an excited quantum system or a resonator that accumulates energy in the form of standing waves. The engineering of dielectric environment allows to modify the emission rate due to the Purcell effect without changing the properties of the emitter itself. Here we study the Purcell effect for several photonic systems described by quantum and classical approaches. Since Edward Purcell published his landmark note [1] on the modification of quantum transition rates due to a cavity, this effect was considered in the framework of the quantum electrodynamics. Recently, it was reported that the Purcell effect in antennas with current loops can be described classically [2, 3]. Here we suggest a classical counterpart of the Purcell effect for pure photonic modes in a microcavity [4].

We describve the Purcell effect in a waveguide with a pair of partially reflecting defects forming an effective environment for a side-coupled resonator. This system was considered earlier as a system with a sharp Fano resonance [5], and it is described phenomenologically by means of the transfer-matrix method. We find the expression the Purcell factor in the form

$$f = \frac{\gamma}{\gamma_0} = (1 - r^2)\frac{1 + r^2 - r[\cos(2\delta_1) + \cos(2\delta_2)]}{(1 + r^2)^2 - 4r^2\cos^2\delta}. \quad (1)$$

Here γ and γ_0 are the resonator damping rate with and without environment respectively, r is reflection coefficient of the defects, $\delta_{1,2} = kd_{1,2}$, $\delta = \delta_1 + \delta_2$, k is wavenumber, $d_{1,2}$ is the distance between left or right defect and the resonator.

We implement the system in a photonic crystal composed of a square array of silicon rods with radius $r = 0.2a$ (a is the lattice constant) and refractive $n = 3.4$ (silicon in near infrared range). A waveguide is formed by removing a row of dielectric rods, and a resonant cavity is created by reducing the radius of a single rod to $0.1a$. The cavity is placed at the distance $3a$ away from the waveguide. Such a cavity supports a localized monopole-like defect mode with the resonant frequency $\omega_0 = 0.32821 \cdot (2\pi c/a)$ and the half-width at half minimum $\gamma_0 = 0.00026 \cdot (2\pi c/a)$. Cylinders of radius $0.1a$ introduce the pair of defects in the waveguide. The transmission spectra in this structure are calculated by employing the frequency-domain Wannier functions approach [6] that enables us accurate modeling of high-Q resonances. The calculated data appear to be in excellent agreement with the results of transfer matrix based theory. The adjustment of the distance between defects changes the damping rate over 25 times (the Purcell factor is in the interval from 0.18 to 5)

To analyze this result we calculate Purcell factor for a two-level quantum particle instead of the resonator using conventional quantum electrodynamic approach explaining the Purcell effect by modification of local density of photonic states (DOS), which can be evaluated through the imaginary part of Green's function for electric field. Quasi-one-dimensional structures considered in the present study allow the calculating of the Green's function by means of transfer matrix method. It appears that the Purcell factor found from the Green's function is exactly the same as one defined by Eq. (1).

For experimental confirmation of results obtained by the Green's function for quasi-one-dimensional structures calculated by transfer matrix method we examine photoluminescence from a photonic crystal. The density of photonic states is known to increase at the edges of photonic gaps. However the local DOS has a strong dependence on the emitter position relative the photonic crystal environment. For the regions occupied with a higher refractive index material the local DOS has a maximum at the low-frequency edge, while for a lower refractive index layers the local DOS has the maximum at the high-frequency edge. To measure experimental data allowing unambiguous interpretation we should take into account a number of circumstances. Emission centers have to be localized either in high-index layers or low-index ones. The width of photoluminescence contour has to be comparable with the photonic band gap, since we need to compare the luminescence intensity at the different edges at the same measurements.

We fabricate one-dimensional photonic crystal being an alternating a-$Si_{0.5}$:$C_{0.5}$:H and a-SiO_2 layers. A gradient in layer thickness is introduced for adjusting the photonic band gap with photoluminescence band. The addition of carbon to amorphous hydrogenated silicon allows a broadening of photoluminescence band (to be compatible with the photonic band gap) and an increasing quantum yield at room temperature. We excite the sample with a 405 nm continuous-wave semiconductor laser (the corresponding phonon energy exceeds the electronic energy gap width of a-$Si_{0.5}$:$C_{0.5}$:H). In addition, this wavelength falls outside the excitation spectrum of the photoluminescence associated with oxygen vacancies in a-SiO_2 films. As a result we obtain the increasing of the luminescence intensity at the low-frequency edge in a good agreement with spectra evaluated theoretically, which are obtained by means of the quasi-one-dimensional Green's function calculated using the transfer matrix method.

In summary, we have studied the Purcell effect in silicon-based photonic structures. The classical counterpart of the Purcell effect for pure photonic modes enables us to discuss Purcell effect in a more intuitive terms of interference. In quasi-one-dimension systems Purcell effect can be evaluated by Green's function calculated by transfer matrix method. This Green's function allows the description of experimentally measured photoluminescence of the layered photonic crystals.

ACKNOWLEDGMENT

This work has been supported by the Ministry of Education and Science of the Russian Federation (Zadanie No. 3.1500.2017/PCh) and by the Australian Research Council.

REFERENCES

1. Purcell, E. M., "Spontaneous emission probabilities at radio frequencies," *Phys. Rev.*, Vol. 69, 681, 1946.
2. Eggleston, M. S., K. Messer, K., L. Zhang, E. Yablonovitch and M. C. Wu, "Optical antenna enhanced spontaneous emission," *Proc. Nat. Acad. Sci.*, Vol. 112, 1704-1709, 2015.
3. Krasnok, A. E., A. P. Slobozhanyuk, C. R. Simovski, S. A. Tretyakov, A. N. Poddubny, A. E. Miroshnichenko, Y. S. Kivshar and P. A. Belov, "An antenna model for the Purcell effect," *Sci. Rep.*, Vol. 5, 12956, 2015.
4. Rybin, M. V., S. F. Mingaleev, M.F. Limonov and Y.S. Kivshar, "Purcell effect and Lamb shift as interference phenomena," *Sci. Rep.*, Vol. 6, 20599, 2016.
5. Fan, S., "Sharp asymmetric line shapes in side-coupled waveguide-cavity systems," *Appl. Phys. Lett.*, Vol. 80, 908, 2002.
6. Busch, K., S. F. Mingaleev, A. Garcia-Martin, M. Schillinger and D. Hermann, "The Wannier function approach to photonic crystal circuits," *J. Phys.: Cond. Matt.*, Vol. 15, R1233, 2003.

Towards chip-scale light manipulation on silicon platform

(Invited Paper)

Jian Wang*

Wuhan National Laboratory for Optoelectronics, School of Optical and Electronic Information, Huazhong University of Science and Technology, Wuhan 430074, Hubei, China

*Corresponding author: jwang@hust.edu.cn

Abstract-Silicon photonics provides a promising integration platform facilitating chip-scale light manipulation. We will review our recent research progress in the fabrication of silicon nanophotonic devices and their wide applications in chip-scale light manipulation. We will talk about 1) design and fabrication of various silicon nanophotonic devices (ridge/slot/hybrid plasmonic waveguides, couplers, gratings, microring resonators, photonic crystal nanocavities, comb filter/interleaver, plasmonic/dielectric metasurfaces); 2) chip-scale optical interconnects (terabit-scale signaling); 3) chip-scale photonic signal processing (wavelength conversion, signal regeneration, optical computing); 4) chip-scale spatial light modulation (generation of orbital angular momentum light beams). The obtained results show favorable performance of chip-scale light manipulation on silicon platform.

In recent years, silicon photonics has become one of the most promising photonic integration platforms owing to its small footprint, low power consumption, and availability of complementary metal-oxide-semiconductor (CMOS) fabrication technology for low-cost mass production [1]. Typical silicon nanophotonic devices include waveguides, microring resonators, photonic crystal nanocavities and metasurfaces, showing unprecedented small size for potential large scale integration. The great success of silicon photonics facilitates miscellaneous chip-scale 1D and 2D light manipulation on silicon platform. In this paper, we will review our recent research progress in chip-scale light manipulation using silicon nanophotonic devices.

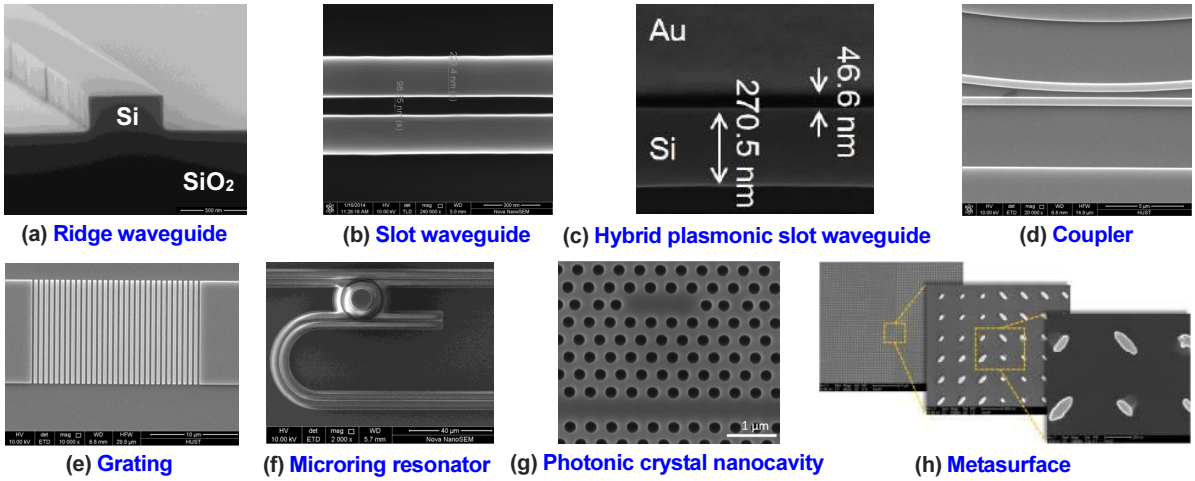

Fig. 1. Measured scanning electron microscope (SEM) images of the fabricated (a) silicon ridge waveguide, (b) silicon slot waveguide, (c) hybrid plasmonic slot waveguide, (d) silicon coupler, (e) silicon grating, (f) silicon microring resonator, (g) silicon photonic crystal nanocavity, and (h) silicon metasurface.

Design and Fabrication of Various Silicon Nanophotonic Devices: The designed various silicon nanophotonic devices were fabricated on silicon-on-insulator (SOI) using electron-beam lithography (EBL) followed by induced coupled plasma (ICP) etching. Shown in Fig. 1 are measured scanning electron microscope (SEM) images of the fabricated silicon ridge waveguide, silicon slot waveguide, hybrid plasmonic slot waveguide, silicon coupler, silicon grating, silicon microring resonator, silicon photonic crystal nanocavity, and silicon metasurface. Some more silicon nanophotonic devices, e.g. silicon comb filter/interleaver, plasmonic metasurface were also fabricated in the experiment. Using these fabricated silicon nanophotonic devices, chip-scale optical interconnects, photonic signal processing and spatial light modulation were demonstrated.

Chip-Scale Optical Interconnects [2, 3]: By exploiting the fabricated silicon microring resonator, silicon vertical slot waveguide and hybrid plasmonic slot waveguide, we demonstrated chip-scale data transmission with advanced multi-carrier multi-level modulation signals, e.g. orthogonal frequency division multiplexing based on offset quadrature amplitude modulation (OFDM/OQAM). OFDM/OQAM 64-QAM, 128-QAM, 256-QAM, 512-QAM signaling and 1.8-Tbit/s wavelength-division multiplexing (WDM) signaling were demonstrated in the experiment, showing potential chip-scale optical interconnects.

Chip-Scale Photonic Signal Processing [4-6]: By exploiting the fabricated silicon ridge waveguides and graphene-assisted silicon microring resonators, we demonstrated chip-scale wavelength conversion of OFDM m-QAM and Nyquist m-QAM signals, chip-scale signal regeneration of 4-ary pulse amplitude modulation (PAM-4) signals, and chip-scale high-base optical computing (quaternary/octal/decimal addition/subtraction).

Chip-Scale Spatial Light Modulation [7-9]: By exploiting the fabricated plasmonic metasurface and silicon metasurface, we presented broadband generation of orbital angular momentum (OAM) carrying vector beams and chip-scale N-fold OAM multicasting. We further demonstrated the generation and detection of different OAM beams in the experiment.

Acknowledgements: This work was supported by the National Natural Science Foundation of China (NSFC) under grants 11574001, 11274131 and 61222502, the National Basic Research Program of China (973 Program) under grant 2014CB340004, and the National Program for Support of Top-notch Young Professionals.

REFERENCES

1. Jalali, B. and Fathpour, S. “Silicon photonics,” *J. Lightwave Technol.*, Vol. 24, No. 12, 4600–4615, 2006.
2. Gui, C. and Wang, J. “Experimental performance evaluation of quadrature amplitude modulation signal transmission in a silicon microring,” *Photon. Res.*, Vol. 4, No. 5, 168–172, 2016.
3. Gui, C., Li, C., Yang, Q. and Wang, J. “Demonstration of terabit-scale data transmission in silicon vertical slot waveguides,” *Opt. Express*, Vol. 23, No. 8, 9736–9745, 2015.
4. Long, Y., Liu, J., Hu, X., Wang, A., Zhou, L., Zou, K., Zhu, Y., Zhang, F. and Wang, J. “All-optical multi-channel wavelength conversion of Nyquist 16-QAM signal using a silicon waveguide,” *Opt. Lett.*, Vol. 40, No. 23, 5475–5478, 2015.
5. Long, Y., Wang, A., Zhou, L. and Wang, J. “All-optical wavelength conversion and signal regeneration of PAM-4 signal using a silicon waveguide,” *Opt. Express*, Vol. 24, No. 7, 7158–7167 (2016).
6. Wang, A., Long, Y., Zhu, Z., Zhou, L. and Wang, J. “Silicon waveguide based two-input octal addition/subtraction using non-degenerate FWM and 8PSK”, *Proc. ACP2015,* postdeadline paper AM4A.5, 2015.
7. Zhao, Z., Wang, J., Li, S. H. and Willner, A. E. “Metamaterials-based broadband generation of orbital angular momentum carrying vector beams,” *Opt. Lett.*, Vol. 38, No. 6, 932–934, 2013.
8. Du, J. and Wang, J. “Design of on-chip N-fold orbital angular momentum multicasting using V-shaped antenna array,” *Sci. Rep.*, Vol. 5, 9662, 2015.
9. Du, J., Li, X. H., Li, S. H., Zhu, L., Zhou, N., Liu, J., Chen, S., Zhao, Y. F. and Wang, J. “Experimental demonstration of chip-scale orbital angular momentum (OAM) beams generation and detection using nanophotonic dielectric metasurface array,” *Proc. OFC2016*, Optical Society of America (OSA), paper W2A.13, 2016.

Ultra-high efficiency, fast graphene micro-heater on silicon

Siqi Yan [1, 2], Xiaolong Zhu[1,3], Lars Hagedorn Frandsen[1], Sanshui Xiao [1,3], N. Asger Mortensen[1,3], Jianji Dong[2] and Yunhong Ding[1,*]

[1]Department of Photonics Engineering, Technical University of Denmark, DK-2800 Kongens Lyngby, Denmark

[2]Wuhan National Laboratory for Optoelectronics, Huazhong University of Science and Technology, 430074, Wuhan, China.

[3]Center for Nanostructured Graphene, Technical University of Denmark, DK-2800 Kongens Lyngby, Denmark

[*]corresponding author: yudin@fotonik.dtu.dk

Abstract-We demonstrate an ultra-high efficiency and fast graphene microheater on silicon photonic crystal waveguide. By taking advantage of slow-light effect, a tuning efficiency of 1.07 nm/mW and power consumption per free spectral range of 3.99 mW. A fast rise and decay times (10% to 90%) of only 750 ns and 525 ns are achieved. The corresponding figure of merit of the device is 2.543 nW • s, one order of magnitude better than results reported in previous studies**.**

Micro-heater on silicon waveguide is one of the most important building blocks in silicon photonics. Silicon photonic integrated circuits based reconfigurable switches are relying on micro-heaters [1], which requires low power consumption and fast tuning. Traditional metallic microheater design requires a thick silicon dioxide layer introduced between the silicon waveguide and the metallic heater to avoid the light-absorption loss, inevitably impeding heat transport and dissipation owing to the low thermal conductivity of SiO_2. The unique properties of graphene, e.g. low optical absorption loss, high thermal conductivity (~5300 W • m^{-1} • K^{-1}) make graphene rather attractive as a heating material. Graphene heater can be in close contact to the silicon waveguide which significantly improves the tuning efficiency. However, the current performances of devices using graphene heaters are limited either by their relatively high power consumptions [2] or by their microsecond response times [3].

Here we report a new concept of enhancing the heater efficiency by the use of slow light in a silicon photonic crystal waveguide with a monolayer of graphene working as a heater. We demonstrate an energy-efficient graphene microheater with a tuning efficiency of 1.07 nm/mW and power consumption per free spectral range (FSR) of 3.99 mW, with the rise and decay times (10% to 90%) of only 750 ns and 525 ns.

A schematic of the slow-light-enhanced graphene microheater is shown in Fig. 1(a). A graphene monolayer is deposited onto the core-region of the silicon PhCW. The graphene is contacted by two gold/titanium (Au/Ti) pads. Ohmic heating is generated in the graphene via an applied voltage bias between two Au/Ti pads. The width of the graphene overlapping the photonic crystal line defect is designed to be narrower than the other part of the graphene to locally increase the Ohmic dissipation, which results in a more effective heating.

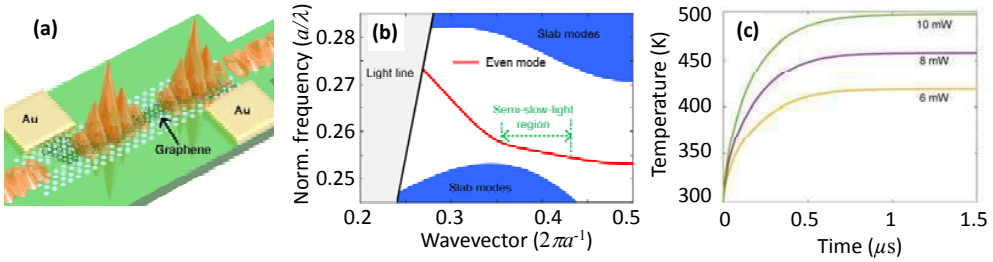

Fig. 1. (a) Schematic of the slow-light-enhanced graphene heater. (b) Band structure of the photonic crystal waveguide. The even guiding mode (red curve) consists of a semi-slow-light region (green dashed line). (c) The temperature response for different heating power.

The tuning efficiency is significantly enhanced owing to the semi-slow light effect that is obtained in the PhCW, which increases the effective interaction length between the heater and the waveguides [5]. By optimizing the positions of the first and second rows of holes adjacent to the line-defect, the band structure with semi-slow light effect is obtained (see Fig. 1(b)). Fig. 1(c) indicates the theoretical response time of the proposed microheater, 420 ns response time is achieved, which is faster than most previous reported microheaters.

The slow-light-enhanced graphene heater was fabricated by CMOS fabrication process and the graphene wet transfer process. The false-color SEM image is shown in Fig. 2(a). In order to test the efficiency, the device is incorporated in a Mach–Zehnder interferometer. By applying external voltage on the device, both the static (see Fig. 2(b)) and the dynamic response (see Fig. 2(c) and 2(d)) of the device are measured. The interference dips shift at 1533.71 nm and 1525.12 nm as functions of the tuning power is represented, and tuning efficiencies of 1.07 nm/mW and 0.65 nm/mW are achieved, respectively. A fast rising and decaying times (between 10% and 90%) are measured to be 750 ns and 525 ns, respectively, as indicated in Fig. 2(d). The corresponding figure of merit of the device [6], i.e. the product of the power consumption per FSR and the average response time, is 2.543 nW·s, which is one order of magnitude better than previous reported results [6].

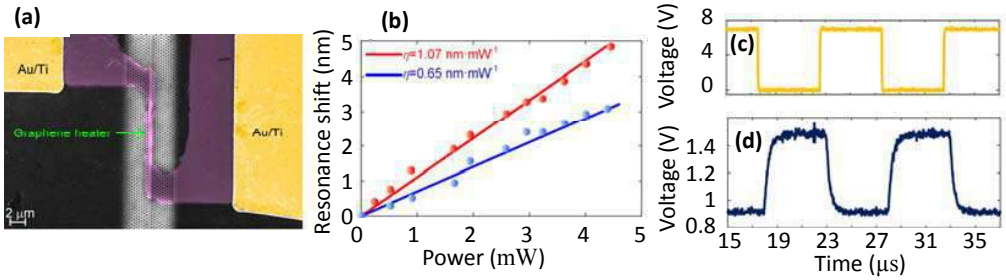

Fig. 2. (a) False-color SEM image of the slow-light-enhanced graphene heater. (b) Measured resonance shifts for the interference dips at 1525.12 nm (blue) and 1533.71 nm (red) as functions of the applied heating power. (c) Driving electrical signal and (d) corresponding temporal response signal.

In summary, we demonstrate an ultra-high efficiency and fast graphene microheater on semi-slow light silicon photonic crystal waveguide. We achieved ultra-high tuning efficiency of 1.07 nm/mW and power consumption per FSR of 3.99 mW. A fast response times (10% to 90%) of only 750 ns and 525 ns is demonstrated.

Acknowledgements, This work is supported by the Danish Council for Independent Research (DFF-1337−00152 and DFF-1335−00771) and the National Natural Science Foundation of China (Grant No. 61622502 and 61475052)..

REFERENCES

1. Y. Ding et al., "Reconfigurable SDM switching using novel silicon photonic integrated circuit," *Sci. Rep.*, Vol. 6, 39058, 2016.
2. S. Gan *et al.* "A highly efficient thermo-optic microring modulator assisted by graphene," *Nanoscale*, Vol. **7**, 20249-20255 (2015).
3. L. Yu et al. "Thermally tunable silicon photonic microdisk resonator with transparent graphene nanoheaters," *Optica*, Vol. 3, 159-166 (2016).
4. S. Yan et al., "Slow-light-enhanced energy efficiency for graphene microheaters on silicon photonic crystal waveguides," *Nature Commun.*, Vol. 8, 14411, 2017.
5. D. Schall *et al.* "Infrared transparent graphene heater for silicon photonic integrated circuits," *Opt. Express*, Vol. 24, 7871-7878 (2016).

Silicon-Photonics-Based Optical Phased-Array

Kyoungsik Yu[1] **and Hyo-Hoon Park**[1*]

[1]School of Electrical Engineering, KAIST (Korea Advanced Institute of Science and Technology), Korea

[*]corresponding author: parkhh@kaist.ac.kr

Abstract-We present the structures and performances of silicon-photonics-based optical phased-arrays (OPAs) to achieve wide beam-forming angles for LiDAR applications. Beam-forming and steering are experimentally demonstrated with 1x16 OPAs in which power splitters, phase shifters, and radiators are integrated on a silicon photonics platform. For wide transversal steering over 45°, two radiator types are examined; the grating- and photonic crystal-based structures. We will compare the detailed performances and tradeoffs for such structures.

The optical phased-array (OPA) has received considerable attention as a compact laser beam scanning/steering device for real-time 3D scene acquisition in the LiDAR (light detection and raging) systems. To attain a wide field of view while maintaining a single-beam characteristic and a high power throughput to the free space, the radiator element in the OPA needs to be carefully designed. In this paper, we present our ongoing works on the integrated OPAs based on the silicon photonics platform with a special emphasis on the radiator structures that can address such issues. Fig. 1(a) shows an example of a 1x16 OPA with 16 tunable phase shifters and 16 grating-based radiators operating near 1550 nm wavelengths.

For wide transversal beam steering in the azimuthal direction, two types of radiator structures were examined, namely a grating radiator structure (Fig. 1(a)) based on the Bragg diffraction and a nano-hole array radiator (Fig. 1(b)) based on the one-dimensional photonic crystal. For longitudinal steering, thermally tunable grating radiators were employed (Fig. 1(c)). The performances of these radiators were compared through 1x16 OPAs in which multi-mode interferometer-based splitters and electro-optic p-i-n phase shifters were integrated with the radiators on the silicon-on-insulator wafer. The radiator pitch was varied in a range of 1.5 μm ~ 2.0 μm.

Both the grating and hole-based radiators showed wide beam-steering ranges above 45° in the transverse direction. Especially, the nano-hole radiators showed a possibility of even wider beam-forming angles with a narrower pitch due to less interference between the neighboring radiators. The thermo-optic tunable grating radiator showed a vertical steering of up to 7° with a current injection of 6 mA into the radiator region. For the examined OPA structures, the overall performances and tradeoffs on the radiation efficiency, beam shapes, power consumption, and phase control speed as well as the steering range will be compared.

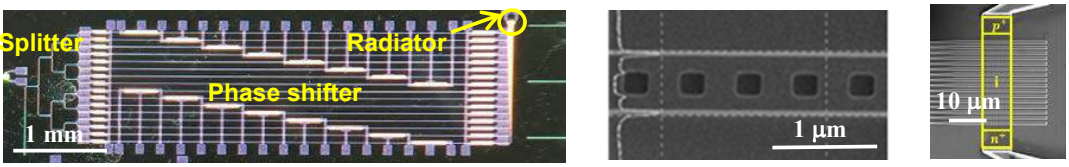

(a) (b) (c)

Figure 1. (a) Optical microscope photographs of a 1x16 optical phased array with grating radiators. Scanning electron micrographs of (b) a nano-holed radiator and (c) tunable grating radiators.

Acknowledgements: This work was supported by the Civil-Military Technology Cooperation Program of Korea (Project no. N04140260). Authors acknowledge cooperation of NNFC Korea for the fabrication of OPA devices.

3D Integrated Optical Vortex Devices

Xinlun Cai[1*]

[1]State Key Laboratory of Optoelectronic Materials and Technologies and School of Physics and Engineering, Sun Yat-sen University, Guangzhou 510275, China.

[*]caixlun5@mail.sysu.edu.cn

Orbital angular momentum (OAM) multiplexing is a promising technology to expand the transmission capacity of either free space optical communication or fiber communication. Previously, we have demonstrated a compact silicon photonic OAM emitter capable of generating single but arbitrary OAM states. The operation principle of the device is based on the coupling of whispering gallery modes (WGMs) in a micro-ring resonator to OAM modes through an angular grating embedded within the micro-resonator. This device is capable of generating any OAM states by simply changing the input wavelength. However, this wavelength dependent approach made it difficult to achieve OAM multiplexing, which is of vital importance for the application of OAM-based optical communications.

Here, we demonstrate a 3D integrated OAM multiplexer, which can be used to combine or multiplexing up to four OAM modes. As shown in Fig. 1, the device consists of two layers of silicon microring resonator with angular grating embedded in the innerwall. The 3D structure is fabricated through a wafer bonding process.

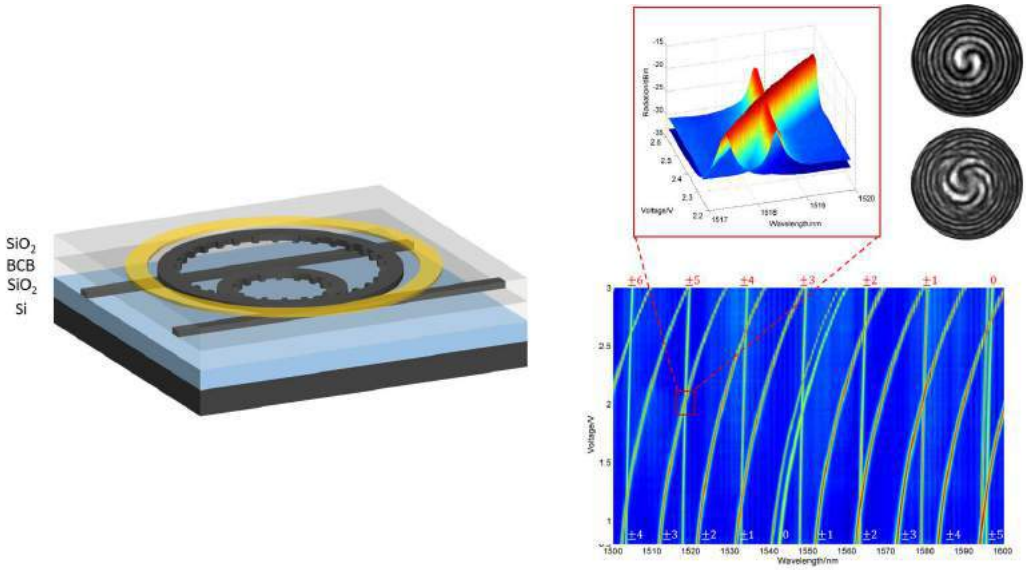

Fig 1 The device layout and the measurement results

Experimental investigation of ultra-compact Si-GST hybrid photonic devices

Linjie Zhou*, Hanyu Zhang, Liangjun Lu, and Jianping Chen
State Key Laboratory of Advanced Optical Communication Systems and Networks
Department of Electronic Engineering, Shanghai Jiao Tong University, Shanghai 200240, China
*corresponding author: ljzhou@sjtu.edu.cn

Abstract- We report our recent progress on hybrid silicon photonic devices based on the phase change of GST. The Si-GST hybrid waveguide loss is extracted from the measurement of straight waveguides and ring resonators. A MZI switch enabled by the electrically-driven GST is realized. Experimental results reveal that the GST can undergo repeatable phase change induced by electrical pulses, giving rise to a switching extinction ratio variation of 5 dB.

To make a large-scale photonic integrated circuit, the individual optical components should be as compact as possible to reduce the chip footprint and power consumption. Silicon-on-insulator based photonic devices are extremely attractive due to its compactness and compatibility with microelectronic circuits using the well-developed CMOS technology [1, 2]. The active tuning in silicon is usually realized by the thermo-optic or free-carrier plasma dispersion effects. However, the thermal effect is slow in the order of microsecond [2]. The free-carrier effect, on the other hand, is fast but relatively weak with a refractive index change only in the order of 0.001[1]. Resonant structures, such as ring resonators, disk resonators, Bragg gratings and photonic crystals, can be employed to reduce the device size [3, 4]. However, this is achieved with the sacrifice of the optical bandwidth. The resonant devices are quite sensitive to temperature change, leading to potential stability issue [5]. One solution to overcome the fundamental limitation in today's silicon photonic devices is to use the exotic materials with a much larger refractive index modulation. The phase-change material (PCM) is one of the materials that can serve for this purpose. There exist at least two phases with significantly different optical properties, which can be repeatedly and rapidly cycled. The $Ge_2Sb_2Te_5$ (GST) is a widely-used PCM in which the phase change can be thermally, optically or electrically induced potentially with an ultrahigh speed. The GST possesses the "self-holding" feature, and consequently there is no static power consumption to maintain the states.

We first investigated the phase change of a GST thin film by using thermal stimulus. Crystalline GST turns to amorphous when it is heated beyond the melting point and quenched rapidly. On the contrary, amorphous GST turns to crystalline when it is heated to above the crystallization temperature (but below the melting temperature). The change in the real part of the refractive index leads to phase shift, while the change in the imaginary part leads to attenuation. We measured straight waveguides and micro-ring resonators to extract the relevant parameters of the GST. The silicon waveguide dimension is 500 nm (width) by 220 nm (height). The GST film thickness is 10 nm, covering a part of the silicon waveguide. By comparing the transmission spectra before and after GST phase change, we obtained the loss and phase change of the GST-covered waveguide section. The GST phase change from the amorphous state to the crystalline change was enabled by heating the devices at 200 °C for 3 min on a hot-plate. For the straight waveguides, we extracted the change in attenuation from the measured waveguide loss. It revealed that the waveguide loss increases by around 1.4 dB after phase change

from the amorphous to the crystalline state for every micron length of active waveguide. For the micro-ring resonator, we fitted the measured resonance spectrum with the resonator transfer function. Upon fitting, we obtained the waveguide losses of 1.38 dB/μm and 0.1 dB/μm for the crystalline and amorphous states, respectively. The phase change induced resonance wavelength shift per unit length of GST was measured to be 0.375 nm/um.

We next implemented a Mach-Zehnder interferometer (MZI) optical switch based on the phase change of electrically-driven GST as shown in Fig. 1. One arm waveguide of the MZI is partially covered with a stack of ITO/GST/ITO film. As the GST has a self-holding characteristic, the two switching states can be maintained without any electrical supply. Electrical power is only consumed during the dynamic phase change process, leading to much lower power consumption if the switching frequency is low. We performed the phase change experiment using electrical pulses as stimuli. Preliminary experimental results reveal that the GST can undergo repeatable phase change induced by electrical pulses. The phase change has a significant effect on the optical performance of the MZI switch. The extinction ratio varies by 5 dB. The proof-of-principle experiment proves the possibility of hybrid integration of GST with silicon waveguides for potential ultra-compact photonic integration.

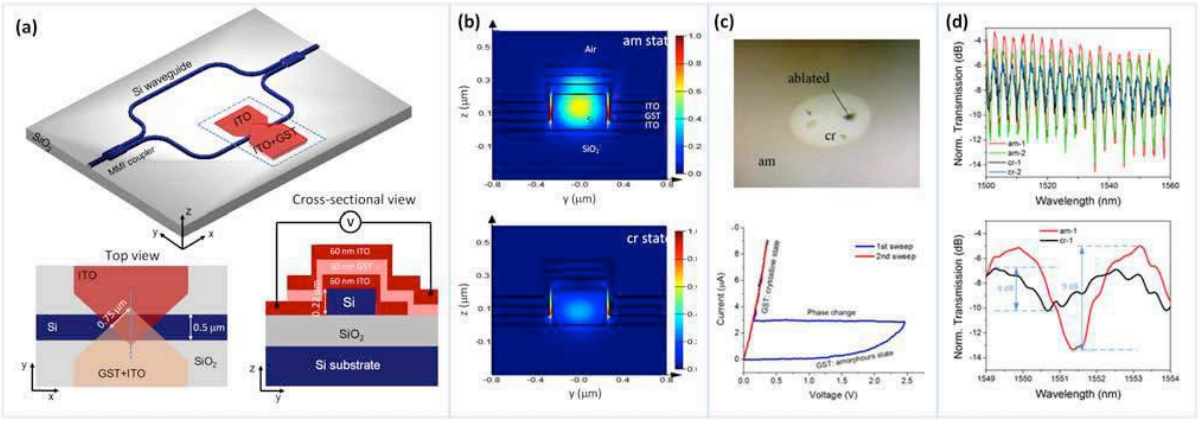

Fig. 1. (a) Schematic structure of the optical switch using GST. (b) Simulated electric-field intensity profiles of the active waveguide when the GST is at the amorphous and the crystalline states. (c) I-V curve measurement before and after GST phase change. (d) Measured transmission spectra of the MZI in two cycles of GST phase change.

References:

[1]. L. Lu, S. Zhao, L. Zhou, D. Li, Z. Li, M. Wang, X. Li, and J. Chen, "16x16 non-blocking silicon optical switch based on electro-optic Mach-Zehnder interferometers," Opt. Express **24**, 9295-9307 (2016).

[2]. S. Zhao, L. Lu, L. Zhou, D. Li, Z. Guo, and J. Chen, "16x16 silicon Mach-Zehnder interferometer switch actuated with waveguide microheaters," Photon. Res. **4**, 202-207 (2016).

[3]. L. Lu, L. Zhou, Z. Li, D. Li, S. Zhao, X. Li, and J. Chen, "4×4 silicon optical switch based on double-ring assisted Mach-Zehnder interferometers," IEEE Photon. Technol. Lett. **27**, 2457-2460 (2015).

[4]. Z. Zou, L. Zhou, X. Li, and J. Chen, "60-nm-thick basic photonic components and Bragg gratings on the silicon-on-insulator platform," Opt. Express **23**, 20784-20795 (2015).

[5]. L. Lu, L. Zhou, X. Sun, J. Xie, Z. Zou, H. Zhu, X. Li, and J. Chen, "CMOS-compatible temperature-independent tunable silicon optical lattice filters," Opt. Express **21**, 9447-9456 (2013).

A flat-top bandpass mode order convertor based on two dimensional Bragg gratings

Yuechun Shi*, Rulei Xiang, and Xiangfei Chen
National Laboratory of Solid State Microstructures & Collaborative Innovation Center of Advanced Microstructure & College of Engineering and Applied Sciences, Microwave-Photonics Technology Laboratory, Nanjing University, Nanjing, 210093, China
*corresponding author: shiyc@nju.edu.cn

Abstract- We propose a new scheme for forward mode order conversion in a multimode waveguide based on cascaded two dimensional Bragg gratings. Usually, the waveguide grating structure, i.e. long period grating or Bragg grating with small period, is an important way to realize mode order conversion for its advantages such as bandpass conversion and easy to control wavelength. But for the long period structure, the device length is very long due to the long period in nature and the conversion spectrum is hard to realize flat-top shape. While for the Bragg grating structure, only backward conversion can be realized up to now. In order to overcome these issues, we employ two Bragg reflections along with twice mode conversions to achieve a flat-top bandpass and forward convertor. Thinks to the Bragg grating structure, the device size is much more compact than that based on long period grating. And the wavelength and bandwidth can be easily adjusted by grating parameters. The simulation results show high mode conversion efficiency (nearly 100%) and low inter-modal crosstalk (<-20dB). In addition, the improved convertors can be obtained by carefully designing grating profiles, such as apodizaion structure for rectangle shape conversion spectrum. Therefore, we believe the proposed scheme may provide a new method for high-performance mode order converter in on-chip mode-division multiplexing.

Figure 1(a) shows the schematic of the proposed converter from mode TE_1 to TE_2 as an example. It includes two BGs, i.e., G_{02} (front section) and G_{01} (rear section). Here, G_{01} and G_{02} are used for reflection-type mode conversion between TE_0 and TE_1, and between TE_0 and TE_2, respectively. The waveguide is designed to support the first-three-order transverse electric (TE) modes, which is sandwiched by an upper silicon-dioxide cladding and a buried oxide (BOX) layer. The whole mode conversion process is described in the following. When the mode TE_1 with a specific wavelength is launched and propagates in the waveguide, it first passes through G_{02} without any reflection until gets to G_{01}. Then, TE_1 is reflected along with mode conversion to TE_0. The resulting mode TE_0 backward propagates and gets to G_{02}. Then, the following mode conversion from TE_0 to TE_2 occurs in G_{02} and subsequently the mode TE_2 pass through the G_{01}. Thus the forward mode conversion from TE_1 to TE_2 is achieved. Figure 1(b) shows the corresponding phase match condition. This condition for two arbitrary order mode conversion from mode i to mode j can be expressed as,

$$\beta_j = \beta_i + K_{mj} - K_{im}. \tag{1}$$

where, $\beta_i = 2\pi n_i/\lambda$, $\beta_j = 2\pi n_j/\lambda$, $\beta_m = 2\pi n_m/\lambda$, and $K_{im}=2\pi/\Lambda_{im}$, $K_{mj}=2\pi/\Lambda_{mj}$. n_i, n_j and n_m are the effective refractive indices of i_{th}, j_{th} and m_{th} order mode, respectively. Λ_{im} and Λ_{mj} are the grating periods for mode conversion between the i_{th} and m_{th} order modes, the m_{th} and j_{th} order modes

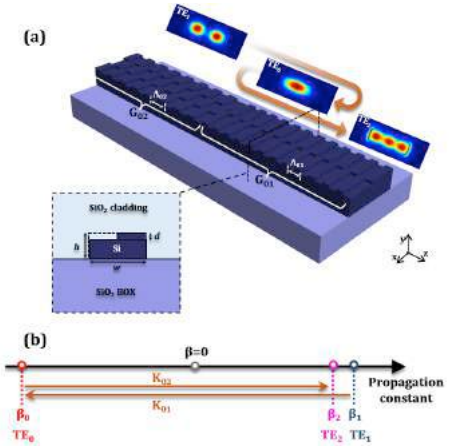

Fig. 1. Schematic of (a) the proposed device structure for conversion from mode TE1 to TE2. The detailed figure shows the cross section of the waveguide. (b) The corresponding phase matching condition.

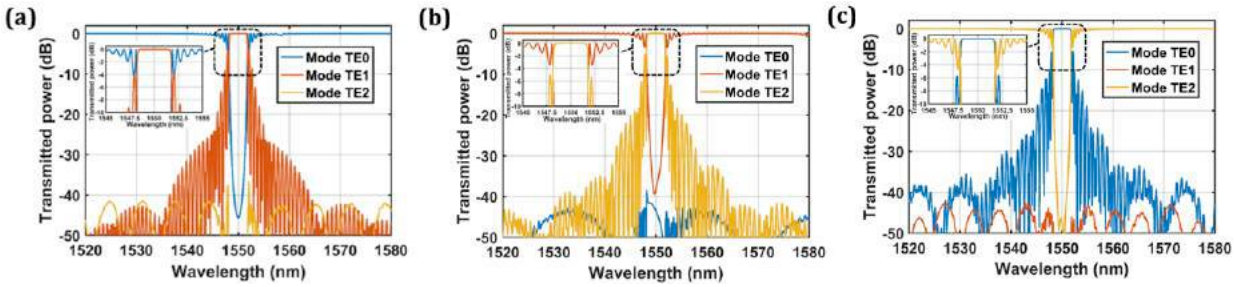

Fig. 2. Transmission spectra for the forward conversions (a) from mode TE_0 to TE_1, (b) from mode TE_1 to TE_2, and (c) from mode TE_2 to TE_0, respectively. The inserted figures show the detailed spectra around the Bragg wavelength.

Arbitrary two gratings from G_{01}, G_{02} and G_{12} are used to achieve one of the three kinds of forward mode conversions. As shown in Fig. 2(a), the mode conversion is wavelength-dependent due to the phase match condition. The designed Bragg wavelengths are both 1550 nm and the bandwidth is ~ 3.7 nm. Within the bandwidth, the mode TE_0 is converted to mode TE_1 with a high conversion efficiency (nearly 100%) and the inter-modal crosstalk is very low (<-20dB). By combining the G_{02} and the G_{01}, we can also obtain the mode conversion from mode TE_1 to TE_2. Simulation results show that the bandwidth is also about 3.7 nm. High conversion efficiency and low inter-modal crosstalk are obtained as shown in Fig. 2(b). Figure 2(c) shows the conversion spectra from mode TE_2 to mode TE_0 with the similar performances. Here, G_{01} and G_{12} are used.

Acknowledgements, National Natural Science Foundation of China (61306068), Jiangsu Province Natural Science Foundation of China (BK20141168, and BK20140414), the National "863" project of China (2015AA016902).

Metasurfaces and 2D Metamaterials in microwave region

Generation of vector beams based on Field Transformation metasurface.

Cheng Wang, Ke Chen, Junming Zhao*, and Yijun Feng
Department of Electronic Engineering, School of Electronic Science and Engineering
Nanjing University, Nanjing,China
*jmzhao@nju.edu.cn

Abstract-The microwave beam whose polarization is radially polarized is called vector beam. Because of its unique properties and potential applications, there has been a rapid increase of the number of publications on vector beams. Different approaches have been proposed to generate vector beams through these studies. Here, for the first time, we use one field transformation(FT)[1] approach to design a metasurface which can generate vector beams. Such vector beam generation metasurface can be easily realized with 3D printer.

Vector beam has great potentialities in various scientific and engineering realms, and it has been extensively explored in helicon inspection and microwave devices. Recently, many types of vector beams have been proposed, such as cylindrical vector beam[2], double-ring-shaped vector beams[3], tractor beams[4] etc. However, most of these vector beam generation methods have limitations that the generation devices are not easy to fabricate. Our previous studies have shown a remarkable degree of fundamental and conceptual advances by applying the FT technique in the design of wave-plates utilizing artificial anisotropic dielectrics[5]. Thus, we utilize the FT theory into designing metasurfaces which can generate vector beam. As Fig 1 shown, the permittivity of the red material is 10, its height d1 is 1mm and the permittivity of the blue material is 1, its height d2 is 1.5mm. We arranged the two materials intersecting along one direction periodically, and gradually rotate 8 different angles, which are -78.75° ,-56.25° ,-33.75° ,-11.25° ,11.25° ,33.75° ,56.25° ,78.75° , respectively. Then we can get 8 different portions that can produce different outgoing polarization directions. The whole metasurface is shown in Fig. 2, whose thickness is 12.5mm, and simulation result at 11.5GHz is shown in Fig 3. We can see that as the whole effect of the combination of the 8 portions, one radially polarized outgoing beam is generated. Besides such metasurface can be easily fabricated through 3D printer. The effective permittivity of each metasurface portion can be achieved based on effective media theory.

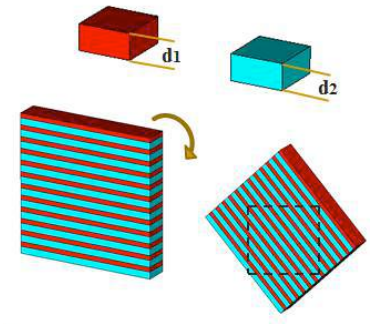

Fig 1. Schematic diagram

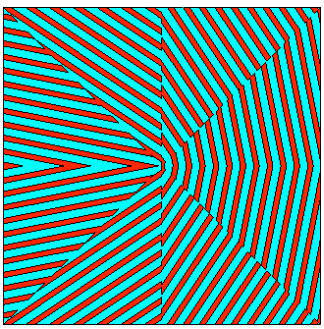

Fig 2. The metasurface to generate vector beam

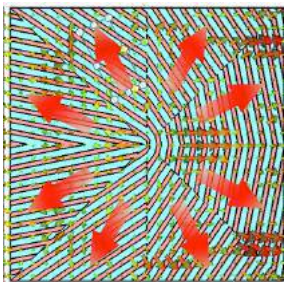

Fig 3. Simulated result

Conclusion

In this paper we propose a new method that utilizing combined metasurfaces through FT theory to generate vector beam, and the metasurface can be easily fabricated by 3D printer.

Acknowledgments

This work is partially supported by the National Nature Science Foundation of China (61671231, 61571218, 61571216, 61301017, 61371034), and partially supported by PAPD of Jiangsu Higher Education Institutions and Jiangsu Key Laboratory of Advanced Techniques for Manipulating Electromagnetic Waves.

REFERENCES

1. Fu Liu, Zixian Liang, and Jensen Li, "Manipulating Polarization and Impedance Signature: A Reciprocal Field Transformation Approach", *Phys. Rev. Lett*, 111, 033901,2013.
2. Qiwen Zhan, "Cylindrical vector beams: from mathematical concepts to applications", *Advances in Optics and Photonics 1*, DOI:10.1364/AOP.1.000001, 1–57,2009.
3. Huan Chen, Xiaohui Ling, Zhihong Chen,"A method for generating double-ring-shaped vector beams", *Chin. Phys. B* ,Vol. 25, No. 7,074201,2016.
4. Carl Pfeiffer, Anthony Grbic "Generating stable tractor beams with dielectric metasurfaces", *Physical Review,* 91, 115408 ,2015.
5. Junming Zhao, Lianhong Zhang, Jensen Li, "A Wide-angle Multi-Octave Broadband Waveplate Based on Field Transformation Approach", *Scientific Reports,*5:17532 ,DOI: 10.1038/srep17532,2015.

Omega-bianisotropic metasurfaces: from controlling radiative fields to manipulating evanescent modes

A. Epstein

Andrew and Erna Viterbi Faculty of Electrical Engineering,
Technion - Israel Institute of Technology, Haifa 3200003, Israel
epsteina@ee.technion.ac.il

Abstract— Omega-bianisotropic metasurfaces (O-BMSs) have been shown to be able to implement any locally power-conserving field transformation via passive lossless meta-atoms. In previous work, we have utilized this theorem to design O-BMSs realizing reflectionless refraction and beam splitting, and perfect reflection. In this talk, we propose a novel O-BMS waveguide, whose eigenmodes are quadruples of surface waves, allowing manipulation of near-field features.

Metasurfaces, ultrathin planar arrangements of subwavelength polarizable particles (meta-atoms), have been intensively investigated in recent years for a myriad of beam manipulation applications [1]. Examining the fundamnetal problem of engineered refraction, early reports have pointed out that to reduce undesirable reflections, it is required, as per the equivalence principle, to use Huygens' metasurfaces (HMSs), allowing induction of *both* electric and magnetic surface currents [2–4]. Nonetheless, subsequent investigations revealed that to guarantee realistic (passive and lossless) design specifications, the field transformation supported by the HMS should satisfy the local power conservation and local impedance equalization conditions [5]. The latter implies that certain reflections are required to compensate the impedance mismatch between the fields on the HMS facets [4].

More recently, we have shown that this restriction can be alleviated by breaking the HMS meta-atom symmetry, introducing omega-type magnetoelectric coupling [6]. The resultant omega-bianisotropic metasurfaces (O-BMSs) are characterized by their electric surface impedance, magnetic surface admittance, and magnetoelectric coupling coefficient, indicating that applied electric fields excite *both* electric and magnetic surface currents, and analogously for magnetic fields [1]. Harnessing this additional (magnetoelectric) degree of freedom, we have proven that *any* (given) field transformation $\{E_x^< (y,z), H_y^< (y,z)\} \leftrightarrow \{E_x^> (y,z), H_y^> (y,z)\}$ which *locally* conserves the real power, i.e., for which $\Re\{E_x^< (y,z)\, H_y^{<*} (y,z)\}_{z\to 0^-} = \Re\{E_x^> (y,z)\, H_y^{>*} (y,z)\}_{z\to 0^+}$, $\forall y \in \mathbb{R}$, can be implemented via a passive lossless O-BMS situated at $z = 0$, whose constituents are given in [6].

While the theorem can be straightforwardly invoked to design reflectionless *refracting* O-BMS [6] (independently derived in [7]), achieving accurate designs becomes less trivial when reflectionless beam splitting or "perfect" engineered *reflection* are considered [7,8]. In these cases, the interference between the incident and (desirable) scattered modes yields non-trivial power profiles on the O-BMS facets, generally difficult to match. In [9] we have proposed an unconventional approach to tackle this problem, requiring auxiliary surface waves (SWs) to be induced by the O-BMS. While the SWs do not affect the functionality in the far field, they can be used to manipulate the flow of real power via interference with the incident and scattered modes. Indeed, by judicious stipulation of the SW properties, we were able to achieve the required local power conservation, leading to accurate optimal analytical designs of passive lossless O-BMSs for these two functionalities [9].

Specifically, to implement engineered plane-wave reflection, we have utilized two SWs propagating on the top facet, the interference between which requires power to be drawn from the lower half-space in the first half of the interference period, and pushes it back downwards at the other half-period; this power profile exactly matches the one exhibited by the interfering incident and anomalously reflected plane waves on the bottom facet [9]. This solution highlighted the possibility to sustain power circulation across the O-BMS facets, supported by interfering SWs.

Inspired by this result, we propose herein a novel *penetrable* O-BMS SW waveguide (SWG), designed to guide a pair of SWs on each of its facets [four SWs overall, Fig. 1(a)]. The SWs below and above the metasurface can have, in general, different amplitudes, propagation constants, and decay coefficients, and they exchange power via the O-BMS while propagating along it. Interestingly, the eigenmodes of this SWG are quadruples of SWs, the properties of which are tailored by the O-BMS design. To synthesize it, we stipulate the fields above and below the O-BMS to follow

$$E_x^>(y,z) = E_1^+ e^{-\alpha_1^+ z} e^{-jk_{t,1}^+ y} + jE_2^+ e^{-\alpha_2^+ z} e^{-jk_{t,2}^+ y};\;\; E_x^<(y,z) = E_1^- e^{\alpha_1^- z} e^{-jk_{t,1}^- y} + jE_2^- e^{\alpha_2^- z} e^{-jk_{t,2}^- y} \quad (1)$$

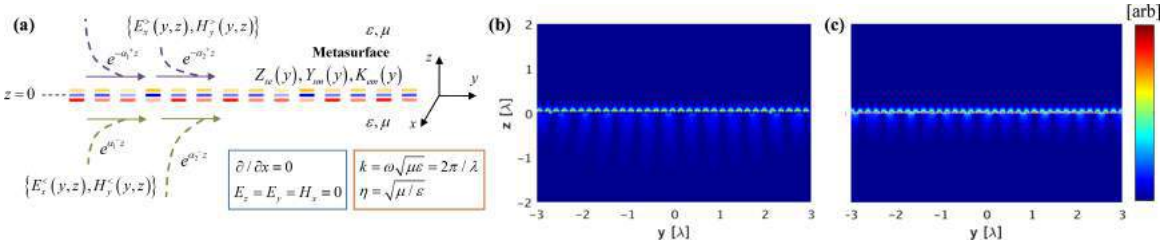

Figure 1: (a) O-BMS SWG configuration. (b) Simulated and (c) analytical field distribution $|\Re\{E_x(y,z)\}|$ of the SWG designed in the text (zoomed in around $y \in [-3\lambda, 3\lambda]$).

with complex amplitude $E_n^{\pm}$, transverse wavenumbers $k_{t,n}^{\pm} > k$, and corresponding decay coefficients $\alpha_n^{\pm} = (k_{t,n}^{\pm 2} - k^2)^{1/2}$. To guarantee local power conservation, the SW parameters must satisfy

$$\left(\alpha_2^+ - \alpha_1^+\right)\left|E_1^+ E_2^+\right| = -\left(\alpha_2^- - \alpha_1^-\right)\left|E_1^- E_2^-\right| \quad \wedge \quad \left(k_{t,2}^+ - k_{t,1}^+\right) = \pm\left(k_{t,2}^+ - k_{t,1}^+\right) \quad \wedge \quad \xi^+ = \pm\xi^-, \qquad (2)$$

where the phase shifts $\xi^{\pm}$ are defined as $E_1^{\pm} E_2^{\pm *} \triangleq \left|E_1^{\pm} E_2^{\pm}\right| e^{j\xi^{\pm}}$. Finally, the SW quadruple of (1), with parameters adhering (2), is substituted into the formulas in [6] to evaluate the O-BMS design.

To verify this new waveguiding concept, we have followed the outlined procedure and designed an O-BMS SWG that simultaneously guides SWs with long ($\alpha_1^+ = \alpha_2^- = 16.78[\lambda^{-1}]$) and short ($\alpha_2^+ = \alpha_1^- = 4.00[\lambda^{-1}]$) evanescent tails, with different balance on each facet ($E_1^+/E_2^+ = 46.3$, $E_2^-/E_1^- = 0.463$). A 25λ-long O-BMS SWG was defined in ANSYS HFSS, using abstract three-layer impedance sheet structures to implement the O-BMS meta-atoms (*cf.* [6,9]), excited by an electric line source at $y = -12.5\lambda$. Comparison between full-wave simulated [Fig. 1(b)] and analytically-predicted [Fig. 1(c)] field distributions reveals good agreement, validating our theoretical concept.

Although extensive research has been conducted on metasurface-based SWGs in the past decade, it was restricted to *impenetrable* structures, and focused on controlling the trajectories of the SWs, or their coupling to leaky-wave radiation [10]. In contrast, the ability to support propagation of "surface wave packets" on the *penetrable* O-BMS holds great potential for generating exotic near-field features by controlling the interference between the guided evanescent waves.

REFERENCES

1. Tretyakov, S. A., "Metasurfaces for general transformations of electromagnetic fields," *Phil. Trans. R. Soc. A*, Vol. 373, 20140362, 2015.
2. Pfeiffer, C. and A. Grbic, "Metamaterial Huygens' surfaces: tailoring wave fronts with reflectionless sheets," *Phys. Rev. Lett.*, Vol. 110, No. 19, 197401, 2013.
3. Monticone, F., N. M. Estakhri and A. Alù, "Full control of nanoscale optical transmission with a composite metascreen," *Phys. Rev. Lett.*, Vol. 110, No. 20, 203903, 2013.
4. Selvanayagam, M. and G. V. Eleftheriades, "Discontinuous electromagnetic fields using orthogonal electric and magnetic currents for wavefront manipulation," *Opt. Express*, Vol. 21, No. 12, 14409–14429, 2013.
5. Epstein, A. and G. V. Eleftheriades, "Huygens' metasurfaces via the equivalence principle: design and applications," *J. Opt. Soc. Am. B*, Vol. 33, A31–A50, 2016.
6. Epstein, A. and G. V. Eleftheriades, "Arbitrary power-conserving field transformations with passive lossless omega-type bianisotropic metasurfaces," *IEEE Trans. Antennas Propag.*, Vol. 64, No. 9, 3880–3895, 2016.
7. Asadchy, V. S., M. Albooyeh, S. N. Tcvetkova, A. Díaz-Rubio, Y. Ra'di and S. A. Tretyakov, "Perfect control of reflection and refraction using spatially dispersive metasurfaces," *Phys. Rev. B*, Vol. 94, 075142, 2016.
8. Mohammadi Estakhri, N. and A. Alù, "Wave-front transformation with gradient metasurfaces," *Phys. Rev. X*, Vol. 6, No. 4, 041008, 2016.
9. Epstein, A. and G. V. Eleftheriades, "Synthesis of passive lossless metasurfaces using auxiliary fields for reflectionless beam splitting and perfect reflection," *Phys. Rev. Lett.*, Vol. 117, 256103, 2016.
10. Maci, S., G. Minatti, M. Casaletti and M. Bosiljevac, "Metasurfing: Addressing waves on impenetrable metasurfaces," *IEEE Antennas Wireless Propag. Lett.*, Vol. 10, 1499–1502, 2011.

Terahertz optical properties of planar all-carbon metamaterials fabricated by laser drawing

M. S. Komlenok[1, 2*], S. P. Lebedev[1], G. A. Komandin[1], S. G. Tikhodeev[1], and V. I. Konov[1, 2]

[1]A. M. Prokhorov General Physics Institute RAS, Russian Federation

[2] National Research Nuclear University MEPhI (Moscow Engineering Physics Institute), Russian Federation

[*]corresponding author: komlenok@nsc.gpi.ru

Abstract-We report on the optical properties of metal-less diamond-based planar metamaterials in terahertz (THz) frequency range. A conductive 200 nm-thick graphitized layer was formed on a surface of CVD polycrystalline diamond by excimer KrF-laser. Optical properties of a diamond plate with a graphitized layer were measured and simulated according to the Drude model. A polarizer with a graphitized subwavelength grating as a prototype of metamaterial device was tested in THz range and had shown different loss for orthogonal polarizations.

Recently, significant progress has been achieved in technologies of generation and detection of terahertz (THz) radiation. As the result a new class of high power sources has been appeared – free electron lasers [1]. These high power coherent sources need new elements with high damage threshold to manipulate radiation. Composite materials, consisted of conductive areas on the surface of dielectric, called metamaterials, are the best candidate for this purpose. Among the methods of fabrication of planar metamaterials may be pointed out following: lithography [2], laser printing [3] and laser-induced forward transfer [4]. However all known for today methods propose to cover conductive layer (metal film) on the dielectric substrate, that induce number of limitations on produced composites (adhesion, damage threshold) and on fabrication techniques in turn. In this work another solution for the formation of conductive planar structures on the dielectric substrate is proposed. It is based on laser-induced graphitization of the diamond surface. In this case fabricated metamaterials will be completely carbon, and conductive graphitized structures will be strong bonded with diamond substrate, that will provide high adhesion and thermal contact –so valuable for the use in high power beam. And the diamond plate will serve as cooler and withdraw heat from working metasurface. The aim of this work was to fabricate graphitized structures on the transparent CVD diamond substrates by means of excimer KrF-laser and to investigate their optical properties in THz frequency range.

In the first step the surface area with size of 4200x4000 μm^2 was irradiated with excimer laser at the fluence of 35 J/cm^2, which was significant larger than the threshold of graphitization of polycrystalline diamond. As the result a graphitized layer with thickness of 200 nm was formed on diamond. Transmittance spectra of the pure diamond with thickness of 574μm and formed graphitized layer on a diamond surface were analyzed in the range of 10-1000 cm^{-1} by Fourier spectrometer BRUKER IFS113v. Modeling of transmittance spectra was carried out according to the formulas for transmission coefficient T as a function of conductivity σ for single – or bilayer medium and plane electromagnetic waves [5]. The dielectric properties of the graphitic layer were simulated according to the Drude model. Fitting the values of scattering rate γ and plasma frequency ν_p has provided to minimize the deviation of the calculated transmittance spectrum from the experimental values for a graphitized layer on the diamond substrate. The best result was achieved for following values: γ=5000 cm^{-1} and ν_p=16340 cm^{-1}. Obtained value of the optical conductivity σ_{DC}=890 $Ohm^{-1}cm^{-1}$ of the graphitized layer in THz frequency

range is in good agreement with the value, measured by the four-probe method.

To demonstrate the possibilities of proposed laser method for the fabrication of metamaterials, the periodic grid, consisting of graphitized lines of a width of 15 μm, a length of 4400 μm and a period of 30 μm, was made by the same laser technique on the surface of the diamond. The obtained sample should act as a polarizer for radiation in the THz frequency range. Transmittance spectra of the structured sample were measured on the spectrometer "Epsilon" [6] in the range of 31 – 39 cm^{-1} for parallel (s-) and perpendicular (p-) orientation of polarization of the radiation relative to the graphitized lines on the diamond surface and are presented in figure 1. It is seen from the obtained spectra that the grid is transparent for waves with p-polarization, and is reflective for waves with s-polarization. Thus, the periodic subwavelength grid created by the laser irradiation acts as a metamaterial polarizer for the THz radiation.

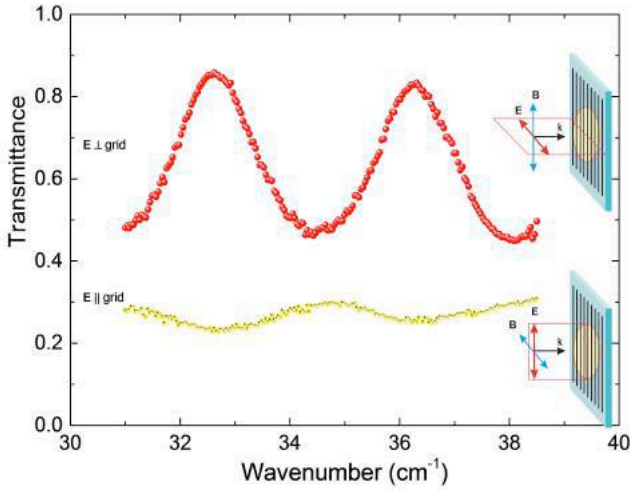

Figure 1. Transmittance of the periodic graphitized grid on the diamond surface for different polarizations of probe beam in THz range.

Acknowledgements This work was supported by the Russian Science Foundation (project "Carbon photonics"). M.S. Komlenok acknowledges funding from Russian Foundation for Basic Research grant 16-32-60179.

REFERENCES

1. Kulipanov, G.N., et al., "Novosibirsk Free Electron Laser-Facility Description and Recent Experiments," *IEEE Transactions on Terahertz Science and Technology*, Vol. 5, No. 5, 798-809. 2015.
2. Gwinner, M.C., et al., "Periodic Large-Area Metallic Split-Ring Resonator Metamaterial Fabrication Based on Shadow Nanosphere Lithography," *Small*, 2009. Vol. 5, No. 3, 400-406, 2009.
3. Walther, M., et al., "Terahertz metamaterials fabricated by inkjet printing," *Appl Phys Lett*, Vol. 95, No. 25, 251107, 2009.
4. Kim, H., et al., "Fabrication of terahertz metamaterials by laser printing," *Optics Letters*, Vol. 35, No. 23, 4039-4041, 2010.
5. Dressel, M. and G. Grüner, *Electrodynamics of Solids: Optical Properties of Electrons in Matter*, Cambridge University Press, Cambridge, 2002.
6. Kozlov, G. and A. Volkov, *Millimeter and submillimeter spectroscopy of solids: Topics in applied physics*, Springer, Berlin, 1998

Inductively reconfigurable periodic structures for synchronous and wideband tuning

Yih-Dar Chen and Chien-Hao Liu

National Taiwan University, Taipei, Taiwan
r04522545@ntu.edu.tw and cliu82@ntu.edu.tw

Abstract— In this research, we propose a planar reconfigurable periodic structure that its frequency response can be tuned continuously over a wide frequency range. Each element is composed of three metallic strips pinned as a deformable triangle acting as an equivalent series LC resonator illuminated by vertically-polarized normal incident electromagnetic waves. By manipulating the induced surface current path on each element, the resulting variations of the equivalent inductance can shift the resonant frequency. In addition, a linkage mechanism is exploited in this research to synchronously alter each element for large area applications. Two prototypes with the dimension of 15 by 18 unit cells was designed, fabricated, and examined with field tests. It was demonstrated that the resonant frequency of the fabricated structure was shift from 5.6 GHz to 7.5 GHz with a wide range of 1.9 GHz (29 % in terms of fractional bandwidth). The research results are expected to be beneficial for wideband reconfigurable periodic structures and large-area applications.

1. INTRODUCTION

In recent years, various techniques have been exploited for developing reconfigurable periodic structures that their frequency responses can be tuned continuously or switched on/off by manipulating each element. Most periodic structures are composed of equivalent LC resonators for providing band-pass or band-stop responses. Since the resonant frequency is inversely proportional to the square root of inductance and capacitance, the resonant frequency can be shifted by altering the equivalent capacitance such as varactors [1] and liquids. However, these methods have some disadvantages including bulky, complicated manufacturing, and parasite harmonics.

In this research, we propose a planar inductively reconfigurable periodic structure that its frequency response can be tuned continuously by varying the equivalent inductances. Each element of the proposed periodic structure is composed of three metallic strips pinned as a triangle with a gap at one edge shown in Fig. 1. The vertically strips are fixed in free space and the two side strips deformable due to the combinations of the slots and pins. For normal incident electromagnetic (EM) waves with vertically polarizations, the induced capacitive gaps and the surface currents on the strips represent the capacitors and inductors of each unit forming a series LC resonator with a band-stop response. The resonant frequency can be shifted by shrinking (short current pathes) and enlarging (long current pathes) the triangles shown in Fig. 1(a) and (b). For synchronously adjusting each unit cell, all the elements are connected via the mechanical linkages for large-area tuning applications.

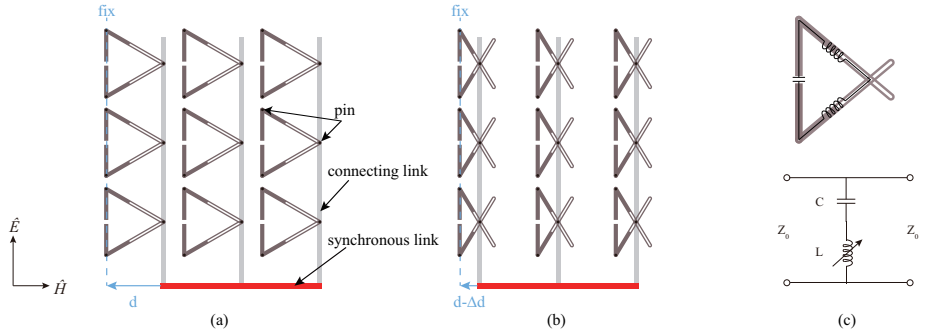

Figure 1: Schematic diagram of the proposed periodic structure under vertically-polarized normal incident EM waves (a) before and (b) after deformations. (c) The equivalent circuit model.

2. DESIGN

Fig. 1(c) shows the equivalent circuit model of the propose triangular element which is composed of a capacitive gap and variable inductor due to the induced surface current on the metallic strips under vertically-polarized EM waves. The resonant frequency was designed at 5.6 GHz before deformations via full-wave EM simulations and circuit simulation tools. As the triangle shrinks, the decrease of the induced current path on the metallic strips results in decrease of the inductance and increase of the resonant frequency shown in Fig. 2(c).

3. FABRICATIONS AND MEASUREMENTS

The proposed triangular periodic structure and the linkage were fabricated via chemical etching and laser cutting shown in Fig. 2(a). However, the linkage did not function correctly due to fabrication errors and tolerance which needed a second fabrication. In stead, three triangles with different sizes corresponding to the three tuning stages of the aforementioned periodic structure with the linkage was fabricated via PCB boards shown in Fig. 2(b). They were examined with the experimental setup reported in [2]. Fig. 2(c) shows the simulated and measured transmission coefficients before and after deformations. As can be seen, the resonant frequency was shifted from 5.6 GHz to 7.5 GHz with a wide range of 1.9 GHz (29 % in terms of fractional bandwidth).

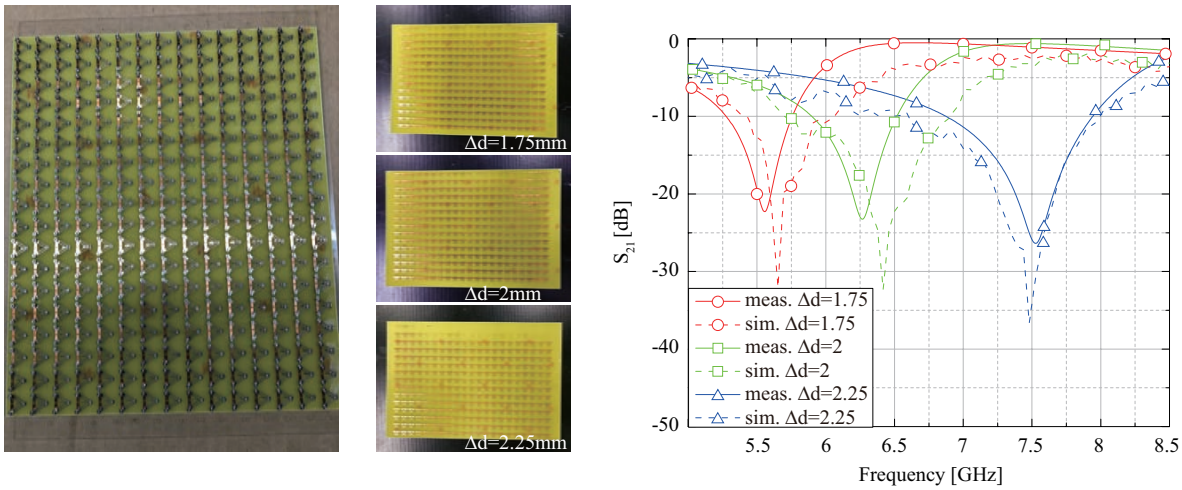

(a) (b) (c)

Figure 2: (a) The fabricated periodic structure with a linkage. (b) Three different triangular periodic structures fabricated on PCB corresponding to the three tuning stages of (a). (c) The simulated and measured transmission coefficients for the three triangles shown in (b).

4. CONCLUSION

In this research, we proposed a relatively large-area reconfigurable periodic structure. By altering the inductive surface current path of each unit cell, its resonant frequency could be shifted from 5.6 GHz to 7.5 GHz with a wide range. The research results are expected to be beneficial for wide-band tunable applications.

ACKNOWLEDGMENT

This work was supported by Ministry of Science and Technology, Taiwan, under funding No. 105-2221-E002-215.

REFERENCES

1. Mias, C. and Yap, J. H., "A Varactor-Tunable High Impedance Surface With a Resistive-Lumped-Element Biasing Grid," *IEEE Trans. Antennas Propag.*, Vol. 55, No. 7, pp. 1955–1962, 2007.
2. Hung, Y. C. and Liu, C. H., "Stretchable Frequency Selective Surfaces for Large-Area-Tuning and High-Power Applications," *International sympposium on antennas and propagation*, Sec. 116, No. 20383, Japan, 2016.

Exploiting Linkage Mechanisms for Synchronously Tunable Dual-Band Frequency Selective Surfaces with Large Areas

Yu-Chieh Hung and Chien-Hao Liu

National Taiwan University, Taipei, Taiwan
r04522543@ntu.edu.tw and cliu82@ntu.edu.tw

Abstract— In this research, we propose a double-rocker linkage mechanism for synchronously tuning the frequency responses of the dual-band FSSs with large areas. Each unit cell is composed of a patch and a loop forming a combination of a series and parallel resonators. Since the patches and loops are connected separately with two rocker linkages, their frequency responses can be synchronously tuned by two linear driving actuators. A prototype of the dual-band FSS with the dimensions of 16 by 16 unit cells was design, fabricated, and examined with field tests. By rotating the patches (loops) via the driving linkages, the pass-band (stop-band) was shifted 7.8% (11.4%). The research results are expected to be beneficial for large-area tuning and high-power microwave applications.

1. INTRODUCTION

Tunable frequency selective surfaces (FSSs) have long been used in modern communications and military applications for providing switching or continuous tuning of the frequency responses. Various tuning approaches have been proposed including electronics, liquid, plasma, memory alloy, and optics. However, the main challenge is to synchronously alter the frequency response of each unit cell for creating desired frequency deviations. For large-area FSSs, it may need millions of bias circuits or actuators to change the frequency response of each unit which is impractical. Take the commonly-used electronic approach as an example, an FSS operating at 10 GHz with a dimension of 1 m $\times$ 1 m and 1 period of 5 mm (i.e. 40,000 unit cells), it needs more than thousands of components for actuation. Therefore, in this research, we propose a dual-rocker linkages for mechanically tuning the frequency responses of the dual-band FSS shown in Fig. 1. Each unit cell is compose of a patch and a loop. For normal incident electromagnetic waves, the patch and loop correspond to the pass- and stop- bands of the FSS. In Fig. 1(a), all the patches and loops are connected separately via two linkage and controlled by two linear driving actuators. By rotating the patches via the driving linkage shown in Fig. 1(b), the corresponding pass-band can be tuned synchronously and continuously. In the other hand, the stop-band responses of the FSS can be tuned synchronously by rotating the the loops via the driving linkage shown in Fig. 1(c).

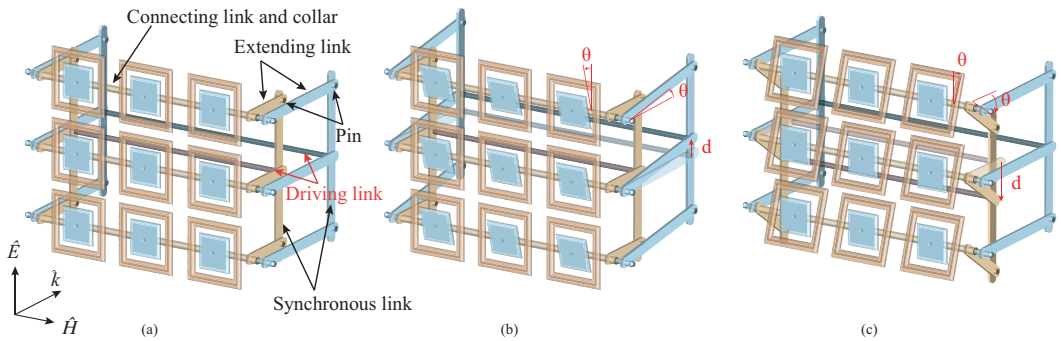

Figure 1: (a) The dual-band FSS composed of patches corresponding to the stop-band and loops corresponding to the pass band for normal incident electromagnetic waves. (b) The pass-band was tuned synchronously by rotating the patches based on the displacement of the driving linkage. (c) The stop-band was tuned synchronously by rotating the loops based on the displacement of the driving linkage.

2. DESIGNS AND FABRICATIONS

The propose dual-band FSS is composed of patches and loops forming a combination of series and parallel resonators illuminated by a normal incident electromagnetic waves shown in Fig. 3(a). The gap between the patch and the loop (loops) acts as an variable capacitor, C_2 (C_1), corresponding to the frequency shift of the pass-band (stop-band). A prototype was fabricated via standard PCB photolithography shown in Fig. 3(b).

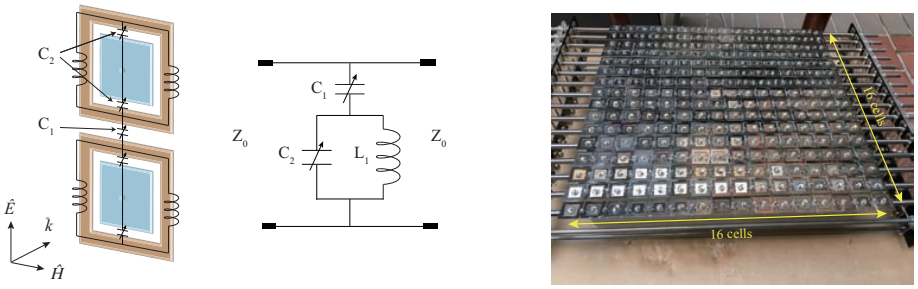

Figure 2: (a)The equivalent circuit model. (b) The photo of the prototype. The patches, loops, collar, and the connecting link were made of stainless metals. The rest components were made of acrylic.

3. MEASUREMENTS

The fabricated prototype was examined with an experiment setup reported in [1]. By synchronously rotating the patches, the pass-band shifted with a 7.8%. Similarly, by rotating the loops, the stop-band shifted with a 11.4%. It was demonstrated that by controlling the driving links separatively, the pass- and stop- bands of the dual-band FSS could be adjusted individually. The measured results (solid lines) deviated from the simulated results (dashed lines) due to fabrication errors.

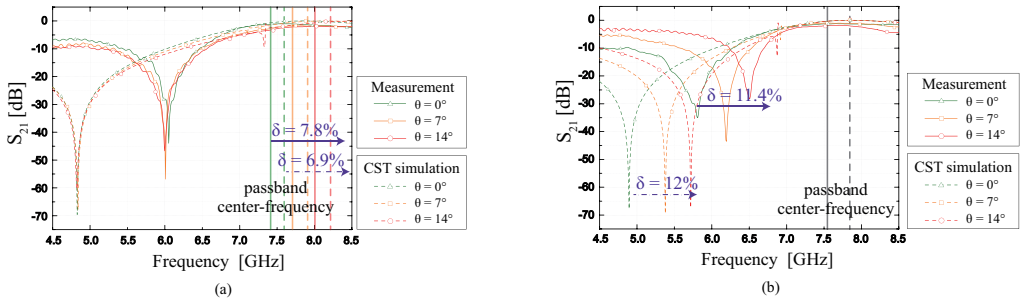

Figure 3: (a) Rotating the patches resulting in shifting of pass-band. (b)Rotating the loops resulting in shifting of stop-band.

4. CONCLUSION

In this research, we proposed a linkage-mechanism based tunable dual-band frequency selective surface with a large area of 16 by 16 unit cells (total: 256 unit cells). By individually recreating the displacements of the two driving linkages, the pass- and stop- bands could be continuously tuned with 7.8% and 11.4%, respectively. The research results are expected to be helpful for large scale tuning applications.

ACKNOWLEDGMENT

This work was supported by Ministry of Science and Technology, Taiwan, under funding No. 105-2221-E002-215.

REFERENCES

1. Hung, Y. C. and Liu, C. H., "Stretchable Frequency Selective Surfaces for Large-Area-Tuning and High-Power Applications," *International sympposium on antennas and propagation*, Sec. 116, No. 20383, Japan, 2016.

Active metasurface for reconfigurable reflector antennas

B. Ratni[1], A. de Lustrac[1,2], G.-P. Piau[3], and S. N. Burokur[4]

[1]Centre de Nanosciences et de Nanotechnologies, CNRS, Univ. Paris-Sud, Université Paris-Saclay, C2N – Orsay, 91405 Orsay cedex, France

[2]Université Paris Ouest, 92410 Ville d'Avray, France

[3]AIRBUS Group Innovations, 92150 Suresnes, France

[4]LEME, EA 4416, Université Paris Ouest, 92410 Ville d'Avray, France

[*]corresponding author: sburokur@u-paris10.fr

Abstract-A planar active metasurface composed of meta-atoms incorporating voltage-controlled varactor diodes, is used as reflector for microwave antenna applications. The dispersion responses of the cells are individually tailored for reconfigurability mechanisms. The phase characteristics of a several reflectors is engineered by judiciously controlling the bias voltage of the varactor diodes on the planar metasurface.

Metasurfaces have been proposed to manipulate light propagation [1]. They present the main advantage of having reduced profile and therefore reduced losses. By controlling the reflection and/or transmission characteristics of metasurfaces, they have been successfully implemented in planar lens antennas [2-4], cavity antennas [5-6], and leaky-wave antennas [7] to achieve high directivity.

In this study, we propose a planar reflecting metasurface as an interesting alternative to classical reflectors. Passive metasurfaces in most cases operate for a single functionality and at a single frequency or on a very narrow frequency band and therefore present limitations in terms of bandwidth due to the intrinsic characteristics of resonant cells. An active metasurface allows integrating multiple functionalities into a single metasurface, and paves the way to new possibilities in controlling the path of electromagnetic waves. In this context, a reconfigurable metasurface composed of resonant meta-atoms is designed, fabricated and tested. Each individual meta-atom incorporates a varactor diode that can be controlled by an external direct current (DC) voltage. Such an active metasurface allows to tailor individual properties from the resonant cells and particularly to control the reflectivity so as to overcome the unique response limitations of passive ones. As such, we show that the proposed metasurface is able to mimic both a corner reflector and a parabolic reflector. The corresponding phase profile can be engineered and can be electronically modified to mimic the corner and parabolic reflector designs, as illustrated by the schematic in Fig. 1.

B. Ratni acknowledges partial support of his PhD works from Airbus Group Innovations

REFERENCES

1. Holloway, C. L., Kuester, E. F., Gordon, J. A., O'Hara, J., Booth, J. and Smith, D. R., "An overview of the theory and applications of metasurfaces: the two-dimensional equivalents of metamaterials," *IEEE Antennas Propag. Mag.*, Vol. 54, No. 2, 10-35, 2012.
2. Cheng, Q., Ma, H. F. and Cui, T. J., "Broadband planar Luneburg lens based on complementary metamaterials," *Appl. Phys. Lett.*, Vol. 95, No. 18, 181901, 2009.

3. Pfeiffer C. and Grbic, A., "A Printed, Broadband Luneburg Lens Antenna," *IEEE Trans. Antennas Propag*., Vol. 58, No. 9, 3055-3059, 2010.
4. Dhouibi, A., Burokur, S. N., de Lustrac, A. and Priou, A., "Metamaterial-based half Maxwell fish-eye lens for broadband directive emissions," *Appl. Phys. Lett.*, Vol. 102, No. 2, 024102, 2013.
5. Ghasemi, A., Burokur, S. N., Dhouibi, A. and de Lustrac, A., "High beam steering in Fabry-Pérot leaky-wave antennas," *IEEE Antennas Wireless Propag. Lett*., Vol. 12, 261-264, 2013.
6. Epstein, A., Wong J. P. S. and Eleftheriades, G. V., "Cavity-excited Huygens' metasurface antennas for near-unity aperture illumination efficiency from arbitrarily large apertures," *Nat. Commun*., Vol. 7, 10360, 2016.
7. Minatti, G., Faenzi, M., Martini, E., Caminita, F., De Vita, P., Gonzalez-Ovejero, D., Sabbadini, M. and Maci, S., "Modulated metasurface antennas for space: Synthesis, analysis and realizations," *IEEE Trans. Antennas Propag*., Vol. 63, No. 4, 1288-1300, 2015.

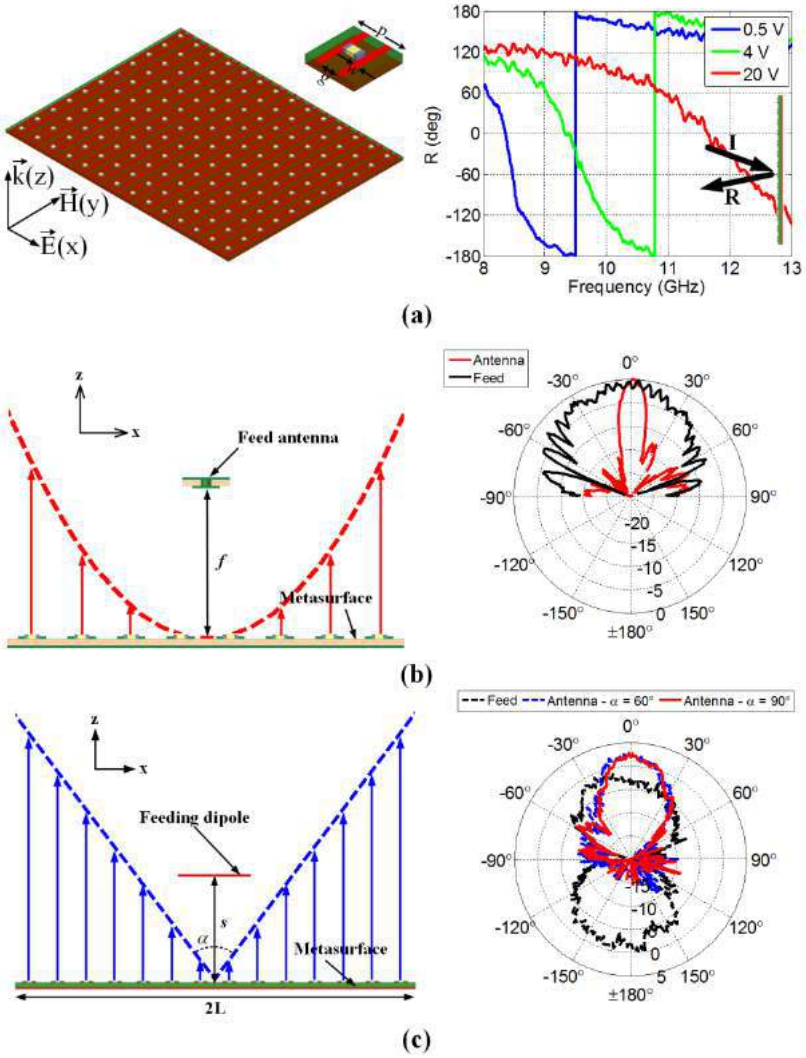

Fig. 1: (a) Schematic of the active metasurface and measured phase responses. (c) Parabolic phase profile and measured antenna performances. (c) Corner reflector phase profile and measured antenna performances.

Design of lumped resistor based broadband metamaterial structure from 2 to 18 GHz

Tanveer Suchu, Ravi Panwar*, and Rajesh Khanna*
Department of Electronics and Communication Engineering
Thapar University, Patiala-147004, Punjab, India
*corresponding author: ravi.panwar@thapar.edu, rkhanna@thapar.edu

Abstract-A wideband metamaterial structure (MMS) using frequency selective surface (FSS) loaded with lumped resistor has been designed in the range of 2 to 18 GHz. The MMS consists of a resistor loaded FSS, a dielectric sheet and a metallic ground. The results show that the MMA covers the wide frequency range of 5.5 GHz with reflection loss of -31.7 dB at normal incidence. The broadband absorption is mainly resulted from the strong electromagnetic (EM) resonance. The obtained result reflects the potential of lumped resistor based MMSs for distinct EM applications.

MMSs are getting significant interest of researchers in the field of electromagnetics due to their diverse practical applications [1]-[5]. But it is still a very challenging task to obtain good absorption with wide bandwidth. However, the requirement of broadband frequency response can be fulfilled by adopting advanced electromagnetic (EM) structures like FSSs [6]. It is well known that the FSS geometry, its dimensions, inter-element spacing, and substrate greatly affects the EM performance of MMSs. A very good pioneer work on MMSs has been reported by the researchers, but still there is a need to introduce the strategies which can further improve the absorption characteristics of the MMSs. Therefore, in this study an effort has been made to critically analyze the effect of the patch and aperture FSS geometries over the performance of MMSs. Further, the bandwidth of MMS has been enhanced by incorporating lumped resistive circuit elements.

The proposed MMS unit cell of size 10 × 10 mm consists of a square patch and square aperture geometries impacted dielectric layer of FR4 material (with thickness- 3.0 mm, dielectric constant 4.3 and loss tangent tan δ=0.025) backed with a perfect electric conductor designed using the CST microwave studio as depicted in the Fig. 1 (a). The Floquet theorem has been utilized in order to develop periodic structures followed by periodic boundary conditions (PBCs). Figs. 1(b) and 1 (c) sketches the square patch and square aperture geometries and corresponding design variables, where grey region represents the conductive surface of the copper.

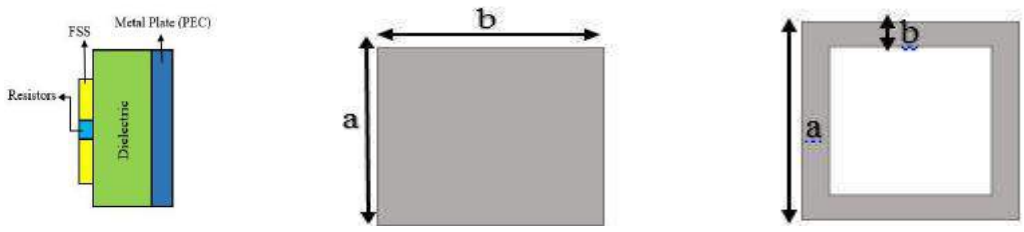

(a) (b) (c)

Figure 1. MMS design (a) 3D view, (b) & (c). Corresponding square patch and square aperture FSS geometries.

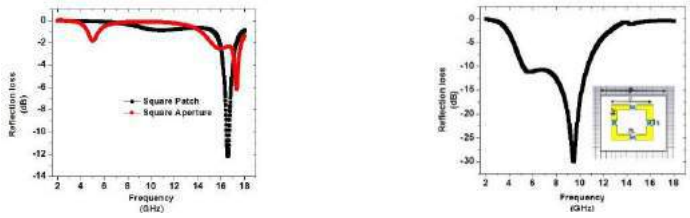

(a) (b)

Figure 2. RL characteristics of MMSs (a) square patch and square aperture geometries based MMSs and (b). Resistive element loaded FSS based MMS.

The RL values for square patch and square aperture geometries based MMSs is shown in the Figure 2 (a). It has been observed that the peak RL value of the square patch (a=b= 4.0 mm) is -11.543 dB at 12.3 GHz. While, the square aperture (a =8.0 mm, b=1.0 mm) based MMS possess a peak RL value of -6.1 dB at 17.3 GHz. The RL characteristics of patch geometry are comparatively better than aperture geometries, however the results are not as per the expectations as far as the wide bandwidth is considered. The resistive lumped circuit elements play an active role in order to provide good absorption [3]. Based on analysis reported by Ghosh et al. [3], the lumped resistive elements have been incorporated with FSSs to improve the bandwidth of aperture square based MMS. Figure 2 (b) depicts a square aperture FSS geometry loaded with resistive circuit elements and corresponding RL characteristics. The optimal design variables are p=12.5 mm, d= 8.0 mm, w= 1.25 mm, R_c =100 Ω, g= 1.2 mm. A critical analysis has been carried out to examine the effect of dielectric thickness and resistance value over absorption properties of MMS. An optimal MMS has been found to provide a peak RL value of -31.7 dB at 9.4 GHz in the range of 2.0 to 18 GHz. Most importantly, the MMS has been found to possess a wide absorption bandwidth of 5.5 GHz in the range of 10.6 GHz to 5.1 GHz. The obtained results clearly reflect the effectiveness of designed MMS for distinct commercial applications.

REFERENCES

1. Panwar, R., S. Puthucheri, V. Agarwala and D. Singh, “Fractal frequency-selective surface embedded thin broadband microwave absorber coatings using heterogeneous composites,” IEEE Trans. Microw. Theory Techn.,Vol. 63, No. 8, 2438-2448, 2015.
2. Panwar, R, S. Puthucheri, D. Singh and V. Agarwala, “Design of ferrite–graphene-based thin broadband radar wave absorber for stealth application,” IEEE Trans. Magn., Vol. 51, No. 11, 1-4, 2015.
3. Ghosh, S, S. Bhattacharyya and K. V. Srivastava, “Design and analysis of a broadband single layer circuit analog absorber,” *2016 46th European Microw. Conf. (EuMC)*, London, 584-587, 2016.
4. Costa, F and A. Monorchio, “A frequency selective radome with wideband absorbing properties,” IEEE Trans. Antennas Propag, Vol. 60, No. 6, 2740-2747, 2012.
5. Ghosh, S and K. V. Srivastava, “Polarization insensitive single and broadband switchable absorber/reflector and its realization using a novel biasing technique,” IEEE Trans. Antennas Propag,Vol. 64, No. 8, 3665-3670, 2016.
6. Panwar R, J.R. Lee, Progress in frequency selective surface based advanced electromagnetic structures: A critical review, Aerospace Sci. Tech., Vol. 66, 216-234, 2017.

Left Handed Meta-Surface Absorber for Tri Band Application

M. M. Hasan[1*], M. R. I. Faruque[1], M. T. Islam[2]

[1]Space Science Centre (ANGKASA), Universiti Kebangsaan Malaysia, Bangi 43600, Malaysia
[2]Department of Electrical, Electronic and Systems Engineering, Universiti Kebangsaan Malaysia, Bangi 43600, Malaysia
*corresponding author: mehedi20.kuet@gmail.com

Abstract

A new tri-band perfect meta-surface absorber based on square shaped metallic resonator, where the circular rings are in the middle of the resonator is investigated in this paper. The proposed absorber structure shows a wide bandwidth and applicable for C-, X- and Ku-band application. Due to the effective medium ratio 6.48 absorber structure compact in size and shows three absorption peaks are 82%, 67%, and 93% respectively in 6.22, 8.76, and 13.05 GHz. In addition, the lumped element model based equivalent circuit has been designed, where for calculation the resonance point, total inductance and capacitance formulas are also developed. In the circuit model the inductance is formed by the metal strips and gaps or splits are induced the capacitance. Besides, the proposed meta-surface absorber structure also exhibits left handed characteristics from 9.10 to 11.34 GHz and the surface impedance is -443.14-158.06j.

1. Introduction

Electromagnetic meta-surfaces are composed of artificial atoms, whose electric and magnetic response could be flexibly tailored to meet desired macroscopic properties. Benefiting from these novel properties, meta-surface absorbers have produced many exotic effects, such as negative refraction, negative permeability, sub-wavelength imaging super-lens, antenna performance enhancing, SAR reduction, and invisible cloaking. The development of the perfect meta-surface absorber utilizes the intrinsic loss of the system, with the help of structural design, to obtain near unity or perfect absorption at a certain frequency. Because of many advantages over the conventional ones, such as ultra-thin dielectric layer thickness, high absorption coefficient, and simple unit design, the research on meta-surface absorbers is in full swing. Perfect meta-surface absorbers have been broad applications in the fields of microwave, terahertz, infrared, and optical frequencies. In spite of high absorption of meta-surface absorbers, the absorption bandwidth of meta-surface absorber is often narrow, i.e., typically no larger than 10% with respect to the central frequency. Few reviewed on the meta-surface and meta-surface absorber have been reported in this paper. In 1996, Pendry et al. anticipated the negative permittivity from thin wire configuration and in 1999 negative permeability from split ring resonator [1]. In 2000, Smith et al. introduced a material that shown simultaneously negative permittivity and permeability with some exceptional properties at microwave frequency [2]. In 2008, N. I. Landy and a group of scientists from Boston College first demonstrated a microwave metamaterial absorber by using a classic sandwiched structure composed of a split ring resonator, a dielectric substrate, and a metallic cut wire. They generate electric and magnetic resonances that were independently manipulated for effective permittivity and permeability, respectively and the absorption of 88% at 11.50 GHz [3]. In 2016, Hasan et al. proposed a z-shaped double negative metamaterial for wide band applications. The 10×10 mm^2 structure metamaterial unit cell was applicable for C- and X-band operations [4]. In 2016, a compact square split z-shape metamaterial with left handed meta-atom for S-, C-, X- and Ku-band application and had 5.67 GHz wide bandwidth. The compact meta-atom had effective medium ratio of 9.10 and exhibited left handed characteristics in 8.50 GHz [5]. A wearable metamaterial microwave absorber (WMMA) for indoor radar clear applications was proposed for dual resonances in 9.0 and 9.8 GHz. The proposed WMMA was composed of two square ring resonators with different sizes, a backing ground plane, and a felt substrate with a 1.0 mm thickness. The grid array of different square ring resonators provided two broad absorptivity peaks greater than 90% due to the polarization angle of the electromagnetic waves and deformation effect as well as a full width at half maximum (FWHM) of 18.9% in 9.48 GHz [6]. In [7] a multi band split S-shape metamaterial was suggested for absorption analyses, which shown resonances in S-, X- and Ku-band in microwave frequency. The absorption spectra for the proposed absorber was 45% achieved at S-band. Moreover, after reducing the coupling capacitance in the z-axis absorption was reached up to 55% but in the y-axis absorption was extended up to 47%. Besides the absorption the proposed metamaterial could be used for various applications like, near zero refractive index, epsilon negative, mu negative, and double negative application. An ultra-thin polarisation-insensitive metamaterial structure has variable absorption bandwidth, which composed of three different cross-dipole-shaped metallic patches and each of which is printed on a very thin dielectric substrate where the ground was metal plane. The designed absorber displayed high absorptions (<80%) up to 45° incident angle for both TE and TM polarisation [8]. A microwave metamaterial absorber was designed that resonance at C-, X- and Ku-band with double negative characteristics as well as the absorption peaks were respectively, 82%, 67%, and 93% at 6.22, 8.76, and 13.05

GHz in [9]. An infrared dual-band metamaterial absorber consisted of a cross resonator ringed by four split-ring resonators spaced a distance above a gold ground plane with a dielectric layer of SiO_2 and exhibited two absorption peaks of 90.3% and 88.4% respectively at 4.17 μm and 4.86 μm [10]. An octave bandwidth metamaterial absorber structure consisted of geometrical patches placed diagonally on the top surface of the structure. The structure had a large bandwidth from 6.86 to 15.16 GHz, covering the entire X-band with absorptivity <90%. In addition, the peak absorptivity of 97.4%, 99.9%, and 97.8% had been observed respectively in 7.24, 10.18, and 14.32 GHz. Moreover, the structure was sensitive to polarisation of the incident field exhibiting maximum absorption at 0° and 90° with no absorption taking place at 45° angle of polarisation [11]. A graphene based terahertz absorber consisted of a single layer periodically arranged grapheme electric resonant and the ground plane was spaced out by SiO_2 dielectric layer. The designed graphene based structure displayed absorption of 99% at 35 μm and 97% at 59 μm [12]. In [13] frequency selective surface metamaterial absorber structures based on resonators like, omega, plus, cross shapes with and without a rectangular frame printed on the dielectric materials were presented and investigated for both microwave and terahertz frequency. In case of structure 1, in 4.0 and 5.60 GHz the simulated and measured absorptions were respectively 99%, 84% and 99%, 79%. Structure 2 displayed simulation absorption of 99.69% around 10 GHz in microwave frequency range. In addition, structure 3 exhibited maximum absorption of 99.78% and 98.80% respectively at 10.66 and 11.23 GHz for the simulation. Further, three different resonances occur at around 8.82, 9.95, and 10.91 GHz and the absorption in those resonance peaks were respectively 74.86%, 99.34%, and 88.86% for the structure 4. Moreover, for terahertz range lowest absorption was around 0.83 THz as 97.14% for 120° and the highest absorption almost 0.88 THz as 99.98% for 60° for structure 5. Besides, structure 6 shown lowest absorption in 1.05 THz as 46.95% for 60° and highest absorption in 0.99 THz as 99.98% for 90°. Besides, it had seen that the structure 6 provided good absorption for 0°, 120°, and 150° with the absorptions of 88.11%, 98.07%, and 87.22% respectively.

A left handed meta-surface absorber is presented in this paper, which consists of square ring resonator with the inner circular ring. The finite integration technique based CST microwave studio electromagnetic simulator has been used for achieving the reflection and transmission parameters. The measured and simulated results are well compiled together, where the measured transmittance resonance are in5.14 GHz (C-band), 7.29 GHz (C-band), 11.83 GHz (X-band), and 16.34 GHz (Ku-band) and the simulated resonance are in 5.35 GHz (C-band), 7.29 GHz (C-band), 11.85 GHz (X-band), and 16.45 GHz (Ku-band). The designed meta-surface compact in size, where the effective medium ratio is 6.48 and the absorption in 6.22 GHz is 82%, 8.76 GHz is 67%, and 13.05 GHz is 93%. Besides, left handed characteristics are shown from 9.10 to 11.34 GHz for any frequency points in that frequency range.

2. Meta-surface Absorber Design

Meta-surface structure operates like a lumped resonant circuit, which can be formed by incorporating inductive and capacitive effect by using the magnetic structures. This inductive and capacitive effect can be produced by adopting printed metallic stripe and gap between the stripes. The length of the metal strip is responsible for creating inductive effect and the spilt between the stripes is responsible for capacitive effect. By increasing the length of the metal line, inductance can be increased and by varying the gap, capacitance can be controlled. Consequently, by increasing the inductance, the effective medium ratio can be improved and this can be achieved as well by lowering the gap between the stripes. These lumped resonant elements has various advantages compared to the traditional microwave absorbers such as supplementary miniaturization, wider adaptability and increased effectiveness. The proposed absorber structure is consisting of a square shaped metallic resonator, where the circular rings are in the middle of the resonator. Meta-surface is usually designed on dielectric substrate material. The thickness and dielectric constant has effects on the properties of meta-surface. Thickness is more important when resonators are etched at the both side of the dielectric slab. Substrate material with high thickness cause low dielectric constant. Similarly, Substrate materials with low dielectric constant produce low bandwidth at higher frequency region. The metallic structure of the proposed meta-surface is designed on a FR-4 dielectric material, which has dielectric constant of 4.50, tangent loss of 0.002 and the thickness of 1.60 mm shown in figure 1(a) and the fabricated array structure in figure 1(b). Copper is used as a resonator on the dielectric substrate with an electrical conductivity of $\sigma=5\times8$ s/m. Moreover, the optimized geometry dimension parameters of the proposed absorber single unit cell are given in table 1 with the detail specifications.

Table 1: Specification of the tri-band meta-surface absorber.

Design parameters	Size (mm)	Design parameters	Size (mm)
Length of the substrate, A	9.0	Radius of outer circle, r1	3.0
Width of the substrate, B	9.0	Radius of inner circle, r2	2.25
Length of the outer RR, L1	8.5	Length of inner metal line, P	3.0
Width of the outer RR, W1	8.5	Length of inner metal line, q	3.0
Length of the inner RR, L2	7.5	Width of the metal strip, d	0.5
Width of the inner RR, W2	7.5	Gap between the rings, g	0.25

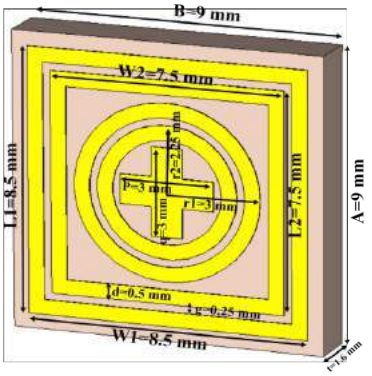

(a)

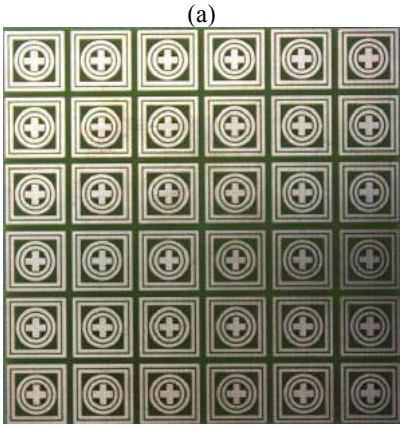

(b)

Figure 1. Proposed absorber: (a) Design single unit cell structure, (b) Fabricated array structure.

3. Methodology and Measurement Set-up

Electromagnetic simulation helps evaluating the fundamental field quantities from Maxwell's equation adopting some numerical technique. In this research, finite integration technique is adopted for numerical analysis. This is a spatial discretization method to solve electromagnetic field problems numerically in frequency domain. The technique provides high flexibility in complex geometric structure modelling as well as boundary handling. Periodic boundary conditions are applied for simulation. Moreover, two converse boundaries are connected here with a perceptible phase shift in such a way that the simulation process is forwarded periodically in the relevant direction. The PEMC boundary condition is the generalization of perfect electric and perfect magnetic boundary. Perfect electrical boundary condition is applied along the *x*-axis, and a perfect magnetic boundary is applied along *y*-axis as well as electromagnetic waves are excited the absorber along the z-axis. However, the permittivity, permeability and refractive index are retrieval by the following procedure [14],

$$S_{11} \approx \left\{ \frac{R_1\left(1-e^{j2nk_0d}\right)}{1-R_1^2e^{j2nk_0d}} \right\} and, S_{21} \approx \left\{ \frac{\left(1-R_1^2\right)e^{j2nk_0d}}{1-R_1^2e^{j2nk_0d}} \right\} \quad 1$$

$$e^{j2nk_0d} \approx T \pm j\sqrt{(1-T^2)}, T = \left\{ \frac{1-S_{11}^2+S_{21}^2}{2S_{21}} \right\} \quad 2$$

$$k_0 \approx \frac{2\pi f}{c} and, Z \approx \pm\sqrt{\frac{\left(1+S_{11}\right)^2+S_{21}^2}{\left(1-S_{11}\right)^2+S_{21}^2}} \quad 3$$

$$Refractive\ index,\ \eta_r \approx \frac{2}{jkd}\sqrt{\left\{ \frac{\left(S_{21}-1\right)^2-S_{11}^2}{\left(S_{21}+1\right)^2-S_{11}^2} \right\}} \quad 4$$

$$Permittivity, \varepsilon_r \approx \left(n_r \middle/ Z \right) \quad 5$$

$$Permeability, \mu_r \approx \left(n_r \times Z \right) \quad 6$$

In the equivalent lumped circuit based on the combination of inductors and capacitors both in parallel is shown in figure 2. In the circuit model inductors are included for the metal strips and a capacitor for the strip gaps or splits. The capacitors located in the circuit maintained the raise of total inductance, similarly inductors are minimized the raise of total capacitance in the circuit for fixing the resonance peaks. However, with the change of geometric structure of the proposed structure the inductance and capacitance will be varied and change the resonance peaks but the resonance band will be similar like before changing structure [5, 15]. So, the total inductance and capacitance of the designed structure can be figure out by the developed equation (7-9),

$$L_T \approx \mu_0 t^2 \left\{ \frac{\left(L_2+g-q\right)^2}{\left(2t^2+\pi d^2\right)} + \frac{\sqrt{A^2+B^2-L_1^2}}{\sqrt{r_1^2+r_2^2-P^2}} \right\} \quad 7$$

$$C_T \approx \varepsilon_0 \left[\frac{\pi\left(L_1+W_1-P\right)}{2\left(P+q+t\right)} \ln\left(\frac{L_2+W_2-d}{r_1+r_2} \right) \right] \quad 8$$

$$f_r = \frac{1}{2\pi\sqrt{L_TC_T}} \quad 9$$

$$Equivalent\ Impedance,\ Z_{eq} \approx \left(\frac{1}{C_{eq} + 1 \middle/ L_{eq}} \right) \quad 10$$

where '*d*' is the thickness of the substrate, '*Z*' is the normalize impedance, 'k_0' is the wave vector, '*c*' is the velocity of light. In addition, the free-space permeability is $4\pi\times10^{-7}$ H/m and the permittivity is 8.85×10^{-12} F/m. The EM-waves incident on the meta-surface absorber and the absorption response of the meta-surface structure described by transmittance $T(\omega)$ and reflectance $R(\omega)$ which are frequency dependent quantities can be calculated from,

$$Absorption, A(\omega) \approx \left[1-R(\omega)-T(\omega)\right] \quad 11$$

Reflectance and transmittance rate on the other hand depend on the scattering parameters, $R(\omega)= S_{11}^2$ and $T(\omega)= S_{21}^2$ which are given at bottom,

$$S_{11} = \frac{\sqrt{Reflected\ Power}}{\sqrt{Incident\ Power}} \text{ and } S_{21} = \frac{\sqrt{Transmitted\ Power}}{\sqrt{Incident\ Power}}$$

In order to optimize the absorptivity of the proposed structure reflection and transmission coefficients must be minimized to obtain minimum feasible values. However, the absorption of the designed mwta0surface absorber is obtained by,

$$Absorption, A(\omega) \approx \left[1 - |S_{11}|^2 - |S_{21}|^2\right] \quad 12$$

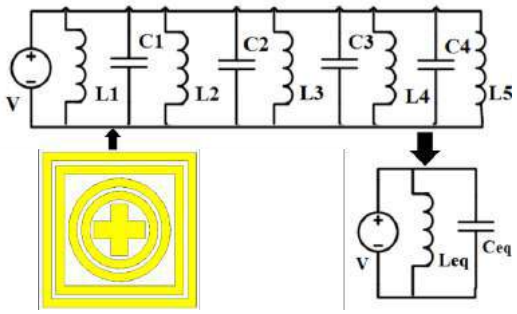

Figure 2. Equvalent lumped circuit model of the proposed meta-surface absorber.

In order to check the accuracy of the simulations, experimental study is also performed. The free space measurements are obtained by using two horn antennas. Antennas are placed far enough from each other to provide far-field conditions. Since the backward side of the structure is covered by a metal, there will be no transmission. Therefore, only the reflection measurements are carried out to evaluate the absorption coefficient. To verify the results, the simulation and measurement results of the absorption coefficient are plotted on the same graph as shown in figure 4(d) to compare them with each other. The measurements are carried out without connecting resistive loads by using an Agilent N5227A vector network analyser and two linearly polarized microwave horn antennas. The VNA supplies frequency range from 2.0 to 18.0 GHz and used to obtain the reflection (S_{11}) and transmission (S_{21}) coefficients to calculate the effective medium parameters.

4. Result Analysis of the Meta-Surface Absorber

The design absorber shows left handed characteristics with high absorption peak due to the electric and magnetic resonance by the inductive and capacitive element. This phenomenon can be explained with the help of surface current density, electric field and magnetic field pattern shown in the figure 3 (a-c). Electric field distribution shows charge accumulation on the oppositely facing strips and indicates capacitive effect. When external magnetic field is applied along the axis of the ring under the effect of the magnetic induction the current to flow in each half of the ring. This current lags with respect to the external magnetic field thereby giving a strong magnetic response. Besides, the flow of current at opposite direction causes the stop band and the colour and arrows indicates the intensity and direction of current flow.

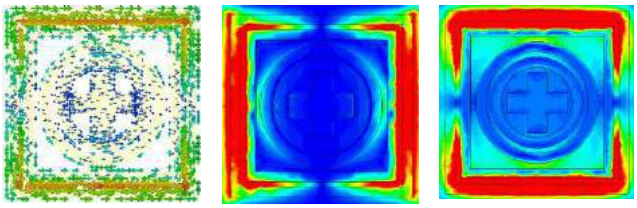

(a) (b) (c)

Figure 3. (a) Surface current distribution, (b) Electric field, (c) Magnetic field, of the proposed meta-surface absorber single unit cell in 5.14 GHz.

The absorber shows tri-band resonance, where the measured exhibited good arrangement with the simulated results in figure 4(a). The figure shows the simulated resonance in 5.35 GHz (C-band), 7.29 GHz (C-band), 11.85 GHz (X-band), and 16.45 GHz (Ku-band), whereas the measured resonances in 5.14 GHz (C-band), 7.29 GHz (C-band), 11.83 GHz (X-band), and 16.34 GHz (Ku-band). The measured resonance peaks in 5.14 GHz, 7.29 GHz, 11.83 GHz, and 16.34 GHz are slightly shifted from the simulated results due to the fabrication tolerance and environmental inferences. In figure 4(b), the effective medium parameters represent the left handed characteristics. The permittivity shows the real value of negative portion from 3.39 to 5.97 GHz, 6.37 to 7.76 GHz, and 8.75 to 11.34 GHz, which covers the bandwidth of 2.58 GHz, 1.39 GHz, and 2.59 GHz. In addition, in case of permeability negative curve from 9.10 to 18.0 GHz. Moreover, it shows that there is variation between the curves of permittivity and permeability due to the polarization effect of the interior construction of the materials. However, the refractive index shows negative real regime from 2.94 to 5.04 GHz, 9.20 to 13.91 GHz, and 16.30 to 18.0 GHz. As we know, when the both real part of permeability and permittivity go to the frequency area with negative value, which indicates the properties of left handed or double negative. From figure 4(b), the negative regime from 9.10 to 11.34 GHz, the effective medium parameters, i.e. permittivity, permeability and refractive index all are negative. As a result, the proposed perfect meta-surface absorber structure can be characterised as left handed for any frequency point from 9.10 to 11.34 GHz frequency range. Such as, in 9.26 GHz the real values of the permittivity, permeability and refractive index are respectively, -10.70, -194.79, and -45.65. From figurer 4(c) the reactance or surface impedance is -443.14-158.06j in 9.15 GHz. The absorption of the designed absorber is figure out from the equation (11). The absorption the proposed absorber at reflection (S_{11}) resonance point are 82% at 6.22 GHz, 67%8.76 GHz, and 93% at 13.05 GHz shown in figure 4(d). The absorption value is obtained from the reflection value by using the absorption equation. It should also be stated that the frequency range is high enough to be affected by small quality. Therefore, the proposed meta-surface absorber based having a high absorption level and a wide bandwidth

nature can be a good candidate for absorbing and future energy harvesting applications in communication bands.

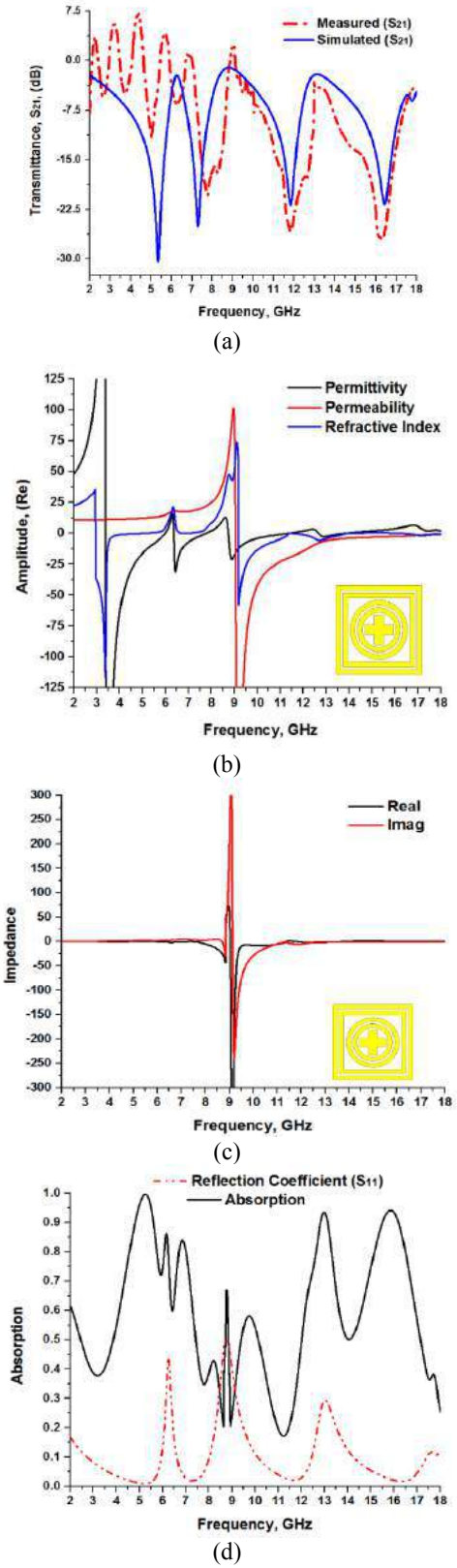

Figure 4. Amplitude of the proposed meta-surface: (a) Reflection and transmission coefficient, (b) Effective medium parameters, (c) Reactance impedance, (d) Absorption.

5. Conclusion

In summary, the absorption characteristics of a novel multi band meta-surface absorber based harvester has been designed, investigated, fabricated, and experimentally verified in this paper. Both numerically and experimentally results are well complied. Measured results show three absorption peaks and the absorption is greater than 93%. Distributions of the electric and magnetic fields are investigated to gain a better understanding of the resonance mechanism. Moreover, the lumped circuit model has been designed to calculate the resonance peaks by the developed total inductance and capacitance formulas. However, compared with the previous studies, the proposed meta-surface absorber has some significant advantages: such as compact unit size, resonance mechanism, and high absorption. Finally, due to the above advantages the proposed absorber structure makes it a good candidate in absorption, detection, sensing, imaging, and so on.

Acknowledgements

This work was supported by the Research Universiti Grant, Geran Universiti Penyelidikan (GUP), code: 2016-028.

.

References

[1] J. B. Pendry, A. J. Holden; D. J. Robbins, W. J. Stewart; "Magnetism from conductors and enhanced nonlinear phenomena", *IEEE Transactions on Microwave Theory and Techniques*, 47:2075- 2084, 1999.

[2] D. R. Smith, W. J. Padilla, D. C. Vier, S. C. Nemat-Nasser, S. Schultz, "Composite medium with simultaneously negative permeability and permittivity", *Physical Review Letters*, 84:4184-4187, 2000.

[3] N. I. Landy, S. Sajuyigbe, J. J. Mock, D. R. Smith, W. J. Padilla, "A perfect metamaterial absorber", *Physical Review Letter*, 100:1–4, 2008.

[4] M. M. Hasan, M. R. I. Faruque, S. S. Islam, M. T. Islam, "A new compact double-negative miniaturized metamaterial for wideband operation", *Materials*, 9(10):830, 2016.

[5] M. M. Hasan, M. R. I. Faruque, M. T. Islam, "Left-Handed Metamaterial using Z-Shaped SRR for Multiband Application by Azimuthal Angular Rotations", *Materials Research Express* 4:4, 2017.

[6] J. Tak, J. Choi, "A wearable metamaterial microwave absorber", *IEEE Antennas and Wireless Propagation Letters*, 2015, Doi: 10.1109/LAWP.2016.2604257.

[7] S. S. Islam, M. R. I. Faruque, M. T. Islam, "Design and absorption analysis of a new multiband split s shaped Metamatrial", *Science and Engineering of Composite Materials*, 2015, Doi: 10.1515/secm-2014-0376.

[8] S. Ghosh, S. Bhattacharyya, D. Chaurasiya, K.V. Srivastava, "Polarisation-insensitive and wide-angle multi-layer metamaterial absorber with variable bandwidths", *Electronics Letters*, 51:1050–1052, 2015.

[9] M. M. Hasan, M. R. I. Faruque, M. T. Islam, "A Tri-Band Microwave Perfect Metamaterial Absorber", Microwave and Optical Technology Letters, 2017, Doi: 10.1002/mop.30726.

[10] W. Ma, Y. Wen, X. Yu, "Theoretical and experimental demonstrations of a dual-band metamaterial absorber at mid-infrared", *IEEE Photonics Technology Letters*, 26:1940-1943, 2014.

[11] S. Bhattacharyya, S. Ghosh, D. Chaurasiya, K. V. Srivastava, "Wide-angle broadband microwave metamaterial absorber with octave bandwidth", *IET Microwaves, Antennas & Propagation*, 9:1160–1166, 2015.

[12] M. H. G. Yao, F. Ling, J. Yue, C. Luo, J. Ji, J. Yao, "Dual-band tunable perfect metamaterial absorber in the THz range", *Optics Express*, 24:1518-1527, 2016.

[13] C. Sabah, F. Dincer, M. Karaaslan, E. Unal, O. Akgol, "Polarization-insensitive FSS-based perfect metamaterial absorbers for GHz and THz frequencies", *Radio Science*, 49:306–314, 2014.

[14] M. M. Hasan, M. R. I. Faruque1, M. T. Islam, "Multiband left handed biaxial meta atom at microwave frequency", *Materials Research Express*, 4: 035015, 2017.

[15] M. M. Hasan, M. R. I. Faruque, M. T. Islam, "A mirror shape chiral meta atom for C-band communication", *IEEE Access*, Doi: 10.1109/ACCESS.2017.2677463.

Singularity Points in Acoustic Metamaterials: Physics and Applications

Acoustic Energy Harvesting Based on Metamaterials and Metasurfaces

Badreddine Assouar[1,2 *], **Shuibao Qi**[1,2] **& Yong Li**[1,2]

[1] Institut Jean Lamour, CNRS, Nancy, France

[2] Institut Jean Lamour, Université de Lorraine, Nancy, France

[*]corresponding author: Badreddine.Assouar@univ-lorraine.fr

Abstract-Acoustic energy harvesting based on acoustic metamaterials and metasurfaces are proposed and investigated. The proposed concepts are based on the idea of using plate-type metamaterial and multilateral metasurface to confine the acoustic energy, and subsequently convert it into the electrical one by a structured piezoelectric material connecting with optimized circuits. The properties of proposed acoustic energy harvesters will be presented and discussed.

As a kind of clean, ubiquitous and renewable form of energy, sound/noise may act as a promising sustainable power source for energy production and micro autonomous devices, such as wireless sensors, mobile electronics and so forth. Due to low power densities in ordinary surroundings, sound/noise generally needs to be focused or confined through effective conversion media for better acoustic energy harvesting (AEH). Intuitively, classical Helmholtz and other chamber resonators could be used to enhance the acoustic confinement and subsequently realize AEH. In general, the strategy based on the resonators suffers from defect of the bulky structures and uncontrolled wave field, thus hampering the applicable energy harvesting. In a different context, the recent emergence of the artificially engineered acoustic metamaterials and metasurfaces has significantly broadened the horizon of acoustic wave and wavefront manipulations. They possess a variety of advantageous and anomalous properties and capabilities.

In this research, we theoretically and numerically report on innovative and practical acoustic energy harvesters based on acoustic metamaterials and metasurfaces [1, 2]. The ideas of AEH and acoustic confinement with the acoustic metamaterials metasurfaces will be demonstrated and analyzed. More specifically, we will present here some recent works and advances on acoustic energy harvesting making use of a defected plate-type metamaterial and a multilateral metasurface based on the coiling up space geometry. Different concepts and designs of the AEH will be presented and discussed as well as and their physical and electrical properties.

REFERENCES

1. S. Qi, M. Oudich, Y. Li & M. B. Assouar. Appl. Phys. Lett., 108 (2016) 263501.
2 M. B. Assouar, S. Qi & Y. Li. Proceeding of SPIE 1011 (2017) 101112B-1.

Topological transition in soft acoustic metamaterials

Shuaifeng Li[1,2,4], Hanchuan Tang[1,4], Lei Ye[1,4], Degang Zhao[3,4], Xuefeng Zhu[3,4], Jianfeng Zang[1,4*]

[1] School of Optical and Electronic Information, Huazhong University of Science and Technology, Wuhan 430074, People's Republic of China

[2] School of Materials Science and Engineering, Huazhong University of Science and Technology, Wuhan 430074, People's Republic of China

[3] School of Physics, Huazhong University of Science and Technology, Wuhan 430074, People's Republic of China

[4] Innovation Institute, Huazhong University of Science and Technology, Wuhan 430074, People's Republic of China

[*]corresponding author: jfzang@hust.edu.cn

Abstract-Here, we report a novel soft acoustic metamaterial with tunable topological phase by applied mechanical deformation. Harnessing deformation Dirac point in our acoustic system can be switched on and off, resulting in energy band inversion. Our finding offers a new approach to generate an interface state at topological domain wall. Besides, the frequency of interface state can also be tuned continuously. Importantly, we provide a general topological phase diagram to design desired tunable topological state by deforming soft acoustic metamaterials.

Acoustic metamaterials are useful in controlling sound waves in the way that does not exhibit in nature, with practical applications in noise reduction and wave guiding technologies. Particularly, recent study on phononic periodic system in view of topological order has drawn increased attention such as phononic analogue of quantum spin Hall effect(QSHE)[1]. Elastic wave, also known as small elastic oscillation in solid, is that motion occurs in a deformed body. It has special advantages in information carrying, seismic detection and geologic prospecting[3]. Due to the nature of low frequency elastic waves, which attenuate more slowly and propagate more stable than high frequency ones, long-wavelength elastic waves play a significant role in information processing. Thanks to the development of advanced fabrication technique, elastically anisotropic and isotropic materials, elastic properties varying from direction, can be fabricated successfully. Nonetheless, a common feature of most such materials is having a fixed geometry, resulting in fixed properties of a system. Thus, soft materials and structures associated with mechanics capable of configuring its global and partial geometry are introduced to tune the functionality of a system[2]. Here, we achieve a dynamically tunable topological elastic metamaterial realized by soft materials. By harnessing deformation, the topological property of our elastic system can be switched. And the interface state can be generated at the boundary separating two elastic metamaterials that are placed at different geometry states respectively, corresponding to opposite style of symmetry in reciprocal space. Finally, we offer a general topological phase diagram to design desired interface state. This strategy gives us possibility to realize and then control topological interface state both statically and dynamically. Note that in our study we only focus on unit cell of millimeter scale, the proposed design can be more complex and has various scales depending on the phonon frequency. The ability to dynamically control interface state in soft materials may be used in other smaller or larger phononic system such as thermal management and help to develop flexible acoustic devices. The interesting phenomenon of robust topological sound wave propagation in soft

materials, which is tuned by mechanical deformation, may have potential applications in military and communication field.

Acknowledgements. We are grateful to Yugui Peng and Yaxi Shen from Huazhong University of Science and Technology for theoretical and experimental discussion.

REFERENCES

1. He, C., Ni, X., Ge, H., Sun, X. C., Chen, Y. B., Lu, M. H., Liu, X. P. and Chen, Y. F. "Acoustic topological insulator and robust one-way sound transport," *Nat. Phys*, Vol. 12, No. 12, 1124–1129, 2016.
2. Wang, P., F. Casadei, Shan, S. C., JC. Weaver and K. Bertoldi, "Harnessing Buckling to Design Tunable Locally Resonant Acoustic Metamaterial," *Phys. Rev. Lett.*, Vol. 113, No. 1, 014301, 2014.
3. Royer, D., Dieulesaint, E. *Elastic waves in solids I: Free and Guided propagation*, Springer Science & Business Media, New York, 2000.

Ultrathin binary metalens of 1/250 Lambda for sound manipulation

Hanchuan Tang[1], Zesi Chen[1], Shuaifeng Li[1,3], Xuefeng Zhu[1,2,4], and Jianfeng Zang[1,2*]

[1] School of Optical and Electronic Information, Huazhong University of Science and Technology, Wuhan 430074, China

[2] Innovation Institute, Huazhong University of Science and Technology, Wuhan 430074, China

[3] School of Materials Science and Engineering, Huazhong University of Science and Technology, Wuhan 430074, China

[4] School of Physics, Huazhong University of Science and Technology, Wuhan 430074, China

[*]corresponding author: jfzang@hust.edu.cn

Abstract. Acoustic metamaterial is extremely attractive due to its unprecedented manipulating properties of acoustic wave. Here we proposed a fiber-beads metamembrane that can cause π phase shift and maintain a 0.9 transmittance with 1/250 lambda thickness at low frequency range. Based on this, we construct a binary metalens with different arrangement modes, which can manipulate the diversity of sound and realize focusing. Meanwhile, our work lay the foundation for the following research about transformation acoustics and so on.

Advanced materials with deep-subwavelength thickness as well as unprecedented controls of propagation of acoustic wave have been vigorously pursued for broad applications such as negative refraction[1]. Popular approach is to manipulate the characteristics of the materials and further adjust the reflection or transmission phase. In this context, emerging acoustic metamaterials are fabricated artificially to achieve some novel properties that don't exist in natural constitutive materials[2]. Common acoustic metamaterial has been designed based on local resonance theory[3]. However, most LC resonant devices even like DMR[4] are not thin enough so as to limiting their application in more scenarios. Here, we report an ultrathin fiber-beads membrane that causes a π phase shift with 90% transmittance at low frequency range. It's worth mentioning that the thickness of membrane reaches to a deep subwavelength scale, as thin as 1/250 λ of the feature size, which is a significant advance compared with previous work[4,5]. Our fiber-beads membrane is inspired by a conventional spring-mass resonator principle: soft polymer fiber embedded with hard beads forms 3-dimensional network membrane. On this basis, unprecedented controls of acoustic wave can be achieved just by manipulating the amplitude and phase of acoustic wavelets at every point in the plane that is perpendicular to incident direction. Moreover, we build a metalens with our membranes to manipulate the directivity of sound and then shift the energy of incident wave to the surrounding, which can be used to reduce far-filed sound intensity or applied to other field requiring specific diversity of sound.

Acknowledgement. This work was supported by the National Natural Science Foundation of China (51572096) and the National 1000 Talents Program, China. We are grateful to Yaxi Shen and Yugui Peng from HUST for useful discussion, and Analytic Testing Center as well as Flexible Electronics Research Center of HUST for measurement support.

REFERENCES

1. Brunet, T., Leng, J. & Mondain-Monval, O., "Soft Acoustic Metamaterials," *Science*, 342 (6156), 323-324, 2013.
2. Fok, L., Ambati, M. & Zhang, X., "Acoustic metamaterials, " *Mrs. Bull*, **33** 931, 2008.
3. Liu, Z. *et al.*, Locally resonant sonic materials. *Science*, **289** 1734, 2000.
4. Ma, G., Yang, M., Xiao, S., Yang, Z. & Sheng, P., "Acoustic metasurface with hybrid resonances," *Nat. Mater*,**13** 873, 2014.
5. Cheng, Y. Zhou C. & Yuan B. G. et al, "Ultra-sparse metasurface for high reflection of low-frequency sound based on artificial Mie resonances," *Nat. Mater*, 14 (10), 1013-1019, 2015.

Topological States in Nanophononic Structures

M. Esmann[1], **F. R. Lamberti**[1], **L. Lanco**[1], **P. Senellart**[1], **A. Lemaitre**[1], **N. D. Lanzillotti-Kimura**[1*]

[1] Centre de Nanosciences et de Nanotechnologies, CNRS, Univ. Paris Sud, France

[*]corresponding author: daniel.kimura@lpn.cnrs.fr

Abstract-We report novel strategies to study topologically protected states in nanophononic systems working at frequencies around 300 GHz. We theoretically predict the existence of such modes in multilayer GaAs/AlAs structures. High resolution Raman scattering unveils features related to the maxima in the phononic local density of states associated to topologically protected states.

A nanophononic cavity shapes the local phononic density of states and can dramatically modify the interactions between mechanical vibrations and other excitations in solids.[1,2] It usually consists of two distributed Bragg reflectors (DBR) enclosing an acoustic spacer. A DBR inherits the topological properties of the associated infinite periodic structure -symmetries and characteristic energies- determining the confinement properties of an acoustic cavity. Despite the obvious relation between the acoustic bandgap structure and the performance of the DBRs, the study of topological states in nanophononic systems remained unexplored.

In this work, we report two novel design strategies for the study of topological states of longitudinal acoustic phonons with frequencies around 300 GHz. In the first approach we concatenate two GaAs/AlAs DBRs presenting inverted band structures for a given gap to create an interface state.[3,4] We study the influence of the choice of unit cell and different interface configurations on the confinement characteristics of these states. In the second approach we mimic the SSH model of polyacetylene[5] by means of a nanophononic multilayered system. We demonstrate the existence of topologically protected nanophononic states. We also discuss the potential application of these novel design strategies into 3D structures.

We have fabricated nanocavities allowing the confinement of phonons based on the aforementioned ideas. We performed high resolution Raman scattering measurements at room temperature.[6] Clear features related to the maxima of the acoustic density of states were measured and reproduced by photoelastic model calculations. The presented results open a new playground in the control of acoustic vibrations in solids, providing new tools not only to confine and control the dynamics of ultra-high frequency phonons but also a new platform to study topological and general localization effects.

Acknowledgements. This project has received funding from the European Research Council (ERC) under the European Union's Horizon 2020 research and innovation programme (grant agreement n° 715939).

REFERENCES

1. M. Trigo, A. Bruchhausen, A. Fainstein, B. Jusserand, and V. Thierry-Mieg, “Confinement of Acoustical Vibrations in a Semiconductor Planar Phonon Cavity,” *Phys. Rev. Lett.* **89**, 227402 (2002)

2. A. Fainstein, N. D. Lanzillotti-Kimura, B. Jusserand, and B. Perrin, “Strong Optical-Mechanical Coupling in a Vertical GaAs/AlAs Microcavity for Subterahertz Phonons and Near-Infrared Light,” *Phys. Rev. Lett.* 110, 037403 (2013)
3. F. R. Lamberti et al, s**ubmitted** (2017)
4. M. Xiao, G. Ma, Z. Yang et al., “Geometric phase and band inversion in periodic acoustic systems,” *Nature Physics* **11**, 240-244 (2015)
5. W. P. Su, J. R. Schrieffer, and A. J. Heeger, “Solitons in Polyacetylene ,” *Phys. Rev. Lett.* **42**, 1698 (1979)
6. N.D. Lanzillotti-Kimura, A. Fainstein, B. Jusserand et al., “Resonant Raman scattering of nanocavity-confined acoustic phonons,” *Phys. Rev. B* **79**, 035404 (2009)

Topological Distinction of Single Negative Metamaterials: from Phononics to Acoustics

Weiwei Zhu[1],Shanshan Hou,[1] Hong Chen,[1]and Jie Ren[1,2]

[1] School of Physics Science and Engineering, Tongji University, 200092 Shanghai, P. R. China
[2] Center for Phononics and Thermal Energy Science, The Institute for Advanced Study, Tongji University, 200092 Shanghai, P. R. China

Topological insulators are new class of states, which are insulating in the bulk but conducting on their surface, protected from the disorder. Similar effects are extended to photonic/micro-wave systems, and so on. In this work, we use a simple circuit model unifies all the different physics of different systems, beyond electronics, ranging from phononics to acoustics, even to microwave photonics. We confirm from the topological band theory and further from continuous Dirac equation method that the single negative metamaterials are topologically distinct, eg., the ENG is topologically different from the MNG. We also analytically study and experimentally measure the reflection phase that is related to the Zak phase through bulk-boundary relation. We observe the field distribution of the interface state, the same as the relativistic Jackiw-Rebby topological solution. The analytical result of the circuit model has a good agreement with the experimental results based on microwave photonics, which however is universal to phononics and acoustics.

Singularity point applications of acoustic vortices

Z. Y. Hong*
Department of Applied Physics, Northwestern Polytechnical University, Xi'an 710072, China
*corresponding author: hongzy@nwpu.edu.cn

Abstract-Single singularity point in water has been yielded by integer-order acoustic vortices, which can be used to trap, move and rotate a single particle or particle cluster. Multiple singularity points in water have been created by generating fractional-order acoustic vortices or superposing two or more first-order acoustic vortices, which can be used to manipulate two or more particles at the same time. Moreover, singularity points of acoustic vortices in air are able to levitate and rotate diverse objects.

REFERENCES

1. Courtney C. R. P., Demore C. E. M., Wu H. X., Grinenko A., Wilcox P. D., Cochran S. and Drinkwater B. W., "Independent trapping and manipulation of microparticles using dexterous acoustic tweezers," Appl. Phys. Lett., Vol. 104, No. 15, 154103, 2014.
2. Hong Z. Y., Zhang J. and Drinkwater B. W., "Observation of orbital angular momentum transfer from Bessel-shaped acoustic vortices to diphasic liquid-microparticle mixtures," Phys. Rev. Lett., Vol. 114, No. 21, 214301, 2015.
3. Hong Z. Y., Zhang J. and Drinkwater B. W., "On the radiation force fields of fractional-order acoustic vortices," Europhys. Lett., Vol. 110, No. 1, 14002, 2015.

Photonic topological insulators: fundamental physics â€¢

Experimental observation of optical Weyl points

J. Noh[1], **S. Huang**[2], **D. Leykam**[3], **Y. D. Chong**[3,4], **K. Chen**[2], **and M. C. Rechtsman**[1]

[1]Department of Physics, The Pennsylvania State University, University Park, PA, USA
[2]Department of Electrical and Computer Engineering, University of Pittsburgh, Pittsburgh, PA, USA
[3]School of Physical and Mathematical Sciences, Nanyang Technological University, Singapore
[4]Centre for Disruptive Photonic Technologies, Nanyang Technological University, Singapore
dleykam@ntu.edu.sg

Abstract— We demonstrate a laser-written photonic lattice exhibiting topologically-protected Weyl point degeneracies in its three-dimensional band structure. Probing the lattice at various wavelengths, we observe topological surface modes and conical diffraction characteristic of an anisotropic "type-II" Weyl point. This constitutes the first realization of a photonic Weyl point at optical frequencies, allowing further study of their novel properties in a wide class of linear and nonlinear photonic systems.

In three dimensional band structures Weyl points are degeneracies that form monopoles of Berry curvature protected by a quantized topological charge. This charge results in novel properties such as arcs of robust surface modes and chiral anomalies [1, 2]. Two different types of Weyl points can occur, depending on the anisotropy of the system. At a "type-I" Weyl point the density of states vanishes, whereas the "type-II" Weyl point illustrated in Fig. 1(a) has a strongly anisotropic conical dispersion with a nonzero density of states at all frequencies [3, 4]. The former has been observed in photonics in microwave photonic crystals [5], however scaling to the important optical wavelength regime is a challenging task requiring the fabrication of complicated 3D structures with high refractive index contrast.

Here we report the observation of "type-II" Weyl points using the three-dimensional photonic lattice of evanescently coupled helical optical waveguides shown in Fig. 1(b). The waveguides are written in borosilicate glass using a femtosecond laser. Monochromatic light propagation along the waveguide axis z is governed by the paraxial equation

$$i\partial_z\psi = -\frac{1}{2k_0}\nabla_\perp^2\psi - \frac{k_0\delta n(x,y,z)}{n_0}\psi, \tag{1}$$

where ψ is the beam envelope slowly varying in z, $k_0 = 2\pi n_0/\lambda$ is the wavenumber, n_0 is the ambient refractive index, λ is the input wavelength, and δn is the refractive index modulation of the waveguides. The three dimensional photonic band structure associated with our periodic index modulation $\delta n(x, y, z)$ hosts a type-II Weyl point at a critical wavelength [6].

We probe the lattice at various wavelengths (1450–1650nm) and observe that the protected surface modes only exist above the Weyl point wavelength, i.e. they form arcs terminating at the Weyl point. Meanwhile, bulk propagation at the Weyl point generates a conical diffraction pattern characteristic of a type-II Weyl point's conical isofrequency surface, see Fig. 1(c). These experimental observations are the first demonstration of a Weyl point at optical wavelengths, and the first realization of a type-II Weyl point in photonics. In future it would be interesting to explore other linear, nonlinear, and quantum propagation dynamics in this class of lattices [7].

ACKNOWLEDGMENT

M.C.R. acknowledges the National Science Foundation under award number ECCS-1509546, the Penn State MRSEC, Center for Nanoscale Science, under award number NSF DMR-1420620, and the Alfred P. Sloan Foundation under fellowship number FG-2016-6418. D.L. and C.Y.D. acknowledge support by the Singapore National Research Foundation under grant No. NRFF2012-02, by the Singapore MOE Academic Research Fund Tier 2 Grant No. MOE2015-T2-2-008, and by the Singapore MOE Academic Research Fund Tier 3 grant MOE2011-T3-1-005. K.C. acknowledges the National Science Foundation under award number ECCS-159199.

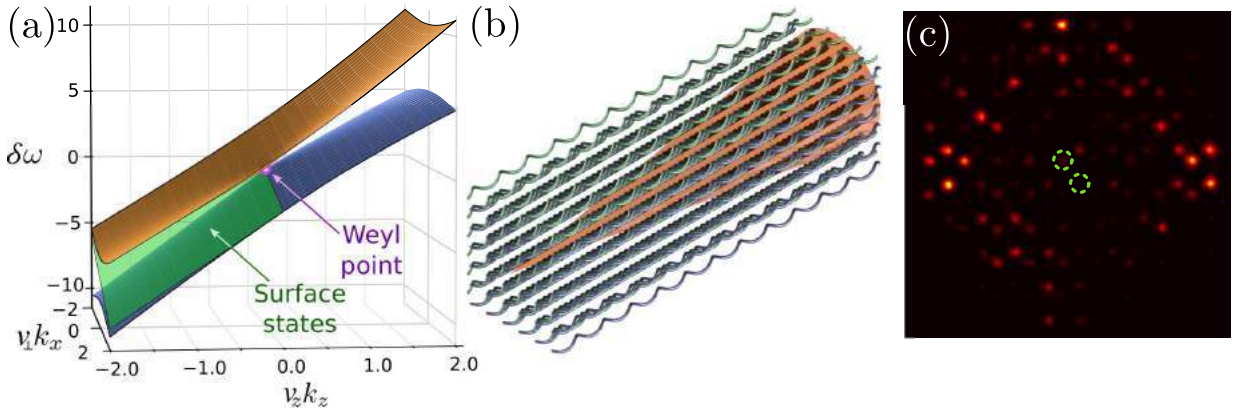

Figure 1: (a) Dispersion of a type-II Weyl point in the (k_x, k_z) plane. $\delta\omega$ is the shift of the modal frequency ω with respect to the Weyl point frequency. (b) Schematic of conical diffraction through the helical waveguide array at the Weyl point frequency. (c) Observed intensity at the output facet, displaying the conical diffraction. Green circles indicate the pair of input waveguides.

REFERENCES

1. Xu, S.-Y. et al., "Discovery of a Weyl fermion semimetal and topological Fermi arcs," *Science*, Vol. 349, No. 6248, 613 2015.
2. Lv, B. Q. et al., "Experimental discovery of Weyl semimetal TaAs," *Phys. Rev. X*, Vol. 5, No. 3, 031013 2015.
3. Xu, Y., F. Zhang and C. Zhang, "Structured Weyl points in spin-orbit coupled fermionic superfluids," *Phys. Rev. Lett.*, Vol. 115, No. 26, 265304 2015.
4. Soluyanov, A. A., D. Gresch, Z. Wang, Q.S. Wu, M. Troyer, X. Dai and B. A. Bernevig, "Type-II Weyl semimetals," *Nature*, Vol. 527, 496 2015.
5. Lu, L., Z. Wang, D. Ye, L. Ran, L. Fu, J. D. Joannopoulos and M. Soljačić, "Experimental observation of Weyl points," *Science*, Vol. 349, No. 6248, 622 2015.
6. Noh, J., S. Huang, D. Leykam, Y. D. Chong, K. Chen and M. C. Rechtsman, "Experimental observation of optical Weyl points," arXiv preprint arXiv:1610.01033 2016.
7. Leykam, D. and Y. D. Chong, "Edge solitons in nonlinear-photonic topological insulators," *Phys. Rev. Lett.*, Vol. 117, No. 14, 143901 2016.

Topological phase transition in acoustic systems

Yu-Gui Peng[1,2] and Xue-Feng Zhu[1,2,*]

[1] School of Physics, Huazhong University of Science and Technology, Wuhan, Hubei 430074, China

[2] Innovation Institute, Huazhong University of Science and Technology, Wuhan, Hubei 430074, China

[*]corresponding author: xfzhu@hust.edu.cn

HP 21/2/17 15:38

Supprimé: ,

Abstract-Topological insulators have inspired analogues in acoustics, in which one-way gapless edge/surface states, featured with absence of scatterings, have been widely achieved via synthetic magnetic field or pseudo-spins. Varied mechanisms to realize topologically protected sound transportation have been realized, as characterized by Chern number, Z2 number as well as winding number. We present that topological phases can be tuned into trivial phases by distorting the geometry of 1D Helmholtz resonator chain or breaking the inherent symmetry of 2D resonator/cylinder array.

REFERENCES

1. Xiao, M. et al. Geometric phase and band inversion in periodic acoustic systems. Nat. Phys. 11, 240, 2015.
2. Peng Y.G. et al. Experimental demonstration of anomalous Floquet topological insulator for sound. Nat. Commun. 7, 13368, 2016.
3. He C. et al. Acoustic topological insulator and robust one-way sound transport. Nat. Phys. 12, 1124, 2016.
4. Lu J. et al. Observation of topological valley transport of sound in sonic crystals. Nat. Phys. 2016. DOI:|10.1038/nphys3999

Experiment Realization of Synthetic Weyl Points In Optical Regime

Qiang Wang[1], Meng Xiao[2,3], Hui Liu[1,*], Shining Zhu[1] and C. T. Chan[2]

[1]National Laboratory of Solid State Microstructures, School of Physics, Collaborative Innovation Center of Advanced Microstructures, Nanjing University, Nanjing 210093, China

[2]Department of Physics and the Institute for Advanced Study, the Hong Kong University of Science and Technology, Clear Water Bay, Kowloon, Hong Kong

[*]corresponding author: liuhui@nju.edu.cn

Abstract- We demonstrate that generalized Weyl points can exist in a parameter space and we report the first observation of such nodal points in one-dimensional photonic crystals in the optical range. The reflection phase inside the band gap of a truncated photonic crystal exhibits vortexes in the parameter space where the Weyl points are defined and they share the same topological charges as the Weyl points.

Great efforts have been devoted to investigating the intriguing phenomena associated with Weyl points[1-3], such as the Fermi arc surface states[4,5] and the chiral anomaly[2] associated with electronic systems. Besides electronic systems, Weyl points have also been found in photonic [6-9], and plasmonic[10] systems. Up to now, Weyl points have mostly been identified as momentum space magnetic monopoles, i.e. sources or sinks of Berry curvature defined in the momentum space. As such, Weyl points are usually perceived as topological nodal points in the 3D momentum space defined by Bloch momentum coordinates. We show that topological nodal points can in fact also be meaningfully defined in a generalized phase space in which some of the dimensions are not Bloch momentum, and yet their topological characteristics make them analogues of Fermi-arc-like interface states in much the same way that ordinary Weyl points are defined in the 3D k-space. We use photonic crystals (PCs) to realize the idea of generalized Weyl points experimentally in the optical frequency regime.

To illustrate the idea of synthetic Weyl points in a generalized parameter space, we consider a 1D PC consisting of four layers per unit cell, as shown in the inset in Fig. 1a. In our experiments, the first and third layers (blue) are made of H_fO_2 with refractive index n_a=2.00, and the second and fourth layers (red) are made of S_iO_2 with refractive index n_b=1.45. where p and q both fall within [-1,1]. The total optical length L inside the unit cell is a constant $2(n_a d_a + n_b d_b)$ for the whole p-q space. As illustrated in Fig. 1a, the structural parameters p and q, together with one Bloch wave vector k, form a 3D parameter space in which Weyl physics can be studied. The band dispersion is plotted in Fig. 1b in red. Fig. 1c shows the band dispersions in the p-q space with $k = 0.5k_0$, where $k_0 = \pi/(d_a + d_b)$. To characterize this degenerate point, we derive an effective Hamiltonian for parameters around it:

$$H = pv_{pz}\sigma_z + qv_{qy}\sigma_y + \xi_k v_{kx}\sigma_x \quad (1)$$

where $\xi_k = (k - 0.5k_0)/k_0$, $v_{pz} = 0.1073$, $v_{qy} = -0.0946$ and $v_{kx} = -1.985$ for our system. This Hamiltonian possesses a standard Weyl Hamiltonian form and with the Weyl node located at $(p,q,k) = (0,0,0.5k_0)$ carrying a "charge" of -1 according to the usual definition. If we consider the Weyl points on the fourth and fifth bands. There are a total of eight Weyl points: six with charge -1 and the remaining two with charge +1. We then set the working frequency to the frequency of the Weyl point with a positive charge (303THz) and truncate the PCs at the center of the first layer. In Fig. 4a, we show the reflection phase in the parameter space, where gray areas within black dashed lines mark the regions of the bulk band. The reflection phase of the silver film coated is measured to be $(-0.95 \pm 0.0471)\pi$ at 303THz. White dashed lines in Fig. 2a show the trajectories of interface states. In addition to

interface states connecting Weyl points with different charges, there are also trajectories of interface states terminating at the boundary of our parameter space. We emphasize here that the existence of interface states is "robust" to the property of the reflecting substrates: we can always find trajectories of interface states that link the two Weyl points with opposite charges no matter what the reflecting substrate is.

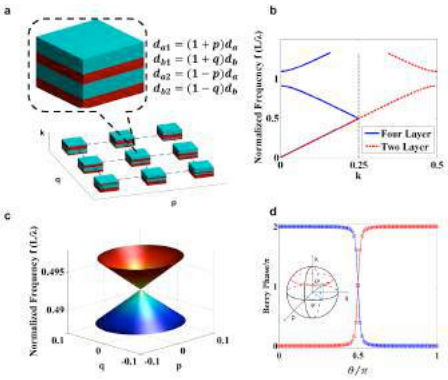

Fig. 1 **(a)** Photonic crystals (PCs) with different p, q values. (b) The band dispersion of PCs with different unit cells. **(c)** The dispersion of PCs in the p-q space with $k = 0.5k_0$. Here two bands form a conical intersection. **(d)** Berry phases defined on the spherical surface with a fixed θ (see the inset).

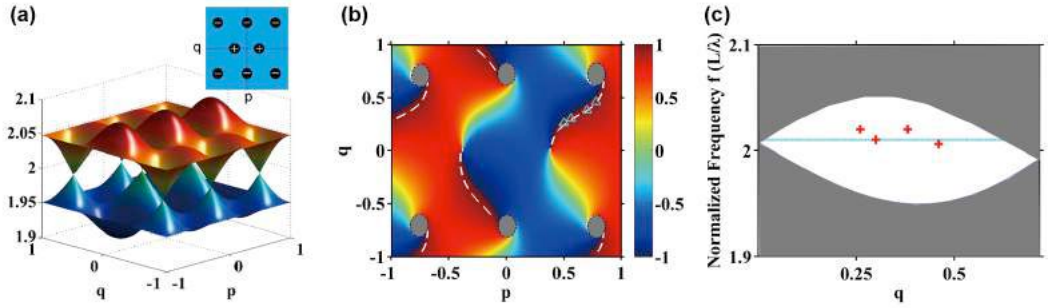

Fig. 2 (a) The band dispersions of band 4 and band 5 in the parameter space; (b) The reflection phase of the PCs at the frequency of Weyl points with charge +1. These interface state trajectories are analogues of Fermi arc states. The triangles mark the and values of the four samples in the experiment. (c) The cyan line indicates the working frequency used in a, and the red crosses label the experimental results.

REFERENCES

[1] H. Weyl, Zeitschr. Phys. **56**, 330 (1929).

[2] P. Hosur and X. Qi, Comp. Rend. Phys. **14**, 857 (2013).

[3] B. Q. Lv, H. M. Weng, B. B. Fu, X. P. Wang, H. Miao *et al.*, Phys. Rev. X **5**, 031013 (2015).

[4] T.-R. Chang, S.-Y. Xu, G. Chang, C.-C. Lee, S.-M. Huang *et al.*, Nat. Commun. **7**, 10639 (2016).

[5] S.-Y. Xu, N. Alidoust, I. Belopolski, Z. Yuan, G. Bian *et al.*, Nat. Phys. **11**, 748 (2015).

[6] L. Lu, L. Fu, J. D. Joannopoulos, and M. Soljacic, Nat. Photon **7**, 294 (2013).

[7] B.-A. Jorge, L. Ling, F. Liang, B. Hrvoje, and S. Marin, 2D Mater. **2**, 034013 (2015).

[8] M. Xiao, Q. Lin, and S. Fan, Phys. Rev. Lett. **117**, 057401 (2016).

[9] W.-J. Chen, M. Xiao, and C. T. Chan, Nat. Commun. **7**, 13038 (2016).

[10] W. Gao, B. Yang, M. Lawrence, F. Fang, B. Beri *et al.*, Nat. Commun. **7**, 12435 (2016).

Crystalline metamaterials for topological properties at subwavelength scales

S. Yves[1*], R. Fleury[2], T. Berthelot[3], M. Fink[1], F. Lemoult[1] and G. Lerosey[1]

[1]Institut Langevin, CNRS UMR 7587, ESPCI Paris, PSL Research University, 1 rue Jussieu, 75005 Paris, France
[2]Laboratory of Wave Engineering, EPFL, Station 11, route cantonale, 1015 Lausanne, Switzerland
[3] CEA Saclay, IRAMIS, NIMBE, LICSEN, UMR 3685, F-91191, Gif sur Yvette, France
[*]corresponding author: simon.yves@espci.fr

Abstract-The intriguing concept of topological insulators has been transposed from condensed matter to optics/acoustics. However, these photonic/phononic topological insulators are inherently physically wavelength scaled. Here, we explain how structural modifications of locally resonant metamaterials, although deep-subwavelength scaled, also induce a topological phase transition. This experimental and numerical demonstration allows to envision applications benefiting the compactness of metamaterials and the amazing potential of topological insulators.

In this talk, we will show how going beyond the usual description of locally resonant metamaterials in terms of effective parameters allows to induce topological properties on a subwavelength scale[1]. Without any loss of generality, we take the particular case of quarter-wavelength-resonators in the microwave domain. First we show numerically that, thanks to multiple scattering[2], it is possible to engineer the band structure of a subwavelength scaled lattice of such resonators in order to obtain Dirac cones.

Then, following the previous work of Wu and Hu[3], we operate adiabatic subwavelength structural changes within the metamaterial. We show that these modifications lead to a phenomenon of band inversion which, added to the computation of the topological invariant, is a proof of the topological nature of the metamaterial crystals we designed. This band inversion is demonstrated both numerically and experimentally comparing the symmetries of the measured modes within the samples. This phenomenon is completely explained from a polaritonic point of view.

Moreover, the interface between media which present different topological behavior supports topological edge modes. Therefore we will show that this phenomenon occurs in the case of our subwavelength microwave topological insulator. We measure experimentally, and corroborate numerically, the propagation of subwavelength topological edge modes along the interface between two topologically different samples. This demonstrate the guiding of microwave on a subwavelength scale. We finally show that this work can be directly transposed to the acoustic domain[4].

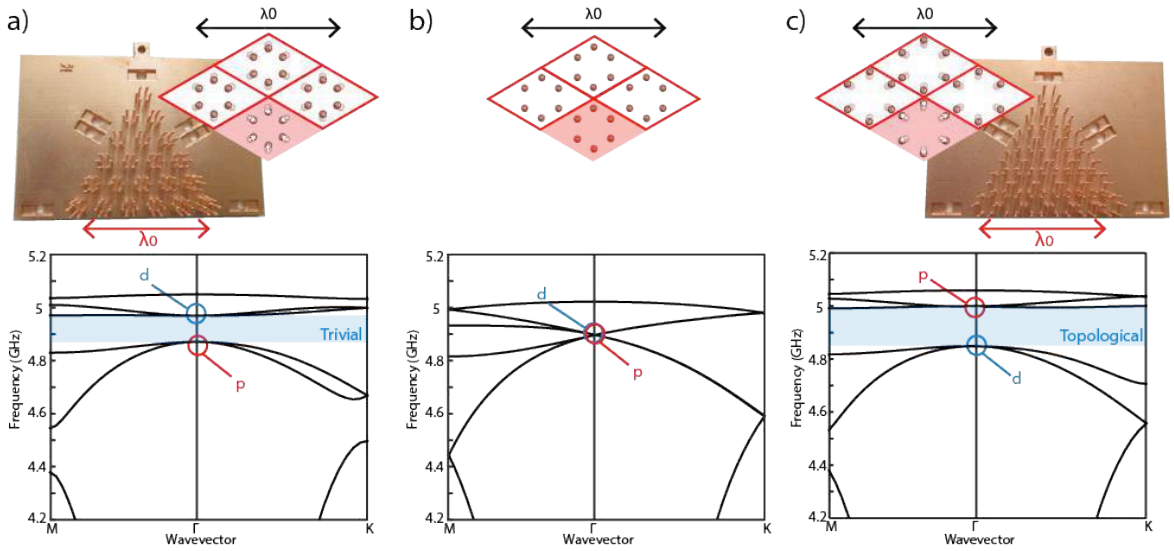

Fig. 1. Tailoring the deep-subwavelength structure of a honeycomb lattice of wires (b), we demonstrate that we can induce a topologically trivial (a) or non-trivial (c) bandgap.

Acknowledgements, the research leading to these results has received funding from the People Program (Marie Curie Actions) of the European Union's Seventh Framework Program (FP7/2007-2013) under REA grant agreement n. PCOFUND-GA-2013-609102, through the PRESTIGE program coordinated by Campus France. This work is also supported by LABEX WIFI (Laboratory of Excellence within the French Program "Investments for the Future") under references ANR-10-LABX-24 and ANR-10-IDEX-0001-02 PSL* and by French National Research Agency under reference ANR-13-JS09-0001-01. S.Y. acknowledges funding from French Direction Générale de l'Armement.

REFERENCES

1. Yves S., R. Fleury, T. Berthelot, M. Fink, F. Lemoult and G. Lerosey, "Crystalline metamaterials for topological properties at subwavelength scales", Under review, *Nat. Commun.* (2017).
2. Kaina, N., F. Lemoult, M. Fink and G. Lerosey, "Negative refractive index and acoustic superlens from multiple scattering in single negative metamaterials", *Nature* 525, 77–81 (2015).
3. Wu, L.-H. and X. Hu, "Scheme for Achieving a Topological Photonic Crystal by Using Dielectric Material", *Phys. Rev. Lett.* 114, 223901 (2015).
4. Yves, S., R. Fleury, M. Fink, F. Lemoult and G. Lerosey, "Topological acoustic polaritons: robust sound manipulation at the subwavelength scale", Under review, *New J. Phys.* (2017).

Directly Measuring Photonic Band Topology in A Dimerized Designer-Surface-Plasmon Chain

Fei Gao[1], **Yidong Chong**[1,2], **and Baile Zhang**[1,2*]

[1]Division of Physics and Applied Physics, School of Physical and Mathematical Sciences, Nanyang Technological University, Singapore 637371, Singapore

[2]Centre for Disruptive Photonic Technologies, Nanyang Technological University, Singapore 637371, Singapore

[*]corresponding author: blzhang@ntu.edu.sg

Abstract-Photonic band topology in a dimerized chain is defined with the winding of pseudo spin along the Brillouin zone. However, no experiment has measured the winding process in any photonic system so far. Here we present the direct measurement of pseudo-spin winding in a dimerized designer-surface-plasmon chain.

Recently, many efforts are devoted to the measurement of photonic band topology in one-dimensional (1D) dimerized chain which relates to the winding of pseudo spin in the Brillouin zone [1, 2]. However, photonic pseudo spins, which can be represented by the in-phase and out-of-phase hybridized wavefunctions in a unit cell, are not easy to characterize in photonic structures [2]. Furthermore, sweeping the pseudo spin across the whole Brillouin zone, which requires physical realizations of tuning wavevectors k, is also difficult to implement in photonic structures. Therefore, it is very challenging to measure the winding of pseudo spins.

Designer-surface-plasmon structures, in which field patterns with phase information can be easily captured, shows promising potentiality to demonstrate the winding of photonic pseudo spins [3, 4, 5]. Based on this platform, tuning k is also feasible. Here, we present the direct measurement of windings of pseudo spins in a 1D designer-surface-plasmon dimer chain.

Acknowledgements, This work was partially supported by Nanyang Technological University for NAP Start-up Grants, Singapore Ministry of Education under Grant No. MOE2015-T2-1-070 and Grant No. MOE2011-T3-1-005.

REFERENCES

1. Xiao, M., Zhang, Z. Q., and Chan, C. T. "Surface Impedance and Bulk Band Geometric Phases in One-Dimensional Systems," *Phys. Rev. X* 4, 021017 (2014).
2. Wang, Q., Xiao, M., Liu, H., Zhu, S., and Chan, C. T. "Measurement of the Zak phase of photonic bands through the interface states of a metasurface/photonic crystal," *Phys. Rev. B* 93, 041415 (2016).
3. Gao, F., *et al*., "Vertical transport of subwavelength localized surface electromagnetic modes," *Laser Photon. Rev*., 9, 571-576 (2015).
4. Gao, F., *et al*., "Probing topological protection using a designer surface plasmon structure," *Nat. Commun*., 7:11619 doi:10.1038/ncomms1619 (2016).
5. Gao, F., *et al*., "Invisibility Dips of Near-Field Energy Transport in a Spoof Plasmonic Metadimer," *Adv. Funct. Mater*., doi:10.1002/adfm.201602233 (2016).

Visualization of unidirectional electromagnetic waveguide using topological photonic crystals made of dielectric materials

Y. Yang[1], Z. H. Hang[1*], and X. Hu[2]

[1]College of Physics, Optoelectronics and Energy & Collaborative Innovation Center of Suzhou Nano Science and Technology, Soochow University, Suzhou 215006, China

[2]International Center for Materials Nanoarchitectonics (WPI-MANA), National Institute for Materials Science, Tsukuba 305-0044, Japan

[*]corresponding author: zhhang@suda.edu.cn

Abstract- The introduction of topology unravels a new chapter of physics, where photonic systems can also benefit from. Engineering locally in real space a honeycomb photonic crystal (PC) with double Dirac cone in its photonic dispersion, topology transition in photonic band structure is induced and a pseudospin unidirectional photonic channel is created and demonstrated by the backscattering immune electromagnetic transportation.

In electronic system, the intrinsically Kramers pair associated with electronic spin states is crucial for the helical edge states in quantum spin Hall effect with time-reversal symmetry (TRS). In order to realize topology protected electromagnetic propagations, a direction mapping of Kramers pair in photonic system is needed.

In this paper, the experimental demonstration of a unidirectional electromagnetic waveguide is conducted using dielectric PCs as previously theoretically schemed.[1] Hexagonal clusters of six neighboring dielectric rods are arranged in a triangular lattice (Fig. 1a). Two competing lengths exist in such a composite lattice (Fig. 1c & d): the intra couple distance h_1 defined as the distance between neighboring rods within the same cluster and the inter couple distance h_2 defined as the distance between the nearest rods in neighboring clusters. By tuning the ratio between h_1 and h_2, the original double Dirac cone photonic dispersion (Fig. 1b) can be engineered and PCs with inversed bulk band properties can be created.

Unidirectional backscattering immune photonic pathway forms at the interface between two PCs with inversed bulk bands and its wave propagation properties is characterized with proof-of-principle microwave experiments using dielectric materials. An antenna array is designed as the source of electromagnetic wave to mimic Kramers pairs in this photonic system with TRS. Direct experimental visualization of the unidirectional waveguide is achieved even in the frequency bands where the topological edge state is buried in bulk photonic band edges. As only dielectric materials with reasonable permittivity are adopted, the structure can be readily available at near-infrared or even optical wavelengths and the present design of topological PC will contribute to future optical communication technology.

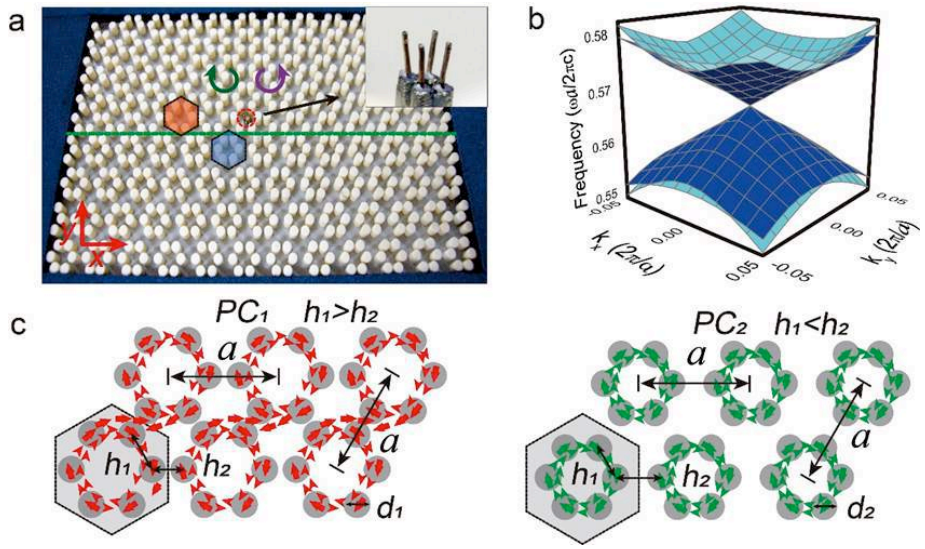

Fig. 1: (a) Experimental setup of dielectric PCs to realize unidirectional microwave propagation. (b) Double degenerate Dirac cone appears at the Brillion zone center of a honeycomb PC. (c) and (d): By tuning the ratio between intra couple distance h_1 and inter couple distance h_2, PCs with topological/trivial band diagrams can be created and unidirectional electromagnetic waveguide can thus be created at the interface between a topological PC and a trivial one.

Acknowledgements The work in Soochow University is supported by National Natural Science Foundation of China (Grant Nos. 11304215, 11574226 and 11675116) and a Project Funded by the Priority Academic Program Development of Jiangsu Higher Education Institutions (PAPD). X.H. is supported by the WPI Initiative on Materials Nanoarchitectonics, Ministry of Education, Cultures, Sports, Science and Technology, Japan.

REFERENCES

1. Wu, L.-H. and X. Hu, "Scheme for achieving a topological photonic crystal by using dielectric material," *Phys. Rev. Lett.* Vol. 114, 223901, 2015
2. Yang, Y., Y. F. Xu, T. Xu, H.-X. Wang, J.-H. Jiang, X. Hu, and Z. H. Hang, "Visualization of unidirectional electromagnetic waveguide using topological photonic crystals made of dielectric materials," *arXiv:1610.07780*

Building Photonic Topological Insulators with Reconfigurable Multipost Re-Entrant Meta-Cavities

M. Goryachev[1*]**, and M. E. Tobar**[1]
[1] ARC Centre of Excellence for Engineered Quantum Systems,
University of Western Australia, Australia
[*]corresponding author: maxim.goryachev@uwa.edu.au

Abstract-The concept of multiple post re-entrant metastructures scaling from a double post cavity to a lattice with nontrivial topological properties is considered. We demonstrate reconfigurable photonic analogues of topological insulators on a regular lattice of tunable posts in a re-entrant 3D lumped element type system. High post tunability allows dynamical in-situ change of media chirality and other properties via alteration of the same parameter for all posts. This provides great flexibility in choice of bulk/edge configurations. Also, one way photon transport without an external magnetic field is demonstrated.Applications in quantum hybrid systems and fundamental physics tests are be discussed.

Being a universal probe of the electromagnetic field, microwave cavities are important tools used in many areas of physics and engineering. In particular, they are employed in many experiments of Quantum Electrodynamics (QED) enhancing field-matter interaction and searches for fundamental particles, forces and symmetries such as Lorentz violating interactions and dark matter particles. The success in many of these areas is related to the ability to produce cavity-like structures with the given field geometries at given frequencies and possibility of *in-situ* reconfigurability. An interesting method to approach the cavity design problem comes from the field of photonic metamaterials. In particular, we will consider photonic meta-cavities built of multiple re-entrant posts.

A single post re-entrant resonator is a well known closed electromagnetic cavity that is widely used in accelerators and some other areas. It may be understood as a 3D version of a split-ring resonator with the rotation symmetry around the post centre. The post is characterized inductance around itself and capacitance in the gap underneath. Due to the high concentration of the electric field in the gap, the resonant frequency of the structure is highly turnable. A natural generalisation of the concept is introduction of several posts in the same closed cavity[1]. In such a case, a number of resonances equals a number of posts, and mutual orientation of post currents for every resonances gives a full control over the distribution of magnetic field inside the cavity. This idea was used to achieve strong and superstrong coupling with spins in solids for QED applications [2-4]. For system with a relatively large number of posts in such a meat-cavity, one can speak of mode bands of different polarisation with possible bandgaps between them that have been demonstrated both in one and two dimensions[1,5]. Moreover, it is possible to control these bands and having control over the gaps under the structure posts. Thus, it makes possible to introduce a concept of programable cavity arrays similar in spirit to the widely used programable gate arrays (FPGAs), where one my control frequencies and mode shapes over a large number of regular posts[5].

The post gaps and thus electromagnetic properties of re-entrant post meta-cavities can be controlled either mechanically or electronically. In the first case, the gap is changed by a piezoelectric actuator that is attached to the post or the opposite cavity wall. In the second case, a varactor diode is introduced between the post and the opposite wall and the equivalent electrical distance in the gap is controlled via the DC between them.

After demonstrating the band properties in closed multiple post meta-cavities, the further important step is to achieve topologically nontrivial phenomena. Unfortunately, each straight re-entrant post is a trivial object that os lumped in the cavity plane. On the other hand, instead of having a lattice of single posts, one may introduce an array of a group of closely positioned posts. Such a group may be understood as a ‘meta-molecule’ constituting the lattice and have non-trivial shapes in the cavity plane[6]. In particular, it is possible to introduce chirality for such an object, for example, through varying the post gaps in the clockwise or counter-clockwise direction across the molecule. Such method has an advantage of being reconfigurable *in-situ* through gap modification. Thus, it is possible to design a meta-cavity with reconfigurable chiral post objects that may compose a lattice with nontrivial topological properties.

To demonstrate nontrivial topological properties of multiple-post arrays, we consider a lattice of four post square molecules where the gap size changes clock-wise or counter-clockwise. Moreover, in order to make the

entire lattice as regular as possible, the inter-molecule spacing is set equal to the square size. This constitutes a regular array of posts where the molecules are distinguished only by gap variations. The system is modelled using both Hamiltonian eigenmode approach and full 3D electromagnetic modelling. We show that the system exhibits band gaps and edge modes in both 2D and 1D arrays. These modes arise on the boundary between lattices with different chirality. Additionally, one way photon transport without an external magnetic field is demonstrated. The ability to change configuration of the system in any spot gives an advantage of changing the system topology 'on the fly'. High localisation of edge modes together with its reconfigurability may be exploited to address certain areas of the system coupling to some small objects 'on-demand'. This is a vital property in the scope of QED where magnetic crystals or qubits should be strongly coupled to condition to some other signals. In other words, the concept implements multi-purpose random access systems, e.g. memories. The other possible applications inspired by the reconfigurability property is topological signal processing and sensing.

Acknowledgements, This work was supported by the Australian Research Council Grant No. CE110001013 and DP160100253.

REFERENCES

1. Goryachev, M. and Tobar M. "The 3D split-ring cavity lattice: a new metastructure for engineering arrays of coupled microwave harmonic oscillators," *New J. Phys*, Vol. 17, 023003, 2015.
2. Goryachev, M., Farr, W.G., Creedon D.L., Fan, Ya., Kostylev, M. and Tobar, M.E., "High-Cooperativity Cavity QED with Magnons at Microwave Frequencies," *Phys. Rev. Applied*, Vol. 2, 054002, 2014.
3. Kostylev, N., Goryachev, M., and Tobar, M.E., "Superstrong coupling of a microwave cavity to yttrium iron garnet magnons," *Appl. Phys. Lett.*, 108, 062402, 2016.
4. Creedon, D.L., Le Floch, J.M., Goryachev, M., Farr, W.G., Castelletto, S., and Tobar, M.E., "Strong Coupling Between P1 Diamond Impurity Centres and 3D Lumped Photonic Microwave Cavity", *Phys. Rev. B*, 91, 140408(R), 2014.
5. Goryachev, M. and Tobar M. "Creating tuneable microwave media from a two-dimensional lattice of re-entrant posts," *J. Appl. Phys.*, Vol. 118, 204504, 2015.
6. Goryachev, M. and Tobar M. "Recongurable Microwave Photonic Topological Insulator," *Phys. Rev. Applied,* Vol. 6, 064006, 2016.

Towards copolymer self-assembly of photonic Weyl metamaterials

M. Fruchart and **V. Vitelli**

Leiden University, The Netherlands
fruchart (at) lorentz.leidenuniv.nl

Abstract— Block copolymers are soft materials made of different types of monomers glued together by covalent bonds. They self-assemble into highly structured phases which can replicate at the mesoscopic scale the symmetry of atomic crystals. Here, we present a bottom-up approach based on copolymer-self assembly to engineer photonic crystals with topologically protected Weyl points. These photonic metamaterials exhibit a frequency and angle selective optical response, lack of Anderson localization and chiral edge states, even in the absence of time-reversal symmetry breaking.

Dynamic long-range couplings in low-symmetry topological photonic systems

Kin Hung Fung*

The Hong Kong Polytechnic University, China
khfung@polyu.edu.hk

Abstract— Non-Hermitian and Lorentz non-reciprocal photonic resonators have attracted intense attention due to their complexities which are strongly dependent on their spatial and temporal structures. Recently, it has been found that arrays of these resonators could also form interesting topological bands and edge modes, which has provided alternatives for realizations of new topological states. Classical photonic systems are different from electronic systems in that the fields near photonic resonators are usually not very localized. However, many traditional theories for the topological bands and edge modes were based on oscillator models with nearest neighbor couplings, ignoring many interesting effects. We try to understand the roles of radiative long range couplings on topological bands and edge modes. In this talk, we will discuss the dynamic radiative effects on the bands and edge modes in these low-symmetry topological photonic systems. Arrays of plasmonic nanoparticles and gyromagnetic resonators will be used as examples to illustrate the effects. The roles of various symmetries including Lorentz reciprocity, time-reversal symmetries, and other spatial-temporal symmetries will also be discussed.

ACKNOWLEDGMENT

This research was partly supported by the Hong Kong Research Grant Council through General Research Fund Scheme (Grant nos. 15300315 and 509813) and Area of Excellence Scheme (Grant no. AoE/P-02/12). The authors also acknowledge the support from the Hong Kong Polytechnic University (G-UC70, G-YBPT). The results to be presented were mostly contributed by C. W. Ling, Raymond P. H. Wu, Ka Hei Choi, K. F. Lee, Jin Wang, and Yongliang Zhang.

REFERENCES

1. Raymond P. H. Wu, K. F. Lee, Ka Hei Choi, Yongliang Zhang, and Kin Hung Fung, "Dynamic effects in non-reciprocal topological arrays made of gyromagnetic resonators," (to be published) (2017).
2. C. W. Ling, Ka Hei Choi, T. C. Mok, Zhao-Qing Zhang, and Kin Hung Fung, "Anomalous Light Scattering by Topological PT-symmetric Particle Arrays," *Scientific Reports* **6**, 38049 (2016).
3. Jin Wang, Hui Yuan Dong, C. W. Ling, C. T. Chan, Kin Hung Fung, "Nonreciprocal mu-near-zero mode in PT-symmetric magnetic domains," *Physical Review B* **91**, 235410 (2015).
4. C. W. Ling, Meng Xiao, C. T. Chan, S. F. Yu, and Kin Hung Fung, "Plasmonic Topological Edge States between Diatomic Chains of Nanoparticles," *Optics Express* **23**, 2021-2031 (2015).
5. C. W. Ling, Jin Wang, and Kin Hung Fung, "Formation of Non-reciprocal Bands in Magnetized Diatomic Plasmonic Chains," *Physical Review B* **92**, 165430 (2015).

Topological and noreciprocal sound and light in quantum well structures

A. V. Poshakinskiy[1], **and A. N. Poddubny**[1,2*]

[1] Ioffe Institute, 194021 St. Petersburg, Russia
[2] ITMO University, 199034 St. Petersburg, Russia
corresponding author: poddubny@coherent.ioffe.ru

Abstract— We study optomechanical effects in the laser-pumped periodic multiple-quantum-well structures. The light-sound interaction is strongly enhanced at the exciton resonance of the quantum wells and the hybrid exciton-light-phonon quasiparticles, termed as phonoritons, are formed. The phonoritons exhibit pumping-induced synthetic magnetic field in the artificial "coordinate-energy" space that makes transmission of left- and right- going waves different. The transmission nonreciprocity allows to use such phonoritonic crystals with realistic parameters as optically controlled nanoscale acoustic diodes and one-way lasers.

In layered multiple quantum well structures the photoelastic interaction is enhanced by several orders of magnitude at the exciton resonance [1], boosting the optomechanical effects. So far the optomechanics of such structures has been analyzed only in the weak exciton-light coupling regime [2]. Here, we study the laser-pumped quantum well structures depending on the relative strength of exciton-photon and exciton-sound interaction. We consider the strong exciton-light coupling and add a new dimension to the phase diagram of coupled light and matter [3], see Fig. 1. In the regime, when both these interactions are strong the eigenmodes are phonoritons, i.e., a hybrid of phonons, photons, and excitons.

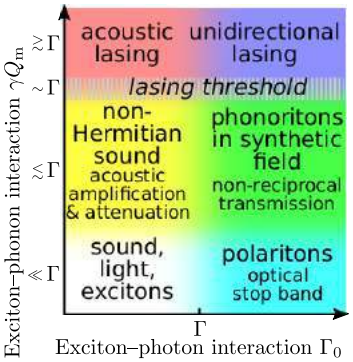

Figure 1: Effects in laser-pumped quantum wells, depending on the exciton-photon and exciton-phonon interactions.

We demonstrate that the propagation of phonoritons through the 1D structure is equivalent to the quantum walk on a stripe of a 2D lattice in the virtual "coordinate–energy" space. Finite pump laser wave vector induces synthetic magnetic field on the lattice, making the wave transport nonreciprocal. The structure can controllably amplify phonons transmitted in one direction while attenuating those transmitted in the opposite direction, enabling construction of an acoustic diode and and unidirectional laser. The proposed devices are can be realized using the mature planar growth technology, are easily integrable with existing optoelectronic platforms and might be promising for phononic computing.

ACKNOWLEDGMENT

This work has been supported by Russian President Grants No. MK-8500.2016.2 and SP-2912.2016.5

REFERENCES

1. B. Jusserand, A.N. Poddubny, A.V. Poshakinskiy, A. Fainstein, and A. Lemaitre, "Polariton resonances for ultra-strong coupling cavity optomechanics in GaAs/AlAs multiple quantum wells", Phys. Rev. Lett., Vol. 115, 267402, 2015.
2. A.V. Poshakinskiy, A.N. Poddubny, and A. Fainstein, "Multiple Quantum Wells for $\mathcal{PT}$-Symmetric Phononic Crystals," Phys. Rev. Lett., Vol. 117, 224302, 2016.
3. A.V. Poshakinskiy and A.N. Poddubny, "Phonoritonic crystals with synthetic magnetic field for acoustic diode," arXiv:1611.07970.

The effect of topology on quantum photonic states in silicon

A. Blanco-Redondo[1*], B. Bell[1], M. Segev[2] and B. J. Eggleton[1]

[1] Centre for Ultrahigh bandwidth Devices for Optical Systems (CUDOS), Institute of Photonics and Optical Science (IPOS), School of Physics, The University of Sydney, New South Wales 2006, Australia

[2] Department of Physics, Technion - Israel Institute of Technology, Haifa 32000, Israel

[*]corresponding author: andrea.blancoredondo@sydney.edu.au

Abstract – We study the effect of topology on quantum walks using on-chip generated correlated photon pairs in an array of silicon waveguides. By using single-photon measurements and simulations we demonstrate the transition between the characteristic path entanglement in random quantum walks and topological localization of the quantum states. Further, we show the robustness of that topological localization to disorder.

Quantum walks are one of many fascinating aspects in quantum information, which are receiving increasing interest since it was shown that they can efficiently perform tasks that are computationally hard in a classical computer [1]. The intrinsically low decoherence of photons, combined with the capability of easily engineered optical platforms, make photonic systems ideal to study different phenomena in quantum walks [2]. In particular, the study of topological phenomena in quantum walks is interesting since it provides a route to robust transport of multiphoton states [3].

We recently demonstrated topological localization of light in an array of silicon waveguides [4], in close analogy with the SSH model [5]. Here, by single-photon measurements and simulations, we demonstrate that a similar platform can be used to study the effect of topology in quantum walks. In particular, we take advantage of the high nonlinearity of silicon waveguides that leads to the generation of correlated photon pairs via four-wave mixing (FWM). In a purely random quantum walk scenario, with equidistant waveguides, the correlated photon pairs spread across the lattice (Fig. 1a). This yields the path entanglement shown in the correlation map at the output of the lattice (Fig. 1b) and the measured correlation counts in the nine center waveguides shown in Fig. 1c.

Next we introduce non-trivial topology in the array by alternating the distances between waveguides and creating long-long defects [4,6]. When exciting the center waveguide of the long-long defect we observe topological localization of the photon pairs (Fig. 1c) giving rise to an output correlation map (Fig 1d) in which the initially spread path entanglement collapses into the center waveguide waveguides. This is further evidenced by the correlation counts measured at the output, shown in Fig. 1f.

The most striking effects of topology in quantum walks are observed when the system is subject to disorder. In this particular implementation, we introduce disorder in the position of the waveguides (the width of the waveguides remains unchanged). Introducing disorder in the purely random quantum walk leads to strong disturbances of the propagation of the photon pairs, which lead to a correlation map strongly affected by disorder (Fig. 1g). When the same level of disorder is introduced in the array with nontrivial topology the propagation of the photon pairs and the correlation map at the output (Fig. 1h) remain unaffected. This robustness is due to the existence of a topological phase that is preserved as long as the chiral symmetry of the structure is conserved.

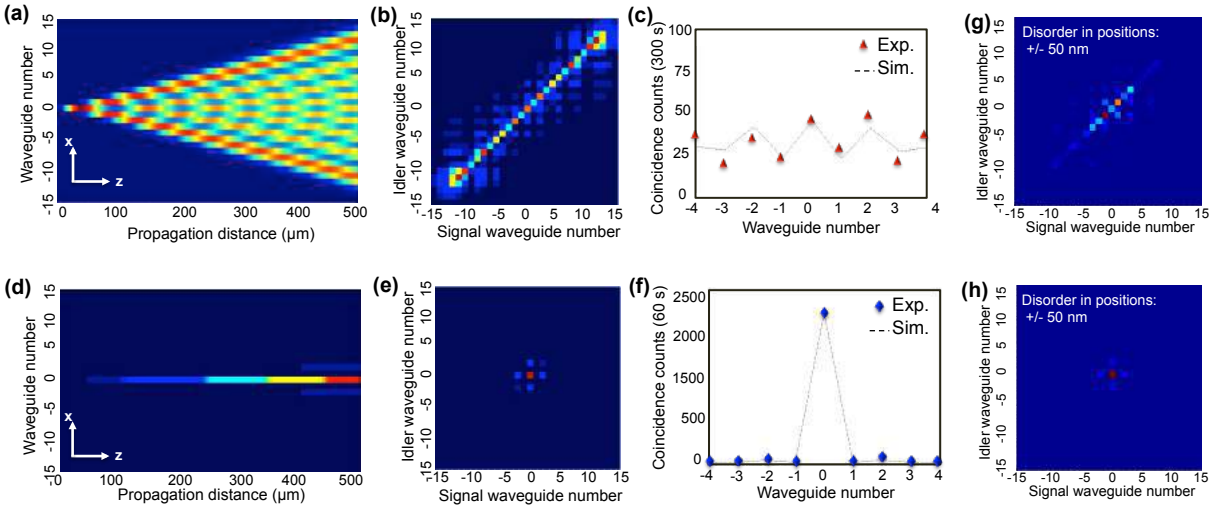

Figure 1. Comparison between random quantum walk and topological quantum walk: (a) Simulated photon pair propagation, (b) simulated output correlation map, and (c) measured correlation counts at the output of the random quantum walk; (d-f) Similar for the topological quantum walk; (g) Correlation map at the output of the random quantum walk and (h) the topological quantum walk when disorder in the position of the waveguides is introduced.

Acknowledgements, This work was supported by The University of Sydney and the Technion collaborative photonics research project funded by The Technion Society of Australia (NSW) and the NSW Department of Industry. The work was also funded by the Center of Excellence CUDOS (CE110001018) and Laureate Fellowship (FL120100029) schemes of the Australian Research Council (ARC).

REFERENCES

1. Aaronson, S., and A. Arkhipov, "The computational complexity of linear optics" Proceedings of the 43rd Annual ACM Symposium on Theory of Computing (ACM, New York), 333, 2011.
2. Peruzzo, A., Lobino, M., Matthews, J. C. F., Matsuda, N., Politi, A., Poulios, K., Zhou, X.-Q., Lahini, Y., Ismail, N., Wörhoff, K., Bromberg, Y., Silberberg, Y., Thompson, M. G., and OBrien, J. L., "Quantum walks of correlated photons," *Science* Vol. 329, 1500–1503, 2010.
3. Rechtsman, M. C., Lumer, Y, Plotnik, Y, Perez-Leija, A., Szameit, A., and Segev, M., "Topological protection of path entanglement," Optica, Vol. 3, No. 9, 925-930, 2016.
4. Blanco-Redondo, A., Andonegui, I., Collins, M. J., Harari, G., Lumer, Y., Rechtsman, M. C., Eggleton, B. J., and Segev, M., "Topological optical waveguiding in silicon and transition between topological and trivial defect states," *Phys. Rev. Lett.*, Vol. 34, No. 16, 163901-5, 2016.
5. Su, W. P., Schrieffer, J. R., and Heeger, A. J., "Solitons in Polyacetylene" *Phys. Rev. Lett*. Vol. 42, No. 25, 1698-1701, 1979.
6. Malkova, N., Hromada, I., Wang, X., Bryant, G. and Chen, Z., "Observation of optical Shockley-like surface states in photonic superlattices," *Opt. Lett.* Vol. 34, No. 11, 1633-1635, 2009.

Three-Dimensional All-Dielectric Photonic Topological Metacrystal

A. Slobozhanyuk[1,2,3], **S. H. Mousavi**[2], **X. Ni**[1], **D. Smirnova**[2], **Y. S. Kivshar**[3], **A. B. Khanikaev**[1,2]*
[1]*Department of Nanophotonics and Metamaterials, ITMO University, St. Petersburg 197101, Russia,*
[2]*Electrical Engineering Department, City College College of New York,NY, NY 11031, USA*
[3]*Nonlinear Physics Centre, Australian National University, Canberra ACT 0200, Australia*
*akhanikaev@ccny.cuny.edu

Abstract-We demonstrate that a symmetry protected topological (SPT) state can be engineered in a three-dimensional (3D) all-dielectric metacrystal where the electromagnetic duality between electric and magnetic fields is ensured by the meta-atoms design. Magneto-electric coupling results in a complete topological photonic bandgap and an emergence of spin-polarized surface states with conical Dirac dispersion on 2D topological domain walls.

Following the footsteps of condensed matter topological systems, a significant progress has been recently made in understanding and realizing topological states of light [1]. Here demonstrate that that topological state protected by the electromagnetic duality can be engineered in a 3D metacrystal. The duality, which is reflected in the symmetry of the Maxwell equations with respect to electric and magnetic field components, responsible for the SPT phase of the electromagnetic eigenmodes, otherwise broken by materials response [2,3], is restored by careful design of building blocks of the 3D photonic lattice – meta-atoms. We demonstrate a 3D photonic metacrystal based on the all-dielectric metamaterial platform, which is thus free of very restrictive requirement earlier concepts, including time-reversal violating systems, where magnets or temporal modulation are required, and SPT approaches utilizing lossy metallic/metamaterial components [2,3]. The suggested design can therefore be readily implemented across entire electromagnetic spectrum from microwave to visible.

The topological photonic metacrystal introduced here is schematically shown in Fig. 1a. It represents a 3D hexagonal lattice of dielectric disks with the permittivity ϵ_d=81 embedded into a matrix of permittivity ϵ_b=3. The dielectric disks - meta-atoms - and their 3D periodic arrangement are designed in a way that the photonic band structure exhibits two overlaid 3D Dirac points near the K-point in the Brillouin zone as in Fig. 1b. Each of the observed Dirac bands originates from the electric and magnetic dipolar modes of the disks with their dipole moments aligned in the *xy* plane, perpendicular to their axes. It is important that the very possibility to emulate a true 3D Dirac point found for relativistic massless spin-½ fermions described by the Dirac equation, i.e. the four linear bands which are overlaid in a pairwise manner, is enabled by the duality symmetry. The presence of these two independent sets of modes, the magnetic-dipole and electric-dipole degrees can also be understood as the result of inversion symmetry in the z-direction, present in the case of gapes structure Fig.1b, as the electric (magnetic) modes are odd (even) with respect to the σ_z ($z\rightarrow -z$) transformation. Any reduction of the σ_z symmetry results in the coupling of the in-plane electric and magnetic orbitals and opening of a band gap in the place of Dirac points. This magneto-electric coupling, also referred to as bianisotropy, has an effect equivalent to the spin-orbital interaction in condensed matter [2,3].

An example of the metacrystal with σ_z symmetry broken by removing part of the dielectric cylinder is shown in Fig. 1a, right panel, with its band structure in Fig. 1(c), which reveals a full 3D bandgap. The modes of such gapped structure no longer represent pure electric and magnetic modes, but are mixed states with the phases between their electric and magnetic components being locked. The dipolar electric and magnetic moments of these modes always appear to be tilted by 90 deg and -90 deg with respect to each other, thus constituting two sets of eigenmodes $\psi^{\uparrow}$ and $\psi^{\downarrow}$, where the superscript indicates up (↑) or down (↓) pseudo-spin value, both for lower and upper bands.

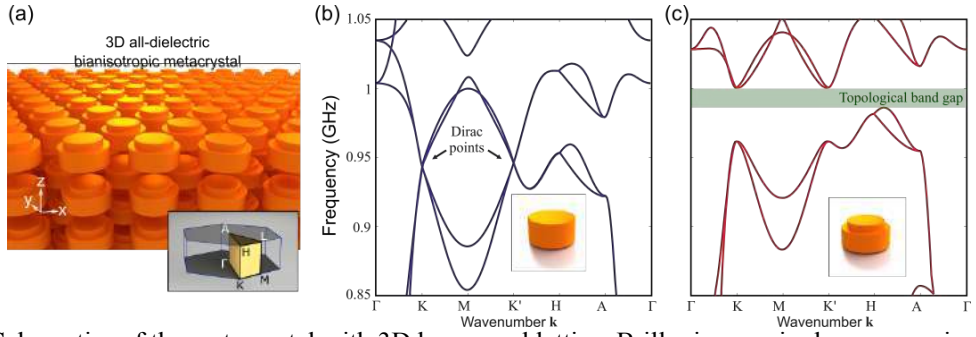

Fig 1. (a) Schematics of the metacrystal with 3D hexagonal lattice. Brillouin zone is shown as an inset. (b,c) Photonic band structures calculated along the high symmetry directions for crystals without and with bianisotropy.

One of the most important consequences of topological order is the emergence of gapless surface states, which may occur either on the external interfaces with topologically trivial system or at the domain walls separating topological systems of distinct classification. Here we consider the topological domain wall along the *yz*-cut which represents an interface between two topological crystals inverted with respect to each other along the z-direction, which results in the reversal of bianisotropy. The corresponding structure is shown in Fig. 2a with the photonic band structure in Fig. 2(b,c). The left and central panels in Fig. 2(b) show two cuts of two-dimensional band structure $\omega(k_y,k_z)$ and reveal two pairs of surface states. The surface states appear within the band gap region interconnecting lower and upper bulk bands. The 3D band diagram shown in Fig. 2(c) exposes one of the Dirac cones corresponding to the surface states near K-point. As in the case of 3D electronic topological insulators, the surface states in our system also have a property of spin-locking which endows them with topological robustness.

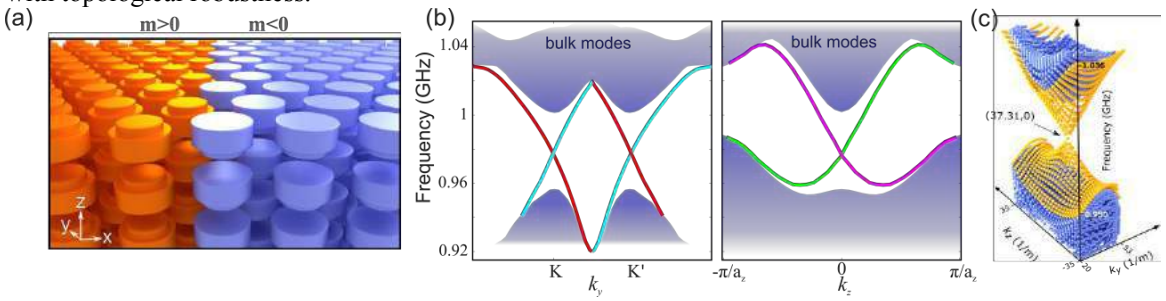

Fig 1. (a) The schematics of the domain wall formed by the reversal of the mass term induced by the bianisotropy in the middle of the metacrystal. (b) Band diagrams of topological surface states supported by the domain wall. (c) The conical Dirac-like dispersion of the surface states.

In summary, we propose an all-dielectric photonic platform which can be used for implementation of topologically robust 3D photonic circuitry in entire electromagnetic spectrum from microwave frequencies to optical domain. The proposed all-dielectric metacrystals may allow avoiding undesirable effects of Ohmic loss unavoidable in metallic structures, and, in addition, facilitates topological order in photonics-compatible dielectric and semiconductor materials, thus avoiding technical difficulties associated with the use of magnetic materials and external magnets required to induce topological order in systems with broken TR symmetry.

REFERENCES

1. L. Lu, J. D. Joannopoulos, and M. Soljaćić, "Topological photonics," Nature Photon. **8**, 821-829 (2014).
2. A. B. Khanikaev, et al., "Photonic topological insulators," Nature Mater. **12**, 233–239 (2013).
3. A. Slobozhanyuk, S. H. Mousavi, X. Ni, D. Smirnova, Y. S. Kivshar, A. B. Khanikaev, "Three-Dimensional All-Dielectric Photonic Topological Insulator", Nature Photon. 11, 130–136 (2017).
4. X. Cheng, C. Jouvaud, X. Ni, S. H. Mousavi, A. Z. Genack, and **A. B. Khanikaev**, "Robust propagation along reconfigurable pathways within a photonic topological insulator", Nature Mater. 15, 542–548 (2016).

Exciting Reflectionless Unidirectional Edge Modes in a Reciprocal Photonic Topological Insulator Medium

Bo Xiao,[1] Kueifu Lai,[2] Yang Yu,[2] Tzuhsuan Ma,[2] Gennady Shvets,[2] and Steven M. Anlage[1]*

[1] Department of Physics and Department of Electrical and Computer Engineering
University of Maryland, College Park, MD 20742-4111, USA

[2] Applied and Engineering Physics, Cornell University, Ithaca, NY 14853-3501, USA

*corresponding author: anlage@umd.edu

Abstract- Photonic topological insulators are an interesting class of materials whose photonic band structure can have a band gap in the bulk while supporting topologically protected unidirectional edge modes. Recent studies on bianisotropic metamaterials that emulate the electronic quantum spin Hall effect using its electromagnetic analog are examples of such systems with a relatively simple and elegant design. In this presentation, we present a rotating magnetic dipole antenna, composed of two perpendicularly oriented coils, that can efficiently excite the unidirectional topologically protected surface waves in the bianisotropic metawaveguide (BMW) structure recently realized by T. Ma *et al.* [Phys. Rev. Lett. **114**, 127401 (2015)] despite the fact that the BMW medium does not break time-reversal invariance. In addition to achieving a high directivity, the antenna can be tuned continuously to excite reflectionless edge modes in the two opposite directions at various amplitude ratios. We demonstrate its performance through experiments and compare to simulation results. For details, see Phys. Rev. B **94**, 195427 (2016).

Acknowledgements, This work was supported by the ONR under Grant No. N000141512134, AFOSR COE Grant FA9550-15-1-0171, and the National Science Foundation under Grant Nos. NSF PHY-1415547; AFOSR FA9550-15-1-0075; ARO W911NF-16-1-0319, and NSF ECCS-1158644.

Transformation Optics concept and applications

Detecting the spatial chirp signals by fractional Fourier lens with transformation materials

J. Chen and J. Hu*
School of Information and Electronics, Beijing Institute of Technology, China
*corresponding author: bithj@bit.edu.cn

Abstract- Detecting the rate of frequency change or chirp rate (CR) of a spatial chirp signal is important in some optical applications. With the help of transformation optics, the improved fractional Fourier lens can be designed to adjust the CR as well as the focusing location of the given input chirp signals. In consequence the CR detection precision can be improved and the range of the input signals can be extended. The numerical simulations verified the design.

Transformation optics (TO) provides an intuitive and direct way to control electromagnetic wave propagation by designing appropriate materials [1]. Lu et al. [2] utilized TO to widen the input spatial frequency bandwidth of the graded index (GRIN) lens by isotropic transformation media and pointed out its potential in fractional Fourier transform (FrFT). In this study, we explore the application of the FrFT lens proposed by Lu et al. [2] in detecting the CR of a spatial chirp signal with enhanced precision and range. Detecting the CR of a spatial chirp signal is important in some optical application. For example, the Newton's rings are two dimensional (2D) chirps and their CRs are important in optical measurements.

It is known that if $f(x)$ is a chirp signal and the FrFT has proper order corresponding to the CR, the FrFT result of $f(x)$ is an impulse [3]. In view of this, the FrFT lens can be used to detect the CR of an input chirp. The chirp will focus at the location within the lens where the corresponding FrFT order can be found [4], in turn the CR can be calculated [3]. The higher the CR is, the smaller the FrFT order will be, and the closer the impulse will locate to the input facet. As the traditional GRIN lens is work under the paraxial approximation, the short propagate distance of high CR signal will lead to considerable error. The proposed lens compress the input facet and maintain the output facet length [2], as a result, although the input signal is the same, it can be viewed as a compressed chirp and is equivalent to a uncompressed chirp in the original space according to TO principle. That is, the proposed lens can reduce the input CR. Compared to the signal with higher CR, the one with lower CR can focus farther in the lens and makes the paraxial approximation satisfied better, thus the detection precision can be improved, which also means the range of the input chirp signals can be extended for the given error.

The 2D numerical simulations results are shown in Fig. 1 and Tab. 1. The compression factor of the input facet is 2.3819 and the input test chirps are transverse electric (TE) waves, with wavelength= 0.09m. One should note that the proposed lens has different method from the traditional GRIN lens in obtaining the FrFT order [2]. It is clear that with the help of the proposed FrFT lens, the detection precision of the CR can be greatly improved. The proposed device may boost the applications of optical FrFT, and the idea proposed here also implies that TO has broad prospects in the field of spatial signal processing.

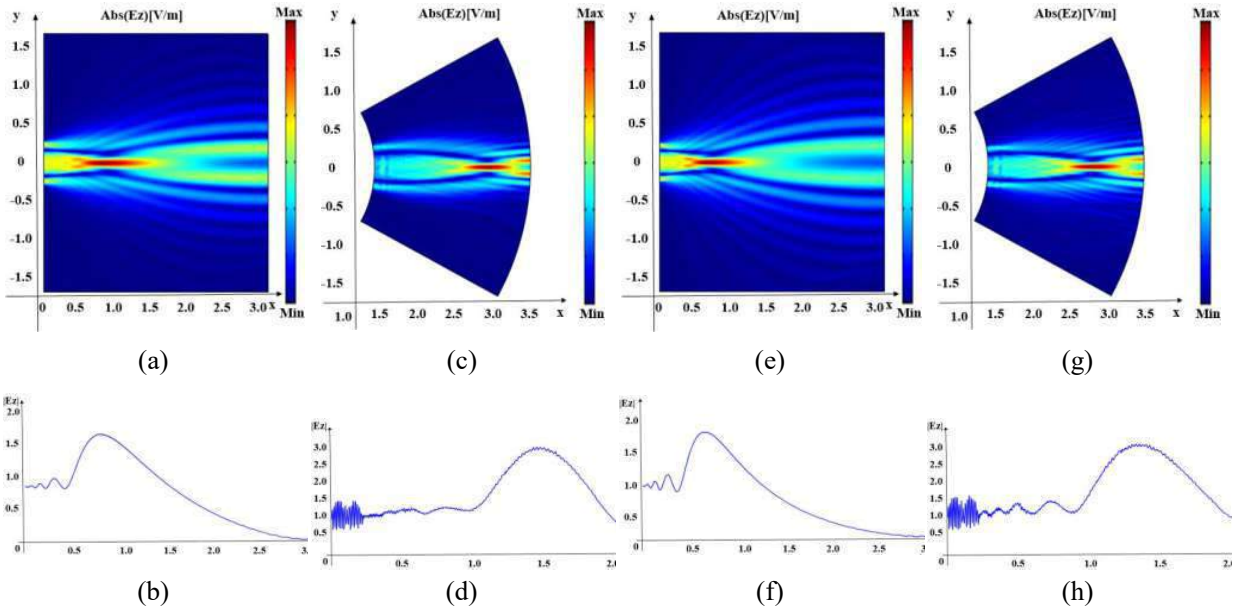

Figure 1. The electric fields |Ez| distributions in the devices and the corresponding amplitude spectrums along the optical axis. (a),(b),(c) and (d): traditional and proposed lens for input CR=50, respectively; (e),(f),(g) and (h): traditional and proposed lens for input CR=60, respectively.

Lens	Input test CR	Theoretical FrFT order	Focusing location	Obtained FrFT order	Obtained CR	FrFT Order error (%)	CR error (%)
Traditional	50	0.3159	0.8189	0.2696	60.0678	14.66	20.14
Proposed			1.4527	0.3055	52.0110	3.28	4.02
Traditional	60	0.2698	0.6578	0.2165	76.5005	19.74	27.5
Proposed			1.3578	0.2603	62.4880	3.53	4.15

Table 1. The comparison of the CR detection precisions between the two kinds of lenses in Fig. 1.

Acknowledgements This work was supported by the National Natural Science Foundation of China (61575022).

REFERENCES

1. J. B. Pendry, D. Schurig, and D. R. Smith, "Controlling electromagnetic fields," *Science* 312(5781), 1780–1782 (2006).
2. X. Lu, J. Hu, and R. Tao, "Enhanced fractional Fourier lens with isotropic transformation media," *Opt. Eng*., 52, 060501 (2013).
3. R. Tao, Y. Li, Y. Wang, "Short-Time Fractional Fourier Transform and Its Applications," *IEEE Trans. Signal Process*. 58(5), 2568–2580 (2010)
4. D. Mendlovic and H. M. Ozaktas, "Fractional Fourier transforms and their optical implement: I," *J. Opt. Soc. Am. A* 10(9), 1875–1881 (1993).

Designing transformation optics devices for wave vectors manipulation

Mircea Giloan*, **Robert Gutt**, **and Gavril Saplacan**

Company for Applied Informatics, Cluj-Napoca, Romania,
*corresponding author: mircea_giloan@cianet.ro

Abstract— The devices designed using a transformation optics approach are mainly accomplishing their functionality by inducing specific manipulations of the wave paths through coordinate transformations. In this study we analyze how the wave vectors can be manipulated as the waves propagate in transformation media derived from a specific class of coordinate transformations. We provide a powerful method for designing electromagnetic devices able to accomplish different functions by inducing proper manipulations of the wave vectors generated by appropriate coordinate transformations.

An electromagnetic device alters the wave path and/or the wave vector of an incident wave according to the desired functionality. So far, the concept of transformation optics was used to design different devices, mainly by focusing on the manipulation of the wave path of the electromagnetic waves [1]-[3].

In this study we present the design of a flat device consisting of a medium delimited by two parallel planes. The required functionality of the device is a proper manipulation of the wave vector in order to provide a specific wave vector distribution at the output plane of the device. The wave vector distribution at the output plane will determine the propagation path of the wave into the homogeneous medium which surrounds the device. This theoretical study shows a general method to retrieve the proper coordinate transformation, and consequently the corresponding permittivity and permeability of the transformed medium, which will generate the desired wave vector distribution at the output plane of the device [4].

Figure 1 shows the main geometrical characteristics of the designed device, the trajectories of the wave paths inside the device and after leaving the device, and the components of the wave vectors of the incident and emergent waves. The device consists in a medium delimited by two planes perpendicular on $z-$axis. The wave path of a normally incident wave is constrained to a parallel line to $z-$axis. In order to manipulate the wave vector inside the device the following coordinate transformation of the original space was used:

$$\left\{ \begin{array}{l} x' = x \\ y' = y \\ z' = zf(x,y) \end{array} \right\} \tag{1}$$

where $f(x,y)$ is a function of two variables which transforms the z coordinate with respect to x and y coordinates.

Considering that the original space is the free space the relative electric permittivity ε and magnetic permeability μ of the anisotropic medium, having an identical electromagnetic behavior as the transformed space described by equations (1), are given by the same symmetric tensor, denoted by n:

$$n = \frac{1}{f(x,y)} \begin{bmatrix} 1 & 0 & \frac{z\partial_x f(x,y)}{f(x,y)} \\ 0 & 1 & \frac{z\partial_y f(x,y)}{f(x,y)} \\ \frac{z\partial_x f(x,y)}{f(x,y)} & \frac{z\partial_y f(x,y)}{f(x,y)} & \frac{z^2((\partial_x f(x,y))^2 + (\partial_y f(x,y))^2)}{f^2(x,y)} + f^2(x,y) \end{bmatrix} \tag{2}$$

where $\partial_x f$ and $\partial_y f$ denote the partial derivatives of the f function with respect to x and y variables,respectively. Note that, tensor n described by equation (2) is expressed in terms of x', y', and z' coordinates of the transformed space where, for simplicity, the primes have been dropped.

After performing some mathematical computations we proved that at normal incidence (i.e. the wave vector of the incident wave has the form $\mathbf{k}_i^T = (0, 0, k_{zi})$, where the superscript $(\cdot)^T$ denotes

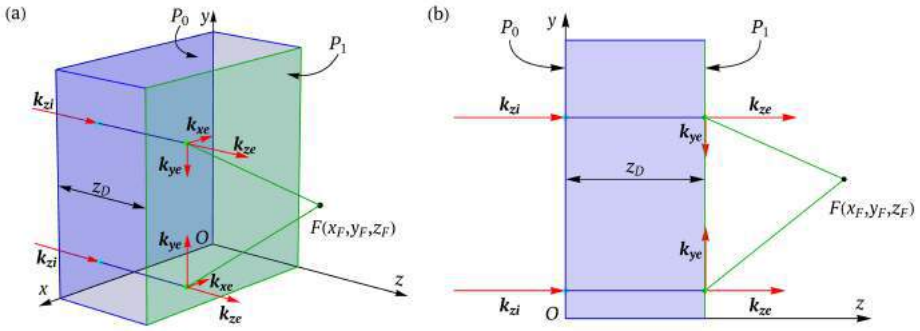

Figure 1: **(a)** 3D view and **(b)** yz plane view, of a reduce area of the device. The device is delimited by the input ($P0$) and output ($P1$) planes perpendicular on $z-$axis and displaced by z_D. The wave paths are depicted inside and outside the device by blue and green lines, respectively. The incident and emergent wave vector components are depicted by red arrows. F denotes an arbitrary point of convergence for the emergent wave vectors (i.e. a focal point) in the particular case of a converging flat lens design.

the transpose operator) the transverse components of the wave vector k_x and k_y are changing linearly with respect to z coordinate so that the $x-$ and $y-$axis components of the emergent wave vector $\mathbf{k}_e^T = (k_{xe}, k_{ye}, k_{ze})$ are described by the following equations:

$$k_{xe} = \frac{\partial h}{\partial x} z_D, \quad k_{ye} = \frac{\partial h}{\partial y} z_D \tag{3}$$

where z_D is the thickness of the device and $h(x, y) = 1/f(x, y)$ (see Fig. 1 and ref. [4]). Since the emergent wave propagates in the free space the components of the wave vector are satisfying also the relation:

$$k_{xe}^2 + k_{ye}^2 + k_{ze}^2 = 1. \tag{4}$$

Equations (3) are the most important result of our theoretical study. In completion with equation (4) these equations allow us to retrieve the function $f(x, y)$ which describes the transformation media able to produce at the output interface of the device the wave vector distribution required by the functionality of the device. Once this function is found the material parameters of the device are easily found from equation (2).

In our presentation we will show through numerical simulations using Finite-Difference Time-Domain (FDTD) algorithms how this theoretical result, which enables a flexible manipulation of the wave vectors, can be applied to design optical devices for the following fields:

- generation of Bessel and angular momentum beams;
- optical information processing;
- super-resolution imaging;
- optical cloaking.

ACKNOWLEDGMENT

This work was developed by the Company for Applied Informatics using infrastructure obtained through the program POSCCE-A2-O2.3.2-2012-1 (ID: 1542/SMIS: 44023), and partially supported by the program PNII/2014-nr. 153/2014.

REFERENCES

1. D. Schurig, J. B. Pendry and D. R. Smith, "Calculation of material properties and ray tracing in transformation media", *Opt. Express* 14, 9794 (2006).
2. D. Schurig, "An aberration-free lens with zero F-number", *New J. Phys.* 10, 115034 (2008).
3. N. Kundtz, and D. R. Smith, "Extreme-angle broadband metamaterial lens", *Nat. Mater.* 9, 129-132 (2010).
4. M. Giloan "Designing wave vector manipulation devices using a transformation optics approach", arXiv:1612.09488 [physics.optics] (2017).

Transformational Fluctuation Electrodynamics: Application to Thermal Radiation Illusion

A. Alwakil[1]*, M. Zerrad[1], M. Bellieud[2], D. Veynante[3], F. Enguehard[3], N. Rolland[4], S. Volz[3] and C. Amra[1]

[1]Aix Marseille Univ, CNRS, Centrale Marseille, Institut Fresnel, Marseille, France
[2]Université Montpellier 2, CNRS, LMGC, France
[3]Ecole Centrale Paris, CNRS, EM2C, France
[4]Université de Lille 1, CNRS, IEMN, France
*corresponding author: ahmed.alwakil@fresnel.fr

Abstract-We apply transformation optics to the field of thermal radiation where fluctuational electrodynamics is shown to be invariant under transformation optics. We show that thermal camouflage/cloaking can be possibly realized using the proposed theory.

In this paper, we extend transformation optics theory [1-2] to thermal radiation physics [3] in order to control thermally radiated signatures emitted from an arbitrary object. Applications concern countermeasure effects in a way similar to other thermal camouflage techniques [4-8].

Starting with fluctuation dissipation theorem [4-6] where thermally fluctuating current sources are related to radiative losses, we show that it is possible for objects residing in virtual and physical space to have the same spectral thermal signature. To reach this goal the complex permittivities and permeabilities should be related by the typical transformation optics such that the fluctuation electrodynamics problem [7] is invariant under transformation. Furthermore the thermal current sources are transformed in a way similar to that of coherent sources according to source transformation [14]. These two properties are the basis for the invariance of fluctuation electrodynamics and allow the illusion procedure in thermal radiation.

We illustrate the concept using the cloaking/illusion paradigm in the two dimensional space [15], where an object is coated with a transformation optics designed cylindrical coat in order to mimic [16] the emitted thermal signature of two other different objects, one for its Transverse Electric polarization and the other for its Transverse Magnetic polarization. Finally we discuss possible extensions to other transformations and physical limitations of their realizations.

Acknowledgements, This work was supported by the French National Research Agency (ANR- INPACT project).

References:

1. Pendry, J. B., Schurig, D. and D. R. Smith, " Controlling electromagnetic fields," *science*, Vol. 312, No. 5781, 1780-1782, 2006.
2. Schurig, D., Pendry, J. B. and D. R. Smith, "Calculation of material properties and ray tracing in transformation media," *Optics Express*, Vol. 14, No. 21, 9794-9804, 2006.
3. Howell, J. R., Menguc, M. P. and R. Siegel, *Thermal radiation heat transfer*, CRC press, 2010.
4. Burkinshaw, S. M., Hallas, G. and A. D. Towns, "*Infrared camouflage*," *Review of Progress in*

Coloration and Related Topics, Vol. 26, No. 1, 47-53, 1996.
5. Wijewardane, S. and D. Y. Goswami, "A review on surface control of thermal radiation by paints and coatings for new energy applications," *Renewable and Sustainable Energy Reviews*, Vol. 16, No. 4, 1863-1873, 2012.
6. Bamfield, P. and M. G. Hutchings, *Chromic phenomena: technological applications of colour chemistry*, Royal Society of Chemistry, 2010.
7. Gupta, K. K., Nishkam, A. and N. Kasturiya, "Camouflage in the non-visible region," *Journal of Industrial Textiles*, Vol. 31, No.1, 27-42, 2001.
8. Kats, M. A., Blanchard, R., Zhang, S., Genevet, P., Ko, C., Ramanathan, S. and F. Capasso, "Vanadium dioxide as a natural disordered metamaterial: perfect thermal emission and large broadband negative differential thermal emittance," *Physical Review X*, Vol. 3, No. 4, 2013.
9. Callen, H. B. and T. A. Welton, "Irreversibility and generalized noise," *Physical Review* Vol. 83, No. 1, 34, 1951.
10. Weber, J. "Fluctuation dissipation theorem," *Physical Review,* Vol. 101, No. 6, 1620, 1956.
11. Kubo, R. "The fluctuation-dissipation theorem," *Reports on progress in physics,* Vol. 29, No. 1, 255, 1966.
12. Rytov, S.M. "Theory of electric fluctuations and thermal radiation," *Air Force Cambridge Research Center, Bedford MA*, 1959.
13. Henkel, C. "Nanoscale Thermal Transfer–An Invitation to Fluctuation Electrodynamics," *Zeitschrift für Naturforschung* A, 2016.
14. Kundtz, N., Roberts, D. A., Allen, J., Cummer, S. and D. R. Smith, "Optical source transformations," *Optics express* Vol. 16, No. 26, 21215-21222, 2008.
15. Guenneau, S., Petiteau, D., Zerrad, M., and C. Amra, "Bicephalous transformed media: concentrator versus rotator and cloak versus superscatterer," *Optics express*, Vol. 22, No.19, 23614-23619, 2014.
16. Alwakil, A., Zerrad, M., Bellieud, M., and C. Amra, "Inverse Heat mimicking of Given Objects," *Scientific Reports* (Accepted, to be published on March 2017).

Practical Realization of a Transformation Optics based Dielectric Superstrate for Patch Antenna using 3D printing

C. Joshi[1], A.C. Lepage[1], X. Begaud[1] and G.P. Piau[2]
[1]LTCI, Télécom ParisTech, Université Paris-Saclay, France
[2] Airbus Group Innovations, Suresnes, France
[*]corresponding author: chetan.joshi.fr@ieee.org

Abstract- Transformation Optics (TO) based superstrates allow modifying radiation patterns of antennas but generally required anisotropic magnetic and dielectric materials or metamaterials. Previously, we presented a TO-based all dielectric solution which allows achieving in-plane radiation from planar antennas. In this paper, we will present the approach to design the superstrate prototype using 3D printing process and the performances achieved.

First introduced in seminal work of Pendry [1], Transformation Optics (TO) is a great tool for electromagnetic design that offers new perspective to long studied electromagnetic problems. One such problem is achieving in plane radiation from planar antennas. Traditionally such radiation can be achieved with leaky wave antennas or end-fire arrays. In [2], design of a dielectric superstrate was proposed that allows reorienting the broadside radiation pattern of a patch antenna in its azimuthal plane. Using TO and optimization techniques, permittivity values are found to interpret the transformation of a rectangular Cartesian space according to a virtual space comprised of 2 opposed quarter ellipses (Figure 1). When placed over a patch antenna, superstrate allows achieving an antipodal radiation pattern with two opposite radiation lobes in the azimuth, and a null in the broadside. Furthermore, a 3D solution is also discussed with a profile comprised of 48 pixels arranged in 3 layers with 16 pixels each, and with permittivity values ranging between 1 and 14. Such a superstrate is shown to provide the desired reorientation behavior for a patch antenna designed to function at 1.25 GHz. The profile is shown in Figure 2.

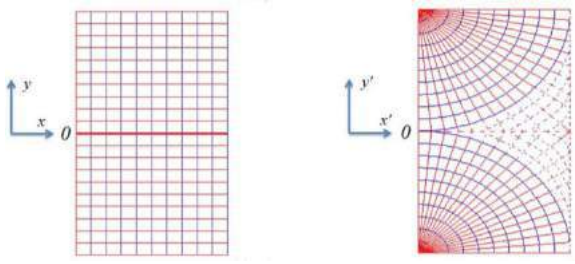

a) b)

Figure 1 (a) Physical space, (b) Virtual Space

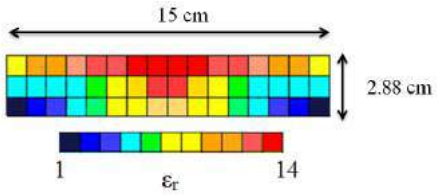

Figure 2 Dielectric TO profile with 48 pixels

While permittivity gradients can be designed by drilling holes of variable radii in a single dielectric medium, implementing the dielectric profile of [2], presented in Figure 2, is very complex using only one material due to the wide-varying permittivity profile. Indeed, materials with high-ε_r values are difficult to find and particularly to

machine. Alternatively, multiple materials can be used. For example, a three material dielectric magnifying lens has been presented in [3], where the high permittivity regions are interpreted using a single high permittivity material (F4B).

In the present work, we adopt a similar approach to address the concern of high permittivity values. Alumina ($\varepsilon_{r\text{-}high} = 9.9$) is used to interpret high permittivity region i.e. all pixels with permittivity value higher than that of alumina. Remaining values are interpreted by a single permittivity value ($\varepsilon_{r\text{-}low}$), corresponding to the permittivity of a 3D printer material. For $\varepsilon_{r\text{-}low}$ realization, two different materials were considered: Objet-FullCure photo curable resin ($\varepsilon_r = 2.8$) and PLA Thermoplastic ($\varepsilon_r = 2.56$, $\tan\delta = 0.031$). In practice, this leads to a two materials design, as shown in Figure 3. Plexiglas sheet is screwed on top face of the receptacle to secure alumina slabs.

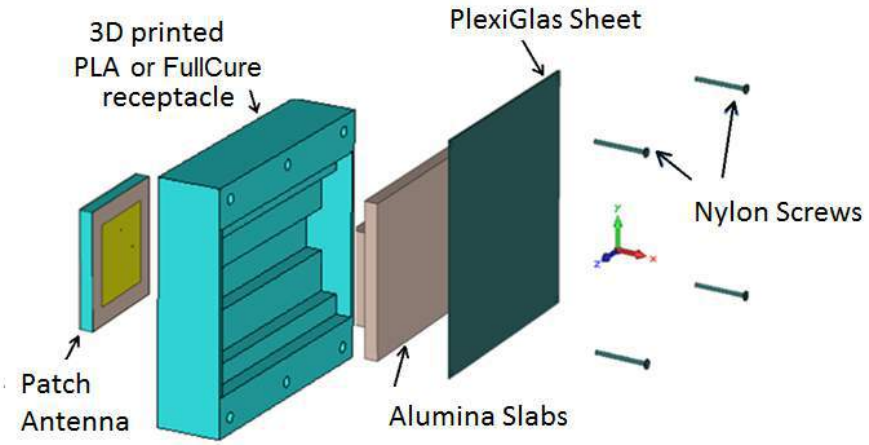

Figure 3 Representative image of the fabricated prototype

The performance achieved with these two different configurations of the superstrate placed over a classical patch antenna will be presented during the conference.

Acknowledgements: This work is supported by the NanoDesign project funded by IDEX Paris-Saclay, ANR-11-IDEX-0003-02.

REFERENCES

1. Pendry, J.B., Schurig, D. and Smith, D.R., "Controlling Electromagnetic Fields," *Science*, Vol. 312, No. 5781, 1780-1782, June 2006.
2. Joshi, C., Lepage, A.C. and Begaud, X., "A dielectric-only superstrate inspired from transformation optics for complete reorientation of electromagnetic waves in azimuthal plane," *EPJ Applied Metamaterials*, Vol. 3, No. 5, 2016.
3. Jiang, W.X. *et al.*, "Broadband all-dielectric magnifying lens for far field high resolution imaging," *Nature Communications*, Vol. 25, No. 48, 6963–6968, Dec. 2013.

Functional Metamaterial Devices for Manipulation of Waves in Microwave Region based on Transformation Optics

K. Zhang[1*], J. Mei[2], X. Ding[1], J. Fu[1], G. Yang[1] and Q. Wu[1]

[1]Harbin Institute of Technology, China

[2]Harbin University of Science and Technology, China

[*]corresponding author: zhangkuang@hit.edu.cn

Abstract-As an effective approach for manipulating propagation of waves, transformation optics has inspired many novel applications in past decades. In this paper, our recent efforts in metamaterial devices for manipulation of waves in microwave region are reviewed with emphasis on (1) multifunctional device with three different kinds of electromagnetic properties, (2) homogeneous illusion device exhibiting transformed and shifted scattering effect and (3) wave bending devices with homogeneous complementary material.

Transformation optics has attracted great attentions of scientists in optics and magnetic since proposed [1]. Based on theory of optical transformation, novel applications in manipulation of waves were proposed and analyzed in theory, including cloaks, illusion device, to name a few [2-4]. In this paper, we briefly review our recent work on metamaterial device for manipulation of waves based on transformation optics. Multifunctional device with three electromagnetic properties, homogeneous illusion device exhibiting transformed and shifted scattering effect and wave bending device with homogeneous complementary material will be introduced.

First, a multifunctional device with invisible, transparent and illusion electromagnetic properties is proposed. This device can be used as complementary cloak, as shown in Fig.1a and 1b. Scattering fields of the circular object in Fig. 1a is cancelled by corresponding anti-object, as shown in Fig.1b. Meanwhile, this device can be used as transparent device, as shown in Fig.1c and 1d. It can be seen that the field distributions of the device of horn antenna in free space are is same as with that of a horn antenna in proposed device free space. Second, a kind of homogenous illusion device exhibiting shifted and transformed scattering effect is proposed. Fig. 2a, 2c and 2e show the electrical field distributions of different PECs in shifting device with linearly minified, magnified and reshaped properties, respectively. Compared electrical field distributions of practical PEC with that of equivalent PEC (shown in Fig. 2b, 2d and 2f), we can see that the field distributions of two PECs are same although they have different size and locate in different location. Third, we adopt homogeneous complementary material to manipulate the propagation property of waves. Fig. 3a and 3b show the wave deflects with a given angle moving through the refractor and splitter. Fig. 3c and 3d show electric field distributions and the time average power outflow of waveguide bend respectively. It is clear that the guiding mode pattern is not distorted and the nearly all the energies are transmitted.

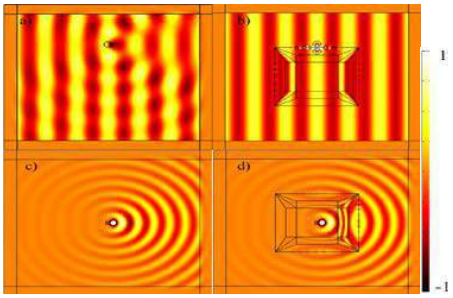

Fig. 1 Electrical field distributions of (a) circular object in free space, (b) circular object in the device, (c) horn antenna in free space and (d) horn antenna in the device.

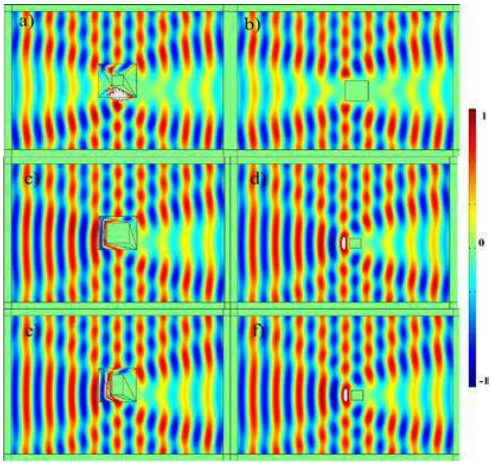

Fig. 2 Electrical field distributions of (a) small PEC, (b) equivalent big PEC, (c) big PEC, (d) equivalent small PEC, (e) rectangle PEC and (f) equivalent square PEC.

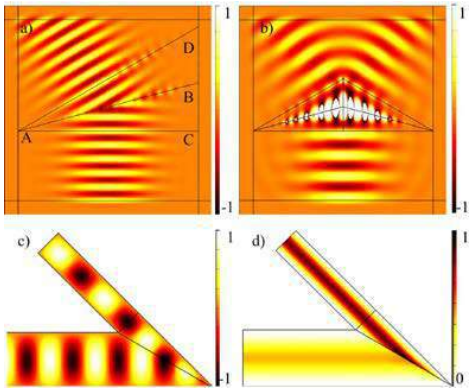

Fig. 3 Electrical field distributions of (a) wave refractor, (b) wave splitter, (c) waveguide bend and (d) time average power outflow of waveguide bend

Acknowledgements, This work is financially supported by National Science Foundation of China (No. 61401122).

REFERENCES

1. Pendry, J. B., Schuring, D. and Smith, D. R."Controlling electromagnetic fields," *Science*, vol. 312, 1780-1782, 2006.
2. Lai, Y., Chen, H. Y., Zhang, Z. Q. and Chan, C. T. "Complementary media invisibility cloak that cloaks objects at a distance outside the cloaking shell," *Phys. Rev. Lett.*, vol.102, 093901, 2009.
3. Jiang, W. X., Qiu, C. W., Han, T. C., Zhang, S. and Cui, T. J. "Creation of ghost illusion using wave dynamics in metamaterials," *Adv. Funct. Mater.* , vol. 23, 4028-4034, 2013.
4. Tichit, P. H., Burokur, S. N. and Lustrac, A. "Waveguide taper engineering using coordinate transformation technology," *Opt. Express*, vol. 18, 767-772, 2010.

QCTO-based lens antennas

J. Yi[1], T. Ding[1,2], H. Li[3], H. Zhang[1], A. de Lustrac[4] and S. N. Burokur[5,*]

[1]State Key Laboratory of Integrated Services Networks, Xidian University, Xi'an 710071, Shaanxi, China
[2]School of Information Engineering, Jimei University, Xiamen 361021, Fujian, China
[3]Department of Biomedical Engineering, Stony Brook University, State University of New York, Stony Brook, New York 11794, USA
[4]Centre de Nanosciences et de Nanotechnologies, CNRS, Univ. Paris-Sud, Université Paris-Saclay, C2N – Orsay, 91405 Orsay cedex, France
[5]LEME, EA 4416, Université Paris Nanterre, 92410 Ville d'Avray, France
[*]corresponding author: sburokur@u-paris10.fr

Abstract-A 3D lens calculated by spatial light transformation method for electromagnetic field shaping is proposed. The lens is capable of transforming cylindrical wavefronts into planar ones, and therefore generating a directive emission. Such manipulation is simulated and analyzed by solving the Laplace's equation. A potential 3D realization with all-dielectric gradient refractive index metamaterials is presented.

Transformation Optics (TO) concept [1,2], known as a powerful and effective method to simultaneously control electromagnetic (EM) fields, has been widely used to design new classes of optical and electromagnetic devices. The best known design by TO approach is the invisibility cloak [3]. Moreover, quasi-conformal transformation optics (QCTO) provides the possibility to design arbitrary shapes and avoid singularities in material parameter value. Thus it has been widely applied to design arbitrary broadband devices such as the carpet cloak [4] and functional lenses [5] with all-dielectric materials. In this study, we propose the design of a 3D lens with a mushroom shape that can significantly enhance the directivity of a conical horn antenna. Such a 3D lens is based on a former 2D one that is capable of restoring in-phase emissions from a conformal array of antennas so as to obtain performances similar to a linear one [6].

The designed model is based on quasi-conformal transformation optics (QCTO) and achieved by solving Laplace's equation. For fields' equivalence at the outer boundaries with the virtual space, Neumann and Dirichlet sliding boundary conditions are set at the edges of the cap lens:

$$\begin{aligned} &x\big|_{B'C',C'D',D'A'} = x', \quad \hat{n}\cdot\nabla x\big|_{A'B'} = 0 \\ &y\big|_{A'B'} = 0, \quad y\big|_{B'C',C'D'} = y', \quad \hat{n}\cdot\nabla y\big|_{D'A'} = 0 \end{aligned} \tag{1}$$

The range of ε_{zz} is related to the deformation between the physical space and the virtual space. We consider the initial parameters as t = 4 cm, r = 14.5 cm and θ = 0.761 rad (Fig. 1). In this case, the permittivity distribution ranges from 0 to 2.8. To refrain from using resonant metamaterials and to support a potential all-dielectric realization process, we have to consider ε_{zz} values below 1 as unity. The discrete lens is designed from dielectric-hole structures for broadband performances, as illustrated in Fig. 2.

This work was supported in part by the National Natural Science Foundation of China under grant No.

61601345 and Educational Commission of Fujian Province, China (JZ160449). J.Yi acknowledges the partial support from the Fundamental Research Funds for the Central Universities (XJS16046, JB160109) and 111 Project under Grant B08038.

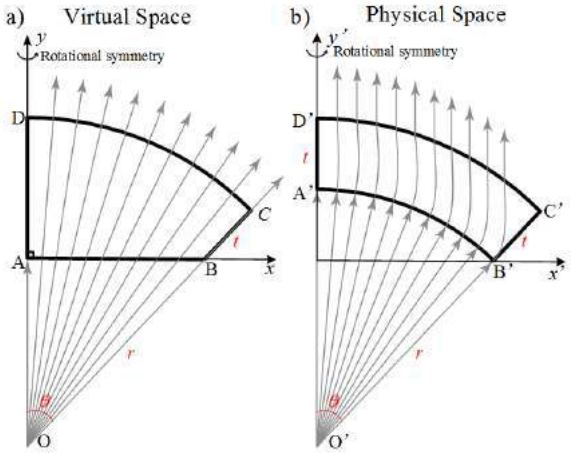

Fig. 1: Illustration showing the space mapping from the virtual space to the physical space.

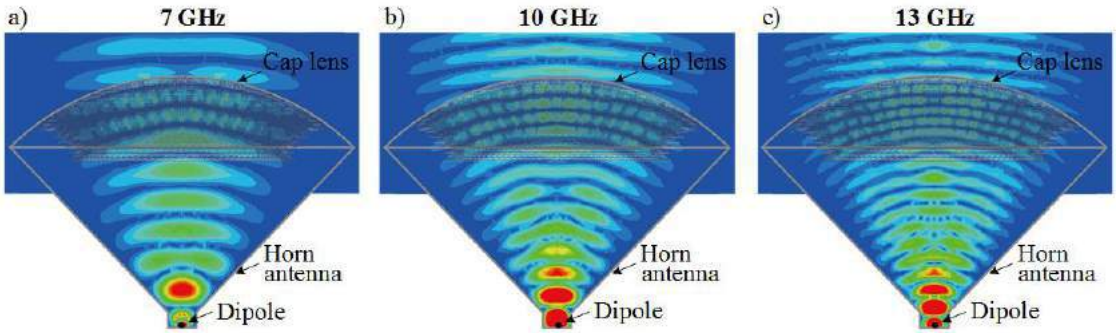

Fig. 2: Simulated electric near field distributions of 3D discrete lens in the *x-y* plane.

REFERENCES

1. Leonhardt, U., "Optical conformal mapping," *Science*, Vol. 312, No. 5781, 1777-1780, 2006.
2. Pendry, J. B., Schurig, D. and Smith, D. R., "Controlling electromagnetic fields," *Science*, Vol. 312, No. 5781, 1780-1782, 2006.
3. Schurig, D., Mock, J. J., Justice, B. J., Cummer, S. A., Pendry, J. B., Starr, A. F. and Smith, D. R., "Metamaterial electromagnetic cloak at microwave frequencies," *Science*, Vol. 314, No. 5801, 977-980, 2006.
4. Li, J. and Pendry, J. B., "Hiding under the carpet: A new strategy for cloaking," *Phys. Rev. Lett*., Vol. 101, No. 20, 203901, 2008.
5. Yi, J., Burokur, S. N., Piau, G.-P., de Lustrac, A., "Coherent beam control with an all-dielectric transformation optics based lens," *Scientific Reports*, Vol. 6, 18819, 2016.
6. Yi, J., Burokur, S. N., Piau, G.-P., de Lustrac, A., "Restoring in-phase emissions from non-planar radiating elements using a transformation optics based lens," *Appl. Phys. Lett*., Vol. 107, No. 2, 024101, 2015.

Free-standing and conformable Optical Metasurfaces

Gauthier Briere[(1)], Peinan Ni[(1)], Jun Rong Ong[(2)], Hong Son Chu [(2)], and Patrice Genevet[(1)]
(1) Université Côte d'Azur, Centre de recherche sur l'hétéro-épitaxie et ses applications, Rue Bernard Gregory, 06560, France;
(2) Institute of High Performance Computing, 1 Fusionopolis Way, 16-16 Connexis, 138632, Singapore
e-mail:patrice.genevet@crhea.cnrs.fr

Keywords: Metasurfaces, boundary optics, optical antenna.

Abrupt modifications of the fields across an interface can be engineered by depositing an array of sub-wavelength resonators specifically tailored to address local amplitude, phase and polarization changes [1]. Physically, ultrathin nanostructure arrays ($\delta \ll \lambda$), also called ''optical metasurfaces'', control light by engineering artificial boundary conditions of Maxwell's equations. Metasurfaces have been implemented to obtain various sorts of optical functionalities, ranging from the basic control of the transmission and reflection of light[1-2], to the control of the radiation patterns for comprehensive wavefront engineering and holography[3]. In the introduction, we will review the recent works in this field and we will explain the physical mechanisms required for the design of efficient planar optical components.
In this presentation, we will discuss recent works on free standing visible (GaN based) and mid-infrared (Si-based) metasurfaces [4]. We will explain which physical mechanisms are utilized for the design of efficient ultrathin planar optical components and show that these conditions are connected with the well-known Kerker conditions already proposed for isolated scatterers.

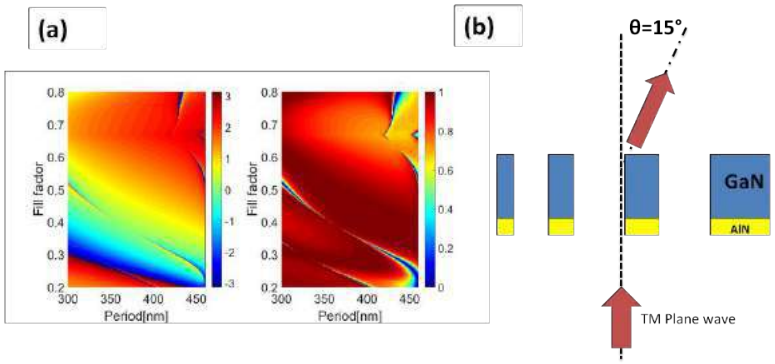

Figure 1 : (a) Phase introduce by the gratings as a function of the fill factor and the period (right) Contour of the transmission versus the fill factor and the period of the grating (b) Schematic diagram of the grating.

Beam deflectors are designed and optimised through sequential particle swarm and gradient descent optimisation in order to maximise transmission efficiency and reduce unwanted grating lobes. We have designed and optimised freestanding silicon nanohole array beam deflector for the visible and the mid-IR. Our metasurfaces, made of GaN for visible and Si for mid-infrared, are fabrication friendly and have high transmission due to the lack of substrate and the fulfillment of Kerker's conditions (fig1 and 2).

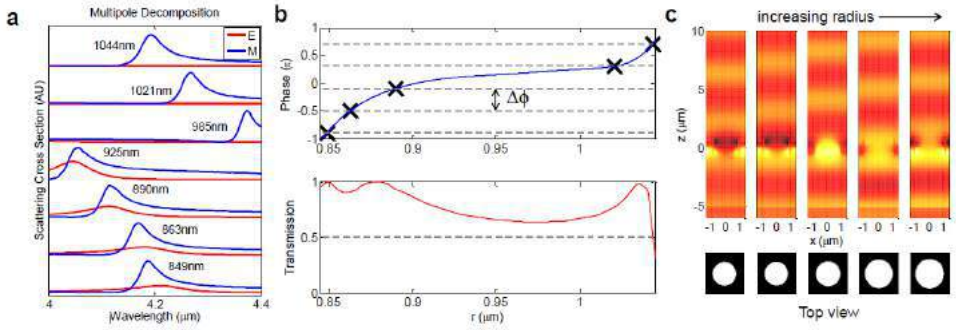

Figure 2. (a) Electric and magnetic dipolar contributions at several selected hole radii. (b) Crosses mark the chosen hole radii for the metasurface beam deflector, showing the constant phase shift difference Df and corresponding high transmission. (c) Field amplitudes before and after incidence on nanohole arrays with different radii, showing the linear phase gradient.

Similar principles can be used to design various other optical metasurfaces, e.g. flat lenses, phase plates, waveplates, helical wavefront generators, and holograms. Rectangular, elliptical, or other asymmetrical hole shapes can be used to impart birefringence to different light polarisations, as required in waveplates or polarisation beam splitters. We will conclude our presentation with a discussion on the concept of **conformal boundary optics**: an analytical method based on novel, first-principle derivations that allows us to engineer transmission and reflection at will for any interface geometry and any given incident wave[5].

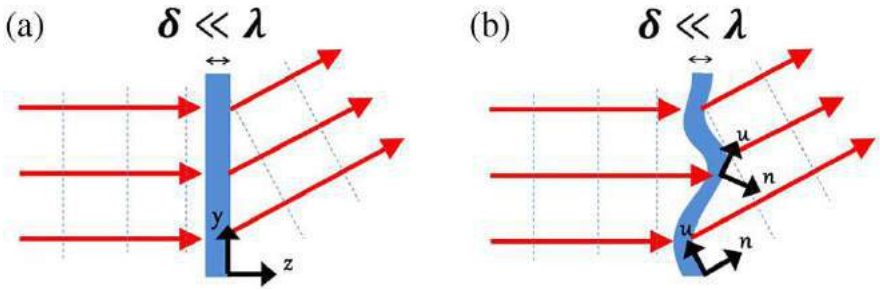

Fig. 1: 2D planar metasurface of subwavelength thickness. For planar interfaces, generalized sheet boundary conditions readily apply, and the surface susceptibility tensors can be calculated. (b) The local coordinate system of the surface follows its local curvature, changing with the position along the interface. Boundary conditions of the fields are obtained in the coordinate system of the interface and are therefore position dependent. To produce an effect equivalent to that in (a), the surface susceptibilities of the optical interface have to be engineered to account for the effect of the physical distortion. The dashed blue lines denote the equiphase fronts of the electromagnetic fields.

References:

[1] N. Yu, P. Genevet, et al., Z. Gaburro, Science 334,333 (2011)
[2] P. Genevet, F. Capasso et al., Optica, Vol. 4,139-152 (2017)
[3] P. Genevet and F. Capasso, Reports of Progress in Physics, 78, 024401 (2015)
[4] Jun Rong Ong, et al.t, Acs Photonics (submitted 2017).
[5] Han, J. T. H., Wong, L.J., Molardi C. & Genevet P., Controlling Electromagnetic Fields at Boundaries of Arbitrary Geometries, PRA 94, 023820 (2016) (2016).

Acknowledgments: PG acknowledges support from the European Research Council (ERC) under the European Union's Horizon 2020 research and innovation programme (Grant agreement no. 639109).

Advanced passive and active metasurfaces

Passive, Active, and Nonlinear Chiral Metasurfaces

Wenshan Cai
School of Electrical and Computer Engineering, Georgia Institute of Technology, USA
corresponding author: wcai@gatech.edu

Abstract- Metasurfaces can be designed to exhibit extraordinarily strong chiral responses, commonly described in terms of the circular dichroism and polarization rotation. Here we present a set of photonic metasurfaces that possess pronounced chiroptical features in both the linear and the nonlinear regimes. These structures are further exploited for chiral-selective two-photon luminescence from quantum emitters and a photon-drag effect with helicity-sensitive generation of photocurrent. Finally, we report a noticeable shift in the chiroptical responses under a modest level of excitation power.

The past few years have witnessed an explosive development of chiral photonic nanostructures that exhibit circular dichroism and optical rotation orders of magnitude larger than conventional materials. Though chirality is most commonly applied in linear optical regime, opposing circularly polarized waves can also display parity as a property of higher order optics. In this talk, we present a set of photonic metasurfaces that possess pronounced chiroptical features in both the linear and the nonlinear regimes.

In addition to gigantic linear chiroptical responses, including the circular dichroism and optical activity that are many times stronger than those found in naturally occurring media, the metasurfaces demonstrates a 20x contrast between second harmonic responses from the two circular polarizations. Linear and nonlinear response images probed with circularly polarized lights show strongly defined contrast, and the second-harmonic circular-dichroism images are produced to reveal the chiral characteristics of a metasurface pattern consisting of opposite meta-enantiomers.

The chiral hotspots created at the center of the chiral meta-atoms can be made accessible to nanoscale probes. By both exposing the resonant near field of the chiral nanostructure via plasma etching and inserting quantum dots as indicators of localized chiral hotspots, we observed substantially enhanced and chiral-selective two-photon luminescence from the hybrid meta-system. The giant chiral response in the metasurface facilitates circular dichroic manipulation of the far-field intensity of locally emitted nonlinear signals, and the strength of the two-photon signal is directly correlated to the chiral resonance in the linear regime.

In the end, we report a chiral metasurface based on topologically continuous metallic layers, which supports a photon-drag effect with helicity-sensitive generation of photocurrent. The structure is further exploited under varying illumination intensity, with which we observe an intensity-dependent modulation of optically active signals, including the circular dichroism and polarization rotation, under a modest level of excitation power..

Acknowledgements. We acknowledge supports from the National Science Foundation under Grant No. ECCS-1609567 and from the Air Force Research Laboratory through Azimuth subcontract 238-5404-GIT.

REFERENCES

1. Y. Cui, L. Kang, S. Lan, S. P. Rodrigues, and W. Cai, "Giant chiral optical response from a twisted-arc metamaterial," *Nano Letters*, Vol. 14, No. 2, 1021-1025, 2014.
2. S. P. Rodrigues, S. Lan, L. Kang, Y. Cui, and W. Cai, "Nonlinear imaging and spectroscopy of chiral metamaterials," *Advanced Materials*, Vol. 26, No. 35, 6157-6162, 2014.
3. S. P. Rodrigues, Y. Cui, S. Lan, L. Kang, and W. Cai, "Metamaterials enable chiral-selective enhancement of two-photon luminescence from quantum emitters," *Advanced Materials*, Vol. 27, No. 6, 1124-1130, 2015.
4. L. Kang, S. Lan, Y. Cui, S. P. Rodrigues, Y. Liu, D. H. Werner, and W. Cai, "An active metamaterial platform for chiral responsive optoelectronics," *Advanced Materials*, Vol. 27, No. 29, 4377-4383, 2015.
5. S. P. Rodrigues, S. Lan, L. Kang, Y. Cui, P. W. Panuski, S. Wang, A. M. Urbas, and W. Cai, "Intensity-dependent modulation of optically active signals in a chiral metamaterial," *Nature Communications*, in press, 2017.

Metasurface for polarization-controllable multichannel superpositions of orbital angular momentum states

X. Chen[1*], F. Yue[1], D. Wen[1], C. Zhang[1], B. D. Gerardot[1], W. Wang[1], S. Zhang[2]

1. Institute of Photonics and Quantum Sciences, School of Engineering and Physical Sciences, Heriot-Watt University, Edinburgh, EH14 4AS, UK
2. School of Physics & Astronomy, University of Birmingham, Birmingham, B15 2TT, UK

[*]corresponding author: x.chen@hw.ac.uk

Abstract- For practical applications of orbital angular momentum (OAM) states, a simple approach is highly desirable for the generation of OAM beams and the manipulation of their superpositions in multiple channels. We propose and experimentally demonstrate a facile metasurface approach to realize polarization-controllable multichannel superpositions of OAM states at will. Four OAM beams in separate channels are observed for an incident Gaussian beam with circular polarization. By manipulating the polarization state of the incident light, arbitrary control of the superpositions of various OAM states in multiple channels is realized using a single plasmonic metasurface.

Light possessing OAM (namely optical vortex) has a helical phase structure described by $\exp(il\theta)$, where θ is the azimuthal angle, l is the topological charge of optical vortex corresponding to an orbital angular momentum of $l\hbar$ per photon. Recently, the OAM of light has attracted considerable attention due to its promising applications, including optical tweezers, quantum memories, and metrology. Specially, a superposition of OAM states is of importance in classical physics and quantum sciences. Despite the diverse applications of OAM ranging from metrology to quantum entanglements, there are fundamental or technical challenges for current techniques to efficiently generate and manipulate multi-OAM-state of light.

Metasurfaces, the two-dimensional analog of conventional metamaterials, have drawn considerable attention in the scientific community due to their exotic electromagnetic properties and potential breakthroughs for light manipulation [1, 2]. In this paper, we propose and experimentally demonstrate an efficient approach to generate multiple OAM states and arbitrarily control their superpositions [3]. Figure 1 shows the superposition of OAM states with topological charges of same absolute values but opposite signs in four output channels. Under the illumination of RCP light, two pairs of off-axis OAM beams are generated, i.e., $|R,\ l_i\rangle$ (denoted by black dots along the horizontal direction) and $|R,\ l_j\rangle$ (yellow dots along the vertical direction), respectively (see Fig. 1a (i)). Here l_i, l_j are the topological charges. By changing the helicity of the incident light from RCP to LCP, the signs of all the topological charges of output OAM states are flipped (see Fig. 1a (ii)), and the positions of the beams are changed to the corresponding centrosymmetric positions with respect to the center, accordingly. A linearly polarized (LP) incident light can be decomposed into two equal-weighted RCP and LCP components with a phase difference, the states of the output beams generated by the metasurface are $e^{i\vartheta}|R,\ l_i\rangle + e^{-i\vartheta}|L,\ -l_i\rangle$ and $e^{i\vartheta}|R,\ l_j\rangle + e^{-i\vartheta}|L,\ -l_j\rangle$, respectively. Consequently, the superpositions of OAM states are realized. The combination of multichannel OAM generation, polarization-controlled OAM superposition, subwavelength resolution, broad spectral band, and compactness

renders this technology very attractive for diverse applications in both classical physics and quantum sciences.

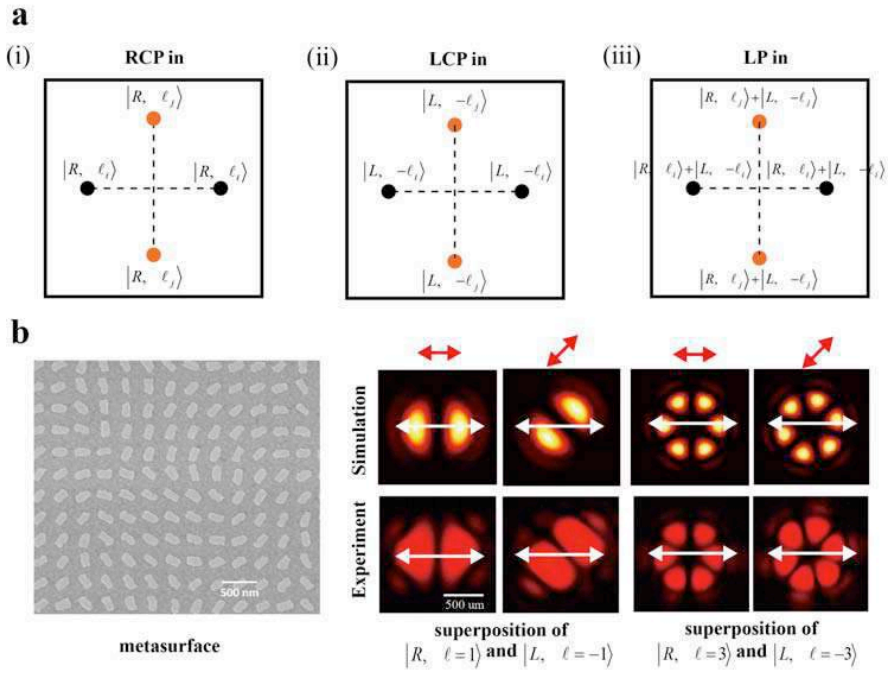

Figure 1 Schematic of the four-channel OAM superpositions, SEM images of metasurfaces, and numerically calculated and experimentally observed superpositions of OAM states. a, The generation of two kinds of OAM modes and their superpositions in four channels. (i) Upon the illumination of RCP input light, two pairs of off-axis OAM beams are generated, i.e., $|R,\ l_i\rangle$(denoted by black dots) and $|R,\ l_j\rangle$(denoted by yellow dots), respectively. (ii) The positions of OAM states and their signs are changed for LCP input light. (iii) Equal-weighted OAM states superpositions occur under the illumination of linearly polarized (LP) input light. b**,** SEM image and numerically calculated and experimentally observed superpositions of OAM states. This metasurface produces two kinds of superpositions, one for OAM states with $l = 1$ and $l = -1$, and another one for OAM states with $l = 3$ and $l = -3$. The polarization angle of incident linearly polarized light and the direction of the polarizer's transmission axis in front of the CCD camera are respectively denoted by the red double-headed arrows and the white double-headed arrows.

Acknowledgements, X.C. acknowledges the Engineering and Physical Sciences Research Council of the United Kingdom (Grant Ref: EP/M003175/1).

REFERENCES

1. Yu, N.*, et al.,* "Light propagation with phase discontinuities: Generalized laws of reflection and refraction", *Science,* Vol. 334, 333-337, 2011.
2. Wen, D., et al., "Helicity multiplexed broadband metasurface holograms", *Nat. Commun.,* Vol.6, 8241, 2015.
3. Yue, F., et al., "Multichannel polarization-controllable superpositions of orbital angular momentum states", *Advanced Materials*, in press.

Chirality-dependent surface plasmon meta-coupler and transmission -type photonic Spin hall effect with nearly 100% efficiency

Shulin Sun[1]*, Weijie Luo[2], Jingwen Duan[1], Huijie Guo[2], Qiong He[2], and Lei Zhou[2]*

[1]Department of Optical Science and Engineering, Fudan University, Shanghai 200433, China
[2] Physics Department, Fudan University, Shanghai 200433, China

Abstract- Recently, Pancharatnam–Berry (PB) metasurfaces exhibit strong abilities to control spin-polarized light. However, low frequency issue becomes a great challenge in their realistic applications. Here, we propose theoretical criterions of high-efficiency PB devices, that guide us realizing several novel effects in microwave regime. These findings can inspire the high efficiency spin-dependent wave-front manipulations in other frequency domains

Pancharatnam–Berry (PB) metasurfaces exhibit strong abilities to control spin-polarized light, leading to fascinating effects such as photonic spin-Hall effect (PSHE), optic-vortex generation and spin-dependent surface plasmon excitations. However, many previous works related to PB devices suffered from the low frequency issues [1-3]. To solve these issues, we have proposed the theoretical criterions for the design of high-efficiency PB devices and performed two different effects to demonstrate our idea.

First, we propose a new scheme to design high efficiency chirality-modulated surface plasmon meta-coupler. It solve the two key issues limiting the performances of previous related devices, that are direct reflections at the coupler surface and the mode mismatch between the coupler and the guiding-out plasmonic structure. We designed and fabricated a realistic device working in the microwave regime, and demonstrate experimentally that it can achieve an spoof SPP conversion efficiency ~78%. Full-wave simulations are in good agreement with experiments, showing that the efficiency can be further pushed to 92% with optimized designs [4]. Second, we demonstrate theoretically that 100%-efficiency PSHE can be realized in PB metasurfaces exhibiting both electric and magnetic responses satisfying certain criterions. Such criterions help us design a microwave transmissive PB metasurface with ultra-thin thickness, yet exhibiting a maximum PSHE efficiency ~91% experimentally. These findings can stimulate many high-performance PB meta-devices with diversified functionalities. As an example, we fabricate several vortex-beam generators with ultra-high working efficiencies [5].

Acknowledgment- This work is supported by National Natural Science Foundation China and Shanghai Science and Technology Committee.

REFERENCES

1. Shitrit, et al. "Optical Spin Hall Effects in Plasmonic Chains". *Nano letters* 11, 2038–2042 (2011).
2. Huang, L., et al. "Helicity dependent directional surface plasmon polariton excitation using a metasurface with interfacial phase discontinuity " *Light: Science & Applications* 2, e70 (2013).
3. Lin, J., et al. "Polarization-Controlled Tunable Directional Coupling of Surface Plasmon Polaritons ".*Science* 340, 331–334 (2013).
4. Duan, J., et al. "High-efficiency chirality-modulated spoof surface plasmon meta-coupler". *Submitted*.
5. Luo, W., et al. "Transmissive Pancharatnam–Berry Metasurfaces with Nearly 100% Efficiency". *Submitted*.

Negative refraction of highly squeezed polaritons in graphene-boron nitride heterostructures

Xiao Lin[1,†,*], Yi Yang[2,†], Nicholas Rivera[3], Josué J. López[2], Yichen Shen[3], Ido Kaminer[3], Hongsheng Chen[4,5], Baile Zhang[1,6,*], John D. Joannopoulos[3], and Marin Soljačić[3]

[1]Division of Physics and Applied Physics, School of Physical and Mathematical Sciences, Nanyang Technological University, Singapore 637371, Singapore.
[2]Department of Electrical Engineering and Computer Science, Massachusetts Institute of Technology, Cambridge, MA 02139, USA.
[3]Department of Physics, Massachusetts Institute of Technology, Cambridge, MA 02139, USA.
[4]State Key Laboratory of Modern Optical Instrumentation, Zhejiang University, Hangzhou 310027, China
[5]The Electromagnetics Academy at Zhejiang University, State Key Laboratory of Modern Optical Instrumentation, Zhejiang University, Hangzhou 310027, China.
[6]Centre for Disruptive Photonic Technologies, Nanyang Technological University, Singapore 637371, Singapore.
[†]These authors contribute equally to this work.
[*]corresponding author: xiaolinbnwj@ntu.edu.sg; blzhang@ntu.edu.sg.

Abstract*:* It is fundamental to achieve negative refraction of highly squeezed polaritons, such as plasmon polaritons in graphene and phonon polaritons in BN with their wavelengths squeezed by a factor over 100, because this could enable many unique nanoscale applications. However, this still remains challenging. We reveal that graphene-BN heterostructures provide a versatile platform to flexibly tune the sign of the group velocity of hybrid plasmon-phonon-polaritons, enabling negative refraction between graphene plasmons, BN's phonon polaritons and their hybrid polaritons.

Polaritons with extreme spatial confinement [1] are crucial for the control over the propagation of light at the nanoscale. A fundamental building block in nano-photonics and plasmonics is the ability to achieve negative refraction of polaritons, because it can offer a novel way of controlling the flow of light and can enable the demonstration of many exotic phenomena and unique applications such as deep-subwavelength imaging, superlens, and novel guiding. However, to do this for highly squeezed polaritons, such as plasmon polaritons in graphene and phonon polaritons in boron nitride (BN) with their wavelengths being able to be squeezed by a factor over 100, requires an ability to flip the sign of their group velocities, which has not been observed nor predicted so far. Therefore, demonstrating negative refraction of highly squeezed polaritons remains an open challenge that is highly sought after due to its importance for the manipulation of light at the extreme nanoscale.

In this work, we predict that utilizing the strong coupling between graphene plasmons and BN's phonon polaritons in graphene-BN heterostructures can flip both signs of their group velocities. This enables us to predict the all-angle negative refraction phenomena between graphene's plasmons and BN's phonon polaritons, and even more surprisingly, between two kinds of graphene plasmons, or between two kinds of BN's phonon polaritons, where the polaritonic wavelengths are all squeezed by a factor over 100. Moreover, unlike

conventional all-angle negative refraction of metal plasmons that are restricted to work at a given fixed frequency, the working frequency of all-angle polaritonic negative refraction demonstrated here can be flexibly tunable within BN's first reststrahlen band, thanks to the tunability of the chemical potential in graphene.

Due to the combined advantages of tunability, low loss, and ultra-confinement provided by these polaritons on the platform of graphene-BN heterostructures, we believe that the negative polaritonic refraction presented in this work will have fundamental and far-reaching impacts. Even more important is the ability to flip the sign of group velocities of highly squeezed graphene plasmons and BN's phonon polaritons. Graphene-BN heterostructures thus provide new fundamental tools to explore other novel actively-tunable polaritonic effects and to design advanced polaritonic devices such as metasurfaces and superlens.

REFERENCES

1. Basov, D. N.; Fogler, M. M.; García de Abajo, F. J. "Polaritons in van der Waals materials," *Science* 354, aag1992, 2016.

Ultrathin metasurfaces for wide-angle spectrum splitting

Z. Li, Z. Liu, F. Callewaert, S. Butun, and K. Aydin*

[1]Department of Electrical Engineering and Computer Science, Northwestern University, Evanston IL, USA

*corresponding author: aydin@northwestern.edu

Abstract-We present flat metasurfaces and metamaterials that enable broadband spectrum splitting and anomalous light reflection and transmission. We will also describe a phase-transition material based dynamic metasurface for beam steering.

Spectrum-splitting, directing different wavelength components of a broadband light source to different directions, has wide range of applications including imaging, spectroscopy, astronomy and solar energy. Conventional optical devices such as lenses, prisms and gratings offer limited control of photon flow due to design constraints and material dispersion. Recently, metasurfaces have emerged as potential and reliable candidates for replacing conventional optical devices. Metasurfaces with desired optical properties can be designed at will by controlling the size, shape, position, and arrangement of metallic and/or dielectric nanostructures enabling extreme manipulation of light-matter interactions at the subwavelength scale[1].

We will present the design and realization of spectrum-splitting ultrathin, flat metasurfaces with unparalleled optical properties that cannot be offered by conventional optical devices. One metasurface design is composed of trapezoid nanoresonator arrays operating in the reflection mode and enabling broadband, highly efficient anomalous reflection at the visible frequency range. We will also demonstrate a novel spectrum splitter capable of directing different wavelengths of light to opposite directions resulting in an ultra-wide ($> 90°$) angular splitting[3]. Utilizing two different size of silver nano-trapezoid resonators as a building block, we engineer the phase gradients imparted by the metasurface beyond the monotonic trend to exhibit frequency-selective characteristics. Spectrum splitting for different visible-frequency component light (blue, green and red light) to completely different or even contrary directions have been demonstrated theoretically and experimentally. When white light is incident normally on a flat metasurface, the red light is reflected at an off-normal, positive angle while green light is reflected at a negative angle. To the best of our knowledge, such counterintuitive, directional wide-angle spectrum splitting and asymmetric light steering cannot be realized by any existing conventional optical devices with a single light-matter interaction.

Such unconventional metasurface building blocks when arranged using a mirror-symmetry at the center, enable the design of a multi-functional optical meta-devices that can behave as a convex, a concave or a planar mirror for different colors of visible light[3]. We believe the first theoretical and experimental demonstration of wide-angle, directional spectrum splitting, asymmetric light steering and multi-functional mirror functionalities based on versatility of the metasurfaces is of significant interest to the broad optics and photonics field[4].

References

1. Yu, N.; Capasso, F. *Nature Materials* **2014,** 13, (2), 139-150.
2. Li, Z.; Palacios, E.; Butun, S.; Aydin, K. *Nano Letters* **2015,** 15, (3), 1615-1621.
3. Li, Z.; Palacios, E.; Butun, S.; Aydin, K. *Advanced Optical Materials* **2016,** 4, (6), 953-958.
4. Pile, D. *Nature Photonics* **2015,** 9, (4), 210-210.

Tunable Quantum Metasurfaces

Yuzhe Xiao[1], Haoliang Qian[1], Zhaowei Liu[1,2,3*]

[1]Department of Electrical and Computer Engineering, University of California, San Diego, 9500 Gilman Dr, La Jolla, CA, USA 92093

[2]Material Science and Engineering, University of California, San Diego, 9500 Gilman Dr, La Jolla, CA, USA 92093

[3]Center for Magnetic Recording Research, University of California, San Diego, 9500 Gilman Dr, La Jolla, CA, USA 92093

[*]corresponding author: zhaowei@ucsd.edu

Abstract-We propose new kinds of tunable metasurfaces based on multilayers of gold quantum well. By changing the laser intensity, the tunability is implemented through the ultrahigh Kerr nonlinearity of gold quantum well that we experimentally demonstrated recently.

Metasurface uses the fact that the phase of light can be changed by interaction with sub-wavelength optical scatters, such as metallic or dielectric nanoparticles [1]. Unlike the bulky conventional optical devices that modify the properties of light through the propagation phase which requires device sizes of wavelength scale, metasurface can accomplish the same functionalities within a much shorter length scale. Therefore, metasurface is promising for integrated on-chip optics. Over the past few years, metasurfaces with specific functionalities have been demonstrated using ultrathin layered structures. Examples of such planar devices include optical lens [2], beam redirector [3], wave plate [4], and optical filter [5]. Most of these metasurfaces are designed on linear optics and can only function passively. It is highly desirable to have active metasurfaces to enable tunable functionality, such as through optical nonlinearity. However, since the strength of the nonlinearity of the existing optical scatters is limited, it is extremely challenging to generate strong nonlinear interaction within ultrathin metasurface.

Recently, we found that the optical properties of ultrathin gold films (thickness <3nm) are drastically different from the bulk values due to the quantum size effect [6-7]. More importantly, findings of the optical Kerr nonlinearity of such quantum-sized gold film show a 4 order enhancement as compared to that of bulk gold [7]. Such giant Kerr response indicates that these ultrathin gold film can be used to achieve strong nonlinear interaction over much shorter length than conventional nonlinear materials. Based on this, we propose a new kind of quantum metasurface made of multilayer structures of quantum sized gold film. In the low power region where the nonlinearity is negligibly small, the quantum metasurface is similar to the existing metasurfaces. In the high power region, material properties can be modified considerably by light through optical Kerr effect. More specifically, the phase of the reemitted light of each scatter depends on the light intensity and functionality of the quantum metasurface can be tuned through light intensity. In the presentation, we will talk about our recent work on such tunable quantum metasurface.

REFERENCES

1. Yu, Nanfang, and Federico Capasso. "Flat optics with designer metasurfaces." *Nature materials* 13.2 (2014): 139-150.
2. Aieta, Francesco, et al. "Aberration-free ultrathin flat lenses and axicons at telecom wavelengths based on plasmonic metasurfaces." *Nano letters* 12.9 (2012): 4932-4936.
3. Pfeiffer, Carl, and Anthony Grbic. "Metamaterial Huygens' surfaces: tailoring wave fronts with reflectionless sheets." *Physical review letters* 110.19 (2013): 197401.
4. Yu, N. *et al.* A broadband, background-free quarter-wave plate based on plasmonic metasurfaces. *Nano Lett.* **12,** 6328–6333 (2012).
5. Jiang, Z. H. *et al.* Tailoring dispersion for broadband low-loss optical metamaterials using deep-subwavelength inclusions. *Sci. Rep.* **3,** 1571 (2013).
6. Qian, Haoliang, et al. "Quantum Electrostatic Model for Optical Properties of Nanoscale Gold Films." *Nanophotonics* 4.1 (2015).
7. Qian, Haoliang, et al. "Giant Kerr response of ultrathin gold films from quantum size effect." *Nature communications* 7 (2016).

Exceptional points in PT-symmetric metasurfaces

Jie Luo[1], Jensen Li[2], and Yun Lai[1*]

[1]College of Physics, Optoelectronics and Energy & Collaborative Innovation Center of Suzhou Nano Science and Technology, Soochow University, Suzhou 215006, China

[2]School of Physics and Astronomy, University of Birmingham, Birmingham B15 2TT, United Kingdom

Abstract-We investigate the systems consisting of a pair of PT-symmetric metasurfaces sandwiching a slab made of metamaterials. We observe two types of exceptional points in such unique systems, at which unidirectional impedance matching is established. By using an epsilon-near-zero slab, a robust one-way cloaking phenomenon is established.

We consider wave incident from dielectric medium with relative permittivity of ε_1 into dielectric medium with relative permittivity of ε_2. An ultrathin metasurface can function as an anti-reflection coating (ARC) for the two dielectric media. Under normal incidence, we find that the relative permittivity of the metasurface ($\mu = 1$) is required to be,

$$\varepsilon = i\frac{\sqrt{\varepsilon_1} - \sqrt{\varepsilon_2}}{k_0 d}. \qquad (1)$$

Equation (1) indicates that the required permittivity is pure imaginary. Both lossy and gain media can operate as the antireflection coatings [1, 2].

For a slab of dielectric or metamaterial, we can sandwich it by a pair of PT-symmetric metasurfaces. In such a system, two types of exceptional points are observed at which unidirectional propagation is established, where the PT-symmetric metasurfaces function as either a CPA-Laser pair [3], or an ARC-ARC pair. Here CPA indicates coherent perfect absorber. By changing the slab to be an epsilon-near-zero slab, an interesting robust one-way cloaking phenomenon can be established, where the cloaking effect is unidirectional.

REFERENCES

1. Luo, J., Li, S., Hou, B., Lai, Y. "Loss/gain-induced ultrathin antireflection coatings", *Scientific Reports* Vol. 6, 28681, 2016.
2. Luo, J., Li, S., Hou, B., Lai, Y. "Unified theory for perfect absorption in ultrathin absorptive films with constant tangential electric or magnetic fields," *Phys. Rev. B* Vol. 90, 165128, 2014.
3. Fleury, R., Sounas, D. L., Alù, A. "Negative refraction and planar focusing based on parity-time symmetric metasurfaces," *Phys. Rev. Lett.* Vol. 113, 023903, 2014.

Nonlinear optics at the nanoscale with metallic, dielectric, and hybrid nanostructures

S. A. Maier[1]

[1] Imperial College London, London SW7 2AZ, UK

Abstract – We discuss a number of schemes for the enhancement of nonlinear processes such as second and third harmonic generation, as well as four wave mixing, focusing on plasmonic, dielectric, and hybrid materials systems. For dielectric systems, anapole modes in Ge disks are shown to allow for maximizing electric field concentration in the material, leading to highly enhanced conversion efficiencies. GaP nanopillars enable localization throughout the visible regime under low-loss conditions, and hybrid structures consisting of both Au and Si elements combine "the best of both worlds" from plasmonics and semiconductor nanophotonics.

Plasmonic nanoantennas with nanoscale gaps act as efficient transducers of electromagnetic energy from the far to the near field at optical frequencies, creating hot spots of field energy utilized extensively in surface-enhanced spectroscopy and sensing. We will review applications of such nanoantennas for nonlinear light conversion on the nanoscale, and then compare with new results obtained on dielectric and hybrid plasmonic/dielectric systems. While not breaking the diffraction limit, dielectric nanoantennas can sustain Mie resonances under low-loss conditions, and we will show that this can be beneficially exploited for applications in nanoscale nonlinear optics. In particular, we will show that anapole modes in germanium disks maximize electric field concentration within the structure itself, hence leading to record nonlinear conversion efficiencies [1]. Wide-bandgap semiconductors such as GaP further enable low-loss operation throughout the visible regime [2].

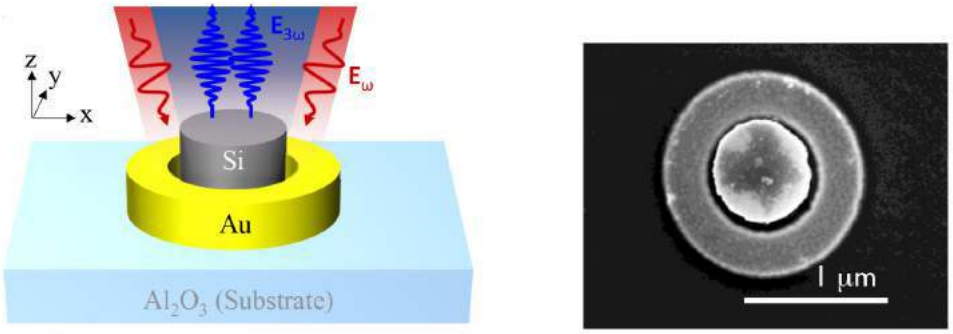

Fig. 1. A hybrid Au/Si nanoantenna structure examined for its performance as a highly efficient generator of third-harmonic radiation at the nanoscale.

We will also present as yet unpublished results on hybrid systems (Figure 1), where higher order plasmon modes of a metallic ring hybridize with modes in a concentric dielectric nanodisk, leading to a boost in conversion efficiencies via both plasmonic light localization and re-radiation, as well as concentration of energy within the dielectric material itself.

REFERENCES

[1] Grinblat et al, ACS Nano 22, 953 (2017); Grinblat et al, Nano Letters 16, 4635 (2016)

[2] Cambiasso et al, “Bridging the gap between dielectric nanophotonics and the visible regime with effectively lossless GaP antennas”, Nano Letters (accepted 2017)

Manipulating the Polarization State of Smith-Purcell Emission by Metasurfaces

Zuojia Wang[1,2], **Kan Yao**[3], **Hongsheng Chen**[2] **and Yongmin Liu**[1,3,*]

[1] Department of Mechanical and Industrial Engineering, Northeastern University, Boston, USA

[2] College of Information Science and Electronic Engineering, Zhejiang University, Hangzhou, China

[3] Department of Electrical and Computer Engineering, Northeastern University, Boston, USA

[*]corresponding author: y.liu@northeastern.edu

Abstract- Smith-Purcell emission is far-field radiation of light from swift electrons when electrons move closely above a periodic structure. Here we show that designer metasurfaces composed of C-aperture resonators can control the polarization state of Smith-Purcell emission on demand with high efficiency, which is very difficult to achieve via traditional gratings. These findings open up new opportunities to manipulate electron-beam-induced emission, and to develop compact, tunable and efficient light sources and particle detectors.

The sophisticated interactions between electrons and materials lay the foundation for advanced electron microscopy including electron energy-loss spectroscopy, and cathodoluminescence emission including transition radiation, Cherenkov radiation and diffraction radiation [1]. The recent advances of artificially engineered materials provide new approaches to tailoring electron-matter interactions [2]. For instance, reversed Cherenkov radiation has been theoretically proposed [3] and experimentally observed [4] in left-handed metamaterials. Swift electrons traveling above a metallic film can excite surface plasmon polaritons, which can be thereafter transformed into Cherenkov radiation with enhanced intensity [5]. In addition, researchers have reported the manipulation of Cherenkov emission by photonic crystals [6] and anisotropic metamaterials [7,8].

Here we show that the polarization state of Smith-Purcell emission, a well-known example of diffraction radiation excited by swift electrons, can be effectively controlled by metasurfaces consisting of C-aperture resonators [9]. When the speed of electrons is smaller than the speed of light in the surrounding medium, the fields associated with the electrons are non-radiative. Traditionally we can place a periodic grating close to electrons to couple the near-field energy to the far-field, leading to Smith-Purcell emission. However, the resulting wave is transverse magnetic polarized only. To overcome this limitation, we have designed C-aperture Babinet metasurfaces resonant at terahertz frequencies to control the polarization of the far-field wave, by coupling the non-radiative energy of moving electrons to the inherent electric dipole and magnetic dipole of the C-aperture resonator. Numerical simulations demonstrate that the polarization angle of the radiated light is determined by the orientation of the C-aperture resonators. We have also employed Stokes parameters to characterize the polarization state of the Smith-Purcell emission. Moreover, the efficiency of the Smith-Purcell emission from the metasurfaces is remarkably increased by 84% in comparison with the case of conventional gratings, indicating that the resonant nature of metasurfaces can significantly enhance the radiation efficiency. These results provide a new strategy to develop a compact, tunable and high power terahertz source based on the Smith-Purcell emission, polarization-sensitive detectors and other novel photonic devices.

REFERENCES

1. F. G. De Abajo, Rev. Mod. Phys. **82**, 209 (2010).
2. H. Chen and M. Chen, Mater. Today **14**, 34 (2011).
3. V. G. Veselago, Sov. Phys. Usp. **10**, 509 (1968).
4. S. Xi, H. Chen, T. Jiang, L. Ran, J. Huangfu, B.-I. Wu, J. A. Kong, and M. Chen, Phys. Rev. Lett. **103**, 194801 (2009).
5. S. Liu, P. Zhang, W. Liu, S. Gong, R. Zhong, Y. Zhang, and M. Hu, Phys. Rev. Lett. **109**, 153902 (2012).
6. C. Luo, M. Ibanescu, S. G. Johnson, and J. Joannopoulos, Science **299**, 368 (2003).
7. G. Adamo, K. F. MacDonald, Y. Fu, C. Wang, D. Tsai, F. G. de Abajo, and N. Zheludev, Phys. Rev. Lett. **103**, 113901 (2009).
8. V. V. Vorobev and A. V. Tyukhtin, Phys. Rev. Lett. **108**, 184801 (2012).
9. Z. J. Wang, K. Yao, M. Chen, H. S. Chen and Y. M. Liu, Phys. Rev. Lett. **108**, 184801 (2012).

Silicon metasurfaces for beam bending and high NA flat lenses

Ye Feng Yu*, Ramon Paniagua-Dominguez, Yuan Hsing Fu, Egor Khaidarov, Liang Xinan, Reuben M. Bakker, Han Fang Hao, Vytautas Valuckas, and Arseniy I. Kuznetsov

Data Storage Institute, A*STAR (Agency for Science, Technology and Research),
2 Fusionopolis Way, #08-01 Innovis, 138634, Singapore
*corresponding author: Yu_Yefeng@dsi.a-star.edu.sg

Abstract In the present work, we demonstrate large angle, optical beam bending using dielectric metasurfaces based on asymmetric, silicon nano-structures. The largest bending angle exceeds 82 degrees. Based on the bending results we design and demonstrate an ultra-high numerical aperture (NA) flat lens, which has a NA around 0.99 at the working wavelength of 720 nm.

Dielectric metasurfaces, two dimensional arrays of resonant dielectric nanostructures, attracts increasing attention and represents a rapidly developing research direction in nanophotonics due to its low intrinsic losses [1] and fascinating functionalities, stemming from their capability to control the amplitude, polarization and phase of light in subwavelength scales. A gradient metasurface, inducing a linear phase shift in the wavefront, is one of these devices, with applications in beam bending [2]. However, in the gradient metasurface one needs several (> 2) elements for a correct phase mapping, which typically means that the so called super-cell (mapping the 0-2π linear phase) will be relatively large if the metasurface inclusions are not deeply sub-wavelength. When the super-cell is larger than the working wavelength, the bending angle cannot be close to 90 degree because of the generalized Snell's law [3]. The limited bending angle will directly connect to the maximum acceptance angle of a dielectric metasurface based flat lens, thus limiting its numerical aperture.

Here, we propose a new dielectric nanoantenna based metasurfaces to cover the large angle bending region. In these metasurfaces, each nanoantenna is tailored to scatter the incoming light into a certain desired diffraction order and to suppress energy channeling into all the other orders, thus causing light bending. The design rule here is to realize asymmetric, directional scattering into the right direction through interference of the different Mie-resonances supported by the antennas. This, in turn, can be achieved by manipulation of their geometrical parameters. Numerical results show that a carefully designed asymmetric silicon dimer can serve this purpose.

Based on this new concept, in combination with the standard gradient metasurfaces [2], we design a flat lens with sub-wavelength thickness and a NA around 0.99 at the operating wavelength (~720 nm). The maximum acceptance angle of the designed lens exceeds 82 degrees and the size of focus spot approaches the diffraction limit.

In the experimental demonstration, the silicon flat lens has a diameter of 599 μm and a focal length around 44 μm (i.e. NA ~ 0.989) at operating wavelength of 720 nm and the measured focal spot size is around 400 nm.

REFERENCES

1. A. I. Kuznetsov et al., "Optically resonant dielectric nanostructures", Science 354, (2016).
2. Y. F. Yu et al., "High-transmission dielectric metasurface with 2π phase control at visible wavelengths," Laser Photon. Rev. 9, 412-418 (2015).
3. N. Yu et al., "Light Propagation with Phase Discontinuities: Generalized Laws of Reflection and Refraction," Science 334, (2011).

Overcoming the constraints of high angle visible light beam bending with asymmetric nanoantenna-based titanium dioxide metasurfaces

Egor Khaidarov[1, 2*], Hanfang Hao[1], Ramón Paniagua-Domínguez[1], Ye Feng Yu[1], Yuan Hsing Fu[1], Vytautas Valuckas[1], and Arseniy Kuznetsov[1]

[1]Data Storage Institute, A*STAR (Agency for Science, Technology and Research), 138634, Singapore

[2]School of Electrical and Electronic Engineering, Nanyang Technological University, 639798, Singapore

[*]egor-khaidarov@dsi.a-star.edu.sg

Abstract-We propose a novel method for energy redistribution between diffraction orders in diffractive arrays of dielectric nanoantennas and demonstrate its application for visible light beam bending using subwavelength-size TiO_2 nanoantenna elements. We prove this concept numerically and experimentally for medium (~45°) and extra-high-angle (~80°) beam bending. The designed systems show highly efficient, broadband operation for green and blue frequencies, significantly surpassing the commonly used discrete phase mapping approach.

Phase control in metasurfaces is commonly realized via discrete mapping of the desired phase with a finite number of nanoantenna elements. In particular, beam bending functionality requires a linear phase profile [1]. However, in the case of a low number of elements, corresponding to high bending angles, the efficiency dramatically drops, imposing limitations to the applicability of this method. In this work, we suggest a novel approach for large angle beam bending, exploiting a combination of nanoantenna and grating concepts. By engineering the radiation pattern of the elements/nanoantennas constituting the grating, the energy between the supported diffraction orders is redistributed; hence, the different orders can be enhanced or suppressed at will. By suppression of all reflection and undesired transmission orders all the energy can be channeled into a single transmission order, with an angle defined by the grating period and corresponding to the desired bending angle.

For the experimental demonstration, we choose dielectric nanoantenna arrays due to their lower losses, compared to plasmonics, and broader design flexibility, resulting from the interaction between the electric and magnetic multipole resonances [2]. We design TiO_2 nanostructures and experimentally confirmed high efficiency at different bending angles, spanning from medium (~45°) to very large (>80°) angles. All proposed designs show broadband operation in the green and blue regions of the visible spectrum. Moreover, the proposed concept is general and the structures can be redesigned to work at any desired wavelength, polarization and angle (with a suitable choice of materials) both in transmission and reflection configurations. Possible applications include polarization beam splitters and high numerical aperture (NA) lenses. The largest efficient bending angle obtained in our experiments is 75.5°, with around 50% transmission efficiency into the designed order, which corresponds to the numerical aperture NA~0.97 exceeding most of the commercially available objective lenses and previously reported flat lenses [3,4].

REFERENCES

1. Yu, N. et al., "Light Propagation with Phase Discontinuities: Generalized Laws of Reflection and Refraction," Science 334, 333-337 (2011).
2. Kuznetsov, A. I. et al., “Optically resonant dielectric nanostructures”, Science 354, aag2472 (2016).
3. Arbabi, A. et al., “Dielectric metasurfaces for complete control of phase and polarization with subwavelength spatial resolution and high transmission,” Nat. Nanotech. 10, 937 (2015).
4. Khorasaninejad, M. et al., “Polarization-Insensitive Metalenses at Visible Wavelengths”, Nano Lett. 16**,** 7229 (2016).

Flat and conformal optics with dielectric metasurfaces

Andrei Faraon, Amir Arbabi, Ehsan Arbabi, Seyedeh Mahsa Kamali, Yu Horie
T.J. Watson Laboratory of Applied Physics, California Institute of Technology, Pasadena, CA, USA
*corresponding author: userid@institution.edu

Abstract- In this talk I will give an overview of our progress towards design and fabrication of flat or conformal dielectric metasurface devices with multiple functionalities

Flat optical devices based on lithographically patterned sub-wavelength dielectric nano-structures provide precise control over optical wavefronts, and thus promise to revolutionize the field of free-space optics. I discuss our work on high contrast transmitarrays and reflectarrays composed of silicon nano-posts located on top of low index substrates like silica glass or transparent polymers. Complete control of both phase and polarization is achieved at the level of single nano-post, which enables control of the optical wavefront with sub-wavelength spatial resolution. Using this nano-post platform, we demonstrate lenses, waveplates, polarizers, arbitrary beam splitters and holograms. Devices that provide multiple functionalities, like simultaneous polarization beam splitting and focusing are implemented. By embedding the metasurfaces in flexible substrates, conformal optical devices that decouple the geometrical shape and optical function are shown. Multiple flat optical elements are integrated in optical systems such as planar retro-reflectors and Fourier lens systems with applications in ultra-compact imaging systems. Applications in microscopy and the prospects for tunable devices are discussed.

Low-Loss and Tunable Huygens-Source Optical Metasurfaces

A. Ollanik[1], Y. Ji[1], D. Bar-Or[1], N. Kurtz[1], and M.D. Escarra[1,*]
[1]Tulane University, New Orleans, LA, USA
[*]corresponding author: escarra@tulane.edu

Abstract- This work reports on the development of low-loss (>90% efficient), dynamically tunable (e.g. >85% modulation of transmission) Huygens-source optical metasurfaces composed of arrays of elliptical nanoantennas patterned into dielectric and phase-change materials.

Fundamental new materials insights are required to manipulate the phase and amplitude of light at the nanoscale through optical metasurfaces that are both low-loss and easily tunable. Successful platforms may serve as a key building block for a range of applications, such as high speed encoding of orbital angular momentum for optical communications. In this work, we report on advances towards low loss and dynamically tunable optical metasurfaces. These metasurfaces are composed of elliptical nanoscale antennas that are highly resonant with both the electric and magnetic field of incident light. Numerical analysis shows that these antennas can produce anomalous refraction from the UV (e.g. 378 nm) into the infrared (e.g. 1340 nm) with ~80-90% of incident light deflected into the desired direction [1]. We show bandwidth of 6% and incident angle tolerance of 30°. Experimental verification of our designs is performed using amorphous silicon antennas embedded in a SiO_2/PDMS matrix.

Due to the highly resonant nature of these metasurfaces, their optical response is easily tuned by changes in either metasurface geometry or constituent material properties. We analyze the potential of metasurfaces composed of a wide range of tunable materials, with a particular focus on vanadium dioxide, a material with a strong metal-insulator transition at relatively low temperature (~70°C). Models show that VO_2 metasurfaces may be tuned to provide >85% modulation of transmission (or reflection) and >180° modulation in phase shift within the first 10% of the VO_2 metal-insulator transition. We synthesize VO_2 via pulsed laser deposition and characterize its electronic and optical properties vs. external stimuli (e.g. temperature tuning). A clear metal-insulator transition is attained, providing a large change in the optical properties of the material. The VO_2 is then patterned into Huygens-source optical metasurfaces. The tunability of performance is experimentally measured in several ways, including direct measurement of the phase shift in the material and mapping of the metasurface's ability to guide and redirect incident light vs. external stimuli.

Future directions for this effort include the fabrication of multi-layer metasurfaces, and initial designs will be reported, including 4-way spectrum splitters. Spatially addressable, pixelated tunable metasurfaces and applications of these materials will also be discussed.

Acknowledgements: This work is supported in part by The Louisiana Board of Regents Support Fund (Contract #: LEQSF(2014-17)-RD-A-08).

REFERENCES

1. Ollanik, A., *et. al.* "Highly Efficient, All-Dielectric, Transmissive Gradient Metasurfaces from the Ultraviolet to the Infrared", *CLEO*, OSA Technical Digest (2016), paper JW2A.34

Nonlinear Scattering and Time Resolved Nonlinear Properties of Metasurfaces and Plasmonic Materials

A.M. Urbas
Air Force Research Lab, Dayton, Ohio
augustine.urbas@gmail.com

Metamaterials provide the ability to design materials properties to meet the unique needs of applications beyond what is possible with conventional materials. From spatially tailored dielectrics to tunable, dynamic material properties and unique nonlinear behavior, these systems offer tremendous flexibility to application engineers. In this presentation, we focus on studying the nonlinear properties of plasmonic and metamaterial systems where the careful balance of multipolar components allows for control of linear and nonlinear scattering cross sections and directionality. Ultimately, this will lead to tailored nonlinear response from metasurfaces. This work drives detailed studies on characterizing the nonlinearities of component materials to be used in metasurfaces. Nonlinearity in the component materials can enable controllable nonlinear excitation of multipoles leading to enhancement, suppression, directional control of nonlinear generation (as diagramed to the left), and nonreciprocal response. The overall system response is dictated by the design of the plasmonic dimer, i.e. the thicknesses and size of metallic and spacer components, and the design process is enabled by tools we have developed to retrieve dimer polarizabilities. These effects arise due to the nonlinear response of the component materials and we are actively pursuing novel materials systems and growth procedures to produce structures with controlled response. A significant part of this work focuses on the characterization of time resolved nonlinear response in plasmonic and dielectric materials. We employ the beam deflection method to measure the nonlinear refraction and absorption of thin films. Beam deflection is a pump probe technique which offers extreme sensitivity to nonlinear response in materials. This allows us to measure the response of films at the dimensions relevant to our dimer designs deposited using the same techniques and reveal thickness and process dependent changes in the properties of nonlinear materials. An example material is graphene.

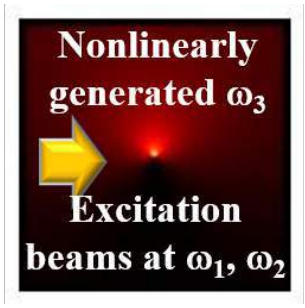

Graphene is a challenging material to measure and is among the materials of interest due to its unique properties such as high thermal conductivity, damage threshold, optical nonlinearity, and broadband saturable absorption. These characteristics are useful in designing nonlinear response from structured materials. The understanding of the time dynamics of the mechanisms is relevant to the design process and of interest to the community. In this work we present nonlinear refraction, $nn2$, and nonlinear absorption, $\alpha\alpha 2$, measurements taken by the Beam Deflection (BD) technique of several plasmonic and dielectric materials, including Graphene shown above, in order to determine the response mechanisms and their associated parameters and the impact on their potential use in nonlinear plasmonics.

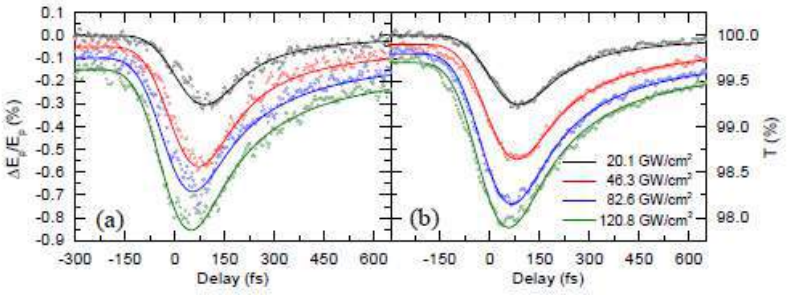

Topological Line Wave based on Impedance Surfaces

Dia'aaldin J. Bisharat[1,2*] and Daniel F. Sievenpiper[2]
[1]Department of Electronic Engineering, City University of Hong Kong, Kowloon, Hong Kong, China
[2]Electrical and Computer Engineering Department, University of California, San Diego, California, 92093, USA
[*]dbisharat2-c@my.cityu.edu.hk

Abstract-Analogous to surface wave formation at the interface of two semi-infinite spaces, we show a one-dimensional electromagnetic mode at the line interface of two semi-infinite planes that are characterized by complementary surface impedances. The proposed mode possesses singular field enhancement, tunable spatial confinement, extensive bandwidth, and robust wavevector-locked propagation, which may advance topological photonics applications. Here, we specify criteria for the line wave existence and present implementations using metasurfaces and graphene that are suitable for microwave, terahertz and optical applications.*n*

The ability to manipulate fields and energy flow of electromagnetic (EM) waves, such as light, is fundamental to modern sensing and communication technologies, as well as quantum information processing schemes. Due to their peak field property at the planar interfaces of dissimilar media, surface waves have been researched for over a century and have recently been exploited to realize topological photonic insulators (TPIs) exhibiting reflection-free unidirectional propagation [1]. However, current designs rely on magnetic field effects or nonplanar structures, which are not suitable for optical applications, and are limited in bandwidth due to band gaps and band inversion requirements. Here, we introduce a new EM mode that has intrinsic topological properties and other unique features, which surpass the limitations of earlier TPI concepts.

The proposed mode is analogous to surface waves, which can propagate without the need for any enclosing structure but is rather confined to a one-dimensional line at the interface between two planar surfaces. The two surfaces are characterized by complementary isotropic surface impedances, Z_{TE} and Z_{TM} which support surface modes of equal phase velocities but opposite polarizations, transverse magnetic (TM) and transverse electric (TE), respectively as follows [2],

$$Z_{TM} = \eta_0 \sqrt{1-(\frac{k_z}{k_0})^2} = j\eta_0 / \zeta \quad , \quad Z_{TE} = \eta_0 / \sqrt{1-(\frac{k_z}{k_0})^2} = -j\eta_0 \times \zeta \tag{1}$$

When interfacing the two surfaces, a new localized hybrid mode appears at the interface, as shown in Fig. 1(a). Due to the open boundary configuration and the fact that neither TM nor TE surface mode could exist at the opposite side, the line mode has a singular field concentration and decays away from the interface as shown in Fig. 1(b). In the case where ζ, a real number, tends to infinity, the TM (TE) surface becomes a perfect electric (magnetic) conductor. PEC and PMC boundaries, as ε-negative and μ-negative materials, possess different topological orders as they have opposite effects on the electric and magnetic fields components [3]. Clearly, both surfaces support evanescent waves but possess opposite signs of imaginary impedance. However, when the two boundaries are joined, EM duality, which is otherwise broken, is restored; hence new modes emerge that are a combination of magnetic and electric modes with specific phase relationships, i.e. conserved pseudo-spin values [4]. Moreover, since the pseudo-spin configuration is uniquely defined by the direction of the mode wavevector (k_z), the interface constitutes a spin-filtered channel as depicted in Fig 1(c).

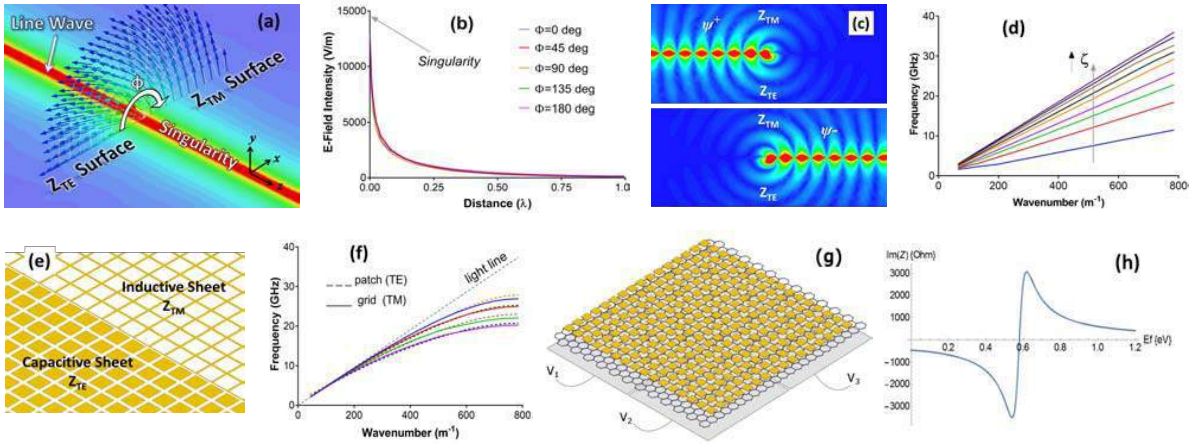

Figure 1. (a) Surface distribution and vector plot of the electric field across the interface of the line wave, (b) decay curves of the electric field at different directions around the interface, (c) pseudo-spin states excited by electric and magnetic hertzian dipoles in phase (above) and out of phase (below), (d) dispersion curves of the line mode at different ζ values, (e) implementation based on complementary FSS cells, (f) dispersion curves of TM and TE FSS cells of different sizes, (g) implementation based on graphene as a reconfigurable platform, and (h) effective impedance of the graphene metasurface at 6 THz at different chemical potentials.

This paradigm applies in general to interfacing complementary impedance surfaces, i.e. inductive/capacitive surfaces with identical ζ value. This enables stronger cross coupling between TM and TE modes and control over the line wave confinement as shown Fig. 1(d). An example of line wave implementation is shown in Fig. 1(e) based on simple frequency-selective surfaces (FSS). Fig. 1(f) shows that the respective surface modes of the complementary FSSs have dispersion curves (phase velocities) that overlap over a wide frequency band, thus giving rise to a line wave at their interface. This is clearly advantageous compared to the typical TPIs based on photonic crystals, which are limited in bandwidth [1]. Furthermore, our effective medium approach based on surface impedance allows for line waves with reconfigurable pathways through electrostatic biasing in graphene as shown in Fig. 1(g). Here, while the patch metasurface has a capacitive effect, tuning the inductive impedance of graphene sheet enables variable net impedance as shown in Fig 1(h).

This is the first demonstration of an entirely planar photonic system with wavevector-locked states that is suitable for both microwave and optical regimes. This makes the line wave an attractive candidate for robust integrated photonic circuits while being potentially the smallest waveguide possible. The exhibited strong mode confinement is a prerequisite for enhanced light-matter interactions, while the field singularity and having an air channel makes the line wave ideal for sensing applications and vacuum based electronic devices. In addition, the tuning capability can be exploited for reconfigurable systems as well as switching and modulation applications. Moreover, our approach provides a flexible and simple platform for investigating and manipulating topological states with subwavelength resolution.

REFERENCES

1. Lu, L., Joannopoulos, J. D. and Soljačić, M. "Topological photonics," *Nat. Photon*, Vol. 8, 821–829, 2014.
2. Bisharat, D. J. and Sievenpiper, D. F. "Guiding light along an infinitesimal line between impedance surfaces," *To be published,* arXiv:1702.05550, 2017.
3. Shi, X., Xue, C., Jiang, H., and Chen, H. "Topological description for gaps of one-dimensional symmetric all-dielectric photonic crystals," *Opt. Exp.*, Vol. 24, No. 16, 18580-18591, 2016.
4. Chen, W.-J., Zhang, Z.-Q., Dong, J.-W., and Chan, C. T. "Symmetry-protected transport in a pseudospin-polarized waveguide," *Nat. Commun.*, Vol. 6, 8183, 2015.

Absorption band engineering by metamaterials

Takuo Tanaka
[1]RIKEN Metamaterials Laboratory, Japan
[2]RIKEN Center for Advanced Photonics, Japan
[3]Tokyo Institute of Technology, Japan
[*]corresponding author: t-tanaka@riken.jp

Abstract-Recent progresses on metamaterials absorber will be presented. As an application of IR metamaterial absorbers, high sensitive molecular detection technique using resonant coupling between metamaterial and molecule is proposed and attomole level sensitivity is demonstrated. As an application of absorption engineering by metamaterial in the visible range, ink-free full color printing with controllable color attributes like hue, brightness and saturation is also demonstrated.

Recent advances in plasmonic metamaterials enable us to create unprecedented optical materials, and perfect absorptive material surfaces within a certain frequency range were demonstrated. Since the metamaterial absorber offers a unique surface condition with tailored absorption properties, a wide variety of potential applications have been proposed, such as high-efficiency thermal emitter and high-sensitive bio-chemical sensing. As an application of metamaterial absorber in IR region, we demonstrate high sensitive background-suppressed surface enhanced IR absorption (SEIRA) of molecules adsorbed on the metamaterial.

Figure 1(a) shows a unit cell cross-section of a metamaterial IR absorber, consisting of a 50-nm Au micro-ribbon on a thick Au film separated by a 30-nm MgF_2 gap layer [1]. The width (w) and unit cell dimension (Λ) were 1.5 μm and 3 μm, respectively. The surface structure was designed to exhibit an anomalous IR absorption at ~ 3000 cm^{-1}, which spectrally overlapped with symmetric/anti-symmetric C-H stretching vibrational modes. Fig. 1(b) shows a photograph of the fabricated metamaterial absorber and its SEM image.

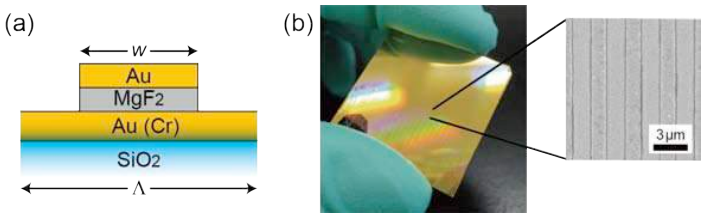

Figure 1 Metamterial IR absorber

Since the metamaterial absorber offers not only strong plasmonic enhancement but also significant background suppression, this unique surface environment improves the sensitivity of the conventional SIERA. In our experiment, 16-Mercaptohexadecanoic acid was used as a target molecule, exhibiting symmetric/ anti-symmetric C-H stretching vibrational modes at ~2855/2920 cm^{-1}. A 21.5-Å thick self-assembled monolayer (SAM) of the 16-MHDA was formed with their thiol head-group chemisorbed on the Au surface. For the reference, a bare Au sample was also prepared by the same process.

Figure 2(a) shows the measured reflection spectrum of the 16-MHDA SAM on a bare Au surface at incident angle of 80º and Fig. 2(b) shows the spectrum from the metamaterial absorber at the incident angle of θ = 40º.

For the bare Au case, the spectrum was suffered from extremely low signal quality, thus the respective absorption dips are undetectable. Moreover, it is notable that the bias of the spectral signal is more than 98% in reflectance. The metamaterial, on the other hand, exhibited a broad plasmonic absorption at 2921.9 cm^{-1}. When the molecules were in the vicinity of the surface structure, their vibrational modes resonantly coupled with the plasmonic modes of the metamaterial. This in turn produced distinct Fano-like anti-resonant peaks within a broad absorption of the metamaterial. Using the SAM packing density of 21.4 $Å^2$/molecule, we estimated the amount of the molecules with the diffraction limited IR beam spot to be ~1.8 attomoles (1.8×10^{-18} mole).

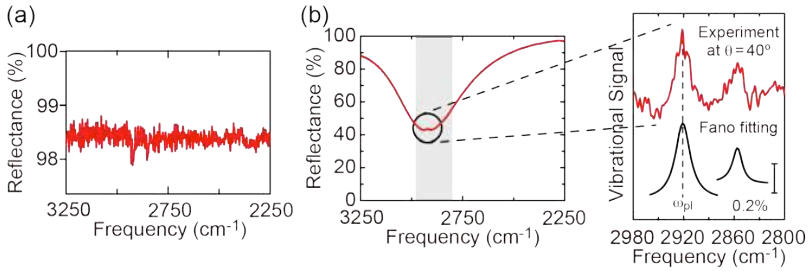

Figure 2 Background suppressed SEIRA for high sensitive molecular detection.

When we make the size of unit cell of metamaterial absorber down to several hundreds nanometers, the absorption bands move to the visible light region. We present a simple yet efficient approach for ink-free color printing employing sub-micrometer scale plasmonic pixels of single constituent metal structure that supports near unity broadband light absorption at two distinct wavelengths, facilitating the creation of saturated colors [2]. The dependence of these resonances on two different parameters of the same pixel enables controllable color attributes such as hue, brightness and saturation across the visible spectrum. Here we present an up scalable color printing scheme using plasmonic pixels of single constituent metal structure, enabling the design of full colors with controllable color attributes. Figure 3 shows the experimental results; Fig. 3(a) is RIKEN's logo observed by optical microscope and (b) is its structure observed by SEM. Fig. 3(c) shows a full color palette made by controlling the size of unit cell of the metamaterial.

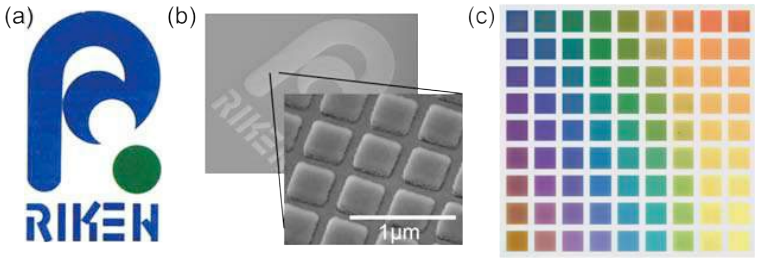

Figure 3 Full color printing by metamaterial absorber.

Acknowledgements, This work was partially supported by Innovative Science and Technology Initiative for Security, ATLA, Japan.

REFERENCES

1. A. Ishikawa and T. Tanaka, "Metamaterial Absorbers for Infrared Detection of Molecular Self-Assembled Monolayers," Scientific Reports **5**, 12570 (2015).
2. R. Mudachathi and T. Tanaka, "Up Scalable Full Colour Plasmonic Pixels with Controllable Hue, Brightness and Saturation," Sci. Rep. (accepted for publication) (2017).

Merging Metamaterial and Optical Fiber Technologies

N. I. Zheludev[1, 2*], K. F. MacDonald[1], E. Plum[1], A. Karvounis[1], D. Piccinotti[1], A. Xomalis[1], I. Demirtzioglou[1], V. Savinov[1], B. Gholipour[1, 3], Y. Jung[1], P. Petropoulos[1], D. J. Richardson[1]

[1]Optoelectronics Research Centre & Centre for Photonic Metamaterials, University of Southampton, UK

[2]Centre for Disruptive Photonic Technologies, SPMS & TPI, Nanyang Technological University, Singapore

[3]Department of Chemistry, University of Southampton, UK

[*]corresponding author: niz@orc.soton.ac.uk

Abstract- We will review recent advances in metamaterials research directed towards the development of switchable and tunable functional nanostructures. Metamaterials research has migrated from the study of exclusively metallic plasmonic structures to embraces a large variety of advanced material platforms, including dielectrics, semiconductors, superconductors, topological insulators and complex hybrid systems. We will discuss coherent control of metasurfaces, all-optical and electro-optical switching with reconfigurable nano-opto-mechanical and phase-change metamaterials and ways in which functional metamaterials can be integrated with optical fiber platforms.

A three-dimensional negative index medium and a miniature surface plasmon polariton amplitude modulator

Ta-Jen Yen,[1,*] Ting-Tso Yeh,[1] Tsung-Yu Huang,[1] Cheng-Wei Chang,[1] Chu-En Lin,[2] and Chih-Jen Yu[3]

[1]*Department of Materials Science and Engineering, National Tsing Hua University, Hsinchu, Taiwan, R.O.C.*

[2]*Department of Mechanical Engineering, National Chin-Yi University of Technology, Taichung, Taiwan, R.O.C.*

[3]*Graduate Institute of Electro-Optical Engineering, Chang Gung University, Taoyuan, Taiwan, R.O.C.*

**E-mail: tjyen@mx.nthu.edu.tw*

In this talk, I introduce two metadevices. Firstly, we design and construct a three-dimensional (3D) negative index medium (NIM) composed of gold hemispherical shells to supplant an integration of a split-ring resonator and a discrete plasmonic wire for both negative permeability and permittivity at THz gap. [1] With the proposed highly symmetric gold hemispherical shells, the negative index is preserved at multiple incident angles ranging from 0° to 85° for both TE and TM waves, which is further evidenced by negative phase flows in animated field distributions and outweighs conventional fishnet structures with operating frequency shifts when varying incident angles. Finally, the fabrication of the gold hemispherical shells is facilitated via standard UV lithographic and isotropic wet etching processes and characterized by μ-FTIR. The measurement results agree the simulated ones very well. Next, we present a miniature surface plasmon polariton amplitude modulator (SPPAM) by directing and interfering surface plasmon polaritons on a nanofabricated chip. [2] Our results show that this SPPAM enables two kinds of modulations. The first kind of modulation is controlled by encoding angular-frequency difference from a Zeeman laser, with a beat frequency of 1.66 MHz; the second of modulation is validated by periodically varying the polarization states from a polarization generator, with rotation frequencies of 0.5-10k Hz. In addition, the normalized extinction ratio of our plasmonic structure reaches 100. Such miniaturized beat-frequency and polarization-controlled amplitude modulators open an avenue for the exploration of ultrasensitive nanosensors, nanocircuits, and other integrated nanophotonic devices.

References

[1] Ting-Tso Yeh, Tsung-Yu Huang, and Ta-Jen Yen, *Scientific Reports* **2017 (*accepted*)**

[2] Cheng-Wei Chang, Chu-En Lin, Chih-Jen Yu, Ting-Tso Yeh, Ta-Jen Yen, *Scientific Reports* **2016**, *6,* Article number: 32098

Transformation behind equivalent metamaterial chains for caustic generation

F. Zhong[1], H. Liu[1], S. Zhu[1] and J. Li[2]

[1]National Laboratory of Solid State Microstructures & School of Physics, Collaborative Innovation Center of Advanced Microstructures, Nanjing University, China

[2]School of Physics and Astronomy, University of Birmingham, UK

[*]corresponding authors: liuhui@nju.edu.cn, j.li@bham.ac.uk

Abstract- We establish a metric interpretation to generate plasmonic caustic using one-dimensional chain of metamaterial atoms with variable orientation profile. Such an approach can be straight-forwardly applied to generate caustic with arbitrarily given shape. We also explore the relationship of the metric interpretation of caustic to motion in curved space-time using a Lorentz-like transformation between equivalent trajectories with experimental realizations.

In 2015, Capasso's group used a line of metallic nano-holes to generate surface plasmon wakes with circular polarized light and interpreted it as analogue Cherenkov radiation[1]. The effect is achieved by the variation of the orientation of the nano-holes, the generated surface plasmon polariton (SPP) signal carries an additional geometric phase[2] and provides a way to generate the wave-front. In terms of the analog motion of the charged particle, it corresponds to a constant velocity.

On the other hand, if the orientation profile of metallic nano-holes on the straight trajectory is non-linear or the trajectory of the nano-holes is curved, a caustic, instead of a planar wavefront, forms[3,4]. In the current work, we would like to investigate the analogy of such a scenario to accelerated particle motion, and explore the transformation between equivalent nano-hole trajectories to generate the same caustic.

For a given caustic to generate, we can write it as a parametric function $\big(X(\tau), Y(\tau)\big)$. If we instruct a one-dimensional chain of nano-slots with variable orientation profile $\alpha(l)$ along a curved trajectory l to generate such a caustic, we have established the metric of problem as

$$d\tau^2 = |\nabla\tau|^2(dl^2 - (4/k_{SPP}^2)d\alpha^2) \tag{1}$$

where τ is the caustic parameter connecting to the trajectory, l is the length along trajectory and k_{SPP} is the wave-number of the surface plasmon polariton. With such a metric interpretation, the orientation profile $\alpha(l)$ can be straight-forwardly obtained by integrating the metric using

$$\alpha(l) = \frac{k_{SPP}}{2}\int\sqrt{dl^2 - \frac{1}{|\nabla\tau|^2}d\tau^2} \tag{2}$$

Fig.1(a), (b) and (c) shows the simulation, experimentally measured SPP profile and SEM (scanning electron microscopy) picture of the sample for generating a given caustic by shining LCP (left-handed circular polarization) light to the sample, showing the validity of such a metric interpretation.

Such a metric interpretation also allows us to establish a coordinate transformation between equivalent trajectories (along l and along l') to generate the same caustic as

$$|\nabla\tau|\begin{pmatrix}\Delta l\\ 2\frac{\Delta\alpha}{k_{SPP}}\end{pmatrix} = |\nabla\tau|'\begin{pmatrix}\cosh\zeta & \sinh\zeta\\ \sinh\zeta & \cosh\zeta\end{pmatrix}\begin{pmatrix}\Delta l'\\ 2\frac{\Delta\alpha'}{k_{SPP}}\end{pmatrix} \tag{3}$$

The coordinate transformation is in analogy to a Lorentz transformation where ζ plays the role of rapidity in conserving the metric in Eq. (1). The rapidity between the two frames also satisfy an analog velocity subtraction formula in relativity:

$$\tanh\zeta = 2\left(\frac{d\alpha}{dl} - \frac{d\alpha}{dl'}\right) / \left(k_{SPP}^2 - 4\frac{d\alpha}{dl}\frac{d\alpha'}{dl'}\right) \quad (4)$$

Fig.1(d), (e) and (f) shows such an equivalence using again simulation, experimentally measured SPP profile and SEM picture of the sample for generating the same caustic but along a different trajectory (Fig. 1(f)) by shining LCP (left-handed circular polarization) light to the sample. There is a caustic marked in white dashed line appearing both in simulation and experiment for the two cases (flat and curved trajectories). In some cases, there might be another caustic due to the SPP signal without carrying geometric phase.

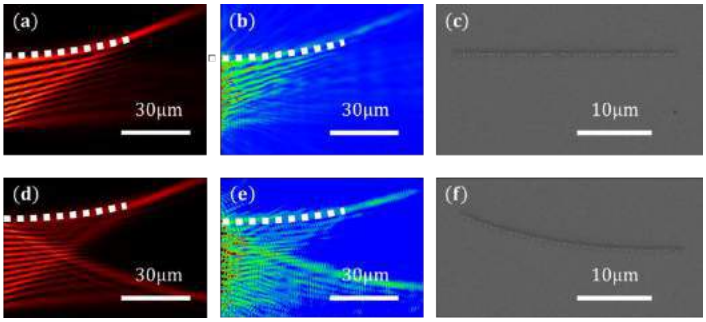

Figure 1 (a) simulation, (b) experimental results of using LCP to excite metallic nano-holes placed in a straight line as in (c) SEM picture. (d) simulation, (e) experimental results of using LCP to excite metallic nano-holes placed in a curved line as in (f) SEM picture.

In summary, we have provided a metric interpretation to generate plasmonic caustic using one-dimensional chain of metamaterial atoms with variable orientation profile. Such an approach can be straight-forwardly applied to generate caustic with arbitrarily given shape. We also explore the relationship of the metric interpretation of caustic to motion in curved space-time.

Acknowledgements, J. L. acknowledges funding from the European Union's Seven Framework Programme under Grant Agreement No. 630979. F. Z., H. L. acknowledge funding from the National Natural Science Foundation of China (No. 11321063, 61425018, 11374151) and the support of travel to University of Birmingham for carrying out the collaboration.

REFERENCES

1. Genevet, P. et al., "Controlled steering of Cherenkov surface plasmon wakes with a one-dimensional metamaterial," *Nature Nanotech.* , Vol. 10, No. 9, 804-809, 2015.
2. Xiao, S. et al., "Flexible coherent control of plasmonic spin-Hall effect," *Nat. Commun.*, Vol. 6, 8360, 2015.
3. Minovich, A. et.al., "Generation and near-field imaging of airy surface pasmoncs", Phys. Rev. Lett. 107, 116902, 2011.
4. Lin, J. et.al., "Mode-matching metasurfaces: coherent reconstruction and multiplexing of surface waves", Sci. Rep. 5, 10529, 2015.

Reconfigurable beam steering using gate-tunable metagratings

Ragip A. Pala,[1,2] Ghazaleh Kafaie Shirmanesh,[1, 2] Ruzan Sokhoyan,[1] Yao-Wei Huang,[1,2] Ho Wai Howard Lee,[1,2] and Harry A. Atwater[1, 2]

[1] Thomas J. Watson Laboratory of Applied Physics, California Institute of Technology, Pasadena, California 91125, USA

[2] Kavli Nanoscience Institute, California Institute of Technology, Pasadena, California 91125, USA

Abstract - *We experimentally demonstrate gate-tunable metasurfaces that enable electrical control of the phase of the plane wave reflected from the metasurface. Our design utilizes field-effect modulation of the complex refractive index of indium tin oxide (ITO) layers incorporated into metasurface antenna elements which are configured in reflectarray geometry[1]. We measured a phase shift of 180^o by analyzing the reflection phase from the metasurface elements at their design wavelength of 1550nm using Michelson Interferometry. We also show possibility of controllable beam steering up to 40^o by applying independent bias on individual antenna elements. This work provides insight towards reconfigurable beam steering devices, dynamic holograms, and tunable ultrathin lenses based on electrically tunable metasurfaces.*

Novel ultrathin optical components based on metasurfaces were recently proposed such as flat lenses, wave plates, holographic surfaces and surfaces with angular momentum manipulation and detection. However, while metasurfaces hold considerable promise for fundamental advances and novel applications, lack of dynamic tunability and low optical efficiency limits their use in a wide range of applications. A successful implementation of tunable metasurfaces requires large phase shifts ($\theta > 270^o$), moderately large amplitude response, and robustness to structural variations and surface roughness. To enable a large phase shift, a substantial change in the permittivity is required to sufficiently shift the resonances, while a small loss parameter is necessary to enable a resonance bandwidth smaller than the spectral bandwidth of the phase shift. On the other hand, in any dispersive material system, these quantities are coupled to each other which imposes a limit on the achievable phase shift. Due to these limitations, it's critical to develop effective resonant metasurface designs to achieve large phase tunability under applied bias.

In this work, I discuss several optical designs that we have critically evaluated for effective beam steering, exploiting tunable electronic properties of conducting oxide materials. For the phase control, a gate-tunable metasurface enables dynamic electrical control of the plane wave reflected from the metasurface (Fig. 1A-B). Tunability arises from field-effect modulation of the complex refractive index of conducting oxide layers incorporated into metasurface antenna elements of fishbone shape (Fig. 1C-D). The fishbone structure provides an additional parameter to independently control the resonance properties through the length of antenna, which is an essential element for realization of 2-dimensional phase control of the metasurface array.

Reflectance spectra of metasurfaces with different antenna lengths (160 nm to 200 nm) are shown in Fig. 1E. By choosing an appropriate antenna length, we can ensure that the magnetic dipole plasmon resonance occurs at a target wavelength in the near-infrared region. We measure a phase shift of 180° and ~30% change in the reflectance by applying 2.5 V gate bias at our operation wavelength of 1550nm with modulation frequencies exceeding 10 MHz (Fig. 1F). Additionally, we demonstrate electrical switching of ±1 order diffracted beams by electrical control over subgroups of metasurface elements and show controllable beam steering up to 40° by applying independent bias on individual antenna elements, a basic requirement for electrically tunable beam-steering phased array metasurfaces (Fig. 1G). This demonstration at NIR frequencies opens the path to applications in ultrathin optical components for imaging and sensing technologies, such as reconfigurable beam steering devices, dynamic holograms, tunable ultrathin lenses, nanoprojectors, and nanoscale spatial light modulators.

1. Huang, Y.-W. et al. Gate-Tunable Conducting Oxide Metasurfaces. Nano Letters 16, 5319 (2016).

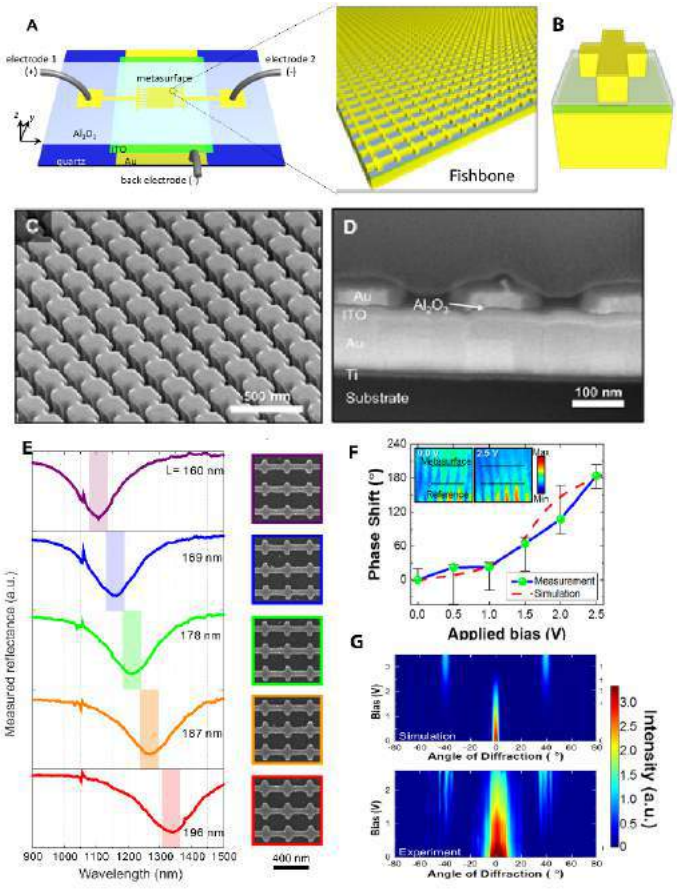

Figure 1: (A) Schematic of the tunable metasurface where voltage is applied between the stripe antenna via the external gold pads and the bottom gold mirror. (B) Individual antenna element. (C) Scanning electron microscopic (SEM) images of the sample (oblique incidence of 52 degrees) before the lift-off process. (D) The cross-section of the fabricated metasurface after the lift-off process. (E) Typical measured reflectance spectra of the metasurfaces where the resonance wavelength can be finely tuned by changing antenna length L. (F) Measured and simulated phase shift as a function of applied bias for applied voltage between 0 and 2.5 V (From Ref 1). Inset: the interference fringes for applied bias 0 and 2.5 V. (G) Simulated (top) and experimental (below) far-field intensity profiles of the diffracted beam versus applied bias. The color map shows far-field intensity of the light beam reflected from the metasurface as a function of diffraction angles and applied voltages.

Tunable Conducting Oxide Epsilon-Near-Zero Metasurface as Broadband Perfect Absorbers

Aleksei Anopchenko[1], Long Tao[1], and Ho Wai Howard Lee[1,2,*]

[1]Department of Physics and Baylor Research and Innovation Collaborative, Baylor University, Waco, United States

[2]The Institute for Quantum Science and Engineering, Texas A&M University, College Station, United States

[*]corresponding author: Howard_Lee@Baylor.edu

Abstract- We present our recent development on the use of tunable transparent conducting oxides to demonstrate an electrically tunable metasurfaces that can tune the optical phase and amplitude for on-chip beam steering devices and perfect absorbers. We find that ultrathin epsilon-near-zero (ENZ) conducting oxide multilayers absorb >95% of light in 1-1.5 μm wavelength range with field-effect tunability.

Light harvesting and high-resolution optical technologies demand optical coatings with strong light absorption. Recent studies suggest that epsilon-near-zero (ENZ) materials can be useful to make perfect ultrathin film absorbers [1-3]. The ultrathin ENZ layers support radiative Berreman and bound ENZ modes [2, 4]. Excitation of these modes in two different incident light configurations leads to resonant absorption. In this work, a broadband perfect absorber has been demonstrated by using a stack of ITO nanolayers with gradually varying electron concentration and hence ENZ frequency. The light absorption dependence on the ENZ layer thickness in the multilayer stack was optimized so that absorption >95% was achieved at deep subwavelength ENZ thicknesses. Electronically tunable absorption via formation of electron accumulation/depletion layer in the field-effect devices was studied.

The ENZ multilayers are composed of 4 ITO nanolayers. The TM-polarized light absorptance as a function of the wavelength is shown in Fig. 1c. The carrier concentrations of the ITO nanolayers are $N_1 = 1\times10^{21}$ cm^{-3}, $N_2 = 8\times10^{20}$ cm^{-3}, $N_3 = 6.1\times10^{20}$ cm^{-3}, and $N_4 = 4.9\times10^{20}$ cm^{-3}. The optical properties of the ITO are modelled using free electron Drude model. We found that the highest absorption can be achieved with the ITO thickness of ~ 10-30 nm in the ENZ multilayers. The absorptance is attributed to the excitation of the radiative Berreman mode. The ENZ multilayer is supported by a thick gold reflector. The electron concentration decreases, and ENZ wavelength increases, from the top to the bottom of the multilayer stack. Broadband maximum absorption >95% and field enhancement are observed at the ENZ wavelengths by exciting Berreman mode. Excitation of the bound ENZ mode in the Kretschmann-Raether configuration) results in resonant light absorption with much borader bandwidth than the Berreman mode. The absorptance of >95% for more than 500 nm wavelength range is observed for the multilayer stack with 8-nm thin ITO layers.

Tunable absorption can be enabled by the field-effect dynamic in metal-oxide-semiconductor (MOS) configuration. The MOS device consists of a metal substrate, single 8-nm thin ITO layer, and 5-nm-thin HfO_2 layer between them. Electron accumulation occurs in ITO at the ITO-HfO_2 interface when bias is applied between metal and ITO, thus modifying the complex dielectric constant of the ITO. Electron accumulation increases plasma and ENZ frequency and therefore leads to a blue shift of the absorption peak in wavelength [5].

The larger absorptance change (> 300%) is observed at shorter wavelengths due to larger field enhancement in the accumulation layer. These results open the path to develop ultrathin tunable ENZ absorbers and thin-film modulators.

REFERENCES

[1] M. A. Badsha, Y. C. Jun, and C. K. Hwangbo, Opt. Commun. 332, 206-213, 2014.

[2] S. Campione, I. Kim, D. de Ceglia, G. A. Keeler, and T. S. Luk, Opt. Express 24, 18782-18789, 2016.

[3] J. Yoon, M. Zhou, M. A. Badsha, T. Y. Kim, Y. C. Jun, and C. K. Hwangbo, Sci. Rep. 5, 12788, 2015.

[4] S. Vassant, J.-P. Hugonin, F. Marquier, and J.-J. Greffet, *Opt. Express* **20**, 23971-23977, 2012.

[5] Y. W. Huang *et al.*, "Gate-tunable conducting oxide metasurfaces," *Nano Lett.* **16**, 5319-5325, 2016.

Epsilon-near-zero substrate engineering for ultra-thin-film perfect absorbers

Federico Capasso[1], Jura Rensberg[2], You Zhou[1], Steffen Richter[3], Chenghao Wan[4, 5], Shuyan Zhang[1], Philipp Schöppe[2], Rüdiger Schmidt-Grund[3], Shriram Ramanathan[6], , Mikhail A. Kats[4, 5], Carsten Ronning[2]

capasso@seas.harvard.edu

[1]John A. Paulson School of Engineering and Applied Sciences, Harvard University, Cambridge, MA 02138, USA.

[2]Institute for Solid State Physics, Friedrich-Schiller-Universität Jena, 07743 Jena, Germany

[3]Institute for Experimental Physics II, Universität Leipzig, 04109 Leipzig, Germany

[4]Department of Materials Science and Engineering, University of Wisconsin - Madison, Madison, Wisconsin 53706, USA

[5]Department of Electrical and Computer Engineering, University of Wisconsin - Madison, Madison, Wisconsin 53706, USA

[6]School of Materials Engineering, Purdue University, West Lafayette, IN 47907, USA

Efficient suppression of reflection is a key requirement for perfect absorption of light. Recently, it has been shown that reflection can be effectively suppressed utilizing a single ultra-thin film deposited on metals or polar materials featuring phonon resonances. The wavelength at which reflection can be fully suppressed is primarily determined by the nature of these substrates, and is pinned to particular values near plasma or phonon resonances – the former typically in the ultraviolet or visible, the latter in the infrared. Here, we explicitly identify the required optical properties of films and substrates for the design of absorbing anti-reflection coatings based on ultra-thin films. We find that completely suppressed reflection using films with thicknesses much smaller than the wavelength of light occurs within a spectral region where the real part of the refractive index of the substrate is $n \lesssim 1$, which is characteristic of materials with permittivity close to zero. We experimentally verify this condition by using an ultra-thin vanadium dioxide film with dynamically tunable optical properties on several epsilon-near-zero materials, including aluminum-doped zinc oxide (AZO). By tailoring the plasma frequency of the AZO, we were able to tune the epsilon-near-zero point, thus achieving suppressed reflection and near-perfect absorption at wavelengths that continuously span the near-infrared and long-wave mid-infrared ranges.

Hot Electron Enhanced Thermionic Emission (HEETE) converters for all-metal optical power generation.

N. Hogan[1], S. Wu[1], and M. Sheldon*[1,2]
[1]Departmetn of Chemistry, Texas A&M University, USA
[2]Department of Materials Science & Engineering, Texas A&M University, USA
*corresponding author: sheldonm@tamu.edu

Abstract- We report on our studies of photo-induced charge transport from nanostructured metal metasurface absorbers. In particular, we outline how the remarkable thermal and optical energy concentration provided by plasmonic resonances can enable a new thermodynamic power cycle whereby photo-excited 'hot' electrons and resonant photothermal heating provides a dual excitation mechanism for electron emission. Because this process is closely related to purely thermionic emission, we label an optical power-converting device based on this mechanism a Hot Electron Enhanced Thermionic Emission (HEETE) converter. The strong enhancement of both thermal and optical energy channels, may enable a significantly more efficient strategy for optical power conversion, and one that can theoretically out-perform traditional semiconductor-based solar cells.

Our study emphasizes theoretical and experimental development of refined models for electronic distributions in metals, specifically when characteristic structural features are smaller than the mean free path of excited carriers. In addition, we have developed a mechanistic model of the photo-thermal response of optimized plasmonic absorbers accounting for factors such as spectral width of absorbance and emissivity, as well the role of thermal damping pathways such as conduction and convection. When radiative loss is the dominant cooling mechanism, as can be achieved with thermionic devices in vacuum, we anticipate solar-induced temperature increases over 1500 K without additional optical concentration, and consequent photo-induced current densities with 10^{15} enhancement compared with purely thermionic emission at the equivalent temperature.

The optimal structures to achieve these temperatures have high absorption (> 90%) with spectral bandwidth that spans the visible up to 1100 nm, and emissivity of ~2% throughout the infrared. Importantly, properly designed surfaces also significantly constrain the angular dependence of thermal emission, enabling absorbers that can approach the theoretical maximum temperature achievable under direct sunlight (5800 K). We show a variety of noble metal nanostructures (Au, Ag, Cu), and high melting point metals (W, Ir, Pt), combined with refractory dielectric cladding that can provide these ideal optoelectronic properties due to their thermal tolerance, highly absorbing and tunable plasmon resonances in the visible, and naturally low and tunable emissivity in the infrared. In combination with full-wave optical simulations that guide optimized designs, we have fabricated HEETE device test structures and measured the spectral and temperature performance in vacuum, outlining opportunities for optical power conversion.

Acknowledgements This material is based upon work supported by the Air Force Office of Scientific Research under award number FA9550-16-1-0154. M. S. also acknowledges support from the Welch Foundation (A-1886).

Polarization anomalies of plasmonic singular fields

Denis Garoli[1], Pierfrancesco Zilio[1], Francesco De Angelis[1], and Yuri Gorodetski[2]*

[1]Istituto Italiano di Tecnologia, via Morego 30, I-16163, Genova, Italy
[2]Ariel University, Mechanical Engineering & Mechatronics department and Electrical Engineering & Electronics department, Ariel, 40
*corresponding author, E-mail: yurig@ariel.ac.il

Abstract

We experimentally demonstrate an anomalous polarization state emitted by a propagating singular plasmonic field from an adiabatically tapered nano cone. This phenomenon is attributed to the specific 3D geometry of the system allowing the increase and the full transfer of the intrinsic transverse plasmonic spin to the far-field. Our model is numerically tested and experimentally verified in this work..

1. Introduction

Structured light beams have been the subject of an intense work in the last years [1, 2] due to the numerous potential applications they may offer in several disparate technological and research fields, ranging from super-resolution imaging [3] to optical tweezing [4] and nanomanipulation [5] to telecommunications [6].

The possibility to produce and analyze singular optical beams at the micro and the nanoscale led to focus on the interaction of light with metallic nanostructures, resulting in Surface Plasmon Polaritons (SPPs) carrying angular momentum (AM) [7, 8, 9, 10, 11, 12, 13, 14]. We will refer to these waves as Plasmonic Vortices (PVs). Such modes are generally surface confined helical electromagnetic distributions with a field singularity. The strength of the singularity, termed the topological charge of a vortex, is defined by the phase ramp acquired in one round trip about the singularity center. This charge is proportional to the AM carried by the field [15, 2].

Several intriguing phenomena have been already studied in these plasmonic wavefronts, such as particle trapping, plasmonic focusing, optical switching etc [16]. Here, we investigate the interaction of these near-field distributions with the far-field beam. Specifically, we propose a system capable of coupling the PV to the far-field with the given AM and at a given polarization state. Moreover, we study a peculiar phenomenon of the helicity locking due to the transverse plasmonic spin carried by the PV. This angular momentum component is shown to significantly affect the far-field emission in our system. We present a geometric model predicting the resulting far-field helicity and demonstrate its application in an experiment with nanofabricated plasmonic system.

2. Far-field coupling of PV by acelleration on a smoothed taper

As was recently shown, PVs can be generated by using spiral grating couplers, which have been sometimes called plasmonic vortex lenses (PVLs) [9]. We assume an Archimede's spiral whose radius are given by $R_m(\varphi) = R_0 + m \cdot \varphi/k_{SP}$, where R_0 is the smallest radius of the groove, m is the topological order of the spiral and φ is the azimuthal angle. The field distribution of the PV consists of a helical plasmonic wavefront of the form $E_{SP} \propto e^{-il\varphi}$, where l - a quantum azimuthal number is commonly called the topological charge. The AM of the resulting PV is then given by its topological charge, $l = \sigma_i + m$, where σ_i is the circular polarization handedness of the incident light ($\sigma_i = +1, -1$ for right-handed and left-handed state respectively). In contrast with propagating vortices the PV is surface-confined and propagates towards the center of the grating [17, 18, 19] (its z componenmt of the momentum is a purely imaginary number). Accordingly, this near-field distribution is not capable of transmitting AM to the far-field. While propagating optical vortices can play a role of AM transducer for nano-manipulations or an optical communication channel [4, 5, 6] plasmonic structures provide a compact and convenient solution for field manipulation and PV generation. In this context there has been a significant concern as for the far-field coupling of the PVs by means of a nanostructure. Such a component should bring about an important functionality of a PV generation and manipulation in the near-field [13, 20, 12].

In this context we have designed a system comprising of a plasmonic spiral grating with a smoothed conical golden tip placed at its geometrical center [14, 21]. Due to its high guiding and efficiency directionality this plasmonic 3D design have been recently presented as useful tool for nanoscale chemical mapping [22] for enhanced IR plasmonics [23] and intracellular plasmonic sensing [24].

The geometry of the system is presented in Fig. 1 along with the scanning electron micrograph of the fabricated system. We analyze the electromagnetic field distribution by means of the COMSOL ®multiphysics software considering a $\lambda_0 = 780nm$ circularly polarized beam impinging on the grating grooves from the bottom. In Fig. 1 it is clearly seen that by modifying a curvature radius, r_c of the tip base the coupling of the plasmonic vortex to the conical

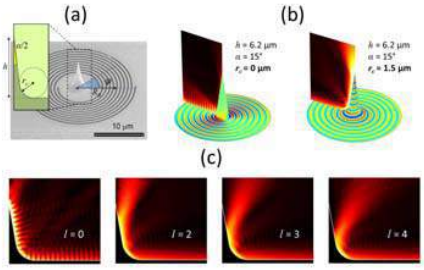

Figure 1: Coupling of PV to the far-field. (a) SEM image of the structure with its geometrical parameters. (b) Comparison of the plasmonic mode coupling to the cone with zero basis curvature versus an optimized one. (c) Plasmonic field distribution on the tip for different PV topological charges.

waveguide can be sufficiently increased. In Fig 1b the two cases are compared - (i) $r_c = 0$ and (ii) the optimized value, $r_c = 1.5\mu m$.

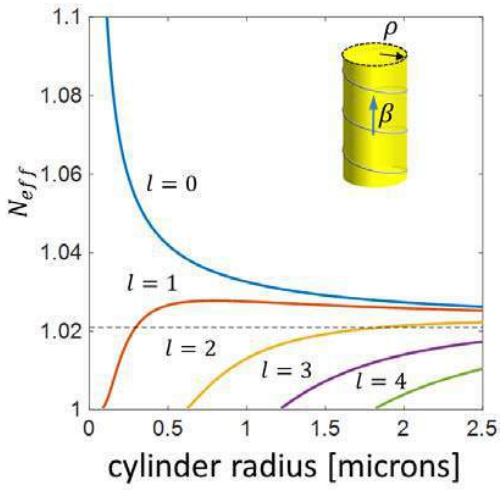

Figure 2: Dispersion of the effective index of the PV mode propagating on a metallic cylinder versus radius.

While in the first case it is evident from the fringes on the surface that most of the PV power is reflected back from the tip, the second case shows a smooth coupling of most of the energy to the guided mode. We also note that this mode is then perfectly coupled to the far-field. The best far-field beaming is obtained for a PV with the topological charge of $l = 1$ (See Fig. 1c) in a form of a point-like source. Higher topological orders produce beams with divergence proportional to their l. We have recently shown that these are Laguerre-Gauss distributions carrying an AM of $l_o \pm \sigma_o$, where σ_o is the emerging light's spin state. The beam was shown to detach from the tip surface at a point where the momentum of the guided mode perfectly matches the one of the corresponding free-space beam.

In Fig. 2 we show a dispersion of the guided mode's effective index, $N_{eff} = \beta/k_0$ (here β is the mode's propagation constant derived from the direct boundary condition solution and $k_0 = 2\pi/\lambda_0$ is the free space momentum) on a metallic cylinder versus the cylinder radius ρ (see the inset). Apparently the mode with $l = 0$ has an increasing index which is manifested by a strong light localization at the apex (Fig. 1). Nevertheless, other modes with $l > 1$ accelerate, and their effective index drops with decreasing radius. At the point where $N_{eff} = 1$ the mode detaches and propagates to the far-field. The mode with $l = 1$ is the only one that survives to the end of the tip, which can be deduced from the asymptotic behavior of the index.

3. Helicity locking

We calculate the transverse field distribution slightly above the detachment points (shown by the yellow dashed line in the insets). The complex field values are used to calculate the local polarization ellipse that is graphically presented on the top of the intensity distribution (Fig. 3). The emerging polarization handedness, $\sigma_o = +1$ is shown in red while $\sigma_o = -1$ is in magenta. Note that the emerging modes are both right-handed and very close to the circular state.

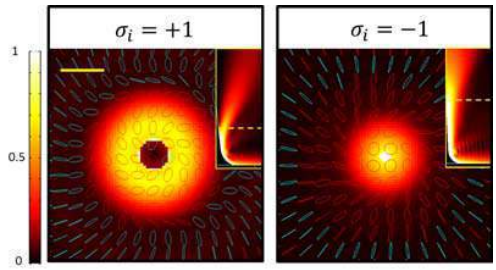

Figure 3: Calculated intensity and polarization distribution at the vortex detachment point for different incident spin states. The insets show the intensity flow along the tip and the yellow dashed line represent the height at which the distribution was taken. The scalebar is 1 μm.

In other words our system emits $\sigma_o = 1$ *independently* on the incident handedness. Apparently, most of the previously discussed axially symmetric scattering architectures, such as circular or coaxial apertures were shown to couple PVs to radially polarized beam, that naturally consisted of almost equal amounts of right and left CP [7, 9, 13]. Here we link the emission of a single-handed polarization to the so-called transverse spin (TS) of the plasmonic mode. The TS of the surface wave propagating in x direction on a metal-air interface is given as

$$\mathbf{s}_\perp \propto \frac{Re\mathbf{k} \times Im\mathbf{k}}{(Re\mathbf{k})^2} \qquad (1)$$

where $\mathbf{k} = k_{SP}\hat{\mathbf{x}} + i\kappa\hat{\mathbf{z}}$ is the the complex valued evanescent wave vector, $\kappa = \sqrt{k_{SP}^2 - k_0^2}$, $k_0 = 2\pi/\lambda_0$ is the vacuum wavenumber and k_{SP} is the in-plane plasmonic wavenumber [25]. This transverse spin results from the

rotation of the resultant of the vectorial plasmonic field, $\mathbf{E}_{SP} = E_p(\hat{\mathbf{z}} - i\chi\hat{\mathbf{x}})$ in a transverse plane with respect to the propagation. Remarkably, the TS is independent of the polarization and solely arises from the amplitude ratio between the longitudinal and the transverse field components χ, that is directly obtained from Maxwell's equations, $s_\perp = \chi = \frac{\kappa}{k_{SP}}$. Accordingly, $s_\perp$ is locked to the SPs propagation direction and can appear with a single handedness. This property has been already utilized for spin-dependent unidirectional plasmonic excitation [26, 27], for nanoparticle tweezing [28, 29, 30, 31] and for study of quantum plasmonic effects [32].

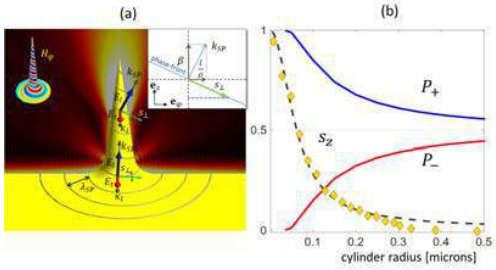

Figure 4: Geometric model of the helicity locking. (a) A conceptual scheme of the TS projection in PV. Details are in the text. (b) Local helicity currents (blue and red lines), TS projection on z axis (dashed) and simulated values of the emerging spin (rhombuses) versus the cylinder radius.

We investigate this phenomenon using the geometry of the system as shown in Fig. 3a. A helical phase-front of the PV (represented as a line spiraling around the cone) propagates on a smoothed cone with a local wave vector k_{SP}. The transverse and the longitudinal components of the local plasmonic field are denoted in the Figure as E_t and E_l, respectively. As can be seen the incidence plane follows the phase-front and gets tilted as the mode propagates upwards. Accordingly, the z projection of the local TS (green arrow) grows.

In a local tangential reference frame $(\mathbf{e}_z, \mathbf{e}_\varphi)$ the complex plasmonic wave vector is represented as $\mathbf{k}_l = \beta\mathbf{e}_z + \frac{l}{\rho}\mathbf{e}_\varphi + i\kappa_l\mathbf{e}_\rho$. By substituting the $\mathbf{k}_l$ in Eq. 1 the TS of the plasmonic wave can be calculated. The z component of the plasmonic TS is then given as,

$$s_z = -\frac{\kappa_l}{k_{SP}^2}\frac{l}{\rho} \tag{2}$$

where $\kappa_l = \sqrt{\beta^2 + \left(\frac{l}{\rho}\right)^2 - (2\pi/\lambda_0)^2}$ and $k_{SP}^2 = \beta^2 + (l/\rho)^2$. The mode detaches from the tip where the effective index becomes unity, i.e. where $\beta = k_0$. The emerging spin at that point is then $s_z = -\left[k_0^2(\rho/l)^2 + 1\right]^{-1}$.

In Fig. 3b we analyze the mode $l = 1$ propagating on a cylinder. We use the calculated fields in the circular basis, $\mathbf{E}_\pm = |\mathbf{E} \pm iZ_0\mathbf{H}|$ (Z_0 is the vacuum impedance) to derive the local field helicity current [33], $\mathbf{P}_\pm = \pm\epsilon_0 k_0 Im\left[\mathbf{E}_\pm^* \times \mathbf{E}_\pm\right] / |\mathbf{E}_\pm|^2$ and depict its integrated value in Fig. 3b. At the same Figure we present the calculated s_z (Eq. 2) as a function of the cylinder radius by using previously derived β values. Finally, we simulate an SP mode propagating on the metallic cone with realistic parameters and directly calculate the TSAM in the vicinity of the cone at different heights. Its integrated values are shown in Fig. 3b as yellow rhombuses. We note that the values of s_z calculated at the real tip fully correspond to the ones extracted from the modal analysis of the cylinder. Moreover, it is clearly visible that for the small radius both, the far-field ellipticity P_+ and the s_z become unity, which indicates the emission of a pure circular polarization with $\sigma_o = sgn(l)$. On the other hand, for large radii the s_z tends to zero. This indicates that if the field was emitted from this point its polarization would contain equal amounts of right handed and left handed CP. The latter behavior is expected from the metal due to its non-duality and was widely discussed elsewhere [34]. Obviously, the described effect of anomalous spin selectivity can be expected from all helical plasmonic modes. This can be understood from Eq. 2 with the real cutoff radius values, where s_z rapidly goes to unity as a function of l.

4. Experiment

The samples were fabricated using a sophisticated multi-step nanofabrication process described elsewhere [35]. The 150 nm gold film was prepared on a Si_3N_4 membrane and a spiral with $m = 0$ and $m = 2$ were milled in it. Then the tip with optimized parameters was formed in the center($r_c = 1.5\mu m$, $h = 6.3\mu m$ and $\alpha = 7.5$ deg). The SEM picture of the sample is shown in Fig. 1. We illuminated this structure from the membrane side with a collimated pigtail CW laser at $\lambda_0 = 780nm$ and by manipulating circular polarizer and analyzer the incident and the emerging polarization state could be controlled. We captured the far-field images by using CMOS camera.

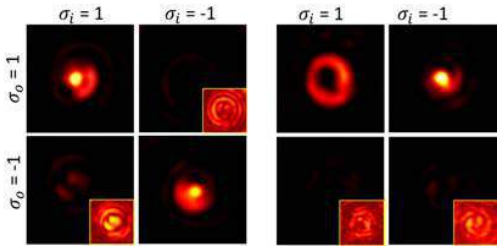

Figure 5: Experimental verification of the helicity locked emission. (a) Cross polarization measurements of the intensities emerging from the tip with $m = 0$ spiral, and (b) with $m = 2$ spiral.

In Fig. 4 the resulting distributions are presented in a table according to the polarization states. We note that for the case of $m = 0$ the system is axially symmetric and as

expected the PV with $l = \pm 1$ is obtained for $\sigma_0 = \pm 1$. In the case of $m = 2$ we obtain a PV with $l = 1, 3$. In this latter case both vortices have positive helicities which results in the only emerging light with $\sigma_o = +1$. In both experiments we measured ratios of at least 1:7 in the intensities of the two emerging polarization components. This high polarization contrast is attributed to the helicity locking of the plasmonic modes due to its intrinsic TS. Note also, that the two presented systems generate the $l = 1$ mode from different incident polarization states. Nevertheless, the emerging polarization state depends *only* on the sign of the topological charge of the PV and not on the incident handedness.

5. Summary

In summary, we have demonstrated a nanoscale plasmonic system capable of producing far-field beaming of a given AM and polarization state. The coupling of light into the system is obtained by a plasmonic spiral grating which generates a PV with a necessary charge. The vortex is then coupled to the far-field by rather a 2D coupling mechanism icorporating MIM waveguiding or a 3D system based on a smooth tip on which the PV propagets untill it detaches to the far-field carrying a desired AM. The helicity locking that stems from the intrinsic transverse spin of the plasmons leads to a purely circularly polarized emission. We beleive that this system can bear an interesting underlying physics as well as technological potential for nanophotonics.

Acknowledgement

This work was supported by the Ministry of Science Technology & Space, Israel.

References

[1] F. Cardano and L. Marrucci, "Spin-orbit photonics," *Nature Photonics*, vol. 9, no. 12, pp. 776–778, 2015.

[2] D. L. Andrews and M. Babiker, *The angular momentum of light*. Cambridge University Press, 2012.

[3] F. Tamburini, G. Anzolin, G. Umbriaco, A. Bianchini, and C. Barbieri, "Overcoming the rayleigh criterion limit with optical vortices," *Physical review letters*, vol. 97, no. 16, p. 163903, 2006.

[4] M. Padgett and R. Bowman, "Tweezers with a twist," *Nature Photonics*, vol. 5, no. 6, pp. 343–348, 2011.

[5] K. Toyoda, K. Miyamoto, N. Aoki, R. Morita, and T. Omatsu, "Using optical vortex to control the chirality of twisted metal nanostructures," *Nano letters*, vol. 12, no. 7, pp. 3645–3649, 2012.

[6] N. Bozinovic, Y. Yue, Y. Ren, M. Tur, P. Kristensen, H. Huang, A. E. Willner, and S. Ramachandran, "Terabit-scale orbital angular momentum mode division multiplexing in fibers," *Science*, vol. 340, no. 6140, pp. 1545–1548, 2013.

[7] Y. Gorodetski, A. Niv, V. Kleiner, and E. Hasman, "Observation of the spin-based plasmonic effect in nanoscale structures," *Physical Review Letters*, vol. 101, no. 4, p. 043903, 2008.

[8] K. Bliokh, F. Rodríguez-Fortuño, F. Nori, and A. V. Zayats, "Spin-orbit interactions of light," *Nature Photonics*, vol. 9, no. 12, pp. 796–808, 2015.

[9] Y. Gorodetski, N. Shitrit, I. Bretner, V. Kleiner, and E. Hasman, "Observation of optical spin symmetry breaking in nanoapertures," *Nano Letters*, vol. 9, no. 8, pp. 3016–3019, 2009.

[10] P. Zilio, E. Mari, G. Parisi, F. Tamburini, and F. Romanato, "Angular momentum properties of electromagnetic field transmitted through holey plasmonic vortex lenses," *Optics lLetters*, vol. 37, no. 15, pp. 3234–3236, 2012.

[11] S.-W. Cho, J. Park, S.-Y. Lee, H. Kim, and B. Lee, "Coupling of spin and angular momentum of light in plasmonic vortex," *Optics Express*, vol. 20, no. 9, pp. 10 083–10 094, 2012.

[12] D. Garoli, P. Zilio, Y. Gorodetski, F. Tantussi, and F. De Angelis, "Optical vortex beam generator at nanoscale level," *Scientific Reports*, vol. 6, 2016.

[13] Y. Gorodetski, A. Drezet, C. Genet, and T. W. Ebbesen, "Generating far-field orbital angular momenta from near-field optical chirality," *Physical Review Letters*, vol. 110, p. 203906, 2013.

[14] D. Garoli, P. Zilio, Y. Gorodetski, F. Tantussi, and F. De Angelis, "Beaming of helical light from plasmonic vortices via adiabatically tapered nanotip," *Nano Letters*, vol. 16, no. 10, pp. 6636–6643, 2016.

[15] L. Allen, S. M. Barnett, and M. J. Padgett, *Optical angular momentum*. CRC Press, 2003.

[16] K. Iniewski, *Nanoplasmonics: Advanced Device Applications*. CRC Press, 2013.

[17] M. Carli, P. Zilio, D. Garoli, V. Giorgis, and F. Romanato, "Sub-wavelength confinement of the orbital angular momentum of light probed by plasmonic nanorods resonances," *Optics express*, vol. 22, no. 21, pp. 26 302–26 311, 2014.

[18] D. Garoli, T. Ongarello, P. Zilio, M. Carli, and F. Romanato, "Nanofocusing on circularly distributed tapered metallic waveguides by means of plasmonic vortex lenses," *Applied optics*, vol. 54, no. 5, pp. 1161–1166, 2015.

[19] T. Ongarello, G. Parisi, D. Garoli, E. Mari, P. Zilio, and F. Romanato, "Focusing dynamics on circular distributed tapered metallic waveguides by means of plasmonic vortex lenses," *Optics letters*, vol. 37, no. 21, pp. 4516–4518, 2012.

[20] P. Zilio, G. Parisi, D. Garoli, M. Carli, and F. Romanato, "Bilayer holey plasmonic vortex lenses for the far field transmission of pure orbital angular momentum light states," *Optics letters*, vol. 39, no. 16, pp. 4899–4902, 2014.

[21] D. Garoli, P. Zilio, F. De Angelis, and Y. Gorodetski, "Helicity locking of chiral light emitted from a plasmonic nanotaper," *Nanoscale*, vol. 9, pp. 6965–6969, 2017. [Online]. Available: http://dx.doi.org/10.1039/C7NR01674C

[22] F. De Angelis, G. Das, P. Candeloro, M. Patrini, M. Galli, A. Bek, M. Lazzarino, I. Maksymov, C. Liberale, and L. C. Andreani, "Nanoscale chemical mapping using three-dimensional adiabatic compression of surface plasmon polaritons," *Nature Nanotechnology*, vol. 5, no. 1, pp. 67–72, 2010.

[23] M. Malerba, A. Alabastri, E. Miele, P. Zilio, M. Patrini, D. Bajoni, G. C. Messina, M. Dipalo, A. Toma, R. P. Zaccaria *et al.*, "3d vertical nanostructures for enhanced infrared plasmonics," *Scientific reports*, vol. 5, p. 16436, 2015.

[24] M. Dipalo, H. Amin, L. Lovato, F. Moia, V. Caprettini, G. C. Messina, F. Tantussi, L. Berdondini, and F. De Angelis, "Intracellular and extracellular recording of spontaneous action potentials in mammalian neurons and cardiac cells with 3d plasmonic nanoelectrodes," *Nano Letters*, 2017.

[25] K. Y. Bliokh and F. Nori, "Transverse and longitudinal angular momenta of light," *Physics Reports*, vol. 592, pp. 1–38, 2015.

[26] A. E. Miroshnichenko and Y. S. Kivshar, "Polarization traffic control for surface plasmons," *Science*, vol. 340, no. 6130, pp. 283–284, 2013.

[27] D. O'Connor, P. Ginzburg, F. Rodríguez-Fortuño, G. Wurtz, and A. Zayats, "Spin–orbit coupling in surface plasmon scattering by nanostructures," *Nature Communications*, vol. 5, 2014.

[28] S.-Y. Lee, I.-M. Lee, J. Park, S. Oh, W. Lee, K.-Y. Kim, and B. Lee, "Role of magnetic induction currents in nanoslit excitation of surface plasmon polaritons," *Physical Review Letters*, vol. 108, no. 21, p. 213907, 2012.

[29] M. Antognozzi, C. R. Bermingham, R. L. Harniman, S. Simpson, J. Senior, R. Hayward, H. Hoerber, M. R. Dennis, A. Y. Bekshaev, K. Y. Bliokh, and F. Nori, "Direct measurements of the extraordinary optical momentum and transverse spin-dependent force using a nano-cantilever," *Nature Physics*, 2016.

[30] M. Neugebauer, T. Bauer, A. Aiello, and P. Banzer, "Measuring the transverse spin density of light," *Physical Review Letters*, vol. 114, no. 6, p. 063901, 2015.

[31] A. Canaguier-Durand and C. Genet, "Transverse spinning of a sphere in a plasmonic field," *Physical Review A*, vol. 89, no. 3, p. 033841, 2014.

[32] K. Y. Bliokh, D. Smirnova, and F. Nori, "Quantum spin hall effect of light," *Science*, vol. 348, no. 6242, pp. 1448–1451, 2015.

[33] A. Aiello and M. V. Berry, "Note on the helicity decomposition of spin and orbital optical currents," *Journal of Optics*, vol. 17, no. 6, p. 062001, 2015.

[34] I. Fernandez-Corbaton, X. Zambrana-Puyalto, and G. Molina-Terriza, "Helicity and angular momentum: A symmetry-based framework for the study of light-matter interactions," *Physical Review A*, vol. 86, no. 4, p. 042103, 2012.

[35] F. De Angelis, M. Malerba, M. Patrini, E. Miele, G. Das, A. Toma, R. P. Zaccaria, and E. Di Fabrizio, "3d hollow nanostructures as building blocks for multifunctional plasmonics," *Nano letters*, vol. 13, no. 8, pp. 3553–3558, 2013.

A bottom-up approach towards metamaterials and plasmonics

About Optical Games with Eutectics $ZnO/ZnWO_4$

A. Belardini[1], P. Osewski[2], E. Petronijevic[1], D. Pawlak[2], R. Li Voti[1], G. Lehau[1], M. Centini[1], C. Sibilia[1,*]

1. Università di Roma La Sapienza, Dipartimento SBAI, Via Scarpa 16, 00161 Roma, Italy
2. Institute of Electronic Materials Technology, ul. Wólczyńska 133, 01-919 Warsaw, Poland

[*]corresponding author: concita.sibilia@uniroma1.it

Abstract - We report an overview of optical properties of eutectics $ZnO/ZnWO_4$. Filtering properties and polarization dependent properties, with together nonlinear optical characterizations in the visible region are presented.

Many different optical interesting and unusual properties of eutectics [1] $ZnO/ZnWO_4$ are presented, ranging from linear up to nonlinear optical properties.

In our experiment, we use a set-up similar to the one used in [2]: a pulsed Ti:Sapphire laser with 130 fs pulse duration, wavelength of 800 nm and repetition rate of 1 kHz is used as a light source. The polarization of the fundamental beam at the laser's output is in p state and it can be tuned by means of rotating a half-wave plate at 800 nm. In order to suppress the SHG signal generated from the half-wave plate, a long pass filter is placed after the plate. The sample is placed on a rotational stage which enables tuning of the angle of incidence α. The light coming out of the sample is then filtered by a shortpass filter and set to p or s state by a polarization analyzer before the detector. With this set-up we measure the intensity of s or p SHG signal at the output as a function of the input polarization or α, and evaluate the corresponding conversion efficiency.

Spectral measurements done with Hamamatsu Spectral Analyzer show that there is a sharp, strong emission peak at λ~400 nm (i.e. SHG), much stronger for the annealed sample as well as a strong supercontinuum generation. For the s output, there is a strong SHG signal at a normal incidence only for the p polarization, while for the p output the α dependence is negligible.

REFERENCES

[1] D. A. Pawlak et al, *Advanced Functional Materials* **20**, 1116-1124 (2010).

[2] A. Belardini, A. Benedetti, M. Centini, G. Leahu, F. Mura, S. Sennato, C. Sibilia, V. Robbiano, M. C. Giordano, C. Martella, D. Comoretto, F. Buatier de Mongeot, "Second Harmonic Generation Circular Dichroism from Self-Ordered Hybrid Plasmonic-Photonic Nanosurfaces," Adv. Opt. Mat. **2(3)**: 208-213 (2014).

[3] C. J. Spengler, S. O'Hara, "Zinc Tungstate – Some Optical Properties," App. Optics Vol. 3, No. **9** (1964).

Self-organized ZnO-$ZnWO_4$ eutectic composite doped with Al and Ga ions, as a NIR nanoplasmonic metamaterial

P. Osewski[1*], A. Antolik[1], J. Toudert[2], B. Surma[1] and D. A. Pawlak[1,3]

[1] Institute of Electronic Materials Technology, 01-919 Warsaw, Poland,

[2] Laser Processing Group, Instituto de Óptica, CSIC, C/Serrano 121, 28006 Madrid, Spain

[3] Centre of New Technologies, University of Warsaw, Warsaw, Poland

[*]corresponding author: Pawel.Osewski@itme.edu.pl

Abstract- We report properties of a self-organized eutectic composite made of ZnO (Transparent conducting oxide - TCO) phase precipitates embedded in $ZnWO_4$ [1] matrix, doped with Al or Ga ions. The ZnO precipitates, with plasmonic properties, are formed as pseudo-periodically dispersed thin (~200 nm in width) layers separated by crystalline matrix. Optical properties, microstructure, chemical analysis, XRD, Raman spectra and photoluminescence will be presented.

In recent years the field of metamaterials and nanoplasmonics developed rapidly. The novel field of metamaterials and nanoplasmonics need new material fabrication techniques, especially bottom-up approaches such as self-organization. Eutectic composites are very promising candidates due to various structural motifs (fibrous/rodlike, globular, lamellar with micron or nanosized precipitates and even split-ring-resonators [2, 3, 4]) and many different component materials. Eutectics can be described as two intersecting crystals in one solid. It means that the eutectic composite in the same time is a monolith and a multiphase material. Eutectic composites can offer many interesting optical properties such as strong second harmonic generation, filtering properties, Faraday effect or nanoplasmonic properties [3], which can be even tunable [4].

Transparent conducting oxides (TCO) such as Al- and Ga- doped zinc oxide (AZO, GZO) are good candidates as plasmonic materials in the near infrared frequency. Dopants (Al^{3+} and Ga^{3+}) substitute Zn^{2+} ions, which enables increase of the free carriers concentration, and results in higher plasma frequency. In such materials carrier concentration is higher than 10^{20} cm^{-3}, so they exhibit metal-like behavior in NIR with low optical losses comparable to the noble metals at this wavelength range. TCOs as alternative plasmonic materials could be used in applications like surface-plasmon-polariton waveguides, metamaterials with hyperbolic dispersion and epsilon-near-zero materials. Plasmonic properties of TCO can be tunable [5, 6].

In this work we present self-organized nanostructure of ZnO-$ZnWO_4$ eutectic doped with different concentrations (1%, 5%, 10% at.) of Al and Ga grown by the micro-pulling down method. The optical properties of the eutectic in visible and IR, as well as polarization studies, and chemical studies will be presented.

References:

(1) P. Osewski, A. Belardini, E. Petronijevic, M. Centini, G. Leahu, R. Diduszko, D. A. Pawlak, C. Sibilia, *accepted in Scientific Reports,* **2017**

(2) D. A. Pawlak, S. Turczynski; M. Gajc; K. Kolodziejak; R. Diduszko; K. Rozniatowski; J. Smalc; I. Vendik *Adv. Funct. Mater.* **2010**, 7, 1116-1124.

(3) K. Sadecka, M. Gajc, K. Orlinski, H. B. Surma, A. Klos, I. Jozwik-Biala, K. Sobczak, P. Dluzewski, J. Toudert,

D. A. Pawlak, *Adv. Opt. Mat.* **2015** *3*, 381-389.

(4) K. Sadecka; J. Toudert; H.B. Surma; D.A. Pawlak *Opt. Express* **2015**, *23*, 19098.

(5) G.V. Naik; N.K. Emani; U. Guler; A. Boltasseva *IEEE J. Sel. Top. Quantum Electron* **2013**, *19*, 4601907.

(6) G.V. Naik; A. Boltasseva *Metamaterials* **2011**, *5*, 1–7.

Studying the properties of bottom-up meta-atoms based on their T-matrix.

M. Fruhnert[1], R. N. S. Suryadharma[1], A. Rahimzadegan[1], C. Rockstuhl[1,2*] and I. Fernandez-Corbaton[2]
[1]Institute of Theoretical Solid State Physics, Karlsruhe Institute of Technology, 76131 Karlsruhe, Germany
[2]Institute of Nanotechnology, Karlsruhe Institute of Technology, 76021 Karlsruhe, Germany
[*]corresponding author: carsten.rockstuhl@kit.edu

Abstract-The T-matrix of a scatterer expresses how it couples an incident mode to a scattered mode at a given frequency. Here, we outline our recent contributions to develop methods to compute the T-matrix for arbitrary scatterers; possibly composed of many sub-elements. Based on the T-matrix, properties of these scatterers are discussed and applications are explored, e.g. scattering cancelation structures, maximal electromagnetic chiral structures, or bi-anisotropic scatterers. Emphasis is put on meta-atoms amenable for a fabrication with bottom-up approaches.

Meta-atoms that can be realized by self-assembly techniques based on bottom-up approaches are often made from a larger number of small metallic nanoparticles in complicated shapes [1]. They usually exist in solution where they can freely rotate and orient to an external illumination. To study and to quantify their properties, means are required that allow the investigation of these meta-atoms without explicitly considering a specific illumination. This means is provided by the T-matrix. The T-matrix of a scatterer expresses how, at a certain frequency, any incident field expanded in a basis set of orthonormal incident modes is coupled to a basis set of orthonormal scattered modes. In most cases and for scatterers localized in space, vector spherical harmonics are used as a basis set but this is not a strict constraint. The T-matrix can be expressed in any different basis set and, indeed, converting it among different sets can provide complementary insights.

In our contribution, we describe how to compute the T-matrix for an arbitrarily shaped scatterer [2]. This usually requires the solution of multiple full-wave simulations where the scattering response of the object to a specific illumination is solved. Projecting the scattered field on the basis sets allows to deduce the T-matrix by solving a system of linear equations in a least-square sense or exactly, depending on whether a single incident mode has been used for the illumination. In our work, we use finite-element-simulations based on the program JCMsuite and rely on a plane wave basis for the illumination.

Once the T-matrix is known, multiple properties can be deduced thereof immediately. This concerns properties of specific entries such as, e.g. a specific bi-anisotropic response, or properties that can be deduced from the T-matrix as a whole, e.g. the electromagnetic chirality [3]. Moreover, insights into the properties of the meta-atoms can be obtained from analyzing the eigenvalues and eigenvectors of the T-matrix or its singular values [4].

We focus on, but do not wish to restrict our consideration exclusively to, meta-atoms that can be fabricated with self-assembly techniques. These meta-atoms consist of a larger number of metallic nanoparticles that are assembled into complicated geometries. As an example of the analysis, Fig. 1 shows some illustrative results of our approach along with some further explanations.

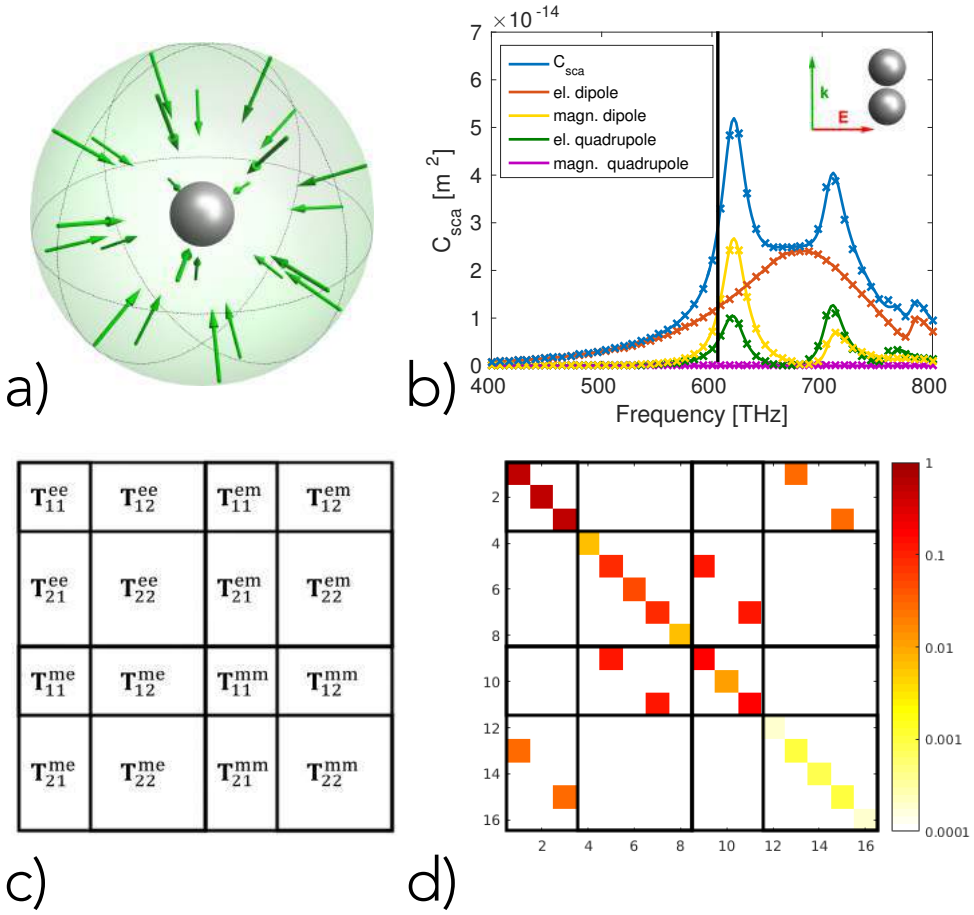

Figure 1: a) General configuration to compute the T-matrix of an arbitrarily shaped object. Many individual plane waves are considered as illumination, the full-wave response is computed and from the scattered field of each plane wave the T-matrix is constructed. b) Basic example of a silver dimer made from spheres with a radius of 30 nm and a center-to-center separation of 63 nm. The scattering cross section for a specific illumination as shown in inset has been solved with Mie theory (solid line) and a finite-element solver (crosses). c) The overall structure how we present the T-matrix, where the different electric, magnetic, and electric-magnetic entries are seen. We consider here up to a quadrupolar order. d) Amplitude of the entries of the T-matrix for the dimer at the frequency indicated by the solid line in b).

Acknowledgements: This work was supported by the German Science Foundation (project RO 3640/4-1).

REFERENCES

1. Rockstuhl C. and T. Scharf, *Amorphous Nanophotonics* Springer 2013.
2. Fruhnert M., I. Fernandez-Corbaton, V. Yannopapas, and C. Rockstuhl, "Computing the T-matrix of a scattering object with multiple plane wave illuminations" accepted for publication in Beilstein Journal of Nanotechnology.
3. Fernandez-Corbaton I., M. Fruhnert, and C. Rockstuhl, Phys. Rev. X, Vol. 6, 031013, 2016.
4. Suryadharma R. N. S., M. Fruhnert, C. Rockstuhl, and I. Fernandez-Corbaton, "Orthogonal modes of an electromagnetic scatterer" submitted to Phys. Rev. A

Reconfigurable plasmonic nanostructures with engineered stimuli responses.

A. Kuzyk[1,2*], F. Ricci[3], M. Endo[4], N. Liu[2,5]

[1]Department of Neuroscience and Biomedical Engineering, Aalto University School of Science, Finland.

[2]Max Planck Institute for Intelligent Systems, Stuttgart, Germany.

[3]Chemistry Department, University of Rome Tor Vergata, Italy.

[4]Institute for Integrated Cell-Material Sciences, Kyoto University, Japan

[5]Kirchhoff Institute for Physics, University of Heidelberg, Germany.

[*]corresponding author: anton.kuzyk@aalto.fi

Spatial reconfiguration of plasmonic nanostructures has remained challenging using both top-down and bottom-up approaches in the field of active plasmonics. In this talk, I will introduce our work on DNA origami[1] based reconfigurable plasmonic metamolecules. The spatial configuration, and hence, the optical response of such metamolecules can be regulated by external stimuli, such as, excess of fuel DNA strands[1], light[2], change in pH[3]. The spatial reconfiguration is transduced into plasmonic circular dichroism change in the visible wavelength range.

We anticipate that such reconfigurable plasmonic nanostructures with engineered stimuli responses will advance the development of smart nanomaterials with tailored optical functionalities.

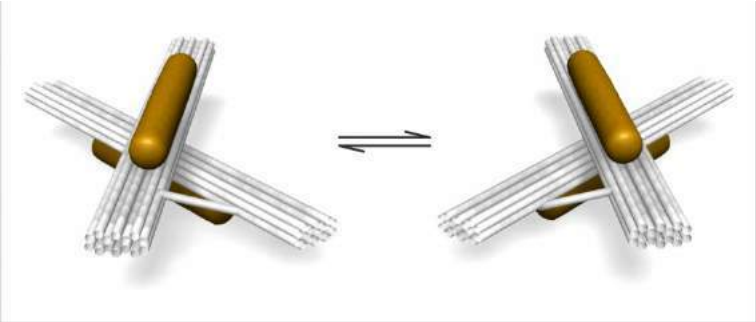

Figure 1. Schematics of reconfigurable plasmonic metamolecules. The metamolecules consist of gold nanorods hosted on switchable DNA origami templates. The precise spatial arrangement of nanorods can be control with external stimulus, e.g. excess of fuel DNA strands, light, change in pH.

REFERENCES

1. Rothemund, P. W. K. “Folding DNA to create nanoscale shapes and patterns,” *Nature* Vol. 440, 297-302, 2006.
2. Kuzyk, A. *et al.* “Reconfigurable 3D plasmonic metamolecules”. *Nat. Mater*. Vol. 13, 862-866, 2014.
3. Kuzyk, A. *et al.* “A light-driven three-dimensional plasmonic nanosystem that translates molecular motion into reversible chiroptical function.” *Nat. Commun.* Vol. 7, 10591, 2016
4. Kuzyk, A. *et al.* “Selective control of reconfigurable chiral plasmonic metamolecules” *Science Advances* 2017. In press.

Visible-range hyperbolic dispersion and generalised Brewster extinction in copolymer-nanoparticle self-assembled composites

X. Wang[1], C. Tallet[1], J. Toudert[1], K. Ehrhardt[1], M. Kildemo[2], A. Baron[1], M. Warenghem[1], P. Barois[1], A. Aradian[1*], V. Ponsinet[1]

[1]Univ. Bordeaux - CNRS, Centre de Recherche Paul Pascal, UPR 8641, Pessac, France
[2]Physics Department, NTNU, Trondheim, Norway
[*]corresponding author: aradian@crpp-bordeaux.cnrs.fr

Abstract- Lamellar block copolymer nanostructures were self-assembled on a substrate, with one of the constituent phases including variable amounts of plasmonic nanoparticles. The assembly's uniaxial optical properties were measured using spectroscopic ellipsometry. The presence of an extinction of the TM wave due to a generalised Brewster effet ("topological darkness") is demonstrated, opening interesting perspectives for sensing applications. More importantly, due to high loadings in nanoparticles, we demonstrate that, within a frequency range, the parallel component of the dielectric permittivity tensor becomes negative, of opposite sign to the perpendicular component, revealing a regime of so-called hyperbolic dispersion. This is to our knowledge the first demonstration of hyperbolic behaviour in a bulk, bottom-up, self-assembled structure.

Diblock copolymer thin film engineering [1] offers a genuine technological platform for the generation of nanostructured thin films with different morphologies. The lamellar phase presents a high degree of order and uniaxial symmetry, with layers parallel to the substrate. Here, we use spun-cast lamellar poly(styrene)-b-poly(2-vinyl pyridine) (PS-P2VP) copolymer films. We spin-cast flat and homogeneous films, of controlled thickness between 200 and 700 nm and of large lateral dimensions, which spontaneously develop a multilayered structurally uniaxial thin film of alternate poly(styrene) and poly(2-vinyl pyridine) layers, each of size $d_o/2$=16 nm. We then grow in-situ gold (Au) nanoparticles selectively within the P2VP layers, thus producing a structure of alternating pure polymer (P) and Au nanoparticles: P2VP nanocomposite (NC) layers. This is achieved by dipping successively the film-bearing wafer into an Au salt solution and then into a reducing agent solution. This infiltration procedure is repeated N times, and N controls the final volume fraction of nanoparticles in the (NC) layers. An example of such a film is shown in Figure 1.

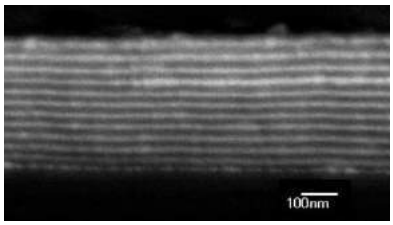

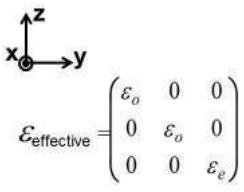

Figure 1. (left) Scanning electron microscopy side-view image (SEM) of a 370 nm-thick film of alternating pure polymer (appearing black) and Au nanoparticles - P2VP nano-composite (appearing white) layers. **(right)** Tensorial form of the anisotropic dielectric permittivity with ordinary ε_o and extraordinary ε_e components.

Variable angle spectroscopic ellipsometry (VASE) was performed in reflection. Figure 2-a shows, on one example of a sample, that for specific angles of incidence and photon energies, the ellipsometric angle Ψ cancels while Δ undergoes a near 180° jump [2]. The sensitivity of this phase jump to modifications of the optical index in the close vicinity of film provides a scheme for high-precision sensing applications.

Next, to evidence hyperbolic dispersion properties of the sample (taken as a whole, effective medium), each multilayer film was measured as a function of the number (N) of gold loading cycles. The VASE data were carefully analyzed [3] using several steps and extracted results were cross-checked with two different methods, so as to finally obtain the uniaxial effective permittivities of the multilayer film. Results (Figure 2-b) show that the components ε_o and ε_e both present a resonance close to 550 nm, with a significantly stronger amplitude for ε_o. For high gold loadings (N=25), the values of the real part of ε_o become negative close to the resonance, and opposite in sign to ε_e, thereby demonstrating the hyperbolic nature of the material.

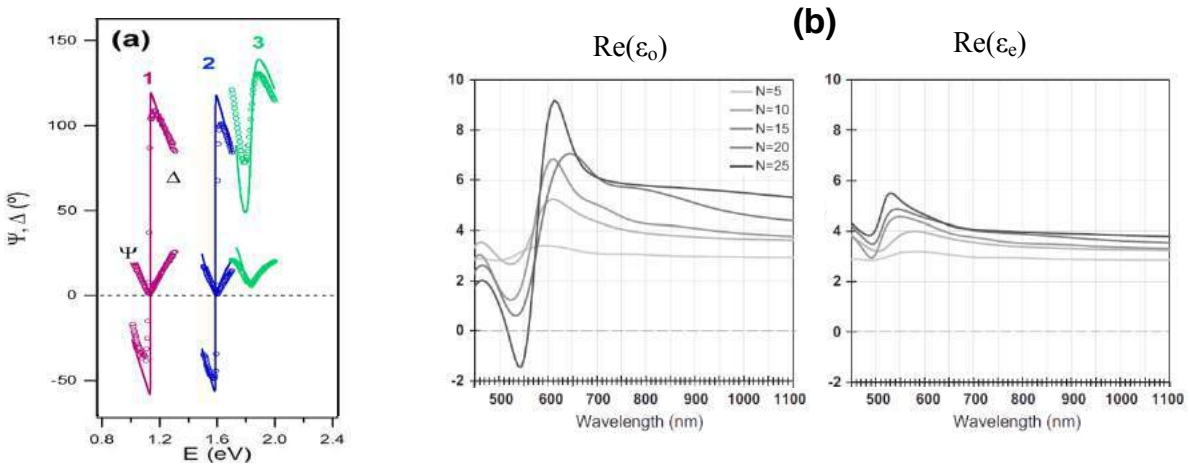

Figure 2. (a) Extinction of Ψ and jump of Δ for two different angles of incidence (trace 1 : 70.35° and trace 2 : 65.71°), while a third angle is shown to be out of extinction (trace 3 : 56.40°). Lines are simulated data for a perfect (defect-free) sample, circles are experimental values. **(b)** Real part of the ordinary and extraordinary components of the dielectric permittivity, showing the strong optical anisotropy of the film, and demonstrating the hyperbolic nature for N=25.

REFERENCES

1. Ponsinet, V., in *Polymer Surfaces in Motion - Unconventional Patterning Methods*, J.Rodríguez-Hernández, C. Drummond, Eds., Springer International Publishing, 2015.
2. Toudert, J., X. Wang, C. Tallet, P. Barois, A. Aradian, and V. Ponsinet, "Plasmonic Optical Interferences for Phase-Monitored Nanoscale Sensing in Low-Loss Three-Dimensional Metamaterials,"*ACS Photonics*, Vol. 2, 1443−1450, 2015.
3. Wang, X., K. Ehrhardt , C. Tallet, M. Warenghem , A. Baron, A. Aradian, M. Kildemo , and V. Ponsinet, "Hyperbolic-by-design self-assembled metamaterial based on block copolymers lamellar phases," *Opt. Laser Tech*., Vol.88, 85–95, 2017.

Acknowledgements. This work was supported by the LabEx AMADEus (ANR-10-LABX-42) in the framework of IdEx Bordeaux (ANR-10-IDEX-03-02), France.

Interband Plasmonic Materials: A promising Platform for Nanophotonics

J. Toudert[1#*], and R. Serna[1]

[1]Laser Processing Group, Instituto de Óptica, CSIC, Madrid, Spain

[#]currently at: ICFO – Institut de Ciències Fotòniques, The Barcelona Institute of Science and Technology, Castelldefels (Barcelona), Spain

[*]corresponding author: johann.toudert@gmail.com

Abstract-We describe the optical properties of "interband plasmonic" materials and their potential for the design of active optical metamaterials for switching and sensing applications.

Research in plasmonics and metamaterials has shown ways to manipulate light down to the nanoscale by creating artificial media with properties not available in nature. These fields were first developed using noble metal nanostructures as building blocks, and in the latest years they have been enriched by employing alternative plasmonic materials, such as transparent conducting oxides or metal nitrides.[1] The plasmonic response of most of these materials is based on the optical excitation of volume free carriers.

However recently plasmonic effects at visible frequencies have been observed in nanostructures made of semi-metals (bismuth[2]) and chalcogenides (bismuth telluride[3], BSTS[4]). These materials present no optical absorption due to volume free carriers in this spectral region. Nevertheless, they share a common feature with the earlier plasmonic materials: they show a negative bulk dielectric permittivity. In this case, this feature is due to the excitation of strong interband transitions rather than volume free carriers.[4,5,6] Therefore, interband polaritons and surface conducting states have been proposed to drive the plasmonic effects observed in the nanostructures. In this presentation, we will describe the optical properties of this new type of so-called "interband plasmonic" materials in relation with their electronic structure. Their performance will be compared with that of the earlier plasmonic materials, and their potential for the design of active optical metamaterials for switching and sensing applications will be presented.

REFERENCES

1. Naik, F. M., Shalaev, V.M. and Boltasseva, A., "Alternative plasmonic materials: beyond gold and silver" *Adv. Mater.* 25, 3264, 2013.
2. Toudert, J., Serna, R., and Jiménez de Castro, M., "Exploring the optical potential of nano-bismuth: tunable surface plasmon resonances in the near-ultraviolet to near-infrared range" *J. Phys. Chem. C* 116, 20530, 2012.
3. Zhao, M. et al., "Actively tunable visible surface plasmons in Bi_2Te_3 and their energy harvesting applications", *Adv. Mater*. 28, 3138, 2016.
4. Ou, J.-Y., So, J.-K., Adamo, G., Sulaev, A., Wang, L., and Zheludev, N.I., "Ultraviolet and visible range plasmonics in the topological insulator $Bi_{1.5}Sb_{0.5}Te_{1.8}Se_{1.2}$", *Nature Comm*. 5, 5139, 2014.
5. Toudert, J., and Serna, R., "Ultraviolet-visible interband plasmonics with p-block elements", *Opt. Mat. Expr.* 7, 2434, 2016.
6. Toudert, J., Serna, R., Camps, I., Wojcik, J., Mascher, P., Rebollar, E., and Ezquerra, T.A., "Unveiling the far infrared to ultraviolet optical properties of bismuth for applications in plasmonics and nanophotonics", *J. Phys. Chem. C* 121, 3511, 2017.

Nanoparticle trapping, sorting, and ratcheting using light forces near photonic crystal slabs

S.-H. Wu[1], A. Krishnan[1], N. Huang[1], E. Jaquay[1], L.J. Martínez[1,2] and M.L. Povinelli[1*]

[1]University of Southern California, USA

[2]*Current address:* J.M: Laboratoire Charles Coulomb UMR 5221 CNRS-UM2, Université Montpellier 2, France

[*]corresponding author: povinell@usc.edu

Abstract-We use the near field of a photonic crystal slab for nanoparticle manipulation. The holes of the photonic crystals form an array of optical traps. In addition to assembling regular arrays of dielectric and metallic particles, we have used this system to demonstrate nanoparticle size selection and optical ratchet motion.

In earlier work, we introduced a technique for creating an array of optical traps in the near field of a photonic crystal [1]. The photonic crystal is designed to support a guided resonance mode for normally-incident light. The mode has high field intensity in the holes of the photonic crystal, making the holes act like optical traps. Previously, we have trapped 2D periodic arrays of dielectric [2] and metallic nanoparticles [3], which can be assembled and released on demand by turning the laser on and off. This capability suggests the ability to dynamically and reconfigurably assemble photonic, plasmonic, and/or metamaterial structures "from the bottom up." Here we demonstrate two new applications of our optical trapping method: *nanoparticle size selection* [4] and *on-chip ratcheting motion* [5].

We demonstrated nanoparticle size selection using a slot-graphite photonic crystal [4]. This structure consists of a silicon slab etched with holes and slots in a pattern based on the graphite lattice [6]. The slots strongly confine light, acting as optical trapping sites. We were able to select one size of particles out of a binary mixture, creating an "optical sieve." In this case, the mixture contained equal concentrations of polystyrene particles with larger (520nm) and smaller (380nm) diameters. 94% of the particles trapped on the photonic crystal were those of the smaller size. This result provides a new method for sorting nanoparticles by size. It also suggests that uniform photonic structures and/or metamaterials can be assembled, even from a nanoparticle solution that is not monodisperse.

Brownian ratchets provide a fundamental mechanism for rectifying random motion, via breaking of spatiotemporal symmetry. We have implemented the first on-chip, near field optical Brownian ratchet [5]. We used a template with nearly triangular holes to break spatial symmetry and modulated the trapping laser. By tracing and analyzing particle trajectories, we conclusively demonstrated ratcheting motion with transport speeds of approximately 1 μm/s.

Acknowledgements: This work was funded by an Army Research Office PECASE Award under Grant W911NF-09-1-0473.

REFERENCES

1. C. A. Mejia, A. Dutt, and M. L. Povinelli, "Light-assisted templated self assembly using photonic crystal slabs," *Optics Express* Vol. 19, 11422-11428, 2011.
2. E. Jaquay, L. J. Martinez, C. A. Mejia, and M. L. Povinelli, "Light-assisted, templated self assembly using a photonic-crystal slab," *Nano Letters* Vol. 13, 2290-2294, 2013.
3. N. Huang, L. J. Martinez, E. Jaquay, A. Nakano, and M. L. Povinelli, "Optical epitaxial growth of gold nanoparticle arrays," *Nano Letters* Vol. 15, 5841-5845, 2015.
4. A. Krishnan, N. Huang, S.-H. Wu, L. J. Martínez, and M. L. Povinelli, "Enhanced and selective optical trapping in a slot-graphite photonic crystal," *Optics Express* Vol. 24, 23271-23279, 2016.
5. S.-H. Wu, N. Huang, E. Jaquay, and M. L. Povinelli, "Near-field, on-chip optical Brownian ratchets," *Nano Letters* Vol. 16, 5261-5266, 2016.
6. L. J. Martínez, N. Huang, J. Ma, C. Lin, E. Jaquay, and M. L. Povinelli, "Design and optical characterization of high-Q guided resonant modes in the slot-graphite photonic crystal lattice," *Optics Express* Vol. 21, 30975 (2013).

Plasmonic applications using air-like refractive index aerogel

Kyoungsik Kim[1*], Dongheok Shin[1], Junhyun Kim[1] and Changuk Kim[1]
[1]School of Mechanical Engineering, Yonsei University,
50 Yonsei-ro, Seodaemun-gu, Seoul 03722, Republic of Korea
[*]corresponding author: kks@yonsei.ac.kr

Abstract
Plasmonic nano-structures have been of great interest in bio-sensing, photonic, optoelectronic, and thermos-plasmonic applications because of their ability to control the light behavior in nanoscale. Aerogels, composed of silica nano-granules with high porosity, have air-like low refractive index and allow us exotic plasmonic phenomena. I introduce our recent results about the plasmonic applications using air-like aerogels such as plasmon resonance, SERS, and so on.

Exploiting structural versatility and fidelity of 3D plasmonic metamolecule, self-assembled on DNA origami pegboard

J. Lee[1], J. Huh[1], W. M. Shih[2], and S. Lee[1,3*]

[1] SKKU Advanced Institute of Nanotechnology (SAINT), Sungkyunkwan University (SKKU), 440-746 Suwon, Republic of Korea

[2] Wyss Institute for Biologically Inspired Engineering at Harvard University, Dana-Farber Cancer Institute, Department of Biological Chemistry and Molecular Pharmacology at Harvard Medical School, Boston, Massachusetts 02115, United States

[3] Department of Nano Engineering and School of Chemical Engineering, Sungkyunkwan University (SKKU), 440-746 Suwon, Republic of Korea

[*]corresponding author: seungwoo@skku.edu

Abstract-Tailoring optical properties of plasmonic nanoclusters (plasmonic metamolecules) has gained special interest in the field of nanophotonics. However, the difficulties in arranging plasmonic nanoparticle in deterministic way have limited the advancement of the relevant field. To address this challenge, we report a deterministic strategy for assembling 3D cluster using DNA origami as a molecular pegboard.

Self-assembled plasmonic metamolecule, a properly tailored metallic nanocluster which exhibits unnatural electromagnetic property (e.g. artificial magnetic resonance and magnetic based Fano scattering resonance), has been extensively studied as the one of the central idea in the field of metamaterials (1-4). Recently, several studies have shown that optical magnetism can be finely tuned by controlling geometry, dimensionality, and number of nanoparticles (NPs) in nanocluster (3-4). However, reliable assembly of the 3D cluster with high structural integrity and versatility is still lacking, owing to i) difficulties in producing highly uniform metallic NPs and ii) limited ability to arbitrary control the 3D cluster geometries (i.e. symmetry and asymmetry).

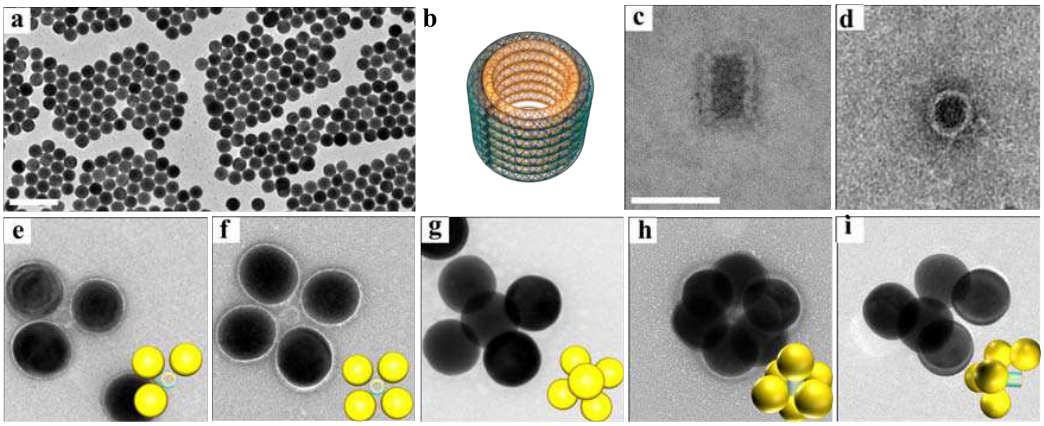

Fig. 1. Extremely uniform AuNPs were arranged into custom geometries by exploiting programmability of

DNA origami. (a) Representative TEM image of synthesized AuNPs. (b-d) Schematic image of Barrel-like DNA origami structure (b) and TEM image viewed at side (c) and top (d). (e-i) Self-assembled plasmonic metamolecules: trimer (e), tetramer (f), 3D pentamer (g), 3D hexamer(h), 3D pentamer with broken symmetry(i). Scale bars are 100nm.

In this work, to tackle these challenges, we first synthesized highly uniform and smooth AuNPs by adopting iterative reductive growth and oxidative dissolution as presented Fig. 1(a). Then, we utilized DNA origami method which provide few nanometer precision for 3D positioning NPs, molecules, and quantum dots in programmable way (6-7). To arrange AuNPs into various geometries (e.g., 3D cluster with broken symmetry) which have been challenging for other self-assembly methods, we designed 3D cylindrical DNA origami structure as depicted in Fig. 1(b-d). The surface of DNA cylinder was encoded with single-stranded DNA sticky ends to host AuNPs in programmable way. As presented in transmission electron microscope (TEM) image, the individual structures were well synthesized in high structural intactness.

Finally, we assembled 3D clusters by assigning programmable location of AuNPs on the DNA origami surface. Fig. 1(e-i) illustrates our current progress of this research. As clearly figured out, the structural fidelity and versatility of spherical AuNPs assemblies were elegantly controlled. Especially, the symmetry breaking was successfully achieved in 3D cluster by applying exotic programmability of DNA origami.

Our ultimate goal is to show that we can gain supremacy over controlling self-assembled plasmonic metamolecule by assembling extremely uniform AuNPs into custom geometry. Our results convincingly demonstrate that programmability of DNA nanotechnology provides an ultimate mean for it. Thus, we believe that our work will pave one of the ways toward a limit of engineering optical properties in nanophotonics.

Acknowledgements, This work was supported by Samsung Research Funding Center of Samsung Electronics under Project Number SRFC-MA1402-09.

REFERENCES

1. Alu, A., A. Salandrino and N. Engheta, “Negative effective permeability and left-handed materials at optical frequencies,” *Opt. Express*, Vol. 14, No. 4, 1557–1567, 2006.
2. Alu, A., N. Engheta, “The quest for magnetic plasmons at optical frequencies,” *Opt. Express*, Vol. 17, No. 7, 5723–5730, 2009.
3. Fan, J. A., C. Wu, K. Bao, J. Bao, R. Bardhan, N. J. Halas, V. N. Manoharan, P. Nordlander, G. Shvets and F. Capasso, “Self-assembled plasmonic nanoparticle clusters,” *Science*, Vol. 328, No. 5982, 1135–1138, 2010.
4. Shafiei, F., F. Monticone, K. Q. Le, X. Liu, T. Hartsfield, A. Alú and X. Li, “A subwavelength plasmonic metamolecule exhibiting magnetic-based optical Fano resonance,” *Nat Nanotechnol*, Vol. 8, No. 2, 95–99, 2010.
5. Douglas, S. M., H. Dietz, T. Liedl, B. Högberg, F. Graf and W. M. Shih, “Self-assembly of DNA into nanoscale three-dimensional shapes,” *Nature*, vol. 459, 414–418, 2009
6. Bui, H., O. Craig, K. Carson, T. YerPeng, G. Elton, K. Wan, L. Jeunghoon, B. K. William, Y. Bernard and W. L. Hughes, “Programmable periodicity of quantum dot arrays with DNA origami nanotubes,” *Nano Lett,* Vol. 10, No. 9, 3367–3372, 2010

Large Area Printed Flexible Hybrid Photonic-Electronic Systems

Debashis Chanda
NanoScience Technology Center CREOL, College of Optics and Photonics
University of Central Florida
*corresponding author: Debashis.Chanda@creol.ucf.edu

Abstract: The talk will focus on high throughput, large area and low cost fabrication of quasi-3D and 3D optical nanostructures based on various printing techniques. Based on these techniques functional devices like uncooled neural sensors, mid-IR detectors, flexible reflective color displays and others are realized.

Optically active metastable defects in NBP:nAg,Er^{3+} nanoplasmonic material

B. Surma[1], M. Gajc[1], D. A. Pawlak[1,2]
[1]Institute of Electronic Materials Technology, Warsaw, Poland
[2]Centre of New Technologies, University of Warsaw, Warsaw, Poland
[*]corresponding author: Barbara.Surma@itme.edu.pl

Abstract- We report on the optical properties of the NBP glass nanocomposite doped with silver nanoparticles, nAg, and erbium ions, grown by the NanoParticle Direct Doping (NPDD) method. We observe formation of optically active metastable defects that we interpret as a result of the interaction of the glass matrix ions with the dangling bonds at the surface of silver particles and with erbium ions. Optical features of the defects were explained by using coordinational coordinate model, CC. Additionally we show that the presence of the silver particles leads also to the decreasing the free-OH absorption in boron-phosphate glass.

Most of current fabrication processes of plasmonic materials and materials with plasmonic-related functionalities arrange metal nanostructures at the dielectric surfaces but the fabrication of volumetric nanoplasmonic composites still remains a challenge. Recently we have developed new approach to obtain volumetric plasmonic nanocomposites through a non-chemical process called NanoParticle Direct Doping (NPDD) method.[1] The NPDD method is based on the directional solidification of dielectric matrices and allows to carry out the doping process during the pulling of the glass fiber with any chemical agents and, plasmonic , semiconductor or anisotropic nanoparticles.

In this work by using NPDD method we obtained nanocomposite NBP (sodium borophosphate glass 30%mol P2O5 50%mol Na2O 17%mol B2O3) doped with erbium ions and Ag nanoparticles (20nm in diameter), NBP:nAg:Er3+. The absorption and luminescence measurements at temperature range (4K-300K) were used to study the optical properties of these nanocomposites.

Low temperature luminescence revealed that defect related emissions X2(1.185eV) and X1(1.085eV) appear in NBP:nAg and NBP:Er^{3+},nAg, composites, respectively. Both defects responsible for these emissions have metastable states. Optical features of the defects were explained by using coordinational coordinate model, CC.

For low (residual) erbium concentration the twofold increase of the emission at 1532nm was observed when X2 defect was in the metastable state.

Surface atoms of nAg have a very large number of dangling bonds as the coordination is not completed. These features can give rise to the formation of any localized defect states at the interface formed between nAg and surrounding environment. Recent studies [2] made by using high-resolution transmission electron microscopy revealed that Ag nanoparticles even at room temperature can be deformed like liquid droplet remaining crystalline in their volume. It means that the nanoparticle can be sensitive to the forces of the crystalline field in the glass.

We have stated that presence of nAg in NBP glass leads to the decreasing of free-OH group as compared

to the pure NBP glass. The fact suggests decreasing the amount of the so called non-bridging oxygens that instead of forming the hydrogen-like bounding with free-OH groups can form some kind of connections with silver particle surface.

Acknowledgements, The authors thank the MAESTRO project 'New Generation plasmonic materials' financed from the National Science Centre of Poland (G.A. 2011/02/A/ST5/00471) for their support of this work.

REFERENCES

1. M, Gajc, B. H. Surma, A. Klos, K. Sadecka, K. Orlinski, A. E. Nikolaenko, K. Zdunek, D. A. Pawlak, "Nanoparticle Direct Doping: Novel Method for Manufacturing Three-Dimensional Bulk Plasmonic Nanocomposites," *Adv. Funct. Mater.*, Vol. 27, 3443, 2013.
2. J. Sun, L. He, Yu-Ch. Lo, T. Xu, H. Bi, L. Sun, Ze Zhang, S. X. Mao, Ju Li, "Liquid-like pseudoelasticity of sub-10-nm crystalline silver particles," Nature Materials, Vol.13, 1007, 2014.

3D bulk material with isotropic magnetic permeability at optical frequencies

S. Gomez-Grana,[a] A. Le Beulze,[a] S. Mornet,[a] E. Duguet,[a] V. Ponsinet,[b] P. Richetti,[b] A. Baron,[b] D. Torrent,[b] P. Barois,[b] J. Leng,[c] J.-B. Salmon,[c] V. G. Kravets,[d] A. N. Grigorenko,[d] and M. Treguer-Delapierre[a]

[a] University of Bordeaux, CNRS, ICMCB, UPR 9048, 33600 Pessac, France
[b] University of Bordeaux, CNRS, CRPP, UPR 8641, 33608 Pessac, France
[c] University of Bordeaux, CNRS, Solvay, LOF, UMR 5258, 33608 Pessac, France
[d] School of Physics and Astronomy, University of Manchester, Manchester, M13 9PL, UK
[*]corresponding author: Treguer@icmcb-bordeaux.cnrs.fr

Abstract- Controlling the magnetic permeability m of artificial materials is expected to offer an unprecedented control of the flow of light in optical devices. Unfortunately, the magnetic response of natural materials is negligible at optical frequencies. A rational design of nano-composites $SiO_2@Ag_n$ enables here the operational extension of the concept of magnetic permeability to visible light. Up to now, artificial optical magnetism has been observed in anisotropic structures thinner than the wavelength of light as a non-local effect which is too complex to be described by an effective magnetic permeability tensor, hence precluding the use of the usual laws of reflection and refraction. In contrast, the reflection of light by the novel magnetic metamaterial described in this talk obeys the classical laws of optics at variable incidence. This fundamental approach, based on the precise control of the structural symmetry of the material at all steps of a hierarchical self-assembly process, provides strict guidelines for the design of magnetic materials described by a valid permeability parameter. This strategy can be readily extended to the future generation of low-loss, all-dielectric metamaterials, hence renewing the interest for extraordinary applications of metamaterials based on non natural values of μ.

Self-organized silver-based eutectic metamaterial

B. Surma[1], K. Sadecka[1], D. A. Pawlak[1,2]
[1]Institute of Electronic Materials Technology, Warsaw, Poland
[2]Centre of New Technologies, University of Warsaw, Warsaw, Poland
[*]corresponding author: Barbara.Surma@itme.edu.pl

Abstract- We report on the optical properties of the Bi_2O_3-Ag eutectic nanocomposite with plasmonic properties, grown by the Micro pulling down method. We will present the optical response of metamaterials built from silver, bismuth, bismuth oxides and highlight the tunability in their structure and optical response. The introduction of rare-earth ions to this eutectic material should promote the enhancement of important optical properties, like photoluminescence or up-conversion processes.

Bottom-up manufacturing methods, like self-organization and chemical methods are powerful for obtaining metamaterials with controlled optical properties. One particularly promising approach relies on the growth of self-organized nano- and micro-structures by directional solidification of eutectics.

This work reports the development of a bulk nanoplasmonic Bi_2O_3-Ag eutectic-based metamaterial. Annealing at 600 °C further refined the structure and introduced metallic nanoparticles that exhibited plasmonic resonance in the optical region of the spectrum [1]. Different atmospheres can affect on the intensity and position of the plasmonic resonance, so the plasmonic resonance can be tune between orange and green wavelengths [2].

Demonstration of the impact of LSPR exhibited by the Bi_2O_3-Ag eutectic composite doped with rare earth ions on its optical properties, such as luminescence and nonlinear properties like upconversion will be presented.

For the annealed Bi_2O_3-Ag: Er^{3+} material (which has plasmonic resonance) two-fold enhancement of the Er3+ ions photoluminescence in the range of 520 nm to 570 nm (excitation wavelength of 488 nm) is observed with respect to the as-grown material. Also strong 19-fold enhancement of the luminescence up-conversion from 980 nm to visible in the annealed Bi_2O_3-Ag-doped with Er^{3+} material is observed. Bi_2O_3 as high refractive index material is often added to types of glass to improve their nonlinear properties such as upconversion i.e. the conversion of luminescence from longer to shorter wavelengths. That is why it was interesting to investigate the effect of the material's plasmonic properties on this phenomenon. Measurements of luminescence showed that the upconversion is strongly enhanced for the Bi_2O_3-Ag: Er^{3+} eutectic material exhibiting the LSPR in comparison to the as-grown Bi_2O_3-Ag: Er^{3+} composite (without LSPR) and the Bi_2O_3: Er^{3+} crystal. This is thanks to the fact that the position of the localized surface plasmon resonance in Bi_2O_3-Ag: Er^{3+} material (after annealing) overlaps the up-converting luminescence bands obtained for erbium, which preliminarily confirms the plasmonic enhancement of the upconversion. Moreover Bi_2O_3-Ag doped with rare earth ions may be potentially used as an element in solar cells. Upconverters with properties strengthened by plasmonic resonances may, when used in a solar cell, enable enhancement of its efficiency.

Acknowledgements, The authors thank the HARMONIA project 'New Generation plasmonic materials' financed from the National Science Centre of Poland (G.A. 2013/10/M/ST5/00650) for their support of this work.

REFERENCES

1. K. Sadecka, M. Gajc, K. Orlinski, H. B. Surma, A. Klos, I. Jozwik-Biala, K. Sobczak, P. Dluzewski, J. Toudert, D. A. Pawlak, "When Eutectics Meet Plasmonics: Nanoplasmonic, Volumetric, Self-Organized, Silver-Based Eutectic", *Adv. Opt. Mater.* Vol. 3, 381-389, 2015.
2. K. Sadecka, J. Toudert, H. B. Surma, D. A. Pawlak, "Temperature and atmosphere tunability of the nanoplasmonic resonance of a volumetric eutectic-based Bi2O3-Ag metamaterial", *Opt. Express* Vol. 23, No 14, 19098-19111, 2015.

Active, Nonlinear, Quantum, and Reconfigurable Plasmonics and Metamaterials

Nonlinear optics of epsilon near zero material using CdO

Ting S. Luk[1,2*], Yuanmu Yang[1,2], Domenico de Ceglia[3], Michael Scalora[4], Kyle Kelley[5], Jon-Paul Maria[5], Gordon A. Keeler[1], and Salvatore Campione[1]

[1]Sandia National Laboratories, P.O. Box 5800, Albuquerque, New Mexico 87185, USA

[2]Center for Integrated Nanotechnologies (CINT), Sandia National Laboratories, P.O. Box 5800, Albuquerque, New Mexico 87185, USA

[3]AEgis Technologies Group, 410 Jan Davis Dr., Huntsville, Alabama 35806, USA

[4]Charles M. Bowden Research Laboratory, AMRDEC, U.S. Army RDECOM, Redstone Arsenal, Alabama 35898, USA

[5]Department of Materials Science, North Carolina State University, Raleigh, North Carolina 27695, USA

[*]corresponding author: tsluk@sandia.gov

Abstract- The banner of strong field confinement using plasmonic material has been waved for quite some time. In many cases, strong field confinement comes with high loss which has hampered many potential applications. In this paper we show two remarkable examples of nonlinear effects of plasmonic material: third harmonic generation and p-polarization reflectance modulation, using high mobility doped semiconductor of CdO where high absorption and strong field confinement can co-exist.

A quintessential property of surface plasmon polariton mode in metal is the ability to produce nanoscale field confinement. This mode is normally not accessible from free-space due to momentum mismatch. However, when the thickness of the material is of the order the Fermi wavelength, surface plasmon polaritons of the two interfaces couple to a hybridized mode called epsilon-near-zero mode which allows free-space coupling and produces a large uniform field enhancement inside the material[1]. When impedance matched to this mode, 100% of the incident field is absorbed (perfect absorption) and large nonlinear polarization field is generated. Efficient third harmonic generation was shown[2] using indium tin oxide. Recently, using defect equilibrium

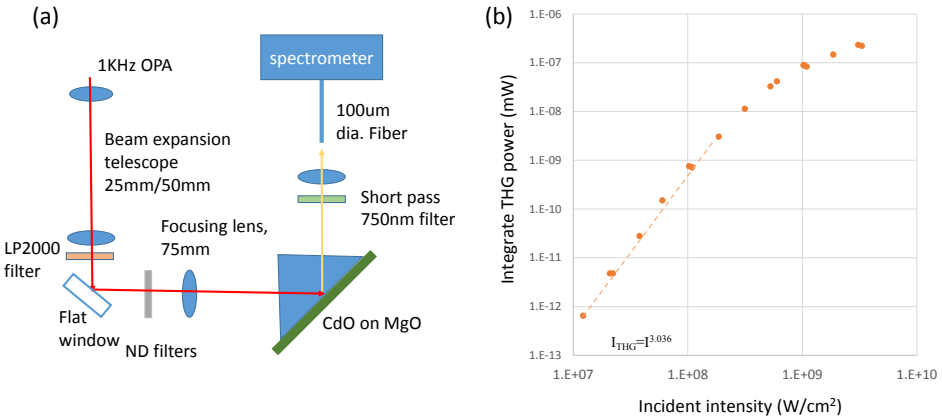

Fig. 1: (a) Schematic representation of the third harmonic generation experiment. (b) Third harmonic power versus incident laser intensity at the fundamental wavelength of 2.1mm. The In:CdO film is 19nm thick and has a carrier density of 2.0×10^{20} cm^{-3} and mobility of 375 cm^2/Vs.

engineering[3], crystalline high mobility conductive oxide can be grown to enable larger field enhancement and

hence higher third harmonic conversion efficiency.

In this paper, we report more than three orders of magnitude enhancement in conversion efficiency $8.3x10^{-22}$ $\%cm^4/W^2$ for In:CdO compared to $5.7x10^{-25}$ $\%cm^4/W^2$ for indium tin oxide[2]. The conversion efficiency metric used here is defined as the ratio of third harmonic to incident power in percent normalized by the square of the incident intensity. Fig. 1 shows the third harmonic generation behavior with pump intensity.

Another nonlinear effect that utilizes strong absorption is reflectance modulator. Low intensity p-polarized probe light at frequency near the epsilon-near-zero value (2.08μm) can be completely absorbed when the impedance matching condition is met as in the case of a 75nm thick In:CdO film with similar properties on an Au[4] substrate. This p-polarized probe beam reflectance can be dramatically increased when a separate high intensity intraband pump pulse is applied to change the carrier temperatures and effective mass. The new epsilon-near-zero frequency is shifted to 2.23μm. Fig. 2 shows that the reflectance at 2.08 μm is switched from 1% to 86% within 200fs. Simultaneously, the reflectance at 2.23μm is dramatically reduced from 73% to 10%.

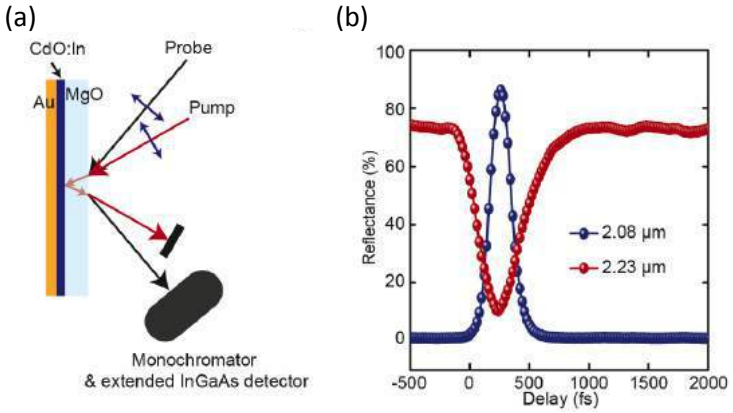

Fig. 2: (a) Schematic representation of the pump-probe reflectance modulation experiment. (b) Shows the temporal p-polarized reflectance response of 2.08 and 2.23 μm at 50 deg angle of incidence after the sample was pumped by another 2.08 μm p-polarized incident angle of 30 deg.

Acknowledgements: Portions of this work were supported by the U.S. Department of Energy, Office of Basic Energy Sciences, Division of Materials Sciences and Engineering, by the Laboratory Directed Research and Development program at Sandia National Laboratories, and were performed, in part, at the Center for Integrated Nanotechnologies, a U.S. Department of Energy, Office of Basic Energy Sciences user facility. Sandia National Laboratories is a multi-program
laboratory managed and operated by Sandia Corporation, a wholly owned subsidiary of Lockheed Martin Corporation,
for the U.S. Department of Energy's National Nuclear Security Administration under Contract No. DE-AC04-94AL85000.

REFERENCES

1. Campione, S.; Brener, I.; Marquier, F. *Physical Review B* **2015,** 91, (12), 121408.

2. Luk, T. S.; de Ceglia, D.; Liu, S.; Keeler, G. A.; Prasankumar, R. P.; Vincenti, M. A.; Scalora, M.; Sinclair, M. B.; Campione, S. *Applied Physics Letters* **2015,** 106, (15), 151103.

3. Sachet, E.; Shelton, C. T.; Harris, J. S.; Gaddy, B. E.; Irving, D. L.; Curtarolo, S.; Donovan, B. F.; Hopkins, P. E.; Sharma, P. A.; Sharma, A. L.; Ihlefeld, J.; Franzen, S.; Maria, J.-P. *Nature Materials* **2015,** 14, (4), 414-420.

4. Luk, T. S.; Campione, S.; Kim, I.; Feng, S.; Jun, Y. C.; Liu, S.; Wright, J. B.; Brener, I.; Catrysse, P. B.; Fan, S.; Sinclair, M. B. *Physical Review B* **2014,** 90, (8), 085411.

Nonlinear Circular Dichroism from plasmonic Metasurfaces

Bernhard Reineke[1], Guixin Li[1], Shumei Chen [2, 5], Franziska Zeuner[1], Martin Weismann[3], Ventsislav Kolev Valev[4], Kok Wai Cheah[5], Nicolae Coriolan Panoiu[3], Shuang Zhang[2], and Thomas Zentgraf[1]

[1]Department of Physics, University of Paderborn, Warburger Straße 100 D-33098 Paderborn, Germany
[2]School of Physics & Astronomy, University of Birmingham, Birmingham B15 2TT, UK
[3]Department of Electronic and Electrical Engineering, University College London, Torrington Place, London, WC1 E7JE, UK
[4]Department of Physics, University of Bath, Claverton Down, Bath, BA2 7AY, UK
[5]Department of Physics, Hong Kong Baptist University, Kowloon Tong, Hong Kong

Abstract- Circular Dichroism is the differential absorption of left or right circularly polarized light. In planar artificial structures, like metamaterials, this effect is rather weak. In contrast to that, second harmonic generation circular dichroism (SHG-CD) in artificial materials is more sensitive, than its linear counterpart. Here, we report about a near unity nonlinear circular dichroism for second- (SHG) and third- harmonic generation (THG) from specially designed plasmonic metasurfaces.

Plasmonic metasurfaces are interesting systems to study nonlinear phenomena, due to their strong light-matter interaction. Since, their strong light-matter interaction leads to a strong electric nearfield enhancement, which in turn leads to strong nonlinear response, plasmonic metasurfaces are a perfect tool to investigate nonlinear phenomena. One of these phenomena is SHG-CD, the differential harmonic generation of left or right circularly polarized light, if the material is illuminated with light of different handedness. Strong CD from metamaterials has been demonstrated but the observed CD in most experiments arises from the chirality of 3D nanostructure or from the extrinsic contribution in 2D structures illuminated under an oblique angel. [1-10] In this work, we demonstrate a strong CD for SHG and THG from planar chiral plasmonic metasurfaces.

Experiment

An array of trisceli-type (for SHG) and gammadion-type (for THG) nanostructures were fabricated by electron beam lithography and a lift-off procedure. The Plasmon resonance of the nanostructures was determined to respectively 1165 nm (trisceli-type) and 1230 nm (gammadion-type) by Fourier Transform Infrared Spectroscopy.

The nonlinear experiments were executed by using a femtosecond laser under normal incidence to the metasurface surface. To characterize the nonlinear CD, the nonlinear response of the Metasurface was measured for right and left circularly polarized light. Furthermore, the fundamental wavelength of the laser was tuned between 1100 nm and 1400 nm, to gain information about the wavelength dependents. The results show that for one polarization state the nonlinear responses have local minima at 1275 nm for SHG and 1300 nm for THG, which corresponds to the wavelengths of the strongest nonlinear CD (fig. 1), which was calculated from the nonlinear measurements by using the definition: $CD = (I_{LCP} - I_{RCP})/(I_{LCP}+I_{RCP})$.

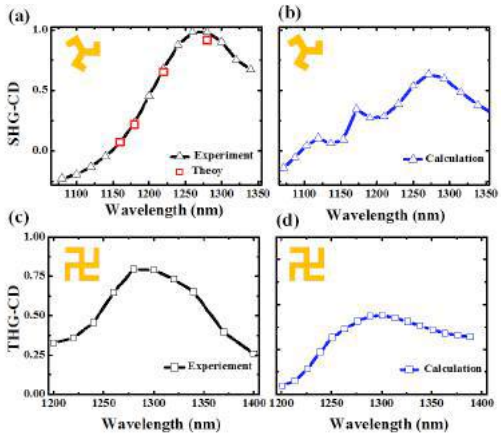

Figure 1. Nonlinear CD for SHG from the trisceli-type structure (a, b) and the nonlinear CD for THG from the gammadion structure (c, d). The values of the squares in (a) are obtained from experimentally determined values of the effective nonlinear susceptibilities of the trisceli-type structure.

Conclusion

In summary, near unity nonlinear circular dichroism for second- and third-harmonic generation with ultrathin trisceli- and gammadion-type plasmonic nanostructures was shown. Moreover, a symmetry controlled generation of left or right handed SHG and THG was demonstrated. Strong SHG-CD and THG-CD are experimentally observed for these planar plasmonic structures with negligible linear optical activity. Especially, the observed SHG-CD is identified to have an achiral origin. In the future, these results, together with simple fabrication methods for plasmonic metasurfaces enable a greater freedom in designing nonlinear optoelectronic devices.

Acknowledgements

The authors would like to acknowledge the support from Cedrik Meier for providing his EBL System. The work was financially supported by EPSRC (Grant No EP/J018473/1), Leverhulme (Grant No. RPG-2012-674) and the DFG (Grant No. ZE953/7-1).

REFERENCES

1. M. Kauranen, A. V. Zayats, Nature Photon. 6, 737, 2012.
2. N. I. Zheludev and Y. S. Kivshar, Nature Mater. 11, 917 (2012).
3. M. Lapine, I. V. Shadrivov, Y. S. Kivshar, Rev. Mod. Phys. 86, 1093, 2014.
4. K. Konishi et al. , Phys. Rev. Lett. 112, 135502, 2014.
5. S. M. Chen et al., Phys. Rev. Lett. 113, 033901, 2014.
6. G. X. Li et al., Nature Mater. 14, 607, 2015.
7. M. Ren, et al.,Giant nonlinear optical activity in a plasmonic metamaterial Nat. Comm. 3, 833 (2012).
8. A. Papakostas, et al., Phys. Rev. Lett. 90, 107404 (2003).
9. M. Kuwata-Gonokami, et al., Phys. Rev. Lett. 95, 227401 (2005).
10. M. Decker, et.al. OPTICS LETTERS,Vol. 32, No. 7,April 1, 2007.

Non-local absorption in quantum hydrodynamictheory: application to plasmonic systems

C. Ciracì[1]

[1]Center for Biomolecular Nanotechnologies (CBN), Istituto Italiano di Tecnologia (IIT), Via Barsanti 14, 73010 Arnesano (LE), Italy.
cristian.ciraci@iit.it

Abstract— The quantum hydrodynamic theory is a promising method for describing microscopic details of macroscopic systems. The hydrodynamic equation is directly obtained from a single particle Kohn-Sham equation. This derivation allows to straightforwardly incorporate in the hydrodynamic equation a viscoelastic term, so that broadening of collective excitation can be taken into account, as well as a correction to the plasmon dispersion. The result is an accurate and computationally efficient hydrodynamic description of the free electron gas.

A reliable description of optical properties of plasmonic nanostructures with different length scalesrequires methods beyond classical electromagnetism. In this context, it becomes very important to develop simulation techniques to take into account quantum microscopic features at the scale of billions of atoms. Density functional theory (DFT) methods are generally unsuitable because their computational cost grows as fast as $O(N_e^3)$ such that their reach is limited to systems with few thousands electrons. Conversely, methods based on effective descriptions have also been proposed [1, 2], although their applicability depends on *a priori* calculations usually relying on a different method and it is limited to the linear response regime.

A promising alternative is given by orbital-free techniques where electron energy functionals are expressed in terms of the electron density n rather than the single electronic orbitals. To this category belongs the *hydrodynamic theory* (HT), in which the quantum dynamics is solved via macroscopic observable quantities, such as, n and the current density $\mathbf{J}$ or the velocity $\mathbf{v}$. The HT has a long history [3, 4] and recently, it has vigorously reemerged in the context of nano-photonics [5, 6], strongly fueled by the proliferation of self-assembling colloidal plasmonic structures [7, 8]. Because of the complexity of the systems involved, however the HT has usually been considered within the limit of the Thomas-Fermi (TF) approximation with the assumption of a constant ground density, neglecting essential effects such as electron spill-out and quantum tunneling. The TF-HT however can be greatly improved by adding a ∇n-dependent contribution to the TF kinetic energy of the free-electron gas. In this way, a space dependent ground density can be easily taken into account. This model usually denominated *quantum hydrodynamic theory* (QHT). A self-consistent approach based on the QHT coupled to Maxwell's equations was recently introduced by Toscano *et al.*, who applied it to show size-dependent blue shift in small noble metal nanowires [9]. Systematic comparisons of QHT with DFT results [10, 11] however pointed out that in order to describe well both near- and far-field features of plasmonic systems, one might need to sacrifice the self-consistency of the method [11]. A precise prediction of the fields near the surface is in fact extremely important for tunneling regimes and nonlinear applications. Moreover, in its present form the QHT does not take into account size-dependent broadening of the plasmonic resonances, although a recent effort in this direction [12] suggested the use of a density-dependent damping rate. As for all orbital-free methods, the challenge is to find an appropriate energy functional that correctly accounts for the electron gas total energy.

In this talk, I first show that the QHT equation can be formally derived form the single particle Kohn-Sham (KS) equation. This non-trivial derivation clearly shows the degree of approximations that are made when using the QHT. This derivation allows to straightforwardly incorporate in the hydrodynamic equation a viscoelastic term, so that broadening of collective excitation can be taken into account, as well as a correction to the plasmon dispersion. Because the QHT intrinsically describes both longitudinal and transverse fields, it is then possible to include in the hamiltonian a current-dependent exchange-correlation (XC) vector potential. Such potential has been developed by Vignale and Kohn [13] in the context current density functional theory (CDFT). The peculiarity of this functional is that it has the form of a divergence of a viscoelastic stress tensor, offering an intuitive and unprecedented way to improve the theory. The results is a theory that can be applied

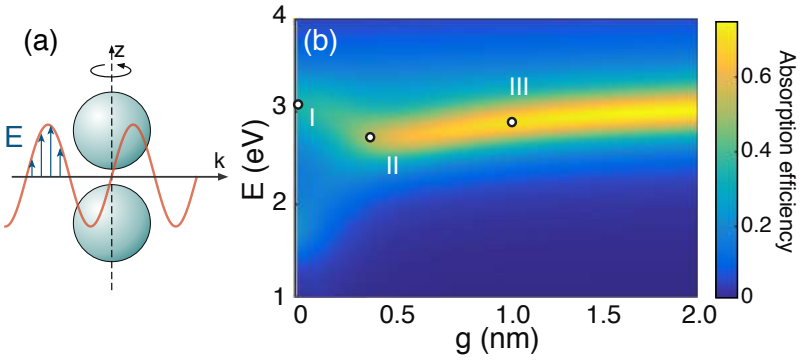

Figure 1: Dimer of Na spheres constituted by $N_e = 398$ electrons each.

to a class of much larger problems compared to DFT techniques, with comparable accuracy. The theory correctly predicts size-dependent plasmon energies and broadening, as well as near-field properties. Application tonanoparticle dimers also show good agreement with DFT calculations previously published, down to the tunneling regime (see Fig. 1).

REFERENCES

1. W. Yan, M. Wubs, and N. Asger Mortensen, "Projected Dipole Model for Quantum Plasmonics," *Phys. Rev. Lett.*, vol. 115, p. 137403, Sept. 2015.
2. R. Esteban, A. G. Borisov, and P. Nordlander, "Bridging quantum and classical plasmonics with a quantum-corrected model," *Nat. Comm.*, vol. 3, p. 825, 2012.
3. E. Madelung, "Quantentheorie in hydrodynamischer Form," *Z. Physik*, vol. 40, pp. 322–326, Mar. 1927.
4. F. Bloch, "Bremsvermögen von Atomen mit mehreren Elektronen," *Z. Physik*, vol. 81, no. 5-6, pp. 363–376, 1933.
5. C. Ciracì, J. B. Pendry, and D. R. Smith, "Hydrodynamic Model for Plasmonics: A Macroscopic Approach to a Microscopic Problem," *ChemPhysChem*, vol. 14, no. 6, pp. 1109–1116, 2013.
6. S. Raza, S. I. Bozhevolnyi, M. Wubs, and N. A. Mortensen, "Nonlocal optical response in metallic nanostructures," *J. Phys.: Condens. Mat.*, vol. 27, p. 183204, Apr. 2015.
7. C. Ciracì, R. T. Hill, J. J. Mock, Y. A. Urzhumov, A. I. Fernandez-Dominguez, S. A. Maier, P. J B, A. Chilkoti, and D. R. Smith, "Probing the ultimate limits of plasmonic enhancement," *Science*, vol. 337, no. 6098, pp. 1072–1074, 2012.
8. L. Lin, M. Zapata, M. Xiong, Z. Liu, S. Wang, H. Xu, A. G. Borisov, H. Gu, P. Nordlander, J. Aizpurua, and J. Ye, "Nanooptics of Plasmonic Nanomatryoshkas: Shrinking the Size of a Core–Shell Junction to Subnanometer," *Nano Lett.*, vol. 15, pp. 6419–6428, Oct. 2015.
9. G. Toscano, J. Straubel, A. Kwiatkowski, C. Rockstuhl, F. Evers, H. Xu, N. A. Mortensen, and M. Wubs, "Resonance shifts and spill-out effects in self-consistent hydrodynamic nanoplasmonics," *Nat. Comm.*, vol. 6, p. 7132, 2015.
10. W. Yan, "Hydrodynamic theory for quantum plasmonics: Linear-response dynamics of the inhomogeneous electron gas," *Phys. Rev. B*, vol. 91, p. 115416, Mar. 2015.
11. C. Ciracì and F. Della Sala, "Quantum hydrodynamic theory for plasmonics: Impact of the electron density tail," *Phys. Rev. B*, vol. 93, p. 205405, May 2016.
12. X. Li, H. Fang, X. Weng, L. Zhang, X. Dou, A. Yang, and X. Yuan, "Electronic spill-out induced spectral broadening in quantum hydrodynamic nanoplasmonics," *Opt. Express*, vol. 23, no. 23, pp. 29738–8, 2015.
13. G. Vignale and W. Kohn, "Current-Dependent Exchange-Correlation Potential for Dynamical Linear Response Theory," *Phys. Rev. Lett.*, vol. 77, pp. 2037–2040, Sept. 1996.

Spatio-temporal dynamics of strongly-coupled emitters with multiple plasmonic modes

A. Demetriadou[1], **J. M. Hamm**[1], **Y. Luo**[2], **J. B. Pendry**[1], **J. J. Baumberg**[3], **and O. Hess**[1]

[1]Blackett Laboratory, Imperial College London, London, SW7 2AZ, United Kingdom
[2]School of Electrical & Electronic Engineering College of Engineering, Nanyang Technological University, Singapore
[3]NanoPhotonics Centre, Cavendish Laboratory, University of Cambridge, Cambridge, CB3 0HE, United Kingdom
a.demetriadou06@imperial.ac.uk

Abstract— Plasmonic nano-cavities provide the ideal conditions to realize light-matter strong-coupling at room temperature. However, they support multiple types of modes that can be spectrally degenerate, but with different radiative behaviour and field profiles. We demonstrate that quantum emitters simultaneously couple to all modes in plasmonic nano-cavities, a process dominating the spatio-temporal dynamics of the Rabi-oscillations.

Plasmonic nano-cavities provide the ideal conditions to strongly-couple emitters and plasmons, due to the high-field enhancement associated with the plasmon excitation and the radiative nature of higher-order modes that suppresses quenching [1]. This unique combination of properties allows for a single molecule to strongly-couple with a plasmon mode at room temperature [2], which opens the route to bring in ambient conditions quantum information systems.

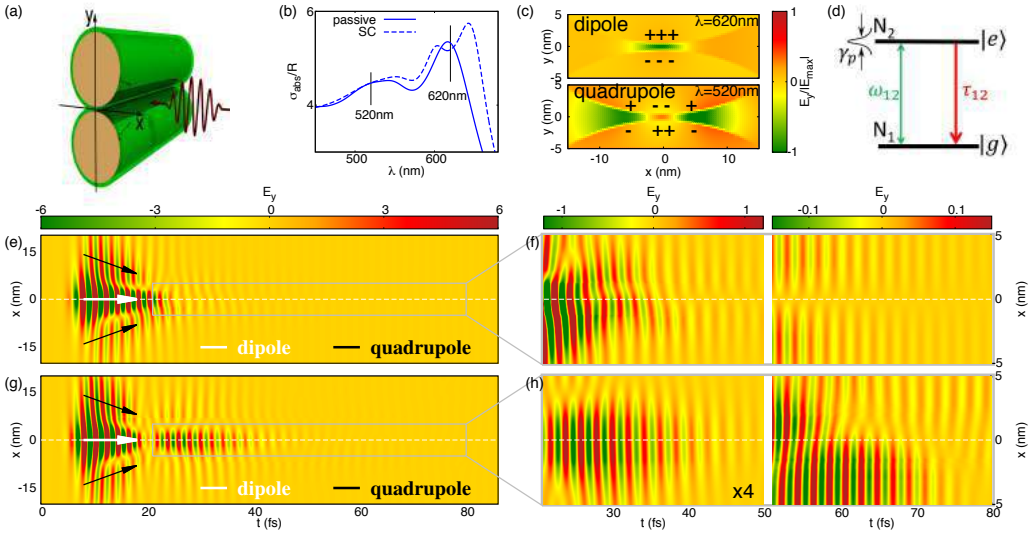

Figure 1: (a) Plasmonic dimer structure, surrounded with a homogeneous layer of QEs (green colour) (b) the absorption cross-section spectra for the plasmonic structure without (passive) and with QEs. (c) The profile of the first two even-bonding modes. (d) QEs are represented by a 2-level system. The spatio-temporal map of (e,f) the passive and (g,h) strongly-coupled system.

In this paper, we explore the coupling of emitters with the multiple type of modes that are present in plasmonic structures. We show that external radiation excites both the even and odd bonding modes of a plasmonic dimer, which are simultaneously exciting and exchanging energy with the QEs. For the plasmonic dimer, these two types of modes occur at the same frequency:

$$\omega_n^{even} = \sqrt{\frac{R_2^n - R_1^n}{2R_2^n}}\omega_p - i\left(\frac{\gamma_m}{2} + \frac{n\pi\gamma_m^4\omega_p^3}{8R_0^2c_0^2}\left(\frac{R_1}{R_2}\right)^2\sqrt{\frac{R_2^n - R_1^n}{2R_2^n}}\right) \quad (1)$$

$$\omega_n^{odd} = \sqrt{\frac{R_2^n - R_1^n}{2R_2^n}}\omega_p - i\frac{\gamma_m}{2} \quad (2)$$

where ω_p and γ_m is the plasma frequency and damping of the metal and R_1, R_2 is the radii of the two cylindrical structures. The two modes have different radiative properties with the even-bonding mode coupling more efficiently to the even continuum (i.e. bright mode), while the odd mode is darker. We model a homogeneous layer of QEs surrounding the dimer structure as a two-level system, whose dynamics are governed by the decay lifetime of the excited state (τ_{12}) and dephasing rate (γ_p). The QEs couple to both modes simultaneously, which leads to spatially asymmetrical Rabi-oscillations and mode beating characteristics (Figure 1).

To excite either type of modes alone, we need to preserve the parity symmetry of the system. We achieve this by exciting the plasmonic dimer structure with two plane-wave sources, incident from opposite directions. The parity symmetry is controlled by the phase difference of the two sources: when in-phase only the even modes are excited, and out-of-phase excitation couples only to odd modes. As expected, odd modes continue to exchange energy with the emitters for much longer times than even modes [3]. Most importantly though, despite their smaller field enhancement, odd modes exhibit identical coupling strength to even mode coupling.

In conclusion, we show that parity symmetry in plasmonic nano-cavities dominates the spatio-temporal dynamics of the plasmon-exciton in the cavity. By tailoring the illumination set-up of the plasmonic structure, we can dynamically control the hybrid states of the strongly-coupled system, and therefore specifically adapt the dressing of molecules with light.

ACKNOWLEDGMENT

We acknowledge financial support from EPSRC grants EP/L027151/1 and EP/L024926/1

REFERENCES

1. Kongsuwan, N., Demetriadou, A., Chikkaraddy, R., Benz, F., Turek, V. A., Keyser, U. F., Baumberg, J. J. and O. Hess, "Suppressed Quenching and Strong-Coupling of Purcell-Enhanced Single-Molecule Emission in Plasmonic Nanocavities," arXiv:1612.02611, 2017
2. Chikkaraddy, R., de Nijs, B., Barrow, S. J., Scherman, O. A., Rosta, E., Demetriadou, A., Fox, P., Hess, O. and J.J. Baumberg, "Single-molecule strong coupling at room temperature in plasmonic nanocavities," *Nature*, Vol. 535, 127, 2016.
3. Demetriadou, A.,Hamm, J. M., Luo, Y., Pendry, J. B., Baumberg, J. J. and O. Hess, "Spatio-temporal dynamics and control of strong coupling in plasmonic nano-cavities," submitted, 2017.

Laser processing of VO_2 for metamaterials applications and THz devices

Alberto Piqué, Nicholas Charipar, Heungsoo Kim, Scott Mathews, Kristin Charipar and Ray Auyeung

[1] Materials Science and Technology Division, Naval Research Laboratory, Washington DC, USA
[*]corresponding author: alberto.pique@nrl.navy.mil

Abstract- Vanadium dioxide (VO_2) undergoes a metal-insulator transition (MIT) whereby its electrical resistivity changes by several orders of magnitude. The combination of fast switching times and response to a broad range of external stimuli make VO_2 an ideal material for a variety of novel devices and sensors. In this talk, we will present details of laser processed VO_2 films and their application for metamaterial devices such as THz emitters and THz modulators.

Vanadium dioxide (VO_2) has been investigated as a tunable functional material because it undergoes a structural phase change between an insulating monoclinic phase and metallic tetragonal phase. This phase change can be induced thermally, mechanically, electrically, or optically and it can occur at ultrafast timescales (~100fs). The combination of fast switching times and response to a broad range of external stimuli make VO_2 an ideal material for a variety of novel devices and sensors. While the MIT in VO_2 has been exploited for a variety of microwave/terahertz applications (i.e. tunable filters and modulators), very few devices exploiting the fast switching time of VO_2 have been reported. The electrical properties of thin film VO_2 (conductivity, carrier concentration, switching speed, etc.) are highly dependent on growth and post-processing conditions. For example, the transition temperature can be tuned via doping or by introducing lattice strain via strain engineering during the growth process [1, 2] (Figure 1).

Metamaterial devices based on the phase changing properties of VO_2 films are very promising as the resonant frequency can be tuned by adjusting the properties of VO_2. For example, hybrid metamaterial devices designed for THz frequency range have been demonstrated by combining split ring resonators (SRRs) with phase changing VO_2 films. In this configuration, changing the conductivity of VO_2 via temperature tunes the behavior of the SRR gap from capacitive to resistive thus modulating the THz beam transmission at the SRR resonance frequencies [3] (Figure 2). Furthermore, VO_2 based devices can also be used for the generation of electromagnetic radiation in the millimeter and terahertz region of the electromagnetic spectrum. We have investigated the use of the ultrafast metal-insulator transition in VO_2 thin films to produce broadband THz radiation [4]. This talk will discuss the effects of various pulsed laser deposition (PLD) growth conditions on the stress/strain state of VO_2 films and the subsequent change in their electrical properties. Finally, results from various VO_2 devices such as THz modulators and THz emitters will be presented.

Acknowledgements, This work was sponsored by The Office of Naval Research (ONR) through the Naval Research Laboratory Basic Research Program.

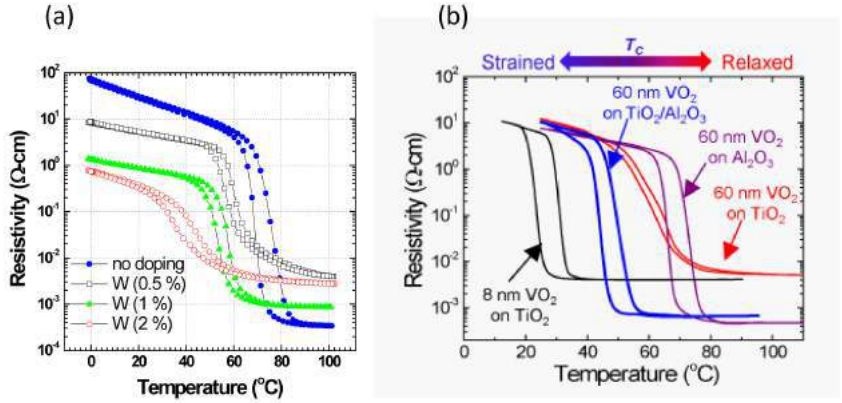

Figure 1. Electrical properties of various VO_2 thin films grown by PLD showing (a) the effect of tungsten-doping and (b) the effect of TiO_2 buffer layers on the VO2 transition temperature.

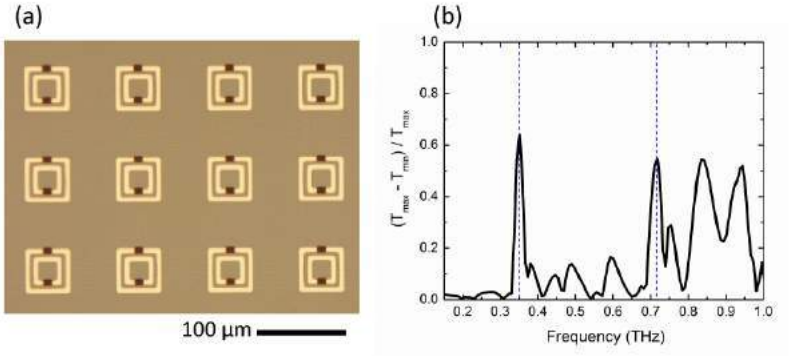

Figure 2 (a) Optical image of an array of SRR structures with patterned VO_2 pads on the gaps of the SRR. (b) Transmission modulation efficiency for a hybrid SRR-VO_2 device, showing ~60% and 54% tunability at 0.35THz and 0.72THz, respectively.

REFERENCES

1. Kim, H., Charipar, N., Osofsky, M., Qadri, S. B., and Piqué, A., "Optimization of the semiconductor-metal transition in VO_2 eptitaxial thin films as a function of oxygen growth pressure," Appl. Phys. Lett. **104**, 081913, 2014.
2. Breckenfeld, E. Kim, H., Burgess, K., Charipar, N., Cheng, S.F., Stroud, R. Piqué, A., "Strain Effects in Epitaxial VO_2 Thin Films on Columnar Buffer-Layer TiO_2/Al_2O_3 Virtual Substrates," ACS App. Mater. Interfaces, **9**(2), 1577–1584, 2017.
3. Kim, H., Charipar, N., Breckenfeld, E., Rosenberg, A., Piqué, A., "Active terahertz metamaterials based on the phase transition of VO_2 thin films," Thin Solid Films **596**, 45-50, 2015.
4. Charipar, N. A., Kim, H., Mathews, S. A. and Piqué, A., "Broadband terahertz generation using the semiconductor-metal transition in VO_2", AIP Advances, **6**(1), 015113, 2016.

Frequency conversion in THz metal-insulator-metal disk resonators coupled to semiconductor quantum wells

C. G. Derntl*, M. Wenclawiak, K. Unterrainer, and J. Darmo
Photonics Institute, TU Wien, Gußhausstraße 27-29, 1040 Vienna, Austria
*corresponding author: christian.g.derntl@tuwien.ac.at

Abstract- We present our investigations of asymmetric quantum wells in the THz regime. The combination with 3D full wave simulations and measurements of modified circular patch resonators allows us to study efficient nonlinear frequency conversion when the resonators are coupled to intersubband transitions in asymmetric quantum wells. The flexible tuning of the eigenmodes and the wide range of the cavity modes' quality factors (13-40) allow to optimize the internal nonlinear conversion process as well as the in- and out-coupling of light.

Cavity field enhanced nonlinear frequency conversion processes are already used in many devices, such as lasers, detectors and parametric amplifiers. However, their applications are limited by the need of high input power. To maintain the same field strength for reduced pump power, either the photon lifetime in the cavity has to be increased or the mode volume is reduced. For the latter case plasmonic resonators have the outstanding ability of extraordinary high field confinement, which reaches effective mode volumes smaller than 10^{-3} of λ_0^3 for metal-insulator-metal (MIM) designs [1]. Nonlinear frequency conversion processes can be further improved by using tailored high non-linear susceptibility materials such as semiconductor quantum wells (QW) [2]. Recently, Lee et al. demonstrated experimentally a second harmonic conversion efficiency of 2×10^{-6} W/W^2 in the mid-infrared [3] using a doubly resonant metamaterial (MM) coupled to intersubband transitions (ISBT) in QWs. Furthermore, theoretical investigations predict a conversion efficiency of 1.3×10^{-2} W/W^2 with split ring resonators strongly coupled to ISBTs [4].

Here, we transfer this concept of enhanced nonlinear susceptibility of MM strongly coupled to semiconductor heterostructures to the THz regime and investigate the induced parametric frequency conversion for MIM type resonators. In our study of circular patch resonators, see Figure 1(a), we showed the capability of selective excitation of their eigenmodes, even if they are degenerated [5]. These selection rules for the excitation of the eigenmodes are introduced by breaking the rotational symmetry with slits that additionally offer the control of generating additional eigenmode and eliminating others. Especially the control of the eigenmodes with a wide range of quality factors from 13 to 40 and the high field confinement of circular patch resonators makes this system suitable for doubly and triply resonant frequency conversion in cavity quantum electrodynamic systems, see Figure 2(b). Thus, the generated field mode is out-coupled using a low quality factor, while for the idler mode a high quality factor is chosen to maximize the conversion efficiency. The pumped eigenmode is matched to the spectrum of the pump beam.

On the other hand, for an efficient second order conversion process asymmetric QWs are required (e.g. SHG in [4]) providing a high second order non-linear term of susceptibility $\chi_{zzz}^{(2)}(\omega - \omega_i, \omega, \omega_i) \sim N\, z_{31}\, z_{23}\, z_{12}$, with doping concentration N. The matrix elements z_{ij} are the QW parameters that can be optimized by the well design for improving the conversion process. In Figure 1(c) a step QW and its wavefunctions are shown. The QW is

optimized for the highest product of the matrix elements z_{ij} for the material system GaAs/AlGaAs in the THz regime. We used a Schrödinger-Poisson self-consistent solver to optimize the design of a step quantum well for SHG at terahertz frequencies.

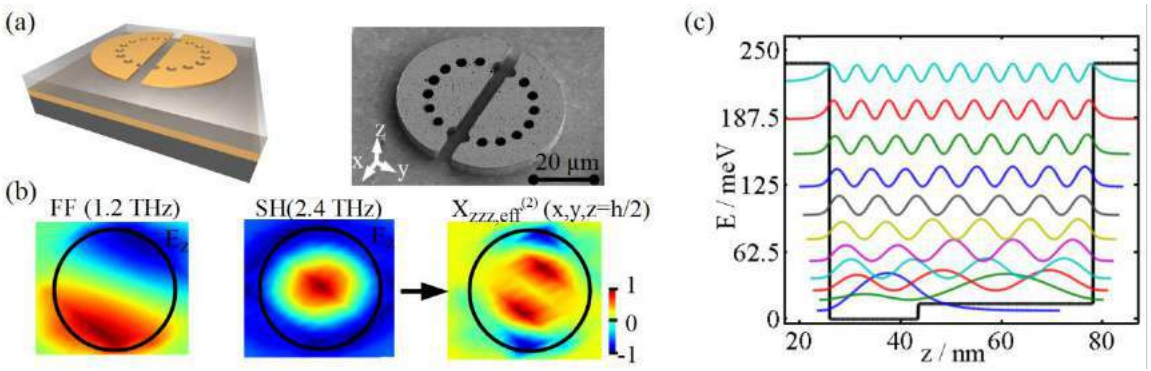

Figures 1: (a) Schematics and SEM micrograph of a MIM disk resonator with broke symmetry. (b) Illustration of a doubly resonant second harmonic generation process. The cavity mode at the fundamental frequency (FF) and the one at the second harmonic frequency (SH) result in an effective distribution of the local electric susceptibility. (c) Step quantum well: E_2-E_1= 10meV, $z_{12}\, z_{23}\, z_{31}$ = 128nm^3, $\chi_{zzz}^{(2)}$ ~ 10^{-4} m/V.

The authors acknowledge partial financial support by the Austrian Science Fund (FWF) through the DK CoQuS W1210 and the SFB NextLite (F4902), and the NATO SfP Program through project NOTES (984698).

REFERENCES

1. Kuttge, M., Garcia de Abajo, F. J, and Polman, A., "Ultrasmall Mode Volume Plasmonic Nanodisk Resonators," *Nano Lett*. 10, 1537-1541 (2010).
2. Rosencher, E., Bois, P., Nagle, J., and Delaitre, S., "Second harmonic generation by intersub-band transitions in compositionally asymmetrical MQWs," Electron. Lett., vol. 25, pp. 1063-1065, 1989.
3. Lee, J., Chen, P. Y., Argyropoulos, C., Alu, A., and Belkin, M. A., "Metamaterials based on intersubband polaritons," Metamaterials Congress, Bordeaux, France, 2013.
4. Campione, S., Benz, A., Sinclair, M.B., Capolino, F., and Brener, I., "Second harmonic generation from metamaterials strongly coupled to intersubband transitions in quantum wells," Appl. Phys. Lett., vol. 104, pp. 131104, 2014.
5. Derntl, C. G., Bachmann, D., Unterrainer, K., Darmo, J., "Circular patch resonators for cavity quantum electrodynamics in the terahertz region," submitted to Opt. Express.

Magnetic-Free Non-Reciprocal Graphene Plasmonics

D. Correas-Serrano and J. S. Gomez-Diaz
University of California, Davis, United States
dcorreas@ucdavis.edu, jsgomez@ucdavis.edu

Abstract – *We discuss recent advances in magnetic-free non-reciprocal plasmonic devices and antennas based on spatiotemporally modulated graphene. We first review the exciting properties and novel functionalities that this technology offers, focusing on achieving large non-reciprocal responses with fully integrated structures. We then address the main challenges that remain to be addressed, including limitations associated to plasmon damping and modulation speed. Finally, we investigate novel routes towards optimal designs. To this purpose, we examine two types of isolators, based on indirect interband photonic transitions and on asymmetric bandgaps for the plasmonic modes. We envision that this technology will open new exciting venues in the field of plasmonics.*

The myriad of graphene plasmonic devices envisioned by researchers in the past decade successfully exploit graphene's field effect to achieve quasi-real-time reconfiguration of devices like waveguides, filters, antennas, and metasurfaces [1] or to realize modulators [2], [3]. Recently, the ultrafast field effect in graphene has been proposed as a mechanism to realize magnet-less non-reciprocal plasmons at THz and infrared [4], achieved by modulating the conductivity of graphene in space and time through multiple gating pads. This imparts linear or angular momentum to the supported plasmons, creating an effective moving medium able to break time-reversal symmetry. Judicious design of the bias voltage signals, namely their phase difference, frequency, and amplitude, allows to create very strong non-reciprocity in compact, fully planar and integrated waveguides [5], antennas [6], or phase shifters [7] without the need of magneto-optic effects. There have been, however, no comprehensive studies on the ultimate capabilities of this technology, or how to realize optimal designs for a given set of constraints. This is particularly important for graphene plasmonics, as loss is arguably the biggest obstacle to practical viability for most graphene devices.

In this talk, we will first review the use of spatiotemporally modulated graphene to realize magnetic-free fully-integrated non-reciprocal devices and leaky-wave antennas, as well as the novel functionalities that this exciting technology enables. Then, will discuss optimal designs in terms of trade-offs between isolation and insertion loss, using an analytical theoretical framework based on coupled-mode theory and finite-element multi-harmonic frequency domain numerical simulations. Fig. 1 illustrates this type of compromise for an isolator based on indirect interband photonic transitions operating at 12 THz. The spatiotemporal modulation imparted to one of the layers ($\sigma_2 = \sigma_0[1 + M\cos(2\pi f_m t - \beta z)]$) creates perfect phase-matching between the odd and even modes in the isolated direction, leading to complete mode and frequency conversion, while full transmission ideally occurs in the opposite one [4]. We note that in this type of isolator maximum isolation requires that both the real and imaginary parts of the modal wavevectors must be matched, and the latter cannot be fully compensated by the simple modulation scheme considered here. Figs. 1b and 1c illustrate this response by plotting the maximum isolation possible and the associated insertion loss for an isolator at 12 THz with M = 0.1, $\tau = 1$ ps and $f_m = 50$ GHz versus layer separation d and chemical potential μ_c. Very large isolation, greater than 30 dBs, can be achieved for those values of d and μ_c for which the damping of odd and even modes is similar, thus defining a clear design

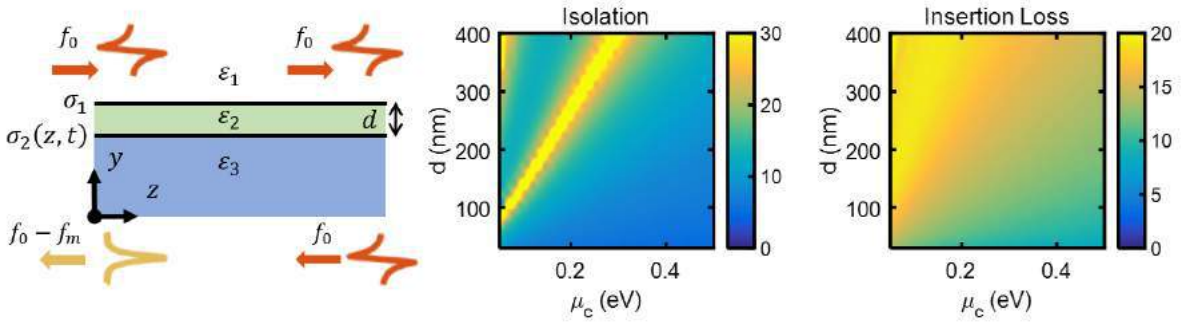

Figure 1. (a) Plasmonic isolator based on indirect transitions between the fundamental modes of a graphene parallel plate waveguide with $\varepsilon_1 = \varepsilon_2 = \varepsilon_3 = 1$, operating at 12 THz, for a relaxation time of 1 ps. The conductivity of the bottom layer σ_2 is modulated simultaneously in space and time as $\sigma_2 = \sigma_0(1 + M\cos[\omega_m t - \beta_m z])$, inducing non-reciprocal phase matching between the modes that translates into unidirectional isolation at f_0. (b) Maximum possible isolation versus chemical potential μ_c and sheet separation d (c) Insertion loss in the transmitting direction for the optimal designs of panel b.

rule to realize quasi-optimal designs. Another key factor is related to the undesired partial mode conversion that inevitably occurs in the transmitting direction due to the finite line width of the modes [5]. This effect may be considered a type of loss that depends on the magnitude of the phase mismatch and the modulation amplitude, and its minimization conflicts with that of dissipation loss due to finite carrier mobility in graphene. We will further discuss these trade-offs at the conference, also for isolators based on asymmetric bandgaps.

Recent great strides being made in experimental graphene plasmonics [8] are enabling the emergence of spatiotemporally modulating graphene as novel, multi-functional, and magnetic-free plasmonic platform able to fulfill many of the currently unmet needs for non-reciprocal devices at terahertz and infrared frequencies.

REFERENCES

[1] J. S. Gomez-Diaz and A. Alu, "Flatland Optics with Hyperbolic Metasurfaces," *ACS Photonics*, vol. 3, no. 12, p. acsphotonics.6b00645, 2016.

[2] B. Sensale-Rodriguez *et al.*, "Broadband graphene terahertz modulators enabled by intraband transitions.," *Nat. Commun.*, vol. 3, p. 780, 2012.

[3] C. T. Phare, Y. D. Lee, J. Cardenas, and M. Lipson, "Graphene electro-optic modulator with 30 GHz bandwidth," *Nat. Photonics*, vol. 9, no. 8, pp. 511–514, 2015.

[4] D. Correas Serrano, J. S. Gomez-Diaz, D. L. Sounas, Y. Hadad, A. Alvarez-Melcon, and A. Alù, "Non-reciprocal graphene devices and antennas based on spatio-temporal modulation," *IEEE Antennas Wirel. Propag. Lett.*, vol. 1225, no. c, pp. 1–1, 2015.

[5] D. Correas-Serrano, J. S. Gomez-Diaz, D. L. Sounas, A. Alvarez-Melcon, and A. Alù, "Non-reciprocal THz components based on spatiotemporally modulated graphene," in *2016 10th European Conference on Antennas and Propagation (EuCAP)*, 2016.

[6] D. Correas-Serrano, A. Alvarez-Melcon, J. S. Gomez-Diaz, D. L. Sounas, and A. Alu, "Non-reciprocal leaky-wave antenna at THz based on spatiotemporally modulated graphene," in *2016 IEEE Antennas and Propagation Society International Symposium*, 2016, no. 1, pp. 1399–1400.

[7] C. Qin, B. Wang, H. Long, K. Wang, and P. Lu, "Non-reciprocal Phase Shift and Mode Modulation in Dynamic Graphene Waveguides," *J. Light. Technol.*, vol. 8724, no. c, pp. 1–1, 2016.

[8] A. Woessner *et al.*, "Highly confined low-loss plasmons in graphene–boron nitride heterostructures," *Nat. Mater.*, vol. 14, no. 4, pp. 421–425, 2014.

Antenna-coupled Photon Emission from Tunnel Junctions

Palash Bharadwaj[1*], Markus Parzefall[2], Achint Jain[2], and Lukas Novotny[2]
[1] Electrical and Computer Engineering, Rice University, Houston, TX 77005
[2] Photonics Laboratory, ETH Zurich, 8093 Zurich, Switzerland
[*]corresponding author: pb22@rice.edu

Abstract- We have studied the ultrafast conversion of electrons localized in vertical Au-hBN-Au tunnel junctions to free-space photons, mediated by resonant slot antennas. We achieve polarized, directional and resonantly enhanced light emission from inelastic electron tunneling and establish a novel platform for studying the interaction of electrons with strong electromagnetic fields.

Optical antennas are elements that couple free space radiation to nanoscale volumes. To date, optical antennas have been driven using light, in contrast to their radio frequency counterparts which are driven by electrical currents. We have realized ultrafast solid-state light-emitting tunnel devices based on arrays of electrically driven optical antennas that significantly alter this paradigm. To achieve this electro-optical transduction, we use vertical Au-hBN-Au tunnel junctions. Electrons tunnel from one electrode to the other

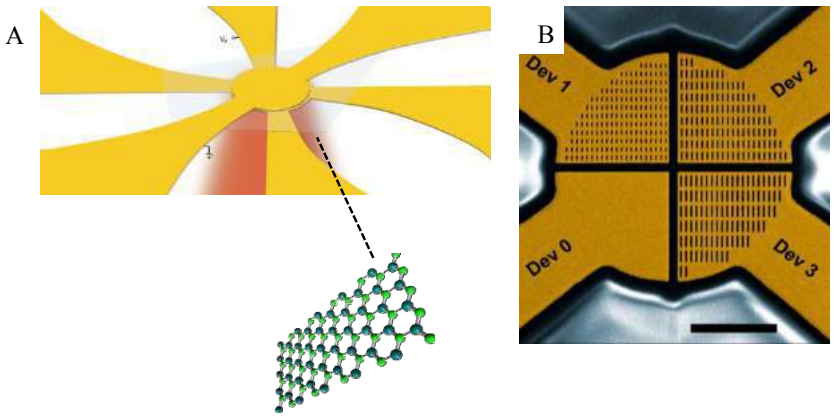

Figure 1. (A) Schematic of the fabricated device comprising two gold electrodes and a thin flake of hBN between them. **(B)** A false color scanning electron micrograph of the bottom electrode before transferring the hBN. The slot antennas in different sectors are different aspect ratios and hence varying spectral resonances. The scale bar is 1 micron.

under an applied bias, and generate highly-confined surface plasmons by inelastic tunneling. Because it does not rely on intermediate excitations such as electron–hole pairs, the response time of such a device is fundamentally only limited by the tunneling time of electrons through the junction, a process that takes place on a femtosecond timescale.

We demonstrate ultrafast temporal modulation of light emission from such h-BN tunnel junctions. The device is driven with an RF signal of frequency f, and a histogram of interphoton arrival times in the resulting photon stream is recorded by employing time-correlated single-photon counting (TCSPC). Figure 2 shows histograms recorded for different modulation frequencies of demonstrating that the photon stream is indeed

time-modulated at the same frequency.

The efficiency of photon emission from our vertical tunnel junction is low, ~1e-5 photons per electron. We show that this can be improved by an order of magnitude by employing Hertzian nanoparticle dimer antennas. Further increase in efficiency can be expected by engineering the tunnel barrier to slow down the electron as they traverse across the gap thus increasing their interaction strength with plasmons (photons). With our tunneling devices we have presented a novel platform to combine electrons and plasmons in nanoscopic volumes. We expect these devices to be useful for ultrafast optoelectronic applications, and also to explore fundamental issues such as plasmon lasing.

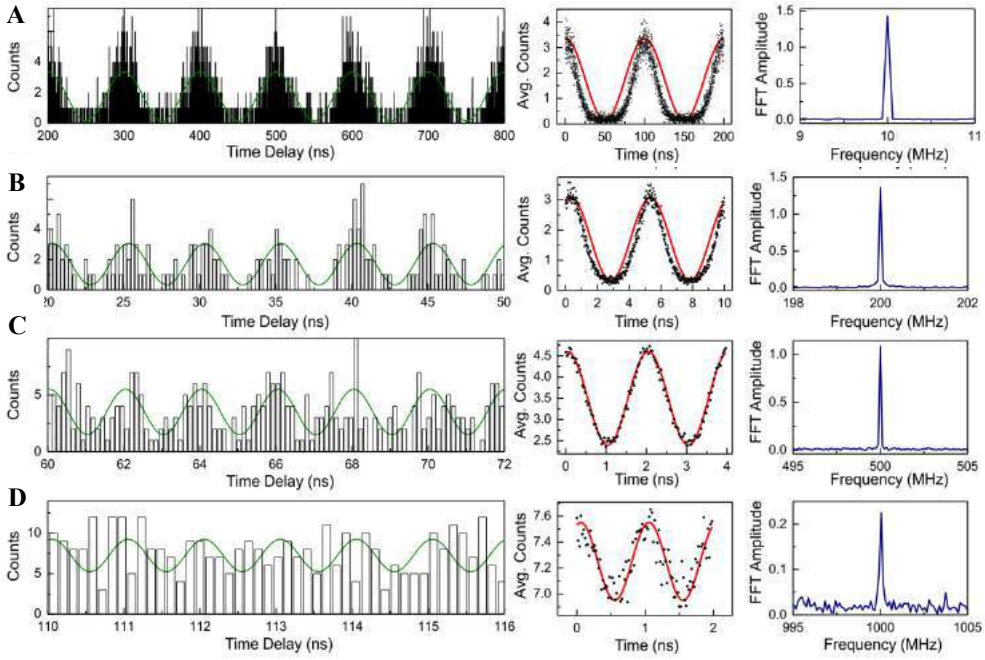

Figure 2: Modulation of light emission from the tunnel junction from 10 MHz up to 1 GHz **. (A)-(D)** show the raw interphoton arrival time histograms as well as the averaged data, together with the Fourier transforms of the raw histograms.

REFERENCES

1. M. Parzefall *et al*, "Antenna-coupled photon emission from hexagonal boron nitride tunnel junctions", *Nature Nanotech.* 10, 1058-1063, 2015.

Strong couplings of many-body quantum emitters in plasmonic metal nanocavities

Aeshah Muqri[1], **and Jae Yong Suh**[1*]
[1]Michigan Technological University, United States
[*]corresponding author: jsuh@mtu.edu

Abstract We report Rabi splitting in the optical reflection and emission spectra from different types of quantum emitters interacting with metal nanostructures in periodic arrays. Metal-insulator-metal (MIM) nanodiscs show two localized surface plasmon (LSP) flat bands as well as surface lattice resonances (SLRs), which is dipolar particle-particle interactions along the diffraction order. The strong coupling between the SLR and quantum emitters observed in MIM nanocavities exhibits both the narrow line-width and enhanced local fields.

Anti-crossing found in energy-momentum dispersion is a characteristic feature of strong couplings between various quasiparticles excited on semiconductor microcavities or periodic nanostructures. A nanoscale analogy of the macroscopic two-mirror cavity is two metal nanodiscs separated by an insulator of a thickness less than its light wavelength. We fabricated metal-insulator (MI) and metal-insulator-metal (MIM) nanodiscs embedded in various kinds of quantum emitters. We first report strong coupling with MI structure that consists of single metal nanodisc overcoated with J-aggregate cyanine dye molecules in dielectric matrix.

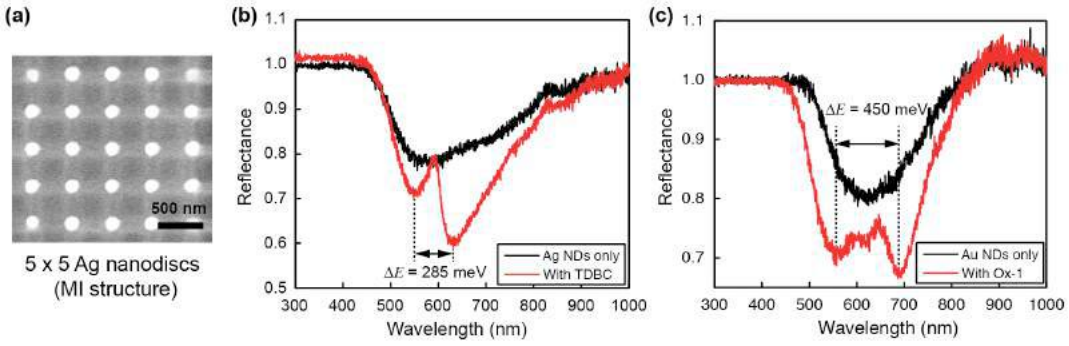

Figure 1. (a) SEM images of Ag nanodiscs in array of 500 nm periodicity. Normalized reflection spectra from (b) TDBC J-aggregates on Ag nanodisc array, and (c) Oxazine-1 dye molecules in PMMA on Au nanodisc array.

The spectral locations of localized plasmon resonances can be engineered by the size and dielectric functions of constituent materials. Figure 1(a) shows silver nanodiscs fabricated by a combination of photolithography and FIB etching. Figure 1(b) shows the experimental reflection spectra from Ag nanodiscs of 140 nm diameter in a square array, overcoated by TDBC molecules in polymer matrix. When there were no TDBC molecules, only the broad LSP resonance of Ag nanodiscs existed centered at 580 nm as shown in black curve. In the presence of the QEs whose absorption band overlapped with the of LSP resonances, the reflectance spectrum clearly showed the

Rabi splitting of frequencies below and above the resonance maximum.

MIM geometry, on the other hand, can support highly localized electromagnetic fields in the gap region due to the near-field interaction between the two metal nanodiscs [1-3]. Specifically, when the coupled LSP resonance at a longer wavelength can interact with SLR mode, an anticrossing can occur at non-zero in-plane *k* vector. This coupling maintains both high local field intensity nearby the MIM structures and relatively narrower line-width, representing a longer lifetime of the plasmon-exciton-polariton quasiparticles in the presence of quantum emitters. Therefore, MIM nanocavities that support extremely small effective mass of the quasiparticle in periodic array can be a good platform to realize exciton-plasmon Bose-Einstein condensates at room temperature [4, 5]

REFERENCES

[1] M. Kuttge, F.J.G. de Abajo, A. Polman, Ultrasmall Mode Volume Plasmonic Nanodisk Resonators, Nano Lett 10 (2010) 1537-1541.

[2] E. Hao, G.C. Schatz, Electromagnetic fields around silver nanoparticles and dimers, J Chem Phys 120 (2004) 357-366.

[3] P. Nordlander, C. Oubre, E. Prodan, K. Li, M.I. Stockman, Plasmon hybridizaton in nanoparticle dimers, Nano Lett 4 (2004) 899-903.

[4] S.R.K. Rodriguez, J. Feist, M.A. Verschuuren, F.J. Garcia Vidal, J.G. Rivas, Thermalization and Cooling of Plasmon-Exciton Polaritons: Towards Quantum Condensation, Phys Rev Lett 111 (2013).

[5] J.P. Martikainen, M.O.J. Heikkinen, P. Torma, Condensation phenomena in plasmonics, Phys Rev A 90 (2014).

Plasmons in superlattices of graphene on hexagonal boron nitride

Jeil Jung[1*]

[1]ADepartment of Physics, University of Seoul, Seoul 02504, Korea

[*]corresponding author: jeiljung@uos.ac.kr

Abstract- Recent experiments have shown the presence of strong of moire superlattice features in the electronic structure of graphene on hexagonal boron nitride. Our analysis shows that the moire superlattices formed at the graphene-hBN interface offer a rich platform for plasmonics where control of the plasmon modes can be introduced both through carrier doping and twist angle control.

The Recent experiments have shown the presence of strong of moire superlattice features in the electronic structure of graphene on hexagonal boron nitride. The conductivity of graphene on a boron nitride substrate exhibits features in the terahertz (THz) and infrared (IR) frequency regimes that are associated with the periodic moire pattern formed by weakly coupled two-dimensional materials. The THz and IR features are strongest when the two honeycomb lattices are orientationally aligned, and in this case they are Pauli blocked unless the Fermi level is close to ±150 meV relative to the graphene sheet Dirac point. The substrate-induced band splitting is larger at energies below the Dirac point and it can lead to sharp features at THz and IR frequencies in p-doped graphene. We explain how the strongest few THz and IR features arise from critical points in the moire-band joint density of states, which in turn depend sensitively on the way the superlattice Hamiltonian is modeled. Based on the calculations for the plasmon excitation spectrum of massless Dirac fermions in the moire superlattice of graphene on hexagonal boron nitride, our analysis shows that the moire superlattices formed at the graphene-hBN interface offer a rich platform for plasmonics where control of the plasmon modes can be introduced both through carrier doping and twist angle control.

Acknowledgements, Korean National Research Foundation through grant NRF-2016R1A2B4010105.

REFERENCES

1. Jung, Jeil and Raoux, Arnaud and Qiao, Zhenhua and MacDonald, "Ab initio theory of moiré superlattice bands in layered two-dimensional materials," *Physical Review B*, Vol. 89, No. 20, 205414, 2014.
2. Jung, Jeil and DaSilva, Ashley M. and MacDonald, Allan H. and Adam, Shaffique, "Origin of band gaps in graphene on hexagonal boron nitrideT," *Nature Communications* 6:6308 doi: 10.1038/ncomms7308, 2015.
3. Tomadin, Andrea and Guinea, Francisco and Polini, Marco, "Generation and morphing of plasmons in graphene superlattices," *Physical Review B*, Vol. 90, No. 16, 161406, 2014.

Nonreciprocal Metasurfaces with Temporal Modulation

Xingjie Ni*

Department of Electrical Engineering, Pennsylvania State University, University Park, PA 16802, USA
*corresponding author: *xingjie@psu.edu*

Abstract – We demonstrated a distinct class of active metasurfaces with temporal modulation that truly breaks the Lorentz reciprocity of light propagation. The technique would pave a viable way to realize practical magnetic-free compact nonreciprocal optical components that could enable numerous applications.

Nonreciprocal optical components, which are indispensable building blocks in m any modern optical and communication systems, are almost exclusively based on the magneto-optic effect, making the devices bulky and preventing them from integration. It is in great demand to have a magnetic-free route to achieve on-chip nonreciprocal light propagation in order to isolate and stabilize optical elements. The newly emerging metasurface - an optically thin layer consisting of subwavelength-sized elements that offers tremendous power for manipulating light - is a great platform for building miniaturized optical components. [1, 2] However, the metasurfaces so far all function in static states and there are fundamental limitations. In particular, to violate Lorentz reciprocity in a non-power dependent fashion without resorting to magneto-optic effects, a time-varying response is required. [3] Here, by incorporating an additional temporal modulation, we demonstrate that it is possible to break time-reversal symmetry of the system and thereby achieve nonreciprocal light propagation with an active metasurface.

REFERENCES

[1] A. V. Kildishev, A. Boltasseva, and V. M. Shalaev, "Planar Photonics with Metasurfaces," *Science,* vol. 339, p. 1232009, 2013.

[2] N. Yu and F. Capasso, "Flat optics with designer metasurfaces," *Nat Mater,* vol. 13, pp. 139-150, 2014.

[3] Y. Shi, Z. Yu, and S. Fan, "Limitations of nonlinear optical isolators due to dynamic reciprocity," *Nat Photon,* vol. 9, pp. 388-392, 2015.

Efficient broadband Huygens sources made of spherical nanoclusters.

Romain Dezert, **Philippe Richetti**, **Virginie Ponsinet**, **Olivier Mondain-Monval**, **Philippe Barois**, **and Alexandre Baron**

[1]University of Bordeaux, CNRS, CRPP, UPR 8641, 115 avenue Scwheitzer, 33600, Pessac, France
alexandre.baron@u-bordeaux.com

Abstract— We present spherical nanoclusters made of spherical inclusions which act as efficient and broadband Huygens sources. The system is versatile enough that several materials may be used as inclusions and different bands may be targeted by varying some of the parameters. They may serve as the basic building blocks of Huygens metasurfaces and are particularly suited to bottom-up fabrication and self-assembly. We also investigate how these sources interact with ultra-short pulses of light.

1. HUYGENS SOURCES AND THEIR APPLICATIONS

Huygens sources are secondary sources of spherical wavelets which spread in the forward direction with respect to the primary source of light (usually a plane wave). Such sources consist of in-phase superimposed electric and magnetic dipoles of equal amplitudes. Recently, it has been shown that by carefully arranging such sources into a two-dimensionnal periodic array, Huygens metasurfaces could be produced which have the elegant property of imparting a 2π phase shift to an impinging plane wave with a near unity transmittance [1, 2, 3]. Such a coverage enables both spatial and temporal wavefront shaping, making it possible to produce flat optical components such as lenses, polarizers and pulse compressors. However all Huygens metasurfaces that have been proposed up to now have been fabricated by top-down approaches and rely on silicon. This is limiting in many aspects, because it makes it difficult to produce large area metasurfaces and usually imposes the substrate on which the metasurface will be formed.

Here we propose an alternative geometry as Huygens sources, which we believe is very well suited to *bottom-up* approaches. They consist of spherical nanoclusters which can potentially be produced in very large amounts by self-assembly and as a result cover very large areas. They could come in the form of inks consisting of colloidal suspensions making it easy to spray over virtually any substrate. This paper will restrict the discussion to the theoretical description of these nanoclusters, but preliminary experimental results will be presented orally. Not only is it possible to make efficient Huygens dipoles, but the geometry is versatile enough that it can easily be made to satisfy the so-called *generalized Huygens condition*, whereby to higher-order multipolar scattering, which is of particular interest to metasurfaces that require broadband operation and polarization control. We also describe the interaction of theses sources with ultra-short pulses.

2. THEORY : NUMERICAL AND ANALYTICAL APPROACH

We consider spherical clusters made of spherical inclusions. Several inclusions of varying materials are considered: silicon, gold and silver. The clusters are generated by considering the closest packing of equal spheres into a sphere that interact repulsively, which likely describes the formation of pseudo-homogenous colloidal aggragates [4]. The scattering properties of the nanoclusters are computed both by using a T-matrix simulator developped by Mackowski [5] and the commercial finite-element solver COMSOL Multiphysics. The parameter space explored consists in the material of the inclusion, the inclusion size, the numbers of inclusions, the volume fraction of inclusions in the cluster and the refractive index contrast between the inclusions and the host material. Many solutions are found which reveals the extreme versatility of the system. One such solution is shown on Fig. 1. It consists in an icosahedral cluster of 13 closely-packed identical silicon spheres. This shape is the solution to the kissing number problem [6].

Figure 1(a) shows the scattering cross-section efficiency of the electric and magnetic dipoles of the nanocluster as well as the multipolar and total efficiency. We see that both electric and magnetic dipoles scatter with equal amplitudes and phase over a broad band of optical frequencies

of almost 100 nm. The radiation diagram of the cluster is provided in Fig. 1(b) along with the spatial distribution of the near field in Fig. 1(c&d) and shows that virtually the scattered energy is radiated in the forward direction. The operation wavelength can be tuned by varying the volume fraction or else the number of inclusions per cluster.

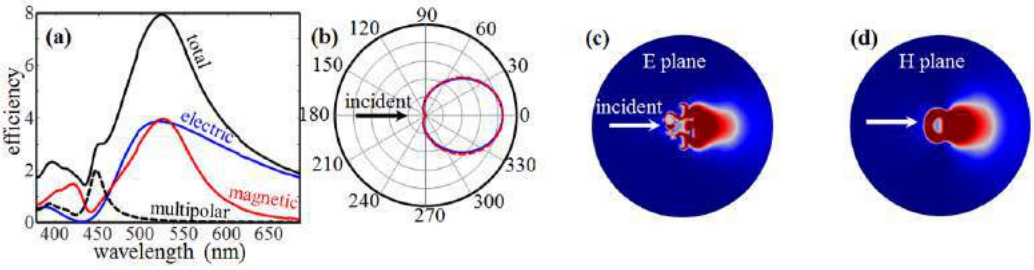

Figure 1: Huygens sources made of spherical clusters

We also adopt an analytical approach which very closely follows the results predicted by our simulations. We consider the nanocluster to be a spherical homogenous nanoparticle made of an effective medium. The effective medium properties (namely the electric permittiy ϵ and magnetic permeability μ) are given by extended Maxwell-Garnett theory which provides

$$\epsilon_{\text{eff}} = \epsilon_{\text{h}} \frac{x^3 + i3fa_1}{x^3 - i\frac{3}{2}fa_1} \tag{1}$$

$$\mu_{\text{eff}} = \frac{x^3 + i3fb_1}{x^3 - i\frac{3}{2}fb_1} \tag{2}$$

where ϵ_{h} is the host dielectric constant, $x = ka$ is the size parameter of the inclusion in which k is the wave vector in the host medium and a is the size of the inclusion. f is the volume fraction and a_1 (b_1) is the first order Mie coefficient describing electric-like (magnetic-like) dipole scattering. Then these effective parameters are used in classical Mie theory to compute the scattering of the nanoclusters and correctly describe the Huygens features exhibited by the system.

3. APPLICATION TO PULSE COMPRESSION

An application will also be described, by considering the interaction of a pulse of light with these sources, which show that femtosecond pulses can be compressed so as to compensate for the strong chromatic dispersion undergone by ultra-short pulses when they propagate through optical components. As noted by Decker *et al.* [1], this is due to the strong group velocity dispersion provided by the Hyugens sources near the simultaneous resonance of the electric and magnetic dipoles.

ACKNOWLEDGMENT

This work is supported by the LabEx AMADEus (ANR-10-LABX-42) in the framework of IdEx Bordeaux (ANR-10-IDEX-03-02), France.

REFERENCES

1. M. Decker *et al.*, "High-Efficiency Dielectric Huygens' surfaces" *Adv. Opt. Mat.*, Vol. 3, No. 6, 813–820, 2015.
2. Y. Tang *et al.*, "All-dielectric metasurface analogue of electromagnetically induced transparency," *Nat. Comm.*, Vol. 5, 5753, 2014.
3. C. Wu *et al.*, "Spectrally chiral silicon metasurfaces on infrared Fano resonances," *Nat. Comm.*, Vol. 5,3892, 2014.
4. V. N. Manoharan, "Solid spheres confined by liquid droplets: geometry, physics, and physical chemistry," *Solid State Comm.*, Vol. 139,557–561, 2006.
5. http://www.eng.auburn.edu/users/dmckwski/scatcodes/
6. O. R. Musin, and A. S. Tarasov, "The strong thirteen spheres problem," *Discrete and Computational Geometry.*, Vol. 48,128-141, 2012.

DNA-mediated self-assembly of plasmonic nanocavities

M. Pilo-Pais[1], **F. Nicoli**[1], **C. Argyropolous**[2], **A. Högele**[1], **and T. Liedl**[1]

[1]Faculty of Physics and Center for NanoScience (CeNS), Ludwig-Maximilians-Universität (LMU), Germany
[2]Department of Electrical and Computer Engineering, University of Nebraska-Lincoln, USA
m.pilopais@lmu.de

Abstract— In this talk, I will discuss our current progress toward assembling DNA-mediated plasmonic nanocavities incorporating single quantum emitters. DNA complementarity allows the controllable placement of individual colloidal quantum dots or fluorescence molecules within closely-spaced metallic nanoparticles. Using this pre-programmable approach, we greatly enhance the emission, and the coupling strength of individual emitters with plasmonic modes. The rational engineering of these self-assembled systems are ideally suited to study plasmon-single exciton interactions.

DNA can be used as a pre-programmable tool to rationally engineer metallic nanoparticles (NPs) with nanometer spacing gaps and tunable plasmon resonance. We have recently shown the feasibility of using DNA origami to fabricate plasmonic cavities able to achieve strong coupling between plasmons and molecular aggregates [1]. Here, we use DNA complementary to place individual quantum emitters, such as colloidal quantum dots and fluorescent molecules, within the NPs cavity. As a proof of concept, we show the placement of single QDs between gold nanoparticles (Fig. 1a) displaying several orders of magnitude emission enhancement compared to individual quantum dots. By varying the NP size, the plasmonic nanocavity resonance is off-tuned in respect to the emitter's emission to prevent quenching. On a second example, we demonstrate the assembly capabilities of the DNA-origami technique to fabricate systems with small mode volumes (Fig. 1b). It has recently been shown that one can achieve strong-coupling between plasmons and individual single emitters using plasmonic cavities [2-3]. Since the mode volume of an open cavity depends on the NP radius R and the gap distance d, $V_{eff} \propto R d^2$ [4], it is desired to use small NPs to increase the coupling-strength g which scales as $g \propto 1/\sqrt{V_{eff}}$. Figure 1b shows an array of 15 nm NPs dimers with nanometer-sized gaps assembled with DNA Origami. The DNA template further allows the placement of individual molecules inside the plasmonic cavity. The flexibility of the design of using DNA as an assembly methodology is an ideal approach to study plasmon - single emitters coupling and to integrate nanocompoents for optical applications.

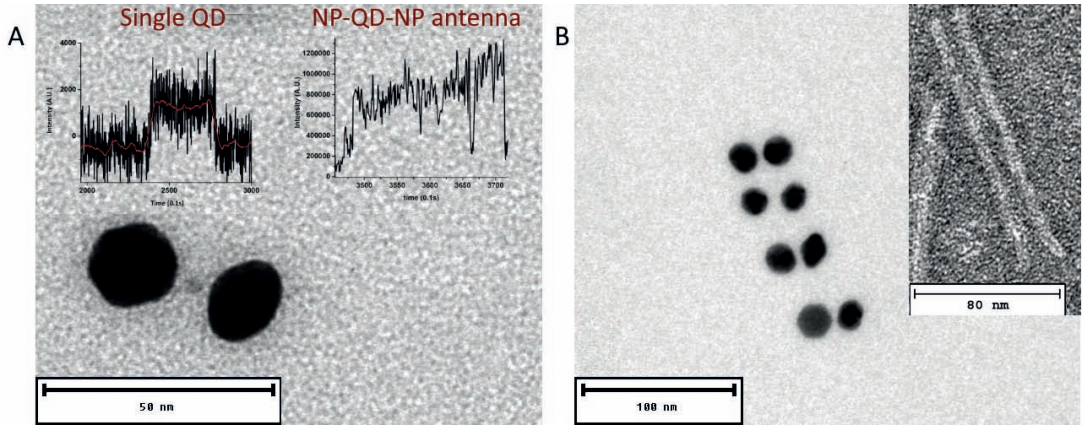

Figure 1: **A)** Individual CdS/ZnS quantum dot placed between 30 nm gold nanoparticles assembled using DNA complementary. The resonance of the cavity is tuned to be blue-shifted in respect to the emitter to avoid quenching. Inset: Fluorescent emission of individual QDs (left) and NP-QD-NP antennas (right). **B)** Array of 15 nm gold nanoparticles assembled using DNA-origami. The DNA template (inset) used for the assembly allows the placement of individual emitters within the plasmonic cavity.

ACKNOWLEDGMENT

This work was funded by the Volkswagen Foundation, the DFG through the Nanosystems Initiative Munich (NIM), and the ERC through the Starting Grant ORCA. A.H. acknowledges funding by the ERC starting grant No. 336749. C.A. would like to acknowledge support by the Office of Research and Economic Development at University of Nebraska Lincoln and the NSF Nebraska MRSEC.

REFERENCES

1. Roller, E.-M., Argyropoulos, C., Högele, A., Liedl, T., and Pilo-Pais, M. (2016). PlasmonExciton Coupling Using DNA Templates. Nano Letters, 16(9), 59625966. http://doi.org/10.1021/acs.nanolett.6b03015
2. Savage, K. J., Hawkeye, M. M., Esteban, R., Borisov, A. G., Aizpurua, J., and Baumberg, J. J. (2012). Revealing the quantum regime in tunnelling plasmonics. Nature, 491(7425), 5747. http://doi.org/10.1038/nature11653
3. Chikkaraddy, R., de Nijs, B., Benz, F., Barrow, S. J., Scherman, O. A., Rosta, E., Demetriadou, A., Fox, P., Hess, O., Baumberg, J. J. (2016). Single-molecule strong coupling at room temperature in plasmonic nanocavities. Nature, 535(7610), 127130. http://doi.org/10.1038/nature17974
4. Santhosh, K., Bitton, O., Chuntonov, L., and Haran, G. (2016). Vacuum Rabi splitting in a plasmonic cavity at the single quantum emitter limit. Nature Communications, 7(May), ncomms11823. http://doi.org/10.1038/ncomms11823

2D materials polaritons

Tony Low
Electrical & Computer Engineering,
University of Minnesota, Minneapolis, USA

Abstract:
In recent years, enhanced light-matter interactions through a plethora of dipole-type polaritonic excitations have been observed in two-dimensional (2D) layered materials. In graphene, electrically tunable and highly confined plasmon-polaritons were predicted and observed, opening up opportunities for optoelectronics, bio-sensing and other mid-infrared applications. In hexagonal boron nitride, low-loss infrared-active phonon-polaritons exhibit hyperbolic behavior for some frequencies, allowing for ray-like propagation exhibiting high quality factors and hyperlensing effects. In transition metal dichalcogenides, reduced screening in the 2D limit leads to optically prominent excitons with large binding energy, with these polaritonic modes having been recently observed with scanning near field optical microscopy. Here, we review recent progress in state-of-the-art experiments, survey the vast library of polaritonic modes in 2D materials, their optical spectral properties, figures-of-merit and application space. Taken together, the emerging field of 2D material polaritonics and their hybrids provide enticing avenues for manipulating light-matter interactions across the visible, infrared to terahertz spectral ranges, with new optical control beyond what can be achieved using traditional bulk materials.

[1] Low T, Chaves A, Caldwell JD, Kumar A, Fang NX, Avouris P, Heinz TF, Guinea F, Martin-Moreno L, Koppens F. Polaritons in layered two-dimensional materials. Nature Materials. 2016 Nov 28.

Short Bio:
Tony Low leads the theory and computational nanoscience group in the department of Electrical & Computer Engineering at the University of Minnesota. Low obtained his doctoral degree from the National University of Singapore in 2008. Prior to joining University of Minnesota, Low worked as an in-house theorist at various experimental groups at Columbia University, Yale University and IBM Thomas J. Watson Research. While at IBM, from 2011-2014, Low served as an industry liaison to various Universities under the Nanoelectronics Research Initiative with the goal of finding the next electronics switch. Low received the several awards from IBM and was recipient of various fellowships.

Ultrafast Spontaneous Emission Sources Based on Plasmonic Nanoantennas

Gleb M. Akselrod

For optical interconnects, a need exists for sources of spontaneous emission (LEDs) that rival or exceed the modulation speeds possible with stimulated emission sources (lasers). In particular, LEDs offer the advantages of being more compact and lower energy due to the lack of threshold. The fundamental limitation to the modulation speed of LEDs is the slow spontaneous emission lifetime of typical semiconductors (~1 ns or more). In this talk I will show how plasmonic nanoantennas can be used to dramatically modify the radiative properties of luminescent emitters. Semincoductor quantum dots integrated into the small mode volume, high-field region of the antenna experience ~1,000-fold enhancement in the spontaneous emission rate, resulting in emission lifetimes of ~10 ps. If excited using electrical injection, this emission lifetime points towards LED light sources with modulation rates up to 100 GHz, equaling or surpassing the performance of semiconductor lasers.

New concepts for energy harvesting and photon management

V_2O_5-Sn bilayer thin film mesh electrode for polymer solar cells

M. Kovendhan[1], K. Sowri Babu[2], and D. Paul Joseph[2,3*]

[1] Center for Condensed Matter Sciences, National Taiwan University, Taipei 10617, Taiwan.

[2] Department of Physics, National Institute of Technology, Warangal, Telangana State – 506 004, India.

[3] Center for Advanced Materials, National Institute of Technology, Warangal, Telangana State – 506 004, India.

[*]corresponding author: paul@nitw.ac.in

Abstract: Electrode modification with suitable metal oxides and or metal buffer layer is an important strategy to improve the light harvesting ability of organic and polymeric solar cells. In this work, square regions of tin (Sn) metal layer over V_2O_5 islands are thermally evaporated onto ITO substrate. The deposited V_2O_5-Sn is expected to act as plasmonic layer improving the carrier collecting ability. Structural, optical and electrical properties of modified electrode are explored and the performance is studied by fabricating polymer solar cells.

Heterojunction polymer solar cells have attracted renowned attention due to advantages like easy fabrication, light weight, potential for low cost solar electricity, portability, compatibility with flexible substrates and scalability [1-5]. However, these devices need improvement in terms of power conversion efficiency, stability and ease of production. Usage of a suitable buffer layer between the active layer and electrode in a polymer or organic solar cell is an important strategy for improving the performance of the cell. Several studies focus mainly on the surface modification of metal oxide by altering their property with self-assembled monolayers by manipulating its morphology, surface energy, etc. Numerous work has been performed in this direction [3, 6-10]. However an exploration by combining metal oxide and a thin layer of metal as a bilayer, especially as a square mesh structure at the active layer-electrode interface is scarce.

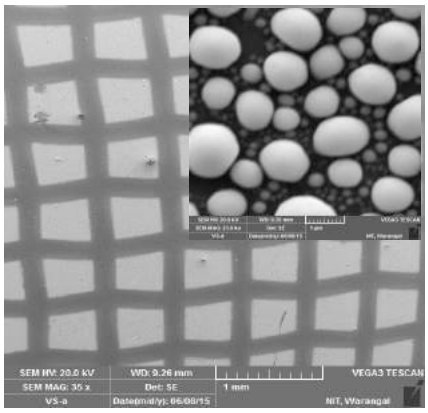

Fig. 1. SEM image of V_2O_5-Sn bilayer mesh on ITO. Inset is the metallic 'Sn' globules.

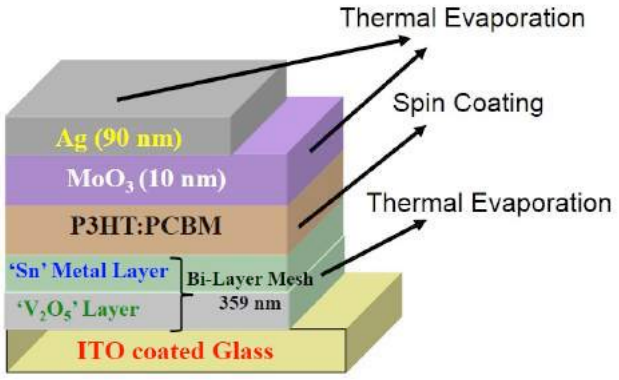

Fig. 2. Device structure of the fabricated polymer solar cell.

Table 1. Electrical transport parameters of the V_2O_5-Sn bilayer mesh film and the measured parameters of the fabricated polymer solar cell device

Carrier concentration (N_b) Cm^3	Mobility (μ) Cm^2/Vs	Resistivity (ρ) Ohm Cm	Conductivity (σ) Ohm Cm^{-1}	V_{OC} (mV)	J_{Sc} (mA/Cm^2)	Fill Factor	Efficiency (%)
1.789×10^{19}	4.251×10^{1}	8.209×10^{-3}	1.218×10^{2}	600	2.24	46.78	0.63

In this work, electrode modification was done by depositing square regions of 'Sn' metal layer over V_2O_5 (Fig. 1) through a shadow mask onto an ITO coated glass substrate by thermal evaporation technique. The deposited metallic tin (Sn) is expected to act as a plasmonic layer to enhance its electron collecting ability. X-ray diffraction showed peaks corresponding to ITO, Sn and V_2O_5. The average thickness of the deposited Sn over V_2O_5 bilayer film was 359 nm as estimated by stylus profiler. The deposited films were having a mesh pattern as seen from the SEM images and the 'Sn' was found to have formed globules. The UV-Vis spectral data showed around 35% transmittance in the visible region. The electrical transport properties of the modified electrode were also obtained by Hall effect measurements (Table 1). We have also fabricated polymer solar cell using the modified electrode showing an efficiency of 0.63% (Fig. 2). These results will be discussed.

Acknowledgements: Financial support for procuring thermal evaporation unit by TEQIP-II sanctioned to NIT-W is acknowledged. The author DPJ thanks SERB for research grant under the file No.: YSS/2014/000191.

REFERENCES

1. W.F. Xu, M.C. Tsai, et al., Efficiency enhancement of organic solar cells using peroxo-polytitanic acid coated silver nanowires as transparent electrodes, *RSC Adv*., Vol. 5, No. 24, 18990-18996, 2015
2. W. Guo, C. Liu, J. Lin and S. Ruan, Improving efficiency of inverted polymer solar cells by introducing inorganic dopants, *Phys. Chem. Chem. Phys*., Vol. 17, No. 12, 7960-7965, 2015.
3. J.L. Lan, S.J. Cherng et al., The effects of Ta_2O_5-ZnO films as cathodic buffer layers in inverted polymer solar cells, *J. Mater. Chem. A*, Vol. 2, No. 24, 9361-9370, 2014.
4. J.W. Kim, Y. Suh, et al., A nano-grid structure made of perovskite $SrTiO_3$nanowires for efficient electron transport layers in inverted polymer solar cells, *Nanoscale*, Vol. 7, No. 10, 4367-4371, 2015.
5. S. K. Hau, H.L. Yip, A.K.Y. Jen, A review on the development of the inverted *polymer* solar cell architecture, *Polym. Rev*. Vol. 50, No. 4, 474–510, 2010.
6. S. K. Hau, et al., Effect of Chemical Modification of Fullerene-Based Self-Assembled Monolayers on the Performance of Inverted Polymer Solar Cells, *ACS Appl. Mater. Interfaces*, Vol. 2, No. 7, 1892–1902, 2010.
7. Z. Liang, Q. Zhang et al., Effects of the Morphology of a ZnO Buffer Layer on the Photovoltaic Performance of Inverted Polymer Solar Cells, *Adv. Funct. Mater.*, Vol. 22, No. 10, 2194–2201, 2012.
8. S. Park, S.J. Tark, et al., Effects of intrinsic ZnO buffer layer based on P3HT/PCBM organic solar cells with Al-doped ZnO electrode, *Sol. Energy Mater. Sol. Cells*, Vol. 93, No. 6–7, 1020–1023, 2009.
9. J.-L. Lan, Z. Lianga, et al., The effect of $SrTiO_3$:ZnO as cathodic buffer layer for inverted polymer solar cells, *Nano Energy*, Vol. 4, 140–149, 2014.
10. M. Thambidurai, J.Y. Kim, et al., Enhanced photovoltaic performance of inverted organic solar cells with In-doped ZnO as an electron extraction layer, *Renewable Energy*, 66, 433–442, 2014.

Increasing of light absorption in perovskite thin film by utilization silicon nanoparticles

A. Chebykin[1*], E. Tiguntseva[1], A. Ishteev[2], E. Ushakova[1], A. Zalogina[1],A. Tsypkin[1], D. Zuev[1], S.Makarov[1] and A. Zakhidov[1,2,3]

[1]ITMO University, St. Petersburg 197101, Russia

[2]MISiS, Moscow 119991, Russia

[3]Texas University at Dallas, Dallas, USA

[*]corresponding author: chebykin.alexandr@gmail.com

Abstract-We have demonstrated experimentally and theoretically that one can use silicon nanoparticles to significantly enhance light absorption in thin perovskite films. We have compared the cases with nanoparticles embedded into the layer and deposited on the perovskite surface. According to our results, absorption in the film with silicon nanoparticles can be increased up to 39% comparing to the film without nanoparticles. Our results are promissing for development and fabrication highly effective perovskite based optoelectronic devices.

In this work, we have investigated the phenomenon of total absorption growth by embedding in volume or deposition on the surface of perovskite film silicon resonant nanoparticles (NPs). For our experiment we have fabricated perovskite films with embedded silicon NPs by the following method: firstly precursor $MAPbI_3$ and solution of toluene with silicon NPs were applied on substrate, which rotated on spinner (1000-5000 t/min), then film was annealing at the temperature of 100 C up to crystallization of the samples and "black phase" formation. To obtain samples with NPs on the surface we have used laser printing method [1]. For measurement of optical transmission (T) and reflection (R) we used normal incidence of linearly polarized light from a halogen lamp and commercial spectrometer with camera. For transmission measurements, the excitation and collection objective with NA=0.95 and NA=0.7 were used, respectively. For reflection measurement, objective with NA=0.42 was used.

We have performed numerical simulations of absorption spectra in Lumerical FDTD Solution as well. We have shown that the absorption coefficient significantly increases in all spectrum from 650 to 950 nm for the case when NPs deposited on the surface. It was demonstrated numerically that the highest absorption increase is equal to around 39% (it's value of integral enhancement of absorption) for the 2% concentration of NPs with radius 130 nm. For the case of the NPs embedded in the perovskite, the maximum of integral absorption is observed for the radius 150 nm and it's around 17%. From our numerical results, one can conclude that the Si NPs deposition on perovskite film surface is more effective than embedded NPs in the volume. We believe that our results will be useful for improve efficiency of perovskite based optoelectronic devices.

REFERENCES

1. Dmitriev, P.A., Makarov, S.V., Milichko, V.A., Mukhin, I.S., Gudovskikh, A., Sitnikova, A.A., Samusev, A.K., Krasnok, A.E., and Belov, P.A. "Laser fabrication of crystalline silicon nanoresonators from an amorphous film for low-loss all-dielectric nanophotonics," *Nanoscale*, Vol. 8, No. 9, 5043–5048, 2016.

Measuring and Exploiting Optical Anisotropies in Nanophotonic Device Architectures

S.J. Brown, R.A. DeCrescent and J. A. Schuller
Electrical and Computer Engineering Department, UC Santa Barbara, CA, USA
*corresponding author: jonschuller@ucsb.edu

Abstract- Nanophotonic architetures provide an attractive approach for enhancing light-matter interactions. A little-discussed aspect of photonic architectures is the presence of strong anisotropies in the electromagnetic field enhancements. These anisotropies are of particular importance in relation to nanostructured materials that possess intrinsic structure-dependent optical anisotropies. In this talk, we describe a novel class of momentum-resolved spectroscopies that provide new insight into structure-dependent optical properties of thin-film material and discuss approaches to exploit these effects in photovoltaic devices that incorporated nanophotonic enhancements.

We use Fourier imaging techniques to measure or control the momentum distribution of in-coming or out-going light rays respectively[1]. These techniques are applied to test-case organic optoelectronic materials that can be deposited with distinct morphologies depending on processing conditions. Using momentum-resolved photoluminescence, we determine the morphology-dependent orientation of transmission and absorption dipoles[2]. We subsequently demonstrate the use of momentum-resolved reflectometry to perform "model-free" measurements of optical constants[3]. The approach provides precise and accurate optical constants with quantified error estimates, obviating the complications associated with highly model-dependent, multi-parameter spectral fitting procedures used in ellipsometry**.** We conclude by describing ongoing efforts to exploit optical anisotropies to enhance light absorption and emission in nanostructured optoelectronics[4].

Acknowledgements, This work was supported by National Science Foundation CAREER award (DMR-1454260).

REFERENCES

1. Schuller, J.A., Karaveli, S.,. Schiros, T., Keliang, H., Yang, S., Kymissis, I., Shan, J. and Zia, R. "Orientation of Luminescent Excitons in Layered Nanomaterials" *Nature Nanotech.* Vol. 8, 271, 2013.
2. Brown, S.J., Schlitz, R.A., Chabinyc, M.L., Schuller J.A. "Morphology-Dependent Optical Anisotropies in the N-Type Polymer P(NDI2OD-T2)" *Phys. Rev. B*. Vol. 94,165105, 2016.
3. DeCrescent, R.A., Brown, S.J., Schlitz, R.A., Chabinyc, M.L., and Schuller J.A. "Model-blind Characterization of Thin Film Optical Constants with Momentum Resolved Reflectometry". *Opt. Express*. Vol. 24, 28842, 2016.
4. Grotet, R.R., Brown, S.J., Driscoll, J.B., Osgood, R.M., and Schuller J.A. "Morphology-dependent Light Trapping in Thin-Film Organic Solar Cells". *Opt. Express*. Vol. 21, A847, 2013.

High Refractive Index dielectric nanoparticles as enhancers of energy harvesting in solar cells: Geometry considerations.

A. I. Barreda[1], F. González[1], and F. Moreno[1*]
[1]Group of Optics, Department of Applied Physics, University of Cantabria, Cantabria 39005, Spain.
[*]corresponding author: morenof@unican.es

Abstract High Refractive Index Dielectric (HRID) nanoparticles have shown to be an alternative to metallic ones. Here, we analyze the possibility of using them for improving the performance of thin film solar cells by studying their Scattering Directionality Conditions (SDCs) as a function of their shape. We demonstrate that cylinders and cubes are the most promising geometries for redirecting the incident radiation into the photosensitive substrate.

At present, solar energy constitute one of the most important renewable energy sources. Its clean and non-polluting energy can be converted into electricity by photovoltaic devices like solar cells, which have become a powerful alternative for solving the problem of climate change. However, the high manufacturing costs, due to great thicknesses of crystalline silicon wafer, which they are made of, make them no competitive with the actual fossil fuel energy resources. For decreasing expenses, thin-film solar cells have been proposed. One of the main drawbacks of these new configurations is the low absorbance of the incident radiation. To increase it, the use of small metallic nanoparticles on top of the photosensitive surface has been suggested[1,2].

Despite the good response of metallic particles in infrared and visible spectral regions, their inherent ohmic losses make them less effective. High Refractive Index Dielectric (HRID) nanoparticles seems to be a promising alternative to address this issue due to their low losses in the infrared spectral region. In addition, HRID nanoparticles can be used for controlling the direction of the scattered radiation. Under some specific conditions, known as Kerker's conditions[3-9], scattered radiation obtained from a single HRID particle can be concentrated either in the backscattering region or in the forward region. In this work, we analyze the scattering directionality conditions of a silicon nanoparticle as a function of its shape. With this contribution, we will show that cylinders and cubes are the most promising geometries for redirecting the incident radiation into the photosensitive substrate.

Acknowledgements: This research has been supported by MICINN (Spanish Ministry of Science and Innovation, Project No. FIS2013-45854-P). A.I.B. thanks the University of Cantabria for her FPU grant and Foundation IBERDROLA-ESPAÑA for its support through its Research on Energy and the Environment Program.

REFERENCES

1. Catchpole, K.R. and A. Polman, "Plasmonic solar cells," *Opt. Express*, Vol. 16, No. 26, 21793-21800, 2008.
2. Catchpole, K.R. and A. Polman, "Design principles for particle plasmon enhanced solar cells," *Appl. Phys. Lett*., Vol. 93, No. 191113, 1-3, 2008.

3. Kerker, M., et al, “Electromagnetic scattering by magnetic spheres,” *J. Opt. Soc. Am.*, Vol. 73, No. 6, 765–767, 1983.
4. Geffrin, J. M. et al, “Magnetic and electric coherence in forward- and back-scattered electromagnetic waves by a single dielectric subwavelength sphere,” *Nat. Commun.*, Vol. 3, No. 1171, 1-8, 2012.
5. Zambrana-Puyalto, X., et al, “Duality symmetry and Kerker conditions,” *Opt. Lett.*, Vol. 38, No. 11, 1857–1859, 2013.
6. García-Cámara, B. et al, “Directionality in scattering by nanoparticles: Kerker’s null-scattering conditions revisited,” *Opt. Lett.*, Vol. 36, No. 5, 728–730, 2011.
7. Laee, R. A., et al, “A generalized Kerker condition for highly directive nanoantennas,” *Opt. Lett.*, Vol. 40, No. 11, 2645–2648, 2015.
8. Fu, Y. H., et al, “Directional visible light scattering by silicon nanoparticles,” *Nat. Commun.*, Vol. 4, No. 1527, 1-6, 2013.
9. Zhang, Y., et al, “Dielectric spheres with maximum forward scattering and zero backscattering: a search for their material composition,” *J. Opt.*, Vol. 17, No. 105612, 1-4, 2013.

Near-field Imaging of Confined Excitons in Monolayer Semiconductors

Jeongyong Kim[1,2]
[1]Center for Integrated Nanostructure Physics, Institute for Basic Science, Republic of Korea
[2]Department of Energy Science, Sungkyunkwan University, Republic of Korea
[*]corresponding author: j.kim@skku.edu

Abstract- Excitons predominate optical properties of monolayer transition dichalcogenides (1L-TMDs) due to their two-dimensional confined nature. Nanoscale spatial emission profiles of excitons, trions and defect-bound localized excitons in monolayer tungsten disulfide obtained by using near-field imaging, revealing a close correlation between local charge population and the formation of trions.

Monolayer transition metal dichalcogenides (TMDs) have tremendous potential as atomically thin, direct bandgap semiconductors [1]. They are ideal platforms to study two-dimensionally confined exciton systems and can be used as convenient building blocks for quantum photonic devices. They host various exciton complexes of not only neutral excitons also trions and biexcitons consisting of three or four electrons or holes, routinely observable in room temperature. We used near-field photoluminescence (PL) imaging with ~70 nm spatial resolution and identified the nanoscale structural defects of CVD grown monolayer MoS_2, which were not distinguished by conventional confocal PL imaging [2]. we present nanoscale spatial emission profiles of excitons, trions and defect-bound localized excitons in monolayer tungsten disulfide (1L-WS_2) obtained by using near-field scanning optical spectroscopy and imaging techniques with 70 nm spatial resolution [3]. By providing separate profiles of excitons and trions with their spatially varying peak energies, we were able to visualize maps of local trion dissociation energy and the Fermi level, revealing a close correlation between local charge population and the formation of trions.

REFERENCES

1. K. F. Mak, C. Lee, J. Hone, J. Shan and T. F. Heinz, "Atomically thin MoS_2: a new direct-gap semiconductor" *Phys. Rev. Lett.*, **105**, 136805 (2010).
2. Y. Lee, S. Park, H. Kim, G. H. Han, Y. H. Lee and J. Kim, "Characterization of the structural defects in CVD-grown monolayer MoS_2 using near-field photoluminescence imaging" *Nanoscale*, **7**, 11909 (2015).
3. Y. Lee, S. J. Yun, Y. Kim, M. S. Kim, G. H. Han, A. K. Sood and J. Kim, "Near-field Spectral Mapping of Individual Exciton Complexes of Monolayer WS_2 Correlated with Local Defects and Charge Populations" *Nanoscale*, **9**, 2272 (2017).

Efficient Hot-Electron Harvesting by Hyperbolic Metamaterials

Pai-Yen Chen[1] and Mohamed Farhat
[1]Department of Electrical and Computer Engineering, Wayne State University, Detroit, Michigan 48202, USA
[2]Qatar Environment and Energy Research Institute (QEERI), Hamad Bin Khalifa University, Qatar Foundation, Doha, Qatar
[*]corresponding author: pychen@wayne.edu

Abstract- Hot-electron (internal-photoemission) devices have recently emerged as promising candidates for transducing photons into electrical currents, enabling the sub-bandgap photodetection and solar/infrared energy harvesting. However, practical challenges resides in how to improve their poor photoconversion quantum yields and comparatively narrow bandwidth of operation. In this talk, I will present a new hyperbolic metamaterial structure, as a vertically-integrated hot-electron device, for efficiently coupling light into plasmonically-excited hot electrons, which can be efficiently collected with high external quantum efficiency approaching the physical limit. I will theoretically show that this metamaterial-based hot-electron device can exhibit efficient, broadband and omnidirectional photoconversion for infrared and visible light. Finally, I will also discuss how to experimentally realize this metamaterial optoelectronic device with nanofabrication techniques and 2D materials. Results presented here may shed some light on designing energy-efficient photodetectors and energy harvesters beyond the bandgap spectral limit.

Nanophotonics for Light Management in Luminescent Solar Concentrators

Vivian E. Ferry[1*]
[1]Department of Chemical Engineering and Materials Science, University of Minnesota – Twin Cities, Minneapolis, MN 55455 USA
[*]corresponding author: veferry@umn.edu

Abstract-This talk will discuss strategies to improve the performance of luminescent solar concentrators to harvest both direct and diffuse sunlight. We will discuss the combination of nanophotonic light management strategies with different types of luminophores based on their spectral overlap and quantum yield, and show experimental strategies that maintain high quantum yield of nanocrystals in polymer matrices.

Luminescent solar concentrators (LSCs) concentrate both direct and diffuse sunlight onto solar cells, both enabling the use of smaller devices and changing the form factor of the panel for architectural applications. The concentrator consists of a plastic sheet with embedded luminophores and an edge-mounted solar cell; incident sunlight is absorbed by the luminophore, emitted at a longer wavelength, trapped in the concentrator via total internal reflection, and ultimately collected by the photovoltaic device.

Efficient operation requires several highly performing components. First, the luminophore must have a high quantum yield and small overlap between the absorption and emission bands. Second, the luminophore must be soluble and stable in a high-index polymer matrix with desirable mechanical properties, as many luminophores suffer from reduced quantum yields upon integration with polymer matrices. Finally, the emitted light has to reach the edge of the concentrator, avoiding coupling to the escape cone of the waveguide. If the concentrator is intended as a window replacement, then it must be made sufficiently transparent for daytime use, whereas if it is intended as a different type of architectural panel or in non-architectural applications the surrounding mirrors must be low enough loss to promote collection at the edge by the solar cell.

This presentation will discuss several ways where photonic structures are useful to overcome the limitations of luminophores. First we will discuss strategies for core-shell CdSe/CdS luminophores, which have high quantum yields in solution, somewhat reduced quantum yields in the polymer matrix, narrow emission bands, and small overlap between absorption and emission. In this case, integrating a one-dimensional spectral filter on the front surface traps light that would otherwise be lost to the escape cone, but these trapped photons propagate at steep angles and are frequently lost to other processes before reaching the edge. We show that metasurfaces that shift the angle of the propagating photons are one way to overcome this problem. Our calculations indicate that this design achieves equivalent performance from 76% quantum yield nanocrystals as a standard LSC with 99% efficient nanocrystals. We will describe the design of this surface in more detail, including the desired angles of propagation. We will then discuss other ways to integrate photonics into these LSCs, including modifying the angles of emission from the luminophore, and strategies for other luminescent materials with broad emission spectra but negligible reabsorption losses.

Finally, we will discuss our recent experimental work on embedding luminophores into various polymer

matrices while maintaining high quantum yield and radiative efficiency, based on controlling the surface chemistry of the nanocrystals and their subsequent interactions with the polymer matrix.

Acknowledgements. We are grateful to the National Science Foundation CAREER program, award number 1553234.

REFERENCES

1. Connell, R., and V. E. Ferry. "Integrating photonics with luminescent solar concentrators: optical transport in the presence of photonic mirrors," *J. Phys. Chem. C*, Vol. 120, 20991–20997, 2016.
2. Bronstein, N. D., Y. Yao, L. Xu, E. O'Brien, A. S. Powers, V. E. Ferry, A. P. Alivisatos, R. G. Nuzzo, "Quantum dot luminescent concentrator cavity exhibiting 30-fold concentration," *ACS Photonics*, Vol. 2, 1576–1583, 2015.
3. Khan, M. R.., X. Wang, P. Bermel, and M.. A. Alam, "Enhanced light trapping in solar cells with a meta-mirror following generalized Snell's law," *Opt. Express*, Vol. 22, A973 – A985, 2014.

A New Type of Heat Engine, Using LED's as Refrigerators

Eli Yablonovitch
Electrical Engineering and Computer Sciences Dept., University of California, Berkeley, USA

Abstract- Very efficient light emitting diodes (LED's), surprisingly, do actually become cold as they operate, since LED light carries away entropy. This cooling requires superb LED efficiency. Of course, we now know that the photovoltaic cell and the LED are really the reciprocal of one another. The slogan: "A great solar cell has to be a great LED" has led to all the new solar cell efficiency records.

What if the electrical output of a photovoltaic cell drives an LED, and the LED light in turn drives the photovoltaic cell? You might fear that it would become a perpetual motion machine. Instead it becomes a heat engine in which a small amount electricity can efficiently provide refrigeration, or conversely a small temperature difference can generate electricity. Such an electro-luminescent heat engine, in which photons are the working fluid, can be more efficient than the competing science, thermo-electrics, in which electrons are the working fluid.

A two-resonance tapping cavity for an optimal light trapping

Jordi Martorell[1, 2*] **Quan Liu,**[1] **Pablo Romero-Gomez,**[1] **Paola Mantilla-Perez,**[1] **Silvia Colodrero,**[1] **and Johann Toudert**[1]

[1]ICFO-Institut de Ciencies Fotoniques, The Barcelona Institute of Science and Technology, 08860 Castelldefels (Barcelona), Spain

[2]Departament de Física, Universitat Politècnica de Catalunya, 08222 Terrassa, Spain

[*]corresponding author: jordi.martorell@icfo.es

Abstract- A two-resonance tapping cavity is proposed and implemented to obtain an effective broadband light trapping in the absorber layer of thin-film solar cells. When this new optical cavity is applied to high performance polymer cells, an optimal light harvesting enhancement is achieved. This leads to a ~20% increase in power conversion efficiency, corresponding to a record performing polymer cell.

Light trapping and guiding in thin films is essential to obtain energy-efficient light harvesting devices. Several decades ago following a ray optics approach, Yablonovitch established that the maximum light trapping in a dielectric slab is equal to $2n^2$ times the incident intensity, being n the refractive index of the slab.[1] To achieve this limit requires a random texturing of both film surfaces to produce a random distribution of light regardless of which direction the beam is coming in.[1,2] Over decades of thin film photovoltaic technology development, many different physical phenomena have been considered and partial success has been reached when a certain degree of light trapping has been demonstrated. However, light trapping or confinement has never been shown to be critical to achieve record performing thin film cells.

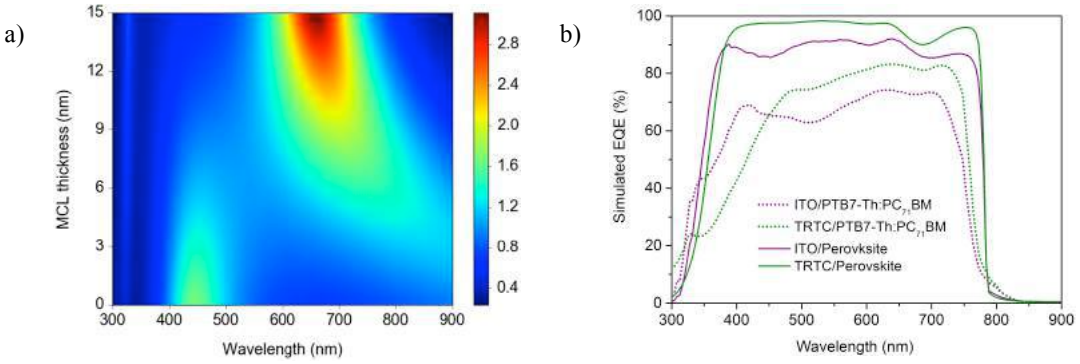

Figure 1 a) Field amplitude inside the cavity. b) External quantum efficiency (EQE).

In this work, we implement a two resonance tapping cavity (TRTC) to reach an optimal broadband confinement for electromagnetic waves.[3] We demonstrate that the combination of an insulator cavity layer with a metal cavity layer (MCL) leads to the formation of an optical cavity that can exhibit a resonant character at two non-harmonic frequencies (See Fig. 1a). The increase in energy storage capacity relies in the inharmonicity of the electromagnetic field propagation within such TRTC. We demonstrate that the energy confinement capacity

seen is to a large extent independent of the material composition or thickness of the active layer, and can be applied to reach efficiency limit performances for any kind of thin film photovoltaic device. We experimentally measured record efficiencies for the PTB7-Th polymer cell and predicted that in the event the TRTC is applied to perovskite cells, as seen in Figure 1b, the EQE would closely match the IQE for a broad frequency range.

REFERENCES

1. Yablonovitch E, *J Opt Soc Am* 1982; **72**: 899-907
2. Yu ZF, Raman A, Fan SH, *Proc Nat Acad Sci USA* 2010; **107**: 17491-17496
3. Q. Liu et al., to be published in *Adv. Energy Materials*

Time-Delayed Interaction of an Excitonic Dimer System with Phonons: non-Markovianity through Memory Effects.

M. Farhat[1*], S. Kais[2], and F. H. Alharbi[1,3]

[1]Qatar Environment and Energy Research Institute (QEERI), Hamad Bin Khalifa University, Qatar Foundation, Doha, Qatar

[2]Department of Chemistry, Department of Physics and Birck Nanotechnology Center, Purdue University, West Lafayette, IN 47907, USA

[3]College of Science and Engineering, Hamad Bin Khalifa University, Doha, Qatar

[*]corresponding author: mfarhat@hbku.edu.qa

We utilize a modeling of non-Markovian open quantum systems, consisting of an excitonic dimer system that displays memory effect due to time delayed interaction with a bath of phonons. We, thus study the effect of delay in the interaction on photosynthetic coherence and excitons dynamics in the time domain investigated experimentally (few hundred femtoseconds). In particular, we show that for high time delays, the coherence is maintained for longer periods. Additionally, if delay is taken into account, coupling to environment can be tuned to lower values, unlike in previous studies.

Hybrid Plasmonics with Quantum Confined Materials and Devices

Superradiance and PT symmetry with plasmonic waveguides

Ying Li and Christos Argyropoulos*

Department of Electrical and Computer Engineering, University of Nebraska-Lincoln, Lincoln, Nebraska, 68588, USA

*corresponding author: christos.argyropoulos@unl.edu

Abstract-Plasmonic waveguides exhibit an effective epsilon-near-zero operation in their cut-off wavelength and Fabry-Perot resonances at lower wavelengths. In this work, we demonstrate a plasmonic route to control coherent collective spontaneous emission effects, such as superradiance and subradiance, from emitters located inside plasmonic waveguides. Our findings will be important to optical computing systems, quantum entanglement of qubits, and efficient sensors. In addition, we will demonstrate a nanoscale parity-time symmetric nanophotonic device, designed based on gain medium embedded inside the plasmonic waveguide nanochannels.

In recent years, realistic metamaterials with effective epsilon-near-zero (ENZ) permittivity response have raised increased interest, especially due to their peculiar transmission properties that provide, in principle, infinite phase velocity combined with anomalous impedance-matching phenomena. This anomalous quasi-static response can be theoretically and experimentally obtained using narrow plasmonic waveguides operating at their cut-off wavelength [1]. Uniform phase distribution and large field enhancement is achieved inside the nanochannels of these narrow waveguides and has been used to enhance fluorescence, squeeze and tunnel light, and boost optical bistability. Moreover, large and uniform local density of states obtained inside the nanochannels are ideal conditions to increase the collective spontaneous emission rate of several emitters [1].

As a collective spontaneous emission response, superradiance has attracted much attention leading to several intriguing applications in laser, sensor, and optical communication technologies [2]. It was proposed that the radiation intensity emitted by N atoms placed in subwavelength distances was proportional to N^2 instead of the usual N. This phenomenon is based on the constructive interference between emitted waves, which can improve the directivity and coherence of the total emitted radiation by an ensemble of quantum emitters. However, this photonic coherent emission effect can be achieved only when the neighboring quantum emitters are placed very closely to each other at highly subwavelength distances, which limits its practical applications.

In this talk, we will present a way to obtain superradiance effects from emitters separated by distances comparable and even larger to the operating wavelength. The superradiance mode is stimulated by a collection of two-level emitters embedded in plasmonic waveguides. The waveguide unit cell is shown in the inset of Fig. 1(a), which is composed of a narrow rectangular glass slit carved in a sliver (Ag) screen. The transmission and reflection spectrum of this waveguide is illustrated in Fig. 1(b) (black lines) and this structure can sustain an ENZ resonance at its cut-off wavelength (λ=1012 nm). At this wavelength point, the electric field enhancement is large and homogeneous along the nanochannel [1]. Below the cut-off wavelength, the first-order Fabry-Perot (FP) resonance (λ=922 nm) is obtained with a typical standing wave field pattern distribution [1]. We use classical electromagnetic calculations to compute the normalized decay factor γ of a pair of emitters embedded inside the channel at ENZ and FP resonances. As it is shown in Fig. 1(a), perfect superradiance (γ=2) is obtained at the ENZ wavelength that is independent of the emitter's separation distance d. Interestingly, the superradiant

mode (γ >1) can be dynamically changed to a subradiant mode (γ <1) at the FP resonance by changing the emitters' separation distance and location. We will also present the collective emission of N emitters uniformly located inside the plasmonic channel at the ENZ wavelength. Our findings can be applied to improve the response of optical computing systems and quantum communications, such as the efficient control of long distance entanglement between qubits [3].

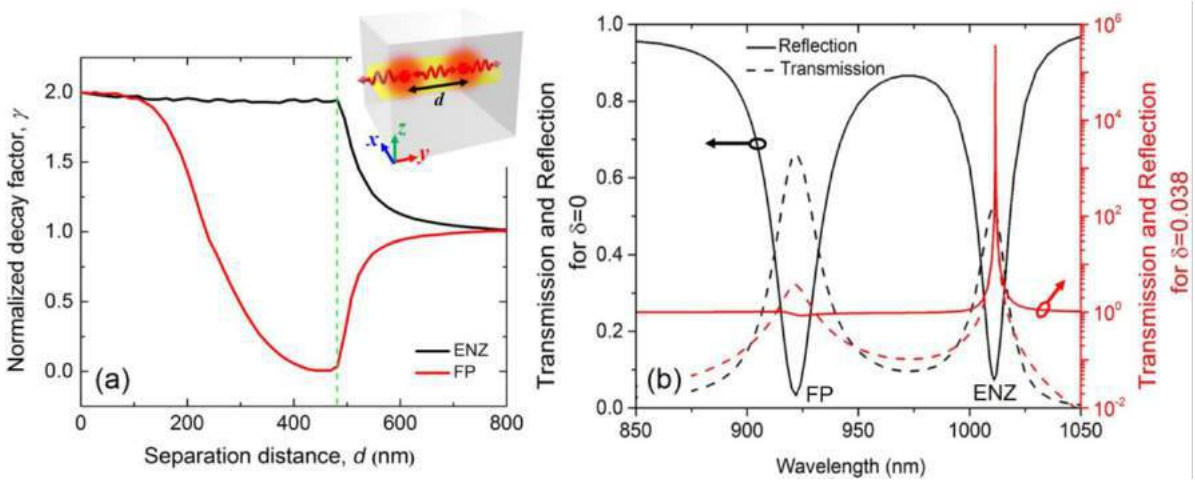

Figure 1 (a) Normalized collective decay factor γ versus separation distance d at ENZ and FP resonances. The green dashed line depicts the end of the waveguide. The inset shows the plasmonic waveguide unit cell loaded with a pair of emitters. (b) Transmission and reflection of the plasmonic waveguide as a function of the incident wavelength with (red) and without (black) gain.

Our plasmonic waveguide can also be used to design a nanoscale parity-time (PT) symmetric system when we introduce an active dielectric material ($\varepsilon = \varepsilon_{glass}+i\delta$) with small gain permittivity coefficient δ inside the nanochannel. The optical loss is introduced by the negative imaginary part of the silver screen permittivity. The effect of introducing gain is more than loss compensation and the strong interplay between loss and gain inside the waveguide will lead to super scattering at exceptional points obtained close to the ENZ resonance. As the red lines demonstrate in Fig. 1(b), giant and narrow transmittance and reflectance can be simultaneously obtained at the exceptional ENZ point (λ=1011.66 nm), when we introduce a small gain coefficient δ=0.038. During our talk, we will also present unidirectional perfect absorption and lasing when the proposed active waveguide is illuminated by two counter-propagating plane waves. Our findings provide a new platform to design nanoscale optical modulators, low threshold nanolasers, and unidirectional coherent perfect absorbers. The addition of optical nonlinearities in this PT-symmetric system will also be studied leading to strong optical bistability and switching around the ENZ exceptional point resonance.

REFERENCES

1. Li, Y., and Argyropoulos, C., "Controlling collective spontaneous emission with plasmonic waveguides," *Opt. Express*, Vol. 24, No. 23, 26696–26708, 2016.
2. Scully, M. O., and Svidzinsky, A. A., "The Super of Superradiance," *Science*, Vol. 325, No. 5947, 1510–1511, 2009.
3. Gonzalez-Tudela, A., *et al*., "Entanglement of Two Qubits Mediated by One-Dimensional Plasmonic Waveguides," *Phys. Rev. Lett*., Vol. 106, No. 2, 20501, 2011.

Molecular optomechanical effects in Surface Enhanced Raman Spectroscopy

R. Esteban[1,2], M. K. Schmidt[3], T. Neuman[3], A González-Tudela[4], G. Giedke[1,2], J. Aizpurua[1,3]

[1]Donostia International Physics Center, 20018 Donostia-San Sebastián, Spain

[2]IKERBASQUE, Basque Foundation for Science, 48013 Bilbao, Spain

[3]Centro de Física de Materiales CSIC-UPV/EHU, 20018 Donostia-San Sebastián, Spain

[4]Max-Planck-Institut für Quantenoptik, 85748 Garching, Germany

[*]corresponding author: ruben_esteban@ehu.eus

Abstract We discuss a novel quantum description of Surface Enhanced Raman Spectroscopy based on the framework of quantum optomechanics. This theory allows interpreting recent experiment and predicts new effects such as unexpected non-linearities, large correlations of the emitted photons and rich control of the population of molecular vibrational states, which may open new possibilities in the study of molecules coupled with plasmonic systems.

Surface Enhanced Raman Spectroscopy (SERS) exploits the strong plasmonic resonances supported by metallic nanoparticles to enable Raman studies of very small quantities of analyte, up to single molecules. Normally, SERS studies use a simple model based on the classical plasmonic response. However, recent work has established a close connection between SERS and quantum optomechanic systems[1]. This new perspective, combined with recent advances on experimental control of Raman systems[2,3], offer the promise of revealing new phenomena and applications.

We use a Quantum Electrodynamics (QED) treatment based on this new framework to study both off-resonant and resonant SERS. The system considered is sketched in Fig. 1a, where the interaction between the vibrations of a molecule and a laser is mediated by a plasmonic cavity. For off-resonant SERS, no electronic level is excited resonantly and the Hamiltonian is characterized by a coupling term $\mathbf{H_I=-g a^\dagger a(b^\dagger+b)}$, where **g** is the coupling strength and $\mathbf{a^\dagger}$ ($\mathbf{b^\dagger}$) and **a**(**b**) are the rising and lowering operators, respectively, of the plasmonic mode (molecular vibrations) [1,4]. This description is identical to the one found in standard quantum optomechanical systems, but with very different values of the parameters. Notably, the large plasmonic losses can be compensated by huge coupling strengths, leading to large cooperatives and potentially the exploration of optomechanic regimes not available to other alternatives.

Our quantum model captures the emission at smaller (Stokes) and larger (anti-Stokes) energies of the incoming laser (Fig. 1b-c), and allows studying the relative influence of thermal pumping (vibrations populated due to the temperature) and vibrational pumping (vibrations excited via the Stokes process). We find an unexpected non-linearity of the Stokes signal for very intense lasers, which may be of interest for experiments. In contrast with typical situations in quantum optomechanics, this non-linearity is found also when the laser is tuned to the plasmon frequency. Last, we analyze the correlations between Stokes and anti-Stokes photons and find that, not only very large correlations, but even non-classical states may be reachable. We demonstrate the usefulness of our model by applying it to pico-cavities at cryogenic temperatures, formed due to wandering of gold atoms in nanometer gaps[5]. These picocavities allow to excite single vibrations, and are characterized by

very large optomechanical coupling strengths, in the order of 10s of meV.

Similarly, resonant SERS accepts a description typical of hybrid optomechanics[6]. In this picture, the electronic level of the molecule couples with the plasmon via a Jaynes-Cummings term, and the Franck-Condon approximation is used to model the interaction between molecular vibrational and electronic levels. We find interesting effects, such as avoided crossings in the emitted spectra of, when the sidepeaks of the Mollow triplet associated with the electronic levels cross the Raman lines. The resulting interaction also allows a particularly flexible control of vibrational populations, which may eventually find applications for photochemistry.

We thus show how going beyond standard descriptions to consider the quantum nature of the molecule-plasmon coupling in SERS experiments can open new perspectives in Raman spectroscopy, and may also offer an interesting platform for quantum optomechanical studies

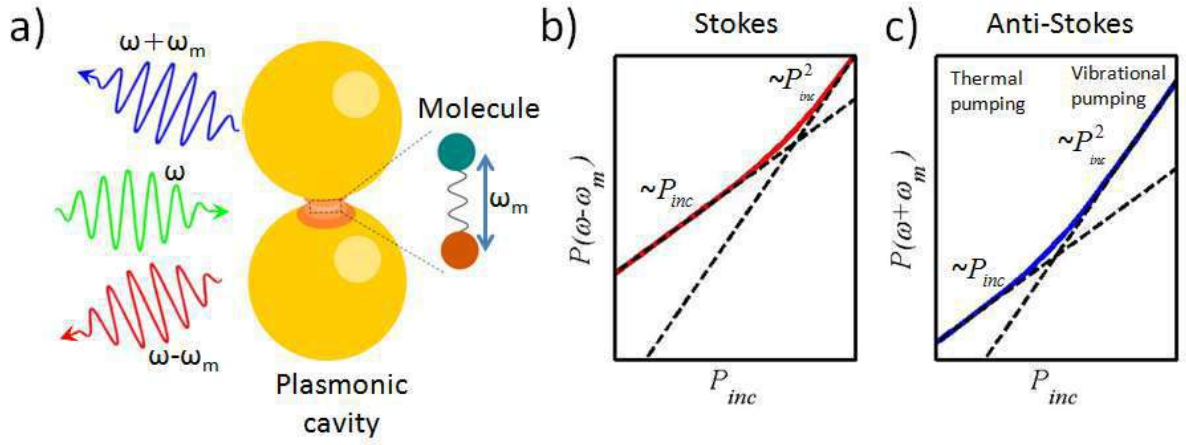

Figures 1: (a) Scheme of the SERS system being studied, where an incoming photon at frequency ω excites a plasmonic cavity coupled with a molecule. The molecular vibrations of ω_m frequency lead to the emission of Raman photons at ω-ω_m (Stokes) and ω+ω_m (anti-Stokes). Sketch of the Evolution of the **(b)** Stokes and **(c)** Anti-Stokes signal with laser power (P_{inc}), for off-resonant Raman. The quadratic dependence of the Stokes signal with P_{inc} at large intensities is not explained by standard SERS models. The change from linear (at low intensity) to quadratic (at large intensity) dependence of the Anti-Stokes signal with P_{inc} is a signature of vibrational pumping. Dashed black lines indicate linear and quadratic dependences for reference.

REFERENCES

1. P. Roelli, C. Galland, N. Piro, and T. J. Kippenberg. "Molecular cavity optomechanics as a theory of plasmon-enhanced Raman scattering." *Nature nanotechnology* 11, 164 (2016).
2. R. Zhang, Y. Zhang, Z.C. Dong, S. Jiang, C. Zhang, L. G. Chen, L. Zhang, Y. Liao, J. Aizpurua, Y. E. Luo, J. L. Yang. "Chemical mapping of a single molecule by plasmon-enhanced Raman scattering" *Nature*, 498, 82 (2013)
3. W. Zhu and K. B. Crozier, "Quantum mechanical limit to plasmonic enhancement as observed by surface-enhanced Raman scattering" *Nature communications* 5, 5228 (2014)
4. M. K. Schmidt, R. Esteban, A. González-Tudela, G. Giedke, and J. Aizpurua. "Quantum Mechanical Description of Raman Scattering from Molecules in Plasmonic Cavities." *ACS nano* 10, 6291 (2016).
5. F. Benz, M. K. Schmidt, A. Dreismann, R. Chikkaraddy, Y. Zhang, A. Demetriadou, C. Carnegie et al. "Single-molecule optomechanics in "picocavities"." *Science* 354, 726 (2016)
6. T. Ramos, V. Sudhir, K. Stannigel, P. Zoller and T. J. Kippenberg, "Nonlinear quantum optomechanics via individual intrinsic two-level defects". *Physical review letters*, *110*(19), 193602. (2013)

Quantum Defects of Carbon Nanotubes: Room Temperature, 1.5 μm Single Photon Emitters for Quantum Plasmonic Circuits.

H. Htoon
Center for Integrated Nanotechnologies, Materials Physics and Applications Division,
Los Alamos National Laboratory, USA
*corresponding author: htoon@lanl.gov

Abstract- We demonstrate that exciton localization at covalently-introduced aryl sp3 defect sites in single-wall carbon nanotubes provides a route to room-T single photon emission (SPE) with ultra-high single-photon purity (99%) and the shot-noise limited emission stability. The inherent optical tunability of SWCNTs allows us to generate room-T SPE spanning over 1.3 to 1.55 μm telecom band. We integrate these novel quantum emitters with plasmonic and photonic structures toward achieving control on SPE characteristics and realization of quantum photonic/plasmonic functionality.

Quantum light sources capable of supplying a regular stream of single as well as entangled photon pairs lie at the heart of quantum photonic/plasmonic circuits that are needed for realization of novel quantum information technologies. For practical implementation, these quantum light sources are required to operate at room temperature and telecommunication wavelengths. A compatibility with well-established Si/SiO_2 based microelectronic fabrication technology is also highly desirable. Despite intensive research effort, an ideal quantum material system capable of meeting all of these requirements has not emerged as of today. InGaAs self-assembled quantum dot, one of the materials intensely investigated for this purpose can emit quantum light at 1.3-1.5 micron telecommunication wavelength but operate only at cryogenic temperatures. Another material system, nitrogen vacancy centers in diamond, can operate at room temperature but emit quantum light only in visible spectral range.

Last year, we have demonstrated that room T single photon emission at wavelength approaching 1.3 μm can be achieved via introduction of quantum defect states by covalent oxygen functionalization of (6,5) single wall carbon nanotubes (SWCNTs).[1,2] Because these quantum defect states are created relative to the band edge of the SWCNT, it becomes possible to tune this emission to 1.3 and 1.55 μm via functionalizing larger diameter nanotubes that have smaller ban gap. However, oxygen functionalization becomes difficult to control with the increase of tube diameter. Furthermore, the single photon emission of these oxygen dopant states also becomes unstable at room temperature. As a result, long-desired goal of establishing room-T single photon emission in telecommunication wavelength remain unfulfilled.

Here in this work, we utilize highly controllable aryl diazonium reaction chemistry to create quantum defect states on large diameter, (7,5) and (10,3) SWCNTs and *successfully demonstrate room-T single photon emission*

at wavelengths extending from 1.1 μm to the deep center of the telecom C band, 1.55 μm. We achieved 99% single photon purity, a critical milestone for applications such as quantum key distribution, logic gates, and memory. This figure exceeds the best single photon purity reported in other RT single photon emitters such as NV centers (70%-90%). The single photon emission is also characterized with exceptional, shot-noise limited count rate stability. Under strong CW excitation, we achieve count rates up to 120 kHz despite a low combined photon collection and detection efficiency (0.05%) for the near-IR emission of our dopant states. Direct coupling of emission to waveguides,[3] paired with higher efficiency detectors, can make 10-100 MHz count rates feasible. The defect-state emission rates are thus comparable to the high rates obtained from diamond color centers and InAs quantum dots. Correcting for detection efficiency, we estimate a single photon emission quantum efficiency of ~12%.

These results establish quantum defects states of diazonium functionalized SWCNTs as near perfect single photon sources meeting almost all the key technological requirements. Furthermore, SWCNTs' compatibility with variety of soft nano-lithography and assembly techniques present unique opportunity for integration into nano-optoelectronic devices and incorporation into plasmonic and photonic cavities for further enhancement and manipulation of photoluminescence (PL) behaviors. I will present a few results we have attained in this area.

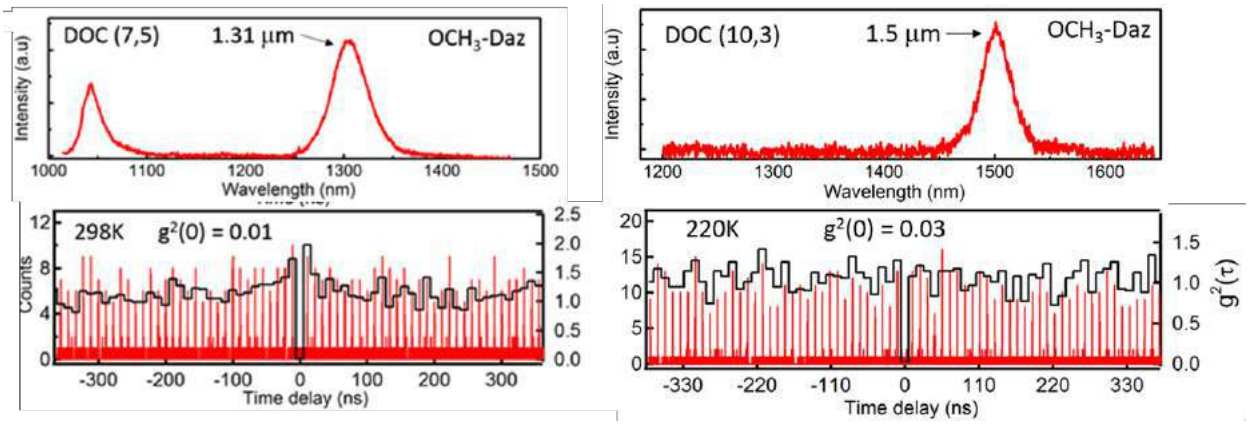

Figure Caption. PL emission spectra (top row) and 2nd order photon correlation trace of 2 quantum defect states

REFERENCES

1. Ma, X.; Hartmann, N. F.; Baldwin, J. K. S.; Doorn, S. K.; Htoon, H. Room-temperature single-photon generation from solitary dopants of carbon nanotubes. *Nature Nanotech*. Vol. 10, 671-675, 2015.
2. Ma, X.; Baldwin, J. K. S.; Hartmann, N. F.; Doorn, S. K.; Htoon, H. Solid-state approach for fabrication of photostable, oxygen-doped carbon nanotubes. *Adv. Funct. Mater.* Vol. 25, 6157-6164, 2015.
3. Khasminskaya, S., *et al*. Fully integrated quantum photonic circuit with an electrically driven light source. *Nature Photon*. Vol. 10, 727-732, 2016.

Metallic/dielectric nanoantennas for high-resolution color printing and giant enhancement of second-harmonic generation

Zhaogang Dong[1,*], **and Joel K. W. Yang**[2,1,*]
[1]Institute of Materials Research and Engineering, A*STAR (Agency for Science, Technology and Research), 2 Fusionopolis Way, #08-03 Innovis, 138634 Singapore
[2]Singapore University of Technology and Design, 8 Somapah Road, 487372, Singapore
[*]corresponding author: dongz@imre.a-star.edu.sg
[*]corresponding author: joel_yang@sutd.edu.sg

Abstract-The fast development of top-down fabrication has enabled investigations towards the interaction mechanism between optical fields and metallic/dielectric nanoantennas. In this talk, we will present our recent work on silicon antenna for high-resolution color printing beyond diffraction limit, where we could achieve a color gamut of more than 100% of sRGB. In addition, we will also present our recent work on metallic nanoantenna for the giant enhancement of photoluminescence (PL) and second-harmonic generation (SHG) from monolayer tungsten diselenide (WSe_2).

The plasmonic response of metallic nanostructures has enabled high resolution color prints beyond the optical diffraction limit, with a resolution of ~100,000 dots per inch (d.p.i.).[1] However, plasmonic colors continue to suffer from poor color vibrancy, with a gamut that occupies only a small subset of perceivable colors on the International Commission on Illumination (CIE) 1931 chromaticity diagram.[2] In this presentation, we will present our recent work on using the local magnetic/electric dipole resonances of silicon nanostructures so as to achieve a CMOS compatible, high-resolution, and a color gamut of more than 100% of sRGB. Moreover, tungsten diselenide (WSe_2) is an attractive two-dimensional (2D) transition-metal dichalcogenide (TMDC) with direct bandgap, and it has great potential for various optoelectronic applications.[3] However, the optical interactions with monolayer WSe_2 and optical fields are very weak due to their characteristic of being atomically thin. In this presentation, we will present our recent work on using metallic nanoantennas to enhance the interaction between monolayer WSe2 and the incidence optical fields, so as to achieve a giant enhancement of both photoluminescence and second-harmonic generation emissions.

Acknowledgements We would like to acknowledge the funding support from Agency for Science, Technology and Research (A*STAR) SERC Pharos project (grant number 1527300025), A*STAR Young Investigatorship (grant number 0926030138), SERC (grant number 092154099), National Research Foundation grant award No. NRF-CRP 8-2011-07, and A*STAR-JCO under project number 1437C00135.

REFERENCES

1. Kumar, K.; Duan, H.; Hegde, R. S.; Koh, S. C. W.; Wei, J. N.; Yang, J. K. W. "Printing colour at the optical diffraction limit," *Nat. Nano.*, Vol. 7, 557-561, 2012.
2. Kristensen, A.; Yang, J. K. W.; Bozhevolnyi, S. I.; Link, S.; Nordlander, P.; Halas, N. J.; Mortensen, N. A. "Plasmonic colour generation," *Nature Reviews Materials*, Vol. 2, 16088, 2016.
3. Ross, J. S.; Klement, P.; Jones, A. M.; Ghimire, N. J.; Yan, J.; Mandrus, D. G.; Taniguchi, T.; Watanabe, K.; Kitamura, K.; Yao, W.; Cobden, D. H.; Xu, X. "Electrically tunable excitonic light-emitting diodes based on monolayer WSe2 p-n junctions," *Nat. Nano.* Vol. 9, 268-272, 2014.

Optically Controlled Molecular Switching: Redox in Plasmonic Nanostructures.

B. de Nijs[1], R. Chikkaraddy[1], F. Benz[1], C. Carnegie[2], S. J. Barrow[2], A. Palma[2], R. Sundararaman[3], P. Narang[4], O. A. Scherman[2], J. J. Baumberg[1]*.

[1]NanoPhotonics Centre, Cavendish Laboratory, Department of Physics, JJ Thompson Ave, University of Cambridge, Cambridge, CB3 0HE, UK.

[2]Melville Laboratory for Polymer Synthesis, Department of Chemistry, University of Cambridge, Lensfield Road, Cambridge CB2 1EW, UK.

[3]Department of Materials Science and Engineering, Rensselaer Polytechnic Institute, Troy, NY, USA.

[4]Faculty of Arts and Sciences, Harvard University, Cambridge, MA.

*corresponding author: jjb12@cam.ac.uk

Abstract Self-assembled plasmonic structures provide enough field-enhancement for single molecule sensitivity in Surface Enhanced Raman Spectroscopy (SERS). We combine this effect with the capability of plasmonic structures to generate high-energy charge carriers to study the oxidation and reduction of single molecules in the plasmonic hot-spot, and demonstrate we can optically control the redox state of these trapped molecules.

Bringing plasmonic nanoparticles close together allows for the coupling of their optical fields. This coupling results in the formation of intense plasmonic hot-spots. Rigid barrel shaped molecular spacers can be utilized to reducibly control the inter-particle spacing between nanoparticles to sub-nm separations.[1] The resulting structure yields field enhancements approaching 3 orders of magnitude.[2] Such high field enhancements allow for sensing guest molecules inside the molecular spacers at the single molecule level by Surface Enhanced Raman Spectroscopy (SERS), and the tracking of their evolution over time.[3]

The non-radiative relaxation pathways of the plasmons provide high energy charge carriers[4] that can be transferred to the molecules captured in the hot-spot. Trapping the charge carriers on molecules sequestered in the spacers results in the oxidation/reduction of these molecules. On account of the high field enhancements in the nanogap, these processes can also be followed in real time via SERS. Here we demonstrate that we can not only follow these processes in real time but also manipulate their redox state.

The redox state of the trapped molecules can be optically controlled by changing the laser intensity, by providing an electron source (see Fig. 1), in this case a molecular reducing agent, for the gold nanostructure to replenish their donated electrons. This reducing agent on itself is not strong enough to reduce the molecules in this configuration. However, switching between a low and high power exposure, after a short delay, switches the molecules' redox state between 2+ and neutral. Demonstrating that optically controlled molecular switches can be made using hot-electron transport between plasmonic structures and molecules.

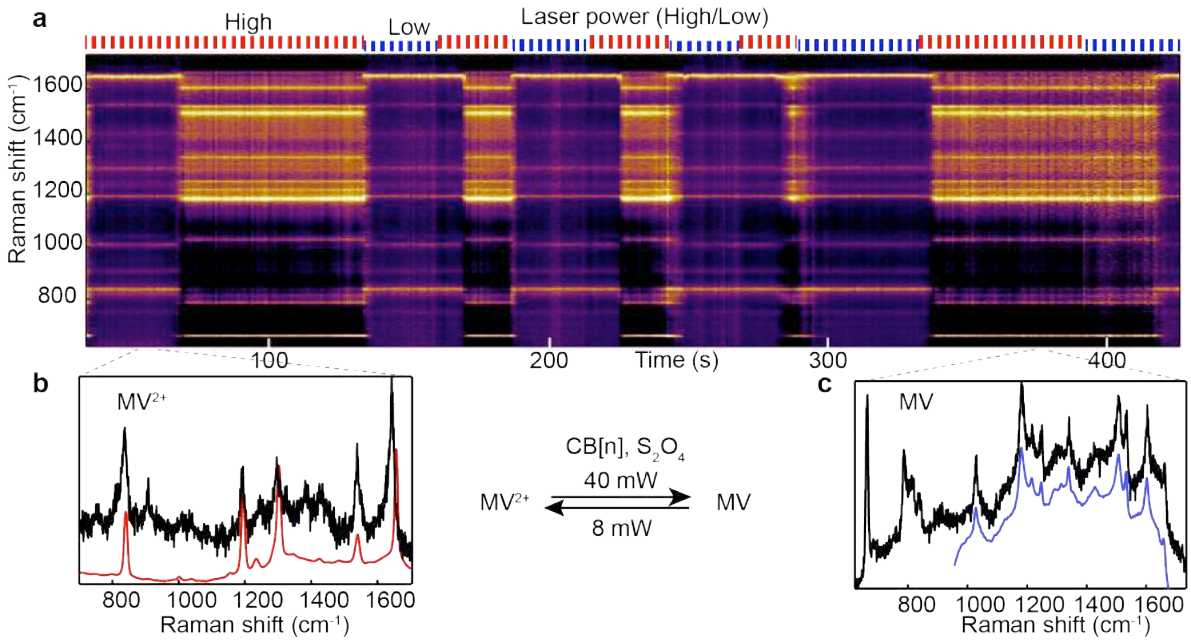

Figure 1: Surface enhanced time scan of self-assembled gold nanoparticles using cucurbit[*n*]uril and a suitable guest (methyl viologen: MV). The redox state of the guest can be switched between MV^{2+} and MV^{0} by switching the laser power. Raman spectra before and after switching match bulk spectra taken of the unreduced and reduced MV respectively.

Acknowledgements, We acknowledge financial support from EPSRC grants EP/G060649/1, EP/I012060/1, EP/L027151/1, ERC grant LINASS 320503. FB acknowledges support from the Winton Programme for the Physics of Sustainability. SJB thanks the European Commission for a Marie Curie Fellowship (NANOSPHERE, 658360). RC acknowledges support from the Dr. Manmohan Singh scholarship from St. John's College. CC acknowledges support from the UK National Physical Laboratories.

REFERENCES

1. de Nijs, B. *et al.* Unfolding the contents of sub-nm plasmonic gaps using normalising plasmon resonance spectroscopy. *Faraday Discuss.* **178,** 185–193 (2015).
2. Benz, F. *et al.* "Single-molecule optomechanics in "picocavities" Science, Vol. 354, No. 6313, 726-729, 2016.
3. Etchegoin, P. G. and Le Ru, E. C. A perspective on single molecule SERS: current status and future challenges. *Phys. Chem. Chem. Phys.* **10,** 6079 (2008).
4. Brongersma, M. L., Halas, N. J. & Nordlander, P. Plasmon-induced hot carrier science and technology. *Nat. Nanotechnol.* **10,** 25–34 (2015).

Quantum and Classical Phenomena in Metal Nanostructures with Hot Spots: Coherent Transfer of Plasmons, Hot Electrons and Heat Generation

Alexander O. Govorov

Department of Physics and Astronomy, Ohio University, Athens, OH, 45701
govorov@ohio.edu

Metal nanocrystals exhibit strong plasmon resonances and have the ability to absorb and scatter light very efficiently. This study concerns special designs of plasmonic nanostructures with electromagnetic hot spots, where the electromagnetic field becomes strongly enhanced. Overall plasmonic nanostructures with hot spots demonstrate strongly amplified optical and energy-related effects.

(1) Using nanoparticle arrays made of different metals, one can transfer plasmonic signals coherently and with small losses [1].
(2) Plasmonic hot spots efficiently generate energetic electrons, which can be used for photochemistry and photodetection [2,3].
(3) Using nanostructures with hot spots, one can strongly enhance optical generation of heat and also confine high photo-temperatures in small volumes [4,5].
(4) Colloidal nanocrystal assemblies with plasmon resonances allow us to strongly enhance chiral optical responses (circular dichroism) of biomolecules and drugs [6,7].

[1] E.-M. Roller, et al., arXiv:1701.04672.
[2] A.O. Govorov, H. Zhang, H.V. Demir and Y. K. Gun'ko, *Nano Today* 9, 85 (2014).
[3] H. Harutyunyan, et al., *Nature Nanotech*. 10, 770 (2015).
[4] A. O. Govorov and H. Richardson, *Nano Today* 2, 20 (2007).
[5] C. Jack, et al., *Nat. Commun.* 7, 10946 (2016).
[6] A. O. Govorov, et al., *Nano Letters 10,* 1374–1382 (2010).
[7] A. Kuzyk, et al., *Nature* 483, 311 (2012).

Strong Coupling Between Individual Plasmonic Metal Nanostructures and Quantum Dots

M. Pelton
[1]University of Maryland Baltimore County, Baltimore, MD, U.S.A.
mpelton@umbc.edu

Abstract-Coupling between plasmons in metal nanoparticles and exctions in quantum dots can lead to novel optical properties and phenomena. We predict that a single colloidal quantum dot can induce nearly complete transparency in the much stronger absorption and scattering of a metal nanostructure, and this induced transparency can be switched on and off with control laser pulses. For more than one quantum dot coupled to the same nanostructure, we predict that laser pulses can induce entanglement among the quantum-dot states.

We have developed a model-Hamiltonian formalism to describe plasmonic metal nanostructures coupled to excitons in quantum dots, taking into account the quantum-mechanical nature of both the excitons and the plasmons. Using this model, we have shown that strong plasmon-exciton coupling leads to novel optical properties and phenomena, beyond the enhancement of optical processes that have been widely investigated so far.

For example, we have predicted that a single colloidal quantum dot has the potential to induce nearly complete transparency in the much stronger absorption and scattering spectrum of a metal nanostructure. Short laser pulses can remove or even reverse the induced-transparency dip, changing it into a superscattering pulse (see Figure 1). If more than one quantum dot is coupled to the same metal nanostructure, laser pulses can induce quantum-mechanical entanglement between the occupation states of the quantum dots. Applying our formalism to an idealized model of a dye-sensitized solar cell, we have shown that there is a fundamental limit to the degree to which plasmons can enhance photocurrent.

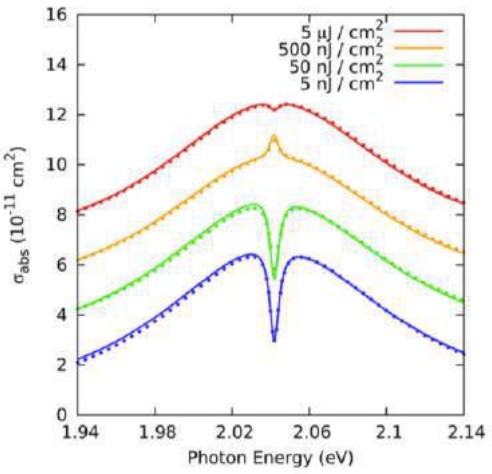

Figure 1. Calculated absorption spectra for a system consisting of a single semiconductor nanocrystal between a pair of gold nanoparticles, for different amounts of energy in an incident laser pulse.

We are currently working on realizing strongly coupled plasmon-exciton systems experimentally. We expect that these systems will enable optoelectronic devices operating at the limit of miniaturization and power consumption, all-optical quantum information processing at the nanoscale, and new paradigms for optical harvesting of solar energy.

Broadband Second-Harmonic Generation based on Active Nonlinear Metasurfaces

J. Yoo and J. Lee*
Ulsan National Institute of Science and Technology, South Korea
*corresponding author: jongwonlee@unist.ac.kr

Abstract-Broadband second-harmonic generation based on Stark-tunable intersubband nonlinearities in multiple-quantum-well structures combined with plasmonic resonators was studied. Theoretically, 5 times broader second-harmonic generation wavelength compared to passive nonlinear metasurfaces and over 0.1% of the maximum conversion efficiency were achieved.

Nonlinear response from optical metasurfaces have opened a new direction in research, with interesting applications such as super-resolution imaging and efficient frequency conversion in subwavelength thin-film with greatly-relaxed phase-matching constraints [1,2]. In a different context, it is well known that intersubband transitions in n-doped multi-quantum-well (MQW) structures may be used to design materials with record second-order nonlinearities up to 4-5 orders of magnitude larger than in traditional bulk nonlinear materials.

Recently, nonlinear metasurfaces with record-high nonlinear optical response up to 1.2×10^6 pm/V for second-harmonic generation (SHG) based on coupling electromagnetic modes in plasmonic nanoresonators with quantum-engineered intersubband nonlinearities in MQW semiconductor heterostructures have been demonstrated [2,3]. However, efficient SHG from the metasurface is only possible near the intersubband resonant frequency due to the resonant characteristics of the intersubband nonlinearities, and thus the operating wavelength for the SHG (SHG bandwidth) is very limited. In this work, we theoretically study active nonlinear metasurfaces for broadband SHG based on Start-tunable intersubband nonlinearities in which the intersubband transition energies in the MQW are modulated from bias voltages applied on the MQW layer. We designed plasmonic resonators to achieve the maximum SHG conversion efficiencies at each bias voltages.

For SHG in the mid-infrared region, we designed a 400nm-thick nonlinear MQW layer that contains 20 repetitions of the $In_{0.53}Ga_{0.47}As/Al_{0.52}In_{0.48}As$ coupled-quantum well structure. One period of the quantum well structure shown in Fig. 1(a) consists of three quantum wells in which the intersubband transition energies between electron subbands for 1 to 2 level (E_{12}) and for 1 to 3 level (E_{13}) can both modulated for bias voltages by quantum confined Stark effect. The modulated intersubband transition energies in the MQW leads to spectral shift of the nonlinear susceptibilities, as shown in Fig. 1(b).

In order to achieve efficient SHG under normal incidence of input pump, the MQW layer is sandwiched between a metal ground plane (bottom contact) and a patterned array of complementary split-ring-resonators (top contact) and the portion of MQW layer without top metal pattern is removed to boost the conversion efficiency (see Fig. 2(a, b))[3]. The nanostructures are designed to induce the enhanced local E_z-field in the MQW layer at both fundamental frequency (FF) ω and SH frequency 2ω for *x*- and *y*-polarized input light, respectively. In this configuration, the highest effective nonlinear susceptibility out of the metasurface is expected for *yxx* polarization combination (the first letter refers to the SH polarization and the last two letters refer to the FF input wave polarization).

For theoretical calculations of SHG conversion efficiencies, we used the input pump intensity of 40 kW/cm^2 for the input pump wavelength range from λ_{FF}=7 to 13μm. The calculated maximum SHG conversion efficiencies and the spectral response of the normalized SH power for the bias voltages from -4V to 4V with 1V step are shown in Fig. 2(c). We obtained a conversion efficiencies over 0.1% for all bias voltages and 5 times broader SHG operation wavelength compared to the passive device (0V). The active nonlinear metasurfaces proposed in this work may have significant practical impact on variety of applications, including broadband frequency up- and down-conversion, spectroscopy and imaging systems requiring broadband operation.

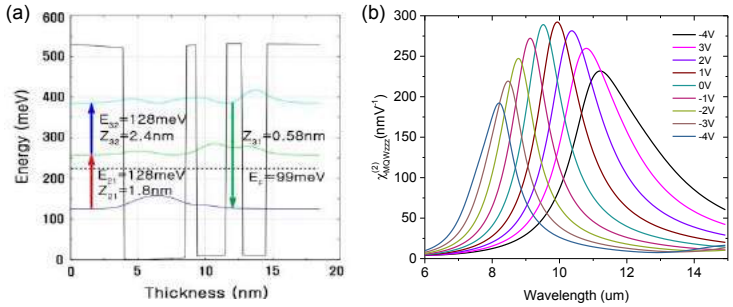

Figure 1. (a) Conduction band diagram of one period of an $In_{0.53}Ga_{0.47}As/Al_{0.48}In_{0.52}As$ MQW structure. The layer sequence (in nm) is **4.0**/4.6/**0.8**/2.2/**1.2**/1.8/**4.0** where barriers are shown in bold, and the first 4.6nm well is n-doped to 3.7×10^{18}cm^{-3}. (b) Calculated intersubband nonlinear susceptibility of the structure for bias voltages from -4V to 4V with 1V step.

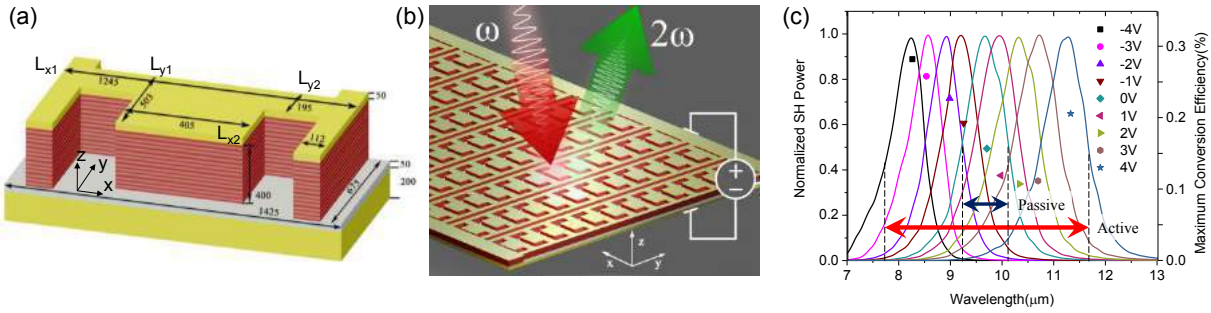

Figure 2. (a) Unit cell of the metasurface with dimensions in nm. (b) Schematic of the active nonlinear metasurface operation. (c) Calculated maximum conversion efficiencies (dot, right axis) and normalized SH power (line, left axis) as a function of wavelength for applied bias voltages.

Acknowledgements, This work was supported by Ulsan National Institute of Science and Technology (UNIST, Grant No. 1.150141.01) and the National Research Foundation of Korea (NRF, Grant No. 2.160257.01)

REFERENCES

1. Pendry, J. B. "Time reversal and negative refraction," *Science*, Vol. 322, 71–73, 2008.
2. Lee, J. et. al., "Giant nonlinear response from plasmonic metasurfaces coupled to intersubband transitions," *Nature*, Vol. 511, 65–69, 2014.
3. Lee, J. et. al., "Ultrathin second-harmonic metasurfaces with record-high nonlinear optical response," *Adv. Opt. Mat.*, Vol. 4, 664-670, 2016.

Visible-frequency Surface Plasmon Resonators and Lasers with High Quality Factors

S. Divitt[1,2], W. Zhu[1,2], J. Strait[1], H. J. Lezec[1] and A. Agrawa[1,2*]
[1]Center for Nanoscale Science and Technology, National Institute of Standards and Technology, Gaithersburg, MD 20899, USA
[2] Maryland Nanocenter, University of Maryland, College Park, MD 20742, USA
[*]corresponding author: amit.agrawal@nist.gov

Abstract - We experimentally demonstrate novel geometries of surface-plasmon-polariton based resonators that exhibit record-high quality factors (>750) in the visible frequency range, and use them to achieve narrow-linewidth lasing.

Coherent optical sources with small device footprints, narrow-linewidth, and room-temperature operation are desirable for potential applications in on-chip optical communications [1]. Surface plasmons, under the form of both stationary localized surface plasmons (LSPs) or propagating surface plasmon polaritons (SPPs), offer an effective route towards achieving lasing at micro- and nano-scale dimensions when integrated with a suitable optical gain media [2]. However, intrinsic absorption and scattering losses have limited the quality factors (Q) associated with plasmonic cavity resonators to <50, thereby limiting the threshold and emission linewidth of plasmonic lasers based on them or requiring low-temperature operation [3, 4]. Recent publications utilizing the template-stripping approach to achieve ultrasmooth metal surfaces have pushed the Q-factors of plasmonic resonators beyond 300, resulting in successful room-temperature lasing operation [5, 6]. In this talk, we will describe recent developments in the field of plasmonic resonators and lasers including our work on experimental realization of plasmon-resonators exhibiting record high Q-factors exceeding 750 in the visible frequency range. The SPP-modes we focus on are bound to the inner metal-dielectric interface of the cylindrical cavity, and exhibit high-Q due to their reflectionless propagation, analogous to the whispering gallery modes in a dielectric resonator. The unique cylindrical open-cavity architecture of the cylindrical plasmonic resonators also makes them suitable for high figure-of-merit optical sensing; for example, the evanescent interaction between analytes and localized electromagnetic fields within a lasing cavity can result in their detection with high sensitivity in a label-free manner [7].

Acknowledgements, S. D., W. Z. and A. A. acknowledge support under the Cooperative Research Agreement between the University of Maryland and the National Institute of Standards and Technology, Center for Nanoscale Science and Technology, Award#70NANB10H193, through the University of Maryland.

REFERENCES

[1] M. T. Hill and M. C. Gather, "Advances in small lasers," *Nat. Photonics* **8**, 908–918 (2014).
[2] P. Berini and I. De Leon, "Surface plasmon-polariton amplifiers and lasers," *Nat. Photonics* **6**, 16–24 (2011).
[3] M. A. Noginov, G. Zhu, A. M. Belgrave, R. Bakker, V. M. Shalaev, E. E. Narimanov, S. Stout, E. Herz, T. Su- teewong, and U. Wiesner, "Demonstration of a spaser-based nanolaser," *Nature* **460**, 1110–1112 (2009).
[4] R. F. Oulton, V. J. Sorger, T. Zentgraf, R.-M. Ma, C. Gladden, L. Dai, G. Bartal, and X. Zhang, "Plasmon lasers at deep subwavelength scale," *Nature* **461**, 629–632 (2009).
[5] S. J. P. Kress, J. Cui, P. Rohner, D. K. Kim, F. V. Antolinez, K.-A. Zaininger, S. V. Jayanti, P. Richner, K. M. McPeak, D. Poulikakos, and D. J. Norris, "Colloidal-quantum-dot spasers and plasmonic amplifiers," arXiv:1611.09792 (2016).

[6] W. Zhu, T. Xu, A. Agrawal, and H. J. Lezec, "Surface-Plasmon-Polariton laser based on an Open-Cavity Fabry-Perot resonator," arXiv:1610.03864 (2016).

[7] R.-M. Ma, S. Ota, Y. Li, S. Yang, and X. Zhang, "Explosives detection in a lasing plasmon nanocavity," *Nat. Nanotechnol*. **9**, 600–604 (2014).

Nanogap-enhanced Electronic Trapping of Quantum Emitters and Nanoparticles

Avijit Barik[1,2], **Xiaoshu Chen**[1], **and Sang-Hyun Oh**[1,2*]
[1]Department of Electrical and Computer Engineering and [2]Department of Biomedical Engineering,
University of Minnesota, Minneapolis, Minnesota 55455, United States.
[*]corresponding author: sang@umn.edu

We demonstrate ultralow-power dielectrophoretic trapping of quantum dots, diamond nanoparticles, and gold nanoparticles using sub-10 nm nanogap electrodes. Dielectrophoresis is a scalable electronic method to trap polarizable objects such as molecules or nanoparticles via gradient forces. Using nanometer-scale gaps, we show rapid trapping and positioning of quantum emitters on a chip using sub-1 V AC bias.

These structures were made using atomic layer lithography, which combines standard lithography and atomic layer deposition (ALD) to create ultra-small gaps at the wafer scale. Using an ultra-bright light source, we are able to monitor the trapping process for single nanodiamond particle in real time.

We will discuss applications of this platform for plasmonics and nanophotonics.

Acknowledgements. This work was supported by the U.S. National Science Foundation (ECCS #1610333).

REFERENCES

1. A. Barik, X. Chen, S.-H. Oh, "Ultralow-power Electronic Trapping of Nanoparticles with Sub-10 nm Gold Nanogap Electrodes," *Nano Letters*, 16, 6317-6324, 2016.
2. Jose, J.; Kress, S.; Barik, A.; Otto, L.M.; Shaver, J.; Johnson, T. W.; Lapin, Z. J.; Bharadwaj, P.; Novotny, L.; Oh, S.-H. "Individual template-stripped conductive gold pyramids for tip-enhanced dielectrophoresis," *ACS Photonics*, Vol. 1, 464-470, 2014.

Transient Extinction in Gold Bipyramids and Doped Oxide Nanostructures

P. Guo[1,2], M.S. Kirschner[1], B.T. Diroll[2], L.X. Chen[1,2], S.K. Gray[2], A.B.F. Martinson[2], X.M. Lin[2], R.P.H. Chang[1]and R.D. Schaller[1,2*]

[1]Northwestern University, United States of America

[2]Argonne National Laboratory, United States of America

[*]corresponding author: schaller@anl.gov

Abstract-We investigate dynamics of three classes of plasmonic structures for applications such as ultrafast switching. Through transient extinction and finite difference time domain simulation, we analyze coherence time of mode-specific acoustic phonon distortions for a series of gold bipyramids. We probe the impact of conformally coated phase change material, VO_2, on a doped oxide nanorod array for broadband infrared optical switching. And finally, we examine transient plasmon responses in colloidally prepared doped oxide nanoparticles that exhibit pump-wavelength dependent spectral responses.

We implement static and transient extinction spectroscopy to probe ensembles of plasmonic structures. In particular, we present efforts on gold bipyramids with particularly narrow ensemble size distributions for a wide range of localized surface plasmon resonance (LSPR) energy, nanofabricated doped oxides with an atomic-layer-deposited phase change material that can be optically switched, and colloidally synthesized doped oxides.

LSPRs arising from metallic nanoparticles offer an array of prospective applications that span chemical sensing to biotherapies. Bipyramidal particles exhibit particularly narrow ensemble LSPR resonances that reflect small dispersity of size and shape but until recently were only synthetically accessible over a limited range of sizes with corresponding aspect ratios. Narrow size dispersion offers the opportunity to examine ensemble dynamical phenomena such as coherent phonons that induce periodic oscillations of the LSPR energy. Here, we characterize transient optical behavior of a large range of gold bipyramid sizes, as well as higher aspect ratio nanojavelin ensembles with specific attention to the lowest-order acoustic phonon mode of these nanoparticles. We report coherent phonon-driven oscillations of the LSPR position for particles with resonances spanning 670 to 1330 nm. Nanojavelins were shown to behave similarly to bipyramids but offer the prospect of separate control over LSPR energy and coherent phonon oscillation period. We develop a new methodology for quantitatively measuring mechanical expansion caused by photogenerated coherent phonons. Using this method, we find an elongation of approximately 1% per photon absorbed per unit cell and that particle expansion along the lowest frequency acoustic phonon mode is linearly proportional to excitation fluence for the fluence range studied. These characterizations provide insight regarding means to manipulate phonon period and transient mechanical deformation

Actively tunable optical transmission through artificial metamaterials offers promise for next-generation nanophotonic devices and metasurfaces. Plasmonic nanostructures and phase change materials have been extensively studied to this end due to their respective strong interactions with light and tunable dielectric constants under external stimuli. Integrating plasmonic components with phase change materials, as described, can facilitate phase change by plasmonically enabled light confinement and meanwhile make use of the high sensitivity of plasmon resonances to the variation of dielectric constant associated with the phase change. The platform described is composed of plasmonic indium tin-oxide nanorod arrays (ITO-NRAs) conformally coated with an ultrathin layer of a prototypical phase change material, VO_2, grown via atomic layer deposition, which enables all-optical modulation of the infrared as well as the visible spectral ranges. The interplay between the intrinsic plasmonic nonlinearity of ITO-NRAs and the phase transition-induced permittivity change of VO_2 gives rise to spectral and temporal responses that cannot be achieved with individual material components alone.

Colloidal doped oxide nanocrystals exhibit large magnitude subpicosecond switching of infrared LSPRs. Such nanocrystals offer a solution-processable, scalable source of tunable metamaterials compatible with arbitrary substrates. Under intraband excitation, these nanocrystals display a red-shift of the plasmon feature arising from the low electron heat capacities and conduction band nonparabolicity of the oxide. Under interband pumping, they show an ultrafast blueshift of the plasmon resonance due to transient increases in the carrier density. Combined with their high-quality factor, large changes in relative transmittance (+86%) and index of refraction (+85%) at modest control fluences (<5 mJ/cm^2) suggest that these materials offer use in all-optical switching, wavefront engineering, and beam steering operating at terahertz switching frequencies.

Acknowledgement. This work was performed in part at the Center for Nanoscale Materials, a U.S. Department of Energy, Office of Science, Office of Basic Energy Sciences User Facility, under Contract No. DE-AC02-06CH11357. We acknowledge support from the Ultrafast Initiative of the U. S. Department of Energy, Office of Science, Office of Basic Energy Sciences, through Argonne National Laboratory under Contract No. DE-AC02-06CH11357.

REFERENCES

1. Kirschner, M. S. *et al.* "Size-dependent coherent-phonon plasmon modulation and deformation characterization in gold bipyramids and nanojavelins," *ACS Photonics*, Vol. 3, 758-763, 2016.
2. Guo, P. *et al.* "Conformal coating of a phase change material on ordered plasmonic nanorod arrays for broadband all-optical switching," *ACS Nano*, Vol. 11, 693–701, 2017.
3. Diroll, B. T. *et al.* "Large transient optical modulation of epsilon-near-zero colloidal nanocrystals," *ACS Nano*, Vol. 10, 10099–10105, 2016.

Fano resonances in optics and microwaves: Physics and application

Explicit demonstration of how path interference can enhance plasmonic nonlinearity

Mehmet Emre Tasgin[1]

[1]Institute of Nuclear Sciences, Hacettepe University, 06800 Ankara, Turkey
metasgin@hacettepe.edu.tr

Abstract— We demonstrate why nonlinear frequency generation, e.g. second harmonic generation and four-wave mixing, can be enhanced via interference of conversion paths. We derive a single equation for the amplitude of the generated nonlinear oscillations. On this equation we show that cancellation in the denominator gives rise to conversion enhancement. We utilize this phenomenon to obtain further enhancement using interference of the multiple conversion paths.

Fano resonances on the linear response are shown to enhance the lifetime of plasmon oscillations and can lead to enhanced florescence of the molecules [1, 2]. Enhancement in the plasmon lifetime leads to the observation of spaser [3] —surface plasmon amplification by stimulated emission of radiation. Fano resonances in plasmonic materials are also shown to enhance the degree of the quantum entanglement [4].

Besides the linear response, Fano resonances are shown to enhance and suppress the nonlinear frequency conversion processes [5, 6]. 2 to 3 orders of magnitude enhancement can be achieved on top of the enhancement due to field localization [6, 7]. We explicitly demonstrate —on an expression for the steady-state SHG amplitude— how the presence of a Fano resonance leads to cancellation of nonresonant terms in a SHG process. Cancellation in the denominator gives rise to enhancement in the nonlinearity. The explicit demonstration, we present here, guides one to a method for achieving even larger enhancement factors by introducing additional coupling terms. The method is also applicable to Fano resonances induced by all-plasmonic couplings [8], which are easier to control in experiments.

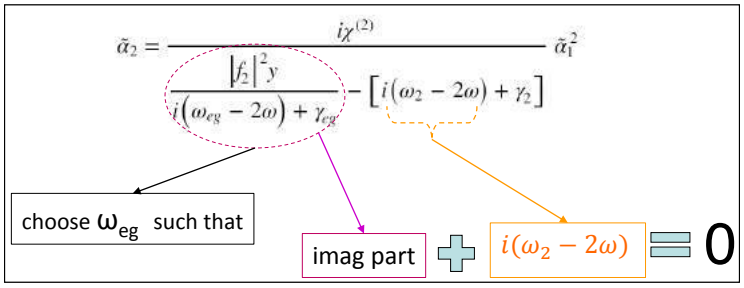

Figure 1: A quick demonstration of how cancellation in the denominator enhances the second harmonic generated plasmons, that is $|\tilde{\alpha}_2|^2$. ω_{eg} (γ_{eg}) is the level spacing (spectral width) of the quantum-emitter (QE), f_2 is the MNP-QE coupling strength, ω_2 (γ_2) is the resonance plasmon frequency (damping rate) of the MNP converter into which SHG take place, y is the population inversion in the QE, $\chi^{(2)}$ is proportional with the nonlinear susceptibility.

ACKNOWLEDGMENT

We acknowledge support from TUBITAK-1001 Project No. 114F170 and Hacettepe University BAP.

REFERENCES

1. M. E. Taşgın, Nanoscale **5**,*Metal nanoparticle plasmons operating within a quantum lifetime*, 8616 (2013).
2. P.Anger, P. Bharadwaj, and L. Novotny,*Enhancement and quenching of single-molecule fluorescence*, Phys. Rev. Lett. **96**, 113002 (2006).

3. M. A. Noginov, G. Zhu, A. M. Belgrave, R. Bakker, V. M. Shalaev, E. E. Narimanov, S. Stout, E. Herz, T. Suteewong and U. Wiesner, *Demonstration of a spaser-based nanolaser*, Nature **490**, 1110 (2009).
4. Guang-Yin Chen and Yueh-Nan Chen, *Correspondence between entanglement and Fano resonance of surface plasmons*, Opt. Lett. **37**, 4023 (2012).
5. D. Turkpence, G. B. Akguc, A. Bek, and M. E. Tasgin, *Engineering nonlinear response of nanomaterials using Fano resonances*, J. Opt. **16**, 105009 (2014).
6. S. K. Singh, M. Kurtulus Abak, and Mehmet Emre Tasgin, *Enhancement of Four-Wave Mixing via interference of multiple plasmonic conversion paths*, Phys. Rev. B **93**, 035410 (2016).
7. M. E. Tasgin, I. Salakhutdinov, D. Kendziora, M. K. Abak, D. Turkpence, L. Piantanida, L. Fruk, M. Lazzarino, Alpan Bek, *Fluorescence Excitation by Enhanced Plasmon Upconversion under Continuous Wave Illumination*, Photonics and Nanostructures - Fundamentals and Applications **21**, 32 (2016).
8. B. C. Yildiz, M. E. Tasgin, M. K. Abak, S. Coskun, H. E. Unalan, and A. Bek, *Enhanced Second Harmonic Generation from Coupled Asymmetric Plasmonic Metal Nanostructures*, J. Opt. **17**, 125005 (2015).

Cross-polarization mode excitation and cross-polarization mode coupling in photonic crystal slabs.

D. A. Bykov[1,2], **L. L. Doskolovich**[1,2], **and N. V. Golovastikov**[1,2]

[1]Samara National Research University, Russia
[2]Image Processing Systems Institute — Branch of the Federal Scientific Research Center "Crystallography and photonics" of Russian Academy of Sciences, Russia
bykovd@gmail.com

Abstract—We study Fano resonances in photonic crystal slabs in conical diffraction mounting. Using two-dimensional coupled-mode theory we obtain simple approximations of the structure's reflection and transmission coefficients. These approximations, which can be interpreted as multivariable generalizations of the Fano line shape, allow to describe a number of important optical effects arising in conical diffraction mounting: cross-polarization excitation of the structure's quasiguided modes, coupling of TE-like and TM-like modes, and emergence of exceptional points.

Photonic crystal slabs (PCS or guided-mode resonant gratings) have found wide use in various optical devices including spectral filters, polarizers, sensors, and pulse shapers. A number of theoretical models were proposed to describe PCS spectra [1, 2, 3, 4]. The simplest models are based on the Fano formula and represent the transmission (reflection) spectrum as a function of incident light frequency ω or in-plane wave vector component k_x [1]. More general approximations consider scattering amplitudes as functions of both ω and k_x [2, 3, 4]. These approximations do not describe a number of important resonant effects arising in conical diffraction mounting when the wave vector of the incident light has two non-zero in-plane components, k_x and k_y.

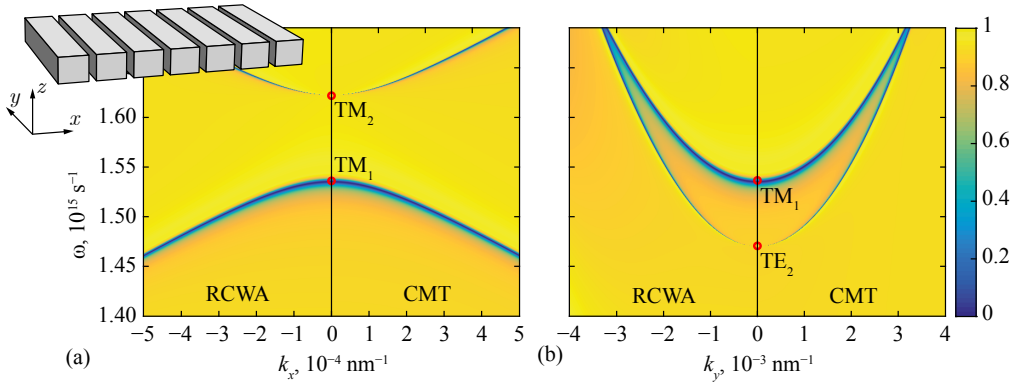

Figure 1: Transmission coefficient $|T(k_x, k_y, \omega)|^2$: calculated using rigorous coupled-wave analysis (at $k_x, k_y < 0$) and approximated using coupled-mode theory (at $k_x, k_y > 0$). Incident wave is TM-polarized. (a) Planar diffraction ($k_y = 0$); (b) conical diffraction at $k_x = 0$. (inset) Photonic crystal slab (period 1000 nm, height 700 nm, fill-factor 4/5; surrounding medium is air, grating permittivity is $\varepsilon = 2$).

Consider 1D PCS shown in the inset of Fig. 1. In this work, we develop 2D spatiotemporal coupled mode theory to describe optical properties of the considered structure. The coupled-mode equations for the PCS in the case of conical mount take the following form [5]:

$$\begin{cases} \dfrac{\partial u}{\partial t} + v_g \dfrac{\partial u}{\partial x} - \dfrac{\mathrm{i}v_g}{2k_1}\dfrac{\partial^2 u}{\partial y^2} + \mathrm{i}\omega_0 u = -\hat{\mathbf{c}}_1 u + \hat{\mathbf{c}}_2 v + \hat{\mathbf{c}}_{e1} f, \\ \dfrac{\partial v}{\partial t} - v_g \dfrac{\partial v}{\partial x} - \dfrac{\mathrm{i}v_g}{2k_1}\dfrac{\partial^2 v}{\partial y^2} + \mathrm{i}\omega_0 v = -\hat{\mathbf{c}}_1 v + \hat{\mathbf{c}}_2 u + \hat{\mathbf{c}}_{e2} f, \\ f_T = t_0 f + \hat{\mathbf{c}}_{t1} u + \hat{\mathbf{c}}_{t2} v. \end{cases} \tag{1}$$

Here ω_0 is light angular frequency; k_1 and v_g are the wave number and group velocity of the mode. To obtain system (1) we considered two paraxial unidirectional wave equations, which describe two counter-propagating modes of the PCS, u and v. These equations are coupled by the terms in the right-hand sides of the equations. The terms contain coupling operators $\hat{\mathbf{c}}$, which are linear differential operators matched with the symmetry of the structure. The third equation of system (1) relates the amplitude of the incident field $f(x, y, z)$ with the amplitude of the transmitted field f_T. A similar equation holds for the reflected field.

We solve system (1) in the Fourier domain to obtain the transmission coefficient of the PCS as a ratio of the transmitted and incident light spectra. The solution has the following form:

$$T = t_0 \frac{v_g^2 k_x^2 - \left(\omega - \omega_{zt} - \eta_{zt} k_y^2\right)\left(\omega - \omega_{p2} - \eta_{p2} k_y^2\right)}{v_g^2 k_x^2 - \left(\omega - \omega_{p1} - \eta_{p1} k_y^2\right)\left(\omega - \omega_{p2} - \eta_{p2} k_y^2\right)}. \quad (2)$$

Here t_0 is non-resonant transmission coefficient, while the other parameters define the ω–k_x–k_y line shape of the resonance. These parameters can be estimated using the rigorous coupled-wave analysis (RCWA) and the scattering matrix approach [4, 5]. Equation (2) provides analytical approximation of the PCS ω–k_x–k_y transmission spectra. This approximation allows to investigate mode excitation conditions and angular tolerances of guided-mode resonant filters.

Figure 1 shows the transmission spectra of the considered PCS. The left part of each subfigure was calculated using the RCWA, while the right part was obtained using approximation (2). It is evident that the obtained formula (2) provides a good approximation of the PCS transmission spectrum. Figure 1(a) shows the transmission spectrum in the case of planar diffraction. In this case no polarization transformation occurs: TM-polarized incident light excites only TM-polarized modes (TM_1 and TM_2). In the case of conical diffraction mounting (Fig. 1(b)) polarization transformation effects result in the excitation of the cross-polarized mode. In this case only one — antisymmetric — cross-polarized mode (TE_2) is exited, due to symmetry considerations.

Another interesting optical effect can be obtained if the frequencies of the TE- and TM-polarized modes are close to each other. In the case of planar diffraction the dispersion curves of these modes are crossing. However, if we introduce non-zero k_y, the cross-polarization light coupling will occur resulting in the coupling of the dispersion curves of the TE and TM modes. To describe this optical effect one can write down the system of coupled-mode equations, similar to Eq. (1). Solution of this system is an analytical approximation of the transmission coefficient as a function of ω, k_x, and k_y. By analyzing this expression one can show that the proper choice of k_x and k_y allows us to obtain an exceptional point. In this case the transmission ω-spectrum will have the pole of the second order: $T(\omega) \approx t + b/(\omega - \omega_p) + c/(\omega - \omega_p)^2$.

In conclusion, we studied optical effects arising in conical diffraction mount in photonic crystal slabs. Let us note, that similar effects can be obtained in the case of planar diffraction of light by *magnetized* PCS. Of particular interest is longitudinal magnetization geometry when magnetization vector is parallel to the y-axis. In this case magnetization of the sample at $k_y = 0$ results in symmetry breaking, analogous to that induced by introducing non-zero k_y for non-magnetized structures. The proposed theory can be used to describe optical and magneto-optical properties of guided-mode resonant gratings. Other applications include spatio-temporal pulse shaping using PCS and guided-mode resonant gratings.

ACKNOWLEDGMENT

This work was funded by the Russian Science Foundation grant 14-19-00796.

REFERENCES

1. Fan, S., W. Suh and J. D. Joannopoulos, "Temporal coupled-mode theory for the Fano resonance in optical resonators," *J. Opt. Soc. Am. A*, Vol. 20, 569, 2003.
2. Shipman, S. P. and S. Venakides "Resonant transmission near nonrobust periodic slab modes," *Phys. Rev. E*, Vol. 71, 026611, 2005.
3. Liu, H. and P. Lalanne "Microscopic theory of the extraordinary optical transmission," *Nature*, Vol. 452, 728–731, 2008.
4. Bykov, D. A. and L. L. Doskolovich "$\omega - k_x$ Fano line shape in photonic crystal slabs," *Phys. Rev. A*, Vol. 92, 013845, 2015.
5. Bykov, D. A., L. L. Doskolovich and V. A. Soifer "Coupled-mode theory and Fano resonances in guided-mode resonant gratings: the conical diffraction mounting," *Opt. Express*, to be published, 2017.

Coherent all-optical information processing on metasurfaces

E. Plum[1*], M. Papaioannou[1], A. Xomalis[1], Y. Jung[1], I. Demirtzioglou[1], E. T. F. Rogers[1], K. F. MacDonald[1], P. Petropoulos[1], David J. Richardson[1], and N. I. Zheludev[1,2]

[1] Optoelectronics Research Centre and Centre for Photonic Metamaterials, University of Southampton, UK

[2] Centre for Disruptive Photonic Technologies and The Photonics Institute, Nanyang Technological University, Singapore

[*]corresponding author: erp@orc.soton.ac.uk

Abstract-Exponentially growing bandwidth requirements of our information society introduce major capacity and energy challenges. We exploit coherent control of light with light on Fano-metamaterials of nanoscale thickness to demonstrate an approach promising massively parallel all-optical information processing at arbitrarily low intensities and with up to 100 THz bandwidth. We experimentally demonstrate parallel all-optical data processing, all-optical pattern recognition and image analysis as well as a fully packaged fiberized metadevice performing several logical operations at GHz bitrates.

Conventional approaches to all-optical information processing rely on nonlinear optical processes to influence one optical signal with another, resulting in tradeoffs between modulation rates and power requirements as fast nonlinearities are weak. However, it is a common misconception that modulation of light with light requires nonlinear optical materials. Consider the interaction between counterpropagating coherent optical signals and a material of substantially sub-wavelength thickness. The thin film can be placed at a node or anti-node of the standing wave formed by the counterpropagating optical signals. At a node, there is no electric field and therefore no light-matter interaction, while constructive interference at the anti-node enhances the light-matter interaction. This linear mechanism allows one optical signal to control absorption of the other almost from 0% to 100%, at arbitrarily low intensities down to the quantum regime and with many THz bandwidth.

We exploit such coherent interaction of light with light on a freestanding gold Fano-metasurface of 60 nm thickness to control intensity of light in spatially distributed optical information channels. Based on optically controlled coherent perfect absorption and coherent transparency of the metasurface (Figure 1), we perform logical operations such as XOR and AND between selected information channels, identify similarities and differences between images, perform pattern recognition by quantifying the similarity between images or data patterns of arbitrary complexity and perform advanced optical image analysis, for example of satellite images to detect the Arctic ice cover, its growth and melting over several decades.

We also demonstrate the first fully integrated data processing metadevice based on coherent interaction of light with light on a gold Fano-metasurface (Figure 2). The fully packaged fibre device is based on a metasurface fabricated on the end face of a polarization maintaining single-mode telecommunications fibre. It can act as an optical logic NOT, XOR and AND gate and has been tested up to GHz frequencies.

In summary, we report a novel, linear approach to all-optical information processing that could deliver orders-of-magnitude improvements in speed and energy efficiency. We illustrate this with a diverse range of experiments ranging from parallel optical processing, recognition and analysis of data and images to

demonstration of a fully integrated fiberized metadevice performing various logical operations at least up to GHz data rates.

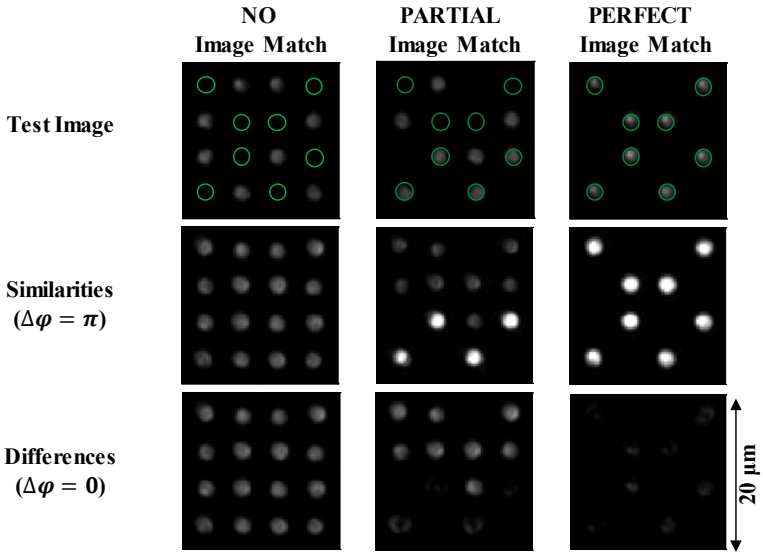

Figure 1. Pattern recognition. Test images (row 1) are compared to a target image (green circles) by projection onto opposite sides of a lossy metasurface using coherent light of 790 nm wavelength. Depending on the optical phase difference Δφ on the metasurface, overlapping image features are perfectly transmitted (row 2) or fully absorbed (row 3), revealing similarities and differences.

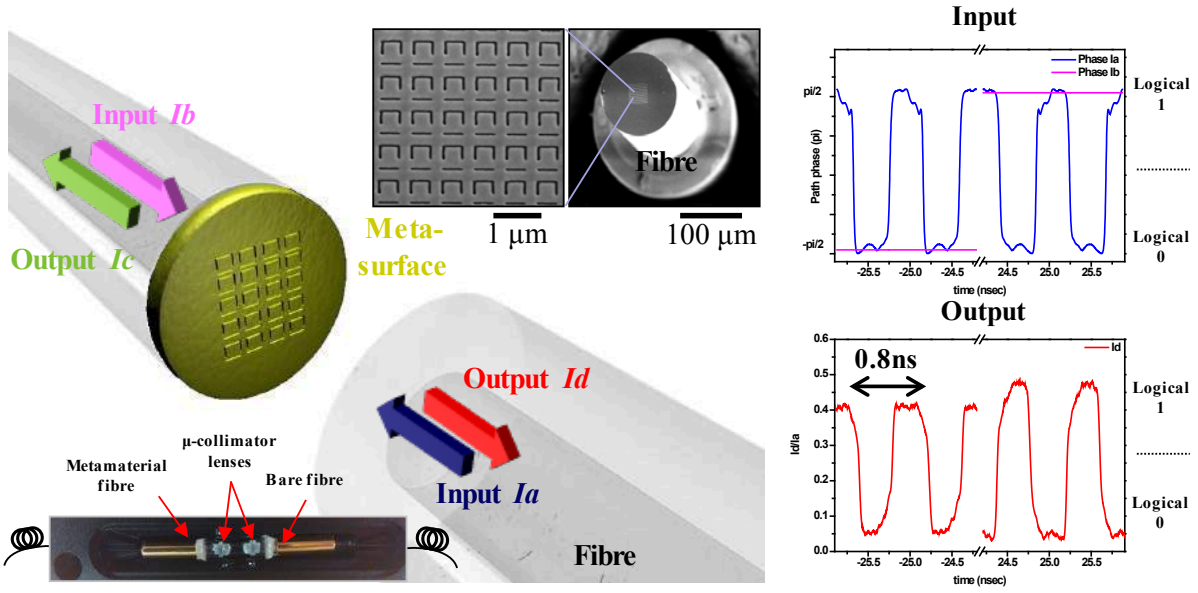

Figure 2. Data processing metadevice based on coherent interaction of input light beams *Ia* and *Ib* on a 70-nm-thick plasmonic metamaterial absorber fabricated on the end face of a single-mode telecoms fibre (1550 nm wavelength). Insets show the nanostructured fibre end and the assembled metadevice. Measurements show an all-optical XOR operation between phase-modulated signals at a data rate of 1.2 GHz: High output (logical 1) results from opposite input bits and low output (logical 0) results from identical input bits.

Mid-Infrared Nonlinear Nanophotonics in Anisotropic Dielectrics Using Surface Phonon Polaritons

I. Razdolski[1], **N. C. Passler**[1], **J. D. Caldwell**[2], **M. Wolf**[1], and **A. Paarmann**[1]

[1]Fritz Haber Institute of the Max Planck Society, Berlin, Germany
[2]Naval Research Laboratory, Washington D.C, USA
alexander.paarmann@fhi-berlin.mpg.de

Abstract— Surface phonon polaritons provide a unique plattform for mid-infrared nonlinear nanophotonics due to broken inversion symmetry and pronounced crystal anisotropy in many of the host materials. Here we experimentally demonstrate resonant enhancement of second harmonic generation due to excitation of localized and propagating surface phonon polaritons in Silicon Carbide. In particular, we observe drastic additional enhancement of the second harmonic response for resonant interactions of the surface phonon polaritons with anisotropic weak phonon modes in subdiffractional nanostructures.

Surface polaritons are the key building block of nanophotonics, since these excitations provide sub-diffractional light localization accompanied by significant optical field enhancements. Many previous studies have focused on surface plasmon polaritons (SPPs) at the surface of noble metals. Recently, an alternative approach was introduced using surface phonon polaritons[1] (SPhPs) which can be excited in the mid-infrared at the surface of polar dielectrics, where optical phonon resonances lead to the negative dielectric permittivity required for the surface polariton formation.

Here, we undertake a first step towards the largely unexplored domain of mid-infrared nonlinear nanophononics. We study the nonlinear-optical response of (i) localized SPhPs in sub-diffractional nanostructures[2] and (ii) propagating SPhPs using Otto-type prism coupling.[3] Employing an infrared free-electron laser as an intense, narrowband, and tunable excitation source for second harmonic generation (SHG) spectroscopy[4] in both approaches, we observe drastic enhancement of the SHG yield for resonant excitation of SPhPs.

We discuss several unique features of the SPhPs as opposed to SPPs, including the large selection of non-centrosymmetric SPhP materials leading to a wide spectral tunability with large bulk nonlinearity. Additionally, many of the host materials are anisotropic, leading to novel effects of resonant interaction of the surface polaritons with anisotropic material resonances. Specifically for 6H-SiC, a Fano-like interaction between zone-folded weak phonon modes and localized SPhPs has been observed in subdiffractional nanostructures.[5] Here, we observe a drastic enhancement of the SHG yield if localized SPhPs are tuned into resonance with zone-folded weak phonon modes.[2] Surprisingly however, no such enhancement is observed for propagating SPhPs excited in the Otto geometry for the same material system.[3] Our results pave the way for efficient control over the mid-infrared nonlinear-optical properties of nanophotonic systems based on anisotropic dielectrics.

REFERENCES

1. Caldwell, J. D. *et al.*, "Low-loss, infrared and terahertz nanophotonics using surface phonon polaritons," *Nanophotonics*, Vol. 4, 1-26, 2015.
2. Razdolski, I. *et al.*, "Resonant Enhancement of Second-Harmonic Generation in the Mid-Infrared Using Localized Surface Phonon Polaritons in Subdiffractional Nanostructures," *Nano Letters*, Vol. 16, 6954-6959, 2016.
3. Passler, N. C. *et al.*, "Second Harmonic Generation from Critically Coupled Surface Phonon Polaritons," *arXiv preprint*, http://arxiv.org/abs/1702.03705, 2017.
4. Paarmann, A. *et al.*, "Second harmonic generation spectroscopy in the Reststrahl band of SiC using an infrared free-electron laser," *Applied Physics Letters* Vol. 107, 081101, 2015.
5. Caldwell, J. D. *et al.*, "Low-Loss, Extreme Subdiffraction Photon Confinement via Silicon Carbide Localized Surface Phonon Polariton Resonators," *Nano Letters* Vol. 13, 3690-3697, 2013.

Fano resonance in Bose-Fermi mixtures

M. V. Boev[1], **V. M. Kovalev**[1,2], **and I. G. Savenko**[3,4,5]

[1]Institute of Semiconductor Physics, Siberian Branch of Russian AoS, Novosibirsk 630090, Russia
[2]Novosibirsk State Technical University, Novosibirsk 630073, Russia
[3]Center for Theoretical Physics of Complex Systems, IBS, Daejeon 34051, Republic of Korea
[4]ITMO University, St. Petersburg 197101, Russia
[5]Nonlinear Physics Centre, Research School of Physics and Engineering, The Australian National University, Canberra ACT 2601, Australia
ivan.savenko@pcs.ibs.re.kr

Abstract— This is a theoretical study of the Fano resonance in a hybrid system consisting of spatially separated two-dimensional layers of electrons and excitons interacting by the Coulomb force and exposed to weak magnetic field and light (electromagnetic field). We investigate the conductivity of electrons in this system and show that the electromagnetic power absorption spectrum has a Fano profile. Further we phenomenologically account for the disorder in the system.

1. INTRODUCTION

Bose-Fermi mixtures exist in hybrid complex systems which serve as unique laboratories to study many-body interactions [1]. In the solid-state physics, such systems usually employ exciton gases localized in quantum wells (QWs). They interact with 2D electron gas (2DEG) in neighbouring layers [2].

Motion of particles and their interaction reveals different quantum paths for the system, moreover, these trajectories can interfere among each other. If the interference is destructive, it results in a partial or full suppression of the particle transport. In our paper [3] we investigate the Fano resonance in such a hybrid systems.

2. CYCLOTRON RESONANCE

Let us consider a system which represents two parallel layers of electrons and excitons, see left hand side panel in Fig. 1. The system is exposed to an external electromagnetic (EM) field, $\mathbf{E}(\mathbf{r},t)=(E_0,0,0)e^{i\mathbf{kr}-i\omega t}$. It results in the deviation of the electronic density, $\delta n(\mathbf{r},t)=n(\mathbf{r},t)-n_0$, where $\mathbf{r}$ is a 2D coordinate, and $\mathbf{k}$ is the wave vector. The excitons feel the presence of the EM field indirectly: via the interaction with electrons. A weak uniform magnetic field, $\mathbf{B}$, is applied perpendicular to the layers and we consider zero-temperature case.

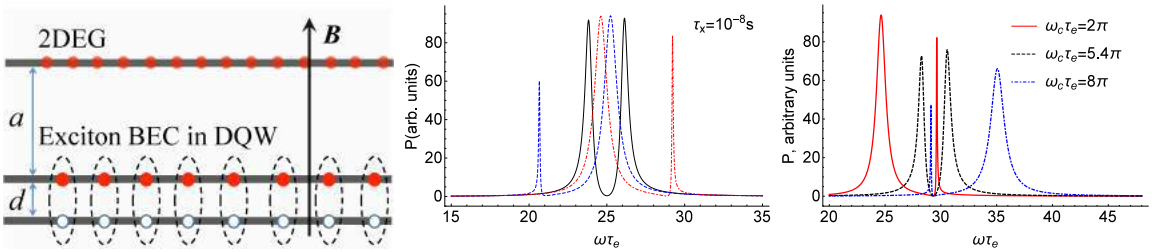

Figure 1: (Left Panel) Structure: excitons are localized in the double quantum well (DQW) structure. The 2DEG lives in other QW at the distance a. (Middle Panel) The power absorption as a function of frequency for the increasing s from (a) to (c) for $\tau_X=10^{-8}$ s (solid curves) and $\tau_X=5\cdot10^{-10}$ s (dashed curves). (Right Panel) Magnetic field effect: power absorption spectrum at $s=7\cdot10^5$ cm/s and different values of magnetic field in units of $\omega_c\tau_e$.

We treat the electrons classically via the continuity equation, $\dot{\rho} + \operatorname{div} \mathbf{j} = 0$: $\delta n_{k\omega} = -\frac{k}{e\omega} j_{k\omega}$. In the Ohm's law,

$$j_{k\omega} = \sigma_B \left(E_0 - \frac{1}{e} F_{k\omega} \right), \tag{1}$$

σ_B is 'xx' component of the conductivity tensor, $F_{k\omega}$ is 'x' component of the applied electromagnetic force, coming from the electron-electron and electron-exciton interaction:

$$F_{k\omega} = -ik(U_k \delta n_{k\omega} + V_k \delta N_{k\omega}), \text{ where } U_k = \frac{2\pi e^2}{\epsilon k}, \; V_k = \frac{2\pi e^2}{\epsilon k} \left(1 - e^{-kd}\right) e^{-ka}, \tag{2}$$

where ϵ is the dielectric function; $\delta N_{k\omega}$ is the fluctuating exciton density in the BEC. The elementary excitations of the BEC are bogolons, we use the model of weakly-interacting Bose gas, and the dispersion then reads: $\varepsilon_k = \sqrt{\frac{k^2}{2M}\left(\frac{k^2}{2M} + 2g_0 n_c\right)}$, where, n_c is exciton density in the condensate, g_0 is exciton-exciton interacting constant,$g_0 \approx 4\pi e^2 d/\epsilon$, and M is the exciton mass. In the long-wavelength limit we come up with the sound quanta, $\varepsilon_k \approx sk$, where $s = \sqrt{g_0 n_c / M}$.

Using the Gross-Pitaevskii equation,

$$i\partial_t \Psi(\mathbf{r}, t) = \left(\frac{(\hbar \hat{\mathbf{k}})^2}{2M} - \mu + g_0 |\Psi(\mathbf{r}, t)|^2 \right) \Psi(\mathbf{r}, t) + \Psi(\mathbf{r}, t) \int d\mathbf{r}' V(\mathbf{r} - \mathbf{r}') \delta n(\mathbf{r}', t), \tag{3}$$

where the last term is treated as a perturbation, we can find the wave function of the condensed particles, $\Psi(\mathbf{r}, t) = \sqrt{n_c} + \psi(\mathbf{r}, t)$.

Finally, the renormalized conductivity, defined as $j_{k\omega} = \tilde{\sigma}_{k\omega} E_0$, reads:

$$\tilde{\sigma}_{k\omega} = \frac{1}{\sigma_B^{-1} + i\frac{k^2}{e^2\omega}\left[U_{k\omega} + V_{k\omega}^2 R_{k\omega}\right]}, \quad \sigma_B = \sigma_0 \frac{i(\omega\tau_e + i)}{(\omega\tau_e + i)^2 - \omega_c^2 \tau_e^2}, \tag{4}$$

where $\omega_c = eB/mc$ is electron cyclotron frequency and $\sigma_0 = e^2 n_0 \tau_e / m$ is the Drude conductivity of 2DEG, $R_{k\omega}$ is the response function. From this main formula, we can calculate the electromagnetic power absorption: $P_{k\omega} = \frac{1}{2} E_0^2 \operatorname{Re} \tilde{\sigma}_{k\omega}$.

3. RESULTS AND DISCUSSION

We calculated the power absorption function using the following parameters: $d = 10^{-6}$ cm, $a = 10^{-5}$ cm, $k = 4.2 \cdot 10^4$ cm^{-1}, and $\sigma_0 = 3.2 \cdot 10^{-5}$ cm/s.

Middle panel in Fig. 1 manifests the Fano resonance in the power absorption spectrum. With the increase of the velocity of the bogolons, s, one can shift the Fano resonance in frequency and even change the disposition of the peaks and the dip of the asymmetric profile.

Right hand side panel in Fig. 1 explains the dependence of the power absorption function on the magnitude of the external applied magnetic field.

ACKNOWLEDGMENT

We thank A. Chaplik, A. Miroshnichenko and S. Flach for useful discussions. V.M.K and M.V.B. acknowledge the support from RFBR grant $\#16 - 02 - 00565a$. I.G.S. acknowledges support of IBS-R024-D1, the Australian Research Council's Discovery Projects funding scheme (project DE160100167), President of Russian Federation (Project No. MK-5903.2016.2). I.G.S. and M.V.B. also thank the Dynasty Foundation.

REFERENCES

1. Cotlet, O., Zeytinoglu, S., Sigrist, M., Demler, E., and Imamoglu, A., *Phys. Rev. B* Vol. 93, 054510, 2016.
2. Matuszewski, M., Taylor, T., and Kavokin, A. V., *Phys. Rev. Lett.* Vol. 108, 060401, 2012.
3. Boev, M. V., Kovalev, V. M., and Savenko, I. G., *Phys. Rev. B Rapid Comminucations* Vol. 94, 241408(R), 2016.

Coupling between photonic crystal cavities and waveguides for ultrafast optical switching

Yanhui Zhao, Chenjiang Qian, Kangsheng Qiu, Jing Tang, Yue Sun, and Xiulai Xu*

Beijing National Laboratory for Condensed Matter Physics, Institute of Physics, Chinese Academy of Sciences, Beijing 100190, P. R. China

*corresponding author: xlxu@iphy.ac.cn

Abstract- We propose a coupled photonic crystal cavity-waveguide structure to achieve Fano resonance by placing partially reflecting elements in waveguide, and the Fano resonance can be greatly enhanced by introducing optical gain material into the cavity. Additionally, coupling between photonic molecules and waveguides in photonic crystal slab structures are investigated for ultrafast optical switching with a time scale of a few picoseconds by optimizing the radii of air holes between two cavities of photonic molecule.

To improve the optical device performance, Fano resonance with asymmetric and steep spectral line shape has been intensively used, which arises from the interference between discrete resonance states and continuum states. By modulating the coupling between photonic crystal (PhC) cavity and waveguide, Fano resonance can be achieved due to the constructive and destructive interference of discrete cavity resonance states with broadband continuum waveguide states. In this work, we design a PhC cavity and waveguide structure using Finite-difference time-domain (FDTD) simulation. By placing partially reflecting elements in the PhC waveguide, Fano type transmission line shape is achieved. In addition, gain materials are introduced into PhC cavities to enhance Fano resonance. With introducing the gain materials into cavity, the transmission line shape of the Fano resonance is greatly steepened and a large contrast is achieved by a small frequency shift. In our structure, the transmissivity in the waveguide is increased by a factor of six, which is potentially applicable for optical switches and optical sensors.

In addition, the coupling between photonic molecules and waveguides in PhC slab structures are studied using FDTD method and coupled mode theory. In a photonic molecule with two cavities, the coupling of cavity modes results in two super-modes with symmetric and anti-symmetric field distributions. When two super-modes are excited simultaneously, the energy of electric field oscillates between the two cavities. To excite and probe the energy oscillation, we integrate photonic molecule with two PhC waveguides. In coupled structure, we find that the quality factors of two super-modes might be different because of different field distributions of super-modes. After optimizing the radii of air holes between two cavities of photonic molecule, nearly equal quality factors of two super-modes are achieved, and coupling strengths between the waveguide modes and two super-modes are almost the same. In this case, complete energy oscillations between two cavities can be obtained with a pumping source in one waveguide, which can be read out by another waveguide. Finally, we demonstrate that the designed structure can be used for ultrafast optical switching with a time scale of a few picoseconds.

Acknowledgements, This work was supported by the National Basic Research Program of China under Grant No. 2013CB328706 and 2014CB921003; the National Natural Science Foundation of China under Grant No. 91436101 and 61275060; the Strategic Priority Research Program of the Chinese Academy of Sciences under Grant No. XDB07030200.

REFERENCES

1. Yanhui Zhao, Chenjiang Qian, Kangsheng Qiu, Jing Tang, Yue Sun, Kuijuan Jin & Xiulai Xu, Gain enhanced Fano resonance in a coupled photonic crystal cavity-waveguide structure, *Scientific Reports*, Vol. 6, 33645 (2016)
2. Zhao Yan-Hui, Qian Chen-Jiang, Tang Jing, Sun Yue, Peng Kai, Xu Xiu-Lai, Effects of location and polarization of a dipole source on the excitation of a photonic crystal H1 cavity, *Acta Physica Sinica*, Vol. 65, No, 13, 134206 (2016)
3. Yanhui Zhao, Chenjiang Qian, Kangsheng Qiu, Yunan Gao and Xiulai Xu, Ultrafast optical switching using photonic molecules in photonic crystal waveguides, *Optics Express,* Vol. 23, No. 7, 9211–9220 (2015)

Control of electromagnetically-induced-transparency-like effect in metamaterials for coherent storage of electromagnetic waves

T. Nakanishi, S. Tohi, and M. Kitano

Department of Electronic Science and Engineering, Kyoto University, Japan
t-naka@kuee.kyoto-u.ac.jp

Abstract— We propose tunable metamaterials, which realize the storage and retrieval of electromagnetic waves, in analogy with electromagnetically induced transparency (EIT) effect in atomic systems. The basic concepts are introduced with coupled resonator models, and we experimentally demonstrate the storage and retrieval of electromagnetic waves in microwave regions. Owing to coherent process, the phase information is also recovered in the retrieved signal.

Electromagnetically induced transparency, or EIT, is a nonlinear optical phenomenon, where an opaque medium becomes transparent in an extremely narrow spectral region by the incidence of auxiliary light called control light, and the EIT effect has been intensively investigated in atomic systems. In the transparency region, the dispersive properties are dramatically modified and the group velocity of the light is significantly reduced. In addition, it is possible even to stop the propagating light in the medium by gradually turning the control light off. In this process, the light is coherently captured in the medium, and the stored light can be released by the reverse process without losing the phase information.

The EIT effect can be emulated by artificial media or metamaterials, and various types of the metamaterials have demonstrated the EIT-like effects, such as sharp transparency and slow propagation, in wide frequency regions from microwave to visible light. The EIT-like metamaterials have two resonant modes, called radiative mode and trapped mode, which are coupled with each other. The radiative mode interacts with propagating waves and the quality factor as a resonator is low owing to the radiation loss. On the other hand, the trapped mode is uncoupled with the propagating waves and the intrinsic quality factor is extremely high. In the presence of the coupling between the two modes, the energy received through the radiative mode is transferred into the trapped mode with low loss, and then is released into free space through the radiative mode. The temporal storage in the trapped mode induces the propagation delay with low loss and contributes to the slow propagation in the metamaterial.

In order to extend the slow-light effect to the storage in the metamaterials, the EIT-like effects in the metamaterial have to be dynamically controlled by external signals in the same manner as the optical storage in atomic EIT medium. In this paper, we propose two types of tunable metamaterials to control the EIT-like effect and demonstrate the storage of electromagnetic waves in microwave regions.

We first introduce an EIT-like metamaterial, which controls coupling between a radiative mode and a trapped mode by external electric signals [1]. The transmission spectra are shown in Fig. 1(a).

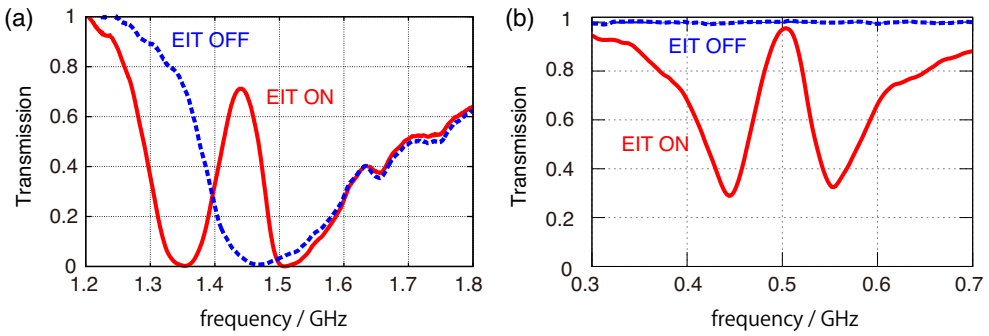

Figure 1: Tunable EIT-like metamaterials. (a) Coupling-controlled metamaterial (b) Radiative-mode-controlled metamaterial.

In the case of "EIT OFF" state denoted by the dotted line, there is no coupling between two modes, and the broad transmission dip attributed to the resonance of the radiative mode is observed. On the other hand, in the "EIT ON" state denoted by the solid line, the coupling is turned on, and a transmission window owing to the EIT-like effect is clearly observed.

As a second example, we introduce another tunable EIT-like metamaterial [2], whose transmission spectra are shown in Fig. 1(b). In this case, the radiative mode and the trapped mode are always coupled with each other. In the metamaterial, a switching element is installed in the radiative mode, in order to control the resonance of the radiative mode. In "EIT OFF" state denoted by the dotted line, the function of the radiative mode as a resonator is deactivated, and the metamaterial shows high transmission in a whole spectrum due to the absence of the resonance mode interacting with external fields. In "EIT ON" state denoted by the solid line, the radiative mode works as the resonator, and the EIT property can be observed.

Both metamaterials realize the storage of electromagnetic waves through the same procedure. First, the EIT state is turned on, and the electromagnetic waves tuned to the transparent region slowly propagate through the metamaterial owing to the EIT effect. In this process, electromagnetic energy is concentrated in the trapped mode. During the propagation, the EIT state is turned off, and the energy is completely captured in the trapped mode. The stored waves can be retrieved by recovering the EIT state.

In this paper, we have proposed two types of EIT-like metamaterials, whose EIT effect can be controlled. The metamaterials have realized the storage of the electromagnetic waves. It is noted that the processes of the storage and retrieval are coherent and the original waves are retrieved without losing the phase information. The experimental demonstration has been conducted in the microwave regions, but the fundamental concept can be applied to higher frequencies.

ACKNOWLEDGMENT

This research was financially supported by JSPS KAKENHI Grants No. 22109004, No. 25790065, No. 25287101, and No. 16K13699.

REFERENCES

1. T. Nakanishi, T. Otani, Y. Tamayama, and M. Kitano, "Storage of electromagnetic waves in a metamaterial that mimics electromagnetically induced transparency," *Phys. Rev. B*, Vol. 87, No. 16, 161110, 2013.
2. S. Tohi, T. Nakanishi, and M. Kitano, "Storage of Electromagnetic Waves in Metamaterial via Conductivity Modulation," in *proceedings of the 9th Int. Congr. Adv. Electromagn. Mater. Microw. Opt.* Oxford, UK, September 2015.
3. T. Nakanishi and M. Kitano, "Implementation of Electromagnetically Induced Transparency in a Metamaterial Controlled with Auxiliary Waves," *Phys. Rev. Applied*, Vol. 4, No. 2, 024013, 2015.

High-Q Fano resonances and SERS applications of 3D metamaterials

C. Z. Gu[1,2], Z. Liu[1], S. Y. Yang[1], J. J. Li[1]

[1] Beijing National Laboratory for Condensed Matter Physics, Institute of Physics, Chinese Academy of Sciences, Beijing 100190, China

[2] Collaborative Innovation Center of Quantum Matter, Beijing 100871, China

[*]corresponding author: czgu@iphy.ac.cn

Abstract-We report a series of studies on 3D folded metamaterial, by which Fano resonances can be excited and the line shape, intensity and Q factor can be modulated. Different combinations of the vertical and planar building blocks of the 3D folded metamaterials result in diverse properties of the Fano resonance, which have practical applications in filter, ultrasensitive biosensor, active SERS substrate, etc.

Fano resonance can be excited in plasmonic metamaterials by destructive interference between a bright continuum mode and a discrete dark mode. 3D folded metamaterial has been used for Fano resonance excitation due to its unique configuration - it is composed of vertical part and planar complementary part[1]. Resonance modes are excited on both parts by evanescent field of surface wave and grating coupling of incident light respectively, and the destructive interference results in Fano resonance with asymmetric line shape[2]. Although the sensing[1] and modulation[3] property of 3D metamaterials have been studied recently, the quality factors of these resonance modes are relatively low. Excitation of high-Q factor resonances are usually accompanied with the generation of extremely strong field at subwavelength scale and low energy losses[4], thus a high-Q 3D metamaterial can be a promising candidate for improving the limitation of detection in SERS analysis.

Recently, we found that through judicious design of the building blocks in shape and size, high-Q resonance can be achieved with extremely large spatial electromagnetic field enhancement. The high-Q Fano resonance can be engineered to the target wavelength by modulating the geometric parameters of the building blocks, and it was used for ultrasensitive SERS detection of bio-molecules.

Acknowledgements: This work was supported by the National Natural Science Foundation of China (Grants Nos 91323304, 11504414, 11174362, 61390503, 11574369 and 11434017) and the National Basic Research Program of China (Grant Nos 2016YFA0200803 and 2016YFA0200400).

REFERENCES

1. Cui, A. et al. “Directly patterned substrate-free plasmonic “nanograter” structures with unusual Fano resonances,” *Light Sci Appl*, Vol. 4, e308.
2. Liu, Z. et al. “3D conductive coupling for efficient generation of prominent Fano resonances in metamaterials,” *Sci. Rep.*, Vol. 6, 27817, 2016.
3. Liu, Z. et al. “Spatially oriented plasmonic ‘nanograter’ structures,” *Sci. Rep.*, Vol. 6, 28764, 2016.
4. Yang, S. et al. “Excitation of ultrasharp trapped-mode resonances in mirror-symmetric metamaterials,” *Phys. Rev. B*, Vol. 93, 235407, 2016.

Light-tunable Fano resonances in metal-dielectric multilayer structures

S. Hayashi[1,2*], D. V. Nesterenko[2], A. Rahmouni[2] and Z. Sekkat[2,3,4]
[1]Kobe University, Japan
[2]Moroccan Foundation for Advanced Science, Innovation and Research (MAScIR), Morocco
[3]University Mohammed V, Morocco
[4]Osaka University, Japan
[*]corresponding author: s.hayashi@dragon.kobe-u.ac.jp

Abstract-Extending our previous work on Fano resonances in metal-dielectric multilayer structures we demonstrate here the tuning of Fano resonance by light irradiation. The photo-tuning was made possible by incorporating azo-dye molecules in a dielectric waveguide layer. Due to the photoisomerization of the molecules, the refractive index of the waveguide layer changes upon pump light irradiation, resulting in the shift of the Fano line shape. The change in the refractive index estimated from the experimental data falls in a range less than ~7.0×10^{-4}.

Recently, we have demonstrated both theoretically and experimentally the generation of high-Q Fano resonances in planar metal-dielectric multilayer structures [1-3]. The multilayer structures studied consist of a metal layer and two insulator layers (MII structure), which can be regarded as a combination of a metal-insulator interface that supports a surface plasmon polariton (SPP) mode and a planar waveguide structure that supports a planar waveguide (PWG) mode. The appearance of the Fano line shapes in their attenuated reflection (ATR) spectra is due to the interaction between the broad SPP mode and the sharp PWG mode. The Fano MII structure can be fabricated easily without any nanofabrication technique and is applicable to high resolution optical sensing and enhanced spectroscopies.

In recent years, tuning of the Fano resonances in plasmonic nanostructures by applying mechanical stress and electric field has been demonstrated. However, clear experimental evidence of the tuning by light has not been reported yet. We extended our previous work to realize the photo-tuning of the Fano resonance [4]. Our previous Fano MII structure was prepared by depositing an Ag film onto a substrate and successively depositing a low-index Cytop spacer layer and a high-index PMMA waveguide layer. To achieve the photo-tuning, we used a DR1-doped PMMA waveguide layer instead of a pure PMMA layer as schematically shown in Fig. 1b. The DR-1 molecule is one of the azobenzene derivatives that undergoes the *trans-cis* transformation under blue

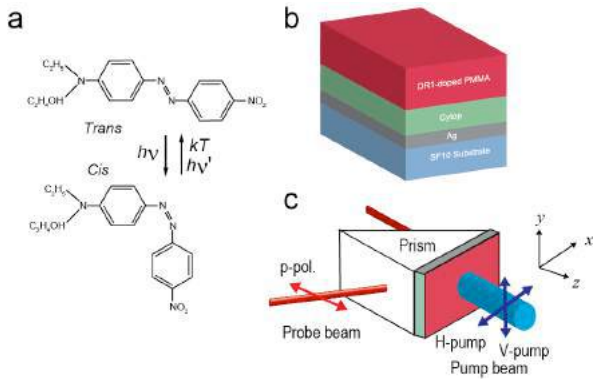

Fig.1 (a) Photoisomerization of DR1 molecule, (b) multilayer sample with a DR1-doped PMMA waveguide layer and (c) Kretschmann configuration of pump-probe ATR measurements.

light irradiation (photoisomerization) (Fig. 1a). Due to the photoisomerization, the refractive index of the DR1-doped waveguide layer decreases upon pump irradiation. We performed pump-probe ATR measurements of the samples attached to a prism in a Kretschmann configuration as schematically shown in Fig. 1c.

Figure 2a shows an angle-scan ATR spectrum under dark probed by a He-Ne laser beam with a wavelength of λ=632.8 nm. We see clearly a Fano line shape around 55° located at the high-angle side of the SPP dip. The Fano resonance is a consequence of the interference between the TM_0 PWG mode and the SPP mode. As can be seen clearly in Fig. 2b, the Fano line shape shifts to a lower angle under the irradiation of blue pump light with a wavelength of λ=488.0 nm. Figure 2c represents the results of systematic measurements performed by varying the power density of pump light for both the vertical and horizontal polarizations of pump light. We see that the Fano resonance shifts more and more as the pump power density increases.

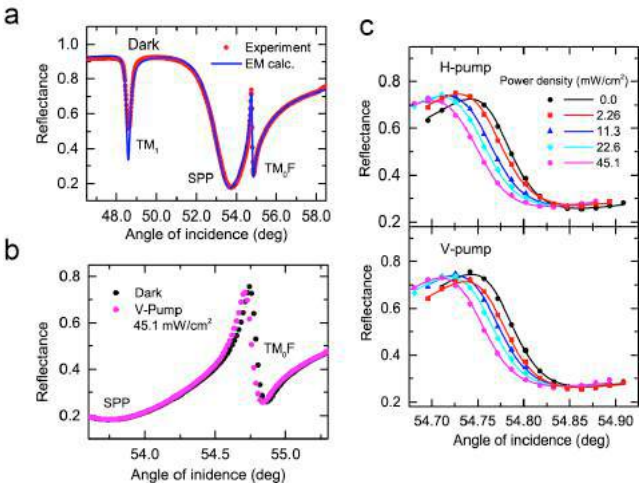

Fig.3 (a) Angle-scan ATR spectrum obtained under dark, (b) shift of Fano line shape caused by optical pumping, and (c) results of systematic observations performed by varying the pump power density for both the horizontal and vertical polarizations.

We analyzed the photo-induced shift of the Fano resonance based on electromagnetic calculations of the ATR spectra and estimated the amount of change in the refractive index of the DR1-doped PMMA waveguide layer. The estimated change in the refractive index falls in a range less than $\sim 7.0 \times 10^{-4}$. This implies that the Fano line shape is very sensitive to the change in the refractive index of the waveguide layer. The photo-tuning of the Fano resonance demonstrated here may open a new avenue for realizing novel optical devices, such as optically tunable sensors and all optical switching elements.−

–

Acknowledgements, This work was supported by Osaka University International Joint Research Promotion Program: the Handai project and by JSPS KAKENHI grant number 16K04979.

REFERENCES

1. Hayashi, S., D.V. Nesterenko and Z. Sekkat, "Fano resonance and plasmon-induced transparency in waveguide-coupled surface plasmon resonance sensors," *Appl. Phys. Express*, Vol. 8, 022201, 2015.
2. Hayashi, S., D.V. Nesterenko and Z. Sekkat, "Waveguide-coupled surface plasmon resonance sensor structures: Fano lineshape engineering for ultrahigh-resolution sensing," *J. Phys. D: Appl. Phys.*, Vol. 48, 325303, 2015.
3. Hayashi, S., D.V. Nesterenko, A. Rahmouni and Z. Sekkat, "Observation of Fano line shape arising from coupling between surface plasmon polariton and waveguide modes," *Appl. Phys. Lett.*, Vol. 104, 051101, 2016.
4. Hayashi, S., D.V. Nesterenko, A. Rahmouni, H. Ishitobi, Y. Inoue, S. Kawata and Z. Sekkat, "Light-tunable Fano resonance in metal-dielectric multilayer structures," *Sci. Rep.*, Vol. 6, 33144, 2016.

Interference of plasmonic vortex fields with different angular momenta

Keiji Sasaki*
Research Institute for Electronic Science, Hokkaido University, Japan
*corresponding author: sasaki@es.hokudai.ac.jp

Abstract-We showed that the optical vortex field can be confined into nano-space using plasmonic multimer structures. In this transfer from chiral photons to plasmons, the total angular momentum is conserved, while the orbital and spin angular momenta can be exchanged. Here, we demonstrate that plasmonic nano-vortex field is formed as interference of chiral photons having different angular momenta. We also show that this interference field induces optical torque and central force, which leads to orbital rotation of nanoparticles in nano-space.

Recently, we clarified that multipolar plasmons of metal nano-disks can be selectively excited by circularly-polarized optical vortex beams, i.e., Laguerre-Gaussian (LG) beams [1,2]. The total angular momenta, that is the sum of orbital and spin angular momenta, are transferred from chiral photons to localized surface plasmons. Unfortunately, the mode volume of this plasmonic nanodisk resonator is sub-micrometer dimension that is restricted by the diffraction limit of the surface plasmon wave. In order to realize single-nanometer-sized cavities, we design the tailored plasmonic structure consisting of metal multimer surrounding a nano-gap. We theoretically showed that this metal structure makes it possible to localize the optical vortex field into the gap space with conserving the total angular momenta. However, the orbital and spin angular momenta of the vortex field can be exchanged in accordance with the boundary conditions at the metal surfaces. Therefore, the nano-vortex field is formed as interference of LG-modes having different angular momenta even when the single LG-mode beam is incident on the plasmonic multimer structure.

The transfer of the angular momenta from this interference nano-field to molecules or nanoparticles induces rotational radiation pressure, i.e., optical torque and gradient force directed to the center [3,4], which causes nano-vortex flow of molecules/particles and may lead to chiral structuring of molecule/particle assemblies. We succeeded in rotational manipulation of a 100-nm polymer bead with a gold nano-triangle trimer structure. The plasmonic structure was illuminated with a circularly polarized beam of a near-infrared laser, so that the nano-sized field with the orbital angular momentum as well as the spin is formed within the gap. We will present detailed analyses of the rotational motions and their relations to the chirality of the plasmonic fields.

REFERENCES

1. K. Sakai, K. Nomura, T. Yamamoto, and K. Sasaki, *Sci. Rep.* 5, 8431 (2015).
2. K. Sakai, K. Nomura, T. Yamamoto, T. Omura, and K. Sasaki, *Sci. Rep.* 6, 34967 (2016).
3. Y. Tanaka, S. Kaneda, and K. Sasaki, *Nano Lett.* 13, 2146 (2013).
4. Y. Tanaka, M. Komatsu, H. Fujiwara, and K. Sasaki, *Nano Lett.* 15, 7086 (2015).

Tuning of Fano resonances by rotation of continuum: wave faucet.

A.F. Sadreev, A.S. Pilipchuk, and A.A. Lyapina
Kirensky Institute of Physics, Federal Research Center KSC SB RAS, 660036 Krasnoyarsk, Russia

Abstract— We consider wave transmission in a non-axisymmetric waveguide which consists of cylindrical resonator and two semi-infinite cylindrical waveguides whose axes are shifted relative to the resonator. Rotation by the azimuthal angle $\Delta\phi$ of input waveguide does not change the eigenfrequency spectrum of the resonator, it tunes the Fano resonances and respectively gives rise to an analog of a faucet opening and closing wave flux under rotation. Moreover under the rotation of the waveguide numerous events of the Fano resonance collapse occur to evidence for the bound states in the continuum.

Beauty of complex wave fields observed in different areas of physics is related to phase of the field. The first demonstration of the phase effect was done by Thomas Young in 1803 in the historic experiment on double-slit interference [1]. Among numerous phase features we mark bound states in the continuum, Aharonov-Bohm oscillations, asymmetric Fano resonances, and topological singularities which millstone the phase effects in the last century. Typically the Fano resonance asymmetric shape is tuned by reconstruction of eigenvalue spectrum by, for example, application of finger gate potential in quantum dots or magnetic field in rings [2]. But in fact the resonances of open quantum system are given by poles of the S-matrix or the complex eigenvalues of the effective non Hermitian Hamiltonian [3] $\widehat{H}_{eff} = \widehat{H}_R - i\widehat{W}\widehat{W}^\dagger$ where $\widehat{H}_R$ describes the closed system (resonator) with discrete eigenvalue spectrum and $\widehat{W}$ describes the coupling matrix between the closed system and the continua (of attached waveguides). Typically the real parts of complex eigenvalues of the effective Hamiltonian which define the resonance positions follow the eigenvalues of the closed resonator when the coupling is weak. However with growth of the coupling the resonances become to interfere to give rise to tune the Fano resonance profiles. First this way to tune the Fano resonance was demonstrated by Rotter *et al* [4] by implementation of changeable diaphragms at the waveguide junctions. In this letter we consider a system which changes only a

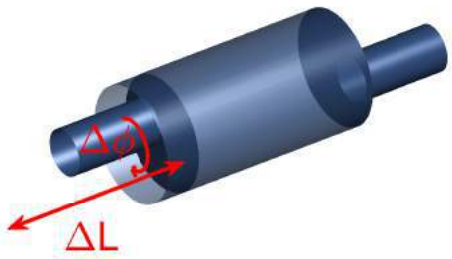

Figure 1: Cylindrical resonator of length L with two non-axially attached cylindrical waveguides. The input waveguide can freely move along the resonator axis and as well as rotate about it.

phase of the coupling matrix by rotation of one of waveguides and show that gives rise to drastic effects beginning with opening and closing the wave transmission (wave faucet) and ending by the bound states in the continuum (BSC). The setup shown in Fig. 1 consists of cylindrical resonator of radius R and length L with two attached semi-infinite cylindrical waveguides with radius $r < R$. If the waveguides were attached coaxially the total system would be invariant relative to azimuthal rotation to split the total Hilbert space of the system into independent subspaces given by the orbital angular momentum (OAM) m (the order of the Bessel functions m also defining the charge of topological singularity). Respectively the wave scattering would not interfere the m sectors with prohibition for OAM conversion. The sound transmission in axisymmetric cylindrical waveguide in the sector $m = 0$ and corresponding BSCs were considered in our first paper [6].

However attachment of the waveguides in a non-coaxial way breaks the azimuthal symmetry giving rise to the OAM conversion. Moreover we assume that one of the waveguides, say the left, can move along the resonator axis to change the resonator length, and rotate by the angle $\Delta\phi$ as shown in Fig. 1. Tuning the shape of the resonator could be performed in a realistic acoustic or electromagnetic experiment by the use of piston-like hollow-stem waveguides tightly fit to the interior boundaries of a cylindric cavity [6] as shown in Fig. 1. This setup unites all above listed phase features. The most striking effect of the rotation is a collapse of the Fano resonances that evidences an occurrence of bound states in the continuum (BSCs) when the resonator traps the propagating mode inside. The last has become one of the actively studied phenomena in different areas of physics [6].

ACKNOWLEDGMENT

This work was supported by Russian Science Foundation through Grant 14-12-00266.

REFERENCES

1. Young, T., "Bakerian Lecture: Experiments and calculations relative to physical optics", *Phil. Trans. Royal Soc.*, Vol. 94, 1–15 1803.
2. Miroshnichenko A.E. , Flach S., Kivshar Yu.S.,"Fano resonances in nanoscale structures," *Rev. Mod. Phys.*, Vol. 82, 2258–2298, 2010 .
3. Feshbach H., "Unified Theory of Nuclear reactions", *Ann. Phys. N.Y.*, Vol. 5, 357–390, 1958.
4. Rotter, S., Libisch, F., Burgoffer, J., Kuhl, U., and Stöckmann, H.-J., " Tunable Fano resonances in transport through microwave billiards", *Phys. Rev. E*, Vol. 69, 046208 2004.
5. Lyapina, A.a., Maksimov, D.N., Pilipchuk,A.S., and Sadreev, A.F., "Bound states in the continuum in open acoustic resonators," *J.Fluid Mech.*, Vol. 780, 370–387, 2015.
6. Chia Wei Hsu, Bo Zhen, Stone A.D., Joannopoulos J.D. and Soljačić M., "Bound states in the continuum", *Nature Rev. Mat.*, Vol. 1, 16048, 2016.

Helical bound states in a microwave-field continuum with an embedded MDM ferrite particle

E. O. Kamenetskii

Microwave Magnetic Laboratory,
Department of Electrical and Computer Engineering,
Ben Gurion University of the Negev, Beer Sheva, Israel
*Email: kmntsk@bgu.ac.il

Abstract-We consider multiple discrete states of magnetostatic oscillations in a quasi-2D ferrite disk embedded in a common microwave continuum. We examine the microwave transport properties of such a system including the appearance of Fano resonances.

Magnetic-dipolar modes (MDMs) in a quasi-2D ferrite disk are microwave energy eigenstate oscillations with topologically distinct structures of rotating fields and unidirectional power-flow circulations [1, 2]. Quantized vortices in MDM oscillations manifest the long-range phase coherence of magnetic dipole-dipole interaction which are described by a complex-valued order parameter field – the magnetostatic-potential (MS-potential) scalar wave function. Sharp multiresonance oscillations, observed experimentally in microwave structures with an embedded quasi-2D ferrite disk, are related to magnetization dynamics in the sample. For given disk sizes and a given quantity of saturation magnetization of ferrite material M_0, there are two different mechanisms of energy quantization: (*i*) by a bias magnetic field H_0 at a constant signal frequency ω and (*ii*) by a signal frequency ω at a constant bias magnetic field H_0. The fact that there are different mechanisms of quantization allows to conclude that for MDM oscillations in a qusi-2D ferrite disk both discrete energy eigenstate and a continuum of energy can exist. The microwave measurement reflects interaction between a classical device – the microwave structure – and a MDM particle [3].

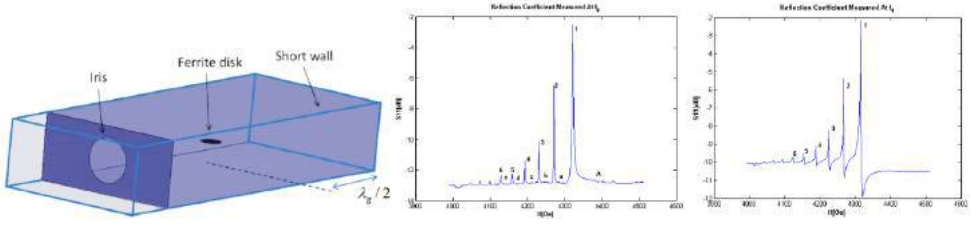

Fig.1. MDM resonances in a microwave cavity in dependence on a bias magnetic field and at different frequencies.

At the cavity resonance frequency f_0 , the bound states are localized in a ferrite disk. The bound states

have a square integrable wave function. When the frequency is shifted from f_0, the edge states flow around the disk. The resonances retain distinctive properties of the bound states. The MDM bound states in a microwave-field continuum have a helical structure with a power-flow current circulating around a quasi-2D ferrite disk [4]. The interference of the resonances results in the formation of a bound state embedded into the continuum of the edge states flowing around the disk [2, 5]. One can say that the MDM disk effectively creates specific boundary conditions for the EM waves in a microwave structure.

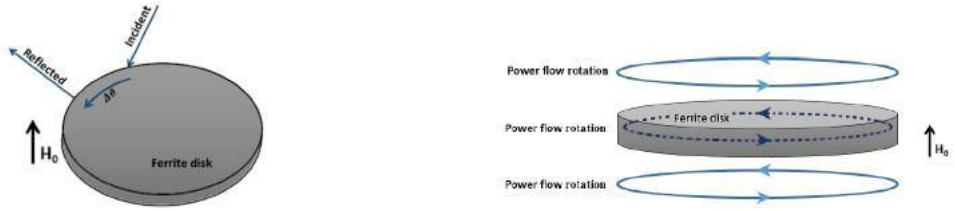

(*a*) (*b*)

Fig. 2. (*a*) The topological nature of the rotating fields in a MDM ferrite disk. On a lateral surface of a normally magnetized ferrite disk, one has an azimuthally nonreciprocal phase shift of electromagnetic waves reflected from a ferrite. (*b*) Power- flow circulations at the MDM resonances. For a given direction of a bias magnetic field, the power flow circulations have the same directions inside a ferrite and in the vacuum near-field regions outside the disk.

A MDM ferrite disk is an open *PT*-symmetry system. In the description of such a system, a non-Hermitian effective Hamiltonian can be derived from the Hermitian Hamiltonian including the environment. Because of strong spin–orbit interaction in MDM magnetization dynamics these bound states in the continuum have a helical structure. The MDM bound states are embedded in the microwave continuum but not coupled to it, so it appears unclear how one could actually probe them. We show that the probing becomes possible due to vortex currents induced on metal parts of a microwave structure [5].

REFERENCES

1. E. O. Kamenetskii, “Energy eigenstates of magnetostatic waves and oscillations”, Phys. Rev. E **63**, 066612 (2001).
2. M. Sigalov, E. O. Kamenetskii, and R Shavit, “Magnetic-dipolar and electromagnetic vortices in quasi-2D ferrite discs”, J. Phys.: Condens. Matter **21**, 016003 (2009).
3. E. O. Kamenetskii, G. Vaisman, and R. Shavit, “Fano resonances of microwave structures with embedded magneto-dipolar quantum dots”, J. Appl. Phys. **114**, 173902 (2013).
4. E. O. Kamenetskii, "Helical-mode magnetostatic resonances in small ferrite particles and singular metamaterials", J. Phys.: Condens. Matter **22**, 486005 (2010).
5. R. Joffe, E. O. Kamenetskii, and R. Shavit, “Azimuthally unidirectional transport of energy in magnetoelectric fields: Topological Lenz’s effect“, arXiv: 1701.05185.

Photonic-crystal Fano structures for lasers and nonlinear optical signal processing

Y. Yu*, D. A. Bekele, E. Semenova, L. Ottaviano, H. Hu, P. Guan, M. Galili, L. K. Oxenløwe, K. Yvind, and J. Mork

DTU Fotonik, Technical University of Denmark, Denmark

*yiyu@fotonik.dtu.dk

Abstract-We present our recent work on photonic-crystal structures based on Fano resonance. We show that the use of Fano interference in combination with optical nonlinearity can enable single-mode operation and self-pulsing in a nanolaser, as well as fast, low-energy all-optical signal processing.

Ultra-compact photonic structures suitable for optical communication at high-speed with low-energy consumption are essential for enabling integrated photonic chips that can meet the growing demand for information capacity [1]. Here we present our recent work on photonic-crystal (PhC) nanocavity structures exploring Fano resonances, and their applications to lasers, switching, nonreciprocity and power limiting, etc.

As for lasers, rather than conventional semiconductor lasers [2]-[5], we demonstrate a new laser concept based on Fano resonance [6], [7]. The structure (Fig. 1(a)) is an InP PhC waveguide sandwiched by a conventional broadband left mirror and a narrowband right mirror, which is realized by the Fano interference between the waveguide continuum and a discrete mode of a side-coupled H0 nanocavity [8]. The laser has 3 layers of InAs quantum dots as active region and is operated at room temperature by exciting with a continuous-wave light source vertically. It was found that the very narrowband feature of the Fano resonance can lead to single mode lasing, with its wavelength almost unaffected by the cavity length. This is in contrast to ordinary PhC line-defect lasers [9]. In addition, when combined with optical nonlinearity, the highly dispersive feature of the Fano resonance can promote self-pulsations at gigahertz frequencies [8] (Fig. 1(b)), which was previously observed only in macroscopic lasers [10].

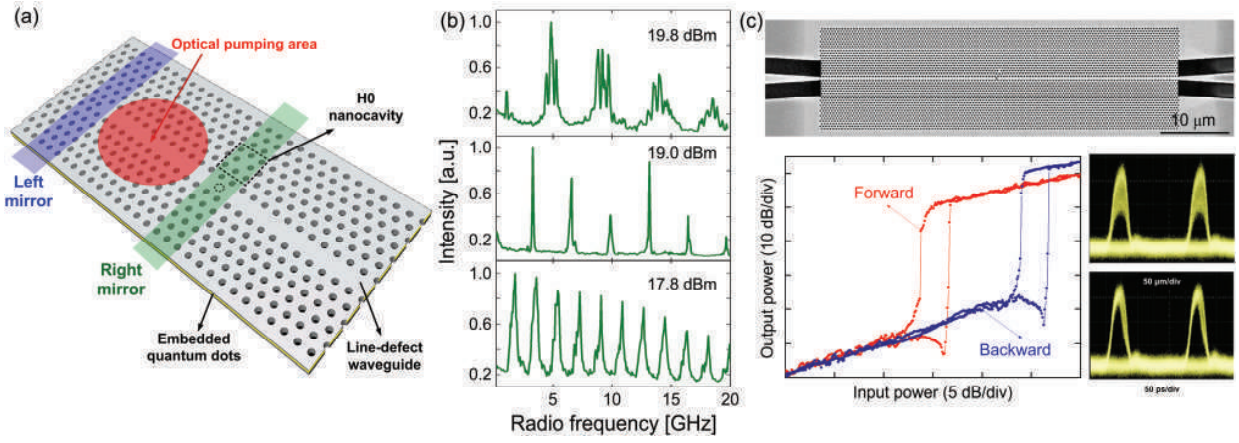

Fig. 1. (a) Schematic of PhC Fano laser. (b) Measured radio frequency spectra of the laser power for different pump powers. (c) SEM image of a fabricated InP PhC Fano switch (top) and its applications for nonreciprocal transmission (bottom left) and power limiting (bottom right).

Compared to traditional Lorentzian structures, Fano resonances can exhibit a sharp spectral shape [11] which enhances the sensitivity of the device to external perturbation, making it especially advantageous for low-energy nonlinear signal processing such as all-optical switching [12]-[13]. Fig. 1(c) shows a fabricated InP PhC 2-port Fano switch, where an H0 nanocavity is side-coupled to a waveguide. A blockade hole is incorporated in the waveguide below the cavity, giving the device's transfer function an asymmetric sharp Fano line shape. By exploiting carrier nonlinearities in the nanocavity, the input signal can be efficiently modulated by itself. This leads to applications such as device nonreciprocity: the forward and backward signal has different transmission coefficients [14] (bottom left panel of Fig. 1(c)); and power limiting: the noise on the injected pulses can be suppressed (bottom right panel of Fig. 1(c)). All the operations are carried out with low energy consumptions on the order of fJ/bit. In the conference, more details about the device fabrication, experimental characterization and the theoretical model will be presented.

Acknowledgements: The authors acknowledge financial support from Villum Fonden via the NATEC (NAnophotonics for Terabit Communications) Centre (grant no. 8692) and YIP QUEENs.

REFERENCES

[1] Miller, D. A. B., "Device requirements for optical interconnects to silicon chips." *Proc. IEEE*, vol. 97, 1166, 2009.

[2] Siegman, A. E., *Lasers*, University Science Books, 1986.

[3] Noda, S. *et al*., "Polarization mode control of two-dimensional photonic crystal laser by unit cell structure design," *Science*, vol. 293, 1123−1125, 2001.

[4] Spillane, S. M. *et al*., "Ultralow-threshold Raman laser using a spherical dielectric microcavity," *Nature*, vol. 415, 621−623, 2002.

[5] Matsuo, S. *et al*., "High-speed ultracompact buried heterostructure photonic-crystal laser with 13 fJ of energy consumed per bit transmitted," *Nat. Photon*., vol. 4, 648–654, 2010.

[6] Fano, U., "Effects of configuration interaction on intensities and phase shifts," *Phys. Rev*., vol. 124, 1866−1878, 1961.

[7] Mork, J. *et al*., "Photonic crystal Fano laser: terahertz modulation and ultrashort pulse generation," *Phys. Rev. Lett*., vol. 113, 163901, 2014.

[8] Yu, Y. *et al*., "Demonstration of a self-pulsing photonic crystal Fano laser," *Nat. Photon*., vol. 11, 81–84, 2017.

[9] Xue, W. *et al*., "Threshold characteristics of slow-light photonic crystal lasers," *Phys. Rev. Lett*., vol. 116, 063901, 2016.

[10] Keller, U. *et al*., "Semiconductor saturable absorber mirrors (SESAM's) for femtosecond to nanosecond pulse generation in solid-state lasers," *IEEE J. Quantum Electron*., vol. 2, 435−453, 1996.

[11] Fan, S. H. *et al*., "Temporal coupled-mode theory for the Fano resonance in optical resonators," *J. Opt. Soc. Am. A*., vol. 20, 569–572, 2003.

[12] Heuck, M. *et al*., "Improved switching using Fano resonances in photonic crystal structures," *Opt. Lett*., vol. 38, 2466–2468, 2013.

[13] Yu, Y. *et al*., "Fano resonance control in a photonic crystal structure and its application to ultrafast switching," *Appl. Phys. Lett*., vol. 105, 061117, 2014.

[14] Yu, Y. *et al*., "Nonreciprocal transmission in a nonlinear photonic-crystal Fano structure with broken symmetry," *Laser & Photon. Rev*., vol. 9, 241–247, 2015.

Fano-resonant excitations of generalized optical spin waves

Xianji Piao*, Sunkyu Yu, Minpyo Lee, and Namkyoo Park
Photonic Systems Laboratory, Department of ECE, Seoul National University, Seoul 08826, Korea
*corresponding author: xjpiao227@gmail.com

Abstract-Here we show the Fano-resonant excitation of optical spin waves, for longitudinal and transverse axes with respect to the propagation direction. By implementing two linearly-polarized scattering paths to chiral materials, antisymmetric Fano resonances of longitudinal spins are derived with the handedness-dependent asymmetry. We will also introduce the realization of transverse spin guided mode and its Fano-resonant excitations.

The spin angular momentum of light, which corresponds to the handedness of polarization evolutions, is one of the most significant physical quantities of photons. With respect to the propagation direction, three components of electric fields (E_x, E_y, E_z) can derive three pairs of spin components: one for longitudinal spin (Fig. 1a,b) and two for transverse spins [1,2] (Fig. 2a,b). To exploit full degrees of freedom in light-matter interactions [3], topological properties [4], and singularity [5] from these 3-dimensional spins, efficient excitation schemes each for longitudinal and transverse spins should be addressed. In this talk, we introduce the excitation of longitudinal and transverse spins from linearly-polarized incidences, achieving lossless and spectrally-controllable performance features.

First, we will talk about the net achievement of longitudinal spin angular momentum of light, through the mixing of birefringence and chiral resonances (Fig. 1c, [6]). A chiral resonator alone, without the circular dichroism, cannot lead to any net longitudinal spin due to the resonance overlap between two longitudinal spin components. We thus introduce two scattering pathways from birefringent mirrors, which derive antisymmetric Fano resonances (Fig. 1d) from the interaction between each spin mode. The net achievement of the longitudinal spin from the opposite shift of Fano dips, and the realization based on metamaterials are also discussed.

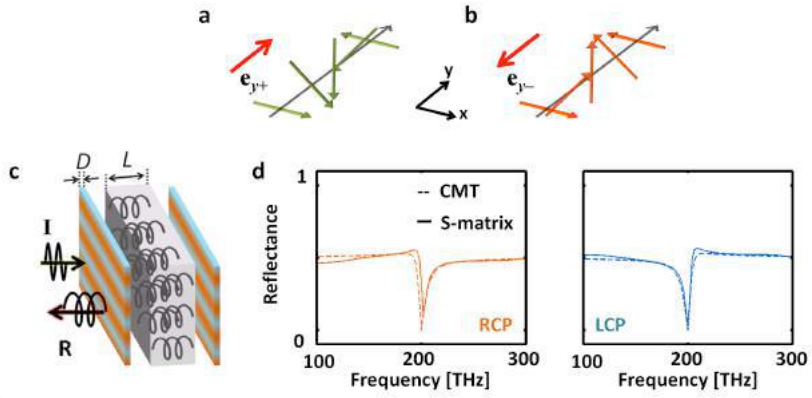

Figure 1. (a,b) Polarization evolutions of longitudinal spins for *y*-propagating wave: (a) positive spin, (b) negative spin. Red arrows denote the spin direction. (c) A schematic of the chiral resonator enclosed within birefringent mirrors for Fano-resonant excitation of longitudinal spins. (d) Reflectance spectra for each longitudinal spin component (RCP and LCP).

In the talk, we will also introduce the realization of guided transverse-spin waves, having a dark-mode feature. The excitation of transverse-spinor dark modes through the grating structure is discussed, revealing the standing wave polarization evolution from opposite transverse spin modes.

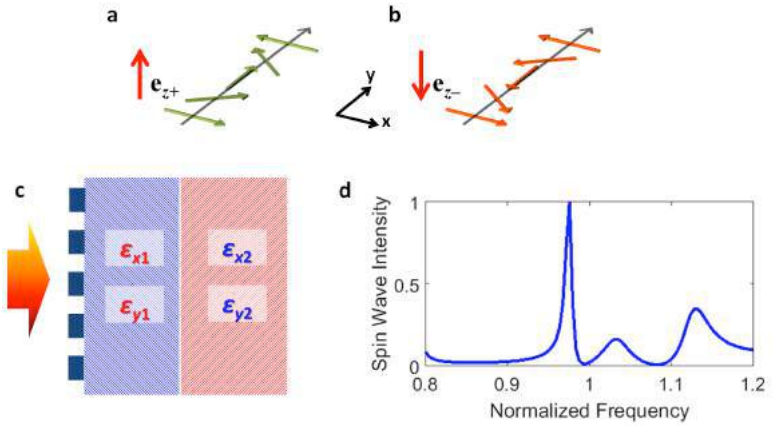

Figure 2. (a,b) Polarization evolutions of transverse spins for *y*-propagating wave: (a) positive spin, (b) negative spin. Red arrows denote the spin direction. (c) A schematic for transverse-spin wave excitations by Fano resonances. (d) Excitation spectra of transverse spin components at the interface.

REFERENCES

1. Bliokh, K. Y. and Nori, F., "Transverse and longitudinal angular momenta of light," *Phys. Rep.* Vol. 592, 1-38, 2015.
2. Aiello, A., Banzer, P., Neugebauer, M., and Leuchs, G. "From transverse angular momentum to photonic wheels," *Nat. Photon.* Vol. 9, 789-795, 2015.
3. Canaguier-Durand, A., Cuche, A., Genet, C., and Ebbesen, T. W. "Force and torque on an electric dipole by spinning light fields," *Phys. Rev. A* Vol. 88, 033831, 2013.
4. Bliokh, K. Y., Smirnova, D., and Nori, F. "Quantum spin Hall effect of light," *Science* Vol. 348, 1448-1451, 2015.
5. Yu, S.†, Park, H. S.†, Piao, X., Min, B., and Park, N. "Low-dimensional optical chirality in complex potentials," *Optica* Vol. 3, 1025, 2016.
6. Piao, X., Yu, S., Hong, J., and Park, N. "Spectral separation of optical spin based on antisymmetric Fano resonances," *Sci. Rep.* Vol. 5, 16585, 2015.

Perturbation theory for bound states in the continuum on periodic structures

Lijun Yuan[1], **Ya Yan Lu**[2,*]

[1]Chongqing Technology and Business University, China
[2]City University of Hong Kong, Hong Kong
*mayylu@cityu.edu.hk

Abstract— On periodic structures with proper symmetries, guided Bloch modes could exist above the lightline, and they are examples of bound states in the continuum (BICs). Certain BICs on periodic structure are not protected by symmetry in obvious ways. Using a rigorous perturbation theory, we show that these BICs are in fact still closely related to the symmetries.

Periodic structures sandwiched between two homogeneous media are often studied in diffration problems when incident waves are specified, and they can also be regarded as wave-guiding structures on which guided Bloch modes may exist without any incident waves. Typically, the Bloch modes on the periodic structures are found below the lightline, that is, the wavenumber in the homogeneous media is less than the magnitude of the Bloch wavevector, so that there exist no propagationg diffraction channels. The bound states in the continuum (BICs) on periodic structures are special guided Bloch modes existing above the lightline, where one or more diffration channels are still open, but the modes exhibit no radiation. The existence of certain BICs (symmetry-protected BICs) which have incompatible symmetry with the radiating waves are well understood, but there are also BICs that cannot be explained by simple symmetry arguments, and these BICs are often classified as "unprotected by symmetry" [1, 2, 3].

In fact, certain BICs labeled as "unprotected by symmetry" depend strongly on the symmetries. The simplest examples can be found on 2D structures given by a real dielectric function $\epsilon(x, z)$ which is periodic in x, even in x, and even in z (with a properly chosen origin), and bounded by identical homogeneous media (e.g. air) for $z > d/2$ and $z < -d/2$. On such 2D periodic structures, there could be propagating BICs with a nonzero Bloch wavenumber, and they are regarded as "unprotected by symmetry" [2, 3]. However, numerical results indicate that these BICs strongly depend on symmetry. If the structure is perturbed with a perturbation that breaks the reflection symmetry in x or z, the BICs usually disappear and become resonances with finite Q values, and if the perturbation keeps the symmetry, the BIC typically continues to exist with a slightly different frequency and slightly different Bloch wavenumber.

In this paper, we present a perturbation theory that clearly reveals the importance of symmetry. Given a structure described by a real $\epsilon_*(x, z)$, and a BIC with a real frequency ω_* and a real Bloch wavenumber β_*, we consider a perturbed structure given by $\epsilon_*(x, z) + \delta\epsilon_1(x, z)$, and derive a linear system for frequency ω and Bloch wavenumber β for a perturbed Bloch mode near the original BIC. It is shown that if ϵ_1 keeps the reflection symmetries in x and z, then the perturbed frequency and wavenumber are real and can be solved from a real 2×2 linear system, and when ϵ_1 breaks the symmetry, the linear system becomes complex in geneal. Therefore, the perturbation theory reveals the hidden dependence on symmetry for these BICs usually labeled as "unprotected by symmetry". It should be pointed out that our perturbation theory is very different from the standard one which only gives a perturbed frequency for a fixed Bloch wavenumber. Numerical results are provided to validate the perturbation theory.

This research is supported by the Research Grants Council of Hong Kong Special Administrative Region, China (project No. CityU 11301914).

REFERENCES

1. Hsu, C. W., B. Zhen, J. Lee, S.-L. Chua, S. G. John- son, J. D. Joannopoulos, and M. Soljaci c, "Observation of trapped light within the radiation continuum," *Nature*, Vol. 499, 188–191, 2013.
2. Bulgakov, E. N. and A. F. Sadreev, "Bloch bound states in the radiation continuum in a periodic array of dielectric rods," *Phys. Rev. A*, Vol. 90, 053801, 2014.
3. Yuan, L. and Y. Y. Lu, "Propagating Bloch modes above the lightline on a periodic array of cylinders," *J. Phys. B.*, Vol. 50, 05LT01, 2017.

Fano-Feshbach resonance in metallic nanohole arrays

M. Nishida, and Y. Kadoya

Graduate School of Advanced Science of Matter, Hiroshima University, Higashi-Hiroshima, 739-8530, Japan
mnishida@hiroshima-u.ac.jp

Abstract— Surface bound modes in thin metallic film with an array of nanoholes produce complicated band structure owing to the diffraction caused by the periodicity and the coupling between the surface plasmon polaritons through the holes. If the different branches co-exist adjacently, multiple bound modes contribute to a resonance and cause a Fano-Feshbach resonance, such as electromagnetically induced transparency (EIT) or coupled-resonator induced transparency (CRIT). In this study, we show that appropriate lattice structure of metallic nanohole array yields sharp reflection-transmission spectra. The origin of this resonance is attributed to the CRIT between the two surface bound modes based on the analyses using spatial and temporal coupled mode methods.

In a metallic film perforated by an array of nanoholes, Bloch-wave surface plasmon polaritons (BW-SPPs) on the upper and lower surfaces of the film are coupled by the wave-guide modes of nanoholes and produce variety of surface bound modes [1]. Especially, in a system with mirror symmetry in the direction perpendicular to the film surface, there are two types of surface bound modes, bonding and anti-bonding modes, which have symmetric and anti-symmetric charge distributions, respectively. These modes respond quite differently to incident light.

As an example, Fig. 1 (a) shows the transmission spectrum for the square lattice with period $L_x = L_y = 0.5\mu$m of the holes with the radius of 0.15μm. The dashed (dashed-dotted) lines indicate the dispersion relations of bonding (anti-bonding) modes. Due to the difference of symmetry, the bonding and anti-bonding modes do not have interaction to lead level anti-crossing, and a degenerate point appears in the dispersion relations. At the degenerate point, the interference between the radiations from two bound modes suppress both of reflection and transmission, and nearly perfect absorption is realized [2]. This phenomenon is a kind of Fano-Feshbach resonance which occurs when multiple resonances interfere [3].

On the other hand, another kind of Fano-Feshbach resonance is expected to occur when two modes with same mirror symmetry are located close together in the $\omega - k$ space. These two modes interact with each other via the coupling with radiation fields, and behave as two coupled modes with closer eigenfrequencies. Moreover, one of the widths of resonance becomes narrower and the other becomes broader. These effects yield a sharp dip structure in the resonance spectrum when two bright modes are located close together. This phenomenon is known as coupled-resonator induced transparency (CRIT) [2,3].

In this study, we show that CRIT phenomena can occur in metallic nanohole array systems by using rectangular lattices of nanoholes which are elongated in one direction. Fig. 1 (b) shows the

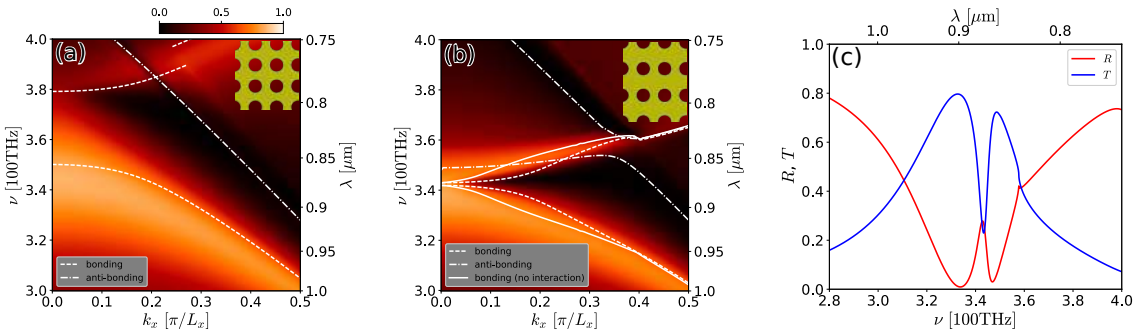

Figure 1: (a) Transmission spectra and dispersion relations of surface bound modes for $L_x = L_y = 0.5\mu$m, and (b) those for for $L_x = 0.5, L_y = 0.63\mu$m. (c) Reflection (R) and transmission (T) spectra at $k_x = 0.1\pi/L_x$.

transmission spectrum and the dispersion relations of bound modes for a rectangle lattice whose period in y direction is elongated to $L_y = 0.63\mu$m from the system used in (a). The solid lines indicate the dispersion relations of bound modes without coupling to radiation field, which are calculated using temporal coupled mode method [4]. We can see that the interaction between these two modes via the coupling with radiation fields put the resonant positions closer and produce quite sharp dip-structure. The panel (c) shows reflection and transmission spectra when the in-plane wave-number is $0.1\pi/L_x$, which have EIT-like profile.

Thus, in metallic nanohole array systems, variety of Fano-Feshbach resonances appear everywhere in the band structure, and yield complicated resonant structures. In the presentation, I will show the general picture of resonant phenomena of this system based on the analyses by the spatial and temporal coupled mode methods.

REFERENCES

1. Nishida, M., N. Hatakenaka, and Y. Kadoya, "Multipole surface plasmons in metallic nanohole arrays," *Phys. Rev. B*, Vol. 91, No. 23, 235406, 2015.
2. Nishida, M., N. Hatakenaka, and Y. Kadoya, "Degenerate Fano resonance between multipole surface plasmons in a metallic nanohole array," *META2016*, Spain, Malaga, 2016.
3. Miroshnichenko, A. E., S. Flach, Y. S. Kivshar, "Fano resonances in nanoscale structures", *Rev. Mod. Phys.*, Vol. 82, No. 3, 2257–2298, 2010.
4. Suh, W., Z. Wang, and S. Fan, "Temporal Coupled-Mode Theory and the Presence of Non-Orthogonal Modes in Lossless Multimode Cavities," *IEEE J. Quantum Electron.*, Vol. 40, No. 10, 1511–1518, 2004.

Fano resonances in light scattering by finite obstacles.

A. E. Miroshnichenko

[1]Nonlinear Physics Centre, The Australian National University, Australia

[*] andrey.miroshnichenko@anu.edu.au

Abstract-Light scattering by finite obstacles, either single particle or a number of particles in arbitrary configuration, exhibits various resonant effects. It turns out that almost any resonant response, either in directional or total scattering light scattering, can be efficiently described in terms of Fano resonance. One of the peculiar feature of the Fano resonance is complete destructive interference, which can be associated with radiationless excitations, such as nontrivial anapole modes.

Fano resonance is a generic phenomenon appearing in various systems where wave interference is permitted. One of the essential features of the Fano resonance is constructive and destructive interferences taking place in a narrow frequency range resulting in asymmetric line shape [1]. Light scattering by a finite obstacle can be unequally described in terms of partial wave scattering coefficients, based on multipolar decomposition. Various multipoles can interfere in a given direction either in phase or out-of-phase producing asymmetric line shape, which can be associated with Fano profile [2]. Such feature was employed to design effective optical nanoantenans.

Alternatively, due to partial waves orthogonality each scattering coefficient can be analyzed independently. It turns out that high index dielectric particles exhibit infinite series of sharp asymmetric Fano resonance in any given partial wave scattering, including complete suppression of scattering [3]. To explain their origin and identify various contributions to destructive interference we analyze the properties of induced field inside dielectric particle by using Cartesian multipoles. In particular, the first zero of the electric dipole partial wave can be described in terms of excitation of anapole mode [4], which is a result of destructive interference electric and toroidal dipole moments [5] in the far-field due to their identical radiation profiles (see Fig.1).

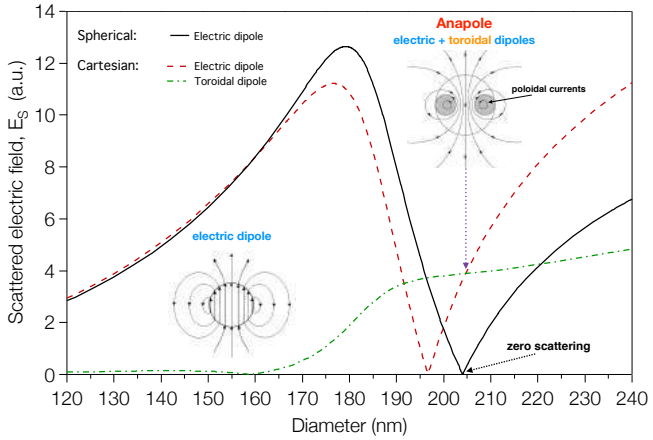

Figure 1. First Fano resonance of electric dipole partial wave scattering (black solid line) and corresponding description of the complete destructive interference in terms of our-of-phase contribution of electric (red dashed line) and toroidal dipole (green dotted line) moments to the far-field.

It can also be considered as an example of localized source excitation, which produces no radiation in the far-field. It now suggests that higher-order zeros of any partial wave scattering can be treated as nontrivial radiationless localized sources. To describe them properly in terms of Fano resonances one needs to introduce higher-order toroidal multipoles.

REFERENCES

1. Miroshnichenko, A. E., S. Flach and Y. Kivshar, "Fano resonances in nanoscale structures," *Reviews of Modern Physics*, Vol. 82, 2257, 2010.
2. Luk'yanchuk, B. et al., "The Fano resonance in plasmonic nanostructures and metamaterials," *Nature Materials*, Vol. 9, 707–715, 2010.
3. Tribelsky, M. and A. E. Miroshnichenko, "Giant in-particle field concentration and Fano resonances at light scattering by high-refractive-index particles," *Physical Review A*, Vol. 93, 053837, 2016.
4. Miroshnichenko, A. E. et al., "Nonradiating anapole modes in dielectric nanoparticles," *Nature Communications*, Vol. 6, 8069, 2015.
5. Papasimakis, N. et al., "Electromagnetic toroidal excitations in matter and free space," *Nature Materials*, Vol. 15, 263–271, 2016.

Parity control of Fano resonances and its application for signal regeneration and pulse carving

D. A. Bekele, Y. Yu, H. Hu, P. Guan, L. Ottaviano, M. Galili, L. K. Oxenløwe, K. Yvind, and J. Mørk[!]

DTU Fotonik, Technical University of Denmark DK-2800 Kongens Lyngby, Denmark
corresponding author: jesm@fotonik.dtu.dk

Abstract— Parity control of Fano resonances in a photonic crystal waveguide coupled to a nanocavity is implemented by controlling the position of a partially transmitting element (PTE) in the waveguide. We experimentally demonstrate regeneration and pulse carving of optical signals by exploiting nonlinearities in the nanocavity in combination with the asymmetrical Fano shape.

Fano resonances can be realized in photonic crystal membrane structures by exploiting the interference between a waveguide continuum and the discrete resonances of a nanocavity [1]. Further, by controlling the details of the coupling between the nanocavity and the waveguide, one can control the sign of the so-called parity of the Fano resonance, i.e., whether the spectral location of the minimum of the transmission is blue (blue-parity) or red (red-parity) shifted with respect to the maximum [2]. In this work, we demonstrate that red-parity can be used for power limiting and pulse carving while blue-parity for signal regeneration applications.

Our device is an InP photonic crystal membrane consisting of a nanocavity side coupled to a line defect waveguide cf. Fig. 1(a). A partially transmitting element (PTE) is placed in the waveguide in two different configurations. In the first case, the PTE is placed in the mirror plane passing through the center of the cavity. This results in red-parity Fano resonance indicated by the red line in Fig. 1(b). In the second configuration, the PTE is placed one lattice constant to the left of the mirror plane leading to blue-parity Fano resonance shown by the blue line in Fig. 1 (b). The structure configurations are shown in the insets of Fig. 1(b).

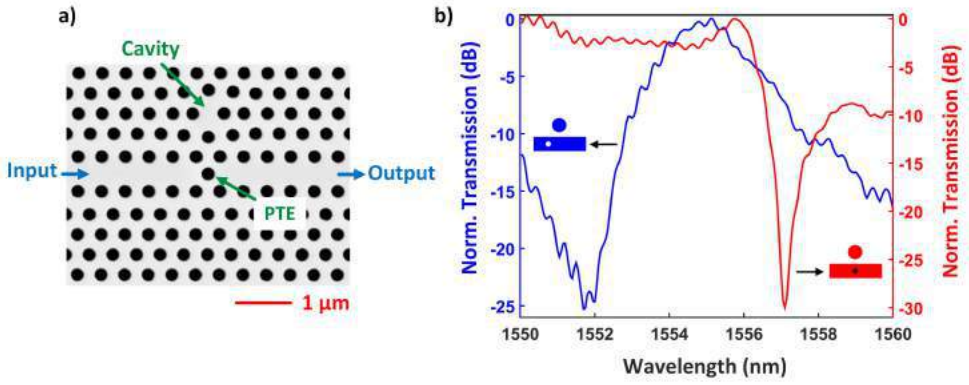

Figure 1: (a) Scanning electron microscope (SEM) image of the fabricated device. It consists of a nanocavity side coupled to a photonic crystal waveguide and a partially transmitting element (PTE) placed in the middle of the waveguide. (b) Measured transmission spectra of two devices with different PTE arrangement giving rise to blue and red-parity Fano resonances.

When an optical signal couples to the nanocavity with Q-factor in the order of 1000, strong intra-cavity field generates free carriers through two-photon absorption leading to free-carrier dispersion and band-filling effects. These nonlinear processes induce changes in refractive index inside the nanocavity resulting in blue shift of the Fano resonance [3]. Depending on the parity of the Fano resonance, very different nonlinear behavior is observed. In the case of blue-parity, the Fano

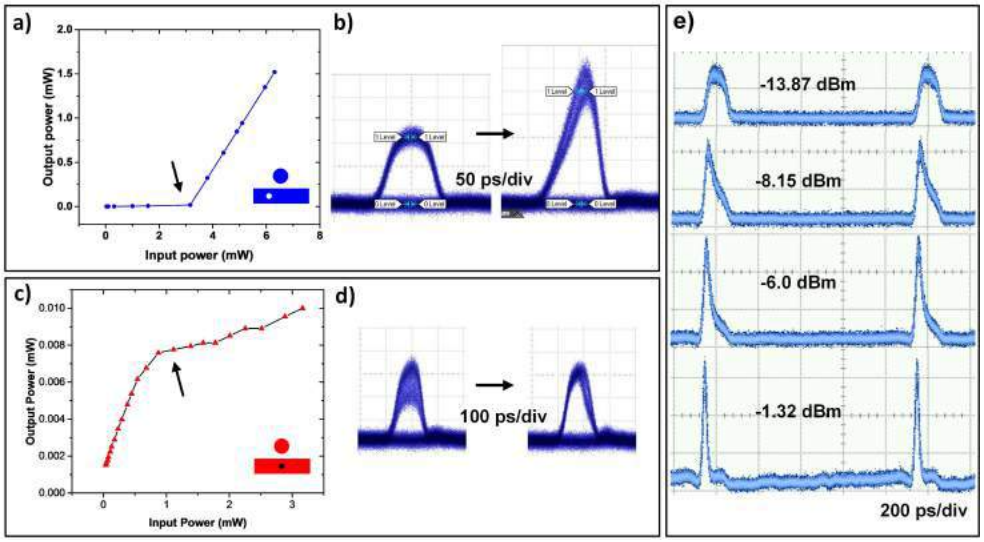

Figure 2: (a) Simulated transfer function of blue-parity Fano resonance. The black arrow indicates the region of operation for extinction ratio improvement. (b) Eye diagram of the input RZ signal (left) and the regenerated signal (right) with approximately 7 dB extinction ratio improvement. (c) Measured transfer function of red-parity Fano resonance used for power limiting experiments. (d) Eye diagram of the degraded input signal (left) and the regenerated signal (right) with reduced intensity noise. (e) Eye diagram for pulse carving of a 93 ps long pulse to a 20 ps pulse. As the input power is increases, the 1 GHz pulse become shorter and shorter.

resonance together with the nonlinear shift possess the transfer function shown in Fig. 2(a) calculated using coupled-mode theory [4]. When the device is operated at the transition point (indicated by the black arrow in Fig. 2(a)), the logical bit 1 experiences a larger transmission than that of the bit 0, which increases the power difference between them, leading to signal regeneration with improved extinction ratio up to 7 dB (Fig. 2(b)).

The red-parity Fano resonance, on the other hand, exhibits a power limiting function Fig. 2(c). Initially, the output power follows the linear increase of the input power, however, as the input power exceeds 1 mW, the output power saturates leading to the power limiting functionality. This can be used to suppress intensity noise in optical signals, hence increasing the signal quality, cf. Fig. 2(d). Compared to the power limiting using Lorentzian resonance [5], the Fano device can show a stronger power saturation as a result of the steeper slope of its spectral shape.

Another interesting application of red-parity Fano resonance is in creating narrow pulses (Fig. 2(e)): when a long pulse spectrally located at the peak of the Fano resonance couples to the cavity, shift in the resonance occurs as a result of nonlinear effects caused by the high peak power of the leading edge of the pulse. This results in reduced transmission for the latter part of the pulse, carving out a short optical pulse from a long one, and at the same time acting as a detector of the long pulse.

REFERENCES

1. Fan, S., "Sharp asymmetric line shapes in side-coupled waveguide-cavity systems," *Appl. Phys. Lett.*, Vol. 80, No. 6, 2002.
2. Osterkryger, A. D. *et al.*, "Spectral symmetry of Fano resonances in a waveguide coupled to a microcavity," *Opt. Lett.*, Vol. 41, 2065–2068, 2016.
3. Yu, Y. *et al.*, "Switching characteristics of an InP photonic crystal nanocavity: Experiment and theory," *Opt. Express* Vol. 21, 31047–31061, 2013.
4. Suh, W. *et al.*, "Temporal coupled-mode theory and the presence of non-orthogonal modes in lossless multimode cavities," *IEEE J. Quantum Electron.* Vol. 40, 1511–1518, 2004.
5. Lenglé, K. *et al.*, "Fast all-optical 10 Gb/s NRZ wavelength conversion and power limiting function using hybrid InP on SOI nanocavity," in *Proceeding of ECOC* , Amsterdam, Netherlands, 2012, 1–3.

Sharp Ultrafast Fano Resonances in Superconducting THz Metamaterials

Yogesh Kumar Srivastava[1,2], Manukumara Manjappa[1,2], Harish N. S. Krishnamoorthy[1,2], and Ranjan Singh[1,2,*]

[1]Division of Physics and Applied Physics, School of Physical and Mathematical Sciences, Nanyang Technological University, 21 Nanyang Link, Singapore 637371
[2]Center for Disruptive Photonic Technologies, The Photonics Institute, Nanyang Technological University, 50 Nanyang Avenue, Singapore 639798
*corresponding author: ranjans@ntu.edu.sg,

Abstract- Superconductor based metamaterial structures pave the way to design switchable metamaterial devices operating at terahertz frequencies. Since, metals possess very high conductivity at terahertz frequencies, the role of superconductors in exciting lossless high Q resonances remains unclear. Here, we used high-Tc superconductor YBCO to design a low asymmetry Fano resonator which supports sharp resonance at extremely low asymmetries but identical metallic meta-atom fails to support any resonance response. We also present the ultrafast switching of sharp Fano resonances in superconductors.

REFERENCES

1.Srivastava Y. K., Manjappa M., Cong L., Cao W., Al-Naib I., Zhang W. and Singh R., *Adv. Opt. Mater.,* Vol. No. 4, 457, 2016.
2. Srivastava Y. K., Manjappa M., Krishnamoorthy H. N. S. and Singh R., *Adv. Opt. Mater.*,Vol. No. 4, 1857, 2016.

Magnetic interactions and transport properties of parallel coupled magnetic molecules.

S. Alwan, J. D. Vasquez Jaramillo, H. Hammar, and J. Fransson*
Department of Physics and Astronomy, Uppsala university, Uppsala, Sweden
*corresponding author: Jonas.Fransson@physics.uu.se

Abstract-Parallel coupled quantum dots embedded in a tunnel junction is a typical system that exhibits Fano resonances. Here, we consider magnetic molecules in a similar geometry and consider the electronically mediated magnetic interactions between the localized spins as function of the gate and bias voltages as well as temperature differences between the leads. In addition to regimes of ferromagnetic and anti-ferromagnetic coupling, we show that Fano resonances give rise to vanishing exchange between the localized spins.

Previous predictions of electrical and thermal control of magnetic exchange interactions between localized spin moments in, e.g., magnetic molecules have revealed the ability to fine tune gate and bias voltages in order to deliberately go between regimes of ferromagnetic and anti-ferromagnetic exchange [1,2]. These studies have been focused on serially coupled molecules in which it is well known that interference phenomena such as Fano resonances are normally not occurring. In quantum dots coupled in parallel, however, Fano resonances are known to exist and are well captured within the traditional two-path structure, see e.g., [3], which serve as a prerequisite for the effect. Here, we consider the electronically mediated magnetic interactions between the localizes spin in magnetic molecules, pertaining to e.g, *M*-porhyrins or *M*-phthalocyanines where *M* is a transition metal element (Cu, Fe, Ni, Co, Mn), or analogous compounds. In particular, we address the dependence of the magnetic interactions on the gate and bias voltages as well as on the temperature difference between the leads. In a quite similar fashion as in the serially coupled system, we show that the exchange interaction can be controllably fine tuned between ferromagnetic and anti-ferromagnetic by means of the external control variables. In addition to this control, we also show that sudden absences of the exchange are correlated with Fano resonances and since the transport properties are deeply connected with the magnetic configuration of the spin dimer, this provides a unique way to study the Fano interference phenomena and its influence on magnetic systems.

REFERENCES

1. Fransson, J, Ren, J, and Zhu, J.-X. “Electrical and Thermal Control of Magnetic Exchange Interactions”, *Phys. Rev. Lett.*, Vol. 113, 257201, 2014.
2. Saygun, T, Bylin, J, Hammar, H, and Fransson, J, “Voltage-Induced Switching Dynamics of a Coupled Spin Pair in a Molecular Junction”, *Nano Lett.*, Vol. 16, 2824–2829, 2016.
3. Fransson, J and Balatsky, A. V., “Exchange interaction and Fano resonances in diatomic molecular systems”, *Phys. Rev. B*, Vol. 75, 153309, 2007.

Effect of substrate on Q-factor of optical bound states in the continuum

A. A. Bogdanov[1], Z. F. Sadrieva[1], I. S. Sinev[1], K. L. Koshelev[1], A. K. Samusev[1], I. V. Iorsh[1], O. Takayama[2], R. Malureanu[2], A. V. Lavrinenko[1,2]

[1] ITMO University, Russia
[2] Technical University of Denmark, Denmark
a.bogdanov@metalab.ifmo.ru

Abstract— We experimentally and theoretically analyze the role of substrate on the optical bound states in the continuum (BICs). We reveal that a high-index substrate could destroy even in-plane symmetry protected BIC due to leakage into the diffraction channels opening in the substrate. We show how two concurrent loss mechanisms – scattering due to surface roughness and leakage into substrate – contribute to the suppression of the resonance lifetime.

Optical bound states in the continuum (BICs) are localized states with energy lying above the light line and having infinite lifetime [1]. The concept of BIC was firstly proposed by von Neumann and Wigner in 1929 for electron placed in a specific potential [2]. In optics, the term bound state in the continuum first appeared around 2008 [3]. Experimental observation of optical BIC followed only in 2011 [4]. Any losses taking place in real systems result in transformation of the bound states into resonant states with finite lifetime. In this work we theoretically and experimentally analyze transformation of optical BICs into resonant states due to surface roughness and high-index substrate beneath the photonic structure.

The design of the photonic structure under study is shown in Fig. 1(a). It consists of rectangular bars made of crystalline silicon surrounded by fused silica. The parameters of the sample are following: The parameters of the sample (period $a = 1$ μm, bar width $w = 150$ nm, bar height $t = 330$ nm, thickness of SiO_2 spacer $H = 1$ μm) were chosen so that the guided modes are excited in the near-infrared spectral range, where the absorption of silicon is negligible. Wavelength of at-Γ BIC in the considered structure is 1450 nm.

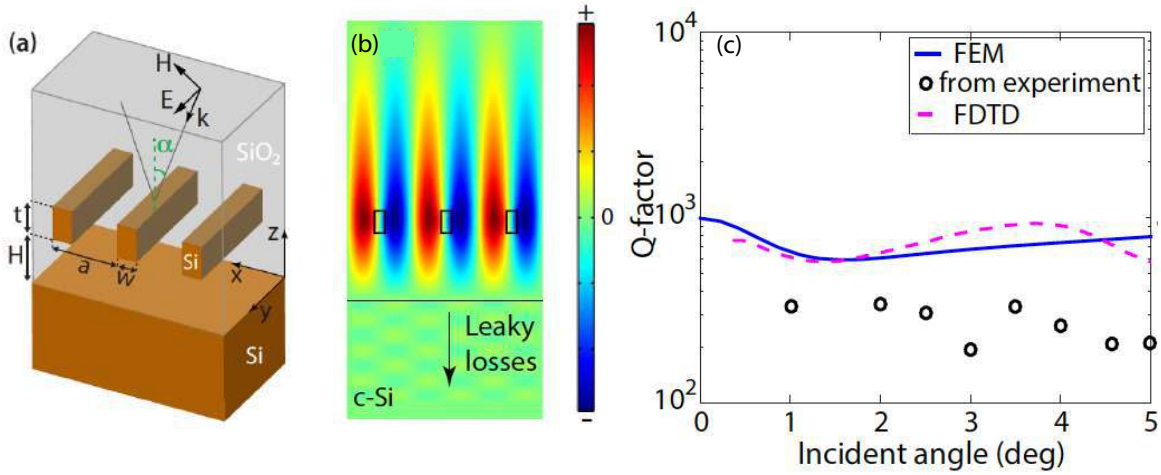

Figure 1: (a) Schematic image of photonic structure under consideration. (b) Calculated distribution of E_y component for TE_1 mode in Γ point. (c) Q-factor versus incident angle extracted from experimental (shown with dots) and FDTD (dashed line) data and calculated with FEM.

To characterize the eigenmode of the system, we carried out the angle-resolved reflectivity measurements. Then we extract the dependence of the Q-factor on the angle of incidence and compare it with results of numerical simulations [see Fig. 1(c)]. One can see that even in the

lossless case the at-Γ BIC transforms into a resonant state in spite of the fact that at-Γ BIC is protected by in-plane symmetry of the structure. Actually, the in-plane symmetry does not protect at-Γ BIC against leakage in diffractions channels opening in the silicon substrate. Figure 1(b) shows how the energy stored in BIC leaks into the silicon substrate via open diffraction channels forming the characteristic interference pattern. Increase of the spacer thickness H results in exponential decay of the leakage. At high H, when the leakage into the substrate is negligible, the scattering due to roughness makes the contribution into the total losses. Therefore, the critical thickness of the spacer, when both loss mechanisms make the same contribution strongly depends on the fabrication quality.

The obtained results provide useful guidelines for practical implementations of structures supporting optical bound states in the continuum and could find a number of applications in optical communications, on-chip photonics, laser physics and sensing.

ACKNOWLEDGMENT

Theoretical part of this work is supported by the Ministry of Education and Science of the Russian Federation (Zadanie No.3.1668.2017) and Grant of the President of the Russian Federation (-6462.2016.2). Experimental part of this work is supported by the Russian Science Foundation (Grant 17-12-01581)

REFERENCES

1. Hsu, C. W., Zhen, B., Stone, A. D., Joannopoulos, J. D. and M. Soljačić, "Bound states in the continuum," *Nat. Rev. Mater.*, Vol. 1, No. 9, 16048, 2016.
2. von Neumann, J. and Wigner, E., "Über merkwürdige diskrete Eigenwerte," *Phys. Z.* Vol. 30, 465–467, 1929.
3. Marinica, D. C., Borisov, A. G., Shabanov, S. V., "Bound States in the Continuum in Photonics," *Phys. Rev. Lett.*, Vol. 100, No. 18, 183902, 2008.
4. Plotnik, Y., Peleg, O., Dreisow, F., Heinrich, M., Nolte, S., Szameit, A., and Segev, M., "Experimental Observation of Optical Bound States in the Continuum," *Phys. Rev. Lett.*, Vol. 107, No. 18, 183901, 2011.

Harnessing Fano resonances for optomechanics

Simone Zanotto[1]
[1]Istituto Nanoscienze – CNR and NEST Laboratory, Piazza San Silvestro 12, 56127 Pisa, Italy
[*]corresponding author: simone.zanotto@nano.cnr.it

Abstract-Cavity optomechanics relies on the interplay between light and mechanical resonant degrees of freedom in a micro- or nanophotonic environment. In this contribution we will explore the physics of optomechanical devices based on optical Fano resonances, with insights towards self-sustained mechanical oscillations and electro-opto-mechanical interaction in piezoelectric metasurfaces.

The interplay between light science and mechanics dates back to the discovery of radiation pressure force, postulated more than a century ago and subsequently observed in several contexts. Recently the interaction of light with mechanics has experienced a surge of interest, mostly thanks to the potentials of nanophotonics, giving rise to the new field of cavity optomechanics [1]. The interest of mechanical interactions with nanostructured photonic devices is twofold: on one side, the optical forces induce a deformation of the structure, with an increased efficiency due to the optical resonant field enhancement. On the other side, a mechanical perturbation effectively converts into an optical response, with an enhancement which is now governed by the mechanical quality factor. In this contribution I will review some recent results about the mechanical actuation of photonic crystal resonators, i.e., of guided-mode resonant filter metasurfaces. When the geometry is perturbed - for instance, stretched along an axis - the Fano resonances occurring in reflection and in transmission will be tuned by a significant amount. In this sense, the system acts as a tunable optical filter. Moreover, if the resonator is loaded with an absorbing material, also its absorption resonance will be shifted. This effect can be harnessed to synthesize self-oscillating components supplied by a simple steady optical source [2]. To implement these effects two main technological approaches have been explored. First, we employed responsive polymers, which strongly deform through a thermo-optic mechanism. Second, we analyzed piezoelectric semiconductors, where the additional electric degree of freedom could provide further flexibility in view of quantum optomechanics experiments [3].

ACKNOWLEDGEMENTS
The author acknowledges financial support from the European Research Council through the FET-open PHENOMEN, GA 713450

REFERENCES

1. Aspelmeyer, Markus, Tobias J. Kippenberg, and Florian Marquardt. 2014. “Cavity Optomechanics.” *Reviews of Modern Physics* 86 (4): 1391–1452. doi:10.1103/RevModPhys.86.1391.
2. Zhu, Hai, Fei Yi, and Ertugrul Cubukcu. 2016. “Plasmonic Metamaterial Absorber for Broadband Manipulation of Mechanical Resonances.” *Nature Photonics* 10 (11). Nature Publishing Group: 709–14. doi:10.1038/nphoton.2016.183.
3. Balram, Krishna C., Marcelo Davanco, Jin Dong Song, and Kartik Srinivasan. 2015. “Coherent Coupling

between Radio Frequency, Optical, and Acoustic Waves in Piezo-Optomechanical Circuits." *Nature Photonics* 10 (5). Nature Publishing Group: 1–20. doi:10.1038/nphoton.2016.46.

New type of the Fano resonance in the core-level absorption spectrum of an impurity in one-dimensional superlattice

Satoshi Tanaka[1,*], **Taku Fukuta**[1], **Tomio Petrosky**[2,3]

[1]Department of Physical Science, Osaka Prefecture University, Japan
[2]Center for Studies in Statistical Mechanics and Complex Systems, The University of Texas at Austin, USA
[3]Institute of Industrial Science, University of Tokyo, Japan
*stanaka@p.s.osakafu-u.ac.jp

Abstract—Core absorption spectrum of an impurity embedded in a one-dimensional tight-binding chain is theoretically investigated in terms of complex spectral analysis. The spectrum shows a distinct Fano-profile only with a single intra-atomic transition. The asymmetric Fano absorption profile is attributed to the complex oscillator strength of the transitions to the discrete resonance states belonging to the extended Hilbert space. Nonlinear nature of the effective non-Hermitian Hamiltonian enhances the asymmetric Fano profile of the absorption spectrum.

The Fano effect was first discovered in the photoionization process of an atom, where the two optical transitions are interfered with each other through the autoionization interaction, which brings about the characteristic asymmetric absorption profile known as the *Fano profile* [1]. Since then, the Fano effect has been found to appear ubiquitously in various physical systems, having been interested as a manifestation of a quantum interference in multiple decay processes [3, 4, 5]. According to the progress of nanoscience, the Fano physics is now flourishing as one of the hot topics in modern physics.

It has been considered that, since the Fano effect is the interference of alternative decay processes, multiple decay channels are necessary to cause the Fano effect, for example, the intra-atomic excitation transition followed by the autoionization decay in addition to the direct ionization decay [2]. In this work, we reveal another process of the Fano profile in terms of the complex spectral analysis.

In this work, we study the optical absorption spectrum of a two-level impurity atom embedded in a semi-infinite tight-binding chain as shown in Fig.1, where the two optical transitions from the core level, $\hat{\mu}_d$ and $\hat{\mu}_0$, are taken into account. We describe the electronic system in terms of the single impurity Fano-Anderson model, and have derived the non-Hermitian effective Hamiltonian with the Brillouin-Wigner-Feschbach projection method. The complex eigenvalue problem of the effective Hamiltonian is nonlinear in the sense that the effective Hamiltonian itself depends on its eigenvalue. We have solved the complex eigenvalue problem to obtain the resonance state in the extended Hilbert space by non-perturbative method [6]. Due to the nonlinearity of the eigenvalue problem of the effective Hamiltonian, there appear several discrete resonance states even though the system carries only a single unperturbed state $|d\rangle$ [7].

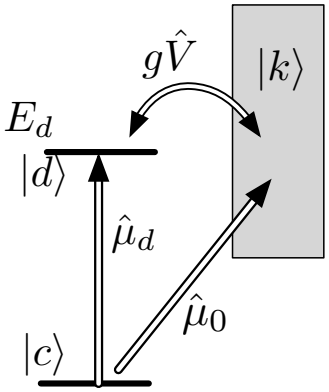

Figure 1: Core-level absorption of the two-level impurity atom in a semi-infinite chain continuum: The ground and excited states are denoted by $|c\rangle$ and $|d\rangle$, respectively, and $|d\rangle$ is coupled with the continuum $|k\rangle$ with $g\hat{V}$. The intra-atomic transition $\hat{\mu}_d$ and the direct transition $\hat{\mu}_0$ to the continuum are taken into account.

In terms of the complex spectral analysis, we found that spectral features are almost exclusively determined by the independent sum of the transitions to the discrete resonance states in the extended Hilbert space. The absorption spectrum due to the transition to a resonance state is then represented by

$$f_j(\omega) = -\frac{1}{\pi}\mathrm{Im}\left[\frac{\mu_d^2}{\omega - z_j}\langle d|\varphi_j\rangle\langle\tilde{\varphi}_j|d\rangle\left\{1 + \frac{\mu_0\, g}{\mu_d\, V}\Sigma^+(z_j)\right\}^2\right], \quad (1)$$

where $|\varphi_j\rangle$ ($\langle\tilde{\varphi}_j|$) is the right(left)-eigenstate of the Hamiltonian with a complex eigenvalue z_j, and $\Sigma^+(z)$ is the self-energy. For $\mu_0 \neq 0$ the second term in the curly bracket causes the ordinary Fano

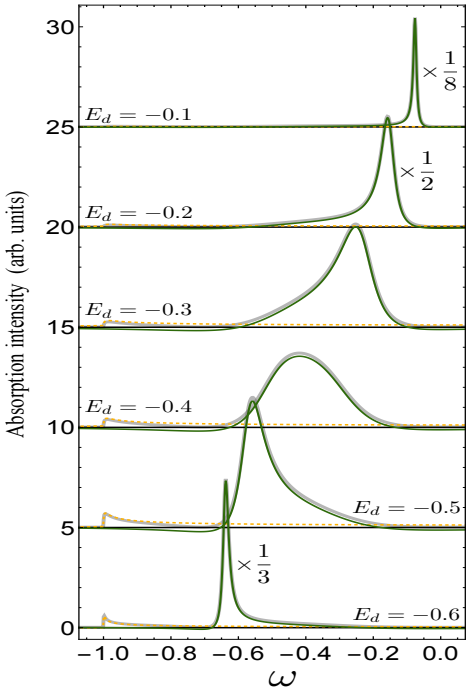

Figure 2: Absorption spectrum of the impurity atom in a semi-infinite chain.

profile, corresponding to the interference between the two optical transition paths of $\hat{\mu}_d$ and $\hat{\mu}_0$. In addition, since the resonance states belong to the extended Hilbert space, $\langle\tilde{\varphi}_j|$ is not a Hermitian conjugate to $|\varphi_j\rangle$, so the factor of $\langle d|\varphi_j\rangle\langle\tilde{\varphi}_j|d\rangle$ becomes complex, which can give rise to the Fano profile. This is very interesting because even with a single optical transition, such as the case with $\mu_d \neq 0$ and $\mu_0 = 0$, we may find the Fano effect in the absorption spectrum, in contrast to the conventional idea that an interference of the alternative transitions is necessary for the Fano effect.

Figure 2 is the result of the absorption spectrum for various values of the impurity state energy E_d for the weak coupling case ($g \ll 1$), where $\mu_d = 1$ while $\mu_0 = 0$. The spectral profile is changed as the bare impurity energy E_d is changed in the continuum. We find that even with the single transition path of μ_d the spectral profile is not at all a simple Lorentzian but a strongly asymmetric Fano type.

This alternative mechanism of the Fano effect is qualitatively different from the ordinary Fano effect, where the several transition channels are interfered with each other. We shall show that the complex spectral analysis is useful to interpret the different types of the Fano effect in the absorption spectrum and applicable to other higher order optical spectroscopies.

REFERENCES

1. H. Beautler, Z. Physik A**93,** 177 (1935), U. Fano, Nuovo Cimento **12,** 154 (1935)
2. U. Fano, Phys. Rev. **124,** 1866 (1961).
3. C. Cohen-Tannoudji and J. Dupont-Roc, *Atom-Photon Interactions: Basic Processes and Applications* (Wiley-VCH, 1998).
4. M. Kroner, *et al.,* Nature **451,** 311 (2008).
5. A. E. Miroshnichenko, S. Flach, Y. S. Kivshar, Rev. Mod. Phys.**82,** 2257 (2010).
6. T. Petrosky, I. Prigogine, and S. Tasaki, Physica A **173** 175 (1991).
7. S. Tanaka, S.Garmon, and T. Petrosky, Phys. Rev. B**73,** 115340 (2006).

Metasurfaces for dark mode resonance characteristics

E. Bochkova[1], S. N. Burokur[2,*], A. de Lustrac[1,3], and A. Lupu[1]

[1]Centre de Nanosciences et de Nanotechnologies, CNRS, Univ. Paris-Sud, Université Paris-Saclay, C2N – Orsay, 91405 Orsay cedex, France

[2]LEME, EA 4416, Université Paris Nanterre, 92410 Ville d'Avray, France

[3]Université Paris Nanterre, 92410 Ville d'Avray, France

[*]corresponding author: sburokur@u-paris10.fr

Abstract-The engineering of metasurfaces intended to obtain sharp features in their spectral response is studied. We show that in contrast to the conventional hybridization approach exploiting Fano type interference between dark and bright resonant elements, a more flexible and efficient engineering of the spectral response can be achieved by using distinctly different mechanisms for the excitation of dark modes.

The aim of the current contribution is to show that electromagnetically induced transparency [1] and dark mode excitation [2, 3] are not necessary associated. We bring theoretical and experimental evidence in the microwave domain that dark mode excitation can be achieved in an independent manner by using direct excitation mechanisms through symmetry matching of the resonant element and that of the incident electromagnetic field. The presented approach provides higher flexibility for the metasurfaces engineering and results in a great improvement of their spectral performances. Furthermore, by using Babinet's principle to design complementary resonant elements, steep variations in the spectral response can be achieved either in transmission or reflection.

Since the initial seminal paper by Fedotov [4], the concept of trapped or dark mode weakly coupled to free space started to be associated with the phenomenon of EIT transparency. However, recent theoretical advances lead to revisit this commonly shared interpretation. In particular, it was pointed that no dark mode excitation is necessary for EIT resonances. They can be described by the interference of bright modes only [5-7]. In contrast, the Fano interference of two modes with substantially different radiative strength results in a very weak EIT effect. The origin of this apparent contradiction stems from the fact that the eigenmodes of the coupled system can significantly differ from those of the individual elements, and in general they are not orthogonal.

In this study, we show that a metasurface composed of identical Z-shaped resonating elements (Fig. 1a) is able to show dark mode resonance (Fig. 1c and 1e). The dark mode in this case is associated with the first higher order mode of odd symmetry. The excitation of this antisymmetric mode is forbidden under normal incidence but becomes allowed for oblique one when the magnetic component of the incident field intersects the magnetic loops formed by the two V-antennas forming the Z resonant element. By using Babinet's principle we demonstrate in the current contribution direct excitation of the antisymmetric dark mode resulting in a maximum in transmission in a complementary Z resonator (Fig. 1b, 1d and 1f).

REFERENCES

1. S. Zhang, D. A. Genov, Y. Wang, M.Liu, and X. Zhang "Plasmon-induced transparency in metamaterials," *Phys. Rev. Lett*., vol. 101, no. 4, 047401, 2008.

2. B. Gallinet and O. J. F. Martin, “Refractive index sensing with subradiant modes: a framework to reduce losses in plasmonic nanostructures,” *ACS Nano*, vol. 7, no. 8, 6978-6987, 2013.
3. B. Gallinet and O. J. F. Martin, “Influence of electromagnetic interactions on the line shape of plasmonic Fano resonances,” *ACS Nano*, vol. 5, no. 11, 8999–9008, 2011.
4. V. A. Fedotov, M. Rose, S. L. Prosvirnin, N. Papasimakis, and N. I. Zheludev, “Sharp trapped-mode resonances in planar metamaterials with a broken structural symmetry,” *Phys. Rev. Lett*., vol. 99, no. 14, 147401, 2007.
5. C. Forestiere, L. Dal Negro, and G. Miano, “Theory of coupled plasmon modes and Fano-like resonances in subwavelength metal structures,” *Phys. Rev. B*, vol. 88, no. 15, 155411, 2013.
6. A. Lovera, B. Gallinet, P. Nordlander, and O. J. F. Martin, “Mechanisms of Fano resonances in coupled plasmonic systems,” *ACS Nano*, vol. 7, no. 5, 4527-4536, 2013.
7. B. Hopkins, A. N. Poddubny, A. E. Miroshnichenko, and Y. S. Kivshar, “Revisiting the physics of Fano resonances for nanoparticle oligomers,” *Phys. Rev. A*, vol. 88, no. 5, 053819, 2013.

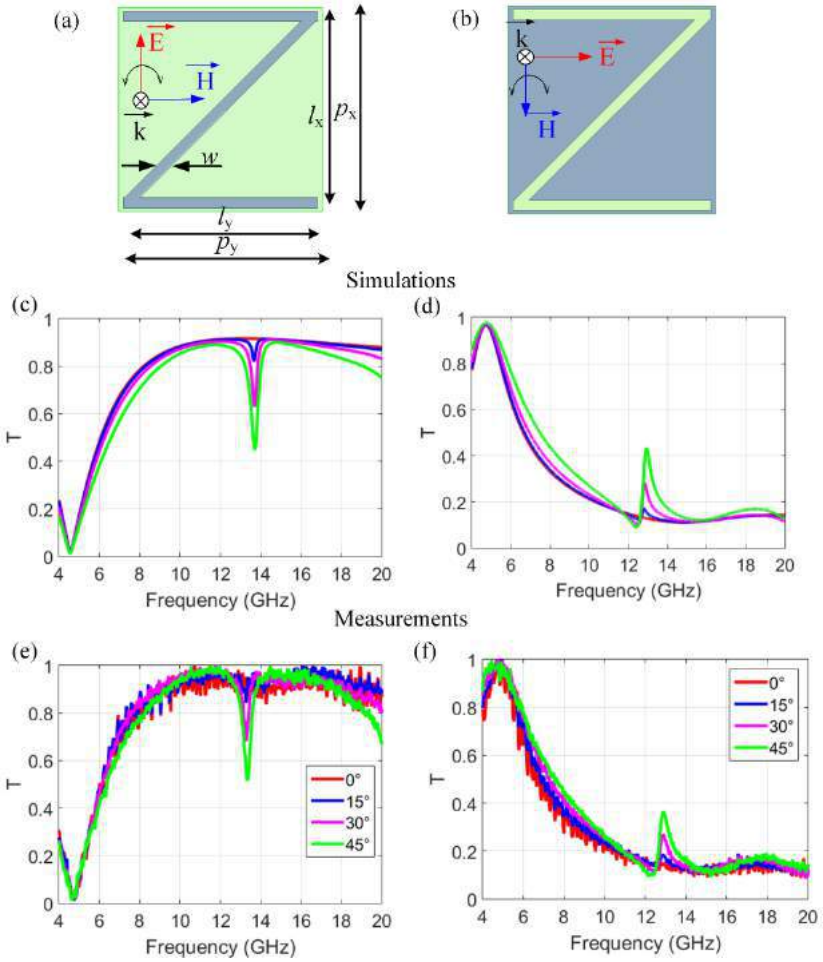

Fig. 1. Incident field polarizations for the Z-shaped (a) and complementary Z-shaped resonator (b). The geometrical dimensions are $p_x = p_y = 6$ mm, $l_x = 5.8$ mm, $l_y = 5.7$ mm, and $w = 0.3$ mm. Computed and measured transmission coefficients under normal and oblique incidence for Z (c, e) and complementary Z (d, f) respectively.

Tuning the directional scattering of light with silicon nanowires.

P. R. Wiecha[1], **A. Cuche**[1], **C. Girard**[1], **G. Colas des Francs**[2], **A. Lecestre**[3], **G. Larrieu**[3], **V. Larrey**[4], **F. Fournel**[4], **T. Baron**[5], **A. Arbouet**[1] **and V. Paillard**[1]

[1]CNRS-CEMES, Université de Toulouse, France
[2]ICB, CNRS, Université de Bourgogne, France
[3]CNRS-LAAS, Université de Toulouse, France
[4]CEA-LETI, Minatec Campus, Université de Grenoble-Alpes, France
[5]LTM, CNRS, Université de Grenoble-Alpes, France
vincent.paillard@cemes.fr

Abstract— The interference between electric and magnetic resonance modes in high refractive index dielectric nanostructures can be exploited to control the directionality of the light scattering. Usually, the directional Fano resonances occur either in spherical dielectric nanoparticles or in coupled nanostructures such as silicon sphere dimers. We show both theoretically and experimentally that directionality can be controlled in single silicon cylindrical nanowires, even by exciting either pure electric ou pure magnetic resonances. The directionality can be further tailored using asymmetric nanowires of rectangular cross section.

Recently, high refractive index nanostructures, such as silicon nanoparticles or nanowires, have proven to offer very interesting optical properties thanks to optical Mie resonances. Theses resonances that can be of electric or magnetic nature can be tuned from the near UV to the near IR. Applications are expected in field-enhanced spectroscopies, near field imaging, nonlinear optics or improved photovoltaic devices. [1]
The coupling between electric and magnetic resonances also results in a strong directional scattering of light, which offers new possibilities to design efficient optical nanoantennas. Evidence of pure forward or backward scattering has been shown using semiconductor nanodisk or nanosphere dimers, a phenomenon also associated with Fano resonances. [1, 2]
We show both theoretically and experimentally that directionality can also be controlled in single silicon cylindrical nanowires, in a first step via the nanowire diameter. The polarization of the incident light (TE or TM) with respect to the nanowire axis adds another degree of freedom compared to spheroidal nanostructures as pure TE or TM excitation allows to excite either pure electric or pure magnetic modes, respectively. However, the interference between intense electric fields is still possible in each case and arises from the coupling of either pure electric or pure magnetic modes of different orders. The exception is the smallest nanowires supporting a single nondegenerate TM mode, leading to omnidirectional scattering in that case. [3]
We finally investigate nanowires obtained by electron beam lithography of silicon on quartz substrates. We show that the forward over backward scattering ratio can be engineered as function of the nanowire size and the asymmetry of its cross-section. Fano-like resonances arising for specific wavelengths and geometries can strongly modify the FW/BW scattering ratio compared to nanowires with more symmetric cross sections.
In conclusion, we show that directional scattering of light by high refractive index nanowires can be tuned as function of both shape and dimensions of the nanowire cross-section, and that it can be controlled by the incident light polarization.

ACKNOWLEDGMENT

The numerical simulations were performed at the computing facility center CALMIP of the University of Toulouse under grant P12167.

REFERENCES

1. Kuznetsov, A. I., *et al.*, "Optically resonant dielectric nanostructures," *Science*, Vol. 354, aag/2472, 2016.
2. Yan, Y., *et al.*, "Directional Fano resonance in a silicon nanosphere dimer," *ACS Nano*, Vol. 9, No. 3, 2968–2980, 2015.
3. Wiecha, P. R., *et al.*, "Strong directional scattering from dielectric nanowires," to be published.

A Spectral Method for the Analysis of Fano-like Resonances of Nanoparticles in the Full-Retarded Regime.

C. Forestiere[1], **M. Pascale**[1], **R. Tricarico**[1], **and G. Miano**[1]

[1] Department of Electrical Engineering and Information Technology, Università degli Studi di Napoli Federico II, via Claudio 21, Napoli, 80125, Italy carlo.forestiere@unina.it

Abstract— In this work, we introduce a full-retarded spectral technique to identify the interfering modes responsible for the peaks and the dips of the scattered power spectrum in spherical nanoparticles. Moreover, we show that the interaction of non-orthogonal modes determines the onset of Fano-like resonances. We also investigate the role played by the material properties in enabling or preventing the interference effects behind Fano-like resonances.

The past two decades have witnessed a rapid rise of interest in the resonant electromagnetic scattering from metal and dielectric nanoparticles (NPs). In particular, asymmetric scattering profiles, often referred to as Fano resonances [1], have been observed in metal nanostructures excited by an electromagnetic field at optical frequencies. They generated large interest, particularly in relation to optical sensors which, taking advantage of the sharp resonant lineshape, could potentially offer a significant improvement in sensitivity.

However, despite many advancement in the understanding of NPs electromagnetic scattering, several fundamental questions remain unanswered. First, the resonances in metal or dielectric NPs of size comparable to the wavelength are currently found either experimentally or numerically by exciting the NP with radiation of various frequencies and locating the peaks of the corresponding scattered power spectra. However, this procedure is flawed and can be often misleading. Generally speaking, a peak of the scattered power spectrum cannot be univocally associated to the action of a unique *resonant mode* but may arise from the interplay of several modes. The correct identification of the resonant modes is essential in the description of anomalous scattering behaviours such as the appearance of asymmetric resonant line-shapes where interference phenomena play a key role. Second, why silicon and metal NPs of comparable size exhibit deeply different resonant behaviours in the visible spectral range? In particular, why asymmetric lineshapes in the total scattering spectrum have been observed for Si spheres, but not for metal spheres? In this work, we tackle these issues, introducing a general method to identify the modes responsible for the peaks and the dips of the scattered power spectrum.

We recently introduced a spectral solution for the electric field $\mathbf{E}_S$ scattered from a homogeneous spherical particle of permittivity $\varepsilon_r(\omega)$ [2]:

$$\mathbf{E}_S(\mathbf{r}) = (\varepsilon_r - 1)\sum_{pmnl}\left(\frac{A_{pmnl}}{\alpha_{nl}-\varepsilon_r}\mathbf{C}^{(\alpha)}_{pmnl}(\mathbf{r}) + \frac{B_{pmnl}}{\beta_{nl}-\varepsilon_r}\mathbf{C}^{(\beta)}_{pmnl}(\mathbf{r})\right), \tag{1}$$

where the eigenvalues α_{nl}, β_{nl} and the corresponding eigenfunctions $\mathbf{C}^{(\alpha)}_{pmnl}$, $\mathbf{C}^{(\beta)}_{pmnl}$ are provided in Ref. [2], and

$$A_{pmnl} = \frac{\langle \mathbf{C}^{(\alpha)}_{pmnl}, \mathbf{E}_i\rangle_\Omega}{\langle \mathbf{C}^{(\alpha)}_{pmnl}, \mathbf{C}^{(\alpha)}_{pmnl}\rangle_\Omega}, \qquad B_{pmnl} = \frac{\langle \mathbf{C}^{(\beta)}_{pmnl}, \mathbf{E}_i\rangle_\Omega}{\langle \mathbf{C}^{(\beta)}_{pmnl}, \mathbf{C}^{(\beta)}_{pmnl}\rangle_\Omega}, \tag{2}$$

$$\sum_{pnml} = \sum_{p\in\{e,o\}}\sum_{n=1}^{\infty}\sum_{m=0}^{n}\sum_{l=1}^{\infty}, \qquad \langle \mathbf{A}, \mathbf{B}\rangle_V = \iiint_V \mathbf{A}\cdot\mathbf{B}\,\mathrm{dV}. \tag{3}$$

The modes $\mathbf{C}^{(\alpha)}_{pmnl}$ are of electric type and the modes $\mathbf{C}^{(\beta)}_{pmnl}$ are of magnetic type. We have $p \in \{e, o\}$, $n \in \mathbb{N}$, and $0 \le m \le n$. The number n is associated to the number of lobes of the mode amplitude at any given radial distance. In particular, the modes with $n = 1$ are the dipolar modes, those with $n = 2$ are the quadrupolar modes, and so on. The mode number $l \in \mathbb{N}$ gives the number of maxima of the mode amplitude along the radial direction inside the sphere. We denote the electric and magnetic

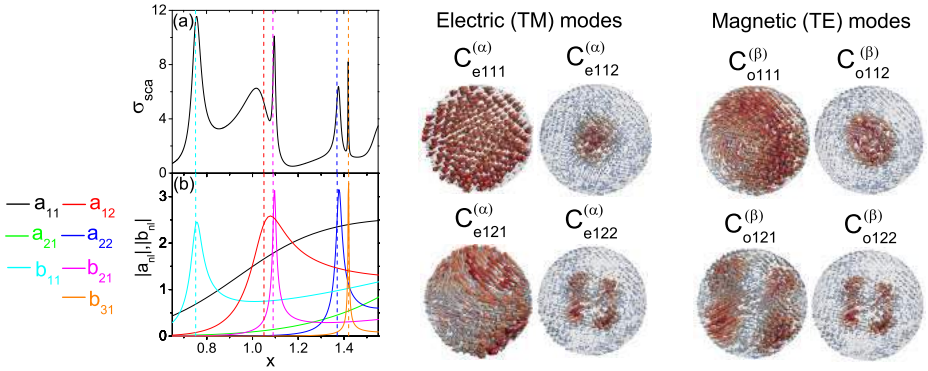

Figure 1: Scattering efficiency σ_{sca} of the Si spheres with $R = 100nm$ as function of $x = 2\pi R/\lambda$. Absolute value of the coefficients a_{nl} and b_{nl} as a function of x. The cone plot of some exemplificative modes is also shown.

modes as *fundamental* when $l = 1$, and as *higher order* modes when $l \geq 2$. In general, we have $\langle \mathbf{C}^{(\delta)}_{pmnl}\, \mathbf{C}^{(\delta')}_{p'm'n'l'} \rangle_\Omega = 0$, $\forall\, (\delta, p, m, n, l) \neq (\delta', p', m', n', l')$, where $\delta, \delta' \in \{\alpha, \beta\}$. Furthermore, due to the spherical symmetry, we also have $\langle \left(\mathbf{C}^{(\delta)}_{pmnl}\right)^*\, , \mathbf{C}^{(\delta')}_{p'm'n'l'} \rangle_\Omega = 0$, $\forall\, (\delta, p, m, n) \neq (\delta', p', m', n')$.

In this work, we show that the only modes that can be resonantly excited in an isolated metal sphere ($\mathrm{Re}\{\varepsilon_r\} < 0$) are the modes with $l = 1$. These modes constitute an orthogonal set, this fact prevents interference phenomena in the total scattered power. Vice versa, the modes that can be resonantly excited in a dielectric sphere with $\mathrm{Re}\{\varepsilon_r\} > 0$ are the magnetic modes and the higher order electric modes ($l \geq 2$). Some of these modes are non-orthogonal, enabling Fano-like resonance phenomena.

Then we apply this approach to investigate the resonances of a silicon (Si) sphere with radius $R = 100$nm and $\varepsilon_{r,Si} = 16$. The scattering efficiency σ_{sca} of the sphere excited by a linearly polarized plane wave is

$$\sigma_{sca} = x^{-2} \sum_n \left(\Big| \sum_l a_{nl} \Big|^2 + \Big| \sum_l b_{nl} \Big|^2 \right), \tag{4}$$

where $x = 2\pi R/\lambda$, λ is the wavelength, $a_{nl} = (\alpha_{nl} - \varepsilon_r)^{-1}\, \tilde{A}_{nl}$ and $b_{nl} = (\beta_{nl} - \varepsilon_r)^{-1}\, \tilde{B}_{nl}$. The coefficients $\tilde{A}_{nl}$, $\tilde{B}_{nl}$ do not depend on ε_r; they vary linearly on $\mathbf{E}_i$, and very slowly on x. Their expression can be found in Ref. [2].

We plot in Fig. 1 (a) σ_{sca}, and in Fig. 1 (b) the magnitude of the coefficients a_{nl} and b_{nl}, corresponding to the contribution of the specific modes. All peaks but one can be attributed to the dominant contribution of a single mode. In particular, the first peak from the left is due to $\mathbf{C}^{(\beta)}_{o111}$, the third one to $\mathbf{C}^{(\beta)}_{o121}$, the fourth one to $\mathbf{C}^{(\alpha)}_{e122}$, and the fifth one to $\mathbf{C}^{(\beta)}_{o131}$. Instead, the second peak arises at $x = 1.02$ from the interplay between $\mathbf{C}^{(\alpha)}_{e111}$ and $\mathbf{C}^{(\alpha)}_{e112}$, as suggested by Fig. 1 (b). In addition, the destructive interference between these two modes, which are not orthogonal, is responsible for the scattering dip enclosed by peaks 2 and 3 at $x = 1.076$, and of the corresponding asymmetry of σ_{sca}. In correspondence of this dip the values of the coefficients are $a_{11} = 0.78 - 0.95i$ and $a_{12} = 0.063 + 1.83i$. It is worth to note that, although the scattering dip is in the close proximity of the third peak, the magnetic dipole $\mathbf{C}^{(\beta)}_{o121}$ cannot be held responsible for it, because it is orthogonal to both $\mathbf{C}^{(\alpha)}_{e111}$ and $\mathbf{C}^{(\alpha)}_{e112}$, and interference cannot take place.

REFERENCES

1. B. Luk'yanchuk, N. I. Zheludev, S. A. Maier, N. J. Halas, P. Nordlander, H. Giessen, and C. T. Chong, "The Fano resonance in plasmonic nanostructures and metamaterials," Nature materials **9**, 707 (2010).
2. C. Forestiere and G. Miano, "Material-independent modes for electromagnetic scattering," *Phys. Rev. B* **94**, 201406 (2016).
3. C. Forestiere and L. Dal Negro, G. Miano, "Theory of coupled plasmon modes and Fano-like resonances in subwavelength metal structures," *Phys. Rev. B* **88**, 155411 (2013).

Dark and bright mode hybridization in plasmonic nanostructures: from electric to magnetic Fano resonances

A. Cerea[1], S. Panaro[1], R. Proietti Zaccaria[1,2], and A. Toma[1*]

[1]Istituto Italiano di Tecnologia, Genova, Italy

[2] Cixi Institute of Biomedical Engineering, CNITECH, Chinese Academy of Sciences, Ningbo, P.R. China

[*]corresponding author: andrea.toma@iit.it

Abstract-Strongly coupled plasmonic nano-architectures are ideal systems for promoting Fano resonance excitation. Here we analyze, both theoretically and experimentally, different trimer configurations supporting, respectively, electric and magnetic Fano modes. In particular, by controlling the dark-mode spectral position and the localized surface plasmon resonance retardation (de-phasing), we were able to clarify the role that these two parameters play in the super- and sub-radiant mode hybridization.

Over the last few years, controlling subwavelength-scale light matter interaction has become an essential focus in nanophotonics. The great field enhancements and highly localized hot-spots associated to plasmonic nanoassemblies have enabled wide applications in the field of near-field microscopy, surface enhanced spectroscopy and biosensing [1]. While electric field manipulation at subwavelength regime constitutes the state-of-the-art in plasmonics [2], handling of the magnetic fields at optical frequencies is still at an embryonic stage. Recently, this study has grown in interest within the context of plasmonic Fano resonances [3], exploiting circulating current configurations in resonance condition [4] via properly tailored plasmonic nano-architectures.

Fano resonances are a general phenomenon occurring, for example, through the coupling between a super-radiant ‘’bright’’ mode and a sub-radiant ‘’dark’’ mode, together with an intrinsic de-phasing among localized surface plasmons (LSPs) [5]. Here, we would like to consider two different trimer architectures in which we could control respectively the dark resonance position and the LSPs retardation, thus clarifying the role that these two parameters play in the super- and sub-radiant mode hybridization. In particular, we will introduce T-shape nanoantennas (see Figure 1a), where the excitation of the horizontal single nanostructure can induce out-of-phase charge oscillation into the vertical dimer and the consequent formation of a dark mode. A direct result of the spectral overlapping between super- and sub-radiant modes consists in the generation of resonant hot-spots inside the inter-particle gap regions. Indeed, if we consider the distribution of the electric field enhancement in correspondence of the Fano condition, we can recognize two identical “electric” hot-spots inside the 10 nm inter-particle separations (see Figure 1a, inset).

The case is totally different if we want to generate intense and localized “magnetic” hot-spots under Fano resonance conditions. Dedicated plasmonic devices able to support close circulating current modes instead of linearly oscillating plasmons are required. A possible strategy consists in replacing the horizontal antenna (Figure 1a, inset) employed in T-shape configuration with a nanodisk structure. The resulting layout is schematically shown in Figure 1b. In Fano resonance condition the plasmonic currents, initially in phase (see Figure 1b,d), undergo a re-arrangement, thus producing a Coil-like plasmonic mode (Figure 1c) and the

consequent formation of a magnetic hot-spot. This transition has been experimentally confirmed by optical characterizing ad-hoc fabricated plasmonic structures. The spectral results are summarized in Figure 1f. The magnetic character of the Fano resonance is clarified by the near-field analysis inside the trimer gap region, as illustrated in Figure 1e where a clear magnetic field enhancement can be recognized. In conclusion, plasmonic Fano resonances represent a key-element in nano-photonics, thanks to their local field enhancement and far-field spectral selectivity (see Figure 1). Furthermore, interesting scenarios can be envisioned in the field of "artificial magnetism" where Fano coil-like resonances could play a prominent role for the local manipulation of the magnetic properties of matter, especially in frequency ranges where the saturation of the magnetic response strongly hinders resonant phenomena [4-5].

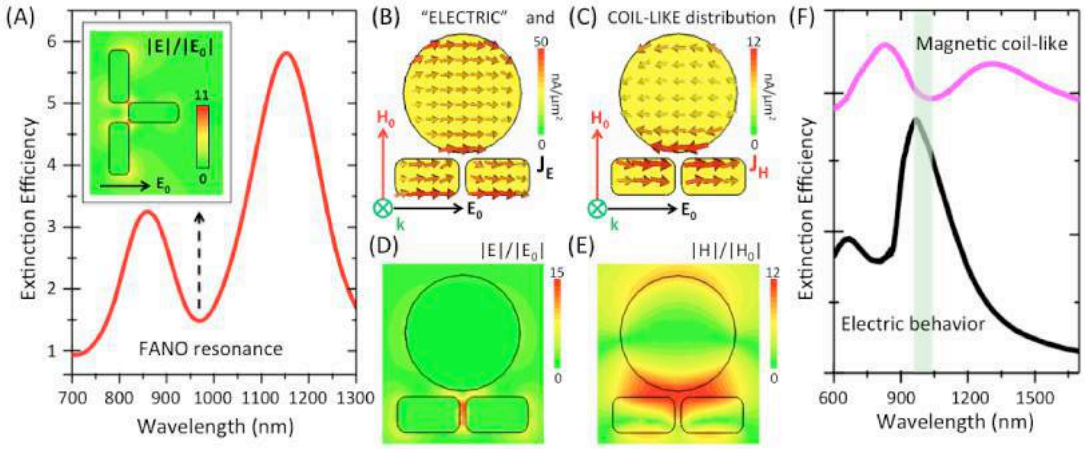

Figure 1: (a) Extinction efficiency spectrum of T-shape trimer with antenna length = 210 nm. The inset shows a 2D plot of the electric field enhancement distribution in correspondence of the Fano resonance. (b, d) Simulated charge current density (JE) and electric field enhancement distributions associated to the "electric" configuration. (d, e) Respectively simulated charge current density (JH) and magnetic field enhancement distributions associated to the Coil-like condition. (f) Measured extinction efficiency spectra of trimer arrays supporting in-phase (black line) and out-of-phase (purple line) plasmonic oscillations.

REFERENCES

1. Anker, J. N. et al. "Biosensing with plasmonic nanosensors", *Nat. Materials,* Vol. 7, 442-453 2008.
2. Schuller, J. A. et al. "Plasmonics for extreme light concentration and manipulation", *Nat. Materials*, Vol. 9, 193-204, 2010.
3. Shafiei, F. et al. "A subwavelength plasmonic metamolecule exhibiting magnetic-based optical Fano resonance", *Nat. Nanotechnol.,* Vol. 8, 95-99, 2013.
4. Nazir, A. et al., "Fano Coil-Type Resonance for Magnetic Hot-Spot Generation", *Nano Lett.* Vol. 14, 3166-3171, 2014.
5. Panaro, S. et al. "Dark to Bright Mode Conversion on Dipolar Nanoantennas: A Symmetry-Breaking Approach", *ACS Photonics*, Vol. 1, 310-314, 2014.

Resonant-state expansion in open quantum systems

Naomichi Hatano

Institute of Industrial Science, University of Tokyo, 5-1-5 Kashiwanoha, Kashiwa, Chiba 277-8574, Japan
hatano@iis.u-tokyo.ac.jp

Abstract— A novel complete set of the Hilbert space of open quantum systems is introduced. The complete set contains all possible states with discrete eigenvalues, including the resonant, anti-resonant, bound and anti-bound states. The Fano resonance is microscopically explained in terms of the interference between discrete eigenstates.

We consider here open quantum systems given by the tight-binding model, typically represented by the T-shaped quantum dot. We first introduce a novel complete set of the Hilbert space of open quantum systems [1, 2, 3]. The complete set consists of all possible discrete eigenstates, namely the resonant, anti-resonant, bound and anti-bound states.

We next break down the transmission coefficient into the summation of the discrete eigenstates. It reveals that the asymmetric Fano resonance is caused by interference between two discrete eigenstates. More precisely, we classify the Fano resonance into the following three categories: (i) the interference between a resonant state and an anti-resonant state; (ii) the interference between a resonant-state pair (a resonant state and the corresponding anti-resonant state) and a bound state; (iii) the interference between a resonant-state pair and another resonant-state pair. We thereby give a microscopic description of the Fano asymmetric parameter, which was originally introduced only phenomenologically. One of the expressions indicates that the corresponding Fano parameter becomes complex under an external magnetic field.

In summary, we explain the Fano asymmetry microscopically from the perspective of the resonant state of open quantum systems.

ACKNOWLEDGMENT

The study is supported by Kakenhi Grants Nos. 15K05200, 15K05207, and 26400409 from Japan Society for the Pro- motion of Science.

REFERENCES

1. Sasada, K., N. Hatano and G. Ordonez, "Resonant Spectrum Analysis of the Conductance of an Open Quantum System and Three Types of Fano Parameter," *J. Phys. Soc. Jpn.*, Vol. 80, No. 10, 104707-1–27, 2011.
2. Hatano, N and G. Ordonez, "Time-reversal symmetric resolution of unity without background integrals in open quantum systems," *J. Math. Phys.*, Vol. 55, No. 12, 122106-1–40, 2014.
3. Ordonez, G. and N. Hatano, "Self-generated breaking of time-reversal symmetry in open quantum systems." arXiv:1610.01548, 2016.

Fano resonance and spontaneous emission of an atom near a plasmonic nanoshell

Tiago J. Arruda[1], Romain Bachelard[2], John Weiner[1], Sebastian Slama[3], and Philippe W. Courteille[1]

[1]São Carlos Institute of Physics (IFSC), University of São Paulo (USP), São Paulo, Brazil
[2]Department of Physics, Federal University of São Carlos (UFSCar), São Paulo, Brazil
[3]Physikalisches Institut, Eberhardt-Karls-Universität Tübingen, Tübingen, Germany
*corresponding author, E-mail: tiagojarruda@gmail.com

Abstract

We analytically study the spontaneous emission of an optical emitter in the vicinity of a plasmonic nanoshell [1]. Based on classical electrodynamics, we show that the fluorescence enhancement can be tuned by the aspect ratio of the coated nanosphere and the distance between optical emitter and spherical surface. In particular, we show that both the enhancement and quenching of the fluorescence are associated with plasmonic Fano resonances induced by near-field interactions.

1. Introduction

With the advent of nanoplasmonics and metamaterials, the Fano interference has become an essential tool for tailoring and controlling light-matter interaction at the nanoscale [2, 3, 4]. In plasmonic systems, the Fano effect can appear due to the interaction of a localized plasmon resonance with a broad Mie scattering resonance [2].

Here, we study the impact of a Fano resonance of a plasmonic nanoshell on an optical dipole emitter in its vicinity [1]. It is well-known that using the first-order perturbation theory, one can formally calculate from quantum electrodynamics the variation on linewidth and energy level shift of a single atom due to the environment (boundary conditions) [5]. In the weak-coupling regime, the spontaneous emission of an atom follows Fermi's golden rule, in which the atom decays exponentially. A remarkable feature of this approximation is that the emission rate of an atom in the vicinity of a body (normalized by the spontaneous emission rate in vacuum), Γ/Γ_0, can be calculated in the framework of classical electrodynamics [5, 6]. Indeed, by taking the total power emitted by a classical dipole in the vicinity of a body (normalized by the power emitted in vacuum), P/P_0, one can demonstrate that $P/P_0 = \Gamma/\Gamma_0$ [6].

Bearing this equivalence in mind, let us consider a coated nanosphere of inner radius $a = 50$ nm and outer radius $b = 70$ nm embedded in the vacuum. The nanosphere has a lossless dielectric core with refractive index $n_1 = 3.5$ and a dispersive silver shell with a realistic refractive index $n_2 = n_{\rm Ag}(\omega)$ [7]. Now, consider that this sphere interacts with a single optical emitter located at $r_0 = b + \Delta r$ (the spherical coordinate system has its origin at the center of the sphere) with dipole moment $\mathbf{d}_0$ and transition frequency ω_0. The spontaneous decay rate of an electric dipole oscillating orthogonally to the spherical surface reads [1, 5]

$$\frac{\Gamma_\perp}{\Gamma_0} = 1 - \frac{3}{2}\mathrm{Re}\sum_{\ell=1}^{\infty}\frac{\ell(\ell+1)(2\ell+1)}{(k_0 r_0)^4} a_\ell \left[\xi_\ell(k_0 r_0)\right]^2, \quad (1)$$

$$\frac{\Gamma_{||}}{\Gamma_0} = 1 - \frac{3}{4}\mathrm{Re}\sum_{\ell=1}^{\infty}\frac{(2\ell+1)}{(k_0 r_0)^2}\Big\{ a_\ell \left[\xi'_\ell(k_0 r_0)\right]^2 + b_\ell \left[\xi_\ell(k_0 r_0)\right]^2 \Big\}, \quad (2)$$

where ξ_ℓ is the Riccati-Henkel function of first kind, and a_ℓ and b_ℓ are the well-known TE and TM Lorenz-Mie coefficients [8], respectively. The expression for a dipole oscillating tangentially to the spherical surface is analogous [5]. It is worth mentioning that coated spheres can exhibit Fano resonances in the total scattering cross section ($\propto |a_\ell|^2$) and these resonances can be analysed via the Lorenz-Mie coefficient a_ℓ [9, 10, 11, 12, 13].

The fluorescence enhancement factor, $F_{\mathbf{d}_0}$, is defined as the ratio between the observed emission intensities in the presence and in the absence of the sphere in the vicinity of the optical emitter [14]:

$$F^{\omega_0}_{\mathbf{d}_0}(r_0,\omega) = \mathcal{G}_{\mathbf{d}_0}(r_0,\omega) Q^{\omega_0}_{\mathbf{d}_0}(r_0), \quad (3)$$

where the quantities $\mathcal{G}_{\mathbf{d}_0} = |\mathbf{d}_0 \cdot (\mathbf{E}_{\rm in} + \mathbf{E}_{\rm sca})|^2 / |\mathbf{d}_0 \cdot \mathbf{E}_{\rm in}|^2$ and $Q^{\omega_0}_{\mathbf{d}_0} = \Gamma^{\rm rad}_{\mathbf{d}_0}/(\Gamma^{\rm rad}_{\mathbf{d}_0} + \Gamma^{\rm nrad}_{\mathbf{d}_0})$ are the intensity enhancement factor (which depends on ω, the *excitation* frequency) and the quantum efficiency (which depends on ω_0, the *transition* frequency), respectively, with $\mathbf{E}_{\rm in}(\omega)$ and $\mathbf{E}_{\rm sca}(\omega)$ being the incoming and scattered electric fields [1].

2. Results and discussion

In Figs. 1(a) and 1(b), we plot the fluorescence enhancement response as a function of the excitation wavelength. Note that the $F_{||}$ profile changes continuously from a Lorentzian lineshape ($\Delta r = 5$ nm) to a Fano lineshape as we increase Δr, whereas $F_\perp$ remains a Fano lineshape profile from the beginning to the end. This change in $F_{||}$ behavior seems to occur around $\Delta r = 20$ nm and $\Delta r = 30$ nm, which is a local minimum region for the quantum efficiency $Q_{||}$ (see Ref. [1]). Furthermore, being a Fano lineshape described by $f_q(\epsilon) = (q+\epsilon)^2/(1+\epsilon^2)$, where q is the Fano asymmetry parameter, the Fano profiles obtained in the insets of Figs. 1(a) and 1(b) have asymmetry parameters with different sign, namely $q_\perp \approx 2.2$ and $q_{||} \approx -2.9$.

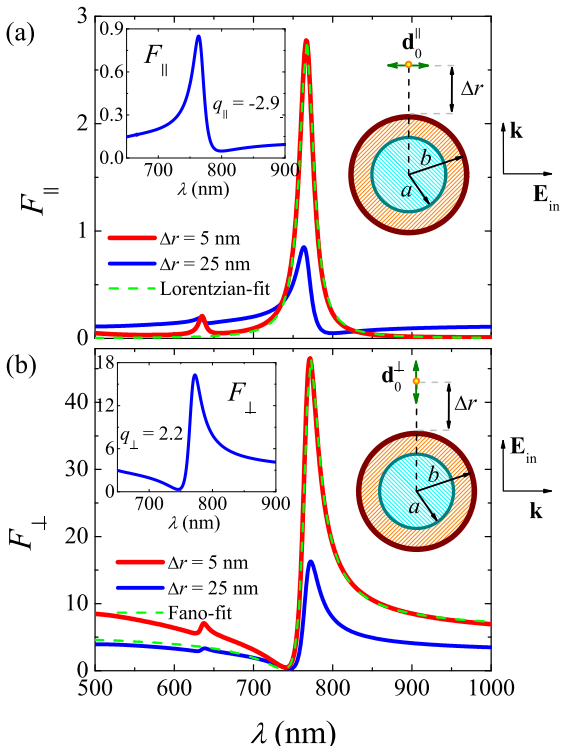

Figure 1: Fluorescence enhancement response associated with an optical emitter (transition wavelength $\lambda_0 = 780$ nm) in the vicinity of a silver nanoshell. The inner sphere has refractive index $n_1 = 3.5$ and radius $a = 50$ nm, whereas the silver nanoshell has radius $b = 70$ nm. (a) The plot shows the Lorentzian lineshape of $F_{||}$ for $\Delta r = 5$ nm (maximum enhancement). The inset shows a Fano lineshape for $\Delta r = 25$ nm with negative asymmetry parameter $q_{||} = -2.9$. (b) The plot shows the Fano lineshape of $F_{\perp}$ for $\Delta r = 5$ nm (maximum enhancement). The inset shows a Fano lineshape for $\Delta r = 25$ nm with positive asymmetry parameter $q_{\perp} = 2.2$.

The sign difference between $q_{\perp}$ and $q_{||}$ and the transition between Lorentzian and Fano lineshapes appear in association with a singular point in the near-field energy flow induced by the Fano effect [3, 15]. For $\ell = 1$, which is the dominant scattering channel for $kb < 1$, we obtain after some algebra [1] the Fano asymmetry parameters of the fluorescence enhancement curves:

$$q_{\perp} = \frac{1}{1+\epsilon''(\omega)}\left[\frac{qy_1(kr_0) - j_1(kr_0)}{qj_1(kr_0) + y_1(kr_0)}\right], \quad (4)$$

$$q_{||} = -\frac{1}{1+\epsilon''(\omega)}\left[\frac{q\chi_1'(kr_0) + \psi_1'(kr_0)}{q\psi_1'(kr_0) - \chi_1'(kr_0)}\right], \quad (5)$$

where $q = \chi_1'(kb)/\psi_1'(kb)$, with j_1, y_1, ψ_1 and χ_1 being the Bessel, Neumann, Riccati-Bessel and Riccati-Neumann functions, respectively. The function $\epsilon''(\omega)$ has a very complicated analytical expression, and it can be estimated from the maximum scattering cross section or the Fano resonance. More details can be found in Ref. [1].

Here, the Lorentzian lineshape in $F_{||}(\lambda)$ in the near-field that changes into a Fano lineshape in the far-field is a consequence of the (dielectric) core-shell (metal) geometry. Physically, the atomic dipole moment $\mathbf{d}_0^{||}$ induces an oppositely directed dipole moment on the plasmonic nanoshell surface, with almost the same amplitude. This interaction cancels out the broad dipole mode at the surrounding medium/plasmonic shell interface, but does not cancel out the narrow dipole mode at the plasmonic shell/dielectric core interface. As the distance between the dipole and the nanoshell becomes greater, the influence of the broad dipole mode in the fluorescence enhancement increases. From the experimental point of view, this result can be applied to control both the enhancement and quenching of the fluorescence response of quantum emitters in the vicinity of plasmonic nanoshells.

3. Conclusion

We have investigated the fluorescence enhancement of an optical emitter in the vicinity of a plasmonic silver nanoshell in the weak-coupling regime. We have demonstrated that a Fano resonance in the total scattering cross section leads to a Fano lineshape response in the fluorescence enhancement as a function of the distance between dipole and sphere. For an optical emitter with dipole moment oriented tangentially to the spherical surface, we have obtained a symmetric Lorentzian lineshape response in the near-field for the fluorescence enhancement. These results may have interesting applications for fluorescence enhancement and/or quenching of optical dipole emitters near plasmonic nanoshells.

Acknowledgement

T.J.A, R.B, and Ph.W.C hold Grants from Sao Paulo Research Foundation (FAPESP) (Grant Nos. 2015/21194-3, 2014/01491-0, and 2013/04162-5, respectively). S.S is supported by the Fulbright-Cottrell Award.

References

[1] T.J. Arruda, R. Bachelard, J. Weiner, S. Slama, Ph.W. Courteille, Fano resonances and spontaneous emission of an atomic dipole near a plasmonic nanoshell, *arXiv*:1706.04856, 2017.

[2] A.E. Miroshnichenko, S. Flach, Y.S. Kivshar, Fano resonances in nanoscale structures, *Rev. Mod. Phys.* 82: 2257, 2010.

[3] Y. Xu, A.E. Miroshnichenko, A.S. Desyatnikov, Optical vortices at Fano resonances, *Opt. Lett.* 37: 4985, 2012.

[4] C. Stehle, C. Zimmermann, S. Slama, Cooperative coupling of ultracold atoms and surface plasmons, *Nat. Phys.* 10: 937, 2014.

[5] H. Chew, Transition rates of atoms near spherical surfaces, *J. Chem. Phys.* 87: 1355, 1987.

[6] V. Klimov, M. Ducloy, V.S. Letokhov, Radiative frequency shift and linewidth of an atom dipole in the vicinity of a dielectric microsphere, *J. Mod. Opt.* 43: 2251, 1996.

[7] P.B. Johnson, R.W. Christy, Optical constants of the noble metals, *Phys. Rev. B* 6: 4370, 1972.

[8] T.J. Arruda, F.A. Pinheiro, A.S. Martinez, Electromagnetic energy within coated spheres containing dispersive metamaterials, *J. Opt.* 14: 065101, 2012.

[9] M.I. Tribelsky, A.E. Miroshnichenko, Y.S. Kivshar, Unconventional Fano resonances in light scattering by small particles, *Europhys. Lett.* 97: 44005, 2012.

[10] T.J. Arruda, A.S. Martinez, F.A. Pinheiro, Unconventional Fano effect and off-resonance field enhancement in plasmonic coated spheres, *Phys. Rev. A* 87: 043841, 2013.

[11] T.J. Arruda, A.S. Martinez, F.A. Pinheiro, Tunable multiple Fano resonances in magnetic single-layered core-shell particles, *Phys. Rev. A* 92: 023835, 2015.

[12] T.J. Arruda, A.S. Martinez, F.A. Pinheiro, Electromagnetic energy and negative asymmetry parameters in coated magneto-optical cylinders: Applications to tunable light transport in disordered systems, *Phys. Rev. A* 94: 033825, 2016.

[13] M.I. Tribelsky, A.E. Miroshnichenko, Giant in-particle field concentration and Fano resonances at light scattering by high-refractive-index particles, *Phys. Rev. A* 93: 053837, 2016.

[14] D.V. Guzatov, S.V. Vaschenko, V.V. Stankevich, A.Ya. Lunevich, Y.F. Glukhov, S.V. Gaponenko, Plasmonic Enhancement of Molecular Fluorescence near Silver Nanoparticles: Theory, Modeling, and Experiment, *J. Phys. Chem. C* 116: 10723, 2012.

[15] B.S. Luk'yanchuk, A.E. Miroshnichenko, Y.S. Kivshar, Fano resonances and topological optics: an interplay of far- and near-field interference phenomena, *J. Opt.* 15: 073001, 2013.

Parity-Time and related symmetries in Photonics, Plasmonics, Acoustics

Non-Hermitian edge modes and topological winding numbers in $\mathcal{PT}$-symmetric systems

D. Leykam[1], **K. Y. Bliokh**[2,3], **C. Huang**[1,4], **Y. D. Chong**[1,5], **and F. Nori**[2,6]

[1]School of Physical and Mathematical Sciences, Nanyang Technological University, Singapore
[2]Center for Emergent Matter Science, RIKEN, Wako-shi, Saitama, Japan
[3]Nonlinear Physics Centre, RSPE, The Australian National University, Canberra, Australia
[4]Department of Physics, National Tsing Hua University, Hsinchu, Taiwan
[5]Centre for Disruptive Photonic Technologies, Nanyang Technological University, Singapore
[6]Physics Department, University of Michigan, Ann Arbor, Michigan, USA
dleykam@ntu.edu.sg

Abstract— Generalizing Hermitian topological phases and edge modes to non-Hermitian systems is a pressing open problem. We study edge modes of a non-Hermitian two dimensional Dirac equation, characterizing its three distinct types of edge modes by two topological winding numbers: the Berry phase and a "non-Hermitian charge" carried by non-Hermitian degeneracies of the bulk spectrum. This provides an important step towards a complete topological description of non-Hermitian quantum systems and may be realized in PT-symmetric honeycomb lattices.

The topological properties and classification of Hermitian quantum Hamiltonians has been thoroughly studied in the past decade. Gapped periodic media can be characterized by quantized topological invariants that can only change by tuning the system through a topological phase transition, i.e. a spectral degeneracy. Boundaries between topologically distinct systems host edge modes that cannot be removed without closing the bulk band gap. These "protected" edge modes have potential photonic applications as disorder-robust non-reciprocal waveguides [1].

The generalization of these concepts to non-Hermitian systems is comparatively less well understood, despite the enormous recent interest in non-Hermitian wave effects such as parity-time ($\mathcal{PT}$) symmetry [2], occurring in photonic systems with spatially structured gain and loss. Non-Hermitian wave systems exhibit distinct *exceptional point* (EP) spectral degeneracies which form branch points where the Hamiltonian becomes non-diagonalizable. A natural question is whether these EPs can be associated with non-Hermitian topological invariants and protected edge states, and how they relate to Hermitian topological phases. Under weak gain or loss Hermitian topological edge modes can retain some of their original characteristics [3, 4], but stronger non-Hermiticity combined with a chiral or sublattice symmetry results in EPs and new "anomalous" edge modes qualitatively different from the Hermitian limit, embedded in a gapless spectrum [5, 6].

We study a continuum model of two-dimensional non-Hermitian topological edge modes analogous to the Hermitian Dirac equation [7],

$$\hat{H} = \begin{pmatrix} k_x - isk_y & m \\ m & -k_x + isk_y \end{pmatrix} \equiv (k_x - isk_y)\,\hat{\sigma}_z + m\hat{\sigma}_x \tag{1}$$

parametrized by the momentum (k_x, k_y), the "Dirac mass" m, and the "non-Hermitian charge" s, which determines the sign of the non-Hermitian part of $\hat{H}$. This Hamiltonian has the chiral symmetry $\{\hat{H}, \hat{\sigma}_y\} = 0$ and $\mathcal{PT}$ symmetry ($\mathcal{T}$ is complex conjugation and $\mathcal{P}$ is an x reflection), and can hence have real energy eigenvalues $\hat{H}\psi = \lambda\psi$. The bulk spectrum $\lambda = \pm\sqrt{(k_x - isk_y)^2 + m^2}$ (real part plotted in Fig. 1(a)) hosts EPs when $\lambda = 0$.

Interfaces between domains with different (m, s) host localized zero energy ($\lambda = 0$) edge modes with parametric regions of existence determined by the EPs of the bulk spectrum. We consider in Fig. 1(b,c) an interface in the x direction and find that the edge modes form three classes: "Hermitian-like", "non-Hermitian", and "mixed", distinguished by two topological winding numbers (w_1, w_2) associated with each EP. w_1 is the non-Hermitian generalization of the Berry phase, while w_2 characterizes the chirality of energy eigenvalues in the vicinity of the EP. We find that the difference in these two bulk winding numbers across the interface, $(\Delta w_1, \Delta w_2)$, completely characterizes the edge modes. For example the "mixed" edge modes only occur when $\Delta w_2 = -\frac{1}{2}$ and resemble the "anomalous" edge modes found in Ref. [6].

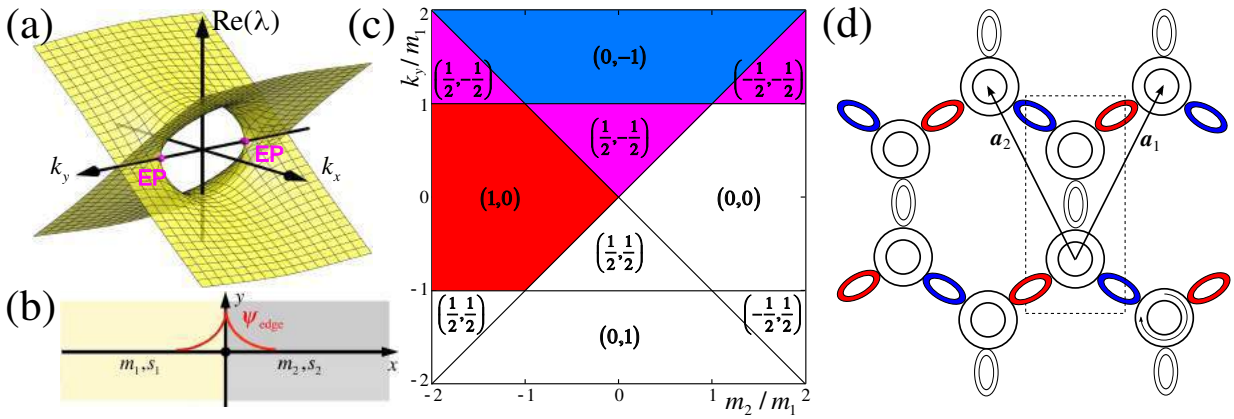

Figure 1: (a) Real part of the bulk spectrum of Eq. (1), hosting two non-Hermitian degeneracies (EPs) separating gapped and gapless regions. (b) Topological edge modes are hosted by interfaces between media with different masses m and non-Hermitian charges s. (c) Phase diagram of edge modes as a function of k_y and relative masses, for media with opposite non-Hermitian charges $s_1 = -s_2 = 1$. Red, purple, and blue regions indicate existence regions of "Hermitian-like", "mixed" and "non-Hermitian" edge modes respectively. Numbers in brackets denote the differences in winding numbers $(\Delta w_1, \Delta w_2)$ across the interface. (d) Possible realization of the model Eq. (1) using a honeycomb lattice of ring resonators with gain (red) and loss (blue) in link rings, with unit cell and lattice vectors indicated by dashed and solid lines respectively.

A possible lattice realization of the effective Hamiltonian Eq. (1) is the 2D photonic ring resonator lattice shown in Fig. 1(d). The required non-Hermitian coupling may be implemented by embedding $\mathcal{PT}$-symmetric gain and loss into the non-resonant link rings. We confirm the existence of zero energy edge modes in this model through diagonalization of the corresponding tight binding Hamiltonian [7]. We therefore anticipate that the zero energy edge modes captured by our continuum model may be observable in a wide variety of non-Hermitian wave systems.

ACKNOWLEDGMENT

This research was supported by the Singapore National Research Foundation (grant NRFF2012-02), the Singapore MOE Academic Research Fund Tier 2 (grant MOE2015-T2-2-008), the RIKEN iTHES Project, the MURI Center for Dynamic Magneto-Optics via the AFOSR (grant FA9550-14-1-0040), Grant-in-Aid for Scientific Research (A), the John Templeton Foundation, and the Australian Research Council.

REFERENCES

1. Lu, L., J. D. Joannopoulos and M. Soljačić, "Topological photonics," *Nature Photon*, Vol. 8, 821 2014.
2. Moiseyev, N., *Non-Hermitian Quantum Mechanics*, Cambridge University Press, Cambridge, 2011.
3. Esaki, K., M. Sato, K. Hasebe and M. Kohmoto, "Edge states and topological phases in non-Hermitian systems," *Phys. Rev. B*, Vol. 84, No. 20, 205128 2011.
4. Hu, Y. C. and T. L. Hughes, "Absence of topological insulator phases in non-Hermitian PT-symmetric Hamiltonians," *Phys. Rev. B*, Vol. 84, No. 15, 153101 2011.
5. Malzard, S., C. Poli and H. Schomerus, "Topologically protected defect states in open photonic systems with non-Hermitian charge-conjugation and parity-time symmetry," *Phys. Rev. Lett.*, Vol. 115, No. 20, 200402 2015.
6. Lee, T. E., "Anomalous edge state in a non-Hermitian lattice," *Phys. Rev. Lett.*, Vol. 116, No. 13, 133903 2016.
7. Leykam, D., K. Y. Bliokh, C. Huang, Y. D. Chong and F. Nori, "Edge Modes, Degeneracies, and Topological Numbers in Non-Hermitian Systems," *Phys. Rev. Lett.*, Vol. 118, No. 4, 040401, 2017.

Lorentz-force picture for controlling optical polarizations in non-Hermitian potentials

Sunkyu Yu, Xianji Piao, Choonlae Cho, and Namkyoo Park*
Photonic Systems Laboratory, Department of ECE, Seoul National University, Seoul 08826, Korea
*corresponding author: nkpark@snu.ac.kr

Abstract-We introduce the manipulation of optical polarizations in non-Hermitian potentials, applying the Lorentz-force picture defined by effective material parameters. From the analogy with relativistic E×B drift in electrodynamics, the collective evolution of the states of polarization to the designer pole is demonstrated on the Poincaré sphere. We will also introduce the criteria for the metamaterial realization toward the E×B drift analogy.

Parity-Time (PT) symmetry [1] has opened a pathway toward the unidirectional transition of optical states [2], due to nonorthogonal eigenmodes which also have strong spatiospectral asymmetry. In this talk, we introduce the interpretation of PT symmetry based on the analogy between electrodynamics and classical Maxwell's equations [3], in terms of Lorentz-force picture founded by effective material parameters.

Figure 1a represents the effective Lorentz-force exerted on the state of polarization (SOP) on the Poincaré sphere. The effective electric and magnetic fields are determined by the material parameters of permittivity, permeability, and optical chirality. It is noted that the resulting evolution of the SOP at the exceptional point of PT-symmetric potentials (Fig. 1b) is analogous to the relativistic behavior of the particle (Fig. 1c) driven by electromagnetic fields at $|E| = |B|$ [4].

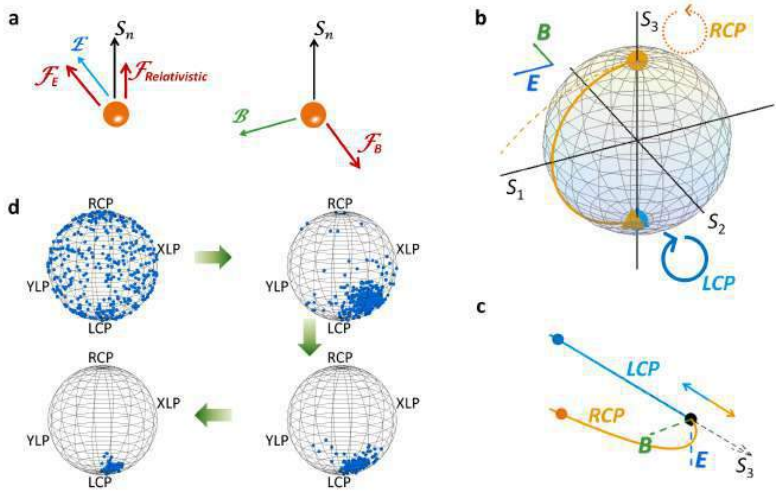

Figure 1. (a) Effective Lorentz force on the SOPs on the Poincaré sphere. (b,c) The analogy between (b) classical polarization evolutions in non-Hermitian optical potentials at the exceptional point, and (c) relativistic particle dynamics driven by E×B drift at $|E| = |B|$. (d) Polarization black hole dynamics to the singularity at the exceptional point in the polarization domain.

To implement the |E| = |B| Lorentz force exerted on the SOP, artificial material realization is necessary to achieve the desired anisotropic complex parameters. Figure 2a,b represents the criteria for the metamaterial design [5], deriving the strong chiral conversion which corresponds to the collective flow of particles by the E×B drift at $|E| = |B|$. In the talk, we will also discuss the singularity at the linear polarization, having the directionality from optical chirality.

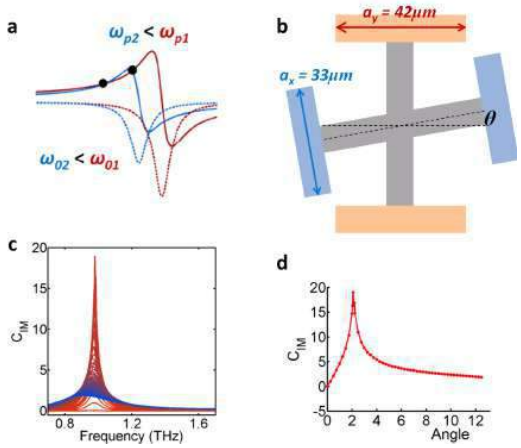

Figure 2. Criteria for the metamaterial design: (a) required permittivity spectrum for each polarization meta-atom. (b) Polarization meta-molecule for the analogy of the E×B polarization drift. Modal chirality of the designed metamaterial (c) in spectral domain and (d) for the tuning of design parameter.

REFERENCES

1. Bender, C. M. and Boettcher, S. "Real spectra in non-Hermitian Hamiltonians having PT symmetry," *Phys. Rev. Lett.* Vol. 80, 5243, 1998.
2. Yu, S., Mason, D. R., Piao, X., and Park, N. "Phase-dependent reversible nonreciprocity in complex metamolecules," *Phys. Rev. B* Vol. 87, 125143, 2013.
3. Kuratsuji, H. and Kakigi, S. "Maxwell-Schrödinger equation for polarized light and evolution of the Stokes parameters," *Phys. Rev. Lett.* Vol. 80, 1888, 1998.
4. Yu, S., Piao, X., and Park, N. "Acceleration toward polarization singularity inspired by relativistic E×B drift," *Sci. Rep.* Vol. 6, 37754, 2016.
5. Yu, S.†, Park, H. S.†, Piao, X., Min, B., and Park, N. "Low-dimensional optical chirality in complex potentials," *Optica* Vol. 3, 1025, 2016.

Self-collimation in 2D Complex P- and PT-symmetric systems

M. Botey[1],W. W. Ahmed[1], R. Herrero[1], , and K. Staliunas[1,2]

[1]Departament de Física, Universitat Politècnica de Catalunya (UPC), Barcelona, Spain
[2]Institució Catalana de Recerca i Estudis Avançats (ICREA), Barcelona, Spain
[*]corresponding author: muriel.botey@upc.edu

Abstract-We predict the self-collimation phenomena (or equivalently, dynamical localization) in 2-dimensional P-symmetric and PT-symmetric complex potentials, with periodic modulations of both gain/loss and refractive index. Non diffractive propagation is analytically predicted and further confirmed by numerical integration of a paraxial model. The parameter space is explored to identify the self-collimation regime in crystals with different complex symmetries.

Artificial structured materials provide the ability to tailor the diffraction of propagating beams leading to the self-collimation phenomena (quantum mechanical analog of the dynamical localization, occurring in modulated lattices); and effect accounted by the appearance of flat segments in the dispersion curves of propagating modes. First predicted in Photonic Crystals (PhCs)1,2,3, the effect was latter shown that also Gain and Loss Materials (GLM) modulated in the wavelength scale 4,5. However, is both cases, either due to the unavoidable presence of losses in PhCs or to the anisotropy of gain in GLM, the absence of diffraction is generally accompanied by diffusive broadening. Yet complex materials allow the independent management of diffraction and diffusion of light beams, by independently modulating refractive index and gain/loss, representing therefore an ideal platform for beam tailoring.

In the present work we demonstrate self-collimation in 2-dimensional (2D) Parity (P) symmetric and Parity Time (PT) symmetric complex crystals (where index and gain/loss modulations are either in phase/counter-phase or de-phased a quarter of the wavelength of the modulation7). In this later case, we consider PT-symmetry eitherthe transverse (or longitudinal) direction and simultaneously in both transverse and longitudinal directions, see Fig.1.

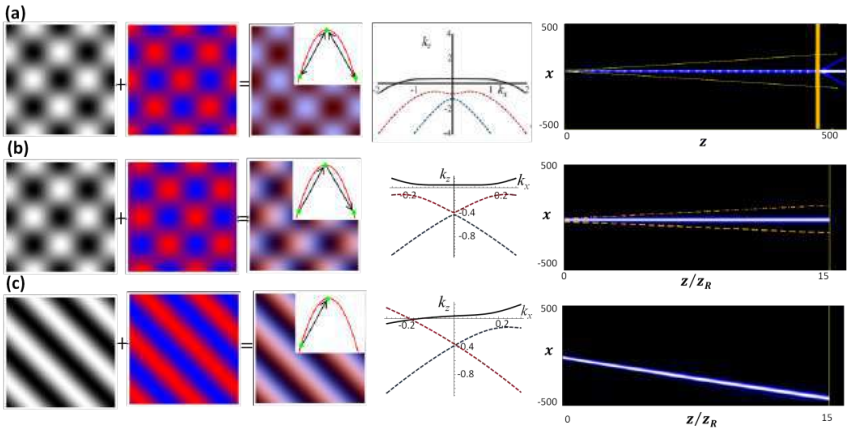

Figure 1. *Self-collimation in 2D complex crystals. The first/second rows display a schematic representation of the real/imaginary modulations of the optical potential, and the third merges both modulations where the inset indicates the coupling provided by the reciprocal lattice vectors — symmetric in (a) and asymmetric in (b) and*

(c)—. The forth row depicts the dispersion for the specific geometries and modulations amplitudes supporting self-collimation and the firth shows the corresponding numerical simulation of non diffractive light beam propagation within the corresponding crystal: (a) P-symmetric 2D lattice; (b) PT-symmetric lattice in the transverse, x, direction, while P-symmetric in z; (c) PT-symmetric lattice both in x and z. The yellow curves in the fifth row of a) and b) denote propagation of the considered beam in an homogeneous medium and are displayed for comparison.

The characteristics required for the suppression of diffraction, specific geometries and relative amplitudes of the gain/loss and index modulations, are analytically explored by a coupled mode analysis (some examples of flat dispersion bands supported for specific complex lattices are displayed in the third column of Fig.1, forth column)

For the case of P-symmetric complex crystals we find regimes of simultaneous suppression of diffusion and diffraction, self-collimated narrow light beams propagate without any distortion while being amplified, see Fig. 1a (since the amplitude of the beam is amplified, is here depicted renormalized at each propagation step). Besides, self-collimation is found either for collinear and non-collinear propagation in such complex crystals.

PT-symmetric lattices also offer the possibility to suppress diffraction. We analytically explore the characteristics of the spatial modulations required for the suppression of diffraction, for situations ranging from the pure PhC limit (system displaying real eigenvalues as for Figs. 1b,1c) to the pure GLM limit, that is to say, at either sides of the PT-transition exceptional point. Non-diffractive beams in GLM-like systems always experience self-broadening due to intrinsic diffusion. We analytically determine the self-collimation regimes for PT-symmetry in the transverse (Fig. 1b), longitudinal (found to be almost equivalent to the transverse one, except for the symmetric /asymmetric energy distribution among modes) and simultaneously in both directions (Fig. 1c). The analytical predictions are further confirmed by numerical simulations performed in paraxial approximation, finding a good agreement (see the last column of Fig. 1).

Finally, we analyze the beam dynamics in such regimes, in particular how the PT-symmetric potentials determine the energy distribution between spatial modes of the self-collimated beams either by the symmetric and or the asymmetric mode coupling. We show how complex lattices open the way to control the energy distribution among spatial modes. The predicted self-collimation effect in complex lattices may be useful to shape the beam profile in integrated optics or optical devices.

Acknowledgement, the work is financially supported by Spanish Ministerio de Educación y Ciencia through project FIS2015-65998-C2-1-P, NATO project SPS-985048 and Erasmus Mundus Doctorate Program Europhotonics (Grant No. 159224-1-2009- 1-FR-ERA MUNDUS-EMJD).

REFERENCES

1. R. Zengerle, J. Mod. Opt. 34, 1589-1617(1987).
2. D.Chigrin, S.Enoch, C. Sotomayor Torres, and G.Tayeb, Opt. Exp.**11**, 1203-1211 (2003).
3. K. Staliunas, R. Herrero, Physical Review E **73**,016601 (2006)
4. K. Staliunas R. Herrero, and R. Vilaseca, Phys. Rev. A **80**, 013821 (2009),
5. M. Botey, R. Herrero and K. Staliunas, Phys. Rev. A **82**, 013828 (2010)
6. R. Herrero, M. Botey, M., and K. Staliunas, Phys. Rev. A **89**, 063811. (2014).
7. A. Guo, G. J. Salamo, D. Duchesne, R. Morandotti, M. Volatier-Ravat, V. Aimez, G. A. Siviloglou, and D. N. Christodoulides, Phys. Rev. Lett. **103**, 093902 (2009).

Invisibility on Demand

Z.Hayran[1], R.Herrero[2], M. Botey[2], H. Kurt[1], and K.Staliunas[2,3*]

[1] Nanophotonics Research Laboratory, TOBB University of Economics and Technology, Ankara, Turkey

[2] Department of Physics, Universitat Politecnica Catalunya (UPC), Barcelona, Spain

[3] Institucio Catalana de Reserca i Estudis Avancats (ICREA), Barcelona, Spain

[*]corresponding author: kestutis.staliunas@icrea.cat

Abstract- We propose a universal integral relation (a generalized Hilbert transform) relating the real and imaginary parts of the complex permittivity function of an object, which can provide invisibility with respect to particular range of directions, and for particular frequency ranges, i.e. on a specific demand. We demonstrate such invisibility by finite-difference-time-domain numerical calculations.

The Kramers-Kronig relation (or more generally the Hilbert transform) in spectrum is related to causality in time. Yet temporal causality implies "invisibility of the future". Analogously, the spatial Kramers-Kronig relation in space [1] can be related with unidirectional invisibility (disappearance of reflections) for waves propagating from a particular direction, either from the left or from the right.

We derive a general procedure to generate the invisibility on demand in two- or three dimensional space, i.e. we propose the modification of the complex permittivity or equivalently the complex refractive index in such a way, that it prevents the scattering of waves (wave reflections) in particular directions ranges and in particular frequency ranges. Such invisibility on demand is respectively less demanding than the conventional Kramers-Kronig relation providing a full unidirectional invisibility.

The procedure, shortly speaking, is the following: starting from the demanded invisibility area in wavenumber domain, and $\theta(\mathbf{k})$ (where $\mathbf{k}$ is a vector in the two-dimensional space $\mathbf{k}=(k_x,k_y)$) one generates its Fourier image $\theta(\mathbf{r})$ which serves as a kernel for a generalized Hilbert transform for complex refraction index: $n_1(\mathbf{r})=n_0(\mathbf{r})-\int n_0(\mathbf{r}_1)\theta(\mathbf{r}-\mathbf{r}_1)d\mathbf{r}_1$. This integral relation (generalized Hilbert transform) allows to modify the refraction index profile of the object from $n_0(\mathbf{r})$ to $n_1(\mathbf{r})$, and the object thus becomes invisible for reflections with respect to the demanded invisibility function $\theta(\mathbf{k})$.

The specific details of the generalized Hilbert transform will be provided [2]. Here we just present finite-difference-time-domain numerical simulations which prove correctness of such transform. Fig.1. shows a complex object (a figure of glass, described by a given real valued refraction index profile), which is visible for reflections, as it scatters incident waves generated at a point source (see Fig.1.a). However when the refraction index is modified according to the above proposed generalized Hilbert transform, the reflections vanish in a particular range of directions (see Fig.2.b), while reflections to other directions remain unaffected (see Fig.1.c).

The proposed transform allows to build the objects with given invisibility geometry from the very beginning, or alternatively to modify the refraction index of the given objects to create the invisibility on demand.

Moreover, it is also possible to follow an iterative procedure based on a chain of generalized Hilbert transforms to provide the invisibility on demand under additional restrictions, for instance restricting allowed

refraction index ranges. In particular it is possible to build the invisible object under the restriction that the refraction index of modified object everywhere remains in a "normal" range $n_{Re}(\mathbf{r})>1$, and that the imaginary parts of the refraction index remains everywhere positive $n_{Im}(\mathbf{r})>0$ (i.e. contains only losses, and no gain).

In the presentation we will provide different cases with invisibility shapes resulting in analytic forms of invisibility kernel; with invisibility shapes ensuring the minimum "expenses" of embedding to achieve invisibility; with invisibility shapes with "smooth" boundaries. We will demonstrate the effect on different complicated objects (the Fig.1. just proves the principles of the idea on a very simple object).

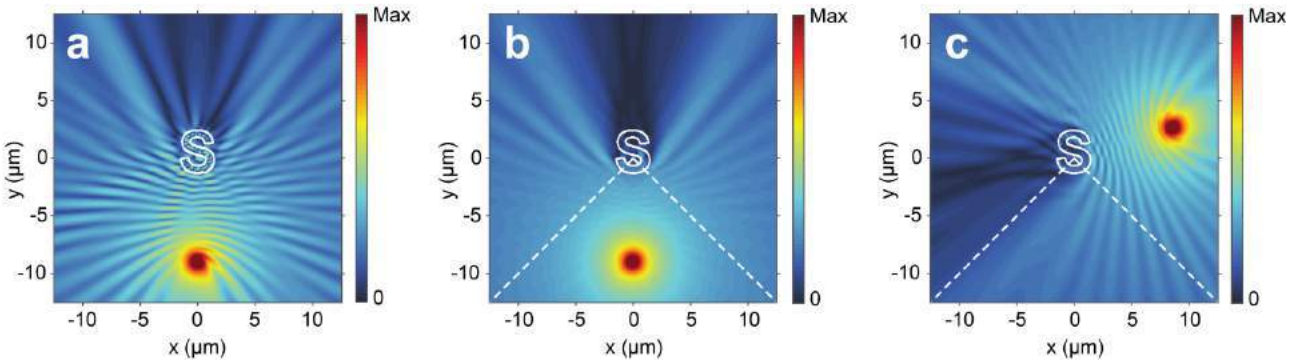

Fig.1 Invisibility on demand: a) the visible object (in this case a pieces of glass), scatters the incoming waves from point source. Back-reflections are evident from the fringed structure between the source and the object. Invisibility is created for particular reflection angles (limited by the dashed lines). b) When the source is within the invisibility area, then back-reflections vanish (since fringes disappear). c) When the source illuminates from some "wrong" angles back-reflections remain unaffected.

Acknowledgements, The work is financially supported by Spanish Ministerio de Educación y Ciencia, European FEDER through project FIS2015-65998-C2-01, by NATO SPS-985048 grant, and of the Turkish Academy of Sciences.

REFERENCES

1. Horsley, S. A. R., Artoni, M. and La Rocca, G. C., "Spatial Kramers-Kronig relations and the reflection of waves", Nat.Photonics **9**, 436 (2015)
2. Hayran, Z., Herrero, R., Botey, M., Kurt, H. and Staliunas, K., "Invisibility on demand", in preparation, 2017.

PT symmetry and pseudo-unitarity of nonunitrary quantum walks

Ken Mochizuki and Hideaki Obuse
Department of Applied Physics, Hokkaido University, Japan
ken_mochizuki@eng.hokudai.ac.jp, hideaki.obuse@eng.hokudai.ac.jp

Abstract-We study *PT* symmetry of the nonunitary quantum walks whose parameters depend on position and time. At first, we clarify that correlations of parameters in spatial and time directions are necessary to preserve *PT* symmetry. Then, we numerically show that the system can have entirely real spectra even when parameters of coin operators are spatially random and *PT* symmetry is broken. This implies that the system possesses pseudo-unitarity.

Recently, many interesting phenomena have been observed in PT symmetric non-Hermitian systems. However, most experimental systems have only a small number of elements, due to difficulty in controlling gain and loss effects. In contrast, quantum walks can overcome this difficulty. Quantum walks recently attract attentions as a versatile platform for quantum computations and quantum simulations. Quantum walks describe quantum dynamics of particles (walkers) with several internal states by a time-evolution operator, which is composed of coin operators, shift operators, and so on. The coin operator varies the internal states of walkers, and the shift operator changes the positions of walkers depending on the internal states. Quantum dynamics is described by acting the time-evolution operator to a quantum state at each time step.

In 2012, a quantum walk built by optical fiber loops was experimentally implemented, in which highly tunable gain and loss effects are included with additional optical amplifiers [1]. Effects of gain and loss make the time-evolution operator nonunitary, which means the effective Hamiltonian is non-Hermitian. It is known that, in certain parameter regions, the system has entirely real quasienergy.

In the present work, we explicitly show that the reality of quasienergy obtained in Ref [1] stems from *PT* symmetry [2]. We find that parameters of operators must have correlations not only in spatial direction but also in time direction in order to preserve *PT* symmetry of the time-evolution operator. Nevertheless, we numerically show that the system can have entirely real quasienergy, in the case parameters of the coin operators are random over the position space and the time-evolution operator does not hold *PT* symmetry in the explicit sense. This suggests that reality of quasienergy is guaranteed by pseudo-unitarity.

REFERENCES

1. A. Regensburger, *et al*., “Parity time synthetic photonic lattices”, Nature **488** 167 (2012).
2. K. Mochizuki, D. Kim, and H. Obuse, “Explicit definition of *PT* symmetry for nonunitary quantum walks with gain and loss”, Phys. Rev. A **93** 062116 (2016).
3. K. Mochizuki and H. Obuse, “Effects of disorder on non-unitary *PT* symmetric quantum walks”, arXiv:1608.00719 (accepted in Interdisciplinary Information Science).

Stationary regimes of Fiber Ring PT laser with saturable gain.

S.V. Smirnov[1], **M. O. Makarenko**[1], **S. V. Suchkov**[2], **I. D. Vatnik**[1], **D. V. Churkin**[1], and **A. A. Sukhorukov**[2]

[1]Novosibirsk State University, Pirogova St. 2, Novosibirsk, 630090, Russia
[2]Nonlinear Physics Centre, Research School of Physics and Engineering, The Australian National University, Canberra, ACT 2601 Australia
sergey.v.suchkov@gmail.com

Abstract— We propose a fiber laser composed of coupled ring cavities with gain and loss, featuring parity-time transition between symmetry-broken single-mode and bistable symmetric regimes, controllable by static phase shifters without active modulation.

The concept of parity-time (PT) symmetry in optics attracts great deal of attention. Recently, a parity-time symmetry-breaking microring laser has been experimentally demonstrated [1, 2]. The latter paper considered two coupled microrings, one ring with losses and another one with gain. A single-mode operation in an initially multi-mode system was achieved through stronger mode discrimination close to a PT-symmetry breaking transition. Further on, a single transverse mode operation in a system of coupled microring lasers was demonstrated near the exceptional point [3]. In a pair of coupled microdisk quantum cascade lasers, the reversal of generated power dependence was identified in the vicinity of exceptional points [4]. Further on, a realization of the PT symmetry based mode-locking has been theoretically proposed [5], and PT fiber cavity laser was developed [6].

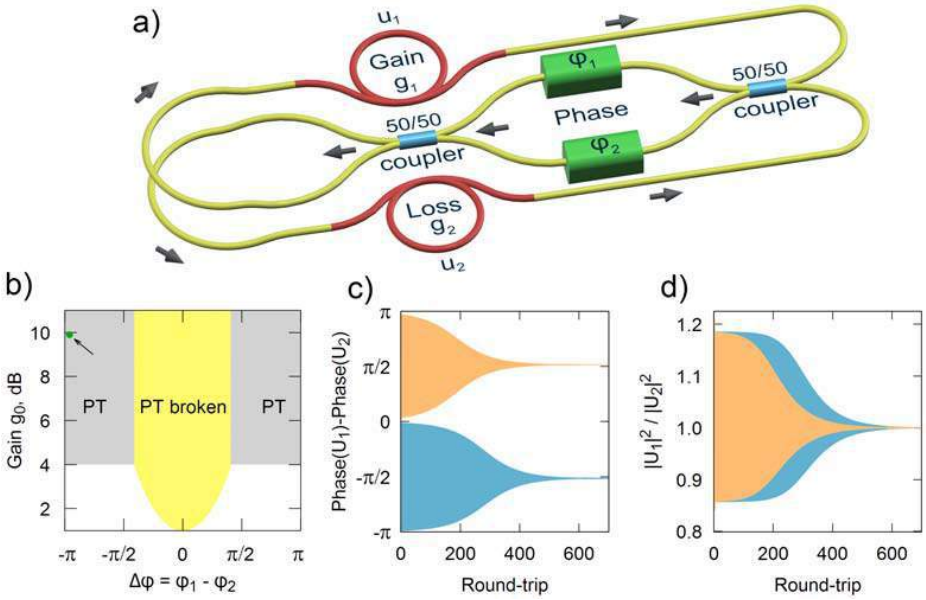

Figure 1: (a) Schematic of the PT-symmetric fiber ring, composed of two cross-coupled fiber cavities with gain and loss. (b) Parameter regions of broken and unbroken PT-symmetry, (c,d) Laser dynamics converging to one of two bistable states in PT-symmetric regime [parameters correspond to a point indicted by arrow in plot (b)] depending on the initial excitation, having (c) different phases but (d) identical intensity profiles in gain/loss regions.

In this work, we propose a design of PT-symmetric fiber ring laser. The scheme comprises two cross-coupled fiber cavities of the same length, as shown schematically in Fig. 1(a). The cavities are coupled via a set of two fiber 50:50 couplers with incorporated adjustable phase shifts (φ_1, φ_2) between them. In the case of zero phase shifts, the ring cavities are uncoupled, then the active cavity acts as a conventional ring fiber laser under appropriate pumping (operating via

Raman gain for example), while the second acts as a passive unpumped fiber cavity. We predict that by changing the phase shift difference, one can switch between PT-symmetric and PT-broken generation regimes.

To describe the system, we use the simplest discrete model governing the evolution of the field amplitudes in both fiber cavities at successive cavity round-trips. Field evolution on a cavity round-trip is modeled via multiplication by a product of matrices corresponding to the discrete cavity elements starting at the middle of gain / loss sections:

$$\mathbf{L} = \begin{pmatrix} e^{g_1/2} & 0 \\ 0 & e^{g_2/2} \end{pmatrix} \begin{pmatrix} 0 & 1 \\ 1 & 0 \end{pmatrix} \begin{pmatrix} \frac{1}{\sqrt{2}} & \frac{i}{\sqrt{2}} \\ \frac{i}{\sqrt{2}} & \frac{1}{\sqrt{2}} \end{pmatrix} \begin{pmatrix} e^{i\varphi_1} & 0 \\ 0 & e^{i\varphi_2} \end{pmatrix} \begin{pmatrix} \frac{1}{\sqrt{2}} & \frac{i}{\sqrt{2}} \\ \frac{i}{\sqrt{2}} & \frac{1}{\sqrt{2}} \end{pmatrix} \begin{pmatrix} e^{g_1/2} & 0 \\ 0 & e^{g_2/2} \end{pmatrix}, \tag{1}$$

where $g_2 < 0$ is a constant loss coefficient and $g_1 > 0$ characterizes gain.

We establish that the round-trip operator $\mathbf{L}$ possesses PT symmetry if gain and loss are balanced, $g_1 = -g_2$. The parity operator $\mathbf{P}$ swaps the two fibers, which interchanges the gain and phase coefficients: $g_1 \leftrightarrow g_2$, $\varphi_1 \leftrightarrow \varphi_2$. The time-reversal operator $\mathbf{T}$ performs complex conjugation and also swaps the propagation direction, which is expressed as $\mathbf{TL} = (\mathbf{L}^{-1})^*\mathbf{T}$. Then, it can be checked that the PT symmetry is satisfied as $\mathbf{PTL} = \mathbf{LPT}$. The optical cavity modes possess PT symmetry if the phase difference exceeds a critical value, $|\Delta\varphi| > \Delta\varphi_{PT}$, where $\exp(-g_2) = [1 + |\sin(\Delta\varphi_{PT}/2)|]\cos^{-1}(\Delta\varphi_{PT}/2)$ and $\Delta\varphi = \varphi_1 - \varphi_2$. Conversely, PT-broken modes are present for $|\Delta\varphi| < \Delta\varphi_{PT}$. It is remarkable that PT symmetry arises for a broad range of phase shifts. Importantly, cross over coupling as described by the second matrix in Eq. (1) facilitates PT symmetry with static elements, whereas active modulation was required in previous realizations of mesh lattices [7].

We model the onset of lasing by considering saturable gain as $g_1 = g_0/(1 + P_1) - g_h$, where P_1 is the normalized power at the input of the gain element at the current round-trip. The model assumes that amplifier introduces g_h loss at high power limit, whereas its amplification of weak field is $(g_0 - g_h)$. In numerical simulations, we assign $g_h = 1$ dB$=10^{-0.05}$. We find that in the PT-symmetric regime with $|\Delta\varphi| > \Delta\varphi_{PT}$ and for $g_0 - g_h + g_2 > 0$, the laser selects a stationary generation power level such that the saturated gain balances total optical losses, and condition $g_1 = -g_2$ is satisfied, see take regions marked 'PT' in Fig. 1(b). Interestingly, optical bistability appears in this regime, i.e. the laser can generate one of two stable modes. In contrast, for the phase difference below a threshold, a PT-broken regime is realized, where only single lasing mode is supported, associated with a stronger light concentration in the fiber cavity with a gain. Accordingly, such PT-broken mode has a lower lasing threshold, see a central shaded region marked 'PT broken' in Fig. 1(b).

In laser experiments, the most direct way to characterize the PT-transition is to measure generation dynamics in both active and passive fiber cavities. We show the relative phase and intensities in the middle of gain and loss sections after each round-trip in Figs. 1(c) and (d), respectively. The parameters are chosen within a PT-symmetric region, and we show the evolution for two different initial conditions with blue and green coloured lines. We observe that for all initial conditions, the intensity ratio converges to unity [Fig. 1(d)], according to PT symmetry property of the lasing mode. However, stationary modes with two different phase structures can emerge [Fig. 1(c)], which illustrates bistable laser operation.

This work was supported by the Russian Science Foundation (16-12-10402) and the Australian Research Council (DP160100619).

REFERENCES

1. L. Feng *et al.*, "Single-mode laser by parity-time symmetry breaking", *Science* **346**, 972–975, 2014.
2. H. Hodaei*et al.*, "Parity-time-symmetric microring lasers", *Science* **346**, 975–978, 2014.
3. H. Hodaei *et al.*, "Single mode lasing in transversely multi-moded PT-symmetric microring resonators", *Laser Photon. Rev.* **10**, 494–499, 2016.
4. M. Brandstetter *et al.*, "Reversing the pump dependence of a laser at an exceptional point", *Nat. Commun.* **5**, 4034–7, 2014.
5. S. Longhi, "PT-symmetric mode-locking", *Opt. Lett.* **41**, 4518–4521, 2016.
6. A. K. Jahromi *et al.*, "Robust statistical parity-time symmetric lasers in fiber cavities", *Frontiers in Optics*, page JW4A.100. OSA, 2016.
7. A. Regensburger *et al.*, "Parity-time synthetic photonic lattices", *Nature* **488**, 167–171, 2012.

Floqeut Topological Phases in PT Symmetric Passive Hadamard Quantum Walks

Hideaki Obuse[1], **Ken Mochizuki**[1], **Dakyeong Kim**[1], **and Norio Kawakami**[2]

[1]Hokkaido University, Sapporo 060-8628, Japan
[2]Kyoto University, Kyoto 606-8502, Japan
hideaki.obuse@eng.hokudai.ac.jp

Abstract— We theoretically study Floquet topological phases of PT symmetric non-unitary quantum walks. Especially, by considering feasibility of experiments, we focus on passive Hadamard quantum walks which have effects of only losses and whose coin operators are described by Hadamard matrices. We clarify Floquet topological phases of this quantum walk and find that after compensating the loss effect, the corrected probability corresponding to edge states exponentially increases with time due to PT symmetry breaking.

A quantum walk, that is, a synthetic quantum system mainly implemented by photonic systems, whose dynamics is described by a time-evolution operator, provides potential applications for quantum computing and information. It is further interesting that the quantum walk possesses novel topological phases akin to those of Floquet topological insulators, which are topological insulators driven by a time-periodic field[1,2]. Recently, a one-dimensional quantum walk dynamics associated with gain and loss is experimentally implemented by optical fiber loops [3]. The experiment shows that the energy of the system is kept to be real as a manifestation of PT symmetry (combined parity and time- reversal symmetry) in spite of the open quantum system. In the previous work, motivated by the above experiment, we theoretically studied Floquet topological phases driven by the PT symmetric non-unitary time evolution. We have found the presence of combined parity and chiral symmetry, in addition to PT symmetry[4]. The presence of these symmetries allows us to study Floquet topological phases in open quantum systems by using a procedure for ordinal quantum walks belonging to class BDI[5]. We have confirmed that the number of edge states originating from Floquet topological phases and topological numbers satisfy the bulk-edge correspondence, while a modification due to the imaginary energy is required due to breaking of PT symmetry.

In the present work, we extend this work to passive Hadamard quantum walks which have effects of only losses and whose coin operators are described by Hadamard matrices. This setup can be easily realized by using bulk optics. We find that, after proper treatments of the effect of losses, the fundamentally same Floquet topological phase is defined for the passive Hadamard quantum walks. We also show that, by considering the connection between the passive quantum walk and quantum walks with gain and loss, a corrected probability corresponding to edge states exponentially increases with time because only edge states break PT symmetry. This provides a way to observe effectively high probabilities originating from edge states in actual experimental setups even in quantum regime.

REFERENCES

1. T. Kitagawa, M. S. Rudner, E. Berg, and E. Demler, "Exploring topological phases with quantum walks", Phys. Rev. A 82, 033429 (2010).
2. J. K. Asboth and H. Obuse, "Bulk-boundary correspondence for chiral symmetric quantum walks", Phys. Rev. B 88, 121406(R) (2013).
3. A. Regensburger, C. Bersch, M-A. Miri, G. Onishchukov, D. N. Christodoulides, and U. Peschel, "Parity-time synthetic photonic lattices", Nature 488, 167 (2012).
4. K. Mochizuki, D. Kim, and H. Obuse, "Explicit definition of PT symmetry for nonunitary quantum walks with gain and loss", Phys. Rev. A 93, 062116 (2016).
5. D. Kim, K. Mochizuki, N. Kawakami, and H. Obuse, "Floquet Topological Phases Driven by PT symmetric Nonunitary Time evolution", arXiv :1609.09650.

Parametric Parity-Time Symmetric Waveguide Array

S. Phang[1], **G. Gradoni**[1,2], **S. C. Creagh**[1], **A. Vukovic**[2], **and T. M. Benson**[2]

[1]School of Mathematical Sciences, University of Nottingham, NG7 2RD, UK
[2]George Green Institute for Electromagnetics Research, University of Nottingham, NG7 2RD, UK
sendy.phang@nottingham.ac.uk

Abstract— A parameteric PT-coupler in which the PT-symmetry is satisfied both in transverse and longitudinal directions is presented in this summary paper. The stability of this structure resembles that of parametric amplifiers, such that the stability of the system not only depends on the gain/loss but also on the parametric parameter. This structure exhibits unique behaviour such as thresholdless lasing and stability re-emergence.

In photonics, an *ideal* PT-symmetric system translates to an optical structure with a judicious profile of complex refractive index that requires the combination of both gain and loss [1–5]. PT-symmetric photonic structures can have purely real spectra, i.e. zero net-power amplification or dissipation, despite having both gain and loss in the system. However, there exists an exceptional point defined by certain system parameters for which the PT-system undergoes a spontaneous PT-symmetry breaking. Above this point the eigenfrequencies become complex and power grows exponentially. In [1–5], we have studied the spectral properties and the dynamics of various PT-symmetric structures, and also demonstrated interesting properties of PT-photonic structures such as loss-induced invisibility and laser generation that effectively reverses the effect of loss at threshold [1–5].

In the context of PT-waveguide structures, most of the studies on PT-symmetry have been limited to systems in one-dimension, in which the PT-symmetry is satisfied either transversely (in a PT-waveguide array) or longitudinally (in a PT-grating). In this summary paper, we consider PT-waveguide arrays (see Fig. 1) which satisfies PT-symmetry both longitudinally and transversely, referred to as parametric PT-waveguide array.

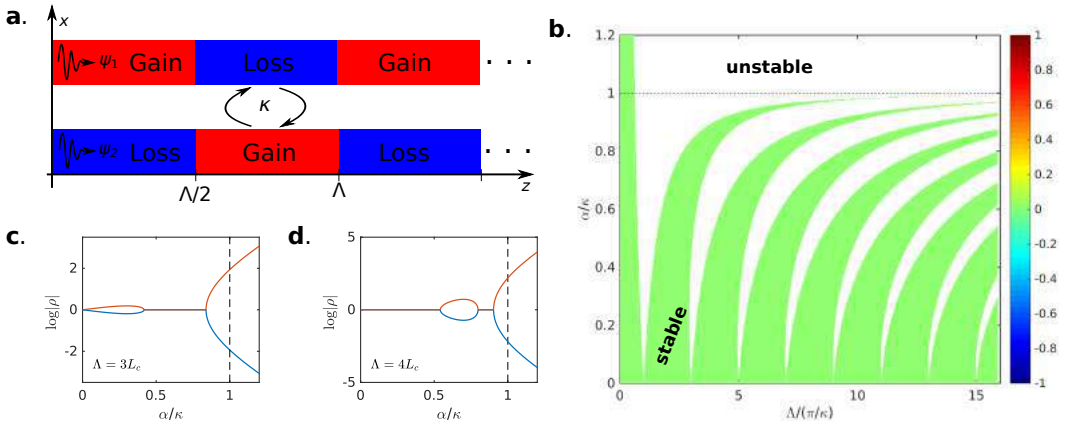

Figure 1: (a) Schematic illustration of parametric PT-coupler with gain/loss spatial modulation parameter Λ; (b) The stability criteria of the parametric PT-coupler as a function of gain/loss parameter α and Λ; (c,d) Eigenvalue ρ of the state transition matrix Φ of the parametric PT-coupler as a function of gain/loss parameter α for $\Lambda = 3L_c$ and $\Lambda = 4L_c$, where $L_c = \pi/\kappa$ denotes the coupling length of the waveguide coupler.

The parametric PT-coupler considered here is comprised of a uniform real part of refractive index with an alternating gain/loss region along the propagation direction z. Its state transition matrix, which describes the state at particular distance z for a given initial state at z_0, is given by

$$\Phi(\Lambda) = \frac{4\mathrm{e}^{j(\beta_0\Lambda+2\theta)}}{(1+\mathrm{e}^{2j\theta})^2}\begin{pmatrix} A & B \\ C & A \end{pmatrix}; \qquad \theta = \arcsin\left(\left|\frac{\alpha}{\kappa}\right|\right), \tag{1}$$

with the matrix entries being given by,

$$
\begin{aligned}
A &= \cos(\kappa\Lambda\cos\theta) + \frac{1}{2}\left(\cos(2\theta)\,!\;\;1\right), \\
B &= 2j\cos\left(\kappa\frac{\Lambda}{2}\cos\theta+\theta\right)\sin\left(\kappa\frac{\Lambda}{2}\cos\theta\right), \\
C &= 2j\cos\left(\kappa\frac{\Lambda}{2}\cos\theta\,!\;\;\theta\right)\sin\left(\kappa\frac{\Lambda}{2}\cos\theta\right).
\end{aligned}
\tag{2}
$$

In (1) and (2), β_0 denotes the phase propagation constant, α is the gain/loss parameter and κ is the coupling strength of the waveguide coupler.

The parametric PT-coupler has a stability behaviour similar to that of a parametric amplifier, as shown in Fig. 1(b), such that its stability depends not only on the gain/loss present [3] in the structure but also on the gain/loss spatial modulation Λ. There also exists a thresholdless condition at which the structure becomes unstable for an infinitesimal amount of gain/loss α. This thresholdless condition occurs on every odd-multiple of the coupling length, $\Lambda = (2n\,!\;\;1)L_c$. Furthermore, we note stability re-emergence as gain/loss increases in the system; a counter-intuitive behaviour in which stability can be attained from an unstable state by increasing gain/loss further in the system.

ACKNOWLEDGMENT

Support from the European Commission H2020 (NEMF21 - project grant No. 664828) is gratefully acknowledged. The authors also acknowledge the support of The University of Nottingham for access to their Minerva HPC.

REFERENCES

1. S. Phang, A. Vukovic, H. Susanto, T. M. Benson, and P. Sewell, "Impact of dispersive and saturable gain/loss on bistability of nonlinear parity-time bragg gratings," *Optics Letters*, vol. 39, no. 9, pp. 2603–2606, 2014.
2. S. Phang, A. Vukovic, S. C. Creagh, T. M. Benson, P. D. Sewell, and G. Gradoni, "Parity-time symmetric coupled microresonators with a dispersive gain/loss," *Optics Express*, vol. 23, no. 9, pp. 11 493–11 507, 2015.
3. S. Phang, A. Vukovic, S. C. Creagh, P. D. Sewell, G. Gradoni, and T. M. Benson, "Localized single frequency lasing states in a finite parity-time symmetric resonator chain," *Scientific Reports*, vol. 6, no. 20499, 2016.
4. S. Phang, A. Vukovic, G. Gradoni, P. Sewell, T. M. Benson, and S. C. Creagh, "Theory and numerical modelling of parity-time symmetric structures in photonics: Boundary integral equation for coupled microresonator structures," in *Recent Trends in Computational Photonics*. Springer Nature, 2017.
5. S. Phang, T. M. Benson, H. Susanto, S. C. Creagh, G. Gradoni, P. D. Sewell, and A. Vukovic, "Theory and numerical modelling of parity-time symmetric structures in photonics: Introduction and grating structures in one dimension," in *Recent Trends in Computational Photonics*. Springer Nature, 2017.

Smith-Purcell radiation in the presence of short-range disorder and from low-energy electrons

I. Kaminer[1], S. E. Kooi[3*], A. Massuda[1,2], C. Roques-Carmes[1,2], R. Shiloh[4], B. Zhen[2,5], Y. Shen[1], R. Remez[4], S. A. Skirlo[1], Y. Yang[2], K.K. Berggren[2], J. D. Joannopoulos[1,3], A. Arie[4], and M. Soljačić[1]

[1]*Department of Physics, Massachusetts Institute of Technology, USA*

[2]*Department of Electrical Engineering, Massachusetts Institute of Technology, USA*

[3]*Institute for Soldier Nanotechnologies, Massachusetts Institute of Technology, USA*

[4]*School of Electrical Engineering, Fleischman Faculty of Engineering, Tel-Aviv University, Israel*

[5]*Physics Department and Solid State Institute, Technion, Israel*

[*]corresponding author: skooi@mit.edu

Abstract- The emission of light from electrons passing in proximity to periodic grating structures includes both resonant plasmonic features and Smith-Purcell collective excitations. We observe both and distinguish between them, finding surprising robustness to disorder in the Smith-Purcell radiation. We also demonstrate the emission of visible light induced by low-energy electrons (1.5 - 6 kV) from sub 60 nm pitch gratings. The experimental results compare nicely to numerical simulations.

The conventional Smith-Purcell effect [1] describes light emission by a collective excitation that is induced by a free electron when it couples through its near-field to the electromagnetic modes of a grating or a periodic structure. Advances in nanoscale fabrication techniques in recent years have created new opportunities to explore the Smith-Purcell effect in plasmonic structures and metasurfaces and new applications are possible based on the Smith-Purcell effect in modern nanophotonic structures.

Over the years, the use of free electrons has become a significant tool in studying plasmonic resonances. Localized plasmonic resonances often appear due to nanoscale disorder and roughness on metal surfaces, with surface-enhanced Raman spectroscopy being a prominent example. At the same time, the effects of disorder on collective modes in periodic structure have been widely studied through the theory of Anderson localization. However, there is no existing theory or experiment studying the effects of disorder on collective excitations of electron-photon interactions, such as the Smith-Purcell effect. Our work studies and observes physical phenomena involving localized resonances and effects of disorder co-existing with collective excitations in the coupling of free electrons with modes of light [2]. While these phenomena usually appear in completely different settings, they can occur simultaneously given the proper nanophotonic structure and the proper experimental setup.

The experimental setup is comprised of a conventional scanning electron microscope (SEM) with the sample mounted almost parallel to the electron beam. A microscope objective is placed on the SEM stage to collect and image the light emission from the surface. The light collected by the objective passes through a viewport and is sent through a series of free space optics that includes a beam splitter, allowing simultaneous measurement of the spectrum and imaging of the spatial emission pattern. The SEM is operated in spot mode, which we control precisely to align the beam so that it passes near to the surface in the desired area of the sample. The spectral

signature contains multiple mechanisms of emitted radiation – the collective effect of conventional Smith-Purcell radiation, the localized plasmonic resonance (if present) and potentially background cathodoluminescence. These signals are separated and analyzed and compared to theory.

Such periodic systems can be used as light sources that are completely tunable by changing the electron velocity. The possibility of observing shorter wavelength emission from relatively low-energy electrons (accessible with regular scanning or transmission electron microscopes, SEM or TEM) is a promising field of research, because of the numerous applications [3].

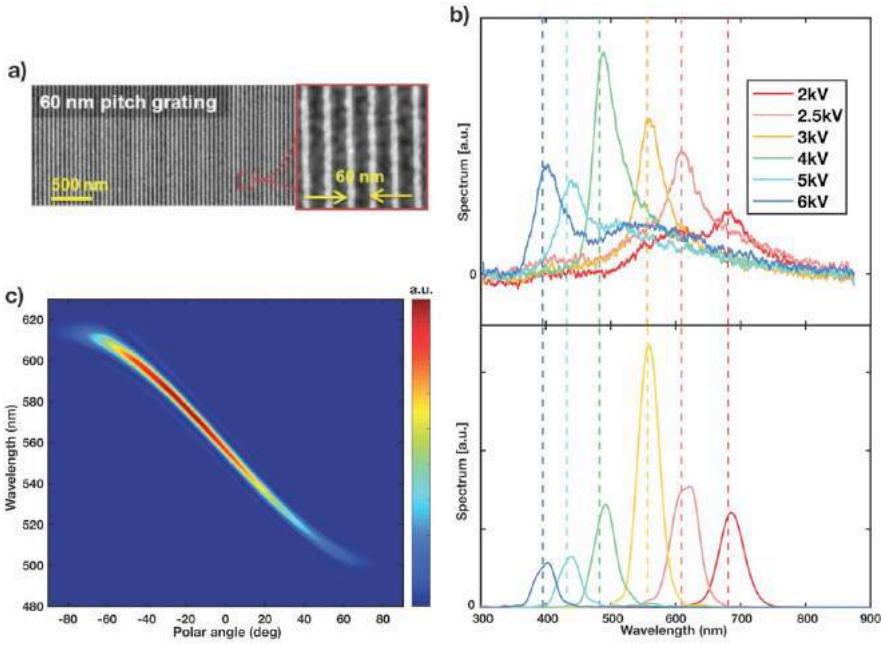

Figure 1. Measured and simulated radiation patterns. (a) SEM images of 60 nm pitch gratings. (b) Upper plot: measured spectra for different kinetic energies. Lower plot: time-domain far-field distribution computed with N = 20 unit cells and integration over an angle corresponding to the numerical aperture of the objective used in our experiment. The dashed vertical lines are calculated according to the conventional Smith-Purcell theory at normal emission, with the color corresponding to the same kinetic energies. (c) Simulation of the angular distribution for a kinetic energy of 3 keV and a grating of N = 100 unit cells. The polar angle is measured from the direction normal to the beam propagation. At each angle, we verify the wavelength radiated with maximum intensity corresponding to the theoretical prediction.

REFERENCES

1. Smith, S. J. and Purcell, E. M., "Visible Light from Localized Surface Charges Moving across a Grating," *Physical Review,* vol. 92, pp. 1069-1069, 1953.
2. Kaminer, I. E.*, et al.*, "Spectrally and spatially resolved Smith-Purcell radiation in plasmonic crystals with short-range disorder," *Phys. Rev. X.,* 7, 011003, 2017.
3. Wong, L. J. et al., "Towards graphene plasmon-based free-electron infrared to X-ray sources," *Nat Photon,* vol. 10, pp. 46-52, 2016.

PT symmetric structures for single-sided diffraction and broadband non-reciprocity

C. Hahn[1], Y. Choi[2], J. W. Yoon[2], S. H. Song[2], C. H. Oh[2], and P. Berini[1,3,4*]
[1]School of Electrical Engineering and Computer Science, University of Ottawa, Canada
[2]Department of Physics, Hanyang University, Seoul, Korea
[3]Department of Physics, University of Ottawa, Canada
[4]Centre for Research in Photonics, University of Ottawa, Canada
[*]corresponding author: pberini@uottawa.ca

Abstract- We discuss single-sided diffraction gratings and waveguide isolators based on exceptional-point optical structures.

Synthetic optical materials having a carefully structured complex refractive index distribution, following non-Hermitian Hamiltonian analogs, have attracted significant attention because of their non-orthogonal eigensystems. Such materials enable functions such as uni-directionality, non-reciprocity, and unconventional beam dynamics. In this paper, we discuss non-Hermitian diffraction gratings formed by optical pumping, in a method offering control of the real and imaginary parts of the complex refractive index distribution defining the grating. The grating was formed by vector-field holographic interference of two elliptically polarized pump beams incident on an azobenzene-doped polymer film. We experimentally observed single-sided grating diffraction, whereby the negative diffraction order is significantly suppressed (by almost 3 orders of magnitude) relative to the positive diffraction order due to operation of the grating at an exceptional point [1].

We also show that interactions based on encircling-an-exceptional-point, which are reciprocal in the linear regime, may become nonreciprocal in the nonlinear regime over a very broad optical bandwidth (limited mainly by the bandwidth of the nonlinearity). We describe a coupled-waveguide structure that supports an encircling-an-exceptional-point parametric evolution based on a gain saturation nonlinearity [2]. The structure is capable of low-loss nonreciprocal optical transmission with an isolation greater than 10 dB over an optical bandwidth approaching 100 THz. We describe progress on the experimental realization of the proposed concept, aiming towards an integrated on-chip optical isolator.

REFERENCES

1. C. Hahn, Y. Choi, J. W. Yoon, S. H. Song, C. H. Oh and P. Berini, "Observation of exceptional points in reconfigurable non-Hermitian vector-field holographic lattices," Nature Communications, Vol. 7, 12201, 2016.
2. Y. Choi, C. Hahn, J. W. Yoon, S. H. Song and P. Berini, "Extremely broadband, on-chip optical nonreciprocity enabled by mimicking nonlinear anti-adiabatic quantum jumps near exceptional points," Nature Communications, Vol. 8, 14154, 2017.

Stable transport with nonlinear PT-broken active couplers

Sergej Flach
Center for Theoretical Physics of Complex Systems
Institute for Basic Science, Daejeon, South Korea
sflach@ibs.re.kr

Abstract

I will discuss two examples of nonlinear PT-broken active couplers. First, I consider light propagation through a pair of nonlinear optical waveguides with absorption, placed in a medium with power gain. The active medium boosts the in-phase component of the overlapping evanescent fields of the guides, while the nonlinearity of the guides couples it to the damped out-of-phase component creating a feedback loop. As a result, the structure exhibits stable stationary and oscillatory regimes in a wide range of gain-loss ratios. I show that the pair of actively coupled (AC) waveguides can act as a stationary or integrate-and-fire comparator sensitive to tiny differences in their input powers [1].

This first example is in sharp contrast to nonlinear active couplers with PT symmetry, which are known to display unstable dynamics [2]. To explore the degree of symmetry breaking needed to achieve stable propagation, I consider a slightly PT-broken system [3]. This asymmetric active coupler (AAC) consists of two coupled dissimilar waveguides with gain and loss. I show that under generic conditions, not restricted by parity-time symmetry, there exist finite-power, constant-intensity nonlinear supermodes (NS), resulting from the balance between gain, loss, nonlinearity, coupling and dissimilarity. The system is shown to possess non-reciprocal dynamics enabling directed power transport functionality and stability with respect to modulations [4].

References

[1] N. V. Alexeeva, I. V. Barashenkov, K. Rayanov and S. Flach, *Actively coupled optical waveguides*, Phys. Rev. A **89**, 013848 (2014).

[2] I. V. Barashenkov, G. S. Jackson and S. Flach, *Blow-up regimes in the PT-symmetric coupler and the actively coupled dimer*, Phys. Rev. A **88**, 053817 (2013).

[3] Yannis Kominis, Tassos Bountis and Sergej Flach, *The Asymmetric Active Coupler: Stable Nonlinear Supermodes and Directed Transport*, Scientific Reports **6**, 33699 (2016).

[4] Y Kominis, T Bountis and S Flach, *Stability Through Asymmetry: Modulationally Stable Nonlinear Supermodes of Asymmetric non-Hermitian Optical Couplers*, arXiv:1702.04980 .

PT systems with time-delayed gain and loss

Y.N. Joglekar[1]

[1]*Indiana University Purdue University Indianapolis (IUPUI), Indianapolis, USA*
E-mail: yojoglek@iupui.edu

In recent years, Floquet PT-symmetric systems, with time-periodic Hermitian or non-Hermitian parts, have become a topic of increasing interest. This interest is driven by their rich PT phase diagram and ability to induce PT transitions in the presence of minimal gain-loss strength. However, in all cases, the system of interest – classical or quantum – is described by a local (instantaneous) Hamiltonian.
In this talk, I will introduce the concept of PT systems with time-delayed gain and loss, where the non-Hermitian, balanced gain and loss terms depend *not on the fields at that time, but on fields at an earlier time.* Formally, such a system is described by delayed differential equations (DDE) that are commonplace in population biology and lasers with feedback. I will show that a PT system with time-delayed gain and loss undergoes transitions from a stable, off state to an unstable state that is similar to the PT broken phase, and present a theoretical phase diagram that results from analysis of DDEs with complex coefficients. I will then show that, under appropriate conditions, such a system is realized in two coupled semiconductor lasers, and that the experimental results show the signatures of these transitions.

This is joint work with Prof. Vemuri's group at IUPUI (NSF grant DMR-1054020).

Experimental realization of the manipulation of exceptional points using magnetic fields

Xu-Lin Zhang[1], **C. T. Chan**[1*]

[1] Department of Physics and Institute for Advanced Study, The Hong Kong University of Science and Technology, Clear Water Bay, Hong Kong, China

[*]corresponding author: phchan@ust.hk

Abstract- We study a pair of coupled ferromagnetic waveguides under an external magnetic field. We find this two-state non-Hermitian system has an exceptional point and a subsequent symmetry recovery due to the presence of accidental degeneracy points when the system has no loss. Experimental measurements on the transmission spectra and field distributions clearly demonstrate the presence of the exceptional point and symmetry recovery.

Non-Hermitian systems with parity-time (PT) symmetric complex potentials undergo a transition at an exceptional point when the degree of non-Hermiticity is increased. Such PT-symmetric systems have drawn a lot of attentions recently [1,2]. It is commonly believed that a two-state PT-symmetric system has only one exceptional point beyond which the eigenvalues become complex and eigenmodes are PT-symmetry broken. The so-called "symmetry recovery" (i.e. the eigenvalues become real again and eigenmodes become PT-symmetric again after the system parameters extend beyond the exceptional point) will not occur for a two-state system, but it can appear in multi-state systems (say three or four-state systems) [3,4].

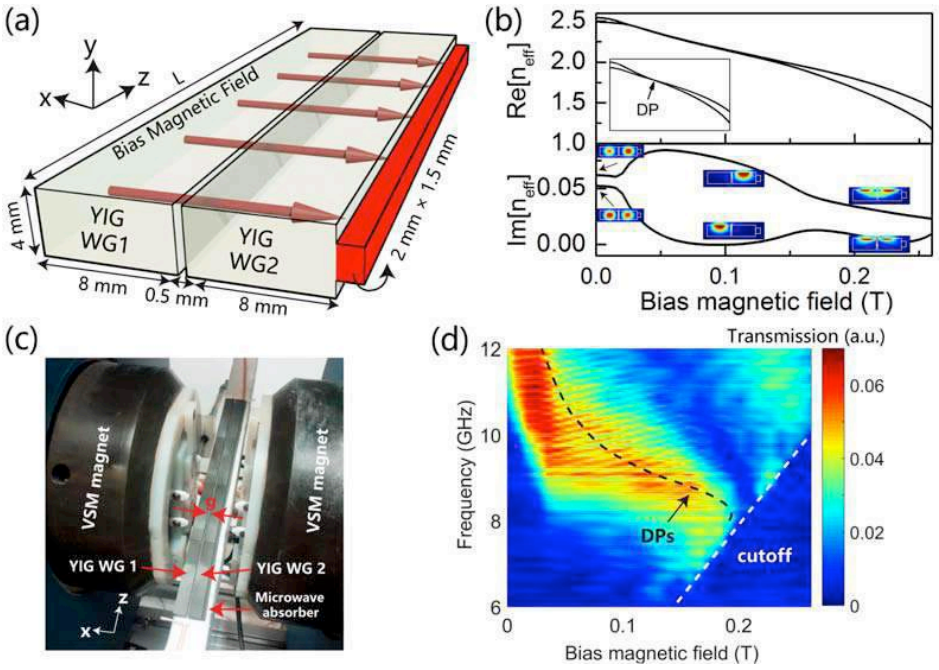

Figure 1 (a) Schematic of a passive coupled YIG waveguide system with microwave absorbers attached to the side of one waveguide. (b) Calculated real part and imaginary part of the effective mode index as a function of the bias field. (c) Experimental setup. (d) Measured transmission spectra under different bias magnetic fields.

Here, we show theoretically that a two-state non-Hermitian system can have symmetry recovery and we performed an experiment to demonstrate for the first time that such phenomena can be realized and observed in a system consisting of a pair of coupled ferromagnetic waveguides under an external magnetic field (see Fig. 1(a)). We show theoretically that the symmetry recovery is made possible by the presence of accidental degeneracy points in the Hamiltonian governing the waveguide system if it is lossless, and each degeneracy point must break up into one pair of exceptional points when loss is introduced and such a process will ensure that the system can have symmetry recovery even though it has only two internal degrees of freedom (see Fig. 1(b)). We performed microwave experiments to verify the theoretical design. The experimental set up is shown in Fig. 1(c), where a pair of yttrium iron garnet (YIG) dielectric waveguides are placed inside a vibrating sample magnetometer. We measured the transmission spectra under different bias fields and found that the transmission was enhanced at specific bias fields for different frequencies due to the presence of broken phase regions (see Fig. 1(d)).

The tuning process in this work is both adiabatic and continuous. As a result, our system serves as a good candidate to be further employed to tune system parameters to encircle an exceptional point to manifest the topological properties unique to PT-symmetric systems.

Acknowledgements: This work is supported by the Hong Kong Research Grants Council through grant AoE/P-02/12.

REFERENCES

1. Rüter, C. E., K. G. Makris, R. EI-Ganainy, D. N. Christodoulides, M. Segev, and D. Kip, "Observation of parity–time symmetry in optics," *Nature Physics*, Vol. 6, 192-195, 2010.
2. Guo, A., G. J. Salamo, D. Duchesne, R. Morandotti, M. Volatier-Ravat, V. Aimez, G. A. Siviloglou, and D. N. Christodoulides, "Observation of PT-symmetry breaking in complex optical potentials," *Physical Review Letters*, Vol. 103, 093902, 2009.
3. Ding, K., G. Ma, M. Xiao, Z. Q. Zhang, and C. T. Chan, "Emergence, coalescence, and topological properties of multiple exceptional points and their experimental realization," *Physical Review X*, Vol. 6, 021007, 2016.
4. Benisty, H., A. Lupu, and A. Degiron, "Transverse periodic PT symmetry for modal demultiplexing in optical waveguides," *Physical Review A*, Vol. 91, 053825, 2015.

Parity-Time Symmetry Based Lasers

Ren-Min Ma[1*]

[1]State Key Lab for Mesoscopic Physics and School of Physics, Peking University,
Beijing 100871, China

[*]corresponding author: renminma@pku.edu.cn

Abstract. This talk will describe how to construct novel microscale laser devices by parity-time symmetry in a non-Hermitian micro-ring cavity system.

Parity-time (PT) symmetric systems have attracted increasing attention over the past few decades for its rich physics and applications. PT symmetry was originally developed in the framework of quantum mechanics to characterize non-Hermitian systems with real eigenspectra. In optics, a system with can be considered as an analogue of a PT symmetric system in quantum mechanics. These PT symmetric optical systems exhibit numerous exotic features and functionalities, such as unidirectional invisibility, loss-induced transparency, coherent perfect absorption and lasing, and nonreciprocal light transmission. Very recently, PT symmetry has been introduced in microscale lasers as a powerful tool of mode manipulation. In a PT symmetric system, there are three phases, i.e. PT symmetric phase, exceptional point and PT symmetry broken phase. In the PT symmetric phase, the coupled modes in the system experience a balanced gain and loss, and thus no lasing can be observed. The transition from the PT symmetric phase to PT symmetry broken phase must experience a singular point, named the exceptional point at which not only eigenvalues but also the eigenstates coalesce. Novel vortex lasers that can directly emit optical beams carrying orbital angular momentum of light has been proposed based on exceptional points [1]. At the PT symmetry broken phase, the coupled modes in the system share the same eigenfrequency, but possess conjugate modal gain/loss coefficients. This phase has been utilized to make single mode microscale lasers [2].

Reference

[1] Xing-Yuan Wang, Hua-Zhou Chen, Ying Li, Bo Li, Ren-Min Ma*, Microscale Vortex Laser with controlled topological charge, *Chinese Physics B* **25**, 124211 (2016).

[2] L. Feng[‡], Z. J. Wong[‡], R. M. Ma[‡], Y. Wang, and X. Zhang[*], Single-mode laser by parity-time symmetry breaking, *Science* **346**, 972 (2014).

Cross/bar Switch using longitudinal gain redistribution and modified parity-time symmetry

Anatole Lupu [1] and Henri Benisty[2*]

[1] Centre de Nanosciences et de Nanotechnologies, CNRS, Univ. Paris-Sud, Université Paris-Saclay, C2N – Orsay, 91405 Orsay cedex, France

[2] Laboratoire Charles Fabry, Institut d'Optique Graduate School, CNRS, Univ Paris Sud, Université Paris-Saclay, 2 Avenue Augustin Fresnel, 91127 Palaiseau, France

[*]corresponding author: henri.benisty@institutoptique.fr

Abstract- The concept of parity-time symmetry has inspired new switch architectures. Here, we explore a 2x2 cross/bar switch architecture that mostly works by redistributing the longitudinal gain along one of the waveguides, which then features either gain in its center or at its edges. The other guide can then be of purely loss type, as occurs in plasmonic or hybrid waveguides. The advantage is to work with more stable space- and time-averaged parameters than previous parity-time symmetric designs.

The design of new devices in optics has recently taken advantage of the parity-time symmetric concept. By implementing gain and losses in adequate fashion onto a pair of coupled waveguides, the two basic "cross" and "bar" states of a 2x2 switch can be realized [1-3].

The advantages of using gain instead of real-index modulation are clear when material such as glass or metals (in plasmonics) are used as the basis of waveguiding [1-3], with adequate care to take into account realistic parameters of real cases [4, 5]. The physics of PT-symmetry (parity-time symmetry) indicates the combination of gain, loss and coupling parameters that ensures an operation close to a conservative condition (conserved power for signals).

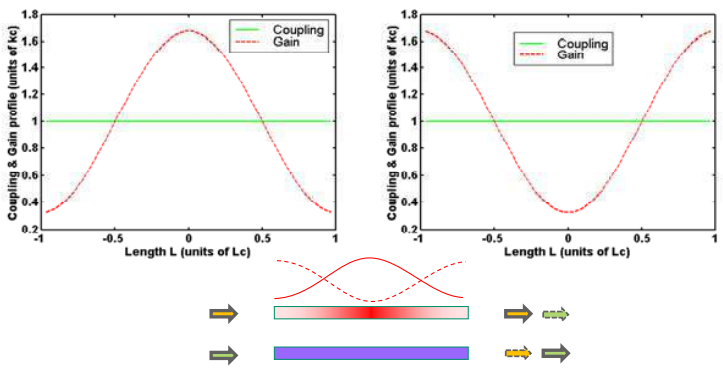

Fig.1: Two different longitudinal distribution of gain in a variant of a PT symmetric device of two coupled waveguide. The bottom scheme illustrates the two distributions and the targeted 2x2 cross/bar switching result.

Another practical quantity whose “conservation” can be interesting is the gain itself. Switching the gain entails heat dissipation and a number of inhomogeneous effects and related engineering issues that can eventually plague a device and incur severe penalties to its implementation. So it is tempting to think of switching by modifying a spatial gain distribution with a constant integral of the gain rather than switching the whole gain on or off in waveguide branches.

We will propose such a device, based on a variable cosine or anti-cosine repartition as pictured in Fig.1, whereby the gain is gently variable between a weak value and a maximum value. The overall gain is the same, but due to the longitudinal distribution change, the result will be shown to be reasonably close to the expected target. Here the other guide is purely lossy and does not undergo any tuning.

More characteristics will be studied to assess the perspectives of the proposed design approach.

Acknowledgements, This work is supported by a public grant overseen by the French National Research Agency (ANR) as part of the “Investissements d’Avenir” program (Labex NanoSaclay, reference: ANR-10-LABX-0035).

REFERENCES

1. H. Benisty, A. Degiron, A. Lupu, A. De Lustrac, S. Chénais, S. Forget, M. Besbes, G. Barbillon, A. Bruyant, S. Blaize, and G. Lérondel, "Implementation of PT symmetric devices using plasmonics: principle and applications," Optics Express, vol. 19, pp. 18004-18019, 2011.
2. A. Lupu, H. Benisty, and A. Degiron, "Using optical PT-symmetry for switching applications," Photonics and Nanostructures-Fundamentals and Applications, vol. 12, pp. 305-311, 2014.
3. A. Lupu, H. Benisty, and A. Degiron, "Switching using PT symmetry in plasmonic systems: positive role of the losses," Opt. Express, vol. 21, pp. 21651-21668, 2013.
4. H. Benisty, C. Yan, A. T. Lupu, and A. Degiron, "Healing Near-PT-Symmetric Structures to Restore Their Characteristic Singularities: Analysis and Examples," IEEE J. Lightwave Technol., vol. 30, pp. 2675-2683, 2012.
5. N. B. Nguyen, S. A. Maier, M. Hong, and R. Oulton, "Recovering parity-time symmetry in highly dispersive coupled optical waveguides," New J. Phys., vol. 18, p. 12502, 2016.

Anomalous transmission due to topological edge modes in low-symmetry photonic systems

C. W. Ling[1], **Jin Wang**[2], **Ka Hei Choi**[1], **K. F. Lee**[1], **Raymond P. H. Wu**[1], **Kin Hung Fung**[1,*]

[1]The Hong Kong Polytechnic University, China
[2]Southeast University, China
khfung@polyu.edu.hk

Abstract— Low-symmetry photonic elements with most symmetries broken but other spatial-temporal symmetries maintained could support exceptional points separating different interesting phases, such as PT-exact and PT-broken phases. Periodic arrays of these units may also support different classifications of topological bands, where the local symmetries in unit cell including material permittivity and permeability tensors play crucial roles. In recent years, it has been found that magneto-photonic crystals can form interesting one-way bands and topological edge modes, which could be used to design compact (Lorentz) non-reciprocal devices such as one-way waveguides and optical isolators. These photonic systems require the breaking of many spatial-temporal symmetries in addition to pure spatial and temporal symmetries. Meanwhile, some other spatial-temporal symmetries can be kept to support exceptional points and different phases similar to PT phases. We aims to understand the scattering and transmission properties associated with these topological photonic bands and edge states. In this talk, we discuss our recent findings on anomalous transmission associated with topological edge modes in Lorentz non-reciprocal and non-Hermitian systems with different spatial-temporal symmetries maintained. Arrays of plasmonic, gyroelectric and gyromagnetic resonators will be used to illustrate the roles of various symmetries including Lorentz reciprocity, time-reversal symmetries, and other spatial-temporal symmetries on these effects.

ACKNOWLEDGMENT

This research was partly supported by the Hong Kong Research Grant Council through General Research Fund Scheme (Grant no. 15300315) and Area of Excellence Scheme (Grant no. AoE/P-02/12). The authors also acknowledge the support from the Hong Kong Polytechnic University (G-YBPT, G-YBCH).

REFERENCES

1. C. W. Ling, Ka Hei Choi, T. C. Mok, Zhao-Qing Zhang, and Kin Hung Fung, "Anomalous Light Scattering by Topological PT-symmetric Particle Arrays," *Scientific Reports* **6**, 38049 (2016).
2. Jin Wang, Hui Yuan Dong, C. W. Ling, C. T. Chan, Kin Hung Fung, "Nonreciprocal mu-near-zero mode in PT-symmetric magnetic domains," *Physical Review B* **91**, 235410 (2015).
3. C. W. Ling, Meng Xiao, C. T. Chan, S. F. Yu, and Kin Hung Fung, "Plasmonic Topological Edge States between Diatomic Chains of Nanoparticles," *Optics Express* **23**, 2021-2031 (2015).
4. C. W. Ling, Jin Wang, and Kin Hung Fung, "Formation of Non-reciprocal Bands in Magnetized Diatomic Plasmonic Chains," *Physical Review B* **92**, 165430 (2015).
5. Jin Wang, Hui Yuan Dong, Raymond P. H. Wu, T. C. Mok, and Kin Hung Fung, "Electrical tunability due to coalescence of exceptional points in parity-time symmetric waveguides," *Optics Letters* **42**, 535 (2017).
6. Ka Hei Choi, C. W. Ling, K. F. Lee, Y. H. Tsang, and Kin Hung Fung, "Simultaneous Multi-frequency Topological Edge Modes between One-dimensional Photonic Crystals," *Optics Letters* **41**, 1644 (2016).

Topological and nonreciprocal dynamics in optomechanical systems with exceptional points.

J. G. E. Harris[1,2*], **H. Xu**[1], **D. Mason**,[1] **Luyao Jiang**[1]
[1]Department of Physics, Yale University, New Haven, CT, USA
[2]Department of Applied Physics, Yale University, New Haven, CT, USA
[*]corresponding author: jack.harris@yale.edu

Abstract-We demonstrate that adiabatic closed-loop operations on a system of damped oscillators can be used to achieve topological control and nonreciprocity.

In classical mechanics the time evolution of N coupled harmonic oscillators may be described by an $N\times N$ Hamiltonian matrix **H**. For undamped oscillators, **H** is Hermitian and has N pairs of real eigenvalues $\{\pm\omega_1, \pm\omega_2, ..., \pm\omega_N\}$ (corresponding to the normal frequencies) and N distinct orthogonal eigenvectors (corresponding to the normal modes). If **H** depends on a set of parameters λ_j which define a space V, then the ω_i are distinct except in isolated subsets of V. Even when degeneracies are present, the eigenvalue "surfaces" (i.e., the ω_i viewed as functions of the λ_j) can be represented by holomorphic functions of the λ_j.[1] These surfaces may be ordered unambiguously throughout V.[1] A smooth path defined by smoothly varying the λ_j will remain on a single surface, provided that it avoids the degeneracies. As a consequence, a closed-loop variation of the λ_j (that avoids degeneracies) will result in a path that remains on a single eigenvalue surface and returns to its starting point.

The situation is substantially different with damped oscillators, for which **H** is non-Hermitian. A system of N damped oscillators possesses N pairs of complex eigenvalues (i.e., ω_1 and $-\omega_1$*, etc.) and $2N$ distinct eigenvectors (which are not in general orthogonal).[2] Degeneracies among the ω_i still occur only for isolated subsets of V, but these degeneracies may be qualitatively different from those of undamped systems. For example, such a system may possess degeneracies (known as "exceptional points" or EPs) at which **H** cannot be diagonalized. In the vicinity of an EP the eigenvalue surfaces are represented by a Puiseux series in the λ_j. As a result the surfaces cannot be ordered unambiguously in a domain of V that contains an EP.[1] A smooth path (even one that avoids all degeneracies) need not remain on a single surface, and a closed-loop variation of the λ_j will not in general return to its starting point on the eigenvalue surfaces.

These features have important consequences for the dynamics of systems of oscillators. It was pointed out in Ref.[3] that if a system of damped coupled oscillators is prepared in one of its normal modes and then **H** is varied slowly in a loop that encloses an EP, the system will be in a different normal mode at the end of the loop. It was later pointed out that this is only true for choices of the initial normal mode and control loop that ensure that the system is in its least-damped mode for the majority of the operation; otherwise non-adiabatic effects will prevent the system from following a smooth path through the eigenvalue surfaces (regardless of how slow the control loop may be).[4,5] Thus, closed-loop operations may be used to achieve topological control *and* nonreciprocal dynamics in systems of damped oscillators.

We have demonstrated the topological control and nonreciprocal dynamics discussed in Refs.[3,4,5] by using two vibrational modes of a SiN membrane as the damped oscillators.[6] The membrane is placed in an optical cavity, and we use the optical spring effect to vary the oscillators' **H** and to carry out the loop operations. Figs.

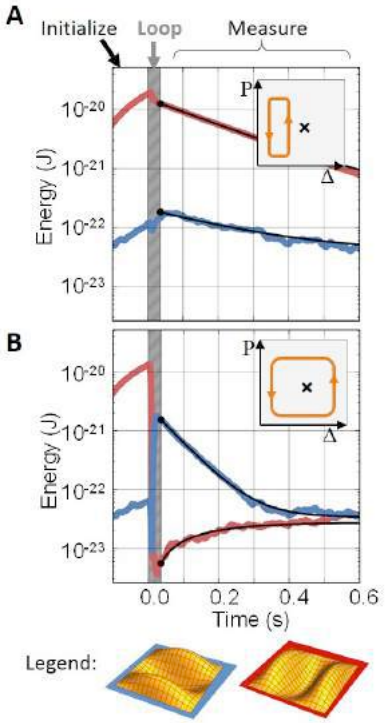

Figure 1. Amplitudes of the two modes (shown in the legend) as a function of time. Each inset shows a cartoon of the control loop in the Δ–*P* plane ("×" indicates the EP).

1(a)&(b) show typical measurements. In each case, one mode is initially driven to a large amplitude. At time t = 0 ms the drive is switched off and the control loop is executed by varying the detuning Δ and power P of a laser incident on the cavity. The control loop finishes at t = 40 ms. After the control loop is complete, the amplitude of each mode is fit (black lines) to determine the mode's energy just after the loop is complete (black dot). In Fig. 1(a) the loop does not enclose the EP, and the energy remaining after the loop is predominantly in the mode that was initially driven. In Fig. 1(b) the loop encloses the EP, and the energy remaining after the loop is predominantly in the mode that was not initially driven.

Fig. 2 shows the transfer efficiency E, defined as the fraction of the energy (after the loop) in the mode that was not initially driven. E is plotted as a function of the loop shape; in Fig. 2(a) the maximum value of Δ is varied, while in Fig. 2(a) the maximum value of P is varied. Loops that remain far from the EP without encircling it show $E \approx 0$, while loops that remain far from the EP and encircle it show $E \approx 1$. Loops passing close to the EP are less likely to result in quasi-adiabatic behavior and show intermediate values of E.

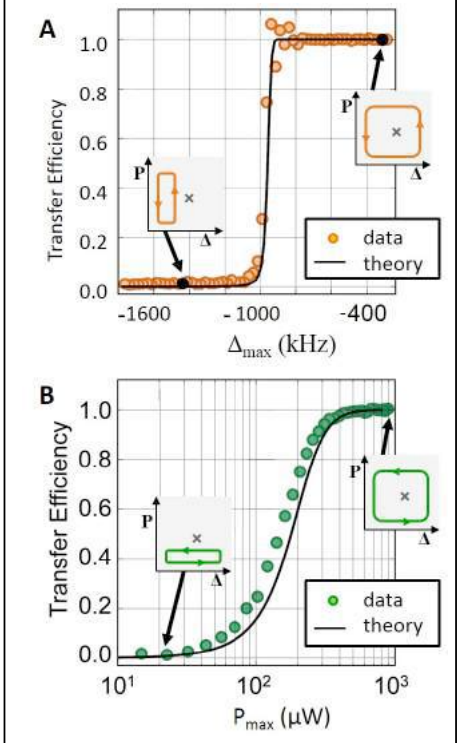

Figure 2. Dependence of the transfer efficiency E upon the control loop's shape.

Acknowledgements: This work was supported by AFOSR grant FA9550-15-1-0270.

REFERENCES

1. Kato, T., *A Short Introduction to Perturbation Theory for Linear Operators*, Springer-Verlag, New York, 1982.
2. Goebel, C. J. and S. T. Epstein "Motion of Damped Oscillators," *Am. J. Phys*, Vol. 48, No. 4, 289–290, 1980.
3. Heiss, W. D. "Phases of wave functions and level repulsion," *Euro. Phys. J. D* Vol. **7**, 1–4, 1999.
4. Uzdin, R., A. Mailybaev, and N. Moiseyev, "On the observability and asymmetry of adiabatic state flips generated by exceptional points," *J. Phys. A* Vol. 44, 435302, 2011.
5. Milburn, T. J. *et al*. "General description of quasiadiabatic dynamical phenomena near exceptional points," *Phys. Rev. A* Vol. 92, 052124, 2015.
6. Xu, H., D. Mason, L. Jiang, and J. G. E. Harris, "Topological energy transfer in an optomechanical system with exceptional points," *Nature* Vol. 537, 80–83, 2016.

Plasmonic Nanocircuits: Fundamentals and Devices

Nonlinear imaging with plasmonic metasurfaces

T. Zentgraf[1*], C. Schlickriede[1], N. Waterman[2], B. Reineke[1], P. Georgi[1], G. Li[3], and S. Zhang[2]

[1]Department of Physics, University of Paderborn, D-33098 Paderborn, Germany

[2]School of Physics & Astronomy, University of Birmingham, Birmingham, B15 2TT, UK

[3]Department of Materials Science and Engineering,

Southern University of Science and Engineering, Shenzhen, 518055, China

[*]corresponding author: thomas.zentgraf@uni-paderborn.de

Abstract- Tailoring the beam propagation is crucial in nonlinear optics. Here we will demonstrate a nonlinear meta-lens that works in a nonlinear way by simultaneously converting the collected light in a second harmonic wave while performing an imaging of the object. We demonstrate the concept by imaging fundamental beams in the infrared wavelength region into a second harmonic image.

We design and experimentally investigate a plasmonic metasurface, which can work as a lens for nonlinear imaging with simultaneous frequency conversion for the incident near-infrared light. With our approach, we take advantage of the Pancharatnam-Berry phase [1,2] in the nonlinear regime originating from the arrangement of meta-atoms with threefold rotational geometry [3]. Due to the strong light-matter interaction of the plasmonic antennas, the nonlinear metalenses have only a thickness of 30 nm. Based on the design concept the nonlinear metalens shows different operation modes, which depend on the spin angular momentum of light. By using a particular circular polarization state, the nonlinear lens can either work as a focusing or defocusing lens while simultaneously converting the illumination light to SHG light. At the same time, no imaging effect will appear for the fundamental wavelength. We investigate the beam propagation of our nonlinear metalenses and determine the evolution of the real and virtual focal planes for illumination with Gaussian beams. To underline the strength and the design flexibility we fabricated and analyzed different types of more complex nonlinear devices featured by different focusing abilities. In addition to that, we present intriguing spin angular momentum depending nonlinear imaging abilities giving rise to real and virtual SHG images of real objects as well as nonlinear Fourier transformations. The images are thereby generated at visible wavelength, which enables this device for revealing new avenues in integrated nano-optoelectronics, quantum communication technologies or other future device applications. Such nonlinear metalenses feature a symbiotic relationship between generation and modulation of frequency conversion within an ultrathin element.

REFERENCES

[1] Berry, M. V. Quantal phase factors accompanying adiabatic changes. *Proc. R. Soc. Lond.* ***392****, 45–57 (1984)*.

[2] Bomzon, Z., Kleiner, V. & Hasman, E. Pancharatnam-Berry phase in space-variant polarization state manipulations with subwavelength gratings. *Opt. Lett.* ***26****, 1424–1426 (2001)*.

[3] Li, G., Chen, S., Pholchai, N., Reineke, B., Wong, P. W. H., Pun, E. Y. B., Cheah, K. W., Zentgraf, T. & Zhang, S. Continuous control of the nonlinearity phase for harmonic generations. *Nature Materials* ***14****, 607-612 (2015)*.

Graphene based plasmonic modulator

Tao Li*, Yulin Wang, and S. N. Zhu
National Laboratory of Solid State Microstructures, School of Physics, College of Engineering and Applied Sciences, Nanjing University, Nanjing 210093, China.
*corresponding author: taoli@nju.edu.cn

Abstract-We proposed a plasmonic modulator design with a graphene covered groove-structured metasurface, which show excellent modulation performance on plamsonic waves. For comparison, several types of graphene-based modulators on dielectric waveguides, planar and wedge surface plasmons are theoretically investigated in detail. The results indicate great advantage of our proposed design and promise potential applications in compact optical circuits.

Graphene holds a great potential to provide efficient modulation in optoelectronic integrated circuits due to its excellent tunablity in conductivity, and several types of graphene-based photonic modulators have already been demonstrated [1,2]. In this work, a plasmonic modulator was proposed based on groove-structured metasurfaces covered by a graphene, in which a transverse electrical (TE) like mode is accommodated. Our design takes the advantage of field enhancement of plasmonic mode, and meanwhile overcome the mismatch of electrical field orientations of the surface plasmon polaritons (SPPs) and that required by graphene conductivity [3]. Therefore, this graphene based plasmonic modulator exhibits greatly improved modulation depth compared with the conventional SPP ones [4]. Moreover, we carried out detailed comparative investigations on different types of graphene modulated waveguides system including Si waveguide, planar SPPs, wedge SPPs. Our results show that this proposed groove-structured metasurface design holds significant advantages in modulation depth (see Fig. 1). Moreover, the theoretical results also show this modulator has a broadband property with acceptable insertion loss, indicating possible applications in nanophotonic integrations.

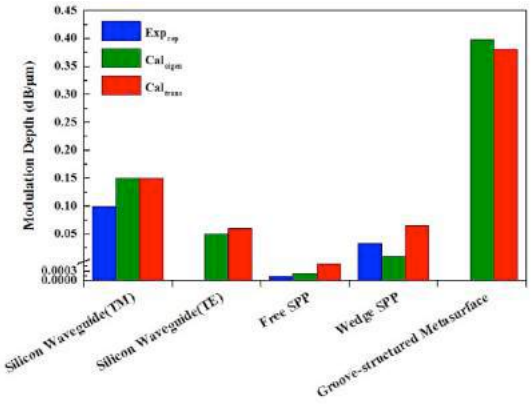

Fig.1 Comparison of the modulation performance of several waveguide systems.

Acknowledgements. This work was supported by from National Program on Key Basic Research Project of China (2016YFA0202103), the National Natural Science Foundation of China (Nos. 11674167 and 11621091).

REFERENCES

1. Liu, M., Yin, X. B., Ulin-Avila, E., Geng, B. S., Zentgraf, T., Ju, L., Wang, F., Zhang, X. "A graphene-based broadband optical modulator," *Nature* Vol. 474, 64-67, 2011.
2. Liu, M., Yin, X. B., Zhang, X. "Double-layer graphene optical modulator," *Nano. Lett.* Vol. 12, 1482-1485, 2012.
3. Wang, Y. L., Li, T., Zhu, S. N. " Graphene based Plasmonic Modulator on Groove-Structured Metasurfaces," unpublished.
4. Ansell, D., Radko, I. P., Han, Z., Rodriguez, F. J. Bozhevolnyi, S. I., Grigorenko, A. N. " Hybrid graphene plasmonic waveguide modulators," *Nat. Commun.* Vol. 6, 8846, 2015.

Multimodes and their hybridization in plasmonic nanostructures

Ru-Wen Peng[1*], Qing Hu[1], Kun Zhang[1], Wen-Bo Shi[1], Yue Xu[1], Nicholas X. Fang[2], Xian-Rong Huang[3], and Mu Wang[1]

[1]National Laboratory of Solid State Microstructures, School of Physics, and Collaborative Innovation Center of Advanced Microstructures, Nanjing University, Nanjing 210093, China

[2] Department of Mechanical Engineering, Massachusetts Institute of Technology, Cambridge, Massachusetts 02139, USA

[3] Advanced Photon Source, Argonne National Laboratory, Argonne, Illinois 60439, USA

[*]Email address: rwpeng@nju.edu.cn

Abstract- In this work, we study the multimodes and their hybridization in several plasmonic nanostructures. First, we present multimodes in a plasmonic nanowire and the applications on plasmonic circuits. Second, we show the multiple hybrid polariton bands in organic-dye-doped plasmonic nanostructures. Third, we explore hybrid strong coupling between multiple photonic modes and excitons in an organic-dyeattached photonic quasicrystal. Our investigations may inspire related studies on hybrid light-matter interactions, and achieve potential applications on multimode polariton lasers and optical spectroscopy.

With the capabilities of confining light into subwavelength volumes, plasmonics has attracted much attention, due to both fundamental interests and practical applications. Here we provide several examples to show the multimodes and their hybridization in the plasmonic nanostructures, and the related applications are also discussed.

Firstly, we demonstrate that by cascading nano-corrugation gratings with different periodicities on silver nanowires atop silicon, multiple plasmonic bands are achieved in the system, and then different colors are spatially separated and chronologically released at different grating junctions [1,2]. The released light frequency depends on the grating arrangement and corrugation periodicities. Hence the nanowire acts as a spectral splitter for sorting/demultiplexing photons at different nano-scale positions with a ten-femtosecond-level interval. Such nanowires can be constructed further into compact two-dimensioanl networks or circuits. We believe that this study provides a promising approach for realizing spatiotemporal-sensitive spectral splitting and optical signal processing on nanoscales, and for general integration of nanophotonics with microelectronics.

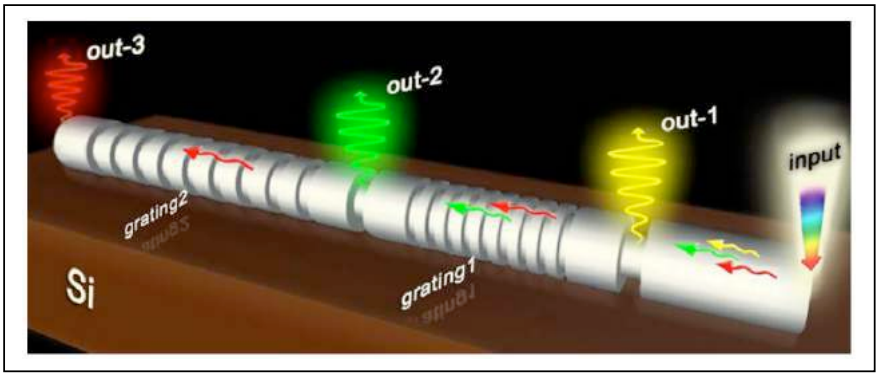

Figure 1. The principle of the wavelength division multiplexing with a plasmonic nanowire.

In the second, we present the possibilities to realize hybrid light-matter interactions, which can effectively achieve multiple hybrid polariton bands in organic-dye-doped nanostructures. We demonstrate experimentally the hybrid coupling among molecular excitons, surface plasmon polaritons (SPPs), and Fabry-Perot (FP) mode in a nanostructured cavity [3], where a J-aggregates doped PVA (polyvinyl alcohol) layer is inserted between a silver grating and a thick silver film. By tuning the thickness of the doped PVA layer, the FP cavity mode efficiently couples with the molecular excitons, forming two nearly dispersion-free modes. The dispersive SPPs interact with these two modes while increasing the incident angle, leading to the formation of three hybrid polariton bands. By retrieving the mixing fractions of the polariton band components from the measured angular reflection spectra, we find all these three bands result from the strong coupling among SPPs, FP mode, and excitons.

Thirdly, we have also experimentally explored multimode photon-exciton coupling in an organic-dye-attached photonic quasicrystal [4]. We show hybrid strong coupling between multiple photonic modes and excitons in an organic-dyeattached photonic quasicrystal. The excitons effectively interact with the photonic modes offered by the photonic quasicrystal, and multiple hybrid polariton bands are verified in both experiments and calculations. Our investigations may inspire related studies on hybrid light-matter interactions, and achieve potential applications on multimode polariton lasers and optical spectroscopy.

REFERENCES

1. Qing Hu, Di-Hu Xu, Yu Zhou, Ru-Wen Peng, Ren-Hao Fan, Nicholas X. Fang, Qian-Jin Wang, Xian-Rong Huang, and Mu Wang, “Position-sensitive spectral splitting with a plasmonic nanowire on silicon chip”, Scientific Reports 3, 3095 (2013).
2. Di-Hu Xu, Qing Hu, Ru-Wen Peng, Yu Zhou, and Mu Wang, "Plasmonic propagation and spectral splitting in nanostructured metal wires", *Acta Phys. Sin.* 64, 097803 (2015).
3. Kun Zhang, Wen-Bo Shi, Di Wang, Yue Xu, Ru-Wen Peng, Ren-Hao Fan, Qian-Jin Wang, and Mu Wang, “Couple molecular excitons to surface plasmon polaritons in an organic-dye-doped nanostructured cavity”, *Appl. Phys. Lett.* 108, 193111 (2016).
4. Kun Zhang, Yue Xu, T. Y. Chen, Hao Jing, W. B. Shi, Bo Xiong, R. W. Peng, and Mu Wang, "Multimode photon-exciton coupling in an organic-dye-attached photonic quasicrystal", *Optics Letters* 41, 5740 (2016).

Plasmonic Nanostructures with Strong Circular Dichroism Effects for Chirality Sensing

W. J. Zhao[1], R.Y. Wang[1*], H. Wei,[2] X. C. Wu,[3] and X. D. Zhang[1]

[1]School of Physics, Beijing Institute of Technology, 100081 Beijing, China

[2] Beijing National Laboratory for Condensed Matter, Institute of Physics, Chinese Academy of Sciences, 100190 Beijing, China

[3]CAS Key Laboratory of Standardization and Measurement for Nanotechnology, CAS Center for Excellence in Nanoscience, National Center for Nanoscience and Technology, 100190 Beijing, China

[*]corresponding author: wangry@bit.edu.cn

Abstract- We report here the plasmon-based chiroptical nanosensors for (1) discriminating the enantiomeric pair of chiral molecules; (2) quantifying enantiomeric purity of the chiral analytes; and (3) recognizing homo/heterochiral zwitterionic interactions in solutions with different pH values (Figure 1). Self-assemblies of gold nanoparticles were designed to achieve chiral or achiral nanostructures with remarkable circular dichroism (CD) responses at plasmon resonance wavelengths[1-5]. Their chiroplasmon spectral responses to chiral molecules provide a new strategy of chiral analyses, which may find important applications in bioscience and biomedicine.

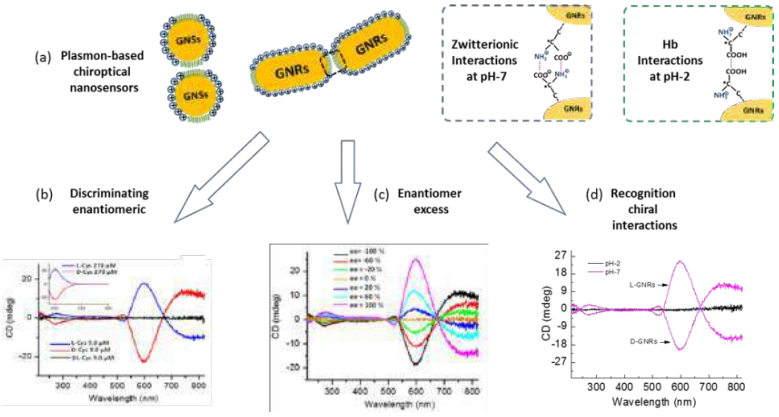

Figure 1. Functions of Plasmonic CD based chiroptical nanosensors.

Acknowledgements, WJZ and RYW gratefully acknowledge the fruitful discussions with Prof. Hongxing Xu from Wu Han University. This work was supported by National Natural Science Foundation of China (Grant Nos.11574030, 11174033, 11422436，91127013)

REFERENCES

1. Wang, R.Y.,* Wang H., Wu X. C., Ji Y., Wang P., Qu Y., and Chung T. S. “Chiral assembly of gold nanorods with collective plasmonic circular dichroism response,” *Soft Matter,* Vol. 7, 8370 – 8375, 2011.

2. Wang, P., Chen, L. Wang, R. Y.,* Ji, Y., Zhai, D., Wu, X., Liu, Y., Chen, K., and Xu, H. “Giant optical activity from the radiative electromagnetic interactions in plasmonic nanoantennas,” *Nanoscale*, Vol. 5, 3889–3894, 2013.
3. Hou, S., Wen, T., Zhang, H., Liu, W., Hu, X., Wang, R. Y., Hu, Z., and Wu, X.* “Fabrication of chiral plasmonic oligomers using cysteine-modified gold nanorods as monomers,” *Nano Research,* Vol. 11, 1699-1705, 2014.
4. Wang, R. Y., Wang, P., Liu, Y., Zhao, W., Zhai, D., Hong, X., Ji, Y., Wu, X., Wang, F., Zhang, D., Zhang, W., Liu, R., and Zhang, X., “Experimental Observation of Giant Chiroptical Amplification of Small Chiral Molecules by Gold Nanosphere Clusters,” *J. Phys. Chem. C.*, Vol. 118, 9690-9695, 2014.
5. Zhai, D., Wang, P., Wang, R. Y., * Tian, X., Ji, Y., Zhao, W., Wang, L., Wei, H., Wu, X., and Zhang, X. “Plasmonic Polymers with Strong Chiroptical Response for Sensing Molecular Chirality,” *Nanoscale*, Vol. 7, 10690 – 10698, 2015.

Surface-assisted carrier excitation in plasmonic nanostructures

Tigran V. Shahbazyan
Department of Physics, Jackson State University, Jackson, MS 39217 USA
shahbazyan@jsums.edu

We present a quantum-mechanical model for surface-assisted plasmon decay into electron-hole pairs (Landau damping) in metal nanostructures of arbitrary shape. The surface absorbed power and scattering rate are highly sensitive to local field polarization relative to the surface. Our model can be used for efficient calculations of plasmon-induced hot carrier generation rates in photovoltaics.

Plasmon-assisted hot carrier excitation and transfer across the interfaces has recently attracted intense interest due to wide-ranging applications in photovoltaics and photochemistry [1]. In metal nanostructures with characteristic size below the diffraction limit, excitation of hot carriers is enhanced due to resonant plasmon absorption followed by plasmon decay into electron-hole pairs. In small nanostructures, the dominant decay mechanism is Landau damping facilitated by carrier scattering from the metal-dielectric interface [2].

We developed a quantum-mechanical model for surface-assisted carrier excitation by alternating electric field **E** in metal nanostructures of arbitrary geometry. We found that the power absorbed in the metal due to carrier surface scattering has the form

$$Q_s = \frac{e^2}{2\pi^2\hbar}\frac{E_F^2}{(\hbar\omega)^2}\int dS\,|E_n|^2$$

where E_n is the normal field component, E_F is the Fermi energy, and integration takes place over the metal surface. We provide simple expressions for surface enhancement factors for plasmon-assisted carrier excitation in terms of surface scattering rates γ_s, which are highly sensitive to field polarization relative to the metal-dielectric interface and can be tuned in a wide range with an appropriate choice of system geometry [3]. In Fig. 1, the surface scattering rates are plotted for nanorods and nanodiscs modeled by prolate and oblate spheroids. The rates for longitudinal and transverse modes exhibit dramatic differences in behavior with changing the system geometry.

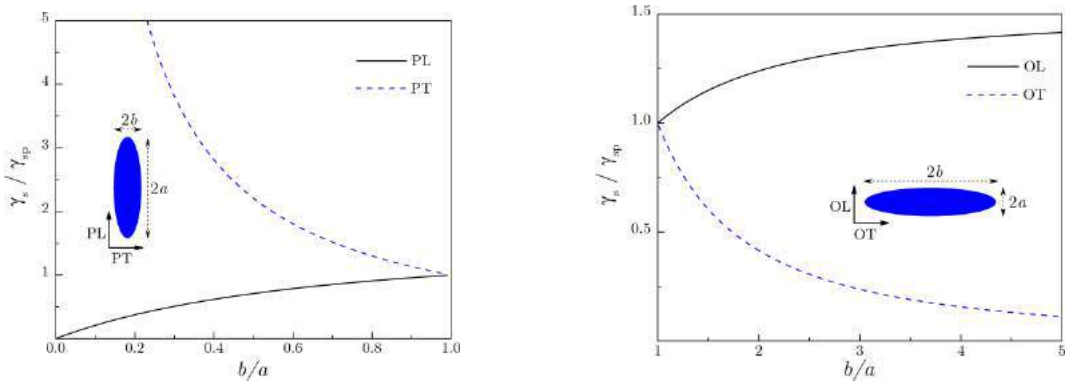

Fig. 1. Surface scattering rates for nanorods (left panel) and nanodisks (right panel) are plotted vs. aspect ratio for longitudinal (PL and OL) and transverse (PR and OR) polarizations.

This work was supported by NSF under grants No. DMR-1610427 and No. HRD-1547754.

REFERENCES

1. M. L. Brongersma, N. J. Halas, and P. Nordlander, Nat. Nanotechnol. **10**, 25 (2015).
2. K. L. Kelly, E. Coronado, L. L. Zhao, and G. C. Schatz, J. Phys. Chem. B **107**, 668 (2003
3. T. V. Shahbazyan, Phys. Rev. B **94**, 235431 (2016).

Quantum plasmon resonance and plasmon-enhanced photocatalytic activity of gold nanoparticles

Si-Jing Ding[1], Da-Jie Yang[2], Li Zhou[1], and Qu-Quan Wang[1,2,*]

[1]Department of Physics, Key Laboratory of Artificial Micro- and Nano-structures of the Ministry of Education, Wuhan University, Wuhan 430072, P. R. China

[2]The Institute for Advanced Studies, Wuhan University, Wuhan 430072, P. R. China

[*]corresponding author: qqwang@whu.edu.cn

Abstract-We demonstrate the nonmonotonous surface plasmom resonance (SPR) red-shift caused by resonant electron transitions and photocatalytic activity enhanced by the quantum plasmon resonance of colloidal gold nanoparticles. A maximal SPR wavelength and the largest photocatalytic activity are observed in the quantum regime for the first time for the gold nanoparticles with a diameter of 3.6 nm. Theoretical analysis based on a quantum-corrected model reveals the evolution of SPR with quantized electron transitions and well explains the observations.

The surface plasmom resonance (SPR) of metal nanoparticles is strongly influenced by their size, morphology, composition, surface chemistry, and surrounding environment. In the nanometer size regime, SPR is more sensitive to the quantum nature of conduction electrons and surface composition. A blue-shift of SPR has been observed in individual and aggregate silver nanospheres with sizes ranging from 20 nm to 2.0 nm.[1,2] This SPR blue-shift has been attributed to the quantum transitions of the conduction electrons of silver particles. Different theoretical approaches have been developed to describe the size-dependent SPR of quantum-sized metal nanostructures; different SPR shifting behaviors are revealed when the finite or infinite barriers and spill out effect are taken into account. But the understanding of quantum plasmon resonance, in particular its size-dependent energy shift in the classical-to-quantum transition regime, remains limited.

Here, colloidal Au nanoparticles have been synthesized by a hydrothermal etching technique.[3] The nanoparticle size is tuned by controlling the etching temperature. Double-reversed size-dependence of the SPR wavelength is observed in the classical and quantum size regimes at the diameter of 20.0 nm and 3.6 nm. The theoretical calculations from the quantum-corrected model reveal that the maximum SPR wavelength at 3.6 nm corresponds to the quantum limits of the SPR of colloidal Au nanoparticles, which is attributed to the competition and the collaboration of surface scattering and resonant quantum transitions of free electrons. The SPR of colloidal Au nanoparticles with diameters smaller than 2.2 nm is substantially broadened and difficult to observe owing to the strong damping by the *d* electrons and the strong individual quantum transitions of conduction electrons. Moreover, the photocatalytic activity reaches a maximum at the diameter of 3.6 nm, and there is no enhancement of reaction rate as the plasmon resonance disappears. This result indicates that the photocatalytic activity is enhanced by the quantum plasmon resonance of Au nanoparticles. These observations offer insight into the nature of the optical responses of quantum-sized Au nanoparticles and have general significance for their prospective applications in photophysics and photochemistry.

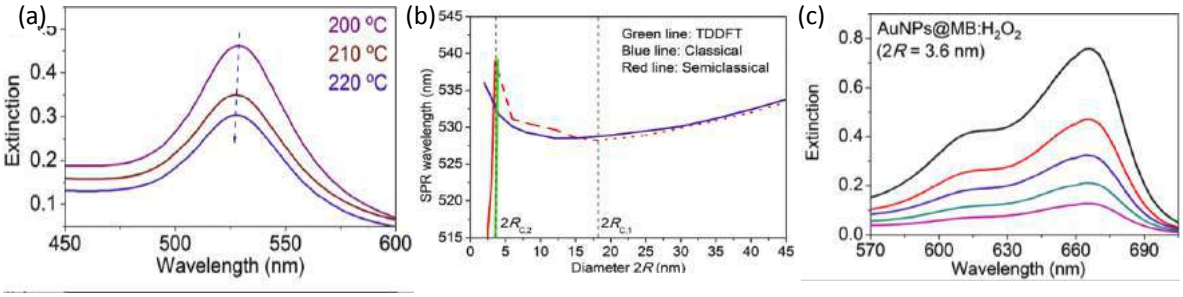

Figure 1. Size-dependences of SPR wavelength and photocatalytic activity for Au nanoparticles. (a) Measured size-dependence of SPR wavelength. (b) Calculated size-dependencies of SPR wavelength by classical and semi-classical Mie models (blue and red lines) and TDDFT (green line, from ref. 4). (c) Reaction rate K as a function of diameter of Au nanoparticles.

Acknowledgements. This work was supported by the National Program on Key Science Research of China, the NSFC (11374236), and China Postdoctoral Science Foundation (2016M602338).

REFERENCES

1. J. A. Scholl, A. L. Koh and J. A. Dionne, *Nature*, 483, 421–428, 2012.
2. L. Genzel, T. P. Martin and U. Kreibig, *Z. Phys. B: Condens. Matter Quanta*, 21, 339–346, 1975.
3. S. J. Ding, D. J. Yang, J. L. Li, G. M. Pan, L. Ma, Y. J. Lin, J. H. Wang, L. Zhou, M. Feng, H. Xu, S. Gao and Q. Q. Wang, *Nanoscale*, DOI: 10.1039/C6NR08962C, 2017.
4. S. Berciaud, L. Cognet, P. Tamarat and B. Lounis, *Nano Lett.*, 5, 515–518, 2005.

Control of Emission Photon Statistics from a Single Quantum Dot Using Plasmonic Nanostructures

S. Masuo*

Department of Applied Chemistry for Environment, Kwansei Gakuin University, Japan

*corresponding author: masuo@kwansei.ac.jp

Abstract-One of the important emission behavior of semiconductor nanocrystal quantum dots (NQDs) is the emission photon statistics, i.e., single-photon and multiphoton emission. Generally, the emission photon statistics of the NQDs are governed by the multiexciton dynamics based on the quantum confinement depending on the size, shape, and atomic composition of NQDs themselves. We demonstrated that the emission photon statistics from a single NQD could be controlled by the interaction with the plasmonic nanostructures.

The emission photon statistics, i.e., single-photon and multiphoton emission from a single semiconductor quantum dot (NQD) are one of the important emission behavior. Generally, the emission photon statistics of the NQD are governed by the multiexciton dynamics based on the quantum confinement depending on the size, shape, and atomic composition of NQDs themselves. We have recently demonstrated that the emission photon statistics from single NQDs could be controlled by the interaction with the plasmonic nanostructures.[1-7] To elucidate the possibility of the control of the photon statistics using the plasmonic nanostructure, the best way is the direct observation of the emission behavior accompanying the interaction with the plasmonic nanostructure. In this work, the enhancement of multiphoton emission from a NQD interacting with a plasmonic nanostructure was investigated using a silver-coated atomic force microscopy tip (AgTip) as the plasmonic nanostructure.[3] Using the AgTip, which exhibited a well-defined localized surface plasmon (LSP) resonance band, we controlled the spectral overlap and the distance between the single NQD and the AgTip. The emission behavior of the single NQD when approaching the AgTip at the nanometer scale was measured using off-resonance (405 nm) and resonance (465 nm) excitation of the LSP (Fig.1).

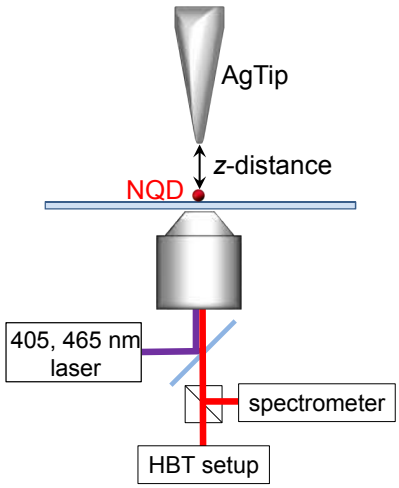

Figure 1. Schematic of the experimental setup for the observation of emission behavior of a single NQD by approaching the AgTip.

We directly observed the conversion of the single-photon emission from a single NQD to multiphoton emission with reduction of the emission lifetime at both excitation wavelengths as the NQD-AgTip distance decreased, whereas a decrease and increase in the emission intensity were observed at 405 nm and 465 nm excitation, respectively. By combining theoretical analysis and the numerical simulation of the AgTip, we deduced that the enhancement of the multiphoton emission was caused by the quenching of the single-exciton

state due to the energy transfer from the NQD to the AgTip and that the emission intensity was increased by enhancement of the excitation rate due to the electric field of the LSP on the AgTip. These results provide evidence that the photon statistics and the photon flux from the single NQD can be manipulated by the plasmonic nanostructure through control of the spectral overlap and the distance.

Acknowledgements, We thank Prof. H. Fujiwara and Prof. K. Sasaki at Hokkaido University for the scattering spectrum measurement of the AgTip and also thank Prof. N. Tamai and Dr. L. Wang at Kwansei Gakuin University for the numerical simulation of the AgTip. This work was partly supported by JSPS KAKENHI Grant Number JP26390023, JP26107005 in Scientific Research on Innovation Areas "Photosynergetics".

REFERENCES

1. Naiki, H., Uedao, T., Wang, L., Tamai, N., and Masuo, S. "Multiphoton Emission Enhancement from a Single Colloidal Quantum Dot Using SiO_2-Coated Silver Nanoparticles" *ACS Omega*, accepted.
2. Naiki, H., Oikawa, H., and Masuo, S. "Modification of Emission Photon Statistics from Single Quantum Dots Using Metal/SiO_2 Core/Shell Nanostructures." *Photochem. Photobiol. Sci.*, accepted.
3. Takata, H., Naiki, H., Wang, L., Fujiwara, H., Sasaki, K., Tamai, N, and Masuo, S. "Detailed Observation of Multiphoton Emission Enhancement from a Single Colloidal Quantum Dot Using a Silver-coated AFM Tip" *Nano Lett*, Vol. 16, 5770–5778, 2016.
4. Masuo, S., Tanaka, T., Machida, S., and Itaya, A. "Photon Antibunching in Enhanced Photoluminescence of a Single CdSe/ZnS Nanocrystal by Silver Nanostructures" *J. Photochem. Photobiol. A*, Vol. 237, 24–30, 2012.
5. Naiki, H., Masuo, S., Machida, S., and Itaya, A. "Single-Photon Emission Behavior of Isolated CdSe/ZnS Quantum Dots Interacting with the Localized Surface Plasmon Resonance of Silver Nanoparticles" *J. Phys. Chem. C*, Vol. 115, 23299–23304, 2011.
6. Masuo, S., Naiki, H., Machida, S., and Itaya, A. "Photon Statistics in Enhanced Fluorescence from a Single CdSe/ZnS Quantum Dot in the Vicinity of Silver Nanoparticles" *Appl. Phys. Lett.,* Vol. 95, 193106, 2009.

Towards atto-Joule efficient Electro-optic Modulators

Z. Ma[1], R. Armin[1], V. J. Sorger[1*]

[1]Department of Electrical and Computer Engineering, George Washington University, Washington, D.C. 20052, USA

[*]corresponding author: sorger@gwu.edu

Abstract- Here we report the optical and electrical concepts to achieve atto-joule per bit efficient and compact on-chip electro-optic modulators. We show that the interplay between the active material and the optical mode properties define the modulator performance. Based on physical tradeoffs, we find combinations of bias, material, and optical-mode that yield efficient phase or amplitude modulation with acceptable insertion loss. Furthermore, we show how material properties in the epsilon near zero (ENZ) regime enable reduction of device-length by 15x.

Photonic integrated circuits (PIC's) are an important enabling technology in today's communication networks and in future chip-to-chip and potentially on-chip interconnects for information processing. The development of PIC has been historically hindered by the inherently weak interaction of light and matter, which requires fundamental size (footprint), speed, and power (S^2P) limits for photonic-based information processing technologies. Among the active PIC components, the high-efficiency, low-noise sources (lasers) and detectors have seen rapid improvement in their performance in the last decade, but the third key active PIC component, light modulators, still remain far from achieving S^2P characteristics. While for a long time there has been no shortage of speculations about achieving all-optical control of signals in PIC's, in the foreseeable future the electrical control of optical signals or, in short, electro-optic (EO) conversion remains the only practical option. Efficient light–matter interaction (LMI) within the active material is key to any optical modulation and strong modulation requires active material that exhibits adequate interaction with the light [1-5]. EO modulation can be enabled by either changing the real part (n) of the modal refractive index leading to phase shifting-based interferometer-like devices termed electro-optic modulators (EOM), or by modulating the imaginary part (k) of the modal index of linear electro-absorptive modulators (EAM). In both types, the

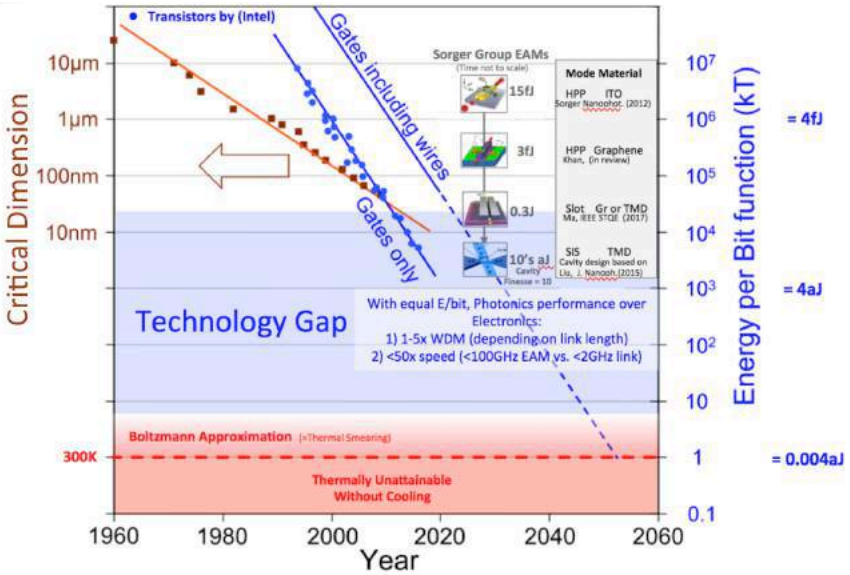

Figure 1. The other Moore's Law: Energy/bit vs. time. Optoelectronics, however, is classically limited to 10-100+ fJ/bit efficiencies, dramatically lagging electronic transistors performance. This illustratively highlights the weak light-matter-interaction. A holistic approach including material choice, optical mode, and cavity feedback enables possible sub-100aJbit EOM performance, as shown by the Sorger group.

fundamental complex index of refraction is altered electrically inside the active material, which in turn modifies the propagation constant of the mode inside the respective waveguide. Electrically driven modulators are classified by the physical mechanism responsible for the change of the complex index. One can distinguish between the current-driven and voltage-driven modulators [1-3]. In the current driven modulators, the change in index is achieved when carriers are injected in (removed from) the active region thus enabling (disabling) the optical transitions and therefore adding (subtracting) to the oscillators strength. Silicon, ITO and graphene modulators are current-driven. In contrast voltage-driven EO modulators no conductivity current flows in/out of the active region, and the change in index is engendered by the energy level shifts and oscillator strength change caused by the electric field (Stark effect), such as in lithium niobate modulators based on Pockels effect and III-V semiconductor based quantum-confined Stark effect. The performance characteristics of current-driven and voltage driven modulators are essentially similar, except that the voltage-driven devices by their nature require active regions capable of avoiding electrical breakdown at high fields which is difficult to achieve in the active regions that are only a few hundred nanometers thick. Given the present state of technology, almost all novel miniaturized modulators appeared over the last few years have been current-driven. The challenge facing EOMs is fundamental in nature; the Kramers–Kronig relations dictate that changing the real part of the complex index independent from simultaneously altering the imaginary part is impossible, unless one operates far from the resonance with any optical transition as is the case when the photon energy is deeply inside the bandgap of modulator material. Yet, both real and imaginary index changes are enhanced near the resonance and any attempt to increase the efficiency of modulation inevitably leads to the increased insertion loss [xxx]. We recently showed that the switching E/bit of EO modulators are able to approach that of electronic transistors of about 10^3-10^4 in fundamental units of k_BT **(Fig. 1)**. For a polaritonic mode, high-index changing material, and cavity enhancement (Finesse = 10), 10's to 100 aJ/bit are possible, matching our earlier optoelectronics scaling law study [4]. Such switching energy is comparable to <10nm scaled FETs is enabling since the performance improvement over electronic links using WDM and medium fast EOM drivers (10's GHz) can approach 250x, depending on link details such as length [6].

Acknowledgements, V.S. is supported by Air Force Office of Scientific Research-Young Investigator Program under grant FA9550-14-1-0215, and under the Army Research Office under the contract number W911NF-16-2-0194.

REFERENCES

1. S. K. Pickus, S. Khan, C. Ye, Z. Li, and V. J. Sorger, “Silicon Plasmon Modulators: Breaking Photonic Limits” *IEEE Photonic Society*, 27, 6 (2013).
2. K. Liu, Z.R. Li, S. Khan, C. Ye, V. J. Sorger, “Ultra-fast electro-optic modulators for high-density photonic integration” *Laser & Photonics Review,* 10, 11-15 (2015). R. Amin, C. Suer, Z. Ma, J. Khurgin, R. Agarwal,
3. V. J. Sorger, “Active Material, Optical Mode and Cavity Impact on electro-optic Modulation Performance” *arXiv:*1612.02494 (2016).
4. K. Liu, A. Majumdar, V. J. Sorger, “Fundamental Scaling Laws in Nanophotonics” Scientific Reports, 6, 37419 (2016).
5. Z. Ma, M. H. Tahersima, S. Khan and V. J. Sorger, "Two-Dimensional Material-Based Mode Confinement Engineering in Electro-Optic Modulators," *IEEE Journal of Selected Topics in Quantum Electronics*, vol. 23, no. 1, 1-8 (2017).
6. S. Sun, A. Badaway, T. El-Ghazawi, V. J. Sorger, “Photonic-Plasmonic Hybrid Interconnects: Efficient Links with Low latency, Energy and Footprint”, *IEEE Photonics*, 7, 6, 15 (2015).

Phase Control and Nonlinear Holography in Composite 3d Metamaterials

Yehiam Prior and Euclides Almeida
Department of Chemical Physics, Weizmann Institute of Science, Rehovot 76100, Israel
*corresponding author: yehiam.prior@weizmann.ac.il

Abstract –The accurate control over the phase and amplitude response of nanoantennas, individual and in arrays, offers a wide range of opportunities for linear and nonlinear shaping of light beams. Optimization of the nonlinear response has been demonstrated, as well as generation of nonlinear holograms at the third harmonic frequency. More recently we introduced a new methodology for the fabrication of three dimensional multilayer metamaterials. Implementation of the 3D materials for phase controlled holography will be discussed, as well as composite multispectral elements such as an RGB lens which is chromatic-aberration-corrected over the visible range.

Metamaterials provide a platform for the study of light-matter interaction in the subwavelength regime, where the material properties can be tailored to give rise to exotic optical phenomena, such as negative refraction, electromagnetic cloaking and superlensing. The current generation metasurfaces rely mostly on quasi 2D structures for the control of amplitude, phase and polarization, and operate mostly in the linear regime. Here we discuss full local phase control of the nonlinear susceptibility tensor in 3D multilayer metasurfaces and show how this control can lead to functional metamaterials operating in the nonlinear regime.

Directional emission of electromagnetic radiation can be achieved from a properly shaped single antenna or from a phased array of individual antennas. Control of the individual phases within an array enables scanning or other manipulations of the emission, and it is this property of the phased arrays that makes them attractive in modern systems. Likewise, the propagation of Surface Plasmons at the interface between metal films and dielectric materials can be controlled by similar approaches. The generic situation of plasmonic surface propagation that is different on both sides of a metal film provides a unique opportunity for such control: plasmons propagating on the slower side feed into the side with the faster propagation, creating a phased array of interfering antennas, and thus controlling the directionality of the wake fields. We show that by shaping the individual nanoantennas we can generate asymmetric propagation geometry as well.

The amplitude and phase control of nonlinear signals in wave mixing experiments can be achieved by tuning the resonance of dipolar nanoantennas. By changing the geometry of these plasmonic elements, the cavity plasmonic resonances are tuned and a continuous, nearly 2π radians, relative phase among nonlinear signals can be attained. This continuous phase-span enables the fabrication of nonlinear metasurface optical elements, such as beam deflector or nonlinear lenses.

The approach for nonlinear phase control described above can be extended to other nonlinear processes and to three dimensions. Polarization dependent 3D metamaterial holograms were fabricated. When illuminated by an

infrared beam, they generate holographic images at the third-harmonic frequency in the blue. The phase information of the nonlinear susceptibility is encoded in nanometric gold antennas (this time V-shaped), fabricated by e-Beam lithography, with stamping accuracy of 10 nm between layers. Because the hologram is generated at a new frequency (the third harmonic), these multilayer metamaterial holograms are background-free and enable high density storage of optical information.

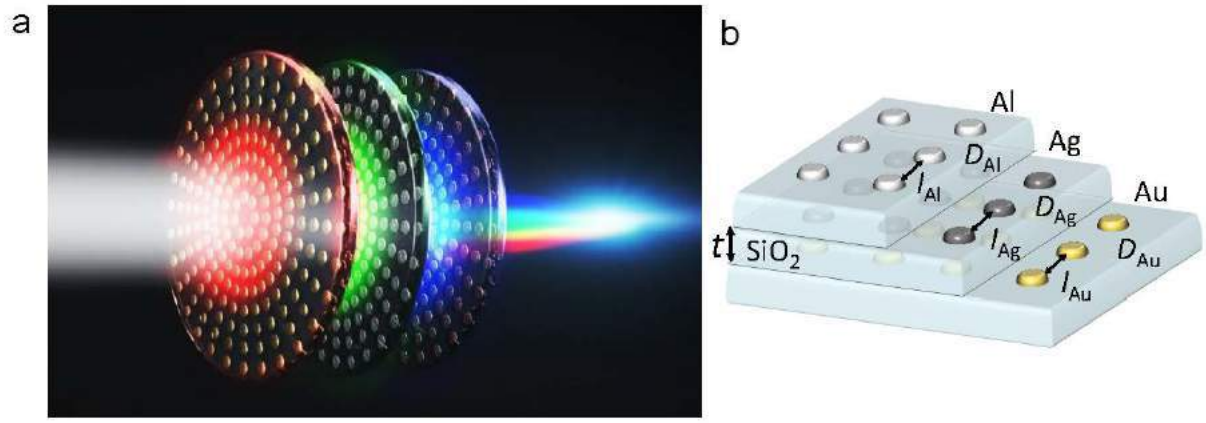

Figure 1. Multilayered RGB lens. A three layers lens, consisting of three different metals each individually designed for a specific wavelength, delivering achromatic operation over the visible range.

Last but not least, based on the ability to assemble multilayer structures, where each layer consists of different metal particles and is separately controlled, Figure 1, we fabricated functional 3D elements, including an aberration free RGB lens and STED elements where different color beams are manipulated differently by the same thin nano element.

Acknowledgements The expert help of Ora Bitton is gratefully acknowledged. This work was partially supported by the Israeli Science Foundation, the ICORE program, by an FTA grant and by the Minerva Foundation.

REFERENCES

1. E. Almeida and Yehiam Prior, Rational design of metallic nanocavities for resonantly enhanced four-wave mixing, **Scientific Reports**, 5:10033 | DOI: 10.1038/srep10033 (2015)
2. E. Almeida Guy Shalem and Yehiam Prior, Nonlinear Phase Control and Anomalous Phase Matching in Plasmonic Metasurfaces, **Nature Communications,** 7:10367 | DOI: 10.1038/ncomms10367 (2016)
3. E. Almeida Ora Bitton and Yehiam Prior, Nonlinear Metamaterials for Holography, **Nature Communications** 7:12533 | DOI: 10.1038/ncomms12533 (2016)
4. Ori Avayu*, Euclides Almeida*, Yehiam Prior, Tal Ellenbogen, Composite Functional Metasurfaces for Multispectral Achromatic Optics, **Nature Communications**, In Press (2017) and **arXiv:1609.08275**

Photonic noise in deep-subwavelength plasmonic structures with gain and fundamental limitations on data transfer rates

A. A. Vyshnevyy and D. Yu. Fedyanin*
Laboratory of Nanooptics and Plasmonics, Moscow Institute of Physics and Technology, Russian Federation
*corresponding author: dmitry.fedyanin@phystech.edu

Abstract – Surface plasmon amplification by stimulated emission of radiation gives the possibility to compensate for high ohmic losses in the metal and design virtually losses devices. However, stimulated emission is inevitably accompanied by spontaneous emission, which greatly reduces the signal-to-noise ratio and impairs the performance characteristics. Here, we present a comprehensive framework to evaluate noise in plasmonic structures with gain and present a strategy for noise reduction to a level sufficient for practical applications in high-density on-chip optical interconnects.

The main obstacle currently faced by plasmonics is strong signal attenuation due to absorption in the metal. High ohmic losses can be compensated by optical gain in an adjacent medium. At the same time, the process of stimulated emission is accompanied by spontaneous emission [1]. If the spectral linewidth of the optical signal is narrow, spontaneous emission can be filtered out. However, according to the laws of thermodynamics, signal amplification unavoidably reduces the signal-to-noise ratio. The higher the material gain, the higher the power of spontaneous emission, which goes into the plasmonic mode, and therefore the stronger the noise. In deep-subwavelength plasmonic structures, where an extremely high optical gain is needed to compensate for high ohmic losses, the spontaneous emission power can significantly exceed the signal power. This greatly affects the noise characteristics.

Here, we develop a comprehensive framework to study photonic noise produced by spontaneous emission [2]. We present our results in a ready-to-use form, which can be immediately applied with no change to different plasmonic and nanophotonic systems, such as optical amplifiers based on semiconductors, quantum dots and dye molecules. Using the developed approaches and comprehensive numerical simulations, we study the influence of spontaneous emission on the performance of truly nanoscale active plasmonic waveguides, which simultaneously provide deep-subwavelength (˜λ2/100) mode confinement and full compensation of the propagation loss (Figure 1). We find that the power of spontaneous emission at the end of the 1-mm-long waveguide exceeds 100 μW and the role of the spontaneous-spontaneous beat noise is crucial due to the relatively large bandwidth of the spontaneous emission spectrum in the semiconductor gain medium. We show that similar to the spontaneous emission power, the spontaneous-spontaneous beat noise can be suppressed using optical filtering. At the same time, the signal-spontaneous beat noise can not be affected by optical filtering, since its spectral properties are determined by the bandwidth of the photodetector [2]. Nevertheless, we demonstrate that deep-subwavelength plasmonic waveguides with gain can be efficiently used for data transfer at distances below ˜1 mm, which is a typical distance for on-chip interconnects, while longer communication distances could be problematic due to the strong photonic noise (Figure 1).

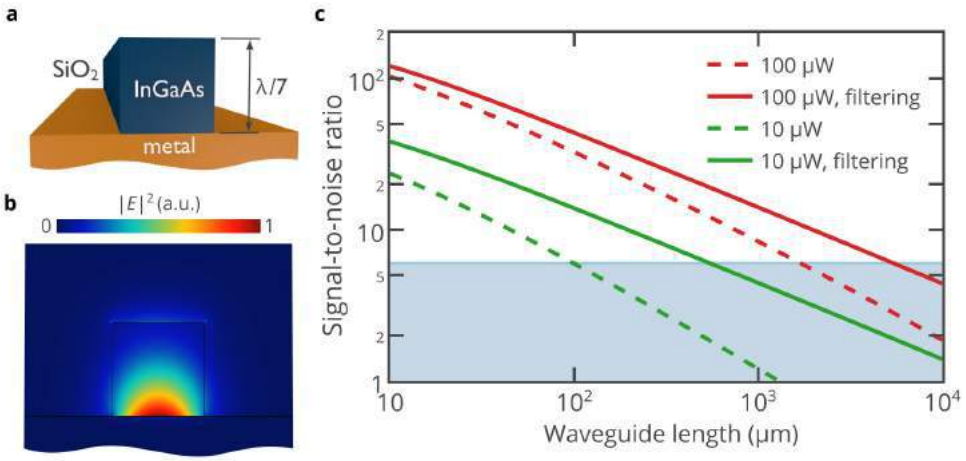

Figure 1. (a) Schematic of the single-mode subwavelength plasmonic waveguide with the InGaAs active medium. (b) Electric field distribution of the plasmonic mode at a light wavelength of 1550 nm. (c) Signal-to-noise ratio versus waveguide length for two different signal powers. The solid curves correspond to the system with a narrow bandpass optical filter, and the dashed curves correspond to the systems without optical filters. The blue area shows the region of high bit error ratios, where high-speed communication is complicated.

REFERENCES

1. Suhara, T. *Semiconductor Laser Fundamentals,* CRC Press, 2004.
2. Vyshnevyy, A. A. and Fedyanin, D. Y., "Spontaneous emission and fundamental limitations on the signal-to-noise ratio in deep-subwavelength plasmonic waveguide structures with gain," *Physical Review Applied* Vol. 6, 064024, 2016.

Chiral Plasmonic Nanoparticles with Chiroptical Activity Engineerable in the UV-visible region

Z. F. Huang[1*]

[1]Department of Physics, Hong Kong Baptist University, Kowloon Tong, Kowloon, Hong Kong SAR, China

[*]corresponding author: zfhuang@hkbu.edu.hk

Abstract-Chiral plasmon is expected to markedly enhance the optical chirality of the electromagnetic field on the nanostructure surfaces. An accessibility of chiral molecules to the irradiation with enhanced optical chirality will give rise to a wide range of vital chirality-related applications. To develop these applications, it is a prerequisite to understand and control the chiroptical activity of chiral plasmonic nanostructures, which is generally characterized by circular dichroism (CD) monitoring the differential absorption of left- and right-handed circularly polarized light. However, the understanding of the chiroptical activity is ambiguous currently. In this talk, the author will present that when plasmonic nanoparticles (NPs) are sculptured in a (hidden) helical shape using, e.g. glancing angle deposition, the NPs exhibit chiroptical activity intrinsically originating from the spiral structures. The chiroptical activity can be flexibly controlled in terms of the CD amplitude and CD resonance wavelength in the UV-visible regime, by engineering the plasmonic material, handedness, and helical dimensions. Numerical and analytical simulations are operated to understand the chiroptical activity of the chiral plasmonic NPs.

Integrated graphene waveguide modulators based on low-loss plasmonic slot waveguides

Sanshui Xiao*
DTU Fotonik, Department of Photonics Engineering, Center for Nanostructured Graphene,
Technical University of Denmark, 2800, Kgs. Lyngby, Denmark
saxi@fotonik.dtu.dk

Abstract- Graphene based electro-absorption modulators involving dielectric optical waveguides have been recently explored, suffering however from weak graphene-light interaction. Surface plasmon polaritons enable light concentration within subwavelength regions opening thereby new avenues for strengthening graphene-light interactions. I present novel integrated graphene plasmonic waveguide modulator showing high modulation depth and low insertion loss, thus giving a promising way to miniaturize the device without jeopardizing the performance of the device.

In recent years, the unique optical and electronic properties of graphene attracts wide interest, ranging from light-emitting devices to photodetectors, and touch screen [1]. In particular, the opportunity to control optoelectronic properties through Fermi-level tuning enables electro-optical modulation, optical-optical switching, and other optoelectronics applications. The deployment of graphene on top of a silicon waveguide is an efficient mean to make graphene−silicon hybrid devices [2-3]. However, it remains a big challenge to achieve high modulation depth because of the modest graphene light interaction in the graphene-silicon waveguide hybrid systems. Surface plasmon polaritons are broadband with the ability to manipulate light on the subwavelength scale [4], while at the same time giving possibility to direct more optical energy to the material interface where graphene could reside. Here I present novel graphene plasmonic waveguide modulators that are interfaced with silicon waveguides and are thus fully integrated in the silicon-on-insulator platform [5],

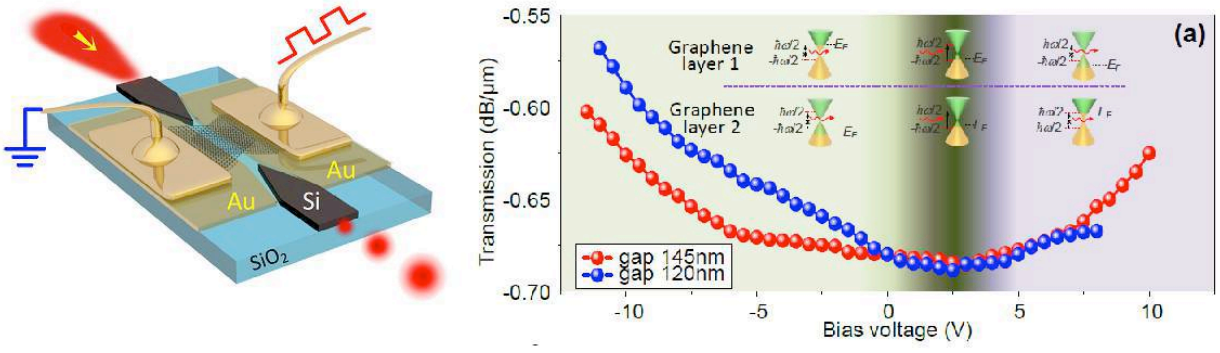

Figure 1. (a) 3D schematic of the graphene plasmonic waveguide modulator; (b) Modulated transmission for 20um-long graphene plasmonic hybrid slot waveguides.

Figure 1(a) shows the illustration of proposed graphene plasmonic waveguide modulator, where the plasmonic slot waveguide is coupled in/out by silicon waveguides with inverse tapering tips. The plasmonic waveguide can confine modes beyond diffraction limit, while at the same time suffering with large propagation loss. Here we propose plasmonic slot waveguides relying on the concept of leaky mode, giving us extremely low loss of 0.25dB/μm. The good alignment of the coupling part (between the silicon and plasmonic waveguide) leads to high in/out coupling efficiency of 1.45 dB.

Transmissions of the light at 1.55 μm through 20 μm-long leaky-mode graphene-plasmonic waveguides at different bias voltages are presented in Fig. 1(b) for two slot widths of 120 nm and 145 nm. One can find that the transmission through the graphene-plasmonic hybrid waveguides is effectively tuned by applying bias voltages on the graphene. An efficient attenuation tunability of 0.13 dB/μm is achieved for the plasmonic slot width of 120 nm at low gating voltages. The modulation depth of 0.13 dB/μm achieved here exceeds that for reported graphene-plasmonic hybrid device [6].

The Center for Nanostructured Graphene is sponsored by the Danish National Research Foundation, Project DNRF103.

REFERENCES

1. F. Bonaccorso, Z. Sun, T. Hasan and A. C. Ferrari, “Graphene photonics and optoelectronics”, Nature Photon., 4, 611 (2010).
2. M. Liu, X.B. Yin, E. Ulin-Avila, B.S. Geng, T. Zentgraf, L. Ju, F. Wang, and X. Zhang, “A graphene-based broadband optical modulator”, Nature 474, 64 (2011).
3. Y. Ding, X. Zhu, S. Xiao, H. Hu, L.H. Frandsen, N.A. Mortensen, and K. Yvind, “Effective electro-optical modulation with high extinction ratio by a grapheme-silicon microring resonator”, Nano. Lett., 15, 4393 (2015).
4. S.I. Bozhevolnyi, V.S. Volkov, E. Devaux, J.Y.Laluet, and T.W. Ebbesen, “Channel plasmon subwavelength waveguide components including interferometers and ring resonators”, Nature 440, 508 (2006).
5. Y. Ding, X. Guan, X. Zhu, H. Hu, S. I. Bozhevolnyi, L.K. Oxenloewe, N.A. Mortensen, S. Xiao, “Integrated graphene plasmonic electro-optical modulator based on leaky-mode slot waveguides”, arXiv:1610.05352.
6. D. Ansell, I. Radko, Z. Han, F. Rodriguez, S.I. Bozhevolnyi, and A.N. Grigorenko, “Hybrid graphene plasmonic waveguide modulators”. Nature Commun., 6, 8846 (2015).

Simple autocorrelation function for analysis of collective and quantum effects in radiation from nanocavities and plasmonic nanostructures

I. E. Protsenko[1], **E.C. André**[2], **M. Wubs**[2], **A. V. Uskov**[1,3] **and J. Mørk**[2]

[1]Lebedev Physical Institute of RAS, Leninsky prospect, 53, Moscow, 119991, Russia
[2]Department of Photonics Engineering, Technical University of Denmark, DK-2800 Kgs. Lyngby, Denmark
[3]ITMO University, Kronverksky pr. 49, St. Petersburg, 197101, Russia
protsenk@gmail.com

Abstract— Analytical expression for fourth-order autocorrelation function of laser field shows strong influence of collective effects to laser coherency and helps to identify parameters for coherent, incoherent (thermal), sub- and associated with superradiance super-thermal lasing. Below-, above- and thresholdless lasing of micro- and nano-lasers are analyzed in the model without adiabatic elimination of active medium polarization. We show that collective effects reduce beta-factor and number of photons below the threshold.

Our model includes two sequences of Heisenberg equations. The first one – for mean values of binary products of operators, describing dynamics of total energy in the system: emitter populations, cavity mode photon number, dipole interaction of emitters with the cavity mode and with each other. Quantum mechanical relations between operators of emitters lead to terms responsible for spontaneous emission into lasing mode. Thus we can describe lasing below, at and above the threshold. The second sequence of equations is for mean value products of four operators, beginning with $\langle a^+a^+aa\rangle$, where a is Bose-operator of the cavity mode, $\langle ...\rangle$ means quantum-mechanical averaging. We break some mean value products of four operators in products of mean values of two operators and arrive to closed set of equations. We approximately neglect by fluctuations in populations of states of emitters, that is good approximation in a weak coupling limit. From the first and the second sets we found, respectively, the stationary photon number $n = \langle a^+a\rangle$ and the normalized autocorrelation function $g_2 = \langle a^+a^+aa\rangle / n^2$.

The model takes into account and shows explicitly the contribution of collective radiation from emitters. A part of the energy from the pump goes to collective radiation, reducing the incoherent spontaneous emission to the lasing mode. As a result, we found a reduction of β-factor respectively to one calculated in the rate equation approach [1] without taking into account collective radiation from emitters. The competition between collective and "individual" (incoherent) spontaneous emission causes the decrease in the number of photons below the threshold, which correlates with results of numerical analysis, for example, in [2]. We also found a feature of two-level active medium corresponding, for example, to q-dots: it permits "thresholdless" lasing even at $\beta \ll 1$ – if the number of emitters is small, that the threshold population inversion per emitter is close to 1.

The approach beyond limits of laser rate equations allows us carefully take into account up to fourth-order correlations between the cavity mode and the active medium polarization. We analytically calculate autocorrelation function g_2 for cavity mode field and identify conditions and laser parameters for various photon statistics. In particular, how large the photon number n must be for $g_2 \to 1$ – coherent field generation; when we obtain $g_2 = 2$ – for thermal field, or $g_2 > 2$ - for super-thermal field and $1 < g_2 < 2$ – for sub-thermal field generation.

Super-thermal field generation $g_2 > 2$ clearly appears below the lasing threshold, when the threshold population inversion per emitter is small: $\Delta_{th} \ll 1$, and for relatively low polarization relaxation (de-phasing) rate γ_h: $\gamma_h/2\kappa < 1$, where κ is the lasing cavity mode damping rate. $g_2 > 2$ means photon bunching because of collective spontaneous emission into lasing mode, which has been shown numerically in [3, 4]. We also see, that lasers with low threshold $\Delta_{th} \ll 1$ and low de-phasing $\gamma_h/2\kappa < 1$ easily demonstrate collective nature not only in spontaneous emission below, but also in stimulated emission above the threshold: there the coherency $g_2 \to 1$ appears at relatively small number of photons.

ACKNOWLEDGMENT

IP acknowledges COST-STSM-MP1403-34800 short scientific mission action for support. The work of AU was supported in part by the Government of the Russian Federation (Grant 074-U01) through the ITMO Visiting Professorship program.

REFERENCES

1. Rice, P., R., and H. J. Carmichael, "Photon statistics of a cavity-QED laser: A comment on the laser-phase-transition analogy," *Phys. Rev. A*, Vol. 50, No. 5, 4318–4329, 1994.
2. Jahnke, F., Gies, G., Aβmann, M., Bayer, M., Leymann, H. A. M., Foerster, A., Wiersig, J., Schneider, C., Kamp, M. and S. H$\ddot{o}$fling, "Giant photon bunching, superradiant pulse emission and excitation trapping in quantum-dot nanolasers," *Nature Commun*, Vol. 7, doi:10.1038/ncomms11540, 2016.
3. Leymann, H. A. M., Foerster, A., Jahnke, F., Wiersig, J. and C. Gies, "Sub- and superradiance in nanolasers," *Phys. Rev. Appl.*, Vol. 4, No. 044018, 2015.
4. Auffeves, A., Gerace, D., Portolan, S., Drezet. A. and M. Franca Santos, "Few emitters in a cavity: from cooperative emission to individualization," *New J. Phys.*, Vol. 13, 093020, 2011.

Plasmonic-Electronic Transducers Based on Tunneling

Christian A. Nijhuis

National University of Singapore. Department of Chemistry and Centre for Advanced 2D Materials, 3 Science Drive 3, Singapore 117543, Singapore

Email: chmca@nus.edu.sg

Abstract-This paper describes highly efficient plasmonic-electronic transducers based on tunneling. The plasmons are excited and detected via plasmon assisted tunneling. By electrically detecting the plasmon, the plasmon excitation efficiencies can be estimated which are 1000 times higher than estimates based on photon out coupling efficiencies.

Recently, the use of tunnel junctions as plasmon sources have regained interest [1,2]. In these devices, currents are directly converted to plasmons in a single step. The reverse process is also possible – optical rectification – and plasmons can couple to tunneling currents also in a single step (i.e., without the need of free photons or excitons). Therefore, tunnel junctions may find applications in plasmonic-electronic circuitry. Till date, it is unclear whether tunnel junctions can excite and detect plasmons efficiently enough for practical applications. From a fundamental point of view, the exact mechanisms of plasmon-electron coupling are not clear in these junction [3].

During the talk I will discuss our recent progress in the development of molecular tunnel junctions based on self-assembled monolayers (SAMs) and how we apply them as electrical excitation sources of plasmons [4-7]. The bottom-electrode is made of gold which also serves as the plasmonic waveguide. By simply applying a bias between the top and bottom electrode, a tunnelling current will flow. The tunnelling charges carriers that reach the gold electrode excite plasmons. Since the tunnelling rate and the tunnelling direction can be controlled by simply changing the chemical structure of the SAM, we have the ability to control the plasmonic properties of the devices and launch plasmons [8,9]. Our experiments indicate that these plasmon sources behave as point sources whose blinking properties can also be controlled by simply changing the molecular structure. Finally, by integrating two tunnel junctions with one wave-guide, we demonstrate that the tunnel junctions are also promising as plasmon detectors [9]. The latter devices make it possible to estimate the plasmon-electron coupling efficiency. Our results indicate that the plasmon-electron coupling efficiency is 1000 times higher than previously estimates based on photon out coupling rates [1-3]. Our results show that molecular electronics combined with plasmonics makes it possible to control plasmonic properties and to study new phenomena at the molecular length-scales and the tunnel junctions are interesting for applications in plasmonic-electronics in more general.

Acknowledgements We acknowledge the National Research Foundation (NRF) for supporting this research under Prime Minister's Office, Singapore under its Medium sized centre programme, and the Competitive Research Programme (CRP) program (NRF-CRP 8-2011-07 and NRF2016-CRP001-111)

REFERENCES

[1] Parzefall, M.; Bharadwaj, P.; Jain, A.; Taniguchi, T.; Watanabe, K. *Nat. Nanotechnol*. **10,** 1058–1063

(2015)
[2] Kern, J.; Kullock, R.; Prangsma, J.; Emmerling, M.; Kamp, M.; Hecht. B. *Nat. Photon*. **9,** 582–586 (2015)
[3] Ward, D. R., Hüser, F., Pauly, F., Cuevas, J. C. & Natelson, D. Optical rectification and field enhancement in a plasmonic nanogap. *Nature Nanotechnol*. **5,** 732-736 (2010).
[4]Nerngchanmnong, N.; Yuan, L.; Qi, D. C.; Jiang, L.; Thompson, D.; Nijhuis, C. A. *Nat. Nanotechnol.* **2013**, *8*, 113.
[5] Wan, A.; Jiang, L.; Suchand Sangeeth, C. S.; Nijhuis, C. A. *Adv. Funct. Mater.* **2014***, 24*, 4442.
[6] Yuan, L.; Jiang, L.; Zhang, B.; Nijhuis, C. A. *Angew. Chem. Int. Ed.* **2014**, *53*, 3377.
[7] Jiang, L.; Yuan, L.; Cao, L.; Nijhuis, C. A. *J. Am. Chem. Soc.* **2014**, *136*, 1982.
[8] Du, W.; Wang, T.; Chu, H.; Wu, L.; Liu, R.; Sun, S.; Phua, W.K.; Wang, L.; Tomczak, N.; Nijhuis, C. A. *Nature Photon.* **2016***, 10*, 274 - 280
[9] Tan, S. F., Wu, L., Yang, K. L. W., Bai, P., Bosman, M., Nijhuis, C. A. *Science*, **2014**, *343*, 1496.
[10] Du, W.; Wang, T.; Chu, H.; Nijhuis, C. A. *submitted*

Plasmofluidic assembly of nanometallic structures: from single-molecule SERS to dynamic lithography

Partha Pratim Patra, Junsuk Rho
Department of Mechanical Engineering, POSTECH, South Korea
ppptra@gmail.com

Sub-wavelength control and manipulation of light is one of the most desirable issues in science and technology. To destine this, surface plasmon polariton (SPP) plays a significant role and to harness SPP, the nanometallic architectures have unprecedented ability to concentrate and transport light. The sophisticated and versatile applications of SPPs mostly rely on the geometry and the arrangement of the nanostructures. Thus innovative 'preparation and assembly' of nanometallic architectures is crucial. Especially, by assembling the nanostructures in a controlled way, one can deploy the plasmon-coupling for subtle modulation of light wave. Recently, the assembly of nanostructures has opened up a promising field of research which is directly linked to many other important subjects, e.g. biophotonic sensing, metamaterials, optical nanoscopy, thermoplasmonics, nonlinear plasmonics, photovoltaics, catalysis etc.

Herein we present how to harness plasmofluidic field (plasmonic field in fluid) to create efficient electromagnetic hot-spots by assembling colloidal nanoparticles to detect single-molecule SERS signals[1]. Also we shall discuss how the extension of this technique can lead to a preamble of reconfigurable dynamic lithography of plasmonic nanostructures at metal-fluid interface[2].

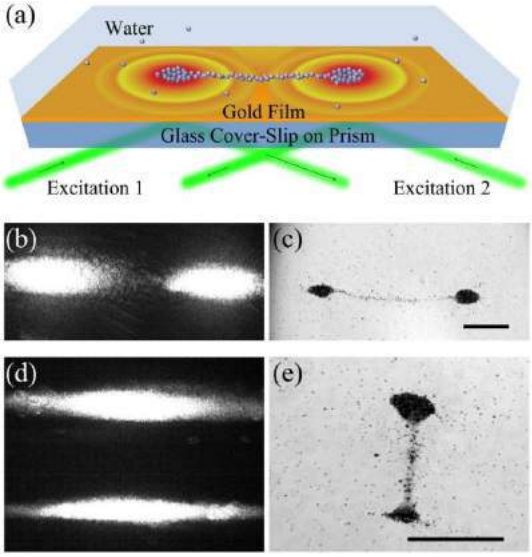

Figure 1 Schematic illustration of experimental geometry and the resulting dynamic assembly of nanoparticles.

Acknowledgements, These works are done in Photonics and Optical Nanoscopy Laboratory, Indian Institute of Science Education and Research (IISER), Pune, India and supported by IISER, Pune and DST, India funding.

REFERENCES

1. Patra P P, Chikkaraddy R, Tripathi R P N, Dasgupta A and Kumar G V P, " Plasmofluidic single-molecule surface-enhanced Raman scattering from dynamic assembly of plasmonic nanoparticles," *Nat*. *Commun*. 5 4357, 2014.
2. Patra P P, Chikkaraddy R, Thampi S, Tripathi RPN, Kumar GVP, "Large-scale dynamic assembly of metal nanostructures in plasmofluidic field," *Faraday discussions* 186, 95-106, 2016.

Modal plasmonic logic gates.

Upkar Kumar[1*], Sviatlana Viarbitskaya[1,2], Aurélien Cuche[1], Alexandre Bouhelier[2], Gérard Colas des Francs[2], Jadab Sharma[1], Christian Girard[1], Erik Dujardin[1]

[1] *CEMES CNRS UPR 8011 and Université Fédérale de Toulouse, 29 rue J. Marvig, 31055 Toulouse, France*

[2] *LICB, CNRS UMR 6303, Université de Bourgogne, 9 Av. A. Savary, Dijon, France.*

[*]corresponding author: dujardin@cemes.fr

Abstract-Two dimensional colloidal plasmonic cavities spatially and spectrally shape the near-field. By designing these two degres of freedom, transduction function can be implemented in single cavities that perform Boolean logic functions. The wealth of available plasmonic modes allow to implement complex logic funcitons without the need of concatenating building blocks but rather by redesigning the ransfer function.

2D plasmonic systems with mesoscopic sizes sustain higher order plasmonic modes and combine the properties of surface plasmon polaritons (SPP) and localized surface plasmon (LSP). Such multimodal plasmonic systems open a new realm in which the modal behavior is better described by the Surface Plasmon local density of states (SP-LDOS), which is solely governed by the material properties and the boundary conditions set by the structure shape, but is independent of the illumination parameters. SP-LDOS can be rationally designed to tailor the local spatial and spectral characteristics of the SP modes, while allowing information transfer over micrometer-sized distances.

The next level of information processing consists in performing Boolean logic from the incoming signal. Here again, the tailoring of the modal properties of confined plasmonic cavities can be exploited to designing reconfigurable universal logic gates that can be converted into one another, this opens the way to the integration of complex functions at the nanoscale.

Acknowledgements. The financial support of the European Research Council (ERC) (contract number ERC-2 2007-StG Nr 203872 COMOSYEL), Agence Nationale de la Recherche (ANR) (ANR-13-BS10-0007-PlaCoRe) and the computing center CALMIP in Toulouse.

REFERENCES

1. S. Viarbitskaya, A. Teulle, R. Marty, J. Sharma, C. Girard, A. Arbouet and E. Dujardin. "Tailoring and imaging the plasmonic local density of states in crystalline nanoprisms." *Nature Materials* 12, 426, 2013.
2. A. Teulle, M. Bosman, C. Girard, K. L. Gurunatha, M. Li, S. Mann, E. Dujardin, "Multimodal plasmonics in fused colloidal networks." *Nature Materials*, 14, 87, 2015.
3. A. Cuche, S. Viarbitskaya, J. Sharma, A. Arbouet, C. Girard, E. Dujardin. "Modal engineering of surface plasmons in apertured Au Nanoprisms." *Sci. Rep.*, 5, 16635, 2015.
4. A. Cuche, S. Viarbitskaya, U. Kumar, J. Sharma, A. Arbouet, C. Girard, E. Dujardin. "*Beyond dipolar regime in high-order plasmon mode bowtie antenna".* Opt. Comm., 2017, 387, 48-54..
5. A. Cuche, M. Berthel, U. Kumar, G. Colas des Francs, S. Huant, E. Dujardin, C. Girard, A. Drezet. " *Near-field hyperspectral quantum probing of multimodal plasmonic resonators".* Phys. Rev. B., 2017, 95, 121402(R)

Classical and Quantum Applications using Fast and Slow Light Photonics

Demonstration of broadband slow light in genetically optimized Silicon based coupled-cavity waveguides with group-index bandwidth product exceeding 0.45

Yiming Lai[1,2], Mohamed Sabry Abdel-Aliem[3], Momchil Minkov[3,4], Boshen Gao[5], Robert W. Boyd[5,6], Vincenzo Savona[3], Romuald Houdré[3], Antonio Badolato[6]

[1] Department of Physics and Astronomy, University of Rochester, Rochester, NY 14627, USA

[2] Current address: DiCon Fiberoptics, 1689 Regatta Blvd, Richmond, CA 94804, USA

[3] Institute of Physics, Ecole Polytechnique Fédérale de Lausanne EPFL, CH-1015 Lausanne, Switzerland

[4] Current address: Ginzton Laboratory, Stanford University, Stanford, CA 94305, USA

[5] The Institute of Optics, University of Rochester, Rochester, NY 14627, USA

[6] Department of Physics and Max Planck Centre for Extreme and Quantum Photonics, University of Ottawa, Ottawa, Ontario K1N 6N5, Canada

[*]corresponding author: romuald.houdre@epfl.ch

Abstract-Synthesizing the optical response of material through photonic band engineering is a means of slowing down light, in effort to achieve enhanced light-matter interaction or optical buffering. State-of-the-art, photonic crystal (PhC)-based slow light devices however suffer from limited bandwidth, group velocity dispersion, and non-flat transmission. Here, we report on the experimental measurements on structures, based on genetically optimized PhC coupled cavity waveguide (CCW) design, with largest bandwidth and the highest group-index bandwidth product. CCWs of length ranging between 50 and 800 cavities were measured with a very homogeneous flat-top transmission profile and losses value below 67 dB/ns.

Slow light propagation through engineered band dispersion in photonic structures is a highly promising tool for realizing integrated optical delay lines and efficient photonic devices through enhanced optical nonlinearities [1,2]. A primary goal is to achieve devices over the largest possible bandwidth with large group index and minimal dispersion (*i.e.* approximately constant group index), flat transmission spectrum, which otherwise would hinders their use for pulse propagation, with setbacks such as pulse distortion and generation of echoes, thus enabling multimode and pulsed operation [2].

We present an experimental proof of record-high group-index bandwidth product (GBP = $n_g \Delta\omega/\omega$) [2] in genetically optimized coupled-cavity waveguides (CCWs) made of staggered modified L3 photonic crystal cavities (Fig.1(a) and (b)). The optimization procedure [3] was applied to the unit cell (Fig. 1(a)) to achieve maximal GBP combined with low losses. The resulting designs [4] were realized in Si slabs (Fig. 1(b)), where CCWs of length ranging between 50 and 800 cavities were fabricated. The samples were characterized by measuring the CCW transmission (Fig. 1(c) and (d)), the mode dispersion through Fourier-space imaging (FSI), and the group index n_g independently with FSI and Mach-Zehnder interferometry (Fig. 1(e)).

Various cavity designs were investigated, with theoretical group index ranging from $n_g = 37$ to $n_g > 100$. Record-high GBP = 0.45 was demonstrated over a bandwidth approaching 20 nm (Fig. 1(e)), with $n_g = 37$, a very homogeneous flat-top transmission profile (Fig. 1(c) and (d), exhibiting variations lower than 10 dB) and losses value below 67 dB/ns. On a different design [3], an average $n_g = 107$ with 15 % variation over 7.4 nm was measured. These values range among the best ever demonstrated for a silicon device.

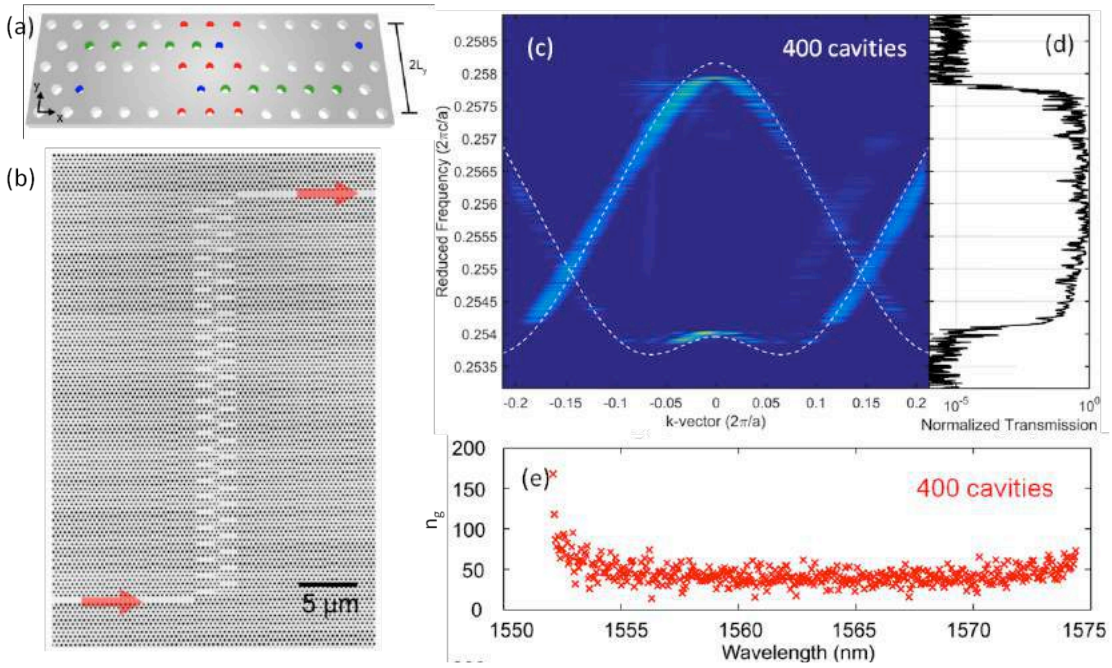

Fig. 1 *: (a) Sketch of the unit cell of the CCW. The radii of the red and green holes, and the radius and x-position of the blue holes, were used as variational parameters to optimize the GBP and the loss rate of the CCW. (b) SEM picture of a 50-cavity CCW. (c) Dispersion of the guided modes of a 400-cavity CCW measured through Fourier-space imaging. Dashed lines: fit with a tight-binding model. (d) Measured transmission of a 400-cavity CCW. (e) Wavelength resolved group index, as measured for a 400-cavity CCW using Mach-Zehnder interferometry.*

REFERENCES

1. T. Baba, "Slow Light in Photonic Crystals," *Nat. Photon.* 2, 465 (2008).
2. S. A. Schulz, et al., "Dispersion Engineered Slow Light in Photonic Crystals: A Comparison," *J. Opt.* 12, 104004 (2010).
3. M. Minkov, and V. Savona, "Wide-band Slow Light in Compact Photonic Crystal Coupled-Cavity Waveguides," *Optica* 2, 631 (2015).
4. M. Minkov, and V. Savona, "Automated Optimization of Photonic Crystal Slab Cavities," *Sci. Rep.* 4, 5124 (2014).

Soliton pulse propagation in the presence of disorder-induced multiple scattering in slow-light photonic crystal waveguides

N. Mann and S. Hughes

Department of Physics, Queen's University, Kingston, Ontario, Canada K7L 3N6

Abstract— We describe a new coupled mode theory to model nonlinear Schrödinger equations for counter-propagating Bloch modes that include disorder-induced multiple scattering effects on nonlinear soliton propagation in photonic crystal waveguides. Our numerical simulations of nonlinear pulse propagation are in excellent qualitative agreement with recent experiments and provide fresh insight into how disorder inhibits soliton propagation and other nonlinear propagation effects in photonic crystal waveguides.

Slow light in photonic crystal waveguides (PCWs) can be exploited for enhancing nonlinear optical (NLO) interactions [1]. For example, self phase modulation (SPM) in the presence of two photon absorption (2PA) and free carrier effects was observed by Monat *et al.* [2], while non-trivial scaling of SPM and three-photon absorption (3PA) was investigated by Husko *et al.* [3]. Colman *et al.* [4] utilized dispersion engineered PCWs to suppress 3PA which was critical in the demonstration of temporal pulse compression of higher order solitons. Other demonstrated NLO effects include third harmonic generation and highly efficient four wave mixing [5–7].

Despite these successes, one of the major limiting factors for exploiting NLO effects in PCWs is disorder-induced multiple scattering which roughly scales as n_g^2, where n_g is the group index [8]. This limitation is somewhat suppressed through dispersion-engineering [9, 10] or by reducing the length of the PCW to less than 500 unit cells which lowers losses but typically increases the required pump power [2]. Regardless, in the slow light regime, coupling to disorder is unavoidable and any realistic model must include such effects. The theory of disorder on linear propagation in PCWs is well developed [8, 11–13]. For modelling NLO effects in PCs, Bhat and Sipe [14] used multiple scales analysis and $k{\cdot}p$ theory to derive a *dynamical* nonlinear Schrödinger equation (NLSE), which is first-order in time, and their nonlinear coefficients use unit-cell averaged Bloch modes; however, the previously mentioned NLO works use the NLSE model adapted from the nonlinear fiber optics literature [15], where the NLSE is *first-order in space* and the nonlinear coefficients are generalized by a unit cell integration involving only the *periodic part* of the Bloch mode.

A severe shortcoming of current NLSEs applied to PCWs is their naive modelling of disorder-induced losses (if at all) as an effective loss parameter α, which follows the Beer-Lambert law, known to breakdown in the regime of multiple scattering, arising from coupling between contra-propagating modes [16]. The effect of multiple scattering on soliton propagation is shown schematically in Fig. 1 (though the pulse profiles are from actual calculations for 2 ps pulses). Although some works have partly studied coupling between contra-propagating modes in the context of examining nonlinear

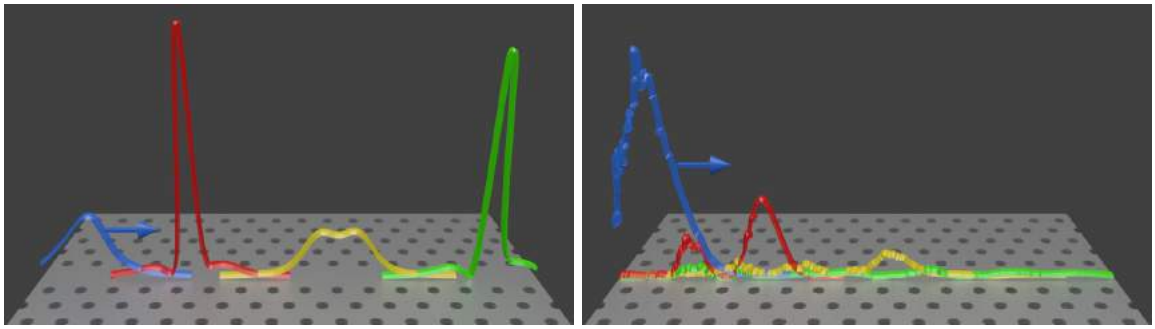

Figure 1: Spatial profiles at various times of a soliton injected from the left side of a W1 PCW in the absence (left) and presence (right) of disorder-induced multiple scattering and localization. For comparing the two schematics, the two leftmost pulses (blue) are of the same magnitude.

bistability in finite periodic media [17, 18], it was for weak scattering and in the *absence* of group velocity dispersion (GVD). For PCWs, neither of these assumptions holds true.

In this work, we will describe our recently developed coupled-mode theory (CMT) to model two coupled NLSEs for counter-propagating Bloch modes, including the effects of GVD, disorder-induced multiple scattering, SPM and cross-phase modulation (XPM) [20]. Unlike previous works, our nonlinear coupling coefficients are positional dependent because they involve an integration over the cross-section of the PCW and utilize the full 3D vectorial Bloch modes. We also introduce a characteristic length scale corresponding to each coupling coefficient, including a length scale associated with multiple scattering, which denotes the spatial extent associated with a disorder-induced localized mode. Using the W1 PCW, we model solitons propagating in the presence of multiple scattering for several n_g ranging from fast light to the slow light regime, and connect to a range of experimental observables. When nonlinearities dominate over multiple scattering, the soliton's spectra shows a random fine peak structure, whereas when multiple scattering dominates, the soliton's spectra exhibits narrow spectral peaks indicative of disorder-induced photon localization. Our numerical results are able to capture hitherto unexplained experimental features related to multiple scattering [2, 3, 19]. Moreover, our formalism can be generalized to assess the impact of multiple scattering on other nonlinearities such as 2PA, 3PA, and four-wave mixing.

References

[1] Thomas F. Krauss. *Nat. Photonics*, 2(8):448–450, aug 2008.

[2] Christelle Monat *et al.*, *Opt. Express*, 17(4):2944, feb 2009.

[3] Chad Husko *et al.*, *Opt. Express*, 17(25):22442, nov 2009.

[4] Pierre Colman *et al.*, *Nat. Photonics*, 4(12):862–868, nov 2010.

[5] Christelle Monat *et al.*, *Opt. Lett.*, 36(15):2818, jul 2011.

[6] C. Xiong *et al.*, *Opt. Lett.*, 36(17):3413, aug 2011.

[7] J. Li, L. O'Faolain, and T. F. Krauss. *Opt. Express*, 20(16):17474, jul 2012.

[8] S. Hughes, L. Ramunno, J.F. Young, and J.E. Sipe. *Phys. Rev. Lett.*, 94(3):033903, jan 2005.

[9] L O'Faolain *et al.*, *Opt. Express*, 18(26):27627–38, dec 2010.

[10] N. Mann, S. Combrié, P. Colman, M. Patterson, A. De Rossi, and S. Hughes. *Opt. Lett.*, 38 (20):4244, oct 2013.

[11] B. Wang *et al.*, *Phys. Rev. B*, 78(24):245108, dec 2008.

[12] S. Mazoyer *et al.*, *Phys. Rev. Lett.*, 103(6):063903, aug 2009.

[13] M. Patterson, S. Hughes, S. Combrié, N. V Quynh Tran, A. De Rossi, R. Gabet, and Y. Jaouën. *Phys. Rev. Lett.*, 102(25):253903, jun 2009.

[14] N. A. R. Bhat and J. E. Sipe. *Phys. Rev. E*, 64(5):56604, oct 2001.

[15] G P Agrawal. *Nonlinear Fiber Optics*. Electronics & Electrical. Academic Press, 4th ed, 2007.

[16] M. Patterson, S. Hughes, S Schulz, D. M. Beggs, T. P. White, L. O'Faolain, and T. F. Krauss. *Phys. Rev. B*, 80(19):195305, nov 2009.

[17] Herbert G. Winful and Gene D. Cooperman *Appl. Phys. Lett.*, 40(4):298, feb 1982.

[18] C. Martijn de Sterke and J. E. Sipe. *Phys. Rev. A*, 42(5):2858–2869, sep 1990.

[19] C. Husko, M. Wulf, S. Lefrancois, S. Combrié, G. Lehoucq, A. De Rossi, B. J. Eggleton, and L. Kuipers. *Nat. Commun.*, 7:11332, apr 2016.

[20] Nishan Mann and Stephen Hughes, e-print: arXiv:1608.08281, aug 2016.

Photonic crystal waveguide designs for optimised chiral light-matter interactions at polarisation singularities.

D. M. Beggs[1*], B. Lang[2*], and R. Oulton[2]

[1]School of Physics & Astronomy, Cardiff University, Queen's Buildings, The Parade, Cardiff CF24 3AA, UK

[2]Quantum Engineering Technology Labs, H. H. Wills Physics Laboratory and Department of Electrical & Electronic Engineering, University of Bristol, BS8 1FD, UK

[*]corresponding author: BeggsD@cardiff.ac.uk

Abstract-Slow-light photonic crystal waveguide designs that support chiral C-point polarisation singularities are shown. Using FDTD simulations, we have confirmed spin-photon entanglement with a correlation >99% for a quantum dot placed at a C-point. Photonic crystal waveguide designs that optimise the chiral light-matter interaction are provided, with a factor 8.6 enhancement of the local optical density of states found. The existence and location of C-points in the waveguide is confirmed to be remarkably robust to disorder in the waveguide.

Photonic crystal waveguides support polarisation singularities such as C-points, which are expected to be useful in future quantum information applications for several reasons. Firstly, thanks to the ability to tailor their dispersion properties [1], photonic crystal waveguides provide a flexible, integrated and miniaturised technology platform for quantum information applications. Secondly, quantum emitters such as quantum dots can be coupled on-chip and in-plane. And thanks to the very tight mode confinement and high density of optical states in the slow-light waveguide mode, the photon emission into the waveguide can be made near-deterministic – e.g. coupling with $\beta > 98\%$ between a slow-light mode and an quantum dot has been demonstrated [2]. Thirdly, the existence of C-points allows the waveguide to display local chirality. The global chirality is zero, as the C-points occur in pairs of left- and right-handed points. The local chirality has consequences for the photons emitted by quantum dots positioned at a C-point. The photons emitted by quantum dot transitions possess an angular momentum which is dependent on the spin state of the electrons. At a C-point, this angular momentum interacts with the chirality to give unidirectional emission dependent on the spin of the electron. The propagation direction of the light is what gives rise to the symmetry breaking needed. Such spin-dependent unidirectional emission is an attractive property for quantum information applications [3].

Here we report on the use of C-points in photonic crystal waveguides for quantum information applications. We use FDTD simulations to show that C-points can be used to entangle spin-encoded static qubits with path-encoded flying qubits [4] – see Fig. 1 – and we have optimised the waveguide design to use slow-light to enhance the local density of optical states at the C-point by a factor of 8.6 [5]. Further increases are constrained by temporal symmetry and the reciprocal nature of light. We find that C-points cannot exist at the bandedge due to the symmetry of the forward and backward modes found there, and this places limits on the use of C-points for unidirectional emission in the slow-light regime [6].

We also investigated the effect that disorder in the waveguide has on the existence and position of the C-points (see Fig. 2), and find that the C-points are remarkably robust to the introduction of disorder [7].

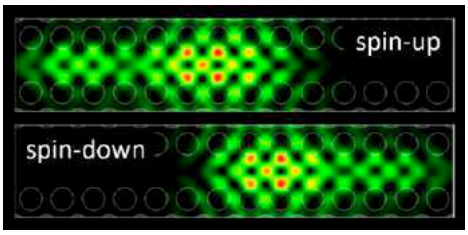

Figure 1. Spin-dependent unidirectional emission from a quantum dot at a C-point. There is >99% correlation between electron spin and emission direction: spin-up electrons always emit photons to the left and spin-down to the right.

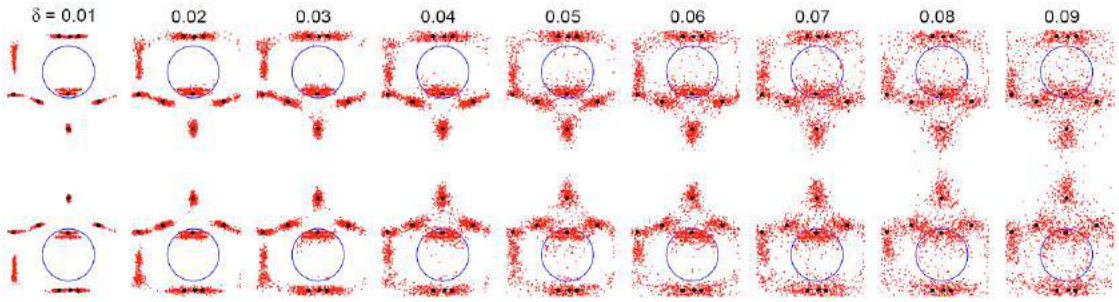

Figure 2. C-points are robust to disorder. Red dots show the calculated positions of C-points in a statistical ensemble of disordered waveguides for increasing values of the disorder parameter δ (indicated). Black dots show positions of C-points in the ideal waveguide.

Acknowledgements, This work has been funded by SPANGL4Q, under FET-Open grant number: FP7-284743. RO was sponsored by the EPSRC under grant no. EP/G004366/1. DMB acknowledges support from a Marie Curie individual fellowship QUIPS. BL gratefully acknowledges funding from EPSRC (DTA). GW4 supported this work. This work was carried out using the computational facilities of the Advanced Computing Research Centre, University of Bristol http://www.bris.ac.uk/acrc/.

REFERENCES

1. S. A. Schulz, *et al.* "Dispersion engineered slow light in photonic crystals: a comparison," *J. Optics*, Vol. 12, No. 10, 104004, 2010.
2. M. Arcari, *et al.* "Near-unity coupling efficiency of a quantum emitter to a photonic crystal waveguide," *Phys. Rev. Lett.*, Vol. 113, 093603, 2014.
3. P. Lodahl, et al. "Chiral quantum optics," *Nature*, Vol. 541, 473–480, 2017.
4. A. B. Young, et al. "Polarization engineering in photonic crystal waveguides for spin-photon entanglers," *Phys. Rev. Lett.*, Vol. 115, 153901, 2015.
5. B. Lang, *et al.* "Optimised photonic crystal waveguide for chiral light-matter interactions," *J. Opt.*, at press, doi: 10.1088/2040-8986/aa5f5f, 2017.
6. B. Lang, *et al.* "Time reversal constraint limits unidirectional photon mission in slow-light photonic crystals," *Phil. Trans. R. Soc. A*, Vol. 374, 20150263, 2016.
7. B. Lang, *et al.* "Stability of polarization singularities in disordered photonic crystal waveguides," *Phys. Rev. A*, Vol. 92, 063819, 2015.

Cavityless plasmonic nanoresonator

I. M. Fradkin* **and D. Yu. Fedyanin**
Laboratory of Nanooptics and Plasmonics, Moscow Institute of Physics and Technology, Russian Federation
*corresponding author: fradkin@phystech.edu

Abstract-Optical resonators are one of the most critical components in optoelectronics owing to their ability to strengthen light-matter interaction. Here, we demonstrate a cavityless nanoresonator based on an extremely slow mode of the metal-insulator-metal plasmonic waveguide. Its operating principle does not rely on the geometric resonances, and thus the device characteristics are almost independent of the structure dimensions. This feature makes such a resonator attractive for diverse applications at the deep-subwavelength scale, where accurate fabrication is still a challenge.

Development of highly efficient nanophotonic devices requires the ability to localize light in order to strengthen the light-matter interaction. This can be achieved with optical cavities, which store the electromagnetic energy in the form of standing waves. The resonance frequencies are determined by the geometry of the cavity, which discretizes the possible dimensions of such a resonator. Here, we discuss and demonstrate a fundamentally different type of resonators: a cavityless resonator, - which paves the way to a whole new approach for the electromagnetic field enhancement. The operating principle of such a resonator is not based on reflection from the cavity boundaries and, therefore, the resonant modes almost do not depend on the geometrical parameters [1,2]. This gives the possibility to reduce the fabrication tolerance and makes this type of resonators highly attractive for nanoscale LEDs [3], lasers [4], detectors and other active nanophotonic devices. The cavityless resonator can be realized using an optical waveguide, in which the energy velocity is close to zero, i.e. light is almost stopped. If the electromagnetic energy dissipates faster than it flows out of the small region of the waveguide, the decay time does not depend on the waveguide length. In this work, we present a cavityless nanoresonator based on the metal-insulator-metal (MIM) plasmonic waveguide (Fig. 1). Its operating frequency can be easily adjusted by choosing the insulator material. We show that even in the presence of Joule heating losses the MIM structure is able to decrease the energy velocity to near zero, which gives the possibility to achieve a high quality factor of the cavityless plasmonic resonator.

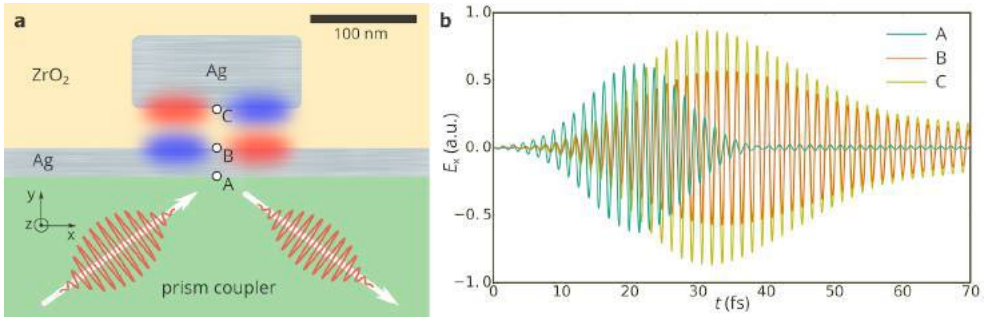

Figure 1. (a) Schematic of the cavityless MIM nanoresonator excited using an ultrashort optical pulse and Kretschmann geometry. (b) Time dependence of the electric field at points A, B and C (see panel a).

This work is supported by the Russian Foundation for Basic Research (16-37-00509-mol) and by the grant of the President of the Russian Federation (MK-2602.2017.9).

REFERENCES

1. Fedyanin, D. Yu. and A. V. Arsenin, "Stored light in a plasmonic nanocavity based on extremely-small-energy-velocity modes," *Phot. Nano. Fund. Appl.*, Vol. 8, No. 4, 264–272, 2010.
2. Fedyanin, D. Yu., A. V. Arsenin, V. G. Leiman and A. D. Gladun, "Detection of ultrashort pulses with a plasmonic nanocavity based on the insulator-insulator-metal waveguide," *36th European Conference and Exhibition on Optical Communication*, 2010.
3. Yao, P., C. V. Vlack, A. Reza, M. Patterson, M. M. Dignam and S. Hughes, "Ultrahigh Purcell factors and Lamb shifts in slow-light metamaterial waveguides," *Phys. Rev. B*, Vol. 80, No. 19, 195106, 2009.
4. Pickering, T., J. M. Hamm, A. F. Page, S. Wuestner and O. Hess, "Cavity-free plasmonic nanolasing enabled by dispersionless stopped light," *Nat. Commun.*, Vol. 5, 4972, 2014.

Coherent optical storage using acoustic phonons in chips

M. Merklein[1*], B. Stiller[1], K. Vu[2], S. J. Madden[2] and B. J. Eggleton[1]

[1]Centre for Ultrahigh bandwidth Devices for Optical Systems (CUDOS), Institute of Photonics and Optical Science (IPOS), School of Physics, University of Sydney, Sydney, New South Wales 2006, Australia

[2]CUDOS, Laser Physics Centre, Research School of Physics and Engineering, Australian National University, Canberra, Australian Capital Territory 0200, Australia

[*]corresponding author: moritz.merklein@sydney.edu.au

Abstract- Here we present an on-chip photonic memory based on a coherent transfer of optical data pulses to acoustic phonons and vice versa. We show that this process is fully coherent by encoding different phase states. The ultra large Brillouin gain in our photonic chips allows us to reach GHz bandwidth. We furthermore show storage of different amplitude levels, which increases the capacity of our memory even further.

Optical communication techniques are the only way to deliver the necessary speed and bandwidth to cope with the exponential increasing amount of data transferred today. The fast speed of light allows to send large amounts of data over long distances, however imposes a challenge when processing, rerouting or synchronising signals. Therefore, it is required to reduce the speed of optical data packets, or in some cases even completely stop the signal stream in a controlled way to enable processing, buffering or rerouting. Achieving this challenging goal in an integrated platform at room temperature has attracted a lot of interest, in particular slow-light in photonic crystals[1], [2] and stimulated Brillouin scattering (SBS) based slow-light in optical fibers [3]. The latter harnesses a change in the group velocity due to the resonant Stokes amplification and is a direct consequence of the Kramers-Kronig relation.

Here, we show a different way to use stimulated Brillouin scattering to delay light signals by storing optical data pulses as acoustic phonons for a certain amount of time and subsequently convert the stored information back to the optical domain [4], [5]. The optical data pulses at frequency ω_{Data} are resonantly transferred to an acoustic wave Ω via a counter-propagating write pulse at frequency $\omega_{W/R}$ that is frequency offset to the data pulse ω_{Data} by the Brillouin frequency shift Ω. The acoustic wave travels 5-orders of magnitude slower than the optical data pulses therefore efficiently delaying the optical signal. Afterwards the optical signals are retrieved by a second counter propagating optical pulse $\omega_{W/R}$, in this case depleting the acoustic wave and retrieving the original data pulse ω_{Data}.

This concept was first demonstrated in highly nonlinear fiber [6], showing, in a proof-of-principle experiment, that several nanosecond long pulses can be stored and retrieved afterwards. However, the potential of this memory greatly exceeds this early demonstration. In our work, we show that the transfer photon-phonon-photon is fully coherent by encoding different phase levels. We also show that we can store and retrieve several amplitude levels and the strict phase-matching condition of stimulated Brillouin scattering allows multi-wavelength operation. As a storage medium we use ultra-high Brillouin gain chalcogenide spiral waveguides. The on-chip waveguides not only greatly reduce the form factor of our memory but also enable to store pulses with much wider bandwidth, i.e. much shorter pulses. As a consequence, the Brillouin gain is spread out over a wide bandwidth, hence ultra-high Brillouin gain in the overlap region of the pulses is required.

In conclusion we demonstrated an optical memory based on a coherent transfer of photons to phonons and vice versa. The optical information is stored in a small-footprint spiral waveguide at room temperature. The ultra-high Brillouin gain of these waveguides allows us to store pulses with sub-ns length. We demonstrate that our Brillouin based memory is fully coherent and show storage and retrieval of multiple phase and amplitude levels.

Acknowledgements, Australian Research Council (ARC) Council Centre of Excellence (CUDOS CE110001010, Laureate Fellowship (FL120100029).

REFERENCES

[1] T. Baba, "Slow light in photonic crystals," *Nat. Photonics*, vol. 2, no. 8, pp. 465–473, Aug. 2008.

[2] T. F. Krauss, "Why do we need slow light?," *Nat. Photonics*, vol. 2, no. 8, pp. 448–450, Aug. 2008.

[3] L. Thévenaz, "Slow and fast light in optical fibres," *Nat. Photonics*, vol. 2, no. 8, pp. 474–481, Aug. 2008.

[4] M. Merklein, B. Stiller, K. Vu, S. J. Madden, and B. Eggleton, "Storing Light as Sound in a Photonic Integrated Circuit," in *Frontiers in Optics 2015*, 2015, p. FW6C.6.

[5] B. Stiller, M. Merklein, K. Vu, S. J. Madden, and B. J. Eggleton, "A coherent on-chip optical memory: storing amplitude and phase as acoustic phonons," in *Photonics and Fiber Technology 2016 (ACOFT, BGPP, NP)*, 2016, p. JW6A.1.

[6] Z. Zhu, D. J. Gauthier, and R. W. Boyd, "Stored light in an optical fiber via stimulated Brillouin scattering.," *Science*, vol. 318, no. 5857, pp. 1748–50, Dec. 2007.

Co- and Counter-Propagating Slow Light Pulses and Their Applications

T. Baba* and K. Kondo
Yokohama National University, Japan
*corresponding author: baba-toshihiko-zm@ynu.ac.jp

Abstract-Optical nonlinearity allows various control of light, while their effects is usually small. Si photonic crystal waveguides enhance the nonlinearity on a chip, thanks to the strong optical confinement and slow-light effect. Here, we present co-/counter-propagating slow-light systems, in which two slow-light pulses propagate simultaneously and exhibit unique interactions. The enhanced nonlinearity as well as engineered group-delay and dispersion in slow light gives unique functions such as adiabatic wavelength conversion, fast delay tuning, pulse compression, Doppler shift and auto-correlation.

REFERENCS

1. T. Baba, “Slow light in photonic crystals,” Nature Photon., vol. 2, pp. 465-473, 2008.
2. M. Shinkawa, N. Ishikura, Y. Hama, K. Suzuki and T. Baba, “Nonlinear enhancement in photonic crystal slow light waveguides fabricated using CMOS-compatible process,” Opt. Express, vol. 19, pp. 22208-22218, 2011.
3. N. Ishikura, R. Hayakawa, R. Hosoi, T. Tamanuki, M. Shinkawa and T. Baba, “Photonic crystal tunable slow light device integrated with multi-heaters,” Appl. Phys. Lett., vol. 100, pp. 221110, 2012.
4. K. Kondo, M. Shinkawa, Y. Hamachi, Y. Saito, Y. Arita, and T. Baba, “Ultrafast slow-light tuning beyond the carrier lifetime using photonic crystal waveguides,” Phys. Rev. Lett., vol. 110, pp. 053902, 2013.
5. K. Kondo and T. Baba, "Dynamic wavelength conversion in copropagating slow-light pulses", Phys. Rev. Lett., vol. 112, no. 22, pp. 223904, 2014.
6. K. Kondo, N. Ishikura, T. Tamura and T. Baba, "Temporal pulse compression by dynamic slow-light tuning in photonic crystal waveguides", Phys. Rev. A, vol. 91, no. 02, pp. 023831, 2015.
7. K. Kondo and T. Baba, “Slow-light-induced Doppler shift in photonic-crystal waveguides”, Phys. Rev. A (Rapid Commun.), vol. 93, no. 1, pp. 011802(R), 2016.
8. K. Kondo and T. Baba, “On-chip auto-correlator using two-photon-absorption photodiode array and counter-propagating slow light,” CLEO, 2016

Slow-light enabled photonic integrated microwave filter.

S. Combrié[1], **J. Bourderionnet**[1], **D. Martin**[1], **A. De Rossi**[1], **Z. Han**[2], **X. Checoury**[2], **M. Gay**[3], **L. Bramerie**[3], **C. Peucheret**[3], and **J-C. Simon**[3]

[1]Thales Research and Technology, France
[2]Centre de Nanosciences et de Nanotechnologies (C2N), Université Paris-Saclay, France
[3]Foton Laboratory, CNRS, University of Rennes 1, Lannion, France
sylvain.combrie@thalesgroup.com

Abstract— A reconfigurable multi-tap microwave filter is demonstrated on a silicon-on-insulator platform. Compactness and low-power operation are achieved owing to slow-light in photonic crystals. As an example, a microwave band-pass and a stop-band filters are obtained. Channel equalization is also demonstrated on an unitary filter cell.

1. INTRODUCTION

The use of optical technology brings unprecedented advantages to manipulate and process microwave signals. Initially mainly reserved to the distribution of signals over long distance, microwave photonics, which exploits optics to process high-speed analog signals, is quickly advancing thanks to the development of photonic integrated circuits (PIC), promising compact, robust, low-power, lightweight devices which can be mass produced. This will have a tremendous impact in wireless and space communication and radar.
In this context, filtering is considered as the most relevant function [1], as superior agility and broadband operation, in addition to immunity to electromagnetic interference, are expected to be an obvious advantage of a photonic microwave device, compared to its electronic counterpart. Our microwave photonic filter implements a finite impulse response owing to the interference of 4 delayed and weighted replicas of the signal in the optical domain. The coherent summation of the fields allows to cover a broader range of response functions. In this architecture, reconfigurability and tunability is provided by adjustable switches and optical delay lines. As the size of these devices is constrained by the dispersion of the waveguide, dispersion engineering and slow light are crucial assets [2].

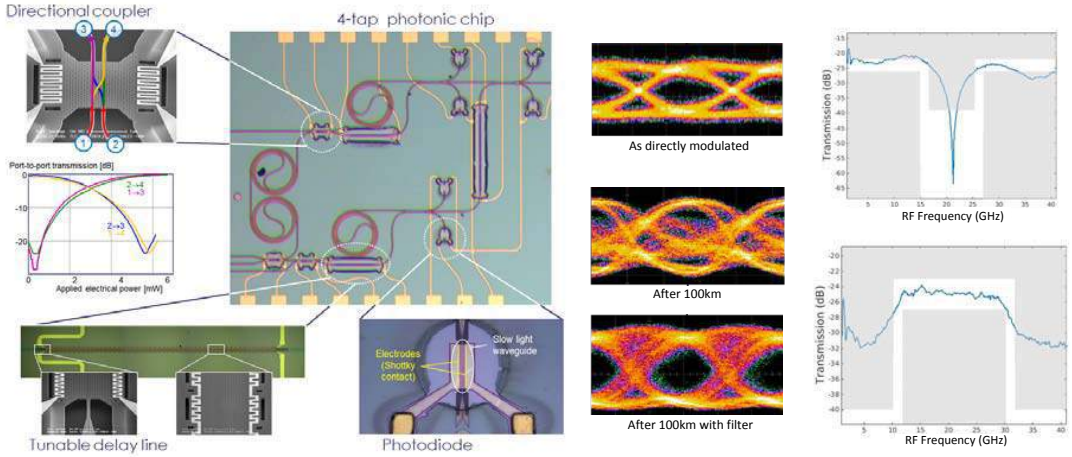

Figure 1: On the left, image of a 4-tap photonic integrated microwave filter and magnified images (SEM) of its constitutive elements: PhC photodetector, PhC tunable delay-line and PhC directional coupler. Signal processing using the device (right): eye diagram before and after dispersion compensation and example of synthesised transfer functions.

2. IMPLEMENTATION OF A SLOW-LIGHT BASED MICROWAVE FILTER

The architecture of the filter (figure 1) is based on nested cells consisting of a Mach-Zehnder (MZ) interferometer formed with a PhC directional coupler (DC), a tunable PhC delay-line (DL) and a 250 μm-long fixed spiral delay ($\sim$ 25 ps) and a multi-mode interferometer (MMI). The device shown here uses two lower level cells nested in a third one. The performances of the filter depends largely on the properties of the tunable delay line, which is a photonic crystal waveguide operating in the so-called slow light regime [5]. The range of the delay determines the central frequency and the free spectral range. The dispersion is tailored to provide a very steep change of the delay as the temperature of the PhC suspended slab is modified. A different design of the dispersion is exploited to reduce the size of the directional coupler [3] at the heart of the 2×2 switch to $10\mu m$ (figure). Because of the tiny active volume and the large thermal resistance of the suspended slabs, the switch provides a large contrast ($> 20dB$) by consuming only (3 mW) of electric power, and its thermal tunability is fairly fast ($1\mu s$). Similarly, the delay line covers a range of 80 ps with a maximum of 80 mW.

The two arms of each interferometer are recombined by a 2x3 MMI interferometer, allowing the use of two photodetectors to measure the state of the interferometer, which is crucial to set the desired parameters of the filter. We use germanium-free photodetectors [4] based on nonlinear and surface absorption, which are remarkably effective in silicon photonic nanostructures in telecom spectral range. Under the operating condition, the responsivity is $\sim$ 0.1 A/W, which is sufficient for our purpose. The structures were fabricated in a standard clean room environment, on a silicon-on-insulator (SOI) platform.

3. DEVICE OPERATION

Each interferometer is stabilized using a small amplitude and low frequency modulation of the current applied to the heaters of the delay lines. Using a standard lock-in technique, the resulting phase modulation of the optical signal is used to unambiguously measure and stabilize the optical phase. The residual phase error of the stability loop is as low as $\lambda/80$ rms . Using a single stabilized filter cell, we have demonstrated [6] the compensation of the dispersion in an optical link based on a directly modulated laser diode. This is apparent in the eye diagram in figure 1.

The transfer function of the 4-tap filter is measured using a modulator, a detector and a vector network analyser (VNA). This is shown in figure 1(right), where a variety of responses are obtained by setting the currents applied to the heaters suitably. As an example, a "stop band" or "bandpass" function are obtained. The slope of the filter edges will increase with the number of coefficients (hence taps), which is allowed by the inherently scalable architecture used here. This opens the way to structures with larger number of taps thanks to silicon photonics capabilities in terms of integration.

REFERENCES

1. J. Capmany, B. Ortega, D. Pastor, "A tutorial on microwave photonic filters", *Journal of Lightwave Technology*, vol. 24, p. 201, 2006.
2. T. Baba, H. C. Nguyen, N. Ishikura, K. Suzuki, M. Shinkawa, R. Hayakawa, K. Kondo, "Photonic crystal slow light devices fabricated by CMOS-compatible process", *IEICE Electronics Express*, vol. 10, p. =20132002, 2013.
3. Z. Han, G. Moille, X. Checoury, J. Bourderionnet, P. Boucaud, A. De Rossi, S. Combrié, "High-performance and power-efficient $2\times$ 2 optical switch on Silicon-on-Insulator", *Optics Express*, vol. 23, p. 24163, 2015.
4. L. D. Haret, X. Checoury, Z. Han, P. Boucaud, S. Combrié, A. De Rossi, "All-silicon photonic crystal photoconductor on silicon-on-insulator at telecom wavelength", *Optics express*, vol. 18, p. 23965, 2010.
5. J. Sancho, J. Bourderionnet, J. Lloret, S. Combrié, I. Gasulla, S. Xavier, S. Sales, P. Colman, G. Lehoucq, D. Dolfi, and al., "Integrable microwave filter based on a photonic crystal delay line", *Nature communications*, vol. 3, p. 1075, 2012.
6. M. Gay, L. Bramerie, L. A. Neto, S. D. Le, J-C. Simon, C. Peucheret, Z. Han, X. Checoury, G. Moille, J. Bourderionnet, A. De Rossi, S. Combrié, "Silicon-on-Insulator RF Filter Based on Photonic Crystal Functions for Channel Equalization", *IEEE Photonics Technology Letters*, vol. 28, p. 2756, 2016

Towards integrated quantum photonics: materials, designs, technologiesâ€

On-chip frequency combs for scalable quantum state generation

M. Kues[1,2], C. Reimer[1], P. Roztocki[1], B. Wetzel[1,3], F. Grazioso[1], B. E. Little[4], S. T. Chu[5], T. Johnston[1], Y. Bromberg[6], L. Caspani[1,7], D. J. Moss[8], R. Morandotti[1]

[1]Centre Énergie Matériaux Télécommunications, Institut National de la Recherche Scientifique, Canada;

[2]School of Engineering, University of Glasgow, UK

[3]Department of Physics and Astronomy, University of Sussex, UK

[4]State Key Laboratory of Transient Optics and Photonics, Xi'an Institute of Optics and Precision Mechanics, China

[5]Department of Physics and Material Science, City University of Hong Kong, China

[6]Racah Institute of Physics, The Hebrew University of Jerusalem, Israel

[7]Institute of Photonics, Department of Physics, University of Strathclyde, UK

[8]Center for Micro-Photonics, Swinburne University of Technology, Australia.

Abstract- Optical non-classical states are fundamental resources for applications in quantum information processing. We show that integrated frequency comb sources, operating in the quantum regime, can provide a scalable and versatile platform for non-classical state generation.

With recent advances in optical quantum information processing (e.g. the realization of quantum cryptography systems), it is foreseeable that reliable, low-cost, and scalable on-chip sources of complex optical quantum states will represent a key enabling technology for quantum applications [1-4]. The requirements of such sources vary for different applications, but typically include long-term operational stability and insensitivity to environmental perturbations, compatibility with quantum memories, operation at telecomm wavelengths (around 1550 nm), and compatibility with mass-producible electronic chip fabrication standards (CMOS). More importantly, source characteristics, such as frequency multiplexing to enable multi-user/channel operation, polarization diversity to implement polarization-based operations, and the generation of more complex quantum states are necessary to enable new functionalities in the fields of quantum information science. Therefore, the realization of integrated quantum sources has attracted considerable attention from the scientific community [1]. However, major difficulties arise when sources need to satisfy several requirements at the same time, i.e. a narrow spectral bandwidth, high-purity single-mode generation, high production rates, multiplexed broadband operation, and / or entanglement shared between several photons.

We demonstrate that integrated quantum frequency combs (based on on-chip, high-Q micro-ring resonators [5]) can address these requirements and enable the generation of *pure heralded single photons, cross-polarized photon pairs,* as well as *bi- and multi-photon entangled qubit states* over a broad frequency comb covering the full S, C, and L telecommunication bands.

2. Heralded single photon source

Exploiting a self-locked, intra-cavity excitation configuration [6], a highly stable integrated source of frequency-multiplexed heralded single photons is demonstrated without the need for active stabilization (of e.g. excitation frequency) [6]. The photons are generated though four-wave mixing (FWM) within an integrated micro-ring resonator. The measured photon bandwidth of 110 MHz is compatible with state-of-the-art quantum memories and repeaters, and the high purity of the emitted photons was confirmed through single-photon auto-correlation measurements [6,7]. We report nearly single-frequency-mode operation and demonstrate

heralded single photons with an anti-bunching dip as low as 0.144.

3. Cross-polarized photon pair source

By simultaneously exciting two resonances corresponding to orthogonal polarization modes, while suppressing stimulated degenerate four-wave mixing (FWM) through a mode family frequency offset, we introduce a new type of spontaneous FWM to the toolbox of integrated photonics [7]. In particular, we demonstrate the first realization of type-II spontaneous FWM (in analogy to type-II spontaneous parametric down-conversion in second-order media), which enables the direct generation of orthogonally-polarized photon pairs on a chip [7]. The measured photon bandwidths (320 MHz), excellent coincidence-to-accidental ratios, and high purity single-frequency-mode operation in the single-photon regime underline the source utility.

4. Two- and multi-photon entangled state source

Through the double-pulse excitation of a high-Q micro-resonator, we demonstrate the generation of time-bin entangled photon pairs [8] over the entire frequency comb spectrum. We measure qubit entanglement with fidelities above 90% both on co- as well as cross-polarized photon pairs. The measured density matrix of the two-photon state also agrees very well with the expected ideal state, confirmed by a measured fidelity of 96%.

Finally, the generation of multi-photon states [9] is experimentally very challenging. In our quantum comb, the excitation field and the generated photons are intrinsically bandwidth-matched due to the resonant characteristics of the ring cavity, enabling the multiplication of Bell states and the generation of a four-photon time-bin entangled state. We confirm the generation of this four-photon entangled state through four-photon quantum interference [10]. The measured density matrix of the four-photon entangled qubit state exhibits a fidelity of 64%, comparable in quality four-photon states generated in other, non-integrated platforms.

3. Conclusion

Integrated quantum frequency combs based on third-order nonlinearities are shown to be a scalable and versatile platform for quantum state generation and a practical technology towards optical quantum information processing.

REFERENCES

1. D. Bonneau, J. W. Silverstone, M. G. Thompson, *in Silicon Photonics III*, L. Pavesi, D. J. Lockwood, Springer, pp. 41–82, 2016.

2. H.J. Kimble, “The quantum internet” *Nature* 453, 1023, 2008.

3. M. Kolobov, “The spatial behavior of nonclassical light” *Rev. Mod. Phys*., 71, 1539, 1999.

4. P. Walther et al., “Experimental one-way quantum computing” *Nature*, 434, 169, 2005.

5. D. J. Moss et al., “New CMOS-compatible platforms based on silicon nitride and Hydex for nonlinear optics,” *Nature Photon.*, 7, 597, 2013.

6. C. Reimer et al., “Integrated frequency comb source of heralded single photons” *Opt. Express,* 22, 1023, 2014.

7. C. Reimer et al., “Cross-polarized photon-pair generation and bi-chromatically pumped optical parametric oscillation on a chip” *Nat. Commun.* 6, 8236, 2015.

8 J. Brendel et al., “Pulsed energy-time entangled twin-photon source for quantum communication” *Phys. Rev. Lett.,* 82, 2594, 1999.

9. H.J. Briegel et al., “Persistent entanglement in arrays of interacting particles” *Phys. Rev. Lett.*, 86, 910, 2001.

10. C. Reimer et al., “Generation of multiphoton entangled quantum states by means of integrated frequency combs” *Science* 351(6278), 1176-1180, 2016.

Nearly 90% collection efficiency from a single-photon source on diamond with a plasmonic nanoantenna

I. M. Fradkin[1], M Agio[2,3] and D. Yu. Fedyanin[1,*]

[1]Laboratory of Nanooptics and Plasmonics, Moscow Institute of Physics and Technology, Russian Federation

[2]Laboratory of Nano-Optics, University of Siegen, Germany

[3]National Institute of Optics (CNR-INO) and Center for Quantum Science and Technology in Arcetri (QSTAR), Italy

[*]corresponding author: dmitry.fedyanin@phystech.edu

Abstract – Efficient single-photon source is a key milestone in the development of optical quantum computers and secure communication lines. Color centers in diamond and related materials are considered to be the best candidates for practical single-photon sources. However, the low quantum yield and poor collection efficiency of these emitters are a serious obstacle. Here, we present a plasmonic nanoantenna for single-photon sources on diamond which increases the radiation efficiency about 30 times and enhances the collection efficiency up to 90%.

The ability to generate single photons on demand is the key to the development of quantum communications and quantum computing technologies. Color centers in diamond give a unique opportunity to design single-photon sources that operate at room and higher temperatures [1–4]. However, it is still a challenge to achieve a high quantum yield and efficiently collect light emitted by these defects in the crystal lattice of diamond. For example, the silicon-vacancy (SiV) center demonstrates a very narrow emission spectrum, but the quantum efficiency is only of the order of 5% [5]. In addition, due to the high refractive index of diamond, it is possible to collect only a few percent of emitted photons [5]. This problem can be solved using an optical antenna.

In our work, we demonstrate a plasmonic nanoantenna, which is simultaneously used to increase the quantum yield and improve the directivity of photon emission. Remarkable is that the proposed relatively simple design (see Figure 1) enables to substantially reduce the dimensions of the single-photon source and greatly improves its efficiency. This approach can be efficiently used for both optically and electrically pumped single-photon sources. Our results show that the Purcell factor is as high as 30, which increases the quantum efficiency of the SiV center more than tenfold. Moreover, the highly directional far-field emission pattern gives the possibility to achieve an ultrahigh collection efficiency of more than 85% using a conventional immersion objective with a numerical aperture of 1.25. These numbers can be further improved by optimizing the materials and geometry. We believe that our findings pave the way towards the development of highly efficient room-temperature practical single-photon sources.

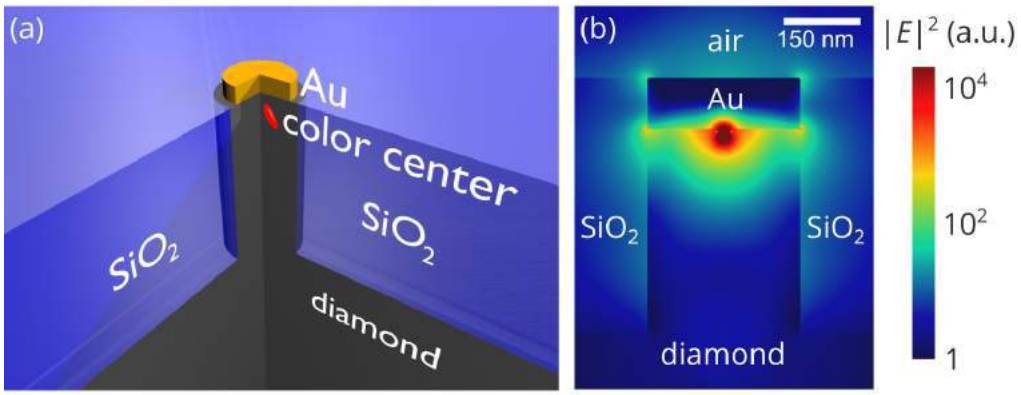

Figure 1. (a) Schematic of the diamond based single-photon source with a plasmonic nanoantenna. (b) Electric field distribution of silicon vacancy in diamond incorporated near the nanoantenna.

This work was supported by the Russian Foundation for Basic Research (16-37-00509-mol-a) and by the grant of the President of the Russian Federation (MK-2602.2017.9).

REFERENCES

1. Boretti, A., Alberto, B., Lorenzo, R., Andrew, M. and Stefania, C., "Electrically driven quantum light sources," *Advanced Optical Materials* Vol. 3, 1012, 2015.
2. Fedyanin, D. Y. and Agio, M., "Ultrabright single-photon source on diamond with electrical pumping at room and high temperatures," *New Journal of Physics* Vol. 18, 073012, 2016.
3. Lagomarsino, S. et al. "Robust luminescence of the silicon-vacancy center in diamond at high temperatures," *AIP Advances* Vol. 5, 127117, 2015.
4. Pezzagna, S., Rogalla, D., Wildanger, D., Meijer, J. and Zaitsev, A., "Creation and nature of optical centres in diamond for single-photon emission—overview and critical remarks," *New Journal of Physics* Vol. 13, 035024, 2011.
5. Prawer, S. and Aharonovich, I., *Quantum Information Processing with Diamond: Principles and Applications,* Woodhead Publishing, 2014.

Engineering quantum light on micro/nanophotonic chips

Qiang Lin[1]

[1]Department of Electrical and Computer Engineering, University of Rochester, Rochester, NY 14627, USA
qiang.lin@rochester.edu

Abstract— In this talk, we will discuss our recent progress in engineering micro/nanophotonic device structures for producing and manipulating photonic quantum states on chip.

Recent advances in quantum photonics have resulted in broad applications ranging from secure communication, metrology, sensing, to advanced computing. Chip-scale implementation would not only enhance the complexity and capacity of information processing, but also enable novel functionalities which are otherwise inaccessible in room-wide/table-top experiments.

Lying in the heart of these applications is the capability of generating versatile high-purity entangled photonic quantum states. In this talk, we will discuss our recent effort in engineering micro/nanophotonic device structures for producing and manipulating photonic quantum states on various chip-scale device platforms, by taking advantage of enhanced four-wave mixing and parametric down conversion processes, via the second-order and third-order optical nonlinearities.

Improved single-photon sources for quantum photonic integrated circuits

A. Fiore[1*], M. Petruzzella[1], F.M. Pagliano[1], Ž. Zobenica[1], S. Birindelli[1], D. Pellegrino[1], M. Cotrufo, R.W. van der Heijden, F.W.M. van Otten[1], L.H. Li[2] and E.H. Linfield[2]

[1] Eindhoven University of Technology, The Netherlands

[2] School of Electronic and Electrical Engineering, University of Leeds, United Kingdom

[*]corresponding author: a.fiore@tue.nl

Abstract- Large-scale quantum photonic circuits require deterministic sources of indistinguishable single photons exhibiting very high efficiency. Single semiconductor quantum dots embedded in nanophotonic cavities and coupled to waveguide circuits can provide the required efficiency. We will discuss our recent progress in improving these integrated sources, including advanced tuning schemes and electrical injection into photonic crystal cavities

Single photons can be efficiently generated from the recombination of single excitons in quantum dots embedded inside photonic crystal (PhCs) cavities [1] and then coupled to waveguides in quantum photonic integrated circuits [2]. The applicability of these sources is however limited by practical problems such as their relative energy detuning and the complexity of optical pumping. In this talk, after reviewing our approach to fully-tuneable on-chip single-photon sources using nano-opto-electromechanical actuation, we will discuss recent progress in their electrical injection.

Electrical injection in PhCs is difficult due to the need of combining a low-resistance electrical path and low optical loss. Here we report the first demonstration of electroluminescence from single QD lines within PhC cavities. A double-membrane electromechanically tuneable [3] PhC structure was used (Fig 1, top), where the top membrane hosts an additional vertical p-i-n junction in order to inject current in the embedded QD layer. The cavity resonance can be reversibly tuned over almost 20 nm by electrostatically actuating the intermembrane distance. Low-temperature electroluminescence spectra clearly show single QD lines, which become enhanced when they cross the cavity mode. The measurement of the second-order autocorrelation function from a cavity-enhanced line (Fig. 1, bottom) proves the antibunched character of the emitted light, and allows deducing a Purcell enhancement of a factor of 3.5 in its emission rate.

As electrical injection does not require focusing a pump spot on the cavity and does not involve stray pump photons, it makes the implementation of large arrays of single-photon sources much more feasible. The large-scale integration of such tuneable single-photon sources, passive optics and waveguide detectors [4] may enable the implementation of boson sampling circuits [5] able to process tens of photons.

REFERENCES

1. Dietrich C.P. et al, “GaAs integrated quantum photonics: Towards compact and multi-functional quantum photonic integrated circuits”, *Laser&Photonics Reviews* Vol. 10, No. 6, 870-894, 2016
2. Fattah poor, S. et al. “Efficient coupling of single photons to ridge-waveguide photonic integrated circuits,” *Appl. Phys. Lett.*, Vol. 102, No. 13, 131105, 2013.

3. Petruzzella, M. et al., “Fully tuneable, Purcell-enhanced solid-state quantum emitters,” *Appl. Phys. Lett.*, Vol. 107, No. 14, 141109, 2015.
4. Sprengers, J.P. et al., “Waveguide superconducting single-photon detectors for integrated quantum photonic circuits,” *Appl. Phys. Lett.*, Vol. 99, No. 18, 181110, 2011.
5. Aaronson, S. and Arkhipov, A., “The Computational Complexity of Linear Optics,” *Theory of Computing,* Vol.4, 143, 2013.

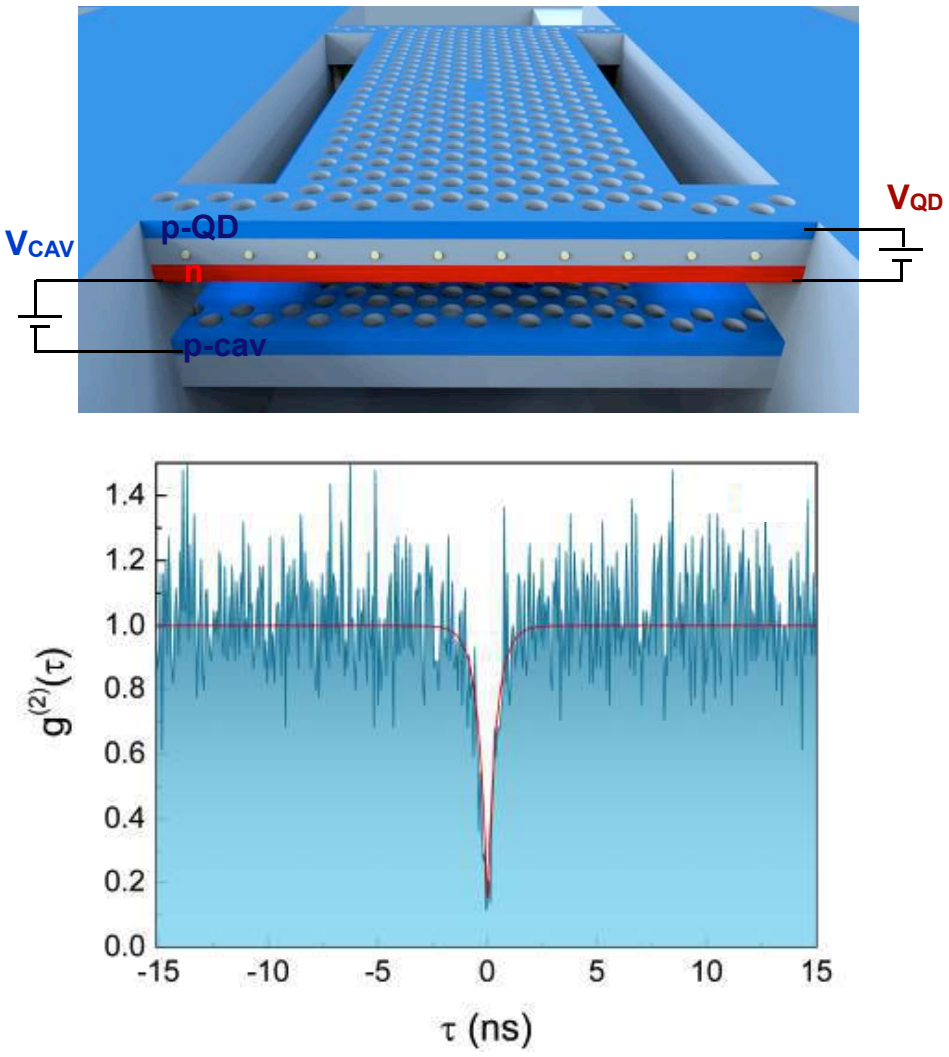

Fig. 1: (top) Schematics of a tuneable photonic crystal LED. (bottom) Antibunching in the electroluminescence of single excitons within a PhC LED

Quantum photonics for novel quantum computing and testing quantum physics foundations

Philip Walther

University of Vienna, Faculty of Physics Quantum Optics, Austria

Abstract- The advantages of the photons makes optical quantum system ideally suited for fundamental quantum physics experiments and a variety of applications in quantum information processing. Here I will discuss multi-photon processing using integrated waveguides as well as experimental benchmark values for hyper-complex extensions of quantum mechanics (such as quaternions) that exploited a metamaterial. As outlook I will briefly discuss the scale-up of photonic quantum information processing by using high-efficient detectors and solid-state single-photon sources.

Photonic circuitry with quantum dots

L. Midolo[1*] and **P. Lodahl**[1]
[1]Niels Bohr Institute, University of Copenhagen, Blegdamsvej 17, DK-2100, Copenhagen, Denmark
[*]corresponding author: midolo@nbi.ku.dk

Abstract-The recent advances in building scalable photonic quantum devices based on semiconductor quantum dots in Gallium Arsenide are reported. The excellent properties of quantum dots as efficient and coherent single-photon resources in this platform allows us to explore novel functionalities by combining them with photonic integrated circuits. Recent results include methods for the efficient out coupling of single photons to optical fibers using tapered waveguides with 80% efficiency, and the on-chip electro-optical routing of single quantum dot emission with sub-μs speed.

Semiconductor quantum dots are excellent sources of single photons for quantum-information processing [1]. The integration with planar photonic nanostructures such as photonic crystal waveguides, nano-beams, and electrically gated devices, provides an exciting platform to perform solid-state quantum optics experiments. We have recently demonstrated near-unity emitter-mode coupling efficiency [2], single-photon nonlinearity [3], directional emission [4], and indistinguishable photon generation [5]. With the proliferation of photonic integrated technologies it is becoming more and more attractive to combine quantum dot sources with passive and active optical elements such as beam-splitters, phase shifters, and input-output couplers. Such integration would open up new possibilities to implement low-loss and scalable photonic quantum devices with embedded capabilities for signal routing. In particular, such capabilities would enable de-multiplexing a single-photon source into an Nx1-photon resource for multi-qubit experiments [6].

A major challenge in this direction is to efficiently couple photons from an optical chip to a fiber without incurring in high losses. We have demonstrated different out-coupling strategies including gratings, inverted tapers [5], and evanescent coupling to nanofibers [7]. The latter method resulted in chip-to-fiber efficiencies exceeding 80% and a total source efficiency of 10.9%.

Another outstanding problem for single-photon de-multiplexing is to realize fast (sub-μs) and low-loss optical switches operating at cryogenic temperatures, i.e. without resorting to thermo-optic effects. We have devised a method for integrating a phase-shifter based on the electro-optic effect in a compact (<250x250 μm^2) Mach-Zehnder interferometer built with free-standing GaAs waveguides. The electric field is applied across a p-i-n junction embedded in the waveguide itself [5]. Switching of quantum dot emission spectra has been demonstrated by a series of electro-optical measurements performed at 10 K, at a <500 ns modulation speed.

Acknowledgements: We gratefully acknowledge financial support from the European research Council (ERC Advanced Grant "SCALE") and the Danish Council for Independent Research, technology and production (DFF-FTP).

REFERENCES

1. Lodahl P., Mahmoodian S. and Stobbe S. "Interfacing single photons and single quantum dots with photonic

nanostructures", *Rev. Mod. Phys* Vol. 87, 347 2015.

2. Arcari M., Söllner I., Javadi A., Hansen S. L., Mahmoodian S., Liu J., Thyrrestrup H., Lee E. H., Song J. D., Stobbe S and Lodahl P. "Near-Unity Coupling Efficiency of a Quantum Emitter to a Photonic Crystal Waveguide", *Phys. Rev. Lett.* Vol. 113, 093603, 2014.
3. Javadi A., Söllner I., Arcari M., Hansen S. L., Midolo L., Mahmoodian S., Kiršanskė G., Pregnolato T., Lee E. H., Song J. D., Stobbe S. and Lodahl P., "Single photon nonlinear optics with a quantum dot in a waveguide", *Nat. Comm.* Vol. 6, 8655, 2015.
4. Söllner I., Mahmoodian S., Hansen S. L., Midolo L., Javadi A., Kiršanskė G., Pregnolato T., El-Ella H., Lee E.-H., Song J.D., Stobbe S. and Lodahl P., "Deterministic photon-emitter coupling in chiral photonic circuits", *Nat. Nanotech.* Vol. 10, 775, 2015.
5. Kiršanskė G., Thyrrestrup H., Daveau R. S., Dreeßen C. L., Pregnolato T., Midolo L., Tighineanu P., Stobbe S., Schott R., Ludwig A., Wieck A. D., Park S. I., Song J. D., Kuhlmann A. V., Söllner I., Löbl M. C., Warburton R. J. and Lodahl P., "Indistinguishable and efficient single photons from a quantum dot in a planar nanobeam waveguide", arXiv:1701.08131, 2017.
6. Lenzini F., Haylock B., Loredo J. C., Abrahao R. A., Zakaria N. A., Kasture S., Sagnes I., Lemaitre A., Phan H.-P., Dao D. V., Senellart P., Almeida M. P., White A. G. and Lobino M., "Active demultiplexing of single-photons from a solid-state source", arXiv:1611.02294, 2017
7. Daveau R. S., Balram K. C., Pregnolato T., Liu J., Lee E. H., Song J. D., Verma V., Mirin R., Nam S.-W., Midolo L., Stobbe S., Srinivasan K. and Lodahl P., "Efficient fiber-coupled single-photon source based on quantum dots in a photonic-crystal waveguide" *Optica* Vol. 4, 178-184 (2017).

Integrated photonic circuits for time-bin encoded quantum information systems

H. Takesue[1], T. Ikuta[1], H. P. Lo[1], and N. Matsuda[1,2]

[1]NTT Basic Research Laboratories, NTT Corporation
[2]NTT Nanophotonics Center, NTT Corporation
takesue.hiroki@lab.ntt.co.jp

Abstract— Integrated quantum photonics is now drawing attention as a way to realize scalable quantum information systems using photons. We review the recent progress of integrated photonic devices based on silica, silicon and lithium niobate waveguides for quantum information and communication systems based on time-bin qubits and qudits.

Integrated quantum photonics is a promising approach to realize scalable quantum information systems using photons. Since most optical waveguides for integrated photonic circuits shows polarization dependence, polarization qubits are not suitable for integrated quantum photonics systems. A time-bin qubit is a promising candidate of a quantum information carrier for such systems, because of its polarization insensitivity and seamless connectivity with quantum communication systems over optical fiber networks.

Our group has employed planar lightwave circuits (PLC), which are optical waveguides fabricated using silica (SiO_2), to construct 1-bit delayed interferometers for phase difference measurement of time-bin qubits. The PLC interferometers have been key components in various quantum communication experiments such as a quantum key distribution [1, 2], time-bin entanglement generation [3], and quantum teleportation of time-bin qubit [4]. Recently, we applied the PLC interferometers to high-dimensional time-bin quantum states. Using cascaded PLC interferometers, we demonstrated a violation of Collins-Gisin-Linden-Massar-Popescu inequality for four-dimensional time-bin entangled photons [5], and also showed that a resource-efficient quantum state tomography for high-dimensional time-bin states could be implemented [6].

We have also been studying silicon (Si) waveguides as a promising platform to realize active functions on photonic chips [7]. In nanoscale silicon waveguides, the nonlinear effect is significantly enhanced by the tight confinement of light inside the very small effective area. Using this enhanced nonlinearity, we demonstrated the first entanglement generation experiment using SFWM in a 1-cm silicon waveguide, where a time-bin qubit was used to encode quantum information [8]. To enhance the nonlinearity further, we employed a slow-light device based on a coupled resonator optical waveguide (CROW) consisted of silicon photonic crystal (PhC) cavities [9]. We realized on-chip time-bin entangled photon pair source using a silicon PhC CROW whose length was as short as 420 μm [10]. We also showed that the silicon PhC CROW could be used as an on-chip single-photon buffer with a tunable temporal delay [11].

A lithium niobate (LN) waveguide is another important platform for integrated quantum photonics since it can be used as an electro-optic device for manipulating single photons. We proposed and demonstrated that a 2-input, 2-output LN switch could be used as two-qubit gate for time-bin qubits [12]. In our most recent experiment, we used an optical single sideband modulator based on an LN waveguide to erase the frequency distinguishability between two single photons [13]. This technology enables us to tune the frequency of single photons with the precision of the frequency of an RF signal that drives the modulator.

ACKNOWLEDGMENT

This work was supported by the Japan Society for the Promotion of Science with a Grant-in-Aid for Scientific Research (No. 22360034).

REFERENCES

1. T. Honjo, K. Inoue, and H. Takahashi, "Differential-phase-shift quantum key distribution experiment with a planar light-wave circuit Mach-Zehnder interferometer," *Opt. Lett.* 29, 2797-2799 (2004).

2. H. Takesue, S. W. Nam, Q. Zhang, R. H. Hadfield, T. Honjo, K. Tamaki and Y. Yamamoto, "Quantum key distribution over 40 dB channel loss using superconducting single-photon detectors," *Nature Photon.* 1, 343-348 (2007).
3. H. Takesue and K. Inoue, "Generation of 1.5-μm band time-bin entanglement using spontaneous fiber four-wave mixing and planar lightwave circuit interferometers," *Phys. Rev. A* 72, 041804(R) (2005).
4. H. Takesue, S. D. Dyer, M. J. Stevens, V. Verma, R. P. Mirin, and S. W. Nam, "Quantum teleportation over 100 km of fiber using highly efficient superconducting nanowire single-photon detectors," *Optica* 2, 832-835 (2015).
5. T. Ikuta and H. Takesue, "Enhanced violation of the Collins-Gisin-Linden-Massar-Popescu inequality with optimized time-bin-entangled ququarts," *Phys. Rev. A* 93, 022307 (2016).
6. T. Ikuta and H. Takesue, "Implementation of quantum state tomography for time-bin qudits," *New J. Phys.* 19, 013039 (2017).
7. H. Takesue, "Entangled photon pair generation using silicon wire waveguides," *IEEE J. Selected Topics in Quantum Electronics* 18, 1722-1732 (2012) .
8. H. Takesue, Y. Tokura, H. Fukuda, T. Tsuchizawa, T. Watanabe, K. Yamada, and S. Itabashi, "Entanglement generation using silicon wire waveguide," *Appl. Phys. Lett.* 91, 201108 (2007).
9. M. Notomi, E. Kuramochi, and T. Tanabe, "Large-scale arrays of ultrahigh-Q coupled nanocavities," *Nature Photon.* 2, 741-747 (2008).
10. H. Takesue, N. Matsuda, E. Kuramochi, and M. Notomi, "Entangled photons from on-chip slow light," *Scientific Reports* 4, 3913 (2014)
11. H. Takesue, N. Matsuda, E. Kuramochi, W. J. Munro, and M. Notomi, "An on-chip coupled resonator optical waveguide single-photon buffer," *Nature Communications* 4, 2725 (2013).
12. H. Takesue, "Entangling time-bin qubits with a switch," *Phys. Rev. A* 89, 062328 (2014).
13. H. P. Lo and H. Takesue, "Erasing frequency distinguishability of single photons using optical single sideband modulator," to be presented at CLEO Pacific Rim 2017.

Frequency conversion in the single photon regime in silicon waveguides

B.A. Bell, C. Xiong, B.J. Eggleton
Centre for Ultrahigh Bandwidth Devices for Optical Systems (CUDOS), Institute of Photonics and Optical Science (IPOS), School of Physics, University of Sydney, Sydney, NSW 2006, Australia.
*corresponding author: bryn.bell@sydney.edu.au

Abstract-Four-wave mixing Bragg scattering in silicon waveguides is demonstrated as a low-noise frequency converter for single photon level signals. The limits to conversion efficiency due to nonlinear losses and parasitic processes are considered. Stable interference between separate input frequencies is observed, and it is shown that a birefringent phase-matching scheme can provide additional control over the unwanted processes and could lead to higher conversion efficiencies.

Four-wave mixing Bragg scattering (FWM-BS) is a $\chi^{(3)}$ nonlinear process which enables the frequency conversion of weak signals using two strong pump lasers [1], as illustrated in Fig.1(a). In particular, the signal can be translated by the frequency difference between the pumps, and this is in principle a noiseless process – unlike other four-wave mixing processes such as parametric amplification or phase conjugation, no excess noise photons are introduced into the signal. For this reason, FWM-BS can be applied to single photon level or quantum signals, and could be used in quantum communications, either for routing signals across a network with wavelength division multiplexing or for aligning a photon with the operating wavelength of a particular quantum memory or matter qubit.

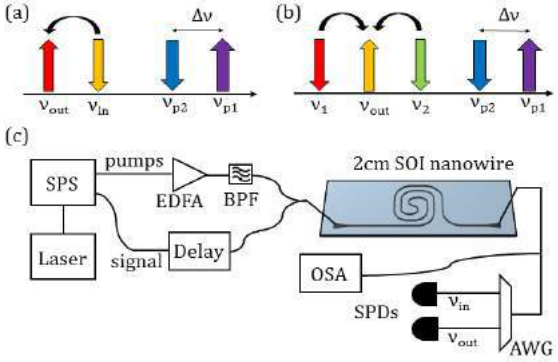

Figure 1. (a) Four-wave mixing Bragg scattering for frequency translation of a weak signal from ν_{in} to ν_{out} using two pump lasers. (b) Two input frequencies at ν_1 and ν_2 are coherently combined at ν_{out} giving rise to stable interference. (c) Experimental setup: a broadband mode-locked laser is filtered into two pumps and a signal using a spectral pulse shaper (SPS). The pumps are amplified by an erbium doped fibre amplifier (EDFA) then a band-pass filter (BPF) removes spontaneous emission from the EDFA. A delay line is used to resynchronize the signal with the pumps in a silicon waveguide. The output is measured with an optical spectrum analyzer (OSA) for classical characterization or filtered by an arrayed waveguide grating (AWG) and measured with single photon detectors.

Here, FWM-BS is demonstrated in silicon waveguides, with the experimental setup shown in Fig. 1(c). Silicon has the advantages of a high $\chi^{(3)}$ nonlinearity and a narrow Raman gain peak, compared to silica fibres [2] or silicon nitride waveguides [3], where the broad Raman spectrum created by the pumps is a source of noise for the signal. First, a 2cm silicon nanowire is used to apply up and down-shifts of 200GHz to a laser attenuated to the single photon regime, within the telecommunications C-band. Maximum internal conversion efficiencies of 11% for up-shifting and 12% for down-shifting are largely limited by nonlinear loss in the waveguide, which increases with the pump power. When this loss is normalized out, up to 32% of the signal power can be transferred to a particular shifted frequency; this limitation is due to the fact that FWM-BS in a short waveguide with relatively small frequency shifts is almost unconstrained by phase-matching, so a photon is equally likely to be up- or down-shifted, and can be shifted multiple times at higher pump powers. This reduces the proportion of the signal which ends up at the intended output frequency.

Despite the limited conversion efficiency, this technique can be used to investigate interference effects between different frequencies. When the input contains two frequencies, they can be overlapped and measured at a single output frequency as in Fig. 1(b). A stable interference fringe is observed with 80% visibility, demonstrating the coherence of the FWM-BS, and this could be useful in some quantum key distribution schemes as a test of frequency-time entanglement. Finally, an example of FWM-BS where the pumps are orthogonally polarized to one another is shown, in a silicon waveguide with a much larger cross-section and a weak birefringence. It is found that the birefringence is useful in controlling the phase-matching of the different FWM-BS processes, so that up-shifting or down-shifting in frequency can be selected using the input polarization of the signal, and the unwanted process is suppressed.

REFERENCES

1. McKinstrie, C.J., Harvey, J.D., Radic, S. and Raymer, M.G. “Translation of quantum states by four-wave mixing in fibers,” *Opt. Express*, 13, 9131-9142, 2005.
2. Clark, A.S. et al., “High-efficiency frequency conversion in the single-photon regime,” *Opt. Lett.*, Vol. 38, 947, 2013.
3. Li, Q., Davanço, M., and Srinivasan, K. “Efficient and low-noise single-photon-level frequency conversion interfaces using silicon nanophotonics,” *Nat. Phot.*, Vol. 10, 406–414, 2016.

Silicon photonic sources of nonclassical states of light.

Daniele Bajoni[1,*]

[1]Dipartimento di Ingegneria Industriale e dell'Informazione, Università di Pavia, Italy
[*]corresponding author: daniele.bajoni@unipv.it

Abstract-We review recent advances in silicon integrated quantum photonics, with particular emphasis on integrated sources of nonclassical states of light. We show how the third optical nonlinearity of silicon and silicon compatible materials can be enhanced via the use of resonators, and how this can be exploited to generate entangled states of the electromagnetic field as well as heralded single photons.

Quantum technologies offer compelling new ways to improve creation, manipulation and transmission of information [1]. Quantum cryptography, for instance, leverages on the properties of single photon states to improve data security in telecommunication networks [2], one of the most critical challenges in communication technologies. Quantum imaging techniques use correlations between photons to improve resolution and signal to noise ratio [3]. Quantum computing protocols point to the use of the laws of quantum mechanics to perform tasks like factorisation or searches in large random databases in a much more efficient way than what can be obtained for classical computers [4].

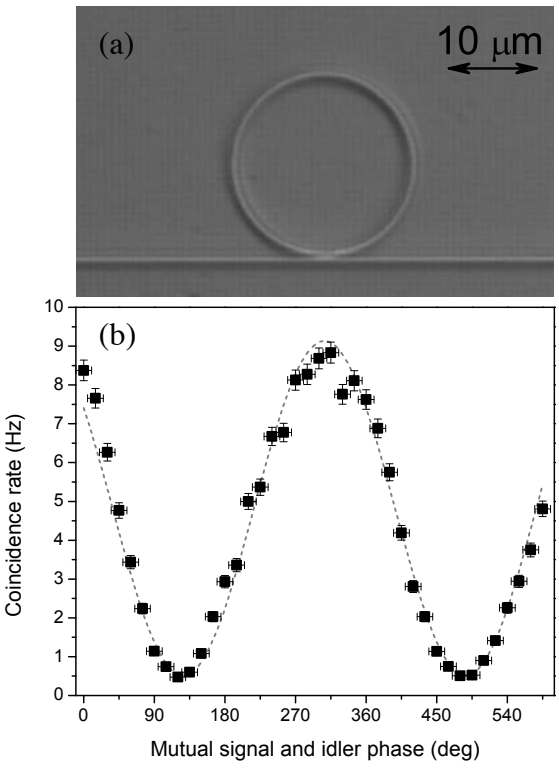

Figure 1: (a) Optical image of a 10 micron radius silicon ring resonator. (b)Dependence of coincidences on the mutual signal and idler phase in a time energy entanglement experiment performed on the ring in (a). The data are taken from ref. [8]. The grey line is the best fit to the experimental data and corresponds to a visibility of about 90% implying a violation of Bell's inequality by 7.1 standard deviations.

Many different systems are being researched as substrates for quantum information protocols, ranging from cold atomic systems, to superconductors, to semiconductor quantum dots. Photons offer an attractive medium for quantum information technologies due to their long coherence times even at room temperature, and can be easily manipulated using the tools of photonics [5]. Photons are also the mostly used medium for the transmission of information via fiber networks. Silicon photonics devices have seen a dramatic development in recent years as Multi Project Wafer (MPW) and application-specific integrated circuit (ASIC) design are becoming increasingly widespread [6]. This offers an unprecedented opportunity to bridge quantum technologies from laboratory environments to actual industrial applications.

In this presentation we review recent advances on the integration of one of the fundamental components of quantum photonics: sources of nonclassical states of light. We start discussing Four Wave Mixing, the most widely used process to achieve emission of quantum states in silicon samples, and how it can be enhanced via the use of resonators. We will in particular describe ring resonators, which are among the most efficient and most used silicon integrated sources reported so far. We will review recent results on silicon integrated sources of photon pairs [7], heralded single photons and entangled photon pairs [8], both in silicon and silicon compatible high band-gap

materials [9,10]. Finally, we will discuss how sources can be integrated with other photonic components on a chip and review promising alternatives and perspectives.

REFERENCES

1. M.A. Nielsen, I.L. Chuang, “Quantum Computation and Quantum Information”, Cambridge University Press (2011).
2. N. Gisin et al., “Quantum cryptography” Rev. Mod. Phys. 74, 145 (2002).
3. Y. Shih, "Quantum Imaging," IEEE Journal of Selected Topics in Quantum Electronics, 13, 1016 (2007).
4. T.D. Ladd et al., “Quantum Computers”, Nature 464, 45 (2010).
5. A. Politi et al., Science 320, 646 (2008).
6. M. Streshinsky et al., “The Road to Affordable, Large-Scale Silicon Photonics,” Opt. Photon. News 24, 32-39 (2013).
7. Azzini et al.,”Ultra-low power generation of twin photons in a compact silicon ring resonator” Opt. Exp. 21, 23100 (2012).
8. Grassani et al., “Micrometer-scale integrated silicon source of time-energy entangled photons”, Optica 2, 88 (2015).
9. C. Reimer et al., “Integrated frequency comb source of heralded single photons”, Opt. Expr. 22, 6535 (2014).
10. C. Reimer et al., “Generation of multiphoton entangled quantum states by means of integrated frequency combs”, Science 351, 6278 (2016).

Femtosecond laser writing of 3D integrated quantum photonic circuits.

R. Osellame
Institute for Photonics and Nanotechnologies – National Research Council (IFN-CNR), Italy
corresponding author: roberto.osellame@polimi.it

Abstract The use of integrated photonics in quantum optics experiments has introduced dramatic improvements in terms of stability and scalability of the experiments. In particular, femtosecond laser direct writing of photonic circuits enabled the manipulation of polarization-encoded single photons and the realization of 3D photonic circuits. These unique capabilities opened the door to advanced quantum simulation and computation tasks.

Femtosecond laser waveguide writing is a recently developed technology to fabricate integrated photonic circuits. It exploits focused ultrafast laser pulses for the direct inscription of waveguides in the bulk of dielectric substrates [1]: the laser beam can be indeed used as an optical pen, able to draw in the three dimensions an optical circuit with arbitrary geometry.

This technology presents several advantages and potentials, with respect to conventional planar lithographic processes. One of its distinctive features is the possibility to produce circuits with arbitrary three-dimensional design inside the substrate. In addition, no lithographic masks are needed and this allows to produce devices with novel design and unique flexibility, rapid turnaround and cost-effective process.

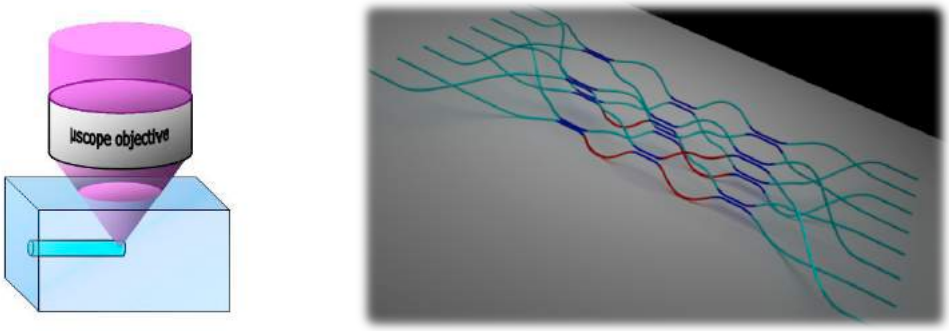

Figure 1. Schematic of the direct laser writing process (left). Example of a 3D layout for a photonic circuit performing the Fourier transform over the optical modes (right).

Femtosecond-laser written circuits have also shown specific advantages in the flourishing field of integrated quantum photonics. In fact, femtosecond-laser written waveguides have typically low birefringence, which enables the propagation and manipulation of polarization encoded qubits [2]. Several components have been reported for the integrated manipulation of the polarization degree of freedom, such as polarization sensitive or insensitive integrated beam splitters [3, 4], and rotated waveplates [5].

A remarkable control in the circuit fabrication has been demonstrated, enabling the realization of complex

circuits for quantum simulation [6, 7] or to implement arbitrary unitary transformations over the optical modes [8, 9, 10], useful e.g. for boson sampling applications.

A further capability of this technology is the possibility to process different materials besides glasses, for example crystals. We have demonstrated the possibility to write waveguides in Pr:YSO [11], implementing an integrated waveguide memory, as well as in diamond [12], where it can be combined with the laser generation of NV centers [13,14].

Acknowledgements The author would like to acknowledge financial support by the H2020-FETPROACT-2014 Grant QUCHIP (Quantum Simulation on a Photonic Chip; grant agreement no. 641039) and by the FP7-PEOPLE-2013-ITN Grant PICQUE (Photonic Integrated Compound Quantum Encoding, grant agreement no. 608062).

REFERENCES

1. Gattass, R., and E. Mazur, "Femtosecond laser micromachining in transparent materials," *Nature Photonics*, Vol. 2, 219–225, 2008.
2. Sansoni, L., et al., "Polarization entangled state measurement on a chip," *Phys. Rev. Lett.*, Vol. 105, 200503, 2010.
3. Crespi, A., et al., "Integrated photonic quantum gates for polarization qubits," *Nature Commun.*, Vol. 2, 566, 2011.
4. Sansoni, L., et al., "Two-particle bosonic-fermionic quantum walk via integrated photonics," *Phys. Rev. Lett.*, Vol. 108, 010502, 2012.
5. Corrielli, G., et al., "Rotated waveplates in integrated waveguide optics," *Nature Commun*., Vol. 5, 4249, 2014.
6. Crespi, A., et al., "Anderson localization of entangled photons in an integrated quantum walk," *Nature Photonics*, Vol. 7, 322-328, 2013.
7. A. Crespi, A., et al., "Particle statistics affects quantum decay and Fano interference," *Phys. Rev. Lett*., Vol. 114, 090201, 2015.
8. Crespi, A., et al., "Integrated multimode interferometers with arbitrary designs for photonic boson sampling," *Nature Photonics*, Vol. 7, 545-549, 2013.
9. Spagnolo, N., et al., "Experimental validation of photonic boson sampling," *Nature Photonics*, Vol. 8, 615-620, 2014.
10. Bentivegna, M., et al., "Experimental scattershot boson sampling," *Science Advances*, Vol. 1, e1400255, 2015.
11. Corrielli, G., A. Seri, M. Mazzera, R. Osellame, and H. de Riedmatten, "An Integrated Optical Memory based on Laser Written Waveguides," *Phys. Rev. Applied*, Vol. 5, 054013, 2016.
12. Sotillo, B., et al., "Diamond photonics platform enabled by femtosecond laser writing," *Scientific Reports*, Vol. 6, 35566, 2016.
13. Chen, Y.-C., et al., "Laser writing of coherent colour centres in diamond," *Nature Photonics*, Vol. 11, 77–80, 2017.
14. Hadden, J.P., et al., "Waveguide-coupled single NV in diamond enabled by femtosecond laser writing," *preprint arXiv:1701.05885*.

High Purcell Factor Generation of Coherent, On-Chip Single Photons

A. Brash[1*], F. Liu[1], J. O'Hara[1], L.M.P.P. Martins[1], R. J. Coles[1], C.L. Phillips[1], B. Royall[1], N. Prtljaga[1], C. Bentham[1], E. Clarke[2], I. Itskevich[3], L.R. Wilson[1], M.S. Skolnick[1], and A.M. Fox[1]

[1] Department of Physics and Astronomy, University of Sheffield, Sheffield, S3 7RH, United Kingdom

[2] Department of Electronic and Electrical Engineering, University of Sheffield, Sheffield S1 3JD, UK

[3] School of Engineering and Computer Science, University of Hull, Hull, HU6 7RX, UK

[*]corresponding author: a.brash@sheffield.ac.uk

Abstract- In this work we develop a high-time-resolution double π-pulse resonance fluorescence technique, allowing observation of a record-high Purcell factor of 35 in a low-Q (677) waveguide-coupled photonic crystal cavity. The short radiative lifetime (27 ps) leads to coherent single photon emission regardless of significant dephasing processes and an enhanced photon generation rate. Combining the strong Purcell effect with resonant coherent excitation and electrical tuning, we demonstrate an on-chip, on-demand tunable single photon source that exhibits high purity and indistinguishability without any spectral filtering.

Integrated quantum circuits are an exciting architecture for compact and scalable Quantum Information Processing (QIP). Silicon-on-insulator devices have demonstrated the concept [1], but rely on four-wave mixing sources which have low brightness (kHz) and large space and optical power requirements. It is thus desirable to consider a source based on a single quantum emitter such as a quantum dot (QD) instead. Single photon emission has been observed from continuous resonant excitation of an InGaAs QD coupled to a nanobeam waveguide [2,3]. However, in this work and others [4] poor coherence times ($T_2 < T_1$) have been observed, possibly due to charge noise from the presence of nearby surfaces. An ideal single photon source requires high coherence and thus should operate close to the radiative limit of $T_2 = 2T_1$.

To overcome this issue and demonstrate a near-ideal on-chip single photon source, a waveguide-coupled Photonic Crystal Cavity (PCC) is used to strongly reduce the radiative lifetime (T_1 = 27 ps) of the QD in this work. In addition to the coherence benefits, the cavity also significantly enhances the source emission rate whilst reducing the optical excitation power required. On demand operation is achieved by resonant driving with π-pulses.

The device studied consists of a waveguide-coupled H1 PhCC. InGaAs QDs are embedded in a *p-i-n* diode and may be electrically tuned across the cavity resonance. As the radiative lifetime (T_1) is too fast to resolve with conventional detectors, we develop a double π-pulse resonance fluorescence (DPRF) technique. As the inter-pulse separation is scanned, the RF signal recovers exponentially with T_1. When the QD is resonant with the cavity, T_1 is 27 ps (Fig. 1(a)), corresponding to a record-high F_P of 35. The short T_1 and near-radiatively-limited coherence ($T_2 = 2T_1$) are verified by a large (~95 %) sub-natural linewidth resonant Rayleigh scattering (RRS) [5] component under weak continuous excitation (Fig. 1(b)). Whilst this super-natural linewidth indicates excellent coherence of the emission, the weak excitation limit means that the process is fundamentally inefficient and cannot operate "on-demand".

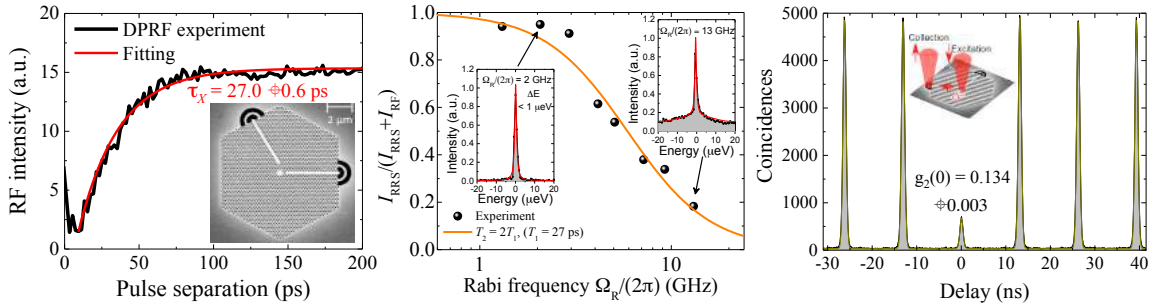

Figure 1. (a) DPRF signal versus pulse separation. An exponential fit (red line) gives T1 of 27 ps. Inset: SEM image of an H1 PhCC coupled to W1 waveguides. (b) Plot of the ratio of the coherently scattered laser photons (I_{RRS}) over the total QD emission ($I_{total} = I_{RRS} + I_{RF}$) versus Rabi frequency. Orange line: Fitting with $T_2 = 2T_1$, ($T_1 = 27$ ps). Insets: QD emission under weak (left) and strong (right) continuous resonant driving. (c) $g^{(2)}(t)$ of the waveguide-coupled QD emission measured with resonant π-pulse excitation and no spectral filtering. Inset: Spatially separated excitation and collection scheme.

To demonstrate an efficient, on-demand single photon source, we perform correlation measurements on the waveguide emission under resonant π-pulse excitation. Unlike most studies to date, no spectral filtering is used, as such these measurements represent a lower-bound to the true on-chip performance of the device. A Hanbury-Brown-Twiss measurement (Fig. 1(c)) yields $g^{(2)}(0) = 0.134$ whilst Hong-ou-Mandel interference gives a two-photon interference visibility of $V = 78$ % at a delay of 2 ns, corresponding to 25 excitation cycles of the source at pulsed RF saturation. This indistinguishability exceeds all QD-based on-chip sources to date, indicating a clear path toward fully-integrated chip devices for QIP. In addition, the short radiative lifetime demonstrated here also lends itself to other important QIP proposals such as fast single photon switching and photonic cluster state generation.

Acknowledgements: This work was funded by the EPSRC (UK) programme grant EP/J007544/1.

REFERENCES

1. J. W. Silverstone et al. “On-chip quantum interference between silicon photon-pair sources,” *Nat. Photon.* Vol. 8**,** 104-108, 2014.
2. M. N. Makhonin et al. "Waveguide coupled resonance fluorescence from on-chip quantum emitter," *Nano Lett.* Vol. 14, 6997, 2014.
3. S. Kalliakos et al. “Enhanced indistinguishability of in-plane single photons by resonance fluorescence on an integrated quantum dot” *Appl. Phys. Lett.* Vol. 109, 151112, 2016.
4. C. P. Dietrich et al. “GaAs integrated quantum photonics: Towards compact and multi-functional quantum photonic integrated circuits” *Laser and Photonics Reviews* Vol. 10, 870-894, 2016.
5. C. Matthiesen et al. “Subnatural Linewidth Single Photons from a Quantum Dot” *Phys. Rev. Lett.* Vol. 108, 093602, 2012.
6. S. Fan et al. “Input-output formalism for few-photon transport in one-dimensional nanophotonic waveguides coupled to a qubit” *Phys. Rev. A.* Vol. 82, 063821, 2010.
7. N. H. Lindner et al. “Proposal for Pulsed On-Demand Sources of Photonic Cluster State Strings” *Phys. Rev. Lett.* Vol. 103, 113602, 2009.

Quantum Emitters in Flatland

Igor Aharonovich
School of Mathematical and Physical Sciences, University of Technology, Sydney
corresponding author: igor.aharonovich@uts.edu.au

Abstract - Engineering solid state quantum systems is amongst grand challenges in engineering quantum information processing systems. While several 3D systems (such as diamond, silicon carbide, zinc oxide) have been thoroughly studied, solid state emitters in two dimensional (2D) materials have not been observed. 2D materials are becoming major players in modern nanophotonics technologies and engineering quantum emitters in these systems is a vital goal.

In this talk I will discuss the recently discovered single photon emitters in 2D hexagonal boron nitride (hBN). I will present several avenues to engineer these emitters in large exfoliated sheets using ion and electron beam techniques. Density functional theory calculations suggest that that the studied defects are the antisite nitrogen vacancy in hBN. The formed emitters in 2D hBN flakes have extremely promising properties – including high brightness (~ millions counts/s), stability up to high temperatuers and linear polarization at excitation and absorption. Those properties make these emitters extremely attractive for their integration with optical resonators and waveguides. Finally, I will discuss several challenges and promising directions in the field of quantum emitters and nanophotonics with 2D materials and other wide band gap materials.

Infrared single-photon detection with superconducting nanowires

R. H. Hadfield*, R. M. Heath, N. R. Gemmell and A Casaburi
School of Engineering, University of Glasgow, Glasgow, G12 8QQ, United Kingdom
*corresponding author: robert.hadfield@glasgow.ac.uk

Abstract- Single photon detectors based on superconducting nanowires have emerged as a highly promising alternative for single-photon detection. These devices offer single photon sensitivity from visible to mid infrared wavelengths with high efficiency, low dark counts and tens of picoseconds timing resolution. We discuss recent advances in device design, integration and miniaturized cooling. We give an overview of applications where these devices are now being deployed, including optical quantum information processing, single photon remote sensing and dosimetry for laser medicine.

The ability to detect single photons underpins a host of emerging 21st century scientific and technological applications. Over the past decade, superconducting nanowire single photon detectors (SNSPDs) [1] have emerged as a practical alternative to off-the-shelf photon counting technologies such as photomultipliers (PMTs) semiconductor single-photon avalanche diodes (SPADs). The canonical SNSPD device consists of a narrow superconducting wire patterned via electron beam lithography in a thin superconducting film. The device is cooled below the superconducting transition temperature and biased close to the critical current. When an infrared photon (energy ~1eV or even lower) strikes the wire, the current distribution is perturbed triggering a fast voltage pulse which can be rapidly read out with room temperature electronics. Major avenues of development include scale up from single pixel SNSPDs to large area arrays [2], integration with optical waveguides [3] and nanoantennas [4]. At the University of Glasgow we are employing novel superconducting materials and advanced nanofabrication techniques to realize these designs [figure 1 (a),(b)]. We are using a suite of advanced characterization tools, including low temperature photoresponse mapping to characterize these devices from near to mid infrared wavelengths. In tandem our group are addressing the challenge of practical device operation at cryogenic temperatures. We have recently partnered with STFC Rutherford Appleton Laboratory to realize a miniaturized 4 K cooling platform for SNSPDs [figure 1 (c)].

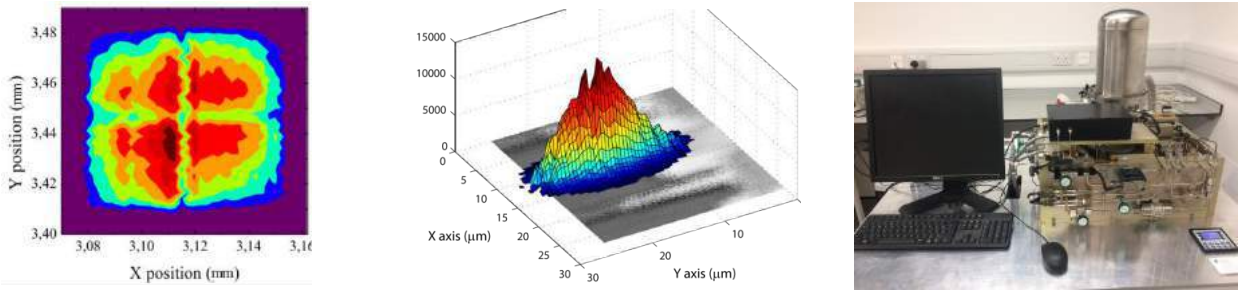

Figure 1 SNSPD development at the University of Glasgow (a) photoresponse map of 60 μm x 60 μm area four-pixel SNSPD array with peak detection efficiency >40%. (b) waveguide integrated SNSPD (c) miniaturized 4 K cooler for SNSPDs

In collaboration with UK and international partners we are deploying SNSPDs in a wide range of advanced photon counting applications. Recent examples of groundbreaking implementations include quantum communication networks [5], on-chip quantum information processing [6], single photon remote sensing [7] and singlet oxygen luminescence dosimetry for photodynamic therapy in the treatment of cancer [8].

Acknowledgements RHH acknowledges support from the UK Engineering and Physical Sciences Research Council (EPSRC) including the UK Quantum Technology Hub in quantum enhanced imaging (QuantIC) and the European Research Council (ERC) through a Consolidator Grant award (IRIS 648604). RHH acknowledges the use of the James Watt Nanofabrication Centre (JWNC) at the University of Glasgow.

REFERENCES

1. CM Natarajan, MG Tanner, RH Hadfield 'Superconducting nanowire single-photon detectors: physics and applications' *Superconductor Science and Technology* 25 063001 (2012) Open Access
2. A Casaburi, A Pizzone, RH Hadfield 'Large Area Superconducting Nanowire Single Photon Detector Arrays' *IEEE Fotonica AEIT Italian Conference on Photonics Technologies*, Naples, Italy (2014), ISBN 9788887237184 (doi:10.1109/Fotonica.2014.6843851)
3. J Li, RA Kirkwood, LJ Baker, B Bosworth, K Erotokritou, A Banerjee, RM Heath, CM Natarajan, ZH Barber, M Sorel, RH Hadfield 'Nano-optical single-photon response mapping of waveguide integrated molybedenum silicide (MoSi) superconducting nanowires' *Optics Express* 24 13931 (2016)
4. RM Heath, MG Tanner, TD Drysdale, S Miki, V Giannini, SA Maier, RH Hadfield 'Nanoantenna enhancement for telecom-wavelength superconducting single photon detectors' *Nano Letters* 15 (2) 819 (2015)
5. L Yu, CM Natarajan, T Horikiri, C Langrock, JS Pelc, MG Tanner, E Abe, S Maier, C Schneider, S Höfling, M Kamp, RH Hadfield, MM Fejer, Y Yamamoto 'Two-photon interference at telecom wavelengths for time-bin entangled single photons from quantum-dot spin qubits' *Nature Communications* 6 8955 (2015)
6. P Sibson, C Erven, M Godfrey, S Miki, T Yamashita, M Fujiwara, M Sasaki, H Terai, MG Tanner, CM Natarajan, RH Hadfield, JL O'Brien, MG Thompson 'Chip-based quantum key distribution' *Nature Communications* 13984 (2017)
7. A McCarthy, N Krichel, X Ren, NR Gemmell, MG Tanner, SN Dorenbos, V Zwiller, RH Hadfield, GS Buller 'Kilometer range time-of-flight depth imaging at 1560 nm wavelength with a superconducting nanowire single-photon detector' *Optics Express* 21 7 8904 (2013)
8. NR Gemmell, A McCarthy, B Liu, MG Tanner, SN Dorenbos, V Zwiller, MS Patterson, GS Buller, BS Wilson, RH Hadfield 'Singlet oxygen luminescence detection with a fiber-coupled superconducting nanowire single-photon detector' *Optics Express* 21 (4) 5005 (2013)

Integration Technologies for Complex Photonic Circuits

G. J. Sharp[1*], Y. Song[1], N. Zhang[1], C. Klitis[1], V. Biryukova[1], S. May[1], J. McPhillimy[2], M. Reza[1], E. Di Gaetano[1], B.M. Holmes[1], M. J. Strain[2], M. Sorel[1]

[1]School of Engineering, University of Glasgow, G12 8LT Glasgow, United Kingdom

[2]Institute of Photonics, University of Strathclyde, G1 1RD Glasgow, United Kingdom

[*]corresponding author: graham.sharp@glasgow.ac.uk

Abstract-Future photonic integrated chips for quantum experiments will demand several thousand of components and a number of diverse functionalities integrated on the same chip. We will discuss some of the challenges faced by the up-scaling of photonic integrated chips with a particular emphasis on robust component trimming and heterogeneous integration of III-V devices on a silicon-on-insulator platform.

The rapid increase in the complexity of quantum experiments demands a shift from bulk optics experiments to integrated circuits that can offer larger stability, compactness and low cost. Amongst the various material platforms, silicon-on-insulator (SOI) is of particular interest thanks to its large third-order nonlinearity, technological maturity and potential for large scale manufacturing. Moreover, its large index contrast allows for the design of very small bend radii that translates into high component density, with figures already exceeding thousands of components per chip[1,2].

However, component numbers and functionalities cannot indefinitely scale up if a number of issues are not effectively addressed. These include the development of algorithms, technologies and designs to mitigate the fabrication process variability, as well as manufacturing processes that allow wafer scale heterogeneous integration. The latter is of particular relevance to all those applications that require components such as optical sources, which cannot be provided by silicon. Here, we will focus on recent advances on trimming of silicon photonic components in complex circuits and on back-end integration of III-V membrane lasers by transfer printing.

An effective way to trim optical components is to thermally cure a cladding layer on top of the silicon waveguide as a means to permanently change the effective index of the optical mode. We will discuss trimming techniques that offer long-term stability and wide tuning range through localised laser irradiation of the upper cladding (see Fig. 1).

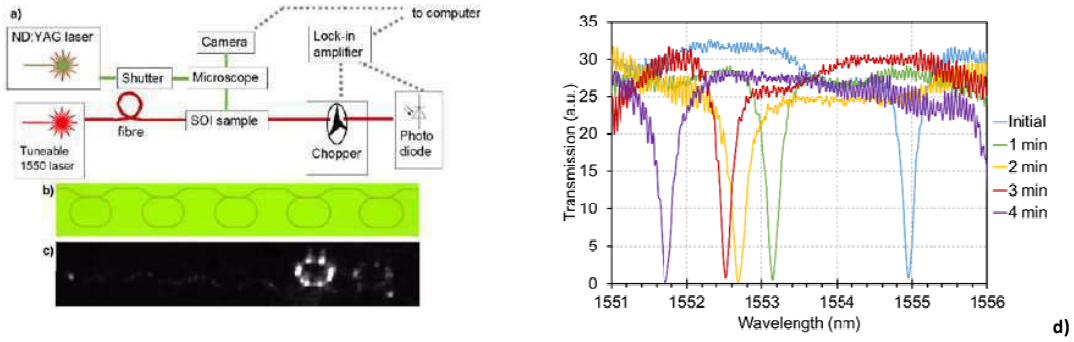

Figures 1 a) Schematic of experimental set-up for localised trimming of SOI components using a frequency-doubled

ND:YAG laser. b) Micrograph of a racetrack resonator array and c) Racetrack array viewed in the infra-red while light is scattered from rings at resonance. d) Transmission spectra of a SOI racetrack resonator following thermal curing at 250℃ at 1 minute increments.

We will also present results on the transfer printing of III-V membrane devices onto silicon substrate with sub-micrometer positioning accuracy[3]. A notable advantage of this method, other than its scalability and precise alignment is the flexibility of the process. In fact, the bonding occurs after device fabrication, thus allowing independent fabrication processing of III-V and SOI wafers. Also, many different III-V membrane devices can be printed onto the SOI host substrate, with the potential for a wide range of heterogeneously integrated photonic devices. One such example is the integration of membrane materials with large Pockels coefficients for the development of ultra-fast electro-optic modulators.

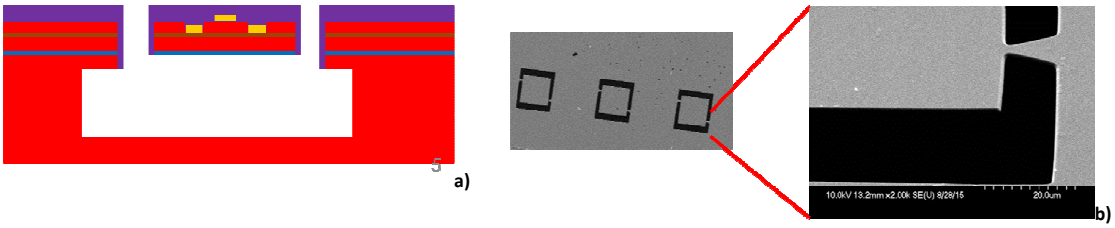

Figures 2 a) Schematic showing the cross-section of a membrane device. b) SEM micrographs of III-V membranes with zooming in on the mechanical support tip

The authors acknowledge support from the technical staff of the James Watt Nanofabrication Center at Glasgow University. The research is supported by the European Union *ROAM* project (grant no. 645361) and by the EPSRC *Cornerstone* project (EP/L021129/1).

REFERENCES

1. Sun J, Timurdogan E, Yaacobi A, Hosseini ES, Watts MR. Large-scale nanophotonic phased array. Nature 2013;493:195–9
2. Harris NC, Steinbrecher GR, Mower J, Lahini Y, Prabhu M, Baehr-Jones T, Hochberg M, Lloyd S, Englund D. Bosonic transport simulations in a large-scale programmable nanophotonic processor. arXiv preprint 2015. arXiv:1507.03406.
3. AJ Trindade, B Guilhabert, D Massoubre, D Zhu, N Laurand, E Gu, IM Watson, CJ Humphreys & MD Dawson, Nanoscale-accuracy transfer printing of ultra-thin AlInGaN light-emitting diodes onto mechanically flexible substrates Appl. Phys. Lett., vol. 103, no. 25, p. 253302, 2013

META-magnetism and interdisciplinary applications

Ultrafast spin dynamics driven by pure phonon excitation

S. Mährlein[1*], I. Radu[2], P. Maldonado[3], A. Paarmann[1], M. Gensch[4], A.M. Kalashnikova[5], R.V. Pisarev[5], M. Wolf[1], P.M. Oppeneer[3], T. Kampfrath[1]

[1]Fritz Haber Institute of the Max Planck Society, Berlin, Germany

[2] Max-Born Institute Berlin, Berlin, Germany

[3]University of Uppsala, Uppsala, Sweden

[4]Helmholtz-Zentrum Dresden-Rossendorf, Dresden, Germany

[5]A.F. Ioffe Physical Technical Institute, St. Petersburg, Russia

[*]corresponding author: s.maehrlein@fhi-berlin.mpg.de

Abstract The future of information processing relies on the rapid manipulation of spin states. Thereupon, we present a novel, non-invasive way to change the spin order of the model ferrimagnet Yttrium Iron Garnet on ultrafast time scales, while keeping its electronic ground state unperturbed. Here, the resonant excitation of high-frequency optical phonons reveals a coupling of lattice vibrations to the spin order within few picoseconds, leading to a novel quasi-equilibrium state of the magnetization that survives for several nanoseconds.

One of the goals of contemporary research is to unveil the fundamental interaction mechanisms of electrons, spins and lattice degrees of freedom in condensed matter. Among them, spin-lattice interaction determines how fast energy and angular momentum is transferred between electron spins and ionic motion. It plays a central role in ultrafast magnetization switching where the crystal lattice acts as the ultimate sink of spin angular momentum[1]. In addition, it is highly relevant for the spin Seebeck effect[2]. The remarkable attention also arises from an application point of view for magnetic data storage technology or future spintronic devices. Surprisingly, despite such wide-area importance, spin-lattice interaction in magnetic solids is still not completely understood.

To reveal the essence of spin-lattice coupling, we reduce the complexity of interactions in a magnetically ordered solid by selectively exciting few optical lattice modes of an insulator in which the electronic degrees of freedom are frozen out. More precisely, we resonantly pump the high-frequency oxygen-iron phonon modes (at ~17 THz) of the insulating two-sublattice ferrimagnet $Y_3Fe_5O_{12}$ (YIG) using intense THz pump pulses (fluence of ~50 mJ/cm , duration of ~200 fs). As the pump photon energy (80 meV) is much smaller than the electronic band gap (2.85 eV), such pumping enables the exclusive excitation of phonons, while leaving the electrons unaffected in their ground state. A subsequent weak probe pulse (duration of 8 fs, photon energy of 1.6 eV) interrogates the transient magnetization change by means of Faraday rotation and ellipticity, on time scales ranging from tens of femtoseconds to hundreds of microseconds.

We find an unexpectedly fast quenching of the transient Faraday signal with a time constant as short as (1.4±0.2) ps. The resulting novel magnetization state persists over a timescale of nanoseconds. Given the long spin-lattice relaxation times in YIG (nanoseconds to microseconds)[3], the observation of such fast phonon-mediated spin dynamics is highly surprising, and indicates a highly efficient energy transfer between ion lattice and spins. Additional temperature dependent measurements suggest distinctively different time scales for

energy and angular momentum transfer between the major part of phonons and the spins. We also present atomistic spin dynamics simulations[4], confirming the scenario of ultrafast inter-sublattice angular momentum transfer. Furthermore, a comprehensive thermodynamic model is presented in order to describe a novel quasi-equilibrium state of the magnetic order accessible via phonon excitation.

Our findings not only give insights to energy and angular momentum transfer between crystal lattice and spins, they also pave the way for spin Seebeck effect based devices operating at THz frequencies and provide implications for the emerging field of antiferromagnetic spintronics[5].

REFERENCES

1. A. Kirilyuk *et al*. "Ultrafast optical manipulation of magnetic order", Rev. Mod. Phys. **82**, 2731 (2010)
2. M. Agrawal *et al*., "Role of bulk-magnon transport in the temporal evolution of the longitudinal spin-Seebeck effect" Phys. Rev. B **89**, 224414 (2014)
3. D. S. Hung *et al*. "Relaxation behaviors of the bismuth-substituted yttrium iron garnet in the microwave range", J. Appl. Phys. **107**, 09A503 (2010)
4. J. Barker *et al*. "Thermal Spin Dynamics of Yttrium Iron Garnet", Phys. Rev. Lett. **117**, 217201 (2016)
5. T. Jungwirth *et al*. "Antiferromagnetic spintronics", Nat Nano **11**, 231 (2016)

Ellipsometric analysis of magneto-optical effects in thin films, nanostructures and spin transport devices

P. Riego[1,2], J. A. Arregi[1], and A. Berger[1*]
[1]CIC nanoGUNE, E-20018 Donostia-San Sebastian, Spain
[2]Departamento de Física de la Materia Condensada, Universidad del País Vasco, E-48080 Bilbao, Spain
[*]corresponding author: a.berger@nanogune.eu

Abstract - We investigate experimentally in how far optical property modifications change magneto-optical responses in films, multilayers and nano-structures. For this purpose, we utilize Generalized Magneto-optical Ellipsometry (GME), a technique that combines high sensitivity of small magneto-optical signal detection with the ability to simultaneously determine both optical and magneto-optical properties by means of a simple experimental setup. Application examples include the detection of magneto-optical anisotropy, optical anisotropy, including in artificial meta-materials, and the investigation of spin transport effects.

Over the last decades, the magneto-optical Kerr effect (MOKE) has gained widespread popularity as a characterization tool for the study of magnetic materials, films and nanostructures [1], and more recently it has been applied also in conjunction with plasmonic structures and devices, for which it allows a magnetic field induced signal modulation [2]. Reasons for its increased popularity are hereby the rather low cost of experimental setups as well as its non-destructive nature and the compatibility with almost any environment. In most experimental approaches, the magneto-optical Kerr effect is measured by using a polarization sensitive detection scheme that is tuned to achieve an optimized sensitivity to at least one MOKE impacted optical property, such as polarization rotation, for instance [1]. While such setups generally achieve excellent sensitivity, they do not track the entirety of available information in reflection experiments and thus, they can be susceptible to data misinterpretation. This is especially relevant in highly excited optical states, such as pump-probe experiments or nano-structured materials, in which temporal or structural modifications lead to variations of not only the magneto-optical effect but also the purely optical response.

Under such circumstances, it is crucially important to fully characterize the optical and magneto-optical properties of the object under investigation, which is possible by means of Generalized Magneto-optical Ellipsometry (GME). This technique combines a high sensitivity of small magneto-optical signal detection with the ability to determine full reflection or diffraction matrices by means of a simple experimental setup [3]. Several examples of its successful application include the detection of magneto-optical anisotropy in films, the detection of optical anisotropy in ferromagnetic grids, and the analysis of Spin Hall Effect induced signals in non-ferromagnetic materials [4-7].

Acknowledgements: We acknowledge support from Basque Government under Project No. PI2015_1_19 and from the Spanish Ministry of economy and competitiveness under Project No. FIS2015-64519-R (MINECO/FEDER).

REFERENCES

1. Z. Q. Qiu, and S.D. Bader, ”Surface magneto-optic Kerr effect (SMOKE)”, J. Magn. Magn. Mater. **200**, 664 (1999)
2. N. Maccaferri, A. Berger, S. Bonetti, V. Bonanni, M. Kataja, Q. H. Qin, S. van Dijken, Z. Pirzadeh, A. Dmitriev, J. Nogués, J. Åkerman, and P. Vavassori, “Plasmonic Phase Tuning of Magneto-Optics in Ferromagnetic Nanostructures”, Phys. Rev. Lett. **111**, 167401 (2013)
3. J. A. Arregi, J.B. Gonzalez-Diaz, E. Bergaretxe, O. Idigoras, T. Unsal, and A. Berger, “Study of Generalized Magneto-Optical Ellipsometry Measurement Reliability”, J. Appl. Phys. **111**, 103912 (2012)
4. J. B. González-Díaz, J. A. Arregi, E. Bergaretxe, M. J. Fertin, O. Idigoras, and A. Berger, “Anomalous Magneto-Optical Behavior of Uniaxial Co/CoO Bilayer Films”, J. Magn. Magn. Mater. **325**, 147 (2013)
5. J. A. Arregi, J. B. González-Díaz, O. Idigoras, and A. Berger, ”Strain induced magneto-optical anisotropy in epitaxial hcp Co-films”, Phys. Rev. **B 92**, 184405 (2015)
6. P. Riego, S. Velez, J. M. Gomez-Perez, J. A. Arregi, L. E. Hueso, F. Casanova, and A. Berger, “Absence of detectable current-induced magneto-optical Kerr effects in Pt, Ta, and W”, Appl. Phys. Lett. **109**, 172402 (2016)
7. J. A. Arregi, P. Riego, and A. Berger, ”What is the longitudinal magneto-optical Kerr effect?”, J. Phys. D: Appl. Phys. **50**, 03LT01 (2017)

Extending Magneto-Plasmonics to the Mid IR by the use of the Magneto Refractive effect.

Alfonso Cebollada*, Fernando García, and Gaspar Armelles
IMM-Instituto de Microelectrónica de Madrid (CNM-CSIC), Isaac Newton 8, PTM, E-28760 Tres Cantos, Madrid, Spain
*corresponding author: alfonso.cebollada@csic.es

Abstract- Magnetoplasmonics combines plasmonic and magneto optic effects, making them to interact and finding great potential in sensing and telecom applications. While this has been so far restricted to the visible and Near IR, here we extend this concept to the Mid IR by substituting the magnetooptic by the magnetorefractive effect (change of refractive index due to magnetic field induced change in electrical resistivity), most effective in the 5-10 microns range. Possible applications of this idea will be introduced.

Plasmonics has proven as a powerful tool to improve the performance of mid-IR devices, resulting in plasmon assited quantum cascade lasers, plasmon enhanced light detection, plasmonic beam steering, plasmonic thermal emiters or plasmonic nanoantenas for vibrational spectroscopy. In this scenario, the possibility of modulating the emission, propagation and/or detection of mid-IR radiation constitutes a promising aspect to expand the limits of the currently used technologies. In this sense, fast and contactless actuation on plasmon resonances via the Magneto-Optical (MO) effect has been put forward by the inclusion of ferromagnetic components into noble metal layers and nanostructures. This magneto-plasmonic concept so far has been restricted to the visible and near-infrared spectral ranges.

Here we present our proposal and initial results on the magnetic field control of plasmon resonances in the mid IR region by the use of the Magneto-Refractive (MR) effect, i.e., a change in the optical properties of the system by magnetic field controlled electrical resistivity. For this we select a Giant Magneto Resistance model system (a Au/Permalloy multilayer), which exhibits changes in resisitivity of the order of 10% by the application of small (of the order of 20 Oe) magnetic fields.

The experiments are carried out in a dedicated FTIR spectrometer with magnetic field capabilities. Due to the low magnetic fields required for the selected GMR structures, it is conceivable to devise potential and easy to implement applications with magnetic field modulation character, improving for example current Mid IR sensing schemes.

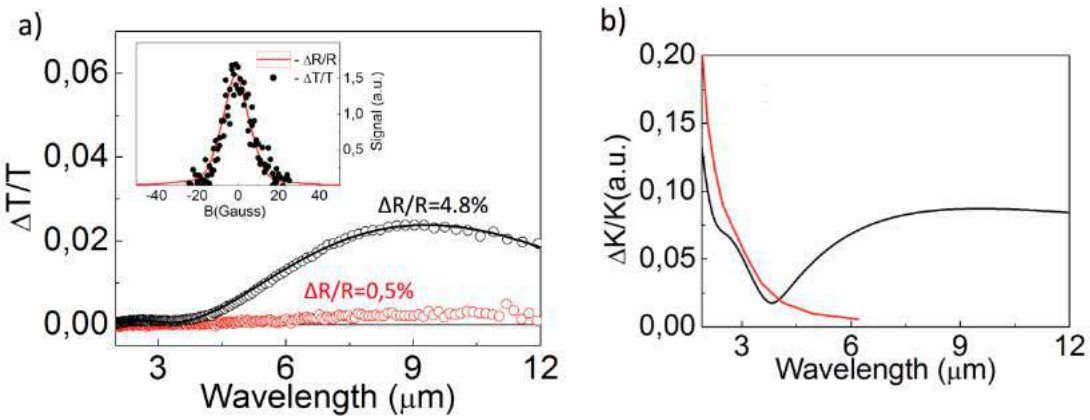

Figure 1: (a) Transmission spectra for two samples with different GMR values (4.8% and 0.5%). INSET: Magnetic field dependence of electrical resistance and integrated transmission in the mid IR region for the 4.8% GMR structure. (b) Calculated magnetic field modulation of propagating plasmons via MO effect (red) and MR effect (black). The modulation is similar for both MO and MR effects up to 3.5 μm, but it is much larger for the MR effect in the whole mid IR range.

REFERENCES

1. Law, S., V. Podolsky and D. Wasserman, "Towards nano-scale photonics with micro-scale photons: the opportunities and challenges of mid-infrared plasmonics," *Nanophotonics*, Vol. 2, No. 2, 103-130, 2013.
2. Jacquet, J. C. and T. Valet "A new magnetooptical effect discovered on magnetic multilayers: the magnetorrefractive effect," *Mat. Res. Soc. Symp. Proc.*, Vol. 384, 477–490, 1995.
3. Parkin, S.S.P., R. F. C. Farrow, R. F. Marks, A. Cebollada, G. R. Harp, and R. J. Savoy, "Oscillations of interlayer exchange coupling and giant magnetoresistance in (111) oriented permalloy/Au multilayers," *Phys. Rev. Lett.*, Vol. 72, No. 23, 3718–3721, 1994.

Magnetic Properties of Nanolaminated Magnetic MAX Phases

R. Salikhov[1*], U. Wiedwald[1], D. Weller[1], J. Rosen[2], and M. Farle[1,3]

[1]Faculty of Physics and Center for Nanointegration (CENIDE), University of Duisburg-Essen, Germany

[2]Thin Film Physics, Department of Physics, Chemistry and Biology (IFM), Linköping University, Sweden

[3]Center for Functionalized Magnetic Materials (FunMagMa), Immanuel Kant Baltic Federal University, Kaliningrad, Russian Federation

[*]corresponding author: ruslan.salikhov@uni-due.de

Abstract-We report on magnetic properties of a new class of inherently nanolaminated materials: magnetic MAX phases. Hexagonal atomically layered MAX phases show exclusive mechanical properties and anisotropic thermal and electrical conductivities. These systems are parent materials of graphene-like transition metal carbides, known as MXenes, which are predicted to be future 2D magnetic materials extending the unique properties of graphene. Magnetic properties of new magnetic MAX phases are presented: magnetic ordering temperature, spin structure, saturation magnetization, magnetocrystalline anisotropy and magnetoresistance.

MAX phases are a family of hexagonal, nanolaminated compounds with the chemical formula $M_{n+1}AX_n$ (n = 1-3) composed of early transition metals *M* (Ti, V, Cr …), *A*-group elements (Al, Ga, Ge …) and *X* (C or N) [1]. Due to their unique structure these materials share properties of ceramics such as high structural stiffness and metals such as good electrical and thermal conductivity [1]. The new class of magnetic MAX phases has been recently discovered substituting or composing the *M*-element by/with Mn in quaternary solid solutions. Also ternary Mn_2GaC magnetic compounds have been synthesized as hetero-epitaxial films containing Mn as the exclusive *M*-element [2]. Significant interest in these systems is rising due to a recently discovered possibility of delamination of layered MAX phase structures leading to 2D graphene-like transition metal carbides and nitrides $M_{n+1}X_n$, known as MXenes [3]. Mn-based MXenes are predicted theoretically to be intrinsic half-metals with full spin polarization and above room temperature ferromagnetism [4].

We report on magnetic and electrical transport properties of recently synthesized magnetic MAX phases. Magnetometry and ferromagnetic resonance (FMR) reveal ferromagnetic (FM) properties of $(Cr_{0.5}Mn_{0.5})_2GaC$ and $(Mo_{0.5}Mn_{0.5})_2GaC$ at temperatures below 220 K. The saturation magnetization is on the order of 0.7 μ_B per M-atom. Both compounds behave as soft magnetic materials possessing small *c*-axis magnetocrystalline anisotropy energy density (MAE) below 5 kJ/m^3 [5-6]. Mn_2GaC at room temperature is antiferromagnetic (AFM) with a Néel temperature of approximately 600 K. At T = 240 K the system undergoes a phase transition to a canted noncollinear spin state [2]. This state is characterized as a metamagnetic state, in which the magnetic field causes a change of the lattice parameters and FM spin alignment. FM Mn_2GaC has a MAE of 40 ± 10 kJ/m^3 with the easy axis perpendicular to the *c*-axis and saturation magnetization of 1.7 μ_B per Mn atom at T = 5 K. All compounds show negative magnetoresistance of about 5% originating from spin-dependent scattering of electrical charge carriers.

Acknowledgements, R. S. acknowledges DFG foundation under Grant No. SA 3095/2-1.

REFERENCES

1. Barsoum, M. W., *MAX Phases. Properties of Machinable Ternary Carbides and Nitrides*, John Wiley and Sons, New York, 2013.
2. Ingason, A. S., M. Dahlqvist and J. Rosen, "Magnetic MAX phases from theory and experiments; a review," *J. Phys.: Condens. Matter*, Vol. 28, 433003 (1-17), 2016.
3. Mashtalir, O., M. Naguib, V. N. Mochalin, Y. Dall'Agnese, M. Heon, M. W. Barsoum and Y. Gogotsi, "Intercalation and delamination of layered carbides and carbonitrides," *Nat. Comm.*, Vol. 4, 1716 (1–7), 2013.
4. He, J., P. Lyu and P. Nachtigall, "New two-dimensional Mn-based MXenes with room-temperature ferromagnetism and half-metallicity," *J. Mater. Chem. C*, Vol. 4, 11143–11149, 2016.
5. Salikhov, R., A. S. Semisalova, A. Petruhins, A. S. Ingason, J. Rosen, U. Wiedwald and M. Farle, "Magnetic Anisotropy in the $(Cr_{0.5}Mn_{0.5})_2GaC$ MAX Phase," *Mater. Res. Lett.*, Vol. 3, 156–160, 2015.
6. Salikhov, R., R. Meshkian, D. Weller, B. Zingsem, D. Spoddig, J. Lu, A. S. Ingason, H. Zhang, J. Rosen, U. Wiedwald and M. Farle, "Magnetic properties of nanolaminated $(Mo_{0.5}Mn_{0.5})_2GaC$ MAX Phase ," submitted.

Materialwissenschaftliches Kolloquium

TECHNISCHE UNIVERSITÄT DARMSTADT

MATERIAL-WISSENSCHAFT

Montag, 30. Januar 2017, 17 Uhr s.t., L2/01 Raum 77

Prof. Dr. Michael Farle
University of Duisburg-Essen
Immanuel Kant Baltic
Federal University, Russia

IEEE Magnetics Society
Distinguished Lecturer for 2017

Functionalized Hybrid Nanomagnets: New Materials for Innovations in Energy Storage and Medical Theranostics

Imagine a future in which food is used to activate specific immune reactions in a human body based on an external noninvasive magnetic stimulus. Dream of a material that stores and releases energy reversibly by temperature changes between day and night. These visions may be realized by using magnetic nanoparticles that are functionalized to be biocompatible, environmentally stable and recyclable, self-healing, and low-cost.

In this presentation I will discuss the basic concepts of magnetic nanomaterials and their magnetic properties with a focus on how to tune specific parameters in a controlled fashion to achieve the dreams of the future. I will highlight state-of-the-art experimental technologies that allow us to understand microscopic properties and interactions in relation to electronic structure changes caused by changes in size, shape, and composition of nanomaterials. Then I will discuss how this understanding is used when nanomagnets are functionalized for targeted drug delivery or composed to form macroscopic materials for new energetic applications like magnetic refrigeration. I will demonstrate that the seemingly complex behavior of hybrid metal/metal, metal/oxide, or oxide/oxide interface materials can be understood from the three fundamental interactions in magnetism: magnetic exchange interaction due to orbital overlap, spin-orbit interaction due to inner- and intra-atomic relativistic corrections (e.g., crystal field effects) and the long-range magnetic dipolar interaction. Several examples will be presented, including the formation of above-room-temperature ferromagnetic interface layers between low-temperature antiferromagnetic layers and the evolution of lattices of magnetic textures (skyrmions) in confined dimensions. The talk will end with an episode in the life of an imaginary golf-playing couple in the year 2040 who use their "Smart Magnet" (SMAG) phone to energize and heal their bodies on the green.

Nach Vortrag Diskussion bei Bier und Brezeln. Eine mögliche Nachsitzung wird mündlich angekündigt.

L. Alff / O. Gutfleisch / W. Jaegermann

MDM ferrite meta atoms and the field chirality in microwaves

E. O. Kamenetskii*, R. Joffe, and R. Shavit

Microwave Magnetic Laboratory,
Department of Electrical and Computer Engineering,
Ben Gurion University of the Negev, Beer Sheva, Israel
*Email: kmntsk@bgu.ac.il

Abstract-Long range dipole-dipole correlation in a ferrimagnetic sample can be treated in terms of collective excitations of the system as a whole. Ferrite samples with linear dimensions smaller than the dephasing length, but still much larger than the exchange-interaction scales, are mesoscopic structures with magneto-dipolar-mode (MDM) oscillations. Recently, it was shown that thin-film yttrium-iron-garnet (YIG) disks, distinguishing by multiresonance MDM spectra, demonstrate unique properties of artificial atomic structures: energy eigenstates and eigen power-flow vortices. Because of these properties, MDMs in a quasi-2D ferrite disk enable strong confinement of microwave radiation to subwavelength scales. In microwave structures with embedded MDM ferrite samples, one can observe quantized fields with topologically distinctive characteristics. These fields are termed magnetoelectric (ME) fields. ME fields are characterized by the helicity parameter which is a pseudoscalar. Newly developed capabilities in microwave sensing using ME probing fields originated the MDM ferrite samples, provide a potential for unprecedented measurements of chiral materials and biological objects with chiral structures.

Subwavelength confinement of light via electrostatic plasmonic resonances has found more demand and has become an important issue in many research fields including integrated photonics, spectroscopy, biological photonics, chemical studies, and so on. In microwaves, however, the effects of the electromagnetic subwavelength confinement due to quasistatic oscillations have not been studied sufficiently. In a series of recent publications [1 – 5], it was shown that small ferrite-disk particles may have unique spectral properties of MDM oscillations and the near fields originated from such particles are microwave chiral fields with strong subwavelength localization of electromagnetic energy.

At microwave frequencies, the spectral properties of the MDM resonances are analyzed based on the Walker equation for magnetostatic-potential wave function. In a normally magnetized quasi-2D ferrite disk, one has real-eigenvalue spectra for scalar wave functions. For such a quasi-Hermitian eigenvalue problem, the analytical spectral solutions can be obtained. Because of special dynamics of the magnetization motion in a ferrite disk, characterizing by symmetry breakings, small ferrite particles with MDM spectra originate near fields with unique topological properties. We term these fields magnetoelectric (ME) fields. The ME fields are characterized by helical structures and power-flow vortices. For incident EM waves, the vortex topological singularities act as traps, providing strong subwavelength confinement of the microwave fields. It appears that a vortex may turn out to generate a “radius of no return", beyond which the incident EM fields falls inevitably towards the vortex singularity. In such a case, the MDM vortex becomes an EM “black hole" in microwaves.

It was shown [6] that at MDM resonances, RF magnetization in a quasi-2D ferrite disk is distinguished by nonzero product $\vec{m}\cdot\left(\nabla\times\vec{m}\right)^{*}$. This pseudoscalar parameter, characterizing the way in which the field lines of magnetization curl themselves, we call magnetization helicity parameter. The magnetization helicity parameter defines the helicity parameters of the ME near fields: $F=\frac{\varepsilon_0}{4}\mathrm{Im}\left[\vec{E}\cdot\left(\nabla\times\vec{E}\right)^{*}\right]=\frac{\omega\varepsilon_0\mu_0}{4}\mathrm{Re}\left(\vec{E}\cdot\vec{H}^{*}\right)$. This gives evidence for the presence of mutually parallel components of the electric and magnetic fields in the ME-field structure. The ME fields, being originated from magnetization dynamics at MDM resonances, appear as the fields of axion electrodynamics. In axion electrodynamics, the coupling between an axion field and the electromagnetic field is expressed by an additional term in the ordinary Maxwell Lagrangian $L_{\vartheta}=\kappa\vartheta\vec{E}\cdot\vec{B}$, where ϑ is an axion field and κ is a coupling constant. The axion field ϑ transforms as a pseudoscalars under space reflection *P* and it is odd under time reversal *T*. MDMs in a quasi-2D ferrite disk are microwave energy-eigenstate oscillations with topologically distinct structures of rotating fields and unidirectional power-flow circulations. The active power flow $\vec{P}=\frac{1}{2}\mathrm{Re}\left(\vec{E}\times\vec{H}^{*}\right)$ has vortex topology. The orbital angular-momentum density of the field is expressed as $\vec{L}=\frac{1}{2}\mathrm{Re}\left[\vec{r}\times\left(\vec{E}\times\vec{H}^{*}\right)\right]$, where $\vec{r}$ is a radius from the disk axis. For a given direction of a bias magnetic field, the power-flow circulations are the same inside a ferrite and in the vacuum near-field regions above and below the disk.

Newly developed capabilities in microwave sensing using ME probing fields originated from multiresonance magnetic-dipolar-mode (MDM) oscillations in quasi-2D YIG disks, provide a potential for unprecedented measurements of chemical and biological objects. Recently, microwave sensors based on ME fields were effectively used for chirality discrimination in enantiomeric liquids [7].

REFERENCES

1. E. O. Kamenetskii, "Vortices and chirality of magnetostatic modes in quasi-2D ferrite disc particles", J. Phys. A: Math. Theor. 40, 6539 (2007).
2. E. O. Kamenetskii, "Helical-mode magnetostatic resonances in small ferrite particles and singular metamaterials", J. Phys.: Condens. Matter 22, 486005 (2010)
3. M. Berezin, E. O. Kamenetskii, and R. Shavit, "Topological-phase effects and path-dependent interference in microwave structures with magnetic-dipolar-mode ferrite particles," J. Opt. 14, 125602 (2012).
4. E. O. Kamenetskii, R. Joffe, and R. Shavit, "Microwave magnetoelectric fields and their role in the matter-field interaction," Phys. Rev. E 87, 023201 (2013).
5. E. O. Kamenetskii, M. Berezin, and R. Shavit, "Microwave magnetoelectric fields: Helicities and reactive power flows", Appl. Phys. B: Lasers Opt. 121, 31 (2015).
6. R. Joffe, E. O. Kamenetskii, and R. Shavit, "Azimuthally unidirectional transport of energy in magnetoelectric fields: Topological Lenz's effect", arXiv: 1701.05185.
7. E. Hollander, E. O. Kamenetskii, and R. Shavit, "Magnetoelectric fields for microwave chirality discrimination in enantiomeric liquids", arXiv:1605.00212.

Ultrafast laser control of magnetic materials

A. Donges, S. Gerlach, D. Hinzke, U. Atxitia, U. Nowak
Department of Physics, University of Konstanz, D-78457 Konstanz, Germany
corresponding author: ulrich.nowak@uni-konstanz.de

Abstract The manipulation of the magnetization with sub-picosecond laser pulses is attractive for potential information storage device applications. Some magnetic materials can already be switched solely by the effect of a laser pulse, without any external magnetic field involved. First, such effects were demonstrated for ferrimagnets but recently also for layered, synthetic ferrimagnets and even for ferromagnets. In this talk we investigate all-optical switching theoretically. We employ multi-scale models linking *ab initio* methods with spin models and mesoscopic theories to explore the spin dynamics, which is triggered by the laser pulse, and to distinguish thermal heating effects from opto-magnetic effects, such as the inverse Faraday effect.

The term all-optical switching (AOS) refers to the fact that some magnetic materials can be switched solely by the effect of a femtosecond laser pulse, without any applied magnetic field involved. Experimentally, such effects were demonstrated for ferrimagnets [1-3] but later also for layered, synthetic ferrimagnets [4] and recently even for ferromagnets [5].

We use a multi-scale approach linking ab-initio calculation for the parameterization of an atomistic spin model with spin dynamics simulations based on the stochastic Landau-Lifshitz-Gilbert equation, to investigate the spin dynamics of the ferrimagnets FeGd and $DyCo_5$, synthetic ferrimagnets consisting of antiferromagnetically coupled bilayers of Fe and Gd, as well as the ferromagnet FePt.

While many aspects of the thermally induced switching in FeGd have been uncovered [1, 2, 3, 6] alternative materials are less understood. In this context, $DyCo_5$ is a very interesting material displaying a reorientation transition. With our model, we are able to compute the complex temperature dependence of the magnetization. The simulations yield a Curie temperature of 1040K and a compensation point at 115K. The spin-reorientation transition is a consequence of competing magneto-crystalline anisotropies in connection with different degrees of thermal demagnetization in the Dy and Co sublattices. We explore the dynamics of the reorientation transition on ultra-fast time scales and in how far this transition affects the thermally induced switching.

For synthetic ferrimagnets we demonstrate and investigate thermally induced magnetic switching. Our findings show that deterministic magnetization reversal occurs above a certain threshold temperature if the ratio of transition metal atoms to rear-earth atoms is sufficiently large. Surprisingly, the total thickness of the multilayer system has little effect on switching. We further provide a simple argument to explain the temperature dependence of the reversal process.

Furthermore, we investigate helicity dependent AOS in FePt. We employ ab initio methods to calculate the laser-power and photon frequency dependence of the inverse Faraday field [7] and the magnetic dichroism and calculate the magnetization dynamics triggered by the laser pulse via the thermal heating effect and the inverse Faraday field based on the Landau-Lifshitz-Bloch equation of

motion for high-temperature magnetization dynamics. Closer analysis suggests the inverse Faraday effect to be strong enough to serve as mechanism for helicity dependent AOS in a multi-shot experiment. Our results are verified by a comparison to recent experiments [8].

Acknowledgements, This work was supported by the EC under Contract No. 281043, FemtoSpin, and via the Center for Applied Photonics in Konstanz.

REFERENCES

1. K. Vahaplar et al., Phys. Rev. Lett. **103**, 117201 (2009)
2. I. Radu et al., Nature **724**, 205 (2011)
3. T. Ostler et al., Nat. Commun. **3**, 666 (2012)
4. S. Mangin et al., Nat. Materials **13**, 287 (2014)
5. C.-H. Lambert et al., Science **345**, 1337 (2014)
6. S. Wienholdt et al., Phys. Rev. B **88**, 020406 (2013)
7. M. Battiato, G. Barbalinardo, and P.M. Oppeneer, Phys. Rev. B **89**, 014413 (2014)
8. R. John et al., arXiv.1606.08723 (2016)

Thermal emission and radiative heat transfer of magneto-optical systems

R. M. Abraham Ekeroth[1,2], A. García-Martín[1], J. C. Cuevas[3,4]

[1]IMM-Instituto de Microelectrónica de Madrid (CNM-CSIC), Isaac Newton 8,PTM, Tres Cantos, E-28760 Madrid, Spain

[2]Instituto de Física Arroyo Seco, Universidad Nacional del Centro de la Provincia de Buenos Aires, Pinto 399, 7000 Tandil, Argentina

[3]Departamento de Física Teórica de la Materia Condensada and Condensed Matter Physics Center (IFIMAC), Universidad Autónoma de Madrid, E-28049 Madrid, Spain

[4]Department of Physics, University of Konstanz, D-78457 Konstanz, Germany

[*]corresponding author: a.garcia.martin@csic.es

Abstract- The thermal emission and the radiative heat transfer between finite objects of arbitrary shape that exhibit magneto-optical activity, is studied using a generalization of the thermal discrete dipole approximation (TDDA).

There is an increasing interest in the study of the radiative heat transfer between nearby objects[1]. This is motivated by the experimental verification of a large enhancement when the objects are placed within the near-filed regime [2-9].

On the other hand, MO objects are of great interest in the context of near field radiative heat transfer. In particular, doped semiconductors under a magnetic field present a sizable MO activity, that can be further controlled by changing the magnitude and the direction of the field. Thus for instance, it has been demonstrated that the radiative heat transfer between two parallel plates made of doped semiconductors can be largely tuned by applying a static external magnetic field [10].

Here, we present the radiative heat transfer between finite objects of arbitrary shape that exhibit magneto-optical activity, using a generalization of the thermal discrete dipole approximation (TDDA). We also describe the thermal emission of a finite object with and without magneto-optical activity, within the same TDDA approach. We will show that employing our TDDA approach one can rigorously demonstrate Kirchhoff's radiation law relating the emissivity and absorptivity of an arbitrary magneto-optical object. Our work paves the way for the theoretical study of the active control of emission and radiative heat transfer between magneto-optical systems of arbitrary size and shape [11].

REFERENCES

[1] B. Song, *et al.*, AIP Advances **5**, 053503 (2015).

[2] Kittel, *et al.*, Phys. Rev. Lett. **95**, 224301 (2005).

[3] E. Rousseau, *et al.,* Nat. Photon. **3**, 514 (2009).

[4] P.J. van Zwol, *et al.*, Phys. Rev. Lett. **109**, 264301 (2012).

[5] B. Song, *et al.*, Nat. Nanotechnol. **10**, 253 (2015).

[6] K. Kim, *et al.*, Nature (London) **528**, 387 (2015).

[7] R. St-Gelais, *et al.*, Nat. Nanotechnol. **11**, 515 (2016).

[8] B. Song, *et al.*, Nat. Nanotechnol. **11**, 509 (2016).
[9] M.P. Bernardi, *et al.*, Nat. Comm. **7**, 12900 (2016).
[10] E. Moncada-Villa, *et al.*, Phys. Rev. B **92**, 125418 (2015).
[11] R. M. Abraham Ekeroth, *et al.*, *submitted* (arXiv:1702.04273).

Light induced magnetization dynamics

M. Aeschlimann
Department of Physics and Research Center OPTIMAS, University of Kaiserslautern, Germany
ma@physik.uni-kl.de

Abstract- New developments in laser-based femtosecond x-ray and extreme-ultraviolet sources make it possible to probe element-specific spin dynamics in multispecies magnetic systems. These nascent optical tools therefore provide new and detailed information that is mostly not accessible by using visible light, and allow for the design of experiments that can help to identify the microscopic mechanisms of ultrafast spin dynamics. Using femtosecond soft X-ray pulses we were able to investigate the ultrafast breakdown of the magnetic coupling in heterogeneous magnetic materials.

The study of magnetism, magnetic materials, and dynamics in magnetic systems is a topic of fundamental interest in our understanding of correlated systems, as well as being directly relevant to technology and information storage. In recent years, magnetism at the ultrafast timescale has been a topic of increasing interest. A thorough understanding of femtosecond magnetism will address the important questions of how fast the magnetization can be reoriented in a material and what physical processes present fundamental limits to this speed. In the spatial domain, magnetism at nanometer length is a topic directly relevant to data storage, since future advances in this technology will require further reduction in device dimensions to increase the storage density. These considerations have motivated a variety of studies using magneto-optic effects in conjunction with ultrafast light pulses to explore these fundamental limits.

Magneto-optical dynamic studies currently make use either of visible-wavelength light from ultrafast lasers, or x-rays from large-scale synchrotron x-ray facilities. Ultrafast lasers produce short pulses (≈10fs), making possible femtosecond time resolution [1,2], but with a spatial resolution that is generally limited by the wavelength of the probe light. Femtosecond X-rays pulses, on the other hand, allow for high spatial resolution and high contrast at the elemental absorption edges of ferromagnetic materials. This is a challenging proposition, but one that can be addressed using newly developed tabletop-scale coherent light sources based on high-harmonic upconversion (HHG) of a femtosecond laser. HHG is an extreme nonlinear process that produces coherent short wavelength beams with the shortest pulse durations demonstrated to date for any light source – in the 0.1 fs to 10 fs range [3,4]. The generated harmonics extend from 10 eV to greater than 2 keV, and retain the polarization and coherence properties of the driving laser under phase-matched generation conditions. Bright HHG beams with sufficient flux for experimental applications can currently be generated with photon energies of up to ≈330 eV [4]. Past 'static' synchrotron measurements have shown that the magnetization can be probed at the M-edges of Fe, Co, and Ni, at photon energies around 55 eV to 65 eV [5]. This is an energy range that is easily accessible using HHG.

In this work, we demonstrate that ultrafast (≈10 fs), coherent, HHG beams can serve as an elementally-sensitive probe of magnetization orientation and demagnetization dynamics [6]. We also show that our measurements are sensitive to the presence of capping layers, making it possible to probe the magnetization state of buried layers and multilayer structures [7,8,9]. The significance of this work is that the ultrafast time-resolution provides a clear pathway for addressing a controversy concerning the timescales and

mechanisms associated with the ultrafast (possibly even attosecond [10]) dynamics of magnetization. The extremely short pulses provided by HHG can address both electron and spin dynamics on an equal footing, which is the prerequisite to studying the mechanisms governing coupling between the electron, spin and lattice subsystems [11]. Finally, the high harmonic source uses a tabletop femtosecond laser that is available in many laboratories worldwide. Therefore, this work represents an accessible new experimental capability for magnetic materials research. The review concludes with a summary and an outlook to the feasibility of laser control of magnetism.

REFERENCES

1. Beaurepaire, E. et al., "Ultrafast Spin Dynamics in Ferromagnetic Nickel," *Physical Review Letters* 76, 4250 (1996)
2. Koopmans, B. et al, "Explaining the paradoxical diversity of ultrafast laser-induced demagnetization" *Nature Mat*. 9, 256 (2010)
3. Kapteyn, H.C.; Murnane, M.M.; Christov, I.R. "Extreme Nonlinear Optics: Coherent X rays from Lasers" *Physics today*, 58, 39 (2005)
4. Popmintchev, T. et al., "Phase matching of high harmonic generation in the soft and hard X-ray regions of the spectrum" *PNAS* 106, 10516 (2009)
5. Höchst, H. et al., "Magnetic linear dichroism effects in reflection spectroscopy: A case study at the Fe $M_{2,3}$ edge" *Journal of Applied Physics* 81, 7584 (1997)
6. Mathias, S. et al. "Probing the timescale of the exchange interaction in a ferromagnetic alloy" *PNAS* 109, 4792 (2012)
7. Rudolf, D. et al., "Ultrafast magnetization enhancement in metallic multilayers driven by superdiffusive spin current" *Nature Communications* Vol. 3, S. 1037 (2012)
8. Mathias, S. et al "Ultrafast element-specific magnetization dynamics of complex magnetic materials on a table-top" *Journal of Electron Spectroscopy and Related Phenomena* Vol. 189, S. 164–170 (2013)
9. Turgut, E. et al., "Controlling the competition between optically induced ultrafast spin-flip scattering and spin transport in magnetic multilayers" *Physical Review Letters*, Vol. 110, Nr. 19, S. 197201 (2013)
10. Tao, Z. et al., "Direct time-domain observation of attosecond final-state lifetimes in photoemission from solids" *Science* 353 (6294), 62 (2016)
11. Turgut, E. et al., "Stoner versus Heisenberg. Ultrafast exchange reduction and magnon generation during laser-induced demagnetization" *Physical Review B*, Vol. 94, Nr. 22, (2016)

Magneto-plasmonic nanostructures and crystals.

P. Vavassori[1,2*]
[1] CIC nanoGUNE, 20018 San Sebastian, Spain
[2] IKERBASQUE Basque Foundation for Science, 48013 Bilbao, Spain
[*]corresponding author: p.vavassori@nanogune.eu

Abstract- The rapidly developing field of magnetoplasmonics merges concepts from plasmonics and magnetism to realize novel and unexpected phenomena and functionalities for the manipulation of light at the nanoscale. Such new functionalities arise from the intertwined optical and magneto-optical properties displayed by magneto-plasmonic nanostructured surfaces. This talk will cover recent advances in the investigation and development of magneto-plasmonic nanostrucutres and crystals, which contributed to broaden the understanding and control of optics at the nanoscale. Applications of such multifunctional optical surfaces and metamaterials to a variety of emerging technologies are presented as an example of their broad scientific and technological perspectives.

Plasmons play a large role in the optical properties of metals. Magnetoplasmonics combines strong local enhancements of electromagnetic fields in surface plasmon excitations with magneto-optically active ferromagnetic materials, which optical properties can be controlled by external magnetic fields.

Owing to the intertwined optical and magneto-optical properties, magnetoplasmonics may offer a smart toolbox for actively tuneable optical ultrathin surfaces and metasurfaces. Here we review recent advances in the research on magnetoplasmonic nanoantennas and two-dimensional magnetoplasmonic crystals. From the one side, they contributed to broaden the understanding and control of optics at the nanoscale. From the other side, magnetoplasmonic nanoantennas and surfaces have already shown a clear path towards applications to variety of emerging technologies as, e.g., ultrasensitive molecular sensing and ultrathin optical devices.

The fundamentals aspects of the physics underlying the optical behavior of magnetoplasmonic metamaterials are first briefly introduced [1-3].

A brief survey of applications to a variety of emerging technologies are presented as an example of their broad scientific and technological perspectives, namely:

- magnetoplasmonic nanoantennas based surfaces allowing for ultra-sensitive and label-free molecular detection, which are expected to have a clear impact on biochemistry and biomedicine and are therefore subject to intense investigation [4-6];
- systems allowing for the control of non-reciprocal light propagation relying on magnetoplasmonic nanoantennas ability to tailor the amplitude and sign of light polarization over a broad spectral range [7-10];
- ultra-thin chiroptical surfaces, built on 2D magnetoplasmonic bimetallic meta-atoms, where the chiral light transmission is modulated by the externally applied magnetic field [11];
- 2D magnetoplasmonic crystals, namely plasmonic crystals made of a periodic array of holes in a ferromagnetic layer, which support surface plasmon polariton modes and display a two-dimensional photonic band structure that can be engineered to obtain tailored and enhanced magneto-optical response [12].

Acknowledgements, support from Basque Government (Project n. PI2015_1_19) and Spanish Ministry of Economy and Competitiveness [Project n. FIS2015-64519-R (MINECO/FEDER)] is acknowledged.

REFERENCES

1. Chen, J., et al., "Plasmonic nickel nanoantennas", *Small* Vol. 7, No. 16, 2341-2347, 2011.
2. Maccaferri, N,. et al., "Tuning the magneto-optical response of nanosize ferromagnetic Ni disks using the phase of localized plasmons", *Phys. Rev. Lett.*, Vol. 111, No. 16, 167401, 2013.
3. Maccaferri, N., et al.," Polarizability and magnetoplasmonic properties of magnetic general nanoellipsoids", *Opt. Express*, Vol 21, No. 8, 9875-9889, 2013.
4. Bonanni, V., et al., "Designer magnetoplasmonics with nickel nanoferromagnets", *Nano Lett.*, Vol. 11, No. 12 , 5333-5338 , 2011.
5. Maccaferri, N., et al., "Ultrasensitive and label-free molecular-level detection enabled by light phase control in magnetoplasmonic nanoantennas", *Nature Commun.*, Vol. 6, 6150, 2015.
6. Zubritskaya, I., et al., "Active magnetoplasmonic ruler", *Nano Lett.*, Vol. 15, No. 5, 3204-3211, 2015.
7. Verre, R., et al., "Polarization conversion-based molecular sensing using anisotropic plasmonic metasurfaces", *Nanoscale*, Vol. 8, No. 20, 10576-10581, 2016.
8. Lodewijks, K., et al., "Magnetoplasmonic Design Rules for Active Magneto-Optics", *Nano Lett.*, Vol. 14, No. 12, 7207-7214, 2014.
9. Maccaferri, N., et al., "Anisotropic Nanoantenna-Based Magnetoplasmonic Crystals for Highly Enhanced and Tunable Magneto-Optical Activity", *Nano Lett.*, Vol. 16, No. 4, 2533-2542, 2016.
10. Kataia, M., et al., "Hybrid plasmonic lattices with tunable magnetooptical activity", *Opt. Express*, Vol. 24, No. 4, 3652-3261, 2016.
11. Zubritskaya, I., et al., "Magnetic control of the chiroptical plasmonic surfaces", submitted to *Nature Photonics*.
12. Maccaferri, N., et al., "Resonant Enhancement of Magneto-Optical Activity Induced by Surface Plasmon Polariton Modes Coupling in 2D Magnetoplasmonic Crystals", *ACS Photonics*, Vol. 2, No. 12, 1769-1779, 2015.

Thin film magnetic metamaterials

Vassilios Kapaklis
Department of Physics & Astronomy, *Uppsala University*, *Sweden*
*corresponding author: Vassilios.kapaklis@physics.uu.se

Abstract-*Lithographically nano-patterned magnetic materials can result in fascinating behaviour exploiting the interactions between individual elements creating novel functionality. The emergent properties in such systems are distinctly different from those of their constituent components, driven by the collective dynamics of the interacting elements and respond to external stimuli such as magnetic or temperature. Further functionality can be realised exploiting the fact that the periodicity and element size in such nano-patterned magnetic arrays matches well the wavelengths of visible light.*

Magnetism has for long been a fertile playground for the study of *phase transitions and dynamics*, as well as the development of elaborate theoretical tools used to describe and explain related experimental observations. This very successful approach has so far mainly focused on properties at the atomic scale and how these result in macroscopic observations, such as magnetic order and magnetization dynamics. Here *we propose a paradigm shift and the study of magnetic phase transitions and dynamics at mesoscopic length-scales*, using interacting ferromagnetic nanostructures of size inferior to the magnetic domain in two-dimensional nanopatterned arrays. These systems exhibit similar phase transitions and dynamics but on different length- and energy-scales, providing also the possibility for direct real-space characterization using a variety of modern magnetic imaging techniques[1]. Furthermore, the mesoscopic length-scales involved, matching well the wavelengths of visible light, present an unprecedented opportunity for the development of new routes to manipulate light with magnetism or vice versa, through plasmons.

Novel functionality can appear in nature from the combination of a large number of interacting elemental building blocks[1]. An example of this are solid materials, where atoms through bonding interactions crystallise in a variety of different structures that define their mechanical, thermal, electronic, magnetic and optical properties. Physicists have attempted to describe and predict such phenomena using models, such as the famous Ising model, where the geometry, interactions and temperature are taken into account providing a route for the identification of phase transitions in real materials. Using the basic concepts of such models, it is possible to engineer condensed matter systems based on thin films that are patterned and consist of a large number of ferroic components that interact (with magnetic dipolar interactions) with each other and result in new functions and properties. The studies of these artificial model systems and their many- particle interactions have grown exponentially in the last few years. It has been demonstrated that these interactions dictate the magnetic order and switching of individual building blocks on surprisingly large length-scales[2-4]. This approach benefits from a further advantage: all the parameters in the Hamiltonian that describes the system can be varied at will during fabrication, resulting in the epithet '*designer matter*'.

Out of the variety of systems that can be designed in this meta-material approach, one of particular interest is *artificial spin ice*, named after their real material analogue, spin ice. Artificial spin ices are lattices of nanomagnets, mimicking the proton arrangement around oxygen atoms in crystalline water ice and arranged

such that their mutual interactions are frustrated, leading to a rich phenomenology associated with the fact they can take up a huge number of reconfigurable metastable states. Artificial spin ice structures can furthermore be directly imaged using real-space techniques. This facilitates the direct determination of their microscopic states experimentally and comparison to well established statistical mechanical models. These systems therefore provide an ideal platform for the investigation of ground state ordering in the presence of frustration[4] and excitations[4,5]. In addition excited states in artificial spin ice possess effective magnetic charges ('monopoles') which might be useful as a new carrier of information[5].

Furthermore, such 2D patterned surfaces (metasurfaces) can affect the polarization/phase of free propagating light – just as the magneto-optical (MO) effects in magnetic materials[6]. The combination of plasmonics, metasurfaces and magnetic materials allows for new perspectives in the long-sought functionality for waveguiding and light manipulation[6-8]. Our developed far-field methodologies already allow for the control of plasmons and their propagation using low magnetic fields and enhancement of the magneto-optic activity due to plasmons[9]. Furthermore, it might also be a possible route for controlling the magnetic state and excitations in material using light that has been "trapped" on metasurfaces through plasmons.

Funding from the Knut and Alice Wallenberg Foundation is greatly acknowledged.

REFERENCES

1. Nisoli C, Kapaklis V and Schiffer P., "Deliberate exotic magnetism via frustration and topology", *Nature Physics*, in press (2016).
2. Kapaklis, V., Arnalds, U. B., Farhan, A., Chopdekar, R. V., Balan, A., Scholl, A., et al., "Thermal fluctuations in artificial spin ice", *Nature Nanotechnology*, *9*(7), 514–519 (2014).
3. Farhan, A., Derlet, P. M., Kleibert, A., Balan, A., Chopdekar, R. V., Wyss, M., et al., "Exploring hyper-cubic energy landscapes in thermally active finite artificial spin-ice systems", *Nature Physics*, *9*, 375 (2013).
4. Kapaklis, V., Arnalds, U. B., Farhan, A., Chopdekar, R. V., Balan, A., Scholl, A., et al., "Thermal fluctuations in artificial spin ice. *Nature Nanotechnology"*, *9*(7), 514–519 (2014).
5. Andersson, M. S., Pappas, S. D., Stopfel, H., Östman, E., Stein, A., Nordblad, P., et al., "Thermally induced magnetic relaxation in square artificial spin ice", *Scientific Reports*, *6*, 37097 (2016).
6. Papaioannou, E. T., Kapaklis, V., Giersig, M., Fumagalli, P., García-Martín, A., Ferreiro-Vila, E., & Ctistis, G. (2010). "Magneto-optic enhancement and magnetic properties in Fe antidot films with hexagonal symmetry", *Physical Review B*, *81*(5), 054424 (2010).
7. Maccaferri, N., Berger, A., Bonetti, S., Bonanni, V., Kataja, M., Qin, Q. H., et al. (2013). Tuning the Magneto-Optical Response of Nanosize Ferromagnetic Ni Disks Using the Phase of Localized Plasmons. *Physical Review Letters*, *111*(16), 167401. http://doi.org/10.1103/PhysRevLett.111.167401
8. Rollinger, M., Thielen, P., Melander, E., Östman, E., Kapaklis, V., Obry, B., et al., "Light Localization and Magneto-Optic Enhancement in Ni Antidot Arrays", *Nano Letters*, *16*(4), 2432–2438 (2016).
9. Melander, E., Östman, E., Keller, J., Schmidt, J., Papaioannou, E. T., Kapaklis, V., et al., "Influence of the magnetic field on the plasmonic properties of transparent Ni anti-dot arrays", *Applied Physics Letters*, *101*(6), 063107 (2012).

Ultrafast All-Optical Manipulation of Magnetization in Hybrid Metal-Ferromagnet Structures

Feng Cheng[1] **and Yongmin Liu**[1,2,*]

[1] Department of Electrical and Computer Engineering, Northeastern University, Boston, USA

2 Department of Mechanical and Industrial Engineering, Northeastern University, Boston, USA

[*]corresponding author: y.liu@northeastern.edu

Abstract- We experimentally demonstrate all-optical helicity-dependent switching (AO-HDS) of magnetization in hybrid metal-ferromagnet thin films, showing very robust AO-HDS effect for a wide range of laser repetition rates and peak powers. The hybrid metal-ferromagnet structures exhibit smaller coercivity and smaller remanent magnetization compared with the bare ferromagnet film, which may facilitate the pronounced HD-AOS feature. This work paves a critical step towards future high-speed, low-power and high-density memory and storage technologies.

The emerging Big Data Era demands the ever increasing speed and capacity of processing and storing information. Recent research has shown that it is possible to use femtosecond circularly polarized laser to switch the magnetization in certain magnetic materials. This helicity-dependent all-optical switching (HD-AOS) was initially discovered in ferrimagnetic systems involving rare-earth elements [1-5], and very recently extended to ferromagnetic materials such as CoPt multilayers [6-7]. Most remarkably, such an extremely fast and novel reversal mechanism does not require an external magnetic field existing in conventional magnetic storage devices such as hard disk drives, and potentially could increase the data storage speed by three orders of magnitude. However, the fundamental mechanism of HD-AOS is still not fully understood [8,9]. In addition, nanoscale optical control of magnetization for high-density storage remains very challenging because of the diffraction limit in classical optics.

Plasmonic nanostructures made of noble metals, such as gold and silver, enable to confine light into deep subwavelength scales and meanwhile significantly increase the local field intensity [10,11]. In order to realize all-optical magnetic switching with lower power and higher density for future memory and storage devices, it has been proposed to combine plasmonic structures with advanced magnetic materials [12,13]. Towards this goal, in this talk we present the HD-AOS effect of CoPt multilayers coated with an additional gold thin film. We demonstrate that this hybrid metal-ferromagnet system exhibits pronounced HD-AOS. We have conducted systematic optical characterizations to explore the dependence of HD-AOS on different repetition rates and peak powers. It is found that better HD-AOS results can be observed for higher repetition rates. By varying the laser power, we have observed the CoPtAu thin films exhibit HD-AOS with a wide range of the threshold fluence (estimated to be larger than 360.5%). This is a significant increase compared with the previous reported results in GdFeCo alloy films [14], which shows HD-AOS only for a narrow window of threshold fluence (estimated to be 1.5%). To reveal the underlying mechanism, we have measured and compared the hysteresis curves of different samples. The hybrid magneto-plasmonic structures show smaller coercivity and smaller remanent magnetization compared with CoPt multilayers, which may be the cause of the pronounced HD-AOS feature [15]. Leveraging

these findings, we have also integrated plasmonic nanostructures with CoPt multilayers. Preliminary results of the plasmonic effect on HD-AOS are obtained.

REFERENCES

1. C. D. Stanciu, F. Hansteen, A. V. Kimel, A. Kirilyuk, A. Tsukamoto, A. Itoh, and T. Rasing, Physical Review Letters **99**, 047601 (2007).
2. J. Hohlfeld, C. D. Stanciu, and A. Rebei, Applied Physics Letters **94**, 152504 (2009).
3. K. Vahaplar, A. M. Kalashnikova, A. V. Kimel, D. Hinzke, U. Nowak, R. Chantrell, A. Tsukamoto, A. Itoh, A. Kirilyuk, and T. Rasing, Physical Review Letters **103**, 117201 (2009).
4. S. Alebrand, A. Hassdenteufel, D. Steil, M. Cinchetti, and M. Aeschlimann, Physical Review B **85**, 092401 (2012).
5. A. Hassdenteufel, B. Hebler, C. Schubert, A. Liebig, M. Teich, M. Helm, M. Aeschlimann, M. Albrecht, and R. Bratschitsch, Advanced Materials **25**, 3122 (2013).
6. C-H. Lambert, S. Mangin, B. S. D. Varaprasad, Y. K. Takahashi, M. Hehn, M. Cinchetti, G. Malinowski, K. Hono, Y. Fainman, M. Aeschlimann and E. E Fullerton, Science **345**, 1337 (2014).
7. M. S. E. Hadri, P. Pirro, C-H. Lambert, N. Bergeard, S. Petit-Watelot, M. Hehn, G. Malinowski, F. Montaigne, Y. Quessab, R. Medapalli, E.E Fullerton and S. Mangin, Applied Physics Letters **108**, 092405 (2016).
8. A. Kirilyuk, A. V. Kimel and T. Rasing, Reviews of Modern Physics **82**, 2731 (2010).
9. A. Kirilyuk, A. V. Kimel and T. Rasing, Reports on Progress in Physics **76**, 026501 (2013).
10. H. Raether, H. Surface plasmons on smooth and rough surfaces and on gratings, Springer Berlin Heidelberg (1988).
11. S. A. Maier, Plasmonics: fundamentals and applications: fundamentals and applications. Springer Science & Business Media (2007).
12. B. Koene, M. Savoini, A. V. Kimel, A. Kirilyuk and T. Rasing, Applied Physics Letters **101**, 013115 (2012).
13. T. M. Liu et al., Nano letters **15**, 6862 (2015).
14. A. R. Khorsand, M. Savoini, A. Kirilyuk, A. V. Kimel, A. Tsukamoto, A. Itoh and Th. Rasing, Phys. Rev. Lett. **108**, 127205 (2012).
15. A. Hassdenteufel, J. Schmidt, C. Schubert, B. Hebler, M. Helm, M. Albrecht and R.Bratschitsch, Phys. Rev. B **91**, 104431 (2015)

Magneto-optic enhancement in 0D-1D- and 2D magneto-plasmonic structures

E. Wiedemann[1], S. Pappas[1], S. Keller[1], C. Dautermann[2], S. Wolff[2], and E. Th. Papaioannou[2*]

[1]Department of Physics and Research Center OPTIMAS, TU Kaiserslautern,
Erwin-Schrödinger-Str. 56, 67663 Kaiserslautern, Germany

[2]Nano Structuring Center TU Kaiserslautern Erwin-Schrödinger-Str. Gebäude 13, 67663 Kaiserslautern, Germany

[*]corresponding author: papaio@rhrk.uni-kl.de

Abstract-The magneto-plasmonic interaction is revealed in 0D, 1D- and 2D magnetic nanostructures. The magneto-optic response is examined in the presence of localized surface plasmons, of propagating surface plasmons and in the geometrical percolation limit. The role of the thickness of the magnetic layer is clarified. Finally, the influence of surface plasmons on the magnetization dynamics is discussed.

The field of magneto-plasmonics is an emergent research field that aims to explore the combination of magnetic and plasmonic functionalities in patterned nanostructures [1, 2]. The presence of magnetic materials in plasmonic structures offers the possibility to influence plasmonic resonances with the magnetization and an external magnetic field. The presence of surface plasmons in magnetic nanostructures on the other side, can boost the magneto-optic response [3].

In this work we show the evolution of the magneto-optic enhancement in zero, one and two dimensions (0D, 1D and 2D) magneto-plasmonic structures. We use Au nanoparticles, Au gratings and Au antidot structures in combination with magnetic films to study the enhancement factor of the polar, longitudinal and transverse Kerr effect. As magnetic films, Yttrium Iron Garnet (YIG) and Co layers are used.

We demonstrate the different degree of magneto-plasmonic interaction when localized surface plasmons (LSPs) or propagating surface plasmons (SPPs) are excited. Furthermore, we reveal the effect on the magneto-optical effects around the dimensionality crossover from 0D to 2D. The transition from LSPs to SPPs is achieved close to the geometrical percolation limit.

We correlate the magneto-optic interaction not only with respect to the transition from LSPs to SPPs but also to the dimensionality of the magnetic layer. The thickness of the magnetic layer plays a decisive role [4]. We present that the spectral features of the magneto-optic enhancement does not only depend on the in-plane structuring of the sample but also on the out-of-plane geometrical parameters, such as the thickness of the magnetic layer.

We furthermore explore how the presence of LSPs and SPPs is modifying the magnetization dynamics of the magnetic layer.

Acknowledgements, The transregional Collaborative Research Center SFB/TRR 173: SPIN+X, Project B07 is gratefully acknowledged.

REFERENCES

1. Armelles, G., Cebollada, A., García-Martín, A. and M. U. Gonzalez, "Magnetoplasmonics: Combining Magnetic and Plasmonic Functionalities," *Adv. Opt. Mater*. Vol 1, 10−35, 2013.
2. Bossini D., Belotelov V. I., Zvezdin A. K., Kalish A. N. and A. V. Kimel, "Magnetoplasmonics and Femtosecond Optomagnetism at the Nanoscale," *ACS Photonics*, Vol 3, 1385–1400, 2016.
3. Rollinger, M, Thielen P., Melander E., Östman E., Kapaklis V., Obry B., Cinchetti M., García Martín A., Aeschlimann M. and E. Th. Papaioannou, "Light Localization and Magneto-Optic Enhancement in Ni Antidot Arrays," *Nano Letters*, Vol. 36, 2432–2438, 2016.
4. Melander, E., George S., Caballero B., Garcia-Martin A., Hjörvarsson B., Kapaklis V. and E. Th. Papaioannou, "Thickness dependent enhancement of the polar magneto-optic Kerr effect in Co magnetoplasmonic nanostructures," *http://arxiv.org/abs/1611.00078*, 2017.

Surface plasmon-polaritons in graphene – antiferromagnet layered structure

I. V. Bychkov[1,2*], **D. A. Kuzmin**[1,2], **and V. G. Shavrov**[3]
[1]Chelyabinsk State University, Chelyabinsk, Russian Federation
[2]South Ural State University (National Research University), Chelyabinsk, Russian Federation
[3]Kotel'nikov Institute of Radio Engineering and Electronics of RAS, Moscow, Russian Federation
[*]corresponding author: bychkov@csu.ru

Abstract-We have investigated surface plasmon-polaritons in graphene-antiferromagnet layered structure. We show the possibility of resonant interaction of the graphene surface plasmon-polaritons with the magnons of antiferromagnet.

Nowadays, in plasmonics great researchers attention is paid to investigation of graphene-based nanostructures and perspectives of its applications in data processing and storage devices[1]. In our recent works we have considered some graphene-containing structures. Some interesting results on speckle-pattern rotation in graphene-coated optical fibers[2], surface plasmon manipulation by magnetic field in the planar gyrotropic waveguide formed by two graphene layers[3], plasmonically induced magnetic field and Faraday rotation of high order modes in graphene-covered nanowires[4, 5] have been obtained.

In this work surface plasmon-polaritons in dielectric – graphene – antiferromagnet structure is investigated. We assume that dielectric is non-dispersive one, antiferromagnet is centrosymmetric few-sublattice magnet (of rhombic symmetry) with exchange spin excitations of electroactive type. Eigen frequencies of exchange modes correspond to infrared and visible spectrum ranges (for example, $YBa_2Cu_3O_{6+x}$, α-Fe_2O_3). Frequency-dependence of graphene conductivity is taken into account.

Calculations are carried out in assumption of decaying length of surface electromagnetic wave is much greater than the lattice constant and phenomenological method may be used. Properties of the structure are depending on dielectric permittivity tensor of antiferromagnet and graphene conductivity.

Different propagation directions of electromagnetic wave with respect to antiferromagnet crystal orientation are considered. Dispersion equations and conditions of excitation of TM- and TE- waves and components of electromagnetic field are obtained. It is shown, that TE- waves, which are non-existing without graphene, may propagates in the structure when some relations between parameters of mediums are satisfied in frequency ranges of exchange modes of antiferromagnet.

The work was financially supported in part by Grant of President of Russian Federation (MK-1653.2017.2), Russian Science Foundation (14-22-00279), Russian Foundation for Basic Reaserches (16-37-00023, 16-07-00751, 16-29-14045, 17-57-150001), Act 211 Government of the Russian Federation (contract № 02.A03.21.0011).

REFERENCES

1. Novoselov, K. S., V. I. Fal'ko, L. Colombo, P. R. Gellert, M. G. Schwab, and K. Kim, "A roadmap for graphene," *Nature*, Vol. 490, 192–200, 2012.
2. Kuzmin, D. A., I. V. Bychkov, and V. G. Shavrov, "Influence of graphene coating on speckle-pattern rotation of light in gyrotropic optical fiber," *Opt. Lett.,* Vol. 40, No 6, 890–893, 2015.
3. Kuzmin, D. A., I. V. Bychkov, and V. G. Shavrov, "Magnetic field control of plasmon polaritons in graphene-covered gyrotropic planar waveguide," *Opt. Lett.,* Vol. 40, No 11, 2557-2560, 2015.
4. Kuzmin, D. A., I. V. Bychkov, V. G. Shavrov, V. V. Temnov, H. I. Lee, J. Mok "Plasmonically induced magnetic field in graphene-coated nanowires," *Optics Letters*, Vol. 41, No. 2, 396-399, 2016.
5. Kuzmin, D. A., I. V. Bychkov, V. G. Shavrov, and V. V. Temnov, "Giant Faraday Rotation of High-Order Plasmonic Modes in Graphene-Covered Nanowires," *Nano Letters*, Vol. 16, 4391, 2016.

Topological magneto-plasmonics of graphene-based meta-structures

D. A. Kuzmin[1,2*], I. V. Bychkov[1,2], V. G. Shavrov[3], and V. V. Temnov[4]
[1]Chelyabinsk State University, Chelyabinsk, Russian Federation
[2]South Ural State University (National Research University), Chelyabinsk, Russian Federation
[3]Kotel'nikov Institute of Radio Engineering and Electronics of RAS, Moscow, Russian Federation
[4]Institut des Molécules et Matériaux du Mans, UMR CNRS 6283, Université du Maine, Le Mans cedex, France
[*]corresponding author: kuzminda@csu.ru

Abstract-In order to explore the non-reciprocal effects, we investigate topological magnetic nanostructures covered with graphene-based meta-surfaces, which consist of a periodic pattern of sub-wavelength stripes of graphene winding around magnetic (meta-)tube or (meta-)torus. We establish the relation between the topological and plasmonic properties in these structures. Elliptical and hyperbolic magneto-plasmonic Fabry-Perot resonances in meta-structures not only manifest the non-reciprocity but display the giant mode splitting.

In recent years, enormous attention of researchers has been paid to metasurfaces, i.e. an artificially created one-layer lattice consisting of sub-wavelength size elements (so-called "meta-atoms") [1-4]. Recently, we have shown that cylindrical graphene-based waveguide filled by gyrotropic (or magnetized) medium demonstrate the giant Faraday rotation of high-order plasmonic modes spiraling around the nanowire axis [5]. Here work we focus on the non-reciprocal cylindrical magneto-plasmonic waveguides based on rolled graphene meta-surfaces (meta-tubes) as well as the finite-length structures serving as meta-cavities (see Fig. 1).

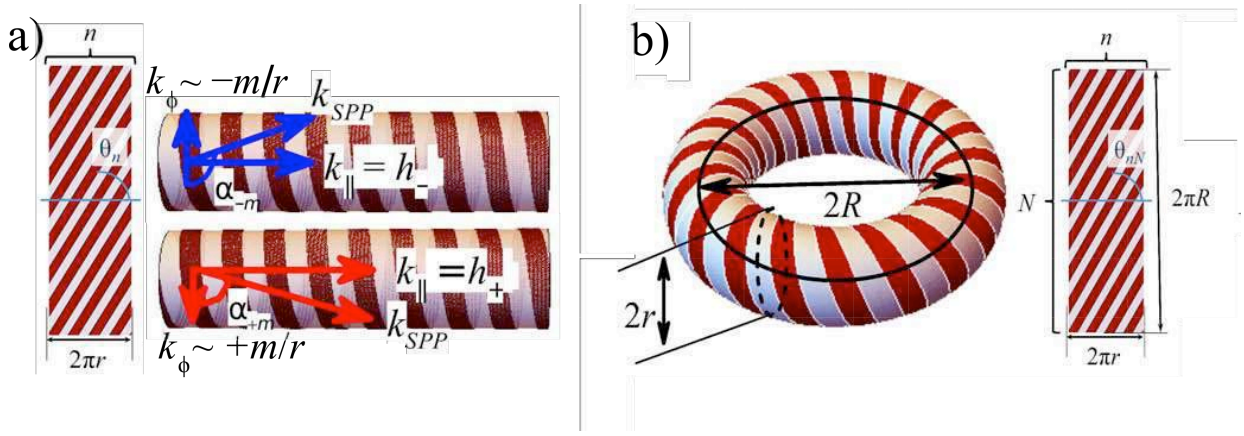

Figure 1. A graphene-based meta-tube (a) is obtained by winding a bunch of n identical graphene stripes around the cylindrical core under the fixed angle θ_n. A meta-torus (b) is characterized of the pair of topological indices of the structure n and N.

A graphene meta-tube may display a giant rotation of azimuthal magneto-plasmonic modes. This structure is

intrinsically non-reciprocal, which plays a crucial role for design of plasmonic devices with one-way propagation resulting in the disappearance of the Fabry-Perot resonances in finite-length meta-tubes. A piece of meta-tube rolled in a torus, possesses a distinct spectrum of azimuthal cavity modes with a large splitting for clock- and counterclockwise propagation directions. Interestingly, the electromagnetic, magnetic and geometrical topological indices of the structure obey simple analytical expressions. Therefore, our results are not limited for graphene-based structures and pave the way for topological non-reciprocal magneto-plasmonics.

The work was financially supported in part by Grant of President of Russian Federation (MK-1653.2017.2), Russian Science Foundation (14-22-00279), Russian Foundation for Basic Reaserches (16-37-00023, 16-07-00751, 16-29-14045, 17-57-150001), Act 211 Government of the Russian Federation (contract № 02.A03.21.0011), Stratégie internationale NNN-Telecom de la Région Pays de La Loire, and Alexander von Humboldt Stiftung.

REFERENCES

1. Kildishev, A. V., A. Boltasseva, and V. M. Shalaev, "Planar photonics with metasurfaces," *Science*, Vol. 339, 1232009, 2013.
2. Yu, N., and F. Capasso, "Flat optics with designer metasurfaces," *Nature Materials*, Vol. 13, 139–150, 2014.
3. Minovich, A. E., A. E. Miroshnichenko, A. Y. Bykov, T. V. Murzina, D. N. Neshev, and Yu. S. Kivshar, "Functional and nonlinear optical metasurfaces," *Laser & Photonics Reviews*, Vol. 9, 195–213, 2015.
4. Gomez-Diaz, J. S., and A. Alù, "Flatland Optics with Hyperbolic Metasurfaces," *ACS Photonics,* Vol.3, No 12, 2211–2224, 2016.
5. Kuzmin, D. A., I. V. Bychkov, V. G. Shavrov, and V. V. Temnov, "Giant Faraday Rotation of High-Order Plasmonic Modes in Graphene-Covered Nanowires," *Nano Letters*, Vol. 16, 4391, 2016.

A modular magneto-optical diffractometer as a toolbox for the characterization of nanostructured magnetoplasmonic crystals

E. Melander[1], I. A. Chioar[1], R. Rowan-Robinson[1], T. Dannegger[1], S. George[1], E. Th. Papaioannou[2], B. Hjörvarsson[1] and V. Kapaklis[1]

[1]Department of Physics and Astronomy, Uppsala University, Box 516, SE-751 20, Uppsala, Sweden
[2]Fachbereich Physik and Forschungszentrum OPTIMAS Technische Universität, Kaiserslautern, 67663 Kaiserslautern, Germany
ioan.chioar@physics.uu.se

Abstract— We present a versatile magneto-optical diffractometer, with ellipsometric capabilities, designed for investigating changes mediated by nano-engineered magnetoplasmonic crystals on the polarization state of the incident light. This facilitates a detailed characterization of metasurface light-tailoring as a function of wavelength and incidence angle, further enabling fundamental studies as well as exploring avenues for potential applications within the flat-optics framework.

The combination between plasmonic resonances, magnetism and nano-scale structuring has opened up exciting possibilities, by which the interplay between these three ingredients can enable an enhanced tailoring of the polarization state of light[1]. This active magnetoplasmonic framework can lead to numerous applications within the flat-optics playground[2]. However, in order to fully capture, quantify and understand the effects of this interplay, an in-depth characterization of the properties of the light scattered from such magnetoplasmonic metasurfaces is necessary. Of a particular interest are periodic arrangements of ferromagnetic nanostructures, for which well-defined grating-coupled plasmonic resonances can arise, given that a Laue-like momentum-matching condition is fulfilled. Such resonances have proven to enhance optical and magneto-optical activities[3] and are characterized by specific dispersion relations within the wavelength-incidence angle parameter space, which can be engineered by the choice of the materials and lattice geometry. For an experimental investigation, however, high-precision angular and wavelength-dependent measurements are required in order to properly identify and further quantify the effects of these plasmonic excitations.

We have developed a modular magneto-optical diffractometer designed to excite such plasmonic resonances while simultaneously characterizing, within a far-field picture, their impact on the polarization state of the incident light[4, 5]. Through the combined use of a high-precision goniometer stage and a supercontinuum laser source, the state of the reflected or transmitted light can be monitored as a function of incidence angle and wavelength, covering the visible and near-infrared ranges. This setup is highly versatile, capable of functioning in different operation modes and it can be regarded as a generalized diffractometer with ellipsometric capabilities. The reflectivity[6], transmission, rotation and ellipticity of the light can thus be recorded and the dispersion relations of effectively propagating plasmonic resonances or surface plasmon polaritons can be directly measured. The effects of complex unit cell geometries and phase gradients can also be investigated. Furthermore, the sample holder is equipped with a quadrupole coil system, enabling measurements under applied magnetic field. This option brings in the possibility of measuring the magneto-optical activity, such as the Transverse Magneto-Optical Kerr Effect (TMOKE) asymmetry[7], as well as exploring the potential for active magnetic tuning of the state of the light.

By using of this instrument, we have been able to experimentally highlight the fingerprints of these network-mediated plasmonic resonances on the optical and magneto-optical properties of different types of two-dimensional magnetoplasmonic crystals. Specifically, we've been able to track and quantify the dispersion relations of grating-coupled plasmonic modes, for both collinear and non-collinear alignments[4, 5, 6], in good agreement with theoretical predictions[8](see Figure1). Furthermore, the role played by the geometry of the lattice element in defining the overall behavior as well as the shape of the plasmonic resonances can been examined and quantified.

In conclusion, this versatile setup allows for an in-depth characterization of light scattered from magnetoplasmonic metasurfaces, incorporating both ellipsometric and magneto-optical functionalities, and can provide a detailed understanding of the underlying plasmonic excitations and dispersions.

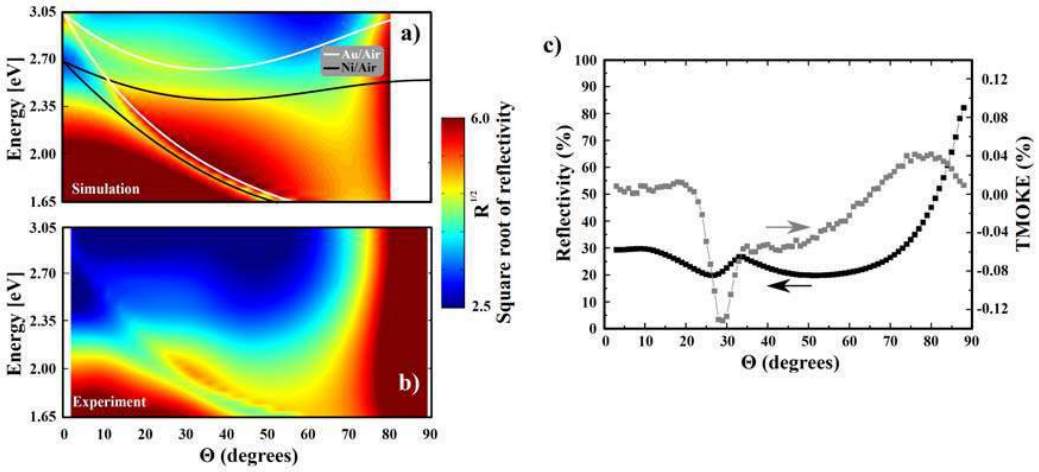

Figure 1: Examples of two-dimensional map representation of simulated (a) and experimental (b) reflectivity responses as a function of wavelength and incidence angle for a Ni/Au-capped hexagonal antidot magnetoplasmonic crystal (sample details in ref.[6]), with incident p-polarized light aligned with the next-nearest neighbor direction of the lattice. The positions found for the dispersion relations are in good agreement with the predicted dispersion relations. (c) Reflectivity and TMOKE asymmetry responses for the same sample for a wavelength of 636nm showing an enhanced magneto-optical activity mediated by the surface plasmon polariton modes.[7]. Figures taken from ref.[4, 5].

ACKNOWLEDGMENT

The authors acknowledge the support of the Swedish Research Council (VR), the Knut and Alice Wallenberg Foundation (KAW) and the Swedish Foundation for International Cooperation in Research and Higher Education (STINT). The authors would also like to thank Antonio García Martín for the SMM simulations.

REFERENCES

1. V. V. Temnov, G. Armelles, U. Woggon, D. Guzatov, A. Cebollada, A. Garcia-Martin, J.-M. Garcia-Martin, T. Thomay, A. Leitenstorfer, and R. Bratschitsch, "Active magneto-plasmonics in hybrid metalferromagnet structures," *Nature Photonics*, Vol. 4, No. 107, 2010.
2. N. Yu and F. Capasso, "Flat optics with designer metasurfaces," *Nature Materials*, Vol. 13, 139, 2014, and references therein.
3. V. I. Belotelov, I. A. Akimov, M. Pohl, V. A. Kotov, S. Kasture, A. S. Vengurlekar, A. V. Gopal, D. R. Yakovlev, A. K. Zvezdin and M. Bayer, "Enhanced magneto-optical effects in magnetoplasmonic crystals," *Nature Nanotechnology*, Vol. 6, 370, 2011.
4. E. Melander - "Magnetoplasmonic nanostructures," *PhD Thesis - Acta Universitatis Upsaliensis*, 2016, URN: http://uu.diva-portal.org/smash/record.jsf?pid=diva2%3A1037156&dswid=2707, Date accessed: 20.02.2017.
5. E. Melander, I. A. Chioar, T. Dannegger, S. George, E. Th. Papaioannou, B. Hjörvarsson and V. Kapaklis, "Modular magneto-optical diffractometer for characterizing nanostructured magnetoplasmonic crystals", *to be submitted to Rev. Sci. Instrum.,* 2017.
6. E. T. Papaioannou, V. Kapaklis, E. Melander, B. Hjörvarsson, S. D. Pappas, P. Patoka, M. Giersig, P. Fumagalli, A. García Martín, and G. Ctistis, "Surface plasmons and magneto-optic activity in hexagonal Ni anti-dot arrays," *Opt. Express*, Vol. 19, 23867 (2011).
7. E. Melander, E. Östman, J. Keller, J. Schmidt, E. T. Papaioannou, V. Kapaklis, U. B. Arnalds, B. Caballero,A. García Martín, J. C. Cuevas and B. Hjörvarsson, "Influence of the magnetic field on the plasmonic properties of transparent Ni anti-dot arrays", *Appl. Phys. Lett.*, Vol. 101, 063107 (2012).
8. B. Caballero, A. García Martín, and J. C. Cuevas, "Generalized scattering-matrix approach for magneto-optics in periodically patterned multilayer systems," *Phys. Rev. B*, Vol. 85, 245103 (2012).

Structural disorder induced magnetization in FeAl and FeRh: The perspectives for laterally patterned magnetic metamaterials

A.S. Semisalova[1,2*], R. Bali[1], S. Wintz[1,3], C. Barton[4], T. Thomson[4], G. Hlawacek[1], C. Fowley[1], J. Ehrler[1,5], R. Böttger[1], K. Potzger[1], J. Lindner[1] and J. Fassbender[1,5]

[1]Helmholtz-Zentrum Dresden – Rossendorf, Institute of Ion Beam Physics and Materials Research, Germany

[2]Lomonosov Moscow State University, Faculty of Physics, Russia

[3]Paul Scherrer Institute, Switzerland

[4]School of Computer Science, The University of Manchester, United Kingdom

[5]Technical University of Dresden, Germany

[*]corresponding author: a.semisalova@hzdr.de

Abstract-The possibilities of fabrication of magnetic nanostructures using ion irradiation will be exampled with the recent achievements in FeAl and FeRh. Magnetization of both alloys at room temperature is highly sensitive to the structural state (ordered or disordered). This opens a way for lateral patterning of nanoscale ferromagnets embedded in paramagnetic (FeAl) or antiferromagnetic (FeRh) ordered matrix and to study the effect of planar geometry of magnetic interfaces.

Nanostructuring of magnetic materials is of vital importance for novel technological applications based on spin and magnon transport, manipulation of domain walls, and artificial spin textures and magnetic metamaterials. A variety of magnetic effects arising on the interfaces in multilayers composed of ferro-, antiferro- and non-magnetic materials boosted the breakthrough in spin-dependent phenomena. Further exploit of nanoscale effects in ferromagnets requires the planar structuring of thin films and lateral patterning. Several binary transition metal based alloys offer a unique opportunity for fabrication of laterally patterned ferromagnetic nanostructures using the structural disordering. The magnetization of $Fe_{60}Al_{40}$ was shown to be highly sensitive to the transition of structure from B2 (ordered) to A2 (bcc, or disordered) [1]. The nearly paramagnetic at room temperature ordered alloy can be turned into a ferromagnet with a saturation magnetization of up to 800 kA/m when the structural disorder is introduced. Similarly, antiferromagnetic in B2 ordered state $Fe_{50}Rh_{50}$ alloy turns into a ferromagnet in disordered state [2].

In this talk, we demonstrate the possibility of a fabrication of embedded ferromagnetic nanostructures using irradiation with neon ions. The magnetic domain structure of the patterned objects can be controlled by the variation of the lateral sizes of the structures and their shape. The fabrication of array of single domain islands surrounded with paramagnetic (FeAl) or antiferromagnetic (FeRh) media might find a response in the emerging field of nanomagnet logic and other applications where nanoscale magnets are required, such as spin-wave propagation materials, artificial spin ice and the lattices of arranged ferromagnetic nanoislands with matrix-mediated coupling.

REFERENCES

1. Bali R. et al., *Nano Letters*, Vol. 14, 435–441, 2014.
2. Heidarian A. et al., *Nucl. Instr. Meth. Phys. Res. B*, Vol. 358, 251-254, 2015.

Impact of the optically-generated dynamical strain on the magnetic anisotropy of metallic films

A. M. Kalashnikova[1*], V. N. Kats[1], T. L. Linnik[2], A. S. Salasyuk[1], A. W. Rushforth[3], A.V. Akimov[3], A. V. Scherbakov[1]

[1]Ioffe Institute, 194021 St. Petersburg, Russia
[2]Department of Theoretical Physics, V. E. Lashkaryov Institute of Semiconductor Physics, 03028 Kyiv, Ukraine
[3]School of Physics and Astronomy, University of Nottingham, Nottingham NG7 2RD, United Kingdom
[*]corresponding author: kalashnikova@mail.ioffe.ru

Abstract We employ femtosecond laser pulses to excite magnetization precession in thin films of magnetostrictive metal galfenol $Fe_{0.81}Ga_{0.19}$, grown on (311)- and (001)-GaAs substrates. We demonstrate unambiguously that dynamical strain, generated due to picosecond lattice temperature increase, can alter magnetic anisotropy of the galfenol film. This dynamical strain-induced change of anisotropy allows excitation of magnetization precession even in relatively high magnetic fields, when the conventional contribution to the magnetic anisotropy change from the temperature increase itself becomes inefficient.

Changing magnetic anisotropy of a medium at the (sub)picosecond time scale can pave the way to the ultrafast control of magnetization orientation [1-3] and excitation of spin waves [4-8]. Ultrafast change of magnetic anisotropy of various media can be achieved via rapid increase of lattice temperature in response to the femtosecond laser pulse [4,5]. Such impact of laser pulses is usually treated as a rapid decrease of temperature-dependent magnetocrystalline anisotropy constants and manifests itself in triggering precession of magnetization. Another approach to change the magnetic anisotropy at ultrafast time scale is based on an effect of inverse magnetostriction. It has been demonstrated that picosecond strain pulses propagating through a magnetic material can change anisotropy of the latter and thus launch magnetization precession [6-8]. These two ways to control magnetic anisotropy are typically considered as alternative to each other.

When the thin magnetic film is excited directly by a femtosecond laser pulses, rapid increase of the lattice temperature sets up a thermal stress, which results in emergence of dynamics strain with complex temporal and spatial profile [9]. Thus, one can expect that in the optically-excited magnetic metallic film dynamical strain can contribute to the magnetic anisotropy change and compete to the conventional thermal change. However, the role of this strain in triggering ultrafast magnetization dynamics upon direct excitation of magnetic media remains unexplored.

Here we report on experimental and theoretical study of the magnetic anisotropy change in the magnetostrictive metallic galfenol ($Fe_{0.81}Ga_{0.19}$) films grown on GaAs substrates subjected to the action of femtosecond laser pulses [10]. By performing optical pump-probe experiments we demonstrate excitation of magnetization precession in the galfenol film, which originate from ultrafast magnetic anisotropy change. Unexpectedly, the trajectories of magnetization precession in the films grown on the high-symmetry (001)- and low-symmetry (311)-GaAs substrates appeared to be very different, indicating that magnetic anisotropy change

in these two cases rely on distinct mechanisms.

The most important result is that in the case of the low-symmetry (311)-galfenol film the ultrafast change of magnetic anisotropy results from both, thermal change of anisotropy constants, and on abrupt emergence of dynamical strain, which modifies anisotropy via inverse magnetostriction. We show that, by tuning applied magnetic field strength, we can change contributions from these two mechanisms to excitation of magnetization precession. While the thermal change of anisotropy allows to launch precession in relatively low magnetic fields, the strain-induced mechanisms remains efficient at fields upto et least 0.5 T. In experiments, competition between these two mechanisms manifests itself in nontrivial changes in magnetization trajectory.

We also show that the impact of optically-induced strain appears to be efficient in the case of low-symmetry film only, while in the high-symmetry (001)-galfenol film the excited precession relies solely on the ultrafast change of magnetic anisotropy parameters occurring due to laser-induced heating. This highlights importance of dynamical shear strain for manipulating magnetization, which occurs in low-symmetry structures only, in contrast to high-symmetry ones, allowing only longitudinal dynamical strain generated under optical excitation.

Acknowledgements, The work at the Ioffe Institute we supported by the Russian Science Foundation (Grant No. 16-12-10485). AWR acknowledges support from a Career Acceleration Fellowship (No.EP/H003487/1) of the Engineering and Physical Sciences Research Council, UK.

REFERENCES

1. De Jong, J. A. et al., “Coherent Control of the Route of an Ultrafast Magnetic Phase Transition via Low-Amplitude Spin Precession,” *Phys. Rev. Lett.*, Vol. 108, 157601, 2012.
2. Afanasiev, D. et al., “Control of the Ultrafast Photoinduced Magnetization across the Morin Transition in $DyFeO_3$,” *Phys. Rev. Lett.*, Vol. 116, 097401, 2016.
3. Stupakiewicz, A. et al., “Ultrafast nonthermal photo-magnetic recording in a transparent medium,” *Nature*, Vol. 542, 71, 2017.
4. Kimel A V. et al., "Laser-induced ultrafast spin reorientation in the antiferromagnet TmFeO3," *Nature* Vol. 429, 850, 2004.
5. Carpene E. et al., “Ultrafast three-dimensional magnetization precession and magnetic anisotropy of a photoexcited thin lm of iron," *Phys. Rev. B* Vol. 81, 060415, 2010.
6. Scherbakov A. V. et al., “Coherent magnetization precession in ferromagnetic (Ga,Mn)As induced by picosecond acoustic pulses”, *Phys. Rev. Lett.*, Vol. 105, 117204, 2010.
7. Kim J.-W. et al., “Ultrafast magnetoacoustics in nickel films,” *Phys. Rev. Lett*. Vol. 109, 166601, 2012.
8. Afanasiev D. et al., “Laser excitation of lattice-driven anharmonic magnetization dynamics in dielectric $FeBO_3$,” *Phys. Rev. Lett*. Vol. 112, 147403, 2014.
9. Thomsen C. et al., “Surface generation and detection of phonons by picosecond light pulses," *Phys. Rev. B* Vol. 34, 4129, 1986.
10. Kats V. N. et al., “Ultrafast changes of magnetic anisotropy driven by laser-generated coherent and noncoherent phonons in metallic films," *Phys. Rev. B* Vol. 93, 214422, 2016.

Magnetization reversal in granular FePt promoted by near-field laser enhancement

L. Le Guyader[1,2,*]

[1]Stanford Institute for Materials and Energy Sciences, SLAC National Accelerator Laboratory, 2575 Sand Hill Road, Menlo Park, CA 94025, USA

[2]Spectroscopy & Coherent Scattering Instrument, European XFEL GmbH, Holzkoppel 4, 22869 Schenefeld, Germany

[*]corresponding author: loic.le.guyader@xfel.eu

Abstract-Using ultrafast small-angle x-ray scattering at an x-ray free-electron laser, the magnetization dynamics of FePt nanoparticles embedded in a carbon matrix after excitation by an optical femtosecond laser pulse is investigated. It is found that some individual FePt nanoparticles neither switch nor demagnetiz, the origin of which is identified as the near-field modification of the incident laser radiation around FePt nanoparticles, as demonstrated by Finite Difference Time Domain simulations.

Light-matter interaction at the nanoscale in magnetic materials is a topic of intense research in view of potential applications in next-generation high-density magnetic recording. Laser-assisted switching provides an eficient pathway for overcoming the material constraints of high-anisotropy and high-packing density media, though much about the dynamics of the switching process remains unexplored. Using ultrafast small-angle x-ray scattering at an x-ray free-electron laser, the magnetization switching dynamics of FePt nanoparticles embedded in a carbon matrix following excitation by an optical femtosecond laser pulse was investigated. We observe that the combination of laser excitation and applied static magnetic field, one order of magnitude smaller than the coercive field, is sufficient to overcome the magnetic anisotropy barrier separating the “up” and “down” magnetic states. However, this magnetic switching is found to be inhomogeneous throughout the material, with some individual FePt nanoparticles neither switching nor demagnetizing. The origin of this surprising behavior is show to be the result of the near-field modification of the incident laser radiation around FePt nanoparticles, as demonstrated by Finite Difference Time Domain simulations of the film’s optical response.

Acknowledgements, Financial support from the Volkswagen-Stiftung through the Peter-Paul-Ewald Fellowship is acknowledged.

REFERENCES

1. Patrick W. Granitzka, Emmanuelle Jal, Loïc Le Guyader, Matteo Savoini, Daniel J. Higley, Tianmin Liu, Zhao Chen, Tyler Chase, Hendrik Ohldag, Georgi L. Dakovsky, William Schlotter, Sebastian Carron, Matthias Hoffman, Padraic Shafer, Elke Arenholz, Olav Hellwig, Virat Mehta, Yukiko K. Takahashi, J. Wang, Eric E. Fullerton, Joachim Stöhr, Alexander H. Reid and Hermann A. Dürr “Magnetic switching in granular FePt layers promoted by near-field laser enhancement,” arXiv:1701.01237 [cond-mat.mtrl-sci]

Magneto-optics at atomic limit with nanoantennas and magnetic control of chiroptical plasmonic surfaces

Alexandre Dmitriev
Department of Physics, University of Gothenburg, Gothenburg 412 96, Sweden
Geballe Laboratory for Advanced Materials, Stanford University, Stanford, California 94305-4045, USA
E-mail address: alexd@physics.gu.se; alexdmi@stanford.edu

Abstract: We show how the combination of optical nanoantennas and ferromagnets produces the sensitivities of the magneto-optical detection down to sub-atomic monolayer amounts of material. This combination also gives the 100%+ dynamic tunability to plasmonic surfaces by introducing the magnetically-tunable optical elements to the 2D plasmonic nanoantennas.

A major challenge facing the plasmon-based nanophotonics is the poor dynamic tunability. A functional adaptive nanophotonic element would feature the real-time large tunability of transmission, reflection of light intensity and/or polarization over a broad range of wavelengths, and would be robust and easy to integrate. Several approaches have been explored so far including mechanical deformation [1-3], thermal [4] or refractive index [5, 6] effects, and all-optical switching [7, 8]. Building on our previous advances of the combination of the plasmonic and ferromagnetic materials (magnetoplasmonics) [9-13], here we devise an ultra-thin chiroptical surface, built on 2D nanoantennas, where the chiral light transmission is controlled by the externally applied magnetic field. The magnetic- field induced modulation of the far-field chiroptical response with this system exceeds 100% in the visible and near-infrared spectral ranges, opening the route for nanometer-thin magnetoplasmonic light-modulating surfaces tuned in real time and featuring a broad spectral response.

We further design the nanoplasmonic antennas to produce tightly confined spot of the optical near-field enhancement. Positioning the magneto-optical dielectric in this spot produces largely enhanced magneto-optical signal from this material, allowing the reliable detection of the sub-atomic monolayer quantities of the material on cm^2-large surfaces.

References

[1] J. Y. Ou et al., An electromechanically reconfigurable plasmonic metamaterial operating in the near-infrared, *Nature Nanotechnol.* **8**, 252 (2013).
[2] J. Valente et al., Reconfiguring photonic metamaterials with currents and magnetic fields, *Appl. Phys. Lett.* **106**, 111905 (2015).
[3] N. I. Zheludev and E. Plum, Reconfigurable nanomechanical photonic metamaterials, *Nature Nanotechnol.* **11**, 16 (2016).
[4] J. Y. Ou et al., Reconfigurable photonic metamaterials, *Nano Lett.* **11**, 2142 (2011).
[5] A. K. Michel et al., Using low-loss phase-change materials for mid-infrared antenna resonance tuning, *Nano Lett.* **13**, 3470 (2013).
[6] Q. Wang et al., Optically reconfigurable metasurfaces and photonic devices based on phase change materials, *Nature Photon.* **10**, 60 (2015).
[7] R. F. Waters et al., Optically switchable photonic metasurfaces, *Appl. Phys. Lett.* **107**, 081102 (2015).
[8] M. Papaioannou et al., Two-dimensional control of light with light on metasurfaces, *Light: Science & Applications* **5**, e16070; doi:10.1038/lsa.2016.70 (2016).
[9] I. Zubritskaya et al., Active magnetoplasmonic ruler, *Nano Lett.* **15**, 3204 (2015).
[10] N. Maccaferri et al., Ultrasensitive and label-free molecular-level detection enabled by light phase control in magnetoplasmonic nanoantennas, *Nat. Commun.* **6**: 6150 (2015).
[11] K. Lodewijks et al., Magnetoplasmonic design rules for active magneto-optics, *Nano Lett.* **14**, 7207 (2014).
[12] Z. Pirzadeh et al., Plasmon−interband coupling in nickel nanoantennas, *ACS Photonics* **1**, 158 (2014).
[13] V. Bonanni et al., Designer magnetoplasmonics with nickel nanoferromagnets, *Nano Lett.* **11**, 5333 (2011).

All-optical magnetic switching: making use of fundamental magnetic interactions

Andrei Kirilyuk
Radboud University, Institute for Molecules and Materials, 6525 AJ Nijmegen, The Netherlands
a.kirilyuk@science.ru.nl

Abstract - The reversal of magnetization solely with the help of femtosecond laser pulses is an expanding area of research with more and more materials that can be switched, and various mechanisms responsible for switching. Here we concentrate on switching in rare-earth - transition metal alloys, where the inter-sublattice exchange is responsible for switching, as well as magnetic garnets, where the precessional switching is driven by the local change of anisotropy.

While the basic possibilities for direct laser manipulation of magnetization have been indicated a long time ago, only recently was it possible to apply such control in magnetically ordered materials [1,2].

The question was immediately triggered whether one could use the same mechanism for practical switching of the magnetization in e.g. recording media. A seemingly straightforward answer came very soon afterwards, with a direct demonstration of all-optical light helicity-dependent magnetic recording in thin films of metallic GdFeCo alloys [3]. In spite of the fact that the switching was clearly reproducible and robust, the exact process and mechanism of it remained elusive for a long time. The most obvious explanation via the inverse Faraday effect could only very qualitatively account for the observed features. Taking into account several factors, all-optical switching of the magnetization in rare-earth - transition metal alloys was assigned to a completely different effect: a combination of ultrafast laser-induced demagnetization with the angular-momentum conservation in the exchanged-coupled sublattices of a ferrimagnet, on a sub-picosecond time scale [4].

In spite of the recent extensive work on all-optical switching of magnetization in a variety of samples [5,6], confusion persists as to its mechanism. Here we demonstrate, using various time-resolved imaging techniques, that this confusion may be largely due to the fact that this phenomenon involves behavior on multiple scales, both in space and time. At 100's fs, independent demagnetization of sublattices is observed accompanied by spin diffusive processes at <10 nm distances, as shown by time-resolved X-ray scattering [7]. This is followed by the exchange spring driven behavior [4] with reversal and formation of skyrmion-like domains [8] at a few ps times.

In order to tune the exchange interaction between the sublattices, the alloyed samples were replaced with multilayers. Intriguingly, very large scale coherent precession could be observed that accompany the growth of large domains [9]. The presence of the compensation point added an extra spatial feature to the reversal dynamics in the multilayer samples.

To be technologically meaningful, the all-optical switching must be able to compete with the bit densities of conventional storage devices, restricting optically-switched magnetic areas to sizes well below the diffraction limit. We have recently demonstrated reproducible all-optical switching of magnetic domains of few tens of nm size [10], in a ferrimagnetic TbFeCo alloy using gold plasmonic antenna structures. It has also been found that the focusing of light to a nm-sized area can be helped by the light interference effects occurring within the magnetic structures themselves [11].

To summarize, such ultrafast exchange-driven ultrafast magnetization dynamics is not only potentially useful, but also provides us with invaluable information about the behavior of magnets away from their thermodynamic equilibrium.

However, the switching mechanisms in these materials are directly related to laser-induced heating close to the Curie temperature. Although several possible routes for achieving all-optical switching in magnetic dielectrics have been discussed, no recording has hitherto been demonstrated. Very recently, an ultrafast all-optical photo-magnetic recording in transparent films of the dielectric cobalt-substituted garnet was demonstrated [12]. A single linearly polarized femtosecond laser pulse resonantly pumps specific d−d transitions in the cobalt ions, breaking the degeneracy between metastable magnetic states. By changing the polarization of the laser pulse, we deterministically steer the net magnetization in the garnet, thus writing '0' and '1' magnetic bits at will. This mechanism outperforms existing alternatives in terms of the speed of the write–read magnetic recording event (less than 20 picoseconds) and the unprecedentedly low heat load (less than 6 joules per cubic centimetre).

To summarize, this is an exciting area that combines speed potential of photonics with the robustness of magnetic materials.

REFERENCES

1. A.V. Kimel et al., Ultrafast non-thermal control of magnetization by instantaneous photomagnetic pulses, *Nature* **435**, 655 (2005).
2. F. Hansteen et al., Femtosecond photomagnetic switching of spins in ferrimagnetic garnet films, *Phys. Rev. Lett.* **95**, 047402 (2005).
3. C.D. Stanciu et al., All-Optical Magnetic Recording with Circularly Polarized Light, *Phys. Rev. Lett.* **99**, 047601 (2007).
4. A. Kirilyuk, A.V. Kimel, and Th. Rasing, Laser-induced magnetization dynamics and reversal in ferrimagnetic alloys, *Rep. Prog. Phys.* **76** , 026501 (2013)
5. C.-H. Lambert et al, All-optical control of ferromagnetic thin films and nanostructures, *Science* **345**, 1337 (2014).
6. S. Mangin et al., Engineered materials for all-optical helicity-dependent magnetic switching, *Nature Materials* **13**, 287 (2014).
7. C.E. Graves et al., Nanoscale spin reversal by non-local angular momentum transfer following ultrafast laser excitation in ferrimagnetic GdFeCo, *Nature Materials* **12**, 293 (2013)
8. M. Finazzi et al., Laser-Induced Magnetic Nanostructures with Tunable Topological Properties, *Phys. Rev. Lett.* **110**, 177205 (2013)
9. Yu. Tsema et al, All-optical magnetization reversal through a strongly inhomogeneous laser-driven dynamics in metallic multilayers, *submitted*
10. T.M. Liu et al, Nanoscale Confinement of All-Optical Magnetic Switching in TbFeCo - Competition with Nanoscale Heterogeneity, *Nano Letters*, Nano Letters **15**, 6862 (2015)
11. L. Le Guyader et al, Nanoscale sub-100 picosecond all-optical magnetization switching in GdFeCo microstructures, *Nature Comm.* **6**, 5839 (2015).
12. A. Stupakiewicz, K. Szerenos, D. Afanasiev, A. Kirilyuk and A. V. Kimel, Ultrafast nonthermal photo-magnetic recording in a transparent medium, *Nature* **542**, 71 (2017).

Phononics in ferromagnets:
coherent phonons to manipulate magnetization at the nanoscale

A. V. Scherbakov
Ioffe Institute, 194021 St. Petersburg, Russia
scherbakov@mail.ioffe.ru

Abstract- We utilize resonant phonon modes of phononic ferromagnetic nanostructures to manipulate their magnetization. Coherent phonons of the resonant frequencies excited by a femtosecond laser pulse remain localized inside a ferromagnetic layer and drive the magnetization precession. By tuning the precession frequency by external magnetic field, we achieve conditions of magnon-phonon resonance, which results in the drastic increase of the precession amplitude and lifetime.

Applications based on magnetic materials have confidently reached the nanoscale. An information bit in conventional magnetic recording or spin torque oscillators in spintronic devices are of nanometer sizes. Phonons are typically considered as a detrimental factor for nanoscale magnetism as they may induce spontaneous reverse of magnetization or spin decoherence. However, phonons may be also an effective instrument. In this research, we utilize coherent phonons for driving magnetization of ferromagnetic nanostructures and demonstrate interplay of phononic and magnetic properties at the nanoscale.

We study experimentally the ferromagnetic structures, whose design leads to formation of high-Q phonic resonances in sub-THz frequency range. As a ferromagnetic material we use Galfenol, which is an alloy of iron and gallium with enhanced magneto-elastic interaction [1]. In our first attempt [2], we examine a ferromagnetic layer of 59-nm width deposited on GaAs/AlAs superlattice. The superlattice serves as phononic Bragg mirror for narrow frequency band. Together with open surface of a ferromagnetic layer they form phonic Fabry-Perot nanoresonator with a ferromagnetic cavity. Such a structure possesses several narrow phonon resonances with frequencies between 10 and 40 GHz. In the second attempt, we use lateral nanogratings produced by the focus ion beam lithography in 100-nm Galfenol film. The gratings possess narrow phonon resonances with frequencies between 15 and 20 GHz depending on their structural parameters and orientations.

At experiment, we use conventional magneto-optical pump-probe technique to monitor in time-domain the response of magnetization on femtosecond optical excitation. In the structures of both types we observe dominant contribution of the optically excited coherent phonons to the time evolution of magnetization. The phonons with resonant frequencies remain localized inside the studied structures and drive the magnetization precession within their lifetimes. The phonon driving achieves maximum efficiency (largest amplitude and longest lifetime of precession) at the resonant conditions when the frequencies of ferromagnetic and phonon resonances are equal.

The suggested approach has prospective uses for sub-THz spin pumping and generation of high-amplitude microwave magnetic fields at the nanoscale.

The presented work is result of collaboration between the Ioffe Institute (A.S. Salasyuk, A.V. Rudkovskaya, A.V. Scherbakov), the University of Nottingham (A.W. Rushforth, A.V. Akimov), Technical University of Dortmund (J. V. Jäger, A.V. Danilov, D.R. Yakovlev, M. Bayer), the Lashkaryov Institute of Semiconductor Physics (B. A. Glavin and S. M. Kukhtaruk) and the Institute of Nanotechnology for Microelectronics (P.A. Nekludova, S. V. Sokolov, A. A. Elistratov)

REFERENCES

1. D. E. Parkes, L. R. Shelford, P. Wadley, V. Holý, M. Wang, A. T. Hindmarch,G. van der Laan, R. P. Campion, K. W. Edmonds, S. A. Cavill, and A. W. Rushforth, "Magnetostrictive thin films for microwave spintronics", *Sci. Reports* Vol. 3, art. N 2220, 2013.
2. J. V. Jäger, A. V. Scherbakov, B. A. Glavin, A. S. Salasyuk, R. P. Campion, A. W. Rushforth, D. R. Yakovlev, A. V. Akimov, and M. Bayer "Resonant driving of magnetization precession in a ferromagnetic layer by coherent monochromatic phonons", *Phys. Rev. B*, Vol. 92, No.2, art. n. 020404, 2015.

Microscopic Electron-Phonon Scattering Dynamics In a Model Ferromagnet

S. Vollmar, K. Leckron, and H. C. Schneider*
Physics Department and Research Center OPTIMAS, University of Kaiserslautern, Germany
*corresponding author: hcsch@physik.uni-kl.de

Abstract-We describe our recent work on electron-phonon scattering in spin-degenerate and ferromagnetic model systems. For the latter, we employ a ferromagnetic Rashba model, in which the exchange interaction and spin-orbit coupling both contribute to the spin splitting. We show that a novel torque matrix element controls the spin-flip that is achievable in a system without precession around effective internal spin-orbit fields. For a combined magnetic and spin-orbit splitting, such precessional dynamics play an important role.

In 3d-ferromagnets, excitation by an ultrashort linearly polarized pulse can reduce the magnetization, as observed by the magneto-optical Kerr effect or X-ray magnetic circular dichroism, by 50% and more, even reaching a complete "quenching" of the magnetization for higher fluences. The spin angular momentum, as determined experimentally, is thus dramatically reduced. Despite the magnitude of this effect, no consensus has been reached as to the microscopic mechanism responsible for it on ultrafast timescales. A similar question has arisen more recently in the context of deterministic optical switching, where there is a contribution from the polarized optical field.

One possible microscopic mechanism for electronic dynamics that leads to a change in magnetization is electronic spin-flip scattering. In the context of demagnetization dynamics, spin-flip scattering is often called Elliott-Yafet scattering after a similar mechanism, which has been identified for semiconductors in the 1960s: In it, electronic spin flips occur due to scattering events with a phonon that connect initial and final states, which have different spin mixtures due to the momentum-dependent spin-orbit coupling.

Studies by Oppeneer and coworkers [1] and by us [2] of electronic density dynamics in ab-initio band-structures of ferromagnetic metals have shown that spin-flip electron scattering with phonons is rather inefficient and cannot explain the experimentally observed ultrafast magnetization dynamics. If one uses a model that includes a time-dependent (mean-field) exchange splitting, the effect of spin-flip scattering of electrons with phonons and other electrons can be amplified to reach the magnitudes observed in experiments [3], but the physics of how the spin angular momentum is "lost" in scattering transitions is hidden in the interaction matrix elements, because in these matrix elements the effects of the interaction and the spin-orbit induced spin mixing cannot be separated.

In this contribution, we describe our recent work on how to correctly describe electronic spin dynamics with spin-orbit coupling and electron-phonon interaction at the level of reduced spin-density matrices. Using this approach, we have reexamined electronic spin dynamics for two cases: (1) the original Elliott-Yafet problem where electronic spin flips occur in a pair of spin-mixed *degenerate* bands [4,5], and (2) a ferromagnetic model system, which contains the contributions of a ferromagnetic exchange "interaction" (at the mean-field level) and spin-orbit coupling.

We show explicitly how spin dynamics due to electron phonon scattering occurs in these cases. For case (1), the spin-dependent part of the electron-phonon interaction plays the most important role, which can be quantified using a torque matrix element. This approach allows us to generalize the original Elliott-Yafet spin relaxation time, so that it also works for strong spin mixing. For case (2), the *spin diagonal* electron-phonon interaction matrix element is mainly responsible for the spin dynamics. This case bears some resemblance to the Dyakonov-Perel mechanism, and we show in microscopic detail how spin dephasing contributes to the magnetization dynamics in the ferromagnetic Rashba model.

We acknowledge support from the DFG through the SFB/TRR 173 "Spin+X". Svenja Vollmar was supported by the Excellence Initiative (DFG/GSC 266).

REFERENCES

1. Carva, K., M. Battiato and P. M. Oppeneer, "Ab initio investigation of the Elliott-Yafet electron-phonon mechanism in laser-induced ultrafast demagnetization," *Physical Review Letters*, Vol. 107, No. 20, 207201, 2011.
2. Essert, S. and H. C. Schneider, "Electron-phonon scattering dynamics in ferromagnetic metals and their influence on ultrafast demagnetization processes," *Physical Review B*, Vol. 84, No. 22, 224405, 2011.
3. Müller, B. Y., A. Baral, S. Vollmar, M. Cinchetti, M. Aeschlimann, H. C. Schneider and B. Rethfeld, "Feedback effect during ultrafast demagnetization dynamics in ferromagnets," *Physical Review Letters*, Vol. 111, No. 16, 167204, 2013.
4. Baral A., S. Vollmar and H. C. Schneider, "Re-examination of the Elliott–Yafet spin-relaxation mechanism," *New Journal of Physics*, Vol. 18, No. 2, 023012, 2016.
5. Vollmar, S., D. J. Hilton and H. C. Schneider, "Generalized Elliott-Yafet spin-relaxation time for arbitrary spin mixing," *arXiv:1612.06249*, to be published 2017.

Ultrafast Magnetization Switching of Ferrimagnetic Oxides

I. Radu[1, *], R. Abrudan[2], M. Hennecke[1], D. Mishra[1], C. von Korff Schmissing[1], T.A. Ostler[3], O. Chubykalo-Fesenko[4], A.M. Kalashnikova[5], R. V. Pisarev[5] and S. Eisebitt[1]

[1]Max-Born Institute Berlin, Max-Born Str. 2A, 12489 Berlin, Germany

[2]Helmholtz-Zentrum Berlin, BESSY II, Berlin, Albert-Einstein-Str. 16, 12489 Berlin, Germany

[3]Département de Physique, Universitè de Liége (B5), B-4000 Liége, Belgium

[4]Instituto de Ciencia de Materiales de Madrid, CSIC, Cantoblanco, 28049 Madrid, Spain

[5]Ioffe Physical Technical Institute, Russian Academy of Sciences, 194021 St. Petersburg, Russia

[*]corresponding author: radu@mbi-berlin.de

Abstract- We report on the latest developments in our studies on ultrafast magnetism, which reveal very intriguing spin switching phenomena by employing a novel experimental approach combining the femtosecond laser excitation with an ultrafast, element-specific X-ray probing of spins. In particular, by investigating the laser-driven magnetization dynamics in *ferrimagnetic iron garnets*, we observe an ultrafast magnetization switching process occurring over an extremely long lived (>>100 ps) transient ferromagnetic-like state. These findings challenge the current understanding of laser-driven magnetization switching phenomena.

Using light to control the magnetic order parameter on ultimate time and length scales is a core research activity of modern magnetism [1]. Of particular interest for both fundamental and applied science is the use of femtosecond (fs) laser pulses to fully switch the magnetization orientation of a spin ensemble on ultrashort time scales [2, 3].

Recent time-resolved XMCD investigations of ferrimagnetic GdFeCo alloys revealed the existence of a transient ferromagnetic-like state mediating the ultrafast magnetization switching of antiferromagnetically coupled Fe and Gd spins [2]. In a subsequent study, this transient ferromagnetic state was shown to drive a novel magnetization reversal mechanism where spin switching is purely thermal, *i.e.* without using any magnetic field [3]. Although groundbreaking, these experiments leave open several intriguing questions on the microscopic driving mechanism of the ultrafast magnetization reversal in the ferrimagnetic compounds. For instance, how does the symmetry and strength of the exchange interaction affect the magnetization switching process? What is the influence of the magnetization damping factor on the duration of the highly non-equilibrium transient ferromagnetic state and implicitly on the ultrafast spin switching? What is the role of the electronic structure of the host material, *i.e.* going for instance from a metallic to an insulating host?

Here, we report on a combined experimental and theoretical study that addresses these questions by investigating *insulating ferrimagnetic iron garnets* $Ho_3Fe_5O_{12}$ and $Gd_3Fe_5O_{12}$ in the close proximity of their magnetization compensation temperatures, T_{comp}=127 K and 291 K, respectively. Using advanced experimental (femtosecond optical excitation combined with ultrafast X-ray measurements) and computational (atomistic spin simulations) approaches, we reveal that femtosecond laser-induced heating of an insulating iron garnet leads to:

1) an ultrafast magnetization switching process over an extremely long lived (hundreds of picoseconds) transient ferromagnetic-like state involving all the constituent magnetic elements of the sample

2) very distinct dynamics of the antiferromagnetically coupled Fe^{3+} (otherwise electronically identical) ions that generates a time lag of about 100 ps between their transient evolution

Moreover, in iron garnets the ferrimagnetic coupling between the iron species (*i.e.* Fe^{3+} ions with tetrahedral and octahedral coordination) and between Fe^{3+} ions, and the rare earth Ho^{3+} and Gd^{3+} sublattices is mediated by super-exchange interaction via the oxygen anions. Therefore, by monitoring the laser-driven spin and electron dynamics in an element- and site-specific manner we obtained, for the very first time, a *direct view on the dynamics of the exchange interaction* itself during the magnetization-switching event.

These highly unexpected and counterintuitive insights challenge the current understanding of ultrafast, laser-driven spin reversal and open new ways for manipulating spins in magnetic solids. Possible implications for the magnetic switching phenomena in ferrimagnetic alloys and heterostructures will be discussed.

Acknowledgements: I.R. and S.E. acknowledge funding from German Ministry for Education and Research (BMBF) through project 05K16BCA Femto-THz-X. T.A.O acknowledges the Marie Curie incoming BeIPD-COFUND fellowship program at the Université de Liége.

REFERENCES

1. Kirilyuk, A., Kimel, A.V. and Rasing, Th. "Ultrafast optical manipulation of magnetic order," *Rev. Mod. Phys.* 82, 2731 (2010).
2. Radu, I. et al., "Transient ferromagnetic-like state mediating ultrafast reversal of antiferromagnetically coupled spins," *Nature* 472, 205–208 (2011).
3. Ostler, T. A. et al., "Ultrafast heating as a sufficient stimulus for magnetization reversal in a ferrimagnet," *Nature Communications* 3, 666 (2012).

Nanophotonics and plasmonics for information applications

Linear crossing dispersion in a multilayered structure with two kinds of single-negative metamaterials

Zhiwei Guo, Feng Wu, Haitao Jiang*, and Hong Chen
MOE Key Laboratory of Advanced Micro-Structured Materials, School of Physics Science and Engineering, Tongji University, Shanghai, 200092, China
*corresponding author: jiang-haitao@tongji.edu.cn

Abstract-We reveal a linear crossing dispersion in a multilayered structure containing two kinds of single-negative metamaterials. Distinct from the elliptical dispersion or the hyperbolic dispersion, linear crossing dispersion can bring about a variety of new phenomena such as beam splitting and negative-refraction imaging.

Topological transition of dispersion from a closed elliptic curve to an open hyperbolic curve can bring about useful physical effects such as the enhancement of the spontaneous emission [1], negative refraction [2], and collimation [3-4]. In fact, the topological transition can also occur when a hyperbolic curve changes from a dielectric-type hyperbolic curve (Fig. 1(a)) to a metal-type hyperbolic curve (Fig. 1(c)). At the transition point, the hyperbolic dispersion becomes a linear crossing dispersion, as is shown in Fig. 1(b). This linear crossing dispersion is very interesting because it has only two (positive and negative) slopes. In this work, we realize the linear crossing dispersion in a multilayered structure composed of ε-negative (ENG) metamaterial ($\varepsilon < 0, \mu > 0$) and μ-negative (MNG) metamaterial ($\varepsilon > 0, \mu < 0$) (i.e. two kinds of single-negative metamaterials). The thickness of each layer is deep subwavelength, which ensures the validity of effect-medium description. Owning to the linear crossing contour, the structure can split the normal incident light along two fixed directions (Fig. 2(a)). Moreover, combining two multilayered structures in which the growth direction of layer is perpendicular to each other, one can realize the negative-refraction imaging, as is shown in Fig. 2(b).

Figures:

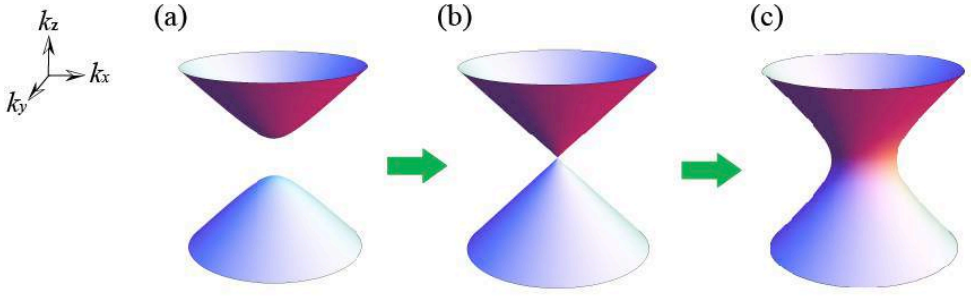

Fig. 1 The topological transition from a dielectric-type hyperbolic curve (Fig. 1(a)) to a metal-type hyperbolic curve (Fig. 1(c)). At the transition point, the hyperbolic dispersion becomes a linear crossing dispersion (Fig. 1(b)).

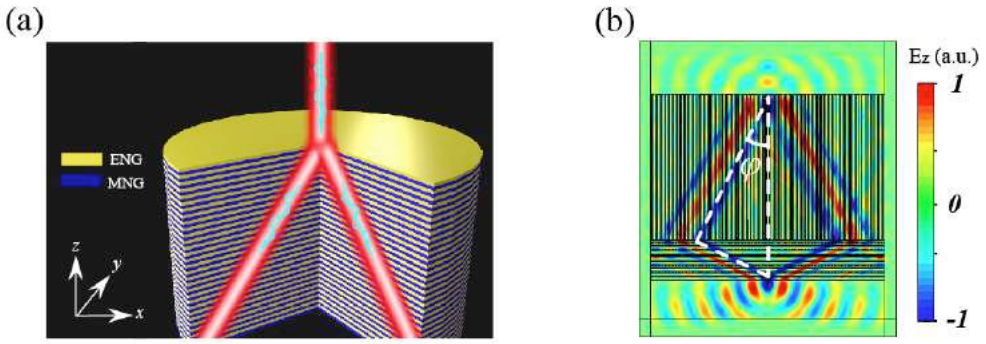

Fig. 2 (a) The schematic diagram of the beam splitting when a light is normally incident on the ENG/MNG multilayer structure. (b) The negative-refraction imaging in a composite multilayered structure.

Acknowledgements, This work is supported by the National Basic Research Program of China (No. 2011CB922001), the NSFC (No. 11474220 and No. 11234010).

REFERENCES

1. Krishnamoorthy, H. N. S., Z. Jacob, E. Narimanov, I. Kretzschmar and V. M. Menon, "Topological transitions in metamaterials," Science Vol. 336, No. 6079, 205–209, 2012.
2. Fang, A., T. Koschny and C. M. Soukoulis, "Optical anisotropic metamaterials: Negative refraction and focusing," Physical Review B Vol. 79, No. 24, 245127, 2009.
3. Yu, K., Z. W. Guo, H. T. Jiang and H. Chen, "Loss-induced topological transition of dispersion in metamaterials," Journal of Applied Physics Vol. 119, No. 20, 203102, 2016.
4. Jiang, H. T., W. W. Liu, K. Yu, K. Fang, Y. Sun, Y. H. Li and H. Chen, "Experimental verification of loss-induced field enhancement and collimation in anisotropic μ-near-zero metamaterials," Physical Review B Vol. 91, No.4 , 045302, 2015.

Cavity quantum electrodynamics based on gap surface plasmons

Juanjuan Ren[1], Ying Gu[1, 2,*], He Hao[1], Dongxing Zhao[1], Fan Zhang[1], Tiancai Zhang[2, 3], Qihuang Gong[1, 2]

[1] State Key Laboratory for Mesoscopic Physics, Collaborative Innovation Center of Quantum Matter, Department of Physics, Peking University, Beijing 100871, China

[2] Collaborative Innovation Center of Extreme Optics, Shanxi University, Taiyuan, Shanxi 030006, China

[3] State Key Laboratory of Quantum Optics and Quantum Optics Devices, Institute of Opto-Electronics, Shanxi University, Taiyuan 030006, China

[*]corresponding author: ygu@pku.edu.cn

Abstract Plasmon nanostructures with ultrasmall mode volume can enhance light-matter interactions in nanostructure based cavity quantum electrodynamics. In the strong coupling regime, taking the evanescent mode provided by single mode nanowire as electromagnetic vacuum, we theoretically demonstrate the enhanced reversible photon-exciton interaction and fluorescence collection. In the weak coupling regime, we theoretically investigate the efficient photon emission of single emitter with metallic nanorod-coupled nanofilm structures. Furthermore, utilizing the liquid crystals, high-contrast switching of spontaneous emission is obtained.

Electromagnetic vacuum engineering plays a fundamental role in controlling light-matter interaction in quantum optics, cavity quantum electrodynamics (CQED), and quantum information devices. In previous studies, evanescent optical modes are thought of as cavity modes rather than providing an electromagnetic vacuum environment that the cavity resides in [1]. Taking the evanescent vacuum provided by a metallic or dielectric single-mode nanowire as the electromagnetic environment, in which a resonant Ag nanorod (AgNR) is embeded, we theoretically demonstrated the enhanced photon-exciton coupling and the increased fluorescence collection efficiency through the careful optical mode design [2]. The AgNR is too small to effect the evanescent optical mode of the nanowire, thus the evanescent mode is taken as the electromagnetic background and the AgNR as plasmon nanocavity, forming the nano-CQED system in evanescent vacuum (Fig. 1(a)). Due to the exponential decay of the evanescent wave (Fig. 1(b)), more localized field at the nanogap is obtained with nanowire (Fig. 1(c,d)). Naturally, the coupling coefficient g0 at the nanogap with nanowire is 4.2 times larger than that without nanowire (Fig. 1(e)). Rabi splitting is signature of strong interaction (Fig.1 (f)). Moreover, 47% of the emitted photons can be collected via the evanescent wave of the nanowire. This CQED in subwavelength-confined quantum vacuum holds promise for exploring the fundamental physics as well as the applications related to on-chip quantum information and scalable quantum networks.

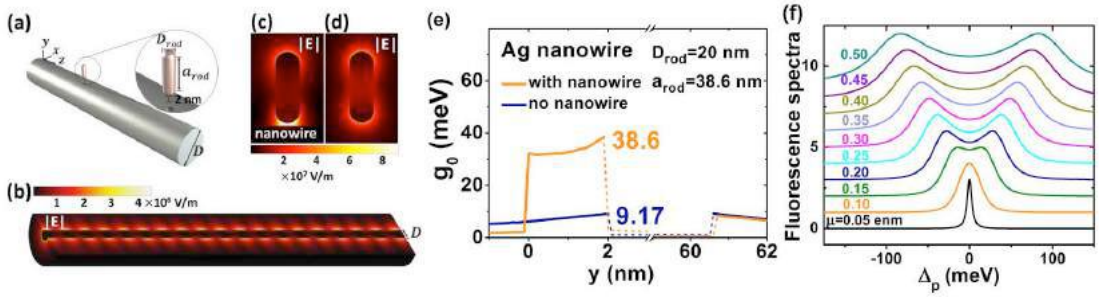

Fig. 1 (a) Schematic diagram of nano-CQED system in evanescent vacuum. (b) Simulation of evanescent electromagnetic mode for Ag nanowire. Electric field distributions of longitudinal modes (c) with nanowire and (d) without nanowire. (e) The coupling coefficient along the central axis of nanorod for μ=0.2 enm. (f) Normalized spontaneous emission spectra for different dipole moments.

The study of single photon emission is of fundamental interest for research in CQED, single photon sources, and cavity-basedlasing processes. Here, combining the advantages of ultrahigh photon emission rates achievable in the gap surface plasmon polaritons with high extraction decay rates into low-loss nanofibers, we theoretically investigated the efficient photon emission of a single emitter and one-dimensional nanoscale guiding of emitted photons in metallic nanorod-coupled nanofilm structures coupled to dielectric nanofibers [3]. Due to the ultra-strong hot spots of gap plasmons, the total decay rates and surface plasmon polariton channel decay rates are orders of magnitude larger than those characteristic of metallic nanofilms alone. Moreover, propagating single photons with decay rates of $290\gamma_0$–$770\gamma_0$ are guided into the phase-matched low-loss nanofibers. The proposed mechanism promises to have an important impact on metal-based optical cavities, on-chip bright single photon sources and plasmon-based nanolasers.

Furthermore, combining the gap surface plasmon with the liquid crystals and low index materials, we theoretically demonstrated both the ultrahigh spontaneous emission rate and a high-contrast switching of spontaneous emission rate [4]. With varying the optical axis of the liquid crystals, total spontaneous emission rate can be switched from $103\gamma_0$ to $8750\gamma_0$ with the contrast ratio of 85, among which the spontaneous emission rate of surface plasmon part is from $42\gamma_0$ to $3726\gamma_0$ with the ratio of 88. The proposed mechanism offers high-contrast, active switching of the spontaneous emission rate, which has potential application for on-chip quantum devices.

Acknowledgements This work was supported by the National Key Basic Research Program under Grant No. 2013CB328700, and by the National Natural Science Foundation of China under Grant Nos. 11525414, 11374025, and 91221304.

REFERENCES

1. Tame M. S., McEnery K. R., Ozdemir S. K., Lee J., Maier S. A. and Kim M. S., "Quantum plasmonics," Nat. Phys., Vol. 9, 329-340, 2013.
2. Ren J., Gu Y., Zhao D., Zhang F., Zhang T. and Gong Q., "Evanescent-vacuum-enhanced photon-exciton coupling and fluorescence collection," accepted by Phys. Rev. Lett.
3. Lian H., Gu Y., Ren J., Zhang F., Wang L. and Gong Q., "Efficient Single Photon Emission and Collection Based on Excitation," Phys. Rev. Lett., Vol. 114, 193002, 2015.
4. Hao H., Ren J., Lu G., Khoo I. C., Gong Q and Gu Y., "High-contrast switching of spontaneous emission enabled by tunable gap surface plasmon," in preparation.

Fully controllable volumetric generation of vortices based on dielectric metasurface

Lingling Huang[1], Xu Song[1], Bernhard Reineke[2], Tianyou Li[1], Xiaowei Li[3], Juan Liu[1], Shuang Zhang[4], Yongtian Wang[1], and Thomas Zentgraf[2]

[1]School of Optoelectronics, Beijing Institute of Technology, Beijing, 100081, China

[2]Department of Physics, University of Paderborn, Warburger Straße 100, D-33098 Paderborn, Germany

[3]Laser Micro/Nano-Fabrication Laboratory, School of Mechanical Engineering, Beijing Institute of Technology, Beijing 100081, China

[4]School of Physics & Astronomy, University of Birmingham, Birmingham, B15 2TT, UK

[*]corresponding author: huanglingling@bit.edu.cn

Abstract- The generation of optical vortex beams, which carry orbital angular momentum, has emerged as a vital approach to applications ranging from high-capacity optical communication to parallel laser fabrication. Here, we propose and experimentally demonstrate volumetric three-dimensional vortex array with space variant topological charges based on dielectric geometric metasurface. By employing the concepts of Dammann vortex gratings and spiral Dammann zone plates, 3D optical vortex arrays with micrometer spatial separation is achieved from visible to near-infrared wavelengths. Importantly, we show that the topological charge distribution can be spatially variant and fully controlled by the design.

Flat optics have attracted great interest for being a promising alternative to control light waves by implementing ultrathin planar elements, namely metasurfaces, with spatially varying phase response instead of relying on phase accumulation along optical paths [1-2]. Metasurfaces have shown the ability to overcome the limitations of conventional optics with a wide range of applications in wave front engineering, information processing, and spin controlled photonics. An important application for metasurfaces is the control and modification of optical beam profiles, and in particular the generation of orbital angular momentum (OAM) for light, which is pivotal in terms of both fundamental physics and practical applications [3-4]. The optical vortex beam has received increasing attention for its various applications, ranging from optical manipulation of microscopic particles and biological cells to free-space optical communication system.

Here, we propose and experimentally demonstrate the generation of a volumetric three-dimensional vortices with independently controllable topological charges that is based on a single ultrathin dielectric metasurfaces [5]. We employ the concepts of Dammann vortex grating (DVG) and spiral Dammann zone plate (SDZP) together with a lens factor to generate the metasurface phase profile with sub-wavelength pixel size. Figure 1 illustrates the generation and reconstruction procedure of such a 3D vortex array. The design technique allows for a well-defined, quantized, and fully controllable spatially variant topological charge distribution.

Such metasurface-based vortex generators can achieve truely 3D vortex arrays over a large volume with high uniformity. Furthermore, the geometric nature of the phase profile (based on a Pancharatnam-Berry-Phase)

enables the reconstruction of the vortices over a broad spectral bandwidth in the near infrared and visible wavelength range. Importantly, the metasurface can be designed to possess the remarkable capability of vortex beam detection. The flexibility of our approach enables on-chip parallel processing to 3D micro- and nano-fabrication, and offers the possibility of ultrahigh-capacity and miniaturized nanophotonic devices for harnessing angular momentum multiplexing and mode sorting.

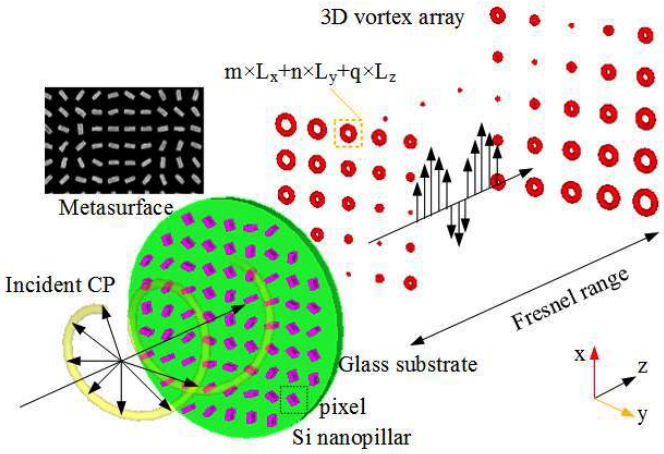

Figure 1. Illustration of the 3D vortex array based on metasurface and the reproducing procedure.

REFERENCES

1. Yu, N. and Capasso F.“Flat optics with designer metasurfaces”, Nat. Mater. 13, 3839 (2014).
2. Meinzer, N., Barnes, W. L., Hooper, L. R.,“Plasmonic meta-atoms and metasurfaces”, Nat. Photon. 2014, 8, 889-898.
3. Padgett M. and Bowman R., “Tweezers with a twist”, Nat. Photon. 2011, 5, 343-348.
4. Wang, J., Yang, J., Fazal, I. M., Ahmed, N., Yan, Y., Huang, H., Ren, Y., Yue, Y., Dolinar, S., Tur, M. and Willner, A. E. “Terabit free-space data transmission employing orbital angular momentum multiplexing”, Nat. Photon. 2012, 6, 488–496.
5. Huang,L., Song,X., Reineke, B., Li, T., Li, X., Liu, J., Zhang,S., Wang,Y., Zentgraf, T. “Volumetric generation of optical vortices with metasurfaces”, ACS Photon. 2017, DOI:10.1021/acsphotonics.6b00808.

On-chip Integrated Free-electron light source

Fang LIU[1*], Long XIAO[1], and Yidong HUANG[1]**

[1] Department of Electronic Engineering, Tsinghua National Laboratory for Information Science and Technology, Tsinghua University, Beijing 100084, China.

[*] liu_fang@tsinghua.edu.cn; [**] yidonghuang@tsinghua.edu.cn

Abstract- To generate Cherenkov radiation (CR) in natural medium, the electron energy threshold is higher than hundreds of keV. Even though various approaches were adopted, the high-energy electrons as high as tens of keV is still required in experiment. We demonstrate in hyperbolic metamaterial that the electron velocity threshold for CR is eliminated, and meanwhile, with this threshold-less CR, the first on-chip integrated free electron light source was realized.

To generate Cherenkov radiation (CR)[1] in natural medium, the electron energy threshold is higher than hundreds of keV[2]. Even though various approaches were adopted, the high-energy electrons as high as tens of keV[3] is still required in experiment. Here we proposed to eliminate the threshold of electron energy to generate CR with the help of hyperbolic metamaterial (HMM). The analytical and simulation results indicate that, even though electron energy is lower than 0.1keV, the CR could be obtained in HMM in a visible and near-infrared frequency region. Further, the on-chip integrated threshold-less CR source, consisted with a planar electron emitter, Au-SiO_2 multilayers HMM, and periodic metal nano-slits, has been realized. It is demonstrated that, with low-energy electrons (0.25-1.4keV), the CR is generated covering λ_0=500~900nm. The electron energy generating CR experimentally is two~three orders of magnitude lower than that in natural media and artificial structures. As we know, this is the first on-chip integrated free electron light source benefiting from the threshold-less CR. Although less than 1% of the light energy could be coupled to free space, the total output light power still reaches 200nW, which is two orders of magnitude higher than free electron light source by using other nanostructures. This work provides a way to realize threshold-less CR, opens up the possibility of exploring high performance on-chip integrated free electron light source and optoelectronic devices, and offers the platform to study the interaction of flying electrons with nanostructures on chip.

Acknowledgements, This work was supported by the National Basic Research Programs of China (973 Program) under Contracts No. 2013CBA01704, the National Natural Science Foundation of China (NSFC-61575104 and 61621064).

REFERENCES

1. García de Abajo, F. J. Optical excitations in electron microscopy. Rev. Mod. Phys. 82, 209–275 (2010).
2. Bolotovskii, B. M. Vavilov – Cherenkov radiation: its discovery and application. Phys.-Uspekhi 52, 1099–1110 (2009).
3. Adamo, G. et al. Light well: a tunable free-electron light source on a chip. Phys. Rev. Lett. 103, 113901 (2009).

Strong couplings among triple Fano resonances in a 3D metamaterial

Jiafang Li,* Zhiguang Liu, and Zhi-Yuan Li
Laboratory of Optical Physics, Institute of Physics, Chinese Academy of Sciences, Beijing, China, 100190
*Email: jiafangli@aphy.iphy.ac.cn

Abstract- We report our recent experimental and theoretical works on strong couplings among triple Fano resonances in a 3D metamaterial, which is formed by integrating vertical asymmetric split-ring-resonators (aSRRs) along a planar metallic hole array with extraordinary optical transmission (EOT) built by means of homemade focused-ion-beam (FIB) manipulations.

In this talk, we report our recent studies on strongly coupled triple Fano resonances in a 3D metamaterial (MM). The 3D MMs are formed by integrating vertical asymmetric split-ring-resonators (aSRRs) along a planar metallic hole array with extraordinary optical transmission (EOT) built by means of homemade focused-ion-beam (FIB) folding technique. In such a configuration, the plasmonic system stably supports triple Fano resonance states. More importantly, the induced Fano resonances are widely tunable and strong coupling among triple Fano resonances occurs during the tuning process. These 3D MMs with significant and robust Fano resonances exhibit an extremely high sensitivity to refractive index of the environments in the near infrared wavelength region.

REFERENCES

1. Cui, A.,[#] Z. Liu,[#] J. Li,[#] T. H. Shen, X. Xia, Z.-Y. Li, Z. Gong, H. Li, B. Wang, J. Li, H. Yang, W. Li,* and C. Gu,* "Directly patterned substrate-free plasmonic 'nanograter' structures with unusual Fano resonances," *Light-Sci. Appl.,* No. 4, e308, 2015.
2. Liu, Z.,[#] Z. Liu,[#] J. Li,* W. Li, J. Li, C. Gu, and Z.-Y. Li, "3D conductive coupling for robust generation of prominent Fano resonances in metamaterials", *Sci Rep-Uk,* No. 6, 27817, (2016).
3. Liu, Z.,[#] J. Li,*[#], Z. Liu,[#] W. Li, J. Li, C. Gu, and Z.-Y. Li, "Fano resonance Rabi splitting of surface plasmons", *submitted*, 2017.

Modeling localized surface plasmon resonance with propagative surface plasmon polaritons in optical nanogap antennas

Haitao Liu[1*], Hongwei Jia[1,2], Fan Yang[3], and Ying Zhong[4]

[1]Key Laboratory of Optical Information Science and Technology, Ministry of Education, Institute of Modern Optics, Nankai University, Tianjin 300350, China

[2]SZU-NUS Collaborative Innovation Center for Optoelectronic Science & Technology, Key Laboratory of Optoelectronic Devices and Systems of Ministry of Education and Guangdong Province, Collage of Optoelectronic Engineering, Shenzhen University, Shenzhen 518060, China.

[3]State Key Laboratory of Low Dimensional Quantum Physics, Department of Physics, Tsinghua University, Beijing 100084, China

[4]State Key Laboratory of Precision Measuring Technology and Instruments, Tianjin University, Tianjin 300072, China

[*]corresponding author: liuht@nankai.edu.cn

Abstract-The resonance behavior of optical antennas is commonly attributed to the excitation of a localized surface plasmon resonance (LSPR), which can be theoretically defined as the quasi normal mode (QNM). To clarify the physical origin of the LSPR, we build up an analytical model of the LSPR by considering a multiple scattering process of propagative surface plasmon polaritons (SPPs) on the antenna arms, which establishes explicit relations between the concepts of the LSPR and the propagative SPP.

Plasmonic optical nanogap antennas can efficiently accelerate the radiation of emitters such as molecules or quantum dots in the nanogap, or reciprocally, allow giant enhancement of near field in the nanogap under far-field illumination. They can be widely used in nonlinear optics, white light super-continuum generation, single-emitter fluorescence enhancement and surface enhanced Raman scattering [1]. The resonance enhancement is commonly attributed to an excitation of LSPR as the illumination frequency matches the eigen-frequency of the LSPR [2]. Theoretically, the LSPR can be defined as the QNM by treating the metallic nano-antenna as an open cavity [3].

To propose an insightful and effective theoretical treatment of nanogap antennas, here we build up an SPP Fabry-Perot model for the QNM of nanogap antennas by considering a multiple scattering process of SPPs on the antenna arms [4] [see Figs. 1(a)-(c)]. The existence of slightly-damped QNMs that cause the resonance nature of nanogap antennas is demonstrated with the model by seeking the solutions of two transcendental equations. The model sets a solid electromagnetic foundation for the intuitive picture that the LSPR (i.e. QNM) of the antenna actually arises from the Fabry-Perot resonance of SPPs at the complex eigen-frequency. With a few assumptions on the frequency-dependence of the field and with the use of complex pole expansion of meromorphic functions (Mittag-Leffler theorem), the field of the nanogap antenna excited by a nearby point emitter can be expanded upon the basis of QNMs, thus providing an analytical description of the frequency response of the field [Figs. 1(d)-(e)]. For calculating the Purcell factor, the model provides a new analytical expression of the mode volume of QNM in terms of the SPP scattering coefficients, which avoids the difficulty

in calculating the mode volume caused by the divergence of the QNM field at infinity that is overcome recently [3]. The present model establishes explicit relations between the concepts of the LSPR and the propagative SPP, and integrates the advantages of the Fabry-Perot and QNM formalisms in understanding the resonance of nanogap antennas, which may inspire new design strategies of antenna devices with different geometries.

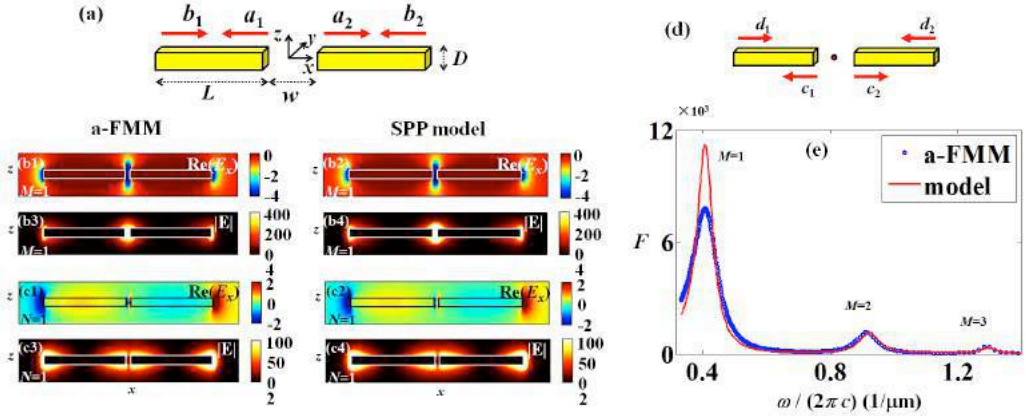

Figure 1 (a) Sketch of the SPP model for the QNM of the nanogap antenna, which is composed of two gold nano-wire arms of length L (with a square cross section of side length D=40nm) separated by a nano-gap (gap width w=30nm). a_1, a_2, b_1 and b_2 denote the complex amplitude coefficients of SPPs at the complex eigen-frequency of QNMs. (b)-(c) Field distributions of the first order symmetric and anti-symmetric QNMs. (d) Nanogap antenna excited by an x-polarized electric point source located at the center of the nanogap. (e) Spontaneous emission rate (normalized by the value in air) of the source versus illumination frequency ω. The results in (b), (c) and (e) are obtained with the full-wave aperiodic Fourier modal method (a-FMM) and the SPP model for L= 0.6μm.

Acknowledgements This work is financially supported by the National Key Basic Research Program of China (973 Program) under Grant No. 2013CB328701, and by the Natural Science Foundation of China under Grant Nos. 61322508, 11504270.

REFERENCES

1. Novotny, L. and N. Van Hulst, "Antennas for light," *Nat. Photonics*, Vol. 5, 83-90, 2011.
2. Esteban, R., G. Aguirregabiria, A. G. Borisov, Y. M. Wang, P. Nordlander, G. W. Bryant and J. Aizpurua, "The morphology of narrow gaps modifies the plasmonic response," *ACS Photonics*, Vol. 2, 295-305, 2015.
3. Sauvan, C., J. P. Hugonin, I. S. Maksymov and P. Lalanne, "Theory of the spontaneous optical emission of nanosize photonic and plasmon resonators," *Phys. Rev. Lett.*, Vol. 110, 237401, 2013.
4. Jia, H., F. Yang, Y. Zhong and H. Liu, "Understanding localized surface plasmon resonance with propagative surface plasmon polaritons in optical nanogap antennas," *Photon. Res.*, Vol. 4, 293-305, 2016.

Resonant cavity modes in plasmonic nanorod and nanotube metamaterials

Junxi Zhang[1, 2], Haojie Song[1], Junfeng Wang[1], Cheng Zhang[3], Pei Wang[3], Lide Zhang[1], Yuri S. Kivshar[4], and Lin Zhang[2]

[1]Key Laboratory of Materials Physics and Anhui Key Laboratory of Nanomaterials and Nanostructures, Institute of Solid State Physics, Chinese Academy of Sciences, Hefei 230031, P. R. China

[2]Aston Institute of Photonic Technologies (AIPT), School of Engineering & Applied Science, Aston University, Birmingham B4 7ET, UK

[3]Department of Optics and Optical Engineering, University of Science and Technology of China, Hefei 230026, P. R. China

[4]Nonlinear Physics Centre, Research School of Physics and Engineering, Australian National University, Canberra ACT 2601, Australia

[*]corresponding author: jxzhang@issp.ac.cn

Abstract-Plasmonic cavity resonators are designed by noble metal nanorod or nanotube metamaterials. A hybrid mode appears due to near-field coupling between plasmonic silver nanorod metamaterials and gold-film substrate. Additionally, T–L hybrid plasmonic modes resulted from the near-field coupling between transversal and longitudinal resonance modes with different order harmonics are found in gold nanotube metamaterials, performing electric fields partially localized into pores and at two ends based on extraordinary optical transmission coupling effect through inner-nanochannels of the gold nanotubes.

Plasmonic resonant cavities are capable of confining light at the nanometer scale due to both enhanced local electromagnetic fields and lower mode volumes, which exhibit promising applications in sources[1], sensing[2], enhanced nonlinear effects[3] etc. It has been noted that the conventional metal nanostrips as cavities with single metal-dielectric interfaces have large Ohmic losses. Whereas enhancement of plasmonic near-field coupling by designing two or multi metal-dielectric interfaces can decrease the Ohmic losses[4-6].

We have studied the near-field coupling of plasmonic nanorod metamaterials consisting of silver nanorod arrays embedded in anodic aluminum oxide (AAO) membranes[5]. Reflectance measurements reveal the

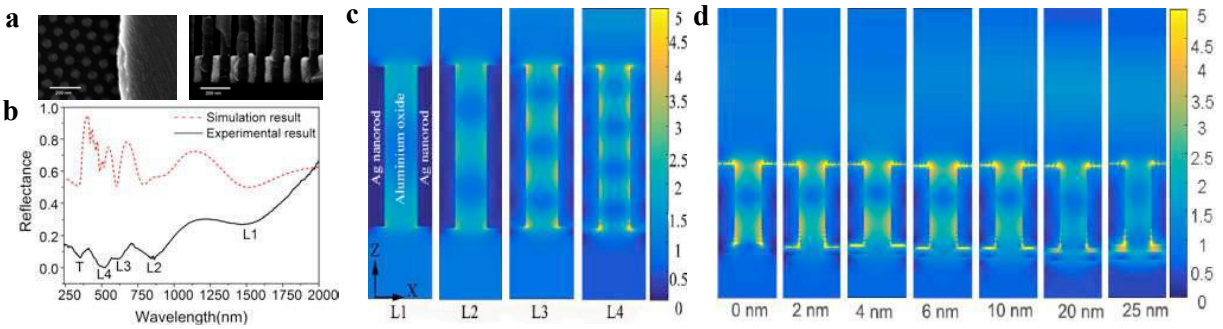

Figure 1. (a) SEM image of silver nanorod metamaterial, (b,c) Reflectance spectra and electric field distributions of the 420 nm long metamaterial, (c) Electric field distributions with the gaps between nanorods and substrate.

existence of multiple resonance modes of the nanorod metamaterials (Fig. 1b). Furthermore, FDTD numerical simulations display that the electromagnetic fields of the higher-order longitudinal resonance modes are focused at the interface between silver nanorods and aluminum oxide, and the electric fields at the interface form standing waves, which indicates that the silver nanorod metamaterials can work as plasmonic cavity resonators (Fig. 1c). An open plasmonic nanocavity exhibits sharp half-wave harmonics with the symmetric distribution of electromagnetic field in the interior of the cavities. A new hybrid mode resulting from the coupling of silver nanorod metamaterials with the gold substrate, and the resonance of the coupling mode gradually become weaker as the gap between the silver nanorod arrays and the gold film substrate increases (Fig. 1d).

On the other hand, plasmonic resonators based on a metamaterial consisting of periodic arrays of gold nanotubes embedded into AAO has been presented[6], and strong confinement of local fields with low losses is demonstrated. Higher-order resonance modes of surface plasmons localized in the gold nanotubes when the nanotube length exceeds some critical values are observed. The FDTD numerical simulations indicate that, the electric fields are associated with some higher-order longitudinal modes for the long nanotubes and some lower-order longitudinal modes for the short nanotubes or the nanotubes with thin walls, odd and even harmonics with standing-wave modes are tuned by the nanotube length. We find a new T-L hybrid plasmonic resonant cavity modes in the gold nanotube metamaterials resulting from the near-field coupling of both transversal and longitudinal modes (Fig. 2 b, c and d), furthermore, the T-L hybrid cavity modes dependent on the wall thickness and the length of the nanotubes, perform electric fields partially localized into pores and at two ends based on extraordinary optical transmission coupling effect through inner-nanochannels.

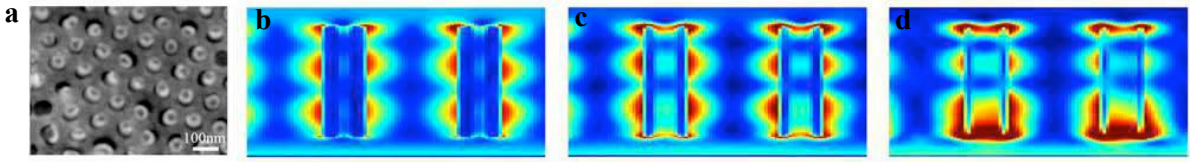

Figure 2. (a) SEM image of gold nanotube metamaterial, (b-d) Electric field distributions of the longitudinal resonance modes of the 5th order harmonics for the 17 nm, 10 nm and the T-L hybrid plasmonic mode for 5 nm thick nanotube walls, respectively.

Acknowledgements, this work was supported by the Seventh Framework Program of the European Union for Research through Marie Curie International Incoming Fellowships (FP7-PEOPLE-2013-IIF, Grant Nos. 623473 and 913473).

REFERENCES

1. Zhou, W., M. Dridi, J.Y. Suh, C.H. Kim, D.T. Co, M.R. Wasielewski, G.C. Schatz and T.W. Odom, "Lasing action in strongly coupled plasmonic nanocavity arrays," *Nat. Nanotechnol.* Vol.8, No.7, 506–511, 2013.
2. Kabashin, A.V., P. Evans, S. Pastkovsky, W. Hendren, G.A. Wurtz, R. Atkinson, R. Pollard, V.A. Podolskiy and A.V. Zayats, "Plasmonic nanorod metamaterials for biosensing," *Nat. Mater.* Vol. 8, No. 11, 867–871, 2009.
3. Kauranen, M. and A.V. Zayats, "Nonlinear plasmonics," *Nat. Photon.* Vol. 6, No. 11, 737-748, 2012.
4. Zhang, J.X. and L.D. Zhang, "Nanostructures for surface plasmons," *Adv. Opt. Photon.* Vol. 4, No. 2, 157–321, 2012.
5. Song, H.J., J.X. Zhang, G.T. Fei, J.F. Wang, K. Jiang, P. Wang, Y.H. Lu, I. Iorsh, W. Xu, J.H. Jia, L.D. Zhang, Y.S. Kivshar and L. Zhang, "Near-field coupling and resonant cavity modes in plasmonic nanorod metamaterials," *Nanotechnology* Vol. 27, No. 41, 415708, 2016.
6. Wang, J.F., C. Zhang, J.X. Zhang, H.J. Song, P. Wang, Y.H. Lu, G.T. Fei, W. Xu, L.D. Zhang, Y.S. Kivshar and L. Zhang, "Hybrid plasmonic cavity modes in arrays of gold nanotubes," *Adv. Opt. Mater.* Vol. 5, No. 4, 1600731, 2017.

Exact theory of Purcell effect and resonant-state expansion

E. A. Muljarov and **W. Langbein**

School of Physics and Astronomy, Cardiff University, Cardiff CF24 3AA, United Kingdom

The Purcell factor (PF) quantifies the change (relative to free space) of the radiative decay of a quantum dipole coupled to an open optical system. For example, the photon emission rate of an optical transition in a quantum dot can be strongly enhanced when the electron (or exciton) level is resonant to a photon cavity mode in an optical resonator, such as a planar microcavity or a dielectric microsphere. Consequently the light-matter interaction is also enhanced. That is why designing the PF is at the heart of photonics technology, striving to develop ever smaller or less lossy optical resonators. Although this well-known effect of enhancement of the spontaneous emission rate was discovered by E. M. Purcell [1] early in 1946, no general exact theory of the Purcell effect was available until recently.

We present here a general analytic theory of the Purcell effect [2], which is based on the expansion of the PF into all relevant resonances of the cavity and exact calculation of their effective mode volumes. We show that the expressions for the mode volumes so far known and used in literature (see e.g. Ref. [3]) are only approximately valid for modes of high quality factor, while in general they are incorrect. We rectify this issue, introducing the exact normalization of modes which we have used earlier to formulate the resonant-state expansion (RSE) [4]. To illustrate and verify our theory of the Purcell effect we use analytically solvable examples of homogeneous dielectric and metal spheres in vacuum.

We also present some illustrations of using the RSE in different geometries. The RSE is a rigorous perturbation theory of resonances in open optical systems, which we have recently invented [4] and subsequently applied to finite one-dimensional (1D), 2D and 3D systems, such as perturbed planar [5,7], cylindrical [6] and spherical resonators [8] with various perturbations, and recently generalized to include frequency dispersion [9], photonic-crystal structures [10] and light propagation in non-uniform waveguides [11]. We have demonstrated the ability of the RSE to accurately and efficiently calculate resonances of a perturbed open optical systems using the spectrum of a simpler, unperturbed one. Furthermore, we have compared the performance of the RSE with commercially available solvers, such as those using the finite difference in time domain (Lumerical) and finite element methods (ComSol), and showed on 2D and 3D examples that the RSE can be several orders of magnitude more computationally efficient [8,10]. The RSE is capable of calculating a numerically complete set of RSs for a given optical system – and this is required by the exact theory of the Purcell effect we present: Indeed, the full Purcell factor is a sum over all RSs of the optical system.

References

[1] E. M. Purcell, Phys. Rev. **69**, 681 (1946).
[2] E. A. Muljarov and W. Langbein, Phys. Rev. B **94**, 235438 (2016).
[3] P.T. Kristensen and S. Hughes, ACS Photonics **1**, 2 (2014).
[4] E. A. Muljarov, W. Langbein, R. Zimmermann, Europhys. Lett. **92**, 50010 (2010).
[5] M. B. Doost, W. Langbein, and E. A. Muljarov, Phys. Rev. A **85**, 023835 (2012).
[6] M. B. Doost, W. Langbein, and E. A. Muljarov, Phys. Rev. A **87**, 043827 (2013).
[7] L. J. Armitage, M. B. Doost, W. Langbein, and E. A. Muljarov, Phys. Rev. A **89**, 053832 (2014).
[8] M. B. Doost, W. Langbein, and E. A. Muljarov, Phys. Rev. A **90**, 03834 (2014).
[9] E. A. Muljarov and W. Langbein, Phys. Rev. B **93**, 075417 (2016).
[10] T. Weiss, M. Mesch, M. Schäferling, H. Giessen, W. Langbein, and E. A. Muljarov
Phys. Rev. Lett. **116**, 237401 (2016).
[11] S. V. Lobanov, G. Zoriniants, W. Langbein, and E. A. Muljarov, arXiv:1611.01441 (2016).

Ultratransparent medium and its applications

Jie Luo, Zhihong Hang, Yun Lai*
College of Physics, Optoelectronics and Energy & Collaborative Innovation Center of Suzhou Nano Science and Technology, Soochow University, Suzhou 215006, China
*corresponding author: laiyun@suda.edu.cn

Abstract- Photonic crystals are well known for exhibiting band gaps that block electromagnetic waves. Here, by designing the nonlocal effective parameters of photonic crystals to have special values, we demonstrate the ultratransparency effect [1] of photonic crystals, which can enhance the transparency of photonic crystals to an extreme level beyond any existing solid materials on earth. In an optimized example, near 100% transmission rate have been realized for almost any incident angle within (-90, 90) degrees. A proof-of-principle microwave experiment has been performed to demonstrate near 100% transmission within (-60, 60) degrees. The ultratransparency effect of photonic crystals opens a new route to approach the ultimate transparency. Its applications include generalized transformation optics, microwave transparent wall, etc.

Transparent media are the foundation of almost all optical systems. However, due to general reflection caused by impedance mismatch, transparency is not perfect in natural materials like dielectrics. In the past decades, artificial electromagnetic materials like photonic crystals (PhCs) and metamaterials have been proposed to realize unusual electromagnetic properties beyond natural materials. However, transparent solid material with the same level of transparency as air or free space is still an extremely difficult task to realize.

In this work, we propose to use pure dielectric PhCs to realize perfectly transparent media with the rare property of omnidirectional impedance matching, which allows 100% transmission of light at all incident angles. Unlike local media with equal frequency contours (EFCs) centered at the Brillouin Zone center, such PhCs are designed to exhibit elliptical EFCs "shifted" in the k-space, and thus contain strong spatial dispersion. Interestingly, the combination of perfect transparency, which eliminates all reflection, and elliptical EFCs, which eliminates aberration in virtual images, satisfies the two essential requirements of optical media for ideal TO devices. As a result, such perfectly transparent PhCs provide a low-loss and feasible platform for transformation optics devices at optical frequencies. Moreover, the "shift" of EFC enables new freedom of phase manipulation beyond the original framework. Since such PhCs are superior to normal transparent media like dielectrics in two major aspects: allowing maximal amount of light to pass through and creating aberration-free virtual images, they are hereby denoted as "ultra-transparent" media.

Acknowledgements – Work in collaboration with Prof. C.T. Chan.

REFERENCES

1. J. Luo *et al.*, Ultratransparent Media and Transformation Optics with Shifted Spatial Dispersions, Physical Review Letters 117, 223901 (2016).
2. Z.Q. Yao *et al.*, Photonic crystals with broadband, wide-angle and polarization-insensitive ultra-high transparency, Optics Letters 41, 5106 (2016).

Fabrication and Nonlinear Effects of Lithium Niobate Microdisk Resonators

F. Bo[1*], J. Wang[1], Z. Hao[1], J. Cui[1], S. Ozdemir[2], Y. Kong[1], F. Gao[1], G. Zhang[1], L. Yang[2], and J. Xu[1]

[1]The MOE Key Laboratory of Weak Light Nonlinear Photonics, TEDA Applied Physics School and School of Physics, Nankai University, Tianjin 300457, China

[2]Department of Electrical and Systems Engineering, Washington University, St. Louis, Missouri 63130, USA

[*]corresponding author: bofang@nankai.edu.cn

Abstract-In this presentation, we will report the mass fabrication of lithium niobate microdisk resonators on a chip. The quality factors for the fabricated resonators can be higher than one million. Nonlinear effects including second harmonic generation, electro-optic effect, and thermo-optic effect were observed in these resonators.

Lithium niobate whispering gallery mode (WGM) micro-resonators provide a platform for the study of nonlinear effects with low pump threshold and photonic devices allowing for active control. Although millimeter-sized lithium niobate WGM resonators with quality factor of the order of ten million can be successfully produced by using traditional optical fabrication techniques, it is difficult to fabricate on-chip lithium niobate micro-resonators with ultra-high quality factors. The fabrication of on-chip lithium niobate resonators recently made a great progress benefiting from the production of lithium niobate film on insulator [1].

In this presentation, we will report the mass fabrication of lithium niobate WGM resonator from lithium niobate film by photolithography, reactive ion etching, and wet etching following the recipe used by Loncar's group [2,3]. Besides, we also made lithium niobate silica hybrid resonators by depositing a layer of polycrystalline lithium niobate film on an inverted-wedge silica resonator [4], that is partially a bottom up method. In the hybrid resonators, thermo-optic effect induced by the absorption of a pump beam and electro-optic effect were realized. Meanwhile, second harmonic generation, electro-optic modulation [2], and two kinds of thermo-optic effects with opposite coefficients [5] were demonstrated in monocrystalline lithium niobate micro-disk resonators made from lithium niobate film. These lithium niobate micro-resonators are good candidates for active photonic devices having potential to be integrated.

Acknowledgements: This work was financially supported by 973 program (2013CB328702); Natural National Science Foundation of China (NSFC) (11374165, 11174153, and 61475077); 111 Project (B07013); PCSIRT (IRT_13R29). F. Bo, F. Gao, Y. Kong, G. Zhang, and J. Xu are also at the Collaborative Innovation Center of Extreme Optics, Shanxi University, Taiyuan, Shanxi 030006, China.

REFERENCES

1. Lin, J., Y. Xu, Z. Fang, M. Wang, J. Song, N. Wang, L. Qiao, W. Fang and Y. Cheng. "Fabrication of high-Q lithium niobate microresonators using femtosecond laser micromachining." Sci. Rep., Vol. 5, 8072 2015.
2. Wang, C., M. J. Burek, Z. Lin, H. A. Atikian, V. Venkataraman, I. C. Huang, P. Stark and M. Loncar.

"Integrated high quality factor lithium niobate microdisk resonators." *Opt. Express* Vol. 22, No. 25, 30924-30933, 2014.

3. Wang, J., F. Bo, S. Wan, W. Li, F. Gao, J. Li, G. Zhang and J. Xu. "High-Q lithium niobate microdisk resonators on a chip for efficient electro-optic modulation." *Opt. Express* Vol. 23, No. 18, 23072-23078, 2015.
4. Bo, F., J. Wang, J. Cui, S. K. Ozdemir, Y. Kong, G. Zhang, J. Xu and L. Yang. "Lithium-Niobate–Silica Hybrid Whispering-Gallery-Mode Resonators." *Adv. Mater.* Vol. 27, No. 48, 8075-8081, 2015.
5. Wang, J., B. Zhu, Z. Hao, F. Bo, X. Wang, F. Gao, Y. Li, G. Zhang and J. Xu. "Thermo-optic effects in on-chip lithium niobate microdisk resonators." *Opt. Express* Vol. 24, No. 19, 21869-21879, 2016.

Nonlinear optical imaging and spectroscopy of gap plasmons in single metal particle-on-film nanocavities

Dangyuan Lei[1,2]

[1]Department of Applied Physics, The Hong Kong Polytechnic University, Hong Kong, China
[2]Shenzhen Research Institute, The Hong Kong Polytechnic University, Shenzhen, China
E-mail: dylei@polyu.edu.hk

Abstract – I will discuss our earlier and recent study on the light scattering response, photoluminescence and nonlinear optical properties of several plasmonic nanocavities comprised of metal film-coupled nanosphere monomers and dimers. Together with 3D full-wave electromagnetic simulations, the plasmon hybridization theory and multipole expansion model will be used to theoretically understood the observed experimental results such as single-particle scattering, polarization-resolved one-photon and two-photon photoluminescence and second-harmonic generation.

Main text – In this talk, I will first review our earlier investigation on the light scattering properties of two particle-on-film systems: a gold nanosphere on top of and partially embedded in a thin gold film [1]. Using polarization-resolved dark-field excitation, we revealed the coexistence of multiple gap plasmon modes in the two systems and the evolution of their scattering intensity and radiation pattern with incident polarization. Our results showed that the former system supports three plasmon resonances, originating from highly confined gap plasmons at the interface while the latter supports two dipolar modes having different orientation and damping rate. Secondly, I will show our recent results on using the polarization-resolved dark-field spectroscopy to study a nanosphere dimer-on-film system [2]. In addition to the two dipole-like plasmon modes sustained in the monomer-film system, the dimer-film system supports two new plasmon modes, one strong yet narrow resonant mode corresponding to a net bonding dipolar moment polarized along the dimer axis and one hybridized high-order resonance mode. Thirdly, I will show that that the spectral linewidth of the dipolar plasmon resonance of a gold nanosphere dimer on silica can be narrowed by a factor of ~4.6 by replacing the substrate with a gold mirror [3]. The measured linewidth is even smaller than its monomer counterpart (~30% reduction). Comprehensive theoretical analyses using multipole expansion model and full-wave electromagnetic simulations reveal that the observed linewidth shrinking originates from gold film-mediated intense plasmon hybridization between the bonding dipolar and quadrupolar gap modes. The intense dipolar-quadrupolar gap plasmon hybridization in the film-coupled system leads to a giant photoluminescence intensity enhancement (~200 times) and a dramatic emission linewidth narrowing in comparison with the dimer on silica. Finally, I will present our preliminary results on the TPL and SHG in a single gold nanosphere-on-film nanocavity, including polarization-dependent nonlinear emission spectroscopy and mapping [4]. We find that the emission pattern of the nanocavity appears as a double-lobe shape, with the axis of the two lobes aligned in the input polarization direction. The emission spectrum of the nanocavity is featured by a narrow SH emission peak and a broad TPL emission peak, and their emission patterns possess a similar double-lobe feature, indicating a same nonlinear emission enhancement mechanism.

References

[1] D. Y. Lei *et al*., ACS Nano **6**, 1380-1386 (2012).
[2] G.-C. Li, Y.-L. Zhang & D. Y. Lei, Nanoscale **8**, 7119-7126 (2016).
[3] G.-C. Li *et al*., "Metal substrate mediated plasmon hybridization in a nanoparticle dimer for photoluminescence linewidth shrinking and intensity enhancement", under revision with ACS Nano (2017).
[4] G.-C. Li *et al*., "Gap plasmon resonance enhanced nonlinear optical emissions in a metal particle-on-film nanocavity: A virtual probe of longitudinal field distribution", under preparation (2017).

Exploiting spin-orbit interactions via engineered transverse spin angular momentum in photonic integrated circuits

Zengkai Shao[1†], Jiangbo Zhu[2†], Ziyang Hu[2], Yujie Chen[1], Yanfeng Zhang[1*], Siyuan Yu[2*]

1. School of Electronics and Information Engineering, State Key Laboratory of Optoelectronic Materials and Technologies, Sun Yat-sen University, Guangzhou 510275, China

2. Photonics Group, Merchant Venturers School of Engineering, University of Bristol, Bristol BS8 1UB, UK

**E-mail address: zhangyf33@mail.sysu.edu.cn, s.yu@bristol.ac.uk*

Abstract - We present the experimental investigation of transverse spin angular momentum engineering in the evanescent fields of whispering-gallery modes in integrated micro-ring resonators. The spin-orbit interactions of light in the transversely confined fields and the cylindrical vector vortices in this structure are exploited for the manipulation of light within the degrees of freedom of optical angular momenta.

Transverse spin angular momentum (T-SAM) of light has been unveiled by recent advances in optics as a new member in the optical angular momentum (AM) family. In sharp contrast to the well-known longitudinal spin angular momentum (SAM), it exhibits spinning directions orthogonal to the propagation of light [1, 2]. T-SAM can typically be studied in highly inhomogeneous structured light fields, including surface plasmon polaritons [3], evanescent fields of guided and un-guided modes [4]. Light fields possessing T-SAM can enable various applications in bio-sensing, nano-photonics, etc. In particular, T-SAM in evanescent fields gives rise to robust spin-controlled directional coupling at optical interfaces [5] also known as the quantum spin Hall effect of light [6]. This effect has its origin in the spin-orbit interaction (SOI) of light, which universally occurs in transversely strongly-confined fields [7].

In this paper, we further introduce a more comprehensive platform for studying and manipulating SOI of light, by including the ability to engineer both the total angular momentum (TAM) and T-SAM in the near-field. The platform combines a whispering-gallery mode (WGM) resonator based optical vortex emitter [8] with precisely controllable global topological charge, and precisely engineered local T-SAM in the evanescent fields of the WGM modes. Enriched SOI effects in this platform can lead to the global conversion between the spin and orbital components of angular momentum in the emitted vortex [9]. The inherent local SOI in vortex emission/reception and global AM conversion allow for nano-photonic chiral interfacing in the full AM domain between travelling and bounded light.

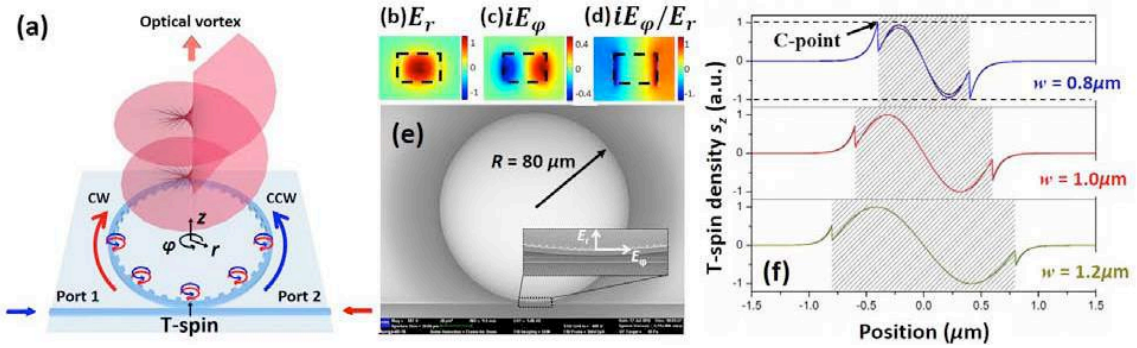

Fig. 1. (a) Device schematic, (b-d) field components of the WG mode, (e) SEM picture of device, and (f) calculated T-SAM density across the waveguide.

The schematic of the structure is shown in Fig. 1(a), where a micro-ring resonator consisting of a close-loop single-transverse mode waveguide is embedded with second-order gratings on the inner sidewall. The micro-ring is coupled with a two-port access waveguide (WG) [8]. In particular, for the quasi-TE mode supported in the high-index ring waveguide, a local tangential component (E_φ) along the sidewalls exists in quadrature phase with respect to the radial component (E_r), as shown in Fig. 1(b-c). Consequently, the local T-SAM of the evanescent field, with the spin axis in the z direction being orthogonal to the local propagation direction ($+\varphi$ or $-\varphi$) of the WGM, is determined by iE_φ/E_r (Fig. 1(d)), or in the form of $s_z \propto \mathrm{Im}[E^* \varphi E_r]$ [10]. The T-SAM at the inner sidewall can be flip-flopped by injecting light from the alternative ports 1 or 2.

The embedded sub-micron grating elements (Fig. 1(e)) scatter the evanescent fields near the inner sidewall, collectively producing a vortex beam travelling perpendicular to the resonator plane [8]. The locally coupled spin and orbital angular momentum (OAM) at each grating point [5] is directed to free-space and transformed into the globally interacting angular momenta in the emitted vortex. We have previously shown that the total angular momentum (TAM) is defined by the near-field topological charge l_{TC} which is only decided by the resonant wavelength and the number of grating elements [8, 9]. The polarization of the emitted field, on the other hand, is defined by the local T-SAM at each grating element, which can be engineered simply by changing the WG geometry. The AM states of the vortex $<l, s>$, where $l+s=l_{TC}$ [9], can therefore

be manipulated to traverse the full higher-order Poincare sphere [11]. By reciprocity, this structure can also be used to selectively receive AM-carrying beams [12] providing a chiral interface between bound and travelling vector vortices.

The simulations and experiments in this paper were both performed with the silicon nitride (SiN_x) resonator/WG fabricated on the silicon wafer. SiN_x is used for its moderate refractive index (n~1.9) so that a larger range of T-SAM density can be accessed over Silicon WGs. An SEM image of a fabricated device of R = 80μm is shown in Fig. 1(e).

The effects of WG geometry on the T-SAM density in the evanescent fields is shown in Fig. 1(f), where the hashed area indicates the WG cross-section as three different widths of WG (w = 0.8μm/1.2μm/1.6μm) are considered. The calculated electric contribution of quasi-TE mode T-SAM density across the WG is plotted along the radial direction also with various WG heights (h = 0.4μm/0.6μm/0.8μm). The T-SAM density generally decays away from the WG sidewalls in accordance with the evanescent fields. However, the peak density in the vicinity of WG sidewall surfaces is strongly dependent on the WG dimensions. Notably, positions of local circular polarizations (CPs) or $s_z = \pm 1$ (also referred to as C-points in singular optics [13]) can be found at the sidewalls with specific WG designs (e.g., as shown in the cases of w = 0.8μm in Fig. 1(f)). Therefore, various T-SAM density values can be achieved with routine WG design.

The measurement of engineered T-SAM and SOI in the emitted vortices was performed with the setup shown in Fig. 2(a). The quasi-TE WGM is excited by launching horizontally (TE) polarized light into one of the ports 1 or 2, and the vertically emitted beam is collimated with a 20X objective lens. Here we employ two separate techniques to measure the SAM state of the global beam. First, a radial polarization converter (RPC) [14] is used to measure the E_φ and E_r contribution in the beam, as the RPC can convert these two spatially variant components into uniformly x- and y-polarized fields, respectively. By detecting the power of the converted fields after a linear polarizer, the polarization ellipticity for various l_{TC} values is obtained and plotted in Fig. 2(b-c), with two different WG heights (0.4μm/0.6μm) and four widths (0.8μm/1.0μm/1.2μm/1.4μm). A wide range of polarization ellipticity (0.3~1.0) is achieved by tailoring the WG width. In particular, light of ellipticity $\sigma \approx 1$ can be observed (e.g., w = 0.8μm in Fig. 2(c)). We also verify these results by comparing the power of left- and right-hand circular-polarized (LHCP/RHCP) components in the light using quarter-wave plate (QWP) and linear polarizer. A ratio ranging from 1 to 16dB can be obtained as shown in Fig. 2(d-e), and the ratio can be inverted by injecting light into the opposite access WG port. These results show that the SAM in the global beam agree well with the local near-field T-SAM density in Fig. 1(f).

The OAM component in the vortices is demonstrated by the interferograms shown in Fig. 2(f). As TAM is only defined by l_{TC}, OAM is subject to the near-field T-SAM manipulation as it decides the far-field SAM. When the local near-field is linearly polarized, the emitted beam is an equal split of states $<l_{TC}\text{-}1, +1>$ and $<l_{TC}\text{+}1, -1>$ [8, 9]. Whereas with particular T-SAM values, for example the C-point of s=+1 as shown in Fig. 2(g), the OAM component of l_{TC}-1 becomes dominant. Vector vortices of arbitrary state $<l, s>$, where l+s is an integer, can be generated/received with this structure.

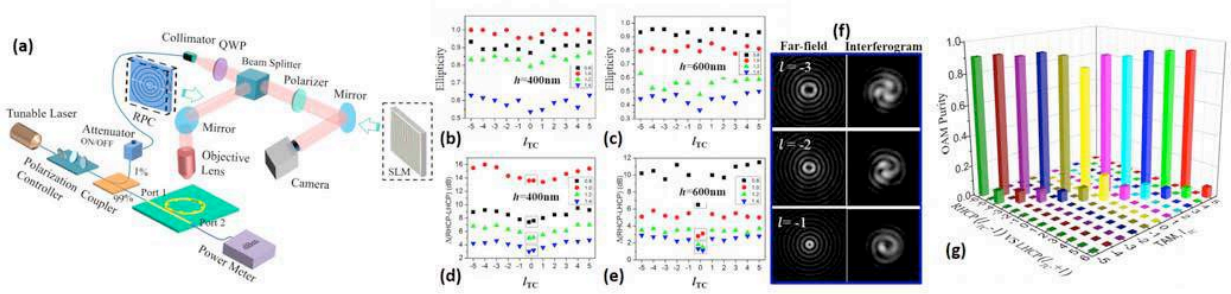

Fig. 2. (a) Experimental setup, (b-c) measured ellipticity, (d-e) measured circular polarization ratio, (f) inteferograms, and (g) polarization purity.

Overall, the two-fold spin-orbit interaction of light is demonstrated which is utilized to manipulate the spin and orbital angular momenta carried by complex vortex light fields. Potential applications include chiral waveguide couplers for vector vortices in quantum and classical information systems, as well as particle manipulation.

Acknowledgement

SYSU is supported by 973 project 2014CB34000, KRDPC project 2016YFB0402503 and NSFC projects 61323001/61490715. UoB is supported by European Union Horizon2020 project ROAM.

References

[1] A. Aiello et al., Phys. Rev. Lett. **103,** 100401 (2009).
[2] A. Aiello et al., Nat. Photon. 9, 789-795 (2015).
[3] K. Y. Bliokh et al., Phys. Rev. A **85**, 061801 (2012).
[4] K. Y. Bliokh et al., Nat. Commun. **5**, 3300 (2014).
[5] J. Petersen et al., Science **346**, 6771 (2014).
[6] K. Y. Bliokh et al., Science **348**, 1448-1451 (2015).
[7] K. Y. Bliokh et al., Nat. Photon. **9**, 796-808 (2015).
[8] X. Cai et al., Science **338**, 363-366 (2012).
[9] J. Zhu et al., Opt. Lett. **39**, 4435-4438 (2014).
[10] M. Neugebauer et al., Phys. Rev. Lett. **114**, 063901 (2015).
[11] G. Milione et al., Phys. Rev. Lett. **107**, 053601 (2011).
[12] K. Cicek et al., Opt. Express **24**, 28529-28539 (2016).
[13] I. Freund, Opt. Commun. **201**, 251 (2002).
[14] M. Stalder et al., Opt. Lett. **21**, 1948-1950 (1996).

Balanced Gain Loss devices in augmented contexts: modulated Bragg structures and some related disordered systems

Henri Benisty [1] and Anatole Lupu [2]

[1] Laboratoire Charles Fabry, Institut d'Optique Graduate School, CNRS, Univ Paris Sud, Université Paris-Saclay, 2 Avenue Augustin Fresnel, 91127 Palaiseau, France

[2]Centre de Nanosciences et de Nanotechnologies, CNRS, Univ. Paris-Sud, Université Paris-Saclay, C2N – Orsay, 91405 Orsay cedex, France

[*]corresponding author: henri.benisty@institutoptique.fr

Abstract- Balanced gain and losses in geometries beyond those of mere trivial compensation have prompted a series of optical counterparts evoking the fascinating physics of parity-time symmetry. We will expose two more complex variants. Firstly, those that arise when tackling such a simple issue as apodizing a complex periodic index sequence. And secondly a very disordered version whereby statistics of the outcome becomes nontrivial, in relation with non-ergodicity and so called Geometric Brownian Motion (GBM), i.e., random walk in multiplicative space.

A bird's view of the dominant paradigms in optoelectronics should undoubtedly emphasize optical coherence. Consequently to that state of matter, it can be said that the *phase* is commonly seen as the crux of most modern optics. Correspondingly, altering the phase through electro-optics, and thus tuning of the real part of the index of refraction, has been the main paradigm for the tuning of the current generation of functional devices. In this picture, a somewhat implicit trend emerged that *gain and losses* should be felt as related to the "incoherent" part of the process, and for instance the laser phenomenon of phase/amplitude coupling as a side complexity.

It is one of the merits of the flourishing of the Parity-Time symmetry concept in optics to trigger a deep revision of this state of matter. The basic enticing characteristics of PT-symmetric operators is to behave, up to a point, as conservative ones even though they have non-Hermitian (gain and loss) character. From this new paradigm, even with fixed material losses − as arise in most instances of envisioned miniature plasmonic devices,− it is possible to build up couplers and other sophisticated "coherent" optoelectronic functions based on tunable gain rather than tunable index [1]. While the case for this approach is now clearer, leading to revisit coupled laser physics for instance, opportunities to *explore the role of complex gain and loss spatial distributions* can be also revisited.

We explore in this paper two roads that, according to our belief, could go beyond mimicking existing functions.

We first discuss more complex form of gain/loss organization: firstly in the case of PT-symmetric Bragg grating [2], known for their unidirectional reflection we show that various flavors of local PT symmetric Bragg gratings that stem from apodization concepts bring rich optogeometric variants. Namely, by considering

separately the apodization of real and imaginary parts of the PT-symmetric Bragg grating, a set of interesting filtering properties can arise, spanning various configuration from flat-top filters to “unilateral” functions with enhanced sidelobe suppressions. Furthermore, we discuss what changes of local “binary” guide properties such as width or gain/loss is most appropriate to implement these effects. This leads us to consider the merits of various “supersymmetric” variants of the real+imaginary index distribution.

Next, we give a hint of unexpected synthetic properties in the case of disordered systems. We do not look at PT-symmetric systems but rather at a simple chain of alternate gain and loss regions. In case the spatial phase evolution can be forgotten (as would be the case for extreme miniature plasmonic resonators), we are essentially left with a multiplicative random walk, also called a Geometric Brownian Motion (GBM) : in such distributions, the logarithm of the intensity evolves like a random walk, and could take the classical Gaussian shape in its more basic form. Thus the intensity distribution is the exponential of a Gaussian, also known as the log-normal distribution. Within some assumptions that can be drawn from recent considerations on such GBM in other fields [3,4], there are non-ergodic effects, with the mean along a given walk not taking the same limit as the mean of an ensemble of walks at a given finite distance from their start. Carrying this concept to gain and loss and plasmonics, we envision a set of plasmonic guides, so that each of them embodies a single random walk. As a consequence of non-ergodicity, the opportunity arises of an information-rich optical output that can carry interesting features from the (plasmonic) disorder, which might be a tunable disorder eventually.

Along this line, we will explore how the core GBM paradigm is modified when minimally realistic ingredients are taken into account rather than the elementary GBM: the phase and the possible coupling between individual walks, i.e. between gain/loss individual channels in our analogy.

We hope to give a different light on disordered systems in plasmonics from such an interdisciplinary perspective.

Acknowledgements, This work is supported by a public grant overseen by the French National Research Agency (ANR) as part of the “Investissements d’Avenir” program (Labex NanoSaclay, reference: ANR-10-LABX-0035).

REFERENCES

1. H. Benisty, A. Degiron, A. Lupu, A. De Lustrac, S. Chénais, S. Forget, M. Besbes, G. Barbillon, A. Bruyant, S. Blaize, and G. Lérondel, "Implementation of PT symmetric devices using plasmonics: principle and applications," Optics Express, vol. 19, pp. 18004-18019, 2011.
2. A. Lupu, H. Benisty, and A. V. Lavrinenko, "Tailoring spectral properties of binary PT-symmetric gratings by using duty cycle methods," J. Sel. Top. Quantum Electron., vol. 22, pp. 4402807 (1-8), September 2016 2016.
3. O. Peters and W. Klein, "Ergodicity breaking in geometric brownian motion," Phys. Rev. Lett., vol. 110, p. 100603, 2013.
4. O. Peters and M. Gell-Mann, "Evaluating gambles using dynamics," Chaos, an Interdisciplinary Journal of Nonlinear Science, vol. 26, p. 023103, 2016.

Surface-Plasmon-Polariton Laser based on an Open-Cavity Fabry-Perot Resonator.

H. J. Lezec[1*], W. Zhu[1,2], T. Xu[1,2,3], C. Zhang[1,2], and A. Agrawal [1,2]
[1]Center for Nanoscale Science and Technology, NIST, Gaithersburg, MD, USA
[2]Maryland Nanocenter, University of Maryland, College Park, MD, USA
[3]National Laboratory of Solid State Microstructures, Nanjing University, Nanjing, China
[*]corresponding author: hlezec@nist.gov

Abstract - We demonstrate visible frequency, room-temperature, ultra-narrow-linewidth lasing of surface plasmon polaritons (SPPs) propagating along the floor of a metallic open-cavity Fabry-Perot resonator formed by template stripping and coated with a subwavelength-thick layer of dye gain medium. The lasing threshold is lowered by pumping the gain medium with an SPP standing wave, generated using a low-profile grating located on the cavity floor. Darkfield transmission sampling of the lasing SPP mode via a recessed nanoslit enables high-contrast, high-figure-of-merit refractive-index sensing of analytes interacting with the open cavity.

Ongoing miniaturization of the footprint of optical systems and circuits requires development of wavelength scale optical elements able to efficiently generate, manipulate and detect light. Achieving coherent optical sources with narrow linewidth and nanoscale mode-confinement in one or more dimensions has been central to this quest. More recently, metal based resonators sustaining surface plasmons have emerged as a promising route to achieve stimulated emission or lasing at nanometer-scale dimensions. For example, optically-pumped lasing plasmon modes formed by localized surface plasmons on dye-coated resonant nanoparticles and nanoparticle arrays (*1–3*), or by gap plasmons confined to a dielectric layer of nanoscale thickness between a metal surface and a semiconductor gain medium (*4–8*), have been recently demonstrated.

Here, we show, for the first time, lasing of propagating surface plasmon polaritons (SPPs) confined to an open Fabry-Perot cavity. Ultra-narrow linewidth, visible frequency lasing is achieved at room-temperature. The cavity consists of a template-stripped (*9*) ultra-smooth flat Ag surface orthogonally bound by a pair of Ag sidewalls (10, 11), forming a trough-shaped, micron-scale width resonator for SPPs exhibiting a record-high quality factor, and a figure-of-merit for refractive-index sensing that is an order of magnitude higher than that of a state-of-the-art surface-plasmon resonance (SPR) sensor (*12*, *13*). By incorporating a subwavelength thickness of DCM-doped (3mM) polymer film on the trough floor, and optically pumping the dye from the open side of the cavity, we demonstrate room-temperature SPP lasing in the red (*14*). We show (Fig. 1) how the lasing threshold and linewidth can be lowered by incorporating a low-profile tapered grating in the cavity floor to couple the excitation beam into a pump SPP, providing strong modal overlap with the gain medium. The record narrow lasing linewidth (≈ 0.24 nm) achieved here is substantially smaller than that of localized–plasmon lasers (*1–3*) and comparable to that of the best semiconductor-based gap–plasmon lasers (*5*, *7*) demonstrated to date. Transmission-configuration sampling of the lasing intensity with minimum perturbation to the both pump and emission SPPs is achieved via an evanescently coupled nanoslit recessed below the cavity floor, opening the way to active, multiplexed platforms for high figure-of-merit refractive index sensing and surface-analyte detection, in which arrays of open-cavity SPP lasers are directly integrated onto electronic imaging chips.

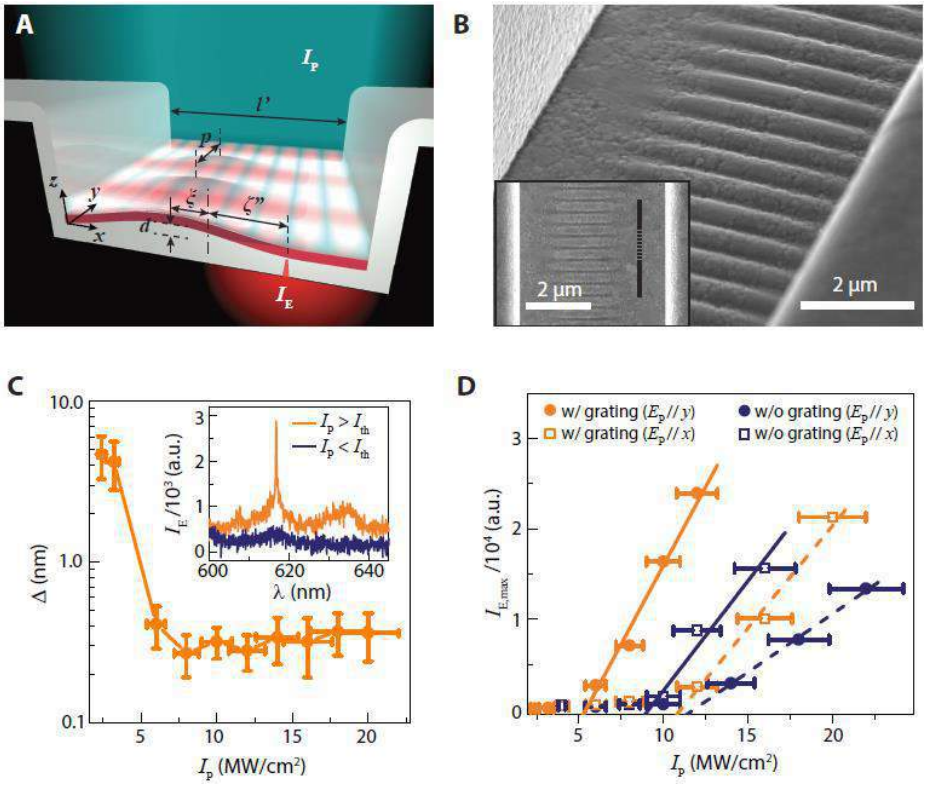

Figure 1: Experimental characterization of grating-decorated SPP-pumped SPP laser. (A) Schematic diagram of a template-stripped, open-cavity SPP laser with cavity metal (Ag) thickness 300 nm, cavity width l' = 4.4 μm and height 2 μm, decorated with a low-profile grating of periodicity p = 350 nm, amplitude d = 40 nm, and offset ξ = 320 nm from the cavity center, coated with a 260-nm thick layer of PMMA:DCM gain medium, illuminated an normal incidence with a nanosecond pulsed pump-beam of wavelength λ_P = 480 nm, intensity I_P, and linear polarization perpendicular to the grating. The schematic blue-green and red standing waves illustrate the grating-coupled pump SPPs and cavity-trapped lasing SPPs, respectively. A 50-nm-wide slit, recessed 50 nm below the cavity floor, offset ζ''= 1.5 μm from cavity center, evanescently samples the lasing SPP mode and transmits a wave of proportional intensity, I_E, into the far-field on the other side of the device (glass substrate). **(B)** Tilted-view SEM image of the template-stripped cavity resonator illustrating the grating-decorated cavity floor. **Inset:** top-view SEM image of the device, where the nominal location of the buried recessed sampling slit is indicated by the dotted black line. **(C)** Evolution of the SPP emission linewidth Δ with increasing pump intensity I_P. **Inset:** representative emission spectra of I_E for I_P below (I_P = 4.0 MW/cm^2) and above (I_P = 6.0 MW/cm^2) the lasing threshold (I_{th} = 5.6 MW/cm^2). **(D)** SPP lasing turn-on characteristics I_E vs. I_P on a linear scale for grating-decorated and grating-free devices as a function of in-plane pump polarization.

REFERENCES

(1) Noginov, M. A., *et al.*, *Nature,* Vol. 460, 1110, 2009. **(2)** Zhou, W. *et al.*, *Nat. Nanotech.,* Vol. 8, 506, 2013. **(3)** Meng, X., *et al.*, *Laser Photonics Rev*., Vol. 8, 896, 2014. **(4)** Hill, M. T., *Nat. Photon.,* Vol. 1, 589, 2007. **(5)** Oulton, R. F., *et al.*, *Nature,* Vol. 461, 629, 2009. **(6)** Khajavikhan, M., *et al.*, *Nature, Vol.* 482, 204, 2012. **(7)** Ma, R., *Nat. Mater.,* Vol. 10, 110, 2010. **(8)** Lu, Y.-J., *Science,* Vol. 337, 450, 2012. **(9)** Nagpal, P., *Science*, Vol. 325, 594, 2009. **(10)** Sorger, V. J., *et al.*, *Nano Lett.,* Vol. 9, 3489, 2009. **(11)** Kress, S. J. P., *et al.*, *Nano Lett.,* Vol. 15, 6267, 2015. **(12)** Wang, X-Y., *et al.*, *Nanophotonics*, Vol. 5, 52, 2016. **(13)** Homola, J., *Surface Plasmon Resonance Based Sensors,* Springer, 2006. **(14)** Zhu, W., *et al.*, arXiv:1610.03864, 2016.

Metamaterial Structures for Healthcare Applications

Thin Metamaterial Antireflection Coating In-vivo Measurements to Test the Transmission Enhancement through Human Tissue

H. Cano-García[1, 2*], S. Saha[1], I. Sotiriou[1], P. Kosmas[2], and E. Kallos[1, 3]
[1]Medical Wireless Sensing Ltd., United Kingdom
[2]King's College London, United Kingdom
[3]Metamaterial Technologies Inc., Canada
[*]corresponding author: helena.cano_garcia@kcl.ac.uk

Abstract-This paper presents for the first time experimental results of a metamaterial antireflection coating designed to work in contact with human tissue. The metamaterial performance is tested using two patch antennas operating between 59 GHz and 62 GHz that send and receive signals through a human hand. The measurements show an average of 4.4 dB enhancement in transmission when the metamaterial is added in front of the hand.

The high value of relative permittivity of the skin compared to air creates an impedance mismatch. This impedance mismatch is present in most of the non-invasive biomedical applications that use electromagnetic radiation (EM). Solving this impedance mismatch problem would help to develop more accurate and less power consuming devices. For example, the sensitivity and specificity of microwave imaging systems would be improved and their limitations, high false negative rate and high false positive rate, would be significantly reduced. The accuracy of microwave hyperthermia treatment would be enhanced, permitting to focus heat on the exact location of the tumor target, without burning healthy tissue. The power levels used in electrosurgery would also be reduced providing a more efficient way of coagulating small blood vessels. And, finally, the precision and reliability of non-invasive blood glucose monitoring would be improved, allowing sensing the blood properties in a more accurate way.

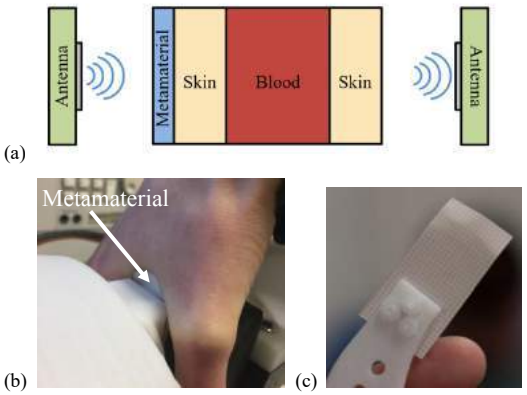

Figure 1: (a) Cross section (not to scale) of the schematic design consisting of an AR metamaterial unit cell placed in contact with a skin-blood-skin slab and excited using patch antennas. (b) Photo showing the experimental setup. (c) Photo showing the metamaterial film

To solve this impedance mismatch, the authors propose to use an antireflection (AR) coating with a similar design than the one presented in [1]. Previously, in [2,3] the authors presented an AR coating design optimized to work in contact of tissue, comprised by 0.5 mm of skin, 1 mm of blood and 0.5 mm of skin. In [2] the authors presented simulations results of this AR metamaterial that achieved 1.4 dB enhancement in the transmitted power. This metamaterial design was fabricated and tested in an in-vivo experimental study using pig subjects, [3], and it achieved 1.9 dB improvement in the transmitted signal.

Here we present in-vivo measurements of this AR metamaterial film when used in presence of human skin. For these measurements, the metamaterial film was placed in front of the skin and two patch antennas,

operating between 59 GHz and 62 GHz, were used as an excitation source (Figure 1a). The antennas were transmitting and receiving signal through the boneless part of the hand located between the index finger and the thumb (Figure 1b). To help the flattening of the skin surface, the antennas were enclosed inside two custom made plastic holders, capable of adjusting the antenna-sample distance.

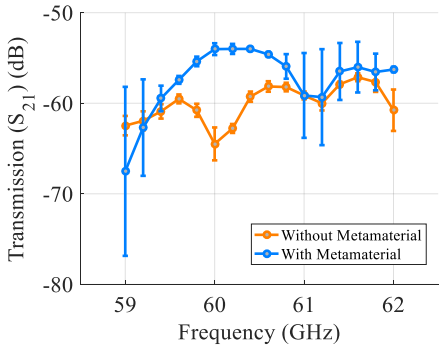

Figure 2. Comparison of the S_{21} recorded signal with and without the presence of the AR metamaterial.

The experimental study was performed at University of Roehampton, London, UK. The transmitted and received signal was measured using a Vector Network Analyzer (Keysight Technologies' E8361A PNA).

To quantify the performance of the metamaterials, two different types of measurements were recorded: (i) antennas transmitting through the tissue without metamaterial; (ii) same as (i) but adding the metamaterial film between the antenna and the hand (Figure 1). Between measurements the holders were slightly moved using micropositioners to facilitate the placement or the removal of the metamaterial between the antenna and the hand.

Figure 2 shows the transmission coefficient (S_{21}) for the two different types of measurements on a single human subject. The error bars represent the standard deviation of two sets of five measurements. Between these two sets the metamaterial was removed and placed again. Between 59.3 GHz and 61 GHz the average increase in transmission achieved when the metamaterial is added is 4.4 dB.

The main reason for the differences between measurements is the possible movement of the hand when the holder was removed to insert or remove the metamaterial. Note that the error bars are more significant on the measurements with the metamaterial. This could be because the position of the metamaterial changed between the two sets of measurements affecting differently to the bending produced on the metamaterial when conforming to the hand shape; and therefore, creating accidental air gaps between the metamaterial and the tissue.

The authors thank Richard Mackenzie and his team from University of Roehampton and Nadine Geddes for their contribution in the human trials. The authors would also want to thank George Palikaras for his support and scientific guidance. Moreover, the authors acknowledge the financial support of InnovateUK and EPSRC for this study.

REFERENCES

1. Chen, H.-T., J. Zhou, J. F. O'Hara, F. Chen, A. K. Azad, and A. J. Taylor, "Antireflection Coating Using Metamaterials and Identification of Its Mechanism," *Physical Review Letters*, Vol. 105, No. 7, 073901, 2010.
2. Cano-Garcia H., P. Kosmas and E. Kallos, "Demonstration of enhancing the transmission of 60 GHz waves through biological tissue using thin metamaterial antireflection coatings," in *10th International Congress on Advanced Electromagnetic Materials in Microwaves and Optics (METAMATERIALS)*, Chania, 2016, pp. 85-87.
3. Cano-Garcia, H., P. Kosmas, and E. Kallos, "Enhancing electromagnetic transmission through biological tissues at millimeter waves using subwavelength metamaterial antireflection coatings," in *9th International Congress on Advanced Electromagnetic Materials in Microwaves and Optics (METAMATERIALS)*, Oxford, 2015, pp.43-45

Tunable Hybrid Metasurfaces for Magnetic Resonance Imaging

Alexey Slobozhanyuk[1,2]
[1]Nonlinear Physics Center, Australian National University, Australia
[2]Department of Nanophotonics and Metamaterials, ITMO University, Russia
[*]corresponding author: aleksei.slobozhaniuk@anu.edu.au

Abstract- Metasurfaces have become a new paradigm in the studies of artificial subwavelength structures due to their potential to overcome many challenges typically associated with metamaterials. However, a majority of demonstrated metasurface structures possess fixed properties, e.g. fixed operational bandwidth or functionality. An active control of metasurface functionalities and bandwidth is highly desirable for engineering an advanced electromagnetic and photonic devices. Here, we suggest and demonstrate experimentally a novel type of tunable metasurface capable of dramatic enhancing the image quality.

Metasurfaces [1] are artificial ultrathin structures representing a planar realisation of metamaterial concept [2]. One important application of metasurfaces is the enhancement of image quality which is crucially important in different fields of biology, medicine and nanotechnologies. In particular it was demonstrated experimentally that the metasurface lens, designed for optical frequencies, can be used to provide diffraction limited focal spots [3] and to resolve features with subwavelength spacing, while parity-time symmetric nonlocal metasurfaces allow ideal aberration-free optical images [4]. Another field where metasurfaces can potentially help is related to Magnetic Resonance Imaging (MRI), known to be one of the most important clinical modalities for detection of various diseases in human bodies. More precise, MR image quality is limited by signal to noise ratio (SNR) that is relatively low for the majority of current machines and therefore MR image acquisition is usually a very time consuming process. Recently a new conceptual idea has been suggested to substantially increase SNR of commercial MRI with the aid of metasurfaces made by resonant metallic inclusions [5]. Later, this effect was confirmed during in-vivo imaging and spectroscopy of the human brain [6].

In this talk, we will review our recent activities with metasurfaces application for MRI and also present a novel hybrid tunable metasurface capable to enhance substantially the MR-image quality, allowing to resolve smaller features of images, e.g. tumours, much faster and more efficiently.

Acknowledgements, This research was supported by the Russian Science Foundation (Grant 15-19-20054) and partially by Ministry of Education and Science of the Russian Federation (Zadanie No. 3.2465.2017/ПЧ).

REFERENCES

1. Holloway, C. et al., "An overview of the theory and applications of metasurfaces: The two-dimensional equivalents of metamaterials," *Antennas and Propagation Magazine, IEEE*, Vol. 54, No. 2, 10–35, 2012.
2. Engheta, N., Ziolkowski R. W., *Metamaterials: Physics and Engineering Explorations*, Hoboken: Wiley-IEEE Press, 2006.
3. Monticone, F., Valagiannopoulos, C. A., Alù, A., "Parity-Time Symmetric Nonlocal Metasurfaces: All-Angle Negative Refraction and Volumetric Imaging," *Phys. Rev. X*, Vol. 6, 041018, 2016.

4. Khorasaninejad, M. et al., "Metalenses at visible wavelengths: Diffraction-limited focusing and subwavelength resolution imaging," *Science*, Vol. 352, No. 6290, 1190-1194, 2016.
5. Slobozhanyuk, A. P. et al., "Enhancement of Magnetic Resonance Imaging with Metasurfaces," *Adv*. *Mater*., Vol. 28, 1832–1838, 2016.
6. Schmidt, R. et al., "Flexible and compact hybrid metasurfaces for enhanced ultra high field in vivo magnetic resonance imaging," arXiv:1612.02721v2, 2016.

Near, Mid and Far Infrared Photonics

van der Waals Materials for Active Infrared Photonics

M. C. Sherrott[1], W. S. Whitney[1], P. W. Hon[1,2], D. M. Jariwala[1], K. T. Fountaine[1,2], L. A. Sweatlock[1,2], H. A. Atwater[1]

[1] California Institute of Technology, USA

[2] Nothrop Grumman Aerospace Systems, USA

[*]corresponding author: msherrot@caltech.edu

Abstract-

In this talk, we will present results on van der Waals materials for active infrared photonics, with a focus on graphene and few-layer black phosphorus. We take advantage of the electrostatically tunable optical properties of graphene to design active devices for controlling absorption, emission, and phase. We additionally consider ultrathin black phosphorus as a novel platform for IR optoelectronics, demonstrating gate-tunable transmittance due to an ambipolar Burstein-Moss and Quantum Confined Franz-Keldysh effect.

van der Waals materials provide an excellent platform for tunable photonics in the infrared (IR). By electrostatically gating these ultrathin materials, tunable absorption, emission, polarization, and phase can be achieved. In this talk, we will present several experiments that take advantage of this dynamic response, establishing new physical mechanisms for achieving tunability, and demonstrating progress towards reconfigurable mid-IR metasurfaces.

Graphene, a monolayer Dirac semi-metal, is an ideal platform for tunable plasmonics in the mid-IR. With a charge carrier density of $\sim 10^{12}$ cm^{-2} which can be controlled with an electrostatic gate, graphene supports IR plasmons which can be spectrally tuned. In this talk, we will present results demonstrating highly confined, tunable plasmons in graphene with confinement factors up to $\lambda_0/\lambda_p \sim 100$ and electromagnetic simulations implying a local density of optical states more than 10^6 larger than free space.[1] This tight confinement results in very strong interactions of the plasmons with their environment, leading to coupling with phonon polaritons in neighboring materials, including other monolayers such as hexagonal boron nitride, which we observed experimentally[2]. By combining these graphene resonators with a quarter-wavelength thick dielectric spacer layer of SiN_x and a gold back reflector, also known as a Salisbury Screen, absorption in the graphene resonators is enhanced up to 24.5%, an order of magnitude higher than without this design.[3] We will also comment on the use of this structure for actively modulation thermal radiation, with kHz switching speeds.[4]

Metasurfaces offer significant potential to control far-field light propagation through the engineering of amplitude, polarization, and phase at an interface. We will present an extension of tunable graphene-based nanophotonics platforms for applications to reconfigurable metasurfaces. Using a gate-tunable graphene-gold resonator geometry, we demonstrate highly tunable reflected phase at multiple wavelengths and show up to 237° phase modulation range at an operating wavelength of 8.50 μm. We observe a smooth monotonic modulation of phase with applied voltage from 0° to 206° at a wavelength of

8.70 μm. Based on these experimental data, we demonstrate with antenna array calculations an average beam steering efficiency of 50% for reflected light for angles up to 30°, relative to a ideal metasurface, confirming the suitability of this geometry for reconfigurable mid-infrared beam steering devices.[5]

Finally, we will present results on field effect optoelectronic modulation of quantum-confined carriers in black phosphorus. We report measurements of the gate-tunable infrared optical response of thin black phosphorus. We interpret the observed spectral changes as a combination of an ambipolar Burstein-Moss (BM) shift of the absorption edge due to band-filling under gate control, and a quantum confined Franz-Keldysh (QCFK) effect, phenomena which have been proposed theoretically to occur for black phosphorus under an applied electric field. Distinct optical responses are observed depending on the flake thickness and starting carrier concentration. Transmission extinction modulation amplitudes of more than two percent are observed, suggesting the potential for use of black phosphorus as an active material in mid-infrared optoelectronic modulator applications.[6]

References:

1. Brar, V. W.; Jang, M. S.; Sherrott, M.; Lopez, J. J.; Atwater, H. A. *Nano Lett* **2013,** 13, (6), 2541-2547.
2. Brar, V. W.; Jang, M. S.; Sherrott, M.; Kim, S.; Lopez, J. J.; Kim, L. B.; Choi, M.; Atwater, H. *Nano Lett* **2014,** 14, (7), 3876-3880.
3. Jang, M. S.; Brar, V. W.; Sherrott, M. C.; Lopez, J. J.; Kim, L.; Kim, S.; Choi, M.; Atwater, H. A. *Phys Rev B* **2014,** 90, (16).
4. Brar, V. W.; Sherrott, M. C.; Jang, M. S.; Kim, S.; Kim, L.; Choi, M.; Sweatlock, L. A.; Atwater, H. A. *Nature Communications* **2015,** 6.
5. Sherrott, M. C.*; Hon, P. W.*; Fountaine, K. T.; Garcia, J. C.; Ponti, S. M.; Brar, V. W.; Sweatlock, L. A.; Atwater, H. A. *arXiv:1701.08221* **2017**.
6. Whitney, W. S*.; Sherrott, M. C.*; Jariwala, D.; Lin, W. H.; Bechtel, H. A.; Rossman, G. R.; Atwater, H. A. *Nano Lett* **2017,** 17, (1), 78-84.

Terahertz-Light Emission in Graphene-Based Active Plasmonic Metamaterial Heterostructures

T. Otsuji[1*], T. Watanabe[1], A. Satou[1], D. Yadav[1], S. Boubanga-Tombet[1], T. Suemitsu[1], and V. Ryzhii[1]
[1]RIEC, Tohoku University, Japan
[*]otsuji@riec.tohoku.ac.jp

Abstract-This paper reviews recent advancement on the research toward graphene-based active plasmonic metamaterials for terahertz (THz) light emission. The dual-gate graphene channel transistor structure serves carrier population inversion, promoting spontaneous broadband THz emission. Active plasmonic meta-surfaces implemented into the gate structure can transcend the incoherent light-emitting action to the amplified stimulated emission of THz radiation.

Carrier-injection pumping of graphene can enable negative-dynamic conductivity in the THz spectral range, which may lead to new types of current-injection THz lasers [1]. The dual-gate graphene channel transistor structure serves carrier population inversion in the lateral p-i-n junctions under complementary dual-gate biased and forward drain-source biased conditions, promoting spontaneous broadband incoherent THz light emission. A distributed feedback (DFB) laser cavity structure implemented into the gate electrodes can transcend the incoherent broadband light-emitting-diode (LED) to the single-mode lasing action. We fabricated the test devices and confirmed aforementioned LED and single-mode laser operations at 100K [2, 3].

To increase the operating temperature and output radiation intensity, further enhancement of the THz gain is mandatory. Asymmetric dual-grating-gate meta-surface structures may promote plasmonic superradiance [4] and/or plasmonic instabilities [5, 6], giving rise to giant THz gain enhancement at plasmonic resonant frequencies. Dyakonov-Shur type instability owing to the Doppler-shift effect at the plasmonic cavity boundaries, Ryzhii-Satou-Shur type instability owing to the carrier transit-time effect in the periodically modulation-doped channel, and plasmonic-boom instability are the possible mechanisms.

ACKNOWLEDGEMENTS
The authors thank G. Tamamushi, J. Mitsushio, T. Hosotani, A.A. Dubinov, V. Ya. Aleshkin, and M. Ryzhii for their contributions. This work is financially supported by JSPS KAKENHI (16H06361, 16K14243), Japan.

REFERENCES

1. Ryzhii, V., Ryzhii, M., Mitin, V. and Otsuji, T., "Toward the creation of terahertz graphene injection laser," *J. Appl. Phys.*, VOl. 110, 094503-1-9, 2011.
2. Tamamushi, G., Watanabe, T., Dubinov, A.A., Mitsushio, J., Wako, H., Satou, A., Suemitsu, T., Fukidome, H., Suemitsu, M., Ryzhii, M., Ryzhii, V., and Otsuji, T., "Single-mode terahertz emission from current-injection graphene-channel transistor under population inversion," *74th Dev. Res. Conf.*, Delaware, USA, June 2016, 225-226.
3. Yadav D., Tobah, Y., Tamamushi, G., Mitsuhio, J., Watanabe, T., Dubinov, A.A., Ryzhii, M., Ryzhii, V., and Otsuji, T., "Current-injection terahertz emission in distributed-feedback dual-gate graphene-channel field-effect transistor," *Int. Conf. Opt. Thz. Sci. Technol.*, London, UK, Apr. 2017.
4. Popov, VV., Polischuk, O.V., Davoyan, A.R., Ryzhii, V., Otsuji, T., and Shur, M.S., "Plasmonic terahertz lasing in an array of graphene nanocavities," *Phys. Rev. B*, Vol. 86, 195437-1-6, 2012.
5. Koseki, Y., Ryzhii, V., Otsuji, T., Popov, V.V., and Satou, A., "Giant plasmon instability in dual-grating-gate graphene field-effect transistor," *Phys. Rev. B*, Vol. 93, 245408-1-5, 2016.
6. Aizin, G.R., Mikalopas, J., and Shur, M., "Current-driven plasmonic boom instability in three-dimensional gated periodic ballistic nanostructures," *Phys. Rev. B*, Vol. 93, 195315-1-8, 2016.

Widely Tunable Semiconductor Antennas for Reconfigurable Metasurfaces

J. A. Schuller
Electrical and Computer Engineering Department, UC Santa Barbara, CA, USA
*corresponding author: jonschuller@ucsb.edu

Abstract-The ability to engineer the optical phase at subwavelength dimensions has led to metasurfaces that provide unprecedented control of electromagnetic waves. To reach their ultimate potential, metasurfaces must incorporate reconfigurable functions. The central challenge is achieving large tunability in subwavelength elements. Here, we describe two different approaches for achieving order-unity refractive index shifts: free-carrier refraction and thermo-optic tuning

We experimentally demonstrate wide tuning of single-particle infrared Mie resonances through doping[1], and demonstrate simulations of electrically reconfigurable III-V heterojunction metasurfaces based on these effects[2,3]. We conclude with recent experimental demonstrations of dyamic, ultrawide tuning of Mie resonators based on two distinct thermo-optic effects: 1) modifying the electron mass and carrier density in InSb and 2) exploiting the anomalous temperature-dependent bandgap of PbTe.

Acknowledgements, This work was supported by the Air Force Office of Scientific Research (FA9550-16-1-0393) and by the UC Office of the President Multicampus Research Programs and Initiatives (MR-15-328528).

REFERENCES

1. Lewi, T., Iyer, P. P., Butakov, N.A., Mikhailovsky, A.A., and Schuller, J.A. "Widely Tunable Infrared Antennas Using Free Carrier Refraction," *Nano Lett.*, Vol. 15, 8188, 2015.
2. Iyer, P.P, Butakov, N.A., and Schuller,J.A. "Reconfigurable Semiconductor Phased Array Metasurfaces," *ACS Photon.*, Vol. 2, 1077, 2015.
3. Iyer, P.P., Pendharkar, M. and Schuller, J.A. "Electrically Reconfigurable Metasurfaces Using Heterojunction Resonators," *Adv. Opt. Mater.*, Vol. 4**,** 1582, 2016.

Rectification in infrared-active, nonlinear metasurfaces

R. M. Osgood[1*], J. M. Xu[2], G. Fernandes[2], M. Kang[3], K-B. Kim[3], L. Parameswaran[4], M. Rothschild[4], Y. Ait-El-Aoud[1], S. A. Giardini[1], and S. Kooi[5]

[1]US Army NSRDEC, USA

[2]Brown University, USA

[3]Seoul National University, Republic of Korea

[4]MIT Lincoln Laboratory

[5]Insitute for Soldier Nanotechnologies, MIT, USA

[*]corresponding author: richard.m.osgood.civ@mail.mil

Abstract- Rectifying stripe-teeth metasurfaces, consisting of microantenna arrays with infrared resonances, coupled to vertical Metal-Insulator-Metal (MIM) diodes having an insulating barrier layer, were designed, fabricated, and characterized with FTIR microscopy and current-voltage (I-V) measurements. Resonances agreed well with FDTD models and the electrical measurements showed that the NbO_x-based diodes have modest large barrier heights and nonlinear I-V curves, allowing for prediction of their rectification response. These, and Al_2O_3-based microrectenna arrays, were illuminated by infrared and visible laser beams, and their direct current was characterized as a function of bias voltage and compared to quantum rectification models.

Absorption in a semiconductor is limited by the band gap. An array of "microrectennas" could theoretically efficiently rectify from near- to far-infrared frequencies, converting the incident THz voltage to direct current via a nonlinear receiver. Vertical metal-insulator-metal (MIM) diodes have produced power from optical-frequency fields, produced by a metamaterial planar stripe-teeth Al or Au antenna array lying above the vertical diode. We have recently published a model of MIM diodes and their predicted current-voltage (I-V) characteristics and rectification[1].

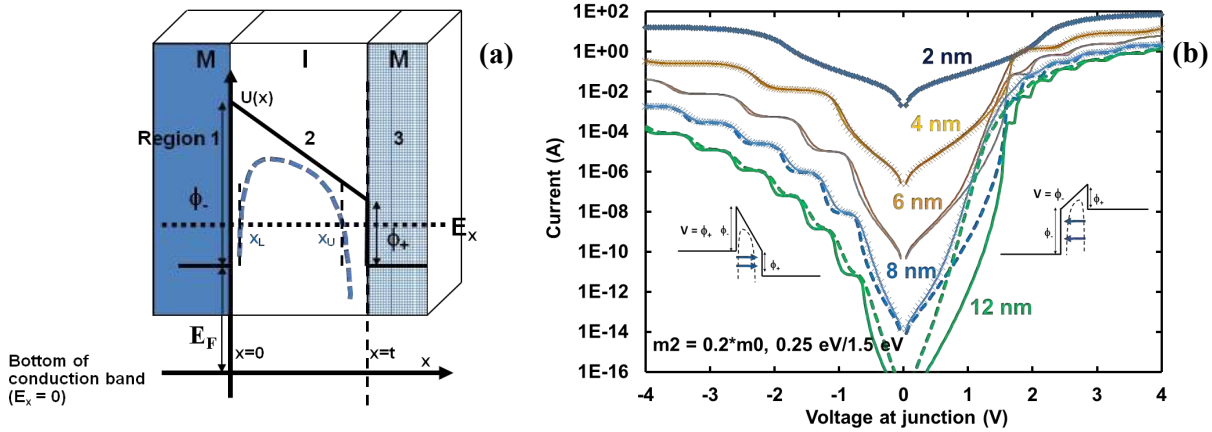

Figure 1: (a) Model of the MIM diode. Region 1 is the metal with larger barrier height, region 2 is the barrier layer (thickness t) with the trapezoidal potential function U(x), and region 3 is the metal with lower barrier height. (b) Predicted I-V curves as a function of barrier thickness and temperature, for both forward bias (V < 0) and reverse bias (V > 0), predicting Fabry-Perot resonance effects.

These stripe-teeth arrays are similar to stripe arrays that have demonstrated, (Wu (2011)) near-perfect absorption in the infrared, except that "teeth" break the left-right symmetry at normal incidence and produce a net a.c. voltage into the substrate, similar to "optical rectification" except that direct current also flows. We designed, fabricated, and analyzed these stripe-teeth microrectenna arrays in the near- and short-wave infrared and planned for LWIR. Stripes extracted the direct current; teeth lay along the x-axis and, when excited by the incident electric field,

produced the resonant a.c. field, determined by the spacing of the teeth along the y-axis. The antenna-amplified z-component of the electric field, was rectified by Atomic-Layer-Deposited (ALD) Au/NbO_x/Nb, Al/Al_2O_3/Au, or Al/Al_2O_3/Al diodes.

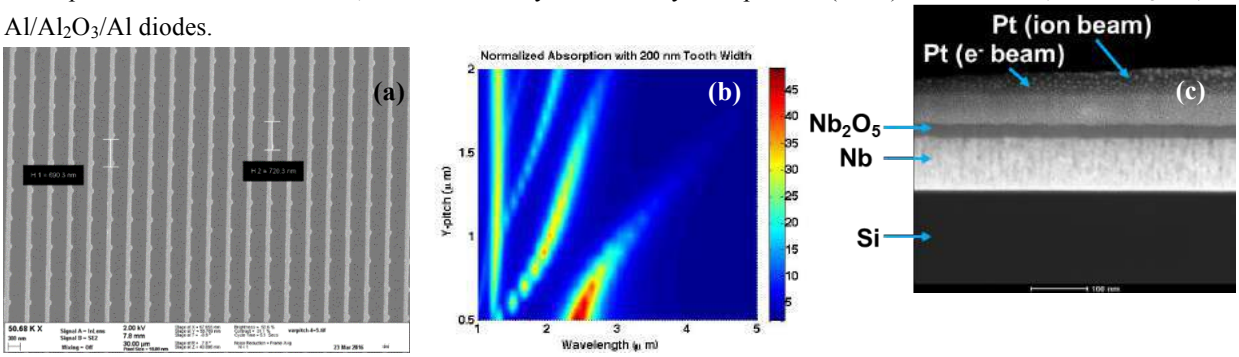

Figure 1: (a) Electron microscopy (EM) image of chirped microrectenna arrays designed at NSRDEC and MITLL (b) Stripe-teeth resonances (normalized absorption) for E-field || x, as a function of wavelength and y-pitch (the vertical line is the fixed cross-stripe resonance); infrared microscopy measurements confirmed this. (c) Transmission EM image of novel NbO_x-Nb based MIM diode.

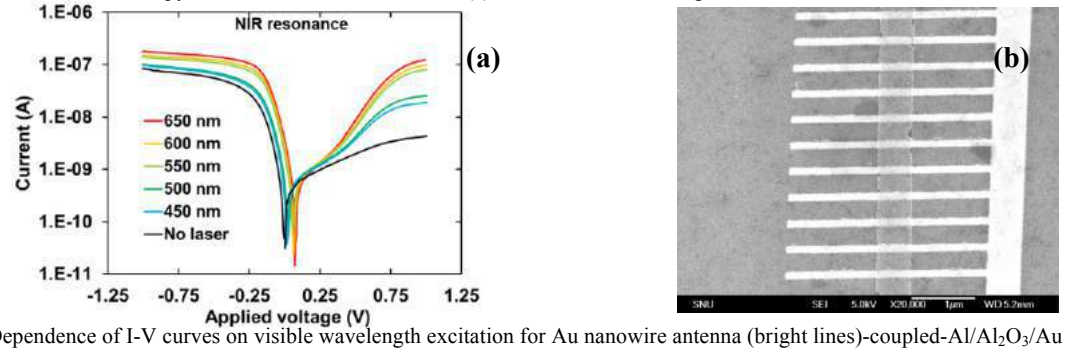

Figure 3: Dependence of I-V curves on visible wavelength excitation for Au nanowire antenna (bright lines)-coupled-Al/Al_2O_3/Au diodes. (b) Plan view EM image of these nanorectennas. Vertical diodes form where the transmissive Al stripe and the Au antennas cross.

I-V measurements from Al/Al_2O_3(22 nm)/Al test diodes gave current densities in the range of μA/cm^2 with an application of +/- 6V, while Au/NbO_x(20 nm)/Nb test diodes produced similar current densities with smaller voltages, due to their smaller (< 1 V) barrier heights. Al/Al_2O_3/Au diodes were much more conductive than their Al/Al_2O_3/Al counterparts, suggesting a reduced barrier height due to a different ALD barrier layer.

These microrectenna arrays are currently being illuminated with visible and infrared cw lasers. For the Au/NbO_x/Nb, and Al/Al_2O_3/Au diodes, if the laser's photon energy is comparable or greater than the voltage scale of the I-V nonlinearity, the Tucker formula for quantum rectification responsivity (R in A/W) is appropriate (Eq. 1, where $\hbar\omega/e$ is the photon energy divided by electronic charge and $I_{dc}(V_0)$ is the direct current under a bias of V_0).[2]

$$R = \frac{e}{\hbar\omega}\left[\frac{I_{dc}\left(V_0+\hbar\omega/e\right) - 2I_{dc}(V_0) + I_{dc}\left(V_0-\hbar\omega/e\right)}{I_{dc}\left(V_0+\hbar\omega/e\right) - I_{dc}\left(V_0-\hbar\omega/e\right)}\right] \quad (1)$$

For the Al/Al_2O_3/Al diodes, it is possible that the formula for classical responsivity may be used instead.[2] Illumination of Pt/NbO_x/Nb and Al/Al_2O_3/Au microrectenna arrays with 514 nm and 450 – 650 nm photons, respectively, produces a significant change in the output current and a shift in the I-V curve and a ~ 5 nA short-circuit current, respectively.[1] Comparison of the experimental measurements with the responsivity prediction is ongoing, and for the Al/Al_2O_3/Au microrectenna arrays may require a new explanation for the observed reduction in diode barrier height.

REFERENCES

1. Osgood, R. M., *et. al.*, "Conduction and rectification in NbOx- and NiO-based metal-insulator-metal diodes," *J. Vac. Sci. Tech. A*, Vol. 34, 051514 – 051527, 2016.

2. Tucker, J. R. and Feldman, M. J. “Quantum detection at millimeter wavelengths,” *Rev. Mod. Phys.*, Vol. 57, 1055-1114, 1985.

Radiative heat transfer in the extreme near-field: from nanometer to ångström-sized gaps

V. Fernández-Hurtado[1*], K. Kim[2], B. Song[2], W. Lee[2], W. Jeong[2], L. Cui[2], D. Thompson[2], J. Feist[1], M. T. H. Reid[3], F. J. Garcia-Vidal[1], J. C. Cuevas[1], E. Meyhofer[2], and P. Reddy[2]

[1]Departamento de Física Teórica de la Materia Condensada and Condensed Matter Physics Center (IFIMAC), Universidad Autónoma de Madrid, Madrid, 28049, Spain

[2]Department of Mechanical Engineering, University of Michigan, Ann Arbor 48109, USA

[3]Department of Mathematics, Massachusetts Institute of Technology Cambridge, Massachusetts 02139, USA

[*]corresponding author: victor.fernandezh@uam.es

Abstract-We present a comprehensive study of radiative heat transfer in ångström and nanometer-sized gaps from both an experimental and theoretical point of view. Our results establish the fundamental validity of fluctuational electrodynamics in modelling near-field radiative heat transfer (NFRHT) down to single-nanometer gaps. Furthermore, our work suggests that unexpectedly large thermal conductances found in previous works are due to the presence of surface contamination.

Radiative heat transfer between objects at different temperatures is of fundamental importance in applications such as energy conversion, thermal management, lithography, data storage, and thermal microscopy [1]. It was predicted long ago that when the separation between objects is smaller than the thermal wavelength, which is of the order of 10 μm at room temperature, the radiative heat transfer can be greatly enhanced due to the contribution of evanescent waves (or photon tunneling). In recent years, different experimental studies have confirmed this long-standing theoretical prediction. However, in spite of this progress, there are still many basic open questions in the context of near-field radiative heat transfer (NFRHT). Thus, for instance, recent experiments exploring the radiative thermal transport in nanometric gaps have seriously questioned the validity of fluctuational electrodynamics [2,3], which is presently the standard theory for the description of NFRHT. In this work, we address the issue of radiative heat transfer in the extreme near-field regime when objects are separated by nanometer-size distances. In particular, we have accomplished a very detailed comparison of novel NFRHT experiments performed with scanning thermal probes with state-of-the-art simulations based on the fluctuating-surface-current formulation of the heat transfer problem. The ensemble of our results clearly show that fluctuational electrodynamics provides an adequate description of the NFRHT between both metals and dielectrics all the way down to nanometer-size gaps [4]. Besides, our analysis of NFRHT in sub-nanometer gaps suggest that past reports of large deviations from the predictions of fluctuational electrodynamics are probably due to surface contamination effects. We also demonstrate, from measurements of apparent tunneling barrier heights, that such deviations can be systematically attenuated by carefully cleaning the surfaces as indicated by an increase in the apparent barrier height [5].

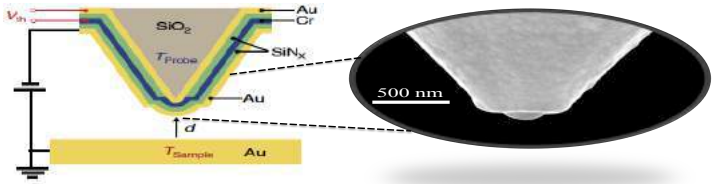

Figure 1. Schematic of the experimental set-up, in which an Au-coated scanning thermal microscopy probe is brought into close proximity of a heated Au substrate. The right inset shows a SEM image of the tip, which has a diameter of 300 nm.

REFERENCES

1. Basu, S., Z. M. Zhang and C. J. Fu "Review of near-field thermal radiation and its application to energy conversion," *Int. J. Energy Res.,* Vol. 33, No. 13, 1203–1232, 2009.
2. Worbes, L., D. Hellman and A. Kittel, "Enhanced near-field heat flow of a monolayer dielectric island," *Phys. Rev. Lett.*, Vol. 13, No. 110, 134302, 2013.
3. Kloppstech, K., N. Könne, S. A. Biehs, A. W. Rodriguez, L. Worbes, D. Hellmann and A. Kittel. "Giant heat transfer in the crossover between conduction and radiation," *Nat. Commun.*, Vol. 8, 14475, 2017.
4. Kim, K., B. Song, V. Fernández-Hurtado, W. Lee, W. Jeong, L. Cui, D. Thompson, J. Feist, M. T. H. Reid, F. J. Garcia-Vidal, J. C. Cuevas, E. Meyhofer, and P. Reddy, "Radiative heat transfer in the extreme near field," *Nature*, Vol. 528, 387–391, 2015.
5. Cui, L., W. Jeong, V. Fernández Hurtado, J. Feist, F. J. Garcia-Vidal, J. C. Cuevas, E. Meyhofer and P. Reddy, "Study of radiative heat transfer in ångström and nanometer-sized gaps," *Nat. Commun.*, Vol. 8, 14479, 2017.

Highly Integrated Dual-Channel Metamaterial Thermal Detector for Mid-IR Optical Gas Sensing

A. Lochbaum[1*], Y. Fedoryshyn[1], C. Hafner[1], and J. Leuthold[1]
[1]Institute of Electromagnetic Fields (IEF), ETH Zurich, 8092 Zurich, Switzerland
[*]corresponding author: alexander.lochbaum@ief.ee.ethz.ch

Abstract- We demonstrate a dual-channel, CMOS-compatible metamaterial thermopile detector, exhibiting near-ideal peak absorptivity values (A=0.99), and narrowband absorption characteristics (Q = 15.1 at 4.29 µm). The ultra-thin metamaterial perfect absorber (MPA) makes additional blackening layers and filter elements obsolete, allowing for highly integrated, low-cost optical gas sensing systems. Employed in a non-dispersive gas sensing setup, the MPA detector leads, in comparison to a non-structured thermopile, to a 3.9-fold increase in analyte resolution, with a simultaneous 6.5-fold decrease in humidity cross sensitivity.

The ubiquitous trend towards low-cost integrated sensing solutions, e.g. for medical or automotive applications, drives the demand for efficient and selective mid-infrared (mid-IR) detectors [1]. Thermopiles (TP) are well known as low-cost detectors for the mid-IR wavelength range and are widely used in non-dispersive infrared (NDIR) gas sensors. However, they suffer from a low spectral selectivity due to their thermal detection principle, and from the low absorptivity values of typical TP membranes. This makes additional filter elements and blackening layers necessary, which limit the size, cost and speed of these detectors. Recently, metamaterials have been investigated as a promising candidate to overcome those limitations by resonantly enhancing their absorptivity in the mid-IR to values close to unity, over a potentially narrow bandwidth [2]. However, the limited resonance quality factors of actually demonstrated metamaterial absorbers restrict their use for selective gas analysis, and the integration of a sufficiently narrowband metamaterial absorber on a thermal detector has not been shown for far. In this paper, we monolithically integrate for the first time narrowband metamaterial perfect absorbers (MPA) on thermopile detectors and demonstrate their performance for sensitive and selective gas analysis in the mid-IR.

The structure of the MPA detector and the MPA unit cell are shown in Figure 1(a). The metamaterial absorber area (270×300 µm^2) is centered on the dielectric TP membrane and comprises a periodic arrangement of subwavelength unit cells. Each unit cell consists of a cross-shaped metal resonator (Cu), separated from the metal backplane (Cu) by means of a

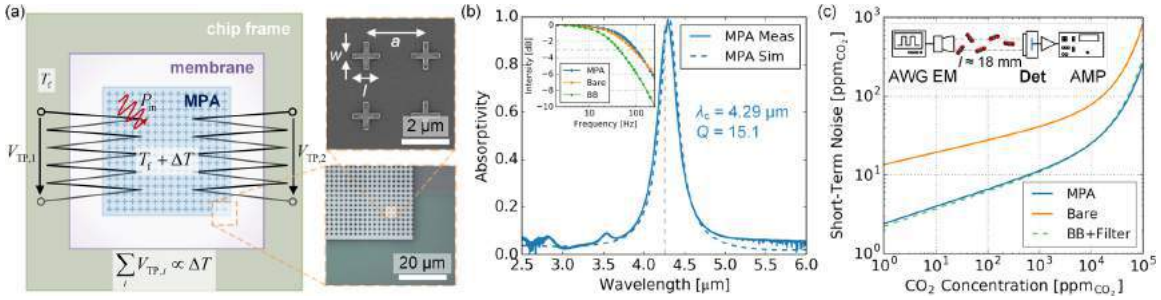

Figure 1. (a) Schematic of the metamaterial detector and details of MPA unit cells. (b) Simulated and measured absorptivity of the MPA structure. Inset: frequency response of the MPA detector in comparison to thermopiles with carbon-black ("BB") and without ("Bare") absorber structure. (c) CO_2 resolution of sensing systems employing MPA, non-structured ("Bare") and dielectrically-filtered ("BB + Filter") thermopiles. Inset: Schematic of non-dispersive gas sensing setup.

dielectric spacer layer (Al_2O_3). Geometrical parameters of the unit cell have been optimized by full-wave simulations for resonant absorption at $\lambda_c = 4.26$ µm, yielding in $a = 2$ µm, $l = 1.03$ µm, $w = 192$ nm, $t_{metal} = 100$ nm, and $t_{dielectric} = 90$ nm. The MPA structure has been fabricated in a series of post-processing steps on top of commercial thermopile substrates. Details on the employed optimization and fabrication processes can be found in [3]. The measured absorptivity of the MPA structure is shown in Figure 1(b). The structure yields a peak absorptivity $A = 0.99$ at the center wavelength $\lambda_c = 4.29$ µm, in very good agreement with the simulation results. In the inset of Figure 1(b), the frequency response of the MPA detector is compared against the frequency response of a carbon-black coated TP and a TP without absorber layer. Due to its low thermal mass, the MPA does not impair the dynamic properties of the underlying detector ($f_{-3db} = 95$ Hz), in contrast to a conventional carbon-black absorber, which increases the detector time constant by a factor of two. Besides its efficient blackening and low thermal mass, the high quality factor $Q = 15.1$ of the MPA enables sensitive and selective gas analysis without the need for additional filter elements, which has been demonstrated in a series of non-dispersive gas sensing experiments using CO_2 (absorption resonance: $\lambda_{CO2} = 4.26$ µm) as an analyte. The experimental setup is displayed in the inset of Figure 1(c). A hotplate emitter (EM) is positioned opposite to the detector under test (DET), separated by a metal-coated absorption channel ($l = 18$ mm). The emitter is driven by a signal generator (AWG), and the TP signal is lock-in amplified (AMP). The performance of the MPA detector in such a setup has been compared against a TP without absorber coating, as well as a TP with carbon-black absorber coating and a commercial dielectric filter ($\lambda_f = 4.26$ µm, FWHM = 180 nm). The measured absolute CO_2 resolution of each system configuration, as derived from the relative analyte sensitivity of the detector signal at various CO_2 concentrations, is shown in Figure 1(c). For the MPA detector system, a resolution of 8.99 ppm_{CO2} at $c_{CO2} = 400$ ppm has been measured, outperforming the non-structured TP by a factor of 3.9 and reaching the resolution of the reference, dielectrically-filtered absorber system. Furthermore, the MPA detector system exhibits a 6.5-fold reduced humidity cross sensitivity (6.4 ppm_{CO2}/%rH) in comparison to the non-structured TP (41.8 ppm_{CO2}/%rH), which can be directly attributed to the narrowband absorption characteristics of the MPA structure. To demonstrate the high integration density of the MPA concept, we realized a dual-channel MPA detector by incorporating two spatially separated MPA areas on the same TP membrane, as shown in the inset of Figure 1(b). The center wavelengths correspond to a sensing ($\lambda_1 = 4.26$ µm) and a reference ($\lambda_2 = 3.91$ µm) channel, with their measured absorptivity spectra shown in Figure 2(a) relative to the atmospheric absorption. The resulting difference signal between both TP areas exhibits excellent stability with virtually no drift, even over extended measurement periods, Figure 2(b), which showcases the MPA technology's potential for advanced detection schemes.

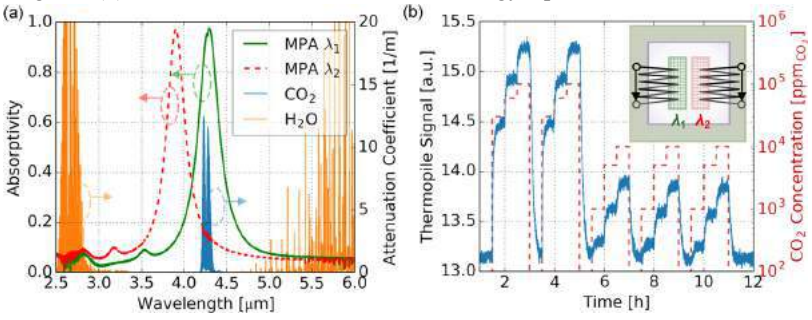

Figure 2. (a) Absorptivity of sensing (λ_1) and reference (λ_2) channel as measured on the dual-channel MPA detector together with the atmospheric attenuation (40 %rH, 400 ppm_{CO2}, at 25°C). (b) Dual-channel detector signal together with the applied gas concentration. Inset: schematic of dual-channel MPA detector.

REFERENCES

1. Hodgkinson, J. and R. P. Tatam, "Optical gas sensing: a review," *Meas. Sci. Technol.,* Vol. 24, No. 1, 2013.
2. Watts, C. M., *et al.*, "Metamaterial electromagnetic wave absorbers," *Advanced Materials,* Vol. 24, No. 23, 2012.
3. Lochbaum, A., *et al.*, "High-Q Metamaterial Mid-IR Emitter on a Membrane Heater for Gas Sensing Applications," Optical Sensors, 2016.

Graphene Plasmon-Assisted Mid-Infrared Light Emission

L. Kim[1], V. W. Brar[2], S. Kim[1], and H. A. Atwater[1*]
[1]California Institute of Technology, USA
[2]University of Wisconsin - Madison, USA
[*]corresponding author: haa@caltech.edu

Abstract – Plasmon emission is predicted to be a highly efficient decay mechanism of photoexcited hot carriers in graphene, competing with optical phonon emission. To facilitate coupling of emitted plasmons with photons, we created graphene nanoribbons whose resonances live above, below and near the optical phonon energy. We observe carrier density-dependent graphene plasmon-assisted light emissions in the mid-infrared under femtosecond laser excitation. We explore how plasmonic modes alter decay pathways for photoexcited hot carriers and affect the resulting infrared radiation.

The decay dynamics of excited carriers in graphene have attracted wide scientific attention, owing to the much lower relaxation rate of excited 'hot' carriers than is seen in many three-dimensional materials. However, plasmons can significantly reduce the photoexcited charge carrier lifetime in graphene, and this plasmon effect on excited state decay gets larger with increasing carrier density, as indicated by recent theoretical calculations and angle-resolved photoemission experiments.[1,2,3,4] We report experimental results suggesting that graphene plasmons excited by ultrafast pumping affect the radiative emission rate. This work has important implications for achieving ultrafast optical control of mid-infrared light emission. While traditionally achieving control of infrared radiation has required heating and cooling of an object – a relatively slow process – plasmon-assisted light emission resulting from sub-100fs decay of hot carriers could provide a method for ultrafast generation and modulation of infrared radiation.

The reported lifetimes of excited carriers in the presence of graphene plasmon emission range from a few femtoseconds to 100s femtoseconds.[3,4] Such timescales suggest that plasmon emission is a decay channel with whose strength is comparable to optical phonon emission, which is widely considered to be the dominant decay mechanism at carrier energies above the "phonon bottleneck" (i.e., the optical phonon energy). In planar continuous graphene sheets, plasmon emission is difficult to observe because emitted plasmons decay non-radiatively, owing to the large momentum mismatch between graphene plasmons and free space light. Radiative emission of graphene plasmons can be dramatically increased by defining nanoribbons in graphene to allow detection of plasmon-coupled light emission. The confined plasmonic resonances of graphene nanoribbons are tunable by changing sizes and carrier densities of graphene nanoribbons, enabling us to spectroscopically tune the detected plasmon energy across the mid-infrared wavelength regime.[5] By creating plasmon resonances above, below and near the optical phonon energy, we can observe how graphene plasmon modes affect the decay mechanisms of photoexcited carriers via measurement of mid-infrared light emission. Photoexcited hot carriers are created in graphene nanoribbons with a 100-fs pulsed laser excitation at $\lambda = 850$ nm, and the resulting infrared emission is collected and analyzed with a Michelson interferometer for varying graphene carrier densities.

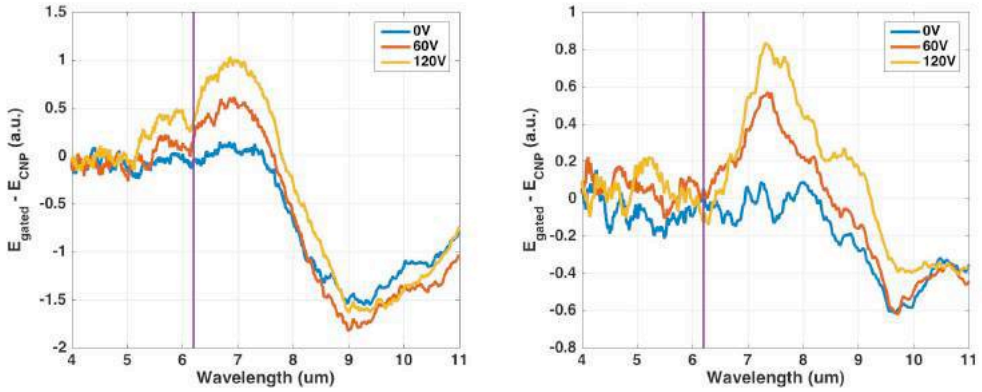

Figure 1. Carrier-dependent emission from bare graphene (left) and 50nm nanoribbons (right) under 100-fs pulsed laser excitation at $\lambda = 850$ nm. The higher gate voltage means higher carrier density. The vertical purple lines indicate the optical phonon energy (200 meV).

Figure 1 shows carrier density-dependent emission spectra from bare graphene (left) and patterned graphene (right). In both cases, the emission intensity is larger for higher graphene carrier density, which is controlled via the changes in applied gate voltage. The emission spectra of bare graphene are broad and show features across a wide energy range – both above and below the optical phonon energy. By contrast, the emission spectra from 50nm ribbons show relatively narrow peaks exclusively at the resonance frequency ($\lambda \sim 7.5$um), and the peaks blue shift with increasing carrier density. By comparing the emission spectra of bare and patterned graphene, we study the effects of propagating plasmons and confined plasmons on hot carrier decay mechanisms and the resulting light emission.

REFERENCES

1. Bostwick, A., T. Ohta, T. Seyller, K. Horn and E. Rotenberg, "Quasiparticle dynamics in graphene," *Nature Phys.* Vol. 3, No. 1, 36-40, 2007.
2. Bostwick, A., F. Speck, T. Seyller, K. Horn, M. Polini, R. Asgari, A. H. MacDonald and E. Rotenberg, "Observation of plasmarons in quasi-freestanding doped graphene," *Science*, Vol 328, No. 5981, 999-1002, 2010.
3. Rana, F., J. H. Strait, H. Wang and C. Manolatou, "Ultrafast carrier recombination and generation rates for plasmon emission and absorption in graphene," *Phys. Rev. B*, Vol. 84, No. 4, 045437, 2011.
4. Kaminer, I., Y. T. Katan, H. Buljan, Y. Shen, O. Llic, J. J. Lopez, L. J. Wong, J. D. Joannopoulos and M. Soljacic, "Efficient plasmonic emission by the quantum Cerenkov effect from hot carriers in graphene," *Nat. Commun*., Vol. 7, 2016.
5. Brar, V. W., M. S. Jang, M. Sherrott, J. J. Lopez and H. A. Atwater, "Highly confined tunable mid-infrared plasmonics in graphene nanoresonators," *Nano Lett.* Vol. 13, No. 6, 2541-2547, 2013.

Topological plasmons in graphene

T. Christensen,[1] **D. Jin**,[2] **L. Lu**,[3] **& M. Soljačić**[1]

[1]Department of Physics, Massachusetts Institute of Technology, Cambridge, MA 02139, USA
[2]Department of Mechanical Engineering, University of California, Berkeley, CA 94720, USA
[3]Institute of Physics, Chinese Academy of Sciences, Beijing 100190, China

Abstract— We discuss recent work on topological plasmonic states in two-dimensional electron gases under an applied magnetic field. By periodic nanostructuring, new high-frequency topological edge states can be synthesized beyond the conventional low-frequency edge magnetoplasmon. In moderately doped graphene, these high-frequency unidirectional edge plasmons can exist at frequencies up to tens of terahertz, reaching the far-infrared regime.

Spurred by the contemporary topological understanding of the quantum Hall effect in fermionic systems, a broad class of nontrivial topological bosonic phases have emerged in recent years. Among these, time-reversal-symmetry ($\mathcal{T}$) broken topological bosonic systems—proposed in a variety of quasiparticles, spanning photons, phonons, excitons, polaritons, and magnons—which host unidirectional and backscattering-immune edge states along structural terminations, hold great promise for the development of nonreciprocal and defect-tolerant devices. So far, however, the achievable operating frequencies of these $\mathcal{T}$-breaking platforms are low, typically in the GHz regime. This restriction, which represents a severe obstruction to applications, is ultimately due to the scarcity of workable high-frequency $\mathcal{T}$-breaking mechanisms.

Recently, efforts to expand the zoo of topological bosons have encompassed plasmonics as well. Notably, it was recently shown [1] that the conventional low-frequency edge magnetoplasmons, which exist along the terminations of two-dimensional electron gases, arise as a consequence of a nontrivial topology of the underlying bulk bands. We will discuss our recent proposal [2] for a new class of high-frequency $\mathcal{T}$-broken topological edge plasmons enabled by periodic nanostructuring of the underlying two-dimensional system. Specifically, in a triangular antidot lattice etched into graphene, we find that a new high-frequency topological edge plasmon emerges under a magnetically induced gapping of a bulk Dirac-degeneracy. This edge plasmon is unidirectional, immune to backscattering by structural defects, and exists at frequencies up to tens of THz, even in moderately doped graphene. Graphene is a particularly attractive candidate material for topological plasmonics by virtue of its low intrinsic loss, tunable carrier density, and chiefly, by its large magneto-optical response. This finding identifies a practical path to topological $\mathcal{T}$-broken operation in the far-infrared regime, and simultaneously enriches the field of topological photonics with the characteristics hallmarks of plasmonics—strong optical confinement and enhanced light–matter interaction.

REFERENCES

1. D. Jin, L. Lu, Z. Wang, J.D. Joannopoulos, M. Soljačić, L. Fu, and N.X. Fang, "Topological magnetoplasmon," *Nat. Commun.*, Vol. 7, 13486, 2016.
2. D. Jin,* T. Christensen,* M. Soljačić, N.X. Fang, X. Zhang, and L. Lu, "Infrared topological plasmons in graphene," *arXiv*:1702.02553, 2017.

Dirac Plasmons in Topological Insulator Bi_2Se_3

Chihun In[1], Sangwan Sim[1], Soonyoung Cha[1], Beom Kim[1], Hyemin Bae[1], and Hyunyong Choi[1*]
[1]School of Electrical and Electronic Engineering, Yonsei University, Seoul 120-749, South Korea
[*]corresponding author: hychoi@yonsei.ac.kr

Abstract- Terahertz (THz) responses of topological insulator Bi_2Se_3 exhibit a strong interaction between Dirac surface plasmon and optical phonon near 2 THz. Employing time-resolved THz spectroscopy, we investigated the spectral manifestation of plasmon-phonon interaction after photoexcition. Ultrafast THz measurements in Bi_2Se_3 micro-ribbon reveal the ultra-high modulation depth of 2,400% assisted by Fano-like plasmon-phonon-destructive interference. When plasmon frequency is controlled by changing the dimension of Bi_2Se_3 micro-slits, we observe the different relaxation dynamics of hot optical phonon after photoexcitation.

Engineering surface plasmon provides an efficient tool to modulate THz wave. A high modulation depth is expected to be emerged in topological insulator (TI) Bi_2Se_3 due to the strong optical modulation capability of Dirac plasmons [1]. In this work, we explore the ultrafast optical modulation of Dirac plasmons in a micro-ribbon array of Bi_2Se_3 by using time-resolved optical-pump THz-probe spectroscopy. Under optical pulse injection, the surface plasmon frequency is shifted beyond the phonon frequency in the THz range, which significantly changes the extinction spectra. As a result, an unprecedented, giant modulation depth up to 2,400% is obtained with very low fluence of optical control pulse (45 $\mu J/cm^2$). Our theoretical calculations show that the plasmon frequency shift arises from the photo-doping of the non-topological two-dimensional electron gas (2DEG) formed due to downward bending of the bulk bands near the surface [2, 3]. Unlike conventional semiconductor-based plasmonics, various species of quantum states, such as Dirac electrons, massive 2DEG and semiconductor-like bulk, which together with plasmon–phonon interference lead to dynamic spectral modulation in TIs, provide a novel platform for controlling plasmons.

The atomic composition of Bi_2Se_3 poses a limit to the control of the phonon resonances. Although prior studies have found that the electron-phonon coupling is a way to manipulate the phonon resonances [4], these methods require a complicate experimental system. Here, using the strong interaction of Dirac surface plasmon and optical phonon [1, 5], we demonstrate a simple methodology of altering the phonon resonances by lithographically-engineered surface plasmons in Bi_2Se_3. Our ultrafast terahertz investigation reveals that the phonon cooling is suppressed when the Dirac plasmon energy exceeds the phonon resonance, resulting in anomalous phonon stiffening. On the other hand, we observe that the phonon cooling is greatly accelerated (within 1 ps) when the plasmon energy is smaller than the bulk phonon, leading to phonon broadening. This observation suggests that engineering the plasmon-phonon coupling provides an alternative to dynamically control the phonon energy without atomic modification. These results thus provide a promising laboratory for novel topological insulator applications, ranging from topological thermoelectric effects to tunable terahertz plasmonic devices.

Acknowledgements- C.I., S.S., S.C., B.K., H.B. and H.C. were supported by the National Research Foundation of Korea (NRF) through the government of Korea (MSIP) (Grant Nos.

NRF-2015R1A2A1A10052520, NRF-2016R1A4A1012929), and Global Frontier Program (2014M3A6B3063709).

REFERENCES

1. Sim, S. *et al*., "Ultra-high modulation depth exceeding 2,400% in optically controlled topological surface plasmons," *Nature Communications*, Vol. 6, 8814, 2015.
2. Pietro, P. D. *et al*., "Observation of Dirac plasmons in a topological insulator," *Nature Nanotechnology*, Vol. 8, No. 8, 556-560, 2013.
3. Stauber, T. *et al*., "Spin-charge separation of plasmonic excitations in thin topological insulators," *Phys. Rev. B*, Vol. 88, No. 20, 2013.
4. Yan, J. *et al*., "Electric field effect tuning of electron-phonon coupling in graphene," *Phys. Rev. Lett*. Vol. 98, No. 16, 166802, 2007.
5. Autore, M. *et al*., "Plasmon-phonon interaction in topological insulator microrings," *Advanced Optical Materials*, Vol. 3, No. 9, 1257-1263, 2015.

THz hollow-core waveguide with metamaterial cladding

S. Atakaramians[1*], H. Li[1,2], R. Lwin[1], X. Tang[1], A. Argyros[1], S. C. Fleming[1], and B. T. Kuhlmey[1]

[1]Institute of Photonics and Optical Science (IPOS), School of Physics, the University of Sydney, New South Wales 2006, Australia

[2]Key Laboratory of All Optical Network and Advanced Telecommunication Network of EMC, Institute of Lightwave Technology, Beijing Jiaotong University, Beijing 100044, China

[*]corresponding author: shaghik.a@sydney.edu.au

Abstract- We theoretically, numerically and experimentally demonstrate hollow core fibres with hyperbolic metamaterial cladding having more than double the single-mode bandwidth of metallic waveguides. In the THz such fibres offer a unique combination of being mechanically flexible, with low optical loss and large single-mode bandwidth.

An essential component in developing compact terahertz devices are waveguides [1]. Among several waveguide solutions proposed for guiding THz radiation, hollow-core waveguides are one of the best options due to low losses of THz waves in air [1]. However, these waveguides usually have diameters of the order of several wavelengths and consequently are rigid, multimode pipes for guiding THz radiation rather than flexible fibres. The emergence of metamaterial opens a new avenue to overcome some of the limitations of hollow-core THz waveguides, by providing new guidance mechanisms and extreme birefringence that guide a single polarization [2,3]. We have demonstrated that fiber-drawing techniques can be used to produce large quantities of metamaterials with electric and magnetic responses [5,6]. Fibers containing arrays of thin metal wires have been produced, which have an electric response depending on the size and spacing of the wires. In this presentation, first we will discuss the characteristic equations for guided modes and the relevant mode existence conditions of a hollow-core waveguides with uniaxial metamaterial claddings [7,8]. Then we will show that a hollow-core waveguide with wire metals in the cladding can only confines transverse magnetic (TM) modes due to extreme anisotropy of wire metamaterials [9]. Finally, we will show experimental results demonstrating how utilizing metal wires in the cladding of a THz hollow-core waveguide can lead to flexible fibres with large single mode operating bandwidth (0.22-0.34 THz), 2.5 times larger than that which can be achieved using metallic hollow core waveguides [9].

ACKNOWLEDGEMENT

The work was supported in part by Australian Research Council (ARC) Centre of Excellence scheme CUDOS (CE110001018), and ARC under the Discovery Early Career Project Award number DE140100614 and Discovery Project DP140104116. This work was performed in part at the Optofab node of the Australian National Fabrication Facility (ANFF), using NCIRS and NSW State Government funding. H.L. acknowledges financial support from the China Scholarship Council.

REFERENCES

1. Tonouchi, M., “Cutting-edge terahertz technology,” Nat. Photonics 1, 97–105 (2007).

2. Atakaramians, S., Afshar, S., Monro, T. M. and D. Abbott, D., "Terahertz dielectric waveguides," *Adv. Opt. Photon.* 5, 169–215, 2013.
3. Cai, W. and Shalaev, V., "Optical Metamaterials: Fundamentals and Applications" (Springer) 2009.
4. Yan, M. and Mortensen, N. A., "Hollow-core infrared fiber incorporating metal-wire metamaterial," *Opt. Express* 17, 14851–14864, 2009.
5. Tuniz, A., Lwin, R., Argyros, A., Fleming, C. S. and Kuhlmey, B. T., "Fabricating metamaterials using the fiber drawing method," *J. Vis.Exp.* 68, e4299, 2012.
6. Tang, X., Kuhlmey, B. T., Stefani, A. , Tuniz, A., Fleming, S. C., Argyros, A., "Electromagnetic Wave Propagation Through Air-Core Waveguide With Metamaterial Cladding" *J. Lightwave Technol.* 34, 5317 (2016).
7. Atakaramians, S., Argyros, A., Fleming, S. C. and Kuhlmey, B. T., "Hollowcore waveguides with uniaxial metamaterial cladding: modal equations and guidance conditions," *J. Opt. Soc. Am. B* 29, 2462–2477, 2012.
8. Atakaramians, S., Argyros, A., Fleming, S. C. and Kuhlmey, B. T., "Hollowcore uniaxial metamaterial clad fibers with dispersive metamaterials," *J. Opt. Soc. Am. B* 30, 851–867, 2013.
9. Li, H., Atakaramians, S., Lwin, R., Tang, X., Yu, Z., Argyros, A., Fleming, S. C. and Kuhlmey, B. T., "Flexible single-mode hollow-core terahertz fiber with metamaterial cladding," *Optica*, Vol. 3, 941-947, 2016.

Symmetry enhanced non-reciprocal polarization rotation in a hybrid metal-graphene metasurface

A. Ottomaniello[1,2]*, S. Zanotto[2], A. Pitanti[2], F. Bianco[2], L. Baldacci[2], V. Miseikis[3], D. Convertino[4], C. Coletti[3], and A. Tredicucci[1,2]

[1]Dipartimento di Fisica "E. Fermi", Università di Pisa, L.go Pontecorvo 3, 56127 Pisa, Italy
[2]NEST, Istituto Nanoscienze - CNR, Piazza San Silvestro 12, 56127 Pisa, Italy
[3]Center for Nanotechnology Innovation @ NEST, Istituto Italiano di Tecnologia, Piazza San Silvestro 12, 56127 Pisa, Italy
[4]Center for Nanotechnology Innovation @ NEST, Scuola Normale Superiore and Istituto Italiano di Tecnologia, Piazza San Silvestro 12, 56127 Pisa (Italy)
*corresponding author: andrea.ottomaniello@df.unipi.it

Abstract— A monolayer graphene is able to produce a Faraday rotation of several degrees in modest magnetic field at terahertz frequencies. Using a metallic metasurface of sub-wavelength optical resonators placed in strong proximity to graphene, an increase of the non-reciprocal effect can be achieved over a broad range of frequencies. We demonstrated via simulations that increasing the geometric symmetry of the single resonator the performances of the device improved. The combination of both a huge polarization rotations (more than 20 degrees) accompanied by a large transmission amplitude, candidates this device as a prototype for sub-wavelength non-reciprocal element, like Faraday rotator and optical isolator.

Among the unique properties of graphene, its giant Faraday rotation ($\sim 6^\circ$) at terahertz (THz) frequencies [1] has attracted a lot of attention in order to approach a new prototype of non-reciprocal element with sub-wavelength dimensions. Focusing on the THz radiation, several works have succeeded to further enhance the non-reciprocal behavior of graphene [2], but most of them achieving this result at the price of losing the intrinsic two-dimensional character provided by graphene itself.
Triggered by the observation that (magneto-)optical response of graphene is strongly influenced by the presence of a planar square array of split-ring resonators (SRRs) at a distance of a few tenths of nanometers from it [3], we have been motivated to investigate by full wave simulations how the non-reciprocal polarization rotation can be greatly enhanced adopting this structure (Figure 1**a**).

We observed that the planar geometry of the specific resonator which constitutes the metasurface has a strong influence on both Faraday rotation angle (θ_F) and transmittance (T) of the system. Even just for common square electric-SRR shape, the hybrid metasurface provides an increase of the Faraday rotation in correspondence of the metasurface resonance. This result, however, comes at the expense of T which results to be very small even after an optimization of the geometric parameters. Nevertheless, devices that aim to work as a Faraday isolator or rotator need to have both high θ_F and T. Their performance can be indeed defined by a dimensionless parameter γ_F which is a function of the transmittance T and of θ_F [4]: $\gamma_\mathrm{F}(\mathrm{T}, \theta_\mathrm{F}) = \frac{|2\mathrm{T}\sin\theta_\mathrm{F}|^2}{(1-\mathrm{T}^2)^2}$. In order to have γ_F as large as possible, several other shapes have been studied. During this process of optimization, we found that shapes characterized by a higher degree of symmetry imply an improvement of the performances. If we take into account also the FWHM of γ_F as function of frequency and we define as figure of merit the product $\frac{\mathrm{FWHM}(\gamma_F)}{\nu(\gamma_\mathrm{F}^{\max})} \times \gamma_\mathrm{F}$, where $\nu(\gamma_\mathrm{F}^{\max})$ is the frequency of maximum γ_F, the improvement of the performances of the system for three symmetry group (C_2,C_4 and C_8) can be seen in Figure 1**b**. Following this trend, the geometry of the resonators which is observed to have the largest value of γ_F is that reported in Figure 1**a**, belonging to C_8 group. The electric and magnetic field spatial distributions of the resonator is shown in Figure 1**c**. The impact of the real part of the refractive index (n) of the substrate on the device performance has also been investigated. We found that lower values of n provide a larger value of the figure of merit, as it clearly appears from the comparison between the red and blue curves in Figure 1**b**, calculated for n equal to 1.5 and 2.5, respectively. In the fabricated device, the used substrate is Cyclic Olefyn Copolymer (COC), which has n$\sim$1.5 and optical losses under 3 cm^{-1} at THz frequencies. The measured transmission spectrum (in the absence of external magnetic field) is shown in Figure 1**d**

in comparison to the corresponding simulation.
Obviously, also the graphene Drude parameters highly influence the non-reciprocal properties. In panel **e** and **f**, the curves for θ_F and γ_F as function of frequency are shown for four values of the Fermi energy, respectively.

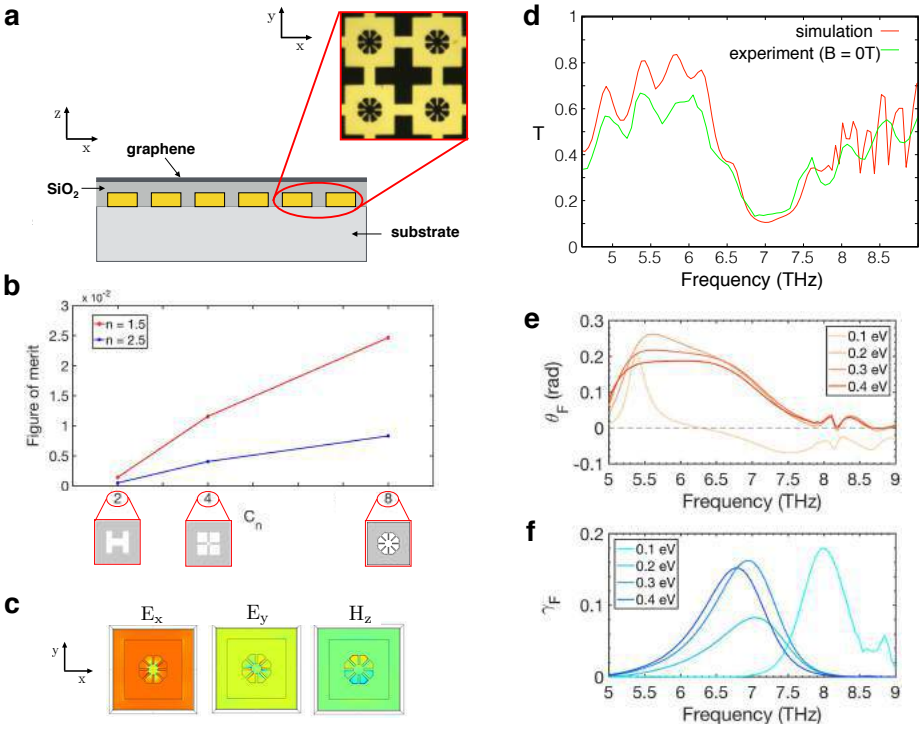

Figure 1: **a)** Device sketch showing the layers of the structure. Graphene, placed on the top, is separated by a 200 nm thick layer of oxide (SiO_2) from the 100 nm thick and 3×3 mm^2 wide metasurface of periodically arranged and interconnected (25 μm long) square resonators. An optical image of the resonators of a fabricated sample is shown. At the bottom a 100 μm thick layer of Cyclic Olefyn Copolymer (COC) is placed as substrate. **b)** Simulated figure of merit of the system for three different planar geometry of the resonators belonging to the symmetry group C_2, C_4 and C_8, respectively. The three geometric shapes are also shown at the bottom of the figure. **d)** Spatial distribution inside the unit cell of the x and y components of the electric field $\vec{E}$ and of the z component of the magnetic field $\vec{H}$ for the excited optical mode of a single resonator belonging to C_8. **d)** Comparison between measured transmission spectrum of fabricated sample in absence of external magnetic field and the corresponding full-wave simulation. In panels **e** and **f**, the simulated Faraday angle θ_F (rad) and dimensionless γ_F factor as function of frequency for the metasurface belonging to the C_8 symmetry group are inserted, respectively. The same quantities are studied for different values of graphene Fermi energy (0.1, 0.2, 0.3 and 0.4 eV). In all simulations the bias magnetic field is set to 7T and the graphene mobility is fixed at 4.000 cm^2/Vs.

In conclusion, we have studied a system consisting of a resonant metasurface put in close proximity to a graphene monolayer at THz frequencies. We demonstrated by simulations that this sub-wavelength structure strongly enhances the graphene Faraday rotation and that the performances can be strongly improved by increasing the symmetry of the unit resonator geometry. Its scalability allows to tune this operating region over the whole THz range, or, provided it is arranged in a connected fashion, it can be used as a back gate to change the Fermi energy of graphene, adding another powerful functionality for the tunability of the system.

REFERENCES

1. Crassee, I., "Giant Faraday rotation in single- and multilayer graphene", *Nature Phys.*, Vol. 7, 48–51, 2011.
2. Tamagnone, M., "Near optimal graphene terahertz non-reciprocal isolator", *Nat. Commun.*, Vol. 7, No. 11216, 2016. .
3. Zanotto, S., "Magneto-optic transmittance modulation observed in a hybrid graphene-split ring resonator terahertz metasurface", *Appl. Phys. Lett.*, Vol. 107, No. 121104, 2015.
4. Tamagnone, M., "Fundamental limits and near-optimal design of graphene modulators and non-reciprocal devices", *Nat. Photon.*, Vol. 8, 556–563, 2014.

Analytical description of nonlinear plasmonic phenomena in nanostructured graphene

J. D. Cox[1]*, R. Yu[1], and F. J. García de Abajo[1,2]

[1]ICFO-Institut de Ciencies Fotoniques, The Barcelona Institute of Science and Technology, Castelldefels, 08860 Barcelona, Spain

[2]ICREA-Institució Catalana de Recerca i Estudis Avançats, Passeig Lluís Companys 23, 08010 Barcelona, Spain

*corresponding author: joel.cox@icfo.eu

Abstract-We present an analytical, classical electromagnetic description of the nonlinear optical response associated with tunable plasmons in graphene nanostructures. Our model uses two-dimensional graphene conductivities as input to obtain the nonlinear response of the desired nanostructures. The results are shown to be in excellent agreement with realistic quantum-mechanical simulations based on a tight-binding description of electrons in graphene combined with the random-phase approximation for the response functions.

Graphene exhibits a remarkably high intrinsic nonlinearity that can be pushed even further when the optical frequency is tuned to the plasmon resonances of the material [1-4]. Atomistic simulations provide an accurate description of these phenomena, although their computational cost is prohibitive for large graphene nanostructures [3,4]. An alternative formalism consists in relying on classical electromagnetism, using the local nonlinear conductivities extracted from models of extended graphene. We show that both of these approaches are in excellent agreement for sufficiently large structures (10s of nm in lateral size) when describing second- and third-harmonic generation, as well as the Kerr effect. Additionally, we exploit an eigenmode decomposition of the optical field in the classical formalism to obtain analytical expressions for the plasmon-driven resonant response of the graphene ribbons and finite islands, in excellent agreement with full numerical calculations. This analytical description constitutes a valuable asset to explore nonlinear optical phenomena in the context of graphene plasmonics, and can also be applied to model nonlinearities in other planar plasmonic materials, such as thin metal layers.

REFERENCES

1. M. Gullans, D. E. Chang, F. H. L. Koppens, F. J. García de Abajo, and M. D. Lukin, Phys. Rev. Lett. **111**, 247401 (2013).
2. X. Yao, M. Tokman, and A. Belyanin, Phys. Rev. Lett. **112**, 055501 (2014).
3. J. D. Cox and F. J. García de Abajo, Nat. Commun. **5**, 5725 (2014).
4. J. D. Cox, I. Silveiro, and F. J. García de Abajo, ACS Nano **10**, 1995 (2016).

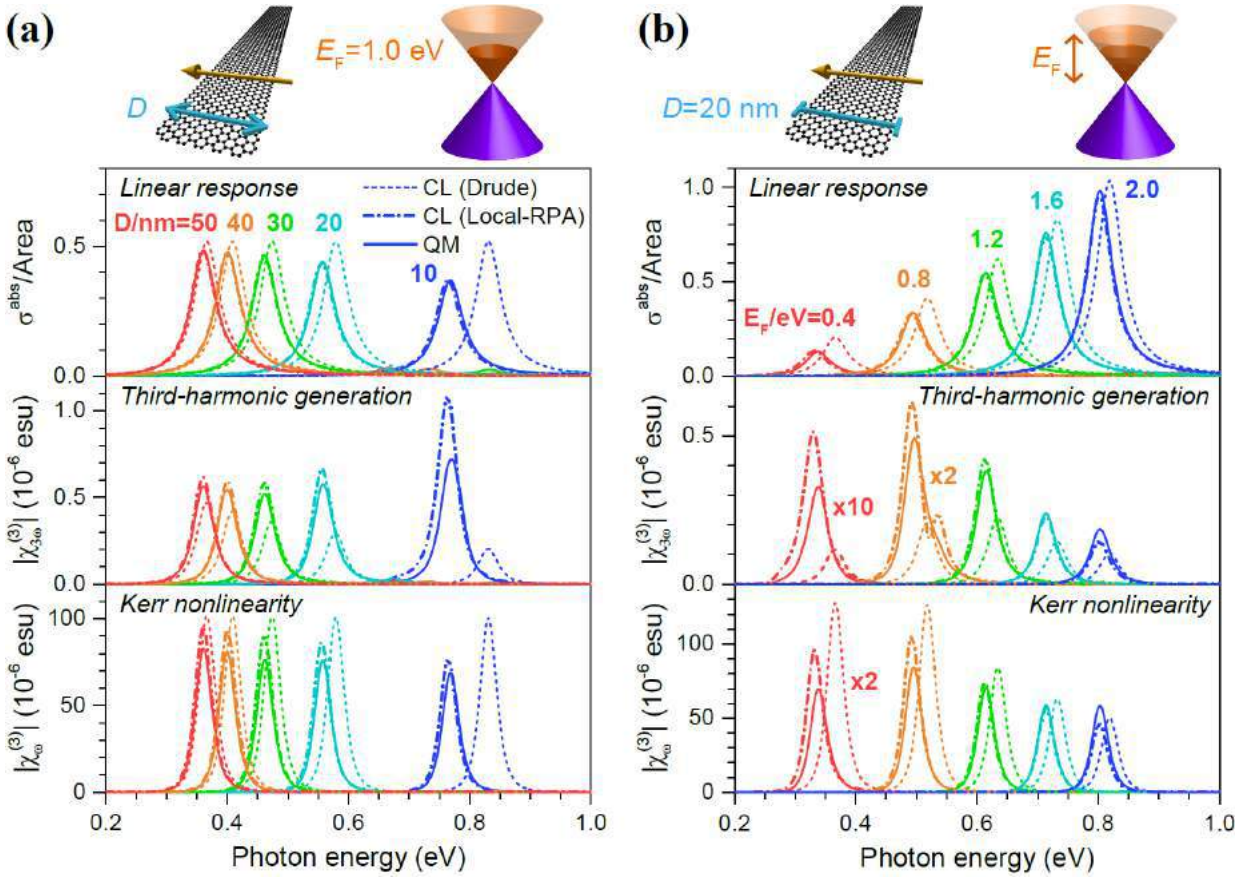

Figure 1. Linear and nonlinear optical response of graphene nanoribbons. We present the linear absorption (top graphs) and the third-order susceptibilities associated with third-harmonic generation (center graphs) and the Kerr nonlinearity (bottom graphs) for graphene nanoribbons of (a) fixed doping of EF=1.0 eV and varying width indicated by the numbers in the top graph (in units of nm) and (b) fixed width of D=20 nm and varying Fermi energy indicated by the numbers in the top graph (in units of eV). Solid curves correspond to atomistic simulations of zigzag-edge-terminated ribbons, dashed (dot-dashed) curves to results from the semi-analytical model employing purely intraband (full inter- and intra-band) graphene conductivities.

Periodic Systems with Glide Symmetry

Chiral Optics of Planar Metamaterials

E. Plum[1*] **and N. I. Zheludev**[1,2]
[1] Optoelectronics Research Centre and Centre for Photonic Metamaterials,
University of Southampton, UK
[2] Centre for Disruptive Photonic Technologies and The Photonics Institute,
Nanyang Technological University, Singapore
[*]corresponding author: erp@orc.soton.ac.uk

Abstract-Any planar structure can be superimposed with its mirror image. Despite lacking conventional chirality, planar metamaterials exhibit stronger and more diverse chiral optical effects than conventional materials. Planar chirality associated with the twist of flat spirals and mirror asymmetry introduced by the direction of illumination give rise to directional transmission asymmetries, giant linear and nonlinear optical activity, circular polarization reflectors and perfect absorbers as well as wavevector selective spectral filters.

It is a common misconception that chiral optical effects require chiral materials, i.e. materials that cannot be superimposed with their mirror image. In fact, chiral optical effects occur in chiral experiments.

A flat spiral does not have conventional chirality as it can be superimposed with its mirror image by flipping it over. Nevertheless, circularly polarized waves of opposite handedness will interact differently with a planar twisted object. As the planar twist reverses for opposite directions of observation, the handedness of the optical effect reverses for opposite directions of illumination, resulting in directionally asymmetric transmission [1]. An effective planar twist can result from oblique incidence onto any planar pattern and thus directionally asymmetric optical properties should be expected for any lossy planar metamaterial [2]. The effect can be engineered to yield perfect absorption for one circular polarization, while the other is reflected without polarization change, providing an opportunity to develop circularly polarized cavities for sensing and lasers [3].

A chiral experiment with an effective three-dimensional twist can result from oblique incidence onto any planar structure lacking two-fold rotational symmetry. For planar metamaterials, this can lead to exceptionally large optical activity for both transmitted [4] and reflected light [5] and exploiting nonlinearity enhancement in plasmonic metamaterials 10-million-fold larger nonlinear optical activity than in natural materials has been observed [6]. The effects are inherently tuneable due to their dependence on the angle of incidence and they allow the realization of switchable circular polarization perfect absorbers [7] as well as resonant spectral passband filters that are directional notch filters [8].

An overview over concepts developed over the last decade and associated experimental breakthroughs will be given.

Acknowledgements. The authors acknowledge fruitful discussions with Vassili A. Fedotov. This work is supported by the Leverhulme Trust, the UK's Engineering and Physical Sciences Research Council (grants EP/G060363/1 and EP/M009122/1) and the MOE Singapore (grant MOE2011-T3-1-005).

REFERENCES

1. V. A. Fedotov, P. L. Mladyonov, S. L. Prosvirnin, A. V. Rogacheva, Y. Chen and N. I. Zheludev, "Asymmetric propagation of electromagnetic waves through a planar chiral structure," *Phys. Rev. Lett.*, Vol. 97, 167401, 2006.
2. E. Plum, V. A. Fedotov, and N. I. Zheludev, "Asymmetric transmission: a generic property of two-dimensional periodic patterns," *J. Opt.*, Vol. 13, 024006, 2011.
3. E. Plum and N. I. Zheludev, "Chiral mirrors," *Appl. Phys. Lett.*, Vol. 106, 221901, 2015.
4. E. Plum, X.-X. Liu, V. A. Fedotov, Y. Chen, D. P. Tsai and N. I. Zheludev, "Metamaterials: optical activity without chirality," *Phys. Rev. Lett.*, Vol. 102, 113902, 2009.
5. E. Plum, V. A. Fedotov and N. I. Zheludev, "Specular optical activity of achiral metasurfaces," *Appl. Phys. Lett.*, Vol. 108, 141905, 2016.
6. M. Ren, E. Plum, J. Xu and N. I. Zheludev, "Giant nonlinear optical activity in a plasmonic metamaterial," *Nat. Commun.*, Vol. 3, 833, 2012.
7. E. Plum, "Extrinsic chirality: Tunable optically active reflectors and perfect absorbers," *Appl. Phys. Lett.*, Vol. 108, 241905, 2016.
8. N. I. Zheludev, E. Plum and V. A. Fedotov, "Metamaterial polarization spectral filter: Isolated transmission line at any prescribed wavelength," *Appl. Phys. Lett.*, Vol. 99, 171915, 2011.

Nonsymmorphic topological photonic crystals

Ling Lu

Instituite of Physics, Chinese Academy of Sciences, Beijing, China
linglu@iphy.ac.cn

Abstract— After discussing the consequences of band dispersions of glide, screw and time-reversal symmetries, I will show examples of 2D photonic crystal waveguides and 3D photonic crystal waveguides with glide and time-reversal symmetries. Then I will go over the discovery of Weyl points in a nonsymmorphic photonic crystal. At last, I will present a 3D magnetic topological photonic crystal hosting a single surface Dirac cone, protected by glide reflections. Such a gapless surface state is fully robust against random disorder of any type.

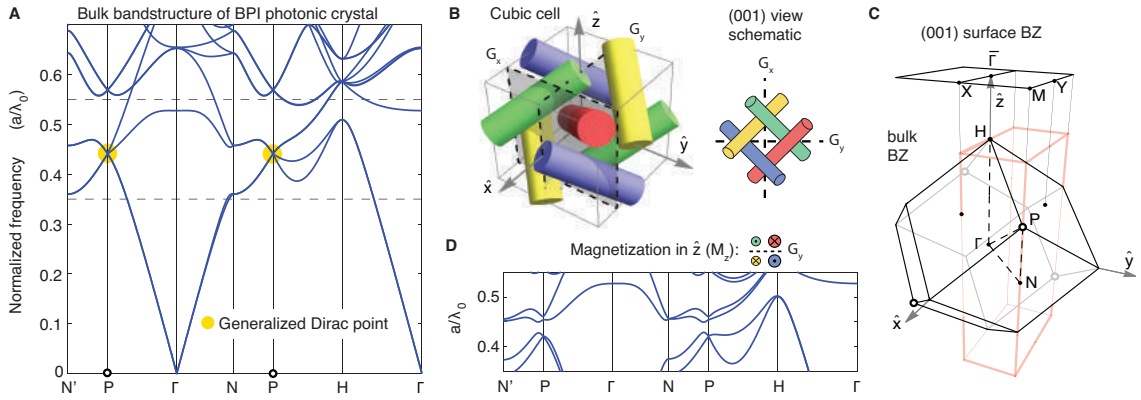

Figure 1: Bulk band structures of the BPI photonic crystal in bcc lattice. A) The GDP is between the first four bands. B) The cubic unit cell of length a consisting of four identical dielectric rods oriented along the bcc lattice vectors of (111) (red), $(11\bar{1})$ (yellow), $(1\bar{1}1)$ (blue) and $(\bar{1}11)$ (green). The rods go through $(0,0,0)a$, $(0,0.5,0)a$. $(0.5,0,0)a$ and $(0,0,0.5)a$ respectively. There are two glide reflection planes (G_x and G_y) in the structure, invariant on the (001) surface. The top-view schematic illustrates the relations between the rods under operations of G_x and G_y. C) The bcc BZ and its projection onto the (001) surface BZ. The transparent red box outlines the volume in the bulk BZ that projects to half of the surface BZ. D) Bulk band structure showing that the GDP opens when magnetization is applied on the rods without breaking G_y.

ACKNOWLEDGMENT

I thank all my collaborators on nonsymmorphic photonic crystals.

REFERENCES

1. Mock, A., Lu, L., & O'Brien, J. (2010). Space group theory and Fourier space analysis of two-dimensional photonic crystal waveguides. Physical Review B, 81(15), 155115.
2. Lu, L., Cheong, L. L., Smith, H. I., Johnson, S. G., Joannopoulos, J. D., & Soljačić, M. (2012). Three-dimensional photonic crystals by large-area membrane stacking. Optics letters, 37(22), 4726-4728.
3. Lu, L., Fu, L., Joannopoulos, J. D., & Soljačić, M. (2013). Weyl points and line nodes in gyroid photonic crystals. Nature photonics, 7(4), 294-299.
4. Lu, L., Fang, C., Fu, L., Johnson, S. G., Joannopoulos, J. D., & Soljačić, M. (2016). Symmetry-protected topological photonic crystal in three dimensions. Nature Physics, 12(4), 337-340.

Rectangular holey glide-symmetric metasurfaces for ultra-wideband anisotropy

B. Majumdar[1*], G. Valerio[2] and O. Quevedo-Teruel[3*]

[1] Indian Institute of Technology, Bombay, India

[2] Laboratoire d'Electronique et Electromagnétisme, Université Pierre et Marie Curie, Paris, France.

[3] Electromagnetic Engineering department (ETK) in School of Electrical Engineering, KTH Royal Institute of Technology, Stockholm, Sweden

[*]corresponding author: oscarqt@kth.se

Abstract- Metasurfaces have recently gained popularity for designing lens antennas. Particularly, fully metallic metasurface lens antennas present low losses and are ideal for space applications. In this work, we present a novel asymmetric unit cell that can be employed for the design of anisotropic lenses. The unit cell consists of two glide-symmetric layers. A rectangular hole is edged at the bottom layer, which is periodically mirrored and translated in the top layer. This unit cell provides low dispersion over a wide band and produces anisotropic high refractive index as required for typical lenses in antennas.

Metasurfaces are two-dimensional versions of metamaterials [1, 2]. By using metasurfaces as in [1-3], flat lenses can be designed, proving high directive beam scanning antennas. These antennas find application for wireless communications, especially at the very high frequencies, where array have a high cost, due to their need of phase shifters [4].

In [3], glide symmetric metasurfaces were proposed to obtain stable refractive indexes over an ultra-broadband frequency range. Those proposed structures were fully metallic, which is an asset for space applications, and inherently have low loss capabilities. Additionally, using this glide-symmetric based approach, it has been demonstrated that glide-symmetric can be employed to produce bandgaps which can be employed for gap waveguide technologies [5].

Glide-symmetric metasurfaces consist of two layers, which are translated half period and mirrored [6-10], and they were extensively studied in the ‘60s and ‘70s in the one dimensional configuration. Although the first studies of two-dimensional glide-symmetric unit cells have provided promising properties [3,5], only isotropic configurations have been proposed.

Here, we propose rectangular holey structures that can be employed to produce an anisotropic response. Our asymmetric unit cell consists of two layers as shown in Fig. 1 with rectangular holes, which are glide-symmetric. Fig. 2 shows the simulated dispersion diagram of the proposed asymmetric unit cell in both x and y directions, with the variation of the depth of the rectangular hole. It is noticed that for the propagating wave along the x direction, the fundamental mode varies with the depth of the hole, but for the waves propagating in y direction, no significant variation is observed. In both cases, the mode is non-dispersive, opening possibilities for the design of ultra wideband anisotropic flat lenses.

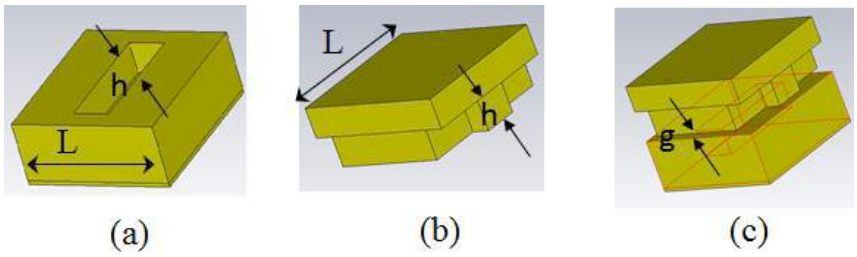

Fig. 1: (a) Bottom layer (b) top layer (c) overall unit cell [L= 4mm, g= 0.15 mm].

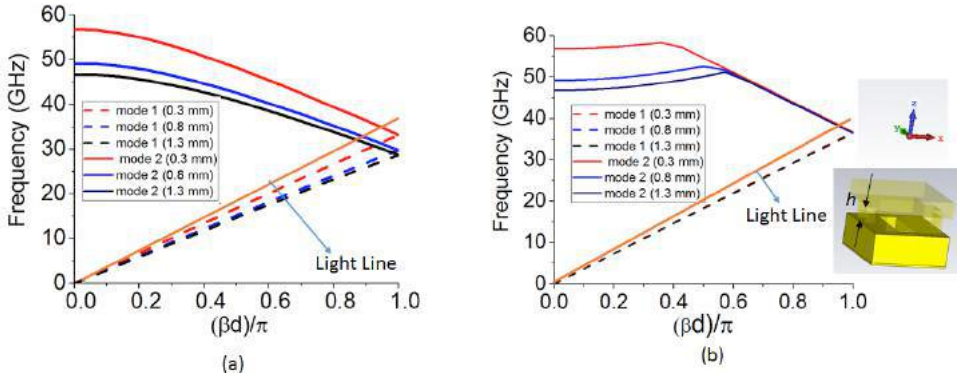

Fig. 2: Dispersion diagram for different h values: (a) x direction (b) y direction.

REFERENCES

1. M. Bosiljevac, M. Casaletti, F. Caminita, Z. Sipus, and S. Maci, "Non- uniform metasurface Luneburg lens antenna design," *IEEE Transactions on Antennas Propagation* , vol. 60, no. 9, pp. 4065–4073, Sep. 2012.
2. A. Dockrey, M. J. Lockyear, S. J. Berry, S. A. R. Horsley, J. R. Sambles, and A. P. Hibbins, "Thin metamaterial Luneburg lens for surface waves," *Physical Review B*, vol. 87, p. 125137, Mar. 2013.
3. O. Quevedo-Teruel, M. Ebrahimpouri, and M. Ng Mou Kehn. "Ultrawideband Metasurface Lenses Based on Off-Shifted Opposite Layers." *IEEE Antennas and Wireless Propagation Letters* 15, pp 484-487, 2016.
4. A. Torki, M. Ebrahimpouri and O. Quevedo-Teruel, "A planar steerable 60 GHz leaky wave antenna with Luneburg lens feed", *In Proc. APSURSI*, pp. 1405-1406, June, 2016.
5. M. Ebrahimpouri, O. Quevedo-Teruel, E. Rajo-Iglesias, "Design Guidelines for Gap Waveguide Technology Based on Glide-Symmetric Holey Structures", in press, *IEEE Microwave and Wireless Component Letters*, 2017.
6. A. Hessel, M. H. Chen, R. C. M. Li, and A. A. Oliner, "Propagation in periodically loaded waveguides with higher symmetries," in *Proceedings of the IEEE*, vol. 61, no. 2, pp. 183–195, Feb. 1973.
7. G. Valerio, Z. Sipus, A. Grbic, O. Quevedo-Teruel, "Accurate equivalent-circuit descriptions of thin glide-symmetric corrugated metasurfaces," in press, *IEEE Transactions on Antennas and Propagation*, 2017.
8. O. Dahlberg, R. Mitchell-Thomas and O. Quevedo-Teruel, "Reducing the Dispersion of Periodic Structures with Twist and Polar Glide Symmetries", *Physical Review Letters*, 2017.
9. F. Ghasemifard, M. Norgren, O. Quevedo-Teruel, "Dispersion Analysis of Two Dimensional Glide-Symmetric Corrugated Metasurfaces Using Mode-Matching Technique", *IEEE Microwave and Wireless Component Letters*, 2017.
10. G. Valerio, Z. Sipus, A. Grbic, O. Quevedo-Teruel, "The Role of Resonances in Plasmonic Holey Metasurfaces for the Design of Artificial Flat Lenses," *Optics Letters*, 2017.

Study of propagation characteristics in a waveguide with twist-symmetric holes

F. Ghasemifard and **O. Quevedo-Teruel**

KTH Royal Institute of Technology, Sweden
fatemehg@kth.se

Abstract— The effect of twist symmetry, a special kind of higher symmetries, in a one dimensional periodic structure has been studied. It has been shown that by adding twist symmetry, achieving less dispersive and denser materials is possible. Moreover, it has been shown that the location of bandgap is changed by adding twist symmetry or changing the degree of twist symmetry.

Glide and twist (screw) symmetries are a certain class of higher symmetries. A glide-symmetric structure is a structure which coincides with itself under a half-period translation followed by mirroring with respect to a glide plane [1]. A p-fold twist-symmetric structure is a structure which coincides with itself under a translation of d/p and a rotation of $2\pi/p$ around the twist axis, where d is the period of the unit cell [1]. Here, we name p as the degree of the twist symmetry. By generalizing the Floquet theorem, periodic structures possessing these higher symmetries were studied in the 1960's and 70's [1, 2, 3, 4].

Recently, glide-symmetric metasurfaces have been proposed. These metasurfaces present low frequency dispersion [5, 6] and can be used to implement wideband flat lens antenna [5]. In these works, it has been shown that a metasurface with glide symmetry acts as a medium with a constant equivalent refractive index over a broad range of frequencies. Moreover, compared to the conventional metasurfaces, higher equivalent refractive indices are achievable by glide-symmetric metasurfaces [5]. Glide-symmetric structures can also be employed in gap waveguide technology [7].

Here, we study the effect of adding twist symmetry to a coaxial waveguide with periodic holes. For this purpose, three different periodic configurations with the same periodicity are investigated. The first one is a coaxial waveguide, composed of an inner and outer conductor, separated by air, with holes located periodically on the inner conductor. Since this structure can be considered as a translation of the holes, it does not possess higher symmetries. However, the second and third configurations are the same coaxial waveguide with 2-fold and 4-fold twist symmetric holes on the inner conductor. The inner conductors of all the cases and their dispersion diagrams have been illustrated in Figure 1. In all cases the inner and outer radii of the coaxial waveguide are, respectively, 1.49 mm ($D/2$ in Figure 1) and 1.59 mm; the periodicity is 12 mm and the sides of the holes $L = 2.4$ mm and $A = 4.69$ mm (A is the length of the arc part of the hole).

The results demonstrate that the dispersive nature of the lowest propagation modes in the coaxial waveguide with periodic holes (Single hole configuration in Figure 1) is reduced or even removed by adding twist symmetry. Moreover, the results reveal that by increasing the degree of the twist symmetry, higher effective refractive indices are achievable. Furthermore, it is clear that the location of bandgaps can be changed by adding twist symmetry or by changing the degree of the twist symmetry. For instance, in the single hole case, there is a bandgap from 10.05 GHz to 13.45 GHz and in 2-fold case, there is a bandgap from 18.26 GHz to 25.91 GHz, whereas, for the frequencies below 30 GHz there is no bandgap in 4-fold case.

In conclusion, by adding glide or twist symmetry to periodic structures, we will have more control on the propagation characteristics of periodic structures. This effect could be used in designing travelling wave antennas such as leaky-wave antennas. Moreover, periodic structures with higher symmetries can be used to realize wideband flat antennas.

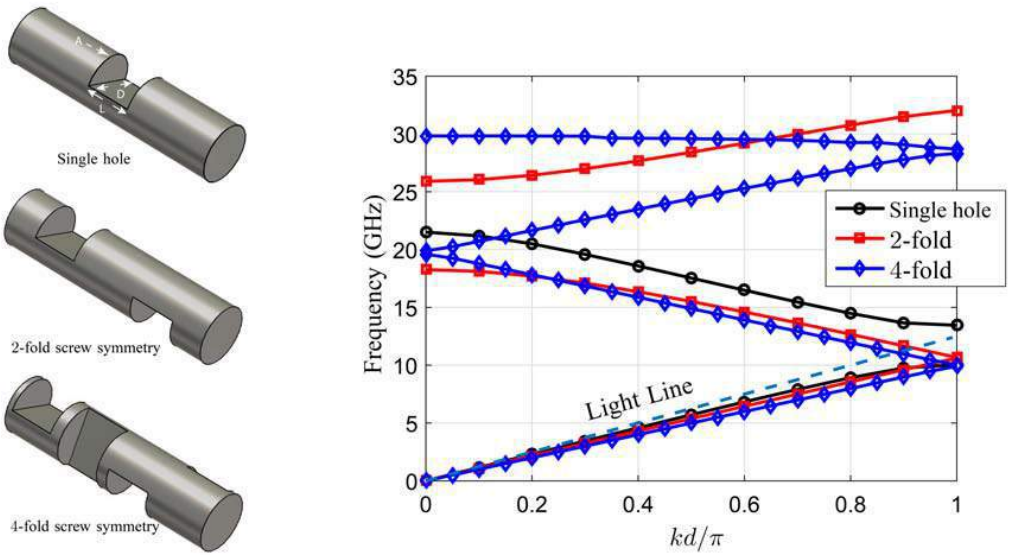

Figure 1: (Left) Inner conductor of a coaxial waveguide with periodic holes (Single hole) and the same coaxial waveguide with 2-fold and 4-fold twist-symmetric holes. In all structures the inner and outer radii of the coaxial waveguide are, respectively, 1.49 mm (which is $D/2$) and 1.59 mm; the periodicity is 12 mm, and the sides of the holes $L = 2.4$ mm and $A = 4.69$ mm (A is the length of the arc part of the hole). (Right) Dispersion diagrams of a coaxial waveguide with periodic holes (Single hole) and the same coaxial waveguide with 2-fold and 4-fold twist-symmetric holes.

REFERENCES

1. Hessel A., Chen M. H., Li R. C. and Oliner A. A., "Propagation in periodically loaded waveguides with higher symmetries," *Proceedings of the IEEE*, Vol. 61, No. 2, 183–195, 1973.
2. Crepeau P. J. and McIsaac P. R., "Consequences of symmetry in periodic structures," *Proc. IEEE*, Vol. 52, 33–43, 1964.
3. Mittra R. and Laxpati S., "Propagation in a waveguide with glide reflection symmetry," *Can. J. Phys.*, Vol. 43, 3353–372, 1965.
4. Kieburtz R. B. and Impagliazzo J., "Multimode propagation on radiating traveling-wave structures with glide-symmetric excitation," *IEEE Trans. Antennas Propagat.*, Vol. AP-18, 3–7, 1970.
5. Quevedo-Teruel O., Ebrahimpouri M. and Kehn M. N., "Ultrawideband metasurface lenses based on off-shifted opposite layers," *IEEE Antennas and Wireless Propagation Letters.*, Vol. 15, 484–487, 2016.
6. Mitchell-Thomas R. C., Hooper I. R., Sambles J. R., Hibbins A. P. and Quevedo-Teruel O., "Broadband metasurface for surface wave lenses," *in 2016 URSI International Symposium on Electromagnetic Theory (EMTS)*, 2016.
7. Ebrahimpouri M., Quevedo-Teruel O. and Rajo-Iglesias E., "Design Guidelines for Gap Waveguide Technology Based on Glide-Symmetric Holey Structures," *IEEE Microwave and Wireless Component Letters*, 2017.

Cost-effective Integrated Waveguide Circuits at High Frequencies Using Glide-Symmetric EBG Structures

M. Ebrahimpouri[1], **O. Quevedo-Teruel**[1*]

[1] Electromagnetic Engineering department (ETK) in School of Electrical Engineering, KTH Royal Institute of Technology, Stockholm, Sweden

[*]oscarqt@kth.se

Abstract- Here, we present a cost-effective and easy method to manufacture integrated waveguide circuits at high frequencies. Glide-symmetric holey EBG structure enables us to realize gap-waveguide technology economically since it only requires drilling holes on metallic plates and larger periodicity of it with respect to the pin-type EBG at the same frequency results in higher accuracy of manufacturing at high frequencies. Introducing this method provides a way for mass production of gap waveguide technology at high frequencies.

Hollow metallic waveguides are one of the earliest types of transmission lines. They have been popular because of their properties like high power handling capacity, low-loss and cross-talk free characteristics. However, these waveguides are expensive and difficult to manufacture at high frequencies. To overcome this problem, substrate integrated waveguide (SIW) [1] and gap waveguide technology [2] were proposed during last years. Although SIW structures are compact and can be manufactured using PCB technology, they are not efficient at high frequencies due to the losses originated by dielectrics. Additionally, SIW requires of metallic vias with diminutive periodicity to minimize leakage, increasing their total cost at high frequencies. Gap waveguide technology is new alternative to hollow metallic waveguides at high frequencies. In gap waveguide, there is no need to have contact between upper and lower plate, due to the use of pin-type EBG at the sides of the wave-guiding region, which is an advantage for manufacturing. Furthermore, waves are guided in the air, which results in less lossy transmission lines. However, at high frequencies thin and tall metal pins are required to prevent leakage in this technology, which increases the costs of manufacturing. To solve this problem, half-height pin-type EBG was proposed [3].

Here, we propose an alternative solution, glide-symmetric holey EBG structures. Manufacturing our proposed EBG structure is easier than pin-type EBG since it only requires drilling holes on metal. Periodicity of this EBG structure is about 3 times larger with respect to pin-type EBG, which results in higher accuracy of manufacturing at high frequencies. A glide-symmetric unit cells is created after a periodic mirror and translation [4-8]. Glide-symmetric structures has demonstrated to produce non-dispersive responses [9] and extraordinary bandgaps [10].

Fig. 1 (a) and (b) present the structure of square lattice of this unit-cell and dispersion diagram over its Brillouin zone, respectively. According to this figure, this EBG structure has a stop-band from 40 GHz to77 GHz. Therefore, this EBG structure can be used with standard rectangular waveguide (WR-19) in U-band (40 GHz- 60 GHz). Fig. 2(a) presents the proposed waveguiding structure. The glide-symmetric holey EBG at the location of gap prevents leakage and provides almost perfect transmission similar to shielded rectangular waveguide (RW). Fig. 2(b) compares transmission in a perfect RW with our proposed waveguiding structure and a

waveguide, which is made in two parts and EBG structure is not placed at the location of gap . Considering Fig. 2(b), a small gap at side walls creates significant leakage, while by placing EBG structure at the location of gap, we can have almost perfect transmission.

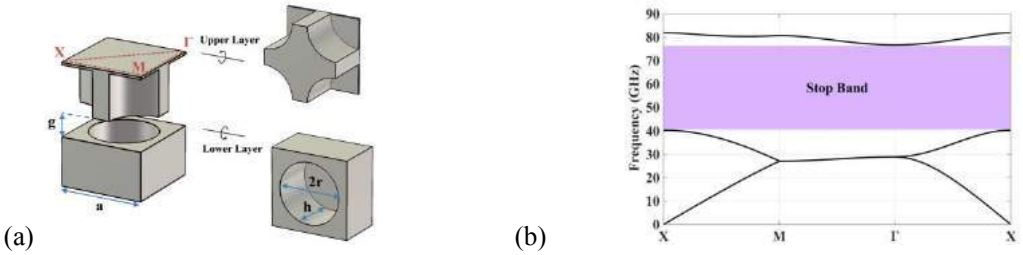

(a) (b)

Figure 1. (a) Structure of the glide-symmetric holey unit-cell. (b) Dispersion diagram over the Brillouin zone, when r=1.4 mm, h=2mm, a=5 mm, g=0.05 mm.

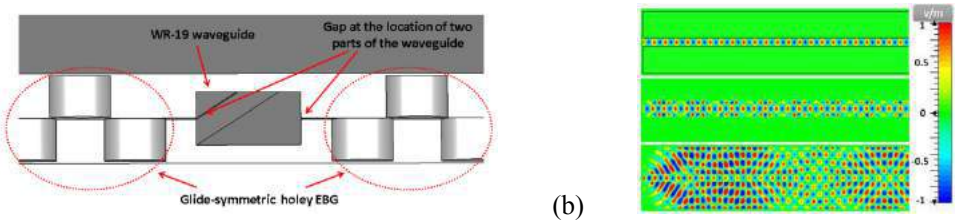

(a) (b)

Figure 2. a) Proposed waveguiding structure. b) Normalized electric field at 50 GHz in perfect RW (top), proposed waveguiding structure (middle) and a waveguide with airgap of 0.05 mm but without EBG (bottom).

REFERENCES

1. F. Shigeki, “Waveguide Line,” *Japanese Patent*, JP6053711, Feb. 1994.
2. P.-S. Kildal, E. Alfonso, A. Valero-Nogueira and E. Rajo-Iglesias, "Local Metamaterial-Based Waveguides in Gaps Between Parallel Metal Plates," *in IEEE Antennas and Wireless Propagation Letters*, vol. 8, pp. 84-87, 2009.
3. F. Fan, J. Yang and P. S. Kildal, "Half-height pins - a new pin form in gap waveguide for easy manufacturing," *10th European Conference on Antennas and Propagation (EuCAP), Davos*, pp. 1-4, 2016.
4. A. Hessel A., M. H. Chen, R. C. M. Li, and A. A. Oliner, “Propagation in periodically loaded waveguides with higher symmetries,” in *Proceedings of the IEEE*, vol. 61, no. 2, pp. 183–195, Feb. 1973.
5. G. Valerio, Z. Sipus, A. Grbic, O. Quevedo-Teruel, “Accurate equivalent-circuit descriptions of thin glide-symmetric corrugated metasurfaces,” in press, *IEEE Transactions on Antennas and Propagation*, 2017.
6. O. Dahlberg, R. Mitchell-Thomas and O. Quevedo-Teruel, “Reducing the Dispersion of Periodic Structures with Twist and Polar Glide Symmetries”, *Physical Review Letters*, 2017.
7. F. Ghasemifard, M. Norgren, O. Quevedo-Teruel, “Dispersion Analysis of Two Dimensional Glide-Symmetric Corrugated Metasurfaces Using Mode-Matching Technique”, *IEEE Microwave and Wireless Component Letters*, 2017.
8. G. Valerio, Z. Sipus, A. Grbic, O. Quevedo-Teruel, “The Role of Resonances in Plasmonic Holey Metasurfaces for the Design of Artificial Flat Lenses,” *Optics Letters*, 2017.
9. O. Quevedo-Teruel, M. Ebrahimpouri and M. Ng Mou Kehn, "Ultrawideband Metasurface Lenses Based on Off-Shifted Opposite Layers," *in IEEE Antennas and Wireless Propagation Letters*, vol. 15, pp. 484-487, Dec. 2016.
10. M. Ebrahimpouri, O. Quevedo-Teruel, E. Rajo-Iglesias, “Design Guidelines for Gap Waveguide Technology Based on Glide-Symmetric Holey Structures”, in press, *IEEE Microwave and Wireless Component Letters*, 2017.

Symmetry properties of planar particle arrays and their role for non-reciprocal and one-way guiding.

Y. Mazor and Ben Z. Steinberg
School of Electrical Engineering, Tel-Aviv University, Israel
steinber@eng.tau.ac.il

Abstract-Resonant particle arrays have been considered as waveguides for various applications. We present a general theory for analyzing the breach of geometrical symmetries required to allow for non-reciprocal guiding and optical isolation. Both, the unit cell symmetry and the properties of the particles themselves play a role in this study. The structure symmetry can be combined with specific particles properties to yield various wave phenomena. Their role in achieving non reciprocity, non-even dispersion, and one-way guiding, will be discussed.

In the context of polarizability theory and discrete dipole approximation, particle arrays response is governed by the difference equation [1]

$$p_n = \alpha_n \sum_{m \neq n} G(r_n - r_m) p_m + \alpha_n E^{inc}(r_n)$$

where p_n and α_n are the equivalent dipole response and polarizability tensor of the n-th particle, located at r_n. Here $G(r)$ is the free space dyadic Green's function. The formulation above holds for any set of particles as long as the particles are electrically small, and the inter-particle distance is large compare to the typical particle size. Specifically, we are interested in cases where at least part of the particles possess non-symmetric polarizability tensor that supports Faraday rotation. This property can be achieved, e.g. by using ferrite particles. In the optical regime, particles made of plasmonic Drude-like material under magnetic bias would possess such properties.

Examples of the particle arrays studied under the present framework are shown in Fig. 1. Any periodic planar strip-like array belongs to at least one group of the seven Frieze symmetry groups schematized in Fig. 1(a). It has been shown, however, that if the particles are merely spherical, then bias magnetization (and the ensuing Faraday rotation) are not sufficient to achieve non-even dispersion and one-way behavior; the associated particle array must possess at least two parallel chains in order to achieve these appealing properties. This observation stems from the obvious geometrical fact that a periodic particle array that consists of a single chain of spherically symmetric particles is "too symmetrical"; it belongs to most of the seven Frieze groups. Non-even dispersion and one-way guiding can reside only in the p1 and p1m1 groups [2].

A single chain particle array can be forced to reside in the aforementioned groups only, if one assign to each particle a property that is not preserved under any type of reflection. A geometrical rotation may provide the solution, in which case the particles must not be spheres, in order to render the rotation meaningful. Indeed, it has been shown that magnetized particle chains of the types shown in Figs. 1(b) and 1(c) possessing conventional and longitudinal chiralities, provide the desires breach of EM symmetries [3,4]. Of particular interest is the structure of Fig. 1(c) as it can be made completely flat, thus it is more convenient for fabrication.

It is interesting to examine the structure's dependence on the rotation step angle $\Delta\theta$. When observed in the "laboratory" frame, these structures seem periodic only for rational $\Delta\theta/\pi$. However, it can be shown that by observing the system in a *rotating* coordinate system $r_n \mapsto T_n r_n$ where T_n is a matrix of rotation by $n\Delta\theta$ about the z axis, the chain in Fig. 1(b) can be made periodic with period d for any $\Delta\theta/\pi$, rational or not. To contrast, there is no coordinate transformation under which the longitudinal chirality chain in Fig. 1(c) can be made periodic if $\Delta\theta/\pi$ is not a rational number. This structure, thus, is much richer in terms of spectral and geometrical features, and optional realizations. Furthermore, it suggests a testbed to study a plethora of fundamental physical phenomena. For example, the passage from a completely symmetric structure, to a one that provides only the basic breach of symmetries permitting one-way behavior, and then on to the case of non-reciprocal quasi-periodic structure (irrational $\Delta\theta/\pi$), are all encapsulated within the same structure. The passage is provided by a slight change of parameter. Figure 1(d) shows the spectral properties of the chain in Fig. 1(c), in the $\Delta\theta/\pi, \omega$ plane, under magnetization. A reminiscent of the Hofstadter's butterfly is seen, where the one-way property is color coded into the plane.

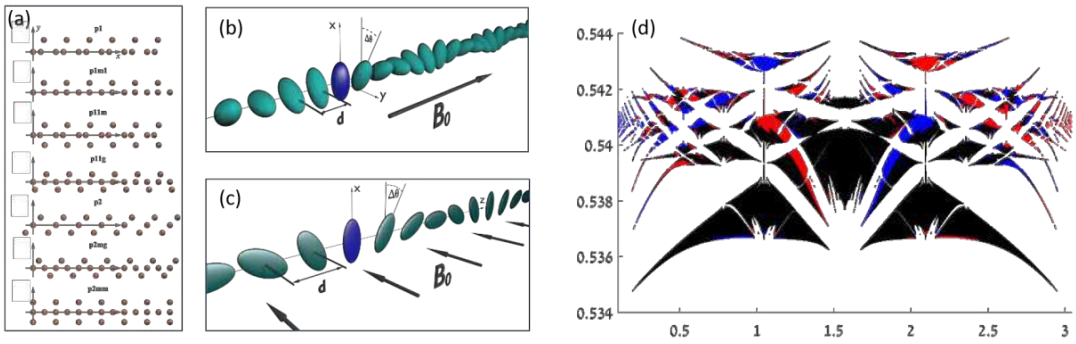

Figure 1. Particle arrays and one-way guiding. (a) The seven Frieze group for strip-like particle arrays. (b), (c) Single chains that provide the required breach of symmetries for one-way guiding (d) Spectral properties of the chain in (c), color coded according to the allowed propagation direction. Black points represent two-way guiding. Red or blue points represent only left or right-way guiding.

In this work the symmetry properties of these interesting structures will be discussed and illuminated via examples.

REFERENCES

1. Alu, A. and N. Engheta, "Theory of linear chains of metamaterial/plasmonic particles as subdiffraction optical nanotransmission lines," *Phys. Rev. B*, Vol. 74, No. 20, 205436 1-17, 2006.
2. Mazor, Y., Y. Hadad and Ben Z. Steinberg, "Planar one-way guiding in periodic particle arrays with asymmetric unit cell and general group symmetry considerations," *Phys. Rev. B*, Vol. 92, No. 12, 125129 1-17, 2015.
3. Hadad, Y. and Ben Z. Steinberg, "Magnetized spiral chains of plasmonic ellipsoid for one-way optical waveguides," *Phys. Rev. Lett.*, Vol. 105, No. 23, 233904 1-4, 2010.
4. Mazor, Y. and Ben Z. Steinberg, "Longitudinal chirality, enhanced non-reciprocity, and nanoscale planar one-way plasmonic guiding," *Phys. Rev. B*, Vol. 86, No. 4, 045120 1-5, 2012.

Generalized glide symmetry and topological edge states in layered media

S. A. R. Horsley[1]

[1]Department of Physics and Astronomy, University of Exeter, Stocker Road, Exeter, UK, EX4 4QL
s.horsley@exeter.ac.uk

Abstract— In this talk I shall discuss the theory of glide symmetry and its generalization to include mixtures of translation and polarization transformation, or translation and time reversal. I shall discuss an example where a wave propagates through a sequence of anistropic slabs, showing how generalized glide symmetry can be used to control the frequency gaps at the Brillouin zone boundary. Following from this I shall discuss the existence of edge states at the interface between two such stacks of slabs, finding the relationship between the Zak phase and the surface impedance of each stack.

Our understanding of wave propagation through periodic media is founded on Bloch's theorem [1]: translation through one spatial period leads to a phase difference, $\varphi(x+a) = \mathrm{e}^{\mathrm{i}Ka}\varphi(x)$. Typically the frequency increases until K reaches the edge of the first Brillouin zone, where there is a frequency gap before the next band of propagation.

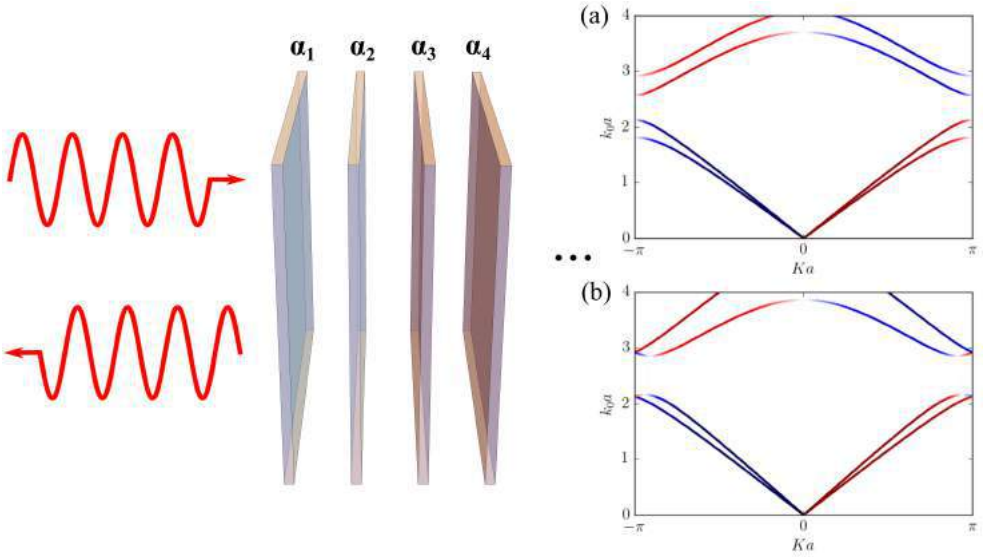

Figure 1: An an example of generalized glide symmetry we consider a series of thin anisotropic slabs characterised by tensors $\boldsymbol{\alpha}_i$. In general such a sequence of slabs exhibit a band gap at $K = \pm\pi/a$ as shown in panel (a) (color indicates direction of power propagation, red positive and blue negative). Panel (b) shows a case where we have imposed a translation–polarization glide symmetry, closing the band gaps at the Brillouin zone boundary.

But this isn't the full story. As usually defined, the first Brillouin zone is only the correct choice if symmetry under translation by a is the most basic symmetry operation. An obvious case where this doesn't hold is a badly chosen unit cell, which might e.g. contain two periods of the structure. In this case the unit–cell transfer matrix $\boldsymbol{T}$ can be written as the square of another transfer matrix $\boldsymbol{t}_{1/2}$

$$\boldsymbol{T} = \boldsymbol{t}_{1/2}^2$$

and the eigenvalue of $\boldsymbol{T}$, $\mathrm{e}^{\mathrm{i}Ka}$ is the square of the eigenvalue of $\boldsymbol{t}_{1/2}$, $\mathrm{e}^{\mathrm{i}Ka/2}$, the band gaps closing at the false Brillouin zone boundary $K = \pm\pi/a$. There are other less trivial cases where there

is a more basic symmetry of the structure, equal to a translation by a/N in addition to another symmetry operation $\boldsymbol{U}$

$$\boldsymbol{T} = \left(\boldsymbol{U} \cdot \boldsymbol{t}_{1/N}\right)^N = \ldots \boldsymbol{U}^{!\ 2} \cdot \boldsymbol{t} \cdot \boldsymbol{U}^2 \cdot \boldsymbol{U}^{!\ 1} \cdot \boldsymbol{t}_{1/N} \cdot \boldsymbol{U} \cdot \boldsymbol{t}_{1/N} \tag{1}$$

One kind of symmetry operation $\boldsymbol{U}$ is a rotation of the structure by an angle $2\pi/N$. When $N = 2$ such structures are said to exhibit *glide* symmetry. This symmetry has attracted some recent interest [2, 3], both in the context of the design of broadband metasurface lenses, and as a useful symmetry in topological photonics. However, it is clear that $\boldsymbol{U}$ is not restricted to spatial rotations. In this talk I shall explore such generalized glide symmetry operations where $\boldsymbol{U}$ can represent a time reversal operation or a transformation of the polarization. In the former case I shall connect generalized glide symmetry with PT–symmetry, and shall illustrate how band gaps can be closed by suitable design of a unit cell, even though the unit cell exhibits no purely spatial sub–division.

As a simple system where we can explore applications of generalized glide symmetry we consider a wave propagating through a sequence of anisotropic plates (see figure 1),

$$\frac{d^2}{dx^2}\begin{pmatrix} E_y \\ E_z \end{pmatrix} + k_0^2 \begin{pmatrix} \epsilon_{yy}(x) & \epsilon_{yz}(x) \\ \epsilon_{zy}(x) & \epsilon_{zz}(x) \end{pmatrix} \begin{pmatrix} E_y \\ E_z \end{pmatrix} = 0$$

where the permittivity tensor is represented as a sequence of delta functions $\boldsymbol{\epsilon}x) = \mathbf{1} + \sum_n \boldsymbol{\alpha}_n \delta(x - x_n)$. I shall discuss how to implement generalized glide symmetry in this system.

Following on from the discussion of glide symmetry I shall cover the criteria for the existence of edge states at an interface between two different sequences of such anisotropic slabs. In this part of the talk I shall discuss a generalization of the result of Xiao et al. where it was found that the closure of a band gap leads to a change in a topological quantity known as the Zak phase, which can be used to characterize layered media that support edge states at their interface.

REFERENCES

1. Singleton, J., "Band theory and electronic properties of solids," Oxford University Press, 2001.
2. Quevedo-Teruel, O., Ebrahimporuri, M. and Ng Mou Ken, M., "Ultrawideband Metasurface Lenses Based on Off-Shifted Opposite Layers" *IEEE Ant. Wire. Prop. Lett.* **15**, 484 (2016)
3. Lu, L., Fang, C., Fu., L., Johnson, S. G., Joannopoulos, J. D. and Soljacic, M., "Symmetry-protected topological photonic crystal in three dimensions" *Nat. Phys.* **12**, 337 (2016).
4. Xiao, M., Zhang, Z., Q., and Chan, C. T., "Surface Impedance and Bulk Band Geometric Phases in One–Dimensional Systems" *Phys. Rev. X* **4**, 021017 (2014).

Symmetry protected topological states of acoustic Kagome lattices

Xiang Ni[1], Maxim A. Gorlach[2], Andrea Alu[3], Alexander B. Khanikaev[1,2*]

[1]Department of Electrical Engineering, City College of New York, New York, NY 10031, USA
[2]ITMO University, Saint Petersburg 197101, Russia
[3]Department of Electrical and Computer Engineering, The University of Texas at Austin, Austin, Texas 78701, USA
khanikaev@gmail.com

Abstract-We demonstrate that an acoustic Kagome lattice formed by an array of interconnected resonant cavities exhibits a new class of topological states protected by C3 symmetry. This acoustic topological metamaterial exhibits a topological transition when a detuning is introduced between the inter-cell and intra-cell hopping amplitudes. The edge states emerge on either truncated ends of the lattice terminated by a cladding layer or at the domain walls between topologically nontrivial and trivial domains.

Recently there has been a significant surge of interest in topological states supported by classical systems, which was inspired by their unique properties such as robustness against various forms of perturbations, as well as the ability to emulate exotic quantum states of matter. A variety of topological systems have been emulated with great success in mechanical, acoustic and electromagnetic structures, encouraging the use of their exotic characteristics in practical applications.

In this work, we study the emergence of a topological state in an acoustic Kagome lattice [33] induced by altering inter-cell and intra-cell hopping amplitudes; the system represents the two-dimensional analogue of the well-established 1D SSH model [1]. We develop a rigorous analytical approach, which allows characterizing the topological state of the system by calculating its topological invariant. The presence of topological edge states on the truncated end interfaced with the cladding layer and at the domain wall, respectively, validates the prediction of existence of the described topological transition. Numerical simulations on the existence of topological edge states and the robustness of edge states to the structure defects with and without C3 symmetry at the boundary are performed and also agree with our analytical prediction.

As in the case of one-dimensional SSH arrays, we expect that in two-dimensional Kagome system the topological transition will be accompanied by the emergence of edge states when a finite system is considered. To verify their existence from first principles, we performed FEM simulations of a supercell with different boundary conditions. A periodic boundary condition was imposed on connectors in the horizontal direction to form an acoustic ribbon that is infinite in the $(\frac{\sqrt{3}}{2}, \frac{1}{2}, 0)$ direction and has a finite width in the vertical $(0,1,0)$ direction. We examined both situations of topologically trivial and topologically nontrivial lattices, and found that only in the topologically nontrivial case (characterized by topological invariant $w = 1$) the bulk band gap hosts additional acoustic modes localized at the opposite truncated ends of the ribbon. Figures 1(a) and (b) show the dispersion of the acoustic ribbon for both respective cases. As shown in figure 1(a), edge states are absent inside the bandgap, while figure 1(b) reveals the presence of the pair of the edge states (shown by red and blue lines, localized at zigzag and armchair cut, respectively) inside the complete acoustic band gap of the bulk acoustic bands (shown by black lines). The field profiles corresponding to the two modes localized at the interfaces of the ribbon are shown in Fig. 1(c). Note that while there are also other non-topological edge modes that appear at the interface of the ribbon in both situations, and which are shown by pink colour bands in Figs. 1(a) and (b), these modes are always present, and coexist with the bulk modes regardless of topological phase

transition, which are similar to Tamm surface states in condensed matter. They therefore represent topologically trivial edge modes not of interest in this paper.

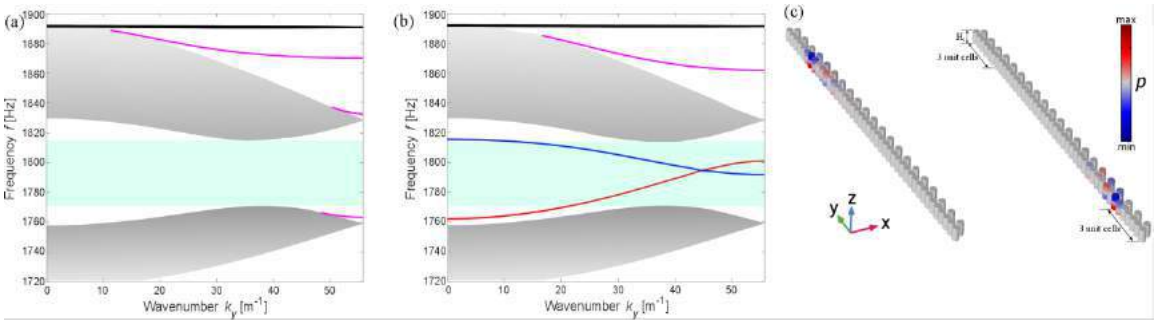

Fig. 1: Two situations of topologically trivial and topologically nontrivial lattices. (a) Trivial band diagram – no edge states go through the complete band gap (green); (b) nontrivial – edge states present inside the complete band gap; and (c) two field profiles corresponding to the blue and red bands in (b), respectively. Pink colour bands show topologically trivial edge modes.

In summary, we have demonstrated the emergence of a topologically nontrivial acoustic phase in distorted Kagome lattices of acoustic resonators. The topological classification based on a tight-binding description and the consequent definition of a meaningful topological invariant were applied to predict the topological transition of this acoustic metamaterial and the existence of topologically protected edge states. To support our analytical results, we performed numerical simulations confirming the presence of topological edge states on both interfaces of the lattice terminated by cladding layer and at domain walls separating topological and trivial crystals. The proposed structure is amenable to physical implementation and the topological edge modes of the Kagome lattice discovered here are worth further investigation based on the real experimental system.

Acknowledgements This work was supported by NSF with a CMMI and an EFRI grant, and by the Simons Foundation. Numerical analysis of the edge states was supported by the Russian Science Foundation (grant No. 16-19-10538).

References

[1] Su W P, Schrieffer J R and Heeger A J 1979 Solitons in polyacetalene *Phys*. *Rev*. *Lett*. **42** 1698

Mesoscopic Crystals with Glide Symmetry Planes for Electric Displacement Manipulation

J. Shin*, T. Chang, and Y. H. Lee
Korea Advanced Institute of Science and Technology, Republic of Korea
*corresponding author: qubit@kaist.ac.kr

Abstract-Mesoscopic crystals or three-dimensional metamaterials with deep-subwavelength unit cells can be designed to manipulate the effective electric permittivity tensor over a broad frequency bandwidth. Especially, crystals with glide planes can have a giant macroscopic electric displacement while the mesoscopic electric displacement field averaged over the dielectric region in a unit cell is very small. The relative magnitudes of the individual elements of the resulting effective permittivity tensors are affected by the symmetry of the crystal. This effect can be used to control linear and nonlinear susceptibilities in unconventional ways.

For the last decade, numerous artificial electromagnetic materials with diverse range of sub-wavelength unit cell designs have been proposed and their unusual properties have been investigated. Though the shapes and sizes of the motifs vary greatly, many of them share the common fact that they are designed for electromagnetic waves with temporal frequencies near specific resonances (often interpreted as the *inductor-capacitor* resonances in analogy with electric circuits) controlled by the constituent materials and their geometries. Direct utilization of the resonances makes it easy to obtain extreme values of effective material properties such as very negative, near zero, or very positive values, but it also imposes constraints on their frequency responses: typically more extreme designs are also more dispersive in frequency, making it challenging to achieve broadband operations.

On the other hand, metamaterial designs with inherently broadband properties have also been explored [1-4]. This class of metamaterials relies on the quasi-static boundary conditions of electric and magnetic fields to control the effective medium properties of an array of deep-subwavelength-scale unit cells. As the phase retardation over a unit cell scale is almost negligible, the effective properties are potentially very broadband. One possible source of frequency dispersion is the absorption and dispersion of the constituent materials themselves: for example, the electric permittivity of metals is a strong function of frequency and it might influence the effective parameters. However, in many cases, the large absolute value of the permittivity of metals minimizes the fields inside the metal and the resulting effective parameters are not very sensitive to the exact values of metal permittivity, showing near-constant values over broad frequency range unless the dielectric is lossy or the metallic region constitutes too much part of the unit cell.

When a 2D crystal has a mirror line like Fig. 1(a) and the macroscopic electric field is parallel to the line, the conductors A and B (C and D) have the same electric potential and the dielectric region between them has negligible electric fields. By contrast, a crystal with a glide reflection like Fig. 1(b) has different mesoscopic field profiles under the same macroscopic electric field condition: the conductors A, B, C, and D have progressively different electric potentials and there can be strong electric fields in all regions of the dielectric. Moreover, if the metallic regions have flat geometries parallel to the mirror line, the mesoscopic electric fields in

the region between two flat metals are almost perpendicular to the mirror line and the direction of the fields is alternating up and down within a unit cell. Hence, if the electric displacement is averaged over the dielectric region in a unit cell, it is nearly cancelled. However, the macroscopic electric displacement can be very large in this situation. This difference in the macroscopic behavior of the two structures in Fig. 1 can be utilized in three dimensional crystals as well. The increased dimension allows many different mirror and glide symmetry configuration possibilities in 3D and it can result in highly anisotropic effective electric susceptibility tensors.

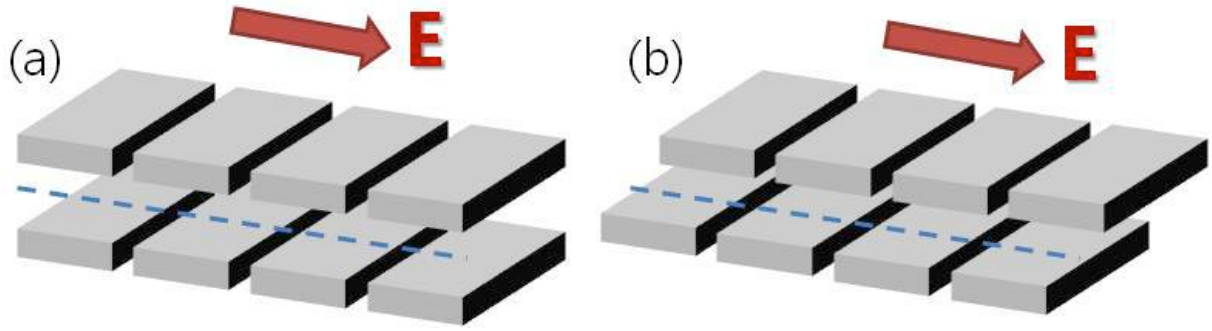

Figure 1 Structures with (a) mirror symmetry and (b) glide symmetry.

REFERENCES

1. Shin, J., J.-T. Shen, P. B. Catrysse and S. Fan "Cut-through metal slit array as an anisotropic metamaterial film," *IEEE J. Sel. Top. Quantum Electron.*, Vol. 12, No. 6, 1116–1122, 2006.
2. Shin, J., J.-T. Shen and S. Fan, "Three-dimensional metamaterials with an ultrahigh effective refractive index over broad bandwidth," *Phys. Rev. Lett.*, Vol. 102, No. 9, 093903/1–4, 2009.
3. Choi, M. *et al.*, "A terahertz metamaterial with unnaturally high refractive index," *Nature*, Vol. 470, No. 7334, 369–373, 2011.
4. Chang, T. *et al*., "Broadband giant-refractive-index material based on mesoscopic space-filling curves," *Nat. Commun.*, Vol. 7, 12661/1–7, 2016.

Reduced Dispersion in Guiding Structures Utilizing Twist Symmetries

O. Dahlberg[1], **R. C. Mitchell-Thomas**[2], **O. Quevedo-Teruel**[1]

[1]Department of Electromagnetic Engineering, Royal Institute of Technology, Stockholm, Sweden
[2]Department of Physics and Astronomy, University of Exeter, UK.
oskdah@kth.se

Abstract— In this paper we investigate the effect of twist symmetries on guiding structures. A reduced dispersive nature of the structure can be seen when the structure possesses twist symmetry. The analysis yields that higher twist-symmetric structures can be used for low dispersive wave guiding. A promising application of this kind of structure is leaky-wave antennas, which can utilize the low dispersion of the structure.

The limitations of metamaterials, e.g the narrow operational bandwidth, reduces the usefulness of such materials in microwave components. Some of these limitations can be addressed by various methods, one of which is to introduce additional symmetries into the structure. If these symmetries are arranged such that the unit cell coincides with itself after more than one linear or angular translation or reflection, the structure can be said to possess higher symmetries [1, 2, 3]. The effective period of a structure possessing higher symmetries is smaller than the actual period of the unit cell [1]. There are mainly two types of higher symmetries discussed in the literature so far, glide and twist symmetries. A structure possesses glide symmetry if the initial unit cell is mirrored in a plane and then translated half its period. Similarly, a structure possesses twist symmetry if instead of a mirroring, a rotation around its axis of symmetry is made together with a translation [1]. The number of rotation operations, p, executed to compose the full unit cell determines the order of twist symmetry, the structure is p-fold twist-symmetric. Several studies on glide symmetry has been presented [4, 5, 6, 7]. Here, we focus on studying the propagation characteristics in a coaxial twist-symmetric structure.

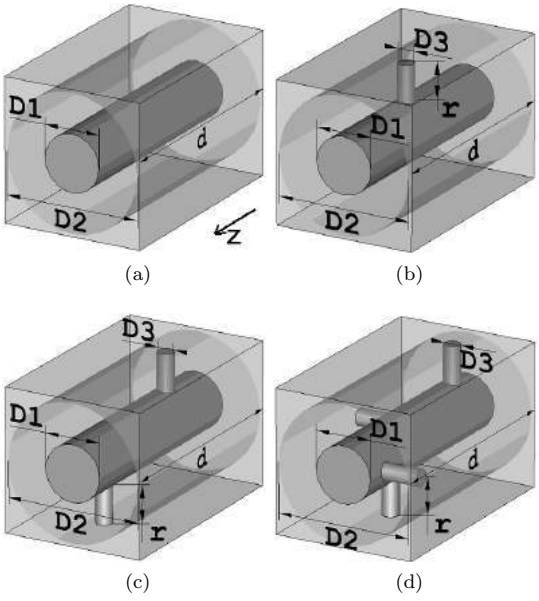

Figure 1: Configurations: (a) Without pins, (b) One pin, (c) 2-fold twist-symmetric structure, (d) 4-fold twist-symmetric structure.

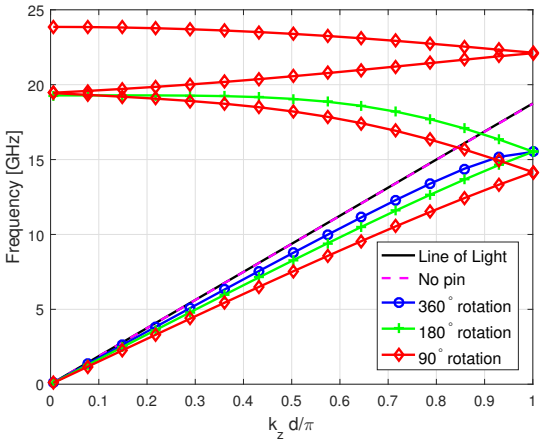

Figure 2: Dispersion diagram for the proposed structures. The dimensions are: $D1 = 2$ mm, $D2 = 4.62$ mm, $D3 = 0.6$ mm, $r = 1.3$ mm and $d = 8$ mm.

The structures considered are variations of a coaxial cable. The symmetries are introduced by placing pins on the inner conductor, terminating close to the outer conductor. There is a small air gap between the pins and the outer conductor. Four twist-symmetric structures are used for the study and they can be seen in Fig. 1. One of the structures, Fig. 1a, is an ordinary coaxial cable. For the rest of the configurations, 1b-d, the rotation between two adjacent pins in the unit cell is 360°, 180° and 90°, respectively.

The chosen dimensions are $D1 = 2$ mm, $D2 = 4.62$ mm, $D3 = 0.6$ mm, $r = 1.3$ mm and $d = 8$ mm. Using these dimensions, the air gap between the pins and the outer conductor becomes 0.1 mm. Simulation with these structures are carried out in *CST Microwave Studio*. The resulting dispersion diagram from these structures is presented in Fig. 2.

If no pins are used, i.e the structure is a coaxial cable, the dispersion diagram is coincident with the light line. When the rotation is either 90° or 180° between two adjacent pins, the guiding structure experiences low dispersion, resulting in a wide operational bandwidth. Since the apparent period is smaller in a twist-symmetric structure, modes from neighboring Brillouin zones are present without band gaps at the Brillouin zone boundaries. These results show similarities with results from studies made on 1D- and 2D-glide symmetry [8, 9, 10]. If only one pin is placed in each unit cell, the structure is periodic by only a translation of the pin and does not possess higher symmetries, the actual period of the structure is the same as the period of the unit cell. The mode is then dispersive and we have band gaps at the Brillouin zone boundary. By placing more pins in each unit cell, the medium is made denser with a higher effective refractive index, thus the structure can be tailored to exhibit the desired propagation characteristics. Promising applications of structures utilizing twist symmetries are leaky-wave antennas, which can utilize the low dispersion as well as the increased control of the effective refractive index.

REFERENCES

1. Hessel, A., Chen, M. H., Li, R. C. M., and Oliner, A. A., "Propagation in periodically loaded waveguides with higher symmetries," *Proceedings of the IEEE*, Vol. 61, No. 2, 183–195, 1973.
2. Crepeau, P.J. and McIsaac, P.R., "Consequences of symmetry in periodic structures," *Proceedings of the IEEE*, Vol. 52, No. 1, 33–43, 1964.
3. Mittra, R. and Laxpati, S., "Propagation in a Wave Guide With Glide Reflection Symmetry," *Canadian Journal of Physics*, Vol. 43, 353–372, 1965.
4. Ebrahimpouri, M., Quevedo-Teruel, O., Rajo-Iglesias, E., "Design Guidelines for Gap Waveguide Technology Based on Glide-Symmetric Holey Structures," *in press, IEEE Microwave and Wireless Component Letters*, 2017.
5. Valerio, G., Sipus, Z., Grbic, A. and Quevedo-Teruel, O., "Accurate equivalent-circuit descriptions of thin glide-symmetric corrugated metasurfaces," *in press, IEEE Transactions on Antennas and Propagation*, 2017.
6. Ghasemifard, F., Norgren, M. and Quevedo-Teruel, O., "Dispersion Analysis of Two Dimensional Glide-Symmetric Corrugated Metasurfaces Using Mode-Matching Technique," *IEEE Microwave and Wireless Component Letters*, 2017.
7. Valerio, G., Sipus, Z., Grbic, A. and Quevedo-Teruel, O., "The Role of Resonances in Plasmonic Holey Metasurfaces for the Design of Artificial Flat Lenses," *Optics Letters*, 2017.
8. Lyu, Y.-L., Liu, X.-X., Wang, P.-Y., Erni, D., and Wu, Q., Wang, C., Kim, N.-Y. and Meng, F.-Y., "Leaky-Wave Antennas Based on Noncutoff Substrate Integrated Waveguide Supporting Beam Scanning From Backward to Forward," *IEEE Transactions on Antennas and Propagation*, Vol. 64, 2155–2164, 2016.
9. Ebrahimpouri, M., Rajo-Iglesias, E., Sipus, Z. and Quevedo-Teruel, O., "Low-cost metasurface using glide symmetry for integrated waveguides," *European Conference on Antennas and Propagation (EuCAP)*, 1–2, 2016.
10. Quevedo-Teruel, O., Ebrahimpouri, M. and Kehn, M.N.M., "Ultrawideband Metasurface Lenses Based on Off-Shifted Opposite Layers," *IEEE Antennas and Wireless Propagation Letters*, Vol. 15, 484–487, 2016.

Advances in Nanolasers

Semiconductor Microlasers with Curve-Side Polygon Resonators

Yong-Zhen Huang, Hai-Zhong Weng, Zhi-Xiong Xiao, Yue-De Yang,
Jin-Long Xiao, and Yun Du
State Key Lab on Integrated Optoelectronics, Institute of Semiconductors & College of Materials Science and Optoelectronic Technology, University of Chinese Academy of Sciences, Chinese Academy of Sciences, Beijing 100083, China,*Email: yzhuang@semi.ac.cn

Unidirectional emission microcavity lasers have been realized by directly connecting an output waveguide to circular and polygon microcavities. However, mode *Q* factors reduce greatly for circular microcavities connecting an output waveguide. In this talk, we propose and demonstrate semiconductor microlasers with curve-side polygon resonators, which can still have ultra-high *Q* factors even as it connected an output waveguide.

For a curve-side square resonator (CSR) in Fig. 1(a), which is a hybrid of circular and square, mode *Q* factors can be greatly enhanced as the transverse mode field patterns are well confined as shown in the inset of Fig. 1(b) with near zero vertices radiation loss. The circular sides can work as concave mirrors for focusing the mode light beam in the CSR. With the enhancement of mode *Q* factors, lasing spectra transfer from single mode at δ = 0.9 μm to dual-mode lasing at δ = 1.1, 1.3, and 1.5 μm as shown in Fig. 1(b). Stable dual-mode lasing was realized with frequency interval of sub-THz suitable for photonic generation of THz wave [1].

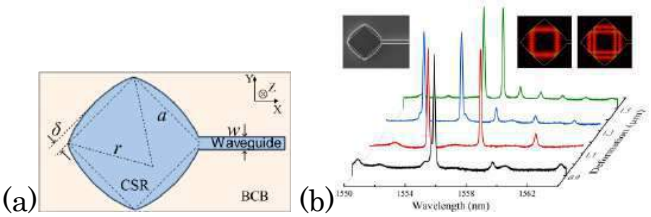

Fig. 1. (a) Schematic diagram of the CSR with a vertex output waveguide, and (b) lasing spectra of CSR lasers at 31 mA with a = 16μm and w = 1.5μm and δ = 0.9, 1.1, 1.3, and 1.5 μm.

For a curve-side hexagonal resonator (CHR) connected an output waveguide, we can have much higher *Q* factor than a microdisk resonator connected with an output waveguide at the same size. For a CHR microlaser with a side-length of 7.5 μm, deformation δ = 0.51 μm, and an output waveguide width of 2 μm, single mode operation is realized with a side-mode suppression ratio of 43 dB [2]. The results indicate that single transverse mode operation is easy to realize for CHR microlasers. Furthermore, flat small signal modulation responses are obtained with a 3-dB bandwidth of 13 GHz.

In conclusion, we have proposed and demonstrated that curve-side polygon microcavites for enhancing mode *Q* factor and controlling lasing spectra.

Reference

[1] Hai-Zhong Weng, Yong-Zhen Huang, Yue-De Yang, Xiu-Wen Ma, Jin-Long Xiao, and Yun Du, "Mode *Q* factor and lasing spectrum controls for deformed square resonator microlasers with circular sides," *Phys. Rev. A* 95, 013833 (2017).
[2] Zhi-Xiong Xiao, Yong-Zhen Huang, Yue-De Yang, Jin-Long Xiao, and Xiu-Wen Ma, "Single mode unidirectional-emission circular-side hexagonal resonator microlasers," Opt. Lett., in press (2017)

Narrow beam emission in PT-axisymmetric lasers

W. W. Ahmed[1] , R. Herrero[1],M. Botey[1], and K. Staliunas[1,2]

[1]Departament de Física, Universitat Politècnica de Catalunya (UPC), Barcelona, Spain
[2]Institució Catalana de Recerca i Estudis Avançats (ICREA), Barcelona, Spain
[*]corresponding author: ramon.herrero@upc.edu

Abstract-We study the field enhancement in lasers with spatial modulations showing PT-symmetry and axial symmetry including a central defect. The merge of these two symmetries created by the modulation of the complex index, strongly directs light to the central point obtaining important localization effects. The concentration capabilities of these potentials is implemented in the Complex Ginzburg-Landau equation as a simple VCSELs model to generate very narrow and bright beams when a central defect is included to avoid field saturation given by the nonlinearities.

The spatial modulation of the complex refractive index, i.e. refractive index and gain-loss modulations, has demonstrated strong capabilities to tailor light dispersion, including diffraction and diffusion, showing different spatial effects in linear light propagation along this kind of potentials[1-3]. Further, the same modulations in nonlinear systems introduce the management of spatial instabilities that intrinsically appear in laser systems and amplifiers[4-6]. One of the most interesting symmetries of complex spatial modulated materials is the PT-symmetry, where the real part of the modulation shows even symmetry while the imaginary part shows odd symmetry[7].

In this work we propose PT-axisymmetric potentials including a central defect for field localization and enhancement in laser systems. The localization of light in a central beam with small width and high intensity opens the possibility to obtain laser light sources with very narrow and bright beams. An important characteristic of PT-potentials is that the coupling between left-propagating modes and right-propagating modes can be strongly unidirectional when the real and gain-loss modulations are balanced leading to new features on light waves such as asymmetric unidirectional reflectors or invisible materials[8]. The merge of the PT-symmetry and axial-symmetry can derive in complex potentials leading to a unidirectional coupling to the left on the right half-space and to the right on the left half-space in the one-dimensional case and equivalently radial inwards couplings in two-dimensional system (see Fig.1a and Fig.1b). The coupling between harmonics always directed to the axis at x=0, allows the field concentration.

The linear light propagation through PT-axisymmetric potentials creates an extreme localization at $x=0$, exhibiting an exponential temporal growth due to the system linearity[9]. On the contrary, the application of such potentials to laser models, and in particular to the Complex Ginzburg-Landau equation as a simplified VCSEL model, shows typical turbulent states with no field concentration. The system nonlinearities introduce field saturation and limit the maximum intensity of the output beam. The inclusion of a central linear defect in the structure avoids saturation and allows the field concentration.

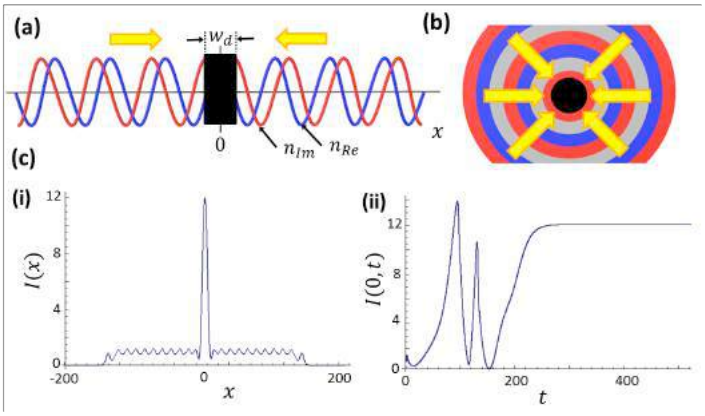

Figure 1. *(a)One-dimensional PT-axisymmetric potential with an axial defect of width w_d at x=0. Index modulations (blue) and shifted gain-loss modulations (red) creates the PT-potential and introduce the directional coupling to the axis.(b)Two dimensional PT-potential with a linear central defect (black).(c) Stationary field for the VCSEL model with pump above threshold and (d) temporal evolution of the field at the central point.*

We explore such potentials in 1D and 2D, scanning the main parameters as laser pump, linewidth enhancement factor of the semiconductor, amplitude of the PT-modulated potential, i.e. refractive index amplitude and gain-loss amplitude, as well as the width of the defect. Results show field concentrations 10 times larger than the saturated laser intensity with stationary behaviors and pulsed regimes. Finally, we include losses in the central part of the VCSEL model to consider the field coupling to an output fiber.

Acknowledgement, the work is financially supported by Spanish Ministerio de Educación y Ciencia through project FIS2015-65998-C2-1-P, NATO project SPS-985048 and Erasmus Mundus Doctorate Program Europhotonics (Grant No. 159224-1-2009- 1-FR-ERA MUNDUS-EMJD).

REFERENCES

1. Staliunas, K., Herrero, R., and Vilaseca, R., "Subdiffraction and spatial filtering due to periodic spatial modulation of the gain-loss profile," Phys. Rev. A 80, 013821 (2009).
2. Botey, M., Herrero, R., and Staliunas, K., "Light in materials with periodic gain-loss modulation on a wavelength scale," Phys. Rev. A 82, 013828 (2010).
3. Herrero, R., Botey, M., Staliunas, K., "Nondiffractive-nondiffusive beams in complex crystals", Phys. Rev. A 89, 063811 (2014).
4. Herrero, R., Botey, M., Radziunas, M., and Staliunas, K. "Beam shaping in spatially modulated broad-area semiconductor amplifiers," Opt. Lett. 37 5253-5255 (2012).
5. Radziunas, M., Botey, M., Herrero, R., and Staliunas, K., "Intrinsic beam shaping mechanism in spatially modulated broad area semiconductor amplifiers, "Appl. Phys. Lett. 103, 132101 (2013).
6. Kumar, S., Herrero, R., Botey, M., Staliunas, K., " Suppression of modulation instability in broad area semiconductor amplifiers, " Optics letters, 39(19), 5598-5601 (2014).
7. Ruter, C.E., Makris, K. G., El-Ganainy, R., Christodoulides, D. N., Segev, M., and Kip, D., "Observation of parity–time symmetry in optics," Nat. Phys. 6, 192–195 (2010).
8. Lin, Z. et al. "Unidirectional invisibility induced by PT-symmetric periodic structures," Phys. Rev. Lett. 106, 213901 (2011)
9. Ahmed, W.W., Herrero, R., Botey, M., Staliunas, K., "Locally Parity-Time Symmetric and globally Parity-Symmetric systems", Phys. Rev. A 94, 053819 (2016).

Fundamental Scaling Laws of Nanophotonics: Case Laser

Ke Liu[1,4], Arka Majumdar[2,3], Volker J. Sorger[1*]
[1]Department of Electrical and Computer Engineering, The George Washington University, Washington, D.C. 20052, USA
[2]Department of Electrical Engineering, University of Washington, Seattle, WA 98195
[3]Physics Department, University of Washington, Seattle, WA 98195
[4]The Key Laboratory of Optoelectronics Technology, Ministry of Education, College of Electronic Information and Control Engineering, Beijing University of Technology, Beijing 100124, P.R. China
[*]corresponding author: sorger@gwu.edu

Abstract-Here we report on an analysis show scaling laws for optoelectronic devices, and how various types of optical cavities directly influence the performance of three classes of photonic devices, namely laser sources, electro-optic-modulators, and photodetectors. The device-underlying optical cavities show Purcell factor maxima as a function of cavity length exceeding 1000, 20, and 200 for a micro ring resonator, Fabry Perot, or plasmonic nanocavity, respectively highlighting the physical tradeoff between optical loss management and field confinement.

Scaling laws based on fundamental physics predict a high potential to improve optoelectronic devices relative to the state-of-the-art applying the FOM = {Datarate/bit} / {Power/bit x Area x Cost}. Ignoring engineering-limited device design constrains, basic physics dictates a lower-bound power consumption for optoelectronic devices of about 0.1aJ/bit. The general switching speed depends on the chosen switching effect, and both the optical and electrical dynamics penalty. The uncertainty principle gives an upper bound for the device speed and can be femtosecond fast in tunnel-based systems. We discuss scaling laws and benchmarks [1] of three prominent opto-electronic devices, namely, laser [2-4], electro-optic modulator [5], and photodetector. The work is based on underlying light-matter-interaction enhancement via optical resonators to include the microring, Fabry-Perot, and plasmonic nanocavity. We raise questions towards establishing a roadmap for optical information processing (i.e. logic and communication) including noise considerations at the detector, quantum entanglement, and realistic integration aspects such as technology hybridization [6] at the link level for high bit-flow-density metrics.

With previous investigations being ad-hoc in their approach to exploit nanoscale device functionality, an understanding leading to fundamental scaling behavior for this new class of devices is outstanding. Here we investigate the fundamental scaling laws for Nanophotonics as a function of nominal device length. Performance criteria of three critical interconnect devices are analyzed with respect to their scaling behavior. Underling to all devices are three types of optical cavities that support enhancing the fundamentally weak interaction between light and matter, namely, microring resonators, Fabry Perot cavities, and plasmonic metal particle-based cavities. An interesting, but actually expected find is, that all cavity types do not perform well for vanishing cavity lengths due to dominance of loss channels. However this critical length is strongly dependent on the cavity properties and varies by more than two orders of magnitude. With the high Purcell factors that can be realized despite high losses in nanoscale cavities, we investigate fundamental achievable optoelectronic device performance.

In our device performance scaling laws results we find that the thought 'smaller-is-better' is not true for nanophotonics and non-monotonic scaling laws are found. With a goal for down-scalability in mind, key results show the possibility the ability to design; 1) laser sources with threshold currents at 1 uA and 100 GHz fast modulation, 2) electro-optic modulators with 10's aJ/bit energy efficiencies and THz fast modulation speeds, and 3) photodetectors with responsivities approaching 1 A/W and ~ps-fast response times. Understanding the potential and limits for Nanophotonics will be a guiding insight not only for device designers, but increasingly also at the circuit level, since a true comparison between both the electronic and photonic technology options is now possible [7-9].

Acknowledgements, V.S. is supported by Air Force Office of Scientific Research-Young Investigator Program under grant FA9550-14-1-0215.

REFERENCES

1. K. Liu, A. Majumdar, V. J. Sorger, "Fundamental Scaling Laws in Nanophotonis" Scientific Reports, 6, 37419 (2016).
2. R.-M. Ma, R. F. Oulton, V. J. Sorger and X. Zhang "Plasmon lasers: coherent light source at molecular scales", *Laser & Photonics Reviews* doi: 10.1002/lpor.201100040 (2012).
3. K. Liu, N. Li, D. K. Sadana, V. J. Sorger, "Integrated nano-cavity plasmon light-sources for on-chip optical interconnects" *ACS Nano***,** DOI: 10.1021/acsphotonics.5b00476 (2016).
4. N. Li, K. Liu, D. K. Sadana, V. J. Sorger, "Nano III-V Plasmonic Light-Sources for Monolithic Integration on Silicon", *Nature: Scientific Reports*, 5, 14067 (2015).
5. K. Liu, Z.R. Li, S. Khan, C. Ye, V. J. Sorger, "Ultra-fast electro-optic modulators for high-density photonic integration" *Laser & Photonics Review,* 10, 11-15 (2015).
6. K. Liu, V. J. Sorger, "Enhanced interaction strength for a square plasmon resonator embedded in photonic crystal nanobeam cavity" *Journal Nanophotonics,* 9, 093790 (2015).
7. R.-M. Ma, R. F. Oulton, V. J. Sorger and X. Zhang "Plasmon lasers: coherent light source at molecular scales", *Laser & Photonics Reviews* doi: 10.1002/lpor.201100040 (2012).
8. V. J. Sorger, R. F. Oulton, R.-M. Ma, X. Zhang "Toward integrated plasmon circuits" *MRS Bulletin* 37, 8, 728-738 (2012).
9. S. Sun, A. Badaway, T. El-Ghazawi, V. J. Sorger, "Photonic-Plasmonic Hybrid Interconnects: Efficient Links with Low latency, Energy and Footprint", *IEEE Photonics*, 7, 6, 15 (2015).

Dynamics of nanolasers and nanoscale light emitters.

Y. Fainman, S. H. Pan, Q. Gu, A. El Amili, and F. Vallini
Department of Electrical and Computer Engineering, University of California, San Diego
9500 Gilman Drive, La Jolla, California, 92093-0407
fainman@ece.ucsd.edu

Abstract-This paper discusses nanoscale engineered metal-dielectric-semiconductor resonant gain geometries confined in all three dimensions used to create a new type of nanolasers and light emitters. When these emitters are driven in a pulsed regime, dynamic hysteresis is observed and characterized.

Achieving the most compact footprint for photonic components is an important factor in the design of integrated optical devices. As the size of a conventional dielectric semiconductor laser is decreased towards λ_0, three effects adversely influence the lasing process. Firstly, the roundtrip path of the optical wave in the gain medium is shortened, secondly radiative losses are increased and finally the field confinement inside the resonator is reduced, resulting in less overlap of the optical mode with the gain medium. All of these effects serve to increase the lasing threshold, so that lasing cannot be achieved below a certain size limit. One approach for alleviating these issues is to incorporate metals into the structure of dielectric cavities, because metals can suppress leaky optical modes and effectively isolate them from their neighbouring environment. The ultimate challenge is to reduce the size of the laser resonator in all three dimensions. A wide spectrum of resonator architectures has been explored, including circular [1, 2] metallo-dielectric cavities, metal-semiconductor coaxial cavities [3], nanopillar/nanowire cavities [4, 5] and plasmonic cavities (SPASERs) [6-9]. To date, the majority of studies on nanocavity lasers have focused on the proof of concept demonstration of lasing behavior. In particular, the measurement of a "kink" in the light-out versus light-in curve (LL-curve) is prevalently used as affirming evidence for lasing and is often the only method adopted to identify the lasing threshold [1-8]. However, it is well known that the "kink" in the LL-curve diminishes as β increases. Therefore, for high-β nanocavity lasers, LL-curve measurement alone can neither fully characterize lasing nor unambiguously identify the lasing threshold. On the other hand, measuring the second order intensity correlation function $g^2(\tau) = \langle I(t) \rangle \langle I(t+\tau) \rangle / \langle I(t) \rangle^2$, where $\langle I(t) \rangle$ represents the expectation value of the nanolaser output intensity at time t, is a more definitive method to confirm lasing [9]. Recently, we demonstrate [10] that by employing nanosecond pump pulses, different emission regimes of a nanolaser can be characterized via the full width at half maximum (FWHM) of a $g^2(\tau)$ peak. We demonstrate the applicability of this technique with a high-β metallo-dielectric nanolaser and further report the first coherence measurement on this type of nanolaser operating at room temperature. We show that while $g^2(\tau)$ peaks narrow in the spontaneous emission (SE) and amplified spontaneous emission (ASE) regimes as stimulated emission increases in proportion, their FWHMs increase in the lasing regime due to dynamical hysteresis (DH), a phenomenon triggered when a laser is driven across

its threshold. The usage of nanosecond pulses is the key to the observation of DH and, therefore, essential to this characterization technique.

Acknowledgements: National Science Foundation (NSF); Office of Naval Research (ONR); Army Research Office (ARO); Cymer Corporation; NSF's San Diego Nanotechnology Infrastructure (SDNI).

REFERENCES

1. M. T. Hill, et. all, *Nat. Photonics **1**, 589-594 (2007).*
2. M. P. Nezhad, et. all, *Nat. Photonics **4**, 395-399 (2010)*.
3. M. Khajavikhan, et. all, *Nature **482**, 204-207 (2012).*
4. R. Chen, et. all, *Nat. Photonics **5**, 170-175 (2011)*.
5. D. Saxena, et. all, *Nat. Photonics 7, 963-968 (2013)*.
6. D. J. Bergman and M. I. Stockman, *Phys. Rev. Lett. **90**, 027402 (2003)*.
7. M. A. Noginov, et. all, *Nature **460**, 1110-1112 (2009)*.
8. R. F. Oulton, et. all, *Nature **461**, 629-632 (2009)*.
9. Y.-J. Lu, et. all,*Science **337**, 450-453 (2012)*.
10. S. H. Pan, et. all, Optica **3**, 1260-1265 (2016).

Manipulating the dispersion characteristics of SPP Nanolasers

Yu-Hsun Chou[1], Kuo-Bin Hong[1], Yi-Cheng Chung[2], Chun-Tse Chang[1], Tzy-Rong Lin[2], and Tien-Chang Lu[1*]

1. Department of Photonics, National Chiao Tung University, Hsinchi, Taiwan
2. Department of Mechanical and Mechatronic Engineering, National Taiwan Ocean University, Keelung, Taiwan
E-mail address: timtclu@mail.nctu.edu.tw

Abstract: Surface plasmon polariton (SPP) nanolasers have recently emerged as a promising candidate to generate coherent light source in nanophotonics integration circuit. The properties of SPP nanolaser such as group velocity, mode area, modulation speed and threshold performance are able to manipulated by the dispersion relation. In this paper we have investigated the characteristics of SPP nanolaser and managed to approach the limit of surface plasmon amplification by stimulated emission radiation (SPASER).

Recently, the development of nanolaser involving surface-plasmon-polariton (SPP) operation has attracted the attention to construct ultra-compact integrated photonic devices and systems [1]-[3]. The characteristics of SPPs can be determined by the dispersion relation of the device structure, which is influenced by the material's permittivity and structural parameters. One straight forward way to manipulate the dispersion relation of the SPP nanolaser relies on the thickness control of the insulator layer in between the semiconductor and the metal thin film for the semiconductor/insulator/metal (SIM) nanolaser structure, which becomes one of the most popular plasmonic structure to confine the optical field and potentially break the optical diffraction limit. However, the tailoring range of the dispersion relation was mainly limited by the materials. To investigate the characteristics of SPP nanolasers with significant dispersion difference, we chose the SPP nanolasers with different metals to compare the properties difference between SPP lasers operating nearby the SP frequency and the SPP laser operating far away from the SP frequency. For more reliable SPP laser operation, ZnO nanowire provides exciton binding energies larger than thermal energy at room temperature (25.6 meV) and strong oscillation strength to interact with SPP. Thus, the ZnO nanowire was chosen in our study for stable SPP laser operation under different circumstances. Since the active emitter was chosen to be ZnO, operated in the near UV range (370-390 nm), aluminum and silver are used to properly generate SPPs. Typically, aluminum has a relatively high surface plasmon frequency. The ZnO nanolaser on Al is operated away from the SP frequency, rendering itself operating as a typical SPP nanolaser with low threshold condition. On the other hand, since Ag has an interband transition at around 350 nm, the dispersion relation of surface plasmon near 370 nm will be significantly bent, leading to ZnO nanolasers operating approaching the limit of surface plasmon amplification by stimulated emission radiation (SPASER). By investigating characteristics of Al- and Ag-based ZnO nanolasers, intriguing phenomena such as the quantum plasmonic effect, ultrafast modulation, strong interaction between the exciton and surface plasmon [4], and high characteristic temperature operation [5] will be discussed.

[1] R. F. Oulton et al., "Plasmon lasers at deep subwavelength scale," Nature, vol. 461, pp. 629–632, 2009.
[2] R.-M. Ma, R. F. Oulton, V. J. Sorger, G. Bartal, and X. Zhang, "Room temperature sub-diffraction-limited plasmon laser by total internal reflection," Nature Mater., vol. 10, pp. 110–113, 2011.
[3] Y.-J. Lu et al., "Plasmonic nanolaser using epitaxially grown silver film," Science, vol. 337, pp. 450–453, 2012.
[4] Y.-H. Chou et al., "Ultrastrong Mode Confinement in ZnO Surface Plasmon Nanolasers," ACS Nano, Vol. 9, pp. 3978-3983, Apr. 2015.
[5] Y. -H. Chou et al., "High-Operation-Temperature Plasmonic Nanolasers on Single-Crystalline Aluminum," Nano Lett. Vol. 16, pp. 3179−3186, Apr. 2016.

Controlled Multi-modal Nanolasing from Plasmonic Superlattices

T. W. Odom[1*]
[1]Northwestern University, Evanston, IL USA
[*]corresponding author: todom@northwestern.edu

Abstract. This talk will describe how to engineer different combinations of nanolasing modes by controlling the structural parameters of the multi-scale plasmlnic nanoparticle arrays.

Band structure engineering is critical for controlling the emission wavelengths and efficiency in electronic and photonic materials. Single band-edge states that show trapped slow light have been used as high-quality optical feedback for lasing from photonic bandgap crystals and metal-dielectric waveguides. Recently, we demonstrated that single band-edge lattice plasmons in periodic metal nanoparticle arrays could contribute to single-mode lasing at room-temperature with directional emission. However, the manipulation of more than a single band-edge mode for nanolasing has not been possible because of limited cavity designs. This talk will describe a new architecture based on plasmonic superlattices—finite-arrays of nanoparticles grouped into microscale arrays—to achieve multi-modal lasing. The underlying mechanism was found to depend on trapped slow light at both zero and non-zero wavevectors. We will discuss how the spectral separation and spatial emission angles of the lasing modes can be tuned by changing patch periodicity. Such characteristics may enable multi-frequency multiplexing and fast-processing of nanoscale coherent light for on-chip photonic integration.

Acknowledgements. This work was supported by the National Science Foundation under DMR-1608258 and DMR-1306514.

REFERENCES

1. A. Yang, T.B. Hoang, M. Dridi, C. Deeb, M.H. Mikkelsen, G.C. Schatz, and T.W. Odom. “Real-time Tunable Lasing from Plasmonic Nanocavity Arrays.” *Nature Comm*. **6**, 1–7 (2015).
2. N.I. Zheludev, S.L. Prosvirnin, N. Papasimakis, and V.A. Fedotov. “Lasing Spaser,” *Nature Phot.* **2**, 351-354 (2008).
3. W. Zhou, M. Dridi, J.Y. Suh, C.H. Kim, D.T. Co, M.R. Wasielewski, G.C. Schatz, and T.W. Odom. “Lasing Action in Strongly Coupled Plasmonic Nanocavity Arrays,” *Nature Nanotech.* **8**, 506–511 (2013).

Optimization of Nanowire Based Light Sources and Their Applications for Super Resolution Imaging

Qing Yang*[1], Xiaowei Liu[1], Pengfei Xu[1], Chenlei Pang[1], Yuanpeng Wu[1], Chao Meng[1], Jiabei Li[1], Zongyin Yang[2], and Delong Wang[1], Tawfique Hasan[2], Michael Geoffrey Somekh[3], Xu Liu[1]

[1]*State Key Laboratory of Modern Optical Instrumentation, College of Optical Science and Engineering, Zhejiang University, Hangzhou, 310027, China*

[2]*Cambridge Graphene Centre, University of Cambridge, CB3 0FA UK*

[3]*Hong Kong Polytechnic University, Elect & Information Engineering, Kowloon, Hong Kong, China*

qingyang@zju.edu.cn

Nanowire (NW)-based light sources, owing to their strong light localization [1, 2], ultra-small footprint [3], high mechanical flexibility [4], large aspect ratio [5, 6], high photoluminesence efficiency and large fractional evanescent field [7], have shown huge potential in areas including communication, diagnosis, and environmental monitoring [8-10]. Optimization of the parameters of NW light sources, such as the emission spectrum and efficiency, is significant for their practical applications. Recently, we have systematically investigated controlling of parameters of nanowire light emitting devices. Using the absorption-emission-absorption effect, we have achieved broad wavelength controlling and tailoring of single NW laser (40 nm for pure CdSe NW and 119 nm for CdSSe bandgap graded NW) (Fig. 1a) [11, 12]. We have also greatly enhanced the external quantum efficiency (up to 0.9%) for a Schottky junction-based NW ultraviolet light emitting diode (LED) by hybridizing single Ag NW with p-GaN substrate (Fig. 1b) [13]. Moreover, we have deeply investigated the modulation of the polarization and emission mode for NW/nanobelt laser sources [14]. Finally, we have successfully applied NW based light sources to break the bottleneck in nanoscopy and achieved the first nanoscale light source-based wide-field and far-field label-free sub-diffraction imaging by hybridizing ring-shaped fluorescent NWs with subwavelength film waveguides (Fig. 1c-d show an experimental result for a 150 nm slot, 100 nm spacing sub-wavelength structure). The reliability and versatility of our approach have been demonstrated by imaging integrated chips, Blu-ray DVDs, biological cells, and various subwavelength 2D patterns, with a viewing area of up to 1000 μm^2, one order of magnitude larger than previous far-field and full-field nanoscopy reports [15]. Our investigation will greatly expand the flexibility of NW based light sources for practical applications in biology, physics, materials science, and so on.

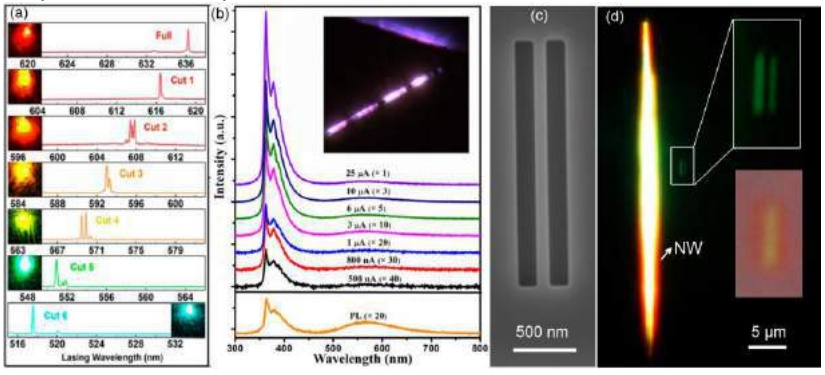

Figure 1. (**a**) Lasing spectra obtained from a bandgap graded CdSSe NW with a forward cutting process. (**b**) Emission spectra of the Schottky junction-based NW ultraviolet LED under injection currents from 500 nA to 25 μA and the PL spectrum of p-GaN under 355 nm pulsed laser excitation. Inset: a typical optical microscope image of the emission of the LED. (**c**) Scanning electron microscope image of a 150 nm slot, 100 (is it 100? Or 150? Ur text says 100) nm spacing sub-wavelength structure. (**d**) Image of the structure under NW ring illumination. A conventional optical microscope image is shown in the lower inset for comparison.

Reference

[1] D.D.D. Ma, C.S. Lee, F.C.K. Au, S.Y. Tong and S.T. Lee, "Small-diameter silicon nanowire surfaces," *Science* **299**, 1874-1877 (2003).

[2] L. Tong, R.R. Gattass, J.B. Ashcom, S. He, J. Lou, M. Shen, I. Maxwell, and E. Mazur, "Subwavelength-diameter silica wires for low-loss optical wave guiding," *Nature* **426**, 816-819 (2003).

[3] Q. Qing, Z. Jiang, L. Xu, R. Gao, L. Mai, and C.M. Lieber, "Free-standing kinked nanowire transistor probes for targeted intracellular recording in three dimensions," *Nat. Nanotech.* **9**, 142-147 (2014).

[4] Q. Yang, W. Wang, S. Xu, and Z.L. Wang, "Enhancing light emission of ZnO microwire-based diodes by piezo-phototronic effect," *Nano Lett.* **11**, 4012-4017 (2011).

[5] M. Law, L.E. Greene, J.C. Johnson, R. Saykally and P. Yang, "Nanowire dye-sensitized solar cells," *Nat. Mater.* **4**, 455-459 (2005).

[6] A. Kolmakov, Y. Zhang, G. Cheng, and M. Moskovits, "Detection of CO and O_2 using tin oxide nanowire sensors," *Adv. Mater.* **15**, 997-1000 (2003).

[7] L. Tong, J. Lou, and E. Mazur, "Single-mode guiding properties of subwavelength-diameter silica and silicon wire waveguides," *Opt. Express* **12**, 1025-1035 (2004).

[8] E. Betzig and J.K. Trautman, "Near-field optics: Microscopy, spectroscopy, and surface modification beyond the diffraction limit," *Science* **257**, 189-195 (1992).

[9] Y. Nakayama, P.J. Pauzauskie, A. Radenovic, R.M. Onorato, R.J. Saykally, J. Liphardt and P. Yang, "Tunable nanowire nonlinear optical probe," *Nature* **447**, 1098-1101 (2007).

[10] B. Tian, T. Cohen-Karni, Q. Qing, X. Duan, P. Xie and C.M. Lieber, "Three-dimensional, flexible nanoscale field-effect transistors as localized bioprobes," *Science* **329**, 830-834 (2010).

[11] Z. Yang, D. Wang, C. Meng, Z. Wu, Y. Wang, Y. Ma, L. Dai, X. Liu, T. Hasan, X. Liu**,** Q. Yang*****, "Broadly Defining Lasing Wavelengths in Single Bandgap-Graded Semiconductor Nanowires", *Nano Lett.* **14**, 3153-3159 (2014).

[12] J. Li , C. Meng , Y. Liu , X. Wu , Y. Lu , Y. Ye , L. Dai , L. Tong, X. Liu , Q. Yang*****, "Wavelength Tunable CdSe Nanowire Lasers Based on the Absorption-Emission-Absorption Process", *Adv. Mater.* **25**, 833-837 (2013).

[13] Y. Wu, T. Hasan, X.Li, P. Xu, Y. Wang, X. Shen, X. Liu, Q. Yang*****, "High efficiency single Ag nanowire/p-GaN substrate Schottky junction-based ultraviolet light emitting diodes", *Appl. Phys. Lett.* 106, 051108 (2015).

[14] W. Yang, Y. Ma, Y. Wang, C. Meng, X. Wu, Y. Ye, L. Dai, L. Tong, X. Liu, and Q. Yang*****, "Bending effects on lasing action of semiconductor nanowires" *Opt. Express* **21** 2024 (2013).

[15] X. Liu, C. Kuang, X. Hao, C. Pang, P. Xu, H. Li, Y. Liu, C. Yu, Y. Xu, D. Nan, W. Shen, Y. Fang, L. He, X. Liu, and Q. Yang*****, "Fluorescent Nanowire Ring Illumination for Wide-Field Far-Field Subdiffraction Imaging", *Phys. Rev. Lett.* **118**, 076101 (2017).

Carrier Dynamics in Nanoscale Light-Emitting Diodes

B. Romeira*, V. Dolores-Calzadilla, A. Higuera-Rodriguez, S. Birindelli, F. Pagliano, P. J. van Veldhoven, E. Smalbrugge, L. E. Black, W. M. M. Kessels, D. Heiss, M. K. Smit and A. Fiore

Institute for Photonic Integration, Eindhoven University of Technology, P.O. Box 513, 5600 MB, Eindhoven, The Netherlands

*corresponding author: b.m.romeira@tue.nl

Abstract-Nanoscale light sources operating efficiently at low powers are required for future optical interconnects. Here, we present, both theoretically and experimentally, the carrier dynamics in metal-dielectric cavity nanopillar light-emitting diodes. The nanoLEDs operate at telecommunications wavelengths, featuring tens of nanoWatt waveguide-coupled powers and GHz-range modulation bandwidths. Furthermore, an extremely low surface recombination velocity of 260 cm/s in passivated InGaAs nanopillars is reported, a result of crucial importance for the development of efficient nanoscale optoelectronic devices for nanophotonic integrated circuits.

Electronic data connections are increasingly becoming a bottleneck in the exponential growth of data traffic worldwide. Future optical interconnects are the obvious successors but will require ultrasmall light sources with sub-micrometer sizes to achieve low energy consumption (<10 fJ/bit), and ultrafast speeds [1]. Nanoscale light sources have been developed recently using either metal, metallo-dielectric or photonic crystal nanocavities [2]. Despite much progress, nanolasers and nano-light-emitting diodes (nanoLEDs) operating efficiently at low powers and suitable for photonic integration are lacking. Among numerous challenges, in both light-emitting diodes and lasers, radiative and nonradiative recombination rates play a key role in the efficiency. Radiative recombination (both spontaneous and stimulated) is affected by the small mode volume in nanoLEDs and nanolasers, potentially leading to strong Purcell enhancements and higher speed [3,4]. On the other hand, nonradiative recombination rates, specifically surface recombination rates, are also very high due to the high surface-to-volume ratios [5], typically leading to low radiative efficiencies.

Here, the authors present recent work on waveguide-coupled metal-dielectric cavity nanopillar LEDs on silicon working at telecommunications wavelengths [5], and featuring more than 20 nW waveguide-coupled powers and GHz-range modulation bandwidths at room-temperature (RT). The efficiency of the reported nanoLEDs currently lies between 0.01 and 1 percent, at RT and at 10 K, respectively, mostly limited by nonradiative recombination effects. We show that a passivation method using sulfur treatment, followed by silicon oxide capping deposited by plasma-enhanced chemical vapor deposition, strongly suppresses the surface recombination at the InGaAs surfaces of nanopillars from a few hundred picoseconds to more than 20 nanoseconds [6]. The estimated surface recombination velocity, decreases from about 2×10^4 cm/s in the untreated nanopillars down to around 260 cm/s. To our knowledge, this is a record low value in undoped InGaAs semiconductors. Most importantly, our passivation studies reveal that the SiO_x capping layer not only protects the pillars' sidewalls against oxidation, as reported in [7], but actively takes part in the passivation process. This will ensure substantial improvements in the efficiency of future nanoLEDs and reduce the threshold current in nanolasers, which are of crucial importance for their application in optical interconnects.

Finally, the performance of the experimental nanoLEDs is analyzed using a rate equations model which properly takes into account the nanocavity effects in the spontaneous emission rate and the spatial and spectral overlap between carriers and photons. The ultimate limits of scaling down these nanoscale light sources leading to Purcell enhancement of the emission and higher speeds are also theoretically analyzed.

Acknowledgements. This work was supported by the Gravitation Zwaartekracht programme and by NanoNextNL, a micro- and nano-technology program of the Dutch Ministry of Economic Affairs and Agriculture and Innovation and 130 partners. A.H-R and M.K.S acknowledge the ERC project NO LIMITS. B.R. acknowledges the financial support of the Marie Skłodowska-Curie IF fellowship NANOLASER (2014-IF-659012).

REFERENCES

1. Miller, D. A. B. "Optical interconnects to electronic chips," *Appl. Opt.*, Vol. 49, No. 25, 59–70, 2010.
2. Hill, M. T., and Gather, M. C. "Advances in small lasers," *Nat. Photon.*, Vol. 8, 908–918, 2014.
3. Purcell, E. M. "Spontaneous emission probabilities at radio frequencies," *Phys. Rev. Lett.*, Vol. 69, 681, 1946.
4. Altug, H., Englund, D., and Vuckovic, J. "Ultrafast photonic crystal nanocavity laser," *Nat. Phys.*, Vol. 2, 484–488, 2006.
5. Dolores-Calzadilla, V., Romeira, B., Pagliano, F., Birindelli, S., Higuera-Rodriguez, A., van Veldhoven, P. J., Smit, M. K., Fiore, A., and Heiss, D. "Waveguide-coupled nanopillar metal-cavity light-emitting-diodes on silicon," *Nat. Comms.*, Vol. 8, 14323, 2017.
6. Higuera Rodriguez, A., Romeira, B., Birindelli, S., Black, L., Smalbrugge, B., Kessels, W. M. M., Smit, M. K., and Fiore., A. "Ultra-low surface recombination for deeply etched III-V semiconductor nano-cavity lasers," *Advanced Photonics Congress 2016*, paper ITu2A, 2016.
7. Crosnier, G., Bazin, A., Ardizzone, V., Monnier, P., Raj, R., and Raineri, F. "Subduing surface recombination for continuous-wave operation of photonic crystal nanolasers integrated on silicon waveguides," *Opt. Express*, Vol. 23, No. 21, 27953–27959, 2015.

Imaging the Dark Emission of Spasers

Hua-Zhou Chen[1], Jia-Qi Hu[1], Suo Wang[1], Bo Li[1], Xing-Yuan Wang[1], Yi-Lun Wang[1], Lun Dai[1,2], Ren-Min Ma[1,2*]

[1] State Key Lab for Mesoscopic Physics and School of Physics, Peking University, Beijing 100871, China.

[2] Collaborative Innovation Center of Quantum Matter, Beijing, China

Corresponding author: renminma@pku.edu.cn.

Abstract- We directly image surface plasmon emission, an intrinsic but unrevealed feature of spasers in spatial, momentum and frequency spaces simultaneously. We demonstrate a nanowire spaser with a coupling efficiency to plasmonic modes of 74%. This coupling efficiency can approach 100% in theory when the diameter of the nanowire becomes smaller than 50 nm. Our results provide clear evidence of the surface plasmon amplifier nature of spasers and will pave the way for their various applications.

The recent rapidly advancing nanoscience and technology calls for a nanoscale laser spot for various technologies, such as nanolithography, high-density data storage and uper resolution imaging. However, conventional lasers amplify photons where diffraction limit puts a forbidden barrier to scaling down its physical size and mode volume. In 2003, David J. Bergman and Mark I. Stockman proposed a new class of amplifier, named spaser, an acronym of surface plasmon amplification by stimulated emission of radiation [1]. In stark contrast to classical laser, spaser amplifies surface plasmons instead of photons providing an optical amplifier with size beyond diffraction limit, which is of major interest for numerous applications, ranging from all-optical computing to biomedical sensing. Because of that, numerous works have been reported on the experimental implementation of spasers [2-14]. However, up to now, spasers have only been characterized by the photons scattered to the optical far field. According to its original definition, a spaser is a surface plasmon amplifier that does not necessarily generate radiative photon output. Its intrinsic surface plasmon emission is yet unrevealed "dark" emission due to its evanescent nature. Consequently, there is a lack of direct evidence of spasing, and the intentional manipulation and utilization of spaser emission becomes difficult to achieve. Here, for the first time, we directly image surface plasmon emission, an intrinsic but unrevealed feature of spasers in spatial, momentum and frequency spaces simultaneously [15]. We demonstrate that spaser can serve as a pure surface plasmon generator with the ratio of surface plasmon emission over total radiation approaching to 100% and experimentally demonstrated 74%. Our results supply an unambiguous evidence of spasing behavior, an intrinsic but unrevealed feature of this intensively studied new class of optical amplifier. Furthermore, in contrast to the scattered photons, the surface plasmon emission of spasers is the crucial element for various nanophotonic applications.

REFERENCES

1. D. J. Bergman, M. I. Stockman, Surface plasmon amplification by stimulated emission of radiation: Quantum generation of coherent surface plasmons in nanosystems. *Phys. Rev. Lett.* **90,** 027402 (2003)
2. M. T. Hill, *et al.* Lasing in metal-insulator-metal sub-wavelength plasmonic waveguides. *Opt. Express* **17,** 11107-11112 (2009)
3. M. A. Noginov, *et al.*, Demonstration of a spaser-based nanolaser. *Nature* **460,** 1110-1112 (2009).
4. R. F. Oulton, *et al.* Plasmon lasers at deep subwavelength scale. *Nature* **461,** 629-632 (2009).

5. R. M. Ma, R. F. Oulton, V. J. Sorger, G. Bartal, X. Zhang, Room-temperature sub-diffraction-limited plasmon laser by total internal reflection. *Nature Mater.* **10,** 110-113 (2011)
6. A. M. Lakhani, M. K. Kim, E. K. Lau, M. C. Wu, Plasmonic crystal defect nanolaser. *Opt. Express* **19**, 18237-18245 (2011).
7. M. Khajavikhan, *et al.* Thresholdless nanoscale coaxial lasers. *Nature* **482,** 204-207 (2012).
8. Y. J. Lu, *et al.* Plasmonic nanolaser using epitaxially grown silver film. *Science* **337,** 450-453 (2012).
9. W. Zhou, *et al.* Lasing action in strongly coupled plasmonic nanocavity arrays. *Nature Nanotech.* **8,** 506-511 (2013).
10. F. van Beijnum, *et al.* Surface plasmon lasing observed in metal hole arrays. *Phys. Rev. Lett.* **110,** 206802 (2013)
11. X. G. Meng, A. V. Kildishev, K. Fujita, K. Tanaka, V. M. Shalaev, Wavelength-tunable spasing in the visible. *Nano Lett.* **13,** 4106-4112 (2013).
12. Q. Zhang, *et al.* A room temperature low-threshold ultraviolet plasmonic nanolaser. *Nature Commun.* **5,** 4953 (2014).
13. Y. J. Lu, *et al.* All-color plasmonic nanolasers with ultralow thresholds: autotuning mechanism for single-mode lasing. *Nano Lett.* **14,** 4381-4388 (2014).
14. C. Zhang, *et al.* Plasmonic lasing of nanocavity embedding in metallic nanoantenna array. *Nano Lett.* **15,** 1382-1387 (2015).
15. H.-Z. Chen, *et al.* Imaging the dark emission of spasers. *Science Advances* **3**, e1601962 (2017).

High-Yield Plasmonic Nanolasers with Excellent Stability for Sensing in Aqueous Solution

Suo Wang[1], Bo Li[1], Xing-Yuan Wang[1], Hua-Zhou Chen[1], Yi-Lun Wang[1], Xiao-Wei Zhang[1], Lun Dai[1,2], Ren-Min Ma[1,2*]

[1] State Key Lab for Mesoscopic Physics and School of Physics, Peking University, Beijing 100871, China.

[2] Collaborative Innovation Center of Quantum Matter, Beijing 100871, China

***** Corresponding author renminma@pku.edu.cn.

Abstract- we report a plasmonic nanolaser with excellent stability in biocompatible aqueous solution by surface passivation. The overall yield of stable operation is over 68%. We demonstrate these passivated plasmonic nanolasers as refractive index sensors. The figure of merit (FOM) of intensity sensing is 8000.

Plasmonic nanolaser with strong field confinement beyond diffraction limit is of major interest for numerous applications, ranging from all-optical computing to biomedical sensing. However, to achieve lasing state, the gain materials in plasmonic nanolasers have to be pumped hard enough for population inversion. In the strong plasmonic lasing field, the optical excited gain materials are easy to experience nonreversible photochemical reactions [1-5], which is a major hurdle for its practical application. And despite the rapidly advanced research in plasmonic nanolasers [6-9], there is no study on their stability and yield yet. Here, for the first time, we demonstrate that the yield of plasmonic nanolasers with excellent stability can be over 68% in water by surface passivation. As a comparison, the as-fabricated plasmonic nanolasers based on CdSe gain material only have a stably lasing yield of about 4%. We further demonstrate that these passivated plasmonic nanolasers can be excellent refractive index sensors in aqueous solution. The figure of merit of intensity sensing is about 8000 which is about 40 times higher than the state-of-the-art surface plasmon resonance sensor. Our results indicate that plasmonic nanolaser can operate stably in biocompatible aqueous solutions with high yield which will pave the way for its real world applications, especially in biomedical research and applications.

Acknowledgments

This work was supported by the National Natural Science Foundation of China (nos.11574012, 61521004, 61125402, 51172004, and 11474007), the Youth 1000 Talent Plan Fund.

.

REFERENCES

[1] E. Ippen, C. Shank & A. Dienes, Rapid photobleaching of organic laser dyes in continuously operated devices. IEEE J. Quantum Electron. **7,** 178-179 (1971).

[2] Q. Zheng, S. Jockusch, Z. Zhou & S. C. Blanchard, The contribution of reactive oxygen species to the photobleaching of organic fluorophores. Photochem. Photobiol. **90,** 448-454 (2014).

[3] Q. Zhang, S. T. Ha, X. F. Liu, T. C. Sum & Q. H. Xiong, Room-temperature near-infrared high-Q perovskite whispering-gallery planar nanolasers. Nano Lett. **14,** 5995-6001 (2014).

[4] H. M. Zhu, Y. P. Fu, F. Meng, X. X. Wu, Z. Z. Gong, Q. Ding, M. V. Gustafsson, M. T. Trinh, S. Jin & X. Y. Zhu, Lead halide perovskite nanowire lasers with low lasing thresholds and high quality factors. Nat. Mater. **14,** 636-642 (2015).

[5] T. A. Berhe, W. N. Su, C. H. Chen, C. J. Pan, J. H. Cheng, H. M. Chen, M. C. Tsai, L. Y. Chen, A. A. Dubale & B. J. Hwang, Organometal halide perovskite solar cells: degradation and stability. Energy Environ. Sci. **9,** 323-356 (2016).

[6] R. F. Oulton, V. J. Sorger, T. Zentgraf, R. M. Ma, C. Gladden, L. Dai, G. Bartal & X. Zhang, Plasmonic nanolasers at deep subwavelength scale. Nature 461, 629-632 (2009).

[7] W. Zhou, M. Dridi, J. Y. Suh, C. H. Kim, D. T. Co, M. R. Wasielewski, G. C. Schatz & T. W. Odom, Lasing action in strongly coupled plasmonic nanocavity arrays. Nature Nanotech. 8, 506-511 (2013).

[8] R. M. Ma, R. F. Oulton, V. J. Sorger, G. Bartal & X. Zhang, Room-temperature sub-diffraction-limited plasmonic nanolaser by total internal reflection. Nature Mater. 10, 110-113 (2011).

[9] R. M. Ma, S. Ota, Y. M. Li, S. Yang & X. Zhang, Explosives detection in a lasing plasmon nanocavity. Nature Nanotech. 9, 600-604 (2014).

Room Temperature Ultralow Threshold Plasmonic Nanolasers with Unusual Scaling Laws

Suo Wang[1], Xing-Yuan Wang[1], Bo Li[1], Hua-Zhou Chen[1], Rupert F. Oulton[3], Ren-Min Ma[1,2*]

[1] State Key Lab for Mesoscopic Physics and School of Physics, Peking University, Beijing 100871, China.

[2] Collaborative Innovation Center of Quantum Matter, Beijing, China

[3] The Blackett Laboratory, Department of Physics, Imperial College London, Prince Consort Road, London SW7 2AZ, UK

***** Corresponding author renminma@pku.edu.cn.

Abstract- we report a room temperature plasmonic nanolaser with threshold on the order of 10 KW cm^{-2} corresponding to a pump density in the range of modern laser diodes. We find unusual scaling laws that allow plasmonic lasers to be more compact, faster, lower threshold and power consumption than photonic nanolasers when the cavity size approaches or surpasses the diffraction limit.

Plasmonic nanolasers are a new class of quantum amplifiers that generate coherent light well below the diffraction barrier bringing fundamentally new capabilities to biochemical sensing, super-resolution imaging and on-chip optical communication. However, a debate about whether metals can enhance the performance of lasers has persisted due to the unavoidable fact that metallic absorption intrinsically scales with field confinement [1-10]. Particularly at room temperature, plasmonic nanolasers still have high thresholds in excess of MW cm^{-2}, preventing their practical usage. Here, we report plasmonic nanolasers with record low thresholds on the order of 10 KW cm^{-2} at room temperature, which are comparable to those found in modern laser diodes. We show that plasmonic nanolaser threshold scales linearly with device volume, which is opposite to the trend seen in conventional lasers. This unusual scaling law means plasmonic lasers have superior performance over photonic lasers in terms of lower thresholds and power consumption when the cavity size is smaller than the diffraction limit. This clarifies the long-standing debate over the viability of metal confinement and feedback strategies in laser technology and identifies situations where plasmonic lasers can have clear practical advantage.

Acknowledgments

This work was supported by the National Natural Science Foundation of China (nos.11574012, 61521004, 61125402, 51172004, and 11474007), the Youth 1000 Talent Plan Fund.

.

REFERENCES

1. Hill, M. T. & Gather, M. C., Advances in small lasers. *Nature Photon.* **8,** 908-918 (2014).
2. Berini, P. & De Leon, I., Surface plasmon–polariton amplifiers and lasers. *Nature Photon.* **6,** 16-24 (2011).
3. Khurgin, J. B. & Sun, G., Practicality of compensating the loss in the plasmonic waveguides using semiconductor gain medium. *Appl. Phys. Lett.* **100,** 11105 (2012).
4. Oulton, R. F. Plasmonics loss and gain. *Nature Photon.* **6,** 219-221 (2012).
5. Ma, R. M., Oulton, R. F., Sorger, V. J. & Zhang, X. Plasmon lasers coherent light source at molecular scales. *Las. Photon. Rev.* **7,** 1-21 (2012).
6. Khurgin, J. B. & Sun, G., Comparative analysis of spasers, vertical-cavity surface-emitting lasers and surface-plasmon-emitting diodes. *Nature Photon.* **8,** 468-473 (2014).
7. Khurgin, J. B., Prospects and merits of metal-clad semiconductor lasers from nearly UV to far IR. *Opt. Express* **23,** 4186-4194 (2015).
8. Ding, K., Diaz1, J. O., Bimberg, D. & Ning, C. Z. Modulation bandwidth and energy efficiency of metallic cavity semiconductor nanolasers with inclusion of noise effects *Las. Photon. Rev.***5,** 488-597 (2015).
9. Yang, A. & Odom, T. W., Breakthroughs in Photonics 2014: Advances in Plasmonic Nanolasers. *IEEE Photonics J* **7,** 0700606 (2015).
10. Gwo, S. & Shih, C. K. Semiconductor plasmonic nanolasers current status and perspectives. *Rep. Prog. Phys.* **79,** 086501 (2016).

High Performance Photonic and Plasmonic Lasers Based on Semiconductor Nanowires

Q. Zhang[1*]

[1] Department of Materials Science and Engineering, College of Engineering, Peking University, Beijing 100871, P. R. China

[*]corresponding author: q_zhang@institution.edu

Abstract- Surface plasmon lasers offer strong light-matter interaction possibilities and many advanced applications in nanophotonics, biology and information technology. However, due to large intrinsic metal Ohmic losses, plasmonic laser suffers from either high threshold or low operation temperature, which limits the practical applications. Here firstly a room-temperature ultra-violet surface plasmon laser using GaN nanowires will be introduced. The lasing threshold is ~3.5 MW/cm^2. Furthermore, we demonstrate a method based on intrinsic self-absorption of semiconductor to tune plasmonic nanowire lasing wavelength.

Acknowledgements

The work is supported by start-up funding support from Peking University and 1000-talents plans of China.

REFERENCES

1. Qing Zhang, Guangyuan Li, Xinfeng Liu, Fang Qian, Yat Li, Tze Chien Sum, Charles M. Lieber[*] and Qihua Xiong[*], A room temperature low-threshold ultraviolet plasmonic nanolaser, Nature Communications, 2014, 5: 4935.
2. Xinfeng Liu[#], Qing Zhang[#], Qihua Xiong[*] and Tze Chien Sum[*], Tailoring the Lasing Modes in Semiconductor Nanowire Cavities Using Intrinsic Self-Absorption, Nano Letters, 2013, 13(3): 1080-1085.
3. Xinfeng Liu[#], Qing Zhang[#], Jing Ngei Yip, Qihua Xiong[*] and Tze Chien Sum[*], Wavelength Tunable Single Nanowire Lasers Based on Surface Plasmon Polariton Enhanced Burstein-Moss Effect, Nano Letters, 2013, 13(11): 5336-5343.
4. Qing Zhang[#], Son Tung Ha[#], Xinfeng Liu[#], Tze Chien Sum[*] and Qihua Xiong[*], Room-Temperature Near-Infrared High-Q Perovskite Whispering-Gallery Planar Nano lasers, Nano Letters, 2014, 14(10): 5995-6001.
5. Qing Zhang[#], Rui Su[#], Xinfeng Liu[#], Jun Xing, Tze Chien Sum[*] and Qihua Xiong[*], High-Quality Whispering-Gallery-Mode Lasing from Cesium Lead Halide Perovskite Nanoplatelets, Advanced Functional Materials, 2016, 26(34): 6238-6245.
6. Qing Zhang, Xinfeng Liu, Muhammad Iqbal Bakti Utama, Guichuan. Xing, Tze Chien Sum[*] and Qihua Xiong[*], Phonon-Assisted Anti-Stokes Lasing in ZnTe Nanoribbons, Advanced Materials, 2015, 28(2): 276-283.
7. Qing Zhang, Xin-Yan Shan, Xiao Feng, Chun-Xiao Wang, Qu-Quan Wang[*], Jin-Feng Jia[*] and Qi-Kun Xue, Modulating Resonance Modes and Q Value of a CdS Nanowire Cavity by Single Ag Nanoparticles, Nano Letters, 2011, 11(10): 4270-4274.
8. Qing Zhang, Xinglin Wen, Guangyuan Li, Qifeng Ruan, Jianfang Wang and Qihua Xiong[*] Multiple Magnetic Mode-Based Fano Resonance in Split-Ring Resonator/Disk Nanocavities, ACS Nano, 2013, 7(12): 11071-11078

Room temperature operation of a Silicon nanobeam laser integrated with a 2D monolayer molybdenum ditelluride

Y.Z. Li[1], J.X. Zhang[1], D.D. Huang[1], H. Sun[1], F. Fan[1,2], J.B. Feng[1], Z. Wang[1], and C.Z. Ning[1,2,*]

[1]*Department of Electronic Engineering, Tsinghua University, Beijing, 100084, China*

[2]*School of Electrical, Computer, and Energy Engineering, Arizona State University, Tempe, AZ 85287, USA*

[*]corresponding author: cning@asu.edu

Abstract This talk will begin with a summary overview of recent efforts in achieving lasing operation using a monolayer of transition metal dichalcogenides. We will then present our recent results in demonstrating the first room temperature laser operation using a monolayer molybdenum ditelluride integrated with a silicon photonic-crystal nanobeam structure. We will show that room temperature lasing can be achieved at very low threshold under a continuous wave laser pumping.

Transition metal dichalcogenides (TMDs) have attracted a great deal of attention due to their distinctive properties and potential applications in electronics and optoelectronic devices [1, 2]. Unlike their bulk counterparts, two-dimensional monolayers of the most of the TMDs are direct bandgaps semiconductors [3], with strong optical emission. Therefore, monolayer TMDs could be an efficient active material, with the thinnest gain medium possible. Laser operation based on monolayers of TMDs were firstly reported at cryogenic temperatures, employing a monolayer WSe_2 coupled onto a GaP photonic-crystal cavity [4], or a monolayer WS_2 with a Si_3N_4 microdisk [5]. These laser demonstrations still have high threshold that prevents their lasing at room temperature, which are necessary for any practical application.

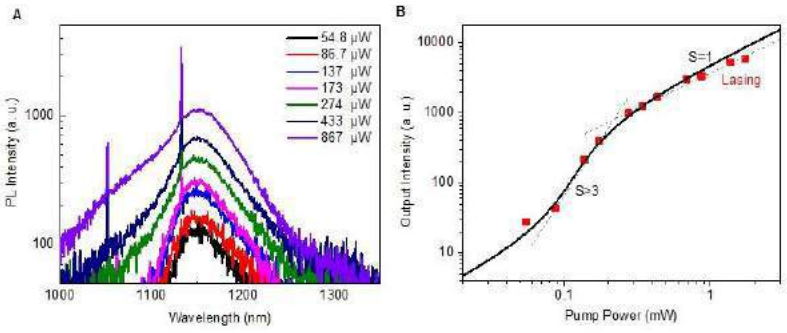

Figure 1 Photoluminescence spectra under different levels of optical excitation (A, left) and intensity output at the lasing peak vs. pumping power (B, right) showing a clear threshold behavior.

Our recent efforts [6] in searching for a high Q cavity to be integrated with a 2D TMD gain material have led us to an interesting combination of a silicon nanobeam cavity and the monolayer of molybdenum ditelluride (MoTe2). Monolayer of MoTe2 is known to have a bandgap around ~1.72 eV, but an excitonic photoluminescence (PL) emission peak at ~1.1 eV,

which is about 50 meV below the silicon bandgap. This makes the MoTe2 a perfect gain material to be integrated with Si cavity structure. The high index of refraction and mature fabrication of Si has resulted in a high Q-cavity. As a result, room temperature operation was achieved under the pumping of a continuous wave laser. Examples of lasing behavior are shown in Figure 1. Details of device design, fabrication, and characterization will be presented, as well as updates about recent progress.

REFERENCES

1. Fengnian Xia, et al. "Two-dimensional material nanophotonics," Nat. Photonics 8, 899-907 (2014).
2. Withers, F. et al. "Light-emitting diodes by band-structure engineering in van der Waals heterostructures," Nat. Mater. **14**, 301–306 (2015).
3. Kin Fai Mak, et al. "Atomically Thin MoS_2: A New Direct-Gap Semiconductor", Phys. Rev. Lett. **105**, 136805 (2010).
4. Wu, S. et al. "Monolayer semiconductor nanocavity lasers with ultralow thresholds," Nature **520**, 69–72 (2015).
5. Ye, Y. et al. "Monolayer excitonic laser," Nat. Photonics **9**, 733–737 (2015).
6. Y.Z. Li et al, "Room-temperature Continuous-wave Lasing from Monolayer Molybdenum Ditelluride with a Silicon Nanobeam Cavity", arXiv:1701.07921,[v1] Fri, 27 Jan 2017 01:44:06 GMT,[cond-mat.mes-hall]; Optics (physics.optics).

Photo/Thermal Conversions and Their Applications

Enhanced near-infrared Photoelectric and Photothermal Response on silicon flatform by metamaterial absorber and omni-schottky junction

Q. Chen and L. Wen
Key Lab of Nanodevices and Applications, Suzhou Institute of Nano-Tech and Nano-Bionics, Chinese Academy of Sciences (CAS), Suzhou 215123, People's Republic of China
*corresponding author: qchen2012@sinano.ac.cn

Abstract-Optical absorption and electron emission/collection are two key factors for improving photoelectric response based on plasmonic hot-electron. Here, we demonstrated plasmonic hot-electron photoresponse as high as 3.3mA/W at 1500nm achieved on a silicon platform by metamaterial absorber (MA) and omni-schottky junction. Furthermore, time-resolved photoresponse shows optical energy transferred to electricity through the photothermal mechanism distinct from the photoelectric process of hot electron.

Plasmonic effects were investigated in a myriad of applications such as biosensing, optoelectronics, thermal therapy, data storage and so on. In particular, the functionality of light harvesting at a nanoscale offers remarkable improvements of the quantum efficiency (QE) of photoelectric energy conversion in both valence-conduction transition [1] and internal photoemission (IPE) processes [2]. In the later one, metal absorbs photons and then generates hot electrons that may cross the metal-semiconductor junction resulting in photocurrent. There are two main limitations on the QE of IPE process, one is the spectral absorption and the other is the emission probability of hot electrons. Localized surface plasmon resonance (LSPR) of regular metal nanostructures only enhances light absorption in a narrow band and the device fabrication relies on the expensive high-resolution lithography technique like electron beam lithography [3]. The small junction area of metal-semiconductor interface limits hot electron emission. In this paper, we present our recent work addressing these two issues by combining both optical and electrical perspectives into the design of plasmonic photodetectors on silicon platform.

As shown in Figure 1, the proposed devices containing Au nanoparticles (NPs) which are sandwiched between two electron-accepting semiconductors (i.e. TiO_2 and silicon) allow high emission probability for the hot electrons due to the formation of the omnidirectional M-S junctions around these tiny plasmonic absorber/emitters. On the other hand, metamaterial perfect absorber (MPA) based optical enhancing scheme is incorporated by a MSM configuration, for the purpose of obtaining highly localized and perfect photon absorption in the mono-layered Au NPs. The measured photoresponse were shown in Figure 2, where we can see that random NPs provide broad band high absorption resulting in a much improved responsivity of the proposed device over the planar reference. The device with TiO2 intermediate layer also showed higher responsivity than the one with ITO layer, supporting the expected benefit for the omni-Schottky junction mechanism (no energy offset in conduction band between TiO_2 and silicon). The results of the time-resolved characterization of the devices differentiate the photoelectric and photothermal response, which will be presented at the conference.

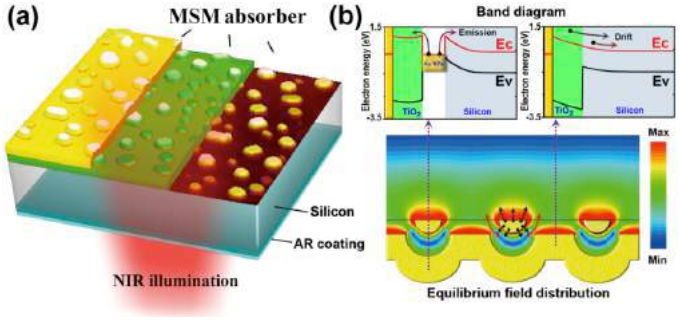

Figure 1 (a) Schematic drawings of the proposed MPA integrated Si photodetectors. A typical morphology of Au NPs via thermal dewetting technique from our experiments is adopted to enhance the illustration. (b) Energy band diagrams (top) and field distributions (bottom) under thermal equilibrium.

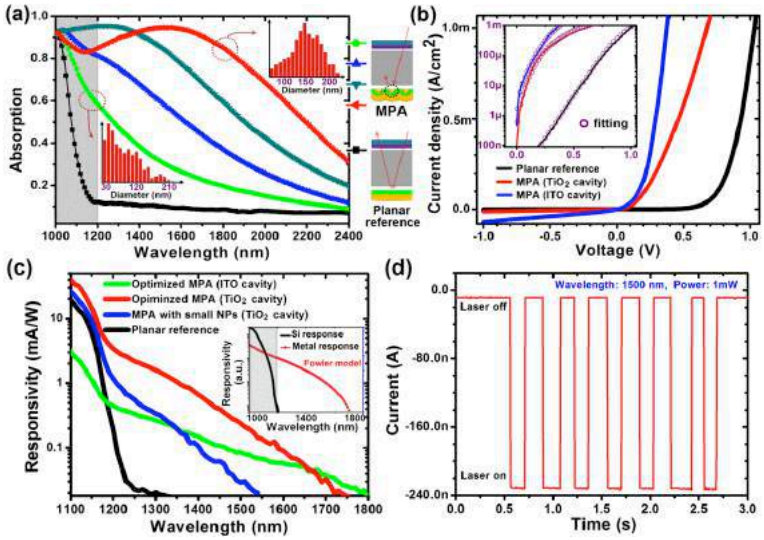

Figure 2 (a) The experimental absorption spectra of the MPA structures with different particle sizes. The inserted histograms illustrate the respective size distributions for two selected MPAs with smallest and largest NPs. The result for planar reference is also given. (b) Typical dark current-voltage curves for the MPA and planar reference devices. MPA devices consisting of TiO_2 and ITO as the cavity materials were considered. (c) Responsivity of the different MPA devices and planar device. The insert shows the theoretical results for two distinct response schemes. (d) Time-dependent current changes under fast switch on-off the laser illumination.

REFERENCES

1. Atwater, H. A. and Polman, A., "Plasmonics for improved photovoltaic devices," *Nature Materials*, Vol. 9, 205-213, 2010.
2. Brongersma, M. L., Halas, N. J. and Nordlander, P., "Plasmon-induced hot carrier science and technology," *Nature Nanotechnology*, Vol. 10, 25-34, 2016.
3. Knight, M. W., Sobhani, H., Nordlander, P., Halas, N. J., "Photodetection with active optical antennas," *Science*, Vol. 332, 702-704, 2011.
4. Wen, L., Chen, Y., Liu, W., Su, Q., Qi, Z., Wang, Q. and Chen, Q., "Enhanced near-infrared Photoelectric and Photothermal Response on silicon flat form by metamaterial absorber and omni-schottky junction," submitted.

Thin multi-layered film of radiation cooling for heat dissipation of LED arrays

Yung-Chiang Lan*, Po Jui Chiu and Bo-Han Cheng
Department of Photonics, National Cheng Kung University, Tainan 701, Taiwan
*corresponding author: lanyc@mail.ncku.edu.tw

Abstract- A three-layered compact film with heat dissipation based on the method of passive radiation cooling for light emitting diode (LED) are developed and analyzed. Electromagnetic and heat diffusion simulations are accomplished to verify that the design of proposed film can effectively decrease the temperature of LED with various input powers.

This work develops and analyzes a three-layered (Si-Ni_3Si-Al) compact film with heat dissipation based on the method of passive radiation cooling for light emitting diode (LED). The proposed film is designed with the feature of high absorptance at atmospheric transmission region (i.e. 8 um – 13 um). According to Kirchhoff's law of thermal radiation, the emissivity of the film will be equal to its absorptivity at thermal equilibrium. The corresponding admittance diagram and absorption spectra are also explored to elucidate the reason of high absorption. Electromagnetic and heat diffusion simulations based on the finite element method (COMSOL) are accomplished to verify that the design of proposed film can effectively decrease the temperature of LED with various input powers. Considering the typical LED in work (e.g. 1 mm square surface area with heat generation of 1 watt), the proposed film can achieve lower temperature with significantly reduced size as compared to LED with traditional heat sink. Figure 1 plots the simulation temperature distribution for LED with the proposed three-layered film (t_1=570 nm, t_2=750 nm, t_3=150 nm) for heat dissipation. The interface temperature can achieve 326.07 K, which is lower than other heat dissipation designs. This work has potential applications in the field of thermal emitter, photovoltaic-based device and high power devices.

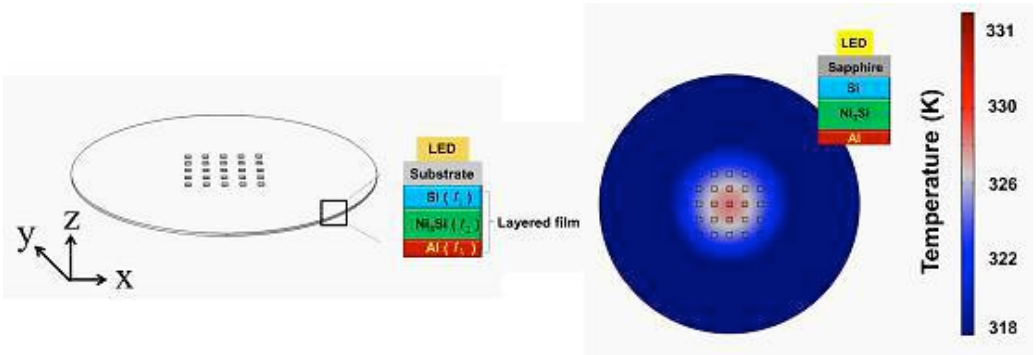

Fig. 1 Simulated structure of LED array and simulated temperature distributions. Heat from each LED is 1 W/ mm^2.

Controlling thermal emission of phonon by magnetic metasurfaces

X. Zhang[1,2], H. Liu[1*], Z. G. Zhang[1], Q. Wang[1], and S. N. Zhu[1]

[1]National laboratory of solid state microstructures & school of physics, Collaborative Innovation Center of Advanced Microstructures, Nanjing University, Nanjing 210093, China

[2]Shandong Province Key Lab of Laser Polarization and Information, Qufu Normal University, Qufu 273165, China

[*]corresponding author: liuhui@nju.edu.cn

Abstract-Our experiment shows that the thermal emission of phonon can be controlled by magnetic resonance (MR) mode in a metasurface (MTS). Through changing the structural parameter of metasurface, the MR wavelength can be tuned to the phonon resonance wavelength. This introduces a strong coupling between phonon and MR, which results in an anticrossing phonon-plasmons mode. In the process, we can manipulate the polarization and angular radiation of thermal emission of phonon. Such metasurface provides a new kind of thermal emission structures for various thermal management applications. *n*

In recent years, the research interest of thermal emission in the infrared wavelength range is growing fast due to its important applications in thermaophotovoltaic (TPV) devices [1], radiative cooling [2,3], incandescent source [4], near-field heat transfer [5], and infrared spectroscopy [6]. Up to now, various structures and systems have been used to control thermal emission, such as gratings [7, 8], nanoantennas [9, 10], photonic crystals [11], surface plasmons [12-14], metamaterials [15-17] and metasurfaces (MTS) [18, 19]. Some properties of thermal emission, such as the emission bandwidth [20], coherent properties [7] and dynamics switching [21, 22, 23] are reported to be controlled in these systems.

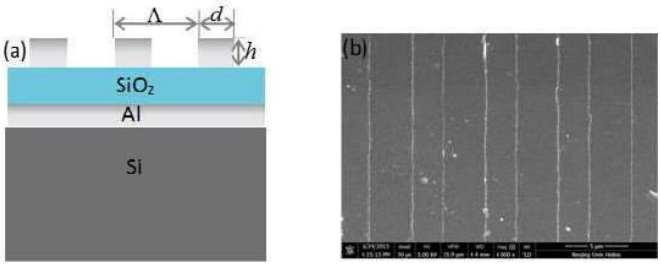

Figure 1 (color online) the sketch plot (a) and SEM top view (b) of sandwiched structure. In experiments, the periodic and height are fixed with $\Lambda = 6.5\mu m$ and $h = 0.05\mu m$, d is changed from 2.6 to 3.6 μm.

In this work, the MIM metasurface is used to control the emission of phonons. Using high temperature synthesized amorphous SiO2, we designed and fabricated the Al/SiO2/Al magnetic MTS with Al grating arrayed on the SiO2/Al film (see figure 1 (a)). The MTS grating width is adjusted to produce the strong coupling between MR and phonon inside SiO2. Differ from the precedent studies about the active optical phonons of silica at $\lambda = 10\mu m$, here, we focus our attention on the relatively inactive optical phonon at $\lambda = 12.5um$. The absorption and thermal emission spectra were measure by Fourier-transform infrared (FTIR) spectrometer in the wavelength range $11-16\mu m$. The anticrossing features in the spectra denoted that strong coupling between

phonon and magnetic resonance, albeit with big difference in radiation intensity of these two resonant states. Using commercial software FDTD solution and coupled mode theory, we analysed the coupling physical mechanism. The theoretical calculations agree with experiments quite well.

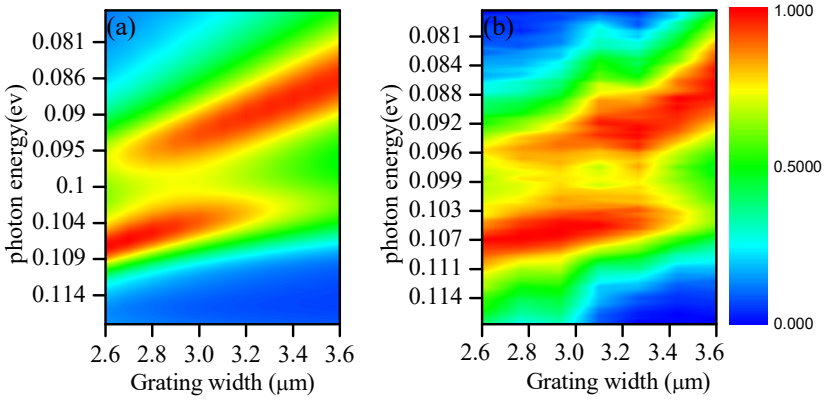

Figure 5. Simulated absorption (a) and measured emission (b) spectra versus photon energy and grating width d.

REFERENCES

1. Lenert, A. et al. Nat Nanotechnol 9, 126-30 (2014).
2. Raman, A.P., Anoma, M.A., Zhu, L., Rephaeli, E. & Fan, S. Nature 515, 540-544 (2014).
3. Shi, N.N. et al. Science 349, 298-301 (2015).
4. Ilic, O. et al. Nat Nano 11, 320-324 (2016).
5. St-Gelais, R., Zhu, L., Fan, S. & Lipson, M. Nat Nano 11, 515-519 (2016).
6. De Wilde, Y. et al. Nature 444, 740-743 (2006).
7. Greffet, J.-J. et al. Nature 416, 61-64 (2002).
8. Dahan, N., Gorodetski, Y., Frischwasser, K., Kleiner, V. & Hasman, E. Phys. Rev. Lett. 105, 136402 (2010).
9. Schuller, J.A., Taubner, T. & Brongersma, M.L. Nat Photon 3, 658-661 (2009).
10. Ingvarsson, S., Klein, L.J., Au, Y.-Y., Lacey, J.A. & Hamann, Optics Express 15, 11249-11254 (2007).
11. Luo, C., Narayanaswamy, A., Chen, G. & Joannopoulos, J.D. Phys. Rev. Lett. 93, 213905 (2004).
12. Wang, C.-M. et al. Optics Express 15, 14673-14678 (2007).
13. Ye, Y.-H. et al. Applied Physics Letters 93, 263106 (2008).
14. Mason, J.A., Smith, S. & Wasserman, D. Applied Physics Letters 98, 241105 (2011).
15. Liu, X. et al. Physical Review Letters 107, 045901 (2011).
16. Guo, Y., Cortes, C.L., Molesky, S. & Jacob, Z. Applied Physics Letters 101, 131106 (2012).
17. Lee, B.J., Wang, L.P. & Zhang, Z.M. Optics Express 16, 11328-11336 (2008).
18. Shitrit, N. et al. Science 340, 724-726 (2013).
19. Costantini, D. et al. Physical Review Applied 4, 014023 (2015).
20. De Zoysa, M. et al. Nat Photon 6, 535-539 (2012).
21. Inoue, T., Zoysa, M.D., Asano, T. & Noda, S. Nat Mater 13, 928-931 (2014).
22. Brar, V.W. et al. Nat Commun 6 (2015)
23. K. Du, et al. Light Sci Appl 6, e16190 (2017).
24. X. Zhang, et.al. Scientific Reports 7:41858 (2017)

Enhancing Near-Field Radiative Heat Transfer with Si-based Metasurfaces

V. Fernández-Hurtado[1,2,3*], F. J. García-Vidal[1,4], S. Fan[2], and J. C. Cuevas[1,3]

[1]Departamento de Física Teórica de la Materia Condensada and Condensed Matter Physics Center (IFIMAC), Universidad Autónoma de Madrid, Madrid, 28049, Spain

[2]Department of Electrical Engineering, and Ginzton Laboratory, Stanford University, Stanford, California 94305, USA

[3]Department of Physics, University of Konstanz, D-78457 Konstanz, Germany

[4]Donostia International Physics Center (DIPC), Donostia/San Sebastián 20018, Spain

[*]corresponding author: victor.fernandezh@uam.es

Abstract-We propose a novel mechanism to further enhance near-field radiative heat transfer (NFRHT) with the use of Si metasurfaces, which is based on the broad spectral bandwidth and the high tunability of the surface-plasmon polaritons that dominate NFRHT in these structures. We have shown that by an appropriate choice of the geometrical parameters, these metamaterials can exhibit room-temperature near-field radiative heat conductances higher than any existent or proposed structure.

Thermal radiation is one of the most ubiquitous physical phenomena. In recent years, there has been a renewed interest in this topic due to the confirmation of the long-standing prediction that radiative heat transfer can be drastically enhanced for bodies separated by small gaps [1]. This enhancement, which occurs when the gaps are smaller than the thermal wavelength (9.6 μm at room temperature), is due to the contribution of evanescent waves that dominate the near-field regime. The fact that this near-field radiative heat transfer (NFRHT) between closely spaced bodies can overcome the far-field limit set by the Stefan-Boltzmann law for black bodies has now been verified in a variety of experiments exploring different materials, geometrical shapes, and gaps ranging from micrometers to a few nanometers [2-4]. We demonstrate in this work that the use of metasurfaces provides a viable strategy to largely tune and enhance near-field radiative heat transfer between extended structures. In particular, using a rigorous coupled wave analysis, we predict that Si-based metasurfaces featuring two-dimensional periodic arrays of holes can exhibit a room-temperature near-field radiative heat conductance much larger than any unstructured material to date [5]. We show that this enhancement, which takes place in a broad range of separations, relies on the possibility to largely tune the properties of the surface plasmon polaritons that dominate the radiative heat transfer in the near-field regime.

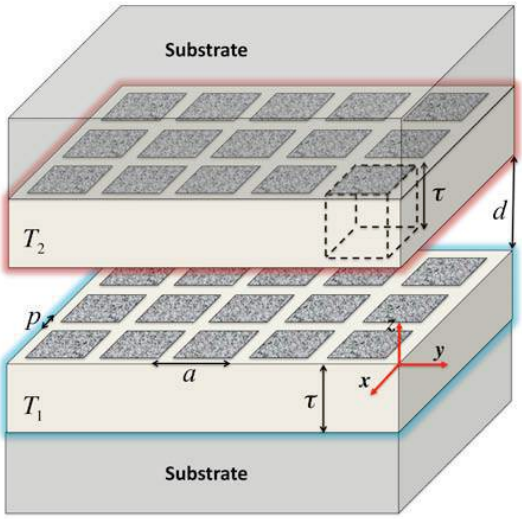

Figure 1. Schematics of two doped-Si metasurfaces made of 2D periodic arrays of square holes placed on semi-infinite planar substrates and held at temperatures T_1 and T_2.

REFERENCES

1. Polder, D. and M. Van Hove, "Theory of radiative heat transfer between closely spaced bodies," *Phys. Rev. B*, Vol. 4, No. 10, 3303-3314, 1971.
2. Shen, S., A. Narayanaswamy and G. Chen, "Surface Phonon Polaritons Mediated Energy Transfer between Nanoscale Gaps," *Nano Lett.*, Vol. 9, No. 8, 2909-2913, 2009.
3. Song, B., Y. Ganjeh, S. Sadat, D. Thompson, A. Fiorino, V. Fernández-Hurtado, J. Feist, F. J. Garcia-Vidal, J. C. Cuevas, P. Reddy, and E. Meyhofer, "Enhancement of near-field radiative heat transfer using polar dielectric thin films," *Nat. Nanotechnol.*, Vol. 10, No. 3, 253–258, 2015.
4. Kim, K., B. Song, V. Fernández-Hurtado, W. Lee, W. Jeong, L. Cui, D. Thompson, J. Feist, M. T. H. Reid, F. J. Garcia-Vidal, J. C. Cuevas, E. Meyhofer, and P. Reddy, "Radiative heat transfer in the extreme near field," *Nature*, Vol. 528, 387–391, 2015.
5. Fernández-Hurtado, V., F. J. Garcia-Vidal, S. Fan and J. C. Cuevas, "Enhancing near-field radiative heat transfer with Si-based metasurfaces," *arXiv preprint*, arXiv:1701.02986 2017.

Resonant Thermoelectric Nanophotonics

K. W. Mauser[1], S. Kim[1], S. Mitrovic[2], D. Fleischman[1], R. Pala[1], K. Schwab[1], and H. A. Atwater[1,3*]

[1]Thomas J. Watson Laboratory of Applied Physics, California Institute of Technology, Pasadena, CA 91125, United States

[2] Joint Center for Artificial Photosynthesis, California Institute of Technology, Pasadena, CA 91125, United States

[2] Kavli Nanoscience Institute, California Institute of Technology, Pasadena, CA 91125, United States

[*]corresponding author: haa@caltech.edu

Abstract- Photodetectors are typically based on photocurrent generation from electron-hole pairs in semiconductor structures and on bolometry for below bandgap absorption. We demonstrate subwavelength thermoelectric nanostructures designed for resonant spectrally selective absorption, which create localized temperature gradients with unfocused, spatially-uniform illumination to generate easily measureable thermoelectric voltages. We show that such structures are tunable with highly wavelength-specific detection, with responsivities up to 38 V/W, and bandwidths of 3 kHz, by combining resonant absorption at thermoelectric junctions, yielding a bandgap-independent photodetection mechanism.

Plasmon excitation enables extreme light confinement at the nanoscale, localizing energy in subwavelength volumes and thus can enable increased absorption in photovoltaic or photoconductive detectors[1]. Nonetheless, plasmon decay also results in energy transfer to the lattice as heat which is detrimental to photovoltaic detector performance[2]. However heat generation in resonant subwavelength nanostructures also represents an energy source for voltage generation, as we demonstrate here via design of resonant thermoelectric (TE) plasmonic absorbers for optical detection. Though TEs have been used to observe resonantly coupled surface plasmon polaritons in noble-metal thin films and microelectrodes[3,4] and have been explored theoretically for generation of ultrafast intense magnetic pulses in a dual-metal split ring resonator[5], they have not been employed as resonant absorbers in functional TE nanophotonic structures.

We demonstrate nanostructures composed of TE thermocouple junctions using established TE materials – chromel/alumel and bismuth telluride/antimony telluride – but patterned so as to support guided mode resonances with sharp absorption profiles, and which thus generate large thermal gradients upon optical excitation and localized heat generation in the TE material. Sample structure geometry and experimental data is shown in Figure 1. Unlike previous TE absorbers[6,7], our structures feature tunable narrowband absorption and measured single junction responsivities 4 times higher than the most similar (albeit broadband) graphene structures, with potential for much higher responsivities in thermopile architectures. For bismuth telluride – antimony telluride single thermocouple structures, we measure a maximum responsivity of 38 V/W, referenced to incident illumination power. We also find that the small heat capacity of optically resonant TE nanowires enables a fast, 3 kHz temporal response, 10-100 times faster than conventional TE detectors[8,9]. Additionally, the resonant TE nanowires exhibit noise only slightly above the Johnson noise level, suggestion a simple pathway for improving detectivity in future devices. We show that TE nanophotonic structures are tunable from the visible to the MIR, with small structure sizes of 50 microns x 100 micons. Our nanophotonic TE

structures are suspended on thin membranes to reduce substrate heat losses and improve thermal isolation between TE structures arranged in arrays suitable for imaging or spectroscopy. Whereas photoconductive and photovoltaic detectors are typically insensitive to sub-bandgap radiation, nanophotonic TEs can be designed to be sensitive to any specific wavelength dictated by nanoscale geometry, without bandgap wavelength cutoff limitations. From the point of view of imaging and spectroscopy, they enable integration of filter and photodetector functions into a single structure.

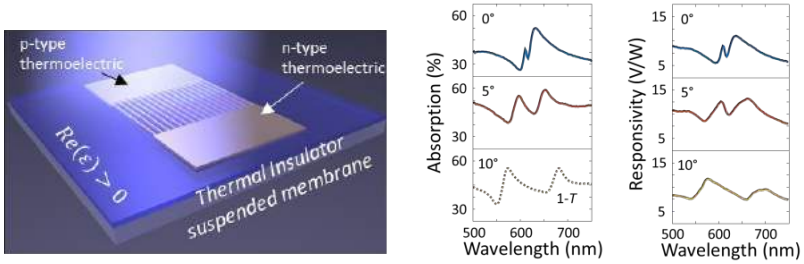

Figures 1. Resonant thermoelectric guided mode resonance structure schematic (left). Absorption (center) and thermoelectric responsivity (right) as a function of off-normal angle of illumination.

Acknowledgements

This work was supported primarily by US Department of Energy (DOE) Office of Science grant DE-FG02-07ER46405. S.K. acknowledges support by a Samsung Scholarship.

REFERENCES

1. Atwater, H. A. and A. Polman, "Plasmonics for improved photovoltaic devices," *Nat Mater* Vol. 9, 205-213, 2010.
2. Skoplaki, E. and J. A. Palyvos, "On the temperature dependence of photovoltaic module electrical performance: A review of efficiency/power correlations," *Solar Energy,* Vol. 83, 614-624, 2009.
3. Innes, R. A. and J.R. Sambles, "Simple Thermal Detection of Surface Plasmon-Polaritons," *Solid State Commun,* Vol. 56, 493-496, 1985.
4. Weeber, J. C. et al. "Thermo-electric detection of waveguided surface plasmon propagation," *Appl Phys Lett* Vol. 99, 031113, 2011.
5. Tsiatmas, A. et al. "Optical generation of intense ultrashort magnetic pulses at the nanoscale," *New J Phys* Vol. 15, 113035, 2013.
6. Cai, X. et al. "Sensitive room-temperature terahertz detection via the photothermoelectric effect in graphene," *Nat Nanotechnol* Vol. 9, 814-819, 2014.
7. Hsu, A. L. et al. "Graphene-Based Thermopile for Thermal Imaging Applications," *Nano Lett* Vol. 15, 7211-7216, 2015.
8. Russer, J. A. et al. "A Nanostructured Long-Wave Infrared Range Thermocouple Detector," *IEEE T Thz Sci Techn,* Vol. 5, 335-343, 2015.
9. Russer, J. A. et al. "High-Speed Antenna-Coupled Terahertz Thermocouple Detectors and Mixers," *IEEE T Microw Theory* Vol. 63, 4236-4246, 2015.

Functionalized Silk Fibroin Thin Films with Gold Nanoparticles as Ultrahigh Broadband Absorber

D. Wan*

[1]Institute of Biomedical Engineering, National Tsing Hua University, Taiwan

*corresponding author: dhwan@mx.nthu.edu.tw

Abstract- In this paper, the phenomenon of white-light-induced heating in silk fibroin (SF) films embedded with gold nanoparticles (Au NPs) is systematically investigated. As far as we are aware, this study is the first to employ Au NPs to develop an ultrahigh broadband absorber and also the first to use a white light source for photothermal generation. Also, the broadband absorptive film is coated on a simple Al/Si Schottky diode and displays a linear, significant, stable photo-thermo-electronic (PTE) response with varying light intensity.

There has been increasing interest in the unique physical and chemical properties of metal nanoparticles (NPs) because of their energy and biomedical applications. For example, metal NPs are attractive for their localized surface plasmon resonance (LSPR) properties. The strong interactions between metallic NPs and incident light originate from excitation of the collective oscillations of conduction electrons within these particles.[1] One of the amazing LSPR-related phenomena is the photothermal effect. When LSPR occurs, the plasmonic particles can efficiently convert optical energy to local heat and rapidly raise the temperature of the surroundings or themselves.

Light-activated Au NPs have been embedded in polymer matrix and widely used in material, biomedical, and photonic applications.[2] To further understand the photothermal process involved in the solid composites, a number of studies have investigated the light-induced heating of various polymers containing Au NPs.[3,4] Note that previous research has focused on the nanocomposites containing low Au contents (typically less than 1 wt%), which induced small temperature increases (few to few tenths °C). The low metal content might be attributed to the limitation of preparation methods or the poor solvent miscibility. In this case, the films exhibited a characteristic absorbance peak with a weak/moderate peak intensity and a narrow spectral bandwidth (ca. 50-100 nm), originated from the LSPR extinction of Au NPs dispersed in the polymer matrix. In other words, the nanocomposites can only absorb a small portion of the incident light energy near LSPR frequency, while most of the light energy within non-LSPR region will propagate through the film without any noticeable loss. This optical phenomenon restricts the choices of the light excitation sources for photoheating. Therefore, for the white-light-induced heat generation, a broadband optical absorber is strongly needed, which can completely trap the light energy over all wavelengths. To our best knowledge, however, no studies of the metallic NP/polymer nanocomposites with wide-range optical absorbance have been reported.

In this study, we fabricated homogeneous Au NP/silk fibroin (SF) composite films exhibiting ultrahigh broadband absorbance in the visible-near infrared (vis-NIR) range through a facile, simple solution process, and systematically investigated their optical properties and white-light-induced photothermal effects (see Figure1). Herein, SF was selected as host material due to a series of advantages: (i) high water solubility to prevent the

aggregation of Au NPs, especially at high colloid concentration; (ii) high T_g (ca. 180 °C) to avoid the heat dissipation induced from the phase change of polymeric matrix, and (iii) high transparency to reduce the light attenuation in the host material. By increasing the Au content in the composite films, the absorbance could be enhanced significantly around the LSPR wavelength and also raised dramatically at the non-LSPR wavelengths. The greater amount of absorbed light led to an increase in the photoheating rate. The optimized composite film exhibits an ultrahigh absorbance of ca. 95% over a wide spectral range of 350-750 nm, and moderate absorbance values (> 60%) in the longer wavelength range of 750-1000 nm. In this case, the composite film could absorb almost all of the incident light and accordingly convert the optical energy to local heat. Therefore, significant temperature increases on the order of ca. 100°C could be readily obtained when the composite film is irradiated by a LED or a halogen lamp. Moreover, the composite films also display a linear light-to-heat response with light intensity and a great photothermal stability. Finally, the broadband absorptive film is coated on a simple Al/Si Schottky diode and displays a linear, significant, stable photo-thermo-electronic (PTE) response with varying light intensity.

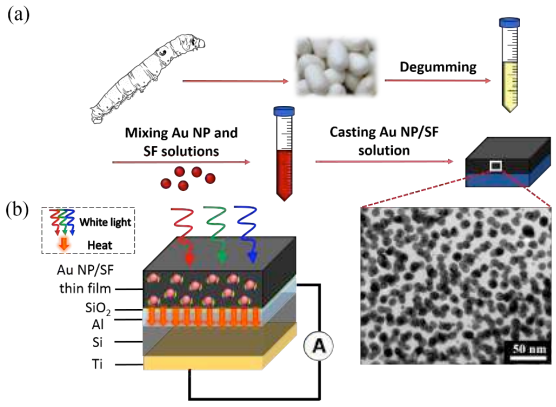

Figure 1. Schematic representations of (a) the fabrication of a hybrid Au NP/SF thin film onto a substrate and (b) white light irradiated into a Au NP/SF thin onto a Al/Si Schottky diode. (Inset) Cross-section TEM image of a SGN/SF thin film.

Acknowledgements This study was supported by the Ministry of Science and Technology, Taiwan (MOST-103-2113-M-007-007-MY2) and Chang Gung Memorial Hospital-National Tsing Hua University Joint Research Grant (104N2744E1).

REFERENCES

1. Kelly, K. L.; Coronado, E.; Zhao, L. L.; Schatz, G. C. The optical properties of metal nanoparticles: The influence of size, shape, and dielectric environment. *J Phys Chem B* 2003, 107, 668-677.
2. Govorov, A. O.; Richardson, H. H. Generating heat with metal nanoparticles. *Nano Today* 2007, 2, 30-38.
3. Heber, A.; Selmke, M.; Cichos, F. Metal Nanoparticle Based All-Optical Photothermal Light Modulator. *ACS Nano* 2014, 8, 1893-1898.
4. Maity, S.; Bochinski, J. R.; Clarke, L. I. Metal Nanoparticles Acting as Light-Activated Heating Elements within Composite Materials. *Adv. Funct. Mater*. 2012, 22, 5259-5270.

Superradiant and superscattering in thermal and light energy conversion

Zongfu Yu

University of Wisconsin Madison

When wave effects of thermal photons become significant, thermal emitters can exhibit intriguing coherent effects. Here, we show that the superradiant emission, which was originally found in quantum emitters, can be realized in resonant thermal emitters. Similar to the superradiance in quantum emitters, the in-phase oscillation of resonant emitters reduces the lifetime of thermal photons in the emitters. Unlike the atomic superradiance, one remarkable consequence of the thermal superradiance is the anomalous power scaling, where the emission power can scale inversely with the number of thermal emitters. More thermal emitters generate less power due to the coherent interference of thermal photons.

Fundamental electrodynamics dictates that the wavelength sets the length scale of the cross section in a resonant scattering process. Diverging cross sections can only be achieved around the DC frequency when the wavelength approaches infinity. Wely points, with a conic dispersion relation like that around the DC point, are shown to exhibit diverging cross sections, regardless of the wavelengths. The decoupling of the resonant cross section and the wavelength could allow, for example a nanoscale optical resonance to have a macroscopic cross section. Extraordinarily large cross section could be very useful for applications in optical energy conversion.

Self-assembled Three Dimensional Plasmonic Absorbers for Solar Thermal Conversion

L. Zhou* and J. Zhu

National Laboratory of Solid State Microstructures, College of Engineering and Applied Sciences, and Collaborative Innovation Center of Advanced Microstructures, Nanjing University, Nanjing 210093, China

*corresponding author: linzhou@nju.edu.cn

Abstract-Nanostructures enabled solar thermal conversion has aroused tremendous interest in the field of solar energy applications. Here we will report our progresses on the self-assembled plasmonic nanostructures assisted solar thermal conversion, which includes the design and fabrication of the most broadband plasmonic absorbers, tunability of absorption bandwidth, as well as the first plasmon enhanced solar desalination device. Our results may provide a competitive solution to the cost-effective and highly efficient solar desalination strategies for personalized applications.

Due to flexible tenability of absorption bandwidth, ability of subwavelength confinement of electromagnetic field and the related hot spots effect, plasmonic absorbers have aroused tremendous interest in solar thermal conversion processes [1,2]. Recently, we have demonstrated the three dimensional metallic nanoparticles as the broadband absorbers with the scalable self-assembled process (Fig. 1b).

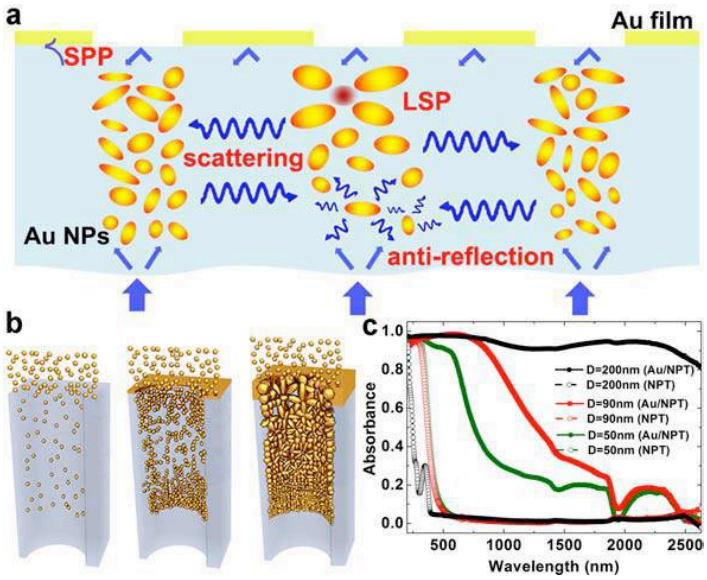

Fig. 1 Optical design (a), self-assembled fabrication (b) and absorption performance (c) for the broadband plasmonic absorbers.

Due to the unique close-packed and highly porous metallic nanoparticle assemblies, the nanostructure is ideal candidate for broadband absorbers due to high density of optical modes by plasmon hybridization, strong

scattering as well as antireflection effect (Fig. 1a) [3]. In addition, the absorption bandwidth can be flexibly tuned by the geometry parameters and/or deposition conditions [4], indicating potential applications for various solar thermal conversion applications. Finally, we for the first time employed the low cost 3D aluminum nanoparticles for the broadband solar absorbers and enabled the plasmon enhanced solar desalination device [5], by which the solar thermal efficiency ~ 90% and ~ 4 orders of magnitude of the ion concentration decrement were achieved. Our results would shed light on the low cost personalized solution for the solar desalination technologies.

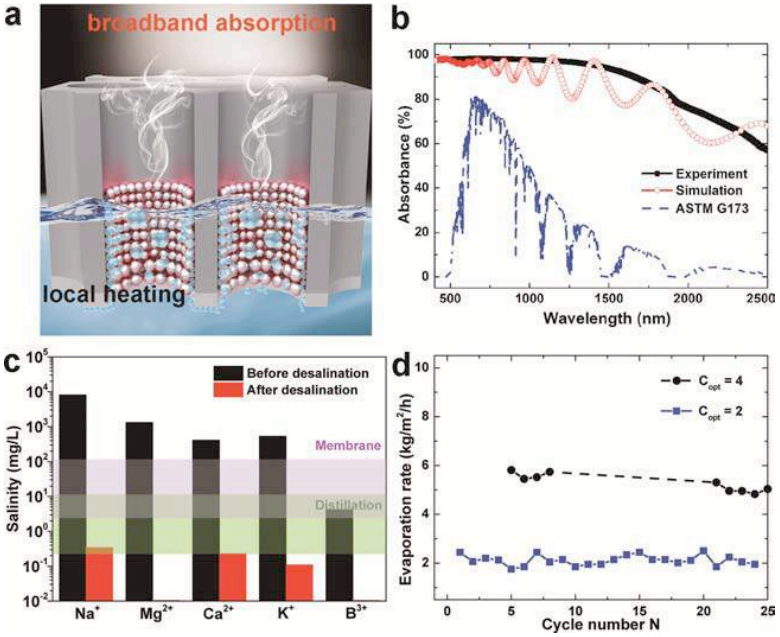

Fig. 2 Three dimensional self assembled aluminum nanoparticles for plasmon enhanced solar desalination. (a) physical mechanism; (b) broadband selective absorption; (c-d) seawater desalination performance.

Acknowledgements, L. Z. thanks the National Natural Science Foundation of China (No. 11204139), Natural Science Foundation (No. BK20151079) and Qing Lan Project of Jiangsu Province.

REFERENCES

1. Liu, Y. *et al*. A bioinspired, reusable, paper-based system for high-performance large-scale evaporation. *Adv. Mater.* Volume **27**, 2768-2774, 2015.
2. Neumann, O. *et al*. Compact solar autoclave based on steam generation using broadband light-harvesting nanoparticles. *Proc. Natl. Acad. Sci.* Volume **110**, 11677-11681, 2013.
3. Zhou, L. *et al*. Self-assembly of highly efficient, broadband plasmonic absorbers for solar steam generation. *Sci. Adv.* Volume **2**, e1501227, 2016.
4. Zhou, L. et al. Self-assembled spectrum selective plasmonic absorbers with tunable bandwidth for solar energy conversion. Nano Energy Volume 32, 195-200, 2017.
5. Zhou, L. *et al*. 3D self-assembly of aluminium nanoparticles for plasmon-enhanced solar desalination. *Nat. Photonics* Volume **10**, 393-398, 2016.

Gap-free thermophotovoltaic systems

M. S. Mirmoosa[1,2], S. A. Biehs[2], and C. R. Simovski[1]

[1]Department of Electronics and Nanoengineering, School of Electrical Engineering, Aalto University, Finland

[2]Institut für Physik, Carl von Ossietzky Universität, D-26111 Oldenburg, Germany

mohammad.mirmoosa@aalto.fi

Abstract— We investigate a *gap-free* thermophotovoltaic system whose engineered emitter is matched to the macroscopic layer of a particular material which has very low absorption at the operation band of the photovoltaic cell and relatively low thermal conductivity. We tailor the radiative heat transfer such that it is maximal and super-Planckian near the bandgap frequency of the photovoltaic cell, and reduced at other frequencies. Therefore, it gives rise to a high ultimate efficiency and high electric output. We believe that our study paves the way toward the new generation of efficient and feasible thermophotovoltaic systems for producing electricity from heat.

Thermophotovoltaics (TPVs) are systems which use a direct energy conversion method to generate electricity from heat. In fact, in TPVs (similar to solar cells) the radiating photons are absorbed by a photovoltaic (PV) cell that operates at room temperature. The absorbed photons are converted into electron-hole pairs and result in the electric current. However, in TPVs the radiating photons are emitted from a source which has a temperature much higher than the room temperature. Emitter and the PV cell are supposed to be separated by a vacuum gap in order to sustain the temperature difference between the emitter and the PV cell [1].

In designing efficient thermophotovoltaic systems, two main points should be taken into account. The first key point is that we have to obtain a super-Planckian radiative heat transfer in order to get a noticeable output power, and the second one is related to the efficiency of the system. Only photons which have higher energy than the bandgap energy of the PV cell ($E > \hbar\omega_{\mathrm{g}}$) can contribute in the generation of the electron-hole pairs. The low-energy photons cause thermal dissipation in the PV cell and may increase its temperature. The same senario is also true for the photons which have very high energy (since the excessive energy $\hbar(\omega\,!\;\;\omega_{\mathrm{g}})$ is not useful and it causes thermal dissipation). Hence, the radiative heat transfer must be frequency-selective such that it is maximum near ω_{g} and negligible at other frequencies [1].

In this conference paper, we introduce a new design of thermophotovoltaic systems which fulfills the above goals: frequency selectivity and super-Planckian radiative heat transfer. However, in contrast to the previous works (see, e.g. [2, 3, 4]) where super-Planckian radiative heat transfer was achieved by using hyperbolic metamaterials (wire media) or decreasing the width of the vacuum gap (to a few nanometres) to have a strong photon-tunelling effect, here, the super-Planckian radiative heat transfer is given by an intermediate material between the emitter and the PV cell. Indeed, the vacuum gap is replaced by the intermediate material which has a large thickness and it is matched to our particular emitter at the frequency near the bandgap frequency of the PV cell. Such a design resolves the difficulty of preserving the nanogap for the sufficient area of a few square centimetres, or fabrication of wire media.

REFERENCES

1. Bauer, T., *Thermophotovoltaics: Basic Principles and Critical Aspects of System Design*, Springer-Verlag, Berlin-Heidelberg, 2011.
2. Simovski, C., S. Maslovski, I. Nefedov and S. Tretyakov, "Optimization of radiative heat transfer in hyperbolic metamaterials for thermophotovoltaic applications," *Opt. Express*, Vol. 21, 186858, 2013.
3. Mirmoosa, M. S., M. Omelyanovich and C. R. Simovski, "Microgap thermophotovoltaic systems with low emission temperature and high electric output," *Journal of Optics*, Vol. 18, 115104, 2016.
4. Messina, R. and P. Ben-Abdallah, "Graphene-based photovoltaic cells for near-field thermal energy conversion," *Scientific Reports*, Vol. 3, 1383, 2013.

Control over emissivity of middle infrared thermal emitters with phase changing material

Qiang Li*, Kaikai Du, Yurui Qu and Min Qiu

State Key Laboratory of Modern Optical Instrumentation, College of Optical Science and Engineering, Zhejiang University, 310027, Hangzhou, China

*corresponding author: qiangli@zju.edu.cn

Controlling the emissivity of a thermal emitter has attracted growing interest with a view towards a new generation of thermal emission devices. So far, all demonstrations have involved sustained external electric or thermal consumption to maintain a desired emissivity. In this invited talk, I will review our recent work on control over the emissivity of a thermal emitter consisting of a phase changing material Ge2Sb2Te5 (GST) film on top of a metal film [1]. This thermal emitter shows broad wavelength-selective spectral emissivity in the mid-infrared. The peak emissivity approaches the ideal blackbody maximum and a maximum extinction ratio of above 10dB is attainable by switching GST between the crystalline and amorphous phases. By controlling the intermediate phases, the emissivity can be continuously tuned. This switchable, tunable, wavelength-selective and thermally stable thermal emitter will pave the way towards the ultimate control of thermal emissivity in the field of fundamental science as well as for energy-harvesting and thermal control applications, including thermophotovoltaics, light sources, infrared imaging and radiative coolers.

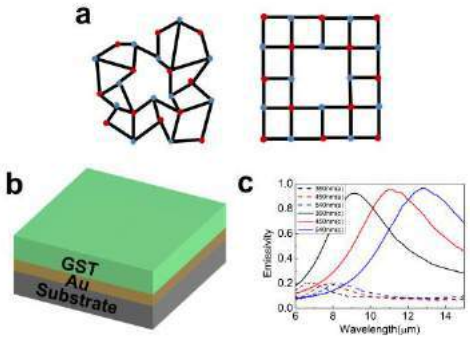

Fig1. (a) Atom distribution diagrams of the two phases (amorphous and crystalline) of the GST. The red and blue dots denote the Ge/Sb atoms and Te atoms, respectively. (b) A 3D schematic of the switchable and tunable thermal emitter composed of a GST film on top of a gold film. (c) Thermal emissivity curves of GST–Au emitters with different GST thicknesses (360, 450 and 540 nm) at 100 °C. Adapted from Ref. [1]

References

1. Kaikai Du, Qiang Li, Yanbiao Lyu, Jichao Ding, Yue Lu, Zhiyuan Cheng and Min Qiu. *Light: Science & Applications*, **6**, e16194 (2017).

Light-induced pulling and pushing by synergic effect of optical force and photophoretic force

Min Qiu, Jinsheng Lu, Hangbo Yang, Lina Zhou, Yuanqing Yang, Si Luo and Qiang Li
State Key Laboratory of Modern Optical Instrumentation, College of Optical Science and Engineering, Zhejiang University, 310027, Hangzhou, China
*corresponding author: minqiu@zju.edu.cn

Optical force has been widely utilized to manipulate microscopic objects, though mostly in vacuum or in liquids. Photophoretic force provides an alternative and effective way to transport light-absorbing particles in ambient gases. However, in most cases these forces work independently. Here, by employing the synergy of optical force and photophoretic force, we propose and experimentally demonstrate a configuration which can drive a micron-size metallic plate moving back and forth on a tapered fiber with supercontinuum light in ambient air [1].

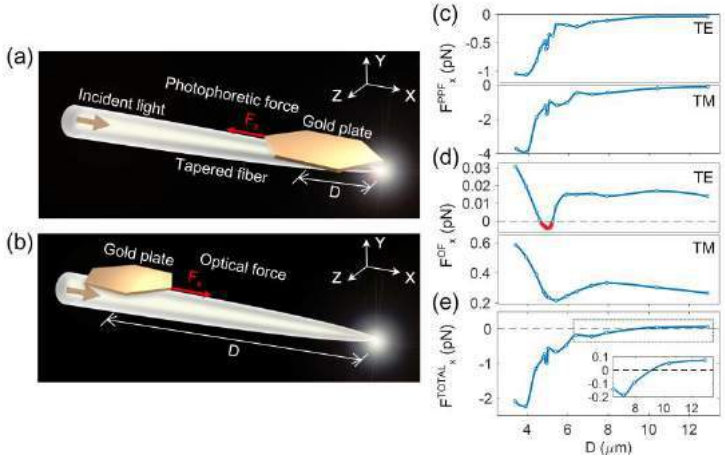

FIG. 1. Numerical modelling of light-induced driving by synergy effect of optical force and photophoretic force. Adapted from Ref. [1]

REFERENCES

1. Jinsheng Lu, Hangbo Yang, Lina Zhou, Yuanqing Yang, Si Luo, Qiang Li, and Min Qiu Light-Induced Pulling and Pushing by the Synergic Effect of Optical Force and Photophoretic Force. Phys. Rev. Lett., Vol. 118, Issue 4, pp. 043601 (2017).

Tungsten based metamaterials and photonic crystals for selective thermal emitters.

Alexander Yu. Petrov[1,9*], Pavel N. Dyachenko[1], Katrin Knopp[1], Slawa Lang[1], Elisabeth W. Leib[2], Jefferson do Rosario[3], Sean Molesky[4], Zubin Jacob[4,5], T. Krekeler[6], M. Ritter[6], Michael Störmer[7], Tobias Vossmeyer[2], Horst Weller[2,8], Gerold Schneider[3], Manfred Eich[1,7]

[1]Institute of Optical and Electronic Materials, Hamburg University of Technology (TUHH), Eißendorfer Straße 38, 21073 Hamburg, Germany

[2]Institute of Physical Chemistry, University of Hamburg, Grindelallee 117, D-20146 Hamburg, Germany.

[3]Institute of Advanced Ceramics, TUHH, Denickestraße 15, 21073 Hamburg, Germany.

[4]University of Alberta, Department of Electrical and Computer Engineering, 9107 - 116 Street, T6G 2V4, Edmonton, Canada.

[5]Birck Nanotechnology Center, School of Electrical and Computer Engineering, Purdue University, West Lafayette, IN 47906, USA

[6]Electron Microscopy Unit, TUHH, Eissendorfer Strasse 42, 21073 Hamburg, Germany.

[7]Institute of Materials Research, Helmholtz-Zentrum Geesthacht Centre for Materials and Coastal Research, Max-Planck-Straße 1, 21502 Geesthacht, Germany.

[8]Department of Chemistry, Faculty of Science, King Abdulaziz Univ., Jeddah, Saudi Arabia

[9]ITMO University, 49 Kronverkskii Ave., 197101, St. Petersburg, Russia,

[*]corresponding author: a.petrov@tuhh.de

Abstract- In order to tailor thermophotovoltaic emitters to match specific photovoltaic receivers we designed spectrally selective emitters that have close to black body emission at short wavelengths and substantially reduced emission at long wavelengths. We demonstrate selective band-edge emitters based on a W-HfO_2 refractive multilayer metamaterial and a ZrO_2 opal monolayer on tungsten both stable up to 1000°C. Conditions for improved selectivity and higher thermal stability will be presented as well.

The efficient thermophotovoltaic conversion requires emitters that demonstrate emissivity close to 1 at frequencies above the band gap frequency of the photovoltaic cell (short wavelengths) and emissivity close to zero for smaller frequencies (longer wavelengths). Two possible routes can be envisaged to produce the required type of the emission. The first is based on materials which have dielectric constants that are matched to vacuum at short wavelengths and are strongly mismatched and thus reflecting at longer wavelengths. The second option is based on structures on a surface that support critically coupled resonances at short wavelengths and no resonances at longer wavelengths.

We are presenting the results obtained by both routes. First we discuss results of a layered metamaterial from W and HfO_2 (Fig. 1a) [1]. The subwavelength combination of dielectric and metal allows shifting the hyperbolic transition of the metamaterial to the NIR. This way the metamaterial has close to one permittivity and thus close to one absorptivity and emissivity at short wavelengths. In the long wavelength range the metamaterial with low absorption has a hyperbolic equi-frequency surface and thus sustains thermally excited modes with only large wavevectors, none of which can couple out into vacuum. The structure shows up to 1000°C stability under

vacuum conditions of ~$2 \cdot 10^{-2}$ mbar. Even though the upper layer of tungsten was protected by 100 nm of HfO_2 the residual oxygen from vacuum leads to oxidation of this first layer of tungsten. The advantage of metamaterial is almost direction independent thermal emission which is connected to the fact that properties are defined by the effective parameters of the metamaterial and not by the accumulated phases. But the metamaterial still shows significant emission at longer wavelengths due to limited reflectivity. This is connected to the high imaginary permittivity of tungsten and large penetration of long wavelength fields into the metamaterial.

Better suppression of long wavelength emission can be obtained using dielectric resonators coupled to lossy metal. This was achieved by deposition of a monolayer of ZrO_2 spheres on a tungsten substrate protected by a thin layer of HfO_2 (Fig. 1b) [2]. The microspheres support resonances which are critically coupled to free space. The dense monolayer of spheres can be approximated and simulated as a PhC with a hexagonal lattice. The resonances of single spheres in this case present a tight-binding approximation of the PhC. The overlapping absorption of different resonances leads to a band of high emission at short wavelengths. At longer wavelength, where no resonances are present, the reflectivity is defined by the flat tungsten substrate. The penetration of the incident fields and thus the absorption is lower at longer wavelength than in the case of metamaterials. Presented PhC emitters have very good suppression of emission at longer wavelengths, but demonstrates angel dependent emission. The stability of this structure is also limited by oxidation of tungsten.

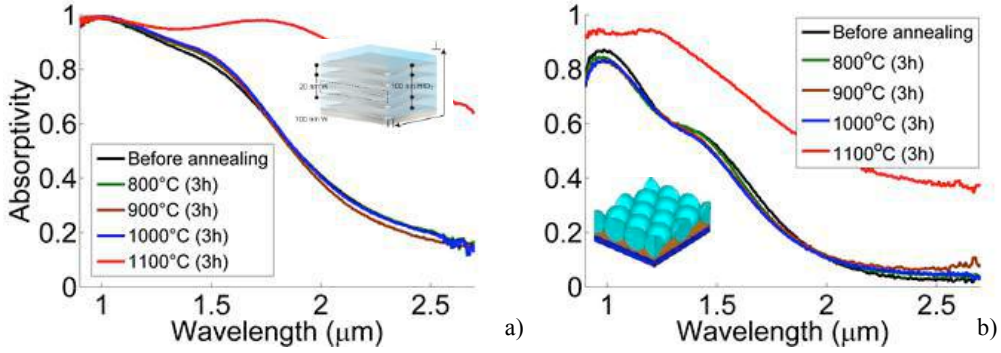

Figure 1: a) Absorptivity of the tungsten based metamaterial after tempering in vacuum ~$2 \cdot 10^{-2}$ mbar. Schematic inset shows the layered structure of W-HfO_2 (20 nm-100 nm) metamaterial. b) Absorptivity of the tungsten emitter coated by a monolayer of ZrO_2 microparticles (660 nm diameter) after tempering in vacuum. Schematic inset shows the structure geometry. (dark blue – W, orange – HfO_2, light blue – ZrO_2).

Acknowledgements, The authors gratefully acknowledge financial support from the German Research Foundation (DFG) via SFB 986 'Tailor-Made Multi-Scale Materials Systems: M3', projects C1, C4, C6, C7 and Z3. The authors also acknowledge the support from CST, Darmstadt, Germany, with their Microwave Studio software.

REFERENCES

1. P. N. Dyachenko et al, „Refractory epsilon-near-zero metamaterials: Controlling thermal emission with topological transitions", *Nat. Comm.*, Vol. 7, No. 11809, 1-8, 2016.
2. P. N. Dyachenko et al, „Tungsten band edge absorber/emitter based on a monolayer of ceramic microspheres", *Opt. Exp.*, Vol. 23, No. 19, A1236-A1244, 2015

Thermoplasmonic energy conversion by self-assembled aluminum oxide meta-structures

Kyoungsik Kim[1*], Kyuyoung Bae[1], Yunha Ryu[1]
[1]School of Mechanical Engineering, Yonsei University,
50 Yonsei-ro, Seodaemun-gu, Seoul 03722, Republic of Korea
[*]corresponding author: kks@yonsei.ac.kr

Abstract

We report on the thermoplasmonic energy conversion by self-assembled meta-structures of aluminum oxide nanostructures. We fabricate aluminum nanowire array, which has high optical transmission haze, and manipulate the optical characteristics by controlling sizes and morphologies. By depositing metal or metal oxide, the array structures absorb broadband light by plasmonic nanofocusing and the absorbed light is converted into the localized heat energy. The converted heat energy can be utilized for solar vapor generation and thermophotovoltaics.

Acknowledgements, This work was supported by Global Research Lab (GRL) Program of the National Research Foundation (NRF) funded by Ministry of Science, ICT (Information and Communication Technologies) and Future Planning (2016K1A1A2912758), the National Research Foundation of Korea (NRF) grant funded by the Korea government (MSIP) (NRF-2015R1A2A2A11001112), Pioneer Research Center Program through the National Research Foundation of Korea funded by the Ministry of Science, ICT & Future Planning (NRF-2013M3C1A3065045), and the Center for Advanced Meta-Materials (CAMM-2014M3A6B3063712) funded by the Ministry of Science, ICT and Future Planning as Global Frontier Project.

REFERENCES

1. Kang, G., Yoo, J., Ahn, J., and Kim, K., "Transparent dielectric nanostructures for efficient light management in optoelectronic applications," *Nano Today*, Vol. 10, No. 1, 22-47, 2015.
2. Kang, G. et al. "Broadband and ultrahigh optical haze thin films with self-aggregated alumina nanowire bundles for photovoltaic applications", *Energy & Environ. Sci.*, Vol. 8, 2650–2656, 2015.
3. Bae, K. et al. "Flexable thin-film black gold membranes with ultrabroadband plasmonic nanofocusing for efficient solar vapour generation", *Nat. Commun.*, Vol. 6, 10103, 2015.
4. Baek, S. et al. "Improvement of Light Extraction Efficiency in Flip-Chip Light Emitting Diodes on SiC Substrate via Transparent Haze Films with Morphology-Controlled Collapsed Alumina Nanorods", ACS Appl. Mater. Interfaces, Vol. 8, No. 1, 135-141, 2016.

Photothermal nanojoining of metallic nanowires

Qiang Li*, Hangbo Yang, and Min Qiu
State Key Laboratory of Modern Optical Instrumentation, College of Optical Science and Engineering, Zhejiang University, 310027, Hangzhou, China
*corresponding author: qiangli@zju.edu.cn

Abstract- Nanojoining of nanomaterials opens up a new emerging set of applications in transparent conductors, thin-film solar cells, nanocatalysis, cancer therapy and nanoscale patterning. Single point nanojoining is highly demanded for building complex nanostructures. In this talk, I will show the precise control of single point nanojoining of silver nanowires in depth, where the nanojoining is laser-induced through the plasmonic resonance enhanced photothermal effect. single point nanojoining technique shows great potentials for high-performance electronic and photonic devices based on nanowires, such as nanoelectronic circuits and plasmonic nanodevices.

As the development of science and technology, integrated device tends gradually into micro-nano scale. For integrated devices based on nanowires elements, nanojoining (including nanowelding [1], nanosoldering [2] and nanobreaking [3]) have shown its necessity for manufacturing integrated nanodevices. In this talk, by taking advantage of photothermal effect of a 532 nm continuous-wave (CW) laser, nanojoining (including nanowelding, nanosoldering and nanobreaking) of nanowires can be achieved.

For the nanowelding and nanosoldering, we investigate the fusing property of a single metallic nanowire after irradiation and take advantage of the concept of match-end to implement nanowelding and nanosoldering. Moreover, we improve the method and test the electrical property after nanowelding. For the nanobreaking (Fig. 1), we study the morphological changes during fusing process and confirm that the critical power required for nanobreaking is much lower for perpendicular polarization than that for parallel polarization both in experiment and simulation. By controlling the polarization and the power of the irradiation laser for nanobreaking, the nanowires can be cut into segments with gap widths ranging from dozens of nanometers to several micrometers.

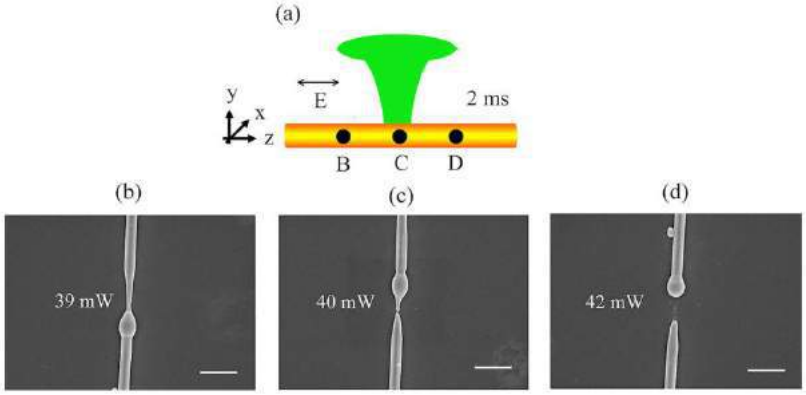

FIG. 2. Morphological changes of a 300-nm-diameter gold nanowire after light irradiation with different power at parallel polarization. (a) A schematic illustration of a focused Gaussian light irradiated on different positions. The irradiation power is (b) 39 mW, (c) 40 mW and (d) 42 mW for positions ‘B’, ‘C’ and ‘D’,

respectively. The formed gap widths are (b) 0 nm, (c) 58 nm and (d) 648 nm. Inset scale bars are 1 μm. (Adapted from Ref. [1])

REFERENCES

1. Lina Zhou, Jinsheng Lu, Hangbo Yang, Si Luo, Wei Wang, Jun Lv, Min Qiu, and Qiang Li Optically controllable nanobreaking of metallic nanowires. Appl. Phys. Lett., Vol. 110, Issue 8, pp. 081101 (2017).
2. Qiang Li, Guoping Liu, Hangbo Yang, Wei Wang, Si Luo, Shuowei Dai, and Min Qiu Optically controlled local nanosoldering of metal nanowires. Appl. Phys. Lett., Vol. 108, Issue 19, pp. 193101 (2016).
3. Shuowei Dai, Qiang Li, Guoping Liu, Hangbo Yang, Yuanqing Yang, Ding Zhao, Wei Wang, and Min Qiu Laser-induced single point nanowelding of silver nanowires. Appl. Phys. Lett., Vol. 108, Issue 12, pp. 121103 (2016).

Spatial and spectral control of thermal emission with nanoantennas.

P. Bouchon[1*], M. Makhsiyan[1,2], J. Jaeck[1] and R. Haïdar[1]

[1]Minao joint Lab., ONERA, The French Aerospace Lab., 91761 Palaiseau, France

[2]Minao joint Lab., Center of nanosciences and nanotechnologies, CNRS, Paris-Saclay University, 91460 Marcoussis, France

[*]corresponding author: Patrick.bouchon@onera.fr

Abstract-Here, we experimentally demonstrate a multispectral metasurface that exhibits controlled inhomogeneous optical properties leading to a spatial modulation of the emissivity up to the wavelength scale in the infrared. A metasurface made of a non-periodic set of 100 million optical nano-antennas that spatially and spectrally control the emitted light up to the diffraction limit has been realized and studied. Each antenna acts as an independent deep subwavelength emitter for a given polarization and wavelength, and their juxtaposition at the wavelength scale can encode far field multispectral and polarized images. Other nanoantennas can be used, like the optical Helmholtz resonator, that allows to control the spectral bandwidth or the radiative losses.

Metasurfaces can be used to tailor the electromagnetic surface on various spectral bands. In particular, metal-insulator-metal (MIM) nanoantennas are known to modify the absorption of a surface due to a Fabry Perot resonance. Here, we first show how the infrared emissivity of a metallic surface, which is nearly zero can be turned into multiple quasi monochromatic emitters thanks to MIM nanoantennas. Then, we show that their subwavelength combination can be used to tailor more complex emissivity spectra, independently for both polarizations. Eventually, an inhomogeneous metasurface is made where the emissivity is spatially modulated at the wavelength scale.

The samples have been studied with a Fourier transform infrared spectrometer coupled to a high resolution cooled HgCdTe camera, and a polarizer.

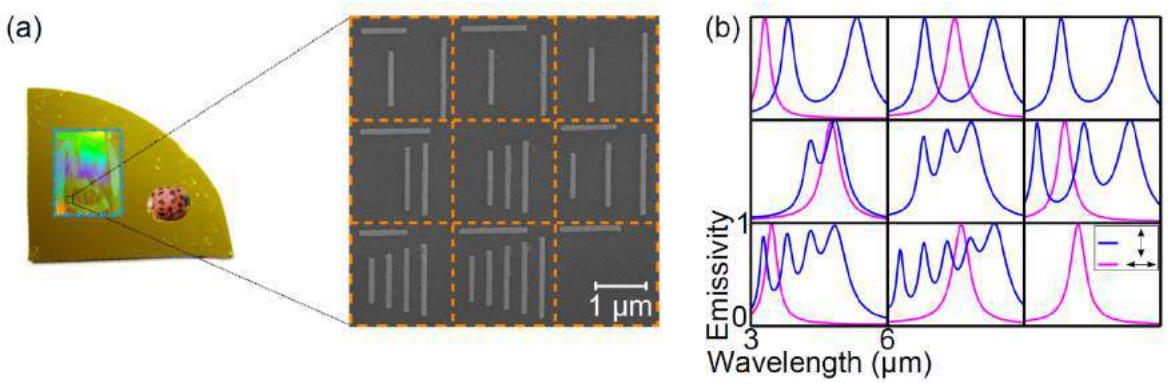

Figure 1: (a) Visible picture of the sample and SEM image of nine elementary cells, each containing various antennas. (b) Computed emissivity spectra for both polarization given for each elementary cell (practically consider as periodic for the computation).

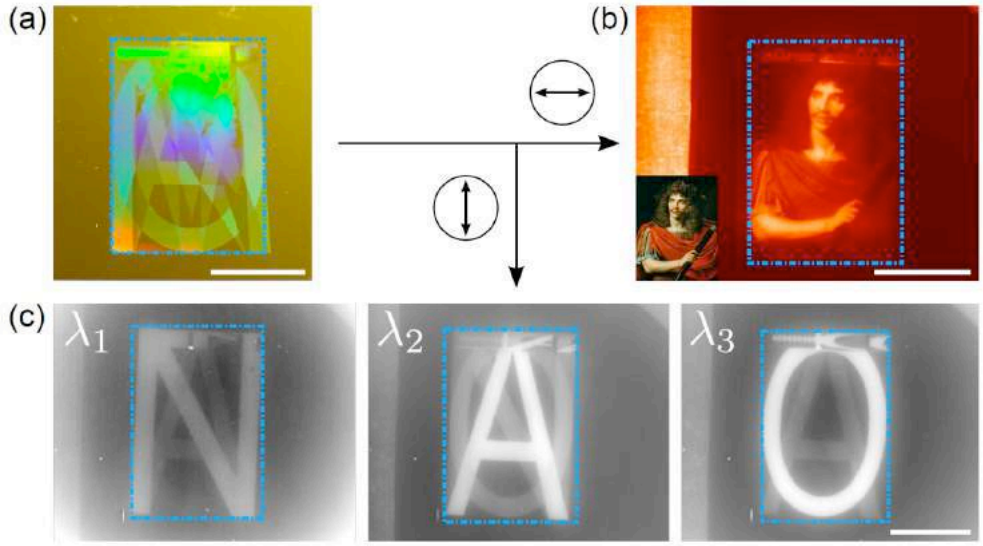

Figure 2: (a) Picture of the sample. (b) Infrared thermal emission on the 3-5 µm band of the sample heated at 100°C for the horizontal polarization. (c) Infrared emission for the vertical polarization, filters were added to select only a part of the emitted spectral band.

REFERENCES

1. Makhsiyan, M., P. Bouchon, J. Jaeck, JL Pelouard and R. Haïdar, "Shaping the spatial and spectral emissivity at the diffraction limit," *Applied Physics Letters*, Vol. 107, 251103, 2015.
2. Chevalier, P., P. Bouchon, R. Haïdar and F. Pardo, "Optical Helmholtz resonators," *Applied Physics Letters*, Vol. 105, 071110, 2014.
3. Chevalier, P., P. Bouchon, R. Haïdar and F. Pardo, "Absorbing metasurface created by diffractionless disordered arrays of nanoantennas," *Applied Physics Letters*, Vol. 107, 251108, 2015.
4. Bouchon, P. , C. Koechlin, F. Pardo, R. Haïdar and JL Pelouard "Wideband omnidirectional infrared absorber with a patchwork of plasmonic nanoantennas," *Applied Physics Letters*, Vol. 34, No. 6, 1038-1040, 2012.

Metamaterials for Spectroscopic Infrared Emitters and Sensors

T. Nagao[1,2], T. D. Dao[1], K. Chen[1], S. Ishii[1], and T. Yokoyama[1]
[1]International Center for Materials Nanoarchitectonics, National Institute for Materials Science, Tsukuba, Japan
[2]Department of Condenced Matter Physics, Hokkaido University, Sapporo, Japan

*corresponding author: NAGAO.Tadaaki@nims.go.jp

Abstract- By adequately designing their size and geometry, metal nano-structures offer highly efficient light/heat absorption with desired spectral features. We report our recent study on the design, fabrication, and characterization of spectrally selective narrow-band plasmonic metamaterial perfect absorbers for the effective applications in wavelength-selective thermal emitters, infrared detectors as well as high-sensitivity molecule-sensing.

Plasmonic metamaterial perfect absorbers can exhibit nearly 100% absorptivity at desired wavelengths, and also emit light at the same wavelengths when they are heated. It has been successfully demonstrated their use such as in wavelength-selective infrared thermal emitters and molecular vibrational sensors [1-4]. We present our recent study on the development of perfect absorbers based on the metal-insulator-metal structures [1-4]. By use of numerical electromagnetic simulations, we optimized the geometrical parameters of the perfect absorbers to have resonances at certain wavelengths depending on their applications from far-infrared to mid-infrared region. The fabricated perfect absorbers exhibit narrowband resonant absorption with efficiency higher than 97 %. We report applications of these devices such as for selective thermal emitters operated above 1273K [1,4], selective surface-enhanced vibrational spectroscopy for high-sensitivity molecular sensing [1,2], and wavelength selective IR detectors based on the combination with pyroelectric device and the metamaterial infrared absorbers [5].

Acknowledgements, This work was supported by CREST program from Japan Science and Technology Agency (JST), and KAKENHI program from Japan Society for the Promotion of Science (JSPS).

REFERENCES

1. Yokoyama, T. Dao T.D., Chen, K., Ishii, S. , Sugavaneshwar, R.P. , Kitajima, M., and Nagao, T., “Spectrally Selective Mid-Infrared Thermal Emission from Molybdenum Plasmonic Metamaterial Operated up to 1000° C,” Advanced Optical Materials 4 (12), 1987-1992, 2016.
2. Chen, K., Dao, T.D., and Nagao, T., "Tunable Nanoantennas for Surface Enhanced Infrared Absorption Spectroscopy by Colloidal Lithography and Post-Fabrication Etching," Sci Rep. 7, 44069, 2017.
3. Chen, K., Dao, T. D., Ishii, S., Aono, M., and Nagao, T., “Infrared aluminum metamaterial perfect absorbers for plasmon-enhanced infrared spectroscopy,” Advanced Functional Materials **42**, 6637-6643, 2015.
4. Dao, T.D., Chen, K., Ishii, S., Ohi, A., Nabatame, T., Kitajima, M., and Nagao, T., “Infrared perfect absorbers fabricated by colloidal mask etching of Al-Al2O3-Al trilayers,” ACS Photonics **2**, 964-970, 2015.
5. Dao, T.D., Ishii, S., Yokoyama, T., Sawada, T., Sugavaneshwar, R.P., Chen, K., and Nagao, T., “Hole Array Perfect Absorbers for Spectrally Selective Midwavelength Infrared Pyroelectric Detectors,” ACS Photonics **3** (7), 1271-1278, 2016.

Tailoring thermal emission with metasurfaces.

L.Wojszvzyk, E. Sakat, I. Doyen, A.L. Coutrot, F. Marquier and J.J. Greffet
Laboratoire Charles Fabry, Institut d'Optique Graduate School, CNTRS, UNiversité Paris-Saclay, France
*corresponding author: jean-jacques.greffet@institutoptique.fr

Abstract- We show that a periodic array of hot nanoparticles embedded in resonant plasmonic antennas can produce thermal emission with an effective emissivity approaching unity.
This type of design allows to control thermal emission by designing the antennas. We expect to modulate thermal emission at a rate exceeding 10 MHz.

The goal of this presentation is to discuss how blackbody radiation can be tailored using nanoantennas. By tailoring blackbody radiation, we mean that the emitted spectrum, the directivity of the source, its polarization can be controlled thereby paving the way to a novel generation of IR sources. Furthermore, we aim at modulating the emitted intensity at a rate faster than 10 MHz.

In the last 15 years, many ideas have completely changed our perspective on what can be done with incandescent sources. Taking advantage of the existence of the spatial coherence of surface waves, highly directional sources have been demonstrated[1]. Taking advantage of the spectral resonances of plasmonic structures, quasimonochromatic sources have been fabricated[2]. Electrical modulation of the absorptivity of a stack of quantum wells has allowed modulating thermal emission at a rate of 600 kHz [3].

In this presentation, we introduce a novel approach. We start by introducing a generalized Kirchhoff law valid for anisothermal bodies. The idea is simple: Kirchhoff law can be extended to objects such as a hot graphene layer deposited on a cold substrate[4]. The power thermally emitted by a hot graphene layer on a cold substrate in a direction and at a given frequency is proportional to the power absorbed in the graphene layer only when illuminating this graphene layer in the same direction and at the same polarization.

The second ingredient of the presentation is to introduce a nanoantenna such as a half-wavelength antenna. By inserting a small hot volume of absorber in the gap of a dimer antenna, it is possible to enhance the power extracted from the small hot volume by more than three orders of magnitude. This can be achieved provided that the absorber has been properly designed in order to verify a critical coupling condition with the antenna. We will discuss in some detail the conditions required to optimize the absorption in a nanoantenna which differs from the maximum enhancement condition.

A key feature of this type of source is the small size of the heated volume. While usual incandescent sources cannot be modulated at high frequency due to their thermal inertia, nanovolumes can be cooled in a few tens of ns offering a new opportunity for high speed modulation. In order to produce a practical emitter, a periodic array of antennas can be fabricated which results in a metasurface for IR emission. Finally, by tuning the properties of the antennas, the metasurface can control the frequency, polarization and direction of emission.

Acknowledgements, JJG acknowledges the Institut Universitaire de France and the Chair Safran-IOGS.

REFERENCES

1. Greffet, J. J. *Nature*, Vol. 416, 61, 2002.
2. Liu, X. et al. *Phys.Rev.Lett.*, Vol. 107, 045901, 2011.
3. Inoue, T. et al. , *Nature Mat.*, Vol. 13, 928, 2014.
4. Rytov S.M., Kravtsov Y.A. and Tatarskii V.I. *Principles of Statistical Radiophysics vol.3*, Springer Verlag, Berlin, 1989.

Thermal emission control by semiconductor photonic crystals

T. Asano[1*], M. Suemitsu[1,2], T. Inoue[1] and S. Noda[1]
[1]Department of Electronic Science and Engineering, Kyoto University, Japan
[2]Energy Technology Laboratories, Osaka Gas Co., Ltd., Japan
[*]tasano@kuee.kyoto-u.ac.jp

Thermal emitters generally exhibit a broad spectrum and are widely used for various light sources from far-infrared to the visible range. However, in many applications involving non-dispersive infrared sensing and thermo-photovoltaics, only a specific spectral component that is much narrower than the original broad spectrum of thermal emitters is utilized, which reduces efficiency. Therefore, it is important to develop a single-mode narrow-bandwidth thermal emitter that achieves high emissivity at a target wavelength while suppressing it as much as possible at other wavelengths. To achieve such an ideal spectrum, we demonstrated mid-infrared thermal emitters by combining multiple quantum wells (MQWs) and two-dimensional photonic crystal (PC) slabs [1]. In our emitters, intersubband transitions of MQWs allow a strong interaction between light and matter around a target wavelength, and a Γ–point resonant effect of PCs further narrow down the thermal emission peak at a target wavelength and enable vertical emission. Ultrafast modulation (~MHz) of thermal emission without changing the temperature of emitters has been also realized by changing the electron density of MQWs using applied electric field [2]. We have also demonstrated near-infrared narrowband thermal emitters recently by using arrays of nano-rods made of intrinsic silicon [3], which can be utilized to increase the efficiency of thermo-photovoltaic power generation. In this emitter, an interband transition of intrinsic silicon emphasized light-matter interaction in the range shorter than the bandgap wavelength of silicon, and a rod-type resonator array with a small material filling factor suppressed the longer wavelength emission components. The details will be reported at the conference.

Acknowledgements: This work was supported in part by Japan Society for the Promotion of Science (JSPS) Grant-in-Aid for Scientific Research (KAKENHI) grant no. 25220607, and the Super Cluster Program of the Japan Science and Technology Agency.

REFERENCES

1. M. De Zoysa, T. Asano, K. Mochizuki, A. Oskooi, T. Inoue, and S. Noda, “Conversion of broadband to narrowband thermal emission through energy recycling,” *Nature Photonics* vol. 6, pp. 535-539, Aug. 2012.
2. T. Inoue, M. D. Zoysa, T. Asano, and S. Noda, "Realization of dynamic thermal emission control", *Nature Materials* vol. 13, no. 10, pp. 928-931, Jul. 2014.
3. T. Asano, M. Suemitsu, K. Hashimoto, M. De Zoysa, T. Shibahara, T. Tsutsumi1 and S. Noda, “Near-infrared–to–visible highly selective thermal emitters based on an intrinsic semiconductor,” *Science Advances* vol. 2, no. 12, e1600499, Jan. 2017.

THz metamaterial and metasurface

Reconfigurable terahertz grating with enhanced transmission of TE polarized light

J. W. He[1,2], Y. Zhang[*], X. K. Wang[1], Z. W. Xie[3], Y. Z. Xue[1], S. Wang[2], and S. F. Feng[1]

[1]Beijing Key Laboratory of Metamaterials and Devices, Key Laboratory of Terahertz Optoelectronics, Ministry of Education, Beijing Advanced Innovation Center for Imaging Technology, and Department of Physics, Capital Normal University, Beijing 100048, P.R. China

[2]Department of Physics, Harbin Institute of Technology, Harbin, 150001, P.R. China

[3]Nanophotonics Research Centre, Shenzhen University & Key Laboratory of Optoelectronic Devices and Systems of Ministry of Education and Guangdong Province, College of Optoelectronic Engineering, Shenzhen University, Shenzhen, 518060, P. R. China

[*]corresponding author: yzhang@cnu.edu.cn

Abstract- We demonstrate an optically reconfigurable grating with enhanced transmission of TE polarized waves in the terahertz (THz) waveband. The grating is realized with periodical photoexcited free carriers strips on a thin Si wafer. For TE polarized THz incident wave, the strips behaviors like metal, resonances between the strips happen and cause the enhanced transmission. The frequency of the transmission peak could be tuned through changing the period and duty cycle of the photoinduced grating.

A pattern with illuminated and dark regions was projected onto a Si wafer with thickness of 10μm. In the illuminated region, carriers are created by photoexcitation. Owing to the fact that the skin depth of Si is 12.2 μm at a wavelength of 800 nm[1], the photoinduced carriers form a freestanding grating, which can be regarded as a metallic wire grating embedded in the Si wafer. Then, a THz beam is incident onto the grating and the transmission spectra are measured with a terahertz time-domain spectroscopy system.

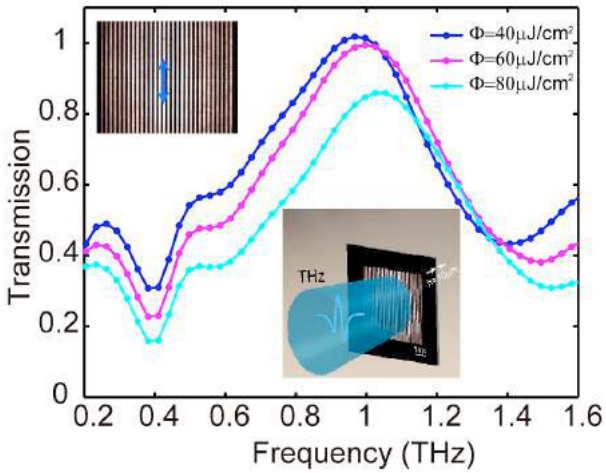

Figure 1 Experimental transmission spectra of the photoinduced grating (P = 200 μm, D = 0.5) for a series of excitation fluences, when the incident THz electric field is TE-polarized.

Extraordinary optical transmission (EOT) through such photoinduced grating is observed for TE-polarized THz incident wave, which is different from the former reports where the incident light is usually TM-polarized [2,3]. In order to verify the measured results, we performed realistic simulations of the photoinduced grating using a commercial software package (FDTD Solutions) based on the FDTD method. The dielectric function of the photoexcited Si wafer is calculated using the Drude model. The physical explanation on the EOT phenomenon with TE-polarized THz incident wave is cavity resonance, which is a rather different process from the excitation of surface plasmons (SPs) that occurs for TM polarization. The field is able to couple in the dielectric and is strongly enhanced in the region between photocarrier strips. The resonator length is determined by the width of the spacing. Thus, the position of the resonance peak shifts towards longer wavelengths when the spacing between the photoinduced stripes increases.

This kind of reconfigurable terahertz grating can be used as a tunable polarization-independent THz filter to avoid the processing of traditional samples and provides flexibility to adjust the structural parameters of the sample. Furthermore, this technique could also be used to produce THz diffractive elements with reconfigurable functionality for more applications.

Acknowledgements, The 973 Program of China (No. 2013CBA01702); National Natural Science Foundation of China (Nos. 11474206, 91233202, 11374216, 11174211, and 11404224); National High Technology Research and Development Program of China (No. 2012AA101608-6); Program for New Century Excellent Talents in University (NCET-12-0607); Scientific Research Project of Beijing Education Commission (KM201310028005); Beijing Youth Top-Notch Talent Training Plan (CIT&TCD201504080); Specialized Research Fund for the Doctoral Program of Higher Education (20121108120009); Scientific Research Base Development Program of the Beijing Municipal Commission of Education.

REFERENCES

1. Palik, E. D., *Handbook of Optical Constants of Solids III*, Academic, 1998.
2. Astilean, S. Lalanne, P. and Palamaru, M. “Light transmission through metallic channels much smaller than the wavelength,” Opt. Commun. Vol. 175, No. 4-6, 265-273, 2000.
3. Treacy, M. M. J. “Dynamical diffraction explanation of the anomalous transmission of light through metallic gratings,” Phys. Rev. B, Vol. 66, No. 19, 195105, 2002.

Sharp dark modes in mirror-asymmetric metamaterials

S. Y. Yang[1,2], C. C. Tang[1], Z. Liu[1], B. Wang[1], C. Wang[1], J. J. Li[1], L. Wang[1], and C. Z. Gu[1,2,3*]

[1]Beijing National Laboratory for Condensed Matter Physics, Institute of Physics, Chinese Academy of Sciences, Beijing 100190, China

[2]School of Physical Sciences, CAS Key Laboratory of Vacuum Physics, University of Chinese Academy of Sciences, Beijing 100190, China

[3]Collaborative Innovation Center of Quantum Matter, Beijing, China

[*]corresponding author: czgu@iphy.ac.cn

Abstract-We report the excitation of extremely high quality-factor (Q-factor) dark mode resonances in metamaterials composed of mirror-asymmetric split ring resonators (MASRRs) in the terahertz region. Breaking the symmetry of the mirror-arranged SRR leads to the occurrence of two distinct otherwise inaccessible ultrahigh Q-factor dark modes. The numerical simulations indicate that the highest Q-factor of the dark mode resonance was 60, which is more than one order of magnitude larger than that of conventional metamaterials.

Metamaterials have attracted tremendous of research interest due to their unusual and exotic electromagnetic properties and functionalities that are not encountered in naturally occurring materials. The unique properties of metamaterials are based on the resonant responses of the constituent building blocks and arrangement. High Q-factor resonances in metamaterials are of particular importance, as they can be utilized to realize slow light devices[1,2], narrow-band filters[3,4], and ultrasensitive sensors[5,6]. However, the performance of conventional metamaterials typically suffer from low Q-factor (<~10)[3,4,6] due to radiative and ohmic losses, which hinder the development of the metamaterial-based devices.

In this paper, we theoretically and experimentally demonstrate a metamaterial composed of mirror asymmetric split ring resonators that sustain multiple high Q-factor resonances. The excitation of sub-radiant dark modes with highly suppressed radiation losses result in the high-Q factor. The metamaterial samples were fabricated using high-resolution electron-beam lithography method, and characterized by terahertz time domain spectroscopy (THz-TDS). The corresponding theoretical calculations were performed by FDTD algorithm. The experimental and simulated results manifest that two extremely sharp resonances appears at ω_1=0.5 THz and ω_2=1.3 THz, respectively. The calculated Q-factor for dark mode ω_1 and ω_2 are 60 and 30, respectively.

This mirror-asymmetric metamaterial supporting multiple high Q-factor resonances may well enable great advances in designing and realization of high-performance photonic devices to overcome the technologically difficulty in terahertz regime.

Acknowledgements: This work is supported by the National Key Research and Development Program of China under Grant No. 2016YFA0200400, and No. 2016YFA0200803, the National Natural Science Foundation of China under Grants No. 91323304, No. 11174362, No. 11504414, No. 11574385, and No. 11574368, Strategic Priority Research Program of the Chinese Academy of Sciences under Grant No. XDB07020200.

REFERENCES

1. Zhang, S., A. Genov, D., Wang, Y., Liu, M., and Zhang, X.,"Plasmon-induced transparency in metamaterials," *Phys. Rev. Lett.*, Vol. 101, No. 047401, 2008.
2. Yang, S. Y., Xia, X. X., Liu, Z., E, Y.W., Wang,Y.J., Tang, C.C., Li, W. X., Li, J. J., Wang, L., and Gu, C. Z.,"Multispectral plasmon-induced transparency in hyperfine terahertz meta-molecules," *J. Phys.: Condens. Matter,* Vol. 28, No. 445002, 2016.
3. Fedotov, V. A., Rose, M., Prosvirnin, S. L., Papasimakis, N., and Zheludev, N. I., "Sharp trapped-mode resonances in planar metamaterials with a broken structural symmetry," *Phys. Rev. Lett.* Vol. 99, No. 147401, 2007.
4. Yang, S. Y., Liu, Z., Xia, X. X., E, Y. W., Tang, C. C., Wang, Y. J., Li, J. J., Wang, L., and Gu, C. Z., "Excitation of ultrasharp trapped-mode resonances in mirror-symmetric metamaterials," *Phys. Rev. B*, Vol. 93, No. 235407, 2016.
5. Cui, A. J., Liu, Z., Li, J. F., Shen, T. H., Xia, X. X., Li, Z. Y., Gong, Z. J., Li, H. Q., Wang, B. L., Li, J. J., Yang, H. F., Li, W. X., and Gu, C. Z., "Directly patterned substrate-free plasmonic "nanograter" structures with unusual Fano resonances," *Light: Science & Applications*, Vol. 4, No. e308, 2015.
6. Singh, R., Cao, W., Al-Naib, I., Cong, L., Withayachumnankul, W., and Zhang, W., "Ultrasensitive terahertz sensing with high-Q Fano resonances in metasurfaces," *Appl. Phys. Lett*., Vol. 105, No. 171101, 2014.

3D Lantern-like metamaterial

S. Hu[1], R. H. Pan[1], Z. Liu[1], S. Y. Yang[1], J. J. Li[1*], and C. Z. Gu[1,2*]

[1] Beijing National Laboratory for Condensed Matter Physics, Institute of Physics, Chinese Academy of Sciences, Beijing 100190, China

[2]Collaborative Innovation Center of Quantum Matter, Beijing 100871, China

[*]corresponding author: jjli@iphy.ac.cn, and czgu@iphy.ac.cn

Abstract-This work presents a 3D metamaterial based on stress induced bending of bilayer or multilayer film. Take advantage of traditional planar process, the lantern-like metamaterial contains a flat pad supported by the substrate and a number of arms connecting to the pad. By changing the number of arms, the transmission spectrum changes correspondingly, and an EIT-like resonance appears when the arm number is above 6 due to the coupling between different arms.

Plasmonic induced transparency (PIT) is an optical phenomenon based on the interference between "dark mode" and "bright mode" of metamaterials, by which a transparency peak appears in the absorption region of the spectrum[1-3]. This phenomenon has great potentials in the application of slow-light devices and sensors. 3D metamaterials usually perform better than 2D structures due to larger degree of freedom and more ways of light-structure interaction. However, up to now, the fabrication of 3D metamaterials is still limited by the existing planar micro/nano-fabrication technique in visible and infrared region, which restricts its application on high frequency EIT devices.

In this work, planar fabrication process including electron beam lithography (EBL), reaction ion etching and metal film deposition was used, and the schematic of 3D structure is shown in figure 1. After released from the substrate, the residual stress and modulus differences between two layers result in the bending of cantilevers[4,5]. This method can flexibly control the structure configuration and different materials can be applied including metal, dielectric and semiconductor. Lantern-like metamaterials were fabricated by this method, and the radius of the curved cantilever is tunable by controlling the thickness and material type of the bilayer film. A series of structures with different numbers of arms were simulated and the transmission spectra are shown in figure 2. The peak at 2 THz is a fundamental mode of the LC resonance in the ring, and at about 6 THz coupling between different arms happens. When the arm number is less than 4, there is only one resonance peak at 6 THz; as the arm number is over 6, a transparent peak appears in the absorption region, which comes from the hybridized coupling effect.

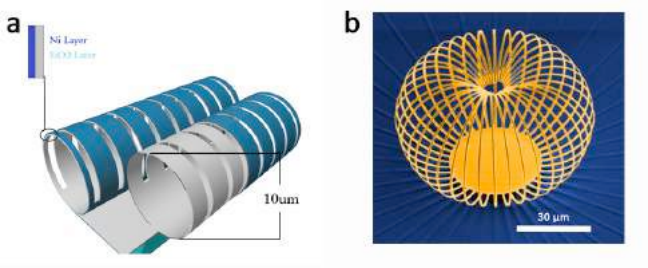

Figure 1 (a) Schematic of stress induced bending methods; (b) SEM image of the lantern-like 3D metamaterial.

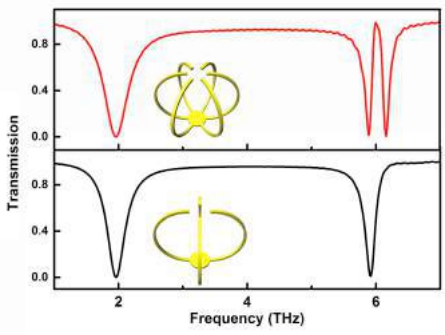

Figure 2 The transmission spectrum of 4-arms and 6-arms lantern.

Acknowledgements: This work was supported by the National Natural Science Foundation of China (Grants Nos 91323304, 11174362, 61390503, 11574369, 11434017 and 11504414) and the Knowledge Innovation Project of CAS (Grant No. KJCX2-EW-W02).

REFERENCES

1 Zhang, S., Genov, D. A., Wang, Y., Liu, M. & Zhang, X. Plasmon-induced transparency in metamaterials. Phys. Rev. Lett. 101, 047401, doi:10.1103/PhysRevLett.101.047401 (2008).

2 Yan, H., Low, T., Guinea, F., Xia, F. & Avouris, P. Tunable phonon-induced transparency in bilayer graphene nanoribbons. Nano Lett. 14, 4581-4586, doi:10.1021/nl501628x (2014).

3 Han, S. et al. Tunable electromagnetically induced transparency in coupled three-dimensional split-ring-resonator metamaterials. Sci. Rep. 6, 20801, doi:10.1038/srep20801 (2016).

4 Huang, M. et al. Nanomechanical Architecture of Strained Bilayer Thin Films: From Design Principles to Experimental Fabrication. Adv. Mater. 17, 2860-2864, doi:10.1002/adma.200501353 (2005).

5 Kuo, J.-N., Lee, G.-B., Pan, W.-F. & Lee, H.-H. Shape and Thermal Effects of Metal Films on Stress-Induced Bending of Micromachined Bilayer Cantilever. Jpn. J. Appl. Phys. 44, 3180-3186, doi:10.1143/jjap.44.3180 (2005).

Determination of dielectric constants of thin films and liquids using terahertz metamaterials

S. J. Park, S. A. N. Yoon and Y. H. Ahn*

Department of Physics, Department of Energy Systems Research, Ajou University, Suwon 16499, Korea

*corresponding author: ahny@ajou.ac.kr

Abstract- We suggest that terahertz (THz) metamaterials can be used to measure the dielectric constant of various dielectric materials. We successfully measure the dielectric constant of various polymers and polar liquid using THz metamaterial devices. Our experimental results were confirmed by finite-difference time-domain simulation.

Recently, we found that THz metamaterial can be used as a sensitive biosensor, enabling us to detect the low-density microorganisms although their scattering cross-section is extremely low against THz waves [1]. This was possible because the detection volume of THz metamaterial is highly confined near the surface, in particular, in the gap area. The vertical range of the detection volume has been estimated to be 3–4 μm, depending of the detailed geometry of the pattern [2]. Therefore, it is highly desirable to use metamaterials to address the dielectric constants of the thin films without necessitating large amount of the materials. More importantly, the narrow detection range will enable us to study the dielectric properties of various polar liquids that attenuate the THz waves substantially.

Here, we introduce a novel method to extract the dielectric constants of the thin polymer film and the polar liquid solution by using THz metamaterial sensors through THz time-domain spectroscopy (THz-TDS) [3]. We demonstrate the dielectric constant measurements of thin polymer films and polar liquid solutions by using THz metamaterial sensors. The resonance shift of the metamaterials exhibits the saturation behavior with the increased film thickness of deposited target material. We found that the saturation frequency shift varies linearly with the real part of the dielectric constant and extracted their correlation explicitly for the particular metamaterials pattern we used. This approach could be very useful to determine the dielectric constants of various materials, without necessitating the large amount of the target materials.

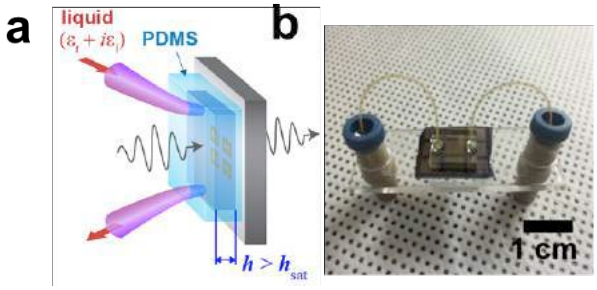

Figure 1. (a) Schematic of the fluidic THz metamaterial device for the sensing of aqueous solutions. (b) Photograph of the fluidic metamaterial device.

More importantly, we were able to measure the dielectric constant of the polar liquids such as distilled water, methanol, and ethanol as schematically shown in Fig. 1. This was possible due to the unique properties of metamaterials whose detection volume is strongly localized at the surface. In other words, the metamaterials allow us to address the THz optical constants without suffering from the large attenuation effects in the polar liquids. In addition, we found that the resonance shift does not depends critically on the imaginary part of the dielectric constants, making our approach a universal technique regardless whether the target specimens are transparent or conductive materials. The results from the FDTD simulation are in good agreement with our experimental results both in the thin film and the liquid cases. We also found that the metamaterial fluidic devices can work as an efficient ion sensor, because the dielectric constant of ionic solutions (such as KCl and NaCl solutions) changes with ionic concentration as shown in Fig. 2(c). For instance, the sensitivity in terms of the molar concentrations of the KCl solutions yielded 10 GHz per M. Our work will contribute to the qualitative and quantitative study on the dielectric properties of various types of materials in THz frequency range as well as to the development of effective future biological and chemical sensors.

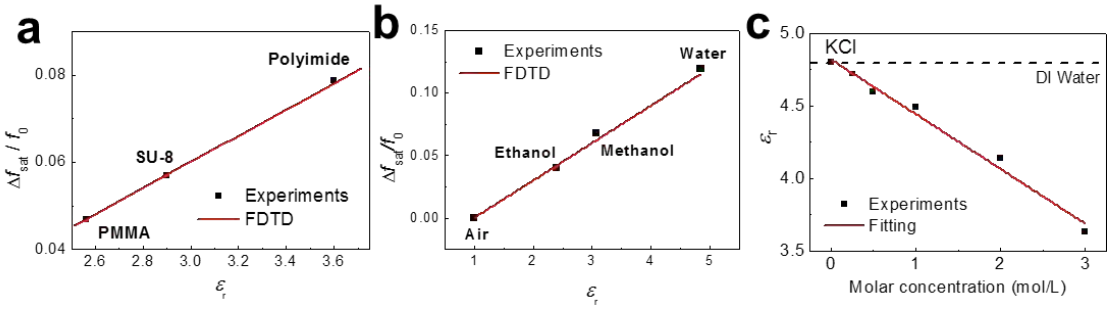

Figure 2. $\Delta f_{sat}/f_0$ as a function of ε_r for the (a) three polymers, and (b) three polar liquids extracted from the THz transmission experiments (black boxes) and from FDTD simulation results (red solid lines). (c) Extracted permittivity of KCl solutions for various molar concentrations

REFERENCES

1. Park, S. J. *et al*, "Detection of microorganisms using terahertz metamaterials," *Sci. Rep.*, Vol. 4, 4988, 2014.
2. Park, S. J. *et al*, "Effective sensing volume of terahertz metamaterial with various gap widths," J. Opt. Soc. Korea, Vol. 20, No. 5, 628, 2016.
3. Park, S. J. *et al*, "Dielectric constant measurements of thin films and liquids using terahertz metamaterials," *RSC Adv.*, Vol. 6, 69381, 2016.

Development of terahertz nano-gap metamaterials for low-density virus detection

S. J. Park[1], G. A. Shin[2] and Y. H. Ahn[1*]

[1]Department of Physics, Department of Energy Systems Research, Ajou University, Suwon 16499, Korea

[2]Department of Environmental Engineering, Ajou University, Suwon 16499, Korea

[*]corresponding author: ahny@ajou.ac.kr

Abstract- We developed terahertz metamaterials with micro- and nano-gaps for the sensitive detection of viruses. Red-shift of resonant frequency occurs as we deposit low-density viruses such as PRD1 and MS2 on the metamaterials due to the change of the effective dielectric constant of the gap structure. Sensitivity increases as we reduce the gap size in the metamaterials, which is due to the size compatibility and the strong field confinement effect in the gap area.

Metamaterials operating in THz frequency range have proven to be an efficient future platform for sensing low-density microorganisms such as fungi and bacteria (with the typical sizes of 1–2 μm). Although their scattering cross-section is extremely low against THz waves, the field-enhancement effects in the gap area enable us to detect the low-density microorganisms [1]. On the other hand, sensing of viruses is still very challenging because their typical sizes ranges ~ 50 nm, which scales only ~λ/10,000 with respect to the incident THz waves. In this work, we used THz metamaterials for sensing low-density viruses and improved the sensitivity by introducing nano-gaps in the metamaterials.

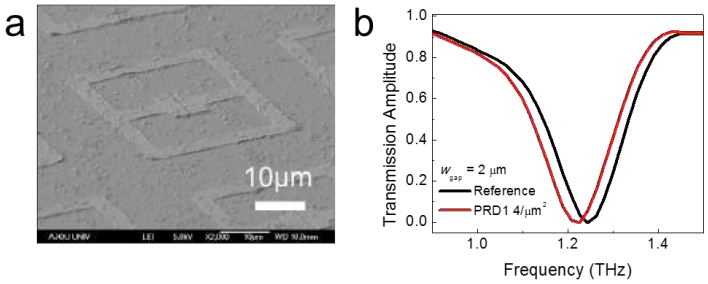

Figure 1. (a) SEM image of metamaterials (with a gap width of 200 nm) coated with PRD1 viruses. (b) THz metamaterials resonances measured before (black line) and after (red line) the deposition.

Our metamaterials consist of split-ring resonators fabricated using conventional e-beam lithography techniques (Fig. 1(a)). We deposited two types of viruses (PRD1 and MS2) on the metamaterials surface from a solution, followed by a drying process in an oven for 5 min at 85 °C. A representative result is shown in Fig. 1(b) for the metamaterial devices with the gap width of 2 μm, for the PRD1 viruses with the surface density of 4/μm^2. The resonant frequency red-shifts as we deposit the viruses and the frequency shift (Δf) increases with an increase in number density. The red-shift in the resonance is due to the change in the effective dielectric constant

of the gap area, consistent with the measured dielectric constant of PRD1 viruses ($\varepsilon_{PRD1} \sim 4.1$, $\varepsilon_{MS2} \sim 3.9$).

More importantly, the sensitivity of THz metamaterials can be improved by reducing the gap width (w_{gap}). In general, THz metamaterials have gap structures typically with the size of ~μm which is compatible with the sizes of the bacteria. In order to optimize the sensitivity, it is highly desirable to develop the metamaterials with the nano-gap, compatible with the size of viruses. In Fig. 2(a), Δf is plotted as a function of PRD1 density for the different w_{gap}'s of 200 nm – 2 μm. Clear saturation behavior was found as the surface density increased and we found that the saturation density is reached at the lower density for the metamaterials with the smaller gaps. We plotted the sensitivity of the metamaterials sensors as a function of w_{gap} in Fig. 2(b). The sensitivity increases by about 8 times for w_{gap} = 200 nm as compared to the case of w_{gap} = 2 μm. The enhanced sensitivity in the nano-gap metamaterials is attributable to the size compatibility between the target substances and the gap size, accompanied by the large field enhancement effects in the gap area [2].

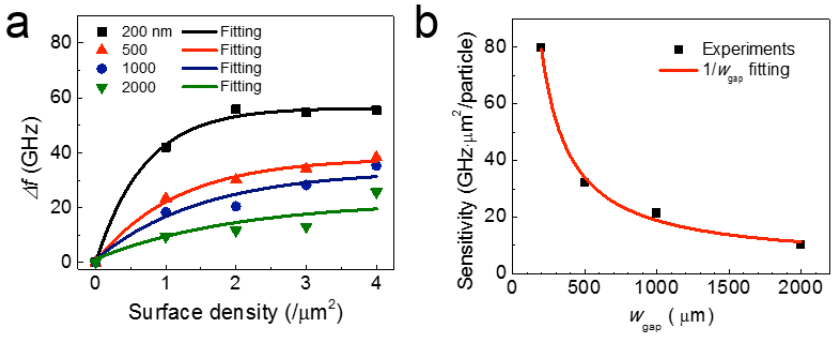

Figure 2. (a) Resonance frequency shift as a function of the surface density of viruses for metamaterials with different gap width (b) The sensitivity of metamaterials sensor as a function of gap width (w_{gap}).

REFERENCES

1. Park, S. J. *et al*, "Detection of microorganisms using terahertz metamaterials," *Sci. Rep.*, Vol. 4, 4988, 2014.
2. Park, S. J. *et al*, "Sensitive detection of yeast using terahertz slot antennas," Opt. Express, Vol. 22, No. 25, 30467, 2014.

Interaction mechanisms in ensembles of planar meta-atoms

M. Wenclawiak[1*], C. Derntl[1], K. Unterrainer[1], and J. Darmo[1]
[1]TU Wien, Institut für Photonik, Gußhausstraße 27-29, 1040 – Vienna, Austria
[*]corresponding author: moritz.wenclawiak@tuwien.ac.at

Abstract-In this contribution we demonstrate the substantial influence of meta-atoms in the terahertz regime on the radiation efficiency when being arranged in a confined environment. The meta-atoms, as the elementary structures of a metasurface, are thereby arranged in separated super cells with varying element density. For such meta-atom ensembles we find a radiative lifetime effect comparable to that known for an ensemble of excited atoms in a sub-wavelength volume.

In the past decades, there have been numerous investigations of the rising phenomena for ensembles of atoms in a confined volume. In 1954, Dicke published a theoretical paper describing a modification of the radiative lifetime for two level atoms confined in a volume smaller than the cubed wavelength corresponding to the optical transition[1]. These effects have later been proven in a variety of experiments, e.g. in gas[2] and as well in solid state[3] environments. Here, we describe a comparable experiment with meta-atoms, structures featuring dimensions shorter than the interacting wavelength. These structures gained a lot of attention in the last years starting with the pioneering experimental work of Pendry *et al.* including phenomena like negative refractive index materials and perfect lensing[4,5].

Our investigation focuses on the radiative lifetime of plasmonic resonators in the terahertz (THz) frequency regime. The used meta-atoms can be regarded as a system of two conductively coupled dipoles oscillating in phase. We measure the transmission properties of various metasurface arrangements by means of time-domain-spectroscopy and extract the resonance frequency and linewidth out of the fitted spectra. Hereby, the frequency position can be compared to a simple analytical model for estimating the resonance behavior of conductively coupled dipoles. The different number of meta-atoms is arranged *randomly* in separated super cells (see Fig.1 (a)) in order to prevent the formation of so called "lattice-modes" due to diffraction of the impinging radiation, which can influence the linewidth of the plasmonic resonators[6].

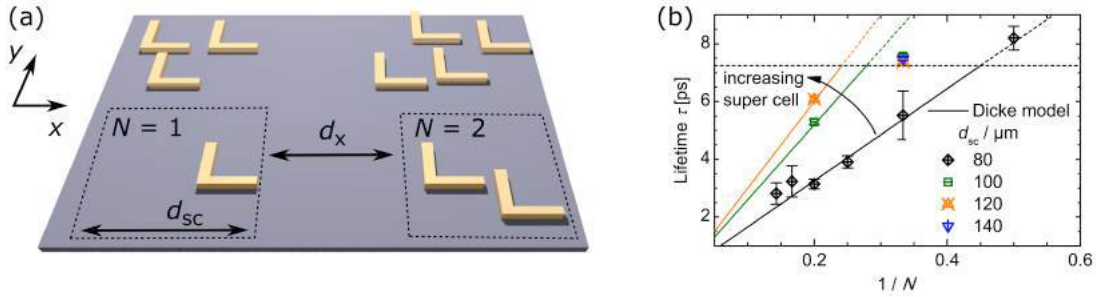

Figure 1: (a) Schematic drawing of the super cell geometry with varying number of randomly arranged meta-atoms. **(b)** Radiative lifetime extracted out of transmission measurements for varying super cell sizes containing an increasing number of meta-atoms.

The radiative lifetime is plotted as a function of the inverse number of confined meta-atoms in one super cell in Fig.1 (b) as it reflects the behavior of the two-level atoms predicted by Dicke. As a result we obtain a proportional dependence between the two parameters restricted only by a critical number of elements in one super cell geometry. In order to confirm the observed behavior, in a subsequent experiment, we change the size of the super cells by keeping the number of elements fixed in order to investigate the critical density showing a modified radiative lifetime response. As schematically shown in the viewgraph of Fig.1 (b), the effect on the radiative lifetime is restricted only to very dense ensembles of meta-atoms.

In the terahertz frequency range, only a few dense meta-atoms already show a strong modification of the radiative lifetime and therefore, influence the rate at which the stored energy is lost.

Acknowledgements: The authors acknowledge partial financial support of the Austrian Science Fund (FWF) through SFB NextLite (F4902), DK CoQus (W1210) and NATO SfP program through NOTES (984698).

REFERENCES

1. Dicke, R. H. "Coherence in spontaneous radiation processes," *Phys. Rev.*, Vol. 93, No. 1, 99–110, 1954.
2. Skribanowitz, N., Herman, I. P., MacGillivray, J. C., and Feld, M. S., "Observation of Dicke superradiance in optically pumped HF gas," *Phys. Rev. Let*, Vol. 30, No. 8, 309–312, 1973.
3. Florian, R., Schwan, L. O., and Schmid, D., "Superradiance and high-gain mirrorless laser activity of O-2-centers in KCl," *Sol. Sta. Com.*, Vol. 42, No. 1, 55–57, 1982.
4. Pendry, J. B., Holden, A. J., Robbins, D. J., and Stewart, W. J., "Magnetism from conductors and enhanced nonlinear phenomena," *Microw. Theo. and Tech., IEEE Trans.*, Vol. 47, No. 11, 2075–2084, 1999.
5. Pendry, J. B., "Negative refraction makes a perfect lens," *Phys. Rev. Let.*, Vol. 85, No. 18, 3966–3969, 2000.
6. Bitzer, A., Wallauer, J., Helm, H., Merbold, H., Feurer, T., and Walther, M., "Lattice modes mediate radiative coupling in metamaterial arrays," *Opt. Let.*, Vol. 35, No. 23, 3859–3861, 2009.

Acousto-elastic metamaterials and phononic crystals

Graded arrays of resonators: focusing, detouring, rainbow trapping and mode conversion of waves with elastic metasurfaces.

A. Colombi[1*] **and R. V. Craster**[1]

[1]Dept of Mathematics, Imperial College London, United Kingdom
[*]a.colombi@imperial.ac.uk

Abstract— Metamaterial designs combining graded arrays of resonators and elastic wave excitation are opening new possibilities to broadband control the propagation of mechanical waves in solid media. In this presentation we report on the recent development of a graded metasurface that supports a variety of phenomena including wave focusing, re-routing, rainbow trapping and mode conversion. Applications of this metamaterial can be envisaged in several fields and lengthscales.

Recent years have witnessed an increasing popularity of metamaterial concepts, based on the so-called local resonance phenomenon, to control the propagation of electromagnetic, acoustics and elastic waves in artificially engineered media. While the momentum initially focused on the subwavelength bandgaps generated by the resonance, the research is now shifting towards more complete forms of control, encompassing tailored graded designs to obtain spatially varying refraction index, wide bandgaps and mode conversion. In the field of photonics and acoustic for instance, this transition has already taken place and new graded design allows a tailored control of the propagation of light, micro-waves and sound. Elastic waves, as opposed to acoustic and electromagnetic waves, are characterized by different compressional and shear wave speeds resulting in mode conversions at the interfaces. On the one hand this makes elastic metamaterials complex to model and the use of computational elastodynamics technique mandatory, on the other hand it offers new control possibilities not achievable in the electromagnetic or acoustic case (e.g. Fig. 1).

In this talk, after a brief introduction on resonant elastic metamaterials, we will discuss few modeling strategies that allow tackling the complexity of the elastodynamic problem. Then, with the help of parallel numerical simulations and ultrasonic experiments, we will explore the physics and the capacities of a recently developed metasurface made of a cluster of rods on an elastic substrate [1, 2]. The metasurface interacts and indeed controls the propagation of flexural waves in plates and Rayleigh waves in halfspaces. Through an appropriate engineering of the resonator's length, we will show how to design a "resonant metalens" for wave focusing and re-routing and a "resonant metawedge" that features not only rainbow trapping capacities but also Rayleigh to shear waves conversion.

To conclude, we will discuss the potential engineering areas, such as geophysics (large-scale), mechanical engineering (micro-scale) and acoustic imaging (nano-scale), where elastic metasurfaces can find application.

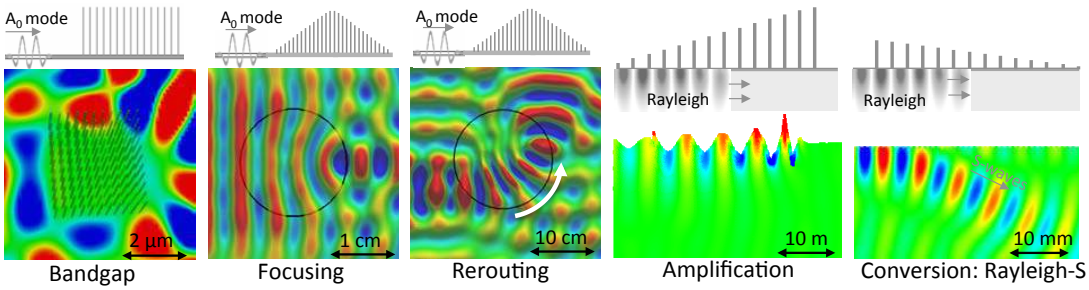

Figure 1: Example of control achieved through one of the discussed resonant metamaterial for different type of waves (Flexural or Rayleigh) and lengthscale.

REFERENCES

1. Colombi, A. Resonant metalenses for flexural waves. *J. Acoust. Soc. Am.* **140**, EL423 (2016).
2. Colquitt, D., Colombi, A., Craster, R., Roux, P. & Guenneau, S. Seismic metasurfaces: Sub-wavelength resonators and rayleigh wave interaction. *J. Mech. Phys. Solids* **99**, 379–393 (2017).

Asymptotic analogies for closely packed photonic and phononic crystals

A. L. Vanel, O. Schnitzer, and R. V. Craster

Department of Mathematics, Imperial College London SW7 2AZ, UK
alice.vanel13@ic.ac.uk

Abstract— Mechanical waves through periodic mass-spring lattices, as developed by Brillouin and others as models in solid state physics, have long acted to motivate, and gain qualitative intuition, about waves through continua containing periodic arrays of inclusions such as photonic and phononic crystals. Our aim here, in the limit of closely arranged inclusions, is to make the qualitative analogy precise, and quantitative, particularly in terms of the band diagrams commonly used for dispersion analysis. Techniques based upon matched asymptotic expansions use the non-dimensional narrow gap between the inclusions, h, as a natural small parameter and allow us to replace a photonic crystal by an effective mass-spring lattice for the whole acoustic band, extract scalings for the frequency variation with gap width, and extend these ideas to higher branches; ultimately a versatile semi-analytic methodology is developed for general inclusion shapes and we illustrate this by comparison with numerical simulations.

One vital task in the design and optimisation of any photonic crystal is the accurate and rapid identification of the dispersion bands, or band surfaces, so that features such as stop-bands, Dirac-like points and local behaviour at stop band edges, can be tuned to enhance specific effects; often this can involve altering material properties, geometric shape or lattice parameters. There are well developed numerical methods for finding band diagrams such as multipole methods for cylindrical and spherical inclusions, plane wave expansion methods and finite element (FE) schemes; in practice many practitioners simply use general purpose commercial FE packages such as COMSOL. Although numerical schemes are highly useful, they provide little physical insight, and can be computationally expensive particularly when resolving the limit of closely spaced inclusions that we treat here. Here we develop an asymptotic theory based entirely upon exploiting the thinness of the gap between inclusions, to be precise we will assume that the inclusions are smooth (with their geometry locally quadratic near the thin gap) and that they have Neumann boundary conditions upon them. We show an illustration of a typical geometry, closely packed cylinders placed on a square array, in Fig. 1. Our aim here is to arrive at an asymptotic description of the closely-packed system and to be able to replace the physical system of Fig. 1(b) with an idealised mass-spring system as in 1(d). Natural questions that arise are how the frequencies at the band-gap edges, or the dispersion curves themselves, scale with the gap width, whether there are analytic formulae for the dispersion curves and, if so, what is the physics behind this. By developing an asymptotic understanding of this thin-gap material we are led to very rapid semi-analytic methods for generating band diagrams that are almost immediate and do not require sophisticated numerical methods and so we anticipate this being a useful alternative to numerical modelling.

The first part of the talk will be an intuitive description of the physics, we do so in terms of the acoustics of a phononic crystal of rigid cylinders in an ideal gas, inspired by Rayleigh 1896. We then proceed formally, using the language of matched asymptotic expansions, to obtain a completely analytical formula for the acoutic branch. We move to analysing the higher branches using coupled modes theory. Finaly, we show that this analysis is not limited to cylindrical inclusions, nor is it limited to a square lattice and the approach is very versatile.

ACKNOWLEDGMENT

Thanks to EPSRC (UK) for their support through research grants EP/L024926/1 & EP/J009636/1.

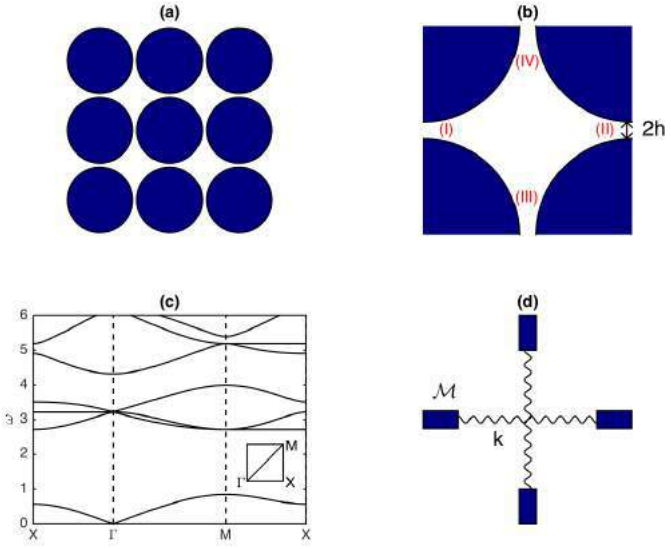

Figure 1: A closely packed array of cylinders shown in (a) with (b) showing the elementary cell with the thin gap of $2h$ and the inner regions (I) to (IV). Panel (c) shows the dispersion curves for $h = 0.02$ taken around the edges of irreducible Brillouin zone (shown in the inset). Panel (d) the analogous mass and springs lattice for the elementary cell of (b).

Perfect Mode Conversion of Elastic Waves: Realization with Anisotropic Metamaterials

Joshua Minwoo Kweun[1], Xiongwei Yang[2], and Yoon Young Kim[1*]

[1] School of Mechanical and Aerospace Engineering, Seoul National University, 1 Gwanak-ro, Gwanak-gu, Seoul 08826, South Korea

[2] BK21 Plus Transformative Program for Creative Mechanical & Aerospace Engineers, Seoul National University, 1 Gwanak-ro, Gwanak-gu, Seoul 08826, South Korea

[*]corresponding author: yykim@snu.ac.kr

Abstract-This work presents a newly-discovered elastic wave mode conversion mechanism called the transmodal Fabry-Pérot resonance (TFPR) which occurs through a special anisotropic medium. When the TFPR occurs at the TFPR frequencies, an incident longitudinal wave becomes maximally transmitted to a transverse wave. The theory of the TFPR phenomenon is presented and the anisotropic medium is realized by elastic metamaterials. Numerical and experimental results show the unique transmodal resonance that maximally transmits an incident wave mode to another without transmitting the incident mode.

When a layer of material of certain size is placed between waveguides, 100% wave transmission through the layer can be possible at certain frequencies. This phenomenon is the well-known Fabry-Pérot resonance [1-2]. This resonance phenomenon has been applied to various wave fields such as wave interferometers and spectroscopes. At the resonance, an incident longitudinal (or transverse) wave is transmitted to a longitudinal (or transverse) wave; the mode at the inlet and the mode at the outlet are identical without mode conversion. When the inserted material is not isotropic, however, an incident longitudinal or transverse wave is transmitted to both longitudinal and transverse waves. On the other hand, we aim to investigate if an incident longitudinal (or transverse) wave can be transmitted only to a transverse (or longitudinal) wave. This transmodal transmission can be extremely useful for generating transverse waves efficiently by using common transducers generating a longitudinal wave.

In this presentation, we report a new type of resonance phenomenon, which is referred to as the transmodal Fabry-Pérot resonance (TFPR) at which an incident longitudinal (or transverse) wave is converted only to a transverse (or longitudinal) wave with highly-efficient transmission through a special anisotropic medium. To reveal this new phenomenon, we establish a simple theoretical model to describe the wave physics in the anisotropic medium and show that inside the medium, longitudinal and shear waves are coupled in a special manner. For the wave analysis, the transfer matrix approach was used [3]. To realize the desired anisotropic medium exhibiting TFPR's, a single-phase elastic metamaterial is designed. Finally, the transmodal conversion mechanism was experimentally confirmed in a plate waveguide, and wave excitation and measurement were done with magnetostrictive patch transducers [3,4].

Acknowledgements: This research was supported by the Global Frontier R&D Program on Center for

Wave Energy Control based on Metamaterials funded by MSIP, contracted through IAMD at SNU in Korea (2014M3A6B3063711).

REFERENCES

1. Perot, A. and Fabry C. "On the application of interference phenomena to the solution of various problems of spectroscopy and metrology," *Astrophys. J.,* Vol. 9, 87–115, 1899.
2. Yariv A. and Yeh P., *Optical waves in crystals*, Wiley, New York, 1984.
3. Kweun, J. M. et al., "Transmodal Fabry-Pérot resonance: Theory and realization with elastic metamaterials," arXiv:1609.05266 [cond-mat.other], 2016.
4. Kim, Y. Y. and Kwon, Y. E., "Review of magnetostrictive patch transducers and applications in ultrasonic nondestructive testing of waveguides," *Ultrasonics* Vol. 62, 3–19, 2015.

Elastic metasurface for high transmission anomalous beam refraction

Hyuk Lee[1], Jun Kyu Lee[1], and Yoon Young Kim[1*]
[1]School of Mechanical and Aerospace Engineering, Seoul National University, Korea
[*]corresponding author: yykim@snu.ac.kr

Abstract-In this work, we realize an elastic metasurface capable of anomalously manipulating the refracted ultrasonic beam with almost full transmission. After the underlying mechanism involving the longitudinal elastic wave motion by the developed mass-spring model is presented, the design of the unique unit cell structure is proposed. For simulation and test, the metasurface is embedded in a thin plate and the anomalous refracting and focusing of the lowest-symmetric Lamb mode within its subwavelength thickness (<0.5λ) are demonstrated.

In order to maximize practicality of the metamaterial devices, bulky metamaterials may need to be miniaturized to compact and thin devices. In this respect, numerous studies on the concept of the metasurface based on the generalized Snell's law [1] have been developed. Compared with vast works performed on optics and acoustics, however, the elastic counterpart has been very rare due to lack of a concrete methodology to control both the transmission and phase especially regarding only a single elastic mode. Our aim is to overcome this limitation by developing an elastic metasurface for high-transmission anomalous beam refraction. As in the electromagnetic and acoustic field, the elastic metasurface can be a powerful tool in solid mechanics as it may be used for non-destructive evaluation and biomedical screening.

We design our elastic metasurface by using a single-phase medium (here, aluminum) to facilitate its fabrication [2, 3]. Relying on our explicit analysis with mass-spring model, we can accurately estimate the transmission coefficient and phase shift through the metasurface structure. By delicately designing the layout and dimension of the unit cell of the elastic metasurface, it was possible to find the proper unit cell configuration realizing both high transmission and the full phase span over 2π. Numerical simulations and experimental results are presented to show how well the propoposed metasurface works.

Said Zouhdi 6/8/17 14:17
Mis en forme: Retrait : Première ligne : 1,63 ch

Acknowledgements

This work was supported by the National Research Foundation of Korea (NRF) Grant [no. 2014M3A6B3063711 (Global Frontier R&D Program on Metamaterials)] funded by the Korean Ministry of Science, ICT and Future Planning (MSIP) contracted through IAMD at Seoul National University.

REFERENCES

1. Yu, N. and F. Capasso, "Flat optics with designer metasurfaces," *Nat. Mat.*, Vol. 13, 139-150, 2014.
2. Oh, J. H., Y. E. Kwon, H. J. Lee and Y. Y. Kim, "Elastic metamaterials for independent realization of negativity density and stiffness," *Sci. Rep.*, Vol. 6, 23630, 2016.
3. Lee, H., J. H. Oh, H. M. Seung, S. H. Cho and Y. Y. Kim, "Extreme stiffness hyperbolic elastic metamaterial for total transmission subwavelength imaging," *Sci. Rep.*, Vol. 6, 24026, 2016.

Nonlinear magneto-granular phononic metawaveguides

F. Allein, V. Tournat, V. Gusev, and G. Theocharis

LAUM, UMR CNRS 6613, Université du Maine, Le Mans, France
florian.allein@univ-lemans.fr

Abstract— We report on the design and operation of magneto-granular phononic structures in two different configurations, line and Γ shaped waveguides. These metawaveguides are composed of steel spherical beads in a properly designed magnetic field, the strength of which induces tunability in their dynamic response. Experimental results reveal the existence of coupled transversal-rotational modes and conversion from longitudinal to transversal-rotational modes. These observations are well supported by a proposed model taking into account all degrees of freedom in translations and rotations. In addition, nonlinearity originated from contact deformations gives rise to nonlinear processes such as amplitude dependent transmission, filtering and conversion to second harmonic frequency. The combination of the non-contact tunability with the potentially strong nonlinear behavior of the granular systems, makes magneto-granular crystals suitable nonlinear tunable mechanical metamaterials for the control of elastic wave propagation.

Granular crystals are periodic arrangements of elastic particles in contact in which the rotational degree of freedom can play an important role on the wave propagation [1]. Here, we present the theoretical and experimental study of 1D magneto-granular metawaveguides composed of steel spherical beads inside a properly designed magnetic field. The latter is induced by an array of permanent magnets. A schematic of the proposed magneto-granular chain is shown on Fig. 1(a). This configuration allows us to tune the dynamic response of the chain by modifying the magnetic strength of the magnets. Tunability of such system have been demonstrated in Ref [2]. As long as the frequency is much below the individual resonances of the beads, the phononic band structure of the granular crystals can be obtained by discrete lattice models, in which the contact deformations are modeled by springs. Due to the finite size of the particles and the friction between them, one should consider not only the normal contact stiffness but also the tangential and torsional ones. Thus, rotational degrees of freedom should be included in the analysis [3].

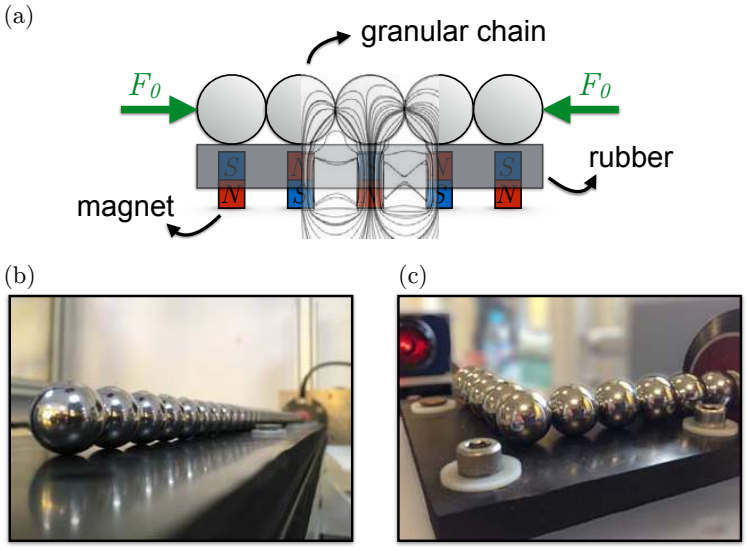

Figure 1: (a) Schematic diagram of the granular waveguide on top of permanent magnets within a rubber. Forces and magnetic flux lines induced by the magnetic field have been superimposed. Photography of (b) the line and (c) Γ-shaped waveguides.

Moreover, a key feature of granular media is the strong nonlinearities at the contact that enable a plethora of nonlinear processes. Granular phononic crystals have recently played a important role in the study of fundamental nonlinear wave phenomena, including harmonic generation [4] and discrete breathers [5]. They have been also applied in various engineering devices, including acoustic lenses [6], and acoustic rectifiers [7, 8].

Here, we intend to design an acoustic device to control the elastic wave propagation taking advantage of the strong contact nonlinearities and geometry. The line-shaped metawaveguide supports the generation of second harmonic for longitudinal motion. The experimental beating in amplitude of this second harmonic is demonstrated in such system. Adding a second chain perpendicular to the first one linked at its extremities gives us a Γ-shaped metawaveguide, see Fig. 1(c). The experimental setup using external magnetic field to create precompression into the chain allows to easily build a two dimensional configuration avoiding mechanical boundary to constrain the system. This system allows mode conversion from longitudinal to transverse-rotational modes. Taking advantage of the nonlinearity, this system supports also amplitude dependent transmission and filtering of harmonics.

To conclude, we have presented the realization and dynamics analysis of magneto-granular metawaveguides composed of spherical steel spheres in contact in the presence of a properly designed magnetic field. The latter can be used to tune the dynamics of the structure. Evidence of conversion from longitudinal to tranverse-rotational modes have been presented in a Γ-shaped waveguides. In addition, nonlinear processes are experimentally shown such as the beating in amplitude of the second harmonic and filtering of harmonics. The combination of the non-contact tunability and the potential strong nonlinear behavior opens the way for the construction of novel nonlinear tunable mechanical metamaterials for the control of elastic wave propagation.

ACKNOWLEDGMENT

G. T. and F. A. acknowledge financial support from FP7-CIG (Project 618322 ComGranSol).

REFERENCES

1. A. Merkel, V. Tournat, and V. Gusev, Experimental Evidence of Rotational Elastic Waves in Granular Phononic Crystals, *Phys. Rev. Lett.*, 107, 225502 (2011).
2. F. Allein, V. Tournat, V. E. Gusev, and G. Theocharis, Tunable magneto-granular phononic crystals, *Appl. Phys. Lett.*, 108, 161903 (2016).
3. F. Allein, V. Tournat, V.E. Gusev, and G. Theocharis, Transversal-rotational and zero group velocity modes in tunable magneto-granular phononic crystals, *Extreme Mechanics Letters*, 12, 65-70 (2017).
4. J. Cabaret, V. Tournat, and P. Béquin, Amplitude-dependent phononic processes in a diatomic granular chain in the weakly nonlinear regime, *Phys. Rev. E.*, 86, 041305 (2012).
5. N. Boechler, G. Theocharis, S. Job, P.G. Kevrekidis, M.A. Porter, and C. Daraio, Discrete Breathers in One-Dimensional Diatomic Granular Crystals, *Phys. Rev. Lett.*, 104, 244302 (2010).
6. A. Spadoni, and C. Daraio, Generation and control of sound bullets with a nonlinear acoustic lens, *Proc. Natl. Acad. Sci.*, USA 107, 7230 (2010).
7. T. Devaux, V. Tournat, O. Richoux, and V. Pagneux, Asymmetric Acoustic Propagation of Wave Packets Via the Self-Demodulation Effect, *Phys. Rev. Lett.*, 115, 234301 (2015).
8. N. Boechler, G. Theocharis, and C. Daraio, Bifurcation-based acoustic switching and rectification, *Nat. Mater*. 10, 665 (2011).

Measurement and Analysis of Lamb Wave Propagating on Plates with Periodic Structures

I-Ling Chang[1*], **Guan-Hua Huang**[1] **and Yun-Chun Lee**[1]
[1] Department of Mechanical Engineering, National Cheng Kung University, Taiwan
[*]corresponding author: ilchang@mail.ncku.edu.tw

Abstract-Both experiment and numerical simulation were carried out to investigate the Lamb wave propagation behavior on phononic crystal plates. The considered periodic structures on the plate are holes and pillars. The dispersion relations of symmetric and antisymmetric Lamb waves extracted from experimental measurement agreed quite well with the numerical results. It was found that the band gaps of the phononic crystal plates with pillars was easier to observe experimentally and narrow banded, which were caused by the local resonance.

In this study, we discussed the behaviors of Lamb wave propagating on the plate with periodic structures, which are so-called phononic crystal plates. Two kinds of periodic structures were considered on the plate, which are "hole-type" and "pillar-type", respectively. We employed finite element method and plane wave expansion approach to investigate the special wave propagating phenomena of the phononic crystal plates, such as band gaps and changes of wave velocity. The effects of the periodic structures, such as the lattice constant, filling ratio, periodic pattern and plate thickness, on the wave propagating behaviors were studied and the band gap mechanisms were also examined. Different Lamb waves, i.e., symmetric and antisymmetric, could be identified from the vibrating mode characteristic.

Then, we utilized PVDF line-focus transducer to experimentally measure the Lamb wave propagating on the phononic crystal plates. The line-focus transducer serves as signal generator and receiver. And the whole experiment was carried out under water. The transducer was first focus on the 50μm thick stainless steel plate with impulse signal and proceeded to a series of de-focusing measurements. After signal processing and data analysis, the dispersion curve could be extracted from a series of receiving signals and the band gap could be identified. Various plate samples with different periodic structures were prepared and measured. The dispersion relations from both experiments and numerical simulations were compared and found good agreement. However due to the design of the transducer, the in-plane shear wave could not be excited. It was found that the band gaps of the phononic crystal plates with pillars was easier to observe experimentally and narrow banded, which were caused by the local resonance.

Acknowledgements, This research work is supported by Ministry of Science and Technology, Taiwan under the grant NSC 103-2923-E-006-004-MY3 and MOST 105-2628-E-006 -003 -MY3.

Omnidirectional Source Illusions of Guided Elastic Waves in Plates using Metasurfaces

Yongquan Liu[1], Zixian Liang[2], Fu Liu[1], Owen Diba[1], Alistair Lamb[1], and Jensen Li[1*]

[1] School of Physics and Astronomy, University of Birmingham, Birmingham B15 2TT, United Kingdom

[2] College of Electronic Science and Technology, Shenzhen University, Shenzhen, 518060, China

[*]corresponding author: j.li@bham.ac.uk

Abstract-We demonstrate source illusion devices to manipulate guided elastic waves using metasurfaces. A source shifter, a transformer and a splitter are proposed, then measured to be broadband and robust against change of source positions. The approach is potentially useful for non-destructive testing, ultrasonography and advanced signal modulation.

The transformation method[1], together with metamaterials, is a powerful tool to achieve invisible cloaking and other illusion effects for electromagnetic waves, acoustic waves, heat flows, and matter waves. However, this approach is non-universal to manipulate elastic waves, as the governing equation in elastodynamics cannot keep its form under a general coordinate transformation, unless further approximations are applied or Willis media are employed. In consequence, the design of generic illusion devices for elastic waves is a challenging task. On the other hand, metasurface[2] has been demonstrated as an effective way to manipulate wavefront in optics and acoustics due to the simplicity in fabrication with low-loss, compact structures, but without losing the extreme functionality of bulk metamaterials. Zhu and Semperlotti[3] presented the first elastic metasurface to achieve anomalous refraction of guided waves in solids recently. Inspired by demonstrations of metasurfaces in achieving reduced versions of electromagnetic cloaks[4], here we develop a theoretical framework and experimental realizations of source illusion devices for flexural waves in plates using elastic metasurfaces. Our approach requires neither the form-invariance of elastodynamics nor bulk metamaterials with negative indices, yet allows us to demonstrate a series of all-angle elastic illusion effects.

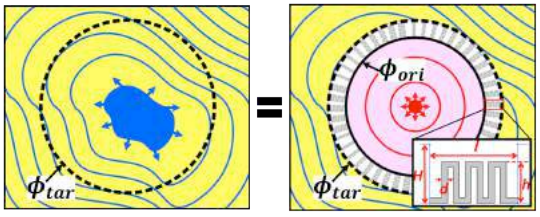

Fig. 1. Schematic of making illusions using metasurfaces. The unit cell is zoomed in the right part.

Fig. 1 shows the schematic diagram of the design strategy. Suppose that we have an original source, with wave field characterized by its phase $\phi_{\text{ori}}(x,y)$, a ring-type metasurface with the phase discontinuity of ϕ_{tar}-ϕ_{ori}, being evaluated at the location of metasurface, will turn this original incident field into an arbitrary target profile $\phi_{\text{tar}}(x,y)$. By doing this, an observer outside the metasurface (the black dashed circle) finds the same target field pattern in the physical space. Next, the phase discontinuity can be achieved by a ring-type metasurface. Each unit cell consists of a curved thin bar with identical width d and height of turns h. Then the wave is restricted to propagate along a zigzag path shaped by the unit cell. Due to the increase of total path length, we can increase the phase discontinuity of transmitted waves.

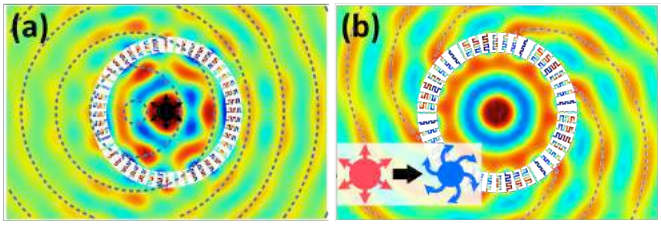

Figure 2 (a) Normalized amplitude of the A0 wave field for the source shifter at 12 kHz. (b) Simulated results for the source transformer at 8 kHz.

A source shifter is firstly proposed to shift the position of a wave source at origin (0,0) horizontally by a distance ΔS to the left. Fig. 2(a) shows the simulated out-of-plane velocity field at 12 kHz. The circular wave fronts are expected from the point source in the metasurface. Out of the metasurface, circular wave fronts are also obtained, centred at about ΔS on the left of the origin. Our elastic metasurfaces can also be used to transform a point source to a prescribed target wavefront. For example, we can impart an additional angular momentum[2] to the point source. The observer outside perceives it is a point source with spiral wave front. As shown in Fig. 2(b), the cylindrical wave shapes into a spiral with evenly-distributed six branches outside metasurface.

In order to validate the present method, we performed experimental investigations for the illusion devices. They all coincide with numerical simulations and theoretical analysis. The proposed approach paves the way to a much wider range of applications of metasurface. For example, the source splitter can be used as compact devices with phased array sources for non-destructive testing, the source transformer with angular momentum provides an additional degree of freedom for signal modulation.

Acknowledgements-J.L. acknowledges funding from the European Union's Seventh Framework Programme under Grant Agreement No. 630979. Y.L. acknowledges the fellowship of future scientist from the China Scholarship Council (CSC). Z.L. acknowledges the financial support by National Natural Science Foundation of China (NSFC) (61505114, 11574216).

REFERENCES

1. Pendry, J. B., D. Schurig, and D. R. Smith, "Controlling electromagnetic fields," *Science*, Vol. 312, No. 5781, 1780-1782, 2006.
2. Yu, N. et al., "Light propagation with phase discontinuities: generalized laws of reflection and refraction," *Science*, Vol. 334, No. 6054, 333-337, 2011.
3. Zhu, H. and F. Semperlotti, "Anomalous refraction of acoustic guided waves in solids with geometrically tapered metasurfaces," *Phys. Rev. Lett.*, Vol. 117, No. 3, 034302, 2016.
4. Ni, X. et al., "An ultrathin invisibility skin cloak for visible light," *Science*, Vol. 349, No. 6254, 1310-1314, 2015.

Bio-Inspired Hierarchical Dissipative Phononic Crystals and Acoustic Metamaterials for Low Frequency Attenuation

M. Miniaci[1,*], A. O. Krushynska[2], F. Bosia[2], B. Morvan[1], N. M. Pugno[3,4,5]

[1]Laboratoire Ondes et Milieux Complexes, University of Le Havre, UMR CNRS 6294, 76600 Le Havre, France

[2]Department of Physics, University of Turin, 10125 Torino, Italy

[3]Laboratory of Bio-Inspired and Graphene Nanomechanics, Department of Civil, Environmental and Mechanical Engineering, University of Trento, 38123, Trento - Italy

[4]School of Engineering and Materials Science, Queen Mary University of London, Mile End Road, E1 4NS London - United Kingdom

[5]Ket-lab, Italian Space Agency, Via del Politecnico snc, 00133 Rome, Italy

[*]presenting author: marco.miniaci@gmail.com; corresponding author: nicola.pugno@unitn.it

Abstract. Many biological systems show extremely efficient structural as well as dynamic properties achieved through their structure, which is often hierarchical. In this study, a hierarchical architecture is introduced in ordinary phononic crystals (PCs) and acoustic metamaterials (AMMs) to investigate modifications of the dispersion diagrams due to increasing structural complexity at different scale levels.

Introduction. Hierarchical structures with constituents over multiple length scales are found in various natural materials like bones, shells, spider silk and others, all of which display enhanced quasi-static mechanical properties, such as high specific strength, stiffness and toughness, attributed to hierarchy[1-3]. At the same time, the role of hierarchy on the dynamic behavior of phononic crystals (PCs) and acoustic metamaterials (AMMs) remains largely unexplored. This study assesses the effect of bio-inspired hierarchical organization as well as of the material viscoelasticity on the wave attenuation properties of continuous mechanical metamaterials[4].

Although optimized ordinary PC and AMM configurations have been proposed so far[5,6], light-weight, practically oriented metastructures with multi-scale wave attenuation abilities remain an open field of research. Indeed, ordinary elementary unit cells comprising single inclusions or cavities, often results into limited frequency band gaps (BGs).

Unit cell organization. One way to potentially overcome this limitation is to exploit fractal-like and bio-inspired structural hierarchy. Structural hierarchy is here understood in the sense that a representative unit cell comprises multiple arrangements of inhomogeneities at various size scales. If the same arrangement occurs at every scale, the pattern is called self-similar. We consider single-phase structures formed by self-similar unit cells with different hierarchical levels and types of hierarchy, as presented in Fig. 1.

Results. The influence of bio-inspired hierarchical organization and material viscoelasticity on wave dispersion in metamaterials with self-similar constituents at various spatial scales (see Figs. 1a and 1b) is numerically and experimentally investigated. Contrary to previous approaches[7,8], our study focuses on porous hierarchical structures, whereby increasing hierarchy entails a weight reduction. Results highlight a number of advantages, such as: (i) conservation of most of the BGs induced by the constitutive regular geometries, in the presence of material damping (we show that even small viscoelastic effects, not treated in the current literature,

are essential in determining this behaviour); (ii) nucleation of additional "hierarchically-induced" BGs and the tuning of the band gap frequencies of regular metamaterial to lower frequencies according to the spatial scale of the hierarchy, with a simultaneous significant reduction of the global structural weight; (iii) similar wave dynamics at low frequencies for hierarchical and corresponding regular structures.

The physical mechanism for the occurrence of the hierarchically induced BGs is discussed and the generality of the observed behavior, which is not limited to a specific configuration, is experimentally proved. A simple equivalent mass-spring model has been developed to predict the observed BG shift to lower frequencies.

In conclusion, this work provides insights on the crucial role of hierarchical structure on the dynamic behavior of metamaterials and reveals that the principles of bio-inspired hierarchical organization can lead to light-weight metamaterials with advanced multi-frequency attenuation properties, providing useful design principles for further practical applications.

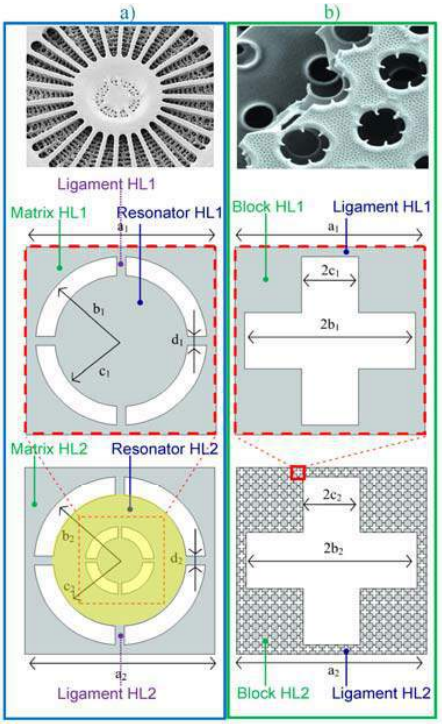

Figure 1 Hierarchical "porous" structures found in natural materials (diatom cell walls) at different spatial scales and the corresponding bioinspired hierarchical metamaterial unit cells: (a) structures with thin connecting elements and nested hierarchical organization (hub-spoke geometry) and (b) cross-like cavities and external hierarchical organization (cross-like porous metamaterial).

Acknowledgements. M. M. acknowledges funding from the European Union's Horizon 2020 research and innovation programme under the Marie Skłodowska-Curie grant agreement N. 658483. A. K. acknowledges funding from the European Union's Seventh Framework programme for research and innovation under the Marie Skłodowska-Curie grant agreement N. 609402-2020 researchers: Train to Move (T2M). N. M. P. is supported by the European Research Council PoC 2015 "Silkene" No. 693670, by the European Commission H2020 under the Graphene Flagship Core 1 No. 696656 (WP14 "Polymer Nanocomposites") and under the FET Proactive "Neurofibres" No. 732344.

REFERENCES

1. M. Meyers, P. Chen, A. Lin and Y. Seki, Prog. Mater. Sci., 53, 1-206, (2008).
2. S. Cranford, A. Tarakanova, N. Pugno and M. Buehler, Nature, 482, 72-91, (2012).
3. M. Miniaci, A. Krushynska, A. B. Movchan, F. Bosia, and N. M. Pugno, Appl. Phys. Lett. 109, 071905 (2016).
4. M. Miniaci, A. Krushynska, F. Bosia, and N. M. Pugno, preprint arXiv:1606.03596, (2017).
5. M. I. Hussein, M. J. Leamy and M. Ruzzene, Appl. Mech. Rev., 66(4), 040802 (2014).
6. M. I. Hussein, K. Hamza, G. M. Hulbert, R. A. Scott and K. Saitou, Struct. Multidisc. Optim., 31, 60-75 (2006).
7. D. Mousanezhad, S. Babaee, H. Ebrahimi, R. Ghosh, A. S. Hamouda, K. Bertoldi and A. Vaziri, Sci. Rep., 5, 18306 (2015).
8. K. H. Matlack, A. Bauhofera, S. Krödel, A. Palermo and C. Daraio, PNAS, 113 (30), 8386-8390 (2016).

Elastic Metamaterial for Extreme Broad Stop Band at Low Frequency Ranges

J. H. Oh[1,*], S. Qi[2,3], Y. Y. Kim[4] and B. Assouar[2,3]

[1]School of Mechanical, Aerospace and Nuclear Engineering, Ulsan National Institute of Science and Technology (UNIST), South Korea

[2]University of Lorraine, Institut Jean Lamour, France

[3]CNRS, Institut Jean Lamour, France

[4]Institute of Advanced Machine and Design, Seoul National University, South Korea

[*]corresponding author: joohwan.oh@unist.ac.kr

Abstract-We propose and realize a new elastic metamaterial having extreme broad low frequency stop band. The stop band achieved with the proposed elastic metamaterial is from 235 to 4520 Hz. To achieve the extreme broad low frequency stop band, we developed a new idea of near-zero rotational stiffness, which is a different mechanism compared with phononic crystals or resonance based metamaterials. We expect that the proposed elastic metamaterial can open a new way in various vibration devices.

Achieving extreme broad stop band at low frequency range, around ~100 Hz, has been a big challenge in the field in elastic metamaterial. If the extreme broad low frequency stop band can be achieved, one can break-through the well-known mass law and realize new vibration shielding devices. Previously, two major physics have been mainly considered to achieve a stop band metamaterial; one is the phononic crystal utilizing Bragg scattering from the crystal's periodicity[1,2], and the other one is the resonance based metamaterial utilizing internal resonance phenomena[3]. However, these two methods have shown a critical limit that they are hard to be applied in achieving the extreme broad stop band at low frequency. The stop band achieved with phononic crystals were generally formed at too high frequency ranges. On the other hand, the stop band achieved with resonance based metamaterials were formed at low frequencies, but they suffered from narrow band width.

In this work, we propose and realize a new elastic metamaterial having the extreme broad stop band at low frequency range. Fig. 1 (a) shows the wave dispersion curve of the proposed elastic metamaterial. In Fig. 1 (a), the stop band is formed from 235 to 4520 Hz, which is not only broad but also very low that covers almost all vibration frequencies. As explained above, such a broad low frequency stop band cannot be achieved by the well-known phononic crystals or the resonance based metamaterials. Here, we developed a new method, called 'near-zero rotational stiffness' method, to achieve extreme broad stop band at low frequency range. As well known, flexural elastic wave is governed by two kinds of stiffness – vertical and rotational stiffness[4]. We found that by lowering the rotational stiffness and increasing the vertical stiffness, one can achieve extreme broad low frequency stop band. Detailed physics and the actual metamaterial design to achieve this will be presented.

Fig. 1 (b) shows the numerically and experimentally measured vibration transmission of the proposed elastic metamaterial structure. As can be seen in Fig. 1 (b), extremely effective vibration shielding from 235 to 4520 Hz can be achieved with the proposed metamaterial. These investigations clearly supports that the proposed elastic metamaterial indeed has the extreme broad low frequency stop band.

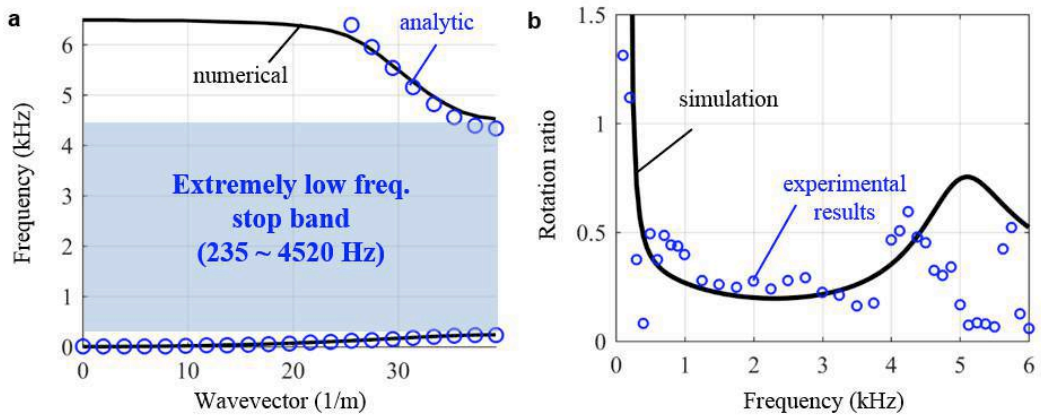

Figure 1 (a) Wave dispersion curve of the proposed elastic metamaterial, (b) numerically and experimentally measured vibration transmission of the proposed elastic metamaterial

This work suggested that by using a new idea of 'near-zero rotational stiffness metamaterial', one can achieve extreme broad stop band at very low frequency ranges. This approach, and the proposed elastic metamaterial structure, can open a new way in vibration devices.

Acknowledgements - This work was supported by the Center for Advanced Meta-Materials(CAMM) funded by the Ministry of Science, ICT and Future Planning as Global Frontier Project" (CAMM-2014M3A6B3063711) and by the new researcher's Research Fund (1.160096.01) of UNIST (Ulsan National Institute of Science & Technology).

REFERENCES

1. Sigalas, M. and Economou, E. N., "Band structure of elastic waves in two dimensional systems," *Solid State Commun.*, Vol. 86, 141-143, 1993.
2. Kushwaha, M. S., Halevi, P., Dobrzynski, L. and Djafari-Rouhani, B., "Acoustic band structure of periodic elastic composites," *Phys. Rev. Lett. B*, Vol. 71, 2022-2025, 1993.
3. Liu, Z., Zhang, X., Mao, Y., Zhu, Y. Y., Yang, Z., Chan, C. T. and Sheng, P., "Locally resonant sonic materials," *Science*, Vol. 8, 1734-1736, 2000.
4. Oh, J. H. and Assouar, B., "Quasi-static stop band with flexural metamaterial having zero rotational stiffness," *Sci. Rep.*, Vol. 6, 33410, 2016

Anisotropic Surface Acoustic Waves in Tungsten / Lithium Niobate Phononic Crystals

Jia-Hog Sun* and Yuan-Hai Yu

Department of Mechanical Engineering, Chang Gung University, Taoyuan, Taiwan
*corresponding author, E-mail: jhsun@mail.cgu.edu.tw

Abstract

Phononic crystals (PnC) were known for acoustic band gaps and applied as filters and reflective gratings for acoustic waves. In this paper, another important property of PnCs, the anisotropic propagation, was studied. A PnC made of circular tungsten films on a lithium niobate substrate was analyzed. Dispersion curves and equal frequency contours of surface acoustic wave were calculated to show the anisotropy. Then negative refraction of group velocity can be observed and used to suppress diffraction of surface waves.

1. Introduction

Phononic crystal (PnC) is an artificial composite for acoustic waves. PnC consists of periodically-arranged elastic materials or geometric structures in a background media. While acoustic waves propagate in PnCs, there are some special phenomena. One is the band gap which can block waves in a frequency range [1-5], and the other one is anisotropic propagation which allows the phase and group velocities aiming at different directions [6-10]. These properties allowed several applications of PnCs. Based on band gaps, PnC were used as the gratings in surface acoustic wave (SAW) device used in SAW resonators, filters and sensors [11-16]. Further, a hybrid design of inter-digital transducers (IDT) and PnCs was proposed to reduce the acoustic loss in SAW devices [17, 18]. On the other hand, PnCs with anisotropic propagation were used as a lens to bend the propagating waves and to focus waves at a certain area [19-21]. Negative refraction of waves in PnC were also reported [22, 23].

In this paper, we analyzed Rayleigh waves in a square lattice PnCs made of circular tungsten films on a piezoelectric substrate. The band structures and equal frequency contours (EFCs) were analyzed. By applying the anisotropic propagation, negative refraction of group velocity were observed at some frequency. Then using the PnC as an acoustic lens to suppress diffraction were demonstrated.

2. Surface acoustic waves in tungsten/lithium niobate PnC

In this paper, the 128˚Y-cut lithium niobate was chosen as the matrix material and a square lattice PnC was formed by circular tungsten films covering on the substrate. We used the finite element method (FEM) to calculate the band structures and EFCs of the PnC [11]. The lattice constant a of unit cell was set as 4 μm, thickness of metal film h is 400 nm and radius r is $0.4a$. The thickness h was chosen by considering the feasibility of fabrication, and a large radius allows more obvious dispersive bands. In order to enhance the anisotropic propagation, we set the x axis of material coordinate toward the ΓM direction of the square lattice coordinate, as the inset shown in Fig. 1.

The dispersion curves of Rayleigh waves, Loves, and high order SAW in the first Brillouin zone were shown in Fig. 1. The irreducible are in the Brillouin zone is the area Γ-M_1-Y-M_2-Γshown in the inset. There are partial band gaps in the ΓY direction while SAW can propagate in ΓM direction. The frequency range from 370 MHz to 460 MHz is the partial band gap of Rayleigh waves, and the range from 385 MHz to 430 MHz is the partial band gap of Love waves. Using the partial band gap, the direction around ΓY is the non-propagation direction to block energy.

The eigenmodes of all wave vectors within the first Brillouin zone formed a dispersive surface SAWs. Then EFCs were determined by cutting three-dimensional band structures at a chosen frequency. EFCs are equivalent to slowness curves. These curves show the relation of propagation property of waves in different directions. Fig 2 showed the EFCs of 445-MHz SAW in 128˚Y-cut $LiNbO_3$ and the W/$LiNbO_3$ PnC. In Fig. 2(a), the EFC is non-circular for SAW in $LiNbO_3$ which present the anisotropy of the piezoelectric materials. By adding the square-lattice tungsten films on $LiNbO_3$ substrate, the anisotropic wave propagation can be enhanced. As shown in Fig. 2(b), partial band gaps for SAWs appeared at the same frequency (445 MHz). We also analyzed another PnC in which the square-lattice pattern rotated 45˚ and the EFC shows more circular contours. Thus the alignment of the PnC can be used to enhance or reduce the anisotropic propagation of SAW in piezoelectric materials.

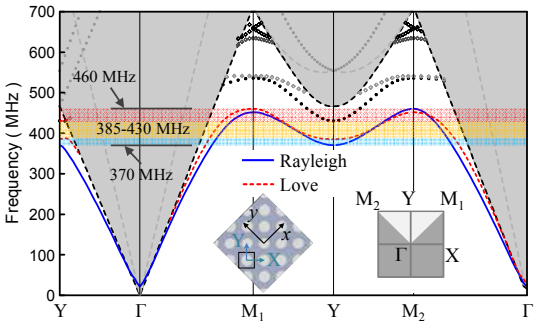

Figure 1: Band structures of W/LiNbO$_3$ PnC (a=4 μm, h = 400 nm, r = 0.4a).

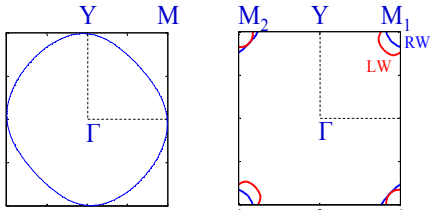

Figure 2: EFCs of 445 MHz SAWs in (a) 128˚Y-cut LiNbO$_3$ and (b) W/LiNbO$_3$ PnC.

The directions of wave propagation were observed from the EFC figures. The direction form the origin to one point on the EFC means the direction of phase velocity, the direction normal to the EFC at the point presented the group velocity (energy velocity). Considering the SAW passing the interface of LiNbO$_3$ area and PnC in Fig. 3, we determined the angle of refraction by the Snell's law. The typical value were list in Table 1. The curve of SAWs in the PnC is concave near the M$_1$ and M$_2$ points in the first Brillouin zone. The directions of group velocity Rayleigh waves were refracted to negative angles near the M$_1$ and M$_2$ points. At the 445 MHz, the refraction angle of group velocity is the minimum -24˚ near M$_1$ point. The result showed that Rayleigh wave at ΓM$_1$ direction has stronger self-collimation effect when passing the LiNbO$_3$-PnC interface. Thus ΓM$_1$ direction, which is parallel to the x axis, was specified in the development of using PnC to suppress diffraction of surface waves.

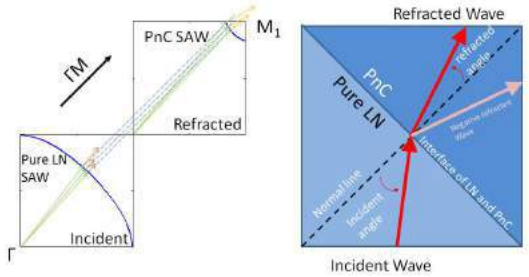

Figure 3: Directions of incident waves and refracted waves at the interface of LiNbO$_3$ and PnC regions.

Table 1: Typical incident and refraction angles of 445 MHz Rayleigh waves. The normal direction of the interface aligns with the ΓM$_1$ direction.

Incident angle in LiNbO$_3$		Angle of refraction in PnC	
θ_{phase}	θ_{group}	θ_{phase}	θ_{group}
7.75˚	4.15˚	5.30˚	-24.0˚
5.00˚	3.00˚	3.50˚	-16.5˚
3.00˚	1.90˚	2.05˚	-8.5˚

3. Lowering diffraction by phononic lens

3.1. Wave trajectory

The negative refraction of energy velocities in the interface supports the development of a PnC lens. Ray trajectories of energy were obtained by calculating the direction of the energy velocity from different incident angles as listed in Table 1. A PnC lens is a simple rectangular PnC. The energy velocity performed negative refraction while entered and leaved a PnC lens, and thus the thickness (the number of layers) of the PnC lens determined the focal area of energy. Fig. 4 showed the directions of wave energy form a point source. Along the ΓM$_1$ direction, rays were converged inside PnC structure due to the negative refraction of energy velocity. When thickness of lens is large enough, rays focused within PnCs, and a secondary focal region outside the lens appears. For different layers of PnCs, the focal length of the secondary focal points changed with the lens thickness, the distance of two boundaries of the lens. In the Fig. 4, there is no focal point behind lens at an 8-layer PnC lens. The focal length is around 11λ if the thickness of lens is 15 layers; the focal length is around 22λ for the 21-layer PnC lens. The focal points are the intersection of ray trajectory of energy velocity and the concentrated energy around those points performed larger displacement.

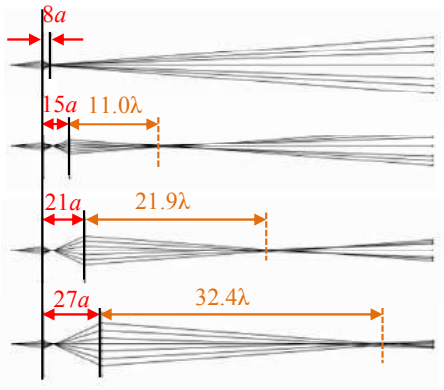

Figure 4: Trajectory of SAW passing PnC lens in different layers.

3.2. SAW passing a phononic lens

To design a lens, the transmission of waves passing the PnC lens was considered. The PnC lens contained lots of tungsten films which may scatter waves, and thus the attenuation of wave inside the PnC lens were calculated. The PnC lens with different thickness was set in FEM model and the amplitude of wave passing the lens was recorded to be compared with the incident waves. The transmission was shown as the dashed line (the standard PnC) in Fig. 5. The transmission did not show a simple trend. This should resulted from the multi-reflection of SAW inside the PnC. According to the theory of matching layer for the equivalent pure material, the transmission can reach to highest value while thickness of lens is an integral number of half wavelength.

The transmission of wave passing a standard PnC lens showed a noticeable energy loss. Thus tapered PnC region was proposed to the design of PnC lens. Tapered structure attached at the boundaries of PnC lens reduced the mismatch of acoustic impedance and discontinuity. A two-layer tapered PnC was defined by adding two-row tungsten film with smaller radii (0.27*a* and 0.35*a*). The radii of the three-layer tapered PnC are 0.23*a*, 0.32*a* and 0.37*a*, respectively. Fig. 5 showed that the tapered structure raised the transmission effectively. The transmission raised from 80% to 95%. Thus the PnC lens was designed with the three-layer tapered structures in the following studies.

The numerical simulation of SAW passing through a PnC lens in a three-dimensional model was present in this section. The PnC lens was designed for the 445 MHz Rayleigh wave. The first case considered the SAW generated by a point source in front of the PnC lens. The amplitude of out-of-plan displacement field was recorded to evaluate the PnC lens. Fig. 6(a) showed the amplitude filed of the SAW in the pure $LiNbO_3$ substrate without a PnC lens. Fig. 6(b) is the result which a 15-layer PnC lens was set. The amplitude fields along the central line were plotted in Fig. 6(c). By comparing these two cases, we observed that the energy was concentrated when SAW through the PnC lens. Thus PnC lens could help to suppress the diffraction of waves.

Further, the SAW launched by line sources were considered and shown in Fig. 7. The length of line source is 3λ, and the thickness of PnC lens is 21-layer. Fig. 7(a) is the displacement amplitude without passing the lens. In the simulation, the SAW from a line source propagated a longer distance before the amplitude field spread because the diffraction occurs mainly at the end points of the line. Therefore, the longer of the source line is, the lower percentage of the energy loss. Thus the effect of suppressing diffraction waves was not as obvious as in the case of point source. In Fig. 7(b), the PnC still converged the energy. Fig. 7(c) showed the amplitude along the central line. The PnC lens did help keep the energy in the central line. These cases with PnC lens really showed low diffraction, and the decrease of energy in the 21-layer PnC lens is lower. The result concluded that PnC could be used in the SAW device to lower the diffraction of surface waves.

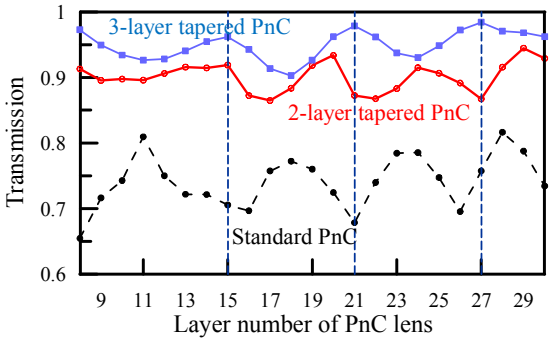

Figure 5: Transmission of SAW passing through three-type PnC lenses of different layers.

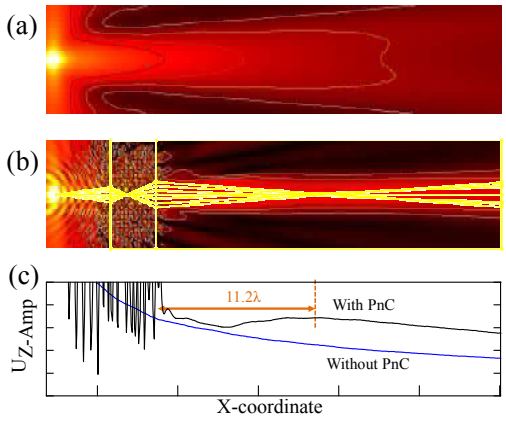

Figure 6: The SAW amplitude fields excited by a point source: (a) without a PnC lens; (b)with a 15 layers PnC lens. (c) Amplitude distribution of cases (a) and (b).

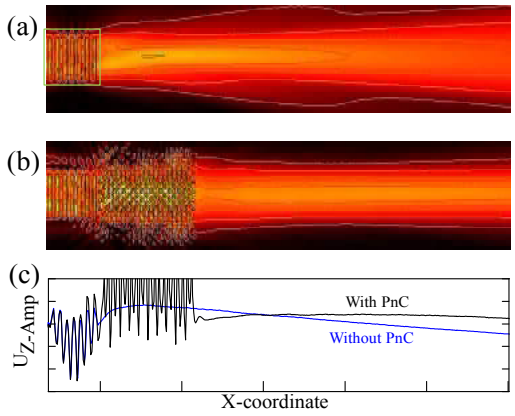

Figure 7: The SAW amplitude fields excited by a IDT: (a) without PnC lens; (b)with a 21 layers PnC lens. (c) Amplitude distribution of cases (a) and (b)

4. Conclusions

In this study, the tungsten/lithium niobate PnCs was analyzed to understand the anisotropic propagation of SAW. The band structure of the PnCs was analyzed the partial band gap and negative reflection of energy velocity were concluded. The PnC was used to be an acoustic lens to suppress diffraction of surface waves at 445MHz along the ΓM1 direction. Considering the energy attenuate inside PnC, three-layer tapered PnCs were proposed to be placed at the interface of PnC lens, and raise the transmission over 90% and the thickness of PnC lens was chosen for higher transmission. Ray trajectory from energy velocity was plotted to predict the distribution of focal points. According to this result, the diffraction of surface waves was suppressed effectively, and this PnC lens could be used to make the low-diffraction SAW device.

Acknowledgements

The authors gratefully thank to the financial supports from and Ministry of Science and Technology, Taiwan (MOST 104-2221-E-182-067), and Chang Gung University (BMRPC67).

References

[1] M.S. Kushwaha, P. Halevi, L. Dobrzynski and B. Djafari-Rouhani, Acoustic Band Structure of Periodic Elastic Composit, *Phys. Rev. Lett.* 71: 2022-2025, 1993.

[2] M.S. Kushwaha, P. Halevi, G. Martínez, L. Dobrzynski and B. Djafari-Rouhani, Theory of acoustic band structure of periodic elastic composites, *Phys. Rev. B* 49: 2313-2322, 1994.

[3] Y. Tanaka and S.I. Tamura, Surface acoustic waves in two-dimensional periodic elastic structures, *Phys. Rev. B* 58: 7958-7965, 1998.

[4] T.-T. Wu, Z.-G. Huang, and S. Lin, Surface and bulk acoustic waves in two-dimensional phononic crystal consisting of materials with general anisotropy, *Phys. Rev. B* 69, 094301, 2004.

[5] J.-H. Sun and T.-T. Wu, Analyses of mode coupling in joined parallel phononic crystal waveguides, *Phys. Rev. B* 71: 174303, 2005.

[6] F. Semperlotti and H. Zhu, Achieving selective interrogation and sub-wavelength resolution in thin plates with embedded metamaterial acoustic lenses, *J. Appl. Phys.* 116: 054906, 2014.

[7] J. F. Robillard, J. Bucay, P. A. Deymier, A. Shelke, K. Muralidharan, B. Merheb, J. O. Vasseur, A. Sukhovich and J. H. Page, Resolution limit of a phononic crystal superlens, *Phys. Rev. B* 83: 224301, 2011.

[8] J. Li, F. Wu, H. Zhong, X. Zhang and Y. Yao, Tuning the acoustic directional radiation by rotating square rods in two-dimensional phononic crystals, *Modern Phys. Lett. B* 28: 1450187, 2014.

[9] J. Li, F. Wu, H. Zhong, Y. Yao and X. Zhang, Acoustic beam splitting in two-dimensional phononic crystals using self-collimation effect, *J. Appl. Phys.* 118: 144903, 2015.

[10] I. A. Veres, T. Berer, O. Matsuda and P. Burgholzer, Focusing and subwavelength imaging of surface acoustic waves in a solid-air phononic crystal, *J. Appl. Phys.* 112: 053504, 2012.

[11] J. H. Sun and J. H. Jhou, Surface acoustic wave resonator using layered phononic crystals, *Jpn. J. Appl. Phys.* 53: 07KB04, 2014.

[12] V. Yantchev, Complete bandgap SAW phononic resonant topologies *Proc. IEEE Ultrasonics Symp.*, pp.475-478, 2014.

[13] M. Solal, J. Gratier and T. Kook, A SAW Resonator With Two-Dimensional Reflectors, *IEEE Trans. Ultrason. Ferroelectr. Freq. Control* 57: 30-37, 2010.

[14] T. T. Wu, W. S. Wang, J. H. Sun, J. C. Hsu and Y. Y. Chen, Utilization of phononic-crystal reflective gratings in a layered surface acoustic wave device, *Appl. Phys. Lett.* 94: 101913, 2009.

[15] T.-W. Liu, Y.-C. Tsai, Y.-C. Lin, T. Ono, S. Tanaka and T.-T. Wu, Design and fabrication of a phononic-crystal-based Love wave resonator in GHz range, *AIP Advances* 4: 124201, 2014.

[16] J. H. Sun and Y. H. Yu, A SAW filter using $SiO_2/LiNbO_3$ layered-structure phononic crystals, *Proc. IEEE Freq. Control Symp.*, pp. 382-384, 2016.

[17] V. Yantchev and V. Plessky, Analysis of two dimensional composite surface grating structures with applications to low loss microacoustic resonators, *J. Appl. Phys.* 114: 074902, 2013.

[18] V. Yantchev, A transversely coupled phononic surface acoustic wave transducer, *Appl. Phys. Lett.* 104: 103503, 2014.

[19] S.-C. S. Lin, T. J. Huang, J.-H. Sun and T.-T. Wu, Gradient-index phononic crystals, *Phys. Rev. B* 79: 094302, 2009.

[20] T.-T. Wu, Y.-T. Chen, J.-H. Sun, S.-C. S. Lin and T. J. Huang, Focusing of the lowest antisymmetric Lamb wave in a gradient-index phononic crystal plate, *Appl. Phys. Lett.* 98: 171911, 2011.

[21] J. Zhao, B. Bonello, L. Becerra, O. Boyko and R. Marchal, Focusing of Rayleigh waves with gradient-index phononic crystals, *Appl. Phys. Lett.* 108: 221905, 2016.

[22] X. Zhou, M. B. Assouar and M. Oudich, Acoustic superfocusing by solid phononic crystals, *Appl. Phys. Lett.* 105: 233506, 2014.

[23] A. Sukhovich, L. Jing and J. H. Page, Negative refraction and focusing of ultrasound in two-dimensional phononic crystals. *Phys. Rev.* B 77: 014301, 2008.

Metamaterials in Communication Systems

Dynamic parameter control of magnet-less non-reciprocal metamaterial (MNM) for adaptive electromagnetic material

Toshiro Kodera
Meisei University, Tokyo Japan
kodera2t@ieee.org

Abstract- Adaptive electromagnetic response control of metamaterial is quite attractive for realizing environment adaptive metamaterial. The magnetic loss of magneto-less non-reciprocal metamaterial (MNM) corresponds to Q-factor of resonant particle and it can be dynamically controlled by the bias condition of the unidirectional active component. In this talk, a precise Q-factor evaluation of MNM is presented and its results are compared to actual prototype device.

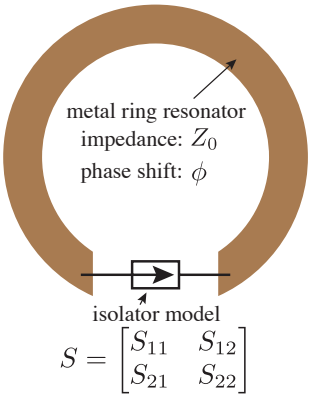

Fig. 1 Simplified MNM model

The magneto-less non-reciprocal matermaterial (MNM)[1] provides an artificial creation of gyrotrpic magnetic response in RF regime, which enables non-reciprocal device realization as same as ferrite material[2].

Figure 1 shows a simplified MNM model consists of metal ring resonator with characteristic impedance Zo with phase shift ϕ and isolator model. Assuming perfect-matched ideal isolator, Q-factor of this model can be derived as [3],

$$Q = \frac{(2n-1)\pi}{2} \left| \frac{2Y_0 R_x S_{21}}{2Y_0 R_x (1+S_{21})+1} \right| \quad (1)$$

, where n is the resonance order and Rx is the loading resistance which corresponds to energy dissipation by electromagnetic coupling with resonator surroundings. The infinite Q-factor leads to oscillation (instability) of MNM and, if S21 has a smaller value than unity, this situation arises only for Rx has infinity value (load-pull situation). The exact magnetic loss of MNM can be estimated by the relation between Q-factor and half-value of magnetic resonance (ΔH). This design guideline will provide the dynamic magnet-loss control of MNM leading to environment adaptive metamaterial.

Acknowledgements, This work has been carried out under the sponsorship KAKENHI Grant-in-Aid for Research Activity # 26289106.

REFERENCES

1. T. Kodera, D. L. Sounas, and C. Caloz, “Artificial Faraday rotation using a ring metamaterial structure without static magnetic field,” Appl. Phys. Lett., vol. 99, pp. 031114:1-3, July 2011.
2. T. Kodera, D. L. Sounas, and C. Caloz, “Magnetless Nonreciprocal Meta- material (MNM) Technology: Application to Microwave Components”, IEEE Trans. MTT, Vol. 61, No. 3, pp. 1030-1042, Mar 2013.
3. T. Ohira, K. Araki “Active Q-Factor and equilibrium stability formulation for sinusoidal oscillators,” IEEE Trans. Circuits and Systems, vol. 54, no. 9, pp. 810–814, Sept. 2007.

Translation of Metamaterial Concepts to Low-Profile Broadband Microwave Antenna Technology (Invited)

Zhi Ning Chen[1*], **Wei Liu**[1], **and Xianming Qing**[2]
[1]Department of Electrical and Computer Engineering, National University of Singapore (NUS), Singapore
[2]Institute for Infocomm Research (I^2R), Agency of Science, Technology and Research, Singapore
[*]corresponding author: eleczn@nus.edu.sg

Abstract-This paper updates the progress in the applications of metamaterials in the designs of low-profile and broadband microwave antennas. First, the development of metamaterials-based antenna technologies is introduced in the designs of artificial magnetic conductor (AMC) loaded substrate-integrated Fabry-Perot cavity antenna, AMC-loaded ultra-high frequency (UHF) radio frequency identification (RFID) reader antenna, high-permittivity meta-slab loaded high gain antenna arrays for 2.5G/3G/LTE cellular base-stations. Then, as an example, the design of a metamaterial-based broadband low-profile mushroom antenna is presented in detail.

As one type of artificially made electromagnetic structures, metamaterials feature the unique electromagnetic properties which have never been found in any nature materials. The important impact of the research into metamaterials is to control the electromagnetic waves and fields in an unusual way. In the past 18 years, the theoretical research into new physical concepts and phenomena has led to many new scientific findings [1–3]. However, translation the scientific findings to engineering technologies for practical applications is critical challenge. So far, more and more metamaterial-based designs have been applied to control the electromagnetic wave transmission and reflection, while we have hardly seen success stories in practical engineering applications of metamaterial-based antenna deigns because of the challenging requirements of antennas, in particular low ohmic loss, wide operating bandwidth, and simple structure for low fabrication cost and ease installation.

The team from NUS and I^2R has paid much effort to translate the physical concepts of metamaterials to antenna engineering technologies in the past ten years. So far, we have developed many solutions for enhancing antenna performance for RFID, WLAN/WiFi, cellular base-stations, radar systems, and so on. Here, we will update the progress in the applications of metamaterials in ultra-low-profile broadband antenna technologies.

A. AMC-loaded substrate-integrated Fabry-Perot cavity antenna and UHF RFID reader antenna

An AMC-based partially reflective sheet and a ground plane are used as the two reflectors of the Fabry-Perot resonant cavity for an ultra-thin design where the cavity is fully dielectric filled as shown in Figure 1(a). With a microstrip patch antenna as a feed, the antenna operating at 10 GHz achieved the high gain of 12.5 dBi with an aperture of $2\lambda \times 2\lambda$ and much reduced thickness of $\lambda/9$ (where λ is the operating wavelength in free space) [4].

Figure 1(b) shows an AMC-loaded UHF RFID reader antenna. The zero-phase-shift-line loop antenna operating at 915 MHz is able to be positioned close to the AMC to achieve directional magnetic field distribution. The ultra-low-profile antenna is with a thickness of less than $\lambda/8$ and enhanced magnetic field intensity.

B. High-permittivity meta-slab loaded high gain antenna

A double layer electromagnetic band gap (EBG) structure with high effective permittivity was loaded in a dipole antenna to achieve wideband high-gain low-profile antenna [5]. The high-permittivity meta-slab loaded

This work was supported by National University of Singapore under Research Grant R-263-000-B62-112.

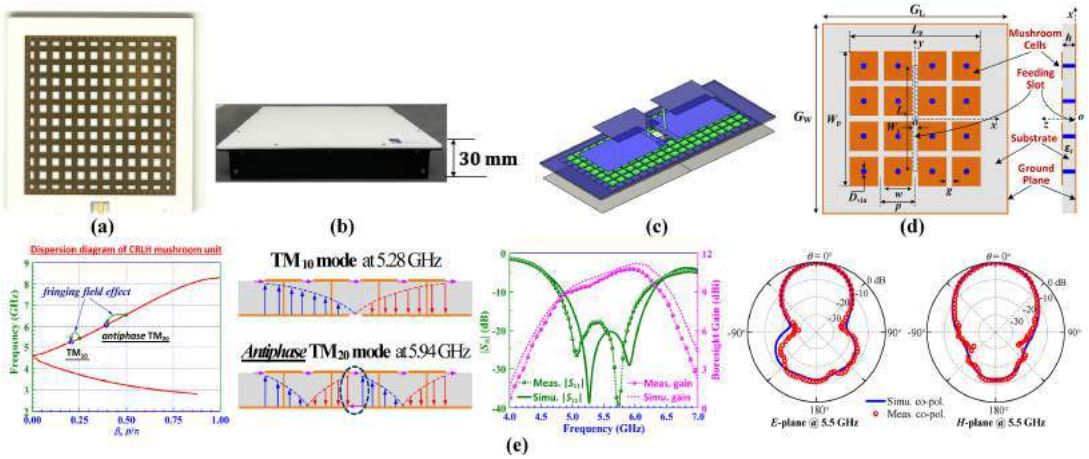

Figure 1. Metamaterial-based antennas

dipole antenna was further developed to realize a maximum gain of 14.2 dBi with aperture efficiency of 94%, and stable radiation patterns over a wide impedance bandwidth of 44.4% (1.67–2.69 GHz) as shown in Figure 1(c). Later, the technology was used to design the cellular base-station antenna with radiation efficiency of >90%, half-power beamwidth of >55±5°, port isolation of >25dB over the bandwidth of ~45% (1710–2690 MHz) at an overall thickness of 20 mm.

C. Metamaterial-based broadband low-profile mushroom antenna

Figure 1(d) shows the metamaterial-based broadband low-profile mushroom antenna fed by a microstrip line thru an aperture on a ground plane [6]. The antenna printed on Rogers RO4003C (ε_r = 3.38, $tan\delta$ = 0.0027) has a patch area of 0.72λ×0.72λ and a thickness of 0.06λ (λ is the free-space wavelength at the center frequency of 5.5 GHz). Figure 1(e) illustrates the dispersion diagram of the mushroom unit cell, sketched electric fields of the dual operating modes, $|S_{11}|$ and gain, radiation patterns of the antenna. Due to the unique composite right/left-handed (CRLH) dispersion of the metamaterial mushroom unit and the feeding scheme, both the adjacent TM_{10} and the antiphase TM_{20} modes are generated for consistent boresight radiation over a wide bandwidth. The achieved bandwidth for $|S_{11}|$<−10 dB is 4.85–6.28 GHz or 26%. The measured average realized boresight gain is 10.2 dBi with consistent radiation patterns over the bandwidth.

REFERENCES

1. D. R. Smith, W. J. Padilla, D. C. Vier, S. C. Nemat-Nasser, and S. Schultz, "Composite medium with simultaneously negative permeability and permittivity," *Phys. Rev. Lett*., vol. 84, no. 18, pp. 4184–4187, May 2000.
2. R. A. Shelby, D. R. Smith, and S. Schultz, "Experimental verification of a negative index of refraction," *Science*, vol. 292, pp. 77–79, Apr. 2001.
3. G. V. Eleftheriades, A. K. Iyer, and P. C. Kremer, "Planar negative refractive index media using periodically *L-C* loaded transmission lines," *IEEE Trans. Microw. Theory Tech*., vol. 50, no. 12, pp. 2702–2712, Dec. 2002.
4. Y. Sun, Z. N. Chen, Y. Zhang, H. Chen, and T. S. P. See, "Subwavelength substrate-integrated Fabry-Pérot cavity antennas using artificial magnetic conductor," *IEEE Trans. Antennas Propag*., vol. 60, no. 1, pp.30–35, Jan. 2012.
5. P. Y. Lau, K. K.-O. Yung, and Z. N. Chen, "A wideband high gain double EBG reflector antenna," 8th *International Conference on Information, Communication and Signal Processing*, Singapore, Dec. 13–16, 2011.
6. W. Liu, Z. N. Chen, and X. Qing, "Metamaterial-based low-profile broadband mushroom antenna," *IEEE Trans. Antennas Propag.*, vol. 62, no. 3, pp. 1165–1172, Mar. 2014.

Modal Dispersions and Propagation Losses along Silver Nanowires Covering Optical Communication Wavelengths

Hung-chun Chang[1,2,3*], **Hsuan-Hao Liu**[1], **Hsiang-Peng Chen**[1], **Pin-Ho Wang**[1], **and Hsin-Mao Hsu**[1]
[1]Graduate Institute of Photonics and Optoelectronics, [2]Department of Electrical Engineering, and [3]Graduate Institute of Communication Engineering, National Taiwan University, Taipei 10617, Taiwan
[*]corresponding author: hungchun@ntu.edu.tw

Abstract-Characteristics of surface plasmon modes, in particular the leaky modes, propagating on dielectric-substrate supported silver nanowires of circular and pentagonal cross-sections are numerically investigated using a finite-element method over the wavelength range covering the optical communication band. Leaky modes are with electric-field guided mainly at the top air-silver interface and with field leakage in the substrate, which are clearly revealed based on high-resolution numerical analysis. Higher order leaky modes are determined for both circular and pentagonal nanowires with their dispersions, cutoff wavelengths, and propagation losses compared.

This work concerns surface plasmon polariton (SPP) modes propagating along a chemically synthesized silver nanowire, in particular for that supported by a dielectric substrate, as depicted in Fig. 1(a). Such nanowires have been investigated for possible applications in optical sensing, optical coupling with nanophotonic components and circuits, interaction with single-photon emitters, etc., and in many related experiments the nanowires often appeared as falling on a dielectric substrate [1, 2]. From the viewpoint of solving electromagnetic modes, the appearance of the substrate results in a more complicated boundary-value problem. Recently, detailed guided-mode solutions based on a finite-element method have been reported for circular-cylinder nanowires with emphasis on single-guiding-mode operation [2, 3]. We have recently conducted mode analysis of similar circular-cylinder silver nanowires using an in-house developed full-vector finite-element imaginary-distance beam propagation method (FV-FE-IDBPM) [4] and disclosed, in addition to the "single-guiding mode" for which the mode fields are mainly guided near the nanowire-substrate interface, the existence of a leaky mode with major electric-field distributions on top of the air-nanowire interface [5]. This analysis method has recently been used to provide high-resolution modal characteristics and detailed modal profiles of leaky modes on a metal stripe plasmonic waveguide with a metal stripe fabricated on top of a substrate [4]. And the possible existence of the leaky mode on the structure of Fig. 1(a) can be understood from the characteristics of the stripe waveguide [5].

The chemically synthesized silver nanowire can possess pentagonal cross-sectional shape [6], as depicted in Fig. 1(b), with the circular cross-sectional shape being an approximation. This paper presents our recent studies of the modal dispersions and propagation losses for silver nanowires of both cross-sectional shapes with the considered wavelength range from 500 nm to 2000 nm, covering the optical communication wavelength band so that waveguiding applications in future photonic circuits can be evaluated [2]. New results include obtaining the higher order leaky modes in addition to the fundamental leaky mode reported in [4]. Possible application in mode-division multiplexing for increasing data transmission channels along a pentagonal nanowire through the existence of multiple leaky plasmon modes was proposed in [6]. Here we are interested in comparing modal characteristics between the circular and pentagonal nanowires. Fig. 1(c) shows the Re[E_y] profile of the first

leaky mode at the wavelength λ = 500 nm when the radius of the circular silver nanowire (*r*) is 400 nm. When the *r* = 400 nm circle is just tangentially surrounded by the five sides of a pentagon, the Re[E_y] profile of the first leaky mode at the wavelength λ = 532 nm of the corresponding pentagonal nanowire is shown in Fig. 1(d). In both Fig. 1(c) and (d), the modal electric field is mainly localized on the top of the nanowire in the air along with down-propagating leakage field in the substrate. For the *r* = 400 nm circular nanowire structure in the considered wavelength range, four leaky modes were found and their propagation length versus wavelength results are shown in Fig. 1(e), where "AML" means "air-metal-leaky" with the subscript specifying the order number. The results show the cutoff wavelength of the AML_1 mode is longer than 1550 nm with the propagation distance larger than 25 μm. The result corresponding to the Fig. 1(d) case is also shown in Fig. 1(e) from which longer cutoff wavelength and larger propagation length are seen. The enough long propagation lengths give the message that such leaky modes can play roles in practical applications.

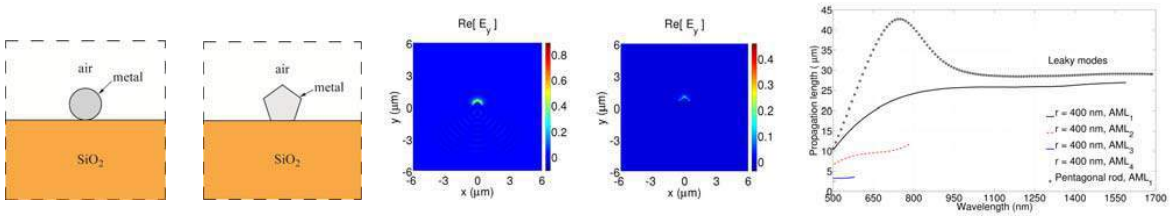

(a) (b) (c) (d) (e)

Fig. 1. (a) Cross-section of the circular nanowire with substrate. (b) Cross-section of the pentagonal nanowire. (c) Re[E_y] profile of the first leaky mode on the structure of (a) with nanowire radius of 400 nm at λ = 500 nm. (d) Re[E_y] profile of the first leaky mode on the structure of (b) at λ = 532 nm. (e) Propagation length versus wavelength curves for the four leaky modes on the structure of (a) with nanowire radius of 400 nm and the first leaky mode on the corresponding structure of (b).

Acknowledgements: This work was supported by the Ministry of Science and Technology of the Republic of China under grants NSC103-2221-E-002-048-MY2, MOST105-2221-E-002-138-MY2, and MOST105-2811-E-002-068.

REFERENCES

1. Li, Z., K. Bao, Y. Fang, Z. Guan, N. J. Halas, P. Nordlander, and H. Xu, "Effect of a proximal substrate on plasmon propagation in silver nanowires," *Phys. Rev. B*, Vol. 82, 241402(R), 2010.
2. Li, Q. Li and M. Qiu, "Plasmonic wave propagation in silver nanowires: guiding modes or not?" *Opt. Express*, Vol. 21, No. 7, 8587–8595, 2013.
3. Wang, Y., Y. Ma, X. Guo, and L. M. Tong, "Single-mode plasmonic waveguiding properties of metal nanowires with dielectric substrates," *Opt. Express*, Vol. 20, No. 17, 19006–19015, 2012.
4. Liu, H. H. and H. C. Chang, "High-resolution analysis of leaky modes in surface plasmon stripe waveguides," *J. Lightwave Technol*., Vol. 34, No. 11, 2752–2757, 2016.
5. Chen, H. P., H. H. Liu, and H. C. Chang, "On the leaky modes for silver nanowires on a silica substrate," in *Proceedings of 15th International Conference on. Numerical Simulation of Optoelectronic Devices* (*NUSOD 2015*), Taipei, Taiwan, September 2015, paper ThPD2.
6. Yang, H., M. Qiu, and Q. Li, "Identification and control of multiple leaky plasmon modes in silver nanowires," *Laser Photonics Rev.*, Vol. 10, No. 2, 278–286, 2016.

Plasmonic Sensor for Biomedical Device

CMOS spoof-SPP optical filter for fluorescence detection

Xiaojian Fu, Yu Jiang and Hao Yu*
School of Electrical and Electronic Engineering, Nanyang Technological University, Singapore 639798
*corresponding author: haoyu@ntu.edu.sg

Abstract-In this work, an optical filter is designed based on spoof surface plasmon polariton resonant cavity constructed by nanoscaled metallic line array. As for fluorescence detection, the numerical results show that the 400~450 nm excitation light is almost 100% absorbed and the 750~850 nm fluorescence is highly transparent. The transmission difference between 400 nm and 800 nm reaches 64dB. Thus, an on-chip high SNR fluorescence detector can be achieved by combining this filter and a high sensitive photon detector.

Fluorescence detection has attracted lots of research interests due to application in materials science and biomedical such as DNA fluorescence detection for early diagnosis of genetic decreases. However, complicated instrument such as fluorescence microscopy is usually employed for traditional fluorescence detection technology. In this work, a kind of novel on-chip plasmonic filter is developed for fluorescence detection. Specifically, a broadband filter is designed based on spoof surface plasmon polariton (spoof-SPP) resonant cavity constructed by nanoscaled metallic line array. As for fluorescence detection, the short-wavelength excitation light will be absorbed by the filter, while the long-wavelength fluorescence beam will have a high transparency. Take the quantum dot source as an example, we estimate the performance of the fluorescence detector using the numerical simulation method. Both the transmission parameter and near-field distribution results show that the 400~450 nm excitation light is almost 100% absorbed and the 750~850 nm fluorescence is highly transparent. The transmission difference between 400 nm and 800 nm reaches up to 64dB. Thus, a broad operating band and high SNR fluorescence detector can be achieved by combining the spoof-SPP based filter and a high sensitive photon detector.

REFERENCES

1. Hong L. Y., S. McManus, H. Yang and K. Sengupta, "A Fully Integrated CMOS Fluorescence Biosensor with on-chip Nanophotonic Filter," 2015 Symposium on VLSI Circuits Digest of Technical Papers C207.

Alternative plasmonic materials

Metal Alloys as Alternative Materials for Plasmonics

Marina S. Leite
Department of Materials Science and Engineering
Institute for Research in Electronics and Applied Physics
University of Maryland – College Park

Steel is an alloy primarily formed by iron, carbon and chromium that have transformed our society. Today, steel is widely in a variety of applications, ranging from building construction to surgical tools, all possible because alloying provides a low-cost material with improved mechanical properties. In the realm of plasmonics, there is still a pressing need to identify materials with superior optical response. Here, we present how the alloying of metals (Ag, Au, Cu, Al) provides materials with permittivity values not found in its pure counterparts. We overcome the constraint imposed by the pre-defined permittivity of noble metals by alloying, where we have recently developed a library of their optical properties [1]. Further, we implement a scalable method for the fabrication of alloyed nanostructures with *on demand* optical response [2]. We resolve the light-alloyed nanostructures interactions by near-field scanning optical microscopy and 3D full-field simulations. We demonstrate that perfect absorbers with superior performance can be obtained by using Al-Cu/semiconductor, where we find near-unity absorption in the visible and NIR range of the spectrum, not possible by using conventional metals [3]. We expect alloyed metals to become a novel platform for the design and fabrication of building blocks for nanophotonics, for applications ranging from metamaterials to displays and catalysis.

[1] C. Gong, M. S. Leite. "Noble Metal Alloys for Plasmonics". *ACS Photonics* **3**, 507 (2016). **Cover**
[2] C. Gong, et al. "Near-Field Optical Properties of Fully Alloyed Noble Metal Nanoparticles". *Advanced Optical Materials* **5**, 1600568 (2017). **Front cover**
[3] M. R. Dias, et al. "Metal Alloys for Perfect Absorbers with Superior Optical Performance". In review.

Plasmonic nanodisc arrays for Luminescence and Raman enhancement

Jörg Schilling[1*], **Neha Sardana**[1,2], **Frank Heyroth**[3], **Yong-Tae Kim**[4]
[1]ZIK SiLi-nano, Martin-Luther-University Halle-Wittenberg, 06120 Halle, Germany
[2] Institute of Nano Science and Technology, Mohali 160062, India
[3] IZM, Martin-Luther-University Halle-Wittenberg, 06120 Halle, Germany
[4] AG μMD, Institut für Physik, Martin-Luther-University Halle-Wittenberg, 06120 Halle, Germany
[*]corresponding author: joerg.schilling@physik.uni-halle.de

Abstract Arrays of gold discs are investigated as substrates for luminescence and Raman enhancement. These nanoantenna arrays exhibit relatively sharp grating resonances leading to increased field concentration and light-matter interaction in their vicinity. This is harnessed for enhanced luminescence of colloidal nanoparticles in the IR-telecom range and surface enhanced Raman scattering in the near IR.

Plasmonic resonances from nanoscopic metal spheres, discs or rods are used frequently to concentrate light in the near field due to their strong localized surface Plasmon resonances. However the large losses due to absorption and scattering of the (mostly) dipole resonances results in rather broad single particle resonances with low Q-factors. This limits the efficient interaction of the light field with matter and impedes the detection of clear peak shifts for e.g. sensing applications. However plasmonic nanoantenna arrays have attracted considerable attention recently, since in addition to the broad single particle plasmonic resonances they offer relatively sharp surface grating resonances [1]. Even lasing at these resonances was observed when semiconductor nanocrystals surrounded the nanoantennas [2].

Here we report on the use of gold nanodisc arrays for luminescence enhancement in the IR telecom range. Au-discs with diameters in the range 150-250nm are arranged in square and rectangular arrays with periods around 900nm. Transmission measurements using a collimated beam clearly show the sharp grating resonances at a wavelength of 1400nm, which appear at the long wavelength tail of the broad single particle resonances [Fig 1].

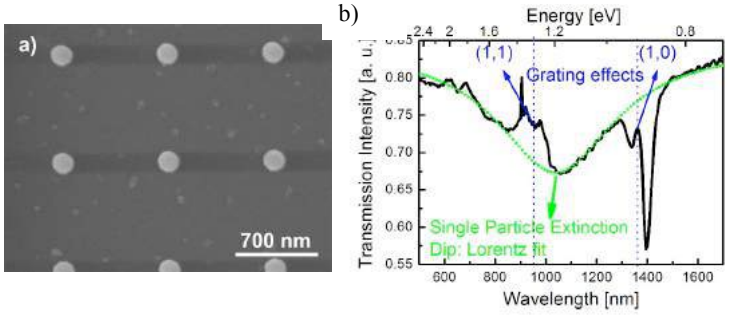

Fig.1: a) SEM-image of Au-Nanodisc array on glass. b) Transmission spectrum of disc array with disc diameter of 250 nm. The experimental curve is shown in black. A Lorentzian fit (green) reveals the underlying single particle surface plasmon resonance. At λ=1400nm the sharp (1 0) grating resonance appears.

Subsequently colloidal PbS-nanoparticles, which emit in the range between 1200-1500nm, were immersed in a PMMA-solution and spread at the nanoantenna array. Photoluminescence (PL) measurements revealed an up to four times enhancement of the emission at the grating resonance [3]. The spectral coincidence of transmission dip and PL-peak, which could be traced for differently sized discs, is a clear indication of their common origin [Fig. 2]. Furthermore the formation of the grating resonances in an asymmetric refractive index environment is studied to

evaluate the applicability of nanoantenna arrays in combination with silicon photonic devices.

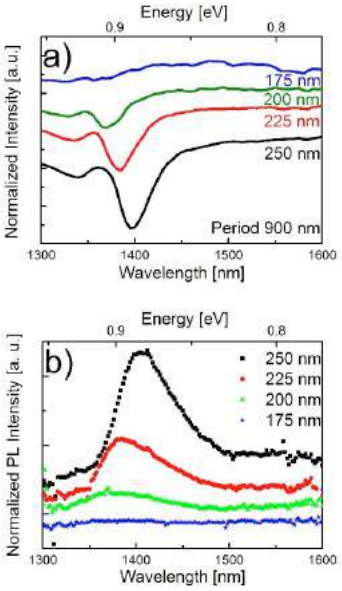

Fig.2: a) Shift of grating resonances with disc diameter observed in transmission. b) Luminescence enhancement of PbS-nanoparticles surrounding the antennas due to the grating resonances.

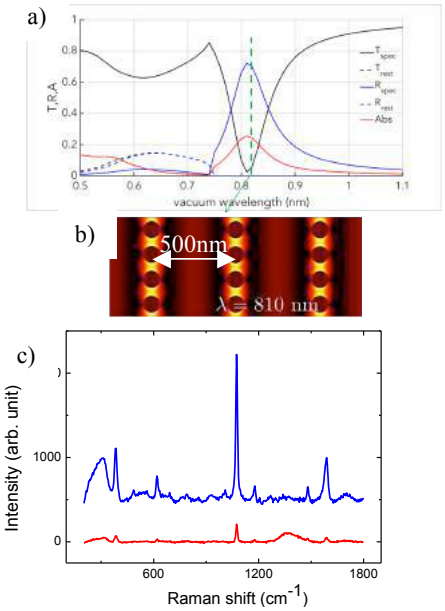

Fig. 3: Periodic Au-disc chains for the combination of near-field hot-spots with the grating resonance a) Simulation of Reflection, Transmission and Absorption for Au-disc chains. b) Field concentration within the chains. c) SERS-measurement showing the importance of polarisation along the chains to observe maximum enhancement: E-field along (blue) or perpendicular (red) to the chain.

To determine the potential of nanoantenna arrays as substrates for surface enhanced Raman scattering, Au-nano-discs were arranged in chains. Near-field hot-spots form in the small spaces between neighbouring discs of the same chain, while the different chains are arranged in a 1D-grating leading to a far-field coupling between the chains. Disc diameters of 100nm and a chain period of 500nm simulations yield a grating resonance at λ=810nm and a clear field concentration between neigbouring discs within the chains is predicted [Fig. 3a,b]. Moreover the experimental investigation of the Raman-effect of 4-methylbenzenethiol (4-MBT) molecules covering the Au-discs showed the remarkable impact of the Laser-polarisation [Fig. 3c]. This can be intuitively understood considering the near- and far-field coupling between Hertzian dipoles. The potentially strong enhancement of the SERS-signals due to the simultaneous combination of the near-field and far-field coupling of particle plasmons might contribute to the development of new large area SERS-substrates operating at non- or lowly focused excitation.

Acknowledgements The authors acknowledge funding from the German Federal Ministry of Research and Education (BMBF) within the ZIK initiative and from the state Sachsen-Anhalt within the program Sachsen-Anhalt WISSENSCHAFT Schwerpunkte.

REFERENCES

1. Auguié, B. and Barnes, W. L. "Collective resonances in gold nanoparticle arrays" *Phys. Rev. Lett.* Vol. 101**,** 1–4 , 2008.

2. Yang, A. *et al.* "Real-time tunable lasing from plasmonic nanocavity arrays" *Nat. Commun.* Vol. 6**,** 6939, 2015.

3. Sardana, N. *et al.* "Localized surface plasmon resonance in the IR regime" *Opt. Express* Vol. 24**,** 254, 2016.

EM response of graphene oxide

A. Thourwal[1], A.K. Singh[1], and N. Sardana [2,*]

[1]Department of Electronics and Communication Engineering, PEC university of Technology, Chandigarh, India

[2]Nanostructured Device Group, Institute of Nano Science and Technology, Mohali, India

[*]corresponding author: nsardana@inst.ac.in

Abstract- This work provides a study the shape dependent resonant properties of the graphene oxide-on FR4, FR4-Cu structures using the GO metamaterials (MMs) patterns. Such different structures are explored for low cost applications in household Wifi antennas.

Recently, metamaterials (MMs) have attracted the attention of many scientists due to their unusual electromagnetic (EM) properties which cannot be found in nature such as negative permittivity and negative permeability [1, 2]. Many researchers have studied the EM response of MMs to use in many applications such as antennas, sensors, lenses, absorbers. Moreover, they can be designed in microwave, millimeter-wave, and optical frequency bands [3]. Furthermore, as an alternative to graphene technology which is expensive and prone to oxidative environments is the use of low cost graphene oxide [4]. It is reasonably easy to produce a large-area of low cost manufacturing grade graphene oxide, having many lucrative nonlinear optical properties [5] for applications in ultrafast photonics and optoelectronics, especially for Kerr effect in optical switching, and fast optical communications [6].

In this work we aim to produce low cost GO and study different shape dependent response GO MM antennas in X, C and S band. The S parameters such as the reflection coefficient (S11) and the transmission coefficient (S 21) were obtained from the simulation and experimental analysis using a VNA. Transmission peaks around 6-8GHz on FR4. From the self-resonance, overlap, and the larger overall current responses with respect to existing SRRs designs, it is clear that the proposed metamaterial's response is the main advantage.

REFERENCES

1. Vesalago V.G., "The Electrodynamics of Substances with simultaneously negative values of ε and μ", *Sov. Phys. Usp*. 10, 509, 1968.
2. Shelby R.A., D. Smith, and S. Schultz," Experimental verification of a negative index of refraction" *Science* 292, 77, 2001.
3. Gokkavas, M., K. Guven, I. Bulu, K. Aydin, R.S. Penciu, M. Kafesaki, C.M. Soukoulis, and E. Ozbay, *Phys. Rev. B*, 73, 193103 (2006).
4. Geim, A. K. and K. S. Novoselov, "The rise of graphene", *Nature Matter*, 6, 183–191, 2007.
5. Khan, M. S., A. D. Capobianco, S. M. Asif, A. Iftikhar, B. D. Braaten, and R. M. Shubair, "A properties comparison between copper and graphene based UWB MMO planar antennas" *IEEE International Symposium on Antennas and Propagation*, 767-1768, 2016 .
6. F. Dincer, "Investigation and Physical Interpretation of H-Shaped Metamaterials in X-Band Waveguide for Microwave Filter Applications", *J. Electron. Mater.*, 45, 1, pp.812-819, 2016.

Coupling of magnetic and electric dipoles to magneto-electric resonancesâ€

Surface-enhanced second harmonic generation and fluorescence using effectively lossless GaP nanoantennas in the visible regime

J. Cambiasso, G. Grinblat, Y. Li, A. Rakovich, E. Cortés and S. A. Maier

The Blackett Laboratory, Department of Physics, Imperial College London, London SW7 2AZ, United Kingdom

*corresponding author: j.cambiasso@imperial.ac.uk

Abstract- Here we show the fabrication of all-dielectric gallium phosphide (GaP) nanostructures with negligible losses in the visible. Second harmonic (SH) generation and surface-enhanced fluorescence and are studied with these platforms. Employing single GaP nanodisks, we observe an increase of more than 3 orders of magnitude in the SH signal with comparison to bulk. We report to the best of our knowledge, the highest yet achieved SH efficiency in the optical region produced by a single nano-object. Furthermore, we show that GaP dimers with 35 nm gap can enhance up to 4000 times the fluorescence emission of dyes located in the gap of the nanoantenna. This is accomplished by a fluorescence lifetime reduction of, at least, 30 times and a high intensity field confinement in the gap region. These results open new venues for low-loss nanophotonics in the optical regime.

The initial motivation on plasmonic nanostructures for the development of nanophotonic devices operating in the optical regime was later partially eclipsed with the observation that losses could, in some cases, overtake actual radiative properties [1, 2]. In this scenario, dielectric nanoantennas have recently emerged as promising alternative candidates to plasmonic systems in the visible range [3, 4]. High-refractive-index dielectric nanostructures can highly concentrate electric and magnetic fields within subwavelength volumes, while presenting ultra-low absorption, compared to metals, when excited above their bandgap energies [5]. In particular, dielectric nanoantennas are expected to boost both nonlinear phenomena and surface-enhanced spectroscopies, without producing significant heating, since locally enhancing the incident light intensity can significantly amplify these processes, as their efficiencies increase with the excitation density.

GaP, in particular, is a dielectric with an associated bandgap wavelength as small as <550 nm and a relatively high refractive index of 3.5, opening interesting opportunities for the development of ultra-low-loss nanophotonic antennas in the optical range. In this presentation, efficient generation of second harmonic light is demonstrated throughout the visible regime by suitably tuning the size of single GaP nanodisks, enhancing their nonlinear response by more than three orders of magnitude with respect to the bulk, via surface effects [6]. Furthermore, by analysing the radiative properties of fluorescent molecules located in the hot-spot of a GaP dimer nanoantenna with 35 nm gap, a fluorescence enhancement factor as high as 2640 is attained when comparing with the bare emitter [6]. Both, high-field confinement effects, and a fluorescence lifetime reduction of more than one order of magnitude, give rise to the measured enhancement factor. The results of this work [6] open new avenues for low-loss nanophotonics in the optical range.

REFERENCES

[1] Albella, P.; Poyli, M. A.; Schmidt, M. K.; Maier, S. A.; Moreno, F.; Sáenz, J. J.; Aizpurua, J. J. Phys. Chem. C 2013, 117, 13573-13584.

[2] Khurgin, J. B. Nat. Nanotech 2015, 10, 2-6.

[3] Caldarola, M.; Albella, P.; Cortés, E.; Rahmani, M.; Roschuk, T.; Grinblat, G.; Oulton, R. F.; Bragas, A. V.; Maier, S. A. Nat. Commun. 2015, 6, 7915.

[4] Regmi, R.; Berthelot, J.; Winkler, P. M.; Mivelle, M.; Proust, J.; Bedu, F.; Ozerov, I.; Begou, T.; Lumeau, J.; Rigneault, H.; García-Parajó, M. F.; Bidault, S.; Wenger, J.; Bonod, N. Nano Lett. 2016, 16, 5143-5151.

[5] Albella, P.; Alcaraz de la Osa, R.; Moreno, G.; Maier S. A. ACS Photonics 2014, 1, 524–529.

[6] Cambiasso, J.; Grinblat, G.; Li, Yi.; Rakovich, A.; Cortés, E.; Maier, S. A., Nano Letters, DOI: 10.1021/acs.nanolett.6b05026.

High-Q resonances in arrays of optically coupled dielectric nanospheres

Evgeny N. Bulgakov[1,2], **and Dmitrii N. Maksimov**[2*]
[1]Siberian Airspace University, Krasnoyarsk, Russia
[2]Kirensky Institute of Physics, Krasnoyarsk, Russia
[*]corresponding author: mdn@tnp.krasn.ru

Abstract-*We consider light trapping by bound states in the continuum (BSCs) in linear periodic arrays of optically coupled high-index dielectric nanospheres. Using a Mie multi-scattering approach we numerically demonstrate that the BSC-related resonances in arrays of silicon nanospheres can be employed for both light guiding and light enhancement in he visible-to-near infrared range. Asymptotic behavior of the resonance Q-factor against the number of spheres is elaborated.*

We consider light trapping in linear periodic arrays of optically coupled high-index dielectric nanospheres. The optical properties of the arrays are examined by a Mie multiscattering approach taking into account electric and magnetic multipoles of all orders [1]. When the array is infinite it is known to support bound states in the radiation continuum (BSCs) [2], i.e. structural resonances with infinite life-time embedded into the continuous spectrum of scattering states. Two classes of the BSCs can be identified, namely, topologically and symmetry protected states. In particular, we demonstrate that there is a Bloch guided BSC mode which is stabilized by a topological singularity in space of the resonance coupling constant. We show numerically that this Bloch BSC can be employed for guiding light pulses above the line of light [3]. If the infinite array is terminated at both ends to form a finite chain of dielectric spheres the BSCs become high-Q resonances. We evaluate the asymptotic behavior of the Q-factor of such resonances against the number of spheres in the array. We demonstrate numerically that under illumination by a plane wave finite arrays of 10-15 silicon nanospheres can be used to enhance the amplitude of the impinging light at least by order of magnitude in the visible-to-near infrared range when the material and geometrical parameters of the systems are tuned to the structural resonance associated with a BSC [4].

Acknowledgments This work was supported by Ministry of Education and Science of Russian Federation (state contract N3.1845.2017) and RFBR grant 16-02-00314.

REFERENCES

1. Linton C.M., V. Zalipaev and I. Thompson, "Electromagnetic guided waves on linear arrays of spheres," *Wave Motion*, Vol. 50, No. 1, 29–40, 2013.
2. Bulgakov E.N. and A.F. Sadreev, "Light trapping above the light cone in a one-dimensional array of dielectric spheres," *Physical Review A*, Vol. 92, 023816, 2015.
3. Bulgakov E.N. and D.N. Maksimov, "Light guiding above the light line in arrays of dielectric nanospheres," *Optics Letters*, Vol. 41 , No. 16, 3888-3891, 2016.
4. Bulgakov E.N. and D.N. Maksimov, "Light Enhancement by dielectric arrays," arXiv:1702.05990, 2017

High Refractive Index Nanostructures as Building Blocks for Optical Devices

A. I. Barreda[1], H. Saleh[2,3], A. Litman[2], F. González[1], J-M Geffrin[2] and F. Moreno[1]*

[1]Group of Optics, Department of Applied Physics, University of Cantabria, Cantabria 39005, Spain.

[2]Aix-Marseille Univ, CNRS, Centrale Marseille, Institut Fresnel, Marseille, France.

[3]Centre Commun de Ressources en Microondes CCRM, 5 rue Enrico Fermi, Marseille 13453, France.

*corresponding author: morenof@unican.es

Abstract-Here, we intend to show a review of our recent investigations in light scattering by nanostructured High Refractive Index Dielectric (HRID) materials and their possible applications for controlling the direction of the scattered light, for switching purposes and, as an alternative to metals, as low-loss near-field enhancers for sensing applications.

Nanostructured high refractive index dielectric (HRID) materials in the VIS and NIR (like Si, Ge, and other semiconductor compounds) have shown to be excellent candidates for building units of more complex optical devices and also, as an alternative to metals for plasmonics and surface enhanced effects (SERS and related techniques)[1,2]. This is because of both their inherent low ohmic losses and the magnetodielectric effects they present in those spectral ranges. These effects are due to the excitation of non-negligible magnetic resonances whose coherent interaction with the electric ones leads to interesting directionality effects which can be the base for constructing nano-antenna elements in the optical range and consequently, leading to advances in the fabrication of more complex optical devices. In this research, for single particles, directionality effects[3-7] and sensing to both particle purity[8] and surrounding medium refractive index[9] will be analyzed. The latter will be also studied for dimer configurations by means of the near field enhancement in the gap[10,11]. Also, for dimer geometries, a novel switching effect will be presented[12].

Acknowledgements: This research has been supported by MICINN (Spanish Ministry of Science and Innovation, Project No. FIS2013-45854-P) and USAITCA (Project No. W911NF-17-2-0023). A.I.B. thanks the University of Cantabria for her FPU grant and Foundation IBERDROLA-ESPAÑA for its support through its Research on Energy and the Environment Program. We also acknowledge the opportunity provided by the Centre Commun de Ressources en Microonde to use its fully equipped anechoic chamber and for financing H.S. PhD grant.

REFERENCES

1. Decker, M. and I. Staude, "Resonant dielectric nanostructures: a low- loss platform for functional nanophotonics," *J. Opt.*, Vol. 18, No. 10, 103001 (31 pp), 2016.
2. Kuznetsov, A. I. et al, "Optically resonant dielectric nanostructures," *Science,* Vol. 354, No. 6314, 2472 (8 pp), 2016.
3. García-Etxarri, A. et al, "Strong magnetic response of submicron Silicon particles in the infrared," *Opt.*

Express, Vol. 19, No. 6, 4815–4826, 2011.
4. Gómez-Medina, R. et al, "Electric and magnetic dipolar response of germanium nanospheres: interference effects, scattering anisotropy and optical forces," *J. Nanophotonics*, Vol. 5, No. 1, 53512 (9 pp), 2011.
5. Geffrin, J. M. et al, "Magnetic and electric coherence in forward- and back-scattered electromagnetic waves by a single dielectric subwavelength sphere," *Nat. Commun.*, Vol. 3, No. 1171, 1-8, 2012.
6. Tribelsky, M. I. et al, "Small Dielectric Spheres with High Refractive Index as New Multifunctional Elements for Optical Devices," *Sci. Rep.*, Vol. 5, No. 12288, 1-7, 2015.
7. Tribelsky, M. I. et al, "Directional Fano Resonances at Light Scattering by a High Refractive Index Dielectric Sphere," *Phys. Rev. B*, Vol. 94, No. 121110 (R), 1-5, 2016.
8. Barreda, A. I. et al, "Using linear polarization to monitor nanoparticle purity," *J. Quant. Spectrosc. Radiat. Transfer*, Vol. 162, 190–196, 2015.
9. Barreda, A. I. et al, "Using linear polarization for sensing and sizing dielectric nanoparticles," *Opt. Express*, Vol. 23, No. 7, 9157-9166, 2015.
10. Albella, P. et al, "Low-Loss Electric and Magnetic Field-Enhanced Spectroscopy with Subwavelength Silicon Dimers," *J. Phys. Chem. C*, Vol. 117, No. 26, 13573−13584, 2013.
11. Albella, P. et al, "Electric and Magnetic Field Enhancement with Ultralow Heat Radiation Dielectric Nanoantennas: Considerations for Surface- Enhanced Spectroscopies," *ACS Photonics*, Vol. 1, No. 6, 524–529, 2014.
12. Barreda, A. I. et al, "Electromagnetic polarization-controlled perfect switching effect with high-refractive-index dimers and the beam-splitter configuration," *Nat. Commun.*, Vol. 8, No. 13910, 1-8, 2017.

Chirality Enhancement at Simultaneous Electric and Magnetic Hotspot

J. Mun[1], and J. Rho[1,2,3*]

[1]Department of Chemical Engineering, Pohang University of Science and Technology (POSTECH), Pohang 37673, Republic of Korea

[2]Department of Mechanical Engineering, Pohang University of Science and Technology (POSTECH), Pohang 37673, Republic of Korea

[3]National Institute of Nanomaterials Technology (NINT), Pohang 37673, Republic of Korea

[*]corresponding author: jsrho@postech.ac.kr

Abstract-Enhanced light-matter interaction near nanostructures have been widely investigated. Chiroptical signal can also be enhanced for a chiral molecule located at the field with enhanced optical chirality. This work investigates globally enhanced optical chirality near achiral nanostructures with simultaneous electric and magnetic resonances.

Chirality, or the absence of symmetry mirror, enables different chemical interaction between enantiomers and a chiral molecule and different optical interaction between circularly-polarized-lights (CPLs) and a chiral molecule. Therefore, chiral sensing has been actively researched in many fields, such as chemistry, biology, and pharmaceutics. The chiroptical properties of chiral molecules can be characterized through circular dichroism (CD), optical rotatory dispersion (ORD), and Raman optical activity (ROA). However, due to large size mismatch between light and molecules, only weak chiroptical signals could be measured, restricting practical measurement. Tang and Cohen discovered the relationship between absorption rate of chiral molecules and local optical chirality [1] and enabled prediction of CD enhancement before actually fabricating a device and measuring a sample. Intense local chirality enhancement near chiral plasmonic nanostructures has been reported [2]. However, the chiroptical signal from the chiral nanostructure was enormous and exceeded the signal from molecules, so their chirality characterization came from its chiroptical peak shift, not from molecular chiroptical signal itself. In addition, simultaneously existing different signs of chirality in volume result decreased overall chirality enhancement and effectiveness of solution-based chirality sensing. Global, not local, enhancement of chirality requires simultaneous electric and magnetic resonance, and high index materials, such as silicon nanoparticles, have been known to exhibit both electric and magnetic resonances [3]. This study investigates optical chirality enhancement near achiral nanostructures with simultaneous electric and magnetic resonances through full-wave numerical simulation. Such structures with high optical chirality enhancement but no chiral signal from themselves can be applied to chiroptical sensors.

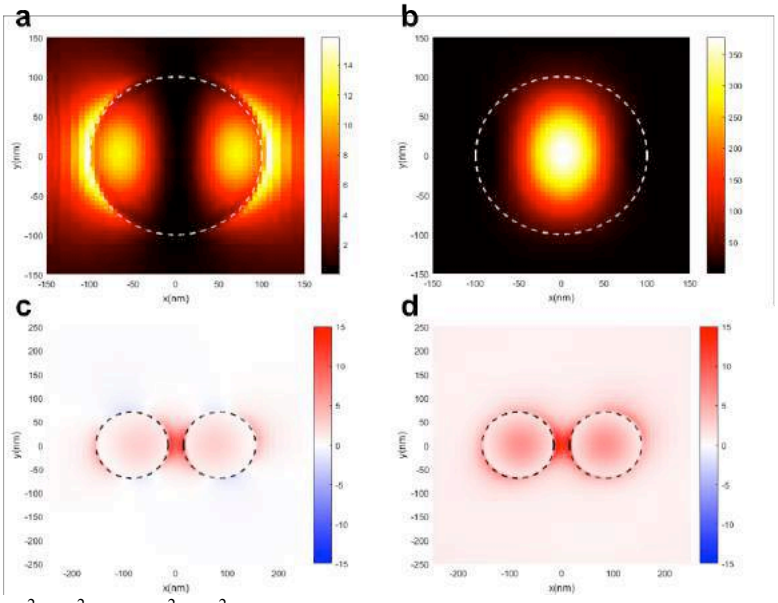

Figure 1. (a,b) $|E|^2/|E_0|^2$ and $|B|^2/|B_0|^2$ near a silicon sphere of radius 100 nm at x polarized light incidence. Electric dipole in x direction and magnetic dipole in y direction are formed. (c,d) Optical chirality enhancement near a spherical silicon dimer aligned in x direction. Electric hotspot formed at x polarized light and magnetic hotspot formed at y polarized light as ref [4] are superposed at the center of the dimer resulting optical chirality enhancement hotspot.

Acknolwledgements. The research was supported by X-Project program (NRF-2015R1C1A1A02036464) and Global Frontier program (CAMM-2014M3A6B3063708) through the National Research Foundation of Korea (NRF) grant funded by the Ministry of Science, ICT and Future Planning (MSIP) of Korean government.

REFERENCES

1. Tang, Y. and Cohen, A. E., "Optical chirality and its interaction with matter," *Phys. Rev. Lett.,* Vol. 104, No. 16, 163901, 2010.
2. M. Schäferling; D. Dregely, M. Hentschel, H. Giessen, "Tailoring enhanced optical chirality: design principles for chiral plasmonic nanostructures," *Phys. Rev. X,* Vol. 2, No. 3, 031010, 2012.
3. A. García-Etxarri; J. A. Dionne, "Surface-enhanced circular dichroism spectroscopy mediated by nonchiral nanoantennas," *Phys. Rev. B*, Vol. 87, No. 23, 235409, 2013.
4. Bakker, R. M. et al., "Magnetic and electric hotspots with silicon nanodimers," *Nano Lett.,* Vol. 15, No. 3, 2137-2142, 2015.

Nanofabrication of silicon Mie resonators and all-dielectric colored metasurfaces

I. Ozerov[1*], J. Proust[2,3], F. Bedu[1], B. Gallas[4], and N. Bonod[2]

[1]Aix Marseille Univ, CNRS, CINAM, 13288 Marseille, France
[2]Aix Marseille Univ, CNRS, Centrale Marseille, Institut Fresnel, 13013 Marseille, France
[3] Université de Technologie de Troyes, CNRS UMR 6281, Laboratoire de Nanotechnologie et d'Instrumentation Optique, Institut Charles Delaunay, 10004 Troyes, France
[4] Sorbonne Universités, UPMC Univ Paris 06, CNRS, Institut des NanoSciences de Paris, UMR7588, 75005 Paris, France
[*]corresponding author: ozerov@cinam.univ-mrs.fr

Abstract – Silicon Mie resonators and metasurfaces were nanofabricated using electron beam lithography followed by wet chemical alkaline etching or reactive ion etching. The fabrication process was adapted for both amorphous and monocrystalline silicon in order to obtain efficient resonant light scattering by individual silicon particles. A large palette of colors was created by tuning the size, shape and aspect ratio of the particles.

Nanoparticles of high-refractive index dielectric materials like silicon are known to efficiently scatter incident electromagnetic waves. The extinction spectra show several well pronounced peaks corresponding to electric and magnetic dipole and quadrupole moments resonantly induced in the particles by the incident light. The spectral positions of these peaks are determined by the shape and the size of the individual particles as well as by coupling between the particles if they are situated close enough from each other. For the visible and near-infrared spectral regions, the typical sizes of individual resonant silicon particles are situated in the range from 70 to 250 nm [1,2].

The nanoparticles can be organized in order to form metasurfaces which allows to control collective effects and to optimize the interaction between the particles. For the metasurfaces constituted by the individual particles, the distances between them should be large enough in order to avoid possible near-field coupling. For example, recently we have fabricated the metasurfaces composed of silicon particles situated at distances larger than 1 μm providing vivid structural colors [2]. On the other hand, a metasurface composed of closely packed resonators has shown to be a very efficient antireflective coating in a large spectral range from the visible to the near infrared and it was fabricated by nanostructuring of monocrystalline silicon [3].

All the fabrication processes need to be carefully adapted to the active material and to the substrate in order to control the size and the shape of the individual nanoparticles and their organization in metasurfaces. We used amorphous and crystalline silicon to fabricate all-dielectric colored metasurfaces, absorbers and antireflective coatings. Amorphous silicon thin films were deposited onto transparent silica glass substrates. Then, the films were patterned by electron beam lithography followed by wet chemical etching in alkaline solutions [1] or by dry reactive ion etching [2]. Different materials such as gold and nickel were used to create hard masks adapted to the etching processes. We will also discuss an original maskless fabrication process using focused ion beam

exposure.

We used wet chemical etching in two different types of alkaline solutions (based on potassium hydroxide and tetramethylammonium hydroxide) and we will discuss their influences on the shapes of the silicon resonators. The fabrication method was applied on both monocrystalline and amorphous silicon. In the case of crystalline silicon, the etching rates strongly depend on the orientation of the silicon crystalline planes, on the temperature and on the composition of the alkaline solution. The etching of monocrystalline silicon patterned with the same mask but in different alkaline solutions can give rise to the formation of nanofeatures with very different shapes [1]. In this case, very careful numerical simulations were needed to control the shape of the obtained features. Contrarily to the case of crystalline silicon, the etching rate of amorphous silicon is isotropic because of the isotropic atomic density. In that case, the final shape depends only on the shape of the mask. Dry reactive ion etching was also applied to both amorphous [2-5] and monocrystalline [3] silicon. This process allows obtaining a very good etching anisotropy and nearly vertical walls of the structures.

The shapes and the sizes of the obtained nanofeatures were controlled by scanning electron microscopy, and then the fabricated arrays of nanoparticles were characterized by optical spectroscopy in reflection mode with a dark-field microscope. The different scattering modes were identified as magnetic and electric dipole and quadrupole Mie resonances by comparing experimental and numerically simulated spectra. We also fabricated silicon monomers [4] and dimers [5] that were used to tailor the spontaneous emission of organic molecules.

In conclusion, we fabricated all-dielectric silicon metasurfaces by electron beam lithography followed by alkaline and reactive ion etching and we observed vivid colors provided by the resonant light scattering by individual silicon particles. The relative strength of the electric and magnetic resonances can be easily tuned with the aspect ratio of the particle. This allowed us to create a large palette of colors when considering the same particle height and simply tuning the aspect ratio of the particle by varying the diameter.

Acknowledgements: All nanofabrication processes were performed in a PLANETE CT PACA cleanroom facility.

REFERENCES

1. Proust, J., F. Bedu, S. Chenot, I. Soumahoro, I. Ozerov, B. Gallas, R. Abdeddaim, and N. Bonod, “Chemical alkaline etching of silicon Mie particles,” *Adv. Opt. Mat.,* Vol. 3, No. 9, 1280–1286, 2015.
2. Proust, J., F. Bedu, B. Gallas, I. Ozerov, and N. Bonod, “All-Dielectric Colored Metasurfaces with Silicon Mie Resonators,” *ACS Nano*, Vol. 10, 7761-7767, 2016.
3. Proust, J., A-L. Fehrembach, F. Bedu, I. Ozerov, and N. Bonod, “Optimized 2D array of thin silicon pillars for efficient antireflective coatings in the visible spectrum”, *Scientific Reports*, Vol. 6, 24947, 2016.
4. Bouchet, D., M. Mivelle, J. Proust, B. Gallas, I. Ozerov, M.F. García-Parajó, A. Gulinatti, I. Rech, Y. De Wilde, N. Bonod, V. Krachmalnicoff, and S. Bidault, “Enhancement and Inhibition of Spontaneous Photon Emission by Resonant Silicon Nanoantennas,” *Phys. Rev. Applied*, Vol. 6, No. 6, 064016, 2016.
5. Regmi, R., J. Berthelot, P.M. Winkler, M. Mivelle, J. Proust, F. Bedu, I. Ozerov, T. Begou, J. Lumeau, H. Rigneault, M.F. García-Parajó, S. Bidault, J. Wenger, and N. Bonod, “All-Dielectric silicon nanogap antennas to enhance the fluorescence of single molecules,” *Nano Lett.*, Vol. 16, 5143-5151, 2016.

Novel photonic and plasmonic structures: theory and applications

Extreme absorption enhancement in ZnTe:O/ZnO intermediate band core-shell nanowires by interplay of dielectric resonance and plasmonic bowtie nanoantennas

Kui-Ying Nie, Fang-Fang Ren, Jiandong Ye*
School of Electronic Science and Engineering, Nanjing University, Nanjing 210093, China
*corresponding author: yejd@nju.edu.cn

Abstract- we explore a rational design of a hybrid structure composed of ZnTe:O/ZnO core/shell NWs with Al bowtie nanoantennas, which exhibits strong ability in tuning and enhancing broadband light response due to the interplay of NW dielectric resonance and plasmonic coupling of metallic nanoantennas.

Intermediate band solar cells (IBSCs) are conceptual and promising for next generation high efficiency photovoltaic devices, whereas, IB impact on the cell performance is still marginal due to the weak absorption of IB states. The demand for IBSCs with higher conversion efficiency and lower cost is driving academic and industrial research efforts in the search for desirable intermediate band materials. Thanks to the strong interaction with light, one dimensional semiconductor nanowires (NWs) have provided an extraordinary platform in applications of photonics and solar energy harvesting [1-2]. To this end, we explore a rational design of a hybrid structure composed of ZnTe:O/ZnO core/shell NWs with Al bowtie nanoantennas, which exhibits strong ability in tuning and enhancing broadband light response due to the interplay of NW dielectric resonance and plasmonic coupling of metallic nanoantennas. The nanowire dimensions are primarily optimized to offer highly confined energy density by engineering leaky-mode dielectric resonances in the visible spectrum region, which maximizes the overlap of the absorption spectrum and the optical transitions in ZnTe:O intermediate-band (IB) photovoltaic materials. By coupling with bowtie antennas composed of low-cost and CMOS-compatible Al metal, the absorption efficiency of ZnTe:O/ZnO core-shell single NW is further enhanced owing to the increase in the radiative loss induced by the excitation of local surface plasmons. The interplay of dielectric and metallic resonance effects in subwavelength-scale nanowires opens up new avenues for overcoming the poor absorption of sub-gap photons by IB states in ZnTe:O to achieve high-efficiency IBSCs.

Acknowledgements This research was supported by National Natural Science Foundation of China (Nos. 61274058 and 61322403), the Natural Science Foundation of Jiangsu Province (Nos. BK2011437 and BK20130013), the Six Talent Peaks Project in Jiangsu Province (2014XXRJ001).

REFERENCES

1. Krogstrup, P. et al. *Nat*. *Photon*. Vol 7, 306-310, 2013.
2. Casadei, A., Pecora, E.F., et al. *Nano Lett*., Vol.14, No.5, 2271-2278, 2014.

Nonlinear polarization rotation of polarization-structured beams through isotropic Kerr nonlinearities

Bing Gu*, Bo Wen, Guanghao Rui, and Yiping Cui
Advanced Photonics Center, Southeast University, Nanjing 210096, China
*corresponding author: gubing@seu.edu.cn

Abstract: Structured intense laser interacting with matter will result in a variety of novel nonlinear optical effects, modulate the light propagation behavior, and change the structural property of a material. In this work, we report a theoretical investigation of the spatial self-phase modulation (SSPM) effect and nonlinear ellipse rotation of both hybridly polarized vector beams and elliptically polarized vector beams through isotropic Kerr nonlinearities. Based on the vectorial Rayleigh-Sommerfeld formulas under the paraxial condition, we obtained the analytical expressions of the focal fields of both the hybridly polarized vector beam and the elliptically polarized vector beam. We determine the isotropic third-order nonlinear refractive indexes of a medium excited by the vector field with arbitrary ellipticity. Then we numerically simulate the far-field vectorial self-diffraction behaviors and nonlinear ellipse rotations of two types of vector beams through isotropic Kerr nonlinearities. We systematically study the dependence of the self-diffraction behaviors on both the physical origin of the optical nonlinearity and the nonlinear phase shift. It is demonstrated that the SSPM intensity pattern, the distribution of state of polarization, and the spin angular momentum (SAM) flux of a hybridly polarized vector beam could be manipulated by tuning the magnitude of the isotropic optical nonlinearity. Interestingly, we observed the radial-variant nonlinear ellipse rotation of elliptically polarized vector beams through isotropic Kerr nonlinearities. Our results may find interesting applications in nonlinear mechanism analysis, nonlinear characterization technique, and SAM manipulation.

Negative refraction in vertically multilayered hyperbolic metamaterials.

S. So[1] **and J.Rho**[1,2,3]

[1]Department of Mechanical Engineering, Pohang University of Science and Technology (POSTECH), Pohang 37673, Republic of Korea

[2] Department of Chemical Engineering, Pohang University of Science and Technology (POSTECH), Pohang 37673, Republic of Korea

[3] National Institute of Nanomaterials Technology (NINT), Pohang 37673, Republic of Korea

[*]corresponding author: jsrho@postech.ac.kr

Abstract- Negative refraction has attracted significant interest of researchers due to its various applications including super-resolution imaging, slow light devices, and cloaking. Although it can be realized in hyperbolic metamaterial, conventional hyperbolic metamaterial has been suffered from high resistive loss and narrow working frequency. In this work, new design of hyperbolic metamaterials of vertically stacked metal-dielectric multilayer is proposed. Comprehensive comparison between two types of vertical and horizontal multilayer hyperbolic metamaterial is followed based on numerical calculation of negative refraction.

Metamaterials have been transforming a number of fields with unprecedented optical phenomena. In particular, hyperbolic metamaterials are highly anisotropic metamatarials, which have opposite signs of permittivity depending on the direction [1,2]. They have shown extraordinary properties such as negative refraction, diverging photonic density of states, and super resolution effect. Conventional hyperbolic metamaterials can be realized by horizontally stacked metal-dielectric multilayer [3,4]. However, according to the Maxwell-Garnet's effective medium theory, the optical resonance is inevitably accompanied in conventional horizontal multilayer structures, restricting their performance with high resistive loss and narrow working frequency.

Here, we suggest new design of hyperbolic metamaterials of vertical metal-dielectric multilayer, which does not require any resonance. Therefore, it shows low loss and broad working frequency, suggesting practical applications of hyperbolic metamaterials. In this study, we compare the two types of vertical/horizontal multilayer hyperbolic metamaterials. Based on the calculated effective permittivity, we report that vertical multilayer broadens the working frequency of hyperbolic metamaterials, compared to conventional horizontal multilayer. Furthermore, the numerical simulation of negative refraction in two types of hyperbolic metamaterials is also conducted, in which vertical multilayer structure suffers much less loss and therefore transmits most of the light. Although the proposed design of new hyperbolic metamaterials has not been experimentally realized yet, it will open the new world, providing the possibility of the realization of various applications of hyperbolic metamaterials.

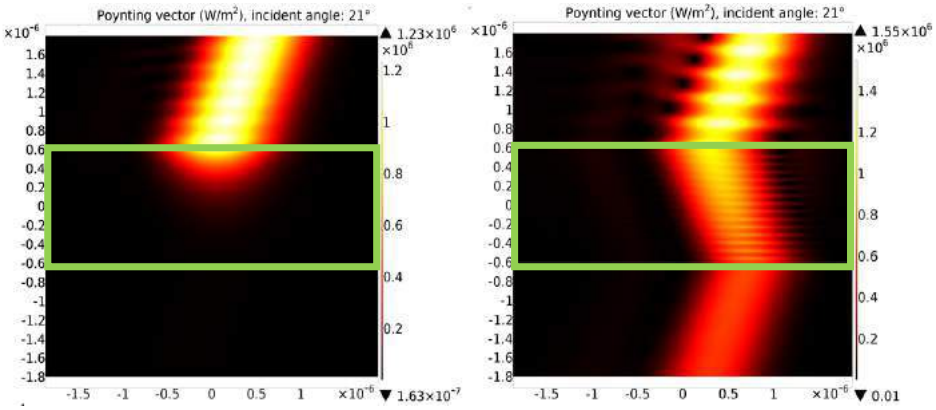

Figure 1. Numerical simulations of negative refraction in two metal-dielectric multilayered hyperbolic metamateirals, which is composed of Ag and Al2O3. The green boxes indicate hyperbolic metamaterials; left and right ones are for horizontal multilayer at 365 nm wavelength and vertical multilayer at 480nm, respectively. Most of light is absorbed and cannot propagate through horizontal multilayer (left) due to high restive loss, whereas most of light propagate through vertical multilayer (right).

Acknowledgements, J.Rho acknowledges the financial support by Engineering Research Center program (2015R1A5A1037668), through the National Research Foundation of Korea (NRF) grant funded by the Ministry of Science, ICT and Future Planning (MSIP) of Korean government.

REFERENCES

1. Poddubny.A. *et al.,* "Hyperbolic metamaterials," *Nat.Phothonics*, Vol. 7, No. 12, 948-957, 2013.
2. Shekhar.P. *et al.,* "Hyperbolic metamaterials: fundamentals and applications," *Nano Converg*, Vol. 1, No. 1, 1-17, 2014.
3. Naik, G. V. *et al.,* "Demonstration of Al:ZnO as a plasmonic component for near-infrared metamaterials," *PNAS.*, Vol. 109, No. 23, 8834-8838, 2012.
4. Lu, D. *et al*., "Enhancing spontaneous emission rates of molecules using nanopatterned multilayer hyperbolic metamaterials," *Nat.Nanotechnol.*, Vol. 9, No. 1, 48-53, 2014.

Resonance splitting in 3D Bi-flake Metamaterial

Z. Liu[1], W. J. Sheng[1], S. Du[1], J. J. Li[1*], and C. Z. Gu[1,2*]

[1]Beijing National Laboratory for Condensed Matter Physics, Institute of Physics, Chinese Academy of Sciences, Beijing 100190, China

[2] Collaborative Innovation Center of Quantum Matter, Beijing 100871, China

[*]corresponding author: jjli@iphy.ac.cn; czgu@iphy.ac.cn

Abstract-A 3D metamaterial composed of two metal flakes with supplementary angles were fabricated by ion beam induced folding technique. Due to its asymmetry configuration, trapped mode can be excited by the destructive coupling between two flakes, and the evanescent wave of surface plasmon plays a leading role. The resonance peak can be split into two peaks, and these steep resonance peaks have great potential for sensing and detecting applications.

In recent years, great interests have been devoted to 3D plasmonic structures with the development of 3D micro/nano fabrication techniques and high demand of spatial optical interconnections. Varieties of 3D fabrication techniques have been developed such as layer-by-layer stacking[1], shadow evaporation[2], and ion-beam folding[3]. Among them, ion-beam folding is a most flexible method to make 3D structures with designable shapes and orientations. The 3D structures have far more ways of inter- or intra-coupling, and can be modulated by external signals such as mechanical, heat or pressure, indicating potentials on active devices.

It has been proved that symmetry-broken structures will lead to trapped-mode with high Q-factor[4]. In this work, we studied a special 3D metamaterial, the building block of which is composed of two metal flakes with supplementary angles. From the simulation and optical measurement data, it can be found that when the inclined angles of both flakes are 90°, there's only one peak in the spectrum. As the inclined angle changes, the peak splits into two peaks, and they gradually shift opposite to each other. These two peaks come from coupling of the LC modes on the edge of the structures, corresponding to normal and trapped modes respectively. The steep peak is a good candidate for sensing devices.

Acknowledgements: This work is supported by the National Key Research and Development Program of China (Grant Nos. 2016YFA0200400 and 2016YFA0200803) and the National Natural Science Foundation of China (Grants Nos. 91323304, 11174362, 11504414, 11574385 and 11574368).

REFERENCES

1. Liu, N. et al. "Three-dimensional photonic metamaterials at optical frequencies," *Nat. Mater.* Vol. 7, 31–37, 2008.
2. Zhang, S. et al. "Midinfrared resonant magnetic nanostructures exhibiting a negative permeability," *Phys. Rev. Lett.* Vol. 95, 037402, 2005.
3. A. J. Cui, et al. "Directly patterned substrate-free plasmonic 'nanograter' structures with unusual Fano resonances," *Light Sci. Technol.* Vol. 4, e308, 2015.
4. Fedotov, V. A. et al. "Sharp Trapped-Mode Resonances in Planar Metamaterials with a Broken Structural Symmetry," *Phys. Rev. Lett.* Vol. 99, 147401, 2007.

Application of Surface Plasmon Antenna To CMOS Terahertz Detectors

X.Ji, J.Peng, Y.Liao, Z. Shen, R.Wu, and F.Yan
School of Electronic Science and Engineering, Nanjing University, Nanjing 210093, China

Abstract- On-chip surface plasmon antenna used for CMOS Terahertz detectors is demonstrated. Unlike the traditional metal antenna, it is designed with heavy-doped polycyrstalline silicon material, backed with an silica layer to prevent radiation from going inside the lossy silicon substrate. By optimizing the antenna pattern using a frequency-domain solver, HFSS, surface plasmon polaritons (SPP) are excited in the antenna and can propagate THz signals to receievers. A CMOS terahertz detector integrated with the proposed antenna at 0.65THz is fabricated in 0.18μm standard CMOS technology. The measurement results show the detector can boost the voltage response by 200% due to the increased local electrical field. The transmission-mode image of the metal blade using the detector is further exhibited. The results demostrate that the designed surface plasmon antenna has a high performance to THz radaition comparable with the conventional radio-wave one.

For using FETs to detect sub-THz waves, FETs are usually integrated with the antennas for collecting THz signals [1-4]. In order to obtain high-performance detection, matching of the input impedance of the antenna and FETs should be carefully considered. However, there remain the challenges to realize antenna with ideal power matching for CMOS devices in THz region [1-2]. New surface plasmon antenna designs [5-8] provide a strategy overcoming this trade-off by converting the input light into the localized surface plasmon polaritons resonances.

Under the normal incidence of electromagnetic waves, the propagation of SPPs (K_{spp}) in the metal-like material can be expressed as

$$K_{SPP} = \frac{2\pi}{\lambda}\sqrt{\frac{\varepsilon_1\varepsilon_2}{\varepsilon_1+\varepsilon_2}}$$

where ε_1 is the dielectric constant of the medium while $\varepsilon_2 = \varepsilon_{r2} + j\varepsilon_{i2}$ is the dielectric constant of the metal-like material. The denotations ε_{r2} and ε_{i2} represent the real and imaginary part of ε_2 respectively. It has been pointed out that the effect of SPP enhanced transmission will increase with a higher value of the ratio between the dielectric constant's real and imaginary part $\varepsilon_{r2}/\varepsilon_{i2}$. From the well-known Drude-type calculation, we calculate the real and imaginary of heavy-doped silicon. The typical ratio is $\varepsilon_{r2}/\varepsilon_{i2} = 0.37$ at 1THz, which suggests a good capacity to support the excitation of SPPs in the terahertz wavelength.

We design on-chip silicon antenna with the modified bowtie structure which combines the advantages of both rod and bowtie to achieve the high localized field enhancement for Thz radiation. As the antenna geometrical parameters have influence on the SPP excitation, the High Frequency Structure Simulator (HFSS) calculation is performed. By monitoring the SPP modes observed as the maximum in electrical field, the most proper structural parameters of the antenna are achieved.

On the basis of the above simulation results, Si surface plasmon antenna coupled NMOS detector at 0.65THz is fabricated using 0.18μm CMOS process on an 8 inch Si wafer with a thickness of 300 μm.

The NMOS channel length and width are 0.18μm and 0.32 μm, respectively. According to the earlier FETs device described in [2], when THz signals coupled to the source terminals of MOSFETs, the transistors under the gate voltage rectify the signals and generate a detectable DC source–drain voltage .

The fabricated detector is then characterized using a Thz source around 0.65 THz with an illumination power of 1 mW. We compare the voltage response–gate bias characteristic of detectors at 0.65THz with and without the surface plasmon antenna. The response from the detector with antenna exhibts about 200 times larger than one without the antenna. Such enhancement of voltage response is a direct experimental evidence of plasmonic effect from Si antenna in Thz region. Furhtermore, the scanned transmission-mode image of a cutter blade embedded in polystyrene foam using the pixel is carried out. These results show that the detector has a high performance to THz radaition comparable with that of conventional radio-wave one. The demonstrated on-chip surface plasmon antenna provides a technology platform for the ease of design and fabrication of CMOS THz detectors without the need of strict matching of the antenna and Si FETs receiever.

Acknowledgement

This work was supported by the National Key R &D Program of China (No.2016YFB0402403), the Natural Science Foundation of Jiangsu Province,China (No. BK20141321), and CAST Project, China (No. 08201601).

REFERENCEs

1 E. Öjefors, U. R. Pfeiffer, A. Lisauskas, and H. G. Roskos, "A 0.65 THz focal-plane array in a quarter-micron CMOS process technology", *IEEE J. Solid-State Circuits*, vol. 44, 1968, 2009.

2 H. Sherry, R. Hadi, J. Grzyb, E. Öjefors, A. Cathelin, A. Kaiser, and U. Pfeiffer, "Lens-integrated THz imaging arrays in 65 nm CMOS technologies", *IEEE Radio Freq. Integr. Circuits Symp.* Jun. 2011, p. 1–4.

3 K. Sengupta, D. J. Seo, and A. Hajimiri, "Silicon Integrated 280GHz Imaging Chipset With 4×4 SiGe Receiver Array and CMOS Source", *IEEE Transactions On Terahertz Science And Technology,* vol. 5, May. 2015.

4 F. Schuster *et al.*, "Broadband terahertz imaging with highly sensitive silicon CMOS detectors," *Opt. Express*, vol. 8, 7827, 2011.

5 Janke C, Rivas J G, Schotsch C, et al. "Optimization of enhanced terahertz transmission through arrays of subwavelength apertures". Physical Review B, vol. 69, 205314,2004.

6 K. Gallo and G. Assanto, "All-optical diode based on second-harmonic generation in an asymmetric waveguide," J. Opt. Soc. Am. B, vol. 16(2), 267,1999.

7 B. R. Masters, "Three-dimensional microscopic tomographic imagings of the cataract in a human lens in vivo," Opt. Express, 3(9), 332, 1998.

8 D. Yelin, D. Oron, S. Thiberge, E. Moses, and Y. Silberberg, "Multiphoton plasmon-resonance microscopy," Opt. Express, 11(12), 1385, 2003.

Zero-admittance all-dielectric planar structures for giant field enhancement

Myriam Zerrad [*], **Fabien Lemarchand, Aude Lereu, Michel Lequime and Claude Amra**
Aix-Marseille Université, Ecole Centrale Marseille, CNRS - Institut Fresnel, UMR 7249, France
[*]corresponding author: myriam.zerrad@fresnel.fr

Abstract-An analytical method to design optical coatings for giant field enhancement under total internal reflection will be presented. Enhancements of several decades can now be localized at arbitrary altitudes within a multi-dielectric component and for different wavelengths.

Volume confinement and field enhancement in optical devices still promote key applications in the field of sensors and micro-sources. Different techniques have been studied and we proposed here an optimized method based on optical interference coatings (OIC). To fit more and more severe requirements, modern design techniques allow producing multidielectric devices with nearly 1000 layers. They are mainly used in free space to control specular properties and less commonly for field enhancement. Narrow-band filters may provide such property, but the enhancement is confined within their spacer, which excludes sensitivity to the surrounding medium.

For this reason several works were devoted to resonances of all-dielectric multilayers in total internal reflection, to build a huge over-intensity at the substrate interface. However, design optimization was not fully achieved, due to a lack of analytic formulation; indeed numerical data are used to identify the reflection poles of the structure, without any additional control. Here, we introduce the concept of zero-admittance layers (ZAL) so as to increase the degrees of freedom and extend the design technique to enhancement optimization. The ZAL are standard dielectric materials whose optical thicknesses are adjusted wrt the total multilayer. Several ZAL are then introduced for a multi-wavelength or multi-angle optimization. We first show how these layers allow reversing the depth field distribution within a stack, and provide giant enhancement. Then the procedure is extended for depth localization. Finally the design technique is generalized to provide huge resonances at a given set of illumination angles and wavelengths that are beforehand chosen.

Simulation and Design of CMOS Terahertz Detector With Surface Plasmon Antenna

Z. Shen[1], X. Ji[1*], Y. Liao[1], J. Peng[1], Q. Lou[1], R. Wu[1], B. Jin[1,3] and F. Yan[1,2]

[1] School of Electronic Science and Engineering, Nanjing University, Nanjing 210093, China

[2] fyan@nju.edu.cn

[3] bbjin@nju.edu.cn

[*]xji@nju.edu.cn

Abstract- In this paper, CMOS terahertz detector integrated with surface plasmon antenna is proposed. The antenna is constructed by the doped silicon material and the simulation results show its capacity to realize strong light concentration at 650GHz. In addition, the effects of the different parameters on the antenna performance are studied and we find that gap spacing of the bow-tie structure is an important factor to determine the antenna's resonant frequency along with its detected field strength. Besides, CMOS terahertz detector integrated with the proposed bowtie antenna is fabricated by the standard CMOS technology. The measured results from the device are well agreed with the simulated ones.

It has been revealed in previous studies that semiconductor based antennas are capable of supporting SPP resonance and achieving strong field confinement[1-2]. Nevertheless, these reported SPP antennas are not fabricated by the standard CMOS technology, such a drawback will become an obstacle for their future utilization. Here, we propose the design of the bowtie antenna which is constructed from the doped silicon material. The antenna model is established in electromagnetic simulation software CST Microwave Studio whose schematic is illustrated in Fig. 1 (a). Open boundary and plane wave excitations are set up to simulate normal incidence of uniform plane wave on the antenna. The antenna lies on the xoy plane of the coordinate system while the plane propagates along the z axis and polarized along the y axis. As is pointed out that the gap spacing between the two arms of the bow tie antenna plays a significant role to influence antenna's behavior, we here also study the effect of the gap spacing on the proposed surface plasmon antenna.

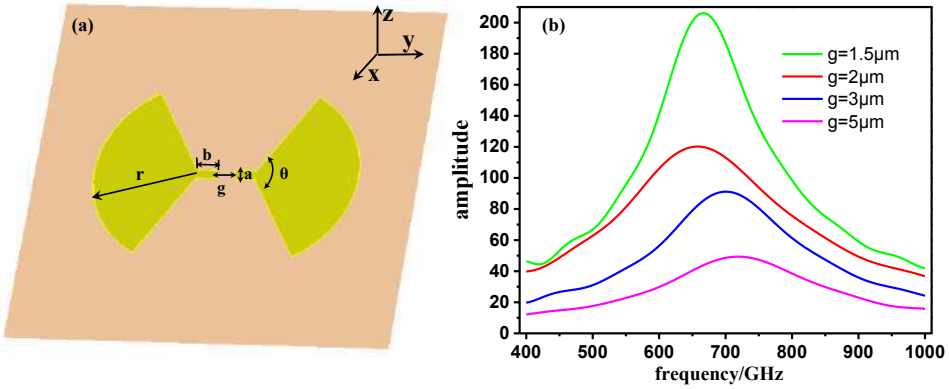

Fig. 1 (a) Schematic of the proposed bow-tie antenna; (b) The detected E-field amplitude versus frequency with respect of different gap spacing values

In the simulation, the gap spacing (g) ranges from 1.5 to 5μm while all the other antenna parameters remain constant as b=14μm, a=1μm, r=54μm and θ =120°.As is shown in Fig. 1 (b), the detected E-field amplitude reaches its maximum value when the gap spacing is 1.5μm. As the value of gap spacing rises, the resonance will occur at a higher frequency end while the detected field amplitude decreases, which conforms to the findings of the bow tie antenna in the optical wavelength[3-6].

Besides, we can insert the excitation port between the two arms of the bow-tie antennas to see their impedance features. The simulated results indicate that SPP resonances occur when the imaginary part of the antenna input impedance changes from inductive (above zero) to capacitive (below zero) at the resonant frequency. In the interested frequency range of 600 to 700GHz, it can be seen that as the gap spacing increases, resonance moves to the higher frequency end. Such results are also agreed with that of the optical bow-tie antenna, for which the extended length of the gap spacing will lead to a decreased capacitance value and a longer resonant wavelength[4].

On the basis of the simulation results above, the bowtie SPP coupled NMOS detector is fabricated using 0.18μm CMOS process on an 8 inch Si wafer with a thickness of 300 μm. The fabricated detector is then characterized using a THz source around 0.65 THz with an illumination power of 1 mW. The measurement results show that the detector has a high performance to THz radiation.

Acknowledgements, This work was supported by the National Key R &D Program of China (No.2016YFB0402403), the Natural Science Foundation of Jiangsu Province, China (No. BK20141321), and CAST Project, China (No. 08201601).

REFERENCES

1 A. Berrier, R. Ulbricht, M. Bonn, and J. Rivas, "Ultrafast active control of localized surface plasmon resonances in silicon bowtie antennas". Opt. Exp. **18**(22), 23226-23235 (2010).

2 G. Georgiou, A. Berrier, C. Schaafsma, H. Tyagi, M. Nagel, and J. Rivas, "THz spectroscopy of semiconducting plasmonic resonators" in Infrared, Millimeter, and Terahertz Waves (IEEE,2013), pp. 1-3

3 A. Cetin, S. Aksu, M. Turkmen, D. Etezadi, and H. Altug, "Theoretical and experimental analysis subwavelength bowtie-shaped antennas", J. Electromagn. Waves Appl. **29**(13), 1686-1698 (2015).

4 Brongersma M L, Kik P G. Surface plasmon nanophotonics[M]. Springer, 2007

5 D.P. Fromm, A. Sundaramurthy, P.J. Schuck, G. Kino,W.E. Moerner: Gap-dependent optical coupling of single "Bowtie" nanoantennas resonant in the visible, Nano Lett. **4**, 957 (2004).

6 J.G. Goodberlet, J.T. Hastings, H.I. Smith: Performance of the Raith 150 electron-beam lithography system, J. Vac. Sci. Technol. B **19**, 2499 (2001).

Recent Progress in Novel Functionalities of Plasmonic and Metamaterial Structures

Enhanced Magneto-chiral Effects at Microwave Frequencies by a Single Metamolecule

Satoshi Tomita

Nara Institute of Science and Technology, Japan
tomita@ms.naist.jp

Abstract— We have experimentally and numerically studied the directional birefringence of X-band microwaves by magneto-chiral (MCh) effects of a single metamolecule at room temperature. By applying a dc magnetic field, we observe an emergence of the MCh effects with simultaneous space-inversion and time-reversal symmetry breaking. The MCh effect is enhanced by using the magnetic resonance of the magnetic meta-atom. Numerical calculation predicts a giant MCh effect by interacting magnetic resonance with a specific resonant structural optical activity.

Symmetry breaking is a fundamental interest in physics. In condensed matter, symmetry breaking causes intriguing electromagnetic properties. The break in space-inversion symmetry in chiral structures like sugars causes reciprocal structural (natural) optical activity. Broken time-reversal symmetry in magnetized materials leads to non-reciprocal magneto-optical (MO) activity; that is to say, MO effects. These optical activities look similar, but have different physical origins. The MO activity is caused by the Lorentz force on electrons, whereas the structural optical activity is due to electromagnetic induction in the chiral structures.

It is natural and interesting to ask what electromagnetic waves will experience when time-reversal and space-inversion symmetries are simultaneously broken. Combination between MO and structural optical activities, gives rise to the directional birefringence independent of polarizations; that is, *magneto-chiral (MCh) effects* [1, 2, 3, 4]. The MCh effect is promising for new functional optics such as a polarization-independent non-reciprocal "one-way mirror". Moreover, the quest for large MCh effects paves a way toward the realization of a synthesized gauge field; for example, an effective magnetic field for electromagnetic waves [5, 6]. The system with the symmetries broken simultaneously is of interest also in terms of topological spin textures like Skyrmion [7]. The MCh effect at room temperature is, however, much weaker than MO and structural optical activities in natural materials.

In a previous study [8], we reported the direct observation of MCh effects in the X-band microwave region by a single metamolecule consisting of a metallic chiral structure and a ferrite rod at room temperature. A weak dc magnetic field of 1 mT was found to induce the MCh effects at frequencies of resonant structural optical activities, referred to as chiral resonances. The MCh effects were increased as the dc magnetic field was increased up to $\pm$200 mT. The difference in non-reciprocal refractive index due to the MCh effect was in the order of 10^{-3}, which was much larger than that observed in natural materials at the visible frequencies [9]. The large MCh effect is associated with the chiral resonance in the metallic chiral structure. However, interaction of the chiral resonance with the magnetic resonance by the ferrite rod remained to be addressed. By applying strong magnetic fields, magnetic resonance of the ferrite rod approaches the chiral resonance frequencies. This motivates a further enhancement of MCh effects.

In this invited talk, we report a comprehensive study of enhanced MCh effects at microwave frequencies by a single metamolecule [10]. Microwave transmission coefficients, S-parameters of S_{21} and S_{12}, are measured through the single metamolecule under magnetic fields up to $\pm$400 mT. We observe the difference between S_{21} and S_{12} in amplitude and phase, which is reproduced by numerical calculation based on a finite element method. The difference is caused by the MCh effect with simultaneous space-inversion and time-reversal symmetry breaking. We demonstrate that the MCh effect can be enhanced by using the ferrite meta-atom magnetic resonance. Moreover, numerical calculation reveals an enormous enhancement of the MCh effect by interacting the magnetic resonance with an exclusive chiral resonance, leading to the giant MCh effect. Non-reciprocal Fano-resonance between the magnetic resonance and exclusive chiral resonance in the meta-atoms is a key in the giant MCh effects. As a consequence, one-way transparency is realized in the MCh metamolecule at room temperature and convenient magnetic field strength. These conditions are quite preferable for practical applications such as a one-way mirror. The present study thus paves

a way toward the realization of a synthetic gauge field for electromagnetic wave [5, 6], and is one further step for *meta-condensed-matter physics* using metamaterials.

ACKNOWLEDGMENT

Financial support of this work by JSPS KAKENHI (No. 25889001 and 26287065) is acknowledged.

REFERENCES

1. N. B. Baranova, Yu. V. Bogdanov, and B.Ya. Zel'dovich, Opt. Commun. **22**, 243 (1977).
2. G. Wagnière and M. Meier, Chem. Phys. Lett. **93**, 78 (1982).
3. L. D. Barron and J. Vrbancich, Molecular Physics **51**, 715 (1984).
4. G. L. J. A. Rikken and E. Raupach, Nature **390**, 493 (1997).
5. K. Sawada and N. Nagaosa, Phys. Rev. Lett. **95**, 237402 (2005).
6. K. Fang, Z. Yu, and S. Fan, Nature Phtonics **6**, 782 (2012).
7. S. Mühlbauer, B. Binz, F. Jonietz, C. Pfleiderer, A. Rosch, A. Neubauer, R. Georgii, and P. Böni, Science **323**, 915 (2009).
8. S. Tomita, K. Sawada, A. Porokhnyuk, and T. Ueda, Phys. Rev. Lett. **113**, 235501, (2014).
9. M. Vallet, R. Ghosh, A. Le Floch, T. Ruchon, F. Bretenaker, and J. -Y. Thépot, Phys. Rev. Lett. **87**, 183003 (2001).
10. S. Tomita, H. Kurosawa, K. Sawada, and T. Ueda, Phys. Rev. B. **95**, 085402 (2017).

Optical Cloaking with Existing Materials

K. Kajikawa

School of Engineering, Tokyo Institute of Technology
kajikawa@ee.e.titech.ac.jp

Abstract— We report macroscopic scattering cancellation caused by difference of local-electric polarization field between core and shell materials. We employ this phenomena to find parameters for the optical cloaking of metallic nanowires.

Optical cloaking is the method to make an object to be transparent. There are a few methods to bring about this phenomenon. One is based on the transformation optics, by covering an object a metamaterial film with appropriate spatial distribution of refractive indices, as the light make a detour around the object [1,2]. Since the realization of the required refractive indices are tough at optical frequency, this method is unrealistic. The other method is to reduce the scattering efficiency to be zero by covering a film of dielectrics or semiconductors [3,4,5]. This method can be realized using the existing materials such as AlAs or Si semiconductors with high refractive index [5]. In this method, macroscopic scattering cancellation is caused by difference of local-electric polarization field between core and shell materials. We employ this to perform realistic optical cloaking for metallic nanowires and found some parameters.

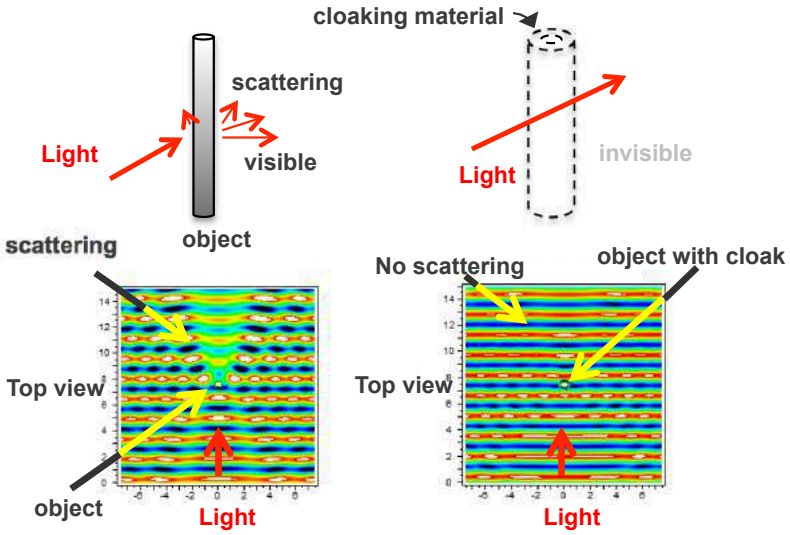

Figure 1: FDTD simulation results of optical cloaking.

To discover the most suitable structure for the cloaking at visible wavelengths with dielectric multilayered structure, we performed analysis of the electromagnetic field by solving classical Maxwell equation. After the determination of the parameters of refractive index and the thickness of the shell, we performed the 2D FDTD simulation to make sure the cloaking. As shown in Figure 1, the strong light scattering was observed from the cylinder core without cloaking, the light front is stable and invisible when the core was covered with a cloak. We found a number of pairs of the core and shell of existing materials: core/shell = dielectrics/dielectrics, dielectrics/metals, metals/dielectrics and even metals/metals.

These cloaking technique can be used for transparent electrodes and electrical-ciruit wires.

ACKNOWLEDGMENT

This work was partially supported by a Grant-in-Aid for Scientific Research (25109707, 26600023, 26286058, 16K13696) and Bilateral Program from the Japan Society for the Promotion of Science.

REFERENCES

1. U. Leonhardt, Science 312, (2006) 1777.
2. D. Schurig et al., Science 314, (2006) 977.
3. F, Bohren "Absorption and Scattering of Light by Small Particles", Wiley (1983).
4. 4. A. Alu and N. Engheta, Phys. Rev. Lett. 100 (2008) 113901.
5. A. Mirzaei, Sci. Rep. 5 (2015) 09574.

Fine Tuning of Plasmonic Properties for Au Nano-Structures by Electrochemical Metal Dissolution/Deposition

Hiro Minamimoto*, Shunpei Oikawa, and Kei Murakoshi
Department of Chemistry, Faculty of Science, Hokkaido University, North 10 West 8, Kita-ku, Sapporo, Hokkaido 060-0810, Japan
*corresponding author: minamimoto@sci.hokudai.ac.jp

Abstract-The control method for plasmonic properties of the metal nanodimer structures has been established via electrochemical metal dissolution reactions. The reaction rate can be precisely tuned by changing the electrochemical conditions. With the progress of the electrochemical reactions, the maximum plasmon resonance wavelength shifted to the shorter wavelength region corresponding to the decrease volume of metal nano-structures. Thorough various attempts, unique optical properties emerged by the structural control in an atomic scale was revealed by *in-situ* electrochemical optical measurements.

Localized surface plasmon resonance (LSPR) which is the collective oscillation of free electrons in the metals is excited in the vicinity of the mental nano-structures under the illumination of the visible or near infrared light. The strong optical field is generated by the excitation of LSPR.[1] Especially for the dimer structures, the intensity of the strong optical field becomes relatively strong compared to the case of the single structures. In order to use the generated optical field efficiently, it is necessary to tune the photo response properties of metal nano-structures by the control of the metal size, shape, composition, and environments. Recently, it has been reported that the nano-dimer structures with the gap distance of less than 1 nm can concentrate the light into the molecules scale before the formation of the tunneling plasmon (charge transfer plasmon) at the center of the gap.[2] At the present stage, fine tuning of the metal nano-structures with the resolution less than 5 nm is quite difficult to be achieved by the ordinary techniques, such as the electron beam lithography method. In this study, we have tried to establish the new method for the control of the plasmon active metal nano-structures with the aim of the arbitrary tuning of plasmon resonance properties. The optical property change was evaluated through *in-situ* electrochemical spectroscopic measurements.

The Au nano-dimer structures on the conductive glass substrate using nano-sphere lithography method (Au-NSL). In addition to this, the well-defined Au structures were also prepared by electron beam lithography technique. Electrochemical dissolution of Au nano-dimer structures were performed with the three-electrode system. Pt plate and Ag/AgCl (sat. KCl) electrode were used as the counter and reference electrodes, respectively. During electrochemical measurements, extinction spectra for the substrate were obtained.

As the first attempts, the tuning of the plasmonic properties for Au-NSL were performed with the system as indicated in Fig. 1. SEM images of Au-NSL structures which were obtained before applying electrode potential were shown in Fig. 1. The *in-situ* electrochemical extinction spectra were obtained under the illumination of polarized light parallel to the long axis. The polarized electrode potentials were 0.89 and 0.87 V corresponding to Fig. 2a and b. As can be seen in extinction spectra, the drastic optical property change was confirmed in the case of 0.89 V. After 600 s, the plasmon resonance peak were disappeared with the resonance wavelength shift.

This phenomenon can be explained by the diminish of the structures due to the fast reaction rate. On the contrary, with the slow dissolution rate at the case for 0.87 V, the scattering cross-sections which reflect volume change of nano-dimer were almost maintained but the maximum plasmon resonance wavelength were slightly shift around 100 nm. It can be considered that this wavelength shift is mainly derived from the gap distance change of dimer structures. Taking into above results, we have succeeded in obtaining appropriate condition for the fine tuning of plasmonic properties for Au nano-structures. Based on the spectroscopic measurement results, we have tried to estimate the gap distance change. From the calculations, the change in the gap distance can be estimated as less than 5 nm, which is difficult to be controlled by the ordinary nano-control methods.

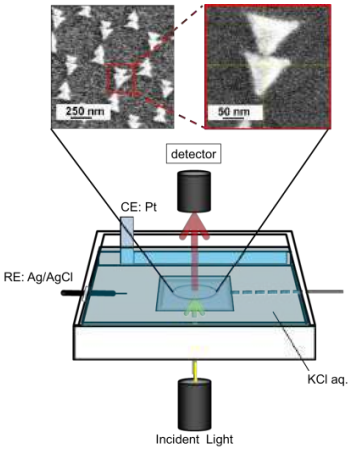

Fig.1 Schematic illustration of electrochemical extinction spectrum measurements cell. SEM images indicate prepared Au-NSL structures.

For further investigations, we have attempted to control of the optical properties using well-defined Au-nanostructures prepared by electron beam lithography technique. By introduction of well defined-structures to the present system, more detail discussion would be realized. As the results for the single Au-nano dimer disk structures obtained with the scattering spectra, we have succeeded in the observation of the drastic optical property change corresponding to each property change of the charge transfer and tunneling plasmon mode. We can say that our results indicate the atomic scale resolution for the present electrochemical method. From all results in our attempts, as conclusions, the present electrochemical method can be considered as the promising technique for the control of the optical properties of the Au nano-structures in an atomic scale.

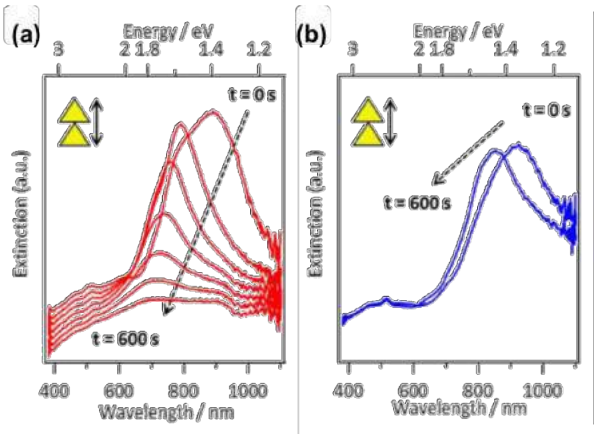

Fig.2 Time dependent extinction spectra of Au-NSL nanodimer obtained under the polarization of (a) 0.89 and (b) 0.87V for 600 s.

REFERENCES

1. Minamimoto, H., Toda, T., Futashima, R., Li, X., Suzuki, K., Yasuda, S., Murakoshi, K., Visualization of Active sites for plasmon-Induced Electron Transfer Reactions Using Photoelectrochemical Polymerization of Pyrrole, *J. Phys. Chem. C*, 120(29)**,** 16051, 2016.,
2. Savage, J. K., Hawkeye, M. M., Esteban, E. R., Borisov, G. A., Aizpurua, J., Baumberg, J. J., Revealing the quantum regime in tunneling plasmonics, *Nature*. 499**,** 574, 2012.

Regulation of microwave propagation in space and frequency domains by plasma-metamaterial composites

O. Sakai[1], **A. Bambina**[1], **A. Iwai**[2], **S. Yamaguchi**[1], **Y. Kabe**[1], **and S. Miyagi**[1]

[1]The University of Shiga Prefecture, Japan
[2]Kyoto University, Japan
sakai.o@e.usp.ac.jp

Abstract— Plasma is suitable for a component and/or an alternative of metamaterial. By installation of plasma into solid metamaterial structure, metamaterial becomes tunable, energetic and nonlinear since the part of the plasma change permittivity even to values in the negative sign with frequency dispersion, and store kinetic energy in electron motions in the level of eV which is sufficient for nonlinear photonics for harmonic wave generation. Plasma also provides spatial gradient of refractive index due to the inherent spatial profile of electron density, and it controls propagation paths of electromagnetic waves, similar to the cloaking devices composed of solid metamaterial. These findings extends roles of metamaterial further to scientific areas that have not been covered by metamaterial.

Metamaterial science opens functions of media for electromagnetic waves, which has not been covered, like negative values of refractive index and cloaking layers [1, 2]. Its motivation is now expanding to potential functionalities that enable us to make it tunable and nonlinear [3]. We have reported plasma-metamaterial composites as examples in the expanded category of metamaterial media [4, 5], and the experimental results suggest nonlinear and cloaking phenomena as well as tunable characteristics.

Plasma has dispersive permittivity ε_{p} which is in the Drude type. ε_{p} becomes negative when the given wave frequency ω is lower than the electron plasma frequency ω_{pe}, and it varies from zero to +1 as ω gets higher than ω_{pe}. The synthesized refractive index in negative-permeability metamaterial takes negative, positive and imaginary values. Furthermore, due to its energetic properties coming from high-energy electrons and rectified current flows in plasma, we observed harmonic wave generation, which makes the frequency dispersive property more rich.

In addition, since plasma has a spatial profile of electron density, ε_{p} changes its value in the balance between ionization and boundary regions, including both positive and negative values. Consequently, such a property leads to a similar spatial profile to that in cloaking layers designed in transformation optics [6]. ε_{p} exhibits a variety of profiles, and the plasma can become an alternative of metamaterial in a cloaking layer and other devices which control a propagation path of electromagnetic waves. We observed wave scattering in plasma layer, and the profiles of the detected signals coincides with numerical results of the finite-difference time-domain method.

Such experimental observations convince us that plasma plays roles that cannot be achieved by conventional solid-state metamaterial, and their functions will increase as concepts and technologies introduced to regulations of plasma generation.

ACKNOWLEDGMENT

This study was supported by Grant-in-Aid for Scientific Research from the Japanese Ministry of Education, Culture, Sports, Science and Technology, Japan, and by Strategic Information and Communications R&D Promotion Programme (SCOPE) from the Ministry of Internal Affairs and Communications, Japan.

REFERENCES

1. Shelby, R. A., D. Smith and S. Schultz, "Experimental verification of a negative index of refraction," *Science*, Vol. 292, No. 5514, 77–79, 2001.
2. Schurig, D., J. J. Mock, B. J. Justice, S. A. Cummer, J. B. Pendry, A. F. Starr, and D. R. Smith, "Metamaterial electromagnetic cloak at microwave frequencies," *Science*, Vol. 314, No. 5801, 977–980, 2006.
3. Lapine, M., I. V. Shadrivov and Y. S. Kivshar, "Colloquium: nonlinear metamaterials," *Rev. Mod. Phys.*, Vol. 86, 1093–1123, 2014.

4. Sakai, O. and K. Tachibana, "Plasmas as metamaterials: a review," *Plasma Sources Sci. Technol.*, Vol. 21, 013001-1–18, 2012.
5. Sakai, O., S. Yamaguchi, A. Bambina, A. Iwai, Y. Nakamura, Y. Tamayama, and S. Miyagi, "Plasma metamaterials as cloaking and nonlinear media," *Plasma Phys. Control. Fusion*, Vol. 59, 014042-1-10, 2017.
6. Leonhardt, U. and T. Philbin, "Geometry and Light: the Science of Invisibility," Dover, New York, 2010.

A generic way for creating topological electromagnetic states

Xiao Hu
International Center for Materials Nanoarchitectonics (WPI-MANA)
National Institute for Materials Science (NIMS), Tsukuba, Japan
*corresponding author: hu.xiao@nims.go.jp

Abstract-Topological photonic phenomena are attracting significant interests from viewpoints of both basic science and potential applications. We have proposed a new way to realize two-dimensional (2D) topological photonic crystals based on honeycomb lattice of dielectric cylinders [1]. The idea can be applied for various systems.

Similar to graphene, Dirac-like linear frequency dispersions exist at K and K' points for the neat honeycomb lattice. We show that deforming the honeycomb lattice in the designed way which preserves the C_{6V} symmetry will open a frequency gap, accompanying with a band inversion between p-orbit- and d-orbit-like electromagnetic modes at Γ point. The system exhibits counter-propagating edge photonic modes with topological protection. Our theoretical prediction has been confirmed by recent experiments [2]. Because only dielectric material is used in the present approach, one can achieve topological photonic properties with working frequency of radio through visible lights by varying merely the lattice constant of photonic crystal. The idea has been extended to 2D waveguides, 3D photonic crystals, phononic and electronic systems [3-7], and is expected to be applicable to other quantum and classic systems, including surface plasmon polariton, BEC, and LC circuits.

REFERENCES

1. L.-H. Wu and X. Hu: Phys. Rev. Lett. vol. 114, 223901 (2015).
2. Y.-T. Yang et al.: arXiv:1610.07780 (2016).
3. S. Barik et al.: N. J. Phys. vol. 18, 113013 (2016).
4. H. X. Wang et al.: Phys. Rev. B vol. 93, 235155 (2016).
5. C. He et al.: Nature Phys. (2016) DOI:10.1038/NPHYS3867.
6. L.-H. Wu and X. Hu: Sci. Rept. vol. 6, 24347 (2016).
7. T. Kariyado and X. Hu: arXiv:1607.08706 (2016)..

Bi-anisotropic response in three-dimensional split ring resonators fabricated by a self-folding method

Yuto Moritake[1*] **and Takuo Tanaka**[1,2,3]
[1]RIKEN Center for Advanced Photonics, Japan
[2]Metamaterial laboratory, RIKEN, Japan
[3]Tokyo Institute of Technology, Japan
[*]corresponding author: yuto.moritake@riken.jp

Abstract-We experimentally demonstrated infrared metamaterials composed of three-dimensional split ring resonators (3D-SRRs) fabricated by a metal-stress-driven self-folding method we developed so far. The self-folding method enables to mass and easy fabrication of 3D SRRs operating in the infrared region due to self-organized nature of the process. By using this method, bi-anisotropic response in 3D-SRRs was controlled, which realizes 3D magnetic materials in the infrared region.

Artificial magnetism in metamaterials has opened a new paradigm to realize intriguing phenomena including negative refractive index, optical cloaking, s-polarization Brewster effects. Especially, negative refractive index materials have attracted significant attention due to exciting functionalities such as negative refraction, sub-wavelength focusing and so on. Split ring resonators (SRRs) are representative metamaterial structures for realizing artificial magnetism. Magnetic component of light can couple to a magnetic resonant mode with induced magnetic dipole and effective permeability at the magnetic resonance in SRRs changes from unity.

To demonstrate artificial magnetism in the optical region using SRRs experimentally, planar type SRRs are generally used due to restriction of sample preparation. However, in planar metamaterials, a magnetic component of light cannot directly couple to the magnetic resonant mode since the excited magnetic dipole in planar SRRs is normal to a substrate at normal incidence. On the other hand, three-dimensional (3D) SRRs allows direct coupling between a magnetic component of light and the magnetic mode in SRRs. However, fabrication of 3D structures for optical metamaterials is still difficult although it can be performed by using some special techniques and state-of-art equipment at the laboratory level [1].

To overcome this issue, we developed a metal-stress-driven self-folding method to fabricate 3D-SRRs [2-4]. Firstly, two-dimensional (2D) gold ribbons are formed on a Si substrate by using electron beam lithography and a conventional lift-off method. The 2D ribbons have two arms connected by a patch. The Si substrate with 2D patterns is isotropically etched using ICP-RIE. When Si under the arms is completely etched and the gold arms are released, intrinsic stress in deposited gold films spontaneously induces folding of the arms as shown in Fig. 1. The role of the center patch is an anchor for the arms not to be peeled off from the substrate after release. Owing to self-organized nature of the process, this method allows mass and easy fabrication of 3D structures.

By using the method, we investigated bi-anisotropic response in infrared metamaterials. General 3D metamaterials show bi-anisotropic response due to luck of inversion symmetry along a propagation axis. In bi-anisotropic materials, electric (magnetic) dipole can be excited by not only electric (magnetic) fields but also magnetic (electric) fields of light, which results in unwanted complex electro-magnetic coupling preventing

purely magnetic resonance in SRRs. Appropriate adjustment of the patch position in gold ribbons enables to control of inversion symmetry along the propagation axis as shown in Fig. 2. Analysis using simulations and effective parameter retrieving revealed elimination of the bi-anisotropic response in 3D-SRRs, which indicates 3D magnetic metamaterials is realized in the infrared region. In the presentation, we will discuss the results in detail.

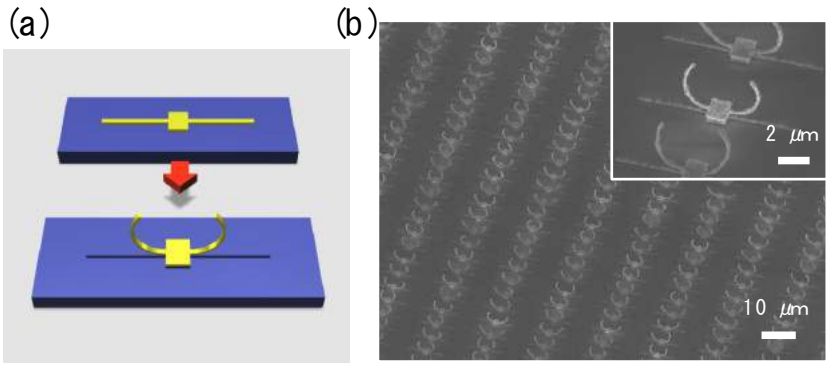

Fig. 1 (a) A schematic of self-folding process of 3D-SRRs. (b) SEM images 3D-SRRs fabricated by the self-folding method.

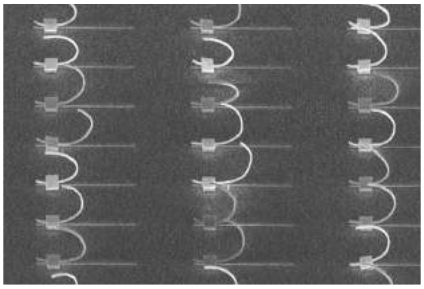

Fig. 2 A SEM image of 3D-SRRs with inversion symmetry along a propagation axis.

Acknowledgements, This work was supported by Innovative Science and Technology Initiative for Security, ATLA, Japan.

REFERENCES

1. Chen, W.-T. *et al.* "Optical magnetic response in there-dimensional metamaterial of upright plasmonic meta-molecules," *Opt. Express*, Vol. 19, No. 13, 12837-12842, 2011.
2. Chen, C.-C. *et al.* "Uniaxial-isotropic Metamaterials by Three Dimensional Split-Ring Resonators," *Adv. Opt. Mater.*, Vol. 3, No. 1, 44-48, 2015.
3. Chen, C.-C. *et al.* "Fabrication of three dimensional split ring resonators by stress-driven assembly method," *Opt. Express*, Vol. 20, No. 9, 9415-9420, 2012.
4. Chen, Y.-H. *et al.* "Interplay of the mutual electric and magnetic coupling between three-dimensional split-ring resonators.," *Opt. Express*, Vol. 25, No. 3, 2909-2917, 2017.

Active terahertz metamaterials utilizing π-conjugated polymers

T. Matsui[1,2,*]

[1]Department of Electrical and Electronic Engineering, Graduate School of Engineering, Mie University, Japan

[2]The Center of Ultimate Technology on Nano-Electronics, Mie University, Japan

[*]corresponding author: matsui@elec.mie-u.ac.jp

Abstract-We demonstrate active tuning of the resonant response of metamaterials utilizing organic π-conjugated materials in terahertz (THz) frequency ranges. Electrochemically grown heavily-doped polypyrrole (PPy) film was used as a linear actuator to slightly shifting relative position of stacked two layers of split-ring resonator (SRR) array. We also show that a stacked closed-ring resonator (CRR) array is also effective to obtain relatively large spectral shift with a small lateral shift.

In recent years, numerous studies have been carried out to develop novel types of metamaterials and metadevices [1]. In metamaterials, artificially designed subwavelength resonant structures, or meta-atoms, such as split-ring resonator (SRR) play crucial roles in obtaining rich variety of unique responses to electromagnetic fields [2]. However, resonant characteristics of such SRRs usually restrict their working frequency only in a narrow range, therefore numerous attempts have been made to add tunability to metamaterials to develop active devices [1]. Based on the fact that resonant condition of meta-molecules or layered metamaterial arrays can be controlled by relative position and/or orientation via near-field interaction between meta-atoms [3, 4], tunable metamaterials and metadevices have been developed [5-8]. Here we demonstrate our recent results on the electro-active metadevices in terahertz (THz) frequency ranges utilizing organic π-conjugated polymers [8].

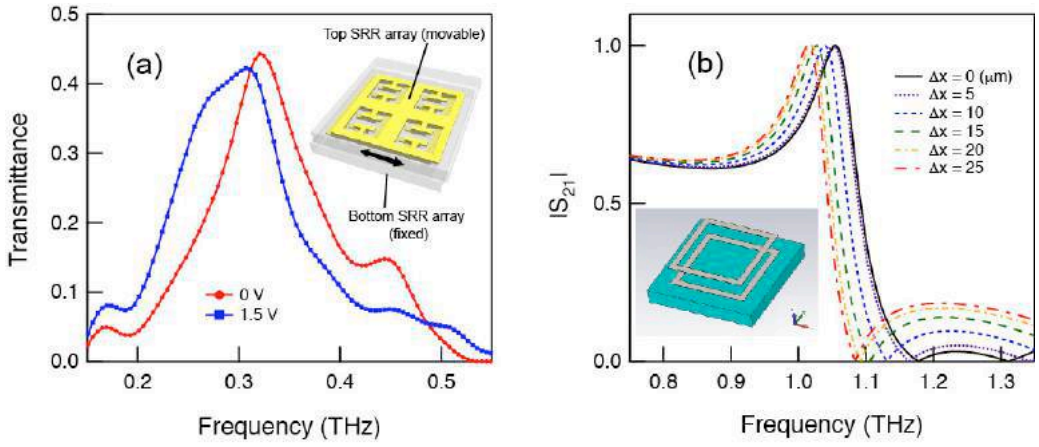

Figure 1 (a) Measured THz transmission spectra of tunable THz device based on PPy(PF6) linear actuator under applied voltage. (inset) Schematics of the double-layered resonator arrays with fixed bottom layer and movable top layer. (b) Simulated THz transmission spectra of stacked CRR array THz metamaterial. (inset) Schematic of stacked CRR array THz metamaterial.

Among rich variety of π-conjugated polymers, doped polypyrrole (PPy) film is unique since its volume can be controlled even in ambient air by applying low voltage of only a few Volts, and thus can be utilized as electro-active polymer actuators [9]. We have synthesized thin films of PPy doped with PF6 ions, PPy(PF6), by electrochemical polymerization and utilized them as linear actuators to laterally shift relative position of stacked SRR arrays (inset of Fig. 1 (a)). By applying voltage to the polymer actuators, a contraction of the polymer film can be induced and this shifts one of the stacked SRR layer. Therefore, a frequency shift of resonant THz transmission can be obtained (Fig. 1 (a)). We also show that the stacked closed-ring resonator (CRR) arrays [10] (inset of Fig. 1 (b)) can be effective to obtain relatively large spectral shift with a small lateral shift. In the numerical simulation, we have obtained spectral shift of the narrow-band transmission by assuming a similar lateral shift of the stacked CRR arrays (Fig. 1 (b)). Our findings might be utilized to develop novel types of electro-active THz metadevices. We also found that resonant frequency can be shifted by changing dielectric constant of dielectrics between CRR arrays, which may be utilized for sensing devices.

Acknowledgements: This project was supported by Open Partnership Joint Projects of Japan Society for the Promotion of Science (JSPS) Bilateral Joint Research Projects and also was partly supported by the Strategic Information and Communications R&D Promotion Programme (SCOPE) from the Ministry of Internal Affairs and Communications of Japan.

REFERENCES

1. Zheludev, N. I. and Y. S. Kivshar, "From metamaterials to metadevices," *Nature Materials*, Vol. 11, No. 11, 917–924, 2012.
2. Pendry, J. B., A. J. Holden, D. J. Robbins and W. J. Stewart, "Magnetism from Conductors, and Enhanced Non-Linear Phenomena," *IEEE Trans. Microwave Theor. Tech.*, Vol. 47, No. 11, 2075–2084, 1999.
3. Lapine, M., D. Powell, M. Gorkunov, I. Shadrivov, R. Marqués and Y. Kivshar, "Structural tunability in metamaterials," *Appl. Phys. Lett.*, Vol. 95, No. 8, 084105-1-3, 2009.
4. Powell, D. A., K. Hannam, I. V. Shadrivov and Y. S. Kivshar, "Near-field interaction of twisted split-ring resonators," *Phys. Rev. B*, Vol. 83, No. 23, 235420-1-6, 2011.
5. Liu, M., Y. Sun, D. A. Powell, I. V. Shadrivov, M. Lapine, R. C. McPhedran and Y. S. Kivshar, "Nonlinear response via intrinsic rotation in metamaterials," *Phys. Rev. B*, Vol. 87, No. 23, 235126-1-6, 2013.
6. Matsui, T., M. Liu, D. A. Powell, I. V. Shadrivov and Y. S. Kivshar, "Electromagnetic tuning of resonant transmission in magnetoelastic metamaterials," *Appl. Phys. Lett.*, Vol. 104, No. 16, 161117-1-4, 2014.
7. Liu, L., W.-C. Chen, D. A. Powell, W. J. Padilla, F. Karouta, H. T. Hattori, D. N. Neshev, and I. V. Shadrivov, "Post-processing approach for tuning multi-layered metamaterials," *Appl. Phys. Lett.*, Vol. 105, No. 15, 151102-1-4, 2014.
8. Matsui, T., Y. Inose, D. A. Powell and I. V. Shadrivov, "Electroactive Tuning of Double-Layered Metamaterials Based on π-Conjugated Polymer Actuators," *Adv. Opt. Mater.*, Vol. 4, No. 1, 135-140, 2016.
9. Okuzaki, H., T. Kuwabara, K. Funasaka, and T. Saido, "Humidity-sensitive polypyrrole films for electro-active polymer actuators," *Adv. Funct. Mater.*, Vol. 23, No. 36, 4400–4407, 2013.
10. Gu, J., J. Han, X. Lu, R. Singh, Z. Tian, Q. Xing, and W. Zhang, "A close-ring pair terahertz metamaterial resonating at normal incidence," *Opt. Express*, Vol. 17, No. 22, 20307-20312, 2009.

Symmetry Classification of Topological Photonic Crystals

Max Lein[1] & **Giuseppe De Nittis**[2]

[1]Advanced Institute of Materials Research, Tohoku University, Japan
[2]Pontificia Universidad Católica de Chile, Chile
maximilian.lein.d2@tohoku.ac.jp

Abstract— As a first step to understand topological effects in photonic crystals via *photonic bulk-boundary correspondences*, we have adapted the Altland-Zirnbauer classification scheme and obtained a classification of topological photonic crystals. Our classification justifies the name "Quantum Hall Effect for light", and suggests that *the Chern number quantifies the net number of edge modes traveling from left to right*. Furthermore, we identify *dual symmetric materials* as a second candidate for exhibiting novel topological effects.

Inspired by ideas from solid state physics, one recent success was the prediction [RH08] and experimental realization [WCJS08, RZP$^+$13] of an analog to the Quantum Hall Effect with electromagnetic waves. The idea here is to exploit periodic patterning to create a photonic bulk *band gap* and choose materials which *break a certain symmetry*. A first principles explanation, starting from Maxwell's equations and culminating in the proof of *photonic bulk-boundary correspondences*, is still missing, and the first step is to adapt the Cartan-Altland-Zirnbauer classification scheme and classify topological photonic crystals according to certain discrete symmetries. After a first attempt [DL14] where we had not taken the real-valuedness of electromagnetic fields correctly into account, we have now obtained a classification of electromagnetic media [DL16] according to discrete symmetries. It turns out only very few symmetries of the form $T_j = (\sigma_j \otimes \mathbb{1})C$ or $U_j = \sigma_j \otimes \mathbb{1}$ are admissible, $(C\Psi)(x) = \overline{\Psi(x)}$ being complex conjugation and σ_j the Pauli matrices in the $(\mathbf{E}, \mathbf{H})$ splitting. That leads to the following classification:

Theorem (Symmetry classification of media) *Suppose the material described by* $W(x) = \left(\begin{smallmatrix} \varepsilon(x) & \chi(x) \\ \chi^*(x) & \mu(x) \end{smallmatrix}\right)$ *is* lossless *and* not negative index. *Then the materials given below possess the following symmetries (*T_j *are time-reversal-type symmetries,* U_2 *a unitary, commuting symmetry):*

Material	Topological Effects	Conditions on W	Symmetries	CAZ Class
Non-gyrotropic materials	*No*	$\varepsilon = \mathrm{Re}\,\varepsilon$, $\mu = \mathrm{Re}\,\mu$, $\chi = 0$	$T_3 : (\mathbf{E}, \mathbf{H}) \mapsto \big(\overline{\mathbf{E}}, -\overline{\mathbf{H}}\big)$	*AI*
Gyrotropic materials	*QHE for light*	$\mathrm{Im}\,\varepsilon \neq 0$ *or* $\mathrm{Im}\,\mu \neq 0$	*None*	*A*
Dual symmetric materials & vacuum	***Unknown***	$\varepsilon = \mathrm{Re}\,\varepsilon = \mu$, $\chi = -\chi^*$	$T_1 : (\mathbf{E}, \mathbf{H}) \mapsto \big(\overline{\mathbf{H}}, \overline{\mathbf{E}}\big)$ $T_3 : (\mathbf{E}, \mathbf{H}) \mapsto \big(\overline{\mathbf{E}}, -\overline{\mathbf{H}}\big)$ $U_2 : (\mathbf{E}, \mathbf{H}) \mapsto \big(-\mathrm{i}\,\mathbf{H}, +\mathrm{i}\,\mathbf{E}\big)$	—

Our classification justifies calling the experiment suggested by Haldane the "Quantum Hall Effect for light", and suggests that in a two-dimensional topological photonic crystal *the Chern number quantifies the net number of edge modes traveling from left to right*. Furthermore, we identify *dual symmetric materials* as a second candidate for exhibiting novel topological effects due to the *presence* of a *second* time-reversal symmetry.

ACKNOWLEDGMENT

M. L. thanks JSPS for support of his research with a WAKATE B grant. G. D. research is supported by the grant *Iniciación en Investigación 2015* - N^o 11150143 funded by FONDECYT.

REFERENCES

[DL14] Giuseppe De Nittis and Max Lein. On the Role of Symmetries in Photonic Crystals. *Annals of Physics*, 350:568–587, 2014.

[DL16] Giuseppe De Nittis and Max Lein. On the Role of Symmetries and Topology in the Theory of Classical Electromagnetism. *in preparation*, 2016.

[RH08] S. Raghu and F. Duncan M. Haldane. Analogs of quantum-Hall-effect edge states in photonic crystals. *Phys. Rev. A*, 78:033834, 2008.

[RZP+13] Mikael C. Rechtsman, Julia M. Zeuner, Yonatan Plotnik, Yaakov Lumer, Daniel Podolsky, Felix Dreisow, Stefan Nolte, Mordechai Segev, and Alexander Szameit. Photonic Floquet topological insulators. *Nature*, 496:196–200, 2013.

[WCJS08] Zheng Wang, Yidong D. Chong, John D. Joannopoulos, and Marin Soljačić. Reflection-Free One-Way Edge Modes in a Gyromagnetic Photonic Crystal. *Phys. Rev. Lett.*, 100(1):013905, 2008.

Chiral metasurfases and photonic crystals for compact sources of circularly polarized light.

S. G. Tikhodeev[1,2*]

[1]M. V. Lomonosov Moscow State University, Leninskie Gory 1, Moscow 119991, Russia
[2]A. M. Prokhorov General Physics Institute, Russian Academy of Sciences, Vavilova Street 38, Moscow 119991, Russia
* tikh@gpi.ru

Abstract— Embedding chiral metasurfaces or photonic crystal slabs into semiconductor nanostructures and/or microcavities allows to create compact sources of circularly polarized light including lasers. The mechanisms to control the circular polarization of light emission by chiral structuring are discussed.

The goal to create compact circularly polarized light sources including lasers without need in bulky wave plates or external magnetic field has drawn a considerable attention in recent years. A monolithic electrically pumped quantum cascade laser with circularly polarized THz emission was demonstrated in [1], using "fishbone" gratings in the surface metallization. Recently, a close to circularly polarized lasing at $\hbar\omega \approx 1.5$ eV was achieved [2] from an AlAs/AlGaAs Bragg microcavity with GaAs quantum wells in the active region and chiral-etched upper distributed Bragg refractor under optical pump at room temperature.

The fabrication of chiral nanostructures from achiral semiconductor materials appeared to be a very effective method to produce a circularly polarized light emission from quantum emitters in the absence of magnetic field [3-6]. They may work as chiral metasurfaces or photonic crystals, depending on the relation between the light wavelength and period of the structure.

The advantage of using chiral semiconductor/air structures with a large contrast of dielectric permittivities is their giant optical activity. This allows one to fabricate a very thin "wave plate", with a thickness of the order of the emitted light wavelength. Unlike the traditional wave plates, chiral nanostructures may have in-plane rotational isotropy due to the C_4 symmetry. Thus, they do not require linearly polarized emission of the active material at some precise polarization direction, which is an important advantage of the demonstrated approach over conventional quarter-wave plates.

ACKNOWLEDGMENT

This work has been funded by Russian Scientific Foundation (grant 16-12-10538).

REFERENCES

1. Konishi, K., Nomura, M., Kumagai, N., Iwamoto, S., Arakawa, Y., and Kuwata-Gonokami, M., "Circularly Polarized Light Emission from Semiconductor Planar Chiral Nanostructures," *Phys. Rev. Lett.*, Vol. 106, 057402, 2011.
2. Rauter, P., Lin, J., Genevet, P., Khanna, S. P., Lachab, M., Giles Davies, A., Linfield, E. H., Capasso, F., "Electrically pumped semiconductor laser with monolithic control of circular polarization" *Proc. Nat. Acad. Sci.*, Vol. 111, E5623-E5632, 2014.
3. Lobanov, S. V., Weiss, T., Gippius, N. A., Tikhodeev, S. G., Kulakovskii, V. D., Konishi, K., and Kuwata-Gonokami, M., "Polarization control of quantum dot emission by chiral photonic crystal slabs," *Opt. Letters* , Vol. 40, 1528–1531, 2015.
4. Maksimov, A. A., Tartakovskii, I. I., Filatov, E. V., Lobanov, S. V., Gippius, N. A., Tikhodeev, S. G., Schneider, C., Kamp, M., Maier, S., Höfling, S., and Kulakovskii, V. D., "Circularly polarized light emission from chiral spatially-structured planar semiconductor microcavities," *Phys. Rev. B*, Vol. 89, 045316, 2014.
5. Lobanov, S. V., Tikhodeev, S. G., Gippius, N. A., Maksimov, A. A., Filatov, E. V., Tartakovskii, I. I., Kulakovskii, V. D., Schneider, C., Geßler, J., Kamp, M., Höfling, S., "Circularly polarized light emission from chiral spatially-structured planar semiconductor microcavities," *Phys. Rev. B*, Vol. 92, 205309, 2015.

6. Demenev, A. A., Kulakovskii, V. D., Schneider, C., Brodbeck, S., Kamp, M., Höfling, S., Lobanov, S. V., Weiss, T., Gippius, N. A., and Tikhodeev, S. G., "Circularly polarized lasing in chiral modulated semiconductor microcavity with GaAs quantum wells," *Appl. Phys. Lett.*, Vol. 109, 171106, 2016.

Polarization dependence of transverse photo-voltage in porous thin metal films

Teruya Ishihara and Marjan Akbari
Deparment of Physics, Graduate School of Science,
Tohoku University, Sendai, Japan
*corresponding author: t-ishihara@m.tohoku.ac.jp

Abstract- Photo-induced voltage is generated in a metallic thin film when the light beam is obliquely incident. The voltage perpendicular to the incident plane (transverse photo-induced voltage: TPIV) is dependent on azimuth angle and ellipticity of the light polarization. By rotating the relative configuration of the film and the electromagnetic field of light, it is possible to deduce its polarization state, which can be utilized to develop a broadband ellipticity meter.

Porous thin metal film can have different optical response from the pristine metal film [1]. When the pore size is smaller than the light wavelength, the film can be considered as a metamaterial. Due to the local DC charge on the metal surface generated by photo-rectification, which is one of the second-order optical nonlinearity, the film may exhibit net DC voltage depending on the symmetry of the applied light field [2-4].

In order to prepare nano porous metallic films we employed two methods. One is to start from an alloy film. By applying nitric acid to a 100 nm-thick white gold leaf (Au : Ag = 50 : 50 wt %) , a bicontinuous porous Au film can be formed [5]. Another method is to use polystyrene spheres as a mask for sputtering. This method is more flexible and various kind of porous metal (including Au, Ag and Al) film can be prepared.

Nanosecond light pulses from an optical parametric oscillator were used as the light source. Polarization states were controlled by achromatic wave plates. Generated voltage was measured with a digital oscilloscope as a function of the incident wavelength or the incident angle. When the transverse voltage is measured as a function of a half-wave plate angle, various patterns are obtained depending on the ellipticity of the incident light. Inversely we can utilize this dependence to deduce ellipticity of unknown polarization [6].

REFERENCES

1. A. Wittstock, J. Biener, J. Erlebacher and M. Bäumer eds, “Nanoporous Gold: From an Ancient Technology to a High-Tech Material,” Royal Society of Chemistry (2012).
2. E. L. Ivchenko, "Circular photogalvanic effect in nanostrucutures," Physics-Uspekhi 45, 1299–1303 (2002).
3. S. D. Ganichev, E. L. Ivchenko, S. N. Danilov, J. Eroms, W. Wegscheider, D. Weiss, and W. Prettl, "Conversion of spin into directed electric current in quantum wells," Phys. Rev. Lett. 86, 4358–4361 (2001).
4. T. Hatano, T. Ishihara, S. G. Tikhodeev and N. A. Gippius, "Transverse photovoltage induced by circularly polarized light," Phys. Rev. Lett. 103, 103906 (2009).
5. M. Akbari, M. Onoda and T. Ishihara, "Photo-induced voltage in nano-porous gold thin film," Opt. Express 23, 823–832 (2015).
6. M. Akbari and T. Ishihara, “Polarization dependence of transverse photo-induced voltage in gold thin film with random nanoholes,” Opt. Express 25, 2143–2152 (2017).

Near-Field Visualization of Plasmons in Single Gold Nanotriangles

K. Imaeda[1], S. Hasegawa[1] and K. Imura[1*]
[1]Graduate School of Science and Engineering, Waseda Univ., Japan
[*]corresponding author: imura@waseda.jp

Abstract-We studied static and dynamic characteristics of plasmons excited in single gold nanotriangles by scanning near-field optical microscope. Near-field transmission images observed near plasmon resonances showed oscillating patterns depending on the observation wavelengths. The observed spatial characteristics are well reproduced by spatial features of eigen functions of a particle confined in a triangular potential well. The dephasing time of the plasmon was visualized by time-resolved near-field imaging, and found that the spatial distribution of the dephasing time varied depending on the excitation positions in the triangle.

Plasmon resonances excited in gold nanoparticles confine light fields spatially and temporally, and consequently induce intense optical fields.[1] To better understand the plasmons, visualization of plasmons is essential. In this study, we performed static and dynamic near-field microscopic measurements on single gold nanotriangles, and revealed the spatio-temporal characteristics of the plasmons excited.[2-4]

Gold nanotriangles were chemically synthesized and dispersed on a coverslip. An aperture-type scanning near-field optical microscope was utilized for optical characterization of the sample. A halogen lamp and a mode-locked Ti:sapphire laser were used for the static transmission and two-photon induced photoluminescence (TPL) measurements, respectively. We also performed time-resolved TPL autocorrelation measurements of the sample to examine the dephasing time of the plasmon.

Near-field transmission spectrum of a single gold nanotriangle shows multiple plasmon resonances from visible to near-infrared spectral region. Figure 1(a) shows a scanning electron micrograph of a gold nanotriangle. Figure 1(b) shows near-field transmission image of the nanotriangle taken at 590 nm. The image shows unique spatial features, which are different from the geometrical shape. The observed spatial features are well reproduced by spatial character of an eigen function calculated for a particle confined in a triangular potential well, as shown in Fig. 1(c). Near-field two-photon excitation image also shows the unique oscillating pattern attributable to plasmon modes excited in the triangle, as is similar to those of the transmission images. We

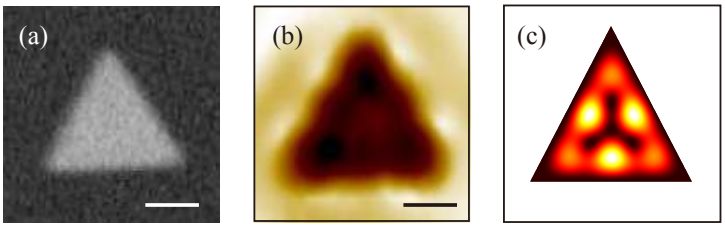

Figure 1(a) A scanning electron micrograph of a single gold nanotriangle. (b) Near-field transmission image of a single gold nanotriangle observed at 590 nm. Scale bars : 200 nm. (c) Calculated eigen function for a particle confined in a triangular potential well.

visualized the spatial distribution of the plasmon dephasing time in a single nanotriangle by time-resolved near-field imaging. We found from the spatial distribution of the dephasing time that the dephasing times varies depending on the internal position on the triangle. The result indicates that the simultaneous excitations of the multiple plasmons are involved in the observation.

REFERENCES

1. Uchida, T., Yoshikawa, Y., Tamura, M. Iida, T., and Imura, K., "Multiple Resonances Induced by Plasmonic Coupling between Gold Nanoparticle Trimers and Hexagonal Assembly of Gold-Coated Polystyrene Microspheres," *J. Phys. Chem. Lett.*, 7, 3652-3658, 2016.
2 Imaeda, K. and Imura, K., "Optical control of plasmonic fields by phase-modulated pulse excitations," *Opt. Express*, 21, 27481-27489, 2013.
3 Nishiyama, Y., Imaeda, K., Imura, K., and Okamoto, H., "Plasmon Dephasing in Single Gold Nanorods Observed By Ultrafast Time-Resolved Near-Field Optical Microscopy," *J. Phys. Chem. C*, 119, 16215-16222, 2015.
4 Nishiyama, Y., Imura, K., and Okamoto, H., "Observation of Plasmon Wave Packet Motions via Femtosecond Time-Resolved Near-Field Imaging Techniques," *Nano. Lett*., 15, 7657-76565, 2015.

Generation of spin waves in nanophotonic structures by femtosecond laser pulses

V. I. Belotelov[1,2*], **M. A. Kozhaev**[1,3], **A. I. Chernov**[1,3], **D. A. Sylgacheva**[1,2], **A. K. Zvezdin**[1,3]

[1]Russian Quantum Center, 143025, Skolkovo, Moscow, Russia

[2]Moscow State University, 119991, Moscow, Russia

[3]Prokhorov General Physics Institute RAS, 119991, Moscow, Russia

[*]corresponding author: v.belotelov@rqc.ru

Abstract Optical non-thermal excitation of magnetostatic spin waves (MSWs) is performed in magnetophotonic crystals (MPCs) and plasmonic structures. It is demonstrated that when excited at the resonance of the MPC the magnetization precession amplitude is enhanced by a factor of 2.5, while the local inverse Faraday effect can be increased up to 5.6 times compared to a stand-alone magnetic film. The origin of the enhancement is the concentration of the electromagnetic energy within the magnetic layer due to the optical confinement.

Ultra-short laser pulses is one of the promising ways for local optical excitation of magnetization dynamics [1], which is highly in demand for various applications. The local spin manipulation is performed only at the light excited area that can be within submicron range and at time scale of femtoseconds. Complex light-matter interaction depends on the type of material studied and light energies used. In iron-garnets, prominent materials for magnonics that demonstrate small damping, non-thermal optical excitation can be performed by photoinduced magnetocrystalline anisotropy, implying the absorption of photons, or via inverse Faraday effect (IFE). Both of the non-thermal excitation types are characterized by the dependence on pump pulses polarization. It has been shown that optical confinement provides a significant enhancement of the direct magnetooptical effects [2] (Faraday rotation, circular and linear birefringence, non-reciprocity).

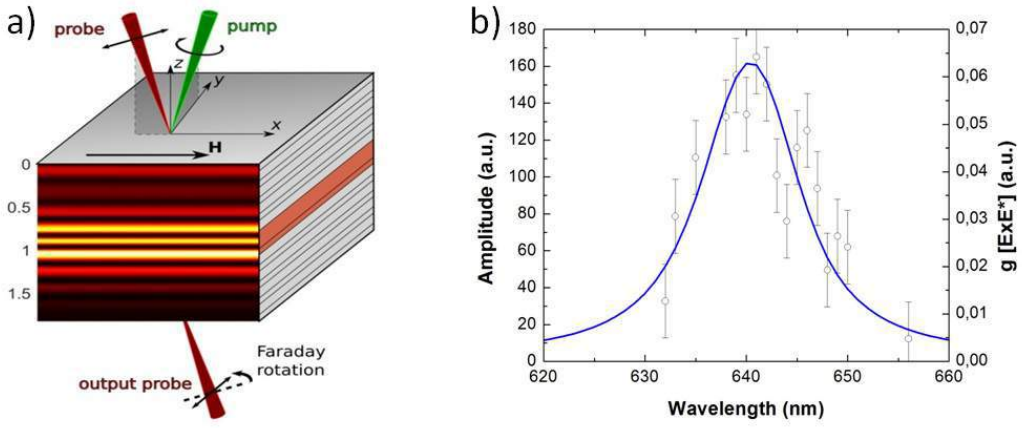

Figure 1 a) Schematic representation of the experiment. Generation of spin waves in magnetophotonic crystal, formed by Bragg mirrors and a transparent magnetic dielectric sandwiched between them. **b)** Amplitude of the magnetization precession and effective field of the inverse Faraday effect versus wavelength of the pump beam.

Micro-structured materials with periodically modulated dielectric constant the so-called magnetophotonic crystals (MPC) have demonstrated the increase of the Faraday effect. Magnetoplasmonic crystals enhance Faraday effect, transversal magneto optic Kerr effect and others up to the orders of a magnitude [3]. It is consistent to expect the possibility of the inverse effects increase in specially tailored periodic structures.

In this work, magnetostatic spin waves (MSWs) have been excited in micro-structured materials (Figure 1). It has been shown that when excited at the resonance of the MPC the magnetization precession amplitude can be enhanced by a factor of 2.5, while the local IFE can be increased up to 5.6 times compared to a stand-alone magnetic film of the same thickness and composition. Alternatively IFE can be enhanced in plasmonic nano-antennas, structures formed by slits or holes in gold-layer or Au-nanoparticles deposited on a magnetic dielectric. Optimal structure parameters that provide effective MSW excitation are found using rigorous coupled-wave approximation. The energy of electromagnetic radiation localized under a nanoparticle is transferred to magnons, which leads to an increase of the effective magnetic field. In both cases optical confinement provides the local impact on the magnetization at spatial scale of several tens of nanometer, which is very promising for holographic memory and quantum information.

Acknowledgements: This work is supported by the Russian President Grant (Project No. MD-1615.2017.2).

REFERENCES

1. Chernov, A. I., Kozhaev, M. A., Savochkin, I. V., Dodonov, D. V., Vetoshko, P. M., Zvezdin A. K., Belotelov, V. I. “Optical excitation of spin waves in epitaxial iron garnet films: MSSW vs BVMSW”, *Opt. Lett.*, Vol. 42, 279, 2017.
2. Shaposhnikov, A. N., Prokopov, A. R., Berzhansky, V. N., Mikhailova, T. V., Karavainikov, A. V., Kharchenko, M. F., Belotelov, V. I., Lukienko, I. M., Miloslavskaya, O. V., Kharchenko, Yu. M., “Magnetooptics of Single and Microresonator Iron-garnet Films at Low Temperatures” *Opt. Mater.*, Vol. 52, 21, 2016.
3. Belotelov, V. I., Akimov, I. A., Pohl, M., Kotov, V. A., Kasture, S., Vengurlekar, A. S., Gopal, A. V., Yakovlev, D. R., Zvezdin, A. K., Bayer, M., “Enhanced magneto-optical effects in magnetoplasmonic crystals” *Nature Nanotech.*, Vol. 6, 370, 2011.

New features of photonic Dirac cones on the Γ point

Kazuaki Sakoda
National Institute for Materials Science
sakoda.kazuaki@nims.go.jp

Abstract- We derive a necessary and sufficient condition for the photonic Dirac cone on the Γ point of periodic metamaterials and photonic crystals. We formulate a Green tensor to show that the propagation direction of the Dirac-cone modes can be controlled by the polarization of the incident wave. We analyze lossy slab modes to show that their group velocity exceeds the light velocity, which apparently contradicts special relativity. This problem of superluminal propagation is resolved by considering the energy velocity.

The Dirac cone is originally an idea to describe the energy spectrum of massless particles. It is characterized by the isotropic linear dependence of their energy on their momentum. A similar energy spectrum was discovered in the dispersion relation of periodic metamaterials in the Brillouin-zone center in the microwave region.[1-4] Such device structures were named CRLH (composite right-/left-handed) transmission lines. To materialize the linear dispersion, it was necessary to make two dispersion curves of the CRLH transmission line degenerate in the zone center, or the Γ point of the Brillouin zone, by the fine tuning of the device structure.

Later the materialization condition of the Dirac cone in the dispersion relation of periodic metamaterials and photonic crystals was clarified for general cases by tight-binding approximation[5-7] and the k-p perturbation theory.[8,9] Mei et al.[8] discussed the formation of the Dirac cone, the Berry phase, and mapping into the Dirac Hamiltonian for phononic and photonic crystals, while the present author derived the sufficient condition for the Dirac-cone formation.[9] Because the effective refractive index is equal to zero at the vertex of the Dirac cone,[10] which is called the Dirac point, quite curious phenomena and their applications are expected. We can also expect novel phenomena like the control of the propagation direction by the polarization of the incident wave.[11]

For the photonic Dirac cone to be materialized, two electromagnetic eigenmodes with particular symmetry combinations should have the same frequency in the Brillouin-zone center by fine-tuning the structure and/or the material parameters. Examples of the photonic Dirac-cone dispersion relation are shown in Fig. 1 where ω_r denotes the Dirac-point frequency. The Dirac cone with an auxiliary quadratic dispersion surface is realized, for example, in metamaterials of the C_{4v} symmetry, while the double Dirac cone is realized in the triangular-lattice metamaterials of the C_{6v} symmetry. The dispersion relation was derived by the first-order perturbation based on the k-p perturbation theory and the group theory.[9] For example, in the case of the degeneracy of an E mode and an A_1 mode in the two-dimensional square lattice of the C4v symmetry, the eigen frequency around ω_r is obtained by diagonalizing the following perturbation matrix, where *b* is a sample parameter.

$$\mathrm{C}_{\mathbf{k}}^{(EA_1)} = \begin{pmatrix} 0 & 0 & bk_x \\ 0 & 0 & bk_y \\ b^*k_x & b^*k_y & 0 \end{pmatrix}$$

By solving the eigen problem, we obtain three solutions, two of which give the isotropic linear dispersion.

We apply our theory to photonic crystal slabs (Fig. 2) to show that the propagation direction of the Dirac-cone mode in the slab can be controlled by the polarization of the incident wave. For this purpose, we

derive the retarded Green tensor to describe the optical response of the Dirac-cone modes.[11] We analyze the dispersion and the propagation speed of the slab Dirac-cone modes with diffraction loss to show that their apparent group velocity can be larger than the light velocity in free space, *c*, which contradicts special relativity. This problem of superluminal propagation is resolved by considering the energy velocity, which remains smaller than *c*.[12]

Acknowledgements

This study was supported by KAKENHI 16K13825.

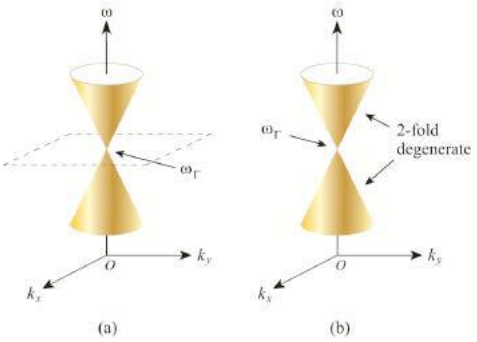

Fig. 1 (a) Dirac cone with a quadratic dispersion surface (broken line). (b) Double Dirac cone.

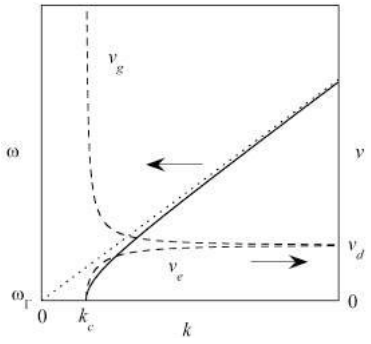

Fig. 2 The dispersion relation and velocity of photonic Dirac-cone modes. The solid (dotted) line is the dispersion curve for the Dirac cone with (without) the diffraction loss. The two broken lines denote v_g (group velocity) and v_e (energy velocity) of the lossy Dirac cone. The left (right) vertical axis is the angular frequency (velocity) of the Dirac-cone mode and the horizontal axis is the wave vector.

REFERENCES

1. Sanada, A. et al., IEEE Microwave Wireless Components Lett. **14** (2), 68-70 (2004).
2. Caloz, C. et al., IEEE Trans. Microwave Theory Tech. **52** (3), 980-992 (2004).
3. Sanada, A. et al., IEEE Trans. Microwave Theory Tech. **52** (4), 1252-1263 (2004).
4. Caloz, C. et al, *Electromagnetic Metamaterials: Transmission Line Theory and Microwave Applications* (Wiley, New York, 2005).
5. Sakoda, K. et al., Opt. Express **18** (26), 27371-27386 (2010).
6. Sakoda, K. et al., Opt. Express **20** (4), 3898-3917 (2012).
7. Sakoda, K., Opt. Express **20** (9), 9925-9939 (2012).
8. Mei, J. et al., Phys. Rev. B **86** (3), 035141 (2012).
9. K. Sakoda, Opt. Express **20** (22), 25181-25194 (2012).
10. Huang, X. et al., Nature Mater. **10**, 582--586 (2011).
11. Sakoda, K., Phys. Rev. A **90** (1), 013835/1-8 (2014).
12. Sakoda, K. et al., Abstract Book of 10th Int. Symp. Modern Opt. Appl. (Bandung), 68–69 (2015).
13. Yao, Y. et al., J. Phys. Soc. Jpn. **85** (6), 065002 (2016).

Advanced numerical and theoretical tools as applied to modern nano photonics â€

Radiative heat-transfer between metallic gratings using adaptive spatial resolution

R. Messina, A. Noto, B. Guizal, and M. Antezza (Invited speaker)
Laboratoire Charles Coulomb - UMR 5221 CNRS, University of Montpellier, Montpellier, France

Contact address: mauro.antezza@umontpellier.fr

Abstract- We calculate the radiative heat transfer between two identical metallic one-dimensional lamellar gratings [1]. To this aim we present and exploit a modification to the widely-used Fourier modal method [2], known as adaptive spatial resolution [3], based on a stretch of the coordinate associated to the periodicity of the grating. We first show that this technique dramatically improves the rate of convergence when calculating the heat flux, allowing to explore smaller separations. We then present a study of heat flux as a function of the grating height, highlighting a remarkable amplification of the exchanged energy, ascribed to the appearance of spoof-plasmon modes, whose behavior is also spectrally investigated. Differently from previous works, our method allows us to explore a range of grating heights extending over several orders of magnitude. By comparing our results to recent studies we find a consistent quantitative disagreement with some previously obtained results going up to 50%. In some cases, this disagreement is explained in terms of an incorrect connection between the reflection operators of the two gratings.

REFERENCES

1. R. Messina, A. Noto, B. Guizal and M. Antezza, "Radiative heat-transfer between metallic gratings using adaptive spatial resolution," arXiv:1612.05516 (2016).
2. G. Granet and B. Guizal, "Efficient implementation of the coupled wave method for metallic lamellar gratings in TM polarization," *J. Opt. Soc. Am. A*, Vol 13, No 5, 1019-1023, (1996).
3. B. Guizal, H. Yala and D. Felbacq, "Reformulation of the eigenvalue problem in the Fourier modal method with spatial adaptive resolution," *Optics Letters*, Vol. 34, N°18, pp 2790-2792, September (2009).

The Fourier Modal Method with Adaptive Spatial Resolution under conical mounting

B. Guizal
Laboratoire Charles Coulomb - UMR 5221 CNRS, University of Montpellier, Montpellier, France

corresponding author: bguizal@montp2.fr

Abstract- The Fourier Modal Method [1] equipped with the concept of Adaptive Spatial Resolution [2] (FMMASR) is derived and presented, in details, in the case of lamellar diffraction gratings under conical mounting. In the present work, we focus on efficiency and reduction of the numerical load. Therefore, special care is given to homogeneous media where we exploit two properties: (i) in such media the Eigen-problem can be simplified and reduced to its half size and (ii) once the solution is obtained for a given homogeneous medium, the solution for any other homogeneous medium can be readily deduced and with extremely low computational cost.

REFERENCES

1. G. Granet and B. Guizal, "Efficient implementation of the coupled wave method for metallic lamellar gratings in TM polarization," *J. Opt. Soc. Am. A*, Vol 13, No 5, 1019-1023, 1996.
2. B. Guizal, H. Yala and D. Felbacq, "Reformulation of the eigenvalue problem in the Fourier modal method with spatial adaptive resolution," *Optics Letters*, Vol. 34, N°18, pp 2790-2792, September 2009.

Graphene based 1D photonic crystals bands via the Fourier Modal Method

M. Ben Rhouma[1], M. Oueslati[1] and B. Guizal[2*]

[1]Université de Tunis El Manar, Unité des Nanomatériaux et Photonique, 2092, El Manar, Tunisie

[2]Laboratoire Charles Coulomb - UMR 5221 CNRS, University of Montpellier, Montpellier, France

[*]corresponding author: bguizal@montp2.fr

Abstract- The Fourier Modal Method (FMM) [1] is used to obtain the band structure of a 1D graphene based photonic crystal. The approach is valid for the first bands where the conductivity of graphene can be described by a Drude model. The structure consists of graphene layers periodically inlayed in a homogeneous lossless dielectric host medium. In the model, the graphene sheet is considered as layer with atomic thickness and its dielectric permittivity is deduced from its surface conductivity. Under these conditions, we show that it is possible to use the FMM in order to obtain a polynomial eigenvalue problem allowing the computation of the band structure. Furthermore, we explore the spatial field-structure of certain modes.

REFERENCES

1. G. Granet and B. Guizal, "Efficient implementation of the coupled wave method for metallic lamellar gratings in TM polarization," *J. Opt. Soc. Am. A*, Vol 13, No 5, 1019-1023, 1996.

Analytical T-matrix solution to the 1D grating diffraction problem.

A. A. Shcherbakov

Moscow Institute of Physics and Technology, Russia
alex.shcherbakov@phystech.edu

Abstract— The combination of two rigorous methods, namely, the C-method and the true modal method for 1D grating diffraction problem allows one, first, to analytically prove the validity of the Rayleigh expansion in the grating region, and, second, to obtain a general analytical solution to the diffraction problem in form of the T-matrix, which elements are written as quadratures involving grating profile function.

The Rayleigh hypothesis (RH) was a subject of intensive debates for quite a long time. Even after establishment of theoretical limits on the validity of the RH [**?**, **?**, **?**, **?**, **?**, **?**] in a series of works, there was evidence calling into question these limits [**?**, **?**]. Moreover, article [**?**] demonstrated that the RH can be successfully used to analyse diffraction by deep sinusoidal gratings, and even for the correct near field calculations. In [**?**] there were formulated a concept and basic steps for an analytical proof of the RH. This work implements these ideas and demonstrates that the association of a basic Chandezon method [**?**] idea, namely, the coordinate transformation, which does not depend on any hypothesis, and the True Modal Method technique [**?**] - a construction of the modal basis of the true permittivity and permeability profile - leads to the required proof, and yields an analytical solution to the grating diffraction problem.

Consider a 1D grating of period Λ which profile is defined by piecewise twice differentiable function $f(x)$. Suppose that this profile defines the interface between upper and lower homogeneous isotropic media with dielectric permittivity and magnetic permeability ε_a, μ_a, and ε_b, μ_b respectively. Then, it is derived that components of the T-matrix of this grating relating upward (sign "+") and downward (sign "−") propagating harmonics of indices p and q at both sides of the interface are given by

$$\begin{aligned}
T_{pq}^{++} &= \zeta_{pq}^{+}\frac{1}{\Lambda}\int_0^{\Lambda}\exp\left[j(q-p)Kx + j(\beta_q^a - \beta_p^b)f(x)\right]dx,\\
T_{pq}^{+-} &= \zeta_{pq}^{-}\frac{1}{\Lambda}\int_0^{\Lambda}\exp\left[j(q-p)Kx - j(\beta_q^a + \beta_p^b)f(x)\right]dx,\\
T_{pq}^{-+} &= \zeta_{pq}^{-}\frac{1}{\Lambda}\int_0^{\Lambda}\exp\left[j(q-p)Kx + j(\beta_q^a + \beta_p^b)f(x)\right]dx,\\
T_{pq}^{--} &= \zeta_{pq}^{+}\frac{1}{\Lambda}\int_0^{\Lambda}\exp\left[j(q-p)Kx - j(\beta_q^a - \beta_p^b)f(x)\right]dx.
\end{aligned} \tag{1}$$

Here $K = 2\pi/\Lambda$, $\beta_q^{a,b} = \sqrt{\omega^2\varepsilon_{a,b}\mu_{a,b} - k_{x,q}^2}$ with $k_{x,q} = k_x^{inc} + Kq$, and factors $\zeta_{pq}^{\pm}$ are rational functions of $\varepsilon_{a,b}$, $\mu_{a,b}$, $\beta_{p,q}^{a,b}$, and $k_{x;p,q}$, different for the TE and the TM polarization. The Rayleigh decomposition

$$F_y = \begin{cases} \displaystyle\sum_{p=-\infty}^{\infty} b_p^{+}\exp\left(jk_{1p}x + j\beta_p^b z\right) + b_p^{-}\exp\left(jk_{1p}x - j\beta_p^b z\right), z \le f(x), \\ \displaystyle\sum_{p=-\infty}^{\infty} a_p^{+}\exp\left(jk_{1p}x + j\beta_p^a z\right) + a_p^{-}\exp\left(jk_{1p}x - j\beta_p^a z\right), z > f(x), \end{cases} \tag{2}$$

is also proven to be valid (here F_y stands for transverse field).

Despite one often searches for a solution to the diffraction problem in S-matrix form, the obtained result presents certain advantages. First, it opens an opportunity to transform the T-matrix analytically. Second, it displays the structure of the T-matrix assisting in its smart transformation. Third, in some cases (like the inverse problem, for example) the solution in the form of a T-matrix can be sufficient.

ACKNOWLEDGMENT

The work was supported in part by the Russian Foundation for Basic Research (No. 16-29-11747-ofi-m). Major contribution to the presented results was made by Prof. Alexandre Tishchenko, who deceased in August 2016.

REFERENCES

1. Uretski, J. L., "The scattering of plane waves from periodic surfaces," *Ann. Phys.*, Vol. 33, 400–427, 1965.
2. Petit, R. and M. Cadilhac, "Sur la diffraction dune onde plane par un réseau infinement conducteur," *C. R. Acad. Sci. Paris*, Vol. 262B, 468–471, 1966.
3. Millar, R. F., "On the rayleigh assumption in scattering by a periodic surface, II," *Proc. Cambridge Philos. Soc.*, Vol. 69, 217–225, 1971.
4. Pavageau, J., "Sur la méthode des spectres d'ondes planes dans les problèmes de diffraction," *C. R. Acad. Sci. Paris*, Vol. 266B, 135–138, 1968.
5. Bates, R. H. T., "Analytic constraints on electromagnetic field computations," *IEEE Trans. Microwave Theory and Tech.*, Vol. MTT-23, 605–623, 1975.
6. Wirgin, A., "On Rayleigh theory of sinusoidal diffraction gratings," *Opt. Acta*, Vol. 27, 1671–1692, 1980.
7. Watanabe, T., Y. Choyal, K. Minami and V. L. Granatstein, "Range of validity of the Rayleigh hypothesis," *Phys. Rev. E*, Vol. 69, 056606, 2004.
8. Elfouhaily, T. and T. Hahn, "Rayleigh's hypothesis and the geometrical optics limit," *Phys. Rev. Lett.*, Vol. 97, 120404, 2006.
9. Tishchenko, A. V., "Numerical demonstration of the validity of the Rayleigh hypothesis," *Opt. Express*, Vol. 17, 17102–17117, 2009.
10. Tishchenko, A. V., "Rayleigh was right: Electromagnetic fields and corrugated interfaces," *Opt. Photon. News*, Vol. 21, 50–54, 2010.
11. Chandezon, J., D. Maystre, and G. Raoult, "A new theoretical method for diffraction gratings and its numerical application," *J. Opt. Paris*, Vol. 11, 235, 1980.
12. Botten, L. C., M. S. Craig and J. L. McPhedran, "The dielectric lamellar diffraction grating," *Opt. Acta*, Vol. 28, 413–428, 1981.

Nitride-on-silicon platform for UV-visible photonics with integrated microlaser sources.

J. Sellés[1], T. Guillet[1], V. Crepel[1], B. Gayral[2,3], B. Damilano[4], M. Leroux[4], M. Mexis[4], S. Rennesson[4], F. Semond[4], F. Tabataba-Vakili[5], I. Roland[5], X. Checoury[5], P. Boucaud[5] and C. Brimont[1*]

[1] Laboratoire Charles Coulomb (L2C), UMR 5221, CNRS-Université de Montpellier, Montpellier, France

[2] Univ. Grenoble Alpes, Grenoble, France

[3] CEA, INAC-PHELIQS, "Nanophysique et Semiconducteurs" group, Grenoble, France

[4] Université Côte d'Azur, CRHEA-CNRS, rue Bernard Grégory, Valbonne-Sophia Antipolis, France

[5] Centre de Nanosciences et de Nanotechnologies, CNRS, Univ. Paris Sud, Univ. Paris-Saclay, Orsay, France

[*]corresponding author: Christelle Brimont@umontpellier.fr

Abstract-Biochemical detection applications and on-chip optical interconnects are examples of the useful applications considered for integrated photonic platforms dedicated to the UV and visible spectral range. This achievement requires the realization of efficient and compact microlaser sources that can be coupled to optical waveguides and are compatible with photonic circuitry. We develop a cost-effective practical approach relying on the controlled growth of thin AlN buffer layers on silicon substrates, followed by the growth of multiple quantum wells (MQW) GaN/AlN (for UV operation), or InGaN/GaN MQWs (for violet and blue operation) with a high radiative efficiency up to T=300K. This unique Nitride-on-Silicon platform could be released into a membrane by the selective under-etching of the silicon substrate.

We present a series of microdisk lasers operating at room temperature under pulsed optical excitation over a broad spectral range extending from 275nm to 470nm. All microdisks present a Q factor above 1000 and reach 4000 in the best resonators. We are able to investigate the gain threshold of the different active layers. The microlasers operate under pulsed optical excitation, and the lasing threshold is reduced by a factor 10 from deep-UV GaN/AlN microdisks to the violet InGaN/GaN ones. This work allows us to expect a variety of integrated photonics applications, including for example multi-color integrated laser sources: we demonstrate here the versatility of this nitride-on-silicon platform, and the first realization on this platform of efficient active layers for a tunable lasing action over a 200nm broad UV to visible spectral range. [1,2].

Acknowledgements: The authors acknowledge support from the projects GANEX (ANR-11-LABX-0014) and QUANONIC (ANR-13-BS10-0010). GANEX belongs to the public funded 'Investissements d'Avenir' program managed by the French ANR agency. This work was also partly supported by the RENATECH network.

REFERENCES

1. Sellés et al., APL 109, 231101 (2016)
2. Sci. Rep. 6, 21650 (2016)

Far and near field optical properties of large scale spherical microparticle arrays

A. A. Shcherbakov[1], **T. Kaempfe**[2], **and Y. Jourlin**[2]

[1]Moscow Institute of Physics and Technology, Laboratory of Nanooptics and Plasmonics, Dolgoprudnyi, Russia

[2]University of Lyon, Lab Hubert Curien UMR CNRS 5516, Saint-Etienne, France

alex.shcherbakov@phystech.edu

Abstract— The work is devoted to experimental and theoretical study of the far and the near field optical properties of 2D monolayer arrays of silica microspheres. In the far field results of measurements of angular dependent diffraction are compared with simulation of realistic monolayers performed by the Generalized Source Method. In the near field simulation results are used to predict geometric parameters of microscale arrays obtained by the colloidal lithography.

Ordered monolayer arrays of silica microspheres attract high interest due to promising applications in photovoltaics, mainly for light trapping functionality. They were demonstrated to increase outcoupling efficiency in organic light-emitting diodes and to possess attractive antireflection properties useful for solar cells. Layers of silica microspheres often represent highly ordered structures thus making diffracted light to be strongly angular dependent. For applications it is then important to be able to carefully predict and optimize both spectral and angular optical characteristics of arranged silica particles.

For preparation of experimental samples we used the Langmuir-Blodgett technique. It is one of the most efficient methods for preparing regular monolayers of microspheres over large areas with homogeneous deposition of the particles. First, 1 μm diameter spherical silica particles were suspended in butanol (concentration was 35 mg/ml). After ultrasonic dispersion during 30 min, the particles were injected into a carrier fluid and brought to liquid surface to form a monolayer array with the aid of surface tension forces. The quality of the self-assembly of particles within the transfer zone was controlled by a camera with a custom image processing software [**?**].

In this work we first present experimental measurements of diffraction efficiency angular dependency for plane wave diffraction on high-quality ordered monolayer of silica microspheres, which supplement data previously published by other authors. Simulation of experimental results was performed by a highly efficient rigorous diffraction calculation method [**?**] taking into account realistic microsphere arrangement and particle size dispersion. This allowed us to obtain reasonably good correspondence between experiment and theory, and to qualitatively explain the shapes of the experimental curves, as well as the observed differences between experimental and theoretical results. Comparison of simulations of freely suspended monolayers and monolayers on a substrate revealed a grating anomaly nature of peculiarities of the obtained curves. Furthermore, simulation of substrate interference effects allowed us to carefully predict the microscopic structure of micropillar arrays obtained with the colloidal lithography technique.

ACKNOWLEDGMENT

The work was supported in part by the Russian Foundation for Basic Research (No. 16-29-11747-ofi-m).

REFERENCES

1. Delléa, O., O. Shavdina, P. Coronel, E. Ollier and S.-F. Désage, "Control methods in microspheres precision assembly for colloidal lithography," *IFIP Advances in Information and Communication Technology*, Vol. 345, 107–117, 2014.
2. Shcherbakov, A. A. and A. V. Tishchenko, "New fast and memory-sparing method for rigorous electromagnetic analysis of 2D periodic dielectric structures," *J. Quant. Spectrosc. Radiat. Transfer,*, Vol. 113, 158–171, 2012.

Treatment of the nonconvergence of the Fourier modal method and the C method arising from field hypersingularities

Haitao Liu[1*], Yanpeng Mei[1], Junda Zhu[1], and Ying Zhong[2]

[1]Key Laboratory of Optical Information Science and Technology, Ministry of Education, Institute of Modern Optics, Nankai University, Tianjin 300350, China

[2]State Key Laboratory of Precision Measuring Technology and Instruments, Tianjin University, Tianjin 300072, China

[*]corresponding author: liuht@nankai.edu.cn

Abstract-Perturbative approaches are reported to overcome the recently observed nonconvergence of the Fourier modal method (FMM) and the coordinate transformation method (C method) arising from field hypersingularities at lossless metal-dielectric edges. Perturbations of profile or refractive index are applied for representative examples of triangular or parallelogram (or rectangular) gratings, respectively. However, for vanishing perturbations, the converged values of the diffraction efficiency can approach a fixed value for some numerical examples but cannot for other examples.

For modeling diffraction gratings the FMM is perhaps the most widely used method due to its simplicity and versatility. Thanks to previous revolutionary works such as the correct Fourier factorization rules and the scattering-matrix propagation algorithm, the convergence and stability of the FMM have been dramatically improved. Despite of this, the FMM still shows nonconvergence for binary gratings with certain sets of grating parameters [1]. This nonconvergence of the FMM is then attributed to the existence of irregular field singularities [2] (or called hypersingularities [3]) at lossless metal-dielectric right-angle edges, for which the transverse electric field components approach infinity as ρ^{-1} near the edge (ρ being the distance to the edge). The nonconvergence of the FMM and the C method for gratings with lossless metal-dielectric arbitrary-angle edges is further proposed and attributed to the field hypersingularities [3].

Here we propose perturbative treatment to overcome the nonconvergence of the FMM and the C method arising from the field hypersingularities [4,5]. Triangular gratings and parallelogram (or rectangular) gratings are taken as representative numerical examples. For triangular gratings with hypersingularities, we replace the sharp edge with a rounded edge to remove the hypersingularities at the edge, and then observe the convergence of diffraction efficiency with the C method. However, by gradually decreasing the radius of the rounded edge, the converged values of the diffraction efficiency do not approach a fixed value (the expected value for the sharp edge) [Figs. 1(c)-(d)]. For the example of parallelogram (or rectangular) gratings with hypersingularities, we smooth the grating boundaries with a medium of gradually varied refractive index to remove the hypersingularities. With the decrease of the width of the perturbative medium, the converged values of the diffraction efficiency can approach a fixed value for some numerical examples [Figs. 1(a)-(b)] but cannot for other examples of parallelogram gratings. While for rectangular gratings the converged diffraction efficiency can always approach a fixed value [4]. We also find that for deep sub-wavelength parallelogram or rectangular gratings, the FMM tends to converge even with the existence of hypersingularities, and the converged value of diffraction efficiency consists well with the theoretical value predicted by the effective medium theory.

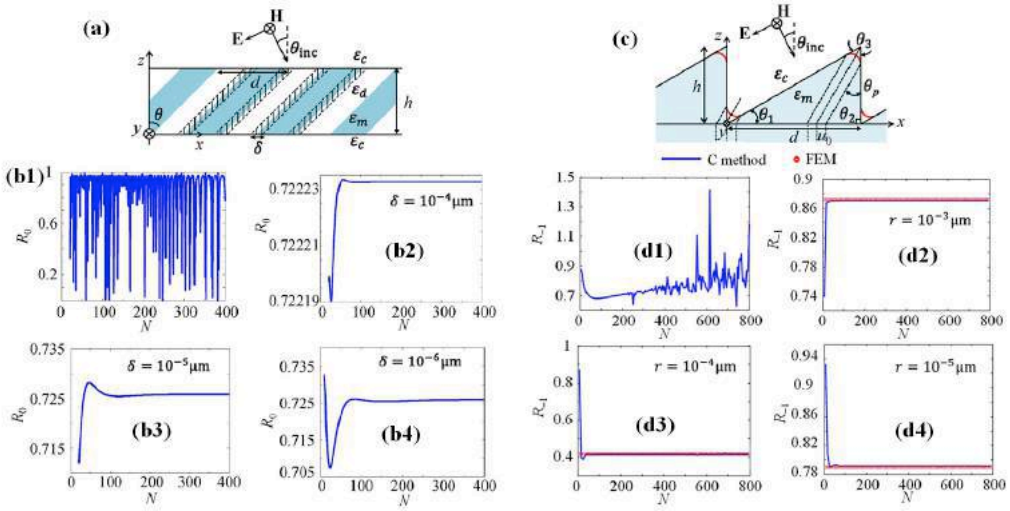

Figure 1 (a) Treatment to overcome the nonconvergence of the FMM for parallelogram or rectangular gratings by smoothing the sharp lamellar boundaries with a gradually-varied medium (with a width δ). (b) Convergence test of the 0th-order reflection efficiency R_0 for the parallelogram grating with different δ. The grating parameters are the same as those in Fig. 6(b) of [3], and (b1) shows the reproduced nonconvergence results. (c) Treatment to overcome the nonconvergence of the C method for triangular gratings by replacing the sharp edge with a rounded edge (with a radius r). (d) Convergence test of the -1st-order reflection efficiency R_{-1} for asymmetric triangular gratings with different r. The grating parameters are the same as those in Fig. 7(b) of [3], and (d1) shows the reproduced nonconvergence results.

Acknowledgements This work is financially supported by the National Key Basic Research Program of China (973 Program) under Grant No. 2013CB328701, and the Natural Science Foundation of China (NSFC) under Grant No. 61322508.

REFERENCES

1. Gundu, K. M. and A. Mafi, "Reliable computation of scattering from metallic binary gratings using Fourier-based modal methods," *J. Opt. Soc. Am. A*, Vol. 27, 1694–1700, 2010.
2. Li, L. and G. Granet, "Field singularities at lossless metal-dielectric right-angle edges and their ramifications to the numerical modeling of gratings," *J. Opt. Soc. Am. A*, Vol. 28, 738–746, 2011.
3. Li, L. "Field singularities at lossless metal-dielectric arbitrary-angle edges and their ramifications to the numerical modeling of gratings," *J. Opt. Soc. Am. A*, Vol. 29, 593–604, 2012.
4. Mei, Y., H. Liu and Y. Zhong, "Treatment of nonconvergence of Fourier modal method arising from irregular field singularities at lossless metal-dielectric right-angle edges," *J. Opt. Soc. Am. A*, Vol. 31, 900–906, 2014.
5. Zhu, J., H. Liu and Y. Zhong, "Treatment of nonconvergence of the Fourier modal method and C method arising from field hypersingularities at lossless metal–dielectric arbitrary-angle edges," *J. Opt. Soc. Am. A*, Vol. 33, 845–853, 2016.

Numerical modeling of biperiodic structures by a vertical mode expansion method

Hualiang Shi[1,*], **Ya Yan Lu**[2]

[1]Beijing Computational Science Research Center, Beijing, China
[2]Department of Mathematics, City University of Hong Kong, Hong Kong, China
shi.hualiang@csrc.ac.cn

Abstract— The vertical mode expansion method (VMEM) is a special numerical method tailor-made for analyzing the scattering of light by structures with multiple finite-height cylindrical objects. In this paper, a VMEM with 2D boundary integral equations is implemented for biperiodic structures consisting of cylindrical objects with arbitrary cross sections.

Due to the existing nanofabrication techniques, many photonic structures can be considered as combinations of numerous cylindrical inclusions. Mathematically, in a Cartesian coordinate system $\{x, y, z\}$ where the z-axis is perpendicular to the substrate surface, a typical cylindrical region is $S_l = \{(x, y, z) : (x, y) \in \Omega_l, -\infty < z < \infty\}$, where Ω_l is the cross section of the l^{th} cylindrical object, and the material parameters depend only on z in S_l. Taking advantage of the periodicity of the entire structure, the problem can be considered only in a unit cell. In the simplest case, a unit cell consists of two regions S_0 and S_1, and we assume S_0 encloses S_1. Examples of a biperiodic structure and its unit cell are shown in Fig. 1. In the vertical mode expansion method

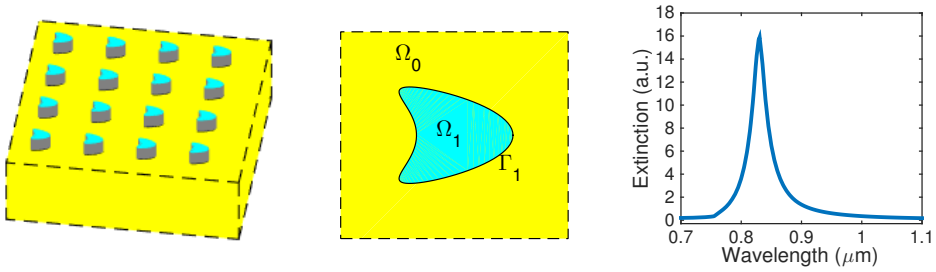

Figure 1: Left: a periodic array of particles on a substrate. Middle: cross section of a unit cell. Right: extinction spectra of the left periodic array of gold elliptic cylinders for a normal incident plane wave.

(VMEM) [1, 2], the field in S_l is expanded in the vertical modes $\phi_j^{(l,p)}(z)$ (where $p = e$ or $p = h$ for two different polarizations) with corresponding expansion "coefficients" $V_j^{(l,p)}(x, y)$. The unknown $V_j^{(l,p)}$ satisfies a 2D Helmholtz equation in Ω_l. An important step in the VMEM is to solve a linear system for all $V_j^{(l,p)}$ or $\partial_\nu V_j^{(l,p)}$ on Γ_l, where Γ_l is the boundary of Ω_l and ν is a unit normal vector to it. In a unit cell, the linear system only need to be set up on Γ_1. To achieve this, we calculate the Neumann-to-Dirichlet operator $\mathcal{N}_j^{(l,p)}$ which maps $\partial_\nu V_j^{(l,p)}$ to $V_j^{(l,p)}$ on Γ_1 for $l = 0, 1$. The operators can be obtained by the boundary integral equation (BIE) method [2]. Particularly, for the domain Ω_0, we need to incorporate the quasi-periodic boundary conditions in the BIEs. To illustrate the method, a numerical example is shown in Fig. 1.

The VMEM gives 2D formulations for 3D problems, and it is relatively simple to implement and highly competitive in terms of efficiency and accuracy.

REFERENCES

1. X. Lu, H. Shi, and Y. Y. Lu, "Vertical mode expansion method for transmission of light through a single circular hole in a slab," *J. Opt. Soc. Am. A*, Vol. 31, No. 2, 293–300, 2014.
2. H. Shi and Y. Y. Lu, "Efficient vertical mode expansion method for scattering by arbitrary layered cylindrical structures," *Opt. Express*, Vol. 23, No. 11, 14618–14629, 2015.

The role of first- and second order light scattering processes in decomposing the 3D nanostructure of butterfly wing scales.

G. I. Márk[1*], K. Kertész[1], G. Piszter[1], Zs. Bálint[2], and L. P. Biró[1]
[1]Institute of Technical Physics and Materials Science, Centre for Energy Research, Budapest, Hungary
[2]Hungarian Natural History Museum, Baross Utca 13, H-1088 Budapest, Hungary
[*]corresponding author: mark@mfa.kfki.hu, www.nanotechnology.hu

Abstract-We identified two different scattering processes characteristic of the low- and high wavelength ranges of optical reflection spectra of butterfly wing scales. Our computer simulations based on the solution of 3D Maxwell equations helps to understand the connection between the wing scale nanoarchitecture and the measured optical spectrum.

The color of various butterflies may originate not only from pigments, but from photonic nanoarchitectures [1], too, found in the scales covering their wings. Most important tools to analyze the structure of wing scales are top-view Scanning Electron Microscopy (SEM) and cross sectional Transmission Electron Microscopy (TEM) imaging. Both methods give only two dimensional (2D) information and it is a non trivial task to decompose the real three dimensional (3D) structure of the scale based on these 2D images. We performed extensive full 3D Maxwell equation calculations to reveal the connection between the 3D structure and the optical spectrum, utilizing many different scale structure models, for the so called "pepper-pot" scale structure, typical of Lycaenid butterflies [2,3]. Our simulations showed that different scattering processes determine the spectrum in different wavelength ranges. For large wavelengths (>350 nm) the optical reflection can be well described by a corresponding effective multilayer model and the peak positions are well represented by a simple first order scattering approximation [4]. One has to include second order scattering processes inside the layers, however, in order to correctly reproduce the small wavelength side of the spectrum (<350 nm). Hence, to calculate the large wavelength part of the spectrum one needs the parameters of the layer structure, which is provided by TEM images. Detailed information on the layer structure, which is provided by the SEM images, is only necessary for calculating the small wavelength part of the spectrum.

REFERENCES

1. Biró, L. P. and Vigneron, J. P. "Photonic nanoarchitectures in butterflies and beetles: valuable sources for bioinspiration", *Laser Photon. Rev.* Vol. 5, 27–51, 2011.
2. Bálint, Z., Kertész, K., Piszter, G., Vértesy, Z., and Biró, L. P. "The well-tuned blues: the role of structural colours as optical signals in the species recognition of a local butterfly fauna (Lepidoptera: Lycaenidae: Polyommatinae)", *J. R. Soc. Interface* Vol 9, 1745–56, 2012.
3. Wilts, B. D., Leertouwer, H. L., and Stavenga, D. G. "Imaging scatterometry and microspectrophotometry of Lycaenid butterfly wing scales with perforated multilayers", *J. R. Soc. Interface* 6 Suppl 2, S185-92 (2009).
4. Márk, G. I., Vértesy, Z., Kertész, K., Bálint, Zs., and Biró, L. P. "Order-disorder effects in structure and color relation of photonic-crystal-type nanostructures in butterfly wing scales", *Phys.Rev.E* Vol 80, 051903-1, 2009.

Polynomial modal method for complex Meta-surfaces modeling

K. Edee[1], **J. P. Plumey**[1], **and A. Moreau**[1]

[1]Université Clermont Auvergne, Institut Pascal, BP 10448,
F-63000 Clermont-Ferrand, France
CNRS, UMR 6602, IP, F-63171 Aubière, France
kofi.edee@uca.fr

Abstract— Metasurfaces are planar metamaterials that consist of a single or a few stack of subwavelength thickness metal-dielectric layers. They could be periodically structured or not with subwavelength scale patterns according to the transverse directions. The strong interaction between an electromagnetic field components and these surfaces, exhibits some properties that could not be found in nature. These artificial properties strongly depend on the shape and arrangement of the elementary patterns and they are often linked to a plasmon resonance phenomenon. Metasurfaces working in the visible range generally consist in periodical arrangments of plasmonic resonators. These resonators are inherently muti-scale, as their responses relie on the excitation of resonances in very small gaps, like in the case of gap-plasmon resonators or for bow-tire antennas. The simulation of their electromagnetic response can be very challenging and may be successfully treated thanks to a modal method holding the complexity of the patterns shape. Here we present a polynomial modal method [1, 2, 3, 4] that is particularly suited for the simulation of metallic structures. Advanced coordinates transformation such as matched coordinates and tilted coordinates are included in order to hold efficiently the complexity of the geometry without any approximation. Such a tool even offers the possibility to control the way the resonators are periodically arranged.

ACKNOWLEDGMENT

This work was financially supported through the Physics of Gap-Plasmons project number ANR-13-JS10-0003 of the French National Research Agency.

REFERENCES

1. K. Edee "Modal method based on subsectional Gegenbauer polynomial expansion for lamellar grating," *JOSA A*, Vol. 28 N^o 9, 2011
2. K. Edee, M. Abboud, G. Granet, J.-F. Cornet and N. A. Gippius "Mode solver based on Gegenbauer polynomial expansion for cylindrical structures with arbitrary cross sections," *JOSA A* Vol. 31, 667-676 2014
3. K. Edee, J.-P. Plumey " Numerical scheme for the modal method based on subsectional Gegenbauer polynomial expansion: application to biperiodic binary grating" *JOSA A* Vol. 31, 402-410 2015
4. K. Edee, J.-P. Plumey, B. Guizal " Unified Numerical Formalism of Modal Methods in Computational Electromagnetics and Latest Advances: Applications in Plasmonics" *Elsevier, Advances in Imaging and Electron Physics* Vol. 197, chapter 2 2016

Tailoring fluctuation-induced interactions with nanostructures.

F. Intravaia

Max-Born-Institut, 12489 Berlin, Germany
francesco.intravaia@mbi-berlin.de

Abstract— We investigate how the strength and the functional dependence of fluctuation-induced interactions are altered by acting on the geometry and the material properties of the system's constituents.

In the constant race towards miniaturization driven by modern technologies, phenomena which are irrelevant at the macroscopic level become more and more important for systems with micro- and nano-scopic size. A large class of these effects are fluctuation-induced interactions which find their origin in the classical and quantum fluctuations of the system. Paradigmatic examples are van der Waals forces and the Casimir effect [1]. The understanding and control of these interactions is essential for opening new avenues for fundamental investigations and for designing new and better performing nanodevices.

Recent investigations have shown that tailoring the geometry and leveraging on the material properties of the system can lead to profound modifications of these phenomena, offering an additional knob to study and to harness these interactions [2]. Along these lines, in this contribution we review some recent results addressing equilibrium and nonequilibrium fluctuation-induced interactions with atomic and mesoscopic systems (e.g. MEMS) [3, 4, 5].

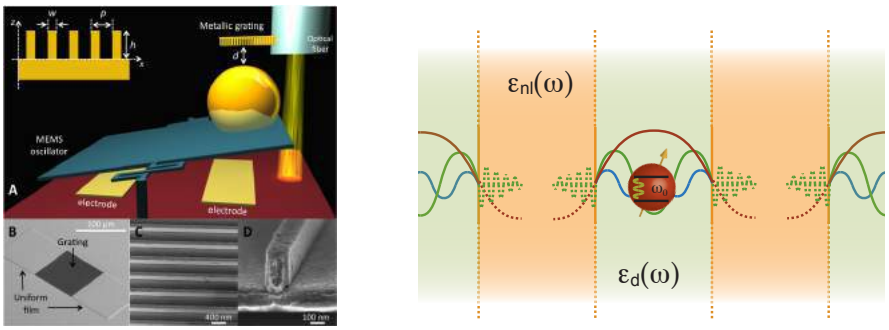

Figure 1: Two examples of nanostructured systems which were used to tailor fluctuation-induced interactions. (Left) Schematic drawing of an experimental configuration used to measure the Casimir force between a gold-coated sphere and a gold 1D grating [3]. (Right) Scheme of an atomic system embedded in the metal/dielectric layered material. This system was analyzed in a framework capable of including local-field corrections in (weakly absorbing) dielectric systems and the nonlocal optical properties of metals [5].

ACKNOWLEDGMENT

We acknowledge support by the Deutsche Forschungsgemeinschaft (DFG) through project B10 within the Collaborative Research Center (CRC) 951 Hybrid Inorganic/Organic Systems for Opto-Electronics (HIOS) and the European Union Marie Curie People program through the Career Integration Grant No. PCIG14- GA-2013-631571.

REFERENCES

1. H. B. G. Casimir, Proc. K. Ned. Akad. Wet. **51**, 793 (1948).
2. A. W. Rodriguez, F. Capasso, and S. G. Johnson, Nat. Photon. **5**, 211 (2011).
3. F. Intravaia *et al.*, Nat. Commun. **4**, 2515 (2013).
4. A. W. Rodriguez *et al.*, Phys. Rev. Lett. **111**, 180402 (2013).
5. F. Intravaia and K. Busch, Phys. Rev. A **91**, 053836 (2015).

Optically-assisted mechanical systems for advanced photonicsâ€

Enhanced second and third harmonic signals achieved by a grating structure from magnetic metamaterials

D. Lee[1], I. Kim[1] and J. Rho[1, 2, 3*]

[1]Department of Mechanical Engineering, Pohang University of Science and Technology (POSTECH), Pohang 37673, Republic of Korea

[2]Department of Chemical Engineering, Pohang University of Science and Technology (POSTECH), Pohang 37673, Republic of Korea

[3]Natioanl Institute of Nanomaterials Technology (NINT), Pohang 37673, Republic of Korea

[*]corresponding author: jsrho@postech.ac.kr

Abstract-Through nonlinear crystals, second and third harmonic signals are obtained. However, such signals are limited to low efficiency as an output. Metamaterials can be used to generate harmonic signals corresponding to nonlinear behaviors. Here, we introduce a new strategy how to amplify the second and third harmonic signals via magnetic metamaterials. We theoretically and numerically show that the higher induced polarization currents with harmonic signals can be achieved by the grating structure and an actual model is suggested and performed.

Metamaterials which consists of artificial structures under sub-wavelength scale have been well studied and gave rise to unusual properties such as negative refractive index [1], invisibility cloak [2], super-resolution imaging [3] and metasurfaces [4]. In addition, nonlinear behaviors based on metamaterials have been researched. Here, we focus on second and third harmonic generation caused by nonlinear behaviors. Conventional second and third harmonic signals are so weak and limited to low efficiency. To overcome such disadvantages, we introduce a new strategy how to amplify the second and third harmonic signals via magnetic metamaterials. First of all, magnetic metamaterials show their nonlinear behaviors at the magnetic resonance, indicating a higher absorption coefficient and higher induced polarization currents [5, 6]. So, the enhanced second and third harmonic signals can be created by the current loop composed of nanostrip metamaterials shown in Fig 1(a). The nanostrip has inversion symmetry in x-direction and no inversion symmetry in y-direction, resulting in third and second harmonic signals, respectively [6]. It is well shown in Fig 1(c) that the x component of polarized current generates the third harmonic signals and the y component of that current generates the second harmonic signals. Moreover, we recognized that the presence of a grating in the metamaterial structure are absolutely related to the good performance of the second and third harmonic signals. The grating has the same width with a unit cell of magnetic metamaterials and is embedded under the glass substrate, which is depicted in Fig. 1(b). We can readily compare the transmission between no grating structure and grating-based structure in Fig. 1 (c) and (d). The amplitude of the second and third harmonic signals in grating-based structure is almost doubled and quadrupled, respectively, compared to the case of no grating structure. We show that enhanced second and third harmonic signals as nonlinear behaviors are indeed achieved by the grating structure from magnetic metamaterials. Finally, we fabricate and measure the model suggested in Fig 1(b) in practice and show whether the amplified second and third harmonic signals are present or not.

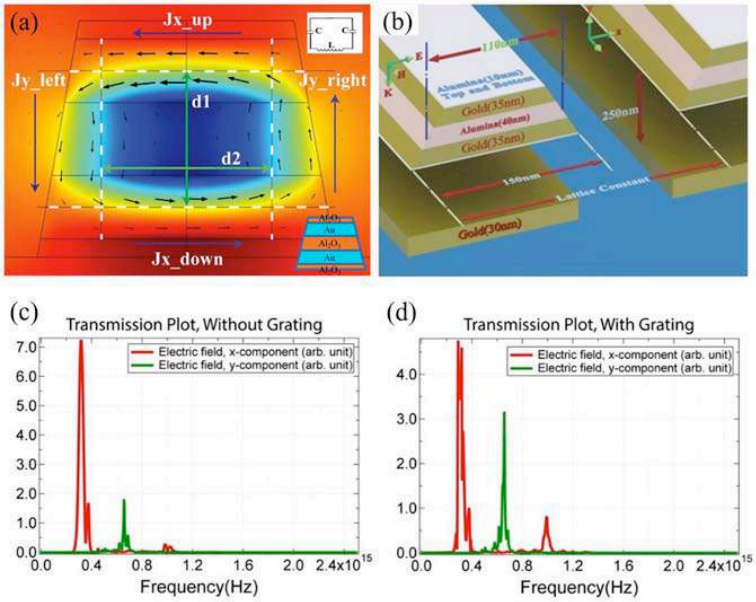

Figure 1. (a) Magnetic field distribution and electric field displacement (black arrows) in magnetic frequency. The external magnetic field induces a current loop which can be divided into two orthogonal groups. (b) Scheme of the actual model. The model is a 5-layer trapezoid placed on a glass substrate upon a grating. The grating is embedded under the glass substrate. (c) and (d) indicate the second and third harmonic signals in the transmitted waves with no grating structure and grating-based structure, respectively.

Acknowledgements. J. Rho acknowledges the financial support by Young Investigator Research program (NRF-2015R1C1A1A02036464), Engineering Research Center program (NRF-2015R1A5A1037668), Global Frontier Research Program (CAMM-2014M3A6B3063708) and I. Kim acknowledges Global Ph.D. Fellowship (NRF-2016H1A2A1906519) through the National Research Foundation of Korea (NRF) grant funded by the Ministry of Science, ICT and Future Planning (MSIP) of Korean government.

REFERENCES

1. Shelby, R. A., D. R. Smith and S. Schultz, "Experimental verification of a negative index of refraction," *Science*, Vol. 292, No. 5514, 77-79, 2001.
2. Schurig, D. *et al*., "Metamaterial electromagnetic cloak at microwave frequencies," *Science*, Vol. 314, No. 5801, 977-980, 2006.
3. Rho, J. *et al*., "Spherical hyperlens for two-dimensional sub-diffractional imaging at visible frequencies," *Nat*. *commun*., Vol. 1, No. 143, 2010.
4. Yin, X. *et al*., "Photonic spin Hall effect at metasurfaces," *Science*, Vol. 339, No. 6126, 1405-1407, 2013.
5. Zeng, Y. *et al*., "Classical theory for second-harmonic generation from metallic nanoparticles," *Phys*. *Rev*. *B*, Vol. 79, No. 235109, 2009.
6. Sajedian, I. et al., "The role of current loop in harmonic generation from magnetic metamaterials in two polarizations," *arXiv preprint arXiv*:1607.07952, 2016.

Experimental realization of ITO based mode-multiplexed nanophotonic modulators

H. Jeong[1], I. Kim[1], and J. Rho[1,2,3*]

[1]Department of Mechanical Engineering, Pohang University of Science and Technology (POSTECH), Pohang 37673, Republic of Korea

[2]Department of Chemical Engineering, Pohang University of Science and Technology (POSTECH), Pohang 37673, Republic of Korea

[3]Natioanl Institute of Nanomaterials Technology (NINT), Pohang 37673, Republic of Korea

[*]corresponding author: jsrho@postech.ac.kr

Abstract-Photonic and optical devices have been improved using the state of the art nanofabrication techniques. Also, photonic modulators have been affected by the nanotechnology, so we has already theoretically designed mode-multiplexed modulator using indium-tin-oxide (ITO) pattern which can distinguish one modes from waveguide modes. Thus this research is to verify that the device can modulate two wave modes by fabricating and experiment the designed structure. The results improve waveguide system multiplying functionality-per-area.

Recently, as nanofabrication enables to create metamaterials and meta-devices, photonic devices have developed with the progress of nanotechnology. Similarly, wave mode modulators have advanced to increasing efficiency and improving performance using transparent conducting oxides (TCOs) [1]. TCOs, such as ITO and aluminum zinc oxide (AZO), are transparent conductive materials which have the both metal and optical properties in near infrared range (NIR). Also, the TCOs' optical properties can be changed by controlling carrier concentration [2]. We used this controllable optical transmission of ITO to create modal dichroism for designing the mode-multiplexed modulator [3]. The modal dichroism obtained by the modulator increase the bandwidth of modulation and functionality-per-area. This research is to fabricate the designed device and prove that it can modulate two wave modes. The schematics of the modulator is shown in Fig. 1(a), and the structure is fabricated following method. After the silicon etching of silicon on insulator (SOI), three patterns are deposited in order of ITO, silicon dioxide and gold using E-beam evaporator as Fig. 1(b), (c). Before deposition, the specimen should be aligned using overlay process. The alignment error is less than 20nm and reproducibility is more than 75% [4], so three alignments are possible to deposit three materials in accurate location on Si layer. Therefore three panels of ITO respond separately to the signal from gold panels insulated with 20nm silicon dioxide layer. The charge density of the ITO panels along vertical axis should be same with the theoretical results in constant doping concentration and voltage of two panels. Thus, annealing is required to stabilize the state of the ITO panel, and defining annealing condition is important to this step. Waveguide input and output section is created by engraving gratings using focused ion beam (FIB) milling or electron beam lithography (EBL). The section should be fabricated to transmit waves maintaining enough propagation efficiency, so the section has already been prepared before the main manufacturing process. Total device image is shown in Fig. 1(d). If the device is fabricated following this method, the device can modulate two modes independently. This means that modal dichroism can be realized and functionality-per-area is multiplied twice. Therefore, when it is required to select

one mode from two or more modes, the designed device is more efficient than other devices. Also, the method of three times overlay process help fabricate other structure design requiring several overlay process.

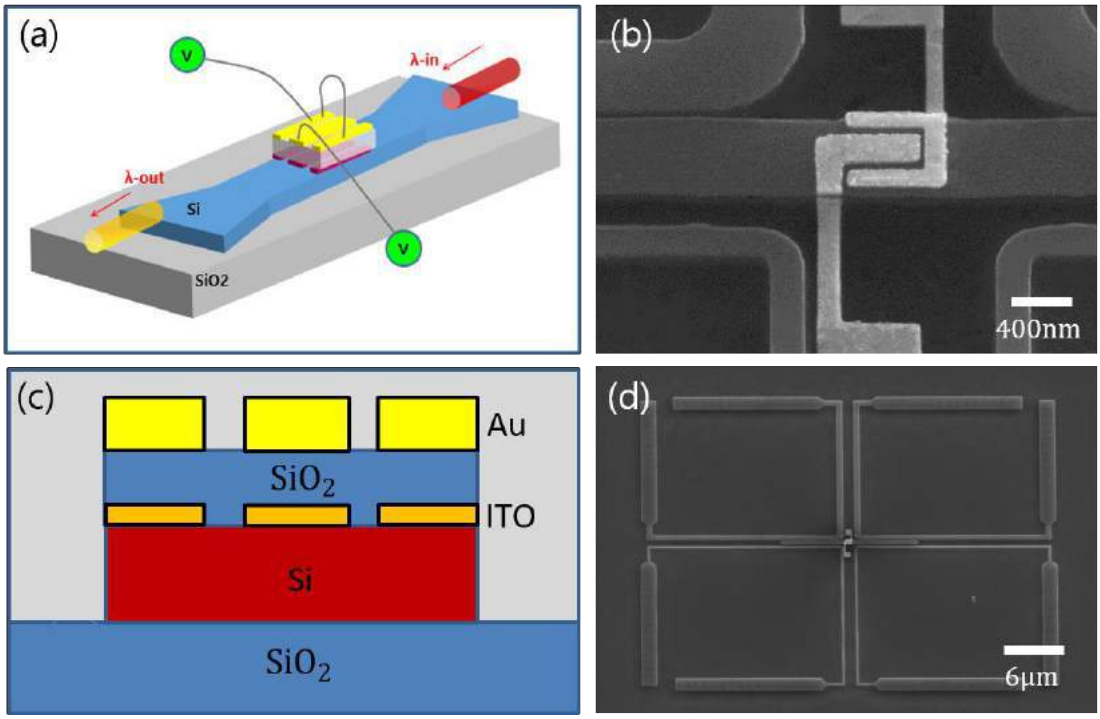

Figure 1. (a) Schematics of the mode-multiplexed modulator. (b) SEM image of the fabricated pattern composed of ITO, silicon dioxide and gold layers. (c) Cross section of the modulator (d) SEM image of the modulator with waveguide input and output section.

Acknowledgements. J. Rho acknowledges the financial support by Young Investigator Research program (NRF-2015R1C1A1A02036464), Engineering Research Center program (NRF-2015R1A5A1037668), Global Frontier Research Program (CAMM-2014M3A6B3063708) and I. Kim acknowledges Global Ph.D. Fellowship (NRF-2016H1A2A1906519) through the National Research Foundation of Korea (NRF) grant funded by the Ministry of Science, ICT and Future Planning (MSIP) of Korean government.

REFERENCES

1. Alok P. V. *et al.*, "Electro-optical modulation of a silicon waveguide with an "epsilon-near" material," *Opt. Exp.*, vol. 21, No. 22, 26387~26397, 2013
2. Gururaj V. N. *et al.*, "Althernative Plasmonic Materials: Beyoud Gold and Silver," *Adv. Mat.*, Vol. 25, No. 24, 3264~3294, 2013
3. Das, S. *et al.*, "Nanophotonic modal dichroism: mode-multiplexed modulators," *Opt. Lett.*, Vol. 41, No. 18, 4394-4397, 2016.
4. Yoon, G. *et al.*, "Ultra-high accurate and precise electron beam lithography overlay for three-dimensional optical metamaterials and hybrid plasmonic nanoantennas," *Sci. Rep.* (in review)

Wafer-scale hyperlens device for biomolecular super-resolution imaging

D. Lee[1], Y. Kim[4], M. Kim[1], H. Choi[4], J. Mun[2], S. So[1], D. M. Nguyen[1], K. Kim[5], J. Ok[6], H. Lee[4], J. Rho[1,2,3,*]

[1]Department of Mechanical Engineering, Pohang University of Science and Technology (POSTECH), Pohang 37673, Republic of Korea

[2]Department of Chemical Engineering, Pohang University of Science and Technology (POSTECH), Pohang 37673, Republic of Korea

[3]National Institute of Nanomaterials Technology (NINT), Pohang 37673, Republic of Korea

[4]School of Materials Science and Engineering, Korea University, Seoul 02841, Republic of Korea

[5]School of Mechanical Engineering, Sungkyunkwan University, Suwon 16419, Republic of Korea

[6]Department of Mechanical and Automotive Engineering, Seoul National University of Science and Technology, Seoul 01811, Republic of Korea

[*]corresponding author: jsrho@postech.ac.kr

Abstract- Hyperlens is an optical imaging method for super-resolution imaging. Due to the unique hyperbolic dispersion relation of hyperlens, sub-diffraction information of objects can be propagated to far-field. Here, we propose a new design consisting of multiple hyperlenses arranged in hexagonal arrays in large scale for high-throughput imaging. With proposed design, we report the experimental demonstration of sub-diffraction imaging on hyperlenses. Biomolecular samples are imaged by visible light through the hyperlens array with resolution down to diffraction limit.

Super-resolution imaging technology has brought interest as a useful tool for observation in biology and nanotechnology [1]. This technology helps to overcome the diffraction limit of conventional imaging system, wherein two objects located closer cannot be resolved clearly in the far field. Recent progress in metamaterials, which are artificial structure never existing in nature, are able to image beyond the diffraction limit. Hyperlens is the kind of special artificial metamaterials with hyperbolic dispersion that can resolve small objects in the optical far field [2-5]. Previous hyperlens research results have been achieved to resolve features down to sub-diffraction limit in visible range [6], still have difficulty to the use of hyperlenses in practical applications. Here, we propose a new design consisting of multiple hyperlenses arranged in arrays in wafer scale for high-throughput imaging and robust to sample positioning. With proposed hyperlens array, we show the experimental result of super-resolution imaging on hyperlenses by combining to conventional microscopy system for imaging biomolecules. Hippocampal neuron cells are imaged by visible light through the hyperlens array with resolution down to 150 nm, beyond the diffraction limit. High resolution imaging result of neuron at sub-diffraction size shows that hyperlens can be used as a useful imaging tools in biology, pathology, medical science and nanotechnology.

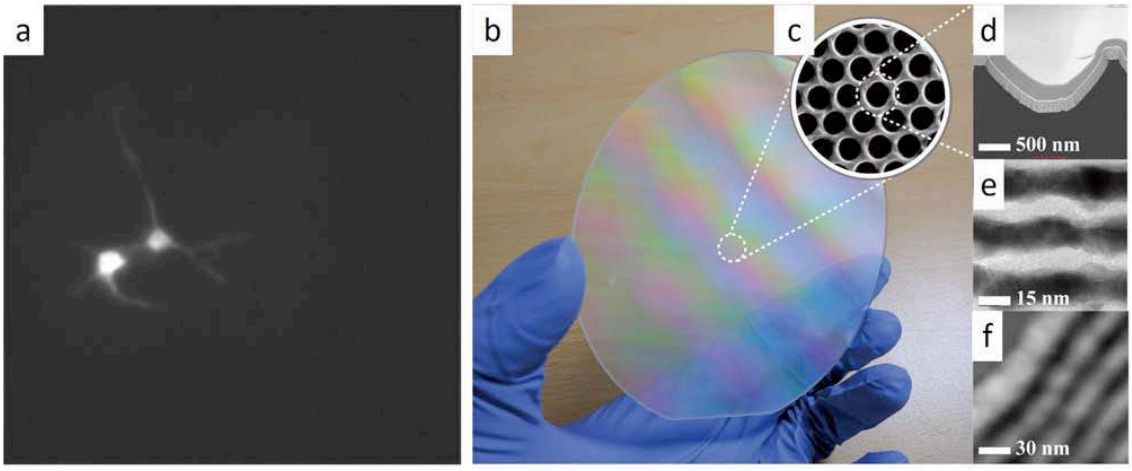

Figure 1. (a) Neuron image captured by hyperlens. (b-f) Fabricated wafer-scale hyperlens array. SEM top-view image(c), cross-sectioned TEM image (d) and magnified image of bottom and side wall region (e-f), respectively [7, 8].

Acknowledgements. J. Rho acknowledges the financial support by Pioneer Research Center program (NRF-2015M3C1A3022550), Young Investigator Research program (NRF-2015R1C1A1A02036464), Engineering Research Center program (NRF-2015R1A5A1037668) and Global Frontier program for the Center for Advanced Metamaterials (CAMM-2015M3A6B3063708) through the National Research Foundation of Korea (NRF) grant funded by the Ministry of Science, ICT and Future Planning (MSIP) of Korean government.

REFERENCES

1. Hao, X. et al., "From microscopy to nanoscopy via visible light", *Light Sci Appl*., Vol. 2, No. 10, e108, 2013.
2. Liu, Z. et al., "Far-Field Optical Hyperlens Magnifying Sub-Diffraction-Limited Objects", *Science*, Vol. 315, No. 5819, 1686-1686, 2007.
3. Salandrino, A. et al., "Far-field subdiffraction optical microscopy using metamaterial crystals: Theory and simulations", *Phys. Rev. B*, Vol. 74, No. 7, 075103, 2006.
4. Jacob, Z. et al., "Optical Hyperlens: Far-field imaging beyond the diffraction limit", *Opt. Express*, Vol. 14, No. 18, 8247-8256, 2006.
5. Pendry, J.B., "Perfect cylindrical lenses", *Opt. Express*, Vol. 11, No. 7, 755-760, 2003.
6. Rho, J. et al., "Spherical hyperlens for two-dimensional sub-diffractional imaging at visible frequencies" *Nat. Commun.*, Vol. 1, No. 143, 2010.
7. Lee, D. et al., "Wafer-scale hyperlens array for neuron imaging", *Science Advances*, (in review).
8. Byun, M. et al., "Demonstration of nanoimprinted hyperlens array for high-throughput sub-diffraction imaging", *Sci. Rep*, (in review).

Gate set tomography on electron spin qubits in diamond

Ji-Won Yun[1], Donghyuck Lee[1], and Dohun Kim[1]

[1]Department of Physics and Astronomy, Seoul National University, Seoul 08826, Korea
[*]corresponding author: dohunkim@snu.ac.kr

Abstract-Nitrogen-vacancy (NV) centers in diamond are excellent candidates for investigating quantum phenomena and constructing quantum two level system due to long coherence time even at room temperature environment [1]. To realize reliable quantum processor, it is essential to confirm performances of single and multiple qubit gates, and traditionally quantum state and process tomography are used to fully reconstruct input and output quantum states under the quantum operator in question [2,3,4]. These methods, however, are prone to state preparation and measurement (SPAM) errors, and number of measurement to complete the characterization grows exponentially with number of qubits. Gate set tomography (GST) is a newly developed method which is self-consistent and overcomes this limit [5]. In this study, we used GST to characterize the gate fidelity of electron spin qubit formed by a nitrogen-vacancy center in diamond. We briefly introduce photo physics of NV centers and GST, and we discuss the accuracy of the single qubit gates we apply to nitrogen-vacancy centers that was obtained using GST. We further discuss the characteristics of main noise source due to nuclear spin bath in diamond, which is deduced from analyzing quantum processes using GST.

Keywords: Nitrogen-vacancy centers, Quantum gates, Quantum tomography, Gate set tomography, Optically detected magnetic resonance

Acknowledgements

This work was supported by the National Research Foundation of Korea(NRF) Grant funded by the Korean Government(MSIP)(No.2015R1A5A1037668), and the Creative Materials Discovery Program through the National Research Foundation of Korea(NRF) funded by the Ministry of Science, ICT and Future Planning(NRF-2015M3D1A1070672)

References

1. F. Jelezko, T. Gaebel, I. Popa, A. Gruber, and J. Wrachtrup, “Observation of Coherent Oscillations in a Single Electron Spin”, Phys. Rev. Lett. 92, 076401 , 2004
2. Leibfried, D. M. Meekhof, B. E. King, C. Monroe, W. M. Itano, and D. J. Wineland,” Experimental Determination of the Motional Quantum State of a Trapped Atom”, Phys. Rev. Lett. 77, 4281, 1996

3. Isaac L. Chuang & M. A. Nielsen (1997) Prescription for experimental determination of the dynamics of a quantum black box, Journal of Modern Optics, 44:11-12, 2455-2467, 2009
4. J. F. Poyatos, J. I. Cirac, and P. Zoller, “Complete Characterization of a Quantum Process: The Two-Bit Quantum Gate, Phys. Rev. Lett. 78, 390, 1996
5. Seth T. Merkel, Jay M. Gambetta, John A. Smolin, Stefano Poletto, Antonio D. Córcoles, Blake R. Johnson, Colm A. Ryan, and Matthias Steffen, “Self-consistent quantum process tomography”, Phys. Rev. A 87, 062119, 2013

3D position tracking confocal microscope based on single-photon-counting for spin resonance experiment in diamond

Donghyuck Lee[1], **Ji-Won Yun**[1], **and Dohun Kim**[1*]
[1]Department of Physics and Astronomy, Seoul National University, Seoul 08826, Korea
[*]corresponding author: dohunkim@snu.ac.kr

Abstract-The confocal microscopy has high resolution and high efficiency, and is used as a major workhorse throughout the entire optical imaging field, and its applications range from cell imaging to quantum information experiment using single molecules. For long-term fluorescence characterization of single molecules or manipulation of single-cell as well as image acquisition, a technique capable of correcting errors caused by external temperature change, sample drift, etc. is required, and previously, a method of periodically locating the local maxima of the intensity spatial distribution such as simulated annealing was used. However, in the quantum information experiment to measure weak atomic light intensity, it is difficult to use the existing motion tracking method because the power is at the femto-watt level and the photon statistical shot noise limit. In this study, we introduce the development of a single-photon-counting three-dimensional position tracking confocal microscope, which mainly aims at quantum information optical experiment of Diamond NV center. Combined with single photon counting and software lock-in modulation, motion tracking in a single molecule level can be performed in real time. As performance verification we show an example of measuring magnetic resonance of single NV center in bulk diamond over several days at a signal to noise ratio of 20:1

Keywords: Position tracking, Confocal microscopy, Nitrogen-vacancy centers, Single-photon-counting, Lock-in modulation, Optically detected magnetic resonance

Acknowledgements, This work was supported by the National Research Foundation of Korea(NRF) Grant funded by the Korean Government(MSIP)(No.2015R1A5A1037668), and the Creative Materials Discovery Program through the National Research Foundation of Korea(NRF) funded by the Ministry of Science, ICT and Future Planning(NRF-2015M3D1A1070672)

A smartphone multi-contrast microscope using a color-coded LED illumination

D. Jung[1], J Choi[2], S. Kim[1], S. Ryu[1], J. Lee[2] and C. Joo[1*]

[1] Department of Mechanical Engineering, Yonsei University, 50 Yonsei-ro, Seodaemoon-gu, Seoul, 03722, Republic of Korea

[2] School of Integrated Technology & Yonsei Institute of Convergence Technology, Yonsei University, 85 Songdogwahak-ro, Yeonsu-gu, Incheon, 21983, Republic of Korea

[*]corresponding author: cjoo@yonsei.ac.kr

Abstract- We present a low-cost multi-contrast microscope operating on a smartphone platform. Our method is based on our recently developed color-coded LED microscopy (cLEDscope). In cLEDscope, LED lights of red, blue and green color illuminate a specimen with different angle, and computation of the acquired images in each color enables bright-field, dark-field and differential phase contrast imaging in a single shot. As cLEDscope can be readily built with inexpensive LED array and CMOS camera, we noted that simple modification of a smartphone, which is already equipped with a color CMOS camera, would transform it into multi-contrast microscope. We designed and fabricated a smartphone adapter composed of micro-LED arrays and specimen stage, so that its installment on a smartphone enables multi-contrast biological imaging. Android-based App was also implemented to acquire images and perform the computation. Details of our cLEDscope adapter and experimental demonstration with biological specimens are presented.

We demonstrated cLEDscope on a smartphone platform. Integration of microLED array as an illuminator and smartphone lens as an objective transformed a smartphone into multi-contrast microscope capable of BF, DF and DPC imaging in a single shot. Its multi-contrast imaging capability was demonstrated by visualizing structures of transparent biological specimens. This method may be utilized for educational purposes as well as diagnostic imaging tool of biological specimens in resource-limited settings.

REFERENCES

1. Donghak Lee, Suho Ryu, Uihan Kim, Daeseong Jung and Chulmin Joo, "Color-coded LED microscopy for multi-contrast and quantitative phase-gradient imaging", Biomedical Optics Express, 2015, Vol. 6, No. 12, 4912
2. Neil. A Switz, Michael V. D'Ambrosio, Daniel A. Fletcher, "Low-Cost Mobile Phone Microscopy with a Reversed Mobile Phone Camera Lens", Plose One, 2014, Vol. 9, e95330.2
3. Ashwin B. Parthasarathy, Kengyeh K. Chu, Tim N. Ford, and Jerome Mertz, "Quantitative phase imaging using a partitioned detection aperture", Optics Letter, 2012, Vol. 38, No. 19, 4062.
4. Shalin B. Mehta, and Colin J. R. Sheppard, " Quantitative phase-gradient imaging at high resolution with asymmetric illumination-based di-erential phase contrast", Optics Letters, 2009, Vol. 34, No. 13, 1924.

in vivo optical coherence tomography imaging of penetration and dissolution characteristics of hyaluronic acid microneedles in human skin

Seungri song[1], Jung-Hyun Bae[2], Soocheol Kim[1], Jung-Dong Kim[2], Hong-Kee Kim[2], and Chulmin Joo[1*]

[1]Department of Mechanical Engineering, Yonsei Univ., 50 Yonsei-ro, Seodaemoon-gu, Seoul, 03722, Republic of Korea

[2] Raphas, AVISON BIOMEDICAL RESERCH CENTER, 50 Yonsei-ro, Seodaemun-gu, Seoul, 03722, Republic of Korea

[*]cjoo@yonsei.ac.kr

Abstract- We present in situ imaging and analysis of the penetration and dissolution characteristics of hyaluronic acid based MNs (HA-MN) with various needle heights in human skin in vivo. In contrast to other studies, we measured the actual penetration depths of the HA-MNs by considering the experimentally measured refractive index of HA in the solid state. For the dissolution dynamics of the HA-MNs, structural alteration of the MNs could be clearly visualized, and the volumetric changes of the MNs were measured.

Transdermal drug delivery (TDD) has been recently highlighted as an alternative to oral delivery and hypodermic injections. Among many methods, drug delivery using a microneedle (MN) is one of the promising administration strategies due to its high skin permeability, minimal invasiveness, and ease of injection. Many researchers have investigated applicability of MN technology to oligonucleotide delivery, insulin delivery, protein vaccine delivery, and DNA vaccine delivry. In addition, microneedle-based TDD is explored for cosmetic and therapeutic purposes, rapidly developing market of microneedle industry for general population.

To date, visualization of microneedles inserted into human skin has primarily been performed *ex-vivo*. MRI, CT and ultrasound imaging do not provide sufficient spatial resolution, and optical microscopy is not suitable because of their limited imaging depth; structure of microneedles located in 0.1~1mm into the skin cannot be visualized.

Optical coherence tomography (OCT) is a non-invasive, cross-sectional optical imaging modality for biological tissue with high spatial resolution and acquisition speed. Compared with ultrasound imaging, it exhibits superior spatial resolution (1~10 um) and high sensitivity, while providing an imaging depth of biological tissue down to 1~2 mm. Here, we present in situ imaging and analysis of the penetration and dissolution characteristics of hyaluronic acid based MNs (HA-MN) with various needle heights in human skin in vivo. In contrast to other studies, we measured the actual penetration depths of the HA-MNs by considering the experimentally measured refractive index of HA in the solid state. For the dissolution dynamics of the HA-MNs, structural alteration of the MNs could be clearly visualized, and the volumetric changes of the MNs were measured with an image analysis algorithm.

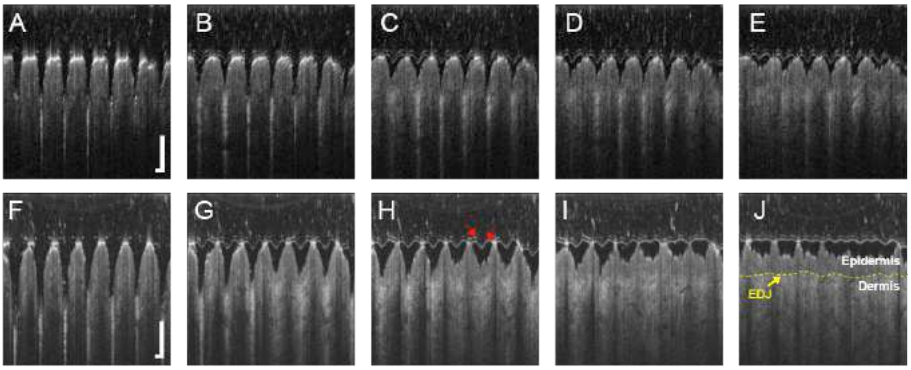

Figure. 1 Time-series image of XZ cross-sectional OCT tomography of human skin tissue from 0 to xx hour after (A-E) 350μm and (F-J) 600μm insertion. Yellow arrow pointed dashed line is epidermal dermal junction (EDJ). the upper layer is epidermis and lower layer is dermis. White line pointed by red arrows is boundary of PU. Scale bar is 500μm.

Acknowledgements, This research was supported by the research programs of the National Research Foundation of Korea (NRF) (NRF-2015R1A5A1037668), and the Ministry of Trade, Industry & Energy(MOTIE), Korea Institute for Advancement of Technology(KIAT) through the Research and Business Development (R&BD) Program.

REFERENCES

1. M.J. Garland, K. Migalska, T.M.T. Mahmood, T.R.R. Singh, A.D.Woolfson, R.F. Donnelly, Microneedle arrays as medical devices for enhanced transdermal drug delivery, Expert review of medical devices, 8 (2011) 459-482.
2. J.W. Lee, J.-H. Park, M.R. Prausnitz, Dissolving microneedles for transdermal drug delivery, Biomaterials, 29 (2008) 2113-2124.
3. Y.A. Gomaa, D.I. Morrow, M.J. Garland, R.F. Donnelly, L.K. El-Khordagui, V.M. Meidan, Effects of microneedle length, density, insertion time and multiple applications on human skin barrier function: assessments by transepidermal water loss, Toxicology in Vitro, 24 (2010) 1971-1978.
4. J.D. Kim, M. Kim, H. Yang, K. Lee, H. Jung, Droplet-born air blowing: Novel dissolving microneedle fabrication, Journal of Controlled Release, 170 (2013) 430-436.
5. In-vivo dynamic characterization of microneedle skin penetration using optical coherence tomography Journal of Biomedical Optics, 15 (2010) 046001-046001-046007.
6. M.-T. Tsai, I.-C. Lee, Z.-F. Lee, H.-L. Liu, C.-C. Wang, Y.-C. Choia, H.-Y. Chou, J.-D. Lee, In vivo investigation of temporal effects and drug delivery induced by transdermal microneedles with optical coherence tomography, Biomedical Optics Express, 7 (2016) 1865-1876.

Single-exposure quantitative phase imaging in color-coded LED microscopy

Wonchan Lee [1], **Daeseong Jung** [1*], **and Chulmin Joo** [1*]

[1]*Department of Mechanical Engineering, Yonsei Univ., 50 Yonsei-ro, Seodaemoon-gu, Seoul, 03722, Republic of Korea*

[*]cjoo@yonsei.ac.kr

Abstract- Here, we demonstrate a strategy for single-shot quantitative phase imaging in color-coded LED microscopy. We employ a circular LED illumination pattern that is trisected into subregions with equal area, assigned to red, green and blue colors, respectively. We also describe computational model and single-shot quantitative phase imaging capability of our method by presenting phase images of calibrated phase sample and dynamics of cells.

we demonstrate single-exposure QPI in the platform of cLEDscope. The LED source pattern is configured as a circle that is trisected in equal angles with red, blue, and green colors. Image acquisition with a color image sensor and computation based on weak object transfer functions allow for the measurement of the phase distribution of transparent biological specimens. We describe a computational model and our phase estimation algorithm for such configuration. Phase measurement accuracy is validated with imaging of precalibrated silica microspheres, and the single-shot phase imaging capability is demonstrated with the static and time-lapse imaging of unlabeled cells.

In cLEDscope, a color LED array replaces the light source of a conventional microscope. Patterned LED illumination and computation with the images in red (R), green (G), and blue (B) colors realize multi-contrast and QPI. The circular LED pattern was trisected into subregions with equal area, and each region was assigned red (R), green (G), and blue (B) colors (Fig. 1). The size of the illumination pattern was set to be larger than the pupil size of the optical microscope.

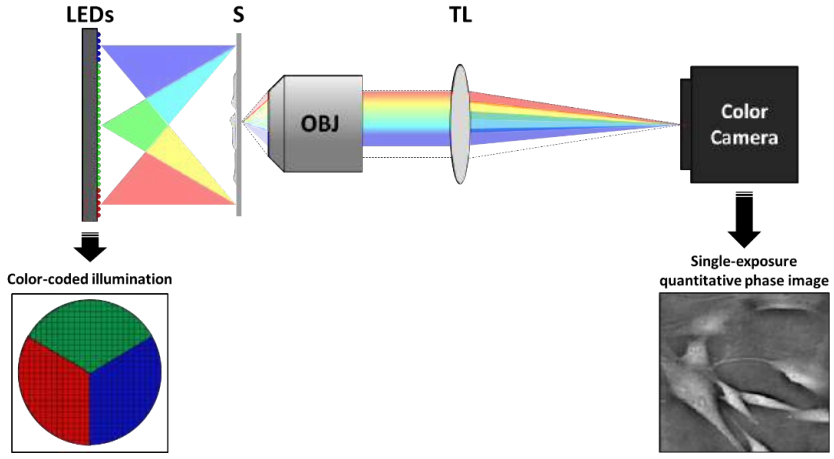

Figure. 1 Schematic of cLEDscope for single-exposure QPI. A color LED array is placed ~100 mm away from the

specimen plane (S). The LED illumination pattern is trisected into subregions with equal area. Each region is assigned red, green, and blue colors. Light passing through a transparent specimen is collected by an objective lens (OBJ), and subsequently detected by a color image sensor. Computation with R, G, and B images in combination with weak object transfer functions results in quantitative phase images. S: specimen plane, TL: tube lens.

Acknowledgements, National Research Foundation of Korea (NRF) (NRF-2015R1A5A1037668 and NRF-2015R1A1A1A05001548)

REFERENCES

1. D. Lee, S. Ryu, U. Kim, D. Jung, and C. Joo, "Color-coded LED microscopy for multi-contrast and quantitative phase-gradient imaging," Biomed. Opt. Express **6**, 4912-4922 (2015)
2. L. Tian, J. Wang, and L. Waller, "3D differential phase-contrast microscopy with computational illumination using an LED array," Opt. Lett. **39**, 1326-1329 (2014).
3. R. A. Claus, P. P. Naulleau, A. R. Neureuther, and L. Waller, "Quantitative phase retrieval with arbitrary pupil and illumination," Opt. Express **23**, 26672-26682 (2015)

Long-term stability enhancement of dynamic spectro-ellipsometry

D. Kim[1*], V. Dembele[1], and I. Choi[1]

[1]Division of Mechanical System Engineering, Chonbuk National University, 567 Baekje-daero, Deokjin-gu, Jeonju 54896, Korea

[*]corresponding author: dashi.kim@jbnu.ac.kr

Abstract: This paper describes a long-term stability enhancement of dynamic spectro-ellipsometry by which we can measure spectral phase difference between p- and s-polarization of the reflected wave from a periodic nano pattern or a thin film with extreme high stability. Long-term stability enhancement scheme is provided for a thin film object by analyzing the spectral ellipsometric parameter $\Delta(\lambda)$ stability.

Typical spectroscopic ellipsometric (SE) system employs mechanical rotating mechanisms or electrical modulation devices to extract the ellipsometric spectral parameters $\Psi(k)$ and $\Delta(k)$. Such time-consuming polarization modulation scheme limits the measurement speed of conventional spectro-ellipsometry. The proposed scheme is highly robust to the external noises and it enables us to extract the ellipsometric spectral parameters of large scale nano-pattern object in real time with high accuracy. [1-2] The newly proposed snapshot spectro-ellipsometry based on an interferometric spectro-polarization modulation technique has no moving parts, and it is extremely robust to external vibration due to its unique optical design. This paper describes how long-term stability of the proposed dynamic spectro-ellipsometry can be improved.

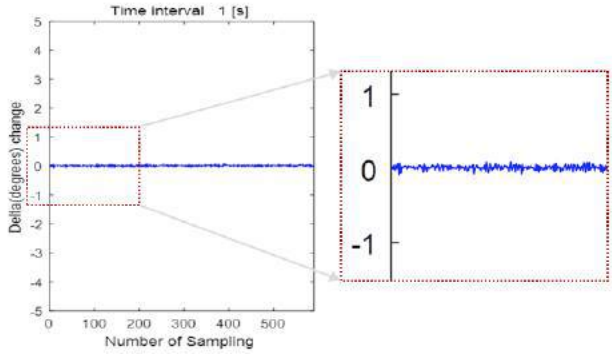

Fig. 1 Long-term stability evaluation of the dynamic spectro-ellipsometric system

Acknowledgements: This work was supported by the National Research Foundation of Korea (NRF) Grant funded by the Korean Government (MSIP) (No. 2015R1A5A1037668 & No. 2015R1A2A2A11001529).

REFERENCES

1. D. Kim, and et al., Opt. Exp. **22**, 17430-17439 (2014).
2. D. Kim, and et al., Opt. Lett. **41**, 2318-2321 (2016).

Graphene quantum dot based nanohybrid material for photoluminescence with surface plasmonic

Byeongho Park[1], Seung Won Cho[1], and Seong Chan Jun[1*]
[1]School of Mechanical Engineering, Yonsei University, Seoul, Republic of Korea
[*]corresponding author: scj@yonsei.ac.kr

Abstract- We made graphene quantum dot (GQD) and Au nanocompound as an innovative fluorescent material. Such sample showed high photoluminescence characteristics and new emission peak in the visible range, since the strong light confinement obtained from the Au nanoparticles as an antenna remarkably enhance the light absorption. Our material with nanosphere structure provided bluish-green emission after the hybridization of GQD and Au (GQD/Au). It exhibited a photoluminescence quantum yield of up to 26.9%, which is better than twice of GQD's (~11%).

We developed a novel nanosphere including GQDs and Au. The UV light was employed to assembly of GQDs and Au with photo-excited electrons and reducing capability of Au^{3+}. The size of the GQD/Au nanospheres was 150–170 nm, which is larger than that of the intrinsic GQDs (4–7 nm). The photoluminescence was improved with two emission peak for blue and green at 468 and 529 nm of wavelength. Our material, GQD/Au nanospheres showed high emission efficiency with 26.9 % of quantum yield over double of typical GQD's. Such fluorescent material can be perceived as exceptional candidates for applications such as light emitting source, optoelectronic devices, and bio-imaging with intriguing emission wavelength and intensity.

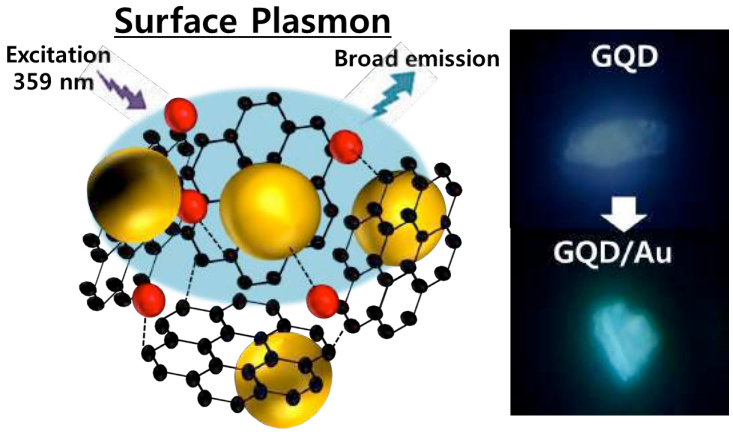

Figure 1. schematic of GQD/Au sample with enhanced photoluminescence of surface plasmon and fluorescence image of GQD and GQD/Au

Effects of micro patterns on negative refractive index of planar surface

J. H. Kim[1], Z. Shoaib[1], H. Choi[1], and M. Y. Jeong[1*]

[1]Department of Cogno-Mechatronics Engineering, Pusan National University, Busan, Korea

[2]Nano-Integrated Cogno-Mechatronics Engineering, BK21 Plus group, Pusan National University, Busan, Korea

[*]corresponding author: myjeong@pusan.ac.kr

Abstract- The metasurfaces which don't appear properties in nature have many interesting properties. Among many properties of metasurfaces, the enhancement of optical signals become more important for optical and electromagnetic field. In this paper, we changed the optical signal by using micro patterned planar surface which can control the permittivity and permeability.

Metasurfaces have many properties which don't appear in nature include anti-refractivity, anti-doppler effect, independence of wavelength and frequency, anti-phase of phase velocity and group delay, and surface plasmon. [1-3] The metasurface's characteristics were appeared by negative permittivity and negative permeability which made negative refractive index.

For negative refractive index equations,

$$n = -\sqrt{\mu \cdot \varepsilon} \tag{1}$$

where n is refractive index, μ is permeability, ε is permittivity. For negative permeability and permittivity,

$$\varepsilon_\gamma(\omega) = 1 - \frac{\omega_{pe}^2}{\omega^2 - j\omega\zeta} = 1 - \frac{\omega_{pe}^2}{\omega^2 + \zeta^2} + j\frac{\zeta\omega_{pe}^2}{\omega(\omega^2 + \zeta^2)} \tag{2}$$

$$\mu_\gamma(\omega) = 1 - \frac{F\omega^2}{\omega^2 - \omega_{0m}^2 + j\omega\zeta} + j\frac{F\omega^2\zeta}{(\omega^2 - \omega_{0m}^2)^2 + (\omega\zeta)^2} \tag{3}$$

Above (2), (3) equation, we can control permeability and permittivity by changing the wavelength or frequency and can make a negative permeability and permittivity.

Photonics techniques in biological and medical have been developed rapidly for new optical bio imaging system and control biological cells. [4,5] The enhancement of optical signal by using metasurfaces can be embedded in certain part of bio imaging system.

REFERENCES

1. Chen, H. T., Taylor, A. J., & Yu, N. "A review of metasurfaces: physics and applications.", *Reports on Progress in Physics*, *79*(7), 07640, 2016
2. Kildishev, A. V., Boltasseva, A., & Shalaev, V. M. " Planar photonics with metasurfaces." *Science*, *339*(6125), 1232009, 2013

3. High, A. A., Devlin, R. C., Dibos, A., Polking, M., Wild, D. S., Perczel, J., ... & Park, H. “Visible-frequency hyperbolic metasurface.” *Nature*, *522*(7555), 192-196.2015
4. Jakšić, Z., Vuković, S., Matovic, J., & Tanasković, D.”Negative refractive index metasurfaces for enhanced biosensing.” *Materials*, *4*(1), 1-36, 2010
5. Slobozhanyuk, A. P., Poddubny, A. N., Raaijmakers, A. J., van den Berg, C. A., Kozachenko, A. V., Dubrovina, I. A., ... & Belov, P. A., “Enhancement of magnetic resonance imaging with metasurfaces.” *Advanced Materials*, 2016

Characteristics of diffusive transport with use of metasurfaces for Spatial resolution of fNIRS

Z. Shoaib[1], J. H. Kim[1], HChoi[1,2], and M. Y. Jeong[1,2*]

[1]Department of Cogno-Mechatronics Engineering, Pusan National University, Busan, Korea

[2]Nano-Integrated Cogno-Mechatronics Engineering, BK21 Plus group, Pusan National University, Busan, Korea

[*]corresponding author: myjeong@pusan.ac.kr

Abstract-Functional near-infrared spectroscopy (fNIRS) is an emerging brain imaging technique. We proposed to use metasurfaces and optical antennas to control the absorption and scattering of light which are the major factors of attenuation of light in the current fNIRS system. Furthermore, with the use of metasurface, we can not only detect the ballistic component but also the diffusive and snake components which in result will enhance the receiving signal intensity of the light.

fNIRS is an optical brain imaging technique which uses near-infrared light of wavelength (690 nm to 820 nm) to detect the hemoglobin (Hb) changes in the brain [1]. Photons introduced at the scalp pass through the most of the tissue, and are either absorbed, scattered, or reflected back from oxy-Hb and deoxy-Hb. Because relatively predictable quantities of photons follow a banana-shaped path back to the surface of the skin, these can be measured using photo detectors. The drawback of current fNIRS system is that it can detect a small amount of light intensity (ballistic component only) of total transmitted intensity of light [2] as shown in Fig. 1. In this study, we will propose to use metasurfaces and optical antennas to enhance the overall performance of the optical brain imaging system by detecting ballistic, snake and diffusive components.

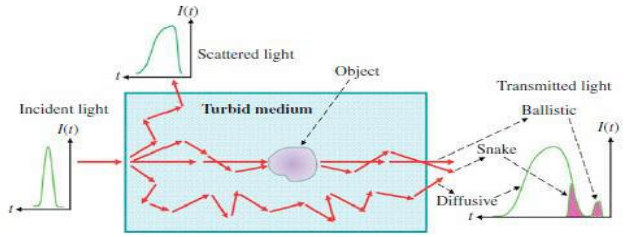

Fig. 1. Schematic diagram of light pulse propagating in a turbid medium showing the ballistic, snake and diffusive photons. Adapted from reference [8].

The two major factors for the attenuation of light in current fNIRS system are absorption and scattering [3]. Changes in the chromophore concentrations cause changes in the reflected light intensity, and are quantified using a modified Beer-Lambert law [1] to detect the ballistic component only [2] given as

$$I = I_0 \exp\{-(\mu_a + \mu_s)L\} \quad (1)$$

Where I is the detected and I_0 is the incident intensity, μ_a is the absorption coefficient, μ_s is the scattering coefficient and L is the differential path length factor.

Photonic techniques in biological and medical research depends on the development of new optically active materials that can measure, control and process biological cells and molecules at an unprecedented level [4]. For example optical nano antennas hold promise for enhancing the efficiency of photon detection, light emission, sensing and spectroscopy [5]. The optical nano antennas are introduced to enhance the transmission efficiency from the transmitter to the receiver [4]. Furthermore, with the use of optical responses of anisotropic plasmonic antennas and a new class of metasurfaces based on arrays of these antennas, we can control the constant interfacial phase gradient that can deflect light into desired direction [6]. With the use of nano structured metasurfaces we can get minimal reflectance (<0.02%) and maximal transmittance (>99.8%) for a wavelength

range, covering visible and near infrared [7]. So that by combining high transmission, low reflectivity and low absorption we can detect a high amount of transmitted intensity.

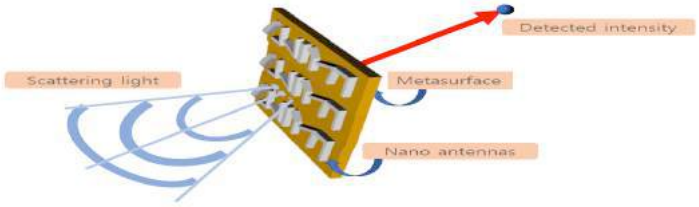

Fig. 2. Schematic of metasurface with optical nanoantennas for fNIRS signal enhancement.

Metasurfaces can be a useful tool to control these parameters which in result will enhance the intensity of the detected light. Moreover, we will use optical antennas [5] in metasurfaces to further enhance the efficiency of the light emission and detection. As discussed above, the major part of the intensity of light is consisted of diffusive component whereas the modified Beer-Lambert law only uses the ballistic component. Therefore, with the use of metasurfaces we can detect the diffusive component which will enhance the intensity of detected light given as [2]

$$I = I_0\left[\exp\{-(\mu_a + \mu_s)L\} + \frac{\Omega}{4\pi}\exp(-\mu_{eff}L)\right] \tag{2}$$

Where $\mu_{eff} = \sqrt{3\mu_a(\mu_s' + \mu_a)}$ and μ_s' is the reduced scattering coefficient. Figure 2 shows the schematic of proposed metasurface with optical antennas.

In our future work, we will use the proposed metasurfaces to develop an efficient optical brain imaging system which can be used as a better brain imaging tool as compared to the current fNIRS system. The enhancement in the detection of intensity of light will give more useful information about the functionality of the brain and this could be useful in diagnosis of many brain diseases and disorders. Furthermore, the use of metasurfaces will improve the spatial resolution of the optical brain imaging system which could be very beneficial for deep brain imaging.

REFERENCES

1. Caffini, M., D. Contini, R. Re, L. M. Zucchelli, R. Cubeddu, A. Torricelli, and L. Spinelli, "Functional near infrared spectroscopy and diffuse optical tomography in neuroscience," In Vikas Chaudhry (ed.) Advances in Brain Imaging (Rijeka, Croatia: InTech), 51–76, 2012.
2. Shi, L., L.A. Sordillo, A. Rodríguez-Contreras, and R. Alfano, "Transmission in near-infrared optical windows for deep brain imaging," *J. Biophoton.,* Vol. 9, 38–43, 2016.
3. Hoshi, Y. "Functional near-infrared spectroscopy: potential and limitations in neuroimaging studies," *Int. Rev. Neurobiol.,* Vol. 66, 237–266, 2005.
4. Wu, Z. et al., "Dual-band moiré metasurface patches for multifunctional biomedical applications," *Nanoscale,* Vol. 8, 18461-18468, 2016.
5. Novontny, L., N. Hulst, "Antennas for light," *Nat. Photon.,* Vol. 5, 83-90, 2011.
6. Yu, N. et al., "Flat optics: Controlling wavefronts with optical antenna metasurfaces," *IEEE J. Sel. Topics Quantum Electron.*, vol. 19, no. 3, 4700423, 2013.
7. Diao, Z. et al., "Nanostructured stealth surfaces for visible and near-infrared light," *Nano Lett.,* Vol. 16, 6610-6616, 2016.
8. Andrews, D. L., "Scientific Foundations, Technology and Applications: Biomedical Photonics, Spectroscopy, and Microscopy, Volume IV", 367-412, USA, Wiley, 2015.

Enhanced mechanical reliability of anti-reflective nanostructured polymer films prepared by sequential heat treatment process

D.-I Kim[1], N. E. Yeo[2], and M. Y. Jeong[3,*]

[1]BK21+ Nano-integrated Cogno-mechatronics Engineering, Pusan National University, Busan 46241, Korea

[2]Department of Opto-mechatronics Engineering, Pusan National University, Busan 46241, Korea

[3]Department of Cogno-mechatronics Engineering, Pusan National University, Busan 46241, Korea

[*]corresponding author: myjeong@pusan.ac.kr

Abstract-Anti-reflection characteristics and mechanical reliability of nanostructured polymer films prepared by nanoimprint process were evaluated to understand effect of the critical imprint parameters on the performance. The nanoscale cone array in hexagonal pattern was fabricated on PET and PMMA films by the thermal imprint process. Characterization of anti-reflection (AR) performance showed that the reflectance and transmittance of the prepared nanopatterned polymeric films were excellent 0.3% and 99%, respectively. However, a pencil hardness test unveiled that the nanostuructred AR film were significantly damaged by the scratch and has poor anti-scratch performance. In this study, the various thermal imprint process with heat treatment process were proposed and the effect of process on the anti-scratch performance were evaluated. It was found that the flat pressing under an elevated temperature higher than a glass transition temperature followed by an immediate cooling improves anti-scratch performance.

The anti-reflection surface treatment technology is highly required for the practical applications such as optical system, large-area display, solar cell panel and handheld devices. In typical optical system, anti-reflective (AR) surface improves the efficiency by minimizing reflection of incident light. One of conventional methods is applying multi-layer AR coating that have different refractive index and induce destructive interference of light [1]. However, it requires expensive and complicated deposition process which hinder fabrication of large-area AR surface. Thus, as an alternative solution, AR film employing nanostructure inspired by AR structures in moth eye was intensely investigated [2], [3]. Nanoimprint lithography technique allows us to fabricate large-area AR nanostructured film with high fidelity. However, nanoimprinted polymer film exposed to harsh condition showed poor mechanical reliability owing to the intrinsic mechanical property of polymer substrate. Therefore, anti-scratch performance of AR nanostructure polymer film is one of main issues should be resolved for the practical applications.

In this work, anti-reflection characteristics and mechanical reliability of nanostructured polymer films prepared by nanoimprint process with heat treatment were evaluated to improve mechanical reliability of AR film. The nanoscale cone array in hexagonal pattern was fabricated on PET and PMMA films by the thermal imprint process as shown in Figure 1(a). Figure 1(b) shows the fabricated nanoscale cone array on PMMA film. It was found that the fabricated Characterization of AR performance showed that the reflectance and transmittance of the prepared nanopatterned polymeric films were excellent 0.3% and 99%, respectively. However, a pencil hardness test unveiled that the nanostructured AR film were significantly damaged by the scratch and has poor anti-scratch performance. The continuous measurements of reflectance across the scratch

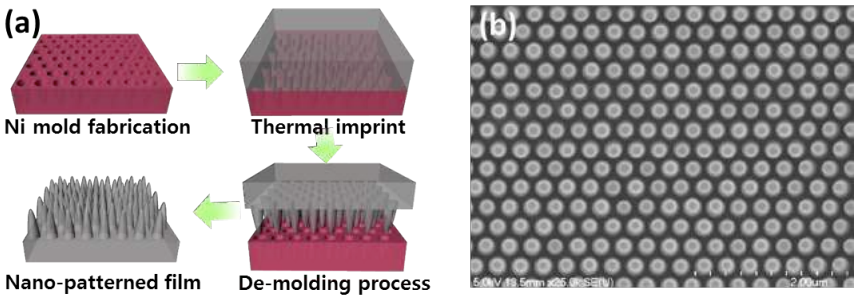

Figure 1: Schematic diagram of Thermal imprint process for AR nanostructure film (a) and the imprinted PMMA film with nanoscale cone array in hexagonal pattern (b)

showed that high reflectance is resulted by the mechanical damage of the nanostructure and the substrate.

To improve anti-scratch performance of AR film, the various thermal imprint process with addtitional heat treatment were proposed and the effect of heat treatment on the anti-scratch performance were evaluated. Figure 2 shows that the maximum reflectance measured form the scratch generated during pencil hardness test on AR films prepared with various heat treatment process. It can be seen that additional flat pressing followed by immediate cooling process is effective in comparison with sample 1, imprinted without suggested heat treatment process. It was found that the flat compression with elevated temperature higher than glass transition temperature followed by an immediate cooling improves anti-scratch performance. It can be concluded that the improved mechanical reliability of the film

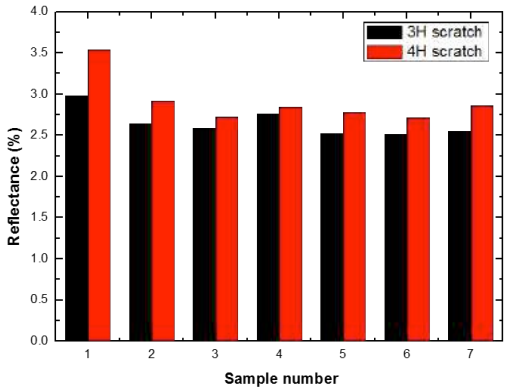

Figure 1: Reflectance measured from the scratches of the nanopatterned films after pencil hardness test.

REFERENCES

1. Raut, H. K., et al. “Anti-reflective coatings: A critical, in-depth review.” *Energy & Environmental Science* Vol. 4, No.10, 3779-3804, 2011.
2. Asadollahbaik, A., et al. “Reflectance properties of silicon moth-eyes in response to variations in angle of incidence, polarisation and azimuth orientation.” *Optics express* Vol. 22, No. 102, A402-A415, 2014.
3. Zhang, J., et al. “Low-cost fabrication of large area sub-wavelength anti-reflective structures on polymer film using a soft PUA mold.” Optics express Vol. 22, No. 2, 1842-1851, 2014.

A Study of Band Gap Effect of Seismic Metamaterials using Leaf Springs

J. Y. Yoon[1], S. J. Lee[1], and N-C. Park[1*]
[1]Yonsei University, Korea
[*]corresponding author: pnch@yonsei.ac.kr

Abstract-Elastic metamaterials that have negative effective properties have been investigated to prevent acoustic or seismic waves. In this study, seismic metamaterials were developed using leaf springs to achieve negative effective properties. We fabricated reduction model of seismic metamaterials and investigated effect of shock absorption using vibration exicter. Finite element model about reduction model was constructed and was verified validity of simulation results. Using similarity analysis, effect of shock absorption of real-size seismic metamaterials was investigated about seismic waves.

Elastic metamaterials can prevent external shock such as acoustic or seismic waves because of negative effective properties in specific frequency range. Seismic metamaterials of various shapes have been investigated and designed. S. Brûlé constructed regular mesh of cylindrical and empty boreholes and implemented seismic test [1]. Y. Yan constructed rubber coated steel of cubic shape [2] and M. Miniaci constructed rubber coated steel of cylinder shape [3]. These seismic metamaterials use tension-compression stiffness of pure material such as rubber or soil. Seismic metamaterials require low stiffness because the seismic wave has low frequency domain (1~10 Hz). However, tension-compression stiffness of pure material has large size to low stiffness, and therefore unit cell sizes of these seismic metamaterials are larger than 3 m. In this study, seismic metamaterials using leaf springs was constructed to reduce unit cell size. The leaf springs can be designed to have low stiffness and small size compared to tension-compression stiffness of pure material. Therefore, seismic metamaterials using leaf springs are more realistic and effective design than other metamaterials.

The unit cell of seismic metamaterials using leaf springs consists of three components: inner mass, outer mass, and leaf springs, as schematically shown in Fig. 1. The inner mass and outer mass are cubic and have length L_i and L_o, respectively. The inner mass is high density material and the outer mass is low density material to widen frequency range when the effective mass is negative. Figure 1 shows one dimensional case of seismic metamaterials. Leaf springs are supplemented in two or three dimensional cases at each axis.

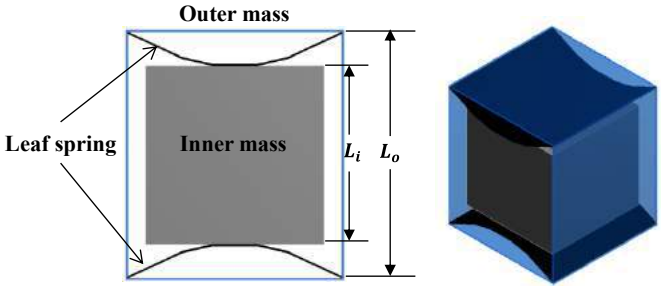

Fig. 1 Schematic diagram of the unit cell of the one dimensional seismic metamaterials using leaf springs

The seismic metamaterials using leaf springs that serialize seven unit cells was investigated using finite element analysis and experiment of reduction model. Input shock is El Centro seismic wave and was applied on side using exicter. Measurement point is the opposite side and experiment results was measured using accelerometer. The shock response of seismic metamaterials had band gap to 5 Hz from 10 Hz. This frequency domain is closed to frequency domain of seismic wave. Therefore, the seismic metamaterials using leaf springs that has 8.4 m total length can absorb shock of earthquake. This simulation and experiment results will be presented in the conference.

Acknowledgements, This work was supported by the National Research Foundation of Korea (NRF) Grant funded by the Korean Government (MSIP) (No. 2015R1A5A1037668)

REFERENCES

1. Brûlé, S., E. H. Javelaud, S. Enoch, and S. Guenneau, "Experiments on seismic metamaterials: molding surface waves," *Physical review letters*, Vol. 112, No.13, 133901, 2014.
2. Yan, Y., Z. Cheng, F. Menq, Y. L. Mo, Y. Tang, and Z. Shi, "Three dimensional periodic foundations for base seismic isolation," *Smart Materials and Structures*, Vol. 24, No. 7, 075006, 2015.
3. Miniaci, M., A. Krushynska, F. Bosia, and N. M. Pugno, "Large scale mechanical metamaterials as seismic shields," *New Journal of Physics*, Vol. 18, No. 8, 083041, 2016.

Variable stiffness using electromagnetic force in acoustic metamaterials.

Dongwook Kim[1], **Junsun Yoo**[2], **and No-Cheol Park**[1*]
[1]Department of Mechanical Engineering, Yonsei University, Koera
[2]Center for Information Storage Devices , Yonsei University, Korea
[*]corresponding author: pnch@yonsei.ac.kr

Abstract- The narrow band gaps of elastic materials is an obstruction for practical applications. In this paper, we proposed a method of changing band gaps through variable stiffness of the proposed lattice structure. We used attractive force between ferromagnetic materials and electromagnets that works like a spring. Electromagnetic circuit was designed to make variable stiffness of the structure. The dispersion equation and attenuation factor of this system was derived.

Elastic materials do not have negative mass density and stiffness in naturally. Recently, some researchers demonstrated that elastic metamaterials with double negativity can be achieved by combining structures.[1-3] However, most of the metamaterials that is aforementioned have negative effective mass and stiffness in narrow frequency region. The band gap of combining structures can be defined by lattice model as shown in Fig.1. The dispersion equation can be derived as below

$$\mathrm{m}_1 m_2 \omega^4 - [(m_1 + m_2)k_2 + 2m_2 k_1(1 - \cos(qL))]\omega^2 + 2k_1 k_2(1 - \cos(qL)) = 0 \quad (1)$$

where, ω is forcing frequency and q is a wave number.

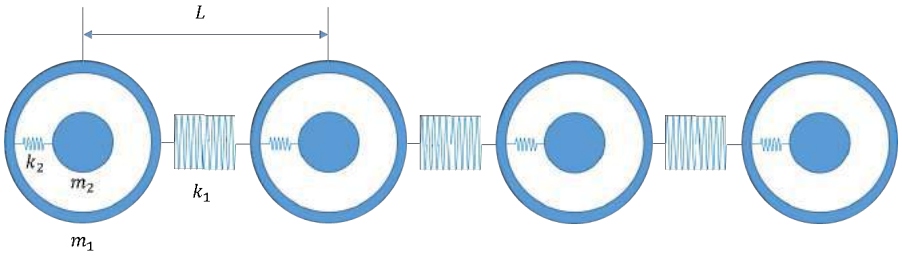

Fig. 1 Lattice model of metamaterials with combining structures

Conventional model has the fixed stiffness k_2 in a unit cell. In this study, the stiffness k_2 could be changed by an electromagnet. Moving mass m_2 is an electromagnet and attracted by another electromagnet. The attractive force can be controlled by flowed current in the coil. An electromagnetic circuit is proposed to have linear force between two electromagnets acting as a stiffness as shown in Fig. 2. Therefore, the band gap can be changed by the changeable stiffness k_2.

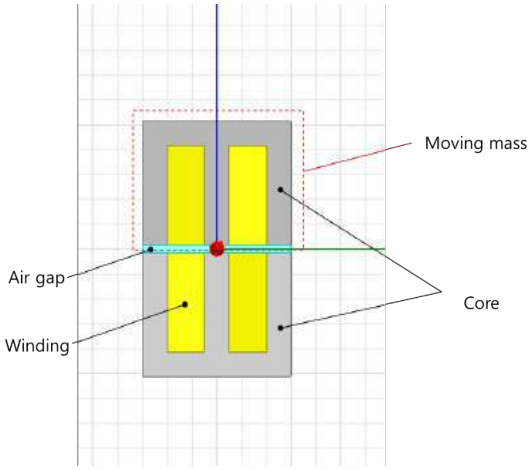

Fig. 2 A electromagnetic circuit of a unit cell

REFERENCES

1. Z. Liu, X. Zhang, Y. Mao, Y.Y. Zhu, Z. Yang, C.T. Chan and P. Sheng, "Locally resonant sonic materials," Science, Vol. 289, 1734–1736, 2000.
2. R.S. Lakes, T. Lee, A. Bersie and Y.C. Wang, "Extreme damping in composite materials with negative-stiffness inclusions," Nature, Vol. 410, 565–567, 2001.
3. N. Fang, D. Xi, J. Xu, M. Ambati, W. Srituravanich, C. Sun and X. Zhang. "Ultrasonic metamaterials with negative modulus," Nat. Mater, Vol. 5, 452–456, 2006.

Quantum manipulation and characterization of electron spin qubits in diamond

Dohun Kim[1]

Department of Physics and Astronomy, Seoul National University, Seoul 08826, Korea
dohunkim@snu.ac.kr

Abstract-Nitrogen-vacancy (NV) centers in diamond are excellent candidates for investigating quantum phenomena, constructing quantum two level system, and realizing quantum limited sensors due to long coherence time even at room temperature environment. In this talk, I briefly introduce optical quantum manipulation and measurements realized using spins in diamond, including electron spins and nuclear spins. For characterizing quantum processes, gate set tomography (GST) is a newly developed method which is self-consistent and overcomes limit of traditional state and process tomography. We apply GST method to electron spins and discuss accuracy of the single qubit gates obtained by analyzing gate sequence data using GST. We further discuss the way toward using GST method to multiple spins and qubits.

Keywords: Nitrogen-vacancy centers, Quantum gates, Quantum tomography, Gate set tomography, Optically detected magnetic resonance

Acknowledgements

This work was supported by the National Research Foundation of Korea(NRF) Grant funded by the Korean Government(MSIP)(No.2015R1A5A1037668), and the Creative Materials Discovery Program through the National Research Foundation of Korea(NRF) funded by the Ministry of Science, ICT and Future Planning(NRF-2015M3D1A1070672)

Highly Sensitive Enhanced Fluorescence DNA Microarray for Diagnosis of Atopic Dermatitis

M. A. Badshah[1], J. Ju[1], X. Lu[1], N. Abbas[1], S. M. Kim[1,*], S. J. Seo[2]

[1]School of Mechanical Engineering, Chung-Ang University, Seoul, 06974, Korea
[2]College of Medicine, Chung-Ang University, Seoul, 06974, Korea
[*]corresponding author: smkim@cau.ac.kr

Abstract-A metal enhanced fluorescence DNA microarray analysis has been demonstrated using glancing angle deposited (GLAD) Ag nanorods substrate for diagnosis of atopic dermatitis. To maximize the fluorescence enhancement factor, the effects of nanorod length on the fluorescence signal were examined. To examine the feasibility of the proposed highly sensitive DNA microarray for real application, a DNA screening chip for diagnosis of Atopic dermatitis was prepared using the fabricated GLAD substrate and the performance of the chip was tested using the real blood sample from the patient.

Metal-enhanced fluorescence (MEF) shows a significant potential to enhance the sensitivity of fluorescence detection by allowing fluorophores to interact with enhanced electromagnetic fields generated by the localized surface plasmon resonance effects of metallic nanostructures. We used a glancing angle deposition (GLAD) process to fabricate Ag nanorods on the whole area of slide glass substrate to serve as an inexpensive and large-area metal-enhanced fluorescence substrate for DNA microarray [1]. To maximize the signal enhancement, the effects of length of Ag nanorods (Ag-NRs) on the signal enhancement were examined. To measure the enhancement factor of GLAD-MEF substrates, a Cy5 conjugated Kallikrein-related peptidase 7 (KLK-7-Cy5) DNA probes, which is one of the DNA marker for atopic dermatitis, were spotted on each substrate and the fluorescence signal was measured after the blocking and washing process. The maximum enhancement factor of ~108x comparing with glass substrate was obtained from Ag-vertical nanorods with 500 nm length. To examine the reliability of GLAD-MEF substrate, we compared the performance of GLAD-MEF substrates with the commercial Amine slide (Amine 2®, Array-it, USA). From the fluorescence measurement experiments, the maximum signal enhancement of ~26x was obtained from the GLAD-MEF substrates compared to commercial amine slides. To examine the feasibility of the proposed MEF substrate for real application, we prepared the atopic dermatitis DNA microarray chip using the optimized Ag-NRs MEF substrate and examine the fluorescence signals repeatability and accuracy by using the blood samples from asthma patient.

Acknowledgements: This study supported by a grant of the Korean Health Technology R&D Project, Ministry of Health & Welfare, Republic of Korea. (HI14C2687), and National Research Foundation of Korea (NRF) grant funded by the Korean Government (MSIP) (No. 2015R1A5A1037668).

REFERENCES

1. Ju, J., Byeon, E., Han, Y., Kim, S.M., "Fabrication of a substrate for Ag-nanorod metal-enhanced fluorescence using the oblique angle deposition process," *Micro Nano Lett*., Vol. 8, No. 7, 370–373, 2013.

Fabrication of Glass micromixer with High chemical resistance

M. R. Haq, Y. K. Kim, and S. M. Kim*
School of Mechanical Engineering, Chung-Ang University, Seoul, 06974, Korea
*corresponding author: smkim@cau.ac.kr

Abstract- A glass micromixer with high chemical resistance was fabricated by glass molding process with vitreous carbon (VC) mold. A VC mold was fabricated by carbonization of replicated furan precursor. The effects of molding temperature and pressure on the replication quality were examined to optimize the glass molding process. The channel shape changes of glass chip during the mixing process with organic solvent as a working fluid were measured and compared with the conventional PDMS chip.

Although the polymer replicated microfluidic chips are generally used in various research fields due to its cost-effectiveness, a glass microfluidic chip offers more advantageous than polymer chips when a high thermal, mechanical and chemical durability are required. In this study, a low-cost glass micromixer fabrication has been realized using glass molding process (GMP) and thermal fusion bonding process (TFB). In the GMP, a mold having durability at high temperature is essentially required. A low cost and high surface quality vitreous carbon (VC) mold was fabricated by carbonization of replicated furan precursor. A photoresist master pattern was fabricated by photolithography technique and the master pattern was transferred to a polydimethyl-siloxane (PDMS) mold by soft lithography. A mixture of 89.9 wt% furan resin, 0.2 wt% p-Tolenesulfunic acid and 10 wt% ethanol were poured into the PDMS mold and a furan precursor having microchannel structure was obtained by curing process. To obtain VC mold with microchannel cavitiy, a carbonization process was carried out with a maximum temperature of 1000˚C in a temperature history programmed furnace [1]. A GMP process was conducted to fabricate glass microchannel structure on a soda line glass substrate at a molding temperature of 720˚C and a pressure of 10 kPa. To test the feasibility of glass micro mixer, the inlets and outlet were drilled of the molded glass micro structure and another soda-lime glass was bonded by thermal fusion bonding process with a temperature of 620˚C, pressure of 16.2 kPa, and holding time of 3 hrs. To examine the advantage of the fabricated glass micromixer, a mixing experiment using toluene with different colors were injected using syringe pump in fabricated glass micromixer and PDMS micromixer which was replicated using the fabricated VC mold. The channel width was decreased in the PDMS chip due to the swelling effects. However, glass chip shows high chemical resistance as expected.

Acknowledgements, This research was supported by the National Research Foundation of Korea (NRF) grant funded by the Korean Government (MSIP) (No. 2015R1A5A1037668) and Technology Innovation Program (No. 10051636) of the Korea Evaluation Institute of Industrial Technology (KEIT) granted financial resource from the Ministry of Trade, Industry & Energy, Republic of Korea.

REFERENCES

1. Ju, J., Lim, S., Seok, J., & Kim, S. M., “A method to fabricate Low-Cost and large area vitreous carbon mold for glass molded microstructures,” *Int. J. Precis. Eng. Manuf.*, Vol. 16, No. 2, 287-291, 2015.

High signal to noise enhanced fluorescence substrate with micro/nano hierarchy structure.

X. Lu, J. Ju, M. A. Badshah, N. Abbas, S. M. Kim*
School of Mechanical Engineering, Chung-Ang University, Seoul, 06974, Korea
*corresponding author: smkim@cau.ac.kr

Abstract-A micro/nano hierarchy structure was fabricated by UV-nano imprinting process and glancing angle deposition (GLAD) technique to improve the signal noise ratio of GLAD metal-enhanced fluorescence (MEF) substrate. Since the metallic nanorod structure formed only on the top of micropillar structure (Spotting area), the non-spot region shows lower background signal than the full metallic nanorod structure substrate, which improve the signal to noise ratio of enhanced fluorescence substrate.

Metal-enhanced fluorescence (MEF) is a powerful technology to improve the sensitivity of fluorescence analysis by allowing fluorophores to interact with enhanced electromagnetic fields generated by the localized surface Plasmon resonance effects of metallic nanostructures [1]. As a low cost and large area MEF substrate fabrication process, a glancing angle deposition (GLAD) has been proposed [2]. GLAD is a physical vapor deposition process in which deposition flux is incident onto the substrate at a large oblique angle to the surface normal (>75°). Although the fluorescence signal from the biomolecules spotted on the GLAD nanostructures increased significantly, the background signal also increased. In this study, a micro/nano hierarchy structure was proposed to improve the signal to noise (S/N) ratio of GLAD MEF substrate. The proposed high S/N ratio MEF substrate was composed of micropillar structures which corresponding to the spotting area and GLAD nanostructures. The micropillar structures were fabricated by UV-nanoimprinting process on a slide glass substrate, and a GLAD process was carried out with a rotation speed of 5 rpm and glancing angle of 85° on the fabricated micropillar structure. During the GLAD process, the nanorod structures formed only on the top of micropillar structure due to the shadowing effect of micropillar. To examine the proposed hierarchy structure, the S/N ratio of Straptavidin-Cy5 spots on the proposed substrate were measured and compared with that on a conventional GLAD substrate. The measured S/N ratio of the proposed substrate was 223.4 and that of the conventional GLAD was 148.6.

Acknowledgements

This work was supported by the National Research Foundation of Korea(NRF) grant funded by the Korean Government(MSIP) (No. 2015R1A5A1037668) and the Technology Transfer Development Program (S2334634) funded by the Small and Medium Business Administration(SMBA, Korea).

REFERENCES

1. Hayakawa T., Selvan S.T., Nogami M., “Field enhancement effect of small Ag particles on the fluorescence from Eu(3 +)-doped SiO2 glass” *Appl. Phys. Lett*, Vol. 74, 1513–1515, 1999.
2. Ju, J., Byeon, E., Han, Y., Kim, S., "Fabrication of a Substrate for Ag Nanorod Metal-Enhanced Fluorescence using the Oblique Angle Deposition Process", *Micro & Nano Letters*, Vol. 8, No. 7, 370–373, 2013.

Solar Energy Harvesting based on Photosynthesis

WonHyoung Ryu[1*]
[1]Department of Mechanical Engineering, Yonsei University, Seoul 03722, Republic of Korea
[*]corresponding author: whryu@yonsei.ac.kr

Abstract-In photosynthesis of plant cells, algae, or cyanobacteria, high energy electrons are generated and transferred in a photosynthetic electron transfer chain. The photosynthetic electrons (PEs) are either used to maintain the life of the plants or stored in a form of carbohydrates. There are multiple approaches to harvest the PEs and utilize them as a clean energy source. In this presentation, recent development of bio-solar cells based on PE harvesting will be introduced and discussed.

Plant cells produce photosynthetic electrons (PEs) by splitting water during photosynthesis. In the beginning of photosynthesis, antenna complex embedded in thylakoid membrane absorbs photon energy and converts them into excited electrons with high quantum efficiency. These excited electrons, known as PEs, are transferred through electron acceptors in order to grow cell or store surplus energy as a form of carbonhydrates. However, since the energy state of the PEs is lowered once they are stored as organic matter, many researchers have tried to extract PEs from photosynthetic electron transfer chain before their conversion into organic matter. Such previous works include collection of PEs by electrochemical oxidizing through mediator as an electron interceptor and use of electrical linker materials such as CNTs, electrically-conducting polymer matrix, or conducting linker to working electrodes between photosynthetic components and the surface of electrodes. Although these works demonstrated the feasibility of harvesting PEs in large scale, there are still issues including efficiency decrease from mediator use and limited stability or requirement of additional electron donors of isolated photosynthetic extracts. In this work, we present nanoelectrode systems to directly extract PEs without mediator. Fabrication of vertically-aligned patterned nanoelectrode systems is explained. Furthermore, we will discuss how the nanoelectrode geometry and illumination conditions affect the longevity of algal cells inserted by the nanoelectrodes during PE extraction. PE extraction for up to 7 days was achieved from nanoelectrode inserted into living algal cells.

Acknowledgements The author would like to thank the financial support by the Center for Advanced Meta-Materials(CAMM) funded by the MSIP as Global Frontier Project (CAMM- 2014M3A6B3063716) and the National Research Foundation of Korea (NRF) Grant funded by the Korean Government (MSIP) (No. 2015R1A5A1037668).

REFERENCES

1. Kim, L. H., Kim, Y. J., Hong, H., Yang, D., Han, M. Yoo, G., Song, H. W., Chae, Y., Pyun, J.-C., Grossman, A. R., Ryu W, “Patterned Nanowire Electrode Array for Direct Extraction of Photosynthetic Electrons from Multiple Living Algal Cells” Adv. Funct. Mater. (2016) 26(42): 7679-7689.

Large-scale fabrication of multilayer dielectric gratings for high power spectral beam combining of fiber lasers

Inki Kim[1], **Jungho Mun**[2], **Sunae So**[1] **and Junsuk Rho**[1, 2, 3*]

[1]Department of Mechanical Engineering, Pohang University of Science and Technology (POSTECH), Pohang 37673, Republic of Korea
[2]Department of Chemical Engineering, Pohang University of Science and Technology (POSTECH), Pohang 37673, Republic of Korea
[3]Natioanl Institute of Nanomaterials Technology (NINT), Pohang 37673, Republic of Korea
[*]corresponding author: jsrho@postech.ac.kr

Spectral Beam Combining (SBC) of multiple fiber lasers is a simple and straightforward method to obtain high power laser beam. The SBC system is typically composed of three parts, fiber laser arrays, transmission optical system, and diffraction grating parts. Performance of the SBC system is mainly determined by the diffraction grating parts where diffraction efficiency and damage threshold problems are dealing with. Thus, many SBC related researches have been focused on a highly efficient and robust diffraction gratings. Metallic gratings exhibit high diffraction efficiency with thin layers, but they have very small laser damage thresholds due to high light absorption in a metal. On the other hand, dielectric gratings can have relatively high-damage thresholds and also by stacking low refractive index and high refractive index medium alternatively, high reflectance mirror can be realized and reflectance become higher as number of layers increases. Moreover, exquisite grating patterns on the uppermost layer can engineer diffracted beam efficiency, but unfortunately most of geometrical parameters, such as number of multilayers, thickness and grating height, in the dielectric gratings are in a trade-off relationship. For instance, increasing number of multilayers is favorable for reflectance, but unfavorable for laser damage threshold. Therefore, all the geometrical parameters in the multilayer dielectric gratings (MLDG) should be optimized [1, 2]. In this abstract, I will discuss our efforts in design and experimental demonstration of MLDG, which is composed of HfO_2 and SiO_2 multilayers. First, I will present two design methodologies, rigorous coupled-wave analysis (RCWA) [3] and finite-difference time-domain (FDTD) method. RCWA is used to optimize different parameters and FDTD is used to calculate near/far-field characteristics. Second, I will present a laser interference lithography (LIL) set-up used in the device manufacturing. Through LIL set up, large-scale MLDG device (35mm x 35mm) is fabricated on a thick fused silica substrate (20mm). Finally, I will introduce optical characterizations for reflectance, diffraction efficiency and laser induced damage threshold. I believe our efforts for design optimization and large-scale fabrication will result in high efficient and robust MLDG for high power SBC.

REFERENCES

1. Varallyay, Z and Dombi, P., "Design of high-efficiency ultrabroadband dielectric gratings," *Appl. Opt.* Vol. 53, No. 25, 5769-5774, 2014

2. Neauports, J. *et al.,* "Effect of electric field on laser induced damage threshold of multilayer dielectric gratings," *Opt. Express* Vol. 15, No. 19 12508-12522, 2007
3. Moharam, M. *et al*., "Stable implementation of the rigorous coupled-wave analysis for surface-relief gratings: enhanced transmittance matrix approach", *J. Opt. Soc. Am. A* Vol. 12, No. 5, 1077-1086, 1995

Design of a flexible metamaterial superlens system for large-area nano patterning below the diffraction limit

Jinhyung Lee[1,2], Changsu Park[1,2] and Shinill Kang[1,2*]
[1]School of Mechanical Engineering, Yonsei University, Seoul, 03722, South Korea
[2]National Center for Optically-assisted Mechanical Systems, Yonsei University, Seoul, 03722, South Korea
[*]corresponding author: snlkang@yonsei.ac.kr

Abstract- We propose a method to design a flexible superlens system for large area nano patterning below the diffraction limit. The superlens structure including silver layer, silicon oxide layer and chrome nano mask was designed through FDTD simulation. To fabricate flexible superlens structure, silicon oxide layer(spacing layer, protective layer), silver layer and chrome grating mask were formed on a silicon substrate as a sacrificial wafer. PDMS was spin coated onto the chrome grating in order to achieve a flexible superlens substrate. After silicon etching, the flexible superlens structure was fabricated. Using the flexible superlens structure, we demonstrated that large-area nano patterns with a 60nm half-pitch below the diffraction limit were achieved at 365 nm illumination wavelength.

Superlens has received much attention for its ability to overcome the diffraction limit by amplifying the exponentially decreasing evanescent wave via surface plasmon resonance of thin metal slab. Since superlens lithography can be integrated with conventional photolithography systems, it is possible to fabricate nanopatterns below the diffraction limit at low cost and high throughput.[1] However, most of the previously reported superlens are fabricated on a rigid substrate(quartz substrate), which makes it difficult to fabricate large-area nanopatterns due to the issue of conformal contact between superlens and photoresist in photolithography process.[2,3]

This study proposes a method to design a flexible superlens system for large area nano patterning below the diffraction limit. By using a flexible superlens, conformal contact between superlens and photoresist can be achieved. First, the superlens structure was designed to amplify the evanescent wave via surface plasmon resonance of silver layer through finite difference time domain(FDTD) analysis. Simulation results show that the intensity of the evanescent wave can be maximized when superlens structure is designed as follows; a 60 nm half-pitch chrome grating mask with a thickness of 35 nm, a silicon oxide layer with a thickness of 30 nm, and a silver layer with a thickness of 30 nm. The light of 365 nm wavelength was illuminated to a superlens in normal incidence.

Based on the FDTD simulation results, the superlens structure was fabricated. A 5nm thick silicon oxide layer(protective layer) was first deposited on a silicon substrate as a sacrificial wafer by electron beam evaporator, and then silver (superlens) with a thickness of 30nm and silicon oxide(spacing layer) with a thickness of 30nm were deposited on a silicon oxide protective layer. A 60nm half-pitch chrome grating with 35nm thick was patterned on top of the spacing layer by using UV nanoimprint lithography. Subsequently,

PDMS was spin coated onto the chrome grating in order to achieve a flexible superlens substrate. After an etching process of silicon in potassium hydroxide(KOH) solution, a flexible superlens structure was fabricated. Superlens lithography was performed using a conventional photolithography system at 365 nm. A nano-pattern with a half-pitch of 60 nm below the diffraction limit was fabricated. Applications of nano patterns fabricated through superlens lithography is a subject of an ongoing research.

Acknowledgements, This work was supported by the National Research Foundation of Korea(NRF) Grant funded by the Korean Government(MSIP) (No. 2015R1A5A1037668)

REFERENCES

1. Fang, Liang, Li Pan, Changtao Wang, Xiangang Luo, "Superlens imaging lithography for high aspect ratio sub-wavelength pattern employing trilayer resist process," *Microelectron. Eng.,* Vol. 110, 35-39, 2013.
2. Chen, Xi, Fan Yang, Cheng Zhang, Jing Zhou, and L. Jay Guo "Large-area high aspect ratio plasmonic interference lithography utilizing a single high□k mode," *ACS NANO*, Vol. 10, No. 4, 4039-4045, 2016.
3. Lee, Hyesog, Yi Xiong, Nicholas Fang, Werayut Srituravanich, Stephane Durant, Muralidhar Ambati, and Cheng Sun, "Realization of optical superlens imaging below the diffraction limit," *New J. Phys.*, Vol. 7, 255, 2005.

High-throughput mechanical nanopatterning for scalable and flexible photonic and plasmonic applications

Jong G. Ok[1*]

[1]Department of Mechanical and Automotive Engineering, Seoul National University of Science and Technology, Seoul, 01811, Korea

[*]corresponding author: jgok@seoultech.ac.kr

Abstract- This talk will address how nanopatterns can be created at high speed and improved scalability, by utilizing continuous mechanical methods highlighted by roll-to-roll imprinting, nanoscale inscribing, and vibrational nanoindentation. Such continuous and scalable mechanical methodologies are based on simpler and cheaper principles, free from ponderous instruments, and applicable to flexible substrates, thereby enabling a big array of tangible applications particularly requiring large-area fabrication. In particular, we focus on two recent results on the plasmonic biosensors and polymer light-emitting diodes.

Acknowledgements

This work is supported by the National Research Foundation of Korea (NRF) Grants funded by the Korean Government (MSIP) (No. 2015R1A5A1037668, No. 2016R1C1B2016182, and No. 2015M2A2A4A01045225).

Facile fabrication of 3D LSPR nanoarchitectures comprising double-bent gold strips on transparent nanogratings via roll-to-roll nanoimprinting and angled metal deposition

J-S. Wi[1], S. Lee[2], S. H. Lee[3], D. K. Oh[2], J. H. Lee[2], J. D. Kim[2], K-T. Lee[4], I. Park[5], M. K. Kwak[3] and J. G. Ok[2*]

[1]Center for Nano-Bio Measurement, Korea Research Institute of Standards and Science, Daejeon, 01811, Korea

[2]Department of Mechanical and Automotive Engineering, Seoul National University of Science and Technology, Seoul, 01811, Korea

[3]School of Mechanical Engineering, Kyungpook National University, Daegu 41566, Korea

[4]Department of Materials Science and Engineering, University of Illinois at Urbana-Champaign, Urbana, Illinois 61801, USA

[5]School of Mechanical and Aerospace Engineering, KAIST, Daejeon 34141, Korea

[*]corresponding author: jgok@seoultehc.ac.kr

Abstract- A more facile nanoarchitecturing methodology for localized surface plasmon resonance (LSPR), particularly securing scalable and cost-effective fabrication procedure, is called for. We develop 3D plasmonic nanoarchitectures comprising the double-bent Au strips (DAS) integrated on transparent nanogratings, which can be continuously fabricated via roll-to-roll nanoimprint lithography along with inclined Au deposition. We also demonstrate the DAS shape can be tuned for optimal LSPR performance simply by controlling the Au deposition angles, towards flexible and transparent plasmonic sensors with high sensitivity.

Localized surface plasmon resonance(LSPR), generating optical absorption peaks at specific wavelengths due to surface plasmon confinement in a nanoscale metallic structure, has been capitalized in many diverse sensing devices. The present methods involving both top-down and bottom-up approaches, such as colloidal nanoparticle synthesis and etching-based nanofabrication, work well but suffer from exacting alignment, high cost, limited processable area, and overall complex procedure. A facile method to create LSPR nanoarchitectures in a scalable and cost-effective fashion is therefore called for.

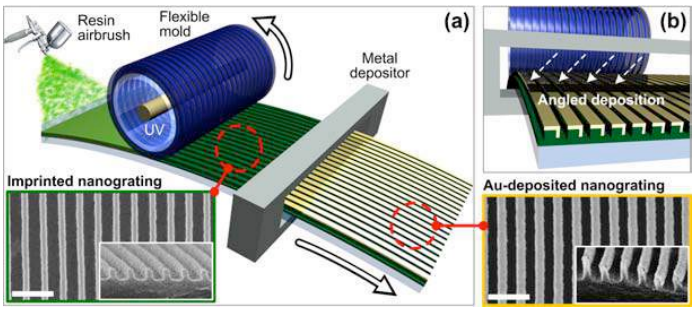

Figure 1. (a) Schematic and conceptual drawing of the overall fabrication procedure based around the continuous R2R NIL. (b) Enlarged conceptual view of the angled Au evaporation over the NIL-ed transparent polymer nanograting structures

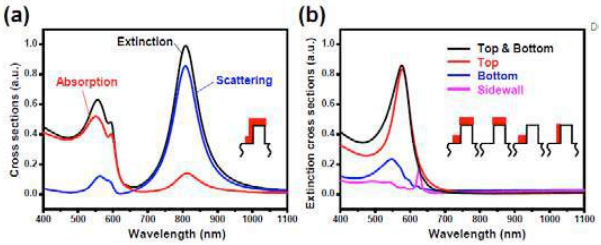

Figure 2. (a) Calculated extinction, absorption and scattering cross-sections of the double-bent Au strips on 1D grating. (b) Calculated extinction cross-sections of the partical segment of the double-bent Au strips.

In this work, we develop a scalable 3D plasmonic nanoarchitecture comprising the double-bent nanoscale Au strip array integrated within the transparent nanograting framework, which can be continuously fabricated on a large-area flexible substrate via roll-to-roll nanoimprint lithography (R2R NIL) and angled Au deposition without resorting to laborious etching or tedious alignment for orderly nanostructures (Figure 1). We first form the polymeric nanograting pattern array by R2R NIL, and then to deposit a metal layer onto the top and/or sidewall of each grating. Here, the long metallic structures can be 'folded' along the nanograting topography in a more compact fashion, compared to the ones simply patterned on a flat surface, thereby yielding the longer oscillation length for surface plasmon polaritons (SPPs) for higher sensitivity in a smaller device footprint. While the nanoscale Au strips can be tuned to unbent, single-bent, or double-bent shapes simply by controlling the Au deposition angle and thickness, (Figure 2b), we investigate that the double-bent Au strips (DAS) shows the best LSPR performance (Figure 2a). Utilizing the DAS formed on a flexible large-area polymer films, we demonstrate one specific example: a plasmonic sensor detecting the biological molecules. The continuous R2R-based manufacturing methodology and straightforward working principle may spur the DAS strip array to further extend the scalability and applicability; it can be conjugated with various antibodies on universal substrates, towards highly-sensitive, reliable, and inexpensive molecular detection platforms.

Acknowledgements

This work is supported by the National Research Foundation of Korea (NRF) Grants funded by the Korean Government (MSIP) (No. 2015R1A5A1037668, No. 2016R1C1B2016182, and No. 2015M2A2A4A01045225).

REFERENCES

1. Ok, J. G., Y. J. Shin, H. J. Park and L. J. Guo, A step toward next-generation nanoimprint lithography: extending productivity and applicability, Appl. Phys. A-Mater. Sci. Process, Vol. 121, No. 2,343-356, 2015.
2. Wi, J-S., S. Tominaka and T. Nagao, Arrays of Nanoscale Gold Dishes Containing Engineered Substructures, Adv. Opt. Mater, Vol. 1, No. 11,814-818, 2013
3. Ok, J. G., H. S. Youn, M. K. Kwak, K. T. Lee, Y. J. Shin, L. J. Guo, A. Greenwald and Y. S. Liu, Continuous and scalable fabrication of flexible metamaterial films via roll-to-roll nanoimprint process for broadband plasmonic infrared filters, Appl. Phys. Lett., Vol. 101, No.22 ,223102, 2012.
4. Koo, S., S. H. Lee, J. D. Kim, J. G. Hong, H. W. Baac, M. K. Kwak and J. G. Ok, Controlled Airbrush Coating of Polymer Resists in Rollto-Roll Nanoimprinting with Regimented Residual Layer Thickness, Int. J. Precis. Eng. Manuf., Vol. 17, No. 7, 943-947, 2016
5. Wi, J-S., S. Lee, S. H. Lee, D. K. Oh, K-T. Lee, I. Park, M. K. Kwak and J. G. Ok, Facile three-dimensional nanoarchitecturing of double-bent gold strips on Roll-to-Roll nanoimprinted transparent nanogratings for flexible and scalable plasmonic sensors, Nanoscale, Vol. 9, No. 4, 1398-1402, 2017.

Fabrication of Glass Microfluidic Devices via Glass Imprinting using a Vitreous Carbon Stamp

H. Jang[1], P. h Oh[1], M. R. Haq[1], J. Ju[1], Y. K. Kim[1], S.-M. Kim[1*], and J. Lim[2*]
[1]School of Mechanical Engineering, Chung-Ang University, Republic of Korea.
[2] School of Mechanical Engineering, Yeungnam University, Republic of Korea.
[*]corresponding author: smkim@cau.ac.kr, jlim@yu.ac.kr

Abstract- This study reports a cost-effective method of replicating glass microfluidic chips using a vitreous carbon (VC) stamp. A glass replica with the required microfluidic microstructures was synthesized without etching. The replication method uses a VC stamp fabricated by combining thermal replication using a furan-based thermally-curable polymer with carbonization. To test the feasibility of this method, a flow focusing droplet generator with flow-focusing and channel widths of 50 µm and 100 µm, respectively, was successfully fabricated in a soda-lime glass substrate.

The VC mold was fabricated via carbonization of a Furan-based replica, which was itself fabricated via a series of replication steps using PDMS and a furan-based thermal curable polymer. Since the demolding properties of the furan-based resin are extremely poor, it is not feasible to replicate a silicon wafer master pattern directly. The first replication step generates an elastomeric intermediate mold made from PDMS. PDMS has superior mechanical and surface properties, and can transfer a pattern to a Furan-based resin with high fidelity. The intermediate PDMS mold was fabricated via a conventional soft-lithography process using 10 parts of Sylgard 184 (Dow Corning, USA) and 1 part of a curing agent. The master pattern of the microfluidic structure was fabricated on a 4 inch silicon wafer via using a photolithography process that employed SU-8 3050 (Microchem Co., USA) as a photoresist. The height of the master pattern was 40 µm.

The second replication step was performed using a mixture that included a furan resin (Kangnam Chemical Co. LTD.), p-TSA (p-Toluenesulfonic acid), and ethanol. The furan mixture was poured onto the PDMS mold. Before solidification, the mixture was degassed to remove air bubbles created during mixing. In the first curing process, the mixture was allowed to polymerize naturally over 5 d under atmospheric conditions. Next, thermal curing was performed in a conduction oven at up to 100 ˚C for 2 d.

The furan precursor synthesized using the aforementioned method was carbonized in a furnace at 1000 ˚C under N2 for 5 d. During this process, pyrolysis phenomena caused shrinkage of the furan precursor to occur. Fig. 1 (a)~(d) shows a schematic diagram of the proposed VC stamp fabrication method.

A soda-lime glass substrate with a thickness of 3 mm was used as imprinting material. Fig. 1(e)~(f) shows the schematic flow diagram of the glass imprinting process. First, the VC mold was installed in the middle of the imprinting system and the glass substrate was placed to cover the VC mold. To prevent the oxidization of the VC mold during the process, the chamber was maintained in an inert environment via nitrogen purging. Meanwhile, the mold and substrate were heated beyond the glass transition temperature of the soda-lime glass, i.e. to 680 °C. Pressure of up to 163.5 kPa was then applied. After cooling to room temperature, the glass replica was removed from the VC mold.

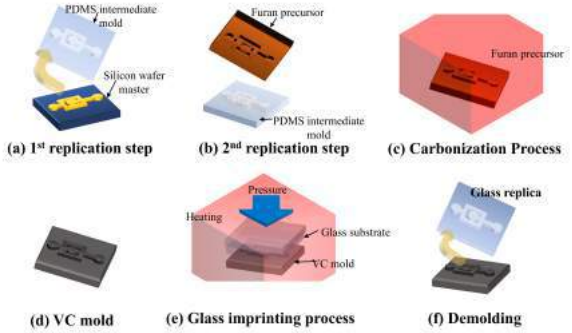

Fig. 1 Proposed fabrication method for the glass microfluidic device

To verify the fidelity of the glass imprinting process, the samples were measured at each step. As shown in Fig. 2, the difference between the surface morphologies of the silicon master (a) and Furan replica (c) is negligible. However, considerable shrinkage occurs during the carbonization process. Based on the measurement results, the sample volume shrinks by approximately 30%.

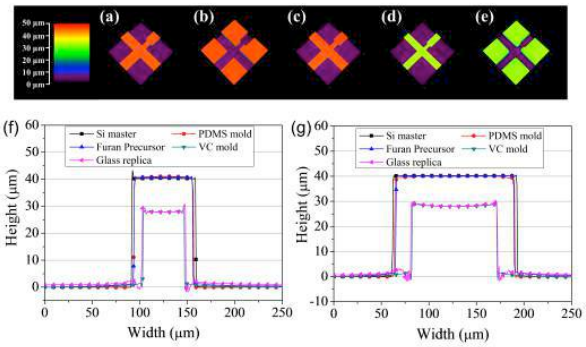

Fig. 2 3D microscope measurement results of (a) the silicon master, (b) the PDMS mold, (c) the furan precursor, (d) the vitreous carbon stamp and (e) the replicated glass microfluidic structure, and comparison of the surface profiles measured in (f) the channel and (g) the orifice.

We demonstrated that our approach can provide cost-effective glass microfluidic chip fabrication. Fabrication of all-glass chips via thermal fusion bonding is the subject of ongoing research.

Acknowledgements, This research was supported by a National Research Foundation of Korea (NRF) grant funded by the Korean Government (MSIP) (No. 2015R1A5A1037668).

REFERENCES

1. Chen Q, Chen Q, Maccioni G (2013) Fabrication of microfluidics structures on different glasses by simplified imprinting technique Current Applied Physics 13:256-261
2. Choi W, Lee J, Kim W-B, Min B-K, Kang S, Lee S-J (2004) Design and fabrication of tungsten carbide mould with micro patterns imprinted by micro lithography Journal of Micromechanics and Microengineering 14:1519

Fabrication of all glass bifurcation microfluidic chip for blood plasma separation

H. Jang[1], M. R. Haq[1], J. Ju[1], Y. K. Kim[1], S.-M. Kim[1*], and J. Lim[2*]
[1]School of Mechanical Engineering, Chung-Ang University, Republic of Korea.
[2] School of Mechanical Engineering, Yeungnam University, Republic of Korea.
[*]corresponding author: smkim@cau.ac.kr, jlim@yu.ac.kr

Abstract- An all-glass bifurcation microfluidic chip for blood plasma separation was fabricated by a cost-effective glass molding process using an amorphous carbon (AC) mold, which in turn was fabricated by the carbonization of a replicated furan precursor. To compensate for the shrinkage during AC mold fabrication, an enlarged photoresist pattern master was designed, and an AC mold with a dimensional error of 2.9% was achieved.

An all-glass bifurcation microfluidic chip for blood plasma separation was fabricated, using the glass molded microchannel plate prepared from an AC mold. To compensate for the shape change during AC mold fabrication, an enlarged silicon master pattern was prepared by conventional photolithography. A furan precursor was obtained by thermal replication using a replicated PDMS mold from the master. After the carbonization of the furan precursor, an AC mold with microchannel cavities was obtained. Finally, the glass bifurcation microfluidic chip was obtained by implementing glass molding for the microchannel plate, micro-drilling for the inlet and outlet connecting holes, and thermal fusion bonding for sealing. To examine the feasibility of the all-glass bifurcation microfluidic chip, the performance of the blood plasma separation was evaluated.

Fig. 1 shows the 3D surface profiles of the fabricated (a) silicon master, (b) PDMS mold, (c) furan precursor, (d) AC mold, and (e) molded glass microfluidic plate, obtained from the confocal microscopy results. It is clearly seen that the positive and negative microfluidic channel structures were uniformly transferred in each fabrication step. The measured widths and heights of microchannels in each sample are summarized in Table 1. Fig. 2 shows the comparisons of the cross-sectional surface profiles of the inlet microchannel (a) between the silicon master, PDMS mold (inverted), furan precursor, and AC mold, and (b) between the AC mold and the glass replica (inverted). Fig. 2(a) shows that a small shape change (shrinkage) occurred during the PDMS and furan precursor replication processes due to polymerization, and a significant shape change took place during the AC mold fabrication because of material decomposition during carbonization. Although an inherent substantial shape change occurred during the AC mold fabrication process, the shape change during the glass molding process is negligible, as shown in Fig. 2(b).

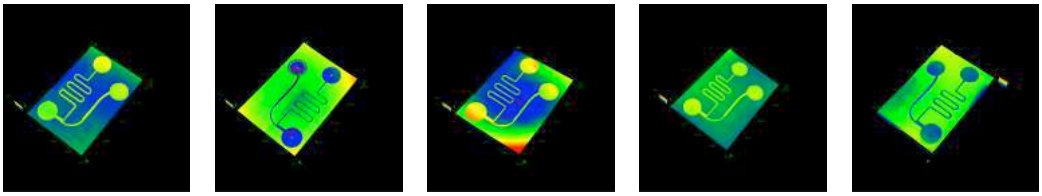

(a) (b) (c) (d) (e)

Fig. 1 3D microscope images of the (a) master pattern on Si wafer, (b) polydimethylsiloxane (PDMS) mold, (c) furan precursor, (d) AC mold, and (e) replicated glass microfluidic structure.

Table 1. Summary of the measured widths and heights of the microchannels for each fabrication step.

Samples	Inlet channel		Outlet channel		Extraction channel	
	Width (μm)	Height (μm)	Width (μm)	Height (μm)	Width (μm)	Height (μm)
Silicon Master	204.5	71.4	600.4	71.9	200.3	71.6
PDMS mold	202.5	71.0	584.9	71.7	190.6	71.1
Furan Precursor	196.4	67.8	585.9	68.2	190.8	68.9
AC mold	153.6	51.6	462.7	53.7	151.0	53.4
Glass replica	154.9	52.9	464.6	54.4	155.4	53.9

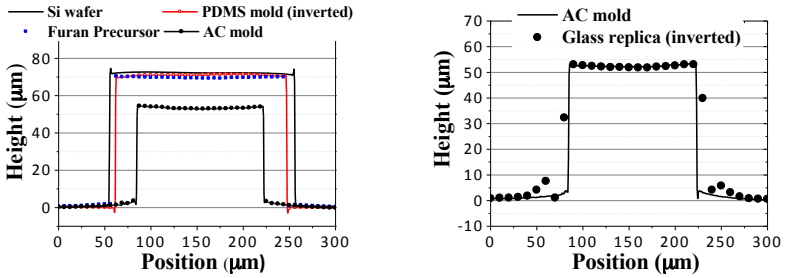

(a) (b)

Fig 2. Comparison of cross-sectional surface profiles of the (a) silicon master, furan precursor, and AC mold, and (b) AC mold and replicated glass microfluidic structure.

Acknowledgements, This work was supported by the National Research Foundation of Korea(NRF) grant funded by the Korean Government (No. 2015R1A5A1037668)

REFERENCES

1. Chong, Z.Z.; Tor, S.B.; Loh, N.H.; Wong, T.N.; Gañán-Calvo, A.M.; Tan, S.H.; Nguyen, N.T. Acoustofluidic control of bubble size in microfluidic flow-focusing configuration. *Lab Chip* **2015**, *15*, 996-999.
2. Kersaudy-Kerhoas, M.; Sollier, E. Micro-scale blood plasma separation: from acoustophoresis to egg-beaters. *Lab Chip* **2013**, *13*, 3323-3346.

Quantitative analysis of e.coli L-asparaginase in pico-liter droplets

E. Cho[1], Y.Lee[2], and J.Lim[2*]

[1] School of Mechanical Engineering, Yonsei University, 50 Yonsei-ro, Seodaemun-gu, Seoul, 120-749, Korea

[2] School of Mechanical engineering, Yeungnam University, Kyongsan, Korea

[*]corresponding author: jlim@yu.ac.kr

Abstract- Screening for enzymatic activities at the single cell level is of particular importance to find variants with specific desired activities, either in the natural diversity or in synthetic libraries obtained through mutagenesis. Droplet-based microfluidics offers promising platforms for the automation and miniaturization of assays, usable for single cell analysis. We demonstrate here a complex coupled assays for the measurement of the enzymatic activity of the bacterial asparginase.

Droplet-based microfluidics technology has become a powerful tool for the quantitative analysis of compartmentalized reactions which can take place in tremendously small volumes. Water-in-oil emulsions have been successfully used to a variety of biotechnological applications serving as diagnostic platforms, set-ups for sample analysis or combinatorial screening. The latest advances in chip design, construction and formation of monodisperse droplets have allowed the generation of volumes in the fL range. Such small volumes have formed a solid basis for the study of single-molecule enzymatic reactions and there has been an explosive interest towards this direction, as evidenced by the numerous high-impact research reports during the recent years. In addition, there have been reported several studies where microfluidic approaches have been successfully applied for high-throughput screening of libraries resulted from directed evolution experiments. The analysis of such libraries aims at the isolation of variants with the desirable properties while the selection pressure can be tuned by the experimental conditions. Notably in cases where, enzyme variants are to be screened for the identification of catalytically improved species, it is very critical to be able to discriminate distinct catalytic properties. Therefore, the success of such high-throughput screening set-ups solely relies on the availability of a highly sensitive enzymatic assay, which allows the quantitative activity characterization of each variant on the single-cell level.

In this paper, the quantitative characterization of single-cell enzymatic reactions using the most recent state-of-the-art droplet-based microfluidic set-ups. For that purpose, we displayed the therapeutic enzyme L-asparaginase II from E.coli (EcASNaseII, EC 3.5.1.1) in the inner membrane of E.coli cells by capitalizing the ApEx (Anchored Periplasmic Expression) system. Upon compartmentalization of single cells displaying EcASNaseII in water-in-oil emulsions, we measured enzymatic activities and performed steady-state kinetic experiments by applying a highly sensitive Amplex Red-based fluorescent assay. Figure 1 shows the enzymatic kinetics of the L-asparaginase.

Acknowledgement

This work was supported by the National Research Foundation of Korea(NRF) Grant funded by the Korean Government(MSIP) (No. 2015R1A5A1037668)

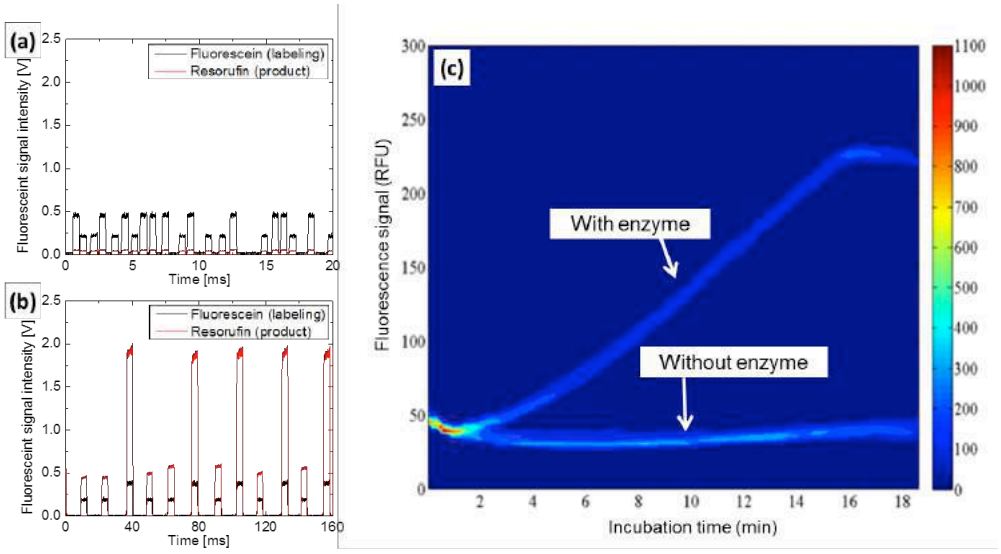

Fig. 1 Recorded fluorescent signal from the enzymatic reaction of the L-asparaginase. (a) Initial fluorescent signal and (b) the saturation point. (c) Kinetic comparison between the negative and positive control of the proposed enzymatic assay.

REFERENCES

1. .Agresti JJ, et al., Ultrahigh-throughput screening in drop-based microfluidics for directed evolution. Proc Natl Acad Sci U S A 107:4004–4009, 2010
2. Sjostrom SL, et al., High-throughput screening for industrial enzyme production hosts by droplet microfluidics. Lab Chip 14:806–813, 2014

High-throughput and scalable micro- and nanopatterning by continuous mechanical inscribing and its application in photonic devices

S. Lee[1], D. K. Oh[1], J. Park[1], J. D. Kim[1], J. H. Lee[1] and J. G. Ok[1*]

[1]Department of Mechanical and Automotive Engineering, Seoul National University of Science and Technology, Seoul 01811, Korea

[*]corresponding author: jgok@seoultech.ac.kr

Abstract- We perform the designing, constructing, and operating of the high-throughput and scalable micro- and nanopatterning system that utilizes continuous mechanical inscribing of a well-cleaved rigid pattern mold edge over a compliant substrate. By controlling the mold shape, inscribing force and speed, and processing temperature, many diverse small-scale patterns including 1D grating and 2D mesh, can be continuously created on any commercial polymer films at high speed. We also demonstrate the applications of such flexible micro- and nanopattern films.

Small-scale patterns have attracted a considerable amount of research and commercialization effort for the performance innovations of existing systems as well as the novel device developments in many fields involving photonics, sensing, bioengineering, metamaterials, displays, and so forth. However, most of the current micro- and nanopatterning processes based on such as photolithography, e-beam lithography, and laser interferometry, have suffered from complicated processes, long processing times, and difficulty in large area processing. A more straightforward and scalable micro- and nanopatterning methodology, hopefully without resorting to complex optical instruments and post-etching, is therefore highly requested.

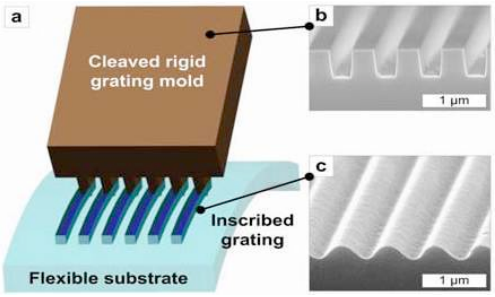

Fig. 1. (a) Schematic overview of continuous micronanopatterning by inscribing a rigid mold edge on a flexible substrate. SEM images of (b) a well-cleaved 700 nm-period SiO2 nanograting mold and (c) a resulting pattern inscribed on a polycarbonate substrate.

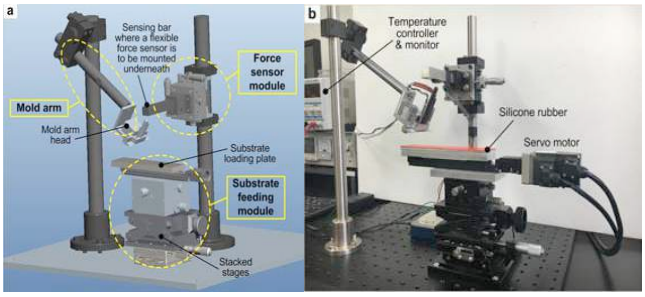

Fig. 2. The high-throughput micronanopatterning system utilizing continuous inscribing principle: (a) a 3D modeling assembly where three main modules are categorized and (b) a completed prototype connected with a servo motor, force sensor, heater, and the controller.

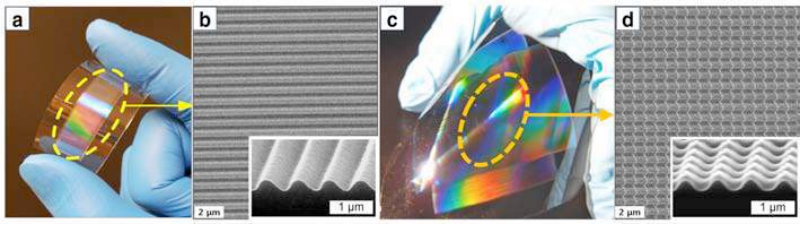

Fig. 3. Fabricated samples applying the continuous inscribing based micronanopatterning system on a flexible PC substrate: (a) 1D and (d) 2D optical view and SEM images of (b) 1D, (e) 2D top and (c) 1D, (f) 2D cross-sectional views.

To this end, we adopt a reliable mechanical machining protocol to small-scale patterning, developing a Dynamic Nano-Inscribing (DNI) process. Figure 1 depicts the overview of DNI; a rigid mold containing desired pattern, typically 1D grating, is cleaved across the grating direction. The edge of a mold then makes conformal contact to the target substrate, usually of compliant polymers. Under proper force and temperature, the mold edge slides over the substrate while continuously inscribing the nanopatterns. DNI enables continuous micro- and nanopatterning at high speed by using a simple and compact system as shown in Figure 2. By controlling the mold shape, inscribing force and direction, many diverse micro- and nanopatterns can be readily created, as demonstrated in Figure 3. Starting from the 1D nanograting structures (Figure 3a-b), we can extend it to multidimensional nanopatterns simply by sequentially performing DNI in multiple directions (Figure 3c-d), which otherwise demand complicated nanofabrication.

Acknowledgements

This work is supported by the National Research Foundation of Korea (NRF) Grants funded by the Korean Government (MSIP) (No. 2015R1A5A1037668, No. 2016R1C1B2016182, and No. 2015M2A2A4A01045225).

REFERENCES

1. Ok, J. G., H. J. Park, M. K. Kwak, C. A. Pina-Hernandez, S. H. Ahn and L. J. Guo, “Continuous patterning of nanogratings by nanochannel-guided lithography on liquid resists”, *Adv. Mater*., Vol. 23, No. 38, 4444-4448, 2011.
2. Ok, J. G., S. H. Ahn, M. K. Kwak and L. J. Guo, “Continuous and high-throughput nano-patterning methodologies based on mechanical deformation”, *J. Mater. Chem. C*, Vol. 1, No. 46, 7681-7691, 2013.
3. Ok, J. G., A. Panday, T. Lee and L. J. Guo, “Continuous fabrication of scalable 2-dimensional (2D) micro- and nanostructures by sequential 1D mechanical patterning processes”, *Nanoscale*, Vol. 6, No. 24, 14636-14642, 2014.
4. Lee, S., D. K. Oh, J. (Jaekyu) Park, J. D. Kim, J. H. Lee, and J. G. Ok, “Development of a High-throughput Micronanopatterning System Based on the Plastic Deformation Driven by Continuous Rigid Mold Edge Inscribing on Flexible Substrates”, *KSMTE*, Vol. 25, No. 5, 368-372, 2016.

Development of a compact roll-to-roll nanoimprinting system equipped with a resin airbrushing module for continuous and high-speed nanopatterning towards large-area and flexible applications in photonics and metastructures

S. Koo[1], S. H. Lee[2], J. D. Kim[1], J (Jeongsoo). Lee[1], J (Jihun). Lee[1], D. K. Oh[1], S. Nam[1], S. Cho[1], Y. Jo[1], M. Go[1], J. H. Lee[1], S. Lee[1], J. G. Hong[2], H. W. Baac[3], M. K. Kwak[2,4], and J. G. Ok[1*]

[1]Department of Mechanical and Automotive Engineering, Seoul National University of Science and Technology, Seoul 01811, Korea

[2]School of Mechanical Engineering, Kyungpook National University, Daegu 41566, Korea

[3]School of Electronic and Electrical Engineering, Sungkyunkwan University, Suwon 16419, Korea

[4] Research Center, Ncoretechnology, Co., Ltd., 80, Daehak-ro, Buk-gu, Daegu 41566, Korea

[*]corresponding author: jgok@seoultech.ac.kr

Abstract- We developed a compact desktop-sized Roll-to-Roll nanoimprinting system equipped with an airbrushing module for high-speed and uniform resin coating. A diluted resin can be smoothly airbrushed on a continuously moving substrate. The resin-coated substrate then makes a conformal contact with a roll bearing a flexible nanopattern mold, where the nanopattern is continuously stamped on a substrate as the rolling proceeds. The system enables the control of initial resin film thickness as well as the residual layer thickness of imprinted pattern.

While micro- and nanoscale patterns are of great interest for both academia and industry due to their extraordinary characteristics particularly in photonic and metastructure fields, the existing nanopatterning methods based on optical lithography and laser interferometry suffer from their low throughput, high cost, and area limitation. Nanoimprint lithography (NIL) can be an alternative solution to improve the nanopatterning productivity by performing direct mechanical stamping on the target substrate using a nanopattern mold. To further expand its scalability and applicability, NIL can be integrated with a continuous roll-to-roll (R2R) processing principle, where the roll wrapped with a flexible nanopattern mold continuously imprints the pattern on a UV-curable resin-coated substrate as rolling proceeds under conformal contact, finalized by UV curing at the outlet (Figure 1). To better utilize R2R NIL in scalable fabrication of diverse devices at high yield, a parametric study on a set of important parameters including rolling speed, contact force, and UV curing conditions is crucial. In this work, we develop a simple, desktop-sized R2R NIL system that realizes facile and handy parametric research without resorting to ponderous and expensive instruments.

Figure 2 schematically depicts the airbrushing process. A UV-curable nonvolatile resin is diluted in volatile solvent, which is smoothly airbrushed onto the desired flexible or rigid substrate to make a uniform thin film. Airbrushing can make uniform thin films over highly topographic surfaces at high speed, which is suitable for the continuous R2R processing principle. By regulating the resin concentration and airbrushing time, the initial thin film thickness as well as the residual layer thickness (RLT) in the R2R NIL-ed pattern can be readily

controlled. Figure 3 shows the core design of the R2R NIL system. The mold roll and backup roll can make conformal contact under a controlled force, while the supporting rolls afford smooth feeding of a substrate. We will demonstrate the detailed parametric investigation of the airbrushing and R2R NIL with varied resin concentration, airbrushing time, and NIL conditions, along with representative nanopatterning results. We will also discuss the effects of key parameters of each process towards optimized R2R NIL and potential applications in flexible and large-area photonic and metastructure devices.

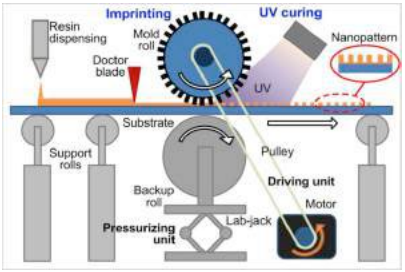

Figure 1 Conceptual scheme of a Roll-to-Roll nanoimprinting. The two main processes, imprinting and UV curing, along with the other necessary processes including the resin coating and motorized rolling are also marked

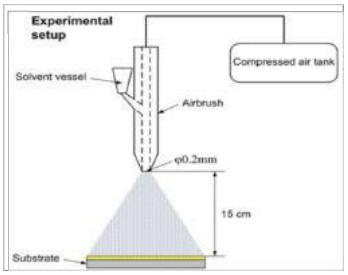

Figure 2 Schematics of airbrushing setup. The airbrushing nozzle is installed at a height 15 cm apart from the substrate, and is sprayed in a vertical direction at an injection pressure of 0.15 MPa.

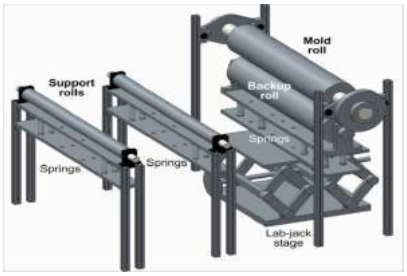

Figure 3 3D CAD drawing of an imprinting module; the mold roll and backup roll are responsible for pressurized imprinting, while the support rolls help secure uniform and continuous substrate feeding.

Acknowledgements

This work is supported by the National Research Foundation of Korea (NRF) Grants funded by the Korean Government (MSIP) (No. 2015R1A5A1037668, No. 2016R1C1B2016182, and No. 2015M2A2A4A01045225).

REFERENCES

1. Ok, J. G., H. S. Youn, M. K. Kwak, K-T. Lee, Y. J. Shin, A. Greenwald, Y. Liu and L. J. Guo, "Continuous and scalable fabrication of flexible metamaterial films via Roll-to-Roll nanoimprint process for broadband plasmonic infrared filters", *Appl. Phys. Lett.*, Vol. 101, No. 22, 223102, 2012.
2. Ok, J. G., S. H. Ahn, M. K Kwak and L. J. Guo, "Continuous and high-throughput nanopatterning methodologies based on mechanical deformation", *J. Mater. Chem*. C, Vol. 1, No. 46, 7681-7691, 2013.
3. Ok, J. G., Shin, Y. J., Park, H. J. and L. J. Guo, "A step toward next-generation nanoimprint lithography: extending productivity and applicability", *Appl. Phys. A*, Vol. 121, No. 2, 343-356, 2015.
4. Koo, S., S. H. Lee, J. D. Kim, J. G. Hong, H. W. Baac, M. K. Kwak, and J. G. Ok, "Controlled Airbrush Coating of Polymer Resists in Roll-to-Roll Nanoimprinting with Regimented Residual Layer Thickness", *IJPEM*, Vol. 17, No 7, 943–947, 2015.

Graphene based nanohybrid material for photoluminescence enhancement with surface plasmon

Byeongho Park[1], Seung Won Cho[1], and Seong Chan Jun[1*]
[1]School of Mechanical Engineering, Yonsei University, Seoul, Republic of Korea
[*]corresponding author: scj@yonsei.ac.kr

Abstract- We made graphene based metal nanocompounds as an innovative fluorescent material. Such sample showed high photoluminescence characteristics and new emission peak in the visible range, since the strong light confinement obtained from the metal nanoparticles as an antenna remarkably enhace the light absorption. Our material with nanosphere structure provided broad emision after the hybridization between materials. It exhibited a photoluminescence quantum yield of ~ 25 %, which is better than twice of graphene's.

We developed a novel nanosphere including GQDs and Au. The UV light was employed to assembly of GQDs and Au with photo-excited electrons and reducing capability of Au^{3+}. The size of the GQD/Au nanospheres was 150–170 nm, which is larger than that of the intrinsic GQDs (4–7 nm). The photoluminescence was improved with two emission peak for blue and green at 468 and 529 nm of wavelength. Our material, GQD/Au nanospheres showed high emission efficiency with 26.9 % of quantum yield over double of typical GQD's. Such fluorescent material can be perceived as exceptional candidates for applications such as light emitting source, optoelectronic devices, and bio-imaging with intriguing emission wavelength and intensity.

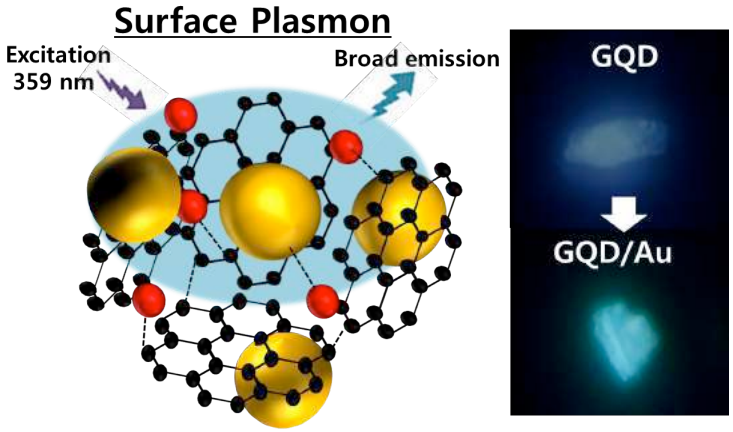

Figure 1. schematic of GQD/Au sample with enhanced photoluminescence of surface plasmon and fluorescence image of GQD and GQD/Au

Wideband metamaterials for antennas and related applications

EMI Shielding Based on MWCNTs/Polyester Composites

Lee Yeng Seng[1,2], F.H. Wee[2], Y.K. You[4], Z. Liyana[1], F. Malek[3], M. A. Jamlos[1] and A.A.M Ezanuddin[1]

[1]Department of Electronic Engineering Technology, Faculty of Engineering Technology, Universiti Malaysia Perlis (UniMAP), Perlis, Malaysia.
[2]Bioelectromagnetics Research Group (BioEM), School of Computer and Communication Engineering, Universiti Malaysia Perlis (UniMAP), Perlis, Malaysia.
[3]Faculty of Engineering and Information Sciences, University of Wollongong in Dubai (UOW).
[4]Radio Communication Engineering Department (RaCED), Faculty of Electrical Engineering, Universiti Teknologi Malaysia, Skudai, Johor, Malaysia.
* Corresponding author: yslee@unimap.edu.my

Abstract- The shielding effectiveness (SE) and complex permittivity of Multi-walled carbon nanotubes and polyester (MWCNTs/PE) composites were investigated in the microwave frequency region from 8.2 to 18 GHz. A rectangular waveguide transmission line method was used to measure the complex permittivity and SE properties of MWCNTs (0-20%) composites. In the microwave range, composite samples with highest conductivity have the greater SE. The results show SE of the composites increased as the amount of the CNTs increased.

SUMMARY

In this work, samples under test were prepared by mixing MWCNT with resin (PE), and methyl ethyl ketone peroxide (MEKP) hardening agent. The MWCNTs/PE composites with different content of MWCNTs were used to fabricate as various shield materials. The MWCNTs weight ratios are shown in Table 1. The MWCNTS/PE samples were fabricated by using two different moulds, i.e., WR-90 and WR-62 moulds. The MWCNTS/PE samples were prepared in two different rectangular shapes, which fit into WR-90 and WR-62 waveguide sample holders.

Table 1. Multi-walled carbon nanotubes composites (%total weight)

Sample code	M1	M2	M3	M4	M5
Multi-walled Carbon nanotube (wt. %)	0	5	10	15	20

In this work, the samples were prepared precisely into 22.86 mm x 10.16 mm x 5mm and 15.799 mm x 7.899 mm x 5 mm to fit into the waveguide sample holder for SE and complex permittivity measurement at 8.2-12.4 and 12.4-18 GHz. The MWCNTS/PE samples were measured using two pairs of WR-90 and WR-62 waveguide flanges that were connected to an Agilent E8362B P-series Network Analyzer (PNA) with Agilent flexible coaxial cables. The complex permittivity of the MWCNTS/PE samples were measured in the frequency range of the X-band and the Ku-band using commercial Agilent Technologies 85071E software. Two pairs of WR-90 and WR-62 waveguide flanges were used to transmit the EM wave to the sample material and to receive transmitted signal. Figure 1 shows the mould (sample holder) that was used to fabricate the rectangular MWCNTS/PE

microwave absorbers.

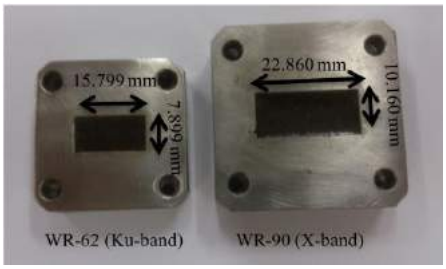

Figure 1. Mould (sample holder) used to fabricate MWCNTS/PE samples

Table 2. Dielectric properties of samples

Samples	Average value		
	Dielectric constant, ε_r'	Loss factor, ε_r"	Conductivity,(S/m)
M1	3.315	0.496	0.36
M2	9.647	3.274	2.33
M3	15.946	8.615	6.09
M4	21.778	15.455	10.92
M5	31.670	26.069	18.14

In this study, Multi-walled carbon nanotubes and polyester composites were successfully prepared. The complex permittivity and the EMI SE were measured in X-band and Ku-band frequency. The results showed that the MWCNTS/PE composite with 20 wt% MWCNTs had excellent EMI shielding ability, with SE > 35 dB in measured frequency range. The MWCNTS/PE composites with high dielectric loss were good candidates for use as EMI shielding materials over the 8.2 to 18-GHz frequency range. The results showed that the MWCNTS/PE composites have potential for applications as EMI shielding materials.

REFERENCES

[1] I. Nam , Lee ,HK and Jang, JH, "Electromagnetic interference shielding/absorbing characteristics of CNT-embedded epoxy composites," *Composites Part A: Applied Science and Manufacturing*, vol. 42, pp. 1110-1118, 2011.

[2] L. Liu, *et al*., "Characterization of Single-and Multiwalled Carbon Nanotube Composites for Electromagnetic Shielding and Tunable Applications," *Electromagnetic Compatibility, IEEE Transactions on*, vol. 53, pp. 943-949, 2011.

[3] D. Micheli, *et al*., "Optimization of multilayer shields made of composite nanostructured materials," *Electromagnetic Compatibility, IEEE Transactions on*, vol. 54, pp. 60-69, 2012.

[4] A. P. Singh, *et al*., "Multiwalled carbon nanotube/cement composites with exceptional electromagnetic interference shielding properties," *Carbon*, vol. 56, pp. 86-96, 2013.

[5] P. Saini, *et al*., "Enhanced microwave absorption behavior of polyaniline-CNT/polystyrene blend in 12.4–18.0 GHz range," *Synthetic Metals*, vol. 161, pp. 1522-1526, 2011.

[6] X. Liu, *et al*., "Fabrication and electromagnetic interference shielding effectiveness of carbon nanotube reinforced carbon fiber/pyrolytic carbon composites," *Carbon*, vol. 68, pp. 501-510, 2014.

Carbon Nanotubes Composite Materials for Dipole Antennas at Sub Terahertz Frequency Band

Yaseen N. Jurn[1], Mohamedfareq Abdulmalek[2], Hasliza A. Rahim[3]
[1]School of Computer and Communication Engineering
University Malaysia Perlis (UniMAP), 02000 Arau, Perlis, Malaysia

[1]Minister of Science and Technology
Baghdad, Iraq

[2]Faculty of Engineering and Information Sciences
University of Wollongong in Dubai (UOWD), Dubai, United Arab Emirates

[3]Bioelectromagnetics Research Group (BioEM),
School of Computer and Communication Engineering, University
Malaysia Perlis (UniMAP), Pauh Putra, Arau, Perlis 02600, Malaysia

[*]Yaseen Naser Jurn: yaseen_nasir@yahoo.com

Abstract-This paper aims to present two types of carbon nanotubes composite materials (CNTs-composite) for antenna applications within sub terahertz (THz) frequency band. These composite materials consist of CNTs coated by copper and silver separately to construct CNTs-copper and CNTs-silver composite materials. The scientific comparisons between the dipole antennas of these structure materials with CNTs and copper dipole antennas are presented to exhibits the performance evaluation of presented dipole antennas. The mathematical modeling of CNTs-composite material is presented in this paper.

The presented CNTs-composite materials consist of CNTs coated by a thin layer of copper and silver separately, where the single-walled carbon nanotube (SWCNT) is the specific structure of CNTs utilized in this work. The main structure of CNTs-composite material is illustrated in Figure (1). In this figure, (r) represent the radius of SWCNT and (t) represent the average thickness layer of coating material. The mathematical model of presented structure derived based on the mixture rule [], for a simple parallel model of the radial interface of coating material and SWNT for a simple parallel model of the radial interface of coating material and SWCNT. The general formula of the electrical conductivity of CNTs-composite material was presented in Equation (1).

$$A_{Compisite}\sigma_{\text{Structure}} = C_{\text{SWCNT}}\sigma_{\text{SWCNT}} + A_{Coat}\ \sigma_{\text{Coat}} \quad (1)$$

Where, ($A_{Composite}$) represent the cross-sectional area of CNTs-composite structure, (C_{SWCNT}) represent the cross-section area of individual SWCNT (circumference of SWCNT) and (A_{Coat}) represent the cross-sectional area of coating material. While, ($\sigma_{Structure}$) represent the electrical conductivity of CNTs-composite material,

(σ_{SWCNT}) represent the electrical conductivity of SWCNT [1], and (σ_{Coat}) represent the conductivity of coating material. Then, the final formula of this conductivity was presented in Equation (2).

$$\sigma_{\text{Structure}}(w) = \frac{1}{(r+t)^2}\left[-j\frac{4e^2V_f}{\pi^2 h(w-jv)} + t^2\sigma_{Coat}\right] \quad (2)$$

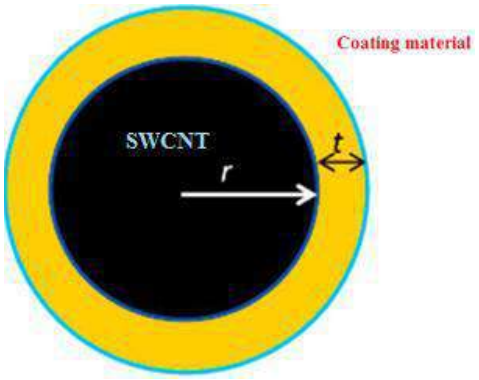

Figure 1: Structure of CNTs-composite material

The comparisons of simulation results for the CNTs-copper and CNTs-silver dipole antennas with SWCNT dipole antenna have been presented based on the similarity of dimensions of these dipole antennas. These comparisons are presented in Table (1).

Table 1: Summary of comparison results for SWCNT and CNTs-copper dipole antennas

L **(*μ*m)**	**SWCNT dipole antenna**				**CNTs-copper dipole antenna**			
	Fr **(GHz)**	**Directivity (dBi)**	**Gain**	**Efficiency**	***Fr*** **(THz)**	**Directivity (dBi)**	**Gain**	**Efficiency**
20	**162**	**2.05**	**9.89×10^{-5}**	**6.18×10^{-5}**	**1.6**	**2.10**	**6.47×10^{-2}**	**5.68×10^{-2}**

REFERENCES

1. Askeland, Donald R., Fulay, Pradeep P. and Wright, Wendelin J. "The Science and Engineering of Materials" (6th ed.). Cengage Learning, 2010.
2. Hanson, G. W. "Fundamental Transmitting Properties of Carbon Nanotube Antennas". *IEEE Transactions on Antennas and Propagation*, Vol.53, No. 11, 3426-3435, 2005.

Compact Tri-band Composite Right/left-handed Patch Antenna

Ting-Yuan Chen and Fu-Chiarng Chen*
Department of Electrical Engineering, National Chiao Tung University, Taiwan
*corresponding author: fchen@faculty.nctu.edu.tw

Abstract- In this paper, a compact tri-band microstrip patch antenna loaded with mushroom-like composite right/left-handed structure is presented. The mushroom-like structure is composed of a mushroom with two L-shaped slots. This composite right/left-handed structure can excite zeroth-order resonance (ZOR) mode and first-positive-order resonance (FPOR) mode. The first order resonance frequency can be adjusted by varying the spacing of two L-shaped slot such that the FPOR frequency can be reduced. As a microstrip upper patch stacked with the mushroom-like structure, the proposed antenna revealed triple-band behavior in 2.31 GHz, 2.92 GHz, and 3.7GHz.

Omini-directional antennas are widely used in the wireless communication systems such as WiFi and mobile communications. Dipole, monopole, and planar inverted F antenna (PIFA) are generally fabricated for producing omidirectional pattern. In recent years, with the rapid progress of metamaterials (MTMs), MTMs which include CRLH and periodic structures are used to design microwave circuits and antennas [1]-[7]. One kind of these applications is the zeroth-order resonance (ZOR) antenna [1]-[3]. ZOR antenna has many unique properties, for instance, the ZOR frequency is independent of the physical length due to the characteristic of infinite wavelength, and therefore the antenna size could be reduced. Mushroom structure is similar to the convention microstrip patch antenna, however, they have substantial different radiation patterns. Mushroom has monopolar radiation pattern because of its unique "equal amplitude/phase" electric-field distribution [4]. Recently, dual mode antennas with omidirectional and directional radiation pattern have been proposed [6]-[7]. In [6], the antenna utilized ZOR and first-order resonance for producing variant radiation patterns. Unfortunately, first-positive-order resonance (FPOR) frequency and first-negative-order resonance (FNOR) are generally restricted by the number of unit cells. Once the number of the unit cells is decided, the FPOR frequency cannot be adjusted. To overcome this drawback, we propose a modified mushroom-like structure by adding two L-shaped slots on a mushroom to control the frequency of the FPOR frequency. Our proposed antenna has dual mode antenna patterns including a monopolar radiation pattern and a patch-like radiation pattern. The ZOR frequency generates a monopolar radiation pattern, while the FPRO frequency generates a patch-like radiation pattern. We apply the stacked antenna technique [8] to add an upper patch over our proposed modified mushroom-like CRLH structure. In [8], dual-frequency behavior of stacked microstrip patch has been investigated. By using the stacking antenna technique, we can excite the third resonance frequency in our proposed antenna. Our proposed antenna only contains a unit cell of the modified mushroom-like structure. Therefore, the size of the antenna is small and easy to be fabricated. The antenna is designed to work in 2.31 GHz, 2.92 GHz and 3.7 GHz. The first operating frequency is the ZOR frequency, the second is the FPOR frequency, and the third frequency is determined by the top microstrip patch size. The antenna radiation patterns are shown in Figure 1. Both simulation and measurement results of the proposed dual-mode tri-band antenna will be presented and discussed.

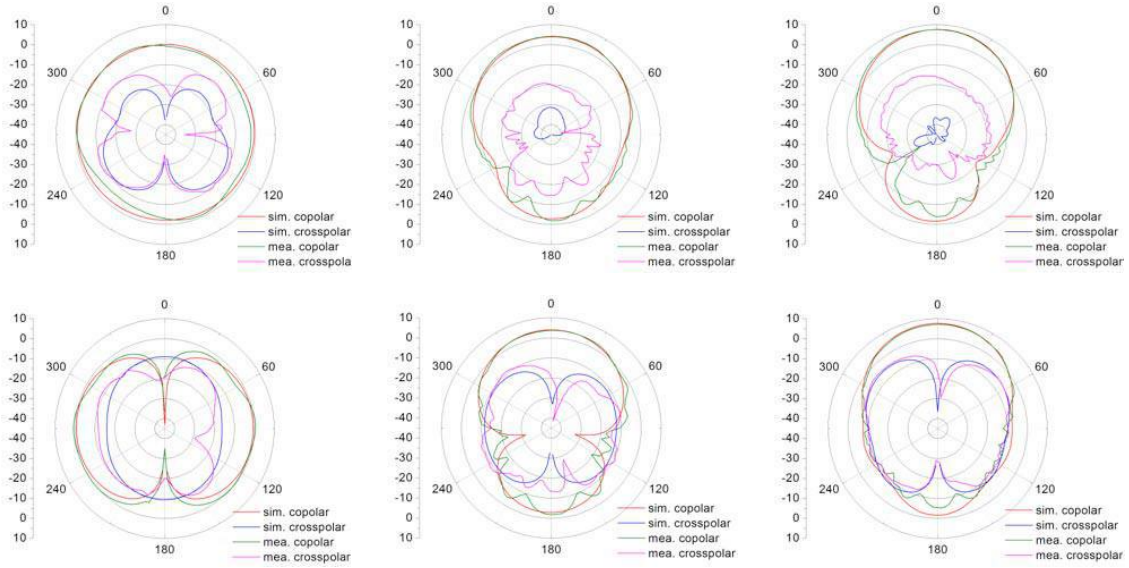

Fig.1. Simulated and measured radiation patterns of the proposed antenna. (a) xy-plane at 2.31GHz. (b) yz-plane at 2.31GHz. (c) xz-plane at 2.92GHz. (d) yz-plane at 2.92 GHz. (e) xz-plane at 3.7 GHz. (f) yz-plane at 3.7 GHz.

REFERENCES

1. M. S. Majedi, and A. R. Attari, "A compact and broadband metamaterial-inspired antenna," *IEEE Antennas Wireless Propag. Lett.*, vol. 12, pp. 345–348, 2013..
2. P.-W. Chen, and F.-C. Chen, "Asymmetric coplanar waveguide (ACPW) zeroth-order resonant (ZOR) antenna with high efficiency and bandwidth enhancement," *IEEE Antennas Wireless Propag. Lett.*, vol. 11, pp. 527–530, 2012.
3. B.-j. Niu, and Q.-Y. Feng,"Bandwidth enhancement of asymmetric coplanar waveguide (ACPW)-fed antenna based on composite right/left-handed transmission line," *IEEE Antennas Wireless Propag. Lett.*, vol. 12, pp. 563–566, 2013.
4. J. K. Ji, G. H. Kim, and W. M. Seong, "Bandwidth Enhancement of Metamaterial Antennas Based on Composite Right/Left-Handed Transmission Line," *IEEE Anten-nas Wireless Propag. Lett.*, pp. 36–39, 2010.
5. A. Lai, K. M. K. H. Leong, and T. Itoh, "Infinite Wavelength Resonant Antennas With Monopolar Radiatio Pattern Based on Periodic Structures," *IEEE Antennas Propagat.*, vol. 55, no. 3, pp. 868–876, Mar. 2007.
6. W. Cao, B. Zhang, A. Liu, T. Yu, D. Guo, and X. Pan," Multi-frequency and dual-mode patch antenna based on electromagnetic band-gap (EBG) structure," *IEEE Antennas Propagat.*, vol. 60, no. 12, pp. 6007–6012, Dec. 2012.
7. A. Lai, K. M. K. H. Leong, and T. Itoh, "Dual-mode compact microstrip antenna based on fundamental backward wave," in *Proc. Asia–Pacific Microw. Conf.*, Suzhou, China, Dec. 2005, vol. 4.
8. T. Fortaki, F. Chebara, and A. Benghalia, "On the dual-frequency behavior of stacked microstrip patches," *IEEE Antennas Wireless Propag. Lett.*, vol. 7, pp. 310–313, Oct. 2008.

A Super Wideband Reconfigurable Antenna for Millimetre Wave Application

M. M. Hasan[1*], M. R. I. Faruque[1], S. Abdullah[1], M. T. Islam[2]

[1]Space Science Centre (ANGKASA), Universiti Kebangsaan Malaysia, Bangi 43600, Malaysia
[2]Department of Electrical, Electronic and Systems Engineering, Universiti Kebangsaan Malaysia, Bangi 43600, Malaysia

*corresponding author: mehedi20.kuet@gmail.com

Abstract

A super wideband microstrip patch antenna based on reconfigurable metamaterial is proposed in this paper. The ground plane of the proposed super wideband antenna is modified with the designed metamaterial structure to obtain the reconfigurable characteristics. The antenna has a zig-zag shape on the patch and the metamaterial structure consists of a ring resonator with two switching configurations. The characteristics of proposed antenna are varied with the effectively activate or deactivate by with the switches. Finite integration technique commercially available electromagnetic simulator is utilized to design and numerical investigation. The return loss (S_{11}) shows the super wideband from 31 to 52.50 GHz. In addition, the performance of the antenna is analysed with the changing of the switch configurations.

1. Introduction

In recent years, for the rapid development of wireless communication technology, the antenna is required to be capable of working with different polarizations or different radiation patterns to satisfy the variation of system working environments. Conventional single-functional antennas can't meet those demands since their characteristics are fixed and inflexible, and thus the system performance will be limited. To this end, antennas with reconfigurable characteristics have drawn much attention in recent years. Moreover, millimetre wave has been attracting attentions of many scientists and engineers of different fields for much higher channel capacity and better resolution in mm-wave radar/imaging systems. In addition, metamaterial is an engineered electromagnetic material having exotic electromagnetic properties and a metamaterial based millimetre wave reconfigurable antenna has the ability to acquire and track moving targets, 5G communication, change radiation pattern, radiation polarization, operating frequency, etc [1]. Few investigation have been done on the previous research in this study. V. G. Veselago first 1968 discussed about metamaterial. After a long time at 2003 R. W. Ziolkowski developed a metamaterial by capacitor loaded strips and split ring resonators, which exhibited negative permittivity and permeability both at the X-band frequency [2]. Later until nowadays a lot of research have been done on the metamaterial characteristics and its applications, such as Hasan et al. proposed a compact z-shaped double negative metamaterial for C- and X-band operations. The metamaterial structure single unit cell was 10×10 mm2 and effective medium ratio was more than 4 [3]. A negative index meta-atom, the resonance at C-, X- and Ku-band with wide negative refractive index bandwidth from 7.0 to 12.81 GHz was presented in [4]. Moreover, the meta-atom presented negative index characteristics at X- and Ku-band. A circularly polarized reconfigurable millimetre wave antenna was presented for achieving low-cost beam steering in 32.5 GHz with the axial ratio <1 dB. The antenna was constructed by placing a periodic array of transverse strips along the surface of a dielectric waveguide [5]. A microstrip line fed star-star fractal antenna with notch loaded semi-elliptical ground plane was proposed for super wideband applications. An impedance bandwidth of 4.60 to 52.0 GHz, which was a bandwidth ratio of 11.31:1 was achieved for VSWR less than 2. The simulated resonances were at the frequencies of 5.60, 8.50, 14.30, 18.0, 21.0, 30.0, 33.50, 36.50, 41.0, 43.50, 46.0, and 48.0 GHz as well as the measured resonances were at 5.60, 8.50, 14.30, 18.0, 29.80, 33.20, 36.20, 41.10, 44.10, 46.30, and 47.40 GHz [6]. A fractal antenna with triangular slot for super bandwidth from 3.0 to 35.0 GHz was suggested, which designed by the triangular slot on a hexagonal metallic patch with tapered microstrip feedline. The SWB antenna total dimension of 20.0×33.4×1.57 mm3, a bandwidth ratio of 11.6:1, and gain varies from 2.2 to 11.2 dBi in the frequency range of 3.0 to 35.0 GHz [7]. A star-triangular fractal monopole SWB antenna with a semi elliptical ground plane was designed to operate the frequency band between 1.0 to 30.0 GHz for VSWR less than 2.0 [8]. In this paper a textile fractal SWB antenna was proposed that the total electrical size of 0.28×0.285×0.00875λ and the antenna based on the triangular circular patch and a modified elliptical ground plane. The proposed SWB antenna showed the operation band from 1.40 to 20.0 GHz [9]. A SWB antenna that consisted of a hexagonal radiation patch with two iterations of Sierpinski square slots for the operating bands, 3.81 to 29.64 GHz and 31.34 to 36.79 GHz [10]. Hossain et *al*. presented a frequency reconfigurable metamaterial antenna using a coupled-resonator structure and the effects of resonator structure are altered by closing and opening the splits using switches [11]. A compact 12.0×12.0×1.128 mm3 antenna was developed in 2017 for

operating higher frequency from 57.0 to 64.0 GHz, high gain <8 dBi, an isolation of better than 25 dB between the transmitting and receiving antenna in [12]. A metamaterial of electromagnetic band gap (EBG) was incorporated to an antenna for frequency re-configurability. The EBG consisted of two identical unit cells that provided multiple band gaps from 1.88 to 1.94 GHz, 2.25 to 2.44 GHz, 2.67 to 2.94 GHz, 3.52 to 3.54 GHz, and 5.04 to 5.70 GHz with different EBG configurations. Subsequently, an EBG structure was added with antenna to achieve different reconfigurable frequencies at 1.60, 1.91, 2.41, 3.26, 2.87, 5.21, and 5.54 GHz respectively. The antenna had the potential to be implemented for Bluetooth, Wi-Fi, WiMAX, LTE, and cognitive radio applications [13]. Further, a planar polarization reconfigurable antenna array using complementary square split ring antenna element based on SIW technique was investigated. The polarization states of the proposed antenna element could be reconfigured between the LP, LHCP, and RHCP modes. The antenna array had an impedance bandwidth (S11<-10dB) of 7.98 to 8.75 GHz and a 3-dB axial ratio bandwidth of 8.18 to 8.45 GHz for the two CP modes, and had an impedance bandwidth of 8.01 to 8.24 GHz for the LP mode. In addition, the maximum gains of the two CP modes and the LP mode were respectively 10.47 dBi, 9.9 dBi and 10.75 dBi [14]. Ding et *al*. introduced a millimetre wave pattern reconfigurable antenna, which adopts a linear array structure with three radiating elements with three reconfigurable modes in 2013. In addition, the three reconfigurable patterns point to -550 to 30 and -550 to +620 in the elevation plane [15]. In 2007 Liu et *al*. invented a dual band reconfigurable fractal patch antenna where the switches etched in the antenna slots and by changing the status of the switches the radiation patterns of the antenna were changed around 60.0 and 80.0 GHz, covering the elevation angles of 130 to 450, -130 to -450 around 60 GHz and of 150 to 500, -150 to - 500 around 80 GHz [16].

In this paper, a super wideband (SWB) antenna based on reconfigurable metamaterial is presented, which has a zig-zag shape on the patch and the metamaterial structure consists of a ring resonator with two switching configurations in the splits on the resonator. By changing the switching state, the performance of proposed antenna is varied. The return loss (S11) of the antenna show the super wideband from 31.0 to 52.50 GHz (bandwidth of 21.50 GHz). At present, in order to support increased traffic capacity, high data rate transmission bandwidths are required in the millimetre wave frequency range (more than 30 GHz) for the communication. This presented antenna includes the frequency bandwidth spectrum from 31.0 GH to 52.50 GHz. As a result, the mentioned bandwidth of the antenna is applicable for the millimetre wave frequency range applications.

2. Reconfigurable Antenna Design

The proposed reconfigurable SWB antenna is designed by a radiating patch where a zig-zag shape on the patch. The slotted ground plane of the antenna is modified with a metamaterial structure to obtain the reconfigurable characteristics. The metamaterial structure consists of a ring resonator with two switching configurations (switch-A and switch-B) between the splits in the resonator. Moreover, the total dimensions of the antenna and the unit cell structure are respectively, 50×40 mm2 and 50×40 mm^2.The schematic views of the radiating patch, metamaterial based ground plane, and the metamaterial single unit cell is shown in figure 1(a-c). The proposed SWB antenna has been printed on a Rogers RT 5880 material (thickness of 1.575 mm, dielectric constant of 2.2 and loss tangent of 0.0009). Copper is used as a resonator on the dielectric substrate with an electrical conductivity of σ=5×8 s/m. The dielectric thickness, mainly helps the coupling between the electric resonance occurred on the metallic resonators with the bottom metallic layer. This coupling creates a magnetic response and makes the effective impedance to be equal to the impedance of the free-space. The fabricated view of the antenna displayed in figure 1(d-e) and optimized dimensions of the designed antenna exhibited in table 1.

Table 1: Optimized dimension (mm) of the proposed SWB reconfigurable antenna.

Para.	L_A	W_A	L_1	W_P	W_f	W_1	W_2
Size	50.0	40.0	38.0	36.0	6.0	23.0	7.0
Para.	L_g	W_g	W_S	H_S	g_2	A	W
Size	9.0	40.0	8.0	2.0	41.0	30.0	22.0

The dimensions of the proposed reconfigurable metamaterial single unit cell structure are: length (A)= 30.0 mm, width (W)= 22.0 mm, metal (copper) width (d)= 4.0 mm, and gap (g)= 4.0 mm. To make the designed metamaterial as reconfigurable metamaterial two switches (S-A and S-B) is placed on the resonator structure in between the splits as shown in figure 1(c). Depending on the state of switches, three different configurations (Conf-1, Conf-2, and Conf-3) are considered. The '0' and '1' states of switch are used for open and close conditions of a switch, respectively. As described in table 2 configuration, Conf-1 consists of both switches (S-A and S-B) are open. The Conf-2, the configuration consists of switch S-A open and switch S-B close state as well as Conf-3 configuration consists of both switches (S-A and S-B) are close.

Table 2: State of the switch on different configuration.

Configuration	State of Switch	
	S-A	S-B
Conf-1	0	0
Conf-2	0	1
Conf-3	1	1

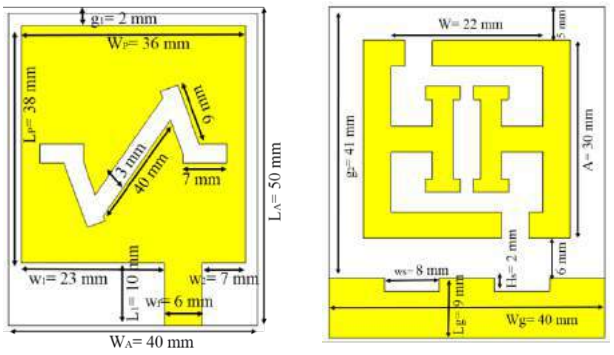

(a) (b)

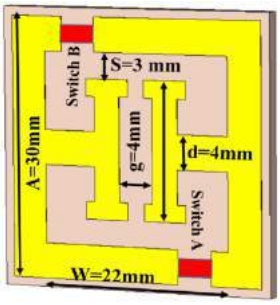

(c)

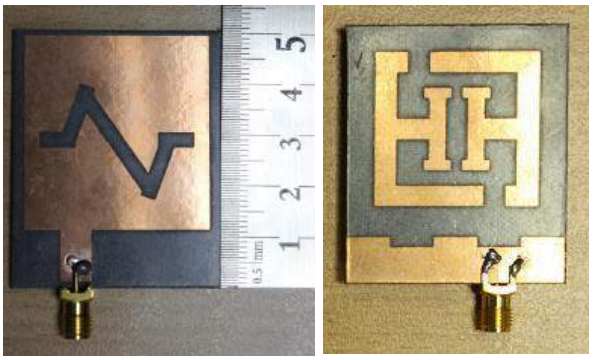

(d) (e)

Figure 1: Schematic prototype of the SWB antenna: (a) Front view, (b) Back view, (c) Schematic view of the reconfigurable metamaterial; Fabricated prototype of the SWB antenna: (d) Front view, (e) Back view with the reconfigurable metamaterial.

The simulation of the proposed antenna is performed by the CST Microwave Studio and measurement is done by the Agilent N5227A vector network analyzer, whereas the network analyzer is calibrated by the Agilent N4694-60001 to achieve the perfect over the entire super wide band (SWB) spectrum. To understand the characteristics of the metamaterial unit cell integrated on the antenna ground plane simulation of the unit cell is done in CST-MWS, whereas the electric boundary is set as an E-field and magnetic boundary is defined H-field. The Nicolson-Ross-Wire method has been utilized to retrieve the effective parameters, which are as follows [17],

$$Permeability, \mu_r \approx \left[\frac{C}{j\pi fd} \left\{ \frac{1-S_{21}+S_{11}}{1+S_{21}-S_{11}} \right\} \right] \quad 1$$

$$Permittivity, \varepsilon_r \approx \left[\frac{C}{j\pi fd} \left\{ \frac{1-S_{21}-S_{11}}{1+S_{21}+S_{11}} \right\} \right] \quad 2$$

$$Refractive\ Index,\ n_r \approx \sqrt{\mu_r \varepsilon_r}$$

$$Refractive\ Index,\ n_r \approx \left[\frac{C}{j\pi fd} \sqrt{\left\{ \frac{(S_{21}-1)^2 - S_{11}^2}{(S_{21}+1)^2 - S_{11}^2} \right\}} \right] \quad 3$$

where, '*d*' is the thickness of the substrate, '*C*' is the velocity of light, 'S_{11}' is the reflection coefficient, and 'S_{21}' is the transmission coefficient.

3. Antenna Performance

The metamaterial structures provide a resonant lumped circuit behavior in some certain frequency bands. The ground metamaterial structure resonator metal strips behave like inductors and the gaps as capacitors. To illustrate how the structure works when placed in an electromagnetic field region, the surface current distribution is presented in figure 2. It can be observed from figure 2 that the current is uniformly distributed along the surface of radiating patch, feed line and the ground plane. The magnetic field shows a similar distribution as the current supports that the resonances are obtained of magnetic type. Moreover, a close examination of the current distribution in figure 2 leads to the observation of some gaps. These gaps occur at current minimum points and this provides an additional capacitance-like response. The electric field is highly localized around these gaps and the reason of the high concentration around the actual gaps is the capacitive effect at these regions.

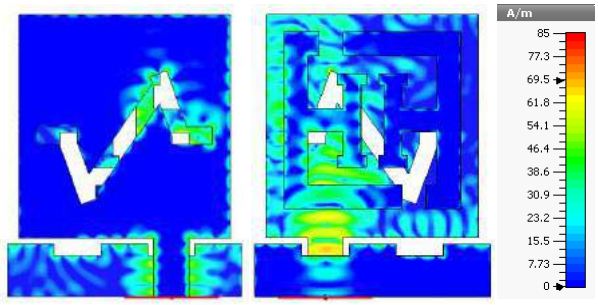

(a) (b)

Figure 2: Surface current distribution at 42.99 GHz in: (a) Radiating patch (front view), (b) Ground plane with the reconfigurable metamaterial (back view).

The full wave simulation of the design antenna with three different switching states, which explained above are shown in figure 3. In figure 3(a) the simulated return loss (S_{11}) of the antenna for three different configurations (Conf-1, Conf-

2, and Conf-3) are displayed. The simulated resonances at 34.14, 43.0, 49.41, and 50.71 GHz are found quite similar to the proposed antenna three different configurations (Conf-1, Conf-2, and Conf-3), whereas the measured results only for Conf-1 in displaying when the both switches (S-A and S-B) are open state. The measured return loss shows resonance peaks at 34.20, 36.96, 41.82, 43.50, and 49.41 GHz when the both switches (S-A and S-B) are open state in figure 3(b). The measured results are slightly different from the simulated results due to the effects from Sub Miniature Version A (SMA) connector soldering with feed line, proper calibration characteristics and toleration of the measurement. Basically, the proposed metamaterial single unit cell structure of the ground plane has strong negative characteristics in the higher frequency and remove the high frequency band of the antenna to create a stop band. Figure 3 (c) depicts the effective medium parameters (permittivity, permeability, and refractive index) curve of the integrated metamaterial. From the graph negative permittivity is from 30.0 to 46.80 GHz and the permeability is shown two negative regions from 35.11 to 40.75 GHz and 48.12 to 51.16 GHz. Moreover, at the resonance points of the reflection coefficient (S_{11}) the amplitude of the permittivity, permeability and refractive index are respectively -0.45-0.29j, 8.33+4.12j, 1.10-1.89j at 34.14 GHz, -0.45+0.12j, 0.64-0.30j, 0.53+0.036j at 43.0 GHz, 0.32-0.05j, -2.53-0.23j, 0.032-0.89j at 49.41 GHz, and 0.37-0.15j, -2.0-0.66j, 0.167+0.88j at 50.71 GHz. There is variation between the results of the permittivity, permeability and refractive index for the polarization effects on the internal structure of the materials. The loss depends on the effective medium parameters and defined by the ratio between the imaginary and the real magnitude of the effective permittivity or permeability. In addition, the imaginary components of the effective medium parameters attributed to bound charge and dipole relaxation, which gives rise to energy loss that is indistinguishable from the loss due to the free charge conduction. However, figure 3(d) shows the simulated results of the VSWR of the proposed antenna at different switching state, which are illustrated in table 2.

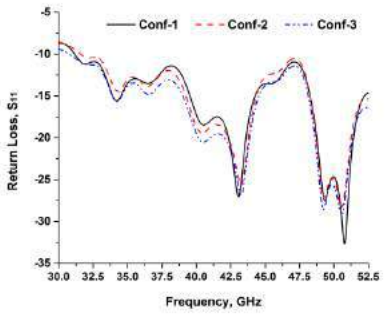

(a)

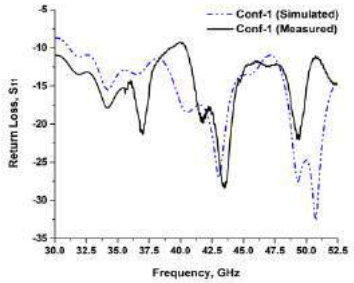

(b)

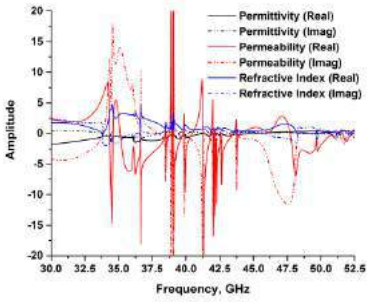

(c)

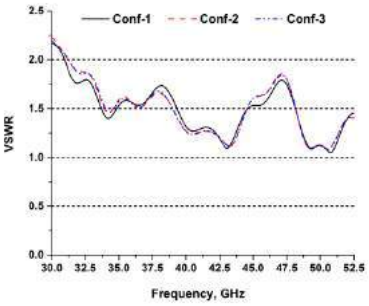

(d)

Figure 3: (a) Simulated return loss (S_{11}) at different switching state (shown in table 2), (b) Measured and simulated return loss of the proposed antenna at both switches (S-A and S-B) are open state, (c) Amplitude of the effective medium parameters of the designed reconfigurable metamaterial at both switches (S-A and S-B) are open state, (d) Simulated VSWR of the proposed SWB antenna at different switching state (shown in table 2).

The *y-z* (E-plane) and *x-z* (H-plane) radiation patterns of the proposed antenna at 42.99 and 49.06 GHz are shown in figure 4(a-c) and figure 5(a-c). It is observed from the plot that the radiation patterns are omnidirectional and stable in the *y-z* plane. In *x-z* plane patterns, few nulls have been observed in the broadside direction due to the diverse electric current distribution. With the raise of the frequency more nulls are observed with some ripples in the amplitude due to many refection into the field.

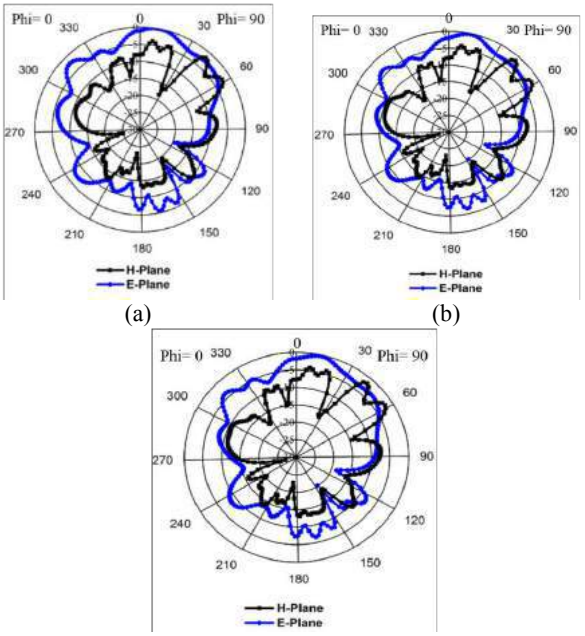

(a) (b)

(c)

Figure 4: Simulated radiation pattern of the proposed SWB reconfigurable antenna at 42.99 GHz: (a) Both switch (S-A and S-B) are open state, (b) Switch S-A open and switch S-B close state, (c) Both switches (S-A and S-B) are close state.

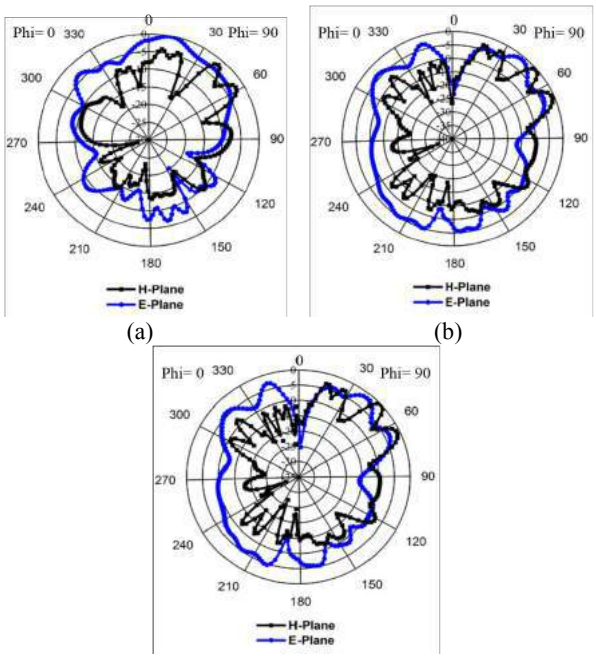

(a) (b)

(c)

Figure 5: Simulated radiation pattern of the proposed SWB reconfigurable antenna at 49.60 GHz: (a) Both switch (S-A and S-B) are open state, (b) Switch S-A open and switch S-B close state, (c) Both switch (S-A and S-B) are close state.

4. Conclusion

A SWB antenna with reconfigurable metamaterial has been analysed in this paper. This proposed antenna takes full advantage of the metallic patch with a zig-zag shape slot in the patch as an effective radiation element without introducing any parasitic elements. The performance of the antenna is significantly affected by the ground plane. Modification of a large ground plane into a partial phase decreased ground plane dependency, enhances the operating band, overcome design complexity and development difficulty. The reconfigurable technology is present in the integrated, switchable metamaterial structure in the ground plane of the antenna. By changing the switching state, the performance of the antenna is changed and the designed antenna shows the large bandwidth of the return loss for the millimetre wave applications. Moreover, a considerable amount of back lobe was observed, possibly because of the utilization of partial ground plane. A full ground plane can reduce this back lobe at the cost of low gain, low efficiency and narrow bandwidth. Finally, the controlling metamaterial structure characteristics of proposed antenna create a new way of designing reconfigurable antenna.

Acknowledgements

This work was supported by the Research Universiti Grant, Geran Universiti Penyelidikan (GUP), Code: 2016-028.

References

[1] D. Tran, P. Aubry, A. Szilagyi, I. E. Lager, O. Yarovyi, L. P. Ligthart, “On the design of super wideband antenna”, In Tech Publication, 2010, pp. 399–426.

[2] R. W. Ziolkowski, “Design, fabrication, and testing of double negative metamaterials”, IEEE Transactions on Antennas and Propagations, 2003, 51 (7): 1516–1529.

[3] M. M. Hasan, M. R. I. Faruque, S. S. Islam, M. T. Islam, “A new compact double-negative miniaturized metamaterial for wideband operation”, Materials, 2016, 9(10), 830.

[4] M. M. Hasan, M. R. I. Faruque, M. T. Islam, “A single layer negative index meta atom at microwave frequencies”, Microwave and Optical Technology Letters, 2017, 59:1450–1454.

[5] C. T. Rodenbeck, M. Y. Li, K. Chang, “Circular-polarized reconfigurable grating antenna for low-cost millimeter-wave beam-steering”, IEEE Transactions on Antennas and Propagation, Vol. 52, No. 10, 2004.

[6] S. Singhal, A. K. Singh, “Modified star-star fractal (MSSF) super-wideband antenna”, Microwave and Optical Technology Letters, Vol. 59, No. 3, 2016.

[7] B. L. Shahu, S. Pal, N. Chattoraj, “Design of super wideband hexagonal-shaped fractal antenna with triangular slot”, Microwave and Optical Technology Letters, Vol. 57, No. 7, 2015.

[8] V. Waladi, N. Mohammadi, Y. Zehforoosh, A. Habashi, J. Nourinia, “A novel modified star-triangular fractal (MSTF) monopole antenna for super-wideband

applications", IEEE Transactions on Antennas and Propagation, Vol. 12, 2013.

[9] M. K. Mohammadabadia, M. A. Dorostkarb, F. Shokuohic, M. Shanbehd, A. Torkand, "Super-wideband textile fractal antenna for wireless body area networks", Journal of Electromagnetic Waves and Applications, 2015, Doi: 10.1080/09205071.2015.1060139.

[10] S. Singhal, A. K. Singh, "CPW-fed hexagonal Sierpinski super wideband fractal antenna", IET Microwaves, Antennas & Propagation, 2016, pp. 1–7.

[11] M. I. Hossain, M. R. I. Faruque, M. T. Islam, M. T. Ali, "Design and analysis of coupled-resonator reconfigurable antenna", Applied Physics A, Doi: 10.1007/s00339-015-9520-6.

[12] S. Liao, Q. Xue, "Dual polarized planar aperture antenna on LTCC for 60-GHz antenna-in-package applications", IEEE Transactions on Antennas and Propagation, Vol. 65, NO. 1, 2017.

[13] R. Dewan, M. K. A. Rahim, M. Himdi, M. R. Hamid, H. A. Majid, M. E. Jalil, "Multiband frequency-reconfigurable antenna using metamaterial structure of electromagnetic band gap", Applied Physics A, 123:16, 2017.

[14] J. Hu, Z. C. Hao, Z. W. Miao, "Design and Implementation of a planar polarization reconfigurable antenna", IEEE Antennas and Wireless Propagation Letters, 2017, Doi: 10.1109/LAWP.2017.2650961.

[15] X. X. Ding, B. Wang, "A millimeter-wave pattern-reconfigurable antenna with a reconfigurable feeding network", Journal of Electromagnetic Waves and Applications, Vol. 27, No. 5, pp. 649–658, 2013.

[16] H. Liu, B. Z. Wang, W. Shao, "Dual-band bi-directional pattern reconfigurable fractal patch antenna for millimeter wave application", Journal of Infrared, Millimeter and Terahertz Waves, 28:25–31, 2007.

[17] M. M. Hasan, M. R. I. Faruque, M. T. Islam, "Multiband Left Handed Biaxial Meta Atom at Microwave Frequency", Materials Research Express, 2017, 4, 035015.

Metamaterial Based Frequency Reconfigurable Antenna for 5G Communication

M. M. Hasan[1*], M. R. I. Faruque[1], M. T. Islam[2]

[1]Space Science Centre (ANGKASA), Universiti Kebangsaan Malaysia, Bangi 43600, Malaysia
[2]Department of Electrical, Electronic and Systems Engineering, Universiti Kebangsaan Malaysia, Bangi 43600, Malaysia

*corresponding author: mehedi20.kuet@gmail.com

Abstract

A metamaterial based frequency reconfigurable antenna is presented for 5G communication. It is composed of a straight feed-line monopole with two double split-ring resonators (DSRR). The DSRR is developed by an outer and inner split ring resonators with inverse E-shape metal strips of copper are connected with the outer ring resonator. Commercially available electromagnetic simulator is utilized to design and numerical investigation. The return loss (S_{11}) shows the resonance in 32.08, 35.07, and 41.60 GHz. The performance of the proposed reconfigurable antenna is analyzed by activate or deactivate the DSRR. However, the designed metamaterial shows left handed characteristics and compact in size.

1. Introduction

The fifth generation (5G) networks are expected to use the higher frequency bandwidths due to the growing need for wider bandwidths and higher data rates. Compared with the cellular networks used today, 5G mobile networks will the proposed bands in the millimetre wave region are, 37.0 to 40.50 GHz, 42.50 to 43.50 GHz, 45.50 to 47.0 GHz, 47.20 to 50.20 GHz, which have allocations to the mobile service on a primary basis. Besides, 31.80 to 33.40 GHz, 40.50 to 42.50 GHz, and 47.0 to 47.20 GHz, which may require additional allocations to the mobile service on a primary basis for 5G wireless communications. Re-configurability of an antenna adds more versatility in the application, like frequency of operation, direction of the main beam, beam width, of a particular antenna. Metamaterials are an artificial material with more compact size compare with conventional structures and have some infrequent properties, which does not exist in the nature materials. Metamaterial based reconfigurable antenna can achieve a high performance by dynamically changing its physical structure. It is equivalent to having multiple antennas with different physical aperture [1]. So, the metamaterial based reconfigurable antenna can reduce the overall cost, weight, and size of a system. Moreover, few metamaterials based reconfigurable antenna has been investigated in this study. V. G. Veselago first 1968 discussed about the concept of metamaterial. After a long time at 2000, D. R. Smith and his colleagues invented a material that shown the negative permittivity and permeability at a same time with some infrequent properties [2]. The use of metamaterial in the antenna structure make the antenna structure compact, flexible for low or high frequency applications, etc. As a result, huge research had been done on metamaterial antenna from the past to present days. Such as a z-shaped double negative metamaterial had been proposed for C- and X-band operations in 2016. The metamaterial structure single unit cell was 10×10 mm^2 and effective medium ratio was more than 4 [3]. A negative index meta-atom, the resonance at C-, X- and Ku-band with wide negative refractive index bandwidth from 7.0 to 12.81 GHz was projected in [4]. A reconfigurable loop antenna with two parasitic Inverted-L grounded strips for modern smartphone devices was presented, which outer metal rim generates three loop modes and the inner parasite grounded strips provided two monopole modes. By merging these two types of antenna modes, it covered GSM 850/900 and LTE 2300/2500 operations with a compact antenna size of 945 mm2. For lower-band (from 824 to 960 MHz), the antenna gains and total efficiencies were approximately 0.3 to 1.7 dBi, and 45 to 60%, respectively, as well as for the upper operating band (from 1710 to 2690 MHz), gains and total efficiencies were respectively about 1.2 to 4.2 dBi and 47% [5]. In this paper a planar polarization reconfigurable antenna with a simple switching topology by utilizing the dual resonating-mode behaviour of the substrate integrated waveguide (SIW) cavity was introduced. Two input-ports were adopted to adjust the phase distributions of the radiating slots etched on the top surface of the SIW cavity. The LHCP, RHCP and linear polarization (LP) could then be realized by using the proper input port. The LHCP had a 3dB axial ratio bandwidth from 5.87 to 5.89 GHz and 5.86 to 5.89 GHz for the RHCP states. The bandwidth of return loss and gain for the LP state were respectively, from 5.65 to 5.9 GHz and 10.0 dBi [6]. A millimetre wave antenna (operation band from 46.0 to 70.0 GHz) consisted of two planar dipoles and a shorted patch, provided over 50% impedance bandwidth and almost 8 dBi gain, but radiates unidirectional with low cross-polarization and back radiation levels [7]. An advanced integration technique for the millimetre wave beam was analysed, where the operational bandwidth and true time delays of the technique were superior to millimetre wave beam steering for 5G wireless networks [8]. A bowtie antenna loaded with a metamaterial to generate a dual beam pattern from 55.0 to 68.0 GHz. The double-sided split-ring resonator structure arrays were integrated and tilted 15° to adapt the radiation beam and the antenna exhibited a high gain of 11.4 dBi in 62.0 GHz [9]. A negative index metamaterial based antenna

was presented, where the narrowband tuned over a broad frequency (from 1.60 to 2.23 GHz), while the higher band remained constant by using a varactor diode (capacitance from around 0.1 to 0.7 pF). Moreover, the total dimension of the antenna ware $0.056\lambda_0 \times 0.047\lambda_0$ and placed over a $0.23\lambda_0 \times 0.111\ \lambda_0$ CPW ground plane [10]. In 2007 Liu et al. invented a dual band reconfigurable fractal patch antenna where the switches etched in the antenna slots and by changing the status of the switches the radiation patterns of the antenna were change around 60.0 and 80.0 GHz, covering the elevation angles of 130 to 450, -130 to -450 around 60 GHz and of 150 to 500, -150 to - 500 around 80 GHz [11]. For the millimetre wave applications a dual band reconfigurable fractal patch antenna was proposed that showed similar operating frequencies, but different radiation patterns between the zeroth-order and the +1 order resonance mode [12]. A chiral metamaterial structure based on the inverse E-shape combined with the outer ring resonator printed on Rogers RT 5880 material was proposed, which showed resonance at C-band and 5.14 GHz bandwidth from 4.0 to 9.14 GHz [13]. A reconfigurable dipole antenna was suggested for 5G applications that maintained by the switches in square patches. The designed antenna was accomplished to switch the polarization among one linearly polarized and two orthogonal circularly polarized states. The antenna shown the bandwidth from 5.07 to 5.95 GHz 8.20 dBi stable gain [14].

In this paper, we present a metamaterial based frequency reconfigurable antenna that is composed of a straight feed-line monopole with two double split-ring resonators for 5G applications. The designed metamaterial single unit cell integrated with the antenna, which is developed by an outer and the inner split ring resonators with inverse E-shape metal strips of copper are connected with the outer ring resonator. The results show the resonances of return loss with DSRR or without DSRR or right side DSRR or left side DSRR are around at 32.08, 35.07, and 41.60 GHz. At present, in order to support increased traffic capacity 5G extend high data rate of transmission for communication. This includes a new spectrum from 30 GH to higher frequency. As a result, all of the mentioned resonance peaks is applicable for the 5G applications.

2. Structural Design of the Proposed Antenna

Figure 1(a-c) shows the detailed configuration of this metamaterial based reconfigurable antenna. As shown in figure 1 the proposed antenna is printed on a Rogers RT 5880 material (thickness of 1.575 mm, dielectric constant of 2.2 and loss tangent of 0.0009). The optimized size of the antenna is 20×22 mm2 and metamaterial single unit cell is 8×8 mm2. Moreover, the antenna is composed of a straight feed-line monopole with two double split-ring resonators (DSRR). The DSRR is developed by an outer and the inner split ring resonator with inverse E-shape metal strips of copper are connected with the outer ring resonator. A connector is attached to the port of the antenna that delivers a 50Ω impedance. However, the fabricated front and back view and the antennas with two DSRR, right side DSRR, left side DSRR, and without DSRR are shown respectively in figure 2(a-b), and figure 3(a-d).

Table 1: Optimized dimension of the proposed SWB reconfigurable antenna.

Parameters	L	W	W_L	W_R	W_f	W_1	W_2
Size (mm)	20.0	22.0	8.0	8.0	3.0	9.5	9.5
Parameters	L_{Lg}	L_{Rg}	L_{Ug}	g_L	g_R	L_g	W_g
Size (mm)	11.50	9.0	3.0	1.0	1.0	7.0	13.0

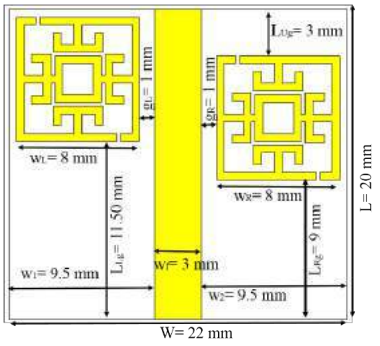

(a)

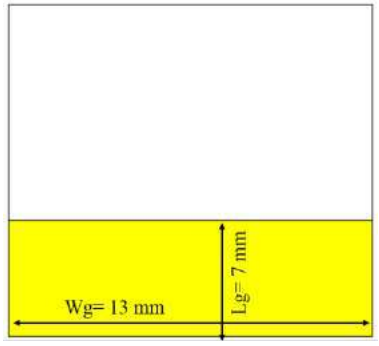

(b)

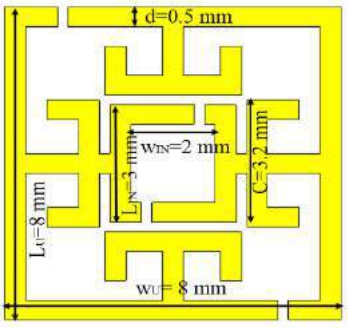

(c)

Figure 1: Schematic view of the proposed reconfigurable antenna: (a) Front view, (b) Back view, and (c) Schematic view of the designed metamaterial single unit cell.

The dimensions of the designed metamaterial single unit cell structure are: outer resonator length (L_L)= 8.0 mm, outer resonator width (W_L)= 8.0 mm, inner resonator length

(L_{IN})= 3.0 mm, inner resonator width (W_{IN})= 2.0 mm, C= 3.2 mm, and resonator metal (copper) width (d)= 0.5 mm.

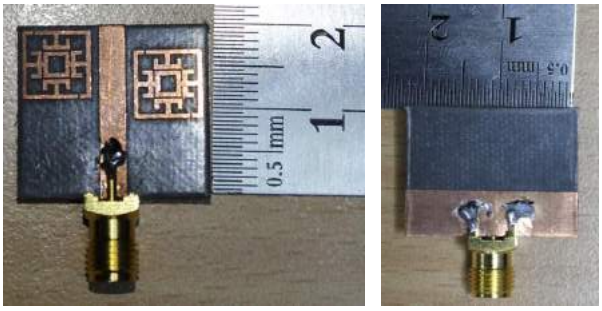

(a) (b)

Figure 2: Fabricated view of the proposed antenna: (a) Front view, and (b) Back view.

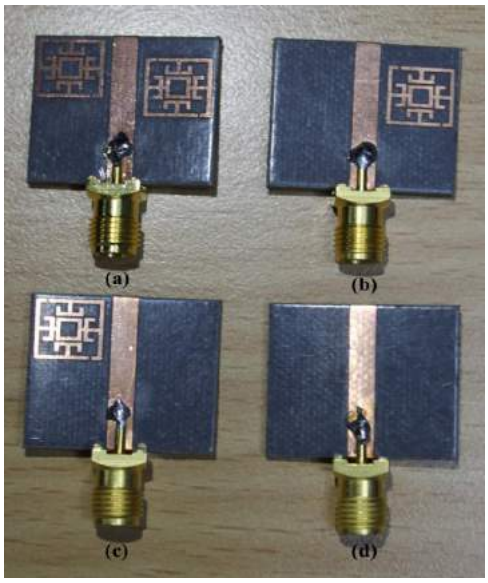

Figure 3: (a) Antenna with two DSRR, (b) Antenna with right handed DSRR, (c) Antenna with left handed DSRR, and (d) Antenna without DSRR.

The simulation of the proposed antenna is performed by the CST Microwave Studio software and measurement is done by the Agilent N5227A vector network analyser, whereas the network analyser is calibrated by the Agilent N4694-60001 to achieve the perfect over the entire super wide band (SWB) spectrum. To understand the characteristics of the metamaterial unit cell integrated on the antenna ground plane simulation of the unit cell is done in CST-MWS, where perfect electric and perfect magnetic boundaries are applied along x and y planes, so that the electric field is oriented along *x*-direction and magnetic field is oriented along *y*-direction. Nicolson-Ross-Wire method has been utilized to retrieve the effective parameters, which are as follows,

$$S_{11} \approx \left\{ \frac{R_1\left(1-e^{-2j\theta}\right)}{1-R_1^2 e^{-2j\theta}} \right\} \quad (1)$$

$$Similarly, S_{21} \approx \left\{ \frac{e^{-2j\theta}\left(1-R_1^2\right)}{1-R_1^2 e^{-2j\theta}} \right\} \quad (2)$$

$$Permeability, \mu_r \approx \left[\frac{C}{j\pi fd} \left\{ \frac{1-S_{21}+S_{11}}{1+S_{21}-S_{11}} \right\} \right] \quad (3)$$

$$Permittivity, \varepsilon_r \approx \left[\frac{C}{j\pi fd} \left\{ \frac{1-S_{21}-S_{11}}{1+S_{21}+S_{11}} \right\} \right] \quad (4)$$

$$Refractive\ Index,\ n_r \approx \sqrt{\mu_r \varepsilon_r}$$

$$Refractive\ Index,\ n_r \approx \left[\frac{C}{j\pi fd} \sqrt{\left\{ \frac{\left(S_{21}-1\right)^2 - S_{11}^2}{\left(S_{21}+1\right)^2 - S_{11}^2} \right\}} \right] \quad (5)$$

where θ= ξd, '*d*' is the thickness of the substrate, 'R_1' is the normalized impedance '*C*' is the velocity of light, 'S_{11}' is the reflection coefficient, and 'S_{21}' is the transmission coefficient.

3. Antenna Performance

To understand the operating principle of the antenna, the current distributions on the proposed antenna at 32.08 GHz is shown in figure 4. The current is distributed parallel and anti-parallel at the surface of metallic patches for the resonance frequencies. Parallel surface current distribution regulates the electrical resonance whereas antiparallel surface currents control magnetic resonance. The source of surface currents is a strong magnetic and electric coupling and the magnetic and electric resonance that pairs with external applied fields. The color in the figure indicates the intensity of the current, besides the directions of the current is shown by the arrows.

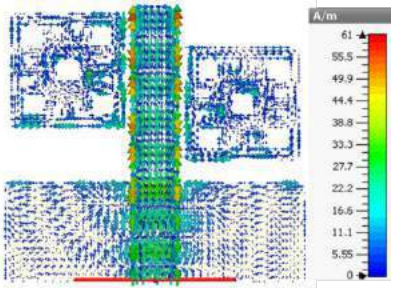

Figure 4: Surface current distribution at 32.08 GHz of the proposed antenna with two DSRR.

The antenna performance is described by the return loss (S_{11}), VSWR, gain, radiation pattern. The performance of the designed antenna is analysed by integrating the metamaterial structure at different position. The simulated and measured results of the proposed antenna are shown in

figure 5(a-b). In figure 5(a) the simulated results resonances at 32.08, 35.07, and 41.60 GHz are around similar for the variation of the proposed antenna configuration, whereas the measured results are in figure 5(b). The measured results are slightly different from the simulated results due to the effects from Sub Miniature Version A (SMA) connector soldering with feed line, proper calibration characteristics and toleration of the measurement. Figure 5(c) display the simulated voltage standing wave ratio (VSWR) of antenna with two DSRR, right side DSRR, left side DSRR, and without any DSRR. The properties of the metamaterial are characteristics by the effective medium parameters (permittivity, permeability, and refractive index ratio). Figure 5(d) exhibited the curve of effective medium ratio. From the curve real magnitude of effective negative permittivity from 30.0 to 44.42 GHz, negative permeability has two negative regions from 33.64 to 36.69 GHz and 41.64 to 47.14 GHz. In addition, at the points of the reflection coefficient (return loss) the permittivity, permeability, and refractive index amplitude are respectively, -1.41+0.40j, 0.62-3.77j, 1.81+0.57j at 32.08 GHz, -1.36-0.93j, -5.87+4.11j, 3.43-0.024j at 35.07 GHz, and -0.026-0.50j, -29.88-73.04j, 1.12+0.93j at 41.60 GHz. There is variation between the results of the permittivity, permeability, refractive index for the polarization effects on the internal structure of the materials.

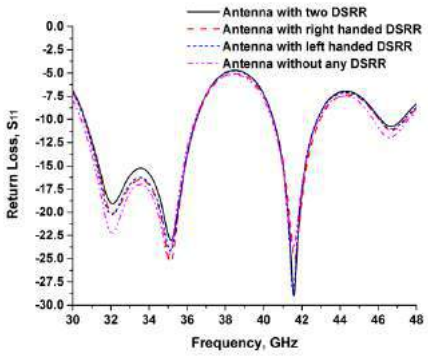

(a)

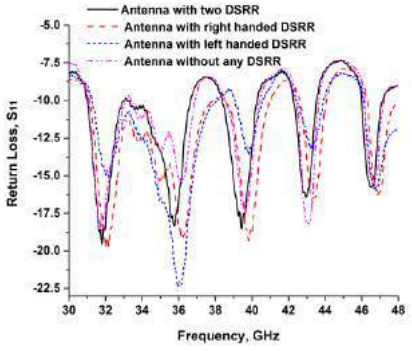

(b)

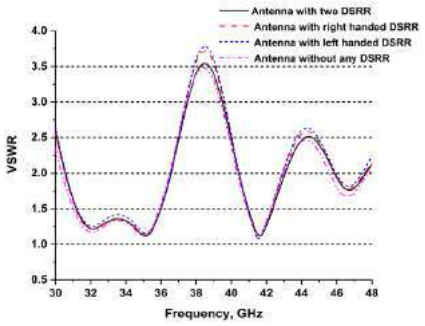

(c)

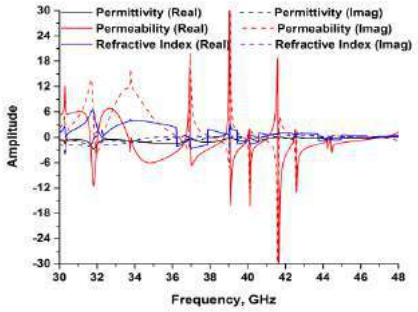

(d)

Figure 5: Proposed reconfigurable antennas: (a) Simulated results of return loss (S_{11}), (b) Measured results of return loss (S_{11}), (c) Simulated VSWR, and (d) Amplitude of the effective medium parameters of the integrated metamaterial.

The material can be characterized by the electrical permittivity and the magnetic permeability. From figure 5(d) the loss of the integrated metamaterial structure is defined by the amplitude ratio of the imaginary value of the (permittivity or permeability) and real value of (permittivity or permeability). If the ratio is more than 1 (<1) then loss positive and when it's less than 1 (>1) loss is negative. Moreover, the two dimensional (2D) radiation patterns at 32.04 and 42.60 GHz are demonstrated in figure 6(a-d) and figure 7(a-d), where both Phi =0° and Phi =90° are included as E-plane and H-plane, whereas the *y*-*z* plane is considered as the E-plane and the *x*-*z* plane is considered as the H-plane. It is seen from figure 6(a-d) and 7(a-d) that the radiation patterns at Phi = 0° are nearly omnidirectional. The results of the *y*-*z* plane in radiation pattern at similar resonance frequency seems almost same for all of the different configuration of the proposed antennas. At the lower frequency the number of the side lobes reasonably less, but with increasing frequency, the patterns have more side lobes and slightly directional. There are few nulls are observed at lower frequencies due to lower order harmonics, the antenna exhibits stable radiation patterns throughout the operating band. The ripples in the radiation patterns may be due to the refection into the field.

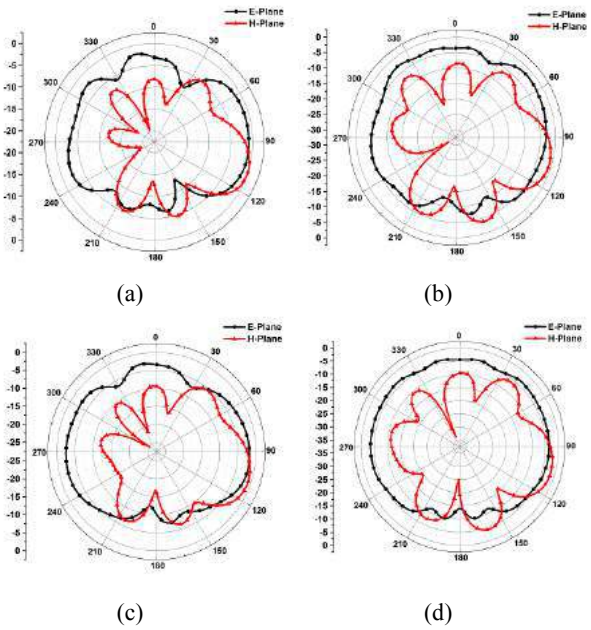

(a) (b)

(c) (d)

Figure 6: Simulated radiation pattern of the proposed antenna at 32.08 GHz: (a) with two DSRR, (b) with right handed DSRR, (c) with left handed DSRR, and (d) without DSRR.

A considerable amount of back lobe was observed, possibly because of the utilization of partial ground plane. A full ground plane can reduce this back lobe at the cost of low gain, low efficiency and narrow bandwidth.

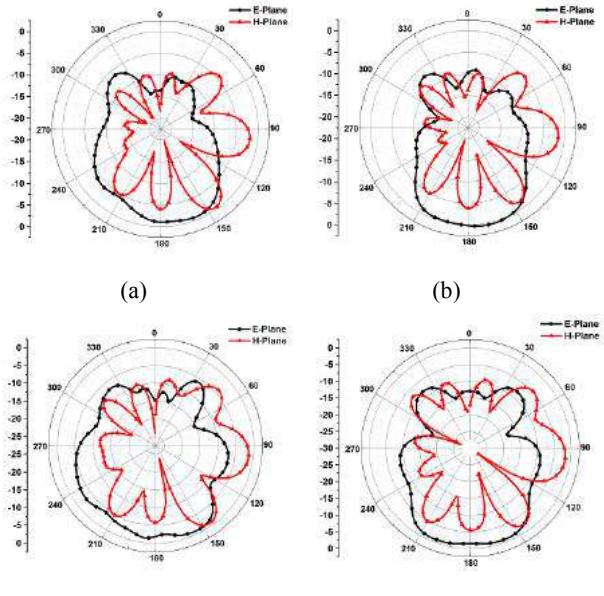

(a) (b)

(c) (d)

Figure 7: Simulated radiation pattern of the proposed antenna at 41.60 GHz: (a) with two DSRR, (b) with right handed DSRR, (c) with left handed DSRR, and (d) without DSRR.

4. Conclusion

The field of wireless communication has witnessed tremendous growth as the technological facility of telecommunications infrastructure, improved significantly in the last decade. Irrespective of the applications, most of the reconfigurable antenna has similar requirements of increased functionality, improved operation, small size and most importantly low system cost. However, the demand on the basic requirement a metamaterial based reconfigurable antenna is proposed by utilizing a metamaterial unit cell integrated with the antenna structure in this paper. The performance of the antenna is varied and investigated by changing the position of the metamaterial with the antenna feed line. As a demonstration, the antennas are designed with a 1.575 mm thickness Rogers RT 5880 substrate material. Experiments are carried out to verify the designs, which show well agreement with the designs. The proposed antenna is showing resonance in higher frequency above 30 GHz, which are desirable for the 5G communication applications. So, the proposed reconfigurable antennas can be used for the diverse applications of the high speed wireless system.

Acknowledgements

This work was supported by the Research Universiti Grant, Geran Universiti Penyelidikan (GUP), Code: 2016-028.

References

[1] W. Roh, J. Y. Seol, J. Park, B. Lee, J. Lee, Y. Kim, J. Cho, K. Cheun, F. Aryanfar, "Millimeter-wave beamforming as an enabling technology for 5 G cellular communications: Theoretical feasibility and prototype results," *IEEE Communications Magazine*, vol. 52, no. 2, pp. 106–113, Feb. 2014.

[2] D. R. Smith, W. J. Padilla, D. C. Vier, S. C. Nemat-Nasser, S. Schultz, "Composite medium with simultaneously negative permeability and permittivity", *Physical Review Letters*, Vol. 84, pp. 4184-4187, 2000.

[3] M. M. Hasan, M. R. I. Faruque, S. S. Islam, M. T. Islam, "A new compact double-negative miniaturized metamaterial for wideband operation", *Materials*, 2016, 9(10), 830.

[4] M. M. Hasan, M. R. I. Faruque, M. T. Islam, "A single layer negative index meta atom at microwave frequencies", Microwave and Optical Technology Letters, 2017, 59:1450–1454.

[5] H. B. Zhang, Y. L. Ban, Y. F. Qiang, J. Guo, Z. F. Yu, "Reconfigurable loop antenna with two parasitic grounded strips for WWAN/LTE unbro-ken-metal-rimmed smartphones", *IEEE Access*, Doi: 10.1109/ACCESS.2017.2686431.

[6] Z. C. Hao, K. Fan, H. Wang, "A planar polarization-reconfigurable antenna", *IEEE Transactions on Antennas and Propagation*, 2017, Doi: 10.1109/TAP.2017.2670440.

[7] M. Li, K. M. Luk, “Wideband magneto-electric dipole antenna for 60-GHz millimetre-wave communications”, *IEEE Transactions on Antennas and Propagation*, Vol. 63, No. 7, 2015.

[8] Z. Cao, Q. Ma, A. B. Smolders, Y. Jiao, M. J. Wale, C. W. Oh, H. Wu, A. M. J. Koonen, “Advanced integration techniques on broadband millimeter-wave beam steering for 5G wireless networks and beyond”, *IEEE Journal of Quantum Electronics*, Vol. 52, No. 1, 2016.

[9] A. Dadgarpour, M. S. Sorkherizi, A. A. Kishk, T. A. Denidni, “Single-element antenna loaded with artificial Mu-near-zero structure for 60 GHz MIMO applications”, *IEEE Transactions on Antennas and Propagation*, Vol. 64, No. 12, 2016.

[10] H. Mirzaei, G. V. Eleftheriades, “A compact frequency-reconfigurable metamaterial inspired antenna”, *IEEE Transactions on Antennas and Propagation*, Vol. 10, 2011.

[11] H. Liu, B. Z. Wang, W. Shao, “Dual band bi-directional pattern reconfigurable fractal patch antenna for millimetre wave application”, *Journal of Infrared, Millimeter and Terahertz Waves*, 28:25–31, 2007.

[12] S. Yan, G. A. E. Vandenbosch, “Radiation pattern reconfigurable wearable antenna based on metamaterial structure”, *IEEE Transactions on Antennas and Propagation*, 2016, Doi: 10.1109/LAWP.2016.2528299.

[13] M. M. Hasan, M. R. I. Faruque, M. T. Islam, “Inverse E-shape chiral metamaterial for long distance telecommunication”, Microwave and Optical Technology Letters, 2017, 59:1772–1776.

[14] L. Ge, X. Yang, D. Zhang, M. Li, H. Wong, “Polarization reconfigurable magneto-electric dipole antenna for 5G WiFi”, *IEEE Antennas and Wireless Propagation Letters*, 2016, Doi: 10.1109/LAWP.2016.2647228.

Structural Color for Displays and Imaging

Dynamic plasmonic colour display

Xiaoyang Duan[1,2], **Simon Kamin**[1], **and Na Liu**[1,2]

[1]Max Planck Institute for Intelligent Systems, Heisenbergstrasse 3, 70569 Stuttgart, Germany

[2]Kirchhoff Institute for Physics, University of Heidelberg, Im Neuenheimer Feld 227, 69120 Heidelberg, Germany

[*]corresponding author: laura.liu@is.mpg.de

Abstract - Plasmonic colour printing based on engineered metasurfaces has revolutionized colour display science due to its unprecedented subwavelength resolution and high-density optical data storage. However, advanced plasmonic displays with novel functionalities have remained in their infancy. Here we demonstrate a dynamic plasmonic colour display technique which enables all the aforementioned functionalities using catalytic magnesium metasurfaces. Controlled hydrogenation and dehydrogenation of the constituent magnesium nanoparticles, which serve as dynamic pixels, allow for plasmonic colour printing, tuning, erasing, and restoration of colour.

In this work, we demonstrate a dynamic plasmonic display technique based on catalytic Mg metasurfaces. Different from other hydrogen-storage metals such as palladium (Pd) and yttrium, which are associated with poor optical response, Mg exhibits excellent plasmonic properties at high frequencies. For example, Mg nanostructures have been used for chiral sensing in the UV spectral range and for hydrogen sensing in the visible spectral range[1-4]. Most importantly, the unique hydrogenation/dehydrogenation kinetics of Mg nanoparticles is ideally suited for creating dynamic plasmonic systems.

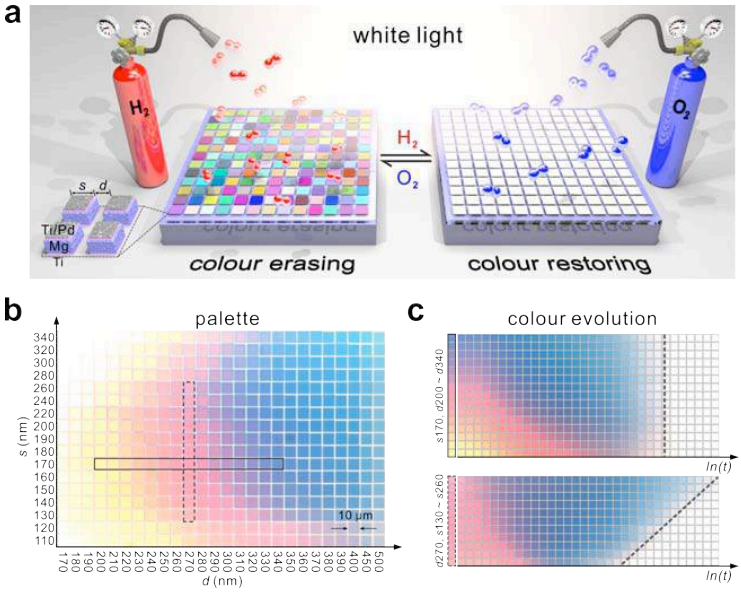

Figure1 | **a**, Schematic of the plasmonic metasurface composed of hydrogen-responsive Mg nanoparticles interacting with incident unpolarized white light. **b**, Colour palette obtained by stepwise tuning of *s* and *d*. **c**, Colour evolutions of the selected colour squares upon hydrogen exposure over time *ln(t)*. The grey-dotted lines indicate the colour vanishing times in the two cases.

Here, we demonstrate successively plasmonic microprint displays with high reversibility, plasmonic animations with subwavelength resolution, and highly secure plasmonic encryption. Our work will stimulate fascinating colour display applications utilizing plasmonic dynamic pixels with nanoscale controllability.

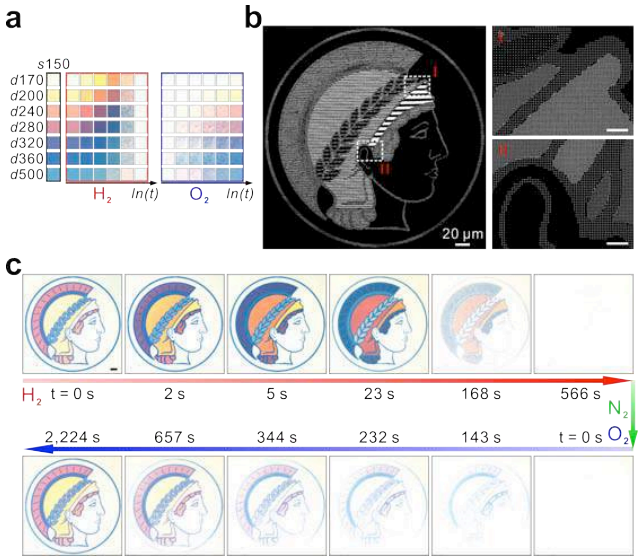

Figure2 | **a,** Colour evolutions of the selected colours used to construct the Minerva logo during hydrogenation and dehydrogenation, respectively. **b**, Overview and enlarged SEM images of the Minerva logo. The scale bars in I and II are 5 μm. **c**, Optical micrographs of the Minerva logo during hydrogenation and dehydrogenation for colour erasing and restoring, respectively. Scale bar: 20 μm.

Acknowledgements: This project was supported by the Sofja Kovalevskaja grant from the Alexander von Humboldt-Foundation, the Marie Curie CIG grant, and the European Research Council (ERC Dynamic Nano) grant.

REFERENCES

1. Kumar, K. *et al.* "Printing colour at the optical diffraction limit." *Nature Nanotechnol*. **7,** 557–561 (2012).
2. Sanz, J. M. *et al.* "UV plasmonic behavior of various metal nanoparticles in the near-and far-field regimes: Geometry and substrate effects." *J. Phys. Chem. C* **117,** 19606–19615 (2013).
3. Sterl, F. *et al.* "Magnesium as novel material for active plasmonics in the visible wavelength range." *Nano Lett.* **15,** 7949–7955 (2015).
4. Duan, X. *et al.* "Hydrogen-regulated chiral nanoplasmonics." *Nano Lett.* **16,** 1462–1466 (2016).

The metamaterial based perfect light absorber for colour generation

Soo-Jung Kim[1], Hye-Won Yun[2], Mi-Hyun Kim[2], Heon Lee[1,*], Sung-Hoon Hong[2,*]

[1] Department of Materials Science and Engineering, Korea University, Anam-dong 5-1, Sungbuk-Ku, Seoul 136-701, Republic of Korea

[2] 3D new device Research Section, ETRI, Daejeon 305-700, Republic of Korea

[*]corresponding author: shong@etri.re.kr

Abstract- In this work, we developed a variety of colour utilizing the metamaterial based perfect absorber based on a coupled nanocrystals (NCs). It is essential to produce two optical absorption spectra with broad bandwidth for the vivid colours. Previously, a conventional metamaterial absorbers, typically made of metals such as silver, gold or aluminum are limited to a narrow bandwidth, and it have difficulty for generation of distinct colours. The chemically coupled NCs (metals, semiconductors and insulators) are newly designed materials in this study for the controlled optical properties of metamaterials. In the corresponding results, the developed NC based absorber in visible wavelength showed the high absorption above 98% in two absorption spectra containing a high reflectance peak, and we tuned the desired colour of varying NC type and nanostructure.

Metamaterial absorbers have great potential in applications for a solar energy harvesting devices, an image application such as digital displays and so on due to their partial absorption spectra. With the point towards higher color resolution and a various color generation in reflective displays, a high absorption property is necessary in partial wavelength. In this study, we focus on the coupled NCs based metamaterial perfect absorber for the color generation in the visible and NIR regions.

NCs can be used as new material in metamaterial building block because their optical properties are different with their type, shape and size. When the coupled NCs which are either same materials or different materials are covalently linked via short ligand on surface of each NC, the optical properties can be controlled. In this study, the coupled Ag NCs and the Ag based hybrid NCs were developed, and the metamaterial structure which consists of NCs were fabricated by nanoimprinting lithography and lift-off method. Also, perfect absorbers were successfully developed containing with the nanodisk array or nanohole array for the variation of absorption wavelength.

Finally, the simulated and fabricated metamaterial perfect absorber using NC showed the high absorption above 98% in visible and NIR range. As the materials are changed and metamaterial structures are controlled in perfect absorbers, the absorption property could be tuned, and the specific vivid colours were generated. Color reproduction, or color gamut, represents about 19%.

This work has been supported by the Pioneer Research Center Program through the National Research Foundation of Korea funded by the Ministry of Science, ICT & Future Planning (NRF-2013M3C1A3063046)

Dual-color plasmonic pixels for high-density information storage

E. Heydari, [1] **J. Sperling,** [1] **S. Neale**[1] **and A.W. Clark**[1*]
[1]School of Engineering, University of Glasgow, UK
[*]corresponding author: Alasdair.clark@glasgow.ac.uk

Abstract- We demonstrate a new plasmonic approach to high-density optical data storage; using dual-color plasmonic nano-pixels to encode two information sets into the same unit area using single arrays of two-state metal nano-apertures.

The ability to effectively separate discrete colors from white-light lies at the heart of how we record and view optical information; whether that be the arrangement of colored inks in painting and printing applications, or the spectral filters that enable many modern image display and recording technologies. In each case, color separation is typically provided by organic compounds; dyes and pigments that absorb and scatter particular wavelengths of light, leading to their distinct color profiles. Recently, structural color systems based on engineered nanophotonic materials have emerged as an appealing alternative to absorptive dyes [1]. Among these examples are color filters based on plasmonics; filters which rely on the resonant interaction between incident photons and the free-electrons of nano-scale metal structures. Plasmonic filters hold several dimensional and stability advantages over their micro-scale, dye-based counterparts. As a result, they have been positioned as new technological solutions for sub-wavelength color printing [1], RGB splitting for image sensors [2], anti-counterfeiting measures [3], and optical data storage [4]; thus representing one of the most promising, commercially relevant areas of current plasmonic research activity.

Here, we demonstrate a method for patterning full-color images and codes, at subwavelength resolutions, that exhibit dual, polarization-dependent information states. Our individual pixels are comprised of asymmetric cross-shaped nano-apertures in a thin film of aluminum; each aperture engineered to exhibit 2 independent plasmonic color resonances that can be individually tuned across the sRGB spectrum. This enables us to encode 2 arbitrary information sets into the same unit area using the same array of nano-pixels. We show that using a standard optical microscope, color separation can be controlled down to 2x2 nano-pixels (approximately 370 x 370 nm), while retaining polarization selectivity. This, in turn, defines our maximum data storage capability; each 2x2 pixel area acting as a 2-state data bit that can be read optically. The maximum data density we can achieve using this technique is approximately 1.46 Gb/cm^2, with the added ability to further encode each of those pixels using the full visible-color spectrum.

Acknowledgements. The work was supported by the Royal Academy of Engineering (grant 10216/103) and the EPSRC (grants EP/P51133X/1 and EP/N016874/1).

References

[1] K. Kumar, H. Duan, R. S. Hegde, S. C. W. Koh, J. 6N. Wei, and J. K. W.Yang, "Printing Colour at the Optical Diffraction Limit", *Nature Nanotechnology*, 7, 557-561 (2012).

[2] S. P. Burgos, S. Yokogawa, H. A. Atwater, "Color Imaging Via Nearest Neighbor Hole Coupling in Plasmonic Color Filters Integrated onto a Complementary Metal-Oxide Semiconductor Image Sensor", *ACS Nano*, 7, 10038-10047 (2013).

[3] Y. H. Zheng, C. Jiang, S.H. Ng, Y. Lu, F. Han, U. Bach, J. J. Gooding, “Unclonable Plasmonic Security Labels Achieved by Shadow-Mask-Lithography-Assisted Self-Assembly”, *Advanced Materials*, 28, 2330-2336 (2016).
[4] M. Gu, X.P. Li, Y. Y. Cao, “Optical Storage Arrays: A Perspective for Future Big Data Storage”, *Light-Science & Applications,* 3 (2014).

High-Resolution Color Prints With Plasmonic and Dielectric Nanoantennas

Joel K.W. Yang[1,2,*]

[1]Engineering Product Development, Singapore University of Technology and Design, 8 Somapah Road, Singapore 487372, Singapore

[2]Institute of Materials Research and Engineering, Agency for Science, Technology and Research (A*STAR), 2 Fusionopolis Way, #08-03 Innovis, Singapore 138634, Singapore

[*]corresponding author: joel_yang@sutd.edu.sg

Abstract- Resonators and antennas that operate in the visible spectrum have enabled color printing by controlling the local geometry of nanostructures. These color prints exhibit unique properties, e.g. polarization dependent colors, ultra-high resolution ~100,000 dpi, and fade resistance. Recent developments of laser printing, active color tuning, stacked plasmonic colors, and scale-up to large areas have been demonstrated. To a large extent, nanostructures of silver, gold, and aluminum have been investigated. However, rapid developments in high-index dielectric nanoantennas have shown great promise in overcoming some of the shortfalls in plasmonic nanostructures, i.e. ohmic losses, and heating effects. In this talk we will discuss our latest investigation of the potential of dielectric nanostructures in high-resolution color prints.

Dynamic Full Color Plasmonic Surface and Active Addressing

D. Franklin[1,2*], **S.T. Wu**[3], **and D. Chanda**[2,3]

[1]Department of Physics, University of Central Florida, Orlando, Florida 32816, USA

[2]NanoScience Technology Center, University of Central Florida, Orlando, Florida 32816, USA

[3]CREOL, The College of Optics and Photonics, University of Central Florida, Orlando, Florida 32816, USA

[*]corresponding author: dan.franklin@knights.ucf.edu

Abstract- We demonstrate a liquid crystal-plasmonic system capable of producing the full RGB color basis set solely as a function of voltage. This is achieved through surface morphology induced polarization dependent color and liquid crystal effects which manifest at different voltages. We further show the integration of such a surface with a thin-film-transistor array to display arbitrary images.

Plasmonic nanostructures have many advantages for novel color and display applications including: diffraction limited color, the ability to control polarization and phase, and post-fabrication tuning through control of the surrounding media. The later of these phenomena could lead to dynamic color changing surfaces and displays, however current demonstrations have been limited in the range of color tuning achieved. Here, we show an increase in this ability and span the full RGB color basis set.

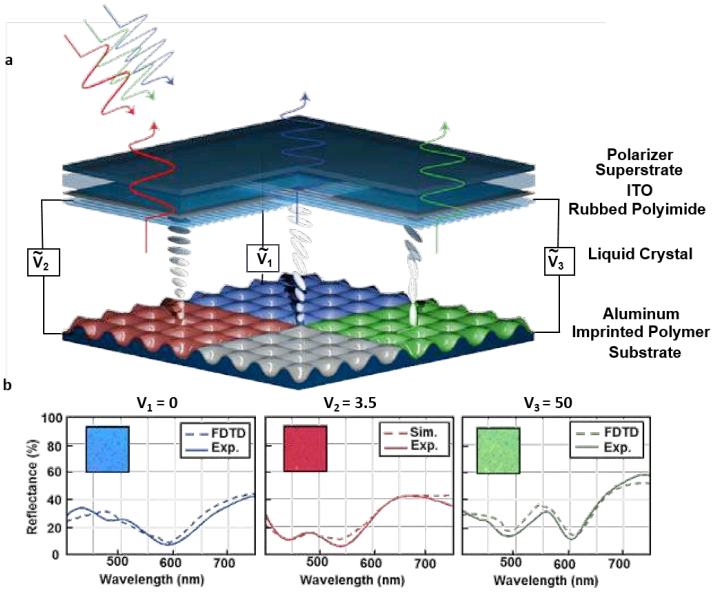

Figure 1 | Liquid crystal-plasmonic device. (**a**) Schematic illustrating the system and its three voltage states which reflect red, green and blue. (**b**) Reflection spectra and matching simulation. Line colors are obtained through the CIE color matching functions and insets are microscope images.

The liquid crystal-plasmonic system is shown in Figure 1a. Ambient white light passes through a polarizer, a traditional LC cell (glass, ITO, rubbed polyimide) and a high birefringent LC (LCM1107). The light is then incident upon a nanostructured plasmonic surface consisting of 30 nm of aluminum deposited on a nanoimprinted polymer. The pattern is a 2D sinusoidal grating 300 nm in periodicity and 100 nm in amplitude. The structure hosts grating coupled surface plasmon resonances within the visible domain, the spectral location of which depends on the orientation of the LC near the surface. The resonance further depends on the surface morphology of the deposited aluminum and through which we control the degree of polarization dependence of the reflected color. We use this to create a device which reflects blue or red light in the 0V (V_1, Off State) given the orientation of the top polarizer. For the given orientation of Figure 1b, this results in a blue reflection.

At voltage V_2 ($3.5V_{rms}$), the bulk LC reorients and rotates the polarization of the incident light to that of the orthogonal state, resulting in a red. Lastly, at the high voltage of V_3 (50 V_{rms}), the LC near the aluminum nanostructured surface reorients to a near vertical state. This red-shifts the plasmonic resonance resulting in a green and the loss of the surface's polarization dependence. These voltages are given for a cell gap of 8.5 um, however we believe they can be lowered by reducing this cell gap.

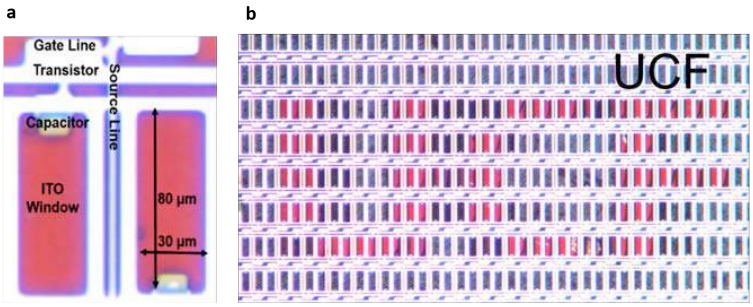

Figure 2 | TFT integrated liquid crystal-plasmonic surface. a) Microscope image (x10) showing the unit cell of the TFT array. (**b**) Display of the text "UCF" through a computer interface.

To show the system's compatibility with preexisting LCD technology, we have integrated the surface with a thin-film-transistor (TFT) array to create an actively addressed plasmonic surface. We procured a conventional transmissive LCD panel (Adafruit, ID: 1680) and harvested the TFT array and attached electronics by removing polarizers, backlight, diffusers and ITO glass. The plasmonic surface is then UV glued onto the TFT with 8.5 um spacers and filled with LCM1107. A microscope image of the device is shown in Figure 2a. Here, the plasmonic surface (red) is imaged through the TFT glass and contacts. By keeping the electronics attached to the TFT intact, individual pixels can be controlled through an HDMI-to-TTL converter and a laptop. Figure 2b shows the letter "UCF" displayed through a text editor. While this device can be used to display arbitrary shapes, images and video, there are several engineering problems to still overcome. Namely, the white reflection from the TFT metallic lines and the lack of high voltage drivers needed to display green.

Here we have shown a dynamically tunable LC-plasmonic surface that spans the full RGB color basis set with a single metallic nanostructure. We further demonstrate the system's compatibility with existing LCD technology by integrating it with a commercial TFT and display arbitrary text. We believe this could lead to a new class of displays.

Acknowledgements: This work at University of Central Florida was supported by NSF grant No. ECCS-1509729.

REFERENCES

1. Kumar, K. et al. "Printing colour at the optical diffraction limit," *Nat. Nano.*, Vol 7, 557-561, 2012.
2. Wan, W. "Full-Color Plasmonic Metasurface Holograms," *ACS Nano*, Vol 10, 10671-10680, 2016.
3. Franklin, D. et al. "Polarization-independent actively tunable colour generation on imprinted plasmonic surfaces," *Nat. Commun.* Vol. 6, 7337, 2015.
4. Franklin, D. et al. "Actively addressed single pixel full-colour plasmonic display," *Nat. Commun.* Vol. 8, 15209, 2017

Military Applications of Metamaterials

Metal oxides for Plasmonic and Metamaterial Applications

H. Kim[1*], N. Sharac[2], N. S. Bingham[2], N. Charipar[1], J. Calame[1], A. Vlasov[1], G. Beadie[1], M. Currie[1], C. Ellis[1], J. Tischler[1], J. Owrutsky[1], J. Caldwell[1] and A. Piqué[1]

[1] U.S. Naval Research Laboratory, 4555 Overlook Ave, S.W., Washington, DC, USA

[2] NRC Postdoctoral Fellow at Naval Research Laboratory, Washington, DC, USA

[*]corresponding author: heungsoo.kim@nrl.navy.mil

Abstract- Transparent conducting oxides (TCOs) exhibit low loss plasmonic properties in the near infrared region of the electromagnetic spectrum and their carrier density can be tuned by doping. In this talk, we will present details on the properties of TCOs, such as Sn-doped In_2O_3 and Al-doped ZnO, and VO_2 along with light trapping metamaterial devices consisting 1D and 2D metallic gratings and TCO, which forms a Schottky contact with Si, for solar cell applications with enhanced photocurrent.

Noble metals such as Au and Ag have been used traditionally for plasmonic devices in the visible spectral range due to their strong interaction with light and good ohmic contact. However, conventional metals are not suitable for near infrared plasmonic applications due to their relatively large optical losses at these wavelengths. Transparent conducting oxides (TCOs), on the other hand, have been considered for low loss metallic components in the near infrared region of the electromagnetic spectrum because they can provide a tunable carrier density (10^{20} - 10^{21} cm^{-3}) by doping. For example, the zero-cross-over permittivity values of TCOs can easily be tuned from 1.2 μm to 3 μm by adjusting doping levels (Figure 1). Optical losses in devices made from these metal oxide materials are generally found to be much lower than those obtained with conventional metals. We have investigated various metal oxides such as Al-doped ZnO, Sn-doped In_2O_3 and VO_2. The details of electrical and optical properties of these metal oxides will be presented [1-3].

In order to extend Si sensitivity to infrared region without impacting visible response in Si solar cells, we have developed light trapping metamaterial devices based on TCO-Si heterostructures. The metamaterial structure consists of metallic 1D or 2D gratings, which couple light through a thin dielectric layer into the thin TCO layer, which forms a Schottky contact with Si. In this configuration, 1) surface plasmons interact strongly with incident light at the plasmon resonance, resulting in enhanced light concentration into the TCO layer, 2) IR photons absorbed as hot electrons in the TCO, and 3) these hot electrons move across a Schottky barrier into the Si substrate, resulting in enhanced photocurrent (Figure 2). We will present details on the optimization of geometric properties of the metal gratings (dimension, pitch) and tunable properties of the TCO layer (thickness, carrier density).

Acknowledgements: This work was funded by the Office of Naval Research (ONR) through the Naval Research Laboratory Basic Research Program.

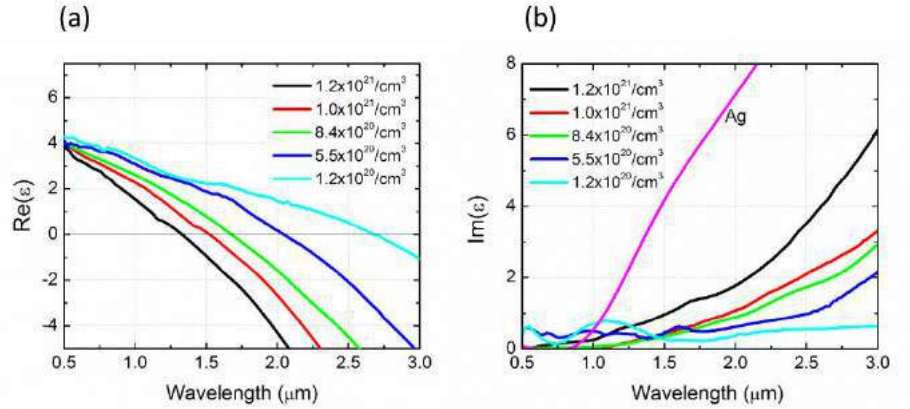

Figure 1. Real (a) and imaginary (b) parts of the dielectric function as function of wavelength for ITO films with various carrier densities from 10^{20} – 10^{21} cm^{-3}. The data for Ag film is added in (b) for comparison.

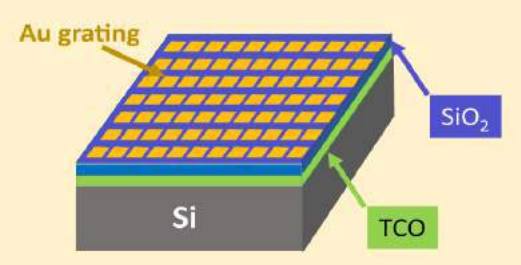

Figure 2. Light trapping metamaterial devices consisting of Au 2D grating and ITO, which forms a Schottky contact with Si, for solar cell applications with enhanced photocurrent.

REFERENCES

1. Kim, H., Osofsky, M., Prokes, S. M., Glembocki, O. J., and Piqué, A., "Optimization of Al-doped ZnO films for low loss plasmonic materials at telecommunication wavelengths," *Appl. Phys. Lett.* **102**, 171103, 2013.
2. Kim, H., Charipar, N., Breckenfeld, E., Rosenberg, A., Piqué, A., "Active terahertz metamaterials based on the phase transition of VO_2 thin films," *Thin Solid Films* **596**, 45-50, 2015.
3. Breckenfeld, E. Kim, H., Burgess, K., Charipar, N., Cheng, S.F., Stroud, R. Piqué, A., "Strain Effects in Epitaxial VO_2 Thin Films on Columnar Buffer-Layer TiO_2/Al_2O_3 Virtual Substrates," *ACS App. Mater. Interfaces*, **9** (2), 1577–1584, 2017.

Compressive sensing and enhanced detectors with plasmonic metasurfaces.

A.M. Urbas
Air Force Research Lab, Dayton, Ohio
augustine.urbas@gmail.com

Metamaterials provide the ability to design materials properties to meet the unique needs of applications beyond what is possible with conventional materials. From spatially tailored dielectrics to tunable, dynamic material properties and unique nonlinear behavior, these systems offer tremendous flexibility to application engineers. Applications across the electromagnetic spectrum have been proposed; from novel RF antennas to devices utilizing optical magnetism. Researchers have pursued optical, RF and acoustic materials and applications. The aim of this work is to gauge the readiness and maturity of metamaterials for the field. Within AFRL, applications spanning the electromagnetic spectrum have leveraged metamaterials. The work we have pursued utilizes the unique traits of meta systems to match broadly different wavelengths and to have dramatic changes in response as a function of wavelength to develop novel communication and sensing systems. Looking to the future, dynamic and tunable metamaterials will be pursued. In the near term, detecting optical signals in the mid and long wave infrared are significant to a range of Air Force technologies and drive the research to increase performance and functionality. Both spectral and spatial information is obtained in images with hyperspectral. New challenges arise as detector pixel counts increase and the information desired from image data is more widely used. Limitations on data communication rates provide a bottle neck for acquiring and processing the increasingly large data sets. Compressive sensing may allow for more efficient acquisition data with higher information content, while preserving mission utility. Our research develops a combined method to integrate plasmonic and micro-optical elements onto detector structures which can both improve the performance of detector systems and provide a means to introduce compressive sensing and computational imaging methods. By coupling a variety of simulation environments which cover the optical, plasmonic, and electronic domains, we can efficiently comprehensively model detector function and performance for a wide range of designs and incorporate compressive sensing into the design loop. We will present the results of several design studies and experimental verification of modeled device performance for several device configurations such as the one pictured below.

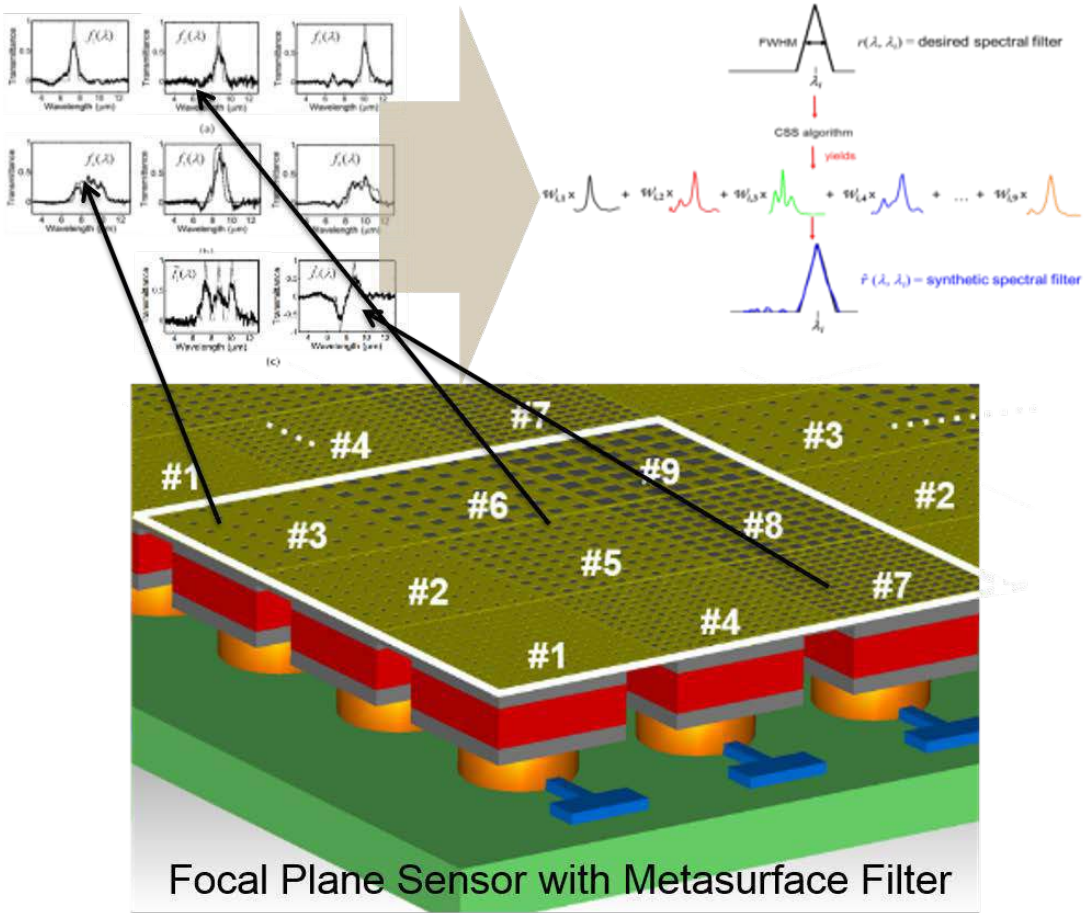

Figure 1: Metasurface filters integrated at the pixel level are engineered to modify the pixel responsivity. This forms the basis set for compressive spectral sensing of images where many spectral bands can be synthesized from linear combinations of the response of the basis set.

The 2D, 1D, and 0D Tightly Coupled Array Antennas

Hakjune Lee[1], **Sangwook Nam**[2*]
[1]Electronics and Telecommunications Research Institute (ETRI), Daejeon, Korea
[2] Department of Electrical and Computer Engineering, INMC, Seoul National University, Seoul, Korea
[*]corresponding author: snam@snu.ac.kr

Abstract-Tightly Coupled Dipole Array (TCDA) is a ultrawideband array antenna proposed by Munk [1]. The operation principle of the TCDA is cancellation between inductive reactance of the ground plane at low frequency and capacitive reactance of coupled capacitance of neighboring element dipoles. In this paper, we present variety dimensions (2D, 1D, and 0D) TCDAs which can be used at electric warfare.

First, we propose the low-profile wideband 2D TCDA. To obtain the low profile and wide bandwidth, we control the impedance of element dipole antenna using vertical gap to operate at low frequency. The common mode and unwanted resonances are adjusted by shorting posts and via holes, respectively. The proposed element antenna is presented in Fig. 1, and its S-parameter response is shown in Fig. 2. The simulation shows that the bandwidth of the proposed array antenna is 3.37:1 (from 1.97 to 6.66 GHz) and low profile of 1/12.7 λ at lowest operating frequency.

Second, we propose the dual-polarized 1D TCDA. To maintain 2D TCDA characteristics, we locate the additional structures which consist of conducting wall with vertical slits and ferrite sheets beside the 1D arranged TCDA as shown in Fig. 3. The simulated -10dB reflection coefficient bandwidth is 2.83:1 (from 1 to 2.83 GHz) for both polarizations with 1/5 λ height at lowest operating frequency when it radiates broadside as shown in Fig.4.

Third, the dual-polarized 0D TCDA is proposed. The additional structures which is used at the 1D TCDA are locates around the horizontal and vertical polarization dipoles that use discrete port feeding at the center of the unit cell, respectively, as shown in Fig. 5. In Fig. 6, the simulated bandwidth of the 0D TCDA is 2.27:1 (from 1.22 to 2.77 GHz) with 1/6 λ height at lowest operating frequency.

The details of the design procedure and other characteristics of the three antennas will be discussed at the conference.

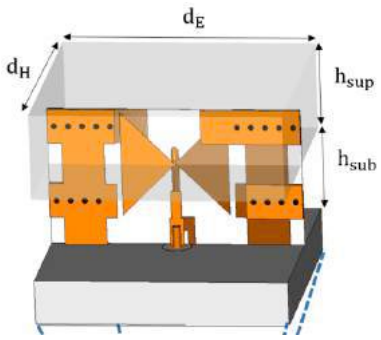

Fig. 1. Configuration of element antenna of the low-profile 2D TCDA.

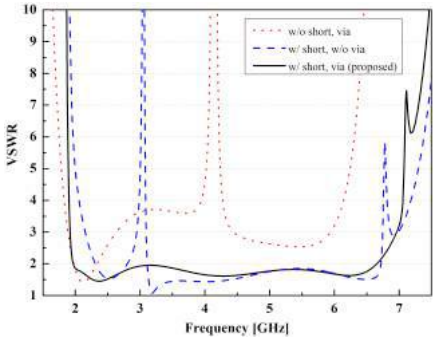

Fig. 2. VSWR of the proposed 2D TCDA.

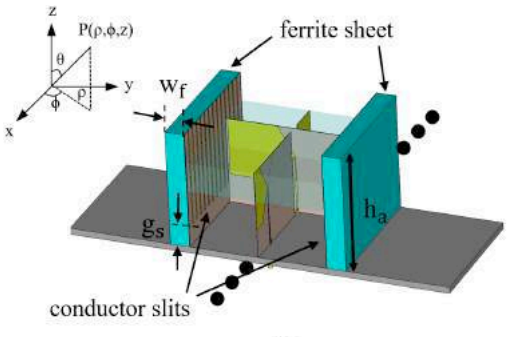

Fig. 3. Unit cell of the 1D TCDA antenna model

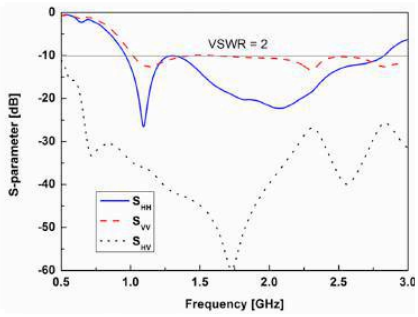

Fig. 4. Simulated S-parameter response of the 1D TCDA

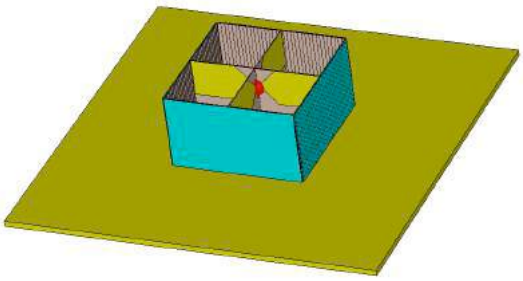

Fig. 5. Unit cell of the 0D TCDA antenna model

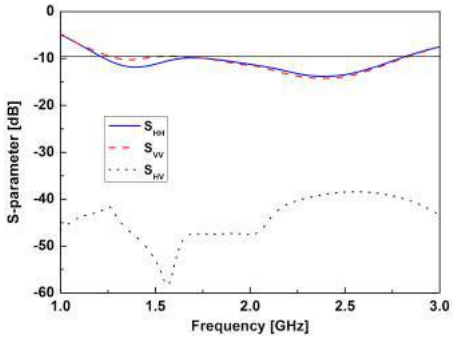

Fig. 6. Simulated S-parameter response of the 0D TCDA

Acknowledgements This work was supported by the Center for Advanced Meta-Material (CAMM) funded by the Ministry of Science, ICT, and Future Planning as Global Frontier Project (CAMM-2014M3A6B3063708).

REFERENCES

1. B. A. Munk, Finite Antenna Arrays and FSSLastname, F. M. “Title of the journal paper,” *Journal Title Abbreviation*, Vol. 34, No. 10, 1064–1076, 1986.

Focusing electromagnetic wave with reconfigurable metasurface.

Jong-Ho Choe[1], **Jin-Soo Kim**[1], **and Q-Han Park**[1*]
[1] Department of Physics, Korea University, Republic of Korea
[*]corresponding author: qpark@korea.ac.kr

Abstract-In this presentation, we demonstrate an electromagnetic wave focusing using reconfigurable metasurface. We made a metasurface which can modulate microwave spatially. Each unit structure constituting the metasurface is controlled electrically. With optimization process, we could concentrate electromagnetic wave energy into a spatially localized spot.

The concept of metasurface was proposed due to readily fabricated using lithography method. Therefore, metasurface is a thin layer made of an array of unit structure with spatially varying geometrical parameters. [1] Because of its strong electromagnetic wave spatial modulation capability even with very thin thickness, metasurface fits to application such as flat optics. Recently, study on metasurface is extending toward accomplishing active and dynamic functionalities with a fast switching speed. [2-5]

In this presentation, we demonstrate a modulating spatial distribution of electromagnetic waves in microwave range using electrically controlled metasurface. We developed a spatial microwave modulating metasurface using readily available electronic components. Each unit structure in the metasurface is controlled electrically and changes electromagnetic wave locally. With optimization process, electromagnetic wave modulated by the device could be localized into a specific spot. Our electromagnetic wave spatial scanner shows that electromagnetic wave modulated by the metasurface can be focused into a localized area and it is different from the beam forming of microwave. We expect our device can be used in many applications such as wireless power transfer, microwave imaging, and indoor radar.

Acknowledgements, This work was supported by the Center for Advanced Meta-Materials (CAMM) funded by the Ministry of Science, ICT and Future Planning as Global Frontier Project (2014M3A6B3063710).

REFERENCES

1. Yu, N. and F. Capasso, "Flat optics with designer metasurfaces," *Nat. Materials*, Vol. 13, 139–150, 2014.
2. Kaina, N., M. Dupre, M. Fink, and G. Lerosey, "Hybridized resonances to design tunable binary phase metasurface unit cells," *Opt. Express*, Vol. 22, No. 16, 18881-18888, 2014.
3. Kaina, N., M. Dupre, G. Lerosey, and M. Fink, "Shaping complex microwave fields in reverberating media with binary tunable metasurfaces," *Sci. Rep.,* Vol. 4, 6693, 2014.
4. Cui, J., C. Huang, W. Pan, M. Pu, Y. Guo, and X. Luo, "Dynamical manipulation of electromagnetic polarization using anisotropic meta-mirror," *Sci. Rep.* Vol. 6, 30771, 2016.
5. Chen, K., Y. Feng, F. Monticone, J. Zhao, B. Zhu, T. Jiang, L. Zhang, Y. Kim. X. Ding, S. Zhang. A. Alu, and C.-W. Qiu, "A Reconfigurable Active Huygens' Metalens," *Adv. Mater.*, 1606422, 2017.

Development of mechanical machining technology for microwave absorber metasurfaces

E. c. Jeon[1*], S. H. Moon[1], J. R. Lee[1], M. S. Heo[2], M. J. Kim[2], J. H. Shin[2], T. J. Je[1] and T. I. Choi[3]

[1]Dept. of Nano Manufacturing Technology, Korea Institute of Machinery and Materials, Korea

[2]Dept. of Materials Science and Engineering, KAIST, Korea

[3]Center for Advanced Meta-Materials, Korea

[*]corresponding author: jeonec@kimm.re.kr

Abstract-We designed microwave absorber metasurfaces consisting of three layers: a patterned conductor, an insulator and a conductor, and developed ultra-fine mechanical machining technologies for manufacturing of the designed metasurfaces. The patterns of the conductor should be accurately machined for avoiding decrease in absorbance of the metasurfaces. We optimized a few machining parameters, and succeeded to manufacture the microwave absorber metasurfaces without machining errors (delamination, warpage and burr). The developed technology can be applied to microwave absorber.

Stealth function is much important for protecting soldiers and expensive weapons. Generally, the paint absorbing the microwaves is used for fighting planes and warships. However, this method needs frequent maintenance which cost too much. Therefore, we suggested a film-type microwave absorber metasurfaces and mechanical machining technologies for easy mass-production in this study.

The suggested metasurfaces consist of three layers: a patterned conductor, an insulator and a conductor. The shape of the patterns on the patterned conductor determines the range of microwaves and the absorbance, thus, it is much important to design the high-performance pattern shapes and to manufacture them accurately. We designed discrete channel patterns having the width of about 100um and verified high absorbance of microwaves by numerical analysis. The ultra-fine planing technology which is one of the mechanical machining technologies was used for manufacturing the designed patterns. A few kinds of machining errors such as delamination, warpage and burr at the machined patterns could be sorted out by optimization of the machining parameters. The width of the cutting tool affected warpage and burr, and the depth of cut affected delamination. Finally, we succeeded to manufacture the accurate microwave absorber metasurfaces having the discrete channel patterns on a conductor.

Acknowledgements, This research was supported by the 'Center for Advanced Meta-Materials(CAMM)' funded by the 'Ministry of Science, ICT and Future Planning' as 'Global Frontier Project (CAMM-2014M3A6B3063707)'.

Absorber using a split eight equal Circular Sectors Resonator

N. T. Trung[1*], and S. Lim[2]
School of Electrical and Electronic Engineering
Chung-Ang University, Seoul 156-756, Korea
sungjoon@cau.ac.kr, nguyentoantrung28190@gmail.com.

Abstract-In this paper, a polarization-insensitive metamaterial absorber is proposed. The unit cell of the metamaterial is designed with a split eight equal Circular Sectors Resonator is introduced for the polarization -insensitivity of the MM absorber. A vertically and horizontally symmetric structure of unit cell enables polarization-insensitivity. The performances of the proposed absorber are demonstrated with full-wave simulation and measurements. Under normal incidence, the fabricated absorber shows 98% absorptivity at 9.26 GHz for all polarization angles, while for oblique incidence, the fabricated absorber maintains an absorptivity higher than 91% for incident angles up to 70˚ for both transverse magnetic (TM) and transverse electric (TE) modes.

Electromagnetic metamaterials (MTMs) are defined as artificial and effectively homogeneous electromagnetic structures with unusual and unique properties that do not exist in the nature. Basically, to design an absorber, we have to maximize the absorption coefficient. It is equivalent to minimize both the transmission (T) and reflection (Γ) coefficients in the Eq. (1), where A is absorption coefficient.

$$A = 1 - \Gamma - T \tag{1}$$

The geometry of the proposed fabricated absorber prototype is shown in Fig. 1. A split eight equal circular sector is realized on the top pattern and the bottom layer is fully covered with a copper sheet. The absorptivity of the unit cell is varied for different incident angles. It is demonstrated from a full-wave simulation that the proposed complementary circular sector enables absorptivity insensitive to incident angles. When the EM wave incident to the absorber, there are the reflected wave and the transmitted wave.

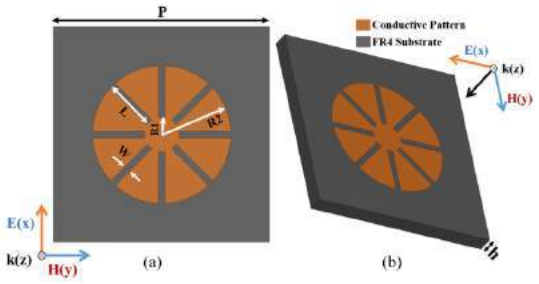

Figure 1: (a) Top view and (b) 3D view of the proposed absorber.

To verify the MM absorber was fabricated consisting of 20×20 unit cells. As shown in Fig. 2, the fabricated prototype is observed. The metallic structures on the top and bottom layers of the substrate are is fully covered with a copper sheet. The substrate of absorber is FR4 with thickness of h = 0.8 mm. Its relative permittivity and dielectric loss tangent are 3.9 and 0.02, respectively.

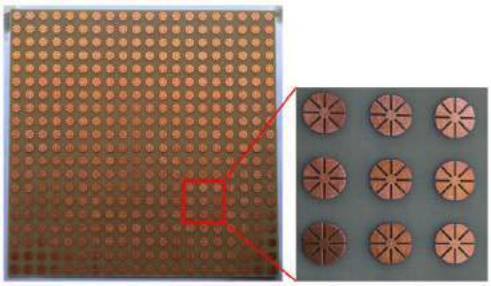

Figure 2: Fabricated absorber prototype absorber

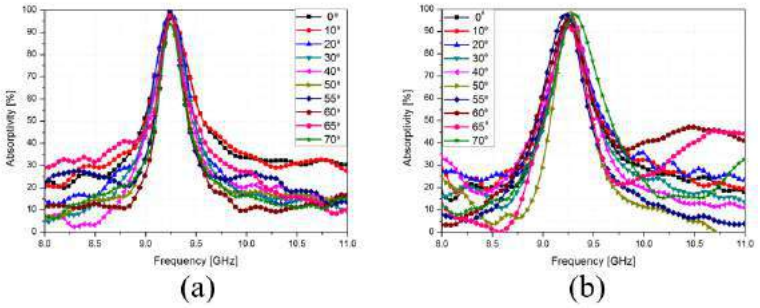

Figure 3: Measured absorptivity of the fabricated prototype absorber (a) for incident angles θ ranging from 0˚ to 70˚ in (b) TE and (c) TM mode.

The measured under oblique incidence, both of TE (Fig. 3. (a)) and TM (Fig. 3. (b)) modes, the absorptivity at 9.26 GHz exceeded 91% even for incident angles (θ) varying from 0˚ to 70˚.

In this paper, a novel planar metamaterial absorber has been proposed. It is observed that the metamaterial absorber is polarization insensitive for both transverse electric (TE) and transverse magnetic(TM) waves. The measurement and simulation results are in very good agreement.

Acknowledgements

This research was supported by the MSIP (Ministry of Science, ICT and Future Planning), Korea, under the ITRC (Information Technology Research Center).

REFERENCES

1. Lim, D., Lee, D. & Lim, S “Angle- and polarization-insensitive metamaterial absorber using via array”, Sci. Rep, Vol. 6, No. 1, 39686, 2016.
2. Lee, D., Hwang, J. G., Lim, D., Hara, T. & Lim, S “Incident angle- and polarization-insensitive metamaterial absorber using circular sectors”, Sci. Rep, Vol. 6, 27155, 2016.
3. Landy, N. I., Sajuyigbe, S., Mock, J. J., Smith, D. R. & Padilla, W. J “Perfect metamaterial absorber”, Physical Review Lett, Vol. 100, No. 20, 207402 – 207406, 2008.
4. Cheng, Y., Yang, H., Cheng, Z. & Wu, N “Perfect metamaterial absorber based on a split-ring-cross resonator”, Applied Physics A: Materials Science and Processing, Vol. 102, No. 1, 99–103, 2011.

Aircraft infrared signature control using metamaterials

Hyung Hee Cho
Department of Mechanical Engineering, Yonsei University, Korea
hhcho@yonsei.ac.kr

Abstract - Infrared signals from the stagnation region where the aerodynamic heating occurs due to supersonic flow and engine and surrounding hot parts of aircraft are detectable and directly related to survivability. To implement the infrared stealth, it is necessary to reduce the contrast radiant intensity (CRI), the difference of intensities between object and background. We have designed metamaterials to control the spectral infrared emissivity, suppresses detectable band emission and enhance non-detectable band. Finally, the infrared stealth performance of metamaterial was evaluated.

The stealth is a technology that prevents detection from enemies and it is being developed to operate independently or integrally with detection areas such as visible, acoustic, infrared, and radar, depending on the operating environment. The most actively developed radar stealth has been studied in the direction of reducing the radar reflection wave of the object and already applied to the aircraft. Thus, the new detection systems have been developed to neutralize radar stealth technology, and the number of weapons systems that detect infrared signal of targets. Infrared is a kind of electromagnetic wave that radiates when all objects have a temperature of above 0K, which is proportional to the surface temperature and the emissivity of surface. Therefore, the infrared signal can be reduced by cooling down surface temperature or controlling surface emissivity. The quantitative index of infrared stealth is evaluated by the difference between the infrared signal of the background and the object, and the lower the CRI value means the better the infrared stealth performance. Therefore, to calculate the reliable CRI value of an aircraft, not only the surface temperature distribution but also the infrared characteristics of the atmosphere should be considered.

The infrared signal of the aircraft analyzed for 3~5 μm and 8~12 μm bands, considering the infrared transmission characteristics of the atmosphere, 5~8 μm opaque band due to strong absorption of CO_2 and H_2O. Infrared signals in the band of 3~5 μm and 8~12 μm were generated in the aircraft engine and surrounding hot parts. In stagnation regions, such as nose, leading edges and engine intake where aerodynamic heating occurs, infrared signals in the 8~12 μm band mainly occurred. In this study, the gas radiation from hot plum was not considered but only aircraft fuselage infrared signal was evaluated.

We analyzed the infrared signal of a combat aircraft of a single jet engine flying at an altitude of 5000 m with Mach 1.5. To accurately calculate the aircraft surface temperature, two numerical analyzes were conducted in an iterative manner. Ansys Fluent was used to obtain aerodynamic heating and heat transfer coefficients on the aircraft surface and RadthermIR was used to calculate conduction, convection, and surface to surface radiation. The bidirectional reflectance distribution function (BRDF) IR image and CRI of the aircraft were calculated by considering the surface temperature distribution of the aircraft and infrared transmittance of atmosphere from the Modtran module of RadthermIR.

In order to reduce the infrared signal of the aircraft, it is necessary to lower the surface temperature or lower the surface emissivity. The method of lowering the surface temperature is not practical because it requires

additional equipment and increases aircraft weigh. Therefore, it is effective to reduce the CRI value by controlling the surface infrared emissivity of the aircraft. However, if the surface emissivity is kept low in the entire infrared band, the radiative cooling performance is significantly reduced, and the surface temperature may increase. Therefore, in this study, we designed and fabricated metamaterials that keeps high emissivity at only undetectable 5 ~ 8 μm band and low emissivity in detectable 3~5 μm and 8~12 μm bands.

The metamaterial composed of metal-dielectric-metal (MDM) can keep the high emissivity in the selected wavelength band depending on the shape, size of the upper metal structure and thickness of the intermediate dielectric layer. And it maintains low emissivity in the non-resonant wavelength region. We fabricated infrared emissivity controlling metamaterial using photo lithography with gold and ZnS. The thickness of metal layer and upper structure was 100 nm and the thickness of intermediate dielectric layer was 200 nm. Since the upper metal structure, circular disk array with same pitch distance, determined resonance wavelength, the selective emission property of MDM structure could be effectively controlled. MDM structure spectral emissivity is measured with FT-IR spectroscope and applied to surface emissivity when calculate CRI of aircraft. Finally, the aircraft CRI is reduced to 1/4 of blackbody surface by applying MDM metamaterials at same flying condition.

REFERENCES

1. Taehwan Kim, Hwanseong Lee, Ji-Yeul Bae, Taeil Kim, Jonghyun Cha, Daetoon Jung and Hyung Hee Cho. "Susceptibility of Combat Aircraft Modeled as an Anisotropic Source of Infrared Radiation," *IEEE Transactions on Aerospace and Electronic Systems,* Vol. 5, No. 5, 2467–2479, 2016.
2. Pekka Alitalo and Sergei Tretyakov, "Electromagnetic cloaking with metamaterials,", *Materials today*, Vol. 12, 22–29, 2009.
3. Wenshan Cai, Uday K. Chettiar, Alexander V. Kildishev and Vladimir M. Shalaev, "Optical cloaking with metamaterials," *Nature Photonics*, Vol. 1, 224–227, 2007.

Lossy acoustic bipolar cylindrical cloak with negative index metamaterial

Y. Y. Lee[1] and D. Ahn[2,3]*

[1]Korea Testing Laboratory,87 Digital-ro 26-gil, Guro-gu, Seoul 08389, Republic of Korea
[2]Department of Electrical and Computer Engineering, University of Seoul, 163 Seoulsiripdae-ro, Tongdaemun-gu, Seoul 02504, Republic of Korea
[3]Physics Department, Charles E. Schmidt College of Science, Florida Atlantic University, 777 Glades Road, Boca Raton, FL 33431-0991, USA
*corresponding author: dahn@uos.ac.kr

Abstract- While, it was shown that for the lossless acoustic cloak the illumination direction independent cloaking can be achieved with the structure with compressed geometry and complementary media, the effect of the material loss have not been fully explored yet. Here, we show that realistic cloaking materials with moderate loss still works when complementary media is introduced but with attenuated back scattering waves. However, the advantages of introducing complementary media are almost lost when the loss tangent of cloaking shell becomes large.

Most of the existing works[1-5] on acoustic cloaking is based on using analogy between the acoustic equations and the transverse electric (TE) polarizations of the 2D electromagnetic field equations. However, it is found that for the electromagnetic fields the cloaking performances of the cloak is superior for the transverse magnetic (TM) polarizations than the TE polarizations because the scattering coefficients for the latter do not vanish completely.[6] Previously, we have the studied[7] the lossless acoustic cloaking using the analogy of acoustic equations and the TM polarizations of the electromagnetic field equations and showed that the acoustic cloak with both cloaking shell and complementary media has the illumination direction independent cloaking properties when the loss can be ignored. The material parameters for the acoustic cloak were obtained by comparing 2D Maxwell's equations in the TM polarization with acoustic field equations for general curvilinear coordinates with the effective medium theory.[7] In this work, we consider a more realistic lossy acoustic cloak and show that the cloak with loss still works but attenuated back scattering waves exist. Dispersive full-wave finite-difference time-domain (FDTD) method[6] is employed for the numerical analysis.

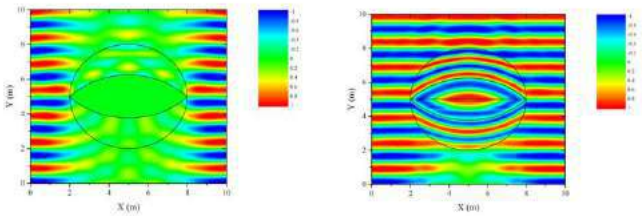

Fig. 1 Comparision of the lossy cloak without (left) and with (right) complementary media.

In Figure 1, the p wave distributions propagating along the negative y direction, respectively, are depicted for the

operation frequency of 1 KHz for a loss bipolar cylindrical exterior cloak without the complementary media (left) and with lossy complementary media (right). We assumed the loss tangent as tan (δ) = 0.01 and tan (a_m) = 0.01 both for the cloak and the complementary media. In the later case, the acoustic cloak is observed to be working, but due to the presence of losses in the cloaking materials, there are shadowing effects on the fields behind the cloaking shell along the direction of wave propagation. It is remarkable that loss in the complementary media does not affect the cloaking performance significantly when the loss tangent is relatively small and one can see that the advantage of employing complementary media.

Acknowledgements, This work were supported by the Global Frontier program of MSIP/NRF 2014M3A6B3063729.

REFERENCES

1 S. A. Cumber and D. Schering, “One path to acoustic cloaking,” New J. Phys. **9**, 45 (2007).
2D. Torrent and J. Sanchez-Dees, “Acoustic cloaking in two dimensions: a feasible approach,” New J. Phys. **10**, 063015 (2008).
3 H. Chen and C. T. Chen, “Acoustic cloaking in three dimensions using acoustic met materials,” Appl. Phys. Let. **91**, 183518 (2007).
3 M. Hua, Q. Shao-Bo, X. Zhuo and W. Jia-Fu, “Acoustic elliptical cylindrical cloaks,” Chinese Phys. B**18**, 1123-1126 (2009).
4 W. Zhu, C. Ding, and X. Zhao, “A numerical method for designing acoustic cloak with homogeneous metamaterials,” Appl. Phys. Lett. **97**, 131902 (2010).
5 S. Zhang, C. Xia, and N. Fang, “Broadband acoustic cloak for ultrasound waves,” Phys. Rev. Lett. **106**, 024301 (2011).
6 Y. Y. Lee and D. Ahn, "Dispersive full-wave finite-difference time-domain analysis of the bipolar cylindrical cloak based on the effective medium approach," J. Opt. Soc. Am. B**30**,140-148 (2013).
7 D. Ahn, Y. Y. Lee, S. Lee and S.-H. Park, “Full wave finite-difference time-domain study of lossless acoustic bipolar cylindrical cloak with compressed geometry and complementary media,” J. Appl. Phys. 118, 044508 (2015).

Air-filled acoustic metamaterials for wide range compressibility tuning

Sam H. Lee[1*], Chung Kyu Han[1], Eun Bok[1], Haejin Choi[1], and Oliver B. Wright[2],
[1] Institute of Physics and Applied Physics, Yonsei University, Seoul 120-749, Korea
[2] Division of Applied Physics, Faculty of Engineering, Hokkaido University, Sapporo 060-8628, Japan
[*]E-mail: samlee@yonsei.ac.kr

Abstract-Metamaterials consisting of Helmholtz resonators exhibit compressibility several times larger than that of air but tuning range is limited. Here we present an acoustic metamaterial based on internally connected double Helmholtz resonators. The wall separating the two Helmholtz resonators has two holes one of which is simply open whereas the other is covered with a thin taut membrane. We experimentally demonstrate tuning the effective compressibility continuously from zero to 10 relative to air. Applications include tunable acoustic lens.

Acknowledgements, This work was supported by the Center for Advanced Meta-Materials (CAMM) funded by the Ministry of Science, ICT and Future Planning as a Global Frontier Project (CAMM-2014M3A6B3063712), and by the National Research Foundation of Korea(NRF) grant funded by the Korea government (MSIP) (No. 2015001948).

Photoelectric Properties of CdSe/ZnS Quantum Dot/Graphene Thin Films Enhanced by Silver Nanowire

Sin-Yi Wang, Kuan-Han Wu and Bo-Tau Liu*
Department of Chemical and Materials Engineering, National Yunlin University of Science and Technology
Yunlin 64002, Taiwan
*corresponding author: liubo@yuntech.edu.tw

Abstract- In this study, we used reduced graphene oxides (rGOs) and CdSe/ZnS QDs to fabricate rGO-QD-rGO sandwich-structure films. The sandwich structure is willing to alleviate the deterioration of QDs in surroundings by virtue of the covering of graphene. We found that the optoelectronic conversion efficiency of the QD-graphene system was significantly improved by incorporating silver nanowires (AgNWs) into the QD layer.

Over the past decade, QDs have been widely studied on the application of solar cells, sensors, light emitters, and bioassays. Recently, many studies revealed that the excited energy of QDs could be transfer effectively to graphene because of the high conductivity and luminescence quenching ability of graphene [1]. In generally, the quenching possible mechanism can be ascribed to the following routes: Forster resonance energy transfer, surface energy transfer and photo-induced electron transfer [2]. Some studies have shown experimentally that the quenching of QDs by graphene was assigned to surface energy transfer. In this study, we prepared the reduced graphene oxide (rGO)-CdSe/ZnS quantum dots (QDs) hybrid films on a three-layer scaffold that the QD layer was sandwiched between two rGO layers. The photocurrent was induced by virtue of the facts that the rGO quenched the photoluminescence of QDs and transferred the excited energy. Unlike graphene, the metal nanostructural surfaces, nanoparticles, or nano-holes not only quench but also enhance the PL of QDs through the excitation of localized surface plasmon resonance (LSPR) of metal nanostructures, which amplifies the local electric field to alter the optical properties of QDs. As a result, both the PL quenching and enhancement are observed after the excitons of QDs coupling with LSPR of metal nanostructures.

Besides exciting and quenching the PL of QDs, AgNWs may absorb and scatter the incident light by the localized surface plasmon resonance and the large diameter, respectively. Therefore, the effect of AgNWs on optoelectronic conversion efficiency of QDs is still vague. We incorporated AgNWs into the QD layer and found the AgNW incorporation can enhance significantly the photocurrent. While the addition of AgNWs changed from 0 to 300 μL, the photocurrent density increased from 22.1 to 80.3 μA cm^{-2}, a near 3.6-fold enhancement. However, too much AgNW incorporation reduced the photocurrent enhancement as a result of the high extinction coefficient and the large scattering effect of AgNWs. In order to realize the mechanism of AgNW enhancement on the photocurrent, the PL spectra of rGO-QDs with/without AgNWs were measured (Figure 1). Although rGO shows the ability of quenching the PL, the AgNW incorporation can enhance the suppression on the PL, being more efficient to transfer the exciton energy. We evaluated the influence of the various shapes of silver (AgNPs, AgNRs, AgNWs) on the optoelectronic conversion efficiency. Figure 2 shows the photocurrent response of the rGO3-QD/AgNW3, rGO3-QD/AgNR, and rGO3-QD/AgNP hybrid films. The photocurrent density increases in the following sequence: rGO3-QD/AgNP < rGO3-QD/AgNR < rGO3-QD/AgNW3. We

infer that the enhancement on the optoelectronic conversion efficiency may arise from the strong quenching ability of silver and the rapid electron transfer of AgNWs.

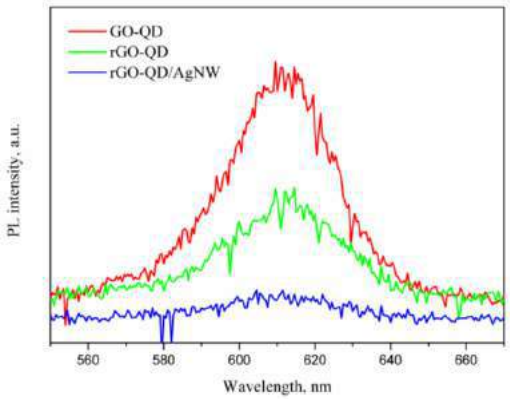

Figure 1. PL spectra of the GO-QD, rGO-QD, and rGO-QD/AgNW hybrid films under 350-nm excitation.

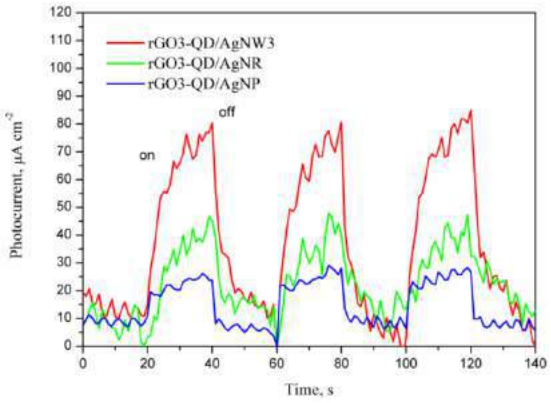

Figure 2. Photocurrent density-time curves of the rGO3-QD/AgNW3, rGO3-QD/AgNR, and rGO3-QD/AgNP hybrid films under on/off-cycle light irradiation.

Acknowledgement This work was financially supported by the Minister of Science and Technology, the Republic of China (MOST 105-2221-E224-059-MY3).

REFERENCES

1. Zedan, A.F., Sappal, S., Moussa, S. and El-Shall, M.S. "Ligand-controlled microwave synthesis of cubic and hexagonal CdSe nanocrystals supported on graphene. Photoluminescence quenching by graphene," *J. Phys. Chem. C*, Vol. 114, 19920-19927, 2010.
2. Li, Z., He, M., Xu, D. and Liu, Z. "Graphene materials-based energy acceptor systems and sensors," *J. Photochem. Photobiol. C*, Vol. 18, 1-17, 2014.

Introduction of Office of Naval Research Global

Simin Feng[1*]
[1] Office of Naval Research Global, USA
[*]corresponding author: simin.feng.civ@mail.mil

Abstract- Office of Naval Research Global (ONRG) is a funding organization within the United States Department of the Navy to support worldwide basic scientific research in the areas of Navy interest. This talk will provide an overview about the ONRG mission and funding opportunities.

The Office of Naval Research (ONR) is an organization within the United States Department of the Navy that coordinates, executes, and promotes science and technology programs of the United States Navy and Marine Corps. ONR-Global is the international arm of the ONR that assists the ONR to execute its mission by fostering international collaborations, promoting fundamental researches, and building partnerships around the world in the areas of mutual interest to the partner countries and United States. Through the positive engagements, the ONRG brings the full spectrum of worldwide science and technology to Navy and Martine Corps. The ONRG has forward physical presence on five continents with headquarter in London, United Kingdom. Other regional offices are located in Chile, Japan, Australia, Singapore, Czech Republic, and India.

We all live on the same planet. Scientific knowledge has led to remarkable innovations that have been of great benefit to humankind. Fundamental research is universal and should be open to general public. The ONRG mission is to foster international collaborations, promote basic scientific researches, build partnerships, and contribute open source data to global technology awareness. The ONRG has three funding programs to execute its mission:

- Collaborative Science Program (CSP): Support international workshops, conferences, and seminars of navy interest held outside the United States.
- Visiting Scientist Program (VSP): Support short term travel for international scientists to US to interact with researchers and socialize S&T ideas/findings with the NRE that advance basic research through collaboration.
- Naval International Cooperative Opportunities in Science Program (NICOP): Provide direct funding support to international scientists to conduct fundamental research and insert innovative science and technology into core ONR and Naval Research Enterprise Programs.

Above programs aim to promote innovative long-rang basic researches, advance sciences and technologies of mutual benefits, and foster a culture of communications and networking. The seed funding from ONRG will provide opportunities for worldwide talented young scientists and engineers, as well as senior professionals, to expand their careers and grow their researches into the full potential.

REFERENCES

https://www.onr.navy.mil/en/Science-Technology/ONR-Global

Innovative Metamaterials

Charge-Transfer Dynamics Controlled by Manipulating Dielectric Permittivities with Hyperbolic Metamaterial Structures as Solvent Analogues

Kwang Jin Lee[1], Yiming Xiao[1,2], Jae Heun Woo[1,3], Eunsun Kim[1], David Kreher[2], André-Jean Attias[2], Fabrice Mathevet[2], Jean-Charles Ribierre[1†], Jeong Weon Wu[1], Pascal André[4]

[1]Department of Physics, Quantum Metamaterials Research Center, Ewha Womans University, Seoul, South Korea.
[2]Sorbonne Universités, UPMC Univ. Paris 06, CNRS, Institut Parisien de Chimie Moléculaire, UMR 8232, Chimie des Polymères, 4 place Jussieu, 75005 Paris, France.
[3]Center for Length, Division of Physical Metrology, Korea Research Institute of Standards and Science (KRISS), Daejeon, South Korea.
[4]RIKEN, Wako, Japan.
† Present Address: OPERA, Kyushu University, Fukuoka, Japan.
[*]corresponding author: kjlee0514@ewha.ac.kr

Abstract - We demonstrate that multilayered hyperbolic metamaterial (HMM) substrates alter charge transfer (CT) dynamics by showing that both charge separation and recombination characteristic times are increased by factors of 2.4 and 1.7, respectively, resulting in longer-lived CT states. We successfully rationalize the experimental data by introducing image dipole interactions in Marcus theory to tune the driving force. The number of metal-dielectric pairs induces a non-local effect formalized in the dielectric permittivity, and is presented as an analogue to local solvent effects.

Charge separation (CS) and recombination (CR) are crucial phenomena which impact numerous phenomena[1], in electronics[2], magnetism[3], biology and photosynthesis[4], and chemistry[5]. Understanding and artificially tuning charge transfer (CT) dynamics are then of the greatest importance. We experimentally evidenced that organic semiconductor CT dynamics depends on substrate nanostructures[6]. Charge separation (CS) and charge recombination (CR) characteristic times from triphenylene donor to perylene acceptor in columnar dyad were both increased by factors up to 2.5 and 1.7, i.e. slower by ~ 140 and 73 %, respectively[7]. Marcus theory could qualitatively describe this trend when including Coulomb interactions and image dipoles in the multi-layered system to reveal the role of HMM image dipole interactions in manipulating dielectric permittivity with non-local effects. The reported control of the CT dynamics is analogous to the use of solvents presenting different dielectric permittivity. This solvent effect is well known, but, to the best of our knowledge, unheard of in solid HMM nanostructured substrates. Furthermore, the relatively small variation of the non-local dielectric permittivity compared to a more traditional solvent effect needed to get a comparable CT dynamic rate alteration is attributed to the very different mechanisms involved. In the former case, directional image dipole interactions apply to a D:A thin films, whereas the latter relies on variation of the polarity of the solvent molecules

surrounding each and every single of the D:A moieties.

Marcus theory finds applications in numerous systems from solutions to interfaces and solids. The present work represents an original extension of it towards solid multi-layered media. Image dipole interactions are influenced by dyad-HMM interface separations, dipole orientations, charge separation within the dipole, as well as HMM periodicity and pair number. From this general features, one can then envisage that more HMM layers should induce a stronger CT dynamic alteration. Similar behaviors are expected for any nanostructured media allowing the periodic formation of image dipoles. We focused on layered Ag:Al_2O_3 but other inorganic and organic materials as well as dissymmetric substrates should provide some control over CT dynamics.

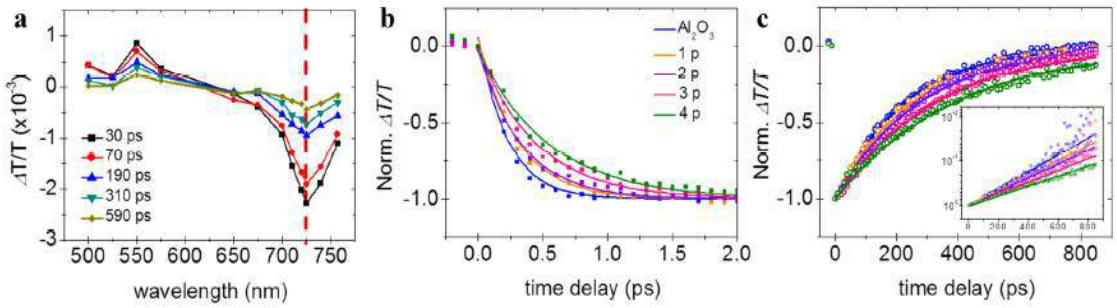

Transient absorption measurements of annealed dyad molecule thin films. a, Relative transmission variation as a function of the wavelength for time delays ranging from 30 to 590 ps measured on fused silica with 325 nm pumping. Time resolved ΔT/T spectra probed at 725 nm monitoring b, the formation and c, the disappearance of the anionic PerDi (inset and SI: semilog plots with inverted scale illustrating the single exponential recovery behaviour). Colored lines are guide-for-the-eyes (a) and exponential fits (b, c).

REFERENCES

1. Marcus, R. A., "Electron Transfer Reations in Chemistry. Theory and Experiment." *Rev. Mod. Phys*. 65, 599-610, 1993.
2. Perrin, M. L., et al., "Large tunable image-charge effects in singlemolecule junctions." *Nat. Nanotech*. 8, 282-287, 2013.
3. Jailaubekov, A. E., et al., "Hot charge-transfer excitons set the time limit for charge separation at donor/acceptor interfaces in organic photovoltaics." *Nat. Mater.* 12, 66-73, 2013.
4. Lambert, N., et al., "Quantum biology" *Nat. Phys.* 9, 10-18, 2012.
5. Canaguier-Durand, A., et al., "Thermodynamics of molecules strongly coupled to the vacuum field." *Angew. Chem. Int. Ed.* 52, 10533-10536, 2013.
6. Kwang Jin Lee et al., "Structure-charge transfer property relationship in self-assembled discotic liquid-crystalline donor?acceptor dyad and triad thin films" *RSC Adv.,* 6, 57811-57819, 2016
7. Kwang Jin Lee et al., "Controlling Charge-Transfer Dynamics with the Effective Dielectric Constant of Hyperbolic Metamaterial Structures as Solvent Analogues ", arXiv:1510.08574

Isospectral transformations for disordered photonics

Sunkyu Yu*, Xianji Piao, Choonlae Cho, and Namkyoo Park
Photonic Systems Laboratory, Department of ECE, Seoul National University, Seoul 08826, Korea
*corresponding author: sk8513e@gmail.com

Abstract-We introduce isospectral transformations for disordered light-matter interactions. Exploiting supersymmetric transformation, we show a novel disorder having perfect bandgap and confined modes, and demonstrate the switching of disordered light without loss of information. We will also discuss the Householder transformation for interdimensional phase matching.

Global phase matching between eigenspectra [1], *i.e.* isospectrality, allows collective controls of multimodes for high information capacity. For the eigenvalue equation $H\psi = \lambda\psi$, a proper transformation operator A constructs the isospectrality $AH\psi = H_s(A\psi) = \lambda(A\psi)$, when the new Hamiltonian H_s is physically allowed. Here we introduce physically allowed isospectrality in optics, imposing disordered properties on optical phenomena.

First, we discuss supersymmetric (SUSY) transformation [2-4] which derives transformed optical potentials while preserving the entire eigenspectrum except the ground state. Figure 1a,b represents SUSY-transformed crystal and quasicrystal having perfect bandgaps despite disordered potential landscapes [3]. We will show that degrees of disorders and spatial widths of eigenmodes (Fig. 1c,d) can be controlled by multiple SUSY transformations, implementing a new type of bandgap media. We also introduce the SUSY transformation for integrated optics, which enables the switching of random waves without any loss of information (Fig. 1e,f, [4]).

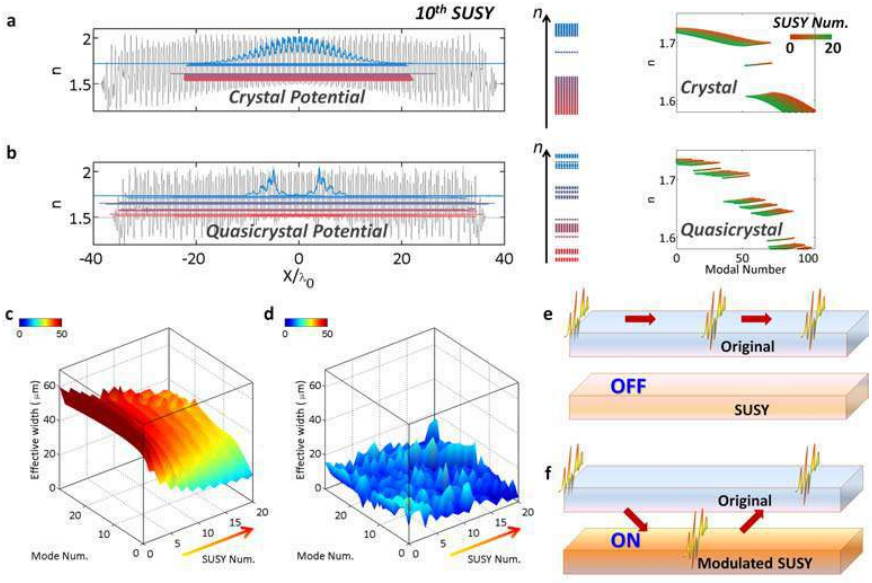

Figure 1. (a,b) SUSY-transformed (a) crystal and (b) quasicrystal with potential landscapes and bandgap evolutions. (c,d) Spatial widths of eigenmodes in SUSY-transformed (c) crystal and (d) quasicrystal. (e,f) SUSY paired potentials for random wave switching: (e) OFF state and (f) ON state.

In the talk, we also discuss the Householder transformation which derives isospectral optical structures each in different dimension [5]. We show that the 2-/3-dimensional disordered structure without degeneracy has a 1D partner structure (Fig. 2a) having a same eigenspectrum (Fig. 2b). From this interdimensional phase matching in a global spectrum, we implement the lossless transfer of light waves between different dimensions (Fig. 2c).

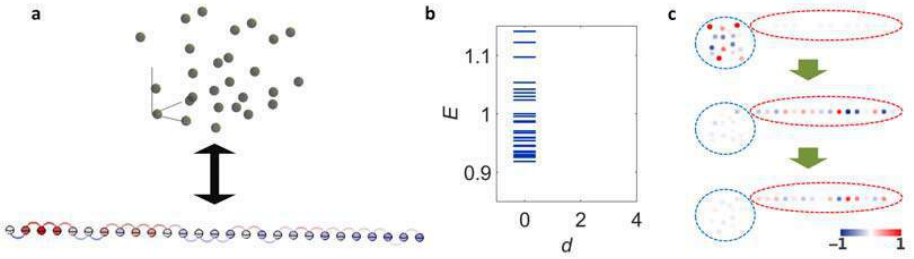

Figure 2. (a) An isospectral pair of different dimensional structures. (b) The identical spectrum of disordered 1D and 3D structures in (a). (c) Wave transfer between 1D and 2D optical structures.

REFERENCES

1. Kac, M. “Can one hear the shape of a drum?,” *Am. Math. Monthly* Vol. 73, 1, 1966.
2. Miri, M.-A., Heinrich, M., El-Ganainy, R. & Christodoulides, D. N. “Supersymmetric optical structures,” *Phys. Rev. Lett.* Vol. 110, 233902, 2013.
3. Yu, S., Piao, X., Hong, J., and Park, N. "Bloch-like waves in random-walk potentials based on supersymmetry," *Nat. Commun.* Vol. 6, 8269, 2015.
4. Yu, S., Piao, X., and Park, N. "Digital building blocks for controlling random waves based on supersymmetry," *arXiv preprint* arXiv:1611.08982.
5. Yu, S., Piao, X., Hong, J., and Park, N. " Interdimensional optical isospectrality inspired by graph networks," *Optica* Vol. 3, 836, 2016.

Direct and quantitative measurement of far-field light scattering of a single optical nanostructure

Jinhyung Kim[1], Donghyeong Kim[1], and Min-Kyo Seo[1*]
[1]Department of Physics and and Institute for the NanoCentury, KAIST, Rep. of Korea
[*]corresponding author: minkyo_seo@kaist.ac.kr

Abstract-We present for the first time the quantitative measurement of the far-field light scattering properties of a single optical nanostructure. A goniometer-based solid angle scanning enables us to overcome the limitations of the conventional back-focal-plane method and quantitatively measure the differential scattering cross-section of a single metal nanorod and its far-field distribution over the full hemisphere. We expect that the angle- and spectrum-resolved far-field measurements will be highly useful for evaluating the performances of optical nano-devices and metamaterials.

Strong light scattering of optical nanostructures enables to effectively interface free-propagating electromagnetic waves to localized near-fields and vice versa[1]. In recent decades, the resonant light scattering has been widely investigated and used to facilitate various applications, including highly-efficient light-emitting, nonlinear signal generation, photovoltaics, spectroscopy, and optomechanics[2]. In the novel applications to optical metasurfaces and metamaterials, it is also required to measure and understand the far-field scattering characteristics of individual nanostructures, which make up the metasurfaces and metamaterials. However, quantitative measurements of the far-field scattering distribution and cross-section of a truly single nanostructure on the wavelength scale or less have not yet been reported. Conventional back-focal plane imaging suffers from optical distortion and aberration and covers only a limited solid angle determined by the numerical aperture of the objective lens[3]. Only the total scattering or extinction cross-section has been measured for an array or colloid of nanostructures[4].

In this study, we demonstrate for the first time the direct and quantitative measurements of the far-field scattering properties of a single metal nanorod. A home-built goniometer-based solid angle scanning system measured the differential scattering cross-section of the single metal nanorod with a high signal-to-noise ratio of ~27.4 dB and its far-field distribution over the full hemisphere of 2π steradians. The differential and total scattering cross-sections are the most fundamental parameters for characterizing the far-field scattering properties. Based on the systematic measurements, we experimentally revealed that the differential and total scattering cross-sections of the metal nanorod depend on different mechanisms, the phase-matching conditions to the free-propagating radiation and the Fabry–Perot resonances of surface plasmon polaritons, respectively. In addition, we also performed angle- and spectrum-resolved far-field measurements of the far-field light scattering of a single metal nanowire and investigated its physical behaviors in the energy (wavelength)–momentum (wavevector) space. The measured far-field scattering cross-section and distribution show excellent agreement with numerical simulations and analytic models. We believe that our novel far-field measurement scheme will be highly useful for investigating and evaluating not only optical nanostructures but also metamaterials and metasurfaces.

Acknowledgements, The authors acknowledged support of this work by National Research Foundation of Korea (NRF) (2016R1D1A1B03935938, 2014M3C1A3052537 and 2014M3A6B3063709).

REFERENCES

1. Novotny, L. and Hulst, N., "Antennas for light," *Nature Photonics,* Vol. 5, 83-90, 2011.
2. Schuller, J. A., Barnard, E. S., Cai, W., Jun, Y. C., White, J. S. and Brongersma, M. L., "Plasmonics for extreme light concentration and manipulation," *Nature Materials*, Vol. 9, 193-204, 2010.
3. Duffieux, P.-M., *The Fourier Transform and its Applications to Optics*, Wiley, New York, 1983.
4. Langhammer, B. Kasemo, I. Zorić, I. Absorption and scattering of light by Pt, Pd, Ag, and Au nanodisks: Absolute cross sections and branching ratios. J. Chem. Phys 126, 194702 (2007).

Overlapped multiple Mie resonances in high-index dielectric structures

I. C. Seo[1], E. Lee[1], B. H. Woo[1], and Y. C. Jun[1*]
[1]*School of Materials Science and Engineering, Ulsan National Institute of Science and Technology (UNIST), Ulsan 44919, Korea*
[*]corresponding author: ycjun@unist.ac.kr

Abstract - We investigate multiple Mie resonances in high-index dielectric structures. Especially, we study spectral (Fano resonances and Superscattering) and spatial (Beam steering) features that occur in overlapped multiple Mie resonances. We also explore the possible applications of these dielectric structures in sensing and spectroscopy.

It is known that high-index dielectric structures (e.g. semiconductor structures) can support various Mie resonances [1]. When these multiple Mie resonances overlap together, various spectral and spatial features can appear: Fano resonances, Superscattering, Beam steering, etc. The spectral positions of Mie resonances can be controlled by engineering the geometry of subwavelength dielectric blocks. And these could find useful applications in sensing and spectroscopy.

For example, we theoretically investigate sharp Fano resonances in the mid-infrared spectral region and consider active tuning of those resonances. Two kinds of dielectric resonators, InSb cylinder and coupled block pair array, are considered [2]. We exploit InSb-based dielectric resonators to take advantages of high refractive index and low optical loss. Firstly, we consider a simple cylinder array. The representative electric field distribution of the Fano resonance is depicted in Fig. 1(a, b), which occurs as a result of the interference between quadrupolar Mie resonance and broad resonance. If the dielectric structure is optically pumped to generate carriers, Fano resonances can be gradually tuned.

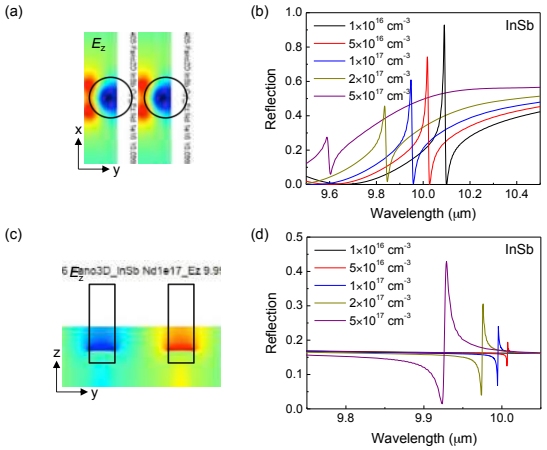

Figure 1 (a) Electric field distribution of Fano resonance and (b) resonance tuning for various carrier densities of cylinder arrays. (c) Electric field distribution of Fano resonance and (d) resonance switching for various carrier densities of block pair arrays.

The block pair array shows different behavior. The two blocks are assumed to have the same physical size, but different carrier density. If only one block is optically pumped, the Fano resonance can be effectively switched on and off. Fig. 1(c, d) depicts the antiparallel displacement field distribution and spectrum of Fano resonance originating from symmetry breaking. Intriguingly, as the carrier density increases, the resonance sharpness decreases but the resonance intensity increases. To understand this behavior, we adopt the two coupled oscillator model. Our studies on multiple Mie resonances can be extended to other spectral region too.

REFERENCES

1. Miroshnichenko, A. E. et. al., "Fano Resonances in All-Dielectric Oligomers," *Nano Lett.* Vol. 12, 6459–6463, 2012.
2. Lee, E. et. al., "Active switching and tuning of sharp Fano resonances in the mid-infrared spectral region", *Opt. Exp.* Vol. 24, 25684, 2016.

Time-resolved pump-probe measurement of optical rotatory dispersion in chiral metamaterial

Jae Heun Woo[1,3], Boyoung Kang[1,4], Minji Gwon[1], Ji Hye Lee[1,5], Dong-Wook Kim[1], William Jo[1], Dong Ho Kim[2], and Jeong Weon Wu[1]

[1]1Department of Physics, Ewha Womans University, Seoul 03760, Korea
[2]Department of Physics, Yeungnam University, Gyeongsan, Korea
[3]Center for Length, Division of Physical Metrology, Korea Research Institute of Standards and Science, 267 Gajeong-ro, Yuseong-gu, Daejeon, Korea
[4]Center for Advanced Meta-Materials, 156 Gajeongbuk-Ro, Yuseong-Gu, Daejeon 34103, Korea
[5]Division of Quantum Phase and Devices, Department of Physics, Konkuk University, Seoul 05029, Korea
jwwu@ewha.ac.kr

Abstract— Transient optical rotatory power (ORP) of chiral metamaterial is measured to clarify the temporal development of ORP by exciting d-band electrons to the conduction p-band of Au using a circularly polarized light pump beam. Three distinct transient behaviors are identified, resulting from different energy relaxation processes of hot electrons that occur during a period of a few picoseconds after pumping. Theoretical analysis of the transient ORP is carried out by introducing a temperature-dependent dielectric function and finite-difference time-domain simulation.

Time-resolved pump-probe measurement is a well-known tool used to clarify microscopic electron dynamics responsible for a macroscopic temporal response in optical materials. For example, temporal evolutions of the spectral shift and broadening of the localized surface plasmon resonance (LSPR) of metallic nanostructures have been studied to relate the geometry of nanostructures with LSPR spectral changes in terms of hot electron energy relaxation processes in the confined geometry. [1, 2, 3]

When chirality is introduced to the geometry of a metallic nanostructure, it becomes circularly birefringent, giving rise to optical rotatory power (ORP) for linearly polarized light. Since chirality exists in an inversion-symmetry broken structure, it carries a sense of right-/left-handedness. Transient dynamics of handedness changes in natural chiral molecules have been studied via an ultrafast, time-resolved chirality measurement. [4]

In this work, we introduce a plasmonic chiral metamaterials (CMM) and investigate how ORP evolves in an ultrafast timescale via a time-resolved pump-probe measurement with circularly-polarized light (CPL) pump beam. Three different temporal regions are identified where distinct behaviors of transient ORP are observed. Nonthermal hot electrons follow the electric field of a pump beam almost instantaneously in region 1, while electron-electron and electron-boundary scatterings are dominant in region 2. In region 3, where an electron-lattice interaction couples two thermal baths of electrons and lattices, electron temperature is determined using a two-temperature model. The dielectric function of Au at an elevated temperature is obtained, with which an FDTD theoretical simulation is performed to find ORP at elevated temperatures.

The transient behavior of chirality can be characterized by measuring circular dichroism or optical rotatory dispersion, which are related by Kramers-Kronig. To compare with the static ORP spectrum, the temporal behavior of ORP is directly measured using a time-resolved pump-probe setup. The polarization-bridge configuration is employed to attain the maximum sensitivity of polarimetric measurement, with the linear polarization direction of the probe beam being horizontal.[5, 6] Parallel and perpendicular polarization-components of a linearly polarized probe beam are separated by a Wollaston prism, and transient ORP at a given wavelength is extracted from the intensities of two orthogonal polarization-components.

First, we study the transient behavior in the temporal region of $t \leq 2ps$. The differences in ORPs for opposite pump beam CPL helicities are negligible at both 640 nm and 720 nm wavelengths. However, the sign of $\delta\theta/\theta$ is negative at both 640 nm and 720 nm, regardless of pump beam CPL helicity. Second, in the temporal region of $0.9 < t < 2ps$, there is a non-vanishing negative value of the difference between differential ORPs $\Delta\theta/\theta$ at both 640 nm and 720 nm .

That is, at both 640 nm and 720 nm, RCP (σ) pumping results in a more weakened ORP than LCP ($\sigma+$) pumping, i.e., the transient ORP depends on pump beam CPL helicity. Third, in the temporal region of $0 < t < 0.9ps$, a large transient ORP occurs with opposite signs of the difference between differential ORPs $\Delta\theta/\theta$. At 640 nm, RCP ($\sigma-$) pumping results in a very large positive $\delta\theta$ and LCP ($\sigma+$) pumping results in a small negative $\delta\theta$. On the other hand, at 720 nm, RCP ($\sigma-$) pumping results in a small positive $\delta\theta$ and LCP ($\sigma+$) pumping results in a very large negative $\delta\theta$. At both 640 nm and 720 nm, RCP ($\sigma-$) pumping gives rise to a positive $\delta\theta$, with the magnitude being larger at 640 nm than at 720 nm, while LCP ($\sigma+$) pumping gives rise to a negative $\delta\theta$, with the magnitude being larger at 720 nm than at 640 nm.

The dynamics of hot electrons in plasmonic chiral metamaterials are studied to relate electron energy relaxation processes with transient optical rotatory power in the visible spectral range. Time-resolved pump-probe measurement in a polarization bridge configuration reveals that there are three distinct temporal regions showing different transient behaviors of optical rotatory power during a period of a few picoseconds after pumping using a circularly polarized light beam.

In the first and second temporal regions ($0 < t < 2ps$), nonthermal hot electrons experience the Lorentz force from an inverse Faraday effect and electron-boundary scattering, yielding a pump beam circularly polarized light helicity-dependent transient optical rotatory power. In the third temporal region ($t \geq 2ps$), hot electrons are in thermal equilibrium with the lattice due to electron-lattice coupling, where electron energy is distributed among occupied states, as described by Fermi-Dirac statistics. In $t \geq 2ps$, the transient optical rotatory power is found to be independent of pump beam circularly polarized light helicity. For thermal hot electrons, the temporal behavior and pump beam circularly polarized light helicity independence of optical rotatory power are well explained by a two-temperature model of the electron cooling process and the selection rule of electron excitations.

Theoretical analysis of the transient optical rotatory power in terms of the energy relaxation of thermal hot electrons is carried out by introducing a temperature-dependent dielectric function and finite difference time domain theoretical simulation of the optical rotatory dispersion. It is found that the magnitude of optical rotatory power at an elevated temperature is reduced to less than that at room temperature. Identification of three distinct temporal behaviors of hot electron energy relaxation processes elucidates how information regarding the handedness of a chiral nanostructure is carried to a transient optical rotatory power during a period of a few picoseconds after pumping. [7]

ACKNOWLEDGMENT

This work is supported by the Ministry of Science, ICT and Future Planning, Korea (2015001948, 2014M3A6B3063706). The authors are also grateful to Dr M. Vomir, Dr. M. Barthelemy and Dr J.-Y. Bigot at IPCMS, University of Strasbourg, France, for their contributions in helping the femtosecond pump-probe measurement in this study.

REFERENCES

1. J.-Y. Bigot, J.-Y. Merle, O. Cregut, and A. Daunois, "Electron dynamics in copper metallic nanoparticles probed with femtosecond optical pulses," Physical review letters **75**, 4702 (1995).
2. R. D. Averitt, S. L. Westcott, and N. J. Halas, "Ultrafast optical properties of gold nanoshells," JOSA B **16**, 1814–1823 (1999).
3. J.-Y. Bigot, V. Halté, J.-C. Merle, and A. Daunois, "Electron dynamics in metallic nanoparticles," Chemical Physics **251**, 181–203 (2000).
4. J. Meyer-Ilse, D. Akimov, and B. Dietzek, "Recent advances in ultrafast time-resolved chirality measurements: perspective and outlook," Laser & Photonics Reviews **7**, 495–505 (2013).
5. V. Zapasskii, "Highly sensitive polarimetric techniques (review)," Journal of Applied Spectroscopy **37**, 857–869 (1982).
6. C.-Y. Chang, L. Wang, J.-T. Shy, C.-E. Lin, and C. Chou, "Sensitive faraday rotation measurement with auto-balanced photodetection," Review of Scientific Instruments **82**, 063112 (2011).
7. J. H. Woo, B. Kang, M. Gwon, J. H. Lee, D.-W. Kim, W. Jo, D. H. Kim, and J. W. Wu, "Time-resolved pump-probe measurement of optical rotatory dispersion in chiral metamaterial," Advanced Optcal Materials (*In press*, 2017).

All-Dielectric metamolecules assembled using perovskite nanoparticles for low-loss magnetic resonances.

Y. Cho[1], K. Kim[1], and S. Lee[1, 2 *]

[1]SKKU Advanced Institute of Nanotechnology (SAINT), [2]Department of Nano Engineering, and School of Chemical Engineering, Sungkyunkwan University (SKKU), 440-746 Suwon, Republic of Korea

[*]corresponding author: seungwoo@skku.edu

Abstract- High-refractive-index dielectric nanoparticle (NP) has been extensively viewed as one of a prominent building block for optical metamaterial. Recent progresses have shown that a strong magnetic responses with a significantly low loss can be driven from silicon (Si) NP. However, currently available synthesis methods hinders its practical and universal application in devising all-dielectric nanoantenna and nanophotonic device. Here we report high-index-dielectric perovskite NPs by one-pot and mild method and their assembly as a practical way for efficient optical magnetism.

Split ring resonators (SRRs), landmark features of metamaterial, have been conventionally used for artificial magnetism at gigahertz [ref1], terahertz [ref2], and near infrared domains [ref3]. However, at visible range, such structural motifs doesn't hold promise anymore due to inherent losses in noble metal and technological limitations for fabrication [ref3]. Different approaches have undertaken to circumvent these limitations including assembly of metallic nanoparticles (NPs) into ring motifs [ref4]. However, these metallic NP assembly methods still suffers from intrinsic ohmic losses.

Seungwoo Lee 23/3/17 13:14
Supprimé: .

To harness low loss, yet strong magnetic response, high-refractive-index dielectric material has paved new road map for metamaterial [ref5]. According to theoretical prediction based on Mie theory, a single dielectric NP with high-refractive-index can exhibit low loss and strong magnetic responses at visible frequency [ref6]. Thus, growing consensus of using high-refractive-index NP, for example, silicon (Si), has been considered extensively as building block for low loss metamaterial. However, practical access to uniform Si NP poses great challenges, as harsh chemical conditions with extremely high pressure and temperature and multiple reaction steps are required. [ref5, 7].

In this work, we suggest another type of dielectric NP made of high-refractive index perovskite (refractive index: ~2.4), which can be accessible with relatively versatile hydrothermal synthesis method. [ref8]. Various shapes and sizes of perovskite NPs with high uniformity were successfully obtained in a reliable and simple way.

Subsequently, AFM nanomanipulation was used for a deterministic assembly of perovskite NP into the rationally designed cluster. As such, the peculiar resonance features resulting from an isolated or coupled magnetic mode were systematically studied including directional scattering and Fano resonance. This low-loss magnetic resonance available with perovskite NP enriches the material library for all-dielectric metamolecules and metamaterials, which could be widely used toward highly efficient nanoantennas and optical filters.

Seungwoo Lee 23/3/17 13:25
Supprimé: .

Acknowledgements, This work was supported by Samsung Research Funding Center of Samsung Electronics under Project Number SRFC-MA1402-09.

REFERENCES

1. Smith, D. R., W. J. Padilla, D. C. Vier, S. C. Nemat-Nasser and S. Schultz, "Composite Medium with Simultaneously Negative Permeability and Permittivity," *Phy. Rev. Lett.*, Vol. 84, 4184–4187, 2000.
2. Yen, T. J., W. J. Padilla, N. Fang, D.C. Vier, D. R. Smith, J. B. Pendry, D. N. Basov and X Zhang, "Terahertz Magnetic Response from Artificial Materials," *Science*, Vol. 303, 1494–1496, 2004.
3. Enkrich, C., M. Wegener, S. Linden, S. Burger, l. Zschiedrich, F. Schmidt, J. F. Zhou, Th. Koschny, and C. M. Soukoulis, "Magnetic Metamaterials at Telecommunication and visible Frequencies," *Phys. Rev. Lett.,*, Vol. 95, 293901, 2005.
4. Fan J. A., W. Chihihui, B. Kui, B. Jiming, B. Rizia, N. J. Halas, V. N. Manoharan, P. Nordlander, G. Shvets and F. Capasso, "Self-Assembled Plasmonic Nanoparticle Cluster," *Science*, Vol. 328, No. 5982, 1135–1138, 2010.
5. Arseniy I. Kuznetsov, A. E. Miroshnichenko, Y. H. Fu, J. Zhang and B. Luk'yanchuk, "Magnetic light," *Sci. Rep.*, Vol. 2, No. 492, 2012.
6. Bohren, C. F. and D. R. Huffman, *Absorption and scattering of light by Small particle*, Wiley-Interscience, New York, 1983.
7. Lei Shi, Justin T Harris, R. Fenollosa, L. Rodriguez, X. Lu, B. A. Korgel and F. Meseguer. "Monodisperse silicon nanocavities and photonic crystal with magnetic response in the optical region," *nature comm.*, Vol. 4, No. 1904, 2013
8. Wemple SH, M. Jr. Didomenico, I. Camlibel, "Dielectric and optical properties of melt-grown BaTiO3," *J. Phys. Chem. Solid*, Vol. 29 1797-1803, 1968

Charge transfer emission control by nonlocal dielectric constant near hyperbolic metamaterial structure

Kwang Jin Lee[1], Yeon Ui Lee[1], Frédéric Fages[2], Jean-Charles Ribierre[1], Jeong Weon Wu[1]*, & Anthony D'Aléo[1, 2]*

[1] Dept. of Physics, Quantum Metamaterial Research Center, Ewha Womans University, South Korea

[2] Aix Marseille University, CNRS, CINaM UMR 7325, France

*corresponding author: daleo@cinam.univ-mrs.fr

Abstract- Hyperbolic metamaterial (HMM) enables to manipulate nonlocal dielectric environment to control photo-induced energy and charge transfers. Here, we address how nonlocal effect of HMM modifies ICT emission spectral features in a way distinct from local effect. A 7nm blueshift is observed in intramolecular charge emission from DCM dye dispersed into a polymer matrix, accounted for by 7% reduction of nonlocal dielectric constant based on Lippert-Mataga formalism. Such a capability of spectral shift control opens new means of designing devices.

Tuning of the photophysical properties of dyes (*i.e* spectral shift, photoluminescence quantum yield (PLQY), decay rates) is essential to obtain efficient devices that could be readily commercialized. To this end, plasmonic nanostructures have been extensively used in order to control photophysical processes such as spontaneous emission and energy transfer owing to the importance of technological applications such as optical sensing, imaging, solar cells, and light-emitting devices.[1] Among the plasmonic nanostructures, hyperbolic metamaterials (HMMs) displaying hyperbolic dispersion have been studied intensively for emission rate control making use of high photonic density of states over a broad spectral range, characteristic of hyperbolic dispersion.[2-8] However, little is known on the nonlocal effect of HMM structure on photoluminescence of organic dyes. In this context, we inspected this effect on photoluminescence arising from π-π* transition and intramolecular charge transfer transition (ICT *i.e.* in push-pull type of systems) by using perylene bisimide and 4-dicyanomethylene-2-methyl-6-(*p*-dimethylaminostyryl)-4*H*-pyran (DCM) laser dye, respectively, blended in polymethyl methacrylate films. To this end, HMM structure consisting of 10 nm thick Ag and Al_2O_3 alternative thin films deposited on fused silica were used with the number of bilayer varying from 1 to 4 and compared the photophysical properties to the one obtained on fused silica. We demonstrate that various thin films containing ICT dyes could result in emission blueshifted by using HMM structure. In addition to the spectral shift, we examined the fluorescence radiative decay rate and non-radiative decay rate as well as photoluminescence quantum yield (PLQY) and found significant changes in these properties based on the effect of HMM structure. In particular, we focus on the effects of local and nonlocal dielectric constants on the emission characteristics of dyes dispersed into polymeric thin films. As such, we used Lippert-Mataga (L-M) formalism to elucidate the difference and similarities between local and nonlocal dielectric constant in evidencing the appearance of spectral changes of the ICT emission. Within those dyes, the decrease of PLQY and of fluorescence lifetimes originate mainly from the hyperbolic dispersion effect as observed with other dyes on HMM structures. However, a noticeable spectral blueshift of ICT emission in the presence of HMM substrate was evidenced, which

indicates that HMM structure can nonlocally affect the ICT energy level which cannot be related to hyperbolic dispersion. This shift continuously increases as the number of metal-dielectric pair increases. We demonstrated that this phenomenon has the same analogue as negative solvatochromic (hypsochromic) shift based on L-M formalism. Around up to 7.2 % decrease in non-local dielectric constant was demonstrated by comparing DCM monomer with liquid solution. From this study, not only the experimental observation of CT energy level variation but also the same experimental realization of solvatochromic shift is evidenced. We believe that whole description of nonlocal effect from HMM structure is addressed in terms of both temporal and spectral properties of CT. As such, we established that fundamental underlying mechanism of nonlocal effect is the quasi electrostatic Coulomb interaction yielding a nonlocal dielectric constant affecting the film properties.

Acknowledgements, This work is supported from the Ministry of Science, ICT and Future Planning, Korea (2015001948, 2014M3A6B3063706).

REFERENCES

1. Noginov, M. A., *et al.* "Controlling spontaneous emission with metamaterials." Opt. Lett. 35, 1863-1865 (2010).
2. Iorsh, Ivan, *et al.* "Spontaneous emission enhancement in metal–dielectric metamaterials." Phys. Lett. A 376, 185-187 (2012).
3. Gu, L. *et al.* "Blue shift of Spontaneous Emission in hyperbolic metamaterial. " Sci. Rep. 4, 4969 (2014).
4. Kim, J., *et al.* "Improving the radiative decay rate for dye molecules with hyperbolic metamaterials." Opt. Express 20, 8100-8116 (2012).
5. Tumkur, T., *et al.* "Control of spontaneous emission in a volume of functionalized hyperbolic metamaterial." Appl. Phys. Lett. 99, 151115 (2011).
6. Lu, Dylan, *et al.* "Enhancing spontaneous emission rates of molecules using nanopatterned multilayer hyperbolic metamaterials." Nat. Nanotech.9, 48-53 (2014).
7. Jacob, Zubin, *et al.* "Broadband Purcell effect: Radiative decay engineering with metamaterials." Appl. Phys. Lett. 100, 181105 (2012).
8. Sreekanth, Kandammathe Valiyaveedu, et al. "Large spontaneous emission rate enhancement in grating coupled hyperbolic metamaterials." Sci. Rep. 4, 6340 (2014)

Metasurfaces for chiral sensing

SeokJae Yoo and Q-Han Park*
Department of Physics, Korea University, Seoul, Korea
**E-mail:qpark@korea.ac.kr*

Metasurfaces as ultrathin flat metamaterials induce substantial phase changes in the propagating light thereby enabling a new field of planar photonics. However, the ability of metasurfaces to create non-trivial strongly localized near fields has not received much attention. Here, we address applications of metasurfaces to the sensing chiral molecules by utilizing highly inhomogeneous near fields created by metasurfaces. We establish underlying physical theories for chiral molecule sensing and explain the role of metasurfaces in enhancing sensing signals.

The circular dichroism (CD) spectroscopy is the optical technique to measure signals of chiral molecules, containing their stereochemical information. Recently, it has been demonstrated that CD signals of chiral molecules can be enhanced by plasmonic nanostructures and metamaterials [1-4]. Few theoretical models have been suggested to describe the surface-enhanced CD signals of chiral molecules adsorbed on the surfaces of nanostructures and metamaterials: the chiral field generation (Figure 1) [1, 2] and (2) the circular differential scattering (Figure 2) [3]. In particular, CD signals of chiral molecules is shown to be proportional to the optical helicity of the local electromagnetic fields[1]. Therefore, the strong optical helicity generated by nanostructures and metamaterials can be used to enhance molecular CD signals [1, 2]. Equally important, but so far ignored, factor to the enhancement is the asymmetric scattering of left- and right-circularly polarized lights by nanostructures and metamaterials in the presence of chiral molecules [3].

Here, we provide a complete description on the metasurface-enhanced CD signals of chiral molecules [5]. We provide a simple theoretical account for the two major mechanisms of the surface-enhanced CD signals. We show that the circular differential scattering of nanostructures and metamaterials plays a crucial role in the surface-enhanced CD signals, rather than the chiral field generation. We exlain how our results can provide a design principle for the surface-enhanced CD spectroscopy using nanostructures and metamaterials.

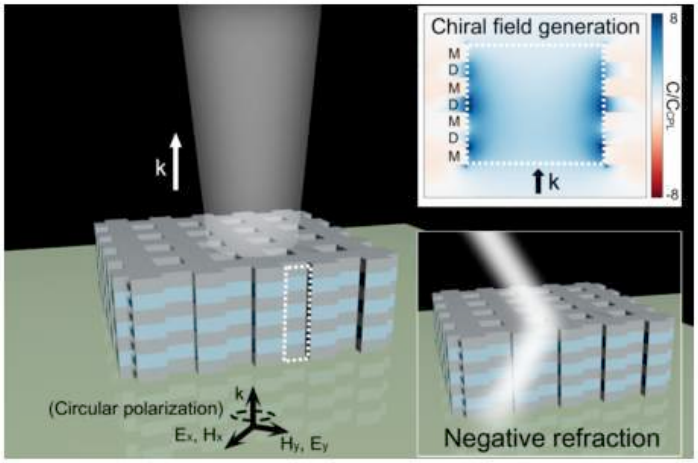

Figure 1. The chiral field generation in the negative-index metamaterials.[4]

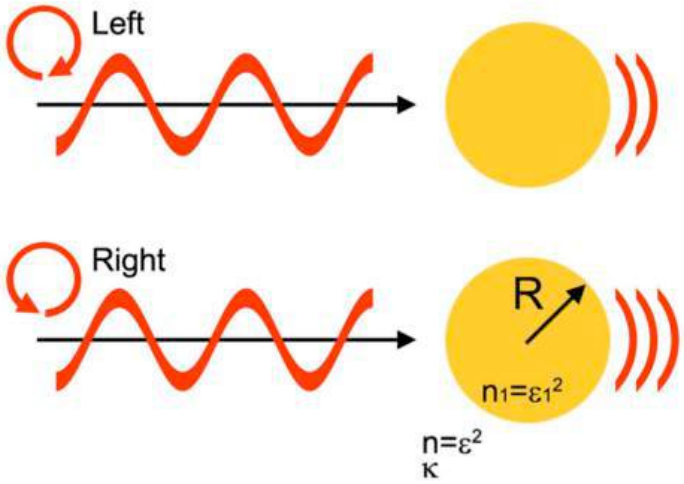

Figure 2. The circular differential scattering in nanospheres embedded in the chiral medium [4].

References

1. Y. Tang, and A. E. Cohen, Phys. Rev. Lett. 104, 16, 163901 (2010).
2. S.J. Yoo, and Q.H. Park, Phys. Rev. Lett. 114, 20, 203003 (2015).
3. S.J. Yoo, and Q.H. Park, Sci. Rep. 5, 14463 (2015).
4. S.J. Yoo, M.H. Cho, and Q.H. Park, Phys. Rev. B. 89, 16, 161405(R) (2014).
5. S. Lee, S.J. Yoo, and Q.H. Park, to appear.

Emergent and Nonlinear Properties of Macroscopic Quantum Superconducting Metamaterials

Melissa Trepanier,[1] Daimeng Zhang,[1,2] Edward Ott,[2] Thomas Antonsen,[2] Steven M. Anlage[1,2]*

[1]Center for Nanophysics and Advanced Materials, Physics Department, University of Maryland, College Park, Maryland 20742-4111 USA

[2]Department of Electrical and Computer Engineering, University of Maryland, College Park, Maryland 20742-3285 USA

[*]corresponding author: anlage@umd.edu

Abstract- Through experiments, numerical simulations, and theory we explore the behavior of 2D rf SQUID (radiofrequency superconducting quantum interference device) metamaterials, which show extreme tunability and nonlinearity [1 - 2]. The emergent properties are sensitive to the degree of coherent response of the driven metamaterial. Coherence suffers in the presence of disorder, which is experimentally found to be mainly due to a dc flux gradient. We investigate methods to recover the coherence, specifically by varying the coupling between the SQUID meta-atoms and reducing the SQUID tunability [3]. We also investigate the SQUID metamaterial as a nonlinear medium through detailed two-tone intermodulation (IM) measurement over a broad range of tone frequencies and tone powers [4]. The response of nonlinear metamaterials and superconducting electronics to two-tone excitation is critical for understanding their use as low-noise amplifiers and tunable filters, for example. A sharp onset followed by a surprising strongly suppressed IM region near the resonance is observed. Using a two time scale analysis technique, we present an analytical theory that successfully explains our experimental observations. The theory predicts that the IM can be manipulated with tone power, center frequency, frequency difference between the two tones, and temperature. This quantitative understanding potentially allows for the design of rf-SQUID metamaterials with either very low or very high IM response.

Acknowledgements This work is supported by the NSF-GOALI Program through Grant No. ECCS-1158644 and CNAM.

REFERENCES

1 M. Trepanier, Daimeng Zhang, Steven M. Anlage, Oleg Mukhanov, "Realization and Modeling of Metamaterials Made of rf Superconducting Quantum-Interference Devices," Phys. Rev. X **3**, 041029 (2013).

2 Daimeng Zhang, Melissa Trepanier, Oleg Mukhanov, and Steven M. Anlage, "Tunable Broadband Transparency of Macroscopic Quantum Superconducting Metamaterials," Phys Rev. X **5**, 041045 (2015).

3 Melissa Trepanier, Daimeng Zhang, Oleg Mukhanov, V. P. Koshelets, Philipp Jung, Susanne Butz, Edward Ott, Thomas M. Antonsen, Alexey V. Ustinov, Steven M. Anlage, "Coherent Oscillations of Driven rf SQUID Metamaterials," Phys. Rev. E **95**, 050201(R) (2017).

4 Daimeng Zhang, Melissa Trepanier, Thomas Antonsen, Edward Ott, Steven M. Anlage, "Intermodulation in Nonlinear SQUID Metamaterials: Experiment and Theory," Phys. Rev. B **94**, 174507 (2016).

New Avenue in dielectric cavities; Transformation optics perspective

Muhan Choi[1*], Yushin Kim[2], Jung-Wan Ryu[3], Inbo Kim[1], and Bumki Min[2]

[1]School of Electronics Engineering, Kyungpook National University Daegu, 41566, South Korea

[2]Department of Mechanical Engineering, Korea Advanced Institute of Science and Technology, Daejeon, 34141, South Korea.

[3]Center for Theoretical Physics of Complex Systems, Institute for Basic Science, Daejeon 34051, South Korea

[*]corresponding author: mhchoi@ee.knu.ac.kr

Abstract-We have proposed a new methodology based on transformation optics to manipulate mode properties of dielectric cavity such as directionality, chirality of resonance modes while maintaining High-Q values. The novel mode properties can be realized in inhomogeneous dielectric cavities which can be defined by imposing spatially-varying refractive index derived from the transformation optics theory.

Optical whispering gallery modes (WGMs) in a dielectric disk cavity exhibit a very long lifetime (ultrahigh Q-factor), and this extreme feature is a crucial requirement for cutting-edge photonic devices, such as ultralow threshold micro-lasers, nonlinear optical oscillators, and highly sensitive sensors[1]. Despite this outstanding merit, the WGMs have been considered inefficient in certain practical optoelectronic applications due to their rotationally uniform (isotropic) radiation. Hence, considerable efforts have been devoted over the last 15 years to achieving directional emission without Q-spoiling. However, in all methods that have been proposed to date, the introduction of directionality inevitably causes substantial Q-spoiling due to the destruction of WGMs. Here, we showed that the optical mode properties of dielectric cavities, such as quality factor and emission directionality, can be tailored at will by using transformation optics[2-3]. In this work, we present a novel scheme to manipulate mode properties of dielectric cavity such as directionality, chirality of resonance modes, without Q-spoiling. The key idea is to restore Whispering Gallery mode in a deformed dielectric cavity by utilizing the angle-preserving feature of conformal mapping from the transformation optics. The spatially varying refractive index profile can be implemented by drilling subwavelength-scale air holes in a dielectric slab. The proposed design scheme of microcavities based on the transformation optics will open a new horizon of application beyond the conventional microcavity application

REFERENCES

1. Vahala, K. J. “Optical microcavities,” *Nature*, Vol. 424, 839-846, 2003
2. Pendry, J. B., Schuring,D., and Smith, D. R. “Controlling Electromagnetic Fields,” *Science* , Vol. 312, 1780-1782, 2006.
3. Leonhardt, U., “Optical conformal mapping,” *Science*, Vol. 312, Vol. 1777-1780, 2006.

Experimental Investigation of Transparent Conducting Oxide N-CNT doped ZnO

Maryama Hammi1[1], Naseem Abbas2[2]*, Younes Ziat3[3], Amine SLASSI4[3], and Anas Benyounes5[1]

[1]Department of Chemistry, Faculty of Science, University of Mohammed V, BP1014 Rabat, Morocco
[2]Department of Mechanical Engineering, University of Central Punjab - Lahore, Pakistan
[3]LMPHE (URAC 12), Faculte´ des Sciences, Universite´ Mohammed V-Rabat, Morocco
*corresponding author, E-mail: naseem.abbas@ucp.edu.pk

Abstract

CNT/ZnO and N-CNT/ZnO thin films were prepared using sol gel method, to extract their usefulness in photovoltaic applications. The optical and electrical properties have been investigated in this research. The electrical conductivity has found to be more imperative for ZnO films filled with N-CNTs. This finding is pretty explained by the electronic conduction hold by nitrogen as charge carriers within carbon nanotubes which provide higher performance to the active layer.

1. Introduction

Transparent conductive oxides (TCOs) are required as a front side electrode for efficient thin film solar cells, since a metallic grid as used in crystalline silicon solar cells cannot be used. Numerous metal oxides with different doping materials can be used as a TCO. In general, a compromise between conductivity and transparency of the TCO must be made. Transparent conducting oxides (TCOs) are employed as transparent electrodes in electrochromic windows, flat-panel displays (FPDs), solar cells and light-emitting diodes (LEDs) [1–4]. Many researchers reviewed on many Photovoltaic applications recently [5], where TCOs are working as front electrode in solar cells. Although there are imperative secondary requirements for such transparent electrodes such as chemical stability, interfacial properties, etc.), the primary requirements are good visible transparency (in thin film form) and high electronic conductivity. In addition, band alignment matching with the active absorber components is important. For organic conductors, the band alignment at the TCO interface is expected to depend directly on TCO work function [6, 7]. For inorganic thin film solar cells, knowledge of the TCO surface potentials such as Fermi level and ionization potential) provides important standards for interpreting band alignment at TCO/inorganic interfaces. Typical TCOs employed in several types of solar cells, adapted from Fortunato et al. [5], including CdTe solar cells, which commonly employ F-doped SnO2 front electrodes [8,9]. Although these same oxides have been employed for organic photovoltaics (OPVs), Fortunato et al. highlight the need for TCOs with higher work functions than are currently available [5].

The aim of this work is to prepare ZnO; CNT/ZnO and N-CNT/ZnO systems using sol-gel method. Several analyses of prepared samples have been performed by optical and electrical characterization techniques. It is found that, the calculated fundamental band gap of ZnO is close to the experimental one and in a good agreement with other theoretical calculations.

2. Experimental Methodology

Sol-gel method was used to make the N-CNT/ZnO thin films. Initial material Zinc acetate dihydrate $Zn(CH_3COO)_2$. $2H_2O$ was selected to proceed the experiment. Two-methoxy ethanol was used as solvent and monoethanolamide (MEA) was used as a stabilizer. Zinc acetate dihydrate and N-CNT were first dissolved in a mixture of solvent (MEA) and stabilizer (two-methoxy ethanol) at room temperature. The zinc acetate concentration was about 0.35 M while the molar ratio of MEA to zinc acetate $Zn(CH_3COO)_2$ was 1.0. To get a clear and homogeneous solution, this mixture was stirred at 60 °C temperature for time of 2 h. After cooling the mixture at room temperature, it was served as the coating solution. After the 24 hour preparation of mixture, coating was made. The solution was poured onto glass substrates, with the rotation cycles of 1000 rpm for time of only 30 s. Once the spin coating has been done, the gained films were dried at a temperature of 400°C for the time of 20 min on a hot plate. The purpose of this experimental process was to evaporate the solvent and remove organic residuals. This whole procedure was repeated twelve times so that the thickness of the sintered films should approach 800 nm.

3. Results and Discussion

The XRD characterization was carried out using a diffractometer of Bruker D8 Type where X-radiation from the Kα emission of copper, with wavelength λ = 1.5406 Å, X-ray diffraction provides information on the crystallographic growth directions of the ZnO layers. The

comparison with the data of the ASTM files indicated that the obtained layer of undoped ZnO is of wurtzite structure.

The measured optical transmittance revealed that the ZnO films are more transparent in the visible region (600nm) 87%. It can also be observed that the MWCNT addition has a profound effect on the film's optical transparency; with decrease in transparency down to 65% and great decrease in N-CNTs/ZnO samples Fig. 1. (a). The reduction in optical transmittance is due to the fact that the CNTs are not transparent and absorb the incoming light and increase the light scattering. The optical bandgap of the ZnO/CNTs and ZnO/N-CNTs thin films was determined by assuming that ZnO is a direct band-gap semiconductor.

From the transmission spectra we deduced the optical gap of the ZnO films using the relationship that links the coefficient of absorption α to the photon energy hv:

$$(\alpha .h\nu)^2 = B\,(h\nu - Eg) \qquad (1)$$

From the plotted graph of $(\alpha h\nu)^2$ versus the incident photon energy (hν), where α is denoted as the absorption coefficient, one can estimate the optical band gap by extrapolation of the straight line region into the x-axis $(\alpha h\nu)^2$. For MWCNT/ ZnO composite, the bandgap of around 2eV was obtained from the film doped with 0.5wt% of CNTs, whereas for N-CNT/ZnO thin film at the same doping rate, the extracted bandgap is around 1.5eV.The obtained band gap deviates from the pure ZnO due to the addition of MWCNTs which influences the overall carrier concentration and reduces the bandgap. The bandgap narrowing effect has been clearly observed in ZnO films doped with N-MWCNT. In fact, bandgap reduction is beneficial towards the photovoltaic efficiency of wide band semiconductors such as ZnO as it is more effective in utilizing the visible light.

The effect of number of CNTs and N-CNTS concentration as a function of conductivity has also been investigated in this research, which express high increase with the increase of concentration, however it's noteworthy that most significant increase happens when N-CNTs are inserted according to previous study this phenomenon is explained by the conduction mechanism of nitrogen as dopant element 15.

Several approaches have been suggested to understand the relationship about the optical properties and the electrical properties. One of these approaches can be utilized to guide the study of our materials it is written as follow16.

$$\sigma = ne\mu \qquad (2)$$

Where the σ is the conductivity of the materials, n is the number of charge carriers, e is the quantity of the charge, μ is the mobility. All of the mentioned parameters are supposed to be explaining the charge transport within the conductive materials, and obviously the conductivity is related to the number of the charge carrier and the mobility of materials which is conventionally translating the movement of electrons within the conductive solid materials 10, also it has been proved that the mobility is proportional to the magnitude of the band gap17.

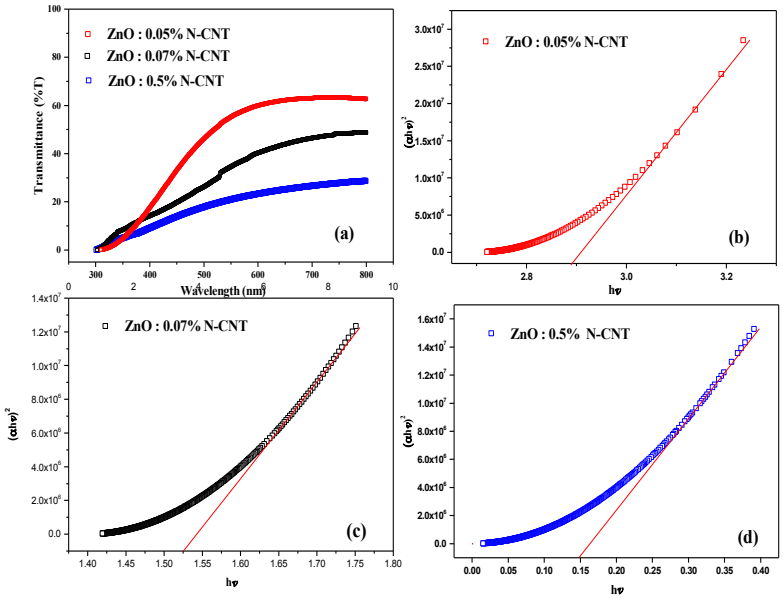

Figure.1. (a): Optical transmittance of the N-CNT/ ZnO samples and (b), (c), (d): $(\alpha h\nu)^2$ versus energy plot for Tauc gap extraction

4. Conclusion

In this work, we have successfully prepared via sol-gel method N-CNT/ZnO which is regarded as a semi-transparent p-type TCO with 80 % visible transmission. The undoped ZnO films were confirmed to be amorphous by X-ray diffraction experiment. We succeeded to see the effect of growing the dopant concentration of our material. For doped ZnO cases, the average transmittances in the visible region are decreased owing to the induced N-CNT and CNT as absorption elements. Fundamental structural, optical and electronic properties of prepared thin-films were significantly studied. Observed results exhibit an enhanced opto-electronic property than undoped and merit further exploration for advanced-device development.

References

[1] H.L. Hartnagel, A.L. Dawar, A.K. Jain, C. Jagadish, Semiconducting Transparent Thin Films, *Institute of Physics Publishing*, Bristol, UK, 1995.

[2] D.S. Ginley, C. Bright, Transparent Conducting Oxides, *MRS Bulletin* 25: 15–18, 2000.

[3] C.G. Granqvist, Transparent conductors as solar energy materials: A panoramic review, *Sol. Energy Mat. Sol. Cells* 91: 1529–1598, 2007.

[4] K. Ellmer, A. Klein, B. Rech, *Transparent Conductive Zinc Oxide: Basics and Applications in Thin Film Solar Cells*, Springer-Verlag publisher, Berlin, Germany, 2008.

[5] E. Fortunato, D. Ginley, H. Hosono, D.C. Paine, Transparent conducting oxides for photovoltaics, *MRS Bulletin* 32: 242–247, 2007.

[6] H. Ishii, K. Sugiyama, E. Ito, K. Seki, Energy Level Alignment and Interfacial Electronic Structures at Organic/Metal and Organic/Organic Interfaces, *Adv. Mater* 11: 605–625. 1999.

[7] W.R. Salaneck, M. Luglund, M. Fahlmann, G. Greczynski, T. Kugler, The electronic structure of polymer-metal interfaces studied by ultraviolet photoelectron spectroscopy, *Mater. Sci. Eng*. 34: 121–146, 2001.

[8] D.H. Rose, F.S. Hasoon, R.G. Dhere, D.S. Albin, R.M. Ribelin, X.S. Li, Y. Mahathongdy, T.A. Gessert, P. Sheldon, Fabrication procedures and process sensitivities for CdS/CdTe solar cells, *Prog. Photovolt. Res. Appl.* 7: 331–340, 1999.

[9] C.S. Ferekides, R. Mamazza, U. Balasubramanian, D.L. Morel, Transparent conductors and buffer layers for CdTe solar cells. *Thin Solid Films*, 480–481, 224–229, 2005.

Applications of nanophotonics and metamaterials in bio-imaging

Image delivery from far-field waves to the surface plasmon polaritons using disordered array of nanoholes

W. Choi[1,2], Y. Jo[1,2], J. Ahn[1,2,3], E. Seo[1,2], Q-H. Park[2], Y. M. Jhon[3], and W. Choi[1,2]

[1]Center for Molecular Spectroscopy and Dynamics, Institute for Basic Science, Seoul 02841, Korea

[2]Department of Physics, Korea University, Seoul 02841, Korea

[3]Sensor System Research Center, Korea Institute of Science and Technology, Seoul 02792, Korea

[*]corresponding author: wonshik@korea.ac.kr

Abstract- Merging multiple microprocessors with high-speed optical networks has been considered a promising strategy for the improvement of overall computation power. However, the loss of the optical communication bandwidth is inevitable when interfacing between optical and electronic components. Here we present an on-chip plasmonic switching device consisting of a two-dimensional (2D) disordered array of nanoholes on a thin metal film that can provide multiple-input and multiple-output channels for transferring information from a photonic to an electronic platform. In this device, the surface plasmon polaritons (SPPs) generated at individual nanoholes become uncorrelated on their way to the detection channel due to random multiple scattering. We exploit this decorrelation effect to use individual nanoholes as independent antennas, and demonstrated that more than 40 far-field incident channels can be delivered simultaneously to the SPP channels, an order of magnitude improvement over conventional 2D patterned devices. With the increased channel capacity, we demonstrated the delivery of far-field optical image to the output channels of SPPs.

Acknowledgements: This research was supported by IBS-R023-D1 and the Global Frontier Project (2014M3A6B3063710) through the National Research Foundation of Korea (NRF) funded by the Ministry of Science, ICT and Future Planning. It was also supported by the Korea Health Technology R&D Project (HI14C0748) funded by the Ministry of Health and Welfare, Republic of Korea.

REFERENCES

1. Choi, W., Jo Y. et al., "Control of randomly scattered surface plasmon polaritons for multiple-input and multiple-output plasmonic switching devices," *Nature Comm.*, 8:14636, 2017.

Wavefront engineering for high resolution in-vivo deep tissue imaging

J. H. Park[1]
[1]Department of Biomedical Engineering, UNIST, Republic of Korea
[*]corresponding author: jh.park@unist.ac.kr

Abstract- Multiple scattering of light is a general phenomenon that occurs in all types of tissue. In this work, we describe methods to control the wavefront of the incident beam to enable subcellular resolution imaging deep inside living animals.

Optical imaging holds unique advantages for bio imaging with its molecular specificity, non-invasiveness, and high spatiotemporal resolution. However, due to multiple scattering induced by the inhomogeneous distribution of cells constituting tissues, high resolution imaging is typically confined to superficial layers or require sectioning of samples. To understand life, we must image it dynamically while in its true state of function. In this regard, controlling the incident light for high resolution deep tissue imaging, without harming the subject of interest, holds many opportunities for bio imaging. Here, we will describe our recent developments that enable high resolution imaging through the skull as well as large area functional imaging of the deep brain.

Aberration Correction of an Optical System for High-resolution Synthetic Aperture Imaging

Changsoon Choi, Kyung-Deok Song, Sungsam Kang, and Wonshik Choi*
Center for Molecular Spectroscopy and Dynamics, Institute for Basic Science, Seoul 02841, Republic of Korea
Department of Physics, Korea University, Seoul 02841, Republic of Korea
*corresponding author: wonshik@korea.ac.kr

Abstract- Short working distance of objective lenses often limits high-resolution imaging of targets located deep within a tissue. Condenser lens supporting high numerical aperture and long working distance can be a good alternative, but strong aberrations induced by the lens causes strong image distortion. Here we propose a method that can eliminate aberrations of condenser lens up to the numerical aperture of 1.2, and demonstrate high-resolution synthetic aperture imaging of biological cells and *c. elegans*.

High numerical aperture (NA) objectives are one of the most essential elements for high-resolution optical imaging. However, their relatively short working distance, which typically ranges up to a few hundred microns for oil-immersion type objectives, has been a major limiting factor for deep-tissue and high-resolution imaging.

As a solution for this problem, we used a pair of oil-immersion type microscope condenser lenses (1.4 NA, Nikon MBL78700) for both illumination and detection, and set up a holographic phase microscope in transmission geometry. Since their working distance is an order of magnitude longer than that of objective lenses, our optical system can deliver images of relatively thick targets up to high NA. However, the condenser lenses are not manufactured for imaging, but for introducing incoherent illumination to the samples. Therefore, they tend to have strong aberrations that distort images and degrade spatial resolution.

We acquire three sets of holographic phase images with a few thousand different illumination directions. The number of required images depends on field of view and NA. Each set consists of images of illumination, the specimen, and a test target positioned at different image planes, respectively. From these data, input and output aberration maps are identified by maximizing intensity of the synthetic aperture image. By applying the identified aberration maps of the imaging system to the acquired images of biological specimens, we could recover diffraction-limit resolution up to 1.2 NA. We demonstrated high-resolution imaging for the working distance of a few millimeters, an order of magnitude improvement over conventional microscopes.

ACKNOWLEDGEMENT

This research was supported by IBS-R023-D1, and the Global Frontier Program (2014M3A6B3063710) through the National Research Foundation of Korea (NRF) funded by the Ministry of Science, ICT & Future Planning. It was also supported by the Korea Health Technology R&D Project (HI14C0748) funded by the Ministry of Health & Welfare, Republic of Korea.

REFERENCES

1. Choi, W., Fang-Yen, C., Badizadegan, K., Oh, S., Lue, N., Dasari, R. R., and Feld, M. S. “Tomographic

phase microscopy", *Nat. Methods,* Vol. 4, No. 9, 717-719, 2007.
2. Choi, Y., Kim, M., Yoon, C., Yang., T. D., Lee, K. J., and Choi, W. "Synthetic aperture microscopy for high resolution imaging through a turbid medium", *Opt. Lett.* Vol. 36, No. 21, 4263-4265, 2011.

Imaging Photonic Structures at Micro and Nano Scales

Ki-Hun Jeong

Department of Bio and Brain Engineering, Korea Advanced Institute of Science and Engineering (KAIST), Republic of Korea

*corresponding author: kjeong@kaist.ac.kr

Abstract- Micro and nanophotonic structures allow miniaturization of diverse and broadband imaging systems. Spherically arranged microlenses mimic insect's eyes and provides wide FOV imaging, fast motion detection, and enhanced image resolution. Binocular microprisms also enable an ultrathin stereoscopic camera in the visible range. Furthermore, optically patternable metamaterial simply defines polymer patterns below the diffraction limit and also subwavelength silicon hole arrays can serve as a planar silicon lens. In this work, we overview diverse photonic structures for broadband compact imaging systems.

Small scale photonic structures allow miniaturization of diverse and broadband imaging systems such as ultraviolet nanolithography, wide field-of-view (FOV) and stereoscopic visible imaging, and even THz spectroscopic imaging. Spherically arranged microlens arrays mimic insect's eyes and the biologically inspired ultrathin camera with multi-apertures provides wide FOV imaging, fast motion detection, and enhanced image resolution [1-5]. Some examples inspired from ultrastructures of a firefly lantern enhance light extraction from LED or OLED for lighting applications [6-8]. Binocular microprism arrays also enable an ultrathin stereoscopic camera that can be utilized for mobile or endoscopic imaging applications in the visible range [9]. Plasmonic nanoantennas also enhance laser induced acoustic signals for highly sensitive photoacoustic imaging [10]. In addition, optically patternable metamaterial with negative effective permittivity simply defines nanoscale polymer patterns below the diffraction limit using a conventional photolithographic equipment. Subwavelength silicon hole arrays can also control effective index of silicon and serve as a planar silicon lens with a diffraction limit [11-17].

Acknowledgements, This work was supported by a grant of the Korean Health Technology R&D Project, Ministry of Health & Welfare, Republic of Korea (HI13C2181, HI16C1111), the Global Frontier Project (2016924609) of the Korea government, and the Ministry of Science ICT & Future Planning (2016013061).

REFERENCES

1. K. H. Jeong, J. J. Kim, and L. P. Lee, "Biologically inspired artificial compound eyes," Science, vol. 312, pp. 557-561, Apr 28 2006.
2. H. Jung and K. H. Jeong, "Monolithic Polymer Microlens Arrays with Antireflective Nanostructures", Applied Physics Letters, vol. 101, 2012.
3. Y.-J. Oh, J.-J. Kim, and K.-H. Jeong, "Biologically Inspired Biophotonic Surfaces with Self-Antireflection", Small, vol. 10, pp. 2558–2563, 2014.
4. H. Jung and K.-H. Jeong, "Monolithic polymer microlens arrays with high numerical aperture and high packing density", ACS Applied Materials & Interfaces, vol. 7, pp. 2160-2165, 2015

5. K. H. Jeong, G. L. Liu, N. Chronis, and L. P. Lee, "Tunable microdoublet lens array," Optics Express, vol. 12, pp. 2494-2500, 2004.
6. J. J. Kim, Y. Lee, H. G. Kim, K. J. Choi, H. S.Kweon, S. Park, and K. H. Jeong, "Biologically Inspired LED Lens from Cuticular Nanostructures of Firefly Lantern", Proceedings of the National Academy of Sciences, vol. 10946, pp. -, Nov. 13 2012.
7. J.-J. Kim, S.-P. Yang, D. Keum, and K.-H. Jeong, "Asymmetric optical microstructures driven by geometry guided resist reflow", Optics Express, vol. 22, pp. 22089-22094, 2014.
8. J. -J. Kim, J. -H. Lee, S. -P. Yang, H. -G. Kim, H. -S. Kweon, S. -H. Yoo, and K. -H. Jeong, "Biologically Inspired Organic Light-Emitting Diodes", Nano Letters, vol. 16 (5), pp 2994–3000, March 2016
9. S. -P. Yang, J. -J. Kim, K. -W. Jang, W. -K. Song, and K.-H. Jeong, "Compact Stereo Endoscopic Camera using Microprism Arrays", Optics Letters, vol. 9, issue 6, pp. 1285 - 1288, March 2016
10. S.-G. Park, S.-B. Yang, M.-S. An, Y.-J. Oh, Y.T. Kim and K.H. Jeong, "Plasmon Enhanced Photoacoustic Generation from Volumetric Electromagnetic Hotspots", Nanoscale vol.8,,757-761, January 2016
11. S. G. Park+, Y. Choi+, Y.-J. Oh, and K. H. Jeong," Terahertz Photoconductive Antenna with Metal Nanoislands", Optics Express, vol. 20, pp. 25530-25535, 2012. +equally contributed to this work.
12. S.G. Park, K.H. Jin, M. Yi, J.C. Ye, J. Ahn, and K.H. Jeong, "Enhancement of Terahertz Pulse Emission by Optical Nanoantenna", ACS Nano, Vol. 6, 2026–2031, 2012
13. S.-G. Park, K. Lee, D. Han, J. Ahn, and K.-H. Jeong, "Subwavelength silicon through-hole arrays as an all-dielectric broadband terahertz gradient index metamaterial", Applied Physics Letters, vol. 105, pp.091101, 2014.
14. H. C. Park*, J. H. Lee*, S. G. Park, D. S. Yee, and K. H. Jeong, “Millimeter scale electrostatic mirror with sub-wavelength holes for terahertz wave scanning”, Applied Physics Letters, vol. 102, pp. -, 2013. +equally contributed to this work.
15. S.-G. Park, K. Lee, D. Han, J. Ahn, and K.-H. Jeong, "Subwavelength silicon through-hole arrays as an all-dielectric broadband terahertz gradient index metamaterial", Applied Physics Letters, vol. 105, pp.091101, 2014.
16. S. G. Park+, Y. Choi+, Y.-J. Oh, and K. H. Jeong," Terahertz Photoconductive Antenna with Metal Nanoislands", Optics Express, vol. 20, pp. 25530-25535, 2012. +equally contributed to this work.
17. S.G. Park, K.H. Jin, M. Yi, J.C. Ye, J. Ahn, and K.H. Jeong, "Enhancement of Terahertz Pulse Emission by Optical Nanoantenna", ACS Nano, vol. 6 , pp 2026–2031, Feb. 17 2012

High-resolution reflectance endomicroscopy free from back-reflection noise occurring at ultrathin imaging probes

C. Yoon[1,2], M. Kang[1,2], Y. Choi[3,*], and W. Choi[1,2,*]

[1]Center for Molecular Spectroscopy and Dynamics, Institute for Basic Science, Seoul 02841, Korea

[2]Department of Physics, Korea University, Seoul 02841, Korea

[3]Department of Biomedical Engineering, Korea University, Seoul 02841, Korea

[*]corresponding author: youngwoon@korea.ac.kr, wonshik@korea.ac.kr

Abstract-We present a high-resolution endoscopic microscope free from back-reflection noise generated at an ultrathin image bundle fiber. To eliminate the back-reflection noise, we illuminate a sample through single individual core fibers in the bundle and detect the reflected signal from the sample by the other core fibers. The transmission matrix method is used for the pixelation-free sample image reconstruction. We confirm that our method enhances the signal to noise ratio of imaging 3.2 times better than conventional illumination-detection scheme.

Acknowledgements: This research was supported by IBS-R023-D1 and the Global Frontier Project (2014M3A6B3063710) through the National Research Foundation of Korea (NRF) funded by the Ministry of Science, ICT and Future Planning. It was also supported by the Korea Health Technology R&D Project (HI14C0748) funded by the Ministry of Health and Welfare, Repulic of Korea.

REFERENCES

1. Y. Choi, C. Yoon, M. Kim, W. Choi, and W. Choi, "Optical Imaging With the Use of a Scattering Lens," *IEEE J. Sel. Top. Quantum Electron*. Vol. 20, No. 2, 6800213, 2014
2. Y. Choi, C. Yoon, M. Kim, T. D. Yang, C. Fang-Yen, R. R. Dasari, K. J. Lee, and W. Choi, "Scanner-Free and Wide-Field Endoscopic Imaging by Using a Single Multimode Optical Fiber," *Phys. Rev. Lett.* Vol. 109, No. 20, 203901, 2012

Wide-field high-resolution fluorescence imaging using wavefront control through a random metasurface

Mooseok Jang[1, 3,†,*], **Atsushi Shibukawa**[1,†], **Horie Yu**[2,†], **Andrei Faraon**[2], **and Changhuei Yang**[1]

[1]Electrical Engineering, California Institute of Technology, 1200 E. California Blvd., Pasadena, California 91125, USA

[2]T. J. Watson Laboratory of Applied Physics, California Institute of Technology, 1200 E. California Blvd., Pasadena, California 91125, USA

[3]Present address: Department of Physics, Korea University, Seoul 136-701, Korea

†These authors contributed equally to the work.

[*]corresponding author: mjang@korea.edu

Abstract- The advanced spatial light modulator technology typically offers controllable degrees of freedom up to ~10^6, but it is still bounded to the trade-off between the modulation's spatial extent and bandwidth. Here we challenge the traditional limitation using an ultrathin random metasurface as a static spatial frequency mixer rendering the ability to arbitrarily control optical wavefronts over their highest possible spatial bandwidth (i.e. the reciprocal of half-wavelength). We furthermore apply this technique for wide-field high-resolution imaging of fluorescence samples.

Optical metasurfaces, which are rationally designed arrays of subwavelength scatterers, have shown promise for manipulating an optical wavefront with unprecedented degrees of freedom, albeit passive to date[1–3]. The versatility in metasurface design has been proven effective to replicate various conventional optical elements, including high numerical aperture (NA) lenses and gratings, over a broad range of operating wavelengths. Nanofabrication technology provides a precise control of subwavelength scatterers that imprint a desired light manipulation at desired locations, allowing the arbitrary control of wavefront over a full range of transverse wavevector components up to k_0 ($=2\pi/\lambda$; λ is wavelength) in free space. The scalability of nanofabrication methods typically allows for the control of more than 10^8 individual scatterers, which are inherently orders of magnitude larger than the degrees of freedom available in state-of-the-art spatial light modulators.

Here we present a method to challenge the conventional trade-off limitation for spatial light modulation by leveraging the ultra-high degrees of freedom in a random metasurface. Random metasurface serves as a programmable scattering surface, providing a gateway to the maximal spatial bandwidth. The concept of "interferometric focusing" is then employed to reconstruct an arbitrary wavefront on demand through a random metasurface by controlling the limited degrees of freedom in SLM ($<\sim10^6$) [4,5]. This approach provides the addressable degrees of freedom in light modulation, which is equivalent to that of the random metasurface ($>10^8$), exactly at the price of the loss in efficiency.

With the scheme of Figure 1, we experimentally demonstrate an unprecedented flexibility for light focusing - scanning of more than 10^8 diffraction-limited spots with a tunable NA ranging from 0 to 0.95. Fluorescence imaging with this capability is shown to yield a high-resolution image of an enlarged field-of-view, which will be particularly useful for studying complex biological systems.

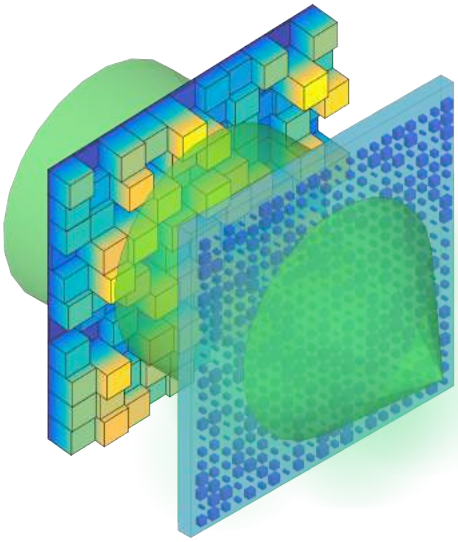

Figure 1. Schematic of an optical focusing system using a random metasurface.

ACKNOWLEDGEMENTS

This work is supported by the National Institutes of Health (1DP2OD007307-01), the National Institutes of Health BRAIN Initiative (1U01NS090577-01), and a GIST-Caltech Collaborative Research Proposal (CG2012).

REFERENCES

1. Kildishev, A. V., Boltasseva, A. & Shalaev, V. M. Planar photonics with metasurfaces. *Science* **339,** 1232009 (2013).
2. Yu, N. & Capasso, F. Flat optics with designer metasurfaces. *Nat. Mater.* **13,** 139–150 (2014).
3. Kamali, S. M., Arbabi, E., Arbabi, A., Horie, Y. & Faraon, A. Highly tunable elastic dielectric metasurface lenses. *Laser Photon. Rev.* **10,** 1002–1008 (2016).
4. Vellekoop, I. M., Lagendijk, A. & Mosk, A. P. Exploiting disorder for perfect focusing. *Nat. Photonics* **4,** 4 (2009).
5. Mosk, A. P., Lagendijk, A., Lerosey, G. & Fink, M. Controlling waves in space and time for imaging and focusing in complex media. *Nat. Photonics* **6,** 283–292 (2012).

Hyperbolic metamaterials and imaging

Junsuk Rho[1,2*]

[1]Department of Mechanical Engineering, Pohang University of Science and Technology (POSTECH), Pohang 37673, Republic of Korea

[2]Department of Chemical Engineering, Pohang University of Science and Technology (POSTECH), Pohang 37673, Republic of Korea

[*]corresponding author: jsrho@postech.ac.kr

Metamaterials, artificially structured nanomaterials, have enabled unprecedented phenomena such as negative refraction. However, despite the great and promising science, making practical devices based on metamaterials have been one of the most important issues due to the difficulty in fabrication. In this abstract, I will discuss recent development of scalable large-scale nanofabrication efforts to make practical metamaterials-based devices. The example is realizing a super-resolution imaging device of wafer-scale hyperlens, which is the first experimental demonstration of near- to far-field imaging of biological living objects at visible light with resolution beyond the diffraction limit in two lateral dimensions. With proposed hyperlens array, we show the first bio-sample imaging experimental result of super-resolution imaging on hyperlenses by combining to conventional microscopy system for imaging biomolecules. Hippocampal neuron cells are imaged by visible light through the hyperlens array with resolution down to 150 nm, beyond the diffraction limit. The super-resolution imaging result of neuron at sub-diffraction size shows that hyperlens can be used as a useful imaging tool in biology, pathology, medical science and nanotechnology. Also, such a unique fabrication techniques mentioned in this talk will provide the opportunity to achieve practical metamaterial devices as the significant step making nanoscience to nanotechnology.

Acknowledgements. J. Rho acknowledges the financial support by Pioneer Research Center program (NRF-2015M3C1A3022550), Young Investigator Research program (NRF-2015R1C1A1A02036464), Engineering Research Center program (NRF-2015R1A5A1037668) and Global Frontier program for the Center for Advanced Metamaterials (CAMM-2015M3A6B3063708) through the National Research Foundation of Korea (NRF) grant funded by the Ministry of Science, ICT and Future Planning (MSIP) of Korean government.

Measurement of Optical Anisotropy for Living Cells

Taeseok D. Yang[1], Kwanjun Park[2], Beop-Min Kim[1,2], and Youngwoon Choi[1,2,*]
[1]School of Biomedical Engineering, Korea University, Seoul 02855, Korea
[2]Department of Bio-Convergence Engineering, Korea University, Seoul 02855, Korea
[*]corresponding author: youngwoon@korea.ac.kr

Abstract We demonstrated the measurement of optical anisotropy, which is called birefringence, of living cells. Multiple images were taken by using a 3D phase microscopic method and then processed into an enhanced 2D or a volumetric 3D image. Quantitative analysis was also presented.

Optical anisotropy, such as birefringence, is an unusual optical characteristic of a sample caused by the alignment of molecular structures in micro-scale. Materials having the optical anisotropy are present in substances constituting cytoskeletons, bones, cartilages, skins, and connective tissues. The anisotropic materials can be selectively imaged in label-free fashion using the characteristic polarization response to light. Quantitative phase microscopy has been used for quantifying the anisotropy of an object, however, its applications are limited only to non-biological specimens with large amount of birefringence. Due to the low level of polarization response, the birefringence associated with living cells has been difficult to be investigated in a quantitative manner.

Here we demonstrated the quantitative measurement of optical anisotropy for single living cells by using a 3D phase microscopic method. To achieve sufficient sensitivity for the measurements of such a small polarization response, multiple object images were taken by the standard tomographic measurements. The images were processed into a single 2D image to suppress the background noise. By the enhanced signal to noise ratio, the amount of birefringence of living cells was quantitatively evaluated. In addition, we also used the 3D tomographic reconstruction for the taken images to produce a spatially-resolved anisotropy map of the living cells.

Plasmonics and nanophotonics

Physical and chemical origin of spectral fluctuation in surface enhanced resonance Raman scattering at single hotspot between silver nanoparticle dimer

T. Itoh*

[1]National Institute of Advanced Industrial Science and Technology (AIST), Japan

*corresponding author: tamitake-itou@aist.go.jp

Abstract- Single molecule (SM) surface-enhanced resonance Raman scattering (SERRS) at a hotspot has exhibited both intensity and spectral fluctuations, resulting in difficulty in SERS reliable analysis. To reduce the degree of complexity, we quantitatively investigate the origin of SERS spectral fluctuation based on the EM mechanism. The physical origin is analyzed as molecular motion within several angstroms and the chemical origin is analyzed as creation-annihilation of defects inside the molecule. SERRS is only method to investigate such extremely fine fluctuations (Abstract).*n*

Raman cross-sections of single molecules (~10^{-29} cm^2) located in gaps or crevasses of a metal nanoparticle (NP) aggregate are enhanced by a factor of <10^{10} by plasmonic resonance.[1] This phenomenon is called surface-enhanced Raman scattering (SERS), and the locations are called SERS hotspots. SERS enables vibrational spectroscopy of single molecules (SMs) with the assistance of resonance Raman effect. SERS boosted by resonance Raman effect is called SERRS. SERRS opens up a research field for in situ probing few or single molecules on metal surfaces. SM SERRS has been applied to in situ ultrasensitive detection of analyte molecules, especially biomolecule under various conditions. Recently, SERRS is also expected to be a potential tool for clarifying such plasmon-modified molecular optical responses e.g. strong coupling molecular exciton and plasmon, ultrafast fluorescence, and so on.[2-3]

SERRS signals under ultralow analyte concentration conditions of <10^{-9} M are usually observed with both temporal and spectral fluctuations, known as “blinking”.[4] SERRS fluctuation itself has been an indirect evidence of SM observation. In 2007, a direct evidence of SM SERRS observation was achieved by a lack of simultaneous detection of isotopically differentiated dye molecules at hotspots in a concentration of ~10^{-9} M. Thus, the studies of the SERRS fluctuation can be now related to various physical and chemical processes, including ground state and excited state dynamics of single molecules such as molecular movement, desorption, structural rearrangement, chemical reaction, and decomposition. However, there are still many complexities in interpretations of the SERRS fluctuation because many of the aforementioned phenomena simultaneously taking place. Furthermore, the existence of two types of SERS mechanisms (i.e., EM and chemical ones) makes the interpretations difficult.

To reduce the complexities in the SERRS fluctuation, a basic understanding of the fluctuations is important. Thus, the presentation is focused on the SERRS fluctuation caused dominantly by EM and resonance Raman mechanisms. On the basis of these demonstrations, we introduce two kinds of studies of extracting detailed information of fluctuation with resolutions (not image resolutions) from several nanometers to a few angstroms.[4-6]

(1) We analyze blinking in SERRS and surface enhanced fluorescence (SEF) of rhodamine 6G (R6G) molecules as intensity and spectral instability by EM mechanism.[4,5] We systematically analyze SERRS and SEF from stable to unstable using single Ag nanoparticle (NP) dimers. The analysis reveals physical insights into fluctuation as follows. The intensity instability is inversely proportional to the enhancement factors of decay rate of molecules. The estimation using the proportionality suggests that separation of the molecules from Ag NP surfaces is several angstroms. This analysis provides us with a quantitative picture for intensity and spectral instability in SERRS and SEF within the framework of EM mechanism. The results are shown in Fig. 1. (2) We evaluate spectral changes in SERRS of near-single dye molecules in hotspots of single Ag NP dimers.[4,6] During the laser excitation, the number of SERRS lines decreased until finally two lines remained around 1600 and 1350 cm^{-1}, those are evidence of *G* and *D* lines of single sp^2 carbon clusters. Analysis of the *G* and *D* line intensity ratios reveals the fluctuation in the crystallite size of the clusters within several angstroms; whereas, splitting in the lines enable us for identifying directly the dynamics of various defects in the clusters. This analysis would be impossible to gain with other microscopic methods.

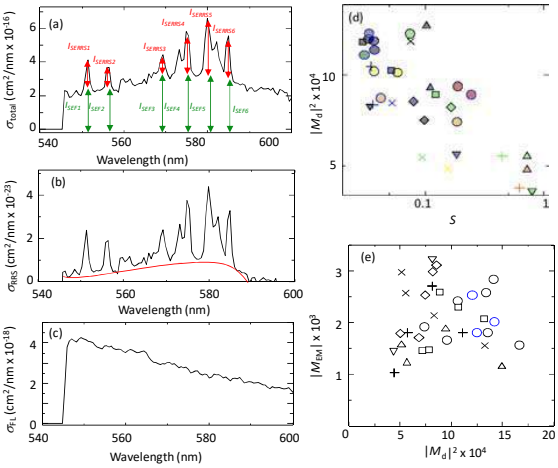

Fig. 1. (Color online) (a) Evaluation of I_{SERRS}/I_{SEF} for panels in (d). Total SERRS intensity I_{SERRS} and SEF intensity I_{SEF} were averaged over I_{SERRS1}/I_{SERRS6} (red arrows) and I_{SEF1}/I_{SEF6} (green arrows), respectively. (b) σ_{RRS} of spectrum R6G in an aqueous solution. Raman intensity is defined as the part above the red curve, which indicates back ground fluorescence. (c) σ_{FL} spectrum of R6G in an aqueous solution. (d) Normalized standard deviation scores S dependence of $|M_d|^2$ in the range of $0 < S < 0.6$ for eight dimers denoted by symbols (○, ○, □, Δ, ▽, ◊, +, and ×). (e) $|M_1|^2$ (~ $(I_{SERRS}/\sigma_{RRS})^{1/2}$) dependence of $|M_d|^2$ (= $I_{SERRS}/I_{SEF} \times \sigma_{RRS}/\sigma_{FL}$) for the same eight dimers as those in (d).

REFERENCES

1. Yoshida, K., Itoh, T. et al. "Quantitative evaluation of electromagnetic enhancement in surface-enhanced resonance Raman scattering from plasmonic properties and morphologies of individual Ag nanostructures," *Phys. Rev. B*, Vol. 81, 115406, 2010.
2. Itoh, T. et al., "Excitation laser energy dependence of surface-enhanced fluorescence showing plasmon-induced ultrafast electronic dynamics in dye molecules," *Phys. Rev. B*, Vol. 87, 235408, 2013.
3. Itoh, T. et al., "Single-molecular surface-enhanced resonance Raman scattering as a quantitative probe of local electromagnetic field: the case of strong coupling between plasmonic and excitonic resonance," *Phys. Rev. B*, Vol. 89, 195436, 2014.
4. Itoh, T. et al., "Recent topics on single-molecule fluctuation analysis using blinking in surface-enhanced resonance Raman scattering: clarification by the electromagnetic mechanism," *Analyst*, Vol. 141, 5000-5009, 2016.
5. Itoh, T. et al., "Quantitative evaluation of blinking in surface enhanced resonance Raman scattering and fluorescence by electromagnetic mechanism," *J. Chem. Phys.*, Vol. 136, 024703, 2012.
6. Itoh, T. et al., "Fluctuating single sp 2 carbon clusters at single hotspots of silver nanoparticle dimers investigated by surface-enhanced resonance Raman scattering," *AIP Adv.*, Vol. 5, 127113, 2015.

Super-radiant photoluminescence of plasmonic cube-in-cube nanoparticles

Jeong-Eun Park, Sungi Kim, Jiwoong Son, Yeonhee Lee, and Jwa-Min Nam*
Department of Chemistry, Seoul National University, Seoul, 08826, Republic of Korea
*corresponding author: jmnam@snu.ac.kr

Photostability of photoluminescence (PL) from plasmonic nanostructures such as non-photoblinking and non-photobleaching is beneficial to exploit them as reliable optical probes. Antenna effect of the localized surface plasmon of plasmonic nanostructures concentrates light at the nanoscale allowing strong interaction with electromagnetic radiation, which can compensate relatively low quantum yield. However, recent studies on PL from plasmonic nanostructures have mostly been limited to lithographically fabricated structures or simple nanoparticles. Here we designed and synthesized interior nanogap-engineered cube-in-cube nanoparticles in high precision and a high yield via a galvanic void formation process.1 The cube-in-cube nanoparticles show significantly enhanced PL and the PL intensity and quantum yield are 31 times and 16 times higher than those of Au nanocubes, respectively, which have the highest PL intensity and quantum yield reported for metallic nanostructures. Based on plasmon hybridization model, we interpret the intense PL with super-radiant character of plasmon mode arisen from plasmonic coupling between the core and the shell. Finally, we check the long-term photostability of the PL signal under continuous illumination for 1 h.

REFERENCES

1. Park, J.-E., Kim, S., Son, J., Lee, Y. & Nam, J.-M. Highly Controlled Synthesis and Super-Radiant Photoluminescence of Plasmonic Cube-in-Cube Nanoparticles. Nano Lett. 16, 7962–7967 (2016).

Ultrafast Transient Dynamics of Optical Loss Compensation in Aggregated Gain-Plasmon Polymeric Films

Alireza. R. Rashed[1, *], M. Elkabbash[2], B. Kucukoz[3], Quang Nguyen[2], A. Karatay[3], G. Yaglioglu[3], G. Strangi[2], E. Ozbay[1], and H. Caglayan[1]

[1]Nanotechnology Research Center, Bilkent University, Bilkent, Ankara 06800, Turkey

[2]Nanotechnology Research Center, Bilkent University, 06800 Ankara, Turkey

[3]Department of Engineering Physics, Faculty of Engineering, Ankara University, Besevler, Ankara 06100, Turkey

[*]corresponding author: alireza.rashed@bilkent.edu.tr

Abstract- We present a comprehensive study via transient absorption spectroscopy (TAS) to investigate ultrafast exciton-plasmon dynamics of hybrid aggregates consisted of core-shell quantum dots (QDs) and Au Nanoparticles (NPs) leading to optical loss mitigation. The results suggest modifying the way of analyzing the transient absorption spectra of loss mitigated systems. We show that appropriate choice of the pump wavelength and by changing the pump power we can conclusively prove the existence of loss mitigation using UTAS.

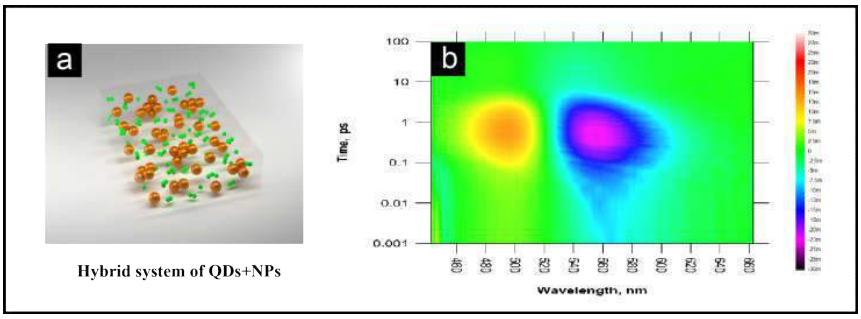

Fig. 1 a) A schematic of fabricated nanocomposite PDMS films with embedded mixture of Au NPs and QDs. **b)** Bird-eye view diagrams of NPs+QDs hybrid system for pump wavelength of 400 nm.

The extraordinary properties of the plasmonic systems arise from confinement of the electromagnetic wave beyond the diffraction limit, as a result of surface plasmons. However, the surface plasmons can be damped due to electron scattering events. In fact, the strong absorption and optical losses in the available plasmonic materials are the main obstacles for their promising applications. One of the most successful approaches to compensate the optical losses, while maintaining the electromagnetic sub-wavelength confinement, is to incorporate gain material in plasmonic systems, such that the gain emission spectrally overlaps with the plasmon resonance. The approach maintains the self-sustaining oscillation of the electromagnetic field while keeping the sub-wavelength field confinement in the vicinity of the NP.

In this work, we report a systematic and detailed transient pump-probe absorption spectroscopy study on loss compensation process of hybrid systems consisted of core-shell QDs aggregates and Au NPs (Fig. 1a). Our study provides a clear understanding of the ultrafast gain-plasmon dynamics to control optical losses in plasmonic

nanostructures, paving the way towards further promising scientific research aimed to enable their practical applications. We highlight that generating hot electrons in plasmonic NPs contribute to the transient differential absorption spectrum under optical excitation and is of great significance. The results suggest modifying the way of analyzing the transient absorption spectra of loss mitigated systems by taking into account the enhanced transmission due to permittivity modification of pumped NPs.

Frequency *pulling like effect* of the transient bleach signal towards the emission maximum of the gain material is reported based on power dependence TAS results as an evidence for loss mitigation process. Furthermore, considerably enhanced bleach signal of the hybrid systems than the combined bleach of only plasmonic NPs and core-shell QDs quantitatively proves the existence of loss mitigation.

Additionally, we study the implications of the coupling strength between the electron oscillation frequency and the phonon modes of aggregated NPs on loss mitigation efficiency and the transient quality factor of the plasmon band. Finally, we investigated the transient kinetics of all systems and showed that hybrid gain-plasmon systems have unique decay kinetics.

REFERENCES

1. Ozbay, E. "Plasmonics: Merging Photonics and Electronics at Nanoscale Dimensions," *Science*, Vol. 311, No. 5758, 189–193, 2006.
2. Khurgin, J. B. "How to Deal with the Loss in Plasmonics and Metamaterials," *Nat. Nanotechnol*., Vol. 10, 2 6, 2015.
3. El Kabbash, M., R. A. Rashed, K. V. Sreekanth, A. De Luca, M. Infusino and G. Strangi, "Plasmon-Exciton Resonant Energy Transfer: Across Scales Hybrid Systems," *J. Nanomat*., Vol. 2016, 1–21, 2016.
4. De Luca, A., M. P. Grzelczak, I. Pastoriza-Santos, L. M. Liz-Marzan, M. La Deda, M Striccoli and G. Strangi, "Dispersed and Encapsulated Gain Medium in Plasmonic Nanoparticles: A Multipronged Approach to Mitigate Optical Losses," *ACS Nano*, Vol. 5, No. 7, 5823–5829. 2011.
5. Quinten, M. and U. Kreibig, "Optical Properties of Aggregates of Small Metal Particles," *Surf. Sci.*, Vol. 172, No. 3, 557 577, 1986.
6. Link, S. and M. A. El-Sayed, "Spectral Properties and Relaxation Dynamics of Surface Plasmon Electronic Oscillations in Gold and Silver Nanodots and Nanorods*," J. Phys. Chem. B*. Vol. 103, No. 40, 8410–8426. 1999.
7. Burda, C., S. Link, T. C. Green and M. A. El-Sayed, "New Transient Absorption Observed in the Spectrum of Colloidal CdSe Nanoparticles Pumped with High-Power Femtosecond Pulses," *J. Phys. Chem. B*, Vol. 103, No. 49, 10775–10780, 1999.
8. Wuestner, S. A. Pusch, K. L.Tsakmakidis, J. M. Hamm and O. Hess, "Overcoming Losses with Gain in a Negative Refractive Index Metamaterial," *Phys. Rev. Lett*., Vol. 105, 127401-4. 2010.
9. Grant, C. D., A. M. Schwartzberg, T. J. Norman, Jr., and J. Z. Zhang, "Ultrafast Electronic Relaxation and Coherent Vibrational Oscillation of Strongly Coupled Gold Nanoparticle Aggregates," *J. Am. Chem. Soc.*, Vol. 125, No. 2, 549–553. 2003.

Bright off-axis directional light harvesting with plasmonic corrugations

Alireza. R. Rashed[1, *], **H. Sattari**[1,2], **E. Ozbay**[1], **and H. Caglayan**[1]
[1]Nanotechnology Research Center, Bilkent University, Bilkent, Ankara 06800, Turkey
[2]Q-LAB, Ecole Polytechnique Fédérale de Lausanne (EPFL), CH-1015, Lausanne, Switzerland
[*]corresponding author: alireza.rashed@bilkent.edu.tr

Abstract- We introduce a new plasmonic bulls-eye antenna to efficiently harvest the emitted light from diamond Nitrogen Vacancy (NV) centers. The designed structure shows a great performance even better than double-side corrugated structures. In addition, we study for the first time asymmetric structures to steer emitted beam in two-axis. Our results show that spatial off-axial steering angle over a cone is approachable by applying optimal asymmetries to grooves and ridges of the plasmonic antenna.

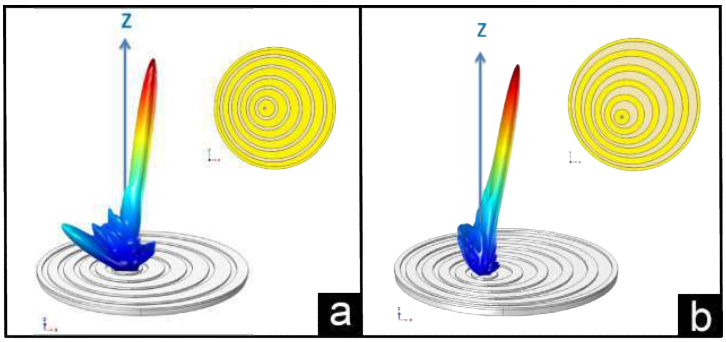

Fig. 1 3D far-field intensity distribution for a Bulls-eye plasmonic antenna with **a)** one main asymmetry plane and ridge asymmetry **b)** with two main asymmetry plane and groove asymmetry. The scheme of each configuration is presented in figure insets.

Sub-wavelength diffracted light sources are rapidly growing cutting edge research field for promising nano-photonic applications. Enhancing the photon collection efficiency and narrowing the emission directivity of such light sources are two critical aspects for their practical applications. For attaining this, one promising approach is to introduce symmetric or asymmetric periodic corrugations on the exit side of a single aperture in a metallic substrate. In this approach, the emitted light of nano-emitter is coupled into the antenna plasmonic modes, and then out-coupled by the antenna to the far-field, resulting in the enhanced light with desired orientation. Accordingly, various applications ranging from efficient photovoltaic light harvesting, polarization sensitive transmission control to precise bio-sensing are enabled. For such applications, recently diamond nitrogen vacancy centers (NV centers) have gained remarkable attention.

Here, we propose a new design of bulls-eye antenna by introducing a metallic sub-plate and dielectric layer below conventional structure. Our proposed design provides high degree of directionality and enhanced out-coupled field intensity of nano-emitter sources as compared to conventional designs. The antenna parameters

are optimized for the emission peak of diamond NV centers. In our model, we have considered diamond NV centers to be doped to dielectric layer and placed inside the central cavity. The structure is optimized by considering the underlying physics of the dielectric layer sandwiched between metal layers. Such an engineered structure provides higher out-coupled light intensity efficiency even better than double-side corrugated antenna.

It is also desirable to have control on the emission angle of out-coupled directive beam from plasmonic antennas. Several studies have been reported to approach angled emission or transmission from such structures. Here, we present trends for steering the radiated beam over the plate of the Bulls-eye plasmonic antenna. By introducing a modification on design of the proposed structure, a considerable off-axis beaming angle retaining high out-coupled light intensity is attainable. A full-asymmetric design approach is introduced for the first time to steer the directive beam on spatial angles over the antenna plate. Our results show that by introducing optimal asymmetries to grooves and ridges of the structure high degree off-axial steering angle are achievable in single-lobe or double-lobe regimes (see Fig. 1).

Finally, our investigations reveal that the far-field intensity for the asymmetric configuration with metal sub-plate is higher than that of a conventional symmetric structure, without perturbing directivity.

REFERENCES

1. Ferry, V. E., L. A. Sweatlock, D. Pacifici and H. A. Atwater "Plasmonic nanostructure design for efficient light coupling into solar cells," *Nano Lett.*, Vol. 8, No. 12, 4391-4397, 2008.
2. Aouani, H., O. Mahboub, N. Bonod, E. Devaux, E. Popov, H. Rigneault, T. W. Ebbesen and J. Wenger "Bright unidirectional fluorescence emission of molecules in a nanoaperture with plasmonic corrugations," *Nano Lett.*, Vol.11, No. 2, 637-644, 2011.
3. Harats, M. G., N. Livneh, G. Zaiats, S. Yochelis, Y. Paltiel, E. Lifshitz and R. Rapaport "Full spectral and angular characterization of highly directional emission from nanocrystal quantum dots positioned on circular plasmonic lenses," *Nano Lett.*, Vol, 14, No, 10, 5766-5771, 2014.
4. Livneh, N., M. G. Harats, D. Istrati, H. S. Eisenberg and R. Rapaport, "Highly Directional Room-Temperature Single Photon Device," *Nano Lett.*, Vol, 16, No. 4, 2527-2532, 2016.
5. Choy, J. T., I. Bulu, B. J. M. Hausmann, E. Janitz, I-C. Huang and M. Loncar, "Spontaneous emission and collection efficiency enhancement of single emitters in diamond via plasmonic cavities and gratings," *Appl. Phys. Let.*, Vol.103, No. 16, 161101, 2013.
6. Li, L., E. H. Chen, J. Zheng, S. L. Mouradian, F. Dolde, T. Schröder, S. Karaveli, M. L. Markham, D. J. Twitchen and D. Englund, "Efficient photon collection from a nitrogen vacancy center in a circular bullseye grating," *Nano Lett.*, Vol. 15, No. 3, 1493-1497, 2015.
7. Caglayan, H., I. Bulu, and E. Ozbay. "Off-axis beaming from subwavelength apertures," *J. Appl. Phys.*, Vol. 104, No. 7, 073108, 2008.
8. Aouani, H., O. Mahboub, E. Devaux, H. Rigneault, T. W. Ebbesen and J. Wenger, "Plasmonic antennas for directional sorting of fluorescence emission." *Nano Lett.*, Vol, 11, No. 6, 2400-2406, 2011.
9. Caglayan, H., I. Bulu, and E. Ozbay. "Observation of off-axis directional beaming via subwavelength asymmetric metallic gratings," *J. Appl. Phys. D*: *Appl. Phys.*, Vol. 42, No, 4, 045105, 2009.

Fe_3O_4@Au Core-shell Nanoparticle with Suprastructure Au shell for SERS

Dong Kyu Lee[1], Van Tan Tran[1], Younseong Song[1], Jeonghyo Kim[1], Jaebeom Lee[1*]

[1] Department of Cogno-Mechatronics Engineering, Pusan National University, Busan, 609-735, Republic of Korea

[*]jaebeom@pusna.ac.kr

Abstract- Suprastructure has unique optical properties so many researchers try to make this kind of structure. In this study we specially synthesized suprastructure like core-shell nanoparticle under the wet chemistry environment. Covering Fe_3O_4 nanoparticles with Au shell has been tried and fully covered self-assembly of AuNPs on Fe_3O_4 nanoparticle was observed by TEM. Au shell can protects the magnetic core against oxidation and produces multifunctionality, special optical properties from suprastructure like Au shell and magnetic properties from magnetic nanoparticles. To form suprastructure like Au NP coating on Fe_3O_4 nanoparticles, ion reducing method assisted with layer-by-layer (LBL) structure of AuNPs and PEI on the surface of Fe_3O_4 nanoparticle were proceeded. This material was used as surface enhanced Raman scattering (SERS) substrate of rhodamine-B and graphene quantum dots (GQDs). Magnetically 1D self-assembled structure of the prepared core-shell nanoparticles and separately deposited nanoparticles were prepared as SERS substrate. Raman signals on these two substrate were obtained and compared.

Summary- Suprastructure like Fe_3O_4@Au core-shell nanoparticles were synthesized through a simple wet chemistry method. Core-shell nanocomposite with unique Au shell was obsereved by TEM. Highly enhanced raman signal was observed on this materials. When this nanoparticle was self-assembled with external magnetic field 3−4 fold greater enhancement of the Raman signal was obtained. Because of its novel structure with simple synthesis methods, this material can be applied for characterizing the electronics and magnetism in the nano-system.

Figures and Tables

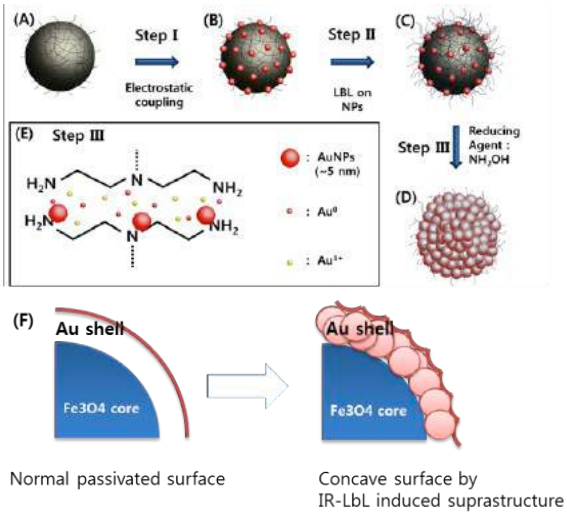

Figure 1. Schematic illustration of preparation of supraparticles (SPs) by ion-reducible layer-by-layer (IR-LbL) method.

Acknowledgements, This work was supported by a 2-Year Research Grant from Pusan National University.

REFERENCES

1. B. Jankiewicz, D. Jamiola, J. Choma, M. Jaroniec, "Silica–metal core–shell nanostructures", *Advances in colloid and interface science*, Vol. 170, No. 1, 28-47, 2012.
2. R. Ghosh Chaudhuri, S. Paria, "Core/shell nanoparticles: classes, properties, synthesis mechanisms, characterization, and applications", *Chemical reviews*, Vol. 112, No. 4, 2373-2433, 2011.
3. J. Du, C. Jing, "Preparation of thiol modified Fe3O4@ Ag magnetic SERS probe for PAHs detection and identification", *The Journal of Physical Chemistry C*, Vol. 115, No. 36, 17829-17835, 2011.
4. H. Zhou, S. Kim, J. Lee, J. Kim, F. Zou, J. Kim, J.Y. Park, J. Lee, "Self-assembled magnetoplasmonic nanochain for DNA sensing", *Sensors and Actuators B: Chemical*, Vol. 203, 817-823, 2014.
5. H. Zhou, J.Y. Park, J. Kim, J. Lee, "Silver-enhanced conductivity of magnetoplasmonic nanochains", *Current Applied Physics*, Vol. 15, No. 2, 110-114, 2015.
6. Zhang, Qingfeng, Nicolas Large, and Hui Wang. "Gold nanoparticles with tipped surface structures as substrates for single-particle surface-enhanced Raman spectroscopy: concave nanocubes, nanotrisoctahedra, and nanostars.", *ACS applied materials & interfaces,* Vol. 6, No.19, 17255-17267, 2014.
7. H. Zhou, J.P. Kim, J.H. Bahng, N.A. Kotov, J. Lee, "Self-Assembly Mechanism of Spiky Magnetoplasmonic Supraparticles", *Advanced Functional Materials*, Vol. 24, No. 10, 1439-1448, 2014.

Magnetoplasmonic core-shell Au@FeCo nanoparticles and their magnetic property compared with solid and hollow types

Junyoung Kwon[1], Menqi Wei[1], and Jaebeom Lee[1]*

[1]Department of Cogno-Mechatronics Engineering, Pusan National University, Busan, 609-735, Republic of Korea

*corresponding author: nanoleelab@gmail.com

Abstract-Recently, the relationship between magneto-optics and plasmonics has been actively studied. But, localized surface plamonic resonance (LSPR) effect on magnetic phase, especially on the motion of magnetic dipole moments, is not confirmed yet. Here, solid, core-shell, and hollow-type of iron-based magnetoplasmonic (MagPlas) nanoparticles (NPs) are produced via thermolysis synthesis route. Different magnetic behaviors inside the magnetic NPs at the presence of plasmonic material are demonstrated based on Landau-Lifshitz-Gilbert (LLG) theory which represents ferromagnetic flux. It is experimentally proved, for the first time as we know, that adding electric field from plasmonic absorption and scattering of Au NPs to LLG equation adjusts magnetic anisotropic energy and thermal energy, which visualizes and explains by OOMMF and COMSOL micromagnetic simulation tool.

The design and synthesis of magnetoplasmonic (MagPlas) nanostructures have been attracted since they have the extraordinary properties not only for those combined functional natures of magnetic and plasmonic optical property but also for the characteristics of quantum mechanics such as size and shape-dependent differences in physicochemical property unlike their bulk counterparts [1, 2]. But plasmonic effects on magnetic property in these MagPlas nanostructure have been hardly described.

In this study, we synthesized MagPlas Au@FeCo and Au@FeNi core-shell, hollow FeCo nanocrystals to compare MagPlas properties. Previously reported studies related with plasmonic and magnetic nano-complexes usually have focused on magnetite as magnetic component or transition metals in core part, but we use soft magnetic element and apply it to shell on Au template. Furthermore, micro magnetic flux of the coated magnetic shell was simulated based on Landau-Lifshitz-Gilbert theory that describes ferromagnetic flux. Many studies on magneto-optic and MagPlas NPs explain magnetic effect on optical and plasmonic component. But, plasmonic effect on magnetic property in ferromagnetic NP regime was figured out here. It was observed that core-shell Au@FeCo NPs have the lowest magnetic anisotropy value among solid FeCo, MagPlas core-shell Au@FeCo, hollow FeCo NPs. This MagPlas nanomaterials can provide promising well-designed magnetic behavior as well as plasmonic property inside NPs to be one candidate for recording media, spintronics, optical device, magnetic hyperthermia, bi-functional medicine.

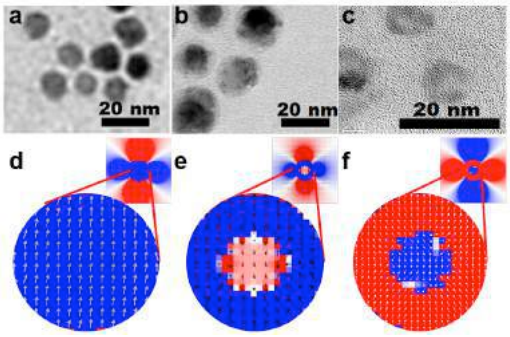

Figures and Tables: TEM and magnetization motion images of solid FeCo(a, d), MasPlas Au@FeCo core-shell(b, c), hollow FeCo NPs (c, f).

REFERENCES

1. R. Jin, Y.C. Cao, E. Hao, G.S. Métraux, G.C. Schatz, C.A. Mirkin, Controlling anisotropic nanoparticle growth through plasmon excitation, Nature, 425, 487-490, 2003.
2. Y. Xia, Y. Xiong, B. Lim, S.E. Skrabalak, Shape‐Controlled Synthesis of Metal Nanocrystals: Simple Chemistry Meets Complex Physics?, Angewandte Chemie International Edition, 48, 60-103, 2009.

Fabrication, Properties and Applications of Multidimensional Magnetoplasmonic Assembled Structures

Van Tan Tran, Younseong Song, Jeonghyo Kim, Sangjin Oh, Jaebeom Lee*

Department of Cogno-Mechatronics Engineering, Pusan National University, Busan, 609-735, Republic of Korea

*Corresponding author: E-mail: jaebeom@pusan.ac.kr

Abstract

Controlling and understanding the assembly of colloidal nanoparticles remain a challenging issue for optimizing magnetic-plasmonic devices for various applications including sensors, displays, bio-imaging and therapy. A magnetic field is successfully utilized to induce the fabrication of multidimensional structures composed of magnetite coated silver core/shell ($Ag@Fe_3O_4$) particles, which exhibit intriguing optical properties. An effective and highly controlled dip-coating technique for fabrication of one-dimensional (1D) structure of magnetoplasmonic particles on large-area surface is proposed by combining electrostatic and magnetic dipole interactions. This technique is demonstrated to be a very powerful approach to modulate optical properties of magnetoplasmonic particles. Moreover, a magnetic-field assisted coating technique for fabrication of two-dimensional (2D) amorphous photonic crystal (APC) film of the magnetoplasmonic particles on a filter membrane is proposed. The fabrication technique relies on combination of high porosity of filter membrane accelerating evaporation-mediated arrangement of particles and strong magnetic response of particles to external magnetic field. The magnetoplasmonic 2D APC exhibits strong dual reflected colors caused by structural scattering and plasmon resonance scattering. The water absorption ability of the membrane and

the high refractive index sensitivity of plasmon resonance scattering are utilized to fabricate a simple colorimetric humidity sensor. Additionally, a mechanical colorimetric sensor that exhibits instantly responses to both bending and stretching forces is fabricated by embedding the 2D APC film into PDMS substrate. Because of unique features including dual-color characteristic, flexibility and high plasmonic sensitivity, these kinds of platform could be highly promising as wearable devices for physical, chemical and biological sensing with naked eye detection.

Plasmonic Trapping and Antitrapping of Nanoparticles.

Aliaksandra Ivinskaya[1], Mihail I. Petrov[1], Andrey A. Bogdanov[1], Pavel Ginzburg[1,2] and Alexander S. Shalin[1,*]

[1]ITMO University, St. Petersburg 197101, Russia

[2]School of Electrical Engineering, Tel Aviv University, Ramat Aviv, Tel Aviv 69978, Israel

[*]corresponding author: alexandesh@gmail.com

Abstract-Optical tweezers performance is investigated when the Gaussian beam is focused on the metal substrate with nanoparticle. When the beam is focused above the substrate optical force increases about an order of magnitude due to evanescent field of surface plasmon. Novel effect of repulsion from Gaussian beam ("anti-trapping") is obtained when the beam waist is moved below the substrate which is confirmed by both the analytical approach and finite element simulation.

The ability to manipulate small objects with focused laser beams opened a venue for investigating dynamical phenomena relevant to both fundamental and applied science. Nanophotonic and plasmonic structures enable achieving superior performance in optical trapping due to highly confined near-fields. In this case, the interplay between the excitation field, re-scattered fields and the eigenmodes of a structure can lead to remarkable effects, as it is shown here with an example of a particle trapped by laser light in a vicinity of metal surface. Surface plasmon excitation at the metal substrate plays a key role in tailoring optical forces acting on a nearby particle. Depending on whether the illuminating Gaussian beam is focused above or below the metal-dielectric interface, an order of magnitude enhancement or reduction of trap stiffness is achieved in comparison to standard glass substrates. Furthermore, a novel plasmon-assisted anti-trapping effect (particle repulsion from the beam axis) is predicted and studied. Highly accurate particles sorting scheme based on the anti-trapping effect is analyzed. The ability to distinguish and configure various electromagnetic channels through the developed analytical theory provides the guidelines for designing auxiliary nanostructures and achieving an ultimate control over the mechanical motion at the micro- and nano-scales [1].

Optical trapping characteristics in the proximity of the beam waist and the impact of the focus position with respect to the surface were studied. Gaussian beam is focused above or below the substrate and the force acting on a dielectric bead ($\varepsilon=3$) of radius R=15 nm is calculated. Three different scenarios were considered: glass ($\varepsilon_2=2.25$) and silver substrates, and in the latter case the plasmonic contribution to optical forces can be switched 'on' and 'off' by either including evanescent harmonics or not. For f=100 μm the bead lying on the substrate (centered at z=15 nm) experiences attraction to the beam center (trapping) at all the cases (Figure 1B). This is a typical behavior for a deeply subwavelength low-index bead which has no resonances and is usually attracted towards the axis of free-space Gaussian beam. Comparison between the force values favors the silver substrate,

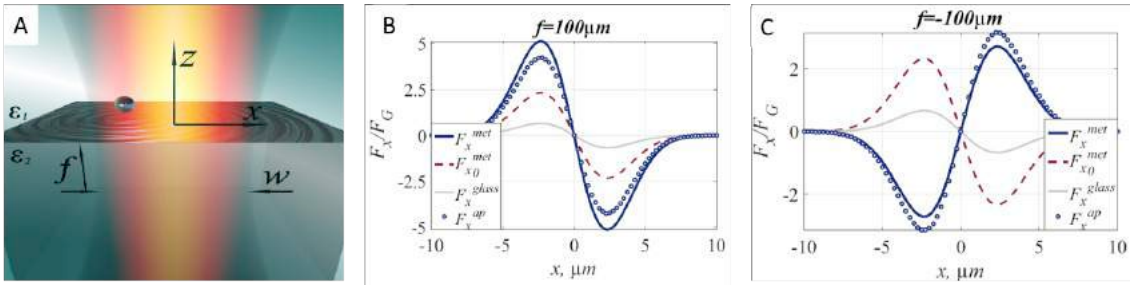

Figure 1. A) Schematics of the system. Gaussian beam with waist w is normally incident on a flat silver substrate; the focal position f along the z axis can be either above or below the interface. Optical forces acting on a spherical dielectric particle are formed by beam-particle, beam-substrate, and particle-substrate interactions. Optical force acting on a particle (ε=3, radius R=15 nm) in the Gaussian beam focused above (f=100 μm, B) and below (f=-100 μm, C) the substrate interface. Blue solid lines correspond to silver substrate; red dashed lines to the model without plasmon contribution; grey solid lines to the glass substrate. The beam waist diameter is w=10λ, the particle is touching the substrate.

which provides about an order of magnitude enhancement compared to the glass. Thus, the auxiliary metal substrate allows increasing the trap stiffness.

At the other hand, focusing the beam below the substrate (f=-100 μm) leads to completely different behavior (Figure 1C). While in both glass and 'silver with plasmon excluded' cases optical trapping is observed, real silver substrate leads to optical repulsion from the beam axis – anti-trapping, pushing the particle away from the region of high optical intensity. Anti-trapping stiffness (derivative of the force with respect to the coordinate) is several times larger than in the case of the glass substrate.

Acknowledgements, This work has been supported in part by the Government of the Russian Federation (No. 074-U01) and the Russian Fund for Basic Research within the Project No. 16-52-00112, 17-02-01058, 17-02-01032. The investigation of optical force distributions has been supported by the Russian Science Foundation (No. 14-12-01227). A.S.S. acknowledges the support of the President of Russian Federation in the frame of Scholarship SP-4248.2016.1 and the support of Ministry of Education and Science of the Russian Federation (GOSZADANIE).

REFERENCES

1. Ivinskaya, A., M.I. Petrov, A. A. Bogdanov, I. Shishkin, P. Ginzburg and A. S. Shalin, "Plasmon-assisted optical trapping and anti-trapping", *Light: Science and Applications*, 2017 (accepted).

Magneto-Plasmonics of Checkerboard Au-Ni Nanoparticle Arrays

M. Kataja[1], S. Pourjamal[1*], N. Maccaferri[2], P. Vavassori[2,3], T. K. Hakala[4], M. J. Huttunen[4], P. Törmä[4] and S. van Dijken[1]

[1]NanoSpin, Department of Applied Physics, Aalto University School of Science, P.O. Box, 15100, FI-00076 Aalto, Finland

[2]CIC nanoGUNE, 20018 Donostia-San Sebastian, Spain

[3]IKERBASQUE, Basque Foundation for Science, 48011 Bilbao, Spain

[4]COMP Centre of Excellence, Department of Applied Physics, Aalto University, FI-00076 Aalto, Finland

*corresponding author: sara.pourjamal@aalto.fi

Abstract-We report a new method of integrating ferromagnetic and noble metal plasmonic nanostructures leading to strong magneto-optical (MO) responses with enhanced optical reflectivity. The structures under study consist of Ni and Au nanoparticles ordered into periodic checkerboard arrays. Diffractive far-field coupling between the individual emitters of the lattice results in the excitation of two orthogonal surface lattice resonance (SLR) modes. Local analyses of the radiation fields indicate that both the Ni and Au nanoparticles actively contribute to these collective resonance modes and, thereby, the MO activity of the hybrid arrays.

Ordering of ferromagnetic nanoparticles into a periodic array enhances the optical and MO activity due to the excitation of SLR modes [1,2]. Coupling between broad localized surface plasmon resonances (LSPRs) of single ferromagnetic nanoparticles [3] and diffracted orders of the array generates sharp and asymmetrical SLRs in the optical and MO spectra. Here, we report on the integration of Au nanoparticles into ferromagnetic nanoparticle arrays [4]. In our experiments, we use periodic arrays comprising a checkerboard pattern of Au and Ni nanoparticles (Fig. 1(a)). The ferromagnetic and noble metal emitters are separated by 450 nm and the diameter of the Au nanoparticles is varied from 80 to 120 nm to gauge its influence on the optical and MO activity (the diameter of Ni nanoparticles is fixed at 120 nm). All nanoparticles have a thickness of 30 nm.

The integration of Au nanoparticles into Ni nanoparticle arrays considerably increases the optical activity as demonstrated by high reflectivity (Fig. 1(b)). Yet, compared to pure nickel nanoparticle arrays, the orthogonal magneto-optical dipole retains its intensity (Fig. 1(c)). In other words, the MO activity is conserved while the optical response is substantially enhanced. Our results are explained by far-field diffractive coupling between the ferromagnetic and noble metal emitters, causing two main effects: (1) A magneto-optical dipole is induced on the Au nanoparticles and, consequently, the non-magnetic noble metal emitters actively contribute to the MO activity of the hybrid array. (2) Far-field diffractive coupling to Au nanoparticles enhances the optical and magneto-optical activity of the Ni emitters. Numerical calculations based on the discrete dipole approximation (DDA) and finite-difference time-domain (FDTD) simulations substantiate our experimental findings. Label-free biosensors based on the measurement of very small refractive index changes [5] and other magneto-plasmonic devices could make use of strong optical and magneto-optical responses in hybrid nanoparticle arrays.

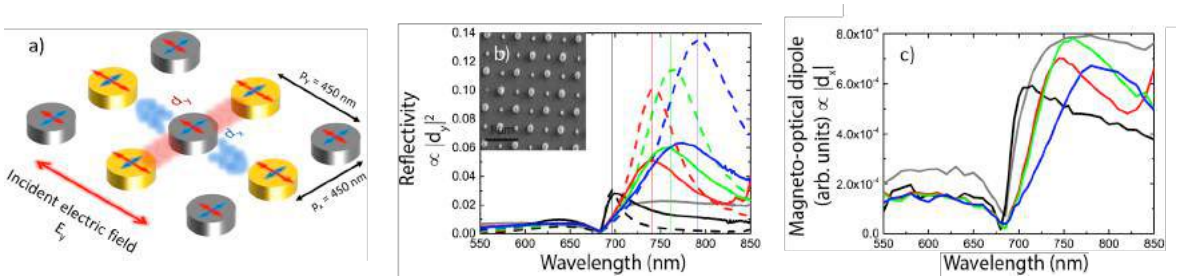

Figure 1 (a) Schematic illustration of a checkerboard array of Ni (grey) and Au (yellow) nanoparticles. (b) Optical reflectivity of Au-Ni nanoparticle arrays (black, red, green, and blue lines). Results for pure Au nanoparticle arrays (dashed lines) and a pure Ni nanoparticle array (grey line) are shown for comparison. (c) Magneto-optical dipole signal for Au-Ni nanoparticle arrays (black, red, green, and blue lines) and a pure Ni nanoparticle array (grey line). The colors of the spectra in (b) and (c) indicate results for Au nanoparticle with different diameter: d_{Au} = 80, 100, 110, 120 nm.

REFERENCES

1. M. Kataja, T. K. Hakala, A. Julku, M. J. Huttunen, S. van Dijken and P. Törmä, "Surface lattice resonances and magneto-optical response in magnetic nanoparticle arrays," *Nat. Commun*. 6, 7072, 2015.

2. N. Maccaferri, L. Bergamini, M. Pancaldi, M. K. Schmidt, M. Kataja, S. van Dijken, N. Zabala, J. Aizpurua and P. Vavassori, "Anisotropic nanoantenna-based magnetoplasmonic crystals for highly enhanced and tunable magneto-optical activity," *Nano Lett*., 16, 2533−2542, 2016.

3. N. Maccaferri, A. Berger, S. Bonetti, V. Bonanni, M. Kataja, Q. H. Qin, S. van Dijken, Z. Pirzadeh, A. Dmitriev, J. Nogués, J. Åkerman and P. Vavassori, "Tuning the magneto-optical response of nanosize ferromagnetic Ni disks using the phase of localized plasmons," *Phys. Rev. Lett*. 111, 167401, 2013.

4. M. Kataja, S. Pourjamal, N. Maccaferri, P. Vavassori, T. K. Hakala, M. J. Huttunen, P. Törmä and S. van Dijken, "Hybrid plasmonic lattices with tunable magneto-optical activity," *Opt. Express* 24, 3652-3662, 2016.

5. N. Maccaferri, K. E. Gregorczyk, T. V. A. G. Oliveira, M. Kataja, S. van Dijken, Z. Pirzadeh, A. Dmitriev, J. Åkerman, M. Knez and P. Vavassori, "Ultrasensitive and label-free molecular-level detection enabled by light phase control in magnetoplasmonic nanoantennas," *Nat. Commun*. 6, 6150, 2015.

Do Surface Plasmons Convey Geometric Phase?

S. Daniel[1*], K. Saastamoinen[1], T. Saastamoinen[1], I. Vartiainen[1], A. T. Friberg[1] and T. D. Visser[2,3,4]

[1]Institute of Photonics, University of Eastern Finland, Joensuu, Finland

[2]Department of Physics and Astronomy, Vrije Universiteit, Amsterdam, The Netherlands

[3]Department of Physics and Astronomy, University of Rochester, Rochester NY, USA

[4]School of Electronics and Information, Northwestern Polytechnical University, Xi'an, China

[*]corresponding author: salman.daniel@uef.fi

Abstract – Surface plasmons polaritons (SPPs) are electromagnetic surface waves that can be generated by and converted back into freely propagating light beams by applying metallic structures, such as gratings or slits. In this work we investigate experimentally whether SPPs in the process light beam → SPP → light beam convey the geometric (Pancharatnam-Berry) phase, which appears on passing a beam of light cyclically through a series of polarizing components.

Surface plasmon polaritons (SPPs) have been the workhorse in nanophotonics, resulting in the emergence of plasmonics [1] as a separate field covering cross-disciplinary physics, including subwavelength light control [2]. SPPs are known to be highly polarized surface waves [1]. A point on the Poincaré sphere [3] represents the state of polarization of a monochromatic electromagnetic beam. If such a beam passes through a succession of polarizing elements so that the initial and final states are identical, the polarization state traces a closed circuit on the sphere. In doing so the light beam acquires, in addition to the usual dynamic phase, also a geometric phase, known as the Pancharatnam-Berry phase [3]. It is equal to half the solid angle subtended by the circuit from the origin of the sphere [3,4]. Here we investigate experimentally whether, when a beam of light is converted into SPPs and then back into a freely propagating field, the geometric phase does survive? The conceptual scheme of the work is illustrated in Figure 1. The closed path ABCDEA on the Poincaré sphere corresponds to the successive polarization states. The geodesic arc BC (shown in blue) represents the path of the polarization state which results from the conversion of circularly polarized light (state B) first into SPPs and back into linearly polarized light (state C). By varying the solid angle of the closed path on the Poincaré sphere, the geometric phase changes. One way to do this is by rotating a linear polarizer and thereby moving the position of point D along the equator. In practice, the change in the geometric phase can be observed as a shift in the interference pattern [5] when two beams (in states A before and after the cyclic rotation) are combined again.

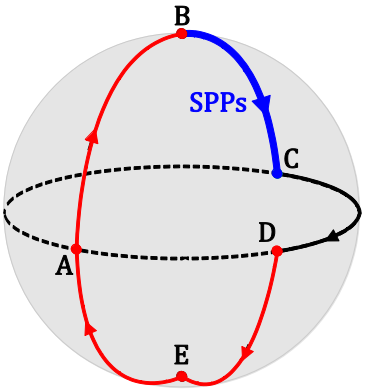

Figure 1. Schematic representation of the polarization-state changes on the Poincaré sphere.

The experimental demonstration [5] is carried out with a Mach-Zehnder interferometer using a He-Ne laser source with a wavelength of 632.8 nm. A linearly polarized light beam from the source is divided into two equal parts. One part undergoes a series of polarization changes, such as linear → right circular → SPPs (linear) → linear → left circular → linear passing through different polarizing elements, and follows the path ABCDEA as

shown in Figure 1. An aluminum grating is applied to generate SPPs which travelled towards a nanoslit that is located at a distance of 25 μm from the grating edge and were converted back into freely propagating field. This output field from the slit is represented as point C on the sphere and its polarization state is opposite to state A. A linear polarizer is placed after the slit with transmission orientation the same as that of the output field C. The polarizer is rotated to change the linear polarization direction along the equator, shown as point D on the sphere. Transformation from state D to left circularly polarized state E is performed using a quarter-wave plate. In the experiment, polarizing elements (linear polarizer and quarter-wave plate) after the slit are joined together. As a starting point, before taking the measurements, the polarizer position is adjusted in such a way that the output intensity is maximum; we call this position as 0°. Measurements are taken by rotating the polarizer left and right of the 0° position with an interval of 20°. This changes the solid angle on the sphere. The beam in the other arm of the Mach-Zehnder interferometer does not go through any polarization-state changes. Finally, both beams are combined and their interference is recorded on a CMOS detector. The presence of the geometric phase in one beam appears as a shift of the interference pattern. The variation of the peak shifts for polarizer rotation angles 20° and 40° on both sides of the maximum position 0° is shown in Figure 2 [5].

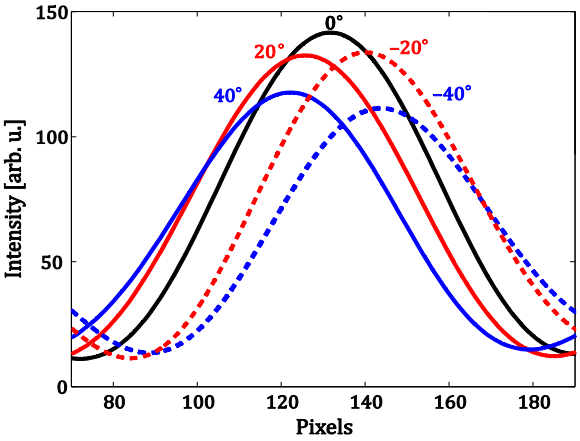

Figure 2. Shift in the interference pattern due to the geometric phase mediated by the SPPs for different angles of rotation of the polarizer. The black solid peak at 0° corresponds to the polarizer position in which the output is maximum (points C and D in Figure 1 coincide). Negative angles -20° and -40° are associated with rotations of the polarizer towards left of the maximum position. Measurements of the interference peak shifts for angles 0°, ±20°, ±40°, and ±60° are in precise agreement with Pancharatnam's rule [5].

The effect of the dynamic phase has been eliminated by aligning all optical components accurately. Hence, a consistent shift of the interference pattern clearly proves the presence of the geometric phase in one of the beams. The conclusion is that surface plasmons mediate the geometric (Pancharantnam-Berry) phase in nanoplasmonic transitions light → SPP → light, and that the geometric phase in such transitions obeys Pancharatnam's theorem.

REFERENCES

1. Maier, S. A., *Plasmonics: Fundamentals and Applications,* Springer, New York, 2007.
2. Daniel, S., K. Saastamoinen, T. Saastamoinen, J. Rahomäki, A. T. Friberg and T. D. Visser, "Dynamic control of optical transmission through a nano-slit using surface plasmons," *Opt. Express,* Vol. 23, No. 17, 22512–22519, 2015.
3. Brosseau, C., *Fundamentals of Polarized Light,* Wiley-Interscience, New York, 1998.
4. Van Dijk, T., H. F. Schouten, W. Ubachs and T. D. Visser, "The Pancharatnam-Berry phase for non-cyclic polarization changes," *Opt. Express,* Vol. 18, No. 10, 10796–10804, 2010.
5. Daniel, S., K. Saastamoinen, T. Saastamoinen, I. Vartiainen, A. T. Friberg and T. D. Visser, "Surface plasmons carry geometric phase," submitted 2017.

Tunable Reflector based on Metal/Insulator/Metal cavity with graphene.

Young Jin Lee[1], Seokhyeon Hong[1], Kihwan Moon[1], and Soon-Hong Kwon[1*]
[1]Dept. of Physics, Chung-Ang University, Republic of Korea
[*]corresponding author: soonhong.kwon@gmail.com

Abstract-We proposed the tunable reflector formed by graphene in Metal/Insulator/Metal cavity. The structure can control the reflectivity not only effectively by strongly confined electric fields but also sensitively by variable permittivity of graphene. Consequently, we can control the reflectivity by modifying the gate voltage of graphene.

Graphene, famous two-dimensional material composed of carbon atoms, has many interesting optical properties due to its unusual band structure as shown in Fig. 1. In this band structure, the optical conductivity is sensitively changed by adjusting Fermi energy induced by gate voltage. The variation of the optical conductivity can be measured by observing change of reflectivity [1]. However, since graphene interacts with the electric field within one atomic width, there is an upper limit to the variation.

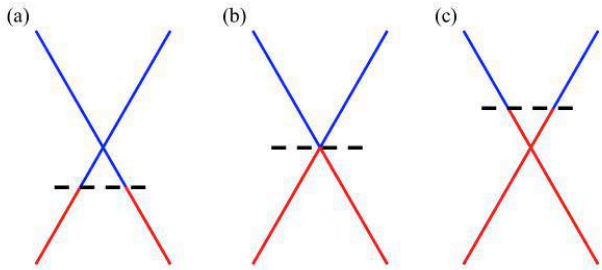

Figure 1: Band structure of graphene when Fermi energy is (a) smaller than, (b) equal to, (c) bigger than Dirac point.

Metal/Insulator/Metal (MIM) structure produces the key of breaking the limit. The MIM cavity strongly confines the lights within sub-wavelength thickness of the insulator layer. When the graphene in the MIM cavity, the light-matter interactions increase by strong field concentration. In addition, since the resonant wavelength of the cavity can be adjusted by changing the distance between the metals, the reflectance can be changed by changing the gate voltage [2]. The reflectivity is also controlled by tuning the resonant wavelength.

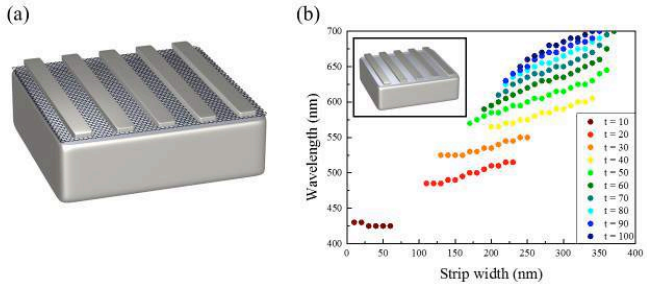

Figure 2: (a) Scheme of Metal/Insulator/Metal cavity with graphene. (b) Maximums of –R (reflectivity) for different width of silver strip and thickness (t) of indium phosphide layer.

In this research, we proposed the structure formed by graphene in MIM cavity as a way to change the reflectivity. The MIM cavity is formed by silver substrate, indium phosphide layer, graphene and periodic silver strips (Fig. 2(a)). As indicated by Fig 2(b), the resonant wavelength is already tunable without graphene by changing the width of silver strip and thickness of indium phosphide layer. However, with graphene, the resonant wavelength can be shifted in situ by using variable permittivity of graphene. The reflectivity is effectively changed because the strongly confined electric fields induced by MIM cavity enhance the interactions between graphene and electric fields. Therefore, we can control the reflectivity sensitively as well as effectively with proposed structure.

REFERENCES

1. Wang, F., Zhang, Y., Tian, C., Girit, C., Zettl, A. Crommie, M. and Shen, Y. R., "Gate-Variable Optical Transitions in Graphene," *Science*, Vol. 320, No. 5873, 206–209, 2008.
2. Kwon, S. –H., "Plasmonic Ruler With Angstrom Distance Resolution Based on Double Metal Blocks," *IEEE Photonics Technol. Lett.*, Vol. 25, No. 16, 1619–1622, 2013.

Enhancing light matter interaction in monolayer MoS_2 with patterned plasmonic nanostructures using two different configurations

Pavithra Sriram[1], Dong-Sheng Su[1], Ta-Jen Yen[1*]
[1] Department of Materials Science and Engineering, National Tsing Hua University, Taiwan, R.O.C
[*]corresponding author: tjyen@mx.nthu.edu.tw

Abstract- Monolayer molybdenum disulfide (MoS_2) has intense attention in recent years for their unique optical properties. However monolayer MoS_2 suffers from insufficient light matter interaction because of its atomically thin nature. Plasmonic nanostructures can be easily integrated and boost the light matter interaction of 2D TMDCs. In this study, we demonstrated the enhanced Photoluminescence of MoS_2 using two different hybrid configurations of Au-MoS_2. Reported results allow us to engineer optical properties of two dimensional materials.

Among two dimensional materials atomically thin transition metal dichalcogenides (TMDCs) exhibit wonderful optical properties because of its optical band gap in the visible regime. Molybdenum disulfide (MoS_2) monolayers are a semiconducting member of TMDCs has unique characteristics to find promising place in future optoelectronics [1]. However monolayer MoS2 suffers from insufficient light matter interaction because of its atomic-thin thickness nature. Plasmonic materials facilitate strong light-matter interaction in Monolayer MoS_2 [2, 3]. In recent years MoS_2-nanoantenna hybrid structures are of great interest owing to its enhanced optical properties. In this study we present two different hybrid configurations of lithography patterned Au nanoantenna and Monolayer MoS_2 for spectrally modified photoluminescence enhancement in monolayer MoS_2.

The nanoantenna arrays were patterned by E-beam lithography technique and lift off process. While large area MoS_2 was grown by CVD method and it was transferred using soft lift-off/ transfer process. Figure 1 depicts the two different configurations of MoS_2-Au nanoantenna hybrid structures. In first configuration MoS_2 was transferred on nanoantenna array, while in second configuration the nanoantenna arrays were patterned on monolayer MoS_2.

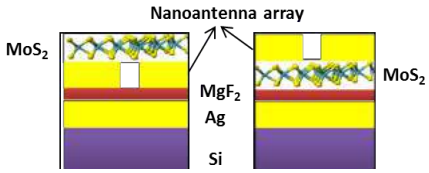

Figure 1: Schematic diagram of two different configurations of MoS2-Au nanoantenna hybrid structures

Figure 2a & 2b shows the optical image of two different configurations of MoS_2-Au nanoantenna hybrid structures. The former shows the successful transfer of MoS_2 on antenna array, whereas the later shows the successful patterning of nanoantenna array on MoS_2.

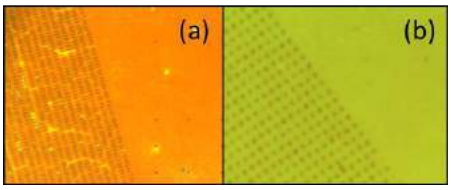

Figure 2: (a) OM image of MoS_2 transferred on nanoantenna array; (b) OM image of antenna array patterned on MoS_2

Using Lumerical FDTD solutions we simulated nanoantenna so as to have resonant wavelength to overlap the emission wavelength of MoS_2 because we are interested in the optical pumping of MoS_2 photoluminescence *via* plasmonic resonance. The blue dotted line in figure 3a shows the emission wavelength of MoS_2 and it's overlapped with the resonant wavelength of designed antenna. Figure 3b depicts the electric filed distribution of nanoantenna with the polarization along the antenna axis at a wavelength of 702nm.

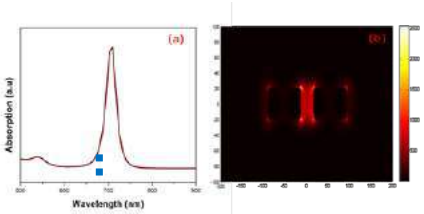

Figure 3: (a) Simulated absorption spectrum of nanoantenna; (b) Electric field distribution of nanoantenna at 702nm (resonant wavelength)

Further PL enhancement studies were carried out for two different hybrid configurations of MoS_2-Au nanoantenna with the 632.5nm laser. Figure 4 shows the PL enhancement for the hybrid structure for both configurations. In both the cases the local near field produced by nanoantenna interacts with the monolayer MoS_2 and this interaction leads to increased optical absorption and number of excitonic pair's photo generated in monolayer MoS_2 leading to PL enhancement of MoS_2. The PL enhancement for MoS_2 on plasmonic structure is high compared to the MoS_2 below the plasmonic structure. This is because of the light extraction efficiency due to plasmonic nanostructures in second configuration dominates the internal quantum efficiency blocking emission from MoS_2.

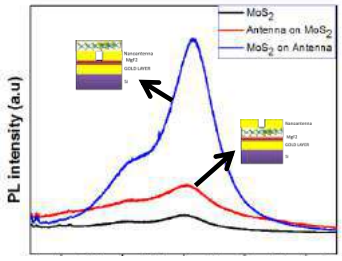

Figure 4: PL enhancement spectrum for two different configuration of MoS_2-nanoantenna hybrid structure

In summary, we have demonstrated the enhanced photoluminescence response of monolayer MoS_2 using surface plasmonic effect based on plasmonic nanostructures. The enhancement is shown when the emission wavelength, resonant wavelength of nanoantenna and incident laser energy is overlapped. The active control of exciton-plasmon coupling would find new opportunities in 2D material based Nanophotonics devices.

Acknowledgements: This project is financially supported by Ministry of Science and Technology (MOST 104-2221-E-007-040-MY3)

References

1. Lopez-Sanchez, O.; Lembke, D.; Kayci, M.; Radenovic, A.; Kis, A. Ultrasensitive Photodetectors Based on Monolayer MoS2. Nat. Nano. 2013, 8, 497–501.
2. Knight, M. W., Sobhani, H., Nordlander, P. & Halas, N. J. Photodetection with Active Optical Antennas. Science 332, 702–704 (2011).
3. Eda, G. & Maier, S. A. Two-Dimensional Crystals: Managing Light for Optoelectronics. ACS Nano 7, 5660–5665 (2013)

Asymmetric Bow-tied Plasmonic Demultiplexer Using Multimode Interference

K. Nakayama[1*], A. Sumimura[1], M. Ota[1,2], R. Watanabe[1], T. Furuki[1], Y. Ishii[1], and M. Fukuda[1]

[1]Department of Electrical and Electric Information Engineering, Toyohashi University of Technology, Japan

[2] JSPS Research Fellow, Japan Society for the Promotion of Science, Japan

[*]corresponding author: knakayama@photon.ee.tut.ac.jp

Abstract- We have demonstrated an asymmetric bow-tied plasmonic demultiplexer for a wavelength division multiplexing system to realize large-capacity information processing. The developed demultiplexer was designed based on a multimode interference structure consisting of patterned SiO_2 on a gold film. This demultiplexer selectively guides 1.31- and 1.55-μm-wavelength plasmonic signals to different output ports. The experimentally measured insertion loss and crosstalk at the developed demultiplexer were ≤ 8.4 dB and ≤ −2.3 dB, respectively.

Integrated circuits using surface plasmon polaritons (SPPs) as signal carriers have attracted attention because the circuits can realize high-speed and large-capacity information processing[1]. The wavelength division multiplexing (WDM) technique, which can transmit different wavelength signals through a single waveguide, is a powerful technique to process a large capacity of information. Recently, several plasmonic demultiplexers, one of the key devices for the WDM technique, have been proposed. Among them, a multimode interference (MMI)-based plasmonic demultiplexer employing dielectric-loaded SPP waveguides (DLSPPWs) enables strong light confinement in the waveguides[2]. Besides, a previous study numerically suggested that the length of the MMI can be shortened by introducing a symmetric bow-tied structure to the photonic MMI devices[3].

In this study, we have demonstrated a MMI-based asymmetric bow-tied plasmonic demultiplexer employing DLSPPWs, which can reduce the size of the demultiplexer and be producible using complementary metal oxide semiconductor compatible processes. Here, we used wavelengths of 1.31- and 1.55-μm-wavelength, which are the optical telecommunication wavelengths. Since the proposed demultiplexer is a linear system, it was necessary to have a long distance to increase the influence of the propagation parameters between the propagation of both wavelengths. The asymmetric structure, which enlarged a second tapered structure, was designed for securing the optical path length. Figure 1 shows a schematic diagram of the proposed demultiplexer. The demultiplexer consisted of four single-mode waveguides and one 1×3 bow-tied MMI structure. The fundamental operation mechanism of the demultiplexer can be explained via the MMI effect[4]. The bow-tied MMI structure can thus reduce the length of MMI devices.

At first, we numerically confirmed the operation of the proposed asymmetric bow-tied demultiplexer using a finite-difference time-domain method (Fujitsu, Poynting for Optics). Next, the designed demultiplexer was fabricated using Au vacuum deposition, SiO_2 sputtering, and subsequent focused ion beam milling (Figure 2). The size of the fabricated demultiplexer was approximately 4.9×11 μm, which cannot be operated at the rectangular MMI devices owing to its size. Figure 3 shows the SPP intensity distributions at the demultiplexer with wavelengths of 1.31 μm and 1.55 μm, as measured using scanning near field optical microscopy. As shown

in Fig. 3, Port1 and Port3 selectively output the 1.55 μm-wavelength signals, and Port2 outputs the 1.31 μm-wavelength signals. The insertion loss and crosstalk were experimentally evaluated to be ≤ 8.4 dB and ≤ −2.3 dB, respectively. The proposed asymmetric bow-tied plasmonic demultiplexer will contribute to the miniaturization of plasmonic demultiplexers and is highly compatible with production processes used to fabricate conventional electronic devices.

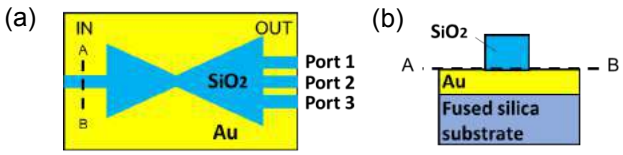

Figure 1. Schematic diagram of the proposed demultiplexer: (a) top view and (b) cross sectional view.

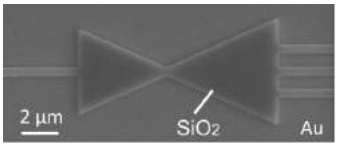

Figure 2. Scanning electron microscope image of the fabricated plasmonic demultiplexer.

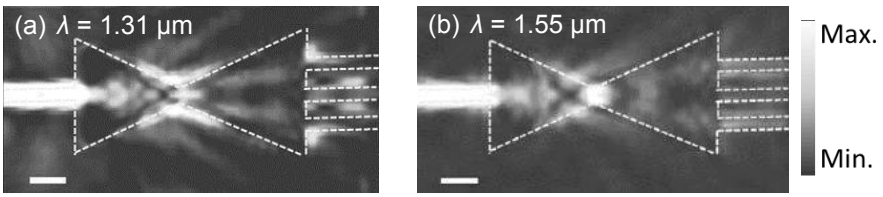

Figure 3. SPP intensity distribution measured at the fabricated demultiplexer, with wavelengths of (a) λ = 1.31 μm and (b) λ = 1.55 μm (scale bar: 2 μm).

Acknowledgements

This work was partially supported by JSPS KAKENHI through Grant Nos. 26289103 and 16K14253 and by a Grant-in-Aid for JSPS Fellows (No. 16J01191).

REFERENCES

1. Ota, M., A. Sumimura, M. Fukuhara, Y. Ishii, and M. Fukuda, "Plasmonic-multimode-interference-based logic circuit with simple phase adjustment," *Sci. Rep.*, Vol. 6, 24546, 2016.
2. Zhu, Z., C. E. Garcia-Ortiz, Z. Han, I. P. Radko, and S. I. Bozhevolnyi, "Compact and broadband directional coupling and demultiplexing in dielectric-loaded surface plasmon polariton waveguides based on the multimode interference effect," *Appl. Phys. Lett.*, Vol. 103, No. 6, 061108, 2013.
3. Lu, H. C. and W. S. Wang, "Analysis of multimode interference coupler with a width of arbitrary-exponent binomial function," *J. Lightw. Technol.*, Vol. 25, No. 9, 2874-2878, 2007.
4. Soldano, L. B. and E. C. Pennings, "Optical multi-mode interference devices based on self-imaging: principles and applications," *J. Lightw. Technol.*, Vol. 13, No. 4, 615-627, 1995.

Fabrication of Al-doped ZnO thin films for plasmonic applications

F. F. Masouleh[1*], I. Sinno[1,2], R. Buckley[3], P. Teal[1], G. Gouws[1], C. Moore[1]
[1]Victoria University of Wellington, P.O. Box 600, Wellington 6140, New Zealand
[2] Callaghan Innovation, 69 Gracefield Road, Lower Hutt 5010, New Zealand
[3] Robinson Research Institute, Victoria University of Wellington, Lower Hutt 5046, New Zealand
[*]corresponding author: fadakafarz@myvuw.ac.nz

Abstract- A sputtering process is presented that enables the deposition of aluminum-doped zinc oxide films with a significant carrier density and thus controllable plasmonic properties. These thin films were characterized using Ultraviolet–visible and Fourier transform infrared spectroscopy, and Hall-effect measurements. Analysis of the results shows a carrier concentration of up to 2.6×10^{20} cm^{-3}, as well as transmission above 80% for 500 nm thick films at wavelengths up to 1900 nm making them well-suited to plasmonic applications.

Transparent conductive oxides (TCOs) have recently been the focus of plasmonics research because of their high density of free electrons and negative permittivity at infrared wavelengths. Conventional gold-, silver-, and aluminium-based plasmonic materials with their very high carrier density of 10^{23} cm^{-3} operate mainly at wavelengths in the visible and UV range, whereas TCOs have the potential to extend plasmonics to a new range of applications in the infrared region of the spectrum that cannot be addressed by metallic plasmonic devices. Among the TCOs, we are especially interested in developing aluminum-doped zinc oxide (AZO) thin films and nanostructures for plasmonic applications [1], due to the relative abundance and non-toxicity of the chemical precursors compared with the widely used indium tin oxide (ITO) [2,3]. In the current study, a fabrication method was investigated that allows for the deposition of high quality AZO thin films with a thickness of 500nm and high transparency at visible and infrared wavelengths, controllable resistivity, and low radiation damage resulting from the fabrication process.

AZO thin films were deposited via off-axis RF magnetron sputtering [4] in order to limit radiation damage from the argon-based plasma used to induce sputtering [5]. This method enables us to achieve highly conductive and transparent AZO films on borofloat33 substrates, paving the way for a variety of plasmonic devices to be fabricated. XRD measurements show that our films have no inherent stresses, and are highly ZnO (002) textured, i.e., they are grown with the ZnO c-axis perpendicular to the substrate surface.

One key goal for our AZO study is to find the frequency where the real part of the permittivity crosses zero, as the film shows metallic behavior below this frequency. We expected this to occur in the near infrared (NIR) part of the spectrum. In order to calculate the exact frequency the carrier concentration of the AZO thin films was measured using Hall-effect system at room temperature with an applied field of 0.55 Tesla. The samples' n-type carrier concentration varies in the range of 3.1×10^{19} to 2.6×10^{20} cm^{-3}, with the higher value comparable to the results reported in [6], indicating desirable plasmonic properties. Using the carrier concentration to calculate the film's plasma frequency resulted in a plasma wavelengths of 1078 nm for the higher carrier concentration, which falls in the NIR part of the spectrum as required.

We are also interested in confirming the transparency of our samples for optical applications. Ultraviolet–visible (UV-Vis) and Fourier-transform infrared spectroscopy (FTIR) measurements indicate that samples are transparent in the visible and infrared ranges, i.e., within the 380 nm to 1900 nm wavelength range, transmission is higher than 80% while reflection is lower than 2%.

In this paper, we have successfully prepared AZO thin films with tuned carrier concentrations and plasma frequencies in the NIR which have the potential of application in plasmonic devices. The goal for future work is to improve the uniformity of our films, and increasing the carrier concentration by 1-2 orders of magnitude.

REFERENCES

1. Grilli, M. L., A. Sytchkova, S. Boycheva and A. Piegari, "Transparent and conductive Al-doped ZnO films for solar cells applications," *Phys. Status Solidi A,* Vol. 210, No. 4, 748–754, 2013.
2. Chen, M. Z. L. Pei, C. Sun, J. Gong, R. F. Huang and L. S. Wen, "ZAO: an attractive potential substitute for ITO in flat display panels," *Mat. Sci. and Eng.: B,* Vol. 85, No. 2-3, 212–217, 2001.
3. Jun, M. C., S. U. Park and J. H. Koh, "Comparative studies of Al-doped ZnO and Ga-doped ZnO transparent conducting oxide thin films," *Nanoscale Res. Lett*, Vol. 7, No. 10, 1064–1076, 2012.
4. Jayaraj, M. K., A. Antony and M. Ramachandran, "Transparent conducting zinc oxide thin film prepared by off-axis rf magnetron sputtering," *B. Mater. Sci.,* Vol. 25, No. 3, 227–230, 2002.
5. Tominaga, K., K. Kuroda and O. Tada, "Radiation Effect due to Energetic Oxygen Atoms on Conductive Al-Doped ZnO Films," *Jpn. J. Appl. Phys.,* Vol. 27, No. 7, 1176–1180, 1988.
6. G. V. Naik, J. Liu, A. V. Kildishev, V. M. Shalaev, and A. Boltasseva, "Demonstration of Al:ZnO as a plasmonic component for near-infrared metamaterials," PNAS, Vol. 109, no. 23, 2012.

High-Performance Metamaterial-Based Transparent Conductive Electrode Using Nano-imprint Lithography Process

Dong-Sheng Su[1], Ta-Jen Yen[1*]

[1] Department of Materials Science and Engineering, National Tsing Hua University, Taiwan, ROC

Corresponding author: tjyen@mx.nthu.edu.tw

(MOST 104-2221-E-007-040-MY3)

Abstract- By applying the beauty of Drude's model, we design metallic meshes to reduce the effective plasmon frequency of metal down to near infrared range, which accomplishes a transparent metal. Due to its metallic nature, the DC conductivity of our designed metallic meshes is still superior to common ITO. Combining these two properties, we successfully realize a metamaterial-based transparent conductive electrode whose transmittance is up to 86.41% in visible spectra and sheet resistance is down to 8.77 Ω/□.

1. Introduction

Currently, indium tin oxide (ITO), which possesses high transmittance (> 80%) and low resistivity (~ 50Ω/□) is the widely used material as a transparent conducting electrode in photovoltaic devices. Yet, ITO suffers from the following five drawbacks including (1) low large-area conductivity, (2) low flexibility, (3) low cost to price value due to scarce indium, (4) low transmittance in blue light region and finally (5) low out-coupling efficiency. Therefore, it becomes a must to develop an alternative material for transparent conducting electrodes to improve the efficiency of photovoltaic devices.

To date, researchers have also focused on a few candidates such as graphenes[1], metal nanowires[2], conducting polymers[3] and so on to replace ITO. Although these alternative techniques own great potentials to replace ITO and even further increase the applications on photovoltaic devices, it is difficult for the abovementioned techniques to integrate with organic light emitting diode (OLED) since an anode should be flat.

On the other hand, low out-coupling efficiency restricts the development of ITO in the field of OLED. The out-coupling efficiency of ITO is only 20% due to mismatched impedances between ITO and free space. Recently, numerous methods have been reported to improve the out-coupling efficiency such as embedding photonic crystals in a glass subtract[4] to overcome the waveguide loss while building a micro-lens array[5] to decrease subtract losses.

In this project, we proposed a metamaterial-based TCE to not only possess high transmittance and low sheet resistance but also could further improve the out-coupling efficiency without any further modification.

2. Metamaterial-based TCE

2.1. Simulation process

We employ finite-difference time-domain (FDTD) simulation software to obtain the transmittance in the visible spectrum of our metamaterial-based TCE with a 1000nm periodicity, a 100nm linewidth and 50nm thickness of gold meshes. Besides, the out-coupling efficiency of our metamaterial-based TCE and ITO could be also extracted out from FDTD simulation by first setting a point light source in emission layer and then measuring the corresponding transmittance through the TCE and ITO beyond a glass substrate. From the simulation, the metamaterial-based TCE possesses reveals a transmittance up to 86% as shown in Fig. 1(a) and an increment out-coupling efficiency of 20% compared of ITO as portrayed in Fig. 1(b).

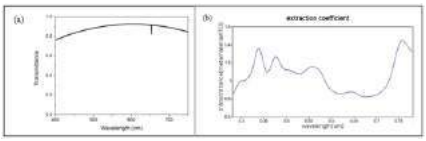

Fig. 1. Finite-difference time-domain (FDTD) simulation result of our metamaterial based TCE. (a) Transmittance in the visible region and (b) out-coupling efficiency normalized by ITO's.

2.2. Fabrication process

We apply a nano-imprint lithography (NIL) process to realize our designed metamaterial-based TCE. We first used an electron beam lithography (EBL) process to define our structure on a silicon substrate as a repeatable mold. We replicate the

pattern from the silicon stamp to a glass substrate with PMMA to define the complementary pattern on the glass substrate. We finally deposited gold on the substrate and carried out lift-off, then we can obtain the realized metamaterial based TCE. Figure 2(a) reveals the flowchart of fabrication process and the corresponding SEM and AFM pictures are shown in Fig. 2(b).

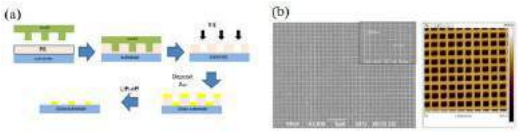

Fig. 2. (a) Fabrication flowchart of the metamaterial based TCE by applying a nano-imprint lithography (NIL) process. (b) SEM and AFM pictures of the metamaterial-based TCE.

3. Result and discussion

Optical transmission measurements were conducted via a UV-Vis with a focal point size of about 50 m in the center of the TCE at the wavelength from 400nm to 700nm, and we further normalize the transmission spectrum by the glass substrate. Figure 3 shows the measurement results of the transmission spectrum. A transmission dip occurs at the wavelength from 600nm to 650nm, which could be attributed to the excitation of surface plasmon polaritons (SPPs) along the individual wires. Furthermore, we also measure the sheet resistance of our metamaterial-based TCE by a multifunctional electrical property system. From the results of Fig. 3, we can conclude that there appears a trade-off between the transmittance and sheet resistance of our metamaterial-based TCE.

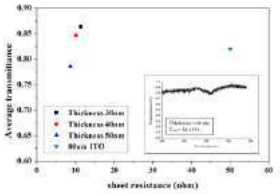

Fig. 3. Measurement result of metamaterial based TCE by UV-Vis with different metal thickness.

4. Conclusion

Metamaterial based TCE possess 3 main advantages to integrate with OLED, which are (1) great opto-electro properties, (2) architecture characteristic, (3) material properties. For opto-electro properties, metamaterial-based TCE could achieve an average transmittance of 86.41% in visible region, meanwhile a sheet resistance of 8.77Ω/□. For architecture characteristic, the nano-grid structure could further improve the out-coupling efficiency and the thin metal film is also beneficial to integrate with opto-electro devices. Finally, the material of metamaterial-based TCE is gold which possesses good ductility, low chemical activity, and high work function. By utilizing these talent of gold, the application of metamaterial based TCE is walking on a road with bright future.

Acknowledgements

This work is supported by National Science Council, Taipei, Taiwan, under Contract No. NSC-104-2221-E-007-040-MY3, NSC-104-2633-M-007-001 and NSC-105-2633-M-007-003

References

[1] S. Bae, H. Kim, Y. Lee, X. Xu, J. S. Park, Y. Zheng, J. Balakrishnan, T. Lei, H. R. Kim, Y. I. Song, Y. J. Kim, K. S. Kim, B. Ozyilmaz, J. H. Ahn, B. H. Hong, S. Iijima, Nature nanotechnology 2010, 5, 574.
[2] H. Wu, L. Hu, M. W. Rowell, D. Kong, J. J. Cha, J. R. McDonough, J. Zhu, Y. Yang, M. D. McGehee, Y. Cui, Nano letters 2010, 10, 4242; H. Wu, D. Kong, Z. Ruan, P. C. Hsu, S. Wang, Z. Yu, T. J. Carney, L. Hu, S. Fan, Y. Cui, Nature nanotechnology 2013, 8, 421.
[3] K. Fehse, K. Walzer, K. Leo, W. Lövenich, A. Elschner, Advanced Materials 2007, 19, 441.
[4] C. Kluge, A. Pradana, J. Adam, M. Gerken, "Multi-Periodic Photonic Crystal Out-Coupling Layers for Flexible OLEDs", presented at *Light, Energy and the Environment*, Canberra, 2014/12/02, 2014.
[5] L. Zhou, H.-Y. Xiang, S. Shen, Y.-Q. Li, J.-D. Chen, H.-J. Xie, I. A. Goldthorpe, L.-S. Chen, S.-T. Lee, J.-X. Tang, ACS Nano 2014, 8, 12796.

Stacked Nanogaps Exciting Strong Fano Resonances

Y. Yu[1], Z. Zhou[2], T. König[1], and A. Fery[1*]

[1]Leibniz-Institut für Polymerforschung Dresden e. V., Germany

[2]State Key Lab of Supramolecular Structure and Materials, Jilin University, China

[*]corresponding author: fery@ipfdd.de

Abstract-In this poster we present a method of fabricating nanogap arrays via a low-cost, versatile method of colloidal lithography. Combing various deposition technologies using colloidal crystal monolayer as initial template, we show here the possibility of obtaining nanogap structures with advanced optical properties with low cost and high throughput. The simulation results show clear Fano resonances occurring because of the presence of nanogap between stacked metallic layers.

Small gaps at nanometer-scale enabled noble metals to be perfect research of interest in the field of plasmonic sensing devices, optical antennas, and nanolasing systems[1]. Due to the ultra-small gap formed in between two metallic components, the coupling effect is usually enormous and hence extreme nanoscale confinement and enhancement of the near electric field intensity[2].

Despite the huge potential in these nanogap devices, challenges still remain in manufacturing the advanced devices with high throughput and reproducibility. Existing fabrication technologies are, in most cases, either time-consuming or of high-cost. Here we propose to fabricate nanogap structures with a combination of bottom-up assembly and top-down patterning strategy in the mean of lower cost and higher throughput. Monolayer of colloidal sphere crystal is used as initial template. By combining various deposition technologies we were able to fabricate nanogap structures of high quality and also over large area. The optical properties proven to be of high electric field enhancement with the possibility of exciting Fano resonances due to the plasmonic hybridization between two metallic parts forming the nanogaps.

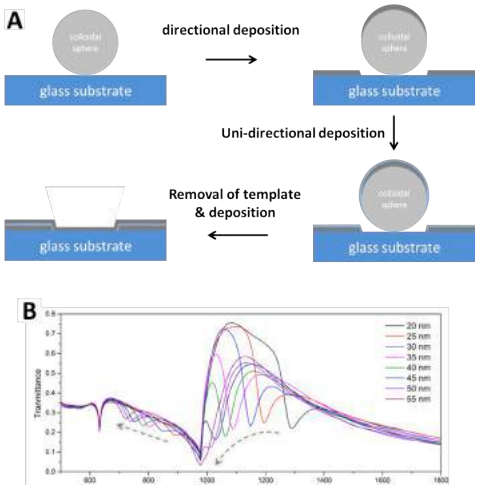

Figure 1: (A) Illustration of the fabrication process of the nanogap arrays by using colloidal lithography. (B)

Evolution of zero-order transmittance upon altering the spacer thickness from 20 nm to 50 nm in step of 5 nm.

Acknowledgements, Y. Yu thanks the Alexander von Humboldt Foundation for the support as Humboldt Postdoctoral Research Fellow. Z. Zhou was supported by the National Natural Science Foundation of China (51673085, 51373066, 51173068) and "111" project (B06009).

REFERENCES

1. Zhou, Z., Zhao, Z., Yu, Y., Ai, B. Möhwald, H., Chiechi, R. C., Yang, J. K. W., and Zhang, G. "From 1D to 3D: Tunable Sub-10 nm Gaps in Large Area Devices," *Adv. Mater.*, Vol. 28, 2956–2963, 2016.
2. Chen, X., Lindquist, N. C., Klemme, D. J., Nagpal, P., Norris, D. J., and Oh, S. –H. "Split-Wedge Antennas with Sub-5 nm Gaps for Plasmonic Nanofocusing," Nano Lett., Vol. 16, 7849-7856, 2016.

Magneto-Optical Effect in Hybrid Plasmonic Nanostructures

Marion Rodier[1], Christopher Kelly[1], Affar Karimullah[1], Calum Jack[1], Ryan Tullius[1] and Malcolm Kadodwala[1]

[1]School of Chemistry, Joseph Black building, University of Glasgow, Glasgow G12 8QQ, UK.

Abstract The magneto-optical effect occurs in magnetic chiral media, and can be detected by use of polarised light. Although this effect is of interest in the study of the light matter interaction, it has not been studied in depth because of the strong magnetic field needed to observe it, and the weakness of the effect. Hybrid plasmonic nanostructures were used to detect a magneto-optical effect. The aim here was also to detect this effect at a low magnetic field with a high intensity.

The magneto-optical effect has been observed, in inorganic material, using strong magnetisation (about 60mT)[3]. The effect is rather small; indeed the change of the angle of polarised light is 1° per T. We propose to study this phenomenon at low magnetic field (8 mT). We therefore used a home design hybrid chiral plasmonic material, consisting of left and right handed nanostructures[4], coated by a layer of 100 nm gold and 100 nm nickel. The nanostructure we used, are called solid-inverse nanostrusture, because they consist in a solid structure (metal layer) and a void (inverse) identical to the structure. These solid and inverse modes can be associated respectably to a bright and a dark mode, by analogy with an orbital molecular diagram. The bright and dark mode being on top of each other can hybridize, giving rise to interferences. The non-linear optical technique, second harmonic generation (SHG) was used to generate S-polarised and P-polarised light. Our material was set up with a magnetic field directed parallel or anti-parallel to the plane of the sample. The absorption of the polarised light, in the magnetised chiral material, relative to the direction of the magnetisation, was recorded. We compared the results from the left and right handed structures with those of non-chiral media. The response changes between P-polarised and S-polarised light, because the polarised light is respectively parallel and perpendicular to the magnetic field. Results show an effect depending on the polarization of the light and the intensity of the magnetic field.

REFERENCES

1. G. H. Wagnière. "*The magnetochiral effect and related optical phenomena*" Chem. Phys. 245 _1999. 165–173.
2. G. L. J. A. Rikken & E. Raupach "*Observation ofmagneto-chiral dichroism*" lett. Nat VOL 390 1997.
3. M. C. Onbasil. et al "Optical and magneto-optical behavior of Cerium Yttrium Iron Garnet thin films at wavelengths of 200–1770 nm" Scientific Reports 6: 23640, 2016.
4. A. S. Karimullah, C. Jack, R. Tullius, V. M. Rotello , G. Cooke, N. Gadegaard , L. D. Barron, and M. Kadodwala: Plasmonics: "*Disposable Plastic Templated Plasmonic Metamaterials with Tunable Chirality*" adv. Mater 201501816.

Infrared tunable absorbers based on electro-optically controlled conducting oxides

D. C. Zografopoulos[1], **G. Sinatkas**[2], **E. Lotfi**[3], **L. A. Shahada**[3], **M. A. Swillam**[4], **E. E. Kriezis**[2], **and R. Beccherelli**[1]

[1] Consiglio Nazionale delle Ricerche, Istituto per la Microelettronica e Microsistemi (CNR-IMM), Via del fosso del cavaliere 100, 00133, Roma, Italy

[2] Department of Electrical and Computer Engineering, Aristotle University of Thessaloniki, Thessaloniki GR-54124, Greece

[3] Department of Chemistry and Earth Sciences, College of Arts and Sciences, Qatar University, P.O. Box 2713, Doha, Qatar

[4] Department of Physics, School of Science and Engineering, The American University in Cairo, New Cairo 11835, Egypt

Abstract— A class of electro-optically tunable infrared plasmonic absorbers is designed and theoretically investigated. The spacer between a subwavelength metallic stripe grating and a ground plane is filled by a bilayer of indium-tin-oxide (ITO) and hafnium oxide (HfO_2). The application of a bias voltage across the dielectric gap induces a free-carrier accumulation layer at the ITO/HfO_2 that locally modulates the ITO permittivity and drastically modifies the optical response of the absorber. The carrier distribution and dynamics are solved via the drift-diffusion model, which is coupled with optical wave propagation studies in a unified finite element method platform. Optimized structures are derived that enable large modulation of the reflected wave amplitude as well as control over the spectral position of the plasmonic resonance.

The dynamic control of the amplitude and/or phase of optical signals is a key property in numerous photonic devices, such as tunable filters, modulators, and switches. Among the various physical platforms employed in the design of tunable photonic components, much attention has been recently focused on the electro-optic control of the free carrier concentration in semiconductors, such as silicon or transparent conducting oxides (TCO). More specifically, it has been demonstrated that the application of a control bias across a metal-dielectric-TCO junction can lead to a free-carrier accumulation layer at the TCO/dielectric interface. Such a layer locally modulates the TCO permittivity and can significantly affect the optical properties of the device, e.g. in the case of epsilon-near-zero-based silicon nanowire modulators [1]. The same effect has been recently extended in the demonstration of mid-infrared amplitude [2] and near-infrared phase [3] free-space modulators, based on plasmonic absorption in thin resonant films [4].

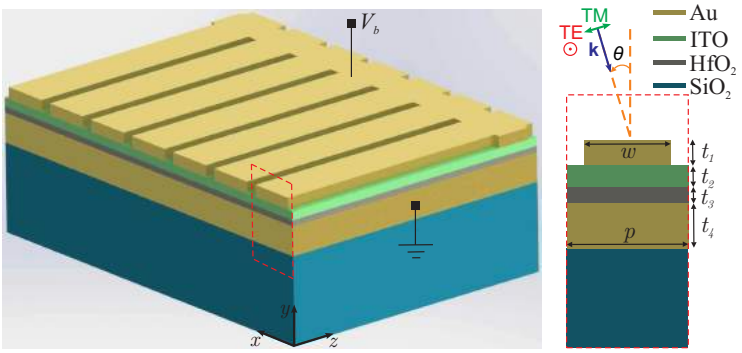

Figure 1: Schematic layout of the proposed electrically tunable near-infrared absorber. The dielectric spacer between the ground plane and an Au grating is composed of two thin films of haffnium oxide and indium-tin-oxide. By applying a bias voltage, a free-carrier accumulation layer is formed at the ITO/HfO_2 interface, which modulates the optical response of the absorber.

In this work, we present the design of electro-optically tunable near-infrared perfect plasmonic absorbers, based on the generic layout of Fig. 1. The resonant plasmonic cavity is formed between a

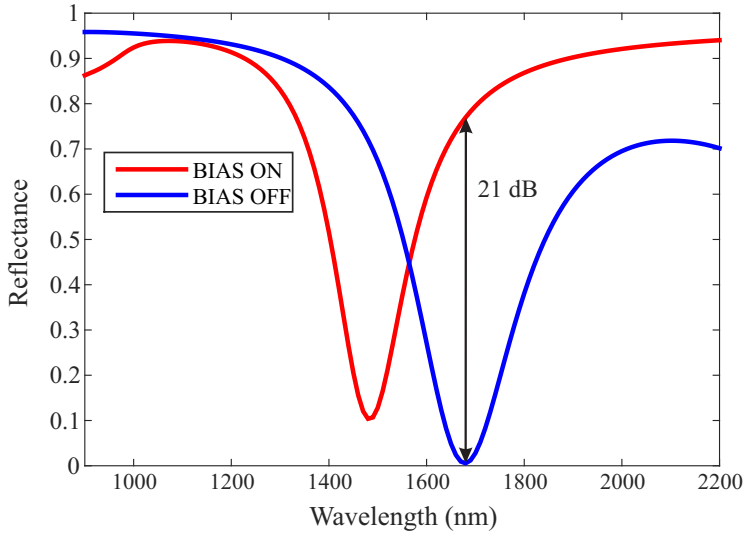

Figure 2: Modulation of the reflected light amplitude by switching ON and OFF the bias control voltage in the proposed TOC-based electro-optically tunable plasmonic absorber.

ground plane and a Au stripe grating patterned on a bilayer consisting of ITO and HfO_2. By properly selecting the geometrical parameters, critical coupling of the impinging planewave is achieved, such that 100% absorption is achieved at the resonant frequency. When a bias voltage V_b is applied, a nanometric thin layer of free-carriers accumulates at the ITO/HfO_2, locally changing the ITO permittivity, which progressively shifts from positive to near-zero and finally negative values. The optimization of the absorber's design leads to large amplitude modulation, as in the case shown in Fig. 2, which corresponds to a structure with $g = 190$ nm, $p = 220$ nm, $t_1 = 100$ nm, $t_2 = 3$ nm, $t_3 = 17$ nm, and $t_4 = 20$ nm.

ACKNOWLEDGMENT

This work was made possible by a NPRP award [NPRP 7456-1-085] from the Qatar National Research Fund (member of the Qatar Foundation). The statements made herein are solely the responsibility of the authors.

REFERENCES

1. G. Sinatkas, A. Pitilakis, D. C. Zografopoulos, R. Beccherelli, and E. E. Kriezis, "Transparent conducting oxide electro-optic modulators on silicon platforms: A comprehensive study based on the drift-diffusion semiconductor model," *J. Appl. Phys.*, Vol. 121, 023109, 2017.
2. J. Park, J.-H. Kang, X. Liu, and M. L. Brongersma, "Electrically tunable epsilon-near-zero (ENZ) metafilm absorbers," *Sci. Rep.*, Vol. 5, 15754, 2015.
3. Y.-W. Huang, H. W. H. Lee, R. Sokhoyan, R. A. Pala, K. Thyagarajan, S. Han, D. P. Tsai, and H. A. Atwater, "Gate-tunable conducting oxide metasurfaces," *Nano Lett.*, Vol. 16, 5319, 2016.
4. C. Wu, B. Neuer, G. Shvets, J. John, A. Milder, B. Zollars, and S. Savoy, "Large-area wide-angle spectrally selective plasmonic absorber," *Phys. Rev. B*, Vol. 84, 075102, 2011.

Surface nanostructuring for high-resolution surface plasmon resonance imaging.

F. A. Banville[1,2,3], M. Sarkar[1,3], C. Colin[1,2], J. Moreau[3], M. Besbes[3], M. Canva[1,2,3], and P. G. Charette[1,2*]

[1]Laboratoire Nanotechnologies Nanosystèmes (LN2) UMI-3463, CNRS-Université de Sherbrooke, Canada
[2]Institut Interdisciplinaire d'Innovation Technologique (3IT), Université de Sherbrooke, Canada
[3]Laboratoire Charles Fabry, Institut d'Optique Graduate School, Université Paris-Saclay, CNRS, France
*corresponding author: Paul.G.Charette@usherbrooke.ca

Abstract— Surface plasmon resonance imaging is a very effective technique for studying surface phenomena in complex biological materials. However, its spatial resolution is limited by the propagative nature of the surface plasmons. In this work, we studied exhaustively by numerical simulations the excitation of surface plasmons on continuous films, and we demonstrate how a higher resolution can be achieved by nanostructuring the metal surface. This method can significantly reduce the surface plasmons propagation length from several micrometers to submicrometer distances.

Surface plasmon resonance imaging (SPRI) is a label-free technique sensitive to small variations of refractive index in a dielectric medium at the surface of a thin metal layer. However, the finite propagation distance of the resonant mode results in a directional blur along the direction of mode propagation, limiting the spatial resolution. It is especially problematic in high magnification microscope objective-based systems [1, 2] where diffraction-limited resolution is expected. In this work, we first give a description of the mechanisms involved in the coupling of a plasmonic mode, in particular the role of phase accumulation. Analytical and numerical calculations will be presented to describe such a mechanism for the simplest configuration used in SPRI, which is a thin continuous metal film. These results are also confirmed experimentally and show that the accumulation of phase required to stabilize the plasmon resonance, which is directly related to the minimum spatial resolution achievable, strongly depends on the system being in resonance or slightly off-resonance. The numerical model used for the simulations is a hybrid of the finite element method (FEM) and the periodic Fourier modal method (FMM) [3].

We studied the impact of nanostructuring the metal surface on the spatial resolution measured in SPRI. This effect is based on the properties of the hybrid plasmonic mode that can be excited in a periodic array of gold nanostructures, fabricated on a continuous gold film [4]. As stated previously, surface nanostructuring can enhance the spatial resolution, but not without compromise. Indeed, sensitivity and image contrast can be significantly diminished depending on the parameters of the grating [5]. To reduce these drawbacks, we have optimized the numerical simulations to take into account all key performance metrics of the plasmonic mode: bulk and surface sensitivity (S_b, S_s), penetration depth of the evanescent wave (L_y), and attenuation length (L_x). The bulk sensitivity represents the intensity variations (ΔR in %) at the operation point (angle of highest variation of reflectivity) for a bulk variation of refractive index in the dielectric medium (Δn=0.07), while the surface sensitivity corresponds to the ΔR resulting of a nanometric biological layer thickness change (n = 1.48). The performance metrics were compared with those of a continuous film (thickness chosen for optimal coupling) to evaluate the impact of nanostructuring. For example, we took a sample of BK7 glass/3 nm Cr/50 nm continuous layer Au/Water @ λ = 800 nm, and obtained the following: L_x = 9.68 μm, L_y = 342 nm, S_b = 42.9% and S_s = 6.47%. When the 50 nm layer was structured with a 2D grating (25 nm of continuous Au, 25 nm of nanostructures, grating period of 400 nm, lines width of 200 nm), we obtained the following: L_x = 2.0635 μm, L_y = 291 nm, S_b = 30.3% and S_s = 2.11%. While there was a drop in sensitivity (ΔS_b = -30%, ΔS_s = -67%) and in penetration depth (ΔL_y = -15%), the attenuation length was improved by a factor of 4.7. Subwavelength resolution can be obtained using a high index glass substrate.

In addition, nanostructuring the metal layer significantly reduces the oscillatory perturbations that arise from an abrupt variation of refractive index in the dielectric medium as shown in figure 1a,

where the reflected electrical field was estimated with an analytical model [6]. In this figure, conditions of resonance are optimized in water, and the abrupt variation of refractive index from water to PDMS (n = 1.33–1.4) results in multiple oscillatory perturbations of the electrical field. Those oscillations are almost completely eliminated due to the rapid attenuation of the hybrid plasmonic mode. Experimental results confirmed this impact on the oscillatory perturbations. Numerical simulations on 3D structures are currently ongoing and should present a higher confinement of the plasmonic mode and a reduced attenuation length.

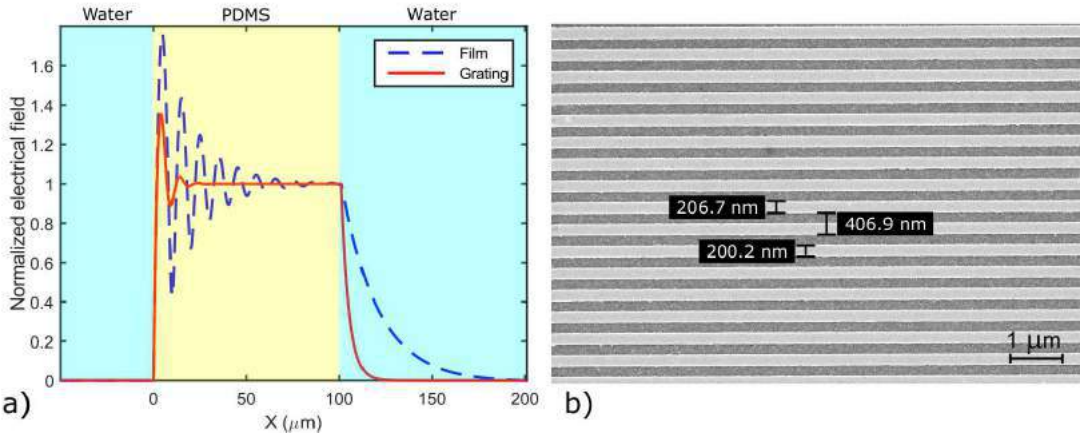

Figure 1: (a) Analytical modelling of an abrupt variation of refractive index in the dielectric medium (Δn=0.07). Amplitude of oscillatory perturbations less important with a grating structure. (b) Nanostructured sample fabricated by electrolithography. Gold line dimensions: 200 nm of width, 400 nm of period, 25 nm of thickness on a 25 nm thick film.

ACKNOWLEDGMENT

This work is supported by the Natural Sciences and Engineering Research Council of Canada (NSERC). FAB is supported by a doctoral scholarship from the Fonds de recherche du Québec - Nature et technologies (FRQNT) and by a French ministerial doctoral contract (MESR) with the Université Paris-Saclay. LN2 is a joint International Research Laboratory (Unité Mixte Internationale UMI 3463) funded and cooperated in Canada by Université de Sherbrooke (UdeS) and in France by CNRS as well as Université de Lyon (UdL, especially including ECL, INSA Lyon, CPE) and Université Grenoble Alpes (UGA). It is also associated to the French national nanofabrication network RENATECH and is supported by the FRQNT.

REFERENCES

1. Huang, B., F. Yu and R. N. Zare, "Surface plasmon resonance imaging using a high numerical aperture microscope objective," *Anal. Chem.*, Vol. 79, No. 7, 2979–2983, 2007.
2. Banville, F. A., T. Söllradl, P.-J. Zermatten, M. Grandbois and P. G. Charette, "Improved resolution in SPR and MCWG microscopy by combining images acquired with distinct mode propagation directions," *Opt. Lett.*, Vol. 40, No. 7, 1165–1168, 2015.
3. Besbes, M., J. P. Hugonin, P. Lalanne et al., "Numerical analysis of a slit-groove diffraction problem," *J. Eur. Opt. Soc, Rapid Publ.*, Vol. 2, 07022, 2007.
4. Sarkar, M., M. Besbes, J. Moreau et al., "Hybrid Plasmonic Mode by Resonant Coupling of Localized Plasmons to Propagating Plasmons in a Kretschmann Configuration," *ACS Photonics*, Vol. 2, No. 2, 237–245, 2015.
5. Kim, D. M. and D. Kim, "Subwavelength grating-based nanoplasmonic modulation for surface plasmon resonance imaging with enhanced resolution," *J. Opt. Soc. Am. B*, Vol. 27, No. 6, 1252–1259, 2010.
6. Berger, C. E. H., R. P. H. Kooyman, and J. Greve, "Resolution in surface plasmon microscopy," *Rev. Sci. Instrum.*, Vol. 65, No. 9, 2829–2836, 1994.

Influence of oxygen on photochemical transformation of silver nanoparticles

KaroliKołątaj[1]*, Jan Krajczewski[1], Andrzej Kudelski[1]
[1]University of Warsaw, Faculty of Chemistry, Poland
*corresponding author: kkolataj@chem.uw.edu.pl

Abstract One way to obtain metallic nanoparticles with different shapes is employment of light in phototransformation method. In this approach one can obtain nanoparticles with the desired final geometry by changing wavelength of light used for irradiation. This method of synthesis of nanoparticles allows obtaining less contaminated nanoobjects. In this work we have also present the first example of phototransformation in oxygen-free environment (as an oxidizing agent 1,4-benzoquinone has been used).

Light is a very valuable tool enabling to obtain various silver nanoparticles. The first report of such approach describes phototransformation of silver spherical nanoparticles into nanoprisms through light illumination. After this report many other works about phototransformation of spherical nanoparticles to structures with different shapes and different optical properties have been published. For example, Zhang group utilized this method to obtain nanorods, and Kitaev group was able to obtain silver decahedrons from once spherical nanoparticles. The main advantage of this method compared with typical chemical approaches of synthesis of anisotropic nanoparticles is that the final solution of nanoparticles after phototransformation is significantly easier to purify. While in a typical chemical synthesis there is a need to use some compounds to drive specific shape transformation, there is no such need in phototransformation method because final geometry of nanoparticles depends on the wavelength of used light.

The phototransformation is a reaction incorporating two independent processes. The first one is a slow dissolution of silver nanoparticles under the influence of an oxidizing agent present in a solution. The second process is a photochemical reduction of silver ions at the specific sites of nanoparticles. As far as we know there was no previous report concerning phototransformation of silver nanoparticles in the deoxygenated solution (in all previous phototransformations oxygen has been used as an oxidizing agent).

In this work, we show the first example of phototransformation with 1,4-benzoquinone used as oxidizing agent instead of oxygen. We also investigated the SERS activity of obtained silver nanopartilces using 3 model Raman scatterers: crystal violet, rhodamine 6G and p-mercaptobenzoic acid. The nanoparticles obtained in the oxygen free phototransformation was about 2.5 times more SERS-active than the Ag nanoparticles transformed under air conditions.

Acknowledgements This project was financed from the funds of the National Science Centre (Poland) allocated on the basis of the decision number DEC-2012/07/B/ST5/02462.

REFERENCES

1. Jin R, Cao, T., Mirkin, Ch. A., Kelly, K. L. and G. C. Schatz, J. G. Zheng, Photoinduced Conversion of

Silver Nanospheres to Nanoprisms. Nature, 294, 1901-1903, 2001
2. Zhang, J., Langille, M. R. and Ch. A. Mirkin, Synthesis of silver nanorods by low energy excitation of spherical plasmonic seeds, Nano Letters, 11, 2495-2498, 2011.
3. Xue, C., Chen X., Hurst S. J. and C. A. Mirkin, Self-Assembled Monolayer Mediated Silica Coating of Silver Triangular Nanoprisms, Adv. Mater., Vol. 19, 4071–4074, 2007.

Full Color display using extraordinary optical transmission in silver block array

Kihwan Moon[1], Young Jin Lee[1], Seokhyeon Hong[1], and Soon-Hong Kwon[1*]
[1]Dept of Physics, Chung-Ang University, Seoul 06974, Korea
[*]corresponding author: soonhong.kwon@gmail.com

Abstract-The transmission-type display requires high intensity of transmitted light. However, the metal structure has high reflectance and absorbance. To overcome disadvantages, we introduced extraordinary optical transmission (EOT). A transmitted light through subwavelength scale metal apertures is enhanced by EOT. In addition, EOT has narrow peak in narrow aperture. We obtained green and red colors, which have high transmittance over 80 %, and blue color transmission spectrum using cross-shape slit array consisted of silver nanoblocks.

Metallic structure with subwavelength scale apertures has transmission peak [1]. Phenomenon that transmission is enhanced in metal apertures, extraordinary optical transmission (EOP), is generated by incident light and various modes of surface plasmons. However Metallic devices using transmitted light need incident light with high intensity because of ohmic loss in metal. Besides, single peak spectrum is required to show vivid color.

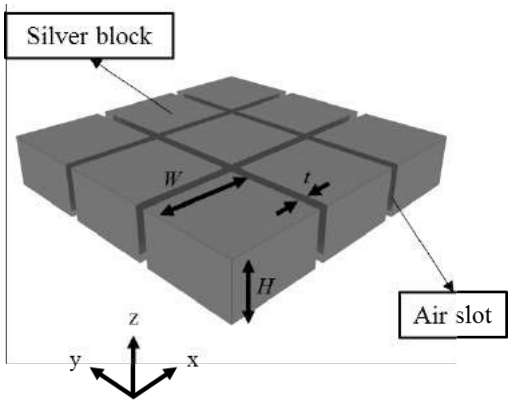

Figure 1. Schematic of color display using silver block array. Transmitted electromagnetic field through the air slit between silver block is enhanced by extraordinary optical transmission.

We demonstrate high transmittance color display using cross shape air slit array that is consisted of silver nanoblocks, as shown in figure 1. Incident light, that is linearly polarized, propagates along the z-direction. The y-direction width of silver block is set to same length with x-direction width for polarization independent transmission. The transmitted light through narrow air slit is enhanced by EOT and the peak wavelength of EOT can be controlled by change of size of silver block. The wavelength of EOT has strong dependence of height (*H*) of silver. The peak of wavelength is increased as the *H* increases.

The width (W) of silver block and thickness (t) of air slit are fixed, W = 250 nm and t =20 nmm as shown in figure 2 (a). In figure 2 (b), Blue color (H = 70 nm) has narrow linewidth and transmission of 60 %. Green (H = 110 nm) and red (H = 150 nm) colors show high transmittance over 80 %. Ex- and Ey-polarized incident light show same transmission spectrum (figure 2 (b)). Optical properties of proposed structure are simulated by using finite-difference time-domain method, and colors are represented by CIE RGB [2].

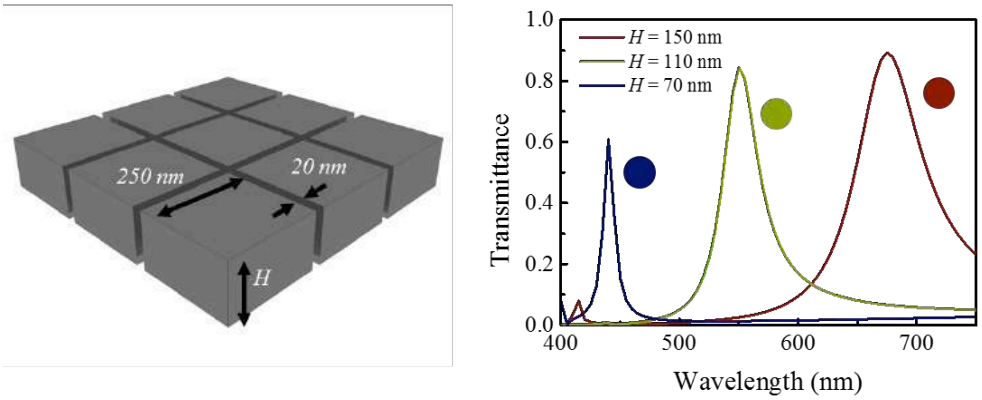

Figure 2. Optimized structure and transmittance spectrum of Red, green, blue. The width of silver block and slit thickness are 250 nm and 20 nm, respectively. Three line colors represent the color samples with heights of 70, 110, 150 nm.

In this research, we suggest the high transmittance color display consisting of silver nanoblock. Blue, green and red colors can be implemented by changing only the size of nanoblock. In addition, proposed structure has advantages, high transmittance in metallic device and low optical loss by independence of polarization. Therefore, silver nanoblock array can be used for full color transmission-type display.

REFERENCES

1. Ebbesen, T. W., H. J. Lezec, H. F. Ghaemi, T. Thio and P. A. Wolff, “Extraordinary optical transmission through sub-wavelength hole arrays” *Nature*, Vol. 391, No. 6668, 667–669, 1998.
2. Rossel, R. A. V., B. Minasny, P. Roudier, A. B. McBratney, “Colour space models for soil science”, *Geodema*, Vol. 133, No. 3–4, 320–337, 2006.

Light enhancement dependence on organic film thickness caused by the generation of surface plasmons in phase and their scattering

Y. Mizoguchi[1], T. Yoneda[1], T. Ishiguro[1], K. Kasahara[1], N. Ikeda[2], and Y. Sugimoto[2]
[1]Ritsumeikan University, Kusatsu, Shiga 525-8577, Japan
[2]Nanotechnology Innovation Center, National Institute for Materials Science, Tsukuba, 305-0047, Japan
*corresponding author: kasahara@se.ritsumei.ac.jp

Abstract- Net Photoluminescence enhancement of Alq_3 on Ag was estimated, changing the Alq_3 thickness by removing the optical interference effect occurring inside the film. Enhancement difference observed for devices with different Alq_3 thicknesses can be explained by aggregate behavior of the energy transfer of excitons to surface plasmons.

Light loss due to surface plasmons (SPs) is still one of the fundamental considerations in the design of high-efficiency organic light emitting diodes. The energy converted from excitons to SPs can be extracted as output light again by SP scattering caused by naturally formed submicrometer-scale surface roughness of the cathode metal. So far, we have pointed out that experimentally obtained light enhancement could not be explained by the previously reported calculation formula for the plasmon scattering rate, and that simultaneous plasmon generation from excitons in phase is probable to occur[1)]. To discuss the phenomenon, it is important to estimate the true light enhancement. To that end, the optical interference effect must be removed from measured results, and the rate of radiation distribution along the film thickness is vital to take into account in the calculation of the optical interference. The distribution of remaining excitons in the direction of film thickness which is involved in light emission, affects the estimation of the interference effect. In this study, angular dependence of light enhancement was measured for Alq_3 films with different thicknesses on Ag. They were compared with the results obtained by the optical interference calculation factoring in the above respect to obtain the net enhancement.

Figure 1 (a) shows the result of photoluminescence enhancement obtained by the light output of Alq_3/Ag/glass divided by that of Alq_3/glass/Ag. The use of Alq_3/glass/Ag as a reference device instead of a normal Alq_3/glass was because when using Alq_3/glass, fluorescence which was emitted toward a glass substrate brought ambiguity to the subsequent optical interference calculation. The both thicknesses of Alq_3 were 60 nm, and the excitation was done with a 405-nm laser diode. Solid lines show the enhancement at 0 (normal to the substrate surface) and 60 degrees.

In the optical interference calculation, the coherence length of photons estimated from a phase coherence time of ~100 fs at room temperature was 36 μm. This was equivalent to an absorption coefficient of 2.8×10^2 cm^{-1}, and was smaller than the Alq_3 absorption coefficient of ~10^3 cm^{-1}. Thus, the latter value was used in the optical interference calculation. Compared to the florescence rise time of ~10 ns of Alq_3, the time of exciton-to-SP conversion was much shorter. Thus, it is reasonable to assume that the exciton distribution is determined a priori before light emission in the calculation[2)]. The radiation rate for *s*-polarization at a certain positon comes from remaining dipoles at that position oscillating parallel to the surface of the metal. Parallel and perpendicular dipoles contribute *p*-polarization. Absorption of the excitation light measured for the two devices

through the reflection was taken into the calculation. Figure 2 (a) shows the observed enhancements and calculated results for 60-nm Alq_3, which reached to 2.3 and 3.1 at 0 and 60 degrees. It was assumed in the calculation that oscillating dipoles below 40 nm didn't emit radiation in our devices. Actually, the emission power lowered rapidly, when the Alq_3 thickness was less than 40 nm. This was probably because nonradiative components were formed in early phase of evaporation. Measured light enhancements were 3.0 and 3.3 at peaks at 0 and 60 degrees, respectively, and were higher than the numerical results. The interference effect from dipoles reaches maximum when they are at the top surface of Alq_3. Compared with the maximum numerical results, experimental results were higher. The results of 200-nm Alq3 are shown in Fig. 1 (b). It was found that measured light enhancement fell below the calculation, and that substantial enhancement was not gained.

The light enhancement at a certain wavelength $M(\lambda)$ is expressed as

$$M(\lambda)=\int_0^d \left\{\eta+\eta(P_s(z)-1)P_g(z)+(1-\eta)\overline{P_s}P_{ng}(z)\right\}dz \Big/ \int_0^d \eta dz \quad (1)$$

Here, z: distance from the metal, d: thickness η : radiative rate without metal, $P_g(z)$: SP generation rate, $P_s(z)$: SP scattering probability, $\overline{P_s}$: scattering probability independent of z, and $P_{ng}(z)$: energy transfer probability of the nonradiative component to SP. As z approaches zero, P_g increases, leading to generation of a higher number of SPs, N. However, on the assumption that these SPs have the same phase, P_s increases in proportion to N . Accordingly, the second term in the integral part of Eq. (1) contributes more to a positive value, which can explain the light enhancement dependence in the film thickness.

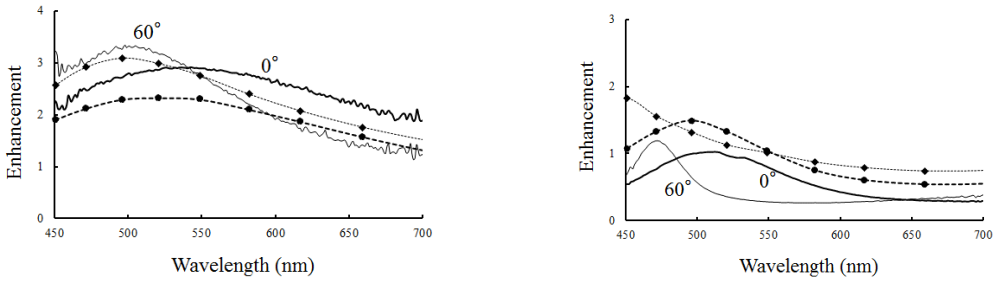

Figure 1 Experimentally observed light enhancement of Alq_3 on Ag (solid lines) and the optical interference effect (dotted lines). Circle: 0 degree and diamond: 60 degree. The thickness of Alq_3 is (a) 60 nm and (b) 200 nm.

REFERENCES

1. T. Inui, Y. Mizoguchi, T. Yoneda, T. Ishiguro, K. Kasahara, N. Ikeda, and Y. Sugimoto, "Enhanced light emission in organic materials caused by constructive surface plasmon generation and scattering", in *Proceedings of* the 7th International Conference on Metamaterials, Photonic Crystals and Plasmonic (META2016), Torremolinos-Malaga, Spain, P15, July 25-28, 2016.
2. W.H. Weber and C.F. Eagen, "Energy transfer from an excited dye molecule to the surface plasmons of an adjacent metal", *Opt. Lett.,* Vol. 4, 236-238, 1979.

High Q-factor dual band tunable polarization independent THz flexible metasurface for chemical sensing applications

M. Janneh[1], A. Tenggara[2*], A. De Marcellis[1], D.Byun[2], and E. Palange[2]

[1]Department of Industrial and Information Engineering and Economics, University of L'Aquila, Italy

2 Department of Mechanical Engineering, Sungkyunkwan University, South Korea

[*] corresponding author: ayodya.tenggara@skku.edu

Abstract - We report on the electromagnetic properties of a flexible dual band THz tunable metasurface able to achieve absorption coefficients and quality-factors up to 99.8% and 120, respectively. The metasurface elemental unit shape and bending capability allow for a polarization insensitive spectral response and for a resonance frequencies fine tuning. Moreover, minimum variations of non-absorbing substances refractive index up to 5×10^{-5} can be identified by using the absorber as a sensing device with detection sensitivities up to 250GHz/RIU.

Among the achievable metasurface (MS) functionalities, perfect THz absorbers emerged for their important potential applications like spectroscopic imagers, high sensitive detectors and chemical and drug sensors [1]. In particular, for these specific applications a polarization insensitive, narrow spectral bandwidth and high quality-factor (Q-factor) of the MS spectral response is essential for optimizing the device performances together with the possibility to tune the MS frequency for which perfect absorption conditions are achieved [2]. However, the main drawback for the enhancement of the MS-based device sensitivity is the low Q-factor achievable that often is unsuitable in detecting extremely small changes of the MS resonance frequency due to the presence of some specific substances close to or adsorbed on the MS. Furthermore, most of the THz absorbers reported in literature operate at fixed resonance frequencies since they are fabricated on rigid dielectric structures. In this communication, we present a novel fine frequency-tunable polarization insensitive high Q-factor dual-band THz absorber. Along the propagation direction of the electromagnetic (EM) radiation, the dual band absorber is composed from top to bottom of a 2D-array of Ag plasmonic nanoantennas (NA) elemental cells realized onto a flexible dielectric polyimide (PI) film that separates the 2D-array from an Ag ground layer covering the whole NA area. Referring to Fig.1a), the NA unit cell is composed of two concentric Ag square rings and a cylinder located at the NA geometrical center that can be realized by employing the electro-hydrodynamic jet printing technique [4]. We performed numerical simulations by using finite element method in the frequency domain to study the MS EM response in terms of the dual band resonance frequencies, the maximum achievable absorption coefficients, the frequency tunability as well as the dependence on the polarization of the impinging EM radiation. For the simulations, the 2D-array was obtained from the NA unit cell by using periodic boundary conditions along the x- and y-axes and the scattering boundary conditions along the EM wave propagation direction, i.e. the z-axis. The simulations were performed by fixing at $|E_0|$=1V/m the value of the electric field of the incident EM radiation, (x;z) the plane of incidence, and the EM properties of the metasurface have been evaluated by employing TM an TE linear polarized EM plane wave. In Fig.1b) we report the MS spectral response in the case of the TM polarization (identical results are obtained for TE polarization due to the symmetry of the NA unit cell). The absorber shows a double resonance behavior centered at f_1=1.80THz and f_2=2.26THz with absorption coefficients equal to 0.998 and 0.996, respectively. Referring to Fig.1a, the NA

geometrical parameters were chosen as L_x=100μm, L_1=85μm, L_2=50μm, d=20μm and the Ag MS film thickness was 0.2μm. The achieved Q-factors are equal to 120 and 95 for the f_1 and f_2 frequency resonances, respectively, being more than 2 times larger than those ones recently reported for a dual band MS absorber [3]. In terms of the resonance frequency bandwidth measured at full-width-half-maximum, we obtain Δf_1=15GHz and Δf_2=24GHz. Since the MS structure is flexible due to the presence of the PI layer, we investigated the possibility to tune the absorber resonances. For a variation of the NA radius-of-curvature from infinity to R=69μm of the NA unit cell, the f_2 resonance presents a blue shift of 110GHz with a 17% decrease of the Q-factor maintaining constant the absorption coefficient. Under the same conditions, the value of the f_1 resonance remain constant with an 8% and 23% decrease of the Q-factor and maximum absorption coefficient, respectively. Furthermore, we investigated the possibility of the proposed dual-band absorber MS to be used as a sensor device to measure the change of the refractive index of substances for chemical/biological applications. For this purpose, a layer of 4μm of a non-absorbing substance (i.e. an analyte) has been superimposed on top of the MS structure (i.e. adsorbed on the NA 2D-array). Fig.1c) shows the frequency shift of both f_1 and f_2 absorber resonance frequencies as a function of the variation of the refractive index of the superimposed substance. In terms of Refractive Index Unit (RIU), the resulting linear dependence allows calculating sensor detection sensitivity equal to 250GHz/RIU and 141.3GHz/RIU for f_1 and f_2 absorber resonance frequencies, respectively. Taking into account the value of Δf_1=15GHz and the resolving power Rayleigh criterion, the minimum change of the refractive index due to any kind of physical/chemical modification is equal to 5×10^{-5}.

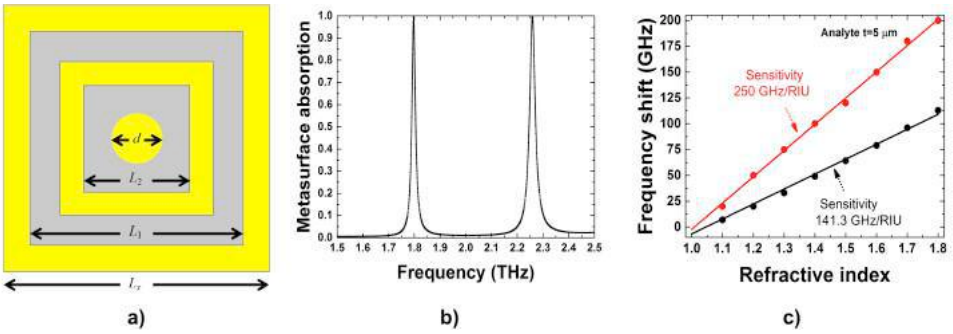

Figure 1: a) top view of the NA 2D-array metasurface unit cell; b) metasurface absorption as a function of the frequency; c) frequency shift of the f_1 (dots) and f_2 (squares) resonance frequencies as a function of the variation of the refractive index of the substance adsorbed on the MS.

REFERENCES

1. F. J. Federici, B. Schulkin, F. Huang, D. Gary, R. Barat, F. Oliveira, D. Zimdars, "THz imaging and sensing for security applications-explosives, weapons, and drugs", *Semicond. Sci. Technol.*, Vol. 20, No. 7, S266–S280, 2005.
2. Y. Q. Wen, W. H. Zhang, S. Y. Xie, H. Q. Yang, and L. Y. Liu "Dual band terahertz metamaterial absorber: design, fabrication, and characterization", *Appl. Phys. Lett.*, Vol. 95, 241111-241114, 2009.
3. B. X. Wang, X. Zhai, G. Z. Wang, W. Q. Huang, and L. L. Wang, "A novel dual-band terahertz metamaterial absorber for a sensor application", *Appl. Phys. Lett.* Vol. 117, 014504-1-014504-5, 2015.
4. A. P. Tenggara, S.J. Park, H. T. Yudistira, Y.H. Ahn and D. Byun "Fabrication of terahertz metamaterials using electrohydrodynamic jet printing for sensitive detection of yeast," *J. Micromech. Microeng*. Vol. 27, 035009, 2017.

Photonic Crystal-based Magnetoplasmonic Heterostructures with Garnet for Surface Plasmon Resonance Sensors

D. O. Ignatyeva[1,2], S. K. Sekatskii[3*], P. O. Kapralov[2], G. A. Knyazev[1,2], M. Nur-E-Alam[4], M. Vasiliev[4], K. Alameh[4], and V. I. Belotelov[1,2]

[1]Lomonosov Moscow State University, Faculty of Physics, Russia

[2]Russian Quantum Center, Russia

[3]École Polytechnique Fédérale de Lausanne, Institute of the Physics of Biological Systems, Switzerland

[4] Edith Cowan University, Electron Science Research Institute, Perth, Australia

[*]corresponding author: serguei.sekatski@epfl.ch

Abstract-The work is devoted to the study of the novel layered heterostructures with 1D photonic crystals and magnetooptical garnet layers providing ultra-high quality factor magnetoplasmonic resonances. Such structures are specially designed to exhibit ultra-narrow resonances due to the excitation of the long-range propagating magnetoplasmon with the experimentally observed propagation distance of 50 um. Experimentally obtained FOM in such structures is up to 2200 which makes it very promising for sensing applications.

We present a novel type of magnetoplasmonic heterostructures containing one-dimentional photonic crystals and magnetooptical garnet layers. Such structures are specially designed to exhibit ultra-narrow resonances of the magnetooptical transverse Kerr effect (TMOKE) due to the excitation of the long-range propagating modes. These ultra-high quality factor resonances as well as the utilization of the magnetooptical measurements instead of the reflection ones observed in ordinary surface plasmon sensors significantly increase their sensitivity to the refractive index of the analyzed medium. Thus usage of such magnetoplasmonic heterostructures is very promising for sensing applications.

We performed the design of the magnetoplasmonic heterostructures and tuned the parameters of the structure in order to enhance the magneto-optical response via excitation of the ultalong-range propagating surface plasmon polariton mode. This structure is designed for gas sensing at the operating wavelength of 790 nm. One-dimensional photonic crystal is used to tune the impedance of the heterostructure so that the long-range propagating modes can be excited. Our sample contains 1D PC made of alternating SiO2 and Ta2O5 layers 164 nm and 119.4 nm correspondingly. PC structure is coated with a 125-nm thick ferromagnetic film of bismuth-substituted iron garnet and 8-nm thick gold film for the excitation of the SPPs.

Magnetoplasmonic sample with a thin gold film demonstrates the width of the surface plasmon resonance 0.13 deg that corresponds to the quality factor of 350. This is extremely narrow resonance for a smooth plasmonic structure with ferromagnetic since typical resonance widths in such structures are about 1 deg. Magnetooptical transversal Kerr effect related to this surface plasmon resonance has even smaller width of 0.06 deg and higher quality factor 700. This causes very high values of the structure sensitivity to the analyzed medium refractive index variation which is $1.8 \cdot 10^3$ deg/RIU.

The work is supported by Russian Science Foundation.

Plasmon-Assisted Positive Photoconductance by Gold Nano-Gradient Structures

Jihye Lee[1,2], Jeong-Hyeon Kim[1,2], and Jong-Souk Yeo[1,2*]
[1] School of Integrated Technology, Yonsei University, Incheon, Republic of Korea
[2] Yonsei Institute of Convergence Technology, Yonsei University, Incheon, Republic of Korea
[*]Corresponding author: jongsoukyeo@yonsei.ac.kr

Abstract Here, we demonstrate the electrically connected gold nano-gradient structure for investigating the positive photoconductance assisted by the plasmons. The gradient nanostructures have an optically graded colors within a visible wavelength so that the interaction of visible light and graded nanostructure shows different positive photoconductive responses depending on the coherency (coherent/incoherent) and wavelength (red, green, blue) of the incident light source. The junction of the graded nanostructure composed of carbon and gold is expected to generate hot carriers by Landau damping.

Introduction

The localized surface plasmon resonance (LSPR) occurs when the metallic nanostructure interacts with the incident light [1]. From the light-matter interaction, the conduction electrons on the surface of metallic nanostructure show the collective oscillation called surface plasmons that are defined by the geometry of the nanostructure. The excitation of surface plasmons in a nanostructure can manipulate the light so that it can be used for developing the plasmon based nanocircuit, sensing platform for bio and chemical field, and processing methods for optical information [2-4].

In order to realize the plasmon based applications, we need to understand the relationship between geometry of nanostructure and optical/electrical response depending on the characteristics of the incident light and analyze the optical-electrical transduction by the plasmon-assisted damping process. In this paper, we have fabricated the gold nano-gradient structure that is connected to the electrical contact pad with a carbon at the junction. By using this structure, we have investigated the optical and electrical responses to understand the relationship.

Results and Discussion

In figure 1 (a), the schematic of gold nano-gradient structure was shown. The types of incident light are incoherent halogen lamp and coherent laser sources. The incoherent halogen lamp has a wideband spectrum while the coherent laser sources have wavelengths of 405, 532, and 632 nm, respectively. These light sources shed light on the fabricated nanostructure as shown in Figure 1 (b). The size of the gradient nanostructure ranges from 100 nm to 600 nm. The photocurrent response from the nano-gradient structure is shown in Figure 2. The photocurrent is increased when the light source is on. Compared to the incoherent white light, the coherent sources induce different levels of photocurrent: 1.07 nA (White incoherent light), 0.78 nA (405 nm, Blue), 1.54 nA (532 nm, Green), 0.31 nA (635 nm, Red). Among them, the green light source provides a maximum photocurrent with 1.54 nA.

Conclusion

The photocurrent has shown a maximum value when the resonance condition is matched for the incident light. The excitation of hot carriers by the plasmons at

the junction of the metal and carbon is believed to affect the positive photocurrent. Further investigation and subsequent understanding of the plasmon-assisted process on the nano-gradient structure may enable the novel design of plasmon based applications.

Acknowledgements

This research was supported by the MSIP(Ministry of Science, ICT and Future Planning), Korea, under the "ICT Consilience Creative Program" (IITP-R0346-16-1008) supervised by the IITP(Institute for Information & communications Technology Promotion) and also under the "Mid-career Researcher Program" (NRF-2016R1A2B2014612) supervised by the NRF(National Research Foundation).

REFERENCES

1. Pelton, M. and Bryant, G. W. *Introduction to metal-nanoparticle plasmonics*, John Wiley & Sons, Inc. New Jersey and Canada, 2013.
2. Kim, J. -H. and Yeo, J. –S. "Enhanced detection of broadband incoherent light with nanoridge plasmonics," *Nano Lett*., Vol. 15, No. 4, 2291-2297, 2015
3. Lee, J., Park, J., Lee, J. –Y and Yeo, J. –S. "Contact Transfer Printing of Side Edge Prefunctionalized Nanoplasmonic Arrays for Flexible microRNA Biosensor," *Adv. Sci*, Vol. 2, No. 9, 1500121, 2015.
4. Lee, J., Lee, J. –Y. and J. –S. Yeo. "Optimally Functionalized Adhesion for Contact Transfer Printing of Plasmonic Nanostructures on Flexible Substrate," *ACS Appl. Mater. Interfaces*, Vol. 9, No. 4, 3251-3259, 2017.

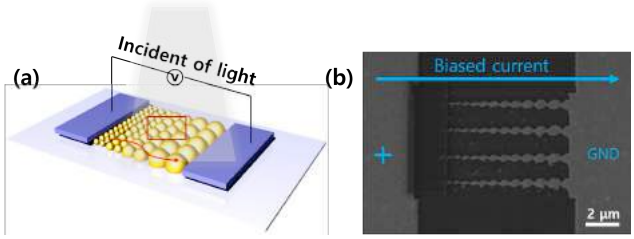

Figure 1 (a) Schematic of gold nano-gradient structure with electrically connected contact pad. The light is incident on the center of the gold nanostructure. (b) Scanning electron microscopy (SEM) image of the fabricated nano-gradient structure.

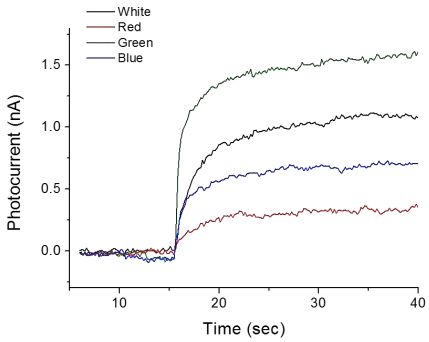

Figure 1 Photocurrent on the nano-gradient structure depending on the light source (Label: White-Incoherent halogen lamp, Red- 635 nm, Green-532 nm, Blue-405 nm coherent laser source)

GHz acoustic modulation of extraordinary optical transmission in a metamaterial based on a square nano-hole array in a gold film

Y. Imade[1*], R. Ulbricht[1], H. Sakuma[1], P. H. Otsuka[1], M. Tomoda[1], O. Matsuda[1], H. Kim[2], G. Park[2], and O. B. Wright[1]

[1]Division of Applied Physics, Graduate School of Engineering, Hokkaido University, Sapporo, Japan

[2]School of Mechanical Engineering, Korea University, Seoul, Republic of Korea

[*]corresponding author: yuta.imade@gmail.com

Abstract- Gigahertz modulation of light transmitted by an extraordinary-optical-transmission (EOT) metamaterial structure is studied using optical pump-probe spectroscopy. The GHz frequency oscillations in the intensity of the transmitted light through a sample consisting of a lattice of square nano-holes in a gold film on a glass substrate are monitored experimentally. Numerical simulations of the transient deformations and strain distributions show that variations in the nano-hole area produce the dominant contribution to the GHz optical modulation.

Extraordinary optical transmission (EOT) through subwavelength-sized holes has been studied over a wide range of electromagnetic frequencies[1]. Light generally cannot go through such small apertures, but interactions with the holes allows light to be converted to surface plasmons, and to pass through more efficiently than expected on the basis of the hole area alone. This phenomenon can be used for filtering electromagnetic (EM) waves at specific wavelengths. Other potential applications are the modulation of the transmitted EM waves by electro-optic modulation (EOM) or acousto-optic modulation (AOM). Such modulations in transmission were demonstrated by combination with electronic circuits[2, 3]. Gigahertz acoustic modulation was also demonstrated: surface acoustic waves can modulate EOT in two-dimensional (2D) nano-hole arrays[4] and 1D nano-slit arrays[5], and bulk waves can modulate EOT in 1D nano-grating geometries[6]. However, quantitative analysis is lacking in the acoustic studies of 2D EOT structures. Questions remain such as how the mechanical vibrational modes excited in such structures can actually modulate the EOT. Here we report on the modulation of the transmitted intensity in a 2D EOT structure made of an array of nano-holes in a gold film on a glass substrate, and show how the GHz vibrational modes contribute to the optical modulation[7]. We conduct experiments by optical pumping and probing, and we also perform numerical simulations to elucidate the transient deformations and strain fields, which point to the hole-area modulation being the dominant effect in modulation.

The sample consists of 1 mm thick glass coated with a 40 nm gold film in which square holes (side 250 nm and pitch 710 nm) were created by electron lithography in a square lattice, as shown by the scanning electron micrograph (SEM) in the inset of Fig. 1(a). This sample shows EOT in the near-infrared region.

GHz acoustic vibrational modes in this 2D EOT structure are excited by optical pump pulses at wavelength 415 nm, and the modulation of the transmitted probe-pulse light intensity is detected at a wavelength of 770 nm. We plot in Fig. 1(a) by the dashed blue line the normalized modulus of the temporal Fourier transform (FT) of the measured transmitted intensity change. The optical pulses are delivered by two synchronized Ti:Sapphire lasers, and the orientations of the linear polarization are set perpendicular to one another and aligned along two symmetry axes of the square-hole array.

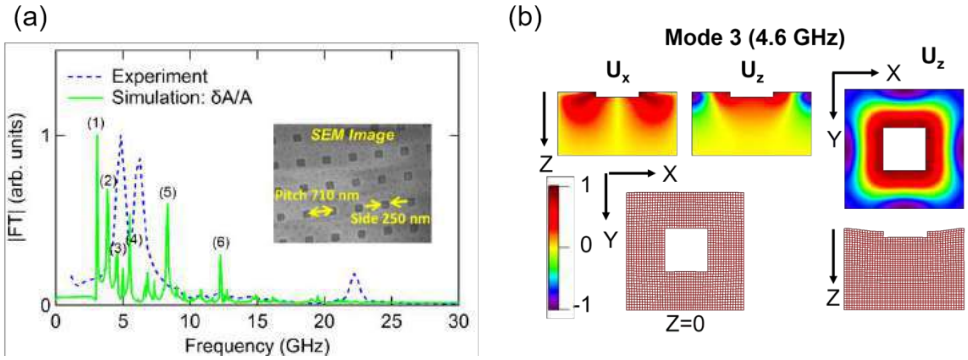

Fig 1: (a) Magnitude of the temporal FT of the experimental relative transmission intensity change (blue dashed line) and simulation of the relative hole-area modulation (green solid line). (b) Simulated deformation fields at 4.6 GHz. X and Y are in-plane coordinates, whereas Z is the out-of-plane coordinate.

We also performed numerical simulations to reveal the vibrational strain distributions in the EOT structure in order to elucidate the acoustic modulation of the transmitted light. Six vibrational modes, involving the opening and closing of the holes, could be identified from temporal Fourier transforms (FT) of the relative area change in the square-hole apertures, as shown in Fig. 1(a) by the solid green line. We show in Fig. 1(b) as an example the displacement and deformation fields for the third resonance indicated by peak (3) in Fig. 1 (a). Analysis of the average volumetric strain over the glass regions in the open holes suggests that it is the hole-modulation that provides the dominant contribution to the transmitted intensity modulation. Applications of this research include novel ultrafast acousto-optic modulators.

REFERENCES

1. T. W. Ebbesen, H. J. Lezec, H. F. Ghaemi, T. Thio, and P. A. Wolff, Extraordinary optical transmission through subwavelength hole arrays, *Nature*, Vol. 391, No. 6668, 667–669, 1998.
2. H.-T. Chen, H. Lu, A. K. Azad, R. D. Averitt, A. C. Gossard, S. A. Trugman, J. F. O'Hara, and A. J. Taylor Electronic control of extraordinary terahertz transmission through subwavelength metal hole arrays, *Opt. Express*, Vol. 16, No. 11, 7641–7648, 2008.
3. W. Gao, J. Shu, K. Reichel, D. V. Nickel, X. He, G. Shi, R. Vajtai, P. M. Ajayan, J. Kono, D. M. Mittleman, and Q. Xu, High-Contrast Terahertz Wave Modulation by Gated Graphene Enhanced by Extraordinary Transmission through Ring Apertures, *Nano Lett.*, Vol. 14, No. 3, 1242–1248, 2014
4. L. L. Guyader, A. Kirilyuk, T. Rasing, G. A. Wurtz, A. V. Zayats, P. F. A. Alkemade, and I. I. Smolyaninov Coherent control of surface plasmon polariton mediated optical transmission, *J. Phys. D: Appl. Phys.*, Vol. 41, No. 19, 195102, 2008.
5. D. Gerard, V. Laude, B. Sadani, A. Khelif, D. V. Labeke, and B. Guizai, Modulation of the extraordinary optical transmission by surface acoustic waves, *Phys. Rev. B*, Vol. 76, No. 23, 235427, 2007.
6. S.-C. Yang, H.-P. Chen, H.-H. Hsiao, H.-C. Chang, and C.-K. Sun, Near-field dynamic study of the nanoacoustic effect on the extraordinary transmission in gold nanogratings, *Opt. Express*, Vol. 20, No. 15, 16186–16194, 2012.
7. R. Ulbricht, H. Sakuma, Y. Imade, P. H. Otsuka, M. Tomoda, O. Matsuda, H. Kim, G.-W. Park, and O. B. Wright, Elucidating gigahertz acoustic modulation of extraordinary optical transmission through a two-dimensional array of nano-holes, *Appl. Phys. Lett.*, Vol. 110, No. 9, 091910, 2017

Steering topological surface lasers

B. Bahari, J. Park, F. Valini, R. Tellez-Limon, A. Kodigala, T. Lepetit, Y. Fainman, and B. Kante*
Country Department of Electrical and Computer Engineering, University of California San Diego, La Jolla, California 92093-0407, USA
* bkante@ucsd.edu

Abstract- We demonstrated topological steering of light sources in which the phase offset to steer the beam is provided by Floquet-Bloch phase in periodic structures. It was shown that in periodic structures there exist singular states in the radiation region of the band diagram that exhibit diverging quality factor, which is useful for light source cavities. The existence of these singular states are topologically protected, and their momentum are very sensitive to any small uniform perturbations. Our experimental demonstrations open new paradigm in the implementation of light steering with applications in data communications, bio imaging and sensing.

Bound States in Continuum (BIC) introduced shown by Von Neumann and Wigner can be achieved in periodic photonic arrays above the diffraction limits where leaky out-going waves interfere destructively resulting in complete confinement of the optical mode inside the structure [1] and has been demonstrated in various passive structures [2-4]. It is possible to achieve low threshold BIC Surface Emitting Lasers (BICSEL) with small foot-prints. BIC points are topologically robust in reciprocal space, meaning that by changing some physical parameters of the cavity they can displace in the reciprocal space [5]. This topological dependence of the BIC points enables the tuning of the lasing beam direction in real space by using the same platform. Moreover, BIC points are the polarization vortex center in the reciprocal space. Basically, polarization of the surface laser operating at the BIC point is the superposition of the all neighboring polarizations making a polarization vortex in the real space.

In this work, we designed and fabricated such cavities to show tunable topological light sources that can lase with any arbitrary angle with many degrees of freedom on controlling the angle and number of the lasing beams. Fig. 1a shows the schematic of the structure, which is a PhC slab made of InGaAsP material on top of glass with PMMA resist interlayer in between and inside the holes. As depicted in the band diagram of the structure (Fig. 1b), there are three modes, with two of them double degenerate modes at Γ. All of the modes have BIC points one of which has BIC always at Γ point (symmetry protected mode) while for double degenerated modes, BIC points are off-Γ (resonantly trapped modes) and their position can be tuned by varying the radius of holes. Off-Γ BICs can move in the band diagram in such a way that they can either go toward the Γ point to annihilate or toward the Brillouin zone edges [5]. These modes can be utilized to design a PhC cavity that lases with an angle as demonstrated in the following. Fig. 2 shows the wavelength scaling by varying the radius of holes. For radii smaller than R=265nm there are one symmetry protected and two resonantly trapped BICs, while for radii larger than 265nm, the two resonantly trapped BICs annihilate and disappear. As we explained in ref. 6, the resonantly trapped mode lases first before the symmetry protected mode (band-edge mode). Therefore, below the radius of 265nm resonantly trapped modes will lase but with different pump thresholds and wavelengths while after this radius symmetry protected mode is the only mode with large quality factor and thus lases. In Fig. 2, solid points are the measurement results, which show lasing at two different wavelengths tracking BIC point along ΓX and

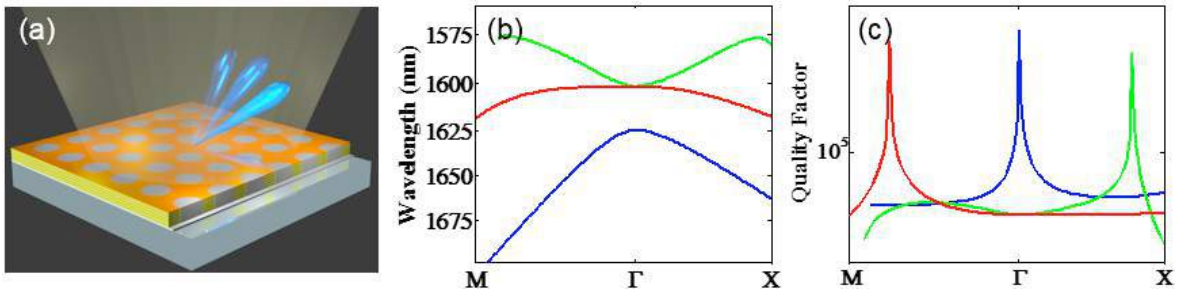

Fig. 1. a) Schematic of the laser cavity made of InGaAsP PhC slab with square lattice of holes filled by PMMA. PhC slab bonded to a glass by using PMMA interlayer and cladding is air. Thickness of the slab and the periodicity are 300 nm and 950 nm, respectively. b) Band diagram and c) quality factor of the structure shown in (a) for the radius of holes equal to 200 nm.

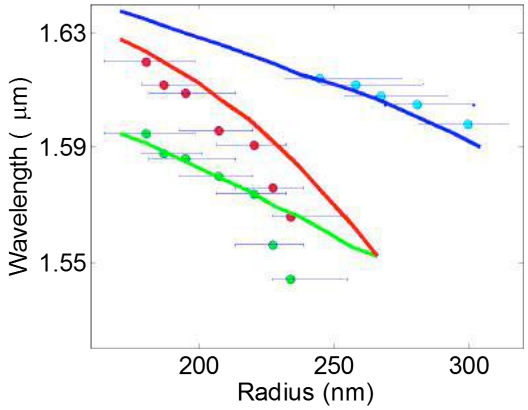

Fig. 2. Wavelength scaling of the structure shown in Fig. 1a as a function of the radius of the holes for symmetry protected and resonantly trapped modes. Solid lines are simulation results and solid points are measurement results. Horizontal lines indicating the error bars for each experimental result.

ΓM directions at smaller radii and lasing at symmetry protected mode at larger radii. We have demonstrated a new type of topological light source in periodic structures that enable steering of the lasing beam in any arbitrary directions depending on the geometrical parameters of the system. In our structure, below the radius of 265nm there are two different modes that can lase at two different lasing thresholds and wavelengths, which can easily be control by using pump power or frequency filters, while above that radius there is just the symmetry protected mode that lases. This novel topological light source opens new doors to design functional and tunable lasers.

REFERENCES

1. J. von Neumann and E. Wigner, “On some peculiar discrete eigenvalues” Phys. Z, 465 (1929).
2. C. Linton et al., “Embedded trapped modes in water waves and acoustics” Wave Motion 45, 16 (2007).
3. D. C. Marinica et al., “Bound states in the continuum in photonics” Phys. Rev. Lett. 100, 183902 (2008).
4. T. Lepetit et. al., “Resonantly trapped bound state in the continuum laser” arXiv: 1508.05164 (2015).
5. B. Zhen et. al., “Topological Nature of Optical Bound States in the Continuum” PRL 113, 257401 (2014).
6. A. Kodigala et. al., “Bound State in the Continuum Nanophotonic Laser” CLEO: Science and Innovations, SM4E. 1, (2016).

A spectroscopic ellipsometry demonstration of ultrasharp subradiant plasmons

M. Taghinejad[1], H. Taghinejad[1], H. Moradinejad[1], A. A. Eftekhar[1], and A. Adibi[1*]
[1]School of Electrical and Computer Engineering, Georgia Institute of Technology, 778 Atlantic Drive NW, Atlanta, Georgia 30332, United States
[*]corresponding author: ali.adibi@ece.gatech.edu

Abstract-We numerically design and experimentally demonstrate ultra-sharp (FWHM $\approx$ 6 nm) and tunable lattice plasmon and Fano-type resonances using plasmonic nanopatch devices, where diffractive coupling of the out-of-plane electric dipoles plays a primary role. Systematic spectroscopic ellipsometry measurements reveals exotic potentials of the investigated nanopatch devices for polarization engineering and enhanced light matter interactions.

Metallic nanoresonators by leveraging the coherent oscillation of free electrons, known as the localized plasmon resonance (LPR), provide spatial resolution beyond the diffraction limit [1]. While diversity of available metals and designs allow accurate control over the spectral location of resonance in plasmonic platforms, the control over the resonance linewidth is in fact challenging. Intrinsic Ohmic loss and radiation loss are the primary effects responsible for the fast detuning and also the broad (~ 50 nm) linewidth of plasmonic resonances. A number of practical strategies for loss management in plasmonic systems have been pursued. One approach is to utilize dark subradiant plasmonic modes, featuring damped net electric-dipole that weakly radiate to far-field photons. Fano-interference is another technique to terminate radiation loss [2]. From a different perspective, lattice plasmons (LPs), owing to the simultaneous reduction of the radiative and Ohmic losses, have attracted growing attention. The LPs take advantage of in-plane dipolar coupling of the scattered light from plasmonic arrays, providing narrow resonances at wavelengths approaching inter-particle distances. This phenomenon was first reported as Wood's anomaly and was explained as the transition of grating orders from an evanescent state to a radiative state [3].

In this study, we demonstrate exceptionally narrow (FWHM $\approx$ 6 nm) lattice plasmon modes using two-dimensional nanopatch arrays (Figure 1(a)-(b)). In our approach, the z-component of the excitation electric-field (Figure 1(c)) induces out-of-plane electric-dipoles inside the nanocubes through which, the diffractive coupling of the incident light to the array becomes possible. Our angle-resolved spectroscopic ellipsometry, Figure 1(d), shows fine tuning of the LP resonance wavelength over an ~ 80 nm range, which is more than 10 times larger than the FWHM of the narrowest measured lattice mode. These modes are only achievable through TM-polarized excitations since TE-polarized light lacks out-of-plane electric-field component (Figure 1(c)). The nanopatch arrays studied here are periodic structures comprised of 30 nm-thick gold (Au) nanocubes separated from a backside Au film by an 8 nm-thick alumina (Al_2O_3) film. The interplay between the induced out-of-plane dipoles and image dipoles (formed inside the Au film) enables formation of such narrow resonances using only 30 nm-thick nanocubes. This is in sharp contrast to previous reports [4] where excitation of narrow resonances, based on out-of-plane dipoles, demands very thick (> 100 nm) metallic nanostructures.

Our utilized plasmonic nanopatch structure, owing to the large refractive index contrast at the nanopatch

edges, supports a second resonance mode (the broad resonance on the longer wavelengths) that is identified as the sub-diffraction Fabry-Pérot (FP)-like mode. In a new design, we prepare the ground for spectral proximity of the subradiant LP and the super-radiant FP modes, which leads to tunable Fano-type lineshapes through interference (Figure 2). Thanks to the polarization sensitivity of the demonstrated LP and Fano-type resonances, the proposed structure reveals great potentials for manipulation of polarization state upon reflection of light from the array. Furthermore, incorporated spacer layer into our designed device can be immediately replaced by a material of interest for various applications seeking plasmonic-enhanced light-matter interactions (e.g., plasmonic lasing and harmonic generation).

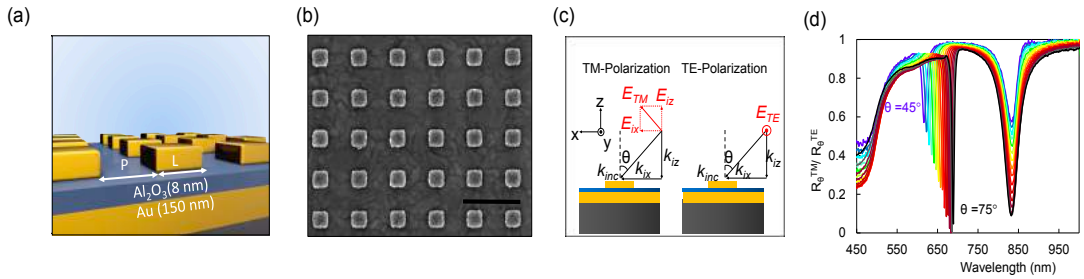

Figure 1. (a) Schematic of the plasmonic nanopatch array. (b) Representative SEM image of the fabricated two-dimensional array (L = 100 nm, P = 250 nm). (c) Designation of polarization states and electric field components of excitation light. (d) Spectroscopic ellipsometry measurements. In this panel we plot ratio of the reflection of TM-polarized light (R_θ^{TM}) to that of TE-polarized light (R_θ^{TE}) at various excitation angles (45° to 75°) with step size of 2°. The tunable and sharp resonance at the shorter wavelength and the broad resonance at longer wavelength are identified as LP and Fabry-Perot (FP) modes, respectively.

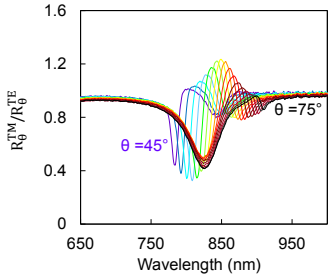

Figure 2. Demonstration of Fano-type resonance in spectroscopic ellipsometry measurements. Here, we use an array with larger period (L= 100 nm, P = 350 nm) in which the spectral vicinity of LP and FP modes allows for effective interference of the modes and generation of Fano lineshapes.

REFERENCES

1. Fang, N., H. Lee, C. Sun and X. Zhang, "Sub-diffraction-limited optical imaging with a silver superlens" *Science*, 308 (5721), 534-537, 2005.
2. Luk'yanchuk, B., N. I. Zheludev, S. A. Maier, N. J. Halas, P. Nordlander, H. Giessen and C. T. Chong, "The Fano resonance in plasmonic nanostructures and metamaterials" *Nat Mater*, 9 (9), 707-715, 2010.
3. Meier, M., A. Wokaun and P. F. Liao, "Enhanced Fields on Rough Surfaces - Dipolar Interactions among Particles of Sizes Exceeding the Rayleigh Limit" *J Opt Soc Am B*, 2 (6), 931-949, 1985.

4. Zhou, W. and T. W. Odom, “Tunable subradiant lattice plasmons by out-of-plane dipolar interactions” *Nat Nanotechnol*, 6 (7), 423-427, 2011.

The dynamic of formation of clusters and Ag nanoparticles in colloidal system and polymer matrix

A. L. Potapov[1*], V. E. Agabekov[1] and V. N. Belyi[2]
[1]Institute of Chemistry of New Materials of the NAS, Minsk, Belarus
[2] B.I. Stepanov Institute of Physics of the NAS, Minsk, Belarus
[*]corresponding author: potapov555@tut.by

Abstract- It is shown that the peak in UV-region (205-235 nm) of absorption spectrum corresponds to the scattering on clusters and nanoparticles (NPs) of Ag. For samples of sol of Ag particles at deficiency in reducing agent (0.5 % PVA) the peak at 290 nm corresponding to Ag clusters is determined. The size and dynamics of formation of clusters and Ag NPs substantially depend on such factors as UV-radiation and acoustochemical influence.

Polymer composites containing Ag NPs are of special interest for obtaining new nanostructural materials and creation of devices on their basis, thanks to the unique properties of Ag NPs.

In spite of a large number of works in this area, the dynamic of formation of clusters and Ag NPs in a colloidal system and a polymer matrix at UV-radiation and acoustochemical influence is not sufficiently studied. The purpose of present work is to determine the influence on the Ag NPs size and dynamic of their formation of such factors as UV-radiation and ultra-sound (US) treatment and also the change of the concentration of PVA – stabilizer and reducing agent for Ag particles.

Using spectroscopy in UV and visible spectral regions, atomic-force microscopy (AFM) and method of dynamic light scattering (DLS) the dynamics of Ag particles growth and their size distribution in 10 % polyvinyl alcohol (PVA) composition, PVA-film and sol are established.

Immediately after homogenization the Rayleigh scattering spectrum of PVA-composition with Ag was obtained. In our experiments we have observed the peak with λ_{max} = 233 nm caused by the scattering of UV-radiation on the clusters (~ 0.5 nm) and Ag NPs (1-10 nm). The SPR-absorption band (390-560 nm) corresponding to Ag NPs did not appear at that.

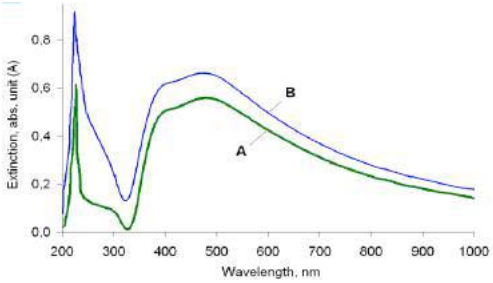

Figure 1 – Spectra of PVA-composition with Ag particles after UV-radiation.
A – UV-influence during 1 h (λ_{max} = 227 nm, A = 0.6, and λ_{max} = 470 nm, A = 0.55).
B – repeated treatment by US (during 1 h) after UV-radiation.

Acoustochemical influence causes the destruction of the clusters and Ag NPs, and the level of this destruction depends on the content of PVA in the composition. So, for example, at 10 % content of PVA under the influence of US full destruction of Ag particles takes place, and at 0.5 % – partial destruction.

After UV-radiation the formation of Ag NPs occurs and there appears deformed (asymmetric) SPR-band at

λ_{max} = 470 nm (Figure 1). The form of SPR-band indicates that the distance between NPs in PVA-composition is several tens of nanometers, i.e. electromagnetic interaction between Ag NPs becomes essential.

The additional repeated treatment by US increases SPR-absorption and, consequently, the quantity of Ag NPs. After comparison of spectra of the sample exposed to UV-radiation and the sample wherein Ag ions reduction takes place only due to PVA-matrix, it is possible to conclude that:

1) for both samples the peak of scattering and SPR-absorption band are observed;
2) SPR-absorption band (395-500 nm) is formed in the sample without UV-influence;
3) due to UV-radiation the acceleration of Ag reduction on the clusters occurs.

Dynamics of SPR-absorption growth is given in Figure 2.

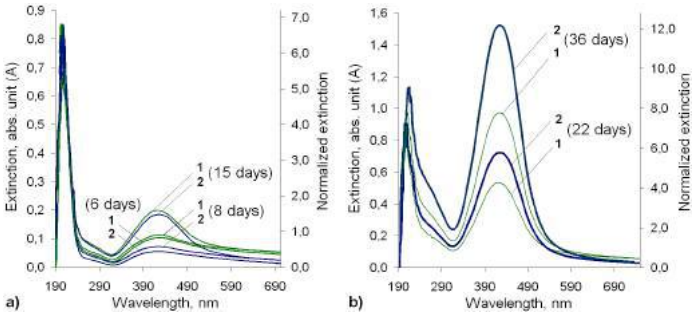

Figure 2 – Spectra of PVA-films with Ag particles after 6, 8, 15 days (a) and 22, 36 days (b). The right scale is the normalized extinction, magnification by 8 times. 1 – PVA-film with Ag after UV-US-treatment (peak of scattering with λ_{max} = 206 nm, SPR-absorption band with λ_{max} = 424 nm); 2 – PVA-film wherein the reduction of Ag^+ occurs only due to PVA-matrix.

At formation of the film Ag clusters and then NPs are intensively formed from Ag ions what is confirmed by the growth of scattering UV-peak. SPR-absorption band of PVA-film corresponding to Ag NPs with the size of 40-45 nm (λ_{max} = 424 nm) becomes symmetric, here the plasmonic absorption prevails over the scattering (Figure 2b). During first 15 days in the sample that was not subjected to UV-US-treatment the value of SPR-absorption is smaller then UV-peak, i.e. the major part of Ag is still in a form of ions (Figure 2a). But after 22 and 36 days (Figure 2b) the dynamics of growth changes, namely, the sample without treatments shows larger value of SPR-absorption. At the change of aggregate state from PVA-composition into the film the hypsochromic shift is fixed for maximum of SPR-absorption (Figures 1 and 2).

If there is not enough reducing agent (0.5 wt.% PVA), the stable sol containing the clusters and Ag NPs is obtained. The peak at 290 nm corresponds to Ag clusters. For sol sample SPR-band with maximum absorption at 490 nm corresponds to Ag NPs with average size of 80 nm. NPs size estimated by λ of SPR agrees with AFM images. According to the DLS method, the diameter of Ag NPs surrounded by ligand shell amounts to 220 nm.

REFERENCE

1. Agabekov, V., Ivanova, N., Dlugunovich, V., and Vostchula, I., "Optical properties of polyvinyl alcohol films modified with silver nanoparticles", *J. Nanomater.*, article ID 206384, 2012.
2. Potapov, A. L., Daineko, O. A., Ivanova, N. A., Agabekov, V. E., and Bin-Hussain, M., "Formation and properties of films based on polyvinyl alcohol and doped with silver nanoparticles", *Appl. Surf. Sci.*, vol. 350, 121–128, 2015.

Exceptional Points in Plasmonic Nanostructures

Ashok Kodigala, Thomas Lepetit, Boubacar Kanté
Department of Electrical and Computer Engineering, University of California at San Diego, La Jolla, CA 92093, USA
akodigala@eng.ucsd.edu

Abstract: We present evidence of the existence of exceptional points (EPs) in three-dimensional (3D) plasmonic nanostructures. The systems are composed of coupled plasmonic nanoresonators and can be judiciously driven to EPs by controlling symmetry-compatible modes.

Plasmonics and its applications have garnered ample attention over the years. These applications range from chemical and biological sensors to enhanced photovoltaics [1-2]. We design 3D plasmonic structures with exceptional point (EP) singularities. Exceptional Points (EPs) are singularities of open systems where at least two complex eigenmodes coalesce [3]. They manifest themselves by the simultaneous degeneracy of both resonant frequencies and linewidths. These points are highly sensitive to external perturbations as even a tiny variation will lift the degeneracy and cause splitting of both resonant frequencies and linewidths. These results make it possible to envision a highly sensitive molecular sensor.

A plasmonic system based on multiple coupled plasmonic bars, depicted in Figure 1(a), is considered. The dimensions of an individual gold bar are chosen such that the dipolar resonance falls in the optical domain at a wavelength of 1.55 μm. Placing these gold bars in close proximity hybridizes their individual plasmon modes into multiple system modes with different symmetries as shown in Figure 1(b) [4-6]. Here, the instantaneous charge profiles of each mode are depicted for a plane wave excitation with the electric field along the length of the bars. The spectral locations of these hybridized plasmon modes can be tuned by spatially shifting one bar in relation to the other two. Essentially, we break the symmetry of the overall shift-bar system by shifting one of the bars. Here, we chose to shift the middle bar by an amount 'dx'.

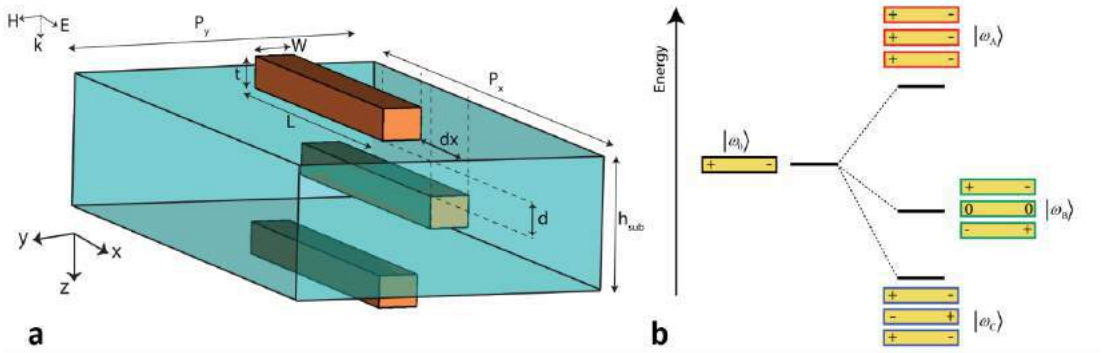

Figure 1: (a) Unit cell setup of plasmonic gold bars with a dielectric (SiO2) spacer given in blue with dimensions: L=450 nm, W=50 nm, t=40 nm, Py=400 nm, Px=800 nm, hsub, dx (variable). The gold bars are described using the Drude model with a plasma frequency (ω_p=1.367x10^{16} rad/sec) and collision frequency (ω_c=6.478x10^{13} rad/sec) based on values from Ref. [5]. (b) Energy-level diagram describing the plasmon hybridization in the shift-bar system with three modes: ω_A, ω_B, ω_C where $\omega_A > \omega_B > \omega_C$ for dx=0. ω_0 is the resonances of an individual bar.

Initially at no shift, mode A, ω_A, has charge in all the bars oscillating in-phase and mode C, ω_C, has charge in all bars oscillating out-of-phase while mode B, ω_B, has no field in the middle bar as seen in Figure 1(b). As such, mode A resides at a higher energy (higher frequency) due to all repelling forces and mode C resides at a lower energy (lower frequency) as a result of repelling forces.

We now examine the effect of shifting the middle bar in the x-direction on all three modes of the plasmonic system. As the middle bar is progressively displaced, the repelling forces associated with mode A weaken to become attractive. Similarly, the attractive forces of mode C weaken to become repulsive. Lastly, the coulomb forces associated with mode B remain constant with shift as there is no field present in the bar. This behavior is observable from the resonances of the system as seen in the figure below.

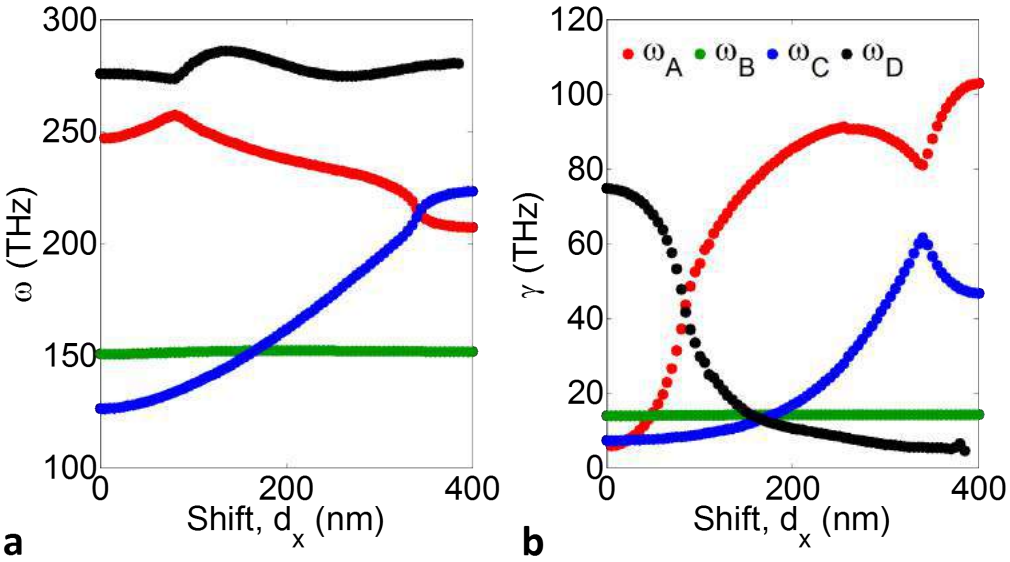

Figure 2: Resonance information in the form of complex poles extracted from scattering parameters and plotted as a function of shift dx (middle bar) (a) Resonance frequency of modes A, B, C and higher order mode D plotted as a function of shift 'dx' and their corresponding (b) linewidths. There is observable coupling between neighboring modes that share a symmetry, i.e., mode A with C at dx = 350 nm and mode A with D at dx = 80 nm. Mode B (green) is unperturbed by both the shift and neighboring modes due to its symmetry. Coupling of modes A (red) and C (blue) leads to an EP singularity where the two modes coalesce.

We see that mode A (red) moves to lower frequencies with shift and mode C (blue) moves to higher frequencies with shift, whereas mode B (green) remains unperturbed [6]. Modes of similar symmetry couple, that is, mode A couples with C at dx=350 nm and mode A with D at dx=80 nm. With additional parameter tuning, the coupling between mode A and C lead to an EP singularity where the two modes coalesce to have the same complex resonance (resonance frequency and linewidth) and eigenvectors. An EP can also be realized in systems with more plasmonic resonators.

We have demonstrated the existence of exceptional points in a three-dimensional system of coupled plasmonic nanoresonators at optical wavelengths (near-IR). Furthermore, the general approach proposed in designing EPs can be used to construct EPs of higher order in physical systems where more than two modes coalesce.

References

[1] H. A. Atwater and A. Polman, "Plasmonics for improved photovoltaic devices," Nature Mater. **9**, 205 (2010).
[2] N. Liu *et al.*, "Three-Dimensional Plasmon Rulers," Science **332**, 1407 (2011).
[3] W. D. Heiss, "The physics of exceptional points," J. Phys. A: Math. Theor. **45**, 444016 (2012).
[4] A. Kodigala, T. Lepetit, and B. Kanté, "Engineering Resonance Dynamics of Plasmon Hybridized Systems," J. Appl. Phys. **117**, 023110 (2015).
[5] E. Prodan *et al.*, "A Hybridization Model for the Plasmon Response of Complex Nanostructures," Science **302**, 419 (2003).
[6] P. B. Johnson and R. W. Christy, "Optical Constant of the Noble Metals," Phys. Rev. B **6**, 4370 (1972).
[7] A. Kodigala, T. Lepetit, and B. Kanté, "Exceptional points in three-dimensional plasmonic nanostructures," Phys. Rev. B **94**, 201103(R) (2016).

Enhancing the infrared absorption of hybrid organic–inorganic perovskites using a high-*Q* metasurfaces

Govind Dayal[1,2] and Ranjan Singh[1,2,*]

[1]Division of Physics and Applied Physics, School of Physical and Mathematical Sciences, Nanyang Technological University, 21 Nanyang Link, Singapore 637371

[2]Center for Disruptive Photonic Technologies, Division of Physics and Applied Physics, School of Physical and Mathematical Sciences, Nanyang Technological University, 21 Nanyang Link, Singapore 637371

We report on design, fabrication, and characterization of high-Q metasurfaces and their multispectral response at near infrared frequencies. The metasurfaces perforated with an array of overlapping annular and rectangular apertures support fundamental and higher order plasmonic resonances which result in high-Q response at mid-infrared frequencies. We show that spectral response of the metasurface can be tuned to a great amount by judicially engineering the hybridization of plasmon resonance in metasurfaces. We then perform the surface enhance infrared spectroscopy of PMMA and solution-processed hybrid organic–inorganic perovskites (HOIPs) with the formula CH3NH3PbI3 using high-Q metamaterial cavity. We show that infrared absorption of extremely weak vibrational modes can be enhanced using well designed high-Q resonances.

Differentiating surface waves and waveguide modes guided by interfaces with one-dimensional photonic crystals

Muhammad Faryad

Department of Physics, Lahore University of Management Sciences
Lahore 54792, Pakistan.
muhammad.faryad@lums.edu.pk

Abstract— One-dimensional photonic crystals are made of multi-layers of different dielectric materials with periodic arrangement. Such photonic crystals support surface waves at their interfaces as well as waveguide modes guided by individual constituent layers. This study examines the differences and similarities between the two types of modes. The differentiation is necessary to fully exploit the promise of photonic crystals in integrated optics.

1. SUMMARY

The interface of a one-dimensional photonic crystal (PC) and a homogeneous material supports surface waves [1, 2, 3], as shown schematically in Fig. 1. If the homogenous material is a metal, surface waves are called surface-plasmon-polariton (SPP) waves [2, 3, 4]. The surface waves are, by definition, independent of the thickness of the partnering materials on both sides of the guiding interface, beyond the critical thickness required to localize the the surface waves. In addition to the surface waves, the waveguide modes can also be guided by the planar layers in a PC, as is schematically also shown in Fig. 1. This figure shows one such waveguide, which is the most important one with respect to the surface waves that are also guided by the same metallic interface.

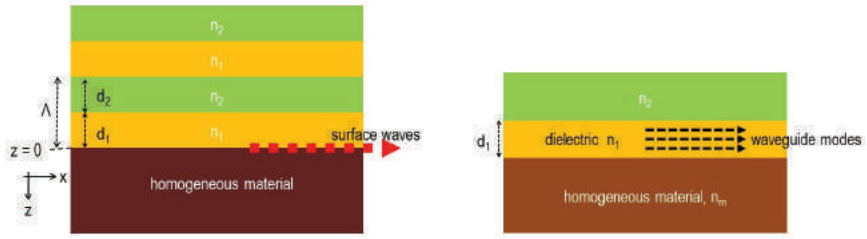

Figure 1: (Left) Schematic geometry of the metal/PC interface showing the guiding of the surface waves. (Right) Schematic geometry of the asymmetrical waveguide formed by the first layer adjacent to the homogeneous material.

The most important feature of the SPP waves guided by an interface of a metal and a one-dimensional PC is the multiplicity of the surface waves, i.e., more than SPP waves of both the *p*- and *s*-polarization states with different phase speeds, spatial profiles, and degree of localization to the metal/PC interface can be excited. This has been shown theoretically [3] and experimentally [4].

Why do we get multiple SPP waves with metal/PC interface? This work was undertaken to address this question. The hypothesis is that the waveguide effect gives rise to multiple SPP waves. As representative results, the real and imaginary parts o f the relative wavenumbers κ/k_0 of the multiple SPP waves that can be guided by the metal/PC interface are given in Fig. 2. For comparison with one set of the waveguide modes, the real and imaginary parts of the relative wavenumbers β/k_0 of the waveguide modes supported by the first layer adjacent to the metal are given in Fig. 3.

A comparison of the results in Figs. 2 and 3 shows that, except for $p1$ branch of SPP waves, all SPP-wave branches have their counterpart in the waveguide modes. Each SPP-wave branch

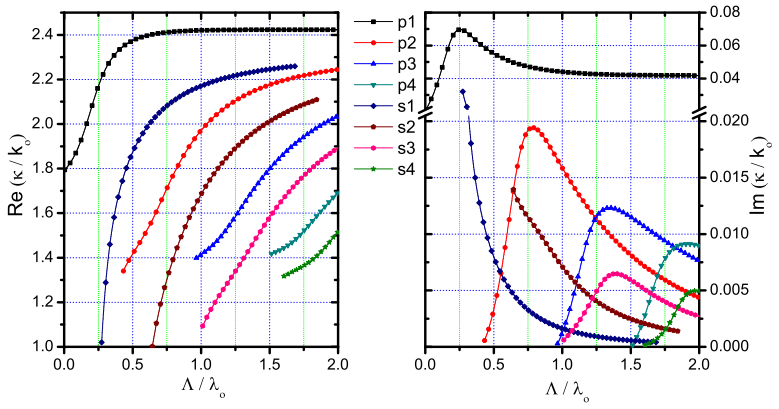

Figure 2: **SPP waves:** (left) Real and (right) imaginary of parts of the relative wavenumbers κ/k_0 of SPP waves as a function of the period $\Lambda = 2d_1 = 2d_2$ of the PC shown in Fig. 1.

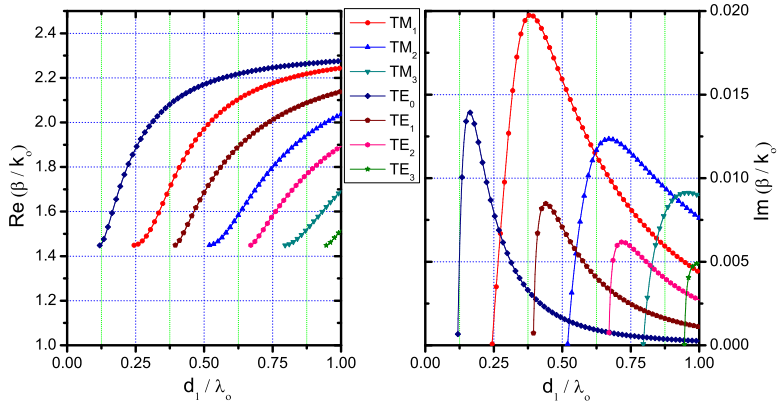

Figure 3: **Waveguide modes:** (left) Real and (right) imaginary of parts of the relative wavenumbers β/k_0 of the waveguide modes as a function of the thickness d_1 of the dielectric waveguide shown in Fig. 1.

is different from the counterpart waveguide branch for small values of d_1; however, it approaches the waveguide branch as d_1 increases. This shows that waveguide modes play a role in generating multiple SPP waves guided by the metal/PC interface. This will be further elucidated by comparing the field profiles of the SPP waves and the waveguide modes. Furthermore, this phenomenon will be explored for Tamm waves as well that guided by an interface of a PC with a homogeneous dielectric material.

REFERENCES

1. Robertson, W. M. and M. S. May, "Surface electromagnetic wave excitation on one-dimensional photonic band-gap arrays," *App. Phys. Lett.*, Vol. 74, No. 13, 1800–1802, 1999.
2. Das, R. and R. Jha, "On the modal characteristics of surface plasmon polaritons at a metal-Bragg interface at optical frequencies," *App. Opt.*, Vol. 48, No. 26, 4904–4908, 2009.
3. Faryad, M. and A. Lakhtakia, "On surface plasmon-polariton waves guided by the interface of a metal and a rugate filter with a sinusoidal refractive-index profile," *J. Opt. Soc. Am. B*, Vol. 27, 2218–2223, 2010.
4. Liu *et al.*, "Experimental excitation of multiple surface-plasmon-polariton waves and waveguide modes in a one dimensional photonic crystal atop a two-dimensional metal grating," *J. Nanophoton.* Vol. 9, 093593, 2015.

Exploring light scattering response by phase diagram

Jeng Yi Lee[1], **and Ray-Kuang Lee**[1,2]

[1]Institute of Photonics Technologies, National Tsing-Hua University, Hsinchu 300, Taiwan
[2]Physics Division, National Center for Theoretical Sciences, Hsinchu 300, Taiwan
johnnyygod2002@hotmail.com

Abstract— By applying power conservation law to absorption cross section, allowable scattering coefficients for any passive electromagnetic scatterers are shown in a phase diagram regardless of geometry, structures, material dispersion and extrinsic operating frequency. This phase diagram not only provides a complete information for energy assignments through radiation loss (scattering cross section) and dissipation loss (absorption cross section), but also offers a clear understanding of all possible extrinsic states. Based on this diagram, we propose a systematic method to design field-controllable devices at subwavelength scales.

In the last decades, passive receivers or scatterers with exotic phenomena have been extensively studied in various wave subjects, from electrodynamic waves, acoustic waves, to quantum matter waves. In particular, invisible cloaking, coherent perfect absorbers, and compact resonant scatterers are revealed with non-trivial scattering solutions [1, 2, 3, 4]. It is undoubted that the concepts behind these structures are relied on our understanding of scattering phenomena. In this work, we propose a phase diagram to revisit these fundamental light scattering processes, with a systematic approach to design functional scatterers.

When incident power is absorbed by passive objects, it would be non-zero in absorption cross section, i.e., $\sigma^{abs} > 0$. With this condition and applying the electromagnetic multi-pole expansions to sources-free Maxwell equation in a surrounding environment, the absorption cross section can be compactly written in an infinite series connected with complex scattering coefficients $C_n^{(TE,TM)}$,

$$\sigma_n^{abs(TE,TM)} \equiv -\frac{(2n+1)\lambda^2}{2\pi}(Re\{C_n^{(TE,TM)}\} + |C_n^{(TE,TM)}|^2) \geq 0. \tag{1}$$

Here, TE and TM represent transverse electric and transverse magnetic modes, respectively. By introducing a phasor representation for scattering coefficients $C_n^{(TE,TM)} = |C_n^{(TE,TM)}| \exp[i\theta_n^{(TE,TM)}]$, one can introduce a phase diagram for passive scatterers, defined by amplitude square and phase of scattering coefficients for each channels. Then, with the inequality shown in Eq. (1), we reveal all allowable scattering solutions $C_n^{(TE,TM)}$ in the phase diagram, i.e., the colored region illustrated in Fig. 1(a).

The finding here is to provide a complete energy information for each channels of TE and TM modes. It shows the maximum value of absorption power is bounded for each channels, corresponding to cancellation of outgoing radiation, i.e., coherent perfect absorption [4]. Another interesting result to be seen from the phase diagram is that, along the constant absorption power contour, the scattering objects could have different scattering signals. This is a useful result to manipulate a subwavelength device with a low scattering field but without sacrificing any energy absorption. In order to further control light responses based on this phase diagram, we introduce two auxiliary parameters: $\alpha_n^{(TE,TM)}$ and $\beta_n^{(TE,TM)}$, into the scattering coefficients $C_n^{(TE,TM)} = -[1 + i(\alpha_n^{(TE,TM)} + i\beta_n^{(TE,TM)})]^{-1}$, as shown in Fig. 1(b).

As the incident wavelength is much larger than optical length of scattering objects, the electrostatic approximation can always provide a good model to describe its radiation. In this scenario, the corresponding scattering coefficients for two-layered structures in a shape of sphere can be found in the analytical form:

$$\alpha_1^{(TM)} + i\beta_1^{(TM)} = \frac{3\lambda^3}{2(2\pi a)^3}\frac{2\gamma^3(1-\epsilon_s)(\epsilon_c-\epsilon_s) - (2+\epsilon_s)(\epsilon_c+2\epsilon_s)}{\gamma^3(\epsilon_s-\epsilon_c)(2\epsilon_s+1) + (1-\epsilon_s)(\epsilon_c+2\epsilon_s)}. \tag{2}$$

Here, λ is the operating wavelength, a is the size of our system, γ is the ratio of the core radius to the size of system, ϵ_s is shell permittivity, and ϵ_c is core permittivity. Once the trajectory is chosen

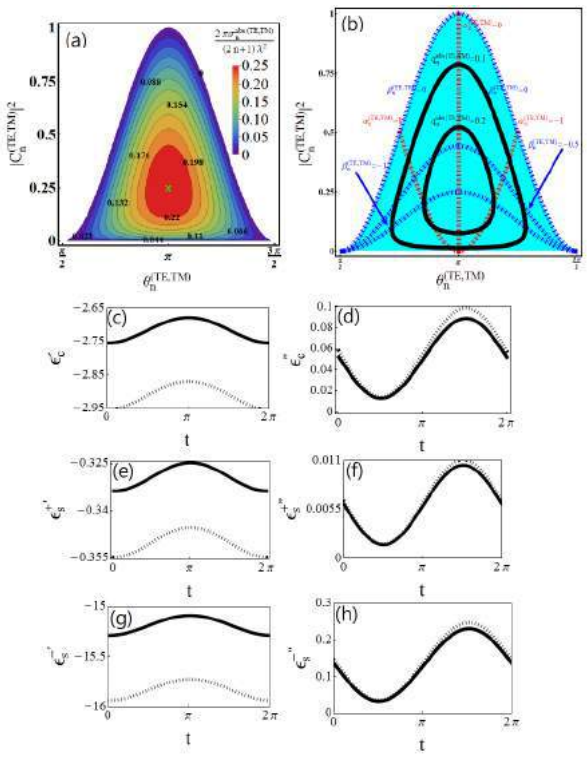

Figure 1: (a) The phase diagram for passive scatterers. The normalized absorption cross section is bounded within $[0, 0.25]$. (b) Trajectories illustrated by two auxiliary parameters $\alpha_n^{(TE,TM)}$ and $\beta_n^{(TE,TM)}$. Here, the black-curves represent constant absorption powers. (c-h) The corresponding dielectric constants to satisfy a given radiation response [5]. Solid curves are obtained from analytical solutions. Dashed curves are obtained from numerical calculation of exact Mie theory. Parameters used are: (c-d), $\epsilon_s = 3.12$, $a = \lambda/24$ and $\gamma = 0.9$; (e-h), $\epsilon_c = 5$, $a = \lambda/24$ and $\gamma = 0.9$.

from the colored region in our phase diagram, the corresponding material parameters, ϵ_s and ϵ_c, can be easily traced back through Eq. (2), which support the required scattering responses, see Fig. 1 (c-h) [5]. Based on phase diagram, our proposed architecture provides a compact way to design devices with required field responses. Obviously, the phase diagram would largely simplify the complicated light scattering phenomena.

In summary, we introduce a phase diagram as a compact tool to link the scattering and absorption powers for each channel. With the supported trajectories in the phase diagram, we reveal a systematic way to find out a variety of solutions in the composited materials to possess the same absorption power.

REFERENCES

1. A. Alú and N. Engheta, "Achieving transparency with plasmonic and metamaterial coatings," *Phys. Rev. E*, Vol. 72, 016623 (2005).
2. J. Y. Lee and R.-K. Lee, "Hiding the interior region of core-shell nanoparticles with quantum invisible cloaks," *Phys. Rev. B*, Vol. 89, 155425 (2014).
3. M. I. Tribelsky, and B. S. Lukyanchuk, "Anomalous light scattering by small particles," *Phys. Rev. Lett.*, Vol. 97, 263902 (2006).
4. H. Noh, Y. Chong, A.D. Stone, and H. Cao, "Perfect coupling of light to surface plasmons by coherent absorption," *Phys. Rev. Lett.*, Vol. 108, 186805 (2012).
5. J. Y. Lee and R.-K. Lee, "Phase diagram for passive electromagnetic scatterers," *Opt. Express*, Vol. 24, 257388 (2016).

Silver nanoparticles with many sharp apexes and edges as efficient nanoresonators for shell-isolated nanoparticle-enhanced Raman spectroscopy.

K. Kołątaj[1*], J.Krajczewski[1], and A. Kudelski[1]
[1]University of Warsaw, Poland
[*]corresponding author: kkolataj@chem.uw.edu.pl

Abstract- One of the tools which is used for investigations of various interfaces, especially in the *in situ* conditions, is shell-isolated nanoparticle-enhanced Raman spectroscopy – SHINERS. In this contribution we tested decahedral and prismatic silver nanoparticles containing a large number of sharp apexes and edges as nanoresonators in SERS and SHINERS measurements. We found that the SERS enhancement factors obtained in the experiments with such anisotropic nanoparticles are *ca.* one order of magnitude larger than in similar experiments with spherical nanostructures.

SHINERS measurements were introduced by Tian et al. in 2010 as the new approach to analyze various surfaces[1]. In this method Raman spectrum was measured from an investigated substrate covered with gold nanopartciles protected by a thin layer of silica or alumina. Gold nanoparticles act as electromagnetic nanoresonators, significantly enhancing electric field of the incident electromagnetic radiation and hence leading to large increase of the Raman signal from studied surface. The inert shell separates metal cores from direct contact with probed molecules and keeps them from agglomeration. Therefore, such systems might find more analytical applications, also for living cells.

In this work, we report the synthesis of decahedral and prismatic silver nanoparticles with silica layer which are very new type of SHINERS nanoresonators with many sharp apexes and edges. We also show their application for Raman studies of some molecules and yeast cells.

To synthesize decahedral and prismatic silver nanoparticles we used methods developed by Kitaev et al. and Mirkin et al. respectively [2,3]. Obtained nanoparticles had mainly decahedral or prismatic shape with average size of 43 and 49 nm respectively. To create silica layer on obtained nanoresonators we used method developed by Mirkin et al. [3].

To compare decahedral and prismatic nanoparticles with spherical nanoresonators we carried out Raman measurements for monolayers of 4–mercaptobenzoic acid (PMBA) deposited on Pt and covered with various nanoresonators (see Fig. 1). As can be seen from Figure 1, nanoparticles with sharp edges enhance Raman signal about one order of magnitude more effectively than spherical nanoresonators.

Decahedral-Ag@SiO_2 nanoparticles have been tested in SHINERS measurements of monolayers of PMBA on Pt and in measurements of model biological samples. Figure 2 shows Raman spectra of *Saccharomyces boulardii* (yeast) cells before and after deposition of decahedral-Ag@SiO_2 nanoparticles. As can be seen in this Figure, in the Raman spectrum recorded with the decahedral-Ag@SiO_2 nanoparticles many Raman bands (e.g., at 1135, 1315, 1346, 1456, 1611, 1665 cm^{-1}) can be clearly identified, whereas in a case of the Raman spectrum recorded without nanoresonators it is very hard to distinguish these bands from the noise.

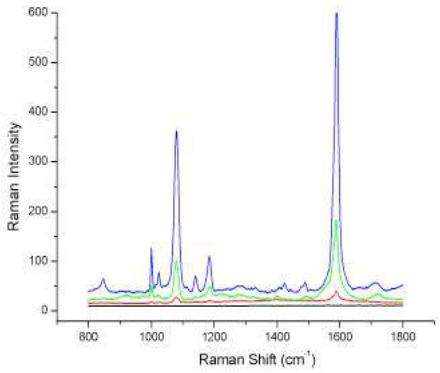

Figure 1. *Raman spectra of monolayer of 4-mercaptobenzoic acid on the platinum surface before deposition of silver nanoparticles (black line) and covered with the spherical (red curve), decahedral (green curve) and prismatic nanoparticles (blue line).*

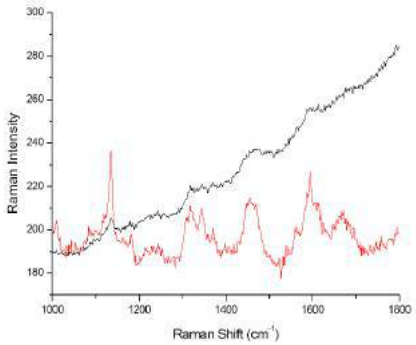

Figure 2. *Raman spectra of Saccharomyces boulardii cells without nanoparticles (black curve) and after addition of decahedral-Ag@SiO_2 nanoparticles (red curve).*

Acknowledgements. This work was financed from the funds of the National Science Centre (Poland) allocated on the basis of the decision number DEC-2013/11/B/ST5/02224.

REFERENCES

1. Li J. F., Huang Y. F., Ding Y., Yang Z. L., Li S. B., Zhou X. S., Fan F. R., Zhang W., Zhou Z. Y., Wu D. Y., Ren B., Wang Z. L. and Z. Q. Tian, Shell-isolated nanoparticle-enhanced Raman spectroscopy, *Nature,* Vol. *46*, 392–395, 2010.
2. Pietrobon B., McEachran M. and V. Kitaev, Synthesis of Size-Controlled Faceted Pentagonal Silver Nanorods with Tunable Plasmonic Properties and Self-Assembly of These Nanorods, *ACS Nano*, Vol. 3, 21–26, 2009.
3. Xue, C., Chen X., Hurst S. J. and C. A. Mirkin, Self-Assembled Monolayer Mediated Silica Coating of Silver Triangular Nanoprisms, *Adv. Mater.*, Vol. 19, 4071–4074, 2007.

Surface plasmon polariton amplification by direct current in semiconductor–graphene–dielectric structure

S. Moiseev[1,2]*, Yu. Dadoenkova[1,3], A. Fotiadi[1,4], A. Abramov[1], A. Kadochkin[1], I. Zolotovskii[1]

[1]Ulyanovsk State University, Ulyanovsk, Russia

[2] Kotelnikov Institute of Radio Engineering and Electronics, Russian Academy of Sciences, Ulyanovsk, Russia

[3]Novgorod State University, Veliky Novgorod, Russia

[4]Universitre de Mons, Mons, Belgium

*corresponding author: serg-moiseev@yandex.ru

Abstract - The interaction of slow surface plasmon polariton waves of far-infrared regime with an electric current induced in the graphene deposited on the boundary between a semiconductor film and dielectric substrate is investigated. It is shown that under the phase matching condition, when phase velocity of a surface plasmon polaritons approaches the drift velocity of charge carriers in graphene, a surface wave can be substantially enhanced by the drift current in graphene.

A surface plasmon polariton in planar structures is an electromagnetic excitation that propagates along the surface of conducting and dielectric media. In contrast to optical beams propagating in three dimensions, surface plasmon polariton is a surface electromagnetic wave, whose electromagnetic field decays exponentially with increasing distance from the interface into each medium. However, ohmic losses are inherent to all plasmonic structures so that further development of integrated plasmonics requires implementation of efficient loss compensation techniques and amplification of surface plasmon polariton waves.

In this work we propose a surface plasmon polariton amplification mechanism due to energy transfer from an electron drift current wave propagating in graphene into a far-infrared slow surface electromagnetic wave propagating along a semiconductor-dielectric boundary in waveguide geometry. A necessary condition of the interaction of these waves is phase matching condition, when the phase velocity of the surface wave approaches the drift velocity of charge carriers in graphene. The current in graphene can be considered to be localized at the interface of the media, which also provides an effective interaction of drift current and a surface wave. It is shown that in the spectral region of the surface plasmon polariton slowing-down its amplification coefficient can reach values substantially exceeding the ohmic loss coefficient of the surface wave in the structure (shown by the color area in Fig.). Moreover, the amplification coefficient can be varied with the applied voltage through the change of the drift velocity.

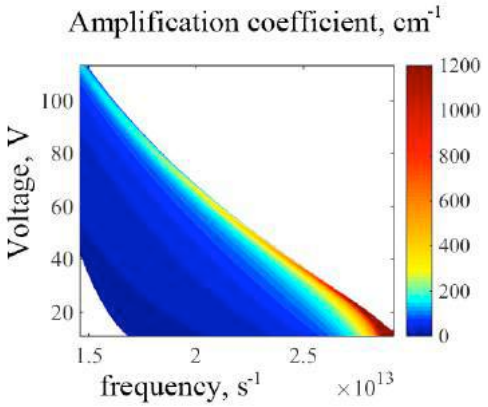

This work was supported by the Ministry of Education and Science of the Russian Federation (Project 14.Z50.31.0015, State Contracts 3.3889.2017, 3.7614.2017/П220 and 3.5698.2017/П220), Russian Foundation for Basic Research (Project 17-02-01382).

Modulation instability of intensive surface plasmon polaritons in a thin film structure

S. Moiseev[1,2]*, D. Korobko[1], I. Zolotovskii[1], A. Fotiadi[1,3]

[1]Ulyanovsk State University, Ulyanovsk, Russia

[2] Kotelnikov Institute of Radio Engineering and Electronics, Russian Academy of Sciences, Ulyanovsk, Russia

[3]Universitre de Mons, Mons, Belgium

*corresponding author: serg-moiseev@yandex.ru

Abstract - The evolution of intensive surface plasmon polariton waves in a metal film-dielectric substrate structure is investigated taking into account absorption properties of metal. The transformation of slightly modulated plasmon polariton wave into a sequence of surface pulses due to modulation instability effect in a structure with amplification is demonstrated.

In this work, the model of modulation instability (MI) of an intensive surface plasmon polariton (SPP) wave in a thin metal film with Kerr nonlinearity is developed. The main feature of this model is that some spatial harmonic perturbations of the SPP wave can be unstable due to the nonlinear optical properties of metal film. Under the influence of MI, the initially weak perturbations grow quickly in time leading to spatial redistribution and longitudinal localization of the SPP energy on the subwavelength scale. However, losses in metal play an important role in plasmonic processes and can lead to reducing of nonlinear effects manifestation. Results of our numerical simulation confirm the necessity for loss compensation and amplification of SPP waves in structure.

The dielectric substrate is considered to be active, which provides enough gain to compensate for the losses in the metal. For this case it is shown that during a time interval of a few picoseconds the modulated SPP wave is transformed into a train of pulses due to nonlinear effects. In the case of the film thickness of 10 nm the pulsation frequency equals 0.2 THz, the duration of each pulse is less than 0.5 ps (Fig. 1). One can see that the time period of SPP wave evolution is picoseconds, and at certain moments the local intensity increases several times in comparison with the initial SPP wave (10^{-2} W/m^2).

This work was supported by the Ministry of Education and Science of the Russian Federation (Project 14.Z50.31.0015, State Contracts 3.3889.2017, 3.5698.2017/П220), RFBR (Project 17-02-01382).

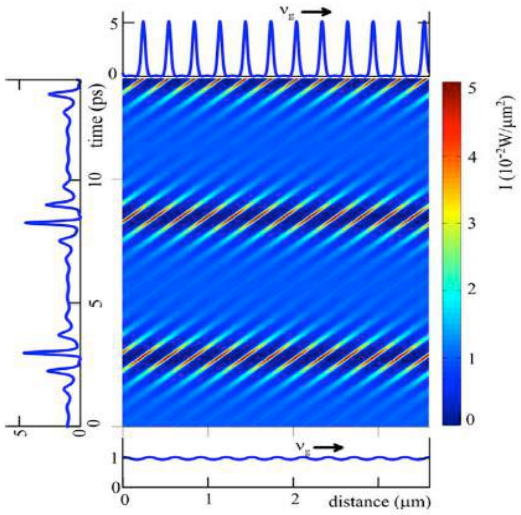

Fig. 1. Evolution of the SPP wave intensity in silver film of thickness 10 nm under condition of loss compensation; the initial wave (at $t = 0$), modulated along x-coordinate (in bottom), time dynamics of the wave intensity at $x = 0$ (left), spatial distribution of the SPP intensity (top) at $t = 14 ps$. The period of the spatial modulation approximately corresponds to the maximum of the modulation instability gain.

Nonlinear Optical Responses under Weak Excitation Regime from Embedded Quantum Dots in Semiconductors Covered by Plasmonic Metasurfaces

Masanobu Iwanaga*, **Takaaki Mano**, **and Naoki Ikeda**

National Institute for Materials Science (NIMS), 1-1 Namiki, Tsukuba 305-0044, Japan
*iwanaga.masanobu@nims.go.jp

Abstract— We fabricated an optimized plasmonic metasurface on bulk semiconductor of GaAs to improve extraction efficiency of photoluminescence (PL) emitted from embedded quantum dots. We found that the PL intensity is approximately square to the excitation power even under weak excitation conditions. The metal-semiconductor system is an essentially nonlinear system, suggesting the potential for high-performance plasmon-merged semiconductor devices.

Plasmonic resonances have been expected to realize significantly enhancing effects for various materials for a few decades. Still, the definite success has been limited to a small number of cases such as enhancements for optical signals (i.e., fluorescence and Raman scattering) from molecules placed properly on plasmonic metasurfaces [1–6] and thresholdless plasmonic nanolasers [7].

We have explored metal-semiconductor systems, in which plasmonic metasurfaces were designed on bulk II-VI semiconductors including quantum dots (QDs) in order to improve extraction of the photoluminescence (PL). Figure 1(a) illustrates a plasmonic metasurface on bulk GaAs. The metasurface is fabricated on the top and comprises a single layer of square hole array. The thickness of Au was 35 nm. As an adhesion layer, Ti of 1 nm thickness was inserted between the Au and GaAs.

Figure 1(b) shows a typical measured PL spectrum at room temperature through the metasurface. The periodicity was set to 250 nm in order to tune the resonance to the peak of PL spectrum. The plasmonic resonance appears as reflectance (R) dip at 910 nm. The PL spectrum is shown with a red solid curve and the R spectra at the normal incidence is shown with a black dashed curve. The PL comes from InAs QDs embedded in GaAs at depth of 50 nm from the outmost surface, as indicated by red dotted lines in Fig. 1(a). Note that a scattered laser line appeared at 1064 nm, which was double to the incident wavelength of 532 nm. The incidence was emitted by a single-mode continuous-wave laser.

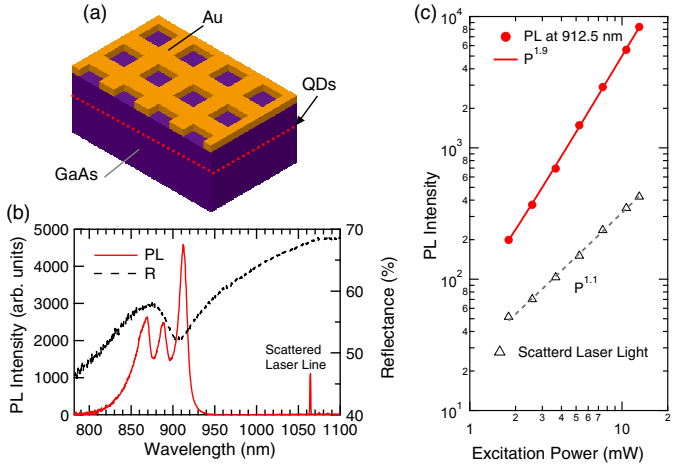

Figure 1: (a) Schematic of on-top Au plasmonic metasurface covering on bulk GaAs, in which QDs are grown at 50-nm depth, indicated by red dotted line. (b) Measured PL and R spectra, shown with red and black dashed curves, respectively. (c) Dependence of the PL intensity at 912.5 nm on the mW-order excitation power.

Figure 1(c) shows excitation-power dependence of the PL peak at 912.5 nm (red dots) and the scattered laser line (gray open triangles). The excitation power was varied in mW order and quite weak. However, the PL-peak intensity is proportional to $P^{1.9}$ (P: excitation power) and approximately square of P. In contrast, the scattered laser line exhibits almost linear response. Thus, we experimentally found unconventional superlinear optical responses from the QDs even under weak excitation. We will discuss the mechanism considering plasmonic hot-electron contributions to the PL processes.

In conclusion, we experimentally found that the metal-semiconductor merged systems incorporating the plasmonic metasurfaces form nonlinear systems even under the weak excitation regime. This result implies that well-designed metal-semiconductor systems substantially improve electronic processes in optoelectronic semiconductors, opening a new route to attain plasmon-assisted high-performance semiconductor devices.

ACKNOWLEDGMENT

This study is partially supported by the 4th mid-term research project in NIMS. M.I. thanks the supports from HPCI system research systems (IDs: hp160035, hp170134).

REFERENCES

1. Iwanaga, M., *Plasmonic Resonators: Fundamentals, Advances, and Applications*, Pan Stanford, Singapore, 2016.
2. Zhang, W., F. Ding, W.-D. Li, Y. Wang, J. Hu, and S. Y. Chou, "Giant and uniform fluorescence enhancement over large areas using plasmonic nanodots in 3D resonant cavity nanoantenna by nanoimprinting," *Nanotechnol.*, Vol. 23, No. 22, 225301, 2012.
3. Zhou, L., F. Ding, H. Chen, W. Ding, W. Zhang, and S. Y. Chou, "Enhancement of Immunoassay's Fluorescence and Detection Sensitivity Using Three-Dimensional Plasmonic Nano-Antenna-Dots Array," *Anal. Chem.*, Vol. 84, No. 10, 4489–4495, 2012.
4. Iwanaga, M. and B. Choi, "Heteroplasmon Hybridization in Stacked Complementary Plasmo-Photonic Crystals," *Nano Lett.*, Vol. 15, No. 3, 1904–1910, 2015.
5. Choi, B, M. Iwanaga, H. T. Miyazaki, Y. Sugimoto, A. Ohtake, and K. Sakoda, , "Overcoming metal-induced fluorescence quenching on plasmo-photonic metasurfaces coated by a self-assembled monolayer," *Chem. Commun.*, Vol. 51, No. 57, 11470–11473, 2015.
6. Iwanaga, M., B. Choi, H. T. Miyazaki, and Y. Sugimoto, "The artificial control of enhanced optical processes in fluorescent molecules on high-emittance metasurfaces," *Nanoscale*, Vol. 8, No. 21, 11099–11107, 2016.
7. Khajavikhan, M., A. Simic, M. Katz, J. H. Lee, B. Slutsky, A. Mizahi, V. Lomakin, and Y. Fainman, "Thresholdless nanoscale coaxial lasers," *Nature*, Vol. 482, No. 7384, 204–207, 2012.

Flexibly tunable plasmonic color filters for wide color display

J. Jang[1], N. Raeis-Hosseini[1], T. Badloe[2], D. Lee[2], H. Jung[2], D. M. Nguyen[2], G. Yoon[2], M. Kim[2], E. Beck[4], J. Rho[1,2,3,*]

[1]Department of Chemical Engineering, Pohang University of Science and Technology (POSTECH), Pohang 37673, Republic of Korea

[2]Department of Mechanical Engineering, Pohang University of Science and Technology (POSTECH), Pohang 37673, Republic of Korea

[3]National Institute of Nanomaterials Technology (NINT), Pohang 37673, Republic of Korea

[4]Department of Photonics, ENSSAT(University of Rennes 1), 6 rue de Kerampont, 22305 Lannion, France

[*]corresponding author: jsrho@postech.ac.kr

Abstract- Artificial subwavelength structures exhibiting multiple resonances in the visible range, known as color filters, are widely used in color printing beyond diffraction limit and color displays. Here, we propose a new reflective color filter structure comprising of a triangle periodic array of cross-shaped aluminum nanorods with various angles of rotation symmetry. Flexible tunability of color in wide color gamut is demonstrated on the device by changing the incident polarization.

Metamaterials for color generation has recently drawn great of interest for sub-wavelength printing and new generation display due to the ability to overcome wavelength diffraction limit and reduce complexity of multiple color printing processes [1]. Plasmonic resonances on metallic nanostructures are normally used to realize color filters such as plasmonic transmission color filters, including additive color filters and subtractive color filters. More recently, reflection color filters are promising due to its potential applications and advantages of angular insensitivity and energy saving [2]. However, reflection type of plasmonic color filter have shown color gamut not enough to illustrate vivid red, blue, and green color. Recently, a number of approaches have been explored to find out new plasmonic nanostructure for improving color performance [3-4]. Here, we propose a new approach to achieve wide color distribution based on new tunable reflection type nanostructure. The device consists of a Al_2O_3 dielectric layer sandwiched by a triangular periodic array of cross-shaped aluminum nanorods at the top layer and a bottom reflector layer as depicted in Fig. 1a. The color can be actively controlled by rotating the incident polarization or rotating the cross-shaped nanorod unit as shown in Fig. 1b. By changing angle of incident polarization and nanorods, together with the lattice period and length of nanorods, we can achieve wide color gamut at CIE 1931 diagram as demonstrated in Fig. 1c, which is wider than the one recently reported in [5].

In summary, we propose a new design of plasmonic color filter, fabricate and demonstrate its color tunability according to the incident polarization and angle of rotation symmetry of each cross-shaped nanorod.

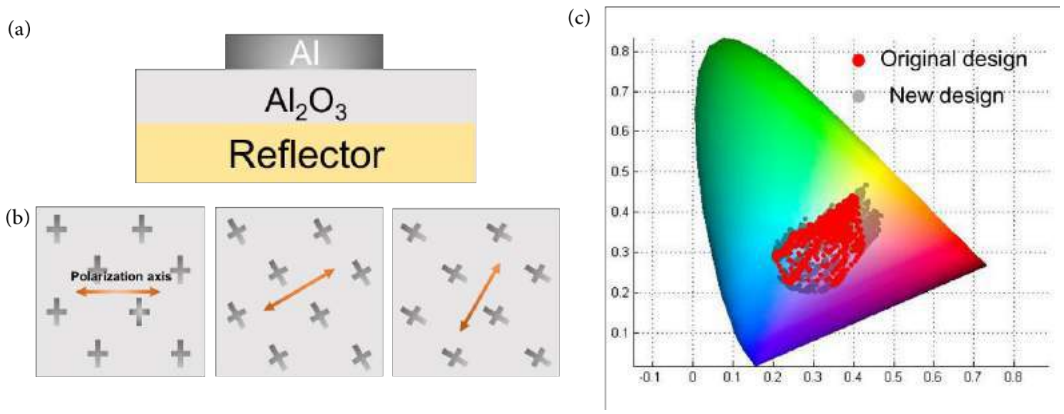

Figure 1. (a) Cross section of the proposed nanostructure. (b) Top view of the nanostructure with incident light axis. (c) CIE 1931 color space of structure published in [6] and in our new design [6].

Acknowledgements. J. Rho acknowledges the financial support by Pioneer Research Center program (NRF-2015M3C1A3022550), Young Investigator Research program (NRF-2015R1C1A1A02036464), Engineering Research Center program (NRF-2015R1A5A1037668) and Global Frontier program for the Center for Advanced Metamaterials (CAMM-2015M3A6B3063708) through the National Research Foundation of Korea (NRF) grant funded by the Ministry of Science, ICT and Future Planning (MSIP) of Korean government.

REFERENCES

1. Yinghong Gu. Et al., “Color generation via subwavelength plasmonic nanostructures”, *Nanoscale.*, Vol. 7, 6409-6419, 2015.
2. Si, Guangyuan, et al. "Reflective plasmonic color filters based on lithographically patterned silver nanorod arrays." *Nanoscale*, Vol. 5, No. 14, 6243-6248, 2013.
3. Timothy D. J. Et al., “The Plasmonic Pixel: Large Area, Wide Gamut Color Reproduction Using Aluminum Nanostructures *Nano Lett*, Vol. 16, 3817−3823, 2016.
4. Seon Uk Lee. Et al., “Wide-gamut plasmonic color filters using a complementary design method”, 7:40649, 2017
5. Ellenbogen, Tal, Kwanyong Seo, and Kenneth B. Crozier. "Chromatic plasmonic polarizers for active visible color filtering and polarimetry." *Nano letters*, Vol. 12, No. 2, 1026-1031, 2012.

Limits on Self-heating in Plasmonic Circuitry with Gain.

A. A. Vyshnevyy[1], **and D. Yu. Fedyanin**[1]

[1]Laboratory of Nanooptics and Plasmonics, Moscow Institute of Physics and Technology 141700, Dolgoprudny, Russian Federation

[*]corresponding author: vyshnevyi.aa@mipt.ru

Abstract-Loss compensation by optical gain in semiconductor media is a promising solution to the problem of high intrinsic losses in nanoscale plasmonic structures. However, any realization of the surface plasmon amplification scheme is unavoidably associated with the heat generation problem. The stronger the pump, the higher heat generation. Here, we estimate the lower bound to the heat generation rate, suggest possible thermal management solutions and discuss limits of plasmonic circuitry.

Plasmonics offers outstanding opportunities for light manipulation at the subwavelength scale, which enables the realization of densely integrated optical circuits for on-chip communication (Fig. 1a). However, due to strong absorption in metal, optical signals in plasmonic structures suffer from strong attenuation. There is a well-known tradeoff between the propagation distance and mode confinement for plasmonic waveguide structures [1]. The use of a gain medium allows to go beyond this general law and greatly increase the propagation distance in deep-subwavelength plasmonic structures with strong field confinement. Loss compensation can be implemented by placing an optically [2] or electrically [3,4] pumped gain medium near the metal surface and ensuring a high overlap with the electric field of the SPP mode (Fig. 1b). The SPP power dissipated due to the propagation losses is resupplied by stimulated emission in the gain medium. However, only a part of the pump energy, transmitted to the gain medium, is transformed into SPP signal, while the rest is radiated to free space and into plasmonic modes, or, which is worse, is converted into heat. Absorption of SPP in metal also contributes to heat generation (Fig. 1c). High heat generation power increases the temperature of the chip, which reduces the energy efficiency of the pumping scheme and can potentially destroy the device.

In this work, we discuss a lower bound to the heat generation rate associated with the amplification scheme, which can guarantee lossless SPP guiding [5]. Due to the high optical gain required for loss compensation in plasmonic nanostructures with strong mode confinement, we limit our consideration to the semiconductor gain medium, which is believed to be the best choice for such devices [6]. The contributions to the heat generation rate can be separated into two groups. The first group is associated with the imperfections of the compensation scheme, while the second is inherent to any plasmonic structure with gain. This second group includes heating due to nonradiative recombination in the inversely populated semiconductor and SPP absorption in metal, which cannot be reduced by improving the amplification scheme. We evaluate the minimum possible heating power produced by plasmonic components with gain and its dependence on the operating light wavelength. These results are then used to find limitations on the maximum integration density of plasmonic components and on other characteristics of plasmonic circuits.

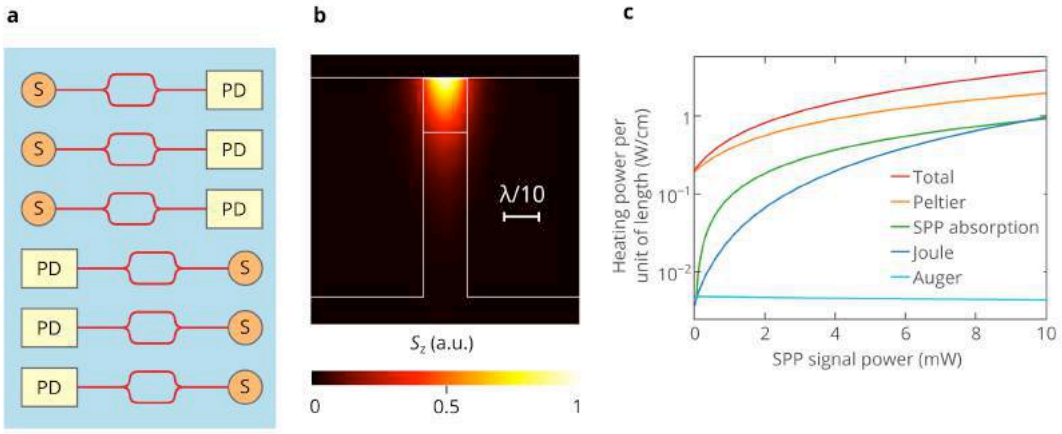

Fig. 1. (a) Schematic view of the on-chip plasmonic circuitry. "S" and "PD" denote SPP sources and photodetectors, respectively. (b) Spatial distribution of the energy flux of the strongly confined plasmonic mode. (c) Heat generation power versus SPP signal power for the electrically pumped lossless plasmonic waveguide.

REFERENCES

1. Oulton, R. F., Bartal, G., Pile, D. F. P. and Zhang, X., "Confinement and propagation characteristics of subwavelength plasmonic modes," *New J. Phys.*, Vol. 10, 105018, 2008.
2. Grandidier, J. et al., "Gain-Assisted Propagation in a Plasmonic Waveguide at Telecom Wavelength," *Nano Lett.*, Vol. 9, 2935–2939, 2009.
3. Fedyanin, D. Yu., Krasavin, A. V., Arsenin, A. V. and Zayats, A. V., "Surface plasmon polariton amplification upon electrical injection in highly integrated plasmonic circuits," *Nano Lett.*, Vol. 12, 2459–2463, 2012.
4. Svintsov, D. A., Arsenin, A. V. and Fedyanin, D. Yu., "Full loss compensation in hybrid plasmonic waveguides under electrical pumping," *Opt. Express*, Vol. 23, 19358–19375 (2015).
5. Vyshnevyy, A. A. and Fedyanin, D. Yu., "Self-Heating and Cooling of Active Plasmonic Waveguides," *ACS Photonics*, Vol. 3, 51–57, 2016.
6. Vallini, F., Gu, Q., Kats, M., Fainman, Y. and Frateschi, N. C., "Carrier saturation in multiple quantum well metallo-dielectric semiconductor nanolaser: is bulk material a better choice for gain media?" *Opt. Express* , Vol. 21, 25985–25998, 2013.

Plasmon resonances of Mid-IR Antennas and localized absorption enhancement in an absorbing substrate

L. Břínek[1,2], T. Šamořil[1,2], O. Tomanec[1,2], M. Hrtoň[1,2], R. Kalousek[1,2], V. Křápek[1,2], P. Dub[1,2], P. Varga[1,2,] and T. Šikola[1,2*]

[1]Central European Institute of Technology, Brno University of Technology, Purkyňova 123, CZ 612 00 Brno, Czech Republic

[2]Institute of Physical Engineering, Brno University of Technology, Technická 2, CZ 616 69 Brno, Czech Republic

[*]corresponding author: sikola@fme.vutbr.cz

Abstract- In the contribution the plasmon resonances of mid-IR antennas fabricated on an absorbing silicon-rich oxinitride substrate and their utilization for spatially localized absorption enhancement of electromagnetic radiation in this substrate will be discussed. The conclusions of this contribution are also applicable for other spectral regions where the materials exhibit strong absorption resonances, for instance in the visible.

It has been demonstrated that interesting phenomena occur if the antennas interact through their near fields with nearby dielectrics possessing absorption peaks or bands at specific wavelengths. This is known from a series of works dealing for instance with intuitive models based on coupled molecular and plasmonic resonators predicting new effects such as the transition between electromagnetically induced transparency (EIT) and enhanced absorption [1].

We will report on the surface plasmon resonances of mid-infrared Au antennas deposited on an absorbing silicon-rich oxinitride (SRON) layer [2], and on their utilization for enhancement of a spatially localized absorption of IR radiation in SRON. The antenna resonances were determined from far-field IR reflection spectra measured over a broad mid-IR range. Due to a strong coupling of localized surface plasmons with vibration modes (optical phonons) in SRON these spectra generally show up Rabi splitting which results in two hybrid branches of resonance wavelengths scaling nonlinearly with the antenna arm length (Fig. 1 left). The corresponding electric field distribution is shown in Fig. 1 right. To maximize spatially localized energy absorption in SRON, a compromise wavelength between that one related to optimum antenna resonances and the SRON absorption wavelengths must be chosen. We stress that the principles of this method can be utilized in other dielectric or semiconductor materials strongly absorbing in the mid-IR range, and, more generally, in other spectral regions, including the visible (e.g. due to excitons). Hence, in addition to the spatially localized heating the principles can be exploited in optimization of the efficiency of IR and light detectors, solar cells, biosensors and other applications.

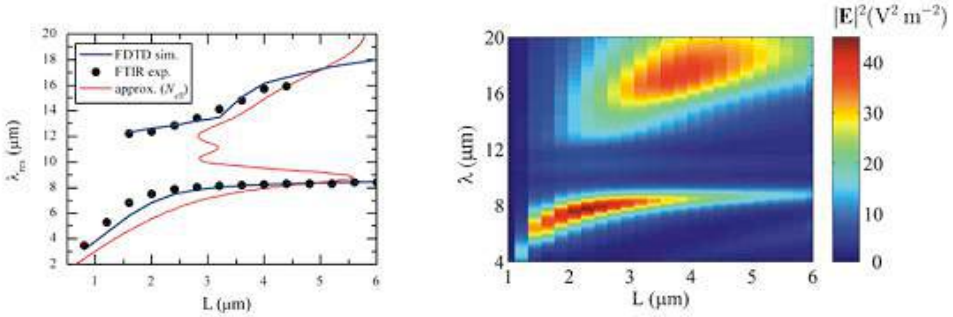

Figure 1: Left: Resonance wavelengths vs. antenna arm lengths (L). The red curve is yielded by the analytical formula $\lambda_{res} = n_{SRON}(\lambda_{res})2L$. Right: The simulated spectra of the square of electric field ($|E|^2$) (V^2m^{-2}) averaged over a domain (with dimensions 1.2 μm x 1 μm x 110 nm) in SRON beneath the antenna gap for different antenna arm lengths.

Acknowledgements

We acknowledge the support by the Grant Agency of the Czech Republic (grant No. 15-21581S), European Regional Development Fund (project No. CZ.1.05/1.1.00/02.0068), MEYS CR (project No. LQ1601 – CEITEC 2020), Technology Agency of the Czech Republic (grant No. TE01020233) and BUT (projects Nrs. FSI-S-17-4482, FSI/STI-J-17-4623,).

REFERENCES

1. Zengin G., Johansson G., Johansson P., Antosiewicz T. J., Käll M., Shegai T., "Approaching the strong coupling limit in single plasmonic nanorods interacting with J-aggregates", *Scientific Report* 3, 3074, 2013.
2. Šikola T., Kekatpure R. D., Barnard E. S., White J. S., Van Dorpe P., Břínek L., Tomanec O., Zlámal J., Lei D. Y., Sonnefraud Y., Maier S. A., Humlíček J., and Brongersma M. L., "Mid - IR plasmonic antennas on silicon-rich oxinitride absorbing substrates: nonlinear scaling of resonance wavelengths with antenna length", *Applied Physics Letters*, **95** (25), 253109-1, 2009.

Plasmofluidic assembly of nanometallic structures: from single-molecule SERS to dynamic lithography

Partha Pratim Patra, Junsuk Rho
Department of Mechanical Engineering, POSTECH, South Korea
ppptra@gmail.com

Sub-wavelength control and manipulation of light is one of the most desirable issues in science and technology. To destine this, surface plasmon polariton (SPP) plays a significant role and to harness SPP, the nanometallic architectures have unprecedented ability to concentrate and transport light. The sophisticated and versatile applications of SPPs mostly rely on the geometry and the arrangement of the nanostructures. Thus innovative 'preparation and assembly' of nanometallic architectures is crucial. Especially, by assembling the nanostructures in a controlled way, one can deploy the plasmon-coupling for subtle modulation of light wave. Recently, the assembly of nanostructures has opened up a promising field of research which is directly linked to many other important subjects, e.g. biophotonic sensing, metamaterials, optical nanoscopy, thermoplasmonics, nonlinear plasmonics, photovoltaics, catalysis etc.

Herein we present how to harness plasmofluidic field (plasmonic field in fluid) to create efficient electromagnetic hot-spots by assembling colloidal nanoparticles to detect single-molecule SERS signals[1]. Also we shall discuss how the extension of this technique can lead to a preamble of reconfigurable dynamic lithography of plasmonic nanostructures at metal-fluid interface[2].

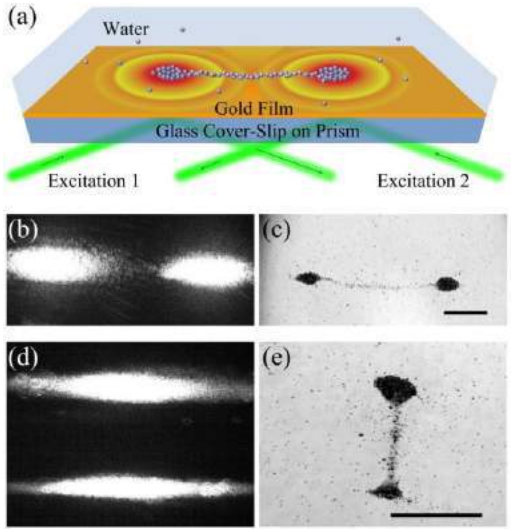

Figure 1 Schematic illustration of experimental geometry and the resulting dynamic assembly of nanoparticles.

Acknowledgements, These works are done in Photonics and Optical Nanoscopy Laboratory, Indian Institute of Science Education and Research (IISER), Pune, India and supported by IISER, Pune and DST, India funding.

REFERENCES

1. Patra P P, Chikkaraddy R, Tripathi R P N, Dasgupta A and Kumar G V P, " Plasmofluidic single-molecule surface-enhanced Raman scattering from dynamic assembly of plasmonic nanoparticles," *Nat*. *Commun*. 5 4357, 2014.
2. Patra P P, Chikkaraddy R, Thampi S, Tripathi RPN, Kumar GVP, "Large-scale dynamic assembly of metal nanostructures in plasmofluidic field," *Faraday discussions* 186, 95-106, 2016.

An in situ strategy to synthesis of plasmonic gold NPs by using plasmonic molybdenum oxide

M. Hosseini[1], **M. Ranjbar**[1*]

Isfahan University of Technology, Isfahan, Iran
[*]corresponding author: ranjbar@cc.iut.ac.ir

Abstract- The reduction of $HAuCl_4$ by molybdenum oxide nanoparticles synthesized via a simple electrochemical anodizing of molybdenum is investigated. By mixing colloidal plasmonic molybdenum oxide with $HAuCl_4$ aqueous solution, the mixed turned to a red-wine color with pronounce SPR properties. By using different analysis involving, X-ray diffraction (XRD), transmission electron microscope (TEM), X-ray photoelectron spectroscopy (XPS), furrier transformed infrared (FTIR) spectroscopy, cyclic voltammetry, and UV-Vis spectroscopy the colloidal nanoparticles of Au/MoO_x be characterized.

Gold and molybdenum oxide belong to material category with plasmonic behavior especially when they are prepared in nanoscale dimensions like colloidal suspensions. Plasmonic nanoparticles show pronounced interactions with visible light caused by collective excitations of conduction electrons [1]. The unique property of localized surface plasmon (LSPR) of nanoparticles is the mystery of its novel development in many applications such as optical sensing [2], photocatalytic [3] and solar energy devices [4].

To obtain composites of gold-metal oxide different synthesis technique are employed such as co-precipitation or deposition-precipitation of gold salt and support metal precursors in the presence of some stabilizing materials and reducing agents [4]. In more cases, removal of these stabilizers and ligand substances can be achieved using thermal and oxidative approaches, while it causes unpleasant changes in the size, shape and crystality of nanoparticles. Comparing with thermal decomposition of gold salt [5], reducing noble metal on a semiconductor substrates directly without any foreign reducing agents and stabilizing molecules, can lead to nanostructures with considerably enhanced activity [6]. This paper reports the reduction of $HAuCl_4$ by blue molybdenum oxide nanosheets, synthesized via a facile electrochemical anodizing of molybdenum. Mixing the colloidal blue molybdenum oxide with $HAuCl_4$ aqueous solution in various molar ratio causes reduction of gold salt into gold nanoparticles. To preparing different MoO_x:$HAuCl_4$ ratios (10:1, 20:1, 30:1 and 40:1), various amount of colloidal blue molybdenum oxide were added drop by drop into 20ml of $HAuCl_4$ aqueous solution. We characterized samples by different conventional techniques including UV–Vis spectrometry, XRD, TEM, XPS, FTIR and cyclic voltammetry.

Fig.1 shows the optical absorption spectra of the initial blue molybdenum oxide suspension and the $HAuCl_4$ solution. The former one displays an optical absorption band in the range of 400–1100 nm. This absorption band is the known characteristic plasmonic peak of molybdenum oxide containing oxygen deficiency [7]. After addition of $HAuCl_4$ solution into the blue molybdenum oxide, the existing blue color gradually disappears due to oxidation of molybdenum oxide and at the same time, the suspension transforms into a pink color due to formation of gold NPs. Optical absorption spectra revealed that localized surface plasmon (LSPR) resonance peak of gold arises after mixing and, depending on Mo:Au ratio, the absorption peak of blue MoO_x decline. At

the same time, optical band gap of molybdenum oxide increases by Au concentration indicating oxidation of blue MoO_x. Moreover, a significant shift in the location of one or two absorption peaks of molybdenum oxide was observed which is attributed to the plasmonic behavior. For most of samples, a red shift for gold LSPR was also observed when blue molybdenum oxide concentration is high due to its upper refraction index comparing with that of MoO_3. XPS, FTIR and cyclic voltametery showed that Mo oxidation state in blue molybdenum oxide colloids is mainly Mo^{5+} and mixing with gold salt leads to formation of Mo^{6+} states.

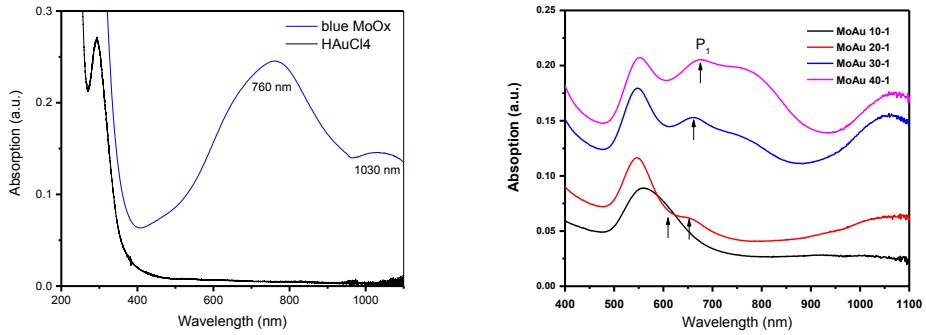

Figure 1: The optical absorption spectra of the initial blue MoOx suspension, the $HAuCl_4$ solution and different concentrations of Mo:Au ratio.

REFERENCES

[1] S. Eustis and M. a El-Sayed, "Why gold nanoparticles are more precious than pretty gold: noble metal surface plasmon resonance and its enhancement of the radiative and nonradiative properties of nanocrystals of different shapes.," *Chem. Soc. Rev.*, vol. 35, no. 3, pp. 209–217, Mar. 2006.

[2] J. Zhao, X. Zhang, C. R. Yonzon, A. J. Haes, and R. P. Van Duyne, "Localized surface plasmon resonance biosensors," *Nanomedicine*, vol. 1, no. 2, pp. 219–228, Aug. 2006.

[3] S. Sarina *et al.*, "Photocatalysis on supported gold and silver nanoparticles under ultraviolet and visible light irradiation," *Green Chem.*, vol. 15, no. 7, p. 1814, 2013.

[4] M. Notarianni, K. Vernon, A. Chou, M. Aljada, J. Liu, and N. Motta, "Plasmonic effect of gold nanoparticles in organic solar cells," *Sol. Energy*, vol. 106, pp. 23–37, 2014.

[5] N. Minh Vuong, D. Kim, and H. Kim, "Porous Au-embedded WO3 Nanowire Structure for Efficient Detection of CH4 and H2S," *Sci. Rep.*, vol. 5, p. 11040, Jun. 2015.

[6] M. E. Aguirre *et al.*, "The spontaneous room temperature reduction of $HAuCl_4$ in ethylene glycol in the presence of ZnO: a simple strategy to obtain stable Au/ZnO nanostructures exhibiting strong surface plasmon resonance and efficient electron storage properties," *New J. Chem.*, vol. 39, no. 2, pp. 909–914, 2015.

[7] H. Cheng, X. Qian, Y. Kuwahara, and K. Mori, "A Plasmonic Molybdenum Oxide Hybrid with Reversible Tunability for Visible-Light-Enhanced Catalytic Reactions," *Adv. Mater.*, no. 27, pp. 4616–4621, 2015.

[8] R. S. Patil, M. D. Uplane, and P. S. Patil, "Structural and optical properties of electrodeposited molybdenum oxide thin films," *Appl. Surf. Sci.*, vol. 252, no. 23, pp. 8050–8056, 2006.

[9] M. Angiola, M. M. Alsaif, K. Kalantar-zadeh, A. Wisitsoraat, W. Wlodarski, and A. Martucci, "Optical Hydrogen Sensing Based on Hybrid 2D MoO 3 /Au Nanoparticles," *Procedia Eng.*, vol. 120, pp. 1141–1144, 2015.

Visible Near-Zero Refractive Index Metamaterials

Andres Ochoa, Mario Gonzalez, and Nantakan Wongkasem*

Department of Electrical Engineering, College of Engineering and Computer Science,
University of Texas Rio Grande Valley, Texas 78539, USA
*corresponding author, E-mail: nantakan.wongkasem@utrgv.edu

Abstract

A near-zero refractive index design based on hyperbolic metamaterials operating in the visible regime is proposed. The structure is composed of a metal-dielectric multilayer, where the dielectric constants are opposite in order to tune the design for a specific wavelength and purpose. The near zero refractive index is designed to be within the visible range.

1. Introduction

Hyperbolic metamaterials (HMM) [1,2] have been implemented in the design and investigation of wave propagation behavior. They are anisotropic media created from structures including multilayer stacks, nanorods and hyperlenses. A similar anisotropic structure has achieved negative refraction in the ultraviolet region [3] using different design methods. Theoretically, similar negative refractive media, and even collimators, could be created systematically using a HMM approach. A considerable challenge arises in bringing HMMs to the visible range. Optical metamaterials have been fabricated using common materials, such as TiO_2 and Ag [4], but with very low transmission. The goal becomes finding materials with special properties that improve transmission and reduce loss from reflection and absorption through careful consideration of desired optical properties and tradeoffs.

2. Research methods

Having epsilon near zero can influence the refractive of the structure to index near zero behavior [5]. The assumptions made in obtaining near zero index in the optical regime is that permeability is unity and a permittivity of zero, or epsilon near zero (ENZ), will carry the most weight in affecting the refractive index of the entire structure.

$$n = \sqrt{\varepsilon\,\mu} \qquad (1)$$

2.1. Proposed potential materials

Designing a metamaterial stack involves using two alternately layered materials with dielectric constants of opposite signs. An ideal pair would have their dielectric functions change at a similar rate across a large band of wavelengths. Available materials in the visible range do not share this quality and must be designed for a narrow bandwidth.

A plasmonic material should be chosen based on its complex dielectric constant. The real part should have a negative value that remains fairly close to zero depending on the wavelength. A few noble metals that are commonly used as conductors have potential. With an increasing wavelength, however, their dielectric constant may drop too low to be effective. This factor limits how far the metamaterial can go from the ultraviolet range into the visible range.

The imaginary part, or loss, of the dielectric constant should be even closer to zero than its real part. Some noble metals and transparent conducting oxides (TCO) have low dielectric loss, but TCOs maintain a positive real dielectric constant in the visible range disqualifying them as plasmonic materials. Compared to other metals, silver has a low dielectric loss. Despite its high dielectric constant, it is the best candidate for a plasmonic material.

A third option for plasmonic materials would be to use nitrides such as HfN, ZrN and TiN [6,7]. Studies into these materials show their real dielectric constant becomes negative halfway through the visible range from green to red. They may act as possible substitutes for noble metals at higher wavelengths, but available nitrides also have high dielectric loss. If this value is too high, they won't produce metamaterial properties. Individual research would be required to understand changes to the dielectric constant of nitrides based on multiple variables presented during different deposition methods.

The real dielectric constant of the dielectric material should be positive and start at a value slightly higher than the magnitude of the dielectric constant of the plasmonic material at the chosen wavelength. This ensures that the HMM remains a Type I HMM and allows the wave to propagate through like an insulator [8]. Similar to plasmonic materials, dielectric materials should have a loss that is very close to zero. Most losses of suitable dielectrics will have values in the micro range.

There is a point where the Type I HMM becomes a Type II HMM as the wavelength increases [2], characterizing HMMs as band pass filters. This crossover occurs when the real dielectric constants of both the plasmonic and dielectric materials are equal, ignoring sign. As a Type II, the metamaterial takes on metallic properties, reflecting a larger amount of light.

2.2. Structure design

With silver having the lowest dielectric loss of metals for optical applications, it is chosen as the plasmonic material. This is confirmed from plotting the reflectance, transmittance and absorptance of four metals with the same thickness of 50 nm in Fig. 1 at an incident angle of 0°.

The alternating layers create a structure with anisotropic properties. Effect Medium Theory is used to obtain the components of permittivity in anisotropic medium [8]. Parallel permittivity is used for x and y components or the ordinary components in a uniaxial crystal and perpendicular permittivity for the z component or the extraordinary component.

$$\varepsilon_{\parallel} = \frac{\varepsilon_1^d L_d + \varepsilon_1^m L_m}{L_d + L_m} \tag{2}$$

$$\varepsilon_{\perp} = \frac{\varepsilon_1^d \varepsilon_1^m (L_d + L_m)}{L_d \varepsilon_1^m + L_m \varepsilon_1^d} \tag{3}$$

Equation (2) provides the fill fraction of plasmonic material by setting epsilon parallel equal to zero and one of the thicknesses as a constant in nanometers and solving for the other thickness. The fill fraction is the ratio of the thickness of a layer of plasmonic material compared to the total thickness of one pair of different layers. It is also taken as the sum of thicknesses of all plasmonic layers per total thickness of the stack.

Using a generalized version of Snell's law for anisotropy, the refractive is found using Equation (4),

$$n = \sqrt{\varepsilon_{\parallel} \varepsilon_{\perp}} \tag{4}$$

where n is the refractive index of the stack [1,2,8,9]. Instead, a set of equations to solve for the angle of refraction θ for the extraordinary angle of incidence [10],

$$\theta_e = \arcsin\left[n_i \sin(\theta_i) \sqrt{\frac{n_o^2 \cos^2\phi + n_e^2 \phi}{n_o^2 n_e^2 - (n_i \sin\theta_i)^2 (n_e^2 - n_o^2)\sin^2\phi}} \right] \tag{5}$$

$$\theta_{kp} = \sin\phi \cos\theta_e \tag{6}$$

$$\tan\theta = \frac{n_o^2}{n_e^2} \tan\theta_{kp} \tag{7}$$

where θ_e is the extraordinary angle of refraction, n_i is the refractive index of the outside medium, θ_i is the incident angle, n_o and n_e are the ordinary and extraordinary indices of refraction, the angle between the y axis and the optical axis is ϕ, and θ_{kp} is the angle between the optical axis and the wave vector at the extraordinary angle. It is later shown that the value of n_o has a significant role in achieving index near zero if the dielectric losses of both the plasmonic and dielectric materials are low.

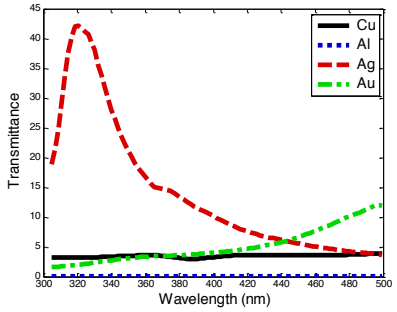

(a)

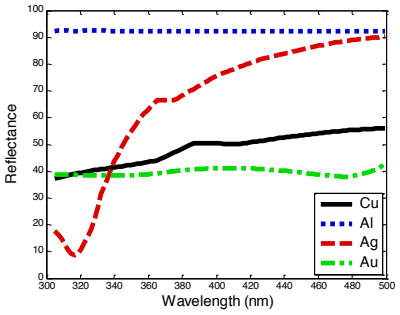

(b)

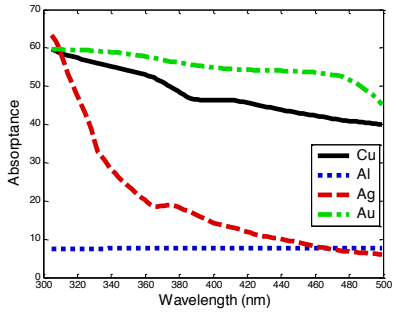

(c)

Figure 1: (a) Transmittance, (b) reflectance and (c) absorptance for 50nm thick metals.

2.3. Results

Comparing Equation (2) and (3), only the epsilon parallel equation has a zero, while epsilon perpendicular has a pole. This can be seen in Fig. 2 (a) where the zero occurs around 58% silver and in Fig. 2 (b) where the pole occurs around 42% silver. The region between the pole and zero where epsilon parallel real is positive and epsilon perpendicular real is negative produces a Type I metamaterial [2]. The fill fraction where we want to produce an ENZ is at zero.

The refractive index of the stack is plotted using equation (4) in Fig. 3. The area between 42% and 58% silver has a refractive index close to zero. According to the results, the best percentage of silver would be slightly above 50%. Taking into account the extinction coefficient, a better percentage would be closer to 58% to reduce the amount of loss. To confirm this, the angle of refraction is calculated with equations (5), (6) and (7) for an incident angle of 20° and plotted in Fig. 4. which shows an angle approaching 0° around 42% and 48%, and an angle below 1° in between.

The transmittance, reflectance and absorptance of three pairs of silver and dielectric material is shown in Fig. 5 with the thickness of silver around 15 nm. 50% transmittance is approximated for a 50 nm thick layer at 405 nm.

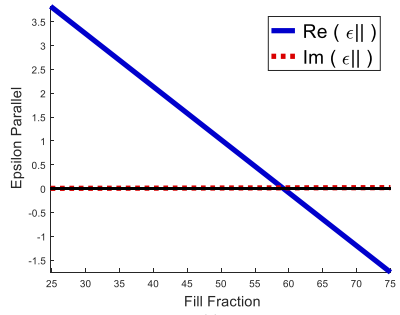

(a)

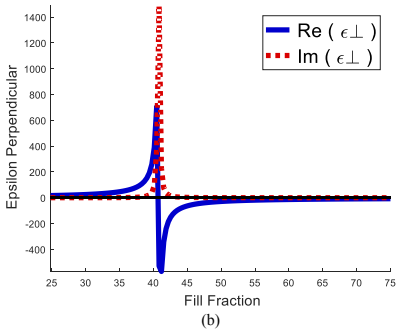

(b)

Figure 2: (a) Epsilon parallel and (b) epsilon perpendicular.

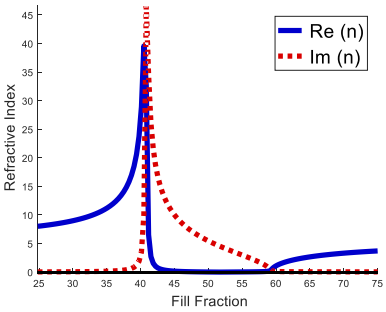

Figure 3: Refractive index.

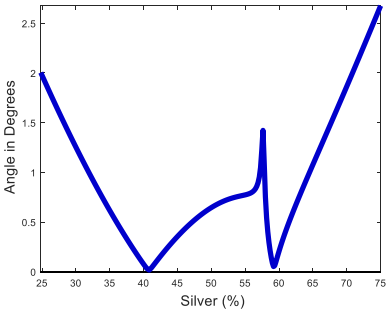

Figure 4: Angle of refraction for an incident angle of 20°.

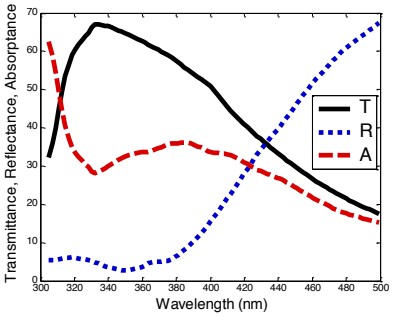

Figure 5: Transmittance, reflectance and absorptance for three pairs of silver/dielectric.

3. Discussion

The final design is a multilayer stack deposited on a thin glass substrate using a magnetron sputtering system with thicknesses set to percentages obtained from the data above. There are three points of interests from the results: 42%, 51% and 48% approximately.

The first percentage corresponds to the pole obtained from the effective medium theory, but has high dielectric loss. 51% is a common solution to achieve both epsilon near zero and epsilon near pole (ENP), but the wavelength is set to a narrow band based on the material characteristics. The key variable in achieving an angle of refraction close to zero is the value of ordinary refractive index in equation (7) which requires an epsilon parallel close to zero. Choosing 48% silver would be the best option for 405 nm. This fill fraction may be changed for different wavelength.

In this paper, permeability is assumed to be unity in the optical regime, however, diamagnetic responses within layers will lower its value [11]. Reaching zero would require an infinite number of layers, but certain materials have a penetration depth which will limit this and the total thickness of the stack. Fig. 6 shows a reduced transmittance down to 20% for the stack doubled to 6 pairs of silver and dielectric material. Decreasing the thicknesses of individual layers to increase the number of layers could increase the transmittance, but it might have an adverse effect on the refractive index of the individual layers. These thicknesses should be chosen based on the magnetron capabilities and the effects on the dielectric constant of the dielectric material.

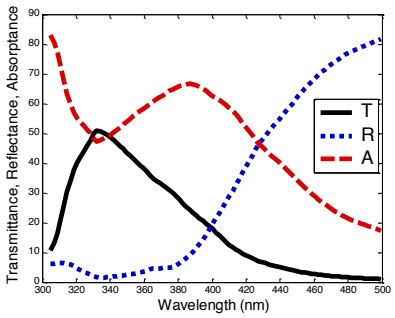

Figure 6: Transmittance, reflectance and absorptance for six pairs of silver/dielectric.

4. Conclusion

Using effective medium theory in combination with low loss materials can produce an epsilon-near-zero metamaterial stack in the visible range. An alternative to silver with both lower dielectric constant and loss is needed to include the higher wavelengths. It may be further altered to form structures such as gratings to increase transmittance and control and possibly form negative index materials. The simplicity of the structure increases the ease of manufacturing and its practical use in larger fabrications.

Acknowledgements

This work is supported by the University of Texas Rio Grande Valley, Office of the Provost.

References

[1] A. Poddubny, I. Iorsh, P. Belov and Y. Kivshar, Hyperbolic metamaterials," *Nature Photonics*, Vol. 7, No. 12, 948-957, 2013.

[2] P. Shekhar, J. Atkinson and Z. Jacob, "Hyperbolic metamaterials: fundamentals and applications," *Nano Convergence*, Vol 1, No. 1, 2014.

[3] T. Xu, A. Agrawal, M. Abashin, K. J. Chau and H. J. Lezec, "All-angle negative refraction and active flat lensing of ultraviolet light," *Nature*, Vol. 497, No. 7454, 470-474, 2013.

[4] G.S.Subramania, A. J. Fischer, T. S. Luk and I. Brener, "Epsilon near zero material for electromagnetic energy transport through sub-wavelength channels," Sandia National laboratories, No. SAND2012-7770s, 2012.

[5] E.J.R. Vesseur, T.Coenen, H. Caglayan, N. Engheta, A. Polman, "Experimental Verification of n=0 Structures for Visible Light," Physical Review Letters, Vol. 110, No. 1, 2013.

[6] P. Patsalas, N. Kalfagiannis and S. Kassavetis, "Optical Properties and Plasmonic Performance of Titanium Nitride," *Materials*, Vol. 8, No. 6, 3128-3154, 2015.

[7] G.V. Naik, J. Kim and A. Boltasseva, "Oxides and nitrides as alternative plasmonic materials in the optical range [Invited]," *Optical Materials Express*, Vol. 1, No. 6, 1090-1099, 2011.

[8] V. Caligiuri, R. Dhama, K. V. Sreekanth, G. Strangi and A. De Luca, "Dielectric singularity in Hyperbolic Metamaterials: the inversion point of coexisting anisotropies," *Scientific Reports*, Vol. 6, No. 20002, 2016.

[9] Z.S. Sacks, D.M. Kingsland, R. Lee, J.-F. Lee, "A perfectly matched anisotropic absorber for use as an absorbing boundary condition," *IEEE Transactions on Antennas and Propagation*, Vol. 43, No. 12, 1460-1463, 1995.

[10] J.F-. Wu, Y.-T. Zhang, "The relation between the propagation of extraordinary ray and the optical axis in the uniaxial crystal," *Optik - International Journal for Light and Electron Optics*, Vol. 124, No. 17, 2667-2669, 2013.

[11] G.T. Papadakis, H.A. Atwater, "Retrieval of material parameters for uniaxial metamaterials," *Physical Review B*, Vol. 91, No. 15, 155406, 2015.

Aj Nantakan 1/5/17 15:25
Supprimé: ,

Aj Nantakan 1/5/17 15:24
Supprimé: A.

Aj Nantakan 1/5/17 15:25
Supprimé: , P.

Aj Nantakan 1/5/17 15:25
Supprimé: , T.

Aj Nantakan 1/5/17 15:25
Supprimé: , G. S.

Aj Nantakan 1/5/17 15:25
Supprimé: , E.J.R.

Aj Nantakan 1/5/17 15:26
Supprimé: , P.

Aj Nantakan 1/5/17 15:26
Supprimé: G. V.

Aj Nantakan 1/5/17 15:26
Supprimé: ,

Aj Nantakan 1/5/17 15:26
Supprimé: V.

Aj Nantakan 1/5/17 15:26
Supprimé: , Z.S.

Aj Nantakan 1/5/17 15:26
Supprimé: , J.-F.

Aj Nantakan 1/5/17 15:26
Supprimé: , G.T.

Positional irregularities in nanowire metamaterials

T. Gric[1*], O. Hess[2]

[1] Vilnius Gediminas Technical University, Sauletekio av. 11, LT-10223, Vilnius, Lithuania
[2] Imperial College London, The Blackett Laboratory, Department of Physics, London SW7 2AZ, U.K.
*corresponding author: tatjana.gric@vgtu.lt

Abstract

Irregularities in metamaterials are usually perceived to have detrimental impacts. Here, we demonstrate that positional irregularities also open up an innovative way to control the properties of interface waves between two layers of materials.

1. Introduction

Nanowire metamaterials have attracted significant attention due to their innovative impact on both fundamental physics and practical applications. Particularly the discovery that hyperbolic metamaterial functionality can be achieved by structures with very simple geometry, such as nanorod arrays [1] and metal-dielectric multilayers [2, 3], really sparked the scientific interest during the past few years. It was proposed, that one-dimensional metallic gratings representing a simple metasurface with practically realistic geometries, are capable of tailoring the dispersion, and thus the propagation characteristics of surface plasmons in an exceptional manner [4]. Here we study the influence of irregularity on the propagation of surface waves at the interface between two different materials.

2. Dispersive relations and properties of the irregular metamaterials

The structure of the metamaterial is shown in Fig.1, where parameters d and S represent the diameter of the metallic nanowire. All the involved media are nonmagnetic, so the magnetic permeability of every medium is the same as that of vacuum. In our numerical calculation, we use a metallic or semiconductor nanowire metamaterial structure as an example to explore the dispersive features of surface plasmon polaritons, where $\varepsilon_{m,s}^{M}(\omega) = \varepsilon_{\infty} - \dfrac{\omega_p^2}{\omega^2 + i\delta\omega}$. By means of effective medium approximation it is possible to evaluate the effective permittivities of the nanowire metamaterial which are described by the following equations:

$$\varepsilon_{\perp}^{M} = \varepsilon_{d}^{M}\left[\frac{\varepsilon_{m,s}^{M}(1+\rho)+\varepsilon_{d}^{M}(1-\rho)}{\varepsilon_{m,s}^{M}(1-\rho)+\varepsilon_{d}^{M}(1+\rho)}\right] \quad (1)$$

$$\varepsilon_{\parallel}^{M} = \varepsilon_{m,s}^{M}\rho^{M} + \varepsilon_{d}^{M}(1-\rho) \quad (2)$$

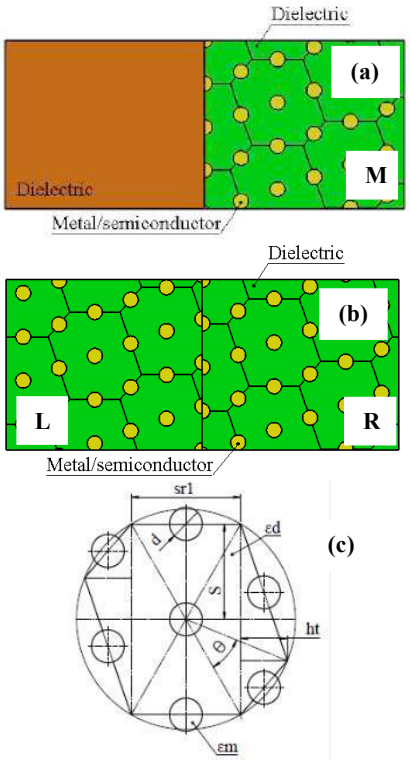

Fig. 1. Fragment of the nanowire metamaterial bounded by either the isotropic medium (dielectric) (a) or ansotropic medium (metamaterial) (b) along with the metmaterial unit cell (c).

Here, subindex M refers to the metamaterial under consideration. Moreover, ρ is the metal fill fraction ratio which is defined as:

$$\rho = \frac{nanowire\ area}{unit\ cell\ area} \quad (3)$$

A possible way to calculate the metal fill fraction (ρ) is to obtain values for pore diameter (d) and spacing (S) and apply the following equation with ht and $sr1$ being the geometrical parameters of the hexagon in case of irregularly positioned metamaterial (Fig. 1).

It is worthwhile mentioning, that

$$ht = \sqrt{2S^2 + \frac{sr1^2}{2} - 2\left(S^2 + \frac{sr1^2}{4}\right)\cos\theta} \times \sin\left(arc\tan\left(\frac{2S}{sr1}\right) - \frac{\theta}{2}\right) \quad (4)$$

with θ being the irregularity angle (Fig. 1).

Under made assumptions, it is possible to derive the dispersion relation for the surface modes localized at the interface between two media with the left one being either isotropic or anisotropic. In case of the metamaterial bounded with the dielectric we evaluate the tangential components of the electric and magnetic fields at the interface and obtain a single surface mode with the propagation constant [5]

$$\beta = k\left(-\frac{\varepsilon_d^M \varepsilon_d a\left(\varepsilon_d - \varepsilon_{m,s}^M \rho + \varepsilon_d^M\left(\rho - 1\right)\right)}{b\left(\varepsilon_d^2 + \frac{\varepsilon_d^M\left(\varepsilon_{m,s}^M \rho - \varepsilon_d^M\left(\rho - 1\right)\right)a}{b}\right)}\right)^{1/2}, \quad (5)$$

Where k is an absolute value of wavevector in vacuum and β is the component of the wavevector parallel to the interface and $a = \varepsilon_d^M\left(\rho - 1\right) - \varepsilon_{m,s}^M\left(\rho + 1\right)$, $b = \varepsilon_d^M\left(\rho + 1\right) - \varepsilon_{m,s}^M\left(\rho - 1\right)$.

To analyze the properties of the surface waves at the interface between two nanowire metamaterials, i.e. anisotropic media, we evaluate the tangential components of the electric and magnetic fields at the interface and obtain a single surface mode with the propagation constant, β. It is interesting to notice that in case of $\varepsilon_m^L = \varepsilon_m^R$ and $\varepsilon_d^L = \varepsilon_d^R$, the obtained result coincides with the dispersion of the surface wave as follows:

$$\beta = k\left(\frac{\varepsilon_d^L\left(\varepsilon_d^L + \varepsilon_m^L - \varepsilon_d^L\rho_L + \varepsilon_m^L\rho_L\right)\left(\varepsilon_d^L + \varepsilon_m^L - \varepsilon_d^L\rho_R \quad \varepsilon_m^L\rho_R\right)}{\sqrt{4\varepsilon_d^L\varepsilon_m^L - \left(\varepsilon_d^L\right)^2\rho_L - \left(\varepsilon_d^L\right)^2\rho_R + \left(\varepsilon_m^L\right)^2\rho_L + \left(\varepsilon_m^L\right)^2\rho_R + 3\left(\varepsilon_d^L\right)^2 + \left(\varepsilon_m^L\right)^2 - \left(\varepsilon_d^L\right)^2\rho_L\rho_R - \left(\varepsilon_m^L\right)^2\rho_L\rho_R \quad 2\varepsilon_d^L\varepsilon_m^L\rho_L\rho_R}}\right) \quad (6)$$

Herein, the sub-indices L and R refer to the left and right metamaterial under consideration, respectively.

3. Discussion

In this section, we investigate SPs supported by the metal and semiconductor nanowire metamaterials presented in Fig. 1. In order to obtain a concise insight into the effect of the losses of the metal nanowires on the modes characteristics, we first consider the lossless case. Then, we revise the results by including the losses in the calculations. The parameters of silver are obtained by fitting this dielectric function to a particular frequency range of bulk dielectric data [6]. It is found [7] that for silver, the values of $\varepsilon_\infty = 5$, $\omega_p = 9.5eV$, $\delta = 0.0987eV$ give a reasonable fit to the bulk dielectric data. It is interesting to notice that heavily doped silicon (n>2.2×10^{19} cm^{-3}) has been shown to exhibit metallic properties at terahertz frequencies [8, 9] and has the potential to replace metals in such applications [10]. The case of a heavy-doped Si is considered, assuming that the doping level is N=5×10^{19} cm^{-3} [11]. Figs. 2-4 show the dispersion curves of the irregular nanowire metamaterial. Although the graphs possess the similar outline with that of traditional metal-SPP, the dispersion curves for the irregular nanowires have some particularities that deserve further considerations.

A. Lossless case

In case the losses are ignored, the plot of Eq. 4, 6 leads to the band structure that can be divided into allowed and forbidden regions. Panels 2 (a), (b) are plotted for different angle θ, i. e. for θ = 10 - 60°. The panel (a) shows the dispersion of the nanowire metamaterial that is bounded with dielectric (ε=4) and the panel (b) – with metamaterial.

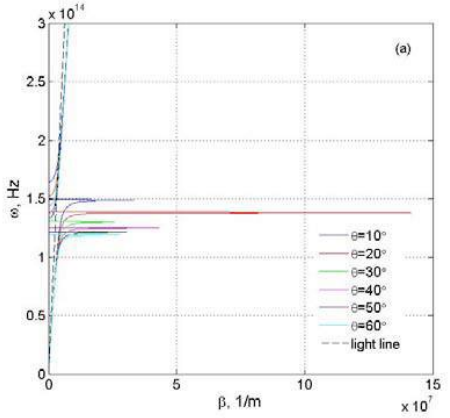

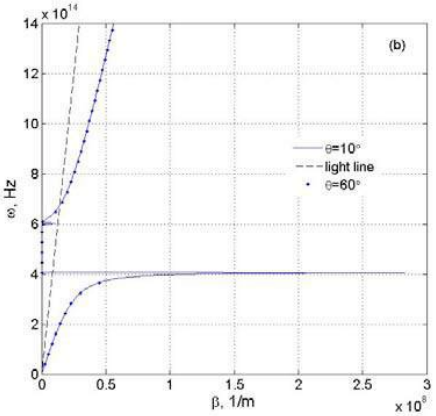

Fig. 2. The dispersion of SPs supported by the lossless metallic nanowire metamaterial bounded by dielectric (a) and metamaterial (b). The black dashed line show the light line.

The allowed modes appear in a wide range of frequency for the specific values of the wavevector β as presented in panel 2 (a), (b). When the metamaterial is bounded with the dielectric, the allowed band shrinks as it is depicted in panel 2 (a). As it is seen from panels 2 (a), (b), by increasing the angle θ, the SPs supported by the system shifted to lower frequencies; the allowed bands shrink to the narrower regions. It should be mentioned that bands deviate significantly from the light line, and this departure is greater in case of the metamaterial bounded with metamaterial. We remark that such dispersion curves exhibited similar behaviors of SPPs propagating along the ordered nanowire metamaterial interface. The asymptotic frequency is tuned by the value of θ, and the maximum value of tuning reaches to 1.6 GHz, if θ=10° and the metamaterial is bound with the dielectric. In the case of the irregular metamaterial, the amendment of θ is equivalent to change in ρ, resulting in the change of asymptotic frequency. For comparison, the dispersion relation of the ordered nanowire metamaterial (θ=60°) is also calculated, as shown in the cyan line in Figs. 2 (a), (b). We observe that the asymptotic frequency of the ordered structure (the cyan line) is lower than that of the irregular structure.

B. Lossy case

Up to now, we have completely ignored the effect of the losses, coming from Re(ε), in our analysis. In the case Im(ε) is involved in the calculations, the wavenumber takes the complex values, i. e. $\beta = \beta' + i\beta''$, and therefore the wavenumber would be complex within the whole frequency region. Panels (a) and (b) of Fig. 3 show the dispersion diagrams and (c) and (d) the propagation length of the surface waves for both cases. While there are visible changes in dispersion curves, the most notable feature is the drastic enhancement of the propagation length as the angle θ is increased.

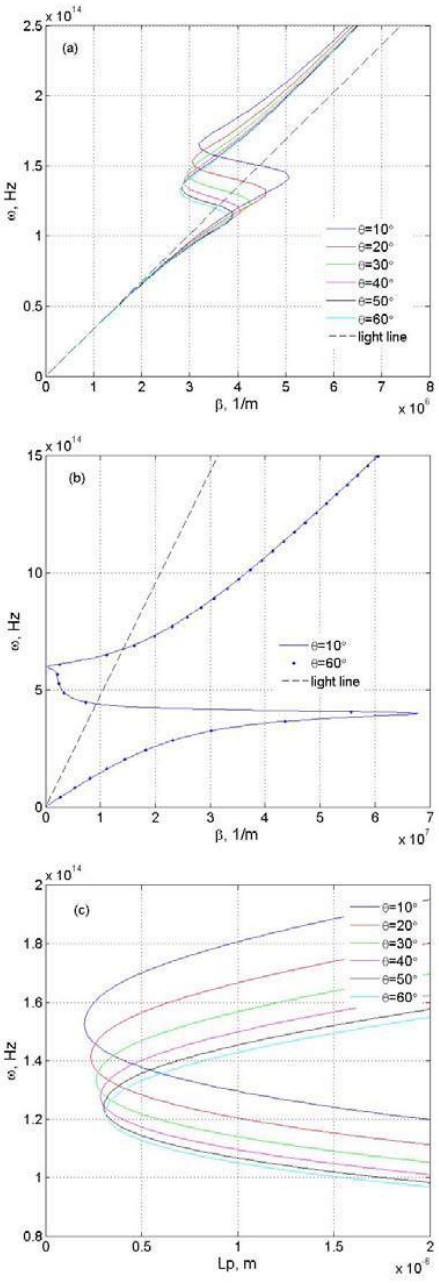

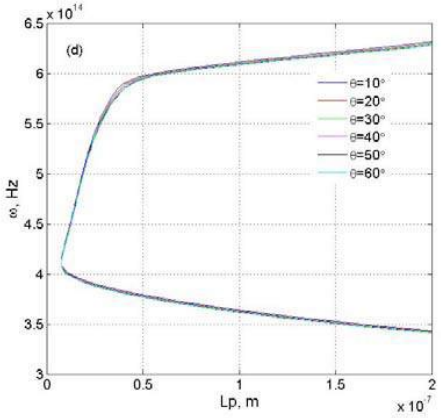

Fig. 3. The dispersion of SPs supported by the lossy metallic nanowire metamaterial bounded by dielectric (a) and metamaterial (b) along with the propagation lengths for different cases (panel (c) – dielectric; panel (b) - metamaterial); the black dashed line shows the light line.

As it is seen from panels (c), (d) of Fig. 3, L_p values of the SPs for θ=60° are considerably smaller than those of θ=10°. This means that when real losses are included, the nanowire metamaterial supports the SPs that are not as efficient as SPs of the irregular metamaterial. By efficient SPs we mean modes with large L_p. From these panels, it can be observed that by decreasing the angle θ from 60 to 10°, the frequency range in which the SPs are supported can be extended. Moreover, the propagation characteristics can also be improved.

Since our goal is to obtain the nanowire metamaterial with the capability of supporting SPs with longer propagation length, for the results presented in Fig. 3 we have replaced metal with the semiconductor. Figure 4 shows dispersion of the SPs in case of the semiconductor nanowire metamaterial.

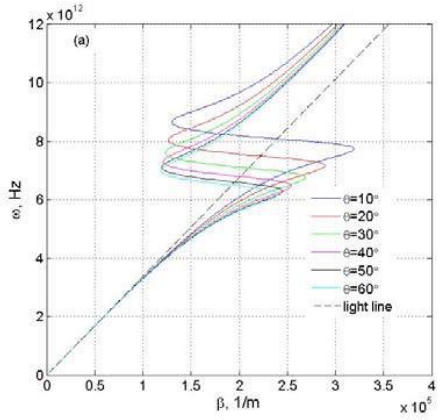

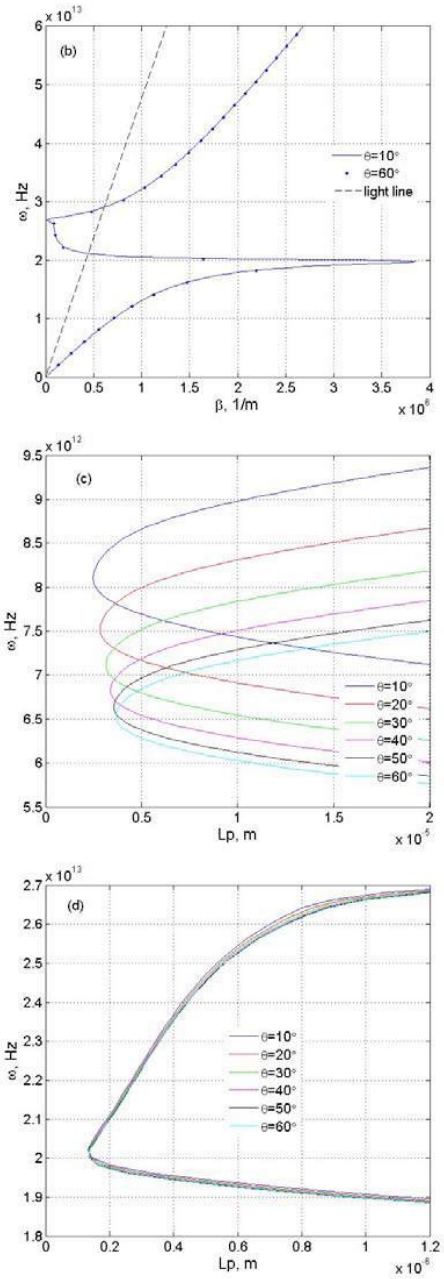

Fig. 4. The dispersion of SPs supported by the lossy semiconductor nanowire metamaterial bounded by dielectric (a) and metamaterial (b) along with the propagation lengths for different cases (panel (c) – dielectric; panel (d) - metamaterial); the black dashed line show the light line.

It can be concluded that the semiconductor nanowire metamaterials support SPs with the longer propagation length. It is clear that the propagation length of semiconductor-SPPs is around 10 times longer than that of metal-SPP. Thus, the propagation loss of semiconductor-SPPs is much lower than that of metal-SPPs. Consequently,

in some circumstances, using the irregular semiconductor nanowire metamaterial structures would result in longer propagation length. And by adjusting the level of irregularity (angle θ), the properties of SPP mode could be tuned.

4. Conclusions

The SPP guided by the irregular nanowire metamaterial was studied theoretically. The dispersion relation of the SPP was derived treating the metamaterial as an anisotropic material by the effective medium theory. It is revealed that semiconductor-SPPs have narrower frequency range than metal. As far as we are concerned, the oscillation of free electrons at the metal surface results with the surface plasmon. Naturally, the decrease of the number of free electrons would lead to the reduction of frequency range. The calculation results also revealed that the semiconductor-SPPs have larger propagation length compared with metal-SPPs. Therefore, at some specific frequency, semiconductors could be more favorable than metal in transmitting signals. Moreover, it should be noticed, that there is a room of possibilities to increase the propagation length of the modes up to two orders by replacing the metallic nanowires with the semiconductor ones. These irregular nanowire metamaterial structures are appropriate for feasibly designing irregular metamaterial, which are beneficial to guiding and sensing applications.

References

[1] M. A. Noginov, Yu. A. Barnakov, G. Zhu, T. Tumkur, H. Li, and E. E. Narimanov, Bulk photonic metamaterial with hyperbolic dispersion, *Appl. Phys. Lett.* 94: 151105, 2009.

[2] Z. Jacob, I. I. Smolyaninov, and E.E. Narimanov, Broadband Purcell effect: Radiative decay engineering with metamaterials, *Appl. Phys. Lett.* 100: 181105, 2012.

[3] T. Gric, Surface-plasmon polaritons at the interface of nanostructured metamaterials, *Prog. Electromagn. Res.* 46: 165-172, 2016.

[4] Y. M. Liu, Plasmonic metamaterials, Ph.D. dissertation, University of California at Berkeley, 2009.

[5] I. Iorsh, A. Orlov, P. Belov, Y. Kivshar, Interface modes in nanostructured metal-dielectric metamaterials, *Appl. Phys. Lett.* 99: 151914, 2011.

[6] P. B. Johnson, R. W. Christy, Optical constants of the noble metals, *Phys. Rev. B* 6: 4370, 1972.

[7] C. Oubre, P. Nordlander, Finite-difference time-domain studies of the optical properties of nanoshell dimers, *J. Phys. Chem. B*. 109(20): 10042-10051, 2005.

[8] S. Li, M. M. Jadidi, T. E. Murphy, G. Kumar, Terahertz surface plasmon polaritons on a semiconductor surface structured with periodic V-grooves, *Opt. Express* 21: 7041–7049, 2013.

[9] G. Kumar, S. Li, M. M. Jadidi, T. E. Murphy, Terahertz surface plasmon waveguide based on a one-dimensional array of silicon pillars, *New J. Phys*. 15: 085031, 2013.

[10] A. Rusina, M. Durach, K. A. Nelson, M. I. Stockman, Nanoconcentration of terahertz radiation in plasmonic waveguides, *Opt. Express* 16: 18576–18589, 2008.

[11] L. Shen, X. Chen, T.-J. Yang, Terahertz surface plasmon polaritons on periodically corrugated metal surfaces, *Opt. Express* 16: 3326–3333, 2008.

Surface plasmon-polaritons and transverse spin angular momentum at the boundary of hyperbolic metamaterial with arbitrary orientation of the optical axis

Vladimir Belyi[1*], Svetlana Kurilkina[1], Nikolai Kazak[1], and Vladimir Agabekov[2]

[1]B.I. Stepanov Institute of Physics of National Academy of Sciences of Belarus, Minsk, Belarus
[2]Institute of Chemistry of New Materials of National Academy of Sciences of Belarus, Minsk, Belarus
*corresponding author, E-mail: v.belyi@ifanbel.bas-net.by

Abstract

The possibility is established and the conditions are found for localization of plasmon-polaritons (PPs) near the boundaries of hyperbolic metamaterials (HMs) of both the I and II types with arbitrary orientation of the optical axis. It is grounded that such surface PP has the transverse spin momentum which depends on the wavelength of the exiting wave, the orientation of the optical axis of the hyperbolic metamaterial, and dielectric properties of bordered media.

1. Introduction

It is known that propagating circularly polarized light beam possesses the longitudinal spin angular momentum (SAM) the direction of which coincides with the wave vector [1]. Meanwhile, each photon transfers the angular momentum $\pm\hbar$ depending on the sign of circular polarization. For linear polarized propagating wave the longitudinal spin angular momentum is absent [1-3].

In the general case the angular momentum carried by the monochromatic light beam represents a superposition of SAM and orbital angular momentum (OAM) related to the optical phase profile of the beam in the plane orthogonal to the propagation direction. Vortex (Laguerre-Gaussian, Bessel-Gaussian) beams with the amplitude of electric vector $E(\rho,\varphi)=E_o(\rho)\exp(im\varphi)$ (ρ,φ are the cylinder coordinates, m is the azimuthal phase index, or topological charge) are examples of the fields possessing OAM. For these vortex beams each photon carries OAM that equals to $m\circ$. When vortex beams interact with microobjects the transfer of spin and orbital momenta to the particles takes place that permits to control them.

Recently it was shown that the spin momentum of evanescent waves (including ones with linear polarization) appears to be nonzero and perpendicular to the wave vector that principally differs these waves from propagating ones [4,5]. Thus, the transverse SAM arises, the origin of which is caused by the rotation of the electric vector of the evanescent wave in the propagation plane. The features of transverse SAM are investigated for evanescent waves at the boundary of isotropic media. But optical anisotropy can essentially influence the conditions of existence of surface waves and transverse spin related to them.

In Ref. [6] the possibility is shown of the presence of transverse spin momentum for plasmon-polariton fields excited at the boundary of the II type hyperbolic metamaterial (HMM) with optical axis perpendicular to this boundary. In this paper we investigate the influence of HMM optical axis orientation on the conditions of existence of surface plasmon-polaritons with transverse spin momentum at the metamaterial interface. As an example, we consider HMM created from multilayered metal-dielectric structures.

2. Surface plasmon-polariton at the boundary of isotropic medium and hyperbolic metamaterial with arbitrary oriented optical axis

2.1. Features of plasmon-polaritons at the boundary of isotropic medium and hyperbolic metamaterial with arbitrary oriented optical axis

Let us consider a metamaterial formed from layered-periodic metal-dielectric medium. In the effective medium theory when the thickness of each layer is sufficiently small, i.e. $|k_d d_d|<<1, |k_m d_m|<<1$ where k_d, k_m are the wave numbers of dielectric and metallic layers, respectively, this multilayered structure can be considered as anisotropic effective medium with the permittivity tensor represented in the form:

$$\varepsilon = diag\{\varepsilon_\perp, \varepsilon_\perp, \varepsilon_\parallel\} = \varepsilon_\perp + \delta \mathbf{c} \otimes \mathbf{c}, \qquad (1)$$

where $\delta = \varepsilon_\parallel - \varepsilon_\perp$, $\varepsilon_\parallel$ and $\varepsilon_\perp$ are the longitudinal (along the Z' axis) and transverse (in the plane orthogonal to Z') main permittivities, $\mathbf{c}$ is the unit vector along the HMM optical axis, and the symbol $\otimes$ denotes the dyadic product of the vectors ($\mathbf{c}\otimes\mathbf{c} = c_i c_k$). The main permittivities of this structure are determined by the following relations:

$$\varepsilon_\perp = (1-f)\varepsilon_d + f\varepsilon_m, \varepsilon_\parallel^{-1} = [(1-f)/\varepsilon_d + f/\varepsilon_m]. \quad (2)$$

Here ε_d and ε_m are the permittivities of dielectric and metallic layer, respectively, f is the filling factor (the volume part of metal in the unit cell). The permittivity of metal ε_m is described by the modified Drude formula:

$$\varepsilon_m(\omega) = \varepsilon_\infty - \omega_p^2/(\omega^2 + i\omega\Gamma) = \\ = \varepsilon_\infty - \omega_p^2/(\omega^2 + \Gamma^2) + i\omega_p^2\Gamma/[\omega(\omega^2 + \Gamma^2)]. \quad (3)$$

Here ω_p is the volume plasma frequency, ε_∞ is the sum of the interband contributions, $\Gamma = V_F/l$ is the damping constant, V_F is the Fermi velocity, l is the electron mean free path in bulk metal. For silver we have $\varepsilon_\infty = 5$, $\omega_p = 14\cdot10^{15}s^{-1}$, $\Gamma = 32\cdot10^{12}s^{-1}$, $V_F = 1.4\cdot10^6 ms^{-1}$[7]. For simplicity of our consideration we suppose that in Eq. (2) $\mathrm{Im}(\varepsilon_l)\approx0$, $\mathrm{Im}(\varepsilon_l)\approx0$. As calculation shows [8] this assumption is correct for spectral regions where parameters $\varepsilon_\perp$ and $\varepsilon_\parallel^{-1}$ significantly differ from zero.

Let the HMM border with the isotropic medium with permittivity ε_1. Meanwhile, the angle between the optical axis of the metamaterial and the normal to the HMM boundary (Z axis) is θ (Fig.1).

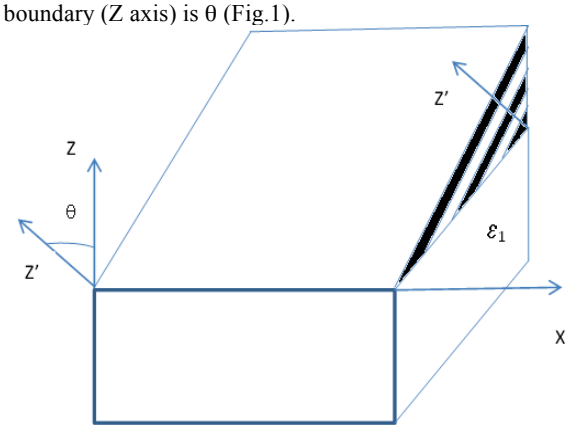

Figure 1: The scheme of the considered structure. The Z′ axis is parallel to the $\mathbf{c}$ vector.

Now we consider *p*-polarized surface waves propagating along the *X* axis in the plane separated the isotropic dielectric with permittivity ε_1 and hyperbolic metamaterial. We'll use the coordinate system *XYZ* (see Fig.1) in which the effective permittivity tensor ε', characterizing the hyperbolic metamaterial, is represented in the form:

$$\varepsilon' = U\varepsilon\widetilde{U}. \quad (4)$$

Here U is the transformation matrix which permits to transfer from the coordinate system related to the HMM main dielectric axes to the system of coordinate XYZ:

$$U = \begin{pmatrix} \cos\theta & 0 & -\sin\theta \\ 0 & 1 & 0 \\ \sin\theta & 0 & \cos\theta \end{pmatrix}, \quad (5)$$

the symbol "tilde" denotes the transposition. As follows from Eqs.(4) and (1)

$$\varepsilon' = U\varepsilon\widetilde{U}.\varepsilon_{xx}\mathbf{e}_x\otimes\mathbf{e}_x + \varepsilon_\perp\mathbf{e}_y\otimes\mathbf{e}_y + \varepsilon_{zz}\mathbf{e}_z\otimes\mathbf{e}_z + \\ + \varepsilon_{xz}(\mathbf{e}_x\otimes\mathbf{e}_z + \mathbf{e}_z\otimes\mathbf{e}_x). \quad (6)$$

Here

$$\varepsilon_{xx} = \varepsilon_\perp\cos^2\theta + \varepsilon_\parallel\sin^2\theta, \\ \varepsilon_{zz} = \varepsilon_\perp\sin^2\theta + \varepsilon_\parallel\cos^2\theta, \quad (7) \\ \varepsilon_{xz} = (\varepsilon_\parallel - \varepsilon_\perp)\sin\theta\cos\theta,$$

$\mathbf{e}_x$, $\mathbf{e}_y$, and $\mathbf{e}_z$ are the unit vectors of the used coordinate system.

Let us represent the vectors of the field inside the dielectric (*d*) and metamaterial (*m*) in the form

$$\mathbf{F} = \begin{cases} \mathbf{F}^d\exp(\kappa_d z + iqx - i\omega t), & z<0 \\ \mathbf{F}^m\exp(-\kappa_m z + iqx - i\omega t), & z>0 \end{cases}, \quad (8)$$

where $\mathbf{F}$ denotes the electric $\mathbf{E} = (E_x, 0, E_z)$ or magnetic $\mathbf{H} = (0, H_y, 0)$ vector, $\kappa_{d,m} > 0$ and q are the decay constant and longitudinal wave number of the surface plasmon-polariton, respectively, $\kappa_d^2 = q^2 - k_0^2\varepsilon_1$, $k_0 = \omega/c$, ω is the cyclic frequency of electromagnetic wave, c is the light velocity in vacuum. Taking into account Eq. (8) from the Maxwell equations one can obtain the relations for electric and magnetic vectors inside the dielectric and metamaterial:

$$\mathbf{E}^d = -\frac{A_0}{\varepsilon_1}(i\frac{\kappa_d}{k_0}\mathbf{e}_x + \frac{q}{k_0}\mathbf{e}_z)e^{iqx+\kappa_d z}, \\ \mathbf{H}^d = A_0\mathbf{e}_y e^{iqx+\kappa_d z}. \quad (9)$$

$$\mathbf{E}^m = \frac{A_0}{sk_0}[(i\kappa_m\varepsilon_{zz} + q\varepsilon_{xz})\mathbf{e}_x - \\ (q\varepsilon_{xx} + i\kappa_m\varepsilon_{xz})\mathbf{e}_z]e^{iqx-\kappa_m z}, \\ \mathbf{H}^m = A_0\mathbf{e}_y e^{iqx-\kappa_m z}. \quad (10)$$

Here $s = \varepsilon_{xx}\varepsilon_{zz} - \varepsilon_{xz}^2$, A_0 is the amplitude, and the phase factor $\exp -i\omega t$ is omitted. Substituting Eq. (10) into the Maxwell equation $rot\mathbf{E} = -(1/c)\partial\mathbf{H}/\partial t$ we find:

$$\kappa_m^2 = aq^2 - bk_0^2 + 2iqd\kappa_m, \quad (11)$$

where $a = \varepsilon_{xx}/\varepsilon_{zz}, b = s/\varepsilon_{zz}, d = \varepsilon_{xz}/\varepsilon_{zz}$. For small and large (close to 90°) values of the θ angle the parameter ε_{xz} (and hence, the d parameter) is small. Owing to this the decay constant κ_m is represented in the form:

$$\kappa_m = \kappa_{mo} + i\kappa_{m1}. \quad (12)$$

It should be noted that $|\kappa_{mo}| >> |\kappa_{m1}|$. Then, squaring Eq. (12) and comparing the result with Eq. (11), we obtain:

$$\kappa_m = \kappa_{mo} + idq = \sqrt{aq^2 - bk_0^2} + idq. \qquad (13)$$

It follows from Eq. (13) that the decay constant is complex. Thereby, the plasmon-polariton has a nonzero propagation constant along the normal to the metamaterial boundary. It means that its phase velocity is directed under the γ angle towards the HMM border:

$$tg\gamma = -d. \qquad (14)$$

As follows from Eq. (14), both for the I type HMM ($\varepsilon_\perp > 0, \varepsilon_{||} < 0$) and the II type HMM ($\varepsilon_\perp < 0, \varepsilon_{||} > 0$) one can realize two different cases of the phase velocity orientation of plasmon-polariton: 1) the phase velocity is directed from the boundary inside the metamaterial, and 2) the phase velocity is directed towards the boundary. The case 1) takes place for the I type HMM at $\gamma > 0$ (positive value of the θ angle relates to the optical axis which is disposed between the Z and X axes of the chosen coordinate system), and for the II type HMM at $\gamma < 0$. The case 2) takes place for the I (or II) type HMM at $\gamma < 0$ (or $\gamma > 0$, respectively). If $\gamma \triangleq 0$ or $\gamma \triangleq \pi/2$ the transverse component of the wave vector of plasmon-polariton disappears, and the equation for the longitudinal wave number of the plasmon-polariton is represented as

$$q = k_0 \sqrt{\frac{\varepsilon_1 \varepsilon_{zz} (\varepsilon_{xx} - \varepsilon_1)}{\varepsilon_{xx}\varepsilon_{zz} - \varepsilon_1^2}} = k_0 \sqrt{\varepsilon_{eff}} \qquad (15)$$

2.2. The condition of the plasmon-polariton localization at the boundary of hyperbolic metamaterial

Now we'll analyze the possibility of localization of the electromagnetic wave on the interface of isotropic medium and hyperbolic metamaterial. Due to the exponentially decaying of the amplitude of this field when moving off the boundary, the wave number *q* has to be larger than modules of wave vectors of the waves propagating inside the dielectric and metamaterial. Thereby,

$$\varepsilon_{eff} > 0,\ \varepsilon_{eff} > \varepsilon_1,\ \kappa_m > 0. \qquad (16)$$

From inequalities (16) the conditions of localization of plasmon-polariton at the boundary of hyperbolic metamaterial follow: $\varepsilon_{zz} > \varepsilon_1$, $\varepsilon_{xx} < 0$. For the hyperbolic metamaterial of the I type these conditions are fulfilled at

$$\sin^2\theta > Y_1 = \sin^2\Theta_1 = \frac{\varepsilon_\perp}{|\varepsilon_{||}| + \varepsilon_\perp}, \qquad (17)$$

$$\sin^2\theta > Y_2 = \sin^2\Theta_2 = \frac{|\varepsilon_{||}| + \varepsilon_1}{|\varepsilon_{||}| + \varepsilon_\perp}. \qquad (18)$$

From Eqs.(17), and (18) it follows the condition of existence of localized plasmon-polaritons at the boundary of the hyperbolic metamaterial of the I type and isotropic dielectric:

$$|\theta| > \theta_1 = \max\{|\Theta_1|, |\Theta_2|\},\quad \Theta_{1,2} = \arcsin\sqrt{Y_{1,2}}. \qquad (19)$$

Similarly, for the hyperbolic metamaterial of the II type the excited plasmon-polariton is localized if the following conditions are fulfilled:

$$\sin^2\theta < Y_3 = \sin^2\Theta_3 = \frac{|\varepsilon_\perp|}{\varepsilon_{||} + |\varepsilon_\perp|}, \qquad (20)$$

$$\sin^2\theta < Y_4 = \sin^2\Theta_4 = \frac{\varepsilon_{||} - \varepsilon_1}{\varepsilon_{||} + |\varepsilon_\perp|}. \qquad (21)$$

From Eqs. (20), and (21) one can obtain the general condition for existence of localized plasmon-polaritons at the boundary of the metamaterial of the II type and isotropic dielectric:

$$|\theta| < \theta_2 = \min\{|\Theta_3|, |\Theta_4|\},\quad \Theta_{3,4} = \arcsin\sqrt{Y_{3,4}}. \qquad (22)$$

Obtained Eqs. (19), and (22) are determined the conditions of localization of surface plasmon-polaritons at the interface of isotropic medium and hyperbolic metamaterial.

2.3. Localized plasmon-polaritons at the boundary of multilayered metal-dielectric nanostructure Ti_3O_5/Ag

As an example we consider the hyperbolic metamaterial created on the basis of the layered-periodic structure Ti_3O_5/Ag the unit cell of which is formed by the nanolayers of silver (Ag) and isotropic dielectric Ti_3O_5.

In Fig.2, 3 the spectral dependences of effective permittivities $\varepsilon_\perp$ and $\varepsilon_{||}$ are represented for hyperbolic metamaterial on the basis of the metal-dielectric layered structure Ti_3O_5/Ag. For calculation here and below we suggested that the thickness of the metal layer was 20 nm, and the filling factor was *f*=0.3. As is seen from Figs.2,3, in the spectral region $320\ nm < \lambda < 390\ nm$ this structure displays the properties of the I type HMM, and for the wavelength $600\ nm < \lambda$ it can be considered as the II type HMM.

Now we support that all layers are deposited on the substrate (for example, fused quartz with dielectric permittivity ε_1=2.1), and the periodicity axis (the optical axis) of the structure is oriented at a certain angle θ to the normal to its border. As is illustrated in Fig.4, for this case the condition (19) is fulfilled for large values of θ. It should be noted that if the parameter $|\varepsilon_{||}|$ increases the value of the angle $\theta_1 = \max\{\Theta_1, \Theta_2\}$ becomes larger.

For hyperbolic metamaterial of the II type created on the basis of metal-dielectric layered structure Ti_3O_5/Ag the condition (22) is fulfilled at small values of the θ angle, i.e. when the optical axis is close to the normal to the HMM

boundary. Meanwhile, the parameter θ_2 increases if $|\varepsilon_\perp|$ becomes larger.

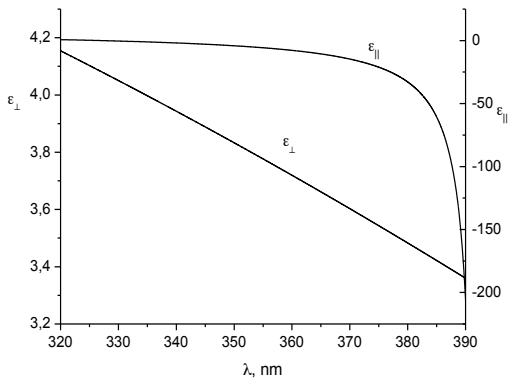

Figure 2: The spectral dependences of main dielectric permittivities of the I type HMM on the base of Ti_3O_5/Ag structure.

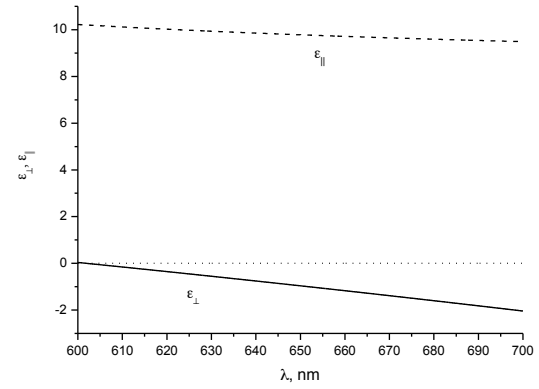

Figure 3: The spectral dependences of main dielectric permittivities of the II type HMM on the basis of Ti_3O_5/Ag structure.

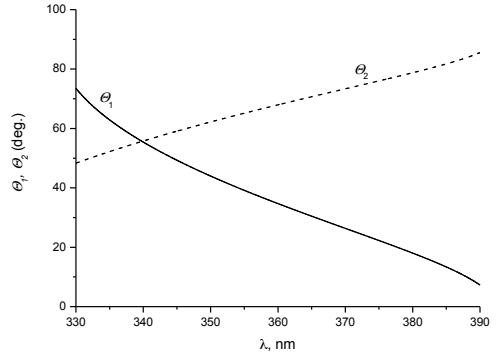

Figure 4: The spectral dependences of the angles $\Theta_{1,2}$=arcsin $(Y_{1,2})^{1/2}$ for the I type HMM on the base of Ti_3O_5/Ag structure.

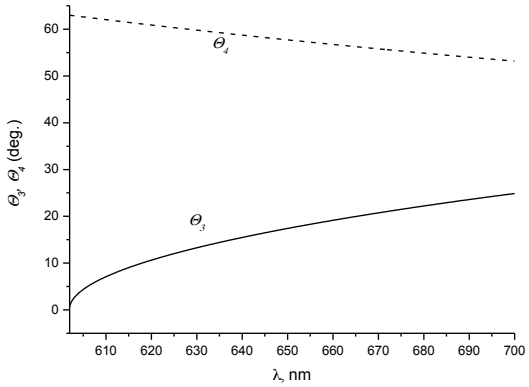

Figure 5: The spectral dependences of the angles $\Theta_{3,4}$=arcsin $(Y_{3,4})^{1/2}$ for the II type HMM on the basis of Ti_3O_5/Ag structure.

3. Transverse spin angular momentum of surface plasmon-polariton

As follows from Eqs. (9), and (10), the electric vector of plasmon-polariton, localized inside the dielectric, is deposited in the propagation plane (*X,Z*) and has both real and imaginary components $\mathbf{k}^d = q\mathbf{e}_x + i\kappa_d\mathbf{e}_z$. Owing to this the phase difference $-\pi/2$ between the components E_x^d and E_z^d appears. This causes the rotation of the electric vector in the propagation plane *(XZ)* and emergence of the transverse component S_y of spin angular momentum [4,5]:

$$\mathbf{S} = \frac{1}{16\pi\omega}\mathrm{Im}\left[\mu^{-1}(\mathbf{E}^*\mathbf{E}) + \varepsilon^{-1}(\mathbf{H}^*\mathbf{H})\right] \quad (23)$$

Then, as follows from Eqs. (23), and (9), the transverse component of SAM is represented in the form:

$$S_y = \frac{|A_0|^2}{8\pi\omega\varepsilon_1^2}\frac{\kappa_d q}{k_0^2}e^{2\kappa_d z}(z<0). \quad (24)$$

Taking into consideration the following relations

$$|A_0|^2 = 8\pi\varepsilon_1 k_0^2 W/q^2,\ W = (\varepsilon_1\mathbf{E}\mathbf{E}^* + \mathbf{H}\mathbf{H}^*)/(16\pi),$$

from Eq. (24) one can obtain:

$$S_y = \frac{W}{\omega\varepsilon_1}\frac{\kappa_d}{q}e^{-2\kappa_d z}. \quad (25)$$

Eq. (25) is applicable for calculation of transverse spin angular momentum carrying by the spatially localized surface wave into a transparent dielectric. In the immediate vicinity of the interface between media, the expression (25) is simplified:

$$S_y = \frac{2\kappa_d q}{q^2 + \kappa_d^2}. \qquad (26)$$

Eq. (26) is convenient to use for calculating the amplitude of the transverse component *Sy* of the spin as a function of the wavelength of the surface plasmon-polariton at the interface between the hyperbolic metamaterial and the dielectric and, in particular, with a liquid or water containing microparticles. In this case, the parameter *Sy* determines the torque momentum acting in the direction of the *Y*-axis on particles near the surface of the metamaterial.

In Figs.6,7 the spectral dependences of expected value of transverse spin (in $\hbar$ units) for plasmon-polariton localized at the boundary of layered-periodic medium Ti_3O_5/Ag and dielectric (water, glyserine, glass). It is seen that the expected value of transverse spin S_y changes with variation of the wavelength. This indicates the possibility of controlling the transverse spin moment and, consequently, the force acting on the microparticles placed in the dielectric near its boundary with the metamaterial, by changing the length of the light wave exciting the surface plasmon-polariton.

However, as is seen in Figs.6,7, dependences $S_y(\lambda)$ are deferent for the spectral regions where considered metal-dielectric structure possesses the properties of HMM of the I and II types. These differences display in the following. If the wavelength increases from the short-wavelength region (where the structure possesses the properties of the I type HMM) up to the wavelength for which $\varepsilon_{\|}^{-1} \to 0$, the expected S_y value decreases (Fig.6). If the wavelength decreases from the long-wavelength region (where the structure possesses the properties of the II type HMM) up to λ for which $\varepsilon_{\perp} \to 0$, the expected value S_y of transverse spin momentum increases (Fig.7).

Moreover, the expected value of transverse spin appears to be dependent on the orientation of the optical axis and permittivity of the medium bordered with the metamaterial. But these dependences are different for spectral regions related to the I and II types of HMMs. In the first case (the I type HMM) the curvature of the $S_y(\lambda)$ curve decreases with increasing the angle θ (Fig.6a). Besides, in this spectral region the S_y value decreases if the permittivity ε_1 increases (Fig.6b). In the second case (the II type HMM) with increasing the angle θ the expected value S_y of transverse spin also increases (Fig.7a), and with increasing ε_1 the curvature of the $S_y(\lambda)$ curve decreases (Fig.7b).

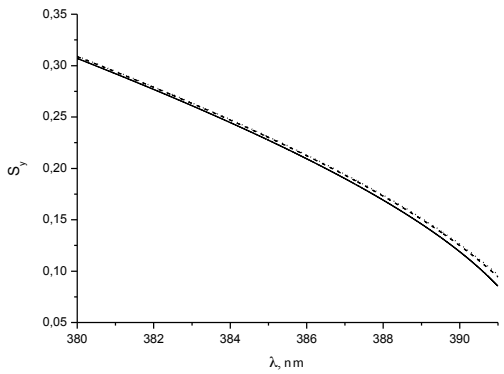

a

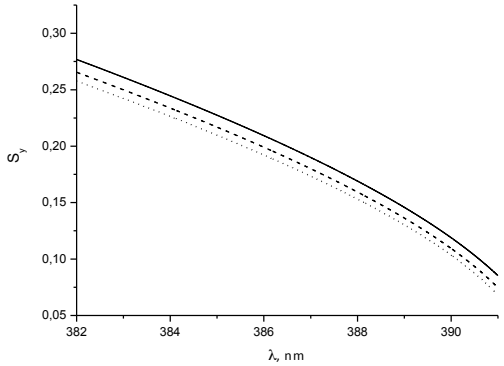

b

Figure 6: The spectral dependence of the expected value of transverse spin (in ħ units) for the localized wave formed at the interface of the metal-dielectric multilayered medium Ti_3O_5/Ag and dielectric: a) water; b) water (solid line), glyserine (dashed line), optical glass BAF 10 (dotted line). The optical axis is oriented at the angle of: a) θ=87.8° (solid line), 89° (dashed line), 90° (dotted line); b) 87.8°.

4. Conclusions

Thus, in this paper we investigated the features of plasmon-polaritons excited at the interface of the hyperbolic metamaterial and dielectric for the case when the optical axis is oriented under the angle towards the boundary. The expressions are obtained for the complex electric and magnetic vectors as well as for the decay constants of the fields on both sides of the interface. It is shown that the propagation constant of plasmon-polariton has the component oriented perpendicular to the boundary inside the metamaterial. Hence, the surface wave has a radiative component propagating inside the HMM under a certain angle to its border. It is established that for hyperbolic metamaterials of different types (the I and II) changing the orientation of the optical axis one can realize the conditions

when the phase velocity of plasmon-polariton is directed from the boundary inside the metamaterial or towards the boundary.

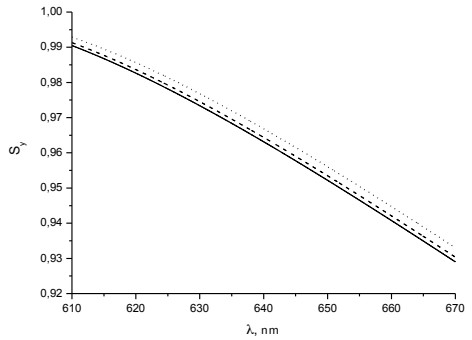

a

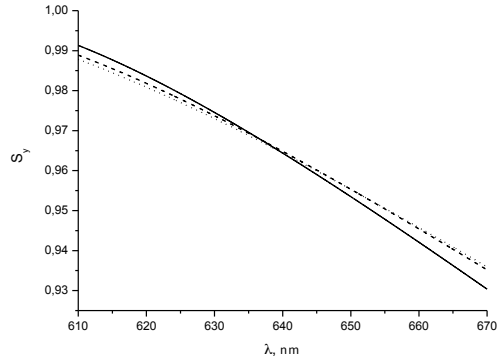

b

Figure 7: The spectral dependence of the expected value of transverse spin (in ħ units) for the localized wave formed at the boundary of the metal-dielectric multilayered medium Ti_3O_5/Ag and dielectric: a) water; b) water (solid line), glyserine (dashed lline), optical glass BAF 10 (dotted line). Optical axis is oriented under the angle: a) $\theta=1^o$ (solid line), 3^o (dashed line), 5^o (dotted line); b) 3^o.

The possibility is shown and the conditions are determined for localization of plasmon-polariton at the boundary of hyperbolic metamaterial of both the I and II types.

It is grounded that surface plasmon-polariton, localized near the interface of isotropic dielectric and hyperbolic metamaterial, possesses the transverse spin angular momentum, the expected value of which depends on the wavelength of exciting radiation, the orientation of the optical axis of HMM, and permittivity of bordered medium.

For illustration of obtained results we carries out a numerical modeling of optical properties of hyperbolic metamaterial formed on the basis of layered-periodic metal-dielectric medium.

References

[1] J. D. Jackson, *Classical Electrodynamics*, Wiley, Berkeley, 1999.

[2] M.V. Berry. Optical currents, *J. Opt. A: Pure Appl. Opt*. 11: 094001, 2009.

[3] A. Bekshaev, K.Y. Bliokh, M. Soskin, Internal flows and energy circulation in light beams, *J. Opt.* 13: 053001, 2011.

[4] K.Y. Bliokh, F. Nori, Transverse spin of a surface polariton, *Phys. Rev. A* 85: 061801, 2012.

[5] K.Y. Bliokh, A.Y. Bekshaev, F. Nori, Dual electromagnetism: helicity, spin, momentum and angular momentum, *New J. Phys*. 15: 033026, 2013.

[6] S.N. Kurilkina, V.N. Belyi, N.S. Kazak, Surface plasmon-polaritons and transverse spin angular momentum at the boundary of hyperbolic metamaterials, *J Appl Specrosc* 83: 965–969, 2017.

[7] W. Cai, V. Shalaev, *Optical Metamaterials. Fundamentals and Applications*, Springer, New York, 2010.

[8] S. N. Kurilkina, M. A. Binhussain, V. N. Belyi, N. S. Kazak, Features of hyperbolic metamaterials with extremal optical characteristics, *J. Opt.* 18: 085102, 2016.

Study on the Transmission Characteristics of the Symmetrical Semi-circular Cavity Filter Based on Surface Plasmon Polaritons

Zhi-shuang Wang, Guan-mao Zhang*, and Hai-rui Liu

Institute of Modern Communication Technology,School of Information Science and Engineering,
Lanzhou University, Lanzhou 730000, P.R.China
*corresponding author, E-mail: zhanggm@lzu.edu.cn

Abstract

A novel structure of the symmetrical semi-circular cavity MIM (metal-insulator-metal) waveguide filter based on the aperture coupled method is proposed. The transmission spectrum of the filter is obtained by using the finite element method (FEM). Using the adjustable characteristics of this filter, the transmission characteristics of the three communication windows (850nm, 1310nm, 1550nm) at optical telecommunication regime can be controlled. The excellent performance of this filter can be applied in the micro-nano optical devices, especially in optical fiber communication.

1. Introduction

Surface Plasmon Polaritons (SPPs) are waves that propagate along the surface of a conductor and a dielectric due to the interaction between the free electrons of the conductor and the incident electromagnetic field [1]. SPPs have promising application on the devices in highly integrated optical circuits because they overcome the conventional diffraction limit and can manipulate light on sub-wavelength scales [2,3]. Among various SPPs based waveguides, metal-insulator-metal (MIM) structure has attracted tremendous interests of the researchers in recent years, because of its potential applications to manipulate and control light in nanoscale[4].

At present, the SPPs based on the MIM structure functional optical devices have made great breakthrough in theoretical and experimental research, such as Bragg reflector[5], splitter[6], interferometer[7], filter[8] and so on, where the filter technology is critically important in the development of micro-nano integrated optical devices, especially in optical communication equipments. Therefore, the study of MIM structure filter is fruitful and different resonant cavity structure filters based on SPPs are proposed. Such as, rectangular resonator[9], rectangular ring resonator[10], nano-disk[11], ring cavity[12], trapezoid cavity[13] , etc. These filters are all based on the evanescent coupling method. Their function is single and the bandwidth of their passband or stopband is relatively narrow. However, wide bandwidth filters can play special roles in some cases. Besides, since the decay length of the field in the metal layer is typically around 20nm, very small gaps ($<$ 20nm) are required to achieve any noticeable coupling. Furthermore, the evanescent coupling is both inefficient and challenging to realize even with state-of-the-art electron beam or ion beam lithography. Compared with the evanescent coupling, aperture coupling can improve coupling efficiency and the coupling strength can be controlled by varying the aperture width and depth[14,15].

In this paper, a new type of symmetric semi-circular cavity MIM waveguide structure filter is constructed based on the aperture coupled method. And the semi-circular cavity can be reduced by half of the size compared to the disk or ring at the same radius. The finite element method (FEM) is used to simulate and analyze the transmission characteristics of the filter. Through the analysis of the structure parameters, the influence of the structure parameters on the transmission characteristics is obtained. And by using the relation between the structure parameters and the transmission characteristics, the optimized structure and the simulation results are achieved. Finally, a single-function filter (band-pass filter) is obtained by improving the filter structure (the left and right semi-circular cavities are changed to disk).

2. Structure and method

As shown in Figure 1, the MIM structure filter is composed of three semi-circular cavities connected with the band waveguide through the rectangular apertures. The structure parameters r, A, d, D, L and W represent the radius of the semi-circular cavity, the width of the rectangular aperture, the gap between the bottom of the semicircular cavity and the waveguide, the distance between the centers of two semi-circular cavities, the distance between the point P/Q and the semi-circular cavity, the waveguide width, respectively. The parameter d is set to 50nm to eliminate evanescent coupling between the semi-circular cavity and the band waveguide [14]. The parameters L and W are fixed to 300nm and 50nm. The tunable structure parameters A, r and D are initialized to 40nm, 100nm and 200nm, respectively.Two power monitors are, respectively, set at the points of P and Q to detect the incident and the transmission fields for calculating the incident power of P_{in} and the transmitted power of P_{out}. The transmission coefficient is defined as $T = P_{out}/P_{in}$[16].

In this paper, the transmission characteristics of this filter can be obtained by COMSOL Multiphysics 5.0 based on the FEM method. The insulator is set as air ($\varepsilon_{r(air)}$= 1)

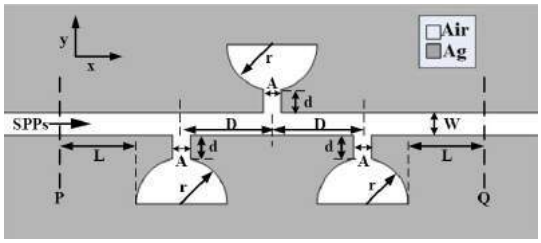

Figure 1: The schematic diagram of the symmetric three semi-circular cavities MIM waveguide filter structure.

and the metal is silver (Ag). The dielectric constant ε_m of silver can be calculated by the standard Drude model,

$$\varepsilon_m = \varepsilon_\infty - \omega_p^2/(\omega^2 - \mathrm{i}\omega\gamma). \quad (1)$$

Here, ε_∞ is the dielectric constant at infinite frequency, γ and ω_p are the electron collision frequency and bulk plasma frequency, respectively. The parameters for silver can be set as ε_∞=3.7, ω_p=9.1eV, and γ=0.018eV [17]. The boundary condition is chosen as the scattering boundary condition [13].

3. Transmission characteristic

Figure 2 shows the transmission spectrum of the filter, in which the tunable structure parameters A, r and D are set as the initial value (A=40nm, r =100nm, D=200nm). As shown in Figure 2, the filter can be treated as multi-functional filter. The first optics communication window of the telecommunication regime is located in its passband and the second and the third windows are in its stopband. The transmission spectrum of this filter appears depression in the passband at the shortwave, but the transmittance of the passband is high and nearly more than 70%. While the transmittance of its stopband is close to 0 and the stopband has the characteristic of flat-bottom. Besides, the falling and the rising edge of this filter are very steep.

4. Analysis of the structure parameters

In order to fully study the transmission characteristics of this filter, the influences caused by the change of the structure parameters A, r and D on the transmission spectrum is analyzed one by one. It is shown in Figure 2 that the passband of the filter at the short-wave has a depression. However, what we expect are the characteristics of the flat-top of the passband and the flat-bottom of the stopband. So, next, we will focus on studying the change trend of the depression of the passband at the shortwave and the bandwidth of the passband and the stopband with the change of the tunable structure parameters.

4.1. Influence of the structure parameter r on the transmission characteristics

When maintaining the structure parameters A and D the initial value unchanged(A=40nm, D=200nm), the transmission spectrum of the structure filter appears obvious red shift with the increase of r, as shown in Figure 3. And with the increase of r, the depression at the shortwave is getting more and more shallow. The bandwidth of the passband increases slowly, but the stopband's increases rapidly. The passband at the long-wave appears a fast drop.

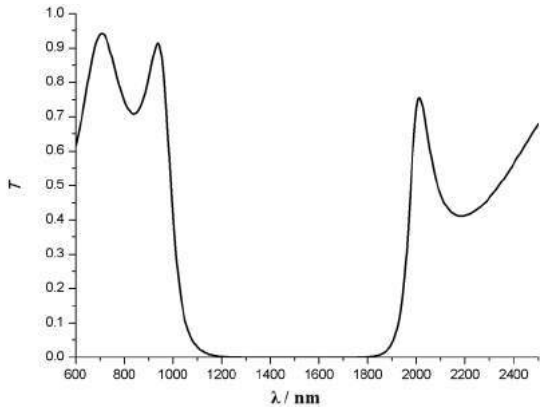

Figure 2: The transmission spectrum of the filter that we proposed with its initial structure parameters (A=40nm, r =100nm, D=200nm).

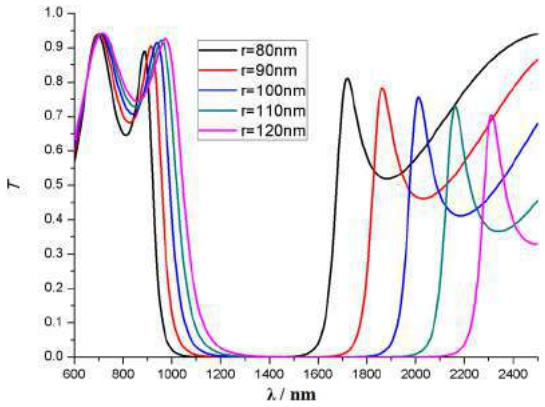

Figure 3: The transmission spectrum of this filter with the increase of r (A=40nm, D=200nm).

4.2. Influence of the structure parameter D on the transmission characteristics

When only changing D and keeping the parameter r and A the initial value the same (r=100nm, A=40nm), the transmission spectrum of the filter appears slight red shift with the increase of D, as shown in Figure 4. And with the increase of D, the depression at the short-wave is getting deeper and deeper; the bandwidth of the passband at the short-wave and the stopband are almost unchanged; the drop degree of the passband at the long-wave slows down.

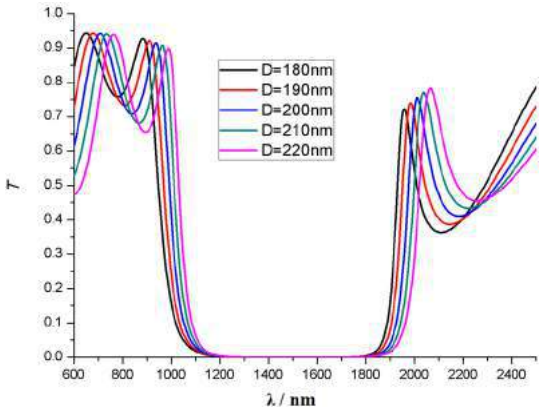

Figure 4: The transmission spectrum of this filter with the increase of D (r=100nm, A=40nm).

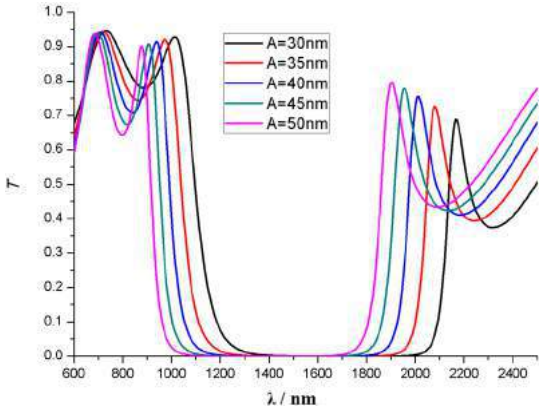

Figure 5: The transmission spectrum of this filter with the increase of A (r=100nm, D=200nm).

4.3. Influence of the structure parameter A on the transmission characteristics

When only changing A and keeping the parameters r and D the initial value unchanged (r=100nm, D=200nm), the transmission spectrum of the filter appears obvious blue shift, as shown in Figure 5. With the increase of A, the depression of the passband at the short-wave is getting deeper and deeper. The bandwidth of the passband at the short-wave decreases and the stopband's almost keeps unchanged; The drop degree of the passband at the long-wave grows up.

Finally, the effects of the structure parameters r, D, and A on the transmission characteristics of the filter are explained. First, the semi-circular cavity and the rectangular aperture can be treated as a "magnetic container". Here, the effective index of the rectangular aperture can be larger than the effective index of the semi-circular cavity and air. So, the waves will flow into "magnetic container" due to the higher effective index of the rectangular aperture, when the

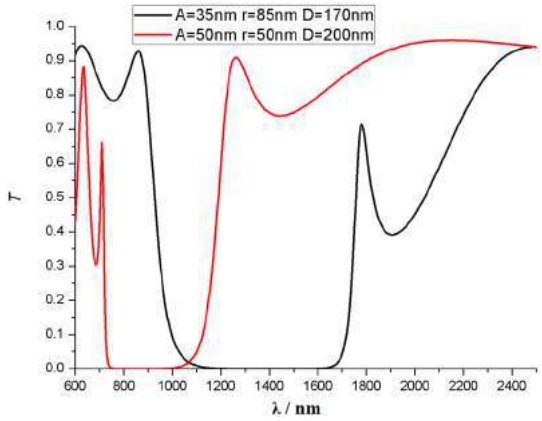

Figure 6: The transmission spectra of the optimized structures.

SPPs waves propagate along the waveguide. And the effect of "magnetic container" causes that the SPPs waves experience a longer propagation length compared with the bare resonator [18, 19]. With the increase of the structure parameters r and D, the red shift of the transmission spectrum is due to the increase of the effective propagation length of the SPPs waves in the MIM filter. Since the parameter r is the parameter of the semi-circular cavity and parameter D is the distance between centers of the three semicircular cavities, so, when increasing r and D to the same degree, the increase of the effective propagation length caused by the semi-circular cavity area with the increase of r will be much greater than that caused by the parameter D. And this is the reason why the red shift of Figure 3 is more visible than that in the Figure 4. At last, we explain the influence of the parameter A on the transmission spectrum. At the same incident wavelength, the effective refractive index of this structure decreases with the increase of the structure parameter A and the resonant wavelength becomes longer with the increase of the effective refractive index of this system [19]. Consequently, with the increase of the structure parameter A, the resonant wavelength of the system moves to the short-wave and the transmission spectrum appears blue shift.

5. Optimization of the structure parameters and the simulation results

First of all, this filter is designed to be used in the telecommunication regime and to control the three optical communication windows on and off. From Section 4, we can learn the different effects of parameters r, D, A on the transmission spectrum. The parameters r, D and A have an effect on the depression of the passband at short-wave. Besides, the parameter r and A have a great influence on the bandwidth of the passband and stopband, while the parameter D has little effect on it. In view of these rules, the tunable parameters can be optimized to get the optimized results,

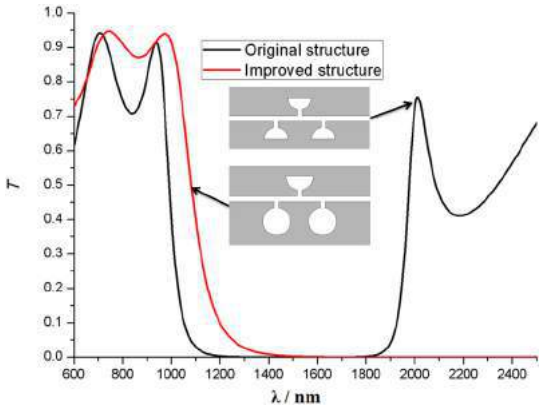

Figure 7: Comparison of transmission spectrum of the improved MIM structure and the original structure filter.

as shown in Figure 6. When the tunable parameters r, D and A are set as 35nm, 85nm and 170nm, respectively, the transmission spectrum of this optimized structure is shown as the black curve. Here, the first optical communication window (850nm) is at the passband of this optimized structure at the short-wave and the center position of the stopband is in the vicinity of 1400nm, which is a good balance between the second and the third optical communication windows. With the decrease of r or the increase of A, the transmission spectrum of this filter is greatly shifted to the direction of the short-wave. And taking advantage of this nature, the tunable parameters are set as A = 50 nm, r = 50 nm and D = 200 nm to obtain another optimized structure shown in the red curve. The first optical communication window is located in its stopband and the second and third optical communication windows are in its passband. Thus, the optimized results are achieved and the control of the three optical communication windows is realized, too.

6. Single functional filter

When keeping the initial tunable structure parameters unchanged (A = 40 nm, r = 100nm, D = 200nm), the left and right semi-circular cavities of the original filter structure are changed to the disk to form an improved MIM structure. As shown in Figure 7, compared with the transmission spectrum of the original structure filter, the transmittance of the improved filter no longer grows up at the wavelength greater than 1800 nm. The transmittance of its passband is higher and the depression of it is very shallow. So, it can be used as a single-functional (band-pass) filter.

7. Conclusions

In summary, a symmetrical semi-circular cavity MIM waveguide structure filter based on SPPs is proposed and studied. This filter has the characteristics of multi-function, tunable and wide bandwidth, etc. By adjusting the structure parameters, the transmission characteristics of the three communication windows (850nm, 1310nm, 1550nm) at optical telecommunication regime can be controlled and the optimized structures and its corresponding transmission spectra can be obtained. Finally, a single-functional (band-pass) filter is achieved with the improved MIM structure. This series filters will have potential engineering application values in micro-nano optics integrated devices, especially in optical fiber communication.

Acknowledgement

This project is supported by the State Key Program of National Natural Science of China (Grant No.61631007), the Fundamental Research Funds for the Central Universities (Lanzhou University) (No.lzujbky-2015-K7) and the Fundamental Research Funds for the Central Universities(No. lzujbky-2017-sp03).

References

[1] W. L. Barnes, A. Dereux, T. W. Ebbesen, Surface plasmon subwavelength optics, *Nature* 424(6950), 824–830, 2003.

[2] C. Genet, T. W. Ebbesen, Light in tiny holes, *Nature* 445(7123), 39–46, 2007.

[3] H. J. Lezec, A. Degiron, E. Devaux, R. A. Linke, L. Martin-Moreno, F. J. Garcia-Vidal, T. W. Ebbesen, Beaming light from a subwavelength aperture, *Science* 297(5582), 820–822, 2002.

[4] F. Hu, H. Yi, Z. Zhou, Band-pass plasmonic slot filter with band selection and spectrally splitting capabilities, *Optics Express*, 19(6):4848–4855, 2011.

[5] B. Wang, G. P. Wang, Plasmon Bragg reflectors and nanocavities on flat metallic surfaces, *Appl. Phys. Lett.* 87(1), 013107, 2005.

[6] G. Veronis, S. Fan, Bend and splitters in metal-dielectric-metal subwavelength plasmonic waveguides, *Appl. Phys. Lett.* 87(13), 131102, 2005.

[7] H.F. Hu, X. Zeng, D.X. Ji, L. Zhu, Q.Q. Gan, Efficient end-fire coupling of surface plasmons on flat metal surfaces for improved plasmonic Mach-Zehnderinterferometer, *J. Appl. Phys.* 113, 053101, 2013.

[8] N. Hu, G. Zhang, H. An, et al, Design and Optimization of the Multifunctional Rectangular Cavity Band-Pass Filter Based on the Surface Plasmon Polariton, *Plasmonics*, 1-6, 2016.

[9] D. Liu, Y. Sun, Q. Fan, et al, Tunable Plasmonically Induced Transparency with Asymmetric Multi-rectangle Resonators, *Plasmonics*, 11(6):1621–1628, 2016.

[10] S. Wang, Y. Li, Q. Xu, et al, A MIM Filter Based on a Side-Coupled Crossbeam Square-Ring Resonator, *Plasmonics*, 11(5):1291–1296, 2016.

[11] G. Zhan, R. Liang, H. Liang, et al, Asymmetric band-pass plasmonic nanodisk filter with mode inhibition and spectrally splitting capabilities, *Optics Express*, 22(8):9912–9919, 2014.

[12] T. B. Wang, X. W. Wen, C. P. Yin, H. Z. Wang, The transmission characteristics of surface plasmon polaritons in ring resonator, *Optics Express* 17(26), 24096–24101, 2009.

[13] C. Song, S. Qu, J. Wang, et al, Plasmonic tunable filter based on trapezoid resonator waveguide, *Journal of Modern Optics*,62(17):1400–1404, 2015.

[14] Z. Han, V. Van, W. N. Herman, et al, Aperture-coupled MIM plasmonic ring resonators with sub-diffraction modal volumes, *Optics Express*, 17(15):12678–12684, 2009.

[15] X. Peng, H. Li, C. Wu, et al, Research on transmission characteristics of aperture-coupled square-ring resonator based filter, *Optics Communications*, 294(5):368–371, 2013.

[16] X. S. Lin, X. G. Huang, Tooth-shaped plasmonic waveguide filters with nanometeric sizes, *Optics Letters*, 33(23), 2874–2876, 2008.

[17] Z. Han, E. Forsberg, S. He, Surface Plasmon Bragg Gratings Formed in Metal-Insulator-Metal Waveguides, *IEEE Photonics Technology Letters*, 19(2):91–93, 2007.

[18] Y. Guo, L. Yan, W. Pan, et al, Characteristics of Plasmonic Filters with a Notch Located Along Rectangular Resonators, *Plasmonics*, 8(2):167–171, 2013.

[19] J. Tao, X. G. Huang, J. H. Zhu, A wavelength demultiplexing structure based on metal-dielectric-metal plasmonic nano-capillary resonators, *Optics Express*, 18(11):11111–11116, 2010.

Combinational Analysis of 2D metamaterials using AFM-IR and s-SNOM

Eoghan Dillon[1*], and Hyuk Woo Jun[2]

[1]Anasys Instruments, USA and [2]Scinco, Korea

[*]corresponding author: eoghan@anasysinstruments.com

Abstract: This talk will focus on techniques and instrumentation for measuring chemical and optical properties of 2D materials with nanometer scale spatial resolution. Conventional infrared spectroscopy is one of the most widely used tools for chemical analysis, but optical diffraction limits its spatial resolution to the scale of many microns. Atomic force microscopy (AFM) enjoys excellent spatial resolution, but has historically lacked the ability to perform robust chemical analysis. This presentation will discuss two techniques (1) AFM-based infrared spectroscopy and (2) scattering scanning near field optical microscopy (s-SNOM). Both of these techniques overcome the diffraction limit, providing the ability to measure and map chemical and optical properties with nanometer scale spatial resolution. As complementary techniques, AFM-IR and s-SNOM together provide an unrivaled capability to perform nanoscale chemical analysis on a diverse range of organic, inorganic, photonic and electronic materials. This talk will focus on the applications of both AFM-IR and s-SNOM to the characterization of a variety of 2D materials, including, nanoantenna arrays and 2D metasurfaces. The applications of nanoantennas are very diverse, ranging from sensing to energy conversion. The ability to measure and tune the resonance structures of these antennas is of vital importance to the construction of accurate and reliable devices. s-SNOM can be readily used as a tool to image the antenna resonance nodes when illuminated at the correct wavelength. In addition to the ability to collect high resolution images of optical phenomenon, the nanoIR2-s provides the capability to spectrally probe nanoscale surface features. This work will show the s-SNOM spectra collected on bar antennas, with the antenna resonance can be clearly resolved, in good agreement with theoretical predictions. AFM-IR and s-SNOM have been used in combination to investigate the role of chirality in the origins of circular dichroism in 2D nanoscale materials. Fully two-dimensional (2D) metamaterials, also known as metasurfaces, comprised of planar-chiral plasmonic metamolecules that are just nanometres thick, have been shown to exhibit chiral dichroism in transmission (CDT).Theoretical calculations indicate that this surprising effect relies on finite non-radiative (Ohmic) losses of the metasurface. Until now this surprising theoretical prediction has never been experimentally verified because of the challenge of measuring non-radiative loss on the nanoscale. s-SNOM is used to map the optical energy distribution when the structures are exposed to RCP and LCP IR radiation while AFM-IR was then used to detect the drastically different Ohmic heating observed under RCP and LCP radiation. For the first time it has been conclusively established the circular dichroism observed in 2D metasurfaces is attributed to handedness dependent Ohmic heating.

.

Enormous Nonresonant THz Field Enhancement with Nanoslits

Om Krishna Suwal and Dai-Sik Kim

Centre for Atom Scale Electromagnetism, Department of Physics and Astronomy, Seoul National University, Seoul 08826, Republic of Korea.

*Corresponding author: dsk@phya.snu.ac.kr

Abstract- Transmission of Terahertz (THz) electromagnetic wave through a substrate is encumbered because of scattering, multiple reflections, absorption, and Fabry–Perot effects when the wave interacts with the substrate. To exclude the undesired interaction of electromagnetic wave with substrates, we investigated THz transmission through a substrate-free nanoslits. We experimentally realized a nonresonant electromagnetic field enhancement by a factor of almost 10^4 in substrate-free 5-nm gold nanoslits. Our nanoslits yielded over 90% normalized electric field transmission in the low-frequency THz region; the slit width was 5 nm, and the gap coverage ratio was 10^{-4} of the entire membrane, 0.42 mm^2. This large field enhancement was attributed to gap plasmons generated by the THz wave, which squeezes the charge cross-section, thus enabling highly dense oscillating charges and strong THz field transmission from the nanoslits.

Previously, we have demonstrated enhancement factors of nearly three orders of magnitude with a 70-nm-wide slit[1]. We assumed that a major obstacle is the substrate, which decreases the transmission and creates undesirable interactions between the gap and the substrate. Here, we demonstrate the experimental realization of nearly four orders of field enhancement by using gold nanoslits on a Si_3N_4 membrane[2]. Our nanoslits had a 5-nm gap that extended up to the entire membrane, with a length of 0.65 mm that was sufficient to surpass the cut-off THz frequency. This structure enabled us to achieve near-maximum field enhancement in the THz region. We observed a straight 1/f-dependent field enhancement factor, as shown in Fig. where f is the frequency. In our case, the gap width was a million times smaller than the wavelength; however, the length of the slit was of the same order as the wavelength. Our experimental results indicates the field enhancement increased by approximately 15 fold at 0.14 THz when Si substrate was removed out from the same nanogap sample (Fig.). Some irregularities in transmission curve was also observed because of the grating modes when the slit array diffracted the incident radiation into the sample plane. We explained the results by poor coupling of THz wave among the evanescent modes because of higher refractive index of substrate.

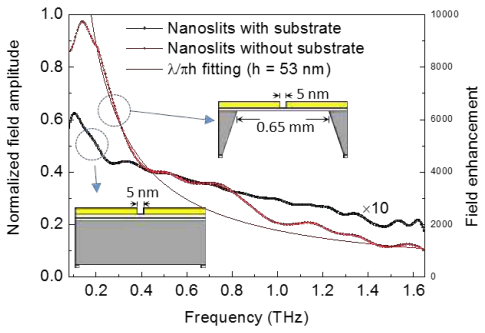

Figure: Normalized field amplitude before and after substrate etched out. The normalization was done with Si substrate and free space for before and after substrate. 1/f fitting seems to be well fitted for the measurement without

Acknowledgements

This work was supported by a NRF Korea (MSIP) (NRF-2005-0093838, NRF-2015R1A3A2031768).

REFERENCES

1 Seo, M. A. *et al.* Terahertz field enhancement by a metallic nano slit operating beyond the skin-depth limit. *Nat Photonics* **3**, 152-156, doi:10.1038/Nphoton.2009.22 (2009).

2 Suwal, O., Rhie, J., Kim, N. & Kim, D. Nonresonant 10 (4) Terahertz Field Enhancement with 5-nm Slits. *Sci Rep-Uk* **7**, 45638 (2017).

Anomalous extinction in lossless index-matched terahertz nanogaps

Jeeyoon Jeong†, Dasom Kim†, Hyeong-Ryeol Park§, Taehee Kang†, Dukhyung Lee†, Sunghwan Kim†, Young-Mi Bahk†, and Dai-Sik Kim*†

† Department of Physics and Astronomy and Center for Atom Scale Electromagnetism, Seoul National University, Seoul 08826, Korea
§ Department of Physics, Chungbuk National University, Chungbuk 28644, Korea

Abstract- Metamaterials are capable of allowing incident wave to neither transmit nor reflect, leading to a perfect absorption. This phenomenon is usually explained in terms of simultaneous manipulation of electric permittivity and magnetic permeability to be impedance-matched to free space[1]. The energy absorption is conceived to occur inside the supporting dielectrics where the electric field amplitude is large, yet systematic study on the actual energy flow has barely been made.

In this work we observe anomalously large extinction of terahertz waves interacting with sub-30nm nanogap arrays even without any absorbing materials within. Simple, exclusive geometry of our nanogap enables analytic study on the origin of the observed phenomena[2]. We find that destructive interference of the diffracted field from the gap and reflected field from metal leads to a giant reflection dip at the resonance, suggesting that absorption might not be the cause of the observed extinction. Nonlinear transmission measurements and calculations indicate that index-matching effect of silicon substrate leads to higher field enhancement at the gap, in which case the extinction further increases to above 60%. Our study provides new insight into how to analyse transmission and reflection signals from nanostructures, and will therefore be of great interest in absorption enhancement or dielectric sensing applications.

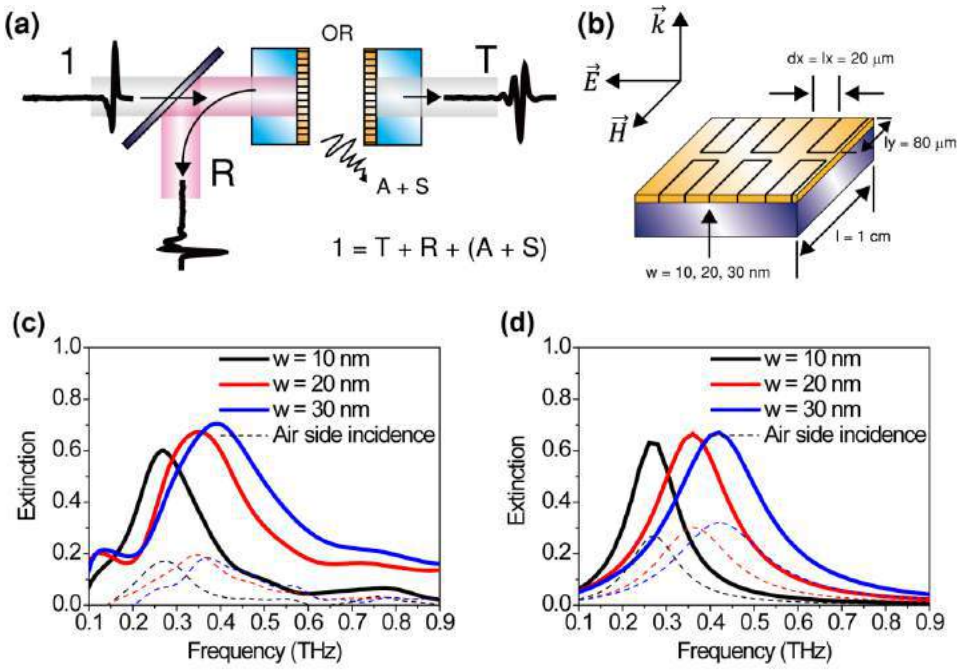

References
1. N. I. Landy et al., Physical Review Letters **100**, 207402 (2008)
2. X. Chen, H.-R. Park et al., Nature Communications 4, 2361 (2013)

Fano resonances in nonlinear photonic structures and its applications for optical bistability/switching

Thu Trang Hoang and Quang Minh Ngo*

Institute of Materials Science, Vietnam Academy of Science and Technology, 18 Hoang Quoc Viet, Cau Giay, Hanoi, Vietnam
Graduate University of Science and Technology, Vietnam Academy of Science and Technology, 18 Hoang Quoc Viet, Cau Giay, Hanoi, Vietnam
*corresponding author, E-mail: minhnq@ims.vast.ac.vn

Abstract

This work presents the spectral properties of Fano resonances generated in nonlinear photonic structures with emphasis on optical switching/bistability. The simple photonic structures such as slab waveguide gratings and coupled slab waveguide gratings in which Fano resonances with various quality and asymmetric factors are designed and their characteristics analyzed with a finite-difference time-domain method. We demonstrate the switching/bistable behaviors of the structure at Fano resonance which provides a significant switching intensity reduction compared to the established Lorentzian resonant structures.

1. Introduction

Various applications of Fano resonance, which rely on its high quality factor due to its sharp and asymmetric profile, have been proposed such as filters, modulators, sensors, broadband reflectors, and lasers [1]. In general, the Fano resonant lineshape in the photonic system is given:

$$R(\varepsilon) = F\frac{(\varepsilon+q)^2}{1+\varepsilon^2} \quad (1)$$

where $\varepsilon = 2\frac{\omega-\omega_o}{\Gamma}$, q is an asymmetric factor, ω_o is a resonant frequency, F is a constant factor which describes the degree of asymmetry, and Γ is a resonant linewidth at half-maximum. The Q-factor is defined by the resonant frequency over the resonant linewidth at half-maximum. The Eq. (1) has been widely used to express the spectrum response of Fano lineshape. It suggests that there are exactly one minimum and one maximum in the Fano lineshape. Fig. 1(a) shows the Fano profiles according to the Eq. (1) for several q-factors. The F-factor is chosen for maximum amplitude of lineshape to unity. The lineshapes for special q-factors are shown in the inset. As $|q|\rightarrow\infty$, the transition to the continuum is too weak, so that the lineshape is entirely determined by the transition through the discrete state only with the standard Lorentzian. As q = 0, it describes a symmetric dip, called the inverted Lorentzian lineshapes. Other cases of q-factors are also shown in Fig. 1 (a), as q-factor changes, the degree and asymmetry of lineshape change and the actual resonant frequency may lie somewhere between the peak (maximum response) and the dip (minimum response) of the asymmetric lineshape. For q = 1, the resonant frequency locates exactly at half of the distance between the peak and dip. In addition, when q-factor changes sign, the reversible of Fano lineshape is also plotted. As a consequence, both changing of amplitude and sign of q- factor hold significant implications for the promising photonic device applications such as sensitive optical filters, lasers, biosensors,

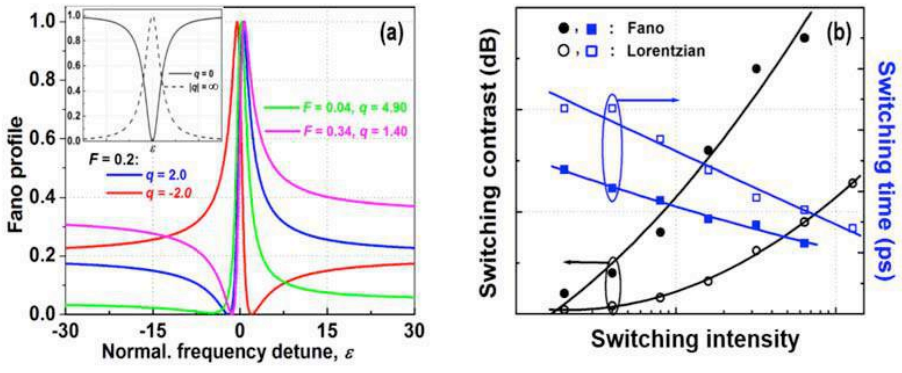

Fig.1. (a) Fano profiles with the formula $F*(\varepsilon + q)^2/(\varepsilon^2 + 1)$ for various values of the asymmetry factor q. The special cases are shown in the inset (Lorentzian lineshapes). (b) Illustration of switching parameters, e.g. switching contrast and switching time vs. switching intensity, based on Fano (solid circle and square dots) and Lorentzian (hollow circle and square shapes) lineshapes with the same of Q-factor and frequency detuning from the resonant peak [1]. The lines are the guides to the eye.

and also switching/bistability.

Recently, Fano resonance has been explored in our works of slab waveguide gratings and optical switching/bistability characteristics based on Fano resonance may provide more bistable switching efficiency than that based on Lorentzian resonance in nonlinear slab waveguide gratings [2,3]. With a given *Q*-factor, asymmetric profiles can provide sharper features than Lorentzian and hence allow more efficient input intensity. Based on the achieved results, Fig. 1(b) shows the illustration of switching parameters, e.g. switching contrast and switching time vs. switching intensity, based on Fano and Lorentzian lineshapes with the same of *Q*-factor and frequency detuning from the resonant peak [4]. In the following sections, we present two examples of Fano resonances in the grating and coupled grating structures and its applications for bistability/switching.

2. Bistability in the nonlinear slab grating with narrow slits

Fano resonances can be simply obtained by using a grating structure with narrow slits as depicted in Fig. 2(a). In this case, a grating structure whose guiding layer is chalcogenide glass (As_2S_3, n = 2.38) with a thickness of 220 nm on a thick glass substrate (n = 1.5). The grating slit aperture (*w*) is formed by a rectangular corrugation in As_2S_3 waveguiding layer with the depth and periodicity (Λ) of 220 nm and 860 nm, respectively. A normally incident wave with transverse electric (TE) polarization is used. Fig. 2(b) shows the calculated linear reflection spectra for three gratings with various slit widths of *w* = 15 nm, *w* = 30 nm, and *w* = 45 nm. Ultra narrow slit (~12 nm) can be fabricated [5], but it is at the border of current electron-beam lithography. In our optimized Fano resonance-based grating design, *Q*-factor of 14,861 can be achieved with the slit width *w* of 15 nm and the resonant peak at 1563.1 nm. As the slit width *w* increases, the resonant wavelength shifts to short wavelength and the *Q*-factor of Fano resonance decreases dramatically. For instance, with the slit width *w* of 45 nm, the resonant wavelength and *Q*-factor are 1516.0 nm and 630, respectively. It means that as the slit width increases, the waveguide mode gets much leaky and hence the linewidth becomes broader leading to a decrease of *Q*-factor. The inset of Fig. 2(b) shows the electric field distributions of the resonances known as TE_0 modes.

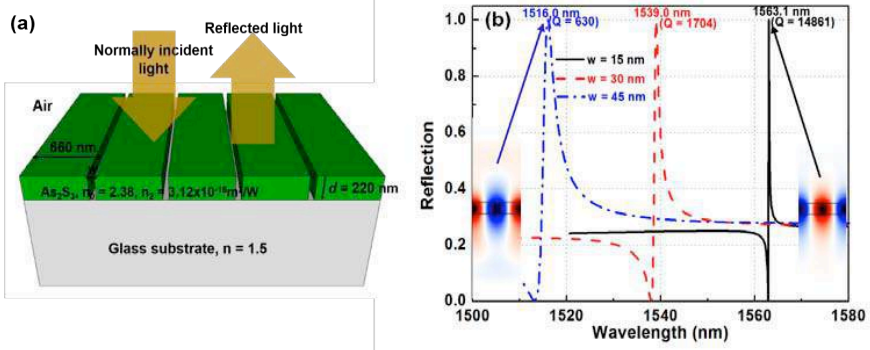

Fig. 2. (a) Sketch of nonlinear grating structure with narrow slits under normally incident light. (b) Reflection spectra for various slit widths (*w*). The insets in (b) show the field distributions at resonances.

In order to see all-optical bistable switching behaviors in nonlinear grating structure with narrow slits, we excite an incident CW source with suitable operating wavelength on the surface of the structure. In general, the operating wavelength is chosen approximately at the center of the all-optical bistability region. In our calculations of all-optical bistable switching for nonlinear grating structure with narrow slits, we choose the operating wavelengths at 50% and 1/e reflection, which locate in the bistability region. In nonlinear calculations, the third-order nonlinear coefficient of As_2S_3 is $n_2 = 3.12\text{x}10^{-18}$ m^2/W [6]. Fig. 3 shows a dependence of reflection on the incident flux intensity of the all-optical bistable switching in the nonlinear grating structure with various narrow slits of (a) *w* = 15 nm, (b) *w* = 30 nm, and (c) *w* = 45 nm, respectively, for the operating wavelength at 50% reflection. It can be seen that the all-optical bistable switching behaviors are formed in all designs. The calculation technique to achieve the bistability behavior was discussed in [2]. In fact, the all-optical bistable switching behaviors have two switching points at the increasing (S_1) and decreasing (S_2) input intensities. The present of S_1 and S_2 in these cases are due to the very short distance between the depths and peaks of linear reflection spectra. The switching times are not mentioned in this work. The incident intensity for switching can be estimated as the input intensity for which the reflection decreases abruptly in the blue and red curves. For example, in Figs. 3(a-c), the estimated switching intensities are 5.6 MW/cm^2, 366.1 MW/cm^2, and 2548.8 MW/cm^2 (at point S_1) and 2.0 MW/cm^2, 181.1 MW/cm^2, and 1306.4 MW/cm^2 (at point S_2) and *Q*-factors of 14861, 1704, and 630 for the slit widths *w* = 15 nm, 30 nm, and 45 nm, respectively. Fig. 3(d) shows the all-optical bistable switching behavior for the slit width *w* of 15 nm with the operating wavelength at 1/e reflection. As seen in Fig. 3(d), the estimated switching intensities are about 25.2 MW/cm^2 at point S_1 and 3.8

MW/cm^2 at point S_2. Compared to the result in Fig. 3(a), it can be seen that the more different the operating wavelength from the resonant wavelength, the higher the switching intensity and the broader the bandwidth of bistability region will be. Because, the detuning of the operating wavelength corresponds to the broad bandwidth and thus the high amount of the resonance shift is required to change the state. In addition, as long as the input intensity exceeds a certain value, the low-reflection state in the bistability region can be maintained. For example, for the slit width w of 15 nm, the bistability regions (between S_1 and S_2) are from 5.6 MW/cm^2 to 2.0 MW/cm^2 and from 25.2 MW/cm^2 to 3.8 MW/cm^2 for the operating wavelengths at 50% and 1/e of reflection, respectively. The all-optical bistable switching behaviors of other slit widths are also shown the same tendency.

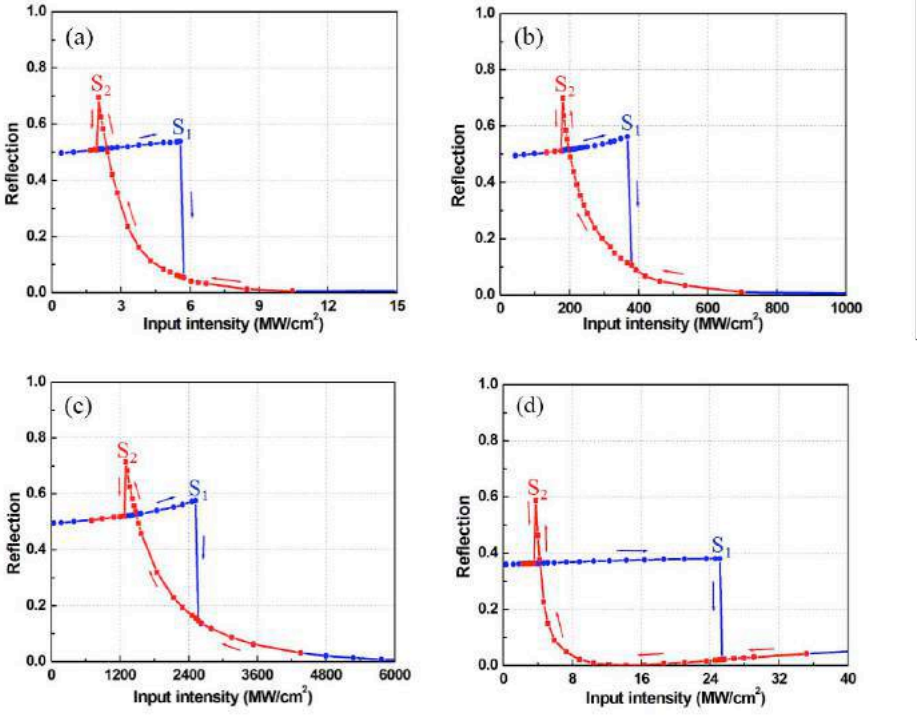

Fig. 3. All-optical bistable switching in the nonlinear grating structure depicted in Fig. 2(a) with the operating wavelength at 50% reflection. (a) w = 15 nm, (b) w = 30 nm, (c) w = 45 nm, (d) operating wavelengths at 1/e reflections for w = 15 nm.

3. Optical bistability in coupled slab waveguide gratings

As presented above, bistability/switching behaviors can be obtained based on Fano resonances in nonlinear slab grating with very narrow slits. The switching intensity depends on Q-factor and the shape of Fano resonances. In general, the dependence of switching intensity and Q-factor is $1/Q^2$. To achieve high Q-factor, the slit width w must be decreased. Due to fabrication limitation, it is a big challenge to reduce the slit width w smaller than 12 nm. High Q-factor, however, can be achieved if two coupled identical slab waveguide gratings facing each other with a gap-distance of d and horizontal shifted-alignment of s is shown in Fig. 4. Each slab waveguide grating supports the Fano resonance, where key structural parameters are defined as the guiding layer with a thickness (h) of 220 nm on a thick glass substrate. Since the Q-factors of Fano resonances in coupled slab waveguide gratings are very sensitive to the gap-distance d and horizontal shifted-alignment s, we treat the Fano resonances in both cases of changing the gap-distance d and horizontal shifted-alignment s as follows:

3.1. Perfect alignment

In the case of perfect alignment (s = 0) of two identical slab waveguide gratings, the coupling strength (determines Q-factor) and resonant wavelength of the system can be easily tuned by changing the gap-distance d. When two slab waveguide gratings are coupled, there are two resonant wavelengths that we called first (F1) and second (F2) Fano resonances. Because of our interest focusing on the F2 shape, Fig. 5(a) shows the reflection spectra at F2 for various the gap-distances d. The gap-distance d is optimized to have the peak (maximum reflection) and depth (minimum reflection) at the resonance close to 1 and 0, respectively. The gap-distance d is important, because the photons can tunnel between them, and then the scattering effect will happen, hence the peak and depth will be not perfect unity and zero in some cases due to scattering loss [7]. This mechanism, therefore, no longer requires the long gap-distance d to achieve high reflectivity and sensitivity. For

the grating width w = 30 nm, the gap-distance d ($d \leq$ 300 nm) is found close to an optimal value. In other words, for a gap-distance d as small as 300 nm, the Fano resonances with high sensitivity can be still existed. As increasing the gap-distance d, the F2's resonant peak shifts to the short wavelength and its Q-factor increases. The resonant peaks, estimated Q-factors, q-factors, and F factors for F2 resonances of the perfect alignment coupled two slab waveguide gratings for various gap-distances d are shown in Table 1. With the gap-distance 50 nm $\leq d \leq$ 300 nm, the resonant wavelengths are in the 1552.2 nm - 1684.9 nm range. The Q-factor increases as the gap-distance d increases due to the long distance of Fabry-Perrot (FB) resonator formed between two slab waveguide gratings [7]. High FP resonator's Q-factor makes the leaky mode from the outside hard to couple into the resonator. It means that as the gap-distance d increases, the Fabry-Perrot mode gets little leaky and hence the linewidth becomes narrower leading to an increase of Q-factor. The Q-factors are 2104, 2543, 3759, and 8522 for the gap-distance d of 50 nm, 100 nm, 170 nm, and 300 nm, respectively. Further importance, as gap-distance d increases, the asymmetric factor q decreases and the reflectivity of side-bands (*RSB*) increases due to the strongly transition to the continuum. Hence, q-factor becomes a function of the R*SB* and Q-factor, $q \rightarrow q$(*RSB*,Q-factor). Our concentration focuses on the positive asymmetric factor q as small as possible. The exact definition for q-factor is not easy to find in the arbitrary photonic systems.

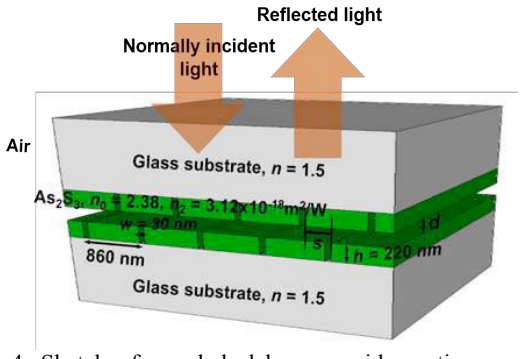

Fig. 4. Sketch of coupled slab waveguide gratings under normally incident light. The gap-distance d and horizontal shifted-alignment s are tuned for exciting Fano resonances.

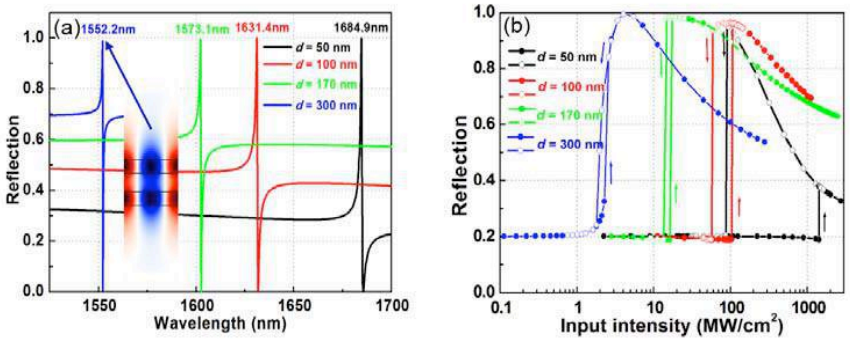

Fig. 5. (a) Reflection spectra of the coupled slab waveguide gratings depicted in Fig. 4 with s = 0. The calculations are done for TE polarized light where electric-field is along to the As_2S_3 strips. The inset shows field distribution at F2 resonance. (b) Bistability curves of the coupled gratings for various gap-distances d of 50 nm, 100 nm, 170 nm, and 300 nm, respectively, with operating wavelength at 20% reflection.

Table 1. Resonant peaks and Q-factors of the coupled slab waveguide gratings for various gap-distances d.

Gap-distance d (nm)	50	100	170	300
Resonant peak (nm)	1684.9	1631.4	1573.1	1552.2
Q-factor	2,104	2,543	3,759	8,522
q-factor	1.696	1.110	0.835	0.655
Switching intensity (MW/cm^2)	1427.1	104.1	16.2	2.2

Fig. 5(b) shows the calculated bistable behaviors of the perfect alignment coupled slab waveguide gratings for the gap-distance d of 50 nm, 100 nm, 170 nm, and 300 nm. Bistable behaviors are clearly observed. In each bistable curve, the incident intensity for switching can be estimated as the input intensity for which the reflection increases abruptly in the dotted solid curve. The estimated switching intensities are 1427.1 MW/cm^2, 104.1 MW/cm^2, 16.2 MW/cm^2, and 2.2 MW/cm^2 corresponding to the quality factors Q = 2104, 2543, 3759, and 8522, and asymmetric factor q = 1.699, 1.110, 0.835, and 0.655 for the gap-distances d = 50 nm, 100 nm, 170 nm, and 300 nm, respectively. In contrast to the Lorentzian resonance, these Fano-based results do not follow the $1/Q^2$ dependence rule of the switching intensity [8-11]. The switching intensity is also influenced by the asymmetric factor q. The asymmetric factor q relates to the Q-factor and the reflectivity of the side-bands. For example, the Q-factors and switching intensities are (2104, 1427.1 MW/cm^2), (2543, 104.1 MW/cm^2), and (8522 and 2.2 MW/cm^2) for the gap-distances d of 50 nm, 100 nm, and 300 nm, respectively. While the Q-factors increase gradually, the switching intensities dramatically decrease due to a reduction of asymmetric factors q. The Q-factor increases 4.0 times but the switching intensity decreases 648.7 times.

We next consider the operating wavelength influence on the switching intensity. We keep the gap-distance d of 300 nm, the optical bistable behaviors for operating wavelengths at 20%, 40%, and 60% reflections corresponding to the shifted-wavelength ($\Delta\lambda$) of 0.088 nm, 0.222 nm, and 0.833 nm from the depth. As seen in Fig. 6, the switching intensities are 2.2 MW/cm^2, 9.7 MW/cm^2, and 140.5 MW/cm^2 for the operating wavelengths at 20%, 40%, and 60% reflections, corresponding to the operating wavelengths of 1552.319 nm, 1552.453 nm, and 1553.064 nm, respectively. It is seen that as we change the operating wavelength ($\Delta\lambda$ = 0.745 nm) from 20% to 60% reflections, the switching intensity increases from 2.2 MW/cm^2 to 140.5 MW/cm^2 (increasing 63.9 times).

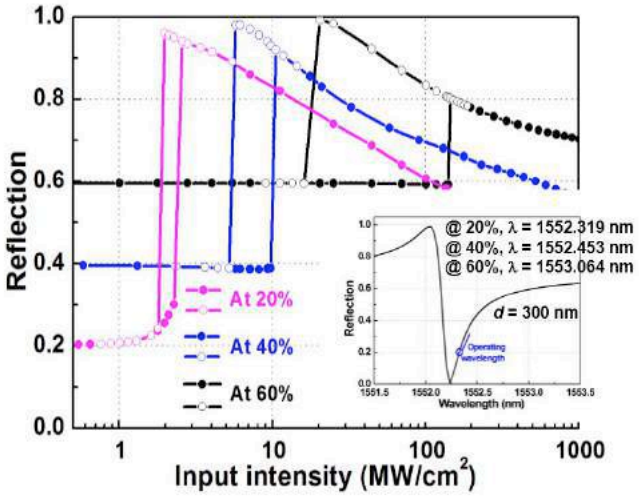

Fig. 6. Bistability behaviors for the gap-distance d = 300 nm. The switching intensities are 2.2 MW/cm^2, 9.7 MW/cm^2, and 140.5 MW/cm^2 for the operating wavelengths at 20%, 40%, and 60% reflections, respectively.

3.2. Horizontal shifted-alignment

Next, we consider coupled slab waveguide gratings with horizontal shifted-alignment. Various shifted-alignment coefficients s are examined while the gap-distance d of 300 nm is fixed as an optimal value to achieve the Fano resonance with high sensitivity and high Q-factor. Our calculated linear reflection spectra for the gratings with various horizontal shifted-alignments s = 100 nm, 150 nm, and 430 nm as shown in Fig. 7 (a). For comparison purpose, the linear reflection spectrum of coupled slab waveguide gratings with perfect alignment is also plotted. The horizontal shifted-alignment s is supposed to mainly change the phase retardation between two slab waveguide gratings. If horizontal shifted-alignment s is 430 nm (half-period), the reflection spectrum is reversed to the case of perfect alignment. So it may cause a phase retardation change of π. The deviations from either of the coupled slab waveguide gratings lead to high Q-factors' states [12].

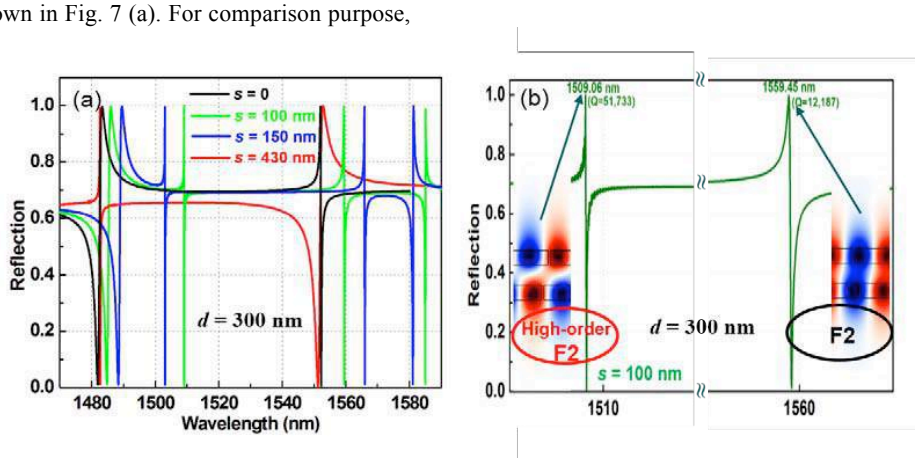

Fig. 7. (a) Full reflection spectra of the coupled slab waveguide grating for various horizontal shifted-alignments and (b) the enlarged F2 regions for horizontal shifted-alignments s of 100 nm. The gap-distance d is fixed at 300 nm.

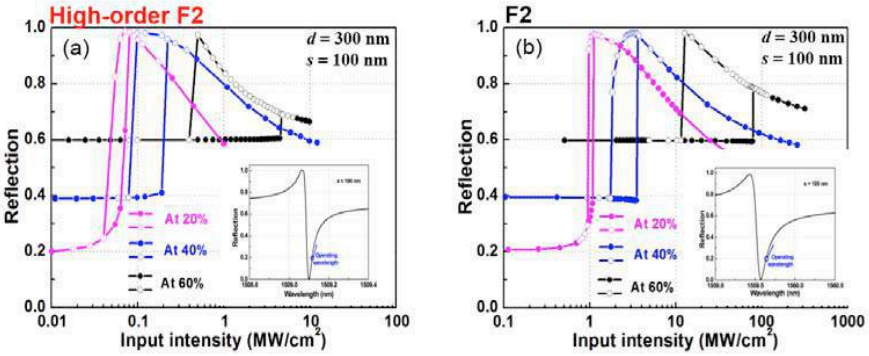

Fig. 8. The bistability behaviors of high-order F2 (a) and F2 (b) resonances for various operating wavelengths of the coupled slab waveguide gratings for the horizontal shifted-alignment *s* of 100 nm.

Table 2. The resonant peaks, *Q*-factors and switching intensities for the horizontal shifted-alignment *s* = 100 nm of the coupled slab waveguide gratings for high-order F2 and F2 Fano resonances.

		High-order F2	F2
Resonant peak (nm)		1509.06	1559.45
Q-factor		51,733	12,187
Switching intensity (MW/cm^2)	20%	0.06	1.08
	40%	0.19	3.43
	60%	4.43	79.97

In our case, we consider the horizontal shifted-alignment *s* of 100 nm and 150 nm and the reflection spectra are plotted in Fig. 7 (a). There are four resonant peaks in each reflection spectrum of horizontal shifted-alignment *s* of 100 nm and 150 nm. The reflectivity of side-bands for all cases of perfect and horizontal shifted-alignment does not change. The reflectivity of side-bands is fixed at around 70%. There exist two Fano resonant F2 shapes, as shown in Fig. 7(b). The F2 and high-order F2 of Fano resonances are located at the longer and shorter wavelengths, respectively. The field distributions and *Q*-factors at resonances are shown in the insets of Fig. 7(b). As the results, the mirror symmetry of the system is broken and brings mainly change in the phase retardation between slab waveguide gratings. It results the higher *Q*-factors. Comparing the field distributions of the perfect alignment (inset of Fig. 5(a)) and the horizontal shifted-alignment cases (insets of Fig. 7(b)), we note that the horizontal shifted-alignment allows the excitation of the state of high-order F2 with a different local modal profile of F2. As seen in Fig. 7(b), the *Q*-factor of high-order F2 resonance is higher than that of F2 resonance. The *Q*-factors for F2 and high-order F2 are 12,187 and 51,733 for the horizontal shifted-alignment *s* = 100 nm. The inset of Fig. 7(b) shows the electric field distributions at F2 and high-order F2 resonances. Table 2 summarizes the resonant peaks, Q-factors and switching intensities for the horizontal shifted-alignment s = 100 nm of the coupled slab waveguide gratings for high-order F2 and F2 Fano resonances.

The optical bistable behaviors for various operating wavelengths of the high-order F2 and F2 resonances in the case of the horizontal shifted-alignment *s* = 100 nm are shown in Figs. 8 (a) and 8(b), respectively. As seen in Fig. 8(a), the high-order F2 case, the switching intensities are 0.06 MW/cm^2, 0.19 MW/cm^2, and 4.43 MW/cm^2 for operating wavelengths at 20%, 40%, and 60% reflections. It is approximately two orders increasing of switching intensity when operating wavelength changes from 20% to 60%. In Fig. 8(b), for the F2 case, 1.08 MW/cm^2, 3.43 MW/cm^2, and 79.97 MW/cm^2 for operating wavelengths at 20%, 40%, and 60% reflections are shown. From Figs. 8(a) and 8(b), the high-order F2 and F2 resonances based the horizontal shifted-aligment, for the operating wavelength at certain reflection. For example, the operating wavelength at 20% refection, *Q*-factors and switching intensities are (12,187 and 1.08 MW/cm^2) and (51,733 and 0.06 MW/cm^2) for the F2 and high-order F2 resonances, respectively. At the F2 resonance, the *Q*-factor is 4.24 times smaller and the switching intensity is 18.0 times higher than those at high-order F2 resonances. In case of operating wavelength at 60% refection, the switching intensity at the F2 resonance is 79.97 MW/cm^2. It is 18.95 times higher than that at the high-order F2 resonances corresponding to the switching intensity of 4.43 MW/cm^2. The other horizontal shifted-alignment *s* are also treated and not shown here, show the same tendency.

Since the *Q*-factors and switching intensities accordingly of the coupled nonlinear gratings are dependent on the horizontal shifted-alignment. In this work, we do not pay much attention on the optimization to achieve the highest *Q*-factor and lowest switching intensity. We instead focus on demonstrating the possibility to significant enhance the *Q*-factor and reduce the switching intensity by using the horizontal shifted-alignment. Based on the enhancement of *Q*-factor and reduce switching intensity accordingly by the horizontal shifted-alignment, the system will undoubtedly facilitate the development of new optical bistable devices towards high efficiency of switching intensity.

4. Conclusion

In conclusion, the Fano resonances have been explored in nonlinear photonic structures such as slab waveguide grating and coupled slab waveguide gratings. The optical

switching/bistability characteristics based on Fano resonance provide more bistable switching efficiency than that based on Lorentzian resonance in nonlinear slab waveguide gratings. We believe that our design and numerical investigation have been a useful guideline for the implementation of Fano resonant configurations for optical devices.

Acknowledgements

This research is funded by Vietnam National Foundation for Science and Technology Development (NAFOSTED) under grant number "103.03-2013.01" and Vietnam Academy of Science and Technology (VAST) under grant number VAST.CTG.01/17-19.

References

[1] A. E. Miroshnichenko, S. Flach and Yu. S. Kivshar, Fano resonances in nanoscale structures, *Rev. Modern Phys.*, 82: 2257-2298, 2010.

[2] Q. M. Ngo, K. Q. Le, L. D. Vu and H. V. Pham, Optical bistability based on Fano resonances in single- and double-layer nonlinear slab waveguide gratings, *J. Opt. Soc. Am. B*, 31(5): 1054-1061, 2014.

[3] Q. M. Ngo, K. Q. Le, T. T. Hoang, D. L. Vu, V. H. Pham, Numerical investigation of tunable Fano-based optical bistability in coupled nonlinear gratings, *Opt. Commun.,* 338: 528-533, 2015.

[4] K. Nozaki, A. Shinya, S. Matsuo, T. Sato, E. Kuramochi, and Notomi, Ultralow-energy and high-contrast all-optical switch involving Fano resonance based on coupled photonic crystal nanocavities, Opt. Express 21: 11877-11888, 20013.

[5] H. Duan, D. Winston, J. K. W. Yang, B. M. Cord, V. R. Manfrinato, and K. K. Berggren, Sub-10-nm half-pitch electron-beam lithography by using PMMA as a negative resist, *J. Vacuum Sci. and Technol. B* 28: C6C58-C6C62, 2010.

[6] J. M. Laniel, N. Ho, and R. Vallee, Nonlinear-refractive-index measurement in As_2S_3 channel waveguides by asymmetric self-phase modulation, *J. Opt. Soc. Am. B* 22(2): 437-445, 2005.

[7] W. Suh, O. Solgaard, and S. Fan, Displacement sensing using evanescent tunneling between guided resonances in photonic crystal slabs, *J. Appl. Phys.* 98: 033102, 2005.

[8] Q. M. Ngo, S. Kim, S. H. Song, and R. Magnusson, Optical bistable devices based on guided-mode resonance in slab waveguide gratings, *Opt. Express* 17: 23459-23467, 2009.

[9] Q. M. Ngo, T. T. Hoang, V. L. Nguyen, D. L. Vu, and V. H. Pham, Metallic assisted guided-mode resonances in slab waveguide gratings for reduced optical switching intensity in bistable devices*, J. Opt.* 15: 055503, 2013.

[10] Q. M. Ngo, S. Kim, J. Lee, and H. Lim, All-optical switches based on multiple cascaded resonators with reduced switching intensity-response time products, *J. Lightwave Technol.* 30: 3525, 2012.

[11] M. Soljacic, M. Ibanescu, S. G. Johnson, Y. Fink, and J. D. Joannopoulos, Optimal bistable switching in nonlinear photonic crystals, *Phys. Rev. E* 66: 055601(R), 2002.

[12] Y. Shuai, D. Zhao, A. S. Chadha, J.-H. Seo, H. Yang, S. Fan, Z. Ma, and W. Zhou, Coupled double-layer Fano resonance photonic crystal filters with lattice-displacement, *Appl. Phys. Lett.* 103:241106, 2013.

Design Considerations for a Very High Near Field Enhancement in a Plasmonic Dimer Geometry

Debadrita Paria[1] and Ambarish Ghosh[1, 2,3]

[1] Centre for Nano Science and Engineering, Indian Institute of Science, Bangalore 560012, India
[2]Department of Physics, Indian Institute of Science, Bangalore 560012, India
[3]Department of Electrical Communication Engineering, Indian Institute of Science, Bangalore, 560012, India
[*]Corresponding author: debadrita@cense.iisc.ernet.in, debadrita.paria@gmail.com

Abstract

There are recent efforts toward the integration of plasmonic nanostructures with graphene, such as to enhance its light-matter interaction which can result in novel optoelectronic technologies. The present work describes numerical efforts to optimize a plasmonic dimer geometry and materials, which results in strongly enhanced electromagnetic near fields that can be coupled with a graphene layer. We used FEM and DDA simulations to understand the details of the coupling mechanism, and also investigate the effect of directionality of the light beam on the plasmonic enhancement.

1. Introduction

One way to improve the light-matter interaction in graphene beyond its intrinsic 2.3% absorption [1] efficiency is to use plasmonic nanostructures in close proximity [2–6]. In a recent effort from our group, we have demonstrated a novel scheme of stacking two arrays of silver nano particles, separated just by a single layer of graphene [7]. The fabrication method was based on layer-by-layer shadow evaporation of different materials, which in the past [8] were used to fabricate three-dimensional arrays of plasmonic nanoparticles separated by a dielectric spacer. The crucial innovation was to use Graphene as the dielectric spacer layer, which allowed placement of two planar arrays of silver nanoparticles separated by 0.34 nm, which is the thickness of single layer graphene. This arrangement gave rise to intense electromagnetic field enhancement at the location of the spacer layer, which resulted in strongly enhanced Raman scattering, as well as a high photocurrent in graphene.

The purpose of this paper is explore design possibilities such as to maximize the field enhancement at the location of graphene in a dimer configuration. Orienting the dimers with respect to the angle of the incident light, as per our simulations, show little or no dependence on the direction of the electric field polarization relative to the dimer axis. This is related to the large electromagnetic retardation [9] in the relatively big particles (radius 70 nm) considered here. The study also indicates that silver gives a better enhancement as compared to gold in the visible range. The numerical simulation assumes the dimer gap to be air. Advanced simulation method using discrete dipole approximation (DDA) [10] reveals that introducing a dielectric to simulate a graphene layer in the dimer gap instead of air has relatively small effect in our field enhancement estimates.

2. Isolated Vs Single Particle

FEM based simulations using a commercial software COMSOL is used to simulate two silver nano particles (diameter=140 nm) separated by a gap of 0.34 nm (thickness of a single layer graphene). The dielectric constants of gold and silver are taken from Johnson and Christy [11]. The surrounding medium is considered to be air. Maximum net electric field enhancement $|\mathbf{E}_{total}/\mathbf{E}_{incident}|^2$ is calculated in a plane perpendicular to the dimer axis, where the graphene spacer lies in our actual experimental system [7]. The electromagnetic (EM) wave propagates along the dimer axis and the polarization is perpendicular to it.

From fig. 1(A) and (B), it can be observed that compared to an isolated nanoparticle, the magnitude of near field enhancement in case of a dimer is about 5 orders of magnitude higher, at their resonance wavelength. Also, the near field is highly confined to a tight spot in the dimer gap. Fig.1 (C) compares the maximum enhancement of a dimer to an isolated particle across various wavelengths. The field enhancement for the dimer is calculated in the dimer gap. Across all wavelengths, the enhancement for a dimer is orders of magnitude higher. The maximum enhancement peaks at the resonance frequencies: 435 nm (quadrupolar resonance) and 510 nm (dipolar resonance) for the dimer and at 365 nm (quadrupolar) for the single particle case. Due to plasmon interactions the resonance peak is red shifted for a dimer as compared to the isolated particle case.

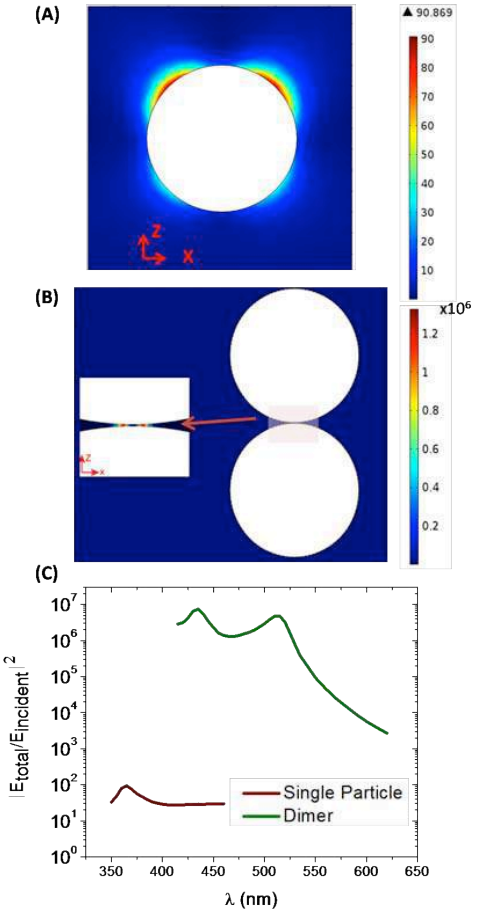

Figure 1: (A) Near field distribution around a single Ag particle; at resonance (365 nm), max($|\mathbf{E_{total}}/\mathbf{E_{incident}}|^2$) is 90.86. (B) Near field distribution around a Ag dimer; at the quadrupolar resonance (435 nm), max($|\mathbf{E_{total}}/\mathbf{E_{incident}}|^2$) is in the order of 10^6. (C) max($|\mathbf{E_{total}}/\mathbf{E_{incident}}|^2$) compared between a dimer and an isolated particle.

3. Dimer Orientation

Heeg et al. have measured the field enhancement in a dimer gap by measuring the SERS signal from a graphene layer on top of two adjacent plasmonic gold nano particles [12]. We compare field enhancement in their configuration to that of our experimental system [7]. We again consider a silver dimer (diameter = 140 nm) separated by a 0.34 nm gap. In the first case, the electromagnetic (EM) wave is propagating perpendicular to the dimer axis while the electric field is polarized parallel to the dimer axis. The enhancement is calculated at the plane, as indicated by the red dotted line in fig. 2 (A), which is similar to the experiments in ref [12]. In the second case, fig. 2 (C), EM wave is propagating parallel to the dimer axis, while the electric field is polarized perpendicular to the dimer axis, which is similar to our experiments [7]. Fig 2 (B) and (D) gives the field distribution for the two orientation in fig. 2 (A) and (C) respectively. It can be observed that in the second case, (orientation in fig. 2(C)) the field is more tightly confined to a very small area. Fig. 2 (E) plots the field enhancement across different wavelengths for both the cases. It can be clearly seen that the enhancement is six orders of magnitude greater in the second case. The arrangement of the dimer in the first case is easily achievable experimentally and has been demonstrated by several groups in the past [3,12]. But the second case where the near field is harnessed right at the dimer gap is extremely difficult to achieve. We were able to achieve such a unique configuration experimentally by the combination of several deposition techniques [7].

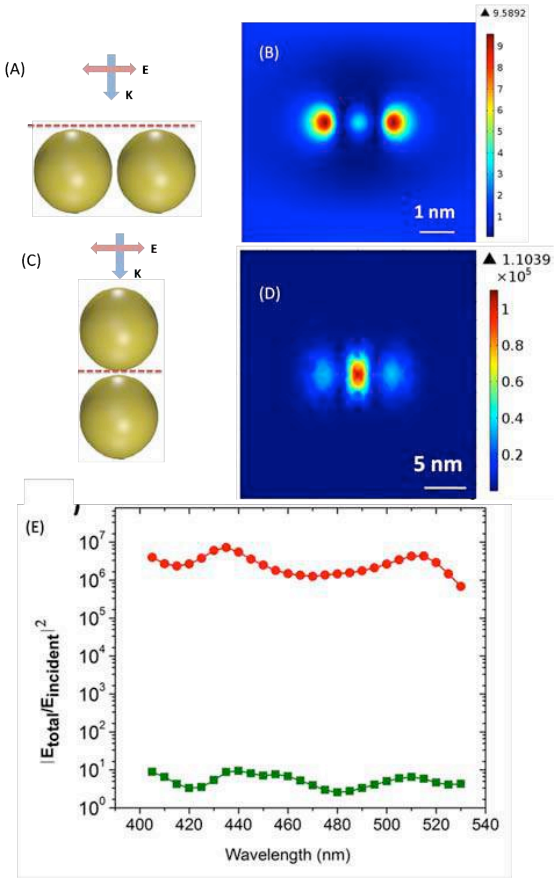

Figure 2: (A) Scheme of simulation similar to the experiments in ref [3,12]; the red dotted line indicates the plane where enhancement is estimated, (B) Corresponding electric field distribution at an incident wavelength of 440 nm. (C) Scheme of simulation similar to our experiments [7]; the red dotted line indicates the plane where enhancement is estimated, (D) Corresponding electric field distribution at an incident wavelength of 440 nm. (E) Comparison of enhancement for the two different orientations. The green and the red lines indicate the orientation similar to case (A) and (C) respectively.

4. Effect of Angle of Incidence

When the angle of incidence of the incident EM wave is varied (0 degree corresponds to **K** vector along dimer axis, 90 degree corresponds to perpendicular to dimer axis), interestingly the maximum field enhancement does not vary drastically, although there is a shift in the resonance peaks (fig. 3). This result is quite contrary to what is usually predicted in the literature [13], which states that if the polarization direction is along the dimer axis, the two nanoparticles couple and give rise to field enhancement, where as if the particles polarize perpendicular to the dimer axis, dipoles in same direction are created in each particle and there is no coupling.

The reason for such strong coupling even when the electric field polarization is in an unfavorable direction is attributed to the retardation effect due to large size [9]. In our case, due to the large size of the particle, retardation is playing an important role and there is almost an equal enhancement in both 0 degree and 90-degree case. By the time the incident EM wave crosses the first particle and reaches the second one, the phase flips, which leads to polarization in dissimilar direction, leading to coupling between the two particles. Our studies on the role of retardation on plasmonic coupling and near field enhancement will be published in near future.

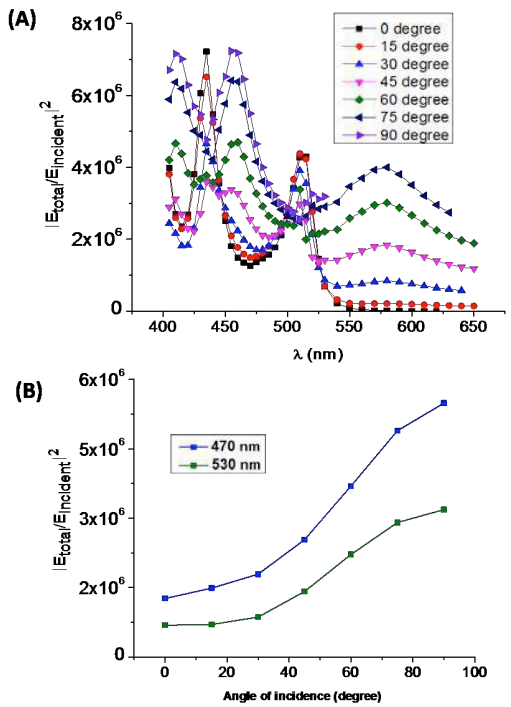

Figure 3: (A) max($|\mathbf{E_{total}}/\mathbf{E_{incident}}|^2$) with different angle of incidences. (B) max($|\mathbf{E_{total}}/\mathbf{E_{incident}}|^2$) plotted for two different wavelengths; it can be clearly observed that the magnitude remains in the same order, with a change in the angle of incidence.

5. Effect of Dielectric Spacer

In all the previous sections, we have considered the dimer gap to be air. In our experimental system, we have a dielectric spacer-graphene in the dimer gap. In order to simulate the actual system, we have tried to put a dielectric slab in the dimer gap and see its effect on the near field enhancement. Including a thin slab of high dielectric constant material in a (finite element method) FEM based simulation was computationally expensive because of the requirement of a very large number of mesh elements. Thus, another computation method known as discrete dipole approximation (DDA) [10,14] is explored for putting the thin dielectric slab in the dimer geometry to simulate our actual experimental system [7]. DDA calculations are also found to be memory intensive and that is why, we could only simulate a slab which was as low as 1.4 nm in thickness; as a thinner slab required more number of dipoles. But even with a slightly thicker dielectric slab than our actual experimental system we are able to achieve an insight about the effect of presence of a dielectric in the dimer gap.

A dielectric spacer of thickness 1.4 nm and refractive index 3 is introduced in the dimer gap. The dipole size is kept smaller than the thickness of the spacer, to ensure enough number of dipoles for discretization of the spacer. The results show that introducing a dielectric layer in the dimer gap changes the magnitude of enhancement minimally, less than 20% (see fig. 4). It is observed, that there is a red shift of the maximum enhancement position by 10 nm, which is expected, as plasmon resonance condition has a direct relation to dielectric constant of the surrounding medium.

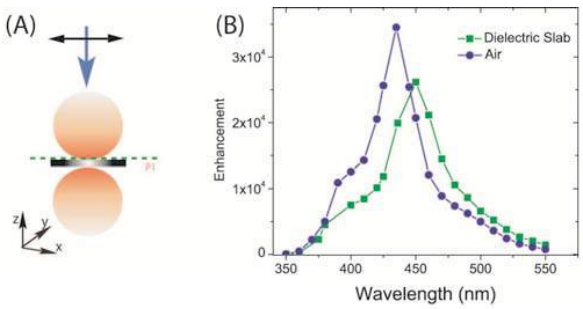

Figure 4: Scheme of DDA simulation for calculating the field enhancement at the dimer gap, in presence of a dielectric spacer. Green dotted line represents the plane considered for calculation of enhancement. (B) Maximum field enhancement at the dimer gap with a dielectric slab compared to that having no dielectric for different wavelengths.

6. Conclusion

In conclusion, we numerically estimate the near field enhancement in a system like an experimental system described before [7]. Compared to an isolated particle, a dimer tightly focuses the near field in a sub-nanometer gap. The plasmon resonance for the dimer is red shifted into the

visible and the near field enhancement is much higher than an isolated particle. Simulations with different orientations of the polarization angle of the incident field is done. Surprisingly, the simulations show that the magnitude of field enhancement varies minimally (within an order of magnitude) for different direction of electric field polarizations relative to the dimer axis. We assumed the gap between the dimers to be air in the FEM simulations. Later we used DDA to introduce a dielectric slab, which has a relative small effect on the resonance peak value and spectral position.

References

[1] R. R. Nair, P. Blake, A. N. Grigorenko, K. S. Novoselov, T. J. Booth, T. Stauber, N. M. R. Peres, and A. K. Geim, Science. **320**, 1308 (2008).

[2] X. Li, J. Zhu, and B. Wei, Chem. Soc. Rev. **45**, (2016).

[3] Y. Liu, R. Cheng, L. Liao, H. Zhou, J. Bai, G. Liu, L. Liu, Y. Huang, and X. Duan, Nat. Commun. **2**, 579 (2011).

[4] T. J. Echtermeyer, L. Britnell, P. K. Jasnos, A. Lombardo, R. V. Gorbachev, A. N. Grigorenko, A. K. Geim, A. C. Ferrari, and K. S. Novoselov, Nat. Commun. **2**, 455 (2011).

[5] Z. Fang, Z. Liu, Y. Wang, P. M. Ajayan, P. Nordlander, and N. J. Halas, Nano Lett. (2012).

[6] A. Fang, J., Wang, D., DeVault, C., Chung, T.F., Chen, Y., Boltasseva, A., Shalaev, V.M. and Kildishev, CLEO QELS_Fundamental Sci. (Pp. FF1B-4). Opt. Soc. Am. (2016).

[7] D. Paria, K. Roy, H. J. Singh, S. Kumar, S. Raghavan, A. Ghosh, and A. Ghosh, Adv. Mater. **27**, 1751 (2015).

[8] H. Johnson Singh and A. Ghosh, J. Phys. Chem. C **116**, 19467 (2012).

[9] J. P. Kottmann and O. J. F. Martin, Opt. Lett. **26**, 1096 (2001).

[10] B. T. Draine and P. J. Flatau, J. Opt. Soc. Am. A **11**, 1491 (1994).

[11] R. W. Johnson, P.B. and Christy, Phys. Rev. B **1318**, (1972).

[12] S. Heeg, R. Fernandez-garcia, A. Oikonomou, R. Narula, S. a Maier, and A. Vijayaraghavan, 1 (2013).

[13] P. K. Jain, S. Eustis, and M. A. El-Sayed, J. Phys. Chem. B **110**, 18243 (2006).

[14] M. A. Yurkin and A. G. Hoekstra, J. Quant. Spectrosc. Radiat. Transf. **112**, 2234 (2011).

Near-field imaging of metamaterials in physical space, reciprocal space and time domain

Xihang Shi[1], **Zhen Gao**[1,2], **and Hongyi Xu**[1*]

[1] Nearfield Imaging Laboratory, Linbou Nearfield Technology Co.,Ltd.,
2-405 Futian Duoli Industrial Park, Shenzhen China 518000

[2] Division of Physics and Applied Physics, School of Physical and Mathematical Sciences,
Nanyang Technological University, 21 Nanyang Link, Singapore 637371

[*] hyxu@linbou.com

ABSTRACT

Near-field imaging has become a versatile technology in metamaterial-related researches, since it not only provides direct imaging of electromagnetic/acoustic wave propagation in and around metamaterials [1-7], but also can visualize the band diagrams in reciprocal space[8,9] and dynamic pulse evolution in time domain[8,10]. LINBOU Nearfield Imaging Systems provide a stable, fast and economic solution to near-field imaging of electromagnetic and acoustic waves in physical space, reciprocal space and time domain, from two dimensions to three dimensions, from near-field measurements to far-field radiation patterns.

REFERENCES

1 Liu, R. *et al.* Broadband Ground-Plane Cloak. ***Science*** 323, 366 (2009).

2 Sun, S. *et al.* Gradient-index meta-surfaces as a bridge linking propagating waves and surface waves. ***Nat. Mater.*** 11, 426-431 (2012).

3 Shen, X., Cui, T. J., Martin-Cano, D. & Garcia-Vidal, F. J. Conformal surface plasmons propagating on ultrathin and flexible films. ***Proc. Natl. Acad. Sci.*** 110, 40-45 (2013).

4 Gao, F. *et al.* Probing topological protection using a designer surface plasmon structure. ***Nat. Commun.*** 7, 11619 (2016).

5 Zigoneanu, L., Popa, B.-I. & Cummer, S. A. Three-dimensional broadband omnidirectional acoustic ground cloak. ***Nat. Mater.*** 13, 352-355 (2014).

6 Li, J., Fok, L., Yin, X., Bartal, G. & Zhang, X. Experimental demonstration of an acoustic

magnifying hyperlens. ***Nat. Mater.*** 8, 931-934 (2009).

7 Schurig, D. *et al.* Metamaterial Electromagnetic Cloak at Microwave Frequencies. ***Science*** 314, 977 (2006).

8 Engelen, R. J. P. *et al.* Ultrafast evolution of photonic eigenstates in k-space. ***Nat. Phys.*** 3, 401-405 (2007).

9 Lu, L. *et al.* Experimental observation of Weyl points. ***Science*** 349, 622 (2015).

10 Gao, Z. *et al.* Surface-wave pulse routing around sharp corners. ***arXiv:***1604.06872 (2017).

Metamaterials and negative index materials

Suppression of Surface Modes in Metamaterial Grounded Slab

R. Borghol[1*], and T. Aguili[2]

[1] University of Tunis El Manar (UTM), National Enginneering School of Tunis (ENIT), Communications Systems Laboratory (SysCom), Tunisia

[2] University of Tunis El Manar (UTM), National Enginneering School of Tunis (ENIT), Communications Systems Laboratory (SysCom), Tunisia

[*]corresponding author: borgholriham@gmail.com

Abstract-This paper investigate the technique of suppression of surface modes in the metamaterial grounded slab. This technique consists to sandwich a left-handed material layer between the air and the metamaterial slab. The purpose of this suppression is to reduce the mutual coupling between the elements of array antennas. The Transverse Resonance Method is applied in this analysis to find the effects of the left-handed material layer on the dispersion characteristics of transverse electric and transverse magnetic polarizations.

The array antennas play in important role in electromagnetic fields. They are used in different applications such as; mobile communications and phased-array radar. The mutual coupling of the elements of array has negative effects on the directivity, the bandwidth and the radiation of antenna. Then, it is necessary to reduce this coupling by the suppression of surface modes using the left-hand material LHM This material has an increasing use thanks to its recent realization (i. e., has a negative index of refraction) and its unusual properties [1]. To suppress the surface modes, the LHM layer is sandwiched between the air and the semi-infinite metamaterial slab, as shown Fig. 1.

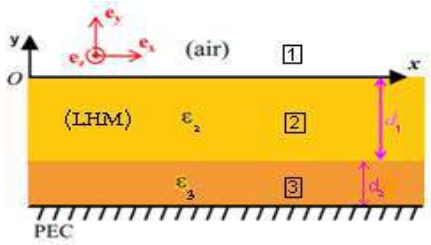

Figure 1. An infinity metamaterial grounded slab with LHM layer characterized by negative parameters ε_2 and μ_2.

Applying the Transverse Resonance Method in order to obtain the equivalent circuit that allows us to find the dispersion equation [2].

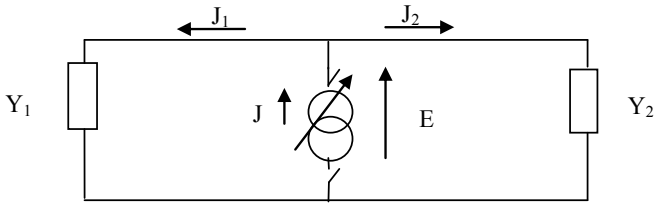

Figure 2. Equivalent circuit used to illustrate the Transverse Resonance Method.

We solve the equivalent circuit from the Kirchhoff's current and Ohm's law to find the dispersion equation:

$$(Y_1 + Y_2)E = 0 \tag{1}$$

For TM and TE polarizations, this dispersion equation may be presented as:

$$\text{TM:} \quad -k_{y2}d_1 - \coth^{-1}\left(\frac{k_{y2}}{k_{y1}\varepsilon_2}\right) - \coth^{-1}\left(\frac{\varepsilon_3 k_{y2}}{k_{y3}\varepsilon_2}\coth(k_{y3}d_2)\right) = 0 \tag{2}$$

$$\text{TE:} \quad -k_{y2}d_1 - \coth^{-1}\left(\frac{k_{y1}\mu_2}{k_{y2}}\right) - \coth^{-1}\left(\frac{k_{y3}\mu_2}{k_{y2}\mu_3}\coth(k_{y3}d_2)\right) = 0 \tag{3}$$

In the numerical study, we consider that our structure is composed by a LHM layer with ε_2= -2, μ_2= -2 and height d_1= 50mm and a metamateriel slab with permittivity $\varepsilon_3(\omega) = 1 - \frac{\omega_p^2}{\omega^2}$ and permeability $\mu_3(\omega) = 1 - \frac{F\omega^2}{\omega^2 - \omega_0^2}$ where $F = 0.56$, $\omega_p/2\pi = 10$ GHz and $\omega_0/2\pi = 4$ GHz according to the drude model and height d_2= 10mm.

The variation of the normalized real constant with the frequency is presented in Fig. 3(a) and (b) for TM and TE polarizations.

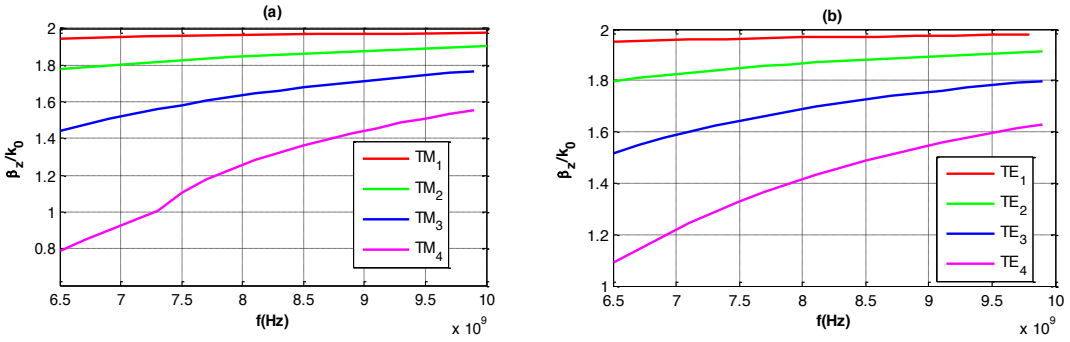

Figure 3. Dispersion of (a) TM and (b) TE surface modes in metamaterial grounded slab with LHM layer.

From these results, we observe that the fundamental modes TM_0 and TE_0 of surface mode do not exist in the metamaterial grounded slab structure with LHM layer. Higher modes of surface modes exist only in particular frequency range and have many remarkable features. When we increase the frequency, the normalized real constant of the higher modes increases approaching the $\sqrt{\varepsilon_2\mu_2}$, but it cannot exceed this value and saturates at a specific value of frequency. The saturation frequency and the normalized real constant are dependent on the mode order. We also observe that the surface mode is suppressed at the frequency band 6.5GHz to 7.4GHz of TM_4 mode because the dispersion curve is below the cutoff frequency.

REFERENCES

1. Taya, S. A. and Elwasife, K. Y. "Guided Modes in a Metal-Clad Waveguide Comprising a Left-Hand Material as a Guiding Layer," *IJRRAS 13*, Vol. 13, 2012.
2. Borghol, R. and Aguili, T. "Analysis of Real and Complex Modes of Grounded Slab with the Transverse Resonance Method," *TinkMind ICWMC*, 2016.

Low Loss Metamaterials for 5G Mobile Networks

B. A. F. Esmail[1], H. A. Majid[1], Z. Z. Abidin[1], M. K. A. Rahim[2], and R. Dewan[2]
[1]Applied Electromagnetic Center, Universiti Tun Hussein Onn Malaysia, Parit Raja, Johor, Malaysia
[2]Faculty of Electrical Engineering, Universiti Teknologi Malaysia, Johor Bahru, Johor, Malaysia
*corresponding author: mhuda@uthm.edu.my

Abstract- A double C-shaped resonator (DCR) unit cell metamaterial (MTM) for 5G mobile network that operates at 28 GHz is proposed. For comparison purpose, three other common unit cells which are the S-shaped resonator, double G-shaped resonator (DGR), and Omega-shaped resonator are optimized to operate at similar operating frequency. Additionally, the approach to reduce MTMs losses is presented and discussed. The losses of the proposed DCR is significantly improved in all unit cells due to the opposite directions of the induced current on both sides of the unit cell and the negativity of the constitutive parameters is maintained.

1. Introduction

MTMs have attracted great attention due to unusual electromagnetic properties such as the negative permittivity, permeability, and refraction index. However, the performance of the MTMs is primarily limited by the MTMs losses. These losses give negative influences toward the realizations of the unique electromagnetic properties of the MTMs. The losses in MTMs consists of two primary components: radiation losses and dissipation losses where losses of the first component is greater than the latter [1, 2]. Millimeter wave frequency range, on the other hand, attracted researchers in the past few years due to its advantages in the wireless communications systems such as high speed, high capacity and availability for large bandwidth. These advantages make this band the best candidate for the fifth generation (5G) cellular networks by exploiting the enormous amount of available spectrum to greatly increase the communication capacity [3]. A suitable configuration of MTM is designed to operate at 28 GHz for 5G mobile phone applications and to the best of our knowledge design an MTM unit cell that operates at this band is the first of its kind. For comparison, three other known unit cells are optimized to operate at 28 GHz. Furthermore, the major component of MTM losses which is the radiation loss is greatly suppressed by applying the principle of the electromagnetically induced transparency (EIT) phenomenon.

2. Unit-Cells Construction, Numerical Results and Discussion

The unit cells in Fig. 1(a)-(d) are constructed on Rogers RT5880 substrate with the relative permittivity of 2.2, tangent-loss of 0.0009, and a thickness of 0.508 mm. The length (L) and width (W) of each unit cells are given in the caption of Fig. 1. The performance comparison between the DCR unit cell and the other three common unit cells shapes which are S-shape, DGR, and Omega-shape to operate at 28 GHz are carried out. Fig. 2 (a) and (b) shows the reflection (S_{11}) and transmission coefficients (S_{21}) of the unit cells. It can be observed that the proposed DCR unit cell achieves a wider bandwidth than the other three unit cells which is 1.1 GHz of bandwidth as opposed to less than 0.5 GHz of bandwidth in other three unit cells. Moreover, the dimension of the proposed DCR unit cell is the smallest over all the studied unit cells with the length L = 2 mm and width W = 1 mm. On the other hand, transmission coefficient of the DCR depicts near zero loss which contribute to nearly full transmission in comparison with the other unit cells where the losses in the S-shape is at the highest, approximately -1 dB. Moreover, the induced surface current of the DCR structure induces the anti-parallel currents on the both sides of the unit cell which causes the destructive interference of the scattering fields. As a consequence, the EIT effect is induced and extremely suppresses the radiation loss. The constitutive parameters are retrieved using the robust method as described in [3]. Fig. 1(a)-(d) depict the real parts of the permittivity ε, permeability μ and refractive index, n of the unit cells at 28 GHz.

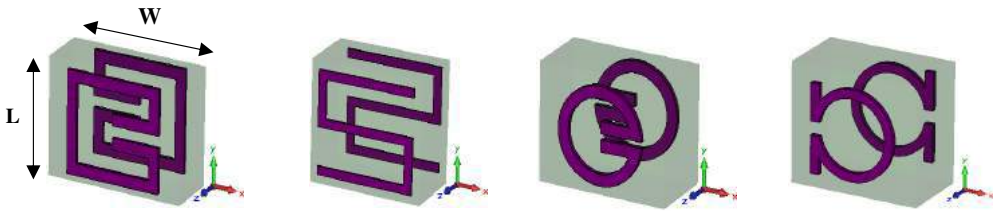

(a) (b) (c) (d)

Fig.1: The unit cells structure a) the proposed DCR (2×1 mm), b) S-shape (2.9×2 mm), c) DGR (1.3×2 mm) and d) Omega-shape (3.7×4 mm)

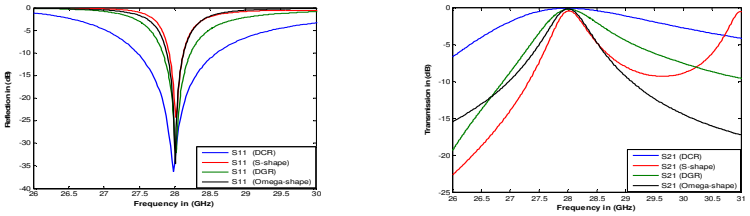

(a) (d)

Fig.2: a) The reflection coefficients b) the transmission coefficient

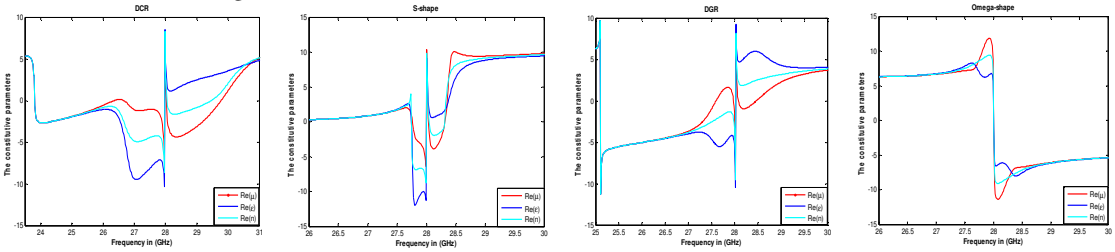

(a) (b) (c) (d)

Fig.3: The retrieved results for the real parts at 28 GHz of a) the proposed DCR b) S-shape c) DGR d) Omega-shape

3. Conclusion

This paper introduces the DCR unit cell which operates at 28 GHz for 5G mobile network application and three others common unit cells are optimized to operate at similar frequency for comparison purposes. The reflection and transmission coefficients of four unit cells are displayed and investigated. The proposed DCR unit cell successfully achieves low radiation loss of nearly full transmission, small size, and wider bandwidth of reflection coefficient and negativity of the constitutive parameters over all other three unit cells.

References

[1] Zhu, Lei, et al. "An ultra-low loss split ring resonator by suppressing the electric dipole moment approach." Progress In Electromagnetics Research 137 (2013): 239-254.

[2]Li, Hai-ming, et al. "Low-loss metamaterial electromagnetically induced transparency based on electric toroidal dipolar response." Applied Physics Letters 106.8 (2015): 083511.

[3]Wang, Peng, et al. "Multi-gigabit millimeter wave wireless communications for 5G: From fixed access to cellular networks." IEEE Communications Magazine 53.1 (2015): 168-178.

[4] Chen, Xudong, et al. "Robust method to retrieve the constitutive effective parameters of metamaterials." Physical Review E 70.1 (2004): 016608.

A broadband optical diode for linearly polarized light using symmetry-breaking metamaterials

M. Kim[1+], K. Yao[2+], G. Yoon[1], I. Kim[1], Y. Liu[2,3*], and J. Rho[1,4,5*]

[1]Department of Mechanical Engineering, Pohang University of Science and Technology (POSTECH), Pohang 37673, Republic of Korea

[2]Department of Electrical and Computer Engineering, Northeastern University, Boston, MA 02115 USA

[3]Department of Mechanical and Industrial Engineering, Northeasterm University, Boston, MA 02115 USA

[4]Department of Chemical Engineering, Pohang University of Science and Technology (POSTECH), Pohang 37673, Republic of Korea

[5]National Institute for Nanomaterials Technology (NINT), Pohang 37673, Republic of Korea

+ These authors contributed equally to this work

[*]corresponding author: jsrho@postech.ac.kr or y.liu@northeastern.edu

Abstract- We experimentally demonstrate a thin bi-layer metamaterial supporting asymmetric transmission for linearly polarized light but not for circularly polarized light over a broad bandwidth in the near-infrared region. We provide a simple and intuitive working principle, along with full-wave simulations that agree well with the experimental results. We also prove that our design is extremely insensitive to spatial misalignment, which might occur during the nanofabrication process.

As an analogue of electrical diodes, optical diodes enable asymmetric transmission, or one-way transmission of light. Such a property is fundamentally interesting, because light transmission is normally symmetric due to the Lorentz reciprocity in time-invariant linear media. Metamaterials, engineered materials with extraordinary optical properties originated from subwavelength scale structures, provide an alternative, simple solution to break the Lorentz symmetry condition via mode conversion between specific modes, even though the system is completely reciprocal. Asymmetric transmission for circularly polarized light [1-5] and for linear polarization [6-11] has been demonstrated with various design.

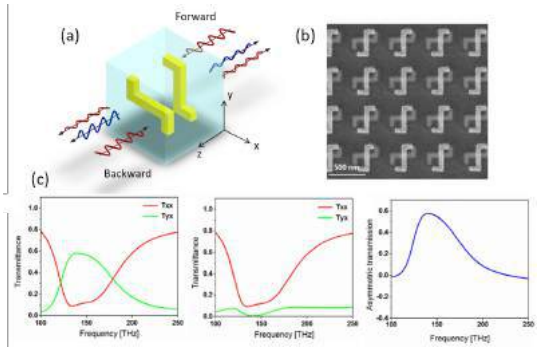

Figure 1. (a) Schematic of the metamaterial unit cell, (b) SEM image of the fabricated sample, (c) simulated transmission characteristics and asymmetric transmission of the metamaterial.

Here, a thin bi-layer metamaterial which works as an optical diode over a broad bandwidth up to 50 terahertz is introduced. Under this bi-layer metamaterial, linearly polarized light transmit the material along one direction, but not the opposite direction while circularly polarized light exhibit symmetric transmission characteristics. A simple and intuitive working principle based on the symmetry inherent in the metamaterial design, along with full-wave simulations that agree well with the experimental results are provided. We also prove that our design is extremely insensitive to spatial misalignment, which might occur during the nanofabrication process. These prominent features promise a wide range of applications, such as ultrafast optical computing, information processing and suppressing undesired interactions in integrated micro- and nano-devices.

Acknowledgements, J. Rho acknowledges the financial support by Young Investigator Research program (NRF-2015R1C1A1A02036464), Engineering Research Center program (NRF-2015R1A5A1037668) and Global Frontier program (CAMM-2014M3A6B3063708), and I. Kim acknowledges the Global Ph.D. Fellowship (NRF-2016H1A2A1906519) through the National Research Foundation of Korea (NRF) grant funded by the Ministry of Science, ICT and Future Planning (MSIP) of Korean government. Y. Liu acknowledges the financial support from the Office of Naval Research under award number N00014-16-1-2049.

REFERENCES

1. Pfeiffer, C., Zhang, C., Ray, V., Guo, L. J. and Grbic, A. High Performance Bianisotropic Metasurfaces: Asymmetric Transmission of Light. *Phys. Rev. Lett*., Vol. 113, 023902, 2014.
2. Schwanecke, A. S. *et al*. Nanostructured Metal Film with Asymmetric Optical Transmission. *Nano Lett.,* Vol. 8, No. 9, 2940-2943, 2008.
3. Singh, R. *et al*. Terahertz metamaterial with asymmetric transmission. *Phys. Rev. B,* Vol. 80, 153104, 2009.
4. Ji, R., Wang, S.-W., Liu, X. and Lu, W. Giant and broadband circular asymmetric transmission based on two cascading polarization conversion cavities. *Nanoscale,* Vol. 8, No. 15, 8189-8194, 2016.
5. Fedotov, V. *et al*. Asymmetric propagation of electromagnetic waves through a planar chiral structure. *Phys. Rev. Lett.,* Vol. 97, 167401, 2006.
6. Xu, T. and Lezec, H. J. Visible-frequency asymmetric transmission devices incorporating a hyperbolic metamaterial. *Nat. Commun.,* Vol. 5, 4141, 2014.
7. Shi, J. *et al.* Dual-band asymmetric transmission of linear polarization in bilayered chiral metamaterial. *Appl. Phys. Lett.* Vol. 102, 191905, 2013.
8. Kang, M., Chen, J., Cui, H.-X., Li, Y. and Wang, H.-T. Asymmetric transmission for linearly polarized electromagnetic radiation. *Opt. Express* Vol. 19, No. 9, 8347-8356, 2011.
9. Mutlu, M., Akosman, A. E., Serebryannikov, A. E. and Ozbay, E. Asymmetric transmission of linearly polarized waves and polarization angle dependent wave rotation using a chiral metamaterial. *Opt. Express* Vol 19, No. 15, 14290-14299, 2011.
10. Mutlu, M., Akosman, A. E., Serebryannikov, A. E. and Ozbay, E. Diodelike asymmetric transmission of linearly polarized waves using magnetoelectric coupling and electromagnetic wave tunneling. *Phys. Rev. Lett.* Vol. 108, 213905, 2012.
11. Menzel, C. *et al*. Asymmetric Transmission of Linearly Polarized Light at Optical Metamaterials. *Phys. Rev. Lett.* Vol. 104, 253902, 2010.

Multi cavity magnetite nanocrystals: preparation and characterization

Hui Wu[1],Jaebeom Lee[2]

1 Department of Nano-Integrated Cogno-mechatronics Engineering (NICE) Pusan National University.
2 Department of Optics and Mechatronics Engineering Pusan National University.
E-mail: jaebeom@pusan.ac.kr

Abstract-A wet chemistry process was designed to synthesize multi cavity magnetite(Fe_3O_4) nanorods using FeOOH as precursor. Both the precursor and magnetite were characterized by XRD. The FeOOH was measured by Thermogravimetric Analyzer (TGA) and Differential Scanning Calorimetry (DSC). And the TEM images indicate that the magnetite has a nanorod structure with multi cavity. The length of the magnetite nanorods are around 50nm. The cavities are quasi-spherical shape with a diameter of 6nm.

Study on the mutual electromagnetic couplings between vertical split ring resonators

Che-Chin Chen[1], Atushi Ishikawa[2,3], Ming-Hua Shiao[1], Yu-Hsin Lin[1], Chien-Nan Hsiao[1], Hai-Pang Chiang[4], and Takuo Tanaka[2]

[1]Instrument Technology Research Center, National Applied Research Laboratories, Hsinchu 30076, Taiwan

[2]Metamaterials Laboratory, RIKEN, 2-1 Hirosawa, Wako, Saitama 351-0198, Japan

[3]Department of Electrical and Electronic Engineering, Okayama University, Okayama 700-8530, Japan

[4]Institute of Optoelectronic Sciences, National Taiwan Ocean University, Keelung 202, Taiwan

[*]corresponding author: ccchen@itrc.narl.org.tw

Abstract- We demonstrate the couplings between vertical SRRs by transmittance experiments and numerical simulations. Two different arrangements inclusive of rectangular and interlacing-rectangular arrays are characterized. For both arrangements, the resonance frequencies are increased while the transmittances are decreased with decreasing distance between vertical SRRs. The weak current densities and magnetic field distribution in the small distance arrays lead to higher resonant frequencies. The interlacing-rectangular array is compared to the similar inter-distance rectangular arrays as well. Slightly increased in current density and significant drop in magnetic field strength are conclude that the electric field strength inside each meta-atom dominates the resonance behaviors.

Unusual electromagnetic properties such as negative refractive index or subwavelength imaging, which is not appeared in nature, are the interaction results while electromagnetic waves passing through the artificial metamaterials[1-2]. Split ring resonators (SRRs) have been investigated since their advent in metamaterials. Until now, they have been widely proved to exhibit negative index of refraction, magnetoinductive coupling, and additionally, extraordinary nonlinear effects and Fano resonance. Down to the scales of nanometers or micrometers, SRRs are often patterned with two dimensional planar structures. There are numerous studies concerning the coupling effects of planar SRRs. However, the studies on the coupling effects of vertical SRRs are limited since the difficulties of the fabrication process. In this work, we fabricated vertical SRRs with an innovative metal stress-driven self-assembled method [3]. The transmittance of the rectangular arrays shows a stronger resonance with blue-shift as the inter-distance decreases, which can be explained from the increased filling factors and reducing capacitances. On the other hand, the rectangular-interlacing array reveals significant transmission deep and approximate resonant frequency comparing to rectangular array with similar inter-distance were based on the fact that the increased filling factors and that the attractive electric force is relatively weak compared to the repulsive electric force between vertical SRRs. More details will be present in the conference.

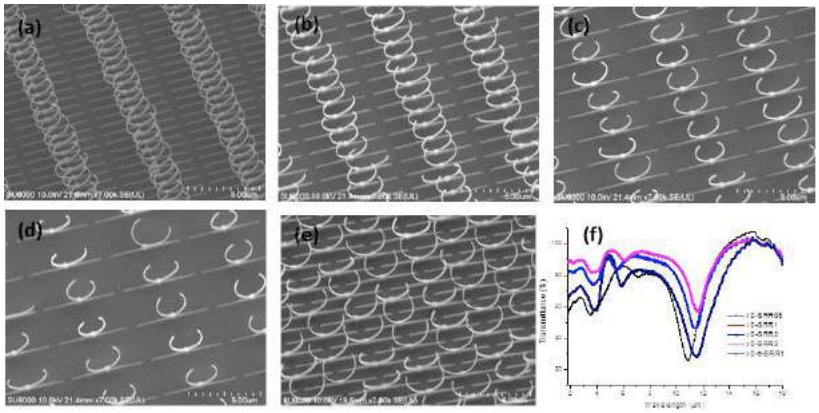

Fig. 1 (a)-(d) The rectangular arrays with inter-distances of 0.5, 1, 2, and 3 μm, respectively. (e) The interlacing-rectangular array by shifting the neighboring rows by half P_x with inter-distance of 1 μm. (f) Transmission spectra of rectangular arrays with inter-distance of 0.5, 1, 2, and 3 μm and interlacing-rectangular array with inter-distance about 1 μm, respectively.

Acknowledgements, The authors thank financial aids from Ministry of Science and Technology, Taiwan (105-2112-M-492−001, 105-2221-E-492−020, 103-2112-M-019 −003 -MY3.

REFERENCES

1. J. B. Pendry, A. J. Holden, D. J. Robbins, and W. J. Stewart, "Magnetism from conductors and enhanced nonlinear phenomena," IEEE Trans. Microw. Theory Techn. **47**, 2075–2084(1999).
2. N. Katsarakis, T. Koschny, M. Kafesaki, E. N. Economou, and C. M. Soukoulis, "Electric coupling to the magnetic resonance of split ring resonators," Appl. Phys. Lett. **84**, 2943–2945 (2004).
3. Che-Chin, Chen, A. Ishikawa, Y.-H. Tang, M.-H. Shiao, D. P. Tsai, and T. Tanaka, "Uniaxial-isotropic Metamaterials by Three-Dimensional Split-Ring Resonators," Adv. Opt. Mater. **3**, 44–48 (2015).

Mutual Coupling Reduction of Two Closely Spaced Meander Line Antennas Using Left-Handed Double-Negative (DNG) Metamaterial Substrate for DSRC V-2-V Application

Imtiaz Islam[1], **Mohd Faizal Jamlos**[1,3*], **Mohd Aminudin Jamlos**[2], **Ping Jack Soh**[1], **Siti Zuraidah Ibrahim**[1], **A.S.M Alqadami**[1] and **Rizalman Mamat**[3]

[1]Advanced Communication Engineering (ACE), School of Computer & Communication Engineering, Universiti Malaysia Perlis (UniMAP), 01000 Kangar, Perlis, Malaysia

[2]Department of Electronic, Faculty of Technology Engineering, UniMAP, 02100, Padang Besar, Malaysia

[3]Faculty of Mechanical Engineering, Universiti Malaysia Pahang (UMP), 26600, Pekan, Malaysia.

[*]corresponding author: mohdfaizaljamlos@gmail.com

Abstract- This paper highlights a mutual coupling reduction of two closely spaced meander line antennas by using left-handed split ring resonator (SRR) metamaterial for 5.9 GHz DSRC application. The antenna consists of two closely spaced meander line antennas where SRR unit cells are placed vertically between two antennas and another 4x3 cells at the ground plane. The SRRs significantly reduce mutual coupling and good MIMO characteristics have been achieved for the designed antennas like diversity gain and effective correlation coefficient.

SUMMARY

Recently in wireless communication, meander strip line antenna has achieved a tremendous attraction for designing small size antennas. Different types of meander line antennas have already investigated in many open kinds of literature as e,g., tapered meandered, tapered meander line and self-resonant MLA [1]. However, the main challenges have come when meander line antennas need to be designed for multi-elements or MIMO application. Mutual coupling effects between two antennas generate distortion in the overall antenna performance [2].

The development of metamaterial concept is treated as a turning point to reduce mutual coupling by utilizing a natural nonexistence property material that enables different characteristics of an antenna [3]. Different types of metamaterial structure have been analyzed briefly include left-handed metamaterial with negative relative permeability and negative permittivity. In this paper, a left-handed Double Negative (DNG) circular split ring resonator (SRR) has been designed for isolation enhancement of MIMO meander strip antennas for Dedicated-Short-Range-Communication (DSRC) Vehicle-to-Vehicle (V-2-V) application working at 5.9 GHz. Fig.1 presents the structure of unit cell, permeability, permittivity and refractive index which have been obtained based from S_{11} and S_{12} [4].

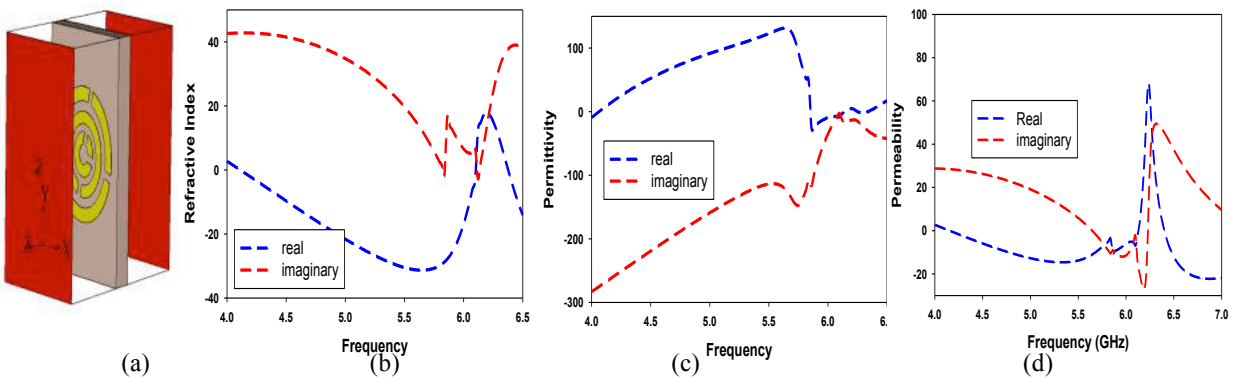

(a) (b) (c) (d)

Figure 1. Left-handed unit cell (a) 3-D configuration (b) Refractive Index (c) Permittivity (d) Permeability

This left-handed circular split ring resonators (SRR) unit cell have been located vertically between meander line antennas as shown in Figure 2(a) while another 4x3 cells are placed at the ground plane, as depicted by Fig. 2(b). The effect of mutual coupling between two antennas is shown in Fig. 2(c). It is clearly seen that the mutual coupling between two antennas improved and shifted to -19 dB at 5.9 GHz when unit cells are applied in the structure. Moreover, less than 0.05 of envelop correlation coefficient (ECC) is stated with more than 9 dB diversity gain which is suit for MIMO application requirements.

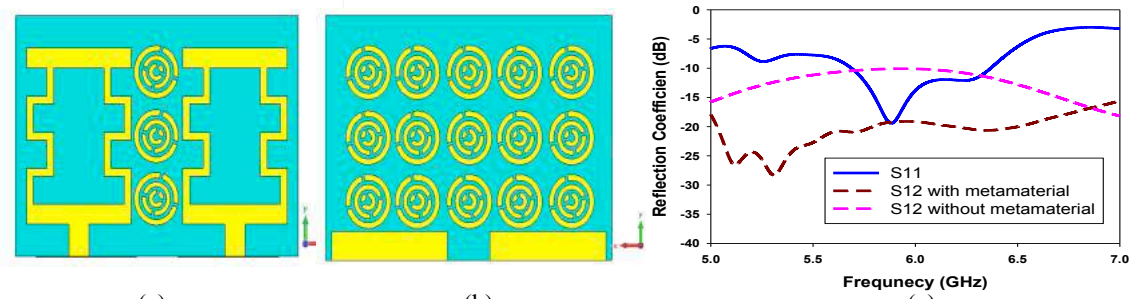

(a) (b) (c)

Figure 2. (a) Front view of meander line antenna (b) back view (c) reflection coefficient.

REFERENCES

1. N.Ibrahim,M.Elamin,T.Abdul Rahman,and A.Y.Abdul Rahman,"New adjustable slot meander patch antenna for4G hand held devices,"*IEEE Antennas Wireless Propagation Letter,* vol. 12, pp. 1077–1080, 2013.
2. J. Ouyang, F. Yang, and Z. M. Wang, "Reducing mutual coupling of closely spaced microstrip MIMO antennas for WLAN application," *IEEE Antennas Wireless Propagation Letter*, vol. 10, pp. 310–312, 2011.
3. M. A. Antoniades and G. V. Eleftheriades, "A folded-monopole model for electrically small NRI-TL metamaterial antennas," *IEEE Antennas Wireless Propagation Letter*, vol. 7, pp. 425–428, 2008.
4. D.R. Smith and S. Schultz , Determination of effective permittivity and permeability of metamaterials from reflection and transmission coefficients, *Phys. Rev*. B65, 195104 (2002).

A Double-Negative Meta-Surface structure for Performance Enhancement of Vehicle-to-Vehicle Circular Array Antenna

Imtiaz Islam[1], **Mohd Faizal Jamlos**[1,3*], **Mohd Aminudin Jamlos**[2], **Ping Jack Soh**[1], **Siti Zuraidah Ibrahim**[1], **A.S.M Alqadami**[1] and **Rizalman Mamat**[3]

[1]Advanced Communication Engineering (ACE), School of Computer & Communication Engineering, Universiti Malaysia Perlis (UniMAP), 01000 Kangar, Perlis, Malaysia

[2]Department of Electronic, Faculty of Technology Engineering, UniMAP, 02100, Padang Besar, Malaysia

[3]Faculty of Mechanical Engineering, Universiti Malaysia Pahang (UMP), 26600, Pekan, Malaysia.

[*]corresponding author: mohdfaizaljamlos@gmail.com

Abstract- A new design of metasurface with double-negative (DNG) characteristic has been proposed for bandwidth and gain improvement of the circular array antenna. The antenna structure is formed by circular radiating patches and DNG metasurface unit cells which are placed at the ground plane in form of 5x3 array. It is found that that DNG metasurface improved the antenna bandwidth from 2.04 GHz to 2.7 GHz and maximum gain enhanced from 5.5 dBi to 5.776 dBi at 5.9 GHz.

SUMMARY

In recent years implementing different types of material in antenna technology has attracted tremendously by researchers. For example artificial metasurface like metamaterial for antenna technology open a way to explore new ideas. Metamaterial is artificial magnetic conductor which can change the material property at certain frequency range [1]. Different types of metamaterial are explored to improve antenna's performances include frequency selective surface (FSS), electromagnetic band gap structure (EBG) and artificial magnetic conductor (AMC) [2]. Nevertheless, those techniques increase thickness of the antenna and produce higher surface wave which degraded the radiation pattern. Furthermore, double negative metasurface (DNG) has widely used where the permittivity and permeability will be negative on certain frequency range [3]. In this paper, a new design of 5x3 double-negative metamaterial array structure have been applied at the ground plane to boost antenna's performances. Figure 1(a-d) presents the metasurface unit cell structure, refractive index, relative permittivity and relative permeability. The extraction procedure has taken from the magnitude and phase of S11 and S21 [4].

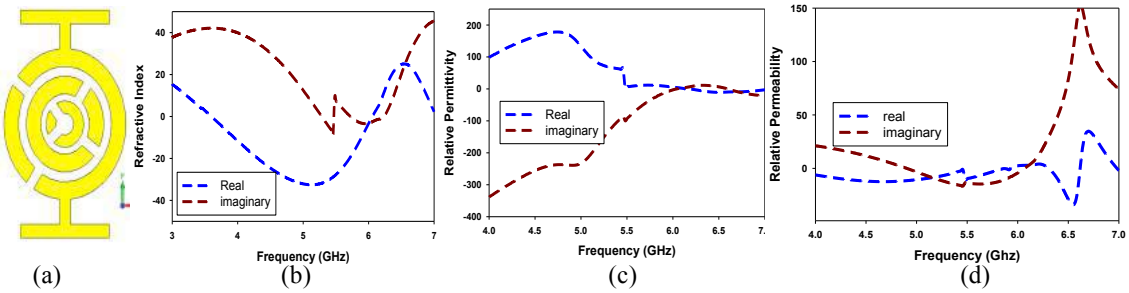

(a) (b) (c) (d)

Figure 1. DNG unit cell (a) 3-D configuration (b) Refractive Index (c) Permittivity (d) Permeability

Figure 2(a) presents the front view of the circular array antenna. This structure contains 8x2 small size circular radiating patches. The diameter of circular patches 8.45 mm. Simple quarter wavelength transmission line is used to develop array structure. This structure produces the bandwidth from 4.26 -6.3 GHz. Figure 2(b) presents the metasurface row which is placed step by step. At first step, it improved the bandwidth from 2.04 GHz to 2.45 GHz. Secondly, when another row of metasurface placed, it improved from 2.45 GHz to 2.57 GHz. Bandwidth is further improved to 2.7 GHz when the third row is added as shown in Figure 2(c). Moreover, the maximum gain is increased from 5.5 dBi to 5.8 dBi at 5.9 GHz.

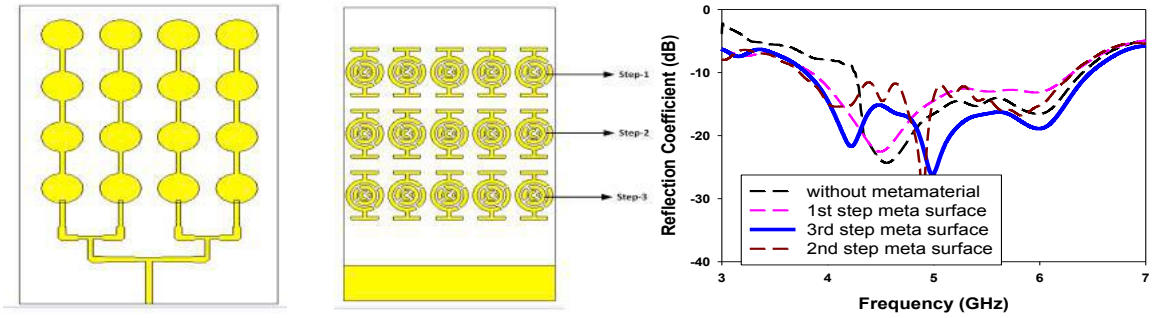

(a) (b) (c)

Figure 2. (a) Front view of array antenna (b) back view (c) reflection coefficient

REFERENCES

1. V.Veselago," The electrodynamics of substances with simultaneously negative values of εand μ." *Sov. Phys. Uspekhi*, 1968, 10, 509–514.
2. Lee, Y.J.; Yeo, J.; Mittra, R.; Park, W.S., "Design of a high-directivity Electromagnetic Band Gap (EBG) resonator antenna using a frequency-selective surface (FSS) superstrate" *Microw. Opt. Technol. Lett.*,243, 462–467,2004.
3. Enoch, S.; Tayeb, G.; Sabouroux, P.; Guérin, N.; Vincent, P. "A metamaterial for directive emission" *Phys. Rev. Lett.*, 89,2002.
4. D.R. Smith and S. Schultz , Determination of effective permittivity and permeability of metamaterials from reflection and transmission coefficients, *Phys. Rev.* B65, 195104 (2002).

Composite Langmuir-Blodgett multilayers of dioctyl sodium sulfosuccinate with oligo phenylenevinilene and gold nanoparticles

A. Salamianski[1], V. Agabekov[1*], N. Karatay[1], A. Agashkov[2], V. Belyi [2], N. Kazak[2]

[1]Institute of Chemistry of New Materials of National Academy of Sciences of Belarus, Minsk, Belarus

[2]Institute of Physics of National Academy of Sciences of Belarus, Minsk, Belarus

[*]corresponding author: ichnm@ichnm.basnet.by

Abstract- Composite Langmuir-Blodgett films (8 layers) of dioctyl sodium sulfosuccinate with oligo phenylenevinylene and gold nanoparticles of size 50 to 80 nm were formed on glass surfaces. Its morphology and optical properties (phase shift) were studied.

Langmuir-Blodgett (LB) films of organic substances with silver or gold particles can be used in the field of photonics to create devices of integrated optics, to develop epsilon-near-zero or negative refraction metamaterials [1, 2]. LB method does not require high temperatures and vacuum [3]. Langmuir layers of amphiphilic compounds are close-packed structures formed at the water surface after their transfer onto a solid substrate by LB method to form defectless mono- and multilayer films [1, 3].

The objective of this work was to create composite LB films of dioctyl sodium sulfosuccinate with gold nanoparticles and investigation of their optical properties.

In order to form of LB multilayers and the hydrophobic shell on the gold particles (Au) we used dioctyl sodium sulfosuccinate (AOT). In order to visualize AOT–Au Langmuir layers at UV light with a wavelength of 365 nm we used 4,4'-(1E,1'E)-2,2'-(2,5-dipropoxy-1,4-phenylene)bis(ethene-2,1-diyl)bis(4,1-phenylene) bis(4-(decyloxy)benzoate) – oligo phenylenevinylene (PhB). AOTPhB coatings and their composition with gold particles were formed on glass plates of rectangle shape with area ~ 4 cm^2. LT – 201 device was used for the measurement of surface pressure – area per molecule (π – A) isotherms of AOTPhB and AOTPhB–Au Langmuir layers and also for the deposition of coatings by vertical deposition method (4 bilayers of Y type) under surface pressure (π) ~ 15 mN/m [3]. Compressibility (K) was calculated for linear portions of the isotherms corresponding to compression of the Langmuir layers in the phase state "solid film" [1]. Gold nanoparticles were synthesized by citrate technique[2]: 1 mM aqueous solution of chloroauric acid was heated to the 100ºC, then 3.8 mM aqueous solution of sodium citrate was added, molar ratio $HAuCl_4$:$Na_3C_6H_5O_7$=2:3.6. Obtained compound was exposed under 100ºC for 5 minutes and then cooled to room temperature. As a result aqueous colloid of gold NPs stabilized by sodium citrate was obtained. After centrifugation and fractionation colloid of gold NP with diameter from 50 to 80 nm was obtained, size of NP was determined by the method of dynamic light scattering on Zetasizer Nano ZS (UK). In order to crate AOTPhB-Au composite LB coatings the NPs aqueous solution was mixed with the 0.4M AOT in isooctane solution containing 1 mg / ml PhB solution in hexane. The thickness of the AOTPhB multilayers was measured by interferometric method using POSTMK1 device (Planar, Belarus). Phase shift of optical radiation passing through the samples measured by using the walk-off interferometer [1]. The He-Ne laser with a wavelength of 632.8 nm was used as radiation source.

The phase shift of 16 nm thick AOTPhB coating (Figure 1) is 6.2°. The incorporation of gold nanoparticles into the structure of the AOTPhB film was accompanied by a decrease in compressibility (from 0.095 to 0.012)

of AOTPhB–Au Langmuir layers relatively to AOTPhB layer. The presence of gold particles with a size from 50 nm to 80 nm in AOTPhB multilayer structure also confirmed by SEM and AFM methods (Figure 2).

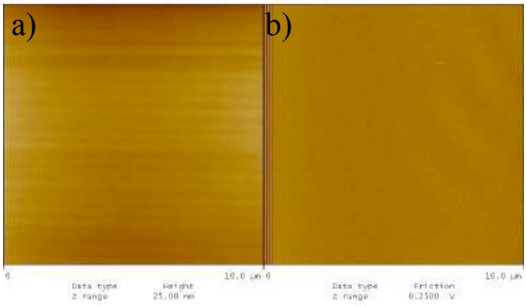

Figure 1 AFM image of topography (a) and phase contrast (b) of AOTPhB multilayer

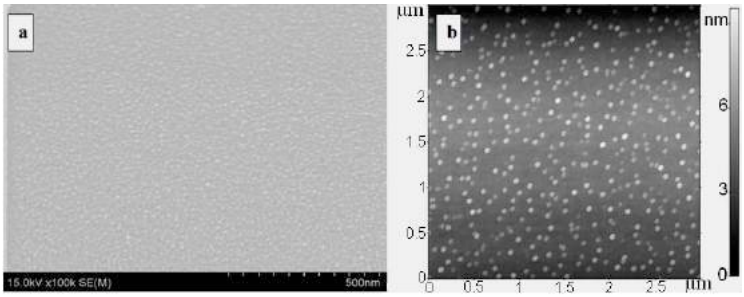

Figure 2 SEM (a) and AFM (b) images of LB multilayer based on gold particles in AOTPhB matrix

The phase shift (δφ) of the composite AOTPhB–Au coating is 1.4°. Partial oxidation of the AOTPhB matrix after 15 min treatment in UV etching with photo Surface processor PL 16-110D (SEN Lights Corp., Japan) – Figure 2 b decreases it's δφ to 0.85°.

Thus composite LB coatings of Au nanoparticles in the dielectric AOTPhB matrix can be used to create epsilon-near-zero materials.

Acknowledgements Authors express gratitude to post-graduate student A. Stankevich for kindly providing oligo phenylenevinylene.

REFERENCES

1. Salamianski A., Skoptsov E., Agashkov A., Binhussain Mohammed A., Agabekov V. "Langmuir-Blodgett films of polystyrene-poly-2-vinylpyridine with silver nanoparticles," in *Proceedings of* 9th International Congress on Advanced Electromagnetic Materials in Microwaves and Optics – Metamaterials 2015, Oxford, United Kingdom, September 2015, 574 – 576.
2. Hao J., Self-Assembled Structures Properties and Applications in Solution and on Surfaces, CRC Press, London, 2010.
3. Patent BY № 15411 Zhavnerko G.K., Agabekov V.E., Salamianski A.E., Chizhik S.A., Suslov A.A. and Chikunov V.V., "Device for forming mono- or multilayers of amphiphilic compounds on a solid surface," Publ. date 28.02.2012.

Optical properties of bulk and waveguide structures based on tunable hyperbolic metamaterials

B. Janaszek[1*], A. Tyszka-Zawadzka[1], and P. Szczepański[1,2]

[1]Institute of Microelectronics and Optoelectronics WUT, Koszykowa 75, 00-662 Warsaw, Poland

[2] National Institute of Telecommunications, Szachowa 1, 04-894 Warsaw, Poland

[*]corresponding author: bjanasze@mion.elka.pw.edu.pl

Abstract-In the last decade hyperbolic metamaterials has become an emerging class of media offering unique electromagnetic response. Within this paper we demonstrate that functionality of such structure can be further extended by employment of stimulus-sensitive functional materials providing control of optical properties of complete Tunable Hyperbolic Metamaterial (THMM) structure. In particular, we put the main emphasis on controllable dispersion, light stopping and gain/absorption in the near- and mid-infrared range of frequency.

Hyperbolic Metamaterials (HMM) are anisotropic media characterized by unclosed surface in wave vector space, known as hyperbolic dispersion. Due to their unusual dispersion properties such media reveal wide variety of potential applications in means of nanophotonics [1]. Particularly, latest researches in field of HMM are focused on employing stimulus-sensitive materials, such as graphene [2-4], vanadium dioxide and chalcogenide glass [5], providing tunability of complete structure and giving rise to completely new potential applications.

In this paper we demonstrate interesting behavior of the passive/active bulk graphene-based HMM structure (GHMM) as well as symmetric planar waveguide composed of Type II HMM core and air cladding. Especially, in the case of bulk GHMM structures we have shown the possibility of voltage-controlling the dispersion regimes i.e., Epsilon-Near-Zero (elliptic), Type I and II HMM (hyperbolic) as well as structure's optical properties. For example, one of the effects resulting from controlling of dispersion is tunability of structure's reflectance, see Figs.1(a)-1(b), also revealing angle-sensitivity.

(a) **(b)**

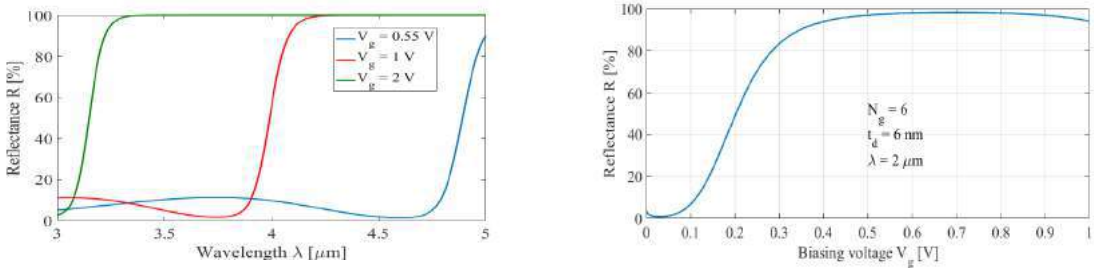

Fig. 1 a): Voltage-controlled [(a)] dispersion regimes and [(b)] reflectance of exemplary bulk THMM structure.

Another interesting behavior arising from dispersion-shape controlling is observed in bulk HMM structure composed of amplifying/absorptive material and functional material. Such structure offers modification of gain/absorption bandwidth of constituent active medium s well controllable electromagnetic transparency. As an

example, we present strong gain/absorption enhancement with significantly narrowed bandwidth, see Figs.2(a)-2(b).

(a) **(b)**

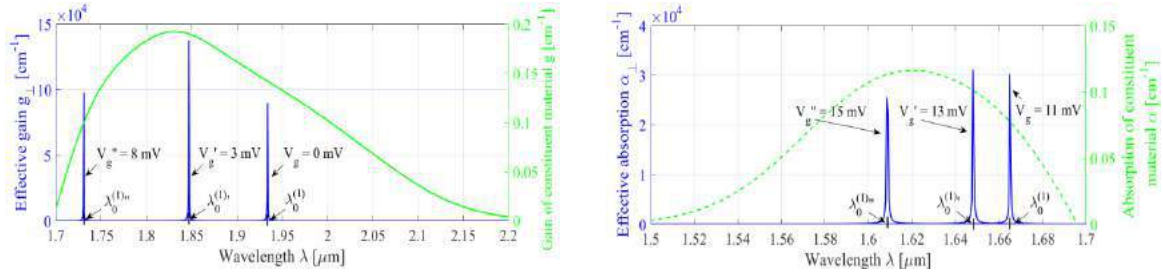

Fig. 2 Controlling of gain [(a)] and absorption [(b)] in active THMM structure.

Finally, our study concerned also the phenomenon of slow light inside a symmetric planar waveguide composed of Type II HMM core and air cladding. It has been shown that proper tailoring of structure's geometry combined with sufficient voltage biasing can lead to stopped light of selected wavelength, for example within SCLU bands (see [3] and its references), for certain waveguide width, see Figs. 3(a)-(b).

(a) **(b)**

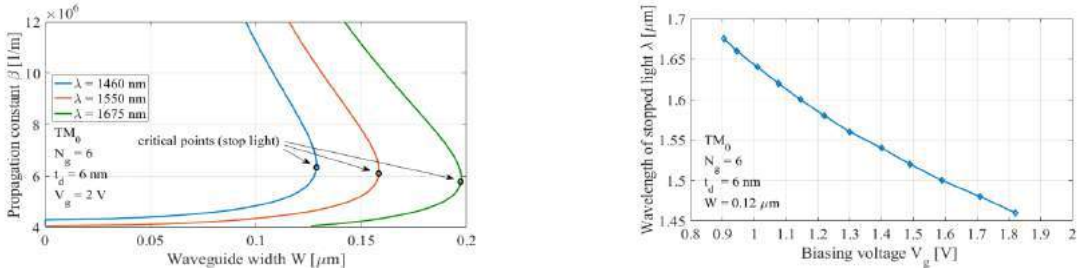

Fig. 3 Controllable light stopping in GHMM-based waveguides.

We believe that these kinds of tunable hyperbolic metamaterials could lay foundations for a new class of novel controllable photonic devices.

REFERENCES

1. Ferrari, L. , C. Wu, D. Lepage, X. Zhang and Z. Liu, "Hyperbolic metamaterials and their applications," *Progress in Quantum Electronics*, Vol. 40, 1-40, 2015.
2. Janaszek, B., A. Tyszka-Zawadzka and P. Szczepański, "Tunable graphene-based hyperbolic metamaterial operating in SCLU telecom bands," *Optics Express* ,Vol. 24, 24129-24136, 2016.
3. Tyszka-Zawadzka, A., B. Janaszek and P. Szczepański, " Tunable slow light in graphene-based hyperbolic metamaterial waveguide operating in SCLU telecom bands," *submitted for publication in Optics Express*, 2017.
4. Janaszek, B., A. Tyszka-Zawadzka and P. Szczepański, " Control of gain/absorption in tunable hyperbolic metamaterials," *submitted for publication in Nature Photonics*, 2017.
5. Krishnamoorthy, H. N., B. Gholipour, N. I. Zheludev and C. Soci, "Reconfigurable hyperbolic metamaterial with negative refraction," *In proceedings of IEEE Conference on Lasers and Electro-Optics (CLEO)*, pp. 1-2 ,2016

Magnetic Purcell effect in magnetic hyperbolic metamaterials

M. S. Mirmoosa, S. Yu. Kosulnikov, and C. R. Simovski

Department of Electronics and Nanoengineering, School of Electrical Engineering, Aalto University, Finland
mohammad.mirmoosa@aalto.fi

Abstract— We study a wire medium comprising high-index wires, and uncover topological phase transition between closed and open types of dispersion for transverse-electric (TE) polarized waves. The transition results in a filamentary pattern and remarkable Purcell factor for a magnetic dipole moment oriented perpendicularly to the optical axis of the medium.

Hyperbolic metamaterials have been widely studied in the past decade [1]. As is well known, since these artificial materials are uniaxially anisotropic and the principal components of the effective permittivity tensor do not possess the same sign, the isofrequency (dispersion) surface is open (a hyperboloid). However, this is only for transverse-magnetic (TM) waves. The isofrequency surface of transverse-electric (TE) waves is a sphere having a certain radius. That is due to the fact that the known hyperbolic metamaterials have no magnetic response. In order to have an open surface for TE waves, the effective permeability tensor should not be unity and its principal components should have different signs.

Recently, in Ref. [2], the authors studied a multilayer fishnet metamaterial, and they experimentally showed that TE waves have an open dispersion surface at optical frequencies. Concurrently with [2], we introduced a novel realization of magnetic hyperbolic metamaterials [3]. It is a wire medium whose wires are made of high-index epsilon-positive materials. It is worth noting that those materials with high refractive index can be found both in microwave and optical ranges. Firstly, we analytically derive the corresponding effective permeability tensor ($\mu_\perp$, $\mu_\perp$, $\mu_\parallel$) and subsequently, we study the isofrequency surfaces at different frequencies according to the dispersion relation of TE waves:

$$\frac{q^2}{\mu_\parallel} + \frac{\beta^2}{\mu_\perp} = k_0^2 \varepsilon_\perp. \tag{1}$$

Here, q and β are the transversal and longitudinal components of the wave vector. Also, $\varepsilon_\perp$ is the transversal component of the effective permittivity tensor and k_0 is the free-space wave number. Intriguingly, we find that at a special frequency, the medium experiences *topological phase transition* [4] between the closed and open types of dispersion. Such effect was investigated in our previous works for a wire medium of polaritonic nanowires. However, in those works, the transition was associated with TM waves [5]. Topological phase transition has a significant influence on radiation pattern and enhancement of subwavelength dipoles. Here, by positioning a magnetic dipole moment inside the medium, we observe that the energy is transferred along the optical axis of the medium at the transition frequency. Also, a strong radiation enhancement is achieved. This noticeable enhancement corresponds to the magnetic moment oriented perpendicularly to the wires axis.

REFERENCES

1. Poddubny, A., I. Iorsh, P. Belov and Y. Kivshar, "Hyperbolic metamaterials," *Nature Photonics*, Vol. 7, 948, 2013.
2. Kruk, S. S., Z. J. Wong, E. Pshenay-Severin, K. O'Brien, D. N. Neshev, Y. S. Kivshar and X. Zhang, "Magnetic hyperbolic optical metamaterials," *Nat. Commun.*, Vol. 7, 11329, 2016.
3. Mirmoosa, M. S., S. Yu. Kosulnikov and C. R. Simovski, "Magnetic hyperbolic metamaterial of high-index nanowires," *Phys. Rev. B*, Vol. 94, 075138, 2016.
4. Krishnamoorthy, H. N. S., Z. Jacob, E. Narimanov, I. Kretzschmar and V. M. Menon, "Topological transitions in metamaterials," *Science*, Vol. 336, 205, 2012.
5. Mirmoosa, M. S., S. Yu. Kosulnikov and C. R. Simovski, "Double resonant wideband Purcell effect in wire metamaterials," *Journal of Optics*, Vol. 18, 095101, 2016.

Miniaturization of Broadband Series Feed Array Antenna Using Double Negative Pi-shaped Metasurface

Imtiaz Islam[1], **Mohd Faizal Jamlos**[1,3*], **Mohd Aminudin Jamlos**[2], **Ping Jack Soh**[1], **Siti Zuraidah Ibrahim**[1], **Toufiq Md Hossain**[1] and **Rizalman Mamat**[3]

[1]Advanced Communication Engineering Centre (ACE), School of Computer & Communication Engineering, Universiti Malaysia Perlis (UniMAP), 01000 Kangar, Perlis, Malaysia

[2]Department of Electronic, Faculty of Technology Engineering, UniMAP, 02100, Padang Besar, Malaysia

[3]Faculty of Mechanical Engineering, Universiti Malaysia Pahang (UMP), 26600, Pekan, Malaysia.

[*]corresponding author: mohdfaizaljamlos@gmail.com

Abstract- This communication presents miniaturization of broadband series feed array antenna using double negative pi-shaped metasurface. The array antenna consists of 3×7 rectangular patches using series feeding operated from 4.38 GHz to 6.07 GHz. Double negative pi-shaped metasurface has applied in the ground plane in 7×5 form which miniaturize the array antenna size by 59.1% in length operating at 4.19 GHz to 6.09 GHz. Moreover, the maximum gain achieved is 6.7 dBi.

SUMMARY

With development of modern era, it is highly required to inflate compact size antennas in order to fulfill the stringent requirements of modern communication system [1]. In last decades, several miniaturization approaches have already demonstrated in the literature for microstrip patch antennas including different types of slots, implementing shorting pins and irregular ground plane [2]. Another conventional technique for antenna miniaturization is to use high dielectric material as antenna substrate [3]. However, those all methods provide narrow impedance bandwidth. Alternatively, a material having both electric and magnetic properties can be used as substrate to reduce antenna size [4]. Nonetheless, it is difficult to find low loss magnetic material for microwave regime in nature.

Recently, metamaterials have been attained much attention in antenna technology for various application like- SAR reduction, antenna performance improvement, invisibility clocking, polarization rotator and filters because of its extraordinary electromagnetic characteristics. In this paper, a pie-shaped metamaterial unit cell having the characteristics of negative permittivity and permeability is used for antenna miniaturization. Figure 1(a) shows unit cell structure where perfect magnetic boundary condition has applied in X-direction while perfect electric boundary condition in Y-axis. The relative permittivity and permeability for this proposed unit cell are presented in Figure 1(b) and Figure 1(c). The series feed array antenna structure presents at Figure 1(d). The array antenna consists of 7×5 radiating patches. The overall size of the antenna is 105mm× 50mm which is 1.5909λ × 0.75λ (wavelength at 4.5 GHz). The overall bandwidth without the unit cells is 1.69 GHz.

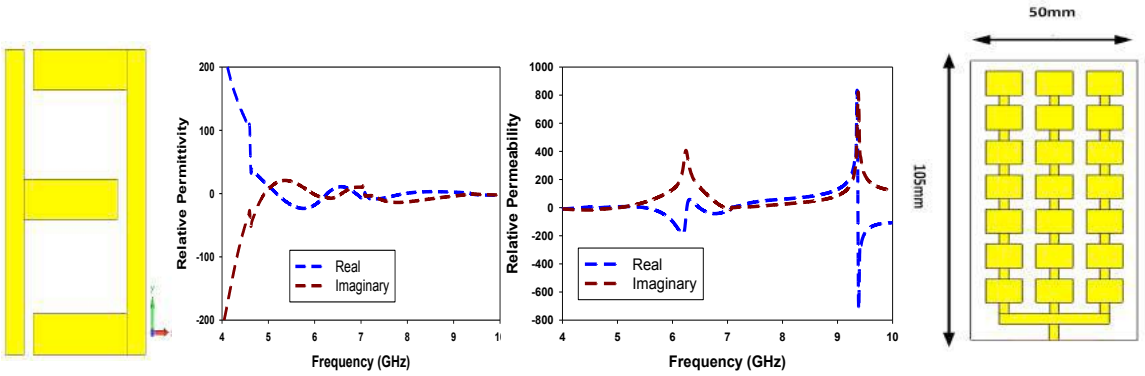

(a) (b) (c) (d)

Figure 1. (a) Pi-shaped unit cell (b) Relative Permittivity (c) Relative Permeability (d) Array Antenna Structure

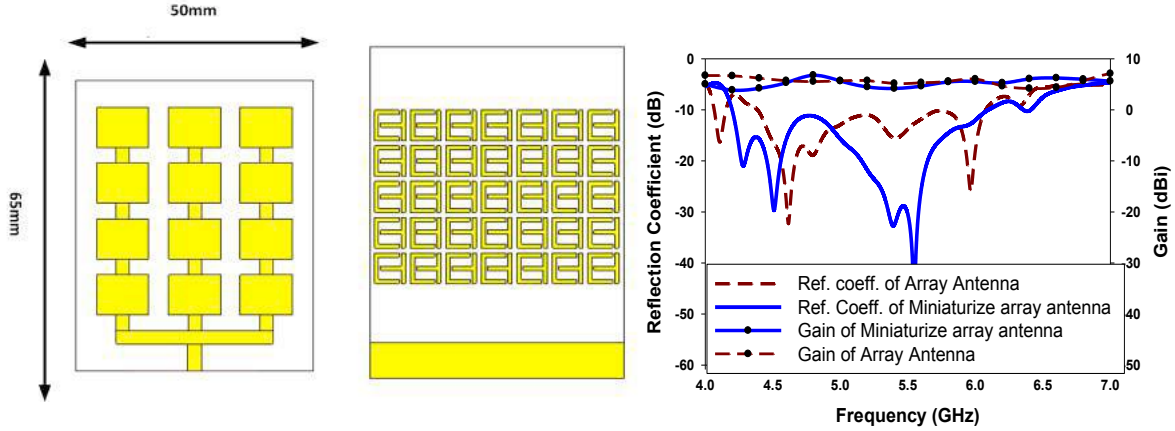

(a) (b) (c)

Figure 2. (a) Miniaturized array antenna structure (b) Back view (c) Reflection coefficient and gain of proposed antenna

The Pi-shaped double negative unit cell has applied in the back side of radiating patches, as shown in Figure 2. It is notified that the overall size of the antenna has reduced to 65mm × 50mm which is 1.0λ × 0.75λ at 4.5 GHz. It can be said that, the size reduced to 59.1% in length from the actual array structure. Furthermore, the overall bandwidth has been increased from 4.19 GHz to 6.09 GHz (1.9 GHz) compared to without unit cell which is 1.69 GHz.

REFERENCES

1. M. L. Wong, H. Wong, and K.-M. Luk, "Small circularly polarised patch antenna" *Electron. Lett*., vol. 41, no. 16, pp. 7–8, Aug. 2005.
2. H. Wong, K. K. So, K. B. Ng, K. M. Luk, C. H. Chan, and Q. Xue, "Virtually shorted patch antenna for circular polarization " *IEEE Antennas Wireless Propag. Lett.*, vol. 9, pp. 1213–1216, 2010.
3. Y. Hwang, Y. P. Zhang, G. X. Zheng, and T. K. C. Lo, "Planar inverted F antenna loaded with high permittivity material" *Electron. Lett.*, vol. 31,no. 20, pp. 1710–1712, Sep. 1995.
4. H. Mosallaei and K. Sarabandi, "Magneto-dielectrics in electromagnetic: Concept and applications," *IEEE Trans. Antennas Propag*., vol. 52, no. 6, pp. 1558–1567, Jun. 2004.

9.5GHz Metamaterial AMC reflector for X-band Applications and Operation

M.M. Gajibo*, M. K. A. Rahim, N. A. Murad, O. Ayop, Raimi Dewan
Department of Communication Engineering, Faculty of Electrical Engineering,
Universiti Teknologi Malaysia, 81310 Johor Bahru, Johor, Malaysia
*corresponding author:*mmgajibo@yahoo.com

Abstract- A single layer structure consisting of a metamaterial (MTM) artificial magnetic conductor (AMC) reflector is presented in this paper. An FR4 substrate with thickness of 1.6mm was used and the incidental wave angles were varied from 0^o to 66^o. A peak reflection of close to 90% was achieved at 9.5GHz by the AMC reflector for both TE and TM polarization

Keywords- *Metamaterial, Reflector, AMC.*

I. Introduction

AMC as the name implies which is sometimes interchanged with electromagnetic bandgap (EBG) [1] is a structure designed with an unusual boundary conditions to be selective in supporting surface wave currents which is different from conventional metallic conductors [2] where as EBG is a high impedance surface consisting of periodic AMCs. In modern antennas, AMC's are used to replace the perfect electric conductor (PEC) ground plane, this is simply because of the AMC's ability to reduce back-radiation as well as increase gain. [3].

II. Proposed Design and Simulation

The proposed MTM structure stages an AMC Reflector on FR4 substrate with a dielectric constant of 4.6, loss tangent of 0.019 and height of 1.60mm. The major part of the AMC's structure comprises of a square box Booleaned with a circular shape as sown in figure 1a & 1b. The square shape measures 6.75mm which is also responsible for the performance of the S_{11} of the AMC. On the other hand, the circular shape measures 5.1mm in diameter and is directly responsible for determining the resonance frequency.

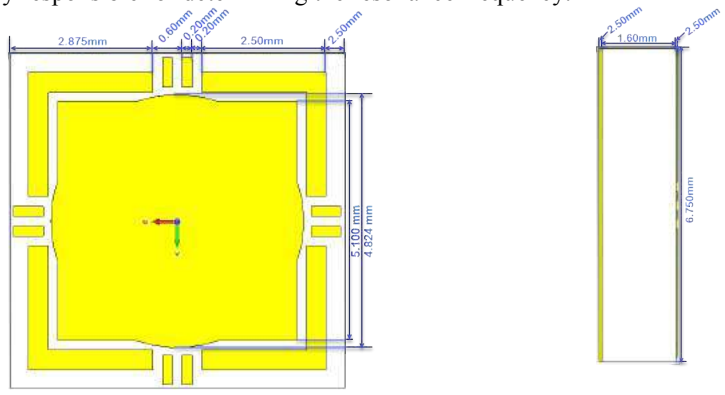

Figure:1 (a) (b)

III. Simulation Results and Discussions

a. Transverse Magnetic mode (TM) AMC's phase reflection

The AMC was simulated with different incidence wave angles (0^0, 15^0, 25^0, 35^0, 47^0 and 66^0) for TM mode and it was observed that, as the incident angle is increased, the resonance frequency across 0^0 (0 degrees) increases gradually. Take for instance, at direct incident wave (0^0) the AMC resonated at 9.50GHz, while as the incident

angle was increased to 15^0 the resonance frequency also increased to 9.54GHz. it is noted that there is no significant difference for angles below 30^0 but above 30^0, the shiftt in the resonance frequency is significantly high, in the cases of 35^0, 47^0 and 66^0, the results were 9.76GHz, 9.96GHz and 10.22GHz respectively.

b. Transverse Electrical mode (TE) AMC's phase reflection

Similar the same simulation was repeated for the same angles and this time it's for TE mode. The results for both the TM and TE mode are similar expect that for the TE mode, the increment in the resonance frequency is less when compared with that of the TM mode. For the first 3 incident angle (0^0, 15^0 and 25^0) the increment is negligible whereas for incident angles (35^0, 47^0 and 66^0) the shift in resonance frequency is high but still lower than that of the TM mode. Figures 2a & b shows the phase reflection for TM & TE respectively.

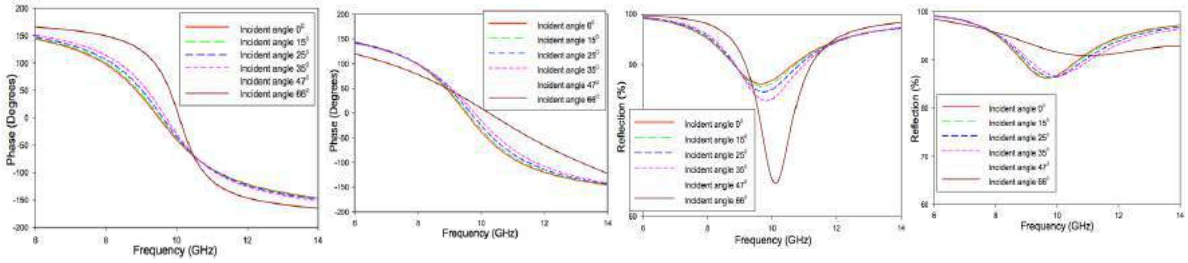

Figure 2: a. b. c. d.

c. *AMC's reflection Magnitude for Different incidental wave angles*

As mentioned earlier, the proposed AMC was simulated with different incidence wave angles (0^0, 15^0, 25^0, 35^0, 47^0 and 66^0. It was observed that for both TE and TM mode there is shift in the resonance frequency. With respect to TE mode, the frequency shift witnessed in the result of incident angles (0^0, 15^0, 25^0 and 35^0) are small and negligible whereas for incident angles (47^0 and 66^0) its considerably large as it jumped into 10.0 GHz. Figures 2c & d shows the phase reflection for TM & TE respectively

IV. Conclusions

MTM AMC reflector was designed and presented. It was simulated for various incident angles (0^0, 15^0, 25^0, 35^0, 47^0 and 66^0 and its performance was tested. It performed excellently at resonance frequency of 9.5GHz for incident angles below 30^0 where as the performance dropped for angles above 30^0 with slight shift in resonance frequency. It demonstrated a usable bandwidth (-90^0 to 90^0) of close to 2.40 GHz.

Acknowledgements: The authors thank the Ministry of Higher Education (MOHE) for supporting the research work, Research Management Centre (RMC), Universiti Teknologi Malaysia (UTM), Faculty of Electrical Engineering for the support of the research under grant no. 12H09, 4L811,4L008

REFERENCES

[1] Raimi Dewan, M. K. A. Rahim, M. R. Hamid, H.A. Majid, M.F.M. Yusoff, M.E. Jalil, "Reconfigurable antenna using capacitive loading to Artificial Magnetic Conductor (AMC)," *Microwave and Optical Technology Letters,* Vol.58, Issue 10, p2422-2429, 2016

[2] Abu, M. and M.K.A. Rahim, "Single-band and dual-band artificial magnetic conductor ground planes for multi-band dipole antenna," *Radio Engineering Journal, issue 4,* p999-1006, 2012

[3] A. Pirhadi, M. Hakkak, F. Keshmiri, and R. Karimzadeh Baee, "Design of compact dual band high directive electromagnetic bandgap (EBG) resonator antenna using artificial magnetic conductor," *IEEE Transactions on Antennas and Propagation*, vol. 55, pp. 1682-1690, 2007

[4] Gajibo. M.M, M. K. A. Rahim, N. A. Murad, O. Ayop, M. R. Hamid and H. A. Majid, "10.7 GHz Switchable Metamaterial Absorber/ Reflector for X-band Applications", *The 7th International Conference on Metamaterials, Photonic Crystals and Plasmonics, meta16,* ISSN 2429-1390 pp2085-2086.

Bifurcation of microwave propagation in a negative-permeability material triggered by high density plasma generation

A. Iwai[1], **Y. Nakamura**[1], **and O. Sakai**[2]

[1]Kyoto University, Japan
[2]The university of Shiga Prefecture, Japan
iwai.akinori.83c@st.kyoto-u.ac.jp

Abstract— We performed a plasma generation experiment with metamaterial using 2.45-GHz microwave, and detected the electron density which decided the effective permittivity and transmitted 2.45-GHz signal at the position in the generated plasma. The transmitted signal sustains relatively high level with both the negative-permittivity plasma and the negative-permeability double-split-ring resonator, although each material works as reflector and absorber. This bifurcation about the wave propagation suggests that the synthesis of the plasma and the DSRR is completed, which compose the *negative-refractive-index material*.

Metamaterials which are the periodic composite of the unit cells, meta atoms, have given the supernatural electromagnetic responses. One of the conventional metamaterials is a double-split-ring resonator (DSRR) which is a good example of the resonance types proposed by Pendry *et al* [1]. DSRR includes large capacitance and inductance, and can exhibits the negative-permeability (μ) reaction to the external magnetic field near the resonance frequency. The refractive index (N) decides the relationship between the frequency and the wavelength whether the wave can propagate or not. The electric permittivity (ε) and the magnetic μ completely decides N, and the negative-μ DSRR generates the novel propagation area, *left-handed material*, with using the negative-ε materials. The experimental verification was performed [2] by using the DSRR and metal wires which were in the effective negative-ε states [3].

On the other hand, metal wires array was used as the experimental simulation for the plasma [4], and the previous researches about the negative N implies that the combination of the DSRR and the plasma, the discharged gas, can provide a negative N state. Our group has focused on this coupling and performed the experiments; we has showed the effective electromagnetic-energy input into the plasma through the DSRR existence [5] and the enhanced nonlinearity [6, 7]. In our previous paper [6, 7], we showed the ability of the dynamic N thanks to the various ε and to the electric connection between the DSRR and the plasma working as the electrode via the plasma vacant area, the plasma sheath. In this report, we focus more on the change of the wave propagation in the DSRR space induced by the plasma generation.

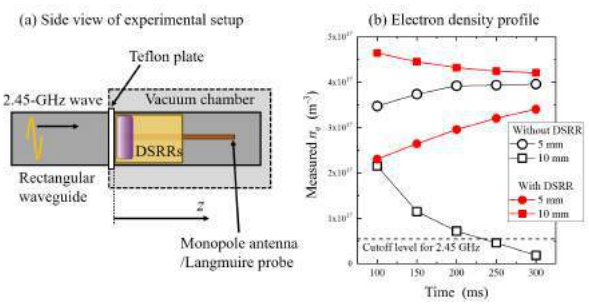

Figure 1: (a) Experimental setup. (b) Time development of measured electron density at $z = 5$ and 10 mm in cases with and without DSRRs. A dash line shows a density whose equavalent permittivity becomes 0.

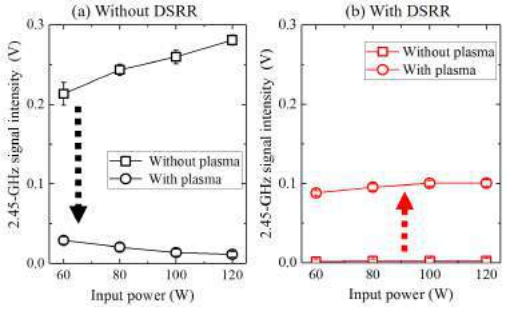

Figure 2: 2.45-GHz detected signal intensity as a function of input power. (a) Without DSRR. (b) With DSRR. Square and circle symboles express results without and with plasma generation, respectively.

Figure 1(a) shows the experimental setup. The input 2.45-GHz microwave propagates into the rectangular waveguide and enters the DSRR space in the vacuum chamber filled with Ar gas. The plasma is generated near the entrance, the Teflon plate, and it diffuses backward.

First, we monitored the electron density (n_e) of the generated plasma at the 5- and 10-mm positions in Fig. 1(a). In this measurement, Ar gas pressure was set at 200 Pa, and the net input power was about 100 and 200 W in cases without and with the DSRR, respectively. The power was the maximum which each generated plasma allowed to enter. Figure 1(b) shows the time development of n_e in the 300-ms initial period of the plasma excitation. Without the DSRR, generated plasma possesses the high n_e for the input microwave frequency, 2.45 GHz, but the density rapidly decreases as the position is far from the entrance because the plasma works like as the absorber and the reflector, which makes thin plasma. On the other hand, the plasma with the DSRR at $z = 10$ mm sustains the high n_e which is clearly beyond the cutoff level. The DSRR extends the penetration length of the input wave into the generated plasma.

We detected the transmitted 2.45-GHz signal intensity ($V_{2.45\mathrm{GHz}}$) at $z = 10$ mm in both cases, and Fig. 2 shows that the plasma generation in 200-Pa Ar gas affects $V_{2.45\mathrm{GHz}}$. In Fig. 2(a), $V_{2.45\mathrm{GHz}}$ increases as the increment of the input power and keeps the high intensity in the vacant waveguide (square symbols), but the plasma generation drastically weakens $V_{2.45\mathrm{GHz}}$ because of the evanescent mode and the energy consumption in the negative-ε plasma.

However, the plasma has the completely opposite role with the DSRR. In Fig. 2(b), $V_{2.45\mathrm{GHz}}$ in the negative-μ DSRR space is suppressed, but the plasma generation induces the higher intensity than that in the DSRR (square symbols in Fig. 2(b)) and in the plasma-filled waveguide (circle symbols in Fig. 2(a)) although the plasma is clearly the absorber/reflector in Fig. 2(a). These results imply that the negative μ of the DSRR cancels the negative ε of the plasma and this synthesization can makes propagation material for 2.45 GHz and helps the effective energy incidence into the generated plasma.

In conclusion, we performed the experiment about the plasma generation and the wave propagation into the plasma with using the DSRR. The generated plasma kept the highly ionized state up to 10 mm along the wave propagation direction, and the detected input signal intensity sustained the higher level with the DSRR and the plasma. Therefore, the DSRR and the plasma can have connection each other and it is possible that this composite works as the negative- and real-N material.

ACKNOWLEDGMENT

This study was supposed by Grant-Aid for Scientific Research from the Japanese Ministry of Education, Culuture, Sports, Science and Technology, Japan and by Grant-in-Aid for JSPS Research Fellow.

REFERENCES

1. Pendry, J. B., A. J. Holden, D. J. Robbins and W. J. Stewart, "Magnetism from Conductors and Enhanced Nonlinear Phenomena," *IEEE Trans. Microwave Theory Tech.*, Vol. 47, No. 11, 2075-2084, 1999.
2. Smith, D. R., Padilla, W. J., Vier, D. C., Nemat-Nasser, S. C. and Schultz. S., "Composite Medium with Simultaneously Negative Permeability and Permittivity," *Phys. Rev. Lett.*, Vol. 84, No. 18, 4184-4187, 2000.
3. Gay-Balmaz, P., C. Maccio and O. J. F. Martin, "Microwire arrays with plasmonic response at microwave frequencies," *Appl. Phys. Lett.*, Vol. 81, No. 15, 2896-2898, 2002.
4. Rotman, W., "Plasma simulation by artificial dielectrics and parallel-plate media," *IRE Trans. Antennas Propag.*, Vol. 10, No. 1, 82-95, 1962.
5. Nakamura, Y. and O. Sakai, "High-density microwave plasma source using negative-permeability metamaterial with tuned wave attenuation," *Jap. J. Appl. Phys.*, Vol. 53, 03DB04-1-5, 2014.
6. Iwai, A., Y. Nakamura and O. Sakai, "Enhanced generation of a second-harmonic wave in a composite of metamaterial andmicrowave plasma with various permittivities," *Phys. Rev. E*, Vol. 92, 033105-1-8, 2015.
7. Iwai, A., Y. Nakamura, A. Bambina and O. Sakai, "Experimental observation and model analysis of second-harmonic generation in a plasma-metamaterial composite," *Appl. Phys. Express*, Vol. 8, 056201-1-4, 2015.

Design of Anisotropic Metamaterials by Topology Optimization

B. Ahn[1*], H. J. Lee[1], and Y. Y. Kim[1]

[1]School of Mechanical and Aerospace Engineering, Seoul National University, Korea

[*]corresponding author: topabs@snu.ac.kr

Abstract- While the resonance mechanism has been utilized for metamaterial design, extreme anisotropy has been less explored. There is indeed a wide range of material properties including extreme anisotropy, which may not be realized without designing metamaterials. Here, we present a design method suitable for anisotropic metamaterials by topology optimization. Specific design problems in consideration are those that require the tailoring of the Equi-Frequency Contour and field polarization. As a design application, we consider the design of wave-mode converting metamaterial.

Because metamaterials are artificially designed to realize various wave-specific phenomena, their design is not a trivial task. Among various design methods, we consider the use of the topology optimization method as an efficient design methodology [1-3]. There were many successful cases of using the topology optimization for metamaterial and phononic crystal design [4-8], but little attention has been paid to the design of elastic metamaterials exhibiting extreme anisotropy [9]. As a specific case, we consider the realization of anomalously polarized elastic wave motion, which can be used to make unique wedges that can convert a longitudinal mode to a shear mode and vice versa.

The phenomenon of anomalous polarization can occur only in special materials exhibiting extreme anisotropy but no progress has been made towards the design of such extreme anisotropy. Now, it may be possible to realize such extreme property by using elastic metamaterials. As the terminology “anomalous polarization” implies, the desired phenomenon requires special Field Polarization (FP). At the same, the Equi-Frequency Contour (EFC) should trace the desire contour shape. However, there appears no topology optimization design considering both the EFC and FP.

While we will discuss possible formulations to design anisotropic elastic metamaterials, we propose a new formulation that simultaneously traces the desired EFC and FP. To facilitate the design optimization process by the proposed formulation, sensitivity analysis was performed to be used for a gradient-based optimizer. We considered several design case studies to demonstrate the effectiveness of the proposed method. Some findings from the convergence behavior will be also discussed.

Acknowledgements, This work was supported by the National Research Foundation of Korea (NRF) Grant [no. 2014M3A6B3063711 (Global Frontier R&D Program on Metamaterials)] funded by the Korean Ministry of Science, ICT and Future Planning (MSIP) contracted through IAMD at Seoul National University.

REFERENCES

1. Bendsøe, M. P. and N. Kikuchi, "Generating optimal topologies in structural design using a homogenization method", *Computer methods in applied mechanics and engineering*, Vol. 71, No. 2, pp. 197-224, 1988.
2. Bendsoe, M. P. and O. Sigmund, "Topology optimization: theory, methods, and applications", *Springer Science & Business Media*, 2013.
3. Kim T. S. and Y. Y. Kim, "Mac-based mode-tracking in structural topology optimization", *Computers & Structures*, Vol. 74, No. 3, pp. 375-383, 2000.
4. Sigmund, O. "Tailoring Materials for Specific Needs", *Journal of intelligent material system and structures*, Vol. 5, No. 6, pp. 736-742, 1994.
5. Ma, P. S., H. J. Lee, Y. Y. Kim, "Dispersion suppression of guided elastic waves by anisotropic metamaterial", *The Journal of the Acoustical Society of America*, Vol. 13, No. 1, pp. EL77-EL82, 2015.
6. Park, J. H., P. S. Ma and Y. Y. Kim, "Design of phononic crystals for self-collimation of elastic waves using topology optimization method", *Structural and Multidisciplinary Optimization*, Vol. 51, No. 6, pp. 1199-1209, 2015.
7. Oh, J. H., Y. K. Ahn and Y. Y. Kim, "Maximization of operating frequency ranges of hyperbolic elastic metamaterials by topology optimization", *Structural Multidisciplinary Optimization*, Vol. 52, pp. 1023-1040, 2015.
8. J. H. Oh, et al., "Elastic metamaterials for independent realization of negativity in density and stiffness", *Scientific reports*, Vol. 6, 2016
9. Helbig, K. and M. Schoenberg, "Anomalous polarization of elastic waves in transversely isotropic media", *The Journal of the Acoustical Society of America*, Vol. 81, No. 5, pp. 1235-1245, 1987.

Phase transitions in periodic photonic structures

M. V. Rybin[1,2], S. V. Li[1], K. B. Samusev[1,2], D. S. Filonov[1], A. V. Nikulin[1], Y. S. Kivshar[1,3], and M. F. Limonov[1,2]

[1]ITMO University, St. Petersburg 197101, Russia
[2]Ioffe Institute, St. Petersburg 194021, Russia
[3]Nonlinear Physics Center, Research School of Physics and Engineering, Australian National University, Canberra ACT 2601, Australia
m.rybin@mail.ioffe.ru

Abstract— We study phase transitions between metamaterials and photonic crystals by employing an inverse dispersion method that allows to construct a phase diagram for periodic structures composed of materials with high dielectric index including silicon and Ge-Sb-Te alloys. Our theoretical results are confirmed by microwave experiments with tunable metacrystals.

Photonic crystals and metamaterials are two important distinct classes of periodic photonic structures usually studied independently. Recently these structures have been considered in a unified approach [1] that analyzes how a typical photonic crystal composed of a square array of dielectric cylindrical rods [2] transforms into a metamaterial that can be characterized by averaged parameters [3]. By varying the cylinder radius and dielectric permittivity, it is possible to build a phase diagram controlled by structural parameters and allowing to introduce metamaterials with negative magnetic permeability. Here we develop deeper the concept of photonic phase transitions initiated in Ref. [1].

We study periodic structures with complex band diagrams employing the information about bands within the gaps related to Mie or Bragg resonances [4]. Usually, to study the band-gap diagrams, one reduces Maxwell's equations to the eigenvalue problem [2]

$$\nabla \times \frac{1}{\varepsilon(\mathbf{r})} \nabla \times \mathbf{H} = \frac{\omega^2}{c^2} \mathbf{H}, \tag{1}$$

where $\mathbf{H}$ is the magnetic field, $\varepsilon(\mathbf{r})$ is the distribution of dielectric permittivity in a periodic structure, ω is the frequency, and c is the vacuum light velocity. The familiar Floquet-Bloch theorem allows to define eigenfrequencies as functions of the wavevector $\mathbf{k}$. If the dielectric permittivity is a real function, the eigenvalue problem (1) is Hermitian, hence eigenfrequencies take real values only, and we cannot find the eigenmodes within bandgaps. An alternative way is to reduce Maxwell's equations to a generalized eigenvalue problem for the wavevector k

$$\begin{pmatrix} i\nabla\times & \omega\mu_0 \\ -\omega\varepsilon_0\varepsilon & i\nabla\times \end{pmatrix} \begin{pmatrix} \mathcal{E} \\ \mathcal{H} \end{pmatrix} = k \begin{pmatrix} \mathbf{n}\times & 0 \\ 0 & \mathbf{n}\times \end{pmatrix} \begin{pmatrix} \mathcal{E} \\ \mathcal{H} \end{pmatrix}, \tag{2}$$

where $\mathbf{n}$ is the direction of the wavevector $\mathbf{k} = k\mathbf{n}$, $\mathcal{E}$ and $\mathcal{H}$ are the Bloch amplitudes of the electric and magnetic fields respectively. After exception of the longitudinal waves the equation (2) can be reduced to the standard eigenvalue problem [4], that represents an inverse problem of finding k for given ω. Since this approach allows us to obtain eigenmodes for frequencies within band gaps, below we analyze the bands behavior typical for both Bragg and Mie resonances.

We consider a complex band-gap diagram calculated for a square lattice of dielectric cylinders with real dielectric constant ε of rods with radius $r = 0.3a$. In this case, the bands collapse at the Brillouin zone boundary (at the X point). However, introducing of weak losses, $\varepsilon = \varepsilon_{cyl}(1+0.002i)$, removes this degeneration. We find that for $\varepsilon_{cyl} < 18.5$ the plot of the real part of wavevector k vs. normalized frequency a/λ demonstrates a crossing behavior (Fig. 1c), so that the distance between the band going from the Γ point at the reciprocal lattice vector $\mathbf{g} = (0, 0)$, and the band going from the Γ point at $\mathbf{g} = (0, 1)$, decreases monotonically with the frequency a/l until the crossing point, then it increases again monotonically. However, for $\varepsilon_{cyl} > 18.5$, the distance between the bands decreases until a certain frequency after which they turn into an anti-crossing regime (Fig. 1d). The critical value $\varepsilon_{cyl} = 18.5$ is in excellent agreement with the value of dielectric constant defining

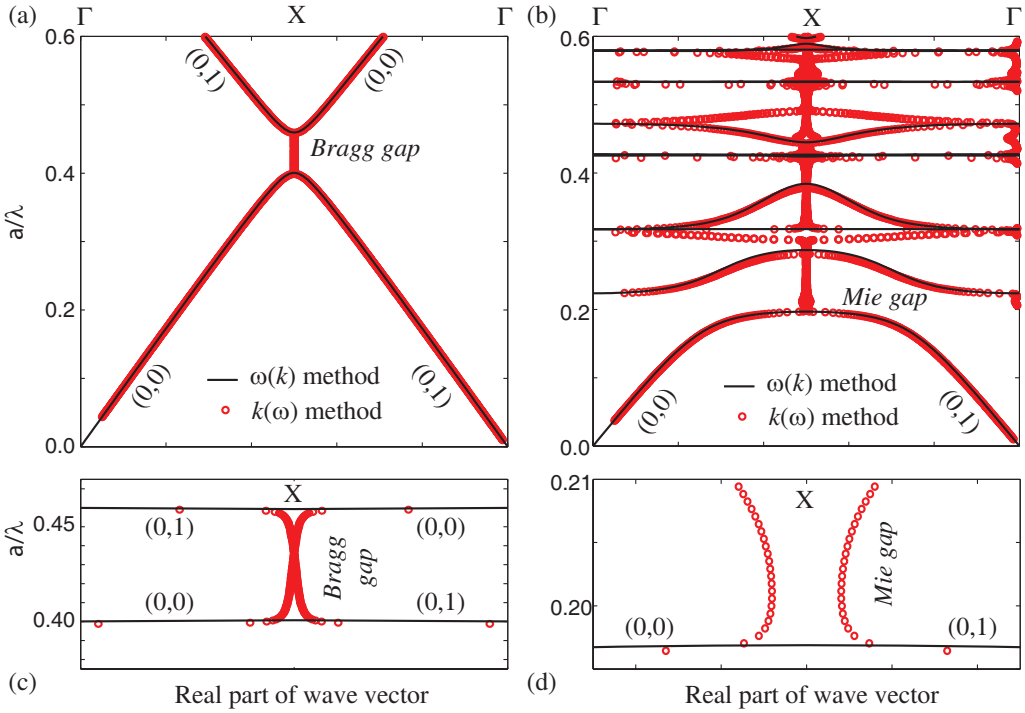

Figure 1: Complex band diagram calculated by the $\omega(k)$ method (solid lines) and inverse $k(\omega)$ method (circles) for the Bragg gap $\varepsilon_{cyl} = 3$ (a) and the Mie gap $\varepsilon_{cyl} = 40$ (b). Details of the band crossing behavior presented in a lager scale of (c) for $\varepsilon_{cyl} = 3$ and (d) for $\varepsilon_{cyl} = 40$. The data calculated by the inverse method correspond to weak losses $\varepsilon'' = 0.002\varepsilon'$. The inverse dispersion method uses 25×25 plane waves.

the boundary between the regime of photonic crystals and the regime of metamaterials obtaining from the direct $\omega(k)$ method. [1].

Since these two methods give the same results, we can use the most appropriate method. With the inverse $k(\omega)$ method we analyze a number of problems that cannot be solved with direct $\omega(k)$ methods. The first one is to build phase diagram for photonic structures composed of common high-refractive index materials such as silicon and Ge-Sb-Te alloys that have strong frequency dispersion of dielectric permittivity $\varepsilon(\omega)$. Arbitrary $\varepsilon(\omega)$ dispersion makes the usage of direct method be problematic since the operator in eigenproblem (1) depends on the eigenvalue ω. At the same time the frequency dispersion $\varepsilon(\omega)$ does not affect inverse $k(\omega)$ method, since its eigenvalue is k. The second problem is to study phase transition due to a higher order Mie modes. We verify our theoretical predictions for higher-order photonic phase transitions experimentally at microwaves. Measured data are shown to be in an excellent agreement with our theory.

ACKNOWLEDGMENT

This work has been supported by the Russian Foundation for Basic Research (No. 15-02-07529) and the Australian Research Council.

REFERENCES

1. Rybin, M. F., D.S. Filonov, K.B. Samusev, P.A. Belov, Y.S. Kivshar and M. F. Limonov, "Phase diagram for the transition from photonic crystals to dielectric metamaterials," *Nature Commun.*, Vol. 6, 10102, 2015.
2. Joannopoulos, J. D., S. G. Johnson, J. N. Winn and R.D. Meade, *Photonic Crystals: Molding the Flow of Light*, 2-nd Ed, Princeton Univ. Press, 2008.
3. O'Brien, S. and J. B. Pendry, "Photonic band-gap effects and magnetic activity in dielectric composites," *J. Phys. Condens. Matter*, Vol. 14, 4035, 2002.
4. Rybin, M. F. and M. F. Limonov, "Inverse dispersion method for calculation of complex photonic band diagram and PT symmetry," *Phys. Rev. B*, Vol. 93, 165132, 2016.

Manipulating the spatial distribution of magnetic near-field by a four-unit coding metamaterial

Lifang Lang, Guo Li, Sheng Ji, Hong Chen and Yunhui Li*

Key Laboratory of Advanced Micro-structured Materials, Ministry of Education, School of Physics Science and Engineering, Tongji University, Shanghai 200092, China

*corresponding author: liyunhui@tongji.edu.cn

Abstract- In this paper a coding metamaterial with '0' or '1'state controlled by a photo-relay is proposed, whose working frequency is about 3.0 MHz or 3.2 MHz. By arranging four units of this coding metamaterial in a square area, some special coding sequences can be easily realized, like '0000' and '0101'. As a consequence, the spatial distribution of magnetic near-field can also be modified. Both numerical and experimental results demonstrate that, under the coding sequence '0000', for instance, the magnetic field distribution are relatively uniform, as well as '0101' provides a diagonal field distribution. This work can also be extended to a large area complex structure with more unit cells.

Recently, vivid applications based on electromagnetic near-field have been emerging, such as near-field communication (NFC), radio frequency identification (RFID) and wireless power transmission (WPT). [1-3] However, the theory and technology of regulating the electromagnetic near field, especially some dynamic control strategies, are still not enough. Metamaterial is a good candidate for the control of electromagnetic waves and fields. However, for classical metamaterials, once the parameters of a metamaterial unit is settled, its electromagnetic properties cannot be changed also. Later, this problem is issued by adding some controllable elements, like variable capacitor, into the metamaterial units. In 2014, Engheta Group develop digital metamaterials , specifically synthesize an electromagnetic metamaterial with a desired permittivity, using as building blocks only two elemental materials with two distinct permittivity functions.[4] Then, T. J. Cui Group proposed the concept of coding metamaterials for convenient switching between different antenna radiation patterns.[5]

In this paper a coding metamaterial with '0' or '1'state controlled by a photo-relay is proposed. By arranging four units of this coding metamaterial in a square area, some special coding sequences can be easily realized, like '0000' and '0101'. As a consequence, the spatial distribution of magnetic near-field can also be modified.

As shown in Fig. 1, a coding metamaterial with 2×2 identical unit cells whose working frequency is about 3.0 MHz or 3.2 MHz is designed and fabricated. Each unit cell includes double-sided copper circuits, two capacity elements, a photo-relay and some connectors for controlling signals. By controlling the photo-relay, the coding metamaterial can work at 3.0 MHz or 3.2 MHz, which are named '0' and '1' states respectively. The total size of each unit cell is $50.8\times50.8\times1mm^3$.

According to the Kirchhoff Voltage Law, the currents in this four-unit coding metamaterial can be determined by the following relation: [6]

$$\begin{pmatrix} Z_1 & i\omega M_1 & i\omega M_2 & i\omega M_1 \\ i\omega M_1 & Z_2 & i\omega M_1 & i\omega M_2 \\ i\omega M_2 & i\omega M_1 & Z_3 & i\omega M_1 \\ i\omega M_1 & i\omega M_2 & i\omega M_1 & Z_4 \end{pmatrix} \begin{pmatrix} I_1 \\ I_2 \\ I_3 \\ I_4 \end{pmatrix} = \begin{pmatrix} U \\ U \\ U \\ U \end{pmatrix} \quad (1)$$

Where, I_n is the current in the n element, $Z_n=R_n+i\omega L_n+1/(i\omega C_n)$ is the self-impedance, L_n is the self-inductance, C_n is the capacitance, M_1 is the mutual inductance between nearest neighbors and M_2 is the mutual inductance between the next nearest neighbors. Consequently, based on the Biot-Savart law and superposition[7], the perpendicular magnetic field at the transfer distance（h=50mm）from surface of the structure can also be deduced, shown in Fig.2. Both numerical calculation and experimental measurement demonstrate that, under the coding sequences '0000', for instance, the magnetic field distribution are relatively uniform, as well as '0101' provides a diagonal magnetic field distribution. This work can also be extended to a large area complex structure with more unit cells.

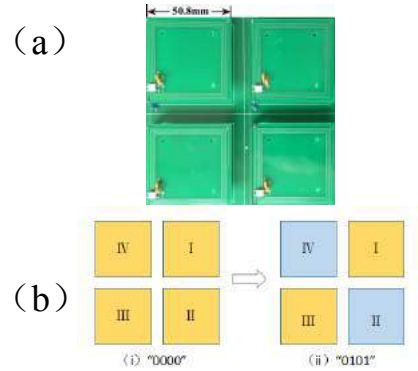

Fig. 1:（a）Photograph of a four-unit coding metamaterial and（b）Schematics of coding sequences '0000' and '0101'. Yellow: '0' state; blue: '1' state.

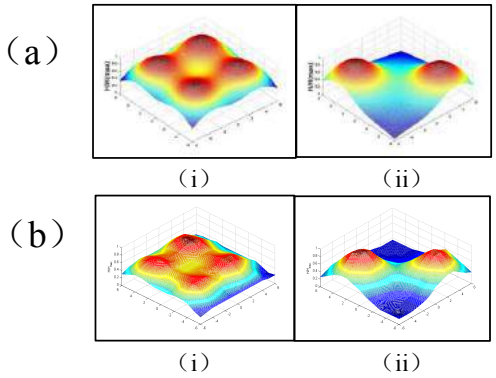

Fig. 2: The calculated (a) and measured (b) results of the spatial distribution of the magnetic near-field at h=50mm: (i), (ii) are the results of '0000' and '0101', respectively.

Acknowledgements, support from the National Key Research and Development Program of China (grant 2016YFA0301100), from the National Natural Science Foundation of China (NSFC) (grants 51377003, 11234010), and from the Fundamental Research Funds for the Central Universities, is gratefully acknowledged.

REFERENCES

1. R.Want, "Near field communication,"*IEEE Pervasive Computing,***10(3)**:4-7,2011.
2. R.Want, "An Introduction to RFID Technology,"*IEEE Pervasive Computing,***5(1)**:25-33,2006
3. A. Kurs, A. Karalis, R. Moffatt, et al., "Wireless power transfer via strongly coupled magnetic resonances," *Science* **317 (5834)**, 83-86 ,2007.
4. D. G. Cristian , E .Nader, "Digital metamaterials," *Nature Materials* **13,** 1115 – 1121, 2014.
5. T. J. Cui, M. Q. Qi,X. Wan,J. Zhao and Q. Cheng, "Coding metamaterials, digital metamaterials and programmable metamaterials ," *Light:Science & Applications* **3**,e218 ,2014.
6. O. Zhuromskyy,E. Shamonina,L. Solymar, "2D metamaterials with hexagonal structure:spatial resonances and near field imaging," *Opt.Express* **13(23),**9299(2005).
7. W. Lee,H. L. Lee,K. Oh and J. Yu, "Uniform magnetic field distribution of a spatially structured resonant coil for wireless power transfer," *Appl. Phys. Lett.* **100**, 214105 (2012).

Enhancement of spontaneous emission in metal-dielectric structures revisited

M. A. Kaliteevski[1,2,3], A. R. Gubaydullin[1,3], K.A. Ivanov[1,3]
[1]Saint- Petersburg Academic University, 194021, St. Petersburg, Russia
[2]Ioffe Physical-Technical Institute of Russian Academy of Science, 194021, St-Petersburg, Russia
[3]Saint Petersburg ITMO University, 197101, St. Petersburg, Russia

Abstract-We have developed the procedure of the quantization of the electromagnetic field in a layered inhomogeneous media, based on the analysis of the eigenvalues of the scattering matrix (S-matrix). We present application of S-quantization for the calculation of spontaneous emission rate for different photonic structures. We study the enhancement of spontaneous emission of the dipole embedded in the layered metal-dielectric structure applying S-quantization.

Metal-dielectric multilayered systems have attracted great scientific interest over the past decade due to their special optical properties emanating primarily from hyperbolic dispersion of isofrequency surface, and therefore are generally called hyperbolic metamaterial (HMM) systems [1]. Recently appeared estimations of ultra-high values of the spontaneous emission rate enhancement of the dipole emitter centered in the stratified metal-dielectric metamaterial [2] are very interesting, offering many fascinating applications. Nevertheless, these results deserve more careful consideration since in these studies, the mode structure of the field in the space with the inhomogeneity was assumed to be identical to the mode structure of a homogeneous medium obtained using periodic BC [3].

However, in the case of an inhomogeneous medium, the approach to the problem of the mode structure of the field on the basis of periodic BC is not rigorous and self-consistent, because the presence of inhomogeneity can lead to significant changes in the mode structure (obtained by applying the periodic BC) discussed in [4],which in turn may lead to inaccuracies in the analysis of layered systems. In our study of layered metal-dielectric structures we present angular dependence of Purcell factor [5] for incidence angles inside the light cone, as proposed initially in [3]. Also we notice that the use of periodic BC limits an applicability of results obtained in [2,3], since only “symmetric” eigenvector is used in approach [3], while the mode corresponding to “antisymmetric” eigenvector is missed.

We have developed a procedure S-quantization [6] of quantization of electromagnetic field that would allow rigorous self-consistent description of the mode structure in the quantization box with inhomogeneity, and providing a way for the calculation of probability of spontaneous emission (Purcell effect) from multilayered structure for modes characterized by arbitrary direction of propagation and polarization, for arbitrary layered structures. S-quantization solves the long-standing problem coupled to normalization of the quasi-stationary electromagnetic modes.

Examples of application of S-quantization for the calculation of spontaneous emission rate for the cases of Bragg reflector and microcavity are demonstrated in [6]. We have compared S-quantization results with experimentally observed photoluminescence pattern measured on Tamm plasmon structure [7], showing a good agreement, what provide the confirmation for S-quantization method. We study the enhancement of spontaneous

emission of the dipole embedded in stratified metal-dielectric structures, illustrating dependence of Purcell factor over the inplane wavevector.

Acknowledgements, this work has been supported by Russian Science Foundation (Project no. 16-12-10503).

REFERENCES

1. Smolyaninov I. I. and Narimanov E. E., *Phys. Rev. Lett.* **105** 067402 (2010)
2. Iorsh I., Poddubny A., Orlov A., Belov P., and Kivshar Y. S., *Physics Letters A* **376** 185187 (2012)
3. Martini F. De, Marrocco M., Mataloni P., Crescentini L., and Loudon R., *Phys. Rev. A.* **43**(5), 2480 (1991)
4. Kaliteevski M.A., Mazlin V.A., Ivanov K.A., Gubaidullin A.R., *Optics and spectroscopy* **119**(5), 832 (2015)
5. Gubaydullin A. R., Kaliteevski M. A., Ivanov K. A., et. al., *Appl. Phys. A* 122:425 (2016)
6. Kaliteevski M. A., Gubaydullin A. R., Ivanov K. A. & Mazlin V.A.,. *Optics and Spectroscopy* 121(3), 410 – 419 (2016).
7. Gubaydullin A.R., Symonds C., Bellessa J., Ivanov K.A., Kolykhalova E.D., Sasin M.E., Lemaitre A., Senellart P., Pozina G. and Kaliteevski M.A., *Scientific Reports*, in press.

Bandwidth Optimization of Trapped-Mode THz Filters Exploiting Adjoint Sensitivity

A. Y. Elsharabasy[1*], M. H. Bakr[1], and M. Jamal Deen[1]
[1]Department of Electrical and Computer Engineering, McMaster University, Canada
[*]corresponding author: elsharay@mcmaster.ca

Abstract—In this work, we present an optimization approach to reduce the bandwidth of metal mesh THz filters on thick substrates. Adjoint sensitivity analysis is exploited to provide the derivatives of the objective function for the optimizer. Through the optimization steps, the trapped-mode response has been improved with the out-of-band rejection reduced. EM simulations are carried out to illustrate the efficiency of the technique in decreasing the filter's bandwidth and enabling integration for detection and sensing applications.

In the last two decades, the THz metamaterials have been of a great interest because they allow for powerful THz applications [1-3]. One crucial and common element in most of these applications, especially in space-based astronomy and sensing, is the THz filter. Metal mesh filter represents a simple design and relatively low-cost in fabrication [4]. The stand-alone metal mesh filters have been widely used for many decades. However, at higher frequencies, their metal sheet thickness becomes electrically thick [5]. A possible remedy is to build the filter on thick and inexpensive substrates. In addition, the out-of-band rejection can be improved by producing a trapped-mode excitation within the structure [6, 7].

Here, the THz filter template shown in Fig. 1 has the vector of control parameters is given by $\boldsymbol{x}$= [*G, J, K, a, b*]^T as shown. The initial values of these points are set and passed to the EM simulator HFSS [8]. HFSS simulates the structure and returns both the S-parameters and their adjoint sensitivities [9, 10] with respect to all the control parameters. These sensitivities are to be utilized within the optimization algorithm. Derivative-based optimization is utilized to reach the optimal set of control variables satisfying the design specifications.

In our example, we utilize a cross absent filter with initial template parameters similar to the design in [7] and a 1-μm thick copper grid operating at 0.37 THz resonant frequency. We carried out the simulations for the filter on a 1-mm thick fused silica substrate. Here, we aim to narrow the bandwidth of the initial filter. The objective function is a weighted version of the transmission response of the filter. The EM simulation is performed for 9 frequency sweep points linearly distributed from 0.34 THz to 0.4 THz. $\boldsymbol{x}_l$ and $\boldsymbol{x}_u$ are, the lower and upper bound constraints on the parameters, respectively. The main objective function can be formulated as,

$$\min_{\boldsymbol{x}} \max_{i} \left\{ \left| S_{21}(f_i, \boldsymbol{x}) \right|^2 \right\}, \quad \text{subject to} \quad \boldsymbol{x}_l \le \boldsymbol{x} \le \boldsymbol{x}_u$$
$$\text{where, } 0.34\,\text{THz} \le f_i \le 0.4\,\text{THz}, i = 1,2,..,9, \text{ and } f_i \ne 0.37\ \text{THz}. \tag{1}$$

The minimax optimizer starting point x_0 and the optimal parameters values x_f are shown in Table I. The optimal response, in Fig. 2, shows that the new bandwidth is reduced from 14% to 6.5%, which is less than half the original one.

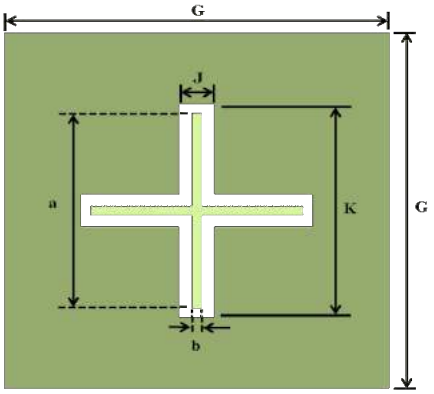

Fig. 1. A top view of one cell of a metal mesh filter.

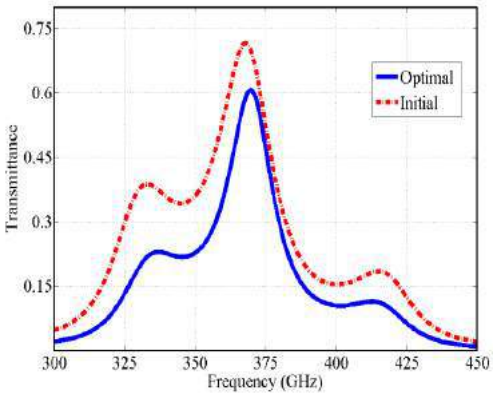

Fig. 2.The transmittance of the initial filter template (…) and of the final (optimal) design (—) of the narrow bandwidth filter.

TABLE I

Parameter	x_0 (μm)	x_f (μm)
G	305	306.2
J	40	28.2
K	194	183.6
a	166	168.0
b	12	7.8

REFERENCES

[1] S. Yoshida, E. Kato, K. Suizu, Y. Nakagomi, Y. Ogawa, and K. Kawase, "Terahertz sensing of thin poly(ethylene terephthalate) film thickness using a metallic mesh," Appl. Phys. Express, vol. 2, pp. 012301-1–012301-3, 2009.

[2] M.J. Deen, Ed., Silicon-based Millimeter-wave Technology, Advances in Imaging and Electron Physics, Academic Press, Amsterdam, vol. 174, 2012

[3] K., Ajito, "Terahertz Spectroscopy for Pharmaceutical and Biomedical Applications," IEEE Trans. Terahertz Science and Technology, vol. 5, no. 6, pp. 1140–1145, 2015.

[4] D. W. Porterfield, J. L. Hesler, R. Densing, E. R. Mueller, T. W. Crowe, R. M. Weikle, "Resonant metal-mesh bandpass filters for the far infrared," Appl. Opt., vol. 33, pp. 6046–6052, 1994.

[5] Y. Wang; B. Yang, Y. Tian, R. S. Donnan, and M. J. Lancaster, "Micromachined thick mesh filters for millimeter-wave and terahertz applications," IEEE Trans. Terahertz Science and Technology, vol. 4, no. 2, pp. 247–253, 2014.

[6] O. Paul, R. Beigang, M. Rahm, "Highly selective terahertz bandpass filters based on trapped mode excitation," Opt. Express, vol. 17, no. 21, pp. 18590–18595, 2009.

[7] W. J. Otter, F. Hu, J. Hazell, S. Lucyszyn, "THz metal mesh filters on electrically thick fused silica substrates," 39th International Conference on Infrared Millimeter and Terahertz waves (IRMMW-THz), 1, 2014.

[8] 'HFSS' ver. 15.0, ANSYS, Inc., Canonsburg, PA, 2015.

[9] M.H. Bakr, Nonlinear Optimization in Electrical Engineering with Applications in Matlab, IET, 2013.

[10] N.K. Nikolova, J. Zhu, D. Li, M.H. Bakr, and J. W. Bandler, "Sensitivity analysis of network parameters with electromagnetic frequency-domain simulators," *IEEE Trans. Microwave Theory Tech.*, vol. 54, no. 2, pp. 670–681, 2006.

New controllable birefringence phase matching method for the 2nd harmonic generation

T.Chang[1], **J. Shin**[1*]
[1]KAIST, Korea
[*]corresponding author: qubit@kaist.ac.kr

Abstract- We show that the new type of the phase matching technique, which is controllable birefringence based on the mesoscopic crystal. The polarization of the pump wave and 2nd harmonic wave can have orthogonal polarization, and the x- and y- directional linear property of the mesoscopic crystal can be independently controlled, and coherence length can be tuned.

1. Introduction

The nonlinear metamaterials draw much interest because of their enhanced nonlinearity. Since the frequency dispersion of the nonlinear metamaterials are generally more severe than natural nonlinear crystal, the phase matching technique for nonlinear metamaterials were also widely studied. However, the many previous phase matching technique for nonlinear metamaterials are limited to special cases, such as zero-index [1], or negative index [2]. Here, we show that the new type of phase matching technique for nonlinearity-enhanced medium based on the controllable birefringence of the mesoscopic crystal. This phase matching method is based on the controlling crystallinity of the mesoscopic structure and polling direction of the nonlinear material.

2. Results

The mesoscopic crystal structure are represented in Fig. 1a and its enhanced linear susceptibility was previously demonstrated [3]. The structural parameters are 'a', 'g', 'h_m', 'h_d', which are lateral unit cell dimension, lateral gap size, metal layer thickness, and dielectric layer thickness, respectively. Here, we assumed the filling dielectric have non-zero 2nd order susceptibility. The effective nonlinear dielectric tensor of the mesoscopic crystal can be obtained by the Lorentz-reciprocal theorem [4,5],

$$\tilde{\chi}_{eff}^{(2)} = v^{-1} \int \tilde{E}^{\mathrm{T}} p \tilde{\chi}^{(2)} \tilde{E}^{(2)} dv, \tag{1}$$

where p = +1, 0, -1 depends on the polling direction for specific points, and (i,j) component of 3-by-3 E matrix, E_i^i, is i-directional component of unitless electric field vector generated and normalized by j-directional applied average electric field. The quantitative E configuration is calculated in ref. [3]. The components of the 6-by-6 $E^{(2)}$ matrix are binomial expansion of the E matrix. Therefore, one can manipulate and enhance the nonlinear susceptibility by mesoscopic field configuration and the polling direction of the mesoscopic crystal. One representative example for the polling direction is depicted in Fig. 1b. For this configuration, the linear susceptibility, and the 2nd order nonlinear susceptibility from Eq. (1) becomes,

$$\tilde{\epsilon} = \epsilon_{33}\begin{pmatrix} \frac{1}{16}\left(\frac{a_x}{h_d}\right)^3 & 0 & 0 \\ 0 & \frac{1}{16}\left(\frac{a_y}{h_d}\right)^3 & 0 \\ 0 & 0 & 2 \end{pmatrix}, \quad \tilde{\chi}^{(2)}_{eff} = \tilde{\chi}^{(2)}_{33}\begin{pmatrix} \frac{1}{16}\left(\frac{a_x}{h_d}\right)^3 & \frac{1}{16}\left(\frac{a_x}{h_d}\right)\left(\frac{a_y}{h_d}\right)^2 & \left(\frac{a_x}{h_d}\right) & 0 & 0 & 0 \\ 0 & 0 & 0 & 0 & \frac{1}{16}\left(\frac{a_x}{h_d}\right)^2\left(\frac{a_y}{h_d}\right) & 0 \\ 0 & 0 & 0 & \left(\frac{a_x}{h_d}\right) & 0 & 0 \end{pmatrix}. \quad \textbf{(2)}$$

It shows that the generated 2nd harmonic wave becomes x-polarization, even if input pump wave is y-polarized. Moreover, the x-component and y-component of linear effective dielectric constant can be controlled by controlling x-, and y-unit cell dimensions. Therefore, the phase matching condition can be accomplished by independent controlling of x- and y- directional dielectric constants even with the dispersion of the metal and dielectric of the mesoscopic crystal. The numerical results is represented in Fig. 1c. It clearly show that the coherence length can be controlled by the controlling of the x- and y- lateral unit cell size.

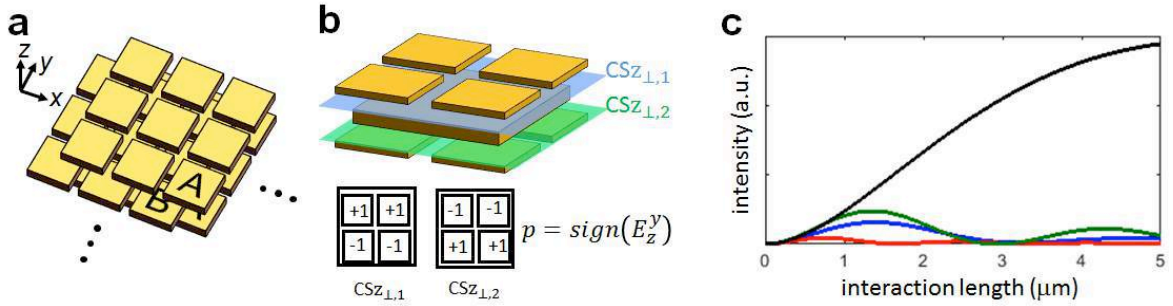

Fig. 1 (a) schematic of mesoscopic crystal (b) one example of polling direction configuration. (c) coherence length controllability (a_x = 160 nm; blue: a_y = 160 nm, red: a_y = 180 nm, green: a_y = 120 nm, black: a_y = 135 nm)

3. Conclusion

We numerically show that the controllable birefringence can be used for new type of the phase matching of second harmonic generation. Together with the enhanced nonlinearity of the mesoscopic crystal, the phased-matched harmonic generation can be widely applicable to nonlinear devices.

REFERENCES

1. Suchowski, H. *et al.* "Phase mismatch-free nonlinear propagation in optical zero-index materials", *Science*, Vol. 342, 1223-1226, 2013
2. Rose, A. Huang, D. and Smith, D. "Controlling the second harmonic in a phase-matched negative-index metamaterial", *Phys. Rev. Lett.* Vol. 107, 063902, 2011
3. Chang, T, *et al*. "Broadband giant-refractive-index material based on mesoscopic space-filling curves", *Nat. Commun.* Vol. 7, 12661, 2016.
4. Lee, J. *et al.* "Giant nonlinear response from plasmonic metasurfaces coupled to intersubband transitions", *Nature* Vol. 511, No. 7507, 65-69, 2014
5. O'Brien, K. *et al.* "Predicting nonlinear properties of metamaterials from the linear response", *Nat. Mater.* Vol. 14, No. 4, 379-383, 2015

Bandwidth Enhanced Metamaterial Inspired Antenna with Bent Monopole at UHF Band

N. A. Borhan[1], **N. A. Murad**[1*], **and M. K. A. Rahim**[1]
[1]Department of Communication Engineering, Faculty of Electrical Engineering,
University of Technology Malaysia, Malaysia

asniza@fke.utm.my

Abstract-In this paper, a design and simulation study of a bandwidth enhanced bent monopole antenna consisting a unit of CSRR, shorting via and a stub is presented. The antenna resonates at 0.75 GHz and 0.9GHz with bandwidth 32.73%. A comparison of return loss between bent monopole and bent monopole with added CSRR is shown to prove the functional of CSRR. The proposed antenna has a moderate 1.789dB and 2.047dB gain at 0.75 GHz and 0.9 GHz respectively.

1. INTRODUCTION

Recently, metamaterials(MTM) have been used widely in microwave devices and antenna application field. Broadband and compact antennas are in high demand with the fast development of modern wireless communication devices. Special properties of MTM such as zero propagation constant and negative refractive index could have enhanced the properties of the antenna [1]–[6]. At the low frequency such as Ultra High Frequency (UHF) band, using a MTM structure would be a great idea to improve the performance of the antenna as the wavelength of the antenna at this band is large. In this paper, a bandwidth enhanced metamaterial inspired antenna is proposed. The antenna is fed by a bent monopole and consists of a square shape complementary split ring resonator (CSRR), shorting via and a stub.

2. ANTENNA DESIGN

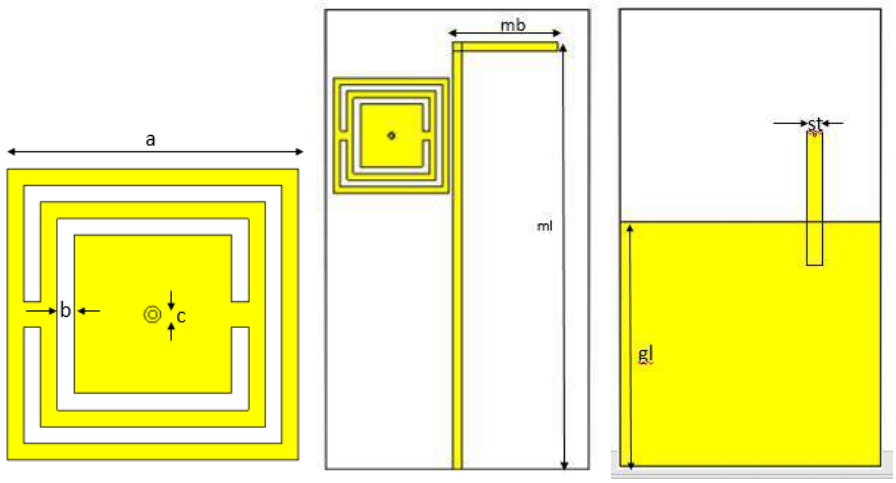

(a) (b) (c)

Figure 1: The geometry of the proposed antenna. (a) CSRR (b) Front view (c) Back view

The geometry of the proposed antenna is shown in Figure 1. The antenna consists of a square shaped CSRR, bent monopole, via and a shorted stub that connects the via to the ground plane with total dimension of 150mm x 80mm. It is designed with basic monopole antenna to be operated at 0.75GHz as the center frequency. The

monopole is bent at the end for the size reduction purpose as the bent has not change much on the antenna performance. The antenna is simulated on FR-4 dielectric substrate of permittivity 5.0, and a thickness of 1.6 mm by using CST microwave software. CSRR is chosen and added to this work for the bandwidth enhancement purpose [2]. A via of radius 0.5 mm at the center of the CSRR connects the stub at the back of the antenna that connected to the ground. Table 1 shows the dimension of the antenna parameters.

Table 1: Proposed antenna dimension

Parameters	a	b	c	mb	ml	gl	st
Dimension (mm)	35	2	2	32	130	65	5

3. RESULTS AND DISCUSSION

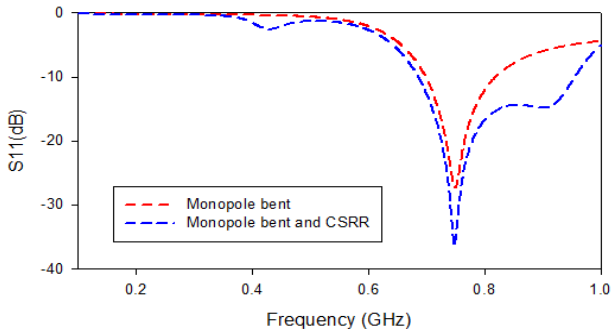

Figure 2: Return loss comparison

Figure 2 shows the comparison of return loss between bent monopole and bent monopole with added CSRR. Bent monopole resonates at 0.75 GHz with bandwidth percentage 17.22%. Then, a CSRR is added next to the monopole and it produced another resonant at 0.9 GHZ with bandwidth 32.73% at -10dB. It shows a single unit of CSRR may enhanced the bandwidth of the antenna. The proposed antenna has a gain of 1.789 dB and 2.047 dB at 0.75 GHz and 0.9GHz respectively.

4. Conclusion

A bandwidth enhanced metamaterial antenna with bent monopole at UHF band is proposed. The antenna consists of a square CSRR, via, stub and monopole bent with size of 150mm x 80mm. The antenna resonates at 0.75 GHz and 0.9 GHz with bandwidth of 32.73%.

REFERENCES

[1] B. D. Bala, M. K. a. Rahim, and N. a. Murad, “Small electrical metamaterial antenna based on coupled electric field resonator with enhanced bandwidth,” *Electron. Lett.*, vol. 50, no. 3, pp. 138–139, 2014.

[2] B. D. Bala, M. K. A. Rahim, and N. A. Murad, “An Epsilon Negative Metamaterial Antenna With Extended Bandwidth,” vol. 2, pp. 372–375, 2013.

[3] P. Feng, X. Chen, and A. A. R. C. A. Covered, “A Non-uniform Design of the metamaterial superstrate for the Resonant Cavity Antenna with Wideband Property,” pp. 10–11, 2016.

[4] B. Garg, A. Samadhiya, and R. D. Verma, “Design of Double-F Metamaterial Structure for Enhancing Bandwidth of Patch Antenna with Negative μ and İ,” no. 5, 2012.

[5] A. Gupta, S. K. Sharma, and R. K. Chaudhary, “A Compact CPW-fed Metamaterial Antenna for High Efficiency and Wideband Applications,” pp. 3–6.

[6] B. Sahu, M. Aggarwal, P. Tripathi, and R. Singh, “Stacked Cylindrical Dielectric Resonator Antenna with Metamaterial as a Superstrate for Enhancing the Bandwidth and Gain,” pp. 4–7, 2013.

Analysis of metamaterial behaviors on $NiAl_2O_4$ based flexible substrate material synthesized by sol-gel method

M. A. Rahman[1*], M. R.I. Faruque[1], and M. T. Islam[2]

[1]Space Science Centre, Universiti Kebangsaan Malaysia, Malaysia
[2]Dept. of electrical, Electronic and Systems Engineering, Universiti Kebangsaan Malaysia, Malaysia
[*]corresponding author: rashed@ukm.my

Abstract- In this study, a flexible substrate for metamaterial based on Nickel Aluminate ($NiAl_2O_4$) synthesized by sol-gel method is presented. The optical and microwave characterization demonstrate that the $NiAl_2O_4$ substrate is consists of a dielectric constant of 4.8, loss tangent of 0.04, and an optical bandgap of 2.8 eV. The metamaterial unit cell is fabricated on prepared flexible composite employing copper coating by magnetron sputtering. The double negative metamaterial behavior is found at a frequency of 6.05 GHz in microwave spectra.

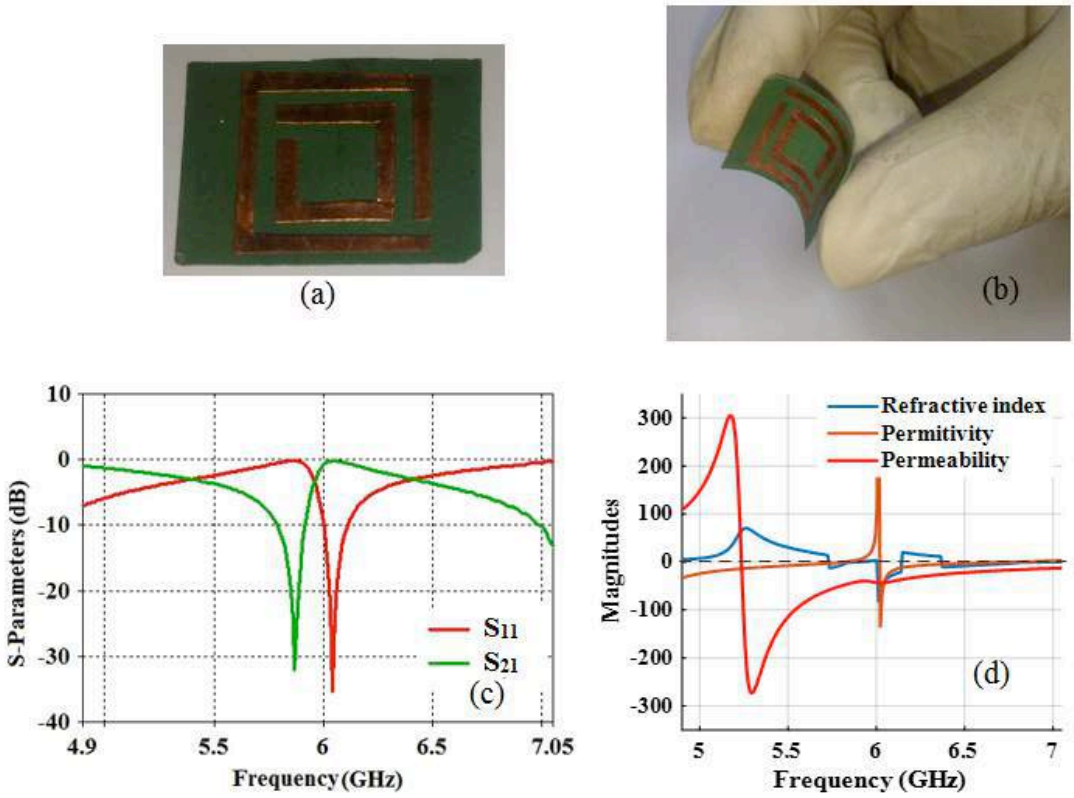

Figure: (a) The fabricated metamaterial unit cell on synthesized substrate, (b) Presentation of flexibility, (c) Reflection and transmission coefficient of metamaterial and (d) The effective parameters.

Improvements in several areas of materials science have resulted in a variety of new materials with strong potential applications to microwave components. In recent years flexible materials have earned immense interest in microwave engineering [1,2], however, there are very limited analyses on the impact of bending structures. Nano-crystalline NiAl2O4 is synthesized by many researchers with several methods [3,4], but they have not been explored much for microwave applications. The microwave dielectric properties of NiAl2O4 were investigated to find their employment as flexible material based metamaterial for microwave uses. The sol–gel method was employed to synthesize the flexible composite. The establishment of spinel assembly and crystalline dimension were assured using X-ray diffraction analysis. Morphology of the samples was clarified by means of the scanning electron microscopy. Relative permittivity and dielectric loss tangent of the specimen were restrained by DAK 200 MHz to 20 GHz dielectric measurement kit and obtained as 4.8 and 0.04, respectively. The energy bandgap was found 2.8 eV from optical analysis, which implies that the synthesized nanoparticles are semiconductors by nature. The flexible substrate layer was prepared by mixing NiAl2O4 nano-powder with polyvinyl acetate (PVA) glue dried up by means of heat. Finally, the metamaterial unit cell is fabricated on 20×18 mm2 NiAl2O4 flexible composite substrate employing 200 nm copper coating over that 1 mm thick substrate by magnetron sputtering shown in Figure (a & b). N5227A PNA microwave network analyzer and 159WCAS A-INFO Microwave waveguides are used to measure reflection and transmission parameters shown in Figure (c) of fabricated unit cell. DRI method [5] is used to extract the effective parameters shown in Figure (d) of the unit cell and double negative metamaterial behavior is found at a frequency of 6.05 GHz in microwave spectra. The overall analysis confirmed that NiAL2O4 is a highly suitable for fabrication of flexible metamaterial and desired operating parameters can be archived by modifying the synthesis and fabrication conditions.

REFERENCES

[1] A. Rahman, M. T. Islam, M. Samsuzzaman, M. J. Singh, and M. Akhtaruzzaman, "Preparation and characterization of flexible substrate material from phenyl-thiophene-2-carbaldehyde compound," *Materials,* vol. 9, p. 358, 2016.

[2] A. Rahman, M. T. Islam, M. J. Singh, and N. Misran, "Sol–gel synthesis of transition-metal doped ferrite compounds with potential flexible, dielectric and electromagnetic properties," *RSC Advances,* vol. 6, pp. 84562-84572, 2016.

[3] M. Aghayan and I. Hussainova, "Fabrication of NiO/NiAl2O4 Nanofibers by Combustion Method," in *Key Engineering Materials*, 2016, pp. 31-34.

[4] M. Maddahfar, M. Ramezani, M. Sadeghi, and A. Sobhani-Nasab, "NiAl2O4 nanoparticles: synthesis and characterization through modify sol–gel method and its photocatalyst application," *Journal of Materials Science: Materials in Electronics,* vol. 26, pp. 7745-7750, 2015.

[5] S. S. Islam, M. R. I. Faruque, and M. T. Islam, "A new direct retrieval method of refractive index for the metamaterial," *Current Science (00113891),* vol. 109, 2015.

Design of metafluids by determining effective parameters of metamolecules-dispersed liquids.

K. Kim[1], S. Yoo[2], J. Huh[1], Q. Park[2*], and S. Lee[1,3*]

[1]SKKU Advanced Institute of Nanotechnology (SAINT), Sungkyunkwan University (SKKU), Suwon, 16419, Republic of Korea

[2]Department of Physics, Korea University, Seoul, 136-713, Korea

[3]Department of Nano Engineering and School of Chemical Engineering, Sungkyunkwan University (SKKU), Suwon, 16419, Republic of Korea

[*] corresponding author: seungwoo@skku.edu

Abstract- We derive a method for calculating effective parameters of metafluids, where the rationally designed 3D metamolecules are homogeneously dispersed in liquid-phase fluid (e.g., water). Using this method, we engineer the effective parameters of solution-processable form of metamaterials by tailoring the shape and size of plasmonic nanoparticle and geometry of cluster.

Metafluids, in which the tailored metallic nanoparticle clusters (i.e., metamolecules) are homogeneously dispersed within fluid medium, have been viewed as a practical way to use metamaterials mainly owing to their solution processability [REF 1, REF 2]. However, *S*-parameter-enabled retrieval methods, which have been widely used in analyzing a periodic metamaterial [REF 3], are not valid for retrieving effective parameters of metafluids, because metamolecules in fluid are randomly rotating and moving in real time.

In this work, we analyze the optical properties of metamolecules, which could be materialized by benefitting from the recent advances in soft matter engineering (e.g., colloidal assembly [REF 4]). Then, we derive the effective parameter determination methods for metafluid based on the Clausius-Mossotti relation combined with dressed polarizability. Finally, we apply this method to various cluster motifs and identify the required concentration of cluster to induce unnatural light-matter interaction such as negative refractive index.

If we assume distance between each cluster and overall size of cluster are relatively small compared with the wavelength, Clausius-Mossotti relation can be applied to retrieve effective parameter (e.g., permittivity) as follows:

$$\frac{\varepsilon_r - 1}{\varepsilon_r + 2} = \frac{N\alpha}{3\varepsilon_0} \tag{1}$$

where $\varepsilon_0, \varepsilon_r$ are permittivity of vacuum and single molecule, respectively. As a representative example of our approach, herein, we exploit the available unnatural electromagnetism by using octahedron cluster motifs (Figure 1a) consisting of six 60 nm metallic nanospheres. This suggested structure has a substantial magnetic and electric dipole resonance by near-field coupling between adjacent metallic nanospheres (Figure 1b).

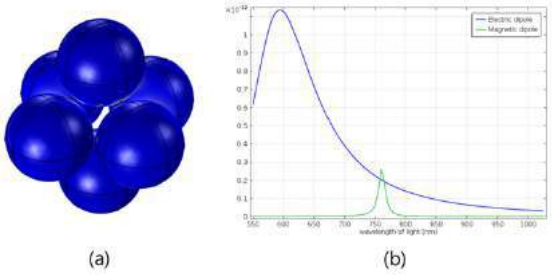

[Fig.1] (a) structure of octahedron. (60[nm] diameter of each constituent particle, 1[nm] gap between neighbor particles) (b)Electric dipole (blue) and Magnetic dipole (green) of this octahedron structure.

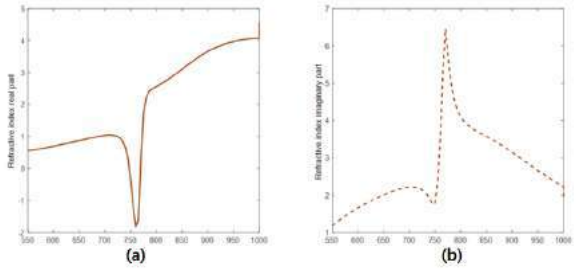

[Fig. 2] Refractive index of 0.77 micro-molar concentarion metafluid calculated by Clausius-Mossotti relation. Real part (a) and imaginary part (b) is shown in graph separately.

When this cluster motif is dispersed in water with 0.77 micro-molar concentrations, the negative refractive index at visible wavelength was found to be achieved (Figure 2). Also, we further engineered the cluster motifs such as broken symmetry to reduce the required concentration of metamolecules for negative refractive index. This design of asymmetric metamolecules was carried out under the umbrella of cluster motifs, which could be available with DNA-based programmable self-assembly [REF 5].

Acknowledgements, This work was supported by Samsung Research Funding Center of Samsung Electronics under Project Number SRFC-MA1402-09.

REFERENCES

1. Urzhumov, Y.A., G. Shvets, J. Fan, F. Capasso, D. Brandl and P. Nordlander, “Plasmonic nanoclusters: a path towards negative-index metafluids,” *Optics Express*, Vol. 15, No. 21, 14129-14145, 2007.
2. Sheiknoleslami, S. N., H. Alaeian, A. L. Koh and J. A. Dionne, “A metafluid exhibiting strong optical magnetism,” *Nano Lett.*, Vol. 13, No. 9, 4137-4141, 2013.
3. Smith, D. R., D. C. Vier, T. Koschny and C. M. Soukoulis, “ Electromagnetic parameter retrieval from inhomogeneous metamaterials,” *Phys. Rev. B*, Vol. 71, No. 3, 1-11, 2005.
4. Fan J. A., W. Chihihui, B. Kui, B. Jiming, B. Rizia, N. J. Halas, V. N. Manoharan, P. Nordlander, G. Shvets and F. Capasso, “Self-Assembled Plasmonic Nanoparticle Cluster,” *Science*, Vol. 328, No. 5982, 1135–1138, 2010.
5. Roller, E. M., L. K. Khorashad, M. Fedoruk, R. Schreiber, A. O. Govorov and T Liedl, “DNA-assembled nanoparticle rings exhibit electric and magnetic resonances at visible frequencies,” *Nano Lett.*, Vol. 15, No. 2, 1368–1373, 2015

Comparison of E-field on Various Patch Split Ring Resonator for Energy Harvesting

M. S. Zainudin, M. K. A. Rahim, N. A. Samsuri,
Faculty of Electrical, Universiti Teknologi Malaysia, Malaysia
mkamal@utm.my, asmawati@utm.my, msyazwan42@live.utm.my

Abstract- The energy harvesting with metamaterial structure (Split Ring Resonator) are proposed. The operating frequency is 1.3GHz. Three design are simulated by using CST software shows square patch give the highest value of absorption, which is 96.57%. For E-field monitoring in CST, the even circle shows the lowest value of absorption frequency wavelength, but its shows that it has the highest value of E-field, which is 181,100 V/m.

Artificial materials showing electromagnetic properties are not attainable in naturally due to their negative value of permittivity and permeability[1]. This artificially called metamaterials. They are made from assemblies of multiple elements fashioned from composite materials such as metals or plastic[2]. The materials are usually arranged in a repeating pattern, with the scale that smaller than their operating wavelength[3]. Split Ring Resonator is the one example of design from metamaterial structure[4]. The ring design as a patch with substrate and ground plane give the negative value of permeability[5]. Since the previous work shows that SRR can be used as an absorber of microwave signal (almost 100% efficiency), here come the challenge to take it as a new platform to harvest an energy, replacing the common method of harvest an RF signal by using rectenna[6]. This research starts from the study the performance of various design for patch split ring resonator[7]. Circle, square and hexagon are the proposed design in the research to optimize which design give the highest performance in absorbing transmitting frequency signal.

The absorption performance of all the structures shows the similarities. The circle shape has absorption value of 92.72%, followed by Hexagon shape by 95.17% and square shape with the highest percentage, which is 96.57%. In this result, all three structure has more than 90% of absorption characteristics, with E-plane must be parallel to the structure. The simulation continued by looking at the E-field characteristic. All mesh value is defined as a constant parameter. The result show vice versa from the absorption result. The circle patch gives the highest value of E-field concentration compared to others two designs. The circle patch gives the value of E-field 181 100 V/m, followed by hexagon patch (158,400 V/m) and square patch (109,200 V/m).

Initial observation shows that the edge of the structure gives an influence of E-field concentration. Since the circle patch didn't have any edge of its shape, the E-field orientation is easier to concentrate at the gap of the structure. Compared to hexagon and square patch, E-field is concentrated more than one point. This makes trapped energy inside the structure spread to several points, and disappear. The propagation of wavelength must be vertical toward the patch. If the structures are rotated 90 degree either clockwise / anticlockwise, the result of E-field decreased. This is due to the reflection coefficient that has been shifted to 800MHz.

Split Ring Resonator Patch Design (0 and 180 degree)	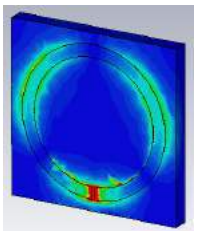 Circle	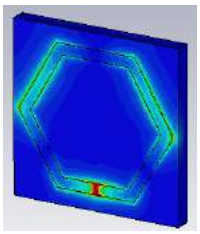 Hexagon	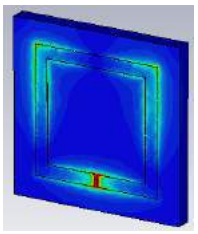 Square
Reflection Coefficient (S11)	-11.405 dB	-13.183 dB	-14.649 dB
E-field (V/m)	181,100	158,400	109,200
Absorption Percentage	92.72%	95.17%	96.57%
E-Field (V/m) (Rotated 90 degree)	4,238	1,527	1,036

In this study, it's important to choose the structure that has high concentration of E-field at the gap. From the table result, even though the square patch has the highest value of reflection coefficient, the circle patch got the better performance on E-field concentration. The absorption percentage of circle patch are the lowest one compared with other two patch, but its capable to capture the highest E-field. Next all three patch structures will be fabricated and measured. The result of measurement will be compared with simulation. Further study, the measurement will be done by using an oscilloscope and measure the potential energy at the gap of the structure by place a passive element (resistor or diode) as a load.

REFERENCES

[1] Muhammad Waqas, Muhammad Abid Saeed, Muhammad Junaid khan, and Muhammad Tayyab Qaiser, "A Circular Split Ringdouble Negative Metamaterial Having Simultaneous Negative Permittivity and Permeability," *IOSR J. Electr. Electron. Eng.*, vol. 9, no. 2, pp. 34–38, 2014.

[2] A. Sihvola, "Metamaterials in electromagnetics," *Metamaterials*, vol. 1, no. 1, pp. 2–11, 2007.

[3] E. Semouchkina, S. Mudunuri, G. Semouchkin, R. Mittra, and E. Furman, "Electromagnetic response of the Split-Ring Resonator placed inside a waveguide," *35th Eur. Microw. Conf. 2005 - Conf. Proc.*, vol. 2, pp. 701–704, 2005.

[4] M. S. Boybay and O. M. Ramahi, "Material Characterization Using Complementary Split-Ring Resonators," vol. 61, no. 11, pp. 3039–3046, 2012.

[5] O. M. Ramahi, T. S. Almoneef, M. Alshareef, and M. S. Boybay, "Metamaterial particles for electromagnetic energy harvesting," *Appl. Phys. Lett.*, vol. 101, no. 2012, 2012.

[6] T. S. Almoneef and O. M. Ramahi, "Harvesting electromagnetic energy using metamaterial particles," *IEEE Antennas Propag. Soc. AP-S Int. Symp.*, pp. 1046–1047, 2013.

[7] K. B. Alici and E. Ozbay, "Electrically small split ring resonator antennas," *J. Appl. Phys.*, vol. 101, no. 8, pp. 1–5, 2007.

A compact printed monopole antenna with double-negative (DNG) metamaterial for super wideband (SWB) wireless application

Samir Salem Al-Bawri[1,2], Mohd. Faizal Jamlos[1,3*], Syed Alwee Aljunid Syed Junid[1], Mohd Aminudin Jamlos[4], Rizwan Khan[1], H. Lago[1] and Ojo Rasheed[1]

[1]Advanced Communication Engineering Centre (ACE), School of Computer & Communication Engineering, Universiti Malaysia Perlis (UniMAP), 01000 Kangar, Perlis, Malaysia
[2]Faculty of Mechanical Engineering, Universiti Malaysia Pahang (UMP), 26600, Pekan, Malaysia.
[3]Department of Electronics & Communication Engineering, Faculty of Engineering, Hadhramout University, Yemen
[4]Department of Electronic, Faculty of Technology Engineering, UniMAP, 02100, Padang Besar, Malaysia
*corresponding author, E-mail: mohdfaizaljamlos@gmail.com

Abstract

A printed super wideband (SWB) monopole antenna for wireless communication applications using a unique double negative (DNG) unit cell metamaterial is presented. A compact key-shaped radiator is designed with electrical dimensions of 0.152 λ_o × 0.140 λ_o with respect to its lowest operating frequency. The proposed design, satisfactory far field radiation pattern, gain features fulfils the requirements to be suitable for SWB spectrum. Moreover, the 10 dB impedance bandwidth of the proposed antenna is from 3.47 to 60 GHz.

1. Introduction

In the past decades, an essential amount of research has been dedicated to microstrip antennas by increasing the utilization of the spectrum depending on the demand of wireless communication systems and the surrounding environment [1]. For instance, the current users of wireless personal area network (WPAN) are excitedly demanding super wideband (SWB) antennas to cover both long and short range transmitting for universal services [2]. These desired antennas have many benefits such as small size, lightweight, low cost, and their conveniently with integrated circuits. However, narrow bandwidth is one of the drawback challenges that limit the usages in the wideband modern wireless applications. Double-negative metamaterial (DNM), which is an example of the metamaterial unit cell can be used to improve and increase the antennas bandwidth due to the tremendous changes of its behavior to produce negative refractive index (NRI) within both negative permeability (μ) and permittivity (ε) [3]. The first engineered materials with simultaneously negative ε and μ was mathematically described by V. Veselago in 1968 [4]. Furthermore, by applying the DNM metamaterial on the antennas design, their performance will be enhanced where a new version of the antennas with an obvious improvement in terms of bandwidth, gain, size and good radiation patterns can be obtained [5].

This paper presents a miniaturized super wideband (SWB) monopole antenna using a new, wideband and compact DNM unit cell for wireless applications. Two rows of the proposed left-handed metamaterial unit cell located on the reverse side of the antenna substrate and some are placed near to the transmission line of the antenna. This structure exhibits negative permittivity and permeability and negative refractive index (NRI), which result in a compact, wide band antenna with omnidirectional radiation pattern.

2. Antenna Design and Unit Cell Geometry

The proposed DNM unit cell consists of several symmetric split ring resonators (SSRRs) assembled and combined to enable the unit cell operation over the wide band range within 3.47–60 GHz.

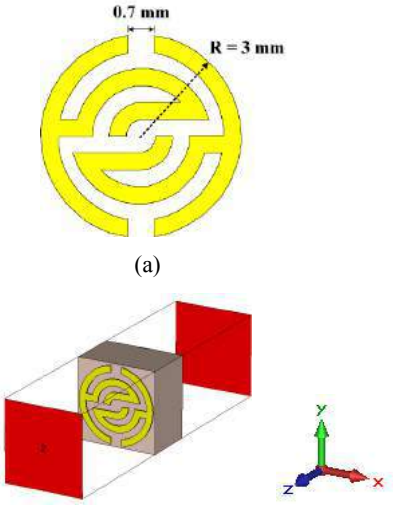

Figure 1: (a) Metamaterial unit cells structure, (b) simulation set.

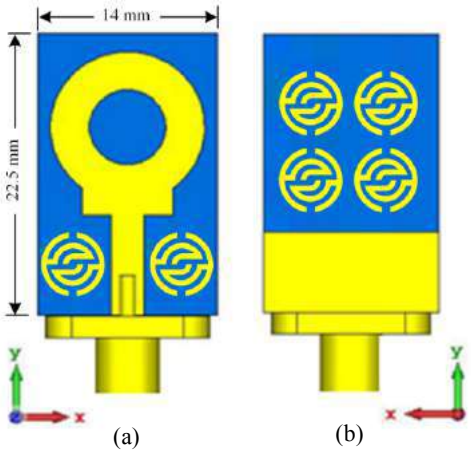

(a) (b)

Figure 2: Proposed antenna with unit cell (a) Front view (b) Back view

It was simulated using Computer Simulation Technology (CST) software for achieving the S-parameters whereas its simulated geometry is shown in Figure 1a. The simulation setup of proposed metamaterial unit cell illustrated in Figure 1b where two waveguide ports are located on each side of the z-axis. However, the proposed miniaturized SWB monopole antenna is shown in Figure 2, which is printed on a low-cost, 1.6 mm-thick FR4 substrate with a relative permittivity of 4.7 and loss tangent of 0.025. The overall size is of substrate is 22.5 × 14 × 1.6 mm^3 where the antenna is fed by 50-Ω SMA connector as shown in Figure 2.

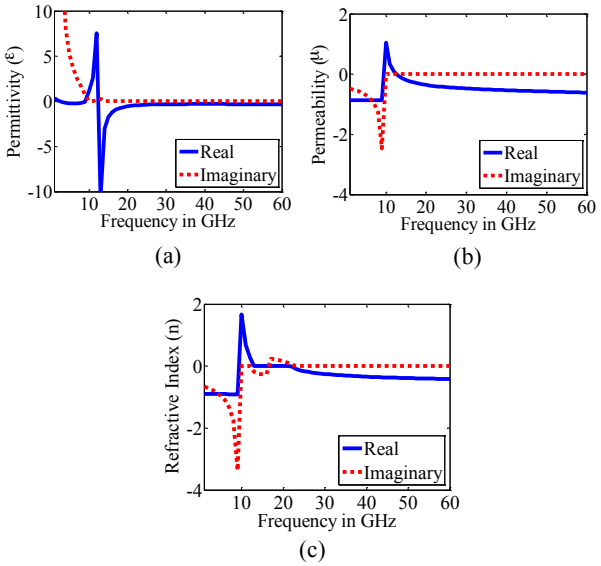

(a) (b)

(c)

Figure 3: Metamaterial unit cell simulated results (a) Permittivity (b) Permeability (c) Refractive Index

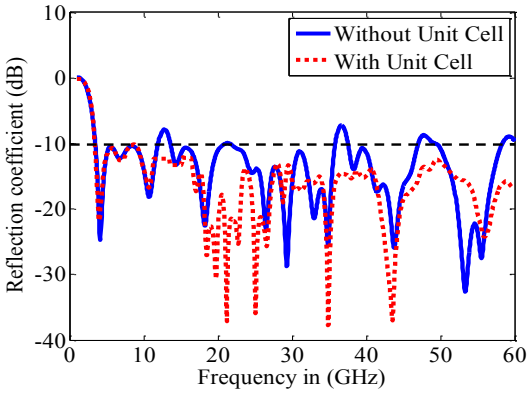

Figure 4: Comparisons of unit cell effects on reflection coefficient

It can be seen clearly that 2 × 2 unit cells are placed on the proposed antenna reverse side above the selected partial ground plane whereas two unit cells are applied horizontally close to the antenna's transmission line.

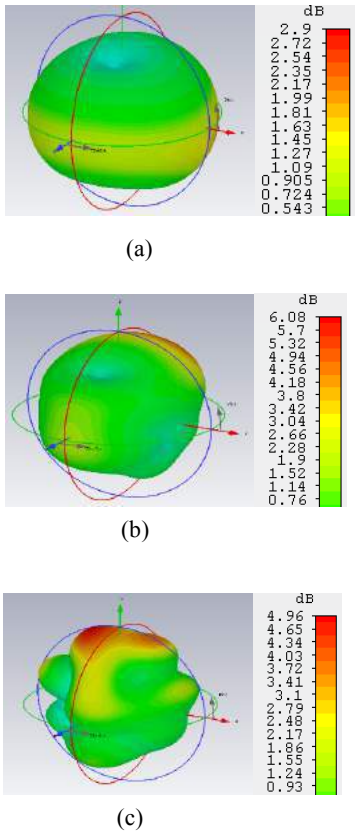

Figure 5: 3-D radiation pattern at (a) 5 GHz, (b) 10 GHz, (c) and 20 GHz.

3. Results and Discussion

Figure 3 (a-c) shows the obtained simulated results of the permeability, permittivity and refractive index within the frequency rang up to 60 GHz. The results showed the acquired wideband range of real negative values for both permeability and permittivity while the achieved real negative refractive index can be observed at the frequency span of (1-9.8 and 16.8-60) GHz as shown in figure 3.
Furthermore, it can be observed in Figure 4 that the proposed SWB antenna incorporates with unit cell can display high bandwidth from 3.47 to 60 GHz with reference to S11 < -10 dB which has too far wide bandwidth against previous antennas. The impedance bandwidth of the proposed antenna reaches 178.13% and the radiation patterns indicate that the SWB antenna radiation patterns are approximately omnidirectional as shown in Figure 5 (a-c).

4. Conclusions

A miniaturized super wideband (SWB) antenna using DNG metamaterials is presented. A novel and compact with left-handed symmetric split ring resonators (SSRRs) metamaterial unit cells is proposed. The features of negative permeability, permittivity, and refractive index (NRI) are validated from the proposed unit cell construction. Several unit cells are then placed on the antenna's backside and nearby the antenna's transmission line. The simulated reflection coefficient (S11) shows a wide bandwidth by 178,13 % (from 3.47 to 60 GHz).

References

[1] T. Aboufoul, C. Parini, X. Chen, and A. Alomainy, "Pattern-reconfigurable planar circular ultra-wideband monopole antenna," *IEEE Transactions on Antennas and Propagation,* vol. 61, pp. 4973-4980, 2013.

[2] K.-R. Chen and J.-S. Row, "A compact monopole antenna for super wideband applications," *IEEE Antennas and Wireless Propagation Letters,* vol. 10, pp. 488-491, 2011.

[3] S. A. Pope, "Double negative elastic metamaterial design through electrical-mechanical circuit analogies," *IEEE transactions on ultrasonics, ferroelectrics, and frequency control,* vol. 60, pp. 1467-1474, 2013.

[4] V.G. Veselago, The electrodynamics of substances with simultaneously negative values of e and l. Sov. Phys. Usp. 10, 509–514 (1968)

[5] A. S. M. Alqadami, M. F. Jamlos, P. J. Soh, S. K. A. Rahim, G. A. Vandenbosch, and A. Narbudowicz, "Miniaturized dual-band antenna array with double-negative (DNG) metamaterial for wireless applications," *Applied Physics A,* vol. 123, p. 22, 2017.

A Compact Modified H-Shaped DNG Metamaterial for Multi-band Microwave Application

Toufiq Md Hossain[1], Mohd. Faizal Jamlos[1, 2*], Md Imtiaz Islam[1], Mohd Aminudin Jamlos[3] and Rizwan Khan [1]

[1]Advanced Communication Engineering (ACE), School of Computer & Communication Engineering, Universiti Malaysia Perlis (UniMAP), 01000 Kangar, Perlis, Malaysia.
[2]Faculty of Mechanical Engineering, Universiti Malaysia Pahang (UMP), 26600, Pekan, Malaysia.
[3]Department of Electronic, Faculty of Technology Engineering, UniMAP, 02100, Padang Besar, Malaysia.
*corresponding author, E-mail: mohdfaizaljamlos@gmail.com

Abstract

This paper highlights a modified compact H-shaped Double Negative (DNG) metamaterial unit cell for X- and Ku-band applications. The unit cell has been constructed with the combination of two pair of L shaped resonators and two rectangular conductor blocks. The unit cell realized a highest DNG bandwidth of 4.32 GHz covering X and Ku-band (10.68 GHz to 15 GHz) with a size of 0.792 cm2. 1x1, 2x1, 2x2 and 4x4 array of the unit cell have also been analyzed.

1. Introduction

Artificial engineered materials or Electromagnetic (EM) Metamaterials (MMs) have been received a lot of attention from researchers with remarkable progress observed over the past decade [1]. The intriguing properties of MMs have inspired the researchers to implement them for various multiband applications and electromagnetic absorption reduction [2]–[4]. Different researchers have designed different alphabet-shaped metamaterial unit cell structures including U-shape, V-Shape, S-shape, H-shape, Z-shape etc. for multiband applications [2], [3], [5]. An "H-shaped" metamaterial has been proposed by Islam et al. [2], but the highest bandwidth was 0.5 GHz in C-band. Moreover Hossain et al. presented "two G-shape" DNG metamaterial for S- and C-band. In this case the highest bandwidth they achieved is 1.05 GHz (2.95 GHz to 4.00 GHz) with the lowest size of 1.2×1.2 cm^2 for the *unit cell-A* [3]. The highest DNG bandwidth in multiband operation has been reported in [5] that is 3.61 GHz which is higher than the other reported works. But in this case the size of the unit cell was 1 cm^2. Few manuscripts have been reported with multiband operation higher than 4 GHz DNG bandwidth associated with miniaturized size less than 1 cm^2.

This paper proposes a DNG multiband meta-material unit cell having negative permittivity and permeability in region of X-band and Ku-band with a highest DNG bandwidth of 4.32 GHz (10.68 GHz to 15 GHz) covering both first and second band.

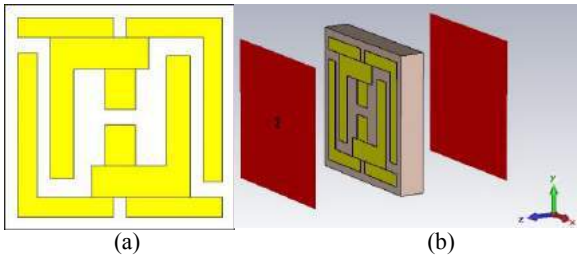

(a) (b)

Figure 1: Proposed Modified H-shaped metamaterial unit cell (a) proposed geometry (b) 3D geometry

This unit cell has realized a size of 0.9×0.88 cm^2 that is less than other unit cell reported in the above mentioned literatures. The proposed unit cell has been analyzed with 1×1 , 2×1 , 2×2 and 4×4 array gestalts. It exhibits resonance in X band and Ku band respectively. Moreover, it has DNG property in these two bands with a highest DNG bandwidth of 4.32 GHz (10.68 GHz to 15 GHz) in covering both bands. For the other array configuration it also shows the DNG properties in the X and Ku bands with a common DNG bandwidth of 10.8~15 GHz.

2. Unit cell design Architecture

The proposed unit cell consists of two pair of L shaped-resonators sandwiched one another. In addition to that it has two rectangular conductors in the middle. These shapes together form a shape of Modified H shaped proposed unit cell. Both of the L shaped resonators are connected with each other as depicted in Figure 2. The whole unit cell is symmetric with respect to the horizontal axis. The unit cell is designed on an FR-4 substrate of relative permittivity, ε_r=4.3 and loss tangent, δ=0.025 , copper thickness of 0.035 mm. The dimensions of the unit cell are presented in Table 1. FDTD based Computer Simulation Technology (CST) Microwave studio is used for the design of the unit cell. In this design the incident wave travels along z axis. Perfect Electric Conductor (PEC) and Perfect Magnetic Conductor (PMC) are deployed along y and x axis

respectively. The design is simulated with a frequency range of 0.1 GHz to 15 GHz using tetrahedral mesh property. Figure 1 illustrates the unit cell's 2D and 3D view. It can be seen that the waveguide port is set in the z direction. The dimensions are elucidated in Figure 2.

Parameter.	Value (mm)	Parameter.	Value (mm)	Parameter.	Value (mm)	Parameter.	Value (mm)
a	9	f	0.95	n	3.9	t	3.75
b	4.4	g	1.2	p	1.58	u	0.68
c	0.5	h	1.22	q	1.2	v	0.75
d	0.5	k	0.5	r	0.6	w	0.7
e	0.5	m	0.8	s	1.2	x	0.6

Table 1: Parameter dimensions of the proposed metamaterial unit cell

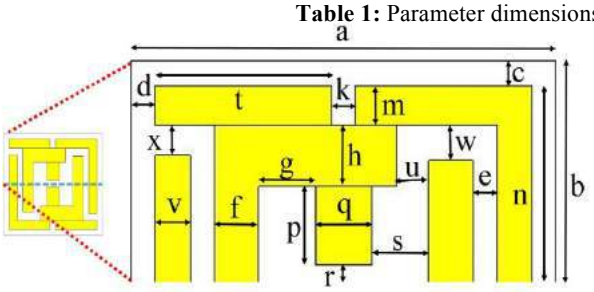

Figure 2: Illustrated proposed geometry of the unit cell

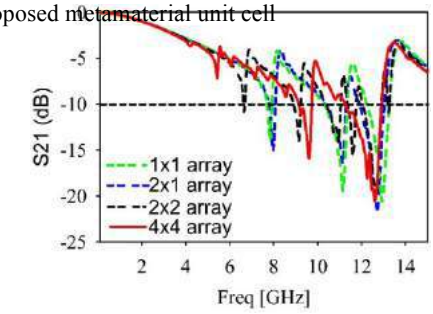

Figure 3: Transmission coefficients for different array structures.

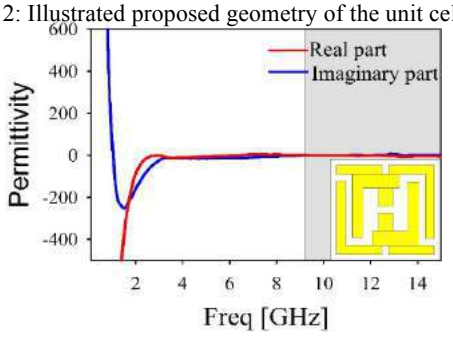

(a)

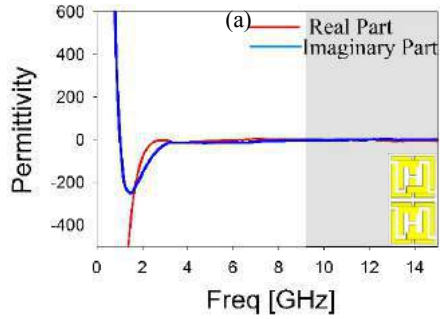

(b)

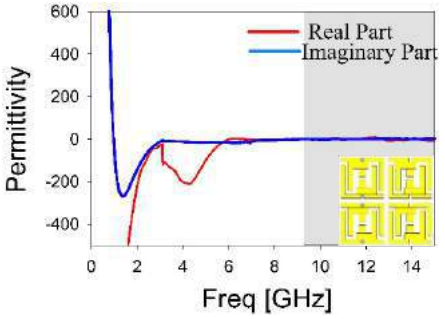

(c)

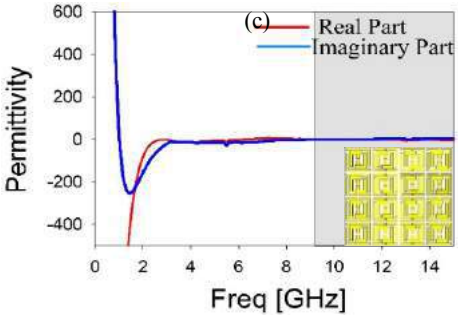

(d)

Figure 4: Relative permittivity of the unit cell with (a) 1×1, (b) 2×1, (c) 2×2 and (d) 4×4 array

3. Results

Figure 3 describes transmission coefficients, S_{21} (dB) the different array of the unit cell. All of the array structures have the resonance in X and Ku band. The 1×1 array structures exhibits resonance at 11.156 GHz and 12.944 GHz in the X and Ku band respectively. Whereas, for the 2×1 array

structure they are at 11.126 GHz and 12.72 GHz. The 2×2 array structures exhibits resonance at 10.962 GHz, 11.618 GHz while the resonances presents at 9.6563 GHz and 12.601 GHz in case of 4×4 array. Figure 4 and 5 respectively delineate the relative permittivity and permeability of different array structures.

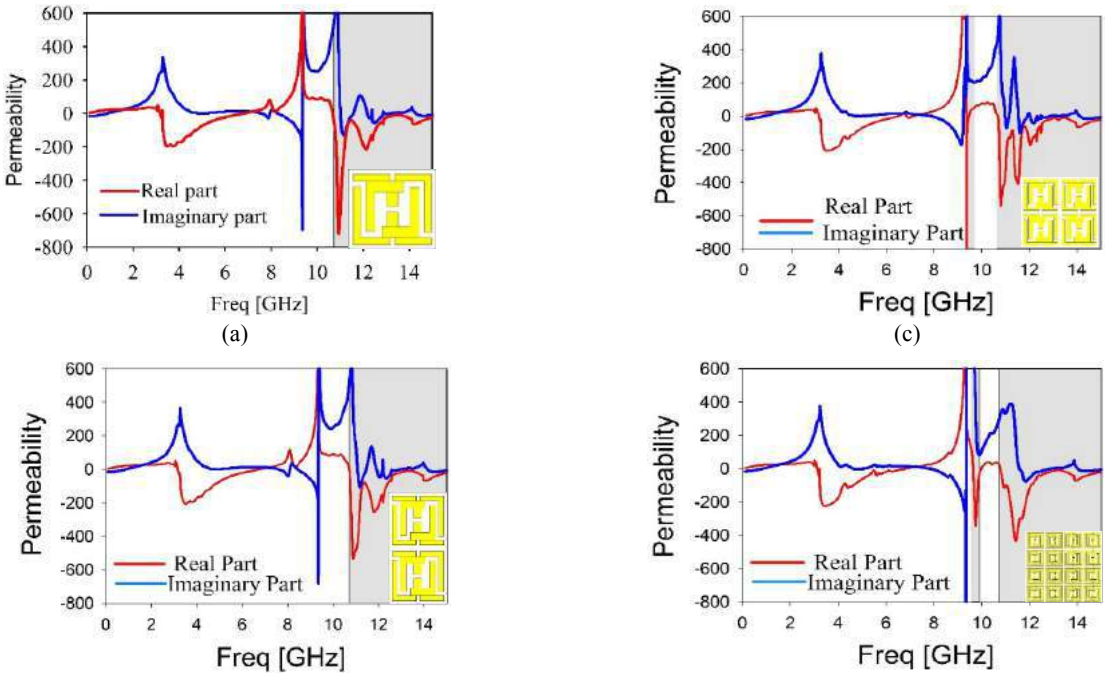

Figure 5: Relative permeability of the unit cell with (a) 1×1, (b) 2×1, (c) 2×2 and (d) 4×4 array.

In Figure 4 and 5, shaded zones in the figures illustrate the negative real part of the permittivity and permeability respectively. In Figure 5, it can be seen that 1×1 and 2×1 array configuration there is only one negative indexed band, while in 2×2 and 4×4 array configuration there is two negative bands. The negative indexed band starts from 10.68 GHz and it stops at 15GHz in case of 1×1 array while it extends from 10.72 GHz to 15 GHz in 2×1 array. For 2×2 array it is 9.37~9.46 GHz and 10.69~15 GHz. In the case of 4×4 array configuration the negative permeability band is found to be in 9.655~9.97 GHz and 10.8~15 GHz zone. From the above results it can be said that the unit cell shows DNG characteristics 10.8~15 GHz band commonly in all of the array configurations.

4. Conclusion

A modified H-shaped Double Negative (DNG) metamaterial has been proposed for the X and Ku band applications. The dimension of the unit cell is 0.9×0.88 cm^2 with a highest DNG bandwidth of 4.32 GHz covering these two band. Different array structures have been analyzed to see the efficacious inclusion of the unit cell for the intended applications. All of the analyzed array combination confirms the possible inclusion of the unit cell for X and Ku band application involving military requirements for satellite uplinks and downlinks in X band, and also for satellite communications and International Space Station (ISS) communications in Ku band.

5. References

[1] Y. Dong, H. Toyao, and T. Itoh, "Design and characterization of miniaturized patch antennas loaded with complementary split-ring resonators," *IEEE Trans. Antennas Propag.*, vol. 60, no. 2 PART 2, pp. 772–785, 2012.

[2] S. S. Islam, M. R. I. Faruque, and M. T. Islam, "The design and analysis of a novel split-H-shaped metamaterial for multi-band microwave applications," *Materials (Basel).*, vol. 7, no. 7, pp. 4994–5011, 2014.

[3] M. I. Hossain, M. R. I. Faruque, M. T. Islam, and M. H. Ullah, "A new wide-band double-negative metamaterial for C- and S-band applications," *Materials (Basel).*, vol. 8, no. 1, pp. 57–71, 2015.

[4] T. Alam, M. R. I. Faruque, and M. T. Islam, "A double-negative metamaterial-inspired mobile wireless antenna for electromagnetic absorption reduction," *Materials (Basel).*, vol. 8, no. 8, pp. 4817–4828, 2015.

[5] M. Hasan, M. Faruque, S. Islam, and M. Islam, "A New Compact Double-Negative Miniaturized Metamaterial for Wideband Operation," *Materials (Basel).*, vol. 9, no. 10, p. 830, 2016.

SNG Split Ring Resonator-based Compact Symmetric Reciprocal Five Port Reflectometer for Early Breast Tumour Detection System

Toufiq Md Hossain[1], Mohd. Faizal Jamlos[1, 2*], Samir Salem Al-Bawri[1, 3] Md Imtiaz Islam[1] and Mohd Aminudin Jamlos[4]

[1]Advanced Communication Engineering (ACE), School of Computer & Communication Engineering, Universiti Malaysia Perlis (UniMAP), 01000 Kangar, Perlis, Malaysia.
[2]Faculty of Mechanical Engineering, Universiti Malaysia Pahang (UMP), 26600, Pekan, Malaysia.
[3]Department of Electronics & Communication Engineering, Faculty of Engineering, Hadhramout University, Al-Mukalla, Yemen.
[4]Department of Electronic, Faculty of Technology Engineering, UniMAP, 02100, Padang Besar, Malaysia.
*corresponding author, E-mail: mohdfaizaljamlos@gmail.com

Abstract

Investigation of Single Negative (SNG) Split Ring Resonator (SRR)-based compact symmetric reciprocal 5 Port Reflectometer (5PR) has been alluded. The 5PR realized a dual bandwidth of 1.072 GHz (0.803 GHz to 1.875 GHz) and 1.056 GHz (3 GHz to 4.956 GHz). The results of 5PR indicate a near zero magnitude of reflection coefficient and ≈ 0.5 for transmission coefficients which agree with theoretical values. The 5PR can be used for portable microwave imaging system for early breast tumour detection.

1. Introduction

Electromagnetic metamaterials have been a concentrated research activity with remarkable progress observed over the past decade [1],[2].The use of different metamaterials including Split Ring Resonators has been presented in various manuscripts for improving bandwidth as well as miniaturization of the antenna [2]. However, to the authors' best knowledge no manuscript has yet been reported to investigate the usability of metamaterial in 5PR for microwave imaging application. Microwave imaging has been proposed as an alternative approach for breast tumour detection by the medical researchers. A portable low-cost reflectometer is needed as an alternative network analyzer in lieu of conventional VNA used in microwave imaging systems which is not only costly but also retards portability owe to its large size. This shortcoming of VNA has inspired the researchers to use reflectometer as an alternative network analyzer. Few researchers have designed reflectometer to be used in breast microwave imaging but specializing for the higher frequency range [3]. This paper presents symmetric reciprocal 5PR reflectometer which can be used for the lower frequencies so as to meet the higher penetration depth as been suggested in [4]. It comprises 4×5 arrays of SNG SRR unit cells in the opposite side of the substrate. The circuitry of the 5PR is based on the microstrip technology. Simulated results shows dual band of 1.072 GHz and 1.052 GHz.

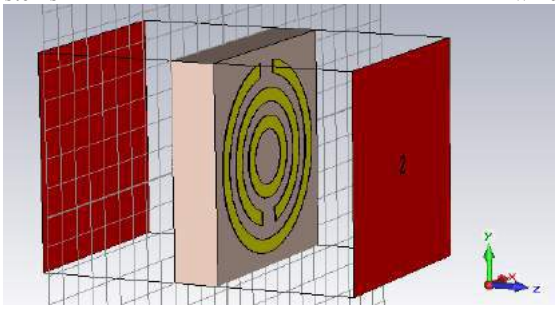

Figure 1: 3D view of the metamaterial unit cell.

2. Reflectometer design

The 5PR have been designed using Advanced Design Software (ADS). The reflectometer consists of the circuitry along with the SNG metamaterial in the ground plane of the reflectometer. The metamaterial unit cell of circular SRR kind consisting two concentric circles. The inner radii of the circles are 2 mm and 3 mm respectively while the outer radii are of 2.5 mm and 3.5 mm respectively. The unit cell is designed using FDTD based Computer Simulation Technology (CST) Microwave studio. Perfect Electrical Conductor (PEC) is placed as the boundary condition in the y axis while Perfect Magnetic Conductor (PMC) is placed in the x axis. The wave-

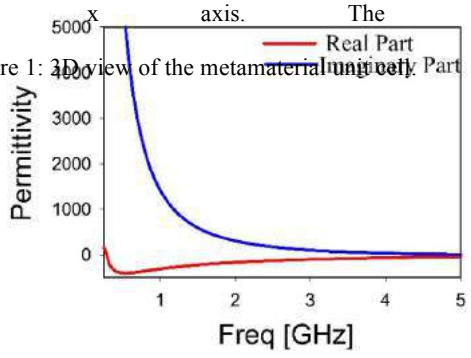

Figure 2: Permittivity characteristics of the unit cell.

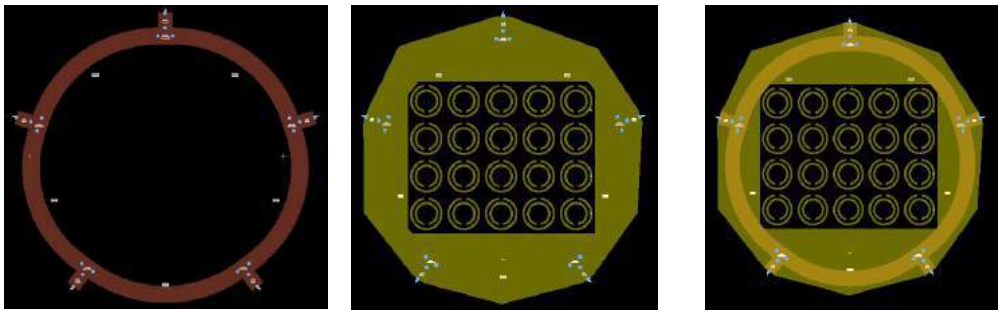

(a) (b) (c)

Figure 3: 2D layout of 5PR (a) conductor layer, (b) SRR unit cell layer and (c) both layers (transparent)

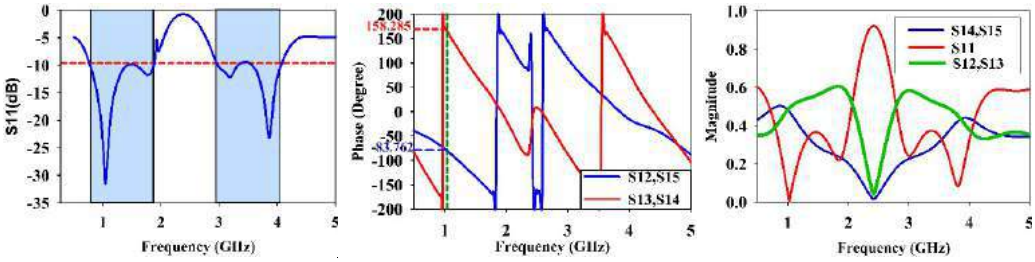

(a) (b) (c)

Figure 4: Simulated Results (a) reflection coefficient, (b) phase and (c) Magnitude of reflection and transmission coefficient

guide ports are applied in z axis and open boundaries are selected for this axis. The split widths of the two circles are 1 mm. which are in line with each other in the vertical direction. The reflectometer consists of 5 ports which are matched to 50 Ω. It consists of 5 curved microstrip lines which are curved by 72 °. 5 microstrip T-junctions are used in each of the ports in the reflectometer circuitry. The unit cells are applied in the opposite side of the substrate by using 4×5 array structures as can be depicted from Figure 3. The five port reflectometer was simulated from 0.5 GHz to 5 GHz. The 5PR has been designed using FR-4 substrate with a relative dielectric constant ε_r=4.3 and a loss tangent, δ=0.025 , copper thickness of 0.035 mm . The Reflectometer is shown in figure 3 in a detailed way.

3. Results

The simulated results are shown in Figure 2 and Figure 4. From Figure 2 it is noticeably seen that the metamaterial unit cell exhibits SNG from 0.5 to 5 GHz as depicted by the red line. Figure 4(a) shows the reflection coefficient of the 5PR. It can be seen that the reflectometer has a resonance of 1.072 GHz (0.803 GHz to 1.875 GHz) and 1.056 GHz (3 GHz to 4.956 GHz) as delineated by the shaded zone. From Figure 4(b) it can be seen that the difference between the phase of S_{12} and S_{13} is (158.285-(-83.762) = 242.047º) at 1.042 GHz (shown by the green dotted line), that is very near to the theoretical value of 240º. Similarly, the magnitude characteristics are also fulfilled by attaining a value of near zero value for S_{11} and a value of approximately 0.5 for the transmission coefficients. The magnitude profile of the proposed 5PR is shown in Figure 3(c).

4. Conclusion

This paper proposes a SNG metamaterial-inspired symmetric reciprocal 5PR for early breast tumour detection system. This 5PR consists of 4×5 array of SNG metamaterial unit cell in the rear part of the substrate and circuitry in the top plane of the substrate. Simulated results shows dual bands of 1.072GHz and 1.056 GHz. This 5PR can be considered as a prominent candidate for the portable early breast tumour detection system.

5. References

[1] S. K. Patel and Y. P. Kosta, “Metamaterial superstrate-loaded meandered microstrip-based radiating structure for bandwidth enhancement.,” *J. Mod. Opt.*, vol. 61, no. 11, pp. 923–930, 2014.

[2] Y. Dong, H. Toyao, and T. Itoh, “Design and characterization of miniaturized patch antennas loaded with complementary split-ring resonators,” *IEEE Trans. Antennas Propag.*, vol. 60, no. 2 PART 2, pp. 772–785, 2012.

[3] S. S. Al-Bawri, M. F. Jamlos, S. Z. Ibrahim, and S. A. Aljunid, “Compact multilayer wideband symmetric five-port reflectometer,” *Microw. Opt. Technol. Lett.*, vol. 59, no. 4, pp. 802–805, Apr. 2017.

[4] X. Li, S. K. Davis, S. C. Hagness, D. W. Van Der Weide, and B. D. Van Veen, “Microwave imaging via space-time beamforming: Experimental investigation of tumor detection in multilayer breast phantoms,” *IEEE Trans. Microw. Theory Tech.*, vol. 52, no. 8 II, pp. 1856–1865, 2004.

Polymeric Magneto Comb Array Antenna for Bandwidth Enhancement in Millimeter Wave Applications

W.A.W. Muhamad[1], R. Ngah[2], Mohd Faizal Jamlos[3,4], P.J. Soh[5]
[1,2]Wireless Communication Centre (WCC), Universiti Teknologi Malaysia, 81310, Skudai, Johor, Malaysia
[3,5]Advanced Communication Engineering Centre (ACE), School of Computer and Communication Engineering, Universiti Malaysia Perlis, 01000, Kangar, Malaysia.
[4]Faculty of Mechanical Engineering, Universiti Malaysia Pahang (UMP), Pekan, Malaysia.
*corresponding author, E-mail: wanasilahwm@gmail.com

Abstract

A new combination polymeric magneto dielectric comb array antenna is presented. The combination substrates of Polydimethylsiloxane (PDMS) and Ferrite III oxide (PDMS-Fe_3O_4) provided huge improvement bandwidth of 49.21 % compared to existing antenna. Combination polymeric magneto dielectric, comb array antenna and PDMS-Fe_3O_4's permeability of 1.85 contributing to such bandwidth ranging from 26.823 GHz to 42.573 GHz and gain of 7.161 GHz. The radiation pattern results are also presented. Furthermore, dimension of 19x33 mm^2 is considered compact in size.

1. Introduction

Currently, modern wireless communication technologies such as medical diagnosis, navigation, and millimeter wave technologies demand robust, small, conformal and lightweight antennas [1]. In millimeter wave technologies, enhancing their bandwidth potentially improves its data-rate transmission [2, 3]. The capability in obtaining a large bandwidth for microstrip patch antenna is contributed by chosen an appropriate types of substrate material [4, 5]. For these reason, this paper introducing a new combination of meta-material substrate; Polydimethylsiloxane (PDMS) and Ferrite III oxide (Fe_3O_4) with a compact microstrip comb array antenna.

2. Polymeric Magneto Comb Array Antenna

PDMS- Fe_3O_4 is a new dielectric substrate contains of silicone based elastomer and (10 nm) nanoparticles of magnetic (Fe_3O_4) iron oxide. The magneto dielectric gives permeability more than unity which is 1.85 lead to bandwidth increment with permittivity of 3.45. The fundamental in getting a huge bandwidth is by reducing its quality factor, Q where Q is inversely proportional to permeability [6]. Hence, high in permeability provides a low Q and enhance the bandwidth.

In this paper, Figure 1(a) shows the comb array antenna which is designed with full ground plane at dimension of 19 x 33 mm^2 for width and length respectively as shown in Figure 1(b). An array structure of comb antenna is organised in zig-zag with main radiating element inclined by -90 degrees. The spacing between each array is $d = \lambda_g/2$ where λ_g is the guided wavelength at the center frequency while length, l of each array is based on formula $l = \lambda_g$ [7].

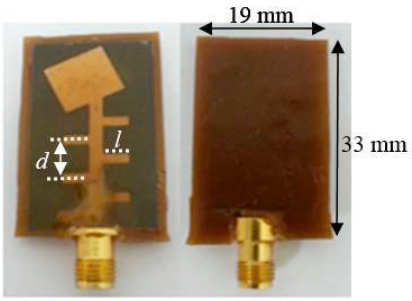

Figure 1. The fabricated polymeric magneto comb array antenna. (a) Front view (b) back view

The PDMS-Fe_3O_4 substrate layer is designed to embed the comb array antenna as depicted in Figure 2 with thickness for upper layer is v=1.4 mm and bottom layer is w=3 mm.

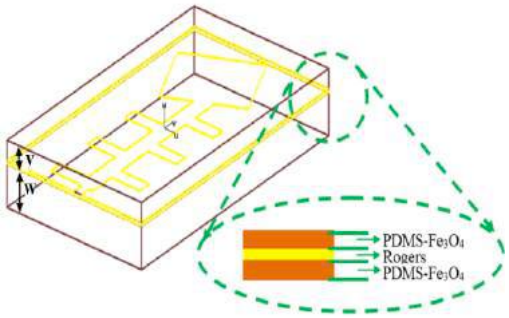

Figure 2. Perspective view for polymeric magneto comb array antenna with PDMS-Fe_3O_4

3. Discussion

Figure 3 shows the reflection coefficient, S_{11} of polymeric magneto comb array antenna. It is observed that the proposed antenna capable to operate in frequency range of 26.823 GHz to 42.573 GHz with 15750 MHz (57.27 %) of bandwidth. Besides, the simulated and measured results for S_{11} agreed well. The polymeric magneto comb array antenna also has a broader bandwidth compared to [7] up to 49.21 %.

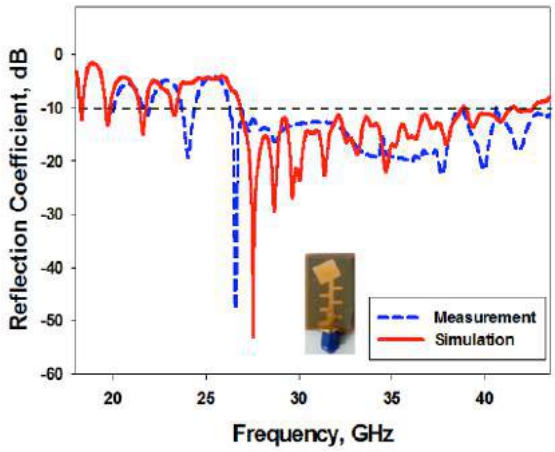

Figure 3. Simulated (solid line) and measured (dotted line) of reflection coefficient for polymeric magneto comb array antenna

Further results is on polar radiation pattern as shown in Figure 4 for XZ-plane and YZ-plane. It is observed that the simulated and measured radiation patterns agreed well. The highest gain of 7.161 dB is recorded.

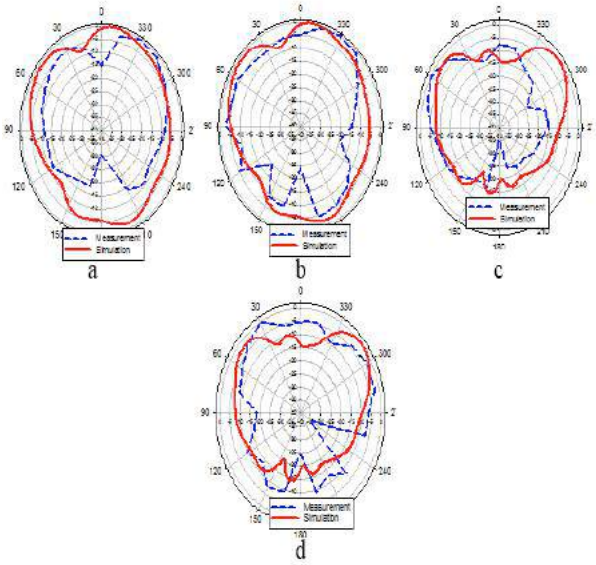

Figure 4. Simulated (solid line) and measured (dotted line) of polar radiation pattern for polymeric magneto comb array antenna

4. Conclusions

As conclusion, the new combination of PDMS-Fe_3O_4 with comb array antenna produces wider bandwidth and good gain as well as compactness of size for millimetre wave applications

Acknowledgements

The authors acknowledge the contribution of Universiti Teknologi Malaysia, Skudai, Johor (UTM) and Universiti Malaysia Perlis, Kangar, Perlis (UniMAP). Our gratitude also goes to grant of FRGS MOHE 9003-00522.

References

[1] Niu, Y., Y. Li, D. Jin, Li Su, A. V. Vasilakos, "A Survey of Millimeter Wave (mmWave) Communications for 5G: Opportunities and Challenges," IEEE Communications Magazine, January 2015.

[2] Sakakibara, K., N. I. Kikuma, H. Hirayama, "Travelling-wave Planar Array Antennas for Beamscanning Systems in Millimeter-wave Band," IEEE Asia-Pacific Conference on Applied Electromagnetics (APACE), December 2014.

[3] Nedil, M., L. Talbi, T. A. Denidni, "Design of Broadband Printed slot Antennas for Wireless millimeter-wave applications," IEEE Topical Conference on Wireless Communication Technology, 2003.

[4] Balanis, C.A., "Antenna Theory: analysis and design," New York: John Wiley & Sons, 2005.

[5] Trajkovikj, J., J.F. Zurcher, A. K. Skrivervik, "Soft and Flexible Antennas on Permittivity Adjustable PDMS Substrates," Loughborough Antennas & Propagation Conference (LAPC). Loughborough, 2012.

[6] Morales, C. A., "Magneto-Dielectric Polymer Nanocomposite Engineered Substrate for RF and Microwave Antennas," 2011.

[7] Zhang L., W. Zhang, Y. P. Zhang, "Microstrip Grid and Comb Array Antennas," IEEE Transactions on Antennas and Propagation, VoL. 59, No. 11, November 2011.

Double Negative (DNG) Left- Handed Metamaterial Radome to Enhance Gain and axial Ratio of Antenna

Ojo Rasheed[1], **Mohd Faizal Jamlos**[1,2*], **P.J. Soh**[1], **Mohd Aminudin Jamlos**[3], **Samir Salem Al-Bawri**[1], and **H. Lago**[1]

[1]Advanced Communication Engineering (ACE), School of Computer & Communication Engineering, Universiti Malaysia Perlis (UniMAP), 01000 Kangar, Perlis, Malaysia
[2]Faculty of Mechanical Engineering, Universiti Malaysia Pahang (UMP), 26600, Pekan, Malaysia.
[3]Department of Electronic, Faculty of Technology Engineering, UniMAP, 02100, Padang Besar, Malaysia
*corresponding author: mohdfaizaljamlos@gmail.com

Abstract

The patch antenna gain and axial ratio enhanced when a dielectric radome double negative (DNG) metamaterial of H-shaped unit cells positioned on top of the patch. The radome is comprising of alternately two layers of negative permeability and permittivity substrate. Circular polarization's axial ratio of 2.329 dB has been realized by the presence of DNG metamaterial radome compared to 5.57 dB of without the radome. The gain has been increased as well from 8.25 dB to 9.57 dB.

1. Introduction

The opportunity of making left-handed metamaterial substrate with -ve permeability, -ve permittivity and refractive index contritely is change radically many fields including antenna design. It is extremely attractive because it shows the opportunity of reducing the difficulties experience in designing a directional antenna. In general directional antennas are either dishes or arrays. [1] They have acquired tricky feeding system. In case of arrays the number of antenna elements is fed with particular phasing and spacing. Since the gain requirement will more advanced of the feed network design becomes a tough task and controlling the side lobe level also becomes dreary. In this paper, we have used the H-shaped and Inverse H-shaped to improve the gain and axial ratio of patch antenna. The antenna gain is increased more than 1.5dB of that of the normal patch antenna. The Circular polarization's axial ratio of 2.329 dB has been realized by the presence of DNG metamaterial radome compared to 5.57 dB of without the radome, which clearly show the existence opportunity to try them as array elements or finding alternative ways of improve the gain and axial ratio of any antenna element. [3] A point-to-point wireless communication usually fails to distribute the threshold signal strength of -51 dBm. It also fails to stabilize the data rates in severe climate conditions. [4] Failing to abide such meshold brings about the slow internet connection or even disconnected. A high efficiency, gain, and circular polarized (CP) microstrip patch antenna will provide a suitable solution to avoid major signal attenuation during such conditions. [5] Rather of CP antenna, two-port MIMO methods to increase channel capacity for higher data rate and better hyperlink stability of a system. Consequently, convergence between CP technique, array antenna configuration and MIMO antenna techniques are studied to deliver effective trusted point-to-point communication. Figure. 1(a-d) presents the permeability, permittivity and refractive index where negative permeability achieved at (5.81-6.82) GHz, negative permittivity achieved (5.8-6.72) GHz and negative refractive index achieved (5.85-6.0) GHz. The effective permeability, permittivity and refractive index has been retrieved from S_{11}.

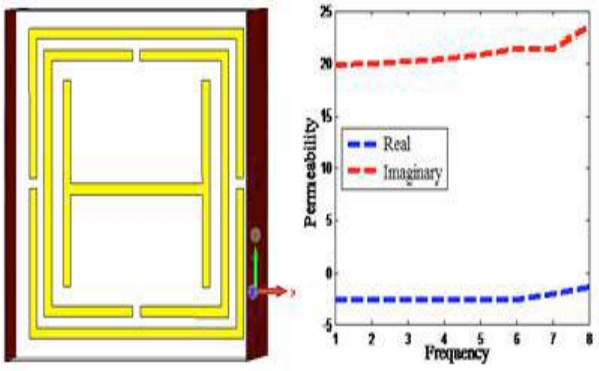

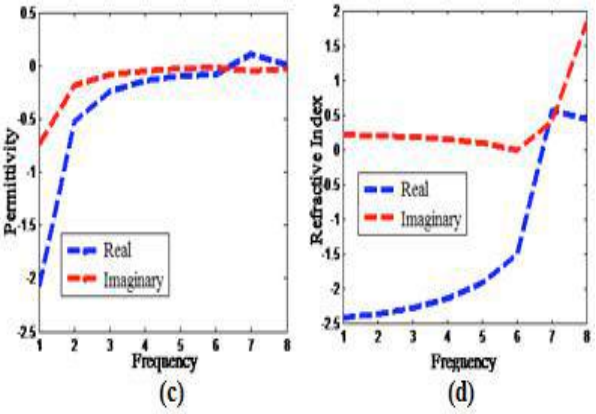

Figure 1: DNG Left-Handed Metamaterial (a) presents the structure simulated, (b) permeability, (c) permittivity and (d) refractive index.

2. Antenna Design Simulated

Metamaterial radome structure with the patch antenna is simulated using CST MICROWAVE STUDIO based 3D for electronic packages and simulated result shows in figure 2 (a-e). Likewise (b-c) shows the axial ratio bandwidth is observed to be 100MHz.As well (d-e) shows the 3D patterns of the patch antenna. The gain is observed to be 1.5dB. It also show that the antenna tunes at 5.8GHz.

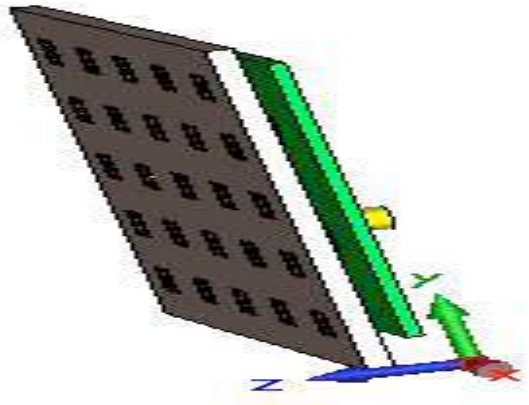

(a)

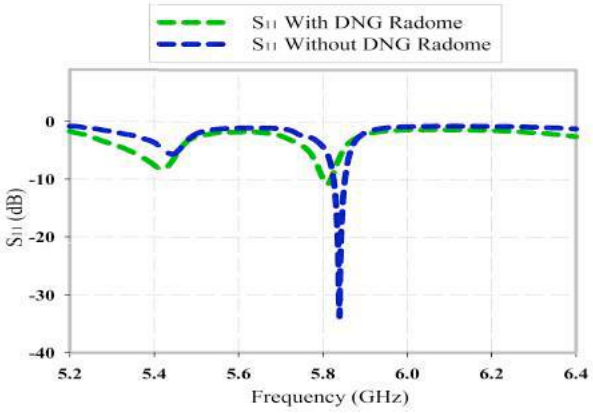

(b)

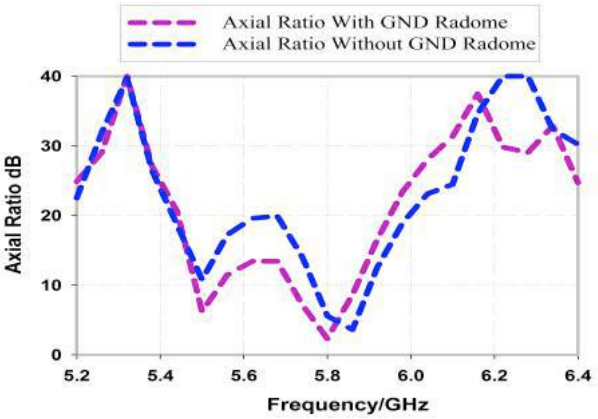

(c)

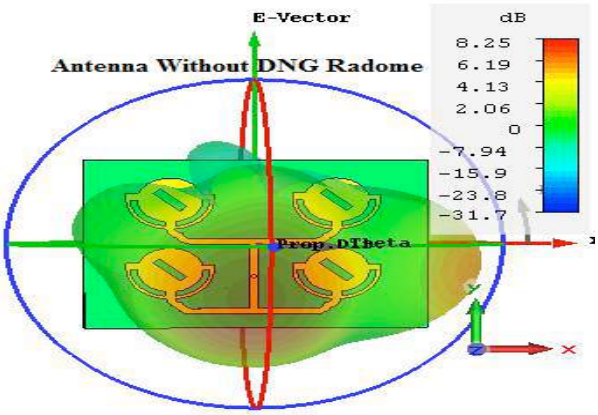

(d)

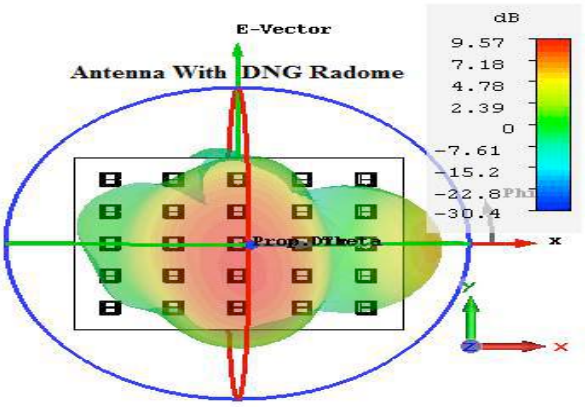

(e)

Figure 2: DNG Left-Handed Metamaterial Radom (a) presents the structure simulated, (b) S11 with and without DNG radome, (c) Axial ratio with and without DNG radome, (d) Gain with DNG radome and (e) Gain without DNG radome.

Table 1: Parameters dimensions of the proposed antenna and (DNG) metamaterial radome.

Para.	Value (mm)	Para.	Value (mm)	Para.	Value (mm)	Para.	Value (mm)	Para.	Value (mm)	Para.	Value (mm)	Para.	Value (mm)
Wsl	2.9	g	0.3	λ_1	42	R_3	10.4	L_{feed}	2.5	W_1	2.6	L_3	16
Ls2	1.7	W_s	60	R_1	7.8	L_{slot}	9	W_{feed}	2.5	L_2	2.8	W_3	2
Ws1	1.2	L_s	40	R_2	9.4	W_{slot}	1.3	L_1	3	W_2	1.85	L_4	23

3. Conclusions

We have studied the structures composed of materials. The (DNG) metamaterial of H-shaped unit cells radome base on dielectric could increase the antenna gain and axial ratio, which could be useful for antenna radome applications. The end-to-end curvy dual-coupled 90° phase shifters that is connected to each circle-segmented patch. (S11) gain in the simulated with (DNG) radome and without (DNG) radome (from 8.25% to 9.57% GHz) and axial ratio simulated with (DNG) radome and without (DNG) radome (from 5.57 to 2.329 GHz) in the axial ratio. CP array antenna radome with 90° triple-coupled phased shift polarizer at 5.8 GHz.

References

[1] Gupta S, Kumar S, "Design and analysis of compact and broadband high gain micro strip patch antennas", *Proceedings of International Conference on Communication and Networking,* pp.11-15, Dec. 2014

[2] J. G. Joshi, Shyam S. Pattnaik, and S. Devi, Metamaterial embedded wearable rectangular microstrip patch antenna, Hindawi *International Journal of Antennas and Propagation*, pp. 1-9, July 2012

[3] K. S. Zheng *et al.*, "Designing and measurement of a single layered planar gain-enhanced antenna radome with metamaterials," *J. Electromagn. Waves Appl.*, vol. 26, no. 4, pp. 436–445, 2012.

[4] R.A.Saed & S. Khatun, "Design of Microstrip Antenna for WLAN", *Journal ofApplied Sciences*. 5 (1), pp 47- 51, February 2005.

[5] M. Rahmani, A. Tavakoli, H. R. Amindavar, A. M. Reza & P. Dehkhoda, "Chalipa, a novel wideband circularly polarized microstrip fractal antenna" in proceedings of the 3rd *European Conference on Antennas and Propagation, EuCAP*, pp. 2389 – 2392, 2009

Split Ring Resonator Based Metamaterial Radome for WLAN MIMO Point-to-Point Communication Antenna

Ojo Rasheed[1], Mohd Faizal Jamlos[1,2*], I. Imtiaz[1], P.J. Soh[1], Mohd Aminudin Jamlos[3], Samir Salem Al-Bawri[1] and H. Lago[1]

[1]Advanced Communication Engineering (ACE), School of Computer & Communication Engineering, Universiti Malaysia Perlis (UniMAP), 01000 Kangar, Perlis, Malaysia
[2]Faculty of Mechanical Engineering, Universiti Malaysia Pahang (UMP), 26600, Pekan, Malaysia.
[3]Department of Electronic, Faculty of Technology Engineering, UniMAP, 02100, Padang Besar, Malaysia
[*]corresponding author: mohdfaizaljamlos@gmail.com

Abstract

This paper presents a split ring resonator based metamaterial radome for point-to-point communication. The radome structure is formed using split ring resonator at 5.8 GHz. Antenna structure has been formed using 2×2 MIMO array structure with high directivity and good isolation between two arrays. Performance of radome characteristics have been evaluated in terms of bandwidth, directivity, radiation pattern and isolation between two antennas. Small degradation has been found for antenna performance in terms of using metamaterial radome.

1. Introduction

A radome plays an important role in the practical application of antennas which are placed over antenna in order to protect from different environment like wind, rain, ice, hot, UV etc. Radome can be different types in several shapes like spherical, geodesic, planar etc. depends on the application (radar, telemetry, tracking, and point-to-point). Radomes can be designed using different types of low losses material like-fiberglass, PTFE-coated with proper integration for indoor and outdoor environment [1]. However, the main challenge for designing radome is the avoiding antenna radiation losses which occurred from attenuation, scattering and depolarization. Thus can effect on the electromagnetic signal by degrading antenna pattern. Furthermore, scattered radiation from radome may affect antenna performance by elevating side lobes which can degrade antenna directivity very highly [2].

Different types of artificial magnetic conductor has been used to design radome as- partially reflecting surfaces, frequency selective surfaces. Metamaterial based radome can be great choice because for designing radome structure because of the unusual electromagnetic property [3]. Metamatrial attains exotic electromagnetic property over certain frequency band which is not normal in nature. It can show totally opposite characteristics compare with naturally existing material in terms of negative permittivity or permeability which is absent in normal material.

2. Split Ring Resonator Based Metamaterial Radome Design

In this paper, a negative permittivity based split ring resonator metamaterial unit cell has been designed for radome structure. Figure 1(a) presents unit cell structure where the negative permittivity achieved from 3.92 GHz up to 10 GHz. Figure 1(b) presents the relative permittivity of the unit cell. This until cell has been applied in 6×4 array on FR-4 substrate which is a radome structure. Than this radome has been placed on the top of array antenna structure maintaining 4mm distance. The MIMO array antenna structure has been formed using 2×2 array. Figure 1(c) presents the MIMO array antenna structure and Figure 1(d) shows the array structure with metamaterial radome.

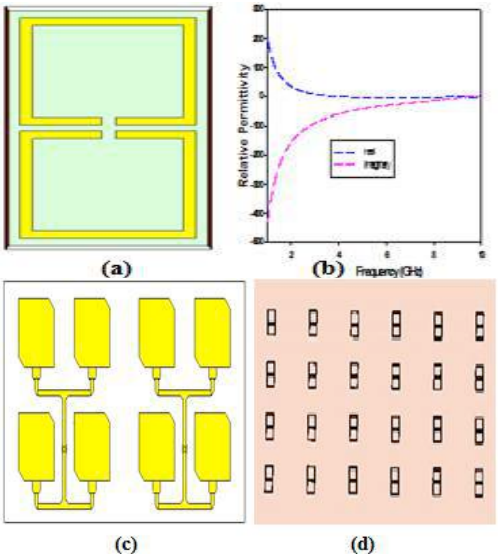

Figure 1: (a) Metamaterial unit cell radome (b) Relative Permittivity (c) Antenna Structure (d) Metamaterial radome (Below is antenna structure).

Table 1 Parameters dimensions of the proposed antenna and metamaterial radome.

Param.	Value (mm)	Param.	Value (mm)	Param.	Value (mm)	Param.	Value (mm)	Param.	Value (mm)	Param.	Value (mm)
lw	1.49	W_s	55	λ_1	27	W_1	3	L_3	13	L_{s1}	55
w	1.49	L_s	58	λ_2	27	L_2	2	W_3	12	W_{s2}	70
g	0.3	W_p	16	L_1	4	W_2	4	L_1	1.4		

3. Results and Discussion

Figure 2 presents the performance of antenna with radome structure. Since the antenna have MIMO characteristics, isolation between two antenna structures is considered as important parameter. Figure 2(a) presents the performance of reflection coefficient and isolation between two antennas with radome structure.

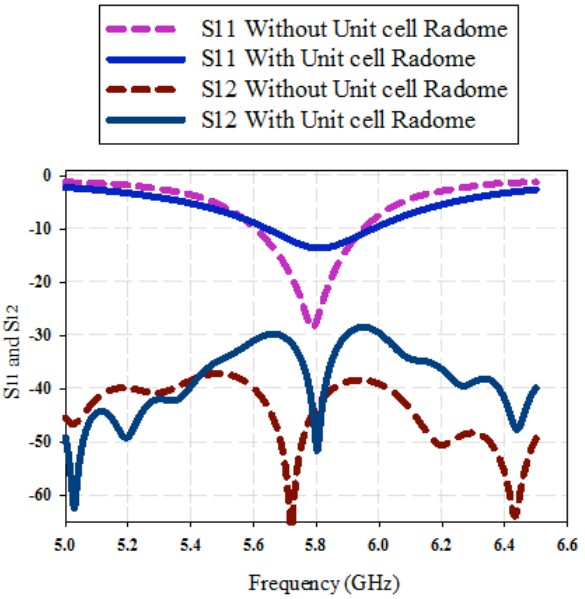

Figure 2: Performance of antenna with and without Metamaterial Radome.

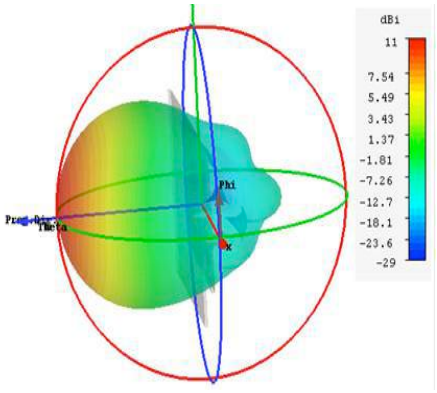

Figure 3: Illustrate the antenna radition pattern based on 3D with Metamaterial Radome.

Figure 3 presents the directivity of the antenna with metamaterial radome. It achieved 11 dBi directivity which is applicable for point-to-point communication.

4. Conclusions

Circularly Polarized Multiple Output Multiple Input (CP-MIMO) Array antenna with isolation between two array and bandwidth has been proposed. The WLAN -MIMO Array antenna's characteristics of directivity, and radiation pattern has been discussed and analyzed to have the optimum performance, which could be useful for point-to-point communication with metamaterial radome, (S11) and (S21) shows a 36% of isolation between two antenna and bandwidth (from 0.311 to 0.401 GHz). Bandwidth achieved with radome structure is 5.8% at 5.8 GHz where without radome it achieved 5.86%. However, the isolation between two antennas with and without radome also satisfactory. At both cases the minimum isolation achieved -39dB and maximum -75 dB.

5. References

[1] M. Kondou, S. Fukuda, and K. Kagoshima, *Radiation characteris-tics of reflector antenna with radome* at 10–30 GHz in rainy condi-tions, Microwave Opt Technol Lett 70 (1987), 119–126

[2] R. Orta, R. Tascone, and R. Zich, *Performance degradation of dielectric radome covered antenna,* IEEE Trans Antennas Propag. 36 (1988), 1707–1713.

[3] M.R.I. Faruque, M.T. Islam, N. Misran, Electromagnetic (EM) *absorption reduction in a muscle cube with metamaterial attachment.* Med. Eng. Phys.33 (5), 646–652 (2011

[4] Asok De, N.S. Raghava, Sagar Malhotra, Pushkar Arora, Rishik Bazaz, "*Effect of different substrates on Compact stacked square Microstrip Antenna",* Journal of Telecommunications, Volume 1, Issue 1, February 2010.

[5] Anzar Khan, Rajesh Nema, *"Analysis of Five Different Dielectric Substrates on Microstrip Patch Antenna*", International Journal of Computer Applications (0975

A Compact Crisscross Slotted Log Periodic Fractal Koch Antenna with AMC Metamaterial for UHF TVWS Applications

Nur Akmal Abd. Rahman[1], Mohd Faizal Jamlos[1,2], Norfatihah Bahari[1], and Md. Imtiaz Islam[1]

[1]Advanced Communication Engineering Centre (ACE), School of Computer and Communication Engineering, Universiti Malaysia Perlis, 01000, Kangar, Malaysia
[2]Faculty of Mechanical Engineering, Universiti Malaysia Pahang, Pekan, 26600, Pahang, Malaysia
*corresponding author, E-mail: mohdfaizaljamlos@gmail.com

Abstract

This paper presents a compact crisscross slotted log periodic fractal Koch antenna (S-LPFKA) with artificial magnetic conductor (AMC) surface that serves as a reflector. This S-LPFKA with AMC is designed to operate from 0.47 to 0.79 GHz with linearly polarized radiation, performing with 36.6% size reduction compared to stand-alone S-LPFKA. With gain from 2.57 dBi to 4.75 dBi, this antenna is suitable and has a great potential for ultra high frequency (UHF) television white space (TVWS) applications.

1. Introduction

In telecommunication, TVWS refers to the unused broadcasting frequencies in wireless spectrum which located within VHF and UHF bands [1-3]. It is very attractive due to its much lower frequency compared to current unlicensed spectrum. Operating Wi-Fi in TVWS will provide several distinct advantages such as longer range, greater speed, more reliable connections and broader coverage compared to traditional 2.4 GHz and 5 GHz frequencies [4].

Microstrip patch antennas are widely applied in various applications because of their small profile, light mass and low budget. However, they suffers from some limitations including narrow bandwidth and low efficiency [5]. Many methods have been proposed to overcome the disadvantages of microstrip patch antennas such as by applying log periodic technique. This technique manage to increase the bandwidth and potentially offer low cross-polarization ratio over a wide frequency range. Nevertheless, it unfortunately results in the expense of a large physical area [6-7].

Nowadays, the inspiration to study AMC design by most researchers are due to the advantages of AMC in increasing gain, reducing back lobe radiation, enhancing bandwidth as well as size miniaturization [8-9]. AMC is one type of metamaterial which consists of periodic structures. It acts like a regular metallic ground plane outside of its bandwidth and has a reflection coefficient phase of 0° [10].

In this paper, a S-LPFKA with AMC metamaterial is designed with a compact size of 190 x 285 mm^2 for the width and length respectively. 36.6% size reduction is obtained for the proposed antenna compared to the stand-alone S-LPFKA. The proposed antenna exhibits gain ranging from 2.57 dBi to 4.75 dBi over UHF TVWS bands. This paper is organized as follows: Section 2 begins by demonstrating an AMC single design. The S-LPFKA with AMC operating from 0.47-0.79 GHz will also be described in this section. Next, the simulated results of S-parameter, gain and radiation patterns are presented and discussed in Section 3. Finally, a conclusion will be drawn in Section 4.

2. Antenna Design

A square patch unit cell is chosen since it is easy to fabricate and provide a large bandwidth performance. A single AMC unit cell is illustrated in Fig. 1(a). The simulations were completed by using periodical unit cell simulation offered in CST Microwave Studio. The structure of AMC unit cell consists of five layers as shown in Fig. 1(b). The ground plane is located at the bottom layer of this structure. This is followed by a layer of FR-4 substrate with dielectric constant of ε_r=4.7 and loss tangent (tan δ) of 0.019, respectively. The AMC plane is located on the third layer. Another layer of substrate is placed on top of this AMC plane. The AMC plane and ground plane are made up using Copper with a conductivity and thickness of 5.8 x 10^7 S/m and 0.035 mm respectively. Finally, a plane wave source is located on the top of the AMC unit cell with a gap of 10 mm. The phase of the reflected wave is about 0° for 0.63 GHz as shown in Fig 2. The operating bandwidth of the AMC plane is defined by a ±90° phase response. The unit cell is then arranged into 2 x 3 array to form the AMC plane.

The AMC plane of the proposed antenna is integrated beneath the antenna substrate as illustrated in Fig. 3. To cover the entire bandwidth from 0.47-0.79 GHz, 10 patches were needed. Series iteration fractal Koch structure with 30° flare angle has been integrated at the radiating elements of log periodic dipole antenna (LPDA). Fractal Koch structure manage to miniaturize the size of conventional LPDA.

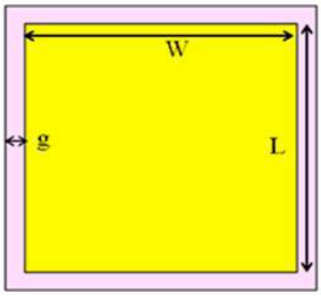

(a)

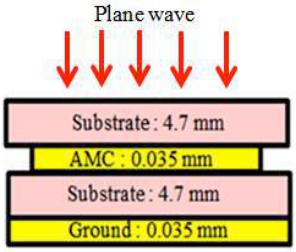

(b)

Figure 1: (a) AMC dimensions (with $L = W = 91$ mm, g = 2 mm), and (b) Side view.

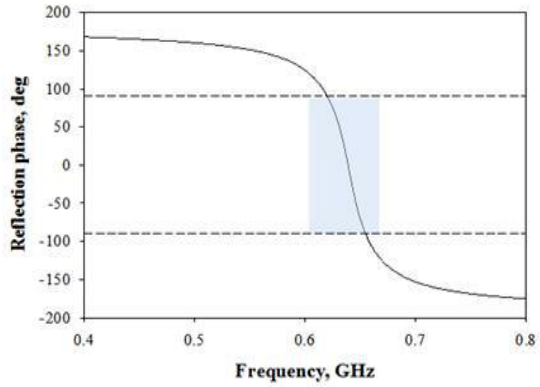

Figure 2: Reflection phase of AMC unit cell.

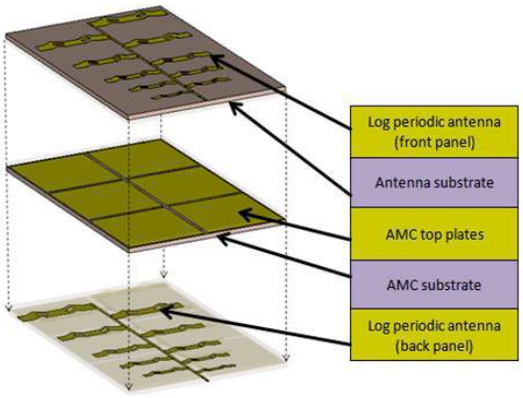

(a)

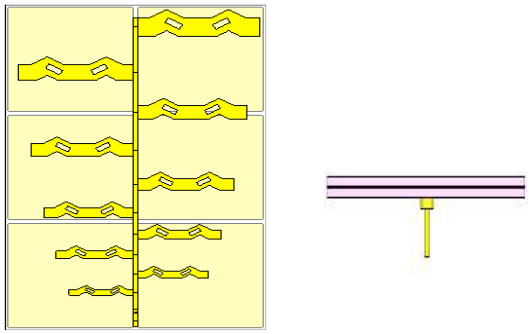

(b) (c)

Figure 3: Proposed antenna (a) 3-D configuration, (b) Top view and (c) Side view.

3. Discussion

The contribution of the AMC plane is evaluated by comparing the antenna performance against a stand-alone S-LPFKA. Fig. 4 shows the comparison of reflection coefficient, S_{11} between stand-alone S-LPFKA and proposed antenna. The graph shows that stand-alone S-LPFKA has impedance bandwidth from 0.47-0.79 GHz which covering the whole UHF TVWS bands but it has larger size which is 305 x 280 mm^2. From the analysis, the optimum dimension of the proposed antenna is 285 x 190 mm^2 which indicate 36.6% size reduction compared to stand-alone S-LPFKA. As can be seen in Fig. 4, the proposed antenna are working on channel 24-25, 28-33, 36-40, 43-46 and 56-60 with the total of 22 channels. Based on the list of TV broadcasters in Malaysia using VHF and UHF, we can notice that there are only 4 channels (channel 27, 33, 39 and 55) which are occupied by the broadcasters in UHF band and the remaining channels are being unused. The polar radiation patterns is illustrated in Fig. 5 and has been performed at 0.47 GHz and 0.79 GHz for both *E*- and *H*-planes. With the gains from 2.57-4.75 dBi, this proposed antenna has become a suitable candidate for UHF TVWS applications

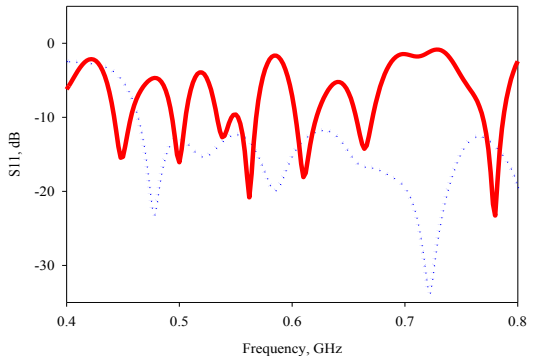

Figure 4: Graph of reflection coefficient; blue dotted line (stand-alone S-LPFKA) and red line (proposed antenna).

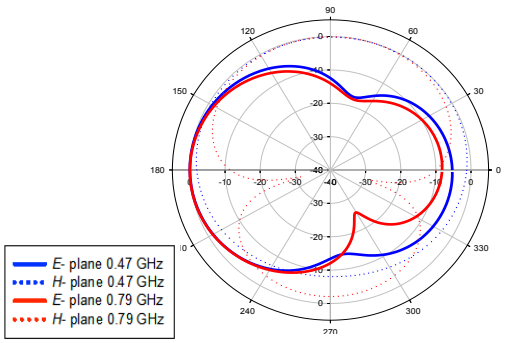

Figure 5: Polar radiation patterns of the proposed antenna.

4. Conclusions

In this work, a S-LPFKA with AMC is proposed with operating frequencies from 0.47-0.79 GHz. The size of proposed antenna is successfully reduced by 36.6% by implementing AMCs with slotted series iteration log periodic fractal Koch techniques. Both simulation and measurement result shows that the proposed antenna satisfies the impedance bandwidth requirements of UHF TVWS bands applications (0.47-0.79 GHz). Overall, the performance of proposed antenna is suitable candidate for UHF TVWS band applications.

Acknowledgements

This project is supported by the Fundamental Research Grant Scheme (FRGS) from the Malaysian Ministry of Higher Education (MOHE) (Grant no: 9003-00522). The authors would like to acknowledge the contribution of Advanced Communication Engineering Centre (ACE), School of Computer and Communication Engineering, Universiti Malaysia Perlis (UniMAP) for their facilities.

References

[1] M.H. Jamaluddin, T.A. Rahman, H. Mohamad, M.T. Islam, Wideband planar U-shaped monopole antenna with meandering technique for TV white space application, *Radioengineering*, vol. 22, no. 3, pp. 708-713, 2013.

[2] J. Acharya, R.D. Yates, A framework for dynamic spectrum sharing between cognitive radio, *IEEE International Conference on Communication,* pp. 5166-5171, 2007.

[3] Razimah Abdul Rahim, Rosdiadee Nordin, Mahamod Ismail, Investigation of channel bonding based on TV white space spectrum occupancy for urban areas in Malaysia, *International Conference on Information and Communication Technology,* pp. 100-105, 2014.

[4] Srikathyayani Srikanteswara, Debabani Choudhury, A review of TV whitespace portable devices, *IEEE Radio and Wireless Symposium*, pp. 480-483, 2010.

[5] Shivangi Verma, Leena Mahajan, Rajesh Kumar, Hardeep Singh Saini, Naveen Kumar, A small microstrip patch antenna for future 5G applications, *International Conference on Reliability, Infocom Technologies and Optimization,* pp. 460-463, 2016.

[6] M.N.A. Karim, M.K.A. Rahim, H.A. Majid, O. Ayop, M. Abu, F. Zubir, Log periodic fractal Koch antenna for UHF bands applications, *Progress In Electromagnetics Research,* vol. 100, pp. 201-218, 2010.

[7] Riska Audina Anindyasari, Achmad Munir, Ultra high frequency log periodic antenna for digital TV application, *2nd International Conference on Wireless and Telematics,* pp. 20-25, 2016.

[8] M. Abu, H. Hassan, M.S.I.M. Zin, S.A.M. Ali, Design of single-band star geometric pattern artificial magnetic conductor, *ARPN Journal of Engineering and Applied Science,* vol. 11, no. 5, pp. 3184-3187, 2016.

[9] Wanchen Yang, Hao Wang, Wenquan Che, Jingjing Wang, A wideband and high-gain edge-fed patch antenna and array using artificial magnetic conductor structures, *IEEE Antennas and Wireless Propagation Letters,* vol. 12, pp. 769-772, 2013.

[10] Juvenal Alarcon, Matthieu Egels, Philipe Pannier, Reduction technique for artificial magnetic conductors, *Loughborough Antennas and Propagation Conference,* pp. 1-5, 2011.

CPW-fed multiband array antenna loaded with wide range double-negative (DNG) metamaterial for wireless applications

Samir Salem Al-Bawri[1,3], Mohd. Faizal Jamlos[1,2*], Syed Alwee Aljunid Syed Junid[1], Mohd Aminudin Jamlos[4], H. Lago[1] and Ojo Rasheed[1]

[1]Advanced Communication Engineering (ACE), School of Computer & Communication Engineering, Universiti Malaysia Perlis (UniMAP), 01000 Kangar, Perlis, Malaysia
[2]Faculty of Mechanical Engineering, Universiti Malaysia Pahang (UMP), 26600, Pekan, Malaysia.
[3]Department of Electronics & Communication Engineering, Faculty of Engineering, Hadhramout University, Yemen
[4]Department of Electronic, Faculty of Technology Engineering, UniMAP, 02100, Padang Besar, Malaysia
*corresponding author, E-mail: mohdfaizaljamlos@gmail.com

Abstract

A multiband coplanar waveguide (CPW) fed antenna array using a novel double negative (DNG) metamaterial unit cell for GSM900, WLAN, LTE-A and 5G Wi-Fi applications is presented in this paper. The investigated DNG structure indicates wide range of negative refractive index in the frequency span (0-3.78 and 5.65-7.2) GHz. Two categories of the proposed metamaterial plane have been applied to enhance the bandwidth up to 1.2 GHz, whereas the maximum attained gain is 6.74 dBi at 3.5 GHz.

1. Introduction

Recently, the development of wireless communication has been grown rapidly especially for 5G Wi-Fi, wireless local area networks (WLANs) and Long Term Evolution-Advanced (LTE-A) [1]. A single hardware to operate in multi frequency bands is highly desired. Furthermore, the metamaterial structures has been developed significantly due to the tremendous change of its physical behaviors that leads to investigate new electromagnetic properties which is not easy to be attained in normal case [2]. Double-negative metamaterial (DNM) is an example of this metamaterial unit cell structure, which has negative properties for both permittivity and permeability to exhibit negative refractive index (NRI) electromagnetic properties [3]. However, antennas performance have been improved dramatically by applying the metamaterial due to its numerous effectiveness to produce a novel version of the antennas design with a noticeable improvement in terms of size miniaturization, gain and bandwidth enhancement, low cost and good radiation patterns [4]. Therefore, antenna design incorporates with metamaterial can offer an ultra-high performance class of these antennas.

In this paper, a multiband CPW fed antenna array using a novel and compact DNM unit cell has been proposed. The investigated DNG structure consists of several symmetric split ring resonators (SSRRs) to exhibit wide range real values of negative permeability and permittivity, hence, leading to negative refractive index (NRI) as well. The proposed antenna is suitable for GSM900 at 0.9 GHz, WLAN at 2.3/2.4/5/5.2/5.8 GHz, 4th generation LTE-A at 3.5 GHz and 5G Wi-Fi in the frequency range of (5.15~5.875) applications, while it is overall size ($0.236\lambda o \times 0.128\lambda o \times 0.005\lambda o$) with respect to its lowest operating frequency. Simulated results (with and without DNG unit cell), including the reflection coefficient and gain at indicated frequency bands are discussed prior to the concluding remarks.

2. Antenna Design and Unit Cell Geometry

The proposed unit cell and the CPW antenna structures are described below:

2.1. Proposed Unit Cell

The proposed DNG unit cell structure is shown in Figure 1a. Its overall size is (6 x 6) mm^2. The optimized line width of each SRR is 0.5 mm with split gap by 0.5 mm is used to generate negative permeability and permittivity where r_1, r_2 and r_3 equal to 2.9 mm, 1.9mm and 0.9 mm respectively. Figure 1b shows the simulation set up testing of proposed metamaterial unit cell structure, which was placed between two waveguide ports located on each side of the z-axis to attaining the S-parameters.

2.2. Antenna Design Geometry

The proposed CPW antenna array is printed on a low-cost, 1.6 mm-thick FR4 substrate with loss tangent of 0.025 and a relative permittivity of 4.7. Figure 2 illustrates the 3-D geometry of the proposed antenna array where two categories of the proposed metamaterial plane have been used, one is placed behind the antenna array and the second will be considered as a reflector within 10 mm away from the antenna. It is an array containing 2-elements; triangular-like structure forms each radiator. The antenna is feeding by narrow micro-strip line with 50-Ω SMA connector.

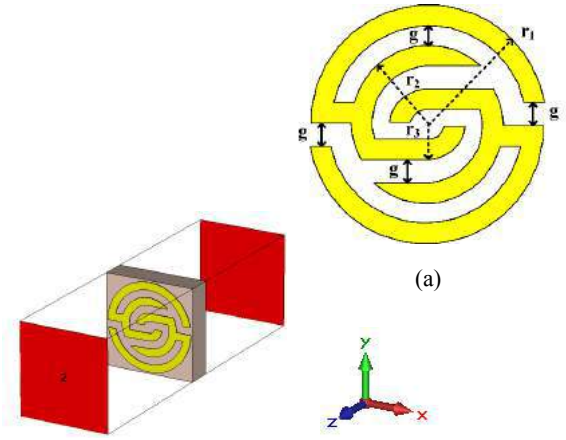

Figure 1: (a) Metamaterial unit cells structure, (b) simulation set

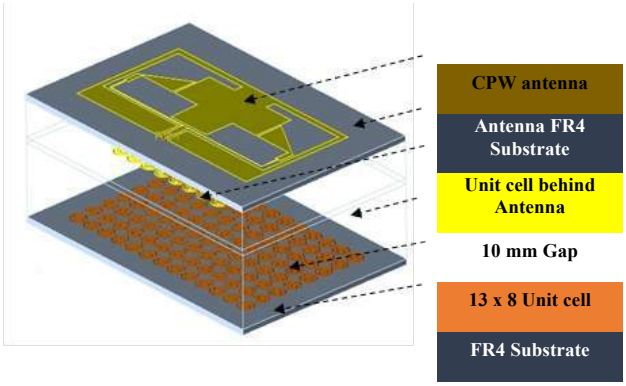

Figure 2: 3-D configuration of the Proposed antenna.

3. Results and Discussion

Figure 3 (a–c) illustrates the obtained real and imaginary values of permittivity, permeability and refractive index. The results indicated that the achieved real negative permittivity, permeability and refractive index at frequency bands of (0 ~ 6.82, 7.22 ~ 10) GHz, (0 ~ 6.96,7.31 ~ 9.36) GHz and(0 ~ 3.78,5.65 ~ 7.2) GHz respectively.

Furthermore, in Figure 4, it can be observed that the proposed antenna with unit cell features high bandwidth of 980 MHz (28 % centered at 3.5 GHz) and 1221 MHz (22.1 % centered at 5.5 GHz). In addition, the achieved gain can be increased from 3.23 dBi to 6.74 at 3.5 GHz for LTE-A and up to 5.98 at 5 GHz. Moreover, two rows structure of unit cell behind the proposed antenna array create additional resonances at 900 MHz and 2.4 GHz for GSM and WLAN applications respectively.

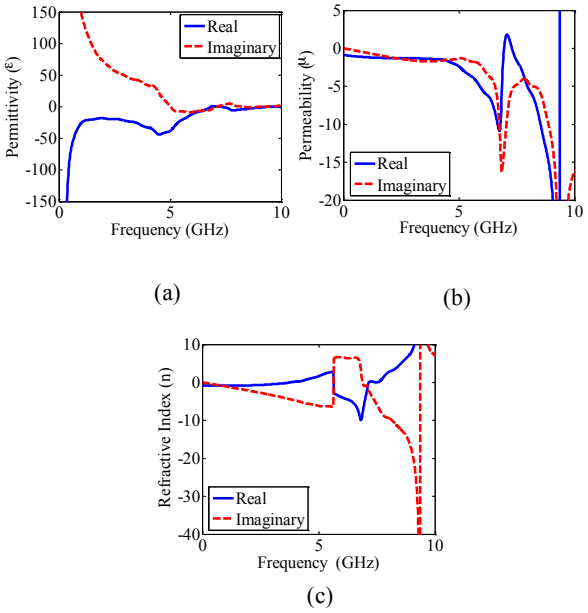

Figure 3: Metamaterial unit cell simulated results (a) Permittivity (b) Permeability (c) Refractive Index.

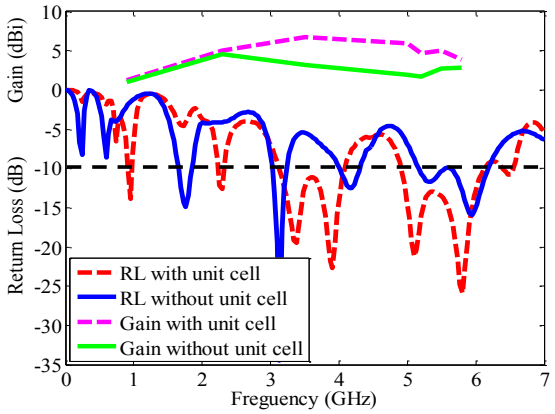

Figure 4: Return loss (S11) and gain.

Figure 5 (a-d) shows the simulated 3D far field radiation pattern at 900 MHz, 2.4 GHz, 3.5 GHz and 5.8 GHz of the proposed CPW antenna along azimuth and elevation plane. The antenna displays almost omnidirectional radiation in the (x-y) plane and (y-z) plane. Moreover, the maximum attained gain is 6.47 dBi considered as an increase of 92.57% after applying the proposed metamaterial unit cell.

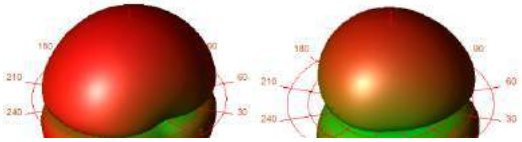

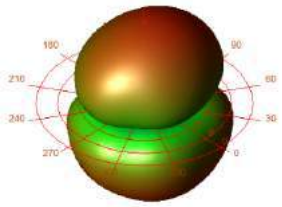

Figure 5: 3-D radiation pattern at (a) 0.9 GHz, (b) 2.4 GHz, (c) 3.5 GHz and (d) 5.8 GHz

4. Conclusions

A quad band antenna array using wide range DNG metamaterials is presented. A novel compact SSRR resonator left-handed metamaterial unit cells is proposed. The features of negative permittivity, permeability and refractive index (NRI) are validated numerically from the proposed unit cells structure. They are then placed as two scenarios on the reverse side of an antenna array. The simulated result shows that the proposed antenna integrated with the compact sized unit cell structure has proper impedance bandwidth covering the required band widths of GSM900, WLAN, LET-A and 5G Wi-Fi in the 0.865–1.06 GHz, 2.24–2.52 GHz, 3.25–4.31 GHz and 4.9–6.5 GHz respectively. The proposed antenna features omnidirectional radiation patterns.

References

[1] H. W. Lai and H. Wong, Substrate integrated magneto-electric dipole antenna for 5G Wi-Fi, *IEEE Transactions on Antennas and Propagation,* vol. 63, pp. 870-874, 2015.

[2] A. Sarkhel, D. Mitra, and S. R. B. Chaudhuri, A compact metamaterial with multi-band negative-index characteristics, *Applied Physics A,* vol. 122, pp. 1-10, 2016.

[3] S. A. Pope, Double negative elastic metamaterial design through electrical-mechanical circuit analogies, *IEEE transactions on ultrasonics, ferroelectrics, and frequency control,* vol. 60, pp. 1467-1474, 2013.

[4] A. S. M. Alqadami, M. F. Jamlos, P. J. Soh, S. K. A. Rahim, G. A. Vandenbosch, and A. Narbudowicz, Miniaturized dual-band antenna array with double-negative (DNG) metamaterial for wireless applications, *Applied Physics A,* vol. 123, p. 22, 2017.

Design and Performance of Polydimethylsiloxane Magnetic Ferrite Micromachine 24GHz Branch-Line Coupler

Noorlindawaty Md.Jizat[1,3] , Mohd Faizal Jamlos[2,3*] , Rizalman Mamat[3]

[1]Centre of Wireless Technology, Faculty of Engineering, Multimedia University, 63100 Cyberjaya, Selangor
[2]Advanced Communication Engineering Centre (ACE), School of Computer and Communication Engineering, Universiti Malaysia Perlis (UniMAP), 01000, Kangar, Perlis, Malaysia.
[3]Faculty of Mechanical Engineering, Universiti Malaysia Pahang (UMP), 26600, Pekan, Malaysia.
*corresponding author, E-mail: mohdfaizaljamlos@gmail.com

Abstract

In this paper, the utilization of flexible polymer polydimethylsiloxane (PDMS) as the substrate for the realization of patch 3dB branch-line coupler (BLC) operated at 24GHz is presented. In advanced, the micromachine technique introduces a magnetization of magnetic filler, Fe_3O_4 into the polydimethylsiloxane (NPDMS) to be applied as transmission line of BLC for Automative Collision Avoidance System (ACAS) application. Promising elements with flexible, lightweight, resistant capability against dust and corrosion are realized. The presented design exhibited considerable return loss, S_{11}, transmission, S_{21}, coupling, S_{31} of (3±1) dB and isolation, S_{41} within ACAS Standard requirement.

1 Introduction

Significantly, enhanced innovation of polymer-based nanocomposite materials by adding magnetic nanofillers, such as carbon nanotubes, carbon nanofibers and iron oxide nanoparticles to polymeric has attracted tremendous interest exclusively on strengthening the electrical conduction, mechanical hardness, chemical stability, resistance of thermal properties as well as the possible improvement of fire behavior properties serve suitable potential applications of microwave absorbing material. These properties showed that the resonance magnetic losses in a ferrocomposite with nanosized magnetite filler are shifted to the higher frequency specifies the compatibility of this method to be applicable for higher frequency applications [1]. Polymer serve as a coupling agent has been demonstrated in preparing elastomer nanocomposites on magnetite nanoparticles [2]. Characterization of magnetic polymer superparamagnetic with good magnetic saturation, improves the permeability and good electrical conductivities [3-4].

In practical, as the higher frequency is desired for ACAS application, the wavelength will be reduced and the device miniaturized. As a proposed technique, micromachining is introduced due to their capabilities of accurately defining structural dimensions, capability to integrate with other integrated circuits and possibly realization at a lower cost [5] which outlines the most development techniques to prepare for polymer magnetic nanocomposites. The high permeability magnetic fillers, Fe_3O_4 are usually employed to increase the permeability and ferromagnetic properties with increased coercive force induced by the non-magnetic polymer spacer [6]. Magnetic nano particles have a wide range of applications, including magnetic fluids recording [7], catalysis, data storage, environmental remediation separation, purification, and biomedical uses [8-10], microwave absorption [11] and medical diagnosis using magnetic resonance imaging [MRI] [12]. The ferromagnetic resonance and intensity are strongly affected by magnetic nanoparticle content in polymer composition which modifies the permeability and permittivity of the microwave devices [13].

In this paper, utilization of magnetic filler, Fe_3O_4 branch-line coupler is designed for vehicle to vehicle beamforming application, at 24GHz ACAS frequency. A PDMS combined with increasing amounts of cross-linker utilized in 3dB branch-line coupler (BLC) as flexible substrate with flexible, lightweight, resistant capability against dust and corrosion. The presented design exhibited promising return loss, S_{11}, transmission, S_{21} and coupling, S_{31} of (3±1) dB and isolation, S_{41} within ACAS ISM Standard with minimal amplitude imbalance properties.

2 Branch-line Coupler Design

Branch-line couplers are utilized for beam forming network due to characteristic of input power divided equally between the output ports. The 3 dB BLCs have a degree of freedom where any of the four ports can be used as an input port. The ports opposite to the chosen input port are the output ports while the adjacent port is the isolated port. By implementing equivalent admittance approach [14-15], the four-port symmetrical network can be split into four circuits by using the two symmetry planes. Due to the decrease of the wavelength (λ_0 = 12.5 mm) at operating frequency of 24GHz, couplers using quarter-wave length lines become feasible. In this paper, a 3dB BLC line is designed using nanocomposite polymeric magneto-ferrite thin film by loading 35% of 10-nm iron oxide Fe3O4 into pure polydimethylsiloxane (PDMS) to generate nanocomposite polymeric magnetic ferrite (NPMDS) branch-line coupler illustrated with blue line with thickness of 300μm, permittivity of 2.8, permeability of 1.4 and loss tangent

0.047 at the operating frequency of 24 GHz for ACAS bandwidth of 200MHz from 24.05GHz to 24.25GHz [16].

3 Experimental Results and Discussion

A pure PDMS (εr = 2.7, loss tangent=0.04) is used as the substrate while ground plane is copper metalized. The multilayer of proposed BLC with the size of 37.49mm x37.49 mm, gap of 0.36mm, depth of 0.2mm and other parameters has been illustrated in Figure 1(a) till Figure 1 (c) and the dimensions of the proposed BLC are listed in Table1.

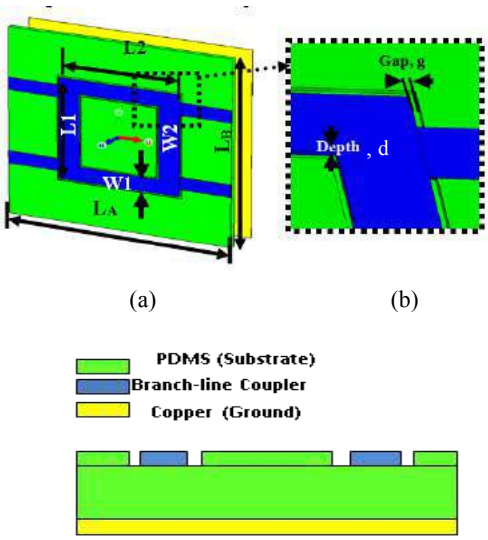

(a) (b)

(c)

Fig. 1: The proposed BLC topology, (a) perspective views, (b) magnification, (c) cross section view.

Table 1: Parameter detailed of the proposed BLC shown in Fig. 1

Para.	Value (mm)	Para.	Value (mm)	Para.	Value
L1	20.30	W2	3.45	Depth, d	300μ
L2	20.30	LA	37.49	Gap, g	0.36mm
W1	2.85	LB	37.49		

Figure 2(a) illustrated S-Parameter performance of the proposed BLC and phase difference in Figure 2(b).

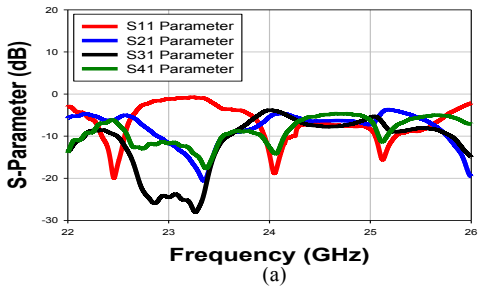

(a)

Fig. 2: Simulated result of the proposed antenna, (a) S- parameters (b) Output phase difference.

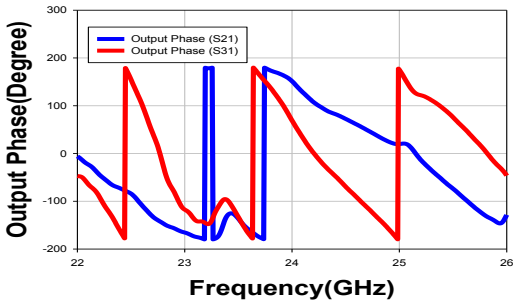

(b)

Table 2 Output simulation results of the proposed BLC

Para.	Value	Para.	Value
S11	-18.63dB	S41	-14.09dB
S21	-4.78dB	Phase Difference	89°
S31	-3.97dB	Bandwidth	(23.95-24.28GHz)

The performance of BLC is determined by the amplitude and phase imbalances, representing the difference in amplitude between the two output ports and the phase differs from the desired 90° between the two output ports. The minimal amplitude imbalance of 0.81dB and promising phase output difference, 89° with minimum variation of 1° error are shown in Figure 2(b) while bandwidth were obtained from 23.95GHz to 24.28GHz which satisfied ACAS requirement. The summarized performance of the proposed BLC is tabulated in Table2.

The magnetic filler PDMS patch is used as radiating patch of the proposed BLC by micromachining channel. Micromachining variation effect parameter depth, d of the channel has been investigated towards the BLC performance of reflection coefficient, S_{11} and isolation value, S_{41}. Once the value of depth, d of radiating magnetic filler is varied, deviations in the BLC performance are observed in Figure 3. As shown in Figure 3(a), as the depth is increased, operating frequency for S_{11} parameter are shifting homogeneously to the lower frequency but with higher percentage of transmission. However the performance at the operating frequency still achieves promising value. Conversely, isolation value didn't reflect the uniform changes due to the depth variation as illustrated in Figure 3 (b) but the value achieve less than -10dB for each depth parameter.

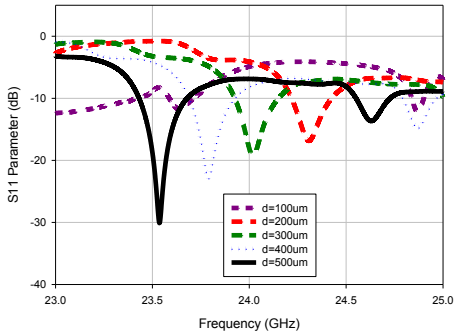

(a)

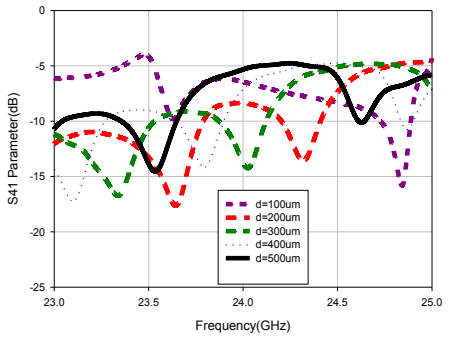

(b)

Fig. 3: Simulation of effect of depth parameter, d variation in term of: (a) S11 parameter, (b) S21 parameter.

Conventionally, amplitude imbalance and phase imbalance due to the depth variation are plotted in Figure 4. Minimal variation of amplitude imbalance can be clearly seen at 24GHz with an average value of 0.75dB. Moreover, phase difference imbalance observed to be uniformly changes with the changes variation of depth, d indicates equally power distributed between output ports. Ideally average of 5.5° consistent value was observed at 24GHz operating frequency with depth variation of 100µm.

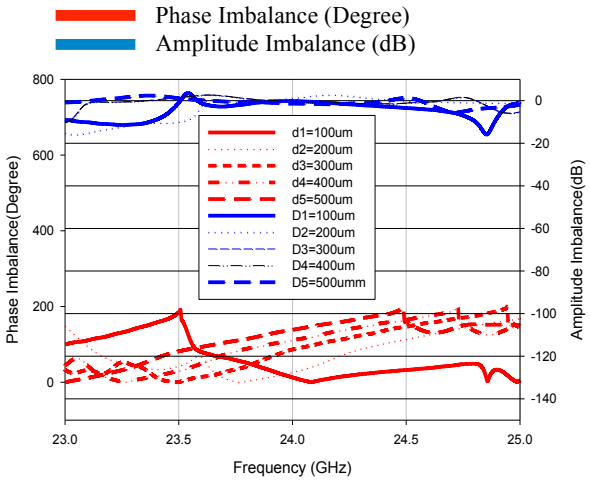

Fig. 4: Amplitude imbalance and phase difference proposed BLC.

4 Conclusions

This paper demonstrated the utilization of 35% of 10-nm iron oxide Fe_3O_4 into polydimethylsiloxane (PDMS) as the BLC transmission line with a flexible polymer PDMS as substrate, for the realization 3dB branch-line coupler (BLC) operated at 24GHz. In particular, accurately defining structural dimensions by micromachine technique contributed to the development of this design. Enhanced properties of the NPDMS is utilized for BLC which is the key element of beamforming network dedicated for vehicle to vehicle application with promising requisites of flexible, lightweight, resistant capability against dust and corrosion properties. In addition, by performing the parameter variation analysis of the polymer nanomagnetic filler radiating patch depth, d between NPDMS and substrate, analysis of BLC performance are presented. The presented design exhibited considerable return loss, S_{11}, promising results of transmission, S_{21}, coupling, S_{31} of minimal amplitude balance (3±1) dB and isolation, S_{41} within ACAS ISM Standard.

Acknowledgements

The authors wish to acknowledge for the support from Research Management Centre, FOE MMU Cyberjaya, (GAMS ID MUI160072), Universiti Malaysia Perlis and Universiti Malaysia Pahang.

References

1. Kolev S, Koutzarova T, Yanev A, Ghelev C, Nedkov I. Microwave properties of polymer composites containing combinations of micro- and nano-sized magnetic fillers, Feb, 8(2):650-4, (2008)
2. Guo J, Zhang X, Gu H, "Reinforced magnetic epoxy nanocomposites with conductive polypyrrole nanocoating on nanomagnetite as a coupling agent," RSC Adv.,4, 36560–36572, (2014)
3. Kakarla Raghava Reddy, Wonjung Park, Byung Cheol Sin, Jaegeun Noh, Youngil Lee, "Synthesis of electrically conductive and superparamagnetic monodispersed iron oxide-conjugated polymer composite nanoparticles by in situ chemical oxidative polymerization," Journal of Colloid and Interface Science 335, 34–39, (2009)
4. M. Vural, O. Gerber, B. P. Pichon, S. Lemonnier, E. Barraud, L. C. Kempel, S. Begin-Colin, and P. Kofinase, "Stretchable Magneto-dielectric Composites Based on Raspberry Shaped Iron Oxide Nanostructures," J. of Material Chemistry, 1-3, (2013)
5. Y. Wang, M. Ke, M. J. Lancaster, F. Huang, "Micromachined Millimeter-wave Rectangular-Coaxial Branch-Line Couplers with Enhanced Bandwidth", IEEE Trans. Microw. Theory Tech, (2009)
6. W. A. W. Muhamad, R. Ngah, M. F. Jamlos, P. J. Soh, M. A. Jamlos, H. Lago, "Antenna array bandwidth enhancement using polymeric nanocomposite substrate, Applied Physics A, (2016).
7. Singamaneni, S., et al, "Magnetic nanoparticles: recent advances in synthesis, self-assembly and applications," Journal of Materials Chemistry, 21(42) p. 16819-16845, (2011)
8. Shylesh S, Schünemann V, Thiel WR, "Magnetically separable nanocatalysts: bridges between homogeneous and heterogeneous catalysis," Angew Chem Int Ed 49:3428–3459, (2010).
9. Laurent S, Forge D, Port M et al, "Magnetic iron oxide nanoparticles: synthesis, stabilization, vectorization, physicochemical characterizations and biological applications," Chem Rev 108:2064–2110, (2008)
10. Colombo M, Carregal-Romero S, Casula MF et al, "Biological applications of magnetic nanoparticles," Chem Soc Rev 41:4306, (2012).
11. A. Muñoz-Bonilla, J. Sánchez-Marcos, P. Herrast, "Magnetic Nanoparticles-Based Conducting Polymer Nanocomposites," Conducting Polymer Hybrids, pp 45-80, (2016).
12. Rashad, M. and I. Ibrahim, "Structural, microstructure and magnetic properties of strontium hexaferrite particles synthesised by modified coprecipitation method," Materials Technology: Advanced Performance Materials, 27(4): p. 308-314, (2012).
13. Jaakko V.I. Timonen, Robin H.A. Ras, Olli Ikkala, Markku Oksanen, Eira Seppälä, Khattiya Chalapat, Jian Li, Gheorghe Sorin Poraoanu, "Magnetic Nanocomposites at Microwave Frequencies," Trends in Nanophysics, pp 257-285, (2010)
14. Seong-Ho Shin ; In-Ho Jeong ; Ju-Hyun Ko ; Man-Lyun Ha ; Young-Se Kwon, "Ka-band branch line coupler using high-performance air-buried microstrip lines," 33rd European Microwave Conference, pp. 951-954, (2004).
15. I. Ohta, et al., "Design of Quadrature Hybrids and Directional Couplers Based on the Equivalent Admittance Approach", IEICE Trans. Electron., pp. 2-14, Jan, (2005).
16. ECC Report 164 Compatibility Between Wide Band Low Activity Mode (WLAM) Automotive Radars in The Frequency Range 24.25 GHz TO 24.5 GHz and other radio communication systems services, May, (2011).

AMC as a Medium to Improve Gain of Microstrip Patch Antenna

Norfatihah Bahari[1], Mohd Faizal Jamlos[1,2*], Mohd Aminudin Jamlos[3], Nur Akmal Abd. Rahman[1], and Imtiaz Islam[1]

[1]Advanced Communication Engineering Centre (ACE), School of Computer & Communication Engineering, Universiti Malaysia Perlis (UniMAP), 01000 Kangar, Perlis, Malaysia

[2]Faculty of Mechanical Engineering, Universiti Malaysia Pahang, Pekan, 26600, Pahang, Malaysia

[3]Department of Electronic, Faculty of Technology Engineering, UniMAP, 02100, Padang Besar, Malaysia

*corresponding author, E-mail: mohdfaizaljamlos@gmail.com

Abstract

This paper proposes a microstrip rectangular patch antenna using a structure of artificial magnetic conductor (AMC). This type of antenna is designed to operate at 16 GHz, where the potential fifth generation (5G) band may be located. By adding AMC structure, the proposed antenna offers about 23.6% size reduction of the conventional antenna. Moreover, higher gain has been achieved, which is from 6.87 dB to 7.99 dB with 494 MHz of frequency bandwidth.

1. Introduction

According to [1], the exploitation of 5G network will emerge between 2020 and 2030. Although there is no standard has been fixed yet, the researchers estimate that 5G frequency band starts from 6 GHz [2]. To realize this newest technology, microstrip patch antenna can be one of the possible candidates as it offers light weight and low volume [3]. However, due to the limited efficiency, low gain and narrow bandwidth, AMC structure is then invented to overcome the drawbacks mentioned. By having reflection phase characteristic of 0°, the frequency bandwidth of an AMC unit cell is determined from 90° to -90° [4-5].

2. Antenna Design

A microstrip rectangular patch antenna with AMC structure is designed on a 44x21 mm^2 Rogers RT5800 substrate with ε_r=2.2 and h=0.508 mm of thickness. The size of the antenna with AMC is reduced by 23.6% of the conventional antenna (antenna without AMC). Figure 1(a) illustrates the arrangement of the antenna, where the AMC structure is placed in between both substrates. This type of metamaterial is formed by 2x4 AMC unit cells, as shown in Figure 1 (b).

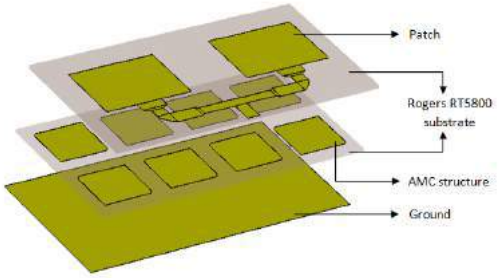

(a)

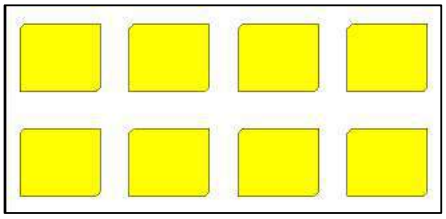

(b)

Figure 1: Proposed antenna with AMC structure (a) 3D view (b) AMC structure.

3. Discussion

To test the utilization of AMC, the performance of the proposed antenna and the conventional antenna has been compared. Figure 2 (a) shows the reflection coefficient (S11) of both antennas. It is clearly indicates that the antenna with AMC structure performs better by having -18.84 dB of S11 and 3.08% (494 MHz) of frequency bandwidth. Besides that, the radiation gain pattern of those antennas also has been analyzed as presented in Figure 2 (b). The proposed antenna obtains 7.99 dB of gain, which is 1.03 dB higher than the conventional antenna.

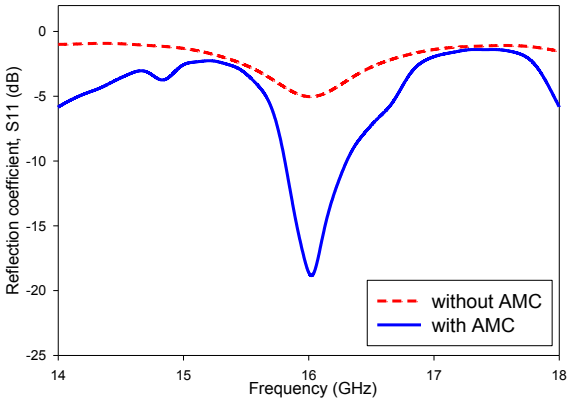

(a)

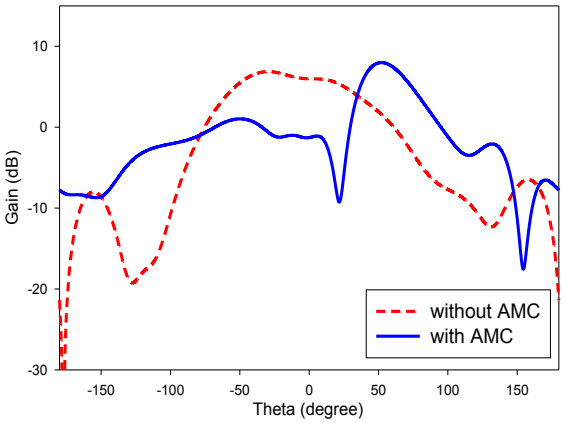

(b)

Figure 2: Performance of the proposed antenna and the conventional antenna (a) Reflection coefficient (b) Gain.

4. Conclusions

A microstrip patch antenna with AMC structure is presented in this paper. The implementation of AMC structure into the microstrip patch antenna offers a lot of advantages especially in antenna size miniaturization and gain enhancement. Due to the high path loss at high frequency, antenna with high gain provides wide area coverage for data exchange, hence the proposed antenna has a potential to be applied in 5G applications.

References

[1] Cheng-Xiang Wang, Fourat Haider, Xiqi Gao, Xiao-Hu You, Yang Yang, Dongfeng Yuan, Hadi M. Aggoune, Harald Haas, Simon Fletcher and Erol Hepsaydir, Cellular Architecture and Key Technologies for 5G Wireless Communication Networks, *IEEE Communications Magazine*, 122–130, 2014.

[2] Laying the foundations for next generation mobile services:update on bands above 6 GHz, 2015.

[3] M. S. Alam, M. T. Islam, N. Misran and J. S. Mandeep, A Wideband Microstrip Patch Antenna for 60 GHz Wireless Applications, *Elektronika Ir Elektrotechnika*, Vol. 19, No. 9, 65-70, 2013.

[4] Maisarah Abu, Maizatun Muhamad, Zahriladha Zakaria and Hasnizom Hasan, Millimeter-Wave Parasitic AMC Patches on the Array Antenna, *International Conference on Computer & Communication Engineering (ICCCE 2016)*, 9-24.

[5] Raimi Dewan and Mohamad Kamal A. Rahim, Antenna Performance Enhancement with Artificial Magnetic Conductor (AMC), *Conference on Antenna Measurements & Applications (CAMA),* 2015.

Bandwidth Enhancement using AMC Metamaterial Structure in Reconfigurable Antenna for 5G Applications

Norfatihah Bahari[1], Mohd Faizal Jamlos[1,2*], Mohd Aminudin Jamlos[3], Nur Akmal Abd. Rahman[1], Imtiaz Islam[1]

[1]Advanced Communication Engineering Centre (ACE), School of Computer & Communication Engineering, Universiti Malaysia Perlis (UniMAP), 01000 Kangar, Perlis, Malaysia

[2]Faculty of Mechanical Engineering, Universiti Malaysia Pahang, Pekan, 26600, Pahang, Malaysia

[3]Department of Electronic, Faculty of Technology Engineering, UniMAP, 02100, Padang Besar, Malaysia

*corresponding author, E-mail: mohdfaizaljamlos@gmail.com

Abstract

This paper presents a reconfigurable U-shaped slot patch antenna with a metamaterial structure of artificial magnetic conductor (AMC). The AMC structure that consists of windmill-shaped slot unit cells are placed in between of two substrates to boost the performances of antenna. Compared to the ordinary antenna, the antenna with AMC structure offers better reflection coefficient and wider bandwidth which is from -10.35 dB to -27 dB and from 64 MHz to 342 MHz, respectively.

1. Introduction

The researchers are recently working very hard to explore the fifth generation (5G) as the users now demand more bandwidths to transmit data at the speed of 1 Gbps and above [1]. As higher frequency needed to realize 5G network, many types of reconfigurable antennas have been proposed but the antenna using RF MEMS switches has a good potential to be applied as they can be operated at high frequency band, have low insertion loss and allow zero standby power consumption compared to others tunable components [2]. The idea of using AMC structure seems to be possible in 5G applications as the ordinary reconfigurable antenna offers narrow bandwidth and poor reflection coefficient. AMC is actually a metamaterial which performs zero degree reflection phase characteristic of Perfect Magnetic Conductor (PMC) at resonance frequency [3-4].

2. Antenna Design

In this paper, a reconfigurable antenna using AMC structure has been designed to operate at 11 GHz, as illustrated in Figure 1. The proposed AMC consists of 2x6 rectangular with windmill-shaped slot unit cells. The structure is placed in between Rogers RT5880 substrates with ε_r=2.2 and thickness, h=1.575 mm.

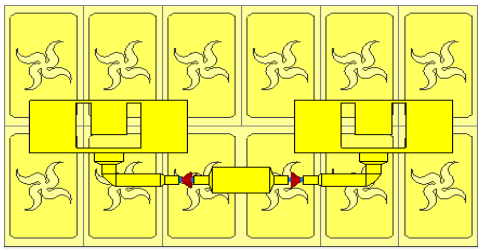

(a)

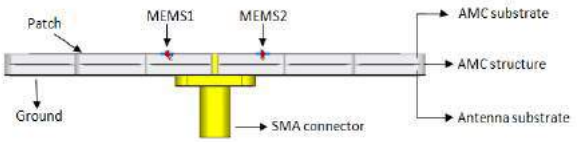

(b)

Figure 1: Proposed reconfigurable antenna with AMC structure (a) Top view (b) Side view

3. Discussion

The phase reflection performance of an AMC unit cell is shown in Figure 2. The bandwidth of AMC is determined when phase shifts between +90° to -90°, therefore the bandwidth of this proposed AMC is 37% at a frequency band from 8.1 to 11.78 GHz.

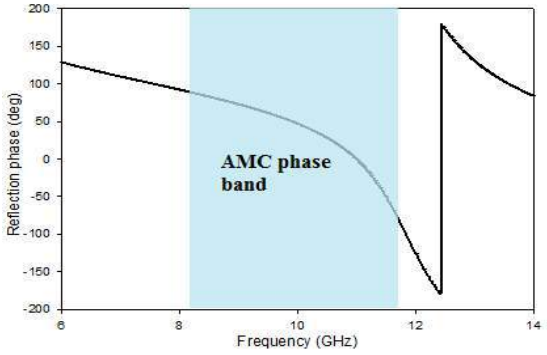

Figure 2: Reflection phase of an AMC unit cell

Table 1: Configurations of RF MEMS switches

State	MEMS1	MEMS2
1	ON	OFF
2	OFF	ON
3	ON	ON
4	OFF	OFF

As two RF MEMS switches have been used in the proposed antenna, four states are defined as tabulated in Table 1. The comparison of reflection coefficient (S11) between the ordinary antenna and antenna with AMC structure has been presented in Figure 3. Based on the figure, the antenna with AMC offers better reflection coefficient and wider bandwidth compared to the ordinary antenna. When MEMS2 is activated or both switches are activated, S11 shifted to the left and vice versa. Besides that, wider overall frequency bandwidth is obtained which is only 64 MHz for ordinary antenna to 342 MHz for antenna with AMC structure.

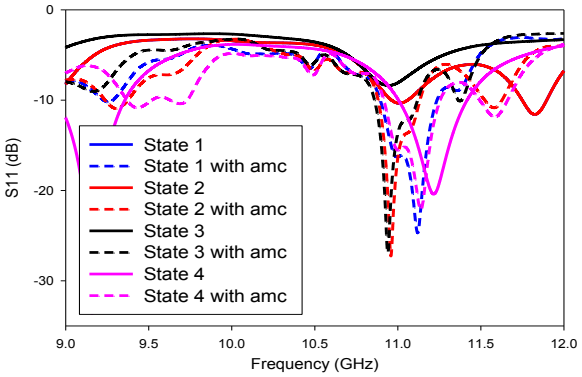

Figure 3: Reflection coefficient of the proposed antenna for each state.

4. Conclusions

A reconfigurable U-slot patch antenna with windmill-shaped slot AMC structure is proposed in this paper. By implementing the AMC structure into the reconfigurable antenna, the proposed antenna offers better reflection coefficient and wider bandwidth compared to the antenna without AMC structure. Therefore the proposed antenna could be the potential candidate to fulfill one of the 5G requirements.

References

[1] Dan Warren and Calum Dewar, Understanding 5G:Perspectives on future technological advancements in mobile, *GSMA Intelligence*, 2014.

[2] H Jaafar, K S Beh, N A M Yunus, W Z W Hasan, S Shafie and O Sidek, A comprehensive study on RF MEMS switch, *Microsystem Technologies* 2014.

[3] Maisarah Abu, Maizatun Muhamad, Zahriladha Zakaria and Hasnizom Hasan, Millimeter-Wave Parasitic AMC Patches on the Array Antenna, *International Conference on Computer & Communication Engineering (ICCCE 2016)*, 9-24.

[4] H. Lago , M. F. Jamlos, N.Bahari and M.R. Hamid, Reconfigurable Beam Pattern Folded Dipole Antenna Based on AMC Structure, *IEEE International RF and Microwave Conference (RFM 2015)*, Sarawak, Malaysia, December 2015, 186-189.

Performance Enhancement of Crescent Shaped Array Antenna using Artificial Magnetic Conductor

H. Lago[1], Mohd Faizal Jamlos[1,2]*, Samir Salem Al-Bawari[1] and Ojo Rasheed[1]

[1]Advanced Communication Engineering Centre (ACE), School of Computer & Communication Engineering
Universiti Malaysia Perlis (UniMAP), 01000, Kangar, Perlis, Malaysia
[2]Faculty of Mechanical Engineering, Universiti Malaysia Pahang (UMP), 26600, Pekan, Malaysia.
*corresponding author, E-mail: mohdfaizaljamlos@gmail.com

Abstract

Integration of crescent shaped array antenna into a metamaterial of single resonant Artificial Magnetic Conductor (AMC) at 9.41 GHz is proposed. AMC plane stacked with crescent shaped array has successfully increased the gain, efficiency and bandwidth of the antenna to 9.73 dB, 97% and 398 MHz respectively compared to 8.46 dB, 96% and 393 MHz without AMC. It is observed that the characteristics of the proposed AMC plane significantly contributed to such results.

1. Introduction

Due to the main characteristic of Perfect Magnetic Conductor (PMC) which exhibits 0o reflected phase, therefore it is potentially to improve the antenna performances [1]. However, the PMC is not available in nature [1]. However, an Artificial Magnetic Conductor (AMC) which is classified as a metamaterial [2] capable to exhibits the PMC characteristic at a specific frequency for each resonant response [3]. This research aims to design an AMC ground layer which can be placed closer to the resonant structure while improve the performance. For that reason, a microstrip array antenna is proposed as the radiating structure due to its fabrication simplicity and low profile characteristics.

2. Results and discussion

In this research, a crescent shaped array antenna has been designed as the radiating structure on the top of AMC plane. The design of the AMC unit cell is illustrated in Figure 1(a). The AMC is capable to exhibit 0^{o} phase response at 9.41 GHz with 2.83 GHz of bandwidth. As depicted in Figure 1(b), the AMC shows positive permittivity and high permeability at the desired operating frequency. To the best of author knowledge, a microstrip patch antenna one of the most popular antenna among researcher. However, this type of antenna is suffered in term of its performance due to the ground effect. Nevertheless, this risk can be eliminated by incorporating the AMC plane at the microstrip antenna as shown in Figure 2. As the result, the proposed antenna with AMC is capable to enhanced the antenna performances especially the gain, bandwidth and efficiency while reducing the radiating surface up to 6%. The performance of the crescent array antenna with and without AMC plane is tabulated in Table 1.

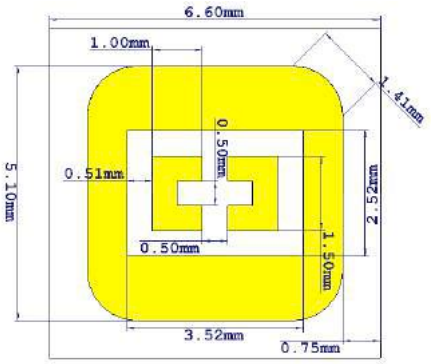

(a)

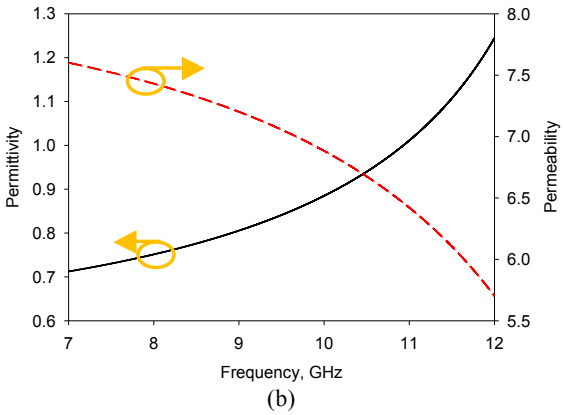

(b)

Figure 1: Simulated AMC unit cell (a) dimension and (b) results of permittivity and permeability.

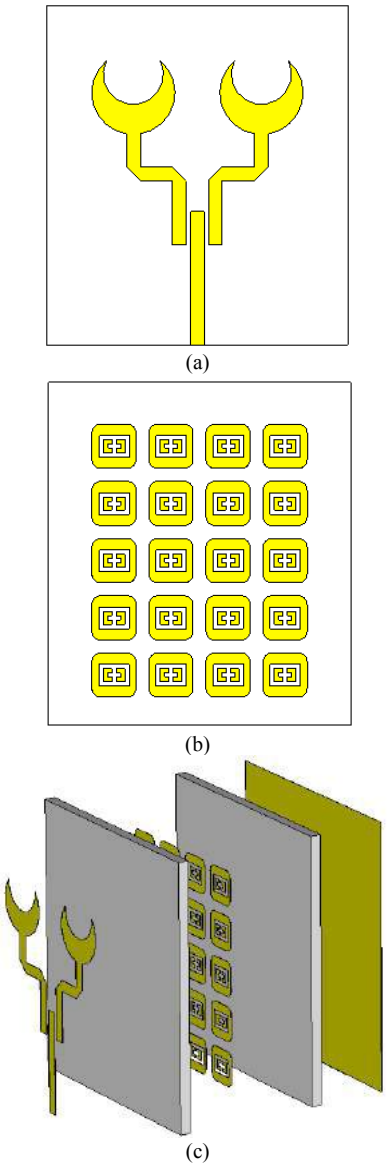

Figure 2: (a) Radiating crescent shaped array antenna, (b) AMC plane and (c) structure of the array antenna with AMC.

Table 1: Comparison performance of the crescent shaped array antenna with and without AMC.

Antenna performance	Crescent array antenna without AMC	Crescent array antenna with AMC
Radiating surface (mm^2)	165.74	155.62
Gain (dB)	8.44	9.73
Bandwidth (MHz)	393	398
Efficiency (%)	96	97

3. Conclusions

An incorporate of crescent shaped array antenna with AMC plane is proposed. Through the simulation process, the AMC plane is capable to be placed near to the radiating element. With aid of AMC plane which potentially exhibits as PMC, therefore the bandwidth, efficiency and gain of the crescent array antenna are enhanced up to 398 MHz, 97% and 9.73 dB respectively.

References

[1] N.A. Abbasi, and R.J Langley, Multiband-integrated antenna/artificial magnetic conductor, *IET Microwaves, Antenna Propag.*, vol. 5, pp. 711-717, 2011.

[2] M.A. Fiddy, and R. Tsu, Understanding metamaterials, *waves in Random and Complex Media*, vol. 20, pp. 202-222, 2010.

[3] S. Yan, P.J. Soh, and G.A.E. Vandenbosch, Low-profile dual-band textile antenna with artificial magnetic conductor plane, *IEEE Trans. Antennas Propag.*, vol. 62, no.12, pp. 6487-6490, 2014.

A Compact UWB MIMO Antenna with Single Ring Resonator (SRR) Metamaterial Structure for Improved Isolation

Mohannad Obaid Katie[1], Mohd Faizal Jamlos[1,2*], Mohd Aminudin Jamlos[3]

[1,2,3] Advanced Communication Engineering Centre (ACE), School of Computer and Communication Engineering, Universiti Malaysia Perlis (UniMAP), 01000, Kangar, Perlis, Malaysia
[2]Faculty of Mechanical Engineering, Universiti Malaysia Pahang (UMP), 26600, Pekan, Malaysia.
[3]Department of Electronic, Faculty of Technology Engineering, UniMAP, 02100, Padang Besar, Malaysia.
*corresponding author, E-mail: mohdfaizaljamlos@gmail.com

Abstract

A compact UWB MIMO antenna with metamaterials Split Ring Resonator (SRR) etched in between elements is presented. Its reverse side integrated with a partial ground plane to enhance bandwidth and improve inter-element isolation. The SRR metamaterial structures are significantly reduced the mutual coupling and improve antenna isolation, through exhibiting the negative characteristics for both permittivity and permeability. Results show that the isolation below than 20 dB in the entire UWB band, from 3.1 to 10.6 GHz.

1. Introduction

The demands of high data rates and channel capacity are the major issues of interest in wireless communication. This attention contributes to the increasing popularity of multiple-input multiple-output (MIMO) systems, which employs diversity techniques to improve communication systems reliability via multipath fading reduction [1]. Meanwhile, the ultra-wideband (UWB) spectrum which ranges between 3.1 and 10.6 GHz is capable of providing high data rates [2], [3]. To simultaneously increase data rates while mitigating multipath fading, the MIMO diversity technology can be integrated within UWB systems [4-6]. Recently, implementing the metamaterial unit cells structures for antenna design enable the performance improvement of MIMO antenna system through the isolation enhancement [7]. The electromagnetic metamaterial is defined as the artificial material structures that can be designed to explain the electromagnetic features that not present in nature [8]. Using the periodic structure of Split Ring Resonator (SRR) with the metal wires, correspondingly the negative relative permittivity and permeability are obtained [9-12]. To decrease the resonant frequency value of an antenna, the metamaterial structures of SRR unit cells are placed along an antenna to be used as a loading structure [13-16].

This work is an effort in designing a compact UWB MIMO antenna with a low inter-element mutual coupling. The proposed antenna operates with from 2.95 to 12.2 GHz and dimensions of ($0.3\lambda \times 0.2\lambda$) at the lower cutoff frequency 2.95 GHz. The Split Ring Structure combination with ground plane effectively reduces inter-element pattern correlation across the operational band with the isolation of 20 dB. Satisfactory diversity performance is confirmed via the envelope correlation coefficient and diversity gain (DG) of 0.2 and 9.8, respectively. Meanwhile, its mean effective gains (MEGs) ratio is nearly unity.

2. Antenna Design Geometry

The structure of the single ring resonator unit cells metamaterial was shown in Figure 1 (a) and (b). The geometrical dimensions of the proposed unit cell are listed in Table 1. The mathematical formulation in [17], [18], were used to evaluate the negative index parameters such as permittivity and permeability that produced through exciting the electric and magnetic fields in the wire SRR unit cells. The real and imaginary values of permittivity, permeability refractive index, and impedance are illustrated in Figure 1 (c), (d), (e) and (f). The geometry of the proposed UWB MIMO antenna was depicted in Figure 2 (a) and (b). It is designed on an FR-4 substrate with a thickness of 1.6 mm, permittivity ϵ_r= 4.7 and loss tangent tan δ = 0.025. The overall structure consists of two identical monopole antenna elements (denoted as MA1 and MA2) placed in parallel on the same side of the substrate with metamaterial structure of unit cells of SRR in between antenna elements. The partial ground plane and long wire of the unit cells are located on the reverse side of the substrate to reduce mutual coupling and improve isolation between ports.

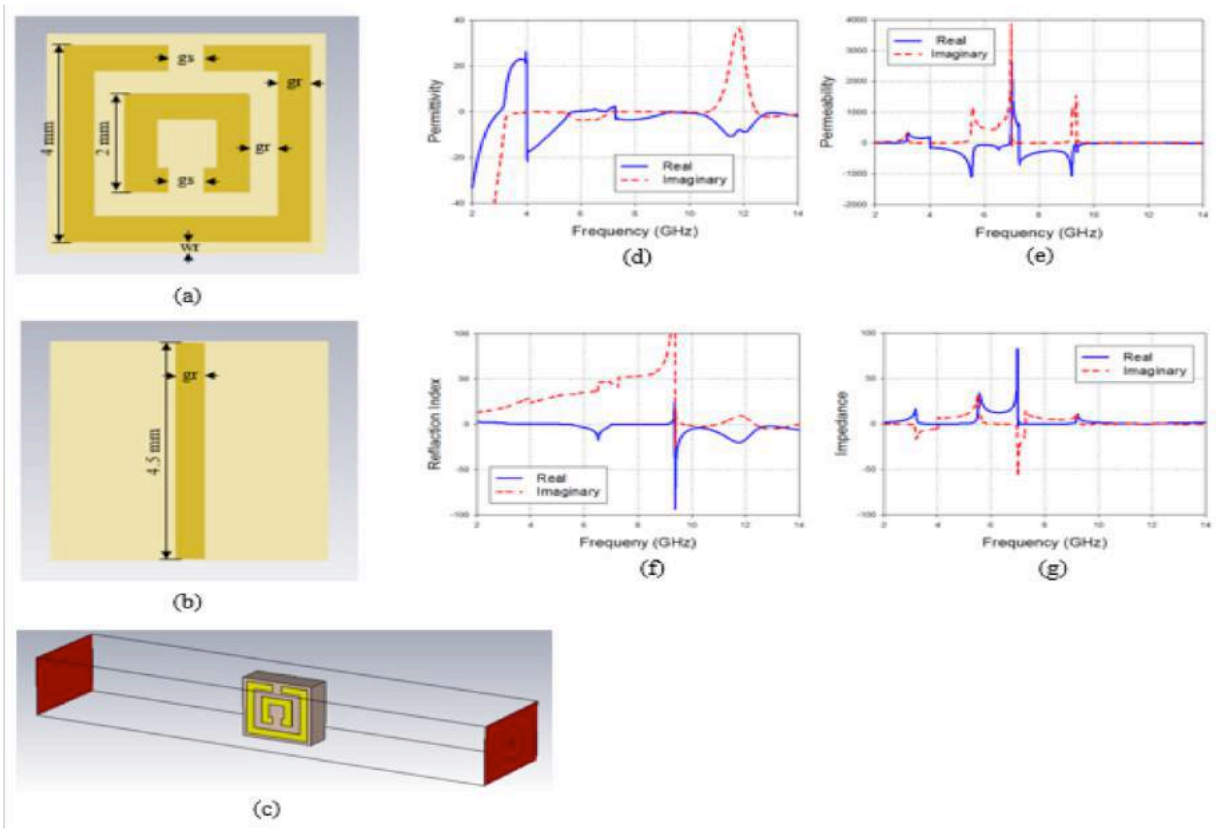

Figure 1: Geometry of the single ring resonator (SRR) unit cell structure, (a) unit cell front view, (b) unit cell back view, (c) simulation setup, (d) permittivity, (e) permeability, (f) refractive index, (g) impedance.

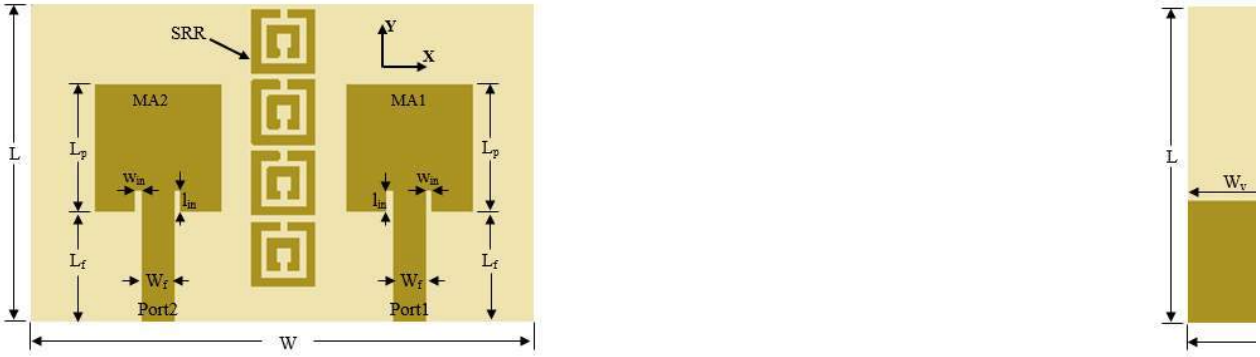

Figure 2: Geometry of the proposed UWB MIMO antenna, (a) front view, (b) back view.

Table 1: Parameters dimensions of the proposed antenna

Para.	Value (mm)	Para.	Value (mm)	Para.	Value (mm)	Para.	Value (mm)	Para.	Value (mm)	Para.	Value (mm)	Para.	Value (mm)
W	32	L_G	6	L_v	3.2	l_{in}	1.3	wr	0.25	W	32	L_G	6
L	20	L_f	7	W_v	6	l_r	16.2	gs	0.6	L	20	L_f	7
L_p	8	W_f	2	w_{in}	0.5	Θ	15°	gr	0.5	L_p	8	W_f	2

3. Results and Discussion

Figure 3 compares the simulated and measured S_{11} and S_{21}. Simulations indicate a bandwidth from 2.95 to 12.2 GHz. A downwards shift is seen as the measured bandwidth covers the UWB band from 2.5 to 11 GHz for the reflection coefficient below -10 dB. The simulated and measured S_{21} shown in Fig. 4 indicate a mutual coupling of less than -20 dB between within the operating band (from 3 to more than 12 GHz).

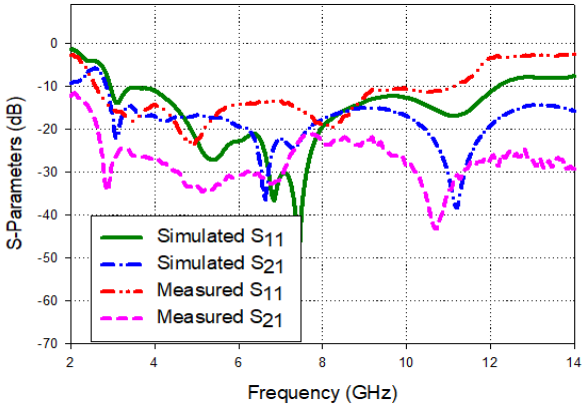

Figure 3: Simulated and measured S_{11} and S_{21} of the proposed UWB MIMO antenna.

The proposed MIMO antenna accomplished a 2:1 VSWR bandwidth of 2.5 to 11 GHz, which enabled operation throughout the whole UWB band and showed isolation better than 20 dB.

References

[1] B. P. Chacko, T. a. Denidni, and G. Augustin, "Uniplanar polarisation diversity antenna for ultra-wideband systems," *IET Microwaves, Antennas Propag.*, vol. 7, no. 10, pp. 851–857, 2013.

[2] T. S. P. See and Z. N. Chen, "An ultrawideband diversity antenna," *IEEE Trans. Antennas Propag.*, vol. 57, no. 6, pp. 1597–1605, 2009.

[3] P. Gao, S. He, X. Wei, Z. Xu, N. Wang, and Y. Zheng, "Compact Printed UWB Diversity Slot Antenna With 5.5-GHz Band-Notched Characteristics," *IEEE Antennas Wirel. Propag. Lett.*, vol. 13, pp. 376–379, 2014.

[4] S. Zhang, B. K. Lau, A. Sunesson, and S. He, "Closely-Packed UWB MIMO / Diversity Antenna With Different Patterns and Polarizations for USB Dongle Applications," *IEEE Trans. Antennas Propag.*, vol. 60, no. 9, pp. 4372–4380, 2012.

[5] J. Li, Q. Chu, Z. Li, and X. Xia, "Compact Dual Band-Notched UWB MIMO Antenna With High Isolation," *IEEE Trans. Antennas Propag.*, vol. 61, no. 9, pp. 4759–4766, 2013.

[6] L. Liu, S. W. Cheung, T. I. Yuk, and A. A. Mimo, "Compact MIMO Antenna for Portable UWB Applications With Band-Notched Characteristic," *IEEE Trans. Antennas Propag.*, vol. 63, no. 5, pp. 1917–1924, 2015.

[7] M. S. Sharawi, A. B. Numan, M. U. Khan, and D. N. Aloi, A dual-element dual-band MIMO antenna system with enhanced isolation for mobile terminals, Antennas and Wireless Propagation Letters, IEEE, vol. 11, pp. 1006-1009, 2012.

[8] P. Mookiah, and K. R. Dandekar, Metamaterial-substrate antenna array for MIMO communication system, IEEE Trans. Antennas Propag., 57(10), 3283-92, 2009.

[9] A. Sarkhel , D. Mitra, and S. R. B. Chaudhuri, A compact metamaterial with multi-band negative-index characteristics, Applied Physics A, 122(4), 1-10, 2016.

[10] M. A. Wan Nordin, M. T. Islam, and N. Misran, A compact wideband coplanar waveguide fed metamaterial-inspired patch antenna for wireless application, Applied Physics A, 109(4), 961–965, 2012.

[11] D. R. Smith, W. J. Padilla, D. C. Vier, S. C. Nemat-Nasser, and S. Schultz, Composite medium with simultaneously negative permeability and permittivity, Phys. Rev. Lett., vol. 84, no. 18, 4184–4187, 2000.

[12] M. M. Bait-Suwailam, Graduate, M. S. Boybay, and O. M. Ramahi, Electromagnetic coupling reduction in high-profile monopole antennas using single-negative magnetic metamaterials for MIMO applications, IEEE Trans. Antennas Propag., 58(9), 2894-902, 2010.

[13] K. Li, C. Zhu, L. Li, Y. M. Cai, and C. H. Liang, Design of electrically small metamaterial antenna with ELC and EBG loading, IEEE Antennas and Wireless Propagation Letters.

[14] J. P. Chen and P. Hsu, A compact strip dipole coupled split-ring resonator antenna for RFID tags, IEEE Transactions on Antennas and Propagation, 61(11), 5372–5376, 2013.

[15] O. S. Kim and O. Breinbjerg, Miniaturised Self-Resonant Split-Ring Resonator Antenna, Electronics Letters, 45(4) 196–197, 2009.

[16] X. H. S. and L. L. C. and C. H. W. and Y. N. Yuan, Study on an SRR-shaped left-handed material patch antenna, Journal of Optics, 13(3) 35402, 2011.

[17] Chen, X., T.M. Grzegorczyk, B.-I.Wu, Jr. Pacheco, and J.A Kong, Robust method to retrieve the constitutive effective parameters of metamaterials, Physical Review E, 70.1, 2004.

[18] D. R. Smith, D. C. Vier, N. Kroll, and S. Schultz, "Direct calculation of permeability and permittivity for a left- handed metamaterial," App. Phys. Lett., 77(14), 2246–2248, 2000

Enhanced Performance of 3dB Branch-Line Coupler with Diamond Shaped Negative Permittivity Metamaterial

Noorlindawaty Md.Jizat[1,3], Mohd Faizal Jamlos[2,3*], Rizalman Mamat[3]

[1]Centre of Wireless Technology, Faculty of Engineering, Multimedia University, 63100 Cyberjaya, Selangor
[2]Advanced Communication Engineering Centre (ACE), School of Computer and Communication Engineering, Universiti Malaysia Perlis (UniMAP), 01000, Kangar, Perlis, Malaysia.
[3]Faculty of Mechanical Engineering, Universiti Malaysia Pahang (UMP), 26600, Pekan, Malaysia.
*corresponding author, E-mail: mohdfaizaljamlos@gmail.com

Abstract

The paper presents enhanced performance of 3dB branch-line coupler (BLC) by implementing diamond shaped unit cell negative permittivity metamaterial with 2×2 array cell configuration. S_{11} of less than -10 dB, equally power distributed of coupling, S_{31} and transmission, S_{21} of less than -3 dB, low magnitude imbalance of 0.01dB and enhanced bandwidth of 103% are achieved from 4.66GHz to 12.54GHz. Such features are highly potential and suitable to be implemented for 5.9GHz automotive Dedicated Short Range Communication (DSRC) application.

1. Introduction

Extraordinary electromagnetic properties possess of negative refractive index revealed initially by Veselago theorized that a left-handed medium (LHM) was implied from the presence of simultaneously negative permeability or permittivity which drastically drawn significant scientific interest [1-2]. Due to the propagation of electromagnetic waves in matter, this unprecedented metamaterials with negative permittivity and negative permeability are artificially constructed into materials design which in turn provides enhanced performance [3-4]. Possessing these intriguing electromagnetic properties, metamaterials widely utilized as a part of applications, such as super-lenses [5], waveguides, filters [6], antenna design, invisibility cloaking, electromagnetic absorbers, and electromagnetic band gaps [7], and branch-line coupler [8-11]. Different techniques of metamaterial was designed in the scaling of artificial structures has already been demonstrated from radio frequencies (RFs) to millimeter-wave application [12-14].

Metamaterials can be classified into three categories: zero-index materials, single-negative media, and double-negative media, where these artificially structured composites potential in the electromagnetic spectrum with material response is limited and the construction of novel devices is simplified. Metamaterial with either a negative permittivity or permeability is known as single-negative (SNG) medium. Significantly, metamaterial emphasis on solving the conventional physical limitations, miniaturization in size, improving gain, bandwidth and efficiency in multi-band operation of the antenna design [15].

In this study, the proposed design of $0.16\lambda_0 \times 0.16\lambda_0$ diamond shaped unit cell array are etched on one side of a FR4 substrate exhibits resonance at DSRC frequency, 5.9GHz for vehicle to vehicle communication elements. The proposed structure exhibits resonance with a wider bandwidth of 50% enhancement in comparison with the BLC design without metamaterial. Moreover, the proposed BLC structure's dimension is 8.72mm × 9.69mm, which is significantly reduced compared to the BLC operating at the same frequency presented in [16]. The results towards enhancement of BLC performance is discussed in detailed in the subsequent part.

2. Branch-line Coupler Design

Specifications for the response of each unit cell are predetermined prior to construction before the entire constructed BLC design is finalized. Fig. 1(a) shows the geometrical parameters and dimension detailed of the proposed diamond shaped unit cell with the size of $0.16\lambda_0 \times 0.16\lambda_0$ in area. As per illustrated in Fig. 1 (b) the unit cells are arranged in the 2×2 array. Subsequently, transmission unit cell is altered by adjusting the shape, size, and configurations of the unit cells, which control over permittivity and magnetic permeability parameters that indicates the propagation of electromagnetic waves in matter.

The negative permittivity and positive permeability behavior are observed through S-parameters response obtained from CST Microwave Studio (MWS) and evaluated by the mathematical formulation in [17-18] which then simulated through Matlab coding. As shown by the frequency-domain solver for the simulation of the metamaterial structure in Fig. 2(a) and (b), negative permittivity was observed with frequency range of 0.5 GHz to 8 GHz. Diamond shaped unit cell array are designed using one side of a FR4 substrate with thickness of 1.6mm, dielectric constant of 4.6, loss tangent of 0.019 and copper thickness of 35μm. The proposed unit cell array was placed

at the center of a waveguide with perfect electric wall in the x−z plane and perfect magnetic wall in the z−y plane to realize TEM mode excitation in the z-direction while the two open ports were in the z-direction.

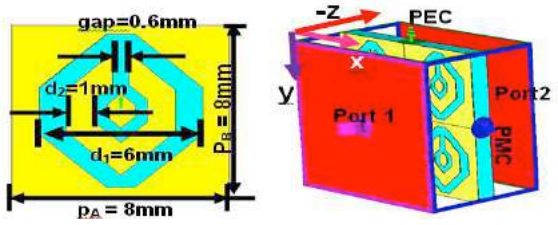

(a) (b)

Figure 1: Diamond shaped unit cell, (a) unit cell (b) 2×2 arrays metamaterial.

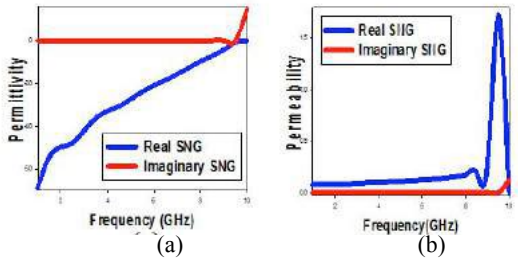

(a) (b)

Figure 2: Unit cell response, (a) permittivity (b) permeability.

Conventionally, directional couplers have four ports, in which the first port is regarded as the input, the second port is regarded as through port, the third port is regarded as the coupler port, and the fourth port is regarded as isolated port. Diamond shaped unit cell metamaterial array is implemented at the bottom layer of the BLC while the center of the substrate is kept metalized serving as a ground plane as shown in Fig. 3 and Fig. 4 accordingly.

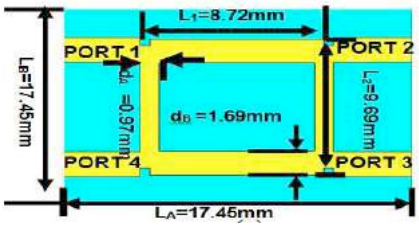

Figure 3: BLC Geometry transmission line dimension.

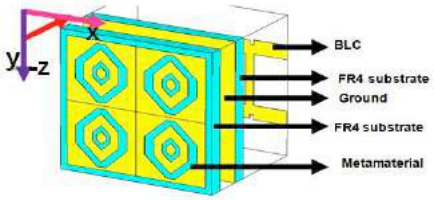

Figure 4: Exploded view structure.

3. Results and Discussion

As can be seen from Fig. 5, simulated results between the BLC design with metamaterial and without metamaterial in term of reflection coefficients (S_{11}), transmission (S_{21}), coupling (S_{31}) and isolation (S_{41}) value is illustrated. Fig. 5(a) and (b) shows S-parameter value of BLC with a good reflection coefficient (S_{11}) value of -20.8dB, transmission (S_{21}) of -3.99dB, tight coupling parameter (S_{31}) of -3± 1 dB, low magnitude imbalance, 0.01dB and isolation (S_{41}) improvement to -28.58 dB at the operating frequency, 5.9 GHz. Fig. 5(c) demonstrates a promising phase output difference between Port 2 and 3, (90°±5) °. Enhanced bandwidth of 103% was obtained from the proposed BLC, operated from 4.66GHz to 12.54GHz. The proposed metamaterial has enabled the concentration of the electromagnetic field and currents nearby radiating elements instead of distributed them along the ground plane which allows BLC to be utilized with enhanced bandwidth as the surface current distribution had been illustrated in Fig. 6.

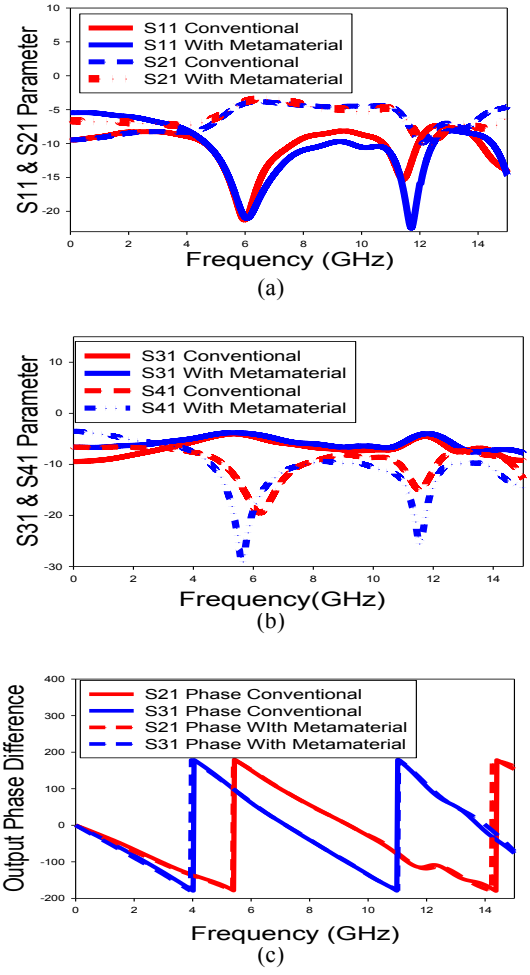

Figure 5: The simulated BLC performance, (a) S11 & S21 (b) S31 & S41 (c) Output phase difference.

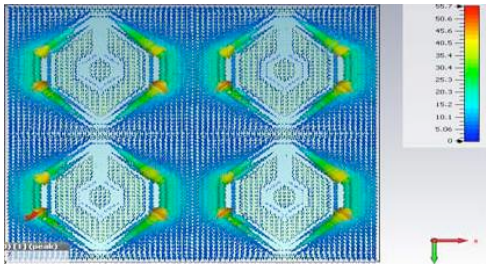

Figure 6: Surface Current distribution in the metamaterial unit cell.

4. Conclusions

In this paper, enhanced performance of BLC operating at 5.9GHz for DSRC application realized using negative refractive index metamaterial unit cell. A novel design of negative permittivity diamond shaped unit cell with considerable small size of $0.16\lambda_0 \times 0.16\lambda_0$ is proposed. The features of negative permittivity are validated numerically from the proposed unit cells structure using Matlab simulator. In advanced, the proposed unit cell array is etched at the bottom layer of the BLC while the center of the substrate is kept metalized serving as a ground plane which provides the higher percentage of transmitted signal into the proposed design. The promising S parameter value in terms of reflection coefficient, S_{11}, insertion loss, S_{21}, coupling, S_{31} and isolation, S_{41} provide promising results to serve as a platform for vehicle to vehicle beamforming element design at DSRC frequency, 5.9GHz.

Acknowledgements

The authors wish to acknowledge for the support from Research Management Centre, FOE MMU Cyberjaya, (GAMS ID MUI160072), Universiti Malaysia Perlis and Universiti Malaysia Pahang.

References

[1] Viktor, G.; Veselago, P.N.L, The electrodynamics of substances with simultaneously negative values of ε and μ, *Sov. Phys. Uspekhi*, *10*, 509–514, 1968.

[2] Loïc Markley and George V. Eleftheriades, A Negative-Refractive-Index Metamaterial for Incident Plane Waves of Arbitrary Polarization, *IEEE Antennas and Wireless Propagation Letters*, Vol. 6, 2007.

[3] Withawat Withayachumnankul ; Derek Abbott, Metamaterials in the Terahertz Regime, *IEEE Photonics Journal* Volume: 1, Issue: 2, pp 99 - 118 ,2009.

[4] Ziolkowski, R.W. Design, fabrication, and testing of double negative metamaterials. *IEEE Trans. Antennas Propag*, 51, 1516–1529, 2003.

[5] Grbic, A.; Eleftheriades, G.V. Overcoming the diffraction limit with a planar left-handed transmission-line lens. *Phys. Rev. Lett.*, *92*, doi:10.1103/PhysRevLett.92.117403, 2004.

[6] Cui, T.J.; Smith, D.; Liu, R. Metamaterials: Theory, Design, and Applications; *Springer*: Berlin, Germany, 2009.

[7] Fang, C.Y.; Gao, J.S.; Liu, H. A novel metamaterial filter with stable passband performance based on frequency selective surface. *AIP Adv*. 4, 077114, 2014.

[8] Md. Mehedi Hasan, Mohammad Rashed Iqbal Faruque, Sikder Sunbeam Islam and Mohammad Tariqul Islam, A New Compact Double-Negative Miniaturized Metamaterial for Wideband Operation, *Materials*, 9, 830, 2016.

[9] Rubaiyat Islam and George V. Eleftheriades, Compact Negative-Refractive-Index Transmission-Line (NRI-TL) Coupler, Filter and Diplexer, *2007 IEEE Antennas and Propagation Society International Symposium*, pp 4957-4960, 2007.

[10] Rubaiyat Islam and George V. Eleftheriades, Phase-Agile Branch-Line Couplers Using Metamaterial Lines, *IEEE Microwave and Wireless Components Letters*, Vol. 14, No. 7, 2004.

[11] Christophe Caloz, Atsushi Sanada, and Tatsuo Itoh, Microwave Circuits Based on Negative Refractive Index Material Structures, 33rd *Eiwopcan .Microwave Conference – Munich,* pp 105-109,2003.

[12] Willie J. Padilla, Dimitri N. Basov, David R. Smith, Negative refractive index metamaterials, *Materials Today*, pp. 28-35, July-August, Volume 9, Number 7-8, 2006.

[13] ITOH T, Metamaterial for RF application, *Int. Conf. on Infrared, Millimeter and Terahertz Waves*, pp. 1– 3, 2008.

[14] Cuong Tran Manh, Habiba Hafdallah Ouslimani1, Geraldine Guida1 Alain Prio , Herve Teillet , and J. Y. Daden, Metamaterial Structures for Compact Millimeter Wave Antenna Applications, *PIERS Proceedings*, Hangzhou, China, pp.1306-1312, March 24-28, 2008.

[15] K. Li, C. Zhu, L. Li, Y. M. Cai, and C. H. Liang, Design of electrically small metamaterial antenna with ELC and EBG loading, *IEEE Antennas and Wireless Propagation Letters*, 2013.

[16] Dakui Wu and Guoxin Zheng, Compact Dual-Band Coupler for Vehicular Beam-Forming Array, *International Journal of Antennas and Propagation,* Volume 2017, 2017.

[17] Alam, T., Faruque, M. R. I., & Islam, M. T, A double-negative metamaterial-inspired mobile wireless antenna for electromagnetic absorption reduction. *Materials*, 8(8), 4817-4828, 2015.

[18] Smith, D., D. Vier, T. Koschny, and C. Soukoulis, Electromagnetic parameter retrieval from inhomogeneous metamaterials. *Physical Review E*. 71, 036617, 2005.

[19] Constantine A. Balanis, Fundamental Parameters and Definitions for Antennas, *Modern Antenna Handbook*, 2007.

Mutual Coupling Reduction for Broadband MIMO Antenna Using SRR Unit Cell Metamaterials

Mohannad Obaid Katie[1], Mohd Faizal Jamlos[1,2*]

[1,2,3] Advanced Communication Engineering Centre (ACE), School of Computer and Communication Engineering, Universiti Malaysia Perlis (UniMAP), 01000, Kangar, Perlis, Malaysia
[2]Faculty of Mechanical Engineering, Universiti Malaysia Pahang (UMP), 26600, Pekan, Malaysia.
*corresponding author, E-mail: mohdfaizaljamlos@gmail.com

Abstract

A broadband MIMO antenna at size 36 × 22 mm^2 is proposed. The antenna consists of two identical monopole antenna elements (MA) with T-shaped stub ground plane and metamaterial Single Ring Resonator (SRR) to reduce mutual coupling and enhanced isolation between antenna elements by exhibiting the negative characteristics for both permittivity and permeability. The overall antenna performance is optimized in terms of the reflection coefficient (S_{11}), and mutual coupling (S_{21}), radiation pattern across frequency from 2.8 to 4.95 GHz. A broadband frequency from 2.8 to 4.95 GHz is achieved, which covers WiMAX and the lower UWB band (3.1–4.8 GHz) operation. The dimension of the proposed MIMO antenna is (0.32λ × 0.21λ) at the lower cutoff frequency 2.8 GHz. The Split Ring Structure combination with ground plane effectively reduces inter-element pattern correlation across the operational band with the isolation of 16 dB. Satisfactory diversity performance is confirmed via the envelope correlation coefficient and diversity gain (DG) of 0.02 and 9.7, respectively. Meanwhile, its mean effective gains (MEGs) ratio is near unity.

1. Introduction

The wireless revolution in recent years has increased the demands for devices which is capable of operating across multiple frequency bands with enhanced radio link performance through using the multiple-input multiple-output (MIMO) technology, which employs diversity techniques to improve communication systems reliability via multipath fading reduction [1], [2]. When applied the MIMO antennas in multi-standards devices, the demand is growing on a wideband and high isolation [3]. Thus, bandwidth enhancement and size reduction are becoming main design requirements for printed antennas in different applications [4-6]. Recently, implementing the metamaterial unit cells structures for antenna design enable the performance improvement of MIMO antenna system through the isolation enhancement [7]. The electromagnetic metamaterial is defined as the artificial material structures that can be designed to explain the electromagnetic features that not present in nature [8]. Using the periodic structure of Split Ring Resonator (SRR) with the metal wires, correspondingly the negative relative permittivity and permeability are obtained [9-12]. To decrease the resonant frequency value of an antenna, the metamaterial structures of SRR unit cells are placed along an antenna to be used as a loading structure [13-16]. This work is an effort in designing a broadband MIMO antenna with a low inter-element mutual coupling.

2. Antenna Design Geometry

The structure of the single ring resonator unit cells metamaterial was shown in Figure 1 (a) and (b). The geometrical dimensions of the proposed unit cell are listed in Table 1. The Using of mathematical formulation in [18], [19], is to evaluate the negative index parameters such as permittivity and permeability that produced through exciting the electric and magnetic fields in the wire SRR unit cells. The real and imaginary values of permittivity, permeability refractive index, and impedance are illustrated in Figures 1 (c), (d), (e) and (f). The geometry of the proposed broadband MIMO antenna was depicted in Figure 2 (a) and (b). It is designed on an FR-4 substrate with a thickness of 1.6 mm, permittivity $\varepsilon_r = 4.7$ and loss tangent tan $\delta = 0.025$. The overall structure consists of two identical monopole antenna elements (denoted as MA1 and MA2) placed in parallel on the same side of the substrate with metamaterial structure of unit cells of SRR in between antenna elements. The ground plane with T-shaped stub and GPA are placed on the other side of substrate, to reduce mutual coupling and enhanced the isolation between antenna elements. The optimized dimensions of the proposed antenna are listed in Table 1, and optimization process will be discussed in the next section.

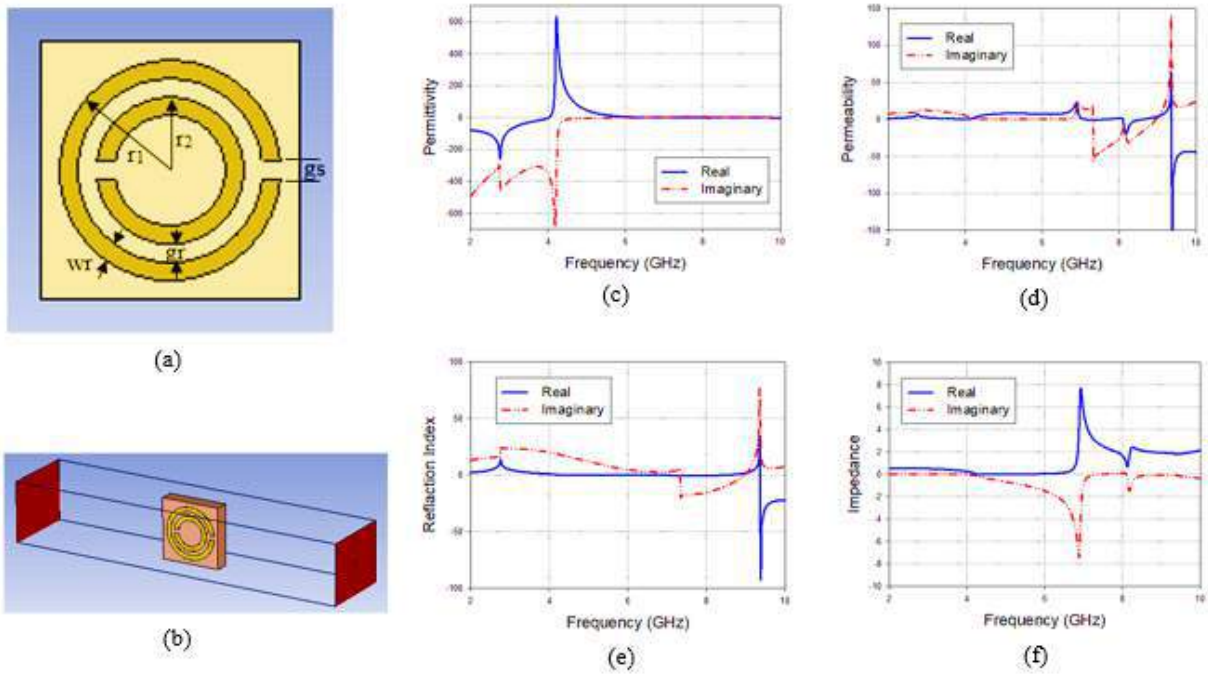

Figure 1: The geometry of single ring resonator (SRR) unit cell structure, (a) unit cell front view, (b), simulation setup, (c) permittivity, (d) permeability, (e) refractive index, (f) impedance.

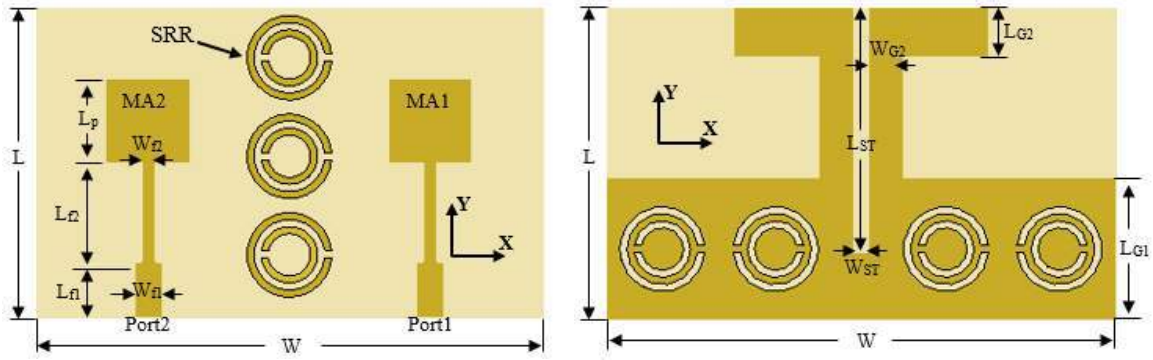

Figure 2: The geometry of proposed Broadband MIMO antenna, (a) front view, (b) back view.

Table 1: Parameters dimensions of the proposed antenna

Para.	Value (mm)	Para.	Value (mm)	Para.	Value (mm)	Para.	Value (mm)	Para.	Value (mm)	Para.	Value (mm)
W	36	L_{f1}	4	L_{G2}	3.5	W_{f2}	1	r1	3	gr	0.5
L	22	L_{f2}	7	L_{ST}	17.2	W_{G2}	2.5	r2	2	gs	0.5
L_p	6	L_{G1}	10	W_{f1}	2	W_{ST}	1	wr	0.5	-	-

3. Results and Discussion

Figure 3 shows the simulated s-parameters of the proposed MIMO antenna, indicating the operation in broadband from 2.5 to 2.85 GHz and from 2.8 to 4.95 GHz. Its operation supports multi-standard operation across WiMAX and the lower band of UWB. Simulated mutual coupling (S_{21}) shown in Fig. 3 indicates the value of -16 dB at lower band and below -20 dB at upper band. This indicates that the proposed antenna is suitable for portable MIMO applications.

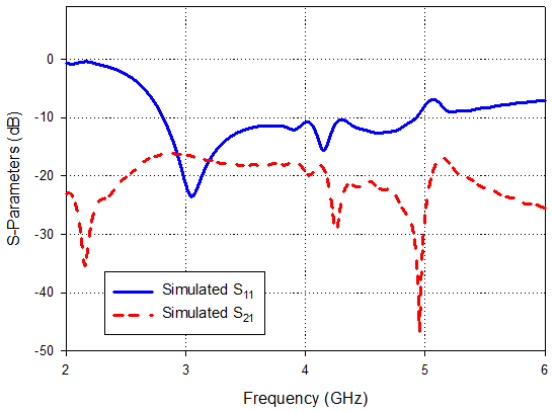

Figure 3: Simulated S_{11} and S_{21} of the proposed broadband MIMO antenna.

The MIMO antenna's radiation patterns evaluated by computer simulation as illustrated in Figure 4. Three dimensions (3D) simulated radiation patterns at the two resonance frequencies 3 GHz and 4.1 GHz are obtained when port 1 is excited, as shown in Figs. 4a and 4c, respectively, Meanwhile 3D radiation patterns exciting from port 2 at the same frequencies are shown in Figs. 4b and 4d, respectively.

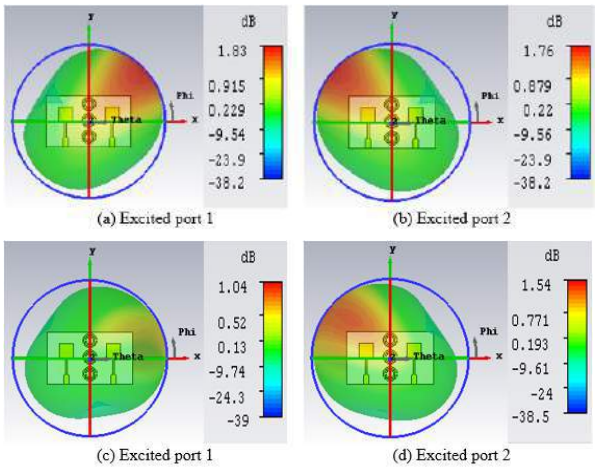

Figure 4: 3D radiation patterns at; (a) 3 GHz and (c) 4.1 GHz when port 1 excited and port 2 terminated with 50-Ω load and 3D radiation patterns at; (b) 3 GHz and (d) 4.1 GHz when port 2 excited and port 1 terminated with 50-Ω load.

4. Conclusions

A compact broadband MIMO antenna sized at 36 × 22 mm^2 is proposed for portable systems. The overall structure consists of two identical planar monopole antennas and a Single Ring Resonator (SRR) metamaterial structure is proposed to reduce the mutual coupling and improve antenna isolation, they located on same side of the substrate. The reverse side contains a ground plane with T-shaped stub designed to reduce mutual coupling and enhance the isolation and Ground Plane aperture (GPA) placed on the other side of substrate, to reduce mutual coupling and enhanced the isolation between antenna elements. The proposed MIMO antenna accomplished a 2:1 VSWR, covered broadband from 2.8 to 4.95 GHz to support multi-standard operation in the WiMAX and the lower band of UWB bands, and featured isolations of at least 16 dB in the desired band. The envelope correlation coefficient of less than 0.05., and its MEG_1/MEG_2 ratio is nearly equal to unity. Its size and results with performance indicated the suitability of the proposed MIMO antenna for portable applications.

References

[1] M. Gallo, E. Antonino-Daviu, M. Ferrando-Bataller, M. Bozzetti, J. M. Molina-Garcia-Pardo, and L. Juan-Llacer, A broadband pattern diversity annular slot antenna, Antennas and Propagation, IEEE Transactions on, vol. 60, 1596-1600, 2012.

[2] Y. Wang and Z. Du, A wideband printed dual-antenna system with a novel neutralization line for mobile terminals, Antennas and Wireless Propagation Letters, IEEE, vol. 12, 1428-1431, 2013.

[3] X. Zhou, X. Quan, and R. Li, A Dual-Broadband MIMO Antenna System for GSM/UMTS/LTE and WLAN Handsets, IEEE Antennas and wireless Propagation letters, vol. 11, 551-554, 2012.

[4] A. Toktas and A. Akdagli, Wideband MIMO antenna with enhanced isolation for LTE, WiMAX and WLAN mobile handsets, Electronics Letters, vol. 50, 723-724, 2014.

[5] J.-F. Li, Q.-X. Chu, and T.-G. Huang, A compact wideband MIMO antenna with two novel bent slits, Antennas and Propagation, IEEE Transactions on, vol. 60, 482-489, 2012.

[6] a. W.-J. L. Shih-Hsun Chang, A Broadband LTE/WWAN Antenna Design for Tablet PC, IEEE Transactions on Antennas and Propagation, vol. 60, no. 9, 4354-4359, 2012.

[7] M. S. Sharawi, A. B. Numan, M. U. Khan, and D. N. Aloi, A dual-element dual-band MIMO antenna system with enhanced isolation for mobile terminals, Antennas and Wireless Propagation Letters, IEEE, vol. 11, pp.

1006-1009, 2012.

[8] P. Mookiah, and K. R. Dandekar, Metamaterial-substrate antenna array for MIMO communication system, IEEE Trans. Antennas Propag., 57(10), 3283-92, 2009.

[9] A. Sarkhel , D. Mitra, and S. R. B. Chaudhuri, A compact metamaterial with multi-band negative-index characteristics, Applied Physics A, 122(4), 1-10, 2016.

[10] M. A. Wan Nordin, M. T. Islam, and N. Misran, A compact wideband coplanar waveguide fed metamaterial-inspired patch antenna for wireless application, Applied Physics A, 109(4), 961–965, 2012.

[11] 11 D. R. Smith, W. J. Padilla, D. C. Vier, S. C. Nemat-Nasser, and S. Schultz, Composite medium with simultaneously negative permeability and permittivity, Phys. Rev. Lett., vol. 84, no. 18, 4184–4187, 2000.

[12] M. Palandoken, A. Grede and H. Henke, "Broadband Microstrip Antenna With Left-Handed Metamaterials, " IEEE Transactions on Antennas and Propagation, vol. 57(2), 331-338, 2009.

[13] Chen, X., T.M. Grzegorczyk, B.-I.Wu, Jr. Pacheco, and J.A Kong, Robust method to retrieve the constitutive effective parameters of metamaterials, Physical Review E, 70.1, 2004.

[14] J. P. Chen and P. Hsu, A compact strip dipole coupled split-ring resonator antenna for RFID tags, IEEE Transactions on Antennas and Propagation, 61(11), 5372–5376, 2013.

[15] O. S. Kim and O. Breinbjerg, Miniaturised Self-Resonant Split-Ring Resonator Antenna, Electronics Letters, 45(4) 196–197, 2009.

[16] M. A. Wan Nordin, M. T. Islam, and N. Misran, A compact wideband coplanar waveguide fed metamaterial-inspired patch antenna for wireless application, Applied Physics A, vol. 109(4), 961–965, (2012).

[17] Y. Ding, Z. Du, K. Gong, and Z. Feng, “A Novel Dual-Band Printed Diversity Antenna for Mobile Terminals,” *IEEE Trans. Antennas Propag.*, vol. 55, no. 7, pp. 2088–2096, 2007.

[18] J. Li, Q. Chu, and T. Huang, “A Compact Wideband MIMO Antenna With Two Novel Bent Slits,” *IEEE Trans. Antennas Propag.*, vol. 60, no. 2, pp. 482–489, 2012.

[19] H. S. Singh, M. Agarwal, G. K. Pandey, and M. K. Meshram, “A Quad-Band Compact Diversity Antenna for GPS L1/Wi Fi/LTE2500/WiMAX/HIPERLAN1 Applications,” *IEEE Antennas Wirel. Propag. Lett.*, vol. 13, pp. 249–252, 2014.

[20] J. Li, Q. Chu, and T. Huang, “A Compact Wideband MIMO Antenna With Two Novel Bent Slits,” *IEEE Trans. Antennas Propag.*, vol. 60, no. 2, pp. 482–489, 2012.

Surface waves guided by metamaterials with rotational disorder

T. Gric[1*], O. Hess[2]

[1] Vilnius Gediminas Technical University, Sauletekio av. 11, LT-10223, Vilnius, Lithuania
[2] Imperial College London, The Blackett Laboratory, Department of Physics, London SW7 2AZ, U.K.
*corresponding author: tatjana.gric@vgtu.lt

Abstract

The analytical analysis of the metamaterial boundary with the rotational disorder reveals both bound and leaky surface plasmon (SP) modes. The dispersion relations of SPs propagating on a surface of these metamaterials are presented along with the propagation lengths. The rigorous modeling and analysis of surface waves at the boundary of two metamaterials possessing rotational disorder are presented. Dispersion properties of two different metamaterial boundaries have been investigated. The results show that the boundary of the metamaterials having different dielectrics employed allows for the presence of the particular modes crossing the light line with the significant portion at lower frequencies lying above the free space light line.

1. Introduction

Guiding the surface wave by artificial metamaterial structures has been the subject of extensive interest over the past decades [1, 2]. This can be explained by two factors. The first one is related to the fact that the dispersion of the surface waves is governed by geometrical considerations. Necessarily, the definite geometry and arrangement of nanoscale enclosures that are typically associated in a periodic lattice determine the unique optical properties of metamaterials [3]. The second favorable factor concerns their sub-wavelength dimensions offering new degrees of freedom for the design of devices [4] with a thickness much shorter than the wavelength.

Since the emergence of the metamaterial, the disorder within artificially structured materials has been a subject of extensive discussions [5-7]. Metamaterial at optical frequency can be considered as a kind of man-made architecture material possessing unusual properties [8]. One of its remarkable features is that the equivalent permittivities on different directions differ from each other and can be varied by designing its structure elaborately [8]. It is worthwhile mentioning, that this property enhanced by the presence of the disorder promises that metamaterial may serve for SP propagating with more flexible performances than conventional metal or ordered metamaterial. For instance, dealing with the photonic crystals, some disorder can dramatically degrade the reflection and transmission properties, which are based on constructive interferences. In contrast, metamaterial media, by taking benefit of strong localization effects is, in theory, not affected by a positional disorder as long as the coupling between these resonators can be avoided [9]. It is worthwhile mentioning, that even in right-handed random media, localization of waves also exists [10-12]. Sometimes the localized modes may accidentally couple to each other and form a propagating channel, the "necklace states" [13]. A variety of metamaterials has been studied from the perspective of applying the disorder to the arrangement of the elements comprising the array. The exceptionally fertile ground to achieve effects of disorder on the electromagnetic properties of two-dimensional metamaterial arrays has been provided by the latest development of techniques for fabrication of metamaterials yielding randomized arrays of metamolecules [14] and new ideas for using metamaterials in coherent sources of electromagnetic radiation [15]. The transmission of randomly distributed circular elements over a series of filling fractions has been explored in [16]. Related findings at terahertz frequencies, demonstrating the ability of periodic hole arrays to support surface plasmon like waves as well as indicating the disability of similar arrays consisting of randomly distributed holes to behave in the same way are reported in [17].

When designing the metamaterials, it is generally assumed that these structures are identical, but in fact, fabrication error will have a dramatic impact on geometrical perturbations thus causing some degree of deviation in their resonant properties. As has been proposed earlier [18, 19] a spreading of the oscillator strengths across a finite bandwidth, arises due to the variation in the geometrical parameters of resonant metamaterial elements. It has been demonstrated [20] that a significant variation of the metamaterial magnetic properties may be caused by the even weak microscopic disorder. Additionally, a substantial suppression of the wave propagation in a wide frequency range may happen due to a 10% deviation in the parameters of the microscopic resonant elements may lead to [20]. The disorder effects of left-handed metamaterials with unitary dendritic structure cell have been proposed in [20]. However, the disordering array and geometrical variations have been achieved separately within this studies, and besides, they are at microwave and infrared wavelengths [21, 22]. In recent times, the negative refractive index and permeability in the visible regime have been recognized by means of a disordered silver metamaterial thin film [23]. To the best of our knowledge the limited number of studies

examining the SPs deals with the disordered metamaterial case [24, 25].

The possibility of reconstructing an image with subwavelength details has provided the fertile background for the the development of SRR/wire media composite metamaterials [26]. However, several studies [27] have shown that disorder suppresses the left-handed behavior, which is critical for this imaging. It is worthwhile mentioning, that robustness to disorder is crucial when scaling a structure down to the scale of THz or optical wavelengths, where precise control of dimensions becomes more difficult.

In this study, we intentionally perturb the perfect checkerboard geometry taking a similar approach to [28]. Doing so, the rotational disorder is introduced by changing the orientation of the nanobeams with respect to the unit cell. However in this case the square size is not fixed and a random rotation is applied to each element with the metamaterial unit cell having the hexagonal shape. We explore how disorder in element rotation affects the dispersion diagrams of the surface plasmon polaritons. It is worthwhile mentioning, that the interface modes in nanostructure metal-dielectric metamaterials have already been considered in [37], however the effect of the rotational disorder has not been taken into consideration.

2. Modeling and the analytical solution

The proposed geometry of the nanobeam composites is shown in Figs. 1, 2. The nanobeams with permittivity ε_m are embedded into a host material with permittivity ε_d..

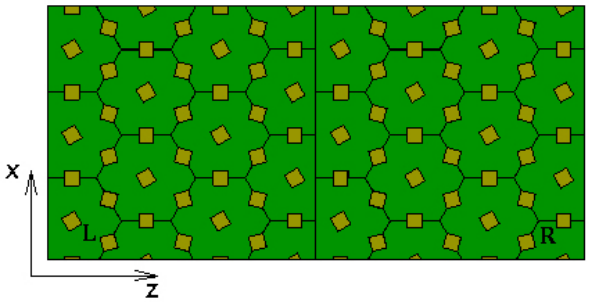

Fig. 1. Schematic view of an interface separating two different nanobeam composites

It should be mentioned, that the optical response of the nanobeam composite resembles that of uniaxial media. It has been proposed that at optical frequencies, Maxwell-Garnett type effective medium theory describes the behavior of the dielectric permittivity tensor components [29-33]. Thus, by means of effective medium approximation it is possible to evaluate the effective permittivities of the nanobeam metamaterial which are described by the following equations:

$$\varepsilon_z^L = \varepsilon_d^L \left[\frac{\varepsilon_m^L \left(1+\rho^L\right) + \varepsilon_d^L \left(1- \rho^L\right)}{\varepsilon_m^L \left(1-\rho^L\right) + \varepsilon_d^L \left(1+\rho^L\right)} \right] \tag{1}$$

$$\varepsilon_z^R = \varepsilon_d^R \left[\frac{\varepsilon_m^R \left(1+\rho^R\right) + \varepsilon_d^R \left(1- \rho^R\right)}{\varepsilon_m^R \left(1-\rho^R\right) + \varepsilon_d^R \left(1+\rho^R\right)} \right] \tag{2}$$

$$\varepsilon_x^L = \varepsilon_m^L \rho^L + \varepsilon_d^L \left(1 - \rho^L\right) \tag{3}$$

$$\varepsilon_x^R = \varepsilon_m^R \rho^R + \varepsilon_d^R \left(1 - \rho^R\right) \tag{4}$$

Here, subindexes *L* and *R* refer to the left and right metamaterial under consideration, respectively. Moreover, ρ is the metal fill fraction ratio enabling to control the metamaterial disorder mechanism and is defined as:

$$\rho = \frac{nanowire\ area}{unit\ cell\ area} \tag{5}$$

To exemplificatively demonstrate the properties of surface waves, we adopt a Drude model to characterize the metal (i. e. silver) in which the permittivity is expressed as $\varepsilon_m(\omega) = \varepsilon_\infty - \dfrac{\omega_p^2}{\omega^2 + i\delta\omega}$.

The parameters are obtained by fitting this dielectric function to a particular frequency range of bulk dielectric data [34]. It is found [35] that for silver, the values of $\varepsilon_\infty = 5$, $\omega_p = 9.5eV$, $\delta = 0.0987eV$ give a reasonable fit to the bulk dielectric data.

A possible way to calculate the metal fill fraction (ρ) is to obtain values for square side (a) and spacing (S) and apply the following equation (assuming perfect hexagonal structure) [36] for the square pore:

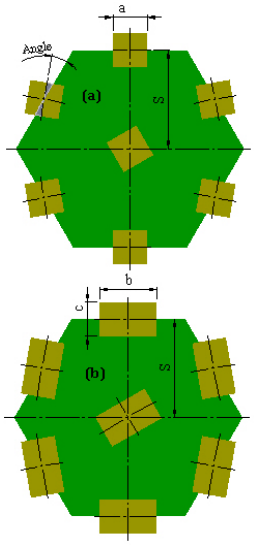

Fig. 2. A metamaterial unit cell with nanobeams having square (a) and rectangular (b) shapes

$$\rho = \frac{2a^2}{\sqrt{3}S^2} \tag{6}$$

and for the rectangular one correspondingly:

$$\rho = \frac{2bc}{\sqrt{3}S^2} \tag{7}$$

Under this assumption, it is possible to derive the dispersion relation for the surface modes localized at the interface between two anisotropic media, we evaluate the tangential components of the electric and magnetic fields at the interface and obtain a single surface mode with the propagation constant [35]

$$\beta = k\left(\frac{\left(\varepsilon_x^R - \varepsilon_x^L\right)\varepsilon_z^R\varepsilon_z^L}{\varepsilon_z^R\varepsilon_x^R - \varepsilon_z^L\varepsilon_x^L}\right)^{1/2}, \tag{8}$$

where k is an absolute value of wavevector in vacuum and β is the component of the wavevector parallel to the interface.

It is worthwhile mentioning, that the reported approach is applicable to any kind of the disordered metamaterial. The effect of the disorder is taken into consideration through the metal fill fraction ρ.

It is interesting to notice that in case of $\varepsilon_m^L = \varepsilon_m^R$ and $\varepsilon_d^L = \varepsilon_d^R$, the obtained result coincides with the dispersion as follows:

$$\beta = k\left(\frac{\varepsilon_d^L\left(\varepsilon_d^L + \varepsilon_m^L - \varepsilon_d^L\rho_L + \varepsilon_m^L\rho_L\right)\left(\varepsilon_d^L + \varepsilon_m^L - \varepsilon_d^L\rho_R \quad \varepsilon_m^L\rho_R\right)}{\sqrt{a+b}}\right) \tag{9}$$

Where

$$a = 4\varepsilon_d^L\varepsilon_m^L - \left(\varepsilon_d^L\right)^2\rho_L - \left(\varepsilon_d^L\right)^2\rho_R + \left(\varepsilon_m^L\right)^2\rho_L + \left(\varepsilon_m^L\right)^2\rho_R + 3\left(\varepsilon_d^L\right)^2$$
$$b = \left(\varepsilon_m^L\right)^2 - \left(\varepsilon_d^L\right)^2\rho_L\rho_R - \left(\varepsilon_m^L\right)^2\rho_L\rho_R \quad 2\varepsilon_d^L\varepsilon_m^L\rho_L\rho_R.$$

On the other hand, the dispersion for the case of $\varepsilon_m^L = \varepsilon_m^R$ and $\varepsilon_d^L \neq \varepsilon_d^R$ depends on the metamaterial parameters as follows:

$$\beta = k\sqrt{\left(\frac{-\left(\varepsilon_d^L\varepsilon_d^R ca\left(\varepsilon_m^L\rho_L - \varepsilon_m^L\rho_R - \varepsilon_d^L\left(\rho_L - 1\right) + \varepsilon_d^R\left(\rho_R \quad 1\right)\right)\right) -}{\left(\frac{\varepsilon_d^L\left(\varepsilon_m^L\rho_L - \varepsilon_d^L\left(\rho_L - 1\right)\right)c}{d} - \frac{\varepsilon_d^R\left(\varepsilon_m^L\rho_R - \varepsilon_d^R\left(\rho_R - 1\right)\right)a}{b}\right)db}\right.} \tag{10}$$

Where

$$a = \varepsilon_d^R\left(\rho^R - 1\right) - \varepsilon_m^L\left(\rho^R + 1\right),\ b = \varepsilon_d^R\left(\rho^R + 1\right) - \varepsilon_m^L\left(\rho^R - 1\right),$$
$$c = \varepsilon_d^L\left(\rho^L - 1\right) - \varepsilon_m^L\left(\rho^L + 1\right),\ d = \varepsilon_d^L\left(\rho^L + 1\right) - \varepsilon_m^L\left(\rho^L - 1\right).$$

3. Discussion

In the following, we study the influence of the square side of the L metamaterial on the surface modes. According to the assumption, the square side varies from 10 nm to 40 nm. Figs. 3-6 show the dispersion curves of the disordered metamaterial. Although the graphs possess the similar outline with that of traditional metal-SP, the dispersion curves for the disordered nanobeams have some particularities that deserve further considerations. Figure 3 is plotted to show the impact of the square side on the surface modes dispersion diagrams. Fig. 3 (a) shows the dispersion curves of the structure under consideration. As a_L increases from 10 to 40 nm, the dispersion curve deviated gradually from that of the a_L=10 nm and is well distinct from the light line and asymptotically approaches different cutoff frequencies. This is similar to the phenomenon originally appearing in the optical frequencies for natural SPPs. The surface modes move to the higher frequencies as the square side increases. Moreover, the frequency range of the waves existence is broadened in comparison with the case of the circular nanowires [38]. Herein, the chosen square side values correspond to the case of the circle inscribed in a square.

Finally, we investigate the influence of the nanobeam shape of the L metamaterial. The square nanobeams are replaced now by the rectangular ones. The side of the rectangle b varies from 10 nm to 70 nm. The surface modes are shown in Fig. 4. As can be seen in Fig. 4, the dispersion curves of the surface modes move to the lower frequencies as b_L decreases.

Generally speaking, the materials composing the metamaterial itself play an important role in studying the surface modes. So it is interesting in the study of the dependence of surface modes on physical parameters of the employed materials. Here, we employ HfO_2 as the dielectric of the R metamaterial. In Fig. 5, we plot the surface modes at the interface of two metamaterials whose parameters are S_L=66 nm, a_R=20 nm, S_R=76 nm, $\varepsilon_m^L = \varepsilon_m^R = \varepsilon_{Ag}$, $\varepsilon_d^L = \varepsilon_{Al_2O_3}$, $\varepsilon_d^R = \varepsilon_{HfO_2}$.

In Fig. 5, the three modes (a_L=10nm, a_L=30nm, a_L=40nm) always lie to the right side of the light line and remain nonradiative (bound) SP modes throughout the certain frequency range. The mode corresponding to the case a_L=20nm is of particular interest due to the fact that its dispersion relation crosses the light line and a significant portion at lower frequencies lies above the free space light line, which usually splits up nonradiative (bound) and radiative (leaky) regions. For the bound modes, longer propagation lengths take place at lower frequencies owning the dispersion that is close to linear. Mode corresponding to the case a_L=30 nm possesses the longer propagation length than the mode corresponding to the case a_L=40 nm.

Looking at the real dispersions of the modes it can be noticed a band bending at frequencies around ω=7·10^{14} Hz. Correspondingly, a divergence in the imaginary parts is observed. Similar deviations are typical of real-frequency (and complex propagation constant) eigenvalue methods. They are not physical and were already reported elsewhere [39-41].

As it is depicted in Figs. 3-6, all the bounded modes always lie to the right side of the light line and remain nonradiative SP modes throughout the whole frequency range. The case presented in Fig. 6 (a) is of particular interest since its dispersion relation crosses the light line and a substantial portion at lower frequencies lies above the free space light line, which typically separates nonradiative (bound) and radiative (leaky) regions. Consequently, the proposed structure will interact with the material via leaky waves. Moreover, the case depicted in Fig. 6 allows the presence of the Ferrell-Berreman modes which exist at energies near the ENZ of the hyperbolic metamaterial to the left of the light line [42-44].

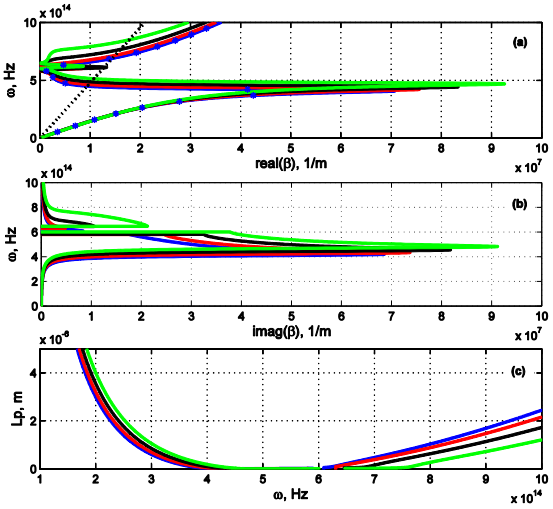

Fig. 3. The dependence of the surface modes on the square side: the dependence of real (a) and imaginary (b) propagation constant on frequency and propagation length (c). The dashed line is the light line in (a); dots represent the numerical simulations by means of the FDTD method in (a). Blue line – a_L=10 nm; red line - a_L=20 nm; black line - a_L=30 nm; green line - a_L=40 nm

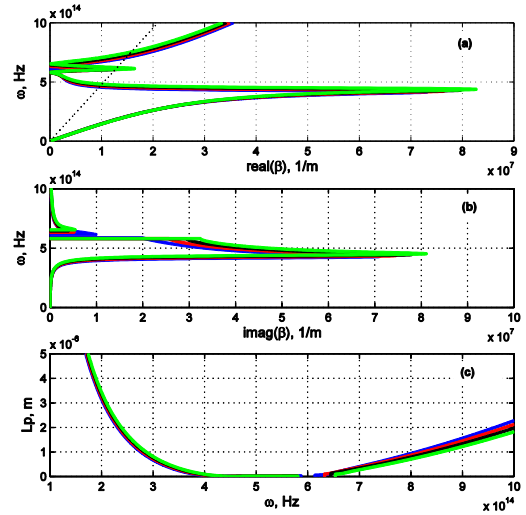

Fig. 4. The dependence of the surface modes on the side of the rectangle b_L: the dependence of real (a) and imaginary (b) propagation constant on frequency and propagation length (c). The dashed line is the light line in (a). Blue line – b_L=10 nm; red line - b_L=30 nm; black line - b_L=50 nm; green line - b_L=70 nm. c_L=10 nm for all the considered cases.

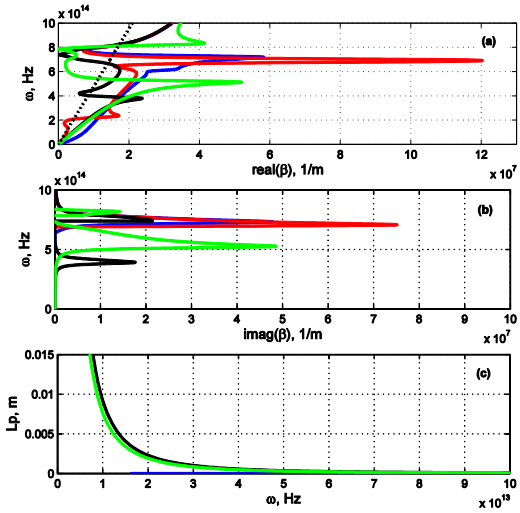

Fig. 5. Calculated surface modes at the interface of two metamateirals composed of different dielectrics included: the dependence of real (a) and imaginary (b) propagation constant on frequency and propagation length (c). The dashed line is the light line in (a). Blue line – a_L=10 nm; red line - a_L=20 nm; black line - a_L=30 nm; green line - a_L=40 nm.

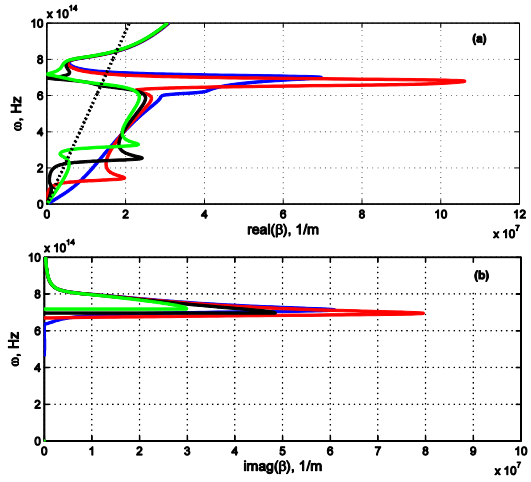

Fig. 6. Calculated surface modes at the interface of two metamateirals composed of different dielectrics included: the dependence of real (a) and imaginary (b) propagation constant on frequency. The dashed line is the light line in (a). Blue line – b_L=10 nm; red line - b_L=30 nm; black line - b_L=50 nm; green line - b_L=70 nm. c_L=10 nm for all the considered cases.

4. Conclusions

We analyzed the boundary of two metamaterials. Despite the simple geometry, the structure allows for rich phenomena. The comparison of both cases (metamaterials with the same dielectric; metamaterials with different dielectrics) gives insight into the differences of the dispersion diagrams. Our results are significant seeking for a better understanding of

the plasmonic properties of SPs in metamaterial, which are useful to design the various metamaterial-based optoelectronic devices.

References

[1] C. J. Zapata-Rodrı´guez, J. J. Miret, S. Vukovic´, M. R. Belic´, Engineered surface waves in hyperbolic metamaterials, *Opt. Express* 21: 19113–19127, 2013.

[2] Z. Jacob, E. E. Narimanov, Optical hyperspace for plasmons: Dyakonov states in metamaterials, *Appl. Phys. Lett.* 93: 221109, 2008.

[3] T. Koschny, M. Kafesaki, E. N. Economou, C. M. Soukoulis, Effective medium theory of left-handed materials, *Phys. Rev. Lett.* 93: 107402, 2004.

[4] N. I. Landy, S. Sajuyigbe, J. J. Mock, D. R. Smith, W. J. Padilla, Perfect metamaterial absorber, *Phys. Rev. Lett.* 100: 207402, 2008.

[5] Y. Nishijima, L. Rosa, S. Juodkazis, Surface plasmon resonances in periodic and random patterns of gold nano-disks for broadband light harvesting, *Opt. Express* 20(10): 11466, 2012.

[6] Y. Nishijima, J. B. Khurgin, L. Rosa, H. Fujiwara, S. Juodkazis, Randomization of gold nano-brick arrays: A tool for SERS enhancement, *Opt. Express* 21(11): 13502–13514, 2013.

[7] A. Moreau, C. Cirac, J. J. Mock, R. T. Hill, Q. Wang, B. J. Wiley, A. Chilkoti, D. R. Smith, Controlled-reflectance surfaces with filmcoupled colloidal nanoantennas, *Nature* 492: 86–90, 2012.

[8] P. Shekhar, J. Atkinson, Z. Jacob, Hyperbolic metamaterials: fundamentals and applications, *Nano Convergence* 1(1): 14, 2014.

[9] J. Hao, É. Lheurette, L. Burgnies, É. Okada, D. Lippens, Bandwidth enhancement in disordered metamaterial absorbers, *Appl. Phys. Lett.* 105: 081102, 2014.

[10] P. W. Anderson, Absence of diffusion in certain random lattices, *Phys. Rev.* 109: 1492, 1958.

[11] A. A. Chabanov, M. Stoytchev, A. Z. Genack, Statistical signatures of photon localization, *Nature* 404: 850-853 2000.

[12] S. Zhang, B. Hu, P. Sebbah, A. Z. Genack, Speckle evolution of diffusive and localized waves, *Phys. Rev. Lett.* 99: 063902, 2007.

[13] Y. Chen, J. A. Newman, K. J. Webb, Circular Bessel statistics: derivation and application to wave propagation in random media, *JOSAA* 31: 2744-2752, 2014.

[14] D. A. Pawlak, Metamaterials and photonic crystals – potential applications for self-organized eutectic micro- and nanostructures, *Scientia Plena* 4: 014801, 2008.

[15] N. I. Zheludev, S. L. Prosvirnin, N. Papasimakis, V. A. Fedotov, Lasing spaser, *Nat. Photonics* 2: 351, 2008.

[16] J. D. Edmunds, Microwave transmissivity of sub-wavelength metallic structures, PhD thesis, University of Exeter (2011).

[17] M. A. Seo, J. W. Lee, S. C. Jeoung, H. Kim, S. Kim, B. Lee, D. S. Kim, Enhanced terahertz transmission: comparisons between metal and absorber, random and periodic arrays of holes, *Proc. of Conference on Lasers and Electro-Optics, and Quantum Electronics and Laser Science Conference CLEO/QELS*, 2006.

[18] I. Shadrivov, D. A. Powell, S. K. Morrison, Yu. S. Kivshar, G. N. Milford, Scattering of electromagnetic waves in metamaterial superlattices, *Appl. Phys. Lett.* 90: 201919-3, 2007.

[19] M. Gorkunov, S. A. Gredeskul, I. V. Shadrivov, Yuri S. Kivshar, Effect of microscopic disorder on magnetic properties of metamaterials, *Phys. Rev. E* 73: 056605, 2006.

[20] X. Zhou, X. P. Zhao, Y. Liu, Disorder effects of left-handed metamaterials with unitary dendritic structure cell, *Opt. Express* 16(11): 7674-7679, 2008.

[21] H. Liu, X. P. Zhao, Metamaterials with dendriticlike structure at infrared frequencies, *Appl. Phys. Lett.* 90: 191904, 2007.

[22] H. Liu, X. P. Zhao, Y. Yang, Q. W. Li, J. Lv, Fabrication of infrared left-handed metamaterials via double template assisted electrochemical deposition, *Adv. Mater.* 20(11): 2050-2054, 2008.

[23] Y.-J. Jen, C.-H. Chen, C.-W. Yu, Deposited metamaterial thin film with negative refractive index and permeability in the visible regime, *Opt. Lett.* 36(6): 1014-1016, 2011.

[24] M. A. Seo, *et al.,* Enhanced terahertz transmission: comparisons between metal and absorber, random and periodic arrays of holes, *Proc. Conference on Lasers and Electro-Optics, and Quantum Electronics and Laser Science Conference CLEO/QELS,* 2006.

[25] Y. Nishijima, L. Rosa, S. Juodkazis, Surface plasmon resonances in periodic and random patterns of gold nano-disks for broadband light harvesting, *Opt. Express* 20: 11466, 2012.

[26] J. B. Pendry, Negative refraction makes a perfect lens, *Phys. Rev. Lett.* 85: 3966, 2000.

[27] J. Gollub, T. Hand, S. Sajuyigbe, S. Mendonca, S. Cummer, D. R. Smith, Characterizing the effects of disorder in metamaterial structures, *Appl. Phys. Lett.* 91: 162907, 2007.

[28] K. Takano, F. Miyamaru, K. Akiyama, H. Miyazaki, M. W. Takeda, Y. Abe, Y. Tokuda, H. Ito, M. Hangyo, Crossover from capacitive to inductive electromagnetic responses in near self- complementary metallic checkerboard patterns, *Opt. Express* 22(20): 24787-24795, 2014.

[29] A. K. Sarychev, R. C. McPhedran, V. M. Shalaev, Electrodynamics of metal-dielectric composites and electromagnetic crystals, *Phys. Rev. B* 62: 8531, 2000.

[30] R. Atkinson et al., Anisotropic optical properties of arrays of gold nanorods embedded in alumina, *Phys. Rev. B* 73: 235402, 2006.

[31] J. Elser et al., Nanowire metamaterials with extreme optical anisotropy, *Appl. Phys. Lett*. 89: 261102, 2006.

[32] G. A. Wurtz et.al., Guided plasmonic modes in nanorod assemblies: strong electromagnetic coupling regime, *Opt. Express* 16: 7460, 2008.

[33] J. C. M. Garnett, Colours in metal glasses and in metallic films, *Philos. Trans. R. Soc. London, Ser. B* 203: 385, 1904.

[34] P. B. Johnson, R. W. Christy, Optical constants of the noble metals, *Phys. Rev. B* 6: 4370, 1972.

[35] C. Oubre, P. Nordlander, Finite-difference time-domain studies of the optical properties of nanoshell dimers, *J. Phys. Chem. B* 109(20): 10042-10051, 2005.

[36] R. Starko-Bowes, J. Atkinson, W. Newman, H. Hu, T. Kallos, G. Palikaras, R. Fedosejevs, S. Pramanik, Z. Jacob,

Optical characterization of Epsilon Near Zero, Epsilon Near Pole and hyperbolic response in nanowire metamaterials, *J. Opt. Soc. Am. B* 32(10): 2074-2080, 2015.
[37] I. Iorsh, A. Orlov, P. Belov, Y. Kivshar, Interface modes in nanostructured metal-dielectric metamaterials, *Appl. Phys. Lett.* 99: 151914, 2011.
[38] T, Gric, O. Hess, Surface plasmon polaritons at the interface of two nanowire metamaterials, *J. Opt.,* 2017.
[39] C. Fietz, Y. Urzhumov, G. Shvets, Complex k band diagrams of 3D metamaterial/photonic crystals, *Opt. Express* 19: 19027, 2011.
[40] K. C. e. a. Huang, Nature of lossy Bloch states in polaritonic photonic crystals, *Phys. Rev. B* 69: 195111, 2004.
[41] Y. Ding, R. Magnusson, Band gaps and leaky-wave effects in resonant photonic-crystal waveguides, *Opt. Express* 15(2): 680-694, 2007.
[42] S. Vassant, J. –P. Hugonin, F. Marquier, and J. –J. Greffet, Berreman mode and epsilon near zero mode, *Opt. Express* 20: 23971-23977, 2012.
[43] S. Vassant, A. Archambault, F. Marquier, F. Pardo, U. Gennser, A. Cavanna, J. Pelouard, J.-J. Greffet, Epsilon-near-zero mode for active optoelectronic devices, *Phys. Rev. Lett.* 109: 237401, 2012.
[44] S. Campione, I. Brener, F. Marquier, Theory of epsilon-near-zero modes in ultrathin films, *Physical Review B* 91: 121408, 2015.

A Modified Theta shaped Double Negative Metamaterial for Satellite Application

Md. Jubaer Alam[1], Mohammad Rashed Iqbal Faruque[1], Mohammad Tariqul Islam[2], Khairul Nizam Abdul Maulud[3]

[1]Space Science Centre (ANGKASA), Institute of Climate Change (IPI), Universiti Kebangsaan Malaysia, 43600 Bangi, Selangor, Malaysia
[2]Department of Electrical, Electronic and Systems Engineering, Universiti Kebangsaan Malaysia, 43600 Bangi, Selangor, Malaysia
[3]Earth Observation Center (EOC), Institute of Climate Change (IPI), Universiti Kebangsaan Malaysia, 43600 Bangi, Selangor, Malaysia
*corresponding author, E-mail: jubaer.alam@iubat.edu

Abstract

The paper imparts the architecture of a modified theta shaped double negative metamaterial unit cell that is felicitous for dual band of microwave frequency. To justify the performance of the proposed resonator an analogy is conferred on transmission coefficient, relative permeability, permittivity and refractive index. A correlation is made on the performance after the analysis of unit cell and array structures. The 9 × 9 mm^2 structure has been printed on FR-4 and a correlation is made between the basic unit cell and array structures to validate the performance of the proposed metamaterial. A great transmission coefficient of 13GHz with a 500MHz band gap in the middle is demonstrated for all of these configurations. The effective parameters of the resonators cover C, X, and Ku-band independently with double negative phenomena at X and Ku-band with a frequency range of about 1.1GHz. Due to its auspicious design, double-negative characteristics and the proposed metamaterial has potential to be used for satellite application.

Keywords Metamaterial, Array Structure, Double negative, satellite communication.

1. Introduction

Metamaterials are the special type of materials that are usually not available in nature. They are actually engineered materials, they need to embed periodic unit cell for their formation to create naturally unavailable electromagnetic properties. Moreover, these materials have the power to control the electromagnetic wave beams to show their unorthodox characteristics. These unusual features of the metamaterials totally depend on the geometry of the atomic construction. It has been started from the year 1968, Veselago et al [1] observed unique properties of materials having negative permittivity (ε) and permeability (μ). But it was not appreciated until 2000 when Smith et al. [2] fortunately validated a new unreal with these unconventional properties (both permittivity and permeability were negative) is called left-handed metamaterial. In case of negativity, it has been categorized as Single-negative (either permittivity is negative or permeability is negative), Double-negative (both permittivity and permeability are negative). There is also a term called near-zero refractive index metamaterial (NZRI) where the permittivity and permeability of a material become approximately to zero on a particular range of frequency. Having these captivating electromagnetic phenomena, necessary applications, like SAR reduction [3-4], super lenses, antenna design [5-7], filters [8], invisibility cloaking [9-10], electromagnetic absorber, and electromagnetic band gaps etc can be employed by metamaterials. In some cases, intrinsic negative permittivity is found. But it is really difficult to find the negative permeability with a natural medium. Even artificial structures can hardly obtain the negative permeability. Concurrently, it is really difficult to get the negative refractive indices. Currently, multi-band metamaterial absorbers have become an auspicious application in the detection of explosives, even in bolometers and thermal detectors. Moreover, a very few studies have been made in designing this type of materials [11-14]. Different alphabetic shapes have become popular for particular operations [15]; like, Benosman et al. [16] introduced a double S-shaped metamaterial that showed negative values of η from 15.67 to 17.43GHz. Mallik et al. proposed various U-shaped rectangular array structures left-handed aspect at approximately 5, 6 and 11GHz. A V-shaped metamaterial was presented by Ekmekci et al. the architecture showed double-negative characteristic. Zhou et al. designed an S-shaped 15 × 15 mm^2 chiral metamaterial for X- and Ku-band application. Though the EMR was not higher than 4. For the purpose of application on S and C bands, Hossain et al. [17] design G-shaped DNG for different unit cells and array sizes.

A metamaterial unit cell of modified theta-shaped has been proposed in this paper. The structure covers multiple bands

(L, C, X, and Ku) of frequencies for the transmission coefficient. And for effective parameters, it covers the X and Ku bands with double negative characteristic.

2. Cell Design

The diagram of the prospective modified Theta-shaped unit cell composition is itemized in Fig. 1. Each unit cell comprises with 9mm in length and 9mm in width. All elements have the thickness of 0.35mm. Each Theta-shaped split resonator has the width of 0.5mm with a same split gap. The outer length of the resonator is 9mm where the split of each of the resonators is 0.5mm. The entire patch (made of copper) is developed on a substrate called FR-4. It has a dielectric constant of $\varepsilon r = 4.3$, a dielectric loss-tangent of $\tan\delta\varepsilon = 0.025$. Sides of the substrate are L = W = 9mm and the thickness is t = 1.6mm. Designed parameters of the proposed metamaterial are enlisted in Table 1.

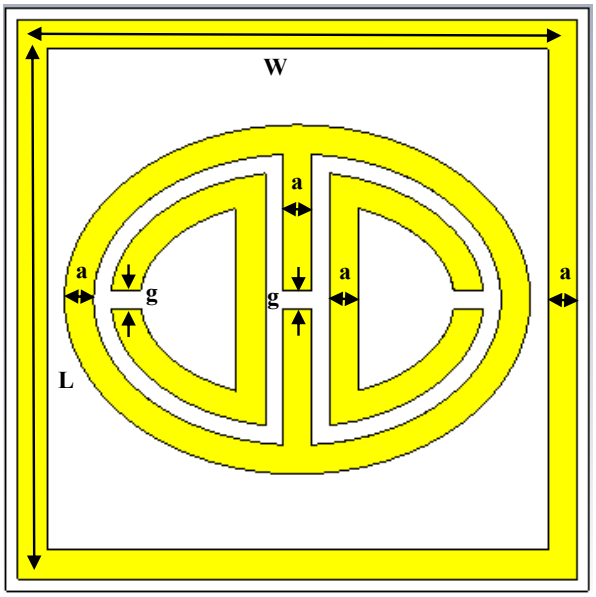

(a)

(b)

(c)

Fig.1: Metamaterial Unit cell: (a) Proposed geometry; (b) Fabricated geometry; (c) Prototype array

A prototype array and a unit cell are fabricated for the purpose of measurement. The area of the array is 36 × 36mm^2. Two waveguide ports are used to propagate the electromagnetic waves to excite the configuration on two opposite direction of Z-axis. PEC and PMC were used along the vertical direction of x and y axis respectively. And for the free-space simulation purposes, a frequency domain solver was utilized. Moreover, for the analysis purpose of these configurations, a tetrahedral mesh was used with a flexible mesh. The normalized impedance was 50 ohms and the system was performed from 1 to 18GHz.

Table 1: Parameters of the unit cell

Parameters	Dimensions (mm)
L	9
W	9
a	0.5
g	0.5

The area of the prototype was 9 × 9 mm,^{2} which was fabricated for the purpose of measurements. By settling the perspective unit cell in between, the waveguides as per the Fig. 2 to actuate the parameters accurately of the metamaterial unit cell. To determine the parameters, we used a vector analyzer commonly known as Agilent N5227A. To calibrate perfectly, an Agilent N4694-60001 was utilized.

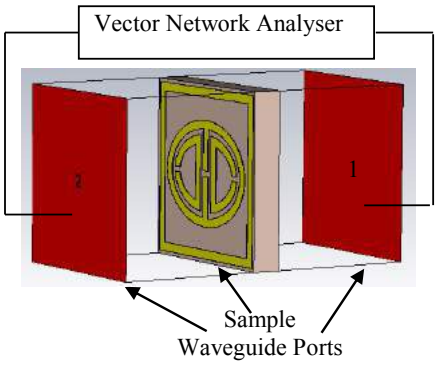

(a)

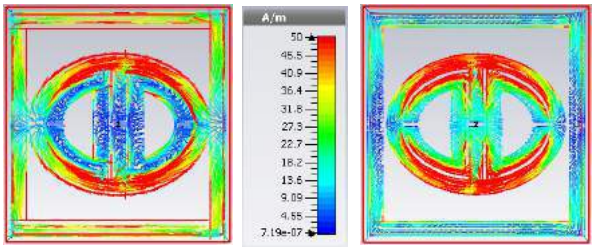

6.5 GHz 13.5 GHz

(b)

Fig.2: (a) Experimental set up for measuring S parameter; (b) Current distribution of the unit cell at various frequencies

3. Results and Discussions

There are plenty of ways to find out the effective parameters of a unit cell like NRW method, DRI, etc. This paper highlights the electromagnetic properties using the real values of ε, μ, and η using S_{11} and S_{21}.

3.1. Analysis of unit cell

As the unit cell is fabricated on a Fr-4 which has an area of 81mm^2, it has been measured within a frequency range of 1 to 18GHz. The simulation was done in the CST microwave studio and the result is compared with the measured one after the fabrication to measure the transmission coefficient (S_{21}). The measured result follows the similar pattern as there is a bit shitting of frequencies in the C-band. The transmission coefficient exhibits a wide band with a coverage of L, C, X, and Ku-band. The first resonance is found in the L-band at frequency 1.63GHz. Then a wide band from 4.68GHz to 17.18GHz with a little band gap of 500MHz. The shifting is occurring due to fabrication error and the free space measurement process.

Fig.2 (b) shows the current distribution of the unit cell at 6.50GHz and 13.5GHz. Due to the antithetical geometry of the structure, a reverse current flow is noticed in the metal fillet of the configuration. Moreover, opposite current flows through the inner and outer surfaces of the resonator creates the stop band at this frequency [18].

Fig.3 (a) shows the magnitude of the transmission coefficient (S_{21}). By using S_{21} and S_{11} parameters, the effective parameters, i.e., effective permeability and effective permittivity can be obtained [19]. Fig.3 (b) and (c) show the result of effective permittivity and effective permeability respectively.
To differentiate the effective permittivity (ε_r) and permeability (μ_r) with S_{11} and S_{21}, the NRW method is applied.

$$\varepsilon_r = \frac{c}{j\pi f d} \times \frac{(1-V_1)}{(1+V_1)} \quad (1)$$

$$\mu_r = \frac{c}{j\pi f d} \times \frac{(1-V_2)}{(1+V_2)} \quad (2)$$

The effective refractive index (η_r) can also be calculated from S_{21} and S_{11} [2]:

$$\eta_r = \frac{c}{j\pi f d} \times \sqrt{\frac{(S_{21}-1)^2 - S_{11}^2}{(S_{21}+1)^2 - S_{11}^2}} \quad (3)$$

Fig.3 (b) shows negative permittivity at resonating points. It shows negativity at 2.60 to 5.16GHz, 6.63 to 9.31GHz and 13.03 to 16.18GHz. Fig.3 (c) exhibits the negative permeability at 7.74 to 13.07GHz and 13.88 to 16.55GHz. At lower frequencies, the current flow matches with the applied field. But in case of higher frequencies, it is not possible for the current to cope up with the applied field when the permeability becomes negative. In the gap, there is a charge produced of a SRR is regulated to a fluctuating magnetic field. Both current and applied field remain in same phase at lower frequencies, but it fails to remain in phase in higher frequencies and as a result, negative permeability produces.
In Fig. 3(d), real and imaginary parts of η are plotted as a function of frequency. The curve shows negativity at 8.13 to 12.14GHz, 13.01 to 15.22GHz and 16.73 to 16.95GHz. Table 2 shows the frequency range of refractive indices with effective parameters of the unit cell at different resonating frequency bands. The refractive index shows negativity when the permittivity and permeability both become negative. Here η shows certain negativity at different bands of frequencies. Hence, the designed unit cell has significant portions, where all the three effective parameters becomes negative. Therefore, this configuration can be allegated as double-negative metamaterial as it has negative peaks at 8.14GHz and 14.01GHz in all the three effective parameters which is shown in Table 2 with bandwidths.

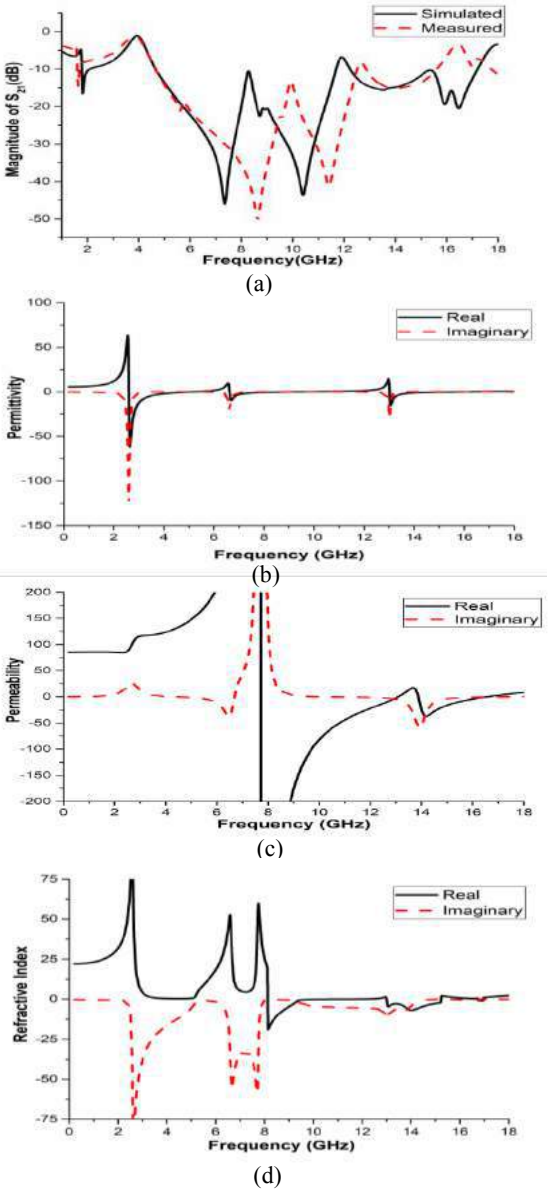

Fig. 3 (a) Measured and simulated results of S_{21} ; Real and imaginary values of (b) effective permittivity (ε) vs frequency; (c) effective permeability (μ) vs frequency; (d) refractive index (η) vs frequency

Table 2: Parameters of the unit cell

Effective parameters	Frequency Range(GHz)	Covered Bands	Values at 8.14 and 14.01GHz
Permittivity (ε)	2.60 to 5.16, 6.63 to 9.31 & 13.03 to 16.18 GHz	S, C, X & Ku	-0.56 & -1.15
Permeability (μ)	7.74 to 13.07 & 13.88 to 16.55GHz	C, X & Ku	-292.49 & -26.21
Refractive Index (η)	8.13 to 12.14, 13.01 to 15.22 & 16.73 to 16.95GHz	X & Ku	-18.32 & -6.99

3.2. Array Analysis

Fig. 4 describes the array formation of the unit structure and unit cell structure which are placed horizontally for 1 × 2 array and both vertically and horizontally on the basic unit structure for higher degrees of arrays on the same Fr-4 substrate. The array structure is measured within the frequency range of 1 to 18GHz. For unit structure, both the patches are placed 0.5mm apart from each other on the substrate. On the other hand, incase of unit cell structure, the gap between the patches is 1mm and the similar approach was used to assess the attainment of the array.

3.2.1. Unit Structure Analysis

Fig.4 (a) shows array formation and (b) shows the transmission coefficient of the array structures. It is apparent that the resonances of the frequencies are found at the same points as the unit cell, but having greater negative magnitudes.

The S21 improves a bit as there is no band gap in between 4.68 to 17.18GHz in case of 1 × 2 array. But it shows a little gap of about 100MHz for 2 × 2 and 4 × 4 array. Fig.4 (c) shows the real values of the permittivity, permeability and refractive index as a function of frequency of array structures.

From Fig.4 (c), it is observed that the negative values for the single unit cell and the array structures are quite similar. The differences among them are the amplitudes or magnitudes and the resonating points shifted a bit to lower frequencies. The negative magnitude decreases in cases of permittivity. But in case of permeability, the negative magnitude increases at resonating points. In case of the refractive index, only the negative qualities are counted. The results of the array structures show similarity with the unit structure. All the effective parameters of these array structures are summarized in table 3. All the arrays show double negative characteristics at 8.14 and 14.01GHz.

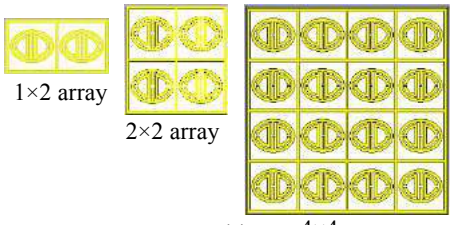

(a)

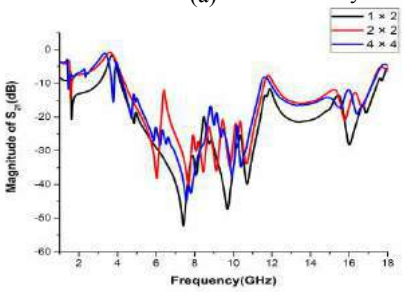

(b)

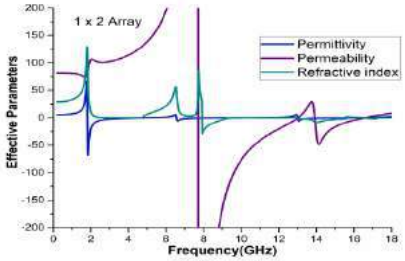

1×2 array

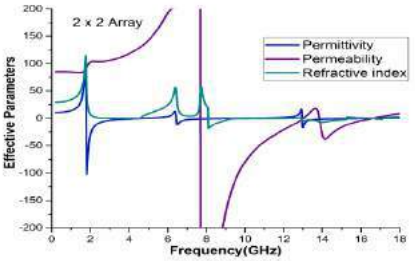

2×2 array

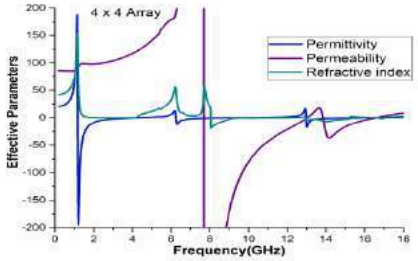

4×4 array

(c)

Fig. 4 Unit structure (a)Different array formation; (b) S_{21} vs frequency; (c) Effective parameters vs frequency for the 1 × 2, 2 × 2, 4 × 4 array.

Table 3: Frequency range of effective parameters of array structures

Effective parameters	Array Structures	Frequency Range (GHz)	Covered Bands
Permittivity (ε)	1 × 2	1.83 – 4.76, 6.55 – 9.19 & 13.92 – 16.45	L, S, C, X & Ku
	2 × 2	1.78 – 4.61, 6.44 – 9.19 & 12.96 – 16.27	
	4 × 4	1.19 – 4.22, 6.27 – 9.12 & 12.98 – 16.20	
Permeability (μ)	1 × 2	7.71 – 13.01 & 13.92 – 16.57	C, X & Ku
	2 × 2	7.71 – 13.01 & 13.85 – 16.58	
	4 × 4	7.69 – 13.03 & 13.87 – 16.55	
Refractive Index (η)	1 × 2	7.92 – 12.32, 12.98 – 15.56 & 16.63 – 17.18	C, X & Ku
	2 × 2	8.10 – 11.98, 12.94 – 15.24 & 16.73 – 17.11	
	4 × 4	2.48 – 3.76, 8.06 – 12.03, 12.96 – 15.24 & 16.73 – 16.96	

3.2.2. Unit Cell structure Analysis

Fig. 5 shows the design of Unit Cell Structures of 1 × 2, 2 × 2 and 4 × 4 array. Here, the total unit cell is arranged horizontally for 1 × 2 array and for higher formations, the unit cells are placed 0.5mm apart both vertically and horizontally based on their degree. And the structures are operated at the frequency range of 1 to 18GHz. The same procedure is followed to evaluate the unit cell and results are compared with the array structures.

The array formations, effective parameters and the transmission coefficient of the unit cell structures are shown in Fig. 5. Array formations are shown in Fig. 5(a), S-parameter is in Fig.5 (b) and Fig.5 (c) contains the real values of effective parameters.

The demonstration was done between two square unit cells. They are actually two different working cells, but the output was quite identical to the single unit cell structure. And the same procedure is repeated for a higher degree of array formations. It is evident from the figure, at lower frequencies, there is a slight deviation in the effective parameters including transmission coefficient. The resonating points shifts a bit from the basic structure. In case of S_{21}, the effect is a bit higher. There is no resonance in the L-band except 2 × 2 formation with a negligible spike. Moreover, instead of getting the double negative at 8.14GHz, the point shifts to 7.94GHz to show the characteristic. But with the increase with frequencies, the unit cell structures showed good commitment to the basic unit cell. However, the unit cell still carries the double-negative characteristic at some extent.

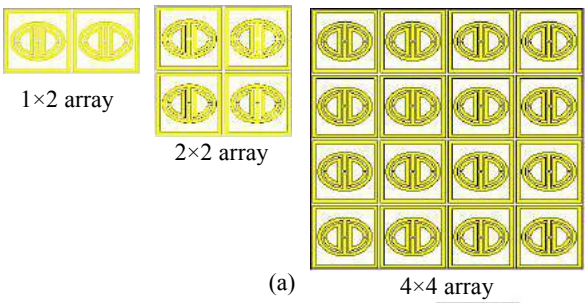

(a)

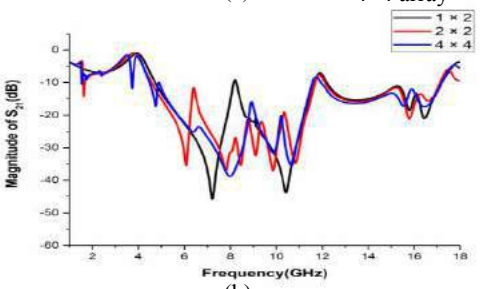

(b)

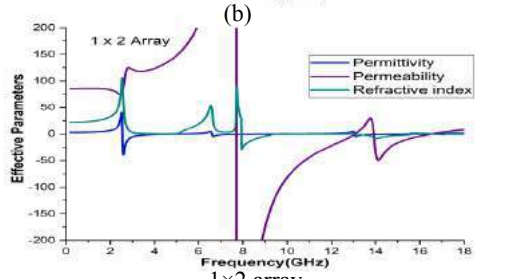

1×2 array

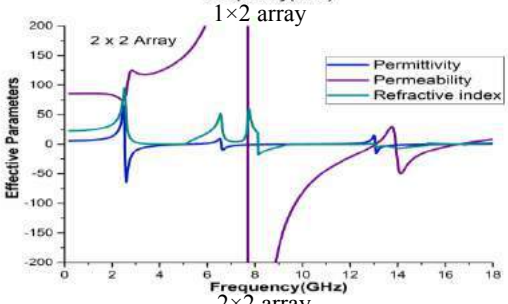

2×2 array

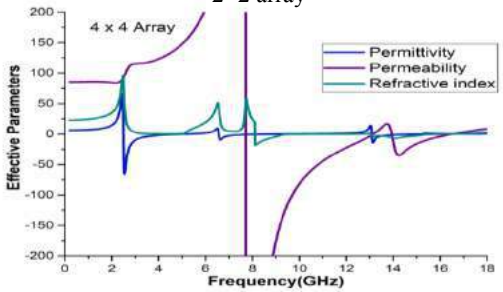

4×4 array

(c)

Fig. 5 (a)Different array formation; (b) S_{21} vs frequency; (c) Effective parameters vs frequency for the 1 × 2, 2 × 2, 4 × 4 array of the unit cell structure.

The transmission coefficient of 13GHz with a 500MHz band gap in the middle is demonstrated for all of these configurations. The effective parameters of the resonators cover C, X, and Ku-band independently with double negative phenomena at X and Ku-band which is similar to basic unit cell. All the effective parameters of these unit cell structures are summarized in table 4

Table 4: Frequency range of effective parameters for unit cell array structures

Effective parameters	Array Structures	Frequency Range (GHz)	Covered Bands
Permittivity (ε)	1 × 2	2.56 – 5.15, 6.59 – 9.28 & 13.05 – 16.41	S, C, X & Ku
	2 × 2	2.55 – 5.15, 6.60 – 9.27 & 13.06 – 16.16	
	4 × 4	2.51 – 5.13, 6.57 – 9.26 & 13.10 – 16.09	
Permeability (μ)	1 × 2	7.73 – 13.06 & 13.92 – 16.55	C, X & Ku
	2 × 2	7.73 – 13.01 & 13.92 – 16.54	
	4 × 4	7.72 – 13.14 & 13.96 – 16.52	
Refractive Index (η)	1 × 2	7.94 – 12.46, 13.01 – 15.58 & 16.61 – 17.12	C, X & Ku
	2 × 2	8.13 – 12.17, 13.07 – 15.25 & 16.77 – 16.86	
	4 × 4	8.12 – 12.21 & 13.07 – 15.28	

4. Comparative Analyses of the configurations

In this paper, total observation is made on S-parameter, effective permittivity, effective permeability, and refractive index. All the results have shown unique, but not contradictory information throughout the methodology. Based on the comparison of 1 × 2, 2 × 2, 4 × 4 arrays and 1 × 2, 2 × 2, 4 × 4 unit structure, it is found that the metamaterial shows double negativity at X and Ku-bands. It has covered 8.13 to 9.31GHz (bandwidth of 1.18GHz) and 13.88 to 15.22 (bandwidth of 1.34 GHz) in basic unit structure. Among these set of results, 8.14 and 14.01GHz is the two frequencies where the double negative character of all sorts of configurations is found. Table 5 shows the covered area and relative bandwidths by the refractive index of different configurations for double negative characteristic.

From the Table 5, it is evident that all the configurations show similar double negative characteristic of the respective frequency range. But more stability is found among basic unit cell, 1 × 2, 2 × 2 and 4 × 4 array with higher bandwidths. Besides 1 × 2, 2 × 2 and 4 × 4 unit cell structures shown fluctuating results with less bandwidth with respect to other configurations.

Table 5: Covered area and relative bandwidths by refractive index of different configurations for double negative characteristic

Structure	Frequency range (GHz)	Band width	Covered Bands	Type of Metamaterial
Unit Cell	8.14 – 9.31 13.80 – 15.22	1.17 1.42	X & Ku	DNG
1 × 2 Structure	7.92 – 9.19 13.92 – 15.56	1.27 1.64	X & Ku	DNG
1 × 2 Unit cell Structure	7.94 – 9.27 13.92 – 15.58	1.33 1.66	X & Ku	DNG
2 × 2 Structure	8.10 – 9.19 13.85 – 15.24	1.09 1.39	X & Ku	DNG
2 × 2 Unit cell Structure	8.13 – 9.27 13.92 – 15.25	1.14 1.33	X & Ku	DNG
4 × 4 Structure	8.06 – 9.12 13.87 – 15.24	1.06 1.37	X & Ku	DNG
4 × 4 Unit Cell Structure	8.12 – 9.26 13.96 – 15.27	1.14 1.31	X & Ku	DNG

5. Conclusions

This paper presents the framework of the modified Theta shaped unit cell and a correlation is contrived on transmission coefficient, relative permeability, permittivity and refractive index. The analyses and the comparisons are made on unit cell, 1 × 2, 2 × 2 and 4 × 4 array structures with 1 × 2, 2 × 2 and 4 × 4 unit cell structures. The transmission coefficient (S_{21}) is calculated and compared with different array formations. The transmission coefficient covered L, C, X and Ku bands for all the configurations. Negative effective parameters are also found in all the structures. However, unit cell, 1 × 2, 2 × 2 and 4 × 4 array structures shown good commitment to the effective parameters. Even the negative values of each of the effective parameters are found on the X and Ku bands at 8.14 and 14.01GHz with a bandwidth of more than 1.20 and 1.32GHz respectively. It certainly represents the dual band double negative characteristic of the proposed compact design. Thus, these structures are valid for the application of dual bands and satellite communication. These can also be a promising choice for double negativity. This modified Theta shaped structure can be an auspicious alternative to new metamaterials, especially in utilizations where metamaterials are the only requirement.

References

[1] V. G. Veselago, The electrodynamics of substances with simultaneously negative values of ε and μ, *Sov. Phys*. 10: 509–514, 1968

[2] D.R. Smith, W.J. Padilla, D.C. Vier, S.C. Nemat-Nasser, S. Schultz, Composite medium with simultaneously negative permeability and permittivity, *Phys. Rev. Lett.* 84: 4184–4187, 2000.

[3] K. Sultan, H. Abdullah, E. Abdallah, Hashish, E. Low-SAR, Miniaturized printed antenna for mobile, ISM, and WLAN services, *IEEE Antennas Wirel. Propag. Lett.* 12: 1106–1109, 2013

[4] M.R.I. Faruque, M.T. Islam, N. Misran, Design analysis of new metamaterial for EM absorption reduction, *Prog. Electromagn. Res.* 124: 119–135, 2012

[5] M. M. Islam, M.T. Islam, M. Samsuzzaman, M.R.I. Faruque, Compact metamaterial antenna for UWB applications, *Electron. Lett.* 51: 1222–1224, 2015

[6] O.M. Khan, Z.U. Islam, Q.U. Islam, F.A. Bhatti, Multiband High-Gain Printed Yagi Array Using Square Spiral Ring Metamaterial Structures for S-Band Applications, *IEEE Antennas Wirel. Propag. Lett.* 13, 2014

[7] Y. Yang, R. Singh, W. Zhang, Anomalous terahertz transmission in bow-tie plasmonic antenna apertures, *Opt. Lett.* 36: 2901–2903, 2011

[8] R. Singh, I. Al-Naib, W. Cao, C. Rockstuhl, M. Koch, W. Zhang, The fano resonance in symmetry broken terahertz metamaterials, *IEEE Trans. Terahertz Sci. Technol.* 3: 1–7, 2013

[9] S.S. Islam, M.R.I. Faruque, M.T. Islam, A Near Zero Refractive Index Metamaterial for Electromagnetic Invisibility Cloaking Operation, *Materials* 8: 4790–4804, 2015

[10] N. Landy, D.R. Smith, A full-parameter unidirectional metamaterial cloak for microwaves, *Nat. Mater.* 12: 25–28, 2013.

[11] B. Gong, X. Zhao, Numerical demonstration of a three-dimensional negative-index metamaterial at optical frequencies, *Opt. Express.* 19: 289–296, 2011.

[12] K. Song, Q. Fu, X. Zhao, U-Shaped multi-band negative-index bulk metamaterials with low loss at visible frequencies, *Phys. Scr.* 84: 035402, 2011.

[13] Y. Huang, J. Wen, Y. Yang, K. Xie, Tunable dual-band ferrite-based metamaterials with dual negative refractions, *Appl. Phys. A* 106: 79–86, 2012.

[14] M.I. Hossain, M.R.I. Faruque, M.T. Islam, M.H. Ullah, A New Wide-Band Double-Negative Metamaterial for C- and S-B and Applications. *Materials* 8: 57–71, 2015

[15] S. S. Islam, M. Rashed, I. Faruque, and M. T. Islam, The Design and Analysis of a Novel Split-H-Shaped Metamaterial for Multi-Band Microwave Applications, *Materials* 7pp. 4994–5011, 2014.

[16] H. Benosman, N.B. Hacene, Design and Simulation of Double "S" Shaped Metamaterial. *Int. J. Comput. Sci.* 9: 534–537, 2012.

[17] Z. Zhou, H. Yang, Triple-Band asymmetric transmission of linear polarization with deformed S-shape bilayer chiral metamaterial, *Appl. Phys. A* 119: 115–119, 2015

[18] M. Hasan, M. Rashed, I. Faruque, and S. S. Islam, A New Compact Double-Negative Miniaturized Metamaterial for Wideband Operation, *Materials* 9pp. 1–12, 2016

[19] O. Luukkonen, S.I. Maslovski, S.A. Tretyakov, A Stepwise Nicolson–Ross–Weir-Based Material Parameter Extraction Method. *IEEE Antennas Wirel. Propag. Lett.* 10: 3588–3596, 2011

Design of a Broad Band – Stop Filter with Metamaterial as Defective Ground System

Md. Jubaer Alam[1], Mohammad Rashed Iqbal Faruque[1], Mohammad Tariqul Islam[2], Khairul Nizam Abdul Maulud[3]

[1]Space Science Centre (ANGKASA), Institute of Climate Change (IPI), Universiti Kebangsaan Malaysia, 43600 Bangi, Selangor, Malaysia
[2]Department of Electrical Electronic and Systems Engineering, Universiti Kebangsaan Malaysia, 43600 Bangi, Selangor, Malaysia
[3]Earth observation Center (EOC), Institute of Climate Change (IPI), Universiti Kebangsaan Malaysia, 43600 Bangi, Selangor, Malaysia
*corresponding author, E-mail: jubaer.alam@iubat.edu

Abstract

In this article, a defected ground structure (DGS) is introduced to design a broad band-stop filter to adjust the resonating characteristics by varying the dimension of the structure. The proposed antenna is embedded into a 50Ω microstrip framework. FR-4 (Lossy) is used as a substrate to design the proposed broad band-stop filter which has a succinct structure. The attainment of the antenna is explored both integrally and experimentally. Here CSRR is introduced in the ground layer. It has been monitored that the level of rejection of the filter in stop band region keeps on going with the introduction of CSRR. This filter is advisable for X-band applications especially on 5.9 to 11.3GHz. It has also been observed by Nicolson-Ross-Weir approach that at the filtering frequency. The effective electromagnetic parameters retrieved from the simulation of the S-parameters imply that metamaterial antenna shows negative refraction bands. This indicates that the proposed antenna has a behaviour to justify the obligation as a Left Handed medium.

Keywords Band-stop filter, Defected ground plane, Left handed medium

1. Introduction

After getting the commercial authorization from Federal Communication Commission (FCC) in February 2002, Ultra-wideband (UWB) applications had become very popular at home and abroad [1]. But this UWB system has to go through probable interferences for WiMax, WLAN and RFID. Thus the use of RF components that operate in multiple bands has become really important to handle this complexity. A lot of researches have been made on the development of filter technology. The context of applications of these filters are included in. In today's world, one of the most essential parameters is confinement among channels in a particular bandwidth. In spite of avoiding possible interferences in a system, Band-stop filter (BSF) is one of the competent arrangements to notify this problem by combining them to the system. In progression, a lot of researches have been done to flourish different kinds of BSF [2].

From last few years, transmission lines have been used with patterned ground structures like spaces, gaps and slots, show interesting characteristics inclusive of band-stop and slow wave phenomena[3-5]. These specially arranged structures are commonly known as slotted ground structure or defected ground structure (DGS) [5]. Park et al. in 1991 proposed this DGS for its improvement quality on filter behaviours and reduction of filter size [6]. Moreover, this DGS has good command over the performance enhancement of stop-band filters, suppression of good harmonics and distinguished periodic system [7]. DGS quenches the response of the effective inductance and capacitance of a microstrip line only by changing the size and shape of it. As a result, the execution of the filter and its circuit can be enhanced. The performance of the filter turned to a different level when matematerials were introduced.

Metamaterials are the special type of materials that are usually not available in nature. They are actually engineered materials, they need embedding periodic unit cell for their formation to create naturally unavailable electromagnetic properties. Moreover, these materials have the power to control the electromagnetic wave beams to show their unorthodox characteristics. These unusual features of the metamaterials totally depend on the geometry of the atomic construction. It has been started from the year 1968, Veselago et al observed unique properties of materials having negative permittivity (ε) and permeability (μ). But it was not appreciated until 2000 when Smith et al. fortunately validated a new unreal with these unconventional properties (both permittivity and permeability were negative) is called left-handed metamaterial. In case of negativity, it has been categorized as Single-negative (either permittivity is negative or permeability is negative), Double-negative (both permittivity and permeability are negative). There is also a term called near-zero refractive index metamaterial (NZRI) where the permittivity and permeability of a material become approximately to zero of a particular range of frequency. Having these captivating electromagnetic

phenomena, necessary applications, like SAR reduction [8], super lenses, antenna design [9], filters [10-11], invisibility cloaking [12], electromagnetic absorber, and electromagnetic band gaps etc can be employed by metamaterials.

Resonant type metamaterials are actually used in filter applications. A variety of sub wavelength resonators are used, such as split ring resonators (SRRs), complimentary split ring resonators (CSRRs), double Slit split-rings resonators (DS-SRRs), double Slit complementary split-rings resonators (DS-CSRRs) [13]etc.
In this paper, a fusion in made by complimentary split ring resonator (CSRR) in the ground plane as defected ground system so that the structure can mostly work in X-band region as broad band-stop band filter.

2. Depiction and configuration

Fig. 1 shows the proposed band-stop filter. The resonating frequency confides on the physical aspects of the structure. The concentration of the structure can be realized depending on the specifications derived from the equivalent circuit Fig. 1 (c) proposed by Woo *et al.* [14]. On the hand, the cut off frequency of this type of filter can be accustomed by maintaining suitable values of the elements of the filter. However, to understand the expected values of lumped filter elements, it is essential to determine the aspects of these transmission lines. The proposed filter is contrived and constructed on a composite material named as glass-reinforced epoxy laminate or FR-4 substrate. This substrate having a height of 1.60 mm and a relative dielectric constant (εr) of 4.4 and loss tangent tan δ=0.02. Defected Ground Structure (DGS) has a direct connection with photonic band gap (PBG). It can be extracted directly from PBG and can be realized when this defected structure is depicted on the ground. This defectiveness in the ground plane interrupts the shield current. This may cause the increment of effective capacitance and inductance in the transmission line [3]. CSRRs are used as DGS under the modified microstrip line. Even resonant frequency can be controlled if the microstrip line and the DGS are modified. This DGS has an influence in implementing compact capacitive coupling to the line is called microstrip DGS. The cut off frequency of the filter depends on the overall slot size. This cut off frequency can be adjusted by varying the slot size. It is essential to reduce the inductance of the strip line if the resonant frequency needs to be shifted up instead of back, or widening the strip line may help to reduce the inductance of the filter. Table 1 shows the parameters of the filter. Commercially available Finite Integration Technique (FIT)-based on Computer Simulation Technology (CST) Microwave Studio software was used to simulate the proposed filter.

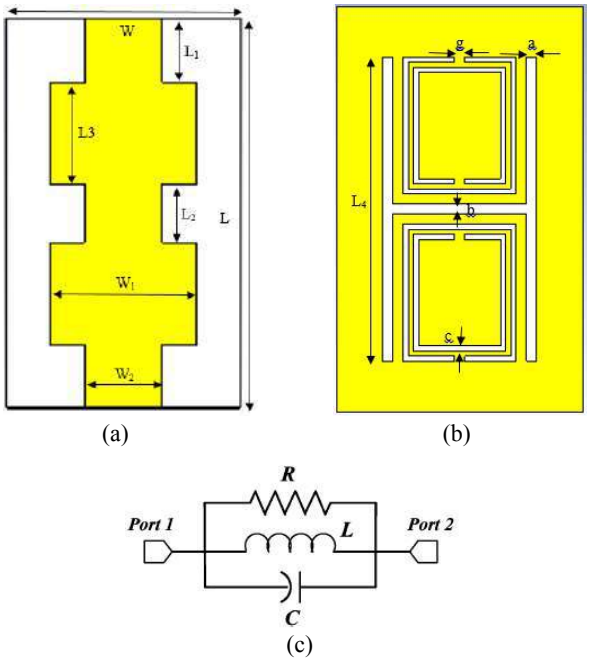

Fig. 1: Geometry of the proposed broad band-stop filter (a) front view; (b) back view and (c) equivalent ckt model of the band stop resonator.

Table 1: Parameters of the unit cell

Parameters	**L**	**L_1**	**L_2**	**L_3**	**L_4**	**W**
Dimensions(mm)	40	6.5	6	10.5	27	24
Parameters	W1	W2	a	b	c	g
Dimensions(mm)	**15**	**8**	**1**	**1**	**0.5**	**0.5**

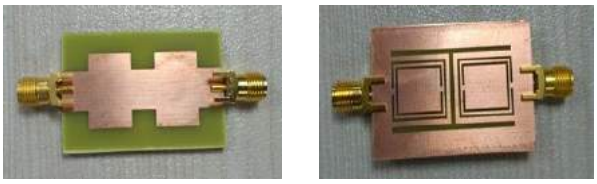

(a) (b)

Figure 2: Prototype of the Band stop filter (a) Front view and (b) Back view

3. Results and Discussions

The filter is designed on FR-4 (substrate) with an area of 24×40 mm^2. A parametric study is made on the dimension of the filter to justify the insertion loss. CSRR in the ground plane is used and the results are compared with the convention one. There are plenty of ways to find out the effective parameters of a unit cell like Nicolson-Ross-Weir (NRW) method, direct retrieval method of refractive index (DRI) etc. This paper highlights the electromagnetic properties using the real values of ε, μ, and η using S_{11} and S_{21}.

Fig. 3 shows the parametric study of the filter and a decision is made on return/ insertion loss characteristics. The simulation is made on 5 to 15 GHz that provides a justification of its unorthodox pattern. In the microstrip line, the width places the main role to adjust the inductive effect. Decrease in inductance shifts the resonant to higher frequencies.

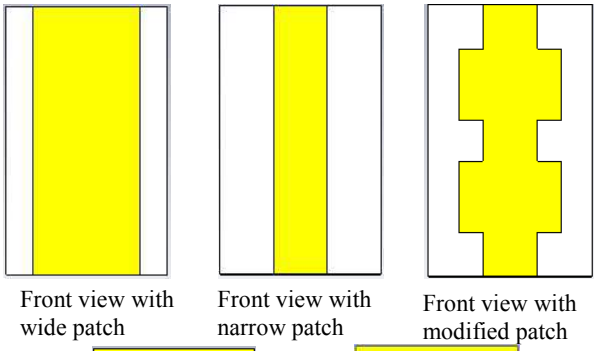

Front view with wide patch | Front view with narrow patch | Front view with modified patch

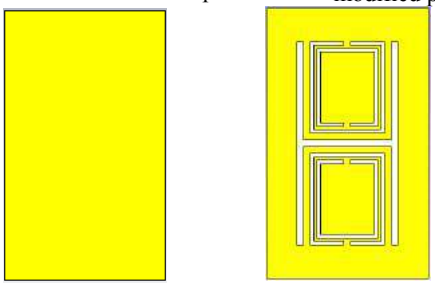

Ground without modification | Front view with wide patch

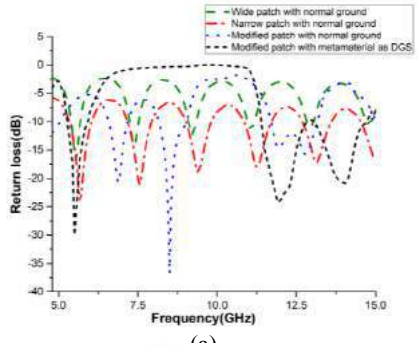

(a)

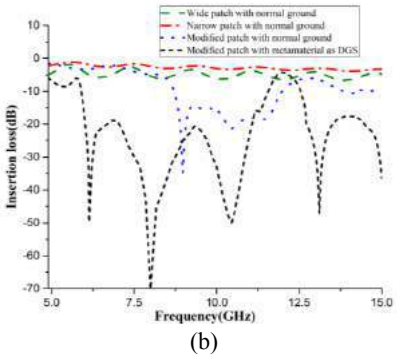

(b)

Fig. 3 Simulated return/ insertion loss characteristics for different structures (a) return loss & (b) insertion loss

Fig. 3 (a) exhibits the return loss of the structure with various shapes of the microstrip line. Keeping the ground unchanged, the microstrip line has been made three different structures. The microstrip line with modification shows less fluctuating response than the other two. But with the use of DGS, the return loss reaches near zero line or less than -10dB line in the frequency range of 5.9 to 11.3 GHz. The application of CSRR has made the band gap in this frequency range.

Fig. 3 (b) exhibits the insertion loss of the configuration with the same three different microstrip lines. Firstly, the loss is observed by applying normal ground and lately, DGS is applied. The modified microstrip line shows better band gap than the other two, so DGS is applied on the ground of the modified microstrip. The insertion loss curves crosses the -10dB line at 5.3GHz and comes back to zero line at 11.3GHz. The influence of CSRR in the ground plane makes the insertion loss wider.

Fig. 4 shows the flat response of return and insertion losses at about 5.9 to 11.9 GHz. Comparatively a wider stop-band has acquired. Moreover, the proposed structure shows broader and deeper band coverage than traditional stop-band filters [15-16]. There is a bit divergence between simulated and measured values. This difference is predominantly due to few parameters like fabrication, dielectric constant and thickness of the substrate, large simulation frequencies and the effect of SMA [17-18]. It is better to check the manufacturing and the measurement process to get a good deal of return loss characteristics for the structure. However, soldering accuracy of the SMA, quality of the substrate and no rusting in the structure need to be considered.

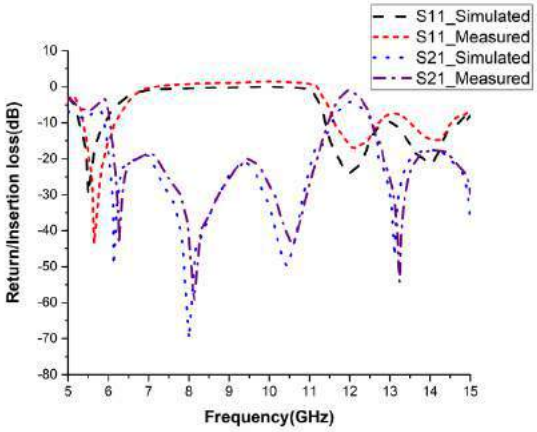

Fig. 4: Simulated and measured return/insertion loss for the proposed band stop filter

3.1. Analysis of Effective parameters

The series of gaps effect the structure for its negative effective permeability. Combining these CSRRs and gaps create a narrow band gap continuously permeability and permittivity emerged close to the resonant frequency [10].

To differentiate the effective permittivity (ε_r) and permeability (μ_r) with S_{11} and S_{21}, the Nicolson-Ross-Weir (NRW) method is applied.

$$\varepsilon_r = \frac{c}{j\pi f d} \times \frac{(1-V_1)}{(1+V_1)} \quad (1)$$

$$\mu_r = \frac{c}{j\pi f d} \times \frac{(1-V_2)}{(1+V_2)} \quad (2)$$

The effective refractive index (η_r) can also be calculated from S_{21} and S_{11} [2]:

$$\eta_r = \frac{c}{j\pi f d} \times \sqrt{\frac{(S_{21}-1)^2 - S_{11}^2}{(S_{21}+1)^2 - S_{11}^2}} \quad (3)$$

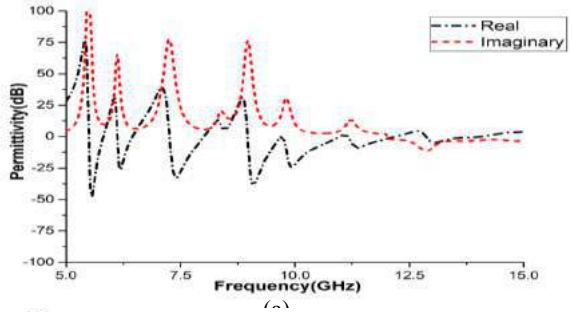

(a)

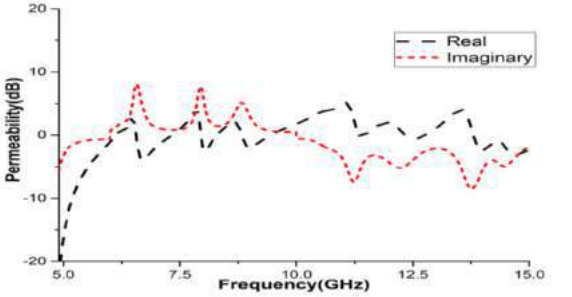

(b)

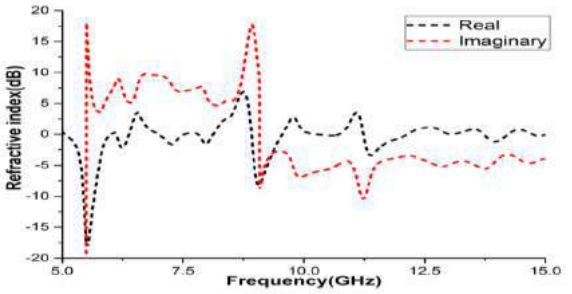

(c)

Fig. 5 (a) Effective permittivity (ε) vs frequency; (b) effective permeability (μ) vs frequency; (c) refractive index (η) vs frequency

Fig.5 (a) shows negative permittivity at resonating points. It shows negativity at 5.49 to 5.81GHz, 6.12 to 6.44GHz, 7025 to 8.01GHz, 8.97 to 10.97GHz, 11.17 to 12.02GHz and 12.86 to 14.08GHz. Fig.5 (b) shows the negative permeability at 5 to 6.11GHz, 6.56 to 7.31GHz, 7.97 to 8.29GHz, 8.84 to 9.44GHz, 11.34 to 11.47GHz, 12.34 to 12.75GHz and 13.80 to 15GHz. At lower frequencies, the current flow matches with the applied field. But in case of higher frequencies, it is not possible for the current to make a go of it with the applied field when the permeability becomes negative. In the gap, there is a charge produced of a CSRR is regulated to a fluctuating magnetic field. At low frequency, the current remains in phase with the applied field, but it fails to remain in phase in higher frequencies and as a result, negative permeability produces.

In Fig. 5(c), real and imaginary parts of η are plotted as a function of frequency. The curve shows negativity at 5.05 to 6.00GHz, 6.11 to 6.38GHz, 7 to 7.52GHz, 7.82 to 8.11GHz, 8.93 to 9.54GHz, 10.25 to 10.73GHz, 11.23 to 12.14GHz, 13.73 to 14.22GHz and 14.74 to 15 GHz. Table 2 shows the frequency range of refractive indices with effective parameters of the filter at different frequency bands. The refractive index shows negativity when the permittivity and permeability both become negative. Here η shows certain negativity at different bands of frequencies. Hence, the designed filter has significant portions where all the three effective parameters becomes negative. Therefore, this band-stop filter can be claimed as double-negative metamaterial as it has negative peaks at 5.51, 7.29, 7.97, 9.05, 11.37 and 13.93GHz in all the three effective parameters which is shown in Table 2 with bandwidths.

Table 2: Parameters of the unit cell

Effective parameters	Frequency Range(GHz)	Covered Bands
Permittivity (ε)	5.49 to 5.81, 6.12 to 6.44, 7025 to 8.01, 8.97 to 10.97, 11.17 to 12.02 & 12.86 to 14.08GHz.	C, X & Ku
Permeability (μ)	5 to 6.11, 6.56 to 7.31, 7.97 to 8.29, 8.84 to 9.44, 11.34 to 11.47, 12.34 to 12.75 & 13.80 to 15GHz.	C, X & Ku
Refractive Index (η)	5.05 to 6.00, 6.11 to 6.38, 7 to 7.52, 7.82 to 8.11, 8.93 to 9.54, 10.25 to 10.73, 11.23 to 12.14, 13.73 to 14.22GHz & 14.74 to 15 GHz.	C, X & Ku

4. Conclusions

This paper presents the framework of the broad band stop filter using modified microstrip line and defected ground structure. Implementation of CSRR in the ground plane creates a constant and flat impedance bandwidth of almost 5.4GHz (5.9 to 11.3 GHz). To justify the performance of the proposed filter an analogy is conferred on transmission coefficient, relative permeability, permittivity and refractive index. The effective parameters of the filter cover C, X, and Ku-band independently with double negative phenomena at C, X and Ku-band. Due to its auspicious design, double-negative characteristics and the proposed structure has potential to be used as Broad band stop filter

References

[1] X. Yin, C. Ruan, S. Mo, C. Ding, and J. Chu, A Compact Ultra-Wideband Microstrip Antenna With Multiple Notches, *Prog. Electromagn. Res.*, 84: 321–332, 2008.

[2] T. Jiang, Y. Wang, and Y. Li, Design and Analysis of a Triple Stop-band Filter Using Ratioed Periodical Defected Microstrip Structure, *De Gruyter,* 71: 1-7, 2016.

[3] V. Radisic, S. Member, and Y. Qian, Novel 2-D Photonic Bandgap Structure for Microstrip Lines, *IEEE Micr. And Guid. Wave Lett.* 8, 2: 69–71, 1998.

[4] D. Ahn, J. Park, A. Member, C. Kim, S. Member, J. Kim, S. Member, Y. Qian, T. Itoh, and L. Fellow, A Design of the Low-Pass Filter Using the Novel Microstrip Defected Ground Structure, *IEEE Trans. Micr. Theory And Tech.*, 49, 1: 86–93, 2001.

[5] C. Caloz, H. Okabe, T. Iwai, and T. Itoh, A Simple and Accurate Model for Microstrip Structures With Slotted Ground Plane, *IEEE Micr. And Wire. Comp. Lett.* 14, 4: 133–135, 2004.

[6] C. Kim, S. Member, J. Park, A. Memeber, D. Ahn, and J. Lim, A Novel 1-D Periodic Defected Ground Structure for Planar Circuits, *IEEE Micr. And Guid. Wave Lett*. 10, 4: 131–133, 2000.

[7] J. Xiaol and Y. Z. J. S. Fu, Non-uniform DGS Low Pass Filter with Ultra-wide Stopband, *IEEE,* 1216–1219, 2010.

[8] M.R.I. Faruque, M.T. Islam, N. Misran, Design analysis of new metamaterial for EM absorption reduction, *Prog. Electromagn. Res.* 124: 119–135, 2012

[9] M. M. Islam, M.T. Islam, M. Samsuzzaman, M.R.I. Faruque, Compact metamaterial antenna for UWB applications, *Electron. Lett.* 51: 1222–1224, 2015

[10] C.Y. Fang, J.S. Gao, H. Liu, A novel metamaterial filter with stable passband performance based on frequency selective surface, *AIP Adv*. 4: 077114, 2014

[11] I. Al-Naib, C. Jansen, R. Singh, M. Walther, M. Koch, Novel THz metamaterial designs: From near- and far-field coupling to high-q resonances, *IEEE Trans. Terahertz Sci. Technol.* 3: 772–782, 2013

[12] N. Landy, D.R. Smith, A full-parameter unidirectional metamaterial cloak for microwaves, *Nat. Mater.* 12: 25–28, 2013.

[13] S. Jindal, Review of Metamaterials in Microstrip Technology for Filter Applications, *Intl. Jour. Comp. App.* 54, 3: 48–54, 2012.

[14] D. Woo, T. Lee, J. Lee, C. Pyo, and W. Choi, Novel U-Slot and V-Slot DGSs for Bandstop, *IEEE Trans. Micr. Theory And Tech*. 54, 6: 2840–2847, 2006.

[15] M. Ojaroudi, N. Ojaroudi, R. Habibi, H. Ebrahimian, Microstrip low-pass fikters by using novel defected ground slot with a pair of protruded t-shaped strips inside the slot, *Adv. Elec. Symp, AES 2012,* Paris, France, Apr. 16-19, 2012

[16] M. Pourbagher, N. Ojaroudi, J. Nourinia, C. Ghobadi, Compact band-stop filter for X-band transceiver in radar applications, *App. Comp. Elec. Society (ACES) Journal,* 30, 4: 423-428, 2015

[17] A. Faraghi, M. Ojaroudi, N. Ghadimi, Compact microstrip low-pass fikter with sharp selection characteristics using triple novel defected structures for UWB applications, *Micro. And Opt. Tech. Lett.* 56, 4 : 1007-1010, 2014

[18] M. Pourbagher, J. Nourinia, C. Ghobadi, Compact Broad Band-Stop Filter with Circular Fractal-Shaped Stubs for X-Band Radar Applications, *App. Comp. Elec. Society (ACES) Journal,32, 1: 56-59, 2017*

A Compact Metamaterial Based Dual Band Patch Antenna for GPS L1/GS Applications

M. Samsuzzaman[1], M. Z. Mahmud[2], M.N. Rahman[2] and M. T. Islam[2]
[1]Dept. of CCE, Patuakhali Science and Technology University, Bangladesh
[2]Dept. Of Electrical, Electronic and Systems Engineering, Universiti Kebangsaan Malaysia, Malaysia
*corresponding author: sobuz@pstu.ac.bd

Abstract

A miniaturized dual band antenna is presented for using GPS L1/GS communication systems. This antenna structure consists of a radiating patch with four mender line resonant elements, and a modified ground plane, which provides a dual band covering from 1.55 GHz to 1.64 GHz frequency. The inductances and capacitances developed due to the ground plane and patterned radiating patch leads to the behavior of the metamaterial. The proposed antenna designed on Rogers's 4350B material substrate with dimension of 25.4 mm × 25.4 mm× 0.70 mm. The proposed antenna shows good omni directional radiation pattern, considerable gain level, and reasonable S11 for using in the GPS L1/GS communication systems.
This is the layout specification and template definition for a paper to be submitted to META Conference.

1. Introduction

Owing to the rapid growth of wireless communication technology, miniature antenna plays a significant role for small size multifunctional devices. In recent days, all communication devices need to be small in size, compact, lightweight, in short should be portable. Moreover, portable devices obligatory to operate dual frequency band applications to use in different areas or countries[1].

Recently, demand of satellite based portable communication devices are increasing noticeably, especially vehicle tracking, mobile communication portable satellite station, weather forecasting etc. A considerable number of patch antenna have been developed targeting better performance for multiple frequency band applications due to lower performance of wired antennas. A low profile, compact, Antenna size reduction with multiband operation capability is still interesting topic for communication engineering researchers. A considerable research effort is given to antenna miniaturization to integrate with small form factor multi frequency devices without compromising the overall performance. There are several techniques have extensively studied by many researchers, such as using reactive impedance substrate [1], artificial magnetic conductor [2], EBG substrate [3], Metamaterials [4-7], Multilayer dielectric substrates [8], etc. Use of ceramic material substrate is one of the effective techniques for antenna miniaturization. Due to higher dielectric constant of the ceramic material substrate, the overall size of antenna can be reduced significantly without compromising the overall performance [9]. Many antenna technology researchers have comprehensively examined the use of ceramic material substrate for miniature antenna design in their article. A miniature antenna was designed using thick truncated textured Ceramic Substrate with the dimension of 14 mm×13.6 mm at 1.88 GHz resonant frequency and obtained 3.5 MHz of bandwidth [10]. A 25 mm×10 mm ×4 mm multiband dielectric resonator antenna designed for multi-standard mobile handheld devices [11]. A miniaturized patch antenna designed with 25.4 mm × 25.4 mm × 6.35 mm dimension using low temperature co-fired-ceramic (LTCC) substrates [12]. On the other hand, Metamaterial-inspired electrically small antennas were proposed in [13] and further developments in the corresponding electric monopole-based electrically small antenna designs have been obtained and confirmed experimentally. Although there is no bulk metamaterial involved in the performance enhancements of these antennas, their radiating elements represent a single unit cell of a metamaterial structure, which leads to the metamaterial-inspired terminology [14, 15]. However, in terms of antenna size reduction or bandwidth enhancement there are still needs to put more research effort for miniaturization with better performance to meet the ever increasing demand for dual band applications.

In this article, a compact (25.4 mm × 25.4 mm×0.762 mm) electrically small, low profile dual band antenna is presented. Multifunctional compact planar versions are introduced by appropriately four meander line elements. These antenna can be used for dual band [GPS L1 and Global star (GS)] linear polarization application. The performance characteristics of the proposed dual band antenna is investigated by Finite Element Method based 3D electromagnetic simulator ANSYS Ansoft High Frequency Structure Simulator (HFSS).

2. Antenna Design

Due to the popularity of satellite positioning and communications, a highly compact, multifunctional antenna that can communicate with satellites to accommodate both voice and data exchanges, while providing GPS

functionality, is of great interest for portable communication device applications. For this perspective, a dual-band GPS L1 (1575.42 MHz) and Global Star (GS, 1610–1621 MHz) electrically small, planar antenna was designed and developed. The proposed dual band antennas geometric layout is presented in Figure 1 (a) top and (b) bottom which is printed on an Rogers 4350B dielectric substrate material with thickness 0.70 mm, dielectric constant 3.66, loss tangent 0.004 and 0.017 copper thickness. The basic architecture of the proposed dual band antenna consists of the radiating patch, a partial ground plane and a coaxial feed-line. The proposed dual band antenna is ported to a 50 Ω SMA connector for signal transmission. To achieve dual band characteristics, the radiating patch consists of some slotted structure with four meander line structure where M1 and M3 meander line elements are responsible for lower band 1.575 (GPS L1 1.575) and M2 and M4 elements is responsible for GS band (1.615 GHz). This can be clearly understand from the surface current distribution of the radiating patch shown in Figure 2 where M1 and M3 are more exciting for the lower band and M2 and M4 are exciting for upper band. The ground plane of the proposed antenna is consists of two near field parasitic elements which is act as single driven elements in the other side of the substrate. By exciting top and bottom driven elements through coaxial fed, both dipoles are the same except for the gaps between the capacitive loads, i.e., the capacitances formed by the gaps between the ends of the arrows. Because of the differences in the resulting capacitances, two independent resonant frequencies were obtained. However, to avoid any unnecessary structural overlaps and to keep the parasitic elements in a one-layer layout, the meander lines were introduced on their legs to increase the overall inductance while allowing a decrease in the requisite capacitances provided by their gaps and still maintaining the desired operating frequency. The choices of the dimensions of the elements were varied according to the usual principles, e.g., thinner traces and longer meander-line segments produce more inductance, and smaller gaps produce more capacitance. A square copper elements also introduced in the center of the radiating patch for widening the total bandwidth. Their final values were optimized with HFSS by studying multiple design iterations and their behaviors. The dimensions of the proposed antenna structure are then optimized using the HFSS simulation software. The final dimensions are: L=25.4 mm, W=25.4 mm, L1= 2.86 mm, L2=2.86 mm, L3=4.57 mm, L4=4.18mm, L5= 1.18 mm, L6=5.23 mm, W1=2.5 mm, R1=8.1 mm.

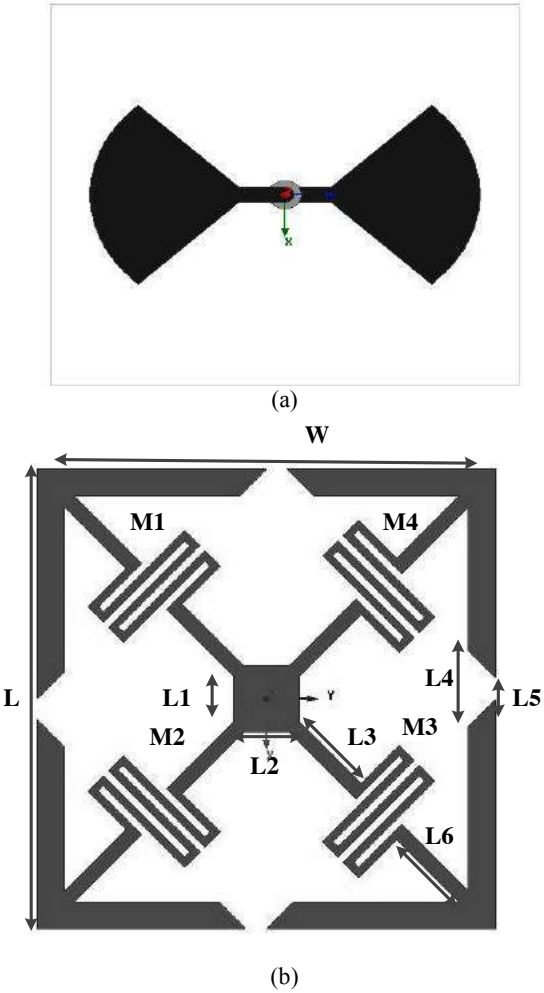

Figure 1: The configuration of the proposed antenna (a) top view (b) bottom view

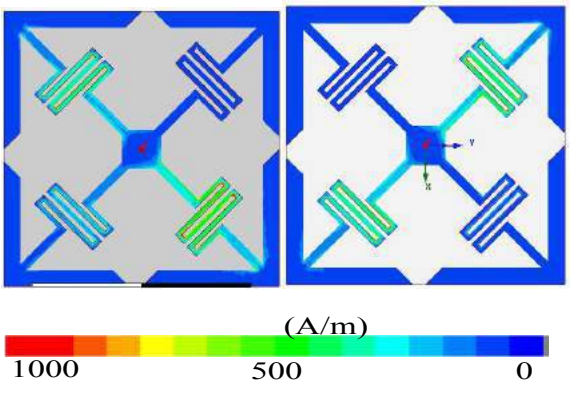

Figure 2: Surface current distribution of the proposed antenna (a) 1.575 GHz, (b) 1.615 GHz

3. Results and Discussions

Fig. 3 shows the simulated reflection coefficient of the proposed dual band antenna. It can be observed from the figure that the proposed antenna achieve -10dB S_{11} (Reflection coefficient) bandwidth from 1.55 GHz to 1.65 GHz which is totally cover the GPS L1 band (1.575 GHz) and GS band (1.615 GHz). The simulated gains and radiation efficiency of the proposed antenna against frequency are shown in Fig. 4. And Fig. 5. At GPS L1 frequency, the corresponding peak gain and radiation efficiencies were 1.44 dB and 92 % respectively. On the other hand, at the GS frequency, the peak gain and radiation efficiencies values were 1.45 dB and 93% respectively. Fig. 6 illustrates the far-field radiation pattern of the proposed antenna at 1.575 GHz and 1.615 GHz, including the xz plane (H-plane) and yz planes (E-plane). It can be seen that omnidirectional radiation pattern can be observed on xz plane and nearly omnidirectional radiation pattern on the yz plane can be observed over the whole operating frequency bands Figure 7 illustrates the 3D radiation pattern of the proposed antenna of the GPS and GS band frequency. The maximum directivity values were 1.72 dB at GPS L1 band and 1.73dB at GS band, respectively.

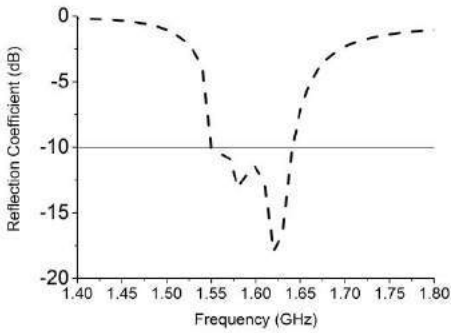

Figure 3: Simulated reflection coefficient of the proposed antenna.

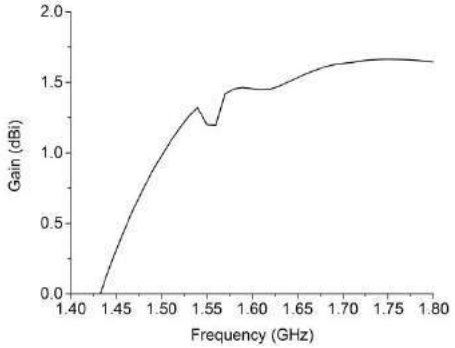

Figure 4: Peak gain of the proposed antenna.

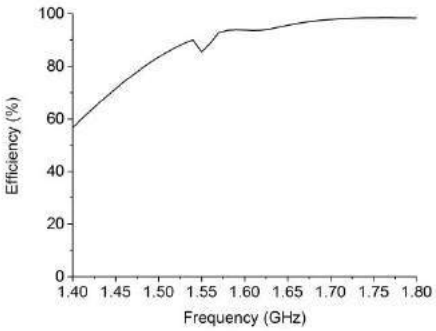

Figure 5: Radiation efficiency of the proposed antenna.

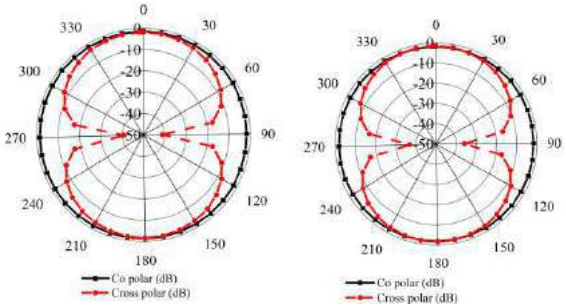

(a)

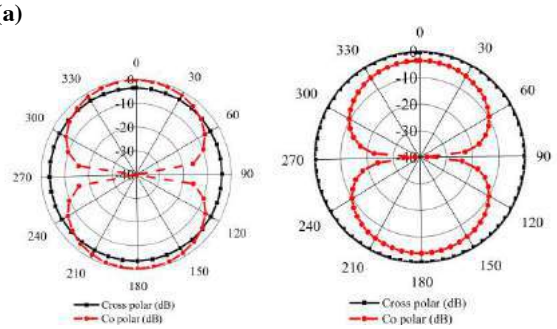

(b)

XZ Plane YZ Plane

Figure 6: Radiation pattern of the proposed antenna, (a) 1.575 GHz, (b) 1.62 GHz

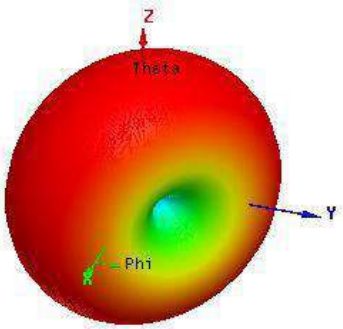

(a)

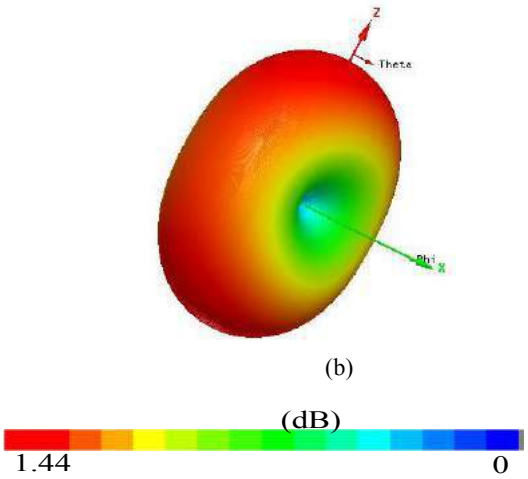

Figure 7: 3D Radiation pattern of the proposed antenna, (a) 1.575 GHz, (b) 1.62 GHz

4. Conclusions

An Omni-directional antenna with dual band characteristic for used in GPS and GS system has been proposed. The designed antenna consists of a radiating patch with four meander line parasitic elements and two Egyptian axe like dipoles to create required dual band frequency. The design antenna faces the -10dB reflection coefficient requirement from 1.55 GHz to 1.64 GHz. The overall antenna dimension is $0.133\lambda \times 0.133\lambda \times 0.004\lambda$ at 1.575 GHz. From the simulated results, it can be shown that the proposed antenna exhibits the dual band characteristic for the GPS L1 and GS band frequency. Reflection coefficient, Gain, radiation pattern and radiation efficiency, directivity of the proposed antenna are analyzed and optimized by using finite element method based 3D-fullwave electromagnetic simulator HFSS. The proposed antenna can be a competitive solution for the current needs to be adopted with small multi technology wireless devices compare to other available dual band antennas.

References

[1] H. Mosallaei and K. Sarabandi, "Antenna miniaturization and bandwidth enhancement using a reactive impedance substrate," *Antennas and Propagation, IEEE Transactions on*, vol. 52, pp. 2403-2414, 2004.

[2] F. Rahmadani and A. Munir, "Microstrip patch antenna miniaturization using artificial magnetic conductor," in *Telecommunication Systems, Services, and Applications (TSSA), 2011 6th International Conference on*, 2011, pp. 219-223.

[3] M. Elayachi, P. Brachat, and J. Ribero, "Novel EBG Structure for Antenna Miniaturization," in *Antennas and Propagation, 2007. EuCAP 2007. The Second European Conference on*, 2007, pp. 1-4.

[4] I. O. Mirza, S. Shi, C. Fazi, and D. W. Prather, "Stacked patch antenna miniaturization using metamaterials," in *Antennas and Propagation Society International Symposium, 2008. AP-S 2008. IEEE*, 2008, pp. 1-4.

[5] H. R. Stuart and A. Pidwerbetsky, "Electrically small antenna elements using negative permittivity resonators," *Antennas and Propagation, IEEE Transactions on*, vol. 54, pp. 1644-1653, 2006.

[6] M. A. Antoniades and G. V. Eleftheriades, "A folded-monopole model for electrically small NRI-TL metamaterial antennas," *Antennas and Wireless Propagation Letters, IEEE,* vol. 7, pp. 425-428, 2008.

[7] C. Caloz, T. Itoh, and A. Rennings, "CRLH metamaterial leaky-wave and resonant antennas," *IEEE Antennas and Propagation Magazine*, vol. 50, pp. 25-39, 2008.

[8] J.-M. Laheurte, L. Katehi, and G. Rebeiz, "CPW-fed slot antennas on multilayer dielectric substrates," *IEEE Transactions on Antennas and Propagation*, vol. 44, pp. 1102-1111, 1996.

[9] M. H. Ullah, M. T. Islam, J. Mandeep, and N. Misran, "Design and analysis of a multi band electrically small antenna using ceramic material substrate," *Przeglad Elektrotechniczny*, vol. 89, pp. 271-274, 2013.

[10] J. Kula, D. Psychoudakis, C.-C. Chen, J. Volakis, and J. Halloran, "Patch antenna miniaturization using thick truncated textured ceramic substrates," in *Antennas and Propagation Society International Symposium, 2004. IEEE*, 2004, pp. 3800-3803.

[11] L. Huitema, M. Koubeissi, M. Mouhamadou, E. Arnaud, C. Decroze, and T. Monediere, "Compact and Multiband Dielectric Resonator Antenna With Pattern Diversity for Multistandard Mobile Handheld Devices," *IEEE Transactions on Antennas and Propagation,* vol. 59, pp. 4201-4208, 2011.

[12] J. Kula, D. Psychoudakis, W.-J. Liao, C.-C. Chen, J. Volakis, and J. Halloran, "Patch-antenna miniaturization using recently available ceramic substrates," *IEEE Antennas and Propagation Magazine,* vol. 48, pp. 13-20, 2006.

[13] A. Erentok and R. Ziolkowski, "Metamaterial-Inspired Efficient Electrically Small Antenna," *IEEE Transactions on Antennas and Propagation,* vol. 56, pp. 691-707, 2008.

[14] R. W. Ziolkowski, "Metamaterial-inspired engineering of antenna systems," in *Antenna Technology and Applied Electromagnetics and the Canadian Radio Science Meeting, 2009. ANTEM/URSI 2009. 13th International Symposium on*, 2009, pp. 1-1.

[15] R. W. Ziolkowski, P. Jin, and C.-C. Lin, "Metamaterial-inspired engineering of antennas," *Proceedings of the IEEE,* vol. 99, pp. 1720-1731, 2011.

Mu-negative metamaterials seen as band-limited non-Foster impedances for magnetic coupled systems

Jorge V. de Almeida[1,2], Gláucio L. Siqueira[1,2], Marbey M. Mosso[1,2], and Carlos A. F. Sartori[3,4]

[1]Center for Telecommunication Studies, Pontifical Catholic University of Rio de Janeiro, Brazil
[2]Dept. of Electrical Engineering, Pontifical Catholic University of Rio de Janeiro, Brazil
[3]Nuclear and Energy Research Institute, University of São Paulo, Brazil
[4]Dept. of Electrical Energy and Automation Engineering, University of São Paulo, Brazil
*corresponding author, E-mail: virgilio@aluno.puc-rio.br

Abstract

In the last decade, various works have demonstrated that a class of artificial material called metamaterials (MTM) can synthesize μ-negative (MNG) media capable of evanescent-wave focusing which largely enhances the magnetic coupling between coils, which is the basic mechanism of Inductive Power Transmission (IPT) systems. In the present work, MTM-enhanced coupling in IPT systems is examined through analytical and numerical results, which are validated by experimental data. Adopting a transmission-line based approach to describe the general MTM-enhanced IPT system, it is evidenced that MNG MTMs can be interpreted as a negative impedance from a circuital point of view.

1. Introduction

The exploitation of evanescent waves in the near field for power transfer purpose has gained a lot of interest recently. In order to prevent radiation, the drivers are high-Q electrically small antennas (ESA). Most of their energy remains stored in the surrounding near field and power transfer occurs primarily via induction. Nonetheless, such inductive power transmission is efficient only for distances smaller than the diameter of the antennas being also quite sensible to misalignment. Electromagnetic MTM slabs presenting effective negative permeability can be used as near-field lenses to improve the overall efficiency of such inductive power transmission systems by enhancing the inductive coupling between the antennas. It has been called MTM-enhanced coupling [1] [2].

This paper describes a transmission-line based approach of the interaction between a MNG MTM and a magnetic link. By introducing the concept of *virtual magnetic transmission line* (VMTL) to describe the magnetic circuit and by calculating an equivalent virtual impedance to represent the MTM slab, the gain mechanism of those lenses can be regarded as a non-Foster impedance matching. Foster's reactance theorem states that any lossless passive one-port network has a reactance (or susceptance) derivative that increases with frequency [3]. According to [4], non-Foster circuits can provide negative resistance, negative inductance and negative capacitance (meaning that their slope varies decreases with frequency). As it will be further shown, a passive MNG MTM behaves as a band-limited negative impedance described by a negative resistor in series with a negative inductor. The negative inductance implies on reduction of the amount of net energy stored in the magnetic circuit while the negative resistance implies on potential gain across the MTM.

This work is organized as follows: In section 2, a generalized theory of transmission lines is presented in order to include a magnetic coupled system. In section 3, an equivalent virtual impedance for the proposed MTM slab is obtained. In section 4, it is demonstrated by means of analytic calculations and numerical results that a magnetic link can be satisfactorily described as virtual transmission line and that the gain introduced by the MTM is due to improvements in the impedance matching between the drivers. The results are supported by experimental evidence.

2. Generalized theory of transmission lines

2.1. Physical and virtual transmission lines

Most of the classical literature on transmission line (TL) concentrates exclusively on electric transmission lines (ELTL) or the guidance of electromagnetic energy using two or multiple electric conductors (two-wire TL, coaxial cable, stripline and so on). Only recently, more general concepts of TLs have been proposed. According to [5], a time-varying magnetic flux can guide EM fields as electric currents in conventional TLs. In [6], it is proposed a generalization for TL theory by introducing the concept of *virtual TLs*.

Since electric and magnetic fluxes have the same dimension of electric and magnetic charges, respectively, a time-varying flux acts as a sort of "virtual current" driving the fields.

It can be easily shown that a time-varying flux is a current:

$$j\omega\psi_m = j\omega \iint \boldsymbol{B}\cdot d\boldsymbol{s} = \iint j\omega\boldsymbol{B}\cdot d\boldsymbol{s} = \iint \boldsymbol{J}_{m,d}\cdot d\boldsymbol{s} = I_{m,d} \quad [V] \qquad (1)$$

According to the Collins Dictionary [7], the word *virtual* means *"sonnearlyntrue that for most purposes it can be regardednasntrue",n"havingnthenessencenornreffectnbutnotnthen appearancenornformnof"* or *"beingnsuchnpracticallynorninn*

effect, although not in actual fact or name". Thus, as fluxes produce *virtually* the same effect as physical charges concerning guidance, the phenomena of electric and magnetic induction can be effectively described through TL equations by taking the displacement currents as *virtual currents*, the fluxes as *virtual charges* and the reluctance to the flux of the medium as *virtual impedances*.

Hence, physical TLs are defined as the ones where EM fields are guided by means of conduction currents, and virtual TLs, as the ones where EM fields are guided by means of displacement currents.

2.2. Propagation equations for virtual magnetic transmission lines

The virtual magnetic transmission line (VMGTL) is defined as a magnetic circuit formed between two insulated drivers (no physical charge is flowing from one driver to the other) coupled by an intervening quasistatic magnetic field. The transmitting driver is the magneto-motive force (MMF) source generating the time-varying magnetic flux (magnetic displacement current) that links the terminals. The receiving driver is the transducer connected to the load that "converts" the virtual magnetic charges (the magnetic flux) to physical ones (see Fig. 1).

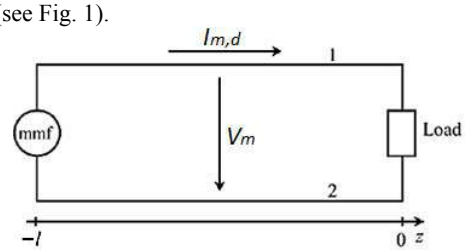

Figure 1: Schematic of a virtual magnetic transmission line.

The total MMF of the virtual line is a real magnetic potential V_m because fluxes going in opposite directions possess inverted magnetic potentials. Consequently, there must be a uniform magnetic field stored between them:

$$MMF = \psi_m \mathcal{R}_m = \int_a^b \boldsymbol{H} \cdot d\boldsymbol{l} = V_m \quad [A] \tag{2}$$

As it is shown in Fig. 2, power flow in a VMGTL is the product of this magnetic field stored between the fluxes and the electric field generated by the time-varying flux in the form of electric-field circulation [8]:

$$P = j\omega \mathcal{R}_m \psi_m^2 = V_m I_{m,d} \quad [W] \tag{3}$$

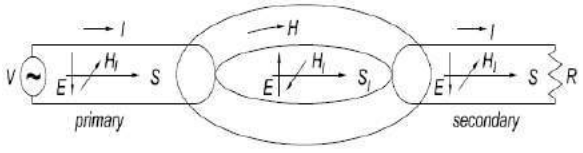

Figure 2: The transversal magnetic field component is responsible for power flow, not the magnetic field parallel to the flux.

Making the simplifying hypothesis that the magnetic flux is mostly confined in a magnetic circuit of fixed transversal section, the virtual TLs can be said to obey propagation equations in terms of potential and current similar to the ones followed by classical ELTLs:

$$\frac{d}{dz} V_m(z) = \left(\frac{\mathcal{R}'_m}{j\omega} + G'_e + j\omega C' \right) I_{m,d}(z) = Y_m I_{m,d}(z) \tag{4}$$

$$\frac{d}{dz} I_{m,d}(z) = (G'_m + j\omega L') V_m(z) = Z_m V_m(z) \tag{5}$$

where Z_m, Y_m, $\mathcal{R}'_m$, G'_e, G'_m, L' and C' denote the series impedance, the shunt admittance and the magnetic reluctance, the electrical conductance, the magnetic conductance, the inductance and the capacitance per unit length, respectively.

Its characteristic impedance Z_0 is given by:

$$Z_0 = \frac{I_{m,d}(z)}{V_m(z)} = \sqrt{\frac{Z_m}{Y_m}} = \sqrt{\frac{G'_m + j\omega L'}{\frac{\mathcal{R}'_m}{j\omega} + G'_e + j\omega C'}} \tag{6}$$

The term $\frac{\mathcal{R}'_m}{j\omega}$ can be said to be a virtual admittance because it neither stores nor dissipate any real power. Like the radiation resistance of an antenna, which is also a virtual impedance [9], it has no relationship with the thermal equilibrium of the circuit that is generating the flux.

The complex propagation constant γ, the load reflection coefficient Γ and the input impedance Z_{in} are given by:

$$\gamma = \sqrt{Z_m Y_m} = \sqrt{\left(\frac{G'_m}{j\omega} + L' \right) \left(-\frac{\mathcal{R}'_m}{\omega^2} + \frac{G'_e}{j\omega} + C' \right)} \tag{7}$$

$$\Gamma = \frac{Z_L - Z_0}{Z_L + Z_0} \tag{8}$$

$$Z_{in} = Z_0 \frac{Z_L + Z_0 \tanh(\gamma l)}{Z_0 + Z_L \tanh(\gamma l)} \tag{9}$$

where Z_L is the load impedance.

The magnetic potential and the virtual current can be identified and converted into the physical electric potential V_e and the physical electric current I_e in the terminals through:

$$V_m(-l) = V_m^{in} = I_e^{in} \tag{10}$$

$$I_{m,d}(-l) = I_{m,d}^{in} = V_e^{in} \tag{11}$$

$$V_{m,v}(0) = V_m^{out} = I_e^{out} \tag{12}$$

$$I_{m,d}(0) = I_{m,d}^{out} = V_e^{out} \tag{13}$$

Note that the magnetic and electric potentials and currents are dimensionally inverted.

Since VMGTLs support the transverse electromagnetic (TEM) mode [5], propagation is described by a one-

dimensional Helmholtz equation [10]. Its generic solution is given by:

$$I_m(z) = I_m(0)e^{-\gamma z}(1 + \Gamma e^{2\gamma z}) \quad (14)$$

$$V_m(z) = \frac{I_m(0)}{Z_0}e^{-\gamma z}(1 - \Gamma e^{2\gamma z}) \quad (15)$$

2.3. Propagation equations for virtual magnetic transmission lines in free space

If there is no ferromagnetic material channeling the flux from the source to the load, the propagation equations of the virtual line must be adapted to compensate the flux leakage. Supposing that the reflection coefficient Γ must increase inversely with the coupling between the terminals of the TL:

$$I_m(z) = I_m(0)e^{-\gamma z}\left(1 + \frac{\Gamma_m}{\kappa_m}e^{2\gamma z}\right) \quad (16)$$

$$V_m(z) = \frac{I_m(0)}{Z_0}e^{-\gamma z}\left(1 - \frac{\Gamma_m}{\kappa_m}e^{2\gamma z}\right) \quad (17)$$

where κ_m is the magnetic coupling coefficient:

$$\kappa_m = \frac{L_m}{\sqrt{L_1 L_2}} \quad (18)$$

3. Equivalent virtual impedance for a μ-negative metamaterial

Table 1: The constitutive parameters of the MTM slab

L_{cell}	$240\ nH$
f_0	$32.4\ MHz$
$C = \frac{1}{\omega_0^2 L}$	$100pF$
Q_{cell}	245
Cell number	49
Periodicity	2.3 cm

The proposed MTM to synthesize a MNG slab is the same model exploited in [1]. Its main characteristics are presented in Table 1.

The Lorentz model can be used to estimate the relative permeability μ_r of the MTM [11]:

$$\mu_{r,MTM} = 1 + \frac{F\omega^2}{\omega^2 - j\omega\xi - \omega_0^2} \quad (19)$$

where F is the coupling coefficient between adjacent cells of the lattice and ξ is the damping ratio of the system.

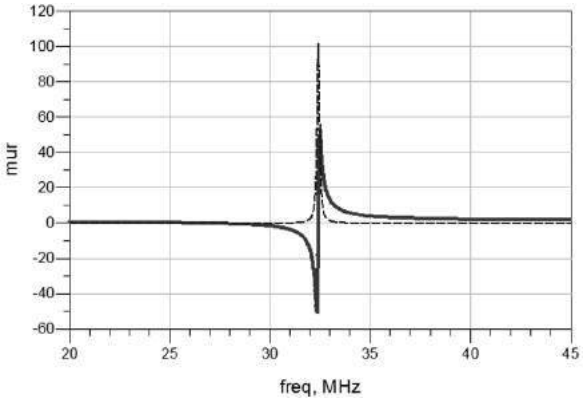

Figure 3: Estimation of the real (solid) and imaginary part (dash) of μ_r.

As it can be seen in Fig. 3, μ_r becomes negative around the resonance frequency ($f_0 = 32.4\ MHz$):

$$\mu_{r,MTM_{analytical}} = -51 - j101.6 \quad (20)$$

The equivalent inductance of the MTM can be determined from its effective parameters:

$$L_{MTM} = \mu_{r,MTM}\mu_0 a = \left(1 + \frac{F\omega^2}{\omega^2 - j\omega\xi - \omega_0^2}\right)\mu_0 a \quad (21)$$

Then, the MTM equivalent virtual impedance is given by:

$$Z_{m,v}(\omega) = jX_{MTM}(\omega) = j\omega L_{MTM}(\omega) \quad (22)$$

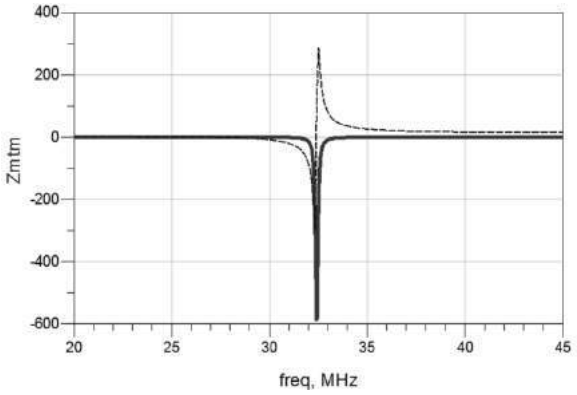

Figure 4: MTM equivalent impedance Z_{MTM} as a function of frequency.

Since the slope of Z_{MTM} does not increases monotonically with the frequency, it can be said to possess a band-limited non-Foster behavior. As it is shown in FIG, the MTM is perceived as negative resistance and a negative reactance around the resonance ($Z_{MTM} \in \mathbb{R}^-$). At the range of sub-resonance frequencies, it is completely invisible to the virtual line ($Z_{MTM} = 0$). And at the over-resonance one, it is seen as a positive reactance ($Z_{MTM} \in Im^+$).

As a negative resistance it acts in the sense of enhancing (restoring) the magnetic current (and consequently the magnetic flux) of the virtual line:

$$\frac{d}{dz}I_{m,d}(z) = -|Re\{Z_{MTM}(\omega_0)\}|V_{m,v}(z) \quad (23)$$

As a negative reactance, it becomes equivalent to a negative inductor and converts the stored energy in the magnetic field into the complementary electric one, reducing the total reactance of the circuit and enhancing the electric potential. On the other hand, as a positive reactance the MTM becomes equivalent to an inductor and stores energy in the surrounding magnetic field. The energy stored by the MTM from higher frequency modes is the energy it uses to amplify the resonance mode.

4. Application

The proposed free-space VMGTL consists of two magnetically coupled loop antennas of radius $r = 5\,cm$ made of copper wire with diameter $p = 1\,mm$ assisted by the MTM described in section 3. The loops operate far from self-resonance. It is assumed that the electrical resistance of wires, the capacitance C and the radiation resistance of the antennas as well as the internal resistance of the source are all negligible. The secondary driver is connected to a load $R_L = 50\,Ohms$. The drivers are separated by a distance $D = 15\,cm$. The amplitude of the tension source is $V_{e,c}^{in} = 1\,V$. The source loop is assumed to have a small internal resistance $R_{source} = 0.5\,Ohms$.

The analytical results are a direct application of the TL model for coupled systems presented in section 2. The numerical results were achieved by the FDTD method on Agilent EMPro and CST studio. The experimental data were obtained using a Vector Network Analyzer.

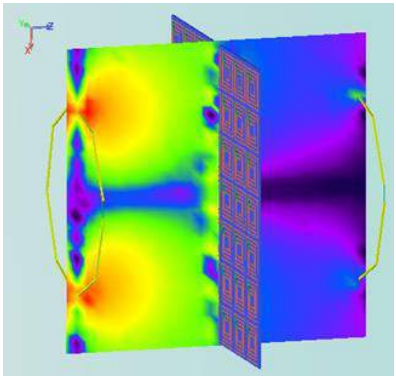

Figure 5: Magnitude of H_x out of the resonance at the plane XZ

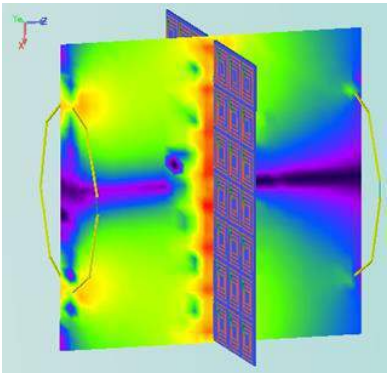

Figure 6: Magnitude of H_x at the resonance at the plane XZ

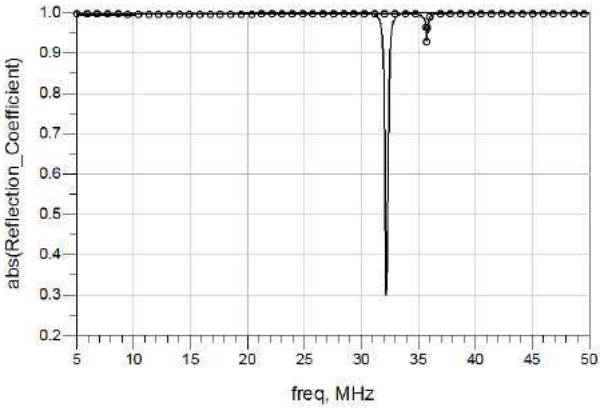

Figure 7: Analytical (solid) and numerical (circle) results for the magnitude of Γ with the MTM slab

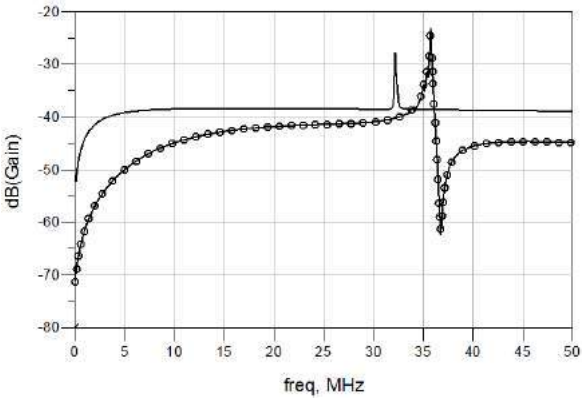

Figure 8: Analytical (solid) and numerical (circle) results for the gain G with the MTM slab inside of the magnetic link

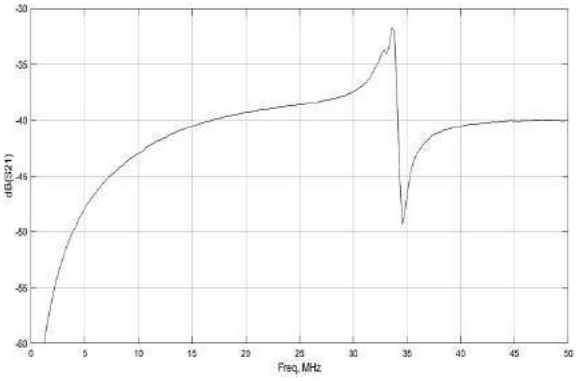

Figure 9: Experimental result for the gain G with the MTM slab

5. Discussion and conclusion

As it is shown in Fig. 5 and Fig. 6, there is a component H_x of the magnetic field inside the link because of the magnetic potential difference V_m between the incoming and the ongoing fluxes trespassing the drivers. It can be clearly seen that the distribution of H_x (thus, the distribution of V_m) is quite improved along the line when the MTM is activated, making the system to behave more similarly to a confined VMGTL with improved transmission. The improvement of the potential distribution along the magnetic link is equivalent to improve the impedance matching of the virtual line as shown in Fig 7.

Table 2: Comparison between the predicted gains and the experimental one

	Gain
Analytical	10 dB
Simulated	15 dB
Experimental	9 dB

As it can be seen in Table 2, the analytical and experimental results for the MTM gain at the resonance present a greater agreement than the one predicted by the numerical simulation, despite the fact that the curve behavior obtained by simulation is more similar to the one obtained with experiment (see Fig. 8 and Fig. 9). The discrepancy between the analytical and experimental curves comes from the simplifying hypotheses concerning the magnetic flux distribution employed by the model.

Finally, one important aspect of the considered system must be pointed out: the relative position of the MTM to the source does not interfere significantly with the gain, which reinforces that such magnetic link has a TL-like behavior.

Acknowledgements

We would like to give a special thanks to the Department of Electrical Engineering of PUC-Rio and particularly to CETUC for the financial support that made possible to us to attend this conference.

References

[1] S. I. Nishimura, J. V. De Almeida, C. Vollaire, C. A. F. Sartori, A. Breard, F. Morel e L. Krähenbühl, "Enhancing the inductive coupling and efficiency of wireless power transmission system by using metamaterials," em 16º SBMO - Simpósio Brasileiro de Micro-ondas e Optoeletrônica e 11º CBMag, Curitiba, 2014.

[2] Y. Urzhumov e D. R. Smith, "Metamaterial-enhanced coupling between magnetic dipoles for efficient wireless power transfer," Phys. Rev. B, vol. 83, nº 205114, 2011.

[3] R. Foster, "A Reactance Theorem," Bell System Technical Journal, 1926.

[4] R. C. Hansen e R. E. Collin, Small Antenna Handbook, New Jersey: John Wiley and Sons, 2011.

[5] J. A. B. Faria e M. P. Pires, "Theory of Magnetic Transmission Lines," IEEE Transactions on Microwave Theory and Techniques, vol. 60, nº 10, 2012.

[6] J. V. de Almeida, Virtual Magnetic Transmission Lines, Rio de Janeiro, 2017.

[7] "Collins Free Online Dictionary," Collins, [Online]. Available: https://www.collinsdictionary.com/dictionary/english/virtual. [Acesso em 2017 02 12].

[8] J. A. B. Faria, "Poynting Vector Flow Analysis for Contactless Energy Transfer in Magnetic Systems," IEEE Transactions on Power Electronics, vol. 27, nº 10, pp. 4292-4300, 10 10 2012.

[9] S. Banerjee, K. Das e B. Rana, Communication Engineering II, Vikas Publishing House, 2015.

[10] R. F. Harrington, Time-Harmonic Electromagnetic Fields, Wiley-IEEE Press , 2001.

[11] [A. D. Boardman e K. Marinov, "Electromagnetic energy in a dispersive metamaterial," Physical Review B, vol. 73, nº 165110, 2006.

Absorption analysis of planar double U-Π shape compact metamaterial for multi-band applications

Mohammad Jakir Hossain[1], Mohd Fais Mansor[2], Mohammad Rashed Iqbal Faruque[1], Mohammad Tariqul Islam[2]

[1]Space Science Centre (ANGKASA), Institute of Climate Change (IPI), Universiti Kebangsaan Malaysia, 43600 Bangi, Selangor, Malaysia
[2]Department of Electrical Electronic and Systems Engineering, Universiti Kebangsaan Malaysia, 43600 Bangi, Selangor, Malaysia
*corresponding author, E-mail: jakir@siswa.ukm.edu.my

Abstract

A new double U-Π shape design, simulation, fabrication and experimental verification of unit cell structure based on a simple configuration was operated in microwave spectra. The proposed structure resonators have magnetic and electric resonances that demonstrate metamaterials properties at different resonance frequency. The finite-difference time-domain (FDTD) based commercially available CST electromagnetic simulator was adopted to investigate the design scattering parameters, effective medium parameters and absorption analysis. The design structure exhibited the resonance frequency within the L-band, C-band, X-band, and Ku-band of the microwave regime. The characteristics and absorption were analyzed using the angular rotation of the structure and different dielectric substrate material. An N5227A vector network analyzer was used for the measurements. The measurement results of the printed prototype were in a better covenant with the simulation results. As a result, the proposed structure enables innumerable application areas such as mobile phones, long-distance radio communications, satellite communications, radar, and space communications.

Keywords: Absorption; Compact; Effective medium ratio; Metamaterials; Multi-band; Planar;

1. Introduction

Metamaterials have attracted noteworthy attention in the past decade due to a number of attractive phenomena not found in nature, such as sub-wavelength focusing, negative refraction, surface wave manipulation, extraordinary transmission, invisible cloaking, super-resolution imaging etc. Negative refractive index metamaterials are engineered materials with negative permittivity (ε less than 0) and permeability (μ less than 0) simultaneously, which have exotic properties in terms of well-known phenomena like Snell's law, and Doppler effect etc. [1]. Due to the interesting properties, the scientific community has been concerned to the metamaterials for strange characteristics and extensive applications in energy harvesting, invisibility clocks [2, 3], filtering, electromagnetic absorber [4] and perfect lenses [5], SAR reduction [6]. A 10×10 mm^2 square split "Z-shape" metamaterials showed Negative refractive index properties at different azimuthal angles, whereas the maximum effective medium ratio (EMR) was 9.1 by Faruque et al. in [7]. A 5×5 mm^2 "Ring-shape" metamaterial was designed by Yang et al. for cloaking effects of frequency range 8-13 GHz. Moreover, the EMR of meta-atom was 6 [8]. Hossain et al. recommended a design structure of 12×12 mm^2 "double C-shape" metamaterial for multi-band operation and reported EMR was 7.44 with negative refractive index from 11.304 to 13.796 GHz [9]. Zhou et al. suggested a "double Z-shape" double negative metamaterial unit cell constructed using coplanar magnetic and electric resonators which obtained an EMR of 4.80 as well as, dimension was 8.5×8.5 mm^2 [10]. Islam et al. recommended a metamaterial unit cell structure with 30×30 mm^2 dimensions and "H-shape" that was applicable microwave regime. The negative refractive indices of the structure were at 0.5 GHz and 0.3 GHz, whereas the EMR was 3.65 [11]. A left-handed "F-shape" metamaterial was designed by Rizwan et al. with 2.3 GHz bandwidth of negative refractive index for K- and Ka-band [12]. Zhou et al. reported a 15×15 mm^2 "S-shape" chiral metamaterial for X- and Ku- band. On the contrary, the EMR of the metamaterial was very small that was less than 4 [13]. However, above authors analyzed Negative refractive index characteristics and compactness but absorption properties did not analyze of their metamaterial. A triple-band metamaterial absorber can be utilized in bolometers, explosives detection and spectroscopic imaging, etc. [14]. Islam et al. [15] proposed multi-band split S-shaped metamaterial structure for absorption analysis, whereas authors obtained maximum 55% absorption. In addition, a paper was proposed by Islam et al. whereas different substrate materials were analyzed for S-band only. Compactness and absorption were not shown in that paper [16]. In this paper, the planar double U-Π shape based metamaterial exhibits, multi resonance at L-, C-, X-, and Ku-bands with different metamaterials properties for

instance, ε-negative, μ-negative and negative refractive index. An absorption, effective medium ratio, and effective medium parameters have been changed by altering the rotation of unit cell and different substrate materials. Moreover, the size of the proposed planar unit cell is 10.5×11 mm^2, which is smaller than the stated metamaterials unit cells in [7, 8, 9, 10, 11, 13] with the terms of EMR. Metamaterial can operate in the sub-wavelength spectra, whether the EMR of the material is greater than 4. Furthermore, the design structure provides high absorption value 99% at 3.79 GHz, 99% at 11.78 GHz, and 96% at 12.24 GHz for RO3010, RT5880 and FR4 substrate materials respectively. It is observed that the absorption of the proposed design is better than the suggested metamaterials unit cells in [17, 18, 19]. To determine the scattering parameters, for example, the reflection coefficient (S_{11}) and transmission coefficient (S_{21}), the CST electromagnetic simulator 2015 was used. The effective medium parameter, for instance, effective permittivity, permeability and refractive index were also retrieved using well-established Nicolson-Ross-Weir method.

2. Design, Numerical simulation, and Measurement

The suggested design consists of two U shape and one Π shape resonators with single split square resonator which was employed to attain unconventional characteristics of metamaterials that were usually not found in nature. The proposed metamaterial structure and structural parameters are shown in Fig. 1(a). The substrate material is low cost FR4 lossy material. All elements of the resonators are made of copper with conductivity of 5.8×10^7 S/m and the thickness of copper resonators are 0.035 mm that is printed on a substrate with standard relative permittivity ε= 4.3 as well as loss tangent δn= 0.025. The parameters of the structure are Lc=10 mm, Wc=10.6 mm, W_1=0.4 mm, W_2=0.65 mm, W_3=0.7 mm, W_4=0.6 mm, W_5=0.7 mm, W_6=0.9 mm, L_1=6.7 mm, g=0.3 mm, s=0.4 mm.

In this paper, the finite-difference time-domain method based CST simulator is implemented to examine this design structure. The electric field and magnetic field have been polarized along the x-axis and the y-axis, respectively, whereas z-axis has been utilized for electromagnetic wave travelling. The boundary conditions of perfect magnetic conductor (PEC) and the perfect electric conductor (PMC) are utilized along the x-axis and y-axis, individually, and two waveguide ports are placed on the positive and negative z-axis. In addition, the periodic boundary conditions with the wave guide port are used in the simulation. The schematic diagram of the proposed design is illustrated in Fig. 1(a). To determine the transmission coefficient and the reflection coefficient in simulation a frequency domain solver is employed. The frequency range 1-15 GHz was used to simulate and measure the design structure.

A fabricated prototype is shown in Fig. 1 (b). The prototype comprises 4×4 arrays of the unit-cell of copper materials and the size of the prototype are 44×42 mm^2. The measurement has been performed with two waveguide in the free-space environment. To allow the incident electromagnetic wave travelling over the prototype that was positioned between the two waveguide in the identical plane, similar to the simulation geometry. In addition, the scattering parameters have been measured by the PNA network analyzer (N5227) where the frequency range of the device is 10 MHz-67 GHz.

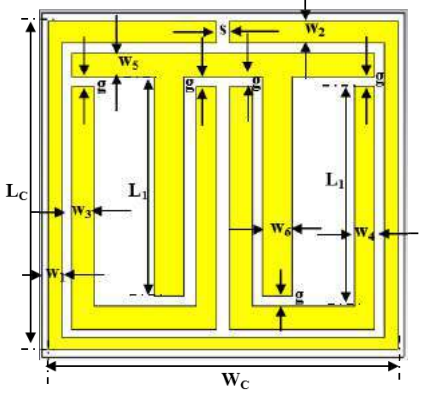

(a)

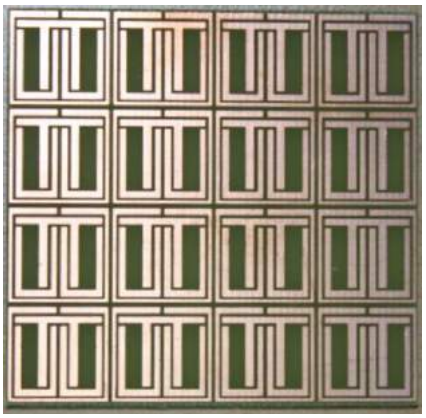

(b)

Figure 1: (a) The proposed metamaterial structure, (b) The fabricated array of structure.

Furthermore, a calibration kit (Agilent N4694-60001) was utilized to calibrate the network analyzer. That is why, the measurements were completed precisely. The Nicolson-Rose-Weir (NRW) method was utilized to determine the medium parameters like effective permeability (μ) and permittivity (ε) from simulated scattering parameters such as transmission coefficient (S_{21}) and reflection coefficient (S_{11}). The direct refractive index method was applied to calculate the effective refractive index (n) from the simulated complex S-parameters. The absorption of the design structure was determined using the following equation, $A(\omega) = 1–R(\omega)–T(\omega)$, where $T(\omega)$, $R(\omega)$, and $A(\omega)$ are the transmittance, reflectance and absorption, respectively. Absorption depends on the scattering parameters, for instance, $|S_{21}|^2 = T(\omega)$, and $|S_{11}|^2 = R(\omega)$. However, from the absorption equation, it can be seen that minimizing the scattering parameters which can maximize the absorption of the metamaterials.

3. Results and Discussions

In this paper, scattering parameters, effective medium parameters, effective medium ratio and absorption of design structure with angular rotation and different type of substrate materials were analyzed..

3.1. Analysis of design structure with angular rotation

The numerical and experimental result of planar double U-Π shape compact metamaterial has been presented. The numerical and measured reflection coefficient (S_{11}), and transmission coefficient (S_{21}) of the design structure has been demonstrated in Fig. 2. It shows the cover band of the resonance frequencies that designates L-, C-, X-, and Ku-bands applications.

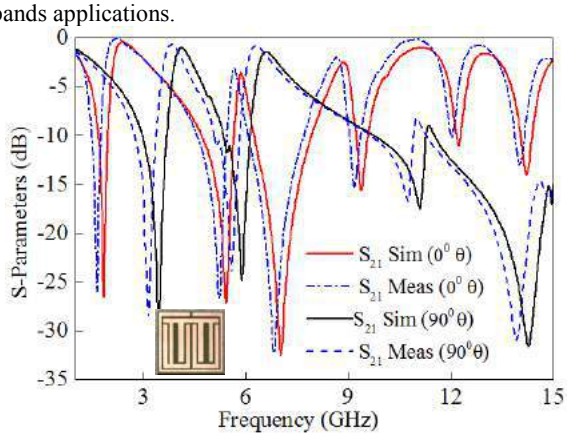

Figure 2: Numerical and measured S-parameters of design structure.

From Fig. 2, the numerical and experimental results are showing good agreement with each other. The measured results have shown the same band comparing with numerical results in Fig. 2. On the contrary, the scattering parameters of measured results have been marginally shifted towards the lower frequency and increase small amount of the magnitude comparing with simulation results. The small amount difference has been occurred for the several fabrication tolerance and open-space measurement procedure. Fig. 3 (a) exhibits the values of the relative negative permittivity 1.658-2.148 GHz, 3.464-5.676 GHz, 5.844-7.37 GHz, 8.84-9.218 GHz, 10.394-11.766 GHz, 12.494-13.012 GHz, and 14.538-14.86 GHz for 0^0 angular rotation. In contrast, 2.512-3.828 GHz, 4.402-6.124 GHz, 6.572-9.456 GHz, 7.622-15 GHz for 90^0 angular rotation of design structure of metamaterial. The electric and magnetic dipole moment can keep route with the applied electromagnetic field at lower frequency. On the other hand, the dipole moment cannot content with the applied field. As a consequence, the fluctuation of scattering parameters have been occurred at higher frequencies. Fig. 3 (b) displays the values of the relative negative permeability 7.93-14.958 GHz and 7.622-15 GHz for 0^0 and 90^0 angular rotation of design structure, respectively. The negative properties of the permittivity and permeability has been altered a small amount as a result of the polarization effect on the interior construction of metamaterial structures. Fig. 3 (c) describes the relative negative refractive index 3.324-5.186 GHz, 6.068-6.726 GHz, 7.636-13.614 GHz, 14.048-15 GHz, and 2.372-3.114 GHz, 4.57-5.382 GHz, 5.564-5.606 GHz, 6.824-8.952 GHz, 11.038-11.388 GHz, 14.146-15 GHz for 0^0 and for 90^0 angular rotation of the design structure.

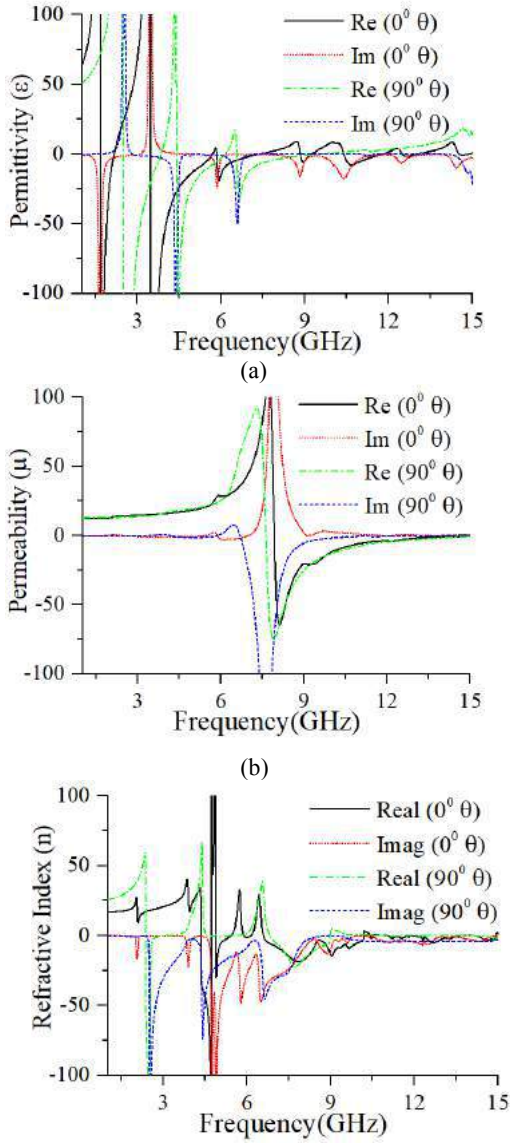

Figure 3: (a) Permittivity (b) permeability and (c) refractive index values of the angular rotation of 0^0 and 90^0 of the design structure.

The curves of the effective refractive index become negative when the curves of the permittivity and permeability are negative, simultaneously. The design structure of material has shown metamaterial properties ε-negative at 1.82 GHz, ε-negative at 5.42 GHz, μ-negative at 9.37 GHz, and negative refractive index at 12.24 GHz that have designated L-, C-, X-, and Ku-bands in the microwave region.

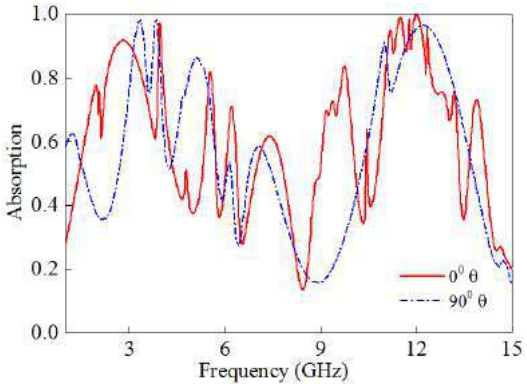

Figure 4: Absorption values of the angular rotation of 0^0 and 90^0 of the design structure.

It is observed from Fig. 4 that the absorption value of design structure are 49% at 1.82 GHz, 73% at 5.42 GHz, 47% at 9.37 GHz, and 96% at 12.24 GHz, respectively for 0^0 angular rotation. On the other hand, the values of the absorption are 95% at 3.42 GHz, 60% at 5.86 GHz, 86% at 11.11 GHz, and 30% at 14.43 GHz, respectively for 90^0 angular rotation of the structure. The absorption value is high while the transmittance value is near zero. However, the reflectance value is less in that point. The angular rotation of the design structure along the propagation direction of electromagnetic wave has changed the resonance frequencies and absorption values due to alter the material properties.

Table 1 describes the overall properties of the structure like EMR, resonance frequencies and metamaterial classification, and absorption for 0^0 and 90^0 angular rotation. The design structure shows the higher EMR at 0^0 angular rotation compares to 90^0 angular rotation. In addition, the absorption value, 96% at resonance frequency, 12.24 GHz for 0^0 angular rotation compares to 90^0 angular rotation of the proposed structure.

Table 1: The values of effective medium parameters, metamaterials properties, and absorption at different resonance frequencies for 0^0 and 90^0 angular rotation of proposed structure.

Rotation angle(θ)	EMR	Resonance frequencies	Metamate-rials properties	Absorption (%)
0^0	14.99	1.82	ENG	49
		5.42	ENG	73
		9.37	MNG	47
		12.24	NRI	96
90^0	7.97	3.42	ENG	95
		5.86	ENG	60
		11.11	MNG	86
		14.43	NRI	30

3.2. Analysis of design structure with different substrate materials

Three types of substrate materials, for example, FR-4(lossy), rogers RO3010(lossy) and rogers RT5880(lossy) have been used as a substrate material in the design structure. In numerical analysis as well as practical implementation, 1.6 mm thick FR4 substrate with permittivity 4.3 and loss tangent 0.025 as well as thermal conductivity 0.3 W/K/m has been utilized. The thickness, electric permittivity, thermal conductivity, loss tangent of rogers RO3010 substrate material are 1.6 mm, 10.2, 0.66 W/K/m and 0.0022. Moreover, the rogers RT5880 substrate material comprises thickness= 1.6 mm, electric permittivity= 2.2, thermal conductivity = 0.2 W/K/m, and loss tangent=0.0009. Three different types of substrate material have been used to observe the metamaterial characteristics, EMR, and absorption in microwave spectra.

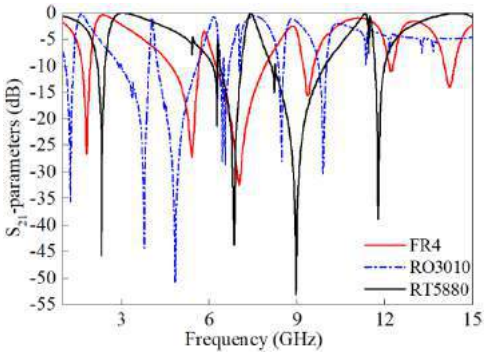

Figure 5: Transmission coefficient of the design structure for different substrate material

Fig. 5 states the transmission coefficient value in dB for different substrate materials like FR4, rogers RO3010, and rogers RT5880. The transmission dip, number of resonance frequency and value of the resonance frequency of the structure have been changed due to different electric properties of the material. In this frequency range, rogers RT5880 has shown the maximum dip. On the other hand, the minimum dip has been obtained by FR4 substrate material. However, rogers RO3010 has displayed the lowest fundamental resonance frequency which has increased the EMR of the structure.

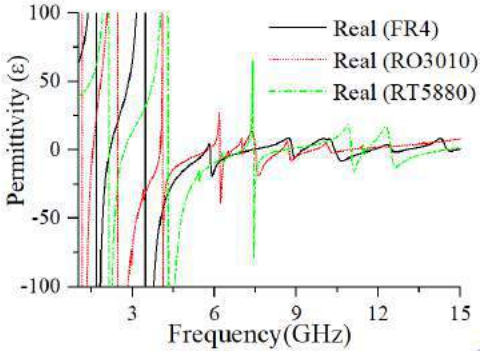

(a)

Fig. 6 (a) displays the ranges of the relative negative permittivity 1.658-2.148 GHz,3.464-5.676 GHz,5.844-7.37 GHz, 8.84-9.218 GHz, 10.394-11.766 GHz, 12.494-13.012 GHz, and 14.538-14.86 GHz; for FR4 substrate in the proposed design. Moreover, 1.154-1.532 GHz, 2.456-3.996

GHz, 4.094-5.746 GHz, 6.208-6.656 GHz, 7.496-8.448 GHz, 8.728-9.624 GHz, and 10.198-10.898 GHz for rogers RO3010 substrate. Furthermore, 2.12-2.694 GHz, 4.304-7.006 GHz, 7.412-8.588 GHz, 11.01-11.542 GHz, and 12.452-14.44 GHz for rogers RT5880 substrate of design structure of metamaterial.

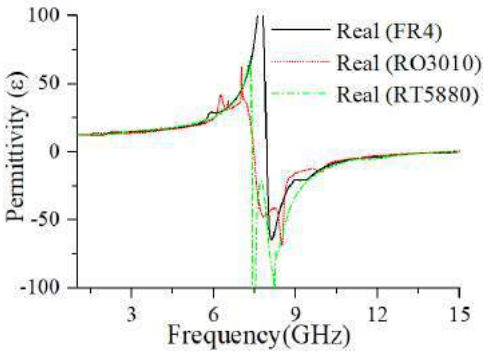

(b)

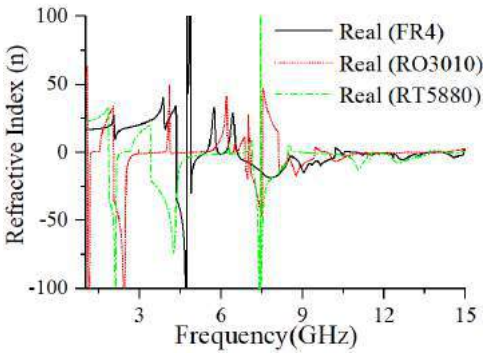

(c)

Figure 6: (a) Permittivity (b) permeability and (c) refractive index values of the angular rotation of 0^0 and 90^0 of the design structure.

The electric and magnetic dipole moment can keep route with the applied electromagnetic field at lower frequency. On the other hand, the dipole moment cannot content with the applied field at higher frequencies. As a result, the fluctuation of effective parameters like permittivity has been occurred more at higher frequencies. Fig. 6 (b) shows the range of the relative negative permeability 7.93-14.958 GHz, 7.468-14.314 GHz, and 7.398-14.608 GHz for FR4, rogers RO3010, and rogers RT5880 substrate materials, correspondingly. Fig. 6 (c) designates the relative negative refractive index 3.324-5.186 GHz, 6.068-6.726 GHz, 7.636-13.614 GHz, 14.048-15 GHz; 1.07-1.21 GHz, 2.036-3.744 GHz, 4.122-4.808 GHz, 6.306-6.418 GHz, 6.88-6.978 GHz, 7.076-7.496 GHz, 8.112-9.428 GHz, 9.89-12.13 GHz, 12.172-12.998 GHz, 13.278-13.46 GHz, 13.67-13.964 GHz; 1.868-2.316 GHz, 3.408-6.25 GHz, 6.292-6.824 GHz, 7.132-8.434 GHz, 8.966-11.514 GHz, 11.78-13.628 GHz, 14.286-14.804 GHz for FR4, rogers RO3010, and rogers RT5880 substrate materials, individually. The negative properties of the permittivity, permeability, and refractive index has altered a bit accordingly of the polarization effect on the materials properties of the structures.The design structure of material has a metamaterial property like single negative, double negative that are shown in Table 3.

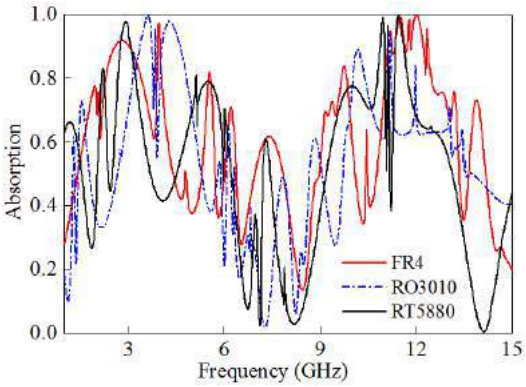

Figure 7: Absorption values of the FR4, rogers RO3010, and rogers RT5880 substrate materials of the design structure.

It is seen from Fig. 7 that the absorption value of design structure are 49% at 1.82 GHz, 73% at 5.42 GHz, 47% at 9.37 GHz, and 96% at 12.24 GHz, respectively for FR4 substrate material. Moreover, the values of the absorption are 22% at 1.25 GHz, 99% at 3.79 GHz, 89% at 4.84 GHz, 35% at 6.45 GHz, 6% at 8.45 GHz, and 50% at 9.90 GHz, correspondingly for rogers R03010 substrate material. Furthermore, absorption values are 63% at 2.33 GHz, 50% at 6.26 GHz, 15% at 8.97 GHz, and 99% at 11.78 GHz, individually for rogers RT5880 substrate material. The absorption value is high while the reflectance value is low. The high absorption value is 99% at 3.79 GHz for rogers R03010 and 99% at 11.78 GHz for rogers RT5880 substrate material. Due to different material properties, the absorption rate has been different at different frequencies.

Table 2: The values of effective medium parameters, metamaterials properties, and absorption at different resonance frequencies for FR4, rogers RO3010, and rogers RT5880 substrate materials of proposed structure.

Substrate type	EMR	Resonance frequencies	Metamate-rials properties	Absorption (%)
FR4	14.99	1.82	ENG	49
		5.42	ENG	73
		7.02	ENG	17
		9.37	MNG	47
		12.24	NRI	96
R03010	21.82	1.25	ENG	22
		3.79	ENG	99
		4.84	ENG	89
		6.45	ENG	35
		8.45	MNG	6
		9.90	NRI	50
RT5880	11.71	2.33	ENG	63
		6.26	ENG	50
		8.97	MNG	15
		11.78	NRI	99

Table 2 designates the overall properties of the structure for instance, EMR, resonance frequencies and metamaterial characteristics, and absorption of different substrate material. The design structure displays the high EMR (21.82) for rogers RO3010 substrate material compares to FR4 and RT5880 substrate material. Additionally, the high absorption value, 99% at resonance frequency, 3.79 GHz for rogers RO3010 compares to FR4 substrate of the proposed structure. It is seen from Table 2, rogers RO3010 substrate material is suitable, in terms of high absorption value and compactness of the design structure.

4. Conclusions

A new design of double U-Π shape compact metamaterial structure was suggested for multi-band, for instance, L-, C-, X-, and Ku-band applications in this paper. This design structure based on rogers RO3010 substrate exhibited 99% absorption with high EMR (21.82) at 3.79 GHz. The CST electromagnetic simulator was utilized to determine the absorption, EMR and metamaterials characteristics. The suggested metamaterials are appropriate for amateur radio, GPS, GSM, radar and satellite communications, long-distance radio telecommunications, space communication and radar terrestrial broadband. A comparative analysis also carried out on the basis of the angular rotation of the unit cell and different substrate material. The open-space measurement method was applied to validate the results of the prototype of the structure. Therefore, the metamaterial structure was compact in size, high absorption and follows better EMR which were more suitable in microwave spectra.

References

[1] V. G. Veselago, The electrodynamics of substances with simultaneously negative values of ε and μ, *Sov. Phys*. 10: 509–514, 1968

[2] D. Schurig, J. Mock, B. Justice, S. A. Cummer, J. B. Pendry, A. Starr*, et al.*, Metamaterial electromagnetic cloak at microwave frequencies, *Science,* 314: 977-980, 2006.

[3] W. Cai, U. K. Chettiar, A. V. Kildishev, and V. M. Shalaev, Optical cloaking with metamaterials, *Nat. photonics,* 1: 224-227, 2007.

[4] P. T. Bowen, A. Baron, and D. R. Smith, Theory of patch-antenna metamaterial perfect absorbers, *Phys. Rev. A,* 93: 063849, 2016.

[5] J. Pendry, Perfect cylindrical lenses, *Opt. Express,* 11: 755-760, 2003.

[6] S. il Kwak, D.-U. Sim, J. H. Kwon, and Y. J. Yoon, Design of PIFA with metamaterials for body-SAR reduction in wearable applications, *IEEE Trans. Electromagn. Comp.,* 59: 297-300, 2017.

[7] M. R. I. Faruque, M. M. Hasan, and M. T. Islam, "Wideband 90° Azimuthal miniaturized meta atom with left-handed characteristics," *IEEE Antenna Wireless Propag. Lett.,* 2016.

[8] S. Yang, P. Liu, M. Yang, Q. Wang, J. Song, and L. Dong, From flexible and stretchable meta-atom to metamaterial: A wearable microwave meta-skin with tunable frequency selective and cloaking effects, *Sci. Rep.,* 6: 21921, 2016.

[9] M. R. I. Faruque, M. J. Hossain, S. S. Islam, M. F. B. Jamlos, and M. T. Islam, Design and analysis of a new double C-shaped miniaturized metamaterial for multiband applications, *Appl. Phys. A.*, 123: 310, 2017.

[10] H. Zhou, C. Wang, and H. Peng, A novel double-incidence and multi-band left-handed metamaterials composed of double Z-shaped structure, *J. Mater. Sci. Mater.,* 27: 2534-2544, 2016.

[11] S. S. Islam, M. R. I. Faruque, and M. T. Islam, The design and analysis of a novel split-H-shaped metamaterial for multi-band microwave applications, *Materials,* 7: 4994-5011, 2014.

[12] M. Rizwan, H.-B. Jin, F. Rehman, Z.-L. Hou, J.-B. Li, F. Butt*, et al.*, Dual-band tunable negative refractive index metamaterial with F-Shape structure, *Open Phys.,* 12: 578-581, 2014.

[13] Z. Zhou and H. Yang, Triple-band asymmetric transmission of linear polarization with deformed S-shape bilayer chiral metamaterial, *Appl. Phys. A,* 119: 115-119, 2015.

[14] X. Shen, T. J. Cui, J. Zhao, H. F. Ma, W. X. Jiang, and H. Li, Polarization-independent wide-angle triple-band metamaterial absorber, *Opt. Express,* 19: 9401-9407, 2011.

[15] S. S. Islam, I. Faruque, M. Rashed, and M. T. Islam, Design and absorption analysis of a new multiband split-S-shaped metamaterial, *Sci. Eng. Compos. Mater.,* 24: 139-148, 2017.

[16] S. S. Islam, M. A. Rahman, M. R. I. Faruque, and M. T. Islam, Design and analysis with different substrate materials of a new metamaterial for satellite applications, *Sci. Eng. Compos. Mater.,*2016.

[17] H.-M. Lee and H. Lee, A metamaterial based microwave absorber composed of coplanar electric-field-coupled resonator and wire array, *Prog. Electromagn. Res. C,* 34: 111-121, 2013.

[18] M. Bakir, M. Karaaslan, F. Dincer, O. Akgol, and C. Sabah, Electromagnetic energy harvesting and density sensor application based on perfect metamaterial absorber, *Int. J. Mod. Phys. B,* 30: 1650133, 2016.

[19] M. Bağmancı, M. Karaaslan, E. Ünal, O. Akgol, F. Karadağ, and C. Sabah, Broad-band polarization-independent metamaterial absorber for solar energy harvesting applications, *Physica E,* 90: 1-6, 2017.

A miniaturized sub-wavelength based wideband negative refractive index metamaterial for quad-band applications

Mohammad Jakir Hossain[1], Mohammad Rashed Iqbal Faruque[1], Mohammad Tariqul Islam[2], Mohd Fais Mansor[2]

[1]Space Science Centre (ANGKASA), Institute of Climate Change (IPI), Universiti Kebangsaan Malaysia, 43600 Bangi, Selangor, Malaysia
[2]Department of Electrical Electronic and Systems Engineering, Universiti Kebangsaan Malaysia, 43600 Bangi, Selangor, Malaysia
*corresponding author, E-mail: jakir@siswa.ukm.edu.my

Abstract

In this manuscript, a new modified hexagonal unit cell structure with wideband negative refractive index metamaterial structure was worked in microwave regime. The proposed structure was designed of two symmetrical metallic patterns printed on the both sides of an FR4 dielectric substrate. The finite-difference time-domain (FDTD) based commercially available CST microwave studio was adopted to investigate scattering parameters of the design. The design structure was analyzed by two orientations with respect to the incident plane wave. For normal wave incidence, the suggested structure displays wideband negative refractive index (3.18 GHz) and (0.9 GHz) with a higher effective medium ratio (17.26) that was indicated small electrical size of the structure, whereas for parallel wave incidence, wideband negative refractive index (2.45 GHz), (1.22 GHz) and (1.93 GHz) bandwidth with a higher effective medium ratio (28.01) was obtained. The negative refractive index was verified by simulation and measurement for quad-band applications. Furthermore, the effective medium ratio (λ/a) of the proposed wideband negative refractive index metamaterial was considerably improved compared to previous suggested multi-band metamaterials.

Keywords: Double-incident, Effective medium ratio, Metamaterial, Quad-band, Negative refractive index, Wideband;

1. Introduction

The composite materials that are called metamaterials, designed to exhibit exotic electromagnetic phenomena not available by natural materials, offer many fascinating ways of handling light and have been intensively examined. The artificial periodic structures comprised of sub-wavelength constituent elements that build the structure perform as an effective medium with negative values of permittivity ($\varepsilon < 0$) and permeability ($\mu < 0$) at the frequencies of interest. The properties of such media were already studied by Veselago over 45 years ago [1]. Negative refractive index materials, i.e., Negative Index Metamaterials (NIMs) are artificial metanmaterials with effective negative permittivity and permeability simultaneously, which have unusual properties in terms of familiar phenomena like Snell's law, Cherenkov radiation, and Doppler effect etc. [1, 2]. Because of these unusual properties of the metamaterials, it can be used many vigorous applications such as antenna design [3], electromagnetic absorption reduction [4], invisibility cloaking [5], absorber design [6], etc. Until now, very few of NIMs designed and tested to perceive an effective negative refractive index materials. On the other hand, most of such NIMs is perceived by the overlapping of effective negative electric permittivity and effective negative magnetic permeability of the materials that are responsible of a metallic wire and engineered magnetic resonator, respectively [7]. The negative electric permittivity perceived by plasma behavior of metallic wire has foremost disadvantages, such as the problem in scheming a NIMs with improved effective medium ratio, for example, the operating wavelength to unit cell size and the subject of strong spatial dispersion [8]. In addition, the refractive negative index has been perceived by artificial S-type resonators and Ω-shaped man-made structure [9, 10]. However, mentioned NIMs have a significant shortcoming for the innovative practical applications due to the single band operation. In addition, in terms of the direction of applied electromagnetic (EM) waves, there are three types of EM incidence are possible, such as parallel, normal and double incidence. The earlier metamaterials are established on the classical incident planar electromagnetic (EM) waves which is parallel to the substrate, like ELC–HSLR pair structure [11], nonlinear metamaterials [12] as well as MTSRR-wire pair structure [13]. The second Metamaterials are also established on the incident planar EM waves that are normal to the substrate, for instance, multiple SSRR pair structure [14] and double C-shaped structures [15]. In case of the third one, the negative refractive index is parallel to both. However, very few researchers are focusing on this way to perceive the metamaterils. On the contrary, very little research has been achieved it. Zhou et al. and Zhu et al. [16, 17] who exhibit multi-bands NIMs founded on double Z-shape pair structure and multiple dendritic cells. It has been displayed the negative refractive index multi-bands for

perpendicular and parallel incidences. Recently, metamaterials for multiband application with negative refractive index and miniaturized sizes are an encouraging research field and a few researchers are focused on such metamaterials. "Π-shape" metamaterial suggested by Islam et al. [18] that was applicable for electromagnetic invisibility cloaking operation in X-band and achieved near zero refractive index of 2 GHz wideband. The effective medium ratio was 3.58 whereas the structure size of the "Π-shape" was 10×10 mm. "Double Z-shape" metamaterials that comprised the electric and magnetic resonators suggested by Zhou et al. in 2015 [16] This structure was built by metal strips of two orthogonal z-shape that exhibited different resonance peak such as 7.3 GHz, 8.1 GHz, and 9.4 GHz, respectively. However, this structure was shown EMR of 4.83 and 4.97 due to the parallel and normal incidence of EM wave. Cumali Sabah recommended a design structure of triangular shape with metal strip for dual-band operation and reported EMR was 7.35 with NIMs properties [19].

In this paper, a new double-incidence miniaturized quad-band NIM with an improved EMR has been introduced. The design structure of metamaterials covers L-, S-, C-, and X-bands with resonance frequencies 1.64 GHz at -18.23 dB, 3.67 GHz at -29.98 dB, 7.90 GHz at -12.55 dB, and 9.41 GHz at -31.94 dB, respectively. The negative refractive indices of the proposed structure are 3.36-3.52 GHz (0.16 GHz bandwidth), 5.34-5.52 GHz (0.18 GHz bandwidth), 5.63-8.69 GHz (3.06 GHz bandwidth), 9.71-10.55 GHz (0.84 GHz bandwidth), and 11.84-13.90 GHz (2.06 GHz bandwidth) for the normal incidence. Moreover, the bandwidths of negative refractive indix due to the parallel incidence of an electromagnetic wave are 1.91-7.33 GHz (5.42 GHz bandwidth), and 12.56-14.30 GHz (1.74 GHz bandwidth). In addition, the dimension of the proposed unit cell is smaller than the reported metamaterials unit cells in [11,12, 13, 14, 16, 19] in respect of EMR. The NIMs characteristics of the suggested structure were tested by numerically and experimentally. The NIM structure is suitable for multi-band applications, for instance, GPS, mobile phones, weather radar, surface ship radar, long-distance radio telecommunications, satellite communications and, space communications from the normal incidence and parallel incidence with the same dimension as well as same structure.

2. Methodology

2.1. Physical geometry of metamaterials

The proposed engineered NIM metamaterial structure has composed the same design structure on the substrate of both sides. The frontside and backside of a dielectric slab are a planar modified hexagonal copper metal structure. A combination of multiple hexagonal shaped split ring resonators with meander line was employed to attain unconventional characteristics of metamaterials that were usually not found in nature. The numerical analysis has been performed using commercially available CST microwave studio. In numerical analysis as well as practical implementation, 1.6 mm thick FR4 substrate with permittivity 4.3 and loss tangent 0.025 as well as permeability 1 has been utilized. All elements of the modified hexagonal resonators are made of copper with electric conductivity of 5.8×107 S/m, thermal conductivity 401 W/K/m, Rho of 8930 kg/m^3, Diffusivity 0.000115141 m^2/s, Young's modulus of 120 KN/mm^2 and the thickness of copper resonators, 35 μm. The elements of all the artificial structure are captured inside a cubic lattice of dimension 10×9.6 mm^2. The design structures are considered the incidence of uniform plane wave propagating along z-direction for normal incident as well as the y-direction for parallel incident. The parameters of the structure are L=9.8 mm, W=9.8 mm, W_1=0.7 mm, W_2=0.8 mm, W_3=0.8 mm, g=0.4.

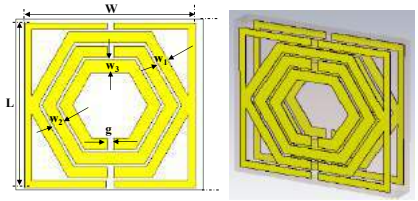

(a) (b)

Figure 1: The proposed engineered structure (a) front side and (b) perspective with both side.

To observe the double incidence operation of the structure, primarily, the z-axis EM plane wave propagation was performed, and then the y-axis EM plane wave propagation was implemented. The schematic diagram of the proposed engineered structure is illustrated in Fig. 1. To determine the transmission coefficient and the reflection coefficient in simulation a frequency domain solver is utilized and 1001 frequency samples were reserved.

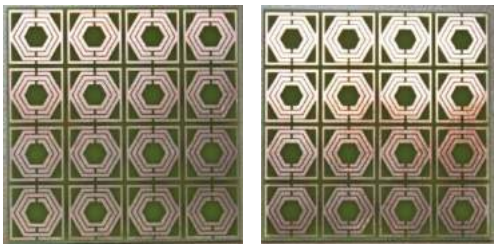

(a) (b)

Figure 2: The fabricated array of proposed engineered structure (a) front side and (b) back side.

A fabricated prototype is shown in Fig. 2. The fabricated sample encloses 5 × 4 arrays of the structure of copper materials and the dimension of the fabricated sample are 55 × 42.5 mm^2. The measurement has been performed with two waveguides in the free-space environment. Besides, the scattering parameters have been measured by the PNA network analyzer (N5227) where the frequency range of the device is 10 MHz-67 GHz. Moreover, a calibration kit (Agilent N4694-60001) was utilized to calibrate the network analyzer. Furthermore, in case of calibration purposes, measurement has been performed with and without of the

prototype. That is why; the measurements have been completed precisely.

2.2. Effective Scattering and medium parameters Calculation

The Nicolson-Rose-Weir method was utilized to retrieve the parameters of the material. The magnetic permeability, $\mu = \mu_0\mu_{eff}$ and the dielectric permittivity, $\varepsilon = \varepsilon_0\varepsilon_{eff}$, the impedance is defined as $Z = \sqrt{\frac{\mu_r}{\varepsilon_r}} Z_0$,

The S-parameters are represented as the addition and subtraction terms as given in equations 1 and 2.

$$v_1 = S_{21} + S_{11}, \quad (1)$$

$$v_2 = S_{21} - S_{11}, \quad (2)$$

The transmission coefficient (S_{21}) and reflection coefficient (S_{11}) are the scattering parameters of the metamaterials. Metamaterials that have finite thickness, $k_{real}d \leq 1$ and complex wave number, $K = \frac{\omega\sqrt{\mu_r\varepsilon_r}}{c} = K_0\sqrt{\mu_r\varepsilon_r}$, to obtain effective magnetic permeability (μ_{eff}), dielectric permittivity (ε_{eff}), and effective refractive index (n_{eff}) are written as follows:

Effective permeability, $\mu_{eff} = \frac{2c}{j\omega d} \times \frac{(1-v_1)}{(1+v_1)}$ (3)

Effective permittivity, $\varepsilon_{eff} = \frac{2c}{j\omega d} \times \frac{(1-v_2)}{(1+v_2)}$ (4)

Refractive index, $n_{eff} = \frac{2c}{j\omega d} \times \left\{ \frac{(S_{21}-1)^2 - S^2{}_{11}}{(S_{21}+1)^2 - S^2{}_{11}} \right\}^{1/2}$ (5)

Where, d, c, and ω are used as the thickness of the substrate, the velocity of light and the angular frequency. The above equations are utilized to determine the effective medium parameters.

3. Results and Discussions

The values of the effective dielectric permittivity, effective magnetic permeability and effective refractive index are verified to characterize the proposed engineered materials. Engineered structure with different type of EM wave propagation, i.e., normal incidence and parallel incidence have been analyzed in this paper.

3.1. Analysis of the Normal Incidents of EM wave

The electric and magnetic field have been polarized along the x-axis and the y-axis, respectively, whereas z-axis has been utilized for electromagnetic wave travelling for normal incident. The PEC and PMC boundary conditions are employed alongside the x-axis and y-axis, individually, and two waveguide ports are placed on the positive and negative z-axis. The numerical and experimental result of the modified hexagonal engineered structure was offered. The numerical and measured reflection coefficient (S_{11}), and transmission coefficient (S_{21}) of the unit-cells were shown in Fig. 3. It illustrates the mathematical values of the four frequency ranges of resonance frequencies are 1.57-1.7 GHz, 3.24-3.95 GHz, 6.44-8.02 GHz and 8.94-11.51 GHz, that designates L-, S-, C, and X-bands applications.

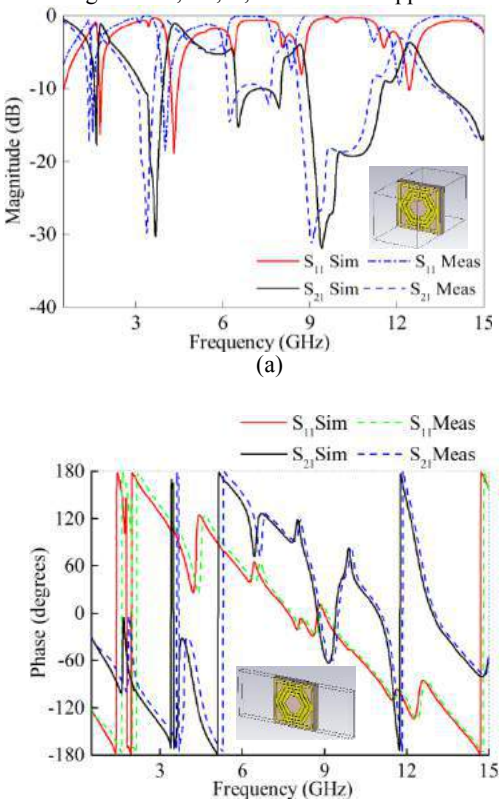

Figure 3: (a) Magnitude (b) phase of simulated and measured S-parameters of engineered structure.

From Fig. 3, the simulation and experimental results for the magnitude and phase of the design structure are showing good agreement with each other. The corresponding magnitude and phases are plotted in Fig. 3(a) and 3(b). Matching occurs at 1.64 GHz, 3.67 GHz, 7.90 GHz, and 9.41 GHz. The value of reflection is highest, whereas the value of transmission is nearly zero at the resonance frequencies. The phase of the transmission and reflection response has a jump at the same frequency which carries a signature of existence the metamaterial's resonance. The experimental results have revealed the same band comparing with simulation results in Fig. 3 (a) and 3(b). On the other hand, the scattering parameters of experimental results have been slightly lifted towards the lower frequency and reduced small amount of magnitude comparing with simulation results. The small amount of difference has been occured for the several fabrication tolerance and open-space measurement procedure. Fig. 4 exhibits the distributions of instantaneous surface current and magnetic field of the resonant four peaks, for instance, 1.64 GHz, 3.67 GHz, 7.90 GHz and 9.41 GHz, where its expose epsilon negative metamaterial, epsilon negative metamaterial, double negative metamaterial and mu negative metamaterial respectively. The flow of the direction of the current on the frontal metallic slabs was

reversely paralleled to the back one. This current produces a heavy charge gathering at the regions where the two opposite flowing currents meet each other and form four magnetic dipoles that show negative magnetic resonances under normal incidence of electromagnetic wave. At 1.64 GHz, the distributions of magnetic field have concentrated on the areas of split gap of middle ring and around the middle ring. Hence, the first epsilon negative is subjected by the magnetic resonance of the areas.

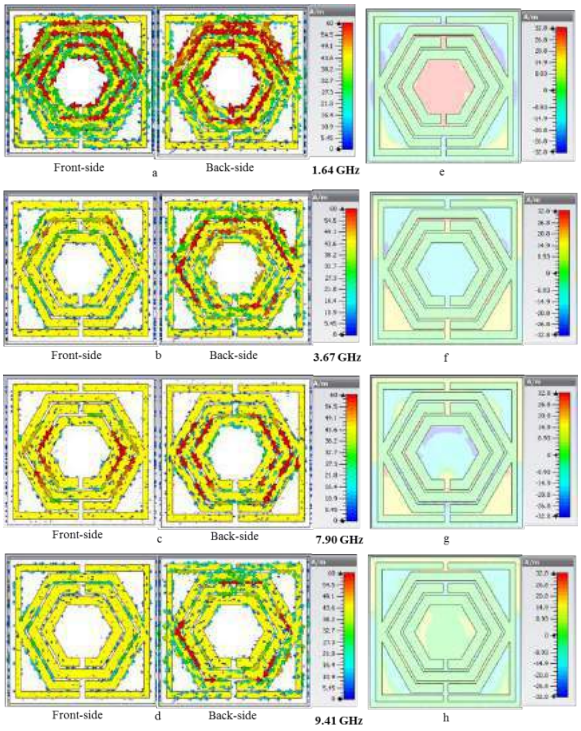

Figure 4: Instantaneous surface current and magnetic field distribution for nermal incidence of EM wave.

Moreover, at 3.67 GHz, the magnetic field's is concentrated in the regions of the left-side, right-side and upper-side of the substrate. Therefore, the second epsilon negative is prevailed by the regions of the magnetic resonance. Furthermore, at 7.90 GHz, the magnetic field's is concentrated in the regions of the left-side, right-side and lower-side of the substrate. So, the double negative is dominated by the magnetic resonance of the areas. Additionally, at 9.41 GHz, the magnetic field's is concentrated in the regions of the left-side and right-side of the substrate. Thus, the mu negative is conquered by the regions of the magnetic resonance. Fig. 5(a) and 5(b) demonstrate the retrieval effective permittivity, $\varepsilon = \varepsilon' + i\varepsilon''$, and effective permeability, $\mu = \mu' + i\mu''$, respectively. Fig. 5(a) shows the real values of the effective negative permittivity, 1.59-1.72 GHz, 2.56-4.05 GHz, 4.60-7.92 GHz, 8.01-8.69 GHz, 12.17-12.56 GHz and 14.86-15.00 GHz for the normal incidence of the EM along the design structure of metamaterials. The real values of the effective negative permeability, 6.21-6.39 GHz, 7.26-8.74 GHz, and 9.10-14.43 GHz, for the propagation direction along the z-axis (normal incidence) of design structure of metamaterials are shown in Fig. 5(b).

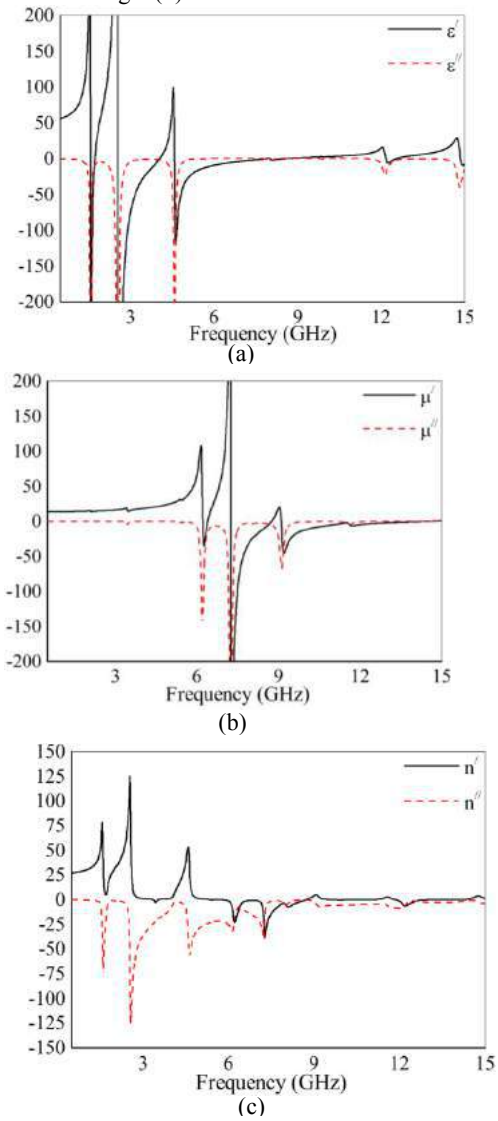

Figure 5: (a) Permittivity (b) permeability (c) Refractive index values of real and imaginary curves for normal incidence of EM.

The negative properties of the permittivity and permeability has altered by a tiny amount due to the polarization effect on the internal construction of metamaterials structures. Anisotropic materials comprise unequal lattice structure that handles the applied electromagnetic field due to the polarization of dipole moment inside materials. Hence, the variety of design structure also alters the properties of the effective permittivity and permeability of the metamaterials. The effective refractive index, $n = n' + in''$, are demonstrated in Fig. 5(c). It can be seen that the magnitude of the real values of the effective negative refractive index are in 3.36-3.52 GHz, 5.34-5.52 GHz, 5.63-8.69 GHz, 9.71-10.55 GHz and 11.84-13.90 GHz of the design structure of metamaterials. The curves of the effective refractive index

become negative when the curves of the permittivity and permeability are negative, simultaneously. The design structure of metamaterials has revealed double negative properties at region of 6.21-6.39 GHz, 7.26-7.92 GHz, 8.01-8.69 GHz, and 12.17-12.56 GHz. It can be considered that the losses are insignificant in those frequency ranges, which designates four efficient pass band.

3.2. Analysis of the Parallel Incidents of EM wave

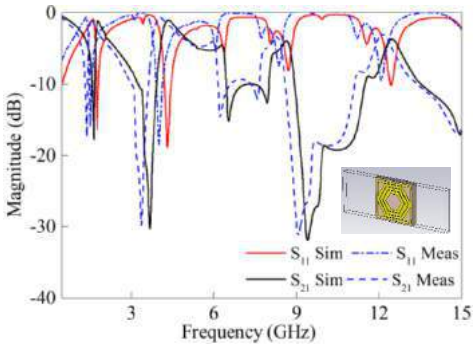

(a)

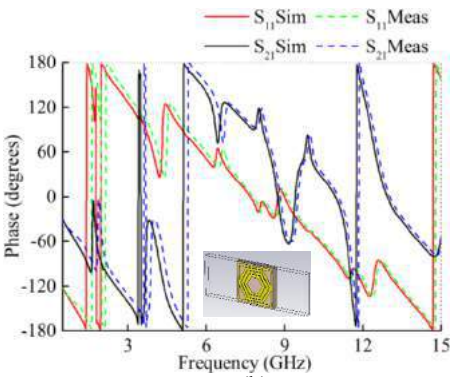

(b)

Figure 6: (a) Magnitude (b) phase of simulated and measuredS-parameters of the structure.

For the parallel incidence, the incident condition was fulfilled by applying PMC and PEC are applied along the y- and z-direction, individually, and two waveguide ports are placed on the positive and negative x-direction. The amplitudes of the real and imaginary values of scattering parameters are shown in Fig. 6(a). Fig. 6 depicts the simulated and measured reflection coefficient (S_{11}), and transmission coefficient (S_{21}) of the artificial material for the direction of EM planar wave propagation along the x-axis.. Fig. 6 (a) demonstrates the values of the dip of the resonances at 1.01 GHz, 3.47 GHz, 6.17 GHz, and 9.81 GHz frequencies, that designates L-, S-, C-, and X-bands applications. The value of transmission is lowest, on the contrary, the value of reflection is nearly zero at the resonance frequencies. The phase of the transmission and reflection follows same phenomena as described in Fig. 3. The distributions of instantaneous surface current and magnetic field of the resonant four peaks are shown in Fig. 7, for instance, 1.01 GHz, 3.47 GHz, 6.17 GHz and 9.81 GHz, where its depict mu negative metamaterial, double negative metamaterial, negative refractive index metamaterial and mu negative metamaterial respectively.

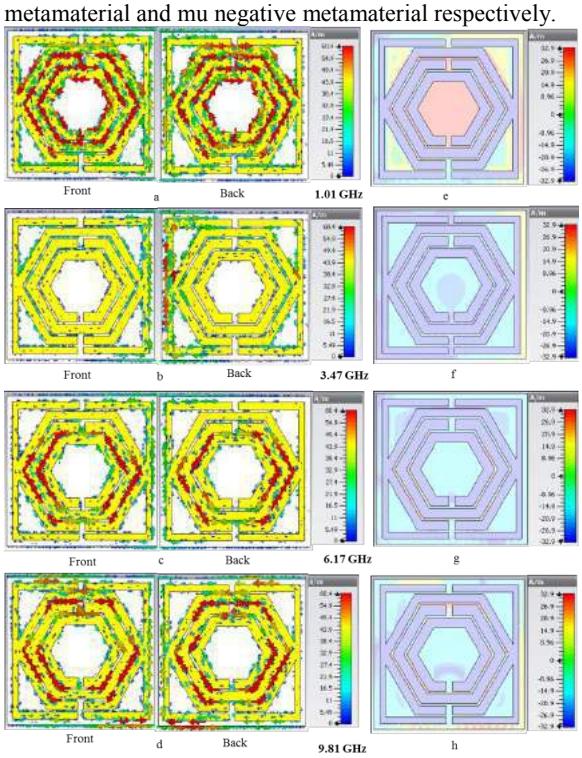

Figure 7: Instantaneous surface current and magnetic field distribution for nermal incidence of EM wave.

The flow of current on the facial metallic pieces is anti-paralleled to the backward or following one, hence, generating a heavy charge buildup at the areas. As a result, four magnetic dipoles formed due to opposite current flow that show negative magnetic resonances under the parallel incidence of EM wave. At 1.01 GHz, the distributions of magnetic field have concentrated on the areas of split gap of inner and middle ring with the surroundings. Hence, the mu negative is exposed by the regions of the magnetic resonance. Moreover, at 3.47 GHz, the magnetic field's is concentrated in the regions of the upper-side and lower-side of the slabs. Therefore, the dual negative is subjugated by the regions of the magnetic resonance. Furthermore, at 6.17 GHz, the magnetic field's is concentrated in the regions of the left-side and right-side of the substrate. So, the negative refractive index is prevailed by the regions of the magnetic resonance Additionally, at 9.81 GHz, the magnetic field's is concentrated on the zones of the left-side, right-side, upper-side and lower-side of the substrate. Thus, the mu negative is prevailed by the regions of the magnetic resonance. Fig. 8 (a) represents the real and imaginary curves of retrieval effective permittivity of the artificial material for the propagation of planar EM wave along the x-axis means parallel incidence. It can be seen that a large span of frequencies, for instance,1.12 to 7.26 GHz and 13.03 to 13.78 GHz of negative amplitude have been attained in the microwave spectra.

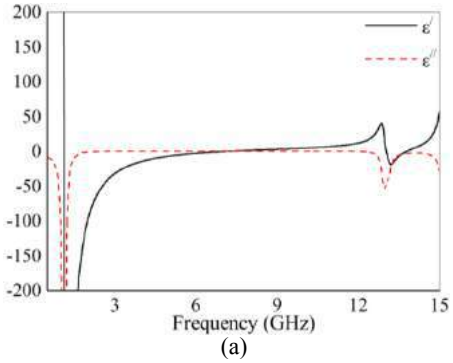

(a)

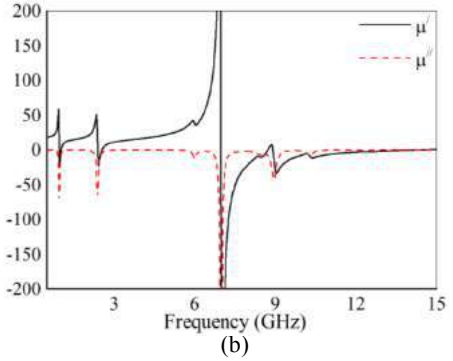

(b)

Likewise, from Fig. 8 (b), it has been perceived that few negative peaks of the effective permeability are 0.95 to 1.01 GHz, 2.39 to 2.53 GHz, 6.98 to 8.71 GHz, and 8.92 to 14.39 GHz.

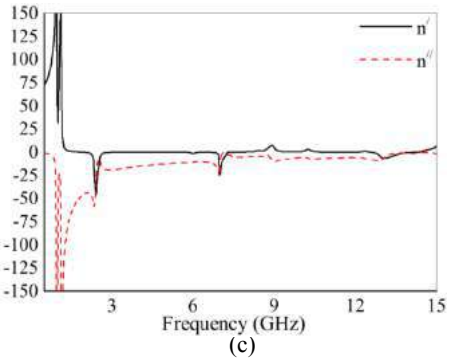

(c)

Figure 8: (a) Permittivity (b) permeability (c) Refractive index values of real and imaginary curves for parallel incidence of EM.

Hence, it is apparent that the artificial material exhibits negative magnitude for both permittivity and permeability at the frequency ranges of 2.39 to 2.53 GHz and 6.98 to 7.26 GHz in the microwave region. Generally, the properties of permittivity and permeability are affected by the polarization that are mentioned previous discussion. Therefore, the refractive index curve of the material also affected by the polarization like as permittivity and permeability. The real and imaginary magnitude of the effective refractive index is shown in Fig. 8 (c) for parallel incident of EM wave, where peak resonances are perceived in the S-, C-, and Ku-band in the microwave region. The bandwidths of the effective refractive index are 1.91-7.33 GHz (5.42 GHz) and 12.56-14.30 GHz (1.74 GHz) for parallel incident of EM wave that indicates the wideband applications of the structure.

Table 1: Comparison of performance with other multi-band metamaterials.

Composition Technique	MHSRR-MHSRR pair	Pair of ELC–HSLR	Orthogonal Z-shaped metallic strip pair	Nonlinear Metamaterial	Pair of MTSRR-wire	Pair of multiple SSRR	Pair of TSRR-wire
Incident direction of EM wave	Parallel Normal	Parallel	Parallel Normal	Parallel	Parallel	Normal	Parallel
Number of frequency bands	5 4	3	2 2	3	1	2	3
Applicable regime	Microwave	Microwave	Microwave	Microwave	Terahertz	Microwave	Microwave
Effective medium ratio(λ/a)	28.02 17.26	19.23	4.83 4.97	6.97	15	7.06	7.35
Number of resonance frequency	5 4	4	3 3	3	2	5	4
Complexity of the structure	Simple	Complex	Simple	Complex	Simple	Simple	Simple
References	This work	11	16	12	13	14	19
Published		2016	2015	2014	2013	2012	2011

Table 1 reveals the comparisons of the incident direction of EM wave, the number of frequency bands, applicable regime, EMR, number of resonance frequency and complexity of the structure of the proposed design. It is seen that EMR of the proposed NIM structure is the uppermost when compared to other suggested metamaterials. Proposed structure has a quad-band, good selectivity, simple construction, and decent characteristics with dual incidence.

4. Conclusions

A new design of miniaturized quad-band negative refractive index operating under the normal and parallel incidence proposed in this manuscript. The metamaterials properties of the suggested structure tested in numerically and experimentally. The FDTD based Computer Simulation Technology was used for the numerical analyses and a vector network analyzer (N5227A) was used for the measurements. For an EM wave of normal incidence, the structure revealed metamaterials properties with wideband negative refractive index (3.18 GHz). In addition, for an EM wave of parallel incidence, the structure has exhibited metamaterials properties with wideband negative refractive index (2.45 GHz). These differences occurred due to changes in the boundary conditions. The proposed NIM considerably improved EMR as compared to other multi-band metamaterials. Furthermore, the proposed structure was appropriate for mobile phones (GSM), microwave communications, radar and satellite communications.

References

[1] V. G. Veselago, The electrodynamics of substances with simultaneously negative values of ε and μ, *Sov. Phys*. 10: 509–514, 1968.

[2] R. A. Shelby, D. R. Smith, and S. Schultz, Experimental verification of a negative index of refraction, *science,* 292: 77-79, 2001.

[3] M. H. Ullah, M. T. Islam, and M. R. I. Faruque, A near-zero refractive index meta-surface structure for antenna performance improvement, *Materials,* 6: 5058-5068, 2013.

[4] S. il Kwak, D.-U. Sim, J. H. Kwon, and Y. J. Yoon, Design of PIFA with metamaterials for body-SAR reduction in wearable applications, *IEEE Trans. Electromagn. Comp.,* 59: 297-300, 2017.

[5] S. S. Islam, M. R. I. Faruque, and M. T. Islam, A dual-polarized metamaterial-based cloak, *Mater. Res. Bull.,* 2017.

[6] P. T. Bowen, A. Baron, and D. R. Smith, Theory of patch-antenna metamaterial perfect absorbers, *Phys. Rev. A,* 93: 063849, 2016.

[7] D. R. Smith, W. J. Padilla, D. Vier, S. C. Nemat-Nasser, and S. Schultz, Composite medium with simultaneously negative permeability and permittivity, *Phys. Rev. Lett.,* 84: 4184, 2000.

[8] R. Liu, A. Degiron, J. J. Mock, and D. R. Smith, Negative index material composed of electric and magnetic resonators, *Appl. Phys. Lett.*, 90:263504, 2007.

[9] H. Chen, L. Ran, J. Huangfu, X. Zhang, K. Chen, T. M. Grzegorczyk*, et al.*, Left-handed materials composed of only S-shaped resonators, *Phys. Rev. E,* 70: 057605, 2004.

[10] J. Huangfu, L. Ran, H. Chen, X.-m. Zhang, K. Chen, T. M. Grzegorczyk*, et al.*, Experimental confirmation of negative refractive index of a metamaterial composed of Ω-like metallic patterns, *Appl. Phys. Lett.,* 84: 1537-1539, 2004.

[11] A. Sarkhel, D. Mitra, and S. R. B. Chaudhuri, A compact metamaterial with multi-band negative-index characteristics, *Phys. Rev. A,* 122,:1-10, 2016.

[12] Y. Liu, X. Zhou, K. Song, S. Gu, Z. Liu, L. Guo*, et al.*, Quasi-phase-matching of the dual-band nonlinear left-handed metamaterial, *Appl. Phys. Lett.,* 105: 201911, 2014.

[13] C. Sabah, Multiband metamaterials based on multiple concentric open-ring resonators topology, *IEEE J. Sel. Top. Quantum Electron.*, 19: 8500808, 2013.

[14] H.-X. Xu, G.-M. Wang, Q. Liu, J.-F. Wang, and J.-Q. Gong, A metamaterial with multi-band left handed characteristic, *Appl. Phys. A.,* 107: 261-268, 2012.

[15] M. R. I. Faruque, M. J. Hossain, S. S. Islam, M. F. B. Jamlos, and M. T. Islam, Design and analysis of a new double C-shaped miniaturized metamaterial for multiband applications, *Appl. Phys. A.,* 123: 310, 2017.

[16] H. Zhou, C. Wang, and H. Peng, A novel double-incidence and multi-band left-handed metamaterials composed of double Z-shaped structure, *J. Mater. Sci. Mater.,* 27: 2534-2544, 2016.

[17] W. Zhu and X. Zhao, Adjusting the resonant frequency and loss of dendritic left-handed metamaterials with fractal dimension, *J. Appl. Phys.,* 106: 093511, 2009.

[18] S. S. Islam, M. R. I. Faruque, and M. T. Islam, A near zero refractive index metamaterial for electromagnetic invisibility cloaking operation, *Materials,* 8: 4790-4804, 2015.

[19] C. Sabah, Multiband planar metamaterials, *Microwave Opt. Technol. Lett.,* 53: 2255-2258, 2011.

Tree-Shape Fractal Meta-Surface with Left Handed Characteristics for Absorption Application

M. M. Hasan[1*], M. R. I. Faruque[1], M. T. Islam[2]

[1]Space Science Centre (ANGKASA), Universiti Kebangsaan Malaysia, Bangi 43600, Malaysia
[2]Department of Electrical, Electronic and Systems Engineering, Universiti Kebangsaan Malaysia, Bangi 43600, Malaysia

*corresponding author: mehedi20.kuet@gmail.com

Abstract

A tri-band fractal meta-surface absorber composed of metallic branches of tree connected with a straight metal strip has been presented in this paper for high absorption application. The proposed tree-shape structure shows resonance in C-, X-, and Ku-band and left handed characteristics in 14.15 GHz. The dimension of the tree-shaped meta-surface single unit cell structure is 9×9 mm^2 and the effective medium ration is 5.50. In addition, the designed absorber structure shows absorption above 84%, whereas the absorber structure printed on epoxy resin fiber substrate material. The FIT-based CST-MWS has been utilized for the design, simulation, and analysis purpose. Fabrication is also done for the experimental validation.

1. Introduction

Meta-surface absorbers, as a branch of metamaterials, with the sub wavelength scale unit cell, currently provoke extensive interests since the first experimental demonstration. The necessity of having low-profile absorbers in microwave frequency is growing rapidly, as a result actuated the researcher toward the development of metamaterial based absorbers. These metamaterial absorbers are formed by the periodic extension of unit cell. On receiving the incident wave, these unit cells get excited due to simultaneous occurrence of electric and magnetic resonances in their structure. High absorption can be achieved by minimizing the reflectance and transmittance as well as impedance must be well matched. Due to ultra-thin dielectric layer thickness, high absorption, and simple design procedure, meta-surface absorbers have been broad applications in the fields of microwave, terahertz, infrared, and optical frequencies. Some metamaterial and metamaterial based absorbers having absorptivity in a single frequency band, dual frequency band, and triple frequency band has been reported in this paper. In 2003 R. W. Ziolkowski successfully developed a capacitor loaded strips and split ring resonators metamaterial that displayed negative permittivity and permeability both at the X-band frequency [1]. After the successfully invention of metamaterial the researcher was being motivated to develop the metamaterial based absorber for high absorption, simple design procedure, cost effective, miniature in size, etc. As a result, first perfect metamaterial absorber was demonstrated by Landy and his colleagues in 2008, which was a classic sandwiched structure composed of a split ring resonator, a dielectric substrate, and a metallic cut wire achieved its peak absorption of 88% in 11.50 GHz [2]. An ultra-wideband metamaterial absorber was presented above 90% absorption and the wide bandwidth from 7.85 to 12.25 GHz (X-band). The structure was designed by composed of two concentric circular split rings imprinted on a metal backed dielectric substrate [3]. In addition, a z-shaped left handed metamaterial for wide band applications was presented, which applicable for C- and X-band application and miniature in size of 10×10 mm^2 but there were no absorption properties had been investigated [4]. Further, a compact square split z-shape metamaterial was presented with left handed features in 8.50 GHz, wide bandwidth of 5.67 GHz for S-, C-, X- and Ku-band application. Besides, the presented meta-atom was investigated in 15^0, 30^0, 45^0, 60^0, 75^0 and 90^0 angular rotations in xy-plane [5]. A left handed metamaterial consisted of a single-sided tree-shaped fractal structure, features triple magnetic resonances and one electric resonance apart from the lower metal plasma response was introduced. Moreover, the resonance points had a value of 2.2, 3.3 and 5.6 dB were clearly observed, respectively in 7.98, 8.68 and 9.0 GHz [6]. An ultrathin and miniaturized FPMA structure was investigated for RCS reduction and the absorption was <90% from 3.17 to 3.22 GHz, whereas the size of the absorber was 0.1λ×0.1λ [7]. Moreover, a fractal shaped square absorber had been proposed and exhibited absorption of 99.1% and 99.7% respectively in 4.17 and 11.16 GHz [8]. Further, a microwave metamaterial absorber was designed that resonance at C-, X- and Ku-band with double negative characteristics as well as the absorption peaks were respectively, 82%, 67%, and 93% in 6.22, 8.76, and 13.05 GHz in [9]. A microwave metamaterial absorber composed of delicate periodic patterned structures and a metallic background plane was separated by a dielectric substrate suggested by Wang and his colleagues. The designed absorber shown absorption peaks were respectively in 28.21, 39.59, 52.78, and 58.63 GHz with the absorption of 99.47%, 99.94%, 99.05%, and 99.55% [10]. An absorber consisted of closed-ring resonator with a metallic patch inside it, and the resonator and the patch were diagonally connected by a metallic arm, shown dual resonance in C-band and broadband absorption in X-band. The absorber

had the peak absorptivity of 95.7%, 99%, and 98.9% in 4.69, 5.19, and 7.15 GHz, for C-band and absorptivity of 99.81% and 99.77 % was obtained in 8.94 and 10.68 GHz for X-band [11]. A wearable microwave metamaterial absorbing for dual resonances in 9.0 and 9.80 GHz and two absorptivity peaks <90%, composed of two square ring resonators with different sizes, a backing ground plane, and a flat substrate with a 1.0 mm thickness in 2016. However, the proposed WMMA has a high absorptivity regardless of the polarization angle of the EM waves and the deformation effect [12]. In [13] Islam et al. proposed a new multi band split S-shape metamaterial for absorption analyses that shown resonance at S-, X- and Ku-bands in microwave spectra. The absorption spectra for the proposed was 45% achieved at S-band. Moreover, after reducing the coupling capacitance in the z-axis absorption was reaching up to 55%, but in the y-axis absorption was extended up to 47%. In [14] a symmetrical circular fractal metamaterial absorber had been proposed for tri-band absorption for both TE and TM polarisations and absorption of 98.7%, 99.4%, and 99.5% respectively in 2.29, 4.28, and 11.71 GHz [14]. A broadband metamaterial absorbing in terahertz frequency range that was made up by two circular split rings, a dielectric substrate and a metallic ground to achieve absorption from 0.85 to 1.926 THz with the absorptivity beyond 90% at normal incidence and the bandwidth was 1.076 THz [15].

In this paper, the proposed fractal meta-surface absorber is completely new by the tree-shaped structure for high absorption application. The designed structure is quite different from the previously designed meta-surface structure. Most of the famous structure was square-, circular-, ring-, or alphabetical-letter shaped, but the proposed fractal meat-surface structure is totally different like a tree-shape structure with lots of branches. The unit cell of the proposed meta-surface structure contains metallic branch tree-shaped fractal metal printed on FR-4 material. The dimension of the tree-shaped structure is 9×9 mm2 and applicable for tri-band (C-, X-, and Ku-band) application. The results of the simulated resonance peaks are in 6.20, 8.13, and 12.23 GHz, whereas the measured transmittances resonance peaks are respectively, 6.06, 7.98, 11.94 GHz. Moreover, the absorption peaks are above 73%, 64% and 84% respectively in 6.50, 8.73, and 14.40 GHz for the designed absorber structure. Besides, the surface impedance of these fractal structures is -2-48i. The paper is organized as follows: in section 2, fractal meta-surface absorber design procedure with specification is described, the methodology and the retrieval of the effective permittivity, permeability and refractive index are explained in section 3, in section 4 measurement procedure and the obtained results are analysed and the paper is concluded by section 5.

2. Fractal Meta-Surface Structural Design

The top view of the proposed fractal meta-surface structure with optimized geometric dimensions is shown in figure 1(a-c). Each single unit cell of the proposed meta-surface structure contains metallic branch tree-shaped fractal metal printed on a 1.60 mm thick epoxy resin fibre substrate material (εr = 4.25 and tanδ = 0.02). However, 'A', 'B', and 't' are respectively the FR-4 substrate material width, length and height. Besides, 'L1', 'W1', and 'd' is the fractal shape length, width and the width of copper metal.

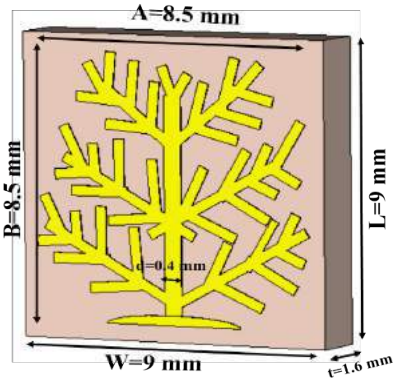

(a)

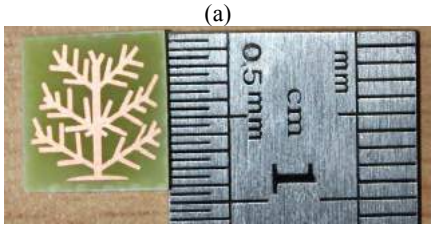

(b)

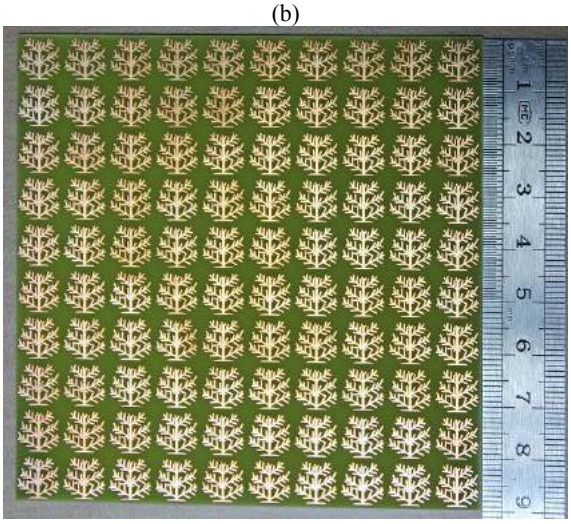

(c)

Figure 1: (a) Schematic view where the geometric dimensions are, A= 9.0 mm, B= 9.0 mm, L_1= 8.50 mm, W_1= 8.50 mm. The metal (copper) has a width (d) of 0.50 mm and thickness (h) of 0.035mm, (b) Fabricated single unit cell structure, (c) Fabricated array structure of the proposed fractal meta-surface absorber.

3. Methodology and Retrieval of Parameters

The finite integration technique has been adopted for all design, simulation, and numerical investigations. This is a spatial discretization technique to solve electromagnetic

field problems numerically in the frequency domain. Basically, in this approach Maxwell's equations are applied in integral form of a set of staggered grids. The utilization of a stable dual orthogonal grid with a precise time integration technique leads the computation process. The technique covers full range of electromagnetic application and a basis for commercially available computer simulation technology microwave studio electromagnetic simulator. Two boundary conditions are commonly used for the computation of meta-surface parameters: periodic boundary condition and perfect electromagnetic conductor boundary condition. Periodic boundary conditions are usually applied for simulating a part of the mass framework by modelling its small part to the absence of proper surface. The perfect electromagnetic conductor boundary condition is the generalization of perfect electric conductor and perfect magnetic conductor. For the simulation of the proposed fractal meta-surface absorber EM-waves are propagating along the z-axis, whereas the x- and y-axis are respectively considered as a perfect electric conductor and perfect magnetic conductor boundaries. The frequency domain solver with tetrahedral mesh have been utilized for the simulation and the impedance has been set to 50Ω. However, the retrieving procedure of the effective medium parameters is given as follows [16],

$$Reflection\ Coefficient,\ S_{11} = \left\{ \frac{R_1\left(1-e^{-2j\theta}\right)}{1-R_1^2 e^{-2j\theta}} \right\} \quad 1$$

$$Transmission\ Coefficient,\ S_{21} = \left\{ \frac{e^{-2j\theta}\left(1-R_1^2\right)}{1-R_1^2 e^{-2j\theta}} \right\} \quad 2$$

$$Permeability,\ \mu_r \approx \left[\frac{2c(1-S_{21}+S_{11})}{j\omega d(1+S_{21}-S_{11})} \right]$$

$$Permeability,\ \mu_r \approx \left[\frac{c(1-S_{21}+S_{11})}{j\pi f d(1+S_{21}-S_{11})} \right] \quad 3$$

$$Permittivity,\ \varepsilon_r \approx (\mu_r + j\frac{2cS_{11}}{\omega d})$$

$$Permittivity,\ \varepsilon_r \approx (\mu_r + j\frac{cS_{11}}{\pi f d}) \quad 4$$

$$Refractive\ Index,\ n_r \approx \left[\frac{2c}{j\omega d}\left\{ \frac{\left(S_{21}-1\right)^2 - S_{11}^2}{\left(S_{21}+1\right)^2 - S_{11}^2} \right\} \right]^{1/2}$$

$$Refractive\ Index,\ n_r \approx \left[\frac{c}{j\pi f d}\left\{ \frac{\left(S_{21}-1\right)^2 - S_{11}^2}{\left(S_{21}+1\right)^2 - S_{11}^2} \right\} \right]^{1/2} \quad 5$$

In addition, the total inductance of the designed structure can be calculated from the equation,

$$L_T = \mu_0 t^2 \left\{ \frac{\sqrt{A^2+B^2}}{3\pi\sqrt{L_1^2+W_1^2+t^2}} + \frac{\sqrt{L_1^2+W_1^2}}{\sqrt{t^2+d^2}} \right\} \quad 6$$

The total capacitance can be calculated from the equation,

$$C_T = \varepsilon_0 \left\{ \frac{\pi(A+B)}{2(L_1+d)} \ln \frac{(L_1+W_1)}{\pi(t+d)} \right\} \quad 7$$

Perfect absorption takes place when the effective impedance of the absorber matches with the impedance of the free space. This condition ensures the zero reflection and transmission of the incident wave. Effective impedance is strongly related with the effective permeability and permittivity of the proposed absorber structure.

$$Impedance,\ Z_{eff} = \sqrt{\varepsilon_r / \mu_r} \quad 8$$

where 'd' is the thickness of the substrate, 'Z_{eff}' is the normalize impedance, 'ω' is the angular frequency, 'c' is the velocity of light, 'S_{11}' is the reflection coefficient, and 'S_{21}' is the transmission coefficient. In addition, the free-space permeability of $4\pi\times10^{-7}$ H/m and permittivity of 8.85×10^{-12} F/m. From the developed equation 6 & 7, the calculated transmittance resonance peaks is 6.18, whereas the simulated and the measured transmittance resonance peaks are respectively in 6.20 GHz and 6.06 GHz. Therefore, the resonance frequency is calculated by,

$$f_r = \frac{1}{2\pi\sqrt{L_T C_T}} \quad 9$$

The total inductance and capacitance describes the resonance points of the proposed meta-surface structure. The variation of any geometrical parameters corresponding to the change of the total inductances and capacitances causes the shift of the resonant frequencies. This analysis provides us a quantitative prediction of residual resonant frequencies whenever a magnetic or electric resonant frequency is given and in turn affords a good guideline for individual control over these resonances. The electromagnetic wave incident on the absorber structure and the absorption can be calculated from the following equation,

$$Absorption,\ A(f) = \left\{ 1 - \left|S_{11}\right|^2 - \left|S_{21}\right|^2 \right\} \quad 10$$

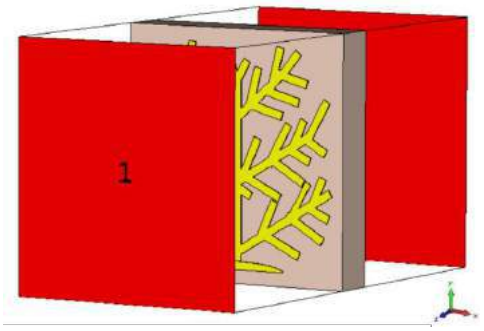

Figure 2: Simulation set-up of the designed fractal meta-surface absorber in the CST-MWS.

4. Experimental Measurement & Result Analysis

A 153×198-mm^2 (17×22 unit cells) array structure has been fabricated for measurement (shown in figure 1(c)). The fabricated tree-shape fractal meta-surface is placed between the horn antennas and the EM-waves are propagated along z-directions to an incident on the fabricated structure, similar to the simulation set-up (shown in figure 2). Antennas are placed far enough from each other to provide far-field conditions. Since the backward side of the structure is covered by a metal, there will be no transmission. Therefore, only the reflection measurements are carried out to evaluate the absorption coefficient. To measure the scattering and effective medium parameters, an Agilent N5227A vector network analyser was connected to the antennas. In addition, an Agilent N4694-60001 device was used to calibrate the vector network analyser (VNA-N5227A) to ensure accuracy of the network analyser in the case of measurement. For the current distribution analysis, the current is flowing inner direction from every branch of the tree-shape structure. At the resonance points the intensity of the current is the highest, whereas the stop bands are created at the null point by the minimization of the current by flowing opposite direction shown in figure 3(a,b). Besides, current loops behave to resemble several independent magnetic dipoles whose dipole moments drill through these loops and are anti-parallel to the external magnetic field. The electric field distributing in the substrate board of proposed fractal structure is plotted at electric and magnetic resonance in figure 3(c-d). The inductive net electric dipole moments yield when current flows on the tree-shaped metal patterns and are anti-parallel to the incident electric fields, providing the negative permittivity. Although th gap is capable of providing a capacitance, it is unable to excite the oscillation of current and play the role of accumulating charges whose dipole moments are anti-parallel to electric fields.

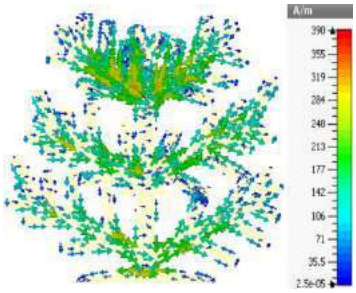

(a)

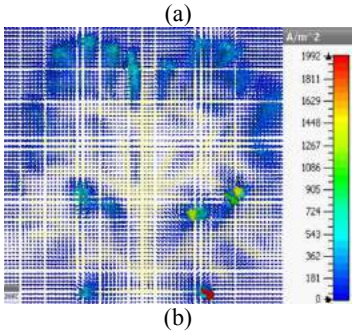

(b)

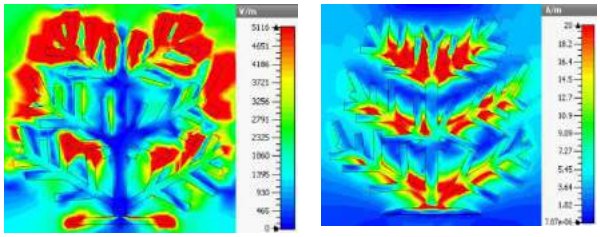

(c) (d)

Figure 3: (a) Surface current distribution, (b) Current density, (c) Electric field, (d) Magnetic field of the proposed fractal meta-surface in 11.94 GHz.

Figure 4(a-b) depicts, the amplitude of the transmission (S_{21}) coefficient and the absorption peaks. In figure 4(a) the simulated transmittance resonances are in 6.20, 8.13, and 12.23 GHz and the amplitude of those simulated peaks are respectively, -15.19, -19.62, and -29.06 dB. Besides, the measured transmittance resonances with the magnitude are respectively, 6.06 GHz (magnitude of -17.10 dB), 7.98 GHz (magnitude of -13.16 dB), 11.94 GHz (magnitude of -34.25 dB), and 15.01 GHz (magnitude of -28.40 dB). Here, the measured and simulated transmittances are a little bit shift due to the fabrication tolerance in figure 4(a). From figure 4(b) the absorption peaks of the proposed fractal meta-surface absorber are more than 73%, 64% and 84% respectively, in 6.50, 8.73, and 14.40 GHz in the case of reflection (S_{11}) coefficient resonance frequencies.

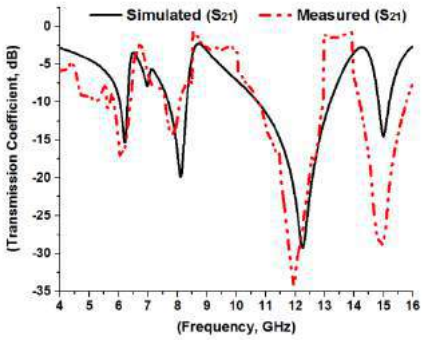

(a)

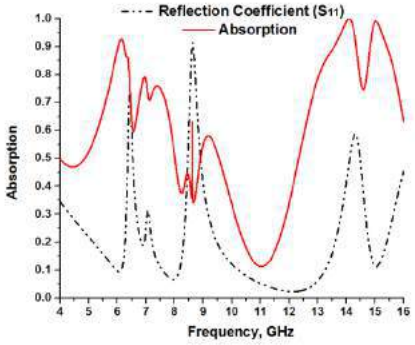

(b)

Figure 4: Amplitude of the proposed meta-surface: (a) Reflection and Transmission coefficient, (b) Absorption.

The amplitude of the effective medium parameters (permittivity, permeability, and refractive index) is shown in figure 5(a-c). The effective permittivity exhibits the negative peaks in 6.50 and 8.68 GHz and the values are respectively, (-28.24-22.03i), and (-12.31-12.98i) in figure 5(a). In figure 5(b) the real value of negative permeability curves shows a negative region from 9.38 to 16.0 GHz and the negative refractive index of real magnitude from 4.0 to 7.90 GHz, 8.87 to 10.94 GHz, and 12.0 to 16.0 GHz in figure 5(c). If the permittivity and permeability are simultaneously negative, then refractive index is also negative. Moreover, in 14.15 GHz the proposed meta-surface absorber exhibits the real value of the permittivity, permeability and refractive index parameters are respectively -1.23, -3.95, and -3.43. However, for the negative magnitude of effective medium parameters in 14.15 GHz the meta-surface absorber structure can be called as a left handed meta-surface. In addition, in 9.95 GHz the reactance impedance (or surface impedance) is (-2-48i) shown in figure 5(d).

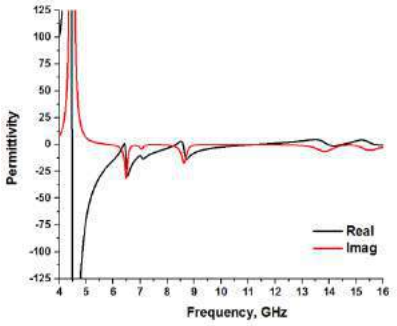

(a)

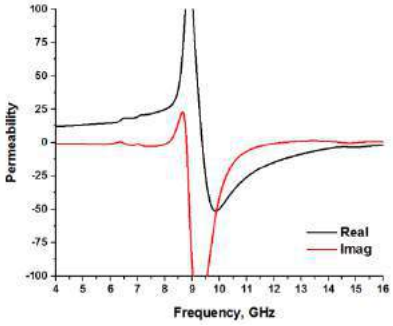

(b)

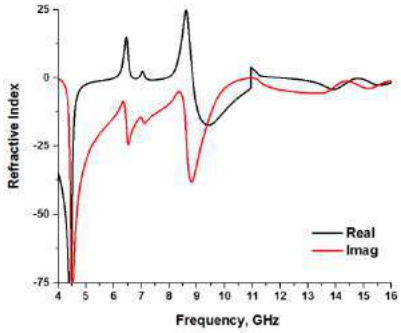

(c)

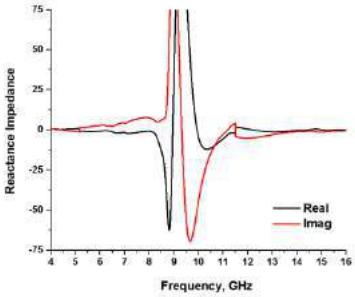

(d)

Figure 5: Amplitude of the proposed fractal meta-surface: (a) Permittivity, (b) Permeability, (c) Refractive index, (d) Reactance impedance.

Further analysis is done with the fractal shape by propagating the electromagnetic waves through the absorber in x-axis displayed in figure 6(a). The resonance of the transmittance (S_{21}) in 8.99 GHz (magnitude of -25.75 dB) is presented in figure 6(b). The permittivity exhibits negative real values from 5.89 to 6.61 GHz and 10.09 to 14.95 GHz in figure 6(c). In addition, surface impedance for x-axis wave propagation is also shown in figure 6(d), which is almost similar highest negative peaks like the z-axis wave propagation.

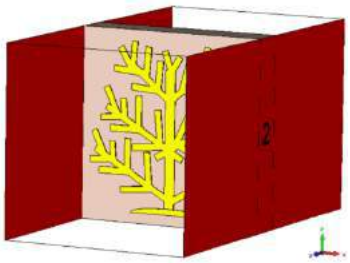

(a)

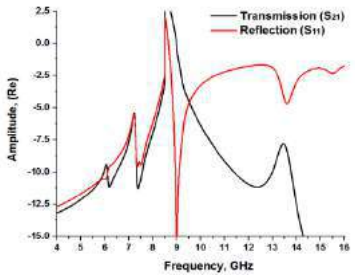

(b)

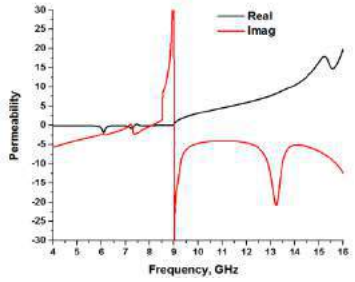

(c)

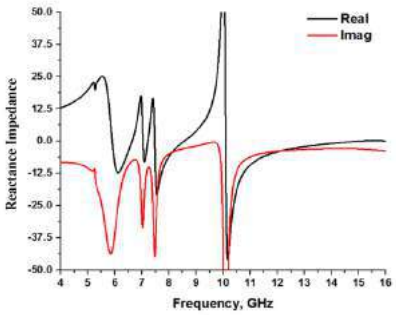

(d)

Figure 6: Amplitude of the proposed fractal meta-surface structure at x-direction wave propagation, (a) Scattering parameters, (b) Permeability, (d) Reactance impedance.

5. Conclusion

A left handed meta-surface absorber inspired by tree-shaped fractal structure with tri-band resonances have been numerically and experimentally analysed in this paper. The resonance of the proposed design is explained by current distribution and field's pattern. The meta-surface structure is compact in size and the absorption in above the 84%. The EM-wave pass through the proposed structure along z-axis. In addition, the impact of the EM-wave on resonance if the EM-wave propagation along x-axis is also investigated here. However, it is obtained that the proposed structure has wider absorption bandwidths as well as better absorption levels in microwave frequency. Besides, for tri-band (C-, X-, and Ku-band) resonance the proposed fractal meta-surface is applicable for high absorption, detection, satellite communication and sensing applications.

Acknowledgements

This work was supported by the Research Universiti Grant, Geran Universiti Penyelidikan (GUP), Code: 2016-028.

References

[1] R. W. Ziolkowski, "Design, fabrication, and testing of double negative metamaterials", *IEEE Transaction on Antennas Propagation*, 5:1516–1529, 2003.

[2] N. I. Landy, S. Sajuyigbe, J. J. Mock, D. R. Smith, W. J. Padilla, "A perfect metamaterial absorber", *Physical Review Letter*, 100:1–4, 2008.

[3] S. Ghosh, S. Bhattacharyya, D. Chaurasiya, K. V. Srivastava, "An ultra-wideband ultra-thin metamaterial absorber based on circular split rings", *IEEE Antennas and Wireless Propagation Letters*, 2015, Doi: 10.1109/LAWP.2015.2396302.

[4] M. M. Hasan, M. R. I. Faruque, M. T. Islam, "Left-Handed Metamaterial using Z-Shaped SRR for Multiband Application by Azimuthal Angular Rotations", 2017, Materials Research Express 4:4.

[5] M. M. Hasan, M. R. I. Faruque, S. S. Islam, M. T. Islam, "A new compact double-negative miniaturized metamaterial for wideband operation", *Materials*, 9(10):830, 2016.

[6] H.-X. Xu, G.-M. Wang, C.-X. Zhang, Q. Liu, Z.-M. Xu, X. Chen, D.-L. Zhai, "Multi-band left-handed metamaterial inspired by tree-shaped fractal geometry", *Photonics and Nanostructures – Fundamentals and Applications*, 11:15–28, 2013.

[7] S. Li, X. Cao, J. Gao, Y. Zheng, D. Zhang, H. Liu, "Fractal metamaterial absorber with three-order Oblique cross dipole slot structure and its application for in-band RCS reduction of array antennas", *Radio Engineering*, 23:1048-1054, 2014.

[8] S. Bhattacharyya, S. Ghosh, A. Bhattacharya, D. Chaurasiya, K. V. Srivastava, "An ultra-thin polarization independent compact fractal shaped metamaterial absorber", *Applied Electromagnetics Conference*, 2016,Doi: 10.1109/AEMC.2015.7509231.

[9] M. M. Hasan, M. R. I. Faruque, M. T. Islam, "A Tri-Band Microwave Perfect Metamaterial Absorber", Microwave and Optical Technology Letters, 2017, Doi: 10.1002/mop.30726.

[10] N. Wang, J. Tong, W. Zhou, W. Jiang, J. Li, X. Dong, S. Hu, "Novel quadruple-band microwave metamaterial absorber", *IEEE Photonics Journal*, 7: 5500506, 2015.

[11] M. Agarwal, A. K. Behera, M. K. Meshram, "Dual resonating C-band with enhanced bandwidth and broad X-band metamaterial absorber", *Applied Physics A*, 122:166, 2016.

[12] J. Tak, J. Choi, "A wearable metamaterial microwave absorber", *IEEE Antennas and Wireless Propagation Letters*, 2015, Doi: 10.1109/LAWP.2016.2604257.

[13] S. S. Islam, M. R. I. Faruque, M. T. Islam, "Design and absorption analysis of a new multiband split s-shaped Metamaterial", *Science Engineering Composite Material*, 2015, Doi: 10.1515/secm-2014-0376.

[14] H. Jiang, Z. Xue, W. Li, W. Ren, "Multiband polarisation insensitive metamaterial absorber based on circular fractal structure", *IET Microwaves, Antennas & Propagation*, 10:1141–1145, 2016.

[15] W. Pan, X. Yu, J. Zhang, W. Zeng, "A broadband terahertz metamaterial absorber based on two circular split rings", *IEEE Journal of Quantum Electronics*, 53: 8500206, 2017.

[16] M. M. Hasan, M. R. I. Faruque, M. T. Islam, "Multiband left handed biaxial meta-atom at microwave frequency", 2017, Materials Research Express 4: 035015

Dynamic behaviour of a two-dimensional elastic metamaterial with eccentric local resonators

Zhengwei Li, Chen Wang, and Xiaodong Wang

Department of Mechanical Engineering,
University of Alberta, Edmonton, Canada T6G 2R3
*Xiaodong Wang, E-mail: Xiaodong.wang@ualberta.ca

Abstract

This article presents a two-dimensional four-component composite, which consists of a periodic arrangement of coated eccentric cylinders embedded in an elastic medium. The engineered composite can generate negative effective mass density due to local resonances. The multiple interaction of the local resonators is studied using a pseudo-incident wave method with the composite subjected to inplane harmonic elastic waves. Then, the dynamic behaviour of the metamaterial system is comprehensively analyzed and the phenomenon of wave attenuation of the systems is presented. This study can provide an initial step of investigating periodic elastic metamaterial systems with eccentric resonators.

1. Introduction

Metamaterials are generally classified as engineered materials exhibiting unique electromagnetic, optic or mechanical properties, such as negative refractive index, negative effective mass, negative effective modulus, which are not readily observed in nature and quite desirable for many engineering applications. Unlike the traditional materials, these unique properties of the metamaterials are not from their chemical compositions, but from the delicately designed sub-wavelength structures.

The concept of metamaterials with negative properties can be traced back to 1968 when the negative refractive index generated by the simultaneously negative permittivity and negative permeability in the electromagnetic materials was theoretically proposed [1]. Subsequently, this novel concept was experimentally justified with delicately built microstructure [2]. Then, the ideas of superlenses overcoming the diffraction limit [3], invisible cloak for electromagnetic waves [4], had been further proposed or demonstrated.

Inspired by the development of electromagnetic metamaterials, research community has placed considerable attention on the study of acoustic/elastic metamaterials [5, 6]. One of the most prominent properties of metamaterials with negative effective mass and/or negative effective modulus is their wave attenuation ability, especially in the low frequency ranges, which usually requires the conventional material to have structures with a spatial period of similar size to the wavelength of the incident wave. The engineered microstructures, as the essence of the acoustic/elastic metamaterials, have intrigued intensive interests. Silicone rubber coated lead spheres have been periodically embedded in epoxy matrix to form an elastic metamateiral system with negative effective mass density, which experimentally showed the sound wave blocking ability by breaking the Bragg limit [7]. The coated cylinders serve as the local resonant inclusions. The relative motion between the local resonant inclusions and the matrix will generate an effective mass density, which is different from the static mass density based on the volume average of the the components of the system. When the inclusions resonate, interesting interactions between the scattered waves from the resonators and the incident wave occurs, inducing negative effective property [8, 9, 10, 11]. Similar phenomenon has been observed with a fluid matrix [12]. Then, this kind of system configuration has become a classic approach to obtain negative effective mass density with wave attenuation ability [13]. To investigate the underlying mechanism of the acoustic/elastic metamaterials and develop a methodology to predict band gaps, mass-spring models have been developed to proposed a new point of view on the elastodynamic equation of the composite materials [14, 15, 16].

There have been a number of efforts in the development of acoustic/elastic metamaterials with greater wave attenuation performance. Multilevel local resonators have been considered to extend the widths of the band gaps to some extent [17, 18]. Graded resonators also have been implemented to obtain flexible tailoring of the attenuation property over the desired frequency ranges [19]. Elliptical inclusions has been chosen to break the geometric symmetry of the resonators and split the attenuation peaks into separate ones, widening band gaps [20]. The rotational motion of the elliptical resonators can contribute to the band gaps in the low frequency ranges, which is vital for wave attenuation application. However, the irregular shape makes the analytical analysis impractical.

A two-dimensional elastic system with periodic eccentric local resonators embedded in the host matrix is proposed and analyzed in this study, based on a semi-analytical method. To evaluate the dynamic behaviour the system when subjected to inplane harmonic elastic waves, the single coated cylinder solution is firstly developed as the building block and then the solutions of the system with multiple interaction between cylinders are formed by using pseudo-incident wave technique [21]. With the wave field

calculated, the effective mass density of the system, which can turn negative under specific frequencies, has been determined based on the boundary effective medium theory [22]. The effective mass density is mainly dominated by the translational motion and the rotational motion of the coated cylinders [23, 24]. The effect of the rotational motion is substantial, especially in the low frequency range. The dynamic behaviour of the system has been studied and the wave attenuation phenomenon of the metamateria system has been illustrated at the frequencies with negative effective mass.

2. Formulation of the problem

Consider a two-dimensional four-component composite material model consisting of a collection of hard cylinders embedded in an elastic matrix with soft coating. In the composite model presented, the basic building block of the representative cell is shown schematically in Fig.1, where the matrix medium is labelled as 4, the coating medium is labelled as 3, and the two mediums of hard cylinders are labelled as 1 and 2 with density ρ_1 and ρ_2 respectively. The inner and outer radii of the coating layer are denoted as r_1 and r_2 respectively, as illustrated in Fig.1(a). The sector with central angle θ_2 is filled with medium 1. The angle between the angular bisector of θ_2 and the horizontal direction is defined as θ_1. The length of the square cell is L.

In this study, mediums 1 and 2 possess high stiffness to make the cylinders rigid compared to the soft coatings and have different densities to realize eccentric resonators, generating unique and interesting phenomena. As illustrated in Fig.1(b), when subjected to an incident longitudinal wave with displacement amplitude u_0, translational and rotational motions of the coated cylinders will be induced. $u_{O,x}$ and $u_{O,y}$ represent the displacements of the centroid, O, in x and y directions respectively. The rotational angle of the cylinder is denoted as $\bar{\theta}$ in Fig.1(b).

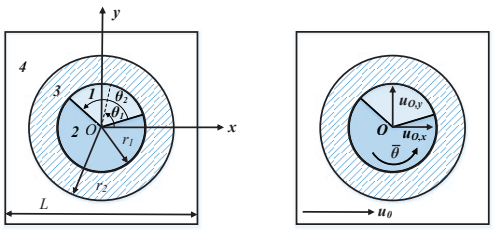

(a) (b)

Figure 1: (a) The configuration of the representative cell, (b) the loading and its corresponding response.

For this two-dimensional metamaterial system, its harmonic response is mostly controlled by the properties of the representative cell.

2.1. The single representative cell

2.1.1. Analysis of the rigid eccentric cylinder

From the geometrical features shown in Fig.1, the following relations can be readily obtained as

$$M_{12} = \frac{1}{2}\theta_2\rho_1 r_1^2 + \frac{1}{2}\left(2\pi - \theta_2\right)\rho_2 r_1^2, \tag{1}$$

$$r_G = \frac{4r_1\left(\rho_1 - \rho_2\right)\sin\left(\theta_2/2\right)}{3\left[\theta_2\left(\rho_1 - \rho_2\right) + 2\pi\rho_2\right]}, \tag{2}$$

where M_{12} is the mass of the cylinder and r_G is defined as the distance between the centroid O and center of mass G of the cylinder. The moment of inertia of the cylinder around its centroid O is

$$I_O = \left\{ \begin{array}{l} \int_0^{r_1}\int_{\theta_1-\theta_2/2}^{\theta_1+\theta_2/2} \rho_1 r^3 d\theta dr \\ + \int_0^{r_1}\int_{\theta_1+\theta_2/2}^{2\pi+\theta_1-\theta_2/2} \rho_2 r^3 d\theta dr \end{array} \right\}. \tag{3}$$

Based on the parallel axis theorem, the moment of inertia of the cylinder around the centre of mass G will be

$$I_G = I_O - M_{12}{r_G}^2. \tag{4}$$

For any point in the outer boundary of the rigid cylinder, its displacements in polar coordinate can be expressed as

$$u_r^{(1,2)}|_{r=r_1} = u_{O,x}\cos\theta + u_{O,y}\sin\theta, \tag{5}$$

$$u_\theta^{(1,2)}|_{r=r_1} = -u_{O,x}\sin\theta + u_{O,y}\cos\theta + r_1\bar{\theta}. \tag{6}$$

The acceleration components of the centre of mass G are in the form of

$$a_{G,x} = -\omega^2 u_{O,x} + \omega^2\bar{\theta} r_G\sin\theta_1 + \omega^2\bar{\theta}^2 r_G\cos\theta_1, \tag{7}$$

$$a_{G,y} = -\omega^2 u_{O,y} - \omega^2\bar{\theta} r_G\cos\theta_1 + \omega^2\bar{\theta}^2 r_G\sin\theta_1. \tag{8}$$

It can be easily observed from equations (7) and (8) that the rotational motions of the eccentric resonators make the system nonlinear. The motion of the rigid cylinders can be determined by the displacements of its center of centroid, $u_{O,x}$ and $u_{O,y}$, and its rotational angle $\bar{\theta}$.

2.1.2. Analysis of the coating

In the coating, the general form of the equation of motion without body force can be written as

$$\left(\lambda_3 + 2\mu_3\right)\nabla\left(\nabla\cdot\vec{u}\right) - \mu_3\nabla\times\nabla\times\vec{u} + \rho_3\omega^2\vec{u} = 0, \tag{9}$$

where ρ_3 is the density of medium 3, λ_3 and μ_3 are the Lamé constants of medium 3. The displacement components in equation (9) are coupled. In order to avoid high-order partial differential equations, displacement potentials are introduced to express the components of the displacement vector with satisfying uncoupled wave equations. For medium 3, the displacement potentials can be expressed as

$$\phi_3\left(r,\theta\right) = \sum_{n=-\infty}^{+\infty}\left\{ \begin{array}{l} J_n\left(K_{L3}r\right)A_n^{(1)} \\ + H_n^{(1)}\left(K_{L3}r\right)A_n^{(2)} \end{array} \right\} e^{in\theta}, \tag{10}$$

$$\psi_3(r,\theta) = \sum_{n=-\infty}^{+\infty} \left\{ \begin{array}{l} J_n(K_{T3}r)\, A_n^{(3)} \\ + H_n^{(1)}(K_{T3}r)\, A_n^{(4)} \end{array} \right\} e^{in\theta}, \quad (11)$$

where $J_n(\cdot)$ and $H_n^{(1)}(\cdot)$ are the n^{th} order Bessel function and Hankel function of the first kind, respectively. The coefficient A_n can be determined by the boundary conditions in the interfaces. The longitudinal wave number K_{L3} and shear wave number K_{T3} are given by

$$K_{L3} = \omega \sqrt{\frac{\rho_3}{(\lambda_3 + 2\mu_3)}}, \quad (12)$$

$$K_{T3} = \omega \sqrt{\frac{\rho_3}{\mu_3}}. \quad (13)$$

Then, the displacement components of the particles in the medium 3 can be expressed in term of the displacement potentials illustrated in equations (10) and (11), as

$$u_r^{(3)} = \frac{\partial \phi_3}{\partial r} + \frac{1}{r}\frac{\partial \psi_3}{\partial \theta}, \quad (14)$$

$$u_\theta^{(3)} = \frac{1}{r}\frac{\partial \phi_3}{\partial \theta} - \frac{\partial \psi_3}{\partial r}. \quad (15)$$

The stress components, $\sigma_{rr}^{(3)}$ and $\sigma_{r\theta}^{(3)}$, will be

$$\sigma_{rr}^{(3)} = \lambda_3 \nabla^2 \phi_3 + 2\mu_3 \left[\frac{\partial^2 \phi_3}{\partial r^2} - \frac{1}{r^2}\frac{\partial \psi_3}{\partial \theta} + \frac{1}{r}\frac{\partial^2 \psi_3}{\partial r \partial \theta} \right] \quad (16)$$

$$\sigma_{r\theta}^{(3)} = \mu_3 \left\{ \begin{array}{l} 2\left(\frac{1}{r}\frac{\partial^2 \phi_3}{\partial r \partial \theta} - \frac{1}{r^2}\frac{\partial \phi_3}{\partial \theta} \right) \\ + \left(\frac{1}{r^2}\frac{\partial^2 \psi_3}{\partial \theta^2} + \frac{1}{r}\frac{\partial \psi_3}{\partial r} - \frac{\partial^2 \psi_3}{\partial r^2} \right) \end{array} \right\} \quad (17)$$

Then, the motion in the soft coating is completely controlled by the material parameters of medium 3 and the coefficient A_n.

2.1.3. Analysis of the matrix

Subjected to an incident harmonic wave, scattered wave will be generated due to the interface between the matrix and the coating. Then, the wave field in the matrix can be considered as the superposition of the incident wave field and the scattered wave field as

$$w^{(4)} = w^{in} + w^{sc}. \quad (18)$$

The displacement potentials in the matrix will be

$$\phi_4(r,\theta) = \sum_{n=-\infty}^{+\infty} \left\{ H_n^{(1)}(K_{L4}r)\, B_n^{(1)} \right\} e^{in\theta}, \quad (19)$$

$$\psi_4(r,\theta) = \sum_{n=-\infty}^{+\infty} \left\{ H_n^{(1)}(K_{T4}r)\, B_n^{(2)} \right\} e^{in\theta}, \quad (20)$$

where $H_n^{(1)}(\cdot)$ is the n^{th} order Hankel function of the first kind and B_n are the undetermined coefficients. The corresponding longitudinal and shear wave number, K_{L4} and K_{T4} are

$$K_{L4} = \omega \sqrt{\frac{\rho_4}{(\lambda_4 + 2\mu_4)}}, \quad (21)$$

$$K_{T4} = \omega \sqrt{\frac{\rho_4}{\mu_4}}. \quad (22)$$

The displacements and stresses of the scattered field in the matrix, u_r^{sc}, u_θ^{sc}, σ_{rr}^{sc} and $\sigma_{r\theta}^{sc}$, can be obtained by following the same procedures in the previous section. From the discussion above, the total displacements in the matrix will be

$$u_r^{(4)} = u_r^{in} + u_r^{sc}, \quad (23)$$

$$u_\theta^{(4)} = u_\theta^{in} + u_\theta^{sc}. \quad (24)$$

Then, the total stresses of $\sigma_{rr}^{(4)}$ and $\sigma_{r\theta}^{(4)}$ in the matrix have the form of

$$\sigma_{rr}^{(4)} = \sigma_{rr}^{in} + \sigma_{rr}^{sc}, \quad (25)$$

$$\sigma_{r\theta}^{(4)} = \sigma_{r\theta}^{in} + \sigma_{r\theta}^{sc}. \quad (26)$$

2.1.4. Analysis of the boundary conditions

There are two interfaces in the unit cell. For the interface between the rigid cylinder and elastic coating, the displacement continuity yields

$$u_r^{(1,2)}|_{r=r_1} = u_r^{(3)}|_{r=r_1}, \quad (27)$$

$$u_\theta^{(1,2)}|_{r=r_1} = u_\theta^{(3)}|_{r=r_1}. \quad (28)$$

From Newton's second law of motion, the equations of motion of the rigid cylinder can be obtained as

$$Ma_{G,x} = \int_0^{2\pi} \left(\sigma_{rr}^{(3)} r_1 \cos\theta - \sigma_{r\theta}^{(3)} r_1 \sin\theta \right) d\theta|_{r=r_1}, \quad (29)$$

$$Ma_{G,y} = \int_0^{2\pi} \left(\sigma_{rr}^{(3)} r_1 \sin\theta + \sigma_{r\theta}^{(3)} r_1 \cos\theta \right) d\theta|_{r=r_1}, \quad (30)$$

$$I_G\alpha = \int_0^{2\pi} \left\{ \begin{array}{l} \sigma_{r\theta}^{(3)} r_1^2 - \sigma_{rr}^{(3)} r_1 r_G \sin(\theta - \theta_1) \\ - \sigma_{r\theta}^{(3)} r_1 r_G \cos(\theta - \theta_1) \end{array} \right\} d\theta|_{r=r_1}, \quad (31)$$

where the angular acceleration of the rigid cylinder, α, is given by

$$\alpha = -\omega^2 \bar{\theta}. \quad (32)$$

The displacement and stress continuity formula also can be applied to the interface between the elastic coating and the matrix. Then, the following relations can be obtained as

$$u_r^{(3)}|_{r=r_2} = u_r^{(4)}|_{r=r_2}, \quad (33)$$

$$u_\theta^{(3)}|_{r=r_2} = u_\theta^{(4)}|_{r=r_2}, \quad (34)$$

$$\sigma_{rr}^{(3)}|_{r=r_2} = \sigma_{rr}^{(4)}|_{r=r_2}, \quad (35)$$

$$\sigma_{r\theta}^{(3)}|_{r=r_2} = \sigma_{r\theta}^{(4)}|_{r=r_2}. \quad (36)$$

To reduce the complexity of the expression of the incident wave $w^{in}|_{r=r_2}$ in local polar coordinate system, an integration method with limited number of collocation points

along the outer interface has been used [25], which can be written as

$$\int_0^{2\pi} w^{in}|_{r=r_2} e^{-in\theta} d\theta \approx \sum_{j=1}^{P} \int_{\theta_j}^{\theta_{j+1}} f_j(\theta)\, e^{-in\theta} d\theta, \tag{37}$$

where P is the number of the collocation points, $f_j(\theta)$ is the linear interpolation function of $w^{in}|_{r=r_2}$ between the angular coordinates θ_j and θ_{j+1}. These angular coordinates for uniformly distributed collocation points are

$$\theta_j = \frac{2\pi\,(j-1)}{P},\ \theta_{j+1} = \frac{2\pi j}{P}. \tag{38}$$

The collocation point density, δ, has been defined as

$$\delta = \frac{\lambda_i P}{2\pi r_2}, \tag{39}$$

where $\lambda_i = \lambda_{L4}$, the longitudinal wave length in medium 4 for longitudinal incident wave or $\lambda_i = \lambda_{T4}$, the transverse wave length in medium 4 for transverse incident wave. Then, with the coefficient vectors defined as

$$\{A\} = \left\{A_{-S}^{(1)} \quad A_{-S}^{(2)} \quad A_{-S}^{(3)} \quad ... \quad A_{S}^{(2)} \quad A_{S}^{(3)} \quad A_{S}^{(4)}\right\}^T, \tag{40}$$

$$\{B\} = \left\{B_{-S}^{(1)} \quad B_{-S}^{(2)} \quad ... \quad B_{S}^{(1)} \quad B_{S}^{(2)}\right\}^T, \tag{41}$$

$$\{C\} = \left\{u_{O,x} \quad u_{O,y} \quad \bar{\theta}\right\}^T, \tag{42}$$

$$\{D\} = \left\{A \quad B \quad C\right\}^T, \tag{43}$$

those coefficients can be calculated as

$$\{D\} = [Q]\,[W], \tag{44}$$

with S being the highest order of the series expansion in equations (10), (11), (19) and (20). $[Q]$ is the known transformation matrix and $[W]$ is comprised of the displacements and stresses due to the incident wave at the collocation points along the interface. After that, the wave field of the system will be readily solved.

This approach, however, can only apply to linear system. It should be mentioned that the rotational motions of the resonators make the system nonlinear, which can be observed from equations (7) and (8). To build a set of linear equations as described in equation (44), $\bar{\theta}^2$ has been replaced with $\beta\bar{\theta}$ to linearize the composite system and then the acceleration components of the mass centre of the cylinder can be rewritten as

$$a_{G,x} = -\omega^2 u_{O,x} + r_G\omega^2\bar{\theta}\,(\sin\theta_1 + \beta\cos\theta_1), \tag{45}$$

$$a_{G,y} = -\omega^2 u_{O,y} + r_G\omega^2\bar{\theta}\,(-\cos\theta_1 + \beta\sin\theta_1). \tag{46}$$

The initial value of parameter β is set as 0 and then calculate the steady-state rotational angle $\bar{\theta}$, which replaces β to calculate the next value of $\bar{\theta}$ until the difference between $\bar{\theta}$ and β is within a specific threshold value.

For the single cell problem, matrix $[Q]$ provides direct transformation from the values of the incident wave at the collocation points to the coefficients A_n, B_n and the motion parameters of the cylinder in matrix $[C]$. From the discussion above, the wave field of the composite system with a single cell can be readily calculated.

2.2. Interaction of multiple cells

For multiple resonators included in the system, pseudo-incident wave method can be introduced to study the dynamic interaction [21]. Then, every coated cylinder in the system can be regarded as a single inhomogeneity subjected to a pseudo incident wave, which consists of the original incident wave and the unknown scattered wave from other cylinders, as shown in Fig.2. Consider N interacting coated cylinders and the pseudo incident wave of the i^{th} cylinder, w_i^{ps}, can be expressed as

$$w_i^{ps} = w^{in} + \sum_{k=1,k\neq i}^{N} w_k^{sc}, \tag{47}$$

with w^{in} being the original incident wave and w_k^{sc} being the displacement due to the scattered wave from k^{th} inhomogeneity. Then, the relation between different inhomogeneities can be established, based on the continuity conditions along the interfaces.

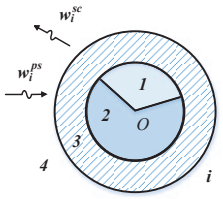

Figure 2: Wave interaction between the matrix and the coating of the i^{th} cell.

Based on the analytical solutions of a single inhomogeneity and the pseudo incident wave method, a set of linear equations for the expansion coefficients can be obtained as

$$\begin{bmatrix} [I]_1 & -\left[\bar{Q}\right]_1[M]_{12} & \cdots & -\left[\bar{Q}\right]_1[M]_{1N} \\ -\left[\bar{Q}\right]_2[M]_{21} & [I]_2 & \cdots & -\left[\bar{Q}\right]_2[M]_{2N} \\ \vdots & \vdots & \vdots & \vdots \\ -\left[\bar{Q}\right]_N[M]_{N1} & -\left[\bar{Q}\right]_N[M]_{N2} & \cdots & [I]_N \end{bmatrix} \bullet \begin{bmatrix} \left\{\bar{D}\right\}^{(1)} \\ \left\{\bar{D}\right\}^{(2)} \\ \vdots \\ \left\{\bar{D}\right\}^{(N)} \end{bmatrix} = \begin{bmatrix} \left[\bar{Q}\right]_1\left[\bar{W}\right]_1 \\ \left[\bar{Q}\right]_2\left[\bar{W}\right]_2 \\ \vdots \\ \left[\bar{Q}\right]_N\left[\bar{W}\right]_N \end{bmatrix}, \tag{48}$$

where matrices $[M]_{kj}$ relate to the effects of the j^{th} inhomogeneity on the k^{th}, matrices $\left\{\bar{D}^{(k)}\right\}$ are the vector composed of the expansion coefficients of the scattered wave

from the k^{th} inhomogeneity given by equation (43), matrices $\left[\bar{W}\right]_k$ represent the displacements and stresses at the collocation points at the interface of the k^{th} inhomogeneity due to the original incident wave, matrix $\left[\bar{Q}\right]_k$ stand for the known transformation matrix from the solution of the single k^{th} inhomogeneity, matrices $[I]_k$ are the identity matrices with a dimension of $(2S+1)$.

Then, the expansion coefficients and kinetic parameters of the rigid cylinders in vectors $\left\{\bar{D}\right\}$ can be determined by solving equation (48), from which the displacement and the stress of the wave field in the matrix and in the soft coating can be readily calculated.

3. Results and discussion

Consider the in-plane problem of the metamaterial system, consisting of 45 distributed eccentric coated cylinders with 5 rows and 9 columns, which are subjected to a harmonic longitudinal wave with excitation frequency ω. The longitudinal incident wave can be generally expressed in the polar coordinates as

$$u_r^{in} = u_0 \cos(\theta - \theta_0) e^{iK_{L4} r \cos(\theta - \theta_0)}, \tag{49}$$

$$u_\theta^{in} = -u_0 \sin(\theta - \theta_0) e^{iK_{L4} r \cos(\theta - \theta_0)}, \tag{50}$$

with u_0 being the displacement amplitude of the incident wave field and the incident wave propagation angle $\theta_0 = 0$. For the geometric parameters shown in Fig.1, $r_1 = 5 \times 10^{-3}$ m, $r_2 = 7.5 \times 10^{-3}$ m, $L = 2.1 \times 10^{-2}$ m and $\theta_2 = \pi/3$. The angles θ_1 of the coated cylinders are in the form of $m\pi/20$ with m as random integers. The materials used are listed in Table 1.

Table 1: Material Parameters.

	Material	Density (Kg/m^3)	λ (Pa)	μ (Pa)
1	Gold	19500	1.62E11	2.70E10
2	Aluminium	2700	5.87E10	2.60E10
3	Silicone rubber	1300	6.00E5	4.00E4
4	Epoxy	1180	4.43E9	1.59E9

In the multiple scattering computation, the highest order of the series expansion in the displacement potentials discussed, S, is set as 30. Also, the collocation point density δ is selected as 1000 for high accuracy.

3.1. Effective mass density

In this study, a square area with 9 cells in the centre of the system has been considered as the targeted element. From the boundary effective medium theory [22], the surface motion of this element, responding to the stimulations exerted by the outside waves, can be calculated in the form of effective displacements, forces on its boundaries. Then, the relation between the net force applied to the element and the average acceleration can be built to calculate the effective mass density.

Due to the symmetry of the system, the effective mass density can be obtained as

$$\rho_e = -\frac{F_{e,x}}{\omega^2 a^2 u_{e,x}}, \tag{51}$$

where a is the length of the element, ρ_e is the effective mass density, $u_{e,x}$ is the effective displacement of the cell in the x direction and it can be expressed as

$$u_{e,x} = \frac{1}{2a}\left(\int_{-a/2}^{a/2} u_x dy|_{x=a/2} + \int_{-a/2}^{a/2} u_x dy|_{x=-a/2}\right), \tag{52}$$

with the centre of the element as the origin of the coordinate system used. Similarly, $F_{e,x}$, the effective force applied to the element in the x direction, can be expressed in the form of

$$F_{e,x} = \left\{ \begin{array}{l} \int_{-a/2}^{a/2} \sigma_{xx} dy|_{x=a/2} - \int_{-a/2}^{a/2} \sigma_{xx} dy|_{x=-a/2} \\ + \int_{-a/2}^{a/2} \sigma_{xy} dx|_{y=a/2} - \int_{-a/2}^{a/2} \sigma_{yx} dx|_{y=-a/2} \end{array} \right\}. \tag{53}$$

3.2. Dynamic behaviour of the metamaterial system

The frequency-dependent mass density is a vital property of elastic metamaterials. The effective mass density of the system designed in the low frequency range has been illustrated in Fig.3. For comparison, the corresponding composite system with uniform resonators have been introduced with the same cylinder density and other parameters.

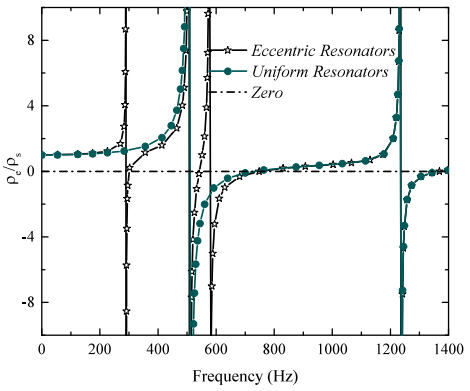

Figure 3: The effective mass density of the system with eccentric resonators and uniform resonators.

It can be easily observed from Fig.3 that there are four resonances in the low frequency range for the eccentric model. The resonances considered can be regarded as oscillations, in which the rigid cylinders serves as the heavy mass and the silicone rubber provides the soft spring. The

first one is the rotational resonance of the rigid eccentric cylinder, occurring at a very low frequency. The frequency range with negative mass density is relatively narrow. The second one is the translational resonance of the cylinder in the θ_1 direction and its corresponding natural frequency coincides with that of the uniform model as expected. For the third resonance, the translational direction of the cylinder is perpendicular to that of the second resonance. The fourth one is the resonance inside of the rubber coating with relatively small translation of the cylinders. It is more about the properties of the coating and the corresponding overall dynamic response of the eccentric model is almost the same with that of the uniform model. In other words, when r_G turns positive from 0, the uniform model will change into the eccentric model. The first resonance mode of the uniform model is split into three modes, as illustrated in Fig.3. The total width of the frequency ranges with negative mass density for the eccentric model is almost equal to that of the uniform model. However, the eccentric model can realize negative mass density at lower frequencies, which is crucial for the related applications.

It should be mentioned that the geometric parameters shown in Fig.1 and the material properties of the components listed in Table 1 can place a substantial influence on the overall dynamic response of the elastic metamaterial system.

For elastic metamaterials with negative mass density, one of their most prominent abilities should come to wave attenuation. The normalized wave displacement amplitudes (u/u_0) of the metamaterial systems have been illustrated in Fig.4, 5, 6 and 7 for the four frequencies from the first four band gaps of the system respectively. For better observation, the displacement inside of the rigid cylinders and elastic coating are not plotted.

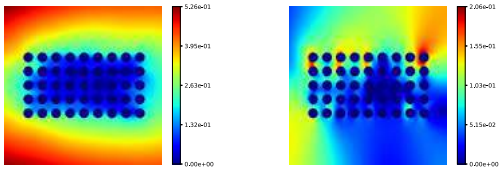

(a) (b)

Figure 4: For $f = 290.46$ Hz, (a) the normalized amplitude of the displacement component in the longitudinal direction, (b) the normalized amplitude of the displacement component in the transverse direction.

It can be directly observed that the wave displacement amplitudes attenuate substantially inside of the metamaterial system. To better evaluate the vibration isolation ability of the system, the normalized displacement amplitudes has been plotted in Fig.8 along the line, which is located in the middle of second and third rows. Fig.8 clearly shows that the normalized displacement amplitudes in the longitudinal direction decrease along the line and reach their minimum values in the middle part. After that, these values begin to increase due to the boundary effect. The normalized displacement amplitudes in the transverse direction are much smaller than those in the longitudinal direction, following a similar changing trend. It should be mentioned that more eccentric resonators can be added to this metamaterial system to further enhance its wave attenuation ability and wave can not propagate through at the frequencies with negative mass density.

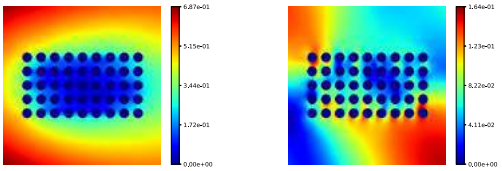

(a) (b)

Figure 5: For $f = 509.30$ Hz, (a) the normalized amplitude of the displacement component in the longitudinal direction, (b) the normalized amplitude of the displacement component in the transverse direction.

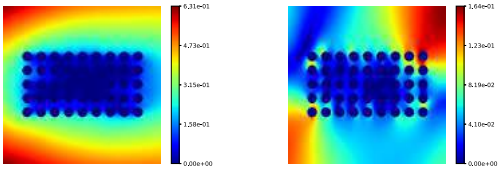

(a) (b)

Figure 6: For $f = 578.53$ Hz, (a) the normalized amplitude of the displacement component in the longitudinal direction, (b) the normalized amplitude of the displacement component in the transverse direction.

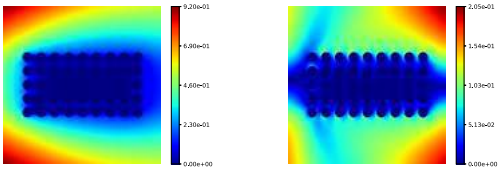

(a) (b)

Figure 7: For $f = 1236.63$ Hz, (a) the normalized amplitude of the displacement component in the longitudinal direction, (b) the normalized amplitude of the displacement component in the transverse direction.

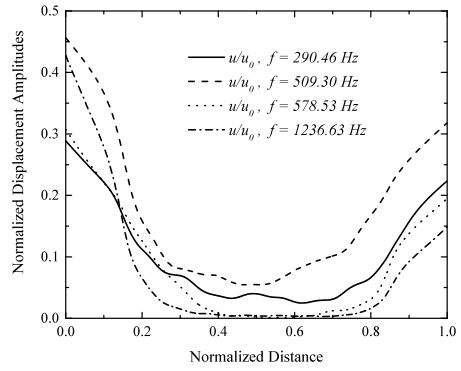

(a)

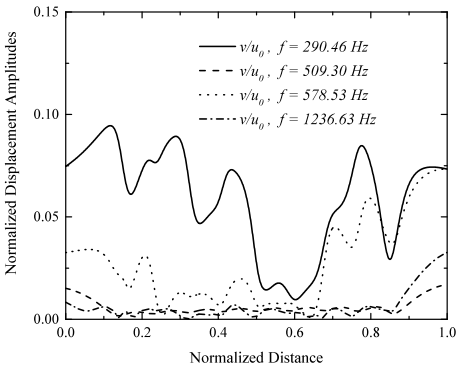

(b)

Figure 8: (a) The normalized amplitude of the displacement component in the longitudinal direction, (b) the normalized amplitude of the displacement component in the transverse direction.

Acknowledgement

This research is supported by the Natural Sciences and Engineering Research Council of Canada (NSERC) and China Scholarship Council (CSC).

References

[1] V.G. Veselago, The electrodynamic of substances with simultaneously negative value of ϵ and μ, *Sov. Phy. Usp.* 10: 509–5141, 1968.

[2] R.A. Shelby, D.R. Smith, S. Schultz, Experimental verification of a negative index of refraction, *Science* 292: 77–79, 2001.

[3] X. Zhang, Z.W. Liu, Superlenses to overcome the diffraction limit, *Nat. Mater.* 7: 435–441, 2008.

[4] N. Kundtz, D.R. Smith, Extreme-angle broadband metamaterial lens, *Nat. Mater.* 9: 129–132, 2010.

[5] G. Wang, X.S. Wen, J.H. Wen, L.H. Shao, Y.Z. Liu, Two-dimensional locally resonant phononic crystals with binary structures, *Phys. Rev. Lett.* 93: 154302, 2004.

[6] M. Hirsekorn, Small-size sonic crystals with strong attenuation bands in the audible frequency size, *Appl. Phys. Lett.* 84: 3364–3366, 2004.

[7] Z.Y. Liu, X.X. Zhang, Y.W. Mao, Y.Y. Zhu, Z.Y. Yang, C.T. Chan, P. Sheng, Locally resonant sonic materials, *Science* 289: 1734–1736, 2000.

[8] Z.Y. Liu, C.T. Chan, P. Sheng, Analytic model of phononic crystals with local resonance, *Phys. Rev. B* 71: 014103, 2005.

[9] X.M. Zhou, X.N. Liu, G.K. Hu, Elastic metamaterials with local resonances: an overview, *Theor. Appl. Mech. Lett.* 2: 041001, 2012.

[10] S.H. Lee, B.W. Wright, Origin of negative density and modulus in acoustic metamaterials, *Phys. Rev. B* 93: 024302, 2016.

[11] G.C. Ma, P. Sheng, Acoustic metamaterials: from local resonances to broad horizons, *Sci. Adv.* 2: e1501595, 2016.

[12] J. Mei, Z.Y. Liu, W.J. Wen, P. Sheng, Effective mass density of fluid-solid composites, *Phys. Rev. Lett.* 96: 024301, 2006.

[13] X.W. Yang, J.S. Lee, Y.Y. Kim, Effective mass density based topology optimization of locally resonant acoustic metamaterials for bandgap maximization, *J. Sound Vib.* 383, 89–107, 2016.

[14] S.S. Yao, X.M. Zhou, G.K. Hu, Experimental study on negative effective mass in a 1D mass-spring system, *New J. Phys.* 10: 043020, 2008.

[15] H.H. Huang, C.T. Sun, G.L. Huang, On the negative effective mass density in acoustic metamaterials, *Int. J. Eng. Sci.* 47: 610–617, 2009.

[16] G.W. Milton, J.R. Willis, On modifications of Newton's second law and linear continuum elastodynamics, *Proc. R. Soc. A* 463: 855–880, 2007.

[17] K.T. Tan, H.H. Huang, C.T. Sun, Optimizing the band gap of effective mass negativity in acoustic metamaterials, *Appl. Phys. Lett.* 101: 241902, 2012.

[18] X.Y. An, F.F. Sun, P.S. Yu, H.L. Fan, S.P. He, D.N. Fang, Negative effective mass density of one-dimensional hierarchical metacomposite, *J. Appl. Mech.* 82, 031002-1-8, 2015.

[19] E. Baravelli, M. Ruzzene, Internally resonating lattices for bandgap generation and low-frequency vibration control, *J. Sound Vib.* 332, 6562–6579, 2013.

[20] M. Hirsekorn, P.P. Delsanto, Elastic wave propagation in locally resonant sonic material: comparison between local interaction simulation approach and modal analysis, *J. Appl. Phys.* 99: 124912, 2006.

[21] X.D. Wang, S.A. Meguid, Diffraction of SH wave by interacting matrix crack and an inhomogeneity, *J. Appl. Mech.* 64(3): 568575, 1997.

[22] Y. Lai, Y. Wu, P. Sheng, Z.Q. Zhang, Hybrid elastic solids, *Nat. Mater.* 10: 620–624, 2011.

[23] X.D. Wang, Dynamic behaviour of a metamateiral system with negative mass and modulus, *Int. J. Solids Struct.* 51: 1534–1541, 2014.

[24] Z.W. Li, X.D. Wang, On the dynamic behaviour of a two-dimensional elastic metamaterial system, *Int. J. Solids Struct.* 7879: 174–181, 2016.

[25] C. Wang, X.D. Wang, Modeling and simulation of wave scattering of multiple inhomogeneities in composite media, *Composites Part B* 90: 341–350, 2016.

Photonic crystals

An experimental study of self-guided unidirectional waveguides by a chain of gyro-magnetic rods

Zhen Li[1,2*], **Rui-xin Wu**[2]

[1] School of Energy and Electrical Engineering,

Nanjing Institute of Industry Technology, Nanjing 210093, China

[2] School of Electronic Science and Engineering, Nanjing University, Nanjing 210093, China

[*]corresponding author, E-mail:li_zane@sina.com, lz@niit.edu.cn

Abstract-We experimentally studied the tunability of an unidirectional waveguides of magnetic photonic crystals(MPCs) which is a straight-line chain with gyro-magnetic rods. By changing the constitution parameters, we could achieve tunable one way transmission (OWT) characteristics. We studied the influence of normalized radius *R* and lattice constant *a* on band width and center frequency of OWT band.

Magnetic photonic crystals (MPCs) have been the focus in recent years for their amazing characteristics[1-3]. Recently a new type of one way waveguide has been proposed which is just a chain of gyro-magnetic rods, this flexible one way waveguide could be arbitrarily bended or curved[4].We theoretically and experimentally investigated the tunability of OWT in this MPCs chain under different constitution parameters in this paper.

First we calculated the band structures of this chain MPCs through multiple-scattering method (MSM)[5], the calculating results of band structure is shown in Figure 1. The chain sample is placed in the parallel-plate waveguide surrounded by absorbers. We specially designed the megnets to fully magnetize the sample. The MPCs chain is stimulated by a probe located at the end of the chain edge and the transmitted signal is detected at another end by Agilent vector network analyzer.

The OWT is originated from (magnetic surface plasmon MSP). The measured results are shown in Figure 2 and Figure 3, the measured results are in good accordance with the band results. Both results showed that we could tune the bandwidth and center frequency by modifying the configuration parameters, the larger normalized radius *R* of the ferrite rods(*R*=*r*/*a, r* is the real radius of ferrite rod) , the wider OWT band, and the higher center frequency. And if we fix the normalized radius, both width and center frequency of the OWT band will decrease with increasing lattice constant. The study illustrates this flexible structure could be widely applied such as tunable isolaters or tunable filters.

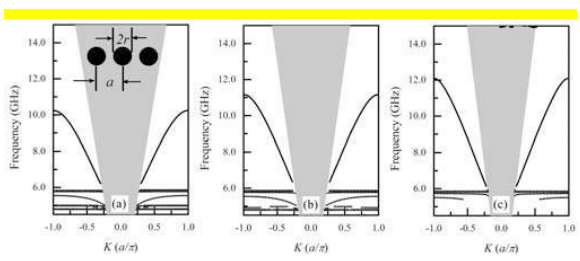

Figure 1: Scheme of MPC chain, and its MSP frequency range with different normalized radius under same magnetic field. (a) MPC chain with *r*/*a*=0.16, (b) MPC chain with *r*/*a*=0.22, (c) MPC chain with *r*/*a*=0.28

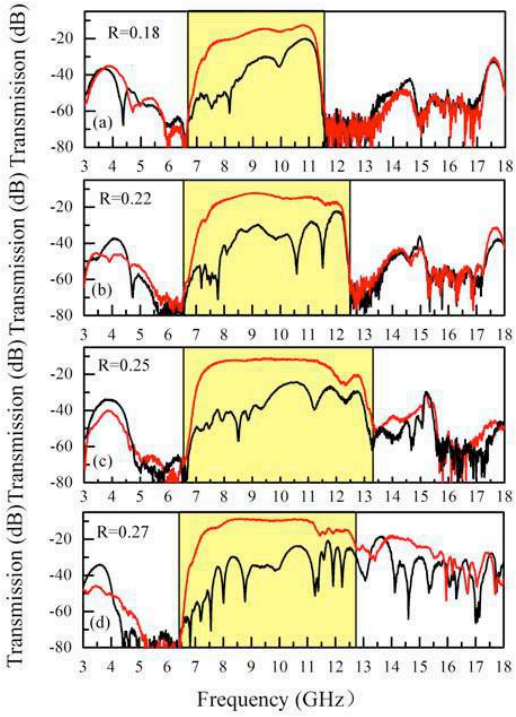

Figure 2: Transmission characteristics of MPC chain with different normalized radius. Red line is forward transmission, black line is backward transmission.(a) R=0.18, (b) R=0.22, (c) R=0.25, (d) R=0.27.

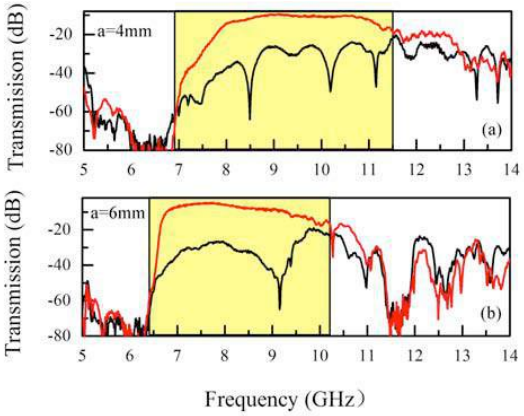

Figure 3: Transmission characteristics of MPC chain with different lattice constant. Red line is forward transmission, black line is backward transmission. (a) a=4mm, (b) a=6mm.

Acknowledgements, This work was supported by the NSFC (61301016, 61271080 and 61071007) and RFDP (20110091110030, 20100091120045).

REFERENCES

1. Z. Yu, G. Veronis, Z. Wang, and S. Fan, One-Way Electromagnetic Waveguide Formed at the Interface between a Plasmonic Metal under a Static Magnetic Field and a Photonic Crystal，Physical Review Letters 100, 023902, 2008.
2. Z.Wang, Y. D. Chong, J. D. Joannopoulos, and M. Soljačić, Reflection-Free One-Way Edge Modes in a Gyromagnetic Photonic Crystal，Phys. Rev.Lett 100, 013905, 2008.
3. Y. Poo, R. X. Wu, Z. F. Lin, Y. Yang, and C. T. Chan, Experimental Realization of Self-Guiding Unidirectional Electromagnetic Edge States，Phys. Rev. Lett 106, 093903, 2011.
4. Z.Li,R.X.Wu,Q.B.Li,Y.Poo,Realization of self-guided unidirectional waveguides by a chain of gyromagneti c rods, Appl. Opt. 54: 1267-1272, 2015.
5. K. M. Leung and Y. Qiu, Multiple-scattering calculation of the two-dimensional photonic band structure，Phys. Rev. B 48：7767-7771, 1993.

Controlling Interface States in 1D Photonic Crystals by tuning Bulk Geometric Phases

Wensheng Gao,[1] Meng Xiao,[2] Baojie Chen,[3] Edwin Y. B. Pun,[3] C. T. Chan,[1,2] and Wing Yim Tam[1,*]

[1] Department of Physics and William Mong Institute of Nano Science and Technology
Hong Kong University of Science and Technology
Clear Water Bay, Kowloon, Hong Kong, China

[2] Department of Physics and Institute for Advanced Study, Hong Kong University of Science and Technology,
Clear Water Bay, Kowloon, Hong Kong, China

[3] Department of Electric Engineering, City University of Hong Kong, Hong Kong, China

[*]corresponding author: phtam@ust.hk

Abstract-Interface states in photonic crystals usually require defects or surface/interface decorations that are susceptible to imperfections. We show here that one can achieve robust interface states through the control of geometrical phase such that interface states can be guaranteed in even or odd, or in all photonic bandgaps of 1D photonic crystals. We verify experimentally the designed interface states in 1D multilayered photonic crystals fabricated by electron beam vapor deposition. We also obtain the geometrical phases by measuring the reflection phases at the bandgaps of the PCs and achieve good agreement with the theory. Our approach could provide a platform for the design of using interface states in photonic crystals for nonlinear optic, sensing, and lasing applications

The existence of interface modes localized at the boundary that separates two materials depend on very much on the details of the system. In principle, one can determine the existence of such interface modes by an explicit calculation or by performing an experiment. However, there are some special cases in which one can predict the existence of interface modes by knowing the properties of the bulk materials. For ideal case there are beautiful mathematical relations that assure the existence of interface modes for periodic media (photonic crystals) if the bulk carries some topological properties that can be labelled by some quantized quantities. A nice example is the geometric Zak phase in 1D crystals [1], which is known to be quantized if the system has inversion symmetry, and which can be used to predict the existence of interface modes [2]. As Zak phases are defined as the integral of "Berry connections" of the bulk bands, one might think that the experimental determination of such a quantity is very difficult. Here, we demonstrate that we can measure the Zak phase of a bulk band simply through the measurement of reflection phases in the band gaps using a thick gap Fabry Perot (FP) interference technique[3], and the measured Zak phases can indeed be used to predict the existence or absence of interface modes. Our results imply we can control the existence of interface modes by controlling the geometric phases of the bulk bands[4]. In our experiment, we can control the interface states' existence in 1st , 2nd or both the band gaps through the designed Zak phase. The results are summarized in below figures. Quantized Zak phases are robust against perturbations, such as fabrication imperfections, enabling the control of the interface states which may find practical applications.

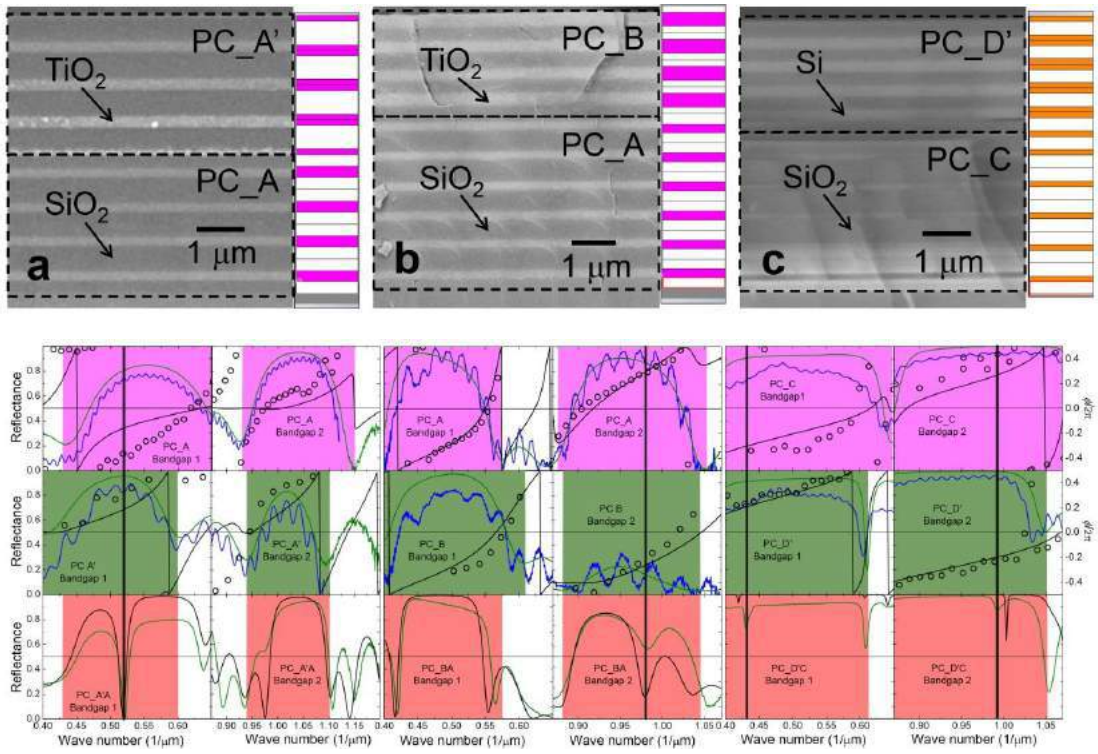

Top Fig. 1: SEM and schematic pictures for 1D photonic crystals.

Bottom Fig. 2: Top and middle rows are reflection spectra (blue and green curves are for samples in FP and bare PC configuration, respectively) and reflection phases (black circles) for the PCs in top Fig. 1 as labeled. The black curves are numerical results for reflection phases calculated using slightly adjusted thicknesses as obtained from the SEM images in top Fig. 1 to account for small difference in layer thickness at the measured areas. The colored regions are bandgaps of the PCs. The last row is reflectance (in green) of the combined PCs. Odd and even columns correspond to bandgaps 1 and 2, respectively. The thick black vertical lines indicate the experimental interface states for the combined PCs. The black curves are calculated reflectance of the combined PCs.

Acknowledgements, Support from Hong Kong RGC grants AoE P-02/12 is gratefully acknowledged. The technical support of the Raith-HKUST Nanotechnology Laboratory for the electron-beam lithography facility at MCPF (SEG_HKUST08) is hereby acknowledged.

REFERENCES

1. J. Zak, "Berry's phase for energy bands in solids," *Phys. Rev. Lett*, Vol. 62, No. 23, 2747, 1989.
2. M. Xiao, Z. Q. Zhang, and C. T. Chan, "Surface Impedance and Bulk Band Geometric Phases in One-Dimensional Systems." *Phys. Rev. X* ,Vol. 4, No. 2,021017 ,2014.
3. W. S. Gao, M. Xiao, C. T. Chan, and W.Y. Tam, "Determination of Zak phase by reflection phase in 1D photonic crystals**,"** *Opt. Lett.* Vol. 40, 5259-5262, 2015.
4. W. S. Gao, M. Xiao, B. J. Chen, C. T. Chan, E. Y. B. Pun and W.Y, Tam, "Controlling Interface States in 1D Photonic Crystals by tuning Bulk Geometric Phases." *Arxiv:*1610.01724, 2016.

Out-of-plane dispersive photonic band structure of a honey-comb photonic crystal

J. D. Valenzuela-Sau[1], **and R. García-Llamas**[2,*]
[1]Physics Doctorate, Universidad de Sonora, México
[2] Physics Research Department, Universidad de Sonora, México
[*]corresponding author: ragal@cifus.uson.mx

Abstract-We present an alternative numerical method for calculating dispersive photonic band structures (DPBS). This method can be implemented considering experimental data or an approximate mathematical model for the dielectric constant and for others types of lattices and cross sections. Out-of-plane propagation is considered for a honey-comb photonic crystal given the high interest in graphene like structures.

Using the plane wave method [1], we implement a numerical method for calculating dispersive electromagnetic out-of-plane modes in two-dimensional Photonic Crystals (PCs). The eigenvalues matrix equation (1) is found and solved numerically by using an iteration algorithm to obtain the eigenfrequencies for both, in-plane (stationary) and out-of-plane (propagating) dispersive electromagnetic modes. This method allows us to consider experimental values or a mathematical model for the dielectric constant. Dispersive photonic bands structures (DPBSs) are obtained for a honey-comb array of cylinders of elliptical (circular) cross section. In-plane (out-of-plane) band structure considers perpendicular (oblique) propagation according to the homogeneous axis of the system. Out-of-plane studies have been made [2-4], however, neither of them considers dispersive media. In-plane dispersive PBS was compared with that presented in reference [5] in order to validate this method.

The eigenvalues matrix equation for the out-of-plane modes is,

$$\sum_{m',n'}\left[\varepsilon_2^{-1}(\omega)_{m-m',n-n'}\right]\left[\left(\vec{k}_{m,n}\times\vec{v}_{m',n'}\right)h_{m',n'}-\left(\vec{k}_{m,n}\times\vec{w}_{m',n'}\right)\left|\vec{k}_{m',n'}\right|^2 e_{m',n'}\right]=\frac{\omega^2}{c^2}\left(\vec{v}_{m,n}\left|\vec{k}_{m,n}\right|e_{m,n}+\vec{w}_{m,n}h_{m,n}\right) \quad (1)$$

Where $[\varepsilon_2^{-1}(\omega)]_{m-m',n-n'}$ are the coefficients of the multiplicative inverse of the dispersive dielectric constant, the vectors $\boldsymbol{v}_{m,n}$ and $\boldsymbol{w}_{m,n}$ are two orthogonal polarizations to the propagation wave vector, and $\boldsymbol{k}_{m,n}=k_{x,m,n}\boldsymbol{i}+k_{y,m,n}\boldsymbol{j}+\gamma\boldsymbol{k}$ is the wave vector which contains the Bloch vector, the reciprocal lattice vectors and the oblique propagation component γ.

In Fig. 1 the PBSs of a square lattice of Alumina (Al_2O_3) rods of circular cross section in vacuum are shown. The dispersive and non-dispersive PBSs correspond to the black and blue lines, respectively. The middle of the first band gap is ν =3.58 THz or λ=83.74 μm. The second band gap shifted towards lower frequencies. Dispersive out-of-plane PBSs of a honey-comb PC are in process of being calculated.

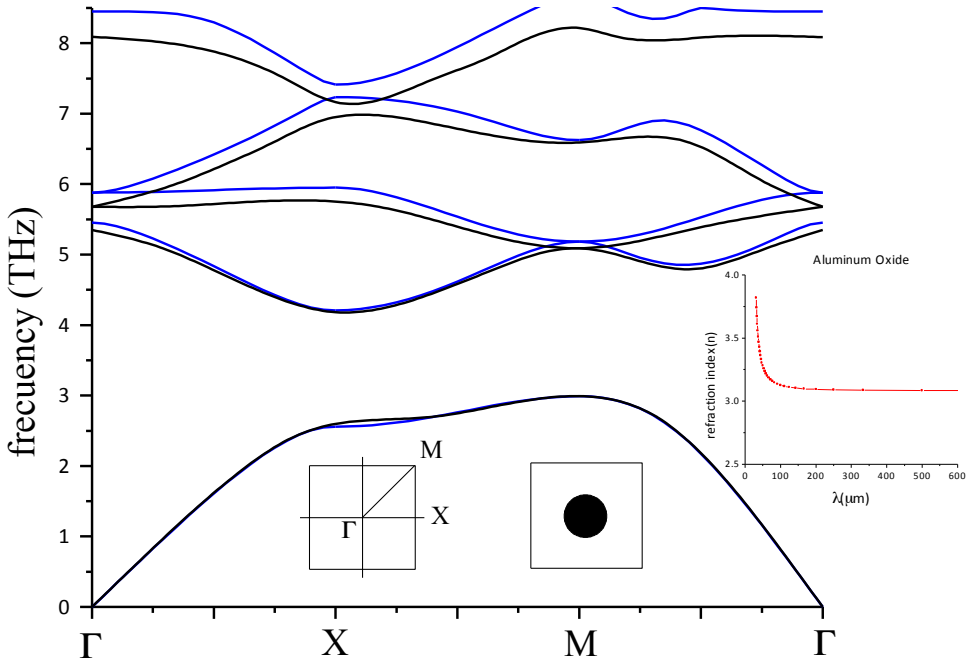

Fig. 1 In-plane photonic band structures of a square lattice of Alumina (Al_2O_3) rods of circular cross section in vacuum. Filling fraction is 0.1256. Dispersive [ε=ε(ω)] (black lines) against non-dispersive [n=3.1256 or ε=9.77] (blue lines) bands are presented. The period of the 2DPC is 31.3819μm. Both PBSs present practically the same band gap between 2.99 and 4.17THz. Inset shows the experimental values of the refraction index (n) of the Alumina as a function of the wavelength (λ) taken from ref. [6] used in this calculation.

Acknowledgements- The author, J. D. Valenzuela-Sau, is grateful for the scholarship granted by CONACyT.

REFERENCES

1. Ho, K. M., C. T. Chan and C. M. Soukoulis, "Existence of a Photonic Band Gap in Periodic Dielectric Structures," *Phys. Rev. Lett.*, Vol. 65, No. 25, 3152–3155, 1990.
2. Meade, R. D., K. M. Brommer, A. M. Rappe and J. D. Joannopoulos, "Existence of a Photonic Band Gap in Two Dimensions," *Appl. Phys. Lett.*, Vol. 61, No. 4, 495–497, 1992.
3. Zhou, L., M. Hu, F. Jia, C. Liao, Z. Feng and X. Feng, "Effect on Bandgap of Two-dimensional Square Photonic Crystal with Different Incidence Angle" *Acta Photonica Sinica*, Vol. 37, No. 11, 2213-2216, 2008.
4. Zhou, L., M. Hu, K. Zhang and X. Chen, "Band Structure of 2D Air-hole-type Triangular Photonic Crystal with Oblique Incidence," *Science & Technology Review*, Vol. 29, No. 7, 46-49, 2011.
5. Guevara-Cabrera, E., M.A. Palomino-Ovando, B. Flores-Desirena, J. A. Gaspar-Armenta, "Dispersive photonic crystals from the plane wave method," Physica B 484, 53-58, 2016.
6. Handbook of Optical Constants of Solids III. Edward D. Palik. Pages 760-780

Fabrication and Optical Characterization of All-biocompatible Photonic Crystals with Fluorescent Carbon-dots

Taeguen Kim[1], Chaeli Lim[1], Soonil Lee[1,2], and Na Young Ha[1,2*]
[1]Department of Energy Systems Research, Ajou University 16499, Suwon, Korea
[2]Department of Physics, Ajou University 16499, Suwon, Korea
[*]corresponding author: nyha@ajou.ac.kr

Abstract-We fabricated biocompatible polymeric films doped with surface-modified Carbon-dots (C-dots) by drop-casting and introduced periodic nanostructures, i.e., photonic crystals on the surface of the C-dots/polymer films using a nanoimprint lithography. The nanostructured polymeric films doped with the C-dots showed strong enhancement of photoluminescence (PL) efficiencies at the specific spectral region depending on the periodicity of the nanostructured films. These nanostructured C-dots/polymer films can be new biocompatible fluorescent sources and photonic devices.

Fluorescent C-dots have been attractive from high water solubility, chemical stability, facile modification, low photo-bleaching, and excellent biocompatibility. However, the lack of understanding of PL origins in C-dots hinders various photonic applications of C-dots, although much progress is achieved in the synthesis of C-dots [1,2]. Here, to obtain surface-modified C-dots with enhanced PL efficiency, we employed a simple and low-cost microwave synthesis route based on citric acid and urea. For various C-dots synthesized under different urea ratios, physical and chemical properties of C-dots were investigated by using the transmission electron microscope (TEM) and the X-ray photoelectron spectroscopy (XPS) systems. The TEM images showed that C-dots were spherical nanoparticles with a size distribution of 2 - 20 nm in diameter and the average lattice spacing of C-dots was 0.23 nm. In the XPS spectra, we found that the surface amino group of the C-dots increased with increasing the urea ratio. These surface-modified C-dots samples with high density of surface amino groups exhibit high PL efficiencies.

Next, biocompatible polymeric films doped with the surface-modified C-dots were fabricated by drop-casting and one- and two-dimensional periodic nanostructures (photonic crystals) were introduced on the surface of the C-dots/polymer films using a nanoimprint lithography. The nanostructured polymeric films doped with the C-dots showed strong enhancement of PL efficiencies at the specific spectral region depending on the periodicity of the nanostructured films. These nanostructured C-dots/polymer films can be new biocompatible fluorescent sources and photonic devices.

REFERENCES

1. Qu, S., X. Wang, Q. Lu, X. Liu, and L. Wang, "A biocompatible fluorescent ink based on water-soluble luminescent carbon nanodots," *Angew. Chem. Int. Ed.*, Vol. 51, No. 49, 12215–12218, 2012.
2. Li. X., S. Zhang, S. A. Kulinich, Y. Liu, and H. Zeng, "Engineering surface states of carbon dots to achieve controllable luminescence for solid-luminescent composites and sensitive Be^{2+} detection," *Sci. Rep.*, Vol. 4, No. 4976, 1–8, 2014.

Optical Characterization of Chiral Photonic Crystals on Nanostructured Perfluoropolymer Films

Heetae Ahn[1], Sooyeon Bae[1], Taeguen Kim[1], and Na Young Ha[1,2*]
[1]Department of Energy Systems Research, Ajou University 16499, Suwon, Korea
[2]Department of Physics, Ajou University 16499, Suwon, Korea
[*]corresponding author: nyha@ajou.ac.kr

Abstract-We investigated optical characteristics of cholesteric liquid crystals (CLCs) on periodically-nanostructured perfluoropolymer films. Here, CLCs with periodic helical structures are chiral photonic crystals and nanostructured perfluoropolymer films are used as alignment layers to control orientations of cholesteric helices. The CLCs on the nanostructured films showed not specular but diffusive reflections at the specific spectral region. This nanostructured perfluoropolymer film can provide new possibility to engineer optical characteristics of the CLCs.

CLCs with periodic helical structures of rodlike molecules are chiral photonic crystals that exhibit photonic band gaps (PBGs) for circularly polarized lights with same handedness as CLC helices. In the CLC, the spectral position of the PBG is equal to an optical pitch of the CLC, related to the distance over which the director of molecules undergoes one full turn. Particularly, the CLC systems engineered to obtain broader widths of PBGs or multiple PBGs in the wide spectral region have been studied in various CLC multilayered films and polymer-based composite materials [1].

An amorphous perfluoropolymer poly[perfluoro(4-viny;ox-l-butene)](PPFVB), used in this study, has been used for antireflective coatings due to its low refractive index of 1.34 and high transmittance over a wide spectral region. Also, the PPFVB film has been investigated as a vertical alignment layer because of its strongly hydrophobic surface with low polarity and low polarizability [2].

In this study, we control molecular orientations of cholesteric helices by introducing a nanostructured PPFVB film as an alignment layer and investigate their optical characteristics such as reflectance, spectral position, width, and incident angle dependences of the PBGs. The nanostructured PPFVB films with various periodicities from 300 nm to 800 nm were fabricated by a nanoimprint lithography and characterized by measurements of atomic force microscope image and transmission spectra. The CLCs on the nanostructured PPFVB films showed not specular but diffusive reflections at the PBG region and this behavior did not depend on the periodicity of nanostructured PPFVB films. The present system with diffusive reflections can extend practical applications of CLCs to new photonic devices.

REFERENCES

1. Mitov, M. “Cholesteric liquid crystals with a broad light reflection band,” *Adv. Mater.*, Vol. 24, No. 47, 6260–6276, 2012.
2. Jeong, S. M., J. K. Kim, Y. Shimbo, F. Araoka, S. Dhara, N. Y. Ha, K. Ishikawa, and H. Takezoe, “Perfluoropolymer surface for shock-free homeotropic alignment of smectic liquid crystals,” *Adv. Mater.*, Vol. 22, No. 1, 34–38, 2010.

Ultrasensitive optical bio- and gas- sensors based on Photonic Crystal Surface Waves

S. K. Sekatskii

Laboratoire de Physique de la Matière Vivante, IPHYS, BSP, Ecole Polytechnique Fédérale de Lausanne, CH1015 Lausanne, Switzerland
corresponding author: Serguei.Sekatski@epfl.ch

Abstract- We report our recent results on development of ultrasensitive optical bio- and gas-sensors based on a properly designed Photonic Crystal supporting the propagation of bounded Electromagnetic Surface Waves along the Photonic Crystal – medium to be studied interface. In particular, extremely narrow magnetoplasmonic resonances have been observed, and kinetics of interactions of certain antibodies with the surfaces of *intact living bacteria* is measured.

Earlier, we have reported our first results on design and development of ultrasensitive optical bio- and gas-sensor based on a properly designed Photonic Crystal (PC) supporting the propagation of bounded Electromagnetic Surface Waves (ESW) along the PC – medium to be studied interface. These results include ultrasensitive hydrogen detection exploiting surface plasmons propagated along thin (8 nm-thick) Pd layers, launch of surface plasmon in blue (405 nm) and UV spectral ranges along thin gold films and their use for ultrasensitive nitrogen dioxide detection, as well as first experiments with metal-free and label-free optical biosensor. Here we would like to present our newest results in these directions.

A specially designed PC has been constructed and then used to support the surface plasmon propagation along thin *ferromagnetic* cobalt layer, which enabled to combine our approach with the magnetoplasmonics. Unprecedently narrow (equal to 0.02^0 thus corresponding to the surface plasmon propagation length exceeding 0.1 mm) for the field magnetoplasmonic resonance (Transversal Magnetooptical Kerr Effect) with 11% magnitude has been recorded [1]. Note, that for bare cobalt layers, without a specially designed PC, here this would be simply meaningless to speak about surface plasmons (similarly to the aforementioned Pd layers and blue plasmons on gold), because the propagation length is just of the order of the wavelength for all these cases. In other experiments, the *dielectric* layer of ferromagnetic bismuth-substituted iron garnet $Bi_{2,1}Dy_{0,9}Fe_{3,9}Ga_{1,1}O_{12}$ coated by thin gold layer has been used in a similar fashion, and excellent magnetooptical parameters were again demonstrated [2].

For biosensing, we used "bare" (no metal coating) PC – external medium (water) interface, specially treated to chemisorb protein layers, for the study of kinetics of the interprotein interactions. Besides quite large sensitivity, 0.2 pg/mm^2, this approach has additional advantages due to the possibility to excite simultaneously *s*- and *p*-polarized surface electromagnetic waves having very different penetration depths into an external medium. This enables to segregate surface and volume effects, thus drastically increasing both the sensitivity and reliability of the data obtained.

Another advantage of our approach is the appearing possibility also to study interactions involving rather thick (of the order of one micron) objects such as bacteria, viruses, and certain cell organells – option unattainable

for usual surface plasmon resonance-based detectors due to the short penetration depth of such plasmons. We have finished the development of a chitosan-based protocol of PC chip functionalization for bacterial attachment and performed experiments on antibody binding to living bacteria measured in real time by the PC ESW-based biosensor, see Fig. 1. Data analysis reveals specific binding and gives the value of the dissociation constant for monoclonal antibodies IgG2b against bacterial lypo-polysaccharides equal to $K_D = 6.2 \pm 3.4$ nM [3, 4]. *To our knowledge, this is a first demonstration of antibody binding kinetics to living bacteria by an optical biosensor*. Already the first obtained data revealed essential difference with the kinetic data on isolated bacterial membrane. For the latter, the binding constant K_D of monoclonal antibodies WN1 222-5 to isolated LPS membranes *E.coli* R-core types ranged from 10^{-8} to 10^{-5} M, that is essentially larger than measured by us for the whole intact living cells, were reported. We believe that this discrepancy may be caused primarily by different accessibility of the binding sites within the pool of membrane LPS molecules for possible intermolecular interactions, and that this circumstance should be taken into account analyzing the results of studies on isolated bacterial membranes, what is very important e.g. for the assessment of drag efficiency.

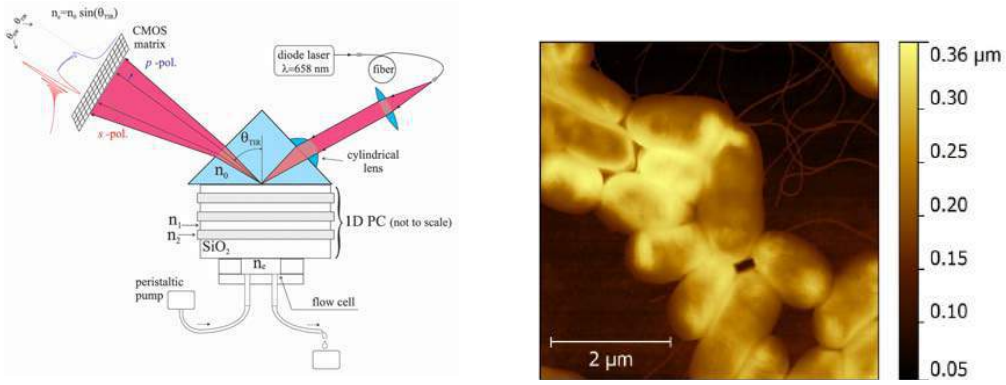

Fig. 1. Left: Schematic of the biosensor. Right: AFM image of (mono)layer of *E. coli* bacteria used as a generic "immobilized receptor layer" in the sensor during the kinetics measurements.

These results pave the way for further sensor and other applications of Photonic Crystal - supported surface waves, and the corresponding perspectives will be discussed.

REFERENCES

1. Ignatyeva, O. D., G. A, Knyazev, P. O. Kapralov, G. Dietler, S. K. Sekatskii and V. I. Belotelov, "Magneto-optical plasmonic heterostructure with ultranarrow resonance for sensing applications", *Sci. Rep*., Vol. 6, P. 28077, 2016.
2. Ignatyeva, O. D., P. O. Kapralov, G. A, Knyazev, S. K. Sekatskii, G. Dietler, M. Nur-E-Alam, M. Vasiliev, K. Alameh and V. I. Belotelov, "High-Q surface modes in photonic crystal/iron garnet film heterostructures for sensor applications", *JETP Lett.*, Vol. 104, No. 10, 679-684, 2016.
3. Rostova, E., G. Dietler and S. K. Sekatskii, "Label-Free Optical Biosensor Based on Photonic Crystal Surface Waves Reveals Binding Kinetics of Antibodies to Living Bacteria in Real Time", *Biophys. J*., 2016, Vol. 110, No. 3, 518A, 2016.
4. Rostova, E., C. Ben Adiba, G. Dietler and S. K. Sekatskii, "Label-free optical biosensor based on photonic crystal reveals binding kinetics of antibodies to living bacterial cells *E. coli*" , *Biosensors*, Vol. 6., 52, 2016.

Fabrication of optical field concentrators based on 3D chirped photonic crystals by direct laser writing technique

V. Mizeikis[1*], Z. Hayran[2], H. Kurt[2], D. Gailevičius[3], M. Malinauskas[3], S. Juodkazis[4], and K. Staliunas[5]

[1]Shizuoka University, Japan

[2]TOBB University of Economics and Technology, Turkey

[3]Vilnius University, Lithuania

[4]Swinburne University of Technology, Australia

[5]Institució Catalana de Recerca i Estudis Avancats (ICREA), Spain

[*]corresponding author: mizeikis.vygantas@shizuoka.ac.jp

Abstract-We describe a class of passive optical devices based on chirped photonic crystals that have structural properties are gradually varied along one direction, and are capable to localize and enhance local intensity of the incident light. We have addressed the challenge of realizing 3D chirped photonic crystals by using Direct Laser Write lithography, and report properties of the fabricated prototype structures for infrared spectral range.

In typical optical detectors, a thin p-n junction or other photosensitive layer is embedded in the bulk of absorbing material, and absorptive losses occurring outside the photosensitive region limit sensitivity of the detector (Fig. 1(a), top schematic). The unwanted losses can be reduced by building an optically transparent artificial structure capable to concentrate optical field near the detector, thus boosting its absorption rate and electronic response. Chirped photonic crystals (ChPhC) whose parameters (lattice period or dielectric filling ratio) are smoothly varied along one direction, can be used as field concentrators. At a certain depth inside the ChPhC, where incident waves encounter local photonic band gap (PBG), light propagation becomes slowed down and reversed, leading to field localization and intensity enhancement (Fig. 1(a) bottom schematic and Fig. 1(b)). This principle [1] can be useful for sensitivity enhancement of optical detectors, and was previously experimentally confirmed at microwave frequencies, where fabrication of 3D ChPhCs can be accomplished by simple mechanical machining and assembly, since large ChPhC lattice periods on the order of centimeters are required at these frequencies. However, realization of 3D ChPhCs for optical frequencies presents a significant fabrication challenge, since ChPhC period must be reduced to micrometer and even sub-micrometer range, and therefore has not been attempted before. One of the few 3D structuring techniques capable of high spatial resolution is Direct Laser Write (DLW) lithography [2], which is based on optical exposure of photoresist by a tightly focused beam of an ultrashort laser. Exposure due to non-linear two-photon absorption is induced selectively at the beam focus, while size of the exposed region can be reduced to less than 100 nm by controlling the exposure level. Thus, complex 3D patterns can be drawn by 3D focus scan. Previously, uniform photonic crystals were successfully fabricated using DLW [2]. Figure 1(c) shows Scanning Electron Microscopy (SEM) images of 3D ChPhC samples fabricated in this study. The samples are based on a 3D woodpile architecture, which is modified by introducing a spatial chirp along the woodpile stacking direction by gradually varying the

corresponding lattice period. Two SEM images shown on the left and right of Fig. 3(c) show spatially uniform (non-chirped) and chirped samples, respectively. In the latter image, gradual decrease of vertical lattice period from 0.58μm (at the top) towards 0.38μm (at the bottom) can be seen, while non-chirped sample has the same lattice period of 0.58μm throughout its thickness. Figure 1(d) compares experimental infra-red (IR) reflectance spectra of spatially uniform and chirped photonic crystals measured along the woodpile stacking direction. As can be seen, both structures exhibit reflectance peaks due to PBG. Spectral broadening and lower peak reflectance in the ChPhC sample can be attributed to the presence of spatial chirp. According to numerical simulations, field intensity enhancement by about five times can be expected in the ChPhC sample. DLW technique in principle allows one to embed thin, transparent detectors into the structures, and thus may enable relatively easy implementation efficient light detection schemes in optical detectors. Factors leading to field enhancement at various wavelengths, and practical possibilities to tune the PBG frequency towards telecommunications spectral range will be discussed.

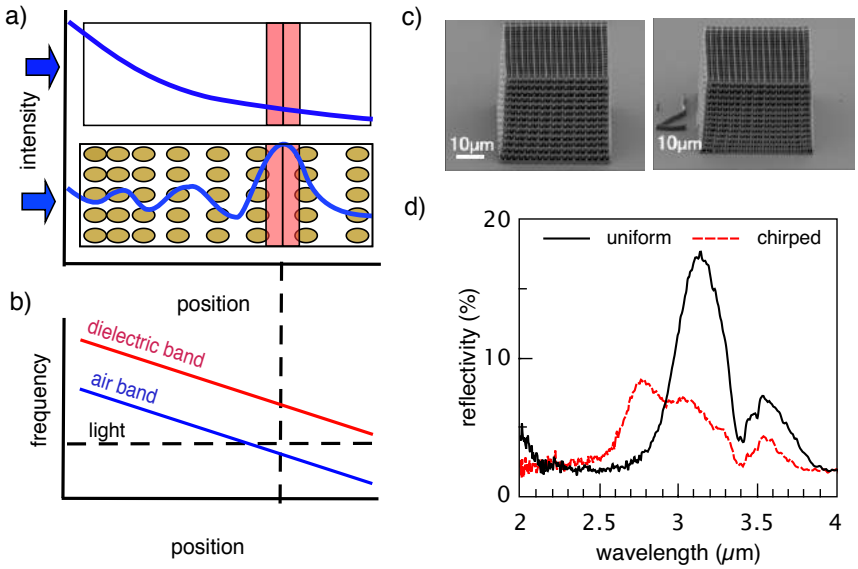

Figure 1. (a) Schematic explanation of field decay in uniform absorbing materials and field concentration in ChPhCs, (b) variation of local PBG frequency with position, (c) SEM images of fabricated uniform and 3D ChPhC woodpile photonic crystals, and (d) comparison between IR reflectance spectra in these samples.

This work was supported by NATO SPS grant No. 985048. VM acknowledges support by JSPS Kakenhii grant No. 15K04637.

REFERENCES

1. Kurt, H., Yilmaz, D. "Rainbow trapping using chirped all-dielectric periodic structures," *Appl Phys B*, Vol. 110, 411, 2013.
2. Mizeikis, V., Seet K.K., Juodkazis, S, Misawa, H., "Three-dimensional woodpile photonic crystal templates for the infrared spectral range", Opt. Lett., Vol. 29, 2061-2063, 2004.

High Quality Photonic Crystal Cavity with low index materials by using Slot Mode

Youngsoo Kim[1], Young Jin Lee[1], Seokhyeun Hong[1], Kihwan Moon[1], Soon-Hong Kwon[1*]
[1]Dept. of Physics, Chung-Ang University, Republic of Korea
*soonhong.kwon@gmail.com

Abstract-We suggest a photonic crystal cavity which confines the photons in low index material for telecommunication wavelength. The photonic crystal consists of periodic Si/SiO□/Si rods. In this cavity, the vertical losses can be reduced by low index slot mode and the horizontal losses can be reduced by photonic bandgap of square lattice photonic crystal slab. For telecommunication wavelength, we can get the highest quality factor 11200 by moving nearest neighborhoods of center defect on suggested photonic crystal structure.

A Si, material used for many electronic devices, has a limit due to its indirect bandgap. Because of its indirect bandgap, we need to another material for example GaAs, as an emitter. However, it is very difficult way to combine Si based electric devices and optical devices that have different lattice structure. We suggest a photonic crystal with low index materials by using slot mode. The vertical loss of cavity can be reduced by low index slot mode and the horizontal loss of cavity can be reduced by photonic band gap of square lattice photonic crystal slab. We used finite-difference time-domain(FDTD) and plane wave expansion(PWE) method to simulation.

In this research, we suggested high quality photonic crystal cavity with low index materials by using slot mode. The photonic crystal has 500 nm lattice constant and 125 nm radius for each cylinder. Each cylinder has a height of 1000 nm, and 10 nm of the center is composed of SiO□ and the rest is composed of Si. (Fig. 1. (a)) The reduced radius defect was positioned at center of entire slab structure for inducing fundamental mode. (Fig. 1. (b))

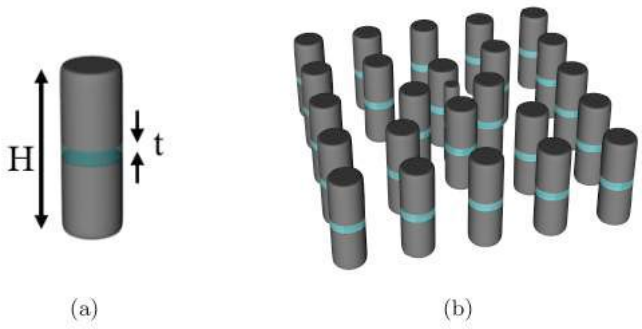

Figure 1: (a) Single cylinder structure. H is height of cylinder. t is thickness of SiO□ slot. (b) Entire photonic crystal structure in air.

For finding proper height of slab, we carried out the FDTD simulation that calculate effective index of Si

plane with height from 200 nm – 1500 nm at 1550 nm wavelength. When the height of plane is higher than 1000 nm of the effective index is saturated to bulk Si (3.47). Thus, we insert SiO□ slot to Si plane with height of 1000 nm. The effective index of combined with Si and SiO□ plane was decreasing while increases thickness of SiO□ slot. For example, when slot thickness is 10 nm, the effective index of combined plane is about 3.30.

Therefore, the 1000 nm Si cylinder with 10 nm SiO□ slot can generate a photonic bandgap. photonic crystal slab has wide bandgap when height of structure approximately 2 - 2.5 times of lattice constant [1]. Therefore, we choose lattice constant of 500 nm when each cylinder has 1000 nm height and the 500 nm lattice constant. Fig. 2. (a) is the photonic band diagram of proposed structure (Fig. 1. (b)) calculated by PWE.

The photonic bandgap was appeared in 1170 - 1690 nm (1620 – 1114 THz) area. The target wavelength (1550 nm) is in the photonic bandgap. Using FDTD simulation, we found the cavity mode appeared in given the defect at center of structure. When the center defect radius is 90 nm and nearest neighborhoods are moved to 70 nm defect toward, we could get the highest Q factor 11200 for 1530 nm wavelength. (Fig. 2. (b))

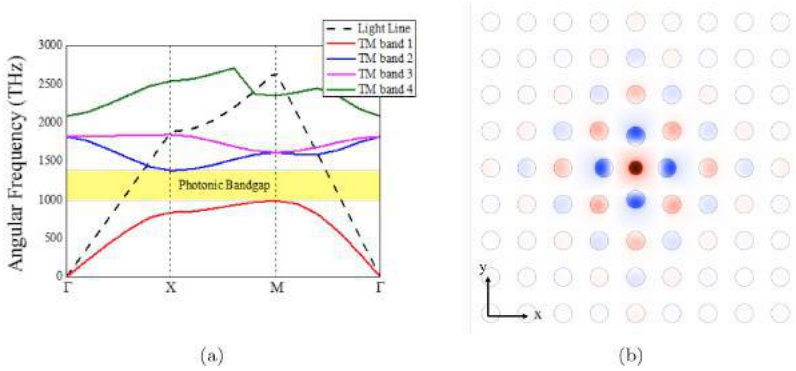

Figure 2: (a) Photonic band structure, cylinder radius = 125 nm, lattice constant = 500 nm. (b) Mode profile of 1530 nm cavity mode, defect radius = 90 nm, nearest neighborhood shift = 70 nm.

We suggested a photonic crystal with low index materials by using slot mode for telecommunication wavelength. We had checked the effective index is approximately 3.3 for height 1000 nm Si cylinder that has 10 nm thickness SiO□ slot. We confirmed that our structure can has enough photonic bandgap when it has square lattice photonic crystal structure. For 500 nm lattice and radius of each cylinder is 125 nm, telecommunication wavelength (1550 nm) was in the photonic bandgap. As a result, when the center defect radius is 90 nm and nearest neighborhoods are moved to 70 nm defect toward, we could get the highest Q factor 11200 for 1530 nm wavelength.

REFERENCES

1. Joannopoulos, J. D., et al. *Photonic crystals: molding the flow of light*. Princeton university press, 2011.
2. F. Riboli, P. Bettotti and L. Pavesi, “Band gap characterization and slow light effects in one dimensional photonic crystals based on silicon slot-waveguides”*, Opt. Express*, Vol. 15, No. 19, 11769-11775, 2007.

Perturbed flat-band modes and anisotropic optical responses in an array of quasi-one-dimensional systems

N. Myoung[1], A. Ramachandran[1], Jung-Wan Ryu[1], E. Lidorikis[2], and H. C. Park[1*]

[1]Center for Theoretical Physics of Complex Systems, Institute for Basic Science, Daejeon 34051, Republic of Korea

[2]Department of Materials Science and Engineering, University of Ioannina, Ioannina 45110, Greece

[*]corresponding author: hcpark@ibs.re.kr

Abstract-We theoretically examine the photonic band structures of an array of quasi-one-dimensional systems where a flat band can exist. Since the interactions in the photonic lattice are not restricted to the nearest neighbor interactions, the flat bands are perturbed by coupling to the dispersive bands, resulting in the avoid crossing nature. The perturbation-induced delocalization is analyzed based on understanding of the life time of localized modes.

Recently, the interest in the flat bands has been remarkably increased in various fields such as condensed matter, optical physics[1-2]. As theoretically predicted by the tight-binding approaches in the condensed matter context, the existence of the flat band is represented by the compact localized states via quantum destructive interferences[2-3], indicating the macroscopic degeneracy. On the other hand, the flat-band formation has been successfully confirmed by realizing the compact localization of light in symmetric cavities of the photonic systems[1,4-5]. While the flat-band modes in either quasi-one-dimensional or two-dimensional photonic lattices have been clearly demonstrated, research on flat bands in an array of quasi-one-dimensional lattices has been unexplored yet because of the existence of unwanted interactions such as next-nearest neighbors coupling, which are simply dismissed in the tight-binding approach. It has been reported that, in bi-layer two-dimensional Lieb lattice, the inter-layer coupling results in the splitting of the flat bands, maintaining their flatness over the in-plane momentum space[6]. In the same context, it is no wonder that the same phenomenon occurs in the case of quasi-one-dimensional lattices: flat bands are still found along the one-dimensional line in the momentum space.

In this work, we consider the more realistic but complicated systems in flat-band photonic lattices, where all possible interactions are taken into account, and examine how the existence of the perturbed flat bands is reflected in optical response spectra and light propagation through the systems. In an array of the quasi-one-dimensional lattices, the one-dimensional flat bands can be still observed whereas two-dimensional flat bands cannot be found. Interestingly, the one-dimensional flat bands exist along both Brillouin zone boundaries, $\Gamma \rightarrow X$ and $\Gamma \rightarrow Y$, at different frequencies (see Fig.1). Anisotropic optical response, obviously, is observed with respect to the propagating direction of the incident waves, and directional dependence of the transmission spectra is also found. Furthermore, it is shown that the presence of perturbations give rise to the delocalization of the flat-band modes, and such delocalization nature is investigated by examining the life time of the perturbed flat-band modes.

By exploring the properties of the perturbed flat band by means of optical response, our results allow for more in-depth understanding of the localization of light in flat-band photonic lattice, which can be easily found

in realistic systems. Anisotropic and directional optical transmission/reflection spectra might be of interest for future optical applications in terms of metamaterials.

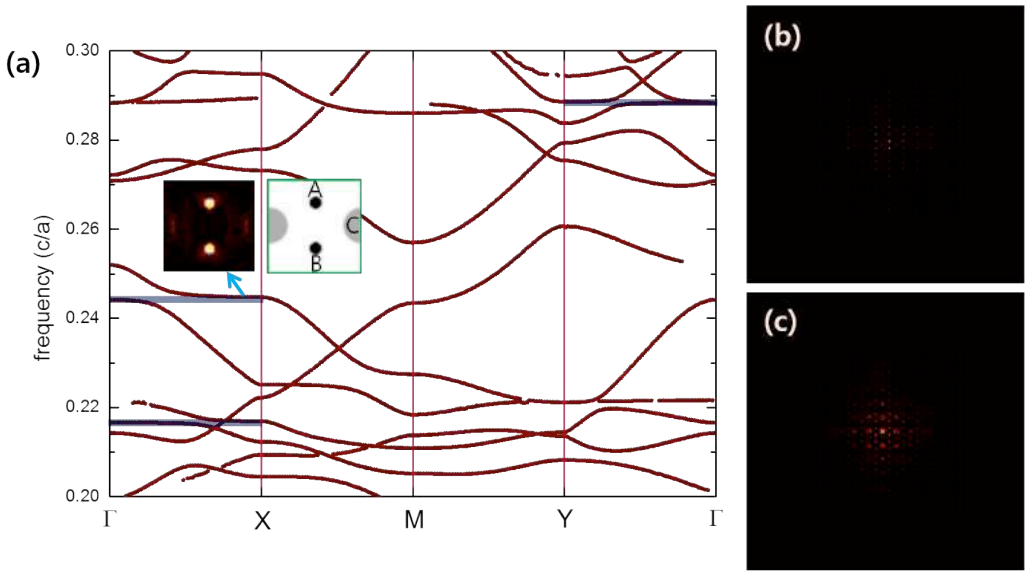

Figure 1. (a) Band structures of the photonic lattices in a given frequency range where perturbed flat bands are found at different frequencies (marked by shaded lines). Insets: Field intensity for the given frequency (~0.244) which corresponds to the perturbed flat band, displaying the strong localization at the symmetric cavities A and B. Unit cell for the photonic band calculation is also shown, where each dielectric cavities labeled by A, B, and C. (b) and (c) Field intensity distributions over finite photonic lattices with a pulsed excitation at A and C sites.

Acknowledgements, This work is supported by Project code (IBS-R024-D1)

REFERENCES

1. Morales-Inostroza, L. and R. A. Rodrigo, "Simple method to construct flat-band lattices" *Phys. Rev. A*, 94, 043831, 2016.
2. Flach, S., D. Leykam, J. D. Bodyfelt, P. Matthies, and A. S. Desyatnikov, "Detangling flat bands into Fano lattices" *Eur. Phys. Lett.*, 105, 30001, 2014.
3. Nishino, S., M. Goda, and K. Kusakabe, "Flat bands of a tight-binding electronic system with hexagonal structure" *J. Phys. Soc. Jpn.*, 77, 2015-2023, 2003.
4. Vicencio, R. A., C. Cantillano, L. Morales-Inostroza, B. Real, C. Mejia-Cortes, S. Weimann, A. Szameit, and M. I. Molina, "Observation of localized states in Lieb photonic lattices" *Phys. Rev. Lett.*, 114, 245503, 2015.
5. Mukherjee, S., A. Spracklen, D. Choudhury, N. Goldman, P. Ohberg, E. Andersson, and R. R. Thomson, "Observation of a localized flat-band state in a photonic Lieb lattice" *Phys. Rev. Lett.*, 114, 045504, 2015.
6. Noda, K., K. Inaba, and M. Tamashita, "Flat-band ferromagnetism in the multilayer Leib optical lattice" *Phys. Rev. A.*, 90, 043624, 2014.

Purcell effect in one-dimensional disordered photonic crystals

A. R. Gubaydullin[1,3], K.A. Ivanov[1,3], V. V. Nikolaev[2], M. A. Kaliteevski[1,2,3]

[1]Saint- Petersburg Academic University, 194021, St. Petersburg, Russia

[2]Ioffe Physical-Technical Institute of Russian Academy of Science, 194021, St-Petersburg, Russia

[3]Saint Petersburg ITMO University, 197101, St. Petersburg, Russia

[*]corresponding author: gubaydullin.azat@gmail.com

Abstract-We have theoretically studied the probability of spontaneous emission rate of the emitter placed in a one-dimensional disordered photonic crystal. It is demonstrated that at high levels of disorder photonic band gap (PBG) is narrowed, and the probability of emission in the center of PBG becomes significantly different from zero, and in the PBG may occur localized states for which the spontaneous emission is significantly enhanced.

Disordered photonic crystals attract interest with the aim of the possibility of light localization [1] in such structures, in analogy with electron localization [2], known as Anderson localization. The aim of this work is to study the influence of disorder on the PBG [3] and the related problem of wave localization in disordered optical media.

We study the probability of spontaneous emission by using S-quantization formalism [4]. We have shown that for a dipole emitter placed in a disordered photonic crystal, the spontaneous emission rate can be enhanced if the frequency corresponds to the optical eigenmode of the structure, and suppression of spontaneous emission can be observed in the case of bandgap, or when the position of the emitter corresponds to a node in the profile of the electric field of the eigenmode. We study the influence of variation of disorder parameter. Particularly, we have demonstrated that at high levels of disorder edge states penetrate into the photonic band gap (PBG), PBG is narrowed, and the probability of emission in the center of PBG becomes significantly different from zero. In addition, in the PBG may occur localized states for which the spontaneous emission can be significantly enhanced.

Acknowledgements, this work has been supported by Russian Science Foundation (Project no. 16-12-10503).

REFERENCES

1. John S., *Phys. Rev. Lett.* 58, 2486 , 1987.
2. Anderson P. W., *Phys. Rev*. 109, 1492, 1958.
3. Kaliteevski M. A., Beggs D. M., Brand S., Abram R. A., Nikolaev V. V., *Phys. Rev. E*, Vol. 73, No. 5, 056616, 2006.
4. Kaliteevski M. A., Gubaydullin A. R., Ivanov K. A., Mazlin V.A.,. *Optics and Spectroscopy*, Vol. 121, No. 3, 410 – 419, 2016.

Applying the Kagome Lattice to 2D Photonic Crystals.

J. Upham[1*], S. A. Schulz[1,2,3], L. O'Faolain[2,3,4], and R. W. Boyd[1,5]

[1]Department of Physics, University of Ottawa, 25 Templeton Street, Ottawa, K1N 6N5, Ontario, Canada.

[2]Centre for Advanced Photonics and Process Analysis, Cork Institute of Technology, Ireland

[3]Tyndall National Institute, Ireland.

[4]School of Physics and Astronomy, SUPA, University of St Andrews, Scotland, UK.

[5]Institute of Optics and Department of Physics and Astronomy, University of Rochester, USA.

[*]corresponding author: jupham@uottawa.ca

Abstract-

Slow light photonic crystal (PhC) waveguides tightly compress propagating light and increase interaction times, yet their practical application is largely limited to moderate group indices (n_g <100). This limitation persists because nearly all research has focused on a single lattice type: the triangular lattice. Here, we present kagome lattice waveguides with an intrinsically high group index for slow light away from the band edge. We experimentally observe n_g >150 and reduced propogation losses compared to traditional PhC waveguides.

Two dimensional photonic crystals have been extensively studied because of their ability to tightly confine light to wavelength order dimensions to form high Q cavities and slow light waveguides [1-3], which are of significant interest for applications in interconnects, sensing and strong light-matter interaction [3]. However, the vast majority of 2D photonic crystal work has focused on only a single crystal structure: the triangular lattice. While this geometry has a demonstrated versatility and been used to develop many different devices, it is not ideal for all applications. For instance, waveguides made in the triangular lattice exhibit slow light near the band-edge, where propagation losses are much higher. Even when heavily optimized, the group index (n_g) in such structures is generally limited to ~100 [4].

Rather than further optimizing such waveguides, we investigated whether the crystal lattice itself could be changed to improve slow light in such structures. The kagome lattice consists of a super lattice of missing holes on top of the triangular lattice (Fig. 1a) and supports multiple photonic bandgaps (Fig. 1b). Intuitively, the kagome lattice can be considered to resemble a tight-binding model, compared to the triangular lattice, which is better approximated by a "free photon" (or free electron for electronic crystals) approximation. This leads to larger photonic band gaps and flatter bands in the kagome lattice [5, 6].

A variety of waveguides can be formed by line defects in the kagome crystal lattice, some of which show some cavity-like behaviour in their propagation modes (Fig. 2a). The propagating mode (Fig. 2b) shows clear cavity-like field behaviour, producing slow light (ng > 150, see Fig. 2c) after only rudimentary dispersion engineering. It is important to note that this slow light section of the dispersion curve is away from the band-edge (light blue dispersion curve in Fig. 1b). Furthermore through use of more sophisticated dispersion engineering of these kagome waveguides, we have observed group indices exceeding 300,000 in numerical simulations.

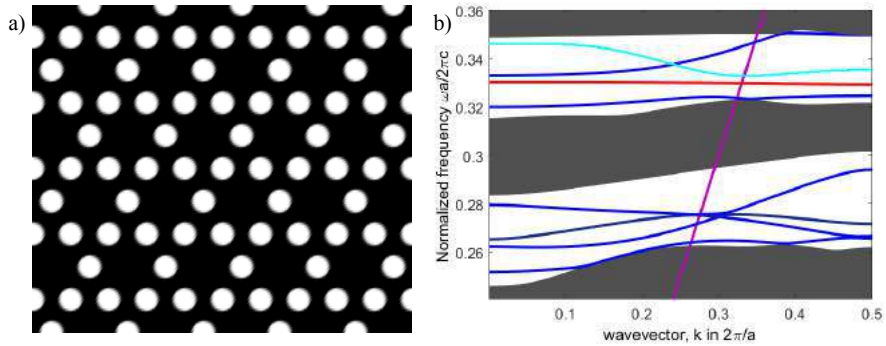

Fig 1: a) Schematic of a bulk kagome lattice. b) Band gaps in dispersion curve of a kagome lattice PhC, with slowlight waveguide modes introduced by a line defect.

We demonstrate that the kagome lattice supports slow light waveguide modes with higher group indices compared to the traditional triangular lattice photonic crystal, even before dispersion engineering. We also consider how the propagation losses in the slow light region are reduced by it being away from the band-edge. We believe that kagome lattice PhCs could thus find practical application for small-footprint, slow light systems as well as providing a medium for fundemental research on slow and stopped light.

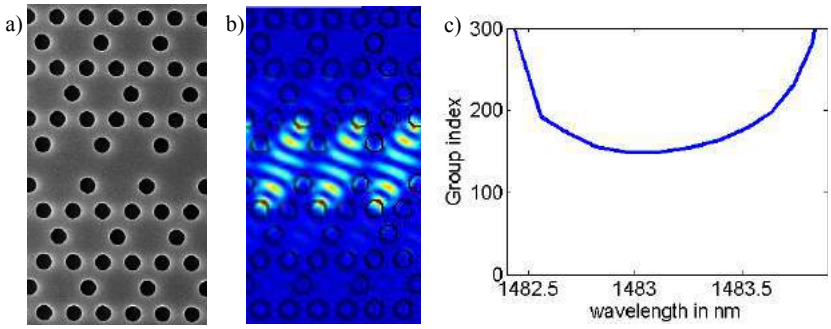

Fig 2: a) Scanning electron microscope image of a kagome lattice waveguide and b) field profile in slow light region, showing cavity-like behaviour of the propagation mode. d) Theoretical group index curve of the mode shown in c).

REFERENCES

1. Akahane, Y. and Noda, S. "High-Q photonic nanocavity in a two-dimensional photonic crystal," *Nature*, Vol. 425, 944–947, 2003.
2. Baba, T, "Slow light in photonic crystals," *Nat. Photon*, Vol. 2, 465–473, 2008.
3. Krauss, T. F., "Why do we need slow light?," *Nat. Photon.*, Vol. 2, 448–450, 2008.
4. Schulz, S. A. O'Faolain, L. Beggs, D. M., White T. P., Melloni, A. and Krauss, T. F., "Dispersion engineered slow light in photonic crystals: a comparison," *J. Optics* Vol. 12, No. 10, 104004 (2010).
5. Garcia-Adeva, J. A., "Band gap atlas of photonic crystals having the symmetry of the kagome and pyrochlore lattices," *New J. Phys*. Vol. 8, No. 86 (2006).
6. Zong, Y., Xia, S., Tang, L., Daohong, S., Hu, Y., Pei, Y., Su, J., Li, Y., and Chen Z., "Observation of localized flat-band states in Kagome photonic lattices," *Opt. Express* Vol 24, 8877-8885 (2016).

An Investigation of Surface Plasmon Effects on Metallic Photonic Crystals in H Polarization

K. L. Low[1*] , M. Z. Mat Jafri[2], and Sohail A. Khan[2]

[1] KDU Penang University College, Penang Malaysia
[2]Universiti Sains Malaysia, Penang Malaysia
* corresponding author: kheelam.low@kdupg.edu.my

Abstract - The surface plasmon effect in metallic photonic crystals has been investigated. The band structure graph is the only graph that can be used to explain the characteristics of photonic crystals. In this work the band structure graph has been used to describe these characteristics, which include the surface plasmon effect of photonic crystals. Recently, band structure graphs for frequency-dependent materials have been analyzed by several researchers. The surface plasmon effect has been found for these materials. This article reports the effect of surface plasmons when the relative permittivity is changed from band structure graphs. The numerical results show the magnetic field distribution of waves on the photonic crystals added for each frequency.

1. Introduction

Photonic crystals have been extensively developed since the prediction and investigation of Yablonovitch and John[1], [2]. This active research has been extended to metallic photonic crystals, and more characteristics of photonic crystals are expected to be discovered compared with the conventional dielectric-dielectric photonic crystals [3]–[23]. It is well known that electromagnetic waves with frequencies lower than the plasma frequency of metals cannot propagate through a bulk metal. But it is possible for electromagnetic waves to be guided below the plasma frequency and attributed to the surface plasmon effect if an array of dielectric components is embedded in the bulk metals [24].

Kuzmiak et al. studied the dispersion relation of photonic crystals containing metallic components in two dimensions (2D) using the plane wave expansion method and the Drude model [10-12]. Low et al. continued their calculation by studying metallic photonic crystals using the modified plane wave expansion method with the Drude model with different dielectric rods in the E polarization mode [24]–[26]. Several characteristics were observed in the dispersion relation graphs, such as flat bands occurring at some of the frequencies, a group velocity anomaly in the band edges, and an effective plasma frequency in the E polarization mode. The H

polarization mode has also been extensively studied by several scientists [8], [10], [11]. Kuzmiak et al. [10], [11] calculated band structure graphs for frequency-dependent materials in a vacuum background using the plane wave expansion method. They also included the damping frequency of the metallic component in his calculation. But unfortunately their calculation was limited to only air or vacuum backgrounds. Their calculation was generalized by Low et al.[27]. Then, Low et al. [24], [26] continued the development of the band structure equation for photonic crystals in metals. The surface plasmon effect was detected in the band structure graphs in this investigation.

In this paper, a plane wave expansion method for metallic photonic crystals with different dielectric rods in H polarization mode is used. Although some results have been published [8], [11], [14], [28], [29], they have not included any extensive discussion of the surface plasmon effect when relative permittivity is changed. The surface plasmon effect is very obvious in the band structure graphs at first glance [24]. So, in this paper, we investigated the surface plasmon effect when the relative permittivity of rods is changed in the metallic photonic crystals. Because the band structure graph presents only the energy change in the metallic photonic crystals, we needed a commercial package to verify whether the surface plasmon effect exists in the metallic photonic crystals. The occurrence of magnetic field distributions at each flat band has been investigated by using COMSOL Multiphysics software.

2. Photonic Band Structure Graph of Metallic Photonic Crystals with Dielectric Rods

We sketch the cross section view of the photonic crystals in Figure 1.

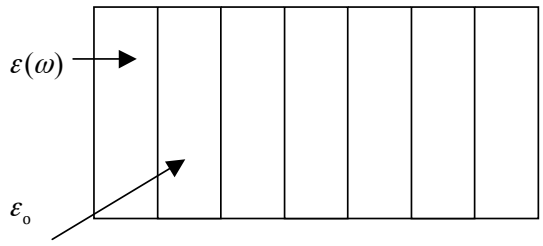

Figure 1 Illustration of the metallic photonic crystals arrangement (square lattice).

The band structure graph has been derived for H polarization for metallic photonic crystals with dielectric rods in Equation (1):

$$\varepsilon_0\mu^2 A(k\,|\,G) - \mu\left[\begin{array}{l}\left(\varepsilon_0 + \varepsilon_0\dfrac{c^2}{\omega_p^2}|k+G|^2\right)A(k\,|\,G) \\ +\left(1-\varepsilon_0\right)\dfrac{c^2}{\omega_p^2}\sum_{G'}(k+G)\mathrm{g}(k+G')2f\dfrac{J_1\left(|\,G-G'\,|\,R\right)}{|\,G-G'\,|\,R}A(k\,|\,G')\end{array}\right] \\ +\frac{c^2}{\omega_p^2}\sum_{G'}(k+G)\mathrm{g}(k+G')2f\frac{J_1\left(|\,G-G'\,|\,R\right)}{|\,G-G'\,|\,R}A(k\,|\,G') = 0 \tag{1}$$

where $\mu = \omega/c$, ε_0 is the relative permittivity, k is the wave vector, G is the reciprocal lattice, J_1 is the first Bessel function, R is the radius of the rods, ω_p is the plasma frequency of the metals, c is the speed of light, and ω is the eigenfrequency. Equation (1) represents a generalized eigenvalue problem. A linearization technique is used. An equation in the following form is obtained:

$$\mu^2\overset{\iota}{J} - \mu\overset{\iota}{K} + \overset{\iota}{L} = 0 \tag{2}$$

where the elements $\overset{\iota}{J}$, $\overset{\iota}{K}$, and $\overset{\iota}{L}$ of $NG \times NG$ matrices are given as

$$\overset{\iota}{J} = \varepsilon_{\mathrm{o}} \tag{3}$$

$$\overset{\mathrm{t}}{K} = \left[\begin{array}{l}\left(\varepsilon_{\mathrm{o}} + \varepsilon_{\mathrm{o}}\dfrac{c^2}{\omega_p^2}|k+G|^2\right)A(k\,|\,G) \\ +\left(1-\varepsilon_{\mathrm{o}}\right)\dfrac{c^2}{\omega_p^2}\sum_{G'}(k+G)\mathrm{g}(k+G')2f\dfrac{J_1\left(|\,G-G'\,|\,R\right)}{|\,G-G'\,|\,R}A(k\,|\,G')\end{array}\right] \tag{4}$$

$$\overset{\mathrm{t}}{L} = \frac{c^2}{\omega_p^2}\sum_{G'}(k+G)\mathrm{g}(k+G')2f\frac{J_1\left(|\,G-G'\,|\,R\right)}{|\,G-G'\,|\,R}A(k\,|\,G') \tag{5}$$

Equation (2) is a second-order eigenvalue problem, which can be represented by the following matrix form:

$$\overset{\text{t}}{M} = \begin{pmatrix} 0 & \overset{\text{ι}}{IJ} \\ \overset{\text{t}}{K} & \overset{\text{t}}{L} \end{pmatrix} \tag{6}$$

The complete solution of Equation (6) is obtained by solving the eigenvalues of $\overset{\text{ι}}{M}$ using the diagonalization of this non-Hermitian matrix.

3. Result and Discussion

In this article, four examples of different materials with the same filling fraction $f = 0.5$ are used as cylindrical rods in a copper medium. The plasma frequency of copper is $\omega_p = 1914 \times 10^{12}$ THz. The band structure graphs are plotted along $M(\pi/a, \pi/a)$ - $\Gamma(0,0)$ - $X(\pi/a, 0)$ in the first irreducible Brillouin zone. The magnetic field distribution graphs are plotted at k = 0 with their respective frequencies. The dimensions of photonic crystals are in micrometers.

From the theory, there should be no wave activities inside the metallic structure below the plasmonic frequency. But from the previous investigation [24], wave activities below the plasmonic frequency are detected. This is because the photonic crystals structure exhibits a very special characteristic, which is the surface plasmon effect. The band structure graph of copper photonic crystals with air rods is plotted in Figure 2(a). The band structure graph has a lot of flat bands. To confirm the effect of surface plasmons, COMSOL Multiphysics software was used to investigate the magnetic field distribution of the photonic crystals at k = 0 at each frequency. Figure 2(b) shows the magnetic field distribution when frequency at 1280 THz ($\omega a/2\pi c = 0.86$). Obviously, there is a surface plasmon effect at this frequency and we find that some of the wave is inside the air rods. Then, the frequency being used in the magnetic field distribution graph is lowered to 537 THz ($\omega a/2\pi c = 0.28$) and the result is shown in Figure 2(c). The wave is only on the surface of the air rods, which is the surface plasmon, and no wave is inside the rods. Then the frequency is further lowered to 185 THz ($\omega a/2\pi c = 0.098$) and the magnetic field distribution graph of this frequency is shown in Figure 2(d). There is a complete wave localized (peak to valley wave) across the air rods. The frequency range shows that the wave is near the surface of the rods. This agrees very well with the band structure graph. Flat bands in all the mentioned frequency points in the band structure graph are evidence of the surface plasmon effect [30]. But

the flat bands vanished when $\omega a/2\pi c \geq 1$. This corresponds to the fundamental metallic characteristic where the wave is able to propagate in a metal when the frequency is larger than the plasmon frequency. The magnetic field distribution graph of photonic crystals at $\omega a/2\pi c = 1.2$ (2255 THz) is plotted in Figure 2(e). The wave is propagating randomly across the air rods. So, it is obvious that the wave is distributed around the rods at frequencies below $\omega a/2\pi c = 1.2$. All the waves below this frequency are surface plasmon waves. This is described very well in the band structure graph.

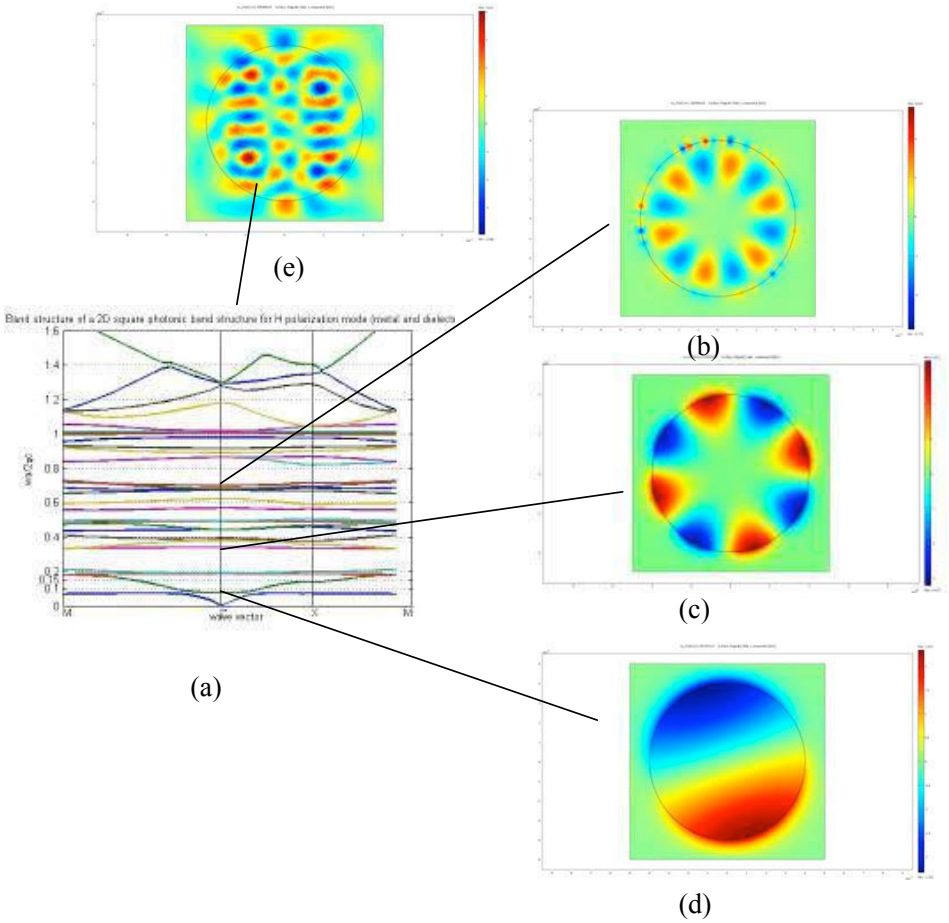

Figure 2 (a) Band structure graph of air rods with filling fraction $f = 0.5$ in copper medium in H polarization mode. Magnetic field distribution at frequency (b) 1280 THz (c) 537 THz (d) 185 THz (e) 2255 THz.

Equation (1) is utilized to plot the band structure graph of a Teflon ($\varepsilon_o = 2$) rod in the copper medium as shown in Figure 3(a). The band structure graph is very similar to the band structure graph of Figure 2(a). It has several flat bands below the normalized frequency, $\omega a/2\pi c = 0.8$ and the frequency is lower than the frequency of the previous structure. A band gap appearing in the frequency range $0.8 \le \omega a/2\pi c \le 1$ shows that this structure is a typical photonic crystal structure. Further, the magnetic field distribution at frequencies 1279 THz, 728 THz, and 138 THz are shown in Figures 3(b), 2(c), and 2(d) respectively. In Figure 3(b), the wave is localized in the Teflon rods and found on the surface of the rods. Figure 3(c) shows the same characteristic with longer wavelength. Then, Figure 3(d) shows that a complete wave is localized in the Teflon rods.

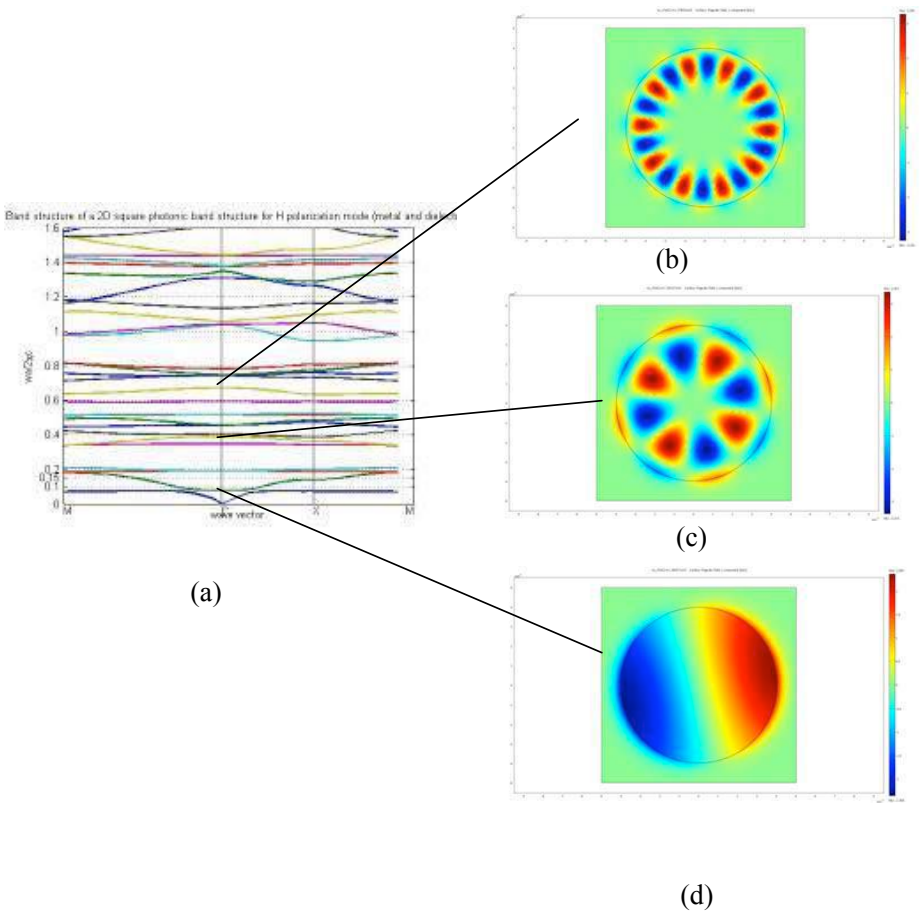

Figure 3 (a) Band structure graph of Teflon rods with filling fraction $f = 0.5$ in copper medium in H polarization mode. Magnetic field distribution at frequencies (b) 1279 THz, (c) 728 THz, and (d) 138 THz.

Then the dielectric constant of rods was increased to $\varepsilon_o = 4.9$ which is FR-4. FR-4 is insulator which is very common in electronic industry. The band structure graph is plotted in Figure 4(a). It is obvious that the flat bands are fewer; they are situated below the normalized frequency $\omega a/2\pi c = 0.6$. The magnetic field distributions of the flat bands at $\omega a/2\pi c = 0.34$(646 THz) and $\omega a/2\pi c = 0.075$ (142 THz) are plotted in Figures 4(c) and 3(d) respectively. In Figure 4(c), the wave is not only localized on the surface of the FR-4 rods but also inside the FR-4 rods. The

wave is in a regular waveform. In Figure 4(d), the waveform is different from the waveform of air and Teflon rods. In the air and Teflon rods, there is a complete wave propagating across the rods. But in the FR-4 rods, the waveform is separated into two complete waves, localized around the surface of the rods. The phenomenon appearing in Figure 2(e) is found in Figure 4(b). The wave is propagating irregularly. But the frequency of Figure 4(b) is lower than the frequency in Figure 2(e). This shows that the wave is propagating in the FR-4 rods at the lower frequency.

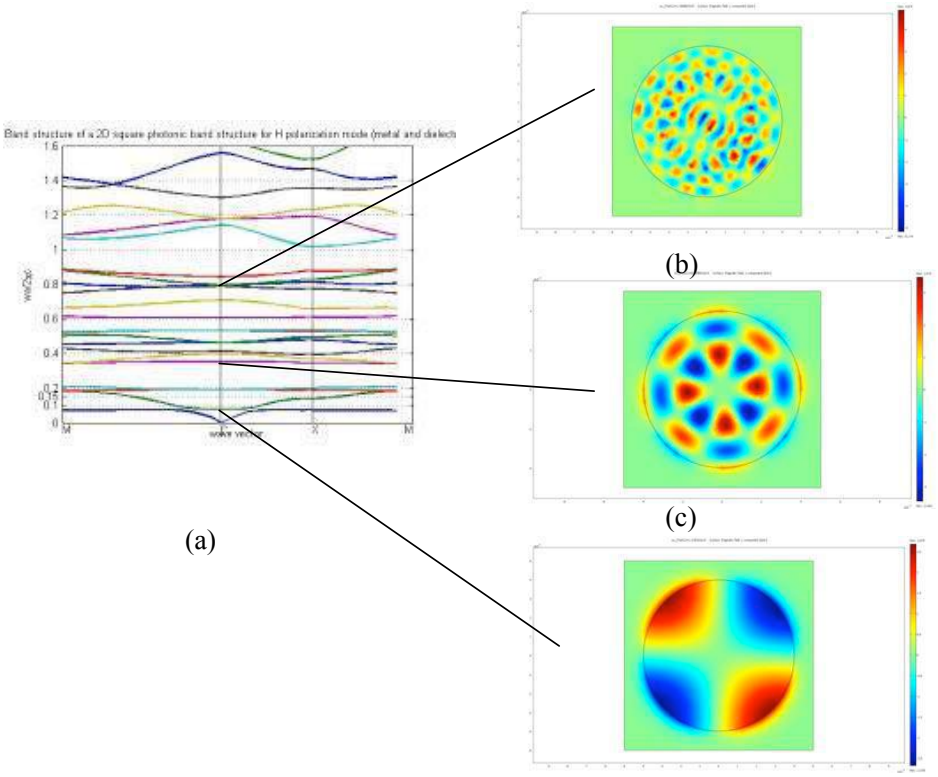

Figure 4 (a) Band structure graph of FR-4 rods with filling fraction $f = 0.5$ in copper medium in H polarization mode. Magnetic field distribution at frequencies (b) 1491 THz, (c) 646 THz, and (d) 142 THz.

The dielectric constant of the rods was further increased to 12.96 in the case of gallium arsenide (GaAs). The band structure graph is plotted in Figure 5(a). The flat bands are less frequent compared to the three materials investigated earlier. This means that the effect of surface

plasmons is reduced. The magnetic field distribution of $\omega a/2\pi c = 0.093$ (176 THz) is shown in Figure 5(d). The waves are localized near the surface of the GaAs rods. But when the frequency is increased to $\omega a/2\pi c = 0.39$ (743 THz), the waves are propagating out from the center of the GaAs rods. The magnetic field distribution graph is shown in Figure 5(c). It no longer shows a surface plasmon effect. Then, the frequency was further increased to $\omega a/2\pi c = 0.80$ (1499 THz); the waves are propagating randomly inside the GaAs rods.

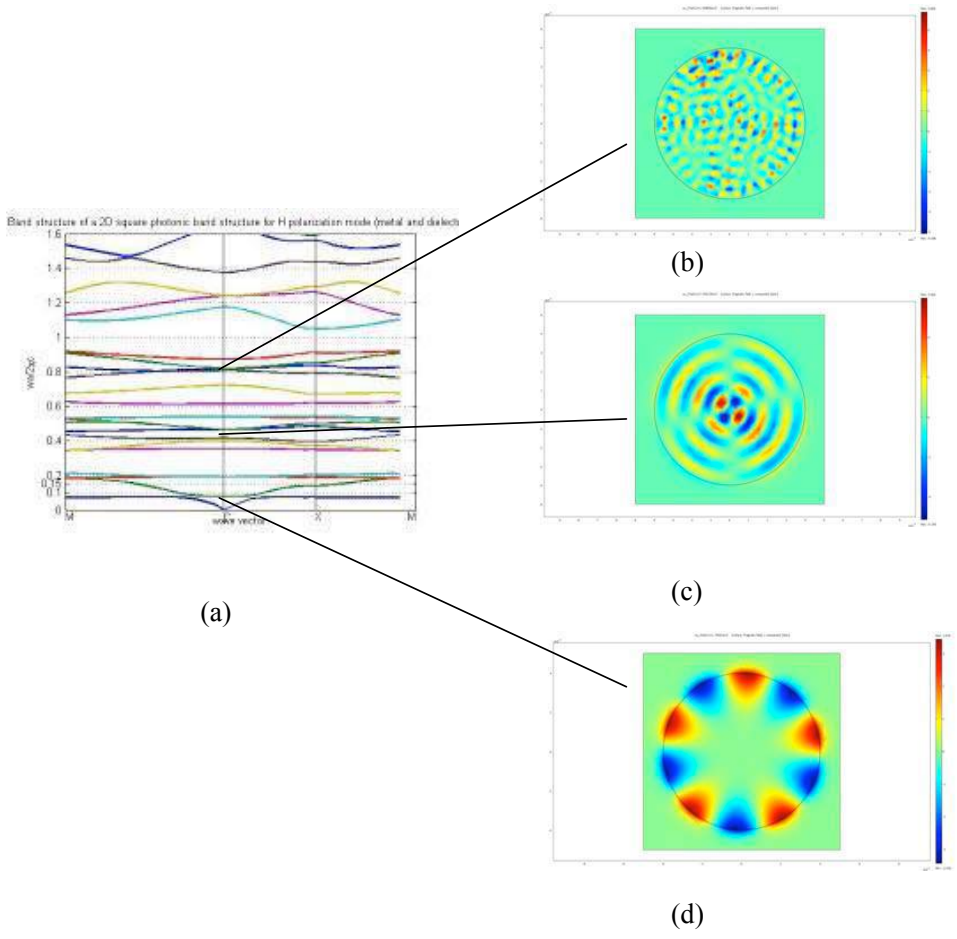

Figure 5 Band structure graph for GaAs rods with filling fraction $f = 0.5$ in copper medium in H polarization. Magnetic field distribution at frequencies (b) 1499 THz, (c) 743 THz, and (d) 176THz

3.1 Effect of Relative Permittivity on Photonic Cystals in Metals

The surface plasmon effect is reduced from vacuum to GaAs. The flat bands that represent the surface plasmon effect are less frequent when the relative permittivity of rods is increased. So, when a high relative permittivity material is coupled with the metals, the surface plasmon effect is not obvious. The structure will act as an ordinary photonic crystal, free of flat bands, while the relative permittivity of rods is increased. From the magnetic field distribution figure, the waves are localized inside the dielectric rods, especially for frequencies lower than the plasma frequency for all materials. The motion of the solid state plasma, whose characteristic is the plasma frequency in metals, is confined to the interior of the dielectric rods. So, the characteristic that an electromagnetic wave cannot penetrate metals can be overcome by insertion of an array of dielectric rods in metals.

4. Conclusion

We have plotted the band structure graphs of several materials rods in a copper medium in the H polarization mode using equations derived from the literature. When the relative permittivity of the rods is increased, the effect of the surface plasmons is reduced. The characteristics of wave propagation in the structure have been investigated using magnetic field distribution plots from COMSOL Multiphysics software. Both of the plots agree very well with each other. The surface plasmon effect is detected for all the materials investigated. The surface plasmon effect is reduced when the dielectric constant of the dielectric rods is increased. We also found that when the dielectric constant of the rods is high, the wave is prone to propagate inside the metallic medium. This phenomenon is found in different types of rods. Our method of calculation can be extended to find the band gap structure of defect modes and wave guide modes of photonic crystals made of metallic slabs.

5. Acknowledgments

This project was carried out using the Fundamental Research Grants Scheme (FRGS) with grant number 203/PFIZIK/6711146 and the Postgraduate Research Grant Scheme with grant number 1001/PFIZIK/841028. We would like to thank the technical staffs who participated in this project. Thanks are extended to USM for the support and encouragement given.

References

[1] E. Yablonovitch, "Photonic band-gap structures," *J. Opt. Soc. Am. B*, vol. 10, no. 2, p. 13, 1993.

[2] S. John, "Strong Localization of photons in Certain Disordered Dielectric Superlattices," *Phys. Rev. Lett.*, vol. 58, no. 23, p. 4, 1987.

[3] H. N. Amir Hosseini and Yehia Massouda, "Triangular lattice plasmonic photonic band gaps in subwavelength metal-insulator-metal waveguide structures," *Appl. Phys. Lett.*, vol. 92, p. 3, 2008.

[4] S. Brand, R. A. Abram, and M. A. Kaliteevski, "Complex photonic band structure and effective plasma frequency of a two-dimensional array of metal rods," *Phys. Rev. B*, vol. 75, p. 7, 2007.

[5] A. Crist, S. G. Tikhodeev, N. A. Gippius, J. Kuhl, and H. Giessen, "Plasmon polaritons in a metallic photonic crystal slab," *Phys. Status Solidi*, vol. 0, p. 4, 2003.

[6] El-Kady, M. M. Sigalas, R. Biswas, K. M. Ho, and C. M. Soukoulis, "Metallic photonic crystals at optical wavelengths," *Phys. Rev. B*, vol. 62, no. 23, p. 4, 2000.

[7] A. Ghoshal and P. G. Kik, "Theory and simulation of surface plasmon excitation using resonant metal nanoparticle arrays," *J. Appl. Phys.*, vol. 103, p. 8, 2008.

[8] T. Ito and K. Sakoda, "Photonic bands of metallic systems. II. Features of surface plasmon polaritons," *Phys. Rev. B*, vol. 64, p. 8, 2001.

[9] M. J. Keskinen, P. Loschialpo, D. Forester, and J. Schelleng, "Photonic band gap structure and transmissivity of frequency-dependent metallic–dielectric systems," *J. Appl. Phys.*, vol. 88, no. 10, p. 6, 2000.

[10] V. Kuzmiak and A. A. Maradudin, "Photonic band structures of one- and two-dimensional periodic systems with metallic components in the presence of dissipation," *Phys. Rev. B*, vol. 55, no. 12, p. 18, 1997.

[11] V. Kuzmiak and A. A. Maradudin, "Distribution of electromagnetic field and group velocities in two-dimensional periodic systems with dissipative metallic components," *Phys. Rev. B*, vol. 58, no. 11, p. 22, 1998.

[12] V. Kuzmiak, A. A. Maradudin, and F. Pincemin, "Photonic band structures of two-dimensional systems containing metallic components," *Phys. Rev. B*, vol. 50, no. 23, p. 10, 1994.

[13] C. Luo, S. G. Johnson, J. D. Joannopoulos, and J. B. Pendry, "Negative refraction without negative index in metallic photonic crystals," *Opt. Express*, vol. 11, no. 7, p. 9, 2003.

[14] E. Moreno, D. Erni, and C. Hafner, "Band structure computations of metallic photonic crystals with the multiple multipole method," *Phys. Rev. B*, vol. 65, p. 10, 2002.

[15] S. O'Brien and J. B. Pendry, "Photonic band-gap effects and magnetic activity in dielectric composites," *J. Physics. Condens. Matter*, vol. 14, no. 15, p. 11, 2002.

[16] R. Ortuno, C. Garcia-Meca, F. J. Rodriguez-Fortuno, J. Marti, and A. Martinez, "Role of surface plasmon polaritons on optical transmission through double layer metallic hole arrays," *Phys. Rev. B*, vol. 79, p. 10, 2009.

[17] J. B. Pendry and A. MacKinnon, "Calculation of Photon Dispersion Relations," *Phys. Rev. Lett.*,

vol. 69, no. 19, p. 4, 1992.

[18] A. Pimenov and A. Loidl, “Conductivity and Permittivity of Two-Dimensional Metallic Photonic Crystals,” *Phys. Rev. Lett.*, vol. 96, p. 4, 2006.

[19] K. Sakoda, N. Kawai, and T. Ito, “Photonic bands of metallic systems. I. Principle of calculation and accuracy,” *Phys. Rev. B*, vol. 64, p. 8, 2001.

[20] M. A. Ustyantsev, L. F. Marsal, J. Ferre′-Borrull, and J. Pallare`s, “Effect of the dielectric background on dispersion characteristics of metallo-dielectric photonic crystals,” *Opt. Commnuications*, vol. 260, p. 5, 2006.

[21] X. Xu, Y. Xi, D. Han, X. Liu, J. Zi, and Z. Zhu, “Effective plasma frequency in one-dimensional metallic-dieletric photonic crystals,” *Appl. Phys. Lett.*, vol. 86, p. 3, 2005.

[22] A. Z. and H. Baudrand, “Electromagnetic Scattering by Metallic Holes and Its Applications in Microwave Circuit Design,” *IEEE Trans. Microw. Theory Tech.*, vol. 50, 2002.

[23] Y. Zhao and D. R. Grischkowsky, “2-D Terahertz Metallic Photonic Crystals in Parallel-Plate Waveguides,” *IEEE Trans. Microw. Theory Tech.*, vol. 55, no. 4, p. 8, 2007.

[24] K. L. Low, M. Z. M. Jafri, and S. A. Khan, “Effective Plasma Frequency For Two- Dimensional Metallic Photonic Crystals,” *Prog. Electromagn. Res. M*, vol. 12, p. 13, 2010.

[25] K. L. Low, M. Z. M. Jafri, and S. A. Khan, “Band Gap Calculation on 2D Square Lattice Metallic Slab Photonic Crystals with Air Rods,” *3rd International Meeting on Frontiers of Physics 2009*. Kuala Lumpur, Malaysia, 2009.

[26] K. L. Low, M. Z. M. Jafri, and S. A. Khan, “Band Gap Study Using Plane Wave Expansion Method for Metallic Slab with Air Rods in E Polarizing Mode,” *Chinese J. Phys.*, vol. 47, no. 6, p. 10, 2009.

[27] K. L. Low, M. Z. M. Jafri, and S. A. Khan, “Dielectric slab photonic crystals containing metallic components for E polarization mode,” *Appl. Phys. Rev.*, vol. 2, 2010.

[28] J. Ferre-Borrull, E. Xifre-Perez, M. Lluis F. Marsal, and J. Pallares, “Real metals in metallo-dielectric photonic crystals in the visible,” in *2007 Spanish Conference on Electron Devices*, 2007, p. 4.

[29] B. Reinhard, G. Torosyan, and R. Beigang, “Band structure of terahertz metallic photonic crystals with high metal filling factor,” *Appl. Phys. Lett.*, vol. 92, 2008.

[30] K. Sakoda, *Optical properties of photonic crystals*. 2005.

On-chip all-optical amplifier on 2D photonic crystal nanocavities

Teanchai Chantakit[1,*], Surasak Chiangga[1], and Preecha P. Yupapin[2,3]

[1]Department of Physics, Faculty of Science, Kasetsart University, Thailand
[2]Faculty of Electrical & Electronics Engineering, Ton Duc Thang University, District 7, Ho Chi Minh City, Vietnam
[3]Department for Management of Science and Technology Development, Ton Duc Thang University, District 7, Ho Chi Minh City, Vietnam
*corresponding author, E-mail: tchantakit@gmail.com

Abstract

The energy efficiency of optical interconnects can address the full performance of chip-scale photonic platforms. However, conventional optical compression designs had fundamentally limited such a device incompatible with the ultra-compact scale integration. Here, we designed a passive all-optical amplifier in a free-space waveguide by using the cavity-field interaction from a 2D photonic crystal (PhC) nanocavity pair. By introducing the controllable nanocavity parameters for a particular resonance frequency, an optical amplification was achieved by the strong oscillation within interfering field radiations from nanocavities. The obtained results had accomplished an occurrence of an amplified light intensity by 2.65% of 4.7 dB optical gain at the wavelength of 1550 nm. This embedded design may form the basis of self-pumping structures in an ultra-compact scale for the future photonic chip integration.

1. Introduction

The energy and cost efficiency of chip-scale light sources have drawn a strong attention to the optical network link devices on their sufficient power consumption which can be enhanced by the optical amplifier [1]. The functionalities of such a device can provide compensating attenuation, and coupling losses of optical interconnect for the multi-photonic chips integration [2]. Conventional approach is performed by the semiconductor optical amplifiers (SOAs) in order to conducts potential applications such as the spectrum narrowing for a single-frequency lasing [3], room-temperature slow light [4–5], high-bandwidth intra-band effects on pulse generation devices [6], controlling ultrafast quantum coherent Rabi oscillations [7] and self-induced transparency [8], and high energy femtosecond laser pulses generation [9]. However, these regimes require an electric current pumping for the optical amplification which faces the challenge to place onto all-optical chip-scale platforms.

The light-matter interaction on 2D photonic crystal (PhC) nanocavities have been attracted to on-chip designs due to their capabilities on the high-quality factor (Q) cavity mode volume, strongly field enhancement with free-space mode excitation in the nanostructure [10–11]. The photonic integration designs based on their structure can demonstrate the novelty theoretical ideas of nanolasers and lab-on-chip devices [12]. In particular, the 2D high-Q PhC nanocavity has been used to manipulate the strong waveguide-cavity coupling, in which produces the emitting photon from a nanocavity [13]. Leaked modes of a nanocavity coupled with the line defect on 2D PhC had been performed in both theoretical and experimental regimes [14] and gained the widely potentials for PhC-based devices and applications. However, one capability of their designs is to enabling the optical linewidth compression [15].

In this research, we have proposed the all-optical amplifier generation in a free space region of 2D photonic crystal waveguide (PCW) which can be embedded in on-chip photonic platforms. The system comprises of the two identical nanocavities formed by rod-type 2D PhC with side-shell layers of a lower dielectric rods material, locating across a three splitter 2D PCWs. Consequently, the radiated fields from high confined light in cavities would combine with the incoming light pulses. This phenomenon leads to the narrower spectral pulses with an amplification detection at the between of these two cavities. The simulation results had confirmed an occurrence of strong field intensity in free space for low-power light injection which depends on dielectric rods parameters of nanocavities.

2. Structure Design

The represented passive optical amplifier design is based on a rod-type 2D PhC nanocavity pair and embedded within a PCW. Because of their compact scale and self-amplification processes in free space, it can take advantage of needed no physical medium which serves as neutral amplifier between different compartments on photonics platforms for links with any on-chip optical interconnects. However, without an external, injection this structure had faced a challenge to changes the physical properties of an incident light in free space. The only existing nanocavities on PCWs had become an important character due to their abilities of the optically coupled with high-Q mode volume and the strong radiation fields from a cavity [16]. Thus, the light-cavity interaction had been considered for only a strong oscillation of localised frequency which matches to incident pulses, result to cavity linewidth narrowing generation [17].

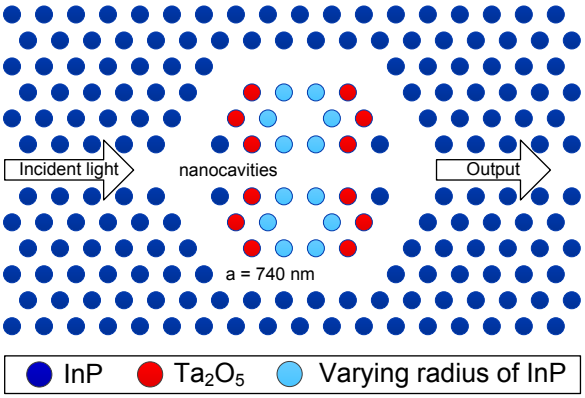

Figure 1: Schematic of an optical amplifier design (top view) which embedded in a three splitter 2D PCW onto a silicon substrate. The central free space area, positioning between nanocavities, represented as an amplification region.

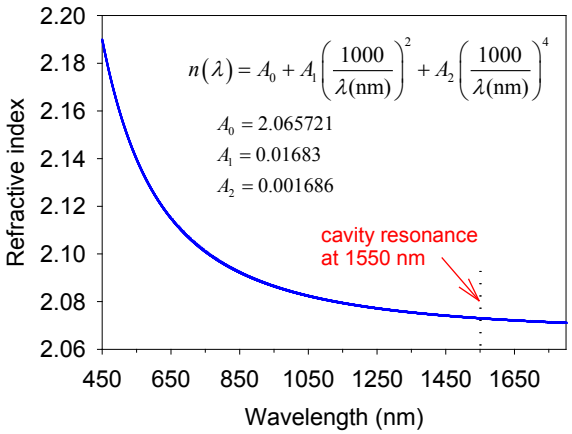

Figure 2: The wavelength dependent refractive index of Ta_2O_5 in a range from 450 nm to 1800 nm.

The design had been performed on a rod-type 2D PhC structure of indium phosphide (InP) on a silicon substrate as depicted in Fig.1. Its 220 nm of radius with the radius-lattice constant ratio (r/a) at 0.2973 was defined for light at a wavelength of 1550 nm for the perfect propagation within PCWs. Symmetrical nanocavities contain the larger InP rods which had been varied their radius from 241 nm to 246 nm, enabling them to realise the interaction between cavities mode and optical amplification. In order to enhance a strong confinement within nanocavities, the 230 nm of tantalum pentoxide (Ta_2O_5) rods have been served as a shell layer of nanocavities, improving the coupling and storage intensity. By performing a highly confined light in 2D PhC, the optical confinement inside nanocavities can be provided by the side-coupling of light in upper and lower waveguides of Y-branch. These branches would allow some fraction of light is conventionally coupling into both nanocavities, in which it generates the optical resonance of localised frequency. The narrow spectral pulse with amplification detection would be observed at a central position between two cavities due to the interference field formed by the cavity emission and directional light from an input port.

In addition to light amplification, the cavity-light field projection for this design has been considered based on three potential features of light-matter interaction. The embedded nanocavities structure can be adapted to the new approach of dynamics coherent controllable light with light for all-optical platforms which allow manipulation of intensity, propagation direction, and polarisation of light [18]. The cavity radiation propagates toward to the central position between two cavities due to an opposite direction of wave vectors as two identical high-Q nanocavities are precisely aligned to each other and support the symmetric leaked mode excitation [19]. Also, the symmetrically interfere with two cavity emission provides the stationary light field due to 2D PhC features [20], and light carries a nonzero transverse mode in the central area has corresponded to the two-wave interference framework [21]. Finally, the optical momentum exchange of the interfering pulse formed by an incident light and a stationary light field for the light-to-light interaction can be achieved due to unstructured paraxial beams intensify the momentum of light along an incidence propagation direction as they carry both angular and spin momentum [22]. Also, the length of middle PCW branch and interfering region formed by nanocavities radiation had unexpectedly been created in a proper position for pulses compression by phase matching of localised frequency between incidence light and field interference, offers the optical amplification phenomena [23] at the central position of PCW, considering energy and momentum conservation.

Importantly, the refractive index and radius of dielectric rods for shell layer have become a key factor in order to achieve the strong confinement in a free space nanocavity and emission decay fraction. The significant lower refractive index of cladding or shell layer than cavity rods would support the localised optical trapping enhancement and field emission into a central branch of PCW. However, the results of highly different in refractive index of dielectric rods between shell layer and cavity showed that the PCW-cavity coupling efficiency is decreased. The highly low refractive index value of dielectric rods in shell layer, compared to the cavity, causes the most fraction of an incoming light only passes through cavity shell without coupling into the cavity. Also, dielectric rods in shell layer act as the light blockage if the refractive index is equivalent or higher than its dielectric rods of nanocavities. As the results, Ta_2O_5 has been selected as the defect rods for shell layer based on high dielectric constant and low absorption material. However, self-amplification phenomenon in this work requires a broadband spectral linewidth of an incidence light, in which initiates the pulse compression. The refractive index wavelength dependence of Ta_2O_5 as illustrated in Fig.2 can be calculated in a function of Cauchy formula [24] as,

$$n(\lambda) = 2.065721 + \frac{0.01683\times10^{6}}{\lambda^{2}(\text{nm}^{2})} + \frac{0.001686\times10^{12}}{\lambda^{4}(\text{nm}^{4})} \qquad (1)$$

where λ is a broadband wavelength in the range from 450 nm to 1800 nm. Although Ta_2O_5 rods ($n \sim 2.0728$ at the wavelength of 1550 nm) shell can improve the capability of light confinement within PhC nanocavities, reaching only fundamental cavity mode resonance has been determined by the cavity size geometry, dielectric rods radius (r_{cavity}), and their material of InP ($n = 3.1$). The correspondence between light-matter interaction of single cavity mode and field radiation of homogeneous structure will experience with the effective cavity mode volume which is defined by [25],

$$V_{eff} = \frac{\int \varepsilon(\vec{r})\left|\vec{E}(\vec{r})\right|^2 d^3\vec{r}}{\varepsilon(\vec{r}_{\max})\max\left[\left|\vec{E}(\vec{r}_{\max})\right|^2\right]} \quad (2)$$

where λ is the wavelength of light in a free-space. r_{max} is defined as the position of the maximum electric field intensity E^2, the related dielectric constant ε and refractive index n. In fact, a nanocavity is based on dielectric rods surrounded by air which leads to the strong resonant at the centre of slot cavity. Therefore, the terms ε in eq.2 can be reduced to the dielectric constant of air, leaving an approximation value of maximum electric field position for modes resonance in a cavity.

3. Simulation Results

The optical amplification in a free-space waveguide based on a light-field interaction of leaked field interference from a nanocavity pair has been observed in the *x*-*y* plane. The finite difference time domain (FDTD) method provided by Freeware 32-bit OptiFDTD was used for light behaviour investigation in the proposed structure which their results were compared with Lumerical simulations software. Each of PhC cavity with identical rods dimension was defined as the emitter which light amplification efficiency satisfies the optical gain. According to the light-matter interaction in the previous context, the amplification wavelength in a central region between PhC cavities was controlled by its geometry breadth which results to the different manifestation of optical gain as illustrated in Fig. 3. Based on wavelength of 1550 nm operation, the 242 nm r_{cavity} of both nanocavities resulted to the maximum optical gain of 6.15 dB at 1548 nm (see green line in Fig. 3) with the Full-Width at Half-Maximum (FWHM) or bandwidth of 42 GHz. However, we also interested the downward amplification capability with r_{cavity} from 243 nm to 245 nm yielded two equivalent results of the negatively skewed curve of 4.63 dB at 1549.9 nm (red line) with bandwidth of 264 GHz, and the 4.70 dB optical gain at 1550 nm (blue line) with 249 GHz FWHM.

Reasonably, we had addressed that this proposed all-optical device has been designed as the neutral compartment for on-chip devices junction. Based on a linear system, the compared intensity of input and output was considered by single-wavelength of 1550 nm, also wavelength shifts were neglected from this investigation. Consequently, even through nanocavities with 242 nm radius of r_{cavity} gave rise to the light amplitude 4.12 times higher than incident power, it provided the blue shift of optical gain and resulted to dramatically drop the output intensity. As the results, the nanocavities formed by 243 nm rod radius had been selected in order to achieve the optical amplifier within a stable system. On the other hand, a blue line in Fig. 3 showed the gain of cavities system matched to incident pulses in both localised frequency and linewidth, offers the frequency and phase matching between the incoming power and light-field interference which gained the ability to amplified optical signals in a free-space 2D PCW.

Moreover, there are no mathematical approaches of electromagnetic field propagation description in the rod-type 2D PhC structure. However, the notion of light amplification occurred by the light-field interference phenomenon had been manipulated by the strong confinement of 2D PhC nanocavities. To evaluate the low power consumption capability of the device within a compact scale, the ratios of

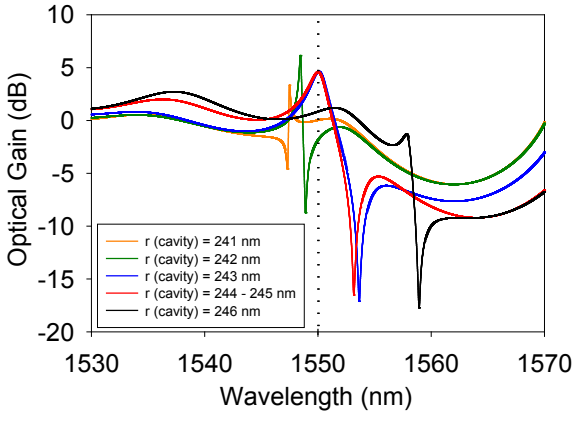

Figure 3: Optical gain of each dielectric rod radius of nanocavities, illustrating light amplification capabilities based on the field interference provided by symmetrically aligned two PhC cavities the difference radial dielectric rods.

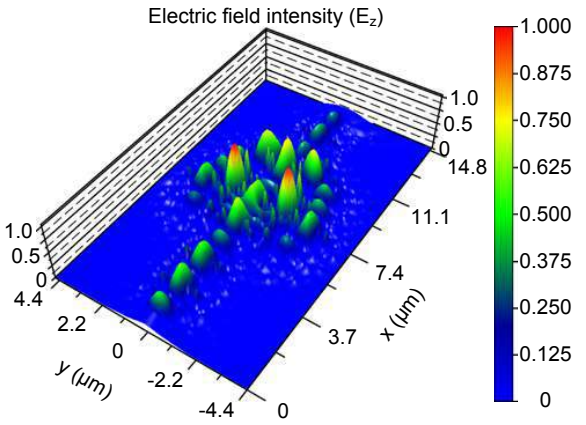

Figure 4: TE simulation at a wavelength of 1550 nm for light propagation in the proposed structure, displaying the strongly confined light in both PhC cavities. Outward optical intensity is increased after passes through the central area between nanocavities.

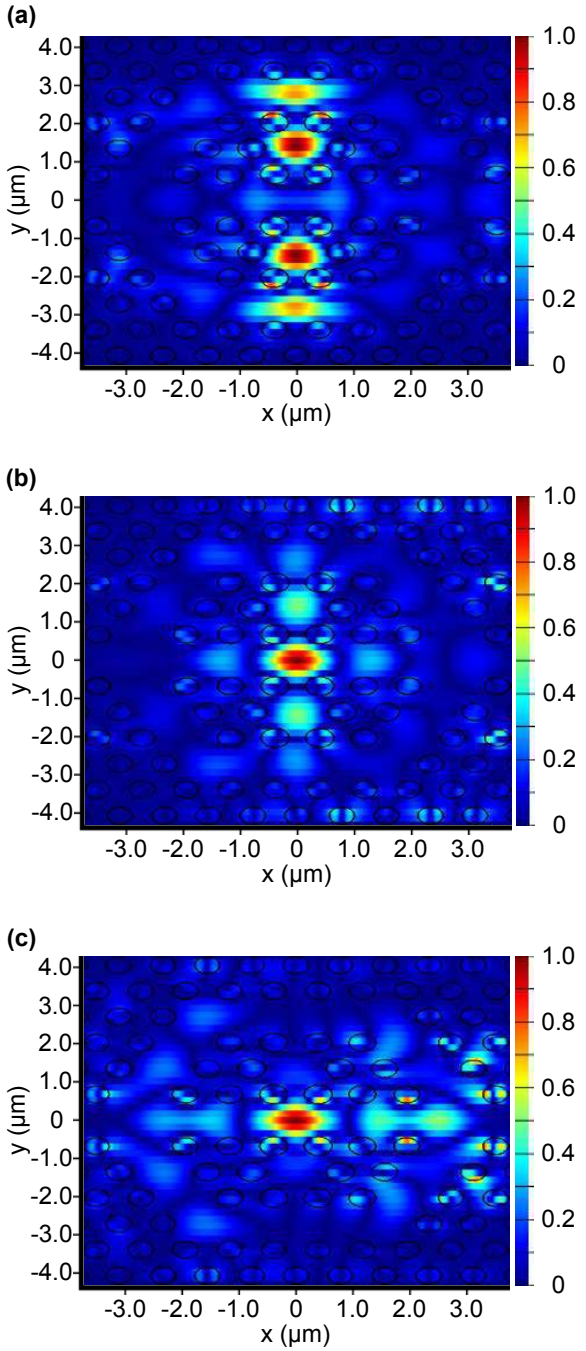

Figure 5: Mode propagation of the total electric field at a wavelength of 1550 nm. (a) Conventional light coupling from upper and lower free-space PCW, offers the strong confinement within the 2D PhC nanocavities. (b) The spatially structured light-field is generated by the cavities leaked mode interference. (c) The incoming light pulses are trapped with the local field, in which results to increase the amplitude of output intensity.

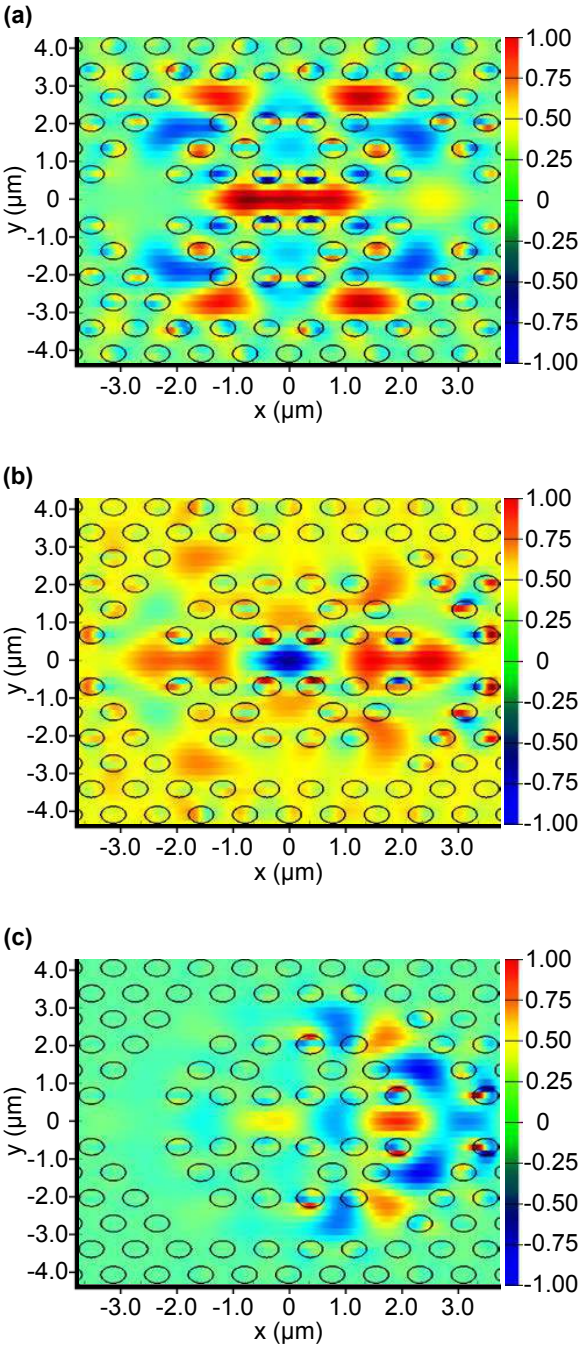

Figure 6: Modes analysis provided by Lumerical MODE solutions. (a) TE wave pattern of the nanocavities emission. (b) Light-field interaction between the leaked field cavity and incoming light pulses. It shows the total field direct toward to the output port. (c) Directional pulse along the propagation direction (*x*-axis) are combined, offers the enhanced optical power level due to the phase matching.

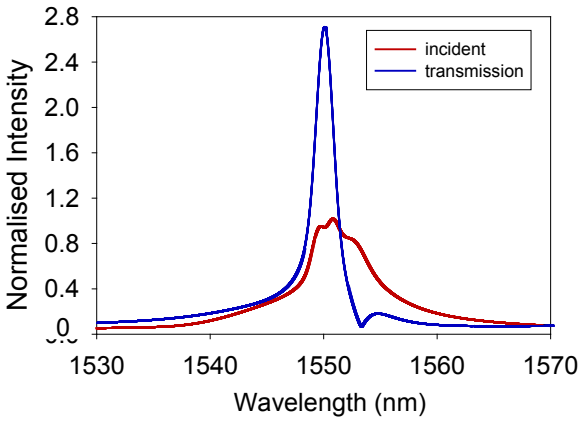

Figure 7: Simulation result of a normalised waveform with 243 nm cavities rod radii. The fluctuated curve at the peak of red line is affected by the interfering light between input and backscattered pulses from a three splitter region.

quality (Q) factor to mode volume (V) was determined as follows. While the coupling in a fundamental mode as dispatched in Fig. 5a, the confined light with Q~9,600 of each cavity offered the Q/V ratio exceeds 10^5, calculated by Lumerical 3D FDTD solutions. Accordingly, the optical effect formed by cavity leaked-field in Fig. 5b contributed Q~3,600, providing the downward Q/V ratio equivalent to 10^5, precisely. Consequently, the significantly dropped of Q factor by 6,000 of the spatially interacting light-field area allowed the incoming light was trapped and matched with the local field frequency. Based on energy and momentum conservation, the result of combined light-field emission increased in its intensity as displayed in Fig. 5c due to the vanished wavelength out of optical gain support its central wavelength energy increased

According to the simulation results, the transmission beam propagation direction direct toward to the output port of amplification region, see Fig. 6b. With the separated upper, lower, and light-field emission beams propagated independently, travelling waves had combined at the end of splitter PCW which results to the increased power level of output pulses due to phase matching as depicted in Fig. 6c. Eventually, the all-optical amplifier device in a free-space was achieved as a result of output intensity increased by 2.65% as illustrated in Fig. 7 wherein the operational light maintain a wavelength within the linear system.

4. Summary

The passive optical amplifier in a free-space waveguide based on 2D PhC nanocavity pair has theoretically been designed and analysed. In doing so, the system operation is performed by launching the beam propagation within 2D PCW to account for the cavity coupling. We focused on the leaked field from a strong confinement of both nanocavities, in which it forms to the spatial structure of dense light-field interference. The cavities with 243 nm rod radius show that optical gain achieves the amplification bandwidth relative to the incident light at 1550 nm. With the field is generated between cavities, the incoming pulses that pass through this region are trapped by the localised field-linewidth due to light-field interaction. This phenomenon diminishes the optical power of wavelengths beyond a local field in order to intensify the incident power, based on energy and momentum conservation. As the results, the calculated transmission power for the linear optical system was increased by approximately 2.65% of the input power. This proposed design may be taken advantage of the neutral system of optical self-amplifier, in which it can be applied for all-optical photonic chips integration platforms.

Acknowledgements

This work was supported fund by the Department of Physics, Faculty of Science, Kasetsart University. We thank the Photonics Research Group for providing Lumerical FDTD and MODE solutions software.

References

[1] S. Cheung, Y. Kawakita, K. Shang, J. Ben Yoo, Highly efficient chip-scale III-V/silicon hybrid optical amplifiers, *Opt. Express* 20: 22431–22443, 2015.

[2] Y. Chen, J. Mørk, Theory of carrier depletion and light amplification in active slow light photonic crystal waveguide, *Opt. Express* 21: 29392–29400, 2013.

[3] L. Wang, Y. Cao, M. Wan, X. Wang, X. Feng, B.-O. Guan, J. Yao, Tunable single-frequency fiber laser based on the spectral narrowing effect in a nonlinear semiconductor optical amplifier, *Opt. Express* 24: 29705–29713, 2016.

[4] N. Laurand, S. Calvez, M.D. Dawson, Slow-light in a vertical-cavity semiconductor optical amplifier, *Opt. Express* 14: 6858–6863, 2006.

[5] M. van der Poel, J. Mørk, J.M. Hvam, Controllable delay of ultrashort pulses in a quantum dot optical amplifier, *Opt. Express* 13: 8032–8037, 2005.

[6] F.G. Sedgwick, B. Pesala, J.-Y. Lin, W.S. Ko, X. Zhao, C.J. Chang-Hasnain, THz-bandwidth tunable slow light in semiconductor optical amplifiers, *Opt. Express* 15: 747–753, 2006.

[7] O. Karni, A.K. Mishra, G. Eisenstein, V. Ivanov, J.P. Reithmaier, Coherent control in room-temperature quantum dot semiconductor optical amplifiers using shaped pulses, *Optica* 3: 570–576, 2016.

[8] O. Karni, A. Capua, G. Eisenstein, V. Sichkovskyi, V. Ivanov, J.P. Reithmaier, Rabi oscillations and self-induced transparency in InAs/InP quantum dot semiconductor optical amplifier operating at room temperature, *Opt. Express* 21: 26786–26796, 2013.

[9] P. Wnuk, Y. Stepanenko, C. Radzewicz, High gain broadband amplification of ultraviolet pulses in optical parametric chirped pulse amplifier, *Opt. Express* 18: 7911–7916, 2010.

[10] J. Kim, A. Shinya, K. Nozaki, H. Taniyama, C.-H. Chen, T. Sato, S. Matsuo, M. Notomi, Narrow linewidth

operation of buried-heterostructure photonic crystal nanolaser, *Opt. Express* 20: 11643–11651, 2012.

[11] X. Zhang, H. Subbaraman, A. Hosseini, R.T. Chen, Highly efficient mode converter for coupling light into wide slot photonic crystal waveguide, *Opt. Express* 22: 20678–20690, 2014.

[12] S. Mahmoodian, J.E. Sipe, C.G. Poulton, K.B. Dossou, L.C. Botten, R.C. McPhedran, C. Martijn de Sterke, First-principles method for high-*Q* photonic crystal cavity mode calculations, *Opt. Express* 20: 22763–22769, 2012.

[13] J. Upham, Y. Tanaka, Y. Kawamoto, Y. Sato, T. Nakamura, B.S. Song, T. Asano, S. Noda, Time-resolved catch and release of an optical pulse from a dynamic photonic crystal nanocavity, *Opt. Express* 19: 23377–23385, 2011.

[14] C. Seassal, Y. Désières, X. Letartre, C. Grillet, P. Rojo-Romeo, P. Viktorovitch, T. Benyattou, Optical coupling between a two-dimensional photonic crystal-based microcavity and single-line defect waveguide on InP membranes, *IEEE J. Quant. Electron.* 19: 811–815, 2002.

[15] Y. Gong, M. Makarova, S. Yerci, R. Li, M.J. Stevens, B. Baek, S. Woo Nam, R.H. Hadfield, S.N. Dorenbos, V. Zwiller, J. Vučković, L.D. Negro, Linewidth narrowing and Purcell enhancement in photonic crystal cavities on an Er-doped silicon nitride platform, *Opt. Express* 18: 2601–2612, 2010.

[16] H. Taniyama, M. Notomi, E. Kuramochi, T. Yamamoto, Y. Yoshikawa, Y. Torii, T. Kuga, Strong radiation force induced in two-dimensional photonic crystal slab cavities, *Phys. Rev. B* 78: 165129, 2008.

[17] M. Sabooni, Q. Li, L. Rippe, R.K. Mohan, S. Kröll, Spectral engineering of slow light, cavity line narrowing, and pulse compression, *Phys. Rev. Lett.* 111: 183602, 2013.

[18] M. Papaioannou, E. Plum, J. Valente, E. TF Rogers, N.I. Zheludev, Two-dimensional control of light with light on metasurfaces, *Light Sci. Appl.* 5: e16070, 2016.

[19] E.N. Bulgakov, K.N. Pichugin, A.F. Sadreev, All-optical light storage in bound states in the continuum and release by demand, *Opt. Express* 23: 22520–22531, 2015.

[20] T.F. Krauss, Slow light in photonic crystal waveguides, *J. Phys. D: Appl. Phys.* 40**:** 2666–2670, 2007.

[21] A.Y. Bekshaev, K.Y. Bliokh, F. Nori, Transverse Spin and Momentum in Two-Wave Interference, *Phys. Rev. X* 5: 011039, 2015.

[22] V. Kajorndejnukul, W. Ding, S. Sukhov, C.-W. Qiu, A. Dogariu, Linear momentum increase and negative optical forces at dielectric interface, *Nat. Photon.* 7: 787–790, 2013.

[23] M. Allgaier, V. Ansari, L. Sansoni, C. Eigner, V. Quiring, R. Ricken, G. Harder, B. Brecht, C. Silberhorn, Highly efficient frequency conversion with bandwidth compression of quantum light, *Nat. Commun.* 8: 14288, 2017.

[24] T.V. Amotchkina, M.K. Trubetskov, V. Pervak, A.V. Tikhonravov, Design, production, and reverse engineering of two-octave antireflection coatings, *Appl. Opt.* 50: 6468–6475, 2011.

[25] P. Seidler, K. Lister, U. Drechsler, J. Hofrichter, T. Stöferle, Slotted photonic crystal nanobeam cavity with an ultrahigh quality factor-to-mode volume ratio, *Opt. Express* 21: 32468–32483, 2013.

Laser and cavities

Photonic Crystal Microchip Laser

D. Gailevicius[1], V. Koliadenko[2], V. Taranenko[2], V. Purlys[1], M. Peckus[1] and K. Staliunas[3,4*]

[1] Laser Research Center, Vilnius University, Vilnius, Lithuania

[2] Institute of Applied Optics, NAS of Ukraine, Kyiv, Ukraine

[3] Institucio Catalana de Reserca i Estudis Avancats (ICREA), Barcelona, Spain

[4] Department of Physics, Universitat Politecnica Catalunya (UPC), Barcelona, Spain

[*]corresponding author: kestutis.staliunas@icrea.cat

Abstract- We show, theoretically and experimentally, that photonic crystals with spatial filtering functionality, inside of a microchip laser cavity, can substantially improve spatial characteristics of the emission of microchip laser. The angular divergence of the emitted beam is reduced, and the radiation brightness is increased.

Microchip lasers (and generally most micro-size lasers, like diode lasers or VCELS) being extremely compact and efficient sources of coherent radiation, suffer from one drawback: the low spatial quality of the emitted beam. Only at low power emission regimes (close from the generation threshold) the microchip lasers can emit the beams and pulses of a reasonable spatial quality. Every attempt to increase the emission power, by increasing the pumping power, or by increasing the pumping area, leads to the deterioration of the spatial quality of the beams, equivalently to large angular divergence, and results to the lower brightness of the emitted radiation.

We proposed that the use of intracavity photonic crystals with spatial filtering functionality, can substantially improve the spatial quality of the emitted beam. Photonic crystals were recently shown to provide the spatial filtering [1]. Both the 1D spatial filtering, as well as axisymmetric 2D spatial filtering, see the left part of Fig.1, were experimentally demonstrated. Positioning of such photonic crystal spatial filters inside the cavity of microchip lasers enables to decrease the divergence of the radiation at high power regimes, and to increase the brightness of emitted radiation, see the right side of Fig.1. Presently we demonstrated an enhancement of brightness of emitted radiation approximately 3 times due to the intracavity photonic crystal spatial filtering, or, equivalently, we achieved a single-transverse-mode emission of approximately 3 times higher emission powers. The reported results [2] are presently limited by fabrication restrictions and imperfections of photonic crystal spatial filters, but potentially can be improved with advance of fabrication technologies.

The experimental measurements are justified by the numerical simulations of mean-field models of microchip lasers.

In summary, we demonstrate a new kind of micro-lasers, the Photonic Crystal Microchip Laser, with substantially improved radiation characteristics due to the intracavity photonic crystal spatial filtering.

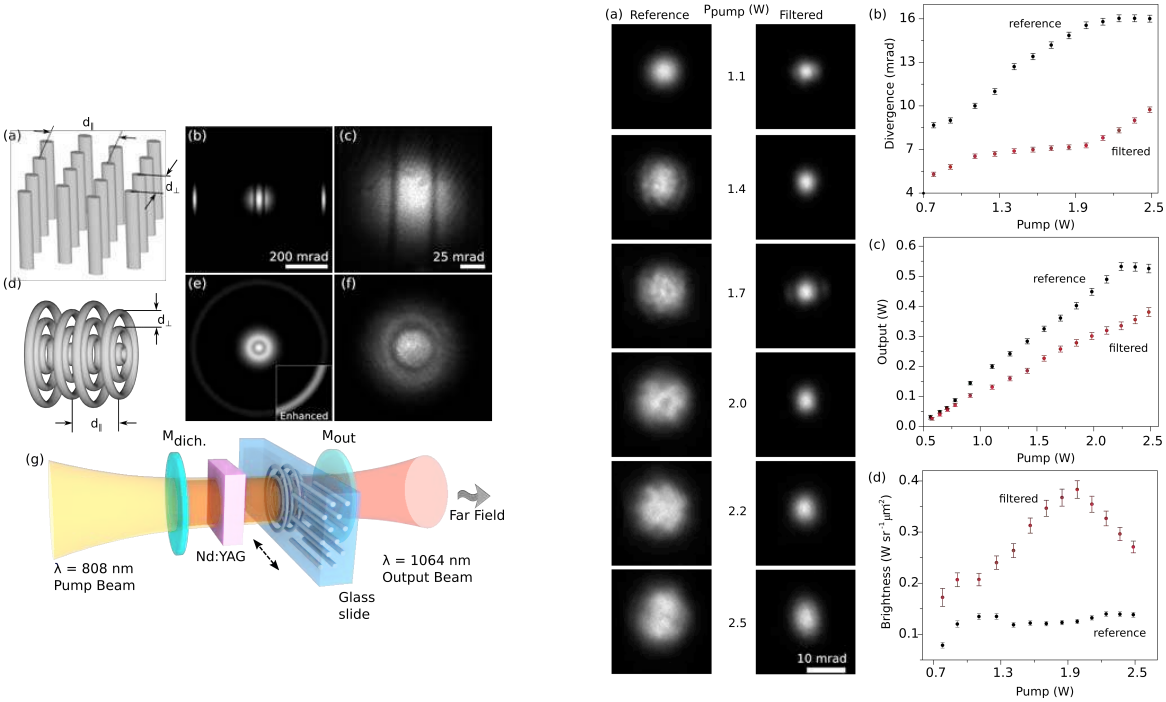

Fig.1 Left: single pass transmission characteristics of photonic prystal spatial filters, in 1D (a,b,c)- and of 2D axisymmetric (d,e,f) configuration. The spatial filters are positioned inside the resonator of microchip lasers (g). Right: whereas the beam divergence increases at increasing pumping power (first column from top to bottom, the far field distributions), the beam remains well collimated in the presence of intracavity Photonic Crystal (second column from top to bottom). Quantitative characteristics: (a) the beam divergence remains substantially lower (b), the generated power increases nearly so much as at the absence of the filtering (b), the brightness of emitted radiation substantially increases (c).

Acknowledgements, The work is financially supported by Spanish Ministerio de Educación y Ciencia, European FEDER through project FIS2015-65998-C2-01 and by NATO SPS-985048 grant.

REFERENCES

1. Maigyte, L. and Staliunas, K. "Spatial filtering with photonic crystals", *Appl. Phys. Rev.* **2,** 011102, 2015.
2. Gailevicius, D., Koliadenko, V., Purlys, V., Taranenko, V. and K. Staliunas, "Photonic Crystal Microchip Laser", Scientific Reports, **6**, 3417 (2016)

Acoustic metamaterials

Design of a double-negative flexural elastic metamaterial

K. Inagaki[1], M. Tomoda[1*], V. E. Gusev[2], O. Matsuda[1], and O. B. Wright[1]
[1],Division of Applied Physics, Faculty of Engineering, Hokkaido University, Sapporo, Japan
[2] Laboratoire d'Acoustique de l'Université du Maine, Le Mans, France
[*]corresponding author: mtomoda@eng.hokudai.ac.jp

Abstract-We present an elastic metamaterial for flexural waves with both negative density and elastic modulus. Nanoscale L-shaped holes are periodically drilled through a Au/Al/Au sandwich-structure plate of micrometer thickness. The structure is shown to have a double-negative frequency band at ~500 GHz for flexural waves by means of finite-element simulations. We calculate the dispersion relation, effective density and effective modulus of the structure, and demonstrating negative refraction of flexural waves in the double-negative band in a prism-shaped geometry.

Double-negative acoustic metamaterials that have negative density and modulus simultaneously over a particular frequency ranges have been recently proposed. In particular, two-dimensional elastic metamaterials for compressional plate waves (symmetrical 0th order Lamb waves) were recently demonstrated [1-2]. In addition, in the case of flexural plate waves (antisymmetrical 0th order Lamb waves) Gusev and Wright theoretically calculated that negative density can be achieved by introducing elements that involve normal-force interactions whereas negative modulus can be achieved by introducing resonant elements that involve lateral forces and rotational inertia [3]. Following on from this work, we designed a two-dimensional GHz flexural elastic metamaterial which can be fabricated by micro/nano machining techniques, and simulated its behavior.

We used the commercial finite-element software COMSOL Multiphysics to calculate the dispersion relation, effective density and effective modulus as the function of frequency and wavenumber. Our design is based on a composite slab in the form of a sandwich (see FIG. 1). In the design, softer parts (Al) are necessary to allow a resonant rotational vibration of harder parts (Au), as prescribed by the general approach of Ref. [3]. We introduce a chiral structure in the outside parts made of Au necessary to create a negative modulus. Making the

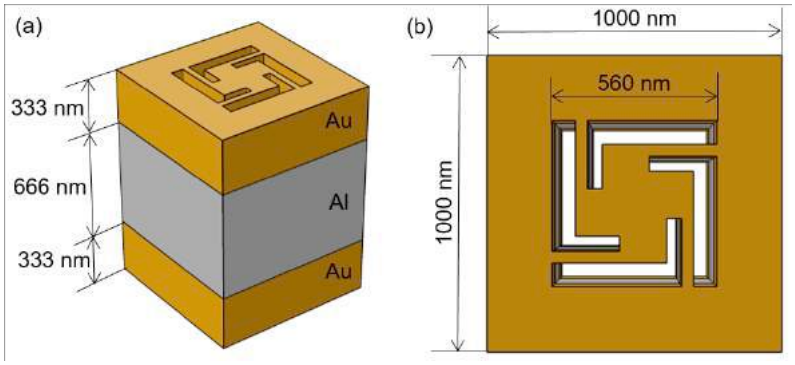

FIG. 1 Unit cell of the flexural elastic metamaterial: views (a) from diagonally above, and (b) from normal to the surface. Four L-shaped holes are drilled through this Au/Al/Au sandwich-plate structure.

inside Al portion of the slab light and the outside (Au) heavy is effective for this purpose, allowing a twisting rotational vibration of the outside portions. After many trials, we arrived the particular design shown in FIG. 1. The elastic metamaterial is designed in the form of a square lattice of unit cells, and is made from drilling a series of L-shaped holes through the Au/Al/Au three-layer plate. It has reflection symmetry in the depth direction and four-fold symmetry for rotation about an axis through the center of each unit-cell. This structure shows double-negative behavior in the frequency range from 510 MHz to 530 MHz, yielding a negative slope of the flexural wave branch in the ΓK direction in **k**-space.

We created a structure of this material in the form of a right-angle isosceles triangular prism to demonstrate negative refraction by simulation (FIG. 2). In the double-negative frequency range, negative refraction is observed. In conclusion, we have demonstrated the first concrete design of a flexural double-negative metamaterial. In future we plan to make samples of this GHz double-negative flexural metamaterial and to image the wave propagation at micron-spatial and picosecond-temporal resolutions by use of a real-time surface-wave imaging method based on an optical ultrafast pump-probe technique [4].

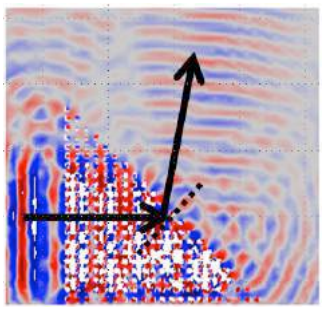

FIG. 2 Demonstration of negative refraction at the double-negative frequency 525 MHz. Flexural waves are incident from the left-hand side of the triangular prism. The colour scale represents the out-of-plane displacement. The arrows show the propagation directions, and dotted line shows normal vector to the interface.

REFERENCES

1. X.N. Liu, G.K. Hu, G.L. Huang, and C.T. Sun, "An elastic metamaterial with simultaneously negative mass density and bulk modulus," *Appl. Phys. Lett.,* Vol. 98, No. 25, 251907, 2011.
2. R. Zhu, X.N. Liu, G.K. Hu, C.T. Sun and G.L. Huang, "Negative refraction of elastic waves at the deep-subwavelength scale in a single-phase metamaterial," *Nature Comm.*, DOI: 10.1038/ncomms6510, 2014.
3. V.E. Gusev and O.B. Wright, "Double-negative flexural acoustic metamaterial," *New J. Phys.*, Vol. 16, 123053, 2014.
4. S. Mezil, P.H. Otsuka, S. Kaneko. O.B. Wright, M. Tomoda and O. Matsuda, "Imaging arbitrary acoustic whispering-gallery modes in the gigahertz range with ultrashort light pulses," *Opt. Lett.,* Vol. 40, No. 10, 2157-2160, 2015

Mimicking metamaterial functionalities in an immersive laboratory with exact boundary conditions

M. Molerón*, D.J. van Manen and J.O.A. Robertsson
Institute of Geophysics, Department of Earth Sciences, ETH Zurich, Switzerland
*corresponding author: miguel.moleron@erdw.ethz.ch

Abstract- This contribution presents an immersive wave propagation laboratory for the study of wave interactions with complex materials. The approach makes use of exact boundary conditions to link a physical experiment to a numerical environment in which a complex material is virtually implemented. This approach makes it possible to mimic exotic wave propagation properties without physically building complex materials.

Usual textbooks conceptions on wave propagation are being challenged by recent advances in metamaterials and parity-time (PT) symmetric media. Metamaterials exploit local resonances in their micro-structure to achieve extreme values of its constitutive parameters, ranging from positive, near-zero to negative. Such properties provide a considerable control on wave propagation, which includes focusing, filtering, negative refraction or cloaking. Complementary, PT-symmetric media, containing balanced loss and gain through the modulation of the imaginary part of the constitutive parameters, offer exciting new possibilities in wave propagation control, including loss-free negative refraction,[1] or unidirectional transparency and cloaking.[2] However, the practical implementation of these exceptional properties is still a major challenge due to, among other factors, inherent losses,[3] narrow bandwidth, or stability issues arising from the presence of active components.[4]

In this contribution, we present an immersive wave experimentation laboratory[5,7] that makes it possible to mimic exotic wave propagating phenomena without the need to physically build a complex material. The proposed approach makes use of exact boundary conditions[5] to link a physical experiment to a numerical environment in which a complex material is virtually implemented. The basic principle of this immersive laboratory is illustrated in Figure 1. The incoming waves from the physical environment are measured on the recording surface S_r and extrapolated to the emitting surface S_e. Then a source distribution on S_e cancels out the incoming waves and simultaneously inject a wave field that takes into account the interaction with the virtual material. This interaction takes place in real time using state of the art computing facilities. The quantities to be injected on the emitting surface are calculated based on a representation theorem between the physical and virtual environments (see References 5-7 for further details).

This approach has been successfully applied to implement broadband holography and cloaking of objects with arbitrary shape.[7] Currently, our research is focused on the experimental realization of PT-symmetric media for elastic and acoustic waves. Additional results from this ongoing research will be presented.

The proposed approach provides a new perspective for investigating wave interactions with complex materials, at the interface between numerical simulations and experimental research.

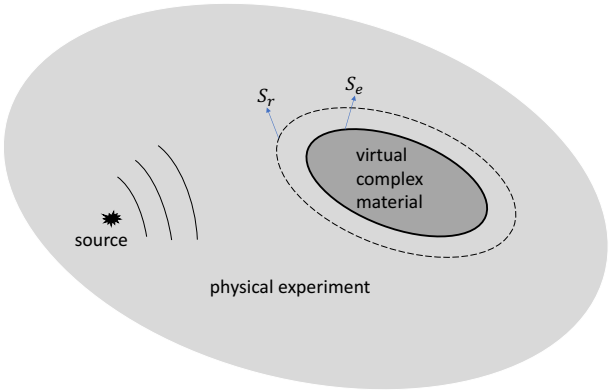

Figure 1. Schematic of the immersive wave experimentation laboratory. Waves emitted in the physical environment are measured on the recording surface S_r and extrapolated to the emitting surface S_e. Then, the emitting surface cancels out the incoming waves and simultaneously inject signals in the physical environment resulting from the interaction with the virtual complex material.

Said Zouhdi 6/8/17 14:12
Mis en forme: Retrait : Première ligne : 1,63 ch

Acknowledgements. Authors gratefully acknowledge support from the European Research Council under the Grant MATRIX-694407.

Said Zouhdi 6/8/17 14:12
Mis en forme: Retrait : Première ligne : 1,63 ch

REFERENCES

1. Fleury, R., Sounas, D. L, and Alù, A., "Negative refraction and planar focusing based on Parity-Time symmetric metasurfaces", Phys. Rev. Lett., Vol. 113, 023903
2. Zhu, X., Ramezani, H., Shi, C., Zhu, J. and Zhang, X., "PT-symmetric acoustics," Phys. Rev. X, Vol. 4, 031042, 2014.
3. Molerón, M. Serra-Garcia, M and Daraio. C, "Viscothermal effects in acoustic metamaterials: from total transmission to total reflection and enhanced absorption", New J. Phys., Vol 18, 033003, 2016.
4. Fleury, R., Sounas, D. L, and Alù, A., "Parity-time symmetry in acoustics: theory, devices, and potential applications", IEEE J. Sel. Top. Quantum Electron., Vol. 22, No. 5, 121-129, 2016.
5. Van Manen, D.J., Robertsson, J.O.A., and Curtis, A., "Modeling of wave propagation in inhomogeneous media", Phys. Rev. Lett., Vol. 94, 164301, 2005.
6. van Manen, D.J., Robertsson, J.O.A. And Curtis, A., "Exact wave field simulations for finite-volume scattering problems", J. Acoust. Soc. Am, Vol. 122, No 4, EL115-EL121, 2007.
7. Vasmel, M., Robertsson, J.O.A., van Manen, D. J., and Curtis, "Immersive experimentation in a wave propagation laboratory", J. Acoust. Soc. Am, Vol. 134, No 6, EL492-EL498, 2013.
8. van Manen, Vasmel, M., D.J., Robertsson, J.O. A. And Curtis, A., "Broadband cloaking and holography using exact boundary conditions", J. Acoust. Soc. Am, Vol. 137, No 6, EL415-EL421, 2014.

Origin of negative permittivity of metamaterials

Sam H. Lee[1*], Eun Bok[1], Haejin Choi[1], Jong Jin Park[1], Chung Kyu Han[1], and Oliver B. Wright[2]

[1] Institute of Physics and Applied Physics, Yonsei University, Seoul 120-749, Korea

[2] Division of Applied Physics, Faculty of Engineering, Hokkaido University, Sapporo 060-8628, Japan

[*]Sam H. Lee: samlee@yonsei.ac.kr

Abstract- Reported methods for retrieval of wave parameters for given metamaterial structures so far have been significantly different from classical theory of dielectrics. Here we demonstrate that the classical treatment, which is familiar with wide range of scientists and engineers, can be extended to the realm of electromagnetic metamaterials for exact accounting of the effective permittivity. Our scheme not only makes the calculations easier but also provides intuitive way of understanding the origins of negative parameters.

Acknowledgements, This work was supported by the Center for Advanced Meta-Materials (CAMM) funded by the Ministry of Science, ICT and Future Planning as a Global Frontier Project (CAMM-2014M3A6B3063712), and by the National Research Foundation of Korea(NRF) grant funded by the Korea government (MSIP) (No. 2015001948).

Acoustic impedance matching of water and air

Haejin Choi [1], Eun Bok[1*], Jong Jin Park[1], Chung Kyu Han[1], Oliver B. Wright[2], and Sam H. Lee[1]

[1] Institute of Physics and Applied Physics, Yonsei University, Seoul 120-749, Korea

[2] Division of Applied Physics, Faculty of Engineering, Hokkaido University, Sapporo 060-8628, Japan

[*] Eun Bok: eunbok81@gmail.com

Abstract- We present the fabrication of an acoustic metasurface of thickness much smaller than the wavelength, which, placed in between water and air, matches impedances of water and air. This impedance matching metasurface is a two-dimensional array of unit cells, each of which consists of a thin cavity covered with five membranes. Experimentally we obtained about 40% power transmission through the interface using the metasurface, which corresponds to over 23.5 dB transmission enhancement.

Acknowledgements, This work was supported by the Center for Advanced Meta-Materials (CAMM) funded by the Ministry of Science, ICT and Future Planning as a Global Frontier Project (CAMM-2014M3A6B3063712), and by the National Research Foundation of Korea(NRF) grant funded by the Korea government (MSIP) (No. 2015001948).

Acoustic Hologram via Decoupled Modulation of Amplitude and Phase in Acoustic Metamaterial

Y. F. Zhu[1], X. F. Zhu[2], X. D. Fan[1], B. Liang[1*], and J. C. Cheng[1]

[1]Key Laboratory of Modern Acoustics, MOE, Institute of Acoustics, Department of Physics, Collaborative Innovation Center of Advanced Microstructures, Nanjing University, Nanjing 210093, P. R. China

[2]School of Physics, Huazhong University of Science and Technology, Wuhan, Hubei 430074, P. R. China

[*]corresponding author: liangbin@nju.edu.cn

Abstract-We have realized acoustic hologram via acoustic metamaterials with simultaneous controls of amplitude and phase. More importantly, the modulation of amplitude and phase is decoupled at specific points in the parameter space, leading to that all possible combinations of amplitude and phase can be accessed. Our method can stably generate hologram with high quality and high fidelity, which are unattainable with previous pure-phase approaches. Our findings will have far-reaching impacts on beam-steering, ultrasonic imaging and particle manipulation, etc.

In this paper, we numerically and experimentally demonstration high-quality acoustic holograms by acoustic metamaterials (AM). Holographic techniques are of fundamental significance to applications such as optical/acoustic tweezers, volumetric displays and medical ultrasound treatment but have high requirement on spatial control of complicated optical/acoustic field. It is known that optical holograms have significantly advanced with the cutting-edge nanotechnology. In ultrasound applications, the acoustic holograms are expected to offer new capabilities in beam-steering and improve medical imaging [1-4].

Figure 1 shows the design of acoustic metamaterials. Figure 1(a) shows the schematic, with the predesigned unit cells. Here we use absorbing boundaries at the back side to introduce controlled energy loss, which capable to modulate both amplitude and phase of reflection at the surface under the illumination of sound on the front side, as indicated by the red arrows in Fig. 1(a). By keeping the back of each unit cell open, as indicated in Fig. 1(e), each unit-cell comprises three components: upper channel, middle channel, and lower channel. The parameters are marked in Fig. 1(a). The operating frequency is 17150Hz. Due to the subwavelength nature, the amplitude and phase of reflection are independent of the incidence direction.

Figures 2(b) and 2(c) show the amplitude and phase responses of the unit cells. The amplitude (A) is modulated by w, and the phase (ϕ) is modulated by h_1. Figure 2(b) and 2(c) show that the tuning of amplitude and phase is decoupled. This decoupled point is achieved by choosing proper h value. As a result, all possible combinations of amplitude and phase can be accessed.

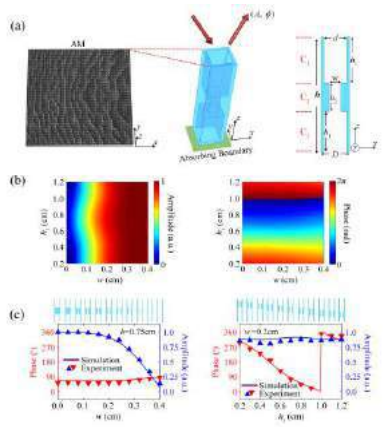

Fig. 1 (a) The design of AM and unit cells. (b) The amplitude and phase response. (c) The simulated and measured amplitude and phase versus w and h_1, respectively.

Figure 2(a) shows the calculated amplitude and phase for generating predesigned Penrose tiling pattern. We record the amplitude and phase information into AM. The photograph of the sample with 79×79 unit-cells is shown in Fig. 2(b). We plot the acoustic pressure amplitude distribution measured on the image plane in Figs. 2(c) and 2(d), showing a good agreement between numerical and experimental results of complicated spatial acoustic field. The hologram with both amplitude and phase modulation have high-quality and high high fidelity, which are unattainable with previous pure-phase approaches [1-4]. Our findings will have far-reaching impacts on beam-steering, ultrasonic imaging and particle manipulation, etc.

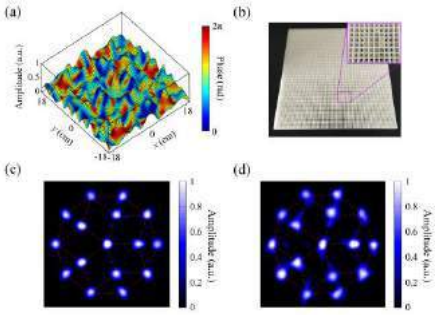

Fig. 2 (a) The calculated amplitude and phase for generating predesigned Penrose tiling pattern. (b) The photograph of sample. (c) The simulated acoustic field pattern. (d) The measured acoustic field pattern.

REFERENCES

1. A. Marzo, S. Seah, B. Drinkwater, D. Sahoo, B. Long, and S. Subramanian, Holographic acoustic elements for manipulation of levitated object. *Nat. Commun.* 6, 8661, 2015.
2. K. Melde, A. G. Mark, T. Qiu, and P. Fischer, Holograms for acoustics. Nature 537, 518–522, 2016.
3. Y. Xie, C. Shen, W. Wang, J. Li, D. Song, B-I. Popa, Y. Jing, and S. A. Cummer, Acoustic Holographic Rendering with Two-dimensional Metamaterial-based Passive Phased Array. *Sci. Rep.* 6, 35437, 2016.
4. Y. Hertzberg, and G. Navon, Bypassing absorbing objects in focused ultrasound using computer generated holographic technique. *Med. Phys.* 38, 6407–6415, 2011.

Experimental Verification of Extraordinary acoustic transmission through Density near zero extremely narrow tubes.

Jong Jin Park[1*], Jun-hyuk Kwak[1], Boyoung Kang[1], and Hakjoo Lee[1]
[1]Center for Advanced Meta-Materials, Korea.
[*]corresponding author: jjpark@kimm.re.kr

Abstract- We experimentally verify recently developed theory of ‘‘supercoupling’’ [Phys. Rev. Lett. 111, 055501 (2013)] by researching uniform acoustic energy squeezing through an extremely narrow acoustic tubes filled with near zero density metamaterials. So, we realized extraordinary acoustic transmission based on impedance matching by installing thin membranes with a subwavelength period along the tube. Potential applications in acoustic treatment, sensing and energy harvesting.

We introduce the concept of acoustic supercoupling associated with impedance matching and anomalous sound tunneling through ultra-narrow tubes. Alu and Engheta, pioneers of this work, have made metamaterials with near-zero permittivity theoretically and experimentally and matched transmission through very narrow channels filled with ENZ materials, also known as ‘‘supercoupling’’ [1]. This is a special phenomenon very different from the general Fabry-Perot (FP) tunneling resonance and is called "Supercoupling". Supercoupling, in theory, delivers the waves regardless of the length, bending and twisting of the tubes made of metamaterials. Alu proposed and theoretically explained acoustic supercoupling which applies the supercoupling phenomenon shown by electromagnetic wave to the sound wave [2]. This paper experimentally implements "acoustic supercoupling" which conveys acoustic energy by focusing acoustic wave to very narrow tube by overcoming acoustic impedance mismatch structure very extreme through acoustic metamaterial structure [3-5].

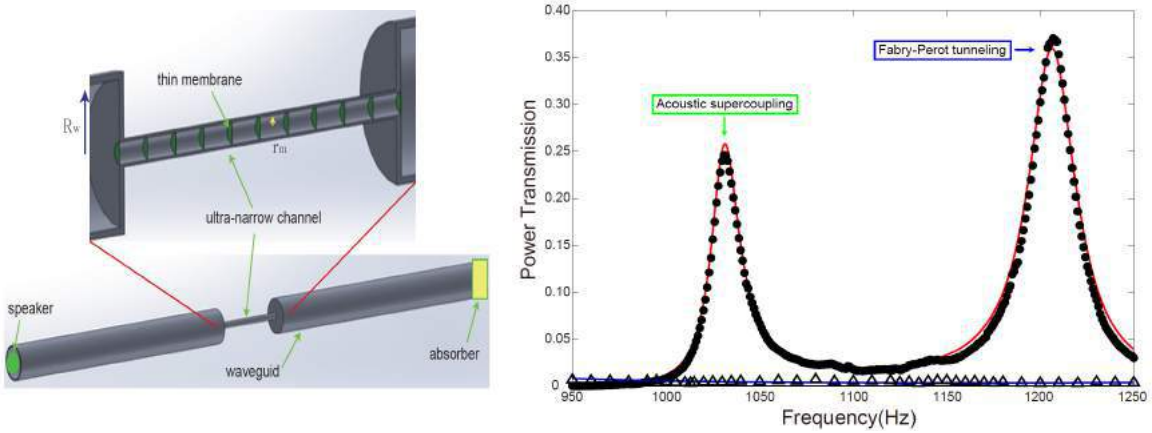

Figures 1. (a) An acoustic metamaterial design that achieves near zero effective density. An extremely narrow tube was connected between two large waveguides. A thin elastic membrane was installed at regular intervals inside the narrow tube. (b) Power transmission coefficient though ultra-narrow channel.

A tube with a narrow cross-section is connected between the same waveguides with the same cross-sectional area as shown in Fig.1 (a). The radius and length of both waveguides are 50 mm and 1 m. The diameter of the narrow tube is 7.5 mm. The length of the narrow tube is 200 mm and installed a thin elastic membrane having a thickness of 0.01 mm at intervals of 20 mm in the narrow tube. The material of the thin elastic membrane installed in the narrow pipe was made of polyethylene and attached with a tension of about 10 N/m. The cut-off frequency of the acoustic metamaterial connected to 10 unit cells is about 1030 Hz. The effective density of the acoustic metamaterial at the cutoff frequency is zero. Sound source was generated from the speaker in the left waveguide. On the other side, the sound absorbing structure was connected to remove the reflected wave.

As shown in Fig. 1(b), the red solid line is the theoretical calculation of the power transmission coefficient when using a narrow tube made of acoustic metamaterial, and the black dotted line is the experimental data. The blue solid line is the theoretical result of the power transmission coefficient when a typical narrow tube is used without the acoustic metamaterial, and the triangular point is the experimental data. As you can see in the result data, you can see two peaks, but the physical phenomena are quite different. The first peak (1032 Hz) is an "acoustic supercoupling" phenomenon where the acoustic impedance of a narrow tube is close to zero and satisfies the acoustic impedance matching conditions. The second peak (1207 Hz) is a characteristic that satisfies the FP resonance condition that is generally known, and is the value that is transmitted because the fundamental resonance mode occurs. The power transmission coefficient of the acoustic wave propagated through the acoustic supercoupling phenomenon is about 25%, and the power transmission coefficient of the general narrow tube with the acoustic metamaterial removed is about 0.3%. In other words, acoustic super coupling showed a power transmission coefficient of about 80 times higher than that of sound energy. By controlling the effective density of the narrow tube using the acoustic metamaterial, the ultra-transmission phenomenon with high transmission efficiency was experimentally realized.

This experimental implementation will play an important role in applications related to noise control, sensing, and sonic energy harvesting. In addition, the technique of concentrating and delivering sonic energy using a very narrow acoustic metamaterial tube can be extended to the ultrasound range and used for diagnosis and treatment by using the ultrasound endoscope.

Acknowledgements, This work was supported by the Center for Advanced Meta-Materials (CAMM) funded by the Ministry of Science, ICT and Future Planning as a Global Frontier Project, and by the Basic Science Research Program through the National Research Foundation of Korea (NRF) funded by the Ministry of Education, Science and Technology (CAMM- 2014M3A6B3063700).

REFERENCES

1. B. Edwards, A. Alu , M. E. Young, M. Silveirinha, and N. Engheta, “Experimental Verification of Epsilon-Near-Zero Metamaterial Coupling and Energy Squeezing Using a Microwave Waveguide,” Phys. Rev. Lett. 100, 033903, 2008.
2. R. Fleury and A. Alu, “Extraordinary Sound Transmission through Density-Near-Zero Ultranarrow Channels,” Phys. Rev. Lett. 111, 055501, 2013.
3. S. H. Lee, C. M. Park, Y. M. Seo, Z. G. Wang, and C. K. Kim, “Acoustic metamaterial with negative density,” Phys. Lett. A 373, 4464, 2009.
4. C. M. Park, J. J. Park, S.H. Lee, Y. M. Seo, C. K. Kim, and S. H. Lee, “Amplification of Acoustic Evanescent Waves Using Metamaterial Slabs,” Phys. Rev. Lett. 107, 194301, 2011.
5. J. J. Park, K.J. B. Lee, O. B. Wright, M. K. Jung, and S. H. Lee, “Giant Acoustic Concentration by Extraordinary Transmission in Zero-Mass Metamaterials,” Phys. Rev. Lett. 110, 244302, 2013.

Deformation Determination of Al doped ZnO Acoustic Cantilever Using Ideal Wurtzite Crystal Structure for Wireless Applications

Md Rabiul Awal[1], Muzammil Jusoh[1], Thennarasan Sabapathy[1], Muhammad Ramlee Kamarudin[2], R. Badlishah Ahmad[1] and Mohamed Nasrun Osman[1]

[1]Bioelectromagnetics Research Group (BioEM), School of Computer and Communication Engineering, Universiti Malaysia Perlis (UniMAP), Kampus Pauh Putra, 02600, Arau, Perlis, Malaysia
[2]Wireless Communication Centre (WCC), Faculty of Electrical Engineering, Universiti Teknologi Malaysia (UTM), 81310 Skudai, Johor, Malaysia
rabiulawal1@gmail.com, muzammil@unimap.edu.my

Abstract— A methodology to calculate the deformation of crystal structure is presented in this paper. Al doped ZnO is used to form the acoustic cantilever in ideal wurtzite crystal structure. The expansion of the applied cantilever is calculated by the proposed methodology and presented accordingly.

1. INTRODUCTION

Recently, acoustic energy transfer (AET) technology has drawn significant industrial attention. Eventually, AET possesses wide range of applications, including, electronic vehicle and portable device charging, implantable devices powering and more [1]. Cantilever approach to propagate acoustic energy is particularly adventurous using multilayer formation. Several materials can be chosen for the cantilever formation. Among them, zinc oxide (ZnO) is one of the common material to use. To calculate the deformation of an acoustic cantilever, usually wave equation is preferable which is complex and difficult to understand. From that motivation, we proposed a set of approach to calculate the deformation of a cantilever in this paper. We have modeled the aluminum doped ZnO for the cantilever formation. The ideal wurtzite crystal structure is applied for the calculation [2, 3].

2. MODELING OF THE CANTILEVER

2.1. Unit cell Modeling

Number of unit cells can be found by applying the deposition length and thickness as follows,

$$\lceil N \rceil = \lceil \overrightarrow{N}^{x,z}_{cell} \rceil = \lceil \frac{\overrightarrow{L}^{x}}{L_{unit\ cell}} \rceil \times \lceil \frac{\overrightarrow{t}^{z}}{h_{unit\ cell}} \rceil \quad (1)$$

Where, $L_{unit\ cell}^{\rightarrow x} = 2\sqrt{ZnO_{slope}^2 + AlO_{slope}^2 - 2ZnO_{slope}AlO_{slope}cos\gamma}$ and $h_{unit\ cell}^{\rightarrow z} = dl_{ZnO} + l_{AlO} + dl_{AlO} = l_{ZnO} * sin(\alpha - 90) + l_{AlO}\{1 + sin(\beta - 90)\}$. Here, $ZnO_{slope} = \sqrt{l_{ZnO}^2 - \{l_{ZnO} * sin(\alpha - 90)\}}$ and $AlO_{slope} = \sqrt{l_{AlO}^2 - \{l_{AlO} * sin(\alpha - 90)\}}$, L and t are the deposition layer length and thickness. α, β and γ are the angles produced by Zn-O, Al-O and Zn-Al bond while l_{ZnO}, l_{AlO} are the bond length and ZnO_{slope}, AlO_{slope} are slopes by the bond.

2.2. Compression to the z-axis of Unit cell

The expansion of an Unit cell to the z axis can be calculated as,

$$|\overrightarrow{C}^{z}| = \sum_{k=1}^{\overrightarrow{N}^{z}} (\overrightarrow{C}^{z}_{ZnO} + \overrightarrow{C}^{z}_{AlO})_k \ where,\ \overrightarrow{C}^{z}_{ZnO} = \sqrt{l_{ZnO}^2 + l_{ZnO_{slope}}^2 - 2l_{ZnO}l_{ZnO_{slope}}cos(\alpha - 90)} \quad (2)$$

$$and\ \overrightarrow{C}^{z}_{AlO} = \sqrt{l_{AlO}^2 + l_{AlO_{slope}}^2 - 2l_{AlO}l_{AlO_{slope}}cos(\beta - 90)}$$

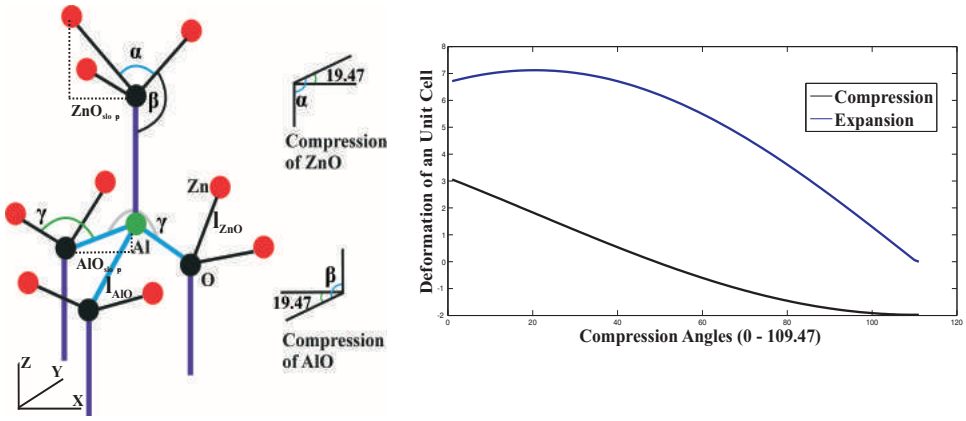

Figure 1: Al doped ZnO unit cell (left); here $\alpha = \beta = 109.47°; \gamma = 141.06°$; $l_{ZnO} = 1.9757$Å, $l_{AlO} = 1.8$Å is considered. Unit cell deformation towards cantilever length.

2.3. Expansion to the x axis of Unit cell

The expansion of an Unit cell to the x axis can be described as,

$$\overrightarrow{E}^{x,y} = \sum_{l=1}^{\overrightarrow{N}^{x}} 2(|\overrightarrow{E}^{x,y}_{ZnO}| + |\overrightarrow{E}^{x,y}_{AlO}|)_l; \; where, \; \overrightarrow{E}^{x,y}_{ZnO} = \overrightarrow{E}^{x,y}_{AlO} = \overrightarrow{E}^{x,y}_{ZnAl} = \sqrt{l^2_{ZnO} + l^2_{AlO} - 2l_{ZnO}l_{AlO}cos\gamma} \quad (3)$$

Which requires the following condition to be satisfied for the maximum deformation,

$$\exists! \; \overrightarrow{E}^{x,y}_{max} = \prod_{k=1}^{n=110} \alpha_k \wedge \beta_k; (0 < \alpha_k < 109.47; \; 0 < \beta_k < 109.47)$$

Table 1: Cantilever dimension and deformation descriptions

Cantilever size	Deposited layer thickness	Unit cell deformation	Total deformation
Length 60 mm Width 10 mm	0.02 mm	0.4072Å (x-axis) 1.2585Å (z-axis)	3.6391e+6 Å (x-axis) 8.22e+5Å (z-axis)

3. CONCLUSION

A geometric approach is proposed in this paper to calculate the deformation from a doped crystal structure. Al doped ZnO is applied for the crystal configuration. By applying the proposed structure, we have calculated the deformation of the Al doped ZnO cantilever. It is found that, the cantilever can be expanded up to 3.6391e+06 Å in length to x-axis with the unit cell expansion 0.4072Å. Results are presented in table 1 and in figure 1.

ACKNOWLEDGMENT

This work is partly supported by the MOHE and UniMAP, Malaysia, under FRGS 9003-00418.

REFERENCES

1. Awal, M. R. et. al., *State-of-the-Art Developments of Acoustic Energy Transfer*, Int. J. Ant. Prop., pp. 1-14, 2016.
2. Hanada, T., *Oxide and Nitride Semiconductors. Wiley-Interscience.*, Springer Berlin Heidelberg, 2009.
3. Morko, H, Ozgur, U., *Zinc Oxide: Fundamentals, Materials and Device Technology.*, Wiley-Interscience, 2009.

Resonance-coupling Effect On Broad Band Gap Formation And Sound Absorption In Locally Resonant Sonic Metamaterials

Meng Chen[1], Heng Jiang[1]*, and Yuren Wang[1]

[1]Key Laboratory of Microgravity, Institute of Mechanics, Chinese Academy of Sciences, Beijing 100190, People's Republic of China

*corresponding author: hengjiang@imech.ac.cn

Abstract- Sonic metamaterials have important applications in both military and commercial fields such as noise control, and acoustic communication. To broaden the resonant band gap and sound-absorbing spectrum, Woodpile structure was introduced into sonic metamaterials. Calculations suggest that Woodpile LRSMs have wider band gaps, which are adaptable to all types of vibration polarizations. Using vibration modes and a mass-spring model, strong coupling effect is confirmed between the orthogonal resonances at the upper edge of the band gap. Moreover, considering viscoelasticity of materials, woodpile LRSMs can implement strong sound-absorbing effect in a wide range.

Locally resonant sonic metamaterials (LRSMs) have attracted much attention for their ability to break through the mass density law and exhibit novel physical properties, such as band gaps [1]. A key issue for the industrial application of an LRSM is the narrow bandwidth produced by the formation mechanism of the resonant band gap. It has been found that relatively wide band gaps can be obtained by changing the LRSM structure [2–3] or by varying the elastic characteristics of the component materials [4]. However, these methods are usually based on changing intrinsic local resonance properties and thus usually limited and ineffective.

The present paper proposes a novel wider bandgap LRSMs with complex lattices: a structure that is Woodpile structure and having orthogonal resonations. The structure of a Woodpile LRSM is shown in Figure 1b and its two-dimensional LRSM variant in Figure 1a. The Woodpile structure can be obtained when the coated square column of the two-dimensional LRSM in the interval position is rotated 90 degrees.

The band structures of the two-dimensional LRSM and Woodpile-structure LRSM are shown in Figures 2 a and b, respectively. The width of the square rods is 0.3 cm. The thickness of the coating materials is 0.1 cm, and the lattice constant is 1 cm. For the Woodpile structure, there is a band gap between 1758.9 and 2411.5 Hz. The bandwidth of the Woodpile-structure LRSM is approximately 652.6 Hz, which is approximately 128 Hz broader than that of the two-dimensional LRSM in the x, y plane. It is thus easier to realize a wider band gap that can be adapted to different polarization states with the Woodpile-structure LRSM. The calculations suggest that two resonances exist in one unit cell at the upper-edge band gap: compression resonance (subject to the tensile modulus) and shear resonance (subject to the shear modulus). The analysis reveals that there is strong coupling between cross resonances at the upper-edge band gap of the Woodpile-structure LRSM originating from the interaction between compression resonance and shear resonance.

In LRSMs, locally resonant absorption coincides with viscoelastic deformation [5]. Considering viscoelasticity of materials, woodpile LRSMs can implement strong sound-absorbing effect in a wide range (as shown in Fig. 3), which provides a new idea for the design and preparation of light weight and low frequency underwater sound-absorbing materials.

Figures and Tables:

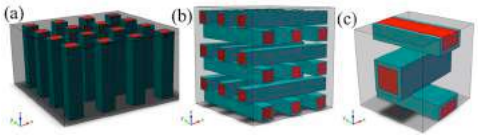

FIG. 1. Schematics of LRSMs: (a) a two-dimensional LRSM, (b) a Woodpile-structure LRSM, and (c) a unit cell of a woodpile structure with a simple cubic lattice.

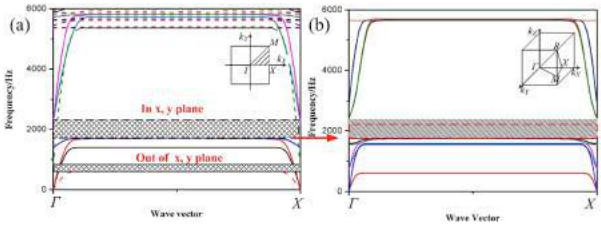

FIG. 2. Band structure of the two-dimensional LRSM (a) and Woodpile structure (b).

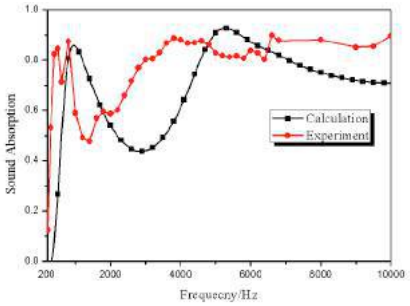

FIG. 3 Underwater absorption coefficients of the Woodpile structure LRSM.

Acknowledgements, We acknowledge project supported by the National Natural Science Foundation of China (Grant Nos. 11202211 and 11602269), the Strategic Priority Research Program of the Chinese Academy of Sciences (Grant No. XDB22040301) and the Research Program of Beijing (Grant No. Z161100002616034 and Z171100000817010).

REFERENCES

1. Liu Z., Zhang X., Mao Y., Zhu Y., Yang Z., Chan C. T., and Sheng P., "Locally resonant sonic materials," *Science*, Vol. **289**, 1734-1736, 2000.
2. Ho K. M., Cheng C. K., Yang Z., Zhang X., and Sheng P., "Broadband locally resonant sonic shields," *Appl. Phys. Lett*. Vol. Vol. **83**, 5566-5568, 2003.
3. Zhang X., Liu Y., Wu F., and Liu Z., "Large two-dimensional band gaps in three-component phononic crystals, " *Phys. Lett. A*, Vol **317**, 144-149, 2003.
4. Gu Y., Luo X., and Ma H., "Optimization of the local resonant sonic material by tuning the shape of the resonator," *J. Phys. D: Appl. Phys.* Vol **41**, 205402 1-7, 2008.
5. Zhao,H. Liu Y., Wen J., Yu D. and Wen X., "Tri-component phononic crystals for underwater anechoic coatings, " *Phys. Lett. A*, Vol **367**, 224-232 2007.

Metasurfaces for perfect transmission of sound from water to air

Eun Bok[1*], Haejin Choi[1], Jong Jin Park[1], Chung Kyu Han[1], Oliver B. Wright[2], and Sam H. Lee[1]

[1] Institute of Physics and Applied Physics, Yonsei University, Seoul 120-749, Korea

[2] Division of Applied Physics, Faculty of Engineering, Hokkaido University, Sapporo 060-8628, Japan

[*] Eun Bok: eunbok81@gmail.com

Abstract- We present the fabrication of an acoustic metasurface of thickness much smaller than the wavelength, which, when placed in between water and air, enhances the transmission by more than two orders of magnitude. This metasurface is a two-dimensional array of unit cells, each of which consists of a thin cavity covered with five membranes. Experimentally we obtained about 40% power transmission through the interface using the metasurface, which corresponds to an over 23.5 dB transmission enhancement.

Acknowledgements, This work was supported by the Center for Advanced Meta-Materials (CAMM) funded by the Ministry of Science, ICT and Future Planning as a Global Frontier Project (CAMM-2014M3A6B3063712), and by the National Research Foundation of Korea(NRF) grant funded by the Korea government (MSIP) (No. 2015001948).

Extraordinary transmission of GHz bulk acoustic waves

T. Devaux[1], **H. Tozawa**[1], **M. Tomoda**[1], **P.H. Otsuka**[1], **S. Mezil**[1], **O. Matsuda**[1], **I.A Veres**[2] and **O.B. Wright**[1]

[1]Division of Applied Physics, Faculty of Engineering, Hokkaido University, Sapporo 060-8628, Japan
[2]Research Center for Non-destructive Testing GMBH (RECENDT), Linz 4040, Austria
thibaut.devaux@eng.hokudai.ac.jp

Abstract— Concentrating acoustic wave energy in tiny sub-wavelength regions is a subject of much recent interest. One method for achieving this is the principle of extraordinary transmission, in which a resonant structure is combined with an aperture to achieve greatly enhanced transmission. Here, we make use of acoustic Fabry-Perot resonances combined with surface-wave resonances in a solid-solid structure to demonstrate bulk-wave acoustic extraordinary transmission. We show by simulation an enhancement in the acoustic amplitude transmission efficiency up to ∼20 times at GHz frequencies. Possible applications are in acoustic imaging or particle sensing.

Acoustic metamaterials are artificial structures designed to manipulate the propagation of sound in ways not possible in naturally occurring materials. One example is their use in extraordinary acoustic transmission, the passage of more acoustic energy than expected through a small sub-wavelength aperture. This has been studied in liquid-solid and air-solid systems [1, 2], but not for waves purely confined to solids. Here, by means of simulations, we investigate extraordinary acoustic transmission (EAT) in a solid-solid structure at GHz frequencies.

Our structure is shown in Fig. 1(a), consisting of a two half-spaces made of tungsten joined by a cylindrical pillar surrounded by a vacuum region. Tungsten is chosen because of its effectively isotropic acoustic behaviour. To enhance the EAT for incident plane longitudinal waves, we also make use of a concentric structure of circular grooves, as shown in Fig. 1(a), by analogy with similar geometries in optics. We consider three cases, one in which there are no grooves, one in which there are grooves only on the input side, and one in which there are grooves only on the output side, termed respectively the no groove case, the input-groove case and the output-groove case. The output-groove case is only analysed qualitatively. The diameter of the pillar is 5 nm, and the groove width and depth are both 5 nm. We adjust the pitch of the groove structure (p) and length of pillar (L) to vary the resonant frequency of the surface-wave and pillar longitudinal resonances. The central groove width is chosen to be 40 nm, measured from the outer diameter of the pillar. Plane longitudinal bulk waves are impulsively excited on the input side, and travel towards the output side. In order to evaluate the extraordinary transmission of longitudinal acoustic waves, we make use of analysis regions for amplitude sampling that are disc-shaped (diameter 700 nm, thickness 5 nm, and 200 nm before the pillar) on the input side and dome-shaped (inner and outer radii 477 nm and 500 nm, and centred on the output end of the pillar) on the output side. The volumes of these two regions are chosen to be the same. We obtain values of the amplitude transmittance $T(f)$ by making use of the average values of the amplitudes A_{in} and A_{out} in these regions at specific frequencies f. We then find, by analogy with the optical case, the EAT efficiency $\eta(f)$ using the following equation:

$$\eta(f) = T(f)^2 \frac{D^2}{W^2}, \tag{1}$$

where D is the diameter of the disc analysis region and W is the pillar diameter. In our case $D^2/W^2 = 196$.

In the the case of no grooves, the EAT is expected to depend on the Fabry-Perot resonance of the pillar at frequency f_n,

$$f_n = \frac{nv_p}{2L}. \tag{2}$$

Here v_p is the wave velocity in the pillar, i.e. the longitudinal velocity of longitudinal acoustic waves in a cylindrical rod, expected from literature values of density and elastic constants to be 4320 m/s for tungsten, and n is the mode number. In our simulations we choose L=50 nm. We

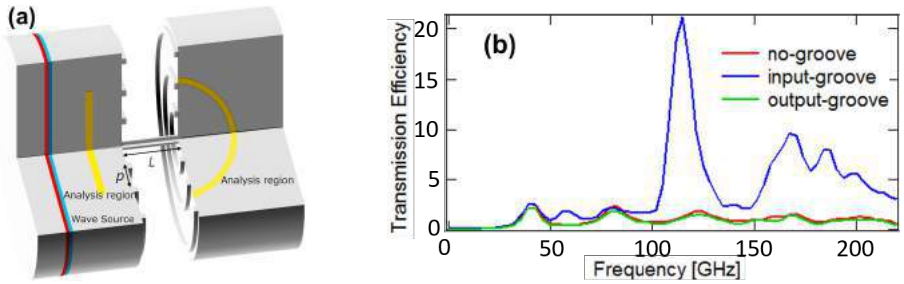

Figure 1: **(a)** Simulation geometry (all grooves shown). **(b)** Transmission efficiency spectra for the no groove case (red line), input-groove case (blue line) and output-groove case (green line).

find $f_1 = 43.2$ GHz from the simulations, indicating that $v_p = 4320$ m/s as expected [3]. In the case of grooves of pitch p being present on the input side, it has been observed that resonances are introduced that depend on surface acoustic waves, for example at a frequency close to [1]

$$f_{gm} = \frac{m v_{\mathrm{SAW}}}{p}, \tag{3}$$

where v_{SAW} is the surface wave velocity, similar to the Rayleigh velocity 2468 m/s for tungsten [4] and m is the mode number. We choose $p = 40$ nm corresponding to $f_{g1} = 61.7$ GHz for both the input and output-groove cases. For the no-groove case (red line in Fig. 1(b)) peaks at integral multiples of about 40 GHz are observed, similar to that expected from the estimated value of $f_1 = 43.2$ GHz. For the input-groove case (blue line), a smaller series of peaks is again observed, this time at integral multiples of about 60 GHz, the first peak similar to that expected from the estimated value of $f_{g1} = 61.7$ GHz. A particularly strong peak appears in the input-groove case at $f = 120$ GHz. This frequency corresponds to $n = 3$ for the longitudinal resonance and also to a surface-wave resonance, and the result is to enhance η by a factor > 10 to a value $\eta = 21$. For the output-groove case (green line), we obtain a spectrum very similar to the no-groove case. Peaks at integral multiples of about 40 GHz are observed, and they are not enhanced. We find that the spectrum does not depend on the pitch of grooves. However, a comparison of the acoustic field for the output-groove case and the input-groove case reveals that the wave patterns in the far-field are modified by the output grooves. In the output-groove case, surface waves decay by radiation of longitudinal waves, giving a strong amplitude perpendicular to the vacuum-solid surface.

In conclusion we have considered the case of extraordinary acoustic transmission in a solid-to-solid system. We chose the generic case of a cylindrical pillar connecting two solid half spaces. We show that concentric grooves installed on the input surface can dramatically improve the transmission efficiency η. Considerably enhanced values of $\eta \sim 20$ can be obtained by tuning the surface-wave resonance to a Fabry-Perot longitudinal resonance of the pillar. In addition, we find that the use of concentric grooves on the output side modifies the the transmitted acoustic waves in the far field but not the transmission efficiency. This work should find future applications in high-resolution acoustic imaging and nano-particle sensing.

REFERENCES

1. Y. Zhou et al., *Phys. Rev. Lett.* 104, 164301, 2010.
2. J. J. Park, K. J. B. Lee, O. B. Wright, M. K. Jung and S. H. Lee, *Phys. Rev. Lett.* 110, 244302, 2013.
3. D. E. Gray, "American Institude of Physics Handbook", 3rd ed., McGraw-Hill, 1982.
4. L. Kelders, J. F. Allard, and W. Lauriks, *J. Acoust. Soc. Am.* 103, 2730, 1998.

Opening Photonic-Plasmonic Hybrid Band Gaps by Lamb Waves

Z.-T. Huang[1], J.-H. Shih[1], T.-R. Lin[1*], and J.-C. Hsu[2*]

[1]Department of Mechanical and Mechatronic Engineering, National Taiwan Ocean University, Taiwan

[2]Department of Mechanical Engineering, National Yunlin University of Science and Technology, Taiwan

[*]corresponding author: trlin@ntou.edu.tw; hsujc@yuntech.edu.tw

Abstract-We propose efficient generation of tunable optical band gaps through acousto-optic (AO) interaction. The optical system proposed in this study consists of a thin dielectric slab coupled to a metal surface with a nanoscale air gap in between and provides hybridization of highly guided photonic–plasmonic gap modes squeezed in the air gap. Enhanced AO interaction occurs through the disturbance of acoustic Lamb waves in the slab, strongly boosting the AO interface effect and scattering the optical fields. As a result, wide optical band gaps are opened.

Acousto-optic (AO) interaction has been widely applied to processing light signal. High-frequency acoustic waves modulate dielectric constants of media so that light can be manipulated [1]. AO interaction can also be an effective contributor to scatter light to influence photon transport. In the past two decades, on the other hand, formation of photonic band gaps (PBGs) in man-made periodic structures has received great interest. However, most PBG materials were immutable while tunable PBGs by external fields were rarely demonstrated.

Photonic-plasmonic hybrid system can lead to tighter spatial confinement of optical energy. Intriguingly, the squeezing features can provide enhanced effects for strong modulation of light by AO interaction. The coupling mechanisms contributing to AO interaction include photoelastic (PE) coupling as a volume interaction effect and the coupling of acoustic field induced mechanical displacement of geometrical boundaries, which are referred to as bulk and interface effects, respectively [2]. To the best of our knowledge, PBG in deep-subwavelength regime opened by AO interaction is still lacking. In this study, we present dynamic modulation of hybrid optical modes in a metal-air-dielectric system using Lamb waves. In the system, a nano air gap is inserted in between an Ag substrate and a GaAs slab, and deep-subwavelength gap modes (TM modes) that hybridize plasmon and photon energy yield to propagate. We show that the system excited with high-frequency Lamb wave eigenmodes in the slab significantly enhance the AO interaction to open tunable PBGs for the squeezed hybrid gap modes.

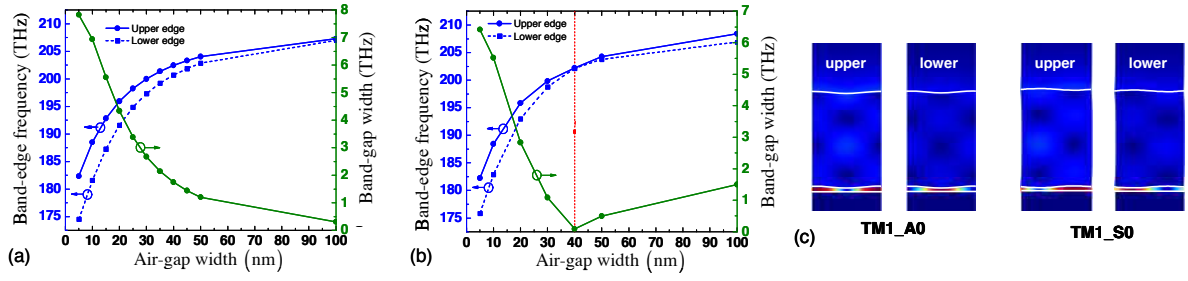

Figure 1. The upper and lower photonic band-edge frequencies of TM1 mode at first BZ boundary separated by the acoustic (a) A0 and (b) S0 modes at acoustic phase $\Omega t = 0$ as a function of air-gap width. (c) Intensity distribution of electric field of TM1 mode at lower and upper edges disturbed by A0 and S0 modes.

We employ a finite-element algorithm in our computational work to deal with elasto-electrodynamics and the AO coupling behavior. The computational procedure follows that the acoustic fields generate a time-varying refractive indices and boundaries, and then effects of AO interaction on the optical fields are calculated in the disturbed system. The interface and bulk effects are introduced by acoustic displacement and strain-optic relation, respectively. The PE coupling and moving mesh technique are used to address the disturbed refractive indices (bulk effect) and geometrical boundaries (interface effect).

We consider the TM1 mode at 193.4 THz and the lowest-order symmetric and antisymmetric eigenmodes A0 and S0. On the basis of co-localization of the optical and acoustic fields, we then calculate the optical bands in an acoustically disturbed system. Figure 1 shows the upper and lower photonic band-edge frequencies of TM1 mode at the first Brillouin zone (BZ) boundary opened by the acoustic A0 and S0 modes as a function of air-gap width. The excited acoustic amplitude is 5 nm. It is observed that a narrower air gap produces a wider PBG by the given acoustic fields because, in the narrow-air-gap regime, the interface variation significantly perturbs the air-gap width, and the effect dominates the PBG opening. Reducing the air-gap width increases the PBG width induced by the Lamb modes. Figure 1(c) shows the TM1 mode at lower and upper edges under the disturbance of A0 and S0 modes. Figure 2 shows the calculated transmission spectrum and propagation decay of TM1 waves passing through A0 waves. Obviously drop off in the PBG range appears at the first BZ boundaries (1.53–1.56 μm). High AO interaction efficiency prohibits the TM1 wave propagation within a 35 μm propagation length.

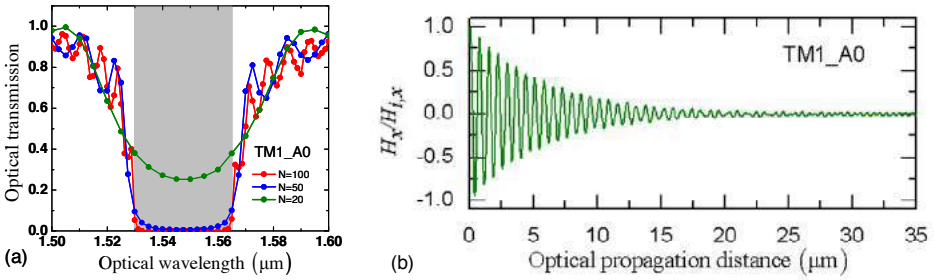

Figure 2. (a) Transmission spectra of TM1 waves passing through A0 acoustic-wave trains composed of N = 20, 50, and 100 waves propagating in the GaAs slab. (c) Transverse magnetic field H_x decay of TM1 waves, divided by the incident intensity $H_{i,x}$, along the z-direction induced by the A0 Lamb waves (N = 100).

In conclusion, we studied the PBG opening in the deep-subwavelength regime through AO interaction. The interface effect can be significantly boosted through an increased ratio of acoustic amplitude to air-gap width and opens wide PBGs. Present study introduces the mechanisms for achieving strong AO and SPP/photon–phonon interaction in deep-subwavelength structures and applications to tunable AO devices in nanometer scales.

Acknowledgements This work is supported by Ministry of Science and Technology (MOST), Taiwan (Grant Nos: MOST 103-2221-E-224-002-MY3 and MOST 103-2221-E-019-028-MY3).

REFERENCES

1. Psarobas, I. E. *et al*. "Enhanced acousto-optic interactions in a one-dimensional phoxonic cavity," *Phys. Rev. B*, Vol. 82, No. 17, 174303, 2010.
2. Lin, T.-R., Lin, C.-H., and Hsu, J.-C. "Strong optomechanical interaction in hybrid plasmonic-photonic crystal nanocavities with surface acoustic waves," *Sci. Rep.*, Vol. 5, 13782, 2013.

A Multilayer Harvester for Acoustic Energy Transfer in Low Power Wireless Applications

Md Rabiul Awal[1], Muzammil Jusoh[1], R. Badlishah Ahmad[1,2], Thennarasan Sabapathy[1], Muhammad Ramlee Kamarudin[2], and Mohamed Nasrun Osman[1]

[1]Bioelectromagnetics Research Group (BioEM), School of Computer and Communication Engineering, Universiti Malaysia Perlis (UniMAP), Kampus Pauh Putra, 02600, Arau, Perlis, Malaysia
[2]Faculty of Informatics and Computing,
Universiti Sultan Zainal Abidin (UniSZA), 22200 Besut, Terengganu, Malaysia
[3]Wireless Communication Centre (WCC), Faculty of Electrical Engineering,
Universiti Teknologi Malaysia (UTM), 81310 Skudai, Johor, Malaysia
rabiulawal1@gmail.com, muzammil@unimap.edu.my, badli@unisza.edu.my

Abstract— This paper presents a multilayer harvester for acoustic energy transfer. A four layer cantilever configuration is used to design the harvester with Aluminum, Silicon and Zinc Oxide. The displacements of the cantilever is obtained through mathematical and simulated analysis and found 5.5e-27 mm and -7e34 mm scale from simulation and mathematical modeling. However, 1.1-4.0 mV output voltage is obtained by the cantilever from minimum finger pressing on tip in open load mode.

1. INTRODUCTION

We propose a cantilever based harvester for acoustic energy transfer in this paper based on the related research works [1, 2, 3]. The cantilever model is designed by following a four layer configuration using Aluminum, Zinc Oxide and Silicon. Zinc Oxide is used for the piezoelectric layer. Top and bottom electrode layers are developed by Aluminum. The base layer is confirmed by Silicon and the thickness is settled to 0.42 mm whereas all other 3 layers has 0.03 mm thickness each. The length and width of the cantilever is 20 mm and 4 mm respectively. Hence, the total device size is $20 \times 4 \times 0.51$ mm^3. Air is used as the medium to analyze the displacement pattern in simulated environment. The proposed and fabricated cantilever is presented in Fig 1. The scope is limited to the study of the receiver end only. Section 2 and 3 presents the governing equations and performances.

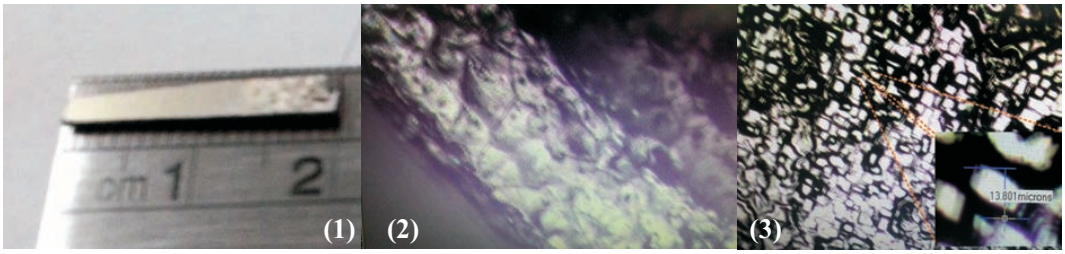

Figure 1: (1)Fabricated Cantilever $20 \times 4 \times 0.51$ mm^3; (2) Deposited Cantilever Layers: Side View; (3) Deposited Aluminum Surface: Top Layer (13.801 microns)

2. GOVERNING EQUATIONS

The bending modulus per unit length for a piezoelectricnonpiezoelectric unimorph is given by [4],

$$D = \frac{E_p^2 t_p^4 + E_{np}^2 t_{np}^4 + 2E_p E_{np} t_p t_{np}(2t_p^2 + 2t_{np}^2 + 3t_p t_{np})}{12(E_p t_p + E_{np} t_{np})} \quad (1)$$

Where, E_p and t_p are the piezoelectric Young's modulus and layer thickness; E_{np} and t_{np} for the non-piezoelectric layers. Bending moments per unit length in the x and y directions resulting from

piezoelectic and non-piezoelectic layers for a four layer cantilever,

$$M_{x,y,p} = \frac{E_{np}^2 t_{np}^2}{(E_{np}t_{np}+E_p t_p)^2} M_E^2 \; and \; M_{x,y,np} = \frac{E_p^2 t_p^2}{(E_{np}t_{np}+E_p t_p)^2} M_E^2; \; here, \; M_E = \frac{E_p E_{np} t_p t_{np}(t_p+t_{np})}{2(E_p t_p + E_{np} t_{np})} d_{31} E$$

$$Hence, \; M_{x,y,p,np} = \frac{3}{2} \frac{E_p^3 E_{np}^3 t_p^3 t_{np}^3 (t_p+t_{np})}{(E_{np}t_{np}+E_p t_p)^5} d_{31} E \tag{2}$$

Here, d_{31} is the piezoelectric coefficient of the piezoelectric layer and E is the applied electric field. Therefore, for a rectangular cantilever with L_x and L_y edges on x and y plane, the displacements can be described as,

$$h = \frac{1}{4}\frac{M'}{D}[x(L_x - x) + y(L_y - y)]; \; where, \; M' \; = M_{x,y,p}(1 - v_p) + M_{x,y,np}(1 + v_{np}) \tag{3}$$

Here v_p and v_{np} is the Poisson ratio of the piezoelectric and nonpiezoelectric layers.

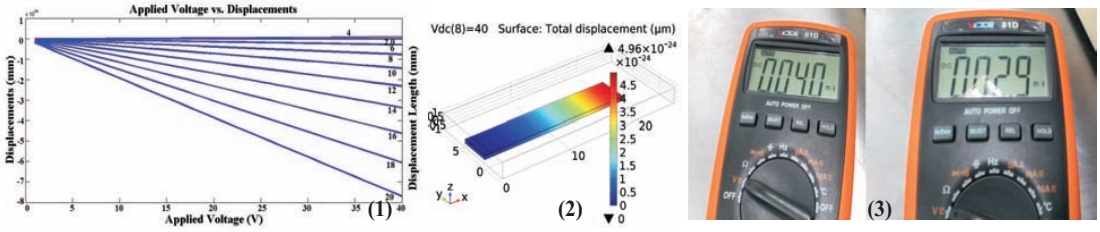

Figure 2: (1)Displacements in Mathematical Analysis; (2) Displacements in Simulated Environment; (3) Finger Pressure Generated Voltage

3. PERFORMANCE ANALYSIS OF THE CANTILEVER

Cantilever displacements is presented in Fig 2. Displacements in Fig 2(1) is calculated by applying equation 3. Fig 2(1) shows, the displacements can be as high as -7e34 mm on the tip of the cantilever and decreases with the occurrence length of the cantilever. Similar effects are found from the simulation as well with 5.5e-27 mm maximum deformation at the tip of the device, as depicted in 2(2). This type of cantilever possesses less displacements and much force by nature, hence, the displacements lie within the nanometer range. Additionally, the finger pressure generated output voltages are found in 1.1-4.0 mV range. The findings are presented in Fig 2(3).

4. CONCLUSION

A multilayer energy harvester based on piezoelectric cantilever is presented in this paper. Cantilever displacements are presented and discussed along with the experimental validation. From the findings, it is obvious that, the proposed harvester can produce voltage as high as 4.0 mV with minimum finger pressure. The obtained displacements from the cantilever is low compared to the conventional ones which lies within nanometer range due to the multilayer configuration. However, it possesses significant energy density due to high stress and can be beneficial in acoustic energy transfer and ambient vibration energy harvesting.

ACKNOWLEDGEMENT

This work is partly supported by the MOHE and UniMAP, Malaysia, under FRGS 9003-00418.

REFERENCES

1. W. C. Tang, T-CH Nguyen, and R. T. Howe, *Laterally driven polysilicon resonant microstructures*, SENSOR ACTUATOR, vol. 20, 25-32, 1989.
2. M. E. Motamedi, *MOEMS: micro-opto-electro-mechanical systems*, vol. 126. SPIE Press, 2005.
3. M. R. Awal, M. Jusoh, T. Sabapathy, M. R. Kamarudin, H. A. Rahim, & M. F. A. Malek, *Analysis of a hybrid wireless power harvester for low power applications*, In 10th European Conf. on Antennas and Propagation (EuCAP), pp. 1-5, 2016.
4. X. Li, W. Y. Shih, I. A. Aksay, & W. H. Shih, *Electromechanical Behavior of PZTBrass Unimorphs*, J. AM. CERAM. SOC., vol. 82(7), pp. 1733-1740, 1999.

Lamb wave focusing by piezoelectric array

Pawel Kudela[1*], Zhibo Yang[2], Maciej Radzienski[1], and Wieslaw Ostachowicz[1,3]

[1]Institute of Fluid Flow Machinery, Polish Academy of Sciences, Poland
[2]Xi'an Jiaotong University, China
[3]Warsaw University of Technology, Poland
*corresponding author, E-mail: pk@imp.gda.pl

Abstract

A novel concept of A0 Lamb wave mode focusing by piezoelectric array transducers is investigated. Instead of phased array approach and beamforming at certain angle, focusing is performed at desired point. Due to dispersive nature of A0 mode of Lamb wave direct implementation of such approach would be ineffective. This problem is overcome by pre-compensation of dispersion in excitation signals. It means that broad band signal at excitation point will change the shape during propagation so that it forms two cycle Hanning windowed signal at certain distance. The designed excitation waveform for each piezoelectric transducer in the array is different and has embedded appropriate time delay so that interference of waves occurs at desired focal point. Developed technique could be useful for damage detection purposes.

1. Introduction

Anomalies of propagating Lamb wave modes are used for damage detection purposes. Lamb wave modes are excited and registered by array of piezoelectric transducers. Some concepts of damage detection and localization algorithms are similar to radar. Thus, there have been attempt to steer the array of actuators so that the wave will propagate at certain angle. This principle is known as beamforming and it is realized mostly as signal processing of appropriate time delay of propagating wave packets [1, 2]. Moreover, the beamforming algorithm is realized mostly only for receiving signal (sensing at different angles) and actuation-sensing is sequential for the whole phased array. This is because devices for multiple piezoelectric transducers actuation is expensive and complex in development. The other idea of steering the waves at certain angle have been proposed by Salas and Cesnik [3]. They manufactured special micro-device called CLoVER which is able to amplify amplitudes of Lamb waves at certain angles (the resolution of the CLoVER is limited). Both mentioned methods relay on extraction of wave packets related to reflections from damage. These wave packets are often dispersive and of low time–space resolution so that it is difficult to obtain precise damage location. The proposed method uses dispersion compensation to improve resolution. Moreover, completely new approach of piezoelectric array steering is used in which waves energy is not sent to certain angle but to certain focal point.

2. The method for Lamb wave focusing

The proposed method is based on ideas given in [4, 5, 6]. It is desired that at selected distance L short time duration signal $f(t)$ will be obtained such as two cycle Hanning windowed toneburst centered at 100 kHz. This can be achieved by applying at piezoelectric transducer specially designed signals according to formula in frequency domain [6]:

$$G(\omega) = F(\omega) \cdot e^{-ik(\omega)\cdot L}, \tag{1}$$

where $F(\omega)$ is the Fourier transform of $f(t)$, $k(\omega)$ is dispersion relation between wavenumber k and angular frequency ω of compensated Lamb wave mode and L is the compensation distance. The dispersion curve $k(\omega)$ can be obtained experimentally. The time domain designed waveform can be obtained by the inverse Fourier transform of (1):

$$g(t) = \frac{1}{2\pi}\int_{-\infty}^{+\infty} F(\omega)\cdot e^{i(-k(\omega)\cdot L+\omega t)}\mathrm{d}\omega. \tag{2}$$

For the given array of piezoelectric transducers and selected focal point (see Fig. 1), distances between actuators and focal point are calculated (L_i). For each actuator excitation is calculated according to formula (2). Since distance L_i can be different for each actuator also excitation signals $g_i(t)$ have different form and have embedded time delay so that they interfere at focal point after the same time. The pre-compensation concept is depicted in Fig. 2. It can be seen that designed waveform in Fig. 2(a) applied to piezoelectric transducer causes that the shape of wave packet is changing with the time so that at 0.5 ms (see Fig. 2(d)) has a form of 2 cycle toneburst. Beyond that time the shape of wavepacket changes again due to dispersive nature of Lamb waves.

The results of A0 Lamb wave mode focusing in the form of full wavefield at the top surface of the plate are presented in Fig 3. The excited wave is dispersed at the beginning then it starts to form more compact waveforms. Finally, at the desired location at the time 0.5 ms particular waveforms interfere giving strong amplification of wave amplitude at focal point. The idea is that if at the focal point is a damage it creates strong reflection. Since reflected

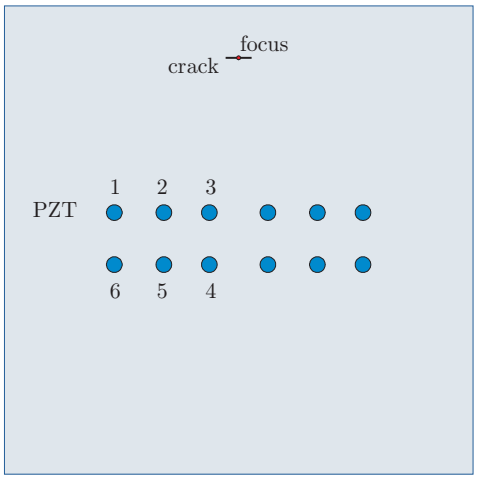

Figure 1: Schematic diagram of piezoelectric transducers array and 20 mm long crack placement on 1 m by 1 m plate.

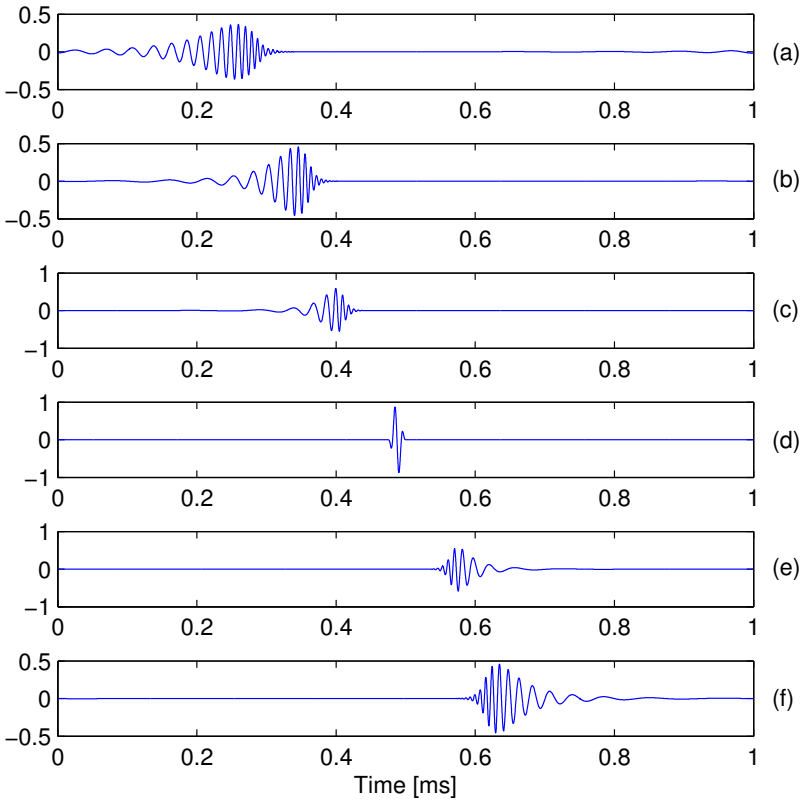

Figure 2: Pre-compensation: (a) response at excitation point (the designed waveform), (b, c) responses between focus and excitation point, (d) response at focus and (e,f) responses beyond focus.

waves are dispersive the signals registered at sensor array have to be post-compensated. Post-compensation of signals registered by sensors is done by using again eqs. (1)–(2) but with positive sign in the exponent. Finally, post-compensated signals from each sensor are summed. The energy value of resulting signal around the designed time (0.5 ms in this case) is a damage indicator. The procedure is repeated for different focal points in order to obtain damage map for the whole surface of the plate.

3. Numerical results

The proof of the concept was conducted by numerical simulation using the time domain spectral element method. 12 piezoelectric transducers were modelled on the 1 mm thick aluminium alloy plate of the size 1 m by 1 m. Transducers were arranged in the form of two rows at the central part of the plate. The distance between the transducers was set to 6 cm. Focal point was selected at coordinates (0, 0.25) m in respect to the origin at the center of the plate (see Fig. 1).

Two cases were considered: undamaged plate and plate with the damage located at the focal point. The signals registered at sensor array for the latter case are shown in Fig. 4. Nothing particular can be said about these signals and it is difficult to indicate a part of signal which corresponds to damage reflection.

However, signal processing described in the previous section connected with post-compensation and summation of signal's contribution from each sensor leads to clear damage indication. The results for the damaged case and undamaged case are presented in Fig. 5 and Fig. 6, respectively. The additional spike in signal caused by the crack has comparable amplitude to the first incoming wave packet. Additionally, it is much stronger than the following part of the signal. It means that it is above certain noise level and can be utilized as damage indicator.

The method can be a little bit modified by utilization of weights assigned to sensors depending on the angle and distance in respect to focal point. Such approach can slightly increase the amplitude of additional spike in signal caused by a damage. The weighted approach is indicated in Fig. 5 by blue color.

The beauty of the proposed method is that it is very easy to extract damage feature from the signal. It can be noticed that the additional spike in the signal caused by the crack is at around the time 0.5 ms which is exactly at the same time as in case of designed pre-compensated signal forming 2 cycle toneburst (vide Fig. 2). It means that the time of interest is known *a priori* and we can calculate signal's energy or maximum value from the interval around this particular moment of time as the damage indicator.

4. Conclusions

New method for Lamb wave focusing was presented. The principle of the method was tested exclusively by numerical methods. It has been found that the proposed method has great potential for damage detection and localization in structures. Further studies will be performed experimentally in order to confirm the effectiveness of the method.

Acknowledgement

The research was funded by the Polish National Science Center under grant agreement number DEC-2013/10/A/ST8/00071 in the frame of MAESTRO project entitled: Excitation and control of mechanical waves in nonlinear media. The second author, Zhibo Yang, would like to thank for the supports given by National Natural Science Foundation of China (No. 51405369) and the China Scholarship Council.

References

[1] P. Malinowski, T. Wandowski, I. Trendafilowa, W. Ostachowicz, A phased array–based method for damage detection and localization in thin plates, *Struct. Health Monit.* 8(1): 5–15, 2009.

[2] M. Engholm, T. Stepinski, T. Olofsson, Imaging and suppression of Lamb modes using adaptive beamforming, *Smart Mater. Struct.* 20, ,2011.

[3] K.I. Salas, C.E.S. Cesnik, Guided wave structural health monitoring using CLoVER transducers in composite materials, *Smart Mater. Struct.* 19: ,2010.

[4] D.N. Alleyne, T.P. Pialucha, P. Cawley, A signal regeneration technique for long–range propagation of dispersive Lamb waves, *Ultrasonics* 31(3): 201-204, 1993.

[5] P.D. Wilcox, A rapid signal processing technique to remove the effect of dispersion from guided wave signals, *IEEE Transactions on Ultrasonics, Ferroelectrics, and Frequency Control* 50(4): 419-427, 2003.

[6] L. Zeng, J. Lin, Y. Lei, H. Xie, Waveform design for high–resolution damage detection using Lamb waves, *IEEE T. Ultrason. Ferr.* 60(5): 1025–1029, 2011.

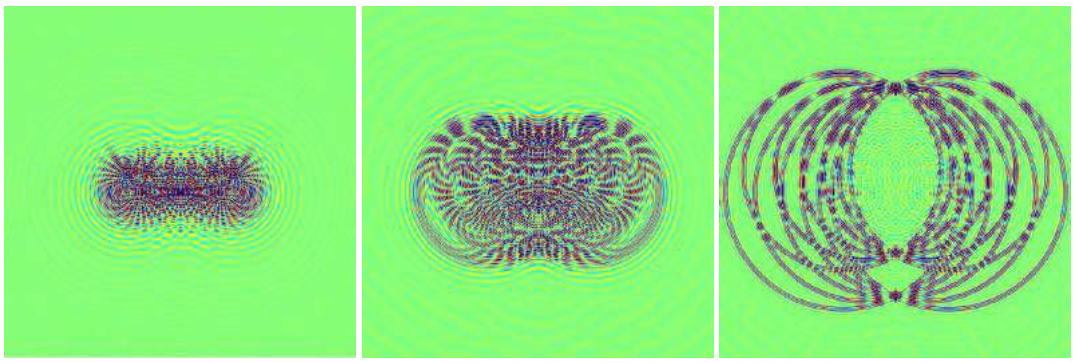

(a) Time: 0.34 ms (b) Time: 0.42 ms (c) Time: 0.50 ms

Figure 3: A0 Lamb wave mode focusing at point (0, 0.25) in undamaged plate.

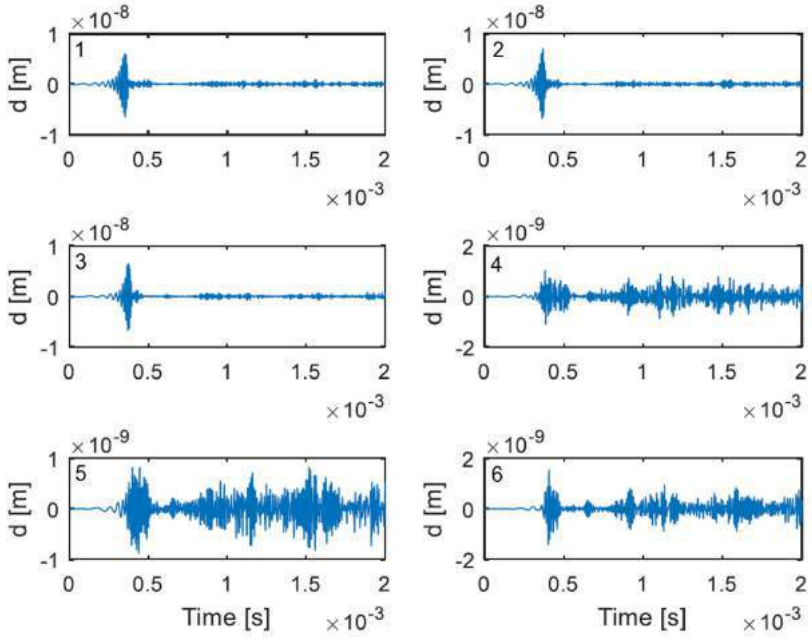

Figure 4: Array responses (only half of array i.e. no. 1-6 are plotted because of the symmetry).

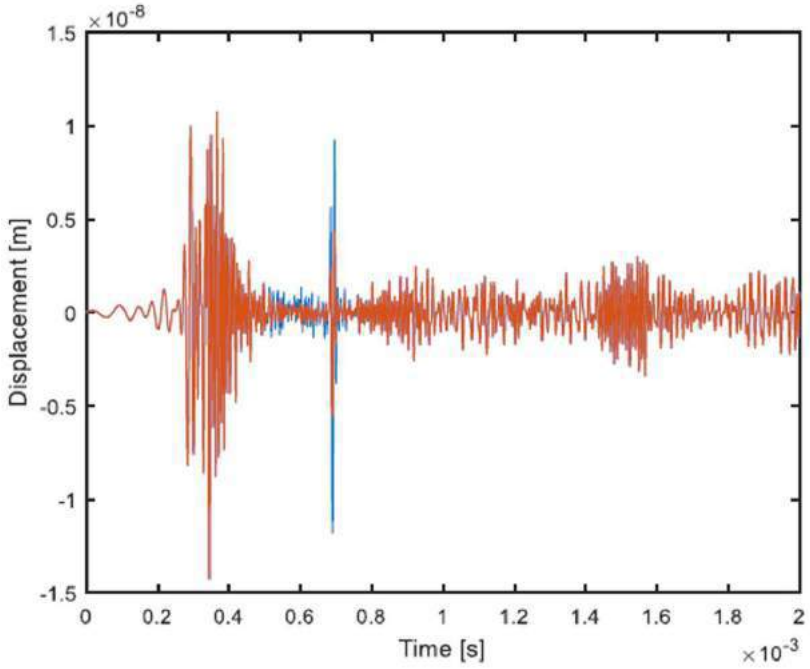

Figure 5: Post-compensated results for the damaged case.

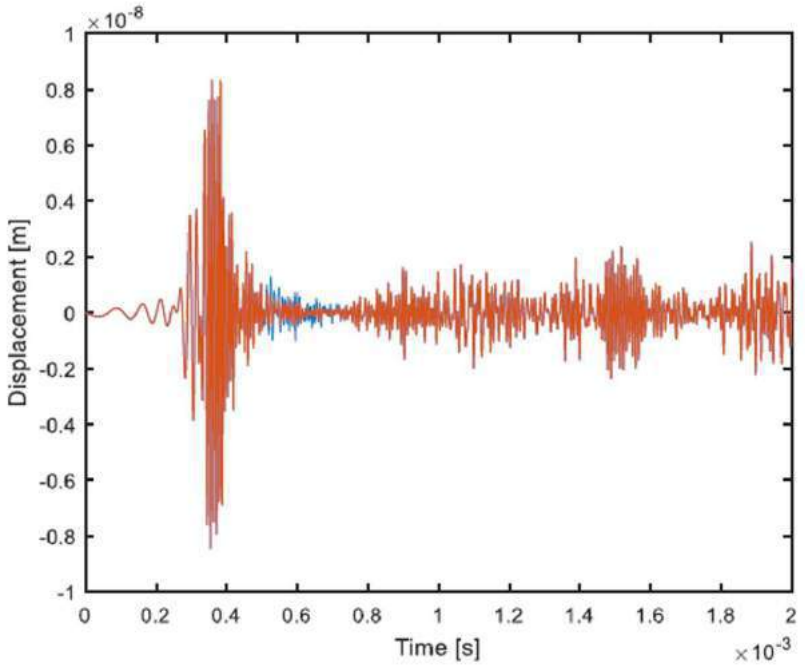

Figure 6: Post-compensated results for the undamaged case.

2D Numerical study of Acoustic Cloaking.

Md.Anzan-Uz-Zaman[1,2], Kyungjun Song[1] ,Eunjoong Lee[1] and **Shin Hur[1,2*]**
[1]Korea Institute of Machinery and Materials, the Republic of Korea
[2]University of Science and Technology, the Republic of Korea
[*]corresponding author: shur@kimm.re.kr

Abstract-It has been observed researchers use triangular bump which is generally called as baseline shape to hide objects under it using Helmholtz resonator[1] or membrane[2] or such kind of metamaterial for manipulating the reflected phase to cloak it. Our approach is to find the surface impedance for a shape analytically and then using it for manipulating the phase to cloak the obstacle. We have confirmed it by 2D numerical simulation.

For getting surface impedance we have mainly focused on the following three relationship:

$$\varphi = -2kh \quad \text{.....(i)}$$

$$R = e^{j\varphi} \quad \text{.....(ii)}$$

$$Z_n = Z_0 \frac{1+R}{1-R} \quad \text{.....(iii)}$$

Using the equations (i)-(iii), we have deduced the required surface impedance and using them, we have got promising result for cloaking the triangular and dome type bump. The figures are given below:

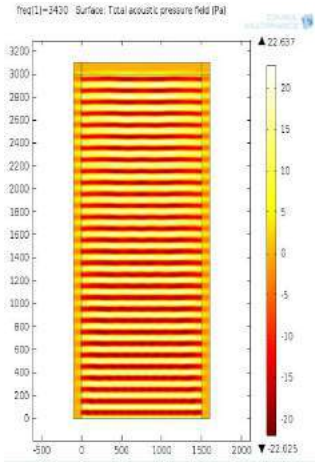

Fig1.a: with wall only

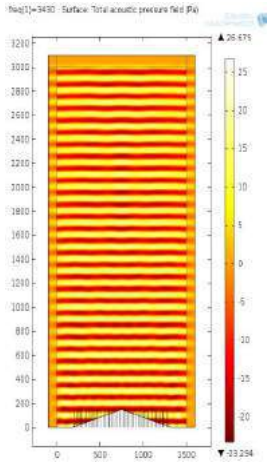

Fig1.b: With the surface impedance on the bump

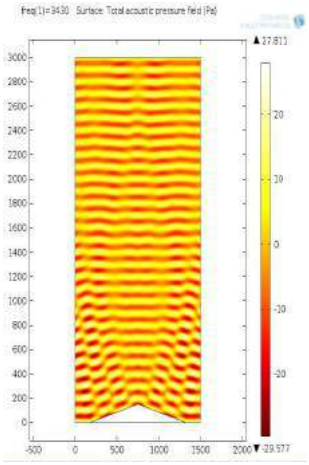

Fig1.c: with bump only

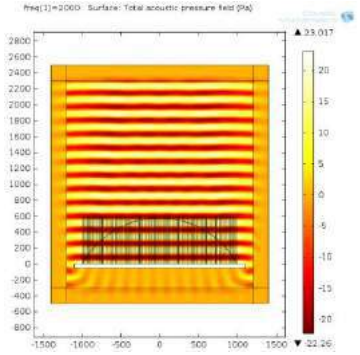
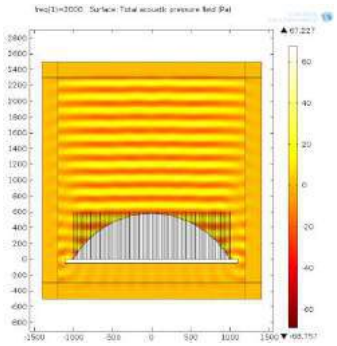
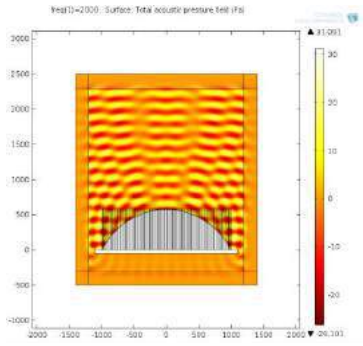

Fig2.a: with wall only Fig2.b: with the surface impedance on the dome Fig2.c: with dome only

If we see fig.1(a) and fig. 1(b), it can be seen that the wave pattern of both figure is similar though at fig1.(b), there is an triangular bump. It seems from fig.1(b) as if the sound is being reflected from a plane wall. From fig1.c, we can see the original scattering behavior of the sound as we didn't use the surface impedance for this case. So, from those figure, we can realize that the bump has been cloaked. Similarly from fig2-(a), (b) and (c), we can realized the dome shaped structure has also been cloaked by the same manner. The main feature of our study is that as we can deduce the required surface impedance at first, have a choice to select a method to design it such as Helmholtz Resonator or Membrane based structure and thus opportunity to cloak a variety types of shapes. This study was done by COMSOL 2D numerical simulation. At next, we have a plan to do it experimentally.

Acknowledgements: This work was supported by the Center for Advanced Meta-Materials (CAMM), funded by the Ministry of Science, ICT, and Future Planning as a Global Frontier Project, and the Korea Institute of Machinery and Materials under Grant NM 8660.

REFERENCES

1. Cedric Faure, Olivier Richoux, Simon F_elix, and Vincent Pagneux "Experiments on metasurface carpet cloaking for audible acoustics," *Appl. Phys. Lett.* 108, 064103 (2016).
2. Hussein Esfahlani, Sami Karkar, and Herve Lissek, "Acoustic carpet cloak based on an ultrathin metasurface," *PHYSICAL REVIEW B* 94, 014302 (2016).

Materials for photonics (Graphene, MoS2, WS2, etc)

The Synthesis of the Novel Fe_3O_4@Void@Ag Yolk-shell Nanostructures from the Fe_3O_4@Carbon@Ag Core-shell Nanoparticles

Di Liu[1], **Jaebeom Lee**[1*]

[1] Department of Cogno-Mechatronics Engineering, Pusan National University, Busan, 609-735, Republic of Korea

[*]corresponding author: J. Lee, nanoleelab@gmail.com

Abstract- Compared with the core-shell and hollow nanoparticles, the yolk-shell nanoparticles (YSNs) with the void space between the core and shell have attracted more attention because of their appealing structures, tunable physical and chemical properties. Here, we tried to synthesis the Fe_3O_4@void@Ag YSNs with removing the carbon shell of Fe_3O_4@carbon@Ag core-shell nanoparticles (CSNs) by the calcination. The area of void space could be adjusted by the thickness of the carbon shell of the Fe_3O_4@carbon@Ag CSNs.

The interspaces provide the place not only for the cores to be freely movable, but also for the storage of the chemicals. Combined with the functional shells, they can endow the YSNs some new properties, and thus render them appealing for more applications, such as nanoreactors, biomedicine, lithium-ion batteries, and photocatalysis[1-6].In the past decade, most researchers focus on the synthesis of YSNs with the template-assisted selective etching approach, however, this approach showed some defects, such as environmentally unfriendly features, low efficiency and complicated processing steps.

Currently, magnetoplasmonic (MagPlas) nanoparticles have attracted more and more attention because of their remarkable combination of the functional natures of magnetic and plasmonic optical property. Fe_3O_4@Ag CSNs, which is one of the representative MagPlas NPs, have been applied in many fields.

In this study, we challenged to fabricate the Fe_3O_4@void@Ag YSNs with a feasible method, which will display better properties than the CSNs. Firstly, the Fe_3O_4@carbon@Ag CSNs were synthesized by the menas of step by step. Secondly, the obtained Fe_3O_4@carbon@Ag CSNs were calcinated by the tube furnace in the pure air atmosphere, which could remove the carbon shell. Finally, we could get the Fe_3O_4@void@Ag YSNs. This approach to the synthesis of Fe_3O_4@void@Ag YSNs exhibited some distinguished advantages. It avoided using the environmentally hazardous alkali, and the synthetic process was simple and feasible. By the control of the synthesis of carbon shell, we could easily acquire the Fe3O4@carbon@Ag YSNs with different void spaces. Hence, the novel Fe_3O_4@void@Ag YSNs would obtain more application in many fields.

REFERENCES

1. Lee, J., Park J. C., Song H. “A Nanoreactor Framework of a Au@SiO2 Yolk/Shell Structure for Catalytic Reduction of p-Nitrophenol,” *Adv. Mater.*, Vol. 20, No. 8, 1523-1528, 2008.
2. Li H., Bian Z., Zhu J., Zhang D., Li G., Huo Y., Li H., Lu Y. “Mesoporous Titania Spheres with Tunable

Chamber Stucture and Enhanced Photocatalytic Activity," *JACS*, Vol. 129, No. 27, 8406-8407, 2007.
3. Li H., Bian Z., Zhu J., Zhang D., Li G., Huo Y., Li H., Lu Y. " Double-Shelled Nanocapsules of V2O5-Based Composites as High-Performance Anode and Cathode Materials for Li Ion Batteries," *JACS*, Vol. 131, No. 34, 12086-12087, 2009.
4. Lou X. W., Li C. M., Archer L. A., " Designed Synthesis of Coaxial SnO2@carbon Hollow Nanospheres for Highly Reversible Lithium Storage," *Adv. Mater.*, Vol. 21, No. 24, 2536-2539, 2009.
5. Van Gough D., Wolosiuk A., Braun P. V. " Mesoporous ZnS Nanorattles: Programmed Size Selected Access to Encapsulated Enzymes," *Nano Lett.*, Vol. 9, No. 5, 1994-1998, 2009.
6. Zhu Y., Ikoma T., Hanagata N., Kaskel S. " Rattle-Type Fe3O4@SiO2 Hollow Mesoporous Spheres as Carriers for Drug Delivery," *Small*, Vol. 6, No. 3, 471-478, 2010.
7. Xia Y., Xiong Y., Lim B., Skrabalak S.E. " Shape‐Controlled Synthesis of Metal Nanocrystals: Simple Chemistry Meets Complex Physics?," *Angew. Chem.-Int. Edit.*, Vol. 48, No. 1, 60-103, 2009.

Topological phase transitions in the photonic local density of states

W. J. M. Kort-Kamp[1, 2*], P. Rodriguez-Lopez[3], A. Manjavacas[4], L. M. Woods[3], and D. A. R. Dalvit[2]

[1]Center for Nonlinear Studies, MS B258, Los Alamos National Laboratory, Los Alamos NM 87545, USA

[2]Theoretical Division, MS B213, Los Alamos National Laboratory, Los Alamos, NM 87545, USA

[3]Department of Physics, University of South Florida, Tampa FL 33620, USA

[4]Department of Physics and Astronomy, University of New Mexico, Albuquerque NM 87131, USA

[*]corresponding author: kortkamp@lanl.gov

Abstract- The expansion of the graphene family by adding silicene, germanene, and stanene opens a promising platform to probe the complex interplay between topology, photonics, and 2D Dirac materials. In this work we investigate the behavior of the photonic local density of states close to buckled materials and show that it can undergo various phase transitions and present topological behavior, all enabled by the rich electronic phase diagram of the graphene family.

In the last few years, notions of topology have been applied to both electronic and photonic systems, opening the field of topological quantum materials [1, 2] and uncovering a myriad of novel effects in classical optics [3, 4]. Even more recently, the expansion of the graphene family by adding silicene, germanene and stanene (2D allotropes of Si, Ge, and Sn) [5], has led to the discovery of various Hall transitions involving the complex interplay between topology, electronic phase transitions, and spin-orbit coupling in such systems. These new 2D van der Waals materials have a layered honeycomb structure similar to graphene, but the two inequivalent atoms in the unit cell are arranged in staggered layers (Fig. 1a) due to strong sp^3 bonding. Owing to their heavier constituent atoms such materials have an intrinsic spin orbit coupling that opens a small gap in the electronic band structure. Under the presence of a static electric field E_z and a circularly polarized laser of coupling strength Λ, the mass gaps of each Dirac cone can be controlled individually and the material can be driven through several topological phase transitions, as shown in the phase diagram in Fig. 1b [6]. Recently we discovered that graphene family materials give origin to Casimir force phase transitions [6].

In this work, we exploit the rich and unique optical properties of the graphene family to examine topological phase transtions in the photonic local density of states (ph-LDOS). The ph-LDOS is a key quantity in the description of the electromagnetic field at the nanoscale, which encodes spatial, spectral, coherence and polarization properties of light. Besides, the ph-LDOS is known drive basic processes in quantum electrodynamics, such as fluorescence, thermal absorption and emission. We show that, in addition to doping, the external static electric field and circularly polarized laser provide extra degrees of freedom to efficiently manipulate the ph-LDOS at the nanoscale. It is shown that the behavior of the ph-LDOS as a function of E_z and Λ resembles the electronic phase diagram of the graphene family materials, with the ph-LDOS being largely enhanced close to phase transition boundaries (Fig. 1c,d). While topology effects are subdominant in the near-field electric ph-LDOS, we discover that the magnetic ph-LDOS presents signatures of the Chern number of each phase of the material.

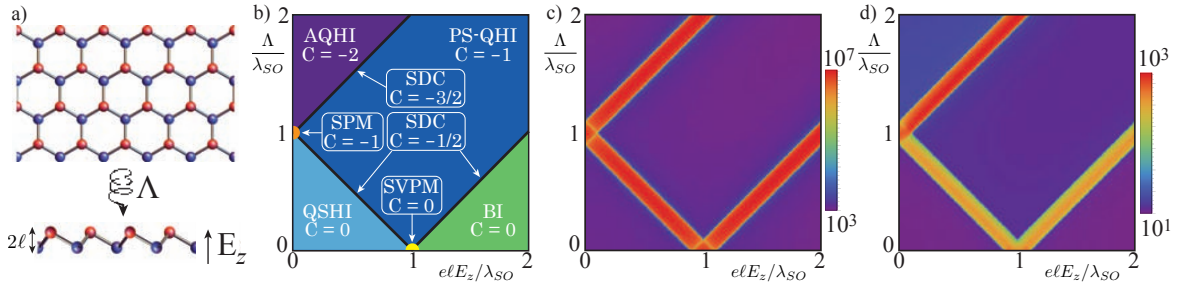

Fig. 1: Topological phase transition in the photonic local density of states. (a) Top view of the hexagonal lattice structure of the graphene family. The red and blue colors represent the two inequivalent atoms in the structure. While graphene has a planar atomic configuration, silicene, germanene, and stanene have a finite staggering 2*l*. (b) Phase diagram of the graphene family materials under the influence of a static electric field E_z and a circularly polarized laser of coupling stregth Λ. The Chern number *C* is shown for each phase and λ_{SO} is the spin-orbit coupling energy. Panels (c) and (d) depict the phase diagram of the electric and magnetic components of the photonic local density of states (normalized by the free space ph-LDOS) near a neutral layer from the graphene family. The distance to the layer is $d = \hbar c/50\lambda_{SO}$, and the frequency $\omega = \lambda_{SO}/10\hbar$.

Acknowledgements: We acknowledge financial support from the US Department of Energy, LANL LDRD program, and CNLS.

REFERENCES

1. Hasan, M. Z. and C. I. Kane, "Colloquim: topological insulators," *Rev. Mod. Phys.*, Vol. 82, 3045, 2010.
2. Qi, X.-L. and S.-C. Zhang, "Topological insulators and superconductors," *Rev. Mod. Phys.*, Vol. 83, 1057, 2011.
3. Lu, L., J. D. Joannopoulous, and M. Soljacic, "Topological photonics," *Nat. Phot.*, Vol. 8, 821, 2014.
4. Bliokh, K. Y., D. Smirnova, and F. Nori, "Quantum Spin Hall effect of light," *Science,* Vol. 348, 1448, 2015.
5. Mannix, A. J. *et. al.*, "Synthesis and chemistry of elemental 2D materials," *Nat. Chem. Reviews*, Vol. 1, 0014, 2017.
6. Rodriguez-Lopez, P., W. J. M. Kort-Kamp, D. A. R. Dalvit, and L. M. Woods, "Casimir force phase transitions in the graphene family," *to appear in Nature Communications,* (2017).

Tip-enhanced exciton-plasmon coupled imaging and control in monolayer WSe_2

Kyoung-Duck Park[1], Vasily Kravtsov[1], Tao Jiang[1], Genevieve Clark[2], Xiaodong Xu[2], and Markus B. Raschke[1*]

[1]Department of Physics, Department of Chemistry, and JILA, University of Colorado, Boulder, Colorado 80309, United States

[2]Department of Physics, Department of Materials Science and Engineering, University of Washington, Seattle, Washington 98195, United States

[*]corresponding author: markus.raschke@colorado.edu

Abstract Combining tip-enhanced Raman and photoluminescence with active atomic force tip interaction, we nano-image the exciton behavior associated with defects, grain boundaries, and local strain. Based on exciton-plasmon coupling we achieve a ~10^5-fold enhancement of photoluminescence yield. This hybrid tip-enhanced nano-spectroscopy and -imaging method also enables to probe and control neutral-, multi-, localized-, and dark-excitons at room temperature.

Since the electronic properties of monolayer (ML) transition metal dichalcogenides (TMDs) are strongly influenced by defects and strain, we present a new hybrid nano-optomechanical tip-enhanced spectroscopy and imaging approach combining nano-Raman (tip-enhanced Raman scattering, TERS), nano-PL (tip-enhanced photoluminescence, TEPL), and atomic force local strain control to investigate the excitonic properties through exciton-plasmon coupling [1]. Fig. 1a shows a TEPL image of the as-grown ML WSe_2 resolving exciton-quenching (47%) at twin boundary (TB) due to nonradiative recombination from midgap states of defects. Given the only atomic-scale dimensions of the TB, the spatial scale of PL quenching (~25 nm) could be associated with the exciton diffusion length. From controlled tip–sample nano-mechanical force interaction we can tune the bandgap reversibly (up to 24 meV) and irreversibly (up to 48 meV) through local nanoscale strain

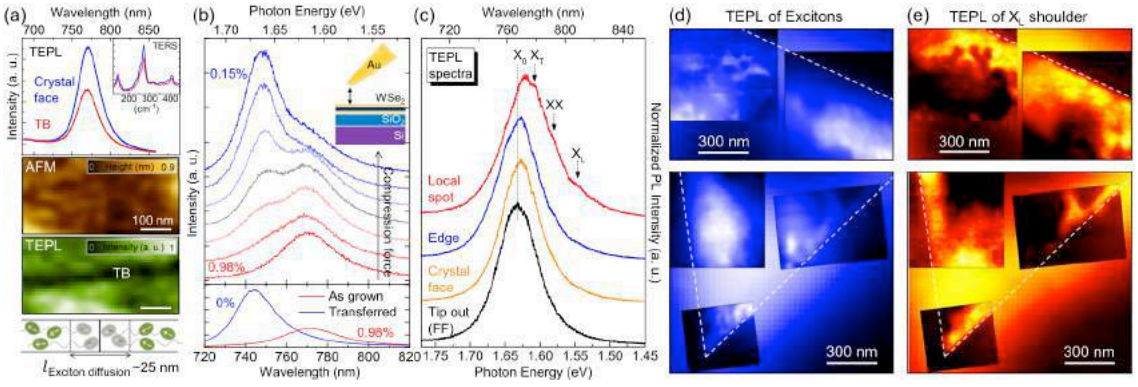

Fig. 1. (a) TEPL spectra and image of the as-grown ML WSe_2 at crystal face and twin boundary regions. (b) Evolution of TEPL spectra with increasing compressive force by the tip, giving rise to a release of the tensile strain of the crystal. Bottom: far-field reference PL spectra for the as-grown (red) and transferred (blue) ML WSe_2. TEPL spectra for various spots (c), and TEPL composite images for the integrated intensity of X_0 (725-760 nm, (d)) and X_L (810-850 nm, (e)).

engineering (0–1%) as shown in Fig. 1b. This allows to actively control the PL energy and quantum yield of nanoscale defects. Further, we achieve a ~10^5-fold enhancement of PL for a ML WSe_2 on the SiO_2/Si substrate as a result of resonant excitation by *in-plane* local plasmon field, the enhanced radiative decay rate in quantum emission through the Purcell effect, and optimization of the exciton-plasmon coupling strength to suppress exciton-quenching. TEPL also enables to observe trions (X_T), bi-excitons (XX), and localized excitons (X_L) signatures even at room temperature (Fig. 1c). These assignments are confirmed by the peak energy difference with neutral exciton peak, and power dependence of PL peak intensities. These plasmon coupled new excitonic properties allow us to investigate spatial local heterogeneity of X_L modes with ~10 nm spatial resolution. As can be seen in Fig. 1d-e, X_L modes concentrate in the vicinity of the crystal edges in contrast to X_0 modes associated with the density of structural defects.

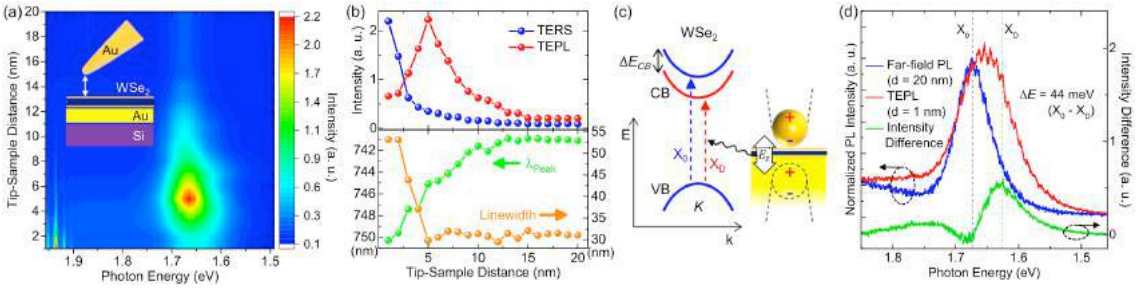

Fig. 2. (a) Tip-sample distance dependence of TERS and TEPL of a ML WSe_2 on the Au substrate. (b) Peak intensity dependence of TERS (273 cm^{-1}) and TEPL (X_0), and peak position and linewidth dependence of TEPL response with respect to the tip-sample distance, derived from (a). (c) Schematic illustration of an optical transition of dark excitons at the *K* point of WSe_2. (d) Normalized PL spectra for the tip-sample distances of 20 nm (blue) and 1 nm (red), and their intensity difference (green) exhibiting peak energy of dark excitons.

We then transferred the sample onto a Au substrate to induce a strongly confined *out-of-plane* optical field to a ML WSe_2 from the plasmonic nano-gap. As shown in distance-dependent spectra (Fig. 2a), the TERS response is significantly enhanced at <5 nm, while the exciton-quenching sets in, as expected. An associated linewidth increase is observed in this regime with significant spectral redshift (Fig. 2b), in contrast to the sample on the SiO_2/Si substrate. We believe the plasmonic tip-sample coupling facilitates transition to intra-valley excitons degenerated in a lower-lying conduction band, i.e., nominally spin-forbidden dark excitons (X_D), as illustrated in Fig. 2c. To estimate an energy gap of dark excitons, far-field PL (d = 20 nm) and TEPL (d = 1 nm) spectra are normalized and their spectral difference is plotted as shown in Fig. 2d. The energy splitting of bright/dark excitons is estimated to ~44 meV, which is comparable to results from recent report at low temperature [2].

In summary, we demonstrate the tip-induced manipulation of excitonic properties of ML WSe_2 from active control of the exciton-plasmon coupling. We expect that this new approach broadens the opportunities for applications of TMDs in novel photonic and optoelectronic devices.

Acknowledgements, Funding was provided by the U.S. Department of Energy, Office of Basic Sciences, Division of Material Sciences and Engineering, under Award No. DE-SC0008807.

REFERENCES

1. Park, K.-D. et al., "Hybrid tip-enhanced nanospectroscopy and nanoimaging of monolayer WSe_2 with local strain control," *Nano Lett.*, Vol. 16, No. 4, 2621–2627, 2016.
2. Zhou, Y. et al., "Probing dark excitons in atomically thin semiconductors via near-field coupling to surface plasmon polaritons," *arXiv:1701.05938*, 2017.

Tunable Graphene-nonlinear sensor

R. J. El-Khozondar[1*], Zeyad I. Al-Sahhar[1], H. J. El-Khozondar[2], and M. M. Shabat[3]
[1]Physics department, Al-Aqsa University, Palestine
[2]Electrical engineering department, Islamic university of Gaza, Palestine
[3]Physics department, Islamic university of Gaza, Palestine
[*]corresponding author: hkhozondar@iugaza.edu

Abstract-Graphene has many exceptional properties such as electrical and optical properties. Therefore, it has attracted attention for applications in electronics, optics and THz technology. The purpose of this work is to study the sensitivity of a composite material made of graphene sandwiched between two layers of dielectric materials. The top layer is linear dielectric and the substrate is nonlinear dielectric. The results will be presented.

Graphene is a two-dimensional crystalline material in which the carbon atoms are arranged in a hexagonal lattice. For this reason, Graphene has particular electronic properties since every carbon atom attached to other atoms by tough sp^2 hybridization. This material has a little overlap between valence and conductance bands; furthermore, high density of electrons or holes can be stimulated by gate voltage applications. In graphene, electrons interact with the hexagonal network; consequently, the electrons act as massless particles. They are named Dirac fermions since they are described by the Dirac equation. The Dirac fermions in graphene can be controlled by electromagnetic fields because they transmit one part of electric charge.

A substantial amount of research are conducted on graphene, which has versatile applications. Papasimakis et al. (2010) proposed a structure comprised a monolayer graphene placed on a metamaterial. They showed that the graphene improved the metamaterial sensitivity indicating that the structure is viable for optical sensing.

El-Khozondar et al. (2017) studied the sensitivity of a composite material made of single graphene layer cladded by dielectric and metamaterial. The concluded that the sensitivity depends on the metamaterial parameters.

We propose to study a graphene layer coated by two dielectric media. The crowned dielectric has a linear permittivity ε_2 and the underlying nonlinear material has permittivity $\varepsilon_{NL}= \varepsilon_1 +\chi^3 |E|^2$. The incident TE waves are considered constant in the y direction.

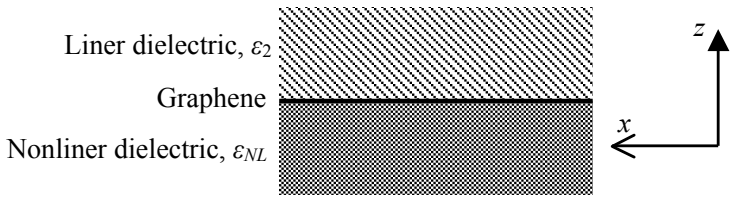

Figure 1. Graphic of a graphene sheet surrounded by linear and nonlinear dielectric media.

The dispersion equation of nonlinear surface polaritons is given by,

$$s\left[p_1^2-\left(\frac{\omega}{c}\right)^2\left|\varepsilon_y\left(0\right)\right|\right]^{1/2}+p_2=i\omega\mu_o\sigma\left(\omega\right), \tag{1}$$

where s=±1 refers to the sign of z_o (the point at which the wave is localized), $p_j^2=k_x^2-\left(\frac{\omega}{c}\right)^2\varepsilon_j; j=1,2$, $\sigma(\omega)$ is the graphene conductivity, which is given by

$$\sigma\left(\omega\right)=\sigma_1+i\sigma_2+\sigma_D \tag{2}$$

$$\sigma_1=\sigma_o\left(1+\frac{1}{\pi}\arctan\frac{\hbar\omega-2E_F}{\hbar\gamma}-\frac{1}{\pi}\arctan\frac{\hbar\omega+2E_F}{\hbar\gamma}\right) \tag{3}$$

$$\sigma_2=-\sigma_o\frac{1}{2\pi}ln\frac{\left(2E_F+\hbar\omega\right)^2+\hbar^2\gamma^2}{\left(2E_F-\hbar\omega\right)^2+\hbar^2\gamma^2} \tag{4}$$

$$\sigma_D=\sigma_o\frac{4E_F}{\pi}\frac{1}{\hbar\gamma-i\hbar\omega} \tag{5}$$

where $\sigma_o=\pi e^2/(2h)$, e is the electron charge, γ is the relaxation rate and E_F indicates for the Fermi level. The sensitivity is defined as the variation of the propagation constant k_x with respect to linear permittivity ε_2. Therefore, differentiating Equation (1) with respect to linear permittivity ε_2, we get the following expression for sensitivity,

$$\frac{dk_x}{d\varepsilon_2}=\frac{k_o^2}{2k_x}\frac{\sqrt{p_1^2-k_o^2\left|E_y\left(0\right)\right|^2}}{sp_2+\sqrt{p_1^2-k_o^2\left|E_y\left(0\right)\right|^2}} \tag{6}$$

Sensitivity in equation (6) depends on the nonlinearity, which make it possible to tune it by changing the field strength. It also depends on ε_2. Therefore, our proposed sensor is capable to detect environmental changes at the cladding area.

REFERENCES

1. Papasimakis, N., Z. Luo, Z. X. Shen, F. De Angelis, E. Di Fabrizio, A. E. Nikolaenko, and N. I. Zheludev, "Graphene in a photonic metamaterial," *Opt Express*, Vol. 18, No. 8, 8353-8359, 2010.
2. El-Khozondar, R. J., H. J. El-Khozondar and M. M. Shabat, "Enhancing Sensor Sensitivity Using Graphene-MTM Interface," *American Journal of Nano Research and Applications*, Vol. 4, No. 5, 43-46, 2017.
3. Bludov, Y. V., D. A. Smirnova, Y. S. Kivshar, N. M. R. Peres and M. I. Vasilevskiy, "Nonlinear TE-polarized surface polaritons on graphene," Phys Rev B, Vol. 89, No. 3, 035406, 2014.

Ultralow-loss copper films for plasmonics: structural morphology is the key to the improvement of optical properties

D. I. Yakubovsky and D. Yu. Fedyanin*
Laboratory of Nanooptics and Plasmonics, Moscow Institute of Physics and Technology, Russian Federation
*corresponding author: dmitry.fedyanin@phystech.edu

Abstract – Plasmonics is widely considered to be a promising candidate for the next generation of chip-scale platforms. However, it is based on noble metals, which are incompatible with the industry-standard manufacturing processes. Here, we demonstrate both experimentally and theoretically that copper can efficiently substitute gold in plasmonic devices and open the prospects for commercialization of plasmonic technologies.

Metal is the essential part of plasmonic and metamaterial devices and components. It gives the possibility to confine light to a space much smaller than the light wavelength and enhance light-matter interaction. However, the performance of metal-based plasmonic devices is severely limited by ohmic losses in the metal, which are determined by electron scattering. For this reason, the most widely used metals in plasmonics are gold and silver due to their exceptional electron conductivity. However, it has been recently reported that thick copper films can exhibit optical constants better than that of gold [1,2], which casts doubt on the previous studies.

In this work, we explain these unexpected experimental results. Furthermore, we have developed a deposition process which gives the possibility to fabricate ultralow-loss thin copper films whose optical properties are superior to gold even at very low film thicknesses (Figure 1a). We have found both theoretically and experimentally that optical properties of copper films are mostly governed by their structural morphology. In turn, the structural morphology is determined by the fabrication process and by the film thickness (see Figure 1). Our findings demonstrate that by controlling the structural morphology in the deposition process, it is possible to greatly decrease ohmic losses in copper and design 'gold quality' plasmonic devices for diverse practical applications.

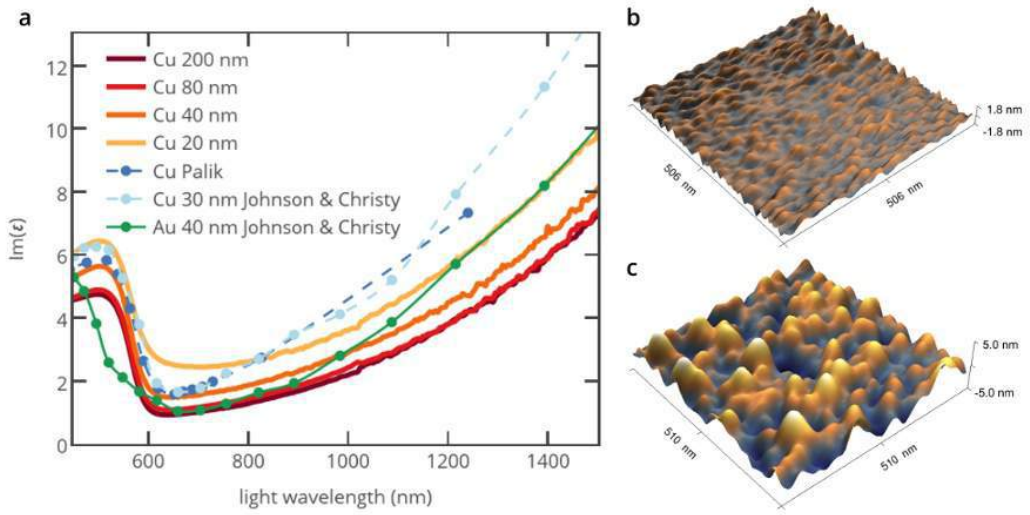

Figure 1. **(a)** Spectral dependence of the imaginary part of the dielectric function, which is responsible for ohmic losses, for the as-deposited copper films and the data from Johnson and Christy [3] and Palik [4]. Despite that the fabrication process was absolutely the same for all samples, the structural morphology of the obtained films is different, which results in different optical properties. **(b,c)** Surface morphology for two copper films of different thicknesses fabricated in same technological process. The grain size for the 200-nm-thick film (panel c) is much larger than for the 20-nm-thick film (panel b), so is the surface roughness.

REFERENCES

1. Fedyanin, D. Y., Yakubovsky, D. I., Kirtaev, R. V. and Volkov, V. S., "Ultralow-Loss CMOS Copper Plasmonic Waveguides," *Nano Letters* Vol. 16, 362–366, 2016.
2. McPeak, K. M. et al. "Plasmonic Films Can Easily Be Better: Rules and Recipes," *ACS Photonics* Vol. 2, 326–333, 2015.
3. Johnson, P. B. and Christy, R. W., "Optical Constants of the Noble Metals," *Physical Review B* Vol. 6, 4370–4379, 1972.
4. Palik, E. D., *Handbook of Optical Constants of Solids*, Academic Press, 1998.

Enhanced Optical Absorption in MoS_2 Layers Grown on Si Nanocone Arrays

Eunah Kim, Yunae Cho, Soyeong Kwon, and Dong-Wook Kim*
Ewha Womans University, Korea
*corresponding author: dwkim@ewha.ac.kr

Abstract-We prepared MoS_2 layers on SiO_2/Si nanocone (NC) arrays and investigated their characteristics. The NCs strongly concentrated incoming light at the surface and increased optical absorption of the MoS_2 layers in broad wavelength range. Finite-difference time-domain simulations were performed to explain the experimental optical properties of the MoS_2-NC integrated structures. The influences of the enhanced absorption on the reflection, photoluminescence, and Raman spectra were investigated.

There has been growing research interest in 2D atomically thin semiconductor, MoS_2, of which physical properties are very distinct from those of conventional 3D semiconductors. MoS_2 has a sizable band gap (1.2 ~ 1.8 eV), which has stimulated active research efforts to realize 2D optoelectronic devices. Extremely small thickness of a few atomic layers, however, limits the optical absorption in MoS_2 despite its very high absorption coefficient. Many researchers have attempted to improve the optical absorption in MoS_2 based on plasmonic effects and interference. In this work, we fabricated integrated structures consisting of 2D MoS_2 layers and 3D SiO_2/Si nanocone (NC) arrays, where the MoS_2 layers were synthesized by chemical vapor deposition method. The periodic arrays of NCs concentrated incoming light near the surface with the help of Mie resonance, multiple reflection, diffraction, and interference. Consequent enhanced optical absorption raised photoresponsivity (R) of MoS_2-NC structures in broad wavelength range: R of the MoS_2-NC structure at wavelength of 532 nm was almost an order of magnitude larger than that of the planar counterpart [1]. Further optical characterizations, such as photoluminescence and Raman measurements, were performed to investigate the influence of the surface concentrated light on the optical properties of the MoS_2 layers on the NC structures. This work demonstrates that the 2D MoS_2 and 3D NC integrated structures could provide a useful means to achieve high-performance optoelectronic devices.

REFERENCES

1. Cho, Y., Cho, B., Kim, Y., Lee, J., Kim, E., Nguyen, T. T. T., Lee, J. H., Yoon, S., Kim, D.-H., Choi, J.-h. and Kim, D.-W., "Broad-Band Photocurrent Enhancement in MoS_2 Layers Directly Grown on Light-Trapping Si Nanocone Arrays," *ACS Mater. & Interfaces*, DOI: 10.1021/acsami.6b15418, 2017.

Strong Coupling between the WS_2 Excitons and Metallic Plasmonic Nanoholes

Xuexian Chen[1], **Huanjun Chen**[1*]

[1]State Key Laboratory of Optoelectronic Materials and Technologies, Guangdong Province Key Lab of Display Material and Technology, School of Electronics and Information Technology, Sun Yat-sen University, Guangzhou 510275, China

[*]corresponding author: chenhj8@mail.sysu.edu.cn

Abstract-We demonstrated that the strong coupling between WS_2 excitons and plasmonic gold nanoholes. By transferring monolayer WS_2 onto the Au nanoholes fabricated by focused ion beam technique (FIB), a hybrid two dimensional optical system has been achieved. Rabi splitting was observed by measuring scattering spectra from the hybrid system. A Rabi splitting of 162 meV is observed at room temperature for this system. Furthermore, the coupling strengths can be tailored by changing the diameter of the hole.

Among the various two-dimensional atomic crystal materials, transition metal dichalcogenides (TMDs), which changes from an indirect to a direct band-gap material when passing from multilayers to a single−layer, have raised much attention in the past five years. On the other hand, tailoring the light−matter interactions from weak to strong coupling regime can endue with a variety of novel physical phenomena, which forms the basis for realization of high performance optoelectronic devices. Metal nanostructures exhibit exceptional electromagnetic field localization due to their surface plasmonic characteristics, which make them excellent platform for achieving strong coupling at room temperature.[1] In the strong coupling regime, upon light irradiation, the electromagnetic coupling between exciton−plasmon yields a hybrid state consisting of two spectrally separated energy bands. The energy separation between these two bands i.e., Rabi splitting energy, was used to measure the coupling strength between the exciton and plasmon.[2] Although such a strong coupling behavior has been reported in the MoS_2 coupled with metal nanostructure arrays,[3] studies using WS_2 which exhibit larger exciton binding energy remained unexplored.[4]

In our study, a hybrid system composed of a monolayer WS_2 and plasmonic gold nanoholes was explored to demonstrate the strong coupling effect. We showed from both of the experiments and numerical simulations that the Rabi splitting can be obtained between the WS_2 excitons and plasmons supported by the gold nanoholes. By changing the diameter of the nanohole, we were able to tailor the coupling strengths facilely. The charge density distributions of a single nanohole coupling with exciton were also studied by a finite-difference time-domain (FDTD) method.

In summary, we have proposed a strong coupling system by integrating the monolayer WS_2 with plasmonic gold nanohole arrays. The coupling strengths can be tailored by tuning the diameter of the nanohole. At lager diameters, charge density distributions were observed to form more circular interference fringes due to the strong coupling process. We strongly believe that such a system can open new avenues to manipulate the light−matter interactions at the nanoscale.

REFERENCES

1. Zakharko, Y.; Graf, A.; Zaumseil, J., "Plasmonic Crystals for Strong Light–Matter Coupling in Carbon Nanotubes," *Nano letter*, Vol. 16, No. 10, 6504–6510, 2016.
2. Wang, H.; Toma, A.; Wang, H. Y.; Bozzola, A.; Miele, E.; Haddadpour, A.; Veronis, G.; De Angelis, F.; Wang, L.; Chen, Q. D.; Xu, H. L.; Su, H. B.; Zaccaria, R. P., "The role of Rabi splitting tuning in the dynamics of strongly coupled J-aggregates and surface plasmon polaritons in nanohole arrays," *Nanoscale*, Vol. 8, No. 27, 13445–13453, 2016.
3. Lee, B.; Park, J.; Han, G. H.; Ee, H. S.; Naylor, C. H.; Liu, W.; Johnson, A.T. C.; Agarwal, R., "Fano Resonance and Spectrally Modified Photoluminescence Enhancement in Monolayer MoS_2 Integrated with Plasmonic Nanoantenna Array," *Nano letters*, Vol. 15, No. 5, 3646–3653, 2015.
4. Wang, S.; Li, S.; Chervy, T.; Shalabney, A.; Azzini, S.; Orgiu, E.; Hutchison, J. A.; Genet, C.; Samorì, P.; Ebbesen, T. W., "Coherent Coupling of WS_2 Monolayers with Metallic Photonic Nanostructures at Room Temperature," *Nano letters*, Vol. 16, No. 7, 4368–4374, 2016.

Highly confined phonon polaritons in thin van der Waals crystal of orthogonal molybdenum trioxide

Zebo Zheng, Huanjun Chen*

State Key Laboratory of Optoelectronic Materials and Technologies, Guangdong Province Key Lab of Display Material and Technology, School of Electronics and Information Technology, Sun Yat-sen University, Guangzhou 510275, China

*corresponding author: chenhj8@mail.sysu.edu.cn

Abstract- Here we report the study on the surface phonon polaritons (SPhPs) in a representative layered oxide crystal, orthogonal molybdenum trioxide (α-MoO_3). The ultra-confined SPhPs waves resulted from the coupling of IR light and optical phonons of α-MoO_3 were launched, detected, and imaged in real space. Our results suggest α-MoO_3 as a new platform for studying on novel regimes of light−matter interactions and the future nanophotonic devices.

Polaritons, the hybrid electromagnetic modes, can offer efficient approach towards subwavelength light trapping and manipulating, which therefore open up new avenues for enhancing light−matter interactions at the nanoscale. In recent years, van der Waals (vdW) layered materials are demonstrated to support a variety of polaritons, which have attracted enormous interests from the nanophotonics community due to their high degree of confinement compared to other materials systems [1][2]. To date, vdW materials such as graphene, hexagonal boron nitride (h-BN), tungsten diselenide (WSe_2) supporting different types of polaritons have been theoretically and experimentally demonstrated by different groups [3-6].

Polar dielectrics can on one hand sustain polaritons (for example, phonon polaritons in h-BN) with confinement comparable to other counterparts (such as plasmon in graphene), and on the other hand offer lower optical loss and higher quality factor. As an expected member of vdW 2D materials, 2D oxides such as α-MoO_3 with rich infrared active optical phonons may lead to the polaritonic functionalities similar to that in h-BN. On one hand, α-MoO_3 is thermally stable and less susceptible to air, making it a potential polaritonic materials with high stability. On the other hand, it tend to react with minority chemicals such as hydrogen and some metal ions, this may benefit the active tuning of polaritons that are limited in the present platform such as h-BN. However, the study on polaritons in 2D oxides have not yet been explored.

In this study, By using scattering-type scanning near-field optical microscopy (s-SNOM), the low-loss ultra-confined SPhPs waves resulted from the coupling of IR light and optical phonons of the α-MoO_3 were launched, detected, and imaged in real space. Our results demonstrated that the α-MoO_3 exhibit natural hyperbolicity results from the strong dielectric anisotropy, where the in- and out-of-plane permittivities have opposite signs. The highest electromagnetic confinement on one hand can reach ~ 10^{-2} λ_0 which is comparable to those in other materials such as grapheme and hexagonal boron nitride, and on the other hand, can be tuned by altering the thickness of the α-MoO_3. Due to the orthogonal lattice structure, the SPhPs in our specimen also showed in-plane anisotropic propagation along different crystalline directions. We further experimentally demonstrated the active controlling of the propagation of SPhPs by applying the facile chemical doping manner. In this manner, metal atoms are intercalated into the gap between adjacent α-MoO_3 layers, resulting in a

reversible lattice disorder, and therefore the annihilation of surface wave.

In summary, We studied the surface phonon polaritons in the layered α-MoO_3 crystal using near-field optical microscopy. Our results suggest the natural optical hyperbolicity of the α-MoO_3 crystal resulted from the in- and out-of-plane dielectric anisotropy. We also demonstrated the tailorable spatial confinement and active controlling of the SPhPs in the α-MoO_3. We believe that our results can offer new avenue for research on 2D oxides and offer guidelines for exploring new 2D polaritonic materials.

REFERENCES

1. Basov. D. N., Fogler. M. M. and Garcia de Abajo. F. J. "Polaritons in van der Waals materials," *Science*, Vol. 354, No. 6309, aag1992, 2016.
2. Low. T. et al. "Polaritons in layerd two-dimensional materials," *Nature Mat*, Vol. 34, No. 10, 1064–1076, 1986.
3. Fei. Z, Rodin. A.S., Andreev. G.O., Bao. W. et al, "Gate-tuning of graphene plasmons revealed by infrared nano-imaging," *Nature*, Vol. 487, No. 7405, 82–85, 2012.
4. Chen. J, Badioli. M, Alonso-Gonzalez. P et al, "Optical nano-imaging of gate-tunable graphene plasmons," *Nature, Vol. 487*, No. 7405, 77–81, 2012.
5. Dai. S., Fei. Z., Ma. Q. et al, "Tunable phonon polaritons in atomically thin van der Waals crystals of boron nitride," Science, *Vol. 343,* No. 6175, 1125–1129, 2014.
6. Fei. Z., Scott. M. E., Gosztola. D. J. et al, "Nano-optical imaging of WSe2 waveguide modes revealing light-exciton interactions," *Phys Rev B*, Vol. 94, No. 8, 081402, 2016.

Anisotropic high field terahertz response of free standing multi walled carbon nanotubes

Byounghwak Lee[1], Ali Mousavian[2], Michael Paul[2], Eunhee Jeang[3], Dai-Sik Kim[4], and Yun-Shik Lee[2*]

[1]Department of Physics and Chemistry, Korea Military Academy, Seoul 01805, South Korea

[2]Department of Physics, Oregon State University, Corvallis, Oregon 97331-6507, USA

[3]National Cancer Center, Goyang-Si 10408, South Korea

[4]Department of Physics and Astronomy, Seoul National University, Seoul 151-747, South Korea

[*]corresponding author: leeys@physics.oregonstate.edu

Abstract-We demonstrate that multi-walled carbon nanotubes (MCNTs) highly aligned on a U-shaped polyethylene reel exhibit distinctly anisotropic terahertz (THz) responses. For THz polarization parallel to the MCNTs axis, strong THz pulses induce nonlinear absorption in the quasi-one-dimensional conducting media, while only linear effect is observed in the perpendicular polarization configuration. A theoretical analysis of transmitted THz pulses measured in THz time-domain spectroscopy (THz-TDS) reveal that intense THz fields enhance permittivity in carbon nanotubes by generating charge carriers.

The high responsivity of CNTs to THz electromagnetic wave which has the spectral regime where photonics and electronics encounter creates great potential for a wide range of applications, including ultrafast nano-photonics[1] and electronics[2]. Recently, high-field electron dynamics become important when CNT devices shrink to nanometer dimensions, where operating frequencies are in the THz range and internal electric fields exceed 100 kV/m. It is, however, rarely studied how electrons in CNTs behave in the presence of strong THz fields.

In this summary, we present an experimental study[3] based on a nonlinear THz transmission spectroscopy performed to investigate THz responses of free-standing MWNTs sheets drawn from the CNT forest[4] synthesized by catalytic chemical vapor deposition (CVD). We generate strong THz pulses ($E_{THz} \geq 1.0$MV/cm) via optical rectification of femtosecond laser pulses with titled pulse front for phase matching between optical and THz pulses in $LiNbO_3$ crystal[5] and detect THz pluses transmitted through the four samples of which areal density is proportion to the deposition number N_w (=2, 5, 10 and 20) on the PE reel, using a liquid-He cooled Si:Bolometer and electro-optic (EO) sampling with a 1-mm ZnTe crystal. When the THz polarization is aligned parallel to the MCNTs axis, THz response of the samples is significantly stronger than that of the perpendicular configuration (Fig1. a-i & ii): The parallel absorption coefficient is 0.47 per deposition and the normalized di□erential transmission (ΔT/T) exhibits a larger change for higher nanotube density, while the perpendicular absorption coe□cient is 0.024 per deposition and ΔT/T is almost zero. To better understand the THz induced nonlinear e□ect for the parallel polarization configuration, we extract the complex refractive indices, $\tilde{n}(\omega) = n_{Re} + in_{Im}$, of the MCNTs samples from the transmitted THz waveforms measured in THz-TDS using the Fresnel transmission coefficient of a layer[3], $t(\omega)$, and an optimization protocol (Taylor approximation and Hessian matrix, and the deviation of the theory),[3,6] . We fit the results to the relative permittivity of a conducting medium based on Drude model:

$$\varepsilon_r(\omega) = \varepsilon_b - \frac{\sigma_0 \tau}{\varepsilon_0} + i\frac{\sigma_0}{\varepsilon_0 \omega} = \tilde{n}(\omega)^2 \qquad (1)$$

where ε_b is the contribution from bound electrons, τ is the scattering time ($\tau \ll \omega^{-1}$), and σ_0 is the DC conductivity of MCNTs. As shown in Fig1.d-iii, the conductivity of the low density sample (N_w =2) increases as the field strength increases, where the e□ect of the carrier generation dominates that of the scattering time reduction. In the high density samples of N_w =5 and 10, the reduction of the conductivity at the high field strength suggests that the scattering rate becomes much higher than the carrier generation rate.

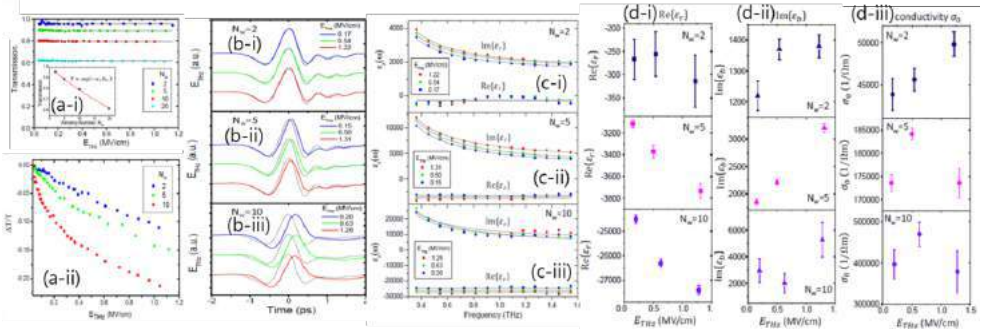

Figure1. THz transmission for THz polarization (a-i) perpendicular / (a-ii) parallel to MWCNT axis measured by a Si:Bolometer. (b-i, ii, & iii) transmitted THz waveforms measured in THz TDS, (c-i, ii, & iii) relative permittivity of MCNTs, and (d-i, ii, & iii) dielectric constant and conductivity depended on N_w =2, 5, 10 and 20 (Transmission through the N_w = 20 sample is too low to acquire meaningful data)

In conclusion, strong THz pulses give rise to highly anisotropic linear and nonlinear responses in freestanding MCNTs. In particular, intense THz fields induce large nonlinear absorption for the polarization parallel to the CNT axis, while no nonlinear response is observed in the perpendicular case. A theoretical analysis based on the Drude model suggests that strong THz fields enhance the permittivity of the MWNTs (Fig1 c-i, ii, & iii) inducing strong nonlinear electron dynamics.

Acknowledgements: The OSU work is supported by the National Science Foundation (DMR-1063632). The SNU work was supported by the National Research Foundation of Korea (NRF) grant funded by the Korea government (MSIP: NRF-2015R1A3A2031768). Poster presentation was supported by Korea Military Academy.

REFERENCES

1. Nikolaenko, Andrey E., Nikitas Papasimakis, Arkadi Chipouline, Francesco De Angelis, Enzo Di Fabrizio, and Nikolay I. Zheludev, "THz bandwidth optical switching with carbon nanotube metamaterial," *Optics Express,* Vol. 20, No. 6, 6068-6079, 2012
2. Fuse, T., Y. Kawano, M. Suzuki, Y. Aoyagi, and K. Ishibashi, "Coulomb peak shifts under terahertz-wave irradiation in carbon nanotube single-electron transistors," *Applied Physics Letters* 90, 013119, 2007.
3. Lee, B., A. Mousavian, M. J. Paul, Z. J. Thompson, A. D. Stickel, D. R. McCuen, E. Y. Jang, Y. H. Kim, J. Kyoung, D.-S. Kim, and Y.-S. Lee, "Anisotropic High-Field Terahertz Response of Free-Standing Carbon Nanotube," *Applied Physics Letters* 108, 241111, 2016.
4. Zhang, M., S. Fang , A. A. Zakhidov , S. B. Lee , A. E. Aliev , C. D. Williams , K. R. Atkinson , and R. H. Baughman, "Strong, Transparent, Multifunctional, Carbon Nanotube Sheets," *Science* 309, 1215, 2005.
5. Paul, M. J., B. Lee , J. L. Wardini , Z. J. Thompson , A. D. Stickel , A. Mousavian , H. Choi , E. D. Minot , and

Y.-S. Lee, “Terahertz induced transparency in single-layer graphene,”*Applied Physics Letters* 105, 221107, 2014.

6. Duvillaret, L., F. Garet, and J.-L. Coutaz, “A reliable method for extraction of material parameters in terahertz time-domain spectroscopy,” *IEEE J. Sel. Top. Quantum Electron*. 2, 739, 1996.

A unique combination of two-stepped in syntesization of high performance graphene antenna

M. A. Jamlos[1], A. H. Ismail[2], M. F. Jamlos[3], and Y. S. Lee[4]

[124]Faculty of Technology Engineering (F-Tech), UniCITI Alam Campus, Universiti Malaysia Perlis (UNIMAP), Malaysia
[3]Advanced Communication Engineering Centre (ACE), School of Computer and Communication Engineering, Universiti Malaysia Perlis (UNIMAP), Malaysia
*corresponding author, E-mail: mohdaminudin@unimap.edu.my

Abstract

A unique two-stepped combination of chemical and microwave reduced method successfully synthesizing the high performance of graphene antenna. The antenna recorded ultra-wide band radiation frequency of 2.5 GHz until 12.2 GHz with high energy produced of 5.5dB to 14.5dB. Small dimension of 90 mm × 45 mm made the antenna suitable enough to be applied and integrated in microwave related system. Most importantly, the measured and simulated results are within in acceptable similarity.

1. Introduction

Graphene is the promising radiating material for the sensor for cancer detection purpose [1]. Since graphene is very expensive to buy, having reduced graphene oxide originated from cheap graphite which has almost the same performance with pure graphene is the ultimate solution for that particular matter. Graphene oxide, a derivative of pure graphene loses most of its electrical conductivity properties during oxidation process. In order to restore back its electrical conductivity, special reduction procedures need to be done [2].

2. Antenna Design and Structure

Two unique methods using a two stepped chemical and microwave method to reduce the graphene are done for that purpose. Figure 1 shows reduced graphene oxide (RGO) in liquid form. It has conductivity of 3.38 × 107 s/m, resistivity of 2.01 × 10-3 Ω.m, voltage of 0.2 V and current of 9.48 × 10-1 I. Test have been done using Four Point Probe device. Meanwhile figure 1 (c) and (d) show antenna views from front and back respectively.

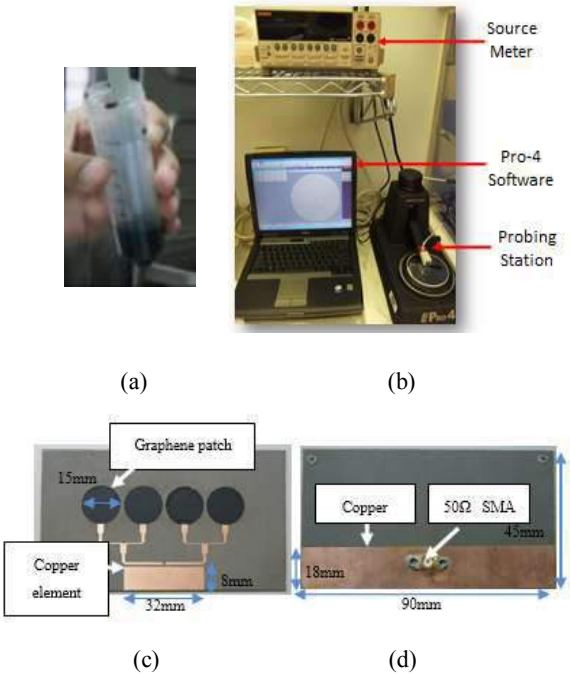

Figure 1: (a) Graphene in liquid form, (b) Four Point Probe, (c) Graphene antenna front view, (d) back view.

3. Discussion

The most intensive peak at 26.60 is recorded by pure graphite [3] as shown in figure 2(a) for XRD pattern. Due to oxidation reaction, the characteristic peak for graphite becomes broader and shifts toward 12.70. However, XRD pattern for RGO display an increasing broader peak which reveals the disappearance of multilayer structures and the formation of graphene single sheets [4] where the broad hump at 2θ = 20-300 indicated the smaller sheet size and an amorphous structure as shown in figure 2(b). The two-stepped processed product for RGO exhibit adequate reduction as seen in other reduction methods [5]. Figure 3 (a) and (b) show the overall performance of the graphene antenna.

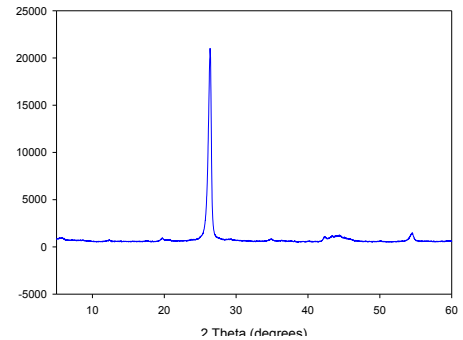

(a)

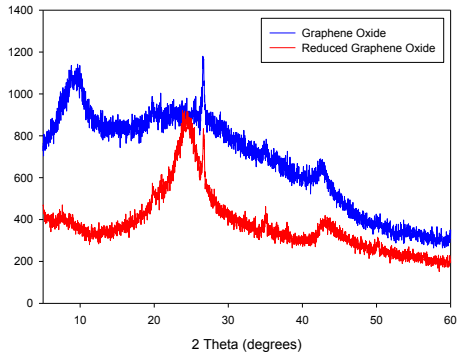

(b)

Figure 2: XRD pattern for (a) graphite, (b) graphene oxide and reduced graphene oxide

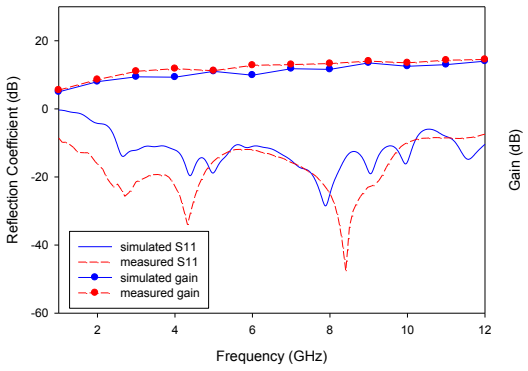

(a)

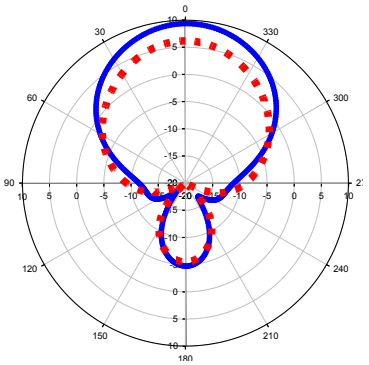

(d)

Figure 3: (a) Antenna measured and simulated S11 and gain, (b) antenna radiation pattern at 2GHz (Azimuth plane)

4. Conclusions

As conclusion, high performance grapheme antenna has been successfully realized. A unique combination of two-stepped utilized in synthesizing RGO as the radiating element of the antenna. Low cost RGO synthesized recorded similar characteristic of pure expensive grapheme.

References

[1] Moon, J. S., Gaskill, D. K., Graphene: Its Fundamentals to Future Applications, *IEEE Transactions on Microwave Theory and Techniques* Vol. 59, No. 10, 2011.

[2] Vashist, S. K., Luong, J. H. T, Recent Advances in Electrochemical Biosensing Schemes Using Graphene and Graphene-based Nanocomposites, *Carbon* 84, 519-550, 2015.

[3] M. M. Viana, M. C. F. S. Lima, J. C. Forsythe, V. S. Gangoli, M. Cho, Y. Cheng, G. G. Silva, M. S. Wong, and V. Caliman, Facile Graphene Oxide Preparation by Microwave-Assisted Acid Method, *J. Braz. Chem. Soc* 26, 978-984, 2015.

[4] W.Chen, L. Yan, P. R. Bangal, Preparation of graphene by the rapid and mild thermal reduction of graphene oxide induced by microwaves, *Carbon* 48, 1146-1152, 2010.

[5] N. Zhao, X. Cheng, J. Yang, M. Yang, S. Zheng, Experimental study on the preparation, characterization and conductivity improvement of reduced graphene-oxide papers, *Journal of Physics and Chemistry of Solids* 75, 1141-1146, 2014.

Fabricated New Polydimethylsiloxane Magnetite Substrates in Bandwidth Enhancement for Cancer Detection Using Specific Absorption Rate Measurement

M. A. Jamlos[1], A. H. Ismail[2], M. F. Jamlos[3], and Y. S. Lee[4]

[124]Faculty of Technology Engineering (F-Tech), UniCITI Alam Campus, Universiti Malaysia Perlis (UNIMAP), Malaysia
[3]Advanced Communication Engineering Centre (ACE), School of Computer and Communication Engineering, Universiti Malaysia Perlis (UNIMAP), Malaysia
*corresponding author, E-mail: mohdaminudin@unimap.edu.my

Abstract

Fabricated Polydimethylsiloxane Magnetite graphene detector successfully detecting brain cancer using SAR measurement. Combination of fabricated PDMS Ferrite as the substrate and graphene sheet as the radiating element realize the ultra-wide band radiation (2.5 GHz-11.2 GHz) with high energy (2.5dB-11.7dB) in microwave frequency ranges. Amount of energy absorbed by the human brain indicated the present of tumor. Human brain with cancer absorbed more energy and recorded higher SAR value (3.98 W/kg) compared with brain without tumor (2.28 W/kg).

1. Introduction

Since beginning, cancer is one of the most complicated disease ever exist in the world. In 2030, according to statistics done before, around 13.2 million people will suffer and die due to cancer [1]. Microwave cancer detection offers several significant advantages compared to others imaging technique including low costs, noninvasive, involves nonionizing radiation and have high accuracy in detecting tumor existence [2]. In Specific Absorption Rate (SAR), microwave cancer detection is realized by the interesting characteristic of the normal tissue and malignant tissue which demonstrated huge difference in term of dielectric property at the microwave frequency. Malignant tissues will record higher dielectric property due to more absorption of electric field compared to normal tissues which help the researcher to identify the tumor presence [3]. The rate could be calculated from following scientific formula (1):

$$SAR = (\sigma|E|2)/\rho \quad (1)$$

where σ is the tissue conductivity (S/m), E is the internal electric field (V/m) and ρ is tissue mass density (Kg/m3).

PDMS is used due to its unique characteristics especially low permittivity, mixable with other inclusions, flexible, transparent, thermally stable and water resistant [4]. In addition, until now there is yet an investigation in exploring the application of magneto-dielectric substrate for UWB antennas in term of its performance such as mutual coupling, correlation coefficient and diversity gain. Recently, graphene as the radiating material has gained much interested among the communication device community. Eventhough Copper patch antennas demonstrated good results yet it is slightly less good as compared to Graphene due to Graphene has slightly higher conductivity compared with Copper (10^8).

2. Substrate Design and Structure

Figure 1(a) shows the geometry of fabricated new Polydimethylsiloxane Magnetite graphene detector for front view and 1(b) for its gain and reflection coefficient (S11).

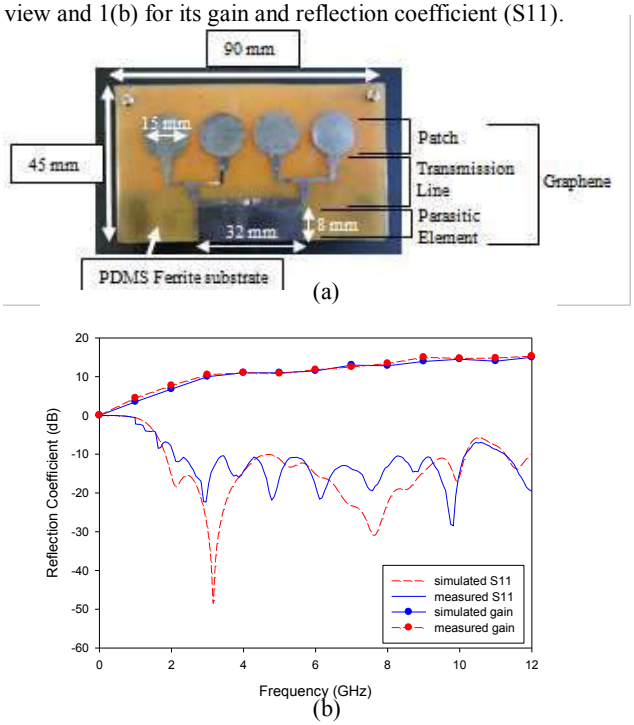

Figure 1: (a) Fabricated PDMS Graphene detector structure, (b) Detector performance in term of gain and S11

3. Discussion

The detector is placed 10 mm away from the multilayer human head phantom as the ideal distance to have maximum energy absorption. The detector radiated the energy towards two different kind of human head phantoms which are the one with tumor present meanwhile another one is without the tumor present to obtain the different SAR value. On the other hand, in order to predict the exact location of the tumor, the detector radiated the energy towards nine different areas to cover the whole one sided area of those two phantoms. The highest different in SAR value among the nine scanned areas between phantom with tumor and without tumor among indicate the tumor position at that particular area. The results are tabulated in table 1 which proposed the tumor position at the area 4 that recorded the highest SAR difference of 1.702 w/kg.

Table 1: SAR measurement result

Scanned Area	Without Tumor (W/Kg)	With Tumor (W/Kg)	Difference
1	0.984	1.563	0.579
2	1.218	1.889	0.671
3	1.439	2.511	1.072
4	**2.284**	**3.984**	**1.702**
5	1.767	1.893	0.126
6	1.102	1.748	0.646
7	1.167	1.951	0.784
8	1.201	1.605	0.404
9	1.323	1.700	0.377

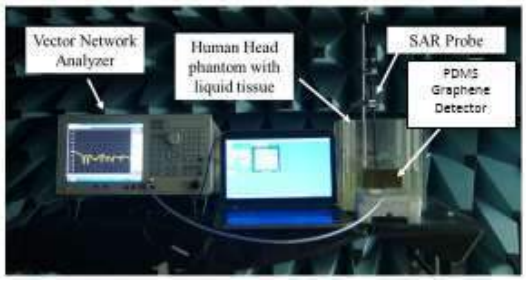

Figure 2: Measurement setup for SAR measurement

4. Conclusions

As conclusion, the detector is successfully detecting human brain tumor based on SAR technique. It is realized by the high performance of the UWB Array antenna which recorded high energy (2.5dB-11.7dB) with wider operated frequency (2.5 GHz-11.2 GHz) due to the presence of grapheme as the radiating material and PDMS-Ferrite as the substrate for the detector. Amount of energy absorbed by the human brain indicated the present of tumor. Human brain with tumor absorbed more energy and recorded higher SAR value (3.98 W/kg) compared with human brain without tumor (2.28 W/kg).

References

[1] Chaudhary, S., Luthra, P. K., Kumar, A., "Use of Graphene as a Patch Material in comparison to the copper and other Carbon Nanomaterials", International Journal of Emerging Technologies in Computational and Applied Sciences, 3(3), Dec.12-Feb.13, pp. 272-279.

[2] Alzabidi, M. A., Aldhaeebi, M. A., and Elshafiey, I., "Optimization of UWB Vivaldi Antenna for Tumor Detection", 2013 First International Conference on Artificial Intelligence, Modelling & Simulation.

[3] Wasusathien, W., Santalunai, S., Thanaset Thosdeekoraphat, T., Thongsopa C., "Ultra Wideband Breast Cancer Detection by Using SAR for Indication the Tumor Location", International Journal of Medical, Health, Pharmaceutical and Biomedical Engineering Vol:8 No:7, 2014.

[4] J. Trajkovikj, J. F. Zurcher and A. K. Skrivervik, "Soft and flexible antennas on permittivity adjustable PDMS substrates," in Antennas and Propagation Conference (LAPC), 2012 Loughborough, pp. 1-4, 2012.

[5] N. Zhao, X. Cheng, J. Yang, M. Yang, S. Zheng, Experimental study on the preparation, characterization and conductivity improvement of reduced graphene-oxide papers, *Journal of Physics and Chemistry of Solids* 75, 1141-1146, 2014.

Printed graphene antenna for 5G applications

Siti Nor Hafizah Sa'don[1], Mohd Haizal Jamaluddin[1*], Fauzan Ahmad[2], and Muhammad Ramlee Kamarudin[3]

[1]Wireless Communication Centre, Universiti Teknologi Malaysia, Johor, Malaysia
[2]Malaysia-Japan International Institute of Technology, Universiti Teknologi Malaysia, Kuala Lumpur, Malaysia
[3]Centre for Electronic Warfare, Information and Cyber, Cranfield University, Shrivenham, United Kingdom
*corresponding author, E-mail: haizal@fke.utm.my

Abstract

In the next generation of mobile communication, fifth generation (5G) will come up with higher frequency band. However, this situation affected reducing antenna size which is more difficult to manufacture especially when using conventional copper as radiating or receiving element. Hence, conductive graphene ink is introduced for smaller antenna and screen printing fabrication. From this conductive ink and approach used, 1 GHz impedance bandwidth is obtained at 15 GHz. The simulated gain achieved is 2 dBi and antenna efficiency is about 80%.

1. Introduction

In every 10 years, communication technology changes from one generation to next generation. Each generation has its own features, improvements and beneficial for mankind. Now, 5G is expected to be a phenomenon in year 2020 at once to overcome the lack of the previous features. In addition, by considering the statements in [1], the spectrum of 5G is above 6 GHz by the time we still do not rule out the statement as reported in [2].

In the latest 4G technology, multi input multi output (MIMO) system is exploited because it has the potential of large capacity gain [3] by enlarging the array of antenna. But in 5G case, enlarge the array of antenna contributes to the increasing of antenna size and then consume extra circuitry area for a particular application. In contrast to small antenna, when it comes in complex design and small element, it cannot be fabricated by copper on Flame Retardant-4 (FR-4) and Rogers easily. Even though the copper possess outstanding conductivities but it is easily oxidized [4]. While silver nanoparticle are popular but it is expensive [5]. Besides, [6] added the increasing printed circuit board (PCB) thickness exceeding 1 mm will directly related to the rising production cost and bulkier design.

Regarding to this situation, the alternative way to manufacture smaller antenna size is by proposing conductive ink as radiating or receiving element and screen printing as the suitable fabrication process. Graphene has ideal properties to be an excellent component of radio frequency integrated circuit (RFIC) [7]. Besides, conductive graphene ink provides chemical stability and flexibility [5], the dimension can be up to centimeter [8], which it is a promising candidate to decrease the antenna size [9] and it is labor-intensive sample preparation compared to the conventional copper [10]. It has lower resistance and inductance caused by its thickness effect [10] where the thickness of graphene in the range of several nanometer. High speed also can be achieved due to special energy band structure and ultrahigh electron mobility in graphene [9]. Hence, several study has been done on graphene ink antenna in order to observe the antenna performance at X-band [5] is, and at lower frequency [11]-[13], respectively. However, very low gain is the main drawback of proposed antenna.

Recently, graphene based antenna employing graphene conductive ink can be achieved through doctor-blading [14], inkjet printing [15], rolling compression method [5] and others. The screen printing technique is proposed because of its simplicity, scalability, environment-friendly process, cost effective and good accuracy [16] on the printed design pattern. It also one of the most versatile and fast [17]. Screen printing is a mass-printing method realized by pressing an ink through a patterned stencil with a squeegee [18]. It has been widely employed for electronics and compatible with a wide variety of functional inks and substrates [18]. Furthermore, it can be used in fine patterning with less than 60 µm of multilayer interconnection in integrated circuit but not suitable for thin film which less than 100µm thickness.

Further details, part 2 will explain the antenna design and its specifications. The screen printing process also was presented to produce the antenna made by conductive graphene ink. Then in part 3, the simulation and measurement result of reflection coefficient magnitude, bandwidth, radiation pattern, gain and antenna efficiency are presented and discussed.

2. Antenna design

The single antenna size consists of its length and width is 11.8 mm and 12.2 mm, respectively. It consists of radiator or receiver element with rectangular shaped of 6.8 mm width and 7.2 mm length, respectively. Then the antenna is

fed by a 50 Ω coplanar waveguide (CPW) with full ground which has chamfer on both side of 1 mm. The gap between ground and transmission line is about 0.08 mm. Figure 1 shows the dimension of graphene antenna. CPW feed is chosen because of its simplicity and ease of fabrication during screen printing process as the radiator or receiver element and the ground plane are printed on the same surface of substrate [19]. The antenna is designed at frequency of 15 GHz. The conductive graphene ink purchase from Sigma Aldrich and characterize with conductivity, σ of 33333.33 S/m with thickness of 0.1 µm, respectively. The substrate used in this work is Kapton polyimide film with dielectric constant, ε_r of 3.5, loss tangent, δ = 0.002, and 0.075 mm thick, respectively.

Screen printing is used to print conductive graphene ink onto a Kapton substrate with simulated design pattern and then the sample is cured for 20 minutes at 250°C. During curing condition, the high temperature does not destroy the Kapton substrate since its maximum operating temperature can be as high as 400°C. Figure 2 shows the fabricated graphene antenna.

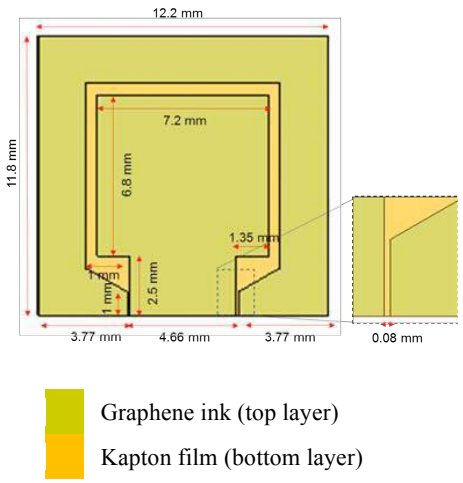

Figure 1: The optimization of antenna parameter length. Green colour is graphene represent as antenna radiator or receiver element on the top layer while yellow colour is Kapton film represent as antenna substrate at bottom layer.

Figure 2: Fabricated antenna after being cured and connected to the 50 ohm SMA connector.

2.1. Screen printing

The advantages of screen printing mentioned in [16] are cost effective since the mesh used in stencil is made by fabric or stainless steel and another one is the alignment between stencil and substrate can be performed easily since the stencil is semi-transparent and both stencil and substrate are planar. In this study, the equipment of screen printing are showed in Figure 3. The wooden frame is stencil contained antenna pattern with mesh resolution of 120 µm. The squeegee rubber is used for spreading the graphene ink on stencil to print the antenna pattern on substrate. Then, to remove the graphene ink is by using solvent 151. The others equipment for safety are disposable mask, disposable glove, disposable dropper and industrial wiper.

Figure 3: Screen printing equipment's'.

The substrate (Kapton film) is placed at the bottom of stencil with spacer between stencil and substrate. The spacer thickness can be in range of 2 mm to 3 mm to avoid the substrate stick to the stencil while printing. Firstly, graphene ink is placed on top of the stencil near to the antenna pattern by using disposable dropper as showed in Figure 4. Then, the ink were spread through antenna pattern by forcing the squeegee rubber and pressing the stencil simultaneously as shown in Figure 5.

Figure 4: The graphene ink is ready to be printed on Kapton film.

Figure 5: The squeegee rubber must be in the incline position, the angle of 45°.

Figure 6 shows the graphene ink antenna after screen printing process. The conductive graphene ink used containing binder of polymer ethyl cellulose (EC) for scalable, efficient production of graphene [20] and providing high conductivity [12]. Since binder are insulator and to increase the conductivity, so high-temperature thermal annealing is required to decompose the binder [5] and made Kapton film being the suitable substrate compared to paper, plastics, textiles, polyethylene terephthalate (PET) and the others sensitive substrate. The graphene ink antenna was cured for 0 minutes at 250°C. The graphene ink antenna after cured was showed in Figure 7.

Figure 6: The antenna pattern made by graphene ink are printed on Kapton film substrate.

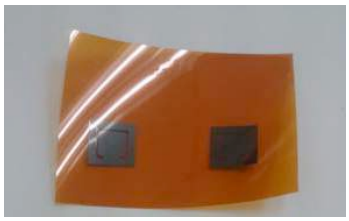

Figure 7: Grey colour appeared after the graphene ink antenna being cured.

3. Discussion

The reflection coefficient magnitude (S11) of this printed graphene antenna was measured using the vector network analyzer (VNA). The simulated and measured results of S_{11} are shown in Figure 8. Simulated S_{11} covering the range between 14.25 GHz to 15.72 GHz, while measured S_{11} ranging between 10.3 GHz to 16.8 GHz at -10 dB level, respectively. The resonance frequency has slightly shifted in S_{11} measurement due to the effect of curing condition on conductive graphene ink. The EC binder contained in the graphene ink may not fully decompose. Hence the bandwidth range of S_{11} measurement is larger than S11 simulation. Moreover, the dielectric constant of Kapton polymide film used as substrate must also changed due to the curing condition in high temperature. Table 1 summarize the comparison between simulation and measurement result obtained.

Figure 9 shows the simulated of normalize radiation pattern of printed graphene antenna where bidirectional at E-plane and nearly omnidirectional at H-plane, respectively. The simulated gain obtained is 2.392 dBi which is higher compared to the graphene antenna produced in [5], [11]-[13]. Then the calculated antenna efficiency is 80.74%, hence it shows that the printed antenna is good.

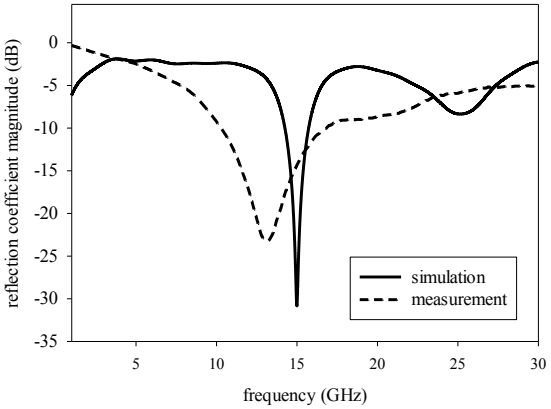

Figure 8: The reflection coefficient magnitude of printed graphene antenna shows straight line for simulation while dash line for measurement.

Table 1: The simulation and measurement of frequency resonance, reflection coefficient magnitude and bandwidth for simulation and measurement.

Characteristics	Simulation	Measurement
Frequency (GHz)	15	13.09
S11 (dB)	-30.82	-23.21
Bandwidth (GHz)	1.47	6.5

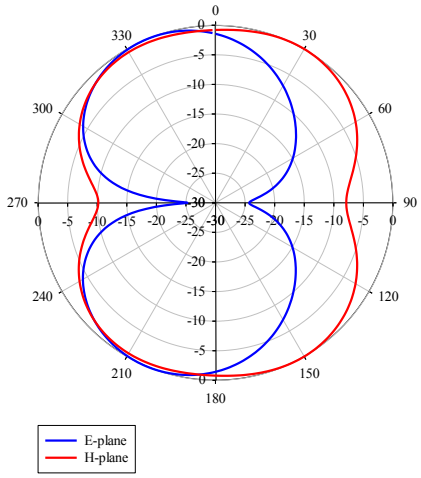

Figure 9: The normalize radiation pattern at E-plane and H-plane at frequency of 15 GHz.

4. Conclusions

High gain of printed graphene antenna has been successfully design for 5G applications and the screen printing technique is used for providing printed graphene antenna. The printed antenna has been through the high temperature process. Therefore the measurement result of printed antenna on Kapton substrate shows that the resonance frequency is slightly shifted and bandwidth is larger. Besides, the dielectric constant of substrate used will change while cure even the physical is not affected. However, the antenna which has smaller size with shaped design still gives high resolution, very light, thin and has a very low cost and fast to produce it. With the proposed antenna and technique used, it will provide one of the alternative ways to produce 5G antenna which needs a very small design and low-cost antenna production.

Acknowledgements

The authors would like to thank the Ministry of Higher Education (MOHE) under FRGS (vote 4F283 and 4F733) and under Research University Grant (votes 05H34, 00G36, 05H62 and 04H36) and Higher Centre of excellence Grant (vote 4J220) for supporting this research work.

References

[1] Ofcom, "Spectrum above 6 GHz for future mobile communications," in *[Online]. Avail- able: http://stakeholders.ofcom.org.uk/binaries/consultations /above- 6ghz/summary/spectrum above 6 GHz CFI.pdf*, 2015, no. February.

[2] T. World and R. Conference, "Studies on frequency-related matters for International Mobile Telecommunications identification including possible additional allocations to the mobile services on a primary basis in portion (s) of the frequency range between 24 . 25 and 86 GHz for the," 2015.

[3] C. X. Wang *et al.*, "Cellular architecture and key technologies for 5G wireless communication networks," *IEEE Commun. Mag.*, vol. 52, no. 2, pp. 122–130, 2014.

[4] L. Huang, Y. Huang, J. Liang, X. Wan, and Y. Chen, "Graphene-based conducting inks for direct inkjet printing of flexible conductive patterns and their applications in electric circuits and chemical sensors," *Nano Res.*, vol. 4, no. 7, pp. 675–684, 2011.

[5] X. Huang *et al.*, "Binder-free highly conductive graphene laminate for low cost printed radio frequency applications," *Appl. Phys. Lett.*, vol. 106, no. 20, p. 203105, 2015.

[6] Wonbin Hong, Kwang-Hyun Baek, Youngju Lee, Yoongeon Kim, and Seung-Tae Ko, "Study and prototyping of practically large-scale mmWave antenna systems for 5G cellular devices," *IEEE Commun. Mag.*, vol. 52, no. 9, pp. 63–69, 2014.

[7] N. A. A. Rahim, M. H. Kara, Z. Awang, and M. R. Mahmood, "High Frequency Characteristics of Graphene Layers," in *2014 IEEE Asia-Pacific Conference on Applied Electromagnetics (APACE)*, 2014, pp. 232–234.

[8] Y. Huang, L. S. Wu, M. Tang, and J. Mao, "Design of a beam reconfigurable thz antenna with graphene-based switchable high-impedance surface," *IEEE Trans. Nanotechnol.*, vol. 11, no. 4, pp. 836–842, 2012.

[9] Z. Xu, X. Dong, and J. Bornemann, "Design of a reconfigurable MIMO system for THz communications based on graphene antennas," *IEEE Trans. Terahertz Sci. Technol.*, vol. 4, no. 5, pp. 609–617, 2014.

[10] H. Lee *et al.*, "Intrinsic characteristics of transmission line of graphenes at microwave frequencies Intrinsic characteristics of transmission line of graphenes at microwave frequencies," *Appl. Phys. Lett.*, vol. 100, no. 223102, p. 223102, 2012.

[11] A. Katsounaros, M. T. Cole, H. M. Tuncer, W. I. Milne, and Y. Hao, "Near-field characterization of chemical vapor deposition graphene in the microwave regime," *Appl. Phys. Lett.*, vol. 102, no. 23, p. 233104, 2013.

[12] X. Huang *et al.*, "Highly Flexible and Conductive Printed Graphene for Wireless Wearable Communications Applications," *Nat. Publ. Gr.*, no. November, pp. 1–8, 2015.

[13] K. Y. Shin, J. Y. Hong, and J. Jang, "Micropatterning of graphene sheets by inkjet printing and its wideband dipole-antenna application," *Adv. Mater.*, vol. 23, no. 18, pp. 2113–2118, 2011.

[14] M. Akbari, M. Khan, M. Hasani, T. Bjorninen, L. Sydanheimo, and L. Ukkonen, "Fabrication and Characterization of Graphene Antenna for Low-Cost and Environmentally Friendly RFID tags," *IEEE Antennas Wirel. Propag. Lett.*, vol. 1, no. c, pp. 1–1, 2015.

[15] H. Subbaraman *et al.*, "Inkjet-Printed Two-Dimensional Phased-Array Antenna on a Flexible Substrate," *Antennas Wirel. Propag. Lett. IEEE*, vol. 12, pp. 170–173, 2013.

[16] X. Cao *et al.*, "Screen printing as a scalable and low-cost approach for rigid and flexible thin-film transistors using separated carbon nanotubes," *ACS Nano*, vol. 8, no. 12, pp. 12769–12776, 2014.

[17] D. A. Pardo, G. E. Jabbour, and N. Peyghambarian, "Application of screen printing in the fabrication of organic light-emitting devices," *Adv. Mater.*, vol. 12, no. 17, pp. 1249–1252, 2000.

[18] W. J. Hyun, E. B. Secor, M. C. Hersam, C. D. Frisbie, and L. F. Francis, "High-resolution patterning of graphene by screen printing with a silicon stencil for highly flexible printed electronics," *Adv. Mater.*, vol. 27, no. 1, pp. 109–115, 2015.

[19] S. Ahmed, F. A. Tahir, A. Shamim, and H. M. Cheema, "A Compact Kapton-Based Inkjet-Printed Multiband Antenna for Flexible Wireless Devices," *IEEE Antennas Wirel. Propag. Lett.*, vol. 14, pp. 1802–

1805, 2015.

[20] B. E. B. Secor and M. C. Hersam, “Graphene Inks for Printed Electronics Inkjet Printable Graphene Ink (793663),” no. c, pp. 2–7, 2016.

Modeling of Millimeter Wave Antenna Conducting Layers Via Adhesive CVD-Graphene on Dielectric Substrate

M. T. Gatte[1 2 *], P. J. Soh[1], M. F. Jamlos[1], R. B. Ahmad[1], M. F. Malek[1,3], H. A. Rahim[1]
[1] Universiti Malaysia Perlis, Malaysia
[2]Ministry of Science and Technology, Bagdad, Iraq
[3]Faculty of Engineering and Information Sciences, University of Wollongong in Dubai, Dubai, United Arab Emirates
*corresponding author, E-mail: mohtaih@gmail.com

Abstract

Due to the difficulties that facing the transfer of graphene onto dielectric substrate of antenna, where sometime the samples produced have tears and cracks due to the process of transfer. A new technique proposed in this study based on adhesion technology. This technique suggest the adhesion of chemical vapor deposition (CVD) graphene to the antenna substrate without removing of the transition metal substrate from the CVD sample. Modeling of antenna based on this technique show promising results, specifically with doped graphene.

1. Introduction

Thanks to its remarkable properties, graphene has been intensively researched, it considers a promising material for devices of next generation wireless communication systems [1], which require high mobility, low power and broadband operation [2]. Graphene can be potentially applied in wireless nanosensors and devices of the THz band [3]. Originally, exfoliating is the commonly standout method for the graphene production of graphene via peeling strips form a graphite. The other method of production is chemical vapor deposition (CVD). The CVD-grow is efficient approach for the production of high-quality monolayer graphene (HQMG) [4]. However, the graphene sheet must be detached from tape or foil, then it transfers to the application substrate [5].

The transfer procedure, of CVD-grow graphene, requires removing the metal substrate beneath the graphene layer to produce HQMG. Supporting layer of polymer (PMMA) has been employed [6]. A simple technique for the graphene transfer from the substrate of copper presented in [7]. However, the process of graphene transfer could be not entirely acceptable, where the samples produced sometime have tears and cracks due to transfer process [4], the solvent cannot completely wash PMMA away [8], PMMA residue tend to behave like scattering centers of charge carriers, which are leading to a degradation in the graphene electrical properties [9].

The bonding between two wafers or substrates represents an important issue in the fabrication, which enables the fabrication of new substrates and also permits for fabricating and packaging of microcomponents[10]. The wafer bonding has used increasingly in the integration of materials [11].

Adhesion technology are used widely in various applications [12]. In adhesive wafer bonding (AWB) an adhesive intermediate layer is employed for bonding between surfaces. The main features of AWB involve, insusceptible to the surface contour, lower bonding temperatures, compatible with processing of integrated circuit wafer, and able to join various wafers. AWB does not need specific treatments to the wafer surface. Textures and particles at wafer surfaces can be overcome via an adhesive material[12]. A review of the recent studies on adhesion with a specific concentration on its mechanisms presented in [14]. According to the above review, the adhesion plays a significant role in the above technologies, while there are no significant studies employ this technique in antennas fabrication. So the employment of adhesion in the fabrication graphene-based antennas is a promised consideration.

In this study a new technique for graphene utilization, adhesion of CVD monolayer graphene without the process of transfer graphene on the target substrate, in the millimeter wave (MMW) microstrip patch antenna design, modeling and characterization. The calculated performance parameters of antenna based on the proposed technique show promising value at the designed resonance frequency, which are shown in Table:1 that elaborate comparison between copper based antenna and adhesive CVD graphene based antenna performance parameters.

Table1: Antenna parameters for non-doped (NDG) and doped graphene (DG) referenced to Copper.

The materials of antenna conductive layers for both Patch and Ground	Patch Width in μm	f_r in THz	S_{11} at f_r in –dB		Gain in dB		η_{rad} at f_r (%)		Prad in watt	
			NDG	*DG*	*NDG*	*DG*	*NDG*	*DG*	*NDG*	*DG*
Adhesive CVD graphene	**1500**	**0.0695**	**21.49**	**24.35**	**6.46**	**6.9**	**80.36**	**89.43**	**0.398**	**0.441**
Copper based	**1500**	**0.0745**	**19.22**		**6.74**		**80.37**		**0.396**	

2. Conclusions

The results that has been gotten in this study considers promising for the researchers of antenna, who are interesting to employ graphene in high frequencies of microwave band and the lower frequencies of millimeter wave band. Where many of antenna engineers and antenna laboratory lack to the facilities and technical knowledge of the graphene production. The new technique based on the modeling design and fabrication of graphene depending on the products of CVD graphene (available in the required dimensions) fabricated from specific factories for graphene production.

References

[1] A. K. Geim and K. S. Novoselov, "The rise of graphene.," *Nat. Mater.*, vol. 6, no. 3, pp. 183–191, 2007.

[2] S. Anand, D. S. Kumar, R. Jang, and M. Chavali, "Graphene nanoribbon based terahertz antenna on polyimide substrate," *Opt. - Int. J. Light Electron Opt.*, vol. 125, no. 19, pp. 5546–5549, 2014.

[3] I. F. Akyildiz and J. M. Jornet, "Electromagnetic wireless nanosensor networks," *Nano Commun. Netw.*, vol. 1, no. 1, pp. 3–19, 2010.

[4] X. Li, W. Cai, J. An, S. Kim, J. Nah, D. Yang, R. Piner, A. Velamakanni, I. Jung, E. Tutuc, S. K. Banerjee, L. Colombo, and R. S. Ruoff, "Large-area synthesis of high-quality and uniform graphene films on copper foils.," *Science (80-.).*, vol. 324, no. 5932, pp. 1312–1314, 2009.

[5] K. S. Novoselov, V. I. Fal′ko, L. Colombo, P. R. Gellert, M. G. Schwab, and K. Kim, "A roadmap for graphene," *Nature*, vol. 490, no. 7419, pp. 192–200, 2012.

[6] N. Liu, L. Fu, B. Dai, K. Yan, X. Liu, R. Zhao, and Y. Zhang, "A Universal Segregation Growth Approach to Wafer-size Graphene from Non-noble Metals," *Nano Lett., ACS*, vol. 11, no. 1, pp. 297–303, 2011.

[7] P. Gupta, P. D. Dongare, S. Grover, S. Dubey, H. Mamgain, A. Bhattacharya, and M. M. Deshmukh, "A facile process for soak-and-peel delamination of CVD graphene from substrates using water.," *Sci. Rep.*, vol. 4, p. 3882, 2014.

[8] M. Her, R. Beams, and L. Novotny, "Graphene transfer with reduced residue," *Phys. Lett. Sect. A Gen. At. Solid State Phys.*, vol. 377, no. 21–22, pp. 1455–1458, 2013.

[9] M. Jang, T. Q. Trung, J. Jung, B. Kim, and N. Lee, "Improved performance and stability of field-effect transistors with polymeric residue-free graphene channel transferred by gold layer.," *Phys. Chem. Chem. Phys.*, vol. 16, no. 9, pp. 4098–105, 2014.

[10] K. Petersen, P. Barth, J. Poydock, J. Brown, J. Mallon, and J. Bryzek, "Silicon fusion bonding for pressure sensors," in *IEEE Technical Digest on Solid-State Sensor and Actuator Workshop*, 1988, pp. 144–147.

[11] U. Gösele, Y. Bluhm, G. Kästner, P. Kopperschmidt, G. Kräuter, R. Scholz, a. Schumacher, S. Senz, Q.-Y. Tong, L.-J. Huang, Y.-L. Chao, and T. H. Lee, "Fundamental issues in wafer bonding," *J. Vac. Sci. Technol. A Vacuum, Surfaces, Film.*, vol. 17, no. 4, p. 1145, 1999.

[12] F. Niklaus, G. Stemme, J. Q. Lu, and R. J. Gutmann, "Adhesive wafer bonding," *J. Appl. Phys.*, vol. 99, no. 3, pp. 4–6, 2006.

[13] H. Guo, Y. Qi, and X. Li, "Adhesion at diamond/metal interfaces: A density functional theory study," *J. Appl. Phys.*, vol. 107, no. 3, 2010.

[14] F. Awaja, M. Gilbert, G. Kelly, B. Fox, and P. J. Pigram, "Adhesion of polymers," *Prog. Polym. Sci.*, vol. 34, no. 9, pp. 948–968, 2009.

Millimeter Wave Antennas Coated using Monolayer Graphene

M. T. Gatte[1 2 *], P. J. Soh[1], M. F. Jamlos[1], R. B. Ahmad[1], M. F. Malek[1,3], H. A. Rahim[1]

[1] Advanced Communication Engineering (ACE) CoE, Sch. of Computer & Communication Engineering, Universiti Malaysia Perlis, Malaysia

[2]Ministry of Science and Technology, Bagdad, Iraq

[3]Faculty of Engineering and Information Sciences, University of Wollongong in Dubai, Dubai, United Arab Emirates

*corresponding author, E-mail: mohtaih@gmail.com

In millimeter-wave (MMW applications, the conducting parts of most communication devices can easily degrade when using conventional metals such as copper. Moreover, oxidation could also take place when such devices are operated in harsh environmental conditions. Conventional conductors such as copper in most of these devices are coated with other materials to overcome this problem. In this study, doped and non-doped monolayer graphene are employed as coating layers of conductors for MMW antennas. Results indicated that coating such antennas using monolayer graphene improves the antenna performance at MMW frequencies.

Graphene, is a single-atom layer of graphite, has an exceptional combined properties that are perfect for corrosion protection coating in different applications, for example, microelectronic parts (interconnects, implantable devices and aircraft components) [1]. Coating is considered an essential technique in enhancing surface quality and giving protection to a substrate or conductor. Attempts have been made to create excellent device properties via coating using graphene [2]. The evaluation, future perspective, and brief description of the production and functionalization of graphene as coating material were studied and proposed in [3]. Many recent pioneering studies have elaborated the ability of graphene to efficiently decouple their underlying surface with the environment Specifically, the inert chemical property of graphene leads to its employment as a defensive metal layer against oxidation and corrosion in electrochemical applications [4]. Besides that, both monolayer and multilayered graphene films have exhibited acceptable transparency [5], indicating that graphene coating does not alter the optical features of the metal placed beneath it [6].. Moreover, the monolayer graphene films are impermeable to the gas molecules [7]. , with a good capability in protecting the underlying metal (copper) against oxidation [8] [1]. The utilization of chemical vapor deposition (CVD) graphene films demonstrates anti-oxidation ability of the metallic surfaces grown on Cu and Cu/Ni alloys [8]. Graphene coating of copper increases their resistance to the electrochemical degradation [9], while low-alloy steels coated with graphene nanocomposite enhanced anticorrosive efficacy by more than three orders in comparison to bare steel [10].

From the antenna design point of view, low loss coating materials are crucial in protecting its existing conductors besides being satisfactory in terms of conductivity, which significantly contributes to antenna performance [11]. In this work, a monolayer graphene is used to coat the metallic surfaces of patch antennas. Coating the patch significantly improved gain, radiated power and radiation efficiency, besides featuring lower losses. .The proposed antennas were coated using two types of coatings: doped and non-doped monolayer graphene. These conductive layers are then utilized as either the patch only or patch and ground of the milimeterwave antenna. The resulting antenna performance is doubled when monolayer graphene is used to coat both conducting layers (the patch and ground) of the proposed microstrip antenna[12]. Moreover, monolayer graphene coating indicated very good results, and this is further enhanced when doped graphene is used at these frequencies. Table 1 summarizes the performance for an elliptical patch antenna when its conducting (copper) layers were coated with gold, non-doped graphene, and doped graphene. The results

indicated that coating copper with doped graphene improved the performance of the antenna most efficiently.

Table 1 Performance of the copper based elliptical patch antenna when the antenna conducting (copper) layers coated with gold, non-doped graphene, and doped graphene.

	PatchWidth W in μm	fr in THz	S_{11} at fr in –dB	Gain in dB	η_{rad} at fr (%)	Prad in watt	Lmet in watt
Copper Based	2000	0.0643	27.261	6.805	82.39	0.401	0.0413
Gold Coating	2000	0.0643	26.79	6.764	81.65	0.397	0.0463
Non-doped Graphene Coating	2000	0.0642	23.574	6.626	78.95	0.381	0.0619
Doped Graphene (0.5eV μc) Coating	2000	0.0645	25.30	7.29	91.85	0.435	0.0014

[1] D. Prasai, J. C. Tuberquia, R. R. Harl, G. K. Jennings, and K. I. Bolotin, "Graphene: Corrosion-inhibiting coating," *ACS Nano*, vol. 6, no. 2, pp. 1102–1108, 2012.

[2] R. Garg, N. Dutta, and N. Choudhury, "Work Function Engineering of Graphene," *Nanomater. MDPI*, vol. 4, no. 2, pp. 267–300, 2014.

[3] Y. Tong, S. Bohmb, and M. Song, "Graphene Based Materials and Their Composites as Coatings," *Austin J. Nanomedicine Nanotechnol.*, vol. 1, no. 1:1003, pp. 1–16, 2013.

[4] T. H. Seo, S. Lee, H. Cho, S. Chandramohan, E.-K. Suh, H. S. Lee, S. K. Bae, S. M. Kim, M. Park, J. K. Lee, and M. J. Kim, "Tailored CVD graphene coating as a transparent and flexible gas barrier.," *Sci. Rep.*, vol. 6, no. January, p. 24143, 2016.

[5] S. Bae, H. Kim, Y. Lee, X. Xu, J.-S. Park, Y. Zheng, J. Balakrishnan, T. Lei, H. Ri Kim, Y. Il Song, Y.-J. Kim, K. S. Kim, B. Özyilmaz, J.-H. Ahn, B. H. Hong, and S. Iijima, "Roll-to-roll production of 30-inch graphene films for transparent electrodes," *Nat. Nanotechnol.*, vol. 5, no. 8, pp. 574–578, 2010.

[6] R. R. Nair, P. Blake, a. N. Grigorenko, K. S. Novoselov, T. J. Booth, T. Stauber, N. M. R. Peres, and a. K. Geim, "Fine Structure Constant Defines Visual Transperency of Graphene," *Science (80-.).*, vol. 320, no. June, p. 2008, 2008.

[7] J. S. Bunch, S. S. Verbridge, J. S. Alden, A. M. Van Der Zande, J. M. Parpia, H. G. Craighead, and P. L. McEuen, "Impermeable atomic membranes from graphene sheets," *Nano Lett.*, vol. 8, no. 8, pp. 2458–2462, 2008.

[8] S. Chen, L. Brown, M. Levendorf, W. Cai, S.-Y. Ju, J. Edgeworth, X. Li, C. W. Magnuson, A. Velamakanni, R. D. Piner, J. Kang, J. Park, and R. S. Ruoff, "Oxidation resistance of graphene-coated Cu and Cu Ni alloy.," *ACS Nano*, vol. 5, no. 2, pp. 1321–7132, 2011.

[9] R. K. Singh Raman, P. Chakraborty Banerjee, D. E. Lobo, H. Gullapalli, M. Sumandasa, A. Kumar, L. Choudhary, R. Tkacz, P. M. Ajayan, and M. Majumder, "Protecting copper from electrochemical degradation by graphene coating," *Carbon N. Y.*, vol. 50, no. 11, pp. 4040–4045, 2012.

[10] B. R. V Dennis, L. T. Viyannalage, and V. Anil, "Nanocomposite Coatings for Protecting Low- Alloy Steels From Corrosion," *Am. Ceram. Soc. Bull.*, vol. 92, no. 5, pp. 18–24, 2013.

[11] Y. Huang and K. Boyle, *ANTENNAS FROM THEORY TO PRACTICE*. John Wiley and Sons, Ltd, 2008.

[12] M. T. Gatte, P. J. Soh, R. B. Ahmad, M. F. Jamlos, M. F. Malek, and H. A. Rahim, "Improvement of Metal-Based THz Patch Antenna Parameters Using Monolayer Graphene," *META'16, 7th Int. Conf. Metamaterials, Photonic Cryst. Plasmon.*, vol. 1, no. July, pp. 25–28, 2016.

Photonics based on 2D materials

Engineering of electronic bands structure and magneto-transport properties in a semimetallic InAs/GaSb superlattice for Terahertz detection

Abderrazak Boutramine, Abdelhakim Nafidi, Driss Barkissy, Abdelkrim Hannour, Mustapha Massaq

Laboratory of Condensed Matter Physics Nano-Re, University Ibn Zphr, 80000 Agadir, Morocco
*corresponding author, E-mail: nafidi21@yahoo.fr

Abstract

We have solved the full 6×6 Kane Hamiltonian within the envelop function formalism to calculate the band structure $E(d_1)$, $E(k_z)$ and $E(k_p)$, respectively, as a function of InAs well width d_1, in the growth direction and in-plan of the long-period InAs(d_1= 160 Å)/GaSb(d_2= 105 Å) type II superlattice (T2SL), with the valence bands offset Λ= 510 meV. The carrier's effective masse $m^*(k_z, k_p)$ is successfully described over the first Brillouin zone. Moreover, for a fixed ratio d_1/d_2= 1.52, the dependencies of SL band gap on d_1 and/or d_2 as well as on Λ and temperature are investigated. The photodetector absorption wavelength, $|\lambda_c|$ is found to be further optimized by the proper choice of d_1 and/or d_2. The semiconductor to semimetal transition is also analyzed in the range of 4.2-300 K. The Fermi energy is relatively insensitive to the temperature and increase from 504.5 to 514.5 meV. At 141 K, using the Boltzmann magnetic-field-dependent Hall coefficient, we have the transport parameters n_e= $3.1.10^{12}cm^{-2}$, n_h= $4.6.10^{12}cm^{-2}$, μ_e= 137343.7 $cm^2/V.s$, μ_h= 442.2 $cm^2/V.s$ and the Hall mobility μ_H= $1.37.10^6 cm^2/V.s$. The conductivity shows the transition from p-type to n-type. In the studied temperature range, the absorption wavelength situates this sample as a terahertz photodetector.

1. Introduction

The broken-gap InAs/GaSb type-II superlattice (T2SL) have proved to be an attractive system for both military and civilian applications [1]. The fabrication of InAs/GaSb SL has stimulated a growing number of experimental and theoretical studies, including the first proposed in 1977 by Sai-Halasz et al.[2] and GaInSb/InAs strained-layer SL infrared detectors proposed by Smith and Mailhiot in 1987 [3]. The intriguing aspect of InAs/GaSb lies in its extreme type-II "broken gap" band alignment, wherein the conduction band (CB) minimum of InAs lies below the valence band (VB) maximum in GaSb. In contrast to conventional SLs such as GaAs/AlAs in which the conducting electrons and holes are located mainly within the same layer. In T2SL the conduction states are found to be confined primarily on the InAs side, whereas the valence states are confined on the GaSb side. Thus, the ground state of this system is separated spatially in different well layers. Therefore, the positions of the SL CB and VB edges can be, to first order, tuned independently. As a result, when it is irradiated by an infrared light, the photon absorption condition can be easily satisfied since the SL band-gap can be tailored to a desired value anywhere from zero to a few hundred meV by choosing the appropriate well and barrier widths. Another distinctive feature of this SL is associated with the relatively light electron mass in InAs layer. Then, the corresponding de Broglie wavelength is so long that, even for thicker GaSb layer thickness, there is considerable tunnelling probability between electrons in successive InAs layers.

From technological perspective, T2SLs have proven to be an excellent material for third-generation infrared (IR) photodetectors [4], tunnel field-effect transistors [5] and high-power light emitting diodes [6]. Recently a good photodetector performance has been demonstrated for focal plane arrays (FPAs) [7]. In the other hand, many fundamental studies on T2SLs material, such as the in-plan and vertical effective masses [8], mobilities [9], and carrier concentration [10], have been conducted for a better understanding of the electronic transport. Despite these impressive progresses, because of their low detection efficiency, such a SLs with long periodicity has been less concerned for photodetection. A good practical applications of T2SLs require a good understanding of their bands structure. In this work, we will prove that with the band structure engineering; this kind of SLs can be used for high-efficiency terahertz (THz) photodetectors.

2. Model and calculation method

Many theories have been conducted for calculating the electronic properties of semiconductor heterostructures. However, different sophisticated theories based on k.p theory, like the envelope-function formalism [11], have been very popular. In this work we show that it is possible to predict the complete photodetector response using only small number of band parameters, together with the widths of the layers in the detector structure.

We have solved the full 6×6 Kane Hamiltonian within the envelop function formalism in the first Brillouin zone. The general dispersion relation of the particles (electrons, light and heavy holes) subbands are given by [11]:

$$\cos[k_z(d_1+d_2)] = \cos(k_1 d_1)\cos(k_2 d_2) - \frac{1}{2}[(\xi+\frac{1}{\xi}) + \frac{k_p}{4k_1k_2}(r+\frac{1}{r} \quad 2)] \times \sin(k_1 d_1)\sin(k_2 d_2) \qquad (1)$$

Here we employ the following notations to describe such a SL. The subscripts 1 and 2 stand to InAs and GaSb layers, respectively. d_1 refers to the InAs layer width, and d_2 to the GaSb layer width. The 2D wave vector $k_p(k_x, k_y)$ describes the motion of particles perpendicularly to k_z. The SL states are labeled by an index i, which identifies the subbands E_i, h_i and HH_i, for electron, light and heavy holes subbands, respectively. The procedure of our band structure computation has been discussed in our previous work [12]. The zero energy is taken at the top of the InAs VB edge.

The temperature dependence of the SL band gap energy is introduced in our calculation by taking into account the temperature dependence of the two bulks band gap energies.

3. Results and discussion

We have calculated, over the first Brillouin zone, the dispersion relations for InAs(d_1= 160 Å)/GaSb(d_2= 105 Å) T2SL at 141 K. Figure.1(a) shows the dispersion results along the in-plan (k_p) (in the left hand panel) and the growth (k_z) (in the right hand panel) directions. Two lowest CBs and three highest VBs are shown. It was necessary to include a second electron subband E_2 for this sample due to the wider InAs layer. The layers are thicker enough that HH_i(i= 1, 2) lie higher in energy than both E_1 and h_1, thus the SL is semimetallic with a small and negative energy gap of $E_g = E_1\text{-}HH_1$= –65.4 meV. The corresponding cut-off wavelength is 24 µm and the cut-off frequency is f_c= 12.5 THz. The latter justify the choice of this sample for THz detection. We have calculated the energy of Fermi level by:

$$E_F(2D) = \frac{h^2 k_F^2(2D)}{2m^*_{HH1}(\Gamma)} \text{ with } k_F(2D) = \sqrt{2\pi|n_h - n_e|} \qquad (2)$$

where $m^*_{HH1}(\Gamma)$ = -0.45 m_0 is our calculated heavy hole effective masse and the measured net hole concentration is $|n_h\text{-}n_e| = 1.51.10^{12}$ cm^{-2} [13]. E_F(2D)= 511.7 meV, indicates that this SL had a p-type conductivity at 141 K.

As seen in Figure.1 (b), when the temperature decreases, the variation of SL band gap E_g is dominated by the contribution of E_1. Note that the HH_i(i=1,2) states remain almost constant in energy. In the studied temperature range, the position of the Fermi energy has been evaluated by (2). When the temperature increases from 4.2 K to 300 K, the SL band gap and the Fermi level increase, respectively, by 50 meV and 11 meV. The latter small variation of E_F indicates that the energy of the Fermi level is constant with a two-dimensional (2D). carrier's gas is

The result plotted in Figure.2 gives the evolutions of the subbands energies and bandwidths as a function of InAs layer width for light particles and heavy-holes at 141 K. All states have **k** vectors at the centre Γ and at the limit of the

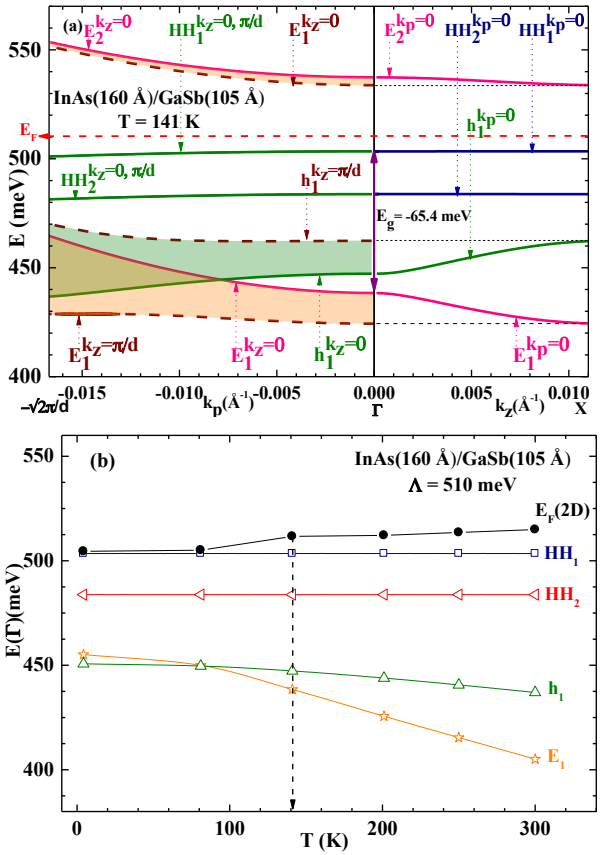

Figure. 1: **(a)** Energy bands structure of InAs(160 Å)/GaSb (105 Å) SL. The growth direction dispersion E(k_z, k_p= 0), the in-plan dispersion E(k_p, k_z=0) and E(k_p, k_z=π/d). HH_i stands to heavy-hole bands, h_1 is the first light hole band, and E_i(i=1,2) refers to the conduction bands. The energy gaps are adjusted according to the given temperature (T= 141 K). E_F stands to the Fermi energy.**(b)** Evolution of the calculated Γ-point energy of light particles, heavy-holes bands and the two-dimensional (2D) Fermi level, plotted as a function of temperature for the investigated InAs/GaSb T2SL.

first Brillouin zone. When d_1 increases, E_1 decreases in the InAs quantum wells. While h_1 and HH_1, located in GaSb quantum wells, increase. It follows that $E_g = E_1\text{-}HH_1$ decreases with increasing d_1. With a further increase in d_1, E_1 and HH_1 invert and the SL becomes semimetallic with overlapping bands. The semiconductor to semimetal conductivity transition occurs at the transition point T_c(d_{1c}= 94.2 Å, E_c= 493.2 meV).

In order to show the effect of InAs (or GaSb) layer thickness on the gap E_g, we have plotted in Figure.3 (a) the variation of E_g, at different temperatures, as a function of d_1. At a fixed InAs layer thickness, $E_g(\Gamma, d_1)$ decreases with increasing temperature.

For each temperature, $E_g(\Gamma, d_1)$ decreases significantly with increasing d_1 and/or d_2, goes to zero at the transition point

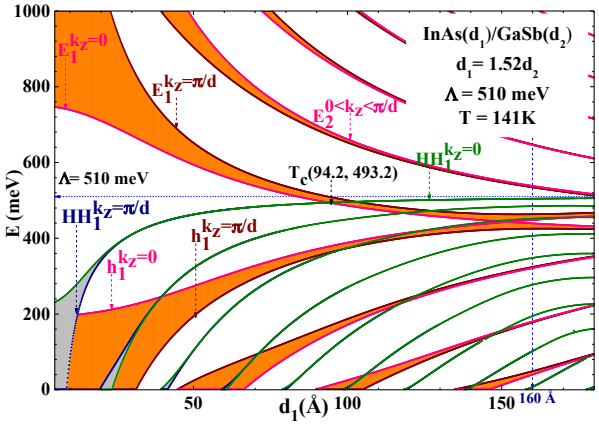

Figure 2. Calculated subband energies and bandwidths at 141K for E_i, HH_i and h_1), at the Γ-point (k_z= 0) and at the limit (k_z= π /d) of the first Brillouin zone, as a function of d_1, with d_1= 1.52d_2 for the investigated SL. The allowed energy bands are hatched. Notice the E_1-HH_1 crossing at T_c(d_{1c}= 94.2 Å, E_c= 493.2 meV) transition point.

T_c(d_{1c}, E_c), with d_{1c}= 104.4, 101, 94.2 and 78.4 Å, respectively, at T= 4.2, 81 , 141 and 300 K. At 141 K for example, when changing InAs well width from 5 to 180 Å, the band gap decreases from 516.6 to -74.2 meV or a 442.5 meV reduction. Using the Tight-binding theory which can describe a system by the location of each constituent atom, Pour et al. [14] calculated the effect of temperature on the energy gap of III–V semiconductors as well as of InAs/GaSb structure. The model suggests that the shifts of our calculated band gap reflect the expansion of the crystal lattice constant which alters the interatomic bonds. Weaker bonds means less energy is needed to break a bond and get an electron in the CB.

Beyond the transition point the band gap becomes negative with a semimetal conductivity. The situation is particularly striking in that a semimetallic SL can be created with two host semiconductors. Accordingly, as shown in the inset of Figure.4, the transition goes to a higher d_1 when the temperature decreases. For this sample, the band gap energy is negative for all studied temperatures, indicating that the SL is in the semimetallic regime, but changes very little with increasing temperature. This variation of E_g is smaller than that observed in our previous study [12] for the shorter period InAs (25Å)/GaSb(25Å) SL. We note that the large band gap observed in figure 3 (a) for small d_1, can be qualitatively understood in terms of the enhancement of the 2D confinement of the wave functions as the layers thicknesses get smaller.

It is interesting to make some remarks about the results reported in Figure.3 (a). For example at 141 K: i) when d_1 approaches zero, the SL band gap tend towards the value of ~ 527 meV. ii) when d_1 get larger, the band gap is obtained to extrapolate to $-\Lambda(1+\varepsilon_2/\varepsilon_1)^{-1}$which is roughly equal to -167 meV in agreement with γ/γ'= -160. The InAs layer width dependence of E_g is described quite well by our deduced expression as shown in Table. 1, where d_1 is expressed in angstroms and E_g in meV.

It is therefore very useful to examine the dependence on d_1 and/or d_2 of the detector absorption wavelength, λ_c(μm). The evolution of $|\lambda_c|$ as a function of d_1 is shown in Figure.3(b). These results were calculated by using the expression:

$$\lambda_c(\mu m)=\frac{1240}{E_g(meV)} \qquad (3)$$

A prominent feature of Figure.3(b) is that $|\lambda_c|$ diverge at T_c. The Figure shows also that the interesting absorption wavelength for infrared detectors around 8-12 μm should correspond at 141K, for example, to the InAs layer width in the range of 45.5 to 56.7 Å which are quite reasonable values from the point of view of the MBE growth. Therefore, in a comparable $In_{1-x}Ga_xAs/GaSb_{1-y}As_y$ alloy, to adequately control λ_c, one must control the compositions x and y with a higher precision.

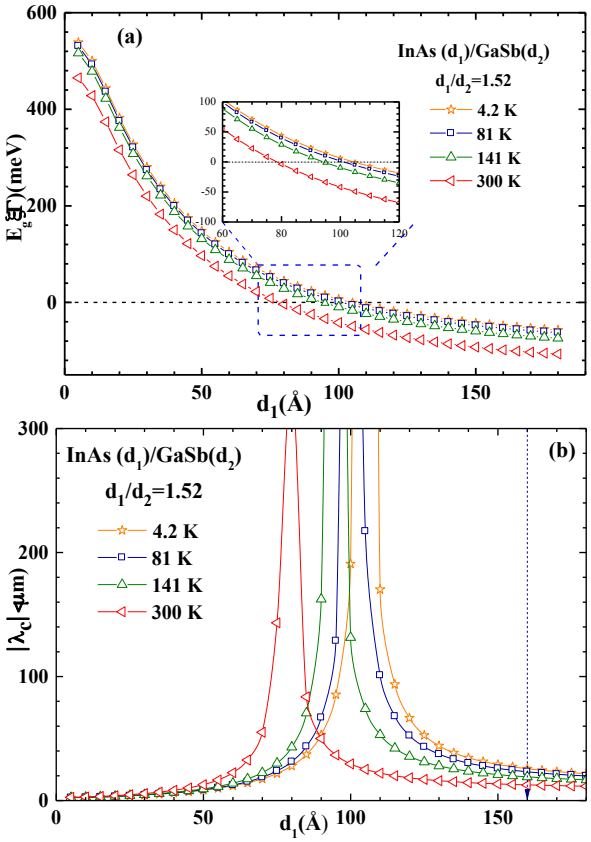

Figure. 3**:** Evolution of **(a)** the band-gap energy between the bottom of the electron miniband in the InAs layer and the top of the heavy-hole miniband in the GaSb layer and **(b)** the corresponding cut-off wavelength, plotted as a function of InAs well width, d_1, with d_1=1.52d_2.

Table. 1: The summary of the parameters that appear in our deduced relation expressing the variation of band gap as a function of InAs layer width for all studied temperatures.

		$E_g(d_1) = (\alpha+\beta d_1+\gamma d_1^2)/(1+\beta' d_1+\gamma' d_1^2)$			
T(K)	α	β	γ	β'	γ'
4.2	550	15.4	-0.195	0.0233	0.0014
81	542	15.5	-0.204	0.024	0.00141
141	527	16.4	-0.232	0.0257	0.00145
300	473	18.8	-0.317	0.0319	0.00159

Based on our calculations, it has been argued that the SL system allows better control over the detector absorption wavelength. For the present sample, the agreement between our results of $|\lambda_c|$(μm)= 25.7, 22.9, 19 and 12.6 and the experimental ones [13] $|\lambda_c|$(μm)= 24.3, 24.8, 24 and 27, respectively for 4.2, 81, 141 and 300 K, is satisfied at low temperature regime. At high temperature regime, the difference is due to the typical measured layer width uncertainty as well as to the fact that InAs and GaSb layers share no-common atoms across the interface. In fact, there are two different types of interfaces in such SLs, namely InSb and GaAs. Many experimental and theoretical studies suggest that the band overlap for an InSb interface is 40 meV larger than that of GaAs. As a consequence the smaller band gap energy can be achieved for InSb interface [15].

Among the most important physical parameter for a given SL is the valence band offset (VBO), at least because it governs the SL band structure and thus many properties of such a SL. Indeed, the quality and even the feasibility of device concepts depend crucially on the value of this VBO. Over the last years there have been a considerable controversy on VBO of InAs/GaSb SL; Srivastava et al. produced Λ= 670 meV [16]. However, M. S. Daly has obtained an average offset of 520 meV [17].

The effect of the VBO on the band structure was investigated by varying the VBO in our script, while holding the other parameters constant for each temperature. In Figure.4 we show the SL band gap, for various temperatures, as a function of Λ. The Figure divides itself into two regimes:

i) For $-200 < \Lambda < \Lambda_c$ meV, the SL is semiconductor with a positive band gap energy. When the offset Λ increases, E_g (Γ, Λ) go to a maximum of 445.7, 439.8, 427.1, and 388.2 meV, respectively, for 4.2, 81, 141 and 300 K at Λ= -60.7 meV. As Λ continues to increase, $E_g(\Gamma)$ shifts strongly to zero yielding a semiconductor to semimetal transition at Λ_c= 463, 457.2, 447.7 and 421.9 meV, respectively, for 4.2 , 81, 141 and 300 K. This can be understood intuitively using this simple model: an increase in the VBO brings the GaSb-VB and the InAs-CB closer to each other, reducing the SL band gap.

ii) For $\Lambda > \Lambda_c$ the system is in the semimetallic regime. Thus, as plotted in the inset of Figure.4, the transition goes to higher Λ_c when the temperature decreases.

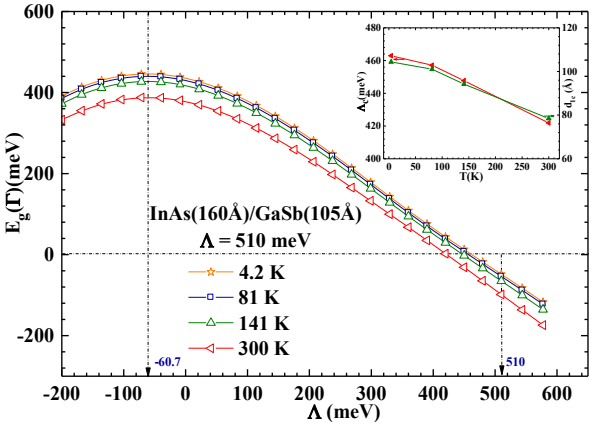

Figure 4: Evolution of the band gap energy of a representative SL with the valence band offset. The calculation includes effects due to temperature. The inset figure shows temperature dependence of the coordinates of the semiconductor-to-semimetal transition point in the investigated InAs/GaSb asymmetric SL.

The most dramatic feature of these results is the rapid variation of the band gap beyond Λ = -60.7 meV.

The effective mass is a necessary parameter for analyzing the carrier transport in materials. A theoretical effective mass in general turns out to be a tensor with nine components m_{ij} defined as [18]:

$$\frac{1}{m^*_{ij}} = \frac{1}{h^2}\frac{\partial^2 E(k)}{\partial k_i \partial k_j} \qquad (4)$$

Where E is the carrier energy and k_{ij} are the components of the wave vector k in a periodic potential of a semiconductor. In Figure.5 (a) we have plotted the carrier's effective mass of two lowest CBs and the first VB, along k_z and k_p, directions, in the reciprocal space. The second derivative of E is obtained directly from the dispersion relations plotted in Figure.1(a). Along k_z direction $m^*_{E1}(k_z, k_p=0)$ varies strongly from the center of the first Brillouin zone, diverges at k_z=3.4.10^{-3}Å^{-1}, and decreases thereafter to 2.510^{-2} m_0 at the limit of the first Brillouin zone. In the two panels, the vertical solid lines correspond to the inflections point of $E(k_p,k_z)$. Since there is no inflection point along k_p, $m^*_{HH1}(k_p, k_z=0)$keep a negative constant value of about -0.45 m_0.

Figure. 5 (b) shows the in-plan carrier's effective masses near k_p= 0, plotted versus temperature. The studied SL , with a relatively small band gaps energies, is seen to have a very small longitudinal light-hole and electron effective masses. This latter decreases slightly from only 3.9.10^{-2} m_0 to 3.7.10^{-2} m_0 when the temperature increases from 4.2 to 300 K. Whereas the heavy-holes effective mass, in the GaSb layer, is constant at about -0.45 m_0 (electron-like). The electron and heavy-hole masses differ from each other and the predicted hole to electron mass ratio $m^*_{HH1}(\Gamma)/m^*_{E1}(\Gamma)$, which increases slightly with temperature, is less than a

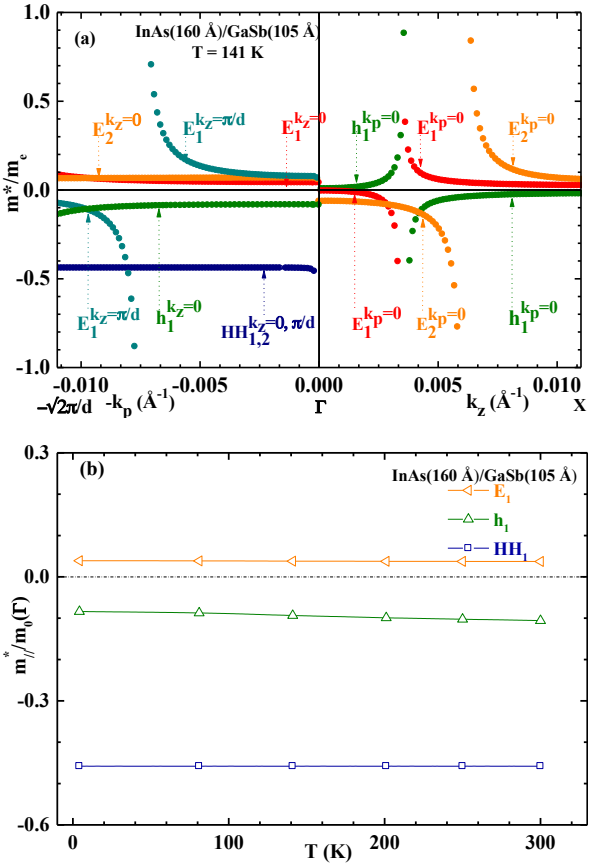

Figure. 5: **(a)** Calculated carriers' effective mass along the growth direction, k_z, and in-plan of the investigated SL at 141K .**(b)** carriers' effective mass as a function of temperature for the representative SL.

factor of 13 over the entire temperature range. This has a significant effect on the in-plan transport properties for free carriers.

4. Hall coefficient and magnetotransport properties

Figure.6 shows the calculated Hall coefficient versus the applied magnetic field at 141 K. Also shown for comparison are the available experimental data. According to the classical expression for the Hall coefficient of two-band model derived from the Boltzmann equation [19]:

$$R_H=[(\mu_h^2 n_h-\mu_e^2 n_e)+(\mu_h\mu_e)^2B^2(n_h-n_e)]/ [e(\mu_e n_e+\mu_h n_h)^2+(\mu_h\mu_e)^2B^2(n_h-n_e)^2] \quad (5)$$

This equation can be simplified as:

$$R_H=(\alpha^2\beta-1)+(\beta-1)\mu_h^2B^2/n_e e(1+\alpha\beta)^2(\beta-1)^2\mu_h^2B^2 \quad (6)$$

Where: $\alpha=\mu_h/\mu_e$ and $\beta=n_h/n_e$

At a weak magnetic fields, the Hall resistance is inversely proportional to n_e and is described by the following formula:

$$R_H^w=e^{-1}(\alpha^2\beta-1)/n_e(1+\alpha\beta)^2 \quad (7)$$

While at high magnetic fields for $\mu B >>1$, Equation (3) is well approximated by:

$$R_H^h=1/e(n_h-n_e) \quad (8)$$

These results show that R_H keep almost magnetic field independent below 10T. However, when the magnetic field increases above 10T, R_H go to zero and changes sign to negative value at:

$$B_0=[(1+\alpha^2\beta)/(\beta-1)\mu_h^2]^{0.5}=32.4\ T \quad (9)$$

A reproducible change of sign of R_H is a clear signature of the coexistence of at least two types of carriers, which suggests a semimetallic character of the conduction mechanism, and also the dominance of holes transport for B ≤ 32.4 T. This was confirmed by the observation of the oxford group regarding the field dependence of Hall resistance [13]. They found that the dependence of the Hall resistance on magnetic field curves go down at high temperature (especially at 141 K), indicating that the hole concentration is slightly larger than that of the electrons ($\beta \backsim 2$). The Hall mobility is given by:

$$\mu_H=\mu_e/(1+\alpha\beta) \quad (10)$$

The difference in carrier concentration, n_h-n_e=1.5.10^{12} cm^{-2} was extracted from the slope ($\backsim R_H^h$) of the Hall resistance at high magnetic fields [13]. This value constitutes strong signature for the existence of interface and donor states. By a simple combination between (7) and (9), we have found: n_e= 3.1.$10^{12}cm^{-2}$, n_h= 4.6.$10^{12}cm^{-2}$, μ_e= 137343.7 cm^2/V.s, μ_h= 442.2 cm^2/V.s and the Hall mobility μ_H= 1.37 10^6 cm^2/V.s. Such a low value of hole mobility carrier's is consistent with high value of the effective masse of heavy holes $m^*_{HH1}(\Gamma)$ = -0.45 m_0.

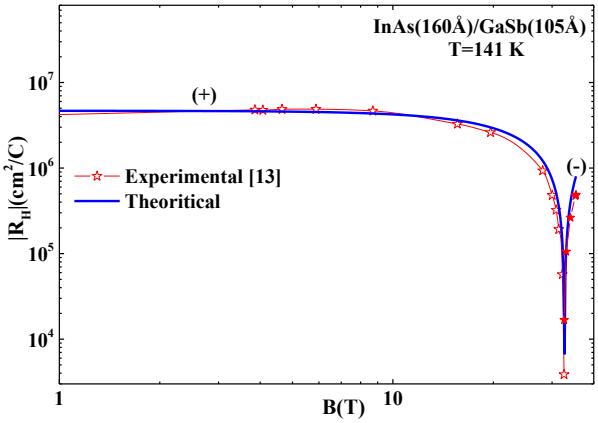

Figure. 6: Hall coefficient versus the magnetic field at 141K for the investigated SL. The open stars are positive values while the solid stars are negative.

5. Conclusion

We have used the envelop function formalism (EFF) for the proper engineering of electronic bands structure of a long-period InAs (d_1= 160 Å)/GaSb (d_2= 105 Å) T2SL for THz photodetection. We have investigated in detail the dispersion relations in the reciprocal space at 141 K. The photodetector parameters like fundamental band gap, absorption wavelength, and the carrier's effective masse were treated as a function of d_1/and or d_2, and temperature for a constant ratio of d_1/d_2=1.52. The band gap E_g decreases when d_1 increases. The evolutions of $E_g(\Gamma)$ as a function of d_1 and Λ, shows that the semiconductor to semimetal transition goes to higher d_{1c} and Λ_c when the temperature decreases.

For T≤ 141 K, our results are in agreement with the experimental data. Further, on the basis of the Boltzmann Hall coefficient magnetic field-dependent, we have interpreted the magnetoresistance results of D. M. Symons et al. We have observed the p-type to n-type conductivity transition. The transport parameters of this SL are: n_e= $3.1.10^{12}cm^{-2}$, n_h= $4.6.10^{12}cm^{-2}$, μ_e= 137343.7 cm^2/V.s, μ_h= 442.2 cm^2/V.s and the Hall mobility μ_H= $1.37.10^6cm^2$/V.s. The Fermi energy is relatively insensitive to the temperature and found to increase from 504.5 to 514.5 meV. The range of absorption wavelength $25.7 \leq |\lambda_c|(\mu m) \leq 12.6$, corresponding to the cut-off frequency $11.6 \leq |f_c|(THz) \leq 23.8$ indicates that this sample can be used as a terahertz (THz) detector.

Acknowledgements

The authors would like to acknowledge Professor Robin Nicholas, leader of the Semiconductor nanostructures group in Clarendon Laboratory, Parks Road, Oxford, OX1 3PU, UK, for permitting us to use the experimental results reported in Fig. 4 cited in [13].

References

[1] M. Razeghi and Binh-Minh Nguyen, Advances in mid-infrared detection and imaging: a key issues review, *Rep. Prog. Phys,* 77: 082401(17pp), 2014.

[2] G. A. Sai-Halasz, R. Tsu, and L. Esaki. A new semiconductor superlattice, *Appl. Phys. Lett*, 30: 651-653, 1977.

[3] D. L. Smith and C. Mailhiot, Proposal for strained type II superlattice infrared detectors, *J.Appl.Phys*, 62: 2545-2548, 1987.

[4] A. Rogalski and P. Martyniuk, InAs/GaInSb superlattices as a promising material system for third generation infrared detectors, *Infrared Phys. Technol.* 48, 39 , 2006.

[5] J.-S. Liu, Y. Zhu, P. S. Goley, and M. K. Hudait, Hetero interface Engineering of Broken-Gap InAs/GaSb Multilayer Structures, *ACS Appl. Mater. Interfaces* 7, 2512 , 2015.

[6] L. M. Murray, D. T. Norton, J. T. Olesberg, T. F. Boggess, and J. P. Prineas, Comparison of tunnel junctions for cascaded InAs/GaSb superlattice light emitting diodes, *J. Vac. Sci. Technol. B* 30, 021203 , 2012.

[7] D. Ting, A. Soibel, L. Hoglund, J. Nguyen, C. Hill, A. Khoshakhlagh, S.D. Gunapala, Chapter 1 – Type-II Superlattice Infrared Detectors, *Semiconductors and semimetals, Adv. Infrared Photodetect*. 84, 1–57, 2011

[8] S. Suchalkin, G. Belenky, S.P. Svensson, B. Laikhtman, D. Smirnov, L.C. Tung, S. Bandara, In plane and growth direction electron cyclotron effective mass in short period InAs/GaSb semiconductor superlattices, *J. Appl. Phys*. 110, 043720, 2011.

[9] F. Szmulowicz, G.J. Brown, Calculation of interface roughness scattering limited vertical and horizontal mobilities in InAs/GaSb superlattices as a function of temperature*, J. Appl. Phys*. 113, 014302, 2013.

[10] X. Guo, W. Ma, J. Huang, Y. Zhang, Y. Wei, K. Cui, Y. Cao, Q. Li, Electrical properties of the absorber layer for mid, long and very long wavelength detection using type-II InAs/GaSb superlattice structures grown by molecular beam epitaxy, Semicond. *Sci. Technol*. 28, 045004, 2013.

[11] G. Bastard, Superlattice band structure in the envelope-function approximation, *Phys. Rev. B*, 24: 5693-5697, 1981.

[12] A Boutramine, A Nafidi, D Barkissy, A Hannour, A Elanique, T El Gouti , "Application of the transition semiconductor to semimetal in type II nanostructure superlattice for mid-infrared optoelectronic devices", *Applied Physics A*, Volume 122, 4, 70-76 , 2016.

[13] D.M. Symons, M. Lakrimi, M. van der Burgt, T.A. Vaughan, R.J. Nicholas, N.J. Mason, P.J. Walker, Temperature dependence of the band overlap in InAs/GaSb structures. *Phys. Rev. B* 51, 1729 ,1995.

[14] S. A. Pour , B. Movaghar and M. Razeghi, Tight-binding theory for the thermal evolution of optical band gaps in semiconductors and superlattices *Phys. Rev. B* 83, 115331, 2011.

[15] R.H Miles, J.N Schulman, D.H Chow and T.C Mc Gill, M, Electronic band structure of far-infrared Ga1-xInxSb/InAs superlattices, *Semi. Sci and Technol* 8.1S 102–105, 1993.

[16] A. K. Srivastava, J. L. Zyskind, R. M. Lum, B. V. Dutt, and J. K. Klingert, Electrical characteristics of InAsSb/GaSb heterojunctions, *Appl. Phys. Lett*, 49: 41, 1986.

[17] M. S. Daly, D. M. Symons, M. Lakrimi, R. J. Nicholas, N. J. Mason, and P. J. Walker, Interface composition dependence of the band offset in InAs/GaSb , *Semicond. Sci. Technol,* 1: 823,1996.

[18] C. Kittel, Introduction to Solid State Physics, Wiley, New York, 3rd edn, pp. 333, 2001.

[19] Y. Sun, T. Taen, T. Yamada, S. Pyon, T. Nishizaki, Z. Shi, T. Tamegai, Multiband effects and possible Dirac fermions in $Fe_{1+y}Te_{0.6}Se_{0.4}$, Phys. Rev. B - *Condens. Matter Mater. Phys*. 89, 1–7, 2014.

Patch antenna enhanced graphene infrared photodetectors

J. Zhou[1*], C. L. Liu[1], D. H. Zhang[1,2], L. Wang[1], X. S. Chen[1], W. Lu[1]

[1] National Laboratory for Infrared Physics, Shanghai Institute of Technical Physics, Chinese Academy of Sciences, China

[2]School of Materials Science and Engineering, Shanghai University, China

[*]corresponding author: jzhou@mail.sitp.ac.cn

Abstract-By integrating a graphene photodetector with an optical patch antenna, the responsivity is enhanced in both optical and electrical way. At resonance, the absorption of the single layer graphene is increased by ~29 times. Besides, the top patches connected with an electrode extend the graphene/contact borderline and hence enlarges the optical sensitive area. The asymmetrical distribution of the top patches over the two contacts allows a net signal under uniform flood illumination.

Graphene has attracted significant attention as a promising candidate for infrared photodetection because of its broadband absorption, ultrafast carrier dynamics, and good controllability through electrostatic doping [1,2]. However, the efficiency of those graphene based photodetectors (PD) is limited by the poor absorption as a consequence of the atomic thickness. Micro photonic structures, such as waveguides and photonic crystal micro cavities, could largely enhance the absorption of graphene, but suffer from the bulky pixel sizes [3,4]. Nano photonic structures, such as plasmonic resonantors and nano antennas, offer a more compact solution [5-7]. However, in order to enhance the practical responsivity of graphene PDs and preserve their unique advantages, designing of the nano photonic structures requires more study with consideration on the optical as well as electrical properties of the devices. For example, the incident light should be converted into a local field as much as possible. The intense local field should be absorbed by the optical sensitive part of the device instead of being dissipated as loss. For the most popular metal-graphene-metal architecture, since the p-n junctions required for photocurrent generation are close to the contacts, the nano photonic structure not only needs to create the intense local field close to the contact but also needs to extend the contact borderline for a better signal collection.

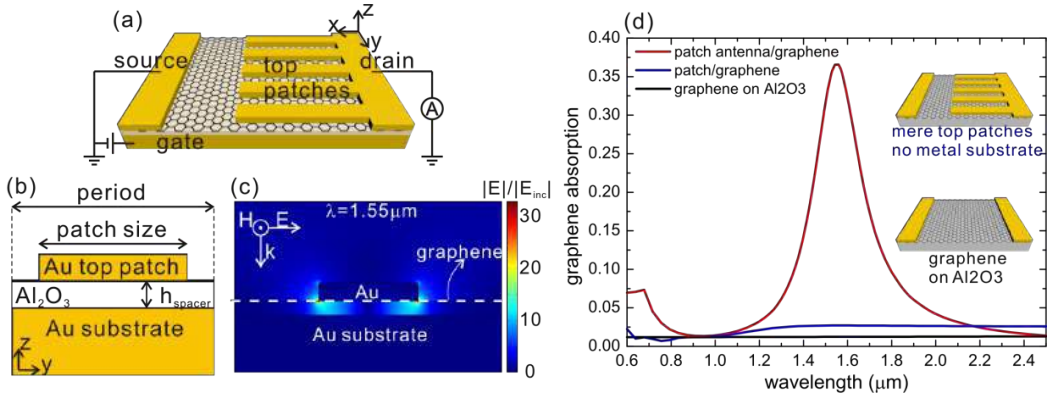

Fig. 1 (a) Sketch of the patch-antenna-graphene PD. (b) One period of the patch-antenna-graphene combination in the *z*-*y* cross section. (c) Simulated electric field distribution of the patch-antenna-graphene combination at the

resonant wavelength of 1.55 μm. The colored surface represents the electric field intensity normalized to the incident light. The patch width is 218 nm; the patch height 40 nm; the period 588 nm; and the spacer thickness 30 nm. (d) Graphene absorption spectra of the patch-antenna-graphene PD, the bare graphene layer on Al_2O_3 and the graphene layer with metal patch array. The metal patches are designed to have a resonance at 1.55 μm. The patch width is 290 nm; the patch height 40 nm; and the period 800 nm.

Based on these considerations, we propose a graphene infrared PD integrated with an optical patch antenna, as shown in Fig. 1 (a). A single layer graphene is transferred onto a metal plane (Au) coated with a dielectric spacer (Al_2O_3). Above the graphene, the contacts and some metal patches are fabricated. The patches together with the bottom metal plane and the dielectric spacer form an optical patch antenna. The cross section is shown in Fig. 1 (b). Due to the Fabry-Perot like resonance of the metal-insulator-metal waveguide mode, the incident light with TM polarization is mostly coupled into a local field as shown in Fig. 1 (c). In this way, the graphene layer just beneath the top patch overlaps with the most intense field and hence has a big absorption. For demonstration, the patch antenna's geometry parameters are designed for the resonance at 1.55 μm. The peak absorption is 37%, ~29 times higher than that of a bare graphene layer on a Al_2O_3 substrate, and ~14 times higher than that of a graphene layer with a common plasmonic structure. The plasmonic structure is represented by a metal patch array (Fig. 1 (d) inset). The geometry parameters are designed to make the resonance around 1.55 μm. Besides the improvement in optical absorption, the patch antenna structure also benefits the signal generation in an electrical manner. First, the top patches serving as the tentacles of the contact greatly extend the borderline and hence increase the optical sensitive area. Second, the asymmetrical distribution of the top patches (all at one contact) induces much stronger light absorption at one contact and thus makes the photocurrent collected by this contact overwhelms the other, leading to a net signal under uniform flood illumination on both contacts of the device. This patch-antenna-graphene PD is suitable for a wide range of wavelengths in the infrared range.

REFERENCES

1. Koppens, F., T. Mueller, Ph. Avouris, A. Ferrari, M. Vitiello, M. Polini, "Photodetectors based on graphene, other two-dimensional materials and hybrid systems", *Nat*. *Nanotechnol*., Vol. 9, 780, 2014.
2. Xia, F., H. Wang, D. Xiao, M. Dubey, A. Ramasubramaniam, "Two-dimensional material nanophotonics", *Nature Photon*., Vol. 8, 899, 2014.
3. Furchi, M., A. Urich, A. Pospischil, G. Lilley, K. Unterrainer, H. Detz, P. Klang, A. Andrews, W. Schrenk, G. Strasser , T. Mueller, "Microcavity-integrated graphene photodetector", *Nano Lett*., Vol. 12, 2773, 2012.
4. Gan, X., R.-J. Shiue, Y. Gao, I. Meric, T. Heinz, K. Shepard, J. Hone, S. Assefa, D. Englund, "Chip-integrated ultrafast graphene photodetector with high responsivity", *Nature Photon*., Vol. 7, 883, 2013.
5. Liu, Y., R. Cheng, L. Liao, H. Zhou, J. Bai, G. Liu, L. Liu, Y. Huang, X. Duan, "Plasmon resonance enhanced multicolour photodetection by graphene", *Nat*. *Commun*., Vol. 2, 579, 2011.
6. Echtermeyer, T., L. Britnell, P. Jasnos, A. Lombardo, R. Gorbachev, A. Grigorenko, A. Geim, A. Ferrari, K. Novoselov, "Strong plasmonic enhancement of photovoltage in graphene", *Nat*. *Commun*., Vol. 2, 458, 2011.
7. Fang, Z., Z. Liu, Y. Wang, P. Ajayan, P. Nordlander, N. Halas, "Graphene-antenna sandwich photodetector", *Nano Lett*., Vol. 12, 3808, 2012.

Nonperturbative theoretical description of graphene saturable absorption

A. Marini[1*], J. D. Cox[1], and F. J. García de Abajo[1,2]
[1]ICFO-Institut de Ciencies Fotoniques, The Barcelona Institute of Science and Technology,
08860 Castelldefels (Barcelona), Spain
[2]ICREA-Institució Catalana de Recerca i Estudis Avançats, Barcelona, Spain
[*]corresponding author: andrea.marini.tlp@gmail.com

Abstract-We theoretically investigate saturable absorption in extended graphene by developing a semi-analytical nonperturbative approach and solving the electron dynamics nonperturbatively. We find a remarkably low saturation intensity along with a large modulation depth that can be electrically manipulated through an externally applied gate voltage. Our results are relevant for the development of graphene-based optoelectronic devices, as well as for application in mode-locking and random lasers.

Saturable absorption (SA) is an inherent property of photonic materials that manifests itself as an absorption quenching at high light intensities and is a key element for passive mode-locking (PML) in laser cavities, where continuous waves break into a train of ultrashort optical pulses. Currently, state-of-the-art semiconductor-based SA mirrors are routinely employed for PML lasers. However, these mirrors operate in a narrow spectral range, are poorly tunable, and require advanced fabrication techniques. Graphene overcomes these limitations thanks to its peculiar conical band structure, providing a universally-resonant wavelength-independent SA at low light intensity [1] that can be further electrically tuned be means of an externally applied gate voltage, thus enabling PML ultrafast laser operation [2]. Here, we calculate intraband and interband contributions to SA of extended graphene by solving non-perturbatively the single-particle Dirac equation for massless Dirac fermions in the presence of an external electromagnetic field. Further, we investigate the dependence of the intensity-saturated graphene conductivity on doping, temperature, and optical frequency. We find a remarkably low intensity-threshold for SA, which is consistent with reported experimental findings. In addition, our calculations indicate a strong quenching of absorption depth ensuing from doping through an externally applied voltage, and a weak dependence on electron temperature. We envisage that our results will be relevant for the engineering of graphene-based PML fibre lasers and single-mode random lasers [3].

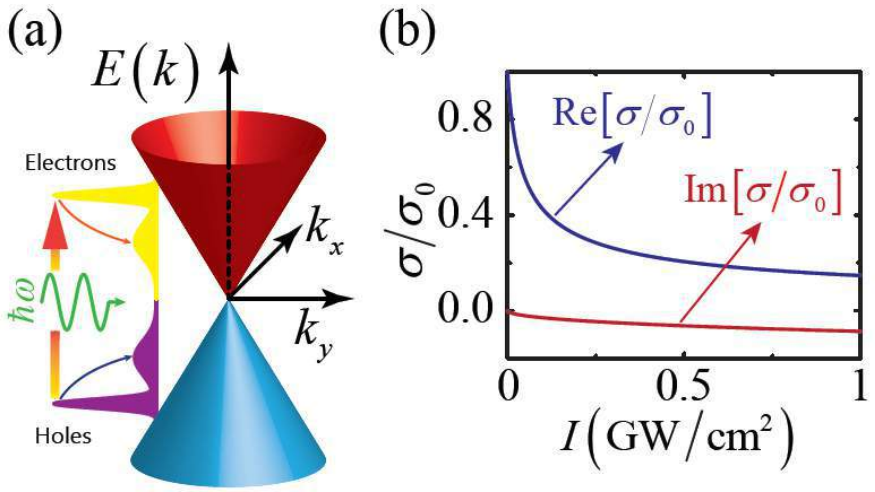

Figure 1: (a) Conical band-structure around the Dirac points. Upper $E_+(k)=+\hbar v_F k$ and lower $E_+(k)=+\hbar v_F k$ energy bands depend linearly on the electron wave-vector k. Interband transitions produced by impinging photons lead to an out-of-equilibrium electron distribution, which then relaxes via electron collisions. After an initial transient time, optical pumping and electron relaxation compensate with each other, and absorption is saturated due to partial Pauli blocking. (b) Intensity-dependent conductivity $\sigma(I)$ normalized to the universal conductivity $\sigma_0 = e^2/(4\hbar)$.

Acknowledgements This work has been partially supported by the Spanish MINECO (MAT2014-59096-P and SEV2015-0522) and the European Commission (Graphene Flagship CNECT-ICT-604391 and FP7-ICT-2013-613024-GRASP).

REFERENCES

1. Hasan, T., Sun, Z., Wang, F., Bonaccorso, F., Tan, P. H., Rozhin, A. G. and Ferrari, A. C., "Nanotube–Polymer Composites for Ultrafast Photonics," Vol 21, 3874–3899, 2009.
2. Sun, Z., Hasan, T., Torrisi, F., Popa, D., Privitera, G., Wang, F., Bonaccorso, F., Basko, D. M. and Ferrari, A. C., "Graphene Mode-Locked Ultrafast Laser," *ACS Nano*, Vol. 4, No.2, 803–810, 2010.
3. Marini, A. and García de Abajo, F. J., "Graphene-Based Active Random Metamaterials for Cavity-Free Lasing," *Phys. Rev. Lett.*, Vol. 116, 217401 (2016).

Low-Loss Non-Reciprocity in Spatiotemporally Modulated Hybrid Dielectric-Graphene Photonic Structures

D. Correas-Serrano[1], D. L. Sounas[2], A. Alù[2*], and J. S. Gomez-Diaz[2*]
[1]University of California, Davis, United States
[2]University of Texas at Austin, United States
[*]corresponding author: alu@mail.utexas.edu, jsgomez@ucdavis.edu

Abstract-We introduce the concept of magnet-less non-reciprocal photonic devices based on spatiotemporally modulated graphene embedded in dielectric structures. Compared to non-reciprocal graphene plasmonic devices based on similar bias schemes [1], graphene is now used as a perturbation of low-loss photonic modes. This approach has important benefits, including significantly reduced losses, much relaxed biasing requirements, and large non-reciprocal responses. We envision that this technology will pave the way to a future low-loss, magnet-free, non-reciprocal photonic platform with wide applications in communication systems, sensing, imaging, and on-chip networks.

Modulating the physical properties of a system in space and time has allowed in recent years the engineering of magnet-less non-reciprocal responses in electromagnetics and acoustics [2], [3], but the use of this concept in practical applications beyond RF remains challenging due to the high modulation frequencies required and the difficulty of modulating the permittivity of silicon [4], [5]. Recently, gated graphene structures with time-varying gate voltages have been introduced as a promising plasmonic platform to implement this paradigm at THz and IR [1], owing to the ultrafast modulations it can support [6] and the numerous attractive features of graphene plasmonics [7]. The most significant challenge in this approach lies in the necessity of high quality graphene able to support plasmons with low damping. To lessen this constraint, here we propose to break reciprocity by using spatiotemporally modulated graphene as a *perturbation* of high-Q photonic modes in dielectric structures. The resulting hybrid graphene-dielectric photonic devices are low-loss, silicon-compatible, robust against graphene's imperfections, and exhibit large non-reciprocal responses using a realistic biasing scheme.

We illustrate this concept through a simple waveguide isolator based on the fundamental transverse electric (TE) mode in a dielectric slab loaded with a closely spaced graphene bilayer, as depicted in Fig. 1a. This configuration allows fast modulation of the effective stack conductivity by applying a time-varying voltage between them [6], [8]. If different voltages with adequate phases are applied along the propagation direction z, an effective linear momentum is imparted to the propagating modes due to the (weak) interaction of the graphene stack with the z-component of the photonic mode. We study the response of the system by (i) analytically solving the eigenmodes of the modulated structure, (ii) using coupled mode theory together with the unmodulated states, and (iii) using coupled multi-harmonic frequency domain numerical simulations – full details will be given at the conference. The operation is as depicted in Fig. 1b: power can only propagate from left to right, with any power in the opposite direction being frequency-shifted and reflected. Fig. 1c shows the insertion loss from left to right and from right to left versus frequency, for a graphene relaxation time of $\tau = 0.1$ ps and a modulation frequency $f_m = 20$ GHz, five hundred times smaller than the operation frequency. We stress that all these parameters are

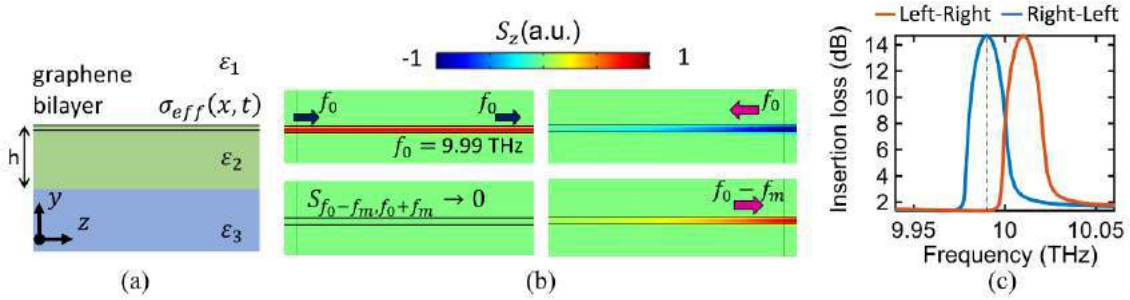

Figure 1. (a) Photonic isolator based on a slab waveguide with relative permittivities $\varepsilon_1 = 1, \varepsilon_2 = 12, \varepsilon_3 = 4$ and $h = 2\ \mu m$, loaded with a spatiotemporally modulated graphene bilayer with effective conductivity $\sigma_{eff} = \sigma_0(1 + M\cos[\omega_m t - \beta_m z])$. (b) Poynting vector for incidence from the left (energy is transmitted to the right) and from the right (energy is frequency converted and reflected). (c) Insertion loss versus frequency for both excitation directions. Dashed line indicates the operation point plotted in panel (b).

easily achieved with state of the art fabrication techniques. Our proposed structure isolates in each direction at different frequencies due to the asymmetric bandgaps opened by the modulation, while loss in the transmitting direction remains very low. These preliminary results are very promising, and they may establish the foundation for a new class of non-reciprocal photonic devices compatible with integrated silicon photonics. We will discuss at the conference alternative implementations based on multimode operation, resonant structures aimed to reduce device footprint, as well as metasurfaces for isolation of plane waves.

REFERENCES

[1] D. Correas Serrano, J. S. Gomez-Diaz, D. L. Sounas, Y. Hadad, A. Alvarez-Melcon, and A. Alù, "Non-reciprocal graphene devices and antennas based on spatio-temporal modulation," *IEEE Antennas Wirel. Propag. Lett.*, vol. 1225, no. c, pp. 1–1, 2015.

[2] N. A. Estep, D. L. Sounas, and A. Alù, "Magnetless microwave circulators based on spatiotemporally modulated rings of coupled resonators," *IEEE Trans. Microw. Theory Tech.*, vol. 64, no. 2, pp. 502–518, 2016.

[3] R. Fleury *et al.*, "Sound Isolation and Giant Linear Nonreciprocity in a Compact Acoustic Circulator," *Science (80-.).*, vol. 20704, no. 2012, pp. 13498–13502, Jan. 2008.

[4] H. Lira, Z. Yu, S. Fan, and M. Lipson, "Electrically driven nonreciprocity induced by interband photonic transition on a silicon chip," *Phys. Rev. Lett.*, vol. 109, no. 3, pp. 1–5, 2012.

[5] D. L. Sounas and A. Alù, "Angular-Momentum-Biased Nanorings To Realize Magnetic-Free Integrated Optical Isolation", ACS Photonics, 2014, 1 (3), pp 198–204, 2014.

[6] C. T. Phare, Y. D. Lee, J. Cardenas, and M. Lipson, "Graphene electro-optic modulator with 30 GHz bandwidth," *Nat. Photonics*, vol. 9, no. 8, pp. 511–514, 2015.

[7] T. Low and P. Avouris, "Graphene plasmonics for terahertz to mid-infrared applications," *ACS Nano*, vol. 8, no. 2, pp. 1086–1101, 2014.

[8] J. S. Gomez-Diaz *et al.*, "Self-biased reconfigurable graphene stacks for terahertz plasmonics," *Nat. Commun.*, vol. 6, no. 6334, pp. 1–8, 2015.

Chiral and bianisotropic materials

Tuning spontaneous radiation of chiral molecules by asymmetric chiral nanoparticles

Dmitry V. Guzatov[1], Vasily V. Klimov[2,3,4,7], Hsun-Chi Chan[5], and Guang-Yu Guo[5,6,8]

[1]Yanka Kupala State University of Grodno, Grodno 230023, Belarus

[2]P.N. Lebedev Physical Institute, Russian Academy of Sciences, Moscow 119991, Russia

[3]All-Russia Research Institute of Automatics, Moscow 127055, Russia

[4]National Research Nuclear University MEPhI, Moscow 115409, Russia

[5]Department of Physics, National Taiwan University, Taipei 10617, Taiwan

[6]Physics Division, National Center for Theoretical Sciences, Hsinchu 30013, Taiwan

[7]klimov256@gmail.com

[8]gyguo@phys.ntu.edu.tw

Abstract- We have derived analytical expressions for the radiative decay rate of the spontaneous emission of a chiral molecule located near a dielectric spherical particle with a chiral nonconcentric spherical shell made of a bi-isotropic material. Our numerical analyses show that for a chiral molecule near a dielectric spherical particle with a shell made of a chiral metamaterial with simultaneously negative permittivity and permeability, the "right" and "left" enantiomers of molecules can exhibit pronounced differences between the radiative decay rates.

The scattering of electromagnetic radiation by a chiral spherical particle was previously investigated [1,2]. However, the problem of scattering of light by an asymmetric chiral particle has not yet received the attention of researchers. In this paper we consider the spontaneous radiation of a chiral molecule located near an asymmetric chiral nanoparticle and as a model of such particles we investigate a spherical dielectric particle with a nonconcentric spherical shell made of a chiral material.

In describing the electric and magnetic fields in the shell of a chiral medium, we use constitutive equations for a bi-isotropic material in the Drude-Born-Fedorov form [3]. We have obtained analytical expressions [4] for the radiative decay rate [2] of the spontaneous emission of such a chiral system. To understand physics of these effects, we also performed independent numerical simulations by using the finite element method as implemented in COMSOL Multiphysics® software [5], as shown in the insets of Fig.1.

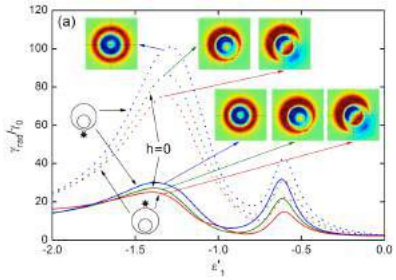

Figure 1. Radiative decay rate of the spontaneous emission of a chiral molecule located close to the surface of a spherical nanoparticle with a dielectric core and a chiral shell as the function of the real part of the permittivity

$\varepsilon_1 = \varepsilon_1' + i0.1$. The solid lines correspond to the "right" molecule ($\mathbf{m}_0 = 0.1\mathbf{d}_0$), and the dashed lines correspond to the "left" molecule ($\mathbf{m}_0 = -0.1\mathbf{d}_0$). The colors represent the cases of the molecule position near the thin (blue), thick (red) parts of a shell, and the case of concentric shell (green). The insets show near-field patterns Re(E_z) at $\varepsilon_1' = -1.33$ on the z=0 plane.

Acknowledgements: The authors are grateful to the Advanced Research Foundation (Contract 7/004/2013-2018 by 23/12/2013) and the Russian Foundation for Basic Research (Grants 14-02-00290 and 15-52-52006) as well as the Ministry of Science and Technology (Grant MOST 104-2923-M-002-004-MY3) and the National Center for Theoretical Sciences of Taiwan for financial support of this work.

REFERENCES

1. Bohren, C. F. "Light scattering by an optically active sphere," *Chem. Phys. Lett.*, Vol. 29, 458–462, 1974.
2. Klimov, V. V., Zabkov, I. V., Pavlov, A. A. & Guzatov, D. V., "Eigen oscillations of a chiral sphere and their influence on radiation of chiral molecules," *Opt. Express*, Vol.22, 18564–18578, 2014.
3. Lindell, I. V., Sihvola, A. H., Tretyakov, S. A. and Viitanen, A. J., *Electromagnetic Waves in Chiral and Bi-isotropic Media*, Artech House Publishers, 1994.
4. Guzatov, D. V., Klimov, V. V., Chan, H. C. and Guo, G. Y., "Tuning spontaneous radiation of chiral molecules by asymmetric chiral nanoparticles," submitted.
5. www.comsol.com

Optical sensing of chiral molecules using metamaterials

S. Yoo, and Q-H. Park*
Department of Physics, Korea University, Republic of Korea
*corresponding author: qpark@korea.ac.kr

Abstract- We present a theory for the microscopic origins underlying the chiroptical spectroscopy using metamaterials. When optical resonators are coupled to chiral molecules, the inherent circular dichroism (CD) of chiral molecules are modified by local fields near resonators, whereas chiral molecules perturb resonant modes of the resonators. We show two origins of CD simultaneously contribute to the CD enhancement in the chiral molecule/resonator coupled system. We propose a design route for the optical resonators that enhance CD of chiral molecules.

Naturally occurring circular dichroism (CD) signals of chiral molecules are inherently weak because the chirality of molecules is much smaller than the wavelength of circularly polarized plane waves, but chiral molecular CD signals can be strongly enhanced when chiral molecules are coupled to optical resonators. In recent years, resonant metamaterials have been applied to the enhancement of molecular CD signals [1]. Unfortunately, however, it has been a significant mismatch between experimentally observed CD enhancement factors and theoretical predictions [1]. Here, we explain two simultaneously contributing mechanisms of the CD enhancement in the chiral molecule/metamaterial coupled systems [2,3].

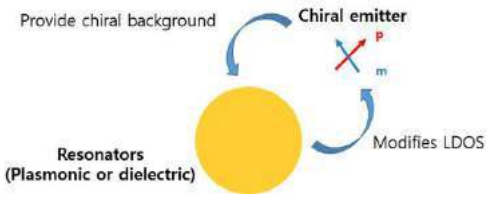

Figure 1. Schematic of two mechanisms for the CD enhancement.

When the chiral molecules are adsorbed on the optical resonators, CD signals can be strongly enhanced. As shown in Fig. 1, the enhancement of CD signals by resonators is originated from two major mechanisms: the chiral Purcell effect and the circular differential scattering effect. The chiral Purcell effect describes the modification of the helicity-dependent spontaneous decay of chiral molecules. Inside the resonator, both the energy and the helicity of light can be strongly localized. As a result of localization of optical energy and helicity, the circular difference in the spontaneous decay rate $\Delta\Gamma$ can be significantly enhanced compared to that in the free space $\Delta\Gamma_0$, as shown in Fig 2 [2,4]. The figure of merit for the resonator to enhance CD signals is called as the chiral Purcell factor F_C, and it is defined by

$$F_C = \frac{1}{4\pi^2}\left(\frac{\lambda_0}{n}\right)^3\left(\frac{Q}{V_C}\right) \quad (1)$$

with the resonance wavelength λ_0, refractive index n, the quality factor Q of the resonator, and the chiral mode

volume V_C [2]. On the other hand, the presence of chiral molecules in the vicinity of optical resonators perturbs the optical response of the resonators [3]. We find that scattering cross sections of light by the optical resonator embedded in chiral medium is different upon two opposite circular polarized incident light although the optical resonators are achiral.

In this presentation, we show that both the chiral Purcell effect and the circular differential scattering effect can simultaneously contribute the measured CD signals. We present a microscopic theory to completely describe the multiple origins for the CD enhancement in the chiral molecule/optical resonator coupled system [5]. We expect that our theory can overcome the limitations of the conventional theory that have a mismatch between experimentally observed CD enhancement factors and theoretical predictions. Our theory also enables analysis and design of the surface-enhanced chiral molecule sensing experiment.

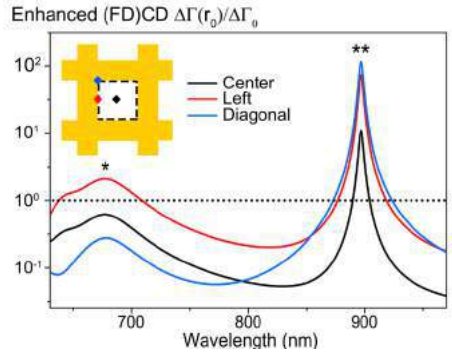

Figure 2. Enhanced CD signals of chiral molecules inside the double fishnet structure corresponding to three different molecule positions.

REFERENCES

1. Hendry E., Carpy T., Johnston J., Popland M., Mikhaylovskiy R. V., Lapthorn A. J., Kadodwala M. "Ultrasensitive detection and characterization of biomolecules using superchiral fields," *Nature Nanotechnology*, 5(11), pp. 783–787, 2010.
2. Yoo S., and Park Q-H., "Chiral Light-Matter Interaction in Optical Resonators," *Physical Review Letters*, 114(20), p.203003, 2015.
3. Yoo S., and Park Q-H., "Enhancement of Chiroptical Signals by Circular Differential Mie Scattering of Nanoparticles," *Scientific Reports*, 5, 14463, 2015.
4. Yoo S., Cho M., and Park Q-H., "Globally enhanced chiral field generation by negative-index metamaterials," *Physical Review B*, 89(16), 161405(R), 2014.
5. Lee S., Yoo S., and Park Q-H., "Microscopic Origin of Surface-enhanced Circular Dichroism," in preparation.

Enhanced Circular Dichroism of Isotropic Au-core/Ag-shell Nanoparticles due to Fano Resonances

J.-W. Park*
Boston University, United States of America
*corresponding author: jwonpark@gmail.com

Abstract-Optical activity of individual Au-nanospheres and Au-core/Ag-shell nanoparticles was observed in aqueous solution. Possible mechanisms are discussed, including the excitation of volume plasmons, multiple scattering, and electron spin polarization. Given the left-handedness of dipolar localized surface plasmons (LSPs) of Au-nanospheres, spherical Au-core/Ag-shell nanoparticles exhibit sign reversal. Strong positive ellipticity from core-shell nanoparticles is attributed to Fano resonances between dipolar and quadrupolar LSPs whereas negative ellipticity of dipolar LSPs originates from nonlocality. Plasmon enhancement via ligand chirality was not observed.

Recent chirality research in nanoparticles concerns only structural dissymmetry, including chiral transfer of ligand molecules to nanoparticles[1] as well as helical arrangement of assembled nanoparticles. This is based on the quantum mechanical theory of optical activity, which is one-electron model associated with formulating the scalar product of electric/magnetic dipole transition moments.[2] Metal nanoparticles are many-body systems, and their dimensions are larger than the Fermi radius of electrons, and thus a direct application of the one-electron model of optical activity to individual nanoparticles may lead to unphysical consequences. Except for helical assemblies of nanoparticles exhibiting dominant CD responses, spatial dispersion (nonlocality) should be considered for individual nanoparticles. In crystals, optical activity is the first order spatial dispersion of electromagnetic waves,[3] which has been neglected since chirality studies of plasmonic nanoparticles gained great interest a decade ago. I experimentally demonstrate that spatial dispersion for individual Au nanosphers leads to optical activity of dipolar LSPs with having left-handedness, although measured ellipticities are generally weak. Longitudinal volume plasmons excited along the direction of light propagation[4] likely generate a electric field gradient, leading to dephasing[5] of the electromagnetic wave. For nanoparticles having strong quadrupolar LSPs such as core-shell structures,[6] however, Fano resonances enhance CD responses,[7] resulting in large positive values of ellipticity. Plasmon enhancement of nanoparticle CD was not observed for L-ascorbic acid functionalized Au-nanospheres, due to homogeneous distribution of the ligands or screened Coulomb interactions between conduction electrons and ligand electrons by the positive jellium background. The CD sign reversal is not related to possible phase variation via multiple scattering as well as possible electron-spin polarization via coupling of Shockley surface states to bulk conduction electrons. The latter effects, which would produce a constant sign of ellipticity, were safely excluded. Under spatial dispersion, Fano resonances produce noticeable CD responses, which is not negligible for optical activity of individual nanoparticles.

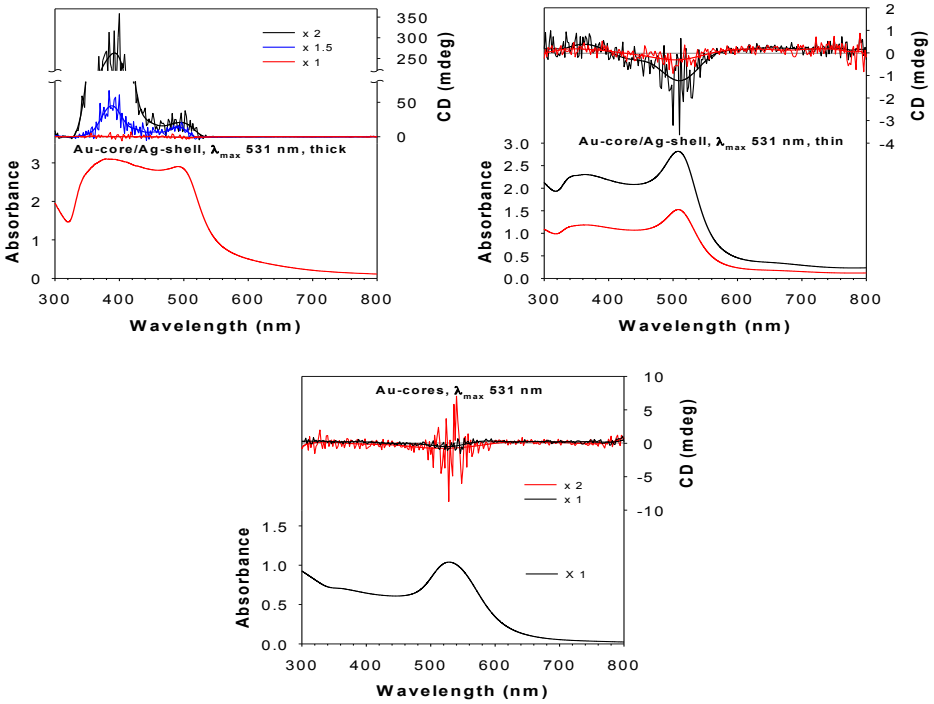

Figure 1. CD and UV-Vis spectra of Au-core/Ag-shell spheres. Ag-shells were grown by reducing Ag^{+} ions with L-ascorbic acid. Thickness of Ag-shells is qualitatively represented as thin/thick.

Acknowledgements, I thank Prof. Björn M. Reinhard at Boston University for generously providing laboratory equipments for conducting experiments and helpful discussion.

REFERENCES

1. Govorov, A. O., Z. Fan, P. Hernandez, J. M. Slocik, and R. R. Naik, "Theory of Circular Dichroism of Nanomaterials Comprising Chiral Molecules and Nanocrystals: Plasmon Enhancement, Dipole Interactions, and Dielectric Effects," *Nano Lett.*, Vol. 10, No.4, 1374−1382, 2010.
2. Mason, S. F., *Molecular optical activity and the chiral discriminations*, Cambridge University Press, New York, 1982.
3. Landau, L. D. and E. M. Lifshitz, *Electrodynamics of Continuous Media*, Pergamon Press, New York, 1960.
4. Höflich, K., U. Gösele and S. Christiansen, "Are Volume Plasmons Excited by Classical Light?," *Phys. Rev. Lett.*, Vol. 103, 087404, 2009.
5. Huang, Y. and L. Gao, "Superscattering of Light from Core-Shell Nonlocal Plasmonic Nanoparticles," *J. Phys. Chem. C*, Vol. 118, No. 51, 30170−30178, 2014.
6. Ren, M., E. Plum, J. Xu and N. I. Zheludev, "Giant nonlinear optical activity in a plasmonic metamaterial," *Nat. Commun.*, Vol. 3, 833, 2012.
7. Hopkins, B., A. N. Poddubny, A. E. Miroshnichenko and Y. S. Kivshar, "Circular dichroism induced by Fano resonances in planar chiral oligomers," *Laser Photonics Rev.*, Vol. 10, No. 1, 137−146, 2016.

Single particle chirality

E. Vinegrad[1], D. Vestler[2], A. Ben-Moshe[2], G. Markovich[2] and O. Cheshnovsky[2,*]
[1] Raymond & Beverly Sackler saklar - School of Physics, Tel Aviv University, Tel Aviv 69978, Israel
[2] Raymond & Beverly Sackler School of Chemistry, Tel Aviv University, Tel Aviv 69978, Israel
[*] **orich@post.tau.ac.il**

Abstract- Chiroptical activity serves as an important tool for manipulating light or for characterizing spatial arrangements in molecules, proteins (and other polymers) crystals and nanostructures. Due to the weak intensity of Circular Dichroism (CD) measurements of CD are all done on an ensemble of particles either in solution, in crystals, or on a large array of meta-particles on a substrate. Here we present an experiment in which the CD spectroscopy of individual, fabricated Gammadions were studied.

Recent studies to measure CD of individual nano-objects have been made, by using near field techniques[1], or dark-field[2] of randomly generated non symmetric structures . Here, we present a study in which CD absorption spectroscopy of individual fabricated (left and right chirality) Gammadions was carried out**.**
Our experimental setup for measuring the spectroscopy of individual nanostructure follows the approach of Sandoghdar and coworkers[3] who demonstrated single molecule detection by optical absorption. Here, we expand the spectral range to the entire visible spectrum together with accurate polarization control to enable CD spectroscopy. We use a broadband Supercontinuum source (SC) filtered by Acousto-optic tunable filter (AOTF). A 50:50 beam-splitter to split the light beam to a probe beam and a reference beam. The reference beam is used to monitor light intensity fluctuations, while the probe beam is passed through the LC retarder and then focused on the sample. We use a moderately high NA polarization maintaining objective to increase the interaction between the beam and particles while still keeping the polarization as pure as possible. . We scan through the spectral range, and spatially over the sample of interest and preform spectroscopic absorption and reflectance measurement on individual particle. The LC retarder cycles 30-100 times between Left/Right circular polarization states to differentiate between the corresponding absorptions and thus measure dissymmetry caused by a single nanoparticle.

Transmission and spatial dissymmetry maps for a 160 nm right handed gold Gammadion, taken at 600 nm, is shown in Figure 1. We show that the chiral gammadion shape leads to a negative dissymmetry value at the shapes center as determined by the transmission data. The dissymmetry shown here is of the order of 10^{-4} and is presented after subtracting the small surface dissymmetry, is attributed to residual dissymmetry-response of the experimental setup. The distinct CD, is reversed in sign when measuring CD on an equivalent left handed Gammadion.

Wide spectral range measurements were performed on 500nm Au Gammadions. For each wavelength the sample was scanned using only right handed circular polarization, and at the end of each such scan the center of the particle was identified by finding the point giving a minima in the transmission. At that point the polarization was square-wave modulated, between right and left circular polarization for 30 cycles. The difference between the left and right set of measurements represents the CD at a specific wavelength. The experimental spectra of the CD of left handed and right handed Gammadions show distinct similarity to our FDTD simulations (See Figure 2)

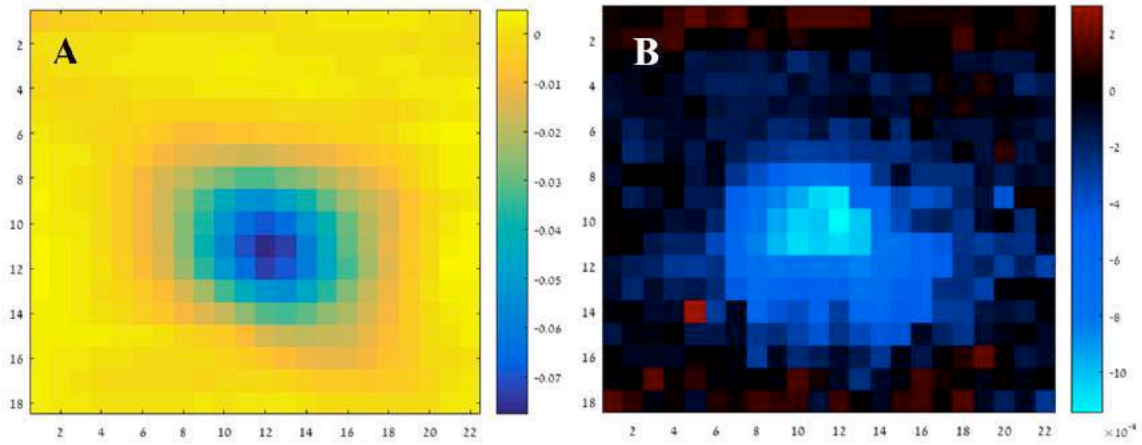

Figure 1 – Transmission and spatial dissymmetry scans at wavelength of 600nm. (**A**) – Transmission scans for a 160nm right handed Gammadion. (**B**) - Dissymmetry scans for the same Gammadion.

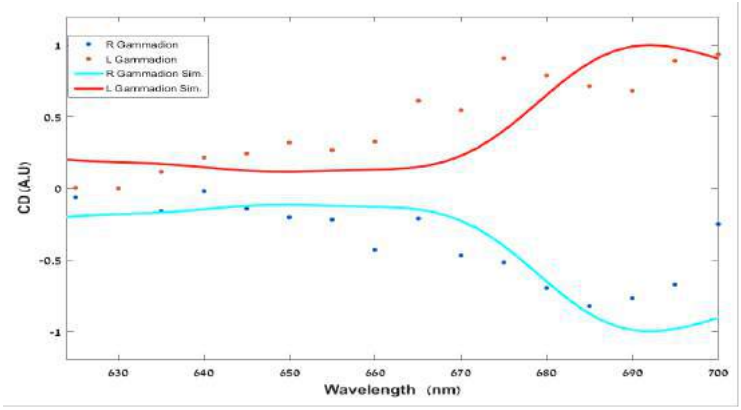

Figure 2 – dissymmetry spectra for 500nm Gammadions. The dots represent measurements on Right/Left handed Gammadions while the solid line is the simulated spectra calculated using FDTD.

In summary, we have successfully shown bright far-field CD spectroscopy of single nano-objects, with a distinct ability to distinguish between the CD responses of two enantiomers and to map the spatial CD distribution on the nanoscale.

REFERENCES

1. Narushima, T. & Okamoto, H. Strong Nanoscale Optical Activity Localized in Two-Dimensional Chiral Metal Nanostructures. *J. Phys. Chem. C* **117,** 23964–23969 (2013).
2. Smith, K. W. *et al.* Chiral and Achiral Nanodumbbell Dimers: The Effect of Geometry on Plasmonic Properties. *ACS Nano* **10,** 6180–6188 (2016).
3. Kukura, P., Celebrano, M., Renn, a & Sandoghdar, V. Imaging a single quantum dot when it is dark. *Nano Lett.* **9,** 926–9 (2009).

Tunable, nondispersive optical activity of bi-layered chiral metamaterials

Hyun Sung Park, Jagang Park, Jaehyeon Son, Yushin Kim, Hyukjoon Cho, and Bumki Min*
Department of Mechanical Engineering, Korea Advanced Institute of Science and Technology (KAIST), Republic of Korea

*corresponding author: bmin@kaist.ac.kr

Abstract- Here we demonstrate that mechanically-tunable, nondispersive optical activity can be achieved in quasi-planar, bi-layered chiral metamaterials where an enhanced magnetic coupling between front- and back layers is present. It is experimentally shown that the polarization state of the transmitted electromagnetic waves through the metamaterial layer is rotated by 30°, regardless of their frequencies in a broad frequency range.

Extremely large optical activity can be realized by chiral metamaterials consisting of strongly-resonant, subwavelength-scale chiral particles. The large optical activity of the chiral metamaterials allows them to be used as ultra-thin polarization rotators. However, the most of chiral metamaterials have highly dispersive optical properties due to their resonant nature, which leads to the narrow operating bandwidth in terms of transmission and optical rotatory power. Recently, nondispersive, strong optical activity has been reported in three-dimensional meshed helical metamaterials [1].

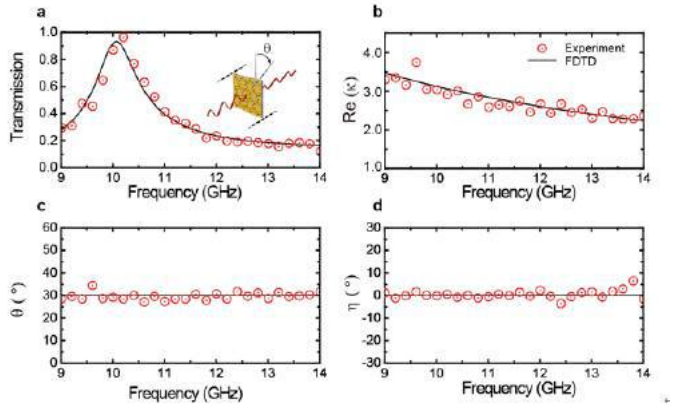

Figure 1 Characterization of the proposed bi-layered chiral metamaterial in the microwave range. (a) Numerically calculated and experimentally measured total transmission amplitude. (b) Numerically- and experimentally retrieved chirality parameter. (c) Nondispersive polarization rotation of the transmitted wave and (d) nearly-zero, flat ellipticity.

Here we demonstrate that mechanically-tunable, nondispersive optical activity can be achieved in quasi-planar, bi-layered chiral metamaterials where an enhanced magnetic coupling between front- and back layers is present. It is experimentally shown that the polarization state of the transmitted electromagnetic waves

through the metamaterial layer is rotated by 30°, regardless of their frequencies in a broad frequency range (see Fig. 1). It is also found that the amount of polarization rotation can be further increased by adding more layers. Furthermore, the rotation angle can be dramatically tuned by changing the interlayer spacing distance. This tunable optical activity seems to originate from the change in interlayer magnetic coupling, which is reasoned by its asymptotic scaling with increasing spacing distance. Since the proposed chiral metamaterial consists of planar structures, we expect that the chiral metamaterials with tunable, nondispersive optical activity at higher frequency regime might be realized by using conventional micro- and nano fabrication techniques.

REFERENCES

1. Park, Hyun Sung, et al. "Nondispersive optical activity of meshed helical metamaterials." Nature communications 5 (2014).

Electrical control of one circular polarization in graphene integrated chiral metamaterials

Teun-Teun Kim[1,2], Hyeon-Don Kim[3], Sang Soon Oh[4], Hyun-Sung Park[3], Ortwin Hess[4], Bumki Min[3*] and Shuang Zhang[2*]

1 Center for Integrated Nanostructure Physics, Institute for Basic Science, Sungkyunkwan University, Suwon,16419 , Republic of Korea

2 School of Astronomy and Physics, University of Birmingham, Birmingham, B15 2TT, United Kingdom

3 Department of Mechanical Engineering, KAIST, Daejeon 34141, Republic of Korea

4 2The Blackett Laboratory, Department of Physics, Imperial College London, South Kensington Campus, London SW7 2AZ, United Kingdom

[*]corresponding author: bmin@kaist.ac.kr, s.zhang@bham.ac.uk

Abstract- We experimentally demonstrate an electrical tuning of the polarization state of terahertz waves with a graphene integrated chiral metamaterial. We validated that the graphene integrated chiral metamaterial achieves a high-intensity modulation depth up to 63% for the RCP wave at the small gate voltage with maintaining high transmission of the LCP wave up to 52%.

Controlling circular polarization states is important in the field of quantum computation and information, optical communication of spin information and circular dichroism spectroscopy. Conventionally, chiral materials such as quartz have been used for the purpose of modifying the state of polarization of light. However, naturally occurring chirality in the form of circular dichroism (CD) and optical activity (OA) is extremely weak, requiring a substantially long propagation length to observe chirality[1]. To overcome this problem, artificial structures called "chiral metamaterials" composed of sub-wavelength metallic building blocks have been proposed for enhancing CD and OA enabling various potential applications such as broadband circular polarizers and wave plates[2].

In this study, it is shown that the transmission of a right- handed circularly polarized (RCP) terahertz wave can be strongly modulated when a voltage is applied to the gate, due to a critical transition followed by the change in the optical conductivity of the graphene.

We used a conjugated double Z metamaterial (CDZM) to control the circular polarization state of the terahertz wave. The metamaterial was fabricated through a general MEMS process. Single layer graphene grown by chemical vapor deposition (CVD) was transferred thereon, and gate voltage was applied to the graphene by side-gate method using ion gel (Figure 1). The fabricated graphene CDZM structures are characterized by THz time-domain spectroscopy (THz-TDS). As shown in the figure 2a, T_{RCP} can be dramatically reduced when we applied gate voltage of $\Delta V(=V_{CNP}-V_G) = 1.8V$, but almost leaves T_{LCP} unchanged at the resonance frequency of 1.1 THz. The maximum modulation depth for the RCP wave, defined as a relative transmission of RCP change $\Delta T_{RCP} / T_{RCP, Min}$ for graphene CDZM, is measured to be 63 % at the resonance. To clarify the mechanism of electrical control of one circular polarization observed in the experiments, we perform numerical simulations and employ the temporal coupled-mode theory (CMT) involving two resonant modes with two ports[3].

Figures and Tables:

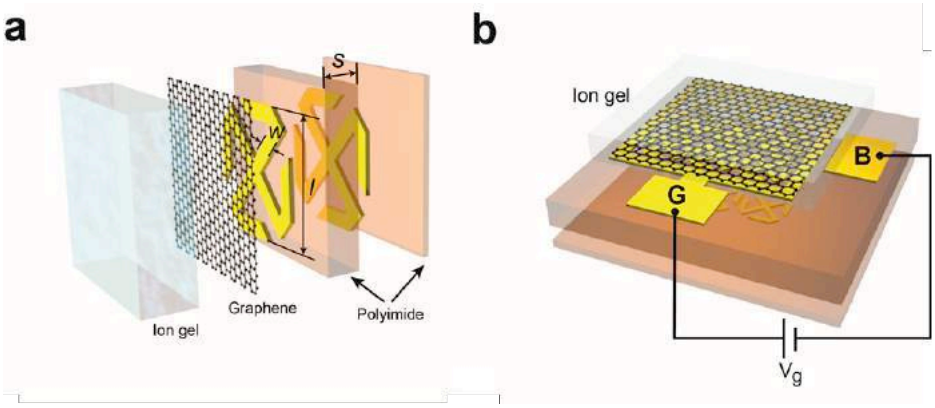

Figure 1. Schematic views and device image of gate-controlled active graphene CDZM.
(a) Schematic rendering of a gate-controlled active graphene CDZM composed of a single layer graphene deposited on the top layer of conjugated double Z metamaterial (CDZM) and subsequently covered by a layer of ion gel (thickness t = 20 μm). (b) Schematic rendering of the fabricated graphene CDZM. B is a base connected to the ion gel and G is a gate connected to the graphene layer.

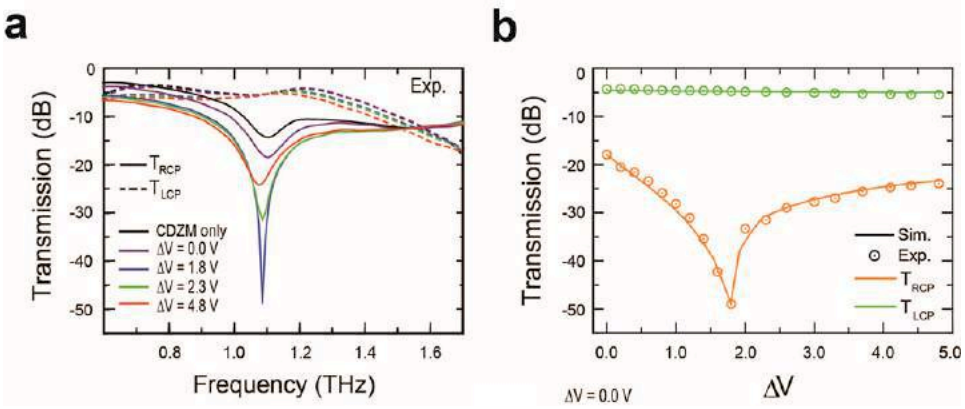

Figure 2. Gate-controlled circular transmission and circular dichroism.
(a) Measured and simulated intensity of transmission spectra for right-handed circularly polarized (T_{RCP}, solid line) and left-handed circularly polarized (T_{LCP}, dashed line) waves are plotted for different gate voltages ΔV. (b) T_{RCP} (orange) and, T_{LCP} (green) at the resonant frequency 1.1 THz as a function of ΔV. While T_{LCP} is almost unchanged, T_{RCP} can be dramatically modified by the applied voltage.

REFERENCES

1. Tinoco, I. & Cantor, C. R., "Application of Optical Rotatory Dispersion and Circular Dichroism to the Study of Biopolymers" (John Wiley & Sons, Inc., 2006).
2. Kim, T.-T., "Optical activity enhanced by strong inter-molecular coupling in planar chiral metamaterials." Sci. Rep. 4, 5864 (2014).
3. S. Fan, W. Suh & J. D. Joannopoulos, Temporal coupled-mode theory for the Fano resonance in optical resonators, J. Opt. Soc. Am. A 20, 569–572 (2003).

Programmable Chiral Plasmonic Nanoparticles with Giant Optical Activity

Hye-Eun Lee[1], Hyo-Yong Ahn[1], Yoon Young Lee[1], Jungho Mun[2], Junsuk Rho[2], Ki Tae Nam [1*]
[1]Department of Materials Science and Engineering, Seoul National University, Korea
[2]Department of Chemical Engineering, Pohang University of Science and Technology (POSTECH), Korea
[*]corresponding author: nkitae@snu.ac.kr

Abstract-We fabricated unprecedented three dimensional chiral plasmonic nanostructures by integrating organic-inorganic interaction in nanoparticle growth. Depending on the functional group in organic molecule, binding energy onto gold surface was modulated and we use this control over shape to address fabrication of asymmetric structure with nanometer controllability. Fabricated chiral gold nanoparticle exhibited extremely high dissymmetry factor at visible range (~0.2 at 622 nm) superior to any other structures produced by bottom-up approaches and showed macroscopic color transformation even in random dispersion.

Nature has remarkable ability to control the shape of inorganic material. Direct contact of biomolecule with inorganic surface at specific site significantly modifies the direction of crystal growth resulting in macroscopic shape change. Inspired from organic modifier in nature, we developed organothiol assisted growth system which is capable of directing morphological development through distinctive interaction between organothiol and gold surface.[1-2] Using rationally designed organothiol molecules, here, we demonstrated unprecedented morphologies with exceptional optical properties. By changing spatial configuration of functional group in organothiol molecule, we constructed nanoparticle with strong optical activity at visible range. The nanoparticle exhibits outstanding anisotropy dissymmetry factor ~0.2 and optical rotatory dispersion effect. In addition, tunable optical response was achieved through tailoring the structure of nanoparticle modulated by spatial control of functional groups.

REFERENCES

1. Lee, H.-E.; Yang, K. D.; Yoon, S. M.; Ahn, H.-Y.; Lee, Y. Y.; Chang, H.; Jeong, D. H.; Lee, Y.-S.; Kim, M. Y.; Nam, K. T. “Concave Rhombic Dodecahedral Au Nanocatalyst with Multiple High-Index Facets for CO_2 Reduction” ACS Nano, 9, 8384-8393, 2015.
2. Ahn, H.-Y.; Lee, H.-E.; Jin, K.; Nam, K. T. “Extended gold nano-morphology diagram: synthesis of rhombic dodecahedra using CTAB and ascorbic acid” J. Mater. Chem. C 1, 6861-6868, 2013.

A Simple Chiral Metamaterial for Broadband Asymmetric Transmission of Linearly Polarized Electromagnetic Waves at Microwave Frequencies

Lincy Stephen[1], Yogesh N.[2], Vasantharajan G.[1], Subramanian V.[1]*N*

[1]Microwave Laboratory, Department of Physics, Indian Institute of Technology Madras, Chennai-600036, India
[2]Department of Nuclear Physics, School of Physical Sciences, University of Madras, Chennai-600025, India
*Lincy Stephen, E-mail: lincy@physics.iitm.ac.in

Abstract

A chiral metamaterial (CMM) based on a complementary metal strip in a single dielectric layer is proposed for achieving broadband asymmetric transmission (AT) of linearly polarized electromagnetic waves. The proposed CMM exhibits AT efficiency of 90% over a bandwidth of 1.15 GHz (8.58 GHz to 9.73 GHz) for forward/backward linearly polarized excitations. Surface current analysis and electric field profiles of the structure elaborates the non-identical interaction of electromagnetic radiation for forward and backward excitations that resulting in the AT effect. Proposed CMM is ultrathin over the operational AT bandwidth and hence it may be useful to replace conventional ferrite based devices for microwave applications.

1. Introduction

Efficient manipulation of polarization state of electromagnetic radiation has always been highly desirable due to its potential applications in molecular biology, analytical chemistry and optoelectronics[1]. Although, conventional chiral materials which lacks mirror symmetry in the propagation direction possess optical activity, its magnitude is very weak. On the other hand, metamaterials which are artificial materials formed by periodic metallic inclusions came out as an excellent candidate for the polarization manipulation. Metamaterial with twisted metal inclusion is sufficient enough to break the mirror symmetry along the direction of propagation and such composite possesses giant optical activity known as chiral metamaterials (CMM). CMM exhibit tailored chiral response which is several magnitudes higher than the natural conventional chiral materials. Initially three-dimensional helical metamaterials were employed for polarization manipulation but due to the difficulty in fabrication and thickness the focus has been shifted to planar CMMs. Twisted rosettes[1], cross wire pairs[2], gammodian structures[3], fractal geometries[4], cut-wire pairs[5], asymmetric split ring resonators including square and V-shaped constituents[6] are few examples of planar CMMs. Apart from giant optical activity CMMs can also show some exciting properties such as polarization transformation, circular or elliptical dichroism and asymmetric transmission (AT).

Asymmetric transmission (AT) is a remarkable effect exhibited by CMMs due to circular conversion dichroism. It is the capability of the structure to allow the electromagnetic wave to propagate in one direction while blocking it completely in the opposite direction. This can be compared to a diode which allows the current in forward direction while blocks it in the backward bias[7]. AT effect in CMMs is different from the non-reciprocity of the Faraday Effect in magneto-optical media and can be explained by de hoop reciprocity as explained by Jones matrix formulation [8]. AT effect is useful in designing non reciprocal devices such as isolators and circulators, especially in the microwave region and also in optical interconnects, ultrafast information processing and integrated photonic circuits [9]. AT effect in metamaterial can be a good replacement for bulky ferrite based conventional ones to help in microwave circuit miniaturization. Hence, over the last decade much research has been carried out to develop metamaterial based AT structures [10-13]. However, many of the designs exhibited only narrow operational bandwidth that restricted its practical applications. Therefore, designs with broadband, high magnitude AT effect is highly desirable.

In this work, we present a novel, broadband asymmetric transmission structure for a linearly polarized wave at microwave frequencies. The designed structure is based on complementary strips patterned on a dielectric substrate. The optimized design is almost transparent for a broadband of 1.15 GHz in one propagation direction while the same polarization is blocked from the other direction. The mechanism of the asymmetric transmission by the proposed design is explored with surface current analysis and electric field maps.

2. Design

Fig. 1 shows the unit cell layout of the proposed AT structure. It is a single dielectric layer design with metal patterns on both the sides of it. The metal patterns are designed to be complementary strips which are kept at an angle of 90° with respect to each other. This rotated geometry breaks the symmetry in the propagation direction and thus gives the asymmetric transmission from the structure by giving different polarization conversion from the two opposite incident directions. Rogers RT 5880 with dielectric constant 2.2 and loss tangent 0.0009 is used as a

substrate and the metal patterns are realized with copper of thickness 0.034 mm and conductivity of 5.8×10^7 S/m.

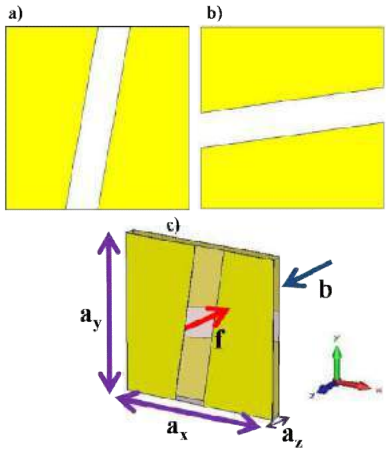

Figure 1: Unit cell of the proposed AT structure. a) Front layer b) back layer c) Perspective view

The geometry of proposed structure is analyzed and optimized by full-wave electromagnetic simulations using CST Microwave studio. In the frequency domain solver, unit cell boundary conditions are applied in the Y and X direction, and electromagnetic radiation is excited along the Z direction. The optimized dimensions of the unit cell parameters are a_x=11.5 mm, a_y=11.5 mm, a_z=0.787mm.

3. Simulation Results

For transverse electric (TE) and transverse magnetic (TM) polarization excitation, all components of co- (T_{xx} and T_{yy}) and cross-polarized (T_{yx} and T_{xy}) transmission coefficients are computed in the frequency range of 4-14 GHz. Transmission coefficients T_{ij} is defined as the ratio of complex amplitude of transmitted electric field to the incident electric field. The subscripts i and j corresponds to the polarization of the transmitted and incident electromagnetic radiation which is either TE (Electric field is oriented along y) or TM (Electric field is oriented along x) linear polarization.

Fig. 2 shows the transmission coefficient from the structure when the electromagnetic radiation incident on it in the a) forward and b) backward directions. For the entire spectrum the cross- polarization terms T_{yx} and T_{xy} show different magnitudes whereas the co-polarization terms T_{xx} and T_{yy} are equal. It is observed that T_{yx} shows a broad, strong peak with values above 0.9 from 8.48 GHz to 9.86 GHz. At the same frequency range co-polarization transmission magnitudes are less than 0.015. This indicates strong cross polarization conversion of the structure. When X-polarized wave is incident on the structure from the forward direction, most of it gets converted to Y polarization and transmitted to the other side. But for Y-polarized incidence, this effect is absent. This large difference in polarization conversion for different incident polarization makes the structure suitable for asymmetric transmission. When the propagation direction is reversed the cross-polarization terms exchange its values (fig. 2 b). That is from the backward direction, the incident Y-polarization gets converted to X-polarization and transmitted to the other side while blocking the incident X-polarization. Also, the co-polarization terms are less than 0.136 for the entire spectrum. The equal magnitudes for T_{xx} and T_{yy} make the asymmetric transmission for circularly polarized light as zero making the structure suitable for asymmetric transmission of linearly polarized wave.

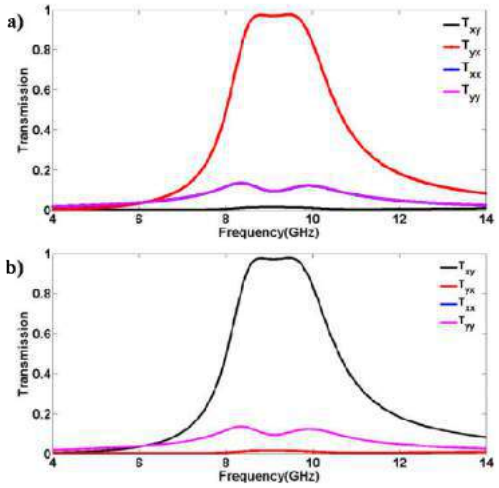

Figure 2: The co- (T_{xx} and T_{yy}) and cross-polarized (T_{yx} and T_{xy}) transmission coefficients of linearly polarized wave in a) forward and b) backward directions.

The large difference in the cross polarization terms causes large difference in the total transmission for a linear polarization from the two propagation directions. Total transmission is calculated as the sum of cross-polarization and co-polarization terms as [14]

$$T_x = |T_{xx}|^2 + |T_{yx}|^2 \qquad (1\ a)$$

$$T_y = |T_{yy}|^2 + |T_{xy}|^2 \qquad (1\ b)$$

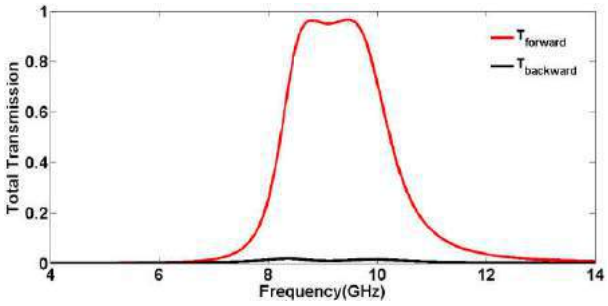

Figure 3: Total transmission for an X- polarized wave from forward and backward directions

From Fig. 3, it is observed that in the forward propagation direction X-polarization shows a peak from

8.56 GHz to 9.75 GHz with a maximum value of 96.6% and in the backward propagation direction it is less than 1.6%. In the opposite propagation direction, Y polarization shows a strong peak in the same frequency band.

Asymmetric transmission is generally characterized by the parameter Δ, which is defined as the difference between the cross-polarization terms [9].

$$\Delta^{x}_{lin} = |T_{yx}|^2 \quad |T_{xy}|^2 = \Delta^{y}_{lin} \qquad (2)$$

Fig.4 shows the calculated asymmetric transmission parameter Δ in the frequency range 4-14 GHz. A Strong, broadband response is observed from 8.58 GHz to 9.73 GHz with magnitude more than 0.9 with a maximum value of 0.95. This strong AT is a result of difference in the partial polarization conversion which is asymmetric in the two propagation directions.

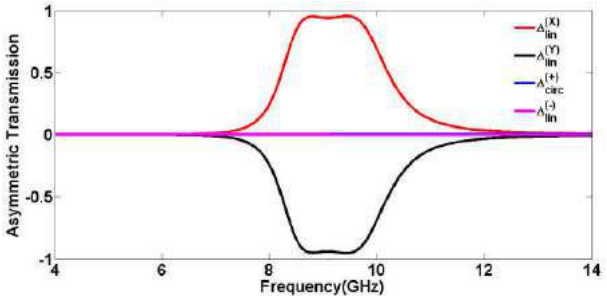

Fig.4 The asymmetric transmission parameter Δ for X and Y polarizations.

The existence of opposite peaks for Δ^x and Δ^y in the spectrum signifies that the asymmetric transmission is contrary for X and Y polarization. That is, in one propagation direction X polarization is allowed while Y polarization is forbidden and in the opposite direction this reverses. Further, owing to the equal magnitudes of the co-polarization terms, Δ for the circular polarizations is observed to be zero.

To elucidate the mechanism of asymmetric transmission, the surface current generated under e-m wave excitation on the structure is analyzed. Surface current distribution of the two metallic layers at 8.78 GHz when X-polarized wave incident on it in the forward direction is presented in Fig. 5. The applied electric field is in the X-direction and magnetic field in the Y direction. From the figure it can be seen that anti parallel currents exist between the front and back layers. This constitute a circulating current in the structure resulting in induced magnetic field which has components in both X and Y directions. The Y component of the induced magnetic field which is perpendicular to the applied electric field does not contribute to the polarization conversion. In contrast, the X component of the induced magnetic field which is in the direction of applied electric field couples strongly with the incident electric field and result in the X to Y polarization conversion. Also, there are induced electric fields along X and Y directions and the induced electric field along the Y direction which is perpendicular to the applied filed contribute in cross polarization conversion.

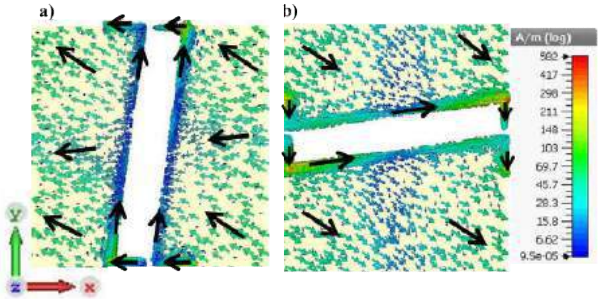

Figure 5: Surface current distribution on the proposed metamaterial structure at 8.78 GHz a) front b) back layers

To substantiate the cross polarization mechanism the electric field profiles of the structure is presented (Fig. 6). When Y polarized wave is incident on the structure in the forward direction (a) most of the incident radiation get reflected and no cross polarization conversion occurs. When Y polarization incident in the backward direction (b), it get converted to X polarization and transmitted to the other side. The change in the field patterns in the structure is noticeable and caused by the cross coupling resulting in the polarization conversion.

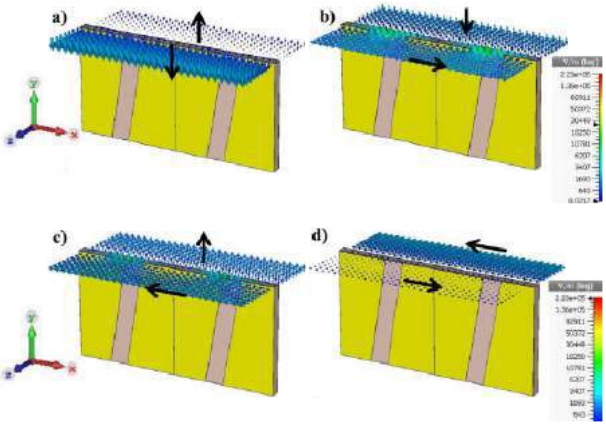

Figure 6: Electric field evolution for X and Y polarization incidence

Similarly when X polarized wave incident in the forward direction (c) cross coupling happens in the structure and the wave gets transmitted to the other side as Y polarization. But when incident in the backward direction (d), most of the radiation gets reflected and no cross polarization conversion occur.

4. Conclusion

In summary, the design and analysis of a metamaterial based broadband asymmetric transmission structure at microwave frequency is presented. In addition to

being planar, simple and ultra-thin, the structure exhibits broadband nature which makes it excellent for practical applications. Full wave simulations show that for a bandwidth of 1.15 GHz from 8.58 GHz to 9.73 GHz, the design produces strong asymmetric transmission for linear polarizations with magnitude more than 0.9. Also, from the calculated total transmission it is found that 96.6% of the incident polarization gets transmitted in one propagation direction while from the other direction the same polarization is restricted to 1.6%. The mechanism of cross polarization conversion is explained with the surface current analysis. Further the electric field profilesof the structure gives a clear visualization of the cross polarization occurring in the structure.

References

[1] E. Plum, J. Zhou, J. Dong, V.A. Fedotov, T. Koschny, C.M. Soukoulis, N.I. Zheludev, Metamaterial with negative index due to chirality, Phys. Rev. B - Condens. Matter Mater. Phys. 79 (2009) 1–6.

[2] J. Zhou, J. Dong, B. Wang, T. Koschny, M. Kafesaki, C.M. Soukoulis, Negative refractive index due to chirality, Phys. Rev. B - Condens. Matter Mater. Phys. 79 (2009) 3–6.

[3] M. Decker, M.W. Klein, M. Wegener, S. Linden, Circular dichroism of planar chiral magnetic metamaterials, Opt. Lett. 32 (2007) 856–858.

[4] D. Zarifi, M. Soleimani, V. Nayyeri, J. Rashed-Mohassel, On the miniaturization of semiplanar chiral metamaterial structures, IEEE Trans. Antennas Propag. 60 (2012) 5768–5776.

[5] G. Dolling, C. Enkrich, M. Wegener, J.F. Zhou, C.M. Soukoulis, S. Linden, Cut-wire pairs and plate pairs as magnetic atoms for optical metamaterials., Opt. Lett. 30 (2005) 3198–3200.

[6] Z. Li, R. Zhao, T. Koschny, M. Kafesaki, K.B. Alici, E. Colak, H. Caglayan, E. Ozbay, C.M. Soukoulis, Chiral metamaterials with negative refractive index based on four “u” split ring resonators, Appl. Phys. Lett. 97 (2010) 1–4.

[7] D. Liu, Z. Xiao, X. Ma, Z. Wang, Broadband asymmetric transmission and multi-band band 90° polarization rotator of linearly polarized wave based on multi-layered metamaterial, Opt. Commun. 354 (2015) 272–276.

[8] T. Pertsch, F. Lederer, Asymmetric Transmission of Linearly Polarized Light at Optical Metamaterials, Phys. Rev. Lett. 253902 (2010) 1–4.

[9] M. Mutlu, A.E. Akosman, A.E. Serebryannikov, E. Ozbay, Diodelike Asymmetric Transmission of Linearly Polarized Waves Using Magnetoelectric Coupling and Electromagnetic Wave Tunneling, Phys. Rev. Lett. 213905 (2012) 1–5.

[10] C. Huang, Y. Feng, J. Zhao, Z. Wang, T. Jiang, Asymmetric electromagnetic wave transmission of linear polarization via polarization conversion through chiral metamaterial structures, Phys. Rev. B. 195131 (2012) 1–5.

[11] L. Wu, M. Zhang, B. Zhu, Dual-band asymmetric electromagnetic wave transmission for dual polarizations in chiral metamaterial structure, Appl. Phys. B Lasers Opt. (2014) 527–531.

[12] J. Shi, X. Liu, S. Yu, T. Lv, Z. Zhu, T.J. Cui, Dual-band asymmetric transmission of linear polarization in bilayered chiral metamaterial, Appl. Phys. Lett. 191905 (2013).

[13] X. Huang, D. Yang, S. Yu, Dual-band asymmetric transmission of linearly polarized wave using P - shaped metamaterial, Appl. Phys. B Lasers Opt. (2014) 633–638.

[14] Z. Li, S. Chen, C. Tang, W. Liu, H. Cheng, Z. Liu, J. Li, P. Yu, Broadband diodelike asymmetric transmission of linearly polarized light in ultrathin hybrid metamaterial, Appl. Phys. Lett. 201103 (2014).

Plasmonics-based devices

Treble-resonance nanohole array structure for selected surface-enhanced Raman scattering substrate

Zhengqing Qi, [1]Jie Yao, [1,2]Chengjun Zhu, [1]Yiping Cui, [1] and Changgui Lu [1,*]

[1]Advanced Photonics Center, Southeast University, Nanjing 210096, China

[2] Nanjing Normal University, Nanjing 210023, China

*Corresponding author: changguilu@seu.edu.cn

Abstract— Here we design a new SERS-active plasmonic nanostructure. Selected enhancement of Raman signals is achieved by this device. We found that the SERS enhancement factor corresponding to the resonant frequency exhibit about one magnitude larger than the enhancement factor mismatched with the resonant frequency.

Structures with one or two plasmon resonant mode have been widely used to realize higher enhancement of Raman signals[1]. Here we design a new SERS-active plasmonic nanostructure with period silver nanoholes upon metallic film separated by a layer of silica spacer. The introduce of silver and silica spacer provides a higher enhanced electric field for the interaction of the LSPR mode and SPP modes with their mirror's resonant modes, respectively.[2-3] The structure we investigate here combines a LSP resonant mode and two SPP resonant modes. Theoretical and experiment studies have been made to realize the selected enhancement of Raman signals. We successfully achieve the enhancement of Raman signals by strengthening the exciting mode and selected enhancements of several specific Raman signals matching with the other two resonant frequencies. Period nanohole without metallic film upon the substrate was introduced for comparison. The SERS enhancement factor (EF) of period silver nanoholes upon metallic film separated by a layer of silica spacer was observed to be more than one order of magnitude larger than that of a regular silver nanohole array on a glass substrate. Besides, we found that the SERS enhancement factors corresponding to the plasmonic resonant modes exhibit more than two times larger than that mismatched with the plasmonic resonant modes, which was almost the same in the period nanoholes with silica substrate only.

In conclusion, we propose a SERS-active substrate with selected enhancement property. Compared to the single layer nanoholes device, the multilayer device possesses not only higher SERS enhancement factors, but also a selective enhancement of specific Raman frequency corresponding to the plasmon resonant mode. This device can also be applied to several molecules with characteristic Raman vibrational frequency detection. Besides, measures like self-assembled[4] or UV nanoimprint lithography[5] can be introduced to reduce the cost of time and economy.

Acknowledgments

This work is supported by the National Science Foundationsof China (Grant No. 11274062)

References

1. Chu, Y.; Banaee, M. G.; Crozier, K. B., "Double-resonance plasmon substrates for surface-

enhanced Raman scattering with enhancement at excitation and stokes frequencies," *Acs Nano*, Vol.4, No.5, 2804-10, 2010.
2. Anna, L.; Angela, D.; Lee, W.; Patrick, A.; Felix, B.; Rohit, C.; Javier, A.; Baumberg, J. J., "Anomalous Spectral Shift of Near- and Far-Field Plasmonic Resonances in Nanogaps," *Acs Photonics*, Vol.3, No.3, 471-477, 2016.
3. Qi, Z.; Yao, J.; Zhao, L.; Cui, Y.; Lu, C., "Tunable double-resonance dimer structure for surface-enhanced Raman scattering substrate in near-infrared region," *Photonics Research*, Vol.3, No.3, 313, 2015.
4. Zheng, P.; Li, M.; Jurevic, R.; Cushing, S. K.; Liu, Y.; Wu, N., "A gold nanohole array based surface-enhanced Raman scattering biosensor for detection of silver(I) and mercury(II) in human saliva," *Nanoscale*, Vol.7, No. 25, 11005-11012, 2015.
5. Chen, J.; Shi, J.; Decanini, D.; Cambril, E.; Chen, Y.; Haghiri-Gosnet, A. M., "Gold nanohole arrays for biochemical sensing fabricated by soft UV nanoimprint lithography," *Microelectronic Engineering*, Vol.86, No.4, 632-635, 2009.

Control of light absorbance using plasmonic grating based metamaterials

D. M. Nguyen[1], G. Yoon[1], D. Lee[1] and J. Rho[1,2,3]

[1] Department of Mechanical Engineering, Pohang University of Science and Technology (POSTECH), Pohang 37673, Republic of Korea

[2]Department of Chemical Engineering, Pohang University of Science and Technology (POSTECH), Pohang 37673, Republic of Korea

[3]National Institute of Nanomaterials Technology (NINT), Pohang 37673, Republic of Korea

[*]corresponding author: jsrho@postech.ac.kr

Abstract - We demonstrate that a conventional polarization-insensitive multilayer absorber can be switched to a highly polarization sensitive perfect absorber by replacing the metallic reflecting layer with a plasmonic grating. Active control of light absorption based on this concept is experimentally and numerically demonstrated for both narrowband and broadband of wavelength.

Perfect absorber, which is a device that neither reflects nor transmits the incident light, has drawn great interest due to many possible applications in photovoltaic solar cells, spatial imaging or highly sensitive detectors. Recently, polarization dependent perfect absorbers, where only lights with specific polarization are perfectly absorbed, have been realized by introducing anisotropy in the design structure. For example, for narrowband polarization sensitive perfect absorber, designs with botte-line and cub-like structures are numerical demonstrated in [1], and the one consisting of arrays of three-dimensional standing U-shaped resonators are fabricated and realized in [2]. Since the control of light absorbance plays a fundamental role in photonics technology with strong impact for light emitting and sensing components, metamaterial designs that can enable active control of light absorbance are necessary.

Here, we report a demonstration of polarization sensitive perfect absorbers for both narrowband and broadband of wavelength based on plasmonic grating, including numerical investigation of the design, fabrication and measurements. We show that a polarization sensitive perfect absorber can be realized by simply replacing the bottom metallic thin film with an appropriate plasmonic grating. The design structures for broadband and narrowband polarization sensitive perfect absorber are presented respectively in Fig. 1a and Fig. 1b. We perform numerical investigations for both cases with different incident angles by using finite element method (FEM) with Lumerical. In fabrication, evaporation for multilayers coating and e-beam lithography technique with parameters optimized for plasmonic grating have been used. Performance of the designed broadband perfect absorber under normal incidence is presented in Fig. 1c. When the incident light is s-polarized, since the permittivity of Cr is closed to the idea metal permittivity in the visible and NIR range, multi-resonance frequencies are created when the beam reflects back to the dielectric layer after approaching the grating [3], leading to high absorption (above 85%) over broad wavelength range of 0.4-1.4 μm. For p-polarized incidence, we can see that absorption decreases rapidly and becomes smaller than 25% for wavelength range of 1.2-1.6 μm. The device is therefore sensitive to the polarization state for a range of 1.2-1.4 μm. In case of narrowband perfect absorber, for s-polarized light, three absorption peaks, denoted as Peak 1 (absorption above 98%), Peak 2 (absorption above 85%) and Peak 3 (absorption above 68%), corresponding to the wavelength of 722 nm, 870

nm and 950 are observed respectively. Similar to the case of the broadband absorber, when the p-polarized light is applied, we can see that all of 3 absorption peaks are diminished. Especially, guided mode resonance absorption (Peak 2) is depleted to below 5%.

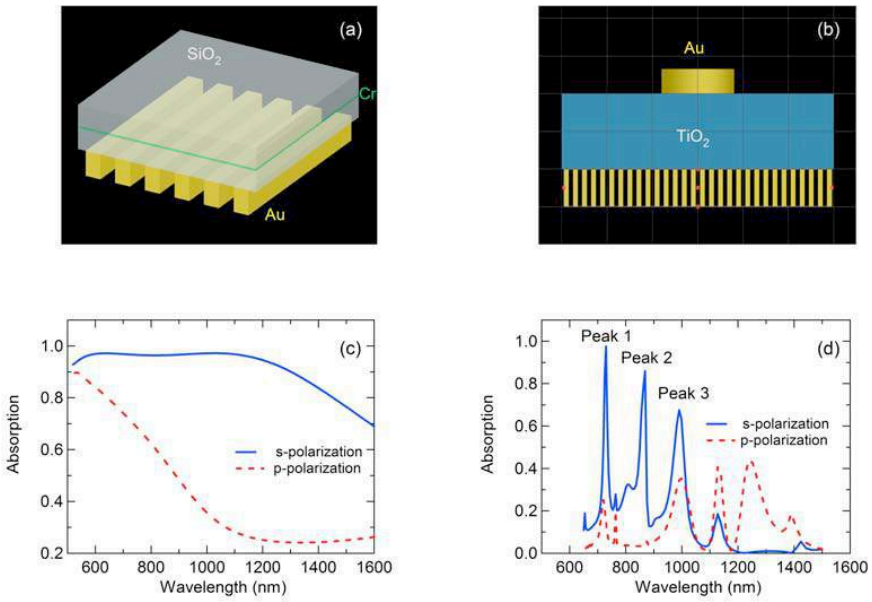

Fig. 1. Design of polarization sensitive perfect absorber for (a) broadband and (b) narrowband range of wavelength. (c) and (d) are absorption under s-polarized and p-polarized incidence for the designed broadband and narrowband perfect absorber respectively.

Overall, this study shows that a conventional multilayer perfect absorber can be switched to polarization sensitive perfect absorber by simply replacing the metallic thin layer with a plasmonic grating. A broadband and a narrowband perfect absorber based on the above concept are designed, fabricated and demonstrated to be polarization dependent. Challenges remain, including the fabrication of grating with tinny period, especially for sizes below 50 nm. The performance tolerance of the absorbers on the grating sizes is therefore also investigated in our work. The proposed absorbers may have potential applications in polarization detectors, polarizers etc.

Acknowledgements. This work is supported by Young Investigator Research program (NRF-2015R1C1A1A02036464), Engineering Research Center program (NRF-2015R1A5A1037668), Global Frontier Research Program (CAMM-2014M3A6B3063708

REFERENCES

1. Meng, L. *et al.*, "Polarization-sensitive perfect absorbers at near-infrared wavelengths," *Opt. Express*, Vol. 21, A111-A122, 2013.
2. Xiong, X. *et al.*, "Polarization-dependent perfect absorbers/reflectors based on a three-dimensional metamaterial*," Phys. Rev. B*, Vol. 88, 115105, 2013.
3. Deng, H. *et al.*, "Broadband perfect absorber based on one ultrathin layer of refractory metal", *Opt. Lett.*, Vol. 40, No. 11, 2592-2595, 2015.

Hybrid plasmonic waveguides by cladding hyperbolic metamaterials

Ruey-Lin Chern

Institute of Applied Mechanics, National Taiwan University, Taipei 106, Taiwan
chernrl@ntu.edu.tw

Abstract— We propose a new type of hybrid plasmonic waveguides by cladding hyperbolic metamaterials, consisting of mutlilayers of metal and dielectric, on a cylindrical plasmonic waveguide. The proposed metal-dielectric-hyperbolic waveguides share the merit of hybrid plasmonic waveguides, that is, a relatively large ratio of propagation length to mode area. We analytically solve the propagation constant, the most important waveguide feature, by locating the complex roots of the multilayered anisotropic cylindrical waveguide dispersion relations.

In the present study, a new design of plasmonic waveguides with the dielectric-coated metal wire as the inner core structure and the hyperbolic metamaterial as the outer cladding, is proposed. The inner core structure is one of the standard optical waveguides for guiding waves in one dimension [1]. The outer cladding is a strongly anisotropic medium, which is carefully arranged to adjust the distribution of field energy within the waveguide. On the one hand, adding an outer cladding on the coated structure forms the so-called metal–dielectric–hyperbolic cylindrical waveguides. The field energy is shown to be highly confined within the dielectric layer as in the metal–dielectric–metal planar [2] or cylindrical [3] waveguides, with minimal interference to nearby optical components. On the other hand, the propagation loss will be reduced because of the somewhat less confinement of the field energy along the transverse (to propagation) direction as in the hyperbolic–dielectric–hyperbolic planar waveguides [4]. The proposed waveguides thus behave in the spirit of hybrid plasmonic waveguides that combine the advantages of two different types of waveguides to reach an optimal performance. Regarding the hyperbolic metamaterial as an effective medium, the radial component of the permittivity tensor is positive in the present configuration, as opposed to being negative for the axial component.

The propagation characteristics of the proposed waveguides are analyzed by the dispersion relation of a multi-layered anisotropic structure in cylindrical coordinates. By taking into account the evanescent nature of surface plasmon waves in the cladding, the dispersion relation can be well approximated by a three-layered compact formula, based on which the propagation constant, propagation length, mode area, and figure of merit are determined in an analytical manner. An optimal waveguide performance is achieved when the propagation loss is substantially reduced at the expense of slight mode confinement. For the plasmonic cylindrical waveguide made of Ag and ZnO at the telecommunication wavelength, the mode area is comparable to that of the metal–dielectric–metal waveguide, while the propagation length is about twice as large.

REFERENCES

1. J. Takahara, S. Yamagishi, H. Taki, A. Morimoto, and T. Kobayashi, Guiding of a one-dimensional optical beam with nanometer diameter, Opt. Lett. **22**, 475–477 (1997).
2. P. Berini, Long-range surface plasmon polaritons, Adv. Opt. Photonics **1**, 484–588 (2009).
3. D. Handapangoda, M. Premaratne, I. D. Rukhlenko, and C. Jagadish, Optimal design of composite nanowires for extended reach of surface plasmon-polaritons, Opt. Express **19**, 16058–16074 (2011).
4. S. Ishii, M. Y. Shalaginov, V. E. Babicheva, A. Boltasseva, and A. V. Kildishev, Plasmonic waveguides cladded by hyperbolic metamaterials, Opt. Lett. **39**, 4663–4666 (2014).

Numerical analysis on propagation compensation for loss in shadow of object by plasma and dielectric layer

S. Yamaguchi[1], **A. Bambina**[1], **A. Iwai**[2], **Y. Kabe**[1], **S. Miyagi**[1] **and O. Sakai**[1]

[1]The University of Shiga Prefecture, Japan
[2]Kyoto University, Japan
ot23syamaguchi@ec.usp.ac.jp

Abstract— We proposed and evaluated a functional layer, a composite of plasma and dielectric, which compensates the propagation of electromagnetic waves for loss in the shadow of an object. The layer hides the object inside the layer from electromagnetic waves like an invisibility cloak. Using the layer, we observed by numerical analyses that electromagnetic waves propagate in the shadow. This layer consists of a dielectric layer and a plasma layer which has a spatial gradient of electron density, and so the structure is simpler than the invisibility cloak composed of metamaterial.

The methods of controlling propagation paths of electromagnetic waves by metamaterial, for instance, cloaking, have been studied extensively[1]. An invisibility cloak decreases scattering from the hidden object and its shadow[2]. In other words, the cloak compensates propagation of electromagnetic waves for loss in the shadow of an object. Metamaterial, which can achieve the cloaking is complex, which is a drawback for future industrial uses. Here we propose that plasma can replace metamaterial in some cases. We observed that the plasma layer and the dielectric layer hide an object roughly like an invisibility cloak without metamaterial by numerical analysis[3]. In addition, combination of plasma and metamaterial works well to make the property tunable[4], which is an advantage of plasma.

In this study, we evaluate this functional composite layer which compensates propagation of electromagnetic waves for loss in the shadow of an object and hides the object from electromagnetic waves. Its structure is simpler than an invisibility cloak of metamaterial.

The two-dimensional model of the layer is shown in Figure 1. We calculated the distribution of the scattered and the total one, which is a sum of vectors of incident and scattered electric fields, by finite-difference time-domain method (FDTD) when the incident plane wave (3.0 GHz) entered the layer. The plane wave is in the TM mode, therefore the electric field is normal to, and the magnetic field is parallel to the plane. The numerical model is shown in Figure 2. Central electron density of plasma n_{e0}, the relative permittivity of dielectric ε_g, the thickness of dielectric d_g and the inner radius of the functional layer r_{in} are model parameters. The observed point is on the circle whose center is the same as the layer and whose radius is $r_{in} + d_g + \lambda$, where λ is the wavelength of the incident filed. We evaluated the layer by the value $E_{trms}(r_{in} + d_g + \lambda, \phi)/E_{irms}(r_{in} + d_g + \lambda, \phi)$, where ϕ is the observed angle, E_{trms} is the root mean square value (RMS) of the total field, and E_{irms} is RMS of the incident field.

RMS distribution of electric field calculated by FDTD and the evaluation value are shown in Figure 3. Figure 3(a) shows the case with the functional layer. In this case, electromagnetic wave cannot propagate in the plasma layer because of its overdense property. This case indicates that the functional layer can hide an object inside the plasma layer. Compared with Figure 3(b), Figure 3(a) shows that electromagnetic waves can propagate behind the layer. Therefore the functional

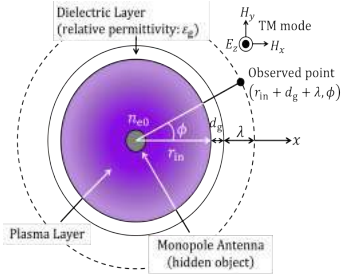

Figure 1: Functional layer.

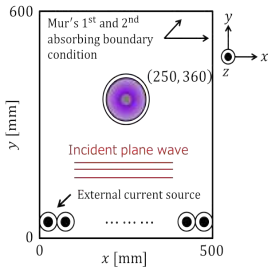

Figure 2: Numerical model

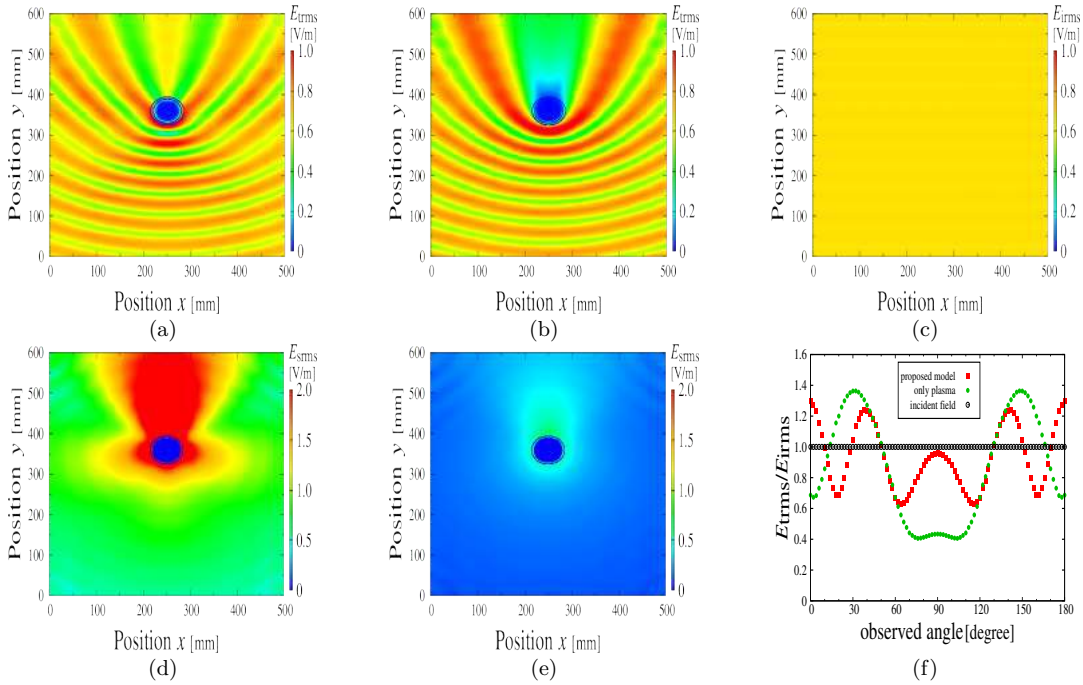

Figure 3: RMS distribution of electric field and evaluation value. Two circles describe inner or outer radius.(a)-(c): total field distribution and (d)-(e): scattered field distribution. (a) and (d): case with the functional layer. n_{e0} is 2.0×10^{19} m^{-3}(overdense plasma), ε_g is 9.0, d_g is 5.0 mm and r_{in} is 30.0 mm. (b) and (e): case with plasma only. Parameters are same as (a) except ε_g. (c): incident electric field. This case corresponds to free space propagation. (f): evaluation value.

layer can hide an object and compensate the propagation for loss in the shadow of the object.

RMS distribution of the scattered field of the functional layer is shown in Figure 3(d). Compared with Figure 3(e), the scattered field in the case with the functional layer is larger than the case of plasma only. In spite of large scattered field, the total field behind the layer is larger than that in the case of plasma only.

Figure 3(f) summarizes the results as an evaluation value. This figure shows that electromagnetic waves can propagate almost as much as the incident field by using the functional layer around 90°. Compared with the case of plasma only, the evaluation value in the case of the layer is bigger than that for plasma only. Therefore the compensation for loss in the shadow is successful.

In conclusion, we proposed the functional layer composed of plasma and dielectric. Its structure is simpler than the invisibility cloak of metamaterial. We observed the layer compensates propagation of electromagnetic waves for loss in the shadow of an object and hides the object from electromagnetic waves by numerical analysis.

ACKNOWLEDGMENT

This study was supported by Grant-in-Aid for Scientific Research from the Japanese Ministry of Education, Culture, Sports, Science and Technology, Japan, and by Strategic Information and Communications R&D Promotion Programme(SCOPE) from the Ministry of Internal Affairs and Communications, Japan.

REFERENCES

1. Schurig, D., Mock, J. J., Justice, B. J., Cummer, S. A., Pendry, J. B., Starr, A. F. and Smith, D. R., "Metamaterial electromagnetic cloak at microwave frequencies," *Science*, Vol. 314, No. 5801, 977– 980, 2006.
2. Cai, W., Chettiar, U. K., Kildishev, A. V. and Shalaev, V. M., "Nonmagnetic cloak with minimized scattering," *Appl. Phys. Lett.*, Vol. 91, 111105-1-3, 2007.
3. Sakai, O., Yamaguchi, S., Bambina, A., Iwai, A., Nakamura, Y., Tamayama., Y. and Miyagi, S., "Plasma metamaterials as cloaking and nonlinear media," *Plasma Phys. Control. Fusion,* Vol. 59, 014042-1-10, 2017.
4. Sakai, O. and Tachibana, K., "Plasmas as metamaterials: a review," *Plasma Sources Sci. Technol.* Vol. 21, 013001-1-18, 2012.

Observation of resonance mode in a MIM plasmonic waveguide with a rectangular resonator

S. Kamada[1], **T. Okamoto**[1], **and M. Haraguchi**[1]

[1]Tokushima University, Japan
c501648001@tokushima-u.ac.jp

Abstract— We proposed a metal/insulator/metal plasmonic waveguide with a rectangular resonator for a compact pressure or refractive index sensor. Transmission spectra of fabricated structure were measured to confirm the resonance mode. Transmission dips by rectangular resonator are appeared at the fabricated structure. It is assume that the transmission dips due to resonance mode in the rectangular resonator.

Plasmonic waveguide poses a potential to realized tiny and simple optical devices, because of strong light confinement [1], [2], [3]. We are working on plasmonic devices for integrated optical circuits based on Metal-Insulator-Metal (MIM) plasmonic waveguides (PWGs). We proposed a MIM PWG with a rectangular resonator. Our rectangular resonator is sensitive to modification of its shape and changing of the refractive index [4]. Therefore, our device is available for pressure and/or temperature sensor.

Our rectangular resonator device could be fabricated by Electron beam lithography techniques. MIM PWGs consist of Ag/PMMA/Ag on a glass substrate. An Ag pattern (thickness: 300nm) of 1st layer is fabricated by EB lithography and lift off process. PMMA films and Ag film (thickness: 20nm) are formed by spin coating and thermal evaporation, respectively. A rectangular resonator was negative type electron beam resist (NEB-22) fabricated by electron beam exposure. Ag films (thickness: 300nm) are deposited on the structure. Finally, the output slit was milling by focused ion beam.

SEM images of the cross section of a part of input slit and PWG with rectangular resonator device are shown as Fig.1 (a) and (b), respectively. As shown in Fig.1 (a), the thickness of PMMA film is approximately 140 nm. The surface plasmon polariton (SPP) can be confined and propagating within the thicknesses PMMA with Ag cladding. The incident light is irradiated from glass substrate for exciting SPP at the MIM PWGs. The height and width of rectangular resonator are 240nm and 2.0μm, respectively.

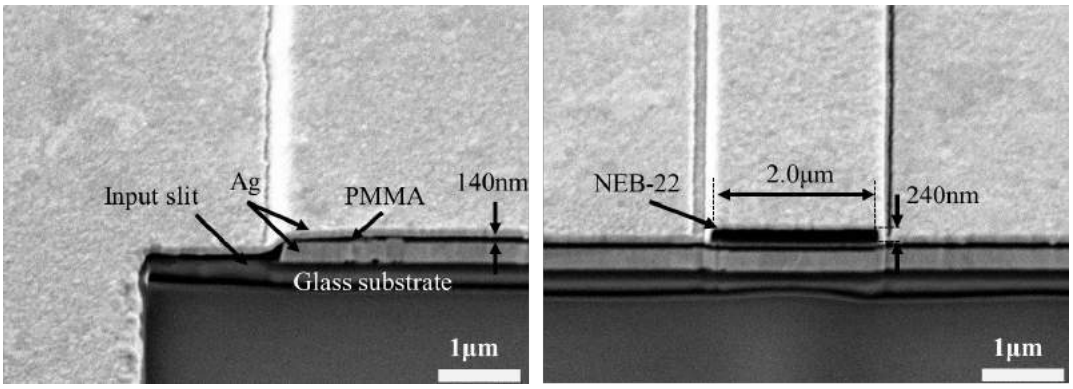

(a) Input slit of plasmonic waveguide (b) Rectangular resonator device

Figure 1: SEM image of cross section of fabricated structures.

Optical setup for measurement of transmission spectra is shown as Fig.2. Xe lamp has been utilized as an incident light source. The TM polarized incident light is irradiated to the input slit from a glass substrate for excitation of the SPPs at a MIM PWG. A distance between input and output slit of a PWG is 20μm.

Transmission spectra of a straight PWG and a PWG with a rectangular resonator are observed in the wavelength range from 600nm to 1000nm. The transmission spectra are shown as Fig.3. Light intensity is decrease to shorter wavelength in the transmission spectrum of a straight PWG as shown Fig.3. It is because of shorter propagation length of SPP in MIM PWGs. There are no dips in this spectrum. On the other hand, there are many dips are appeared in the spectrum of a PWG with a rectangular resonator. Transmission dips appeared at the wavelength 780nm, 840nm and 890nm. When standing waves are occurred in a rectangular resonator, optical energy propagating in PWGs is consumed at a part of the rectangular resonator. Therefore, we believe that transmission dips as shown Fig.3 are resonance modes in a rectangular resonator.

In this study, we proposed a rectangular resonator device, and experimental measurements of transmission dips are succeeded. The device is available for on-chop sensor device.

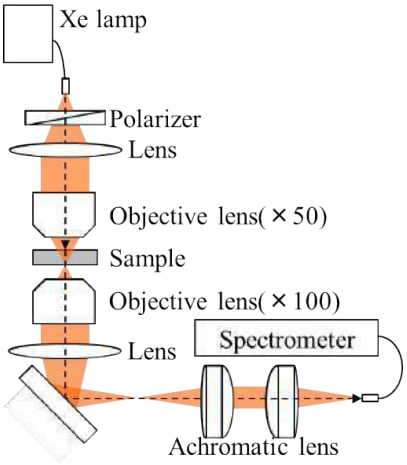

Figure 2: Optical setup

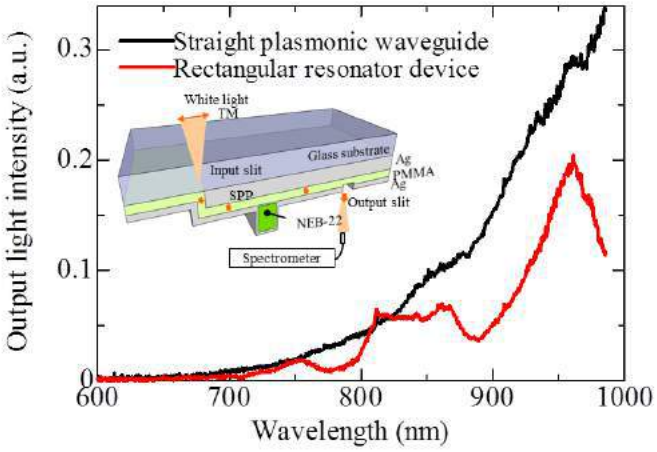

Figure 3: Transmission spectra of a straight plasmonic waveguide and a plasmonic waveguide with a rectangular resonator

REFERENCES

1. H. Lu, X. Liu, D. Mao, Y. Gong, and G. Wang, "Induced transparency in nanoscale plasmonic resonator systems," *Optics Letters*, 36, 3233-3235 (2011).
2. S. Zhan, Y. Peng, Z. He, B. Li, Z. Chen, H. Xu, and H. Li, "Tunable nanoplasmonic sensor based on the asymmetric degree of Fano resonance in MDM waveguide," *Scientific Reports*, 6, 22428(2016).
3. T. Wu, Y. Liu, Z. Yu, Y. Peng, C. Shu, and H. Ye, "The sensing characteristics of plasmonic waveguide with a ring resonator," *Optics Express*, 22, 7669-7677 (2014).
4. S. E. El-Zohary, A. Azzazi, H. Okamoto, T. Okamoto, M. Haraguchi, and M. A. Swillam, "Resonance-based integrated plasmonic nanosensor for lab-on-chip applications," *Journal of Nanophotonics*, 7, 073077(2013).

Demonstration of active plasmonic device on an optical fiber.

K. Yamamoto[1*] and K. Yamaguchi[2*]
[1]Institute for Material Chemistry and Engineering (IMCE), Kyushu University, Japan
[2] Faculty of Engineering, Kagawa University Japan
[*]corresponding author: k_yamamoto@cm.kyushu-u.ac.jp, kenzo@eng.kagawa-u.ac.jp

Abstract-Active and reconfigurable plasmonic devices are expanding their applications. To combine such devices on optical fibers, one easily excites and detects signals from the optical element. We report the design, fabrication and demonstration of active plasmon device on fiber facets. From visible to near- infrared spectral range, we could control the transmission from the device by applying electrical signal.

Plasmonic devices, including sensors, optical filter, ultra-thin lenses, and optical tweezers and so on, are expanding their application based on their strong electric field enhancement and nano-scale localization. However, their properties are determined by the material and structure design, so it is difficult to change the properties after the devices are fabricated. Active and reconfigurable plasmonic devices are paid attention to overcome the difficulties. These device structures can be changed after the fabrication using electric voltage, material expansion, and refractive index change and so on. Yamaguchi et al. proposed and demonstrated the active plasmon filter [1] and the active plasmon lens [2] using micro/nano electro-mechanical system (MEMS/NEMS) technologies.

Optical fibers are the central element of optical information and communication technology and can deliver light energy to long distance with low loss and are easy to handle and connect to other optical elements. Recently, the research areas called “Lab on Fiber [3]” are paid attention due to their advantages. Lab on Fiber technologies covers optical function inside of optical fiber (“Lab in fiber”), and on fiber facet for controlling input and output. To disperse the functionalities of optical network including sensors and switches, such technology is one solution. In this presentation, we propose MEMS/NEMS-based active plasmonic devices on fiber facet for the Lab on fiber technology. We designed and fabricated active plasmon device which control the transmission from the fiber by applying electric signals shown in Fig.1. From optical measurement, we could control the transmission from the visible to near-infrared.

First, we designed the active plasmon device using the finite difference time domain (FDTD) method. Figure 2 show the transmission spectrum for a designed structure. We designed the structure consist of 4 slit grating with slit width is (400, 400, 400, 400) nm. Using electro static MEMS mechanism, the slit width change to (200, 600, 600, 200) nm when we applied the voltage to the structure. As figure 2 shows, around 570 nm the transmission decrease, on the other hand, around 780 nm the transmission increase. These changes come from slit width and plasmonic resonance of slit structures.

Next, we fabricated the active plasmon device on fiber facet using focused ion beam (FIB) milling and selective wet etching. First, we deposited Au/Cr thin film (300 nm/ 5nm) on cleaved fiber facet. We used the dispersion compensated fiber (DCF) for the telecom wavelength. Next, using FIB we milled a part of slit on the fiber core position. These slit act as the window for the following wet etching of optical fiber. Then, the structure was immersed to buffered fluoric acid (BHF). The etching rate for the core and clad of the fiber are different

because of their Ge doping difference. In this case, the etching rate for the core is faster than for the clad, we could release the plasmonic structures above the fiber core. Finally, grating structures were expanded for the decreasing driving voltage and the electrode pads using FIB milling. Figure 3 shows the scanning electron microscope (SEM) image of the fabricated device.

We conducted the transmission measurement of the active plasmonic device. White light incident from the fiber end and the outputted light were collected by optical microscope using 100X objective. The collected light entered the fiber-coupled spectrometer and the transmission spectrum was measured. Figure 4 shows the transmission spectrum of the active plasmonic device. The black point shows the spectrum without applying voltage and the blue point shows the spectrum when we applied 21 V DC voltages to the device. Comparing with the simulated data, the results suggest the grating arms moved about 200 nm to outer by electrostatic force and transmission could be changed by the MEMS mechanism.

In conclusion, we proposed and demonstrated the active plasmon device on the optical fiber. Our device could connect to other fiber or waveguide devices easily and make bundles for the parallel optical processing. In presentation, we will also discuss the combination with the in-fiber ("Lab in fiber") device [4].

Acknowledgements This work was supported by JSPS Grant-in-Aid for Scientific Research (B) (Grant Numbers JP15H03546) and Grant- in-Aid for Young Scientists (B) (Grant Number JP15K21212).

REFERENCES

1. Yamaguchi K, Yamanaka H, Ohtsu T, and Ishi S, "Electrically driven plasmon chip: Active plasmon lens in the visible range," *Appl. Phys. Lett.* Vol. 108, 111903 (2016).
2. Yamaguchi K, Fujii M, Okamoto T and Masanobu H, "Electrically driven plasmon chip: Active plasmon filter," *Applied Physics Express*, Vol. 7, No. 1, 012201 (2014).
3. Patrizio V, Benito C, Marco P, Armando R, Giuseppe Q, Marco C, Alessio C, Emanuela E, and Andrea C, "Lab on Fiber Technology for biological sensing applications," *Laser Photonics Rev.*, Vol. 10, No. 6, 922–961 (2016).
4. Yamamoto K, Yamaguchi K, Yokoyama S and Otomo A, "Plasmonic nanostructures combined with integrated nano-fiber," *META'15 abstract* (2015).

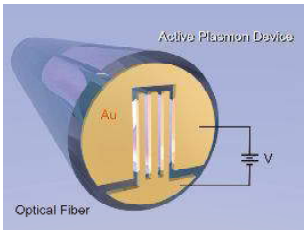

Fig.1 Schematic of active plasmon device on fiber.

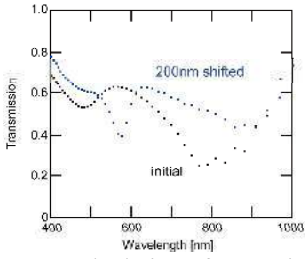

Fig.2 FDTD calculation of transmission.

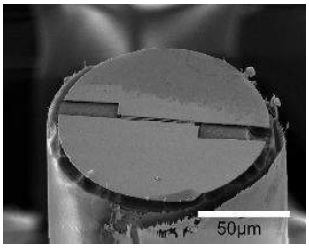

Fig.3 SEM image of fabricated device.

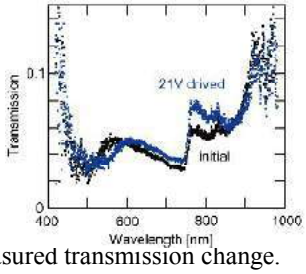

Fig.4 Measured transmission change.

1D subwavelength gratings-dielectric-T2SL detector: Highly improved performance of MWIR polarization detection

Jehwan Hwang[1,2], Daehyeon Ku[1], Jun Oh Kim[1], Eun Kyu Kim[2], Augustine Urbas[3], Zahyun Ku[3], and Sang Jun Lee[1*]

[1]Division of Convergence Technology, Korea Research Institute of Standards and Science, Daejeon, 305-340, Korea

[2]Department of Physics, Hanyang University, Seoul 133-791, South Korea

[3]Materials and Manufacturing Directorate, Air Force Research Laboratory, WPAFB, OH 45433, USA

[*]corresponding author: sjlee@kriss.re.kr

Abstract- We propose and analyze a novel detector structure for linear polarization detection in the mid-infrared regime. 1-dimensional subwavelength grating atop a dielectric layer offers enhanced transmission for transverse magnetic polarized light, thereby enabling a higher extinction ratio as compared with conventional structure. Numerical simulations based on a finite integration technique were used to find the optimized geometric parameters for the structure. Our work can pave the way for practical, easy-to-fabricate detectors, which are highly useful for polarimetric imaging applications.

Infrared (IR) polarimetric imaging has been widely used in remote sensing, military applications and environmental protection[1]. 1-dimensional (1D) subwavelength grating integrated IR sensors have advantages such as polarization discrimination and a significant reduction in cost and complexity of IR camera systems. However, conventional 1D grating structures have low transmission efficiency for transverse magnetic (TM) polarized light due to unwanted reflections. Our design uses a 1D grating on top of the dielectric film, which can be integrated with a Type-II superlattice (T2SL) detector, thereby enabling enhanced responsivity for the TM polarization and thus giving rise to higher figure of merit (extinction ratio), as the measure of linear polarization detection performance than a conventional 1D grating[2]. T2SL structures have been the focus of significant interest recently because of a high device performance and bandgap engineering capabilities[3]. In this study, we employed both the commercial software (CST Microwave Studio[4]) based on a finite integration technique and a rigorous coupled wave analysis[5] for designing the structure of 1D grating atop the dielectric layer. Figure 1(a) shows the calculated extinction ratio color map (1D grating on substrate) as a function of grating parameters (periodicity p and duty cycle r). The grating period p and the ratio r are varied continuously from 0.2 – 2.0 μm and 0 – 1 with fixed gold thickness at 100 nm. The extinction ratio (ER) at 4 μm is found to be from 1 - 10^5 for linear polarized light. The ER for the grating period p = 0.4 μm and duty cycle r = 0.7 can reach up to ~10^3 while maintaining TM transmission higher than 50%. Next, we use SU-8 as the spacer between the 1D grating (p = 0.4 μm and r = 0.7) and substrate. ER is represented in the color map as a function of wavelength and SU-8 dielectric thickness (t_{SU8} is varied from 0 to 2 μm with a step of 0.2 μm) as shown in Figure 1(b). In order to satisfy high TM transmission (>70%) and ER (>10^3) simultaneously, an optimal SU-8 thickness was found to be ~0.4 μm. As indicated in Figure 1(a) and (b), the 1D grating on SU-8 spacer structures show overall performance enhancement (associated with linear polarization detection) as compared with a single layer 1D grating. Finally,

the 1D grating and 1D grating-SU8 (p = 0.4 μm; r = 0.7; t_{SU8} = 0.4 μm) integrated backside-illumination T2SL detector (Figure 1(c)) were simulated for the overall polarization detection performance. Figure 1(d) indicates that TM absorption efficiency in 1D grating-SU8-T2SL can be improved up to ~87% as compared with 1D grating-T2SL and integration of extinction ratio ($\int ER(\lambda)d\lambda$) is also increased by ~ a factor of 10. We expect our design and analysis can be used for various IR polarimetric imaging applications.

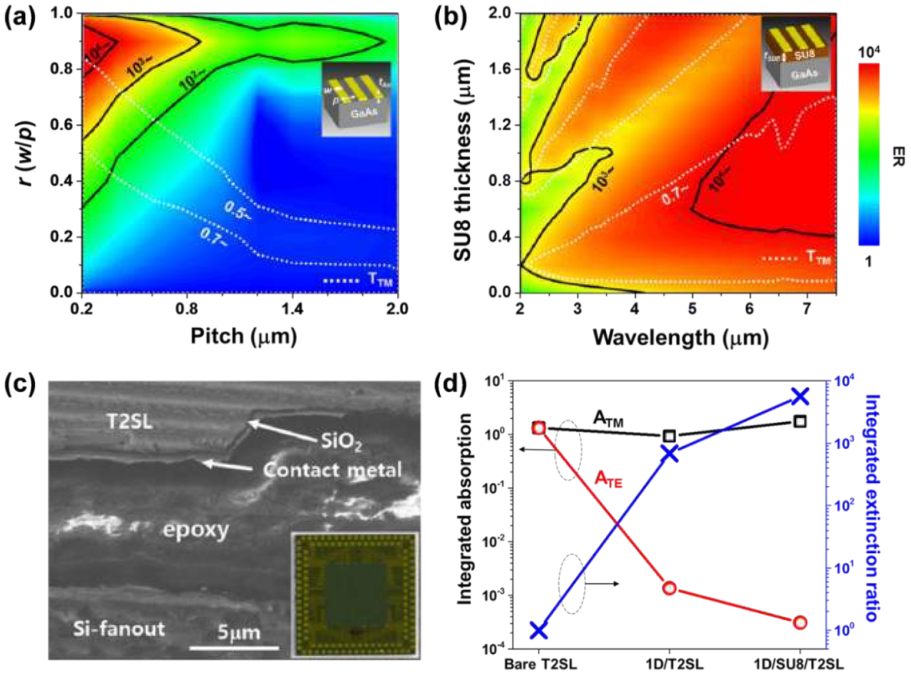

Figure 1. Extinction ratio color maps as a function of (a) p & r (1D grating) and (b) λ & t_{SU8} (1D graing-SU8). (c) Backside illumination T2SL detector. (d) Linear polarization detection performance of bare-T2SL, 1D grating-T2SL and 1D grating-SU8-T2SL detector: Integration of simulated absorption in the active layer for TM (black) and TE (red) modes and integration of ER (blue) with respect to the wavelength.

Acknowledgements

This work was supported by the KRISS grant GP2016-034 and the AOARD grant FA2386-14-1-4094 funded by the U.S. government (AFOSR/AOARD).

REFERENCES

1. Tyo, J. Scott, et al. "Review of passive imaging polarimetry for remote sensing applications," *Appl. Opt.*, Vol. 45, No. 22, 5453-5469, 2006.
2. Wang, Rui, et al. "Subwavelength Gold Grating as Polarizers Integrated with InP-Based InGaAs Sensors," *ACS app mater.*, Vol. 7, No. 10, 14471–14476, 2015.
3. Walther, M., et al. "256×256 focal plane array midwavelength infrared camera based on InAs/GaSb short-period superlattices," *J Electron Mater*, Vol. 34, No. 6, 722–725, 2005.
4. Moharam, M. G. and Gaylord, T. K., "Rigorous coupled-wave analysis of planar-grating diffraction," *J. Opt. Soc. Am.* Vol. 71, No. 7, 811–818, 1981.

Parameterization Study of Dual Polarized Cross Bowtie Nano Antenna for Energy Harvesting Applications

R. Arfin, A. Y. Elsharabasy, M. H. Bakr*, S. Ali, and M. Howlader
McMaster University, Hamilton, Ontario, Canada
*mbakr@mcmaster.ca

Abstract- In this paper, we study the performance of dual polarized cross bowtie gold nano antenna (nantenna) using COMSOL Multiphysics software [1] for energy harvesting applications [2, 3, 4]. Illuminating the bowtie nantenna with an incident plane wave results in a strong local field confinement in the gap. In this work, the electric field in the inner gap of the cross bowtie nantenna is observed and estimated for different values of the geometrical parameters of the nantenna. As it is challenging to fabricate and obtain sharp-tips for such nanostructures, we focus on the changes in the local field for curved-tips as compared to sharp-tips cross bowtie nantenna. Fig. 1 shows the design of cross bowtie gold nanoantenna and the variation of the normalized electric field against frequency for one of the considered parameters.

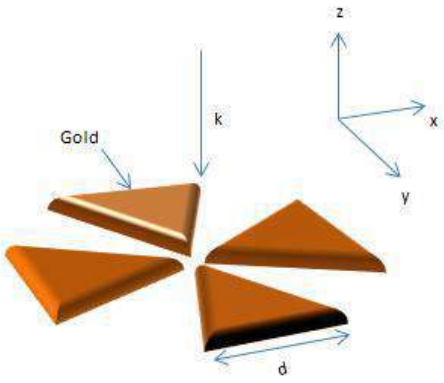

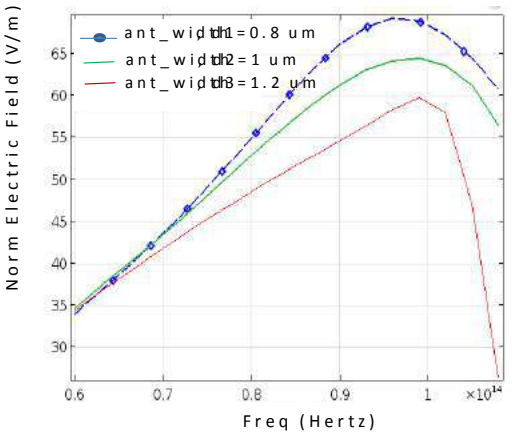

REFERENCES

1. COMSOL Multiphysics Software, Ver. 5.1, COMSOL Inc. Burlington, MA.
2. A. M. A. Sabaawi, C. C.T simenidis and B. S. Sharif, "Planar Bowtie Nanoarray for THz Energy Detection", *IEEE Transactions on Terahertz Science and Technology*, Vol.3, No.5, September, 2013.
3. A. M. A. Sabaawi, C.C.Tsimenidis and B.S. Sharif, "Bow-Tie Nano-Array Rectenna: Design and Optimization", *6th European Conference on Antennas and Propagation (EUCAP)*, pp. 1975-1978, 2011.
4. S. H. Zainud-Deen, N. A. Eltresy, H. A. Malhat and K. H. Awadalla, "Single/Dual-Polarized Infrared Rectenna for Solar Energy Harvesting", *Advanced Electromagnetics*, Vol. 2, No. 2, May 2016.

Surface Plasmonic - Cavity System

J. Jeon[1,2], K. Bhattarai[3], D.-K. Kim[2], J. O. Kim[1], J. Zhou[3], A. Urbas[4], Z. Ku[4] and S. J. Lee[1,*]

[1]Division of Convergence Technology, Korea Research Institute of Standards and Science, Daejeon 34113, Korea

[2]Department of Electrical Engineering, Sejong University, Seoul 05006, Korea

[3]Department of Physics, University of South Florida, Tampa, FL 33620, USA

[4]Air Force Research Laboratory, Wright-Patterson Air Force Base, OH 45433, USA

[*]corresponding author: sjlee@kiriss.re.kr

Abstract-This paper is focused on analyzing the effect of a two-dimensional metal hole array structure and metal mirror back plane in a surface plasmonic-cavity system. Simulation results clearly show anti-crossing behavior resulting from interaction between the surface plasmon resonance and the Fabry-Perot resonance, depending on the thickness of the dielectric spacer. The simulation method detailed in this paper provides a generalized approach to optimize the design of any type of couplers integrated with backside-illuminate IR devices.

In this work, we have investigated the resonances in the surface plasmon[1-3] coupled cavity system. The system is composed of a dielectric spacer (BCB) of variable thickness t_d (from 0.32 μm to 4.52 μm) sandwiched between a gold mirror back plane (t_{MGP} = 0.2 μm) and surface plasmon resonance structure (a gold film perforated with two-dimensional periodic array of subwavelength sized patterns: pitch p = 3.2 μm, diameter of circular aperture d_m = 1.6 μm, gold thickness t_m = 0.05 μm) as shown in the inset of Figure 1. Finite integration technique based simulations (CST Microwave Studio) were carried out to study the physical origins of coupling between surface plasmon (SP) resonance and Farby-Perot (FP) resonance in the cavity[4]. We gradually varied the BCB thickness t_{BCB} and numerically calculated the reflection of the SP-FP system. We present the spectral reflection data using a colormap to show the spectral changes as shown in Figure 1. For t_{BCB} = 0.32 μm, zero reflection is achieved at 5.5 μm, which is the first order SP resonance. Higher order SP resonances can be found at shorter wavelengths. As t_{BCB} increases, the SP resonance is blue-shifted (up to the t_{BCB} of ~1.72 μm). At t_{BCB} = 1.53 μm, anti-crossing behavior is clearly observed due to two resonances, i.e., SP resonance and a half-wavelength ($\lambda/2$) FP mode. The simulated $\lambda/2$ FP mode shows good agreement with theoretically calculated FP mode (green dashed line) for the system bounded by two mirrors. Note that our SP-FP system is bounded by a mirror at one end and an SP structure at the other end, acting as the quasi-open boundary, thus giving rise to a small discrepancy between simulation and theory. Similar anti-crossing behavior can be also found between λ FP mode and 2nd order SP resonance at 3.12 μm. Understanding the underlying mechanism by means of a simulation may offer guidelines for the design of backside-illuminate IR detectors (including IR focal plane array) integrated with any type of resonators because these device structures (semiconductor and metal ground plane consisting of contact metals, under bump metallization, etc.) are similar to the system used here[5]. We are currently testing various sets of geometric parameters (t_{BCB} = 0.32, 1.21, 1.52, 1.7 and 2.12 μm with fixed p, d_m, t_m, t_{MGP} at 3.2, 1.6, 0.05, 0.2 μm, respectively) for experimental verification.

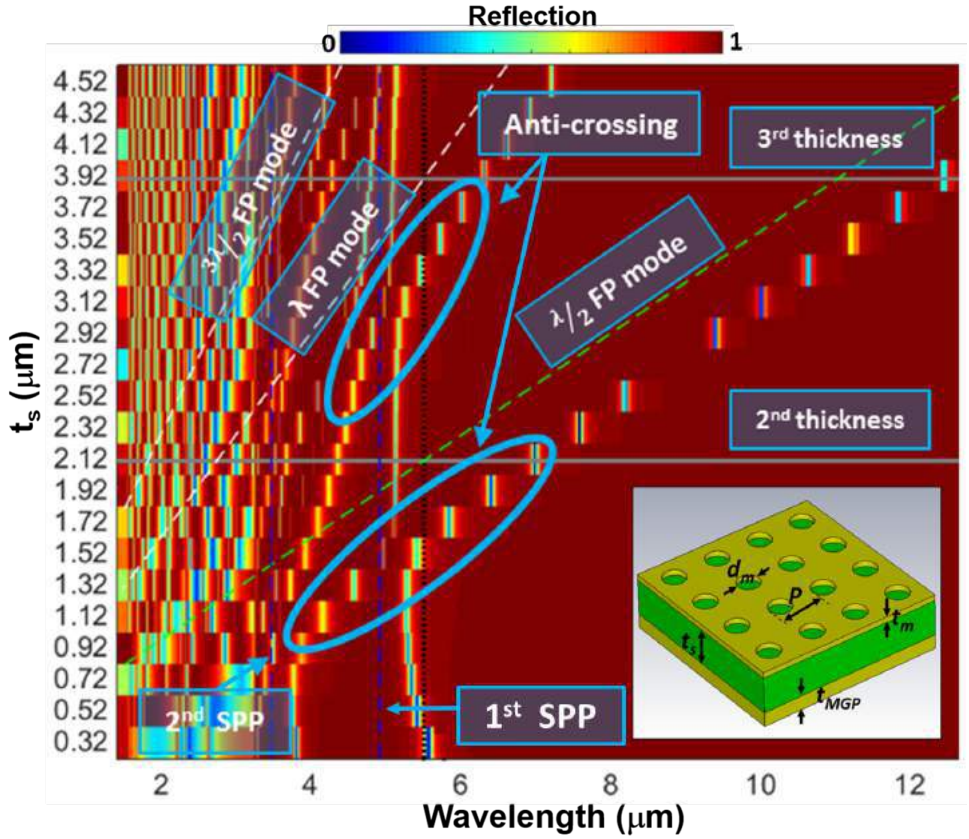

Figure 1. Simulated reflection colormap for SP-FP system (p = 3.2 μm; d_m = 1.6 μm; t_m = 0.05 μm; t_{MGP} = 0.2 μm) as a function of the wavelength and BCB thickness t_d (varying from 0.32 μm to 4.52 μm with a step of 0.2 μm). Inset shows the illustration of unit cell of SP-FP system.

Acknowledgements

The USF portion of this work was supported by the Alfred P. Sloan Research Fellow grant BR2013-123 and by KRISS grant GP2016-034. The KRISS portion of this work was supported by the KRISS grant GP2016-034 and the AOARD grant FA2386-14-1-4094 funded by the U.S. government (AFOSR/AOARD).

REFERENCES

1. Genet, C. and Ebbesen, T. W. "Light in tiny holes," *Nature.*, Vol. 445, No. 7123, 39–46, 2007.
2. Hwang, J., et al. "Surface plasmon resonant splitting and merging due to infrared incidence through thermal imaging lens," *Electron. Lett.*, Vol. 51, No. 15, 1170–1172, 2015.
3. Jeon, J., et al. "A Low – loss Metasurface Antireflection Coating on Dispersive Surface Plasmon Structure," *Sci. Rep.*, 6, 36190; doi:10.1038/srep36190, 2016.
4. Ku, Z., et al. "Analysis of subwavelength metal hole array structure for the enhancement of back-illuminated quantum dot infrared photodetectors," *Opt. Express*, Vol. 21, No. 4, 4709-4716, 2013.
5. Lee, S. J., et al. "A monolithically integrated plasmonic infrared quantum dot camera," *Nat. Commun.*, Vol. 2, No. 286, 2011.

A Monolayer Graphene NIR Plasmonic Super Absorber using High-index Contrast Grating (HCG)

Parag Parashar, Wei-Ming Huang, and Albert Lin*
Department of Electronic Engineering, National Chiao-Tung Univeristy, Hsinchu, Taiwan 30010
*corresponding author: hdtd5746@gmail.com

Abstract- Quasi-guided plasmonic mode excitation based near infrared (NIR) graphene absorber using high index contrast grating (HCG) has been demonstrated. High-Q (=700) narrow-band plasmonic resonance with enhanced (>80%) absorbance in graphene monolayer is reported without incorporating metallic mirrors. The high absorbance achieved is comparable to the magnetic resonance graphene absorption with metal gratings**.** Also**,** only a single-layer of subwavelength dielectric grating is adopted to achieve high TM NIR absorption without the use of distributed Bragg reflectors or 1D Photonic crystals.

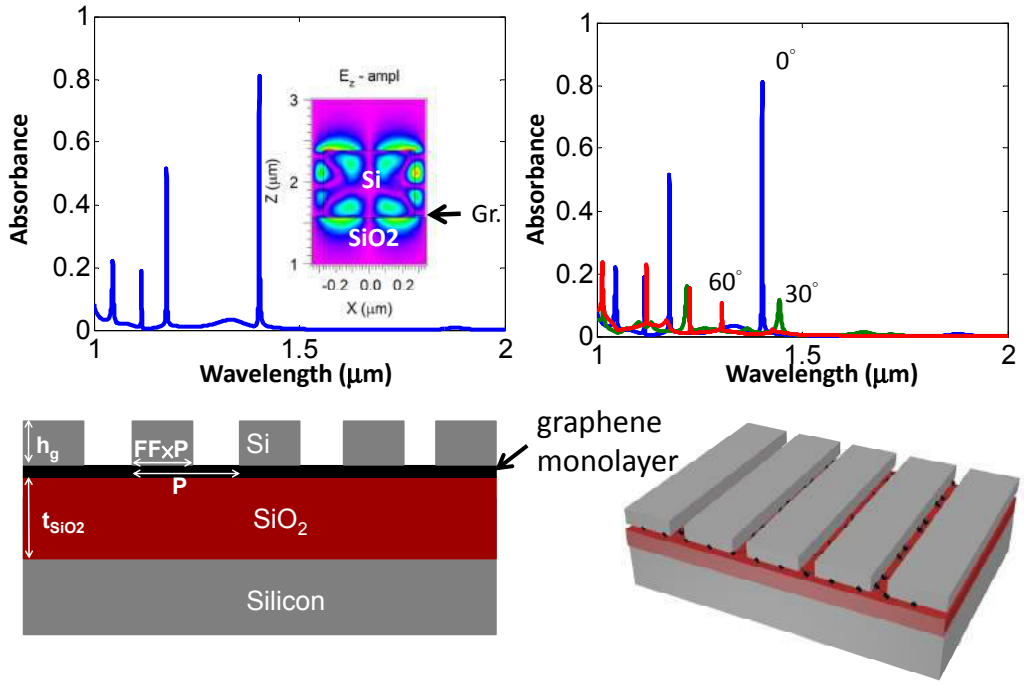

Figure 1 Proposed HCG monolayer graphene plasmonics platform and the corresponding TM spectral absorption curves for the normal and oblique incidences. Surface plasmon polaritons (SPP) are observed at graphene/SiO_2 interface.

Graphene is a 2D monoatomic layer of carbon atoms that possess unique optical and electrical properties. The monolayer graphene absorption enhancement is imperative for optical sensing, photo detecting, and

biomedical applications. High absorption using graphene plasmonics is relatively easy to achieve for a single layer graphene at THz, FIR, and MIR regimes, but the realization of the super absorber at near infrared (NIR) is quite difficult due to the lower free carrier concentration in graphene as compared to noble metals, such as silver and gold. Previously, B. Zhao et al. [1] achieved nearly 70% total absorption in monolayer graphene using metallic gratings to enhance the TM NIR absorption. In contrast to metallic-gratin-based graphene super absorbers, dielectric structures with multiple layers of dielectric gratings, DBR, and 1D PC were also investigated to realize high absorption [2]. Figure 1 shows the structure of our proposed HCG platform for monolayer graphene plasmonics. The graphene monolayer has been sandwiched between top Si grating and bottom SiO_2 spacer.

In the present work, we demonstrated that only one layer of HCG is capable of achieving >80% TM absorption via plasmonic mode excitations. The absorption value achieved here is analogous to the work done by B. Zhao et al. [1] that implemented localized strong electric field resulted from magnetic resonance. However, the quality factor (Q- factor) achieved in our proposed structure is higher than B. Zhao et al. work. As compared to the past dielectric grating structures [2], we have used only a single-layer of subwavelength dielectric grating to achieve high TM NIR absorption without the incorporation of DBR or 1D PC.

RCWA simulations have been conducted for the structure, and high-Q (Q=700) resonance at λ=1.4μm has been achieved for normal incidence through plasmonic mode excitations. The inset shows the field profile variation that manifests the plasmonic nature of the quasi-guided mode. Here, surface plasmon polariton (SPP) at graphene surface is evident at the resonating wavelength. Also, high angular selectivity exists for this structure as <20% absorption is observed at 30^o and 60^o incidences due to the high geometry and angle sensitivity associated with the high-Q narrow band resonances and the ultrathin graphene absorption layer. A very thin etch stop layer above the graphene monolayer could also be included in this design so as to prevent damage to the graphene layer during dry etching process**.**

REFERENCES

1. Zhao, B., J. M. Zhao, and Z. M. Zhao, "Enhancement of near-infrared absorption in graphene with metal gratings," Applied Physics Letters, Vol. 105, 031905, 2014.
2. Piper, J. R. and S. Fan, "Total Absorption in a Graphene Monolayer in the Optical Regime by Critical Coupling with a Photonic Crystal Guided Resonance," ACS Photonics, Vol. 1, 347–353, 2014.

A Capacitor-Loaded Spoof Surface Plasmon Transmission Line (SSP-TL) Design for Flexible Dispersion Properties Control

Xiao-Lan Tang[12], Qingfeng Zhang[1*], Sanming Hu[2] and Yifan Chen[13]

[1]Department of Electrical and Electronic Engineering, South University of Science and Technology of China, China
[2]State Key Laboratory of Millimeter Waves, Southeast University, China
[3]Faculty of Science and Engineering, The University of Waikato, Hamilton, New Zealand
*corresponding author, E-mail: zhangqf@sustc.edu.cn

Abstract

A novel implementation of spoof surface plasmon transmission line (SSP-TL) with loaded capacitors is proposed in this paper. It has been demonstrated that SSP-TL with capacitors can be an alternate candidate of flexible dispersion properties control. As an example, a smaller-line-width SSP-TL with loaded capacitors is designed and its measured performance is compared to the conventional one without capacitors but in larger-line-width configuration. The new method provides design flexibility without any geometrical dimensions modification of the SSP-TL.

1. Introduction

In optics, surface plasmons (SP) are propagating waves along the interface between a conductor and a dielectric medium. These waves decay exponentially in the direction perpendicular to the interface and give rise to highly field confinement near the surface supporting the surface electromagnetic waves [1]. In 2004, Pendry *et al*. has demonstrated that a similar surface plasmonic phenomenon, known as spoof surface plasmon (SSP), can be observed by perforating the conductive surface by parametrical holes [2]. Since then, the SSPs are widely being explored for their potential in microwave and terahertz circuits design, such as low crosstalk SSP transmission lines (SSP-TL), filters, leaky-wave antennas and etc [3-6].

In recently reported works on SSP-TL design, it has been demonstrated that the dispersion properties of such SSP-TL structure can be adjusted by modifying their geometrical dimensions and/or dielectric material parameters [3]. A novel implementation approach of SSP-TLs with loaded capacitors is proposed in this work. The value of capacitors brings another design degree freedom, which can control the dispersion properties of the fabricated SSP-TL structure without any geometrical dimensions modification.

2. SSP-TL Design

The conventional structure of SSP-TL consists of an ultrathin metallic strip with uniform periodic slots without ground plane. The dispersion properties of such SSP-TL can be realized in two ways: by modifying the geometrical parameters or by loading capacitors in the structure. In [3], an electrical equivalent model was proposed according to geometrical parameters as shown in Fig.1(a). The parameters *d*, *h*, *a* and *w* denote the periodic pitch, the slot depth, the slot width and the line width respectively (see Fig.1(b)). Fig.1(c) shows the dispersion curves for conventional SSP-TL with various slot depth *h* and the proposed SSP-TL with loaded capacitors. As expected, the confinement of electromagnetic wave is enhanced as the depth of slots increases. Although a high corrugation depth is good for filed confinement, it inevitably increases the line width which is not preferred in a compact system. To overcome this drawback, we propose the capacitor-loaded SSP-TL in Fig.1(b). As shown in Fig.1(c), the additional loaded capacitors ΔC along the surface brings in an extra

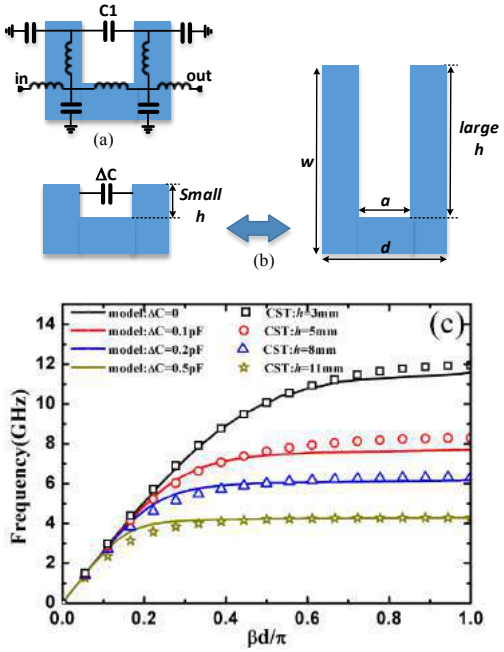

Figure 1: (a) Equivalent circuit model presented in [3]. (b) Proposed SSP-TL and geometrical dimensions. (c) Dispersion curves of conventional SSP-TL and capacitors-loaded SSP-TL.

capacitance, in equivalence to the extra capacitance brought by the increased corrugation depth in conventional SSP-TLs. For a given conventional SSP-TL, one can find a corresponding SSP-TL with smaller line width loaded by capacitors ΔC to analyze a similar dispersion behavior, leading to a control of dispersion properties.

Fig.2 shows the fabricated prototypes of SSP-TL with (Fig.2(a)) and without loaded capacitors (Fig.2(b)). The CPW-SSP transitions are required to achieve momentum, impedance matching and highly efficient SSP mode conversion [4]. The SSP-TLs were implemented on a 1.52 mm-thick Rogers 4003C substrate with ε_r=3.38 and tanδ=0.0027. The geometrical dimensions of SSP-TL in Fig.2(a) are *h*=3 mm, *w*=5 mm, *a*=1 mm, *d*=5 mm and ΔC=0.2 pF (Murata GJM1555C1HR20WB01D), whereas its comparison counterpart in Fig.2(b) were with *h*=8 mm, *w*=10 mm, *a*=1 mm, *d*=5 mm. Fig.2(c) shows the measured performance of both SSP-TLs. From 2 to 6 GHz, the measured S-parameters of proposed SSP-TLs are similar with |S21| and |S11| around -3 dB and lower than -11 dB respectively. The measured cutoff frequency of both SSP-TLs is around 5.8 GHz, corresponding to the one extracted from Fig.1(c). From the graph, it can be clearly seen that the proposed SSP-TL structure with less line width and loaded capacitors is validated, and it can be used as an alternative solution for SSP-TLs with large line width for compact system applications.

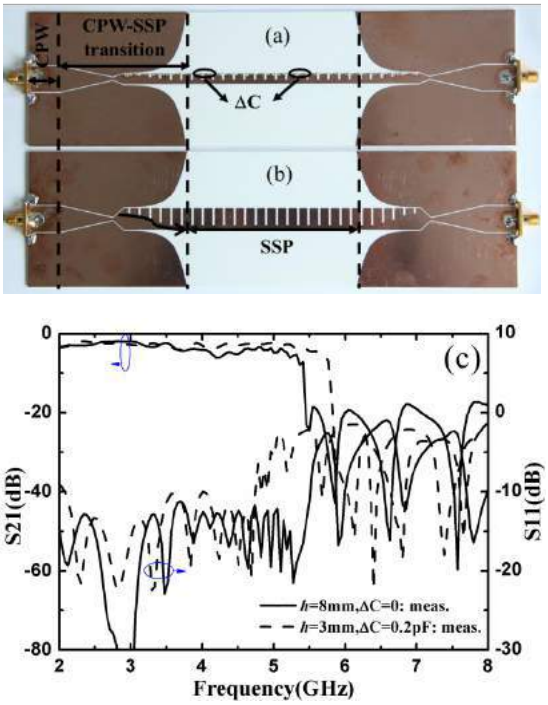

Figure 2: Prototype of SSP-TL (a) with ΔC=0.2pF and *h*=3mm/*w*=5mm, (b) without capacitors and *h*=8mm/*w*=15mm. (c) The measured S-parameters of the fabricated prototypes in (a) and (b).

3. Conclusions

In this paper, we have demonstrated that the use of capacitors in SSP-TL structures is a good solution for systems where large line width SSP-TLs are required. Indeed, the smaller line width SSP-TLs can be employed instead of large line width ones when the capacitors are used. In microwave frequency band, the measured performance of both SSP-TLs is quite similar. Furthermore, with this method, the control of dispersion properties can be done without any geometrical dimensions modification of the fabricated SSP-TL structure, making the SSP-TL design more flexible. In addition, with the proper scaling-down of the dimensions, various and reconfigurable SSP-TLs in terahertz band can be expected.

Acknowledgements

This work is supported by National Natural Science Foundation of China (61401191), Guangdong Natural Science Funds for Distinguished Young Scholar (2015A030306032, S2013050014223), Shenzhen Science and Technology Innovation Committee funds (KQJSCX20160226193445650, JCYJ20150331101823678, KQCX2015033110182368, JCYJ20160301113918121, JSGG20160427105120572), and Shenzhen Development and Reform Commission Funds (Grant [2015]944)..

References

[1] W. L. Barnes, A. Dereux, and T. W. Ebbesen, "Surface plasmon subwavelength optics," *Nature*, vol. 424, no. 6950, pp. 824–830, 2003.

[2] J. B. Pendry, L. Martin-Moreno, and F. J. Garcia-Vidal, "Mimicking surface plasmons with structured surfaces," *Science*, vol. 305, no. 5685, pp. 847–848, 2004.

[3] A. Kianinejad A, Z. N. Chen and C. W. Qiu, "Design and modeling of spoof surface plasmon modes-based microwave slow-wave transmission line," *IEEE Trans. Microw. Theory Tech.*, vol. 63, no. 6, pp.1817-1825, Jun. 2015.

[4] H. F. Ma, X. Shen, Q. Cheng, W. X. Jiang, and T. J. Cui, "Broadband and high-efficiency conversion from guided waves to spoof surface plasmonpolaritons," *Laser Photonics Rev.*, vol. 8, no. 1, pp. 146–151, 2013.

[5] X. Gao, L. Zhou, Z. Liao, H. F. Ma, and T. J. Cui, "An ultra-wideband surface plasmonic filter in microwave frequency," Appl. Phys. Lett., vol. 104, pp. 191603, 2014.

[6] S.K.Gu, H.F. Ma, B.G. Cai and T. J. Cui, "Continuous leaky-wave scanning using periodically modulated spoof plasmonic waveguide," Sci. Rep., vol.6, pp.29600, 2016.

Metamaterial-based devices

Metasurface-based reconfigurable visible light absorber

Gwanho Yoon[1] **and Junsuk Rho**[1,2*]

[1]Department of Mechanical Engineering, Pohang University of Science and Technology (POSTECH), Pohang, 37673, Republic of Korea

[2] Department of Chemical Engineering, Pohang University of Science and Technology (POSTECH), Pohang, 37673, Republic of Korea

[*]corresponding author: jsrho@postech.ac.kr

Abstract – Although metamaterials have shown many extraordinary phenomena, most of the metamaterials have been demonstrated in a passive type which acts as obstacle of its real applications. A few works of active metamaterials have been done, but modulation in the visible region is still challenge. Hereby, we suggest an active mechanism enabling high speed modulation in the visible region and tunable perfect absorber by using this mechanism.

Metamaterials have been explored due to their extraordinary optical properties and unprecedented phenomena such as negative refractive index [1,2], invisibility cloak [3,4], super-resolution imaging [5], artificial chirality [6], electromagnetically induced transparency [7], perfect absorber [8] and so on. Although many interesting phenomena have been introduced, there are technical limitations. Most of the metamaterials demonstrated before were passive type, so their optical properties cannot be changed after fabrication. This limitation is a critical obstacle of conventional metamaterials to outperform typical optical and electronic devices. A few works to control the optical properties of fabricated metamaterial devices by using electrical, optical, thermal and mechanical methods have been reported. However, they have severe problems to solve such as low working frequency, low modulation speed and insufficient integration feasibility.

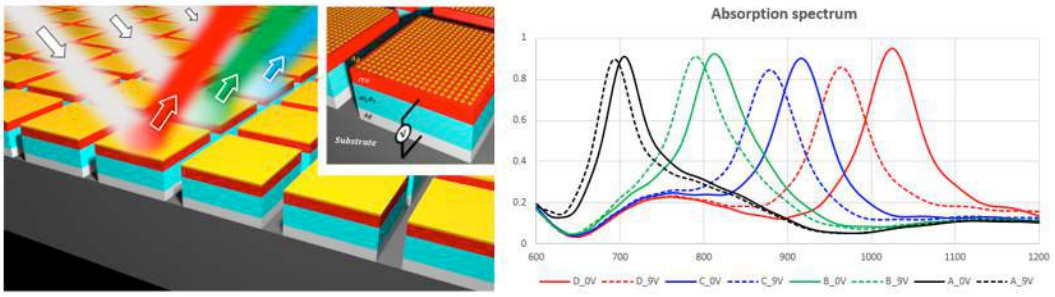

Figure 1. Schematic of the device and simulation result of the voltage application

Hereby, we suggest ITO as an active layer of the tunable metamaterial perfect absorber to solve aforementioned issues. Intrinsic ITO is not suitable for tuning in the visible wavelengths, so its carrier concentration has to be tuned to appropriate value by optimizing fabrication conditions such as annealing process. According to the simulation result, the suggested device can perfectly absorb a certain wavelength and handle the absorption wavelength within the visible region. It has many potential applications such as optical logic elements, ultrafast visible tunable band-pass filter, reflective display and military stealth technology.

Moreover, tuning mechanism of ITO at visible region can convert the past passive metamaterials to the active metamaterials, for example, tunable meta-hologram, ultrafast optical modulation and active wavefront manipulation opening a new generation of photonics beyond metamaterials.

Acknowledgements

This work was supported by Young Investigator Award (No.2015R1C1A1A02036464) and POSCO Green Science program through the National Research Foundation of Korea (NRF) grant funded by the Ministry of Science, ICT and Future Planning (MSIP) of Korean government and POSCO

REFERENCES

1. Veselago, V. G. The electrodynamics of substances with simultaneously negative values of ε and μ. *Sov. Phy. Usp.* Vol. 10, 509-514, 1968.
2. Pendry, J. B. Negative refraction makes a perfect lens. *Phys. Rev. Lett.* Vol. 85, 3966-3969, 2000.
3. Shurig, D. et al. Metamaterial electromagnetic cloak at microwave frequencies. *Science* Vol. 314, 977-980, 2006.
4. Cai, W. et al. Optical cloaking with metamaterials. *Nat. Photon.* Vol. 1, 224-227, 2007.
5. Fang, N. et al. Sub-diffraction-limited optical imaging with a silver superlens. *Science* Vol. 308, 534-537, 2004.
6. Zhang, S. et al. Photoinduced handedness switching in terahertz chiral metamolecules. *Nat. Commun.* Vol. 3, 942, 2012.
7. Zhang, S. et al. Plasmon induced transparency in metamaterials. *Phys. Rev. Lett.* Vol. 101, 047401, 2008.
8. Landy, N. I. et al. Perfect metamaterial absorber. *Phys. Rev. Lett.* Vol. 100, 207402, 2008.

Broadband and Thin Electromagnetic Absorber Based on Non-Foster Metasurface

Jinchao Mou and Zhongxiang Shen *
School of Electrical and Electronic Engineering, Nanyang Technological University, 50 Nanyang Avenue, Singapore
*corresponding author: ezxshen@ntu.edu.sg

Abstract-An ultra-wideband and extremely-thin electromagnetic absorber is presented, containing a grounded magnetic sheet coated with a non-Foster metasurface. The non-Foster metasurface can tailor the dispersion property of the magnetic material for reactance neutralization and compensate the loss in the substrate for power absorption over an ultra-wide band. Experimental measurements demonstrate that a nearly decade-wide absorption bandwidth can be achieved with a total thickness of only 1/255 wavelength at the lowest frequency, effectively breaking the Rozanov limit for passive absorbers.

Manipulating the absorption of electromagnetic (EM) waves is a fascinating and important theme, which can be realized by artificially engineering the dispersion properties with metamaterials or metasurface [1]. However, broadening the absorption bandwidth and thinning the thickness of an EM absorber is always a pair of contradictory propositions, which originates from the natural essence of causality and passivity [2]. To break the theoretical thickness-to-bandwidth ratio formulated as the Rozanov limit [3], active inclusions that can break Foster's limitations are necessary [2], [4]. By tailoring the dispersion property and compensating the loss in a magnetic sheet with a non-Foster metasurface, an ultra-wideband and extremely-thin absorber can be designed.

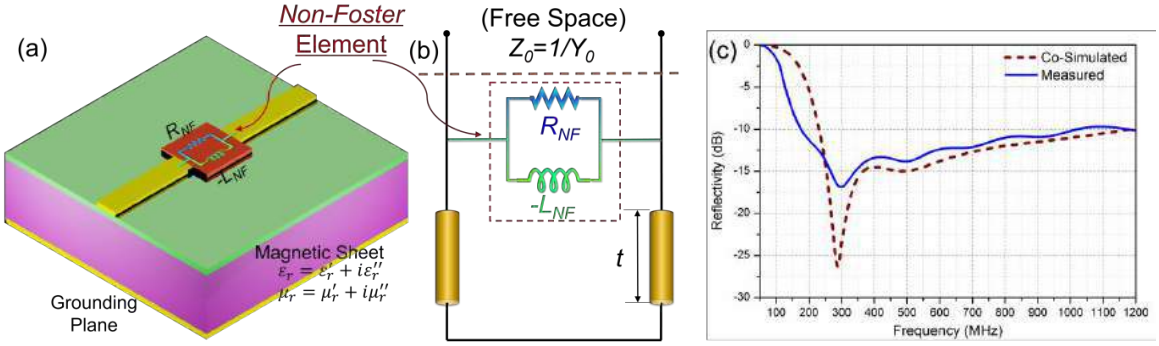

Figure 1. (a) Elementary cell of the proposed non-Foster absorber. (b) Equivalent circuit model of the absorber; (c) Measured and simulated reflectivity of the non-Foster absorber with physical implementation.

Figure 1(a) shows the elementary cell of the proposed absorber, which contains a grounded magnetic sheet topped by a non-Foster metasurface. The non-Foster element with ($-L_{NF}||R_{NF}$) may *re*-phase the current that is induced from the incident plane wave by the metallic gratings, which will then *re*-radiate out-of-phase to facilitate the destructive interference. Therefore, little energy will be reflected back and good absorption can be achieved over a wide frequency range. As the periodicity of the metasurface is smaller than the operating

wavelength, the absorber can be equivalent to a circuit in Figure 1(b). The non-Foster matching condition corresponding to the perfect absorption is L_S-L_{NF}=0 and ($1/R_{NF}$+$1/R_S$)=$1/Z_0$, where Z_0 is the characteristic impedance in free space.

A fabricated non-Foster absorber is demonstrated experimentally for validation, which is optimized with a co-simulation method [4] and fabricated using standard lithographic etching and plated through-hole technology. A test setup based on parallel-plate waveguide is employed for characterizing the fabricated absorber, which is particularly useful for long-wavelength band [5]. In this case, the fabricated absorber placed inside the parallel-plate waveguide will be imaged and equivalent to an infinite array. Figure 1(c) plots the measured reflectivity that is in a good agreement with the co-simulated result. The results exhibit that a reflectivity less than -10 dB can be obtained from 160 to 1000 MHz. The total thickness of the absorber including the non-Foster metasurface is only 7.35 mm, corresponding to 1/255 λ_0 at the lowest frequency of 160 MHz. This thickness is only one sixth of the theoretical minimum from the Rozanov limit [3].

The above analysis and results have validated the concept that the non-Foster metasurface can tailor the dispersion characteristics of a magnetic film for reactance cancellation and loss compensation for wide-band absorption. It may be mentioned that the same concept can be applied to other absorbing structures and readily scaled to other frequency bands.

Acknowledgements

This research was funded by Singapore's DSO National Laboratories (Project Agreement No. DSOCL15066).

REFERENCES

1. N. I. Landy, S. Sajuyigbe, J. J. Mock, D. R. Smith, and W. J. Padilla, "Perfect metamaterial absorber," *Phys. Rev. Lett.*, vol. 100, 207402(1-4), 2008.
2. P. Y. Chen, C. Argyropoulos, and A. Alu, "Broadening the cloaking bandwidth with non-Foster metasurfaces," *Phys. Rev. Lett.*, vol. 111, 23301(1-5), 2013.
3. K. N. Rozanov, "Ultimate thickness to bandwidth ratio of radar absorbers," *IEEE Trans. Antennas Propag.*, vol. 48, no. 8, 1230-1234, 2000.
4. J. Mou and Z. Shen, "Design and experimental demonstration of non-Foster active absorber," *IEEE Trans. Antennas Propag.*, vol. 65, no. 2, 696-704, 2017.
5. Y. Shang, Z. Shen, and S. Xiao, "On the design of single-layer circuit analog absorber using double-square-loop array," *IEEE Trans. Antennas Propag.*, vol. 61, no. 12, 6022-6029, 2013.

Metasurface electrode light emitting diodes for directional emission

Yeonsang Park[1*], Jineun Kim[1], Young-Geun Roh[1], and Q-Han Park[2*]
[1]Device lab., Samsung Advanced Institute of Technology, Korea
[2]Department of Physics, Korea University, Korea
[*]corresponding authors: yeonsang.park@samsung.com, qpark@korea.ac.kr

Abstract-Metasurfaces have attracted great attention in recent years due to their diverse properties. However, the application of metasurfaces to optical source devices has been limited by difficulties in fabrication and the inefficient coupling of unit elements to light due to their small sizes. Here, we present quantum dot light emitting diodes with metasurface-integrated metal electrode and demonstrate direction control of LED emission. By incorporating slot-groove array structures into the metal electrode, we show that LED emission can be directed towards a specific direction determined by metasurfaces.

Metasurfaces are planar structures that can change the polarization, phase, and amplitude of electromagnetic (EM) waves abruptly within thin and planar interfaces.[1,2] Based on their diverse properties and practical advantages, the application of metasurfaces has been extended from long-wavelength regime to optical regime. However, most previous works about optical metasurfaces dealt with passive type such as lens and beamsplitters[3,4] because the small size of optical scatterers causes not only fabrication difficulties but also low coupling efficiency with light emitters such as quantum wells (QWs), quantum dots (QDs), and molecule dyes. In view of practical applications, integrating metasurfaces with electric-driven light devices would provide unprecedented submicron-scale control to achieve improved performance or new functionalities in nanophotonics.

In this report, we present metasurface electrode light emitting diodes (LEDs) that control the direction of emission. Figure 1a shows the schematics of the metasurface electrode LED. Red-emitting colloidal quantum dots (CQDs) are used as a light emitting materials.[5] Its top electrode is made of Al-Ag-Au multilayer metals for the simultaneous operation as optical metasurfaces and electrode. Successful operation of the LED with the multilayer metal electrode was demonstrated by measuring the representative current-voltage (IV) curve and electroluminescence (EL) of the LED as shown in Figure 1b. As optical metasurfaces for direction control, we engraved slot-groove array structure on the top metal electrode. A scanning electron microscope (SEM) image of the fabricated slot-groove unit is given in left of Figure 1c. We demonstrated the control ability of metasurfaces by measuring optical and Fourier-space images of emissions from the LED. The optical image of Figure 1c shows surface emission from metasurface electrode LED. On the contrary, the Fourier-space images of Figure 1c corresponds to each pixel for 4-directional emission and clearly show that EL from the metasurface electrode LED is deflected in four distinct directions. From these results, we conclude that metasurface-integrated electrode not only actuates LEDs but also steers the emission into a directed beam.

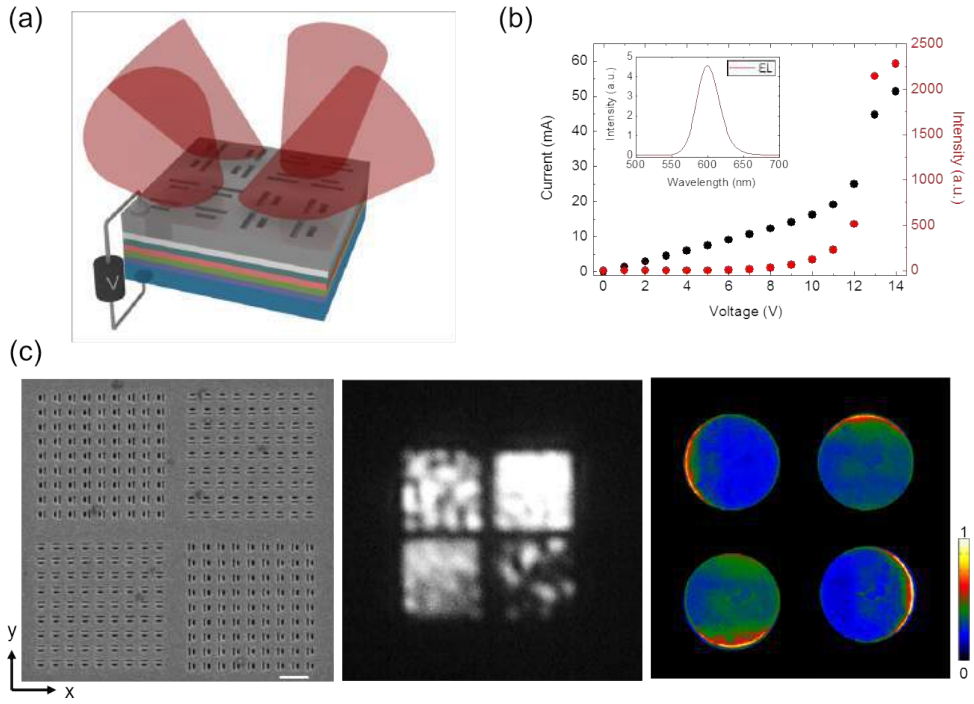

Figure 1. (a) Schematics of metasurface electrode LEDs (b) IV curve and EL spectrum (inset) of metasurface electrode LED (c) SEM image (left), optical images of EL from metasurface electrode LED (middle), and Fourier-space images of 4-directional emissions from metasurface electrode LED (right). White bar in SEM corresponds to 1 μm and the intensity in Fourier-space images are normalized by the maximum.

ACKNOWLEDGMENT

Q-H. P. was supported by the Ministry of Science, ICT and Future Planning as a Global Frontier Project (CAMM-2014M3A6B3063710).

REFERENCES

1 Yu, N. and F. Capasso, "Flat optics with designer metasurfaces," *Nat. Mater.,* Vol. 13, No. 2, 139-150, 2014.

2 Genevet, P., F. Capasso, F. Aieta, M. Khorasaninejad and R. Devlin, "Recent advances in planar optics: from plasmonic to dielectric metasurfaces," *Optica,* Vol. 4, No. 1, 139-152, 2017.

3 Arbabi, A., Y. Horie, M. Bagheri and A. Faraon, "Dielectric metasurfaces for complete control of phase and polarization with subwavelength spatial resolution and high transmission," *Nat. Nanotech.,* Vol. 10, No. 11, 937-943, 2015.

4 Li, Z., E. Palacios, S. Butun and K. Aydin, "Visible-frequency metasurfaces for broadband anomalous reflection and high-efficiency spectrum splitting," *Nano Lett.*, Vol. 15, No. 3, 1615-1621, 2015.

5 Cho, K.-S., E. K. Lee, W.-J. Joo, E. Jang, T.-H. Kim, S. J. Lee, S.-J. Kwon, J. Y. Han, B.-K. Kim and B. L. Choi, "High-performance crosslinked colloidal quantum-dot light-emitting diodes," *Nat. Photon.*, Vol. 3, No. 6, 341-345, 2009.

Dual Band Frequency Reconfigurable Array Antenna Using Metamaterial

Raimi Dewan[1], M.K.A. Rahim[1], Mohamed Himdi[2], M.R. Hamid[1], and M.E. Jalil[1]
[1]Advanced RF and Microwave Research Group, Communication Engineering Department,
Faculty of Electrical Engineering, University Technology Malaysia, 81310 Johor Bahru, Johor, Malaysia
[2]Institut d'Electronique et de Télécommunications de Rennes (IETR), UMR-CNRS 6164, Campus de Beaulieu,
263 Avenue du Général Leclerc, Rennes 35042, France
*corresponding author: raimidewan@gmail.com

Abstract- Metamaterial structure of Electromagnetic Band Gap (EBG) incorporated onto dual band array antenna operate at 2.45 GHz (lower band) and 5.8 GHz (upper band) is proposed. The three EBGs with different diode states introduces dual band gap (S21) properties at 2.45 GHz and 5.8 GHz which is verified using Suspended Transmission Line (STL) method. The EBG successfully realize frequency reconfigurable array antenna which able to configure to operate exclusively at both bands, lower band or upper band.

Introduction

EBG is a High Impedance Surface (HIS) of metamaterial which exhibits unique properties in suppressing the propagating wave within its structure [1]. This characteristic can use to realize a filter [2] for the antenna design in which certain frequency can be block from propagating through the antenna feeding network. In this paper, a dual band array antenna is incorporated with EBG cells at various positions at the feeding network to realize dual band frequency reconfigurable antenna. The antenna has a maximum realized gain of 6.27 dBi and 7.84 dBi at 2.45 GHz (lower band) and 5.8 GHz (upper band respectively).

Result and Discussion

Figure 1(a)-(b) shows the front and back view of EBG cells with region "S0" and "S1" which can be "ON" and "OFF" with connection or removal of copper strips respectively. The "ON" and "OFF" are represented by "1" and "0" respectively. STL method in Figure 1(c) is used to analyzed the band gap, S21 of EBG and the result is shown in Figure 1(d). It can be observed that EBG produces band gap at lower band (2.45 GH) and upper band (5.8GH) with different EBG configurations. EBG is then incorporated to array antenna as shown in Figure 1(e) and 1(f). Different EBG configuration at EBG1, EBG2 and EBG3 as depicted in Figure 1(g) successfully achieve frequency reconfigurability for the array antenna as shown in Figure 1(h) and Figure 1(i). The proposed antenna is very useful to reduces the interference in wireless communication service (WCS) which operate at similar operating frequencies because the proposed antenna with metamaterial can be selectively operates at single band of lower band and upper band or simultaneously at both bands depending on dynamic requirement of the WCS.

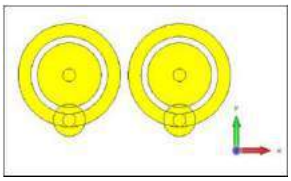

(a)

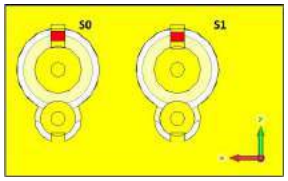

(b)

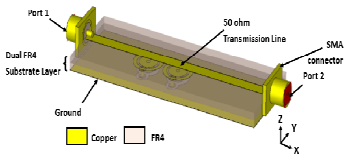

(c)

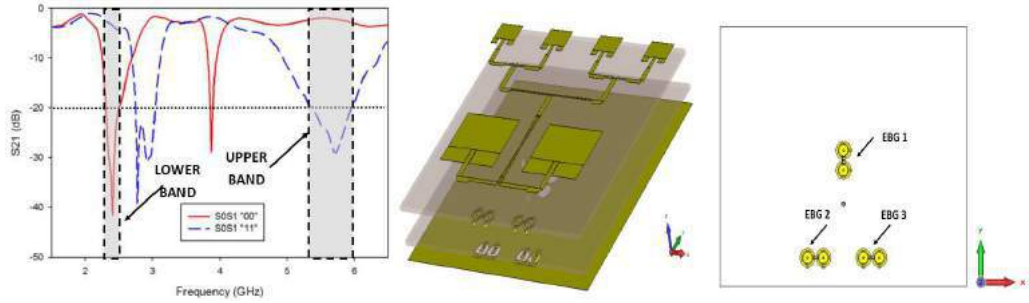

(d) (e) (f)

EBG 1		EBG 2		EBG 3		Frequency
S0	S1	S0	S1	S0	S1	Reconfiguration
0	0	1	1	1	1	Both bands
1	1	1	1	1	1	Lower band only
0	0	0	0	0	0	Upper band only

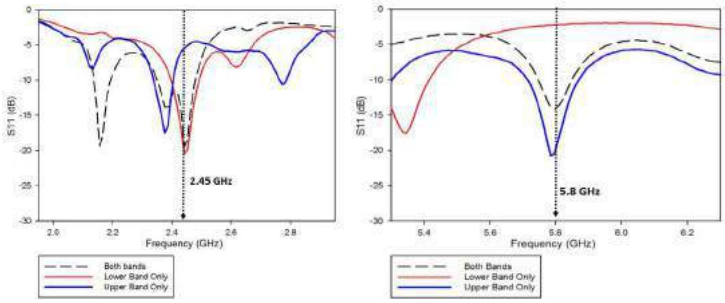

(g) (h) (i)

Figure 1. (a) Front and (b) back view of EBG cells. (c) STL method to analyze band gap (S21) with the corresponding (d) band gap (S21) simulated result. The (e) 3-dimensional and (f) EBG cells at the bottom substrate view of the array antenna. (g) EBG configurations at the array antenna with the corresponding frequency reconfigurability at (h) lower and (i) upper band of 2.45 GHz and 5.8 GHz respectively.

Conclusion: Dual band frequency array antenna using metamaterial EBG is proposed. EBG with different configuration produces band gap at 2.45 GHz and 5.8 GHz. By varying the configuration of EBG1, EBG1 and EBG3, the array antenna successfully achieves frequency reconfigurability to operate either at 2.45 GHz, 5.8 GHz or at both band simultaneously. The potential applications of the proposed antenna are in RFID, WLAN and WiMAX applications.

Acknowledgements The authors thank the Ministry of Education (MOE) for supporting the research work; Research Management Centre (RMC), Faculty of Electrical Engineering (FKE) UTM, School of Graduate Studies (SPS) under grant no. 12H09, 4F360, and 12H08.

REFERENCES

[1] L. F. Shi and D. L. Zhou, "Selectively Embedded Electromagnetic Bandgap Structure for Suppression of Simultaneous Switching Noise," *IEEE Transactions on Electromagnetic Compatibility,* vol. 56, pp. 1370-1376, 2014.

[2] J. d. D. Ruiz, F. L. Martínez-Viviente, and J. Hinojosa, "Optimisation of chirped and tapered microstrip Koch fractal electromagnetic bandgap structures for improved low-pass filter design," *IET Microwaves, Antennas & Propagation,* vol. 9, pp. 889-897, 2015.

Tunable Metatronic Circuits for Biosensing

A. Rahimi Rashed[1], M. Aalizadeh[1], M-H Kim[2], S-J Kim[3], S- H. Hong[2] and H. Caglayan[1*]

[1]Bilkent University NANOTAM, Bilkent 06800 Ankara TURKEY

[2]ETRI, 218, Gajeong-ro, Yuseong-gu, Daejeon, 305-700, Republic of Korea

[3]Department of Materials Science and Engineering, Korea University, Anam-dong 5-1, Sungbuk-Ku, Seoul 136-701, Republic of Korea

[*]corresponding author: hcaglayan@bilkent.edu.tr

Abstract In this work, we enhanced the functionality to metatronic nanocircuits by adding real time tunability feature. We change the surface structure of the ITO surface using nanoimprint lithography. Hence, we will obtain RLC nanocircuits which operates at NIR region. Then, we change the dielectric constant of the nano-gap region dynamically. The capacitance value and the resonance wavelength of optical nanocircuits changes when the dielectric constant of the gap region the nanoscale gap region changes.

In microelectronic devices, radiofrequency signals are controlled and manipulated by 'lumped' circuit elements (i.e., resistors, capacitors, and inductors). It is essential to integrate radiofrequency electronic systems with nanoscale platforms for high speed information processing and high density data-storage technologies. In 2005, Engheta proposed metamaterials inspired optical lumped circuit elements. Properly designed and suitably arranged nanostructures exposed to optical signals function as lumped circuit elements. The optical material dispersion determines the type of lumped nanostructure, with dielectric leading to capacitive behavior and plasmonic materials leading to inductive behavior. Instead of conduction current these optical nanocircuits based primarily on the use of optical displacement field current. This concept of metamaterial-inspired optical nanocircuitry, named as ''metatronics''.

It is shown that an optical circuit is effectively a "stereo-circuit", exhibiting different properties simultaneously for multiple optical signals with different incident angles and polarizations, and thus can significantly improve our capability in parallel information processing at the nanoscale. Recently, 3D lumped nanocircuitry at visible wavelengths by using individually loaded nanoantennas has been experimentally demosntrated.

These state of the art studies shows optical frequency circuit elements in which circuit operations are based on photons rather than electrons. They open up possibilities for optical information processing at the nanoscale. It is possible to tailor the metatronic nanocircuits by changing the geometry or the load of the circuitry as suggested previous works. However, these approaches are lack of enabling real-time control. The ability to tune the values of the lumped circuit element will enable the real-time control of the circuits and add more functionality.

In this work, we fabricate ITO nanorod structures which act as optical RLC nanocircuits and add more functionality to the metatronic nanocircuits changing the dielectric constant of the gap region dynamically. The capacitance value of optical nanocircuits changes when the dielectric constant of the gap region the nanoscale gap region changes. We have changed the resonance of the metatronic circuit by the control of the outside medium. We tuned the optical element values by changing the substrate filling the nanoscale gap region in

real-time Finally, we have tested dielectric materials such as PDMS, glucose and CEMS. Hence, tune the capacitor value and resonance wavelength of the RLC circuitry.

This work has been supported by TUBITAK under Project No 115F560. The author H.C. also acknowledges partial support from the Turkish Academy of Sciences and The Science Academy.

REFERENCES

[1] Engheta, N., Salandrino, A., Alu, A. 2005. "Circuit Elements at Optical Frequencies: Nanoinductors, Nanocapacitors, and Nanoresistors", Phys. Rev. Lett. 95, 095504.

[2] Engheta, N. 2007. "Circuits with Light at Nanoscales: Optical Nanocircuits Inspired by Metamaterials", Science 317, 1698.

[3] Alu A., Engheta, N. 2009. "All Optical Metamaterial Circuit Board at the Nanoscale", Phys. Rev. Lett. 103, 143902.

[4] Sun, Y., Edwards, B., Alu, A., Engheta, N. 2012. "Experimental realization of optical lumped nanocircuits at infrared wavelengths", Nat. Mater. 11, 208.

[5] Caglayan, H., Hong, S. H., Edwards, B., Kagan, C. R., Engheta, N. 2013. "Near-Infrared Metatronic Nanocircuits by Design", Phys. Rev. Lett. 111 073904.

[6] Liu, N., Wen, F., Zhao, Y., Wang, Y., Norlander, P., Halas, N. J., Alu, A. 2013. "Individual Nanoantennas Loaded with Three-Dimensional Optical Nanocircuits", Nanolett. 13(1) 142.

Metasurface-based reconfigurable visible light absorber

G. Yoon[1] and J. Rho[1,2*]

[1]Department of Mechanical Engineering, Pohang University of Science and Technology (POSTECH), Pohang, 37673, Republic of Korea

[2] Department of Chemical Engineering, Pohang University of Science and Technology (POSTECH), Pohang, 37673, Republic of Korea

[*]corresponding author: jsrho@postech.ac.kr

Abstract – Although metamaterials have shown many extraordinary phenomena, most of the metamaterials have been demonstrated in a passive type which acts as obstacle of its real applications. A few works of active metamaterials have been done, but modulation in the visible region is still challenge. Hereby, we suggest an active mechanism enabling high speed modulation in the visible region and tunable perfect absorber by using this mechanism.

Metamaterials have been explored due to their extraordinary optical properties and unprecedented phenomena such as negative refractive index [1,2], invisibility cloak [3,4], super-resolution imaging [5], artificial chirality [6], electromagnetically induced transparency [7], perfect absorber [8] and so on. Although many interesting phenomena have been introduced, there are technical limitations. Most of the metamaterials demonstrated before were passive type, so their optical properties cannot be changed after fabrication. This limitation is a critical obstacle of conventional metamaterials to outperform typical optical and electronic devices. A few works to control the optical properties of fabricated metamaterial devices by using electrical, optical, thermal and mechanical methods have been reported. However, they have severe problems to solve such as low working frequency, low modulation speed and insufficient integration feasibility.

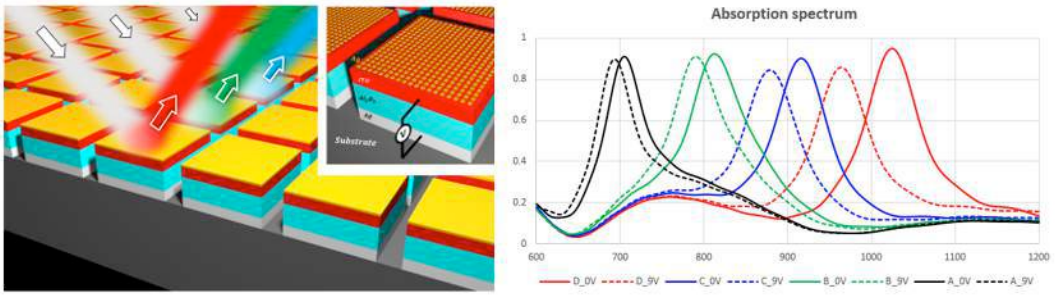

Figure 1. Schematic of the device and simulation result of the voltage application

Hereby, we suggest ITO as an active layer of the tunable metamaterial perfect absorber to solve aforementioned issues. Intrinsic ITO is not suitable for tuning in the visible wavelengths, so its carrier concentration has to be tuned to appropriate value by optimizing fabrication conditions such as annealing process. According to the simulation result, the suggested device can perfectly absorb a certain wavelength and handle the absorption wavelength within the visible region. It has many potential applications such as optical logic elements, ultrafast visible tunable band-pass filter, reflective display and military stealth technology.

Moreover, tuning mechanism of ITO at visible region can convert the past passive metamaterials to the active metamaterials, for example, tunable meta-hologram, ultrafast optical modulation and active wavefront manipulation opening a new generation of photonics beyond metamaterials.

Acknowledgements

This work was supported by Young Investigator Award (No.2015R1C1A1A02036464) and POSCO Green Science program through the National Research Foundation of Korea (NRF) grant funded by the Ministry of Science, ICT and Future Planning (MSIP) of Korean government and POSCO

REFERENCES

1. Veselago, V. G. The electrodynamics of substances with simultaneously negative values of ε and μ. *Sov. Phy. Usp.* Vol. 10, 509-514, 1968.
2. Pendry, J. B. Negative refraction makes a perfect lens. *Phys. Rev. Lett.* Vol. 85, 3966-3969, 2000.
3. Shurig, D. et al. Metamaterial electromagnetic cloak at microwave frequencies. *Science* Vol. 314, 977-980, 2006.
4. Cai, W. et al. Optical cloaking with metamaterials. *Nat. Photon.* Vol. 1, 224-227, 2007.
5. Fang, N. et al. Sub-diffraction-limited optical imaging with a silver superlens. *Science* Vol. 308, 534-537, 2004.
6. Zhang, S. et al. Photoinduced handedness switching in terahertz chiral metamolecules. *Nat. Commun.* Vol. 3, 942, 2012.
7. Zhang, S. et al. Plasmon induced transparency in metamaterials. *Phys. Rev. Lett.* Vol. 101, 047401, 2008.
8. Landy, N. I. et al. Perfect metamaterial absorber. *Phys. Rev. Lett.* Vol. 100, 207402, 2008.

A programmable flexible perfect absorber

N. Raeis-Hosseini[1], G. Yoon[2], and J. S. Rho[1, 2, 3*]

[1]Department of Chemical Engineering, Pohang University of Science and Technology (POSTECH), Pohang 37673, Republic of Korea

[2]Department of Mechanical Engineering, Pohang University of Science and Technology (POSTECH), Pohang 37673, Republic of Korea

[3]National Institute of Nanomaterials Technology (NINT), Pohang 37673, Republic of Korea

*corresponding author: jsrho@postech.ac.kr

Abstract- Phase change metamaterial (PCM) is a potential candidate to be assimilated in planar structures to make a new generation of tunable optical devices. We developed a tunable perfect absorber based on PCM, which also works as a non-volatile optical memory. By exploiting the advantage of switching the PCM between amorphous and crystalline states, we designed and fabricated a flexible programmable perfect absorber. The suggested device reflects the basic requirements of a re-writable and non-volatile memory by absorbing the light into a thin film of a PCM.

MMs as electromagnetic illustrative with artificial operations can get attained by configuring on the sub-wavelength scale.[1] Because the resonant optical characteristics of plasmonic MMs depends on the near-field dielectric circumstances, they specify a vigorous and an adjustable substitute for metals. Although various MMs has been introduced with a representative reflection to induced stimuli such as light and electric field, but the majority of them showed volatile switching state.[2, 3]

To overcome this bottleneck, we integrated a phase change metamaterial (PCM) in the nanophotonic device structure. We take benefits from the loss elements of the optical constant (real components) to establish an elevated absorber. A near-zero reflectivity is achieved by controlling the μ and ε resonances and matching MM impedance to the free space.[4, 5]

Metamaterial-based programmable perfect absorber (MPA) is a reconfigurable device with an absorbance near unity. It has been shown that optically- stimulated PCM specifies a non-volatile MM modulator of transmission and reflection for near- infrared (NIR) to mid-infrared (MIR) wavelengths with a subwavelength thickness.[2] MPAs have been earned appeal owing to their polarization independency, widespread-angle occurrence, high amount of light absorbency, exotic properties, and unity absorptivity of EM waves.[6]

Our design consists of three main layers in a simple metal-insulator-metal (MIM) structure including a dielectric thin film (spacer) which is sandwiched between two metallic layers (Figure 1a-d). The structure is analogous with Fabry-Perot (FP) etalon with an ultrathin cavity according to the top electrode (TE) arrayed nanoparticles. TE is a patterned metallic layer which conveys an electric reply relevant to the grounded bottom electrode (BE) by intensely coupling to the electric field at a specific resonance frequency.[1]

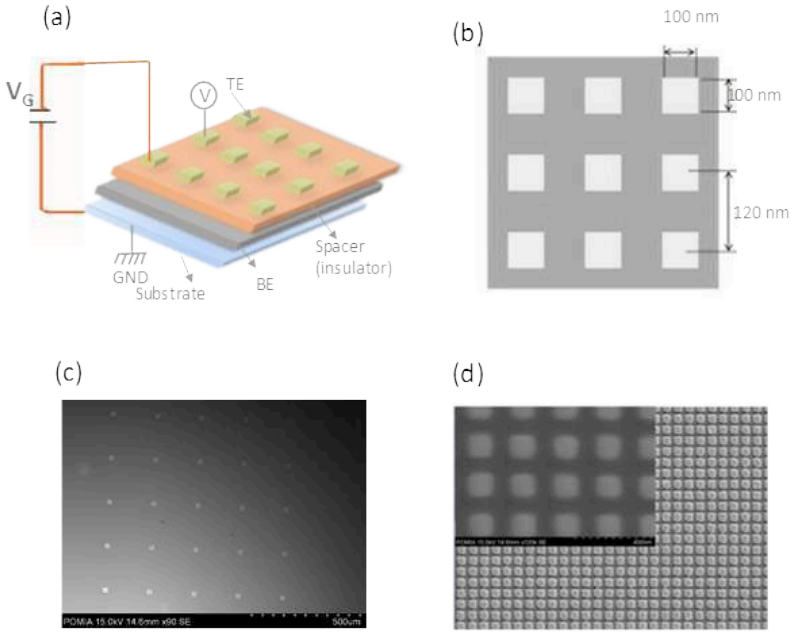

Figure1. (a) Schematic illustration of the dual functional device; the MPA and ReRAM. (b) The device consists of a 100 nm Pt as a BE, an ALD deposited PCM (25nm) and an array of Ag nanoparticles with a 100 nm thickness. The SEM images of the fabricated (c) device with MIM structure, (d) nanoparticles on the MPA.

We demonstrated a reconfigurable and rewritable MPA with two resistance states, which works as a memory device as well. The metal-insulator transition is done opto-electrically in both of the amorphous and insulator states. This programmable MPA device, potentially provides an enhancement in the future digital approaches of optical devices.

Acknowledgements. We acknowledge the financial support by Young Investigator Research program (NRF-2015R1C1A1A02036464), Engineering Research Center program (NRF-2015R1A5A1037668), Global Frontier Research Program (CAMM-2014M3A6B3063708).

REFERENCES

1. Watts, C.M., X. Liu, and W.J. Padilla, "Metamaterial electromagnetic wave absorbers", *Advanced materials,* Vol. 24, No. 23, 98-120, 2012.
2. Gholipour, B., *et al.*, "An all-optical, non-volatile, bidirectional, phase-change meta‐switch", *Advanced Materials*, Vol. 25, No. 22, 3050-3054, 2013.
3. Driscoll, T., *et al.*, "Memory metamaterials"*, Science*, Vol. 325, No. 5947, 1518-1521, 2009.
4. Hedayati, M.K., F. Faupel, and M. Elbahri, "Review of plasmonic nanocomposite metamaterial absorber*", Materials,* Vol. 7, No. 2, 1221-1248, 2014.
5. Landy, N.I., *et al.*, "Perfect metamaterial absorber*", Physical review letters*, Vol. 100, No. 20, 207402, 2008.
6. Cao, T., *et al.*, "Broadband polarization-independent perfect absorber using a phase-change metamaterial at visible frequencies", *Scientific reports,* Vol. 4., 3955, 2014.

A New Meta-atom-based Stop-Band Filter for Ultra Wideband Applications

S. S. Islam[1], M. R.I. Faruque1*, S Abdullah[1], M. M. Hasan[1] and M. T. Islam[2]
[1]Space Science Centre, Universiti Kebangsaan Malaysia, Malaysia
[2]Dept. of Electrical, Electronic and Systems Engineering, Universiti Kebangsaan Malaysia, Malaysia
*corresponding author: sikder_islam@yahoo.co.uk

Abstract-. In this study, a meta-atom-based ultra wideband stop-band filter is presented. Initially, a pi-shaped metamaterial was designed. The metamaterial shows wide band negative refractive index and near zero refractive index property. The metamaterial was then utilized in designing a filter that performs stop-band operation over an ultra wide band region. Measured results were provided for the metamaterial and the filter.

Artificially constructed metamateraial have become a promising field for the researcher. Metmaterial unit cell (meta-atom) can be utilized in designing a wideband filter. In the field of filter design, very few works are found with metamaterial in stop-band applications. For example, a metamaterial-based cut-band filter was proposed in [1] for C-band applications. They utilized different array of same metamaterial for increasing the resonance, but all in C-band of microwave spectra. They also increased bandwidth by increasing the metamaterial array. A split ring resonator (SRR) metamaterial-based microstrip filter was proposed in [2] where stop band performance was achieved from L-band to X-band. Actually, in their work, they obtained sharp resonances for each band with consecutive SRR increment, but their filter could not produce ultra wideband stop-band characteristics. A compact stop-band filter was proposed in [312] for radar application, but the filter was designed for X-band operation only and no metamaterial characteristics were shown.

In this paper, a new pi-shaped metamaterial introduced that was designed on $10\times10mm^2$ FR-4 substrate material with dielectric property 4.3 + j0.002. Finite integration technique (FIT) based CST-microwave studio software was utilized for the calculation of the complex S-parameters S_{21}(transmission co-efficient) and S_{11} (reflection co-efficient) of the metamaterial. The transverse electromagnetic wave was propagated through *z*-axis of the metamaterial unit cell using two waveguide ports. The metamaterial unit cell shows transmittance in the frequency of 8.31 GHz and 12.81 GHz as seen in Figure-1. The effective medium parameters permeability (μ) and permittivity (ε) were extracted from the simulated complex S_{21}(transmission co-efficient) and S_{11} (reflection co-efficient) parameters using Nicolson-Ross-Weir method.

In further step, a filter was constructed using the metamaterial unit cell for stop-band operation. The 20×10 mm^2 filter were designed for the same substrate material. However, in the filter design the copper arms of the unit cell structure were extended up to ending border on two opposite sides. The Figure.2 displays fabricated filter and the numerical and measured results of S-parameters for the filer operation. The stop band region has started from the frequency of 1 GHz to 12.04 GHz. The rejection level was found greater than 20dB from 1GHz to 10 GHz. The return loss was found below -10 dB from the frequency of 12.07 GHz to 12.55 GHz. A small pass band is visible from the frequency of 12.15GHz to 12.28 GHz.

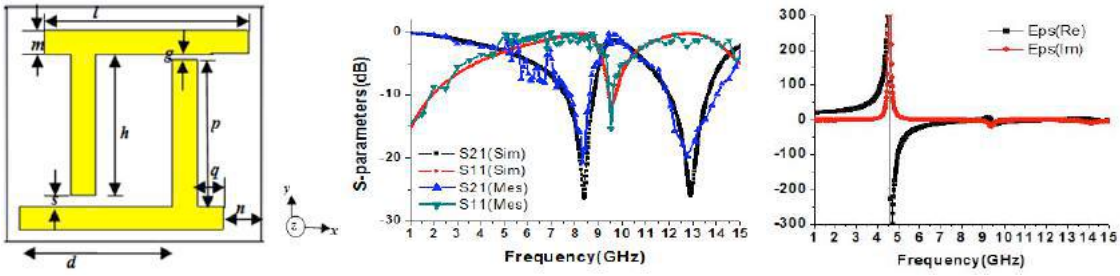

(a) (b) (c)

Figure-1: (a) The pi-shaped metamaterial unit cell where *l=8, m=1,n=1.5, g=0.33, s=0.5, d=6, h=6,p=6.27,q=1* (b) S-parameters for the unit cell (c) negative effective permittivity (ε) for the unit cell.

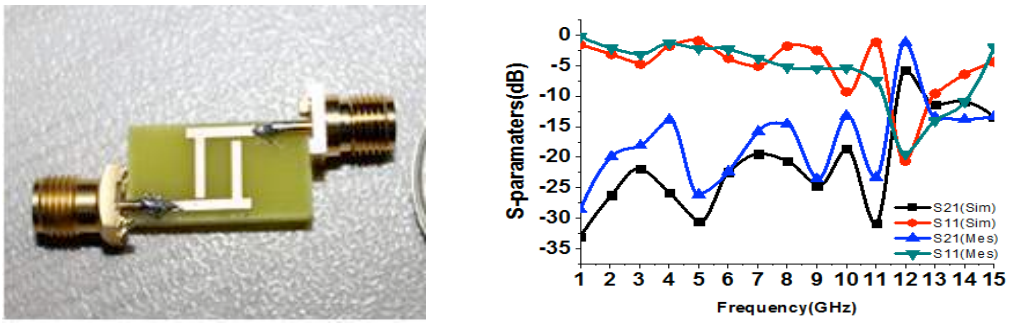

(a) (b)

Figure-2:(a) fabricated metamaterial-based filter (b) S-parameters for the filter

Acknowledgements: This work is supported by the Ministry of Education Malaysia (MOE) under grant no. FRGS/1/2014/TK03/UKM/01/1.

REFERENCES

1. Carver, J., Reignault, V.: Engineering of the metamaterial-based cut-band filter; *Appl. Phys. A*, Vol.117,513-516 2014.
2. Monish, G., Jyoti, S.: Microsrtip filter designing by SRR metamaterial, *Wireless Pers Commun.* Vol.71, 3011-3022 ,2013.
3. Pourbagher,M., Nourinia, J.,Ghobadi, C.: Compact broad band-Stop filter with circular fractal-shaped stubs for X-band radar applications, *ACES J.* ,Vol.32, 56-59,2017.

Left Handed Meta-Surface Absorber for Energy Harvesting Application

M. R. I. Faruque[1*], M. M. Hasan[1]
[1]Space Science Center, Universiti Kebangsaan Malaysia, Malaysia
43600 UKM, Bangi, Selangor, Malaysia
[*]Email: rashed@ukm.edu.my

Abstract- In this paper, the proposed absorber structure shows a wide bandwidth of 4.66 GHz and applicable for C-, X- and Ku-band applications. The absorber is developed by electric-inductive-capacitive resonators that are capable of not only high absorption, but also channelling almost all the absorbed power to a resistive load. The size of every unit cell of the absorber unit cell is 10×10 mm^2 and array slab is 150×200 mm^2. FIT-based CST Microwave Studio has been used for design and analysed purpose. From result analysis, it has been shown the simulated and measured results are well matched together. The measured result show resonance at 5.35 GHz (C-band), 11.85 GHz (X-band), and 16.45 GHz (Ku-band) and the effective medium ratio is 9.85. However, the absorption of the proposed meta-surface absorber at 2.06, 5.05, 9.26, and 13.23 GHz, are respectively, 60%, 95%, 78%, and 93%.

As advances in low power design, power consumption of electronics becomes smaller increasingly, which opens the possibility to harvest energy from the environment to power directly to the electronics or recharge a secondary battery. This kind of new techniques is called energy harvesting. In 2003, a metamaterial by capacitor loaded strips and split ring resonators, which exhibited negative permittivity and negative permeability both at the X-band frequencies developed by Ziolkowski et *al*. [1]. The first perfect metamaterial absorber was introduced by Landy et *al*. in 2008. The absorber with a classic sandwiched structure composed of a split ring resonator, a dielectric substrate, and a metallic cut wire achieved its peak absorption of 88% at 11.50 GHz [2]. A compact square split z-shape meta-atom with left handed features, wide bandwidth for S-, C-, X- and Ku-band applications by Faruque et *al*. presented. The presented meta-atom was investigated at 0^0, 15^0, 30^0, 45^0, 60^0, 75^0 and 90^0 rotation angle. The designed structure shown resonances at S-, C-, X-, and Ku-band with 5.67 GHz wide bandwidth. The compact meta-atom had an effective medium ratio 9.10 and exhibited left handed characteristics at 8.50 GHz [3]. Almoneefa et *al*. presented a metamaterial slab comprised of 13×13 electrically small cells, each loaded with an 82Ω resistor. The designed structure shown power absorption efficiency of 97% and 93%, respectively in 2015 [4].

The designed structure consists of a square outer and an inner metallic resonator, where the circular rings are in the center of the inner resonator. There is splits in every resonator and the circular metallic rings, which formed the capacitance and shift the resonance points toward higher frequency shown in figure 1(a). The simulation results show transmittance (S_{21}) resonance at 4.13, 8.19, 12.01, and 16.63 GHz. The measured result show resonance at 4.16 GHz (C-band), 8.18 GHz (X-band), 12.03 GHz (Ku-band), 16.61 GHz (Ku-band) and the effective medium ratio is 5.50 in figure 1(b). Further, from figure 1(c) the effective permittivity, permeability and refractive index curves show negative values from 9.42 to 11.55 GHz. According to the left handed characteristics, if the permittivity and permeability are simultaneously negative, then the refractive index will be

negative. As a result, the designed structure can be called as a left handed meta-surface absorber. The absorption rate of 2.06, 5.05, 9.26, and 13.23 GHz are, respectively, 60%, 95%, 78%, and 93% exhibited in figure 1(d).

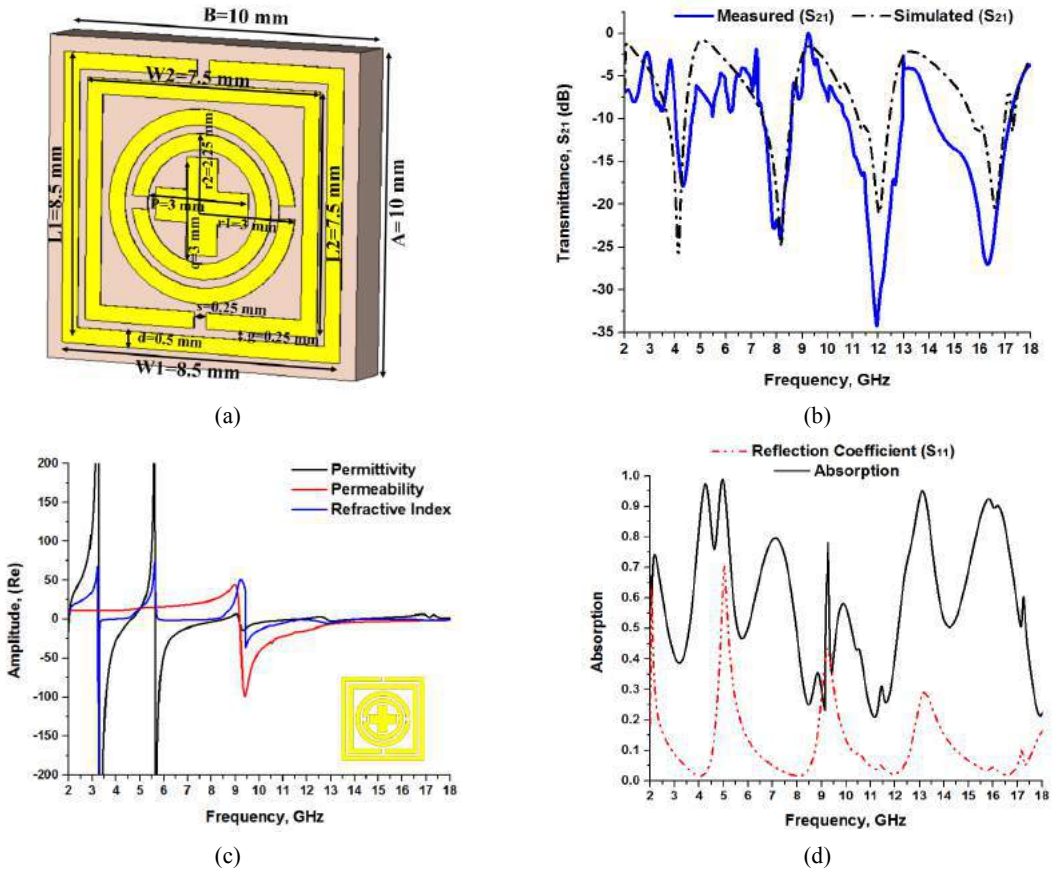

Figure 1. (a) Schematic of the proposed meta-surface absorber (dimensions in millimeters), (b) Results of the scattering parameters, (c) Real amplitude of the effective medium parameters, (d) Absorption of the structure.

REFERENCES

1. Ziolkowski, R. W., "Design, fabrication, and testing of double negative metamaterials", *IEEE Trans. On Antennas Propag., 2003,* 51 (7): 1516–1529.
2. Landy, N. I., Sajuyigbe, S., Mock, J. J., Smith, D. R. and Padilla, W. J., "A perfect metamaterial absorber", *Physical Review Letter*, 100, pp. 1–4, 2008.
3. Faruque, M. R. I., Hasan, M. M. and Islam, M. T., "Wideband 90^0 Azimuthal Miniaturized Meta Atom with Left-Handed Characteristics", IEEE Antennas and Wireless Propagation Letters, 2016, DOI: 10.1109/LAWP.2016.2624757.
4. Almoneefa, T. S. and Ramahib, O. M., "Metamaterial electromagnetic energy harvester with near unity efficiency" Applied Physics Letters, 2015, 106, 153902.

Analysis of Effects of Mobile Casing Materials on Specific Absorption Rate

M. I. Hossain[1*], **M. R. I. Faruque**[2], and **M. T. Islam**[3]
[1]Department of Electrical & Electronic Engineering, International Islamic University Chittagong, Bangladesh
[2]Space Science Center, Universiti Kebangsaan Malaysia, Malaysia
[3]Department of Electrical, Electronic, and System Engineering, Universiti Kebangsaan Malaysia, Malaysia
[*]Email: ipk_eee@yahoo.com

Abstract-The aim of this investigation is to analyze the effects of mobile casing on the specific absorption rate (SAR) in the human head. The effects were analyzed with the variation in casing materials and its thickness. The results show that the SAR values are reduced significantly after using a mobile casing at 0.9 GHz. The maximum SAR reduction can be obtained by using silicon mobile casing (97.8 percent at 0.9 GHz and 24 percent at 1.8 GHz).

Nowadays, the mobile phones are the most popular devices all over the world. But the electromagnetic (EM) radiation from mobile devices is a matter of threat to the human health as it can penetrate the body tissues when the phone is used in the vicinity of human body [1, 2]. The defined parameter for the absorbing power calculation in the human body tissue is SAR, which is directly related to the electric and magnetic field distribution in the human body tissues. Several factors may affect SAR values such as EM source geometry and frequency, the user body tissue size and their properties. SAR values also depend on the medium and distance between source and user body [3]. In [4] effects of mobile component and casing on antenna performances were analyzed. The results showed that the mobile casing with metal ring significantly affected the antenna performances. On the other hand, the cell phone casing also processes significant effects on the SAR values. In [5], a study of materials to reduce the SAR values has been presented. The numerical results showed that the cell phone case box made of materials with higher conductivity produces higher SAR in the human head. In this paper, a study of the effects of mobile casing materials on SAR is presented. This investigation will provide the detail information about the effects of different casing materials on SAR values and antenna radiation efficiency. Six different casing materials comprising Polyimide, Polycarbonate, Aluminium, Rubber, Silicon and Glass are used in this analysis.

Figure 1(a) indicate the geometry of dual band PIFA operates over 900 MHz and 1800 MHz. The casing box is indicated in Figure 1(b). The dimensions of mobile casing are 104 mm × 44 mm × 15.4 mm, where the glass sheet dimensions are 84 mm × 44 mm × 1 mm. The simulation setup of mobile phone with human head and hand phantom is indicated in Figure 1(c) considering cheek position of talk mode. Figure 1(d) indicates SAR values in the human head due to mobile phone with silicon casing. The obtained results indicate that all the cell phone casing can reduce SAR values to the human head significantly at 0.9 GHz. At upper frequency band, SAR values increase for some of casing materials (Polyimide, Polycarbonate, and Rubber) and decrease for other materials (Aluminum, and Silicon). The maximum SAR reduction can be obtained by using silicon mobile casing (97.8 percent at 0.9 GHz and 24 percent at 1.8 GHz).

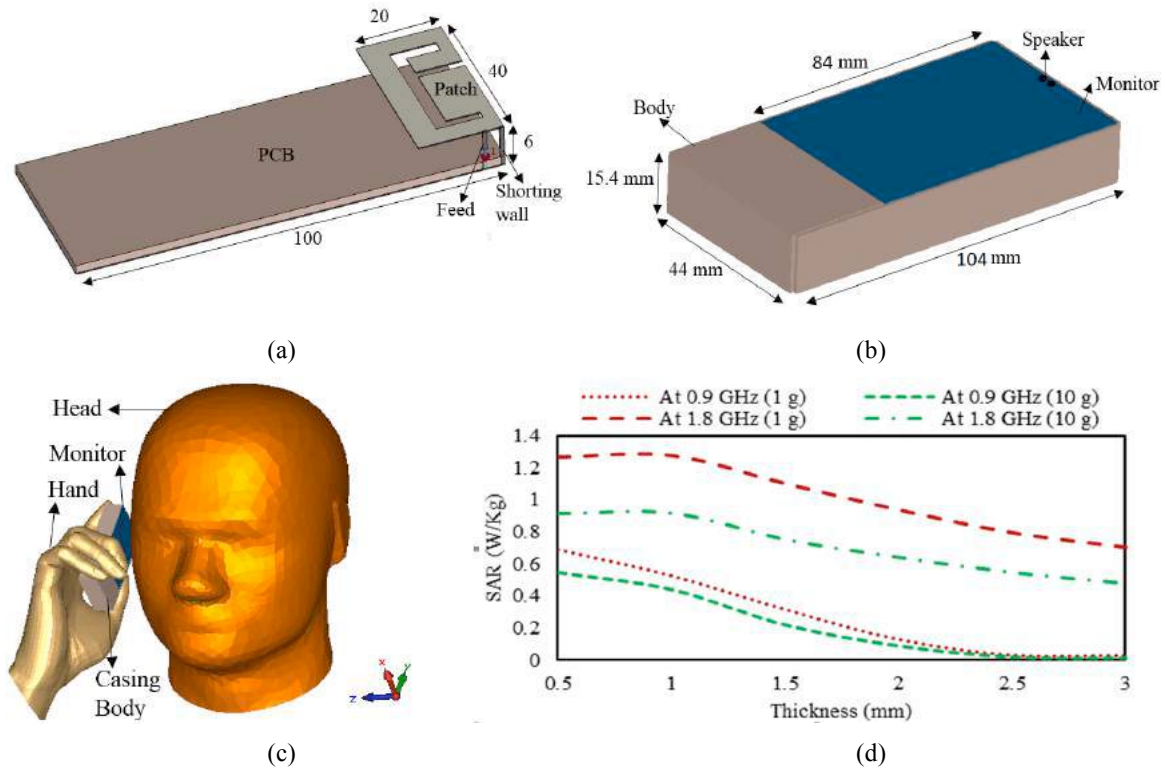

Fig. 1. (a) Geometry of PIFA antenna, (b) geometry of mobile casing with monitor, (c) cheek position of talk mode of mobile phone with head and hand, and (d) values of SAR for silicon mobile casing with different thickness.

REFERENCES

1. M. R. I. Faruque, M. T. Islam, and N. Misran, "Analysis of electromagnetic absorption in mobile phones using metamaterials," *Electromagnetics,* vol. 31, pp. 215-232, 2011.
2. A. H. Kusuma, A.-F. Sheta, I. M. Elshafiey, Z. Siddiqui, M. A. Alkanhal, S. Aldosari, S. A. Alshebeili, and S. F. Mahmoud, "A new low SAR antenna structure for wireless handset applications," *Progress In Electromagnetics Research*, vol. 112, pp. 23–40, 2011.
3. O. Kivekas, J. Ollikainen, T. Lehtiniemi, and P. Vainikainen, "Bandwidth, SAR, and efficiency of internal mobile phone antennas," *Electromagnetic Compatibility, IEEE Transactions on,* vol. 46, pp. 71-86, 2004.
4. Guo, Qingxin, Raj Mittra, Fang Lei, Zengrui Li, Jilong Ju, and Joonho Byun. "Interaction between internal antenna and external antenna of mobile phone and hand effect." *Antennas and Propagation, IEEE Transactions on* 61, no. 2 (2013): 862-870.
5. L. C. Fung, S. W. Leung, and K. H. Chan. "Experimental Study of SAR Reduction on Commercial Products and Shielding Materials in Mobile Phone Applications." *Microwave and optical technology letters* 36, no. 6 (2003): 419-422.

Designing High Gain WiMAX Antenna Using Metamaterial Inspired Technique

M. I. Hossain[1*], **M. R. I. Faruque**[2], and **M. T. Islam**[3]
[1]Department of Electrical & Electronic Engineering, International Islamic University Chittagong, Bangladesh
[2]Space Science Center, Universiti Kebangsaan Malaysia, Selangor, Malaysia
[3]Department of Electrical, Electronic, and System Engineering, Universiti Kebangsaan Malaysia, Malaysia
[*]Email: ipk_eee@yahoo.com

Abstract- In this paper, a high gain microstrip antenna with double negative metamaterial (DNG) is proposed for WiMAX application. The experimental and numerical results show that the proposed metamaterial loaded antenna operates over a wide frequency range about 2 GHz (2.95 to 5 GHz). The DNG metamaterial loading leads to enhance antenna gain more than twice compared to conventional one at 3.5 GHz WiMAX band. The metamaterial loading does not affect the radiation efficiency of antenna.

Nowadays, the wireless communication technology has been spread all over the world and the demand of low profile and high performance antenna is increasing day by day. Although, different types of antennas have been proposed in recent years for WiMAX and WLAN applications, there are still some performances need to be improved. However, metamaterials are being used in antenna engineering due to its extraordinary electromagnetic properties. Recently, metamaterials are proposed to enhance antenna performances and to reduce electromagnetic (EM) radiation toward human [1]. In [2], a metamaterial based helical antenna is designed to get improved radiation characteristics and directivity. The gain improvement of microstrip patch antenna is obtain in [3] using left-handed metamaterial (LHM) structure at 2.4 GHz. The application of proposed LNH detunes the resonance points and alters the radiation pattern greatly. In [4], a microstrip-patch antenna with metamaterial reflecting surface was introduced to improve the antenna gain at 2.4 GHz WLAN frequency. A single layer split ring resonator was utilized with an antenna to enhance gain [5]. This configuration reported significant gain enhancement, but 66.5 mm distance between antenna and metamaterial layer is not applicable for modern compact devices. In this paper, a double negative metamaterial loaded microstrip antenna is presented to enhance antenna gain for WiMAX application. Three-layer planar metamaterial array is proposed as a superstrate of antenna. The presented metamaterial loaded antenna design is compact in size and it is highly suitable for the compact electronic devices.

Figure 1(a) shows the geometry of proposed antenna and Figure 1(b) shows the structure metamaterial unit-cell and array (planar one dimensional array). Figure 1(c) indicates the reflection coefficients for the antenna with and without metamaterial superstrate. The results show that the metamaterial superstrate layers affect resonance points of antenna slightly. The optimized distance between antenna and superstrate is determined 10 mm based on the facts that with metamaterial superstrate does not reduce the bandwidth of antenna. Figure 1(d) exhibits the values simulated and measured gain for the antenna with and without metamaterial superstrate configurations. The results also exhibit that the antenna gain is dramatically increased

due to the influence of proposed double-negative metamaterial layer.

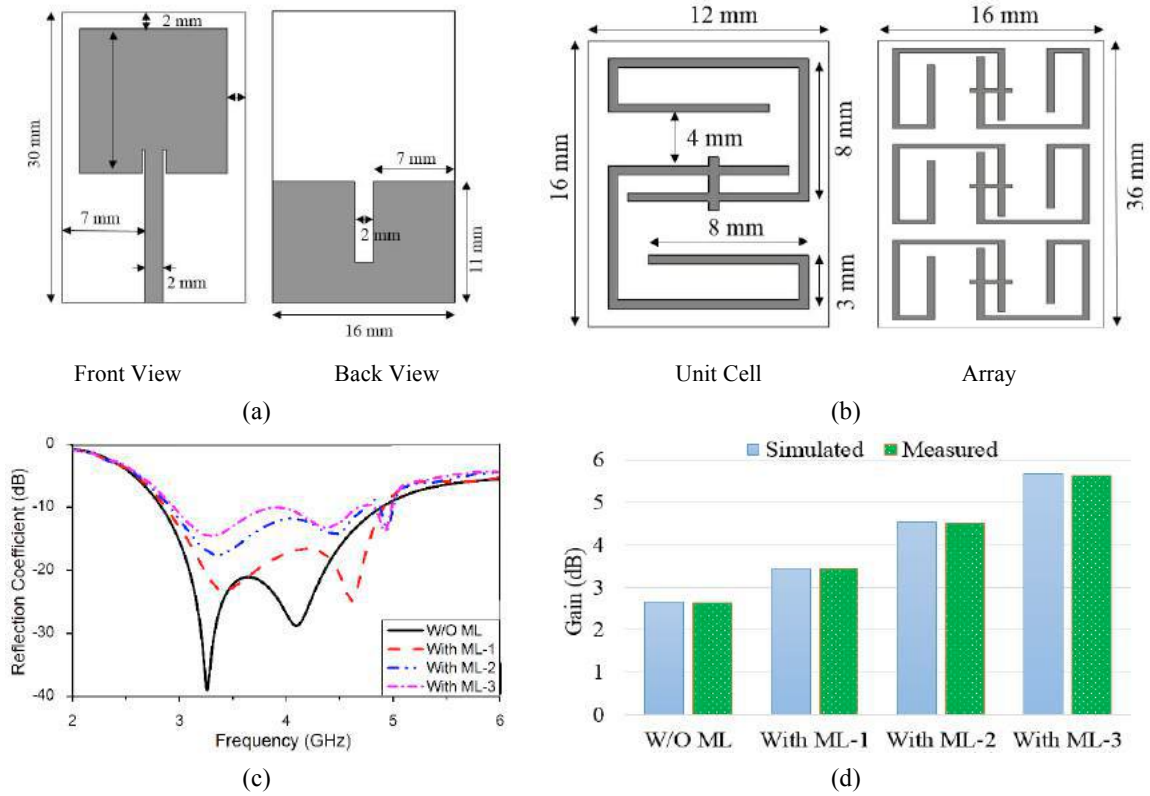

Fig. 1. (a) Geometry of proposed antenna (dimensions in millimeters), (b) metamaterial unit-cell (dimensions in millimeters), (c) return loss characteristics of antenna with and without metamaterial, and (d) antenna gain of proposed antenna with and without metamaterial.

REFERENCES

1. M. I. Hossain, M. R. I. Faruque, and M. T. Islam, "A New Design of Cell Phone Body for the SAR Reduction in the Human Head," *ACES Journal*, vol. 30, no. 7, pp. 792-798, 2015.
2. I. A. Lafmajani and P. Rezaei, "A novel frequency-selective metamaterial to improve helix antenna," *J. Zhejiang Univ. Sci. C*, vol. 13, no. 5, pp. 365–375, 2012.
3. H. A. Majid, M. K. Abd Rahim, and T. Masri, "Microstrip antenna's gain enhancement using left-handed metamaterial structure," *Prog. Electromagn. Res. M*, vol. 8, pp. 235–247, 2009.
4. Chaimool, Sarawuth, Kwok L. Chung, and Prayoot Akkaraekthalin. "A 2.45 GHz WLAN high-gain antenna using a metamaterial reflecting surface." *Proc. ISAP2009*, Bangkok, Thailand (2009).
5. Kasem, Ferhad, Mohammed Al-Husseini, Karim Y. Kabalan, Ali El-Hajj, and Youssef Nasser. "A high gain antenna with a single-layer metamaterial superstrate." *In Mediterranean Microwave Symposium (MMS)*, 2013, pp. 1-4. IEEE, 2013.

AMC- integrated Dual Band Slot Antenna for WBAN Applications

F. N. Giman[1], **P. J. Soh**[1*], **M. F. Jamlos**[1], **H. Lago**[1], **M. Abdulmalek**[2]

[1] Advanced Communication Engineering (ACE) CoE, School of Computer and Communication Engineering,Universiti Malaysia Perlis, Pauh Putra, Arau, Perlis 02600, Malaysia.

[2] Faculty of Engineering & Information Sciences, University of Wollongong in Dubai, Dubai Knowledge Village Dubai, United Arab Emirates.

[*]corresponding author: pjsoh@unimap.edu.my

Abstract- This paper is presents an optimized structure of a slotted dual-band textile antenna integrated with an optimized artificial magnetic conductor (AMC) plane made using felt and ShieldIt Super. These structure operates at 2.45 GHz and 5.8 GHz for WBAN applications. The realized gain of this structure is about 2.38 dB and 6.53 dB at 2.45 GHz and 5.8 GHz, respectively. The antenna has a satisfactory reflection coefficient, bandwidth, and high front-to-back-ratio (FBR) and exhibit properties suitable for wearable applications.

Summary: From our previous research in [1], a planar slot antenna made from textile has been initially proposed, with unsatisfactory gain levels. This paper describes the optimization of a planar C-slotted dual band textile antenna plane with improve antenna performances, especially in terms of gain. The topology of the proposed optimized antenna and the diamond-shaped slotted AMC unit cell are illustrated in Figure 1. Felt was used as its substrate and ShieldIt Super as its conducting element. The 6.51 mm thick overall structure is build using five layers: a ground (bottom), two layers of substrate, a layer of AMC plane in between substrate and patch (top). As shown in Figure 1(c), the optimized AMC indicated a phase response of 1.24^{o} and -1.59^{o} at 2.45 GHz and 5.8 GHz, respectively. The antenna also exhibited a satisfactory simulated reflection coefficient with -15.69 dB at 2.45 GHz and -24.55 dB at 5.8 GHz. The bandwidth of the antenna for lower and upper frequency is 109 MHz and 766 MHz in the lower and upper band, respectively. Besides that, the FBR for both frequencies are more than 19 dB. The directivity of the antenna is 7.31 dBi and 9.88 dBi in the lower and upper frequency, respectively. Deformations in terms of bending when placed on the chest and upper arm are investigated and their SAR values calculated. The detailed results will be presented in the full paper.

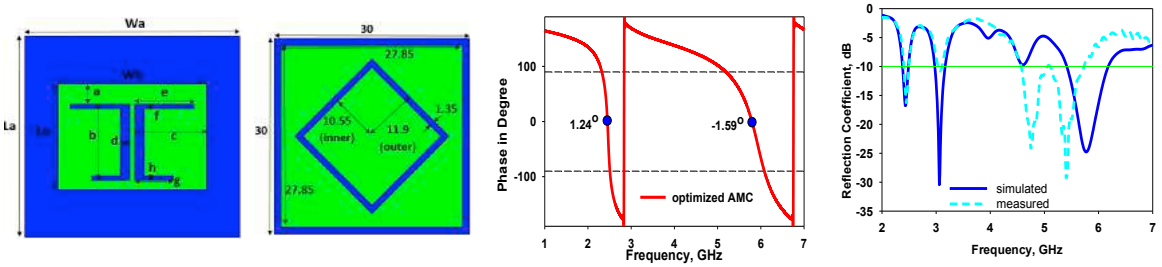

(a) (b) (c) (d)

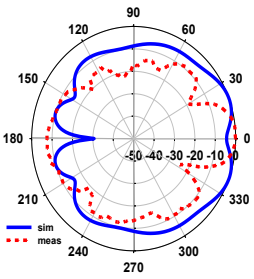

(e)

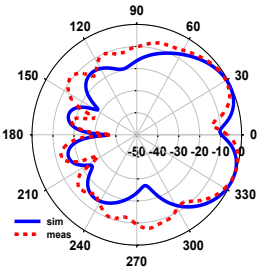

(f)

Figure 1: (a) Topology of the proposed antenna, (b) optimized diamond-shaped slotted AMC, (c) reflection phase of the optimized AMC unit cell, (d) reflection coefficient results, and radiation pattern in the yz-plane (e) at 2.45GHz, (f) at 5.8 GHz. The dimensions of the optimized antenna are La=90mm, Wa=90, Lb=47, Wb=62, a=9, b=34, c=26, d=4, e=21, f=2, g=12, h=2. The dimensions of optimized AMC unit cell are L=30, W=30, L1=27.85, W1=27.85, inner=10.55 and outer=11.9. All dimensions are in mm.

Conclusion: An optimized wearable planar slotted dual band textile antenna integrated with an AMC plane to improve the realized gain and performances of antenna is presented. This structure operates in dual band mode at 2.45 GHz and 5.8 GHz for WBAN and WLAN. The performance of proposed antenna is satisfactory as a wearable antenna in terms of reflection coefficient, bandwidth and gain.

REFERENCES

1 Soh, P. J., F. N. Giman, M. F. Jamlos, H. Lago, and A. A. Al-Hadi, "A C-slotted dual band textile antenna for WBAN applications," in *2016 URSI Asia-Pacific Radio Science Conference, URSI AP-RASC 2016*, 1621-1624, 2016.

2 Afridi, A., S. Ullah, S. Khan, A. Ahmed, A. H. Khalil, M. A. Tarar, "Design of Dual Band Wearable Antenna Using Metamaterials," Journal of Microwave Power and Electromagnetic Energy, Vol. 47, No. 2, 126-137, 2013.

3 Yan, S., P. J. Soh, and G. A. E. Vandenbosch, "Low-Profile Dual-Band Textile Antenna With Artificial Magnetic Conductor Plane," *IEEE Trans. Antennas Propag.,* Vol. 62, No. 12, 6487-6490, Dec 2014.

4 Jiang, Z. H., D. E. Brocker, P. E. Sieber, D. H. Werner, "A Compact, Low-Profile Metasurface-Enabled Antenna for Wearable Medical Body-Area Network Devices*," IEEE Trans. Antennas Propag.,* Vol. 62, No. 8, 4021-4030, Aug 2014.

5 Di, Y. H., X.Y. Liu, M. M. Tentzeris, "A Conformable Dual-Band Antenna Equipped with AMC for WBAN Applications," in *3rd Asia-Pacific Conference on Antennas and Propagation*, 2014.

6 Yan, S., P. J.Soh, and G.A. E. Vandenbosch, "Wearable Dual-Band Magneto-Electric Dipole Antenna for WBAN/WLAN Applications," *IEEE Trans. Antennas Propag.,* Vol. 63, No. 9, 4165-4169, Sept 2015.

A 4x4 Ku-band Array Antenna Excited by Variable CRLH Phase-Shift Lines Network

M. K. Khattak[1], H. Park[1*], M. S. Khattak[1*], A. Rehman[2*], D. Han[2*], C. Lee[2*] and S. Kahng[3*]
[1, 2, 3] Incheon National University, South Korea
s-kahng@incheon.ac.kr

Abstract- A 4x4 (16 element) planar array antenna for Ku-band satellite communication is presented in this paper. The proposed antenna is a two layered structure where the top layer consists of rectangular microstrip patches while the bottom layer consists of corporate feeding structure energizing the antenna patches through aperture. The concept of microstrip feeding array antenna structure was presented in [1] which was improved by various groups [2-4]. In this work, we have used composite right-left hand (CRLH) material to introduce phase-shifts in the feeding lines which can help controlling the direction of the main beam as well as reducing the side-lobe levels. A progressive phase-shift of 0°, 90°, 180°and 270° is achieved by introducing lumped-elements based CRLH lines in the feeding structure [5-6] which reduces the overall size of the feeding structure. The gain of the antenna is approximately 7 dB in the azimuth plane. The design of the proposed antenna is shown in Figure 1.

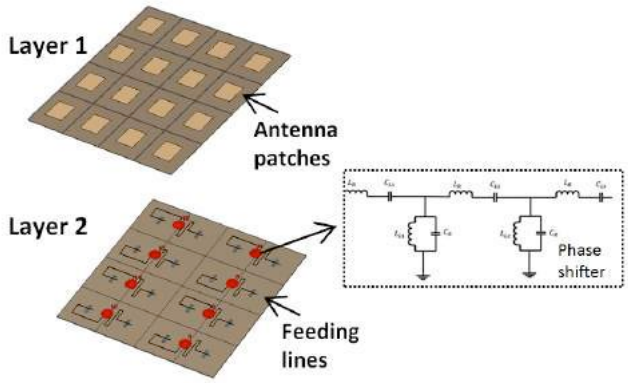

Figure 1. Design of the 4x4 array antenna

CST-MWS is used to design and simulate the proposed antenna. The overall length and width of the antenna is 65mm x 65 mm. RT5880 with the permittivity of 2.2 and thickness of layer 1 = 0.55 mm and layer 2 = 0.25 mm is used as the substrate.

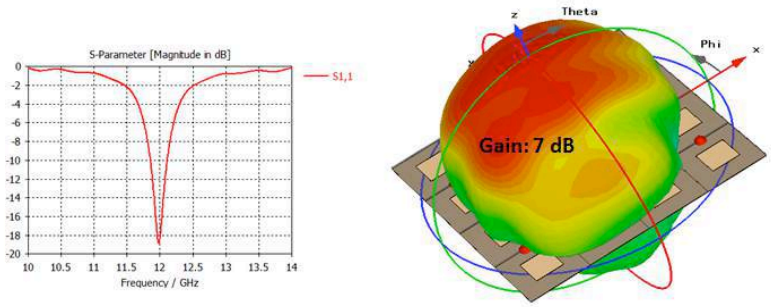

Figure 2. Simulated results of the return-loss and 3D farfield pattern

The simulated results including return-loss and 3D farfield pattern is shown in figure 2.

Acknowledgements: This work is supported by ICT R&D program of MSIP/IITP. [2016-0-00130, Cloud based SW platform development for RF design and EM analysis]

REFERENCES

1. Levine, E., Malamud, G., Shtrikman, S., Travel, D., "A study of microstrip array antennas with the feed network," IEEE Trans. Antennas Propag., vol. 37, pp. 426-434, 1989.
2. Kimura, Y., Miura, Y., et al., " A low-cost and very compact wireless terminal integrated on the back of a waveguide planar array for 26 GHz band fixed wireless access systems," IEEE Trans. Antenna Propag., Vol 53, pp. 2456-2663, 2005.
3. Kan So, K., and Chan, C. H., "Circularly polarized patch antenna array for satellite communication in Ku Band," EuCAP 2016, Switzerland.
4. Shi, W., Qian, Z., et al., "A small Ku-band polarization tracking active phased array for mobile satellite communications," IJAP Hindawi publishing, 2013.
5. Caloz, C., Itoh, T., *Electromagnetic Metamaterials: Transmission Line Theory and microwave applications*, Wiley-IEEE Press, New York, 2005.
6. Khattak, M. K., and Kahng, S., "Novel and compact open-ended CRLH-TL notch filter," Intr. Jour. On Microwave CAD, 2015.

Optical switching of scattering direction in Si rectangle -dimer

Bona Ku[1] , Seokhyeon Hong[1]
and Soon-Hong Kwon[1*]
[1]Dept. of Physics, Chung-Ang University, Seoul 06974, Korea
[*]E-mail: soonhong.kwon@gmail.com

Abstract- Resonant scattering of nanodimer composed of silicon enables controlling of scattering direction depending on the wavelength of incident light. Silicon has two representative resonance based on Mie resonance, called electric and magnetic dipole. We make a dimer structure consisting of silicon rectangles. In this study, the direction of forward scattering in proposed dimer is tuned by changing the wavelength of incident light. The maximum angle of forward scattering is shifted 45°when the wavelength of incident wave is changed 30 nm.

Nanodimer consisting of dielectric particles hold the control of optical scattering for switching and sensing [1]. we simulated scattering cross-section and far-field of scattering light in the dimer as the wavelength changes from electric dipole wavelength to magnetic dipole wavelength of silicon nanorectangle as shown in Fig. 1 (a). In contrast to strong forward scattering with same direction of incident light in the single nanorectangle, the scattering in the hybrid dimer shows deflections of incident light depending on the wavelength.

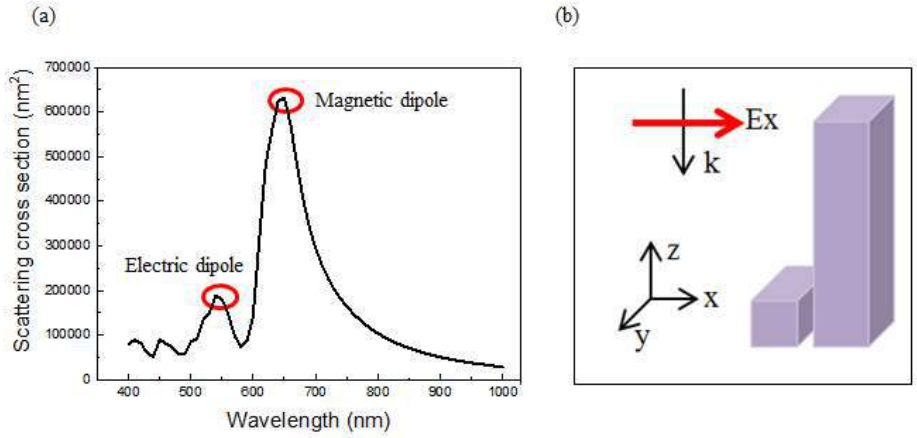

Figures 1: (a) Scattering cross-section by wavelength of rectangle nanodimer (b) Scheme of hybrid dimer composed of rectangles

We simulated hybrid dimer composed of silicon rectangles by using finite-difference time-domain method as shown in Fig. 1 (b).

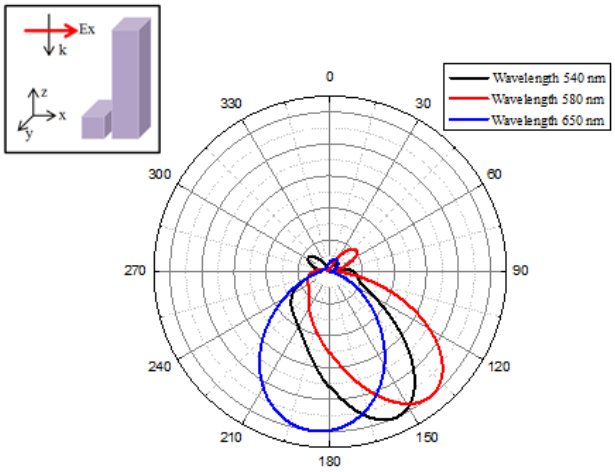

Figures 2 : Scattering direction transition when the wavelength of incident wave is changed from 580 nm 650 nm

When height of two rectangles exist, switching of scattering direction by wavelength is especially prominent. we observed that maximum angle of forward scattering is shifted 45° when the difference of height between two rectangles is 400 nm as shown in Fig. 2.

REFERENCES

1. P. Alabella, T. Shibanuma, S. Maier, "Switchable directional scattering of electromagnetic radiation with subwavelength," *Sci.Rep*, Vol. 5, No. 18322, 2015.

Electrically reconfigurable terahertz meta-molecules

H. Jung[1], J. Koo[2], W. Lee[1], C. In[3], H. Choi[3], M. S. Kang[2], and H. Lee[1*]
[1]School of Electronic Engineering, Soongsil University, Seoul, Korea
[2]Department of Chemical Engineering, Soongsil University, Seoul, Korea
[3]School of Electrical and Electronic Engineering, Yonsei University, Seoul, Korea
[*]corresponding author: hojinl@ssu.ac.kr

Abstract- In this study, we propose an intriguing metamaterial design method to achieve actively customized tuning of terahertz resonance properties. The proposed metamaterial devices are based on the inter-atomic bonding of meta-atoms, which is referred as 'moleculization' of meta-atoms, and realized by controlling the conductance of interconnected graphene bridges. Based on the numerical and experimental results, we confirm that the proposed moleculization system successfully exhibits a broad tuning range of resonance frequency in terahertz regime.

In the past decade, many researchers have attempted to realize the actively tunable metamaterials within the fixed array structures, so that their exotic resonance properties could be controlled in the wide spectrum range [1]. Graphene based metamaterials have recently received extensive attentions as one of the promising tunable metamaterials in THz and optical ranges with various ways [2-4]. However, due to the limited conductivity variation range of graphene materials, they suffered from the unsatisfied tunability of the resonance properties. In this paper, we propose resonance frequency tunable terahertz metamaterials by interconnecting the meta-atoms with the ion-gel gated graphene bridges along the incident polarization direction.

Figure 1a shows the schematic view of our proposed metamaterial array. In this design, the H-shaped meta-atoms are adopted to generate fundamental resonance frequency of the metamaterials with the designated width-to-length ratio of the gap between the adjacent meta-atoms. The graphene bridges are formed between the meta-atoms and connected to two outer electrodes to control their conductivities. One isolated electrode is used as an ion-gel gating electrode.

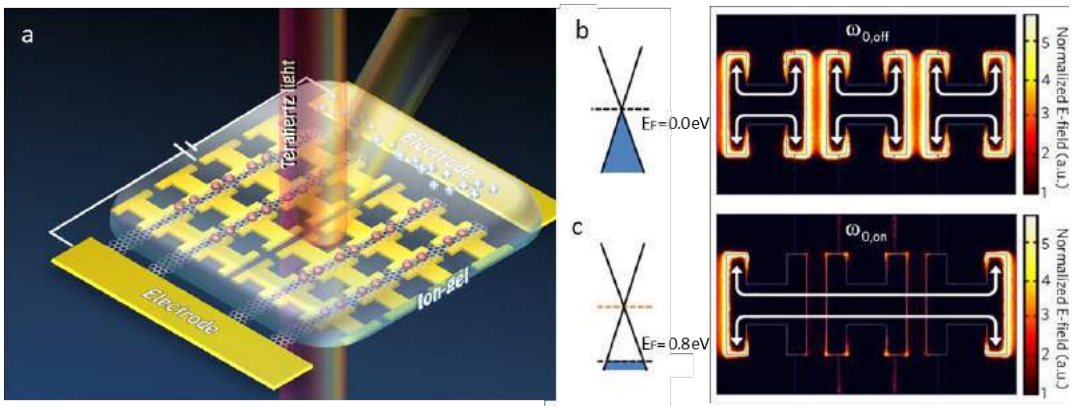

Figure 1. (a) Schematic view of the proposed active meta-atom moleculization system using graphene bridges. (b, c) band structure of the graphene and electric field distribution of the proposed metamaterials at (b) E_F = 0.0 eV and (c) E_F = 0.5 eV.

As shown in Figure 1b, when the fermi energy of graphene bridges E_F is 0.0 eV (V_G = 1.0 V), there are no electrical bridging between the meta-atoms and therefore the proposed metamaterials merely exhibit the resonance of the individual H-shaped meta-atoms ($\omega_{0,\,off}$). However, for the electrically p-doped graphene bridge (E_F = 0.8 eV or V_G = -3.0 V) as shown in Figure 1c, the conductivity of graphene bridges increases and can form electrical connections between adjacent meta-atoms, so that the resonance path of the meta-atoms can be extended as they are connected to each other. Consequently, this extended resonance path makes the resonance frequency red-shifted ($\omega_{0,\,on}$).

Figure 2a shows the optical microscope image of the fabricated graphene bridge metamaterials and the inset shows the position of the graphene bridges between the H-shaped meta-atoms. As shown in Figure 2b, measured transmission spectra of our active moleculization system successfully show that the resonance frequency can be adjusted from 0.8 to 1.28 THz by controlling the conductance of the graphene bridges. These results indicate that the proposed metamaterials can be used as tunable and switchable terahertz and optical meta-surface platforms. Moreover, we can expect that their resonance tuning range can be even extendable and alterable by changing the numbers of interconnected graphene bridges.

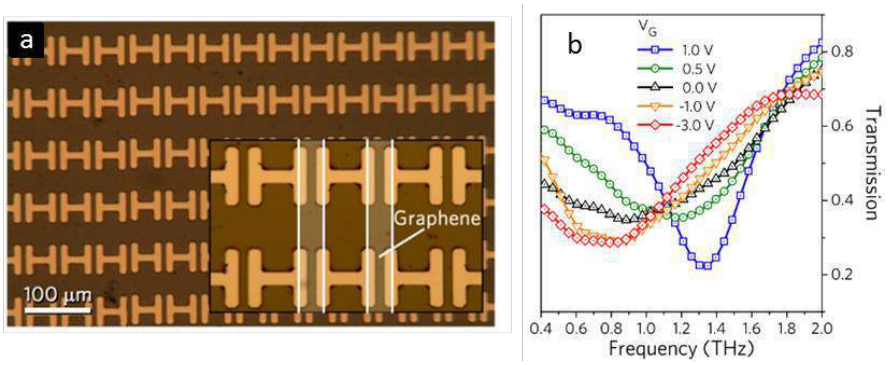

Figure 2. (a) Optical microscope image of the proposed metamaterials. The inset shows the position of the fabricated graphene lines. (b) Measured transmission spectra of proposed meta-atom moleculization system.

Acknowledgements This work was supported by Samsung Research Funding Center of Samsung Electronics under Project Number SRFC-MA1601-02 and the National Research Foundation of Korea (NRF) through the government of Korea (MSIP) (NRF-2016R1A4A1012929).

REFERENCES

1. Fan, K. and Padilla, W. J. "Dynamic electromagnetic metamaterials," *Mater*. *Today*, Vol. 18, 39-50, 2015.
2. Ju, L., Geng, B., Horng, J., Girit, C., Martin, M., Hao, Z., Bechtel, H. A., Liang, X., Zettl, A., Shen, Y. R., and Wang, F. "Graphene plasmonics for tunable terahertz metamaterials," *Nat*. *Nanotech*., Vol. 6, 630-634, 2011.
3. Lee, S. H., Choi, M., Kim, T.-T., Lee, S., Liu, M., Yin, X., Choi, H. K., Lee, S. S., Choi, C.-G., Choi, S.-Y., Zhang, X., and Min, B. "Switching terahertz waves with gate-controlled active graphene metamaterials," *Nat*. *Mater*., Vol. 11, 936-941, 2012.
4. Wu, Y., La-o-vorakiat, C., Qiu, X., Liu, J., Deorani, P., Banerjee, K., Son, J., Chen, Y., Chia, E. E. M., and Yang, H. "Graphene terahertz modulators by ionic liquid gating," *Adv*. *Mater*, Vol. 27, 1874-1879, 2015.

Phase change metamaterial pollution sensor

W. Dong[1*], Y. Qiu[2], X. Zhou[1], A. Banas[3], K. Banas[3], T. Cao[2], and R. E. Simpson[1]

[1] Singapore University of Technology and Design, Singapore

[2] Department of Biomedical Engineering, Dalian University of Technology, China.

[3] Singapore Synchrotron Light Source, National University of Singapore, Singapore

[*]corresponding author: weiling_dong@mymail.sutd.edu.sg

Abstract- We demonstrate a tuneable metamaterial device for gas sensing. The transmission peak of this metamaterial is tuned to over a wide frequency band in the mid-infrared. Upon inducing a structural phase transition in the chalcogenide, the transmission peak is red-shifted by 333 nm. We further engineered the peak transmission wavelength by controlling the geometry of the metamaterial's features. The tuneable chalcogenide metamaterial-based filters will have extensive applications in sensing, displays, and spectroscopy.

Metamaterials have aroused enormous interest in the past decades due to their unusual interaction with electromagnetic waves. The optical properties of these metamaterials can be tailored according to specific requirements for various applications, such as perfect absorbers[1], invisibility cloaking[2] and negative refractive index materials[3]. Our objective here is to use phase change chalcogenides to tune mid-infrared sensors for sensing of pollutant gases, such as SO_2, NO_2, NO, N_2O, HCl, HCHO, CH_4. We demonstrate a tuneable phase change metamaterial that can be tuned over a wide frequency band in the mid-infrared. Upon inducing a structural phase transition in the chalcogenide, the transmission peak is red-shifted by 333 nm. We engineered the peak transmission wavelength by controlling the geometry of the metamaterial's features. The relatively large dimensions of the matamaterial features will enable fabrication of devices over a large area using inexpensive methods such as nano imprinting. Compared with most other metamaterial designs that are passive and show transmission peaks at a fixed frequency, tuneable chalcogenide metamaterial-based filters will have extensive applications in sensing, displays, and spectroscopy.

Key words: chalcogenide, metamaterials, sensing

Acknowledgements, We acknowledge the support from the A-Star Singapore–China joint research program under grant 1420200046.

REFERENCES

[1] T. Cao, L. Zhang, R. E. Simpson, and M. J. Cryan, "Mid-infrared tunable polarization-independent perfect absorber using a phase-change metamaterial," *J. Opt. Soc. Am. B,* vol. 30, pp. 1580-1585, Jun 2013.

[2] I. I. Smolyaninov, V. N. Smolyaninova, A. V. Kildishev, and V. M. Shalaev, "Anisotropic metamaterials emulated by tapered waveguides: application to optical cloaking," *Phys. Rev. Lett.,* vol. 102, p. 213901, 2009.

[3] R. A. Shelby, D. R. Smith, and S. Schultz, "Experimental verification of a negative index of refraction,"

science, vol. 292, pp. 77-79, 2001.

A parasitic resonator based diamond shape microstrip antenna for UWB applications

M. Z. Mahmud*, M. N. Rahman, F. B. Ashraf, M. F. Mansor, and M. T. Islam

[1] Dept. Of Electrical, Electronic and Systems Engineering, Universiti Kebangsaan Malaysia, Malaysia

*corresponding author: zulfikerm@siswa.ukm.edu.my

Abstract- This study proposes a diamond shaped microstrip patch antenna for ultra-wideband applications. The antenna is made up of a diamond shape radiating patch, partial ground plane, and three asterisk shaped parasitic elements. The parasitic elements are positioned above the ground plane to enhance the bandwidth and gain. The proposed antenna has a compact dimension of 30 x 25 x 1.6 mm^3 and achieves an overall bandwidth (S11<-10dB) is 5.8 GHz from 2.7 GHz to 8.5 GHz. The antenna attains more than 4 dBi realized gain and 80% efficiency over the bandwidth with omnidirectional radiation pattern. The design and simulation of the proposed antenna is performed in CST Microwave Studio. The observation during the analysis of the simulated data reveals that the proposed antenna is suitable for UWB applications where high gain is required.

In recent years, UWB communication has been attracted in wireless communication system for its special features like extremely high data transmission rate, low interference and low spectral power density. It is still a challenge to design a proficient compact UWB antenna. Azim *et al.* proposed tapered-shape slot antenna for UWB application with an overall dimension of 22 × 24 mm^2 [1]. Gautam *et al.* proposed a 25 × 25 × 1.6 mm^3 CPW antenna for achieving UWB bands in [2]. In this study, a diamond shaped UWB antenna is proposed using asterisk shaped parasitic elements. The geometric layout of proposed antenna is shown in Figure 1. The proposed antenna is designed on Rogers RT/duroid 5880 substrate material having 2.2 dielectric constant and 0.0009 loss tangent.

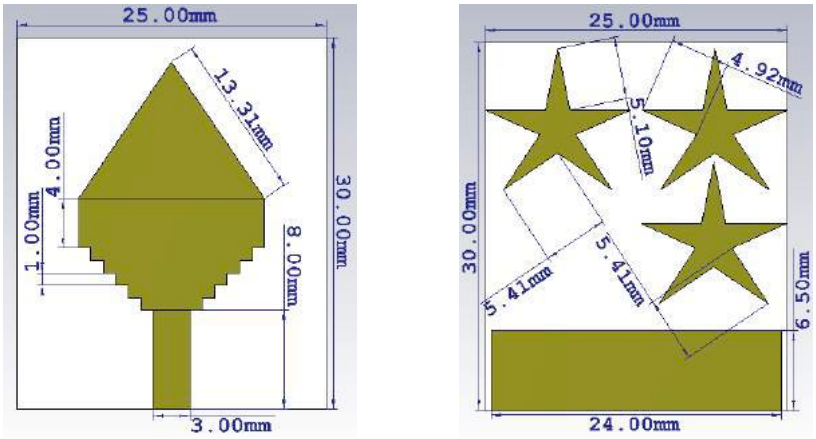

Figure 1. Geometric layout of the proposed UWB antenna-Top view (left) and bottom view (right).

The proposed antenna is designed with a diamond shaped patch, partial ground plane and asterisk shaped parasitic elements on the bottom side of the substrate. The existence parasitic elements and staircase diamond

shape of patch and optimum ground plane has strong effect for the impedance matching. The proposed antenna is feed by a 50 Ω microstrip line.

The reflection coefficient of the proposed diamond shaped antenna is depicted in Figure 2(a). The antenna achieves -10dB impedance bandwidth of 5.8 GHz (2.7- 8.5 GHz).

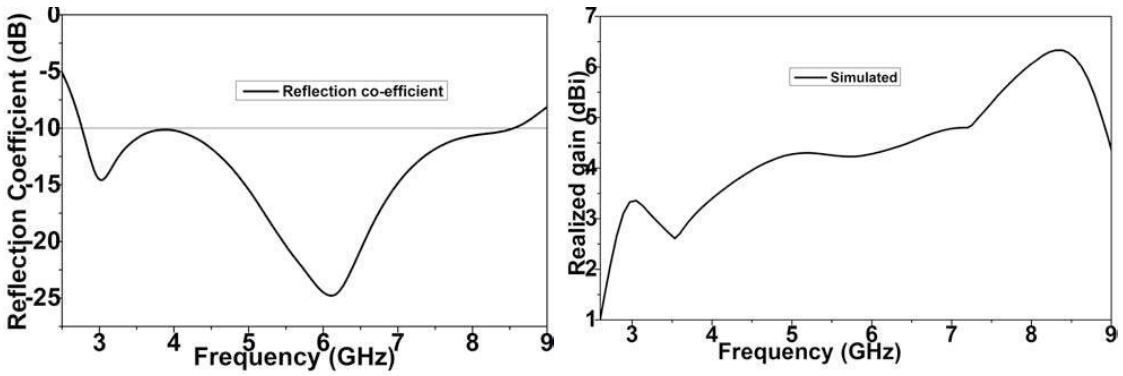

Figure 2. (a) Reflection coefficient (b) Realized gain

Figure 2(b) shows the gain of the proposed diamond shaped antenna. The result reveals that the antenna maintain a more than 4 dBi gain over the entire band with maximum realized gain of 6.2 dBi. Higher gain made the antenna a suitable candidate for the use of UWB applications where high gain is required.

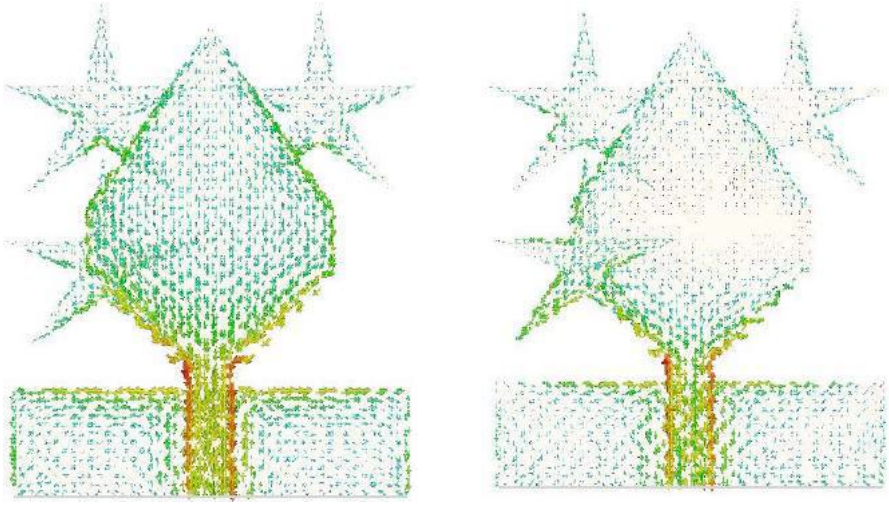

Figure 3. Surface current distribution of the antenna-(a) at 3 GHz and (b) 6.15 GHz

REFERENCES

1. Azim, R., Islam, M. T., & Misran, N. "Compact tapered-shape slot antenna for UWB applications," A*ntennas and Wireless Propagation Letters, IEEE*, Vol. 10, 1190-1193, 2011.
2. Gautam, A. K., Yadav, S., & Kanaujia, B. K. "A CPW-fed compact UWB microstrip antenna," Antennas *and Wireless Propagation Letters, IEEE*, Vol. 12, 151-154, 2013.

Digit 8-Shaped Resonator Based Metamaterial for Sensor Applications

M. N. Rahman[1*], M. T. Islam[1], M. Z. Mahmud[1], M. A. Ullah[1], and GK Beng[1]

[1] Dept. Of Electrical, Electronic and Systems Engineering, Universiti Kebangsaan Malaysia, Malaysia

[*]corresponding author: p86256@siswa.ukm.edu.my

Abstract-This paper presents a metamaterial, based on a digit 8-shaped resonator. The resonator is encompassed by a partial ground plane and excited by a microstrip feeding transmission line. As the digit 8-shaped resonator, partial ground plane, and the feedline are all on a microstrip, the measurement can be executed by using the common laboratory facility instead of using the waveguide. The resonator and the ground are placed on the similar part of the microstrip and the microstrip feeding line is placed on the other part of the microstrip. In metamaterial design, normally numbers of unit cells are needed, whereas this paper presents only one cell which can achieve the metamaterial properties. The characteristic parameters of the metamaterial are fetched and analyzed to find the concurrency between the simulated and measured results. The presented metamaterial is also applied in sensor applications where the simulated and measured results reveal considerable agreement. The presented prototype can be used for several applications where metamaterial properties are required.

From the introduction of the metamaterials, they became popular with the researchers who are working with materials that exhibits negative permittivity and negative permeability. Many researchers suggested different types of resonators for different resonance frequencies and parametric characteristics [1-2]. Currently metamaterials are used in sensors because metamaterial based sensors provide miniaturization facility and large Q-factor values. These advantages make the metamaterials highly sensitive to the environment and for this reason metamaterials are used in sensing applications [3].

In this paper, a metamaterial on a planar surface based on only one unit cell is presented. In the proposed structure, the digit 8-shaped resonator and partial ground frame are placed on the one side of the lossy FR4 substrate, and the feeding transmission line (FTL) is placed on the opposite side of the substrate. This structure provides some advantages and flexibility to design and implementation of the metamaterial. Figure 1 shows the geometric layout of the proposed metamaterial.

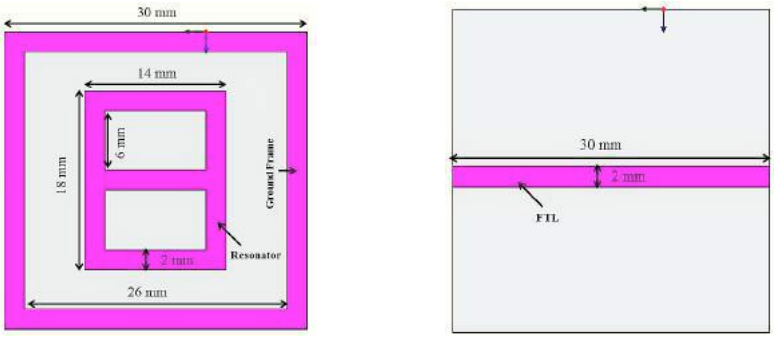

Figure 1. Geometric layout of the proposed UWB antenna-Top view (left) and bottom view (right).

The simulated S-parameters of reflection coefficient and transmission are shown in Figure 2. The figure shows multiple resonances throughout the frequency from 2 GHz to 12 GHz. The resonance at 3 GHz covers highest transmission peak, which is called the left-handed peak.

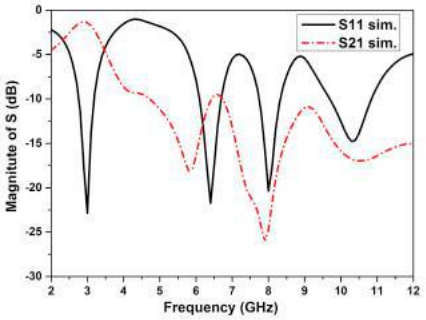

Figure 2. Transmission and Reflection coefficient of the proposed antenna

The metamaterial characteristics of the proposed metamaterial are displayed in Figure 3. From the figure the electromagnetic characteristics of the metamaterial can be observed.

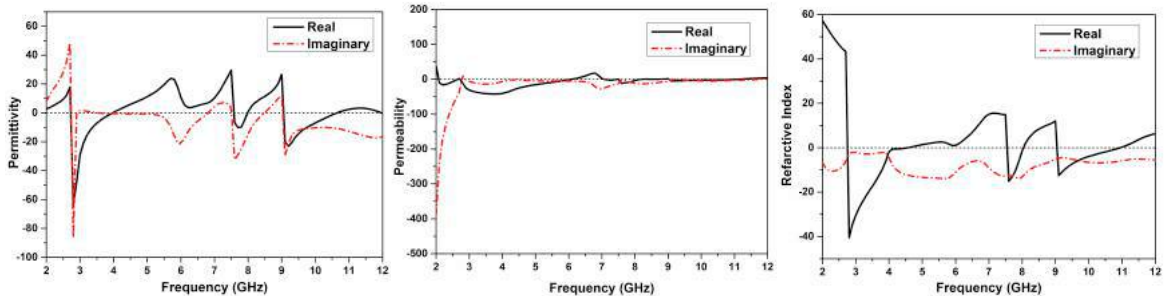

(a) (b) (c)

Figure 3. The simulated parameters such as (a) Permittivity (b) Permeability and (c) Refractive Index of the proposed metamaterial.

REFERENCES

[1] C. Sabah and T. Nesimoglu, "Design and characterization of a resonator-based metamaterial and its sensor application using microstrip technology," *Optical Engineering,* vol. 55, pp. 027107-027107, 2016.

[2] M. M. Islam, M. T. Islam, M. Samsuzzaman, M. R. I. Faruque, N. Misran, and M. F. Mansor, "A miniaturized antenna with negative index metamaterial based on modified SRR and CLS unit cell for UWB microwave imaging applications," *Materials,* vol. 8, pp. 392-407, 2015.

[3] V. Rawat, V. Nadkarni, and S. Kale, "ISM (Industrial Scientific and Medical standard) band flex fuel sensor using electrical metamaterial device," Applied Physics A, vol. 123, p. 75, 2017.

Microstrip Patch Antenna Loaded with Reactive Impedance Surface

A.N. Suraya[1], T.Sabapathy[2], and M.Jusoh[3]

Radio Engineering Research Group, School of Computer and Communication Engineering,[1,2,3]
Universiti Malaysia Perlis, Bangunan Pengkalan Indah, Jalan Pengkalan Asam, 01000, Kangar, Perlis, Malaysia.
Email: mira_anssa@yahoo.com.

Abstract- An investigation on the use of reactive impedance surface (RIS) for wearable antenna is presented. The investigation is conducted with wearable patch antenna that design using RIS at different frequency of unit cells, namely 1.8GHz, 2.45GHz and 5.12GHz. The aim of this project is to observe the miniaturize of antenna if it integrates with RIS. This antenna operates at 2.45 GHz.

In recent years, wearable antenna designs have gained a lot of attention from researchers and industries. Wearable antenna design plays important characteristics such as ease of fabrication and integration, conformal, low profile and high efficiency [1]. Generally, the substrate used to design wearable antenna to have low relative permittivity, εr. According to antenna design theory, this will increase the antenna size. The problem could be further challenging when multi element antenna has to be designed for wearable application that could support emerging communication technologies such as beam steering [2] and MIMO [3].

A two-dimensional (2D) equivalent of metamaterial is basically a surface distribution of electrically small scatters is called metasurface [4]. The RIS is also referred as meta-surface or artificial magnetic surface and used to provide a zero degree reflection phase for further improving the antenna radiations and miniaturization [5-7]. The RIS has a simple design that is composed of metallic patches. In this paper, a miniaturization wearable patch antenna loaded with RIS is proposed. At first, a conventional microstrip patch antenna is designed and optimized with good performance in terms of bandwidth and gain. RIS is introduced as a substrate to miniaturize the size and performance is observed and compared to the RIS operating at different frequencies.

Firstly, the metamaterial unit cell is the initial step of the study based on full structure which is generally consists of unit cell and substrate. A unit cell is design with different dimension based on frequency used; see Figure 1(a). To miniaturize original antenna, RIS is apply as a substrate. The RIS layer consists of 5 × 5 cross-shaped metallic unit cell patch array printed periodically on a grounded low-cost felt substrate. The proposed antenna structure in figure 2(b) is a two layered dielectric geometry made up of felt substrate with the same thickness. As a result, the bandwidth of the all design shows better performance, see Figure 2(c). Felt is used as substrate, this material was chosen because it is easy to cut and sew. As conclusion, the gain and bandwidth is improved as the size of patch is decreased. Overall performance is better compared to original patch antenna.

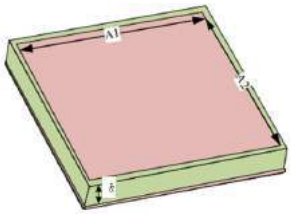

Figure 1: (a) Unit cell

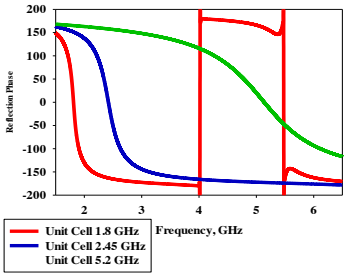

(b) simulation of the reflection phase at three different frequencies

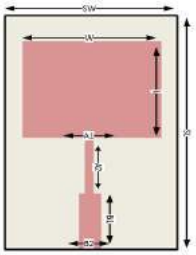

Figure 2(a): The optimized dimension is SW=70mm, SL= 110mm, W=55mm, L=45mm, A1=2.9mm, A2=27mm, B1=26.6mm and B2= 6.3mm.

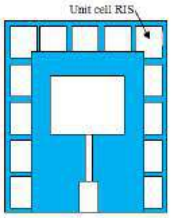

(b):The view of the microstrip patch antenna with 5x5 RIS

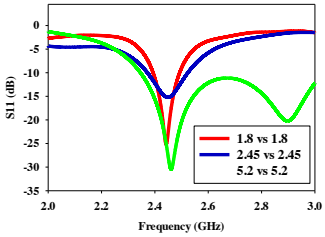

(c): reflection coefficient (S_{11}) result of the patch antenna with RIS.

Acknowledgement

This work is a part of the research project of metasurface develops in ENAC Lab of SCCE UniMAP (Universiti Malaysia Perlis).

REFERENCES

[1] Jaeck, V., & Bernard, L. (2013). Design of an enhanced patch Array on a Reactive Impedance Substrate, (1), 232–235.
[2] Wong, Kin-Lu. *Compact and broadband microstrip antennas*. Vol. 168. John Wiley & Sons, 2004.
[3] Chen, W.S.; Wu, C.K.; Wong, K.L.: Compact circularly polarized microstrip antenna with bent slots. Electron. Lett., 34 (1998),1278–1279.
[4] Werner, Douglas H, and Do-Hoon Kwon. *Transformation Electromagnetics And Metamaterials*. London: Springer, 2014.
[5] Mosallaei, H.; Sarabandi, K.: A novel artificial reactive impedance surface for miniaturized wideband planar antenna design: concept and characterization, in Proc. IEEE Antennas and Propagation. Society. Int. Symp., Columbus, OH, USA, 2003.
[6] Buell, K.; Cruickshank, D.; Mosallaei, H.; Sarabandi, K.: Patch antenna over RIS substrate: a novel miniaturized wideband planar antenna design, in Proc IEEE Antennas and Propagation. Society.Int. Symp., Columbus, OH, USA, 2003.
[7] Mosallaei, H.: Antenna miniaturization and bandwidth enhancement using a reactive impedance substrate. IEEE Trans. Antennas Propag. 52 (2004), 2403–2414.

Chiroptical Spectroscopy Using an On-Resonance Chiral Metasurface

S. Hamed Shams Mousavi[1], Sajanlal R. Panikkanvalappil[2], Ali A. Eftekhar[1], Mostafa A. El-Sayed[2], Ali Adibi[1]

[1] School of Electrical and Computer Engineering, Georgia Institute of Technology, Atlanta, GA, 30332 USA

[2] School of Chemistry and Biochemistry, Georgia Institute of Technology, Atlanta, GA, 30332 USA

*corresponding author: h.mousavi@gatech.edu

Abstract- We present a novel three-dimensional chiral metamaterial design for chiroptical spectroscopy. Utilizing the chiral light-matter interaction between the designed metamaterial and molecule that is chiral in the same wavelength range, we demonstrate chiroptical sensing at the molecular level.

Previously, off-resonance chiroptical sensing has been demonstrated using a planar chiral metamaterial [3]. It was shown that optically active biomolecules can be detected by a planar chiral metamaterial by studying the dissymmetry in the resonance shifts induces on the two enantiomers. The measured change in CD, in this experiment, was fairly modest due to the small chirality of the proposed planar metasurface, as well as the mismatch between the chiral resonance of the metamaterial and that of the target molecules. It has been suggested that in order to achieve a significant CD, at least a bilayer nanostructure, with three-dimensional arrangement of plasmonic nanoantennas is needed [4]. In this paper, we demonstrate a new three-dimensional chiral metamaterial (Fig. 3.1.a-b) that can be used for sensing applications [5]. We show that the interaction between the metamaterial presented here and biomolecules with significant chirality in the same range can result in a large change in the chiroptical response of the overall system, beyond what could be achieved with a planar nanostructure.

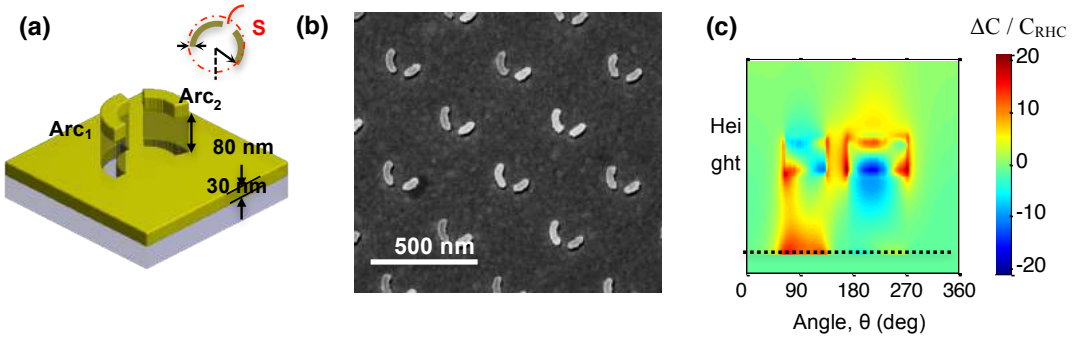

Fig 1. *(a) Schematic view of the bilayer nanoantenna array with geometrical parameters. (b) Scanning electron micrograph from one enantiomer of the designed metamaterial (d) Chirality pseudoscalar over the cylindrical surface 1 nm away form the outer surface of the two arcs.*

In addition this chiral metamaterial can be realized using a simple fabrication process with one-step lithography [6], that preserves the scalability of the embossed nanostructures necessary for practical applications

at lower wavelengths. Figure 1.c shows the chirality pseudoscalar defined in Eq. 1 over a cylindrical surface (S) shown in the inset Fig. 1.a.

$$C(\vec{r}) = \frac{1}{2}\varepsilon_0 \vec{E}(\vec{r}).\nabla \times \vec{E}(\vec{r}) + \frac{1}{2\mu_0}\vec{B}(\vec{r}).\nabla \times \vec{B}(\vec{r}) \quad (1)$$

Figures 2.a-b show the measured change in CD spectra of Enant D and Enant L, when coated by Chlor A and B. As it is evident in the measured ΔCD spectra of Fig. 2, both enantiomers show a giant change of several degrees in the CD in response to the adsorption of the chiral molecules (i.e., Chlor A and Chlor B).

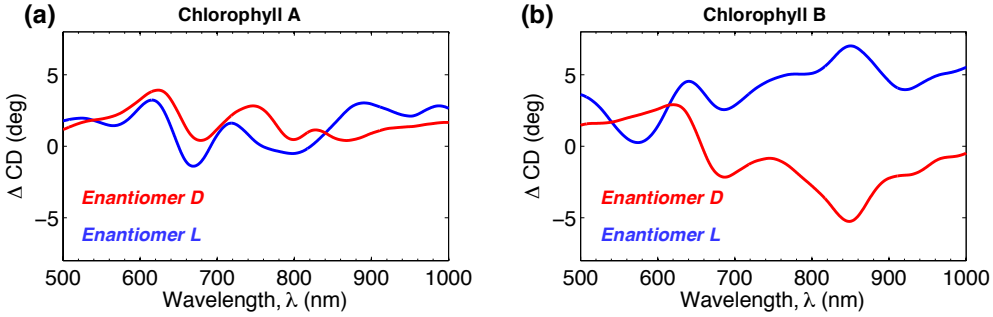

Fig 2. *Differential CD spectra acquired from the two enantiomers of the metamamterial coated with (a) Clor A, (b) Chlor B*

In conclusion, we have demonstrated SECD-based spectral analysis of chiral biomolecules at the molecular level using an on-resonance chiral metamaterial. Using these metamaterials, we measured the superchiral spectra from a monolayer of two biomolecules with very similar atomic compositions, and showed that we can distinguish them from the acquired differential CD. The values of ΔCD reported in this work, show a very large improvement over the non-resonant experiments [7], performed using planar chiral metamaterial, nanoparticle assemblies or non-chiral nanoparticles, owing to the large chirality of the nanostructures and the spectral matching between the CD spectra of the metamaterials and target molecules.

REFERENCES

1. J., Kelly, S. M., Barron, L. D., Gadegaard, N., Kadodwala, M. Ultrasensitive detection and characterization of biomolecules using superchiral fields. *Nature Nanotech.* **5** (2010).

2. Fan, Z., Govorov, A. O. Plasmonic circular dichroism of chiral metal nanoparticle assemblies. *Nano lett.* **10** (2010).

3. S. H. Shams Mousavi, S. R. Panikkanvalappil, A.A. Eftekhar, M.A. El-Sayed, A.Adibi, Chiroptical Sensing Using an On-Resonance Chiral Metamaterial, *rXiv*

4. Shams Mousavi, S. H., Eftekhar, A. A., Atabaki, A. H. & Adibi, A. Band-edge bilayer plasmonic nanostructure for surface enhanced Raman spectroscopy. *Acs Photonics* **2**, 1546-1551 (2015).

5. Hendry, E., Carpy, et al. Ultrasensitive detection and characterization of biomolecules using superchiral fields. *Nature Nanotech.* **5** (2010).

Encoding and Display with 3D Metastructures

X. Xiong[1], Z. H. Wang[1], Y. S. Hu[1], R. W. Peng[1] and M. Wang[1*]

[1]National Laboratory of Solid State Microstructures and School of Physics, Collaborative Innovation Center of Advanced Microstructures, Nanjing University, Nanjing 210093, China

[*]corresponding author: muwang@nju.edu.cn

Abstract- The history of manufactured mirror can be traced back to thousands of years ago. Yet people never imagined that the same object can be used as a reflector (mirror) and an absorber by simply rotating its geometrical orientation. In recent decades, as the development of subwavelength optics and plasmonics, optical properties of a structured metal film become extremely diverse. These properties depend not only on the chemical composition of the material, but also on the subwavelength structural designing. In this work, we report on encoding and display based on stereo standing U-shaped resonator (SUSR) arrays. The SUSR serves as a perfect absorber at a structure-dependent frequency when the polarization of incident light is parallel to the bottom rim of the SUSR. When the incidence polarization is rotated for 90^{o} (perpendicular to the bottom rim of the SUSR), SUSR turns to a perfect reflector at all frequencies. Further, the resonant frequency sensitively depends on the height of the arms of SUSR. By introducing SUSRs with different arm height, resonant absorption state may occur at different frequencies. By defining the resonant absorption state as "Dark" and the reflection state as "Bright", we can encode and display binary patterns. Besides, when SUSR rotates with the direction of the standing arms as axis, different reflectivity, hence different shade will be generated. In this way we may realize gray scale display. Experimentally we demonstrate that this encoding and display scheme indeed works.

Polarization and Pattern Reconfigurable Antenna with EBG Structures.

M. F. Ismail[1,2], M. K. A. Rahim[2], M. R. Hamid[2] and H. A. Majid[3]
[1]Centre for Diploma Studies and [3]Faculty of Engineering Technology
UniversitiTun Hussein Onn Malaysia, Parit Raja 86400 Johor, Malaysia
[2]Faculty of Electrical Engineering,
UniversitiTeknologi Malaysia, Johor Bahru 81310 Johor, Malaysia
[*]corresponding author: ifaizal@uthm.edu.my

Abstract-This paper presents a design of single patch antenna incorporated with an array of electromagnetic band gap (EBG) structure with pattern and polarization reconfigurability. By tuning the characteristics of the EBG structure and the antenna, the radiation pattern and polarization of the patch antenna can be switched or dynamically controlled. The polarization of the proposed antenna can be switched from linear to circular polarization and vice versa. Meanwhile, the radiation pattern is tuned by controlling the connection between the EBG patches and the ground plane. Five elements of EBG is located at both side and higher from of the antenna to give configuration of -14, 0 and 14 degree of radiation pattern. Full EM wave simulation including the PIN diode equivalent circuit will be discussed.

Figure 1 shows the geometry of proposed antenna where Ls = 100mm, Ws = 70 mm, Lp = 32mm, Le = 12.5 mm, and h = 6.08 mm. The EBG structure was located higher than an antenna for pattern reconfigurability occurs. It is due to the properties of EBG can absorb the surface wave. The antenna is designed on a Taconic RF35 board with a relative permittivity of 3.5, tangential loss of 0.0018 and a thickness of 1.52 mm. A BAR50–02V PIN diode is used as the switch. Computer Simulation Technique (CST) software is used to simulate the designed antenna. In the simulation, the switch is represented by the S-parameters of the BAR50–02V diode, obtained from the manufacturer's website. To obtain the linear polarization, diode D1 to D4 is switched ON to give square shape of patch antenna while switched OFF to obtain circular polarization truncated patch antenna. The axial ratio and S11 parameter of both polarization are shown in Figure 2 (b) and (c). The proposed shape gives good 3dB axial ratio at 2.43 GHz radiating frequency and it's comply the ISM band point to point communication.

Meanwhile, the radiation pattern reconfigurable is obtained by switching the group of array EBG at both side of the antenna. The diode configuration as shown in Figure 2 (a). The radiation pattern was tiled about 14 degree for both condition 0:1 and 1:0. However, when both side of EBG are ON and OFF, the radiation pattern are return to 0 degree. Average gain for all condition are 7.2 dBi. The gain of the antenna can be improve by increasing unit of radiating path in array form. The radiation pattern was tilled when one side of EBG was absorb the surface wave from the antenna. The size of EBG and distance from edge of patch will give major contribution to results.

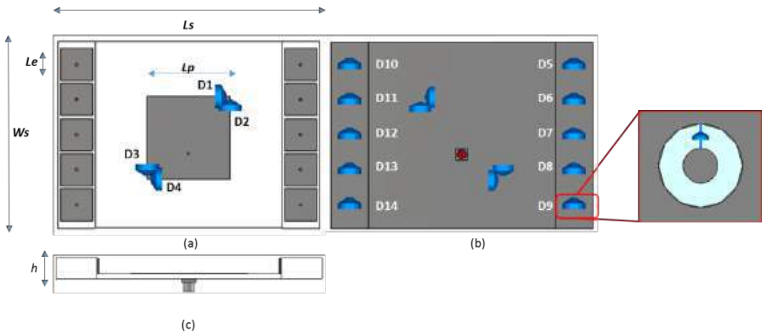

Figure 1 Proposed design with diode model in (a) front, (b) bottom and (c) side view.

Condition	D6 – D9	D11 –D14
0 : 0	OFF	OFF
0 : 1	OFF	ON
1 : 0	ON	OFF
1 : 1	ON	ON

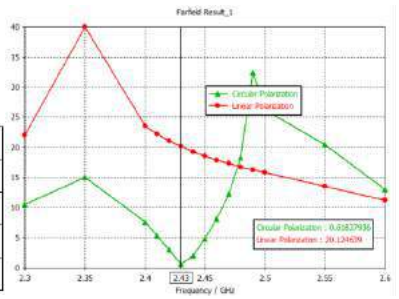

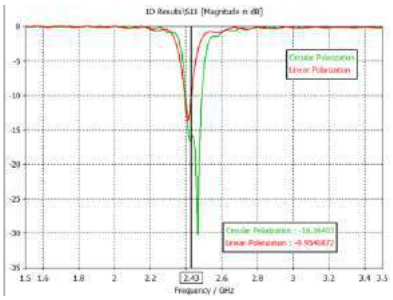

(a) (b) (c)

Figure 2 (a) Diode condition. (b) Simulated result for Axial ratio, and (c) S11 parameter

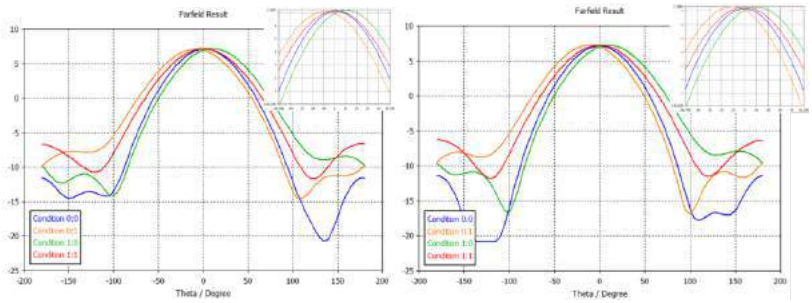

(a) (b)

Figure 3 Simulated Cartesian radiation pattern for (a) circular and (b) linear polarization.

REFERENCES

1. Y. R. Samii, Mosallaei, "Electromagnetic Band Gap Structure: Classification, Characterization and Apllication", *Proceeding of IEEE-ICAP symposium*, pp. 560-4, 2001.
2. H. A. Majid, M. K. A. Rahim, et. all "Frequency Reconfigurable Wideband Monopole Antenna Using EBG Structures", *The 8th European Conference on Antenna and Propagatio*n, pp. 1906-1908, 2014.
3. O. Ayop and M.K.A. Rahim, Analysis of mushroom-like electromagnetic bandgap structure using suspended transmission line technique, In: IEEE International RF and Microwave Conference, December 2011.

Ultrafast Terahertz Active Metamaterials integrated with MSM-2DEG Varactors

Ji Hyun Hwang, Muhammad Tayyab Nouman, Kye-Jeong Lee, and Jae-Hyung Jang*
School of Electrical Engineering and Computer Science, Gwangju Institute of Science and Technology, Gwanjgu 500-712, South Korea
*corresponding author: jjang@gist.ac.kr

Abstract-We propose ultrafast amplitude modulation scheme of terahertz waves based on metamaterials integrated with metal-semiconductor-metal (MSM) two-dimensional electron gas (2DEG) varactors. The MSM-2DEG varactors embedded into the split gap of metamaterials are based on AlGaN/GaN heterostructures, which enable ultrafast modulation. By applying a bias voltage across the split gaps, the effective capacitance of metamaterials changes. This capacitance change leads to resonant frequency shift of metamaterials and amplitude modulation.

The terahertz band of the electromagnetic spectrum (0.3~3 THz) is interesting because of its various applications into imaging, communications, and bio-sensing [1]. Nevertheless, the practical use of the terahertz band is still limited, in the absence of high-performing devices. As one of these, the development of terahertz modulators is highly desirable. Since there are no materials in nature to respond to the terahertz wave, artificially engineered metamaterials have been considered as a solution to manipulate the terahertz wave [2]. In recent years, various modulation techniques have been adopted for metamaterials to actively control the terahertz wave [3]. In particular, electrically controllable metamaterials have received a lot of attention due to its superior characteristics such as the compact size, high modulation speed, and low power consumption.

In this work, we show the full wave electromagnetic simulation result to modulate the incident terahertz wave, as shown in Fig. 1(a). For various bias voltage, the effective capacitance of metal-semiconductor-metal (MSM) two-dimensional electron gas (2DEG) varactors embedded into metamaterials get changed, as shown in Fig. 1(b) [4]. According to this, the resonant frequency of metamaterials is shifted and the amplitude of terahertz wave is modulated for the fixed frequency region. After removing substrate effects, high modulation index (82 %) is obtained from low transmittance (0.15) to high transmittance (0.81). Furthermore, employing AlGaN/GaN heterostructure offers the high speed 2DEG channel by conduction band offset and polarization doping [5]. This high speed 2DEG channel can realize ultrafast modulation of the terahertz wave with reduced RC time constant of the devices. In the optimized design of metamaterials (high Q-factor) and MSM-2DEG varactors (high cutoff frequency), we expect to realize the terahertz modulator with high modulation speed (>10 GHz) and high modulation index (>0.8). Ultimately, the proposed ultrafast terahertz active metamaterials will facilitate seamless terahertz data transmission and real-time terahertz imaging.

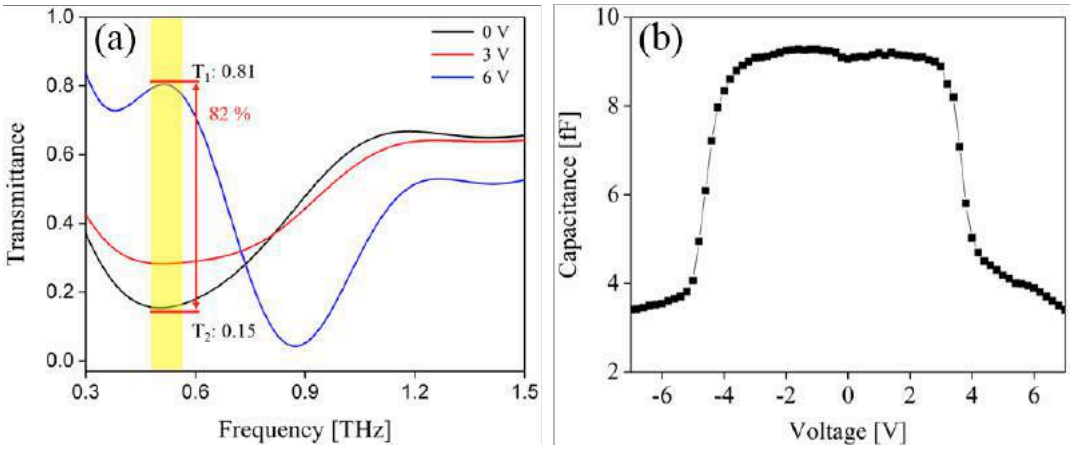

Fig. 1. The proposed terahertz active metamaterials. (a) Simulation results for THz transmittance at various bias voltage. (b) C-V characteristics of MSM-2DEG varactor.

Acknowledgements This work was supported by the Samsung Research Funding Center of Samsung Electronics under Project SRFC-IT1401-08.

REFERENCES

1. Tonouchi, M., "Cutting-edge terahertz technology," *Nat. Photon.*, Vol. 1, 97–105, 2007.
2. Zheludev, N. I. and Kivshar, Y. S., "From metamaterials to metadevices," *Nat. Mater.*, Vol. 11, 917-924, 2012.
3. Rahm, M., Li, J., and Padilla, W. J., "THz Wave Modulators: A Brief Review on Different Modulation Techniques," *J Infrared Millim Terahertz Waves*, Vol. 34, No. 1, 1-27, 2013.
4. Hwang, J. H., "Balanced MSM-2DEG Varactors Based on AlGaN/GaN Heterostructure With Cutoff Frequency of 1.54 THz," *IEEE Elect. Dev. Lett.*, Vol. 38, No. 1, 107-110, 2017.
5. Ambacher, O., Majewski, J., Miskys, C., Link A., Hermann M., Eickhoff M., Stutzmann M., Bernardini F., Fiorentini V., Tilak V., Schaff B., and Eastman L. F., "Pyroelectric properties of Al(In)GaN/GaN hetero- and quantum well structures," *J. Phys. Condens. Matter*, Vol. 14, 3399-3434, 2002.

Near-field acoustic microscope for sub-wavelength imaging based on extraordinary transmission in zero-mass metamaterials

T. Devaux[1], J.J. Park[2], S.H. Lee[2], and O.B. Wright[1]

[1]Division of Applied Physics, Faculty of Engineering, Hokkaido University, Sapporo 060-8628, Japan
[2]Institute of Physics and Applied Physics, Yonsei University, Seoul 120-749, Korea
thibaut.devaux@eng.hokudai.ac.jp

Abstract— Using the principle of extraordinary transmission through a zero-mass metamaterial, a prototype of a near-field acoustic microscope is proposed and built for the audible frequency range. Experimental results reveal the detection of objects of sub-wavelength size ($\sim \lambda/20$) by use of a simple reflection coefficient measurement. This method allows one to work at high resolution compared to the far-field diffraction limit, and introduces new perspectives in acoustic imaging and non-destructive testing.

Concentrating energy through a spot much smaller than the wavelength, so-called extraordinary transmission (ET), has been a recent subject of much interest for both optical and acoustic waves [1, 2]. In particular, ET acoustic audio energy transmission in air was achieved using zero-mass metamaterials [3]. A transmission of ∼80 % of the incident acoustic energy was demonstrated with a filling fraction of only 1%. Here we demonstrate a prototype of a near-field acoustic microscope based on audio ET that allows $\sim \lambda/20$ resolution near 2000 Hz.

In the setup described in [3], acoustic energy is transmitted through a subwavelength hole containing a tensioned membrane maintained by the acoustic wave at the membrane resonance frequency. Our near-field acoustic microscope, as shown on Fig.1, is based on the same concept.

It is composed of an 100-mm internal diameter acrylic tube closed at one end by an anechoic

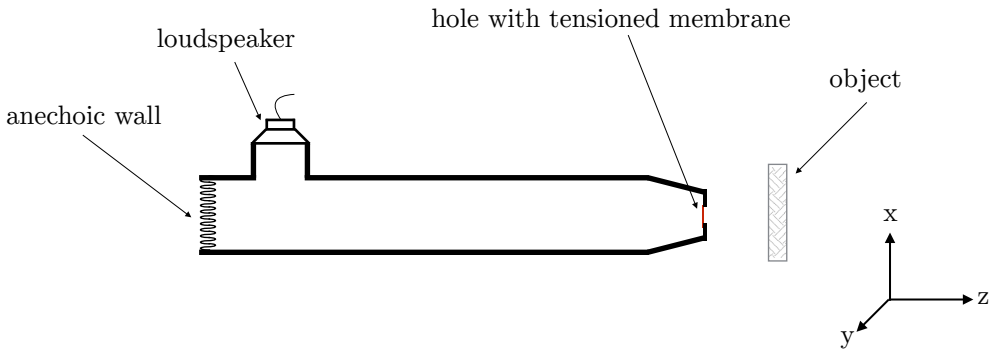

Figure 1: Schematic diagram of the experimental setup. The reflection coefficient of the hole with a tensioned membrane is measured inside the tube with a probe microphone.

wall and at the other end by an hole of diameter 10.5 mm covered with a tensioned membrane. A loudspeaker at the opposite end to the hole provides the audio excitation. The resonance frequency of the tensioned membrane is experimentally determined as $f_r = 1785$ Hz ($\lambda = 0.19$ m), corresponding to a hole diameter of $\lambda/18$.

The principle of microscope is as follows: with no object present in front of the membrane, the zero-mass metamaterial facilities the acoustic energy transmission, so the acoustic reflection coefficient is lowered compared to a bare hole. If an object is placed near the membrane, it frustrates the ET and results in a higher reflection coefficient. To verify this principle, the modulus of the acoustic amplitude reflection coefficient $|R|$ was experimentally determined from the standing wave ratio (SWR) using a probe microphone in the tube.

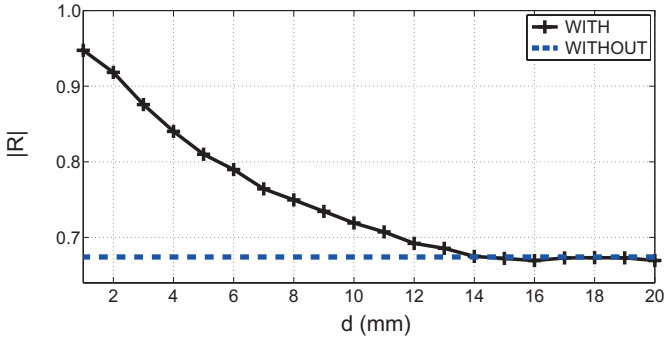

Figure 2: Reflection coefficient of the microscope as a function of the object position d along the z-axis at a frequency of 1785 Hz. The results without any object present are shown by the dashed line.

Figure 2 shows the microscope response when varying the distance between the object position and the membrane (along what we term the z-axis). In the acoustic near-field (i.e. $d \lesssim 15$ mm), the object position influences the reflection coefficient, as expected. $|R|$ decreases monatonically from a maximum value of 0.95 as z increases. For greater object distances, the object position has a negligible influence on $|R|$, and $|R|$ tends to the value (0.67) obtained with no object present. The object position along the z-axis can be deduced by a suitable calibration of these results.

An ET-based scanning acoustic microscope for mapping topography modifications along the x-y-axes can be made by lateral motion of this ET probe. We have demonstrated experimentally that images can be obtained in this way using commonly available materials such as metal, wood and plastic. A lateral resolution of $\sim$10 mm, i.e. $\sim \lambda/20$ could be obtained.

In conclusion, a near-field acoustic microscope based on extraordinary acoustic transmission through a tensioned membrane is proposed with deeply sub-wavelength spatial resolution. By simple measurement of the acoustic reflection coefficient in a tube, one can determine the object position. In future, the use of higher frequencies in the ultrasonic region should expand the possible applications of this microscope.

REFERENCES

1. C. Genet and T. Ebbesen, "Light in tiny holes", *Nature*, 68, 39-46, 2007.
2. M.-H. Lu et al., "Extraordinary acoustic transmission through a 1d grating with very narrow apertures", *Phys. Rev. Lett.*, 99, 174301, 2007.
3. J. J. Park, K. J. B. Lee, O. B. Wright, M. K. Jung and S. H. Lee, "Giant acoustic concentration by extraordinary transmission in zero-mass metamaterial", *Phys. Rev. Lett.* 110, 244302, 2013.

Accurate Prediction of Longitudinal Electromagnetic Mode Profile Sculpting in Wire Media

Jonathan Gratus[1,3], **Taylor Boyd**[1,3], **Paul Kinsler**[1,3], **Rosa Letizia**[2,3]

[1]Physics Department, Lancaster University, Lancaster LA1 4YB, United Kingdom
[2]Engineering Department, Lancaster University, Lancaster LA1 4YB, United Kingdom
[3]Cockcroft Institute, Daresbury, WA4 4AD, United Kingdom
j.gratus@lancaster.ac.uk

Abstract— Using a wire medium with high dielectric wires of varying radius, we can sculpt the longitudinal electromagnetic wave profile. Such sculpted wave profiles have applications in signal processing and accelerator physics. The required design modulation of the wires was calculated using concepts of spatial dispersion, and full 3D CST Studio simulations of the structures were run. Predictions and simulations were in excellent agreement, validating our design process.

In a uniform waveguide the mode profiles along the propagation axis are sinusoidal. Here we show how to customize the wave profile, a process with many possible applications [1, 2, 3, 4]: e.g. a flatter profile like that in figure 1(a) enables us to reduce non linear effects. Further, when controlling the bunch properties in particle accelerators, it would mean that more of the bunch receives the same energy boost, so that it could be used to accelerate longer bunches. In contrast, a peakier profile such as that in fig. 1(b) could be used to enhances nonlinear effects; it would also enhance the signal to noise ratio. In accelerators, it would help in the acceleration of short bunches. Another example is the triangular profile in fig. 1(c), which gives a longer bunch a sustained chirp Further, this wave profile shaping could have utility in high harmonic generation [5].

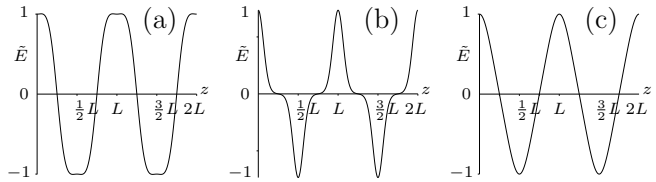

Figure 1: Solutions to Mathieu's equations showing a (a) flatter, (b) peakier and (c) triangular profiles.

Existing methods of mode profile shaping include varying the geometry of the waveguide and adding multiple sinusoidal modes. We consider longitudinal modes in a wire medium with varying radii. The wires had a high dielectric constant. We modelled the three dimensional wire medium using a one dimensional spatially dispersive medium with permittivity of the form

$$\epsilon_{\mathrm{r}}(\omega,k) = 1 + \frac{\omega_{\mathrm{P}}^2}{-\omega^2 + k^2 + \omega_0^2} \tag{1}$$

There exist solutions of the form $\boldsymbol{E} = Ee^{-i\omega t+ikz}\boldsymbol{k}$, $\boldsymbol{D} = 0$ and $\boldsymbol{B} = 0$, so that $\epsilon_{\mathrm{r}}(\omega,k) = 0$. I.e. it is an ENZ medium and the dispersion relation is $\omega^2 - k^2 = \omega_{\mathrm{P}}^2 + \omega_0^2$.

We used CST Microwave studio to examine the modes in a uniform wire. This revelaed a large number of different modes, with a great range of mode profiles and dispersion properties.

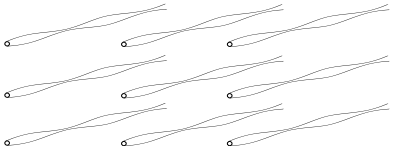

Figure 2: A wire media with varying radii.

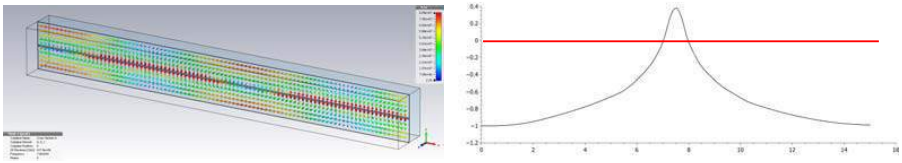

Figure 3: CST simulations of the electric field for a wire medium with fixed radius. This field has the desired properties. (Right) The strength of the electric field as one passes along a line through the wire.

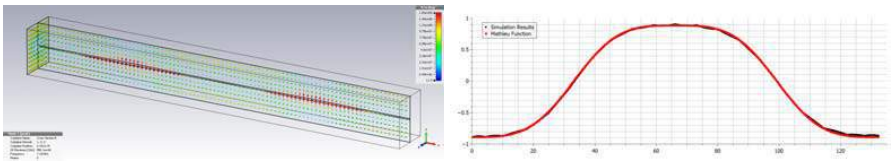

Figure 4: Flat profile: 3D fields from CST simulations (left), and a comparison of predicted (red) and simulated (black) longitudinal electric fields.

A detailed and exhaustive search though these possibilities showed that some of them had the desired properties. It turns out a good case was when the wires are thin and have high $\epsilon_{\rm r}$. We set period $\Delta x = 11$mm, $\Delta y = 15$mm, $\Delta z = 52$mm and $\epsilon_{\rm r} = 1200$. Periodic boundary conditions $\kappa_x = \kappa_y = 360°$, varying κ_z between 0 and 180°. The wire diameter were around 2mm. The wires were in the z-direction. One such is shown in figure 3, in which we can see that:

- The field away between the wires was longitudinal, as needed for on-axis particle acceleration
- Most of the field was between the wires, where it is needed; it is not a wire-localised
- The dispersion relation above is given by to a high degree of accuracy.
- One could control this dispersion by varying the thickness of the wires.

By making the radius depend on position we would get a permittivity that depends both on position z and wave-number k; a scenario that raises interesting issues [2, 6]. We handle it here Fourier transforming the dispersion relation and setting $\Lambda(r(z)) = \omega_{\rm P}(z)^2 + \omega_0^2$; so that we have

$$\tilde{E}'' + \left[\omega^2 - \Lambda\big(r(z)\big)\right]\, \tilde{E} = 0. \tag{2}$$

In all three cases for the wire variation designed to give flat (fig. 4), peakier and triangular profiles, we found very good agreement from frequency domain CST simulations.

Conclusion: We have shown it is possible to sculpt the electric field for longitudinal modes in a 3D wire medium; with results very close to predictions from a 1-dimensional spatially dispersive medium. Our aim is now to verify these modes experimentally.

ACKNOWLEDGMENT

The authors are grateful for the support provided by STFC (the Cockcroft Institute ST/G008248/1), EPSRC (the Alpha-X project EP/J018171/1 and EP/N028694/1) and the Lancaster University studentship program. Figures 3 and 4 are used with permission from [7].

REFERENCES

1. Gratus, J., et al, Letizia, R., McCormack, M., "Spatially dispersive inhomogeneous dielectric wire media with periodic structure," *PIERS 2015 Proceedings.*
2. Gratus, J., McCormack, M., "Spatially dispersive inhomogeneous electromagnetic media with periodic structure," *J. Optics* Vol 17, 25105 2015.
3. Gratus, J., Kinsler, P., Letizia, R., Boyd, T., "Electromagnetic mode profile shaping in waveguides," *Appl. Phys. A* Vol. 123, 108 2017; also see *EMTS2016 Proceedings.*
4. Gratus, J., et al., "Customised Mode Profiles Using Functional Materials," arXiv:1607.04313
5. Radnor, S., et al, "Carrier-wave self-steepening & applications to HHG," *Phys. Rev. A* Vol. 77, 033806 2008.
6. Gratus, J., Tucker, R., "Covariant constitutive relations and relativistic inhomogeneous plasmas," *J. Math. Phys.* Vol. 52, 042901 2011.
7. Gratus, J., Kinsler, P., Letizia, R., Boyd, T., "Customised Mode Profiles," internal report.

Multiband band-stop filters for spoof surface plasmon polaritons

Jiandong Li, Xiaopeng Shen*,Haipeng Li, Kui Han, Chuanlei Jia

School of Physics, China University of Mining and Technology, Xuzhou 221116, China
*corresponding author: xpshen@cumt.edu.cn

Abstract-Ultrathin corrugated metallic strip supports the propagation of spoof surface plasmon polaritons (SSPPs). Band-stop filter or band-rejection filter is a filter that passes most frequencies unaltered, but attenuates those in a specific range to very low levels, it's key component and play a very important role in various communication and radar systems. In this report, we will demonstrate a new type of multiband bandstop filters for SSPPs in the microwave frequency regime. The simulated, measured, and the resonator theory calculated resonant frequencies are in good agreement. The proposed planar filters play an important role for filtering surface plasmon polaritons (SPPs) waves in plasmonic circuits and systems.

REFERENCES

1. X. Shen, T. J. Cui, D. Martin-Cano, and F. J. Garcia-Vidal, "Conformal surface plasmons propagating on ultrathin and flexible films," Proc Natl Acad Sci U S A, vol. 110, pp. 40-5, Jan 02 2013.
2. X. P. Shen and T. J. Cui, "Planar plasmonic metamaterial on a thin film with nearly zero thickness," Applied Physics Letters, vol. 102, p. 211909, May 27 2013.
3. L. Zhao, X. Zhang, J. Wang, W. Yu, J. Li, H. Su, et al., "A Novel Broadband Band-pass Filter Based on Spoof Surface Plasmon Polaritons," Scientific Reports, vol. 6, p. 36069, Oct 31 2016.

Frequency Switchable Microfluidic Metamaterial-Loaded QMSIW Bandpass Filter Using a Liquid Metal Alloy

M. U. Memon, and S. Lim*
School of Electrical and Electronics Engineering, Chung-Ang University, Republic of Korea
*corresponding author: sungjoon@cau.ac.kr

Abstract- Frequency-switchable metamaterial-loaded quarter-mode substrate-integrated-waveguide (QMSIW) band-pass filter is proposed. A liquid metal inside microfluidic channel is used for switching. The microfluidic channels are built using the elastomer polydimethylsiloxane (PDMS) and 3D printed channel molds. This structure has two states. Before injection of the liquid metal, the recorded fractional bandwidth and center frequency of filter are 6.80% and 2.205 GHz, respectively. After injecting liquid metal, the frequency changes from 2.205 GHz to 2.56 GHz.

Figure 1 shows the dimensions of the proposed metamaterial-loaded QMSIW bandpass filter, which is composed of two different substrates. The relative permittivity, thickness, and dielectric loss of the Duroid-5880 substrate are 2.2, 0.51 mm, and 0.0009, respectively. The PDMS substrate is attached on top of the Duroid-5880 substrate to form the microfluidic channels. The relative permittivity, thickness, and dielectric loss of PDMS are 2.8, 1 mm, and 0.02, respectively. The resonant frequency of the QMSIW cavity at the TE_{100} dominant mode is given by [1], [2], [3]:

$$f_{100,QMSIW} = \frac{1}{2\pi\sqrt{\mu\varepsilon}}\sqrt{\left(\frac{\pi}{W_{QMSIW}+\Delta W}\right)^2+\left(\frac{\pi}{L_{QMSIW}+\Delta L}\right)^2} \quad (1)$$

A second-order band-pass filter was implemented using metamaterial-loaded QMSIW cavities with a center frequency of 2.205 GHz, fractional bandwidth of 7.71%, and two transmission zeros at 2.19 GHz and 2.25 GHz. An insertion loss of less than 1.65 dB with an in-band and a return loss greater than 19 dB were achieved.

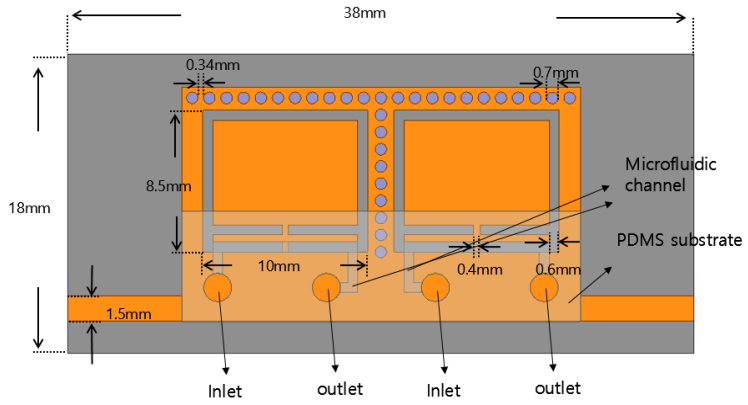

Figure 1. Layout of the proposed metamaterial-loaded QMSIW bandpass filter.

Figure 2a shows the fabricated QMSIW metamaterial filter prototype. The return loss and insertion loss of the filter are recorded using an Anritsu MS2038C vector network analyzer. Figure 2b shows the simulated and measured S-Parameters of the proposed filter along with their comparison. The recorded fractional bandwidths and center frequency are 6.80% and 2.205 GHz, respectively. Two transmission zeros are recorded at 2.18 GHz and 2.25 GHz. An insertion loss of less than 1.8 dB with an in-band and a return loss greater than 14 dB are achieved.

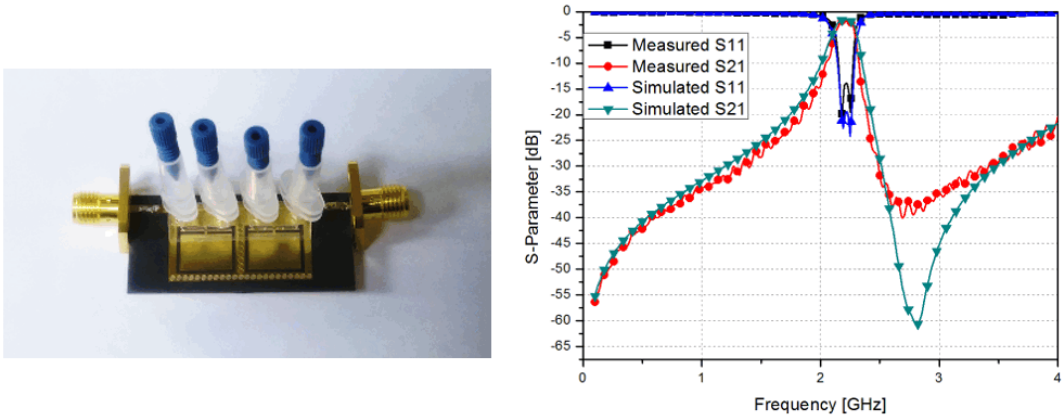

(a) (b)

Figure 2. (a) Fabricated metamaterial-loaded QMSIW filter prototype and (b) simulated and measured S-parameters of the proposed filter.

After the removal of the liquid metal, a small amount of liquid metal remained on the PDMS surface. However, it did not come in contact with the metamaterial directly. Therefore, the measured S-parameter results before and after injecting the liquid metal are practically the same.

Acknowledgements: This research was supported by the MSIP (Ministry of Science, ICT and Future Planning), Korea, under the ITRC (Information Technology Research Center) support program (IITP-2016-H8501-16-1007) supervised by the IITP (Institute for Information and Communications Technology Promotion) and the National Research Foundation of Korea (NRF) grant funded by the Korea government (MSIP) (No. 2014R1A2A1A11050010).

REFERENCES

1. Memon, M.U. and S. Lim, "Review of reconfigurable substrate-integrated-waveguide antennas," *J. Electromagn. Waves Appl.*, Vol. 28, 1815–1833.
2. Memon, M.U. and S. Lim, "Frequency-Tunable Compact Antenna Using Quarter-Mode Substrate Integrated Waveguide," *IEEE Antennas Wirel. Propag. Lett.,* Vol. 14, 1606–1609.
3. Guo, Z., Chin, K. S. Che, W. and C. C. Chang, "Cross-coupled bandpass filters using QMSIW cavities and S-shaped slot coupling structures," *J. Electromagn. Waves Appl.,* Vol. 27, 160–167.

Dispersion-free Tunable Beam Splitter with Gate-controlled Graphene Metadevices

Soojeong Baek[1], Hyeon-Don Kim[1], Kanghee Lee[1], Jagang Park[1], and Bumki Min[1]

[1]Department of Mechanical Engineering, Korea Advanced Institute of Science and Technology(KAIST), Daejeon 305-701, Republic of Korea.

[*]corresponding author: bmin@kaist.ac.kr

Abstract- In this study, we propose a broadband tunable beam splitter, where metamaterials and graphene are hybridized to modulate the splitting ratio in electrically tunable manner.

Terahertz time-domain spectroscopy is dubbed a compelling tool for investigating chemical and physical phenomena. Despite the rapid development of terahertz research, the development of related optical component is still at a late stage. Terahertz beam splitter which is indispensable for interferometers, has recently been suggested. However, in the case of such a beam splitter, the characteristics of the beam splitter are dependent on the specific frequency due to the Fabry-Perot effect. Since temporal distortion of the transmitted terahertz pulse follows such a frequency dependence, the use of a beam splitter with low dispersion characteristics is required. Moreover, once it was fabricated, the splitting ratio could not be changed.

Researches on the modulation of transmission by hybridizing metamaterial with graphene have been proposed. In the case of these studies, there was no focus on modulating the ratio of transmittance to reflectivity even with broadband characteristics. In addition, if the doping concentration of the graphene is changed, the dispersion also changes accordingly. Therefore, it is demanding to modulate the splitting ratio while having nondispersion with transmittance and reflectivity in a wide band. In this regard, we propose broadband THz tunable power splitters based on gated-graphene metadevices. Splitting ratio of the beam splitter can be electrically-modulated. The proposed metadevices were designed to reduce dispersion by combining resonant metamaterials considering the characteristics of transmission modulation according to the Fermi-level change of graphene.

Acknowledgements The work was supported by Pioneer Research Center Program (2014M3C1A3052537) and Quantum Metamaterials Research Center Program (No.2015001948) through the National Research Foundation of Korea (NRF) grant funded by the Korea Government (MSIP). The work was also supported by the center for Advanced Meta-Materials (CAMM) funded by Korea Government (MSIP) as Global Frontier Project (CAMM 2014M3A6B3063709).

REFERENCES

1. Kampfrath, T., et al. "Resonant and nonresonant control over matter and light by intense terahertz transients." *Nature Photonics,* Vol. 7, No. 9, 680-690, 2013.
2. Homes, Christopher C., et al. "Silicon beam splitter for far-infrared and terahertz spectroscopy." *Applied optics,* Vol. 46, No. 32, 7884-7888, 2007.
3. Ung, Benjamin S., et al. “Low-cost ultra-thin broadband terahertz beam-splitter.” *Optics express,*

Vol. 20, No. 5, 4968-4978
4. Lee, Seung Hoon, et al. "Broadband modulation of terahertz waves with non-resonant graphene meta-devices." *IEEE Transactions on Terahertz Science and Technology,* Vol. 3, No. 6, 764-771, 2013.

High-efficiency circular polarizer based on dielectric Huygens surface in microwave band

Huan Jiang[1], Wenyu Zhao[1], and Yongyuan Jiang[1, 2]

[1]Department of Physics, Harbin Institute of Technology, Harbin, China
[2]Key Lab of Micro-Optics and Photonic Technology of Heilongjiang Province, Harbin, China
*corresponding author, E-mail: jiangyy@hit.edu.cn

Abstract

Most previously reported circular polarizers are designed by equivalent circuit model in the microwave region. Here, we demonstrate an all-dielectric circular polarizer with high efficiency and broadband response in the microwave region by leveraging the recently developed Huygens surface. Due to the symmetry breaking of structure in the light propagation, right circularly polarized (RCP) light can pass through freely, while left circularly polarized (LCP) light is largely blocked in the broad band of 46.5-54.6 GHz. The high polarization transmission originates from the simultaneous excitation of the Mie-type electric and magnetic resonances in the rotationally twisted strips array with MgF_2 spacer. The device possesses the merits of high efficiency and simple inclusions, which represents a major advance.

1. Introduction

Circular polarizers are the devices who transmit one state of the circularly polarized light (CPL) and completely block the other state CPL. Conventionally, two most common methods to generate circularly polarized light are cholesteric liquid crystals and a combination of linear polarizer with a quarter-wave plate [1]. The performance of cholesteric liquid crystals is further limited by their high viscosity and poor chemical stabilities. To overcome these limitations on traditional circular polarizer, matermaterials based circular polarizers come to researchers' eyes [2-5]. Most circular polarizers are composed of metal components for the advantages of subwavelength thickness and scalability [3-5]. This will inevitably suffer from strong Ohmic loss and the absence of magnetic response. The intrinsic absorptive loss leads to low transmission efficiency and dissymmetry factor, which is defined as $g = 2(T_L - T_R)/(T_R + T_L)$ (T_L, T_R represent the transmission of LCP and RCP light) [6]. For the nature of lacking magnetic response in metal structure, one has to design the polarization devices with complex structures [7], which are difficult to fabricate and preclude further practical application. Another problem is that the principle of circular polarizers in microwave band are limited in equivalent circuit model [8-10].

To solve these problems, we leverage all-dielectric materials, following the principle of Huygens surface rather than equivalent circuit model, to construct high efficiency and broadband response circular polarizers in microwave band. The high efficiency and broadband response of the circular polarizer originates from the simultaneous excitations of electric and magnetic resonances in the all-dielectric rotationally twisted strips. Symmetric breaking of the Huygens metamaterial leads to the significant difference in transmissions between LCP and RCP wave. Furthermore, all-dielectric metamaterial inherently with electric and magnetic resonances extremely simplify the structure compared with previously reported circular polarizers [11,12]. The proposed circular polarizer shows high polarization transmission ($T_{L\max} = 0.99$) and dissymmetry factor ($g = -1.89$), which means the extension of theoretical method for designing circular polarizer by Huygens surface.

2. Design and simulations

Huygens' principle, treating each point on a wavefront as a secondary source of outgoing waves, is developed by Love and Schelkunoff to specify the secondary sources in terms of fictitious electric and magnetic currents fulfilling rigorous boundary condition. In Huygens' surface, certain equivalent electric and magnetic currents are obtained by designing electric and magnetic dipole resonances with suitable surface polarizabilities [13-15]. Since fields are vectorial at the surface, the general forms of electric and magnetic polarizabilities are tensorial [16]. The transmission coefficients of x- and y-polarized incident light can be controlled independently by electric and magnetic surface polarizabilities [17,18]. In other words, arbitrary polarization transmission can be engineered at will by constructing suitable electric and magnetic polarizabilities [19]. To gain polarization transmission selectivity, we arranged a rotational twist between two strips to break the symmetry of the structure.

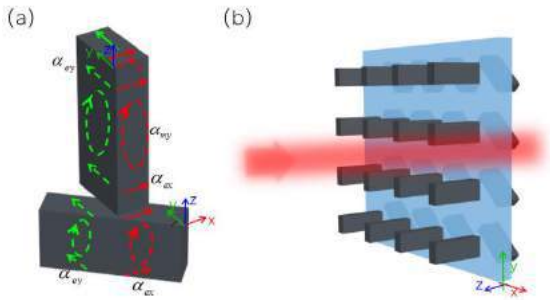

Fig. 1. (a) The design methodology of the circular polarizer. The circles represent the magnetic dipole resonances and the arrows represent the electric dipole resonances. These resonances are excited by the incident waves polarized along x- and y- direction. (b) 3-D scheme of the proposed circular polarizer with two twisted silicon strips arrays on a MgF_2 substrate and the period is 4400 μm.

Figure 1(a) illustrates the design methodology of the circular polarizer. Silicon strips supporting simultaneous excitation of electric and magnetic dipole resonances in each layer for both TE and TM modes are chosen as the basic unit cell of the circular polarizer. The incident CPL can be decomposed into two perpendicular components along x and y directions. Each component will excite corresponding electric and magnetic dipole resonances and they will superimpose together without cross coupling. The fields scattered by orthogonal electric and magnetic dipole resonances can be homogenized by effective electric and magnetic polarizabilities. Fig. 1(b) shows the 3-D scheme of the proposed circular polarizer with two twisted silicon strips arrays on a MgF_2 spacer and the period of the structure is 4400 μm in both x and y directions. The thicknesses of the two strips are 5350 μm and 1650 μm respectively, and the thickness of spacer between two layers is 2000 μm. The Huygens metamaterial is excited by CPL propagating in the direction of -z. Refractive index of silicon strips is 3.5 in the near-infrared range, while the substrate media is MgF_2 (n=1.3) [20]. Transmission spectra and excitations of associated electric and magnetic dipole resonance modes were simulated at the frequency from 46 to 55 GHz using commercial software, CST Microwave Studio. The simulation is based on a frequency-domain finite integration technology (FIT) using a unit cell boundary coupled with the Floquet port, and E-Field monitor and H-Field monitor are used at 54 GHz to detect the distribution of electric and magnetic fields.

3. Results and discussion

Figure 2(a) shows the transmission spectra of the all-dielectric cascaded tensor Huygens surface under the excitation of normal incident CPL. The blue and red lines represent the transmission of LCP light and RCP light, respectively. The transmission of RCP light is above 0.8 in the broad band of 46.5-54.6 GHz, and the maximum transmission of RCP light reaches 0.99 at 48.7 GHz, while the transmission of LCP light is below 0.2. Dissymmetry factor, the key parameter of circular polarizer, further shows the transmitted difference between LCP and RCP light in Fig. 2(b). The maximum dissymmetry factor reaches -1.89 at 54 GHz, which means good performance in polarization selective transmission is obtained in the proposed structure. The high transmission of RCP light results from the spectral overlapping of tensorial electric and magnetic resonances in both layers. The electric field components of orthogonal electric and magnetic dipole resonances are in the same direction, and the contributions of electric, magnetic resonances and the incident electric field in both layers lead to a wideband and nearly unit transmission. Meanwhile, the symmetry breaking in rotationally twisted strips leads to low transmission for LCP light. This is because the electric field components of electric and magnetic resonances are weak, especially in the second layer.

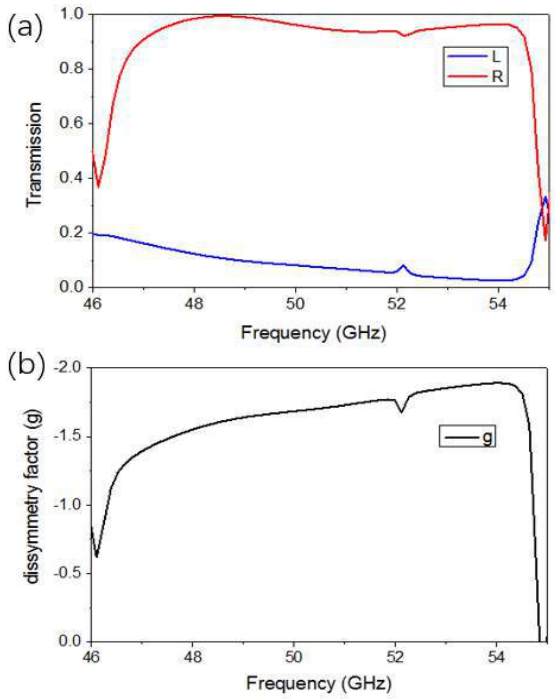

Fig. 2. (a) Transmission spectra of proposed structure simulated by CST. Red and blue lines represent transmission spectra of RCP and LCP light, respectively. (b) Dissymmetry factor spectra of the proposed circular polarizer.

Figure 3 further clarify the origin of the difference in polarization transmission. The black dashed frames in crosscuts along -z direction represent the strips in the proposed structures. Typical electric dipole mode characteristics with opposite polarization charges accumulated at the edges outside resonators and magnetic fields confined at the center of resonators, which mimicked the radiation pattern of electric dipole in the far-field. While the magnetic dipole mode characteristics with polarization charges formed a circle inside strips and the magnetic fields focused inside the resonators. The confined electric fields at the center and the accumulated polarization charges at the edges outside the two-layer strips in Fig. 3(a), (b) represent the magnetic and electric dipole modes in x-z and y-z

planes under the excitation of RCP light. Moreover, the local magnetic fields enhancement at the center of resonators in Fig. 3(e), (f) further demonstrate the simultaneous excitations of electric and magnetic dipole resonances in both x-z and y-z planes of two layers, which is in consistent with the design methodology as shown in Fig. 1(a). Fig. 3(c), (d), (g) and (h) also show the electric and magnetic dipole resonances exist simultaneously in the x-z and y-z planes under the excitation of LCP light. But differently, electric and magnetic resonances of LCP wave is much weaker than the resonances of RCP, especially in the second layer. This is why the transmission of RCP wave is near unit but the transmission of LCP is near zero.

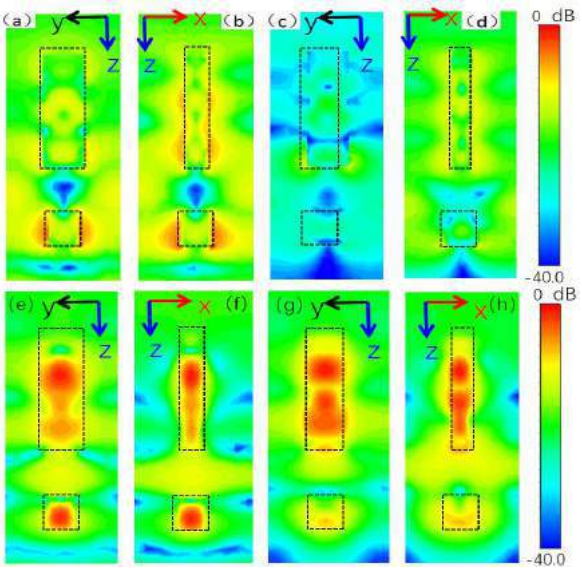

Fig. 3. Field distribution of a unit cell at 54 GHz. (a), (b) absolute value of electric field driven by RCP light at y-z plane and x-z plane, respectively. (c), (d) absolute value of electric field driven by LCP light at y-z plane and x-z plane respectively. (e), (f) absolute value of magnetic field driven by RCP light at y-z plane and x-z plane respectively. (g), (h) absolute value of magnetic field driven by LCP light at y-z plane and x-z plane respectively.

4. Conclusions

In conclusion, a high-efficiency, wideband circular polarizer operating in the microwave band is numerically demonstrated in this paper. The cascaded tensor Huygens surface with asymmetric all-dielectric strips passes nearly all RCP light and blocks most LCP light. The polarization transmission of RCP wave is up to 0.99, which results from the spectral overlapping of the electric and magnetic resonances in both layers. The symmetry breaking of rotationally twisted strips leads to the transmitted difference between LCP and RCP light. The high-efficiency circular polarizer with simple inclusions makes great progress in performance compared to the previously reported structures and paves a way to construct polarization devices by cascading tensor Huygens surfaces with all-dielectric materials.

References

[1] A. Saha, K. Bhattacharya, and A. K. Chakraborty, "Reconfigurable achromatic half-wave and quarter-wave retarder in near infrared using crystalline quartz plates," *Optical Engineering*, vol. 50, no. 3, pp. 034004-034004-4, 2011.

[2] H. Jiang, W. Zhao, and Y. Jiang, "All-dielectric circular polarizer with nearly unit transmission efficiency based on cascaded tensor Huygens surface," *Optics Express*, vol. 24, no. 16, pp. 17738-17745, 2016.

[3] J. Y. Chin, M. Lu, and T. J. Cui, "Metamaterial polarizers by electric-field-coupled resonators," *Applied Physics Letters*, vol. 93, no. 25, pp. 251903, 2008.

[4] X. Huang, D. Yang, and H. Yang, "Multiple-band reflective polarization converter using U-shaped metamaterial," *Journal of Applied Physics*, vol. 115, no. 10, pp. 103505, 2014.

[5] S. Yan, and G. A. Vandenbosch, "Compact circular polarizer based on chiral twisted double split-ring resonator," *Applied Physics Letters*, vol. 102, no. 10, pp. 103503, 2013.

[6] M. Wakabayashi, S. Yokojima, T. Fukaminato, K.-i. Shiino, M. Irie, and S. Nakamura, "Anisotropic dissymmetry factor, g: Theoretical investigation on single molecule chiroptical spectroscopy," *The Journal of Physical Chemistry A*, vol. 118, no. 27, pp. 5046-5057, 2014.

[7] M. Selvanayagam, and G. V. Eleftheriades, "Design And Measurement of Tensor Impedance Transmitarrays For Chiral Polarization Control," *IEEE Transactions on Microwave Theory and Techniques*, vol. 64, no. 2, pp. 414-428, 2016.

[8] J. Q. Hou, L.-F. Shi, S. Chen, and Z.-R. Gou, "Compact broadband circular polariser based on two-layer frequency-selective surfaces," *Electronics Letters*, vol. 51, no. 15, pp. 1134-1136, 2015.

[9] M. Letizia, B. Fuchs, C. Zorraquino, J.-F. Zurcher, and J. R. Mosig, "Oblique incidence design of meander-line polarizers for dielectric lens antennas," *Progress In Electromagnetics Research B*, vol. 45, pp. 309-335, 2012.

[10] L. Martinez-Lopez, J. Rodriguez-Cuevas, J. I. Martinez-Lopez, and A. E. Martynyuk, "A multilayer circular polarizer based on bisected split-ring frequency selective surfaces," *IEEE Antennas and Wireless Propagation Letters*, vol. 13, pp. 153-156, 2014

[11] J. Wang, Z. Shen, W. Wu, and K. Feng, "Wideband circular polarizer based on dielectric gratings with periodic parallel strips," *Optics Express*, vol. 23, no. 10, pp. 12533-12543, 2015.

[12] A. S. Chadha, D. Zhao, and W. Zhou, "Comparative study of metallic and dielectric helix photonic metamaterial," *Optical Materials Express*, vol. 4, no. 12, pp. 2460-2467, 2014.

[13] C. Pfeiffer, and A. Grbic, "Metamaterial Huygens' surfaces," *Microwave Symposium Digest (IMS)*, IEEE MTT-S International, pp. 1-4, 2013.

[14] C. Pfeiffer, and A. Grbic, "Metamaterial Huygens' surfaces: tailoring wave fronts with reflectionless

sheets," *Physical Review Letters*, vol. 110, no. 19, pp. 197401, 2013.
[15] M. Kim, A. M. Wong, and G. V. Eleftheriades, "Optical Huygens' metasurfaces with independent control of the magnitude and phase of the local reflection coefficients," *Physical Review X*, vol. 4, no. 4, pp. 041042, 2014.
[16] M. Selvanayagam, and G. V. Eleftheriades, "Polarization control using tensor Huygens surfaces," *IEEE Transactions on Antennas and Propagation*, vol. 62, no. 12, pp. 6155-6168, 2014.
[17] M. Selvanayagam and G. Eleftheriades, "Tensor huygens surfaces," *IEEE Antennas and Propagation Society International Symposium APSURSI*, pp. 17–18, 2014.
[18] C. L. Holloway, M. A. Mohamed, E. F. Kuester, and A. Dienstfrey, "Reflection and transmission properties of a metafilm: With an application to a controllable surface composed of resonant particles," *IEEE transactions on electromagnetic compatibility*, vol. 47, no. 4, pp. 853-865, 2005.
[19] M. Decker, I. Staude, M. Falkner, J. Dominguez, D. N. Neshev, I. Brener, T. Pertsch, and Y. S. Kivshar, "Highefficiency light-wave control with all-dielectric optical Huygens' metasurfaces," *arXiv:1405*. 5038, 2014.
[20] E. D. Palik, Handbook of optical constants of solids. *Academic press*, 1998.

CPW-fed metamaterial antenna based on mushroom unit cell for dual applications

B. D. Bala[1], M. K. A. Rahim[2], N. A. Murad[2], H. A. Majid[3], M. E. Jalil[2], O. Ayop[2]

[1]Electrical Engineering Department, Faculty of Engineering,
Kano University of Science and Technology, Wudil, 713281, Kano, Nigeria.
[2]Communication Engineering Department, Faculty of Electrical Engineering,
Universiti Teknologi Malaysia (UTM), 81310, Johor-Bahru, Malaysia.
[3]Department of Electrical Engineering Technology, Faculty of Engineering Technology
Universiti Tun Hussein Onn Malaysia (UTHM), Parit Raja, 86400, Batu Pahat, Malaysia

bdbala2@kustwudil.edu.ng, mkamal@fke.utm.my, asniza@fke.utm.my, mhuda@uthm.edu.my, ezwanjalil@gmail.com, osmanayop@utm.my

Abstract

A coplanar waveguide (CPW) fed metamaterial antenna based on mushroom unit cell for dual band applications is proposed. The mushroom unit cell is etched on the host transmission line to engineered left-handed properties. Two resonant modes at 5.2 GHz and 7.3 GHz are obtained for the negative order resonant (NOR) and positive order resonant (POR) modes respectively. The peak realized gain -3.56 dBi and 2.51 dBi are obtained respectively for NOR and POR modes. The antenna has a compact size of 0.4744λo x 0.4934λo at the resonance frequency of 5.2 GHz. The simulated results of the reflection coefficients and surface current distributions are presented. The antenna is suitable for WLAN applications (5.15 GHz-5.25 GHz).

1. Introduction

With the recent development of modern wireless communication system due band antennas are required in this regards [1]. The concept of metamaterials (MTM) among other techniques was developed and applied to antennas design due to its unparalleled advantages. MTMs offers various advantages such as negative electromagnetic constitutive parameters, zero propagation constants, infinite wavelengths and negative group velocities [2]. However, composite left/right-handed transmission line (CRLH-TL) approach provides an intangible method of implementing small resonant antennas. Apart from size reduction, transmission line based MTM offers resonant modes at positive, zero and negative phase constant which can be used for multiband applications [3] . In [4] a CRLH-TL based dual band antenna was obtained which utilizes NOR and POR mode for dual band applications. In [5] a wideband mushroom based antenna was design by merging POR and NOR mode together.

In this paper, a CPW-fed dual band MTM antenna is presented which is loaded with mushroom unit cell. The antenna is compact in size and support dual resonant modes. The NOR mode resonates at 5.2 GHz and the POR mode resonates at 7.3 GHz. The antenna has potential application for WLAN operations (5.15-5.25 GHz).

2. Design and Analysis of the Mushroom based MTM Antenna

The proposed MTM antenna is shown in Figure 1. The antenna is design on Flame retard FR-4 substrate of dielectric permittivity of 4.3, thickness (h) of 1.6 mm and tangential loss of 0.025. The antenna is CPW fed with a MTM unit cell incorporated on the transmission line to engineered composite right/left-handed properties. The transmission line provides the series right-handed intrinsic inductance L_R and the gap (g) etched on the transmission line due to the Mushroom cell provides the series left handed capacitance C_L. The via process connecting the top mushroom patch and the bottom patch is responsible for the shunt left-handed inductance L_L and the right-handed capacitance C_R is obtained due to the coupling between the top and bottom patch. Bloch-Floquet theorem as in [6] can be used to analyzed the unit cell and obtained the dispersion diagram.

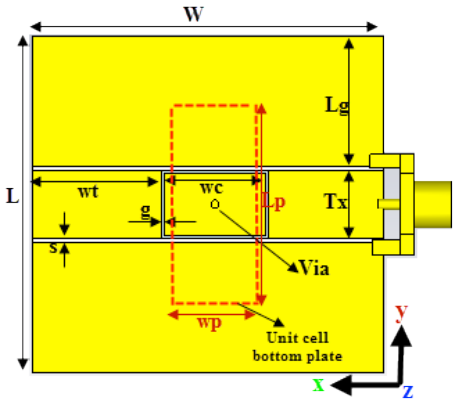

Figure 1: Geometry of the proposed MTM antenna (W = 26 mm, L = 25 mm, Lg = 9.7 mm, wc =7.6 mm, wt = 9.5 mm, h = 1.6 mm, Tx = 5 mm, s = 0.3 mm, g = 0.2 mm, Lp = 16, wp = 6 mm, r = 0.4 mm)

3. Results Discussion

The reflection coefficient of the proposed antenna is shown in Figure 2. The antenna is a dual mode and resonates at 5.2 GHz and 7.3 GHz. The NOR mode at 5.2 GHz is attributed to the left-handed behavior of the composite unit cell while the resonance at 7.3 GHz is due to the right-handed response of the transmission line. The resonance frequency of the NOR can be tuned using the shunt inductance L_L and the POR mode can be tuned through the series intrinsic inductance L_R. Parametric studies on the via which is responsible for the left-handed shunt inductance L_L is investigated in Figure 3. The resonance frequency of the NOR decreases with increase in the inductance of the shorted via from r = 0.4 mm to r = 0.2 mm. The effect of the right-handed series inductance LR on the POR mode is shown in Figure 4. Increase on the length of the signal patch Wt from 25mm to 27 mm decreases the resonance frequency of the POR from 7.28 GHz to 6.50 GHz. The surface current distributions for the resonant modes are shown in Figure 5. High current concentrations can be observed at 5.2 GHz along the shunted via which is a parameter for the NOR. Also, strong current concentrations mainly on the transmission line is indicating that it is the main radiating element as well as parameter for right-handed property. The antennas radiation patterns at both resonant modes for E- and H-plane are shown in Figure 6. A directional pattern is obtained for E-plane and omini-directional pattern for H-plane. The realized gain of -3.5 dBi and 2.51 dBi are obtained for NOR and POR respectively. The radiation efficiencies of 21% and 72% is also obtained for NOR and POR modes respectively. Drops in gain and efficiency of the NOR is due to the un-reflected surface wave cause by the suspended ground plane of the Mushroom cell.

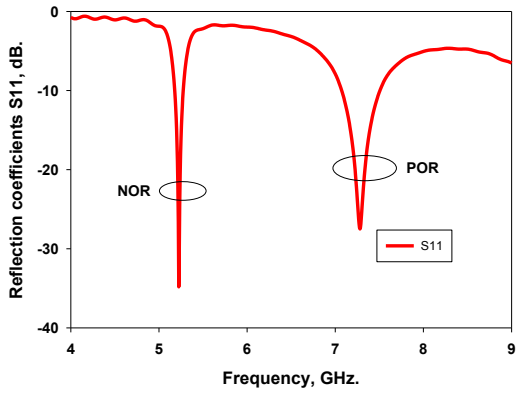

Figure 2: Simulated reflection coefficients of the proposed antenna showing the negative order resonance (NOR) and positive order resonance (POR)

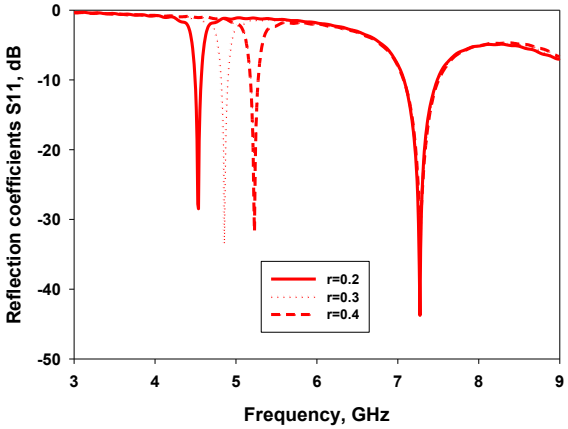

Figure 3: Effect of the Left-handed shunt inductor L_L on the negative order resonance (NOR).

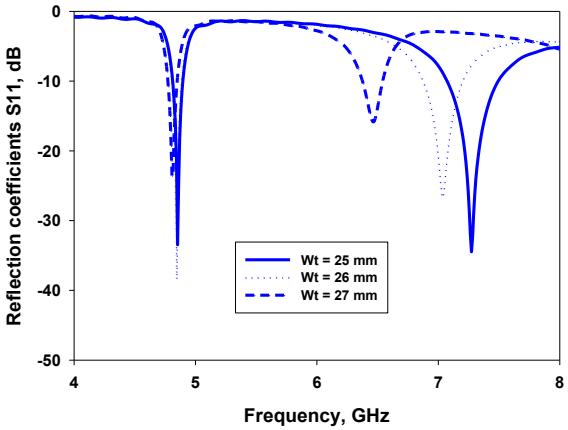

Figure 4: Effect of the series right-handed inductor L_R on the positive order resonance (POR).

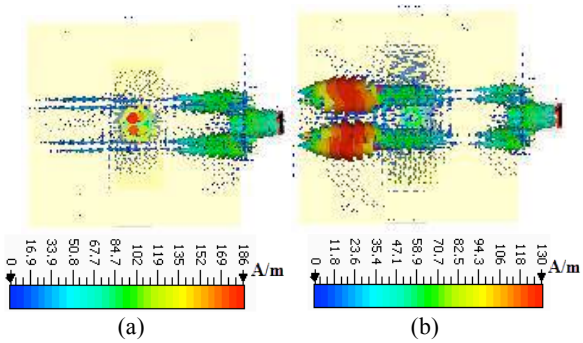

(a) (b)

Figure 5: Surface current distributions (a) NOR at 5.2 GHz (b) POR at 7.3 GHz.

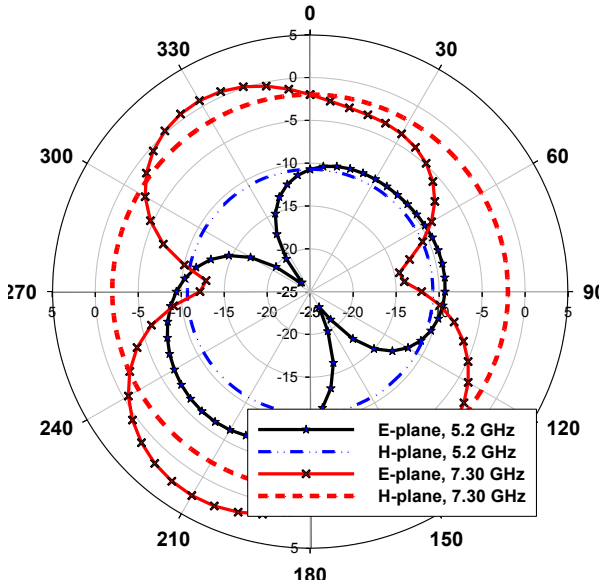

Figure 6: Effect of the series right-handed inductor L_R on the positive order resonance (POR).

4. Conclusions

A CPW fed dual band metamaterial antenna based on mushroom unit cell has been presented. The antenna consists of mushroom unit cell loaded on the host transmission line. The left-handed property was attributed to the composite mushroom cell. The NOR mode was excited by the mushroom cell and the POR was excited by the intrinsic host transmission line. A peak realized gain -3.56 dBi and 2.51 dBi were obtained for NOR and POR modes respectively. The antenna has a compact size of 0.4744λo x 0.4934λo at the resonance frequency of 5.2 GHz. Simulation results presented shows that the designed antenna is suitable for WLAN applications (5.15 GHz-5.25 GHz).

Acknowledgements

This work was supported by Ministry of Higher education (MOHE), Research Management Centre (RMC), Universiti Teknologi Malaysia (UTMJB) Johor Bahru.

References

[1] Y. L. Kuo and K. L. Wong, "Printed double-T monopole antenna for 2.4/5.2 GHz dual-band WLAN operations.," *IEEE Trans. Antennas Propagation.*, vol. vol. 51, no. no. 9, pp. pp. 2187–2192, 2003.

[2] Y. Ryu, J. Park, J. Lee, and H. Tae, "Multiband antenna using +1, -1 and 0 resonant mode of DGS dual composite right/left handed transmission line," *Microw. Opt. Technol. Lett.*, vol. 51, no. 10, pp. 2485–2488, 2009.

[3] B. D. Bala, M. K. A Rahim, and N. A. Murad, "Complementary electric-LC resonator antenna for WLAN applications," *Appl. Phys. A Mater. Sci. Process.*, vol. 117, pp. 635–639, 2014.

[4] B. D. Bala, M. K. A. Rahim, and N. A. Murad, "Composite Right / Left-Handed Dual-Band Metamaterial Antenna with Improved Gain and Efficiency," *Microw. Opt. Technol. Lett.*, vol. 56, no. 7, pp. 1575–1579, 2014.

[5] S. Mok, S. Kahng, and Y. Kim, "A wide band metamaterial ZOR antenna of a patch coupled to a ring mushroom," *J. Electromagn. Waves Appl.*, vol. 26, no. January 2013, pp. 1667–1674, 2012.

[6] C. Caloz and T. Itoh, *Electromagnetic metamaterials: Transmission line theory and microwave applications*. Wiley-IEEE Press, 2005.

Chiral Resonance-Based Microwave Sensors

Mario Gonzalez, Andres Ochoa and Nantakan Wongkasem*

Department of Electrical Engineering, University of Texas Rio Grande Valley, Edinburg, Texas USA
*corresponding author, E-mail: nantakan.wongkasem@utrgv.edu

Abstract

A one turn wire spiral structure is proposed as a sensor element in microwave sensors. Based on the changes of the structure's radius and height, the chiral helical structure is significantly sensitive to circularly polarized waves. The linear optical activity shift is observed within the chirality band. This proposed helical structure is an excellent sensor element to be employed in microwave sensors, which will benefit a multitude of sensor applications.

1. Introduction

Microwave sensors are comprised of a microwave generator and a detecting circuit located before and after the sample [1]. These are then connected to interface circuits and to a computer to analyze the sensing responses. This means that no circuits, wires, tubes, or power supply is needed on the actual sensing element, which gives microwave sensors an advantage over conventional sensing elements.

Metamaterials have been researched as a viable sensing element in microwave sensors using split ring resonators (SRRs). Lee [2] shows how SRRs can be used as sensing elements in the microwave regime. These sensing elements work by measuring the shift in resonance of the structure in response to a structural change to the SSR sensing element. In this way, the structural change can be determined by looking at the electrical response of the structure. This method of sensing is met by problems when introduced into an environment where the sensing element can be affected by multiple sources or contaminants. These problems, however, are addressed by using a chiral structure as the sensing element.

The most well-known chiral structure can be observed in three-dimensional (3D) helix structures [3-8]. This was suggested as a negative refractive index material in the microwave to optical regime. The proposed chiral structure is a much simpler variant of the conventional 3D helix. The chiral structure proposed is a one turn wire helix spiral. Instead of reading the change in resonance frequency, this sensor will read the change in optical activity and give a response to external interaction.

The chiral parameters observed in the simulation results are the circularly polarized transmission coefficients, the polarization azimuth rotation angle, θ, indicating the rotation between the phases of two circular polarized waves and the circular dichroism, η, or the elliptical property, which states the amplitude difference between the two transmission coefficients.

2. Chiral Media

2.1. Optical properties

In order to observe the properties of chiral structures, the mathematical model of bi-isotropic chiral media must be derived. Using this mathematical model in conjunction with simulated or measured results, the optical properties of a structure can be extracted and easily analyzed.

Chiral media belongs to a larger range of bi-isotropic media. The equations that characterize bi-isotropic media are as follows:

$$\mathbf{D} = \epsilon_0\epsilon\mathbf{E} + (\chi + i\kappa)\sqrt{\mu_0\epsilon_0}\mathbf{H} \quad (1)$$

$$\mathbf{B} = \mu_0\mu\mathbf{H} + (\chi - i\kappa)\sqrt{\mu_0\epsilon_0}\mathbf{E} \quad (2)$$

where ϵ is the relative permittivity of the medium and μ is the relative permeability of the medium. The difference between isotropic media and bi-isotropic media in these equations lies in the parameters χ and κ. χ describes the reciprocity of the material, while κ describes the chirality of the material. Because in this instance, we will only be looking at a certain type of bi-isotropic media (Pasteur medium) which has no reciprocity and is chiral, χ will be 0. From these equations, considering Maxwell's equations in the frequency domain and considering plane wave propagation, a wave equation can be obtained for the electric field:

$$\mathbf{k}\times(\mathbf{k}\times\mathbf{E}) = -k_0^2(\epsilon\mu - \kappa^2)\mathbf{E} - 2i\kappa k_0(\mathbf{k}\times\mathbf{E}) \quad (3)$$

where $\mathbf{k}$ is the wavevector in the medium and k_0 is the wavevector in a vacuum. This equation can then be simplified by assuming $\mathbf{k} = k\hat{z}$. The equation then becomes:

$$k_\pm = k_0(n \pm \kappa) \quad (4)$$

The wavevector solution k_+ corresponds to the eigenvector of the RCP wave and k_- corresponds to the eigenvector of the LCP wave. If we were to define the index of refraction of RCP/LCP waves from the relation $k_\pm = n_\pm k_0$, it becomes:

$$n_\pm = n \pm \kappa \quad (5)$$

Next, we need to look at two parameters for chiral media defined as optical activity. This is caused by the rotation of the polarization plane of a linearly polarized light passing through a chiral medium. The first parameter is the polarization azimuth rotation angle of elliptically polarized light, defined as:

$$\theta = \frac{1}{2}\delta = \frac{1}{2}[\arg(T_{++}) - \arg(T_{--})] \quad (6)$$

The first subscript in T indicates the initial polarization and the second subscript indicates the transmitted polarization. This means that T_{++} and T_{--} are the transmission coefficients for RCP and LCP waves respectively.

Because the medium we are working with is chiral (therefore asymmetrical) and the circularly polarized waves are turning as they propagate, LCP and RCP light interacts with the medium differently. We characterize this difference using the difference in absorption and distortion between the two polarizations. This parameter is called circular dichroism. Because we can say the impedance is the same for LCP and RCP waves, the circular dichroism is characterized by the ellipticity of the circular polarization [9].

$$\eta = \frac{1}{2}\sin^{-1}\left(\frac{|T_{++}|^2 - |T_{--}|^2}{|T_{++}|^2 + |T_{--}|^2}\right). \quad (7)$$

2.2. Parameter extraction

In order to extract the previously mentioned chiral parameters, the transmission coefficients for both RCP and LCP waves must be obtained. This can be done directly by exciting the structure with a circularly polarized plane wave using circularly polarized antennas. Another, more common way to obtain the transmission coefficients is to measure the linear cross polarized transmission coefficients and converting them to the circularly polarized transmission coefficients.

The linear cross polarized transmission coefficients are denoted as T_{xx}, T_{xy}, T_{yx}, and T_{yy}, where the first subscript indicates the transmitted field polarization and the second subscript indicates the incident field polarization. Equation (8) shows the conversion from linear transmission to circularly polarized transmission [10].

$$\begin{pmatrix} T_{++} & T_{+-} \\ T_{-+} & T_{--} \end{pmatrix} = \frac{1}{2} \times \begin{pmatrix} (T_{xx} + T_{yy}) + i(T_{xx} - T_{yx}) & (T_{xx} - T_{yy}) - i(T_{xy} + T_{yx}) \\ (T_{xx} - T_{yy}) + i(T_{xy} + T_{yx}) & (T_{xx} + T_{yy}) - i(T_{xy} - T_{yx}) \end{pmatrix} \quad (8)$$

Measurement of the linear cross polarized transmission coefficients can be achieved using two horn antennas set up in much the same way a linear measurement would be done. If both antennas are kept co-polarized, the T_{xx} coefficient will be measured. In order to measure, for example, T_{yx}, the receiving antenna should be rotated ninety degrees from the transmitter. This will cross polarize the two antennas. The two other parameters can be measured by rotating the transmitting and receiving antenna by ninety degrees depending on the subscripts [10].

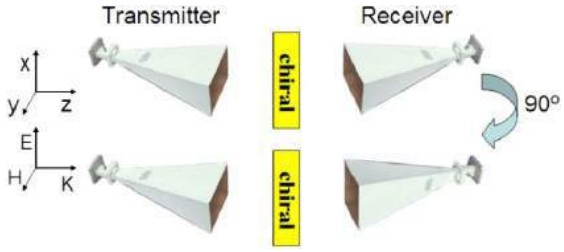

Figure 1: Measurement of chiral media using horn antennas [10].

Since the results shown in this paper will be simulated results, alternative methods will be needed to cross polarize. These will be discussed in the simulation section.

3. Chiral wire helix

The chiral structure will be a wire helix of varying radius and height. The wire is a 22 AWG copper wire. The height will depend on the radius in such a way that the length of the wire will remain constant with changes to the radius. The radius is varied between 2.5cm to 3.4cm by 0.1cm steps. This will create ten data points in the final analysis. The length is kept constant at 25cm throughout the simulation. The propagation direction of the wave is along the length of the spiral.

Equations (9) and (10) show how the height will change according to changes of the radius. Figure (2) shows a visual representation of the spiral if it were uncurled and flattened on a plane. This shows how the structure interacts clearly.

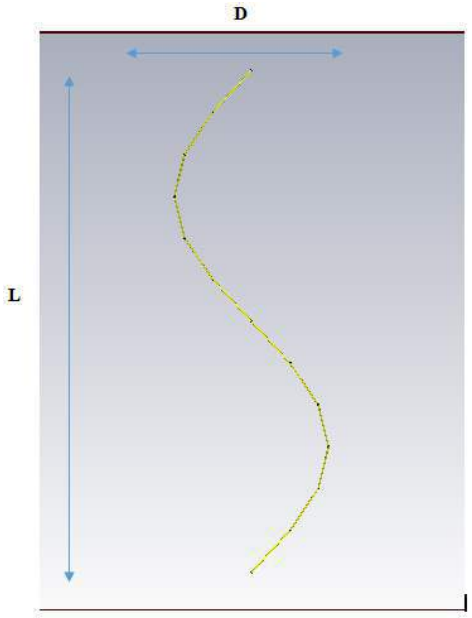

Figure 2: Spiral structure with dimensions labled are L is length and D is diameter.

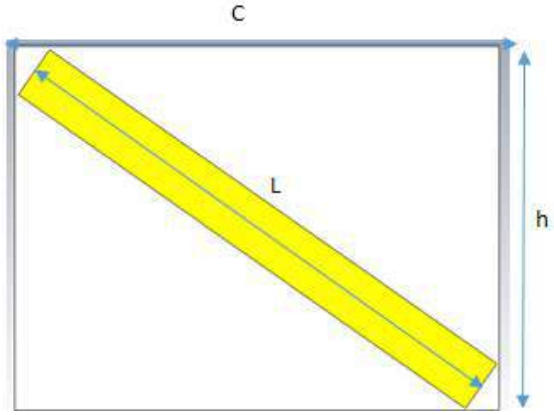

Figure 3: What the spiral would look like if uncurled. This visual representation is useful for understanding how each parameter interacts with the other, where *L* is the length, *C* is the circumference, and *h* is the height.

$$h^2 + (2\pi r)^2 = L^2 \quad (9)$$

$$h = \sqrt{L^2 - (2\pi r)^2} \quad (8)$$

Where *h* is the height, *r* is the radius, and *L* is the length.

4. Simulation

The simulations in this paper are done with CST commercial simulation software. Within this software, a frequency domain solver was used. The boundaries for this simulation were set as open space on all sides and the wave was propagated and received by waveguide ports.

The waveguide ports were set for two modes. In this way, the cross polarized transmission coefficients were simulated by changing the incident and transmitted waves to different modes.

The simulation was carried out with 10 different radii for the spiral.

5. Results and analysis

The optical parameters were extracted from the simulation results. These parameters were then analyzed for recognizable patterns. Figure (4) shows the results of the analysis and parameter extraction. The co/cross-polarization plots are shown, as well as the circular polarization plots. This is to see how patterns emerge as early as these stages. The optical activity was similarly plotted as the transmission plots, but the optical plots were further analyzed to see flawless and concrete patterns.

It can be seen that a clear, linear pattern emerges in the optical parameters of the structure when the radius of the spiral is changed at a linear rate. The peak frequencies for these plots were taken from the first clearly defined peaks that had a linear pattern. This pattern suggests that the radius of a spiral can be easily detected by extracting its optical parameters.

It can be noticed that below a radius of about 2.7cm, the chirality of the structure fails. This is hypothesized to be because the radius is too small to be seen by the wave as a spiral, and begins to see the structure as a straight wire and no longer has any chiral properties.

6. Conclusions

A sensing element in which the main sensing mechanism is the change in optical parameters of a chiral structure is shown to be possible. A clear pattern emerged as a direct effect of outside influence on the structure. Further study is needed on the effects different propagation angles can have as well as what the range of these sensing elements could be.

Acknowledgements

This work is supported by the University of Texas Rio Grande Valley, Office of the Provost.

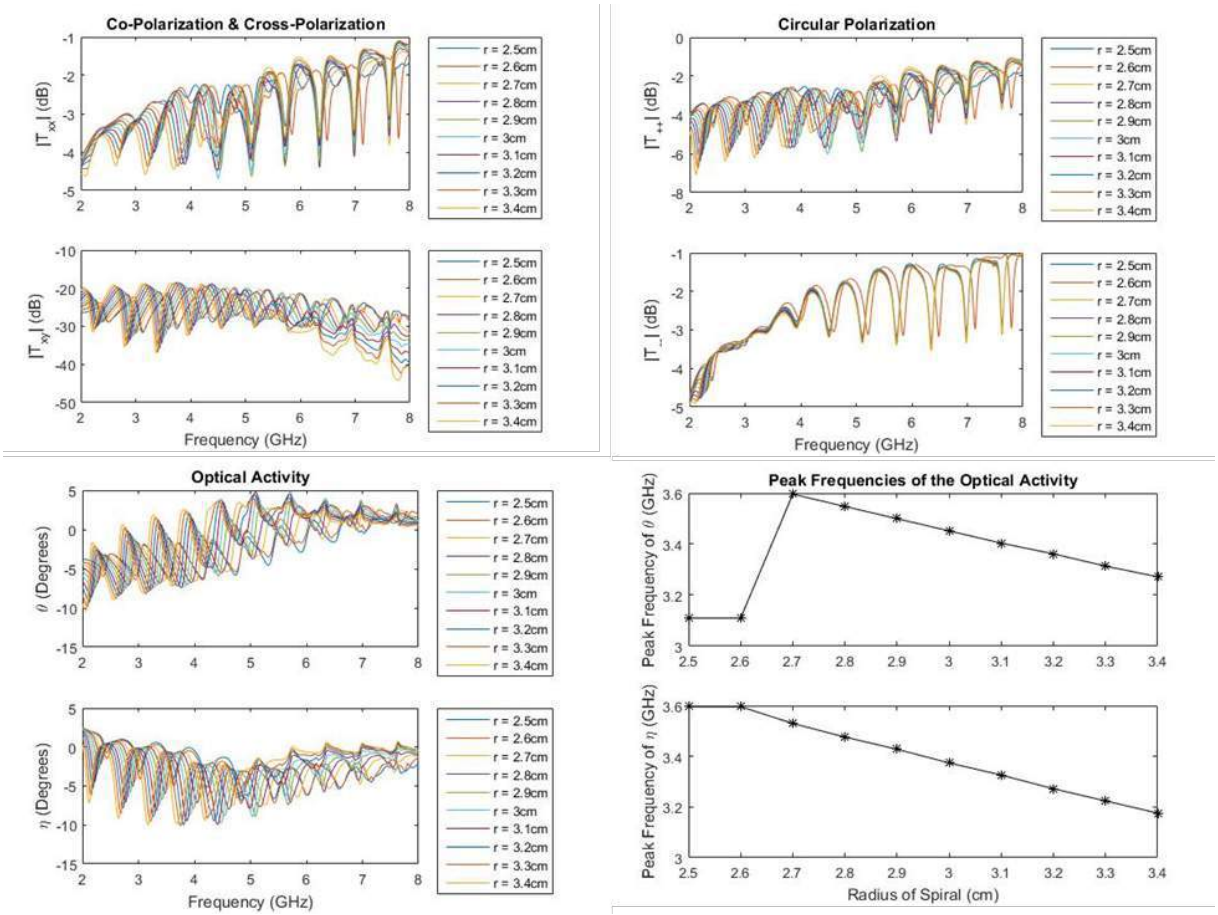

Figure 4: Top Left: Co & Cross-polarization results. Top Right: Circular polarization results. Bottom Left: Optical activity. The frequency shift between different radii can be clearly seen here. Bottom Right: Peak frequencies vs. radius. A clear pattern is seen.

References

[1] M. Huang, , M. Huang, J. J. Yang and E. A. Petrin, Microwave sensor using metamaterials. Intech Press: Vienna, Austria, 13–36, 2011.

[2] H. J. Lee, and J. G. Yook, "Biosensing using split-ring resonators at microwave regime," *Appl Phys Lett*, 92, 254103:1–254103:3, 2008.

[3] J. B. Pendry A chiral route to negative refraction, *Science*, 306 1353–5, 2004

[4] J. K. Gansel, M. Wegener, S. Burger, and S. Linden, Gold helix photonic metamaterials: A numerical parameter study *Opt. Express* **18** 1059, 2010.

[5] N. Wongkasem, C. Kamtongdee, A. Akyurtlu and K. Marx, Artificial multiple helices: EM and polarization properties *J. Opt.* **12** 075102, 2010.

[6] A. Sonsilphong and N. Wongkasem, Three-dimensional artificial double helices with high negative refractive index *J. Opt.* **14** 105103, 2012.

[7] A. Sonsilphong and N. Wongkasem, Low loss circular birefringence in artificial triple helix, *Progress In Electromagnetics Research M* **29** 267-278, 2013.

[8] N. Wongkasem, Circular polarizer by multi-form helices *Software, Telecommunications and Computer Networks (SoftCOM)* 37-40, 2014.

[9] B. Wang, J. Zhou, T. Koschny, M. Kafesaki, C. M Soukoulis. Chiral metamaterials: simulations and experiments. *J. Opt. A: Pure Appl. Opt.* 11, , 114003, 2009.

[10] Z. Li, M. Mutlu, E. Ozbay. Chiral metamaterials: from optical activity and negative refractive index to asymmetric transmission. *J. of Opt.* **15**, No.2, 2013.

Biomass Charcoal Based Graphene Oxide Solution Would Be a Potential Superconducting Electronic Storage Devices under Magnetic Field

Wu-Jang Huang

Dept. of Environmental Engineering and Science, National Pingtung University of Science and Technology, Pingtung, Taiwan
*corresponding author, E-mail: wjhuang@mail.npust.edu.tw

Abstract

For the first time, the directly magneto-voltaic effect in biomass derived graphene sheets oxide solution was observed. The voltage reaches a maximum was observed and the maximum voltage of 3.0 V would be approached at magnetic field of 0.02 T. The possible mechanism of this process is attributed to the superconducting effect of biomass graphene oxide under a magnetic field.

1. Introduction

Graphene is the single layer of graphite, it was just been discovered within 6 six years. Graphene has higher electron conductivity and thermal conductivity than graphite. Currently the usage of graphene in the manufacturing of super-capacitor is very similar with traditional method. This invention demonstrated ability for using graphene oxide solution as electrolytes for super-capacitor and maintains the stored electron current by magnetic force. Therefore we can control the discharging rate of this totally novel biomass derived graphene oxide based super-capacittery pool. In the future we can determine the storage electron-current amount by the used volume of graphene oxide solution rather than the area of electrodes. In our previously publications, we have demonstrate a feasible pathway for preparing graphene sheets carbon materials from biomass derived biochar [1-5]. In this short communication, we would like to report an unpredicted magneto voltaic occurs in biomass derived graphene sheets oxide solution.

2. Experimental Section

Experimental was carried out by homemade biomass derived graphene sheets oxide solution [1], the concentration was 1 wt% with a transparency light brown color. A homemade wireless charging box was built to provide a homogeneous alternative current magnetic field, from 0 T to 0.05 T. 100mL of the battled biomass derived graphene sheets oxide solution was placed directly in the center area in the magnetic field for wireless charging for 0 to 30 min, under a magnetic field strength of 0 to 0.02 T. Results are shown in the following figures. Fig 1 shows the harging curve of biomass derived graphene sheets oxide solution under various charging time. Fig. 2 show the charging curve of biomass derived ed graphene sheets oxide solution under various magnetic field.

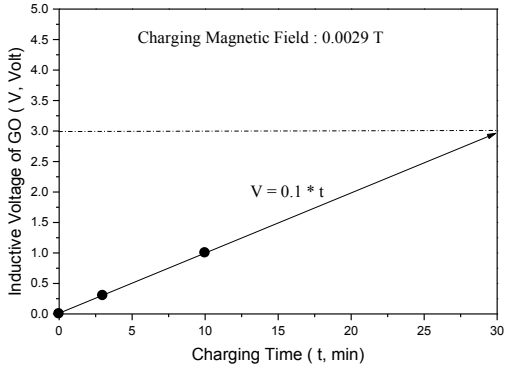

Fig 1 Charging curve of biomass derived graphene sheets oxide solution under various charging time.

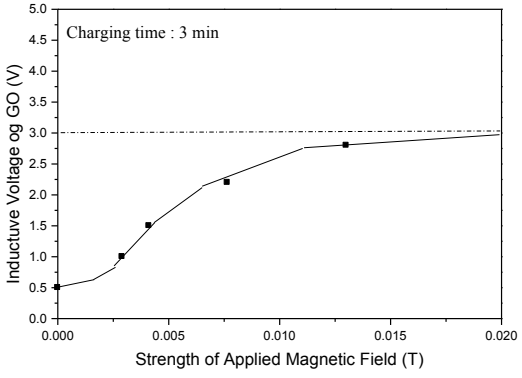

Fig. 2 Charging curve of biomass derived ed graphene sheets oxide solution under various magnetic field.

3. Discussion

For the first time, the directly magneto-voltaic effect in biomass derived graphene sheets oxide solution was observed. The 1% graphene sheets oxide solution is charged by wireless type under low magnetic field (< 0.02 T). The maximum charged voltage is 3.0 V within 30 min, with a charging rate is 0.1 V/min. Figure 1 shows the charging curve for 0 to 30 min under 0.0029 T. The maximum voltage of 1.0 V was measured by a commercial Volta-meter, and the charging rate is 0.1 V/min. Figure 2 shows the voltages of charged biomass derived graphene sheets oxide solution under various magnetic field strength. The voltage reaches a maximum was observed and the maximum voltage of 3.0 V would be approached at magnetic field of 0.02 T. A superconducting storage mechanism of this process is proposed. This invented product is the first demonstration type in the world developed from the idea of the pattern. We predict that the commercial fine product will be produced within future years.

4. Conclusions

For the first time, the directly magneto-voltaic effect in biomass derived graphene sheets oxide solution was observed and s superconducting storage mechanism of this process is proposed.

Acknowledgements

Financial support by National Pingtung University of Science and Technology was fully acknowledged.

References

[1] Yan-Jia Liou, Bo-Da Tsai, Wu-Jang Huang, An Economic Route to Mass Production of Graphene Oxide Solution for Preparing Graphene Oxide Papers, *Materials Science and Engineering B*, 193(1), pp. 37 – 40, 2015.

[2] Yan-Jia Liou, Wu-Jang Huang, The role of sodium ions on the development of micro-sized pores in a high alpha-cellulose content woody biomass under ambient temperature, *Journal of Cleaner Production*, 74(2), 199 – 201, 2014.

[3]Yan-Jia Liou, Wu-Jang Huang, Determination of graphene sheets content in carbon materials by Raman spectroscopy, *Journal of the Chinese Chemical Society*, 61(5), 1045 – 1048, 2014.

[4] Yan-Jia Liou, Wu-Jang Huang, Quantitative Analysis of Graphene Sheet Content in Wood Char Powders during Catalytic Pyrolysis, *Journal of Materials Science & Technology*, 29(5), pp. 406-410, 2013.

[5] Odette Varela Milla, Eva B. Rivera, Wu-Jang Huang, Chuan-Chi Chien, Yu-Ming Wang, Agronomic Properties and Characterization of Rice Husk and Wood Biochars and their Effect on the Growth of Water Spinach in a Field Test, *Journal of Plant Nutrition*, *and Soil Science* I13(2), 251-266, 2013.

Flexible Antenna with Artificial Magnetic Conductor using Liquid Metal at 5.8 GHz

Muhammad Nazrin Ramli[1], Ping Jack Soh[1*], Mohd Faizal Jamlos[1], Mohd Firdaus Ibrahim[2,3] Herwansyah Lago[1], and Azremi Abdullah Al-Hadi[1]

[1]Advance Communication Engineering (ACE) CoE, School of Computer and Communication Engineering, Universiti Malaysia Perlis (UniMAP), Pauh Putra, 02600, Arau, Perlis, Malaysia
[2]Center of Excellence for Advanced Sensor Technology (CEASTech), Universiti Malaysia Perlis (UniMAP), Taman Muhibbah, Jejawi, 02600, Arau, Perlis, Malaysia
[3]School of Bioprocess Engineering, Universiti Malaysia Perlis (UniMAP), Kompleks Pusat Pengajian Jejawi 3, Kawasan Perindustrian Jejawi, 02600, Arau, Perlis, Malaysia
*pjsoh@unimap.edu.my

Abstract

A flexible fluidic antenna embedded in a polydimethylsiloxane (PDMS) structure integrated with a liquid metal Artificial Magnetic Conductor (AMC) plane is presented. The antenna is designed based on the operating principles of a patch antenna to cover its operation in the WLAN ISM 5.8 GHz radio band for wireless communication. The main innovation of this work is the integration of a AMC plane made fully using liquid metal embedded in PDMS to enable a highly flexible antenna, besides potentially adding tunability feature to the structure in the future.

1. Introduction

Flexible antennas to simultaneously support computing and wireless communication functionalities have garnered a great amount of interest in academia and the electronics industry. For wireless transmission requiring of higher data rates, wireless local area network (WLAN) in the 5.725-5.875 GHz band is commonly employed [1]. Antenna design techniques are evolving based on the new and innovative materials available for use. One of such materials which gained attention due to its capability and suitability as the better material for flexible antennas is the liquid metal. This work proposes a flexible and robust antenna with artificial magnetic conductor (AMC) implemented using polydimethylsiloxane (PDMS) as its substrate and eutectic gallium indium alloy (EGaIn) (Ga 75.5% and In 24.5%) as its conductor [2]. The EGaIn liquid metal is injected into microfluidic channels embedded in the multilayered elastomeric substrate. Such structure is advantageous as it provides extra robustness against water and dust, besides enabling better flexibility for the antenna due to the liquid metal's low viscosity [3].

2. Antenna Design

2.1 AMC design

To ensure fabrication simplicity, a simple square AMC unit cell enclosed inside a larger square unit cell sized at 25x25 mm2 is chosen in this work, see figure Figure 1(a). As a result, the proposed AMC realized a bandwidth of 1130 MHz (5.27 GHz to 6.40 GHz) as illustrated in Figure 1(c). Next, 16 elements of the AMC unit cells are arranged into 4x4 array to form the AMC plane and placed behind the radiating element, see Figure 1(b). In this project, the AMC plane is aimed to increase the gain and efficiency [4].

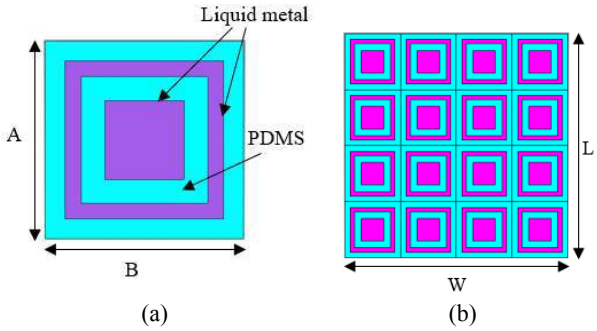

Figure 1(a): Unit cell. The dimension of AMC unit cell (in mm) are, *A*=25, *B*=25, (b): 4x4 array. The dimension of AMC plane 4x4 array (in mm) are, *L*=100, *W*=100

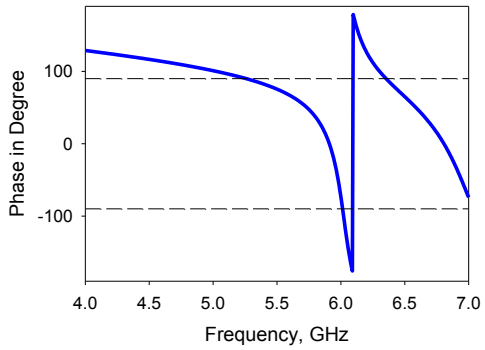

Figure 1(c): Phase response of the proposed AMC.

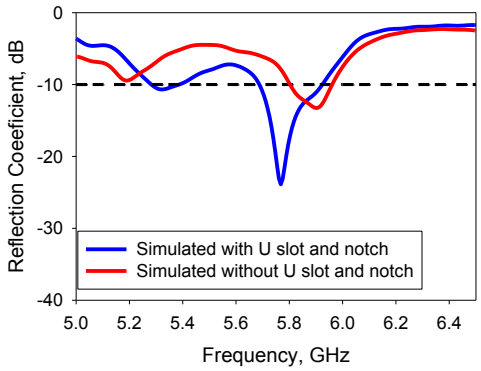

Figure 2(b): Reflection coefficient (S_{11}) of proposed antenna on the AMC plane.

2.2 Radiator Topology

The radiator is designed based on a rectangular patch topology sized at 37 x 43.5 mm2 with a target operating frequency of 5.8 GHz, see Figure 2(a). For the antenna design, a U slot and notches are added onto the patch to increase impedance bandwidth. Consequently, the integration of the AMC layer and the proposed antenna resulted in an operation from 5.68 to 5.92 GHz with 236.4 MHz of bandwidth, see Figure 2(b).

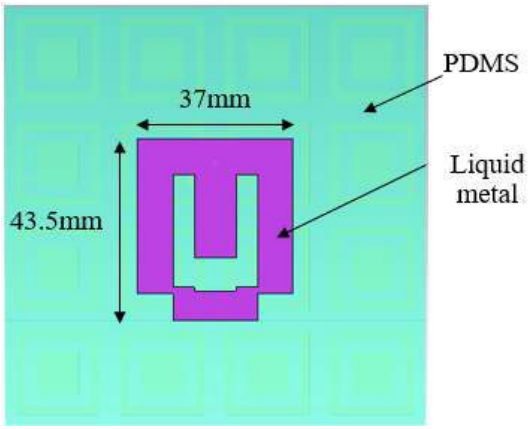

Figure 2(a): Topology of the radiating element

3. Conclusions

As conclusion, the radiator-AMC combination made using PDMS substrate and EGaIn as conductor resulted in satisfactory operation at 5.8 GHz with a gain of 2.570 dB. This result indicates that the antenna operates well and potentially may be used for applications requiring physical flexibility

Acknowledgements

This project is supported by the Fundamental Research Grant Scheme provided by the Malaysian Ministry of Higher Education (MOHE) (grant no: 9003-00537).

References

[1] J. Baviskar and S. Pawar, "Meta-material Lens Embedded 5.8 GHz Wide Band Patch Antenna for Wireless Communication," in *Communication Systems and Network Technologies (CSNT), 2015 Fifth International Conference*, 1–6, 2015.

[2] G. J. Hayes, J.-H. So, A. Qusba, M. D. Dickey, and G. Lazzi, "Flexible Liquid Metal Alloy (EGaIn) Microstrip Patch Antenna,"*IEEE Trans. Antennas Propag.*, Vol. 60, No. 5, 2151–2156, 2012.

[3] J. H. So, J. Thelen, A. Qusba, G. J. Hayes, G. Lazzi, and M. D. Dickey, "Reversibly deformable and mechanically tunable fluidic antennas," *Adv. Funct. Mater.*, Vol. 19, No. 22, 3632–3637, 2009.

[4] Z. H. Jiang, D. E. Brocker, P. E. Sieber, and D. H. Werner, "A compact, low-profile metasurface-enabled antenna for wearable medical body-area network devices," *IEEE Trans. Antennas Propag.*, Vol. 62, No. 8, 4021–4030, 2014.

A Flexible Circularly Polarized Antenna Integrated with AMC for CubeSat Application

A.H. Lokman[1]*, P.J. Soh[1], S. N. Azemi[1], M. F. Jamlos[1], H. Lago[1], and A. A. Al-Hadi[1]

[1]Advanced Communication Engineering Centre (ACE) CoE, School of Computer and Communication Engineering, Universiti Malaysia Perlis, Perlis, Malaysia.
*E-mail: abdhalimlokman@gmail.com

Abstract

This paper proposes the design of circularly polarized antenna operating in the S-band frequency integrated with an Artificial Magnetic Conductor (AMC) plane with a total size of 0.506λ x 0.506λ x 0.0267λ. The AMC provided antenna gain enhancement from 3.52 dB to 5.89 dB at 2.3 GHz. Most importantly, it performed well with circular polarization characteristics centered at 2.3 GHz.

1. Introduction

In recent years, the implementation of CubeSats intensified worldwide due to their cost-effectiveness for various applications. Several antennas have been developed for CubeSat communication aimed at improving gains. These improvements benefited the satellite-to-ground station communication segment, besides other CubeSat applications. The integration of metamaterial-based elements has been proven to improve antenna properties at the desired frequencies by using a number of unit cells [1]. An example of such application is the dual-band crossed asymmetric dipole antenna integrated with a dual-band AMC surface placed beneath it. Such technique resulted in gains of up to 5.1 dBic and 6.2 dBic at 2.4 GHz and 5.2 GHz respectively [2]. Meanwhile, another printed meandered dipole antenna shows gain improvements from 1.8 dB to 5.1 dB by introducing the AMC on its reverse side [3].

2. AMC and Antenna Design

The proposed circularly polarized antenna in this work integrates an AMC plane underneath the antenna and is separated by a 2 mm gap. As depicted in Figure 1(a), four triangular slots were added at each corner of the AMC unit cell for its miniaturization. This unit cell designed on a flexible Kapton film substrate which is 0.635 mm thick to exhibit the behavior of a perfect magnetic conductor (PMC) at 2.4 GHz, as shown in Figure 1(c). This is to enable its application in a deployable format and to save stowage space which is limited on CubeSats. The designed AMC unit cell sized at 33 x 33 mm^2 exhibited a bandwidth of 2.2 % and a zero phase reflection at 2.4 GHz, see Figure 1(c). This unit cell is then arranged in a 2 x 2 array to form the AMC plane with an overall size of 66 x 66 mm^2. Next, a circularly polarized antenna is designed on a thin 0.85 mm Rogers RO4003C substrate to be integrated with this AMC plane. As illustrated in Figure 1(b), the antenna is formed using four elements of dipole antennas placed perpendicular to each other with a phase shifter located at center to generate circular polarization. It is placed over the AMC plane, with an overall size of 66 mm x 66 mm x 3.485 mm. Furthermore, the gain of the antenna has been improved from 3.52 dB up to 5.89 dB at 2.3 GHz by the presence of AMC plane as shown in Figure 1(d).

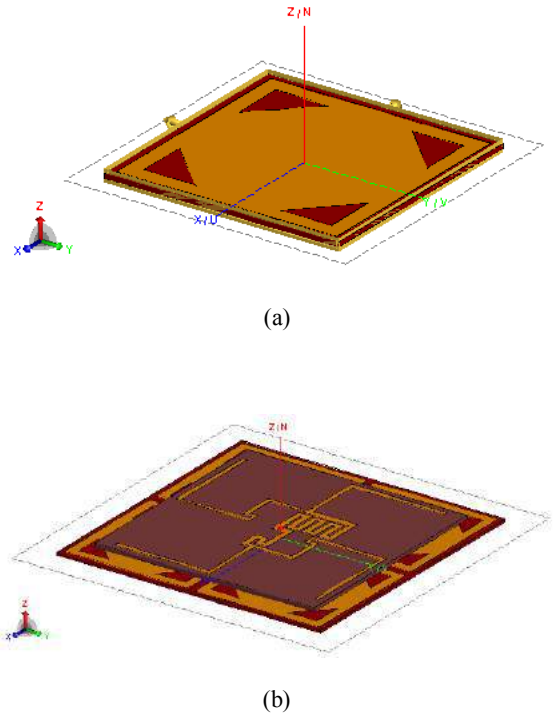

Figure 1: The proposed of (a) AMC unit cell, (b) 2 x 2 AMC plane.

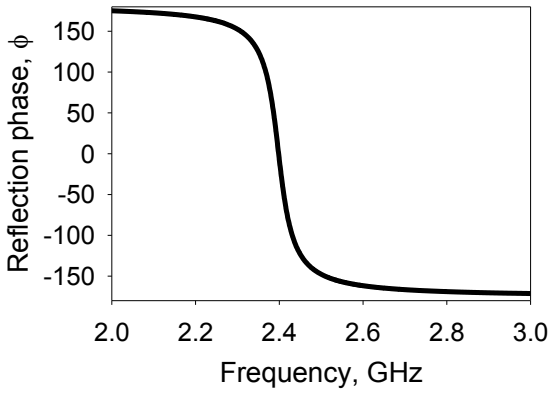

(a)

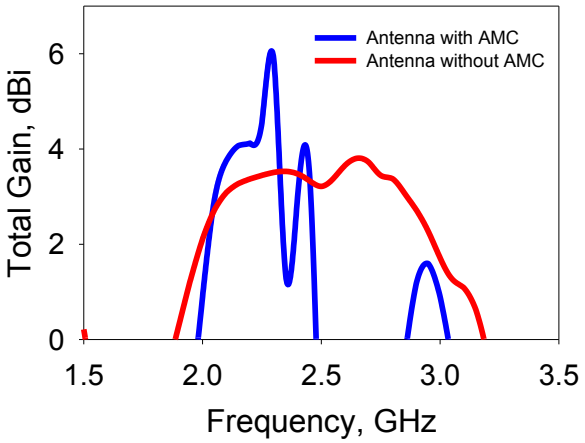

(b)

Figure 2: (a) Phase response of the AMC unit cell, (b) gain comparison of antenna with and without AMC.

3. Conclusions

An AMC plane capable of enhancing antenna gain for a circularly-polarized antenna is proposed in this work. Careful considerations must be taken to ensure that its integration onto the plane does not affect the circular polarization characteristics. The combined antenna and AMC plane fabricated using thin and flexible materials such as Rogers RO4003C and Kapton film enables it to be potentially applied as a deployable antenna. Its operation centered at 2.3 GHz with a total size of 0.506λ x 0.506λ x 0.0267λ. The gain improvements using this technique is aimed at enhancing the gain to suit satellite communication, especially satellite-to-ground station communication in CubeSats.

Acknowledgements

This work has been partly supported by the Malaysian Ministry of Higher Education (MoHE) via the Prototype Development Research Grant Scheme (PRGS) (Grant no. 9013-00024).

References

[1] R. C. Hadarig, M. E. de Cos, and F. Las-Heras, "Novel Miniaturized Artificial Magnetic Conductor," IEEE Antennas Wirel. Propag. Lett., vol. 12, pp. 174–177, 2013.

[2] S. X. Ta and I. Park, "Dual-Band Low-Profile Crossed Asymmetric Dipole Antenna on Dual-Band AMC Surface," IEEE Antennas Wirel. Propag. Lett., vol. 13, pp. 587–590, 2014.

[3] M. Abu, M. K. A. Rahim, and S. A. Hamzah, "A Meandered Triple-band Dipole Antenna with 920 MHz Artificial Magnetic Conductor," Antennas Propag. Soc. Int. Symp., vol. 1, pp. 10–13, 2010.

Study on the Technique to Improve the Isolation in the MIMO Quasi-Yagi AP Antenna by Using Small Metamaterial Phase-Shifters

Changhyeong Lee[1], Dajung Han[2], Heejun Park[3], Abdul Rehman[4], Muhammad Salman Khattak[5], Muhammad Kamran Khattak[6] and Sungtek kahng[7*]

[1234567]Dept. of Information and Telecommunication Eng., Incheon National University
Incheon, 22012, korea
*s-kahng@inu.ac.kr

Abstract

In this paper, we propose a method to handle the isolation problem of a MIMO antenna for Wi-Fi access point (AP). Firstly, a quasi-Yagi antenna is designed with a transmission-line balun at the feed. Secondly, this conventional quasi-Yagi antenna is adopted for the two closely placed MIMO elements for 2.4GHz-AP equipment, and the coupling between them is checked. The 180^{O}delay-line of one element is long and next to the feed of the other element, which is an obstacle to the isolation improvement. Hence, the conventional balun is replaced by right and left-handed phase shifters, which take up a much smaller area of the feed and result in improved isolation. In addition, the MIMO radiating elements based on the metamaterial phase-shifters show less inclination of the main beam from the intended direction. The MIMO quasi-Yagi antennas without and with the metamaterial phase-shifter balun are designed, and their return- loss, beam-patterns and isolation curves are compared. Also, the full-wave simulation results are given with the measured ones.

1. Introduction

Wireless communication technologies have linked distant points over the globe or inside the office building. For quality communication, it goes without saying that the users have up- to-date handheld wireless devices as well as their software- embedded modules. More importantly, the repeaters are responsible for the connection between the users compliant to the required performances in the environment, and represented by the access point (AP) antennas [1].

Clinging to the ceiling, an AP antenna receives the signal from the transmitter and delivers it to the receiver. It handles the reception of the signals propagating on the horizontal plane. In most cases, the monopole antenna is commonly used [2]. However, there are shortcomings in the use of the monopole antenna in reality, and other types of antenna have been sought to replace it. The first weakness of the monopole structure is that its profile is not low. Though modifications are introduced to the monopole design, they tend to be higher than the body of an AP system[3]. And the second shortcoming is that the monopole radiator mounted on the ground structure results in imbalance between the upper and lower beam-patterns, which causes the H-plane gain to fall significantly. These negative factors make the AP system developers hesitate to use the aforementioned antenna.

To tackle the shortcomings of the customarily used antennas, we can think of the quasi-Yagi antenna [4,5]. The two arms of the driving element are fed by a balun that has a 180^{o}-long delay-line. As the antenna emanates the wave in the longitudinal direction that the driving element and directors sit on the substrate, it works as an end-fire type. The beam covers the user of WiFi connection in the hallway of a building and can be held high or low according to the needs.

When the quasi-Yagi antenna has to be applied to the MIMO AP as [6,7] or as seen in commercial products such as Wi-Fi routers, a few undesirable things will occur. The main beam of each quasi-Yagi element is tilted from its longitudinal direction. This comes from the influence of the degraded isolation between the two quasi-Yagi elements. It results from the fact that the delay line of the conventional balun for one element is situated near the feed of the other. To handle this matter by putting the feeding baluns of the two elements apart, we propose compact baluns comprising short metamaterial phase-shifters. The balun is connected through the right- handed 90^{o}-line and left-handed 90^{o}-line to the right and left arms of the driving element, respectively. Like [8-10], the metamaterial phase shifters can produce a 180^{o}-angular difference as a small structure, which is helpful to obtaining a higher isolation. In line with this, the conventional and novel quasi-Yagi MIMO antennas are designed and their simulated and measured characteristics are compared. Especially, the isolation levels of the two cases reveal the improvement by the proposed technique.

2. MIMO Antenna with the conventional quasi-yagi

This section regards a MIMO antenna having two conventional quasi-Yagi elements. As the preliminary form of the multiple antennas, it is needed to present a single quasi- Yagi radiating device. The geometry originates from the Yagi- Uda array antenna which is the

set of metallic rods in parallel. This 3-dimensional geometry is adapted to the microstrip structure which has the metallic strips printed on the top of the substrate that are analogous to the driving and parasitic elements. The reflecting strip does not exist unlike the 3D Yagi-Uda antenna, but the balun comprising the two paths of 180°-phase-difference is utilized to excite the antenna.

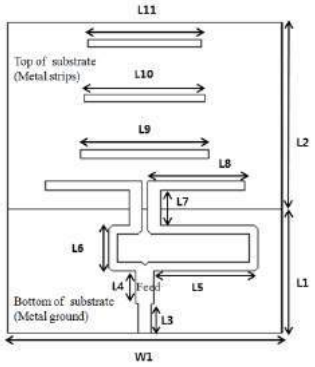

Figure 1: The geometry of the conventional quasi-Yagi antenna

The pattern is printed on FR4 as the substrate of 2-mm thickness. The driver in Fig. 1 has the two arms connected to the shorter and longer paths from left to right. The physical dimensions are given as below for the operation at 2.4 GHz.

Table 1: Physical dimensions of the conventional antenna

Parameter	Length[mm]	parameter	Length[mm]
W1	75	L6	10.5
L1	35	L7	9.5
L2	51	L8	26.5
L3	8	L9	35
L4	9	L10	33
L5	10.5	L11	31

This is applied to the MIMO antenna version of AP device

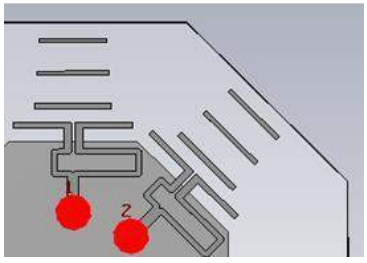

(a)

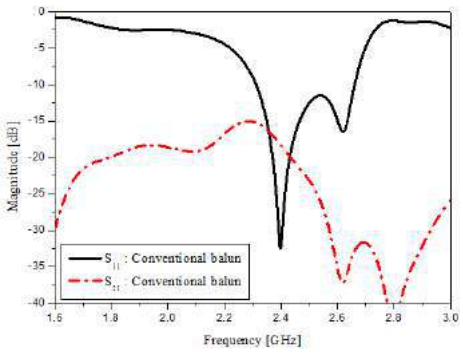

(b)

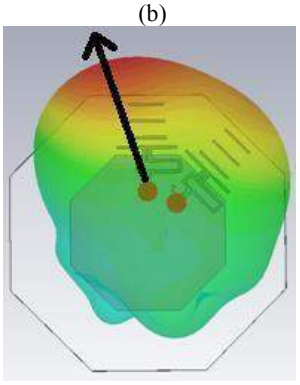

(c)

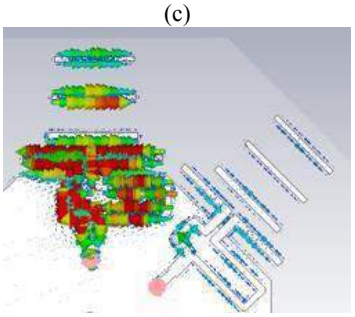

(d)

Figure 2: Electrical and EM phenomena of the MIMO of the conventional quasi- Yagi antenna (a) Geometry (b) Return loss and isolation (c) 3D beam-pattern
(d) Surface current density showing coupling between the two antennas

The ports for the quasi-Yagi antennas are 28 mm away as in Fig. 2(a). The EM simulation gives us S_{11} below -10 dB as shown in Fig. 2(b), meaning good input impedance match for antenna 1. The same applies to the port 2 as antenna 2. The isolation is the inverse of the coupling between antennas 1 and 2 symbolized as S_{21} and it is 17.5 dB in Fig. 2(b). At first sight, it seems to have nothing wrong. But, the unnecessary interaction of one antenna to another causes the problem of asymmetry in radiation characteristics. Fig. 2(c) shows this undesirable effect that the main beam of antenna 1 is off the vertical axis due to the surface current induced by the coupling from antenna 1 in Fig. 2(d).

3. Novel MIMO quasi-yagi antenna

The former MIMO antenna changes to a new one which has the compact balun with metamaterial phase-shifters.

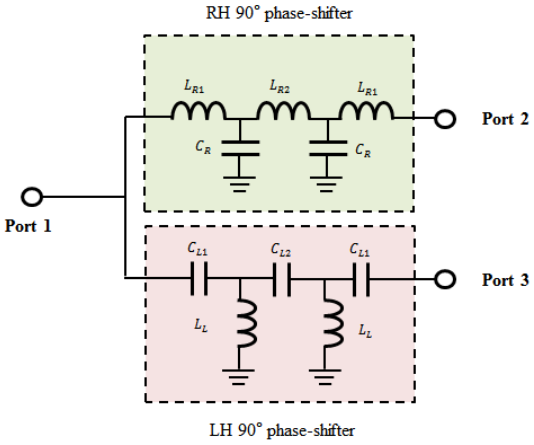

(a)

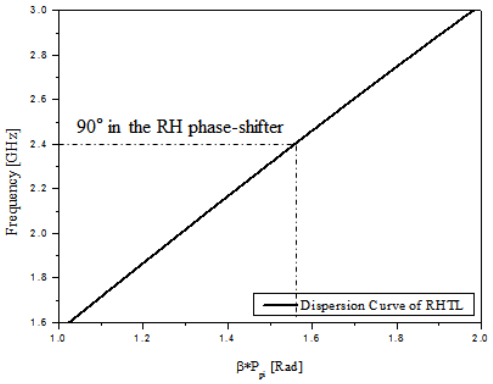

(b)

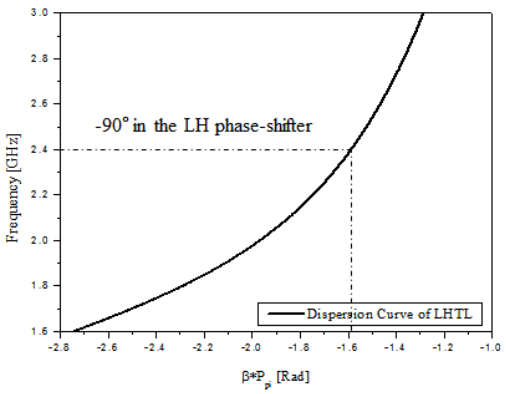

(c)

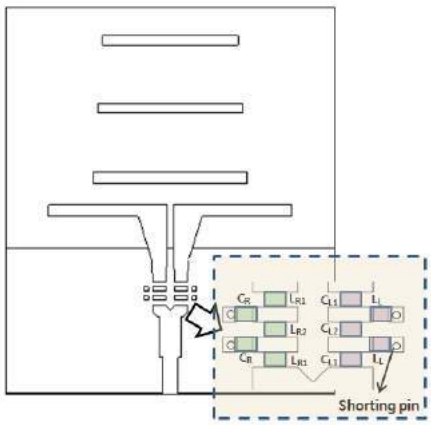

(d)

Figure 3: Small-sized balun of metamaterial phase-shifters and adoption to the quasi-Yagi antenna (a) Equivalent circuit of the balun of metamaterial phase- shifters (b) Dispersion diagram of the RH 90^{O}-phase-shifter (c) Dispersion diagram of the LH 90^{O}-phase-shifter (d) Geometry of the single quasi-Yagi antenna with the metamaterial balun

Fig. 3(a) presents the equivalent circuit of the balun made of the RH 90^{o}-phase-shifter and LH 90^{o}-phase-shifter branches. The values of lumped elements for positive and negative 90^{o} are decided as 2.2 nH, 4.8 nH, 2 pF, 30 pF, 12 pF and 30 nH for L_{R1}, L_{R2}, C_R, C_{L1}, C_{L2} and L_L. The phases of the RH and LH phase-shifting lines amount to 90^{o} and -90^{o} at the operating frequency of 2.4 GHz in Fig. 3(b) and (c), respectively. This renders the 180^{o}-differnce required for the balun. This metamaterial component can be adopted in a small area of the quasi-Yagi antenna as in Fig. 3(d). Now, we apply this structure to the MIMO AP antenna.

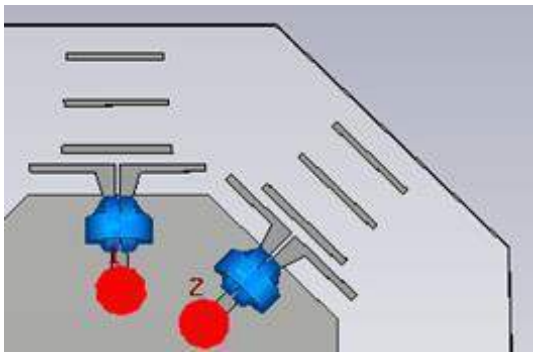

(a)

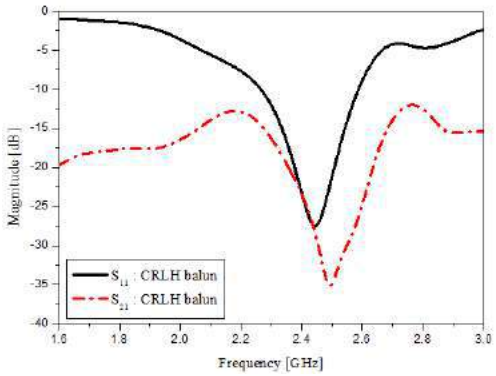

(b)

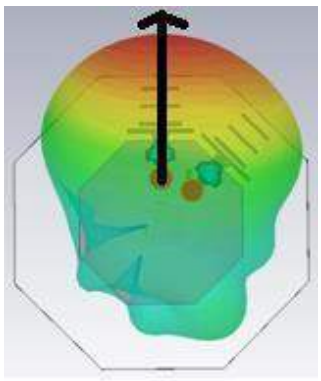

(c)

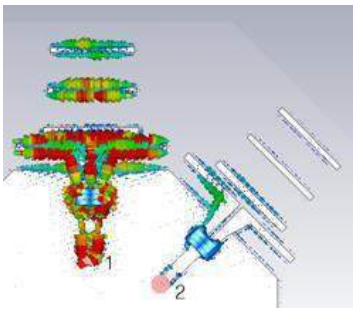

(d)

Fig. 4 : Electrical and EM phenomena of the MIMO of the suggested quasi- Yagi antenna (a) Geometry (b) Return loss and isolation (c) 3D beam-pattern
(d) Surface current density showing the weakened coupling between the two antennas

Fig. 4(a) shows the size-reduced feeds for the two radiating elements copied from Fig. 3(d). This enables the structure to lower S_{21} at 2.4 GHz as the coupling between the adjacently located feeds in Fig. 4(b), meaning improvement in isolation. Also, the main beam returns to the vertical direction in Fig. 4(c). This is explained by much weaker surface current on antenna 2 induced by antenna 1 as shown in Fig. 4(d). The conventional and suggested antennas are fabricated and measured as follows

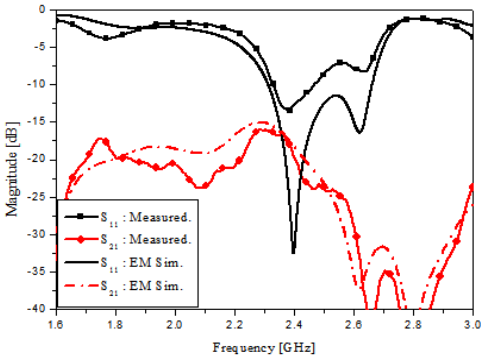

(a)

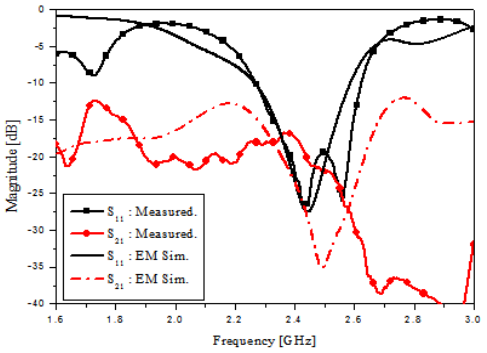

(b)

Fig. 5: Measured return loss and isolation levels of the conventional and suggested MIMO antennas (a) Conventional case (b) Proposed case

The two types of the antennas are fabricated by the PCB manufacturing process. The conventional MIMO structure is tested in terms of S_{11} and S_{21}. Fig. 5(a) shows the degraded return loss and isolation. Contrarily, the input impedance of the metamaterial balun-embedded quasi-Yagi antenna is in good shape in Fig. 5(b). With regard to the isolation, the measurement curve is shifted upward from the simulation curve. The discrepancy is expected to be mended by replacing the used L and C elements by those close to the calculated components.

4. Conclusions

The quasi-Yagi antenna has been adapted to the MIMO AP device. When the MIMO elements are fed through the delay- line type of balun, the current on the longer path of the feed of antenna 1 interacts with the feed of antenna 2, which causes problems in antenna isolation. In order to solve them, a compact balun is suggested and has been implemented by the metamaterial phase-shifters. This balun is very small and used to excite the elements of the MIMO antennas. This antenna system

is developed to perform in an improved manner from the view-point of isolation and far-field radiation.

Acknowledgements

This work was supported by ICT R&D program of MSIP/IITP. [2016-0-00130, Cloud based SW platform development for RF design and EM analysis].

References

[1] Z. N. Chen, et al, "Antennas for WiFi Connectivity," *Proceedings of the IEEE* vol. 100, no. 7, pp.2322-2329, July 2012.

[2] J. D. Kraus, et al, Antennas For All Applications, 3rd ed., New York, USA: *McGraw-Hill Science/Engineering/Math* 2001.

[3] S. Prasadet al, "Experimental study of inverted L-, T-, and related transmission-line antennas", *Journal of Research of the National Bureau of Standards*, vol. 65, no. 5, pp. 449–454, September–October 1961.

[4] Y. Qian, W. R. Deal, N. Kaneda, and T. Itoh, "Microstrip-fed quasi- Yagi antenna with broadband characteristics," *Electronics Letters*, vol. 34, no. 23, pp. 2194-2196, Nov. 1998.

[5] Q. Xu, S. Qin, and Y. E. Wang, "Indented quasi-Yagi antenna array for high-isolation full-duplex radios," *Proc. of 2015 IEEE MTT-S Int'l Microwave Symposium*, (10.1109/MWSYM.2015.7167128), May 2015.

[6] E. Capovilla, A. Tavora, S. E. Barbin, and L. C. Kretly, "Planar Antenna Array Mutual Coupling Identification: A Direct Method Applied to Quasi-Yagi Elements," *PIERS Proceedings*, Vol.1, No. 1, pp.1446-1449, March 23-27, 2009

[7] L. Gu, Y.-W. Zhao, Q. M. Cai, and Z.-P. Zhang, "Wideband Quasi- Yagi Antenna Design and Its Usage in MIMO/Diversity Applications," *Progress In Electromagnetics Research C*, Vol. 71, pp.33–40, 2017

[8] D.-J. Eom, and S. Kahng "Fully Printed Dual-Band Power Divider Miniaturized by CRLH Phase-Shift Lines," *ETRI Journal*, vol.35, no.1, pp.150-153, February 2013.

[9] S. Kahng, J. Lee, K.-T. Kim, and H. Kim, "Metamaterial CRLH Structure-based Balun for Common-Mode Current Indicator," Journal of Electrical Engineering & Technology, vol.9, no.1, pp.301-306, 2014.

[10] K. Jang, S. Kahng, J. Jeon, J. Anguera, "Small Dual-Band 3-Way Metamaterial Power-Divider with the Phase-Compensated Outputs", *Proc, of EuMC 2014*, (10.1109/EuMC.2014.6986434), vol. 1, no.1, October 5-10, 2014.

Infrared broadband absorber utilizing non-resonant metasurface for microbolometer

J. Y. Jung[1*], K. Song[1], J. Lee[1], J. H. Jeong[1], and D. P. Neikirk[2]

[1]Nano-convergence Mechanical Systems Research Division, Korea Institute of Machinery and Materials, Republic of Korea

[2]Department of Electrical and Computer Engineering, The University of Texas at Austin, USA

[*]corresponding author: jjy21211@kimm.re.kr

Abstract-We demonstrate an infrared broadband metasurface absorber that is suitable for increasing the response speed of a microbolometer by reducing its thermal mass. A large fraction of periodic patterned holes in a thin lossy metal layer can be used as a non-resonant metasurface that can be integrated with a Salisbury screen absorber to construct an absorbing membrane for a microbolometer that can significantly reduce the thermal mass while maintaining high infrared broadband absorption in the long wavelength infrared (LWIR) band.

The response speed of an infrared microbolometer may be slow because of the very high thermal resistance required for sensitivity. In other words, the absorbing membrane of microbolometer pixels, which is composed of a resistive absorber layer, bolometric layer, and mechanical support layer, is suspended over the metal mirror layer using high thermal resistance arms to provide thermal isolation. One way to reduce the thermal mass is by using a thinner absorbing membrane. For mechanical support, however, microbolometers require a finite thickness support layer; this limits how much the thermal mass of the microbolometer can be reduced. Another way to reduce the thermal mass is by making patterned holes in the absorbing membrane, but this reduces the fill factor of the absorbing layer. Recently, patterning periodic subwavelength-sized holes in a metal layer or metal elements on a substrate have been shown to produce unique spectral responses through the abrupt changes in the phase and amplitude of the incident light at the surface of the metal layer for various electromagnetic wave bands[1-3]. These two-dimensional structures are known as metasurfaces. They can be treated as thin layers with an equivalent effective surface impedance and have been used as part of narrowband[4] or tunable absorbers[5]. These metasurface absorbers have near-unity absorption, even though the fill factor of the absorbing area of metasurface is small. However, the spectral responses of these metasurface absorbers show wavelength-selective narrowband absorption because the effective surface impedance of metasurfaces having the nature of a resonator that is extremely dispersive around the resonance wavelength

In this study, we demonstrated that infrared broadband metasurface absorbers can reduce the thermal mass of microbolometer pixels by incorporating a metasurface with a non-dispersive effective surface impedance into a Salisbury screen absorber. The retrieved non-dispersive effective surface impedance matched to the free space can be achieved by finding the optimised dc surface resistance of a thin lossy metal for a certain patterned hole size by using the proposed dc approximation method. Experiments with the fabricated metasurface absorbers showed outstanding broadband absorption in the LWIR band, even when the fill factor of the absorbing area was reduced to 27.75%. Therefore, this concept for the metasurface absorber can be used in current state-of-the-art uncooled infrared thermal detectors.

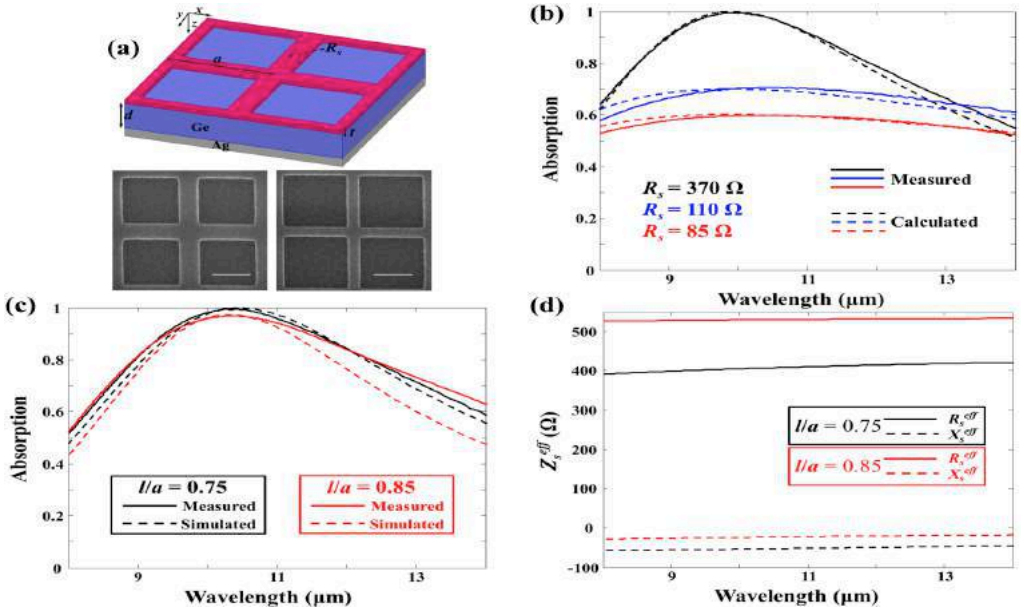

Fig. 1. (a) Schematic and SEM images of the fabricated metasurface absorbers. Scale bar is 500 nm. (b) Measured (solid curves) and calculated (dashed curves) absorption spectral responses of Salisbury screen absorbers with three different surface resistances: R_s = 85 (red curves), 110 (blue curves), and 370 Ω (black curves). (c) Measured (solid curves) and simulated (dashed curves) absorption spectral responses of the metasurface absorbers for l = 0.75 μm with R_s = 110 Ω (black curves) and l = 0.85 μm with R_s = 85 Ω (red curves). (d) Retrieved effective surface impedances of the metasurfaces for l = 0.75 μm with R_s = 110 Ω (black curves) and l = 0.85 μm with R_s = 85 Ω (red curves).

Acknowledgements, This work was supported by the Center for Advanced Meta-Materials (CAMM), funded by the Ministry of Science, ICT, and Future Planning as a Global Frontier Project (CAMM-No. 2014M3A6B3063707).

REFERENCES

1. Ni, X., "Metasurface holograms for visible light," *Nat. Commu.*, 4, 2807, 2013.
2. ElBadawe, M., "True metasurface antenna," *Sci. Rep.*, 6, 19268, 2016.
3. Dabidian, N., "Electrical switching of infrared light using graphene integration with plasmonic Fano resonant metasurfaces," *Acs Photonics*, 2, 216-227, 2015.
4. Jung, J. Y., "Wavelength-selective infrared metasurface absorber for multispectral thermal detection," *IEEE Photon. J.*, 7, 1-10, 2015.
5. Andryieuski, A., "Graphene metamaterials based tunable terahertz absorber: effective surface conductivity approach," *Opt. Express*, 21, 9144-9155, 2013.

Resonator Structure Metamaterial Based Microwave Sensor Using Microstrip Technology

M. N. Rahman[12*], M. T. Islam[1], T. Alam[1], F. B. Ashraf[1], and M. Samsuzzaman[2]

[1] Dept. Of Electrical, Electronic and Systems Engineering, Universiti Kebangsaan Malaysia, Malaysia
[2]Patuakhali Science and Technology University, Bangladesh
*corresponding author, E-mail: tariqul@ukm.edu.my

Abstract

A microwave metamaterial based on resonator structures is proposed in this study for sensor applications. The metamaterial structure consists of a resonator which is surrounded by a partial ground frame and excited by a microstrip feeding transmission line. The metamaterial has a geometric size of 30 mm × 30 mm, which is imprinted on Rogers RO3010 (tm) substrate with the relative permittivity of 10.2 and the dielectric loss tangent of 0.0035. In the metamaterial structure, the resonator, partial ground frame, and the transmission line are all on a microstrip, thus it is easy to measure the metamaterial by using the common laboratory facility instead of using the waveguide. Numbers of unit cells are needed for traditional metamaterial design, whereas the proposed metamaterial structure has only one cell which can achieve the metamaterial properties. The aim of the study is to apply the presented metamaterial in sensor applications and the results exhibit that the metamaterial is quite appropriate for the microwave sensor applications.

1. Introduction

Metamaterials were first introduced by Veselago in 1968. From the introduction, metamaterials became an interesting field of research for industry and researchers who are devoted to finding metamaterial characteristics such as negative permeability and negative permittivity. Since then, a lot of resonator based metamaterials have been suggested by researchers for different operating frequencies [1]. These metamaterials are designed, analyzed, validated and manufactured for practical experiments [2-11]. A split ring resonator (SRR) and capacitance loaded strip (CLS) unit cell inspired metamaterial antenna has been reported for UWB microwave imaging applications [2]. A metamaterial based fuel sensor has been mentioned in [3] which operates in the ISM (Industrial Scientific and Medical Standard) band. Referenced in [4], a split ring resonator based metamaterial has been discussed for terahertz sensing applications. A metamaterial using broadside-coupled triangular split-ring-resonator for terahertz sensing applications has been rendered in [5]. An electric field coupled resonator antenna has been addressed the comparison among the traditional split ring resonator based devices and the electric-field-coupled (ELC) and complementary electric-field-coupled (CELC) resonators based devices [6]. Referenced in [7], a metamaterial based microwave sensor has been focused where the transmission lines (TL) act as a building block for microwave sensors. In [8], the dielectric characterization of a metamaterial based on the complementary, split ring resonators (CSRR) has been described. Having the shape of CSRR, the sensor operates at a 0.8-1.3 GHz band. The performance characteristics and the comparisons of different metamaterial sensors have been reviewed and summarized [9]. A high sensitive metamaterial sensor has been rendered in [10] for the dielectric characterization of microfluidics. A thin film metamaterial sensor has been reported using rectangular asymmetric double split resonators [11].

In this study, a metamaterial based on resonator has been proposed. The metamaterial is based on a single unit cell which exhibits all the metamaterial characteristics. In the proposed configuration, the resonator and the ground frame are sketched on one part of the substrate. The feeding transmission line (FTL) is sketched on the other part of the substrate. This configuration has quite a lot of amenities which are discussed in this study. The resonator based metamaterials are not new and unique. Some of the examples are discussed in the literature review. The reason to choose the proposed resonator for the metamaterial is its simplicity in design and ease to fabricate. The proposed structure is based on the microstrip technology. The effective metamaterial characteristics for both the simulated and experimented results are fetched and analyzed. Both the results are very much close to each other. The proposed metamaterial can be used in various applications such as antennas, filters, sensors, imaging systems, etc. In this study, the proposed metamaterial is used in sensor applications in the GHz operating band. This study is organized in some sections. In the first section, the design, simulations, fabrication, and measurement technique of the metamaterial is discussed. The second section describes the metamaterial characteristics of the proposed prototype. In section three, the surface current distribution and the field distributions are described. Finally, the sensor application of the proposed metamaterial is discussed in section four.

2. Design, Simulation, Fabrication, and Measurement

The metamaterial characteristics are unavailable in conventional materials in nature. In this study, a resonator, ground frame along with an FTL are used to make a metamaterial device which depicts all the metamaterial properties. The proposed structure is designed on Rogers RO3010 (tm) substrate with a thickness of 1.28 mm. The substrate has 10.2 relative permittivity with a loss tangent of 0.0035. The resonator and the ground frame are sketched on the same portion of the substrate. The feeding transmission line (FTL) is sketched on the opposite portion of the substrate. The metamaterial structure is simulated and analyzed by using the High-Frequency Structural Simulator (HFSS). The excitation is supplied to the resonator through the FTL. For the proposed structure, the electric, magnetic, boundary condition is used so that the electromagnetic wave propagates through FTL. Figure 1 shows the layout of the proposed metamaterial.

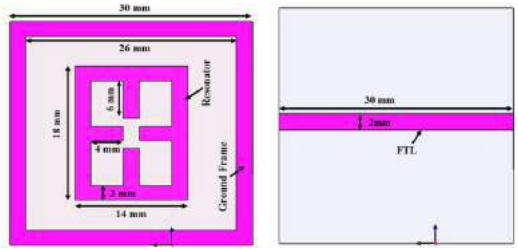

(a) (b)

Figure 1: Geometric layout of the Metamaterial structure. (a) top view and (b) bottom view.

The proposed metamaterial structure is fabricated on the printed circuit board for practical observation. The metamaterial is fabricated using a circuit plotter LPKF, S63. The fabricated prototype of the proposed resonator based metamaterial is illustrated in Figure 2. The measurement was performed in the microwave laboratory at the Department of Electrical, Electronic and Systems Engineering (JKEES), UKM, Malaysia. For the measurement of the proposed antenna, N5227A PNA Microwave Network Analyzer (10MHz- 67GHz) was used. The simulated and measured data are plotted by using data analysis software Origin Pro.

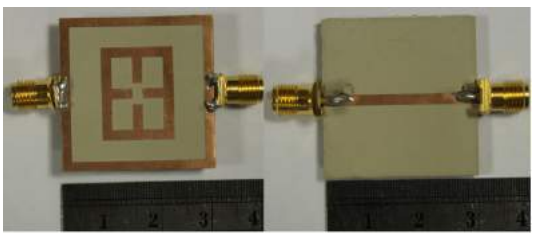

(a) (b)

Figure 2: Picture of the fabricated metamaterial prototype. (a) Top view and (b) bottom view.

Figure 3 shows the reflection and transmission coefficients of the metamaterial. The resonances are found at 2.30 GHz and 7.10 GHz where the reflections are minimum and the transmissions are maximum. The transmission resonance frequency is found at 6.30 GHz. Though there is a little disagreement between the reflection and transmission coefficients between the simulated and measured results, the two results are uniform over the operating band. The disagreement between the simulated and measured results occurs because of the fabrication tolerance, the soldering inaccuracies, and the external reflections.

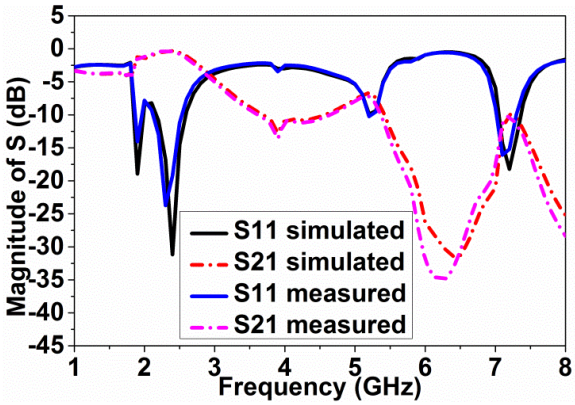

Figure 3: Simulated and measured magnitude of the S-parameter.

3. Metamaterial Characterization

To characterize the metamaterial, the effective metamaterial characteristics are extracted by the Nicolson-Ross-Weir (NRW) method. The method uses the S-parameters of the metamaterial to extract the characteristics. The NRW method is a simple and familiar method to characterize the unknown materials which are utilized for characterizing metamaterials. The refractive index depends on the effective permeability and effective permittivity, but not on reflection and transmission parameters in NRW method. The NRW method is mathematically represented by following equations [12].

$$V_1 = S_{21} + S_{11} \quad (1)$$

$$V_2 = S_{21} - S_{11} \quad (2)$$

$$\mu_r \approx \frac{2}{jk_0 d}\frac{1-V_2}{1+V_2} \quad (3)$$

$$\varepsilon_r \approx \frac{2}{jk_0 d}\frac{1-V_1}{1+V_1} \quad (4)$$

$$\eta = \sqrt{\mu_r \varepsilon_r} \quad (5)$$

Where μr, εr, η, d, and k0 corresponds effective permeability, effective permittivity, refractive index, substrate thickness, and propagation constant, respectively. In NRW method, the calculation of the parameters is based

on the S-parameter. The method does not depend on the calculation of the impedance.

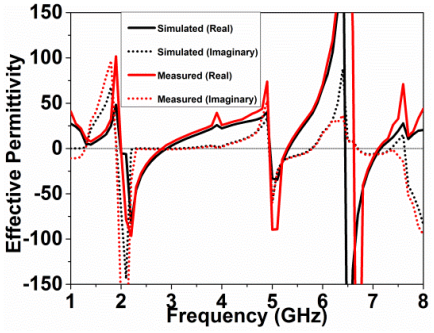

(a)

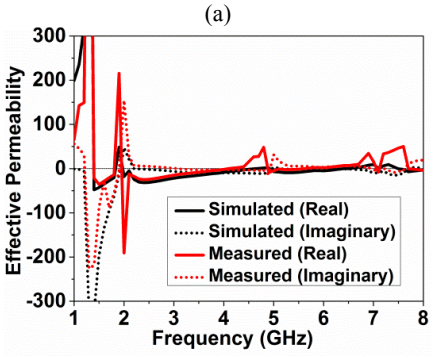

(b)

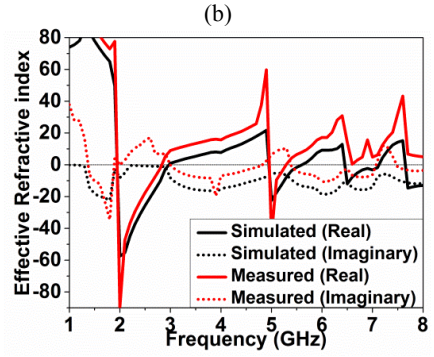

(c)

Figure 4: Simulated and measured effective constitutive parameters of the proposed metamaterial. (a) Effective permittivity, (b) Effective permeability, and (c) Effective refractive index.

At the peak of the transmission coefficient (S21), the effective permittivity and effective permeability should be negative, which is observed from the Figure 4 (a) and Figure 4 (b). From the Figure 4 (a), the effective permittivity is negative from 2.0 GHz to 2.80 GHz, from 4.90 GHz to 5.20 GHz, and from 6.60 GHz to 7.0 GHz. The simulated and measured data are a little bit dissimilar, but two results are unique throughout the operating frequency. Figure 4 (b) shows the negative permeability from 1.40 GHz to 1.80 GHz, from 2.0 GHz to 3.90 GHz, and from 4.90 GHz to 5.20 GHz. Again, there exists a little discrepancy between simulation and measurement. There exists a variation between the permittivity and permeability due to the polarization effect. This effect happens because of the construction of the metamaterial structure. The permittivity and permeability changes because of the change in design. This is for the unequal distribution of electromagnetic waves on the material which affects the properties of the material by the polarization. The refractive index is also affected by the polarization through the same technique. The refractive index will be negative when the permittivity and the permeability become negative. Figure 4 (c) shows the negative refractive index from 2.0 GHz to 2.80 GHz and from 4.90 GHz to 5.20 GHz. Thus, the proposed metamaterial structure shows double negative characteristics as the permittivity, permeability, and the refractive index is negative in the operating bandwidth.

4. Surface Current Distribution and Field Distribution

Surface current distribution is an important parameter to describe the resonance type of the metamaterial. Figure 5 displays the surface current distribution of the proposed resonator based metamaterial.

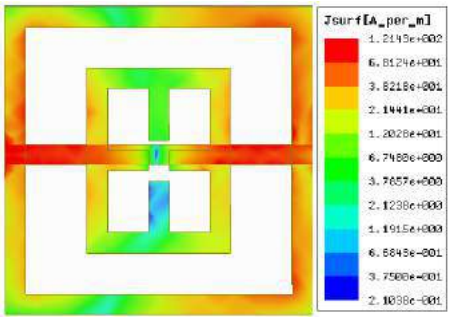

(a)

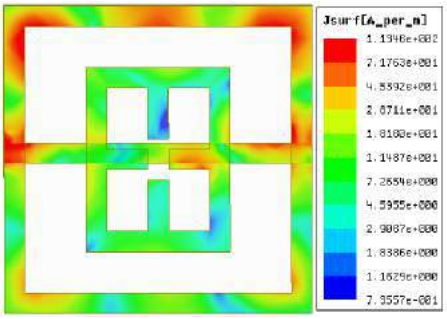

(b)

Figure 5: Distribution of currents of the metamaterial at the resonance frequency. (a) At 2.30 GHz (b) At 7.10 GHz.

From the figure, it is observed that the current density is mainly concentrated on the resonator and the FTL. Two opposite directional magnetic dipoles are formed on the ground frame due to symmetrical rotation of the surface currents on the resonator. Figure 6 shows the induced magnetic field of the metamaterial structure.

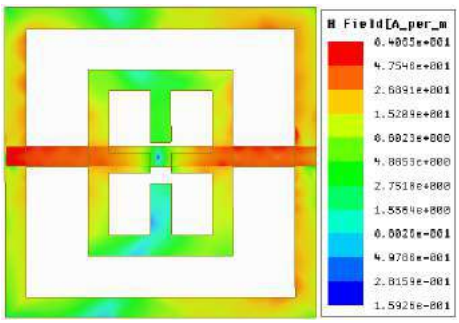

(a)

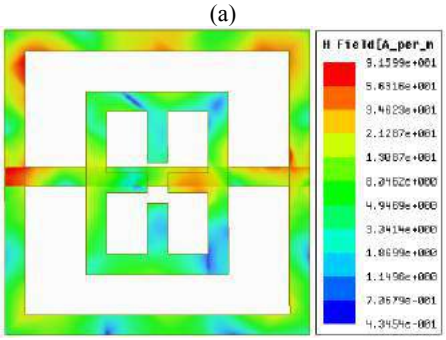

(b)

Figure 6: Distribution of magnetic field of the metamaterial at the resonance frequency. (a) At 2.30 GHz (b) At 7.10 GHz.

From the figure, it is investigated that at the resonance frequency, the FTL is coupled to the ground frame and the resonator with its electric field. At this point, the metamaterial structure shows the inductive and capacitive behavior due to the ground frame and the space between the ground frame and the resonator. The induced magnetic field is opposite to the external magnetic field and hence diamagnetism is generated. Due to the diamagnetism property, the negative permeability is extracted by the metamaterial structure. The magnetic field is vertical to the ground frame and the resonator. Thus, the negative permeability rises through the magnetic field, ground frame, and the resonator. As the metamaterial structure shows negative permittivity as well, the metamaterial gives a negative refractive index which is shown in Figure 4. Due to the collateral combination of the electric field of the structure to the ground frame, resonator, and the FTL, the negative permittivity rises. The presence of the ground frame around the resonator produces additional inductance and capacitance to the metamaterial structure and hence it becomes a crucial factor to create resonance. Moreover, the ground frame also serves as the ground plane, which provides the negative permittivity and negative permeability through the inductive-capacitive properties of the proposed structure.

The electric field distribution of the proposed resonator based metamaterial is shown in Figure 7. According to the figure, the electric field distributions are quite consistent with the surface current distribution and the magnetic field distributions. The electric field is distributed on the resonator, ground frame, and the FTL. The intensity of the electric field is enhanced at the higher frequency.

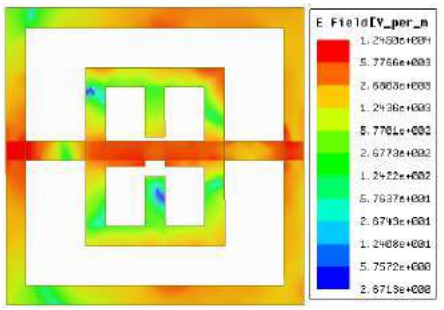

(a)

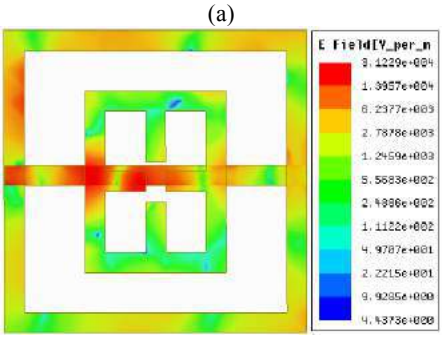

(b)

Figure 7: Electric field distribution of the proposed metamaterial at the resonance frequency. (a) At 2.30 GHz (b) At 7.10 GHz.

5. Metamaterial Sensor Application

The proposed resonator based metamaterial structure is used for the double-sided sensing system. The both front and back side of the proposed metamaterial is used in the sensing application. The unknown material which is to be detected is taken as the overlayer. By changing the thickness and the dielectric constant of the unknown material, the frequency response of the metamaterial sensing device is experimented.

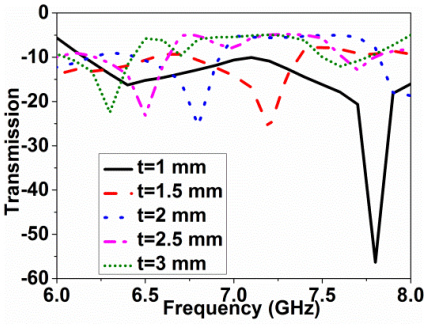

(a)

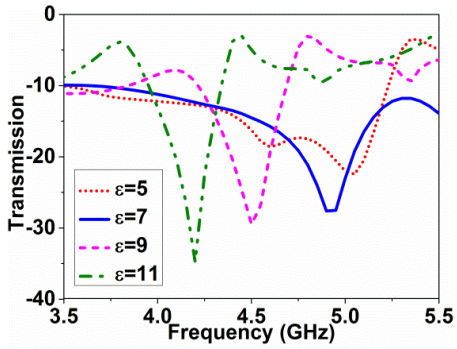

(a)

Figure 8: Change of transmission resonance. (a) for changing overlayer thickness (b) for changing overlayer permittivity.

Firstly, the effect of changing the overlayer thickness is considered to observe the frequency response. For the simulations, an overlayer with dielectric constant 10.0 and 0.0035 loss tangent is considered as it is close to the parameter of the Rogers RO3010 substrate which is used in the proposed metamaterial. Figure 8 (a) shows the simulated results after changing the thickness of the overlayer. From the figure, it is clearly observed that the transmission resonance shifts downward with the increase of the overlayer thickness. The sensing device along with the overlayer can be considered as the RLC resonant circuit in which the resonance frequency is calculated by the effective capacitance and the effective inductance. With the increment of the overlayer thickness, the effective inductance, and capacitance changes. Due to this, the transmission resonance shifts downward as the resonance frequency are directly related to the effective capacitance and the effective inductance. Thus, the proposed metamaterial structure can be effectively used in sensing application in the GHz region.

The frequency response due to changing the overlayer relative permittivity is simulated and analyzed. Figure 8 (b) illustrates the effects of the variation of the overlayer relative permittivity. When the relative permittivity is increasing, the transmission resonance downshifts as well. The higher overlayer permittivity corresponds to a larger downshift of the transmission resonance. Hence, the sensitivity of the metamaterial increases, according to the increment of the overlayer relative permittivity.

For the validation of the simulation, the practical experiments have been performed and the measured results are compared to the simulated results. In the practical observations, the Rogers RO3010 material having a relative permittivity of 10.2 with 0.0035 loss tangent and Rogers TMM 10i material having a relative permittivity of 9.8 with 0.02 loss tangent are used as the overlayers. The thickness of the materials is 1.28 mm and 1.27 mm respectively. The metallic ledge on both portions of the substrates is abolished to have the overlayer having the dielectric materials only. The proposed metamaterial structure with the overlayers is shown in Figure 9.

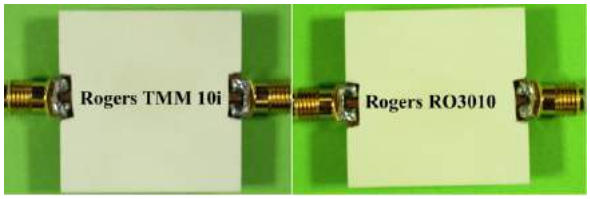

(a) (b)

Figure 9: Picture of the sensing device. (a) Rogers TMM 10i as overlayer (b) Rogers RO3010 as overlayer.

The measured results of the proposed resonator based metamaterial as a sensor along with the simulated results are displayed in Figure 10.

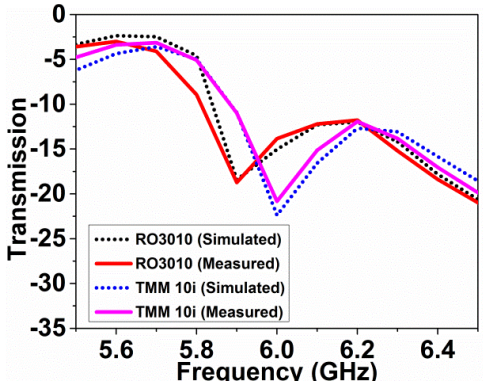

Figure 10: Simulated and measured transmission response with Rogers RO3010 and Rogers TMM 10i overlayer.

From the figure, it is clearly investigated that the resonance frequency shifts downward with the increment of the thickness and the overlayer relative permittivity. As the Rogers RO3010 has a larger thickness and higher relative permittivity than the Rogers TMM 10i material, Rogers RO3010 shifts more downward than the Rogers TMM 10i overlayer with reference to no overlayers which is shown in Figure 3. More specifically, with no overlayer, the transmission resonance is at 6.30 GHz, but using the Rogers TMM 10i and Rogers RO3010 overlayers, the transmission resonance shifts to 6.0 GHz and 5.90 GHz, respectively.

To extend the experiment, double-overlayer structures are considered for perplexing situations. In this scenario, Rogers RO3010+Rogers RO3010 and Rogers TMM 10i+Rogers TMM 10i double-overlayers are used. The simulation and practical investigations are conducted by the similar procedure as described in the previous section. The simulated and measured frequency responses for the double-overlayers are illustrated in Figure 11.

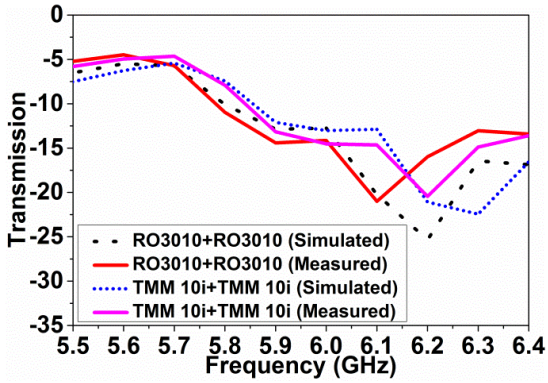

Figure 11: Simulated and measured transmission response with Rogers RO3010+Rogers RO3010 and Rogers TMM 10i+Rogers TMM 10i double-overlayers.

From the figure, it is clear that the resonance frequency shifts downward with the increment of the thickness and the overlayer relative permittivity. With no overlayer, the transmission resonance is at 6.30 GHz, but using the Rogers TMM 10i+Rogers TMM 10i and Rogers RO3010+Rogers RO3010 double-overlayers, the transmission resonance shifts to 6.20 GHz and 6.10 GHz, respectively.

Both in the overlayer and double-overlayer cases, the simulated results vary a little with the measured results. This could be due to the mechanical etching of the metallic layer of the dielectric materials, external reflections during measurements, and soldering inaccuracies. Based on the simulations and measurements performed above, the proposed resonator based metamaterial can detect materials having different values of thickness and relative permittivity. The proposed metamaterial can be used as a sensor in various applications.

6. Conclusions

In this paper, a metamaterial structure on the basis of the resonator is designed, simulated, fabricated, and investigated as a sensor. The resonator is surrounded by a ground frame and is fed by a 50Ω feeding transmission line on the rear side of the substrate. The metamaterial is measured by using common laboratory facilities rather than using of waveguides. Both the results found in the simulation and measurements agree quite well and the proposed metamaterial reveals negative permittivity and negative permeability in the operating band. The proposed metamaterial can be used in various applications including antennas, filters, sensors, imaging systems, etc. In this work, the metamaterial structure is utilized in sensor application where it can detect unknown overlayer materials with good sensitivity. The metamaterial properties with an uncomplicated design, using only one metamaterial unit cell make the structure competent to be used where metamaterial properties are essential.

Acknowledgements

The authors would like to thank the Department of Electrical, Electronic and Systems Engineering (JKEES), Universiti Kebangsaan Malaysia (UKM) and Ministry of Higher Education Malaysia (Grant No. AP-2015-007), for the sponsor of this work.

References

[1] C. Sabah, T. Nesimoglu, Design and characterization of a resonator-based metamaterial and its sensor application using microstrip technology, *Optical Engineering* 55: 027107-027107, 2016.

[2] M. M. Islam, M. T. Islam, M. Samsuzzaman, M. R. I. Faruque, N. Misran, M. F. Mansor, A miniaturized antenna with negative index metamaterial based on modified SRR and CLS unit cell for UWB microwave imaging applications, *Materials* 8: 392-407, 2015.

[3] V. Rawat, V. Nadkarni, S. Kale, ISM (Industrial Scientific and Medical standard) band flex fuel sensor using electrical metamaterial device, *Applied Physics A* 123: 75, 2017.

[4] C. Sabah, H. Roskos, Terahertz sensing application by using planar split-ring-resonator structures, *Microsystem technologies*18: 2071-2076, 2012.

[5] C. Sabah, H. G. Roskos, Broadside-coupled triangular split-ring-resonators for terahertz sensing, *The European Physical Journal Applied Physics* 61: 30402, 2013.

[6] H. Odabasi, F. Teixeira, D. Guney, Electrically small, complementary electric-field-coupled resonator antennas, *Journal of Applied Physics* 113: 084903, 2013.

[7] M. Schueler, C. Mandel, M. Puentes, R. Jakoby, Metamaterial inspired microwave sensors, *IEEE Microwave Magazine* 13: 57-68, 2012.

[8] M. S. Boybay, O. M. Ramahi, Material characterization using complementary split-ring resonators, *IEEE Transactions on Instrumentation and Measurement* 61: 3039-3046, 2012.

[9] T. Chen, S. Li, H. Sun, Metamaterials application in sensing, *Sensors* 12: 2742-2765, 2012.

[10] A. Ebrahimi, W. Withayachumnankul, S. Al-Sarawi, D. Abbott, High-sensitivity metamaterial-inspired sensor for microfluidic dielectric characterization, *IEEE Sensors Journal* 14: 1345-1351, 2014.

[11] I. A. I. Al-Naib, C. Jansen, M. Koch, Thin-film sensing with planar asymmetric metamaterial resonators, *Applied Physics Letters* 93: 083507, 2008.

[12] S. S. Islam, M. R. I. Faruque, M. T. Islam, A new direct retrieval method of refractive index for the metamaterial, *Current Science* 109: 337-342, 2015.

Unloaded-Dodecagon-Shaped Flexible Linear to Circular Polarizer using PDMS

Hidayath Mirza[1, 2], Ping Jack Soh[1, 3*,] Mohd Faizal Jamlos[1], Muhammad Nazrin Ramli[1], Azremi Abdullah Al-Hadi[1], R.Ahmad Sheik[2], Emad S. Hassan[2], and Sen Yan[3]

[1]Advance Communication Engineering (ACE) CoE, School of Computer and Communication Engineering, Universiti Malaysia Perlis (UniMAP), Pauh Putra, 02600, Arau, Perlis, Malaysia.

[2]Dept. of Electrical Engineering, College of Engineering, Jazan University, P. O. Box 706, Jazan 45142 Kingdom of Saudi Arabia.

[3]ESAT-TELEMIC, KU Leuven, Kasteelpark Arenberg 10, Box 2444, 3001 Leuven, Belgium

*corresponding author: pjsoh@unimap.edu.my

Abstract

This paper presents the design of a flexible and robust linear to circular polarizer using Polydimethylsiloxane (PDMS) and ShieldIt fabric. The size of the unit cell is 58 x 48 x 3.17 mm^3, which is about 0.3757 x 0.3109 x 0.0205 in terms of wavelength for operation at 1.94 GHz. The simulated structure demonstrated a 3 dB axial ratio bandwidth of 34.53 % ranging from 1.63 GHz to 2.31 GHz.

1. Introduction

Polarization can be classified into three types, a) linear, b) circular and d) elliptical [1]. In satellite communication, RFID, etc., polarization is pivotal as these systems typically use circularly polarized waves for wireless communication. The polarization of transmitter and the receiver has to be identical to polarization losses [2].

Polarizers have been realized using different shapes, thicknesses and topologies using frequency selective structures (FSS). It is a type of planar metamaterial. Most of these structures originated from meander lines, loops, dipoles, or the combination of them [3-7]. The main innovativeness of the proposed work are as follows. The structure attempts maintain a single-layered and low profile topology to maintain simplicity and conformality. Besides that, the polarizer are built using flexible materials, PDMS and ShieldIt Super conductive fabric. This enables the structure to be flexible and robust (waterproof, dust-proof).

2. Unit cell design

A unit cell of the polarizer is modeled and simulated using the frequency domain solver in CST Microwave Studio. Unit cell boundaries, Floquet ports and template based processing are used in the modeling. To extract the CP wave, the ABS(Tx)=ABS(Ty) criterion has to be meet, as presented in Fig. 2. At the same frequency (1.94 GHz) a phase difference of -89.50^0 is observed in Fig. 3, indicating above 99 % of conversion efficiency. Fig. 4 depicts the axial ratio with its 3 dB bandwidth shown inset, with a minimum AR value of 0.08 dB at 1.94 GHz. It can be concluded that the performance of the polarizer is suited for the conversion of linear to circular polarization for a flexible antenna.

3. Conclusions

In this paper, a new flexible, single layered, linear to circular polarizer has been designed for S-Band operation based on PDMS and ShiedIt conducting fabric. The simulated structure demonstrated a 3 dB axial ratio bandwidth of 34.53 % ranging from 1.63 GHz to 2.31 GHz.

Acknowledgements

This project is supported in part the Malaysian Ministry of Higher Education (MOHE) Prototype Development Research Grant Scheme (PRGS) (grant no: 9013-00024)

and Research Foundation - Flanders (F.W.O.) Postdoctoral Fellowship (No. 12O1217N).

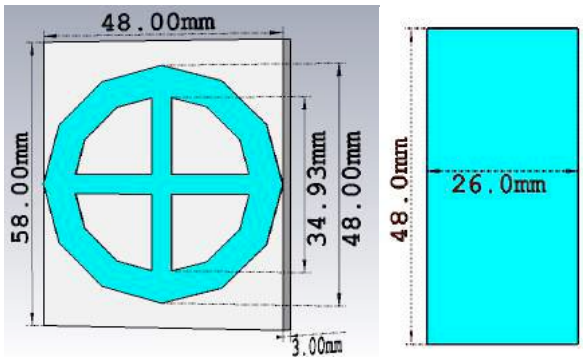

Figure 1: Topology of the proposed polarizer (a) front view (b) back view.

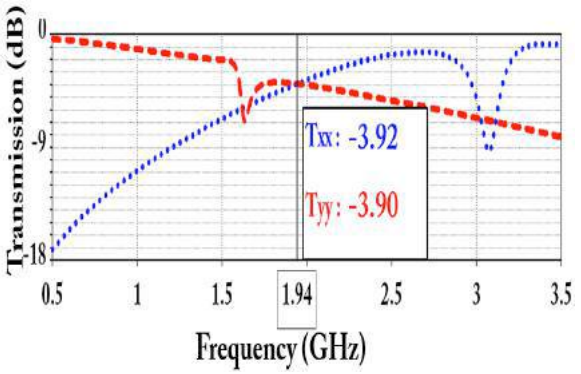

Figure 2 :Tx and Ty component

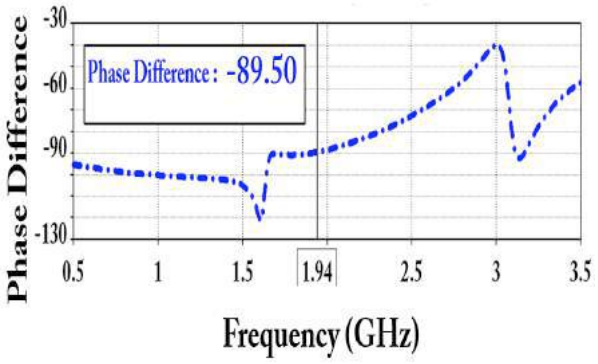

Figure 3 :Phase difference between Ty /Tx

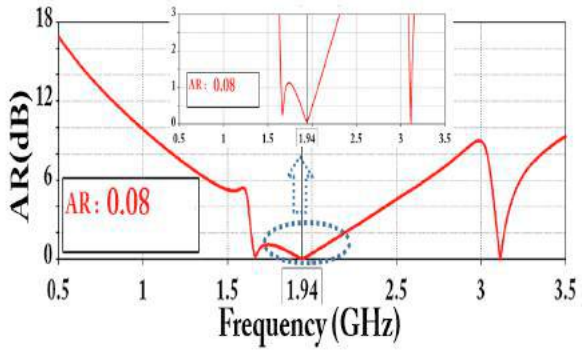

Figure 4: Axial Ratio

References

[1] Jiang Wang, Zhongxiang Shen, Wen Wu, and Keming Feng, Wideband circular polarizer based on dielectric gratings with periodic parallel strips, *Optical Express* 23, 12533-12543, 2015.

[2] H.Mirza and M.F.Elahi, A UHF-RFID tag antenna for commercial applications, 2008 *International Conference on Electrical and Computer Engineering*, Dhaka, pp. 764-767, 2008.

[3] Martinez-Lopez, Lourdes, et al. A multilayer circular polarizer based on bisected split-ring frequency selective surfaces, *IEEE Antennas and Wireless Propagation Letters* 13 153-156, 2014.

[4] Wei Zhang, Jian-ying Li, and Ling Wang, Broadband Circular Polarizer Based on Multilayer Gradual Frequency Selective Surfaces, *International Journal of Antennas and Propagation*, vol. 2016

[5] H. Zhu, K. L. Chung, X. L. Sun, S. W. Cheung and T. I. Yuk, CP metasurfaced antennas excited by LP sources, *Proc IEEE International Symposium on Antennas and Propagation*, Chicago, IL, pp. 1-2 , 2012.

[6] M. Fartookzadeh and S. H. Mohseni Armaki, Dual-Band Reflection-Type Circular Polarizers Based on Anisotropic Impedance Surfaces, *IEEE Transactions on Antennas and Propagation*, vol. 64, no. 2, pp. 826-830, 2016.

[7] Di Palma, L., Clemente, A., Dussopt, L., Sauleau, R., Potier, P., & Pouliguen, P, Circularly-polarized reconfigurable transmitarray in Ka-band with beam scanning and polarization switching capabilities. *IEEE Transactions on Antennas and Propagation*, *65*(2), 529-540, (2017)

Swastika-Shaped Flexible Linear to Circular Polarizer using Textiles

Hidayath Mirza[1, 2], Ping Jack Soh[1], Mohd Faizal Jamlos[1], Muhammad Nazrin Ramli[1], Azremi Abdullah Al-Hadi[1], Emad S. Hassan[2], and Sen Yan[3]

[1]Advance Communication Engineering (ACE) CoE, School of Computer and Communication Engineering, University Malaysia Perlis (UniMAP), Pauh Putra, 02600, Arau, Perlis, Malaysia.

[2]Dept. of Electrical Engineering, College of Engineering, Jazan University, P. O. Box 706, Jazan 45142 Kindom of Saudi Arabia.

[3]ESAT-TELEMIC, KU Leuven, Kasteelpark Arenberg 10, Box 2444, 3001 Leuven, Belgium

*corresponding author: pjsoh@unimap.edu.my

Abstract

In this paper, a flexible linear to circular polarizer (LCP) using Felt as substrate and Shieldit fabric its conducting material is designed. The simulated structure demonstrates a 10 dB fractional bandwidth (FBW) of 13.17 %. Meanwhile, its 3dB axial ratio bandwidth ranges from 2.01 GHz to 2.29 GHz. The size of the unit cell is 56 x 67.2 x 3mm^3 which is about 0.4067 x 0.4881 x 0.0218 λ at 2.04 GHz. A phase difference of 81.78^o is observed, which is equal to about 91 % in terms of conversion ratio.

Introduction

Traditionally, antennas are designed and operated in linear polarization [1,2]. However, several other applications such as GPS and satellite communication require the use of circular polarized antennas [3-5]. This is especially relevant when such antennas are required to support location tracking in a wearable format [6,7]. A simple method to enabling circular polarization is to place a linear-to-circular polarization converter in front of a linearly polarized antenna.

In this paper, an innovative linear to circular polarizer is proposed and designed using such flexible materials.

Unit Cell Design

To realize the flexible polarizer, Felt is used as its substrate and ShiledIt Super as its conducting fabric. It is designed using CST Microwave Studio's frequency domain solver and excited using Floquet ports. To create pure circular polarization using linear polarized antennas, the criteria in equation (1) needs to be met, and its phase difference between Ty and Tx components must be ± 90^0 as per equation (2), (3)[3]. A phase difference of 81.78^0, which is equivalent to 90.86 % in conversion ratio (CR) is achieved at 2.18 GHz, see Figure 4. Figure 5 represents the 3dB AR BW of 13.17 % with a reflection coefficient of at least -10 dB. This indicates its suitability to function as a linear-to-circular polarizer for applications requiring material flexibility.

$$|T_x| = |T_y| \tag{1}$$

$$\begin{aligned} \mathrm{PD}(\varphi) &= \left(\frac{\angle T_y}{\angle T_x}\right)(\text{degrees}) \\ \mathrm{CR} &= \left(\frac{PD}{90^0}\right)*100 \ \ (\%) \end{aligned} \tag{2}$$

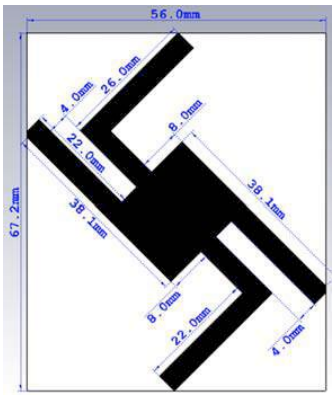

Figure 1 Topology of the swastika-shaped LCP (front view).

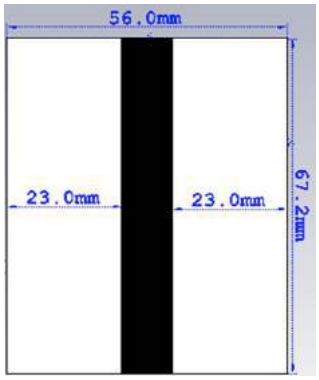

Figure 2 Topology of the swastika-shaped LCP (back view).

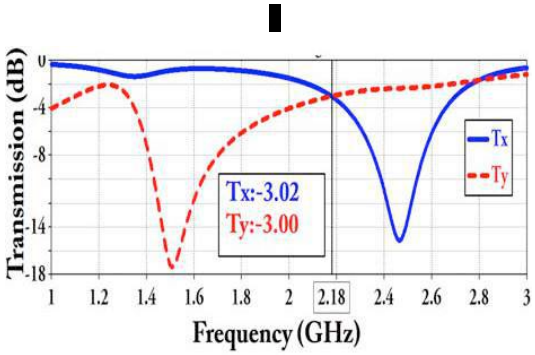

Figure 3 Tx and Ty components

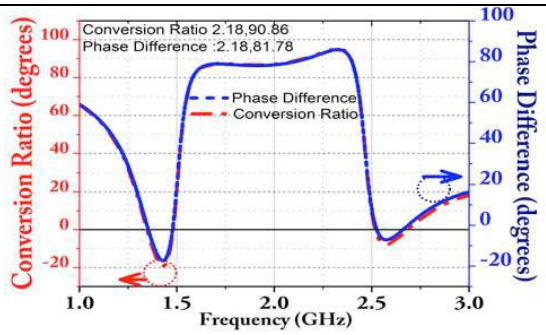

Figure 4 Phase difference and conversion ratio

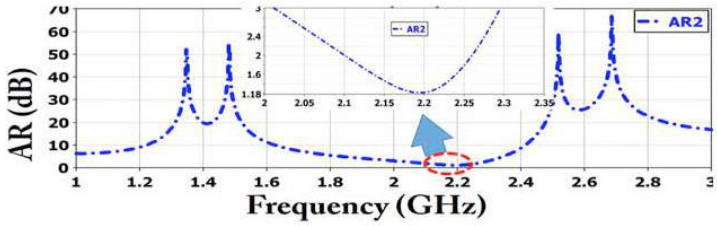

Figure 5 Axial Ratio with 3dB bandwidth

Conclusion

In this paper, an innovative linear to circular polarizer has been designed for operation in the S band using flexible materials such as textile and ShiedlT super conducting fabric based flexible. The single layered structure also ensures design and fabrication simplicity, compactness and about 91 % conversion efficiency.

Acknowledgements

This project is supported in part the Malaysian Ministry of Higher Education (MOHE) Prototype Development and Research Grant Scheme (PRGS) (grant no: 9013-00024) and Research Foundation - Flanders (F.W.O.) Postdoctoral Fellowship (No. 12O1217N).

References

[1] N. H. M. Rais, P. J. Soh, F. Malek, S. Ahmad, N. B. M. Hashim and P. S. Hall, "A review of wearable antenna, *Loughborough Antennas & Propagation Conference2009*, Loughborough, pp. 225-228, 2009,.

[2] P. J. Soh, G. A. E. Vandenbosch, S. L. Ooi and N. H. M. Rais, Design of a Broadband All-Textile Slotted PIFA, *IEEE Transactions on Antennas and Propagation*, vol. 60, no. 1, pp. 379-384, 2012.

[3] Toh, Bee Yen, Robert Cahill, and Vincent F. Fusco, Understanding and measuring circular polarization, *IEEE Transactions on Education* 46.3, 2003

[4] Kaplan, Elliott, and Christopher Hegarty. *Understanding GPS: principles and applications*. Artech house, 2005.

[5] Constantine AB. *Antenna Theory: Analysis And Design. Microstrip Antennas*, third edition, John wiley & sons. 2005.

[6] Soh PJ, Vandenbosch GA, Mercuri M, Schreurs DM. Wearable wireless health monitoring: Current developments, challenges, and future trends. IEEE Microwave Magazine. May;16(4):55-70, 2015

[7] M. I. Jais, M. F. B. Jamlos, M. Jusoh, T. Sabapathy, M. R. Kamarudin, R. B. Ahmad, A. A. A.-H. Azremi, E. I. Bin Azmi, P. J. Soh, G. A. E. Vandenbosch, and N. L. K. Ishak, A novel 2.45 GHz switchable beam textile antenna (sbta) for outdoor wireless body area network (wban) applications, *Progress In Electromagnetics Research*, Vol. 138, 613-627, 2013

[8] Yan, Sen, and Guy AE Vandenbosch, Compact circular polarizer based on chiral twisted double split-ring resonator, *Applied Physics Letters* 102.10,103503, 2013.

[9] Fei,P.,Shen, Z.,Wen,X.,& Nian, F, A single-layer circular polarizer based on hybrid meander line and loop configuration, *IEEE Transactions on Antennas and Propagation*, 3(10), 4609-4614, 2015.

[10] J. D. Baena; S. B. Glybovski; J. P. del Risco; A. P. Slobozhanyuk; P. A. Belov, "Broadband and Thin Linear-to-Circular Polarizers Based on Self-Complementary Zigzag Metasurfaces, *IEEE Transactions on Antennas and Propagation* , vol.PP, no.99, pp.1-1, 2016.

Unloaded & Loaded Circular-Shaped Flexible Linear to Circular Polarizer using Polydimethylsiloxane (PDMS)

Hidayath Mirza[1, 2], Ping Jack Soh[1, 3*], Mohd Faizal Jamlos[1], Muhammad Nazrin Ramli[1], Azremi Abdullah Al-Hadi[1], Emad S. Hassan[2] and Sen Yan[3]

[1]Advance Communication Engineering (ACE) CoE, School of Computer and Communication Engineering, Universiti Malaysia Perlis (UniMAP), Pauh Putra, 02600, Arau, Perlis, Malaysia.

[2]Dept. of Electrical Engineering, College of Engineering, Jazan University, P. O. Box 706, Jazan 45142 Kingdom of Saudi Arabia.

[3]ESAT-TELEMIC, KU Leuven, Kasteelpark Arenberg 10, Box 2444, 3001 Leuven, Belgium

*corresponding author: pjsoh@unimap.edu.my

Abstract

In this paper, a flexible linear to circular polarizer designed on flexible Polydimethylsiloxane (PDMS) and textiles is proposed. PDMS is used as the substrate while the conducting elements are made using a commercial conductive textile, ShieldIt Super. Two structures consisting of loaded and unloaded circular unit elements are proposed. The unloaded circular unit cell design is sized at 46 x 56 x 3 mm^3 to operate at 2.04 GHz, while the loaded version is sized at 68 x 58 x 3 mm^3 for operation at 2.58 GHz. Both structures exhibited 3 dB axial ratio bandwidths of 33.17 % (1.99 GHz to 2.79 GHz) for the unloaded circular and 19.51 % (2.54 GHz to 3.09 GHz) for the loaded circular-shaped element inscribed in a circular patch.

Introduction

The use of circular polarization has become an essential in satellite communication, global positioning system, radar, weather forecasting and RFID. Due to its unique characteristics, propagation using circular polarized antennas minimizes noise interference, enables greater penetration into buildings, reaching difficult areas, reducing multipath and causes smaller changes to signals when propagating in rain and fog [1-5].

In this paper, two unit cell designs are proposed and investigated as follows: a) a circular patch inscribed with unloaded circles (denoted as "unloaded" in Figure 1) and b) a circular patch inscribed with loaded circles (denoted as "loaded" in Figure 2)[6-7].

Unit Cell Design

The polarizer has been designed using the frequency domain solver in CST Microwave Studio and is excited using Floquet ports. To create circular polarization using linear polarization, the phase difference between the phase of Ty and Tx components must be $\pm 90^0$ as in equations (1) and (2) [8-9]. A phase difference of about -94^0 and $+90^0$ is obtained for the unloaded and loaded structure, respectively, see Figure 4. Meanwhile, Figure 5 illustrates its 3 dB axial ratio (AR) bandwidth, indicating a bandwidth of 33.17 % and 19.51 % for the unloaded and loaded structure, respectively.

$$|T_x| = |T_y| \tag{1}$$

$$\mathrm{PD}(\varphi) = \left(\frac{\angle T_y}{\angle T_x} \right) (\text{degrees}) \tag{2}$$

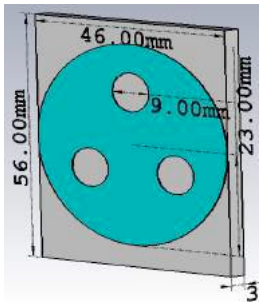

(a)

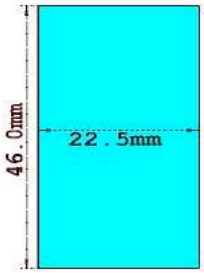

(b)

Figure 1 Topology of the unloaded circles inscribed in a circular-shaped polarizer (a)front view (b) back view

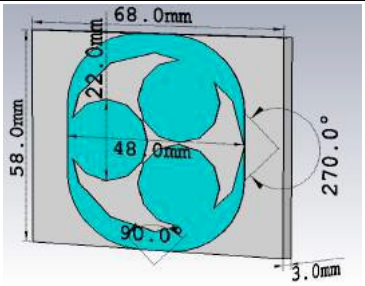

(a)

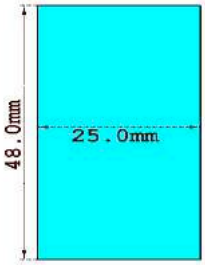

(b)

Figure 2 Topology of the loaded circular shaped polarizer (a)front view (b) back view

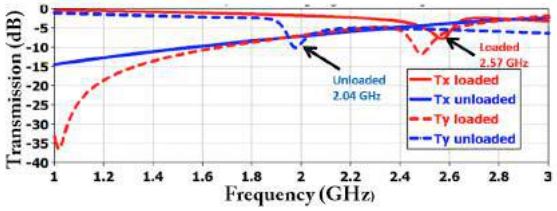

Figure 3 Tx and Ty components

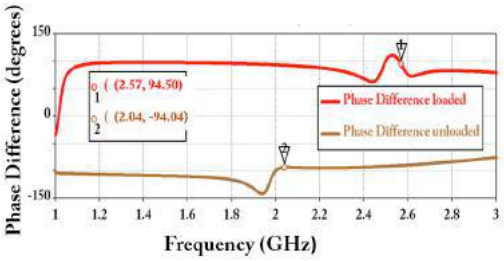

Figure 4 Phase difference

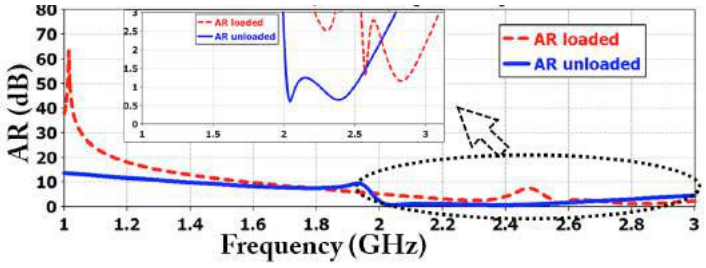

Figure 5 Axial ratio bandwidth

Conclusion

The use of the loaded circular patch unit cell enabled the polarizer to exhibit a wider AR bandwidth compared to the unloaded version. Despite that, both structures exhibited a

satisfactory functionality as a linear-to-circular polarizer at the center frequency of 2.60 GHz and 2.04 GHz for loaded and unloaded circles, respectively.

Acknowledgements

This project is supported in part the Malaysian Ministry of Higher Education (MOHE) Prototype Development Research Grant Scheme (PRGS) (grant no: 9013-00024) and Research Foundation - Flanders (F.W.O.) Postdoctoral Fellowship (No. 12O1217N).

References

[1] Batchelor, John C., and Richard J. Langley, Microstrip annular ring slot antennas for mobile applications, *Electronics Letters* 32.18: 1635, 1996.

[2] A, X., Huang, C., Pu, M., Hu, C., Feng, Q. and Luo, X, Single-layer circular polarizer using metamaterial and its application in antenna. *Microw. Opt. Technol. Lett.,* 54: 1770–1774, 2012.

[3] Mirza, Hidayath, Mohd Imran Ahmed, and Mohammad Fazleh Elahi. Circularly polarized compact passive RFID tag antenna. International Conference in Electrical and Computer Engineering, *ICECE2008*, Bangladesh, pp. 760-763, 2008.

[4] Toh, Bee Yen, Robert Cahill, and Vincent F. Fusco, Understanding and measuring circular polarization, *IEEE Transactions on Education* 46.3, 2003.

[5] Constantine, A. Balanis. *Antenna theory: analysis and design. MICROSTRIP ANTENNAS*, third edition, John wiley & sons, 2005.

[6] B.A.Munk, *Frequency Selective Surfaces: Theory and Design*. New York: Wiley, 2000.

[7] Vardaxoglou, John C, *Frequency selective surfaces: analysis and design*, Research Studies Press, 1997.

[8] J. L. Masa-Campos and F. Gonzalez-Fernandez, Dual linear/circular polarized plannar antenna with low profile double-layer polarizer of 45º tilted metallic strips for WiMAX applications, *Progress In Electromagnetics Research*, Vol. 98, 221-231, 2009

[9] Yan, Sen, and Guy AE Vandenbosch, Compact circular polarizer based on chiral twisted double split-ring resonator, *Applied Physics Letters* 102.10: 103503, 2013.

Adaptive GPS Array Antennas Using the Non-Linear ω-β Metamaterial Feeds

Heejun Park[1], Dajung Han [1], Changhyeong Lee [1], M. Kamran Khattak[1], and Sungtek Kahng[1*], Hosub Lee[2]

[1] Dept. Information & Telecommunication Engineering, Incheon National University, Incheon, Korea
[2] Comunication R&D Center LIG NEX1, Seongnam, Korea
*corresponding author, E-mail: s-kahng@inu.ac.kr

Abstract

This paper presents an approach to enable a typical GPS receiver to be much less susceptible to intentional disruption such as jamming and change in link environment. In order for the GPS receiver to cope with jamming and to get adaptivity, 4x4 or 8x8 elements beamforming antenna is designed using metamaterials. The design results show the antenna gain much higher than 5dBi and the movable various beam patterns.

1. Introduction

Recently, as the necessity of location information has been expanded in all industries where IT is applied such as defense, construction, traffic and etc., the demand of GPS(Global Positioning System) antenna is steadily increasing. The Frequency blocks of GPS system are classified into five types and are named L1, L2, L3, L4 and L5 blocks. Among them, the L1 and L2 block can be used for civil use, and the L1 block is in general use for the navigation message signal.
As a typical GPS receiver has a fixed and wide angular beam, when the receiver is mounted on a vehicle or aircraft that moves, it does not have the adaptivity in beam. To overcome the weakness, the beam can be steered by controlling the electrical phase. The electrical phase of each element is controlled with metamaterial phase shifters.

2. Design procedures

The design starts with the element which is going to be extended to a 4x4 matrix. Coaxial-fed patch antennas are placed periodically, and denoted as (1,1) through (4,4) from left to right in the descending order from the top row.

Fig. 1. An adaptable GPS antenna to be designed

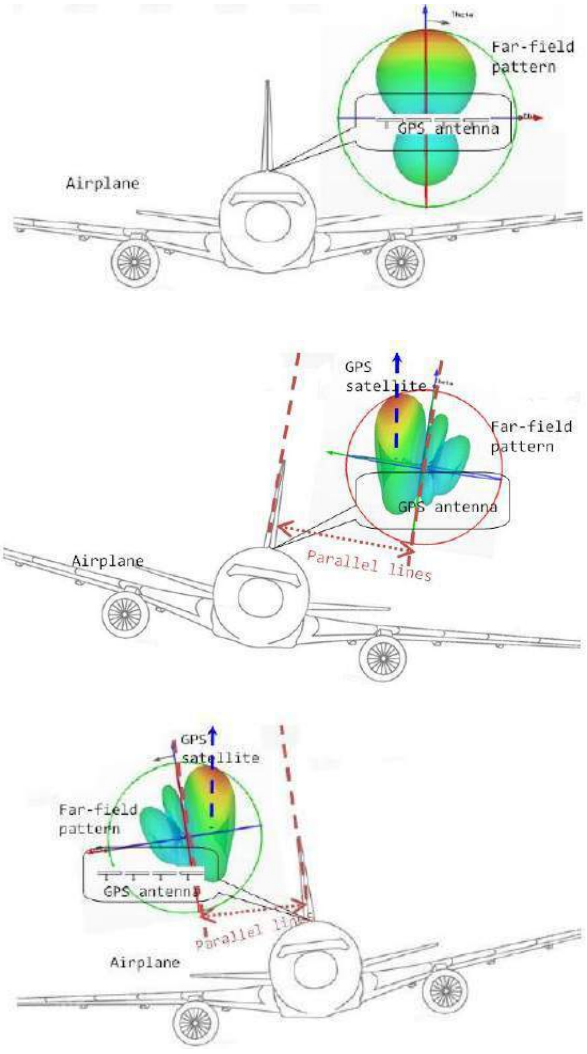

Fig. 2. Adaptivity of the GPS receiver

2.1. Basic design array antenna

Figure 3 shows the 4X4 Array antenna and 16 ways power divider. For ease of matching, the radiator and the feeder line are designed to be connected in aperture coupling. Also, in order to reduce the required area and the convenience of the design, the line at the end connected to the antenna was matched with 100 ohms.

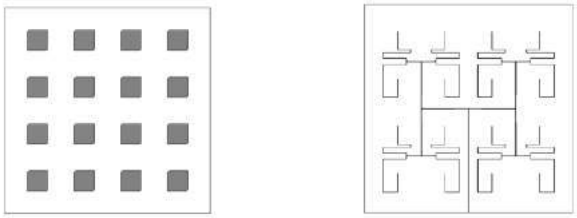

(a) (b)

Fig. 3. The designed array antenna and feed network

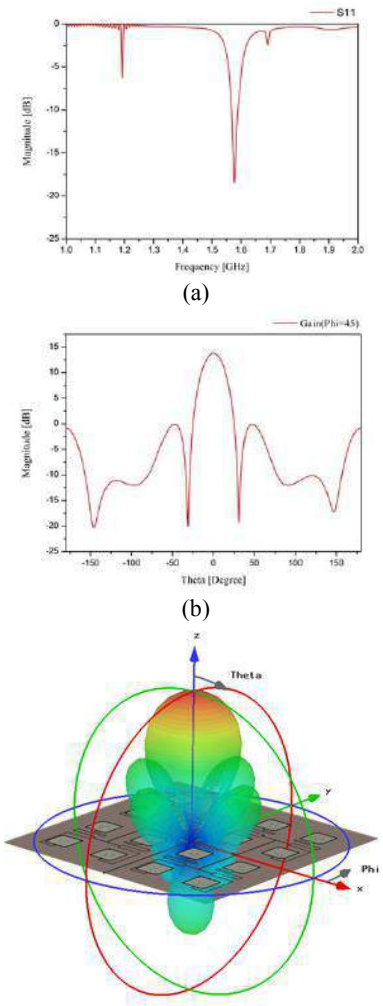

(a)

(b)

(c)

Fig. 4. Design results of GPS array antenna (a)Return loss (b)Radiation pattern(2D) (c)Radiation pattern(3D)

Simulation results is in the figure 4. The antenna gain is 13.79dBi and efficiency is 50.2%. Also, it shows that the direction of the antenna beam is directed to the vertical direction(+z) because of the in-phase feeding.

2.2. Design metamaterial phase shifter

In order for the array antenna to electrically steer the antenna beam, a different phase difference feed must be applied to each radiating element. In order to realize the metamaterial phase shifter, the combination of the RH transmission characteristic component and the LH transmission characteristic component by combining the lumped element and the shorting pin in the microstrip transmission line. The metamaterial phase shifter has different output phases according to the lumped element combination value.

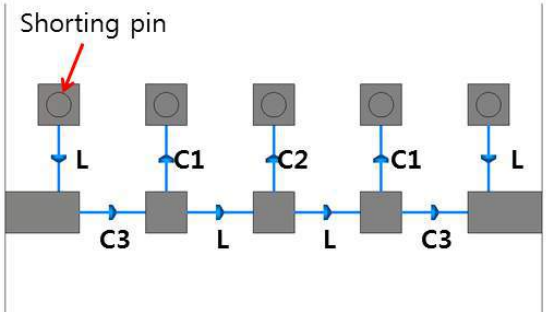

Fig. 5. The proposed metamaterial phase shifter

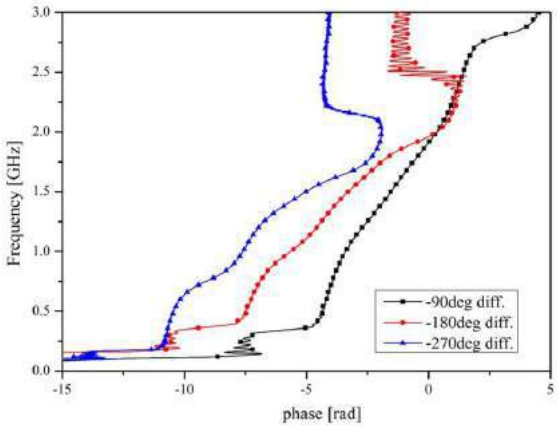

Fig. 6. The phase distribution curve of the proposed CRLH phase shifter

2.3. Combining the array antenna and phase shifter

When azimuth and elevation angle of the main beam are set to 45 degrees, each array elements should have 90 degrees phase differences.

As figure 7 shows, the CRLH phase shifter is combined to the feed network. The results show that the return loss and low mutual coupling are obtained at the L1-band. The antenna gain is 12.54dBi and efficiency is 58.7%. Also when the power was fed so that each adjacent radiator element had a phase difference of 90 degrees, the main beam of the antenna was tilted 43 degrees in the direction of +Theta and +Phi. As well as the null point moved together with the main beam. Thus, by adjusting the appropriate the lumped element value, the beam of the antenna can be steered at various angles and it can increase adaptivity of the antenna.

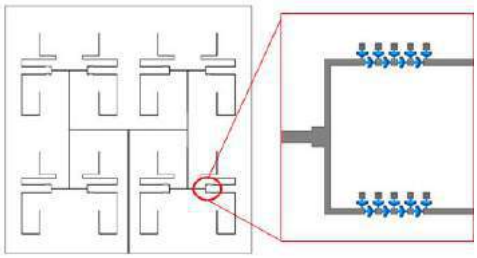

Fig. 7. Combination of array antenna and CRLH phase shifter

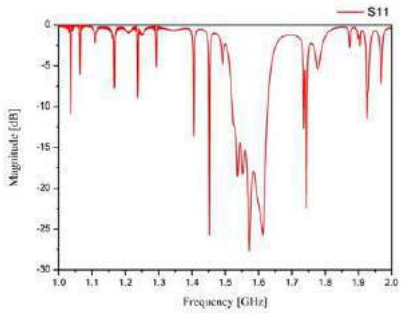

(a)

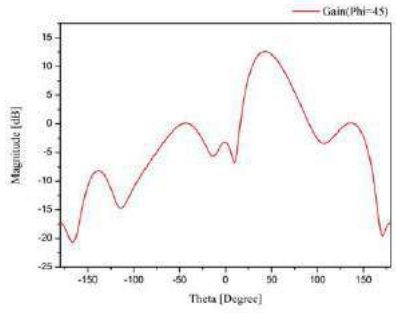

(b)

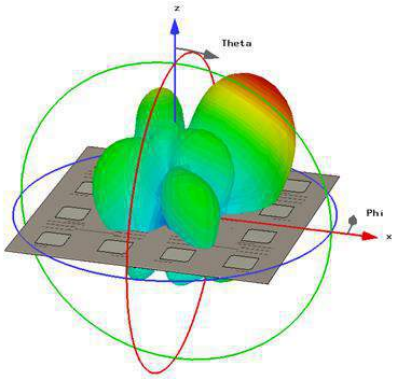

(c)

Fig. 8. The simulation results (a)Return loss (b)Radiation pattern(2D) (c)Radiation pattern(3D)

3. Conclusions

In this paper, we have studied beam tilting method for the antenna beam adaptivity and anti-jamming function of GPS receiver used in vehicle or payload, and verified it by simulation. The results show that the main beam of the GPS receiving antenna can be steered by the CRLH phase shifter. The proposed CRLH phase shifter can output various phase according to the lumped element C value. If the CRLH phase shifter is combined with varactor diode, it can steer the antenna beam in realtime.

Acknowledgements

This work was supported by Space R&D Project of KARI.

References

[1] D. Lu, R. Wu, Z. Su, and W. Huang, "A Two Stage GPS Anti jamming processor for Interference Suppression and Multipath mitigation", *Proc. Of 2007 IEEE Radar Conference*, pp. 746 – 749, 17-20 April 2007.

[2] S. Kahng, et al, "A Low-Profile Dual-Band SIW Slot-Array Antenna based on LH Material Waveguides for a Satellite Communication Receiver", *Proc. of IEEE APS 2014*, p.58, July 6-11, 2014

Dual-UWB T-Slotted AMC for Mandatory UWB Channels

N. F. M. Aun[1*], P. J. Soh[1], M. F. Jamlos[1], H. Lago[1], and A. A. Al-Hadi[1]

[1]Advanced Communication Engineering (ACE) CoE, School of Computer and Communication Engineering (ACE), Pauh Putra Campus, 02600, Arau, Perlis.
farahiyah86@gmail.com

Abstract

A flexible dual band Artificial Magnetic Conductor (AMC) operating in the two Ultra Wideband (UWB) mandatory channels is proposed. Operations are centered at 4 GHz (channel 1) and 8 GHz (channel 6) based on the IEEE 802.15.4 standard for Wireless Body Area Network (WBAN). Upon validation of its dual-UWB performance, the proposed AMC is subsequently incorporated on a quasi-circular patch antenna to determine its contribution in improving the antenna's reflection coefficient and impedance bandwidth.

1. Introduction

Artificial Magnetic Conductor (AMC) is a metamaterial which exhibits a perfect magnetic conductor's (PMC) characteristics within a certain frequency band [1-10]. AMC is an effective approach to significantly widen the bandwidth [4], [7], [8], for radiation suppression towards a certain direction [1], [6], transmission enhancement [3], impedance matching improvement [8] and gain enhancement [2]. Recently, work in [10] presented AMC-integrated antenna for operation of Ultra Wideband (UWB) mandatory channel 6 centered at 8 GHz with combination of upper Wireless Local Area Netwrok (WLAN) band at 5.5 GHz. On the other hand, a T-slotted rectangular AMC element is proposed in this paper to improve the impedance matching and bandwidth of a dual band UWB antenna in the mandatory channels. The proposed antenna is quasi-circular, comprising of two semicircles with different radii to radiate at 4 GHz and 8 GHz. In comparison, the standalone antenna without the AMC plane is poor in terms of impedance matching due to the use of a closely-located ground plane to the radiator. This can be approximated as a perfect electric conductor (PEC) which introduces a negative image current to that of a source.

2. AMC and Antenna Design

In this work, a rectangular T-slot unit cell is designed and optimized before being duplicated and placed periodically to the complete AMC plane. Fig. 1 illustrate the AMC unit cell operation centered at 4 GHz and 8 GHz with about 222.95 MHz and 561.38 MHz of phase reflection bandwidth, respectively, determined within ±90° from the zero-phase reflection (PMC) point. The planar AMC unit cell is then multiplied to form a 3 x 3 AMC plane layer.

The geometry of the proposed quasi-circular patch antenna and the AMC plane layer is shown in Fig. 2(a) and 2(b) respectively. The full structure consists of the AMC plane which is placed underneath the same 1.5 mm thick felt substrate consisting of a radiating patch made from the *ShieldIt*. Fig. 2(c) shows the cross-section of the integrated AMC-antenna structure.

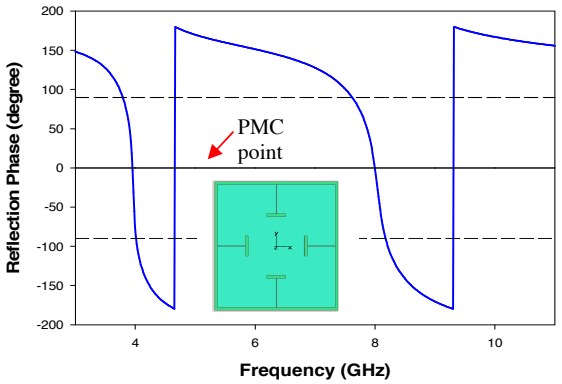

Figure 1: The reflection phase of the AMC unit cell

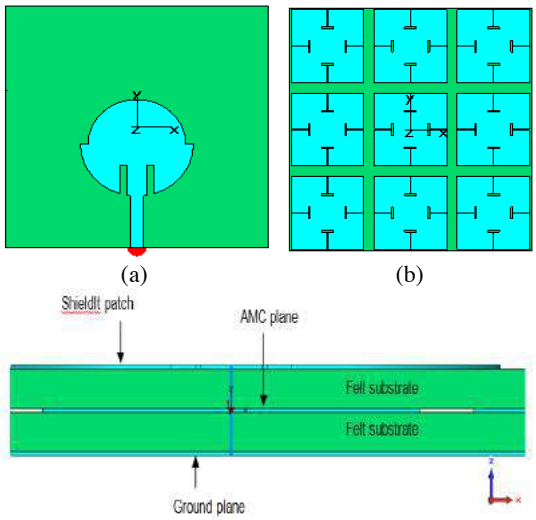

(c)

Figure 2: The quasi-circular patch, (b) 3 x 3 array AMC layer, and (c) overall antenna's cross-section

3. Results and Discussion

As depicted in Fig. 3, the incorporation of the AMC plane into the antenna improved its reflection coefficients. Minimum values of -16.08 dB and -12.22 dB are achieved at 4 GHz and 8 GHz. The performance of the standalone antenna is also provided as a comparison.

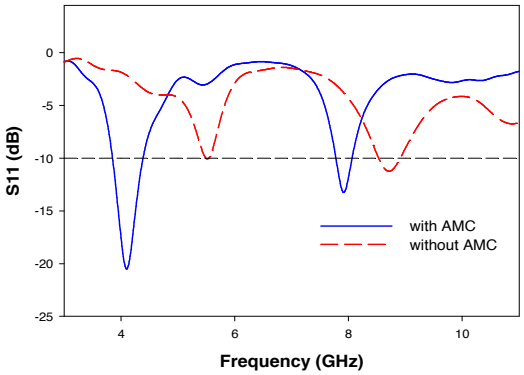

Figure 3: Reflection coefficients of the standalone patch antenna with and without AMC

4. Conclusions

An AMC unit cell based on rectangular patches integrated with T-slots is proposed in this work. Its dual band operation is centered at 4 GHz and 8 GHz with reflection phase bandwidths of 222.95 MHz and 561.38 MHz, respectively. The inclusion of the AMC structure onto a conventional slotted quasi-circular patch antenna successfully lowered its resonances and improved impedance matching at 4 GHz and 8 GHz.

Acknowledgements

This project is supported in part by the Malaysian Ministry of Higher Education (MOHE) MyBrain15 Program and the Fundamental Research Grant Scheme (FRGS) (grant no: 9003-00527).

References

[1] S. Yan, P. J. Soh, and G. A. E. Vandenbosch, "Low-Profile Dual-Band Textile Antenna With Artificial Magnetic Conductor Plane," *IEEE Trans. Antennas Propag.*, vol. 62, no. 12, pp. 6487–6490, 2014.

[2] L.-R. Zhong, G.-M. Yang, and Y.-W. Zhong, "Gain enhancement of bow-tie antenna using fractal wideband artificial magnetic conductor ground," *Electron. Lett.*, vol. 51, no. 4, pp. 315–317, 2015.

[3] M. K. A. Rahim, N. A. Samsuri, K. Kamardin, and P. S. Hall, "Vertical and horizontal transmission enhancement between antennas using textile artificial magnetic conductor waveguide sheet," *Electron. Lett.*, vol. 51, no. 9, pp. 671–673, 2015.

[4] R. Dewan, S. K. A. Rahim, S. F. Ausordin, M. Z. M. Nor, and B. M. Saad, "Crescent moon-shaped artificial magnetic conductor ground plane for patch antenna application," *2013 IEEE Symp. Wirel. Technol. Appl. ISWTA.*, Kuching, Malaysia, pp. 254–258, 2013.

[5] F. Rahmadani and A. Munir, "Microstrip patch antenna miniaturization using artificial magnetic conductor," *2011 6th Int. Conf. Telecommun. Syst. Serv. Appl.*, Bali, Indonesia, pp. 219–223, 2011.

[6] H. R. Raad, A. I. Abbosh, H. M. Al-Rizzo, and D. G. Rucker, "Flexible and compact AMC based antenna for telemedicine applications," *IEEE Trans. Antennas Propag.*, vol. 61, no. 2, pp. 524–531, 2013.

[7] P. Lu, "Combination of Bow-tie Shaped Meander Slot Antenna with Wideband AMC Structure," 2014 *IEEE Antennas and Propagation Society International Symposium (APSURSI).*, Memphis, Tennessee, pp. 2066–2067, 2014.

[8] R. R. Ihsan and A. Munir, "Utilization of artificial magnetic conductor for bandwidth enhancement of square patch antenna," *2012 7th Int. Conf. Telecommun. Syst. Serv. Appl. TSSA 2012.*, Bali, Indonesia, no. 003, pp. 192–195, 2012.

[9] K. Agarwal, Y. X. Guo, B. Salam, L. C. W. Albert, "Latex based near-endfire wearable antenna backed by AMC surface," *Microwave Workshop Series on RF and Wireless Technologies for Biomedical and Healthcare Applications (IMWS-BIO), 2013 IEEE MTT-S International*, 9-11 Dec 2013.

[10] N. F. M. Aun, P. J. Soh, M. F. Jamlos, H. Lago, A. A. Al-Hadi, "A Wideband Corner-Notched Artificial Magnetic Conductor (AMC) Integrated With a Rectangular Ring Antenna", *7th International Conference on Metamaterials, Photonic Crystals and Plasmonic (META 2016)*, 25-28 July 2016, Malaga, Spain.

Investigation of a Resonator Based Metamaterial Fascinating Sensor Applications

M. T. Islam[1*], M. N. Rahman[1], M. Z. Mahmud[1], M. A. Ullah[1], and MJ Singh[1]

[1] Dept. of Electrical, Electronic and Systems Engineering, Universiti Kebangsaan Malaysia, Malaysia
*corresponding author, E-mail: tariqul@ukm.edu.my

Abstract

A resonator based metamaterial for sensor application is studied in this paper. The resonator is encompassed by a partial ground plane and excited by a microstrip feed-line. As the resonator, partial ground frame, and the feeding transmission line (FTL) are on the same microstrip, the measurement can be executed by using the common laboratory facility instead of using the waveguide. The proposed metamaterial occupies a compact size of 20 mm × 20 mm and is imprinted on a low-cost FR4 substrate. The substrate has a relative permittivity of 4.6 with adielectric loss tangent of 0.02. The resonator and the ground frame are placed on the similar part of the substrate and the feed-line is placed on the other part of the substrate. In metamaterial design, normally arrays of metamaterial unit cells are needed, whereas this study presents only one cell which can achieve the metamaterial properties. The characteristic parameters are fetched and analyzed to find the concurrency between the simulated and measured results. The presented metamaterial is applied in sensor applications where the simulated and measured results reveal considerable agreement.

1. Introduction

Metamaterials were first to come into focus by Veselago in 1968. From the introduction, metamaterials became an interesting field of research for industry and researchers who are devoted in metamaterial characteristics such as negative permeability and negative permittivity. Since then, researchers have suggested lots of resonator based metamaterials for different operating frequencies [1]. These metamaterials are designed, analyzed, validated and manufactured for practical observations [2-11]. A split ring resonator (SRR) and capacitance loaded strip (CLS) unit cell inspired metamaterial antenna has been reported in [2] for UWB microwave imaging applications. A metamaterial based fuel sensor has been mentioned in [3] which operates in the ISM (Industrial Scientific and Medical Standard) band. A split ring resonator based metamaterial for terahertz sensing applications has been referenced in [4]. A metamaterial using broadside-coupled triangular split-ring-resonators for terahertz sensing applications has been mentioned in [5]. An electric field coupled resonator antenna has been described in [6] where the comparison among the traditional split ring resonator based devices and the electric-field-coupled (ELC) and complementary electric-field-coupled (CELC) resonators based devices has been addressed. Referenced in [7], a metamaterial based microwave sensor has been focused in which the transmission lines (TL) act as a building block for microwave sensors. In [8], the dielectric characterization of a metamaterial based on the complementary, split ring resonators (CSRR) has been discussed. Having the shape of CSRR, the sensor operates at a 0.8-1.3 GHz band. In [9], the performance characteristics and the comparisons of different metamaterial sensors have been reviewed and summarized. A high sensitive metamaterial sensor has been rendered in [10] for the dielectric characterization of microfluidics. A thin film metamaterial sensor using rectangular asymmetric double split resonators has been reported in [11].

In this study, a metamaterial based on resonator has been introduced. The proposed metamaterial is based on a single unit cell which depicts all the metamaterial characteristics. In the proposed configuration, the resonator and the ground frame are sketched on one part of the substrate. The feeding transmission line (FTL) is sketched on the other part of the substrate. This configuration has quite a lot of amenities which are discussed in this study. The resonator based metamaterials are not new and unique. Some of the examples are discussed in the literature review. The reason to choose the presented resonator for the proposed metamaterial is its simplicity in design and ease to fabricate. The proposed structure is based on the microstrip technology. The effective metamaterial characteristics for both the simulated and experimented results are fetched and analyzed. Both the results are very much close to each other.The proposed metamaterial can be used in various applications such as antennas, filters, sensors, imaging systems, etc. In this study, the proposed metamaterial is used in sensor applications in the GHz operating band. This study is organized in some sections. In the first section, the design, simulations, fabrication, and measurement technique of the metamaterial is discussed. The second section describes the metamaterial characteristics of the proposed prototype. In section three, the surface current distribution and the field distributions are described. Finally, the sensor application of the proposed metamaterial is discussed in section four.

2. Design, Simulation, Fabrication, and Measurement

The metamaterial characteristics are unavailable in conventional materials in nature. In this study, a resonator, ground frame along with an FTL are used to make a metamaterial device which depicts all the metamaterial properties. The proposed structure is designed on a low-cost FR4 dielectric substrate with a thickness of 1.6 mm. The substrate has 4.6 relative permittivity with a loss tangent of 0.02. The resonator and the ground frame are sketched on the same portion of the substrate. The feeding transmission line (FTL) is sketched on the opposite portion of the substrate. The metamaterial structure is simulated and analyzed by using the High-Frequency Structural Simulator (HFSS). The excitation is supplied to the resonator through the FTL. For the proposed structure, the electric, magnetic, boundary condition is used so that the electromagnetic wave propagates through FTL. Figure 1 shows the layout of the proposed metamaterial.

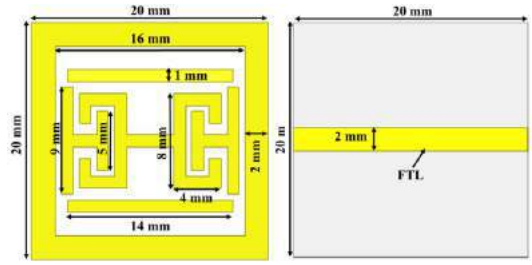

(a)(b)

Figure 1: Geometric layout of the Metamaterial structure. (a) top view and (b) bottom view.

The proposed metamaterial structure is fabricated on the printed circuit board for practical observation. The metamaterial is fabricated using a circuit plotter LPKF, S63. The fabricated prototype of the proposed resonator based metamaterial is illustrated in Figure 2. The measurement was performed in the microwave laboratory at the Department of Electrical, Electronic and Systems Engineering (JKEES), UKM, Malaysia. For the measurement of the proposed antenna, N5227A PNA Microwave Network Analyzer (10MHz- 67GHz) was used. The simulated and measured data are plotted by using data analysis software Origin Pro.

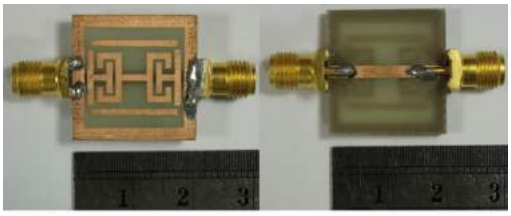

(a)(b)

Figure 2:Picture of the fabricatedmetamaterial prototype. (a) Top view and (b) bottom view.

Figure 3 shows the reflection and transmission coefficients of the metamaterial. The resonances are found at 4.90 GHz and 9.30 GHz where the reflections are minimum and the transmissions are maximum. The transmission resonance frequency is found at 7.60 GHz. Though there is a little disagreement between the reflection and transmission coefficients between the simulated and measured results, the two results are uniform over the operating band. The disagreement between the simulated and measured results occurs because of the fabrication tolerance, the soldering inaccuracies, and the external reflections.

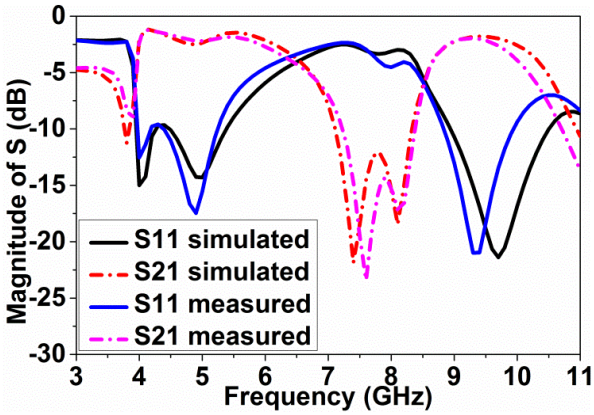

Figure 3:Simulated and measured magnitude of the S-parameter.

3. Metamaterial Characterization

To characterize the metamaterial, the effective metamaterial characteristics are extracted by the Nicolson-Ross-Weir (NRW) method. The method uses the S-parameters of the metamaterial to extract the characteristics. The NRW method is a simple and familiar method to characterize the unknown materials which are utilized for characterizing metamaterials. The refractive index depends on the effective permeability and effective permittivity, but not on reflection and transmission parameters in NRW method. The NRW method is mathematically represented by following equations [12].

$$V_1 = S_{21} + S_{11} \quad (1)$$

$$V_2 = S_{21} - S_{11} \quad (2)$$

$$\mu_r \approx \frac{2}{jk_0 d}\frac{1-V_2}{1+V_2} \quad (3)$$

$$\varepsilon_r \approx \frac{2}{jk_0 d}\frac{1-V_1}{1+V_1} \quad (4)$$

$$\eta = \sqrt{\mu_r \varepsilon_r} \quad (5)$$

Where μr, εr, η, d, and k0 corresponds effective permeability, effective permittivity, refractive index, substrate thickness, and propagation constant, respectively. In NRW method, the calculation of the parameters is based

on the S-parameter. The method does not depend on the calculation of the impedance.

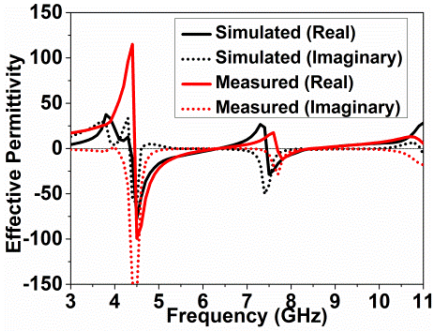

(a)

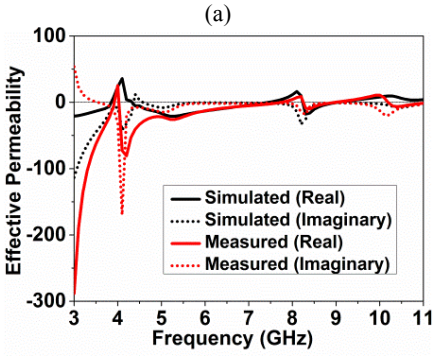

(b)

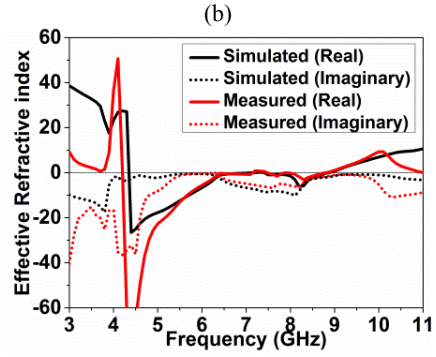

(c)

Figure 4: Simulated and measured effective constitutive parameters of the proposed metamaterial. (a) Effective permittivity, (b) Effective permeability, and (c) Effective refractive index.

At the peak of the transmission coefficient (S21), the effective permittivity and effective permeability should be negative, which is observed from the Figure 4 (a) and Figure 4 (b). From the Figure 4 (a), the effective permittivity is negative from 4.40 GHz to 6.0 GHz and from 7.65 GHz to 8.30 GHz. The simulated and measured data are a little bit dissimilar, but two results are unique throughout the operating frequency. Figure 4 (b) shows the negative permeability from 4.0 GHz to 7.50 GHz and from 8.20 GHz to 8.80 GHz. Again, there exists a little discrepancy between simulation and measurement. There exists a variation between the permittivity and permeability due to the polarization effect. This effect happens because of the construction of the metamaterial structure. The permittivity and permeability changes because of the change in design. This is for the unequal distribution of electromagnetic waves on the material which affects the properties of the material by the polarization. The refractive index is also affected by the polarization through the same technique. The refractive index will be negative when the permittivity and the permeability become negative. Figure 4 (c) shows the negative refractive index from 4.20 GHz to 6.30 GHz and from 8.0 GHz to 8.60 GHz. Thus, the proposed metamaterial structure shows double negative characteristics as the permittivity, permeability, and the refractive index is negative in the operating bandwidth.

4. Surface Current Distribution and Field Distribution

Surface current distribution is an important parameter to describe the resonance type of the metamaterial. Figure 5 displays the surface current distribution of the proposed resonator based metamaterial.

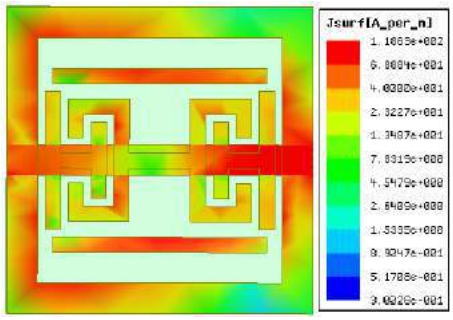

(a)

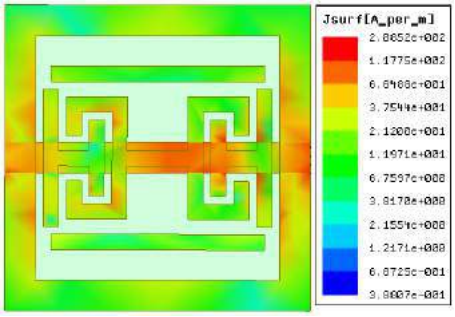

(b)

Figure 5: Distribution of currents of the metamaterial at the resonance frequency. (a) At 4.90 GHz (b) At 9.30 GHz.

From the figure, it is observed that the current density is mainly concentrated on the resonator and the FTL. Two opposite directional magnetic dipoles are formed on the ground frame due to symmetrical rotation of the surface currents on the resonator. Figure 6 shows the induced magnetic field of the metamaterial structure.

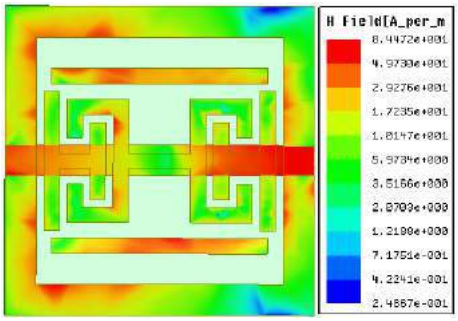

(a)

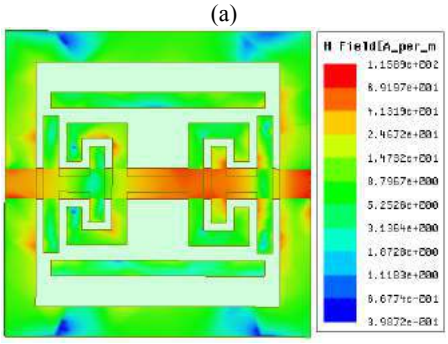

(b)

Figure 6: Distribution of magnetic field of the metamaterial at the resonance frequency. (a) At 4.90 GHz (b) At 9.30 GHz.

From the figure, it is investigated that at the resonance frequency, the FTL is coupled to the ground frame and the resonator with its electric field. At this point, the metamaterial structure shows the inductive and capacitive behavior due to the ground frame and the space between the ground frame and the resonator. The induced magnetic field is opposite to the external magnetic field and hence diamagnetism is generated. Due to the diamagnetism property, the negative permeability is extracted by the metamaterial structure. The magnetic field is vertical to the ground frame and the resonator. Thus, the negative permeability rises through the magnetic field, ground frame, and the resonator. As the metamaterial structure shows negative permittivity as well, the metamaterial gives a negative refractive index which is shown in Figure 4. Due to the collateral combination of the electric field of the structure to the ground frame, resonator, and the FTL, the negative permittivity rises. The presence of the ground frame around the resonator produces additional inductance and capacitance to the metamaterial structure and hence it becomes a crucial factor to create resonance. Moreover, the ground frame also serves as the ground plane, which provides the negative permittivity and negative permeability through the inductive-capacitive properties of the proposed structure.

The electric field distribution of the proposed resonator based metamaterial is shown in Figure 7. According to the figure, the electric field distributions are quite consistent with the surface current distribution and the magnetic field distributions. The electric field is distributed on the resonator, ground frame, and the FTL. The intensity of the electric field is enhanced at the higher frequency.

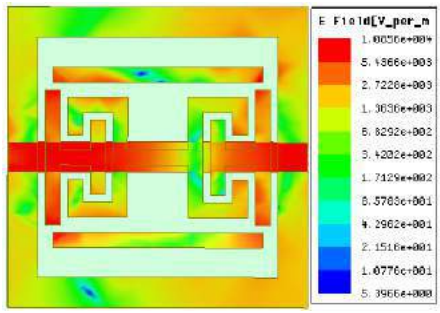

(a)

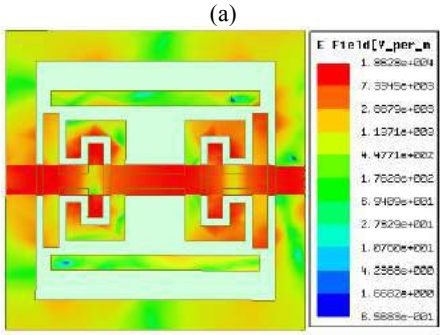

(b)

Figure 7: Electric field distribution of the proposed metamaterial at the resonance frequency. (a) At 4.90 GHz (b) At 9.30 GHz.

5. Metamaterial Sensor Application

The proposed resonator based metamaterial structure is used for the double-sided sensing system. The both front and back side of the proposed metamaterial is used in the sensing application. The unknown material which is to be detected is taken as the over-layer. By changing the thickness and the dielectric constant of the unknown material, the frequency response of the metamaterial sensing device is experimented.

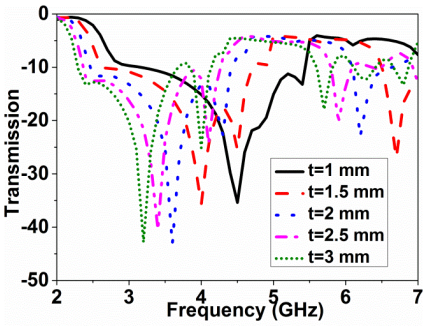

(a)

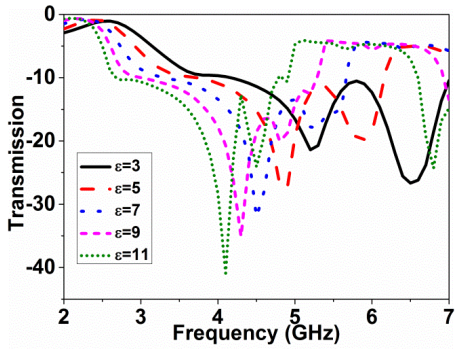

(a)

Figure 8:Change of transmission resonance. (a) for changing overlayerthickness (b) for changing overlayer permittivity.

Firstly, the effect of changing the overlayer thickness is considered to observe the frequency response. For the simulations, an over-layer with dielectric constant 4.4 and 0.025 loss tangent is considered as it is close to the parameter of the FR4 substrate which is used in the proposed metamaterial. Figure 8 (a) shows the simulated results after changing the thickness of the over-layer. From the figure, it is clearly observed that the transmission resonance shifts downward with the increase of the overlayer thickness. The sensing device along with the over-layer can be considered as the RLC resonant circuit in which the resonance frequency is calculated by the effective capacitance and the effective inductance. With the increment of the overlayer thickness, the effective inductance, and capacitance changes. Due to this, the transmission resonance shifts downward as the resonance frequency are directly related to the effective capacitance and the effective inductance. Thus, the proposed metamaterial structure can be effectively used in sensing application in the GHz region.

The frequency response due to changing the overlayer relative permittivity is simulated and analyzed. Figure 8 (b) illustrates the effects of the variation of the overlayer relative permittivity. When the relative permittivity is increasing, the transmission resonance downshifts as well. The higher overlayer permittivity corresponds to a larger downshift of the transmission resonance. Hence, the sensitivity of the metamaterial increases, according to the increment of the overlayer relative permittivity.

For the validation of the simulation, the practical experiments have been performed and the measured results are compared to the simulated results. In the practical observations, the FR4 material having a relative permittivity of 4.6 with 0.02 loss tangent and Rogers RO4350 material having a relative permittivity of 3.66 with 0.004 loss tangent are used as the over-layers. The thickness of the materials is 1.60 mm and 1.53 mm respectively. The metallic ledge on both portions of the substrates is abolished to have the over-layer having the dielectric materials only. The proposed metamaterial structure with the over-layers are shown in Figure 9.

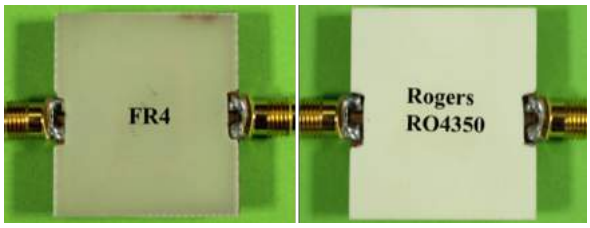

(a) (b)

Figure 9:Picture of the sensing device. (a) FR4 as over-layer (b) Rogers RO4350 as over-layer.

The measured results of the proposed resonator based metamaterial as a sensor along with the simulated results are displayed in Figure 10.

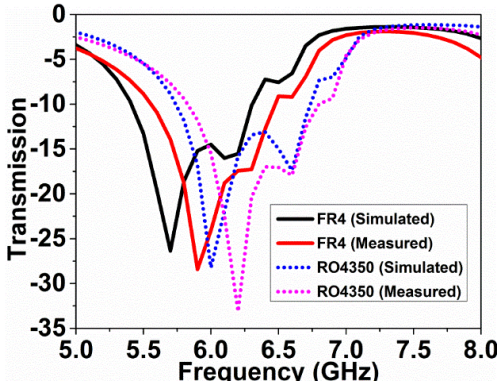

Figure 10:Simulated and measured transmission response with FR4 andRogers RO4350 over-layers.

From the figure, it is clearly investigated that the resonance frequency shifts downward with the increment of the thickness and the overlayer relative permittivity. As the FR4 has a larger thickness and higher relative permittivity than the Rogers RO4350 material, FR4 shifts more downward than the Rogers RO4350 overlayer with reference to no overlayers which is shown in Figure 3. More specifically, with no over-layer, the transmission resonance is at 7.60 GHz, but using the Rogers RO4350 and FR4 over-layers, the transmission resonance shifts to 6.20 GHz and 5.90 GHz, respectively.

To extend the experiment, double-overlayer structures are considered for perplexing situations. In this scenario, FR4+FR4 and Rogers RO4350+Rogers RO4350 double-over-layers are used. The simulation and practical investigations are conducted by the similar procedure as described in the previous section. The simulated and measured frequency responses for the double-over-layers is illustrated in Figure 11.

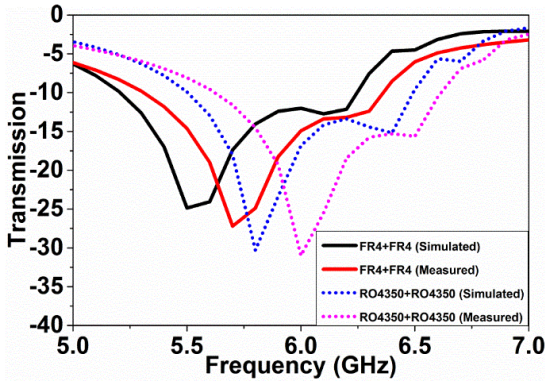

Figure 11:Simulated and measured transmission response with FR4+FR4 andRogers RO4350+Rogers RO4350 double-over-layers.

From the figure, it is clear that the resonance frequency shifts downward with the increment of the thickness and the overlayer relative permittivity. With no over-layer, the transmission resonance is at 7.60 GHz, but using the Rogers RO4350+Rogers RO4350 and FR4+FR4 double-over-layers, the transmission resonance shifts to 6.0 GHz and 5.70 GHz, respectively.

Both in the over-layer and double-over-layer cases, the simulated results vary a little with the measured results. This could be due to the mechanical etching of the metallic layer of the dielectric materials, external reflections during measurements, and soldering inaccuracies. Based on the simulations and measurements performed above, the proposed resonator based metamaterial can detect materials having different values of thickness and relative permittivity. The proposed metamaterial can be used as a sensor in various applications.

6. Conclusions

A resonator based metamaterial structure is designed, simulated, prototyped, and investigated as a sensor in this paper. The resonator is surrounded by a ground frame and is excited by a 50Ω feeding transmission line on the back side of the substrate. The metamaterial is measured by using common laboratory facilities instead of using waveguides. Both the results found in the simulation and measurement agree quite well and the metamaterial shows negative permittivity and negative permeability in the operating band. The proposed metamaterial can be used in various applications such as antennas, filters, sensors, imaging systems, etc. In this study, the metamaterial structure is used in sensor application where it can detect unknown over-layer materials with good sensitivity. The metamaterial properties with an uncomplicated design, using only one metamaterial unit cell make the structure competent to be used where metamaterial characteristics are needed.

Acknowledgements

The authors would like to thank the Department of Electrical, Electronic and Systems Engineering (JKEES), Universiti Kebangsaan Malaysia (UKM) and Ministry of Higher Education Malaysia (Grant No. AP-2015-007), for the sponsor of this work.

References

[1] C. Sabah, T. Nesimoglu, Design and characterization of a resonator-based metamaterial and its sensor application using microstrip technology,*Optical Engineering*55: 027107-027107, 2016.

[2] M. M. Islam, M. T. Islam, M. Samsuzzaman, M. R. I. Faruque, N. Misran, M. F. Mansor, A miniaturized antenna with negative index metamaterial based on modified SRR and CLS unit cell for UWB microwave imaging applications,*Materials* 8: 392-407, 2015.

[3] V. Rawat, V. Nadkarni, S. Kale, ISM (Industrial Scientific and Medical standard) band flex fuel sensor using electrical metamaterial device,*Applied Physics A* 123: 75, 2017.

[4] C. Sabah, H. Roskos, Terahertz sensing application by using planar split-ring-resonator structures,*Microsystem technologies*18: 2071-2076, 2012.

[5] C. Sabah, H. G. Roskos, Broadside-coupled triangular split-ring-resonators for terahertz sensing, *The European Physical Journal Applied Physics* 61: 30402, 2013.

[6] H. Odabasi, F. Teixeira, D. Guney, Electrically small, complementary electric-field-coupled resonator antennas,*Journal of Applied Physics* 113: 084903, 2013.

[7] M. Schueler, C. Mandel, M. Puentes, R. Jakoby, Metamaterial inspired microwave sensors,*IEEE Microwave Magazine* 13: 57-68, 2012.

[8] M. S. Boybay, O. M. Ramahi, Material characterization using complementary split-ring resonators,*IEEE Transactions on Instrumentation and Measurement* 61: 3039-3046, 2012.

[9] T. Chen, S. Li, H. Sun, Metamaterials application in sensing,*Sensors* 12: 2742-2765, 2012.

[10] A. Ebrahimi, W. Withayachumnankul, S. Al-Sarawi, D. Abbott, High-sensitivity metamaterial-inspired sensor for microfluidic dielectric characterization,*IEEE Sensors Journal* 14: 1345-1351, 2014.

[11] I. A. I. Al-Naib, C. Jansen, M. Koch, Thin-film sensing with planar asymmetric metamaterial resonators,*Applied Physics Letters* 93: 083507, 2008.

[12] S. S. Islam, M. R. I. Faruque, M. T. Islam, A new direct retrieval method of refractive index for the metamaterial,*Current Science* 109: 337-342, 2015.

Analysis of Lateral Displacement for Ultrathin Planar Loop Incorporating mu near zero Metamaterials

L. L. Pon[1*], S.K.A. Rahim[2], C.Y. Leow[1], W.Y.Yong[1], M. R. Ramli[1], and B.W. Chew [2]

[1]Wireless Communication Centre, Faculty of Electrical Engineering,
Universiti Teknologi Malaysia, Skudai, 81310, Johor, Malaysia
[2]Intel Microelectronics (M) Sdn. Bhd., Halaman Kampung Jawa, 11900 Penang, Malaysia
*corresponding author, E-mail: lailypon@yahoo.co.uk

Abstract

The aim of this paper is to investigate the inter-relation between lateral displacement and desired axial distance in an integrated planar loop with mu near zero (MNZ) spiral resonators on establishing sustained energy efficiency for low power wireless energy transfer application. The proposed study is done by utilizing RO 4350 from Rogers with dielectric constant of 3.66. Variation ratio of up to 0.37 is observed for operating distance between 20mm to 25mm within quotient value of lateral displacement and distance. It can be discerned that there is potential to achieve robustness towards misalignment with MNZ metamaterials.

1. Introduction

Besides the operating distance between inductive loops, alignment between the transmitter and receiver is also a crucial feature in wireless power transfer as link transfer efficiency is reduced significantly under lateral misalignment condition [1]. Stable power transfer efficiency (PTE) within distance of up to 30 mm is reported in [2] by employing 3 by 3 array of negative permeability metamaterial. This paper provides the examination on the influence of axial distance, z towards efficiency upon integration with metamaterial that possess permeability close to zero. The proposed design is etched on RO 4350 substrate with dielectric constant of 3.66 and thickness of 0.254 mm. The double-sided RO 4350 with the 0.035 mm copper deposited on top is used. The overall dimension of the proposed design is 70 X 70 mm.

2. Design and Output

As shown in Figure 1 (a), inner length of metamaterial unit cell, *Ui* is 13.78 mm whereas the width, *wu* is 1.02 mm. The proposed five turns square spiral resonator is completed with lumped element of 200 pF capacitor to facilitate frequency resonance tuning. The extraction of permeability from single unit cell is retrieved by employing robust method [3, 4]. Figure 1(b) indicates that the permeability is near zero around desired operating frequency of 13.56MHz.

A single turn planar loop with inner diameter length, Di of 58.80mm and loop width, w of 0.85mm is designed on the bottom layer of the substrate as depicted in Figure 1(c). Simulations for axial distances ranging from 20mm till 25mm are performed with the aid from full wave finite element simulator. PTE is derived from s-parameters as $|S_{21}|^2$. Figure 2 reveals that consistency of peak transfer efficiency above 65% is feasible for operating distance between 20mm to 25mm within quotient value up to 0.4. The variation ratios of peak transfer efficiency are tabulated in Table 1. It is observed that optimal axial distance to compensate for lateral displacement, ay for this proposed design is at 20mm with lowest peak transfer efficiency variation ratio of 0.19.

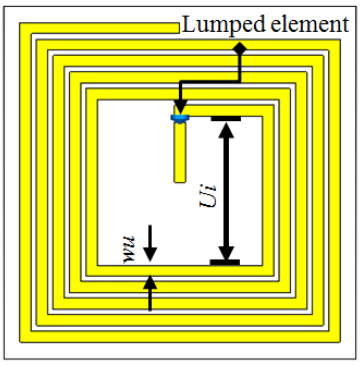

Figure 1(a): Unit cell

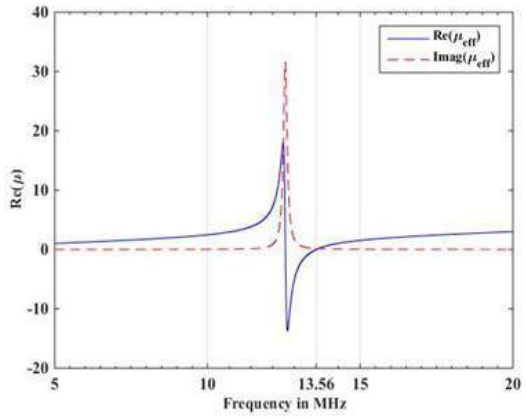

Figure 1(b): Permeability extraction from a unit cell

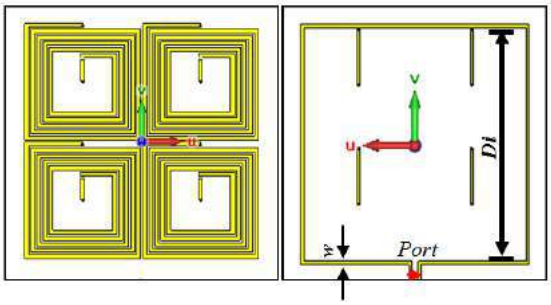

Figure 1(c): Front and bottom layer of proposed design

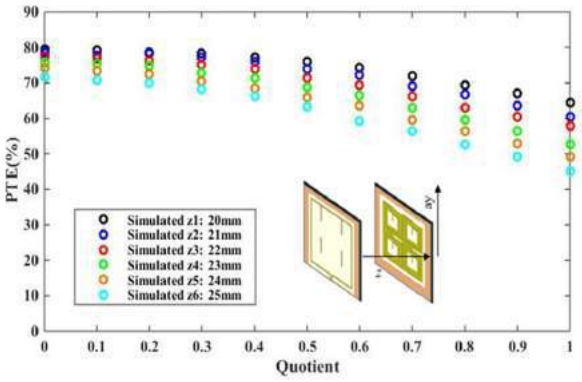

Figure 2: Peak power transfer efficiencies

Table 1: Variation ratio of peak transfer efficiency.

Axial distance (mm)	20	21	22	23	24	25
Variation ratio	0.19	0.23	0.25	0.31	0.34	0.37

3. Conclusions

A single turn planar loop incorporating permeability near zero metamaterial is proposed and analyzed. The capability of permeability near zero metamaterial in enhancing coupling allows a uniform magnetic field and sustained energy efficiency for wireless energy transfer application under lateral displacements condition. This analysis can be further extended to longer axial distances.

Acknowledgements

This work was supported by the Collaborative Research in Engineering, Science and Technology (CREST) fund, Malaysia, under grant number: 4B151 and Universiti Teknologi Malaysia Research University Grant under vot number: 4J299.

References

[1] Eteng, A. A., Rahim, S.K.A, Leow, C.Y., Chew, B.W. and Vandenbosch, G.A.E. "Simple compensation for lateral misalignments in resonant inductive coupling links," *Electronics Letters*, Vol. 52, No. 11, 954–956, 2016.

[2] Senior, D. E and Parimi, P.V., "Planar Wireless Power Transfer System with Embedded Magnetic Metamaterial Resonators," in *2016 IEEE International Symposium on Antennas and Propagation (APSURSI),* Puerto Rico, USA, June 2016, 1947-1491.

[3] W.M Smith, D. R., Schultz, S., Markos, P. and Soukoulis, C.M. "Determination of Effective Permittivity and Permeability of Metamaterials from Reflection and Transmission Coefficients," *Physics Review B*, Vol. 65, No. 19, 195104, 2002.

[4] Chen, X., Grzegorczyk, T. M., Wu, B., Pacheco, J. J. and Kong, J.A. "*Robust Method to Retrieve the Constitutive Effective Parameters of Metamaterials*," *Physics Review E*, Vol. 70, No. 1, 016608, 2004.

Gain Enhancement of a Triple Band CSRR Antenna by Using Frequency Selective Surface Reflector

M. Z. Mahmud[1,2*], M.A. Ullah[1], M. Samsuzzaman[1], T. Alam[1] and M. T. Islam[1]

[1] Dept. Of Electrical, Electronic and Systems Engineering, Universiti Kebangsaan Malaysia, Malaysia

[2]Dept. of AIS, Jagannth University, Bangladesh

[*]corresponding author: zulfikerm@yahoo.com, tariqul@ukm.edu.my

Abstract

A high gain circular split-ring resonator (CSRR) based triple band antenna with Frequency Selective Surface (FSS) is presented in this paper. The proposed FSS structure is used to enhance the gain of the antenna. Significant improvement in gain has been noticed after implementing the proposed FSS layer. The antenna achieved realized gain of 3.5 dBi without the FSS where the same antenna with FSS attained 6.0 dBi of realized gain at the resonant frequency. The reflection coefficient has good agreement of the antenna with the FSS structure. The antenna also exhibited directive radiation pattern after using FSS. The proposed unit cell is structured with S-shaped meandered line on FR4 substrate. The dimension of proposed FSS structure's unit cell is 10 mm×10mm. The design and simulation of the proposed antenna and the FSS structure is performed in CST Microwave Studio.

1. Introduction

At presents antenna with high gain, wide bandwidth, directive radiation and low cost are some the prime interests of the researchers in wireless communication. Several versatile methods are being used to enhance the performance of antenna parameters like tapered shaped slot[1],modified ground plane[2], using coupled resonator[3] and many more. Use of frequency selective surfaces (FSS) is one of the most effective technique to enhance the antenna performance. A number of antenna are presented in[4-6] using FSS to enhance the antenna characteristics. In [7], FSS structure is used to aid the bandwidth backing reflector functions. FSS based corner reflector is used to enhance the performance of a dual band monopole antenna in [8]. In this paper, a S-shaped meandered line FSS structure is presented for gain enhancement along with performance verification using a circular split-ring patch antenna.

2. Unit cell and Antenna configuration

The unit cell and the array of the proposed FSS structure is shown in figure 1. The unit cell consists of S-shaped meandered line. The dimension of unit cell is 10 mm×10 mm. The length of each line is 5 mm and width is .5 mm. The array of unit cell used to form a frequency selective surface. The size of array is 3×4 with 41.5 mm length and 31 mm width. The gap between each unit cell is 5.5 mm.

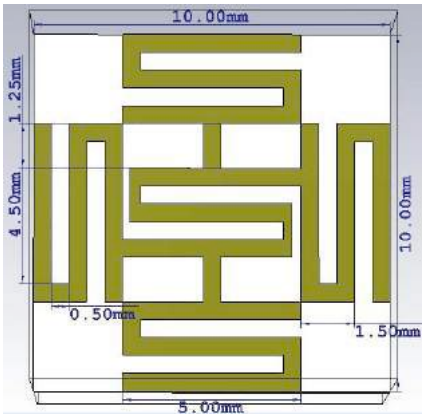

(a)

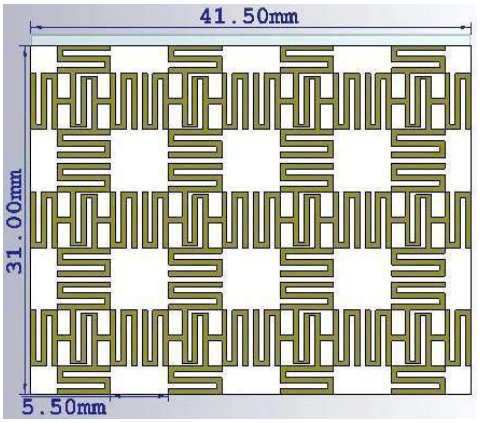

(b)

Figure 1. (a) Unit cell (b) FSS structure

The layout of proposed triple band CSRR antenna is depicted in figure 2(a). The parametric values of propose antenna is illustrated in table 1.

Table 1: Design parameters of propose antenna.

Parameter	Value [mm]	Parameter	Value [mm]
L	35	p	1
W	30	D	24
d	5	g	0.25
n	0.5	h	9.63
f	10.04		

The perspective view of the proposed FSS structure with the antenna is represented in figure 2(b). The antenna and the FSS are combined in a single unit using a spacer vacuum box. The vacuum space between these two layers is 11.85 mm. The appropriate selection of surface-state and accuracy of spacer enhance the antenna performance specially the gain.

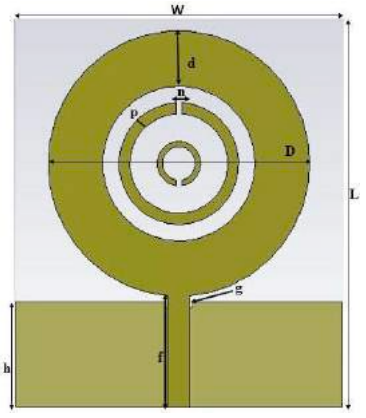

(a)

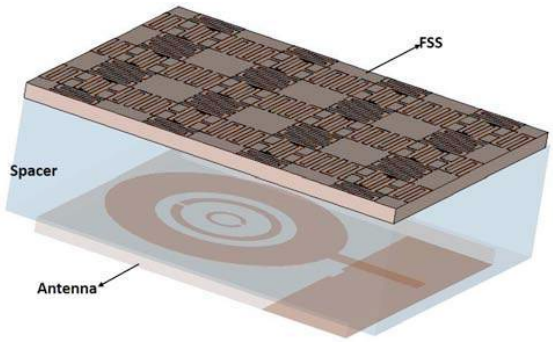

(b)

Figure 2. (a) Antenna without FSS (b) Antenna with Proposed FSS structure.

3. Antenna Performance Analysis

Significant improvement in gain of the antenna is observed after using proposed FSS structure shown in figure 3. Without FSS the realized gain is around 4 dBi, where using FSS the realized gain is reached up to more than 6 dBi. This gain enhancement proofs the effectiveness of FSS structure.

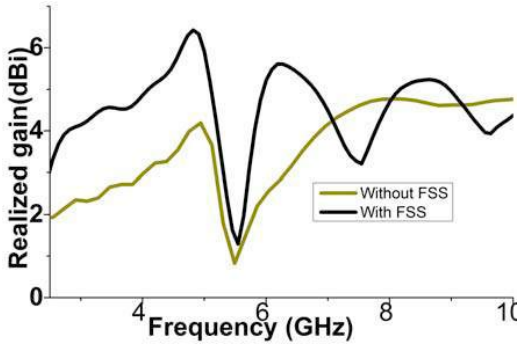

Figure 3. Gain enhancement of proposed antenna using FSS Structure

The reflection co-efficient of proposed antenna is shown in figure 4(a), which shows triple band of -10dB impedance bandwidth from 2.6 GHz to 3.6 GHz, 5.6 GHz to 6.7 GHz and the final band is from 7.9 GHz to 14.3 GHz. The multiband characteristics ensure the use of proposed prototype for multifunctional devices. The proposed CSRR antenna have three working resonance at 3.3, 6, 8.5 and 12.83 GHz.

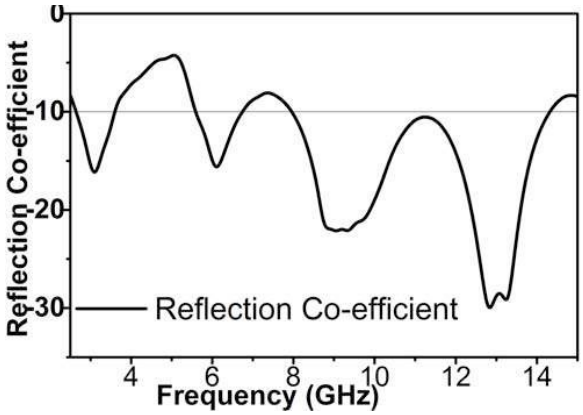

(a)

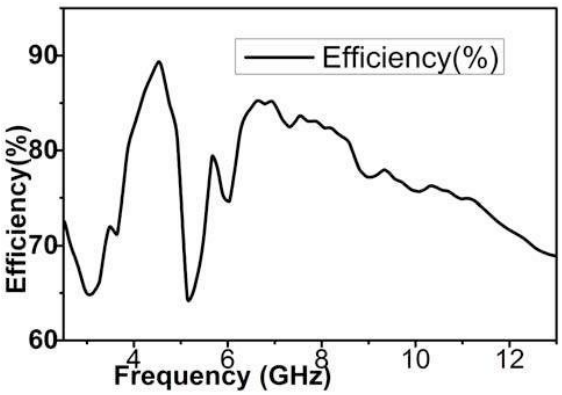

(b)

Figure 4. (a) Reflection co-efficient (b) Efficiency

The efficiency of antenna with FSS structure is depicted in figure 4(b). Overall efficiency is more than 80%. The efficiency is less than 60% in the area where the reflection co-efficient shows out of band.

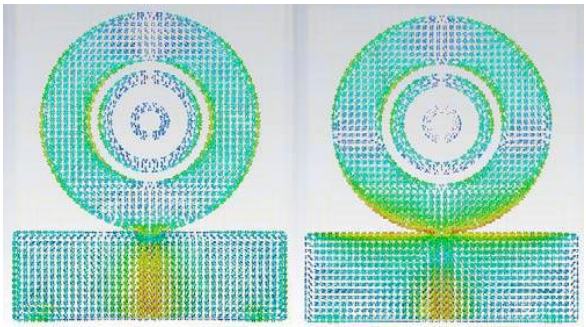

(a) (b)

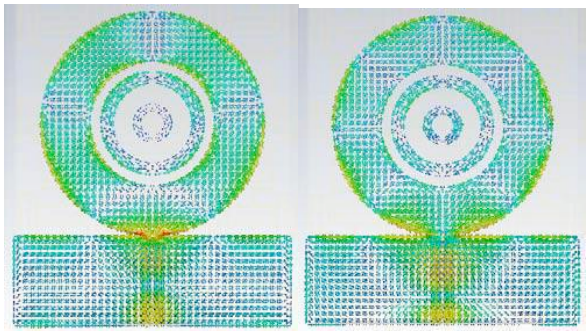

(c) (d)

Figure 5. Surface current of CSRR antenna (a) 3.3 GHz (b) 6 GHz (c) 8.5 GHz (d) 12.83 GHz

The surface current distribution of proposed antenna is shown in figure 5(a-d) at four resonant frequency. The most current conducting area of the proposed prototype is around fed line and lower part of patch. At higher frequencies, there exist few nulls on the patch due to the higher order current mode. The radiation pattern of proposed antenna is presented in figure 6. The antenna is directive to the z direction and at higher frequency the directivity is moves to the phi direction due to the change of current conducting area on the surface.

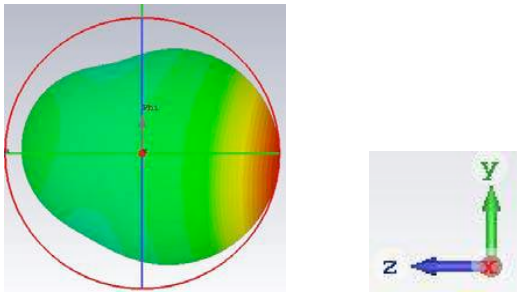

(a)

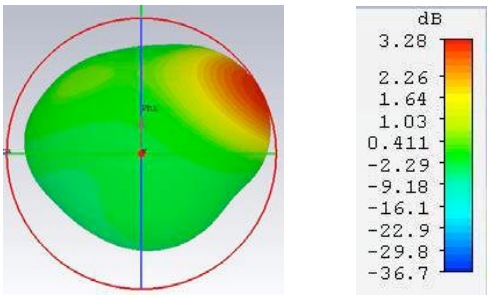

(b)

Figure 6. Radiation pattern (a)3.3 GHz and (b) 6 GHz

4. Conclusion

A triple band frequency selective surface based spit ring

resonator antenna is presented having dimensions 30 mm× 35 mm. FSS structure is implemented with CSRR antenna to enhance the gain. The antenna gain is significantly improved from 3.5 dBi to 6.0 dBi. The antenna also exhibited directive radiation pattern after using FSS. The design and simulation of the proposed antenna and the FSS structure is performed in CST Microwave Studio. The antenna provides triple band over UWB band and be potential candidate for multiband applications.

REFERENCES

[1] R. Azim, M. T. Islam, and N. Misran, "Compact tapered-shape slot antenna for UWB applications," *IEEE Antennas and Wireless Propagation Letters,* vol. 10, pp. 1190-1193, 2011.

[2] P. Jyoti Gogoi, D. Jyoti Gogoi, and N. S. Bhattacharyya, "Modified ground plane of patch antenna for broadband applications in C-band," *Microwave and Optical Technology Letters,* vol. 58, pp. 1074-1078, 2016.

[3] M. Z. Mahmud, T. Alam, and M. T. Islam, "A triangular coupled-resonator antenna for ultra-wideband applications," *Applied Physics A,* vol. 123, p. 20, 2017.

[4] Y. J. Lee, J. Yeo, R. Mittra, and W. S. Park, "Design of a high-directivity Electromagnetic Band Gap (EBG) resonator antenna using a frequency-selective surface (FSS) superstrate," *Microwave and Optical Technology Letters,* vol. 43, pp. 462-467, 2004.

[5] W.-T. Wang, S.-X. Gong, X. Wang, H.-W. Yuan, J. Ling, and T.-T. Wan, "RCS reduction of array antenna by using bandstop FSS reflector," *Journal of Electromagnetic Waves and Applications,* vol. 23, pp. 1505-1514, 2009.

[6] M. Bouslama, M. Traii, A. Gharsallah, and T. A. Denidni, "Analysis of antenna gain enhancement using new frequency selective surface superstate," *Microwave and Optical Technology Letters,* vol. 58, pp. 448-452, 2016.

[7] M. Pasian, S. Monni, A. Neto, M. Ettorre, and G. Gerini, "Frequency selective surfaces for extended bandwidth backing reflector functions," *IEEE Transactions on Antennas and Propagation,* vol. 58, pp. 43-50, 2010.

[8] A. Chatterjee and S. K. Parui, "Performance Enhancement of a Dual-Band Monopole Antenna by Using a Frequency-Selective Surface-Based Corner Reflector," *IEEE Transactions on Antennas and Propagation,* vol. 64, pp. 2165-2171, 2016.

Gain and bandwidth enhancements of a monopole antenna using a dual band stub-loaded AMC

K. N. Paracha[1], S. K. A. Rahim[1], P. J. Soh[2], Y. W. Yan[1], S. A. Babale and M. H. Misran[1]

[1]Wireless Communication Centre (WCC), Faculty of Electrical Engineering,

Universiti Teknologi Malaysia (UTM), 81310, Skudai, Johor, Malaysia

[2]Advanced Communication Engineering (ACE) CoE, School of Computer and Communication Engineering,

Universiti Malaysia Perlis, 02600 Arau, Perlis, Malaysia

[*]corresponding author, E-mail: paracha863@hotmail.com

Abstract

A dual band sub-loaded artificial magnetic conductor (AMC) structure is presented for dual band WLAN application. Detailed evolution of our design has been discussed. It has been shown that the upper AMC band can be tuned by varying the stub length of the structure. The array of the proposed AMC unit cell is then used as a reflector for a monopole antenna. It has been shown that the gain of the antenna is improved up to 6.3 dBi, whereas fractional impedance bandwidth has increased from 14.68 % to 33.87%.

***Index Terms*—Gain, FBR, SAR.**

1. Introduction

Exponential growth of communication systems in real life has necessitate the enhancements of planar antenna performance besides their readily available features such as low profile, light weight, and compliance to rapid prototyping methods which make them easily conformal to the host surface. However, such antennas suffer from several disadvantages such as narrow operational bandwidths, low gains and excitation of surface waves which eventually reduces its radiation efficiencies. Many techniques have been proposed in the literature to overcome these drawbacks such as introducing slots in the patch[1], utilizing thick substrates [2], and employing non-symmetrical CPW feeding[3]. Recently, metasurfaces have also been utilized to increase the radiation performance of microstrip antennas[4]. Among them, AMC/EGBs have gained much attention due to their ability in suppressing surface waves and exhibiting High Impedance Surfaces (HIS) characteristics within their operational frequency bands [5, 6]. AMCs are periodic arrangement of unit cells used as antenna backing surfaces to enhance gain[7], or to improve impedance bandwidth of these antennas[8]. They are also used to mitigate back radiations effects towards human body for wearable antenna applications [8-10].

The most prominent property of the AMC, also known as HIS, is that it exhibits the characteristics of PMC (Perfect Magnetic Conductor) surface reflecting the incident wave with almost zero reflection phase [7]. It is pertinent to note that the opposite of PMC is Perfect Electric Conductor (PEC) plane which exhibits 180^0 phase reflection. The useful bandwidth of AMC is generally defined as the reflection phase between -90^0 to 90^0 on both sides of the zero-phase reflection. Within this phase reflection band, a non-destructive interference between incident and reflected waves [11] occurs, resulting in the impedance bandwidth and gain increase of the antenna, and consequently reducing the back radiation towards the human body for wearable application as reported in [12] .

The AMC design presented in this work enables the higher band to be tuned from 5.2 to 5.8 GHz frequencies with zero reflection phase by increasing only the stubs length. This frequency band is chosen considering its applicability in the WLAN frequencies. Meanwhile, the risk of electromagnetic (EM) radiation towards the human body, defined in terms of the Specific Absorption Rate (SAR) is also evaluated. This limit is defined by the International Commission on Non-Ionizing Radiation Protection (ICNIRP) to be 1.6 W/kg averaged over a 1g of tissue [13-15] in North America and several other countries. The contribution of the AMC array in reducing backward radiation and EM absorption in the human body when worn is assessed using SAR. [9, 10].

In this work, a dual band AMC unit cell to enhance the gain and impedance bandwidth of a monopole antenna with reduced SAR is proposed. The unit cell, as shown in Fig. 1(a), consists of an annular slot loaded with four perpendicular stubs on a simple rectangular patch. Due to inclusion of the stubs in the annular slot, the proposed unit cell reduced resonant frequency from 5.93 to 4.82 GHz (18.72%) compared to the structure consisting of only an annular slot with a radius (r_1) of 5.5 mm on the patch resonating at 6.14 GHz with the same radial length. Impedance bandwidth and gain of the monopole antenna is increased by using our proposed unit-cell as backplane of the antenna. Moreover, reduced values of SAR have been observed due to reduction of back radiations from the antenna.

This paper is organized as follows: the design procedure of

the stub loaded unit cell will be presented in the next section, followed by the CPW-monopole antenna design backed by a 4 x 4-unit cell AMC plane. To validate the safety of the antenna, a SAR analysis to investigate the back-radiation towards the human body is performed prior to the concluding remarks.

2 Unit cell and antenna design

The unit cell and monopole antenna backed by the AMC plane are designed using Computer Simulation Technology (CST) software, which uses the Finite Integration Technique (FIT) for solving Maxwell's equations.

2.1. AMC design

The unit cell of AMC structure is designed on a FR4 substrate with a relative permittivity (ε_r) of 4.5 and a loss tangent (tan δ) of 0.019. It is 3.2 mm thick and sized at 12 x 12 mm^2. The design is based on a simple rectangular patch structure prior to the introduction of an annular ring slot in the patch to enable dual band behavior. Finally, four perpendicular rectangular stubs in the circular patch is added to reduce the second resonant frequency of the structure as shown in the Fig. 1(b). The decrease in the upper frequency band results from the rectangular stubs behaving as interdigital capacitors in the structure. It can be seen in Fig.1(c) that as the length of the rectangular stub is increased from 1 to 3 mm, the higher band of our structure decreased from 5.67 GHz to 4.62 GHz (18.52 %) with slight perturbation (only 3.21 %) in the lower band. This also indicates the miniaturization of the structure with reduced AMC operational bandwidth in the upper band from 656 MHz to 524 MHz with the variation of the stub length.

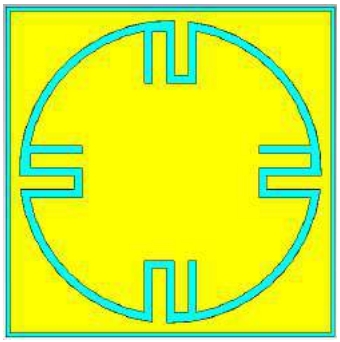

Figure 1:(a) Proposed AMC unit cell

Angular stability is also investigated using a constant stub length of 2 mm. It is observed that for a varying θ angle of the incident TE mode waves, the angular stability of the proposed structure is up to 75^0 for the polarization angle of $\varphi=0^0$.

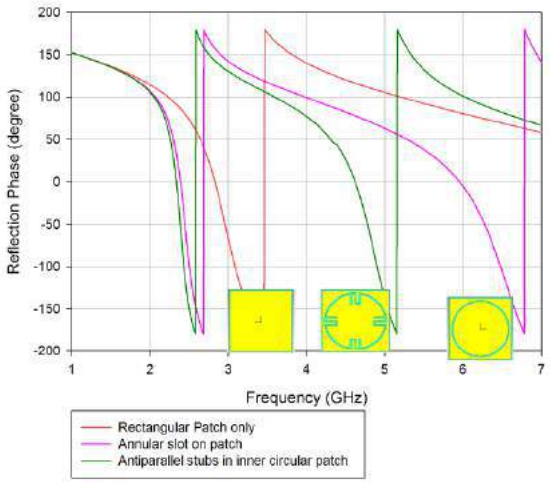

Figure 1:(b) Simulated reflection phase characteristics of the three structures in the design evolution of the proposed unit cell.

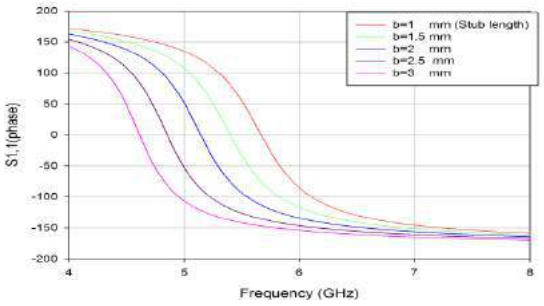

Figure 1:(c) Effect of stub lengths on the upper band of the AMC structure

2.2. AMC backed monopole antenna

A CPW monopole patch antenna is then designed on a 1.6 mm FR4 substrate to validate the functionality of the proposed unit cell design acting as a reflector. Using a 4 x 4-unit cell array to form the AMC plane, a dual band behavior is exhibited to mainly provide operation at 5.2 GHz (upper band) due to the narrow bandwidth in the lower frequency band. The overall size of the AMC backed antenna is 48 x 48 x 9.76 mm^3 including a 4 mm of spacer used to separate the antenna from AMC structure for better impedance matching.

2.3. Results and discussion

The impedance bandwidth of the monopole antenna, as shown in Fig. 2, has been improved from 0.762 GHz (14.68 %) to 1.54 GHz (33.87%) using the proposed AMC structure. Moreover, the gain of the AMC backed antenna increased significantly from 1.07 dBi to 6.3 dBi at 5.2 GHz, which is within the AMC operational bandwidth. This proves that the

proposed structure is behaving as a PMC plane for the monopole antenna. This increased its impedance bandwidth and gain of the antenna.

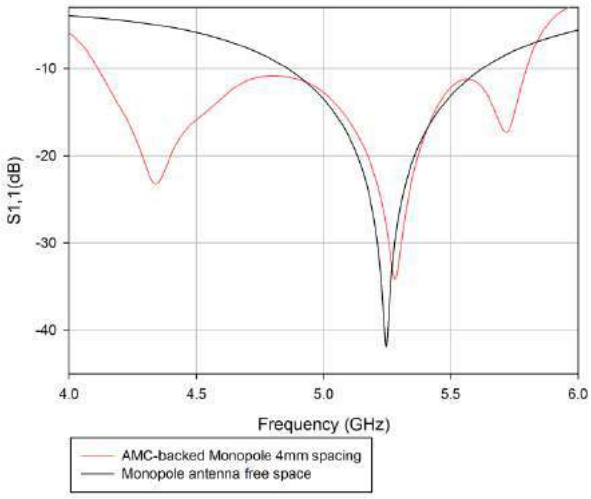

Figure 2: Simulated reflection coefficient of the monopole antenna in free space with and without AMC.

As can be seen in the Fig. 3, the gain of the AMC-backed antenna increased up to 6.3 dBi. The front to back ratio is observed to be more than 12 dB throughout the operational bandwidth of the AMC (4.89-5.45 GHz) with a maximum FBR of 25 dB observed at 4.8 GHz. This indicates its effectiveness in back radiation reduction for wearable antennas.

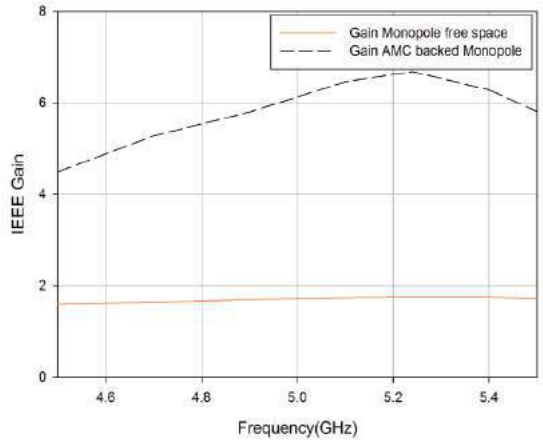

Figure 3:(a) Comparison of the IEEE gain of monopole antenna with AMC-backed Monopole

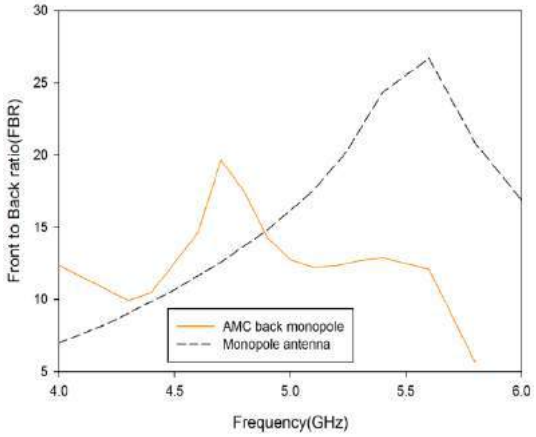

Figure 3:(b) Comparison of the FBR of monopole antenna with AMC-backed Monopole

2.4. Specific Absorption Rate

Due to health concerns resulting from EM radiation towards human body, it is imperative that the SAR of this antenna is evaluated when placed on the human body. For that reason, a series of simulations is performed using a numerical human model consisting of a layer of skin (3 mm thick), fat (7 mm thick), and muscles (60 mm thick). To ensure the $\lambda/4$ margin between the antenna and human tissue model edges, the total volume of the model is taken as 150 x 150 x 80 mm^3. The model and its dielectric properties at 5.2 GHz has been validated in [16, 17]. It has been assigned dielectric values from [18]. The antenna is placed on the body model with and without AMC. The proposed AMC-backed antenna indicated less EM radiation influence on the human body tissues due to the zero-phase reflection provided by the AMC. It can be observed that the maximum SAR is 0.68 kg/W averaged over 1g of tissue, in compliance with the ICNIRP limit of 1.6 kg/W. Generally, the SAR values at the higher frequencies is relatively higher due to the increased conductivity of the human body. Thus it can be expected that the SAR value in the lower ISM band (2.45 GHz) is also relatively lower. The total dimension of the structure also complies with the recommended wearable devices size of 50 x 50 mm^2 [19].

3. Conclusion

A dual band sub-loaded AMC-based structure is proposed and evaluated. It is shown that by varying the stub length of the structure, the higher AMC band can be tuned. The proposed AMC is effective in functioning as a reflector, improving antenna gain up to 6.3 dBi and increasing fractional impedance bandwidth has increased from 14.68 % to 33.87% GHz. It is also validated that the SAR value evaluated in proximity of a simplified human body model is well below the regulatory limits.

References

[1] A. T. Hussein and S. Luhaib, Designing E-Shape microstrip patch antenna in multilayer structures for WiFi 5GHz network, *20th Telecommunications Forum (Telfor),* pp. 366-368, 2012.

[2] H. Malekpoor and S. Jam, Miniaturised asymmetric E-shaped microstrip patch antenna with folded-patch feed, *IET Microwaves, Antennas & Propagation,* vol. 7, pp. 85-91, 2013.

[3] R.-C. Han and S.-S. Zhong, Broadband circularly-polarised chifre-shaped monopole antenna with asymmetric feed, *Electronics Letters,* vol. 52, pp. 256-258, 2016.

[4] D. Yuandan and T. Itoh, Metamaterial based antennas, *Proceedings of the IEEE,* vol. 100, pp. 2271-2285, 2012.

[5] L. Yousefi, B. Mohajer-Iravani, and O. M. Ramahi, Enhanced bandwidth artificial magnetic ground plane for low-profile antennas, *Antennas and Wireless Propagation Letters,* vol. 6, pp. 289-292, 2007.

[6] R. Dewan, M. K. A. Rahim, M. R. Hamid, and M. F. M. Yusoff, Analysis of wideband antenna performance over dual band Artificial Magnetic Conductor (AMC) ground plane, *Applied Mechanics and Materials,* vol. 735, pp. 273-277, 2015.

[7] P. Prakash, M. P. Abegaonkar, A. Basu, and S. K. Koul, Gain enhancement of a CPW-Fed monopole antenna using polarization-insensitive AMC structure, *IEEE Antennas and Wireless Propagation Letters,* vol. 12, pp. 1315-1318, 2013.

[8] H. Malekpoor and S. Jam, Improved radiation performance of low profile printed slot antenna using wideband planar AMC surface, *IEEE Transactions on Antennas and Propagation,* vol. 64, pp. 4626-4638, 2016.

[9] Z. H. Jiang, D. E. Brocker, P. E. Sieber, and D. H. Werner, A compact, low-profile metasurface-enabled antenna for wearable medical body-area network devices, *IEEE Transactions on Antennas and Propagation,* vol. 62, pp. 4021-4030, 2014.

[10] G. K. Pandey, H. S. Singh, and M. K. Meshram, Platform tolerant UWB antenna over multi-band AMC structure, *Microwave and Optical Technology Letters,* vol. 58, pp. 1052-1059, 2016.

[11] J. R. Sohn, K. Y. Kim, and H. S. Tae, Comparative study on various artificial magnetic conductors for low-profile antenna, *Progress in Electromagnetics Research-Pier,* vol. 61, pp. 27-37, 2006.

[12] M. A. B. Abbasi, S. S. Nikolaou, M. A. Antoniades, M. N. Stevanović, and P. Vryonides, Compact EBG-Backed planar monopole for BAN wearable applications, *IEEE Transactions on Antennas and Propagation,* vol. 65, pp. 453-463, 2017.

[13] A. Ahlbom, U. Bergqvist, J. Bernhardt, J. Cesarini, M. Grandolfo, M. Hietanen, Guidelines for limiting exposure to time-varying electric, magnetic, and electromagnetic fields (up to 300 GHz), *Health physics,* vol. 74, pp. 494-521, 1998.

[14] P. J. Soh, G. Vandenbosch, F. H. Wee, A. van den Bosch, M. Martinez-Vazquez, and D. Schreurs, Specific absorption rate (SAR) evaluation of textile antennas, *IEEE Antennas and Propagation Magazine,* vol. 57, pp. 229-240, 2015.

[15] M. R. Faruque, M. I. Hossain, N. Misran, M. Singh, and M. T. Islam, Metamaterial-Embedded low SAR PIFA for cellular phone, *PLoS One,* vol. 10, p. e0142663, 2015.

[16] J. Gemio, J. Parron, and J. Soler, Human body effects on implantable antennas for ISM bands applications: models comparison and propagation losses study, *Progress In Electromagnetics Research,* vol. 110, pp. 437-452, 2010.

[17] C. Gabriel, S. Gabriel, and E. Corthout, The dielectric properties of biological tissues: I. Literature survey, *Physics in medicine and biology,* vol. 41, p. 2231, 1996.

[18] S. Nikolaou and M. A. B. Abbasi, Design and development of a compact UWB monopole antenna with easily-controllable return loss, *IEEE Transactions on Antennas and Propagation,* pp. 1-1, 2017.

[19] M. K. Khattak and S. Kahng, A novel dipole antenna backed by a thin and small-area AMC for good impedance match and low SAR on human tissue, *Journal of Electromagnetic Waves and Applications,* vol. 30, pp. 1591-1602, 2016.

Wearable Textile Antenna with a Dual-band AMC Plane for GPS and WLAN Applications

Ezzaty Faridah Nor Mohd Hussin[1], Ping Jack Soh[1]*, Mohd Faizal Jamlos[1], Herwansyah Lago[1], Azremi Abdullah Al-Hadi[1], Mariana Ricca[2], Sven Kuhn[2], Niels Kuster[2]

[1]Advanced Communication Engineering (ACE) CoE, School of Computer and Communication Engineering, Universiti Malaysia Perlis, Pauh Putra Campus, Arau, Perlis 02600, Malaysia
[2]IT'IS Foundation, Swiss Federal Institute of Technology (ETH) Zurich, Konradstrasse 28, 8005 Zurich, Switzerland
*Corresponding author: pjsoh@unimap.edu.my

Abstract

A wearable planar textile antenna with dual-band AMC plane for GPS and WLAN applications is presented. The antenna design begins with two rectangular slotted octagonal patch to enable miniaturization. This radiator is placed on top of a Kevlar substrate and integrated with an AMC plane beneath it. The AMC unit cells are formed using a corner-truncated square patch with dodecagonal ring for dual-band operation at 1.575 GHz and 2.45 GHz, resulting gain enhancement to 3.05 dB and 3.897 dB, respectively.

1. Introduction

Metamaterial is an artificial structure that is designed to obtain specific characteristics which are not naturally available in nature [1-2]. The unique characteristics of metamaterial have been used extensively in antennas and microwave applications for performance improvement [3].

Artificial magnetic conductor (AMC) has been widely used as a mechanism to enhance antenna performance [1] such as its radiation characteristics on a wideband textile planar antenna [2-5], gain, bandwidth [2-4] and directivity [3, 5]. Many applications also require their antenna to work at two different frequencies simultaneously, resulting in the same requirements for the AMC plane [6]. In this work, a wearable antenna with an AMC plane is designed using textile materials to operate at 1.575 GHz and 2.45 GHz.

This paper is organized as follows. Section 2 presents a description of the materials used in the proposed antenna. Antenna design and results of simulations are presented in Section 3 and finally concluded in Section 4.

2. Textile Materials

Two textiles types were used in this design; ShieldIt Super (as its conductor) and Kevlar (as its substrate). ShieldIt Super is 0.17 mm thick with a conductivity of 1.18 x 105 S/m, whereas Kevlar is a 0.4 mm thick textile with a relative permittivity, (εr) of 1.56 and loss tangent (tan- δ) of 0.0612. The proposed antenna is fed using a 50 Ω SMA connector. CST Microwave Studio software is used for the numerical simulations.

3. Antenna Design

The proposed AMC unit cell is based on a hexagonal patch formed from a square patch and truncated at all corners. A dodecagonal ring slot is then added, as shown in Figure 1. Its resulting reflection phase is plotted in Figure 2, indicating operation at 1.575 GHz and 2.45 GHz. The unit cell is then multiplied to form a 3 x 3 array to form the AMC plane. It is then integrated beneath the optimized antenna as illustrated in Figure 3, resulting in the reflection coefficient seen in Figure 4. This antenna operates at 1.575 GHz and 2.45 GHz.

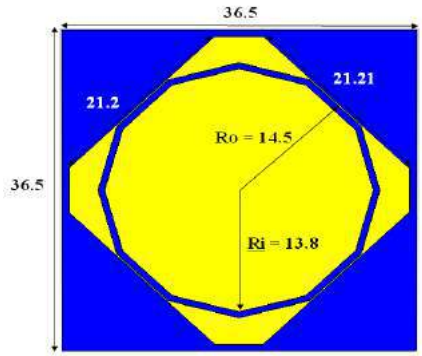

Figure 1: The unit cell of dual-band AMC (all dimension in mm).

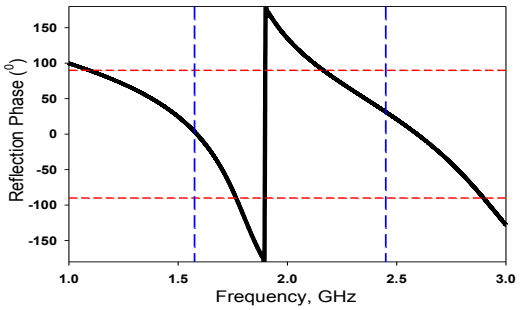

Figure 2: Reflection phase of the proposed unit cell.

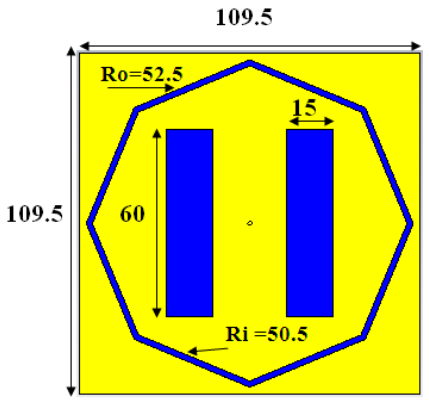

Figure 3: Dual-band textile antenna (all dimensions in mm).

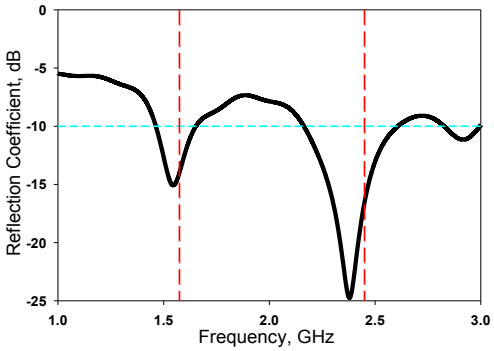

Figure 4: Reflection coefficient of the proposed antenna.

4. Conclusions

A wearable textile antenna with dual-band AMC plane is presented. The radiator is designed using a slotted octagon ring to operate at 1.575 GHz and 2.45 GHz. The AMC plane consisting of 3 x 3 octagon patches slotted with a dodecagon ring operates at 1.575 GHz and 2.45 GHz resulting gain enhancements to 3.05 dB and 3.897 dB in the lower and upper band, respectively.

References

[1] S. X. Ta and I. Park, "Dual-Band Low-Profile Crossed Asymmetric Dipole Antenna on Dual-Band AMC Surface," in *IEEE Antennas and Wireless Propagation Letters*, vol. 13, no. , pp. 587-590, 2014.

[2] G. Gnanagurunathan and K. T. Selvan, "Artificial Magnetic Conductors on Wide-Band Patch Antenna," *Progress In Electromagnetics Research Letters,* vol. 36, 9-19, 2013.

[3] Qu,D., L. Shafai, and A. Foroozesh, "Improving microstrip patch antenna performance using EBG substrates," *IEE Proceedings on Microwaves, Antennas and Propagation,* vol. 153,558-563, 2006.

[4] Elsheakh, D. A., H. A. Elsadek, E. A. Abdallah, H. Elhenawy, and M. F. Iskandar, "Enhancement of microstrip monopole antenna bandwidth by using EBG structures," *IEEE Antennas and Wireless Propagation Letters,* vol. 8, 959-962, 2009.

[5] De Cos, M. E., Y. Alvarez-Lopez, and F. Las-Heras, "On the influence of coupling AMC resonances for RCS reduction in the SHF band," *Progress In Electromagnetics Research,* vol. 117, 103-119, 2011.

[6] SX Ta, and I Park, “Design of Miniaturized Dual-Band Artificial Magnetic Conductor with Easy Control of Second/First Resonant Frequency Ratio”, Journal of Electromagnetic Engineering and Science, vol. 2, no. 2, Jun 2013.

A Rectangular Gap-Coupled Resonators Antenna for Low SAR Mobile Applications

Mohammad Tariqul Islam, Touhidul Alam, Farhad Bin Ashraf, Md. Zulfiker Mahmud, Kamarulzaman Mat.

Dept. Of Electrical, Electronic and Systems Engineering, Universiti Kebangsaan Malaysia, Malaysia
*corresponding author: tariqul@ukm.edu.my

Abstract

A single rectangular gap-coupled resonator inspired mobile wireless antenna is presented for low specific absorption rate applications. The proposed antenna consists of a microstrip fed rectangular with a slotted partial ground plane. The antenna achieves multiband characteristics, which can operate at PCS 1900, WCDMA, Bluetooth, WLAN 2400, WiMAX 2.5 and WLAN 5 GHz frequency band applications. The antenna is fabricated on copper clad bio-degradable substrate material, made of biomass, organic source material, moulding ceramic powder and polymeric binder. The perceptible novelties of the proposed antenna is appreciable SAR reduction with covering most widely used mobile communication bands.

1. Introduction

With the recent advances in wireless technology system, antenna researchers are facing challenges to design antenna for next generation multifunctional mobile applications. Nowadays, antenna researchers have to concentrate on EM radiation from wireless devices and using environment friendly composite material for ensuring safer use of wireless devices.

In recent years, several planar antennas with different shapes and sizes have been introduced for mobile wireless applications [1-9], like slot antenna [1], metamaterial antenna [2], coupled resonator antenna [3], etc. Alam et al. proposed metamaterial unit cell based antenna for wireless mobile application with the 0.26 λ × 0.26 λ× 0.0084 λ at 1.6 GHz lower frequency band [2]. A coupled resonator concept has been adopted in antenna, which has achieved a significant reduction in antenna dimension with satisfying antenna performances [9]. A metamaterial inspired dual frequency bands antenna has been proposed for mobile applications in [10], which can cover DCS, GSM1800, WCDMA, and Bluetooth frequency bands with dimension of 50×50×1.6 mm3.

Moreover, organic multilayer substrate has been introduced in antenna design, where, conventional fossil petroleum-based material is replaced by bio-based substrate materials [11]. Alam et al. developed a bio-substrate based material for wireless mobile communication [11], which can operate at GSM 1800, UMTS (1.92-2.17 GHz), LTE 40 frequency band with antenna size of 48×48×1.95 mm3.

In this communication, we propose a bio-substrate based coupled resonator antenna for multifunctional mobile applications. In order to satisfy the requirement of the next-generation wireless communication, the EM absorption rate of the proposed antenna has also been analyzed with human head phantom.

2. Antenna Design

The geometrical layout of the proposed coupled resonator inspired antenna is shown in Figure. 1. Commercially available CST microwave studio software has been adopted to design and investigate the antenna performances. The antenna is designed on organic or bio plastic-based substrate with dielectric constant of 15.0. The bio-plastic substrate material made of biomass organic source material, molding ceramic powder and polymeric binder. The antenna consists of a rectangular frame shape radiator and inverted L shape slotted ground plane. The antenna is fed by a 1.5 mm L-shape microstrip line. The input impedance of the microstrip line is 50Ω. All the design parameters are listed in Table 1.

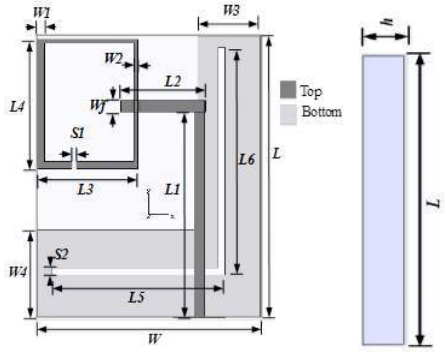

Figure. 1. Schematic design of the proposed antenna

Table 1. The proposed antenna design parameters.

Parameter	Dimension (mm)	Parameter	Dimension (mm)
L	33	S1	0.6
W	32	S2	2.0
h	1.6	L1	28.5
W1	1.0	L2	9.5
W2	0.5	L3	14.5
W3	9.0	L4	16.0
W4	11.5	L5	22.0
Wf	1.5	L6	28.0

3. Antenna Performances

The fabrication of the desired antenna has been performed using a PCB prototyping machine named Protomat S63 from LPKF as depicted in Figure 2. Performance Network Analyzer (PNA Agilent N5227A) has been used to perform the antenna reflection coefficient measurement. The reflection coefficient of the proposed antenna is presented in Figure 3. It is shown from Figure 3 that the measured and simulated reflection coefficients are nearly identical. There is a slight discrepancy between simulation and measurement results, possibly caused by SMA soldering in manual. The antenna shows multi-resonant, which can be used for multi-application of wireless communication. The antenna has achieved two wide impedance bandwidths as, 1.89-4.4 GHz and 4.87-5.84 GHz.

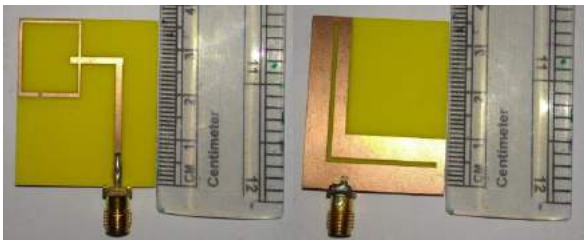

Figure 2: Prototype of the proposed antenna

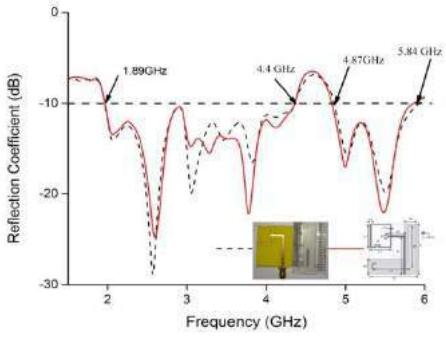

Figure 3: Reflection Coefficients of the proposed antenna

Moreover, the surface current distribution of the proposed antenna at 1.90 and 2.40 GHz are illustrated in Figure 4. From Figure 4, it is seen that at lower frequency the maximum current flows at the rectangular frame patch and for higher order of frequency the main patch has less effect. The far-field radiation pattern of the proposed antenna with human head phantom is shown in Figure 5. The antenna shows directional radiation patterns. The antenna exhibit 4.57 dBi of far-field directivity away from head phantom at 1.90 GHz and 6.81 dBi at 2.4 GHz .

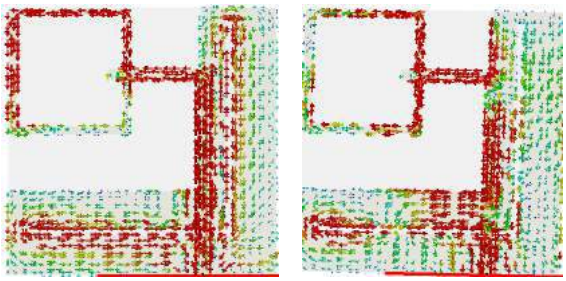

(a) (b)

Figure 4: Surface current distribution of the proposed antenna (a). 1.9 and (c) 2.4 GHz

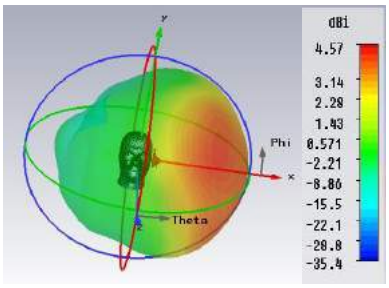

(a)

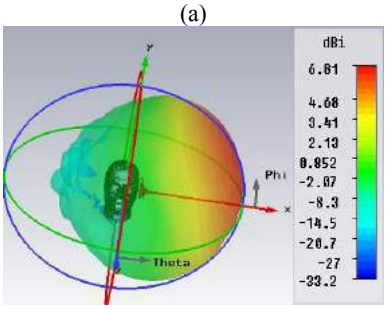

(b)

Figure 5: Far Field radiation pattern of the proposed antenna at (a). 1.9 and (c) 2.4 GHz

In modern society, the wide use of mobile phone can be resulted inimical radiation from the devices. There are several myths about the biological effect for using a mobile phone. Tissue heating is one of them[12-13]. The principal mechanism of tissue heating is the interaction between radio frequency energy and the human body. The specific absorption rate is defined by the power absorbed per unit of mass of biological tissues, which is the measurement system of tissue heating due to RF energy absorption. At present, two established institutions have developed exposure guidelines: IEEE and ICNIRP. The SAR limit

specified in IEEE C95.1:2005 is 1.6 W/kg in a 1 g averaging mass and 2 W/kg in a 10-g averaging mass of tissue [14]. To comply with the guidelines, the specific absorption rates of the proposed antenna have been investigated. The simulated SAR analysis is presented in Figure 6. And measured result is in Figure 7. It is shown from Figure 6 that the proposed antenna shows 1.21 w/kg and 1.19 w/kg of 1g SAR at 1.9 and 2.4 GHz, respectively. Besides this the measured SAR values of the proposed antenna shows 1.34w/kg and 0.98 w/kg of 1g SAR at 1.9 and 2.4 GHz, respectively. There is a discrepancy is observed between simulation and measurement results due to measurement setup and used measurement liquid. But it is observed from both measured and simulated results that the proposed antenna exposed lower SAR values than standard SAR guidelines.

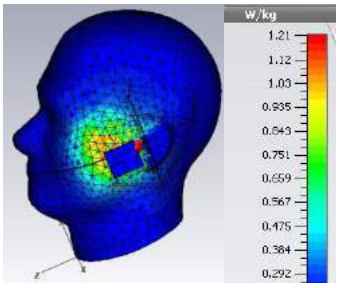

(a)

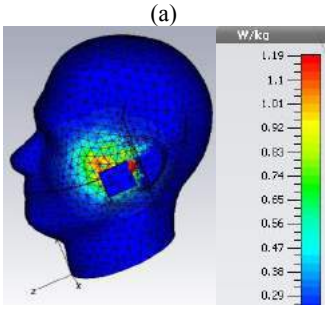

(b)

Figure 6: Simulated specific absorption rate analysis of the proposed antenna
at (a). 1.9 and (c) 2.6 GHz

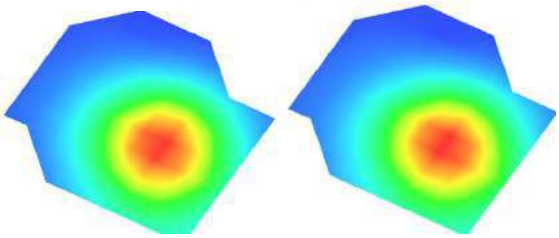

(a) (b)

Figure 7: Measured specific absorption rate analysis of the proposed antenna at (a). 1.9 and (c) 2.6 GHz

4. Conclusions

A coupled resonator based antenna is proposed for multifunctional wireless applications. The antenna enables to operate in the frequency bands of the upper GSM band, Bluetooth, WLAN 2400, WiMAX 2.5 and WLAN 5 band with satisfactory antenna performances. Moreover, the antenna satisfies the EM absorption guidelines established by IEEE and ICNIRP without degrading other antenna performances.

References

[1] C.H. Wu And K.L. Wong, Hexa-band internal printed slot antenna for mobile phone application, *Microwave and optical technology letters* 50(1):35-38, 2008.

[2] Alam, T., Faruque, M.R.I. And Islam, M.T., Specific absorption rate reduction of multi-standard mobile antenna with double-negative metamaterial, *Electronics Letters* 51(13): 970-971, 2015.

[3] Zhou, Tao, Yazi Cao, and Zhiqun Cheng, Compact Multiband Interdigital-Coupled-Fed Planar Antenna with Stepped-Impedance Structures for Mobile Handsets, *International Journal of Antennas and Propagation*, 2017.

[4] Ji, Jeong Keun, Compact Broadband Dual ZOR Antenna for Multiband Smart Mobile Phone Applications." *International Journal of Antennas and Propagation*, 2017.

[5] Huang, Daiwei, Zhengwei Du, and Yan Wang, An Octa-band Monopole Antenna With a Small Nonground Portion Height for LTE/WLAN Mobile Phones, *IEEE Transactions on Antennas and Propagation* 65.2 : 878-882,2017.

[6] Chang, The-Nan, and Shih-Yen Cheng, Ultra Wide Miniaturized Printed antenna, *Electromagnetics*,1-10, 2017.

[7] Cheong, H. R., Yeap, K. H., Lai, K. C., Teh, P. C., & Nisar, H., A compact CPW-fed antenna with fractal S-shaped patches for multiband applications, *Microwave and Optical Technology* Letters 59(3):541-546, 2017.

[8] Mulla, Sajeed, and Shraddha S. Deshpande, Compact multiband antenna fed with wideband coupled line impedance transformer for improvement of impedance matching, *Microwave and Optical Technology Letters* 59(9):2341-2348, 2017.

[9] Hossain, M. I., Faruque, M. R. I., Islam, M. T., & Ali, M. T., Design and analysis of coupled-resonator reconfigurable antenna, *Applied Physics A*, 122(1): 1-4, 2016.

[10] Sharma, S.K. And Chaudhary, R.K., Dual band metamaterial inspired antenna for mobile applications, *Microwave and Optical Technology Letters* 57(6):1444-1447, 2015.

[11] Alam, T., Faruque, M. R. I., Alam, M. S., Islam, M. M., Mahmud, M. Z., & Islam, M. T., Bio-plastic composite substrate material based microstrip-fed printed antenna

for wireless communications, *Materiali in tehnologije* 51(1): 101-104, 2017.

[12] Hirata, Akimasa, and Osamu Fujiwara, Correlation between mass-averaged SAR and temperature elevation in human head model for RF near-field exposure from 1 to 6 GHz, Technical research report of the Institute of Electronics, Information and Communication Engineers (MW) 109.242 : 165-169, 2009.

[13] Hassanin, A. I. M., Biological effect of mobile telephone inside the human brain, IEEE Antennas and Propagation Society International Symposium, 2: 88-91, 2001.

[14] IEEE Standard for Safety Levels With Respect to Human Exposure to Radio Frequency Electromagnetic Fields, 3 kHz to 300 GHz, IEEE Std C95.1-2005, (2006), 0_1-238,doi: 10.1109/IEEESTD.2010.5433227.

A Three-Dimensional Antenna Inspired by Metamaterial for Human Head Imaging

M. A. Ullah[1], T. Alam[1], M. Z. Mahmud[1], G. K. Beng[1], J. S. Mandeep[1], M. T. Islam[1*]

[1] Dept. Of Electrical, Electronic and Systems Engineering, Universiti Kebangsaan Malaysia, Malaysia
*corresponding author: tariqul@ukm.edu.my

Abstract

A 3D antenna design followed by metamaterial unit cell is presented in this paper for portable microwave imaging system to scan human head. The proposed antenna is based on bounded H-shaped 10×10 mm^2 unit cell. FR4 lossy material is used as substrate for the box shaped design. 3×3 array of the unit cell is used as ground. Another array of unit cell is used as reflector on the bottom wall of the box. Finally, the antenna achieved operating band at 2.90-3.24 GHz which is within the operating band suggested by researchers for human head imaging. The overall dimension of the antenna is 50×37×14mm^3. The whole design and simulation process is performed under CST Microwave Studio simulation environment. Finally the optimum design has been fabricated and measured. The simulated and measured results are found in good agreement.

1. Introduction

Distribution of electrical property in the body can be observed through microwave images constructed by microwave imaging system in clinical diagnosis. More precisely, microwave imaging is the technique of using electromagnetic wave to observe internal architecture of objects. Microwave imaging system added more values to medical treatment due to fast and safe diagnosis.

Antennas act as main element of a microwave based imaging system. A good performing antenna can lead to an effective and portable medical diagnosis tool and finally have the potential to pave the way of saving lives. In literatures, different types of antenna have been reported for microwave imaging. Some basic properties of antenna are considered as requirements for microwave imaging. For instance, an antenna to be used for biomedical diagnosis in head imaging should have an operating frequency within 1-4 GHz [1], compact size to make the whole system portable etc.

Apart from that, several types of antennas are found in literature that are used in microwave imaging. An study reported about the use of dipole, monopole, bow-tie, Vivaldi, stacked-patch antennas for breast cancer imaging. 3D antennas are also used in human head imaging, congestive heart failure detection, breast cancer detection etc[2],[3],[4],[5],[6].

In this paper a three-dimensional antenna design is revealed for the application of microwave based human head imaging. The antenna design is followed by two arrays of 10×10mm^2 unit cell. Slotted microstrip feed-line is used for excitation purpose. The final 3D structure achieved operating band in lower microwave spectra. Frequency band at 2.90-3.24 GHz is obtained by the antenna.

2. Design of the antenna

The design and simulation of the antenna is performed using CST Microwave Studio. First of all, a unit cell is designed using 1.6mm thick FR4 lossy substrate. During the designing process, operating frequency between 2-4 GHz has been considered as the antenna is opted for human head imaging. Fig. 1 illustrates the design of the unit cell used to design the antenna. The shape of the unit cell is inspired by alphabet 'H'. Finally the shape is modified to the optimum design of the unit cell that obtained desired result.

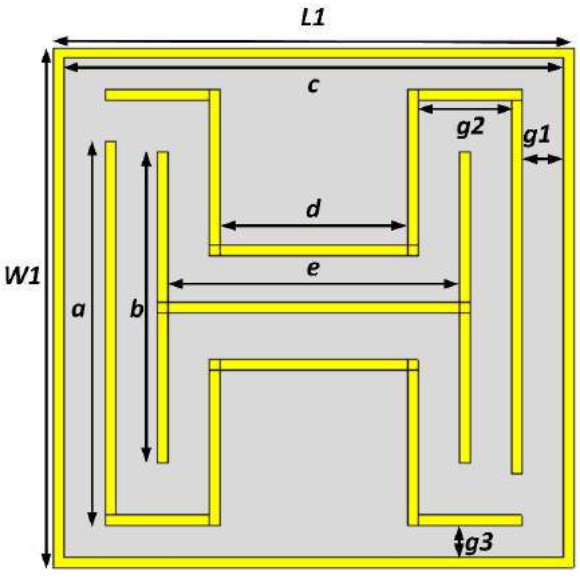

Figure 1: Design configuration of the unit cell

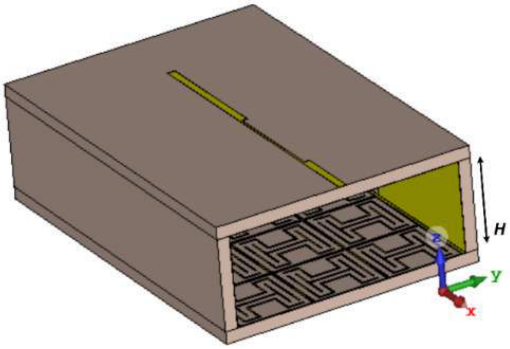

Figure 2: Perspective view of the proposed 3D antenna

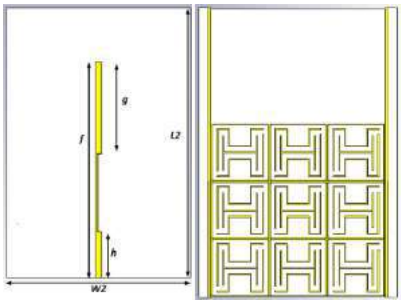

(a) (b)

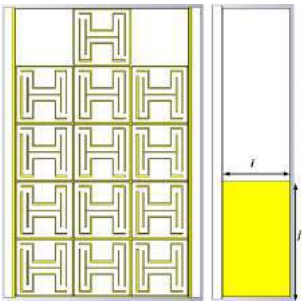

(c) (d)

Figure 3: Configuration of the different part of the proposed antenna, (a) Front view, (b) Ground, (c) Radiating element on lower substrate, (d) Side wall

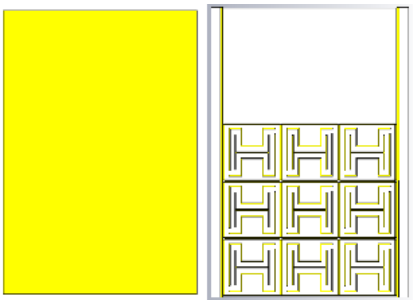

(a) (b)

Figure 4: Change of ground plane; (a) full ground, (b) metamaterial inspired ground

The evolution of the final three-dimensional antenna started from a basic patch antenna, depicted in Fig. 3(a), where 1.6mm FR4 used as substrate and 0.035mm thick copper radiating element. Then the array of the unit cell is placed instead of full ground plane. An array of 3x3 unit cell has been used as a ground plane that enabled the antenna to achieve operating band at lower microwave frequency. Results are shown in Fig. 4.

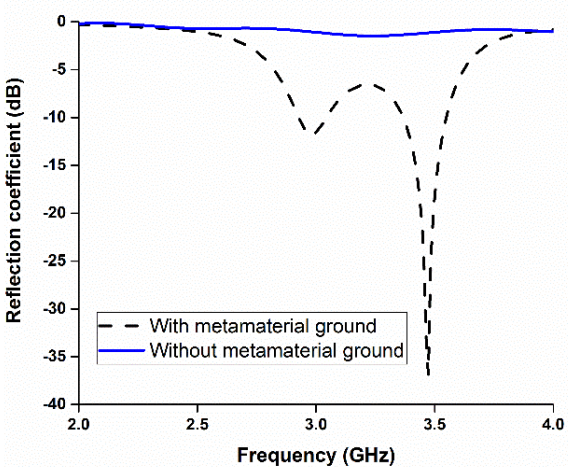

Figure 5: Reflection coefficient of the basic patch antenna

Finally, the antenna is given a rectangular box shaped structure to improve the bandwidth using the sidewalls connected with another array of unit cell on FR4 substrate. The final structure improvised the bandwidth significantly. Meanwhile a parametric study on the length of the feed line is investigated to obtain optimum result.

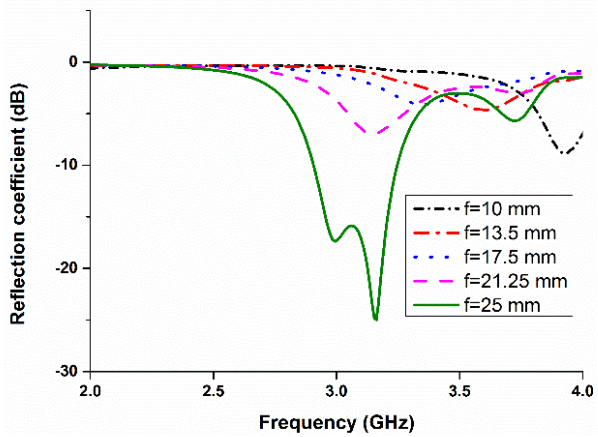

Figure 6: Parametric study on the length of the feedline

The optimum design parameters of the proposed antenna along with the unit cell are represented in Table 1.

Table 1: Design parameters of the proposed unit cell and antenna.

Parameters	Value [mm]
L1	*10*
W1	*10*
L2	*50*
W2	*37*
a	*7.2*
b	*6*
c	*9.6*
d	*4*
e	*6*
g1	*1.8*
g2	*1*
g3	*.8*
f	*25*
g	*17*
h	*8.5*
i	*11.8*
j	*20*
H	*12*

3. Results and discussion

The proposed unit cell that has been used in the antenna has obtained negative permeability, permittivity and refractive index in the operating band.

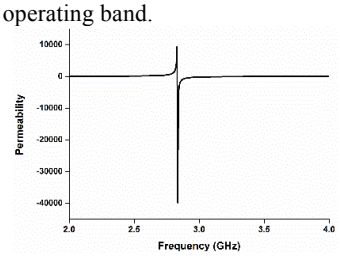

(a)

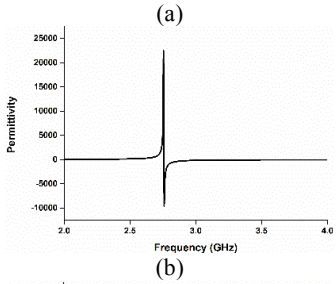

(b)

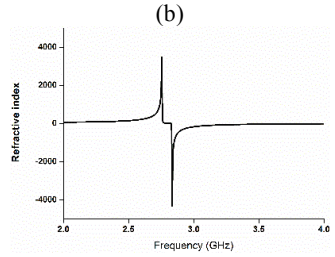

(c)

Figure 7: Calculated (a) permeability, (b) permittivity and (c) refractive index of the proposed unit cell

The final design of the proposed antenna has achieved operating and at 2.90-3.24 GHz in simulation. The fabricated prototype achived opearating band with a larger bandwidth at 3.78-3.34 GHz. The bandwidth increased from 340MHz to 560MHz after fabrication. Possible reason could be fabrication and measurement tolerance. Results are shown below in Fig. 8.

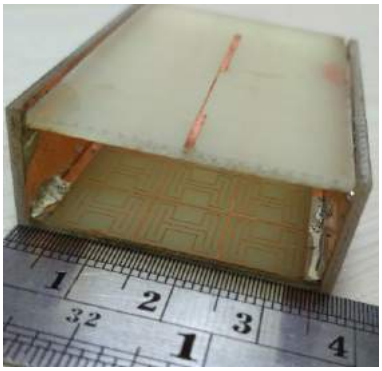

(a)

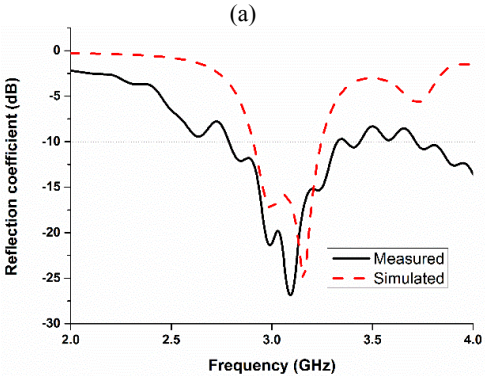

(b)

Figure 5: (a) Fabricated prototype, (b) Reflection coefficient of the proposed antenna

The proposed antenna achieved bidirectional radiation pattern in H plane and almost omnidirectional radiation pattern in E plane.

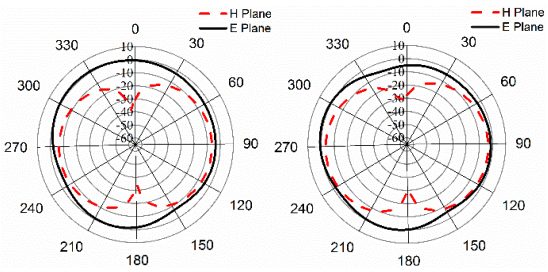

(a) (b)

Fig 5: Radiation pattern at (a) 3.00 GHz (b) 3.15 GHz

Radiation efficiency of the proposed antenna has been shown in Fig. 7. From the figure it can also be noticed that,

efficiency of the proposed antenna is more than just the patch antenna with unit cell. Certainly, introduction of the extra layer of the unit cell below the ground plane has increased the efficiency of the proposed design.

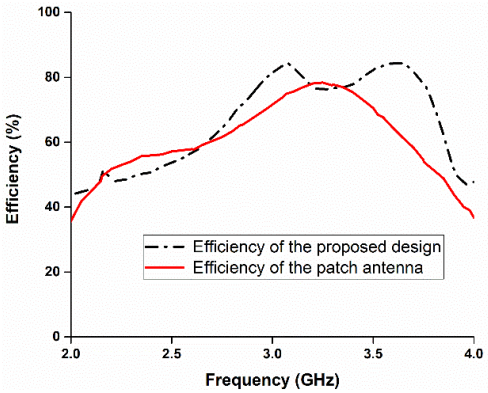

Figure 6: Efficiency of the proposed design and the patch antenna only.

4. Conclusions

A three-dimensional design of a metamaterial inspired antenna has been exposed in this paper. The illustrated unit cell obtained negative permeability, negative permittivity and negative refractive index over the proposed antenna's operating bandwidth. The unit cell is embedded with the antenna's final design. Finally, use of the unit cell and the three dimensional structure aided the antenna to achieve larger bandwidth along with a raise in efficiency level up to 85%. The proposed antenna could be a potential apparatus in for human head imaging using microwave imaging technology because of it's lower band operation.

References

[1] S. Ahdi Rezaeieh, A. Zamani, and A. M. Abbosh, Three Dimensional Wideband Antenna for Head Imaging System with Performance Verification in Brain Tumor Detection, *IEEE Antennas Wirel. Propag. Lett.*, vol. 1, no. c, pp. 1–1, 2015.

[2] A. T. Mobashsher, S. Member, and S. Member, Compact Three-dimensional Slot-Loaded Folded Dipole Antenna with Unidirectional Radiation and Low Impulse Distortion for Head Imaging Applications, *IEEE Transactions on Antennas and Propagation*, Vol. 64, pp. 7–10, 2016.

[3] N. A. Hassan and M. B. Tayel, Basic Evaluation of Antennas Used in Microwave Imaging for Breast Cancer Detection,*The Third International Conference on Computer Science & Engineering*, Dubai, UAE, pp. 55–63, 2016.

[4] Z. Akhter, B. N. Abhijith, and M. J. Akhtar, Hemisphere lens-loaded Vivaldi antenna for time domain microwave imaging of concealed objects, *Journal of Electromagnetic Waves and Applications,* vol. 5071, 2016.

[5] X. Li, M. Jalilvand, Y. L. Sit, and T. Zwick, A Compact Double-Layer On-Body Matched Bowtie Antenna for Medical Diagnosis, *IEEE Trans. Antennas Propag.*, vol. 62, no. 4, pp. 1808–1816, 2014.

[6] L. Ge, M. Li, J. Wang, and H. Gu, Unidirectional Dual - Band Stacked Patch Antenna with Independent Frequency Reconfiguration, *IEEE Antennas and Wireless Propagation Letters*, vol. 16, pp. 113-116, 2016.

Dual-Band Meta-Inspired Microstrip Antenna for WLAN and WiMAX Applications

F. B. Ashraf, M. T. Islam*, T. Alam, M. Z. Mahmud and M. J. Singh

Dept. Of Electrical, Electronic and Systems Engineering, Universiti Kebangsaan Malaysia, Malaysia
*corresponding author: tariqul@ukm.edu.my

Abstract

This paper presents a dual-band meta-inspired antenna operating at WLAN 2.4 GHz and WiMAX 2.5 and 5 GHz. The proposed antenna size is 35×35×1.6 mm^3. A left-handed metasurface providing negative refractive index is used as a patch and as a ground of the antenna. The antenna is fed by microstrip feeding methods. The antenna is designed on fiberglass cloth embedded in epoxy resin substrate and simulated on CST Microwave studio software package. The proposed design consists of a modified split ring resonator and a capacitive loaded strip to achieve metamaterial characteristics. The proposed meta antenna archives resonant frequency at 2.53 GHz and 5.58 GHz bandwidth of 360 MHz and 320 MHz, respectively. The gain of the antenna at 2.5 GHz is 4.19 dBi and 5.58 GHz is 4.16 dBi, respectively.

1. Introduction

In recent years, wireless technology requires compactness. For these, researcher has left space to design an antenna. The WLAN and WiMAX system is one of the most widely used technologies to simplify human communication. Using a metasurface mounted on an antenna can catch up with this compactness. The allocated frequency band for WLAN and WiMAX is between 2.5-2.69 GHz and 4.9-5.9 GHz. Left-handed metamaterials can exhibit simultaneously negative values of electric permittivity (ε) and magnetic permeability (μ) over a specified frequency band [1, 2]. Metamaterial based planar antenna design became popular due to enhanced radiation.

Over the years various designs of microstrip transmission line planar antennas have been reported for WiMAX and WLAN wireless communications. Many metamaterial based low profile antennas has been proposed [3, 4], by using metamaterial resonator as a radiating element. T. Alam *et al.* proposed a triangular shaped antenna 48×48×1.57 mm^3 for mobile wireless application [5]. The gain of the antenna at 2.45 GHz is 2.07 dB, and 5 GHz is 4.06 dB with radiation efficiency of 77.15% and 87.6%. Ali *et al.* proposed a 20×40 mm^2 miniaturized slot antenna for WALN in [6]. A nested inverted-F antenna resonating frequency at 2.5 and 5.5 GHz achieved a radiation efficiency of 92% and 88%, respectively [7].

In this paper, a metamaterial inspired antenna is proposed based on modified split ring resonator (MSRR) and capacitive loaded strip (CLS). The geometric layout of the proposed antenna is depicted in Figure 1. The budget FR-4 has been used as a substrate. The proposed antenna consisted with 2×2 CSRR metamaterial unit cell as a top

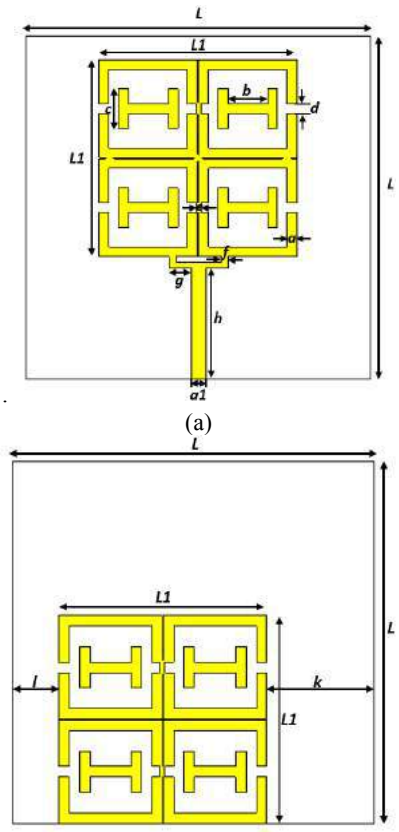

Figure 1. Geometry of the proposed antenna (a) Top View and (b) Bottom view.

Table 1: Dimensions Parameters.

Parameter	Value [mm]	Parameter	Value [mm]
L	35	*e*	0.5
L1	20.1	*f*	0.7
a	1	*g*	2.25
a1	1.5	*h*	11.3
b	4	*k*	10.4
c	4	*l*	4.5
d	1		

and bottom layer. The size is reduced due to the negative electromagnetic properties of the metasurface. A 50 Ω microstrip transmission line is used to feed the antenna. The antenna achieves -10 dB impedance bandwidth of 350 MHz and 300 MHz.

2. Design and Fabrication

The schematic layout of the proposed meta-inspired microstrip antenna is shown in figure 1, while fabricated prototype is in figure 2. The proposed antenna consists of a 2×2 metamaterial unit cell acting as a radiating component in one side of the substrate also on the opposite side acting as a ground plane. The proposed meta antenna has been designed on FR-4, which is a low-cost material, made from fiberglass cloth embedded in epoxy resin with relative permittivity ε_r=4.3, relative permeability μ_r=1 and loss tangent of δ=0.025. The substrate thickness is 1.6 mm and the dimensions of the antenna is 35×35 mm^2. The conductive copper is 0.035mm thick. The design parameters are represented in Table 1.

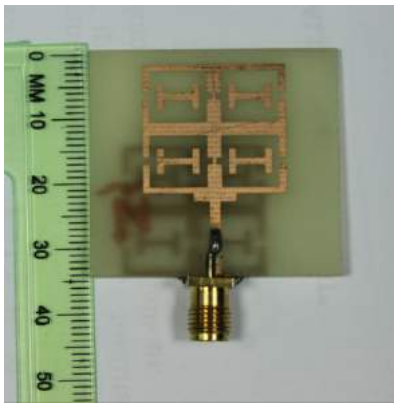

Top view

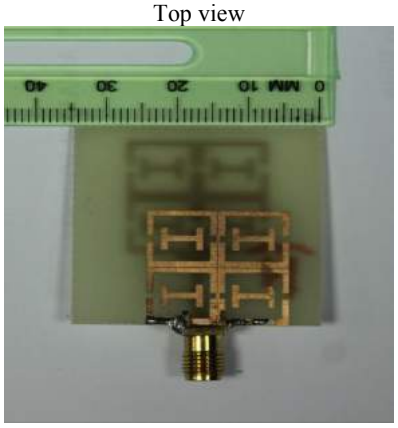

Bottom view

Figure 2. Fabricated prototype of the proposed meta inspired antenna.

3. Metamaterial Characterization

Perfect electric conductor (PEC) and perfect magnetic conductor (PMC) are set as a boundary condition throughout the x and y axis as shown in figure 3. In z-axis, the electromagnetic wave is propagated. The effective parameters of the proposed unit-cell are extracted by using transmission-reflection method [8].

$$z = \pm\sqrt{\frac{(1+S_{11})^2 + S^2_{21}}{(1-S_{11})^2 + S^2_{21}}} \quad (1)$$

$$\eta = \frac{1}{k_0 d}[\{[\ln(e^{ink_0 d})] + 2m\pi\} - i[\ln(e^{ink_0 d})]] \quad (2)$$

$$e^{ink_0 d} = \frac{s_{21}}{1 - s_{11}\dfrac{z-1}{z+1}} \quad (3)$$

$$\varepsilon = \frac{\eta}{z} \quad (4)$$

$$\mu = \eta z \quad (5)$$

Where, S_{11} and S_{21} are the reflection and transmission coefficients, symbol ε is the effective permittivity, μ is the effective permeability, k_0 is the wavenumber, d is the thickness of the substrate, η is the refractive index, m is an integer related to the branch index and z is the relative impedance.

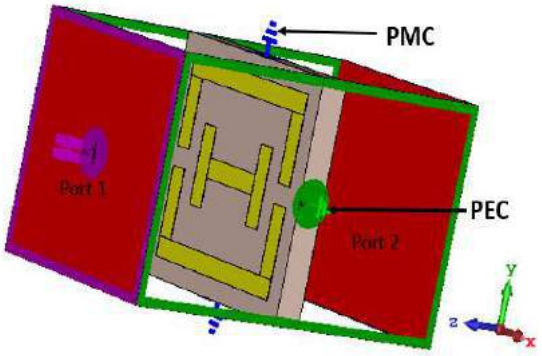

Figure 3. Floquet port arrangement.

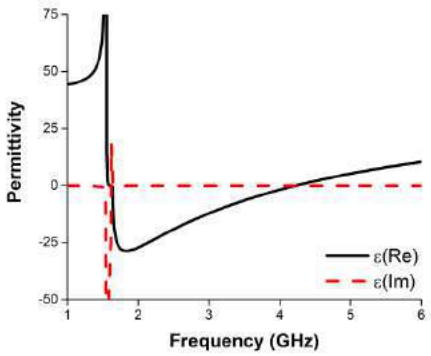

(a)

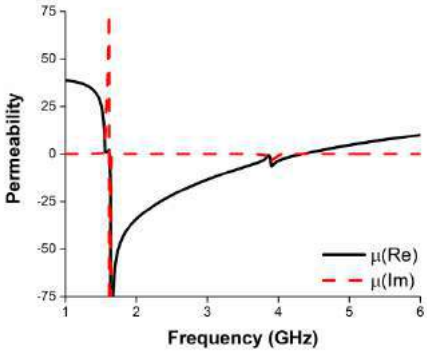

(b)

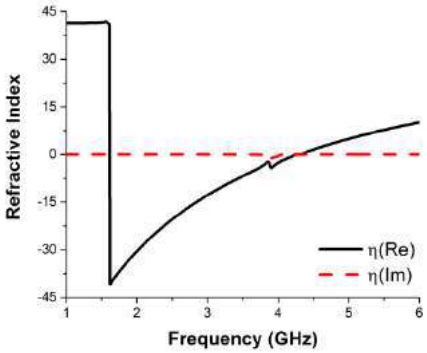

(c)

Figure 4. Effective constitutive parameters of unit-cell (a) Permittivity (b) Permeability and (c) Refractive Index.

4. Antenna Performance

The simulated and measured reflection coefficient (S_{11}) of the proposed meta antenna is depicted in figure 5. It shows a peak below -10 dB from 2.46 GHz to 2.57 GHz bandwidth of 110 MHz and 5.45 GHz to 5.73 GHz bandwidth of 280 MHz predicted by CST. Where the fabricated prototype shows a peak below -10 dB from 2.21 GHz to 2.57 GHz bandwidth of 360 MHz and 5.51 GHz to 5.83 GHz bandwidth of 320 MHz.

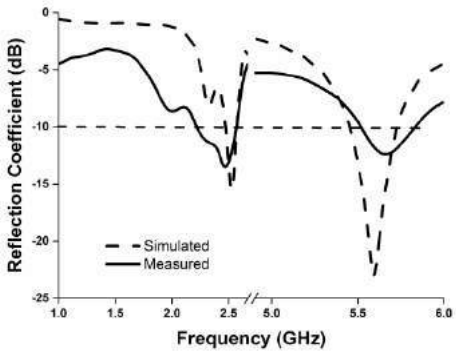

Figure 5. Reflection coefficient of the proposed meta-inspired antenna.

The measured reflection coefficient a bit different from the simulation result. That's because of fabrication tolerance and measurement system loss.

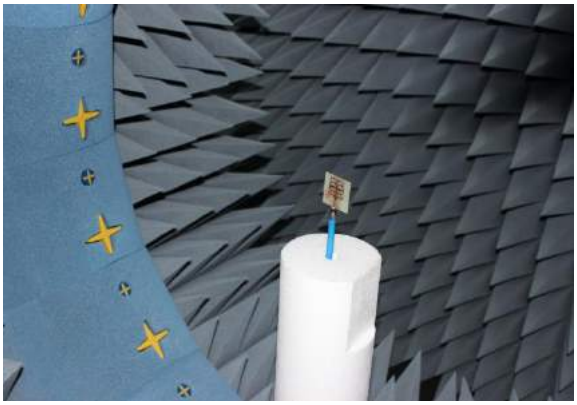

Figure 6. Farfield Characteristics measurement setup.

A near field measurement system of Satimo has been used to analyze the farfield performances of the proposed antenna, as shown in Figure 6.

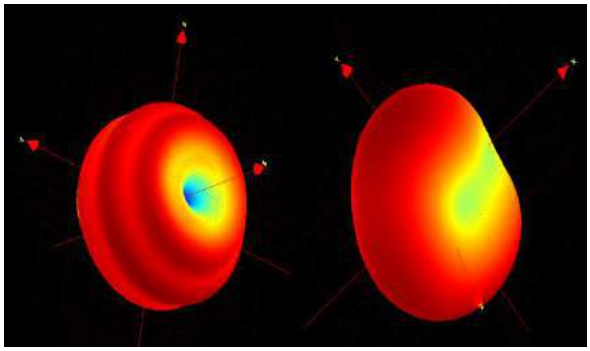

(a) (b)

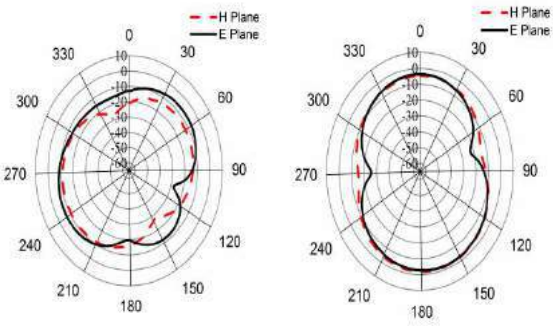

(c) (d)

Figure 7. Measured 3D radiation pattern at (a) 2.53 GHz (b) 5.58 GHz and H plane and E plane radiation pattern at (a) 2.53 GHz (b) 5.58 GHz

Radiation patterns of the proposed antenna have been shown in figure 7. At 2.53 GHz the antenna achieved almost omnidirectional radiation pattern. Near about bidirectional radiation pattern have been obtained at 5.58 GHz. The value of directive gain obtained by the antenna are GHz is 4.19 dBi at 2.53 GHz and 4.16 dBi at 5.58 GHz.

5. Conclusion

A dual band meta-inspired microstrip patch antenna has been presented for 2.53 GHz and 5.58 GHz. The proposed antenna has various slots and slits on the patch resonator and ground plane to obtain dual band characteristics. The tested results demonstrate that the proposed antenna can be a good candidate of wireless communication. Integrating a negative refractive index (NRI) metamaterial structure to the proposed antenna at the same time enhance the performances along with miniaturization are the distinctive novelty. The proposed antenna can be merged in practical small devices demanding dual band WLAN and WiMAX applications.

Acknowledgements

This work is supported by the Ministry of Education Malaysia (MOE) under grant no. FRGS/1/2014/TK03/UKM/01/1, and the University research grant code no. DIP-2014-029.

References

[1] A. Grbic and G. V. Eleftheriades, "Experimental verification of backward-wave radiation from a negative refractive index metamaterial," *Journal of Applied Physics,* vol. 92, no. 10, pp. 5930-5935, 2002.

[2] P. Y. Chen and A. Alu, "Dual-Mode Miniaturized Elliptical Patch Antenna With $\mu $-Negative Metamaterials," *IEEE Antennas and Wireless Propagation Letters,* vol. 9, pp. 351-354, 2010.

[3] F. Qureshi, M. A. Antoniades, and G. V. Eleftheriades, "A compact and low-profile metamaterial ring antenna with vertical polarization," *IEEE Antennas and Wireless Propagation Letters,* vol. 4, no. 1, pp. 333-336, 2005.

[4] M. A. Antoniades and G. V. Eleftheriades, "A broadband dual-mode monopole antenna using NRI-TL metamaterial loading," *IEEE Antennas and Wireless Propagation Letters,* vol. 8, pp. 258-261, 2009.

[5] T. Alam, M. Samsuzzaman, M. R. I. Faruque, and M. T. Islam, "A metamaterial unit cell inspired antenna for mobile wireless applications," *Microwave and Optical Technology Letters,* vol. 58, no. 2, pp. 263-267, 2016.

[6] M. Ali, S. Rahim, M. Sabran, M. Abedian, A. Eteng, and M. T. Islam, "Dual band miniaturized microstrip slot antenna for WLAN applications," *Microwave and Optical Technology Letters,* vol. 58, no. 6, pp. 1358-1362, 2016.

[7] A. Subbarao and S. Raghavan, "Coplanar waveguide-fed ultra-wideband planar antenna with WLAN-band rejection," *Journal of Microwaves, Optoelectronics and Electromagnetic Applications,* vol. 12, no. 1, pp. 50-59, 2013.

[8] Y. Shi, Z.-Y. Li, K. Li, L. Li, and C.-H. Liang, "A Retrieval Method of Effective Electromagnetic Parameters for Inhomogeneous Metamaterials," *IEEE Transactions on Microwave Theory and Techniques,* vol. 65, no. 4, pp. 1160-1178, 2017.

Cost Effective Negative Indexed EMTM for Specific Absorption Rate Reduction

M. T. Islam*, F. B. Ashraf, T. Alam, M. A. Ullah, M. N. Rahman and M. R. I Faruque

Dept. Of Electrical, Electronic and Systems Engineering, Universiti Kebangsaan Malaysia, Malaysia
*corresponding author: tariqul@ukm.edu.my

Abstract

A simply fabricated double negative metamaterial to reduce specific absorption rate (SAR) of wireless mobile antenna is proposed in this article. Low cost of fabrication and photo paper are the main attraction of this paper. Elliptic based metamaterial (EMTM) is used to reduce the SAR for 1g mass of human tissue. The simulation is performed using head phantom integrated in CST Microwave studio. The SAR has been reduced by 53% and 10.5% at 0.9 GHz and 1.8 GHz for 1g, respectively.

1. Introduction

The hazard of electromagnetic (EM) radiation from mobile phone become a key point of consideration for researchers as its increasing demand and use in our daily life. The fundamental parameter in EM absorption is characterized regarding the specific absorption rate (SAR), or the absorbed power in unit mass of tissue. The electromagnetic radiation radiated by wireless devices are analyzed by measuring the specific absorption rate in a human head phantom, defined as [1]:

$$SAR = \frac{\sigma \left|\vec{E}\right|^2}{\rho} = c\frac{dT}{dt}$$

Where, σ is electrical conductivity, ρ is mass density, *c* is specific absorption rate and *dT/dt* is the changing rate of the body tissue temperature. An exposure limits in terms of SAR are set by standards organizations [2].Recently, researchers work on SAR reduction using metamaterial while focused on low cost and easy implementation procedure. In previous research, many folks use metamaterial to reduce SAR [3-5]. Metamaterial structure used for their unique properties on electromagnetic wave, which cannot be found in nature. It depends on how they structured not in their inclusion.

Hwang *et. al.* [6] presented split ring resonator structure to reduce the SAR value for 1g. By placing thin wires periodically negative permittivity can also be obtained [7]. Sultan *et. al*. proposed an electromagnetic bandgap structure embedded with an antenna to reduce the SAR values in [8]. The metamaterials designed on circuit board make it appropriate for integrated into the mobile phone easily.

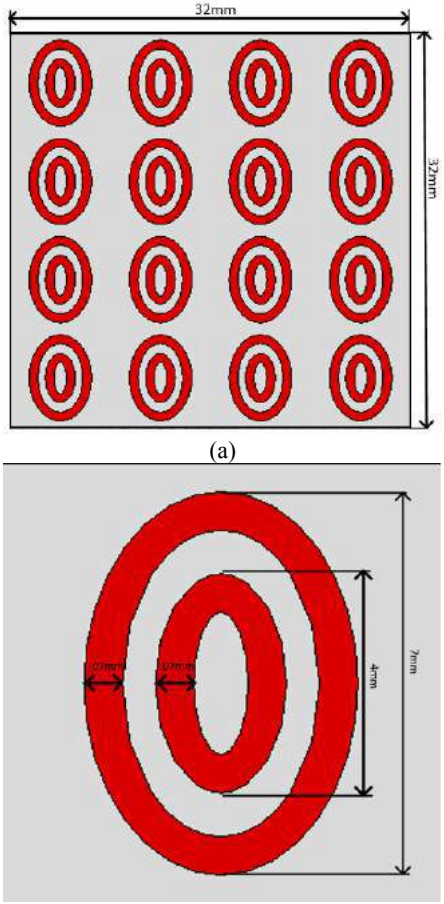

Figure 1. (a) Proposed elliptic based metamaterial and (b) unit-cell design.

2. Metamaterial Deign and Characterization

The proposed EMTM structure is constructed and investigated by using CST Microwave Studio based on finite-difference time-domain method (FDTD). Figure 1, shows the proposed metamaterial. The metamaterial is designed on a photo paper which dielectric constant, ε_r=3.2 and width of the paper is 0.27 mm. The effective characteristics of the presented metamaterial are exemplified in Figure 2. As shown in Figure 2, the effective permittivity of the EMTM is found from 1.98 to 3.98 GHz

and effective permeability from 1.98 to 3.99 GHz. As expected, it shows negative refractive index (NRI) from 1.98 to 3.99 GHz, bandwidth of about 2 GHz. The proposed metamaterial structure doesn't reduce the antenna performance.

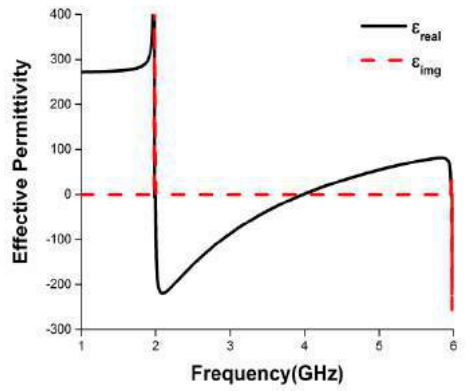

(a)

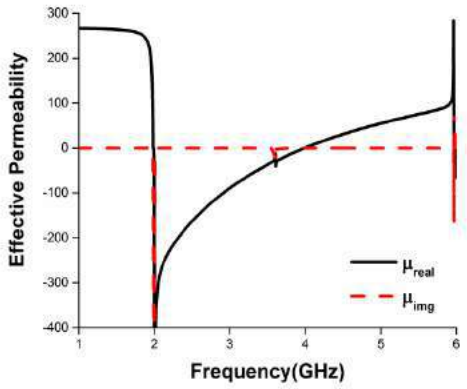

(b)

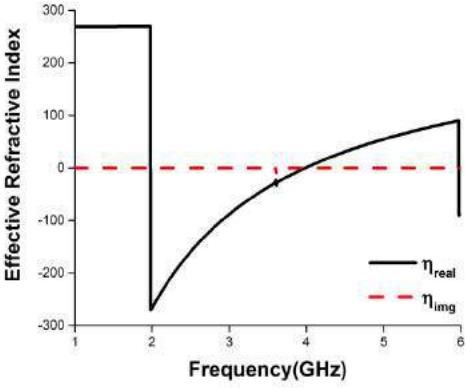

(c)

Figure 2. Extracted effective parameters (a) effective permittivity (b) effective permeability and (c) index of refraction.

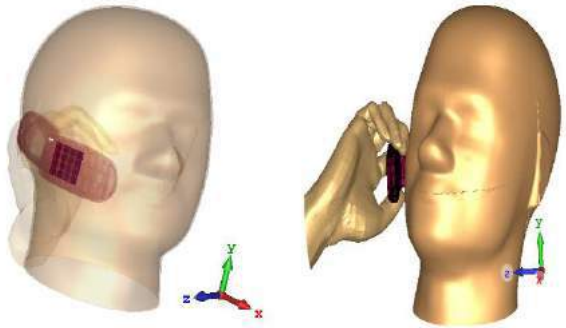

Figure 3. EMTM embedded in hand mobile and SAR simulation head model.

3. Analysis of Specific absorption rate

The SAR values of the presented elliptic metamaterial are observed using CST Microwave Studio 2017. The inbuilt human head phantom of CST has been taken and the reference power has been fixed to 500 mW. The human head model consists of head equivalent fluid with $\varepsilon_r = 40$, $\sigma = 1.4$ and shell with $\varepsilon_r = 5$, tangent delta = 0.05 are set in the SAM head phantom. Moreover, an inbuilt handset model having a circuit board, dial pad, LCD, housing and battery has been combined with the SAM head phantom. The simulation environment has been arranged just as IEEE and Federal Communications Commission standards. The placement of the paper based metamaterial inside the handset model and the full SAR simulation head model are shown in Figure 3.

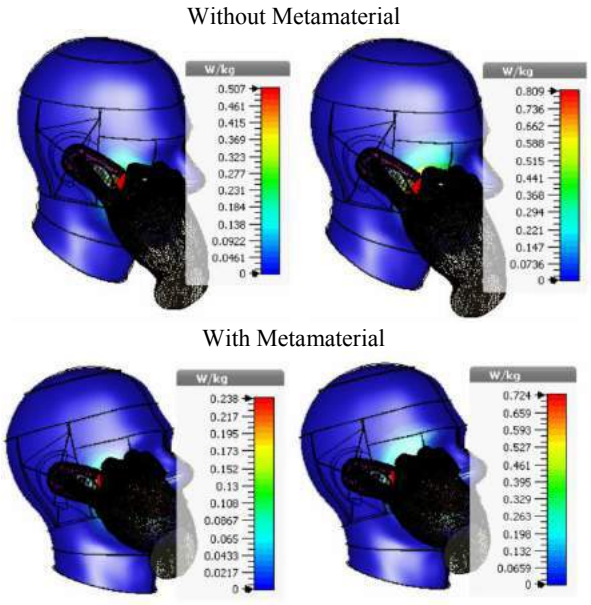

Figure 4. 1g SAR values at .9 GHz and 1.8 GHz.

Without Metamaterial

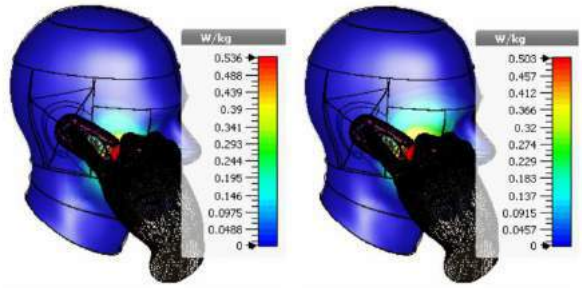

With Metamaterial

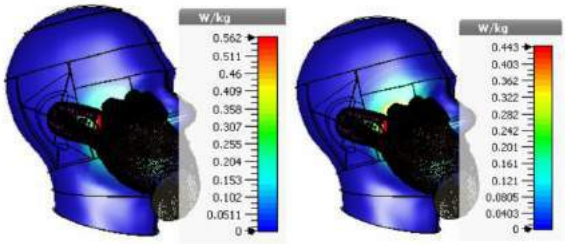

Figure 5. 10g SAR values at .9 GHz and 1.8 GHz.

Initially, the simulation has been done without inserting the proposed paper based metamaterial for 0.9 GHz and 1.8 GHz, presented in figure 4 for 1g and in figure 5 for 10g body tissue. It is shown from figure 4 and 5 that the highest SAR values are shown 0.238 W/Kg and 0.724 W/Kg for 1 g and 0.562 W/Kg and 0.443 W/Kg for 10 g tissue at 0.9 GHz and 1.8 GHz. When inserting the paper based elliptic metamaterial inside the phone model, the highest SAR values are now 0.238 W/kg and 0.724 W/kg for 1g and 0.562 W/kg and 0.443 W/kg for 10 g at 0.9 GHz and 1.8 GHz respectively. A comparison of the SAR values for both 1g and 10g are presented in Table 1.

Table 1: Comparison of SAR values.

Phone Model	Frequency [GHz]	1g SAR [W/Kg]	10g SAR [W/Kg]
With	0.9	0.238	0.562
EMTM	1.8	0.724	0.443
Without	0.9	0.507	0.536
EMTM	1.8	0.809	0.503

The simulated SAR values of the proposed EMTM are lower than the safety guidelines provided by IEEE and FCC. At this point, the presented metamaterial structure plays a vital role in reducing the SAR values.

4. Conclusion

The presented elliptic based metamaterial structure reveals an EM absorption reduction without altering the antenna performances. The newly developed EMTM attachment in the phone model led to a SAR value of 0.238 W/Kg for 1 g and .562 W/Kg for 10 g at 0.9 GHz and 0.724 W/Kg for 1 g and .443 W/Kg for 10 g at 1.8 GHz. Therefore, using a photo paper based elliptic metamaterial (EMTM) can be a remedy from the dangerous effects of electromagnetic wave radiated by the wireless device.

Acknowledgements

This research received funding from the Ministry of Education Malaysia (MOE) under grant no. FRGS/1/2014/TK03/UKM/01/1, and the University research grant code no. DIP-2014-029.

References

[1] M. R. I. Faruque, M. T. Islam, and M. A. M. Ali, "A new design of metamaterials for SAR reduction," *Measurement science review,* vol. 13, no. 2, pp. 70-74, 2013.

[2] ANSI/IEEE, "C95. 6-2002, IEEE Standard for Safety Levels with Respect to Human Exposure to Electromagnetic fields, 0-3 kHz," ed: Institute Electrical Electronics Engineers New York, 2002.

[3] S. il Kwak, D.-U. Sim, J. H. Kwon, and Y. J. Yoon, "Design of PIFA with metamaterials for body-SAR reduction in wearable applications," *IEEE Transactions on Electromagnetic Compatibility,* vol. 59, no. 1, pp. 297-300, 2017.

[4] T. Alam, M. R. I. Faruque, and M. T. Islam, "Specific absorption rate analysis of broadband mobile antenna with negative index metamaterial," *Applied Physics A: Materials Science and Processing,* vol. 122, no. 3, 2016.

[5] Y. Pinto and X. Begaud, "Mobile phone model with metamaterials to reduce the exposure," *Applied Physics A,* vol. 122, no. 4, p. 336, 2016.

[6] J.-N. Hwang and F.-C. Chen, "Reduction of the peak SAR in the human head with metamaterials," *IEEE Transactions on Antennas and Propagation,* vol. 54, no. 12, pp. 3763-3770, 2006.

[7] A. A. Abdelrehim and H. Ghafouri-Shiraz, "High performance patch antenna using circular split ring resonators and thin wires employing electromagnetic coupling improvement," *Photonics and Nanostructures-Fundamentals and Applications,* vol. 21, pp. 19-31, 2016.

[8] K. Sultan, H. Abdullah, E. Abdallah, and E. Hashish, "Low-SAR, miniaturized printed antenna for mobile, ISM, and WLAN services," *IEEE antennas and wireless propagation letters,* vol. 12, pp. 1106-1109, 2013.

A Metamaterial Inspired Patch Antenna for Handheld Mobile Communication

Mohammad Tariqul Islam[1*], Md. Amanath Ullah[1], Farhad Bin Ashraf[1], Md. Naimur Rahman[1] and Mohd Tarmizi Ali[2]

[1] Dept. Of Electrical, Electronic and Systems Engineering, Universiti Kebangsaan Malaysia, Malaysia

[2]Centre for Communication Eng. Studies Universiti Teknologi MaraShah AlamMalaysia

[*]corresponding author: tariqul@ukm.edu.my

Abstract

A metamaterial inspired dual band rectangular patch antenna design is introduced in this paper for feature phones. The proposed antenna design is based on $10\times10mm^2$ grid shaped unit cell. Four unit cells are interconnected with a thin radiating element to achieve operating bandwidth in lower frequency. The ground plane used a 3×5 array of the proposed grid shaped unit cell, accompanied with a single cell on the upper side of the ground. The electrical dimension of the proposed antenna is $0.46\lambda\times0.017\lambda$ at 0.92GHz lower frequency bands. The proposed antenna can operate at most widely used GSM 900MHz and 1900MHz. The design and simulation process of the unit cell and the proposed antenna is computed using CST Microwave Studio. 1.6mm thick lossy FR4 material is used as substrate for the proposed antenna. Finally, Specific Absorption Rate (SAR) of the antenna has also been calculated to investigate if the SAR values of the proposed antenna remain within public exposure limit.

1. Introduction

The present era of smartphones and smart devices is truly undeniable. Even though the enormous popularity of smartphones, demand for feature phones still prevails. Moreover, places like hilly or rural areas and places which are not still blessed with 3G or 4G communication the GSM network is still being used there. In addition to the facts, even the tech giants are emphasizing on smartphone production, they still have not stopped manufacturing the feature phones considering the demands. Furthermore, an antenna that covers the GSM bands is a mandatory apparatus for wireless communication in smartphones too. In [1] a dual band antenna inspired by metamaterial is presented for GSM and Wimax application. The antenna used 'I' shaped unit cell. However the width of the antenna is comparatively bigger than the proposed antenna. Two dual-band antennas for wireless and GSM applications are reported in [2]. These antenna are based on metamaterial structures. Effect of different material structures on size miniaturization are also reported in this study.

There are more metamaterial patch antennas found in literature for various applications like, miniature satellite communication [3], modern wireless communication [4], 4G mobile communication [5], wireless body centric communications[6] etc.

In this paper, a metamaterial inspired dual band antenna has been proposed for the application of wireless communication in feature phones. The proposed antenna covers GSM 900MHz and GSM 1900MHz. The design of the antenna is engendered from a metamaterial unit cell. Finally, arrays of the unit cell are used to make radiating element of the antenna.

2. Design of the antenna

The design and simulation of the antenna is performed using CST Microwave Studio. First of all, a unit cell is designed using 1.6mm thick FR4 lossy substrate. Then the unit cell is embedded as ground and patch of the proposed antenna. Design configuration of the proposed unit cell and antenna is shown in Fig. 1 and Fig. 2.

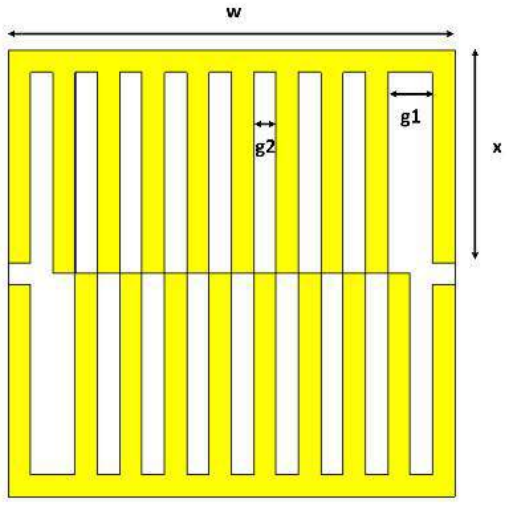

Figure 1: Design configuration of the unit cell

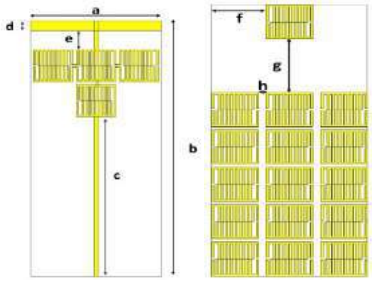

(a) (b)

Figure 2: Configuration of the proposed antenna (a) Front view, (b) Back view.

The patch of the antenna consists of total 4 unit cells where an array of 1x3 unit cell included and they are interconnected. The thickness of the copper radiating patch is considered to be 0.035mm. The ground plane has an array of 5x3 unit cell along with an unit cell placed at the top middle of the ground plane. Design parameters of the proposed antenna are enlisted in Table 1.

Table 1: Design parameters of the proposed unit cell and antenna.

Parameters	Value [mm]
w	10
g1	1
g2	0.5
x	4.75
a	32.2
b	80
c	50
d	3
e	6
f	11.1
g	15.9
h	1.6

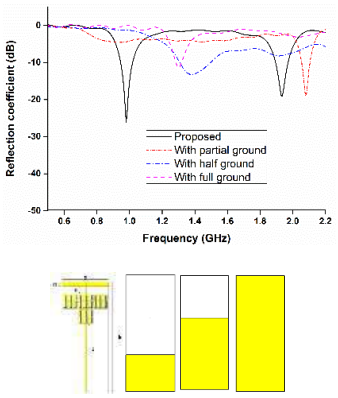

(a) (b) (c) (d)

Figure 3: Reflection coefficient using (a) proposed design, (b) partial ground, (c) half ground, (d) full ground without unit cell.

A parametric study has been investigated to obtain the optimum design. The results are depicted in Fig. 3. From the Fig. 3 it can be observed that the reflection coefficient of the proposed antenna has been significantly better by using metamaterial inspired unit cell.

3. Results and discussion

Fig. 4 depicts the permeability, permittivity and refractive index of the proposed unit cell respectively.

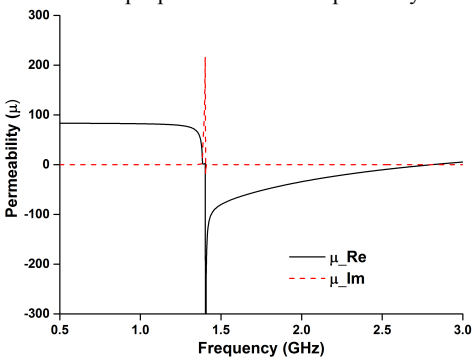

(a)

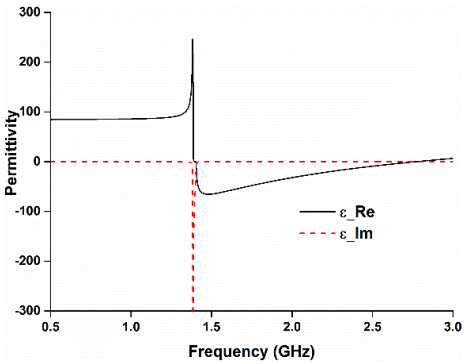

(b)

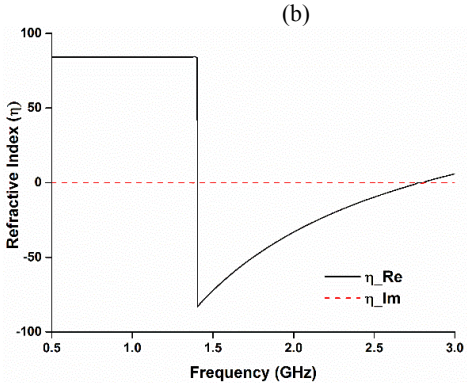

(c)

Figure 4: Calculated (a) permeability, (b) permittivity and (c) refractive index of the proposed unit cell.

It is noticed that, the negative permeability and permittivity has been found at 1.4-2.79 GHz and1.4-2.70 GHz

respectively. The reflection coefficient of the proposed antenna has been presented in Fig. 5. The antenna achieved operating band (<6dB) at 0.92-1.05 GHz and 1.86-2.00 GHz that covers GSM 900 and GSM 1900 bands. The simulated result shifted a bit at the resonances in measured result obtaining a wider bandwidth at 0.88-1.09 GHz and 1.64-2.06 GHz due to fabrication tolerance. However, results of the simulation and fabricated prototype have shown good agreement.

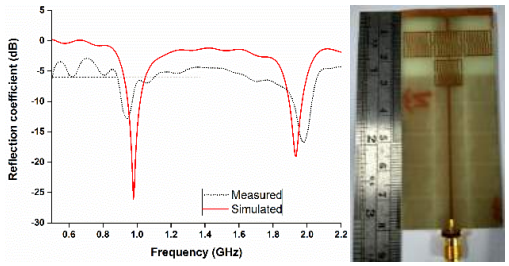

(a) (b)

Figure 5: (a) Reflection coefficient of the proposed antenna, (b) fabricated prototype.

The proposed antenna achieved bidirectional radiation pattern at 0.98 GHz and 1.93 GHz in E plane. Cross polarization is negligible.

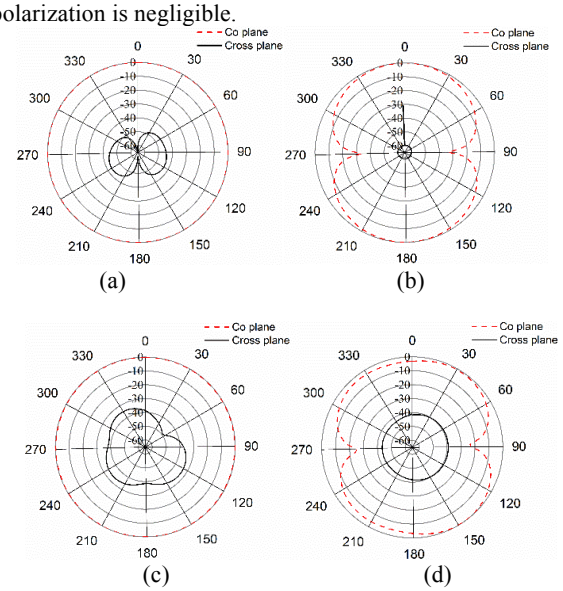

(a) (b)

(c) (d)

Figure 5: 2D radiation pattern at 0.98GHz (a) H Plane (b) E plane and 1.93 GHz (c) H plane (d) E plane

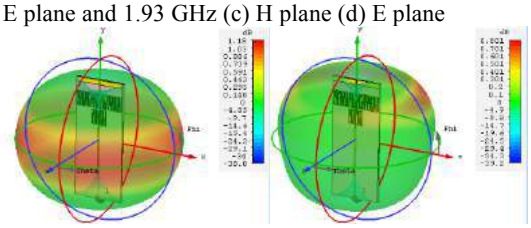

(a) (b)

Figure 6: 3D radiation patterns at (a) 0.98 GHz, (b) 1.93 GHz.

Finally, the proposed antenna has been used in SAR simulation with head model and antenna placed in mobile using CST Microwave Studio. The built-in SAM head phantom is used along with the complete handphone model which includes LCD display, battery, housing case and circuit.

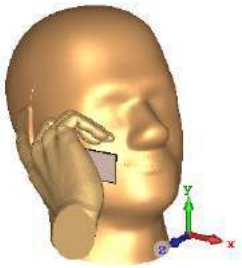

Figure 7: SAR simulation setup of the antenna with head model.

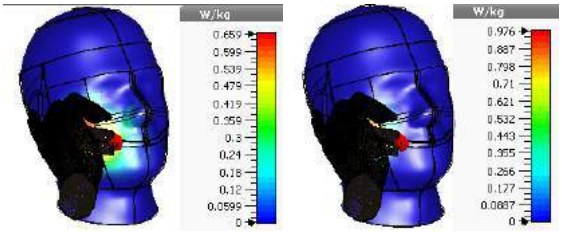

(a) (b)

Figure 8: 1g SAR values of the proposed antenna at (a) 900 MHz and (b) 1900 MHz

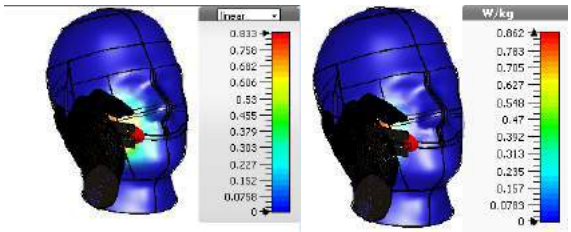

Figure 9: 10g SAR values of the proposed antenna at (a) 900 MHz and (b) 1900 MHz

It can be noticed from the figure 8 and 9 that, 1g SAR value of the proposed antenna are 0.659 and 0.976 W/Kg at 900MHz and 1900 MHz respectively. 10g SAR value at 900MHz is 0.833 W/Kg and at 1900 MHz is 0.862 W/Kg.

4. Conclusions

In this paper, design of a metamaterial inspired patch antenna has been revealed for GSM 900 and GSM 1900 for handheld mobile communication. Metamaterial unit cells have been used to design the patch and ground plane of the antenna. The reflection coefficient has been improvised by using the metamaterial unit cell. The simulation result and measured result of the fabricated prototype have shown good agreement and the designed unit cell aided the antenna to achieve the GSM 900 and GSM 1900 frequency bands.

Moreover, the result of the SAR values are within the public exposure limit of less than 1.6 watts per kilogram, hence making the antenna potential for feature phones.

References

[1] C. Goswami, M. Pal, R. Ghatak, and D. R. Poddar, Metamaterial based miniaturized dual band antenna, *Proc. 2014 2nd Int. Conf. "Emerging Technol. Trends Electron. Commun. Networking", ET2ECN 2014*, pp. 2–5, 2015.

[2] M. Rahimi, F. B. Zarrabi, R. Ahmadian, Z. Mansouri, and A. Keshtkar, Miniaturization of Antenna for Wireless Application With Difference Metamaterial Structures, *Prog. Electromagn. Res.*, vol. 145, no. February, pp. 19–29, 2014.

[3] C. G. M. Ryan and G. V Eleftheriades, Single- and Dual-Band Transparent Circularly Polarized Patch Antennas With Metamaterial Loading, *IEEE Antennas and Wireless Propagation Letters*, vol. 14, pp. 470–473, 2015.

[4] W. Liu, Z. N. Chen, and X. Qing, Metamaterial-Based Low-Profile Broadband Aperture Coupled Grid-Slotted Patch Antenna, *IEEE Transactions on Antennas and Propagation*, vol. 63, pp. 3325-3329, 2015.

[5] C. Zhu, T. Li, K. Li, Z. Su, X. Wang, and H. Zhai, Electrically Small Metamaterial-Inspired Tri-Band Antenna with Meta-mode, *IEEE Antennas and Wireless Propagation Letters*, vol. 14, pp. 1738 - 1741, 2015.

[6] Z. Liu, Y. Guo, and S. Member, Compact Low-Profile Dual Band Metamaterial antenna for body centric communications, *IEEE Antennas and Wireless Propagation Letters*, vol. 14, pp. 863-866, 2014.

A Meta-Inspired Multi-Standard Wideband Antenna for Mobile Applications

Touhidul Alam[1], Md. Amanath Ullah[1], Md. Naimur Rahman[1], Mohd Tarmizi Ali[2], Mohammad Tariqul Islam[1*]

[1]Dept. Of Electrical, Electronic and Systems Engineering, Universiti Kebangsaan Malaysia, Malaysia
[2]Centre for Communication Eng. Studies, Universiti Teknologi Mara, Shah Alam, Malaysia
*corresponding author: tariqul@ukm.edu.my

Abstract

A metamaterial ground planed structured antenna is proposed for multiband wireless mobile applications. The proposed structure consists of microstrip fed polygonal radiator with a meta-structure partial ground plane, which can operate within 1.77 GHz to 4.55 GHz. The antenna covers mostly used mobile application bands, such as GSM 1800, 1900, 2100, WCDMA, Bluetooth, WLAN 2400, WiMAX 2.5. The novel outcomes of this antenna are to achieve wideband with compact size metamaterial structured antenna.

1. Introduction

Nowadays, the mobile antenna design is becoming challenging issue to the antenna researchers due to multifunctional uses of mobile device. Many researches have been performed to design suitable mobile antenna, like as PIFA antenna [1], MIMO antenna [2], metamaterial antenna [3], patch antenna [4] segmented loop antenna [5]. Zhu et al proposed coupled fed triband antenna for mobile wireless applications [2]. In [3], a metamaterial inspired corded shaped antenna has been proposed for mobile applications, which can cover DCS, GSM1800, WCDMA, and Bluetooth frequency bands. Choukiker et. al proposed a fractal antenna for wireless communication which can achieved frequency band of 1.6 to 3.4 GHz with the size of 66 × 27 mm^2 [4]. In [6], a metamaterial unit cell inspired antenna is presented for mobile application with dimension of 48 × 48 × 1.575 mm^3. The antenna covers two bands, one is 1.6–1.97 GHz and another is 2.34–2.72 GHz.
Moreover, mobile antenna must complies the specific absorption rate (SAR) guidelines [7]. The SAR is defined by the power absorbed per unit of mass of biological tissues, which is the measurement system of tissue heating due to RF energy absorption. The SAR limit specified in IEEE C95.1:2005 is 1.6 W/kg in a 1 g averaging mass and 2 W/kg in a 10-g averaging mass of tissue.

In this paper, a compact size antenna is proposed for mobile communication system. Unlike the majority of existing designs, the proposed antenna is both simple in structure and simultaneously has wide impedance with moderate gain and efficiency.

2. Antenna Design and Characterization

The proposed antenna has been designed and characterized using commercially available microwave simulator "CST Microwave Studio" considering substrate material of Rogers 4003, dielectric constant of 3.55 and thickness 0.508 mm. The optimized design is depicted in Figure 1. The antenna consists of a polygonal radiator as main radiator and 3×3 metamaterial array based ground plane. The metamaterial unit cell characteristics has also been analyzed, shown in Figure 2. It is shown from Figure 2 that the negative permittivity of the unit cell shows from 12 GHz to 3.85 GHz and negative permeability shows from 2.635 GHz to 3.62 GHz. The negative refractive index is achieved from 3.08 to 3.70 GHz.

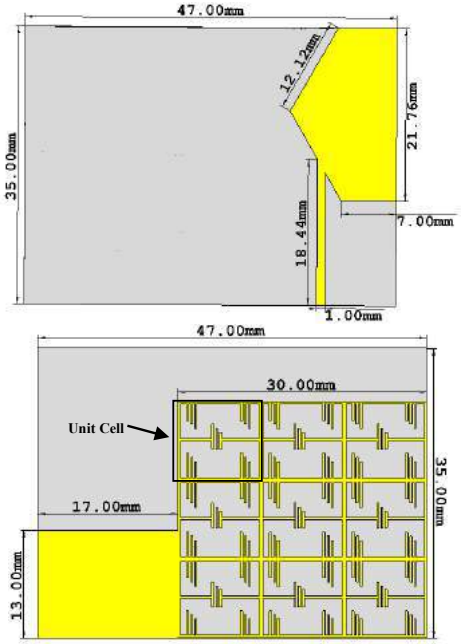

Figure 1: Schematic design of the proposed antenna

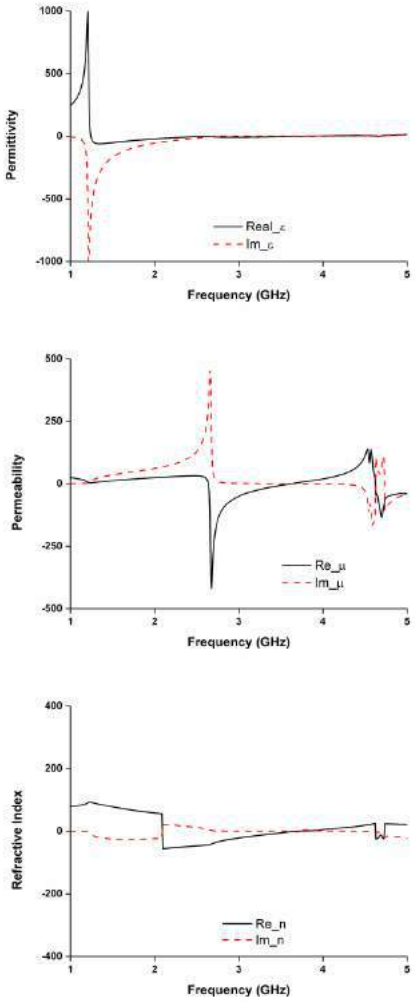

Figure 3: Retrieved metamaterial parameters.

3. Discussion

The optimized antenna shown in Figure 1 has been fabricated to measure the antenna performances, depicted in Figure 3. The measured and simulated reflection coefficient is illustrated in Figure 4. The measured and simulated results matched well though a small disagreement is observed. The possible reason of this mismatch is fabrication and measurement tolerance. The farfield characteristics have also been measured using Satimo nearfield measurement system, illustrated in Figure 5. In Figure 6, 3D farfield radiation is presented. It can be observed from Figure 6 that the antenna shows nearly omni-directional pattern at 1.8 GHz and 2.4 GHz.

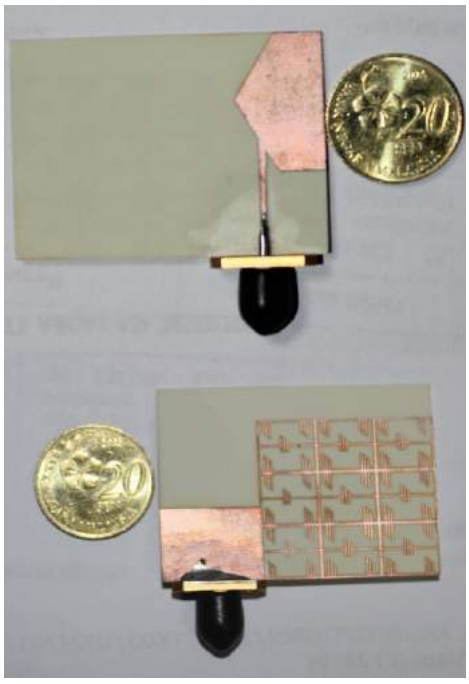

Figure: 3: Fabricated prototype of the proposed antenna

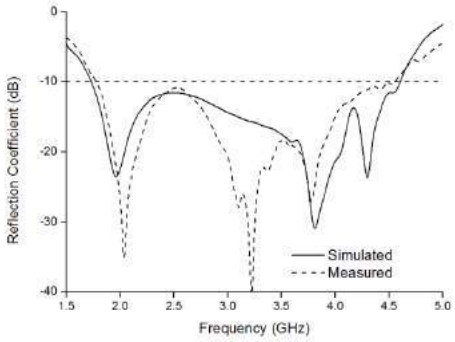

Figure 4: Reflection Coefficients of the proposed antenna

Figure 5: Antenna measurement in Satimo nearfield measurement system.

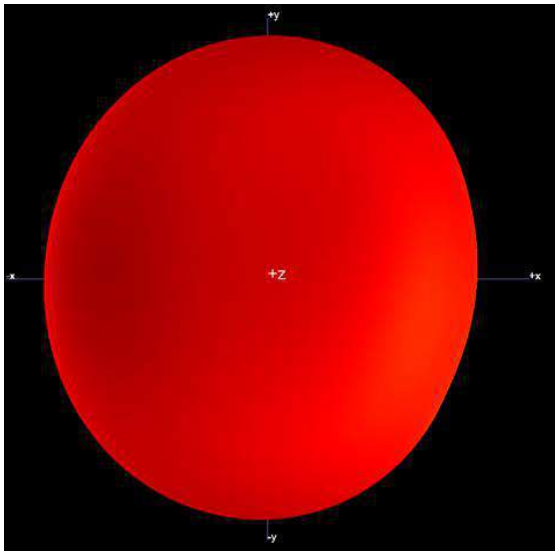

(a)

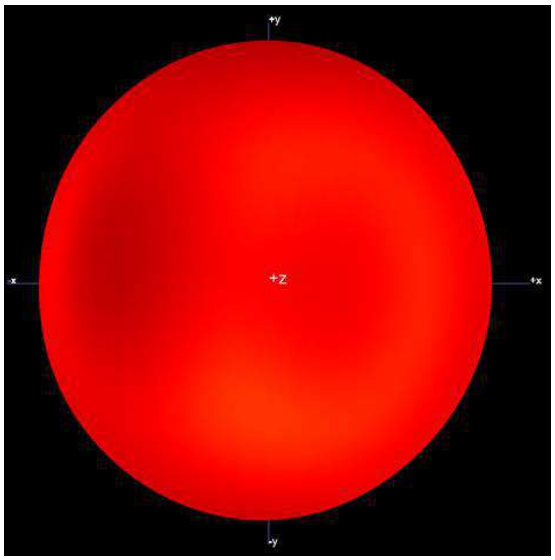

(b)

Figure 6: 3D farfield radiation pattern at (a) 1.8 GHz and (b) 2.4 GHz

The radiation efficiency and the realized gain is presented at Figure 7. The antenna shows -1.53 dB and -2.4 dB of radiation efficiency at 1.8 GHz and 2.4 GHz, respectively. Moreover, the antenna achieves 1.373 dB and 0.38 dB of realized gain at 1.8 GHz and 2.4 GHz, respectively.

The Specific absorption rate (SAR) values of the proposed antenna has been performed to ensure the compatibility with mobile communication system. The SAR measurement setup is demonstrated in Figure 8(a). And Figure 8(b) presents the SAR values at 1.8 GHz for different distance. The antenna shows 0.95 W/Kg of 10-g SAR and 1.62W/Kg of 1-g SAR at 1.8 GHz, which complies the SAR guidelines [7].

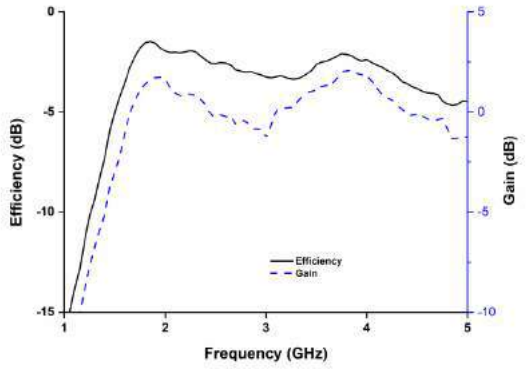

Figure 7: Measured efficiency and realized gain of the proposed antenna

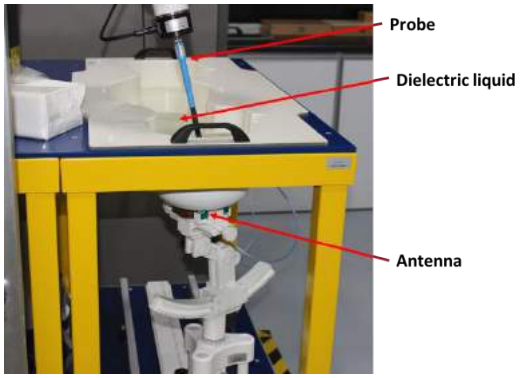

(a)

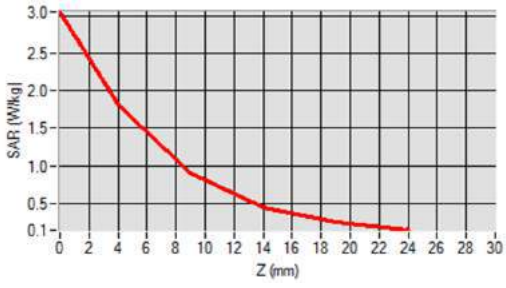

(b)

Figure 8: SAR measurement of the proposed antenna (a) measurement setup (b) SAR at 1.8 GHz for different distance.

4. Conclusions

A metamaterial ground plane inspired has been presented. The antenna has achieved -10 dB impedance band of 1.77 GHz to 4.55 GHz, which can operate at mostly used mobile bands. Moreover, the antenna complies the SAR guidelines and the antenna can be utilized in wireless devices due to its and relatively small size and simple structure.

References

[1] Lee, J. G., & Lee, J. H., SAR Reduction Using Integration of PIFA and AMC Structure for Pentaband Mobile Terminals, *International Journal of Antennas and Propagation*, 2017, doi: https://doi.org/10.1155/2017/6196721.

[2] Zhu, Jianfeng, Botao Feng, Li Deng, Biao Peng, and Shufang Li, Coupled - fed tri - band MIMO mobile antenna for WWAN and LTE applications, *Microwave and Optical Technology Letters* 59(2): 463-468, 2017.

[3] Alam, T., Faruque, M. R. I., & Islam, M. T., Specific absorption rate analysis of broadband mobile antenna with negative index metamaterial, *Applied Physics A: Materials Science and Processing*, 122(3), 2016.

[4] Choukiker, Y., & Mudiganti, J., Compact hybrid fractal antenna for wideband wireless applications, *International Journal of Microwave and Wireless Technologies* 9(5): 1191-1196, 2017.

[5] Zhao, X., Tian, B. N., Yeo, S. P., & Ong, L. C., Wideband Segmented Loop Antenna With Dual-Polarized Omnidirectional Patterns for Mobile Platforms, *IEEE Transactions on Antennas and Propagation* 65(2): 883-886, 2017.

[6] Alam, T., Samsuzzaman, M., Faruque, M. R. I., & Islam, M. T.,A metamaterial unit cell inspired antenna for mobile wireless applications, *Microwave and Optical Technology* Letters 58(2):263-267,2016.

[7] International Commission on Non-Ionizing Radiation Protection, Guidelines for limiting exposure to time-varying electric and magnetic fields (1 Hz to 100 kHz), *Health physics* 99(6): 818-836, 2010.

A New Metamaterial-based Wideband Rectangular Invisibility Cloak

S. S. Islam[1], M. M. Hasan[1], M. R.I. Faruque[1], and M. T. Islam[2]

[1]Space Science Centre, Universiti Kebangsaan Malaysia, Malaysia
[2]Dept. of Electrical, Electronic and Systems Engineering, Universiti Kebangsaan Malaysia, Malaysia

*corresponding author: sikder_islam@yahoo.co.uk

Abstract A new metamaterial-based wideband electromagnetic rectangular cloak is being introduced in this study. The metamaterial unit cell shows sharp transmittances in the C- and X-band and displays wideband negative effective permittivity region there. The metamaterial unit cell was then applied in designing a rectangular-shaped electromagnetic cloak. Scattering reduction technique was adopted for the cloaking operation. The cloak operates in the certain portion of C-and X-band that covers more than 4 GHz bandwidth region. The experimental results were provided as well for the metamaterial and the cloak.

1. Introduction

Artificially constructed metamaterial is now contributing in almost all the fields of electromagnetism including invisibility cloak design. Metamaterial provides essential property to synthesize proper electromagnetic cloak. An electromagnetic cloak can hide an object electromagnetically. Cloaking is usually used in the defense sector for hiding aircraft, satellite or missile from the hostile radar system. An object can be hidden electromagnetically if it does not scatter wave in any direction. In other sense, it does not absorb any power. Utilization of metamaterial guides the applied electromagnetic waves around the object instead of scattering and restores the waves to its original path that results transparency to the observer. Since the first successful attempt was done in [1] based on transformation optics (TO) technique, several research groups adopted numerous approaches to build compact metamaterial and an invisibility cloak [2-5]. In TO-method, a volume of no-field region is formed making the volume electromagnetically undetectable. However, the property requirement for the material that is utilized in designing a TO-cloak is difficult. A material with value of effective permittivity or permeability is between zero and greater than one can be utilized for the construction of TO-based cloak. Moreover, multiple layers are needed for designing metamaterial-based TO-cloak [6]. Among the other cloaking methods, scattering reduction method is easier to obtain the cloaking operation. Usually a good cloak reduces the normalized total scattering cross section (NTSCS) of an object close to zero [7]. Actually, a physical cloak diminishes the normalized total scattering cross section to some non-zero value, below one. A metamaterial with epsilon negative property is suitable for designing a cloak to suppress the scattering of an object [4]. Scattering reduction method was realized as well for the TO-cloak [6]. Previously few studies were performed on metamaterial-based cloak. However, most of the cloaks were cylindrical in shape and very few of them were found operating in C-band. Like, Xiaohui Wang et *al*. in [7], proposed a dielectric resonator based metamaterial X-band cloak but it was cylindrical in shape. They demonstrated that their cloak reduced the total scattering width below one in the X-band. A metamaterial-based cloak was developed in [8] for C-band operation but it was square-shaped and operating over 500 MHz region. A metasurface-based single layer cylindrical cloak was claimed by Matekovits *et al*. in [9] but it was operating in the K-band of microwave region. Another single layer cloak was proposed in [10] for C-band application but it was square-shaped and operating over 900 MHz region.

In this study, a rectangular-shaped wideband cloak is proposed that was designed using a bare-H-metamaterial. The cloak operates over more than 4 GHz frequency ranges. For designing the cloak, only one layer of metamaterial shell has been utilized.

2. Design and characteristics investigations of the metamaterial unit cell

The design and the S-parameters investigation of the metamaterial unit cell was done by the finite integration technique based CST Microwave Studio software. In this study, a bare-H-shape structure was formed on a $12\times12mm^2$ FR-4 substrate material by the combination two inner and outer magnetic copper made resonators of thickness 0.035mm. The inner resonator forms the basic bare-H-shape structure adopting a mirror symmetry, which helps to form negative effective permittivity property. Another split square resonator was added to the basic structure as outer resonator. Two gaps in the top and bottom of the outer resonator was kept 0.46mm. Each arm of the split square-shaped resonator is taking part to generate the inductive effect and the two gaps between the metal arms are responsible for generating the capacitive effect. The inductive and capacitive effects constitute the negative effective medium property for the metamaterial. The dielectric constants and thickness of the substrate material was 4.2mm and 1.6mm respectively. Fig.1a and Fig.1b depicts the new bare-H-shaped metamaterial unit cell and its fabricated sample consecutively. The structure and size of the proposed metamaterial unit cell was finalized to obey the proper effective medium ratio. The effective medium ratio for the metamaterial unit cell was $\lambda/a=6$, where λ is the wavelength.

At each side, 1 mm gap was maintained from the resonator to the end of the substrate. The design parameters were expressed in the Table-1.

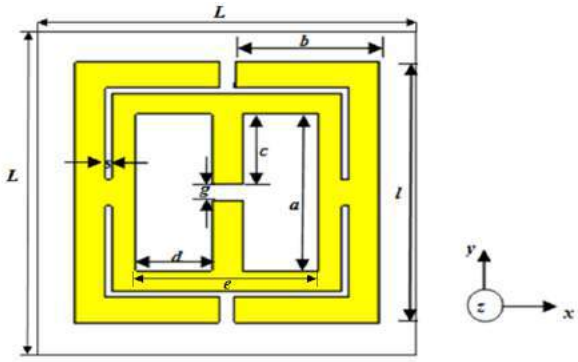

(a)

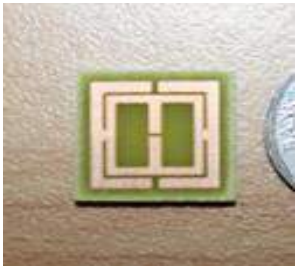

(b)

Figure-1. (a) Schematic diagram of the unit cell (b) Fabricated sample of the metamaterial unit cell

Table-1: Unit cell design parameters

Unit Cell Parameters	Value(mm)
a	6
b	4.77
c	2.77
d	2.50
e	6
g	0.46
s	0.2
l	10
L	12

To calculate the S-parameters of the metamaterial unit cell, electromagnetic wave was propagated through the unit cell using two waveguide ports. Perfect electric-magnetic boundary condition was applied for the simulation. The acquired S-parameters were adopted to evaluate the effective medium property of the material. For the calculation of the effective medium property of the material, Nicolson-Ross-Weir method [11] was utilized.

To perform the measurement of the unit cell, a sample unit cell metamaterial prototype was fabricated using LPKF laser based electronic machine. The fabricated sample was placed between two rectangular C-band waveguides, acting as transmitter and receiver. The waveguides were linked to the vector network analyzer (VNA) N5227A. From the VNA the S-parameters were obtained.

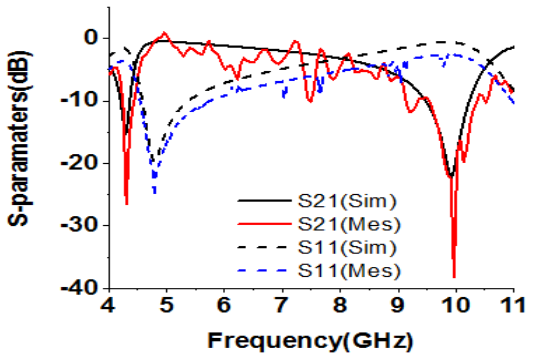

(a)

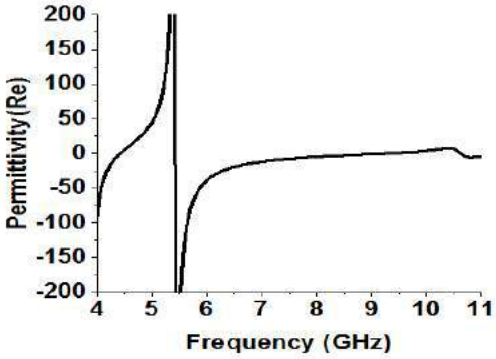

(b)

Figure-2. (a) Simulated and measured S-parameters for the unit cell (b) effective permittivity for the metamaterial unit cell

The simulated and measured results of S-parameters are shown in the Fig.2a for the metamaterial unit cell. Form the Fig.2a, the numerical curve shows transmittances at the frequency of 4.29 GHz and 9.93 GHz. The experimental transmittance also follows the numerical curve well. Similarly, the experimental reflection parameter agrees well with the numerical one. The effective permittivity curve is also presented in the Fig.2b where the curve displays negative peak from 4GHz to 4.43 GHz and 5.42GHz to 9.26 GHz in the frequency range. This negative region has significant effect for creating cloaking zone. This type of negative region regions creates opposite dipole moment that is useful for cloak operation.

3. Development and performance investigations of the metamaterial-based cloak

The newly developed metamaterial was applied for the construction of an electromagnetic cloak. The same CST Microwave Studio tool was also adopted for the design and numerical investigation of the metamaterial-based cloak. Scattering suppression technique was chosen to perform the cloaking operation. In this technique, a kind of dielectric shell or coating is surrounded by the object to be cloaked. The shell helps to reduce the scattering from the object and return the electromagnetic waves back to its usual path at a certain frequency. Therefore, the electromagnetic waves bend around the object and thereby make the object hidden to the observer or radar.

To perform such operation, four unequal walls were prepared where two parallel walls were equal. Two side walls were composed of four unit cells and two width walls were built by two unit cells of the proposed metamaterial in this study. As an object, an aluminium made cylinder was chosen that has 4mm inner and 5mm outer radius with equal height of the cloak. The four metamaterial walls were arranged to form a rectangular shape structure. The object was placed at the center of the cloak. The top view of the square-shaped cloak structure is being displayed in the Fig.3a with the object inside it.

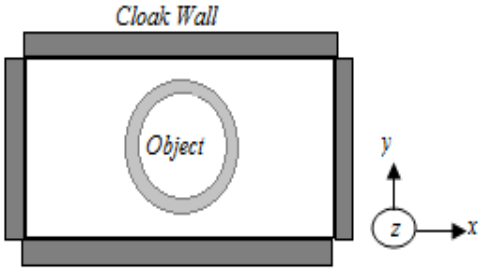

(a)Top view

(b)

Figure-3. (a) The rectangular-shaped cloak structure with an object (b) Fabricated cloak prototype with aluminium made cylider inside.

evaluation of the cloak, the normalized scattering cross section (NSCS) is determined. Total scattering cross section is the ratio of scattered and incident energy from the cloaked object. NSCS is the ratio of total scattering cross section (TSCS) of cloaked object normalized by the TSCS of uncloaked object that can be calculated according to the equation mentioned in [7]. Similarly, for the measurement purpose, according to the design, two 24×24 mm^2 walls and two 24×12 mm^2 walls were fabricated and each of the walls consists of unit cells of the metamaterial. The WR159 and WR112 waveguide sets as well as the VNA (vector network analyzer) N5227A were utilized for the measurement. The metamaterial walls were arranged in such a way that had produced a rectangular-shaped cloak. Aluminium made metal cylinder with diameter 8mm in the inner surface was utilized as object having same height of the cloak so that the metal cylinder can be placed easily inside the cloak. Fig. 3b shows the fabricated cloak sample with a metal object inside.

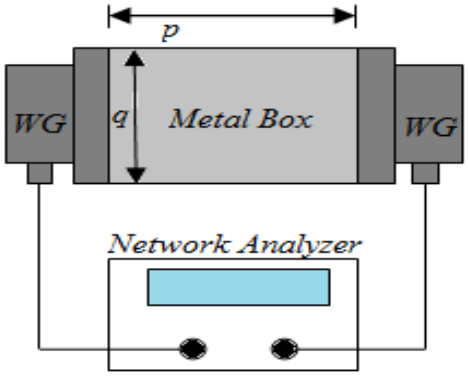

(a)

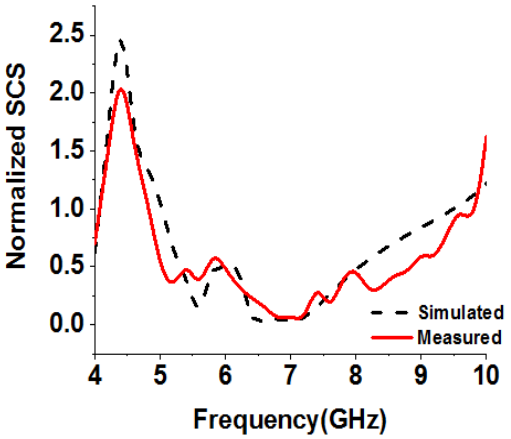

(b)

Figure-4. (a) The measurement setup for the cloak (b) simulated and measured results of TSCS of cloaked object normalized to the TSCS of bare object in the *xy*-plane

waveguides were connected to VNA as well. The whole cloak measurement setup is seen in the Fig.4a.

For the evaluation of NSCS, field status of incoming and scattering were measured. By placing the two waveguides face to face into the metal box, the incoming (Ei) field was measured. Afterwards, the metal object was placed between the waveguides inside the metal box and field parameters were measured that actually integrates total filed (Et) including the incoming and scattering field (Es). Deducting the incoming field from the total filed, the scattering field can be obtained. In addition, field measurement was also performed after placing the cloaked object inside the metal box and the scattering field was measured following the same way as mentioned above.

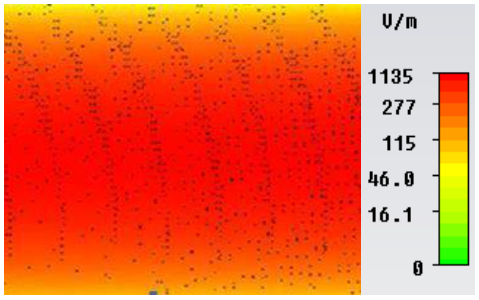

(a)

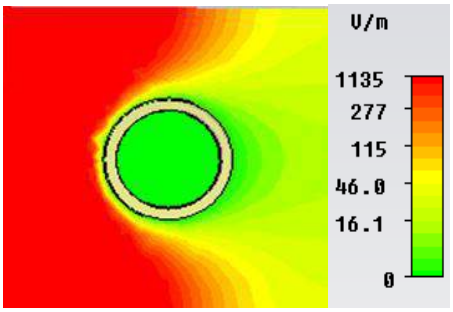

(b)

Figure-5. (a) Free space E-field distribution in the *xy*-plane, (b) E-field distribution for the uncloaked object at the lowest cloaked frequency (7 GHz) in the *xy*-plane.

In the Fig.4b, the simulated and measured result of normalized TSCS of cloaked object normalized by the TSCS of uncloaked object is being displayed. According to the numerical result of Fig.4b, it is evident that the simulated normalized scattering width curve shows value less than one, from 5.04 GHz to 9.47 GHz in the frequency range that covers more than 4 GHz bandwidth in the certain region of C- and X-band of microwave spectra. The lowest value is 0.03 and it was achieved at the frequency of 7 GHz. Moreover, the metamaterial unit cell exhibits epsilon negative region at this lowest point with the complex value ε= -11.80. However, the frequency range 5.04 GHz to 9.47 GHz can be considered as the zone where the cloaking operation is taking place. The measured normalized scattering cross section is found complying well with the numerical result although the lowest point was found at the same frequency of 7 GHz with the value 0.08. The measured curve shows less than zero value from 5 GHz to 9.40 GHz that covers more than 4 GHz bandwidth in the certain portion of C-and X-band. Therefore, this region can be considered as the realistic cloak operating area.

In the Fig.5a, the numerical electric field distribution in the *xy*-plane for the open space condition is being shown. The Fig.5b shows the electric field distribution over the metal object in the *xy*-plane. From the Fig.5b it is evident that, electric field is being scattered in the forward direction by the bare metal object. Moreover, no wave front reconstruction is taking place in the forward direction and therefore zero field region is being created in the forward direction i.e. right side of the object.

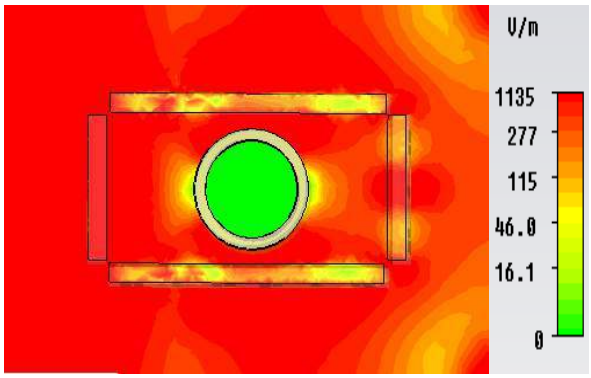

(a)

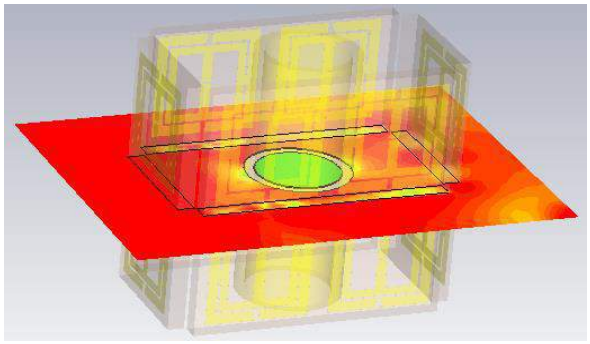

(b)

Figure-6. (a)Distribution of E-field for the cloaked object at the cloaked frequency (7 GHz) in the *xy*-plane, (b) transparent view of E-filed distribution at 7GHz.

In the Fig.6a, the electric field map in the *xy*-plane is revealed at cloaked frequency, where the metal object has been cloaked with the metamaterial-shell. It is seen from the Fig.6 that, no forward scattering was taking place there and reconstruction of wave front in the forward direction was achieved. This reconstruction of wave was gained due to the metamaterial-shell around the object and it points towards the competency of scattering diminution of the metamaterial walls. Therefore, any hostile observer or radar will not be

able to track the object. This has happened due to the epsilon negative property of the metamaterial as it prevents the scattering from the object being cloaked. The Fig.6b shows the transparent side view of the cloaked object that demonstrates the cloaking operation by the bare-H-shape metamaterial wall.

4. Conclusion

In this paper, a new metamaterial unit cell was introduced and its characteristics were evaluated. The characteristics of the metamaterial reveal the epsilon-negative property at certain region of the microwave C-band. Moreover, a rectangular-shaped cloak was designed using the metamaterial and a metal cylinder was cloaked perfectly in the wide region of C-band and some portion of X-band where the metamaterial contains the epsilon-negative property. Experimental results for metamaterial and the cloak was provided to the validated the performance of the metamaterial and the cloak. Therefore, the metamaterial and the cloak can be efficiently utilized for the C-band operation.

Acknowledgements

This work is supported by the Ministry of Education Malaysia (MOE) under grant no. FRGS TOPDOWN/2014/TK03/UKM/01/1 and DIP-2014-03.

References

[1] D. Schurig, J.J. Mock, B.J. Justice, S.A. Cummer, J.B. Pendry, A.F. Starr, D.R. Smith, 'Metamaterial electromagnetic cloak at microwave frequencies'. *Science*, 314, 977–980, 2006.

[2] J. Andkjær and O. Sigmund, 'Topology optimized low-contrast all-dielectric optical cloak'; *Applied Physics Letter*, 98, 021112, 2011.

[3] B. Kante, D. Germain, A.D. Lustrac, 'Experimental demonstration of a nonmagnetic metamaterial cloak at microwave frequencies', *Physical Review B*, 80, 201104, 2009

[4] S. S. Islam, M.R.I Faruque, and M. T. Islam, 'A two-component NZRI metamaterial based rectangular cloak', *AIP Advances*, 5, 107116:1-9, 2015

[5] M. M. Hasan, M. R. I. Faruque, S. S. Islam, M. T. Islam, 'A new compact double-negative miniaturized metamaterial for wideband operation', *Materials*, 9(10):830, 2016

[6] N. Kundtz, D. Gaultney, D.R. Smith, 'Scattering cross-section of a transformation optics-based metamaterial cloak'. *New Journal of Physics*, 12, 043039, 2010.

[7] X. Wang, F. Chen, E. Semouchkina, 'Implementation of low scattering microwave cloaking by all-dielectric metamaterials', *IEEE Microwave Wireless Components Letter*, 23, 63–65, 2013.

[8] S. S. Islam, M. R. I. Faruque, M. T. Islam, 'A near zero refractive index metamaterial for electromagnetic invisibility cloaking operation', *Materials,* 8**,** 4790–4804, 2015.

[9] L. Matekovits, T.S. Bird, 'Width-modulated microstrip-line based mantle cloak for thin single and multiple cylinders'. *IEEE Transactions and Antenna Propagation*, 62, pp.2606–2615, 2014.

[10] S. S. Islam, M. R. I. Faruque, M. T. Islam, 'An Object-Independent ENZ Metamaterial-Based Wideband Electromagnetic Cloak', *Scientific Reports* 6, 33624:1-10, 2016.

[11] M. M. Hasan, M. R. I. Faruque, M. T. Islam, "Multiband left handed biaxial meta atom at microwave frequency", *Materials Research Express*, 4, 035015, 2017.

Metasurfaces and flat optics

Reflection phase measurements by thick-gap Fabry-Pérot interferometry and correction of numerical aperture effect

Tsz Kit Yung* and **Wing Yim Tam**

The Hong Kong University of Science and Technology, Hong Kong

*tkyungaa@connect.ust.hk

Abstract- Metamaterials, artificial materials with sub-wavelength structures capable of exhibiting novel electromagnetic behaviors, have been actively perused as a hot research topic in recent years. The small feature sizes have led to challenges in characterizing the properties of the metamaterials. A new method for measuring the absolute phase change on reflection for small samples in the optical range using converging incident beam is presented as the usual techniques work only for bulk samples and in discrete wavelengths.

To measure the reflection phase of small samples, a Fabry–Pérot interferometer (also name as FP etalon) is used together with a microscopic objective. Figure 1a is an example of the setup. The airgap between the top reference glass and sample can be varied by a micrometer. Using a 5x objective, the detected area can be zoomed down to 100 X 100 μm^2 in the visible range with possible improvement by using higher magnification objective. To model the effect of converging incident beam, a detailed analysis based on a 2-beam interference is presented and correction is applied to the measured interference peak positions.

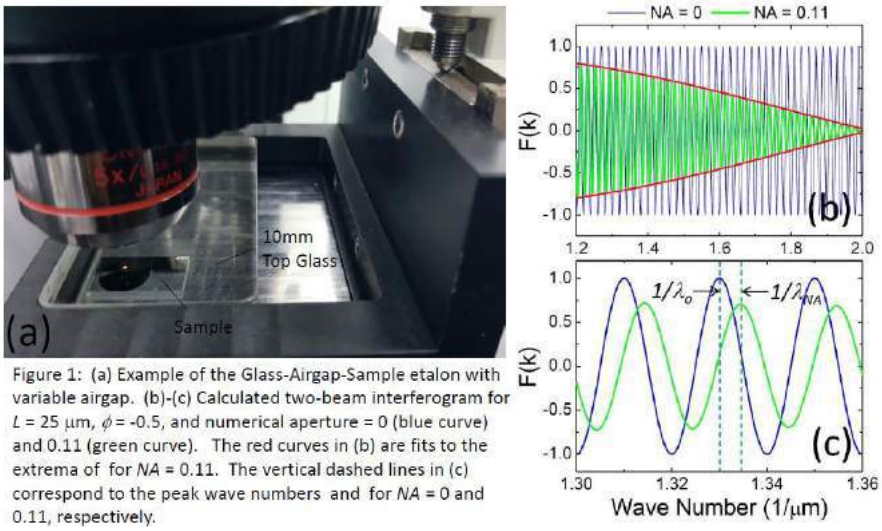

Figure 1: (a) Example of the Glass-Airgap-Sample etalon with variable airgap. (b)-(c) Calculated two-beam interferogram for L = 25 μm, ϕ = -0.5, and numerical aperture = 0 (blue curve) and 0.11 (green curve). The red curves in (b) are fits to the extrema of for NA = 0.11. The vertical dashed lines in (c) correspond to the peak wave numbers and for NA = 0 and 0.11, respectively.

Following the analysis of Kino and Chim[1] the reflected interference intensity $I(k)$ from FP etalon can be written as the weighted sum of the incident beams over all angles. For monochromatic case, the expression is given by Dubois et al[2], which can be generalized to all wavelengths in the visible range by including the dispersion of the objective. The results show that the interference peaks/troughs are shifted by a slowly-varying envelope due to objective 's numerical effect (Shown in Figure 1b and c). To characterize the shift in the interference peak's position, the condition for constructive interference with converging incident beam is derived

from the 1st derivative of reflected intensity. By assuming $L>>\lambda$ with small angular-aperture, the condition for constructive interference can be expressed by equation 1:

$$m = \frac{2L}{\lambda} + \phi + \frac{1}{4} \mp \frac{1}{2} + \frac{1}{2\pi}\arctan\left\{\frac{\cos^2\theta_{\max}\sin\left[4\pi L/\lambda\left(\cos\theta_{\max}-1\right)-\pi\right]}{1+\cos^2\theta_{\max}\cos\left[4\pi L/\lambda\left(\cos\theta_{\max}-1\right)-\pi\right]}\right\} \quad (1)$$

where m is the interference order, L is the airgap between top glass and sample, ϕ is the reflection phase of sample at normal incident normalized by 2π, λ is the wavelength at peak interference under the influence of objective and $\theta_{\max}$ is the half-angular aperture of objective. Due to the arctan term, directly fitting of Eqn. (1) using the measured m and λ, in most of the cases, do not converge. Here, instead of using Eqn. (1), we choose to correct the peak/trough's position such that a simple 2-beam interference model can be used to obtain the correct airgap and absolute reflection phase of the sample expressed as:

$$m = \frac{2L_{fit}}{\lambda_{NA}} + \phi_{fit} \xrightarrow[\lambda_{NA}\to\lambda_0]{correction} m = \frac{2L}{\lambda_0} + \phi \quad (2)$$

and λ_{NA}, λ_0 is the interference peak's position in wavelength with and without influence of objective respectively. L_{fit} and ϕ_{fit} are the as-measured airgap and reflection phase obtained by a direct fitting a simple 2-beam interference model to the data[3].

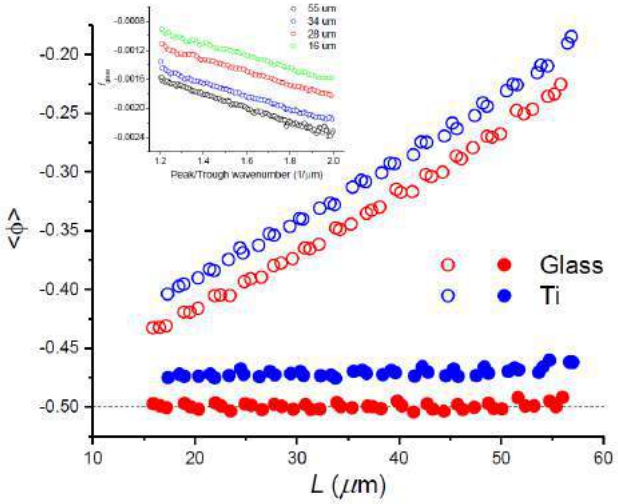

Figure 2: The plot of average reflection phase airgap before (hallow circles) and after the correction by f (solid circles) for glass (red scatters) and 200nm titanium (blue scatters). Inset is the measured value of f plotted at different wavenumbers and airgaps.

The required correction term f can be defined as the relative shift in interference peak/trough's position in wavelength:

$$f = \frac{\lambda_{NA}-\lambda_0}{\lambda_0} \leftrightarrow \frac{1}{\lambda_0} = \frac{1}{\lambda_{NA}}(1+f) \quad (3)$$

By considering its properties under the given experiment conditions, using glass as reference, its value can be fitted from the measured difference of ϕ_{fit} and ϕ as a function of wavelength. The inset in Figure 2 are the measured dispersion of f for glass at different airgaps. As a demonstration, corrections are performed on the measured data from 200nm Titanium on Glass and the obtained average reflection phase before and after correction are also shown in Figure 2.

REFERENCES

1. Kino, G. S., & Chim, S. S. (1990). Mirau correlation microscope. *Applied Optics*, *29*(26), 3775-3783.
2. Dubois, A., Selb, J., Vabre, L., & Boccara, A. C. (2000). Phase measurements with wide-aperture interferometers. *Applied optics*, *39*(14), 2326-2331.
3. Yung, T. K., Gao, W., Leung, H. M., Zhao, Q., Wang, X., & Tam, W. Y. (2016). Measurement of reflection phase using thick-gap Fabry–Perot etalon. *Applied Optics*, *55*(26), 7301-7306.

Tunable beam steering with reconfigurable phase-change metasurface

C. Yu Han[1,*], C. Chen Hung[2], T. Ming Lun[1], W. Hsiang-Chu[1] , C. Ting-Yu. , C. Jie[1] , T. Wei-Yi[1] and T. Din Ping[1,2]

[1] Department of Physics, National Taiwan University, Taipei 10617, Taiwan.

[2] Research Center for Applied Sciences, Academia Sinica, Taipei 11529, Taiwan.

[*]Email: r05222028@ntu.edu.tw

Abstract-We present the tunable optical response of phase change material, which can be used to metasurfaces with varied functionalities. The concept of reconfigurable metasurface, which have different combination of unit cells with various geometries and phase states are proposed. The research is promising to apply to the area of the metadevice.

. . **Introduction**-Due to thermal stability and rapid transition of phase-change material $Ge_2Sb_2Te_5$ (GST) between amorphous and crystalline states, it has been utilized as the recording medium in optical and electronic rewritable data storage. Metamaterials and metasurfaces, the artificial sub-wavelength structures exhibit the abilities to actively control the optical responses and therefore play potential candidates for a number of feasible applications. Recently, the development have been focused on integration of phase-change material into such artifical photonic structures [1, 2]. However, in most of researches, the use of phase-change material is limited as a switchable dielectric environment (a switch between crystalline and amorphous states).

In this paper, we present the tunable optical resonance of phase-change material $Ge_2Sb_2Te_5$ in the near-infrared regime. Further, we propose the concept of reconfigurable metasurfaces, which have different combination of unit cells with various geometries and phase states.

Result&discussion-The optical transmission spectra of amorphous and crystalline $Ge_2Sb_2Te_5$ nanoantennas with various length L are shown in Fig. 1 (a)-(b). The dielectric constants of the $Ge_2Sb_2Te_5$ in crystalline and amorphous states are adopted and transformed from Ref. 2. The height and width of nanoantenna are 50 nm and 150 nm, respectively. When the polarization of the incident light is parallel to the long axis of the nanoantenna, the resonant dips observed in the transmission spectrum. The resonant wavelengths of the nanoantenna are red-shifted with the increased lengths. We also consider the partially crystalline ability of $Ge_2Sb_2Te_5$ for the multi-level optical resonance shown in Fig. 1 (c).

To further investigate the potential of $Ge_2Sb_2Te_5$ in novel metadevice, we design two kinds of reconfigurable metasurfaces. The dolmen structure is composed of a horizontal nanoantenna and a pair of vertical nanoantennas shown in Fig. 2. With different composition of phase-change rods, the transmission spectrum of the dolmen structure changes dramatically. Another one is the gradient metasurface composed of $Ge_2Sb_2Te_5$-SiO_2-Au resonators for realizing the light steering shown in Fig. 3. The super cell of gradient meta-surface consists of a 130-nm-thick Au mirror, 50-nm-thick SiO_2 spacer and twelve $Ge_2Sb_2Te_5$ nanoantennas with various lengths and phase states. The phase delay of each unit cell depends on the phase state and length of nanoantenna. Fig. 3 (b)

shows the scattered electric field of the gradient of metasurface. The reconstruction of wavefront indicated by a dashed line is shown. The scattered electric field intensity of gradient metasurface versus reflection angles at λ = 1550 nm normal incidence is shown in Fig. 3 (c) as well.

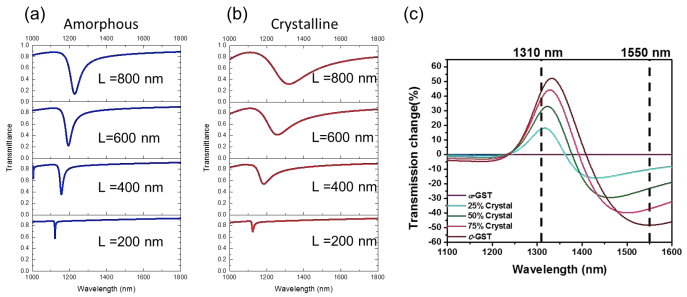

Figure 1 (a)-(b) Transmittance of amorphous and crystalline $Ge_2Sb_2Te_5$ nanoantenna with different length. (c) Transmittance of $Ge_2Sb_2Te_5$ nanoantenna with different crystalline ratio.

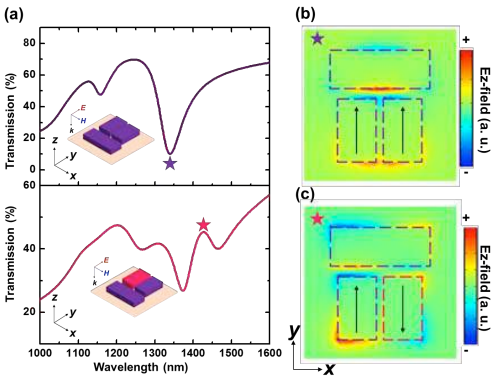

Figure 2 (a) Transmission spectra of dolmen structure and (b-c) corresponding electrical field.

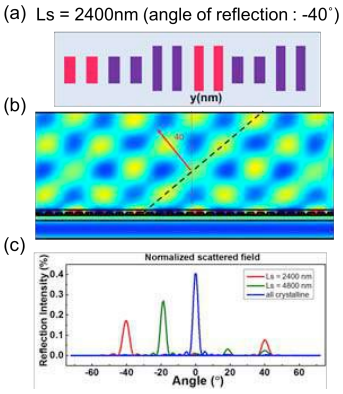

Figure 3 (a) Super cell of gradient metasurface (b) Scattered electric field. (c) Electric field intensity versus reflection angles at λ= 1550nm.

. . . . . **Acknowledgements**-The authors acknowledge financial support from Ministry of Science and Technology, Taiwan(Grant. Nos. 101-2112-M-006-002-MY3, 103-2745-M-002-004-ASP, 102-2911-I-002-505 and 103-2911-I-002-594) and Academia Sinica (Grant No.AS-103-TP-A06).

REFERENCES

1. Tun, C., W. Chenwei, S. Robert E., Z. Lei and Cryan Martin J. "Fast tuning of Fano resonance in metal/phase-change materials/metal metamaterials," *OME.*, Vol. 4, No. 9, 1775–1786, 2014.
2. Behrad, G., Z. Jianfa, M. Kevin F., H. Daniel W. and Z. Nikolay I., "An all-Optical, non-volatile, bidirectional, phase-change meta-switch," *Adv. Mater*, Vol. 25, No. 22, 3050–3054, 2013.

Plasmonic metasurfaces for subwavelength mathematical operations

Yongsop Hwang[1,2,3*], **Timothy J. Davis**[4], **Xiao-Cong Yuan**[1] **and Jiao Lin**[1,2]
[1]College of Optoelectronic Engineering, Shenzhen University, China
[2]School of Engineering, RMIT University, Melbourne, Victoria, Australia
[3]CSIRO Manufacturing, Private bag 10, Clayton South 3169, Victoria, Australia
[4]School of Physics, University of Melbourne, Parkville Victoria 3052, Australia
[*]corresponding author: yongsop@gmail.com

Abstract-We experimentally demonstrated 2-dimensional subwavelength detection of optical phase differences using a metasurface consists of an array of plasmonic nanostructures. The metasurface is fabricated from arrays of coupled gold nanorods where each group of three rods form the circuit to perform the difference operation in one-direction of the *xy*-plane. This metasurface at subwavelength scale can be applied to optical signal processing, ultrafast computing, and biosensing.

Metasurfaces that perform mathematical operations may provide solutions, since they can control the phase, amplitude, and the polarization of light within a thickness smaller than the free space wavelength, forming highly compact optical elements. In this work, we demonstrate plasmonic metasurfaces that perform mathematical operations in two dimensions on an incident light beam, with potential applications in phase-shift key decoding and biosensing.

The plasmonic circuits are fabricated using electron beam lithography. The meta-atom patterns are written on the electron beam resist using the 100 kV electron beam and developed in methyl isobutyl ketone (MIBK): isopropyl alcohol (IPA) solution with the ratio of 1:3. Thereafter, electron beam evaporation was performed to deposit the 2 nm thick germanium adhesion layer and 30 nm gold layer followed by a lift-off process using acetone. Note that the center-to-center distance of the two parallel nanorods used in both circuits to detect differences in the incident light is only 190 nm, which is subwavelength compared with the free space wavelength of 640 nm. The nanorods were designed to be 90 nm long, 40 nm wide, and 30 nm thick.

It is clearly observed that this metasurface performs a two-dimensional mathematical difference operation at the subwavelength scale, which results in it being sensitive to optical phase differences. Phase sensitivity is useful for decoding optical signals carrying data by phase shift keying. The difference operation has potential in nanoscale optical logic operations, since this device behaves like an XOR gate - there is an output if either of the inputs is active, but not both. More generally we have introduced a class of plasmonic devices that can perform a variety of linear mathematical operations with complex coefficients on light fields, determined by the configuration of plasmonic particles. Biosensing for transparent biomaterials is another potential application of this metasurface.

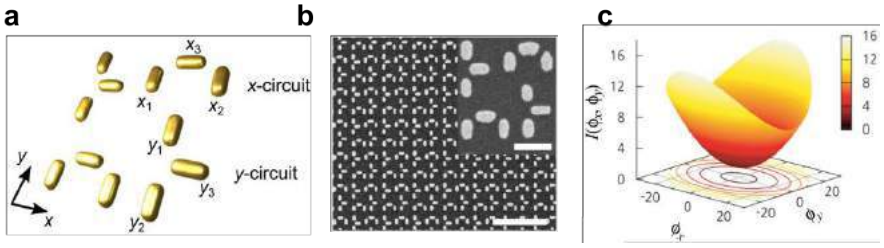

Fig. 1. (a) The unit cell of the metasurface. (b) The SEM image of fabricated metasurface with the magnified image of the unit cell in the inset. Scale bars are 1 μm and 200 nm. (c) Surface plot mapping responses on phase differences in both *x*- and *y*-directions.

REFERENCES

1. Hwang, Y. and Davis, T. J., "Optical metasurfaces for subwavelength difference operations," *Appl. Phys. Lett.*, Vol. 109, No. 18, 181101, 2016.
2. Silva, A. et al., "Performing mathematical operations with metamaterials," *Science*, Vol. 343, No. 6167, 160, 2014.
3. Eftekhari, F., Gómez, D. E., and Davis, T. J., "Measuring subwavelength phase differences with a plasmonic circuit—an example of nanoscale optical signal processing," *Opt. Lett.*, Vol. 39, No. 10, 2994, 2014.

High Performance Hybrid Meta-Surface for Radio Telecommunication

M. M. Hasan[1], **M. R. I. Faruque**[1*], **Fais Mansoor**[2], and **M. T. Islam**[2]
[1]Space Science Center (ANGKASA), Universiti Kebangsaan Malaysia, Malaysia
[2]Department of Electrical, Electronic, and System Engineering, Universiti Kebangsaan Malaysia, Malaysia
[*]Email: rashed@ukm.edu.my

Abstract- Meta-surfaces offer an alternative to bulk three-dimensional metamaterials. Because of the two-dimensional nature of the meta-surface structures, they occupy less physical space and can exhibit lower loss. We have pointed a 2.15 GHz wide bandwidth meta-surface for C-band applications. The proposed structure is consisted of ring resonators, where the dimensions of a single unit cell is 11×11 mm^2 and the effective medium ratio 5.27. Commercial available CST Microwave Studio software is utilized to design and numerical analysis. The numerical and the experiment results are around overlapped together. The measured transmittance shows the resonance at 5.17 GHz, and for simulation it was 5.26 GHz. The proposed design is also described by the equivalent inductive-capacitive circuit model and shows left handed characteristics from 6.35 to 7.72 GHz frequency ranges.

Electromagnetic meta-surfaces are artificial material with more compact size comparable with conventional structures and have some infrequent properties, which does not exist in nature materials. In 2000, Smith et *al*. introduced a material that is shown simultaneously negative permittivity and permeability with some exceptional characteristics of microwave frequency [1]. In 2016, Faruque et *al*. suggested a compact square split z-shape meta-atom with left handed features, wide bandwidth for S-, C-, X- and Ku-band applications. The presented meta-atom was investigated at 0^0, 15^0, 30^0, 45^0, 60^0, 75^0 and 90^0 (xy-axis) rotation angle. The designed structure shown resonances at S-, C-, X-, and Ku-band with 5.67 GHz wide bandwidth. The compact meta-atom had an effective medium ratio 9.10 and exhibited left handed characteristics at 8.50 GHz [4]. In 2016, Pan et *al*. proposed a meta-surface to control the absorption and radiative loss and to reduce the radar cross section, where the meta-surface was designed by metallic square patch and square loop structure inserted with resistors, and absorption in the S-band [11]. In 2016, Hasan et *al*. exhibited a compact z-shaped double negative metamaterial for wideband applications. The 10×10 mm^2 structure metamaterial unit cell was applicable for C- and X-band operations and the effective medium ratio was 4.0 [3].

Figure 1(a) shows the schematic geometry of the proposed structure. In figure 1(b), measured transmittance shows the resonance at 5.17 GHz, which is the C-band and the amplitude of the resonance point is 26 dB. In addition, the simulation results of the transmittance (S_{21}) are also shown in the same figure, where the resonance point at 5.26 GHz and the magnitude of the resonance point is 43 dB. From figure 1(c), the designed structure can be called as a left handed meta-surface for any frequency points in the frequency range of 6.35 to 7.72 GHz. However, figure 1(d) represents the effect on resonance frequency by FR-4, Rogers RT 5880, Rogers RT 5870, Rogers RT 6010, Rogers RT 4350, Rogers RT 4003, Mica, and Polyimide, materials used as substrate.

Table 1: Configurations of the proposed meta-surface single unit cell

Parameters	a	b	l	w	l1	w1
Dimensions (mm)	11	11	10	9.0	8.0	7.0
Parameters	d	s	m	n	l2	r2
Dimensions (mm)	0.5	0.25	4.0	1.2	3.0	1.0

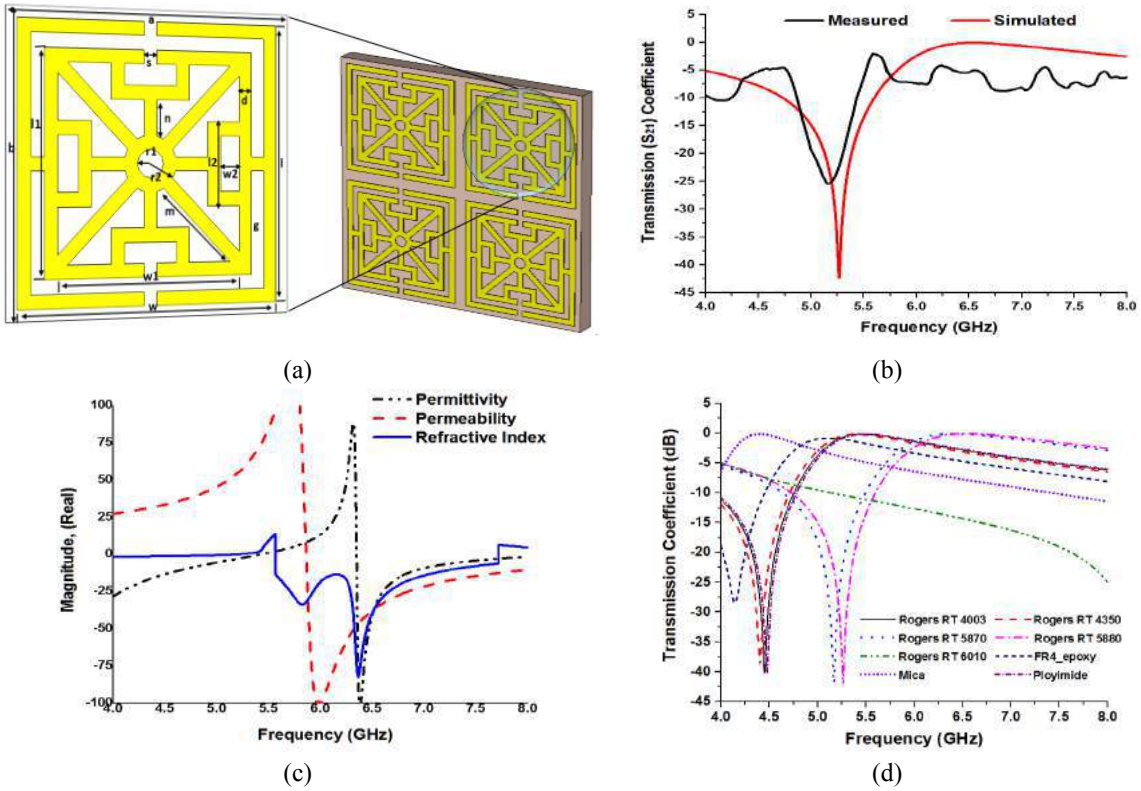

Figure 1. (a) Geometry of proposed meta-surface, (b) Simulated and measured results of the transmission (S_{21}) coefficient, (c) Real magnitude of effective medium parameters and (d) effects of different substrate materials on transmission (S_{21}) coefficient of the proposed meta-surface structure.

REFERENCES

1. Smith, D. R., Pendry, J. B. and Wiltshire, M. C., "Metamaterials with negative refractive index", *Optical Technology*, 2008, Vol. 75, Issue. 4.
2. Faruque, M. R. I., Hasan, M. M. and Islam, M. T., "Wideband 90^0 Azimuthal Miniaturized Meta Atom with Left-Handed Characteristics", *IEEE Antennas and Wireless Propagation Letters*, 2016, DOI: 10.1109/LAWP.2016.2624757.
3. Pan, W., Huang, C., Pu, M., Ma, X., Cui, J., Zhao, B. and Luo, X., "Combining the absorptive and radiative loss in metasurfaces for multispectral shaping of the electromagnetic scattering", *Sci. Rep.* 6, 21462, 2016.
4. Hasan, M. M., Faruque, M. R. I., Islam, S. S. and Islam, M. T., "A New Compact Double-Negative Miniaturized Metamaterial for Wideband Operation", *Materials*, 9(10), 2016, 830.

Designing flat lenses using a transformation optics approach

Mircea Giloan*, **Robert Gutt**, **and Gavril Saplacan**

Company for Applied Informatics, Cluj-Napoca, Romania,
*corresponding author: mircea_giloan@cianet.ro

Abstract— In the context of transformation optics theory we developed a method for designing optical devices able to manipulate the wave vectors in the specific manner required by the functionality of the device. This new approach was applied for designing both diverging and converging flat lenses. As the waves propagate inside the transformation media of the lenses the wave vectors are properly changed in order to impose a converging or diverging propagation of the emergent waves.

The transformation approach is based on the theoretical result which shows that Maxwell's equations have the same form whether we apply a coordinate transformation or introduce specific gradients in the permittivity and permeability of the original space [1]. This approach was successfully used to design a variety of electromagnetic devices including lenses [2]. Recently, a great attention was paid to the design of flat optical devices due to the ability of integration with the planar integrated circuit technology and to the simplicity of fabrication. The concept of optical phase discontinuities was applied to design flat lenses by shaping the wavefront of the emerging wave [3].

In this study we show how the concept of transformation optics can be used to design transformation media able to manipulate the wave vectors in the desired manner, while the alteration of the wave path remains of a secondary importance. In order to manipulate the wave vector inside a flat device having the input and output planes perpendicular to $z-$axis the following class of coordinate transformations was used:

$$\left\{ \begin{array}{l} x^{!} = x \\ y^{!} = y \\ z^{!} = zf(x,y) \end{array} \right\} \tag{1}$$

where $f(x,y)$ is a function of two variables which transforms the z coordinate with respect to x and y coordinates. Following some mathematical computations, detailed in reference [4], we proved that at normal incidence the wave vectors are properly manipulated in order to fulfill the functionality of an aberration-free lens surrounded by the free space when the transformation function has the form:

$$f(x,y) = \frac{1}{\delta - \gamma(\varphi^2 + (x-x_F)^2 + (y-y_F)^2)^{\frac{1}{2}}} \tag{2}$$

where $\gamma = \pm 1/z_D$ (a positive/negative value corresponds to a converging/diverging lens), z_D is the thickness of the lens, $\delta = 1 + \varphi\gamma$, φ is the focal length measured from the output plane of the lens along the $z-$axis, x_F and y_F are the $x-$ and $y-$axis coordinates of the focal point, respectively. The input plane of the designed flat lens coincide with the xy plane of the coordinates system. For the simplified case of a linearly polarized transverse magnetic (TM) plane wave described by the field components $\{E_y, E_z, H_x\}$ and a focal point located on $z-$axis the stretching function f reduces to:

$$f(y) = \frac{1}{\delta - \gamma(\varphi^2 + y^2)^{\frac{1}{2}}} \tag{3}$$

while the permittivity and permeability of the transformed medium are given by the symmetric tensor:

$$\varepsilon = \mu = \begin{bmatrix} h(y) & 0 & 0 \\ 0 & h(y) & -zh^{!}(y) \\ 0 & -zh^{!}(y) & \dfrac{(zh^{!}(y))^2 + 1}{h(y)} \end{bmatrix} \tag{4}$$

where $h(y) = 1/f(y) = \delta - \gamma(\varphi^2 + y^2)^{\frac{1}{2}}$ and $h^{!}(y)$ denotes the derivative of function h. The constitutive parameters tensor given by equation (4) is expressed in terms of the $y^{!}$ coordinate of

the transformed space with the prime dropped for aesthetic reasons. The transformation function given by equation (3) has two singularity points $y_S = \pm\sqrt{z_D(z_D + 2\varphi)}$ where z_D is the thickness and φ is the focal length of the lens.

Figure 1 shows the results of numerical simulations performed using a two-dimensional Finite-Difference Time-Domain (FDTD) algorithm [4]. The thickness and the focal length of the lens were the same ($\varphi = z_D$). Hence, the singularity points of function f are $y_S = \pm z_D\sqrt{3}$. The geometrical dimensions of the lens used in simulations were related to the wavelength of the incident wave as follows: lens thickness $z_D = 5\lambda$ and lens aperture $2y_D = 16\lambda$, where $y_D = (8/5)z_D$ satisfies the inequality $y_D < y_S$ required for positive values of constitutive parameters. The lens was illuminated at normal incidence by a plane wave source of wavelength λ with field components $\{E_y, H_x\}$ of magnitude equal to unity located at $z_S = -z_D$. The simulation area span on $z-$axis from z_S to z_P, where $z_P = 5z_D$. The simulation area was terminated with periodic boundary conditions on $y-$axis and uniaxial perfectly matched layer (UPML) absorbing boundaries on $z-$axis. The simulations have been performed using an orthogonal computational grid with a step resolution $\Delta = \lambda/50$ for each axes and a time step reaching the Courant limit $\Delta t = \Delta/c\sqrt{2}$, where c is the speed of light in free space. Computer simulations show reliable focusing capabilities of the converging flat lens designed in the context of the developed method.

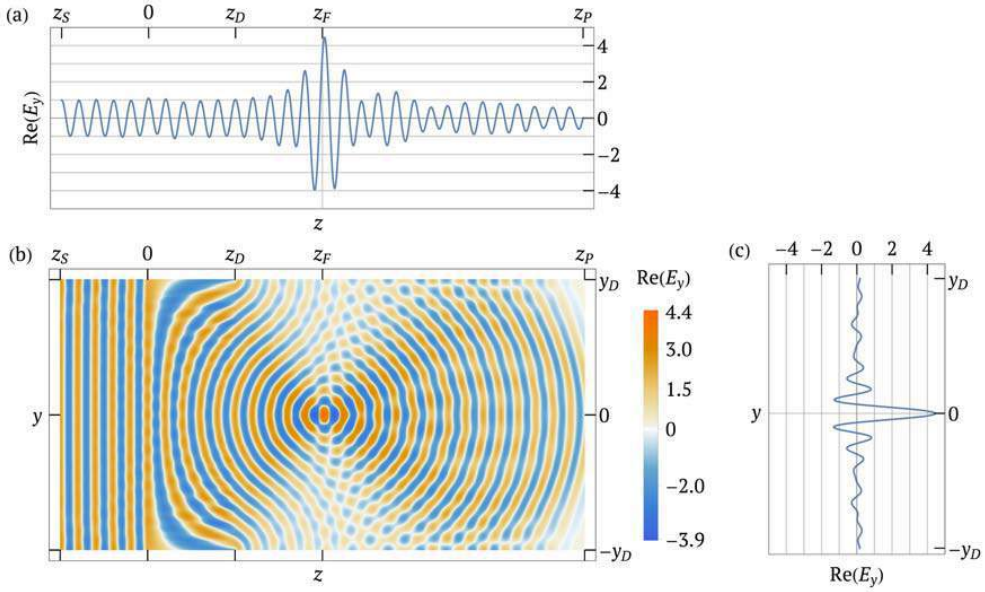

Figure 1: The simulated distribution of the real part of the Ey field component. **(a)** Along $z-$axis, **(b)** on yz plane, and **(c)** along a line parallel to $y-$axis passing through the focus point resulted from simulation.

ACKNOWLEDGMENT

This work was developed by the Company for Applied Informatics using infrastructure obtained through the program POSCCE-A2-O2.3.2-2012-1 (ID: 1542/SMIS: 44023), and partially supported by the program PNII/2014-nr. 153/2014.

REFERENCES

1. D. Schurig, J. B. Pendry and D. R. Smith, "Calculation of material properties and ray tracing in transformation media", *Opt. Express* 14, 9794 (2006).
2. N. Kundtz, and D. R. Smith, "Extreme-angle broadband metamaterial lens", *Nat. Mater.* 9, 129-132 (2010).
3. S. J. Byrnes, A. Lenef, F. Aieta, and F. Capasso, "Designing large, high-efficiency, high-numericalaperture, transmissive meta-lenses for visible light", *Opt. Express* 24, 5110 (2016).
4. M. Giloan "Designing wave vector manipulation devices using a transformation optics approach", arXiv:1612.09488 [physics.optics] (2017).

Holographic and interferometric approach to trap helical light within a metafilm cavity

Sun-Je Kim[1], Seung-Yeol Lee[2], Jangwoon Sung[1], and Byoungho Lee[1*]

[1]Inter-University Semiconductor Research Center and School of Electrical and Computer Engineering, Seoul National University, Seoul 08826, Korea

[2]School of Electronics Engineering, College of IT Engineering, Kyungpook National University, Daegu 41566, Korea

[*]byoungho@snu.ac.kr

Abstract-A novel and simple approach to trap helical light within a subwavelength metafilm cavity is proposed with a theory and numerical calculations. A silver metasurface giving phase-gradient, dielectric thin-film, and a half-infinite silver mirror are stacked in order to form a metafilm cavity. Compared to conventional metal-insulator-metal (MIM) cavity, the proposed scheme is based on generalized Snell's law using geometric phase of the metasurface and strong interference of multiple scatterings. The proposed metafilm cavity is more compact than MIM cavity and the performance is especially depending on a magnitude of light spin. This approach to trap helical light would be very fruitful for compact optical sensor designs and various nano-cavity applications.*n*

In the field of nanophotonics, explosive attention has been paid on the concept of metasurface for the past few years. Metasurface is an artificial surface to control scattering properties of light in an anomalous way. In 2011, Yu *etal.* proposed the concept of generalized Snell's law of reflection and refraction with discontinuous phase-gradient [1]. Since then, many researches have been published using various metasurfaces to implement ultra-thin flat optical devices [2]. Among those, the concept of geometric phase, also known as optical Pancharatnam-Berry phase, has been widely studied for polarization dependent anisotropic scatterings of light by using metallic nanoslits and nanorods [2-4]. Studies on metasurfaces employing geometric phase concept have mainly focused on holographic purposes, implementing specifically engineered optical wavefront in free space or on a metallic plane.

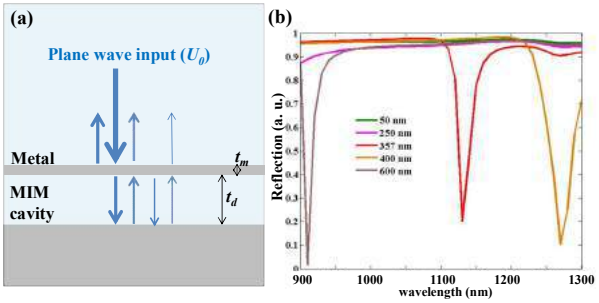

Figure 1. (a) A conventional MIM cavity for Fabry-Perot resonance. t_m is fixed to 30 nm. (b) Calculated reflection spectra using when t_d are 50 nm, 250 nm, 357 nm, 400 nm, and 600 nm, respectively.

However, trapping light within a nanocavity has not been connected with holographic metasurface approach and generalized Snell's law despite the significance of nanocavity and light trapping [5]. Here, we propose a novel scheme to trap helical light using geometric phase of metasurface, generalized Snell's law, and strong interference. As shown in Fig. 1, a simple MIM cavity can also have Fabry-Perot resonance (FPR). To make an FPR in a conventional MIM cavity, at least half-wavelength of optical length is needed for the lowest order resonance. However, the proposed method, named metafilm cavity depicted in Fig. 2(a) and 2(b), is able to make FPR with more compact thickness owing to artificially designed optical paths inside the cavity through generalized Snell's law.

$$\sin\theta = \frac{1}{nk_0}\frac{d\Phi}{dy} = \frac{1}{nk_0}\frac{2\pi}{p_y},\ \theta \approx 48^{\circ}. \tag{1}$$

Discrete subwavelength rotations of silver nanoslits by 45 degrees give phase-gradient and anomalous refraction for cross-polarized right circular polarization (RCP) light as shown in Fig. 2(b). Co-polarized left circular polarization (LCP) light is not affected by phase-gradient in y-direction while reflected or transmitted. As a result, the total 0^{th} order reflection can be approximated as a sum of co-polarized LCP partial waves ($U_{1,LL}$, $U_{2,LL}$, and $U_{3,LL}$). Fig. 2(c) clearly shows that the dips of 0^{th} order reflectance caused by FPR can be obtained with shorter cavity-length rather than those of conventional MIM cavities. We expect that our result would be highly applicable to various flat metafilm absorbers and nanocavity applications in the future.

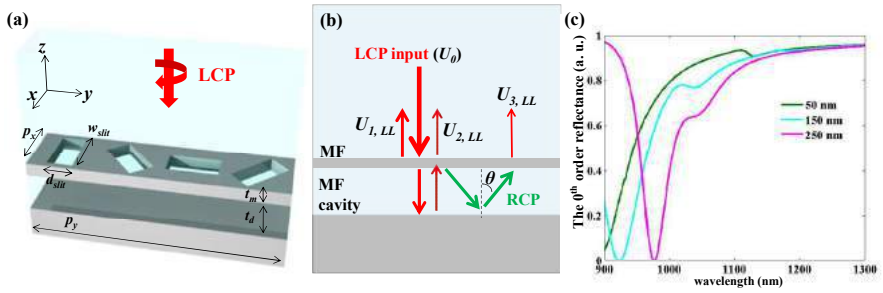

Figure 2. (a) The unit cell scheme of the metafilm cavity. w_{slit}, d_{slit}, t_m, p_x, and p_y are 200 nm, 60 nm, 150 nm, 240 nm, 960 nm. Rotating angle difference between two adjacent silver nanoslits is fixed to 45 degrees. The refractive index of dielectric layers is set to 1.4. (b) A scheme for dominant multiple light scattering processes. Red and green arrows denote lights with left and right handedness, respectively. Total reflectance of LCP light is nearly a sum of $U_{1,LL}$, $U_{2,LL}$, and $U_{3,LL}$. (c) Numerically calculated 0^{th} order reflection for three different values of t_d (50 nm, 150 nm, 250 nm).

Acknowledgements National Research Foundation (NRF) of Korea (21A20131612805)

REFERENCES

1. Yu, N., P. Genevet, M. A. Kats, F. Aieta, J. P. Tetienne, F. Capasso, and Z. Gaburro, *Science*, Vol. 334, No. 6054, 333-337, 2011.
2. Yu, N., and F. Capasso, *Nat.nMater.*, Vol. 13, No. 2, 139-150, 2014.
3. Lin, J., J. B. Mueller, Q. Wang, G. Yuan, N. Antoniou, X. C. Yuan, and F. Capasso, *Science*, Vol. 340, No. 6130, 331-334, 2013.
4. Lee, S.-Y., K. Kim, S.-J. Kim, H. Park, K.-Y. Kim, and B. Lee, *Optica*, Vol. 2, No. 1, pp. 6-13, 2015.
5. Kats, M. A., and F. Capasso, *LasernPhoton.nRev.*, Vol. 10, No. 5, 699-699, 2016.

High-efficiency electro-optic transmission modulation with multiply stacked Si *p-n* junction subwavelength gratings

Ki Young Lee[1], Jae Woong Yoon[1*], and Seok Ho Song[1,*]
[1]Department of Physics, Hanyang University, Seoul 133-791, Korea
[*]corresponding author: jaeong.yoon@gmail.com and shsong@hanyang.ac.kr

Abstract- We propose a free-space electro-optic transmission modulator based on multiple *p-n*-junction semiconductor subwavelength gratings. The proposed device operates with a high-Q guided-mode resonance undergoing electro-optic resonance shift due to direct electrical control. Using rigorous electrical and optical modeling methods, we theoretically demonstrate a modulation depth of 84%, on-state efficiency 85%, and on-off extinction ratio of 19 dB at 1,550 nm wavelength under electrical control signals within a favorably low bias voltage range from –4 V to +1 V. This functionality operates in the transmission mode and sustainable in the high-speed operation regime up to a 10-GHz-scale modulation bandwidth in principle. The theoretical performance prediction is remarkably advantageous over plasmonic tunable metasurfaces in the power-efficiency and absolute modulation-depth aspects

Leaky-mode resonances in nanopatterned thin-film metasurfaces are of interest owing to their great potential for creating integration-compatible, multifunctional devices harnessing desired spectral, polarization, intensity, and phase properties [1,2]. Adding active tunability to these device classes by means of direct electrical controls, free-carrier-induced electro-optic (EO) effects in heavily doped semiconductors and transparent conducting oxides (TCO) at epsilon-near-zero (ENZ) conditions provide an efficient tuning mechanism. In particular, ENZ nanofilms incorporated in metal-oxide-semiconductor (MOS) capacitor arrays have showed remarkable intensity and phase modulation properties driven by field-effect free-carrier accumulation and depletion [3]. In this approach, highly dissipative, deep-subwavelength plasmonic resonances are necessary to induce significant optical interaction with sub-10-nm-thick EO-active layers.

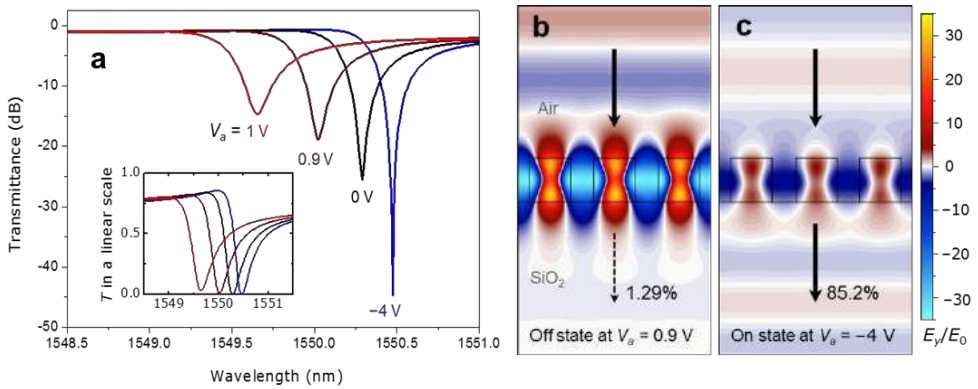

Figure 1. Trasnmission modulation properties. **a** Bias-voltage dependent trasmittance spectrum. **b** Total electric field patterns for off-state and **c** on-state operation regimes.

Pursuing high-performance tunable leaky-mode resonance devices operating in the transmission mode in this paper, we propose an approach based on high-Q GMRs. The proposed device class consists of moderately doped, low-loss semiconductor *p-n* junctions in a resonant subwavelength grating structure. This structure is designed such that a high-Q GMR is supported in the optical domain while in the electrical domain bias voltage across multiple *p-n* junctions effectively control density of conduction electrons and holes, resulting in the associated tuning of the Drude-part optical dielectric constant [4]. we select an interleaved Si *p-n* junction nanograting architecture as one promising example.

We apply the obtained bias-voltage-induced mobile-carrier effect to an example GMR element optimized for the transmission-mode optical modulation in the telecommunications C-band around 1,550 nm. Figure 1 (a) shows the V_a–dependent transmission spectra in dB (a linear scale in the inset) under transverse-electric (TE) polarized planewave incidence at surface-normal angle ($\theta = 0$). Following the standard convention, the TE polarization refers to electric field oscillating in the axis of grating lines (*y*-axis). We use the finite-element method in this calculation involving $\varepsilon_{Si}(z)$ profiles. The transmission spectra show an asymmetric Fano-resonance profile as a result of the configuration interference between resonant and non-resonant pathways. The resonant pathway is created by coupling of the incident wave with a leaky TE_0 mode and its radiation decay toward the transmitted zero-order planewave channel through dominant first-order diffraction processes. This resonance feature possesses remarkably high resonance Q factor ~ 3.69×10^3. Consequently, the design yields a very high field enhancement factor ~ 1.2×10^3 in the 550-nm-thick EO-active Si-*p*-*n*-junction at the resonance center wavelength.

Subtle interaction between the highly enhanced resonant optical fields and bias-voltage-induced mobile-carrier effect results in a resonance-center (λ_c) shift as shown in Fig. 1 (a). Using well-established electrical and optical modeling methods, we theoretically demonstrate a robust transmission modulator with on/off power ratio of 18.9 dB, on-state efficiency of 85.2%, and modulation bandwidth of 54.3 GHz at an operation wavelength of 1550 nm as shown in Fig. 1(b) and (c). These performance characteristics are driven by favorably small bias voltage values in a range of –4 V ~ +1 V and possibly maintained in the high-speed operation regime up to 50 GHz when appropriate in-plane miniaturization schemes are incorporated.

Notably, the obtained properties are supported by the low-loss free-carrier-induced EO effect occurring in the whole device region with 500-nm-thick Si layers as opposed to the transparent-conducting-oxide-based plasmonic metasurface approaches involving a sub-10-nm-thick EO-active region and strong ohmic absorption. Therefore, experimental realization of our proposed device class is of great interest to develop compact, low driving power, and high-speed optical modulators for applications in telecommunications, optical information processing, LIDARs, small-signal detection systems, high-power laser machining, and many others.

Acknowledgement

This research was supported in part by the Basic Science Research Program (NRF-2015R1A2A2A01007553) and by the Global Frontier Program through the National Research Foundation (NRF) of Korea funded by the Ministry of Science, ICT & Future Planning (NRF-2014M3A6B3063708).

REFERENCES

1. Ding, Y. and Magnusson, R. “Resonant leaky-mode spectral-band engineering and device applications”. *Opt*. *Express* **12**, 5661-5674, 2004.
2. Yu, N. & Federico C. “Flat optics with designer metasurfaces” *Nat*. *materials* **13**, 139-150, 2014.
3. Huang, Yao-Wei, et al. “Gate-tunable conducting oxide metasurfaces”. *Nano Lett*. **16**, 5319 – 5325, 2016.
4. Reed, G. T., Mashanovich, G., Gardes, F. Y., & Thomson, D. J. “Silicon optical modulators”. *Nat*. *photonics*, 4, 518-526, 2010.

Active focal tuning of graphene-metal metasurface lenses

Zongduo Huang[1], **Bin Hu**[1*], **Zi Wang**[1], **and Juan Liu**[1]
[1] School of Optoelectronics, Beijing Institute of Technology, Beijing, People's Republic of China
[*]corresponding author: hubin@bit.edu.cn

Abstract- Conventional metallic metasurfaces are difficult to achieve tunable devices once a structure is fabricated. We propose a method to realize metasurfaces with active focal tuning by graphene-metal hybrid structures. Tunable metasurface lenses in both mid-infrared and terahertz frequencies are proposed.

Unlike conventional optical components, which require enough thickness of the media to achieve wavefront shaping, metasurfaces introduce abrupt and controllable changes of optical properties in two-dimensional (2D) space [1]. However, the modulation of each unit cell is hard to change once a metasurface is manufactured, lacking the flexibility for achieving tunable modulators. Graphene is a 2D form of carbon in which the atoms are arranged in a honeycomb lattice. In addition, the Fermi level of the cone-shaped electronic band structure of graphene is modulatable by an external gate voltage [2], which makes graphene a promising material for tunable optical devices. In this work, based on Berry geometrical phase theory [3], we theoretically demonstrate mid-infrared (mid-IR) and terahertz (THz) tunable graphene-metal metasurface lenses to achieve focusing and active focal control by tuning the graphene chemical potential uniformly.

We first give the design of a cylindrical lens for mid-IR frequencies [4]. The schematic structure of the tunable metasurface lens is depicted in Fig.1 (a). It is composed of an array of rectangular apertures etched on a thin Au film. The metallic film is deposited on a monolayer graphene, which is used to change the scattering electromagnetic fields of the apertures. A glass substrate and a transparent conducting film are below the metal layer. A gate voltage V_g is applied to tune the chemical potential of the graphene layer. The incident light is right-handed circularly polarized (RCP). The inducing transmitted field can be divided into a right-handed circularly polarized light and a left-handed circularly polarized (LCP) light with an abrupt phase change of 2φ. Thus a desired phase change of the LCP light can be obtained by the rotation of the aperture. By this principle, a lens with a focal length of f can be designed by [5]:

$$\varphi(x) = \frac{\pi}{\lambda}\left(\sqrt{x^2 + f^2} - f\right) \tag{1}$$

In order to design a tunable metasurface lens, the phase change should be different for each unit on the metasurface when the graphene chemical potential varies uniformly. We find that the phase of the LCP scattering light can be tuned by changing the chemical potential of the graphene layer and the length of the aperture (not depicted here), thus a tunable metasurface lens is expected to be achieved. We choose 17 apertures along the x-direction. The designed result is shown in Fig.1(c). FDTD simulations are then conducted to verify the focal effect and the tunability of the lens. The electric field intensity distributions of the transmitted LCP light are shown in Fig.1(d).

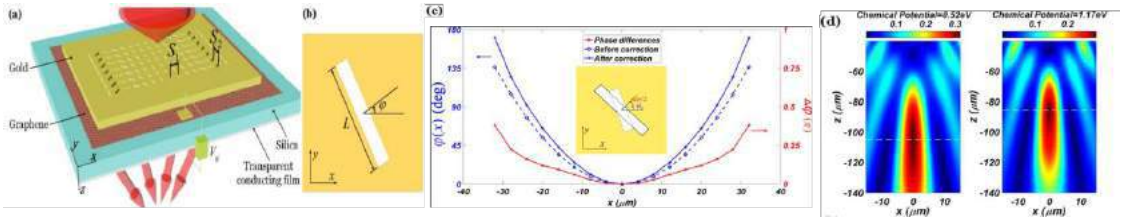

Fig.1 (a) The structure of the cylindarical lens for mid-IR. (b) A unit cell of the metasurface. (c) Rotation angles (blue solid line) corresponding to the 17 slits of the designed lens at different positions. (d) Electric field intensity distributions of the transmitted LCP light corresponding to the chemical potentials of 0.52eV and 1.17eV, respectively. The focal length changes from 105 to 85μm when the incident wavelength is λ=6.6μm.

This method can also be applied to design tunable Thz lenses. We design a tunable metasurface sperical lens in Thz frequencies (λ=400μm). The schematic structure of the metasurface is depicted in Fig.2 (a). When the lens is illuminated by RCP light, the electric field intensity distributions of LCP light are shown in Fig.2(b). The focal length changes from 4.67mm to 5.24mm.

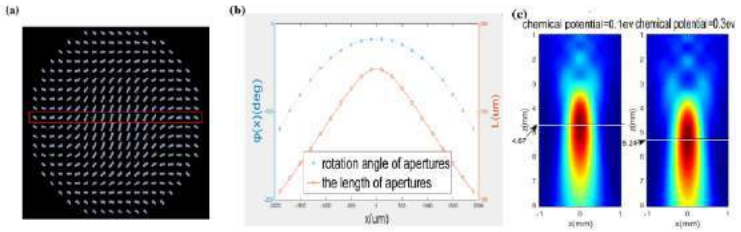

Fig2.(a) The structure of the spherical lens for THz. (b) The distribution of rotation angles and lengths of apertures within the red border in Fig.2(a). (c) Electric field intensity distributions of the transmitted LCP light corresponding to the chemical potentials of 0.1 eV and 0.3eV, respectively.

Acknowledgements, This work is supported by the National Natural Science Founding of China (Grant NOs 61405012 and 61420106014), the National Basic Research Program of China (973 Program Grant No. 2013CBA01702), NCET, Excellent young scholars Research Fund of Beijing Institute of Technology,

REFERENCES

1. Yu, N and Capasso, F, “Flat optics with designer metasurfaces,” *Nat. Mater.*, Vol. 13, 139–50, 2014.
2. Zhe. F, et al. "Gate-tuning of graphene plasmons revealed by infrared nano-imaging," *Nature*, Vol. 487, 82-85, 2012.
3. Huang, L., et al. "Dispersionless phase discontinuities for controlling light propagation." *Nano letters*, Vol. 12, 5750-5755, 2012.
4. Wang, Z., et al. "Active focal control of an ultrathin graphene-metal metasurface lens." *Materials Research Express*, Vol.3, 115011, 2016.
5. Chen, X., et al. "Dual-polarity plasmonic metalens for visible light." *Nature communications*. Vol. 3 1198, 2012.

The SNOM observation of surface plasmon modes from different chiral plasmonic structures

Feng Lin*

School of Physics, State Key Laboratory for Mesoscopic Physics, Peking University, Beijing 100871, China

*corresponding author: linf@pku.edu.cn

Abstract-Au nanostructures can be fabricated to intentionally guide the propagation of surface plasmon polaritons (SPPs), which leads to the varying of propagating directions for the SPP beams, and thus generates the orbital angular momentum (AM) of SPPs. Here, we investigated the coupling of such plasmonic orbital AM with optical spin AM, and found that the chiral characteristics of Au nanostructures impose great effects on the electromagnetic modes of SPPs under this spin-orbit interactions.

The optical spin-orbit interaction is that a coupling of the intrinsic angular momentum (photon spin) and the extrinsic momentum (orbital angular momentum) [1-2]. The effect is usually observed when the light passes through an anisotropic and inhomogeneous medium. For instances, the optical spin Hall effect, beam displacement and momentum shift due to the optical spin, was observed at the medium interface. In plasmonic structures, the surface plasmon polaritons travel along the path that can be defined to within a subwavelength scale by the geometric patterns of the structures, which generate a significant optical orbital angular momentum. In our work, on the Au thin film deposited on glass substrates, we fabricate the subwavelength holes by focused ion beam, which form the ring shape. Using the scanning near-field optical microscope, the different propagation modes of surface plasmon polaritons has been observed for the excitation light with the left and right handed circular polarization, respectively. Based on the conservation of total optical angular momentum in this circular system, the coupling effect of the spin and orbital angular momentum can be deduced from the measured and simulated distribution of electric fields.

REFERENCES

1. Shitrit, N., Bretner, I., Gorodetski, Y., Kleiner, V. and Hasman, E., "Optical spin Hall effects in plasmonic chains," Nano Lett., Vol. 11, 2038-2042, 2011.
2. Shitrit, N.; Yulevich, I.; Maguid, E.; Ozeri, D.; Veksler D.; Kleiner, V.; Hasman, E., "Spin-optical metamaterial route to spin-controlled photonics," Science, Vol. 340, 724-726, 2013.

Terahertz nano-metamaterials for rotation-free performance

Sang-Hun Lee[1, 2], Dong-Kyu Lee[1], Young Min Jhon[1], Joo-Hiuk Son[2], and Minah Seo[1*]

[1] Sensor System Research Center, Korea Institute of Science and Technology (KIST), Republic of Korea

[2]Department of Physics, University of Seoul, Republic of Korea

[*]corresponding author: mseo@kist.re.kr

Abstract-In this work, we designed three types of terahertz (THz) nano-slot-antenna arrays to obtain rotation-free performance in transmission. Honeycomb- and the chlorophyll-shape patterned arrays show multi resonance features in transmission, induced by the strong resonance coupling between adjacent slots, and those are azimuthally rotation-free to normal incidence. For interpreting this interesting phenomena, coupled harmonic oscillator model was applied and the resultant spectra were analyzed in terms of coupling strength.

The electromagnetic near-field enhancement behaviors via nano-slot-antenna structured metamaterials, consisted of subwavelength width of slots in orders of $\lambda/10$ - $\lambda/10{,}000$, can be applied to highly sensitive and selective optical sensors [1, 2]. In such applications, collinearly aligned slot antenna arrays have been usually considered, by taking advantage of maximized transmittance magnitude with clearly defined resonance behavior according to their geometry and effective refractive index of materials [2, 3]. Normally this collinearly aligned antenna array shows strong rotation dependence on both transmission and reflection, which can be issued regarding somewhat inconvenient aligning and unexpected decreasing of efficiency in molecular sensing.

Here, we demonstrate THz transmission control by several uniquely patterned slot antenna arrays, including asterisk, chlorophyll, and honeycomb patterns. These patterns were designed to compensate rotation-induced transmission decreasing of each elementary slot in an array. The elementary slots are identical, which have fundamental resonance at 0.92 THz with 64 μm-length and 500 nm-width, and are fabricated onto the thin gold film (150 nm thickness). Typical collinear pattern shows clear resonance with transmission decreasing by azimuthal rotation as shown in Fig. 1(a). The asterisk pattern also has a single resonance similar to collinear pattern, but has constant transmission efficiency over all measured angles. The honeycomb pattern depicts rotation-free transmission with dual mode resonances: a fundamental mode and an additional secondary mode near 0.7 THz which is induced by strong resonance coupling with adjacent slots, as shown in Fig. 1(b). The transmission efficiencies of fundamental resonance mode in terms of the rotation angle, for four different nano-slot-antenna arrays, are plotted in Fig. 1(c). The suggested three unique patterns represent completely rotation-free performance. We also put the theoretical interpretation for the dual resonance behavior (Fig. 1(b)) using coupled harmonic oscillator model [4] (Fig. 1(d)). The calculated results with the model has an excellent agreement with measured spectra. The resonance peak is split into dual resonance mode with individual transmittance decreasing and the secondary mode has a redshift as coupling constant increasing in the model.

In conclusion, we have made three different types of nano-slot-antenna arrays which have constant transmission efficiencies by rotation angle. Honeycomb- and chlorophyll patterned arrays show dual-resonance spectra, well interpreted using coupled harmonic oscillator model. The model gives analytical information for the resonance tunability for spectral changes by the coupling strength. Finally, we hope that the results presented here will help further applications including rotation-free and controllable multi spectral optical sensors.

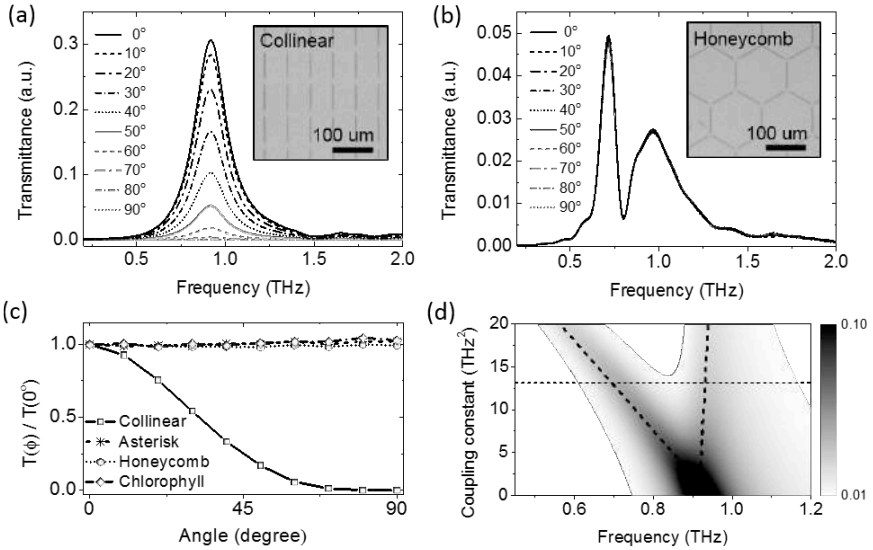

Figure 1 (a-b) Transmission spectra of nano-slot-antenna array of the collinear- and the honeycomb-pattern. Inset is optical microscope images of nano-slot-antenna arrays. (c) Transmission efficiencies depending on rotation angle are plotted. (d) Calculated transmission spectrum of the honeycomb pattern. Horizontal dash line is the coupling constant of the geometry used in the experiment, 13.1.

Acknowledgements This research was supported by the National Research Foundation of Korea (NRF) grant funded by the Korea government (MSIP) (2016R1A2B2010858) and the Global Frontier Program through NRF grant funded by the Ministry of Science, ICT & Future Planning (2016M3A6B3936653) and KIST intramural grants with No. 2E26490 and 2E25723.

REFERENCES

1. M. A. Seo, H. R. Park, S. M. Koo, D. J. Park, J. H. Kang, O. K. Suwal, S. S. Choi, P. C. M. Planken, G. S. Park, N. K. Park, Q. H. Park and D. S. Kim, "Terahertz field enhancement by a metallic nano slit operating beyond the skin-depth limit," Nat. Photonics, Vol. 3, No. 3, 152-156, 2009.
2. D.-K. Lee, J. Kang, J.-S. Lee, H.-S. Kim, C. Kim, J. Hun Kim, T. Lee, J. Son, Q. Park and M. Seo, "Highly sensitive and selective sugar detection by terahertz nano-antennas," Sci. Rep., Vol. 5, No. 15459, 2015.
3. D.-K. Lee, G. Kim, C. Kim, Y. M. Jhon, J. H. Kim, T. Lee, J. Son and M. Seo, "Ultrasensitive Detection of Residual Pesticides Using THz Near-Field Enhancement," IEEE Trans. Terahertz Sci. Technol., Vol. 6, No. 3, 389-395, 2016.
4. S. Yin, X. Lu, N. Xu, S. Wang, Y. E., X. Pan, X. Xu, H. Liu, L. Chen, W. Zhang and L. Wang, "Spoof surface plasmon polaritons in terahertz transmission through subwavelength hole arrays analyzed by coupled oscillator model," Sci. Rep., Vol. 5, No. 16440, 2015.

Dichroic phase modulation at near-infrared wavelengths based on bilayer metasurface

Kyookeun Lee, Gun–Yeal Lee, Hansik Yun, Sang–Eun Mun, Jeong-Geun Yun, and Byoungho Lee*
Inter-University Semiconductor Research Center and School of Electrical and Computer Engineering,
Seoul National University, Seoul 08826, South Korea
* byoungho@snu.ac.kr

Abstract- We present a bilayer metasurface that modulates phase of light at two different wavelengths independently. A unit cell of the metasurface is composed of stacked poly-silicon nanofins with different geometric parameters, including height, length, width, and rotation angle. Each nanofin gives different amplitude and phase at each target wavelength, so that phase of each wavelength can be tailored independently. The proposed metasurface can be applied to dichroic splitters, full-color holography, and achromatic optical elements.

Metasurface, which is an artificially engineered material with a subwavelength scale thickness, gives an entirely new approach to design optical elements. Properties of light, such as polarization, phase, and amplitude profiles can be tailored within a wavelength of propagation using properly designed metasurfaces [1]. More recently, one of the most fundamental optical element, a lens is realized using a metasurface based on titanium dioxide nanofins and their geometric Pancharatnam-Berry phase [2]. The geometric phase is a powerful tool to achieve spatial modulation of phase because rotation angle of a scatterer is directly proportional to phase of output light. However, due to evenness of spatial phase profiles, metasurfaces based on the geometric phase inevitably suffer from the chromatic aberration after diffraction. In order to reduce the chromatic aberration, metasurfaces composed of dielectric resonators with a slot [3], nanopillars, [4] and sub-pixel structure [5] have been proposed, which can give different phase profiles according to wavelengths.

Here, we propose a bilayer metasurface that can manipulate phase of incident light independently at two wavelengths. Two stacked poly-silicon nanofins with a period of 380 nm constitute a unit cell of the metasurface as shown in Fig. 1(a). Each nanofin has different geometric parameters which cause transmission to differ with respect to the wavelength. By superposing two transmitted waves from each nanofin with additional geometric phase 2θ due to rotation angle of the upper nanofin, it is possible to achieve arbitrary phase difference between two wavelengths. If complex-valued transmission coefficients are given by a_1 and a_2 for each nanofin layer, geometric parameters and the rotation angle θ can be found by satisfying the relation:

$$r = \left| a_1 + a_2 e^{i2\theta} \right|, \tag{1}$$

where r is a constant representing modulation efficiency.

Wavelengths are set as 800 nm and 980 nm, and corresponding dielectric constants are $3.58 + j0.001$, $3.68 + j0.005$ for the nanofins, and 2.1124, 2.1045 for the host medium, respectively. At first, a_1 and a_2 at two wavelengths are investigated with auxiliary geometric parameters of h_1 = 350 nm, h_2 = 400 nm, d = 50 nm. Figures 1(c)-1(f) show transmitted phase of left-hand circularly polarized light when right-hand circularly polarized light is incident normally from the bottom. It is seen that phase differences between two wavelengths

are tuned by 161 °, 49 °, −48 °, and −160 °. As well as these examples, more arbitrary phase difference can be achieved based on the proposed design principle.

It is expected that the proposed design method can be applied to more generalized achromatic metasurface, including compact dichroic splitters, full-color holography, and achromatic optical elements.

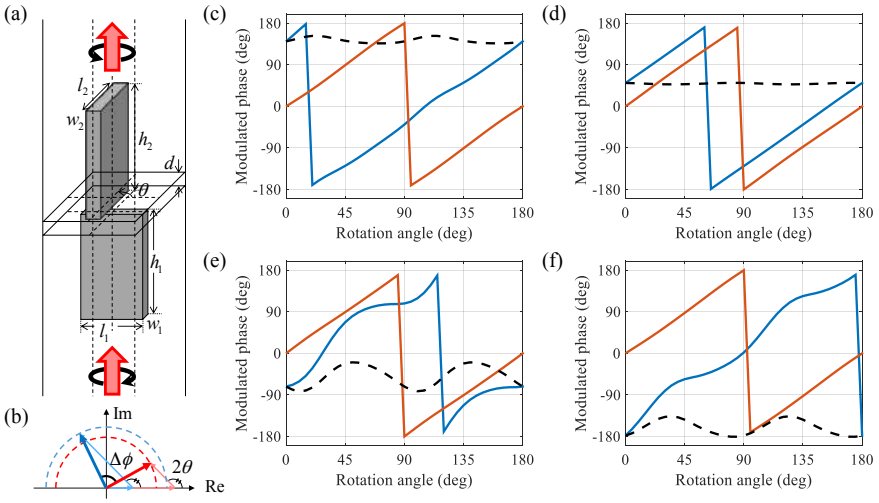

Figure 1. (a) Schematic illustration of a unit cell structure. (b) Vector representation of superposition of two transmitted waves by nanofins at different wavelengths. (c-f) Geometric phase profiles with respect to the rotation angle of the nanofins. Blue solid lines denote 800 nm wavelength, red lines 980 nm, and dashed lines are their difference. Geometric parameters (w_1, l_1, w_2, l_2, θ) are given by (c) (250 nm, 80 nm, 200 nm, 55 nm, 85 °), (d) (230 nm, 60 nm, 200 nm, 60 nm, 115 °), (e) (250 nm, 60 nm, 240 nm, 80 nm, 110 °), and (f) (250 nm, 80 nm, 200 nm, 60 nm, 75 °), respectively.

This work is supported by Brain Korea 21 Plus program through the National Research Foundation (NRF) funded by the Ministry of Education of Korea and the Center for Advanced Meta-Materials (CAMM) funded by the Ministry of Science, ICT and Future Planning as Global Frontier Project (CAMM-2014M3A6B3063710).

REFERENCES

1. Minovich, A. E., Miroshnichenko, A. E., Bykov, A. Y., Murzina, T. V., Neshev, D. N. and Kivshar, Y. S. "Functional and nonlinear optical metasurfaces," *Laser Photon. Rev.*, Vol. 9, No. 2, 195-213, 2015.
2. Khorasaninejad, M., Chen, W. T., Devlin, R. C., Oh, J., Zhu, A. Y. and Capasso, F., "Metalenses at visible wavelengths: Diffraction-limited focusing and subwavelength resolution imaging," *Science*, Vol. 352, No. 6290, 1190-1194, 2016.
3. Aieta, F., Kats, M. A., Genevet, P. and Capasso, F., "Multiwavelength achromatic metasurfaces by dispersive phase compensation," *Science*, Vol. 347, No. 6228, 1342-1345, 2015.
4. Khorasaninejad, M., Shi, Z., Zhu, A., Chen, W. T., Sanjeev, V. and Capasso, F, "Achromatic metalens over 60 nm bandwidth in the visible and metalens with reverse chromatic dispersion," *Nano Lett.*, DOI: 10.1021/acs.nanolett.6b05137, 2017.
5. Wang, B., Dong, F., Li, Q. T., Yang, D., Sun, C., Chen, J., Song, Z., Xu, L., Chu, W., Xiao, Y.-F., Gong, Q. and Li Y., "Visible-frequency dielectric metasurfaces for multiwavelength achromatic and highly dispersive holograms," *Nano Lett.*, Vol. 16, No. 8, 5235-5240, 2016.

Investigating Corresponding Unequal Divided Circles Unit Cells Response as Alternate Electromagnetic Absorbing Matter

A. A. M Ezanuddin[1*], H. Lago[2], and L. Y. Seng[1]
[1]Electronic Department, FETech, UniMAP, Aras 1, Blok S2, Kampus UniCITI Alam, 02100 Sungai Chuchuh, Padang Besar, Perlis, Malaysia.
[2]Advanced Communication Engineering (ACE), CoE, School of Computer and Communication Engineering, UniMAP, Pauh Putra Campus, 02600 Arau, Perlis, Malaysia
[*]mezanuddin85@gmail.com

Abstract-This paper discover ways of exploiting corresponding unequal divided circles (CUDC) unit cells with different formations and its related electromagnetic surface wave behavior using 3D tetrahedral eigenmode computation. Strategically placed unit cells using identified formation, known electromagnetic surface wave can either be allowed to pass through, blocked and redirect to desire angle within designated area. Engineered CUDC presented shows strong resonance at 5.9 GHz and produced stable electromagnetic bandgap (EBg) region from 5.9265 GHz to 5.9516 GHz.

Through extensive literature and Babinet's guideline [1], findings shows that engineered CUDC unit cell will exhibit a semi-static reverberation trademark once energized with an outer period changing electromagnetic field streaming ordinarily towards CUDC unit cell plane. After a CUDC unit cell is etched on the microwave laminate surface closed to or on the positive, negative plane. The EBG condition produced by such unit cells was discovered able to differ undesirable electromagnetic field, spreading on the vertical plane to such conductive layer. To model this CUDC EBg plane, various optimization and algorithm were examined [2]. Hence only a single full wave solver was found suitable which CST MWS is. CST MWS can provide a mish mash full wave electromagnetic wave numerical prediction accompanied by an enhancement calculation algorithm. Utilizing this features, CUDC was found able to produce a bandgap region within the 5.9 GHz possible. CUDC-EBg was imprinted on a FR4 laminate, thickness = 1.6 m and permittivity = 4.3.

CUDC unit cell are proposed to be organized in certain arrangement and it is observed to be adequate in manipulating surface wave. The distinct electromagnetic reaction of CUDC unit cell can be inspected utilizing prominent electromagnetic field hypothesis [3]. Nonetheless, constructing EBg based devices may include larger amount of comprehension of every part [6-8] to function effectively. Therefore, exact quantitative examination of 3D EM field impacts of EBg unit cell can be done utilizing numerical full wave means, for example, computer simulation technology microwave studio (CSTMWS) utilized here to check both scientific and basic modeling [4].

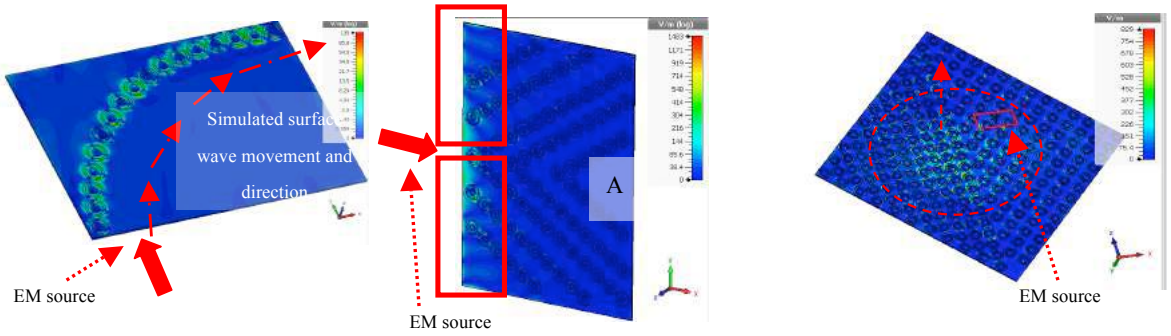

(a) (b) (c)

Figure 1: Simulations of CUDC surface wave (a) Electrical surface movement at 5.9 GHz (b) Electrical field at the wedge are seen lees visible where A is the location with no surface wave and (c) with a denser CUDC region, strong electrical field are found resonating at the middle.

Conclusion: CUDC unit cells frequency response and EBg capability can be simulated by using eigenmode solver. An alternative transmission route can be constructed where energy movement can be seen flowing at its peak from Figure 1(a). From Figure 1(b), A surface wave beam separator was created that can reduce scattering from an object dividing incident wave in a given direction. This type of formation can be used to shield regions on a surface from surface wave incident externally or to prevent interference between two devices on the same platform. Lastly, form Figure 1(c), a rectangular flat panel with CUDC unit cells was patterned with the aim to alter forward and backwards scattering. This can be achieved by placing an angled electromagnetic source near the CUDC surface that reflects incident wave in a different direction. The CUDC unit cells was arranged into two different regions with different formation and volume.

Acknowledgements: Universiti Malaysia Perlis (UniMAP), Short Term Grant (STG) 2017. Account number 9001-0510.

4700

REFERENCES

1. Dwivedi, Surabhi, Vivekanand Mishra, and Yogesh P. Kosta. "Metamaterial inspired patch antenna miniaturization technique for satellite." *Emerging Technology Trends in Electronics, Communication and Networking (ET2ECN), 2012 1st International Conference on*. IEEE, 2012.
2. Urbanec, T., and P. Kovacs. "Electromagnetic band gap structures: Practical tips and advice for antenna engineers." *Radioengineering* (2012).
3. Rajesh, Galaba Sai, and Vijay Kumar. "CSRR Loaded Multi Substrate Antenna for 4G LTE and Wi-MAX Applications." *Indian Journal of Science and Technology* 9.40 (2016).
4. Rajaraman, Gayathri, et al. "Dual-band, miniaturized, enhanced-gain patch antennas using differentially-loaded metastructures." *Indian Journal of Science and Technology* 8.1 (2015): 11.

Exploring Different Metallic Structures Dispersion Attribute to Enhance Future Microwave Absorbing Material

A. A. M Ezanuddin[1*], H. Lago[2], and L. Y. Seng[1]
[1]Electronic Department, FETech, UniMAP, Aras 1, Blok S2, Kampus UniCITI Alam, 02100 Sungai Chuchuh, Padang Besar, Perlis, Malaysia.
[2]Advanced Communication Engineering (ACE), CoE, School of Computer and Communication Engineering, UniMAP, Pauh Putra Campus, 02600 Arau, Perlis, Malaysia
[*]mezanuddin85@gmail.com

Abstract- Not all engineered metallic structures with the same resonance can exhibit acceptable electromagnetic bandgap (EBg). In this paper, several metallic structures consisting of rectangular, deformed, slit patch and unequal divided circles (UDC) were assessed its proneness in manipulating surface wave and producing targeted EBg. Utilizing FR4 laminate, decent EBg can be achieved by using optimized structure with the correct resonance. Results shows a stable and decent EBg region can be gained from UDC specifically from 5.9 to 6 GHz.

There can exists numerous diverse propagation constants at the similar resonance. Each one is known as a particular mode with its own phase velocity, group velocity and electromagnetic field distribution. The relation between phase and frequency response when plotted out and can be referred to as its dispersion attribute. This attributes determines the bandgap behavior of the engineered metallic structure. This dispersion attribute chart is a graph based on frequency versus spatial phase variations of the predefined parameter of phase. Here in this paper, the phase part is selected to be swept from 0 to 180 degrees in 19 steps for an even and understandable pace. Figure 1 shows the simulations done using periodic boundaries in the z-direction. The frequency range of investigation starts from DC to 14 GHz for the first three metallic sample, and then Dc to 8 GHz for the proposed structure. It is essential to monitor the dispersion curve along the phase axis with a periodicity of $2\pi/p$ namely $0 < \beta_{xn} < 2\pi/p_x$, which is also known as the Brillouin zone [xxx]. By simulating the structure in the periodic mode, field distribution of a surface wave is also periodic with a proper phase delay determined by the wavenumber and periodicity. Thus each surface wave mode can be decomposed into an infinite series of space harmonic waves as shown in equation (1):

$$\vec{E} = (x, y, z) = \sum_{-\infty}^{+\infty} \overrightarrow{E_n}(y, z) e^{-j\beta_{xn}x}, \beta_{xn}(\omega) = \beta_x(\omega) + n \quad (1)$$

Conclusion: From all the simulation work done, only metallic structure named unequal divided circles dispersion attribute lead to the formation of desired EBg. A good and stable bandgap region exist which is situated at 5.9265 GHz to 5.9516 GHz as highlighted in Figure 1(d). From all 7 modes investigated, apparently there are six bandgap region. As seen, not all the region can satisfy a proper bandgap along its operating frequency. Most of the modes are found either too wide (plot Γ to X) or too narrow (plot M to Γ) since this unequal divided circles structure uses two different radius size that effect frequency scattering response while introducing coupling effect.

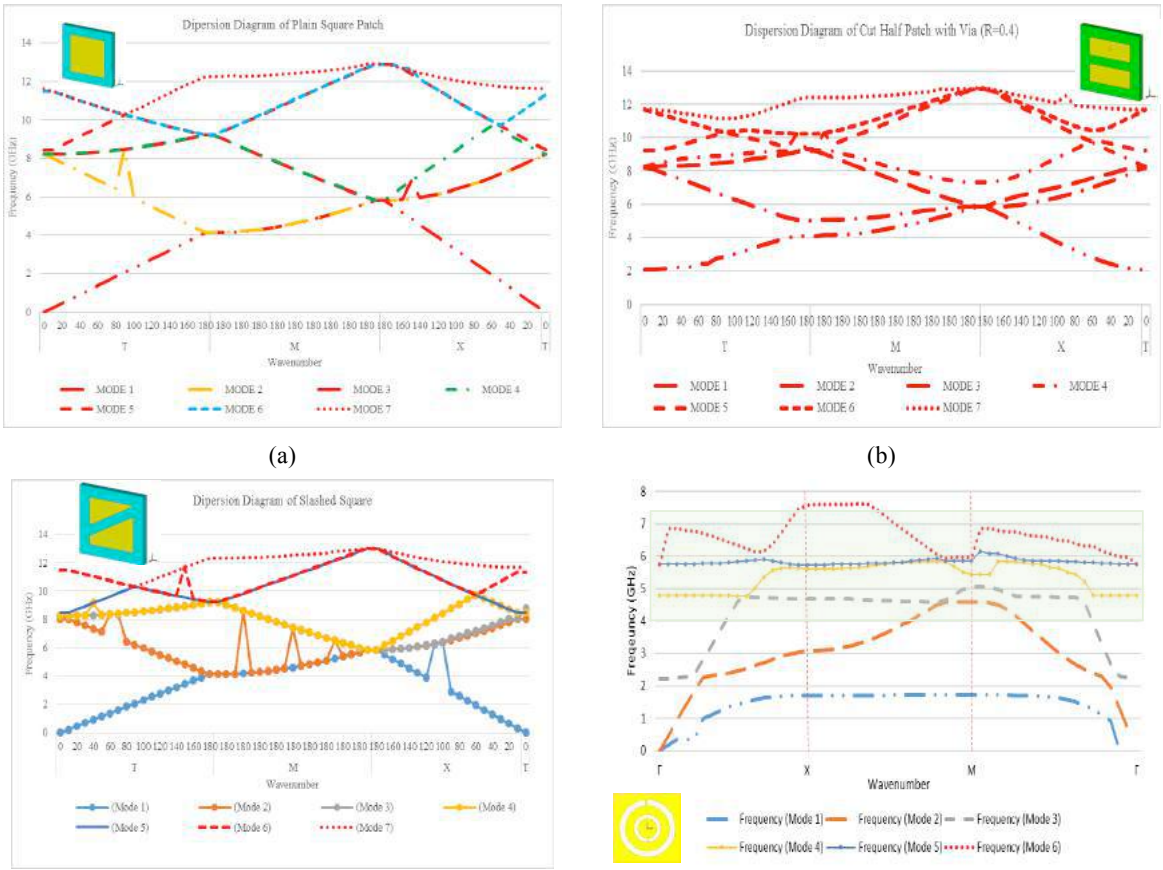

Figure 1: Simulated metallic structures and its corresponding dispersion attribute, a) Rectangular patch – exist potential EBg region, b) Deformed patch – no EBg region due to its narrow phase are, c) Slit patch – no EBg region due interfering resonance spike from different modes, and d) Unequal divided circles – exist a small EBg.

Acknowledgements: Universiti Malaysia Perlis (UniMAP), Short Term Grant (STG) 2017. Account number 9001-0510.

REFERENCES

[1]. Alshargabi, M. A., Z. Z. Abidin, and M. Z. M. Jenu. "Spiral Electromagnetic Bandgap Structure for EMI Reduction." In *RFM 2013*. 2013.

[2]. Polemi, Alessia, Stefano Maci, and P. Kildal. "Dispersion characteristics of a metamaterial-based parallel-plate ridge gap waveguide realized by bed of nails," *Antennas and Propagation, IEEE Transactions on* 59, no. 3 (2011): 904-913.

[3]. Li, Bo, and Zhongxiang Shen. "Synthesis of quasi-elliptic bandpass frequency-selective surface using cascaded loop arrays." *Antennas and Propagation, IEEE Transactions on* 61, no. 6 (2013): 3053-3059.

A Model for Calculating the Far-Field Polarization Response of a Plasmonic Metasurface at UV Wavelengths.

M.S. Davis[1, 2, 3], J. Strait[2], Wenqi Zhu[2,3], J.K. Lee[1], S. Blair[4], H. J. Lezec[2], and A. Agrawal[2,3]

[1]Department of Electrical Engineering and Computer Science, Syracuse University, Syracuse, NY 13244, USA

[2]Center for Nanoscale Science and Technology, National Institute of Standards and Technology,
Gaithersburg, MD 20899, USA

[3]Maryland Nanocenter, University of Maryland, College Park, MD, 20742, USA

[4]Department of Electrical and Computer Engineering, University of Utah,
Salt Lake City, UT 84112, USA

msdavi01@syr.edu

Abstract: UV plasmonic technology has enabled many advanced applications however, the design and implementation of UV interactive metasurfaces remains challenging. To aid in the design of such metasurfaces we demonstrate a model accurately describing the far-field response of a chiral structured metasurface at UV wavelengths. This model is applicable to any arbitrary shape and significantly reduces the reliance on FDTD calculations required to characterize a plasmonic device.

UV plasmonics has produced many useful technological applications such as label-free detection of biomolecules [1], tip-enhanced Raman scattering [2], and enhanced circular dichroism spectroscopy [3]. An application of UV plasmonics that has, until recently, remained largely unrealized at the experimental level is the UV interactive metasurface composed of periodic arrangements of subwavelength surface structures. These structures are designed to act as spatial modulators of both the incident polarization and phase wavefront over subwavelength distances. The design of devices for sophisticated applications such as right and left circular polarization (RCP/LCP) filtering at UV presents several challenges: fabrication remains difficult due to device scaling required at UV, material choice is crucial since typical plasmonic metals are not suitable at UV, and the design of metasurface structures requires immense calculation resources. In regards to the latter, previous work describing chiral nanoparticles as collections of coupled oscillators presents an intuitive picture for chiral nanoparticle behavior [4,5]. Understanding the underlying mechanisms of chiral nanoparticles can lead to significantly reduced design times due to less reliance on numerical solvers.

In this work an analytic model is presented describing the polarization dependent far-field response of a UV interactive metasurface consisting of a periodic arrangement of chiral structures demonstrating strong circular diattenuation (CD) at 350 nm (see Fig. 1), where $\mathrm{CD} = \pm(P_{RCP} - P_{LCP})/(P_{RCP} + P_{LCP})$ and P_{RCP} (P_{LCP}) is the transmitted or reflected power from the metasurface with RCP (LCP) incident light. The metasurface is characterized in Cartesian coordinates by a 2x2 polarization matrix:

$$\vec{\vec{\alpha}} = \begin{pmatrix} \alpha_{1,1} & \alpha_{1,2} \\ \alpha_{2,1} & \alpha_{2,2} \end{pmatrix} \quad (1)$$

where the metasurface far-field response is given by $\vec{E}_{far} = \vec{\vec{\alpha}}\vec{E}_{inc}$ for incident field $\vec{E}_{inc}$. The CD is calculated from eq (1) for RCP and LCP incident fields $\mathrm{CD} = \pm(|E_{RCP}|^2 - |E_{LCP}|^2)/(|E_{RCP}|^2 + |E_{LCP}|^2)$ giving

$$\mathrm{CD} = \frac{1}{2\pi}\int_0^{2\pi}\int_0^{\pi} Im\left\{\frac{\alpha_{1,1}\alpha_{1,2}^* + \alpha_{2,1}\alpha_{2,2}^*}{\|\vec{\vec{\alpha}}\|^2}\right\} sin\theta d\theta d\varphi \quad (2)$$

where the integration is over the transmission or reflection half space, $\#\|\vec{\alpha}\|^2 = \sum_{i,j}|\alpha_{i,j}|^2$ and -1 ≤ CD ≤ 1. The polarization matrix of equation (1) is easily extracted using FDTD calculations for any two incident orthogonal linear polarizations The resulting matrix then describes the device far field response for any arbitrary incident polarization. This work will show the CD response of a plasmonic metasurface is not due to circular dichroism or optical activity, but is characterized by equation (1) and hence originates from the interaction of strongly coupled oscillatory modes in the metasurface structure. The device response can be characterized by constructive or destructive interference in the far-field. This understanding of the far field response of plasmonic metasurfaces can lead to a more general model describing the polarization response for any arbitrary incident angle.

In this talk we discuss the model assisted design, fabrication, and experimental realization of an aluminum chiral structured metasurface exhibiting strong CD at UV wavelengths. The complex interaction of oscillatory modes leading to the circular polarization dependent modes in Figure 2 will be explored in the context of eq (1).

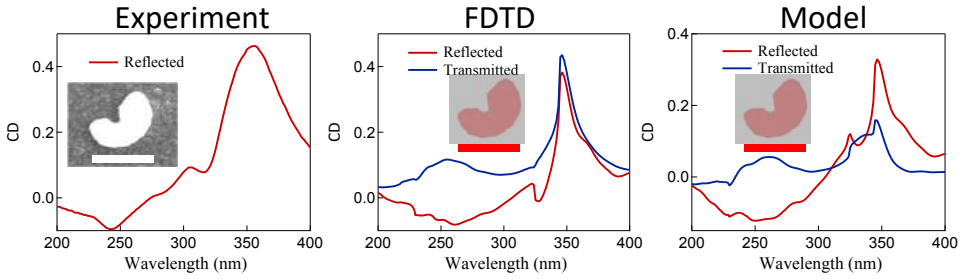

Figure 1. (a) The CD response of a periodic array of Aluminum chiral structures measured with an ellipsometer. The structures are patterned on a fused silica substrate using ebeam lithography and ebeam evaporation (see image inset, scale bar corresponds to 200 nm). (b) Using the SEM image in (a) as a template and ellipsometer measured permittivity of Al, the CD response of the fabricated structure is characterized with FDTD calculations. (c) The CD response of the fabricated structure as predicted by the model described in equations (1) and (2).

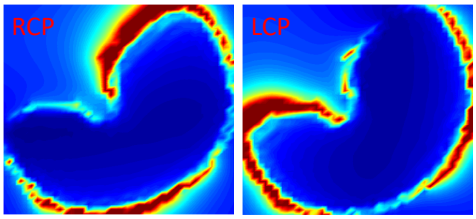

Figure 2. The FDTD calculated field profile $|E|^2$ of the fabricated structure template at wavelength 350 nm demonstrates strongly distinct resonant modes at RCP and LCP.

REFERENCES

1. M.H. Chowdhury, K. Ray, S.K. Gray, J. Pond and J.R. Lakowicz, "Aluminum nanoparticles as substrates for metal-enhanced fluorescence in the ultraviolet for the label-free detection of biomolecules,"*Anal. Chem.*, Vol. 81, No. 4, 1397–1403, 2009.
2. A. Taguchi, N. Hayazawa, K. Furusawa, H. Ishitobi and S. Kawata, "Deep UV tip-enhanced Raman scattering," *J. Raman Spectrosc.*, Vol. 40, 1324–1330, 2009.
3. M.L. Nesterov, X. Yin, M. Schäferling, H. Giessen and T. Weiss, "The role of plasmon-generated near fields for enhanced circular dichroism spectroscopy," *ACS Photonics*, Vol. 3, 578–583, 2016.
4. X. Yin, M. Schäferling, B. Metzger and H. Giessen, "Interpreting chiral nanophotonics spectra: the plasmonic Born-Kuhn model," *Nanoletters.*, Vol. 13, 6238–6243, 2013.
5. F. Eftekhari and T.J. Davis, "Strong chiral optical response from planar arrays of subwavelength metallic structures supporting surface plasmon resonances,"*Phys. Rev. B.*, Vol. 86, 075428, 2012.

Ultrathin linear optical logic gates based on a metasurface beam deflector

S. Kita[1,2,*], A. Shinya[1,2], K. Takata[1,2], K. Nozaki[1,2], and M. Notomi[1,2,*]
[1]NTT Nanophotonic Center, Japan
[2]NTT Basic Research Labs, Japan
[*]corresponding author: kita.shota@lab.ntt.co.jp, notomi.masaya@lab.ntt.co.jp

Abstract We propose all-optical AND gates based on a 120-nm thick metasurface beam deflector. The binary contrast can be maximized up to 9.5 dB by introducing an additional bias input. The insertion loss is also evaluated as 1.5 dB with use of silver at the wavelength of 633 nm. As far as we know, this is the thinnest linear optical logic gate satisfying the better performances. It could be effective to configure lower latency optical computing circuits.

All-optical logic gates have been one of fundamental researches to realize scalable optical computing. Most of them are based on nonlinear optical effects since logic operations should be performed with the nonlinearity between input and output signals [1]. However, it is very though to achieve the device length of < 10 μm because the effective nonlinear coefficient cannot be high enough even with using current nanophotonic devices. On the other hand, linear all-optical logic gates also have been proposed and demonstrated by several groups based on polarization [2], photonic crystals [3], and plasmonic waveguides [4]. Linear devices can operate constantly even with very small input power. The length can be very short as < 5 μm if we use metal-air-metal waveguides [2]. However, most of them do not care the huge insertion loss which constrains the cascadability.

For shorter length with smaller loss, we propose an extremely thin linear optical logic gates as illustrated in Figure 1(a) - the cross section consists of a metasurface beam deflector (trapezoid antenna array), a silica spacer, and a partial reflector on a quartz substrate. The total thickness except for the substrate is only ~120 nm [6]. This gate has 6 ports in total, so we can input 3 signals independently. *BC* can be maximized with an additional bias input (a beam splitter, which has 4 ports, cannot have such a bias input). (b) shows the I/O configuration for AND operation. 2 in-phase signals and 1 out-phase bias input from Port A, B, and D are respectively input. All the inputs are *y*-polarized plane waves with same wavelength of 633 nm. The input intensity from A and B are set as unity. The output to Port C is simply determined by the multiple interference of the inputs at the metasurface. Therefore, the bias intensity from D should be fixed according to the transmittance relationships for the best *BC* (typically around 0.25 – 0.75). By investigating the structural dependences of the transmittances, the three layer thicknesses are determined as (d_{MS}, d_{SP}, d_{BPR}) = (30, 70, 18) nm to obtain the best *BC* with the smallest insertion loss. (c) shows steady state responses of E_y field against all (A, B) combinations. When (A, B) = (1, 1), we have a larger output toward Port C, otherwise less. Table (d) compares the output intensity with different input combinations. The material difference between gold and silver is also investigated in here (in the case of silver, the layer thicknesses are optimized as (d_{MS}, d_{SP}, d_{BPR}) = (30, 80, 10) nm). For both materials, we can obtain *BC* ~ 9.5 dB. When we have an unity output with (A, B) = (1, 1), the insertion loss is regarded as 0 dB. According to this definition, the insertion loss is evaluated to be ~1.5 dB with the use of silver. If we choose a telecom wavelength, the loss can be less because of smaller absorption loss in metal.

In conclusion, we proposed a novel linear optical AND gate by utilizing an extremely thin metasurface beam deflector with a partial reflector. Even with the thin thickness, it has better *BC* of ~ 9.5 dB and smaller loss of ~ 1.5 dB. As far as we know, this concept should be the ultimate one to have the shortest all-optical logic gates. Optical inverters (NOT gate) are also achievable based on the concept of bias input. Such shorter gates would be a key technology for lower latency optical computing.

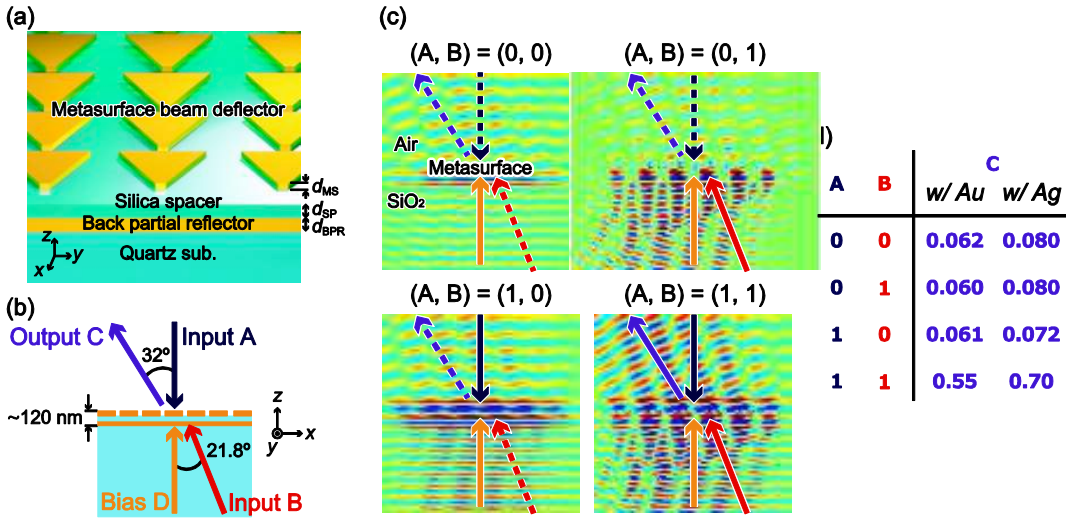

l)

A	B	C w/ Au	C w/ Ag
0	0	0.062	0.080
0	1	0.060	0.080
1	0	0.061	0.072
1	1	0.55	0.70

Fig. 1(a) Schematic of our proposed device (*x* and *y* spacing and length of the trapezoid antenna is respectively fixed to 1.2 μm, 0.2 μm, and 0.8 μm). (b) Schematic of the setup for AND logic operation. (c) Simulated Ey distribution with different input condition. Solid and broken arrows respectively denote whether the input or output is ON or OFF state. (d) Optical I/O table with different metals (Au and Ag).

Acknowledgements This work was supported by JST CREST.

REFERENCES

1. P. Singh, D. Kr. Tripathi, S. Jaiswal, and H. K. Dixit, "All-Optical Logic Gates: Designs, Classification, and Comparison," *Adv. Opt. Tech.*, Vol. 2014, Article ID 275083 (2014).
2. Y. A. Zaghloul, A. R. M. Zaghloul, and A. Adibi, "Passive all-optical polarization switch, binary logic gates, and digital processor," *Opt. Exp.*, Vol. 19, No. 21, pp. 20332-20346 (2011)
3. C. Wang, and Z. Y. Li, "Ultracompact linear on-chip silicon optical logic gates with phase insensitivity," Euro Phys. Lett., Vol. 103, No. 6 (2013).
4. Y. Fu, X. Hu, C. Lu, S. Yue, H. Yang, and Q. Gong, "All-Optical Logic Gates based on Nanoscale Plasmonic Slot Waveguides," *Nano Lett.*, Vol. 12, No. 11, pp. 5784-5790 (2012).
5. S. Kita et al., "Coherent control of high efficiency metasurface beam deflectors with a partial back reflector," *APL Photonics* (2017). (*Accepted*)

Continuous control of complex nonlinear susceptibility for harmonic generation using plasmonic metasurface

Gun-Yeal Lee, Kyookeun Lee, Yohan Lee, Hyeonsoo Park, Chulsoo Choi, and Byoungho Lee*
Inter-University Semiconductor Research Center and School of Electrical and Computer Engineering,
Seoul National University, Gwanak-Gu Gwanakro 1, Seoul 08826, Korea
* byoungho@snu.ac.kr

Abstract-In the field of nonlinear optics, the capability of tailoring nonlinear optical properties in confined area is an important issue. Here, we propose a novel strategy for designing a metasurface that can control magnitude of nonlinear susceptibility continuously. The continuous control of the nonlinear susceptibility is demonstrated by using X-shaped nanoantennas, which induce the third harmonic generation due to its circular symmetry. The proposed metasurface is expected to be applicable to nonlinear applications such as nonlinear holography and data storage.

Metasurfaces are artificially fabricated planar structures whose optical characteristics can be modified by individually adjusting the scattering characteristics of constituent nanoantennas. Recently, metasurfaces have attracted extensive interest owing to their numerous functionalities and potentials [1]. One of the most important application of metasurfaces is holography. Holography is an important technique that can record and reconstruct wavefronts of light with both amplitude and phase information. However, conventional holography, which is based on typical optoelectronic devices such as diffractive optical elements and spatial light modulators, has been suffering from several issues: low resolution and occurrence of noise caused by the diffraction orders and DC components. More importantly, conventional holography techniques are based on the phase- or amplitude-only modulation with incomplete approximations.

Owing to the benefits of metasurfaces such as compactness and the variety of the functionalities, metasrufaces have offered novel methods for holography that overcome the defect of conventional holography. Some studies report metasurfaces that are able to modulate phase, polarization of light, or both [2, 3]. For simultaneous phase and amplitude modulation, metasurface with C-shaped or V-shaped nanostructures were proposed [4, 5], but they have been still deficient; the V-shaped structure only provides imperfect modulation in the sense that the accessible range of complex-amplitude is partial, and the C-shaped structure only operates on Terahertz region. Therefore, full modulation of electromagnetic waves for perfect holography still remains challenging. Recently, several studies have shown that nonlinear metasurfaces can open the new way to realize optical holography with unique advantages. These approaches add functionalities to the optical field modulation and permit the exploration of interesting new possibilities such as generating tailored light at new frequencies, all-optical mode control, and generation of waveform-entangled states [6]. For this reason, nonlinear meatsurfaces are expected to make an advantage which linear metasurfaces are hard to have.

In this study, we propose a metasurface that enables to control both phase and magnitude by manipulating third-order nonlinear susceptibility. We have found that such metasurface can be successfully designed by using X-shaped nanoantennas of which schematic is represented in Figure 1(a). This structure has circular symmetry, especially C2 symmetry, so it can strongly enhance the third harmonic generation (THG).

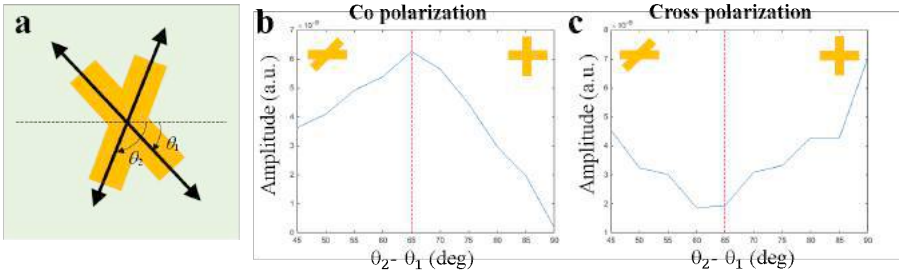

Figure 1. (a) Schematic of X-shaped nanoantenna. (b, c) Amplitude of the transmitted light with (b) co-polarization and (c) cross-polarization from X-shaped structure as a function of the differences between two orientation angles of the X-shaped nanoantenna.

The basic principle of the X-shaped structure is related to Pancharatnam–Berry phase. Pancharatnam–Berry phase can be applied to both linear and nonlinear optical regions due to its robust and dispersion-less nature, so this remarkable nature of the Pancharatnam–Berry phase allows that the X-shaped structure can make it possible to modulate the complex nonlinear third-order susceptibility continuously. The operating scheme was modeled with theoretical analysis based on dipole moment modeling, and the performances of the proposed structure were verified by using a numerical simulation based on finite difference time domain (FDTD) method. As shown in Figure 1(b) and (c), amplitude of the transmitted circularly-polarized light is successfully controlled by the disparity of two orientation angles of the X-shaped nanoantenna. In addition, the phase component can be fully covered by rotating the entire structure because of the nature of Pancharatnam–Berry phase. It means that full modulation of the complex nonlinear susceptibility can be realized. In the presentation, we will explain basic principles of the proposed structure, and then results by numerical simulations will be discussed.

Acknowledgements This work was supported by the Center for Advanced Meta-Materials (CAMM) funded by the Ministry of Science, ICT and Future Planning as Global Frontier Project (CAMM-2014M3A6B3063710). The authors acknowledge support from the Brain Korea 21 (BK21) project.

REFERENCES

1. Meinzer, N., Barnes, W. L. and Hooper, I. R., "Plasmonic meta-atoms and metasurfaces," *Nat. Photon.,* Vol. 8, 889-898, 2014.
2. Genevet, P. and Capasso, F., "Holographic optical metasurfaces: a review of current progress," *Rep. Prog. Phys.*, Vol. 78, 024401, 2015.
3. Arbabi, A., Horie, Y., Bagheri, M. and Faraon A., "Dielectric metasurfaces for complete control of phase nad polarization with subwavelength spatial resolution and high transmission," *Nat. Nanotech.*, Vol. 10, 937-943, 2015.
4. Zhout, F. et al., "Plasmonic holographic imaging with V-shaped nanoantenna array," *Opt. Express*, Vol. 4, 4348-4354, 2013.
5. Liu, L. et al., "Broadband metasurfaces with simultaneous control of phase and amplitude," *Adv. Mater.*, Vol. 26, 5031-5036, 2014.
6. Keren-Zur, S., Avayu, O., Michaeli, L. and Ellenbogen, T., "Nonlinear Beam Shaping with Plasmonic Metasurfaces," *ACS Photonics*, Vol. 3, 117-123, 2016.

Complex Electromagnetics Based on Hybridized Simple Nanoplasmonics in Optical Metasurfaces

Atefeh Fazel Najafabadi and Tavakol Pakizeh*
Faculty of Electrical Engineering, K. N. Toosi University of Technology, Tehran 1631714191, Iran
*corresponding author: t.pakizeh@kntu.ac.ir

Abstract- Electromagnetic coupling of nanoparticles in plasmonic nanostructures leads to effective hybridization and modification in optical properties of the nanostructured metasurfaces in visible region. In the present paper, we study the outstanding optical properties of nanodimers and nanotrimers composed of Ag nanorods in terms of the circular dichroism (CD) and the electromagnetically induced transparency (EIT)-like response. It is shown that breaking symmetry of this configurations boost these optical properties. Therefore, these arrangements can be considered as building blocks for proposing novel optical metasurfaces.

In recent years, the modifications corresponds to different phenomena have been investigated in optical properties to develop various applications in nanooptics, bio-electromagnetism, and complex photonics. Recent studies have revealed that (EIT)-like optical responses as well as chiroptical features such as CD can be obtained classically using on-chip plasmonic and photonic nanoresonators [1-4]. In plasmonic nanostructures, EIT can be controlled with the interaction of the radiant and superradiant modes in the arrangments. Similarly, CD can be tunes with the coupling intensity between nanoparticles and the degree of asymmetry in the nanostructure [4]. In this way, nanodimers and nanotrimers are two of the best candidates for achieving interesting optical properties including CD and EIT. Here, we address the optical interaction of nanoparticles in the dimer and trimer arrangements in order to investigate the optical chirality and EIT. As a classical model, we use the known quasi-static coupled dipoles approximation (CDA) method to study the interaction of nanoparticles and the resulted hybridization phenomenon. In the case of inverted-T nanotrimer, there is a special feature that breaking the symmetry leads to occurring a new mode in contrast to the trimer case composed of nanospheres. Due to the capability of the tuning the hybridized LSPR mode in desired direction and thus having more effective interaction between nanoparticles, we use structures composed of nanorods in the nanodimer and nanotrimer cases to study the optical chirality and EIT. There are different mechanisms applied to the structures in order to break the symmetry in the structure to achieve considerable/effective EIT and CD. Fig. 1(a) illustrate the schematics of a dimer and a trimer composed of Ag nanorods and a plane wave, polarized along the vertical nanorod, incident normally to the structures. Extinction cross section of the considered dimer and trimer versus different separation distance are presented in column two and three, respectively. Figs. 1(c, f) show the numerical results and Figs. 1(d, g) represent the theoretical results obtained via CDA approach. In the CDA method nanorods are approximated with prolate nanospheroids (see Fig. 1(b)), which the quasi-static polarization of them is well known [4]. As seen in Fig. 1, due to the interaction between nanorods two hybridized plasmonic modes are induced in the nanostructures, although the polarization of the incident field is along the

z axis. For a dimer it is shown that for the symmetric T-shape dimer, two hybridized modes merge and a single resonance at the LSPR wavelength of a single nanorod is observed. However, for asymmetric configurations, g=-20, 0 nm, in-phase and out-of-phase hybridized modes separate further. Similarly, in the case nanotrimer, as seen in Figs.1 (f, g), the bright mode of the nanostructure, LSPR resonance of the vertical nanorod, splits to hybridized or dark modes. The bandwidth and the amplitude of the induced modes can be tuned with the separation distance s. Unusual optical properties of the dimer and trimer are shown in Figs. 1(e, h). It can be seen that asymmetric nanodimers reveal significant CD; though, for symmetric configurations, g= 20 nm and g= -30 nm as plotted schematically, CD vanishes. The outstanding results in Fig. 1(h) show the transmission spectra of horizontal double nanorods, a vertical nanorod, and the corresponding trimer while the polarization of the incident field is along the vertical nanorod. Interestingly, the nanotrimer has a EIT-like behavior at the dark modes of the nanostructure; although it is opaque at the bright mode of the nanotrimer. Consequently, the results of this paper are posed to have a general significance for the field of chiral nanoplasmonics and electromagnetically induced transparency.

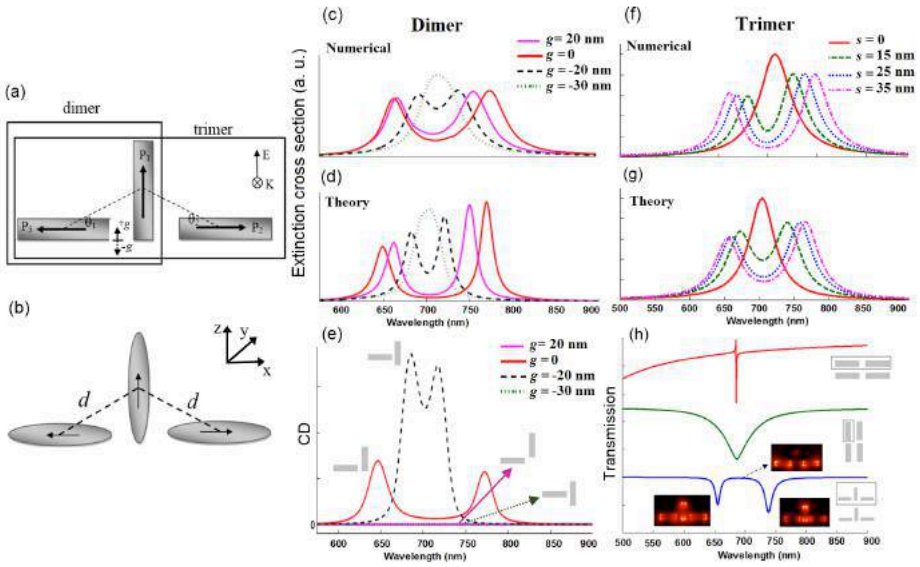

Figure 1. (a) Schematics of the plasmonic nanodimer and nanotrimer (b) Modeling representation of the nanostructures with prolate nanospheroids. (c, d, f, and g) Extinction cross section of the dimer and trimer versus g and $s = d\cos\theta$. (e) CD spectrum of the nanodimer versus different g. (h) Transmission spectra of the horizontal double nanorods, vertical single nanorod, and the considered trimer.

Acknowledgements: The author acknowledge efforts of M. A. Simab, from EE-KNTU.

REFERENCES

1. Aydin, K., Imogen M. Pryce1, and Harry A. Atwater, "*Opt. Express*," Vol. 18, 13407-13416, 2010.
2. Chen, J., P. Wa*ng, C. C*hen, Y. Lu, H. Ming, and Q. Zhan, "*Opt. Express*, " Vol. 19, 5970-5978, 2011.
3. Zu, S., Bao, Y., and Fang, Z., "*Nanoscale,*" Vol. 8, NO. 7, 3900-3905, 2016.
4. Ogier, R., Fang, Y., Svedendahl, M., Johansson, P., and Käll, M., "*ACS Photonics*," Vol. 1, No.10, 1074-1081, 2014.
5. Bohren, C. F. and Huffman, D. R., *Absorption and scattering of light by small particles*, John Wiley & Sons, New York, 1998.

Practical Limits of capacitive coupling between gold nanoparticles toward self-assembled, ultrahigh index optical metamaterial

Ji-Hyeok Huh[1] **and Seungwoo Lee**[1,2*]

[1] SKKU Advanced Institute of Nanotechnology (SAINT), Suwon, Republic of Korea

[2] Department of Nano Engineering and School of Chemical Engineering, Sungkyunkwan University (SKKU), Suwon, Republic of Korea 16419

[*]seungwoo@skku.edu

Abstract – In this work, we demonstrate self-assembly of the closely-packed plasmonic nanoparticles (NPs) superlattice that could exhibit unnaturally high-refractive-index at optical frequencies. We successfully synthesized highly uniform and smooth AuNPs with sphere and cube shapes; by benefitting from this unprecedented quality of AuNPs, we approached to the practical limits of the accessible minimum gap between AuNPs, self-assembled into large-area, close-packed monolayer. Thus, the effect of AuNP shape on capacitive coupling, essential for unnaturally high-refractive-index, was systematically studied; the experimentally available upper limit of permittivity, tuned via capacitive coupling, was figured out in a deterministic fashion.

Subwavelength-scaled noble metallic nanoparticles (plasmonic NPs) have emerged as a promising building block of metamaterials which operate at visible to NIR domain (optical metamaterials).[1] For example, it has already been reported theoretically that the 2D superlattice of metallic NPs with sub-10 nm gap can exhibit unnaturally high-refractive index at optical frequencies.[2,3] Because an incident electromagnetic wave can be resonantly confined to deeply sub-wavelength volume by a strong capacitive coupling between neighboring plasmonic NPs, available effective permittivity ε_{eff} can be significantly enhanced. However, there are stringent requirements to achieve a ultrahigh effective permittivity ε_{eff}, including highly uniform and smooth plasmonic NPs, exquisite control over NP shape, and ultrasmall (less than 10 nm) and uniform gap between NPs. Unfortunately, conventional chemical synthesis (e.g. controlled growth of sodium citrate capped small seed NPs) have allowed for a relatively polygonal shape and disperse size of AuNP.[4] As such, the previous researches on the plasmonic NP superlattice-enabled ultrahigh-refractive-index optical metamaterials have been limited to a theoretical peculiarity.[5]

To address this challenge, we synthesized the highly uniform and smooth Au NPs with a different shape (i.e., nanospheres (NSs) and nanocubes (NCs)) by iterative growth and etching methods. Then, as shown in Figure 1(a)-(d), convective-assembly technique was exploited to obtain large-area Au NSs and NCs superlattice. As capillary force, driven by selective evaporation of solvent at meniscus, can continuously push AuNPs to be closely packed, the gap between AuNPs in principle can be minimized.[6] In particular, the thickness of organic ligand (1~2 nm) defines the minimum gap. More importantly, the unprecedented quality of AuNSs and AuNCs in terms of smoothness and size uniformity allowed us to achieve an experimentally accessible minimum gap over the large area. Thereby, we figured out the practically limits of capacitive coupling between AuNPs and the resultant effective permittivity ε_{eff}. The far-field measurement results including reflection and transmission (Figure 1. (e)-(h)) and their comparison with numerical simulation confirmed an effectively available gap between AuNPs (less than 5 nm). Furthermore, we used a dressed

polarizability theorem to rationalize capacitive coupling and effective permittivity ε_{eff};[7] experimental verification of effective permittivity ε_{eff} also was carried out thorough quantitative phase imaging method (QPIU).[8]

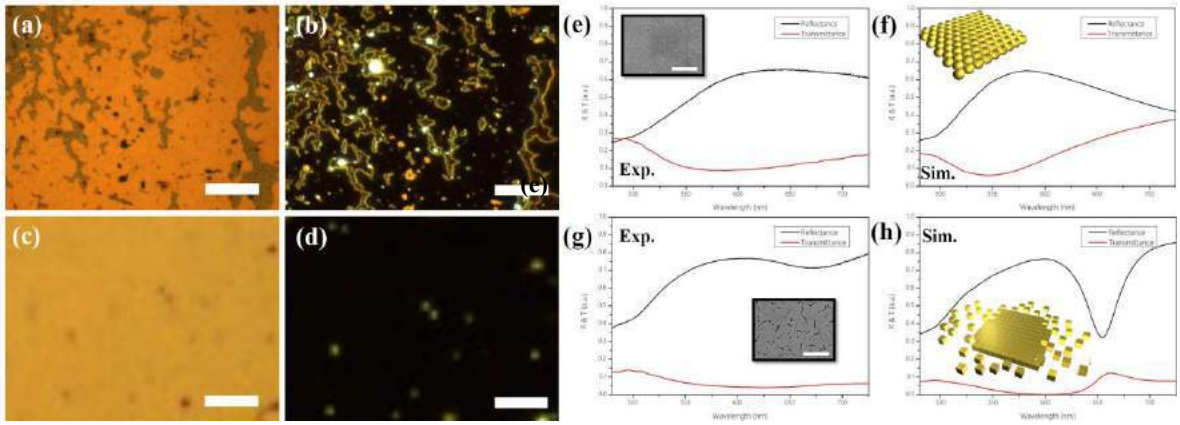

Figure1. Self-Assembled AuNPs Monolayer obtained by convective assembly and far field optical response. (a-b) Optical microscope images of 60nm AuNS monolayer. (a) Bright field, (b) Dark field. (c-d) 60nm AuNC monolayer (c) Bright field, (d) Dark field (scale bar 10μm). (e-f) Reflectance and transmittance of 60mn AuNS monolayer. (e) Experimental result of 60nm AuNS monolayer. (f) Simulation result of periodically hexagonal packed AuNS monolayer with gap 5 nm. (g-h) As with (e-f), (g) and (h) are the results of 60nm AuNC with gap 5nm. Insets in (e),(g) are scanning electron microscope(SEM) images (scale bar 2 μm)

Acknowledgements, This work was supported by Samsung Research Funding Center of Samsung Electronics under Project Number SRFC-MA1402-09.

REFERENCES

1. Rozin M. J., D. A. Rosen, T. J. Dill and A. R. Tao, "Colloidal metasurfaces displaying near-ideal and tunable light absorbance in the infrared" *Nat. Commun.,* Vol. 6, 7325, 2015.
2. Alù A. and E. Nader, "Dynamical theory of artificial optical magnetism produced by rings of plasmonic nanoparticles" *Phys. Rev. B,* Vol. 78, No. 8, 1-10, 2008.
3. Alaeian H., and J. A. Dionne, "Plasmon nanoparticle superlattices as optical-frequency magnetic metamaterials" *Opt. Express,* Vol. 20, No. 14, 15781, 2012.
4. Steven D. P., and C. W. Chan, "Synthesis and Surface Modification of Highly Monodispersed, Spherical Gold Nanoparticles of 50-200 nm" *J. Am. Chem. Soc.,* Vol. 131, No. 47 17042-17043, 2009.
5. Lee S. "Colloidal superlattices for unnaturally high-index metamaterials at broadband optical frequencies" *Opt. Express,* Vol. 23, No. 22, 28170, 2015.
6. Malaquin L., T. Kraus, H. Schmid, E. Delamarche and H. Wolf, "Controlled Particle Placement through Convective and Capillary Assembly" *Langmuir,* Vol. 23, No. 23, 11513-11521, 2007.
7. Yoo S. and Q. Park, "Effective permittivity for resonant plasmonic nanoparticle systems via dressed polarizability" *Opt. Express,* Vol. 20, No. 15, 16480, 2012.
8. Lee K. and Y. Park, "Quantitative phase imaging unit" *Optics Lett.,* Vol. 39, No. 12, 3630-3633, 2014.

Quantitative 3D phase imaging – a tool for plasmonic metasurfaces

J. Babocký[1,2], A. Křížová[1,3], F. Ligmajer[1,4], M. Hrtoň[1,4], P. Dvořák[1,4], M. Týč[1], V. Křápek[1,4], R. Kalousek[1,4], R. Chmelík[1,4], and T. Šikola[1,4*]

[1]Central European Institute of Technology, Brno University of Technology, Purkyňova 123, CZ 612 00 Brno, Czech Republic

[2]TESCAN Brno, s.r.o., Libušina třída 1, CZ 623 00 Brno, Czech Republic

[3]TESCAN Orsay Holding, a.s., Libušina třída 21, CZ 623 00 Brno, Czech Republic

[4]Institute of Physical Engineering, Brno University of Technology, Technická 2, CZ 616 69 Brno, Czech Republic

[*]corresponding author: sikola@fme.vutbr.cz

Abstract- We present coherence-controlled holographic microscopy as an ultimate tool for 3D wide-field phase imaging finding direct application in characterization of optical fields formed by metasurfaces. Proof-of-concept experiments were performed on individual plasmonic antennas and on a specific metasurface – a focusing zone plate made of plasmonic nanodiscs.

Coherence-controlled holographic microscopy (CCHM) is a real-time, wide-field, and quantitative light-microscopy technique enabling 3D imaging of electromagnetic fields, providing complete information about both their intensity and phase. It has been patented by a member of our team and until now utilized exclusively in bio-applications only [1]. However, these attributes make also CCHM a promising candidate for performance assessment of phase-altering metasurfaces, a new class of artificial materials that allow to manipulate the wavefront of passing light and thus provide unprecedented functionalities in optics and nanophotonics.

In our study, we report on our investigation of phase imaging of plasmonic metasurfaces using this technique. We demonstrate its ability to obtain phase information from the whole field of view in a single measurement on a prototypical sample consisting of silver nanodisc arrays. The experimental data were validated using FDTD simulations and a theoretical model that relates the obtained phase image to the optical response of metamaterial building blocks. Finally, in order to reveal the full potential of CCHM, we employed it in the analysis of a simple metasurface represented by a plasmonic zone plate (Fig. 1). By scanning the sample along the optical axis we were able to create a quantitative 3D phase map of fields transmitted through the zone plate. The presented results prove that CCHM is inherently suited to the task of characterization of optical fields formed by metasurfaces. Moreover, as the temporal resolution is limited only by the camera framerate, it can be even applied in analysis of actively tunable metamaterials.

CCHM has no similar limitations one can find in other techniques for the phase imaging, such as ellipsometry (poor lateral resolution and complex evaluation), scanning aperture-less near-field optical microscopy (inherently slow) and current interferometric methods (one sample spot at a time only). Hence, CCHM brings a considerable progress for the quantitative phase imaging in the important and vivid field of photonic metasurfaces and other optical systems.

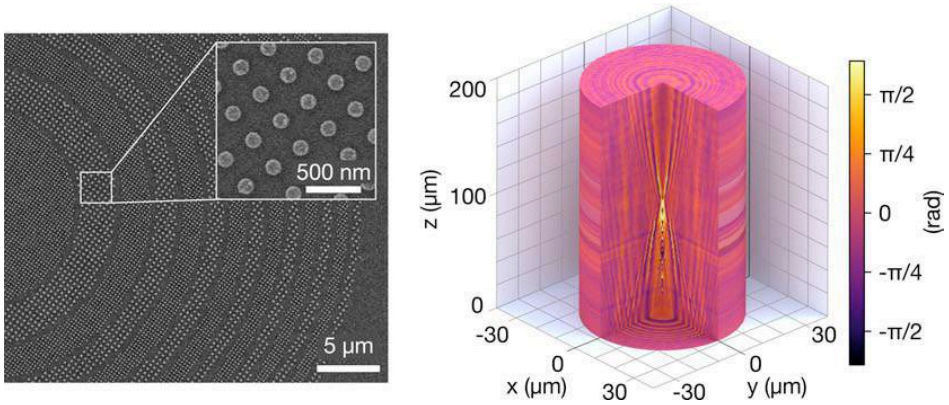

Figure 1. Left: Plasmonic zone plate consisting of concentric rings alternatively filled with silver plasmonic nanodiscs of two different diameters (two distint plasmon resonance frequencies) on a transparent substrate. The plate is illuminated from bottom and the transmitted light (comprising of incident and scattered component) then interferes with the light in the reference arm at an oblique angle, allowing to retrieve the phase and amplitude of the wave at each point of the sample (zone plate) and above it. Right: 3D visualization of the measured total phase distribution in the half-space above the plasmonic zone-plate.

Acknowledgements

We acknowledge the support by the Grant Agency of the Czech Republic (grant No. 15-21581S), European Regional Development Fund (project No. CZ.1.05/1.1.00/02.0068), MEYS CR (project No. LQ1601 – CEITEC 2020), Technology Agency of the Czech Republic (grant No. TE01020233) and BUT (projects Nrs. FSI-S-17-4482, FSI/STI-J-17-4623,).

REFERENCES

1. Lošťak, M., Chmelik R., Slaba M. and Slaby T., "Coherence-controlled holographic microscopy in diffuse media," *Opt. Express,* Vol. 22, 4180-4195, 2014.

Reflection-type plasmonic metasurfaces for reconfigurable wavefront modulation using phase-change materials

Chi-Young Hwang*, Yong-Hae Kim, Gi Heon Kim, Jong-Heon Yang, Jae-Eun Pi, Ji Hun Choi, Kyunghee Choi, and Chi-Sun Hwang

Electronics and Telecommunications Research Institute,
218 Gajeong-ro, Yuseong-gu, Daejeon 34129, Republic of Korea
*corresponding author: cyhwang@etri.re.kr

Abstract - Reflection-type reconfigurable metasurfaces are proposed for spatial light modulation of visible light at subwavelength scale. The structure is based on a subwavelength metal grating that can couple the incident light to the gap plasmon mode and modulate it through cavity resonance. By using chalcogenide phase-change materials, the optical characteristics of the structure can be switched between two states so that it can generate the desired spatial light distributions. Numerical simulations are performed to verify the proposed structure.

Spatial light modulation with subwavelength resolution has the fundamental advantage of continuous wavefront manipulation, which is free from the unwanted high-order diffraction that occurs in conventional diffractive optical devices. In this regard, in recent years, various novel methods have been proposed for subwavelength-scale wavefront control, based mainly on metamaterials and metasurfaces [1]. However, most of them are currently taking a way of passive-type modulation, which is inadequate for dynamic applications.

In this study, a subwavelength plasmonic structure is proposed in order to generate two-level spatial distributions of a wave field that can be reconfigured. Figure 1(a) shows the design of the unit cell, basically a subwavelength grating in which light modulation is performed by cavity resonance of gap plasmons [2], and tunability can be achieved by a thin layer of the phase-change material $Ge_2Sb_2Te_5$ (GST). By either electrical or optical pulses, the state of the GST can be reconfigured between amorphous and crystalline, switching the optical property accordingly [3]. It should be noted that the protective layer of indium tin oxide (ITO) can provide the function of electrical switching of the GST by using Joule heating. Figure 1(b) shows the numerically calculated spectral reflectance and phase difference of the proposed structure with respect to the two GST states. Here, a transverse magnetic wave is normally incident on the structure, and periodic boundary conditions are applied for both x and y directions. The numerical results show that, based on the structure, reflection-type reconfigurable plasmonic metasurfaces can be realized, which can be promising candidates for an advanced holographic display.

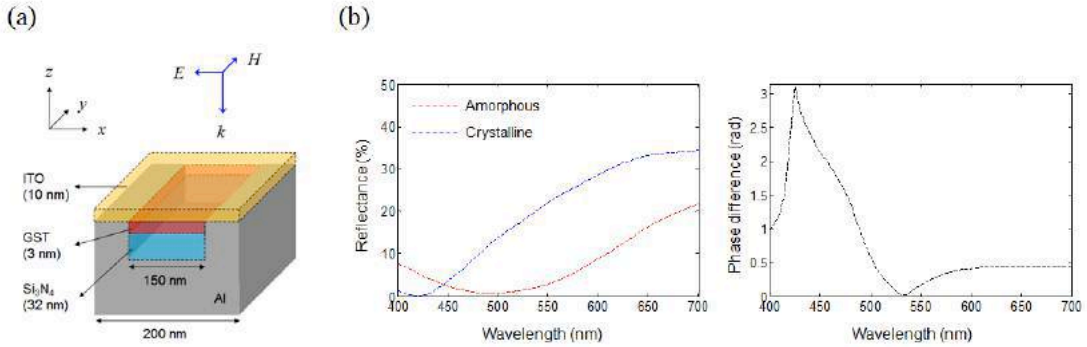

Fig. 1. (a) Unit structure for reconfigurable subwavelength-scale spatial light modulation, using phase-change materials. The thickness of each layer is indicated in parenthesis. (b) Numerically calculated spectral reflectance and phase difference for the two states of the GST layer.

Acknowledgements This work was supported by "The Cross-Ministry Giga KOREA Project" grant from the Ministry of Science, ICT, and Future Planning, Korea [GK16D0100].

REFERENCES

1. N. Yu and F. Capasso, "Flat optics with designer metasurfaces," *Nat. Mater.*, Vol. 13, No. 2, 139–150, 2014.
2. C.-Y. Hwang, Y. Yi, and C.-G. Choi, "Reflection-type spatial amplitude modulation of visible light based on a sub-wavelength plasmonic absorber," *Opt. Lett.*, Vol. 41, No. 5, 990–993, 2016.
3. C. H. Chu, M. L. Tseng, J. Chen, P. C. Wu, Y. H. Chen, H. C. Wang, T. Y. Chen, W. T. Hsieh, H. J. Wu, G. Sun, and D. P. Tsai, "Active dielectric metasurface based on phase-change medium," *Laser Photon. Rev.*, Vol. 10, No. 6, 986–994, 2016.

Polarization Dependent Light-Matter Interaction with Metal Surfaces and Metasurfaces

Pieter G. Kik[1,2,*], Chatdanai Lumdee[2], Vrinda Thareja, Majid Esfandyarpour, and Mark L. Brongersma
[1]Geballe Laboratory for Advanced Materials, Stanford University, Stanford, CA, USA
[2]CREOL, The College of Optics and Photonics, Orlando, FL, USA
[*]corresponding author: kik@creol.ucf.edu

Abstract-The large free charge concentration in metals enables strong light-matter interaction, allowing for nanoscale engineering of emission efficiency and radiation patterns. However, the large conductivity of metals also strongly suppresses lateral fields, reducing excitation and emission rates related to lateral polarization. Here we show that subwavelength patterning of metal surfaces can overcome the deleterious effect of lateral field suppression, resulting a large, reproducible, and quantitatively understood enhancement of Raman scattering from graphene in close contact with a metasurface.

Metals can dramatically alter the optical response of near-surface emitters and scatterers. For example, scattering by plasmon resonant metal nanoparticles can be strongly modified near metal surfaces due to interaction of the nanoparticle with image charges.[1] However, since good conductors efficiently suppress tangential field components, emission and scattering processes that involve polarization along the metal surface are strongly suppressed. As a result, the optical response of scatterers and emitters near metallic surfaces is often dominated by surface-normal polarization contributions. This limitation can be circumvented by modification of the effective surface impedance. Under normal incidence illumination from vacuum, the electric amplitude reflection coefficient is governed by the impedance of vacuum $Z_0 = \sqrt{(\mu_0/\varepsilon_0)}$ and that of the substrate $Z_S = \sqrt{(\mu_S/\varepsilon_S)}$ according to

$$r = \frac{Z_S - Z_0}{Z_S + Z_0} \qquad (1)$$

For metals with large negative permittivity (small negative impedance) this results in large reflection with reversed field amplitude, corresponding to suppressed tangential fields. However by subwavelength patterning of a metal film, its impedance can be modified, and under certain conditions an electric field maximum can be attained near the surface. Thus by engineering the impedance of such metallic metasurfaces, it becomes possible to significantly modify emission and scattering of lateral polarization contributions.

Here we investigate the enhancement of gold photoluminescence (PL) and Raman scattering. We compare the role of polarization in gap-plasmon-enhanced gold PL and magnetic-mirror-enhanced Raman scattering from graphene. Graphene is an ideal reporter of near-surface tangential field enhancement on metasurfaces. First, its two-dimensional extended nature allows it to be in close contact with a large nanostructured region. Second, it features distinct Raman peaks with relatively large shifts. Finally, its 2D nature results in a strongly anisotropic Raman response, making it especially sensitive to tangential fields.

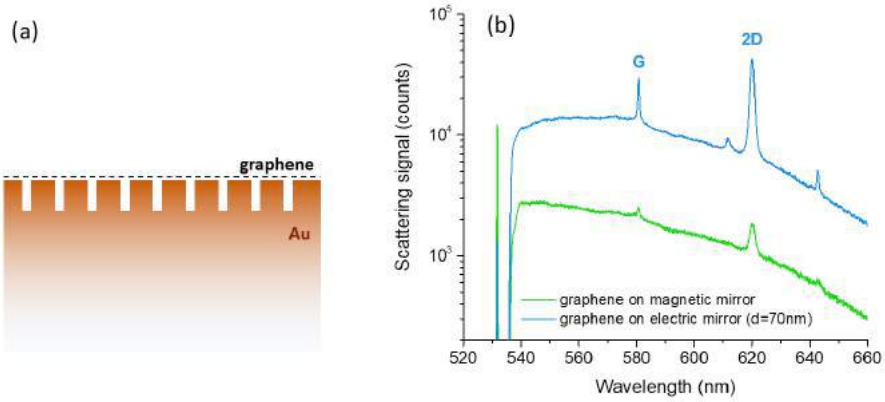

Figure 1: (a) Schematic of a graphene draped metallic metasurface. (b) Scattering spectrum of single-layer graphene on a gold film (green curve) and on a gold metasurface acting as a magnetic mirror (blue curve), showing different enhancement of the gold photoluminescence and of the Raman signal from in-plane graphene phonons.

First it is shown that gold PL enhancement by gap plasmons can be quantitatively described using a combination of numerical simulation and the assumption of reciprocity. Second it is shown that graphene Raman scattering enhancement on metasurfaces consisting of subwavelength groove arrays can be quantitatively described by simulated electromagnetic fields and invoking reciprocity. We show how the full tensorial nature of the graphene Raman response must be taken into account. The results highlight the unique nature of graphene as a reporter of tangential near-fields, and demonstrate the potential of surface impedance engineering for the control of polarization dependent light matter interaction.

REFERENCES

1. Lumdee, C., Yun, B, and Kik, P.G., Wide-band Spectral Control of Au Nanoparticle Plasmon Resonances on a Thermally and Chemically Robust Sensing Platform, J. Phys. Chem. C 117, 19127 (2013)
2. Esfandyarpour, M., Garnett, E. C., Cui, Y., McGehee, M. D. & Brongersma, M. L., Metamaterial mirrors in optoelectronic devices. Nat Nano 9, 542–547 (2014)

Triangular Shape Left-handed Meta-surface based on Meta-Atom Cluster for C-band Operation

M. M. Hasan[1*], M. R. I. Faruque[1], M. T. Islam[2]

[1]Space Science Centre (ANGKASA), Universiti Kebangsaan Malaysia, Bangi 43600, Malaysia
[2]Department of Electrical, Electronic and Systems Engineering, Faculty of Engineering and Built Environment, Universiti Kebangsaan Malaysia, Bangi 43600, Malaysia

*corresponding author: mehedi20.kuet@gmail.com

Abstract

In this paper, a triangular shaped left handed meta-surface based on the meta-atom cluster has been demonstrated for C-band application. A modified version of the resonators is connected together to form like a triangular shape structure. The Finite integration technique based CST Microwave Studio electromagnetic simulator has been used for design, simulation, and investigation. Measurement is also done and the measured and simulated results are well complied together. The measured results show resonance peaks of transmission coefficient in 7.40 GHz and the left handed characteristics is exhibited from 16.66 GHz to 18.0 GHz. In addition, electric lumped circuit model based on the inductor and capacitor of the proposed meta-surface is also design and analysed. Due to the resonance in C-band the proposed meta-surface structure is flexible for EM-cloaking, Imaging, radio communication, etc.

1. Introduction

The concept of metamaterials was originally introduced for electromagnetic waves, which is now classified as electromagnetic meta-surface. In nature, electromagnetic metamaterials are man-made structures patterned on the sub-wavelength scale in order to achieve exotic functionality, which possess peculiar electromagnetic properties not seen in natural materials. The electromagnetic characteristics of electronic materials are primarily determined by the physical parameters of the permittivity, permeability, and conductivity. All loss less electromagnetic materials can be classified as shown in figure 1. According to the signs of permittivity and permeability, where DPS denotes double positive ($\varepsilon>0$ and $\mu>0$), ENG denotes Epsilon negative ($\varepsilon<0$ and $\mu>0$), DNG denotes double negative ($\varepsilon<0$ and $\mu<0$), and MNG denotes Mu negative ($\varepsilon>0$ and $\mu<0$). In particular, materials with simultaneously negative permittivity and permeability are also called left handed or negative-index or double negative metamaterial. With the rapid growth of the communication systems the demand of the meta-surface has been extensively increased not only for the meta-surface exotic electromagnetic properties but also for their promise for applications like invisible cloaking, electromagnetic absorption, specific absorption reduction (SAR), enhanced the antenna performance by using as radiating patch or parasitic elements or ground plane, filter design, perfect lenses, hyper lenses, aberration free lenses, etc. Moreover, few research on these studies has been reviewed for understanding the properties of these man-made artificial materials.

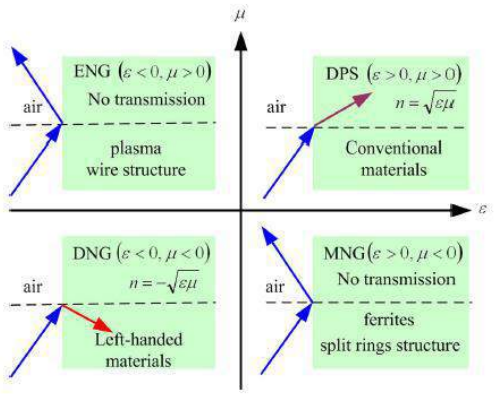

Figure 1. Wave propagation properties through the medium.

Ziolkowski et al. developed a metamaterial by capacitor loaded strips and split ring resonators in 2003, which exhibited negative permittivity and negative permeability both at the X-band frequencies [1]. A periodic array, where the unit cells consists of two symmetrical π-shape wire and the negative-refractive band lies between 11.20 GHz and 13.05 GHz. Besides, high transmission with low loss occurs between 11.95 GHz and 12.50 GHz in case of the designed structure proposed by Chun et al. [2]. A dual band meta-atom as a negative permittivity metamaterial and had two stop bands at around 5.41 and 6.70 GHz, whereas the measured results are almost, 5.55 and 6.80 GHz was introduced in 2015 [3]. In addition, a compact z-shaped double negative metamaterial for wide band applications was presented by Hasan et al. The 10×10 mm^2 structure metamaterial unit cell was applicable for C- and X-band operations and the effective medium ratio was 4.0. Besides, the designed DNG metamaterial different structure are also investigated with the equivalent lumped circuit model [4]. A metamaterial embedded microstrip patch antenna was introduced for microwave C-band (from 3.77 to 6.58 GHz) applications that composed of a rectangular metamaterial

embedded patch, microstrip-fed line and a partial ground plane. The antenna shown fractional bandwidth 54.97 % at the central frequency and the radiation efficiency varied from 85 % to 97 %, whereas the peak gain from 1 dB to 4.5 dB in different frequencies [5]. In addition, a z-shaped left handed metamaterial for wide band applications was presented, which applicable for C- and X-band application. The designed structure shown left handed characteristics in 8.50 GHz, bandwidth of 5.67 GHz, and the effective medium ratio was 9.10 [6]. A metamaterial based microstrip patch antenna, optimized for bandwidth and multiple frequency operations by criss-cross metamaterial structure had been proposed, whereas the criss-cross shape metamaterial structure was inspired from the famous Jerusalem cross. This metamaterial antenna improvement in bandwidth without reducing the gain in the C-band. The results shown the bandwidth of the metamaterial embedded was 610 MHz but the bandwidth of the simple patch was 300 MHz, as a result the enhancement of 310 MHz was achieved with a gain of 4.45 dB [7]. A meta-atom sensor based on planar hexagon split ring resonators was reported which structure was designed to operate in terahertz regime. In addition, a modified version of split ring resonator was simulated for sensing dielectric changes by placing thin dielectric layers as sample materials on the full frontal surface of the sensor. The real part of permittivity and permeability remains from 3.90 to 4.10 THz and the quality factor was 95.0 [8]. A negative index metamaterial with two components analysis for C- and X-band had been introduced by Islam et al. and the structure had two arrows and a metal arm was connected the two arrows that looked like a double arrow shape printed on the epoxy resin fibre and the epoxy resin formation processes were also explained step by step in 2017 [9]. A single layer negative index meta atom was analysed that was developed by an outer and inner split ring resonators with inverse E-shape metal strips of copper were connected with the outer ring resonator. This designed meta-atom structure illustrated the bandwidth of 5.81 GHz, which was applicable for C-, X- and Ku-band applications. Moreover, due to the total dimension of 0.2λ×0.2λ×0.035λ and effective medium ratio of 5.0 the proposed meta-atom structure was suitable for the practical applications [10]. In addition, a microwave metamaterial absorber was designed that resonance at C-, X- and Ku-band with double negative characteristics as well as the absorption peaks were respectively, 82%, 67%, and 93% at 6.22, 8.76, and 13.05 GHz in [11]. In [12] a robust nature inspired optimization technique had been discussed for evolving optimal design for soft, hard and balanced meta-surfaces that would be used as broadband low-loss liners in anisotropic and dispersive boundary mode horn antennas. A double-negative metamaterial for 0.5 to 7 GHz frequency range applications was presented by Ikbal et al. in 2015. They investigated the effects of the size of the single unit cell of the metamaterial structure on the resonance frequency and on the double negative characteristics. However, the designed unit cells were exhibited negative permittivity and permeability simultaneously in the S-band (2.95 to 4.00 GHz), and C-band (4.00 to 4.95 GHz and 5.00 to 5.57 GHz) in microwave frequency range [13].

The aim of this paper is to demonstrate a meta-surface based on meta-atom cluster for C-band application numerically and experimentally. The proposed structure is designed by the metallic strips, where the metallic strips are connected together at a central point and look like a triangular shape. The size of a single unit cell is 7×7 mm^2 and the effective medium ratio is 5.80 that means the proposed meta-surface structure compact in size. Moreover, the measured transmittance (S_{21}) shows resonance in 7.40 GHz and the left handed characteristics exhibits from 16.66 to 18.0 GHz for any of frequency points in this frequency range. In addition, the lumped circuit model for the proposed meta-surface has been designed with the total inductance and capacitance determined equations. In the circuit model the gaps and splits in every resonator produce the capacitance and each metal strip is responsible for generating the inductance. This paper is organized as these manner, the meat-surface structural design with schematic and fabricated view is shown in section 2 and Section 3 illustrated the proposed meta-surface extraction process with the mathematical explanation. Besides, the equivalent lumped element circuit model through the developed total inductance and capacitance equation to calculate the resonance point of the proposed meta-surface in the same section. The measured and simulated results with the effective medium parameters (permittivity, permeability, and refractive index), and reactance impedance (surface impedance) of the designed meta-surface has been discussed in section 4, and section 5 conclude the paper.

2. Meta-surface Design

The meta-atoms are periodically arranged in the form of cluster with optimized geometric dimensions is shown in Fig. 2(c). Every single unit cell of the proposed structure contains metallic strips, where the strips are connected together and form like a triangular shape structure. The designed structure printed on an FR-4 material that permittivity of ε_r= 4.25, loss tangent of tanδ= 0.02, and thickness of t= 1.60 mm. The effect of the dielectric thickness response, as the thickness increases resonance frequency of the proposed structure shifts to the lower frequencies since the increment of the thickness increases the inductance of the structure. This results in reduction of the resonance frequency of the lumped resonance circuit.

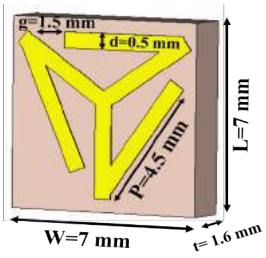

(a)

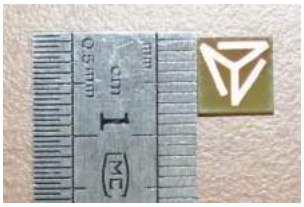

(b)

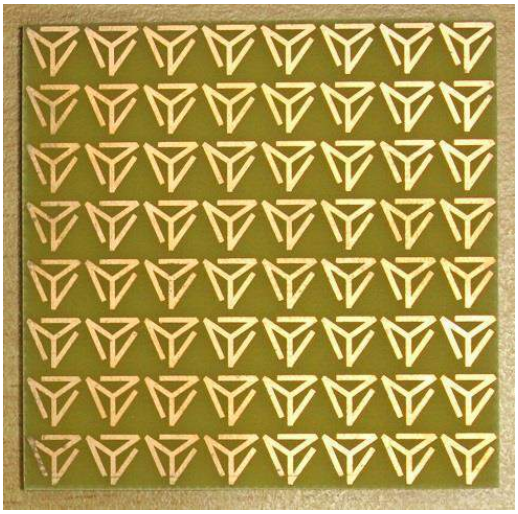

(c)

Figure 2: Proposed Meta-surface: (a) Schematic structure, where the geometric dimensions L= 7.0 mm, W= 9.0 mm, P= 8.50 mm, t=1.60, and g= 1.50 mm. The metal is 0.5 mm in width (d) and 0.035 mm in thickness (h); (b) Fabricated (7×7-mm^2) single unit cell, (c) Fabricated array structure.

3. Methodology and Equivalent Circuit Model

The Finite integration technique based commercially available computer simulation technology Microwave Studio is adopted for all the design and numerical investigations. Two boundary conditions are commonly used for the computation of meta-surface parameters: periodic boundary condition and perfect electromagnetic conductor boundary condition. Periodic boundary conditions are usually applied for simulating a part of the mass framework by modelling its small part with the absence of proper surface. The perfect electromagnetic conductor boundary condition is the generalization of perfect electric conductor and perfect magnetic conductor. For the simulation of the proposed fractal meta-surface absorber EM-waves are propagating along the z-axis, whereas the x- and y-axis are respectively considered as a perfect electric conductor and perfect magnetic conductor boundaries. Frequency domain solver with tetrahedral mesh have been utilized for the simulation and the impedance has been set to 50Ω. However, the retrieving procedure of the effective parameters are given as follows [14],

$$\textit{Reflection Coefficient, } S_{11} \approx \left\{ \frac{R_{01}\left(1-e^{i2nk_0d}\right)}{1-R_{01}^2 e^{i2nk_0d}} \right\} \quad 1$$

$$\textit{Transmission Coefficient, } S_{21} \approx \left\{ \frac{\left(1-R_{01}^2\right)e^{i2nk_0d}}{1-R_{01}^2 e^{i2nk_0d}} \right\} \quad 2$$

$$\textit{Impedance, } Z \approx \pm\sqrt{\frac{\left(1+S_{11}\right)^2+S_{21}^2}{\left(1-S_{11}\right)^2+S_{21}^2}} \quad 3$$

$$e^{\gamma d} = \left\{ \left(\frac{1-S_{11}^2+S_{21}^2}{2S_{21}} \right) + \left(\frac{2S_{11}}{\left(Z-\frac{1}{Z}\right)S_{21}} \right) \right\} \quad 4$$

$$\phi_N = \phi_0 + \sum_{i=1}^{N} \arg\left(\frac{e^{\gamma id}}{e^{\gamma i-d}} \right) \quad 5$$

Refractive index n of N_{th} sample,

$$\sqrt{\left(n_N\right)^2-\left(\frac{\omega_c}{\omega_N}\right)^2} = \frac{1}{k_0 d}\left[-i\ln\left(\left|e^{\gamma Nd}\right|\right)+\phi_N\right] \quad 6$$

$$\sqrt{\left(n_N\right)^2-\left(\frac{\omega_c}{\omega_N}\right)^2} = \frac{1}{k_0 d}\left[-i\ln\left(\left|e^{\gamma Nd}\right|\right)+\phi_0+\sum_{i=1}^{N}\arg\left(\frac{e^{\gamma id}}{e^{\gamma i-d}}\right)\right] \quad 7$$

$$\textit{Refractive Index, } n_r \approx \sqrt{\frac{n^2-\left(\frac{\omega_c}{\omega}\right)^2}{1-\left(\frac{\omega_c}{\omega}\right)^2}} \quad 8$$

$$\textit{Permeability, } \mu_r \approx \left(Z \times n_r\right) \approx Z\sqrt{\frac{n^2-\left(\frac{\omega_c}{\omega}\right)^2}{1-\left(\frac{\omega_c}{\omega}\right)^2}} \quad 9$$

$$\textit{Permittivity, } \varepsilon_r \approx \left(\frac{Z}{n_r}\right) \approx \left(\frac{\pm\sqrt{\frac{\left(1+S_{11}\right)^2+S_{21}^2}{\left(1-S_{11}\right)^2+S_{21}^2}}}{n_r} \right) \quad 10$$

where 'd' is the thickness of the substrate, 'Z' is the normalize impedance, 'k_0' is the wave vector, 'R_{01}' is the sample interface, 'S_{11}' is the reflection coefficient, and 'S_{21}' is the transmission coefficient. From the equivalent lumped circuit of the designed structure [6, 10, 15], the three branch equivalent impedance are respectively,

$$Z_1 = \frac{Z_{C1}Z_{L1}}{Z_{C1}+Z_{L1}}, Z_2 = \frac{Z_{C2}Z_{L2}}{Z_{C2}+Z_{L2}}, Z_3 = \frac{Z_{C3}Z_{L3}}{Z_{C3}+Z_{L3}}.$$

$$Total\ Impedance, Z_T = \frac{Z_1Z_2 + Z_1Z_3}{Z_1 + Z_2 + Z_3} \quad 11$$

$$I_T = C_1\frac{d^2V}{dt} + C_2\frac{d^2V}{dt} + C_3\frac{d^2V}{dt} + \frac{1}{L_1^{'}}V + \frac{1}{L_2^{'}}V + \frac{1}{L_3^{'}}V \quad 12$$

The total inductance of the designed structure can be figure out from the equation,

$$L_T \approx \mu_0 t\left\{\frac{(p+h)^2}{(2t^2 - g^2 - \pi d^2)} + \frac{\sqrt{L^2+W^2}}{\sqrt{p^2+g^2}}\right\} \quad 13$$

In addition, total capacitance can be calculated by,

$$C_T \approx \varepsilon_0\left[\frac{\pi(W+L-d)}{2(g+p+t)}\ln\left(\frac{L+W}{p+d}\right)\right] \quad 14$$

where the free-space permeability is $4\pi\times10^{-7}$ H/m and permittivity is 8.85×10^{-12} F/m. As the proposed structure consist of inductive-capacitive circuit, so the resonance frequency would be,

$$f_r = \frac{1}{2\pi\sqrt{L_TC_T}} \quad 15$$

From figure 3, the inductive effect is formed by the metallic part and the capacitive effect is induced by the gaps and splits. The rise of the inductive and capacitive effect minimizes together. Because, if the inductance raise resonance point shifts toward lower frequency and the resonance points shift to a higher frequency for the increase of capacitive effect. However, the total inductance and capacitance describes the resonance points of the proposed meta-surface structure depend on the design specifications. The variation of any geometrical parameters corresponding to the change of the total inductances and capacitances causes the shift of the resonant frequencies.

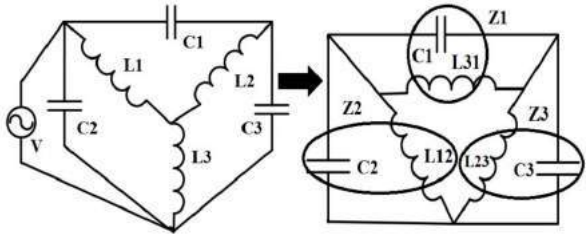

Figure 3: Equivalent lumped circuit model of the proposed triangular shape meta-surface single unit cell structure.

4. Measurement Validation and Result Analysis

The fabricated triangular-shape array of meta-surface is placed between the horn antennas for the measurement validation. The EM-waves are propagated along z-axis to incident on the fabricated structure and the electric and magnetic boundaries are considered x-and y-axes. An Agilent N5227A vector network analyzer was connected to the antennas to measure the scattering and effective medium parameters. From figure 4(a,b) the current is flowing inner and outer direction in every branch of the triangular-shape meta-surface. The arrows indicate the direction and the color describe the intensity of the flowing current. At the resonance point the intensity of the current is the highest, whereas the stop bands are created at the null point by the minimization of the current through flowing currents opposite direction. The field distributing in the substrate board of the proposed structure is plotted in figure 4(c-d). The inductive net electric dipole moments yield when the current flows on the triangular-shaped metal patterns and are anti-parallel to the incident electric fields, providing the negative permittivity. Although the gap is capable of providing a capacitance, it is unable to excite the oscillation of current and play the role of accumulating charges whose dipole moments are anti-parallel to electric fields.

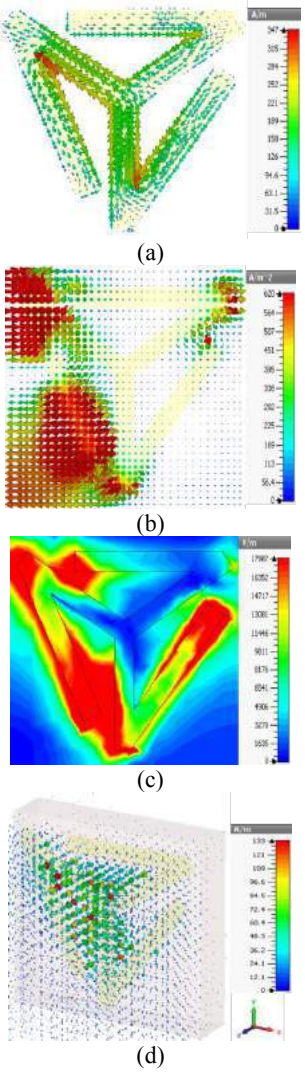

Figure 4: (a) Surface current distribution, (b) Current density, (c) Electric field, and (d) Magnetic field of the proposed meta surface unit cell at 7.40 GHz.

Figure 5(a) represents the simulated and measured transmittance of the triangular shape meta-atom cluster, where the results are well complied together. The simulated result shows transmittance resonance in 7.41 GHz and 13.60 GHz and the magnitude of those resonance points are respectively, -23.17 dB, and -15.22 dB. In addition, the measured results resonance points are around 7.40 GHz (C-band) and 13.61 GHz (Ku-band), whereas the estimation of the magnitudes is respectively, 14.0 dB and 23.5 dB. Figure 5(b) exhibits the reactance impedance of the designed meat-surface structure, where the reactance impedance at 8.61 GHz is -26.69+10.44j.

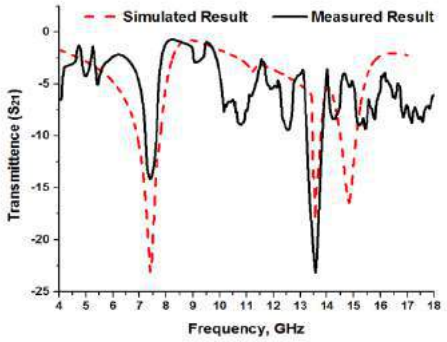

(a)

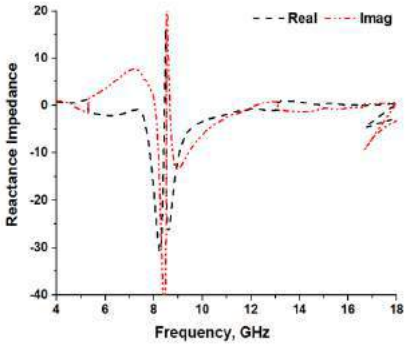

(b)

Figure 5: (a) Simulated and measured transmittance of the meta-atom cluster, (b) Magnitude of the reactance impedance of the proposed structure.

In figure 6(a) the real value of negative permittivity range from 4.68 to 7.68 GHz, 8.58 to 12.15 GHz, and 16.66 to 18.0 GHz respectively bandwidth covers 3.0 GHz, 3.57 GHz, and 1.34 GHz. In addition, the negative real permeability from 8.42 to 16.76 GHz, and 16.66 to 18.0 GHz, where the bandwidth covers respectively, 8.34 GHz and 1.34 GHz in figure 6(b). Further, figure 6(c) shows the negative refractive index absolute value from 4.06 to 7.15 GHz (bandwidth of 3.09 GHz), from 8.08 to 11.63 GHz (bandwidth of 3.55 GHz), and 16.66 to 18.0 GHz (bandwidth of 1.34 GHz). However, from 16.66 to 18.0 GHz the effective medium parameters (permittivity, permeability and refractive index) shows negative regime. So, according to the left handed characterise the proposed meta-surface based on meta-atom cluster can be characterized as left handed meta-surface for any frequency points in the frequency range from 16.66 to 18.0 GHz.

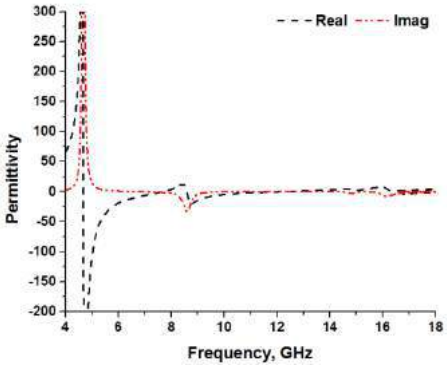

(a)

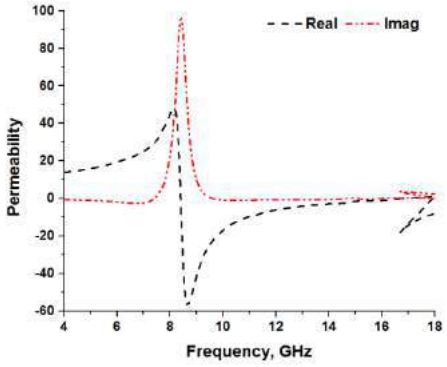

(b)

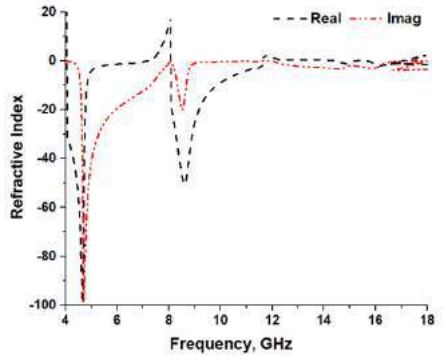

(c)

Figure 6. Real amplitude of the proposed meta-surface, (a) Permittivity, (b) Permeability, (c) Refractive index.

5. Conclusions

The triangular-shape meta-surface by meta-atom cluster exhibits left handed characteristics at microwave frequency is reported in this paper. The results display the transmittance in 7.40 GHz and the size of the single unit cell is 7×7 mm^2. Moreover, the complete circuit model allows to derive an analytical expression of the total inductance and capacitance for the resonance point of the proposed design. It is clearly shown that the proposed meta-surface is insensitive to both TE and TM polarizations as

well as TEM mode throughout the whole of the operating frequency band. This characteristic of the designed meta-atom cluster is very significant since the proposed model has many advantages compared to those in the literature. Moreover, the electric field and surface current distributions are introduced and analysed to better understand of the mechanism. Finally, due to the compactness the designed left handed meta-surface has been potential for the performance enhanced of antenna performance, filter, EM-cloaking, long distance radio communication applications.

Acknowledgements

This work was supported by the Research Universiti Grant, Geran Universiti Penyelidikan (GUP), code: 2016-028.

References

[1] R. W. Ziolkowski, "Design, fabrication, and testing of double negative metamaterials", *IEEE Transactions on Antennas and Propagation*, 51:1516–1529, 2003.

[2] Y. C. Chun, C. Y. Ping, W. Qiong, Z. S. Chuang, "Negative refraction of a symmetrical π-shaped metamaterial", *Chinese Physics Letter*, 25:482-484, 2008.

[3] A. Sarkhel, D. Mitra, S. Paul, S. R. B. Chaudhury, "A compact meta atom for dual band negative permittivity metamaterial", *Microwave and Optical Technology Letter*, 57: 1152-1156, 2015.

[4] M. M. Hasan, M. R. I. Faruque, S. S. Islam, M. T. Islam, "A new compact double-negative miniaturized metamaterial for wideband operation", *Materials*, 9(10):830, 2016.

[5] M. I. Hossain, M. R. I. Faruque, M. T. Islam, A. Rahman, "A metamaterial embedded wideband antenna for the microwave C-band", *Materials and Technology*, 51:25–28, 2017.

[6] M. M. Hasan, M. R. I. Faruque, M. T. Islam, "Left-Handed Metamaterial using Z-Shaped SRR for Multiband Application by Azimuthal Angular Rotations", *Materials Research Express* 4:4, 2017.

[7] Y. K. Inamdar, Y. P. Kosta, S. Patnaik, "Criss-cross metamaterial based radiating structures for C-band applications", *Progress In Electromagnetics Research Symposium*, China, 151-154, 2014.

[8] N. Naeem, A. Ismail, H. Alhawari, A. Reda, M. A. Mahdi, "Terahertz dielectric sensor based on novel hexagon meta-atom cluster", *Applied Computational Electromagnetics Society Journal*, 30:996-1002, 2015.

[9] S. S. Islam, M. M. Hasan, M. R. I. Faruque, M. T. Islam, "Two components NRI metamaterial for dual band applications", *Microwave and Optical Technology Letters*, 59:1092–1096, 2017.

[10] M. M. Hasan, M. R. I. Faruque, M. T. Islam, "A single layer negative index meta atom at microwave frequencies", *Microwave and Optical Technology Letters*, 59:1450–1454, 2017.

[11] M. M. Hasan, M. R. I. Faruque, M. T. Islam, "A Tri-Band Microwave Perfect Metamaterial Absorber", *Microwave and Optical Technology Letters*, 2017, Doi: 10.1002/mop.30726.

[12] Q. Wu, C. P. Scarborough, D. H. Werner, E. Lier, X. Wang, "Design synthesis of metasurfaces for broadband hybrid-mode horn antennas with enhanced radiation pattern and polarization characteristics", *IEEE Transactions on Antennas and Propagation*, 60:3594-3604, 2012.

[13] M. I. Hossain; M. R. I. Faruque, M. T. Islam, M. H. Ullah, "A new wide-band double-negative metamaterial for C- and S-, B-band applications", *Materials*, 8:57-71, 2015.

[14] O. Luukkonen, S. I. Maslovski, S. A. Tretyakov, "A stepwise nicolson–ross–weir-based material parameter extraction method", *IEEE Antennas and Wireless Propagation Letters*, 10:1295-1298, 2011.

[15] M. M. Hasan, M. R. I. Faruque, M. T. Islam, "A mirror shape chiral meta atom for C-band communication", *IEEE Access*, Doi: 10.1109/ACCESS.2017.2677463.

Phase Gradient Silicon Nitride Nanostructures at Visible Wavelength

Jungwoo Park[1] **and Ki-Hun Jeong**[1*]
[1]Department of Bio and Brain Engineering, KAIST, Republic of Korea
[*]corresponding author: kjeong@kaist.ac.kr

Abstract-This work reports a silicon nitride metasurface that can control the refraction angle of transmitted light at visible wavelength for high transmission efficiency. We numerically simulated the refracted wavefront transmitted through metasurface by tuning the length and the width of rectangular nanoantennas and aligning different-sized nanoantennas in a sub-array. The refraction angle can be adjusted by a unit cell size and number of element antennas in a sub-array.

Metasurface, which is a two-dimensional structure composed of subwavelength-sized antennas, can control the amplitude, phase, and polarization of light. For a phase gradient metasurface which manipulates the wavefront of the transmitted light, it is possible to refract light in an anomalous direction by varying the shape or size of the antenna. However, metal metasurfaces are inappropriate for practical uses in visible light, due to Ohmic losses. Dielectric metasurfaces with relatively high refractive indices have been studied, based on silicon[1, 2] and titanium dioxide[3], but their absorption loss at visible wavelength is not negligible. We use silicon nitride, which fully covers 0 to 360 degree phase delay as well as exhibiting high transmittance at visible wavelength.

In this work, we report silicon nitride metasurface composed of rectangular nanoantennas on a quartz wafer (**Fig. 1**). To cover entire 0 to 360 degrees of phase delay at a wavelength of 633 nm, the height and unit cell size should be comparable with the wavelength[4]. Six antennas of different sizes are made up of sub-array of metasurface, and each antenna shows 60 degrees phase increments. The wavefront of light transmitted through this sub-array is refracted in an anomalous direction.

To optimize silicon nitride antennas with consistent phase increments. The width and length of a rectangular nanoantenna with a fixed height of 633 nm and a unit cell size of 500 nm are varied by a finite difference time domain (FDTD) method (**Fig. 2**). Silicon nitride antenna shows an electromagnetic resonance with an abrupt phase change showing zero phase (green) as shown in Figure 2 (b). The transmittance at a width of 380 nm (black line) of Figure 2 shows a consistent values even if the length is varied, and the lowest value shows a relatively high transmittance of 0.72. In addition, the phase at the width of 380 nm includes a phase shifts of 0 to 360 degrees, which is suitable for a phase gradient sub-array.

We choose four, six, and eight antenna elements (phase increment of 90, 60, and 45 degrees) in a sub-array Si_3N_4 metasurface of 380 nm width. The phase of plane wave propagating though the metasurface is numerically calculated **(Fig. 3**). For a sub-array with a unit cell size of 450 nm in Figure 3, the refraction angles are 17.6, 11.9, and 8.9 degrees, respectively. In addition, by changing the unit cell size and number of elements in a sub-array, the refraction angle can be manipulated through the metasurface. This results show possibilities of manipulating shape of an optical wavefront using silicon nitride metasurface.

Acknowledgements This work was supported by the grant funded by the Korea government (if any, including all funding information, should be gathered into a brief statement at the end (No.2016013061, HI16C1111, 2011-0031848).

REFERENCES

1. Zhou, Z. et al. “Efficient Silicon Metasurfaces for Visible Light” ACS Photonics 4.3 (2015): 544-551.
2. Shalaev, M. I. et al. “High-Efficiency All-Dielectric Metasurfaces for Ultracompact Beam Manipulation in Transmission Mode” Nano Letters 15.9 (2015): 6261-6266.
3. Zou, L. et al. “Dielectric Resonator Nanoantennas at Visible Frequencies” Optics Express 21.1 (2013): 1344-1352.
4. Zhan. A. et al. “Low-Contrast Dielectric Metasurface Optics” ACS Photonics 3.2 (2016): 209-214.

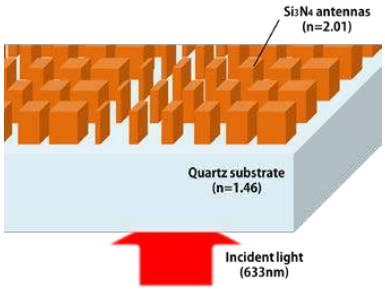

Figure 1. Schematic illustration of silicon nitride metasurface at visible wavelength.

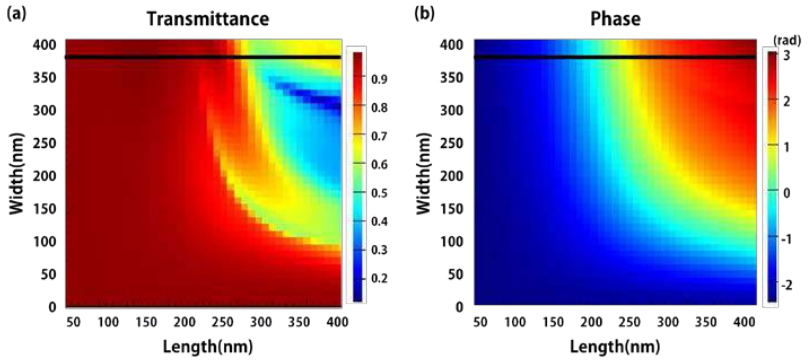

Figure 2. Calculated (a) transmittance and (b) phase as a function of width and length.

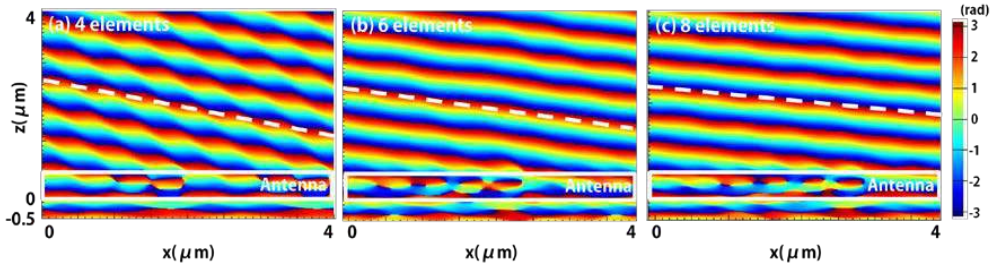

Figure 3. Calculated phase distribution passing through Si_3N_4 metasurface. Each figure has different refraction angles with different number of elements: (a) 4, (b) 6, and (c) 8, respectively.

Optical antennas

Widely Tunable Semiconductor Antennas for Reconfigurable Metasurfaces

J. A. Schuller
Electrical and Computer Engineering Department, UC Santa Barbara, CA, USA
*corresponding author: jonschuller@ucsb.edu

Abstract-The ability to engineer the optical phase at subwavelength dimensions has led to metasurfaces that provide unprecedented control of electromagnetic waves. To reach their ultimate potential, metasurfaces must incorporate reconfigurable functions. The central challenge is achieving large tunability in subwavelength elements. Here, we describe two different approaches for achieving order-unity refractive index shifts: free-carrier refraction and thermo-optic tuning

We experimentally demonstrate wide tuning of single-particle infrared Mie resonances through doping[1], and demonstrate simulations of electrically reconfigurable III-V heterojunction metasurfaces based on these effects[2,3]. We conclude with recent experimental demonstrations of dyamic, ultrawide tuning of Mie resonators based on two distinct thermo-optic effects: 1) modifying the electron mass and carrier density in InSb and 2) exploiting the anomalous temperature-dependent bandgap of PbTe.

Acknowledgements, This work was supported by the Air Force Office of Scientific Research (FA9550-16-1-0393) and by the UC Office of the President Multicampus Research Programs and Initiatives (MR-15-328528).

REFERENCES

1. Lewi, T., Iyer, P. P., Butakov, N.A., Mikhailovsky, A.A., and Schuller, J.A. "Widely Tunable Infrared Antennas Using Free Carrier Refraction," *Nano Lett.*, Vol. 15, 8188, 2015.
2. Iyer, P.P, Butakov, N.A., and Schuller,J.A. "Reconfigurable Semiconductor Phased Array Metasurfaces," *ACS Photon.*, Vol. 2, 1077, 2015.
3. Iyer, P.P., Pendharkar, M. and Schuller, J.A. "Electrically Reconfigurable Metasurfaces Using Heterojunction Resonators," *Adv. Opt. Mater.*, Vol. 4**,** 1582, 2016.

Raman scattering of MoS_2 enhanced by Ag nanoparticles

F. K. Meng[1], and F. Lin[1*]

[1] *School of Physics, Peking University, Beijing* 100871*, China*

[*]corresponding author: linf@pku.edu.cn

Abstract- Raman scattering, a fingerprint method to nondestructively obtain information about the lattice vibration of a crystal, has been widely used to characterize a monolayer of MoS_2. However, the intensity of Raman scattering from the MoS_2 monolayer is usually very weak for the atomic thickness of this materials. Based on localized plasmon resonances of silver nanoparticles (Ag NPs) with the size of several tenths of nanometer, we obtained a dramatic enhancement for Raman scattering of MoS_2 as the Ag NPs were dispersed on the monolayer of MoS_2. We also observed that the intensity of Raman scattering is deeply dependent on the polarization of incident light, which is due to the property of localized plasmon resonances of Ag NPs.

As shown in Fig. 1(a), the sample was prepared by dispersing Ag NPs on the monolayer MoS_2. We focused the laser on the place indicated by the arrow and then got the Raman spectra of the monolayer MoS_2 enhanced by the Ag NPs showed in the Fig. 1 (b) by changing the directions of the linearly polarized light marked above the curves in the Fig.1 (b). The Raman spectra of the MoS_2 without Ag NPs was also obtained as shown by the green curves in the Fig.1 (b).

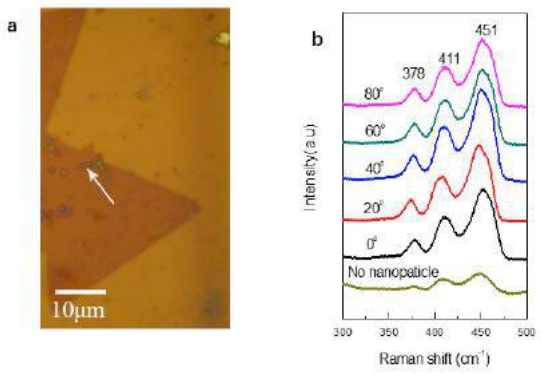

Fig. 1. (a) Optical image of the monolayer MoS_2 with Ag NPs. The light illumination point is indicated by arrows. (b) Raman spectra of the monolayer MoS_2 excited by 633nm laser without Ag nanoparticles(green curves) and with Ag nanoparticles（other curves）. The directions of the linearly polarized light are marked above the curves.

Obviously, a dramatic enhancement for Raman scattering of MoS_2 with the Ag NPs was observed with the enhancement factor about 4~5. Furthermore, the enhancement factor increases when the polarization was varied from 0 to 40°. However, it begins to decrease from 40° to 80°. This phenomenon can be attributed to that the coupling strength of localized plasmon resonances between interparticles which is dependent on the polarization of incident light.

Analyzing a 3D Far Field of Plasmonic Ruler Based on Double Metal Blocks

Eunso Shin[1], Young Jin Lee[1], Seokhyeon Hong[1], Kihwan Moon[1] and Soon-Hong Kwon[1]*
[1]Dept. of Physics, Chung-Ang University, Republic of Korea
*corresponding author: soonhong.kwon@gmail.com

Abstract- In a manufacturing process of a nano-size product, sensing a structure is challenging theme. For sensing the nano-size structure, we propose analyzing the 3D far field of plasmonic ruler which composed of two silver nanoblocks separated by 10 nm thickness of an air gap. When upper nanoblock slightly shifted to x or y-axis, it causes the considerable change of far field of the specific wavelength, which occurs plasmonic coupling, in comparison with original one. This change of far field cans simply detecting structure.

Between the two silver nanoblocks, there is plasmonic coupling at a particular resonant wavelength when the incident light propagated to the structure. We can measure a slight movement of an interval between two metal blocks via observing cavity mode of the resonant wavelength [1]. In addition, since the length of block width and height are different from each other, there is two kinds of resonant wavelength; caused by incident light in the direction of x axis and y axis. When the upper block moved towards x or y axis, it leads to distinct results of resonant wavelength and far field.

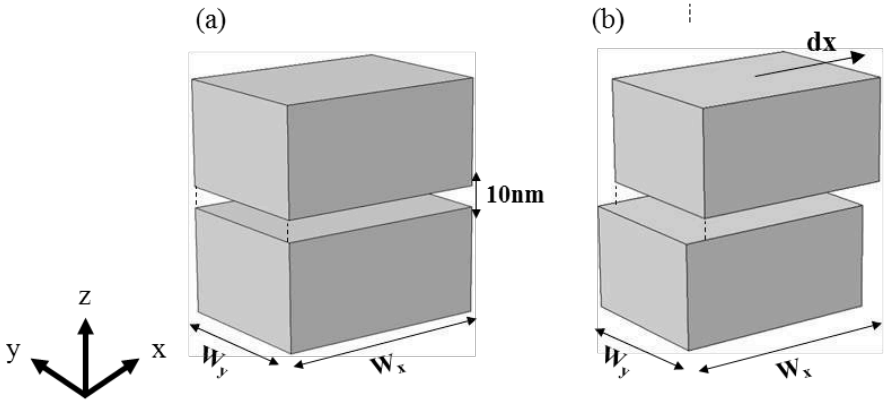

Figure 1: Schematic diagram of proposed a plasmonic ruler composed of two silver nano-blocks. Between the blocks there is an air gap with 10 nm thickness. (a) Original Structure, (b) Shifted Structure.

As shown in figure 1 (a), we propose plasmonic ruler that comprises of two parts, upper silver nanoblock and the lower one. Two blocks, which have the same scale of three dimensions W_x=200 nm, W_y=150 nm and height=100 nm, are separated by 10 nm air gap. When an incident light of X or Y axis heads to the proposed

structure, cavity mode of the resonant wavelength of plasmonic coupling is confined between the silver blocks.

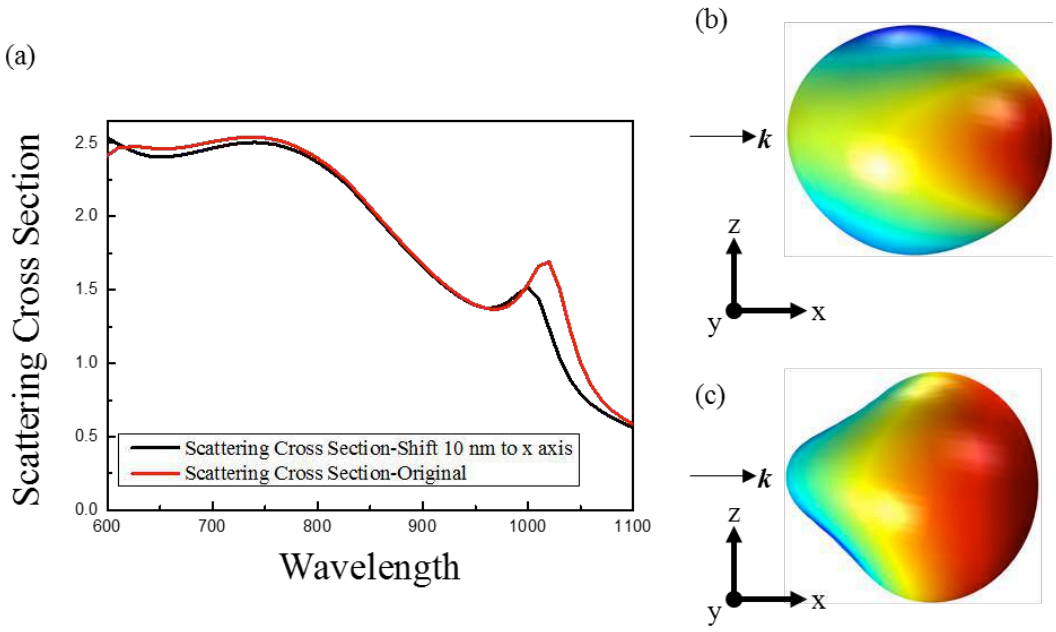

Figure 2: (a) Graph of Scattering Cross Section. The red line presents the original structure of scattering cross section and the black one presents the shifted structure. The 3D far field of resonant wavelength of 1020 nm is confined inside the air gap (b) in the original structure and (c) in the 10 nm shifted structure.

We investigated the 3D far field of the structure with a three-dimensional finite elements method (FEM). For an incident light of X axis, the red line of scattering cross section graph in Figure 2 (a) is shown that plasmonic cavity mode with the resonant wavelength of 1020 nm is highly confined through the gap of air. On resonant wavelength of 1020 nm, the far field is illustrated in Figure 2 (b). As upper block shifts 10 nm to the X axis, resonant wavelength slightly decreases from 1020 nm to 1000 nm, according to scattering cross section graph of Figure 2 (a). In addition, Figure 2 (c) shows the 3D far field of 10 nm shifted structure with the resonant wavelength of 1020 nm, which indicates significant change compared with the former 3D far field. Therefore, analyzing 3D far field allows understanding the structure since slightly shifted structure results in considerable difference of far field

REFERENCES

1. Kwon,S.-H., "Plasmonic Ruler with Angstrom Distance Resolution Based on Double Metal Blocks," *IEEE Photonics Technol. Lett.*, Vol. 25, No. 16, 1619–1622, 2013.

Light scattering by magnetic resonance of crescent-shaped split-ring resonator

Toshihiro Okamoto*, Naoki Tamura and Masanobu Haraguchi
Tokushima University, Japan
*toshi-okamoto@tokushima-u.ac.jp

Abstract- We investigated the optical scattering property of crescent-shaped split-ring resonator (SRR) fabricated by the nanosphere lithography method. The magnetic resonance of single gap SRR was able to be excited in an optical magnetic field by using the total reflection of the prism. It was clarified to contain a polarized component different from the incident light as a result of observing the scattered light from SRR.

The split-ring resonator (SRR) cause magnetic resonance near the LC resonance frequency and change the permeability of the SRR metamaterial. The electric and magnetic fields are expected to be enhanced when magnetic resonance occurs in SRRs. Then, SRR not only is used as a unit cell of the metamaterial but also using it as an antenna of the unit is also interesting. We investigated the optical scattering property of single-gap SRR.

We fabricated single-gap crescent-shaped gold SRR of the diameter of about 100 nm on the glass substrate using the nanosphere lithography (NSL) technique [1,2]. The light of the TE polarization was entered by the configuration shown in Fig.1 (a), and evanescent wave that occurred along with total reflection was entered into SRR. The scattered light spectra of single isolated SRR are shown in Fig.1 (b). The spectral peak of the *Ey* polarization of the same component as the incident light was a wavelength of around 700 nm. This peak means the electric dipole in the same direction as the incident light was excited by the localized surface plasmon resonance of SRR. On the other hand, the scattered light of *Ex* polarized component different from the incident light appeared in the wavelength around 900 and 600 nm. This phenomenon means the loop electric current flowed in SRR by the magnetic resonance of SRR excited in an incident magnetic field.

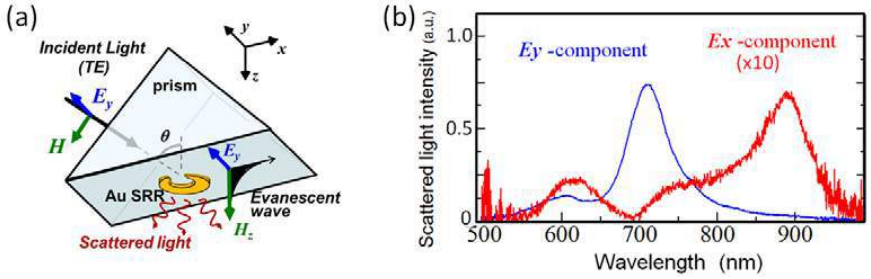

Fig.1 Experimental setup(a) and scattered light spectra of a single SRR(b)

REFERENCES

1. T. Okamoto, et al., "Visible near-infrared light scattering of single silver split-ring structure made by nanosphere lithography," *Opt. Exp.*, Vol. 19, No. 8, 7068–7076, 2011.
2. K. Tanikawa, T. Okamoto et al., "Fabrication of peelable thin films containing crescent-shaped split-ring resonators for three-dimensional optical metamaterials," *Opt. Mat. Exp.*, Vol. 7, No. 1, 1–7, 2017.

Design of New Plasma Antenna for Wi-Fi Wireless Coverage

M. Hilmi[1], M. T. Ali[1], I.Pasya[1], M. T. Islam[2], S.Subahir[1]

[1]Antenna Research Centre (ARC), Faculty of Electrical Engineering, Universiti Teknologi MARA, Shah Alam, Selangor 40450, Malaysia.
[2]Dept. of Electrical, Electronic and Systems Engineering, Faculty of Engineering and Built Environment, Universiti Kebangsaan Malaysia, 43600 Bangi, Malaysia.
*corresponding author, E-mail: musfirah.hilmi@gmail.com

Abstract

This paper presents the design of plasma antenna array for Wi-Fi application, operating at 2.4 GHz. In this experiment, four pieces of a commercially available fluorescent tube function as a plasma antenna, with same length and diameter was used. The proposed antenna is simulated using CST Microwave Studio to study its performance. The measured return loss, radiation pattern and signal propagation of this proposed antenna is also presented. The experimental and analysis of this study are discussed.

1. Introduction

The Plasma is the fourth state of matter after solid, liquid and gases. Therefore, plasma antenna is a type of antenna in which the material conducting element of a metal is replaced by plasma, to either transmit or receive a radio signal. When a plasma tube is energized with sufficient electrical power, the gas inside the tube will be ionized into plasma state, where it becomes conductive. There are many plasma antenna that have been reported, which use plasma elements instead of metal conductors [1–3]. Plasma antennas are also useful in application for stealth [4], radar [5] and re-configurability [6-8]. Reconfigurable antennas have very attractive features such as the capability to reconfigure themselves alone, to adapt to change or with the system to perform entirely different functions. The reconfigurable antenna is also capable of providing a single antenna for the use with multiple systems [9].
Plasma is ionized gas. The ionization degree can vary from 100% which are fully ionized gasses, to very low values or partially ionized. Plasma frequency is a natural frequency of the plasma and is a measure of the amount of ionization in plasma. Equation (1) shows the plasma frequency equation.

$$\omega_p = \sqrt{\frac{e^2 n_e}{\varepsilon_0 m_e}} \tag{1}$$

Where ω_p the plasma frequency [rad/s], e is the charge on electron [C], m_e is the electron mass [kg], n is the electron density [m^{-1}] and ε_0 is the free space permittivity [F/m]. The collision frequency equation is given in Equation (2).

$$v_c = n_e K(T_e) \tag{2}$$

Where n_e is the electron density [$1/m^3$], K is Boltzman's constant and T_e is electron temperature of the plasma elements.
In this paper, an array plasma antenna using a fluorescent tube, operating at 2.4 GHz is designed. This paper is divided into five sections as follows: Section 1 discus the introduction of Plasma Antenna and theory. Section 2 presents the antenna pattern and the structure of array antenna, section 3 presents the analysis of the plasma antenna array, section 4 discusses the simulation and measurement results and Section 5 provides the conclusion of this paper.

2. Antenna Design and Structure

At first, a single monopole plasma antenna with dimension of 586mm length (L) and 24.2mm diameter (D) was constructed on commercially available fluorescent tube. A coupling sleeve was attached to one end of the tube which is made from a copper wire, to energize the plasma ion which then converts it to plasma state. Thus, the fluorescent tube behave as an antenna. Table 1 and Fig. 1 present the dimensions of the monopole plasma antenna.

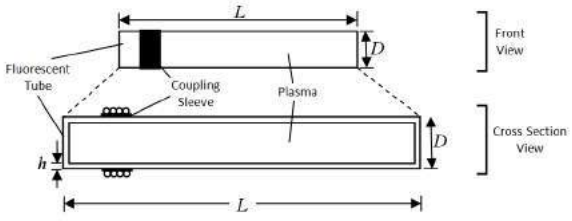

Figure 1: The Geometry of Monopole Plasma Antenna.

Table 1: Dimensions of Monopole Plasma Antenna.

parameter	symbol	dimension
Fluorescent tube length	L	586 mm
Fluorescent tube diameter	D	24.2 mm
Tube thickness	h	1 mm

Then, another 3 pieces of fluorescent tube with the same dimension as the original tube was added parallel to each other with separation distance of 100 mm. A coupling sleeve was attached to one end of each of the tube. The coupling sleeve of all the four tubes were combined as an input signal with a 4-port power divider. The antenna array was constructed to increase the overall gain. Fig. 2 and Table 2 present the dimensions of the plasma antenna array.

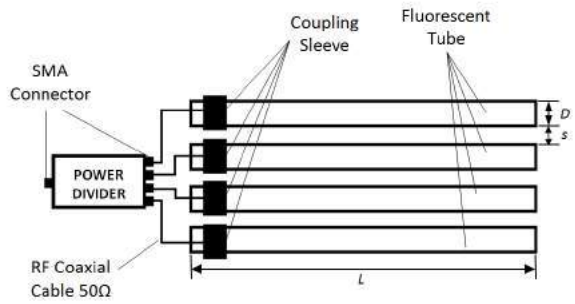

Figure 2: The Geometry of Plasma Antenna Array.

Table 2: Dimensions of Plasma Antenna Array.

parameter	symbol	dimension
fluorescent tube length	L	586 mm
fluorescent tube diameter	D	24.2 mm
Spacing between tube	s	100 mm

3. Analysis of Plasma Antenna Array

In this section, the analysis of parametric study is presented to investigate the effects of design of the plasma antenna. The simulation is performed by using CST Microwave Studio. A parametric study was accomplished to achieve the optimum performance of the antenna.

Fig. 3 shows the simulated parametric studies on the reflection coefficient S11, when the diameter of the copper wire was varied from 0.35 mm until 0.55 mm. Based on the graph, it is noticed that when the diameter of the coil is increased, the operating frequency is shifted to higher frequency.

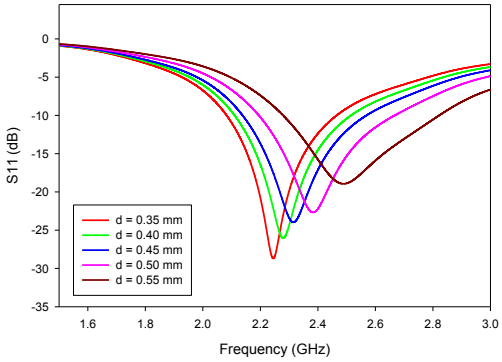

Figure 3: Simulation results as a function of different size of diameter coil.

The spacing of each lamps is determined to avoid mutual coupling effect between antennas. The optimization of the spacing was made to obtain an optimum performance of the plasma antenna array. Fig. 4 shows the simulated result of the return loss when the spacing between the lamps was varied from 90mm to 130mm with increment of 10mm. It can be clearly seen that when the spacing between the lamps was increased, the operating frequency shifted to lower frequency. From the analysis, the optimum result for the antenna to operate at frequency of 2.4 GHz was when s = 100 mm.

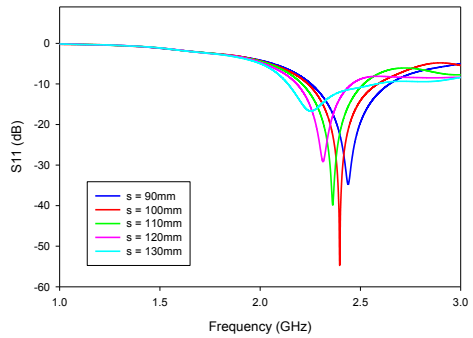

Figure 4: Simulation results as a function of different spacing between lamps.

4. Result and Discussion

The prototype of the 1x4 plasma antenna array has been constructed and measured to validate the simulated result. Fig. 5 shows the photograph of the antenna prototype when all the lamps were switch on.

Figure 5: Photograph of the Fabricated Antenna.

4.1. Return Loss

Fig. 6 shows the comparison between simulated and measured results of S11 when the antenna was operating at 2.4GHz. The blue line represents the simulated result while the red dotted line represents the measured results. Based from the graph, both antennas resonate at 2.4 GHz.

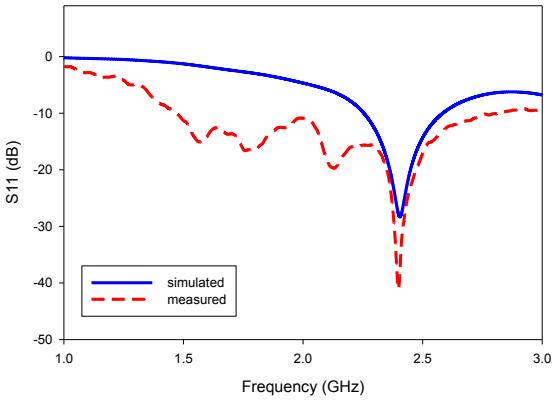

Figure 6: Comparison of simulated and measured S-parameter result for plasma antenna array.

Fig. 7 shows the comparison of S_{11} between monopole plasma antenna and plasma array antenna. It can be seen that both antennas can be operated at 2.4 GHz. The measuremed result agree well with the simulation result.

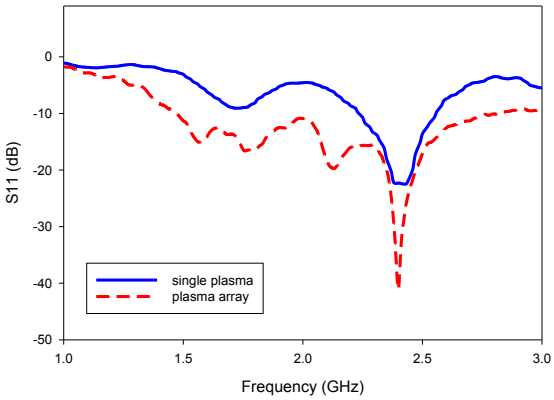

Figure 7: Comparison of measured S-parameter result between single plasma antenna and plasma antenna array.

4.2. Radiation Pattern

Fig. 8 presents the simulated and measured radiation pattern in polar plot at frequency of 2.4GHz. The results shows that there is a slight difference in the radiation pattern between the simulation and the measurement result. This may be attributed to measurement error, since the radiation pattern were measured in a partially anechoic chamber that may lead to inaccuracy.

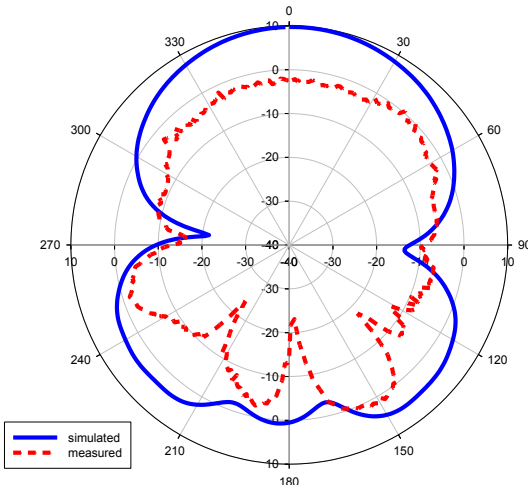

Figure 8: Comparison of simulated and measured radiation pattern for plasma antenna array.

4.3. Antenna Propagation

Outdoor propagation measurement was done in a free space to measure the signal strength of the antenna. The plasma antenna array was used as the receiving antenna. The transmitted antenna and received antenna were set up in point-to-point connections. This experiment was done by

varying the length between transmitted and received antenna and measuring the received power. The signal was measured from 1 meter up to 16 meters. Table 3 represents the results of the propagation measurement. The results show that as the distance between transmitted and received antenna increase, the loss power at the receiving antenna will increase.

Table 3: Result of Propagation Measurement.

Distance between Transmitter and Receiver	Received Power
1 meter	-41.72 dBm
2 meters	-43.44 dBm
3 meters	-44.95 dBm
4 meters	-46.42 dBm
5 meters	-46.53 dBm
6 meters	-47.96 dBm
7 meters	-48.51 dBm
8 meters	-50.09 dBm
9 meters	-51.32 dBm
10 meters	-55.55 dBm
11 meters	-55.23 dBm
12 meters	-55.33 dBm
13 meters	-56.40 dBm
14 meters	-57.61 dBm
15 meters	-58.31 dBm
16 meters	-62.54 dBm

4.4. Antenna Gain

Table 4 shows the difference of antenna gain between a monopole plasma antenna and plasma antenna array. Both antennas were operated at frequency of 2.4 GHz. Antenna gain for plasma antenna array was higher compared to monopole plasma antenna. This proves that by designing an antenna array will increase the overall gain.

Table 4: Plasma Antenna Gain.

plasma antenna	antenna frequency (GHz)	Antenna gain (dB)
monopole	2.4	1.956
array	2.4	9.685

5. Conclusions

In this paper, the design of 1x4 plasma antenna array using fluorescent tube was presented and discussed. Good agreement has been achieved between simulation and measurement results. Future works will concentrate on the measurements of the gain of the plasma antenna array.

Acknowledgements

The authors would like to give appreciation towards Antenna Research Centre (ARC), Faculty of Electrical Engineering, Universiti Teknologi MARA (UiTM), for providing facilities to conduct the present research.

References

[1] Huan Quing Ye, Min Gao, Chang Jian Tang. Radiation theory of the plasma antenna. IEEE Transactions on Antennas and Propagation, 2011, vol. 59, no. 5, p. 1497–1502.

[2] Borg, G. G., Harris, J. H., Miljak, D. J. Application of plasma columns to radiofrequency antennas. Applied Physics Letter, 2014, vol. 74, no. 22, p. 3272–3274.

[3] W. L. Kang, M. Rader, I. Alexeff, "A conceptual study of stealth plasma antenna," Proceedings of the 1996 IEEE International Conference on Plasma Science, pp. 261, 1996.

[4] W. M. Manheimer, “Plasma reflectors for electron beam steering in radar systems,”IEEE Trans. Plasma Sci ., vol. 19, pp. 1228–1234, Dec.1991.

[5] M. Alshershby and J. Lin, “Reconfigurable Plasma Antenna Produced in Air by Laser-induced Filaments : Passive Radar Application,” in Proceedings of the International Conference on Optoelectronics and Microelectronics (ICOM '12), pp. 364–371, August 2012.

[6] H. Ja’afar, M.T. Ali, A.N. Dagang, H.M. Zali, N.A. Halili, "A Reconfigurable Monopole Antenna with Fluorescent Tubes by Using Plasma Windowing Concepts at 4.9GHz", Advanced Materials Research, Vol. 905, pp. 432-435, Apr. 2014

[7] H.Ja’afar, M.T.Ali, A.N.Dagang, H.M.Zali, N.A.Halili, , “A Reconfigurable Monopole Antenna with Fluorescent Tube using Windowing Concept for 4.9 GHz Application” IEEE Transaction on Plasma Science, Vol 43, No 3,March 2015.

[8] H.Ja’afar, M.T.Ali, A.N.Dagang, N.A.Halili, H.M.Zali.,”Reconfigurable Plasma Antenna Array by Using Fluorescent Tube for Wi-Fi Application,” Radio Engineering

[9] Bogaerts, A., Neyts, E., Gijbels, E. Gas discharge plasmas and their applications, Spectrochimica Acta Part B, 2002, vol. 57, no. 4, p. 609–658.

Performance Enhancement of Integrated Light Emitting Diode and Wi-Fi Antenna Using Stacked Microstrip

Hamizan Yon[1], Aziati H. Awang[1], M. T. Ali[1], S. Subahir[1], S.N. Kamarudddin[1], M.T. Islam[2]

[1]Antenna Research Group (ARG), Faculty of Electrical Engineering, Universiti Teknologi MARA, Malaysia.
[2]Department of Electrical, Electronic and Systems Engineering, Universiti Kebangsaan Malaysia, Malaysia.

hamizanyon@gmail.com, aaziatihusna@yahoo.com, mizi732002@yahoo.com, suhailas@salam.uitm.com.my, tariqul@ukm.edu.my

Abstract

The integrated rectangular stacked microstrip antenna with Light Emitting Diode (LED) for Wi-Fi application is presented in this paper. In this paper more LEDs were placed on the top layer to improve the lighting capability, while maintaining the feasibility of working as a Wi-Fi router. Wi-Fi antenna simulated to resonate at 2.45 GHz using Computer Simulation Technology (CST) with permittivity, $\varepsilon_r =$ 4.3 and thickness, h = 1.6mm on FR4 substrate. The LED placed on the top substrate behave as parasitic element to the antenna design. The radiating patch is placed on the second layer of substrate and aperture coupled feeding network was used in this design. The antennas are reasonable well matched at their corresponding frequency of operations. The simulation results have shown that the antenna works well with the integrated LED giving 4.21dB gain, -25.61dB return loss and 106MHz bandwidth while 3.33dB gain, -16.90dB return loss and 103MHz bandwidth design without LED placement. Antenna was measured using Vector network analyzer (VNA) and Anechoic chamber.

1. Intoduction

Development of integrated antenna in order to works with multi-function characteristic had been widely studied nowadays. Currently, plasma antenna is one of the antennas that have dual function development in wireless communication technology especially an indoor Wi-Fi communication as antenna and at the same time as illumination sources. However, plasma antenna technology has limitation due to expensive and difficulties to manufacture. Meanwhile plasma requires energy to be ionized and the gas is more complex and expensive [1]. The volume of mercury inside plasma also can harm the safety and not supporting green technology [3]. Developing antenna with same capabilities and low cost and at the same time support green technology is much more needed.

LED is known as the semiconductor device that can emits light. It has many advantages compare with other traditional light source, such as long life expectancy, high-efficiency light sources, low maintenance, low power consumption and generally very robust and environmentally friendly[3-5]. The structure of LED itself is in principle, can be integrated with other product to create a new multifunctional product. In the communication field the integration LED with antenna has a potential of dual functionality device, as transmission and reception medium for wireless network and simultaneously as light source [1-3]. However, the feasibility of this integrated design is still continuously investigated due to the copper conductor on the LED that can affect the performance of the antenna [1-3].

In this paper, the integration of antenna with LED is studied. The copper material on the bottom of the LED has resulted in resonant frequency shifted as the number of LED are increased has been reported by [1-3]. Therefore, this stacked configuration has been proposed to overcome the frequency shifted problem [4-5]. The simulation has been studied by [5] to design LED circuit connectivity. In this design, the antenna has been design to resonant at 2.45GHz for Wi-Fi application and the LED works as parasitic element to improve antenna performance and as illumination sources. The implementation of LED at the top layer of design, for enhancing the performance in term of gain and return loss and at the same time adding the LED structure on the antenna structure will maintain the resonant frequency.

2. Antenna Design

The antenna with LED as parasitic elements in series parallel connection are designed as shown in figure 1. The antennas are designed on FR4 substrate with permittivity of 4.3 and thickness 1.6mm. LEDs are soldered on the top substrate where the size of substrate fixed at 50mm x 50mm, while patch radiator located on the second substrate. Meanwhile, ground plane and feed line are located on the bottom substrate as shown in figure 2.

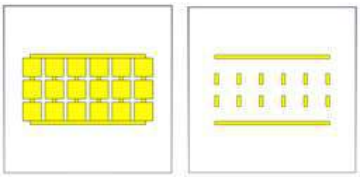

Figure 1: Antenna with LED as parasitic element designed

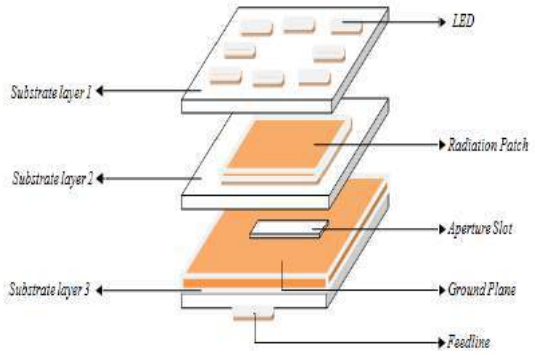

Figure 2: Antenna with LED parasitic element designed on the three substrate layers

The size of patch radiator is determined from numerical analysis using equation (1) to (4).

$$W = \frac{1}{2f_r\sqrt{\mu_o\varepsilon_o}}\sqrt{\frac{2}{\varepsilon_r+1}} \quad (1)$$

$$l = \frac{1}{2f_r\sqrt{\varepsilon_{reff}\sqrt{\mu_o\varepsilon_o}}} - 2\Delta L \quad (2)$$

$$\Delta L = 0.412(h)\frac{(\varepsilon_{reff}-0.3)\,(\frac{W}{h}+0.264)}{(\varepsilon_{reff}-0.258)(\frac{W}{h}-0.8)} \quad (3)$$

$$\varepsilon_{reff} = \frac{\varepsilon_r+1}{2} + \frac{\varepsilon_r-1}{2}\left[1+12\frac{h}{W}\right]^{-1/2} \quad (4)$$

Table 1: Antenna parameter.

Parameter	Value(mm)
Width of Substrated,W	50
Width of LED,W1	5
Width of patch,Wp	38
Width of feedline,Wf	4.23
Width of aperture slot,Ws	15
Length of substrated, L	50
Length of LED, L1	5
Length of patch, Lp	22.28
Length of feedline, Lf	30
Length of aperture slot, Ls	2

In this design, the advantages of allocating LEDs above the designed antenna in order to reduce the shifting frequency effect. The new antenna design focus on designing LED circuit without altering the resonant antenna frequency and at the same time improve the performance of the antenna due to parasitic effect. The LED used in this design is the SMD 5050 LED which is white LED [1] as shown in Figure 3. Meanwhile Figure 4 shown LED circuit diagram. 18 LEDs have been used in the designed antenna in order to get better parasitic effect. Optimization on the LED circuit has been studied using computer simulation software. The simulation process is performed using Computer Simulation Technology (CST) and all the design result is present as shown in table 2

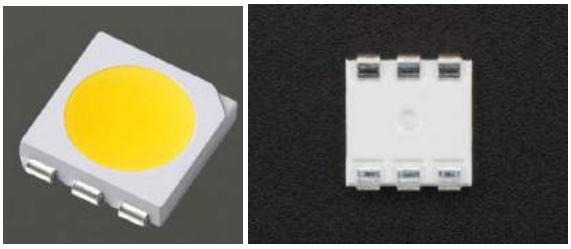

Figure 3: SMD 5050 LED

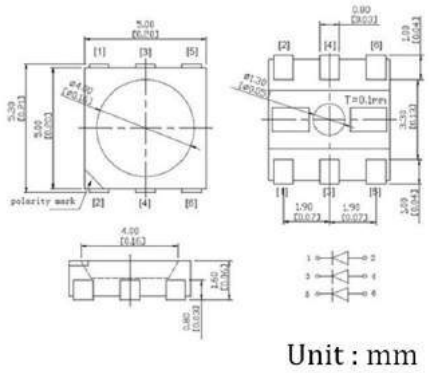

Figure 4: SMD 5050 Circuit diagram

Table 2: Simulation result.

Design Result	Antenna Design *With LED*	*Without LED*
Frequency (GHZ)	2.455	2.453
Return Loss(dB)	-25.61	-16.90
Gain(dB)	4.21	3.33
Bandwidth(MHz)	106.6	103.1
VSWR	1.020	1.054

3. Result and Discussion

3.1. Simulation Result Using Computer Simulation (CST)

The proposed antenna is simulated using CST simulation software and the simulation of the purpose antenna has been studied for antenna design with and without LED. Figure 5 shown antenna return loss result for both condition, with and without LED structure. The figure shown good in result where there are no shifting frequency when the LED is located on the top antenna structure. Furthermore, the return loss, S11 for antenna with LED is higher as compared with without LED. The technique that place LED on the top antenna structure as parasitic element, will improve the antenna performance without altering the antenna resonant frequency, therefore LED can work equally well on other antenna stack design. The radiation pattern of antenna is shown in figure 6 respectively.

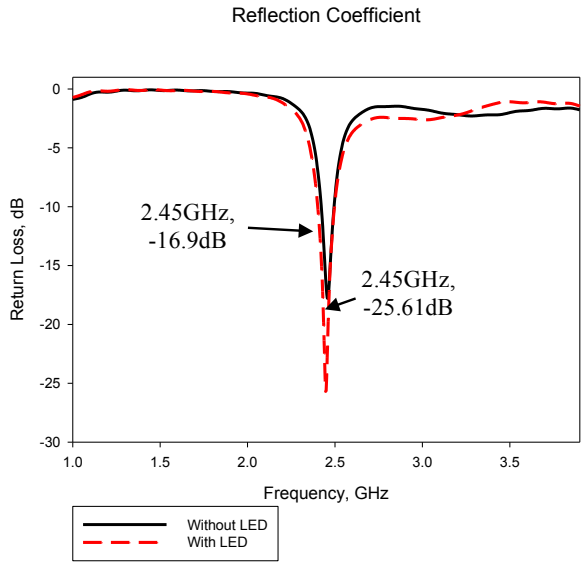

Figure 5: Simulated result return loss, S11 without LED and with LED

Meanwhile Figure 6 shown the antenna radiation pattern for simulation result. From the figure it shown that locating the LED have improve in the antenna gain. Although the figure shown radiation pattern with back loop, the front loop is more dominant compare with back loop. The antenna gain has been increase from 3.33dB without LED to 4.06dB in the design with LED structure.

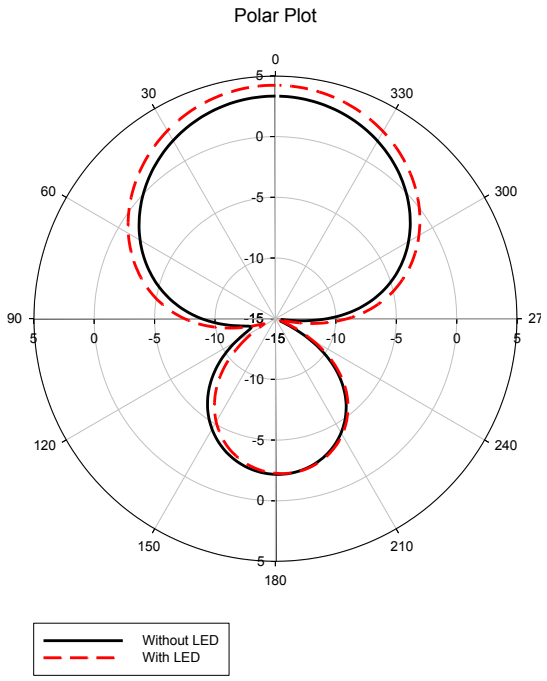

Figure 6: Simulated radiation pattern result with and without LED

3.2. Measurement Result Using Vector Network Analyzer and Anechoic Chamber

The optimized antenna design structure has been fabricated and measured in this section. The return loss of antenna design has been carried out using VNA Keysight module. The return loss of the integrated microstrip antenna with and without LED measurement results were shown in Figure 7. However in measurement result, the resonant frequency is shifted to the right from the simulation result about 2%. This situation is believe due to improper handling on fabrication process. However, the frequency response for both resonant was unchanging at 2.50GHz for antenna structure with and without LED, respectively. On the other hand, return loss value with LED structure is much better as compared to the antenna without LED structure. The corresponding operating bandwidths were 132 MHz without LED and 152MHz on with LED for both conditions as shown in Figure 7.

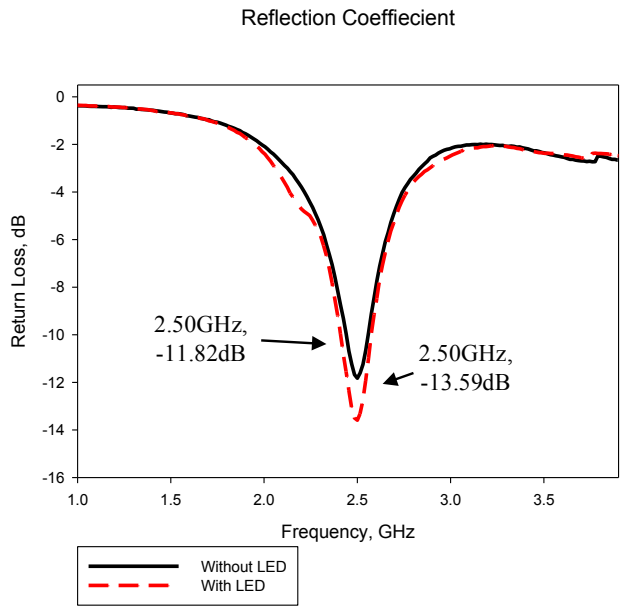

Figure 7: Antenna with and without LED measurement result.

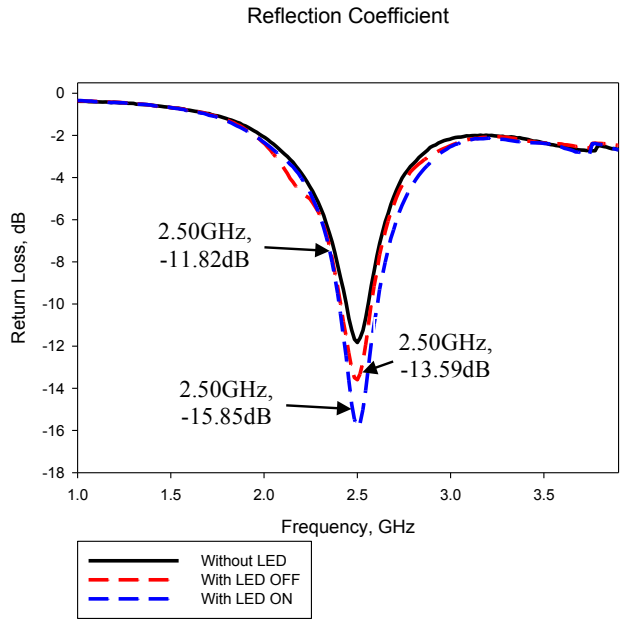

Figure 8: Measurement ON/OFF LED

Meanwhile in Figure 8 shows well matched result at the input of antenna where the return loss for 'OFF' LED is -13.59dB at 2.50GHz and return loss of -15.58dB and 2.50GHz respectively for 'ON' LED. The corresponding operating bandwidth was border to 195 MHz when LED are 'ON' state and 153 MHz at LED OFF state. The results shows that by turning 'ON' and 'OFF' LED the resonant frequency of the antenna is not changing, without and with LED. The bandwidth is slightly increase when LED is in 'ON' stage, it may be caused due to current distribution when turning ON the LEDs and also the fabrication process and soldering effect of LED terminal on the patch and also the return loss is better with LED ON condition.

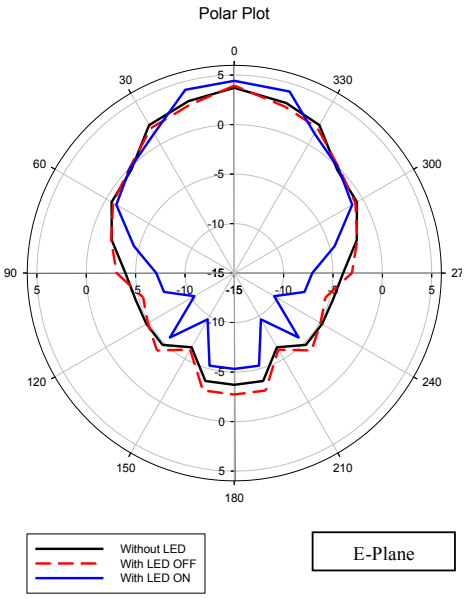

Figure 9: Measurement result with/without LED for E-Plane.

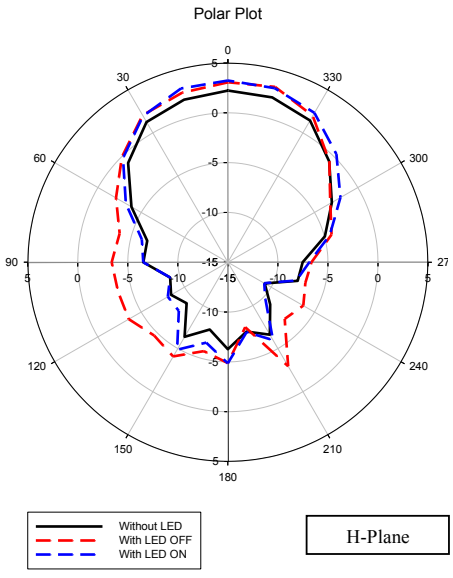

Figure 10: Measurement result with/without LED for H-Plane.

The measured gain curves are also given in figure 9 for E-plane and figure 10 for H-plane result. The maximum power was received by the antenna is match form the simulation result. From the measurement result of the purposed antenna, the maximum gain achieve when adding the LED on the top layer antenna structure was 3.92dB. Meanwhile, the gain for the measurement result on "ON" LED has been increased to 4.41dB. The measured gain was increase in ON LED is believed due to current distribution effect when the current flow into LED structure. Table 3 shown the antenna measurement result for purposed antenna design.

Table 3: Measurement result.

Design Description	Without LED	With LED OFF	With LED ON
Frequency (GHz)	2.50	2.50	2.50
Return Loss (dB)	-11.82	-13.59	-15.85
Gain (dB)	3.70	3.92	4.41
Bandwidth (MHz)	135	153	195

Meanwhile in figure 10 shows antenna radiation pattern in 3D view, (a) without LED (b) with LED OFF mode and (c) with LED ON mode. From the 3D figures we can see that the antenna has more radiates towards z-plane when turning ON the LED. This situation will lead to the improvement in gain value when making the measurement process. Meanwhile figure 11 shown the antenna that has been fabricated (a) with (b) without LED structure.

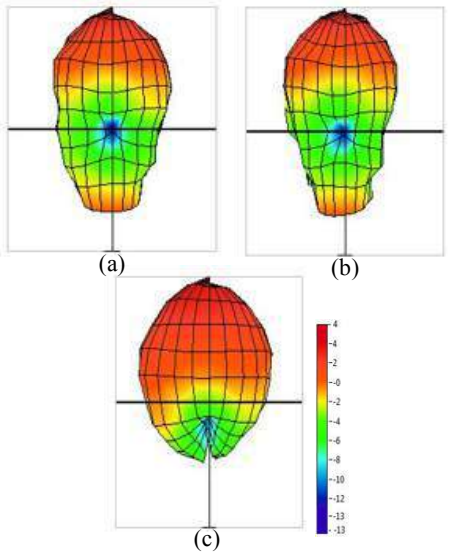

Figure 10: 3D view antenna design

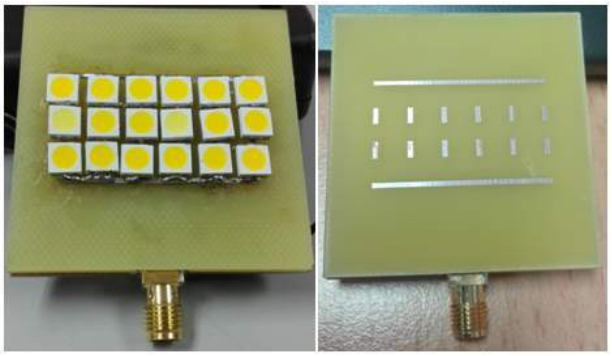

Figure 11: Antenna design With/Without LED

4. Conclusion

The rectangular stack microstrip patch antenna integrated with LED has been designed and investigated. From this research works, it can be concluded that, the designed antenna contributes to dual-function in a device. It can function as an antenna at Wi-Fi application and the same time it gives illumination to user with improved the overall performance of the antenna with and without LED. The measurement proves that LED can assume as a parasitic element to the antenna and well matched to the patch to improve the gain of the antenna. The use of the integrated LED in the design supports the green environment and will contribute better in terms of energy consumption. However, future works will be considered to improve this antenna to have better performance for the both conditions in terms of gain and radiation pattern.

Acknowledgment

The authors would like to thank Universiti Teknologi MARA for sponsoring the work. Express gratitude to the members of the Antenna Research Group (ARG), Faculty of Electrical Engineering, Universiti Teknologi MARA (under RAGS/1/2014/TK03/UITM//11) for supporting the research work.

References

[1] S.N. Kamarudin, M.T. Ali, S. Subahir, A.A. Azlan, S. Muhamud-Kayat, Muhammad Ramlee Kamarudin "Design and Investigation of H-Shaped Patch Antenna Integrated with Light Emitting Diodes", The International Electrical Engineering Congress (iEECON 2015), March 18-20, 2015.

[2] M.S Amari, S.Subahir,M.T.Ali, N.A Ramli, S.N. Kamaruddin " Rectangular Spiral Microstrip Patch Antenna Integrated With LED For Wifi Application", The 2nd IEEE International Symposium on Telecommunication Technologies (ISTT2014)

[3] S.Subahir,M.T.Ali, N.A Ramli, S.N. Kamaruddin, A.H.Awang, M.R. Kamaruddin, "Development of Rectangular Loop Microstrip Antenna Integrated With Light Emitting Diode (LED) for Wi-fi Application", The International Electrical Engineering Congress (iEECON 2015), March 18-20, 2015

[4] Hamizan Yon, Aziati H. Awang, M. T. Ali, S. Subahir, S.N. Kamaruddin , M.A.Aris, Norfishah Ab Wahab, "Integrated Stacked Microstrip Antenna with Light Emitting Diode (LED) for Wi-Fi Application", the international communication and computer engineering conference (ICOCOE 2016), June 25-27,2016

[5] Hamizan Yon, Aziati H. Awang, M. T. Ali, S. Subahir, S.N. Kamaruddin, "Parametric Study of Integrated Stacked Microstrip Antenna with Light Emitting Diode (LED) for Wi-Fi Application", 6th International Conference on. Computer and Communication Engineering 2016. (ICCCE 2016). 25-27 July 2016.

[6] Robert E. Collin, "Antenna and Radiowave Propagation",McGraw-Hill Book Company, New York 1985.

[7] Dawar Awan , Shahid Bashir, Nerijus Riauka, "Parametric Study of UWB Antenna Loaded with Stacked Parasitic Patch and Reflector", Loughborough Antennas & Propagation Conference, 11-12 November, 2013.

[8] M. F. Jamlos, T. A. Rahman, M. R. Kamarudin, M. T. Ali,M. N. Md Tan, P. Saad, "The Gain Effects of Air Gap Quadratic Aperture-coupled Microstrip Antenna Array", PIERS Proceedings, Cambridge, July 5-8, 2010.

[9] Y. F. Weng, S. W. Cheung, and T. I. Yuk, "Band-Notched Characteristic using Meandered Ground Stubs for Compact UWB Antennas," in IEEE Int. Conf. Ultra-Wideband, 2010, pp. 1-4

[10] S. Foo, "Superstrate Performance and Multibeam Gain Enhancement", in 3rd European Conf. Antennas Propag., 2009, pp. 3492-3496.

[11] H. Vettikalladi, O. Lafond, and M. Himdi, "High-Efficient and High-Gain Superstrate Antenna for 60-GHz Indoor Communication," in IEEE Antennas Wireless Propag. Lett., vol. 8, pp. 1422-1425, 2010.

[12] S. I. Latif, L. Shafai, and C. Shafai, "Gain and efficiency enhancement of compact and miniaturised microstrip antennas using multi-layered laminated conductors," in IET Microw. Antennas & Propag., vol.5, pp. 402-411, 2011.

Plasmon-enhanced photovoltaics, photocatalysis, and solar fuels

Energy Tunable Hot Carrier Generation via Surface Plasmon Polaritons for Photocatalysis

W. Ahn[1,*], D. C. Ratchford[2], P. E. Pehrsson[2], and B. S. Simpkins[2]

[1]National Research Council Postdoctoral Associate, U.S. Naval Research Laboratory, Washington, DC 20375, United States

[2]Chemistry Division, U.S. Naval Research Laboratory, Washington, DC 20375, United States

[*]corresponding (presenting) author: wonmi.ahn.ctr.ks@nrl.navy.mil

Abstract-Surface plasmon polaritons (SPPs) on a metal/TiO_2 heterostructure enable plasmon-mediated chemical reactions in a system whose resonance may be continuously tuned simply by altering excitation source and incident angle. We found a strong excitation angle dependence and linear power dependence in the photocurrent, confirming that the photoelectrochemical reactions are SPP-driven. Applicability of the SPP system for energy-tunable hot carrier generation and hot-carrier driven solution chemistry was further investigated using refractory plasmonic materials and SP band gap structures.

The ability of plasmonic nanostructures to create electron-hole pairs with energies much larger than those in thermal equilibrium - so-called "hot carriers" - offers new possibilities to utilize photon energy to drive useful chemical reactions. While the rate of photocatalytic reactions on nearby semiconductors can be optimized by varying the morphology of metal nanoparticles that support localized surface plasmon resonance (LSPR), the LSPR of individual nanoparticles is not tunable. The lack of tunability of the LSPR system hinders the efficient charge transfer from the photoexcited metal nanoparticles to the adsorbate, which is a carrier energy dependent process by aligning hot carrier potentials with redox potentials of adsorbed molecules. Recently, we have shown surface plasmon polaritons (SPPs) generated at the interface between a noble metal/titanium dioxide (TiO_2) heterostructure film and aqueous solution for the simultaneous optical and electrochemical interrogation of plasmon-mediated chemistry in a system whose resonance may be continuously tuned via the incident excitation angle.[1] We found a strong excitation angle dependence and linear power dependence in the photocurrent, confirming that the photoelectrochemical reactions are SPP-driven. A single plasmonic structure was used to generate plasmons with two different energies of 1.6 and 2.3 eV, and at both energies SPP-induced hot carriers drove both solution-based oxidation of methanol and the anodic half-reaction of photoelectrochemical water-splitting in sodium hydroxide solution. The applicability of the SPP system for energy-tunable hot carrier generation and hot-carrier driven solution chemistry was further investigated in a refractory plasmonic material platform using titanium nitride (TiN) and in the periodically textured metal films exhibiting surface plasmon photonic band gaps. Our results demonstrate that the broad and continuous energy tunability of the SPP system can be used to increase the basic knowledge of plasmon-induced hot carrier generation not only for photocatalysis but for many other applications including solar energy conversion, photodetection, and scanning probe imaging.

Figures and Tables:

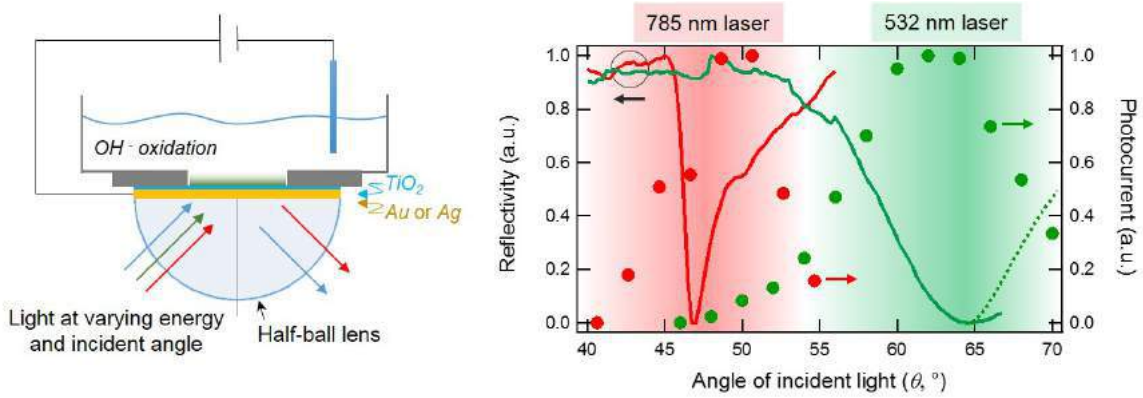

Figure 1. Energy tunable hot carrier generation for photocatalysis: The SPP on a metal/TiO_2 heterostructure enables plasmon-mediated chemical reactions (methanol oxidation and anodic half-reaction of water-splitting) in a system whose resonance may be continuously tuned via excitation angle. A single plasmonic structure can be tuned between two different resonances simply by altering excitation sources (785 and 532 nm laser) and incident angle.

Acknowledgements: This research was performed while the author, Wonmi Ahn, held a National Research Council (NRC) Research Associateship award at the U.S. Naval Research Laboratory. The authors acknowledge I. Vurgaftman and J. J. Petron for insightful comments and discussion, P. Narang for Au and Ag optical constants, and G. Beadie for guidance on developing transfer matrix calculations. This work was supported by the Office of Naval Research and the U.S. Naval Research Laboratory.

REFERENCES

1. Ahn, W., Ratchford, D. C., Pehrsson, P. E., and Simpkins, B. S. "Surface plasmon polariton-induced hot carrier generation for photocatalysis" *Nanoscale*, 2017, Advance Article (DOI: 10.1039/C6NR09280B)

Enhancing Energy Transfer Upconversion in Rare Earth Doped Nano-Crystals using Plasmonic Nano-Arrays

Jon Fisher[1], Amy Hor[1,2], M.T. Berry[2], P. Stanley May[2], Steve Smith[1*]

[1]Nanoscience and Nanoengineering, South Dakota School of Mines and Technology, Rapid City, SD 57701

[2]Chemistry Department, University of South Dakota, Vermillion, SD 57069

*corresponding author, E-mail: Steve_Smith@mailaps.org

Abstract- Spectroscopic imaging is used to investigate surface plasmon polariton (SPP) enhanced energy transfer upconversion (ETU) of rare-earth doped $NaYF_4$:Yb^{3+},Ln^{3+} upconverting nano-particles (UCNPs) on noble metal nano-structured substrates, including arrays of Au nano-pillars and nano-cavities with optical resonances coincident with rare-earth ion absorption (Yb^{3+}) or emission (Er^{3+},Tm^{3+}) energies. The mechanisms for the observed enhancement and power dependence are understood through analytical and computational models, relating the observed enhancement to kinetics of the ETU system and the photonic properties of the substrates.

While upconversion can be achieved through a variety of optical processes, such as two-photon absorption, second-harmonic generation, cooperative luminescence, two-step absorption and energy transfer upconversion, at low excitation intensity, the energy transfer upconversion process is by far the most efficient [1]. With the advent of nano-sized UC materials, the range of applications wherein such materials can be deployed has greatly increased. For instance the areas of bio-imaging, bio-labeling and photodynamic therapy benefit greatly from upconverting nano-particle (UCNP) materials due to the long penetration depth of near-infrared light in biological tissues [2,3]. There are also prospects for spectral conversion in increasing efficiency in solar energy applications [4]. However, low luminescence efficiency still limits the full potential of these materials.

In the vicinity of a metallic nanostructure, luminescence enhancement can be achieved through the amplification of the incident field, where local electromagnetic fields at the UCNP position are intensified due to plasmon resonances, and through the modification of the radiative rates of the phosphors [5-8]. By optimizing the geometry of the metallic nanostructures, and placing them within suitable proximity to the UCNPs, significant enhancement in UC efficiency should be achievable. In this work, we investigate the efficacy of specific plasmonic nanostructures towards radiative control of energy transfer upconversion processes in β -phase $NaYF_4$:Yb:Er[Tm] nanoparticles, using spectroscopic imaging to directly visualize the local enhancement associated with specific noble metal nanostructures.

Figure 1 shows a survey of the UCNPs (figure 1a) and the plasmonic nano-arrays we have investigated (figure 1b-d, and f-g), including representative spectra on and off the arrays [7-14]. Figure 1h shows the power dependence of the energy transfer upconversion enhancement of $NaYF_4$:Yb,Er UCNPs on Au nano-cavity arrays (figure 1f-g)[14]. The nano-cavity arrays support a surface plasmon (SP) resonance at 980nm, coincident with the peak absorption of the Yb^{3+} sensitizer. Spatially-resolved upconversion spectra show a 30X to 3X luminescence intensity enhancement on the nano-cavity array compared to the nearby smooth Au surface, corresponding to varying excitation intensities from 1 W/cm^2 to 300kW/cm^2, spanning the non-linear and saturation power dependence regimes. Figure 1I shows the measured and simulated power dependence of the ETU enhancement on the nano-cavity arrays, the latter obtained by simultaneous solution of a system of coupled rate equations developed by our team [13]. Our analysis shows the power dependent enhancement in upconversion luminescence can be almost entirely accounted for by a constant shift in the effective excitation intensity, which is maintained over five orders of magnitude variation in excitation intensity, limited by the kinetics of the ETU process.

In these measurements, it is shown that the amplification of the excitation field is independent of the emission wavelength, indicating the enhancement in upconversion emission is due to entirely to increased absorption by the Yb^{3+} sensitizer. Analysis of the statistical distribution of emission intensities in the spectroscopic images on and off the nano-cavity arrays provides an estimate of the average enhancement factor independent of fluctuations in nano-particle density. More recent work in random aggregates of Ag nanowires show evidence for collective plasmon resonances which manifest as local “hot-spots” with enhancements factors exceeding

thirty times [15]. These and our most recent results suggest significantly higher upconversion enhancement factors can be achieved under proper conditions by utilizing the surface plasmon polariton interaction with the ETU UCNPs while maintaining optimal ETU kinetics.

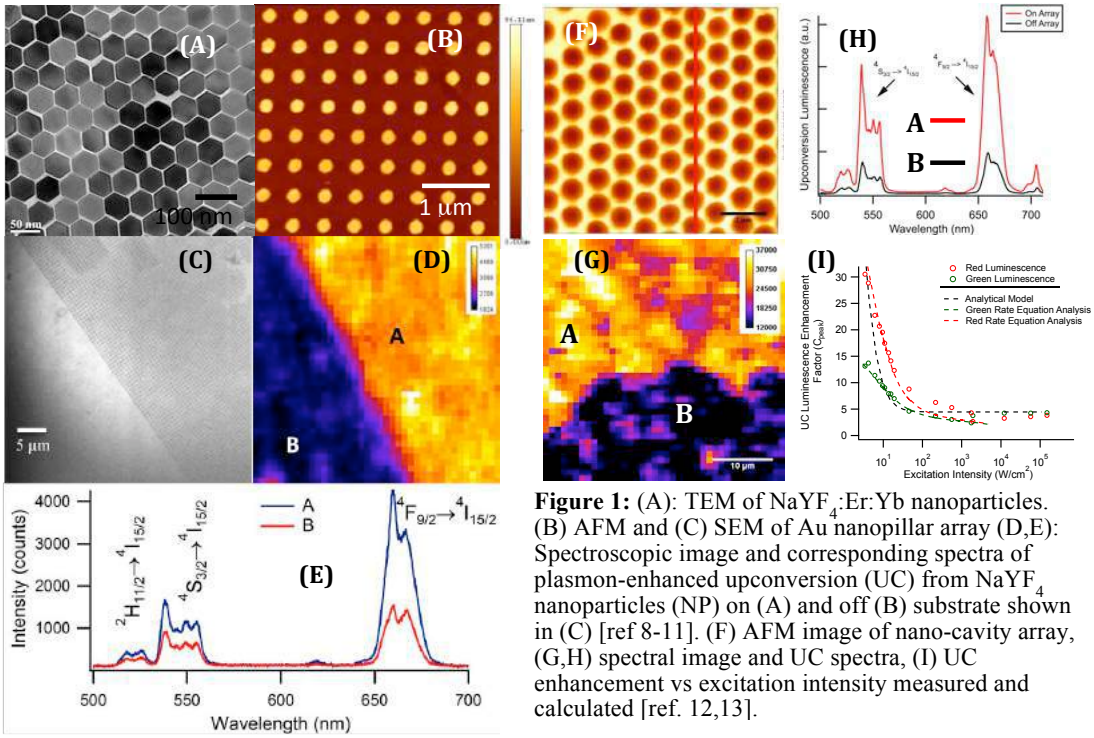

Figure 1: (A): TEM of $NaYF_4$:Er:Yb nanoparticles. (B) AFM and (C) SEM of Au nanopillar array (D,E): Spectroscopic image and corresponding spectra of plasmon-enhanced upconversion (UC) from $NaYF_4$ nanoparticles (NP) on (A) and off (B) substrate shown in (C) [ref 8-11]. (F) AFM image of nano-cavity array, (G,H) spectral image and UC spectra, (I) UC enhancement vs excitation intensity measured and calculated [ref. 12,13].

Acknowledgements: Work supported by NSF 0903685 (IGERT) and NASA Cooperative Agreement Number: NNX13AD31A.

REFERENCES

[1] Auzel, F. *Chem. Rev.* **2004**, *104*, 139–73.

[2] Wang, F.; Banerjee, D.; Liu, Y.; Chen, X.; Liu, X. *Analyst* **2010**, *135*, 1839–54.

[3] Zhang, P.; Steelant, W.; Kumar, M.; Scholfield, M. *J. Am. Chem. Soc.* **2007**, *129*, 4526–7.

[4] Moskovits, M. *Rev. Mod. Phys.* **1985**, *57*, 783.

[5] W. G. van Sark, A. Meijerink and R. E. I. Schropp, Solar Spectrum Conversion for Photovoltaics *DOI: 10.5772/39213*

[6] Lakowicz, J. R. *Anal. Biochem.* **2001**, *298*, 1–24.

[7] Esteban, R.; Laroche, M.; Greffet, J.-J. *J. Appl. Phys.* **2009**, *105*, 033107.

[8] Schietinger, S.; Aichele, T.; Wang, H.-Q.; Nann, T.; Benson, O. *Nano Lett.* **2010**, *10*, 134–8.

[9] C. Lin, M. T. Berry, R. Anderson, S. Smith, and P. Stanley May, *Chem. of Materials* **21** (14), 3406-3413 (2009).

[10] H.P. Paudel, L. Zhong, K. Bayat, M.F. Baroughi, S. Smith, P.S. May *et. al.* , *J. Phys. Chem C* **115** (39), 19028–19036 (2011).

[11] H. Paudel, D. Dachhepati, K. Bayat, *et. al*., S. May, S. Smith, M. Baroughi, *J. Photonics for Energy* **3** 035598 (2013).

[12] Q. Luu, A. Hor, J. Fisher, R.B. Anderson, S. Liu, *et. al*., P. S. May, S. Smith, *J. Phys. Chem C* (2014).

[13] R. B. Anderson, S. J. Smith, P. S. May, and M. T. Berry, *J. Phys. Chem. Lett.* **5** (1), 36–42 (2014).

[14] J. Fisher, B. Zhao, C. Lin, M. Berry, P. Stanley May, S. Smith, *J. Phys. Chem. C* **119** (44), pp 24976–24982 (2015).

[15] A. Hor, Q. A. N. Luu, P. S. May, M. Berry and S. Smith, *MRS Advances* CJO2016 doi:10.1557/adv.2016.356 (2016). *Highlighted in Materials360(r) Newsletter, August 16, 2016.*

Broadband enhancement of photocatalytic efficiency by 3D patterned light trapping structure

Yunha Ryu and Kyoungsik Kim*
Department of Mechanical Engineering, Yonsei University, Seoul, Korea
*corresponding author: kks@yonsei.ac.kr

Abstract- Here we report enhancement of photocatalytic efficiency of TiO_2 by utilizing three dimensional light trapping structure which brings increased the light absorption. We successfully fabricate the 3D structures via self-assembly technique. The fabricated structures show high light absorption and large surface area which are beneficial to photocatalytic effect. Also, we combined TiO_2 structures with plasmonic metal nanostructures to achieve higher light absorption and hot carrier injection.

We fabricated TiO_2 nanotube structures by anodic-anodization method and gold nanoparticles are decorated on the nanotubes to increase the light harvesting efficiency (Fig.1). The optical and electrical properties of the fabricated structure are measured to evaluate the enhancement of photocatalytic efficiency.

Acknowledgements This work was supported by Global Research Lab (GRL) Program of the National Research Fundation (NRF) funded by Ministry of Science, ICT (Information and Communication Technologies) and Future Planning (2016K1A1A2912758),the National Research Foundation of Korea (NRF) grant funded by the Korea government (MSIP) (NRF-2015R1A2A2A11001112), Pioneer Research Center Program through the National Research Foundation of Korea funded by the Ministry of Science, ICT & Future Planning (NRF-2013M3C1A3065045), and the Center for Advanced Meta-Materials (CAMM-2014M3A6B3063712) funded by the Ministry of Science, ICT and Future Planning as Global Frontier Project.

REFERENCES

1. Zhang, Zhonghai. et al.,"Plasmonic Gold Nanocrystals Coupled with Photonic Crystal Seamlessly on TiO2 Nanotube Photoelectrodes for Efficient Visible Light Photoelectrochemical Water Splitting," *Nano Lett.*, Vol. 13, No. 1, 14–20, 2013.
2. Zhang, Xing, "Coupling surface plasmon resonance of gold nanoparticles with slow-photon-effect of TiO2 photonic crystals for synergistically enhanced photoelectrochemical water splitting," *Energy Environ. Sci*, Vol. 7, 1409-1419, 2014.

Plasmonic and Electrochemical Response of Nanostructured Au-Iron Oxide Composite Films

Naresh C. Das[1], Joshua McClure[2], Kyle Grew[2] and Deryn Chu[2]

[1]Semiconductor Optoelectronic Devices Branch
U.S. Army Research Laboratory
2800 Powder Mill Rd., Adelphi, MD 20783

[2]Electrochemistry Branch
US Army research Laboratory
2800 Powder Mill Rd., Adelphi, MD 20783
Corresponding author: naresh.c.das2.civ@mail.mil

Abstract:

We report the plasmonic resonance behavior of nano-structured iron oxide films decorated with Au nanoparticles. Iron oxide (Fe_2O_3) nano-structured films have recently drawn interest for electro-catalytic processes including reactions that involve carbon-carbon (C-C) bond breakage. We deposited iron oxide films using electron-beam evaporation followed by annealing at 450°C in mixed and pure oxygen environments. We deposited Au NPs either in embedded or on top of the Fe_2O_3 nano structured thin films with thicknesses ranging from 25-500 nm. We used ellipsometric as well as UV-Vis reflectance spectroscopy techniques to determine the plasmonic characteristics of the nanostructured films.

Iron oxide (Fe_2O_3) film has recently received much attention among various semiconductor photo-electrode materials due to its favorable optical band gap (~2.2 eV), excellent chemical stability in high pH media, natural abundance, and low cost [1]. However, Fe_2O_3 exhibits a relatively poor absorptivity of photons near its band-edge due to an indirect band gap, poor electronic conductivity (PEC), and picosecond recombination of excited states, thus leading to a photo-generated hole diffusion length of ~2-4 nm [2]. These non-ideal optoelectronic properties hinder the transport of photo-generated carries and increase the recombination rate, which results in a lowering of the PEC efficiency compared to theoretically predicted values. Controlling the nanostructure of Fe_2O_3 may provide an effective technology for overcoming the aforementioned problems of Fe_2O_3 film due to the geometry and mechanism-dependent semiconductor structure [3]. The shape of the Fe_2O_3 structures with cone, cylinder, sphere, etc. features alters the electric field dependent absorption and transport processes.

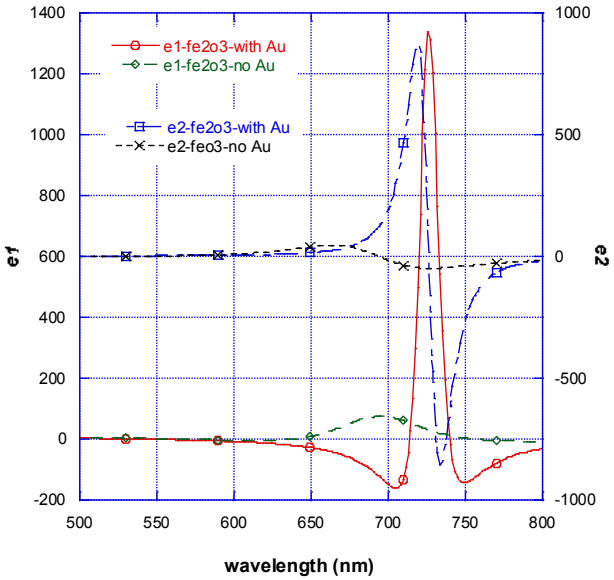

Fig. 1 Real (e1) and Imaginary (e2) parts of the dielectric constant of a representative sample (e.g., a 100 nm of Fe_2O_3 film with and without Au NPs)

In Figure 1, we show the e1and e2 both real and imaginary of dielectric constant of the Fe2O3 film with and without Au nano particles measured by variable angle ellipsometry. The plasmonic resonance occurs in between 700-750 nm as seen in the above figure. In addition, we discuss theoretical modeling of the extinction, scattering and absorption characteristics of the Fe_2O_3 films with varying thickness with and without Au NPs. The Au NP-Fe_2O_3 structure has significant absorption characteristics in visible spectral region. Detailed deposition, annealing, and characterization results of Fe_2O_3 nano plasmonic structures will be presented in a full paper.

Acknowledgements, Funding from Army Research Laboratory director research initiative (DRI) funding is acknowledged.

References:

[1]Wang, G. M.; Ling, Y. C.;Wheeler, D. A.; George, K. E. N.; Horsley, K.; Heske, C.; Zhang, J. Z.; Li, Y. *Nano Lett.* **2011,** *11*, 3503

[2] Cherepy, N. J.; Liston, D. B.; Lovejoy, J. A.; Deng, H. M.; Zhang, J. Z. *J. Phys. Chem. B* **1998,** *102*, 770

[3] Sivula, K.; Zboril, R.; Formal, F. L.; Robert, R.; Weidenkaff, A.; Tucek, J.; Frydrych, J.; Grätzel, M. *J. Am. Chem. Soc.* **2010,** *132*, 7436

Topological photonics

Topological phase transitions in QED: Casimir forces in the graphene family

D. A. R. Dalvit[1*], P. Rodriguez-Lopez[2], W. J. M. Kort-Kamp[1,3], and L. M. Woods[2]
[1]Theoretical Division, MS B213, Los Alamos National Laboratory, Los Alamos, NM 87545, USA
[2]Department of Physics, University of South Florida, Tampa, FL 33620, USA
[3]Center of Nonlinear Studies, MS B213, Los Alamos National Laboratory, Los Alamos, NM 87545, USA

[*]corresponding author: dalvit@lanl.gov

Abstract- The expansion of the graphene family by adding silicene, germanene, and stanene (2D allotropes of Si, Ge, and Sn) lends itself as a platform to probe Dirac-like physics in honeycomb staggered systems in the Casimir interaction. We discover Casimir force phase transitions between these staggered 2D materials induced by the complex interplay between Dirac physics, spin-orbit coupling, and externally applied fields. Furthermore, due to the topological properties of these materials, repulsive and quantized Casimir interactions become possible.

The discovery of systems with reduced dimensions and physics different from the one of standard 3D dielectric, metals, and semiconductors has given a new impetus to the field of van der Waals and Casimir phenomena [1]. In particular, the graphene-family materials has recently been expanded through the synthensis of silicene, germanene, and stanene. Unlike graphene, these new 2D materials gave spatial buckling between the two sublattices and exhibit non-trivial topological insulator features. The application of external fields together with the inherently strong spin-orbit coupling can be used as effective "knobs" for various Hall transitions. We have recently discovered [2] a new effect in the Casimir physics of these materials, namely Casimir force topological phase transitions driven by the complex interplay between Dirac physics, spin-orbit coupling, and externally applied electric fields and circularly polarized light. Novel distance scaling laws, abrupt magnitude changes, force quantization and repulsion, are all manifestations of Casimir force phase transitions occurring in these 2D staggered materials. Thermal effects result in the smoothing out of phase transition boundaries and disappearance of quantized and repulsive Casimir interactions. In order to detect experimentally Casimir force phase transitions, cryogenic atomic force microscope set-ups, such as the one developed in [3], are required. Given the magnitude of the predicted effects [2] and the reported sensitivities of experiments [3], the measurements of Casimir force phase transitions in the graphene family materials should be within reach with current state-of-the-art low-temperature Casimir force experiments.

Acknowledgements, We acknowledge financial support from the US Department of Energy under grant No. DE-FG02-06ER46297, and the LANL CNLS and LDRD program.

REFERENCES

1. Woods, L. M., Dalvit, D. A. R., Tkatchenko, A., Rodriguez-Lopez, P., Rodriguez, A. W., and Podgornik, R.,

"Materials perspective on Casimir and van der Waals interactions," *Rev. Mod. Phys*. **88,** 45003 (2016).

2. Rodriguez-Lopez, P., Kort-Kamp, W. J. M., Dalvit, D. A. R., and Woods, L. M., "Casimir force phase transitions in the graphene family," to appear in *Nature Communications* (2017), arXiv:1609.05193
3. Laurent, J., Sellier, H., Huant, S., Chevrier, J., "Casimir force measurements in Au-Au and Au-Si cavities at low temperature," *Phys. Rev. B* **85**, 035426 (2012).

A group theoretical route to deterministic Weyl points in chiral photonic lattices

M. Saba[1], **J. M. Hamm**[1], **and O. Hess**[1]

[1]Department of Physics, Imperial College London, Prince Consort Road, SW7 2BB, UK
m.saba@ic.ac.uk

Abstract— Point degeneracies in the photonic bandstructure give rise to a variety of exotic properties such as topological phases. Previously identified exceptional points are based on accidental degeneracies and subject to engineering on a case-by-case basis. We here show that symmetry induced (deterministic) pseudo Weyl points with non-trivial topology and hyperconic dispersion exist at the Γ point in the Brillouin zone of chiral cubic systems. We demonstrate the universal behavior by means of interacting plasmonic spheres on a chiral cubic lattice.

The broad interest in topological phases over the past decades, triggered by the discovery of the quantum Hall effect [1] and its theoretical investigation [2], is mainly attributed to the fact that topological features are, due to their discrete nature, insensitive to system perturbations. One of the striking physical implications of non-trivial topology is the existence of topologically induced uni-directional edge states for bulk systems [3, 4]. The plasmonic [5] and single electron surface states of Weyl semi-metals, with an isolated exceptional point of non-trivial topology, in particular are known to be stable against perturbations and to give rise to peculiar dynamics.

In 2004, Onoda *et al.* showed that topological phases occur in entirely classical systems such as 2D photonic crystals [6], sparking a new wave of research on topological photonics [7]. In particular, topologically protected Weyl points with hyperconic dispersion have been identified in double gyroid photonic crystals with broken parity-time symmetry [8].

More recently, Huang *et al.* [9] exploited the linear dispersion in the bandstructure close to accidental pseudo-Dirac points at the Γ point of a square lattice of dielectric rods to form a 2D metamaterial with vanishing refractive index $n = 0$ and finite impedance $Z \neq 0$, with remarkable implications on interface scattering and wave propagation.

On the basis of group and perturbation theory, we here predict the existence of 3D *pseudo Weyl points* with hyperconic dispersion relation at the center of the BZ of chiral cubic lattices. Pseudo Weyl points are in contrast to previously reported pseudo Dirac points [9] deterministic, *i. e.* symmetry protected and hence not subject to careful engineering of geometric parameters. They are shown to be isotropic, to exhibit a Chern characteristic of $C = \pm 2$ (*i. e.* they are topologically non-trivial), and exist in classical and quantum systems with chiral cubic symmetry.

We demonstrate the predicted behavior via a minimalistic model system based on a simple cubic array of plasmonic nano-spheres on a $P2_13$ lattice (Fig. 1**A**). In the limit of small spheres of radius ρ much smaller than the lattice constant a, the polarization vectors $\vec{p}_\mu$ of individual spheres μ (in the frequency domain) are subject to dipole interaction [10]. Using Bloch's theorem, the underlying equation of interaction reduces to a low-dimensional non-linear hermitian eigenproblem, with eigenvalues k_0 and dimension $N = 12$:

$$\alpha^{-1}(k_0)\,\vec{p}_\mu = \sum_\nu M_{\mu\nu}(\vec{k}, k_0)\,\vec{p}_\nu \ . \tag{1}$$

Here, α is the polarizability, and $M_{\mu\nu}(\vec{k}, k_0)$ a lattice sum over Maxwell Green functions. For the particular system, group theory predicts three 3-fold degeneracies, one 2-fold degeneracy and a non-degenerate mode at the Γ point. These are reproduced by the numerical solution of equation (1). The dispersion relation close to one of those points is shown in Fig. 1**C**: a flat band (black) is sandwiched between a pair of hyperconic bands (red) with linear and isotropic dispersion of equal magnitude.

In summary, we show that isotropic hyperconic dispersion can be found at the Γ point of chiral cubic lattices for a broad class of physical systems. Although not strictly speaking in the Weyl class, the associated exceptional points share most features with genuine Weyl points including non-trivial topological characteristics. A natural application for the unique dispersion behavior of these

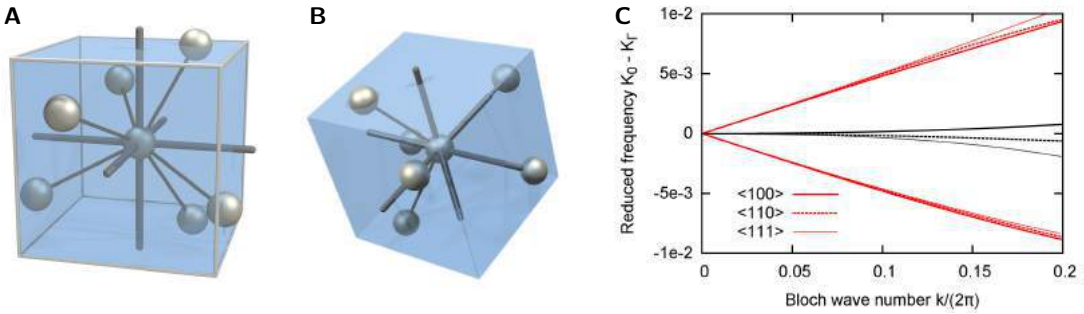

Figure 1: (**A**) Unit cell of the 3D plasmonic sphere packing on a $P2_13$ lattice considered here. Connecting rods, glass cube and Cartesian grid for illustration purposes only. (**B**) View from the $\langle 111 \rangle$ direction. (**C**) Bandstructure close to the Γ point along the cubic high symmetry directions.

pseudo Weyl points are zero refractive index materials that have been suggested previously in the context of accidental Dirac points in two-dimensional photonic crystals [9]. A cubic arrangement of nano-spheres similar to the proposed model could be for example realized by means of DNA origami [11].

ACKNOWLEDGMENT

This research was supported through the Engineering and Physical Science Research Council (EPSRC) via the EP/L027151/1 grant.

REFERENCES

1. Klitzing, K. v., G. Dorda and M. Pepper, "New Method for High-Accuracy Determination of the Fine-Structure Constant Based on Quantized Hall Resistance," *Phys. Rev. Lett.*, Vol. 45, No. 6, 494–497, 1980.
2. Thouless, D. J., M. Kohmoto, M. P. Nightingale and M. d. Nijs, "Quantized Hall Conductance in a Two-Dimensional Periodic Potential," *Phys. Rev. Lett.*, Vol. 49, No. 6, 405–408, 1982.
3. Qi, X.-L. and S.-C. Zhang, "Topological insulators and superconductors," *Rev. Mod. Phys.*, Vol. 83, No. 4, 1057–1110, 2011.
4. Wang, Z., C. Yidong, J. D. Joannopoulos and M. Soljačić, "Observation of unidirectional backscattering-immune topological electromagnetic states," *Nature*, Vol. 461, No. 7265, 772–772, 2009.
5. Hofmann, J. and S. Das Sarma, "Surface plasmon polaritons in topological Weyl semimetals," *Phys. Rev. B*, Vol. 93, No. 24, 241402, 2016.
6. Onoda, M., S. Murakami and N. Nagaosa, "Hall Effect of Light," *Phys. Rev. Lett.*, Vol. 93, No. 8, 083901, 2004.
7. Lu, L., J. D. Joannopoulos and M. Soljačić, "Topological photonics," *Nat. Phot.*, Vol. 8, No. 11, 821–829, 2014.
8. Lu, L., L. Fu, J. D. Joannopoulos and M. Soljačić, "Weyl points and line nodes in gyroid photonic crystals," *Nat. Phot.*, Vol. 7, No. 4, 294–299, 2013.
9. Huang, X., Y. Lai, Z. H. Hang, H. Zheng and C. T. Chan, "Dirac cones induced by accidental degeneracy in photonic crystals and zero-refractive-index materials," *Nat. Mat.*, Vol. 10, No. 8, 582–586, 2011.
10. Weick, G., C. Woollacott, W. L. Barnes, O. Hess and E. Mariani, "Dirac-like Plasmons in Honeycomb Lattices of Metallic Nanoparticles," *Phys. Rev. Lett.*, Vol. 110, No. 10, 106801, 2013.
11. Andersen, E. S. *et al.*, "Self-assembly of a nanoscale DNA box with a controllable lid," *Nature*, Vol. 459, No. 7243, 73–76, 2009.

Quantum photonics

Electronic band structures and quantum Hall effect in $In_{0.53}Ga_{0.47}As$/InP nanostructures superlattices short infrared detectors

Driss Barkissy, Abdelhakim Nafidi, Abderrazak Boutramine, Abdelkrim Hannour and Es-saïd Es-Salhi

Laboratory of Condensed Matter Physics and Nanomaterials for Renewable Energy, Faculty of Sciences, University Ibn Zohr, Agadir, Morocco
*corresponding author, E-mail: nafidi21@yahoo.fr

Abstract

We report here the band structures and transport properties of $In_{0.53}Ga_{0.47}As$ (d_1=10 nm)/InP (d_2=5 nm) lattice matched superlattice, based on the envelope function formalism and the effective mass approximation. We investigated the effect of well thickness, valence band offset and temperature on the band structures as well as the effect of barrier thickness and magnetic field on the density of states. In the later, the existence of a small dispersion indicates weak interactions between adjacent wells. The position of Fermi level predicts that this sample exhibits n-type conductivity. We find out some correlations between band structures and both Shubnikov-de Hass and quantum Hall effects. These results were compared and discussed with the available data in the literature.

1. Introduction

$In_xGa_{1-x}As$/InP superlattices (SLs) have attracted many attention due to their electronic and optical properties, which can be tuned by adjusting layers thicknesses or indium compositions x. The relative small band gap and high mobility of the constituent quantum well ($In_xGa_{1-x}As$) demonstrate that those nanostructures are attractive for high operating temperature devices [1].

These nanostructures have been used in the development of different optoelectronic devices such as photoconductive switches, transistors, and photodetectors [2,3]. They are expected to be promising with the superlattice-emitter resonant tunneling bipolar transistor (SE-RTBT) which have demonstrated a significant potential in high-speed switches and to reduce the functional device circuits complexity [3].

Nevertheless, the lattice matched $In_{0.53}Ga_{0.47}As$/InP quantum well infrared detectors become the choice for low cost, low dark current, high speed and high temperature operation detectors in short wavelength infrared (SWIR) [4]. Such detector's performances can be enhanced significantly when the infrared absorber material is made from a superlattice and the detection wavelength can be extended out to cover 5-9 μm as reported by Majumdar et al. [5], or even further with binary superlattice [6]. The key advantage of superlattice based infrared detectors over conventional ones is that the layer thickness and alloy compositions are chosen to yield the desired energy band gap.

One of the quantities which characterize the reduced dimensionality of the structure is the density of states (DOS). Several optical and electrical properties follow DOS. Thus, it is possible to get useful information by studying this quantity.

Several experimental observations show, at low temperatures and under high magnetic fields, some new features in $In_xGa_{1-x}As$/InP superlattices. Among them, Shubnikov de Haas effect (SDH) and quantum Hall effect (QHE) [7,8]. However, only few attempts have been devoted to study the formation of mini-bands in such system, obtained by magnetotransport and photoluminescence measurements [7], or analysis of Raman data [9].

2. Superlattices band structures theory and computation

The general expression of dispersion relation of $In_xGa_{1-x}As$/InP superlattice, within the envelope function formalism and effective mass approximation, is given by [10,11]:

$$\cos(k_z d) = \cos(k_1 d_1)\cos(k_2 d_2) - \frac{1}{2}\left[\left(\xi + \frac{1}{\xi}\right) + \frac{k_p^2}{4k_1 k_2}\left(r + \frac{1}{2} - 2\right)\right]\sin(k_1 d_1)\sin(k_2 d_2) \quad , \quad (1)$$

With k_z the wave vector in the growth direction and $k_p(k_x,k_y)$ the superlattice in-plane wave vector. The origin of the energy E has been chosen at the top of InP valence band as shown in the Fig.1. In each host material and for a given energy, the two–band Kane model [12] gives the wave vector ($k_i^2+k_p^2$). Therefore, the energy E of the light particles (electron and light hole) is given by:

$$\begin{cases} \frac{2}{3}P_1^2\hbar^2\left(k_1^2 + k_p^2\right) = \left(E - \varepsilon_1 - \Lambda\right)\left(E - \Lambda\right) & for\ In_xGa_{1-x}As \\ \frac{2}{3}P_2^2\hbar^2\left(k_2^2 + k_p^2\right) = E\left(E - \varepsilon_2\right) & for\ InP \end{cases}, \quad (2)$$

The expression of ξ and r in the Eq(1) are:

$$\xi = \frac{k_1}{k_2} r \text{ and } r = \frac{E - \varepsilon_2}{E - \varepsilon_1 - \Lambda}$$

From the same equation (1), the superlattice heavy holes mini-bands can be calculated with the following relations:

$$\begin{cases} -\frac{1}{2}\frac{\hbar^2}{(m^*_{hh})_1}\left(k_1^2 + k_p^2\right) = (E - \Lambda) \quad for\ In_xGa_{1-x}As \\ -\frac{1}{2}\frac{\hbar^2}{(m^*_{hh})_2}\left(k_2^2 + k_p^2\right) = E \quad for\ InP \end{cases}, \qquad (3)$$

with $\xi = \frac{k_1}{k_2} r$ and $r = \frac{(m^*_{hh})_2}{(m^*_{hh})_1}$

The direct band gaps parameters ε_i (i= 1 and 2) used here, as a function of temperature, for x=0.53, are given by the empirical expressions reported in [13,14]. P_i is the Kane matrix element [15]. The heavy holes effective masses of $In_{0.53}Ga_{0.47}As$ and InP are, respectively, $(m^*_{hh})_1 = 0.47 m_0$ and $(m^*_{hh})_2 = 0.6\ m_0$, as given in [1,15].

In this work, we have used the valence band offset Λ between heavy holes sub-bands edges of $In_{0.53}Ga_{0.47}As$ and InP. We adopted in the computation, the experimental Λ= 346 meV measured by Lang et al. [16] with admittance spectroscopy and supported by the theoretical calculations of Ichii et al. [17].

The computation of band structures consists of solving the general dispersion relation with the reported parameters. In the Eq. (1), state energy exists if the right-hand side lies in the range -1 to 1. In other words, $-1 \le \cos(k_z d) \le 1$ which implies $-\pi/d \le k_z \le \pi/d$ in the first Brillouin zone, with $d = d_1 + d_2$ is the superlattice period. In the study of energy E as a function of wave vector in the direction of growth k_z (k_p=0), the solving procedure consists of going with small steps of energy through the studied range. Then finding, for a given E, the value of k_z which is root of the dispersion relations. The same procedure is used for studying E versus the in-plane wave vector k_p (k_z=0 and $k_z = \pi/d$). Note that strain effects are not taking into account here, since

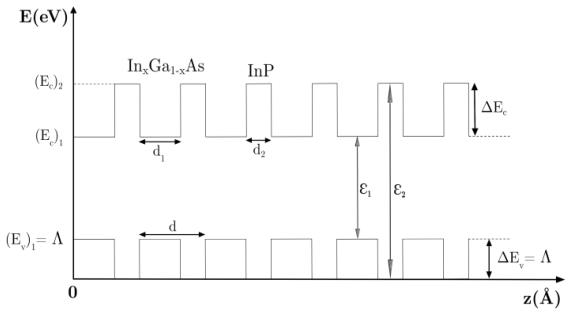

Figure 1: Illustration of band lineup between $In_xGa_{1-x}As$ and InP along the growth direction with different parameters related to electronic band structures. $(E_c)_i$, $(E_v)_i$ and ε_i where i= 1, 2 are the conduction and valence bands edges and band gap of bulks, respectively.

$In_{0.53}Ga_{0.47}As$ is lattice matched to InP [1,14].

The sample studied here consists of alternating $d_1(In_{0.53}Ga_{0.47}As)$= 100Å and d_2(InP)= 50Å with d= d_1+d_2= 150Å.

3. Results and discussions

3.1. Band gap engineering

In the Fig. 2a, we represent the energy of conduction (E_i), light-hole (lh_i) and heavy-hole (hh_i) mini-bands at the center $\Gamma(k_z = 0)$ and the limit ($k_z = \pi/d$) of the first Brillouin zone as a function of well thickness d_1. The calculated band gap, from bottom of the first conduction (E_1) to top of valence mini-bands (hh_1) at T=1.7 K is $E_g(\Gamma) = E_1 - hh_1$= 849 meV. The photoluminescence measurements Pusep et al. on the same sample [8], show a direct band gap of 822 meV.

The observed difference of 27 meV may be due to parameters considered here, particularly, the valence band offset (VBO). The effect of this parameter on the superlattice band gap is shown in Fig. 2b. A Good agreement can be obtained with the optical band gap when the VBO is taken to be 605 meV at 1.7 K. However, in the literature, the experimental Λ of $In_{0.53}Ga_{0.47}As/InP$ hetero-junction is ranging between 0.24 eV and 0.38 eV [18]. Such

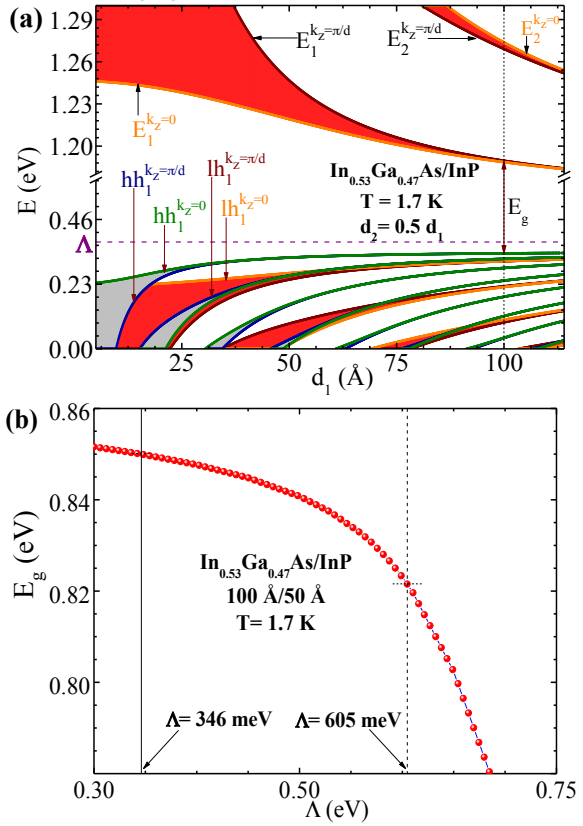

Figure 2: (a) Energy of both conduction (upper part) and valence (lower part) mini-bands versus the well thickness at 1.4 K. Solid areas show the mini-bands width. (b) Band gap as a function of the valence band offset of the studied superlattice.

difference, can be also attributed to the strain effects which could be significant in such low temperature and could modify the band structures by introducing interface states [19]. Also, fluctuations during the growth of both wells and barriers could affect the superlattice band gap, since it depends significantly on thickness.

In addition, we can see, in Fig. 2a that the mini-bands width and band gap decrease and tend to discrete levels of a quantum well as d_1 increases. This can be explained by the creation of more allowed states, available to be occupied by electrons in the forbidden region, since the overlapping orbitals between nearest atoms grow with thickness. As result, the valence and conduction mini-bands separation, starts to narrow, leading to a reduction of band gap.

The effect of temperature on the superlattice band gap is shown in the Fig. 3. At low temperatures, the gap varies hardly and then it decreases when the temperature increases.

For T≥40 K, our theoretical results (green solid squares) are in agreement with the photoluminescence measurements (solid red circles) of Fernandes dos Santos et al. [20]. The difference between the calculated and measured band gaps energies decreases from 8 meV to 3.8 meV when T increases from 40 K to 300 K, may be, are due to the factors discussed above.

Nevertheless, in their paper Pusep et al. [8] suppose that the difference between the experimental and the calculated inter mini-bands gaps is due particularly to the imprecisely known band offsets of $In_{0.53}Ga_{0.47}As/InP$ heterostructure. In Fig. 3, we did the fit of valence band offset Λ and the best agreement is achieved for Λ= 400 meV (brown solid line).

In addition, these results were fitted by the empirical Varshni formula [21] expressed as:

$$E_g(T) = E_g(0) - \alpha \frac{T^2}{T+\beta}, \qquad (4)$$

Where $E_g(T)$ is the band gap at a given temperature T, $E_g(0)$ the gap at absolute zero, α and β are Varshni fitting parameters. The best fitting for the temperature dependence of band gap was obtained with: α= 0.49 meV K^{-1}, β= 323 K and $E_g(0)$= 851 meV. These values are consistent with the reported ones in Ref. [20] of Γ−Γ PL peak energies Varshni fitting.

In order to explain the effect of temperature on the band gap in semi-conductors, Ünlü et al. [22] proposed a thermodynamic model and demonstrate that, the observed behavior is due to the thermal energy and the expansion of the lattice constant with temperature, which cause an increase in the inter-atomic spacing and the potential seen by electrons decreases, leading to a smaller band gap.

In the Fig. 3, the calculated cut-off wavelength is given by:

$$\lambda(nm) = \frac{1240}{E_g(eV)}, \qquad (5)$$

In the investigated temperature range of 1.7 K to 300 K, 1.46 μm ≤ λ_c ≤ 1.59 μm, this is located in the short infrared region.

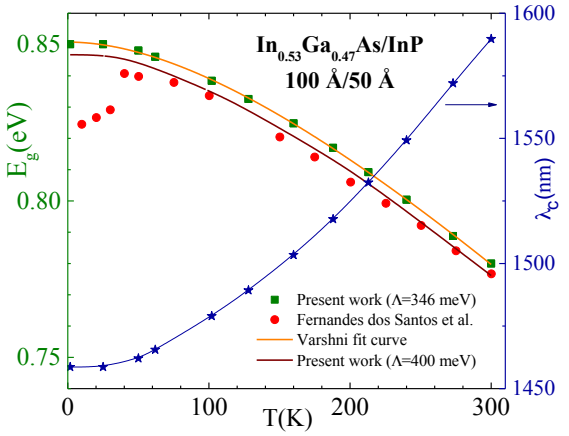

Figure 3: Superlattice band gap Energy and cut-off wavelength λ_c versus temperature.

The Fig. 4a shows the computed band structures from the dispersion relation (Eq. 1). We can see that, the electronic states are quantized and the dispersion $E(k_z)$ along the growth axis, is small compared to the in-plane dispersion $E(k_p)$. This show that, the system's wells are weakly coupled. Consequently, electronic transport is dominated in-plane of this superlattice (InGaAs layers). In addition, for E< 35 meV the heavy holes mini-bands (hh_i) dominate the edge of the valence band.

Carrier's effective mass of the first conduction and valence mini-bands for the in-plane motion and along growth direction are shown in Fig. 4b. The latter, is derived from Fig. 4a, by using following expression:

$$\left(\frac{1}{m^*}\right)_{ij} = \frac{1}{\hbar^2}\frac{\partial^2 E_{k_{ij}}}{\partial k_i \partial k_j}, \qquad (6)$$

Along k_p, effective masses of heavy holes and electrons are almost constant and equal to -0.47m_0 and 0.114m_0, respectively. For light holes it decreases from -0.07m_0 at the center to -0.09m_0 at the limit k_p= -0.03 $Å^{-1}$. The corresponding electron $(m^*_{E1})_{EF}$, light hole $(m^*_{lh1})_{EF}$ and heavy hole $(m^*_{hh1})_{EF}$ effective masses are 0.093m_0, -0.079m_0 and -0.47m_0, respectively.

3.2. Fermi level and density of states

In order to estimate the Fermi level, we used the magneto-resistance measurements of Pusep et al. [8]. It is well known that the transverse magnetoresistance oscillations are periodic with respect to 1/B at very low temperatures and under high magnetic fields. The electron sheet density n_{2D} is related to the period $\Delta_{1/B}$ by:

$$n_{2D} = \left|e/\left(\pi\hbar\Delta_{1/B}\right)\right|, \qquad (7)$$

Thus, the inverse of the minima $1/B_{min}$ as a function of the entire N, Landau level index, follows this expression:

$$1/B_{min} = \Delta_{1/B}\left(N + 1/2\right), \qquad (8)$$

The slope evaluated from the linear line is $\Delta_{1/B}$= 0.11 T^{-1} and

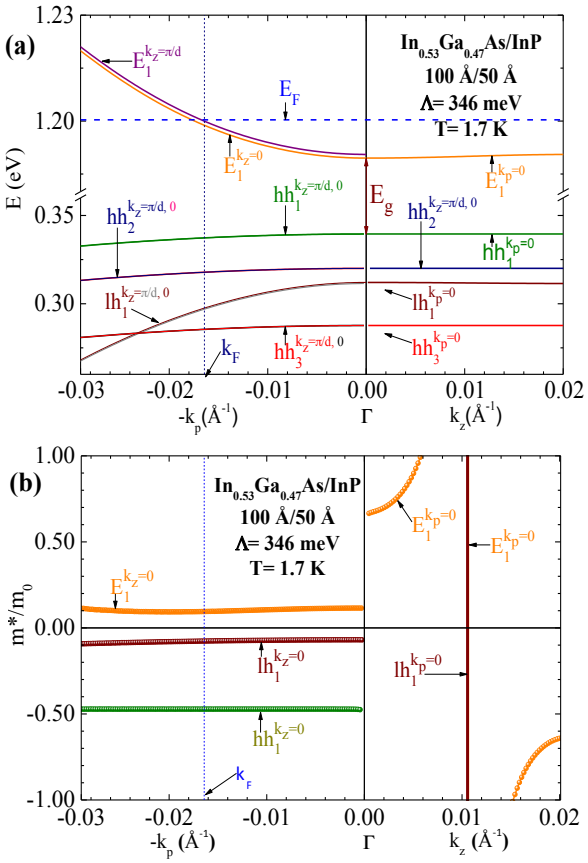

Figure 4: (a) Band structures of the investigated superlattice along the growth direction (k_z) and in-plane (k_p) (b) Carrier's effective mass ratio of the first conduction and valence mini-bands with m_0 the mass of the free electron.

the electron concentration is n_{2D}= 4.3 10^{11} cm^{-2}.

The two dimensional electron gas Fermi wave vector k_F can be calculated with: $k_F^2 = 2\pi\, n_{2D}$. Thus, $|k_F|$= 0.0164 Å^{-1} as indicated in Fig. 4a and b, by vertical dashed line.

At low temperature, the Fermi level is given by:

$$\left|E_F - E_c\right| = \left|e\hbar / \left(m^*_{E_1}\Delta_{1/B}\right)\right| = \left|n_{2D}\pi\hbar^2 / \left(m^*_{E_1}\right)_{E_F}\right|, \qquad (9)$$

Since the edge of conduction band is E_c=1.189 eV, the position of Fermi level E_F= 1.200 eV shows that the studied sample exhibits n type conductivity.

The superlattice density of states (DOS) of ith mini-band with a finite mini-band energy width $\Delta E^{(i)} = E^{(i)}_{max} - E^{(i)}_{min}$, is given by [23]:

$$\rho^{(i)}_{DOS}(E) = \begin{cases} 0 & for \quad E^{(i)}_{min} > E > E^{(i)}_{max} \\ \left(m^*/\pi^2\hbar^2\right)k_z(E) & otherwise \end{cases}, \qquad (10)$$

The sum over all mini-bands of the superlattice can be expressed as:

$$\rho_{DOS}(E) = \sum_{i=1}^{n} \rho^{(i)}_{DOS}(E), \qquad (11)$$

In the Fig. 5, we have computed DOS of the two lowest conduction mini-bands of $In_{0.53}Ga_{0.47}As/InP$ superlattices with the same well thickness (d_1= 100 Å) and different barrier thicknesses d_2= 50 Å and 150 Å. For curve A, only the first conduction mini-band is occupied ($E \le E_F$) and the DOS is quantized in term of $m^*/\pi\hbar^2 d$. Note that, for d_2= 50 Å, the system is quasi two dimensional and very small k_z dispersion occurs. However, as d_2= 150 Å, the mini-bands become discrete states and DOS is a staircase like function (curve B). Therefore, the quantum wells are decoupled from each other and the electrons motion is completely two-dimensional. In the same figure 5, we show $In_{0.53}Ga_{0.47}As$ bulk density of states (curve C), with parabolic shape, which can be obtained from formula 10 with $k_z(E) = (2m^*E)^{1/2}/\hbar$. It is noteworthy that, when the barrier thickness decreases, the superlattice ρ_{DOS} curve becomes higher and approaches to that of bulk material.

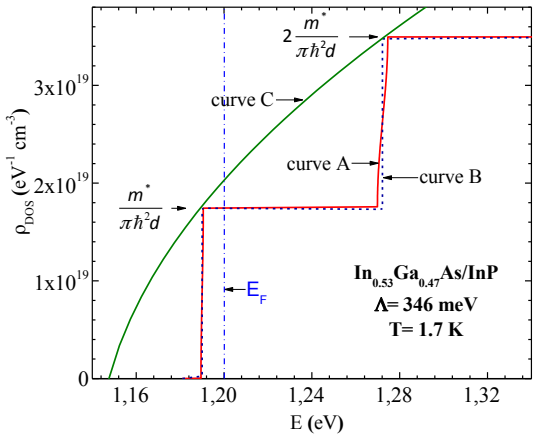

Figure 5: Density of states versus mini-bands energy of $In_{0.53}Ga_{0.47}As/InP$ superlattices with d_1= 100 Å, d_2=50 Å (curve A) and d_2=150 Å (curve B). The parabolic curve C represents $In_{0.53}Ga_{0.47}As$ bulk density of states.

3.3. Quantization of energy and density of states under magnetic field

In the presence of an external magnetic field along the growth axis z, a quantization of DOS in-plane energy spectrum takes place. The quantum states, in the first Brillouin zone, are distributed to distinct sets of Landau mini-bands as represented in Fig. 6a, c and e. The expression of the total energy $E^{(i)}$ of the ith miniband is given by:

$$E^{(i)} = E^{(i)}(k_z) + \left(N^{(i)} + 1/2\right)\hbar\omega_c + E^{(i)}_{Zeeman}, \qquad (12)$$

Where $E^{(i)}(k_z)$ is the carriers charge energy associated with z-motion which remain unaffected and can be obtained from the dispersion relations discussed above. The in-plane carrier's motion energy is completely quantized in terms of $(N^{(i)}+1/2)\hbar\omega_c$ with $N^{(i)}$ the Landau index of ith miniband. In the case of this sample we can assume, that Zeeman spin splitting energy $E_{Zeeman} = \pm\, g^*\mu_B B/2$ is negligible compared to Landau mini-band splitting $\hbar\omega_c = \hbar eB/m^*$.

In an ideal two dimensional systems with no impurities

or other defects, the quantization of DOS can be described as a set of δ functions separated by cyclotron energy $\hbar\omega_c$, and can be written as [24]:

$$\rho_{DOS}^{2D}(E,B) = \frac{|e|B}{\hbar}\sum_i\sum_{N^{(i)}}\delta\left(E - E^{(i)}\right), \qquad (13)$$

The resulting curves, at different magnetic field, are represented in Fig. 6. We can see that the spacing between two adjacent Landau mini-bands increases (Fig. 6a, c and e) and DOS (Fig. 6b, d and f) increases with the magnetic field. It's known that, the highest occupied quantum state corresponds to Fermi level. Thus, when each Landau mini-band pass through Fermi level (Fig. 6c and d) it depopulates and the electrons become free to flow as current, resulting to minima in the longitudinal magnetoresistance R_{xx} and a plateau in the transverse magnetoresistance R_{xy}.

3.4. Interpretation of SDH and QHE

Under high magnetic field, only the ground Landau mini-band with $N^{(1)}= 0$ is populated, as shown on Fig. 6a and Fig. 7. Therefore, when the intensity of magnetic field varies, the number of occupied states changes with B, since the degeneracy of each Landau mini-band, given by $|e|B/h$, changes with B. This will lead to an oscillatory behavior of magnetoresistance known as the Shubnikov-de Haas effect. Such oscillations and quantum Hall effect can be observed only if distinct landau mini-bands exist, which implies that, the mini-band width should be less than the Landau mini-bands spacing $\Delta E^{(i)}<\hbar\omega_c$. According to our calculation for B≤1.2 T, both of SDH and QHE are no longer observed, since all energies above $E^{(1)}_{center}+(1/2)\hbar\omega_c$ are permitted (continuous energy spectrum) as can be seen in Fig. 6e and f. The latter show the limit between classical Hall and quantum Hall effects. These results are in good agreement with the experimental measurements of Pusep et al. [8].

The effect of high magnetic field on band structures and Fermi level is shown in Fig. 7. These results are obtained by using the in-plane wave vectors quantification rule of superlattice given by: $k_p^2= (2N^{(i)}+1)(eB/\hbar)$.

We have calculated the Fermi level energy as a function of B, by using the following formula:

$$n_{2D} = \int_0^{+\infty}\rho_{DOS}^{2D}(E,B)f(E)dE, \qquad (14)$$

with f(E)=1/(1+exp(E-E_F/k_BT)) the Fermi-Dirac distribution.

Table 1. Comparison between experimental observations (ref.[8]) and the calculated magnetic field of R_{xx} minima and maxima, labeled here by B_{min} and B_{max}, respectively.

B_{min}(T)		B_{max}(T)	
Experimental (ref.[8])	Theoretical	Experimental (ref.[8])	Theoretical
7.4	7	5.4	5.1
4	3.9	3.2	3.3
2.6	2.7	2.3	2.4
2	2.1	1.8	1.9

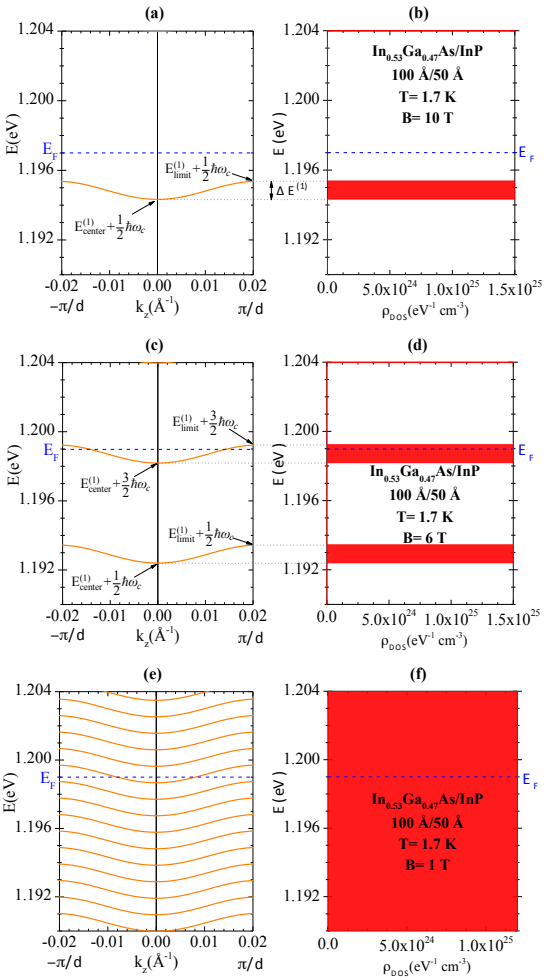

Figure 6: (a), (c) and (e) Quantification of the 1st conduction mini-band (E_1) into Landau mini-bands in first Brillouin zone. (b), (d) and (f) Total energy versus density of states.

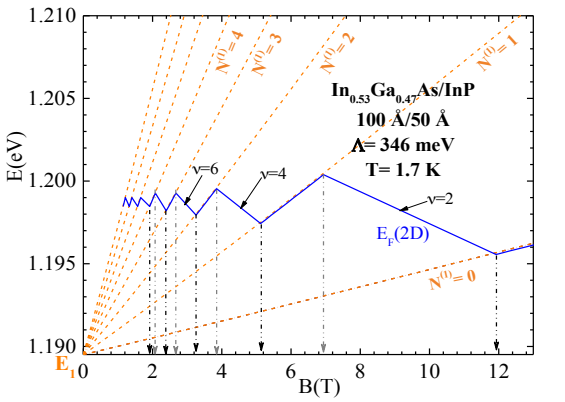

Figure 7: Energy of the conduction Landau mini-bands as a function of magnetic field. The position of Fermi level is also shown. The labeled arrows ν denote the Landau mini-bands filling factors.

with $f(E)=1/(1+\exp(E-E_F/k_BT))$ the Fermi-Dirac distribution. We can notice in the Fig. 7 that, Landau mini-bands energies increase linearly with B. The crossovers between the calculated Landau mini-bands (for $N^{(1)}= 1$ to 4) and Fermi level indicate, almost the same magnetic field of the longitudinal magnetoresistance extrema observed in ref. [8], up to 10 T, as shown in table 1. Note that, under high magnetic fields the peaks in the Shubnikov-de Haas oscillations (R_{xx} maxima) occur at the jumps in the transverse magnetoresistance R_{xy} of quantum Hall effect and each minima of R_{xx} corresponds to a plateau in R_{xy}.

4. Conclusions

In this work, we investigated the band structures properties of $In_{0.53}Ga_{0.47}As/InP$ superlattice, within the envelope function formalism and effective mass approximation. The band gap E_g and mini-bands width decrease and tend to discrete levels of a quantum well when well thickness d_1 increases. We have discussed the supposition of Pusep et al on the effect of valence band offset on the band gap. The computed DOS shows that the system is quasi two dimensional with small k_z dispersion. In addition, the dispersion curves and effective mass m^*/m_0 in the direction of growth and in the plane of this superlattice, show that, the first conduction and valence mini-bands are parabolic and the quasi-two dimensional electron gas effective mass is $0.093m_0$ at 1.7K. The calculated Fermi level of 1.2eV indicates n type conductivity in this sample.

In the presence of quantizing magnetic field, the spacing between Landau mini-bands increases with B and demonstrate the presence of SDH and QHE. According to our calculations both the two effects can be observed only if B> 1.2T. We have interpreted the oscillations of longitudinal magnetoresistance R_{xx} in SDH and R_{xy} in QHE observed by Pusep et al. These results can be used as a guide for the design of $In_xGa_{1-x}As/InP$ nanostructured short infrared detectors.

References

1. Y. A. Goldberg and N. M. Shmidt, in *Handb. Ser. Semicond. Parameters Vol. 2 Ternary Quat. III-V Compd.* (1996), pp. 62–88.
2. T. Asar, S. Özçelik, and E. Özbay, J. Appl. Phys. **115**, 104502 (2014).
3. W.-C. Wang, H.-J. Pan, K.-W. Lin, K.-H. Yu, C.-Z. Wu, L.-W. Laih, S.-Y. Cheng, and W.-C. Liu, Superlattices Microstruct. **29**, 111 (2001).
4. A. Rogalski, in *Infrared Detect. Second Ed.* (CRC Press, 2010), pp. 542–600.
5. L. Pham, X. S. Jiang, and P. K. L. Yu, IEEE Electron Device Lett. **14**, 74 (1993).
6. A. R. Ellis, A. Majumdar, K. K. Choi, J. L. Reno, and D. C. Tsui, Appl. Phys. Lett. **84**, 5127 (2004).
7. A. B. Henriques, L. K. Hanamoto, R. F. Oliveira, P. L. Souza, L. C. D. Gonçalves, and B. Yavich, Brazilian J. Phys. **29**, 707 (1999).
8. Y. A. Pusep, B. G. M. Tavares, M. A. Tito, L. F. dos Santos, and R. R. LaPierre, J. Phys. Condens. Matter **27**, 245601 (2015).
9. A. D. G. Rodrigues, J. C. Galzerani, D. Comedi, and R. R. Lapierre, **36**, 905 (2006).
10. G. Bastard, Phys. Rev. B **25**, 7584 (1982).
11. D. Barkissy, A. Nafidi, A. Boutramine, N. Benchtaber, A. Khalal, and T. El Gouti, Appl. Phys. A **123**, 61 (2017).
12. E. O. Kane, J. Phys. Chem. Solids **1**, 249 (1957).
13. S. Paul, J. B. Roy, and P. K. Basu, J. Appl. Phys. **69**, 827 (1991).
14. Y. A. Goldberg, in *Handb. Ser. Semicond. Parameters Vol. 2 Ternary Quat. III-V Compd.* (1996), pp. 37–61.
15. S. Z. Karazhanov, Semiconductors **39**, 161 (2005).
16. D. V. Lang, M. B. Panish, F. Capasso, J. Allam, R. A. Hamm, A. M. Sergent, and W. T. Tsang, Appl. Phys. Lett. **50**, 736 (1987).
17. A. Ichii, Y. Tsou, and E. Garmire, J. Appl. Phys. **74**, 2112 (1993).
18. C. Ghidoni, R. Magri, and S. Ossicini, Surf. Sci. **489**, 59 (2001).
19. Y. Gusakov, E. Finkman, G. Bahir, and D. Ritter, Appl. Phys. Lett. **79**, 2508 (2001).
20. L. Fernandes dos Santos, Y. Pusep, A. R. Zanatta, and R. R. LaPierre, J. Phys. D. Appl. Phys. **48**, 465101 (2015).
21. Y. P. Varshni, Physica **34**, 149 (1967).
22. H. Ünlü, Solid. State. Electron. **35**, 1343 (1992).
23. H.-S. Cho, J. Vac. Sci. Technol. B Microelectron. Nanom. Struct. **7**, 1363 (1989).
24. T. Ihn, in *Semicond. Nanostructures Quantum States Electron. Transp.* (Oxford University Press, 2009), pp. 287–334.

Parity time symmetry

On-chip optical isolator enabled by adiabatic propagation following an enclosed path in non-Hermitian parametric space

C. Hahn[1], Y. Choi[2], J. W. Yoon[2], S. H. Song[2], and P. Berini[1,3,4*]
[1]School of Electrical Engineering and Computer Science, University of Ottawa, Canada
[2]Department of Physics, Hanyang University, Seoul, Korea
[3]Department of Physics, University of Ottawa, Canada
[4]Centre for Research in Photonics, University of Ottawa, Canada
[*]corresponding author: pberini@uottawa.ca

Abstract- We show that nonreciprocal light propagation occurs following an adiabatic evolution of the parametric path that encircles an exceptional point. Moreover, a device architecture for the nonreciprocal transmission over a broad spectral range is presented. The device is designed for chip-scale operation, and therefore can be applied to a wide range of integration-compatible active photonic devices.

Optical isolators and circulators are important elements that are required in optical signal processing, telecommunications, and for the protection of ultra-short pulsed laser systems. Traditionally, magneto-optic crystals exploiting the Faraday Effect are used to implement efficient nonreciprocal elements in free-space systems. However, realizing on-chip magneto-optic devices integrated with other photonic functions has remained elusive. Different approaches to realize the on-chip nonreciprocal devices suitable with integration have been proposed, including exploiting indirect photonic transitions mediated by dynamic index modulation [1] and nonlinear resonance shifts in asymmetric high-Q microcavities [2]. Such approaches have led to significant nonreciprocal transmission within a chip-scale device footprint, however, other performance limitations such as a high signal power threshold for operation, a low forward-transmission efficiency, and a narrow bandwidth have limited their applications. These limitations should be compensated or eliminated to process broadband signals (including modulation), to respect tight energy-conservation constraints imposed by applications and for stable operation in ambient conditions involving moderate temperature drifts.

Here, we propose a nonlinear coupled-waveguide device which is integration-compatible and nonreciprocal over a broad spectral range. The structure is designed to follow the parametric path that encircles an exceptional point (EP) during the evolution of its non-Hermitian Hamiltonian. Nonreciprocal transmission is achieved due to the non-adiabatic transition during the eigenstate propagation along the path [3]. The parametric path can be built into the coupled waveguide structure by generating the required complex-index distribution along the propagation axis as shown in Fig. 1(a). To realize this in photonic systems, we briefly introduce a lithographic approach to generate the required complex effective-index profile which encircles an EP.

The approach is illustrated in Fig. 1(b). The unidirectional mode converter region consists of two coupled-channel waveguides with an adjacent side patch. In this design, the real effective index profile is created by a z-dependent waveguide-core width, while the imaginary effective index profiles are created via the z-dependent gap-width between the waveguide core and side patch. As represented in Fig. 1(c), the instantaneous eigenvalue diagram of designed unidirectional convertor shows that the two eigenstates

interchange during the parametric evolution. However, as numerically simulated in Fig. 1(d), the eigenstates are uni-directionally converted due to the non-adiabatic transition during propagation following the designed path, which induces nonreciprocity (and isolation) in the device.

We will present theoretical and numerical details for the device architectures and background theories with some experimental results that confirm the proposed nonreciprocal functionalities.

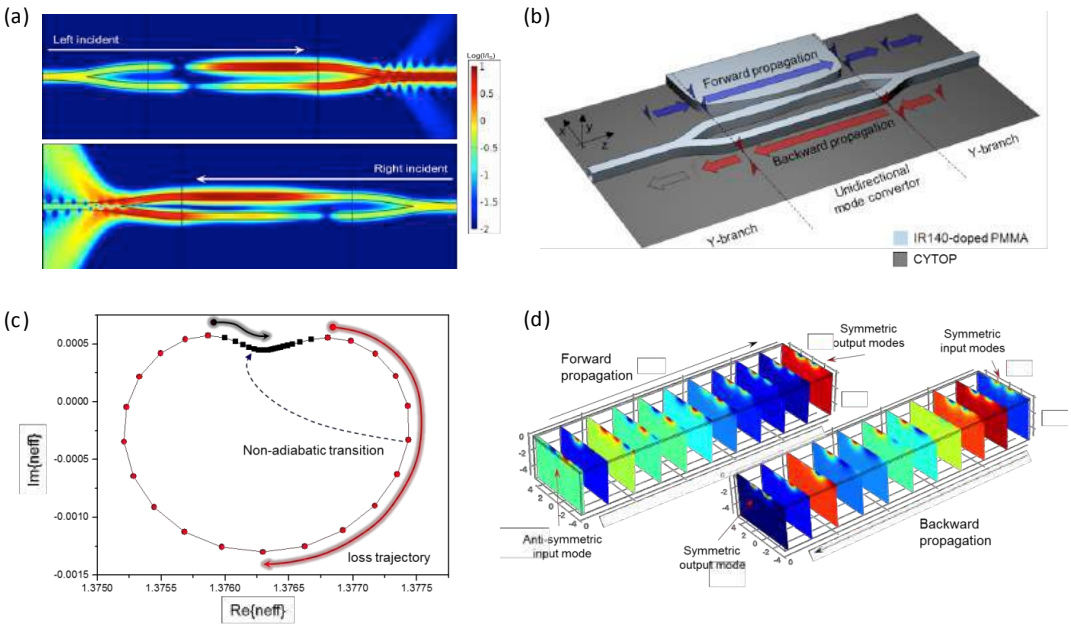

Figure 1. (a) Numerical simulation of nonreciprocity in coupled waveguide system. (b) Schematic illustration of optical isolator with unidirectional mode convertor. (c) Instantaneous eigenvalue diagram for the non-Hermitian path. (d) Unidirectional mode conversion during adiabatic propagation following non-Hermitian path which encircles an exceptional point.

REFERENCES

1. Yu, Z. and Fan, S. "Complete optical isolation created by indirect interband photonic transitions," *Nat. Photonics*, Vol. 3, 91–94, 2009.
2. Fan, L., Wang, J., Verghese, L. T., Shen, H., Niu, B., Xuan, Y., Weiner, A. M. and Qi, M. "An All-Silicon Passive Optical Diode," *Science* Vol. 335, No. 6067, 447–450, 2012.
3. Choi, Y., Hahn, C., Yoon, J. W., Song, S. H. and Berini, P., "Extremely broadband, on-chip optical nonreciprocity enabled by mimicking nonlinear anti-adiabatic quantum jumps near exceptional points," *Nat. Commun.* Vol. 8, 14154, 2017.

Anti-parity-time symmetry
in optical waveguide and electric circuit structures

Youngsun Choi, Choloong Hahn, Jae Woong Yoon, Seok Ho Song*
Department of Physics, Hanyang University, Seoul 133-791, Korea
*corresponding author: shsong@hanyang.ac.kr

Abstract- We demonstrate a spontaneous symmetry breaking and power-difference-conserving light propagation in the anti-parity-time symmetric optical waveguide structures. These optical properties are experimentally realized in the equivalent electric circuit analogy.

Recently, parity-time (PT) symmetric optical systems have been attracted considerable attention due to their unique properties such as unidirectional reflection and nonreciprocal transmission. The anti-PT (APT) symmetry, as a counter part of the PT-symmetry, is expected to exhibit its own unique characteristics. However, experimentally implementing or theoretically designing APT-symmetric optical system is challenging since a strictly APT-symmetric index distribution requires negative index material (NIM) in general [1]. Here we demonstrate an NIM-free optical APT-symmetry and its experimental circuit analogy. In this demonstration, a spontaneous APT-symmetry breaking and anomalous light propagation characteristics are investigated in detail.

To avoid the demand of NIM, which might be an obstacle to experimental implementation, the proposed system is designed to have an APT-symmetric effective Hamiltonian based on all-positive-index materials as shown in Fig. 1(a). The proposed system consists of two gain-guiding waveguides with different core indices. The real refractive index distribution is asymmetric whereas the imaginary refractive index distribution is symmetric. The difference between real parts of core indices is used as a control parameter while imaginary index distributions are maintained.

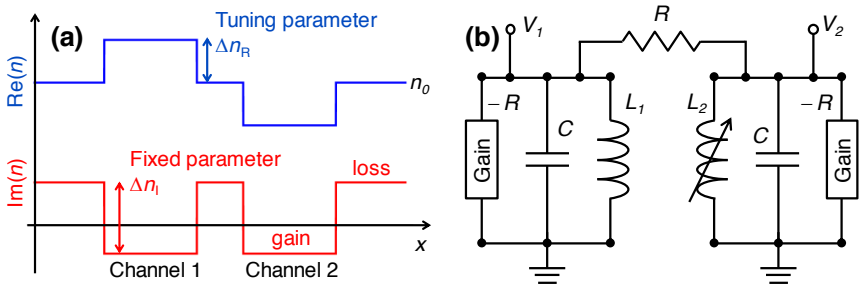

Figure 1. (a) Real and imaginary index distribution in APT-symmetric waveguide coupler. (b) Schematic of APT-symmetric coupled LC-resonators.

In the proposed system, the spontaneous APT-symmetry breaking is manifested as a branch point in the parametric eigenvalue spectrum as shown in Figs. 2(a) and 2(b). The power–difference-conserving light propagations in Figs. 2(c) ~ 2(f) are presented as unique properties that does not appear in the PT symmetric systems. These anomalous dynamics are experimentally investigated with equivalent circuit analogy using two coupled LC-resonators as shown in Fig. 1(b). Taking advantages of the low signal frequency, time-domain measurements are performed with high temporal resolution.

The APT-symmetry may provide opportunities to obtain novel optical properties unattainable in conventional Hermitian or PT-symmetric optical systems.

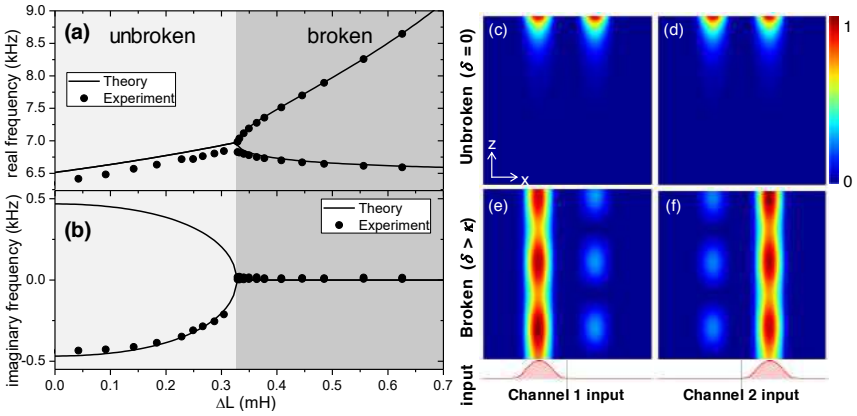

Figure 1. Eigenvalues and dynamics of the APT-symmetric systems. (a, b) Real (a) and imaginary (b) eigenvalues measured in APT-symmetric coupled LC resonator. (c, d) Propagation characteristics in the broken phase of APT-symmetric coupled waveguide.

Acknowledgements, This research was supported in part by the Basic Science Research Program (NRF-2015R1A2A2A01007553) and by the Global Frontier Program through the National Research Foundation (NRF) of Korea funded by the Ministry of Science, ICT & Future Planning (NRF-2014M3A6B3063708).

REFERENCES

1. Ge, L., Tureci, H. E. Antisymmetric PT-photonic structures with balanced positive-negative-indexmaterials. Phys. Rev. A **88**, 053810 (2013).

Quantum states and transport in *PT*-symmetric quasi-one-dimensional lattices

Jung-Wan Ryu[1*], **Nojoon Myoung**[1], **and Hee Chul Park**[1]
[1]Center for Theoretical Physics of Complex Systems, Institute for Basic Science (IBS), Republic of Korea
[*]corresponding author: jungwanryu@gmail.com

Abstract-We study quantum transport in *PT*-symmetric quasi-one-dimensional lattices in which complex band structures appear. Quantum transport in the lattice is measured only in the unbroken *PT*-symmetric phases in the energy band but not in the broken *PT*-symmetric phases. We devise a mechanism for reconfiguration of quantum states that is related to *PT*-phase transition between regions of broken and unbroken *PT*-symmetry.

Non-Hermitian properties in open systems with energy gain and loss has attracted great interest in both theoretical and experimental studies [1]. While we consider a physical system to be isolated, interactions with the environment strongly influence the physical properties of quantum and classical systems by breaking both energy and flux conservation. From a mathematical viewpoint, these open systems can be described by non-Hermitian formalism, with closed ones by Hermitian formalism. In non-Hermitian systems, a potential with a positive imaginary part describes a system that receives energy from its environment but a potential with a negative imaginary part describes a system that loses energy to its environment. Among non-Hermitian systems, parity-time (*PT*)-symmetric systems have the condition that loss and gain are exactly balanced [2]. The *PT*-symmetric systems exhibit a transition from an unbroken *PT*-symmetric phase to a broken phase via exceptional points. While the unbroken phase contains normal dispersive states with real eigenenergies, the broken phase allows for spontaneous symmetry breaking in the eigenstates with complex energies.

In this work, we demonstrate that a bandgap is realized in *PT*-symmetric quasi-one-dimensional lattices by quantum measurement through external leads. The bandgap is shown to be controlled by external parameters such as energy gain and loss, but not by inherent properties such as geometric shape or defects. As a result, we devise a mechanism for reconfiguration of quantum states that is related to *PT*-phase transition between regions of broken and unbroken *PT*-symmetry.

Acknowledgements
This work was supported by Project Code (IBS-R024-D1).

REFERENCES

1. Moiseyev, N., *Non-Hermitian Quantum Mechanics,* Cambridge University Press, New York, 2011.
2. C. M. Bender and S. Boettcher, “Real Spectra in Non-Hermitian Hamiltonians Having *PT* Symmetry,” *Phys. Rev. Lett.* Vol. 80, No. 24, 5243–5246, 1998.

Nanobiophotonics

A freestanding, flexible, tunable, and biocompatible super-resonator and color filter

N. Raeis-Hosseini[1], D. Lee[2], and Junsuk Rho[1, 2, 3*]

[1]Department of Chemical Engineering, Pohang University of Science and Technology (POSTECH), Pohang 37673, Republic of Korea

[2]Department of Mechanical Engineering, Pohang University of Science and Technology (POSTECH), Pohang 37673, Republic of Korea

[3]National Institute of Nanomaterials Technology (NINT), Pohang 37673, Republic of Korea

*corresponding author: jsrho@postech.ac.kr

Abstract- A freestanding resonator based on a natural organic polymer for flexible and biocompatible nano-optics is reported. The device has metal-insulator-metal (M-I-M) structure, which demonstrates perfect absorber and color filter. A facile lithography-free fabrication method based on solution-assisted process and a biocompatible material facilitate the realization of a cost-effective and environmentally benign large-area super absorber. The proposed resonant optical device exhibits a narrow bandwidth absorber with absorption near unity and equivalent functionalities with nano-patterned super absorbers.

Utilization of light at subwavelength with extraordinary optical properties is achieved by nanophotonic materials.[1, 2] Particularly, supernatural transmission and absorption filters based on localized/delocalized resonances have been triumphed by plasmonic metamaterials.[3] However, attainment of large area superior optical filters built on nanoplasmonics under visible wavelength is defying because of high-cost lithography techniques and deficiencies of nanofabrication.[4] We report a planar optical resonator built on a Fabry-Perot (FP) etalon with a lithography-less fabrication[5] process, which is extremely cost-effective.

Multi-layered optical devices have earned research attentions owing to their unique performance and lucrative fabrication in employing of light. The conventional planar resonators encounter deficiencies in sensing abilities due to the inconvenient impact of analytes on the physical variables of the insulator film.[5] We exploited the advantage of a natural biomaterial (NBM) as a bio-inspired material to fabricate an optical device with M-I-M structure, which is capable of being utilized in bio-sensing.

We employ NBM as insulator layer or spacer of the suggested device with biocompatibility, non-toxicity, and biodegradability. The utilized NBM offers exceptional features of the homogeneity, transparency, and hydrogel properties, which makes it a proper material for an absorber and color filter. Through reaction of the insulator thin film with humidified environment, it tunes the resonance wavelengths by swelling. The proposed NBM is sandwiched between two Ag layers, while the substrate is made of NBM (Figure 1a). The NBM, which serves as insulator layer or the spacer of the color filter reacts with the environmental liquids (water) and swells (Figure 1b, c). The resonance mode is altered due to a shift of refractive index (RI) causing an increase in the volume of the spacer.[5] The FP resonances can get tuned by liquid absorption of NBM spacer. During the experiment and measurement, the amount of swelling is governed by changing the liquid type and its pH.

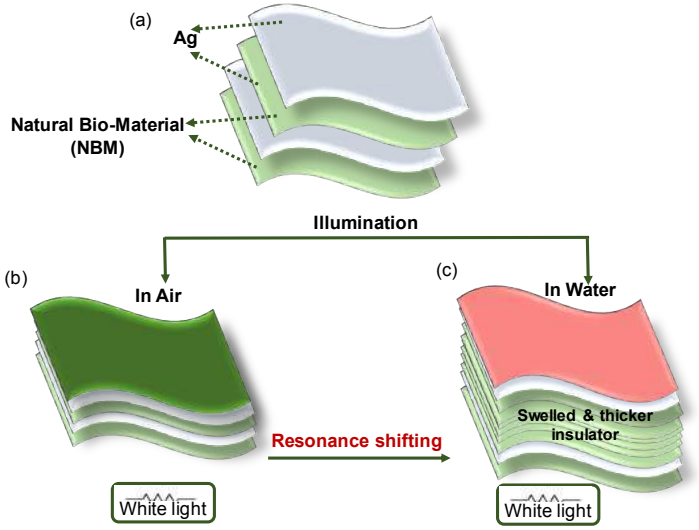

Figure 1. (a) Schematic illustration of a freestanding color filter with M-I-M structure; a natural biomaterial (NBM) is sandwiched between two Ag layers. (b, c) Illumination of the device under white light in air and water, respectively.

In summary, we fabricated and characterized a freestanding perfect absorber and color filter based on NBMs with a facile lithography-less method. Our suggested super absorber shows similar properties of nanostructured plasmonic materials.

Acknowledgements. We acknowledge the financial support by Young Investigator Research program (NRF-2015R1C1A1A02036464), Engineering Research Center program (NRF-2015R1A5A1037668), Global Frontier Research Program (CAMM-2014M3A6B3063708).

REFERENCES

1. Smith, D.R., J.B. Pendry, and M.C. Wiltshire, "Metamaterials and negative refractive index", *Science*, Vol. 305, No. 5685, 788-792, 2004.
2. Zhu, H., F. Yi, and E. Cubukcu, "Plasmonic metamaterial absorber for broadband manipulation of mechanical resonances", *Nature Photonics*, Vol. 10, 709–714, 2016.
3. Burgos, S.P., et al., "A single-layer wide-angle negative-index metamaterial at visible frequencies", *Nature Materials,* Vol. 9, No. 5, 407-412, 2010.
4. Li, Z., S. Butun, and K. Aydin, "Large-area, lithography-free super absorbers and color filters at visible frequencies using ultrathin metallic films", *ACS Photonics*, Vol. 2, No. 2, 183-188, 2015.
5. Kwon, H. and S. Kim, "Chemically tunable, biocompatible, and cost-effective metal–insulator–metal resonators using silk protein and ultrathin silver films", *ACS Photonics*, Vol. 2, No. 12, 1675-1680, 2015.

Early Detection of Gastric Cancer with microRNA-106a using Plasmon Coupling of Hybridized Metal Nanoparticles

Sang-Heon Park[1,2], **Jihye Lee**[1,2], **and Jong-Souk Yeo**[1,2*]
[1] School of Integrated Technology, Yonsei University, Incheon, Republic of Korea
[2] Yonsei Institute of Convergence Technology, Yonsei University, Incheon, Republic of Korea
[*]corresponding author: jongsoukyeo@yonsei.ac.kr

Abstract- To detect miRNA-106a, the promising biomarker for gastric cancer, we demonstrate colorimetric sensing platform based on plasmon coupling effect. The on-chip platform with core-satellite structure is made by conjugation of complementary oligonucleotides between target miRNA-106a and probes which are pre-functionalized on gold nanoparticles, thus enabling to observe the scattering color changes and spectral shift.

1. INTRODUCTION

Although gastric cancer is the second most common cause of cancer-related deaths in the world, early stage detection is still lacking due to the inherent property of cancer cells that are initially small in size and asymptomatic. Thus, early stage detection and prognosis monitoring are very important to avoid the death from later stage presentation of gastric cancer.[1] Current practice for screening gastric cancer completely relies on the endoscopy, however, it is difficult for many people to access endoscopic instruments and expertise for proper screening.

In this paper, we demonstrate an on-chip colorimetric biosensing platform of miR-106a based on the principles of localized surface plasmon resonance (LSPR). The LSPR occurs when the metallic nano particles interact with incident light inducing collective oscillation of conduction electrons on the surface of metallic nanostructure.[2] It can be tuned by the size, shape, materials, and also the plasmon coupling with a nanoscale gap between the particles. When the metallic nanoparticles are sufficiently adjacent to each other, the near-field interaction leads to plasmon oscillations in the particles. This plasmon coupling among the gold nanoparticles (AuNPs) enables our sensing platform.[3, 4]

2. RESULT AND DISCUSSION

In advance of development of the sensing platform, the density of core AuNPs in the detection area needs to be controlled by optimizing the mixing ratio of APTES to OTMS. When the concentration of the APTES is high in a mixing solution with the ratio ranging from 1:0 to 5:1, agglomerated nanoparticles are made so that the bound core AuNPs present a red color. When the concentration of the mixing solution ranges from 3:1 to 3:2, the bound particles show green color. When the concentration is ranging from 1:1 to 0:1, the core AuNPs are not bound to the modified substrate. To observe the colorimetric change and spectral shift clearly, we choose APTES/OTMS mixing ratio of 3:1. By using this mixing solution, we made the substrate with maximum spectral intensity near 550 nm wavelength.

To verify the attachment of nanoparticles via complementary sequence, we have investigated the change in the nanostructure by scanning electron microscopy images (SEM) as shown in Figure 1 (a) and (b). The single AuNPs with 50 nm in diameter are uniformly distributed without the agglomeration (Figure 1 (a)). When the miR-106a is attached, the core-satellite assemblies are made (Figure 1 (b)). These nanoscale assemblies lead to the colorimetric

change, thus enabling the detection of miRNA corresponding to the miRNA concentration. The colorimetric changes are shown in Figure 1 (c) with spectral change and in Figure 1 (d)-(e) with dark-field microscopy. Figure 1 (c) shows the detection of miR-106a by measuring the spectral response from the hybridized core-satellite AuNPs. The single core AuNPs show the green colour (Figure 1 (d)) while the scattering spectrum is red shifted with the formation of core-satellite nanostructure assembly when the 10 μM concentration of miR-106a is applied (Figure 1 (e)).

3. CONCLUSION

In summary, the sensing platform we demonstrated here provides a novel approach of colorimetric detection of miR-106a to use for the early diagnosis of gastric cancer with a potential for clinical application. To make on-chip detection platform, we modified the glass substrate with mixed layer composed of APTES and OTMS to achieve a proper density of core AuNPs. On the modified substrate, we confirm the colorimetric change with the spectral shift of 28.33 nm wavelength for 10 μM concentration of miR-106a. This study proposes the sensing platform for a point of care diagnostics for miR-106a, a potential biomarker for gastric cancer.

Acknowledgements

This research was supported by the MSIP(Ministry of Science, ICT and Future Planning), Korea, under the "ICT Consilience Creative Program" (IITP-R0346-16-1008) supervised by the IITP(Institute for Information & communications Technology Promotion) and also under the "Mid-career Researcher Program" (NRF-2016R1A2B2014612) supervised by the NRF(National Research Foundation).

References

[1] Leung, W. K., Wu, M., Kakugawa, Y., Kim, J. J., Yeoh, K. et al., "Screening for gastric cancer in Asia: current evidence and practice," Lancet oncol.,Vol. 9 No. 3, 279-287, 2008.

[2] Maier, S.A., *Plasmonics: fundamentals and applications*, Springer Science & Business Media, New York, 2007.

[3] Lee, J., Park, J., Lee, J. -Y., and J. -S. Yeo, "Contact Transfer Printing of Side Edge Prefunctionalized Nanoplasmonic Arrays for Flexible microRNA Biosensor," Adv. Sci., Vol. 2, No. 9, 1500121, 2015.

[4] Park, J. and J.-S. Yeo, "Colorimetric detection of microRNA miR-21 based on nanoplasmonic core–satellite assembly," Chem. Commun., Vol. 50, No. 11, 1366-1368, 2014.

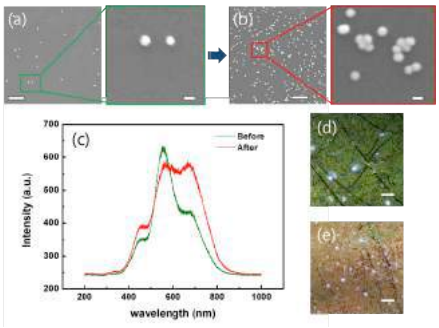

Figure 1. Formation of the core-satellite nanostructures. On the organosilane treated (APTES/OTMS = 3:1) substrate, the 50 nm sized single core AuNPs form core-satellite structure with the 30 nm sized satellite AuNPs by the pairing of complementary sequences between the probes and miRNA-106a. SEM images of (a) the core AuNPs and (b) the core-satellite nanostructures (Scale bars of 1 μm (left) and 100 nm (right) in (a) and (b)). (c) The plot of scattering colour for the core AuNPs and the core-satellite structures. Dark field images of (d) the core AuNPs and (e) the core-satellite nanoparticle structures (Scale bars, 100 μm).

‘Building Up’ NanoMetamaterials Utilizing a Synthetic Biology Approach for Photonic Applications

R. Cullinan[1], C.Liu[2], P.G.Oppenheimer[3] and T.Dafforn[4]
[1]School of Biochemical Engineering, University of Birmingham (DSTL), UK
[2]School of Physics and Astronomy, University of Birmingham, UK
[3]School Biochemical Engineering, University of Birmingham, UK
[4]School of Life Sciences, University of Birmingham, UK

Abstract- *Synthetic biology is a new and emerging field. Utilizing mechanisms found in nature we can reach solutions to problems such as; ‘cloaking’ devices, not currently found within the reaches of traditional science.* [1] *Exploiting the intrinsic nature of M13, a filamentous bacteriophage, to self-assemble we have achieved tuneable 3D nanoarchitectures. Such structures have demonstrated interesting optical characteristics, where a strong non-linear dependence of light induces a resonance shift in the reflected light, and therefore the colour witnessed by you and I.*

Learning from biological processes such as self-assembly can subsequently allow us to contribute to them, from which we can produce endless possibilities in a multitude of applications; from super-lenses to cloaking devices. Taking the principal of the invisibility cloak from ‘Harry Potter’ and translating the idea into real world optical devices *i.e.* through the production of optical metamaterials, is not totally out of reach. Optically interesting materials can be achieved *via* the interaction of nanoparticles with a biomolecule surface. Harvesting the inherent self-assembly nature of biological molecules allows us to develop novel 3D structures capable of displaying metamaterial and/or photonic characteristics. [2]

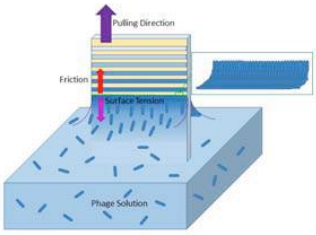

Figure 1. Templating procedure employed to achieve a tuneable 3D scaffold at the air/liquid/solid interface. The scaffold is produced as a result of opposing surface tension and friction forces to create a meniscus at the interface. Templating of M13 (phage) within the solution to the substrate is produced perpendicular to the director axis.

We have utilized the filamentous nature and high aspect ratio of M13 as a scaffold. It’s propensity to self-assemble at the air/liquid/solid interface has been initially set out by Chung et.al. [2] Producing a modified system, we have achieved a tuneable scaffold (Figure 2 and 3).

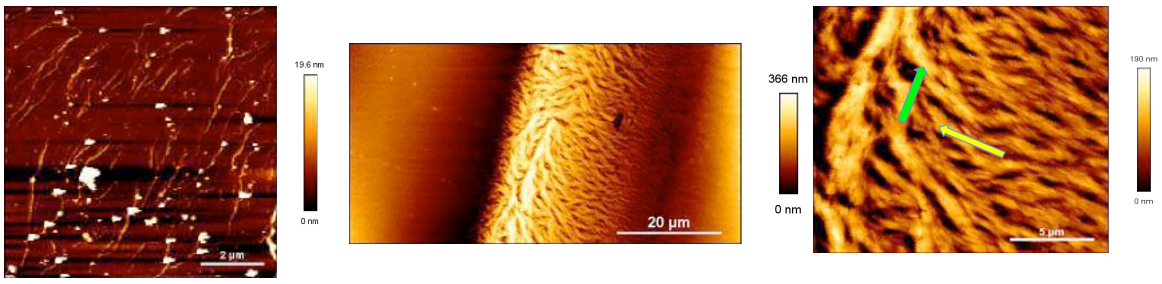

A **B** **C**

Figure 2. Atomic Force Microscopy imaging of M13 phage at 0.01 mg/mL drop casted onto an Au coated silicon (Si) wafer and dried under air (A). 3 mg/mL M13 phage templated at 100 µm/min of vertical shear (B) and a further image at a smaller section of B (C). C demonstrates the ability of M13 to hierarchically self-assemble under suitable conditions.

The tunability of the structure has strong dependence on both the concentration of M13 within the templating solution and speed at which vertical shear onto a substrate is employed (Figure 2). The produced surfaces are able to interfere with visible light to demonstrate non-linear angle dependence, with linearly polarized light when sputter coated with gold (Figure 3) and circularly polarized light when gold (Au) is electrolessly deposited thr

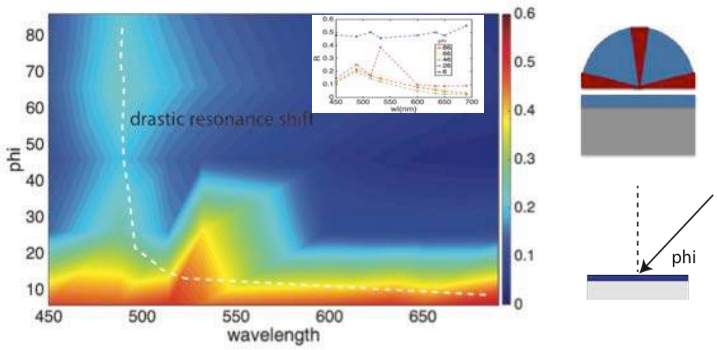

Figure 3. Left, x-polarized light transmitted through a sample of M13 (sputter coated with Au) templated at high speed to yield a densely packed array of ridges and grooves. Inset, the corresponding reflectance data plot. Right, colour respective naked-eye view of the sample.

Acknowledgements, I would like to thank DSTL for funding throughout my PhD, alongside my supervisors Dr Pola G Oppenheimer and Prof. Tim Dafforn for their continued support. I would also like to thank Dr Changxu Liu for the support in gathering of the data for reflectance analysis.

REFERENCES

1. Nie. Z., A. Petukhova A. and E.Kumacheva "Properties and emerging applications of self-assembled structures made from inorganic nanoparticles," *Nat.Nanotechnol,* Vol. 5, No. 1, 15–25, 2010.
2. Wen. A. M., R. Podgornik, G. Strangi and N. F. Steinmetz "Photonics and plasmonics go viral: self-assembly of hierarchical materials," *Rend.Lincei,* Vol. 26, 129-41, 2015.
3. Chung W. -J. "Biomimetic self-templating supramolecular structures," *Nature,* Vol. 478, No. 7369, 364-68, 2011.

Near-field optics and nano-optics

Measurement of far-field to near-field transmission matrix using near-field scanning optical microscopy

E. Seo[1,2], J. Ahn[1,2,3], W. Choi[1,2], Y. Jo[1,2], Q-H Park[2], Y. M. Jhon[3], and W. Choi[1,2]

[1]Center for Molecular Spectroscopy and Dynamics, Institute for Basic Science, Seoul 02841, Korea

[2]Department of Physics, Korea University, Seoul 02841, Korea

[3]Sensor System Research Center, Korea Institute of Science and Technology, Seoul 02792, Korea

[*]corresponding author: wonshik@korea.ac.kr

Abstract- Control of near-field waves is the key to going beyond the diffraction limit in imaging and manipulating target objects. We present the focusing of plasmonic waves, a type of near-field waves, by the wavefront shaping of far-field waves. We coupled far-field waves to a random array of nanoholes on a thin gold film to generate speckled plasmonic waves. By measuring the far-field to near-field transmission matrix and shaping of the far-field wave, we demonstrated the focusing of plasmonic waves at arbitrary position of gold film surface.

Acknowledgements: This research was supported by IBS-R023-D1 and the Global Frontier Project (2014M3A6B3063710) through the National Research Foundation of Korea (NRF) funded by the Ministry of Science, ICT and Future Planning. It was also supported by the Korea Health Technology R&D Project (HI14C0748) funded by the Ministry of Health and Welfare, Republic of Korea.

REFERENCES

1. Seo, E. et al "Far-field control of focusing plasmonic waves through disordered nanoholes," *Opt. Lett.*, Vol. 39, 20, 5838–5841, 2014.

Spectroscopic investigation of localized surface plasmon resonator structure by infrared nanoscopy near the plasma frequency

Y. HUANG[1], J. Vaillant[1], F. Barho[2], F. Barho[2], M. J. Milla[2], M. Bomers[2], F. Gonzalez-Posada[2], L. Cerutti[2], T. Taliercio[2], A. Bruyant[1*]

[1]ICD-LNIO, UMR CNRS 6281, Université de Technologie de Troyes, 12 rue Marie Curie CS 42060, 10004 Troyes, France

[2]CNRS, Institut d´Electronique et des Systèmes, UMR 5214, F-34000, Montpellier, France
[*]corresponding author: aurelien.bruyant@utt.fr

Abstract-We present a nanoscopic investigation of optical modes near plasma frequency of a highly doped semiconductor structure. With a phase sensitive mid-IR s-SNOM [1], we have imaged the complex field distribution of localized surface plasmonic resonators and we have obtained near-field optical amplitude and phase spectrum containing precise information on the dieletric function of the sample, in agreement with simulations. Moreover, our finding corroborates a formal link between Local Density of Optical States and the phase information scattered by a local emitter.

Highly doped InAsSb is an exciting material exhibiting metallic behavior with a plasma frequency ranging from THz to midIR (up 5.5µm) depending on the doping level. Therefore it offers quite unique perspectives for infrared plasmonic devices, notably to create intense Localized Surface Plasmon Resonance (LSPR) for sensing application in the Infrared range, where specificity can be provided by spectroscopic measurement [2].

In our work, a homemade mid-IR scanning near-field microscopy is used to investigate the localized plasmonic modes of submicronic InAsSb ribbon that is 700nm wide and 100nm high. The phase sensitive images reveal the presence of an ultra confined mode on the edge of the ribbon that is confirmed by electromagnetic simulations, shown in figure 1(b). Using the same tool we investigate the peculiar nature of the signal scattered by the probe (a nano-antenna) in the vicinity of the plasma frequency where the permittivity approaches zero, shown in figure 1(d). Finally, we make a link between the obtained phase near-field spectrum and the expected LDOS spectrum.

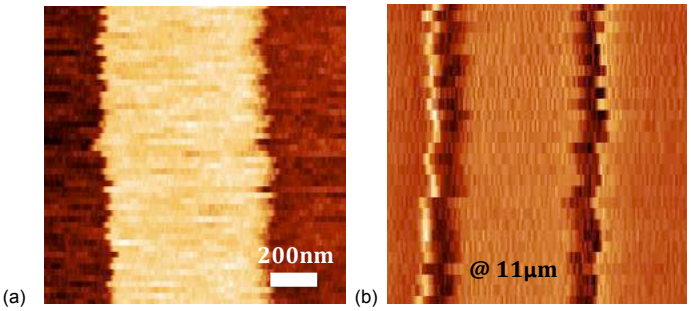

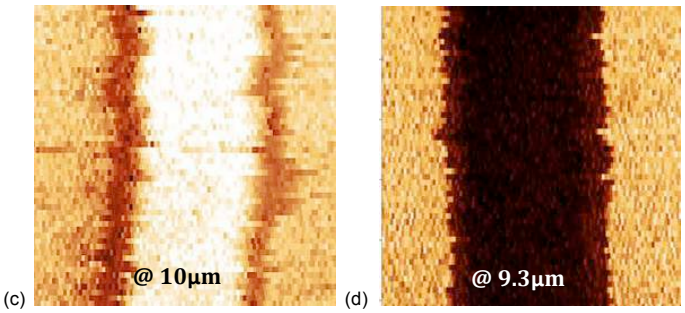

Figure 1: Experimental image of the InAsSb/GaSb gratings: (a) Topography of the ribbon ;(b) Optical Amplitude image at 11µm ;(c) optical amplitude image at 10µm ;(d) optical amplitude image at 9.3µm

REFERENCES

1. Al Mohtar A., Vaillant J., Sedaghat Z., Kazan M., Joly L., Stoeffler C., Cousin J., Khoury A., and Bruyant A. "Generalized lock-in detection for interferometry: application to phase sensitive spectroscopy and near-field nanoscopy". Optics express, 22(18):22232–22245, 2014.
2. Guilengui VN'Tsame, Cerutti L., Rodriguez J-B, Tournié E., and Taliercio T. "Localized surface plasmon resonances in highly doped semiconductors nanostructures". Applied Physics Letters, 101(16):161113, 2012.

Super-resolution imaging

Terahertz dielectric lens for super-resolution images

A.V. Chernyadiev[1*], A.V. Vozianova[1], and M. K. Khodzitsky[1]

[1]ITMO University, 49 Kronverksky pr., Saint-Peterburg, 197101, Russian Federation

[*]corresponding author: alex.chernyadiev@gmail.com

Abstract-In this paper the dependence of the full-width at half-maximun (FWHM) of the terajet from the polarization of the incident light (TE-TM), from the orientation of the structure (two different cross-sections of the composite) is performed. S-parameters and Ey, Hz intensity distributions for TE- and TM-polarized wave was obtained in the COMSOL Multiphysics Software.

In some cases radiation propagating through a microparticle can focus into a narrow, high-intensity electromagnetic beam that continue it's way into the background medium from the shadow-side surface of a plane-wave illuminated lossless dielectric microparticle of a size greater than the illuminating wavelength, λ. This beam can maintain a subwavelength full-width at half-maximun (FWHM) transverse beam width smaller than the classical diffraction limit. It was called «photonic nanojet (PNj)», or simply «nanojet» [1.2]. Due to it's peculiarities nanojet has very promosing applications. Microparticles combined in linear chains close to each other can work as an optical waveguide [3] and assembled in a planar array put on top of a photoresist in a single layer suggests us a maskless subwavelength-resolution direct-write nanopatterning technique [4]. Giant backscattering perturbation phenomenon of PNj allows us to detect and size nanoparticles as small as a few nanometers, that is essential in various biophotonics applications [5-6].

Jet generated in THz frequency range is called «terajet» [7]. In this paper incident wave propagating through the dielectric periodical artificial structure in the shape of the parallelepiped formed a terajet [8]. The structure is perforated. The waist of the terajet (FWHM) was evaluated in COMSOL Multiphysics software using the Finite Element Method (FEM). The value of this parameter defined whether the classical diffraction limit (λ/2) was overcome or not. This parameter depends on: the polarization of the incident wave (TE, TM), the orientation of the structure (in one cross-section the incident light illuminates a rectangle with circle holes and in another one - an alternating layered structure), the permittivity of the photopolymer (ABS $\varepsilon = 2.47$, PLA $\varepsilon = 3.57$, Visijet $\varepsilon = 2.76$) and the permittivity of the 2nd component of the composite (it was air in this case), the period of the holes. The last three items could be united in one parameter – effective permittivity in terms of the effective medium theory. The ratio between this parameter and the range of frequency was obtained – dispersion relations. Devices based on the effect of the terajet could find applications in biological visualization or terahertz microscopy.

Acknowledgements

This work was supported by Government of Russian Federation (Grant 074-U01).

REFERENCES

1. Heifetz A et al "Photonic nanojets" *J. Comput. Theor. Nanosci.*, 6, 1979–92, 2009.
2. Chen Z.G., A. Taflove, and V. Backman "Photonic nanojet enhancement of backscattering of light by nanoparticles: a potential novel visible-light ultramicroscopy technique", *Opt. Express*, 12, 1214, 2004.
3. Yang S. and V. N. Astratov "Experimental demonstration of small-angle bending in an active direct-coupled chain of spherical microcavities", *Appl. Phys. Lett.*, 92, 261111, 2008.
4. Wu W., A. Katsnelson, O. G. Memis, and H. Mohseni "A deep sub-wavelength process for the formation of highly uniform arrays of nanoholes and nanopillars", *Nanotechnology*, 18, 485302, 2007.
5. X. Li, Z. Chen, A. Taflove, and V. Backman "Optical analysis of nanoparticles via enhanced backscattering facilitated by 3-D photonic nanojets", *Opt. Express*, 13, 526 (2005).
6. A. Heifetz, J. J. Simpson, S.-C. Kong, A. Taflove, and V. Backman "Subdiffraction optical resolution of a gold nanosphere located within the nanojet of a Mie-resonant dielectric microsphere", *Opt. Express*, 15, 17334, 2007.
7. Pacheco-Peña V., M. Beruete, I. V. Minin, and O. V. Minin "Terajets produced by dielectric cuboids", *Applied Physics Letters*, 105, 084102, 2014.
8. Khodzitsky M.K., A.V. Vozianova, V.V. Gill, A.V. Chernyadiev, A.N. Grebenchukov, I.V. Minin, O.V. Minin "Formation of terahertz beams produced by artificial dielectric periodical structures" // *Proceedings of SPIE - 2016*, Vol. 9918, pp. 99182X.

Super-Resolution by Nonlinear Photo-Modulated Reflectivity.

O. Tzang, D. Hershkovitz and O. Cheshnovsky*

School of Chemistry, the Sackler Faculty of Exact Sciences, Tel Aviv University, Tel Aviv, Israel

*corresponding author: orich@post.tau.ac.il

Abstract-We introduce a far field label-free SR methodology that is based on the nonlinear reflectance changes induced by photo-modulation. Following an ultra-short pump pulse, an overlapping delayed probe pulse monitors the nonlinear reflectance changes. Spatial resolution within the diffraction limited spot is enhanced as the square root of the nonlinearity order. The method is compatible with semiconductors and metals, in vacuum and air, ultrathin and thick samples alike. Examples of resolution enhancement in several materials (<90nm) are demonstrated.

Far-field super-resolution (SR) microscopy has developed to be an important tool in life sciences. However, it relies on, and therefore is limited by the ability to control the fluorescence of label molecules or nanoparticles. While in many cases, label-free far-field microscopy is required, an equivalent SR technique is not available.

We introduce a new far field label-free SR methodology that is based on the nonlinear response of the reflectance to photo-modulation [1-3]. It relies on the ability to photo-excite a temperature and/or charge-carriers spatial distribution inside the diffraction limited spot by an ultra-short pump pulse. In Nonlinear photo-modulated Reflectivity (NPMR) an overlapping delayed probe pulse monitors the nonlinear reflectance changes. By scanning over the sample and measuring the NPMR, spatial resolution is enhanced. NPMR is measured by recording the high harmonics in the probe laser reflectance. The improvement in resolution scales like $\sqrt{n}$, where n is the nonlinearity order.

In order to achieve a reliable response in high harmonics, pure sine modulation is required. By using an acouto-optic modulator coupled to an arbitrary wave-form generator, we have succeeded in modulating our pump source with harmonic impurity down to 10^{-4}.

Examples of resolution enhancement due to nonlinearities are presented: The change of thermo-reflectance of VO_2 upon its characteristic insulator-to-metal transition, the heating process of a nanostructured silicon or gold surfaces, and the nonlinear response of photo-modulated Raman spectra. Super-resolution down to 85nm is demonstrated with a probe laser of 800nm wavelength. NPMR is suitable to characterize semiconductors and metals in vacuum, ambient, and liquid, semi-transparent and opaque systems, ultrathin and thick samples alike.

REFERENCES

1. Tzang, O., Pevzner A., Marvel, R.E., Haglund, R.F. and Cheshnovsky, O. "Super-Resolution in Label-Free Photomodulated Reflectivity" *Nano Letters*, Vol. 15, 1362 ,2015.

[2] Tzang, O. and Cheshnovsky, O., "New modes in label-free super resolution based on photo-modulated reflectivity" *Optics Express,* Vol. 23, 20926, 2015.

[3] Tzang, O., Azoury, D. and Cheshnovsky, O., "Super resolution methodology based on temperature dependent Raman scattering" *Optics Express*, Vol. 23, 17929, 2015.

Transformational electromagnetics, cloaking

Omnidirectional Invisibility Cloak Based on A Two-step Linear Transformation

Youming Zhang[1], Yu Luo[2], and Baile Zhang[1,3,*]

[1]Division of Physics and Applied Physics, School of Physical and Mathematical Sciences, Nanyang Technological University, Singapore 637371, Singapore

[2]School of Electrical and Electronic Engineering, Nanyang Technological University, Singapore 637371, Singapore

[3]Centre for Disruptive Photonic Technologies, Nanyang Technological University, Singapore 637371, Singapore

[*]corresponding author: blzhang@ntu.edu.sg

Abstract-Realizing an invisibility cloak has drawn great research interests since the theory of transformation optics was proposed. However, previous demonstrations of invisibility cloaks suffered from various problems due to the complex parameters required, though significant achievements have been achieved both in microwave and optical frequencies recently. Here, we propose and demonstrate a cloak based on a two-step linear transformation that works for omnidirection at microwave frequencies. This work could push the research of cloak realizations one step forward.

Rendering an object invisible has long been a fantasy of people for decades. Recently, invisibility cloak has captured wide scientific interests since the theory of transformation optics[1, 2] was proposed in 2006. Significant achievements in invisibility cloak realizations have been achieved both in microwave[3-6] and optical frequencies[7-13]. However, due to the complex parameters required, previous demonstrations still suffer from various problems such as impedance mismatch[3, 10, 11], unidirection[6, 13], single polarization[3, 10, 11], lateral shift[4, 5, 7-9, 14] and narrow bandwidth[3, 6] etc. Here we propose and demonstrate an invisibility cloak based on a two-step linear transformation that works for omnidirection at microwave frequencies. The cloak requires extremely anisotropic media with both zero and infinity which are realized by periodic metallic structures. The work could inspire the study of extremely anisotropic metamaterials and push the research of cloak realization one step forward.

REFERENCES

1. Pendry, J. B., Schurig, D., and Smith, D. R., "Controlling Electromagnetic Fields", *Science*, Vol. 312, No. 5781, 1780-1782, 2006
2. Leonhardt, U., "Optical Conformal Mapping", *Science*, Vol. 312, No. 5781, 1777-1780, 2006
3. Schurig, D., Mock, J. J., Justice, B. J., Cummer, S. A., Pendry, J. B., Starr, A. F., and Smith, D. R., "Metamaterial Electromagnetic Cloak at Microwave Frequencies", *Science*, Vol. 314, No. 5801, 977-980, 2006
4. Liu, R., Ji, C., Mock, J. J., Chin, J. Y., Cui, T. J., and Smith, D. R., "Broadband Ground-Plane Cloak", *Science*, Vol. 323, No. 5912, 366-369, 2009
5. Ma, H. F. and Cui, T. J., "Three-dimensional broadband ground-plane cloak made of metamaterials", *Nature Communications*, Vol. 1, No. 21, 2010

6. Landy, N. and Smith, D. R., "A full-parameter unidirectional metamaterial cloak for microwaves", *Nature Materials*, Vol. 12, No. 1, 25-28, 2013
7. Gabrielli, L. H., Cardenas, J., Poitras, C. B., and Lipson, M., "Silicon nanostructure cloak operating at optical frequencies", *Nat Photon*, Vol. 3, No. 8, 461-463, 2009
8. Valentine, J., Li, J., Zentgraf, T., Bartal, G., and Zhang, X., "An optical cloak made of dielectrics", *Nat Mater*, Vol. 8, No. 7, 568-571, 2009
9. Ergin, T., Stenger, N., Brenner, P., Pendry, J. B., and Wegener, M., "Three-Dimensional Invisibility Cloak at Optical Wavelengths", *Science*, Vol. 328, No. 5976, 337-339, 2010
10. Zhang, B., Luo, Y., Liu, X., and Barbastathis, G., "Macroscopic Invisibility Cloak for Visible Light", *Physical Review Letters*, Vol. 106, No. 3, 033901, 2011
11. Chen, X., Luo, Y., Zhang, J., Jiang, K., Pendry, J. B., and Zhang, S., "Macroscopic invisibility cloaking of visible light", *Nature Communications*, Vol. 2, No. 176, 2011
12. Ni, X., Wong, Z. J., Mrejen, M., Wang, Y., and Zhang, X., "An ultrathin invisibility skin cloak for visible light", *Science*, Vol. 349, No. 6254, 1310-1314, 2015
13. Chen, H., Zheng, B., Shen, L., Wang, H., Zhang, X., Zheludev, N. I., and Zhang, B., "Ray-optics cloaking devices for large objects in incoherent natural light", *Nat Commun*, Vol. 4, No., 2013
14. Zhang, B., Chan, T., and Wu, B.-I., "Lateral Shift Makes a Ground-Plane Cloak Detectable", *Physical Review Letters*, Vol. 104, No. 23, 233903, 2010

Construction methods of auxetic structures with hourglass shaped units and its application to smart transformation optics

Junhyun Kim[1] and Kyoungsik Kim[2]
[1]School of Mechanical Engineering, Yonsei University, Seoul 120-749, Republic of Korea
[*]corresponding author: twosteps@yonsei.ac.kr

Abstract- In this paper, we illustrate the methods of constructing structures with negative Poisson's ratio with rigid sliding units. By numerical evaluation we describe its mechanical properties and show structures exhibit auxetic behavior indeed. We discuss its future productivity and its application to smart transformation optics.

Engineers can control electromagnetic waves through coordinate transform based on invariance of Maxwell's equation [1]. While conventional transformation optics require anisotropic permittivity and permeability, in quasi-conformal mapping, electromagnetic devices require isotropic dielectric materials only [2]. Smart transformation optics regards mechanical deformation of medium as coordinate transformation [3, 4]. Using metamaterials with negative Poisson's ratio (so called auxetic behavior), smart transformation optics satisfy quasi-conformal transformation [3, 4]. Unlike normal object, structures with auxetic behavior exhibit negative Poisson's ratio [5]. In this paper, we show how we can construct auxetic structures with 'hourglass shaped units' [6]. Changing its geometrical condition, we show that the proposed structures always exhibit auxetic behavior indeed. We also derive its mechanical properties such as on axis Young's modulus to quantify its stiffness of the structure. Last we show its possibility to application to smart transformation optics as a basic material of optical medium.

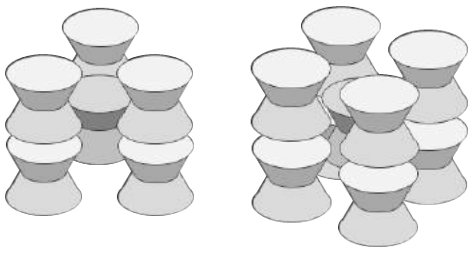

Figure 1 Constructed auxetic structures with hourglass shaped units

Acknowledgements This research was supported by Low Observable Technology Research Center program of the Defense Acquisition Program Administration and Agency for Defense Development.

REFERENCES

1. J. B. Pendry, D. Schurig, and D. R. Smith, "Controlling electromagnetic fields ", Science. 312, 1780-1782 (2006).
2. J. Li, and J. B. Pendry, "Hiding under the carpet: A new strategy for cloaking," Phys. Rev. Lett., vol. 101, p. 203901, 2008
3. D. Shin, Y. Urzhumov, D. Lim, K. Kim, and D. R. Smith, "A versatile smart transformation optics device with

auxetic elasto-electromagnetic metamaterials", Sci. Rep. 4, 1-9(2014)

4. D. Shin, J. Kim, D. Yoo and K. Kim, "Design of 3D isotropic metamaterial device using smart transformation optics", Opt. Express. 17, 21892-21898(2015)
5. D. Attard and J. N. Grima. "A three-dimensional rotating rigid units network exhibiting negative poisson's ratios," *Phys. Status. Solidi B*, 246, 1330–1338, 2011.
6. J. Kim, D. Shin, S. Lee, J. Lee, S. Kwon, S. Yoon, D. Yoo and K. Kim, "Auxetic structures with regularly configured rigid sliding units," *Phys. Status. Solidi B*, DOI 10.1002/pssb.201600335, 1600335, 2017.

Gradient permittivity plasma and metamaterial in numerical analysis to reduce the size of cloaking.

A. Bambina[1], **S. Yamaguchi**[1], **A. Iwai**[2], **Y. Kabe**[1], **S.Miyagi**[1] and **O. Sakai**[1]

[1]The University of Shiga Prefecture, Japan
[2]Kyoto University, Japan
zn68abambina@e.usp.ac.jp

Abstract— Clocking for microwaves is investigated numerically in a model integrating plasma with anisotropic metamaterial. Realization of cloaking requires media with designed permittivity and permeability parameters. Invisibility observed in this study is based on spacial gradient of permittivity in plasma and anisotropic permeability in metamaterial. This report demonstrates our numerical results based on the finite-difference time-domain (FDTD) method. These results indicate potentials and possible advantages coming from spacial gradient of plasma permittivity with anisotropic permeability.

1. INTRODUCTION

Metamaterial has independent control of permeability μ and permittivity ϵ_p; they support all real values in arbitrary directions [1]. Characteristics of independence work as anisotropic properties and, in addition, their values can vary in space to make a gradient [8]. Anisotropie property and gradient existence are key factors for cloaking [4, 7, 8]. Alternatively, plasma can be used in a cylindrical device to change the permittivity ϵ_p, which will be shown in Figure 2(b) [8, 3]. Here we report numerical results to show an advantage about its smooth gradient for a cylindrical cloak. To find the perfect cloaking characteristic, transformation optics was used [8]; in our case the gradient has a slight mismatch between theoretical prediction from transformation optics and possible parameters of plasma. In the interest of the numerical code, we use electric and (hypothetical) magnetic currents in the Maxwell equations to include plasma and metamaterial effects on ϵ_p and permeability μ respectively. In this study, we test the size of our cloak by a numerical code integrating the requirements for cloaking. Our analysis is focused on scattering wave created by different size of cloaking.

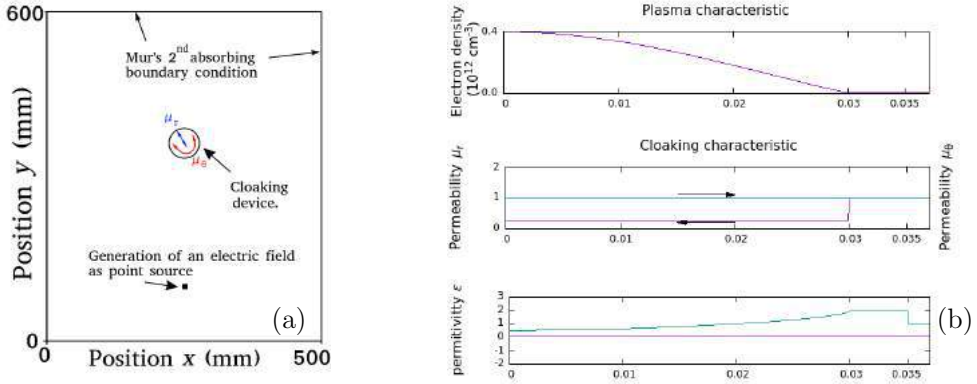

Figures 1: (a) Schema of the numerical code, (b) characteristic use for our cloaking device.

2. NUMERICAL CODE

We developed a code in the finite-difference time-domain (FDTD) method in two-dimension space (500 mm $\times$ 600 mm on the x-y plane), as show in Figure 1. A point microwave source at 6 GHz is placed at $x = 250$ mm and $y = 100$ mm. Our cloaking [4] is made around a metallic monopole placed at $x = 250$ mm and $y = 360$ mm. Integration effect of plasma with ϵ_p and metamaterial

with anisotropic μ is due to electric and magnetic current densities in the Maxwell equations [5, 6]. The time resolution for the Maxwell equations is every 0.5 ps, and the boundary of the delimited space is made of the 2nd Mur's boundary condition to have the perfect absorption boundary. We assume the plasma in a vacuum chamber composed of a dielectric container of 30-mm inner radius, and the smooth gradient of ϵ_{p} is supported by a natural profile of electron density [4], shown in a smooth gradient of permittivity in radial coordinate [2, 3]. We did not fix the permittivity of the container wall to see its impacts, like $\epsilon = 1.0$, 2.0 and 3.0.

3. LIMIT EFFECT OF THE SIZE FOR CLOAKING

Figure 2 (a) and (b) show results of power as square of electric fields at a fixed time for 60-mm- and -80-mm-diameter devices. In Figure 2 (c) we compare the cloaking size with amplitude of the scattering wave; each amplitude is devided by the radius to have calibrated values because of the mismatch between possibility from plasma and perfect cloaking. From Figure 2 (c), we note that the scattering wave is significant when the size is comparable with about quarter of the wavelength in all values of dielectric permittivity $\epsilon_{\mathrm{p}} = 1.0$, 2.0 and 3.0.

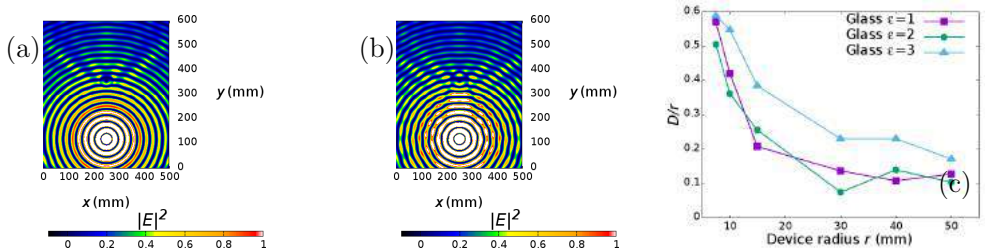

Figures 2: Scattering wave in space with cloaking of (a) 60-mm-radius, (b) 80-mm radius, and (c) fluctuation level of $|E^2|$ (D) normalized by radius r.

4. CONCLUSION

Plasma as metamaterial can be used in cloaking; the cloaking with plasma can be a configuration compressed to a lower limit. The size limit is close to quarter of the wavelength of the electromagnetic wave. The underlying physics on this limit may be based on Rayleigh diffraction, the slope of the plasma and the FDTD grid which is limited by our calculation precision.

ACKNOWLEDGMENT

This study was supposed by Grant-Aid for Scientific Research from the Japanese Ministry of Education, Culture, Sport, Science and Technology, Japan.

REFERENCES

1. Pendry, J. B., A. J. Holden, D. J. Robbins and W. J. Stewart, "Magnetism Conductors and Enhanced Nonlinear Phenomen," *IEEE Trans. on Micro. theory and tech.*, Vol. 47, No. 11, 2075–2084, 1999.
2. Sakai, O. and Tachibana, K., "Plasma as metamaterial: a review," *Plasma Sources Sci. Technol.*, Vol. 21, No. 1,013001-1-18, 1-18, 2012.
3. Lieberman, M. A. and A. J. Lichtenberg, *Principles of plasma Discharges and Materials Processing*, Wiley-Interscience, New Jersey, 2005.
4. Sakai, O., S. Yamaguchi, A. Bambina, A. Iwai, Y. Nakamura, Y. Tamayama and S. Miyagi, "Plasma metamaterials as cloaking and nonlinear media," *Plasma Phys. Control. Fusion.*, Vol. 59, No. 1, 014042-1-10, 2016.
5. Petrin, A., *Wave propagation*, InTech, 2011.
6. Bambina, A., S. Yamaguchi and O. Sakai , "Anisotropic magnetic property in numerical analysis for electromagnetic wave propagation around metamaterial cloaking device," (Submitted)
7. Schuring, D., J. B. Pendry and D. R. Smith, "Calculation of material properties and ray tracing in transformation media," *Opt. Exp.*, Vol. 14, No. 21, 9794–9804, 2006.
8. Schuring, D., J. J. Mock, B. J. Justice, S. A. Cummer, J. B. Pendry, A. F. Starr and D. R. Smith, "Metamaterial Electromagnetic Cloak at Microwave Frequencies," *Phys. Rev. Lett.*, Vol. 314, No. 5801, 977–980, 2006.

Curvature and Transformations

Paul Kinsler[1,2,3], **Jonathan Gratus**[1,2], **and Martin McCall**[3]

[1]Lancaster University, Lancaster LA1 4YB, United Kingdom
[2]Cockcroft Institute, Daresbury, WA4 4AD, United Kingdom
[3]Imperial College London, SW7 2AZ, United Kingdom
dr.paul.kinsler@physics.org

Abstract— We discuss the presence and role of curvature in transformation optics and other transformation fields. Further, we show where and why it is not induced by cloaking transformations, but where and why it can be in other cases.

The original spatial cloak proposals [1] showed how light could be steered around an object in a way intended to make it invisible from all angles. The way the initially straight wavefronts – or ray paths – are transformed into curved ones begs the question: can transformation optics induce curvature? For example, a cloaking device might attempt to mimic an empty space, or a curved waveguide attempt to mimic a straight one. In such cases, despite ray paths becoming curved in the colloquial sense, the mimicry would not work if the true (mathematical) curvature differed between the device and its intended appearance (i.e. its design).

However, we can also consider other constructions, such as the Maxwell's Fisheye Lens [2] stereographic projection which makes a plane look like a sphere; or indeed any transformations between different and obviously curved surfaces. One notable case of such a "topographic transformation" [3] is the pioneering surface wave cloak of Mitchell-Thomas et al. [4]. Since we cannot escape the role of curvature in these cases, we here develop a description of the machinery and concepts needed to handle – and perhaps more importantly, *clarify* – this.

In what follows we will discuss everything in terms of transformation optics; although same arguments can be applied to other transformation fields.

Figure 1: We use device properties to hide the host space metric ($\bar{g}$) and make the space look as if it has some desired design space metric ($\hat{g}$). This means the device does not have a notion of a metric in and of itself – its constitutive properties act as a *transformation* between one metric and another. (Figure reused with permission [5]).

Any given situation, whether it be intended as a design or reference case, or as the device itself, can be codified here in terms of of three things: **First,** the geometry of the background space which will have some metric $g_{\alpha'\beta'}$; **Second,** the effect of the device we have constructed, i.e. the optical medium placed in the background space, which we denote $\mathfrak{M}^{\alpha'\beta'}_{\alpha\beta}$; **Third,** the metric seen by the light travelling within the device is a combination of the background space metric and the optical medium, the net effect giving rise to an effective or optical metric $\mathfrak{C}_{\alpha\beta}$.

We denote (a) the optical/effective metric to be $\mathfrak{C}$, (b) the lab/spacetime/background metric to be g, where the two are linked by (c) material properies $\mathfrak{M}$; so that

$$\mathfrak{C}_{\alpha\beta} = \mathfrak{M}^{\alpha'\beta'}_{\alpha\beta}\ g_{\alpha'\beta'}. \tag{1}$$

This treatment in terms of optical metrics addresses only part of the full electromagnetic system, which is a wave theory based on a full set of constitutive parameters, and contains polarization-dependent properties. However, as we will show, it performs extremely well and covers the most important features with regards to the presence or absence of curvature.

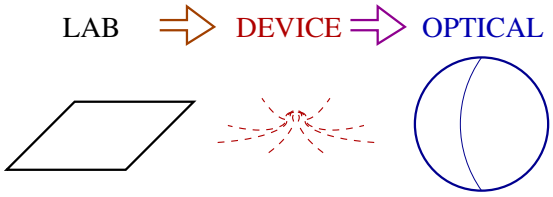

Figure 2: A flat lab space can be transformed into a curved optical space using a device with an inhomogeneous optical properties. The most famous example is the Maxwell's fisheye lens, whose index profile can be calculated by means of a standard stereographic projection from the sphere to the plane. (Figure reused with permission [5]).

From the simple representation of the transformation optics scenario shown in fig . 2, we can see that there are two places where curvature might exist, i.e. in the reference/laboratory space, and in the design space. Because any transformation must be a diffeomorphism, these two curvatures must be identical as far as the relevant optical (wave, ray) properties are concerned. For devices such as illusion generators or cloaks this is indeed the very *point* of the device design; and is independent of whether or not the laboratory space has an underlying curvature or not – e.g. because the spacetime is curved, or because the waves under consideration are confined to a curved sheet.

Despite the clear "no induced curvature" conclusion from earlier, what about Maxwell's fisheye lens? Since this is based on a stereographic projection of a sphere onto a plane, it is clearly possible to point to an initially curved laboratory space (i.e. the sphere), and a final lab space which is flat (i.e. the plane). Although the optical behaviour remains identical – propagation as if on a sphere – some aspects of curvature have altered.

We will show how a more sophisticated re-imagining of the situation shown in fig. 2 can resolve this, with allowances made for alterations in both the lab space and the device, whilst keeping the design criteria fixed.

We demonstrate that all transformation designs never induce curvature – the final in-device wave properties act to all intents and purposes as if travelling on the same space as the reference case: typically these spaces are both flat as far as the propagating wave is concerned. Nevertheless, the "location" of curvature in the system can be shifted from the lab space to the device properties, or vice versa, and we will show how to systematize this process.

ACKNOWLEDGMENT

PK and JG acknowledge support from STFC (the Cockcroft Institute ST/G008248/1) and EPSRC (the Alpha-X project EP/J018171/1 and EP/N028694/1); MWM is grateful for support from EPSRC (EP/K00305/1).

REFERENCES

1. Pendry, J. B., et al., "Controlling Electromagnetic Fields", *Science* Vol. 312, 1780-1782 2006.
2. Luneburg, R. K. "Mathematical Theory of Optics", UC Press, Berkeley, California, 1964.
3. Kinsler, P., McCall, M. W., "Transformation Design: metrics and speeds", arXiv:1510.06890.
4. Mitchell-Thomas, R. C., et al, "Perfect Surface Wave Cloaks", *Phys. Rev. Lett.* Vol. 111, 213901, 2013.
5. Kinsler, P., internal report, 2017.

Space transformation based multi-beam generation lens antenna

R. Feng[1], J. Yi[1,*], H. Zhang[1], A. de Lustrac[2] and S. N. Burokur[3]

[1]State Key Laboratory of Integrated Services Networks, Xidian University, Xi'an 710071, Shaanxi, China
[2]Centre de Nanosciences et de Nanotechnologies, CNRS, Univ. Paris-Sud, Université Paris-Saclay, C2N – Orsay, 91405 Orsay cedex, France
[3]LEME, EA 4416, Université Paris Ouest, 92410 Ville d'Avray, France
[*]corresponding author: jianjia.yi@xidian.edu.cn

Abstract-A 3D flat cuboid shaped lens calculated by spatial light transformation method for electromagnetic field shaping is proposed. The lens is capable of generating multi beams by reshaping the omnidirectional emission of a monopole antenna into four or more beams. Such manipulation is simulated and analyzed by solving the Laplace's equation. The design implies a potential 3D realization with all-dielectric gradient refractive index metamaterials.

Transformation optics (TO) is one of the most powerful conceptual techniques for the design of devices which leverage complex materials. TO enables to alter the field distribution by choosing material parameters which cause light to 'behave' as if it was in a transformed set of coordinates [1,2] and novel applications have been explored rapidly and quantitively. Hu et al. [3] found the equivalence between coordinate transformation and spatial deformation and propose to use Laplace's equation to determine the deformation of coordinate grids. Thus, it has been widely applied to design arbitrary broadband devices such as the carpet cloak [4] and functional lenses [5,6] with all-dielectric materials. In this study, we propose the design of a 3D lens with a flat cuboid shape that can significantly reshape the directivity of a monopole antenna into four directive beams [7]. Such a 3D lens can be obtained by the 2D design extension along *z* direction.

The designed model is based on quasi-conformal transformation optics (QCTO) and achieved by solving Laplace's equation. For fields' equivalence at the outer boundaries with the virtual space, Neumann and Dirichlet sliding boundary conditions are set at the edges of the cap lens:

$$\begin{aligned} x'\big|_{\overset{\frown}{A'B'}} = x, \quad x'\big|_{C'D'} = \sqrt{R^2 - y^2}, \quad \hat{n}\cdot\nabla x'\big|_{B'C',D'A'} = 0 \\ y'\big|_{\overset{\frown}{A'B'}} = y, \quad y'\big|_{C'D'} = \sqrt{R^2 - x^2}, \quad \hat{n}\cdot\nabla y'\big|_{B'C',D'A'} = 0 \end{aligned} \tag{1}$$

The range of ε_{zz} is related to the deformation between the physical space and the virtual space. We consider the initial parameters as $R = 4\sqrt{2}$ cm, r = 1 cm. In this case, the permittivity distribution ranges from 0 to 2.8. To refrain from using resonant metamaterials and to support a potential all-dielectric realization process, we have to consider ε_{zz} values below 1 as unity. The electric near field distribution of the lens for broadband performances is presented as illustrated in Fig. 2.

This work was supported in part by the National Natural Science Foundation of China under grant No. 61601345. J.Yi acknowledges the partial support from the Fundamental Research Funds for the Central

Universities (XJS16046, JB160109) and 111 Project under Grant B08038.

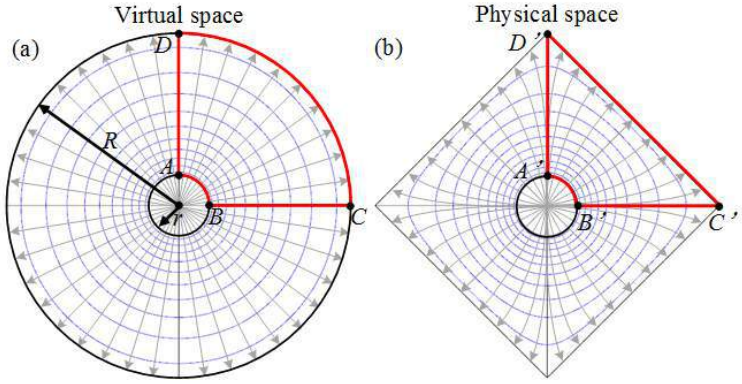

Fig. 1: Illustration showing the space mapping from the virtual space to the physical space.

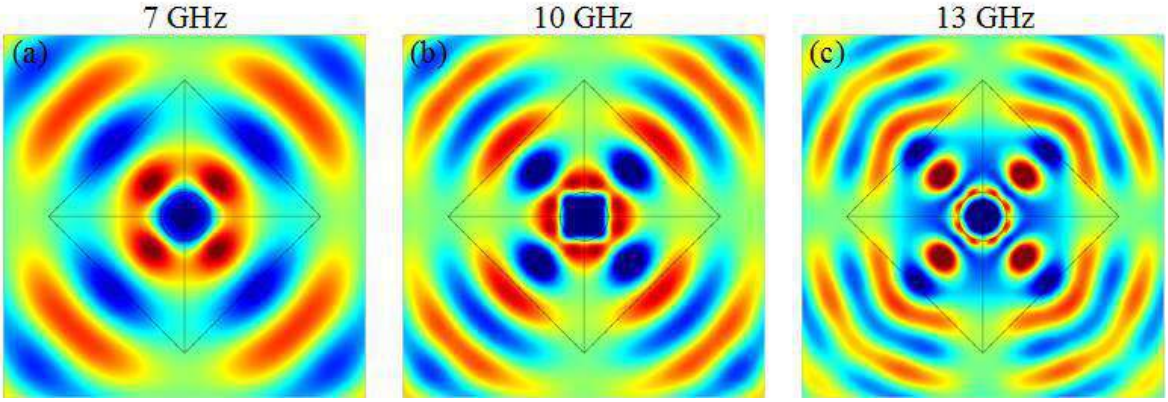

Fig. 2: Simulated electric near field distributions in the *x*-*y* plane, at (a) 7 GHz, (b) 10 GHz and (c) 13 GHz.

REFERENCES

1. Leonhardt, U., "Optical conformal mapping," *Science*, Vol. 312, No. 5781, 1777-1780, 2006.
2. Pendry, J. B., Schurig, D. and Smith, D. R., "Controlling electromagnetic fields," *Science*, Vol. 312, No. 5781, 1780-1782, 2006.
3. J. Hu, X. M. Zhou and G. K. Hu, "Design method for electromagnetic cloak with arbitrary shapes based on Laplace's equation," Opt. Express, Vol. 17, pp. 1308, 2009.
4. Li, J. and Pendry, J. B., "Hiding under the carpet: A new strategy for cloaking," *Phys. Rev. Lett*., Vol. 101, No. 20, 203901, 2008.
5. Yi, J., Burokur, S. N., Piau, G.-P., de Lustrac, A., "Coherent beam control with an all-dielectric transformation optics based lens," *Scientific Reports*, Vol. 6, 18819, 2016.
6. Yi, J., Burokur, S. N., Piau, G.-P., de Lustrac, A., "Restoring in-phase emissions from non-planar radiating elements using a transformation optics based lens," *Appl. Phys. Lett*., Vol. 107, No. 2, 024101, 2015.
7. Zhang, K. Ding, X., Wo, D., Meng, F., Wu, Q., "Experimental validation of ultra-thin metalenses for N-beam emissions based on transformation optics," Appl. Phys. Lett., Vol.108, No. 5, 053508, 2016

FSS, HIS and Extraordinary transmission

A Low-Cost Paper-based Inkjet-Printed Frequency Selective Surface for X-band Screening

W.Y.Yong[1*], **S.K.A.Rahim**[1], **H.A.E.Elobaid**[1], **N.A.Remli**[1] ,**F.C.Seman**[2] and **M.Himdi**[3]
[1] Wireless Communication Centre, Univerisiti Teknologi Malaysia.
[2]Research Centre of Applied Electromagnetic, Universiti Tun Hussein Onn Malaysia.
[3] Institute of Electronics and Telecommunications in Rennes (IETR), University of Rennes 1.
[*]warrenyong92@gmail.com

Abstract- A low-cost paper based frequency selective surface (FSS) for X-band frequency shielding is presented in this paper. The proposed FSS contains the unit cell made of single ring loop element with paper as its novel substrate. The overall thickness of the proposed FSS measured only 0.15mm. The designed FSS provide a band-stop response at 10 GHz with minimum 35 dB shielding effectiveness. Additionally, due to the ring loop FSS is symmetrical in nature, the designed FSS providing the advantage of polarization independency. It also exhibits angular stability up to 45° for both transverse electric (TE mode) and transverse magnetic (TM mode) fields. A prototype with overall dimension of 17.5cm x 26.3 cm of the proposed paper-based FSS is fabricated using inkjet printing method which is a low-cost manufacturing technique. The proposed FSS can be easily applied on the walls and windows of a room to block the unwanted frequency band in order to protect sensitive instruments from possible electromagnetic interference (EMI).

1. Introduction

Frequency Selective Surface (FSS) is commonly used to shield the unwanted signals which will lead to the EMI. FSS defined as either radiating or non-radiating elements that arranged in periodic array manner [1]. The FSS can be designed as either band-pass or band-stop filter respectively to electromagnetic waves [1]. Recently, rapid evolution of the wireless communication industry promote the needs of low-cost, flexible and environmentally-friendly wireless communication devices such as antennas and microwave devices [2]. Choosing the appropriate substrate is one of the most significant method to realize the flexible wireless communication devices. Flexible substrate such as PDMS, polyethylene terephthalate (PET), fabric and paper substrate had been proposed [3]. From all these substrates, paper is considered the best alternative as it is easily available, environmentally-friendly, flexible and most importantly is very low cost. However, the development of the FSS on paper is a big challenge. In the previous research, the development of the FSS on paper substrate was done by shaped the copper tape manually and glued on the paper later [4]. Another approach is to draw the design of the FSS manually using the silver conductive pen [5]. However, both of this approaches will cause high fabrication errors especially when the size of the unit cell become smaller and the design become complicated. In order to overcome the mentioned limitations, in this paper we proposed to develop the FSS on the paper substrate using inkjet printing method. We present a ring slot FSS on low-cost, flexible and environmental friendly paper substrate (permittivity = 3.1, thickness = 0.15mm and lost tangent = 0.05) to shield the X-band signal at 10 GHz.

2. FSS Unit Cell Design and Simulation Results

The proposed FSS is as shown in Figure 1. The designed FSS is made of silver-nanoparticle ink single ring slot with slot thickness of 0.003 mm. The unit cell is deposited on the paper substrate with measured thickness of 0.15 mm and tangent loss of 0.05. The performance of the FSS is evaluated through the simulation by utilizing CST Microwave Studio (CST MWS). Since the FSS is a highly resonant structure and it is important to investigate the angular stability performance, thus the frequency domain solver is utilized for the simulation. In order to reduce the simulation load, the FSS is modelled as infinite array in the software by utilized the full floquet mode to simulate single unit cell. The simulation results are as shown in Figure 2. From the results, we can observe the designed FSS provided attenuation of signal at 10 GHz up to 35dB for both TE and TM polarization. The designed FSS also managed to perform satisfactory for both TE and TM polarization up to 45 degree.

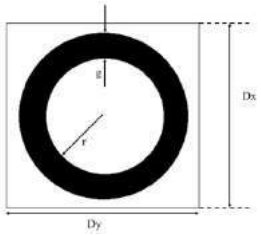

Fig1. Single Loop FSS; Dx=Dy=8.6mm, r=4mm g=0.9mm

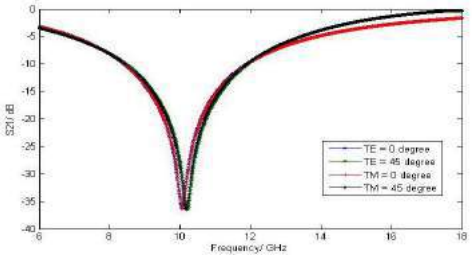

Fig2. Comparison for simulated S21 for both TE and TM polarization up to 45 degree.

3. Conclusion

In this paper, a low cost, environmentally friendly paper-based FSS is proposed. The prototype of the proposed FSS is realized using inkjet printing techniques. The proposed FSS can replaced the conventional FSS that developed on FR-4 and rogers while maintaining the performance of FSS. The fabrication technique proposed in this paper allow the accurate fabrication of the design. The detail explanation will be discussed after the acceptance of abstract.

REFERENCES

1. J.D.Kraus and R.J.Marhefka, *Antenna for All Applications*, Third Edit. McGraw Hill, 2003.
2. H. A. Rahman and S. K. . Rahim, "Dual band PDMS Based Flexible Antenna for Wearable Application," *2015 IEEE MTT-S 2015 Int. Microw. Work. Ser. RF Wirel. Technol. Biomed. Healthc. Appl.*, vol. 1, no. 1, pp. 193–194, 2015.
3. M. Bozzi *et al.*, "Inkjet-printed antennas, sensors and circuits on paper substrate," *IET Microwaves, Antennas Propag.*, vol. 7, no. 10, pp. 858–868, 2013.
4. R. Sivasamy, L. Murugasamy, M. Kanagasabai, E. F. Sundarsingh, and M. Gulam Nabi Alsath, "A Low-Profile Paper Substrate-Based Dual-Band FSS for GSM Shielding," *IEEE Trans. Electromagn. Compat.*, vol. 58, no. 2, pp. 611–614, 2016.
5. N.K.Khalid, "Frequency Selective Surface (FSS) for Cellular Signals Shielding," Universiti Tun Hussein Onn Malaysia, 2015.

A Low-Profile Paper-based Inkjet Printed Frequency Selective Surface using Modified Square Loop for X-band Shielding

W.Y.Yong[1*], S.K.A.Rahim[1], N.A.Remli[1], F.C.Seman[2], and M. Himdi[3]
[1]Wireless Communication Centre, Universiti Teknologi Malaysia.
[2]Research Centre for Applied Electromagnetic, Universiti Tun Hussein Onn Malaysia.
[3] Institute of Electronics and Telecommunications in Rennes (IETR), University of Rennes 1.
[*]warrenyong92@gmail.com

Abstract-A contemporary, flexible and economical frequency selective surface designed for X-band shielding establish from simple inkjet printer using highly conductive silver nanoparticles ink. The resonating element of the FSS is designed using a modified square loop element and printed on top a paper substrate with a measured thickness of 0.15 mm. The performance of the FSS is examined using Computer Simulation Technology (CST) software. From the simulation outcome, the proposed structure offered band stop response at 10 GHz with attenuation up to 30 dB at normal incidence. Moreover, the modified square loop FSS is symmetrical and therefore it managed to offer a stable frequency response at oblique angle up to 45° for both TE and TM polarization. The model of the designed FSS is then developed using inkjet printing technique. The proposed FSS can be cascaded to building easily as wallpaper to block the unwanted X-band signals.

1. Introduction

Frequency Selective Surface (FSS) is commonly used as a spatial filters either as a band-pass or band-stop filter [1]. FSSs are useful as antenna radome, absorbers, antenna reflectors and in many other areas [2]. The performance of the FSSs are mainly reliable on the geometry of the element, size of the unit cell, periodicity and characteristics of dielectric substrate used [1]. In order to achieve a stable frequency response performance, the element geometry playing the most notable role. The compact FSS design will allow the FSS to operate satisfactory under different angle of incident and polarization [3]. Therefore, it is crucial to design a compact FSS element. Recently, with the rapid development of the communication devices, the demand of the flexible wireless devices is become significant [4]. Most of the study reported the development of the wireless devices on PDMS, polyethylene terephthalate (PET) and paper substrate as the dielectric body for the devices [4], [5]. From all these substrate, paper substrate is the most ordinary option as it is easily available in the market and allow the roll-to-roll production which will reduced the cost significantly [6]. To ensure the FSSs manage to perform competently, the metal depositing technique is relatively crucial. Inkjet printing is become a commendatory choice today due to it is low cost and simple to fabricate [6]. In this paper, we offered to develop the modified square loop FSS on the low-cost, flexible and environmentally friendly paper substrate (permittivity = 3.1, thickness = 0.15mm and loss tangent = 0.05) using simple inkjet printing technique to support the screening of the X-band frequency signals.

2. FSS Unit Cell Design and Simulation Results

The objective of this paper is to present a low profile FSS element that can operate satisfactory at

different angle of incident and polarizations. The proposed FSS is as explicated in Figure 1. The designed FSS comprised an unit cell of modified square loop (MSL) with conductor thickness of 0.003 mm deposited on top of a paper substrate with thickness of 0.15 mm, permittivity 3.1 and loss tangent of 0.05. The proposed MSL is transformed from square loop by introduced an inward bending U-shaped stubs to all sites of the square loop. The package density of the FSS has exacerbated when the square loop is evolved to MSL [3]. From the simulation result, we can examine that the frequency response of proposed FSS operate stability at both TE and TM polarization. Although when the angle of incident increase to 45°, the center frequency alter slightly but at 10GHz, the FSS still manage to provide attenuation more than 25 dB for both TE and TM polarizations. In a nutshell, the FSS provide a stable frequency response.

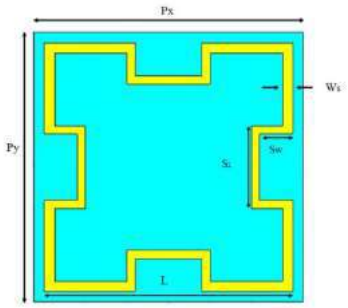

Fig1. Modified Square Loop. Px=Py=6.5mm, L=6mm Ws= 0.5mm, S_L=2mm, S_w=0.8mm

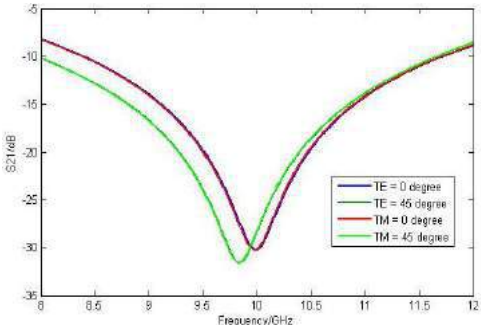

Fig2. Simulated Frequency transmission response of the proposed MSL.

3. Conclusion

In this paper, a MSL FSS deposited on a paper substrate is presented. The proposed FSS is realized using simple inkjet printing technique to deposit the silver nanoparticle ink on the paper substrate. From the simulation result, the proposed FSS provide a stable performance at both TE and TM polarization up to 45°. The detail explanation on fabrication technique, experimental setup for validation will be discussed after the acceptance of abstract.

REFERENCES

1. R.J.Marhefka and J.D.Kraus, *Antenna for All Applications*, Third Edit. McGraw Hill, 2003.
2. L. B. Wang, K. Y. See, J. W. Zhang, B. Salam, and A. C. W. Lu, "Ultrathin and flexible screen-printed metasurfaces for EMI shielding applications," *IEEE Trans. Electromagn. Compat.*, vol. 53, no. 3, pp. 700–705, 2011.
3. F. C. Seman and N. K. Khalid, "Investigations on fractal square loop FSS at oblique incidence for GSM applications," *Proc. - 2014 Electr. Power, Electron. Commun. Control Informatics Semin. EECCIS 2014. conjunction with 1st Jt. Conf. UB-UTHM* , pp. 62–66, 2014.
4. H. A. Rahman and S. K. . Rahim, "Dual band PDMS Based Flexible Antenna for Wearable Application," *2015 IEEE MTT-S 2015 Int. Microw. Work. Ser. RF Wirel. Technol. Biomed. Healthc. Appl.*, vol. 1, no. 1, pp. 193–194, 2015.
5. M. E. Jalil, M. K. A. Rahim, N. A. Samsuri, R. Dewan, and K. Kamardin, "Flexible ultra-wideband antenna incorporated with metamaterial structures: multiple notches for chipless RFID application," *Appl. Phys. A*, vol. 123, no. 1, p. 48, 2017.
6. M. Bozzi *et al.*, "Inkjet-printed antennas, sensors and circuits on paper substrate," *IET Microwaves, Antennas Propag.*, vol. 7, no. 10, pp. 858–868, 2013.

Flexible Microstrip Polymer-Conductive Fabric Grid Array Antenna for Wearable Applications

M. R. Ramli, S. K. A. Rahim, W.Y.Yong and M. I. Sabran
Wireless Communication Centre (WCC), Universiti Teknologi Malaysia
* mridduan2@live.utm.my

Abstract- A flexible microstrip grid array antenna that established using copper conductive fabric as the conducting element deposited on the Polydimethysiloxane (PDMS) as it substrate is presented. The proposed design is made up from a rectangular geometry which consists of 19 cells that build up by 22 radiating elements on the PDMS to provide a resonant frequency at 15 GHz. The proposed design managed to provide a 40% bandwidth at -10 dB bandwidth performance with maximum gain up to 14.6 dBi at normal condition. The study on the bending effect of the proposed antenna is examined using Computer Simulation Technology (CST) software. The bending effect of the proposed antenna is observed by bending the antenna into different bending radius. From the results obtained, it can be examined that the proposed antenna is insensitive toward the bending and thus it is a suitable candidate for wearable applications.

1. Introduction

The introduction of smart devices and Internet of Things (IoT) has leads to the increase demand on the communication data. The 5G communication is envision to support around 1,000 time data than the existing data[1]. As a result, the antenna that going to utilize for 5G must consist the features of large bandwidth, high gain and manage to operate at high frequency. Grid Array antenna which is designed using several number of meshes to form the grid cells with radiating elements and transmission line and a full ground plane [2]. Grid array antenna provide the credit of simple feeding technique, high gain, wide-bandwidth and most importantly it manage to provide a stable performance over high frequency [3]. Besides that, the introduction of the IoT increases the need of the wearable and flexible electronics which include the flexible antennas. One of the propose approach to realize the flexible antenna is to utilize the flexible substrate such as PDMS [4]. In this paper, we present a durable microstrip grid array antenna by using the PDMS substrate and conductive fabric which provide the flexibility characteristics. The proposed antenna manages to provide stable performance when it is bent up to certain level.

2. Flexible Antenna Design and Simulation Results

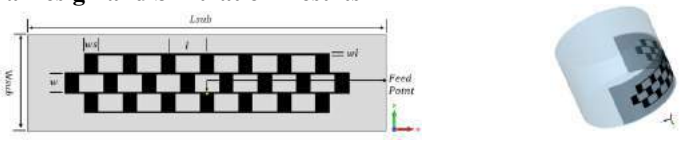

(a) (b)

Fig1. (a) The proposed antenna configuration. (b) Simulation for bending process experiment in CST

Figure 1(a) shows the configuration of the proposed flexible microstrip grid array antenna. The presented

antenna is designed on 1.6 mm thick PDMS substrate (relative permittivity εr = 2.9 and loss tangent tanδ = 0.0019) and 0.035 mm copper conductive fabric with electrical conductivity of 5.8 x 10^7 S/m as the patch and ground plane. The cell element is designed using guided wavelength equation at 15 GHz and simulated using CST Microwave Studio software. The proposed antenna consist of 19 number of cells with 22 radiating elements arranged in rectangular geometry. The optimized antenna parameters is *l*=14 mm, *w*=7 mm, *ws*=5.1 mm, and *wl*= 0.55 mm with total dimension of 130 x 35 mm. Figure 1(b) shows the simulation bending experiment in CST. The proposed antenna was bend correspond to the attached cylinder curved surface where the radius of the cylinder, R will be consider as the parameter of bending. The reflection coefficient of the antenna without bending is compared with the bending antenna in order to examine the bending effect on the antenna performance. Figure 2 shows the simulated reflection coefficient and gain for the proposed antenna with bending and without bending. The antenna provide 40% wideband characteristics at -10 dB with maximum gain of 14.6 dBi at 15 GHz at normal condition. The bending level of the antenna is depend on the radius of the cylinder where smaller radius allow higher level of bending on antenna. From the result, we can examined the proposed antenna manage to provide a stable performance over 15GHz when it is being bent.

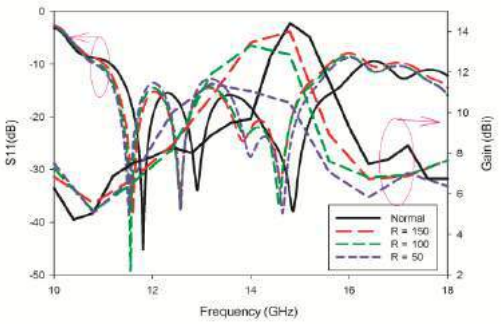

Fig2. Return loss and gain of the proposed antenna with and without bending

3. Conclusion

A flexible microstrip grid array antenna on PDMS and conductive fabric is presented in this paper. Proposed antenna manage to operate satisfactory at 15 GHz when it is bent or without bending. Such feature allow the proposed antenna to be use for wearable applications. The detail explanation about antenna performance and fabrication method will be discussed after the acceptance of abstract.

REFERENCES

[1] M. Agiwal, A. Roy, and N. Saxena, "Next generation 5G wireless networks: A comprehensive survey," *IEEE Commun. Surv. Tutorials*, vol. 18, no. 3, pp. 1617–1655, 2016.

[2] Muhammad Sani Yahya and S. K. A. Rahim, "15 GHz Grid Array Antenna for 5G Mobile Communications System," *Microw. Opt. Technol. Lett.*, vol. 54, no. 12, pp. 2977–2979, 2016.

[3] M. R. Ramli, S. K. A. Rahim, M. I. Sabran, and M. L. Samingan, "Performance Analysis of Microstrip Grid Array Antenna on Different Substrates for 5G Mobile Communication," *J. Telecommun. Electron. Comput. Eng.*, vol. 8, no. 6, pp. 6–9, 2016.

[4] C. P. Lin, C. H. Chang, Y. T. Cheng, and C. F. Jou, "Development of a flexible SU-8/PDMS-based antenna," *IEEE Antennas Wirel. Propag. Lett.*, vol. 10, pp. 1108–1111, 2011.

Branch Line Coupler Using PDMS as Dielectric Substrate and Superstrate at 2.45 GHz

M. L. Samingan[1], S. K. A. Rahim[1*], T. Peter[1*], W.Y. Yong[1*] and D. Schreurs [2*]
[1]Wireless Communication Center, Universiti Teknologi Malaysia, Malaysia
[2]ESAT- TELEMIC, Telecommunications and Microwaves, Belgium
[*] S. K. A. Rahim: sharulkamal@fke.utm.my
[*] T. Peter: tom.peter@live.com
[*]W.Y. Yong: warrenyong92@gmail.com
[*] D. Schreurs: dominique.schreurs@kuleuven.be

Abstract-This paper presents the design of a branch-line coupler (BLC) using a copper fabric sheet as conductive element, mounted on Polydimethylsiloxane (PDMS) substrate and superstrate (cover) dielectric layers. The BLC operates at the 2.45 GHz operating frequency and has a phase difference of 90 degree. The use of PDMS material as a dielectric layer for BLC is to add the special characteristics of PDMS on this passive microwave circuit. The PDMS has very unique properties such as durability, light weight and electromagnetic shielding. By incorporating the copper fabric as a conductive element for BLC it will enhance the durability and the electromagnetic shielding of the BLC.

Realization of electronic and photonic components on flexible, durable and stretchable substrates as opposed to conventional rigid substrates can open doors for the next generation of electronic and microwave circuits with new functionalities [1]. Typically a microwave circuit, such as a Branch Line Coupler (BLC) is commonly fabricated on a solid substrate like FR-4 or RT/duroid board. Although these substrates can give us more advantages in term of high performance, ease of fabrication and low cost, they however, are not reliable when exposed to harsh weather conditions or a mechanically stressed environment [2].

Utilizing the copper fabric sheet as a conductive element, increases the EMI capability of the proposed BLC. It has been proved by previous research [3], that the mesh structure of the copper fabric sheet can reflect the electromagnetic waves by using the principle of the Faraday cage. This material can also strengthen the polymer based substrate for the proposed BLC [3].

The conducting element for the branch-line coupler is designed on a copper fabric sheet with thickness and sheet resistance of 0.08 mm and 0.05 Ω/square, respectively whilst the thickness for PDMS is specified at 1.9 mm. The length and width of the shunt/series transmission lines for the BLC are computed using the transmission line calculator from AWR software, by taking into consideration the thickness of the copper fabric, and dielectric constant εr of the PDMS substrate. The simulated and measured S-parameter results for the planar PDMS-based BLC are shown in Fig. 1. The reflection coefficient (S11) and isolation (S41) in simulation are -31.6 dB and -37.1 dB, respectively. Meanwhile, the measured reflection coefficient and isolation for the PDMS-based BLC are -29.1 dB and -26.6 dB, respectively.

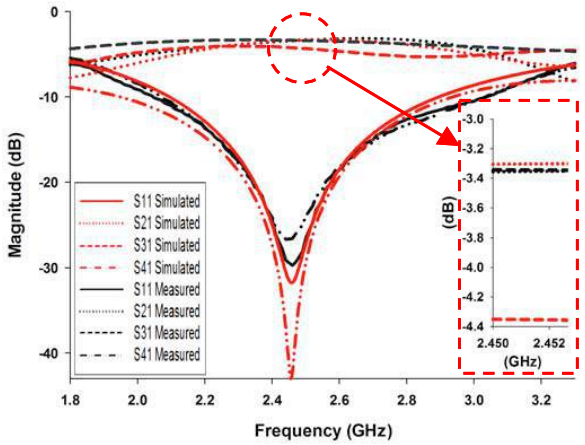

Fig. 1. Simulated and measured S-parameter results for the PDMS-based BLC

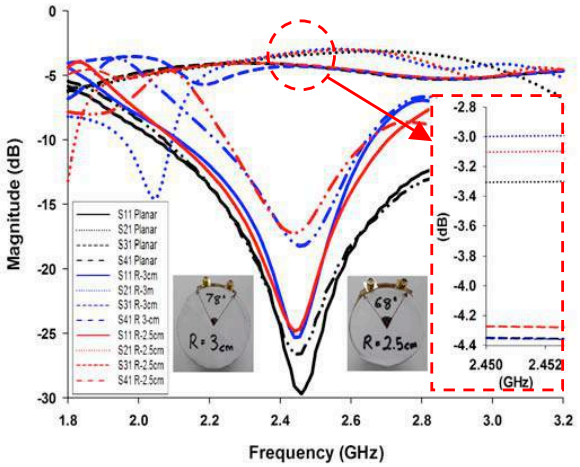

Fig. 2. Measured S-parameter results for the PDMS-based BLC at three different radii and angles.

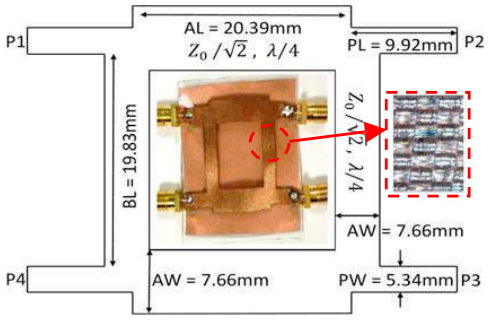

Fig. 3. (a) Design layout of the proposed and fabricated PDMS-based BLC
(b) mesh structure of the copper fabric sheet (x200 magnification)

This may be attributed to fabrication accuracy. The simulation value for coupling (S31) is -3.3 dB whilst for insertion loss (S21) it is -3.4 dB. In measurement, the values for the same are -4.2 dB and -3.5 dB, respectively. Basing on the results, the measured insertion loss of the PDMS based BLC is close to the simulated result. The fabricated prototype figure is embedded in the design layout in Fig. 3. Fig. 2 shows measured S-parameter results for the PDMS-based BLC at different radii of curvature. Although the S11 resonant peak for the 3 cm and 2.5 cm radii of curvature reduces to -25.3 dB and -24.7 dB, respectively it still hovers around 2.45 GHz.

REFERENCES

1. J. A. Rogers, T. Someya, and Y. Huang, "Materials and mechanics for stretchable electronics, "*US National Library of Medicine National Institutes of Health*; 10.1126/science.1182383, 2010
2. P. Lall, M. N. Islam, J. Evans, J. C. Suhling, and T. Shete, "Damage Mechanics of Electronics on Metal-Backed Substrates in Harsh Environments,"*IEEE Trans. on Comp. and Packaging*, Vol. 29, No. 1, 2006
3. R. Perumalraj, B. S. Dasaradan, R. Anbarasu, P. Arokiaraj, and S. Harish, "Electromagnetic shielding effectiveness of copper core-woven fabrics," *The Journal of The Textile Institute*, Vol. 100, No. 10, pp. 512-524, 2009.

Flexible, Ultrathin and Light-weight PET based inkjet-printed FSS for X-band Shielding

W.Y.Yong[1*], S.K.A.Rahim[1], M.R.Ramli[1], N.A.Remli[1] M.L.Samingan[1] and F.C.Seman[2]

[1]Wireless Communication Centre, Universiti Teknologi Malaysia.

[2]Research Centre of Applied Electromagnetics, Universiti Tun Hussein Onn Malaysia.

[*]corresponding author: warrenyong92@gmail.com

Abstract- This paper presents the design of a novel ultrathin, light-weight and flexible X-band band-stop frequency selective surface (FSS) using instant, simple and fast inkjet printing technology. The proposed FSS design is deposited on the 0.125 mm-thick light-weight, ultrathin and flexible PET substrate with dielectric constant of 2.7 and designed to attenuate 10 GHz. The ring slot FSS is proposed as it is easy to design and symmetrical in nature which is insensitive toward the change in polarization and angle. The flexible and ultrathin FSS provide attenuation up to 30 dB for both TE and TM polarization. In addition, the proposed design provided a stable performance up to 45° at both polarization. The proposed FSS has a measured -10 dB bandwidth of 38% and 0.125 mm profile. These advantages greatly enhance the potential applications of the FSS also as a EMI shield that can be mounted onto the glass surface of buildings to shield the unwanted signals caused by the increase of wireless devices.

1. Introduction

Fifth Generation (5G) communication technology envisage to support huge mobile traffic [1]. In other words, more base station will be built to support the demand from the users. However, this will lead to the electromagnetic pollution which will degrade the performance of the electronic devices [2]. The common solution using the metallic shielding to block the electromagnetic waves is impractical in this case as it is costly and labor intensive[2]. Thus, FSS is introduced as spatial filter to block the unwanted frequency. Recently, there has been a growing interest in developing flexible electronics. This trend is also happening in the wireless communication industry where the industries are looking for bendable antennas or microwave devices [3], [4]. To make the flexible communication devices into reality, the substrate used is relatively crucial. One of the common approaches is to design the antennas and microwave devices on top of Polydimethylsiloxane (PDMS) [3]. Although PDMS is the best candidate to realise the flexible wireless devices, but it is challenging to deposit the conductive element on top of it especially for the array types microwave devices such as FSS and reflect-array antenna as the conductive layers are deposited on PDMS manually. To overcome this hindrance, development of the microwave devices on top of a paper substrate and Polyethylene Terephthalate (PET) using inkjet printing technique is then introduced [4]. In this paper, we present a single ring loop FSS on the 0.125 mm-thick light-weight, ultrathin and flexible PET substrate with dielectric constant of 2.7 to provide an attenuation at 10 GHz.

2. FSS Unit Cell Design and Simulation Results

Single ring slot as shown in Figure 1 is used for the FSS element design. Ring slot FSS is chosen as it is easy to design and symmetrical in nature which able to provide a stable performance for both TE and TM polarization and insensitive toward the change of angle of incident [5]. The proposed design is realised using silver nanoparticle ink and supported by a polyethylene terephthalate (PET) substrate with thickness, h of 0.125 mm and dielectric constant ε_r of 2.7 with the tangent loss of 0.004. The unit cell of the proposed ring slot FSS is

simulated using Computer Simulation Technology (CST) Microwave Studio software. The simulated transmission response of the proposed FSS is demonstrated in Figure 2. From the results, it can be examined that the presented FSS provide attenuation at 10 GHz up to 33 dB with -10 dB bandwidth of 39% at normal incidence for TE polarization.

Fig 1. (a) Unit cell of the designed single ring loop FSS; Dx = Dy = 10.75 mm, R1 = 4.2 mm; R2 = 4.9 mm; (b) Fabricated FSS on PET substrate.

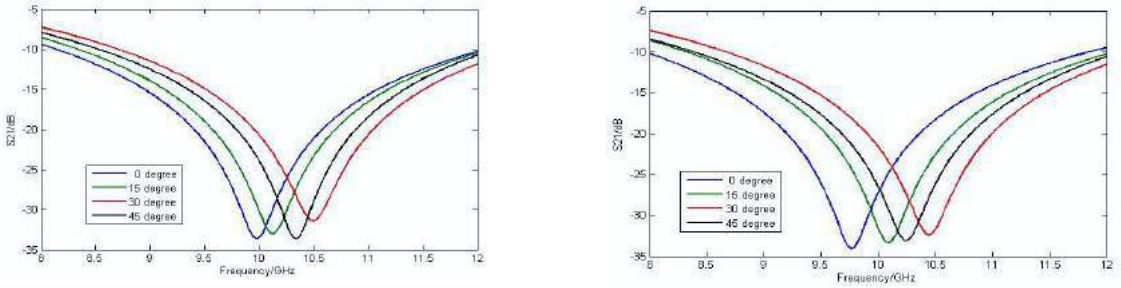

(a) (b)

Fig 2. Transmission Response of the proposed ring shape FSS for (a) TE polarization and (b) TM polarization at various angle of incident.

3. Conclusion

A flexible and low-profile PET-based FSS for X-band signals screening is presented in this paper. The element of the proposed FSS is designed using single ring loop element. The proposed design offers attenuation up to 32 dB at the centre frequency of 10 GHz. The fabrication technique of the proposed FSS and the measurement results will be discussed after the acceptance of abstract.

REFERENCES

[1] Muhammad Sani Yahya and S. K. A. Rahim, "15 GHz Grid Array Antenna for 5G Mobile Communications System," Microw. Opt. Technol. Lett., vol. 54, no. 12, pp. 2977–2979, 2016.

[2] F. C. Seman and N. K. Khalid, "Investigations on fractal square loop FSS at oblique incidence for GSM applications," Proc. - 2014 Electr. Power, Electron. Commun. Control Informatics Semin. EECCIS 2014. conjunction with 1st Jt. Conf. JB-UTHM , pp. 62–66, 2014.

[3] S. A. Babale, S. K. A. Rahim, M. Jusoh, and L. Zahid, "Branch-line coupler using PDMS and Shieldit Super fabric conductor," Appl. Phys. A, vol. 123, no. 2, p. 117, 2017.

[4] M. E. Jalil, M. K. A. Rahim, N. A. Samsuri, R. Dewan, and K. Kamardin, "Flexible ultra-wideband antenna incorporated with metamaterial structures: multiple notches for chipless RFID application," Appl. Phys. A, vol. 123, no. 1, p. 48, 2017.

[5] G. Bharti, G. Singh, K. R. Jha, and R. Jyoti, "Circular ring frequency selective surface: A novel synthesis technique," in 2013 6th International Conference on Contemporary Computing, IC3 2013, 2013, pp. 491–496.

Improving MIMO Fabric Antenna Performance using AMC Octa-rift Structure

H. Lago[1*], A. A. M. Ezanuddin[2], L. Y. Seng[2] and C. M. N. C. Isa[1]

[1] Advanced Communication Engineering (ACE), School of Computer and Communication Engineering, UniMAP, 01000 Kangar, Perlis, Malaysia.

[2] Electronic Department, FETech, UniMAP, Aras 1, Blok S2, Kampus UniCITI Alam, 02100 Sungai Chuchuh, Padang Besar, Perlis, Malaysia

[*]herwansyahlago@gmail.com

Abstract-A textile artificial magnetic conductor (AMC) plane with hexagonal and triangular microstrip patch antenna was proposed. The AMC is designed to function as a perfect magnetic conductor (PMC) at 2.45 GHz to improve the antenna performance. The performances of both antennas with and without the AMC plane were investigated. The results show gain enhancement at the operating frequency while maintaining the antennas' size. Furthermore, the AMC plane has been integrated with three different MIMO orientation and its performance investigated. In addition, the presented AMC plane and both antennas are made of fabric for the entire substrate and conducting parts. For that reason, the AMC plane antennas have big potential to be implemented in wearable applications.

Introduction: Recently, research in wearable communication system has received remarkable attention due to the community needs especially in find and rescue purpose. However, the wearable antenna is suffering performance degradation caused by several factors [1]. One of the factor is human body effect when the antenna is placed near to the body. Textile artificial magnetic conductor (AMC) has been introduced in [2] to overcome the drawback faced by wearable antennas. This research intends to improve and analyze the performance of the wearable antennas on the AMC plane.

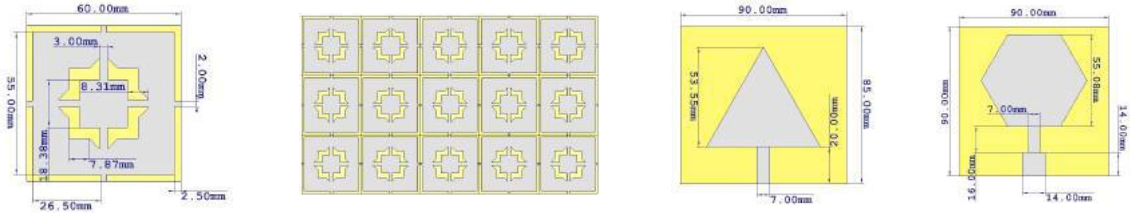

(a) (b) (c) (d)

Figure 1: Proposed (a) AMC octa-rift unit cell, (b) AMC plane, (c) triangular patch and (d) hexagonal patch antenna.

A textile AMC unit cell has been designed which exhibit PMC's characteristics at 2.45 GHz as illustrated in Figure 1(a). Then the AMC unit cell is arranged into 5x3 matrix formation to form the AMC plane (see Figure 1(b)). The triangular and hexagonal patch antennas (see Figure 1(c)) are designed with an operating frequency of 2.45 GHz and placed on the AMC plane. As the result, the antenna gain is enhanced up to 23% with present of the AMC. In addition, the electric density also improved for both patch antennas. To investigate the MIMO

characteristics, the antennas are placed side by side and form three different orientations named as antenna orientation A, B and C (see Figure 2). The reflection coefficient for all antenna orientations remained unchanged. Furthermore, all of these MIMO antenna have shown good performance in term of isolation (S_{21}), diversity gain and envelope correlation coefficient as tabulated in Table 1.

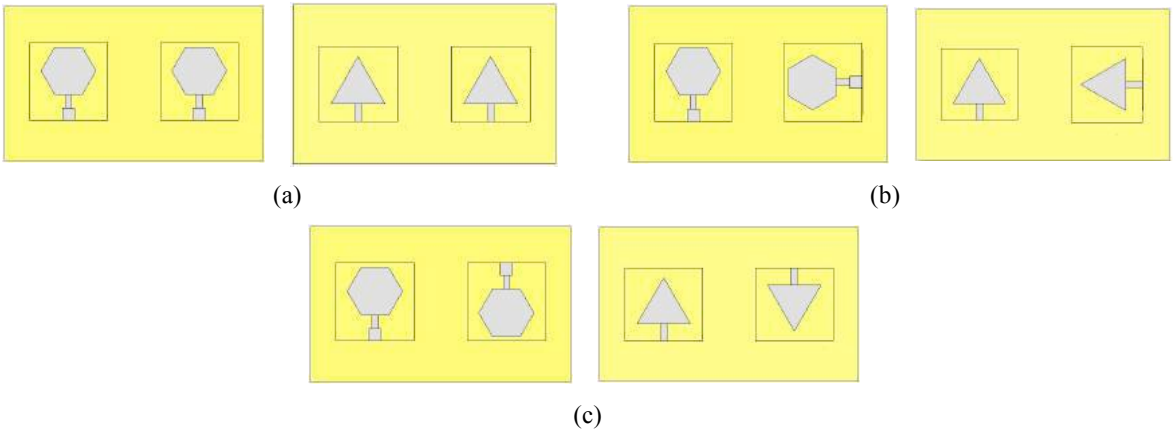

Figure 2: Antenna orientation (a) A, (b) B and (c) C for hexagonal and triangular MIMO antenna.

Table 1. Comparison performance of the crescent shaped array antenna with and without AMC.

Orientation	Antenna	Isolation (dB)	Diversity Gain	Envelope Correlation Coefficient
A	Hexagonal	-45.22	10	0.28m
	Triangular	-53.31	10	0.15m
B	Hexagonal	-55.06	10	65 μ
	Triangular	-56.48	10	68μ
C	Hexagonal	-46.71	10	0.66m
	Triangular	-56.32	10	0.6m

Conclusion: A textile AMC with hexagonal and triangular microstrip patch antenna which operate at 2.45 GHz was proposed. Through the simulation process, the AMC potentially to be placed near to the radiating element without any frequency shifting. The performances of the single and MIMO antenna are potentially to be improved with aid of the proposed AMC plane.

Acknowledgements: This project is supported by UniMAP Short Term Grant (STG) 2017 (grant no.:9001-0510).

REFERENCES

1. Hall, P.S., and Hao, Y., *Antennas and propagation for body centric communications systems*, Artech House, London, 2012.
2. Salonen, P., Yang, F., Rahmat-Samii, Y. and Kivikoski, M., "WEBGA - Wearable Electromagnetic Band-Gap Antenna," in *IEEE International Symposium on Antennas and Propagation*, 2004, 451–454.

A CPW-Fed CSRR Loaded Inkjet Printed Filtenna on Low-Cost Flexible PET Substrate.

N.A.Remli[1], S.K.A.Rahim[1], W.Y.Yong[1] and M.I.Sabran[1]
[1]Wireless Communication Center, Universiti Teknologi Malaysia
[*]afiqahremli16@gmail.com

Abstract-A coplanar waveguide (CPW) loaded complementary split-ring resonator (CSRR) harmonic rejection filtenna designed on low-cost flexible PET substrate operates at 5.8 GHz is presented. The proposed antenna comprised of square slots built-in the rectangular patch structure, developed using inkjet printer with highly conductive nanoparticle silver ink. CSRR is implemented at the transmission line to suppress unwanted harmonics. The antenna performance is simulated and optimized using Computer Simulation Technology (CST) software. The proposed antenna achieved acceptable 2nd and 3rd harmonic rejection with minimum reflection coefficient of -4.56 dB and -3.3 dB respectively, offers efficiency up to 88.66%.

1. Introduction

Filtenna (filter-antenna) is the term used for integration of antenna and the filter into one structure [1]. Filtenna is developed to improve RF front end communication system performance in terms of size, losses, complexity and cost by eliminating the use of band pass filter module [2]. To filter out the unwanted harmonics, it can be achieved by using various shapes of stubs, slits and slots on the antenna structure [2]–[4]. The performance of harmonic rejection and good return loss can be achieved by optimizing the dimensions of the stubs, slits and slots [3]. Complementary split-ring resonator (CSRR) is an alternative solution to achieve frequency notching by implementing the metamaterial in antenna design. It has distinct electromagnetic (EM) characteristic of negative refraction thus make it suitable to be applied as filters in miniaturized design [5]. With the increasing demand on the flexible device, number of researchers starts to develop the antenna on flexible substrate such as SU-8/polydimethylsiloxane (PDMS), paper and Polyethylene (PET) substrates. From that, PET substrate is the best candidate as it is more flexible, thin, foldable, bendable and transparent as compared to others [6]. Recently, inkjet printing has become a promising solution for fast, low-cost and precise way of antenna fabrication especially for flexible materials. In this paper, an attempt of designing a CPW filtenna on low-cost flexible PET substrate is developed using inkjet printing technique and it is realized by introducing CSRR on the transmission line, thereby suppressing the harmonics of the resonance frequency.

2. Filtenna Design and Simulation Results

The design on the proposed CPW antenna is shown in Figure 1. The designed antenna is composed of rectangular radiating shape with square slots, coplanar waveguide (CPW) feeding with CSRR loaded on the transmission line and ground plane (g = 0.17 mm). The structure is printed on 35mmx40mm PET substrate which has thickness of 0.125 mm (ε_r = 2.7, tan δ=0.004). The antenna has parameters of Wp=9 mm, Lp=33.5 mm, Wf=2.5 mm, Lf=16 mm, G_{LP} =0.5 mm, G_{WP}=1.6 mm, L_1=5.5 mm, L_2=12.5 mm, D_1=0.5 mm, D_2=1.7 mm, S_1=2.3 mm, S_2=3 mm, G_1=0.1 mm, G_2=0.2 mm and D_S=0.2 mm. Silver nanoparticles conducting ink has been

used for printing of the radiating elements. Figure 2 illustrates the reflection coefficient performance of the antenna from the conventional basic design until the proposed harmonic suppression technique applied. It can be observed that the initial reflection coefficient, S11 result is improved by integrating the square slots at the radiating element. The antenna structure is further modified by integrating CSRR to the transmission line for harmonic rejection at 10.73 GHz and 19.46 GHz. Although the centered frequency alters slightly, the filtenna manage to achieve suppression of the second and third harmonics with reflection coefficient -4.56 dB and -3.3 dB respectively.

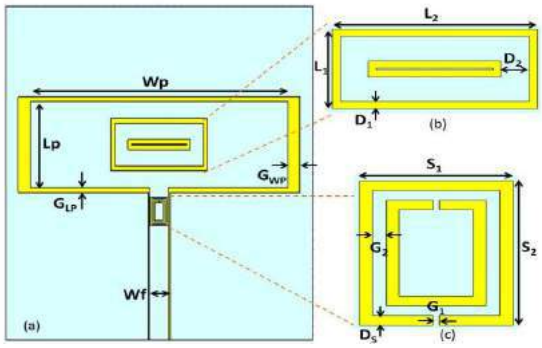

Figure 1: Filter arrangement (a) Proposed antenna structure, (b) Square slots, (c) CSRR loaded on transmission line

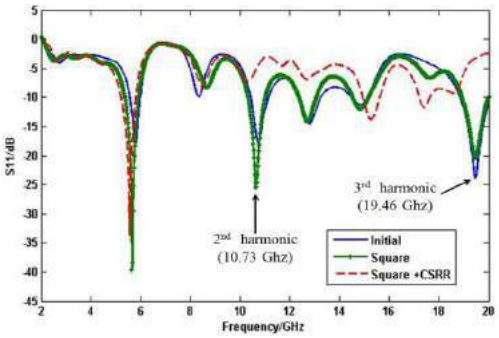

Figure 2: Reflection coefficients performances of the proposed antenna with filter

.

3. Conclusion

A CPW filtenna with CSRR on flexible substrate is presented in this paper. The proposed antenna design is sufficient for the 5.8 GHz with blocked 2nd and 3rd harmonics. The CSRR unit on the transmission line acts as a filter to suppress harmonics, with reflection coefficient -4.56 dB and -3.3 dB respectively. The details of fabrication technique and the measurement result will be discussed after the acceptance of abstract.

REFERENCES

[1] A. Nyangwarimam Obadiah, M. R. Hamid, M. K. A. Rahim, and N. A. Murad, "A Review on Filter-Antennas," *Appl. Mech. Mater.*, vol. 735, pp. 289–293, 2015.

[2] R. H. Zaghloul and H. H. M. Ghouz, "Novel Compact Microstrip Filtenna Structures," *Int. J. Adv. Eng. Appl.*, vol. 7, pp. 1–15, 2014.

[3] M. I. Sabran, S. K. A. Rahim, T. A. Rahman, A. A. Eteng, and Y. Yamda, "U-shaped harmonic rejection filtenna for compact rectenna application," *2014 Asia-Pacific Microw. Conf.*, pp. 1007–1009, 2014.

[4] R. a. Rahim, F. Malek, S. I. S. Hassan, and M. N. Junita, "A 2.45 GHz circular patch antenna with harmonic suppression for wireless power transmission," *2012 IEEE Colloq. Humanit. Sci. Eng.*, no. Chuser, pp. 283–287, 2012.

[5] M. S. A. Rani, S. K. A. Rahim, M. R. Kamarudin, T. Peter, S. W. Cheung, and B. M. Saad, "Electromagnetic behaviors of thin film CPW-Fed CSRR loaded on UWB transparent antenna," *IEEE Antennas Wirel. Propag. Lett.*, vol. 13, no. height mm, pp. 1239–1242, 2014.

[6] A. Hassan, S. Ali, J. Bae, C. H. Lee, J. H. Cho, and H. Y. Kim, "Flexible dual-band antenna for communication and radar applications," *2016 IEEE Radar Conf. RadarConf 2016*, pp. 1–5, 2016.

Flexible Chipless RFID Based Frequency Selective Surface

Mohd Ezwan Jalil[1] Mohamad Kamal A Rahim[1] Asmawati Samsuri[1] Mohamed Himdi[2] Raimi Dewan Kamilia Kamardin[3]

1. Advanced Radio Frequency and Microwave Research Group Communication Engineering Department, Faculty of Electrical Engineering, Universiti Technologi Malaysia, 81310 Johor Bahru, Johor, Malaysia
2. Institut d'Electronique et de Télécommunications de Rennes (IETR), UMR-CNRS 6164, Campus de Beaulieu, 263 Avenue du Général Leclerc, Rennes 35042, France
3. Computer Systems Engineering Group, Advanced Informatics School, Universiti Teknologi Malaysia (UTM), 54100 Kuala Lumpur, Malaysia*corresponding author: ezwanjalil@gmail.com

*corresponding author: ezwanjalil@gmail.com

Abstract- This paper present the design of metamaterial frequency-selective surface for chipless Radio-frequency Identification. Three circular ring with different radius are as resonating elements as main identification element for coding of chipless RFID. The gap of metamaterial-split ring resonators are adjusted using frequency shifting technique to maximize amount of number or bits, From simulated result, the proposed structure archive high transmittance, which is range between 95% and 90% at 3.50, 4.88 and 6.73 GHz The proposed chipless RFID tag offer high amount bit number without any size and capability of operating when mounted on metamaterial.

Introduction- Chipless radio frequency identification (RFID) offer several attractive feature such as compact and high capacity and does not including any silicon chip. [1]. Effort to investigate the potential chipless RFID design and technique has been blooming ever since the discovery of minimizing structure and improving RFID performance[2-3]. Metamaterial structure is one solution for solving the challenge of designing high capacity and compact chipless RFID. One of the popular metamaterial structure is split ring resonator (SRR) was invented by Hardy [4] as shown in Fig 1a. The gaps between two rings determine capacitance and the outer ring store the magnetic field. Pedry [5] was improved the SRR design with combination of two concentric ring with split on opposite side as shown in Fig 1 b) for non-magnetic array effect. The model equivalent circuit has approximated same with the SRR model as shown by Falcon [6] as shown in Fig 2. The complementary SRR are introduced at the back side substrate achieve high magnetic coupling between line and ring resonance by Martin [7].

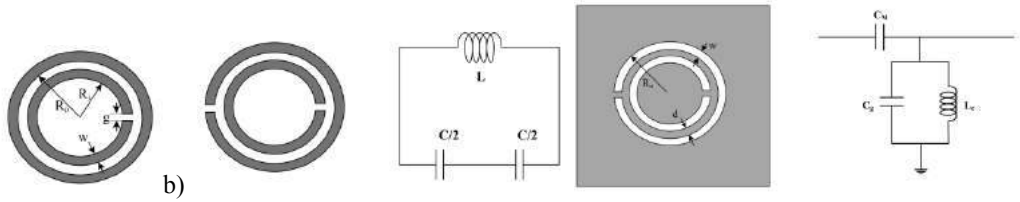

a) b)

Fig 1 a) Hardy's SRR structure, b) Pedry's SRR structure with equivalent circuit c) Complementary SRR and equivalent circuit

Multi-frequency Metamaterial Frequency-Selective Surface- This paper proposed a split ring resonator (SRR) structure for operating at three frequencie bands (3.56, 4.87 and 6.7 GHz) with narrow bandwidth from previous research [8-9]. The structure can absorb the incident of EM wave coming from a direction (+z). The substrate is used Rogers RT 5880 which has dielectric constant of 2.2, loss tangent of 0.0009 and thickness of 0.17mm. The

resonating elements are made by 0.017 mm thick copper. The corresponding dimensions are listed in Table 1. The dimension of the unit cell (W x L x H) is 18 mm x 18 mm x 0.127mm. The frequency shifting approach for chipless RFID as shown in Fig 3 is introduced to improve the amount of bit generated by a single resonator. From the analysis, the length of split ring resonator has inverse relationship with resonant frequency. The addition of gap size reduces the length of resonator and increases the resonant frequency. The simulated reflectance and transmittance of multi-resonant SRR metamaterial are shown in Fig 4. The transmittance of all resonant frequency above 90% show the proposed metamaterial structure enable to produce high transmittance.

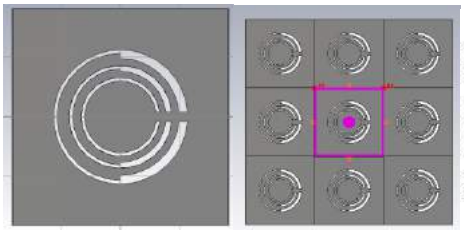

Fig 3. The proposed structure

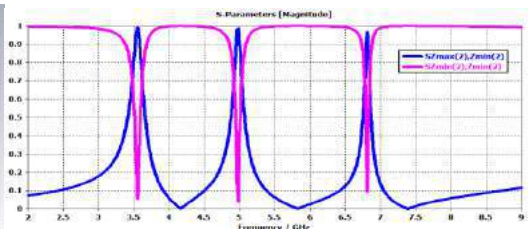

Fig 4. Simulated reflectance and transmittance of proposed structure

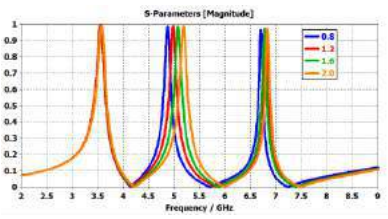

Fig 5 Gap Second Ring vs Resonance Frequency

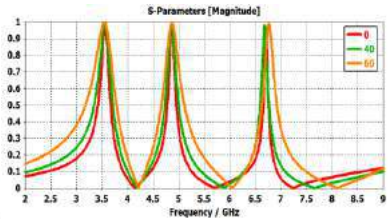

Fig 6. Simulated Transmittance for TE Polarization of Incident Wave

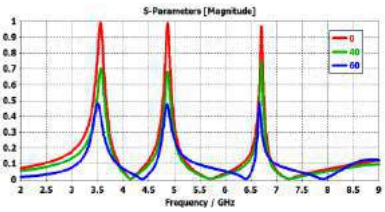

Fig 7. Simulated Transmittance for TM polarization of Incident wave.

Conclusion : A novel chip-less RFID tag base metamaterial structure using split ring resonator on the flexible substrate, Rodger 5880 operates between 2.5 to 6.5 GHz with multiple bits of data have been designed and analysed. The concept of modified complimentary split ring resonator metamaterial based frequency-selective surface is proposed to miniaturize the size and reduces the space consumption for chipless RFID application

Acknowledgements, The authors thank the Ministry of Education (MOE) for supporting the research work; Research Management Centre (RMC), Faculty of Electrical Engineering (FKE) UTM, School of Graduate Studies (SPS) under grant no. 12H09, 4F360, and 12H08.

REFERENCES

1. Preradovic, S.; Karmakar, N.C., "Chipless RFID: Bar Code of the Future," Microwave Magazine, IEEE , vol.11, no.7, pp.87,97, Dec. 2010R.
2. Moscato, S.; Moro, R.; Bozzi, M.; Perregrini, L.; Sakouhi, S.; Dhawadi, F.; Gharsallah, A.; Savazzi, P.; Vizziello, A.; Gamba, P., "Chipless RFID for space applications," *Wireless for Space and Extreme Environments (WiSEE), 2014 IEEE International Conference on* , vol., no., pp.1,5, 30-31 Oct. 2014
3. Vena, A.; Moradi, E.; Koski, K.; Babar, A.A.; Sydanheimo, L.; Ukkonen, L.; Tentzeris, M.M., "Design and realization of stretchable sewn chipless RFID tags and sensors for wearable applications," *RFID (RFID), 2013 IEEE International Conference on* , vol., no., pp.176,183, April 30 2013-May 2 2013

Metamaterial-HIS for Pattern Reconfigurable Multiband Array Antenna

Raimi Dewan[1], M.K.A. Rahim[1], Mohamed Himdi[2], M.R. Hamid[1], and N.A. Samsuri[1]

[1]Advanced RF and Microwave Research Group, Communication Engineering Department,
Faculty of Electrical Engineering, University Technology Malaysia, 81310 Johor Bahru, Johor, Malaysia

[2]Institut d'Electronique et de Télécommunications de Rennes (IETR), UMR-CNRS 6164, Campus de Beaulieu,
263 Avenue du Général Leclerc, Rennes 35042, France

*corresponding author: raimidewan@gmail.com

Abstract- Metamaterial-HIS of Electromagnetic Band Gap (EBG) incorporated onto dual band array antenna operate at 2.45 GHz (lower band) and 5.8 GHz (upper band) is proposed. The four configurations of EBG unit cells successfully realizes a dual band antenna with dedicated pattern reconfigurability. The antenna is suitable for steering the main lobe direction to intended directions.

Introduction

EBG is a High Impedance Surface (HIS) of metamaterial which exhibits unique properties in suppressing the propagating wave within the microwave structure [1] at its resonance frequency. This properties can be used to block away the desired wave of particular frequency in reaching the antenna radiating patch [2]. In this paper, a multiband array antenna which operates at 2.45 GHz and 5.8 GHz with EBG for pattern reconfigurability is presented and discussed.

Result and Discussion

Figure 1(a)-(b) shows the back and front view of the EBG cells with region "S0" and "S1" which can be "ON" and "OFF" with connection or removal of copper strips respectively. The "ON" and "OFF" are represented by "1" and "0" respectively. Suspended Transmission Line (STL) method in Figure 1(c) is used to analyzed the band gap, S21 of EBG and the result is shown in Figure 1(d). It can be observed that EBG produces band gap at lower band (2.45 GH) and upper band (5.8GH) with different EBG configurations. EBG is then incorporated to array antenna as shown in Figure 1(e) and 1(f). Various configuration of EBG1, EBG2, EBG3 and EBG4 have achieved pattern reconfigurability as shown in Figure 1(g). It is observed from Figure 1(h) and 1(i), that the multiband array antenna successfully resonates at 2.45 GHz and 5.8 GHz despite difference in configuration of the EBG unit cells. Figure 1(j) and 1(k) shows the polar plot of the H-field of the array antenna. The proposed antenna is very useful in wireless communication service (WCS) where the antennas are required to direct its pattern at desired coverage or intended receiver in the dynamic environment.

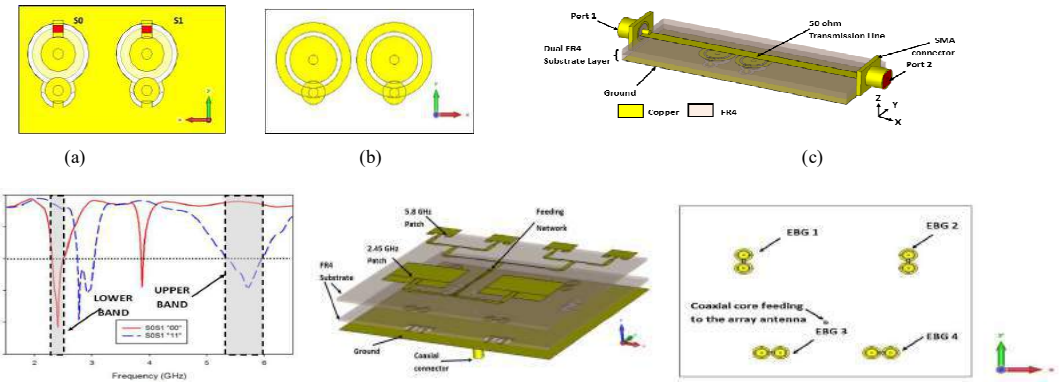

(a) (b) (c)

(d) (e) (f)

EBG state configurations				Pattern (Degree)	
EBG1	EBG2	EBG3	EBG4	2.45 GHz	5.8 GHz
0	0	1	1	0	31
0	0	0	1	342	3
0	0	1	0	18	357
0	1	1	1	1	5
1	0	1	1	359	355

(g)

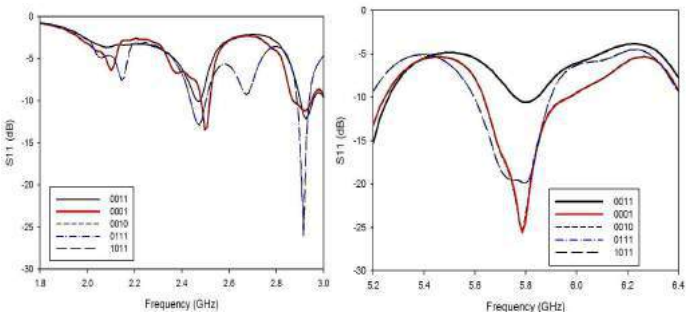

(h) (i)

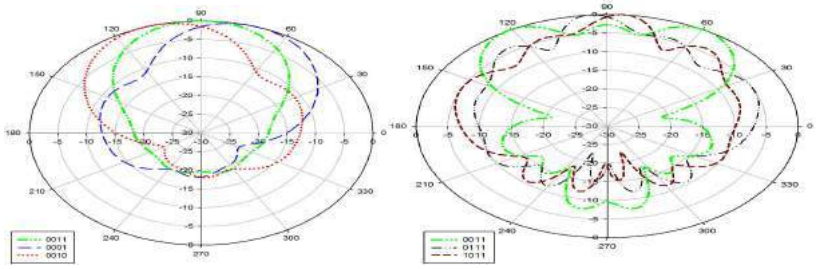

(j) (k)

Figure 1. (a) Back and (b) front view of EBG cells. (c) STL method to analyze band gap (S21) with the corresponding (d) band gap (S21) simulated result. The (e) 3-dimensional exploded diagram and (f) EBG positions at the bottom substrate of the antenna. (g) EBG configurations with corresponding degree of main lobe direction. The reflection coefficients at lower band and upper band of (h) 2.45 GHz and (i) 5.8 GHz respectively. The corresponding H-field polar plot at (j) 2.45 GHz and (k) 5.8 GHz.

Conclusion: Pattern reconfigurable multiband array antenna with EBG is proposed. The antenna pattern can be reconfigured with different EBG configurations. The antenna operates at 2.45 GHz and 5.8 GHz at all EBG configurations.

Acknowledgements The authors thank the Ministry of Education (MOE) for supporting the research work; Research Management Centre (RMC), Faculty of Electrical Engineering (FKE) UTM, School of Graduate Studies (SPS) under grant no. 4F883, 12H08, 12H09 and 4F360,

REFERENCES

[1] R. Dewan, M. K. A. Rahim, M. R. Hamid, M. F. M. Yusoff, N. A. Samsuri, N. A. Murad*, et al.*, "Artificial magnetic conductor for various antenna applications: An overview," *International Journal of RF and Microwave Computer-Aided Engineering,* pp. e21105-n/a, 2017.

[2] J. d. D. Ruiz, F. L. Martínez-Viviente, and J. Hinojosa, "Optimisation of chirped and tapered microstrip Koch fractal electromagnetic bandgap structures for improved low-pass filter design," *IET Microwaves, Antennas & Propagation,* vol. 9, pp. 889-897, 2015.

Passive Sensors using 3D Circular Frequency Selective Surfaces for Structural Health Monitoring System

S. A. Suhaimi[1], S. N. Azemi[1], P. J. Soh[1],

[1]Advanced Communication Engineering Center (ACE),
School of Computer and Communication Engineering,
University Malaysia Perlis, Malaysia
anassuhaimi91@gmail.com, snorlyana@unimap.edu.my, pjsoh@ieee.org

Abstract

This paper is introduced a passive sensor to detect the performance of the structure using three-dimensional (3D) Frequency Selective Surfaces (FSS). The proposed 3D Circular FSS results are proved behave as passive sensor with changing of sensitivity incident angles to be apply in Structural Health Monitoring (SHM) system. Moreover, this 3D Circular FSS capable to operate without stand to any (DC/AC) power and very low cost in term of installation and maintenance.

1. Introduction

Nowadays, SHM system has been offered a huge beneficial for building structure safety and performance. By developing SHM system, it is proved that the percentage of safety increased. SHM is commonly applied to tracking and detect any poor structure performance such as tilting, crack and movement of structure with using various sensors [1].

There are many type of sensors have been proposed and applied in SHM system which are wired and wireless sensors. Besides that, mostly researchers are more concentrating to wireless sensor compared to wired sensor due to their higher active element needed and difficulties in installation [2], [3].Characteristic of passive sensor has been overcome the active sensor problem in term of easier installation and maintenance, less power consumption and long term of endurance element [4].

The 3D Frequency Selective Surfaces with circular shaped was introduced here to act as a passive sensor. A good performance in term of sensitivity angular response for this circular shaped was chosen [5], [6]. A new technique of 3D FSS was proposed in this paper to tracking abnormalities structure performance for SHM system. The electromagnetic wave characteristic will varies by changing the angle of FSS due to the building tilting as shown in Figure 1 (b). The changing (frequency shifting) of different electromagnetic wave characteristics were presenting in two polarizations which is TE- and TM- incident angle. For this case, the TE- and TM- incident angle required to obtain in two different characteristic frequency responses TE and TM angle such sensitive and insensitive angular response respectively. See Figure 1 (b), sensitivity of angular response indicating that the frequency response (band stop) shifting from 3.8GHz to 3.86 GHz with the angle 0° to 20° respectively. Meanwhile, insensitive frequency response (band stop) is maintained in one location of frequency response with various angles up to 60 degrees. Therefore, the building tilting is monitored by a different of sensitivity angular response changing. The 3D Circular FSS design is shown in Figure 1(c), where behaves as a passive sensor and attached on the building structure.

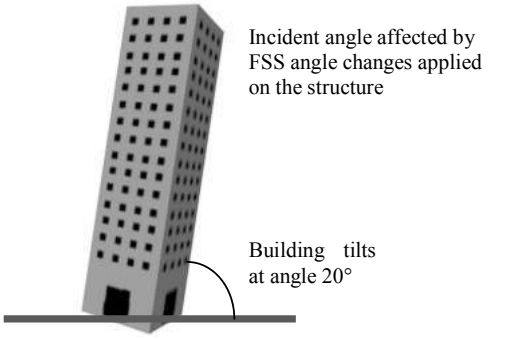

(a)

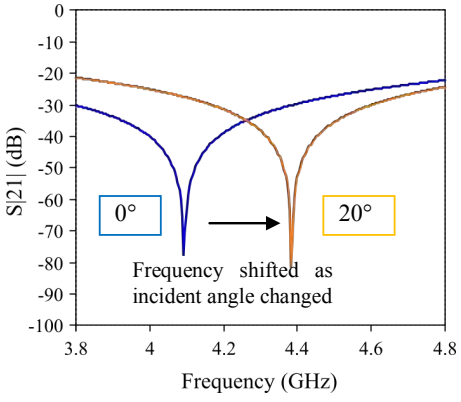

(b)

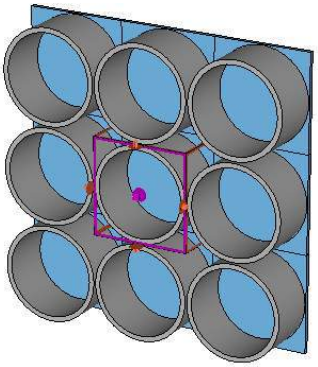

(c)

Figure 1: (a) Incident angle effect as building tilting (b) Frequency response shifting as incident angle changed (from 0° to 20°) (c) 3D Circular FSS design with unit cells.

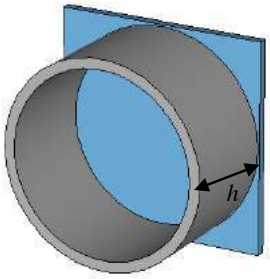

Figure 2: Elevating the height of conducting element.

See Figure 2, by increasing the conducting element will render the frequency characteristic. The geometry FSS play an important role towards the frequency behavior [7]. Therefore the frequency response of FSS can be control in two different polarizations by alter the geometry size.

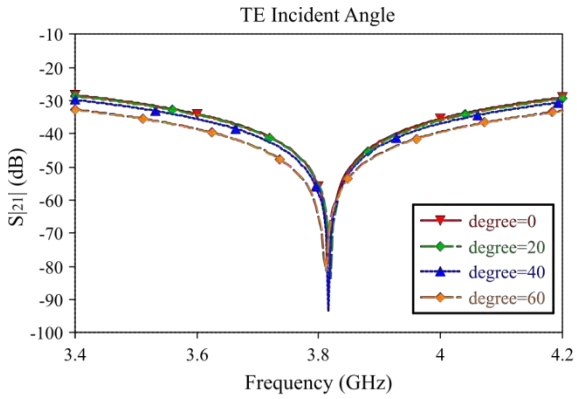

(a)

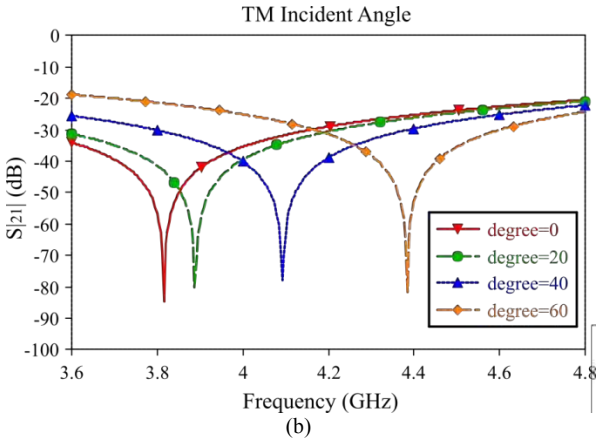

(b)

Figure 3: Frequency response results up to 60° (a) TE incident angle, insensitive (b) TM incident angle, sensitive.

In Figure 3 indicate that two different polarization TE- and TM- incident angle have been simulated. Result in Figure 2 (b) looks sensitive in various angles and will be used for monitoring in SHM system. Table 1 indicated the percentage different center frequencies in each angle as the FSS (building) changed.

Table 1: Values center frequencies of the 3D Circular FSS with different angle.

TE incident angle		
Degree (°)	Frequency (GHz)	Deviation (%)
0	3.81	0
20	3.816	0.15
40	3.816	0.15
60	3.815	0.13
TM incident angle		
0	3.81	0
20	3.893	2.17
40	4.12	8.13
60	4.38	14.9

2. Discussion

The FSS shape was designed in circular geometry. FSS structure was modified by elevating the height of conducting element. Besides that, 3D Circular FSS has shown the different S_{21} band stop results in two polarization TE and TM incident angle. Controllable FSS performance and characteristic made the two polarization results become sensitive and insensitive in various angle. Simulation on 3D FSS has been done from 0° up to 60°.

3. Conclusions

The proposed of 3D Circular FSS was introduced to perform as a passive sensor in SHM system. 3D Circular

FSS able to utilize without depends on the power supply on it. Moreover, various angles S_{21} results shown a sensitivity incident angle (TM-polarized), meanwhile insensitivity (stable) incident angle at TE-polarized. 3D Circular FSS proved that can controlled the sensitivity incident angle in both polarizations instead of 2D FSS structure. A result in Figure 2 (b) has shown a terrific sensitivities frequency shifting as the incident angle of building changed. Therefore, a result will be used as monitoring building performance due to sensitive on different building condition.

Acknowledgements

The authors would like to acknowledge the contributions of Mr. Herwansyah Lago for his technical contributions during the experimental validations.

References

[1] J. M. Lopez-Higuera, L. Rodriguez Cobo, A. Quintela Incera, and A. Cobo, "Fiber Optic Sensors in Structural Health Monitoring," *J. Light. Technol.*, vol. 29, no. 4, pp. 587–608, 2011.

[2] S. A. A. Jabir and N. K. Gupta, "Thick-film ceramic strain sensors for structural health monitoring," *IEEE Trans. Instrum. Meas.*, vol. 60, no. 11, pp. 3669–3676, 2011.

[3] X. Jiang, Y. Tang, and Y. Lei, "Wireless Sensor Networks in Structural Health Monitoring Based on ZigBee Technology," *3rd Int. Conf. Anti-counterfeiting, Secur. Identif. Commun.*, pp. 449–452, 2009.

[4] Y. Ikemoto, S. Suzuki, H. Okamoto, H. Murakami, H. Asama, S. Morishita, T. Mishima, X. Lin, and H. Itoh, "Force sensor system for structural health monitoring using passive RFID tags," *Sens. Rev.*, vol. 29, no. 2, pp. 127–136, 2009.

[5] W. S. T. Rowe, A. R. As-Saber, S. N. Azemi, and K. Ghorbani, "3D frequency selective surfaces with highly selective reponses," *2015 Loughbrgh. Antennas Propag. Conf. LAPC 2015*, pp. 3–6, 2015.

[6] S. N. Azemi, K. Ghorbani, and W. S. T. Rowe, "3D Frequency Selective Surface," *Prog. Electromagn. Res. C, Vol. 29, 191–203, 2012 3D*, vol. 29, no. May, pp. 191–203, 2012.

[7] S. A. Suhaimi, S. N. Azemi, and P. J. Soh, "Structural Health Monitoring System using 3D Frequency Selective Surface," *IEEE Asia-Pacific Conf. Appl. Electromagn.*, pp. 145–149, 2016.

Multiband Salisbury Screen Absorber Using Double Layer Cross Dipole FSS

F. C. Seman[1*], S. Omar[1], W. Y. Yong[2] and S. K. A. Rahim[2]

[1]Research Centre for Applied Electromagnetic, Universiti Tun Hussein Onn, Malaysia
[2]Wireless Communication Centre, Universiti Teknologi Malaysia, Malaysia
[*]corresponding author: fauziahs@uthm.edu.my

Abstract

In this paper the microwave absorbing properties of multiband Salisbury screen absorber design which is constructed using multi-layer FSS is investigated. The structure exhibits triple operating band where the -10 dB reflectivity bandwidth of a Salisbury screen operating at normal incidence is 36.3%, 11.9% and 14.5% at the resonant frequencies of 6.56 GHz, 9.1 GHz and GHz respectively. Reflectivity predictions for normal incidence are shown to be in close agreement with bistatic measured results over the frequency range 8 - 12 GHz.

1. Introduction

The Salisbury screen is a resonant absorber created by placing a 377 Ω/square resistive sheet on a dielectric substrate backed by a metal plate as illustrated in Figure 1(a). The loss mechanism in this dielectric-based and conductor-backed thick (d) absorber exploits the terminating impedance property of an open circuit which is transformed from a short circuit that is presented when the signal is reflected from the ground plane with a phase of 180° [1]. This reduces the amount of energy reflected back to the transmitter, and so effectively reduces the RCS of the structure. Equation (1) defines the phase criteria necessary to generate the reflection null [2];

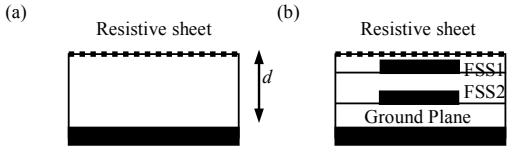

Figure 1 : (a) Conventional Salisbury screen absorber d= λ/4 (b) Salisbury screen with double layer FSS.

$$\emptyset_{GP}(f) + \emptyset_{PL}(f) = 2n\pi \quad [1]$$

Where n = 1,2,3 …

$$\emptyset_{PL}(f) = \frac{2\times 2\pi \times d\sqrt{\varepsilon_r - \sin^2\theta}}{\square} \quad [2]$$

where ϕ_{GP} is the reflection phase (180º) attributed to the ground plane, ϕ_{PL} is the path length phase in the cavity, d is the physical spacing between the resistive sheet and metal backing plate, θ is the angle of incidence and ε_r is the permittivity of the spacer material. In conventional Salisbury screen absorber, additional phase length of 180° is contributed by the λ/4 to provide total phase of 360° at reflection null. The same phase characteristic can be realised by integrating multilayer FSS between the resistive sheet and metal back as illustrated in Fig.1 (b). Here, manipulation of total phase of 360° is obtained multiple times therefore multiband Salisbury screen may be realised.

In this paper, design concept of multiband Salisbury screen is explored by integrating multilayer cross dipole FSS. The phase characteristic in Salisbury screen absorber is discussed in details in relation the reflection phase provided by the conductor layer (solid metal backed or FSS) and the path length phase contributed by the substrate layer. This is designed to generate additional reflection nulls at predetermined frequencies by optimising the size, periodicity and shape of the periodic elements in each FSS unit cell. Later, verification of design concept of multiband Salisbury screen is realised by fabricating a prototype of Salisbury Screen with two layers of cross dipole FSS so that each layer generate the reflection phase of 180° thus generating additional absorbing bands above the inherent absorption band of the structure [3].

2. Cross Dipole and Fundamental

Fig. 2 shows the geometry of cross dipole FSS printed on vacuum spacer (ε_r =1.0) where the geometry can be represented as a series of capacitance and inductance. Note that the vacuum spacer is used to ease explanation of phase changing in Salisbury screen. The resonant frequency of the FSS occurs when the electrical length of the dipole is about λ/4. The cross dipole patch perform as a bandstop filter at its resonant frequency. Fig. 3 shows that a microwave signal is completely reflected by the cross dipole FSS, l =15 mm at 9.41 GHz with reflected phase of 180°. This demonstrates that the FSS behaves as ground plane as in conventional Salisbury screen at the resonant frequency. This phase can be manipulated to compensate the required total phase in the Salisbury screen as given in equation [1] and [2]. Fig. 4 shows the transmission characteristic of a cross dipole FSS. As the dipole length, l increases from 15 mm, 17 mm to 19 mm, the resonant frequency reduces from 9.41 GHz, 8.43 GHz to 7.32 GHz. To obtain FSS reflection phase of 180°, the physical dimension of cross dipole FSS can be varied therefore the absorbing band provided by Salisbury screen

can occur at the specified frequency. Consider for case with FSS l = 15 mm, as the reflection phase from the FSS is 180° at 9.41 GHz, the path length of 180° is required which is a 7.97 mm thick vacuum spacer. Note that absolute value of FSS reflection phase is included as the negative sign indicates out-phase. Therefore total phase of 360° is accomplished and a reflection null is occurred. If a thicker vacuum spacer is employed which bring more than 180° path length phase, the reflection null is expected to occur below 9.41 GHz. Note that the same vacuum spacer will provide different path length phase at other frequencies range then it may compensate the reflection phase from another FSS layer to create another reflection null. On the other side the total phase of 180° in the Salisbury screen absorber will produce a reflection peak.

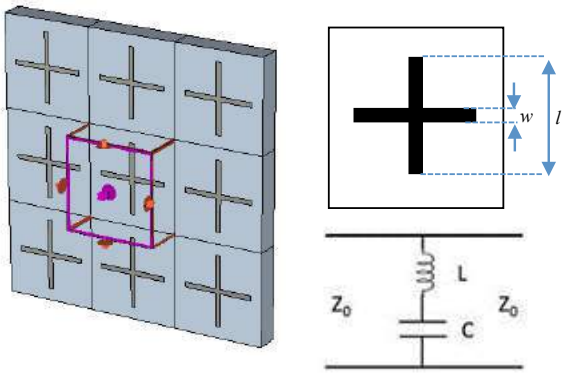

Figure 2 : Unit cell of cross dipole FSS

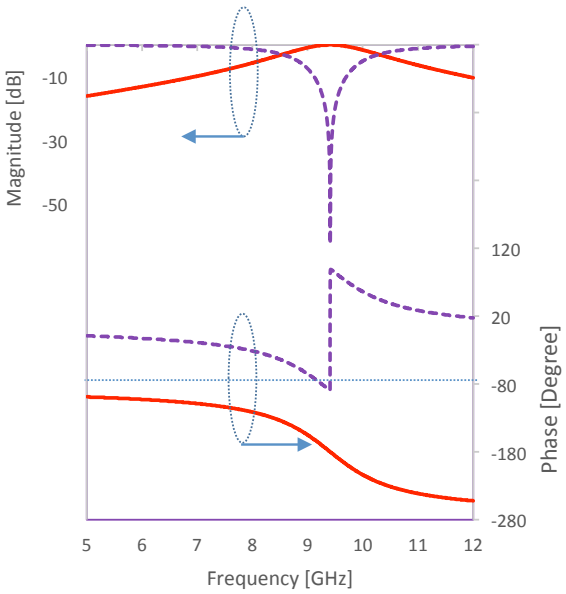

Figure 3 : Scattering parameters for Cross dipole FSS l = 15 mm where —— for reflection, S_{11} and - - - for transmission, S_{21}

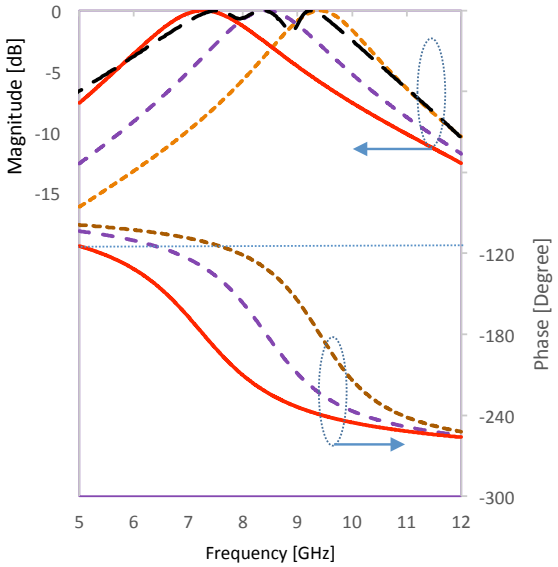

Figure 4 : Scattering parameters for Cross dipole FSS l = 15 mm (- - - - -) , l = 17 mm (- - -), l = 19 mm (——) and cascaded 3 FSSs (— —) mm for transmission, S_{21}

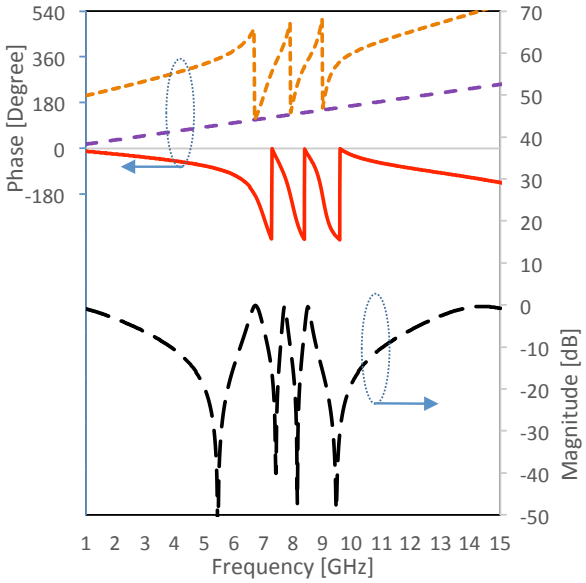

Figure 5 : Phase characteristic in a Salisbury screen, reflection phase, S_{11} for a cascaded FSS1 l = 15 mm, FSS2 = 17 mm, FSS3 l = 19 mm (——), path length phase in 7 mm thick vacuum spacer, (- - -) and total phase (- - - - -), and absorbing band of Salisbury screen absorber, S_{11} (— —) at normal incidence.

Consider for multilayer FSS in the construction of Salisbury Screen, the three layer of cross dipole FSS are cascaded with 1.5 mm separation. Fig. 4 shows that the

transmission characteristics of the cascaded FSS are slightly shifted due to the coupling between each FSS layer. If the FSS are separated to be more than a 1.5/λ, the coupling is not significant then the scattering characteristics of each FSS layer can be maintained. Fig. 5 shows that with 7 mm thick of vacuum spacer, additional path length phase is demonstrated to contribute 17° to 249° phase in frequency range of 1 to 12 GHz. Total phase given by the path length and the cascaded FSS determine the characteristic in the scattering parameters of in Salisbury Screen. The total phase of 360° is achieved to generate four reflection nulls at 5.5, 7.4. 8.1, 9.5 GHz. Here, the reflection phase from each FSS layer is not necessary to be 180°.

3. Fabrication and Measured Results

Multiband Salisbury screens was fabricated and measured to validate the design methodology presented in the previous section. Two layers of cross dipole FSS were fabricated on 1.6 mm thick FR4 substrate, $\varepsilon_r = 4.3$. The first FSS layer with $l = 0.5$ mm and the second FSS layer with $l = 7.5$ mm, and $w = 0.5$ backed by a solid metal plate. Both FSS layers were bonded directly. The manufacture of the Salisbury screen absorbers was completed by glueing the surfaces of a 5 mm thick foam spacer, to the patterned side of the FSS and a 400 Ω/square resistive textile sheet. The Salisbury screen with two cascaded cross dipole FSS layer was fabricated in 30 x 30 cm size. The reflection and transmission measurement were made in a semi anechoic chamber relative which was placed 50 cm distance from the aperture of a pair of standard gain horns which cover the frequency range 8 – 12 GHz. For transmission measurement, the FSS was placed between two antenna horns in a far field region. The reflection measurement was carried out by positioning Salisbury screen absorber in front of two horns placed side by side as shown in Fig. 6.

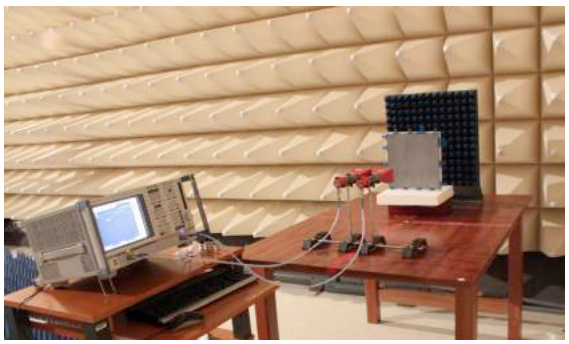

Figure 6 : Measurement setup for scattering parameters for Salisbury screen.

Fig. 7 illustrates the transmission magnitude of the fabricated cross dipole FSS. The FSS with $l = 7.5$ mm resonates at 11.14 GHz while FSS with $l = 6.5$ resonates at frequency 13.26 GHz. However it was observed that when the two FSS layers are attached together, the transmission magnitude produces dual resonances at 9.16 GHz and 12.5 GHz. This demonstrates a significant downward shifts in resonance frequencies because of strong coupling between two electrical closely separation. Both simulation and measurement are in a very good agreement.

Fig. 8 shows the absorbing parameters of constructed Salisbury screen at normal incident. Within 1 – 20 GHz frequency range the multilayer FSS generates three absorption bands of -10 dB bandwidth at 4.96 – 7.3 GHz (38.1%), 8.5 – 9.6 GHz (12.1 %) and 11.7 – 13.9 GHz and (17.2%). The reflection null occurred at 6.56 GHz, 9.1 GHz and 13 GHz due to the total phase of 360° was satisfied at these three conditions. Note that each reflection null was obtained due to reflection at particular virtual ground plane, the lowest reflection null was on the metal backed side, the middle reflection null was on the FSS layer, $l = 6.5$ mm and the highest reflection null on the FSS layer, $l = 7.5$ mm respectively. On the other side the reflection peaks were produced at 6.85 GHz, 7.76 GHz and 8.58 GHz when the total phase in the structure was 180°.

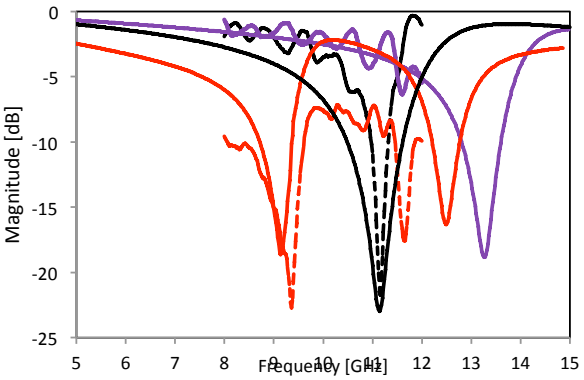

Figure 7 : Transmission magnitude for standalone cross dipole FSS $l = 6.5$ mm, simulated (——), measured (– – –) ; standalone cross dipole FSS $l = 7.5$ mm, simulated (——), measured (– – –) ; cascading both FSSs simulated (——), measured (– – –).

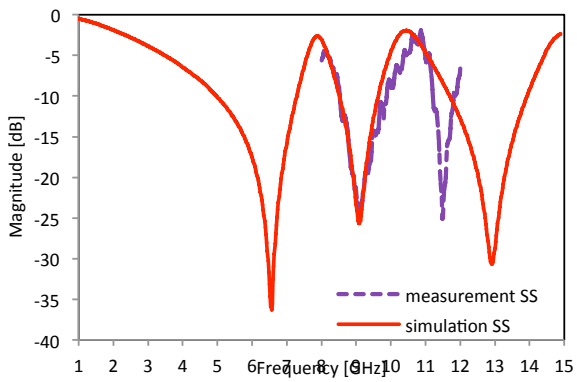

Figure 8 : Scattering parameters for Salisbury screen, simulation (——), measurement (– – –)

4. Conclusions

This paper has presented about phase interaction between path length phase and reflection phase by either a metal backed or an FSS. The concept has been explained in detail by integrating three FSS layers in the Salisbury screen. To validate the concept a prototype of Salisbury screen absorber with two layer FSS has been realised. In this paper the microwave absorbing properties of multiband Salisbury screen absorber design which is constructed using double layer FSS is investigated. The structure exhibits triple operating band where the -10 dB reflectivity bandwidth of a Salisbury screen operating at normal incidence. Reflectivity predictions for normal incidence are shown to be in close agreement with bistatic measured results over the frequency range 8 - 12 GHz.

Acknowledgements

The authors thank the Office for Research, Innovation, Commercialization and Consultation Management (ORICC) of Universiti Tun Hussein Onn Malaysia for supporting the registration funding of the conference under Research and Innovation Fund.

References

[1] B.A. Munk., *Frequency Selective Surfaces -Theory and Design*, John Wiley and Sons Inc, New York, 2000.

[2] F.C. Seman,, and R.Cahill, Frequency Selective Surfaces Based Planar Microwave Absorber. *Progress In Electromagnetics Research Symposium Proceedings*, ,pp 906-909, 2012

[3] F.C. Seman, R. Cahill, V.F.Fusco, G.Goussetis, Design of a Salisbury screen absorber using frequency selective surfaces to improve bandwidth and angular stability performance, *IET Microw. Antennas Propag*ation, Vol. 5, Issue. 2, pp. 149–156, 2011.

Modeling, Computational Techniques and Verification of Theory

Application of the Mathieu's equation for an analysis of photonic crystal – supported surface electromagnetic waves: *s*- and *p*-polarization cases

E. Rostova, S. K. Sekatskii*, and G. Dietler
Laboratoire de Physique de la Matière Vivante, IPHYS, BSP, Ecole Polytechnique Fédérale de Lausanne, CH1015 Lausanne, Switzerland

*corresponding author: Serguei.Sekatski@epfl.ch

Abstract- Recently, we showed that an analogy between a 1D Photonic Crystal and a structure with a sine-modulated refraction index enables to apply the Mathieu's differential equation for an analysis of Photonic Crystal - supported surface electromagnetic waves [1]. Here we present the detailed analysis for *p*- and *s*-polarizations and show that the *s*- polarization case is described exactly by the Mathieu's equation while that corresponding to the *p*-polarization gives rise to a slightly modified equation.

In a recent paper [1] we discussed the general principles of use of the famous Mathieu's differential equation [2] to analyze the 1D photon crystal (PC) – supported electromagnetic waves and to design appropriate structures. Now we give a detailed analysis for both *s*- (TE) and *p*-polarization (TM) cases: it is well known, that metal-free PC-based systems can support electromagnetic waves of both polarizations, and their co-existence is indeed very important for sensor applications to unambiguously separate surface and volume effects [3].

Geometry of the problem is shown in Fig. 1. Let us start with the *p*-polarization. We are interested in the surface modes (electromagnetic waves) strongly confined at the photonic crystal surface and decaying exponentially away from the surface. This property of the surface modes immediately prescribes the choice of the function *f(z)* in the most external medium with the dielectric constant ε_1 as an exponentially decaying function $f_1(z) = \exp(S_1 z)$ for *z<0* and $S_1 > 0$. Here $\vec{H} = \vec{H}_0 f(z)\exp(i\omega t - i\beta x)$ is a magnetic field propagating along the *Ox* axis and for all media $S_i^2 = \beta^2 - \varepsilon_i k^2$ (Fig. 1A), k is a wave number in vacuum, and β is a complex propagation constant. We suppose that our PC with a period *L* is a medium having the sine-modulated dielectric permeability $\varepsilon_3(z) = \varepsilon_{av} + \Delta\varepsilon\cos(2\pi z / L)$ while its magnetic permeability, as it usually takes place in optical frequency range, does not depend on the coordinate. The full forms of the wave equation in a medium are (see, for example, [4]): $\nabla^2\vec{E} - \mu\varepsilon\dfrac{\partial^2\vec{E}}{\partial t^2} + (\nabla\ln\mu)\times(\nabla\times\vec{E}) + \nabla(\vec{E}\cdot\nabla\ln\varepsilon) = 0$,

$\nabla^2\vec{H} - \mu\varepsilon\dfrac{\partial^2\vec{H}}{\partial t^2} + (\nabla\ln\varepsilon)\times(\nabla\times\vec{H}) + \nabla(\vec{H}\cdot\nabla\ln\mu) = 0$, and for our particular case, the equations describing the appropriate magnetic field inside the PC is reduced to the following equation, which is *not* that of Mathieu (but can be written as Hill's equation):

$$\frac{d^2H_y}{du^2} + \frac{2\Delta\varepsilon\sin(2u)}{\varepsilon_{av} + \Delta\varepsilon\cos(2u)}\frac{dH_y}{du} + (a - 2q\cos(2u))H_y = 0 \qquad (1).$$

Considering for the *s*-polarization case an electric field propagating along the *Ox* axis $\vec{E} = \vec{E}_0 f(z)\exp(i\omega t - i\beta x)$, we in a similar fashion obtain the Mathieu's equation

$$\frac{d^2 E_y}{du^2} + (a - 2q\cos(2u))E_y = 0 \qquad (2).$$

For both cases here $u = \pi z / L$, $a = -\beta^2 L^2 \pi^{-2} + \varepsilon_{av} k^2 L^2 \pi^{-2}$, $q = -\frac{1}{2}\Delta\varepsilon k^2 L^2 \pi^{-2}$.

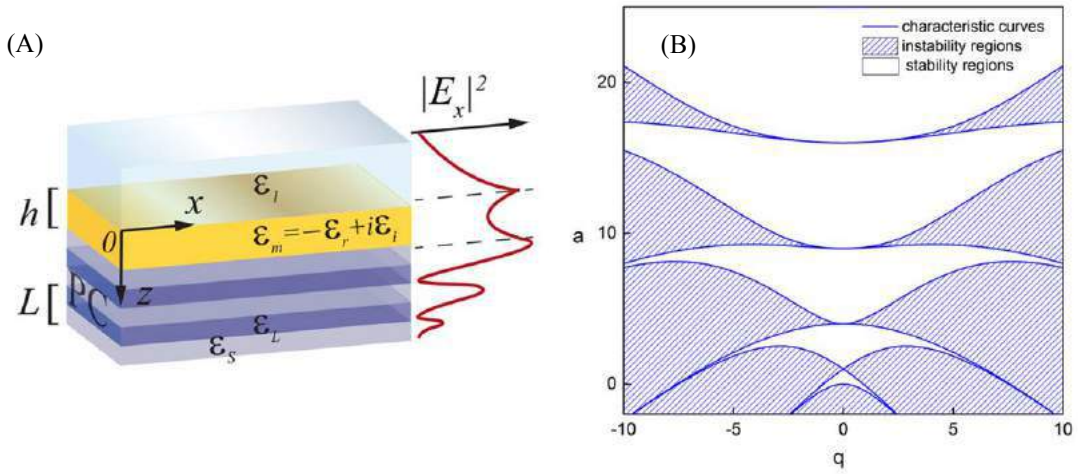

Figure 1. (A) A schematic of the investigated structure: a metal layer surrounded by a dielectric and a photonic crystal. The red line corresponds to the surface wave in the photonic crystal and the surface plasmon at the metal interface. Metal intermediated layer is not necessary present and can be absent (e.g. for the *s*-polarization case) (B) A stability diagram for the Mathieu's equation: the lines display the periodic Mathieu functions, the regions marked "U" belong to the instability regions (*a* and *q* here are the parameters in the Mathieu's equation), adapted from [2].

The procedure how to find the appropriate solution describing the photon crystal – supported electromagnetic waves (that is to fulfill the necessary conditions of continuity of tangential magnetic and electric fields), has been described in [1]. It rests the same, but now for *p*-polarization exponentially decaying to the infinity solution of eq. (1) rather than that of the Mathieu's equation (2) should be taken. Certainly, this modifies the concrete parameters to be applied for specific structures design, as well as the stability and instability regions shown in Fig. 1B. All these questions are analyzed in the present submission. In particular, we show that for real experimental situation neither the difference between two aforementioned differential equations nor that between their solutions and conditions necessary to ensure the existence of PC-supported surface electromagnetic waves are large.

REFERENCES

1. Rostova, E., G. Dietler and S. K. Sekatskii, "Application of the Mathieu's equation for a design of a photonic crystal supporting surface electromagnetic waves", *Adv. Electromagnetics,* Vol. 4, No. 3, 4729–4735, 2015.
2. McLachlan N. W. *Theory and Application of Mathieu Functions*, University Press, Oxford, 1951.
3. Konopsky, V. N., T. Karakouz, E. V. Alieva, C. Vicario, S. K. Sekatskii and G. Dietler "Photonic crystal biosensor based on optical surface waves," *Sensors,* Vol. 13, No. 2, 2566–2578, 2013.
4. Yeh, P. *Optical waves in layered media*, J. Wiley and Sons, New York, 1988.

Performance Prediction of Bundle Carbon Nanotube and Bundle Carbon Nanotube Composite Dipole Antennas

Yaseen N. Jurn[1], Mohamedfareq Abdulmalek[2], Hasliza A. Rahim[3], Sawsen A. Mahmood[4]
[1]School of Computer and Communication Engineering
University Malaysia Perlis (UniMAP), 02000 Arau, Perlis, Malaysia

[1]Minister of Science and Technology
Baghdad, Iraq

[2]Faculty of Engineering and Information Sciences
University of Wollongong in Dubai (UOWD), Dubai, United Arab Emirates

[3]Bioelectromagnetics Research Group (BioEM),
School of Computer and Communication Engineering, University
Malaysia Perlis (UniMAP), Pauh Putra, Arau, Perlis 02600, Malaysia

[4]Department of Computer Science, College of Education
University of Mustansiriyah, Baghdad, Iraq

[*]Yaseen Naser Jurn: yaseen_nasir@yahoo.com

Abstract-The performances of bundle carbon nanotubes (BCNTs) and bundle carbon nanotubes composite (BCNTs-composite) materials for the antenna applications in the terahertz and gigahertz frequency ranges are evaluated. The performances of these bundles are compared based on the electromagnetic properties of their dipole antennas, where the cross sections of bundles are circular geometry. Furthermore, comparative studies are performed to show the size and frequency dependent of these bundles.

In this work, the BCNTs contains (N) a number of metallic single-walled carbon nanotubes SWCNTs which are identical have the same dimensions, radius (r) and length (L_S). While, the BCNTs-composite contains (N) a number of SWCNTs coated by a thin layer of another materials (t) such as, graphite or copper materials, radius ($R = r + t$). Both bundles BCNTs and BCNTs-composite have configuration characterized by closely packed structure with a circular geometrical structure. Also, all tubes are aligned parallel along the axis of bundle and the lattice constant of the bundles is (Δ) to personify the distance between each two contiguous walls of SWCNTs and SWCNTs-composite. The minimum required radius of the cylinder that contains all SWCNTs or SWCNTs-composite is the radius of bundle (R_B). Figure (1) explains the sketch of BCNTs and BCNTs-composite with a circular geometrical structure.

The mathematical model of SWCNTs-composite structure derived based on the mixture rule [1], the simple parallel model of the radial interface of coating material and SWCNT for a simple parallel model of the radial interface of coating material and SWCNT. The general formula of the electrical conductivity of

SWCNTs-composite material was presented in Equation (1).

$$A_{Compisite}\sigma_{Structure} = C_{SWCNT}\sigma_{SWCNT} + A_{Coat}\sigma_{Coat} \quad (1)$$

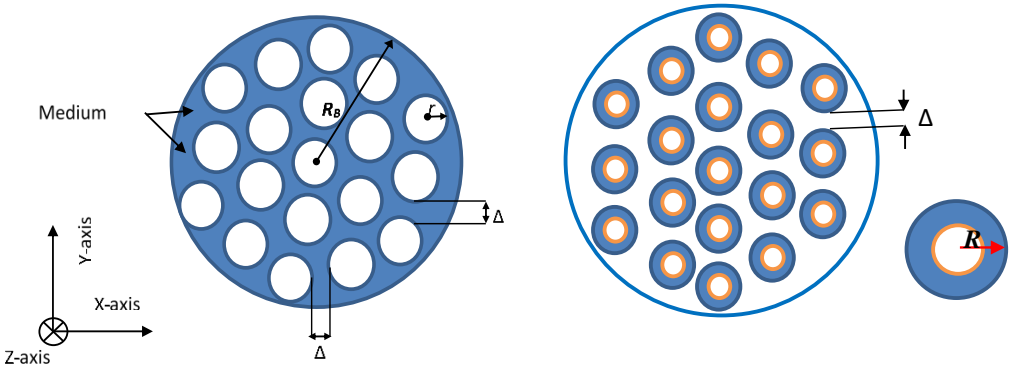

(a) (b)

Figure 1: (a) Schematic configuration of BCNTs and (b) Schematic configuration of a BCNTs-composite

The simulation results for both bundles are compared between each other and with the BCNTs which are presented in previous research [2]. These comparisons carried out based on their electromagnetic behaviors such as, S11 parameters response with various numbers of tubes included in bundles, efficiency, gain and directivity. The simulation results of BCNTs with different numbers of SWCNTs are illustrated in Figure (2).

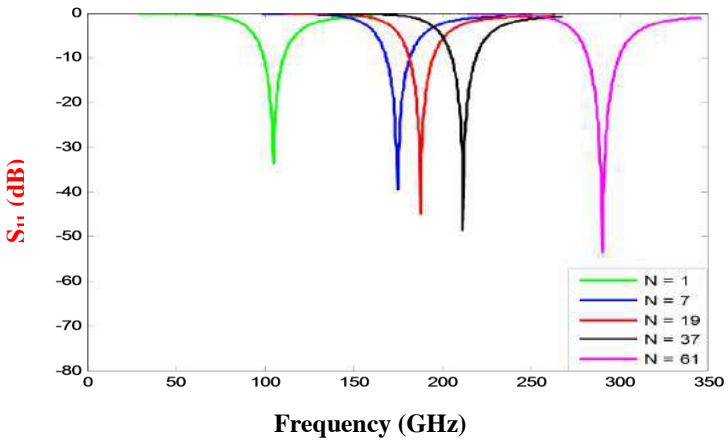

Figure 2: (a) Simulation results of BCNTs dipole antenna at Length = 30 μm and N = (7, 19, 37 and 61)

REFERENCES

1. Askeland, Donald R., Fulay, Pradeep P. and Wright, Wendelin J. "The Science and Engineering of Materials" (6th ed.). Cengage Learning, 2010.
2. Huang, Y., Yin, W.-Y., & Liu, Q. H. "Performance Prediction of Carbon Nanotube Bundle Dipole Antennas". *IEEE Transactions on Nanotechnology*, Vol. 7, No. 3, 331-337, 2008.

Dual-Band Circularly Polarized Wearable Textile Antenna Slotted with Split-Ring Resonator for Off-Body LTE Applications

E. A. Muhammad[1], H. A. Rahim[1*], P. J. Soh[2], M. Abdulmalek[3] and G. A. E. Vandenbosch[4]

[1]Bioelectromagnetics Research Group (BioEM),

[2]Advanced Communication Engineering (ACE),

School of Computer and Communication Engineering, Universiti Malaysia Perlis (UniMAP),

Kampus Pauh Putra, Perlis, Malaysia

[3]Department of Engineering and Information Science, University of Wollongong in Dubai, Block 15,

Dubai Knowledge Village, Dubai, UAE

[4]ESAT-TELEMIC Research Div., Katholieke Universiteit Leuven, Kasteelpark Arenberg 10, 3001

Leuven, Belgium

[*]corresponding author: haslizarahim@unimap.edu.my

Abstract- This paper presents a dual band circularly polarized wearable textile patch antenna slotted with split-ring for WBAN application. The antenna consists of a patch, fed through coaxial probe and is designed to radiate in two bands, 1.8 and 2.6 GHz. A split-ring slot is integrated onto the top radiator. The antenna achieved a 10-dB impedance bandwidth of 3.9 % at 1.8 GHz and 15 % at 2.6 GHz, respectively. The 3-dB axial-ratio bandwidths are 3 % and 13 % at 1.8 GHz and 2.6 GHz, respectively, with a maximum gain of 4.1 dB.

With the fast growth of wireless systems, the demands for reliable and efficient integrated wearable system are increasing. In biomedical applications, for example, researchers have employed wearable health monitoring systems, such as VTAM (Clothes for Teleassistance in Medicine Project), the European Wearable Healthcare System (WEALTHY) and LifeShirt [1]. In addition, these wearable health monitoring systems incorporate enablers which are capable of transmitting collected health information to the healthcare personnel for further diagnosis. This long range transmission at high data rates can be achieved through the established communication networks, e.g., the Global System for Mobile Communication (GSM) and fourth Generation Long Term Evolution (4G-LTE).

To achieve circular polarization in textile patch antennas, several techniques have been introduced, e.g. by annular ring slots [2], single-feed aperture coupled slots [3] and coplanar waveguide feeds (CPW) [4], [5]. The CPW feed technique is especially effective due to its better tolerance on difference body's conditions and it consists of single layer of metal usage. However, the main disadvantage of CPW-fed based technique is the absence of a full ground plane on its reverse side, thus causing higher frequency detuning effect due to the body coupling when the antenna is placed in its vicinity. To solve this, a novel wearable circularly polarized textile antenna slotted with a Split Ring (SR) for Internet-of-Thing (IoT) and home-based wireless wearable healthcare sensing system is presented. The antenna is capable of providing dual band coverage for the entire 1.8 GHz (f_1) and 2.6 GHz (f_2) Long Term Evaluation (LTE).

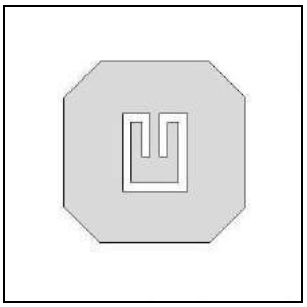

Figure 1: Structure of SSR textile antenna

The simulated 10-dB impedance bandwidths are 3.9 % (from 1.78 to 1.85 GHz) and 15 % (from 2.47 to 2.84 GHz), as shown in Figure 2a. The axial ratio is an indicator of the quality of circular polarization. The 3-dB axial-ratio bandwidth, which is an indicator of the quality of the circular polarization are 3 % (from 1.78 to 1.85 GHz) and 13 % (from 2.47 to 2.84 GHz), respectively. Figure 2b shows the effects of changing the width of split-ring, *w*, from 1 to 5 mm on the antenna resonance. When the *w* increases, the impedance bandwidth is enhanced and the frequency band is shifted down. This change also results in a variation in f_1, where the resonant frequency is shifted to the right when the *w* value increases. Thus, the best 10-dB impedance bandwidth is achieved when *w* is 2 mm. The maximum realized gain for the proposed antenna is 4.1 dB.

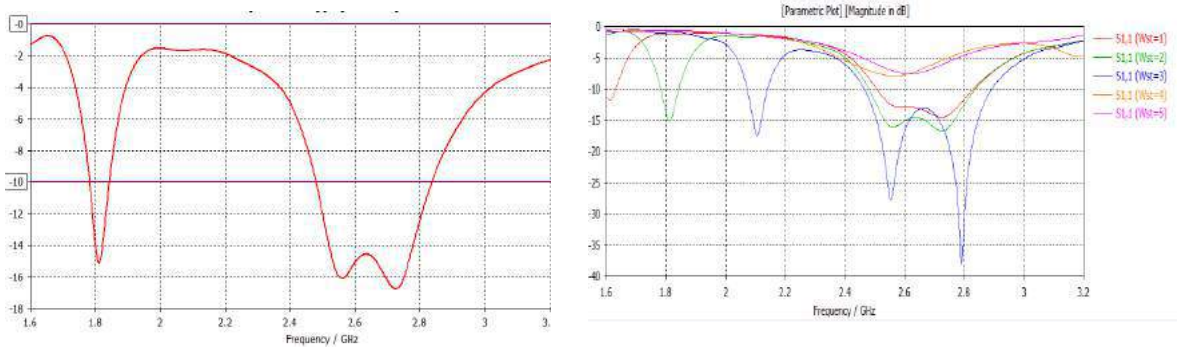

(a) (b)

Figure 2: Reflection coefficient, S11 of (a) antenna, and (b) different values of split ring width (*w*).

REFERENCES

1. Axisa, F., Schmitt, P. M., Gehin, C., Delhomme, G., McAdams, E., & Dittmar, A. (2005). "Flexible technologies and smart clothing for citizen medicine, home healthcare, and disease prevention," *IEEE Transactions on Information Technology in Biomedicine*, 9(3), 325–336.
2. J.-Y. Sze and W.-H. Chen, "Axial-ratio-bandwidth enhancement of a microstrip-line-fed circularly polarized annular-ring slot antenna," *IEEE Trans. Antennas Propag.*, vol. 59, no.7, pp. 2450 – 2456, 2011.
3. Nasimuddin, Z. N. Chen and X. Qing, "Dual-band circularly polarized S-shaped slotted patch antenna with a small-frequency-ratio," *IEEE Trans. Antennas Propag.*, vol. 58, no. 6, pp. 2112-2115, 2010.
4. J.-Y. Sze, C.-I.G. Hsu, Z.-W. Chen and C.-C. Chang, "Broadband CPWfed circularly polarized square slot antenna with lightening-shaped feedline and inverted-L grounded strips," *IEEE Trans. Antennas Propag.*, 58 (3), pp. 973 – 977, 2010.
5. K. W. Lui, O. H. Murphy and C. Toumazou, "A wearable wideband circularly polarized textile antenna for effective power transmission on a wireless-powered sensor platform", *IEEE Trans. Antennas Propag.*, vol. 61, no. 7, pp. 3873 – 3876, 2013.

Wireless Transfer Efficiency Enhancement on Reduced Size Antenna

M.H.Misran[1], S. K. A. Rahim[2], W. Y. Yong[3], K. N. Paracha[4] and M. A. Meor Said[5]
[1, 2, 3, 4]Wireless Communication Centre (WCC), Universiti Teknologi Malaysia
[1, 5]Faculty of Electronics and Computer Engineering, Universiti Teknikal Malaysia Melaka (UTeM), Malaysia
[*] harris@utem.edu.my

Abstract- Paper present a reduced size of patch loop antenna is proposed on glass-reinforced epoxy laminate sheets substrate with copper conductive as a microstrip line for wireless power transfer purpose. Single square loop antenna is designed on each of front and back FR4 layers at 13.56MHz to optimize the used of near-field communication that already embedded in almost middle and high end smartphone. An optimized antenna is able to achieve 13.9% wireless transfer efficiency improvement with 47% size reduction.

1. Introduction

Mobile devices become highly demanding in the evolution of high-end technology. Researchers gain an interest on recharging the batteries wirelessly to enable mobility and inductive coupling is preferred due to its simplicity and safety. This technology already implemented on some contactless transactions applications using RFID and NFC. NFC frequency, 13.56MHz is selected to maximize the benefit of near-field communication (NFC) that available in most smartphones. Therefore, NFC can be used not limited only to wireless data transfer but also for wireless energy transfer (WTE) purpose [1]. Various studies have been done insensitivity using low-cost glass reinforced epoxy laminated boards (FR 4) [2-4]. In WET, wireless transfer efficiency (WTE) is the most important factor to be focused. In short, large size of antenna will offer higher WTE rather than small antenna. However, increasing size of antenna will limit the mobility of the device itself. This paper presents the reduced size of single square loop antenna compared to the initial design. The performance of the antenna will be analyzed and discussed. The reduced size of antenna that offers performance at least equal to initial design is expected at the end of the research.

2. PLA Design and Simulation Results

This WET system use identical antennae as transmitter and receiver as shown in Figure 1(a). Figure 1(b) shows the initial design of antenna configuration. The antenna designed on 80mm x 80mm FR4 with antenna side length, ws_1 = 60mm. Microstripe line wide, wl_1 = 0.5mm, port gap, pg_1 = 10mm and port length, lp_1 are being used. WTE of 44.5% is recorded at 13.56MHz with 50mm distance between transmitter and receiver. Figure 1(c) shows the proposed reduced size of antenna that can operate without any performance degradation. Designed on 50mm x 50mm FR4, side length, ws_2 = 30mm, microstripe line wide, wl_2 = 2mm, port gap, pg_2 = 10mm and port length, lp_2 are used as parameters. Figure 2(a) shows the size of wl_2 that will yield WTE larger than the initial antenna design. Referring to Figure 2(b), the proposed antenna offers WTE = 50.7% with 47% size reduction, which is 13.9%

performance improvement. The results show that the reduced antenna at almost half size can works even better than the original size of antenna version.

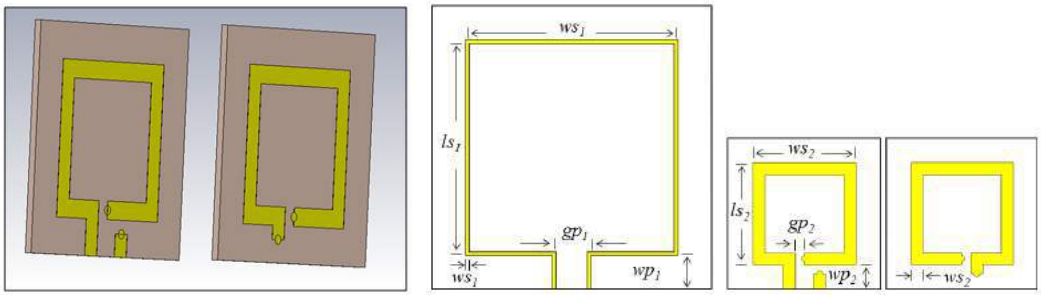

(a) (b) (c)

Fig1. (a) WET system, (b) The initial design of PLA and (c) The reduced size design of PLA (front and back)

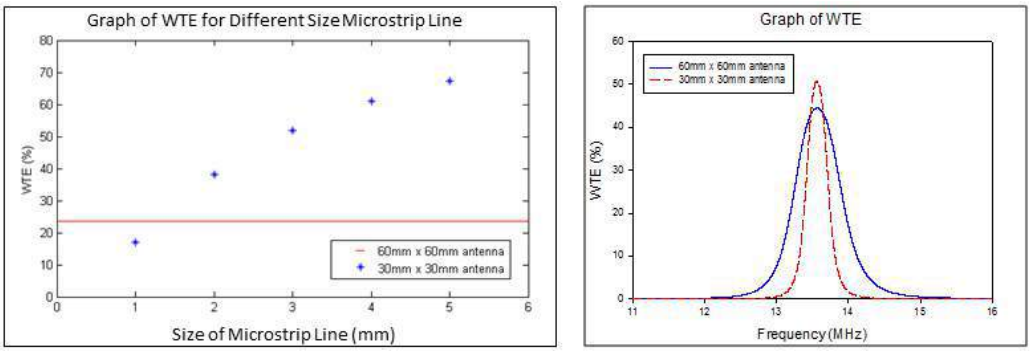

(a) (b)

Fig. 2: Graph of (a) WTE for Different Size Microstrip Line and (b) WTE

3. Conclusion

A reduced size antenna is successfully developed and present. The simulated performance using Matlab and CST were compared and analyzed. The proposed antenna managed to achieve almost half size reduction without any system performance degradation.

REFERENCES

[1] E. Strommer, M. Jurvansuu, T. Tuikka, A. Ylisaukko-oja, H. Rapakko, and J. Vesterinen, "*NFC-Enabled Wireless Charging*", 2012 4th International Workshop on Near Field Communication, pp. 36–41, 2012

[2] F. Jolani, Yigiang Yu, Zhizhang Chen, "*A Novel Planar Wireless Power Transfer System with Strong Coupled Magnetic Resonances*", 2014 IEEE International Wireless Sym/posium (IWS), Pages 1-4, 2014

[3] K. Mori, Hyunkeun Lim, S. Iguchi, K. Ishida, M. Takamiya, T. Sakurai, "Positioning-free resonant wireless power transmission sheet with staggered repeater coil array (SRCA)", *IEEE Antennas and Wireless Propagation Letters*, Volume 11, Pages 1710-1713, 2013

[4] W. Lee, K. OhJ. Yu, “Distance-insensitive wireless power transfer and near-field communication using a current-controlled loop with a loaded capacitance”, *IEEE Transactions on Antennas and Propagation*, Volume 62, Issue 2, Pages 936-940, 2014

Rpi as A Mechanism to Control Reconfigurable Receiver Ability of RSSI Scanning and Tracking System Modeling.

Mohd Ilman Jais[1], Thenarasan. Sabapathy[1], Muzammil Jusoh[1], Md Rabiul Awal[1] and Iszaidy Ismail[1]
[1]Bioelectromagnetics Research Group (BioEM), School of Computer and Communication Engineering,
Universiti Malaysia Perlis (UniMAP), Kampus Pauh Putra, 02600, Arau, Perlis, Malaysia
ilmanjais86@gmail.com

Abstract-This paper presents a scanning and tracking system based on received signal strength indication (RSSI). Deployed raspberry-pi (Rpi) is used as a mechanism to control reconfigurable receiver ability and as a tracking decision maker based on captured incoming RSSI. The proposed prototype is verify by the obtained real-time experimental and found as ±4° and angel error for mode II and III of reconfigurable receiver. Hence, this work validates Rpi as a mechanism to control reconfigurable receiver ability of RSSI scanning and tracking system modeling with minimum angle error.

1. INTRODUCTION

We proposed a scanning and tracking system modeling based on received signal strength indication (RSSI) deployed by raspberry-pi as a switching control mechanism in this paper, based on the related research works [1]–[4]. The scanning and tracking system model is developed by own solitary reconfigurable receiver cooperate with SZ05 ZigBee Module. The core of the proposed system modeling is configured with a single board computer (SBC) raspberry-pi (Rpi) is set as a controller and RSSI processing module. Rpi has limitation in terms of CPU and memory required to develop the algorithm to scan incoming RSSI, process captured RSSI and decision making to control solitary reconfigurable receiver. The main contribution of this work is to introduce an algorithm for scanning RSSI and decision making which will control the switching reconfigurable receiver simultaneously to track the strongest RSSI. The proposed prototype for scanning and tracking system is presented in Fig. 1(a). The scope is limited to the study of the receiver end only. Section 2 and 3 presents the system structure and performance verification respectively.

2. SYSTEM STRUCTURE & MODELING

The proposed prototype is configured by three (3) major components: a single board computer (SBC), SZ05 ZigBee RF Module and a developed reconfigurable receiver as shown in Fig. 1(a). A Python program developed an algorithm was sniff and process the incoming RSSI from various transmitters. Verification of this proposed prototype based on angle error tracking estimation is compared with initial experiment setup. Effect of distance coverage between transmitter and receiver toward angle error tracking estimation is also obtained by applying equation 1.

$$P_R = P_T + G_T + G_R - FSPL \quad (1)$$

Where P_R and P_T are the received power and transmitted power; G_T and G_R are the gains of both receiver

and transmitter antennas; FSPL represents free space path loss. The findings and verification of the proposed scanning and tracking system modeling are presented in section 3.

3. PERFORMANCE VERIFICATIONS & ANALYSIS

The experimental angle error estimation is presented in Fig. 1(b). Five (5) angular positions are considered with 30° angular separation. At each position, angle error tests were performed. The result shown in ±4° angle error between region -30° and 30° because proposed reconfigurable receiver can achieve maximum tilt angle of ±30°. Effect of distance between receiver and transmitter toward angle error tracking estimation are demonstrated in Fig. 1(c). Referred equation (1), the received power inversely proportional to the distance. Thus, the angle error increases with the gap increment between receiver and transmitter.

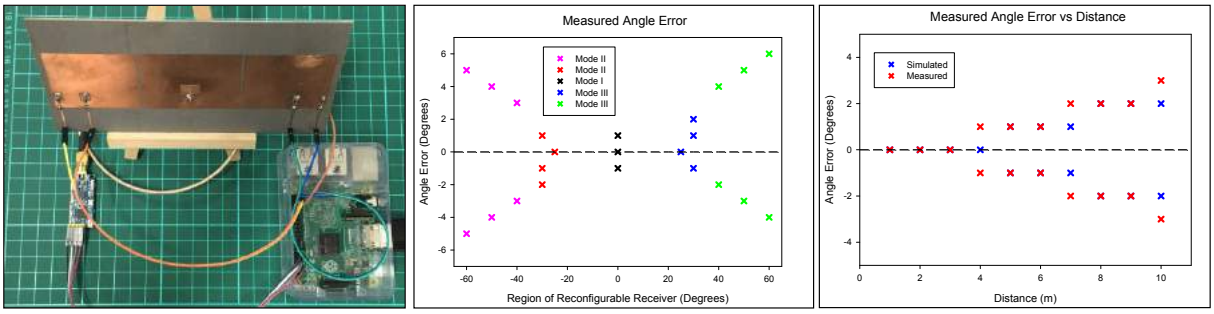

Figure 1:(a) The proposed prototype RSSI scanning and tracking system modeling. (b) Measured angle error by region. (c) Measured Angle Error Result vs Distances.

4. CONCLUSION

A scanning and tracking system modeling are presented in this paper. From the findings, it is obvious that, the proposed prototype can perform the scanning and tracking system with low angle error tracking estimation. Hence, the proposal can meet the requirement Rpi as a mechanism to control reconfigurable receiver in order to reduce angle error tracking and enhanced scanning and tracking coverage. However, this prototype possesses significant indoor experimental result operated at ISM band and can be beneficial in near-field indoor scanning and tracking system.

REFERENCES

[1] B. N. Hood and P. Barooah, "Estimating DoA from radio-frequency rssi measurements using an actuated reflector," *IEEE Sens. J.*, vol. 11, no. 2, pp. 413–417, 2011.

[2] M. R. Kamarudin, Y. I. Nechayev, and P. S. Hall, "Onbody diversity and angle-of-arrival measurement using a pattern switching antenna," *IEEE Trans. Antennas Propag.*, vol. 57, no. 4, pp. 964–971, 2009.

[3] M. I. Jais, P. Ehkan, R. B. Ahmad, I. Ismail, T. Sabapathy, and M. Jusoh, "Review of angle of arrival (AOA) estimations through received signal strength indication (RSSI) for wireless sensors network (WSN)," in *I4CT 2015 - 2015 2nd International Conference on Computer, Communications, and Control Technology, Art Proceeding*, 2015, pp. 354–359.

[4] M. Malajner, Z. Cucej, and D. Gleich, "Angle of arrival estimation using a single omnidirectional rotatable antenna," *IEEE Int. Conf. Wirel. Inf. Technol. Syst.*, vol. 12, no. 6, pp. 2–5, 2012.

Dynamics of harmonically excited irregular cellular metamaterials

S. Adhikari[1], **T. Mukhopadhyay**[2]

[1]Swansea University, United Kingdom
[2]Oxford University, United Kingdom
[1]s.adhikari@swansea.ac.uk

Abstract— Dynamic analysis of hexagonal cellular lattice structures with geometric and material irregularities is considered. Effective in-plane elastic properties for steady-sate harmonic response of the system is discussed. A dynamic stiffness based approach in the frequency domain is developed for this purpose.

Two-dimensional lattice metamaterials have gained considerable attention in the recent years as an advanced material due to its capability of meeting high-performance requirements. The applications range across different length scales such as honeycomb core in sandwich structures to nanomaterials like graphene and boron nitride nanosheets. This paper concerns elastic and dynamic behaviour of such metamaterials.

Equivalent static elastic properties of regular cellular solids [1] using an unit cell approach is the most common approach. However, the underlying analytical methods cannot be directly extended to dynamic analysis or when there are spatial irregularities in the cell geometry or material properties. For predicting equivalent elastic properties of irregular lattices or dynamic analysis, direct finite element simulation has been the predominant method of choice [2]. This is computationally expensive, but perhaps most importantly, does not provide intuitive understanding provided by analytical formulations available for static analysis of regular lattices [1]. We propose a dynamic stiffness based approach in the frequency domain. Individual elements of the lattice have been considered as damped Euler-Bernoulli beams with the equation of motion

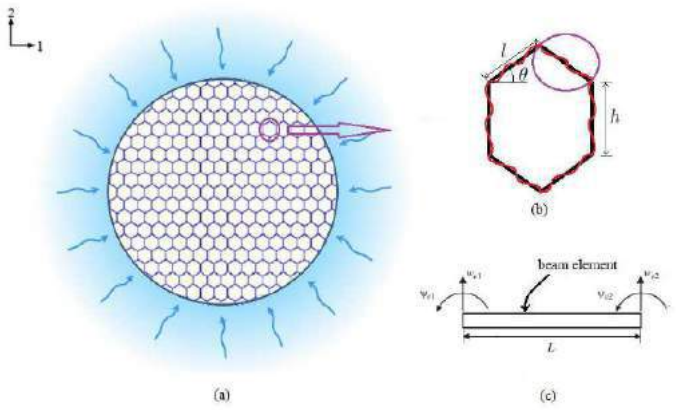

Figure 1: (a) Typical representation of a hexagonal lattice structure in a dynamic environment (e.g., the honeycomb as part of a host structure experiencing wave propagation). (b) One hexagonal unit cell under dynamic environment (c) A dynamic element for the bending vibration of a damped beam with length L. It has two nodes and four degrees of freedom. The displacement field within the element is expressed by complex frequency dependent shape functions.

$$EI\frac{\partial^4 V(x,t)}{\partial x^4} + c_1\frac{\partial^5 V(x,t)}{\partial x^4 \partial t} + m\frac{\partial^2 V(x,t)}{\partial t^2} + c_2\frac{\partial V(x,t)}{\partial t} = 0 \tag{1}$$

Here EI is the bending rigidity, m is mass per unit length, k is the elastic filler modulus, c_1 is the strain-rate-dependent viscous damping coefficient, c_2 is the velocity-dependent viscous damping coefficient and $V(x,t)$ is the transverse displacement. The length of the beam is assumed to be L.

Exact closed-from expressions for effective in-plane elastic moduli of the entire irregular lattice have been derived in the frequency domain. By conducting a limiting analysis, it was shown that the derived values reduced to the classical expressions [1] when the frequency becomes zero (static case). Asymptotic values and convergence of the frequency dependent homogenized properties are discussed for the case when a very large number of cells are present. The closed-form expressions are validated against detailed finite element simulations.

REFERENCES

1. Gibson, M. F. Ashby, Cellular Solids Structure and Properties, Cambridge University Press, Cambridge, UK, 1999.
2. M. J. Silva, W. C. Hayes, L. J. Gibson, The effects of non-periodic microstructure on the elastic properties of two-dimensional cellular solids, International Journal of Mechanical Sciences 37 (11) (1995) 1161-1177.

Emerging applications: Quantum photonic devices, Biophotonics, Plasmonics for health, â€¦

High Efficient Plasmonic Spectral Imaging using Algorithmic Data Compression and Recovery Techniques

W. Y. Jang[1, 2*], Z. Ku[2], J. Park[2], A. Urbas[2], and M. Noyola[2]
[1]University of Dayton Research Institute, U.S.A.
[2]Air Force Research Laboratory, U.S.A.
[*]corresponding author: Woo-Yong.Jang@udri.udayton.edu

Abstract-We report the progress on developing the next generation IR imaging strategy based on plasmonic sensor incorporated by the data-efficient sensing algorithm with compression and recovery techniques. The geometry of the plasmonic coupler was modified to shape the sensor's spectral sensitivity in order to bring the multispectral imaging capability. The technique termed the band-compressive algorithmic spectrometer was incorporated in the plasmonic sensor to compress required number of bands (by minimum band selection) and successfully reconstructed high resolution spectral contents.

Summary –*n*The surface plasmonic structure [1] has been reported as a spectral tuning element for IR imaging application because of its ability to shape the sensor's spectral sensitivity or responsivity by controlling the interaction of light when coupled to the sensor structure. The data processing technique termed the band-compressive algorithmic spectrometry (BAS) [2] was incorporated in the design of plasmonic IR sensor to find sensor's minimum spectral requirements associated with signatures of interest. Key concept behind the BAS is the compressive spectral sensing [3], which effectively compresses the number of required plasmonic spectral sensitivities thereby finding a minimum and essential bandset to be used for recovering signatures of interest. Another key step is the reconstruction or recovery of spectral signatures using a minimum set of plasmonic bands. The reconstruction is done by linearly synthesizing a collection of raw plasmonic output images with a set of weights prescribed by the BAS. This synthetic image reconstructs radiations from targets at a specific wavelength. The reconstruction step is simply repeated for multiple signatures of interest by applying different sets of weights, producing a series of synthetic images. Recently a plasmonic structure was modeled by using a square coaxial aperture (SCA) array and was coupled on a state of the art HgCdTe (MCT) sensor platform operating in the longwave IR (LWIR). By the parameter study, twenty six spectral sensitivities of a plasmonic MCT (P-MCT) sensor were produced as a pitch size of SCA structure was varied from 2.3 to 3.5 μm shown in Fig.1a. The spectral tunability was observed with a peak shift in an 8-12 μm range despite having some overlaps among engineered sensitivities. To realize the P-MCT sensor in actual fabrication, the BAS algorithm was performed to select the subset from original 26 spectral sensitivities based on three following requirements: (1) select 9 bands or less, (2) reconstruct spectral signatures for at least 40 different wavelengths and (3) produce the reconstruction error with 20% or less. As shown in Fig. 1a, the BAS selected a minimal subset with 9 P-MCT bands with a good compression ratio of 9/26 from 26 original bands. The BAS designed narrowband synthetic spectral filters centered at 40 distinct wavelength locations by the weighted synthesis with 9 selected bands. Each synthetic filter represents a signature of interest. This demonstrates an excellent spectral recovery with a 40/9 (i.e., over ×4) reconstruction ratio. Also the designed synthetic filters showed a fine resolution of 250 nm

full-width half maximum and a reconstruction error of 14% in average. Designed synthetic filters were applied to the test scene for extracting high resolution LWIR spectral signatures. Series of synthetic images in Fig. 1b show successful reconstructions of distinct spectral signatures at multiple wavelengths.

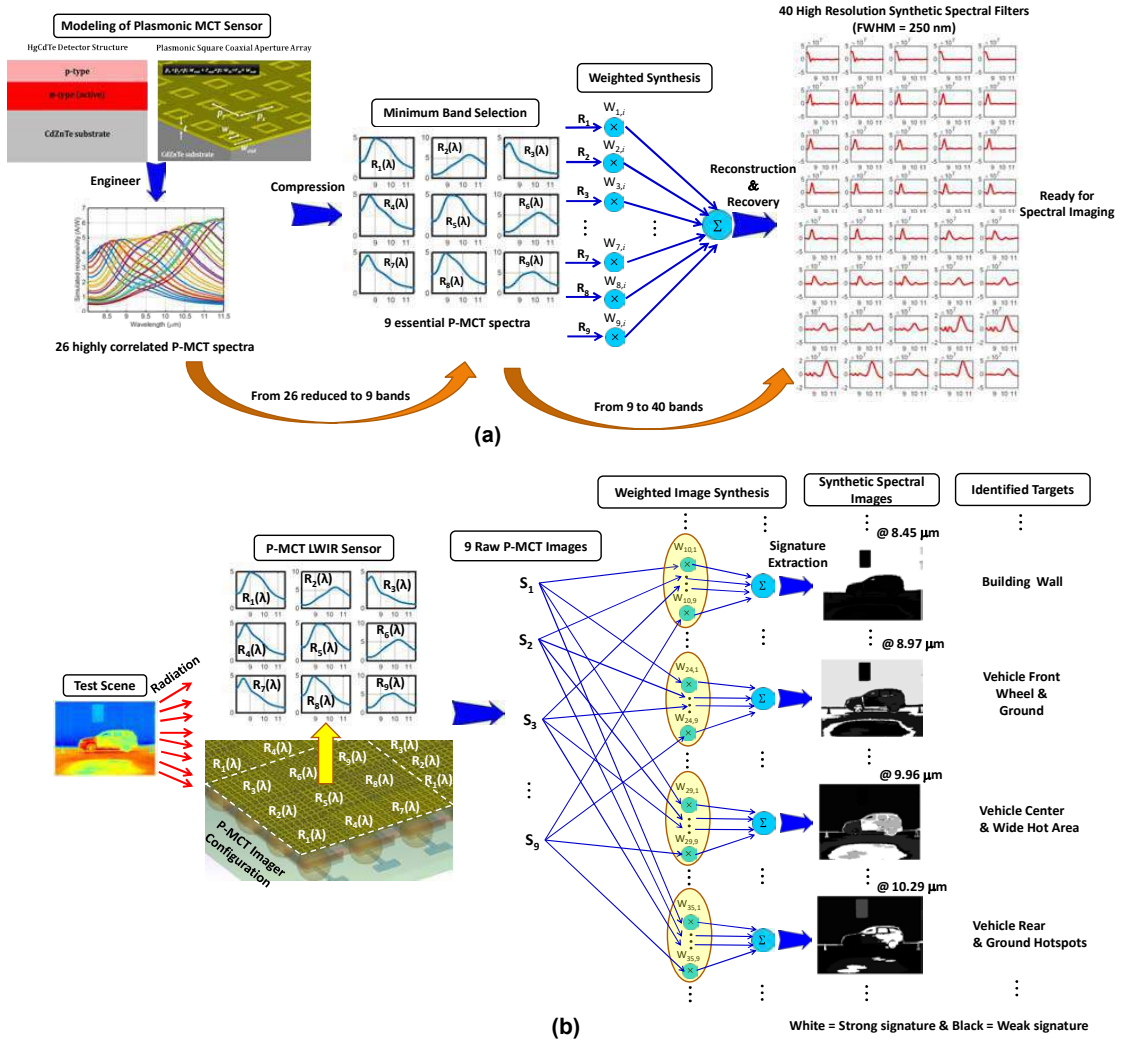

Figure 1. (a) Modeling of plasmonic MCT sensor, band compression and recovery by the BAS algorithm (b) LWIR synthetic spectral imaging using the BAS to extract signatures and identify targets at various wavelengths.

REFERENCES

1. Lee, S. J. *et al*., "A monolithically integrated plasmonic infrared quantum dot camera," *Nat. Commun.*, 2: 286, 1-6, 2011.
2. Jang, W. Y. *et al*., "Plasmonic Super-pixel Sensor for Compressive Spectral Sensing," *IEEE Trans. Geosci. Remote Sens.*, Vol. 53, No. 6, 3471-3480, 2015.
3. Jang, W. Y. *et al*., "Data compressive paradigm for generalized multispectral sensing using tunable DWELL mid-infrared detectors," *Opt. Express*, Vol. 19, No. 20, 19454-19472, 2011.

Terahertz nano-metamaterials for discrimination and quantification of Avian Influenza viruses

D.-K. Lee[1], J.-H. Kang[2], J. Kwon[3], C.-S. Song[3], M. Seo[1*]
[1]Sensor System Research Center, Korea Institute of Science and Technology (KIST), Republic of Korea
[2]Department of Physics, University of California at Berkeley, USA
[3]College of Veterinary Medicine, Konkuk University, Korea
[*]corresponding author: mseo@kist.re.kr

Abstract-Optical characteristics of three different subtyped Avian influenza viruses were measured using nano scaled metamaterial sensing chip based terahertz (THz) time-domain spectroscopy (TDS) system. The enhanced THz field via metamaterial structures can lead to increase absorption cross section of the targeted viruses, in turn, increase the detection sensitivity. The three virus samples can be discriminated by measured optical parameters including normalized transmittance change and shifted frequency at maximum transmittance, assigning subtype of viruses.

Recently, metamaterial sensing chip based terahertz (THz) detection technique has been developed for highly sensitive and selective detection of various bio- and chemical-molecules overcoming the limit of sensitivity of general THz time-domain spectroscopic (TDS) systems. Especially THz spectroscopy with various bio-materials have been attracted great attention, because many intra- and inter-molecular vibration modes of bio-materials such as protein and DNA etc. are located within THz range. One of important viruses as a highly pathogenic Avian Influenza (HPAI), which should be intensively studied for quick and accurate field diagnosis, was investigated in terms of the optical characteristics assisted by the THz metamaterials.

In this research, we analyzed THz optical characteristics of AI viruses using nano-slot-antenna sensing chip and applied them for distinguishing subtype of AI viruses and quantification. In previous studies [1, 2], the sensing chip was designed for increasing of absorption cross section of the targeted sample molecules that is related to the transmitted THz near field enhancement [3]. In contrast to earlier studies, it was noted that there is no specific absorption feature at the reliable frequency for the AI viruses, since they are composed of complex combination of surface proteins as hemagglutinin and neuraminidase. The optical characteristics measurement, therefore, were performed via multi resonances nano antenna sensing chip with a log-periodic alignment [4]. Most sensitive frequency, 1.31 THz was selected by the transmittance measurements with the multi resonance nano antenna sensing chip, then applied for further experiments.

The transmittance spectra for the three subtypes of virus samples such as A/NWS/33 (H1N1), A/wild bird/Korea/K09-652/2009 (H5N2), and A/Korean native chicken/Korea/K040110/2010 (H9N2), are shown in Fig. 1(a) with differences in transmitted intensity (ΔT) and shifted resonance frequency from each fundamental resonance peak of bare nano-slot-antenna (Δf). Each virus sample shows a distinct transmission change and a change in resonance frequency associated with different surface protein and unique strain of it. Further analysis of THz optical characteristics for these viruses was performed through finite-difference time-domain method (FDTD) simulation and the results are shown in Fig 1(b). In addition, the experimental results of the concentration dependent measurement of a virus are well consistent with the simulation results. Depending on

the assigned optical properties, including complex refractive indices, the examined viruses can be classified according to their subtypes (Fig. 1(c)).

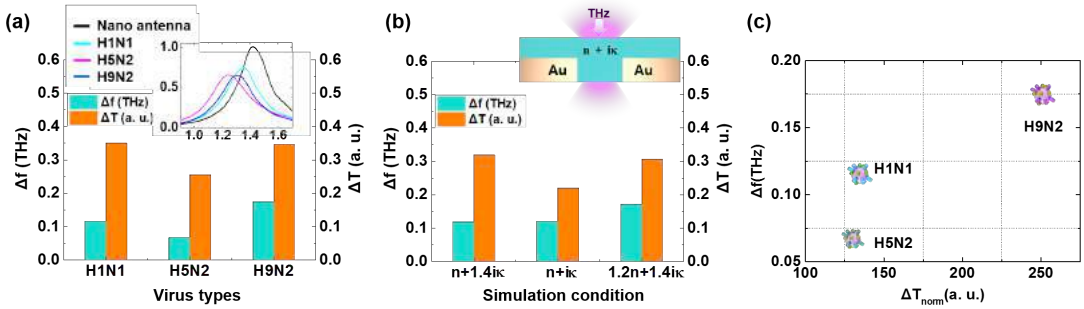

Figures 1. (a) The difference in transmitted intensity (ΔT) and shifted resonance frequency from each fundamental resonance peak of bare nano-slot-antenna (Δf) for three subtype (H1N1, H5N2, H9N2) of virus samples are represented. Inset is transmittance spectrums of three samples and bare nano-slot-antenna. **(b)** FDTD simulation results of the differences in transmitted intensity (ΔT) and shifted resonance frequency (Δf) with various composition of dielectric constants (n and κ) are shown. Inset shows a used geometry for simulation. (c) Mapping of classified viruses in terms of ΔT and Δf.

The THz spectra measured for various virus samples are analyzed as effective optical properties, and FDTD simulations show that the spectral changes can be represented with the optical properties of the sample through the nano-slot-antenna. According to these results, nano-metamaterial based THz spectroscopy can provide a possibility of rapid yet highly accurate solution for discrimination and quantification of AI viruses in non-contact and label-free manner.

Acknowledgements This research was supported by the National Research Foundation of Korea (NRF) grant funded by the Korea government (MSIP) (2016R1A2B2010858) and the Global Frontier Program through NRF grant funded by the Ministry of Science, ICT & Future Planning (2016M3A6B3936653)

REFERENCES

1. Park, H.-R., K. J. Ahn, S. Han, Y.-M. Bahk, N. Park, and D.-S. Kim, "Colossal Absorption of Molecules Inside Single Terahertz Nanoantennas," *Nano lett.,* Vol. 13 (4), 130305151332003–1786, 2013.
2. Lee, D.-K., J. H. Kang, J.-S. Lee, H. S. Kim, C. Kim, J. H. Kim, T. Lee, J.-H. Son, Q.-H. Park and M. Seo, "Highly Sensitive and Selective Sugar Detection by Terahertz Nano-Antennas," *Sci. Rep.* Vol. 5, 15459, 2015.
3. Seo, M. A., H. R. Park, S. M. Koo, D. J. Park, J. H. Kang, O. K. Suwal, S. S. Choi, P. C. M. Planken, G. S. Park, N. K. Park, Q.-H. Park and D. S. Kim, "Terahertz Field Enhancement by a Metallic Nano Slit Operating Beyond the Skin-Depth Limit," *Nat. Photonics* Vol. 3 (3), 152–156, 2009.
4. Park, H. R., Y. M. Park, H. S. Kim, J. S. Kyoung, M. A. Seo, D. J. Park, Y. H. Ahn, K. J. Ahn and D. S. Kim, "Terahertz nanoresonators: Giant field enhancement and ultrabroadband performance," *Appl. Phys. Lett.* Vol. 96, 121106, 2010.

A polarimetric analysis applied to human cells

A. Fernández[1], Y. Gutiérrez[1], J. L. Fernández-Luna[2], F. Moreno[1] and J. M. Saiz[1*].

[1]Departamento de Física Aplicada, Universidad de Cantabria, Avda. Los Castros s/n, 39005, Santander, Spain

[2]Unidad de Genética HUMV - Hospital Universitario Marqués de Valdecilla, Avda. Marqués de Valdecilla s/n, 39008, Santander, Spain

[*]corresponding author: josemaria.saiz@unican.es

Abstract- We measure the image Mueller matrix (MM) of human cancerous cells. We apply three different decomposition and transforming methods (Polar decomposition, Mueller matrix transformation and differential decomposition) over these matrices in order to look for an adequate polarimetric parameter that allow us to characterize and differentiate these tumor cells. Due to the intrinsic difficulty of applying polarimetry to these kind of samples we set out two proposals in order to enhance the sensitivity of the polarimetric parameters.

In recent years, imaging polarimetry has become a field of increasing interest in diagnosis [1] because of its non-invasive nature and its potential to identify abnormal properties in propagating media. Specifically, polarized light has been used to perform studies over tumor tissues [2] such as colon, cervix, thyroid or skin. When light interacts with matter its polarimetric properties are affected by the nature of the material. Consequently, the analysis of polarimetric parameters should give information about the tissue and processes that take place therein.

MM contains all the information relative to polarization for any given working conditions. In order to reveal useful information of the system, there are two important lines of work: one consists in selecting the most adequate conditions (geometry of sample and setup, wavelength, etc). The other one is the adequate manipulation of the MM. Some methods have been widely used to extract the information given by the Mueller matrix (MM), transforming it into useful parameters that may contribute to providing a physical interpretation.

The experimental device used for the measurement of the MM in this work consists basically of a Dynamic Rotating Compensator Polarimeter with a tunable laser source and a microscope objective (Figure 1).

We are focused on the analysis of human cells corresponding either to normal or tumor tissues. We have performed imaging polarimetry and measured the transmission MM of such samples. Over these matrices we have applied three different transforming methods for its analysis. Namely: polar decomposition (MMPD) [3], Mueller matrix transformation (MMT) [4] and differential decomposition

(MMDD) [5], looking for useful parameters that allows us to better characterize the cells and, eventually, to identify them.

Tumor and normal cells present very small differences in their refraction index [6]. This fact, together with its main transparent nature, translates into a low polarimetric activity of the samples, making a challenge to apply polarimetry to the recognition and study of tumor cells. Because of this, we consider two lines of actin: 1) Use of some statistical analysis over the most significant parameters taking advantage of the high number of measurement contained in an image and 2) Try other configurations like dark field in order to make the parameters more sensitive to the small changes in the cells.

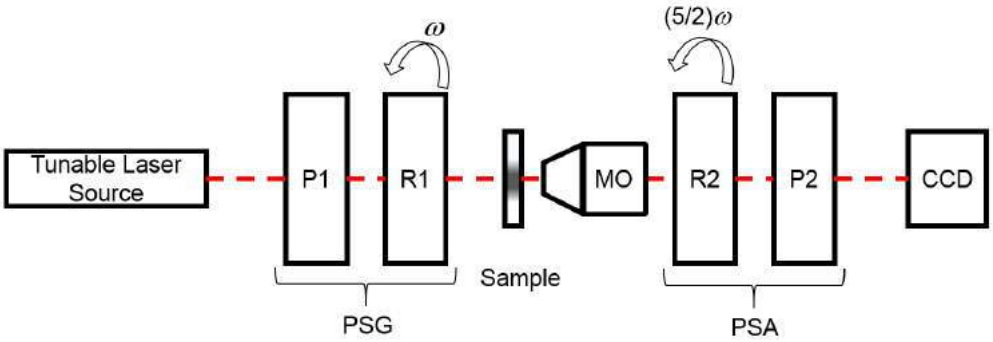

Figure 1. Schematics of the imaging polarimeter. The light source is a supercontinuum laser, P1 and P2 are polarizers, R1 and R2 are retarders (quarter waveplate), MO is the microscope objective, PSG and PSA stand for Polarization State Generator and Analyzer respectively.

References

1. He, H., J. Chang, C. He, and H. Ma. 'Transformation of full 4 × 4 Mueller matrices: a quantitative technique for biomedical diagnosis,' *Proc. of SPIE* Vol. 9707, 97070K-1, 2016.
2. Ghosh, N. (2011). 'Tissue polarimetry: concepts, challenges, applications, and outlook,' *Journal of Biomedical Optics*, Vol. 16 No. 11, 110801, 2011.
3. Lu, S. and R. Chipman, (1996). 'Interpretation of Mueller matrices based on polar decomposition,' *Journal of the Optical Society of America A*, Vol. 13, No. 5, 1106-1113, 1996.
4. Guo, Y., D. Li, and R. Liao. 'A possible quantitative Mueller matrix transformation technique for anisotropic scattering media,' *Photonics and Lasers in Medicine*. Vol. 2, No. 2, 129-137, 2013.
5. Azzam, R. M. 'Propagation of partially polarized light through anisotropic media with or without depolarization: A differential 4 × 4 matrix calculus,' *Journal of the Optical Society of America*, Vol. *68*, No. 12, 1756-1767, 1978.
6. Liu, P. Y., L. K. Chin, et al. (2016). 'Cell refractive index for cell biology and disease diagnosis: past, present and future,' *Lab on a Chip*, Vol. 16, 634–644, 2016.

Nanofabrication Technology, Lithography and etching techniques, Growth and deposition, Self-organized

Fabrication of nanoscale 3D optical metamaterials and metadevices using electron beam lithography overlay process

I. Kim[1], G. Yoon[1], S. So[1], J. Mun[2], M. Kim[1] and J. Rho[1,2,3*]

[1]Department of Mechanical Engineering, Pohang University of Science and Technology (POSTECH), Pohang 37673, Republic of Korea

[2]Department of Chemical Engineering, Pohang University of Science and Technology (POSTECH), Pohang 37673, Republic of Korea

[3]Natioanl Institute of Nanomaterials Technology (NINT), Pohang 37673, Republic of Korea

[*]corresponding author: jsrho@postech.ac.kr

Abstract-Nanofabrication techniques is essential for exploring nanoscience including nanophotonics, plasmonics and optical metamaterials. Recently, 3D nanofabrications have been actively investigated to make sophisticated nanoscale 3D metamaterials and metadevices, but it is still challenging to fabricate elaborate 3D nanostructures. In this work, ultra-high accurate and precise electron beam lithography overlay process is developed for fabricating elaborate nanometers-sized 3D metamaterials and metadevices. Sub-20nm alignment accuracy and over-75% repeatability are achieved through well-defined alignmarks and specific calibrators.

Metamaterials, artificially fabricated materials composed of sub-wavelength unit cells, have enabled unprecedented and extraordinary phenomena such as invisibility cloaking, negative refraction and super-resolution imaging. Especially working frequencies of metamaterials are demonstrated by the size of unit cells called meta-atoms. By shrinking the size of the meta-atoms, the operating frequency of metamaterials have moved to higher frequencies. Now, thanks to nanometer scale fabrication technologies, we can fabricate "optical metamaterials" working at near-infrared, visible, or ultra-violet regions. So far, most of the optical metamaterials have been fabricated on 2D substrates in a forms of planar nanostructures called metasurfaces [1]. Various interesting physics and applications of metasrufaces have been reported, but there are several drawbacks arising from their own 2D structures, such as anisotropic and inhomogeneous properties, polarization and incident angle dependency. In order to tackle these issues, many researchers are investigating 3D nanofabrication technique for 3D metamaterials including, but not limited to, direct laser writing [2], transfer printing [3] and bottom-up based fabrications [4, 5]. In this abstract, I will discuss our efforts in realizing 3D metamaterials and metadevices based on specially-developed ultra-accurate and precise electron beam lithography (EBL) overlay process showing sub-20nm alignment error and over-75% reproducibility. First, I will present the method of highly accurate EBL overlay process including the strategy for designing alignmarks and calibrator and accuracy verifications experiment [6]. Second, I will present the design and fabrication methods for two kinds of 3D metamaterials. One is stacked 3D metamaterials for asymmetric transmission of linearly polarized light like optical isolator. The other one is 3D chiral induced negative index metamaterials working at optical frequencies. Finally, I will present the design and fabrication method of 3D metadevices, which are mode-multiplexed nanophotonic modulators and waveguides system [7]. The mode-multiplexed modulators can suggest new strategy for enhancing functionality per area in the integrated photonic and optoelectronic devices. I believe our efforts for

making a truly 3D metamaterials and metadevices will lead to novel and practical applications of metamaterials in optics, nanoscale science and engineering.

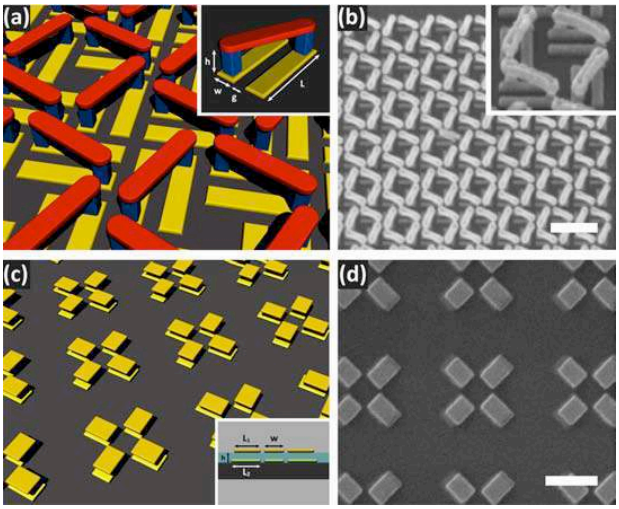

Figure 1. Demonstrated 3D optical metamaterials [6]. (a), (b) show 3D chirality inducing negative index metamaterials working at optical frequency. (c), (d) show 3D nanostructure for artificial toroidal magnetism at optical frequency. All the scale bars represent 500nm.

Acknowledgements. J. Rho acknowledges the financial support by Young Investigator Research program (NRF-2015R1C1A1A02036464), Engineering Research Center program (NRF-2015R1A5A1037668), Global Frontier Research Program (CAMM-2014M3A6B3063708) and I. Kim acknowledges Global Ph.D. Fellowship (NRF-2016H1A2A1906519) through the National Research Foundation of Korea (NRF) grant funded by the Ministry of Science, ICT and Future Planning (MSIP) of Korean government.

REFERENCES

1. Yu, N and Capasso, F., "Flat optics with designer metasurfaces," *Nat. Mater.*, Vol. 13, No. 2, 139-150, 2014.
2. Ergin, T. *et al.*, "Three-dimensional invisibility cloak at optical wavelenghts", *Science*, Vol. 328, No. 5976 337-339, 2010.
3. Chanda, D. *et al.*, "Large-area flexible 3D optical negative index metamaterials formed by nanotransfer printing," *Nat. Nanotechnol.*, Vol. 6, No. 7, 402-407, 2011.
4. Kuzyk, A. *et al.,* "Reconfigurable 3D plasmonic metamolecules," *Nat. Mater.*, Vol. 13, No. 9, 862-866, 2014.
5. Yang, S. *et al.*, "Feedback-driven self-assembly of symmetry-breaking optical metamaterials in solutions," *Nat. Nanotechnol.*, Vol. 9, No. 12, 1002-1006, 2014.
6. Yoon, G. *et al.*, "Ultra-high accurate and precise electron beam lithography overlay for three-dimensional optical metamaterials and hybrid plasmonic nanoantennas," *Sci. Rep.* (in review)
7. Das, S. *et al.*, "Nanophotonic modal dichroism: Mode-multiplexed modulators," *Opt. Lett.*, Vol. 41, No. 18, 4394-4397, 2016.

Self-assembly-assisted gold nanostructure for plasmonic sensor

E.-S. Yu[1,2], S.-H. Lee[1], I.-H. Lee[3], S. H. Lee[1], Y.-S. Ryu[2*], and S.-D. Lee[1*]

[1]School of Electrical Engineering, Seoul National University, Seoul, Korea

[2]Sensor System Research Center, Korea Institute of Science and Technology, Seoul, Korea

[3]School of Electrical and Computer Engineering, University of Minnesota, Twin City, U.S.A.

[*]corresponding author: sidlee@plaza.snu.ac.kr, ysryu82@kist.re.kr

Abstract A self-assembly of gold (Au) nanostructures was employed over a dielectric spacer and an underlying bottom Au layer for a plasmonic refractive index (RI) sensor. Its exposures to distinct surrounding media with different refractive indices result in visible color changes due to plasmonic resonance shifts in the reflectance that are attributed to the changes of the surrounding RI. The resonance absorption occurred at λ = 550.3 nm, 634.7 nm, and 725.3 nm for the RI's of n = 1.000, 1.343, and 1.516, respectively.

Surface plasmon resonance (SPR), collective oscillation of electrons at the interface between metal and dielectric material, has attracted great attention both in scientific and commercial fields for sensing purpose.[1] A conventional SPR sensing system not only requires a huge and expensive Kretschmann configuration but also experiences the difficulty of tracking the changes of the RI in local areas.[2] Instead, localized surface plasmon resonance (LSPR) is advantageous in tracking the RI changes around metallic nanostructures that act as hot-spots of highly localized electromagnetic wave. [3] However, LSPR sensors by serial fabrication processes such as electron beam lithography, and focused ion beam is highly limited on a large-area application.[4, 5] Besides they still require particular sensing equipment to monitor the SPR phenomena.

Here, we report visible RI sensor platform which enable to monitor changes of the RI around the Au-nanostructures with simple and easy fabrication processes for a large-area application. The proposed RI sensor composed of underlying Au layer and self-assembled Au nanostructures, separated by CYTOP (n = 1.4) insulating film (inset; Fig. 1a). The Au nanostructures over the hydrophobic CYTOP layer is achieved by control of deposition conditions, followed by vertically etching process leaving inert Au-nanostructures atop the nano-pillar CYTOP structure. The surrounding medium such as gas (Fig. 1b) or solvents with distinct RI values (Figs. 1c and 1d) infiltrates into etched empty spaces of the insulating layer. This allows changes of effective RI around the Au-nanostructures, resulting in visible color changes. During the measurement process, air (n = 1.000), anisole (n = 1.343) and acetonitrile (n = 1.516) were selected for different refractive indices. The resonance absorption appears at 550.3 nm for the surrounding medium of n = 1.000, 634.7 nm for n = 1.343, and 725.3 nm for n = 1.516 (Fig. 1e).

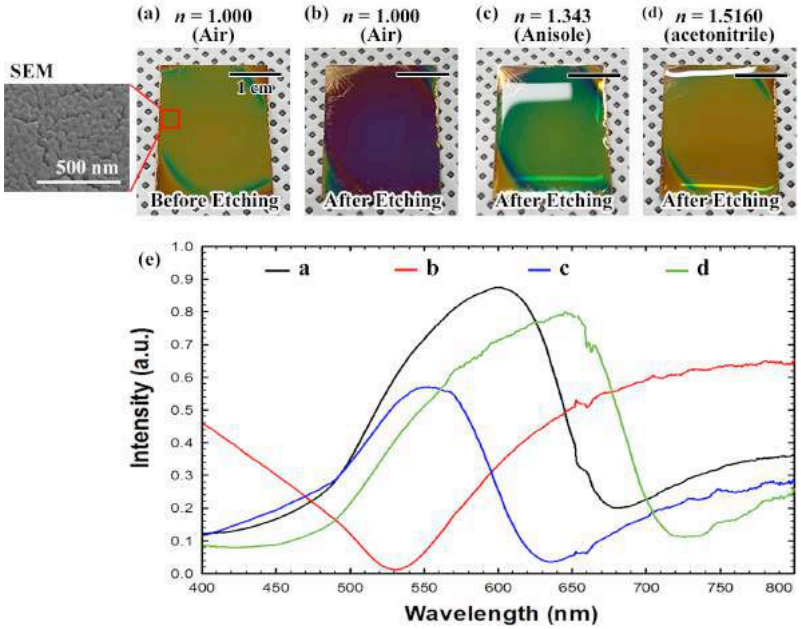

Figure 1: Sample images before (a; inset: SEM image of red square zone) and after O_2 plasma etching process (b - d) in different surrounding media: (b) n = 1.000; air, (c) n = 1.343; anisole, and (d) n = 1.516; acetonitrile. (e) The corresponding reflectance spectrum as a function of wavelength in each different conditions

Acknowledgements, This research was supported by the KIST intramural grant under No. 2E27270 and the Brain Korea 21 Plus Project in 2017.

REFERENCES

1. Barnes, W. L., A. Dereux and T. W. Ebbesen "Surface plasmon subwavelength optics," *Nature*, Vol. 424, No. 6950, 824-830, 2003.

2. Homola, J. "Surface plasmon resonance sensors for detection of chemical and biological species," *Chemical reviews*, Vol. 108, No. 2, 462-493, 2008.

3. Mayer, K. M. and J. H. Hafner "Localized surface plasmon resonance sensors," *Chemical reviews*, Vol. 111, No. 6, 3828-3857, 2011.

4. Sreekanth, K. V., Y. Alapan, M. ElKabbash, E. Ilker, M. Hinczewski, U. A. Gurkan, A. De Luca and G. Strangi "Extreme sensitivity biosensing platform based on hyperbolic metamaterials," *Nat Mater*, Vol. 15, No. 6, 621-627, 2016.

5. Im, H., N. J. Wittenberg, A. Lesuffleur, N. C. Lindquist and S.-H. Oh "Membrane protein biosensing with plasmonic nanopore arrays and pore-spanning lipid membranes," *Chemical Science*, Vol. 1, No. 6, 688-696, 2010.

THz Metamaterials Fabricated using Electrohydrodynamic Jet Printing for Sensitive Detection of Microorganism

A. Tenggara[1], S.J. Park[2], Hadi Teguh Yudistira[3] Y.H. Ahn[2], and D. Byun[1,*]
[1]Department of Mechanical Engineering, Sungkyunkwan University, South Korea
[2]Department of Physics and Department of Energy System Research, Ajou University, South Korea
[2]Mechanical Engineering Program, Institut Teknologi Sumatera (ITERA), Indonesia
[*] corresponding author: dybyun@skku.edu

Abstract - We demonstrated the capability of terahertz metamaterial sensor fabricated using electrohydrodynamic jet printing for the accurate and on-site detection of microorganism (yeast). The ESRR unit structures could be printed on a large area. It was shown that the metamaterial sensor fabricated on a flexible polyimide film had higher sensitivity by more than six times, due to the low refractive index of the PI substrate and the extremely thin substrate thickness which lowers the effective index further.

THz metamaterials with the gap structures characterized by strongly localized and enhanced fields are able to provide sensitive detection of extremely small amounts of chemical or biological substances to overcome the low scattering cross-section of THz spectroscopy to detect small size of substances [1]. THz metamaterials becomes compatible as an ideal platform for the sensitive detection of small size microorganisms such as molds, yeast cells, and bacteria [2]. The resonance frequency shift is considered as a function of the dielectric constant and the density of the microorganism. The sensitivity can be improved by decreasing the effective dielectric constant of metamaterial, such as using a substrate with a low refractive index.

Electrohydrodynamic (EHD) jet printing technology using the drop on demand (DoD) technique of patterning has become an alternative choice for fabricating metamaterial structures on both rigid and thin flexible substrates with low refractive index [3]. Compared to conventional fabrication techniques such as photolithography, e-beam lithography, and focused ion beam, EHD jet printing technology has several advantages, such as being an inexpensive, non-contact, and simple procedure and being environmentally friendly.

In this communication, we present the fabrication of THz metamaterials for the high-speed-on-site detection of microorganism using the DoD technique of EHD jet printing, as shown in Figure 1(a). Yeast was used as the microorganism to be detected due to its high dielectric constant that makes it ideal to test and optimize the microbial sensing system in THz frequency range. The resonance frequency shift of the metamaterial was investigated as a function of the weight of yeast deposited on the metamaterial for two types of substrate: silicon and PI. Due to its lower dielectric constant, the thin PI film has been chosen to decrease the effective dielectric constant of the metamaterial structure in order to improve the sensitivity of the sensor.

Figure 1(b) shows the schematic of THz time-domain spectroscopy used to measure the transmission amplitudes of the metamaterial samples with and without the yeast deposition. The response of THz transmission obtained by Fast Fourier Transform gave the resonance frequency due to the electric field enhancement in the capacitive gap. When the yeasts were deposited on the metamaterial structures, the resonance frequency will be

shifted due to the change of capacitance in the gap by the presence of yeasts. This frequency shift can be used to detect the quantity of the yeast. Figures 1(c) and 1(d) show comparisons of the terahertz transmission response of the metamaterials on the silicon wafer and the PI film, respectively, before and after yeast deposition with the weight of 74 $\boldsymbol{\mu}$g. The frequency shifts of the metamaterials ($\Delta \boldsymbol{f}$) on the silicon wafer and the metamaterial on the PI film were 7 GHz and 47 GHz, respectively. Moreover, the sensor is also possible to be cleaned by a fungicide and to be reused again. After the cleaning of the sensor, the resonance frequency would shift to the initial resonance frequency. The thin flexible PI film also gave higher sensitivity due to its small thickness that made its effective dielectric constant close to the dielectric constant of air. The sensitivity enhancement by about 3 times has been reported when we use the substrate with the lower dielectric constant (i.e., quartz substrate instead of Si substrate) in the case of the slot antenna array sensors [4].This is because the relative change in the effective dielectric constant with the presence of the yeasts is higher for substrates with lower permittivity. The enhancement effects were much better in the case of thin PI films of this work as compared to the quartz substrate, although the dielectric constant values are not far from each other. This unexpected sensitivity enhancement is due to the thin film effects of PI flexible substrates, which lowers the effective dielectric constant as mentioned already. Using substrate with small thickness can offer a useful guideline how to improve the sensitivity significantly in metamaterials sensing. Our work demonstrates a simple, inexpensive, and environmentally friendly fabrication technique without chemical waste that we expect will contribute to the rapid, accurate, and on-site detection of small size microorganisms.

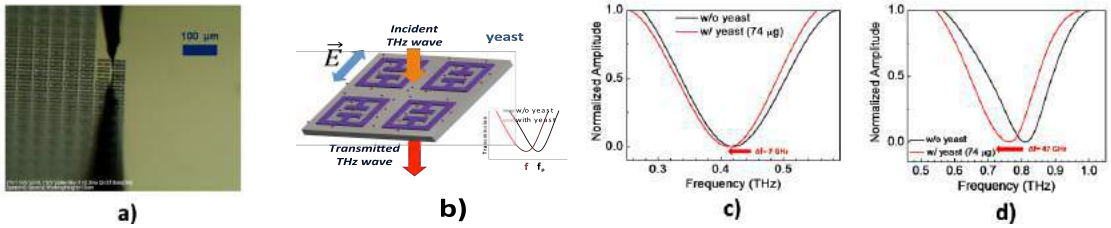

Figure 1: a)) Fabrication process of the metamaterial samples using EHD jet printing with printing speed and the working distance of the nozzle 2 mm/s and 20 μm, respectively; b) Schematic of THz metamaterial sensing of yeast; c) Comparisons of normalized transmission amplitudes of the metamaterial on the silicon wafer. (d) Comparisons of normalized transmission amplitudes of the metamaterial on the PI film.

REFERENCES

1. J. F. O'Hara, R. Singh, I. Brener, E. Smirnova, J. Han, A. J. Taylor and W. Zhang, "Thin-film sensing with planar terahertz metamaterials: sensitivity and limitations", *Opt. Express*, Vol. 16, 1786-95, 2008.
2. S. J. Park, J. T. Hong, S. J. Choi, H. S. Kim, W. K. Park, S. T. Han, J. Y. Park, S. Lee, D. S. Kim and Y. H. Ahn, "Detection of microorganisms using terahertz metamaterials," *Sci. Rep.*, Vol. 4, 4988, 2014.
3. A. P. Tenggara, S.J. Park, H. T. Yudistira, Y.H. Ahn and D. Byun "Fabrication of terahertz metamaterials using electrohydrodynamic jet printing for sensitive detection of yeast," *J. Micromech. Microeng.*, Vol. 27, 035009, 2017.
4. S. J. Park, B. H. Son, S. J. Choi, H. S. Kim and Y. H. Ahn, "Sensitive detection of yeast using terahertz slot antennas," *Opt. Express* Vol. 22, 30467-72, 2014.

Aluminum oxide nanowire metastructure for tailoring the absorption and radiation

Kyuyoung Bae[1] and Kyoungsik Kim[1*]
[1]School of Mechanical Engineering, Yonsei University,
50 Yonsei-ro, Seodaemun-gu, Seoul 03722, Republic of Korea
[*]corresponding author: kks@yonsei.ac.kr

Abstract
Here we establish the fabrication method for self-collapsed aluminum oxide nanowires from anodization process. A lattice and length of nanowire bundle can be controlled readily by anodization time, wet etching, and drying conditions. With the metal or metal-oxide deposition, the optical characteristic dramatically changes to ultra-broadband absorption or selective emission. The nanowires can be transferred onto adhesive tape or polymer films for practical applications as well.

Recently, we developed a dielectric nanowire structure using an anodization process for nanoporous aluminum oxide. The aluminum oxide nanowires are produced by conventional anodization and additional wet etching and drying processes, and the nanowires arrays are formed as by aggregation at the tip of each nanowire. The nanowires are developed as microscale funnel structures composed of thin nanowires of tens of nanometers. We sputtered metal and metal oxide on the structure as well. The nanoscale aluminum nanowires with metal show strong plasmonic absorption of visible and near-infrared light by adiabatic nanofocusing of surface plasmons. For the mid-infrared light, we can change the wavelength range and peak of absorption by controlling the microscale funnel structures and deposited materials. The dielectric and metal-dielectric nanowire array can be applied to control the light behavior in optoelectronic, and thermoplasmonic applications.

Acknowledgements, This work was supported by Global Research Lab (GRL) Program of the National Research Fundation (NRF) funded by Ministry of Science, ICT (Information and Communication Technologies) and Future Planning (2016K1A1A2912758),the National Research Foundation of Korea (NRF) grant funded by the Korea government (MSIP) (NRF-2015R1A2A2A11001112), Pioneer Research Center Program through the National Research Foundation of Korea funded by the Ministry of Science, ICT & Future Planning (NRF-2013M3C1A3065045), and the Center for Advanced Meta-Materials (CAMM-2014M3A6B3063712) funded by the Ministry of Science, ICT and Future Planning as Global Frontier Project.

REFERENCES

1. Kang, G., Yoo, J., Ahn, J., and Kim, K., "Transparent dielectric nanostructures for efficient light management in optoelectronic applications," *Nano Today*, Vol. 10, No. 1, 22-47, 2015.
2. Kang, G. et al. "Broadband and ultrahigh optical haze thin films with self-aggregated alumina nanowire bundles for photovoltaic applications", *Energy & Environ. Sci.*, Vol. 8, 2650–2656, 2015.

3. Bae, K. et al. “Flexable thin-film black gold membranes with ultrabroadband plasmonic nanofocusing for efficient solar vapour generation”, *Nat. Commun.*, Vol. 6, 10103, 2015.

Nanoimprint-lithographically fabricated stacked 1D gratings for improved MWIR polarization detection

B. Oh[1,2,3], X. E. Huang[3], D.-K. Kim[2], J. O. Kim[1], S. J. Lee[1], A. Urbas[4], Z. Ku[4], D. A. Czaplewski[5], I. W. Jung[5], and J. E. Ryu[3*]

[1]Division of Convergence Technology, Korea Research Institute of Standards and Science, Daejeon 34113, Korea

[2]Department of Electronics Engineering, Sejong University, Seoul 05006, Korea

[3]Department of Mechanical Engineering, Indiana University, Indianapolis, (IUPUI), IN 46202, USA

[4]Materials and Manufacturing Directorate, Air Force Research Laboratory, WPAFB, OH 45433, USA

[5]Center for Nanoscale Materials, Argonne National Laboratory, Lemont, IL 60439, USA

[*]corresponding author: jeryu@iu.edu

Abstract: Polarization extinction ratio of a stacked double-layer subwavelength metal grating structure was investigated. Top and bottom grating layers were fabricated with nanoimprint lithography on silicon wafer, separated by a dielectric spacer. We characterized the linear polarization extinction ratio of the stacked gold gratings (100-nm thickness) in the mid-infrared regime with various pitches of 0.4, 0.7, and 1.0 μm, whose width-to-pitch ratio and spacer thickness were 0.7 and 0.45 μm, respectively. Numerical simulations were performed to design the geometrical parameters.

Infrared (IR) imager has been used in a variety of applications from non-invasive medical diagnostics to industrial and military applications such as night vision, overhead intelligence system, and thermal track and search [1,2]. In particular, polarized IR contains richer surface information, such as shading, roughness, and shape, which can enhance image quality and detection capability [3-6]. The ultimate goal of this research is to develop a lightweight, compact IR focal plane array (FPA) monolithically-integrated with a linear polarizer [2,3]. Here, we designed and characterized a stacked double-layer 1-dimensional subwavelength gratings (1dSGs), separated by a dielectric layer, benzocyclobutene (BCB), as illustrated in Figure 1(a), to improve the performance of linear polarization detection, i.e., polarimetry extinction ratio (*ER*) given by

$$ER(\lambda) = \frac{T_{TM}(\lambda)}{T_{TE}(\lambda)} \quad (1)$$

where T_{TM} and T_{TE} are the transmission of transverse magnetic and electric polarization (of note, transmission for the polarized IR incidence perpendicular and parallel to the gratings), respectively. Computational simulation (CST Microwave Studio) was carried out to find the optimized geometrical parameters, pitch (p), width (w), gold (Au) grating thickness (t_{Au}), and BCB thickness (t_{BCB}) as shown in Figure 1(b). Figure 1(b) shows that calculated *ER* of stacked-1dSGs is 10^4 times higher as compared to single-1dSGs, in which the designed p, r (w/p), t_{Au} and t_{BCB} were 0.4 μm, 0.7, 0.1 μm, and 0.45 μm, respectively. In our preliminary results, the single-1dSGs and stacked-1dSGs fabricated by nanoimprint lithography (NIL) show similar trends in T_{TM} and T_{TE} characterization (Figure 1(c)) while measured *ER* in the stacked-1dSGs is only four times greater than the single-1dSGs. We are currently testing various sets of geometry parameters (p = 0.4, 0.7 and 1.0 μm, r (w/p) = 0.7, t_{BCB} = 0.45 μm, and t_{Au} = 0.1 μm).

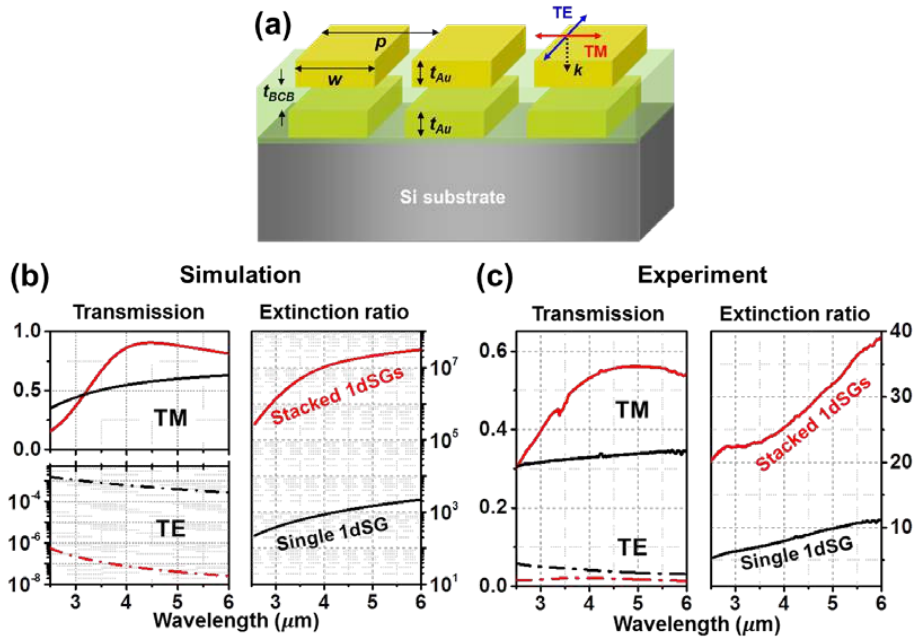

Figure 1. (a) Schematic view of unit cell of stacked-1dSGs on Si substrate. (b) CST-simulated and (c) FTIR-measured transmission / *ER* (λ) of a single- and stacked-1dSGs for TM and TE polarization (*p* and *r* is fixed at 0.4 μm and 0.7, respectively). The figure of merit, as the measure of linear polarization detection performance can be given by $\max\{T_{TM}(\lambda)/T_{TE}(\lambda)\}$.

Acknowledgements This work was supported by the Air Force Research Lab, Materials and Manufacturing Directorate. The use of the Center for Nanoscale Materials was supported by the U. S. Department of Energy, Office of Science, Office of Basic Energy Sciences, under Contract No. DE-AC02-06CH11357. Acknowledgement is also made to the Summer Faculty Fellowship Program funded by US Air Force Office of Scientific Research.

REFERENCES

1. Hutchinson, L. "Imaging: Digital infrared breast scan shows promise for detecting cancer," *Nat Rev Clin Oncol*, Vol. 7, No. 9, 483-483, 2010.
2. Rogalski, A., J. Antoszewski and L. Faraone, "Third-generation infrared photodetector arrays," *J. Appl. Phys.*, Vol. 105, No. 9, 091101, 2009.
3. Lee, S. J., Z. Ku, A. Barve, J. Montoya, W.-Y. Jang, S. R. J. Brueck, M. Sundaram, A. Reisinger, S. Krishna and S. K. Noh, "A monolithically integrated plasmonic infrared quantum dot camera," *Nat. Commun.*, Vol. 2, No. 286, 2011.
4. Tyo, J. S., D. L. Goldstein, D. B. Chenault and J. A. Shaw, "Review of passive imaging polarimetry for remote sensing applications," *Appl. Opt.*, Vol. 45, No. 22, 5453-5469, 2006.
5. Sarkar, M., D. S. S. Bello, C. van Hoof and A. J. P. Theuwissen, "Biologically Inspired CMOS Image Sensor for Fast Motion and Polarization Detection." *IEEE Sensors J.*, Vol. 13, No. 3, 1065-1073, 2013.
6. Gurton, K. P., A. J. Yuffa and G. W. Videen, "Enhanced facial recognition for thermal imagery using polarimetric imaging," *Opt. Lett.*, Vol. 39, No. 13, 3857-3859, 2014.

Self-Assembled Hyperbolic Metamaterials in the Deep-Ultraviolet

S. Skov Campbell[1*], W. P. Wardley[1], M. E. Nasir[1], G. A. Wurtz[2], A. V. Zayats[1] and W. Dickson[1]

[1] King's College London, United Kingdom

[2] University of North Florida, USA

*corresponding author: Serena.campbell@kcl.ac.uk

Abstract -Here we describe a self-assembled, template-assisted approach for the fabrication of anisotropic metamaterials which exhibit dipolar plasmonic resonances in the deep ultraviolet spectral range. This technique is based on the electrochemical deposition of UV plasmonic nanorods in anodic aluminium oxide templates. Such materials exhibit dipolar plasmon resonances, related to the nanorod geometry, with the quality factor determined by the intrinsic loss of the constituent metals. This research advances many applications, including fluorescent enhancement, surface enhanced resonant Raman scattering and bio-sensing.

Ultraviolet (UV) plasmonics has received considerable attention recently due to its many potential applications, such as fluorescent enhancement[1] and UV-surface enhanced resonant Raman scattering[2]. Moreover, it may further enhance the sensitivity of biological detection by taking advantage of many natural resonances displayed by biological molecules in the UV-range[3], as well as enabling control over photochemical reactions[4]. The materials commonly employed for plasmonics, namely gold and silver, do not exhibit plasmonic responses in the deep-UV region which, when combined with practical considerations, has meant that the majority of research has been limited to the visible to infrared (IR) regions.

Self-assembled metamaterials comprised of gold nanorods have been shown to exhibit strong anisotropy, which leads to hyperbolic dispersion at frequencies below the epsilon near zero (ENZ) condition and have been employed as highly sensitive sensors for the detection of biological molecules, ultrasound[5] and hydrogen[6] due to their extraordinary refractive index sensitivity. However, transferring this approach to the ultraviolet has been challenging, due to either poor optical properties of the constituent metals (Pd, Pt) or challenging chemistry (Al).

In this work we discuss the fabrication and optical characterization of a UV-plasmonic metamaterial comprised of arrays of aluminium nanorods and compare the optical properties with the well-known noble metals, palladium and platinum. Investigations in UV-plasmonics[7] have revealed aluminium to be the most suitable choice, due to its low losses in the UV range and is particularly advantageous for scalable techniques and future applications as it also benefits from low cost and high natural abundance.

Self-assembled metallo-dielectric metamaterials based on gold nanorod arrays have been widely studied due to the ability to precisely tailor the optical properties by varying the template geometry (pore separation and diameter) and nanorod length during the electrochemical deposition[8]. This flexibility

allows the epsilon near zero (ENZ) frequency to be varied throughout the visible spectral range and therefore also the onset of hyperbolic dispersion. Until recently, it was not possible to extend this approach to the fabrication of aluminium nanorod based metamaterials due to a paucity of chemical procedures for aluminium, an issue that was solved recently by the development of ionic liquid based electrochemical baths[9]. In order to produce aluminium based metamaterials, templates were first fabricated as described elsewhere[10] followed by the electrodeposition of aluminium from an ionic liquid comprised of a 60:40 molar concentration of $AlCl_3$(99.999%, Alfa Aesar) and organic salt [EMIm]Cl (98+%, Alfa Aesar). This procedure was necessarily carried out in an oxygen and water free (< 1 ppm) glovebox environment to prevent degradation of the electrodeposition solution.

Following fabrication, the aluminum nanorod samples were optically characterized by acquiring the zero order transmission spectra. Collimated light was provided by a deuterium-halogen lamp and the metamaterials illuminated with an incident beam at varying angles and polarizations (TE and TM). The transmitted light was collected by a long working distance, deep-UV objective lens before being passed through a solarisation resistant optical fibre to a spectrometer equipped with a UV enhanced EMCCD. Experimental extinction spectra obtained from a metamaterial comprised of aluminium nanorods with radii of 20 nm, an inter-rod separation of 100 nm and length of approximately 200 nm, are shown below Figure 1.

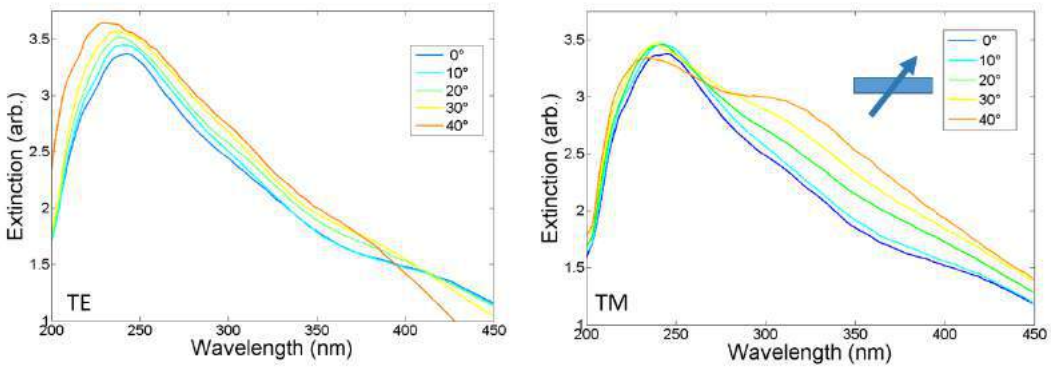

Figure 1 – Extinction spectra for an array comprised of aluminum nanorods having a separation of 100 nm, diameter 20 nm and length of approximately 200 nm measured in (a) TE (b) TM incident polarization. Spectra were taken at various angles of incidence of the illuminating light for both polarizations.

The experimental data in Figure 1, exhibits a transverse mode at 230nm for TE polarized light (left) which is angle independent. In the case of TM polarization however, two dipolar plasmonic resonances are observed; the transverse mode at 230 nm and the angle dependent longitudinal mode at 320 nm, related to the short and long axes of the nanorods respectively.

In summary, we experimentally demonstrate the hyperbolic, and tunable plasmonic response, of self-assembled aluminum nanorod arrays in the deep to near-UV region. The strong plasmonic response in the UV range, tunable by varying the dimensions of the template and length of the rods, can aid in enhancing many plasmonic studies into the deep-UV range; such as the study of non-linear properties, fluorescent enhancement or UV-SERRS as well as research involving quantum dots that operate in the UV-region.

REFERENCES

1. Jha, S. K.; Ahmed, Z.; Agio, M.; Ekinci, Y.; Löffler, J. r. F., Deep-UV surface-enhanced resonance Raman scattering of adenine on aluminum nanoparticle arrays. *Journal of the American Chemical Society* 2012, 134, 1966-1969.
2. Taguchi, A.; Hayazawa, N.; Furusawa, K.; Ishitobi, H.; Kawata, S., Deep-UV tip-enhanced Raman scattering. *Journal of Raman Spectroscopy* 2009, 40, 1324-1330.
3. Hammond, J. L.; Bhalla, N.; Rafiee, S. D.; Estrela, P., Localized surface plasmon resonance as a biosensing platform for developing countries. *Biosensors* 2014, 4, 172-188.
4. Attavar, S.; Diwekar, M.; Blair, S., Photoactivated capture molecule immobilization in plasmonic nanoapertures in the ultraviolet. *Lab on a Chip* 2011, 11, 841-844.
5. Anker, J. N.; Hall, W. P.; Lyandres, O.; Shah, N. C.; Zhao, J.; Van Duyne, R. P., Biosensing with plasmonic nanosensors. *Nature materials* 2008, 7, 442-453.
6. Zhou, L.; Zhang, C.; McClain, M. J.; Manjavacas, A.; Krauter, C. M.; Tian, S.; Berg, F.; Everitt, H. O.; Carter, E. A.; Nordlander, P., Aluminum nanocrystals as a plasmonic photocatalyst for hydrogen dissociation. *Nano letters* 2016, 16, 1478-1484.
7. McMahon, J. M.; Schatz, G. C.; Gray, S. K., Plasmonics in the ultraviolet with the poor metals Al, Ga, In, Sn, Tl, Pb, and Bi. *Physical Chemistry Chemical Physics* 2013, 15, 5415-5423.
8. León Patiño, C.; Aguilar-Reyes, E.; Ruiz-Aguilar, C. In *Fabrication and Characterization of Highly Ordered Porous Alumina Templates by a Two-Step Anodization Process*, Materials Science Forum, Trans Tech Publ: 2013; pp 75-81.
9. Oltean, G.; Nyholm, L.; Edström, K., Galvanostatic electrodeposition of aluminium nano-rods for Li-ion three-dimensional micro-battery current collectors. *Electrochimica Acta* 2011, 56, 3203-3208.
10. Jessensky, O.; Müller, F.; Gösele, U., Self-organized formation of hexagonal pore arrays in anodic alumina. *Applied Physics Letters* 1998, 72, 1173-1175.

Facile fabrication technique of periodically aligned faceted gold nanocrystal array

Minjung Choi[1], Kyuyoung Bae[1], and Kyoungsik Kim[1*]
[1]School of Mechanical Engineering, Yonsei University, 50 Yonsei-ro, Seodaemun-gu, Seoul 03722, Republic of Korea
[*]kks@yonsei.ac.kr

Abstract-We demonstrate a fabrication technique of gold nanocrystals with periodic anodic aluminum oxide groove template by evaporation and high-temperature heat treatment processes. Employing diverse groove templates with different lattice constants and proper evaporation condition, we fabricated gold nanocrystal arrays with few tens of nanometer-diameter. Compare with chemically synthesized gold nanocrystals, our gold nanocrystals are not aggregated nor piled but periodically distributed as a monolayer in accordance with the periodicity of the groove template. With enhanced dipolar plasmon mode supported by faceted nanocrystal shape, the gold nanocrystal array can be used for plasmonic sensing applications.

A-two steps method, first preparing periodic groove template, and then forming nanocrystals via evaporation on the template and high-temperature heat treatment processes, is used. We utilize an anodic aluminum oxide template as the periodic groove with diverse lattice constants of 75, 100, and 140 nm, depend on the template's first anodization voltage; 30, 40, and 52 V, respectively. Thickness optimization of gold evaporation process, leads us to highly regular-sized nanocrystal creation via high-temperature heat treatment. Thanks to well-established manufacturing process of the anodic aluminum oxide template, 40, 65, and 80 nm-diameter gold nanocrystals are fabricated with lattice constants of 75, 100, and 140 nm, respectively.

Acknowledgements

This research was supported by the Low Observable Technology Research Center program of the Defense Acquisition Program Administration and Agency for Defense Development.

REFERENCES

1. H. Masuda and K. Fukuda, "Ordered metal nanohole arrays made by a two-step replication of honeycomb structures of anodic alumina," *Science*, Vol. 268, No. 5216, 1466–1468, 1995.
2. McClain, M. J., Schlather, A. E., Ringe, E., King, N. S., Liu, L., Manjavacas, A., Knight, M. W., Kumar, I., Whitmire, K. H., Everitt, H. O., Nordlander, P. and Halas, N. J., "Aluminum Nanocrystals," *Nano Lett.*, Vol. 15, No. 4, 2751–2755, 2015.
3. Nakayama, K., Tanabe, K. and Atwater, H. A., "Plasmonic nanoparticle enhanced light absorption in GaAs solar cells," *Appl. Phys. Lett.*, Vol. 93, No. 12, 121904, 2008.
4. Lee, J., Bae, K., Kang, G., Choi, M., Baek, S., Yoo, D.-S., Lee, C.-W. and Kim, K., "Graded-lattice AAO photonic crystal heterostructure for high Q refractive index sensing," *RSC Advances*, Vol.5, No. 88, 71770–71777, 2015.

Dr. Marlous Kamp

Cambridge University, Departments of Physics and Chemistry

Plasmon-induced local heating for optically controlled nano-architectures

This poster discusses new results in optically controlled nano-architectures of gold nanoparticles, prepared using the temperature responsive polymer poly(N-isopropylacrylamide) (pNIPAM). We show how assemblies can be selected according to size using local plasmonic heating. We also discuss how these assemblies relate to a type of self-limiting assemblies called actuating nanotransducers (ANTs) prepared in our lab[1].

[1] T. Ding, V. K. Valev, A. R. Salmon, C. J. Formand, S. K. Smoukov, O. A. Scherman, D. Frenkel, and J. J. Baumberg. *Light-induced Actuating Nanotransducers.* PNAS 113:20, 5503-5507 (2016).

Optical Patternable Metamaterial For Nanolithography Below Diffraction Limit

Youngseop Lee[1], Sang-Gil Park[1], SeokJae Yoo[2], Minhee Kang[1], Sang Chul Jeon[3], Young-Su Kim[3], Q-Han Park[2], and Ki-Hun Jeong[1]*

[1]Department of Bio and Brain Engineering, KAIST, Republic of Korea

[2]Department of Physics, Korea University, Republic of Korea

[3]National Nanofab Center, Republic of Korea

*corresponding author: kjeong@kaist.ac.kr

Abstract - This work reports optical patternable metamaterial (OPM) for ultraviolet nanolithography below the diffraction limit. The OPM features mono-dispersed silver nanoislands (AgNs) embedded within photosensitive polymer by using solid-state embedment of AgNs into ultrathin polymer. This unique configuration simultaneously exhibits both negative effective permittivity and high lithographic contrast in the ultraviolet range, which enables the superlens effect for the clear photolithographic definition of 70 nm in minimum feature size beyond the Fraunhofer distance.

Metamaterials become of considerable interest thanks to the miscellaneous and compelling capabilities such as negative index[1,2], which overcomes the optical diffraction limit by compensating the information loss at the sub-diffraction limit scale[3]. Recently, metamaterials have demonstrated the sub-diffraction limit imaging in the ultraviolet (UV) range based on the superlens effect[4-6]. However, most previous works still have intrinsic limitations in defining the nanopatterns on a photoresist thinner than the Fraunhofer distance, because the pattern information passing through the superlens exponentially decays in a dielectric medium of photoresist. Furthermore, the direct patterning of photoresist film on the substrate of a photomask with superlens or hyperlens intrinsically impedes the practical use for nanolithography as well as the subsequent nanofabrication process.

Here we report optical patternable metamaterial (OPM) of mono-dispersed silver nanoislands (AgNs) embedded within photoresist polymer for ultraviolet nanolithography. The OPM exhibits the superlens effect under UV exposure and defines clear sub-diffraction limited photoresist pattern thicker than the Fraunhofer distance (**Fig. 1**). The superlens effect is clearly visualized by using the finite difference time domain (FDTD) method (**Fig. 2**). The electric field intensity of UV at 365 nm clearly maintains the sub-diffraction limited image within the OPM whereas conventional photoresist shows significantly blurred and highly diffracted images. Optical properties of OPM were numerically calculated by using the FDTD method for different width, gap, and thickness of AgNs. The calculated results of permittivity and lithographic contrast show the OPM efficiently exhibits the superlens effect (ε_M' ~ -2.7) and acceptable contrast of $C > 0.5$ for the nanoisland widths relatively larger than the gap spacing.

Ultraviolet nanolithography on a wafer level has been experimentally demonstrated by combining the OPM with a conventional contact mask aligner (**Fig. 3**). The OPM was simply prepared on a 4 inch silicon wafer by using spin-coating of ultrathin photosensitive polymer (SU-8), oblique angle deposition (OAD) of thin silver film, and solid-state embedment of AgNs. The chrome photomask with sub-diffraction limited patterns was fabricated by using an e-beam lithography and metal lift-off process. Nanopatterns were defined in the OPM by using a conventional UV mask aligner. The experimental results clearly demonstrate that the OPM defines the sub-diffraction limited under one-shot UV exposure whereas

conventional photoresist (SU-8) significantly diffracts and broadens the identical images (**Fig. 4**). Based on the topographic measurements with atomic force microscope (AFM), "N" textured patterns of 70 nm (<~λ/5) line width are clearly defined in the OPM but significantly broaden up to 240nm in the SU-8 resist.

Acknowledgements This work was supported by the grant funded by the Korea government (if any, including all funding information, should be gathered into a brief statement at the end (No. 2015036205, CISS-2011-0031866, HI13C2181).

REFERENCES

1. Xu, T. et al. "All-angle negative refraction and active flat lensing of ultraviolet light", *Nature,* Vol. 497, 470-474, 2013.
2. Van de Harr, M. A. et al. "Experimental realization of a polarization-independent ultraviolet/visible coaxial plasmonic metamaterial", *Nano Lett,* Vol. 14, 6356-6360, 2014.
3. Pendry, J. B. "Negative refraction makes a perfect lens", *Phys Rev Lett,* Vol. 85, 3966-3969, 2000.
4. Fang, N. Lee, H. Sun, C. Zhang, X. "Sub-diffraction-limited optical imaging with a silver superlens", *Science,* Vol. 308, 534-537, 2005.
5. Liu, H. et al. "High aspect sub diffraction-limit photolithography via a silver superlens". *Nano Lett*, Vol. 12, 1549-1554, 2012.
6. Liu, Z. et al. "Far-field optical hyperlens magnifying sub-diffraction-limited objects", *Science,* Vol. 315, 1686-1686, 2007.

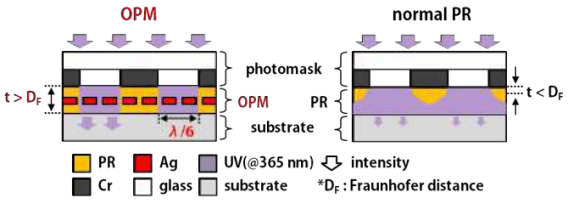

Figure 1. Schematic diagram of optical patternable metamaterial (OPM) for UV nanolithography below the diffraction limit.

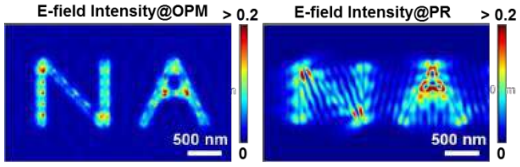

Figure 2. Comparison of electric field intensity through OPM and normal PR by using the FDTD method.

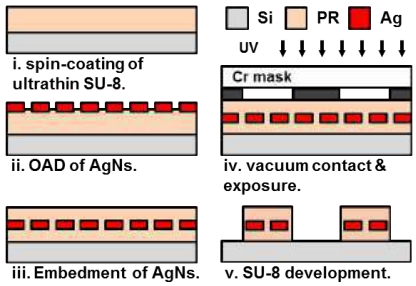

Figure 3. Lithography procedures with OPM.

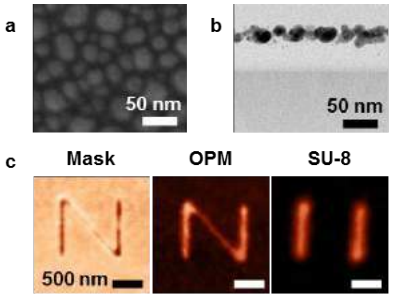

Figure 4. UV nanolithographic results using the OPM. a) The SEM image of top view of AgNs. b) The TEM image of cross-sectional view of AgNs inside SU-8. c) The AFM images of nanolithographic results.

Instrumental Development of FT-IR Spectroscopy in the Meta-Material Characterization and studies

Young Sup Roh[1*], Dan Wu, Denis Czurlok, and Michael Joerger[2]
[1]Bruker Korea Co., Ltd. Seongnam, Gyeonggi-do, Korea
[2]Bruker Optik GmbH, Ettlingen, Germany, Germany
[*]corresponding author: Youngsup.roh@bruker.com

Abstract-In the field of Metamaterials research, FT-IR spectroscopy has played important roles to characterize the optical properties with wavelength dependence. We will review the recent development of our FT-IR spectrometer. We will also introduce state-of-art Instrument, hybrid FT-IR and cw-THz system, covering from 3 to 50,000 cm-1, which corresponds from Terahertz to UV region.

Keyword: Metamaterial, FT-IR, optical spectroscopy, FIR, Terahertz, IR imaging,

Designing plasmonic nanostructure based on two-step organothiol-assisted growth

Hyo-Yong Ahn[1], **Hye-Eun Lee**[1], **Yoon Young Lee**[1], **and Ki Tae Nam**[1*]
[1]Department of Materials Science and Engineering, Seoul National University, Korea
[*]corresponding author: nkitae@snu.ac.kr

Abstract-We developed two-step organothiol-assisted nanoparticle growth system, which is capable to direct morphology of plasmonic nanoparticle in solution. Rationally designed organothiols incorporated in growth process of nanoparticle and induce a distinctive interfacial interaction at the gold nanoparticle surface. We achieved novel nano-morphology control ranging from simple polyhedron to concave rhombic dodecahdron and chiral 432-symmetry structures, which show characteristic extinction, SERS enhancement, and chiroptical property.

Design and fabrication of nanostructure have been essential parts of plasmonics and metamaterial researches. Although lithographic techniques are widely used for making complex and asymmetric nanostructure, simple and large-scale fabrication of geometry-controlled 3D nanostructure is still challenging. In this respect, nature is highly skilled at nano-structuring inorganic materials using organic-inorganic interaction. Here, inspired from organic modifier in nature, we developed organothiol assisted growth system which is capable to direct morphological development through distinctive interaction between organothiol and gold surface. We constructed the morphology diagram describing the morphology development modes of low-index-faceted nanoparticle for the foundational understanding of the colloidal nanoparticle growth in the system we utilized[1]. Based on the morphology diagram, we designed 2nd growth of nanoparticle and produced the unique nanoparticles with high-index-faceted morphology. Addition of organothiol during the growth mediated the formation of substructures in the nanometer resolution which enable the synthesis of concave rhombic dodecahedral nanoparticle[2]. Furthermore, using asymmetric interaction of organothiols and high index surfaces, we successfully synthesized unprecedented chiral morphology with 432 point group symmetry. We expect that this research will open a venue of the solution-based fabrication of plasmonic metamaterials.

Acknowledgements, This work was supported by National Research Foundation of Korea (NRF) funded by the Korean Government (NRF-2014-Global Ph.D. Fellowship Program, Grant No. 2014020809)

REFERENCES

1. Ahn, H. Y., Lee, H. E., Jin, K. & Nam, K. T. Extended gold nano-morphology diagram: synthesis of rhombic dodecahedra using CTAB and ascorbic acid. J Mater. Chem. C 1, 6861-6868 (2013).
2. Lee, H.-E. et al. Concave rhombic dodecahedral Au nanocatalyst with multiple high-index facets for CO2 reduction. ACS Nano 9, 8384-8393 (2015).

Instant Inkjet Printed 3dB Hybrid Coupler with Non-Conventional Output Phase Difference

S. A. Babale[1,2], S.K.A. Rahim[1], H. A. Elmobarak[1] and D. Schreurs[3]

[1]Wireless Communication Centre (WCC) Faculty of Electrical Engineering,
Universiti Teknologi Malaysia, UTM Skudai, 81310, Johor, Malaysia.
[2]Department of Electrical Engineering, Faculty of Engineering,
Bayero University Kano, 3011, Kano, Nigeria.
[3] Electronic Engineering Department, KU Leuven, Leuven 3001, Belgium.

*corresponding author: sababale.ele@buk.edu.ng

Abstract

***Abstract*—In this paper, a design a 3-dB coupler with 45^0 phase difference is implemented using a low-cost instant inkjet silver-nano printing technology. The responses of the coupler show that the return loss and isolation are both below -20dB at the designed frequency. However, for the output phase difference it can be observe that there is 45^0 phase difference and the amplitude imbalance in dB is less than 0.05 at the center frequency.**

***Index Terms*—3dB hybrid coupler, nonstandard phase differences, silver-nano technology.**

1. Introduction

Branch Line Coupler (BLC) is a four port 3dB power divider, with only one input, two equal outputs having 90^0 phase difference, and an isolated port. It is a crucial component in the rapidly growing applications of microwaves in communication systems, electronic warfare and radar systems. It is often used in frequency discriminators, balanced mixers, automatic level controls, and in many wireless applications due to its planar and relatively simple structure[1].

Couplers with quadrature outputs have been reported widely in different techniques such as microstrip [2], substrate integrated waveguide [3], multilayer microstrip [4], coplanar waveguide [5] and inkjet printing technology [6]. Despite their importance, little has been done on arbitrary output phase-difference characteristics.

In this research, new sets of equations for the 3dB coupler utilizing non-standard phase-difference and arbitrary power division ratio is proposed and validated by prototyping the coupler using Inkjet Printed silver-nano technology.

2. Instant Inkjet Printing Process

The printing technique presented in this paper uses inkjet printer manufactured by Brother Industries, Ltd. (DCP–J140w) because it is of low cost, availability, and their nozzles specially eject large amount of ink volume. This translates to deposition of excessive amounts of conductive ink making undistorted conductive [7]. Unlike the inkjet printing technique presented in [6], where it requires curing to achieve high conductivity. Once printed, this desktop inkjet printing technology gives good conductive pattern with resistance less than 0.3 Ω per square in fraction of seconds. This is achieved using Polyethylene terephthalate (PET) as a substrate which is chemically coated by means of photolithography for fast absorption of the ink and effectively prevent coating. This thin, absorbent coating plays a vital role in the chemical sintering process of the silver nanoparticle ink thereby supporting the ink to dry up instantly. The printing technique does not use any special software to drive the printer. But, some customized settings are necessary for achieving optimum performance. With this setting, the ink deposition is done in such a way to ensure that, each 'dot' of ink merging with its neighbors to form a continuous conducting pattern [7].

3. Coupler with 45^0 phase-difference

The transmission line model of the proposed coupler is shown in Fig. 1a. where Z_1, Z_2 and Z_3 are the impedance of the main line and the branch of the coupler. Also, θ_1,θ_2 and θ_3 represent the electrical length of the main line and the branches as shown in Fig. 3. Z_2 is choosing to be equal to Z_3 for simplicity and Port 1 is taken as the input, port 4 and port 3 are the through and the coupled ports respectively while port 2 is completely isolated. Taking the advantage of the symmetrical nature of the coupler, Even-Odd mode nalysis was used to analyzed the circuit. Fig. 1b shows Even and Odd mode equivalent circuit representation of the coupler in

Fig. 1(a). The design criteria are aim at achieving a variable phase difference, variable power division, good return loss and isolation. The power division ratio P(f) and the phase difference ψ between the output ports 2 and 3 are defined as follows:

$$\psi(f) = \angle S_{21} - \angle S_{31} \quad (1)$$

$$P(f)^2 = \left|\frac{S_{21}}{S_{31}}\right|^2 \quad (2)$$

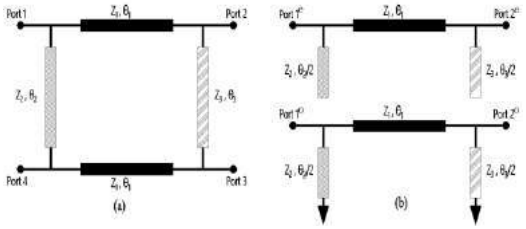

Fig. 1: (a) Schematic representation of the proposed coupler; (b) Even-Odd mode representation

Referring to Fig. 1b, the transmission characteristics of the even or odd mode is obtained using the transmission (ABCD) matrix, The ABCD matrix used in obtaining the overall transmission and reflection characteristics of the network are used to obtained the following designed equation:

$$Z_2 = Z_0 P|\sin\psi| \quad (3)$$

$$Z_1 = Z_3 = \frac{Z_0 P \sin\psi}{\sqrt{1+P^2\sin^2\psi}} \quad (4)$$

$$\theta_1 = \pi - \tan^{-1}\left(\frac{(Z_0\tan\psi)}{Z_1}\right) \quad (5)$$

$$\theta_2 = \frac{\pi}{2} \quad (6)$$

$$\theta_3 = \tan^{-1}\left(\frac{(Z_0\tan\psi)}{Z_1}\right) \quad (7)$$

From the design equations formulated (1) – (7), a 3-dB coupler was designed and implemented using instant inkjet printing technique. The coupler is meant to operate at a frequency of 6.0GHz. By setting the phase difference between the outputs to be 45^0 and the reference impedance $Z_0 = 50\Omega$, for 3dB power division ratio, the impedances of the coupler arms are: $Z_1 = 35.36\Omega$, $Z_2 = Z_3 = 28.87\Omega$, $\theta_1 = 90^0$, $\theta_2 = 120^0$, and $\theta_3 = 60^0$. Fig. 2 shows the layout of the proposed coupler. Other power division ratios is possible using the design equations.

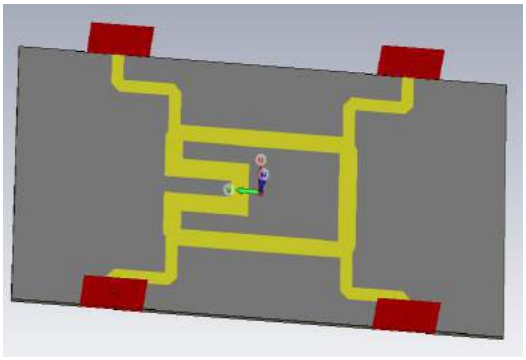

Fig. 2: Layout of the proposed 45^0 Coupler.

The Simulation was carried out in CST Microwave Studio 2005® and fabricated on a transparent Polyethylene terephthalate (PET) substrate specially coated with resin. The measured dielectric constant, thickness, and a loss tangent of the substrate are 0.125mm, εr = 2.72 and 0.043 respectively. Silver-nano printing technology was used to produce the prototype. This technology is accessible and of low cost that support fast prototyping of electronic circuitries [7].

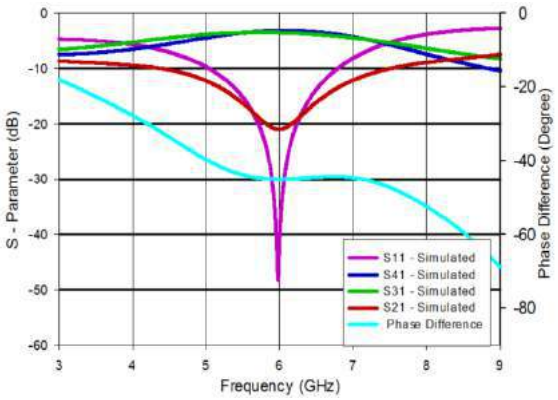

Fig. 3: Simulated S- Parameter Response for the Proposed Coupler. Magnitude in dB and output Phases difference in degrees.

4. Conclusions

In this paper, 3dB hybrid coupler with non-standard phase difference was designed and implemented using low-cost, silver nano inkjet printing technology on a transparent PET substrate. This coupler could be useful in number of applications like in antenna beam steering and in feeding networks for phased antenna array without the use of additional phase shifter. Explicit design equations with variable phase differences ψ was derived and validated by fabricating a prototype of the coupler operating at 6.0 GHz. At the designed frequency, both the measured (not shown

for now) and the full wave simulated results agreed with little discrepancy, this is because of fabrication tolerances.

Acknowledgements

The authors acknowledge the Ministry of Higher Education Malaysia and Universiti Teknologi Malaysia for providing financial support under a vot 4J299. This grant is managed by Research Management Center, Universiti Teknologi Malaysia.

References

[1] D. M. Pozar, "Microwave Engineering 3e," ed: Wiley 2012, pp. 317-380.

[2] S. A. Babale, S. K. A. Rahim, M. Jusoh, and L. Zahid. "Branch-line coupler using PDMS and Shieldit Super fabric conductor." Applied Physics A. vol. 123, no. 2, pp117 Feb. 2017.

[3] J. Haiyan, K. Wang, J. Guo, S. Ding, and K. Wu. "Slow-Wave Effect of Substrate Integrated Waveguide Patterned with Microstrip Polyline." IEEE Trans. Microw. Theory Tech., vol. 64, no. 6, pp1717-1726, 2016.

[4] W. Yongqiang, K. Ma, and S. Mou. "A High Performance Tandem Coupler Using Substrate Integrated Suspended Line Technology." IEEE Microw. Wireless Comp. Lett., vol. 26, no. 5, pp 328-330 May 2016.

[5] K. M. Ben, M. Nedil, N. Kandil, M. C. E. Yagoub, and T. A. Denidni. "Wideband directional elliptic coupler based on CB-CPW technology." Electron. Let., vol. 48, no. 12, 2012.

[6] A. Werner, M. Lee, Y. Kim, E. Ryu, and I. S. Kim. "New inkjet printed wideband 3 dB branch line coupler." In Microw. Sym. Dig., IEEE MTT-S Int., pp. 1-4, 2011.

[7] Y. Kawahara, S. Hodges, B. S. Cook, C. Zhang, and G. D. Abowd, "Instant inkjet circuits: lab-based inkjet printing to support rapid prototyping of UbiComp devices, "in Proceedings of the 2013 ACM int., conf., Pervasive and ubiquitous comp., ", pp. 363-372: ACM, 2013.

A Low-cost PET-based 4x4 Butler Matrix using 3dB Hybrid Coupler with Non-Conventional Output Phase Difference

S. A. Babale[*1,2], S.K.A. Rahim[1] and M. Himdi[3]

[1]Wireless Communication Centre (WCC) Faculty of Electrical Engineering,
Universiti Teknologi Malaysia, UTM Skudai, 81310, Johor, Malaysia.
[2]Department of Electrical Engineering, Faculty of Engineering,
Bayero University Kano, 3011, Kano, Nigeria.
[3]Institute of Electronics and Telecommunications of Rennes (IETR),
University of Rennes, France.

*corresponding author: sababale.ele@buk.edu.ng

***Abstract*—Butler Matrix (BM) utilizing only 3dB hybrid couplers and a crossover is presented. It is implemented on a specially coated PET substrate using a low -cost silver-nano inkjet printing technology. The results show a return loss better than -19 dB at 6.0GHz. When port 1 is exited, the transmission coefficients are $S_{51} = 6.89$dB, $S_{61} = 6.68$dB, $S_{71} = 6.04$dB, and $S_{81} = 6.54$dB at the operating frequency. Similarly, when port 2 is exited, the transmission coefficients are $S_{52} = 6.11$dB, $S_{62} = 6.98$dB, $S_{72} = 6.80$dB, and $S_{82} = 7.11$dB at the center frequency. The proposed design has a good performance in terms of amplitude and progressive phase difference at the output ports.**

***Index Terms*—**Butler Matrix, couplers, crossover, return loss, and amplitude imbalance.

I. INTRODUCTION

A Butler Matrix (BM) is one of the popular beamforming network due to its simplicity, easy fabrication and low power loss. One of the many options for constructing the beamforming network is by the application of BM [1]. 4X4 Conventional BM has four input and four output ports. It comprises of four quadrature hybrid couplers, two Phase Shifters, and two Zero dB Cross-over [2]. By exciting any of its input port, there will be an equal amplitude and progressive phase differences at the output ports. When an antenna array is connected to the outputs, there will be four dissimilar beams in the radiation pattern [3].

Directional couplers are the essential building block of BM, due to the quarter wavelength requirement of the couplers, the layout of the BM is usually very large [4]. Recently, several techniques have been proposed to miniaturize the coupler to reduce the size of the BM. In [5], an artificial transmission line was used in miniaturization of the couplers. Substrate integrated waveguide technology has been proposed in [6]. For the branch line couplers presented in [7], high impedance lines are meandered to achieve size reduction. Reference [8] proposed a low-temperature co-fired ceramic technique.

Most of the above techniques use either lumped elements or phase shifters for the implementation of the BM which tend to reduce the performance of the Butler matrices. To have BM with a better performance, Reference [9] proposes a BM without crossovers. But the multi-layer technique requires the use of vias which increase the fabrication difficulties.

In contrast to the BM presented in [9], this paper present a 4x4 Butler matrix utilizing only microstrip couplers and a crossover in planner structure. Employing 45^0 couplers in the design eliminate the use of phase shifters. This reduces the dimension and transmission loss of the device by shortening transmission line path.

II. INKJET PRINTING

The printing technique presented in this paper uses inkjet printer manufactured by Brother Industries, Ltd. (DCP–J140w) because it is of low cost, availability, and their nozzles specially eject large amount of ink volume. This translates to deposition of excessive amounts of conductive ink making undistorted conductive [10]. Unlike the inkjet printing technique presented in [9], where it requires curing to achieve high conductivity. Once printed, this desktop inkjet printing technology gives good conductive pattern with resistance less than 0.3 Ω per square in fraction of seconds. This is achieved using Polyethylene terephthalate (PET) as a substrate which is chemically coated by means of photolithography for fast absorption of the ink and effectively prevent coating. This thin, absorbent coating plays a vital role in the chemical sintering process of the silver nanoparticle ink thereby supporting the ink to dry up instantly. The printing technique does not use any special software to drive the printer. But, some customized settings are necessary for achieving optimum performance. With this setting, the ink deposition is done in such a way to ensure that, each 'dot' of ink merging with its neighbors to form a continuous conducting pattern [10].

III. BUTLER MATRIX DESIGN

The concept used in the design of this novel 4x4 Butler Matrix is centered around the design of 45^0 hybrid coupler. The use of this hybrid coupler 45^0 phase-difference eliminates the need for additional components in building Butler Matrix, thereby making it compact in size and retain its good performance. This is because it replaces the combination of quadrature coupler and phase shifter in the design of conventional Butler Matrix.

All the components of the BM are designed and fabricated on a transparent Polyethylene terephthalate (PET) substrate specially coated with resin. The measured dielectric constant, thickness, and a loss tangent of the substrate are 0.125mm, εr = 2.72 and 0.043 respectively. A commercial Simulation software (CST) was used throughout the

simulation and a Silver-nano printing technology was used to produce the prototype. Fig. 1 shows the layout of the proposed 4x4 Butler Matrix.

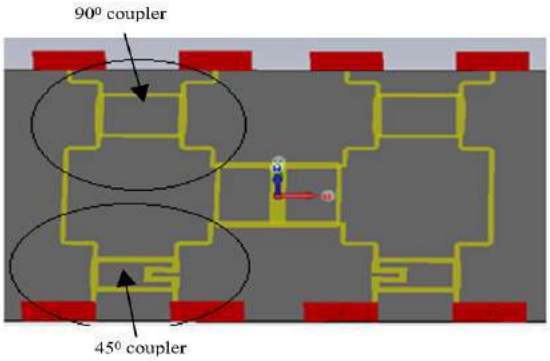

Fig. 1: Layout of the proposed 4x4 Butler Matrix

IV. PERFORMANCES OF THE BUTLER MATRIX

By exciting port 1 of the BM, the simulated return losses and the transmission coefficients at its output ports is shown in Fig. 2.

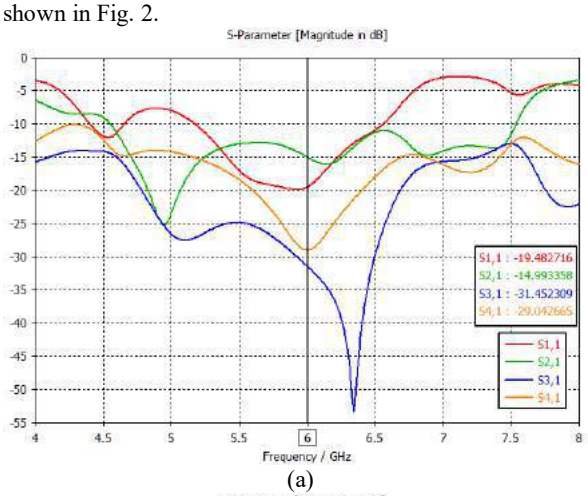

(a)

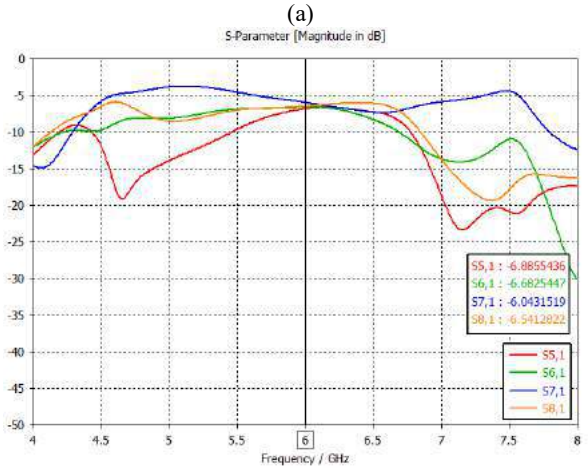

(b)

Fig. 2: Simulated S-Parameter of the 4X4 Butler Matrix when port 1 is exited. (a) Magnitude in dB; (b) Phases in degree.

The simulated return losses and the transmission coefficients at the various output ports when port 1 is fed are shown in Figure 4. The return losses are better than -19 dB and the transmission coefficients are $S_{51} = 6.89\text{dB}$, $S_{61} = 6.68\text{dB}$, $S_{71} = 6.04\text{dB}$, and $S_{81} = 6.54\text{dB}$ at the operating frequency. Similarly, when port 2 is exited, the transmission coefficients are $S_{52} = 6.11\text{dB}$, $S_{62} = 6.98\text{dB}$, $S_{72} = 6.80\text{dB}$, and $S_{82} = 7.11\text{dB}$ at the center frequency.

ACKNOWLEDGEMENTS

The authors acknowledge the Ministry of Higher Education Malaysia and Universiti Teknologi Malaysia for providing financial support under a vot 4J299. This grant is managed by Research Management Center, Universiti Teknologi Malaysia.

V. CONCLUSION

A novel 4×4 Butler matrix has been designed and simulated to operate at center frequency of 6GHz. In this BM, only couplers and cross over are used, phase shifter is not needed as in the design of conventional BM. The result results obtained shows that, the proposed design has a good performance in terms of amplitude and progressive phase difference at the output ports as they are in good agreement with the practical values. Some of the advantages of this design are: its compactness due to the absent of phase shifters and low transmission losses by shortening transmission line path. With this structure, the proposed Butler matrix can serve as a good candidate for the future 5G beam forming network.

REFERENCES

[1] J. Butler, "Beam-forming matrix simplifies design of electronically scanned antennas," Electron. Des., vol. 9, pp. 170-173, 1961.

[2] H. Moody, "The systematic design of the Butler matrix," IEEE Trans. Antennas Propag., vol. 12, pp. 786-788, 1964.

[3] S. K. A. Rahim and P. Gardner. "A novel active antenna beamforming networks using Butler matrices." Progress In Electromagnetics Research C, vol. 11, pp183-198, 2009.

[4] S. A. Babale, S. K. A. Rahim, M. Jusoh, and L. Zahid. "Branch-line coupler using PDMS and Shieldit Super fabric conductor." Applied Physics A. vol. 123, no. 2, pp117 Feb. 2017.

[5] C.-W. Wang, T.-G. Ma, and C.-F. Yang, "A new planar artificial transmission line and its applications to a miniaturized butler matrix," IEEE Trans. Microw. Theory Tech., vol. 55, pp. 2792-2801, 2007.

[6] C.-J. Chen and T.-H. Chu, "Design of a 60-GHz substrate integrated waveguide Butler matrix—A systematic approach," IEEE Trans. Microw. Theory Tech., vol. 58, pp. 1724-1733, 2010.

[7] Q. Wu, Y. Yang, M. Lin, and X. Shi, "Miniaturized broadband branch-line coupler," Microw. Opt. Tech. Lett., vol. 56, pp. 740-743, 2014.

[8] G. Tudosie, H. Barth, and R. Vahldieck, "A compact LTCC Butler matrix realization for phased array applications," in IEEE MTT-S Int. Microw. Symp. Dig., 2006.

[9] A. Werner, M. Lee, Y. Kim, E. Ryu, and I. S. Kim. "New inkjet printed wideband 3 dB branch line coupler." *In Microw. Sym. Dig., IEEE MTT-S Int.*, pp. 1-4, 2011.

[10] Y. Kawahara, S. Hodges, B. S. Cook, C. Zhang, and G. D. Abowd, "Instant inkjet circuits: lab-based inkjet printing to support rapid prototyping of UbiComp devices, "*in Proceedings of the 2013 ACM int., conf., Pervasive and ubiquitous comp.,* ", pp. 363-372: ACM, 2013

Application of microchip laser for high resolution 3D printing.

D. Perevoznik[1*], K. Kurselis[1], R. Kiyan[1], B.N. Chichkov[1]
[1]Laser Zentrum Hannover e.V.
[*]corresponding author: D.Perevoznik@lzh.de

Abstract- Application of Q-switched microchip laser for 3D printing by two-photon polymerization is reported. With optimized laser configuration and photo-resist high resolution high throughput 3D printing of polymer is achieved.

Among 3D nano- and micro-structuring techniques, only two-photon polymerization (2PP) [1-2] technology allows true 3D micro and nano-fabrication. Because of the threshold behavior and nonlinear nature of the 2PP process, resolution beyond the diffraction limit can be achieved by controlling the laser pulse energy and focal spot size. Since the absorption cross-section for two-photon process is very small, a high intensity laser radiation is required. Typically, tightly focused output beam from femtosecond laser is used to achieve high peak power avoiding optical break down of the materials.

2PP technology has been successfully applied for 2D and 3D nano-fabrication in different disciplines [3]. However, wide industrial usage of the 2PP technology is limited due to lack of low cost industrial grade femtosecond lasers. Competitiveness of 2PP in industrial applications will be improved significantly if cheaper and more reliable pico- and nano-second lasers are used. It is especially attractive to apply passively Q-switched microchip lasers for 3D printing of polymers by 2PP. Although successful 2PP structuring by pico- and nano-second lasers has been already demonstrated [4], structuring characteristics achieved with femtosecond lasers are still far superior. The most significant drawback of the standard microchip lasers is low repetition rate of the generated pulses that is not compatible with 2PP technology.

We are presenting for the first time application of the high repetition rate Nd:YVO_4 Q-switched microchip laser with SESAM for 3D micro-/nano-fabrication by 2PP. Energy of the pulses generated by this microchip laser is of about 95 nJ with pulse duration of 90 ps and repetition rate up to 500 kHz. Since the microchip laser is radiating at 1064 nm, optimization of the photosensitive material was necessary. Specifically, various photo-initiators were investigated for application in the 2PP process at this wavelengths. Optimal photo-initiator was selected allowing effective 3D fabrication by 2PP. Examples of the fabricated structures are shown in Fig. 1.

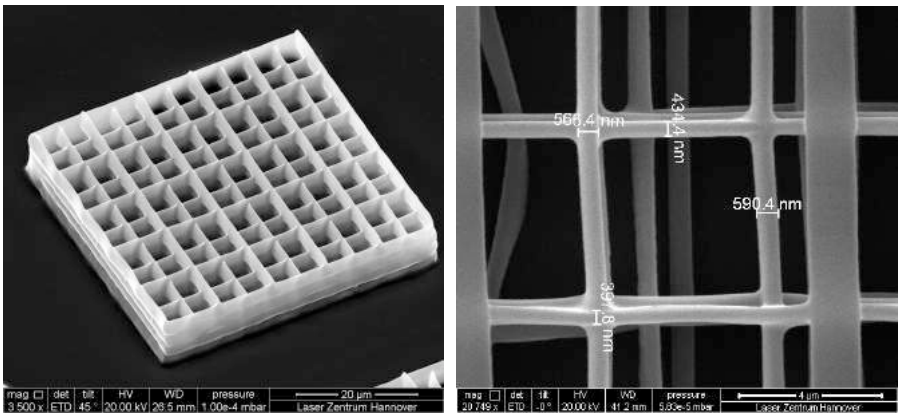

Figure 1. Scanning electron microscope images of photonic crystals fabricated by 2PP with Nd:YVO_4 Q-switched microchip laser.

REFERENCES

1. S. Kawata, H.-B. Sun, T. Tanaka, K. Takada, Nature 412, 697 (2001).

2. J. Serbin, A. Egbert, A. Ostendorf, B. N. Chichkov, R. Houbertz, G. Domann, J. Schulz, J. Cronauer, L. Fröhlich, M. Popall, Opt. Lett. 28, 301 (2003).

3. M. Farsari, B.N. Chichkov, Nature Photonics 3, 450 (2009).

4. B. Kaehr, N. Ertas, R. Nielson, R. Allen, R.T. Hill, M. Plenert, J.B. Shear, Anal. Chem. 78, 3198-3202 (2006)